ICESID
International Conference on Engineering for Sustainable Innovation and Development

Faculty of Engineering, Ahmadu Bello University
ZARIA · NIGERIA

BOOK OF PROCEEDINGS

International Conference on Engineering Innovation for Sustainable Development

ICESID 2026

THEME

Innovating Tomorrow: Harnessing Engineering to Drive Nigeria's Sustainable Development

8–10 September 2026
Faculty of Engineering, Ahmadu Bello University Zaria

EDITED BY

Prof. A. M. S. Tekanyi EDITOR-IN-CHIEF

Prof. S. Y. Sanusi · Dr. J. O. Gaminana · Prof. T. K. Bello · Prof. Y. M. Sani

CONFERENCE PLATFORM & PRODUCTION PARTNER

SayPeace SOLUTIONS

DOI https://doi.org/10.67203/sp.ICESID.2026
https://icesid.org

Saypeace Solutions Ltd. · https://conference.saypeace.ng
support@saypeace.ng · +2347036890546

BOOK OF PROCEEDINGS

International Conference on Engineering Innovation for Sustainable Development (ICESID 2026)

Theme: Innovating Tomorrow: Harnessing Engineering to Drive Nigeria's Sustainable Development

8–10 September 2026 · Faculty of Engineering, Ahmadu Bello University, Zaria, Nigeria

Editors

Prof. A. M. S. Tekanyi (Editor-in-Chief)
Prof. S. Y. Sanusi
Dr. J. O. Gaminana
Prof. T. K. Bello
Prof. Y. M. Sani

Published by the Faculty of Engineering, Ahmadu Bello University, Zaria.

DOI: https://doi.org/10.67203/sp.ICESID.2026

https://icesid.org

© 2026 Faculty of Engineering, Ahmadu Bello University, Zaria. Individual papers © their authors.

All rights reserved. No part of this publication may be reproduced, stored in a retrieval system or transmitted in any form or by any means without the prior permission of the publisher, except for brief quotation with due acknowledgement.

The views and opinions expressed in the papers are those of their authors and do not necessarily reflect those of the editors, the organising committee or the publisher. Authors are responsible for the accuracy of their content and references.

PREFACE

The Faculty of Engineering, Ahmadu Bello University Zaria is happy to introduce the proceedings of the 1st International Conference on Engineering Innovations for Sustainable Development (ICESID 2026) held between 8th–10th September 2026. The Conference drew the attention of researchers, developers and policy makers in academia and industries, from various fields of engineering. The conference was organized by the faculty with theme; Innovating Tomorrow: Harnessing Engineering to Drive Nigeria's Sustainable Development. The theme was later divided into the following sub-themes;

- Smart Infrastructure and Sustainable Systems for National Development
- Engineering Innovations, Technology Commercialization and Industrial Policy
- Emerging Technologies and Digital Transformation in Engineering Education and Practice
- Renewable Energy Integration and Smart Grid Applications in Power Systems
- Intelligent Systems, Automation and Control Engineering
- Strategies for Infrastructural and Industrial Transformation through Engineering Innovations
- Green Mobility and Next Generation Automobile Technologies
- Sustainable Engineering Processes and Systems
- Emerging Technologies for Safe Engineering Practices and Environmental Protection
- Telecommunication Infrastructure for Sustainable Urban Development and Economic Growth
- Advanced Manufacturing, Materials and Sustainable Production

The work of the technical committee is highly appreciated for smooth and effective review of the 167 submitted manuscripts for the conference, the committee did extremely well by completing the peer review process of the technical papers and also compiled a high quality technical program. We are of the belief that the ICESID 2026 provided a good platform for knowledge sharing, networking, research collaborations, which involves researchers, developers and practitioners to discuss recent advancements in various fields of Engineering. We also hope that the next ICESID will be even more stimulating than the just concluded one.

September 2026

Prof. I. A. Mohammed-Dabo
Chairman, LOC

CONFERENCE ORGANIZATION

Dean, Faculty of Engineering, Ahmadu Bello University, Zaria

Prof. J. M. Kaura
Department of Civil Engineering
Ahmadu Bello University, Zaria

Chairman, LOC

Prof. I. A. Mohammed-Dabo
Department of Chemical Engineering
Ahmadu Bello University, Zaria

Co-Chairman, LOC

Prof. A. Y. Atta
Department of Chemical Engineering
Ahmadu Bello University, Zaria

Secretary

Dr. S. Salisu
Department of Electrical Engineering
Ahmadu Bello University, Zaria

Technical Committee

Prof. A. M. S. Tekanyi
Prof. S. Y. Sanusi
Dr. J. O. Gaminana
Prof. T. K. Bello
Prof. Y. M. Sani

Media & Publicity

Dr. N. S. Usman
Dr. H. Ismail

Finance and Sponsorship

Dr. J. Baba-Ali
Dr. A. A. Dandaje

Logistics

Dr. A. S. Abdulrasheed

KEYNOTE ADDRESS

INNOVATING TOMORROW: HARNESSING ENGINEERING TO DRIVE NIGERIA'S SUSTAINABLE DEVELOPMENT

Prof Idris Bugaje
Executive Secretary, National Board for Technical Education (NBTE), Kaduna

A Keynote Address Delivered at the International Engineering Conference (ICESID 2026), Faculty of Engineering, Ahmadu Bello University (ABU), Zaria, Kaduna State, Nigeria, September 8-10, 2026.

PROTOCOLS

- The Vice-Chancellor, Ahmadu Bello University, Zaria,
- The Dean, Faculty of Engineering, Ahmadu Bello University, Zaria,
- Presidents and Executives of Professional Bodies (COREN, NSE, N.Acad.Eng.),
- Distinguished Professors, Scholars, and Researchers,
- Future Engineers, Our Resilient Students,
- Ladies and Gentlemen.

I bring you warm greetings from the National Board for Technical Education (NBTE).

INTRODUCTION: THE ZARIA ENGINEERING LEGACY

It is an extraordinary honour to stand before you today in Zaria, a historic citadel of academic excellence, where I was trained as a Chemical Engineer. For generations, the Ahmadu Bello University has served as the intellectual forge of Nigeria’s technological backbone, producing visionary engineers who built our national grid, designed our transport corridors, and structured our industrial landscape. However, as we gather today, our nation stands at a critical historical junction. Nigeria faces a complex, interlocking set of macroeconomic and environmental challenges: severe grid instability with one of the lowest per capita electric energy, rising energy costs, urban infrastructure collapse, rapid desertification in the North, insecurity, and ecological degradation.

We can no longer afford to rely on traditional, post-colonial engineering models that favor quick imported fixes over long-term structural resilience. The theme of this conference, "Innovating Tomorrow: Harnessing Engineering to Drive Nigeria's Sustainable Development," is therefore not just an academic concept, it is an urgent operational imperative.

First and foremost, as we harness Engineering, Nigeria must allow its Engineers to practice. At the moment, as we speak, most engineering designs are done offshore. From refineries built in the 1950s to 2023, to superhighways till date, the only minor exception being aspects of the building construction industry. This unwholesome practice must stop. Let's own our space.

The theme of this conference, could not be more fitting, nor more urgent. Nigeria stands at a defining moment. Our population is young, our ambitions are large, and our development needs, in power, transportation, water, housing, manufacturing, and digital infrastructure, are immense. Every one of these needs is, at its core, an engineering problem. And every engineering problem, in turn, is a question of whether we have built the human capacity to solve it ourselves, rather than perpetually importing the solution.

I want to use this platform, this morning, to speak plainly about three things: first, the state of engineering and technical capacity in Nigeria today; second, why I believe our informal and technical education systems, if properly harnessed, are Nigeria's most under-utilised engineering assets; and third, a set of concrete commitments the National Board for Technical Education is prepared to make alongside this university, and alongside all of you, to turn today's innovation into tomorrow's national capacity.

THE PILLARS OF ENGINEERING-LED SUSTAINABLE DEVELOPMENT

To engineer a resilient tomorrow for Nigeria, our domestic engineering ecosystem must pivot across these fundamental fronts. Sustainable development is not an abstraction. It is measured in kilometres of durable roads, in megawatts of reliable power, in litres of clean water delivered, in tonnes of locally fabricated machinery that no longer needs to be imported. Every item on that list depends on engineers and, just as critically, on the technicians, artisans, and craftspeople who build, install, operate, and maintain what engineers design.

Too often, our national conversation about engineering capacity begins and ends with our universities and polytechnics. That conversation is necessary, but it is incomplete. Nigeria's true engineering base is broader, more distributed, and more resilient than our formal institutions alone, and nowhere is that clearer than in our informal technical and artisan clusters, the Panteka being a typical example.

The recurring failure of public infrastructure, manifested in building collapses, premature road degradation, and industrial hazards, demands uncompromising regulatory leadership. The Council for the Regulation of Engineering in Nigeria (COREN), through its Engineering Regulation Monitoring (ERM) framework, must maintain strict field oversight. Every project site in Nigeria must be audited for structural calculations, quality material blends, and certified professional supervision. We must enforce strict, proportional consequences for non-compliance, ranging from administrative stop-work orders for minor site log errors, to license cancellations, corporate blacklisting, and criminal prosecution for gross negligence that endangers public safety.

THE UNTAPPED POTENTIAL OF THE INFORMAL SKILLS SECTOR

Allow me to speak of a place many of you may already know, or used: the Panteka market in Kaduna. By our own assessment, and by the assessment of independent observers, this is the largest informal technology and artisan hub in Africa, home to an estimated 38,000 artisans and apprentices working in metal fabrication, mechanics, electrical installation, welding, and allied trades. Panteka was not built by any government. It was not designed by any faculty of engineering. It grew organically, through a master-apprentice tradition, driven by necessity and sustained by the ingenuity of ordinary Nigerians. And yet, within its workshops, one finds the same instincts that animate this conference: the instinct to solve a practical problem with the materials and tools at hand, to innovate under constraint, to build rather than merely import.

The National Board for Technical Education has taken deliberate steps to bring this informal capacity into our national framework. Since November 2017, Kaduna Polytechnic, supported by the NBTE, had worked with Panteka, to formalise skills training within Panteka. In November 2023, the first cohort of Panteka artisans graduated with National Skills Qualification Level 3 certification. And Kaduna Panteka has now been registered under Nigeria's National Skills Qualification Framework (NSQF), alongside similar hubs such as those in Jos, Ikeja, Araria-Aba, etc., a first step towards ensuring that a skill acquired informally is a skill that can be recognised nationally. Recognition of Prior Learning (RPL) is, therefore, taking centre stage across Nigeria’s informal landscape.

We are also looking outward for successful models of upgrading. Pakistan's Ustadh-Shagird apprenticeship tradition, structurally similar to what we see in Panteka, has, over past decades, been formalised and scaled through institutions such as Punjab's Vocational Training Council and the National Vocational and Technical Training Commission (NVTTC), and has helped power industrial clusters such as in Sialkot, and Gujranwala, into globally competitive, export-oriented manufacturing hubs. If Pakistan's informal artisans can become the backbone of an export industry, there is no reason why Panteka cannot follow a similar trajectory. NBTE is actively pursuing this collaboration, and we invite this Faculty of Engineering, and the researchers gathered here, to help us think rigorously about what that upgrading path should look like.

BRIDGING THE GAP BETWEEN CURRICULA AND INDUSTRY

Engineering innovation, however brilliant, does not drive national development if it stays within the walls of a laboratory or the pages of a journal or book of proceedings. This conference's sub-themes (advanced manufacturing and sustainable production, digital transformation in engineering practice,

green mobility, technology commercialisation, and industrial policy, among others) all point to the same underlying imperative: the distance or gap between what we teach, what we research, and what our industries and communities actually need must continue to close.

This is precisely NBTE's statutory mandate: to accredit and coordinate technical and vocational education in a way that keeps curricula honest to the demands of the real economy (within limits of available budgets). We do not do this work alone. We do it through partnerships: with universities such as this one, with polytechnics, international collaborators, and industry players, including engineering firms undertaking major infrastructure works in Nigeria, who are training, mentoring, and absorbing our graduates directly into productive work.

A DIRECT CALL TO ACTION FOR ABU ENGINEERS

To the distinguished lecturers and researchers of ABU: Let your laboratories solve immediate, local challenges. Design low-carbon agricultural ash cement blends to reduce construction costs; engineer precision solar irrigation pumps for northern farmers; build waste gasification systems to convert municipal refuse into clean electricity, and find engineering solutions to the current insecurity.

To our engineering students, the leaders of tomorrow: Reject the illusion that engineering is purely a white-collar office profession. True engineering happens where theory meets real-world application, in construction sites, in bio-processing pilot plants, and in industrial fabrication workshops. You are not just studying to earn degrees; you are training to construct the structural foundation of a sovereign nation, Nigeria.

To the researchers and postgraduate scholars in this hall: let your papers this week be judged not only by their theoretical rigour, but by a simple additional question: could this be built, deployed, and maintained by a Nigerian technician?

To the industry participants: engage seriously with our technical institutions, not as a corporate social responsibility afterthought, but as a genuine talent pipeline and innovation partner.

And to my colleagues in government and academic leadership: let us match today's enthusiasm with the institutional follow-ups, such as funding, accreditation pathways, and policy that innovation requires to survive beyond a conference hall.

CONCLUSION

The future of Nigeria will not be built by policy papers or political rhetoric. It will be drawn on CAD design screens, calculated through rigorous thermodynamics, forged in metal fabrication yards, and verified by strict regulatory inspectors on the ground. Let us leave this conference committed to building a nation where our bridges hold, our power grids remain stable, our local industries thrive on clean energy, and our youth are empowered with practical, globally competitive skills.

'Innovating Tomorrow' is not a slogan we should leave behind when we leave Zaria this week. It is a discipline, one that asks every engineer, every technician, every policymaker in this conference, to treat Nigeria's development challenges as solvable problems, and to treat our own people, from the postgraduate laboratories of Ahmadu Bello University to the workshops of Panteka, as fully capable of solving them. That confidence is the key! On behalf of the National Board for Technical Education, I reaffirm our commitment to walk this path with you, to keep our technical education system honest, responsive, and connected to the real engineering work this nation needs to get done.

I congratulate the Faculty of Engineering, its Dean and the organising committee, for convening this important conference, and I wish all of you a productive and thought-provoking three days in this ancient city of Zaria.

Thank you, God bless the Ahmadu Bello University, and God bless and guide Nigeria.

Prof. Idris Bugaje, ES, NBTE 8th September, 2026
#SkillsNotJustDegrees

COMMUNIQUÉ

THE COMMUNIQUÉ AT THE END OF THE INTERNATIONAL CONFERENCE ON ENGINEERING INNOVATION FOR SUSTAINABLE DEVELOPMENT (ICESID 2026)

Theme: *Innovating Tomorrow: Harnessing Engineering to Drive Nigeria's Growth for Sustainable Development*
Date: 8th–10th September, 2026
Venue: ACENPEE Building, Faculty of Engineering, Ahmadu Bello University, Zaria

The International Conference on Engineering Innovation for Sustainable Development (ICESID 2026), organised by the Faculty of Engineering, Ahmadu Bello University, Zaria, was held from 8th to 10th September, 2026, under the theme *"Innovating Tomorrow: Harnessing Engineering to Drive Nigeria's Growth for Sustainable Development."* The conference brought together researchers, academics, engineers, industry professionals, policymakers, and students to exchange knowledge, present research findings, and deliberate on the role of engineering innovation in addressing Nigeria's developmental challenges.

A total of 205 abstracts were accepted, while 167 research presentations were made during the conference. The presentations covered a broad range of engineering disciplines and emerging areas of technology, reflecting the depth of research and innovation taking place within the engineering community. The conference provided a platform for participants to share research findings, exchange professional knowledge, showcase emerging technologies, and explore opportunities for collaboration.

The keynote address by Professor Idris Muhammad Bugaje, Executive Secretary of the National Board for Technical Education (NBTE), emphasised that Nigeria's engineering capacity should extend beyond universities and polytechnics to include the informal technical sector. He highlighted Panteka Market, Kaduna, with an estimated 38,000 artisans and apprentices, as an important hub for practical engineering skills. Professor Bugaje stressed the need to formalise and integrate such skills into national development, citing collaboration between NBTE, Kaduna Polytechnic, and Panteka. He urged stakeholders to bridge the gap between education, research, industry, and community needs by translating engineering knowledge into practical solutions for sustainable economic development.

RESOLUTIONS

Following the presentations, technical sessions, and deliberations, the conference resolved as follows:

1. Government should increase and sustain funding for engineering research, laboratories, technical education, innovation, and local manufacturing, with priority given to Nigeria's critical development challenges.
2. Universities, researchers, and industry should strengthen collaboration to transform research outcomes into prototypes, patents, products, processes, and commercially viable technologies.
3. Major infrastructure and industrial projects should incorporate technology transfer and deliberate Nigerian capacity development to ensure that imported technologies strengthen local expertise rather than create permanent dependence.
4. Government, educational institutions, and industry should strengthen technical and vocational education, apprenticeships, and practical training while recognizing, certifying, and integrating skilled artisans and technicians into the formal engineering ecosystem.
5. Academic institutions should align engineering curricula, teaching, research, and practical training with industry and societal needs, while providing students with meaningful exposure to real engineering projects.
6. Universities, Government, industry, and professional bodies should provide opportunities for students and young engineers to develop technical, digital, entrepreneurial, and innovation skills that enable them to create solutions and address national challenges.

7. Researchers and institutions should prioritize interdisciplinary research that addresses pressing Nigerian challenges in areas such as energy, infrastructure, manufacturing, agriculture, water, transportation, and the environment.
8. Government, industry, and other stakeholders should support, adopt, finance, and promote credible Nigerian-made technologies through appropriate procurement policies, market access, and other incentives.
9. Professional bodies, universities, polytechnics, research institutions, industry, artisans, technicians, and entrepreneurs should establish and sustain partnerships for skills development, research, innovation, standards, certification, technology development, and knowledge exchange.
10. All stakeholders should work collectively to build a productive national engineering ecosystem in which Government provides enabling policies and funding, institutions generate knowledge, researchers develop solutions, students acquire practical skills, industry commercializes innovations, and artisans and technicians contribute hands-on expertise towards local manufacturing, technological independence, and sustainable national development.

This communiqué signifies and formally declares the conference concluded.

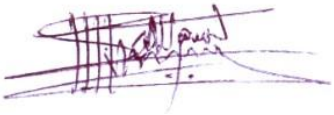

Professor Abdoulie M. S. Tekanyi
Chairman, Technical Committee
International Conference on Engineering Innovation for Sustainable Development (ICESID 2026)
Faculty of Engineering, Ahmadu Bello University, Zaria

10/09/2026

TABLE OF CONTENTS

ADVANCED MANUFACTURING, MATERIALS AND SUSTAINABLE PRODUCTION

1. ADVANCING SUSTAINABLE FRUCTOSE SYRUP PRODUCTION FROM SWEET SORGHUM **2**
Abdulkareem Abubakar, Alhaji Zanna Umara, Suleiman Mohammed Shuwa, Muhammad Bashir Tijjani, Suleiman Yunusa, Toyese Oyegoke & Alewo Opuada Ameh

2. BIODEGRADABLE STRUCTURE-DIRECTING AGENTS FOR SUSTAINABLE SYNTHESIS OF ZSM-5 ZEOLITE: A REVIEW OF AMINO-ACID AND BIOPOLYMER ROUTES **10**
Emmanuel John, Abdulazeez Yusuf Atta, Baba Jibril El-Yakubu & Ajayi Olusegun Ayoola

3. COMPARATIVE STUDY OF THERMAL, ZEOLITE-Y CATALYTIC AND NI-DOPED ZEOLITE-Y CATALYTIC CRACKING OF GAS CONDENSATE **16**
Jonathan Danladi Gaiya, Shuaibu Musa, Suleiman Shehu, Mansur Suleiman, Abdullahi Nuraddeen Bakori, Narcillina Nkechi Adegboro, Muhammad Aminu Abubakar, Aliyu Ibrahim, Abdullahi Bukar, Muazu Ibrahim, Toyese Oyegoke & Abdulazeez Yusuf Atta

4. DENSITY FUNCTIONAL THEORY INVESTIGATION OF METHANE STEAM REFORMING ON NI(111) AND PD1–CU(111) SINGLE-ATOM ALLOY SURFACES **27**
Abdulrauf Onimisi Ibrahim

5. DETERMINATION OF LOW-TEMPERATURE LOW-PRESSURE (LTLP) FILTRATION PROPERTIES OF DRILLING MUD FORMULATED FROM ARAWA BENTONITE CLAY FOR OIL AND GAS DRILLING APPLICATION **34**
Bala Usman, Bilal Sabiu, Hamza Abdulhamid, Muhammad Tukur, Abubakar Sadeeq Hussain & Kabiru Suleman

6. DEVELOPMENT AND MICROSTRUCTURAL CHARACTERIZATION OF AL-SI-MG / GIRO CLAY NANOPARTICLE COMPOSITES FABRICATED VIA STIR CASTING **41**
Youshau Najee Abdusalam, Kasim Auwal, Abdulwahab Malik, Gaminana Jimoh O., Abdullahi Ibrahim & Adegbite Dauda A.

7. EFFECT OF DOUBLE PRESSING AND DOUBLE SINTERING ON THE MECHANICAL AND TRIBOLOGICAL PROPERTIES OF ALUMINIUM MATRIX REINFORCED RICE HUSK ASH COMPOSITES **53**
Abdulrahman Adeiza Musa, Kamilu Adeyemi Bello, Agbo E. Oloture, Mohd A. Maleque, Jimoh O. Gaminana, Rayyan M. Dodo, Hayatu M. Abdullahi & Abdullahi Umma

8. EFFECT OF HEAT TREATMENT AND QUENCHING MEDIA ON THE MECHANICAL, TRIBOLOGICAL, AND MICROSTRUCTURAL BEHAVIOUR OF A6082-SNSA/MWCNT HYBRID COMPOSITES **63**
Abdullahi Mohammed, Malachy Sumaila, Muhammad Dauda & Laminu Shattima Kuburi

9. GEOSPATIAL ASSESSMENT OF SOIL TEXTURAL CLASSES AND THE IMPLICATIONS ON ACHIEVING SDG 2 IN NORTHWESTERN NIGERIA **76**
Garuba H.s, Mujahid, M.m & Mukhtar, M.k

10. INVESTIGATION INTO THE USE OF LOCALLY AVAILABLE MATERIALS FOR THE PRODUCTION OF INVESTMENT CASTING MOULD **83**
Nura Lawal, Mahadi Makoyo, Adamu Umar Alhaji & Yakubu Shuaibu Ochetengwu

11. MECHANICAL, OPTICAL AND ENGINEERING ASSESSMENT OF POLYPROPYLENE/FIBREGLASS COMPOSITES FOR TRANSLUCENT LPG CYLINDER APPLICATIONS **94**
Usman Sani, Fatima Mohammed & Simon N.n

12. PERFORMANCE EVALUATION OF GRANITE POWDER-STABILIZED LATERITIC ADOBE BRICKS: MECHANICAL STRENGTH, MOISTURE RESISTANCE AND THERMAL PERFORMANCE **107**
Yunusa Tsoho Abdullahi, Nasiru Zakari Muhammad, Ado Ma'aruf, Mujitafa Sariyyu & Zaharaddeeen Baffa Baba

13. PRODUCTION OF SILICA FROM AGRICULTURAL WASTES FOR APPLICATION IN FCC/RFCC CATALYST DEVELOPMENT: A MINI REVIEW **114**
Usman Sani, Daniel Adanenche, Mustapha Yusuf, A. Y. Atta & B. J. El-Yakubu

14. SUGARCANE BAGASSE ASH AS A SUSTAINABLE SILICA PRECURSOR FOR ZEOLITE SYNTHESIS: A REVIEW OF EXTRACTION ROUTES **133**
Gabriel Christopher, Abdulazeez Yusuf Atta, Baba Jibril El-Yakubu, Olusegun Ayoola Ajayi & Mustapha Yusuf

EMERGING TECHNOLOGIES AND DIGITAL TRANSFORMATION IN ENGINEERING EDUCATION AND PRACTICE

15. AN EDGE AI-DRIVEN CYBER-PHYSICAL FRAMEWORK FOR GREEN NETWORK OPTIMIZATION AND RESILIENT IT INFRASTRUCTURE IN EMERGING ECONOMIES **140**
Sani Muhammed Hassan, Muhammad Ahmad Abdulkadir, Abdullahi Usman Mohammad, Mohammad Hussaini Faskari, Najib Sayyadi & Mubarak Idris

16. COMPUTATIONAL INVESTIGATION OF ACTIVE PALM OIL COMPONENTS AS ECO-FRIENDLY CORROSION INHIBITORS FOR COPPER METAL **153**
Usman Sani, Abdulazeez Abdulateefa, Amaram Jonah Adams & Toyese Oyegoke

17. DEVELOPMENT OF A HYBRID SUPPORT VECTOR MACHINE AND BAT OPTIMIZATION ALGORITHM FOR ENHANCED **159**
Yahaya Hamisu Abubakar & Mathew Ehikhamenle

18. FACTORS INFLUENCING THE ADOPTION OF MIXED REALITY TECHNOLOGY FOR CONSTRUCTION PROJECTS COST ESTIMATION **182**
Raphael Olarewaju & Olubunmi Comfort Ade-Ojo

19. INTELLIGENT ENERGY MANAGEMENT IN AGRICULTURE: A SYSTEMATIC REVIEW OF INTERNET OF THING, RENEWABLE INTEGRATION, AND ARTIFICIAL INTELLIGENCE TECHNIQUES **198**
Vandi Jusu, Eugene Okenna Agbachi & Jibril Abdullahi Bala

20. MEASUREMENT OF LIQUID FILM HEIGHT IN GAS-LIQUID TWO-PHASE FLOWS USING TWIN-WIRE CONDUCTANCE PROBES..... **214**
Mohammed Kabir Abdullahi

21. STUDENT VERIFICATION ASSISTANT: A LOW-COST MULTIMODAL BIOMETRIC SYSTEM FOR SECURE EXAMINATION IDENTITY AUTHENTICATION..... **225**
Zainab Mukhtar Abubakar, Abdulfatai Dare Adekale, Risikat Folashade Adebiyi, Abubakar Umar, Anas Zakari & Habeeb Bello-Salau

EMERGING TECHNOLOGIES FOR SAFE ENGINEERING PRACTICES AND ENVIRONMENTAL PROTECTION

22. APPLICATION OF ARTIFICIAL INTELLIGENCE IN TRANSPORTATION SAFETY AND ENVIRONMENTAL ADMINISTRATION: A SYSTEMATIC REVIEW **234**
Ahmad Abubakar & Shehu Mohammed Yusuf

23. ASSESSING THE IMPACT OF CLIMATE CHANGE ON GROUNDWATER RECHARGE POTENTIAL IN PALLADAN, ZARIA, KADUNA STATE, NIGERIA. **240**
Samuel Adebamidele Morohunkola, Aliyu Adamu Dandajeh, Nura Idris Abdullahi, Shamsuddeen Jumande Mohammad, Sani Yakubu Khalifa & Bashir Tanimu

24. ASSESSMENT OF ELECTRICAL POWER QUALITY ISSUES IN AIRCRAFT DC SYSTEMS: ANALYSIS OF VOLTAGE DROP AND HARMONIC DISTORTION **253**
Alum Ikechukwu Otu, Muyideen Omuya Momoh, Princess Love David, Abdussalam El-Suleiman, Gowon Sule, Godwin Eseosa Abbe & Kumater Peter Ter

25. CALIFORNIA BEARING RATIO OF GEOPOLYMER-STABILIZED LATERITIC SOIL USING SUGARCANE BAGASSE ASH AND RICE HUSK ASH AS PRECURSORS **260**
Aliyu Mani Umar, Mustapha Amin Muhammad, Ashiru Mohammed, Nura Shehu Aliyu Yaro, Yaseer Adam Nabage, Adam Ado Sabari & Surajo Abubakar Wada

26. COMPARATIVE ASSESSMENT OF PAVEMENT DISTRESS USING CONVENTIONAL MEASUREMENTS AND UAV PHOTOGRAMMETRY ALONG THE GOMBE - KWAMI HIGHWAY, NIGERIA..... **268**
Salisu Ibrahim & Aminu Suleiman

27. COMPARATIVE ASSESSMENT OF CLAY POT AND PLASTIC CONTAINERS ON WATER QUALITY DURING 14-DAY HOUSEHOLD STORAGE IN ZARIA, KADUNA STATE **281**
Aminu Ohueyi Ahmed, Mohammed Aliyu Aliyu, Mohammad Shamsuddeen Jumande & Akinola Abdulwasiu Olalekan

28. REMAINING USEFUL LIFE PREDICTION OF TURBOFAN ENGINE USING ATTENTION AUGMENTED LSTM BASED NETWORK..... **288**
Oluwafemi Daniel Oluwapelumi, Samuel David Iyaghigba, Marcus Aul Maafan, Sadiq Thomas & Abbas Abdullahi

29. DESIGN AND PERFORMANCE EVALUATION OF A DUAL-MEDIA FILTRATION SYSTEM USING PALM KERNEL SHELL ACTIVATED CARBON FOR WASTEWATER TREATMENT **311**
Aminu Ohueyi Ahmed, Mohammed Aliyu Aliyu, Abdullahi Mohammed Dalhatu, Umar Abdullahi & Yakubu Joseph Nlira

30. DESIGN OPTIMISATION AND IMPACT ASSESSMENT OF A BIOGAS-INTEGRATED ANAEROBIC BAFFLED REACTOR WASTEWATER TREATMENT SYSTEM AT NIGERIAN CORRECTIONAL CENTRE **320**
Philip Ayodele Balogun, Donatus Begianpuye Adie, Igboro Sunday Bamidele & Aliyu Adamu Dandajeh

31. DESIGNING ENFORCEMENT FOR SAFETY, NOT HAZARD: EVIDENCE FROM A TRAFFIC MANAGEMENT SYSTEM FAILURE IN KANO METROPOLIS **339**
Muwaffaq Safiyanu Labbo, Abubakar Idris & Suraj Abubakar Wada

32. DEVELOPMENT AND PERFORMANCE EVALUATION OF A WASTE PLASTIC SHREDDER.. **346**
Akeem Adekunle Adebesin & Ogundemuren Victor Oluwatobi

33. DEVELOPMENT OF AN OPTIMAL CONTROL STRATEGY FOR LOAD FREQUENCY CONTROL OF THE TWO-AREA POWER SYSTEM USING ARITHMETIC OPTIMIZATION ALGORITHM**355**
Mustapha Abdullahi & Sani Salisu

34. EFFECT OF MUNICIPAL SOLID WASTE LEACHATE ON PLASTICITY CHARACTERISTICS OF CLAY SOIL **363**
Adamu Umar Chinade, Musa Umar Chinade, Isa Zubairu, Muhammad Abdu Nasara & Yakubu Hyelmura

35. EFFECTS OF HYDROCARBON IMPURITIES ON CONCRETE STRENGTH AND DURABILITY: A COMPREHENSIVE REVIEW **374**
Otu Nnamdi Johnson, James Olayemi James & Abubakar Mahmud

36. EMERGING TECHNOLOGIES FOR SAFE ENGINEERING PRACTICES AND ENVIRONMENTAL PROTECTION: A SYSTEMATICALLY INFORMED, EVIDENCE-GRADED REVIEW WITH A PROPOSED NIGERIAN ADOPTION FRAMEWORK **382**
Emmanuel Adie, John Wasiu & Ibrahim Abdulrazaq Olayinka

37. ENHANCED ANAEROBIC DIGESTION OF COW DUNG AND POULTRY DUNG VIA A COUPLED MICROBIAL ELECTROLYTIC CELL: OPTIMIZATION, KINETICS, AND THERMODYNAMIC STUDIES. **400**
Ijuptil Ndumari, Olakunle Michael Sunday & Auwal Aliyu

38. FLOOD INUNDATION RISK ASSESSMENT OF AN EARTHEN DAM UNDER PIPING FAILURE USING HEC-RAS AND QGIS: **408**
Aliyu Yahaya Muhammad, Auwal Jarmai Babagirei, Alamin D Bello, Khalid Sulaiman, Abdulaziz Ahmad Imam & Raji Olasunkanmi Sheriffdeen

39. GEOSPATIAL ANALYSIS OF ANTHROPOGENIC HEAVY METAL SOURCES AND DISTRIBUTION IN SOIL AND GROUNDWATER IN FUNTUA, KATSINA STATE **419**
Al-Mustapha Abubakar, Aliyu Ishaq, Badruddeen Saulawa Sani, Umar Alfa Abubakr & Abubakar Sadiq Isah

40. HYDRODYNAMIC ASSESSMENT OF PIPING-INDUCED DAM-BREAK AND DOWNSTREAM FLOOD HAZARD CLASSIFICATION AT ZOBE DAM, NIGERIA. AN INTEGRATED HEC-HMS AND HEC-RAS MODELING APPROACH **428**
Abdulaziz Imam Ahmad, Umar Abdullahi, Shamsuddeen Jumande Mohammad, Raji Olasunkanmi Sheriffdeen, Mohammed Aliyu Aliyu, Aliyu Yahaya Muhammad & Auwal Jarmai Babagirei

41. INFLUENCE OF SLICE THICKNESS AND DRYING TEMPERATURE ON THE PROXIMATE COMPOSITION OKRA: IMPLICATIONS FOR NUTRITIONAL QUALITY AND DRYING PROCESS OPTIMIZATION **448**
Muhammad Mujahid Muhammad, Abba Yahaya, Mohammed Abdulsalam, Al-Amin Danladi Bello, Daniel Onwude, Ibrahim Babangida Dalha, Muhammad Bashir Abdulrazaq, Badruddeen Saulawa Sani & Abdullahi Argungu Sule

42. IMPACT OF AGEING WATER INFRASTRUCTURE ON WATER SUPPLY IN NIGER STATE: CASE STUDY OF SULEJA AND MINNA **454**
Stephen Osu & Mohammed Saidu

43. IMPACTS OF ROAD CONSTRUCTION SITE ACTIVITIES ON THE OCCURRENCE OF ACCIDENTS: A CASE STUDY OF THE ZARIA–KADUNA ROAD **463**
Muhammed Mustapha Musa, Kasimu Yusuf Gojara, Ibrahim Bello & Yusuf Ya'u

44. INFRASTRUCTURE CHARACTERIZATION AND PHYSICAL INTEGRITY ASSESSMENT OF URBAN WATER DISTRIBUTION SYSTEMS: A RISK-BASED FRAMEWORK FOR SUSTAINABLE ASSET MANAGEMENT IN MINNA, NIGERIA **483**
Abdulrahman Aminu, Johnson A. Otun & Aliyu Ishaq

45. INTEGRATED EXERGETIC–ECONOMIC ASSESSMENT OF THERMAL AND CATALYTIC PYROLYSIS OF HOUSEHOLD THERMOPLASTIC WASTE FOR SUSTAINABLE WASTE-TO-ENERGY APPLICATIONS **502**

Zhidaya Jude, Eyitayo A. Afolabi & O. S. Azeez

46. MINIMIZATION OF POWER LOSSES IN DISTRIBUTION NETWORKS THROUGH SMART GRID TECHNOLOGIES (SGT): A CASE STUDY OF BWARI 33 KV DISTRIBUTION NETWORK **508**
Francis Igbinosa, Eronu Emmanuel & Ngang Bassey Ngang

47. NON-PARAMETRIC ASSESSMENT OF WIND-SECTOR AND ELEVATION EFFECTS ON CONTAMINANT DISTRIBUTION AROUND A CEMENT FACTORY **524**
Taiwo Abadunmi, Ayodele Olanrewaju Ogunlela & Kamorudeen Olaniyi Yusuf

48. OPTICAL EMISSION SPECTROSCOPY (OES) ANALYSIS OF CORROSION OF HIGH-GRADE CONVENTIONAL 5 MM UKRAINIAN METALLIC PLATE USED IN TANKER TRUCK FABRICATION IN NIGERIA **537**
Jamilu Haruna, Abdulkareem Abubakar, Usman Abubakar Zaria & Abdulmajid M. Nainna

49. PERFORMANCE EVALUATION OF MODEL REFERENCE ADAPTIVE CONTROLLER FOR STRING STABILITY IN HEAVY-DUTY TRUCK PLATOONING **545**
Hassan Maharazu, Z. Haruna, O. Ajayi, Muktar Abubakar & Mohammed Babakolo Adamu

50. PROBABILISTIC FREQUENCY ESTIMATION OF BOILING LIQUID EXPANDING VAPOUR EXPLOSION IN A LIQUEFIED PETROLEUM GAS ADD-ON SKID SYSTEM USING INTEGRATED FAULT TREE AND EVENT TREE ANALYSIS **557**
Shuaibu Musa, Abdullahi, Nuraddeen Bakori & Mohammed-Dabo, I. A.

51. PROCESS INTENSIFICATION OF A 50 BPD MODULAR MINI-REFINERY: A SIMULATION-DRIVEN PINCH ANALYSIS APPROACH FOR ENHANCED HEAT RECOVERY AND SUSTAINABLE REFINING IN NIGERIA **564**
Habib Ahmed Tijjani, Muhammed-Dabo I. A., Waziri S. M. & Mustapha M. Sugungun

52. SPATIAL VARIATION ASSESSMENT OF GROUNDWATER QUALITY IN IWO LOCAL GOVERNMENT AREA, OSUN STATE, NIGERIA. **580**
Yuusuf Oluwaseun Adetona & Kamar Taiwo Oladepo

53. STUDY OF THE CORROSION RATE OF NIGERIAN HIGH-GRADE CONVENTIONAL 5 MM UKRAINIAN METALLIC PLATE USING WEIGHT LOSS (GRAVIMETRIC) METHOD..... **598**
Jamilu Haruna, Abdulkareem Abubakar, Usman Abubakar Zaria, Abdulmajid M. Nainna & Abubakar Ado Datti

ENGINEERING INNOVATIONS, TECHNOLOGY COMMERCIALISATION AND INDUSTRIAL POLICY

54. A COMPREHENSIVE REVIEW ON THE POULTRY BROODING REQUIREMENTS AND FORCED AIR METHODS OF HEAT GENERATION FOR BROODING **608**
George Akwec, Adebayo Segun Emmanuel & Caroline Omoanatse Alenoghena

55. BIOELECTRICITY GENERATION AND NUTRIENT REMOVAL FROM LANDFILL LEACHATE USING DOUBLE-CHAMBER MICROBIAL FUEL CELLS..... **620**
Aliyu Ishaq, Ismail Shafiu Nuhu, Shamsuddeen Jumande Muhammad, Jamila Baba Ali & Kehinde Adeagbo

56. CONCEPTUAL DESIGN, OPERATIONS, AND THEORETICAL MODELING OF A 1 KW PHYSICAL SCALE PROTOTYPE FOR THE KAINJI HYDROPOWER DAM **630**
Abdurrasheed Said Abdurrasheed, Raphael Ejembi, Mujahid Muhammad Mujahid, Aliyu Ishaq, Sambo Mohammed Aminu, Jamila Baba Ali, Williams Ejembi & Islam Sajjad Muhammad

57. A CONCEPTUAL CPS-DRIVEN ADAPTIVE COORDINATION FRAMEWORK FOR HETEROGENEOUS WIRELESS SENSOR NETWORKS IN DYNAMIC AND UNCERTAIN ENVIRONMENTS..... **639**
Matthew Iyobhebhe, Abdoulie Momodou. S. Tekanyi, Athanisius Terlumun Utev, Fatima Ashafa, Asebakeoghene. J. Khama, Botson Ishaya Chollom & Umar Salisu Lawal

58. DESIGN AND FABRICATION OF A 5 BSPD PILOT-SCALE SEMI-REGENERATIVE CATALYTIC NAPHTHA REFORMING UNIT **653**
Lamido Sani Inuwa, Mohammad-Dabo, I. A, Maina, N. S, Aminu Uba Alhassan & Bashir Aliyu Abba

59. DESIRABILITY-BASED MULTI-RESPONSE OPTIMIZATION OF FLEXURAL PERFORMANCE IN BAMBOO AND STEEL REINFORCED CONCRETE BEAMS..... **675**
Chukwu Mbazor, J. M. Kaura, A. Ocholi & J. Ochepo

60. ENERGY-EFFICIENT COMMUNICATION AND ROUTING STRATEGIES IN HETEROGENEOUS WIRELESS SENSOR NETWORKS: A COMPREHENSIVE REVIEW **692**
Matthew Iyobhebhe, Abdoulie Momodou. S. Tekanyi, Athanisius Terlumun Utev, Fatima Ashafa, Asebakeoghene. J. Khama, Botson Ishaya Chollom & Umar Salisu Lawal

61. EVOLUTION, PROSPECTS, AND FUTURE DIRECTIONS OF NIGERIAN CURRENCY IMAGE ANALYSIS: A DECADAL REVIEW **706**
Isaac Yusuf & Isaac Omeiza Avazi

62. FEATURE SELECTION USING RANDOM FOREST FEATURE IMPORTANCE FOR EFFICIENT NETWORK INTRUSION DETECTION ON THE NSL-KDD DATASET **724**
Shafiu Shuaibu, Basira Yahaya, A.d. Adekale & Aminu Yakubu

63. STRUCTURAL RELIABILITY ASSESSMENT OF REINFORCED CONCRETE BEAM INCORPORATING GROUNDNUT SHELL ASH FOR TILAPIA CONCRETE INCUBATOR. **734**
Joseph Ogugua Eze, J.i. Aguwa, A. Mohammed & S.f. Oritola

64. SWOT ANALYSIS OF LOCAL ENGINEERING INNOVATION FOR SUSTAINABLE INDUSTRIAL GROWTH IN NIGERIA: PATHWAY TO SDG REALIZATION **745**
Anas Mahmoud Ibrahim, Umar Ibrahim Kwami, Abdulmajid Aliyu & Shuaibu Babandi Shuaibu

65. THE EFFECTS OF CONCENTRATED SOLAR IRRADIANCE ON THE OVERALL PERFORMANCE OF MONOCRYSTALLINE AND POLYCRYSTALLINE SOLAR CELLS **758**
Lukman Lawal, Uke Douglas Ozoemena & Abdullahi Mohammed SB

GREEN MOBILITY AND NEXT GENERATION AUTOMOBILE TECHNOLOGIES

66. CFD-DRIVEN THERMAL ANALYSIS AND CLIMATE-ADAPTIVE OPTIMIZATION OF LITHIUM-ION EV BATTERY USING DIFFERENT COOLING MEDIA AND STATISTICAL TECHNIQUES **771**
Abubakar Unguwanrimi Yakubu, Fahim Ullah, Wang Jiongfan, Shusheng Xiong, Jiahao Zhao & Xuanhong Ye

67. DEVELOPMENT OF A CYCLONIC LIQUID SPRAY SCRUBBER FOR EMISSION CONTROL... **784**
Hamisu Adamu Dandajeh & Tasiu Salisu Abubakar

68. INVESTIGATION OF THE PHYSICOCHEMICAL PROPERTIES, ENGINE PERFORMANCE AND EMISSION CHARACTERISTICS OF GLYCINE MAX BIODIESEL–DIESEL BLENDS IN A COMPRESSION IGNITION ENGINE **793**
Hamisu Adamu Dandajeh & Yusuf Hafiz

INNOVATIVE RESOURCE UTILIZATION AND MANAGEMENT

69. COMPARATIVE EVALUATION OF AASHTO AND CBR FLEXIBLE PAVEMENT DESIGN METHODS USING LABORATORY-DERIVED SOIL PARAMETERS **800**
Ahmad Idris

70. EFFECT OF POLYCARBONATE PLASTIC ON THE MECHANICAL PROPERTIES OF ASPHALT CONCRETE **807**
Kenneth, Ejike Ibedu, Abdulfatai, Adinoyi Murana, Muhammad, Ashiru & Abdulrahman, Nda'abo Alfa

71. EFFECT OF SOIL LEAD CONTAMINATION ON THE GROWTH CHARACTERISTICS AND PHYTOREMEDIATION POTENTIAL OF SUNFLOWER (HELIANTHUS ANNUUS L.), COMMON DANDELION (TARAXACUM OFFICINALE) AND JATROPHA (JATROPHA CURCAS L.)..... **818**
Sumaila Muhammed Shaibu, Aliyu Adamu Dandajeh, Aliyu Ishaq, Alice Ibrahim Onize & Raphael Owoicho Ejembi

72. ESTIMATING GROUNDWATER RECHARGE IN THE BIDA BASIN USING INTEGRATED SOIL MOISTURE BALANCE AND HEC-HMS MODELLING: A CASE STUDY OF THE NEW BUSSA SUB-BASIN **827**
Salihu Mohammed

73. EVALUATION OF PHOSPHORUS COMPOUND ENRICHMENT AND EUTROPHICATION RISK OF ALAU RESERVOIR, NIGERIA **834**
Yunusa Mamza Usman, Al-Amin Danladi Bello, Badruddeen Saulawa Sani, Umar Alfa Abubakar & Bawu Musami

74. EXPERIMENTAL ASSESSMENT OF SPECTRUM OCCUPANCY AND TVWS AVAILABILITY IN THE UHF TELEVISION BAND (470–694) MHZ IN KANO STATE NIGERIA..... **846**
Yahaya Hamisu Abubakar & Matthew Ehikhamenle

75. HOUSEHOLD WATER SECURITY AND INTEGRATED WATER RESOURCES MANAGEMENT GAPS IN A RAPIDLY URBANISING NIGERIAN CITY: EVIDENCE FROM MINNA, NIGER STATE **868**
Muhammad Ashafa & Mohammed Saidu

76. HYDROLOGICAL MODELLING AND TIME-SERIES STREAMFLOW FORECASTING OF THE KIRI WATERSHED USING SWAT AND ARIMA MODELS **876**

Nura Idris Abdullahi, Hamisu Ahmadu Jalo, Babatunde Karode Adeogun, Jamilu Abdullahi, Aliyu Adamu Dandajeh & Aliyu Ishaq

77. IOT-ENABLED HYBRID SOLAR–RF ENERGY HARVESTING FRAMEWORK FOR BATTERYLESS AGRICULTURAL MONITORING NODES: A PATHWAY TO SUSTAINABLE RURAL DEVELOPMENT IN NIGERIA **888**
Vera Ijeoma, Chinedu Reginald Okpara, Daniel Ikenna Akabuike, Favour Chidera Oruche & Somtoo-Chukwu Samuel Utoh

78. MODIFICATION OF FORWARD AND REVERSE ELECTRIC MOTOR STARTERS **895**
Ismail Yusuf Adubazi

79. SMART SELF-HEALING MATERIALS: A COMPREHENSIVE REVIEW OF EMERGING TECHNOLOGIES AND FUTURE PERSPECTIVES **908**
Yakubu Usman, Ibrahim Mu'azu, J. O. Gaminana & Danjuma Adamu Ismaila

INTELLIGENT SYSTEMS, AUTOMATION AND CONTROL ENGINEERING

80. CGAN-AUGMENTED LIGHTWEIGHT CNN ARCHITECTURES WITH COORDINATE ATTENTION FOR MAIZE LEAF DISEASE RECOGNITION **919**
Sani Saleh Saminu, Musa Idris Shehu, Yusuf Ibrahim, Sani Abdulwahab, Yakubu Abubakar Hassan & Emejuo Nichodemus Chibueze

81. DEEP LEARNING NETWORK FOR AUDIO-BASED ENVIRONMENTAL SOUND RECOGNITION USING YAMNET AND DENSE SELF-ATTENTION MECHANISM..... **938**
Shehu Mohammed Yusuf & Kabiru Muhammed Nasiru

82. DEEP LEARNING-BASED WEAPON CLASSIFICATION FOR INTELLIGENT SURVEILLANCE APPLICATIONS USING RESNET-50..... **949**
Kenneth Okhiria, Joseph Samuel Mshelizah & Saidi Abdulraimi

83. AI-BASED SMART MEDICATION IDENTIFICATION, AUTOMATED DISPENSING, TIMED REMINDER, AND MONITORING DASHBOARD SYSTEM **965**
Oluwafemi Lawal, Oreofe Ajayi, David Ejila Oiwona, Abdulhafeez Tahir Adamu, Mohammed Abubakar & Muhammad U. Nafiu

84. DESIGN AND PERFORMANCE EVALUATION OF AN INTELLIGENT UAV-BASED VISION SYSTEM FOR AUTOMATED POWER TRANSMISSION LINE COMPONENT INSPECTION USING YOLOV8S **972**
Asmau Sanusi Gumbi, S. Salisu, A.s Adamu, Muhammad Dikko Almustaha & Sulaiman Garba

85. DESIGN AND PROOF-OF-CONCEPT EVALUATION OF A GROWTH-STAGE-ORIENTED ESP32-BASED SMART DRIP IRRIGATION SYSTEM FOR BELL PEPPER PRODUCTION IN SEMI-ARID NIGERIA **984**
Bwala Sarah Usman, U.d Idris & Garba H.m

86. DESIGN AND SIMULATION OF ARTIFICIAL INTELLIGENCE-BASED ADAPTIVE PROTECTION SCHEME FOR NIGERIA'S POWER GRIDS USING BIG DATA ANALYTICS .. **990**
Tolulope Adelugba, Eronu Emmanuel & Ogunjuyigbe Jacob Kehinde

87. DEVELOPMENT OF AN AUTOMATIC COIL WINDING MACHINE **1001**
Abubakar Umar, Idris Musa Shehu, Idris Fatima, Zaharuddeen Haruna, Kogi Hephzibah Beulah, Zainab Mukhtar Abubakar & Shittu Shehu Danraka

88. DEVELOPMENT OF AN IOT BASED SMART SYSTEM FOR COLD SUPPLY CHAIN STORAGE AND TRANSPORTATION **1009**
Abubakar Umar, Idris Musa Shehu, Ibrahim Zakariyau Ndagitako, Zaharuddeen Haruna, Zainab Mukhtar Abubakar, Njoku Franklin C & Nafisa Shehu Usman

89. EXTENDED KALMAN FILTER-BASED FORMAL STATE ESTIMATION AND HIDDEN DYNAMIC RECONSTRUCTION FOR REAL-TIME GLUCOSE-INSULIN DIGITAL TWINS IN TYPE 1 DIABETES **1019**
Idris Oladele Muniru, Sani Saminu, Suleiman Abimbola Yahaya & Muhammad Kabir Abdulkadir

90. FAULT CLASSIFICATION IN TRANSMISSION LINE USING ANN, EXTREME GRADIENT BOOSTING AND RANDOM FOREST MACHINE LEARNING MODELS. **1030**
Joshua Alberah, G.a. Olarinoye, A.s. Abubakar, A.b Kunya & S.h Sulaiman

91. FUZZY-INTELLIGENT PID CONTROL FOR ANODE PRESSURE REGULATION IN PEMFC SYSTEMS: A HARDWARE-IN-THE-LOOP VALIDATION STUDY **1037**
Abubakar Unguwanrimi Yakubu, Jiahao Zhao, Xuanhong Ye, Fahim Ullah & Shusheng Xiong

92. INTEGRATION OF CNN-LSTM SHORT-TERM LOAD FORECASTING INTO DISTRIBUTION NETWORK OPERATIONAL PLANNING **1050**
Dorcas A.a Gomna, James Garba Ambafi, Lanre Joseph Olatomiwa & Jibril Abdullahi Bala

93. METAHEURISTIC OPTIMIZATION STRATEGIES FOR SYNTHETIC INERTIA AND LOAD FREQUENCY CONTROL IN ISLANDED MICROGRIDS: A COMPREHENSIVE REVIEW **1058**
Nurudeen Abdulazeez, Abdullahi Bala Kunya, Abdulkarim Abubakar & Abubakar Saidu Adamu

94. MISSION-AWARE OPTIMISATION OF DEPLOYABLE RENEWABLE ENERGY SYSTEMS FOR CRITICAL RURAL SERVICES IN NIGERIA: A RECONFIGURATION FRAMEWORK **1072**
Waliu Musa, Taiwo Emmanuel Okharedia, Muhammed Ibrahim, Aneke Nnamere Ezekiel, Isaac Adekanye, Oluwaseun Adebisi & Umar Abubakar Saleh

95. POWER TRANSFORMER INCIPIENT FAULT PREDICTION USING DISSOLVED GAS ANALYSIS AND ARTIFICIAL BEE COLONY OPTIMIZED RANDOM FOREST MODEL **1084**
Abdulkadir Itopa Isa, Yau Haruna Shuaibu, Abdullahi Amoo, Ganiyu Ayinde Bakare & Mustapha Musa

96. SMALL-SIGNAL STABILITY ASSESSMENT OF DFIG-BASED WIND ENERGY INTEGRATION IN STATCOM-COMPENSATED NIGERIAN TRANSMISSION NETWORK: A MODAL ANALYSIS APPROACH **1090**
Dahiru Musbahu, G.a Olarinoye, A.s Abubakar, Z. Haruna, A.s Musa & B.r Tanko

STRATEGIES FOR INFRASTRUCTURAL AND INDUSTRIAL TRANSFORMATION THROUGH ENGINEERING INNOVATIONS

97. A DOMAIN-INVARIANT SPATIO-TEMPORAL GRAPH ATTENTION NETWORK FOR CROSS-DOMAIN ANOMALY DETECTION IN INDUSTRIAL CONTROL SYSTEMS **1099**
Emejuo Nichodemus Chibueze, Idris Shehu Musa, Basira Yahaya, Sani Saleh Saminu & Mohammed Bashir Abdulrazaq

98. DEVELOPMENT AND VALIDATION OF A FINITE ELEMENT MODEL FOR REINFORCED CONCRETE BEAMS EXTERNALLY STRENGTHENED IN FLEXURE WITH STEEL PLATES**1116**
Ebitei Williams Francis, Auta Samuel, Aguwa James & Abdullahi Aliyu

99. FROM NESI 1.0 TO NESI-X: A HYBRID LEAPFROGGING ARCHITECTURE FOR ADAPTIVE TRANSFORMATION OF NIGERIA'S ELECTRICITY SUPPLY INDUSTRY **1133**
Waliu Musa, Taiwo Emmanuel Okharedia, Muhammed Ibrahim, Aneke Nnamere Ezekiel, Isaac Adekanye, Oluwaseun Adebisi & Umar Abubakar Saleh

100. INTEGRATED HEC-HMS AND IMPROVED SOIL MOISTURE BALANCE MODELLING FOR GROUNDWATER RECHARGE ASSESSMENT IN THE SEMI-ARID SOKOTO BASIN, NIGERIA**1150**
Usman Muhammed Kudu & Richard Adeolu Adesiji

101. PREDICTION MODEL FOR SOIL WATER RETENTION BEHAVIOUR OF UNSATURATED SOILS WITH DIFFERENT VOLUMETRIC WATER CONTENT **1171**
Abdullahi Karaye, Gambo Haruna Yunusa, Abubakar Jibrin Shuaib, Hafiz Ibrahim & Ibrahim Khalil Umar

102. SYSTEMIC FAILURES AND INEFFICIENCIES IN LARGE-SCALE INFRASTRUCTURE EXECUTION: A CRITICAL APPRAISAL OF THE KANO–KATSINA ROAD DUALIZATION PROJECT..... **1190**
Aminu Darda'u Rafindadi, Abubakar Sunusi & Abdullahi Balarabe Bello

SUSTAINABLE ENGINEERING PROCESSES AND SYSTEMS

103. A SECURITY-CONSTRAINED PEER-TO-PEER MARKET FRAMEWORK FOR RESILIENT DISTRIBUTION NETWORKS **1202**
Olatunji Obalowu Mohammed, Shereefdeen O. Sanni, Nabila Ahmed Rufa'í & Olayinka Sikiru Zakariyya

104. ADVANCING SUSTAINABLE URBAN MOBILITY: A TRAFFIC-RELATED AIR QUALITY ASSESSMENT AT MAJOR ROAD INTERSECTIONS IN KANO METROPOLIS, NIGERIA.... **1215**
Nasiru Danlami, Ibrahim Umar Salihi & Muttaka Na'iya Ibrahim

105. ASSESSMENT OF GROUNDWATER QUALITY AND IRRIGATION SUITABILITY IN JERE LGA, BORNO STATE: ENGINEERING SOLUTIONS FOR SUSTAINABLE AGRICULTURAL DEVELOPMENT IN NIGERIA **1229**
Aliyu Salisu Ibrahim, Muhammad Muhammad Abdulsalam & Usman Butu Tukur

106. AWARENESS, BARRIERS, AND ENABLERS OF CIRCULAR ECONOMY ADOPTION IN ABUJA'S CONSTRUCTION SECTOR **1238**
Muhammad Hadi Kabir & Abdulhameed Danjuma Mambo

107. DESIGN AND OPTIMIZATION OF A SHELL AND TUBE HEAT EXCHANGER USING PARTICLE SWARM OPTIMIZATION **1253**
Ernest Ikechukwu Dike, Umar Hassan & Muhammad Auwal Adamu

108. DESIGN AND THERMAL PERFORMANCE OF A HYBRID SOLAR-BIOMASS DRYER FOR DRYING FISH **1260**
Igbinosa Ikpotokin

109. DEVELOPMENT AND CHARACTERIZATION OF CARBON DOT (CD)-ENHANCED SHEA BUTTER AS A PHASE CHANGE MATERIAL FOR THERMAL ENERGY STORAGE **1269**
Yotolmbaye Sylvain, T.o. Ahmadu, F.o. Anafi & L.o.yusuf

110. DEVELOPMENT AND PERFORMANCE EVALUATION OF A MANUALLY OPERATED SINGLE ROW MULTI-PURPOSE WEEDER **1275**
Aminu Saleh, Akande F. B & Ishola T. A

111. DEVELOPMENT OF FAULT DIAGNOSIS FRAMEWORK FOR 132 KV CAPACITOR VOLTAGE TRANSFORMER USING MACHINE LEARNING FRAMEWORK **1284**
Moses Uchendu

112. EFFECT OF SUPERPLASTICIZER DOSAGE ON THE WORKABILITY AND COMPRESSIVE STRENGTH OF RICE HUSK ASH MODIFIED CONCRETE **1295**
Yahaya Muhammad

113. ENHANCING SOYBEAN THRESHER PERFORMANCE: A TAGUCHI DESIGN OF EXPERIMENTS APPROACH TO MODELING THRESHING AND CLEANING EFFICIENCIES**1312**
Abdullahi Saeed Hassan, Jamilu. M. Ahmed, Aminu Mohammed, Danladi Drambi Usman, Abdulwahab D. Ismail, Bala Gambo Jahun & Lawan Garba Abubakar

114. EXPERIMENTAL ASSESSMENT OF ACTIVATED CHARCOAL GRANULES AS WET PAD FOR EVAPORATIVE COOLING IN POSTHARVEST STORAGE SYSTEMS DESIGN..... **1326**
Muhammad Abubakar, Olorunsogo TS & Mohammed Ibrahim Shaba

115. EXPERIMENTAL EVALUATION OF A SOLAR DRYER INTEGRATED WITH A CARBON DOT-ENHANCED SHEA BUTTER PHASE CHANGE MATERIAL (PCM). **1340**
Yotolmbaye Sylvain, T.o. Ahmadu, F.o. Anafi & L.o.yusuf

116. FIELD-VALIDATED FAILURE ANALYSIS OF COMMERCIAL TRICYCLES IN NIGERIA AND THE POTENTIAL OF AGRICULTURAL RESIDUE-REINFORCED ALUMINIUM MATRIX COMPOSITES FOR PISTON DURABILITY ENHANCEMENT..... **1352**
Sikiru Kayode Sanusi & Adebisi Jeleel Adekunle

117. MASS AND ENERGY ASSESSMENT OF THE PYROLYSIS OF LOW LIPID MICROALGAE (DUNALIELLA SALINA)..... **1363**
Yashim Afuwai & Auwal Aliyu

118. MODELLING THE DYNAMIC EVOLUTION OF SUSTAINABILITY RISK IN INFRASTRUCTURE PROJECTS: A BAYESIAN-CALIBRATED MARKOV CHAIN APPROACH**1375**
Emmanuel Adie, John Wasiu & Ibrahim Abdulrazaq Olayinka

119. MOISTURE-DEPENDENT ENGINEERING PROPERTIES OF BEEDI BAMBARA GROUNDNUT (VIGNA SUBTERRANEA (L.) VERDC.) FOR POST-HARVEST PROCESSING DESIGN..... **1390**
Abdullahi Saeed Hassan, Aminu Mohammed, Jamilu. M. Ahmed, Bala Gambo Jahun, Danladi Drambi Usman, Abdulwahab D. Ismail & Lawan Garba Abubakar

120. PERFORMANCE EVALUATION OF A PROTOTYPE THERMO-ELECTRIC GENERATOR (TEG) BASED ENERGY HARVESTER FROM ASPHALT PAVEMENTS **1399**
Mubarak Danladi Muhammad & Abdulazeez Nazif

121. PRELIMINARY SCREENING AND CHARACTERIZATION OF A-CELLULOSE EXTRACTED FROM COTTON STALK, SUGARCANE BAGASSE, AND SAWDUST USING ALKALINE PRETREATMENT **1406**
Hassana Gwandi Audu, • Prof. Ajayi Olusegun Ayoola & M.t Isa

122. RELIABILITY ANALYSIS ON REINFORCED CONCRETE COLUMN CONTAINING SAWDUST ASH FOR STRUCTURAL APPLICATIONS **1418**
Cyprian Chukwudi Ogbobe, Aguwa James I., Abubakar Mahmud & Kolo Daniel N.

123. SCREENING AND IDENTIFICATION OF SIGNIFICANT PROCESS PARAMETERS FOR SOLID STATE FERMENTATION OF TRICHODERMA HARZIANUM..... **1432**
Buhari Uwairu, Habib Adebisi Abubakar & Bilal Sabiu

124. SOLAR-BIOMASS HYBRID SYSTEMS FOR INTEGRATED LIVESTOCK-HORTICULTURE FARMS IN SUB-SAHARAN AFRICA: A REVIEW **1443**
Kouétcha Esaïe Kombetto, James Garba Ambafi & Taliha A. Folorunso

125. UPSCALING SUSTAINABLE COLOURATION: DESIGN, FABRICATION, AND PERFORMANCE EVALUATION OF AN INDUSTRIAL-SCALE NATURAL INDIGO EXTRACTION MACHINE FOR NIGERIA'S TEXTILE SECTOR **1457**
Adam Muhammad Tanko

SUSTAINABLE MATERIALS SYNTHESIS, PROCESSING AND RECYCLING

126. AN ASSESSMENT OF WASTEPAPER MANAGEMENT IN A.B.U. MAIN CAMPUS, SAMARU **1474**
Sabur Alim & Olowodun, Theophilus Mazor

127. AN EVALUATION OF THE MECHANICAL PROPERTIES OF SANDCRETE MORTAR CONTAINING POLYSTYRENE WASTE AND FLY ASH **1483**
Salihu Yazeed, Sanusi Gambo & Abdullahi Getso Ibrahim

128. AN INVESTIGATION INTO THE PHYSICAL PROPERTIES OF METAKAOLIN-BASED GEOPOLYMER MODIFIED ASPHALT BINDER **1493**
Kenneth, Ejike Ibedu, Abdulfatai Adinoyi Murana, Aliyu Usman & Abdulmumin Ahmed Shuaibu

129. DEVELOPMENT AND CHARACTERIZATION OF HYDROPHOBIC SILICA AEROGEL SYNTHESIZED FROM RICE HUSK VIA AMBIENT PRESSURE DRYING **1508**
Isa Zubairu, Badruddeen Saulawa Sani, Salmiati Salmiati, Umar Alfa Abubakar, Sunday Bamidele Igboro & Aliyu Ishaq

130. DYNAMIC MECHANICAL ANALYSIS OF RECYCLED LDPE/HDPE POLYMER BLENDS **1521**
Tijani Abdullahi, Tajudeen Kolawole Bello & Abdulmalik Dahiru Kona

131. EFFECT OF ALKALINE PRE-TREATMENT ON THE MECHANICAL STRENGTH AND BIODEGRADATION BEHAVIOUR OF COIR FIBRE REINFORCED CONCRETE **1529**
Oluwatobi Akin, Ibrahim Aliyu, Bilkisu Sada Amartey & Amana Ocholi

132. ENGINEERING SUSTAINABLE PCL/PLA/HAP-SR/KERATIN FIBRE BIOPOLYMER COMPOSITES FOR BONE TISSUE ENGINEERING APPLICATIONS: MECHANICAL AND CHEMICAL PROPERTIES **1539**
Kazeem Adeniyi Salami, Abdulmumin Akoredeley Alabi, Ibrahim Iliyasu, Muhammad Auwal Adamu & Abdulaziz Abdullahi Bada

133. ENGINEERING SUSTAINABLE SOLID BIOFUELS FOR NIGERIA'S CLEAN ENERGY TRANSITION: COMPARATIVE PERFORMANCE EVALUATION OF INDIVIDUAL AND BLENDED AGRO-RESIDUE BRIQUETTES **1549**
Binta Zakari Bello, Rabiu Kamaldeen & Aisha Talatu Ibrahim

134. ENHANCING THE THERMAL PROPERTIES OF ASPHALT PAVEMENT FOR ENERGY GENERATION USING THERMOELECTRIC GENERATORS **1564**
Farouk Shehu Yakasai & Aminu Suleiman

135. EVALUATION OF THE SYNERGISTIC EFFECT OF CORN COB ASH (CCA) AND DATE PALM SEED ASH (DPSA) AS PARTIAL CEMENT REPLACEMENT ON THE MECHANICAL PROPERTIES OF CONCRETE **1574**
Tukur Sani, Yusuf Yau, Tasiu Ashiru Sulaiman & Yusuf Mansur Hashim

136. EXPERIMENTAL VALIDATION OF EUROCODE 2 PREDICTIONS FOR THE FLEXURAL AND SHEAR CAPACITIES OF REINFORCED METAKAOLIN-BASED GEOPOLYMER CONCRETE BEAMS **1581**
Ibrahim Aliyu, Sholadoye I.o, Idris Abubakar, Jamilu Yau & Aliyu Abubakar Abbas

137. INFLUENCE OF PLASTIC WASTE MORPHOLOGY ON THE COMPACTION PROPERTIES OF MARGINAL LATERITIC SOIL **1588**
Ahmad Idris, Aminu Suleiman & Gambo Haruna Yunusa

138. INFLUENCE OF T6-AGING TREATMENT ON SELECTED MECHANICAL PROPERTIES OF ALUMINIUM ALLOY A356/MELON HUSK ASH NANOCOMPOSITE **1593**
Ibrahim Usman, Kamilu Adeyemi Bello, Malik Abdulwahab & Terver Ause

139. MECHANICAL AND DURABILITY PERFORMANCE OF SUSTAINABLE CONCRETE INCORPORATING RICE HUSK ASH AND 100% RECYCLED CONCRETE AGGREGATE ... **1601**
Raphael Ejembi, Amana Ocholi, Bilkisu Amartey, Williams Ejembi, Samuel Ebiojo Ocheja, Samuel Godwin Obademi & Sumaila Muhammed Shaibu

140. OPTIMIZATION AND PREDICTIVE MODELLING OF DOUM PALM FIBRE-REINFORCED CONCRETE INCORPORATING RICE HUSK ASH **1613**
Musa Abdullahi, Yusuf Yau, Isah Garba, Bashir Usman & Suleiman Yusuf

141. OPTIMIZATION OF ORGANOSOLV LIGNIN EXTRACTION FROM GROUNDNUT SHELL FOR ADHESIVE PRECURSOR APPLICATIONS **1621**
Mustapha Nma Abubakar, M.t Isa, Bello Tijjani Kayode, Adamu Yusuf & Bello Abdullahi

142. PALM FRUIT BUNCH ASH AS A PARTIAL CEMENT REPLACEMENT IN SANDCRETE BLOCK**1635**
Elijah Adaofoyi Adache, Theophilus Yisa Tsado & James Olayemi James

143. PHYSICO-MECHANICAL PROPERTIES OF SUSTAINABLE TERNARY BLENDED CONCRETE INCORPORATING CORN COB ASH AND RICE HUSK ASH AS PARTIAL CEMENT REPLACEMENTS **1645**
Williams Ejembi, Y. D. Amartey, Adamu Lawan, Bilkisu H. S. Amartey, Joseph Kevin Zambwa & Raphael Ejembi

144. PREPARATION OF POROUS WASTE EXPANDED POLYSTRENE/BAMBOO FIBRE NANOCOMPOSITE MATERIAL FOR CO2 CAPTURE..... **1659**
Aliyu Ibrahim Isah & Ibrahim Ibrahim Abdulwahab

145. PROBABILISTIC RELIABILITY ANALYSIS OF REINFORCED METAKAOLIN-BASED GEOPOLYMER CONCRETE BEAMS SUBJECTED TO VARIATIONS IN GEOPOLYMER MIX PARAMETERS **1671**
Ibrahim Aliyu, I.o Sholadoye, J. M. Kaura, A. A. Abbas & Jamilu Yau

146. SILICA-BASED MATRICES FOR MICROBIAL CELL ENCAPSULATION AND IMMOBILIZATION:A REVIEW **1679**
Utibeabasi Okonbaba, H. I. Atta, A.y. Atta & B. J. El-Yakubu

147. THE USE OF GREEN MATERIALS IN BUILDING CONSTRUCTION: A STUDY OF THE NIGERIAN CONSTRUCTION INDUSTRY **1687**
Alhassan Galadima, Umar Ibrahim Kwami & Muazu Bello

148. THERMAL EVALUATION OF ASPHALT CONCRETE FOR PAVEMENT-BASED THERMOELECTRIC ENERGY GENERATION: INFLUENCE OF AGGREGATE TYPE AND GRADATION..... **1706**
Sadiq Muktar Muhammad & Aminu Suleiman

149. TRIBOLOGICAL BEHAVIOUR AND MULTI-OBJECTIVE OPTIMIZATION OF AUSTEMPERED HIGH-CARBON STEEL USING SULFATE SALT-MODIFIED SESAME OIL **1715**
Hafiz Bashir Aminu, Rayyan Mamuda Dodo & Terver Ause

150. VOLUMETRIC AND MARSHALL PROPERTIES OF HOT MIX ASPHALT WITH LDPE-MODIFIED BITUMEN, HIGH RECLAIMED ASPHALT CONTENT PAVEMENT AND WASTE ENGINE OIL **1729**
Abdulmumin Ahmed Shuaibu, Mudassir Rabiu Adam, Ahmad Abdulsalam Amin, Esther Amanosi Nyebe, Asmau Hamdana Kankia, Abdulmumin Nda Mohammed & Ismaila Mohammed Amodu

TELECOMMUNICATIONS INFRASTRUCTURE FOR SUSTAINABLE URBAN DEVELOPMENT AND ECONOMIC GROWTH

151. DEVELOPMENT OF A NARROW BAND INTERNET OF THINGS (NB-IOT) MONITORING AND CONTROL MODEL FOR URBAN DRAINAGE SYSTEM IN KANO, NIGERIA..... **1747**
Abba Abdulhadi, Hassan Sabo Miya & Usman A. Umar

152. DEVELOPMENT OF A Q-LEARNING-DRIVEN INTERFERENCE MANAGEMENT MODEL WITHIN THE ADAPTIVE RRM FRAMEWORK FOR ADAPTIVE TRANSMIT POWER OPTIMIZATION..... **1757**
Abubakar Abdulkadir, H. A. Abdulkareem, ZM Abdullahi, Elvis Obi & Aliyu Umar Abubakar

153. IMPROVED CLUSTERING AND ROUTING APPROACH FOR HOTSPOT MITIGATION IN WIRELESS SENSOR NETWORKS USING LOAD-AWARE CLUSTER-HEAD SELECTION .. **1765**
Samson Bitrus Visa, Abdulqadir Mahmudu Jada, Aliyu Muhammad Isa, Yohanna Ali Mshelia, Okehie M. Baslem & Adamu Muhammad

154. INTERFERENCE MITIGATION OF UNDERLAY SECONDARY USERS USING INTERFERENCE ALIGNMENT..... **1776**
Isiyaku Yau, Mohammed Dikko Amustapha, Shamsuddeen Abdullahi Mika'il, Joshua David, Usman Yau & Nafiu Murtala Kamaluddeen

155. HYBRID TOA–RSS LOCALIZATION BASED ON SOCP WITH HUBER LOSS OPTIMIZATION**1783**

TRACK 1 OF 11

Advanced Manufacturing, Materials and Sustainable Production

International Conference on Engineering Innovation for Sustainable Development (ICESID 2026)

Faculty of Engineering, Ahmadu Bello University Zaria · 8–10 September 2026

https://icesid.org

ADVANCING SUSTAINABLE FRUCTOSE SYRUP PRODUCTION FROM SWEET SORGHUM

Abdulkareem Abubakar[1,*], Alhaji Zanna Umara[1], Suleiman Mohammed Shuwa[1], Muhammad Bashir Tijjani[1], Suleiman Yunusa[1,2], Toyese Oyegoke[1,2], Alewo Opuada Ameh[3]

[1]*Ahmadu Bello University, Zaria*
[2]*Department of Chemical Engineering, Nasarawa State University, Keffi, Nigeria*
[3]*Department of Chemical Engineering, Federal University, Wukari, Nigeria*

Email: aaavazi@gmail.com*, a.sdarni@gmail.com, smshuwa@yahoo.com, bashtj@mail.com, slmnyunus@gmail.com, toyegoke@abu.edu.ng, ameh@fuwukari.edu.ng

***Corresponding author**: Abdulkareem Abubakar

DOI: https://doi.org/10.67203/sp.ICESID.2026

ABSTRACT

The increasing demand for high-fructose syrup, coupled with the need to reduce dependence on imported sweeteners and conventional corn-based production systems, has intensified interest in alternative and renewable feedstock. This review studied the potential of sweet sorghum, sustainable feedstock for fructose syrup production, with particular emphasis on clarification technologies, catalytic conversion pathways and process optimization strategies. The physicochemical characteristics of these feedstocks, together with juice extraction, clarification, hydrolysis, glucose isomerization, and purification approaches, are examined. Sweet sorghum demonstrates considerable potential owing to its high fermentable sugar content, relatively low agricultural input requirements, adaptability to semi-arid environments and suitability for decentralized processing. The review further highlights the importance of effective purification, catalyst selection, reaction-condition optimization and integrated processing systems in improving fructose yield, product quality and process efficiency. Consequently, the utilization of this non-conventional feedstock could support value addition, reduce biomass losses and contribute to more sustainable and locally adaptable sweetener production systems.

Keywords: *Enzymes; feedstock; fructose; optimization; syrup; valorization*

1. INTRODUCTION

Global sweetener industry dwelled on fructose syrup production in food and beverage which is highly cost-effective (Khorshidian *et al.*, 2021; Bulbul *et al.*, 2024). However, conventional corn, sugarcane and sugar beet usage has become a serious problem due to cultivation challenges which necessitate alternative biomass feedstock such as sweet sorghum, (Taylor *et al.*, 2023)

This alternate feedstock is easily cultivated with minimum farming input, care to achieve reasonable outcome (Almodares and Hatamipour, 2011; Velmurugan *et al.*, 2020), waste material like stalk also can be utilized as bagasse in bioenergy production (Appiah-Nkansan *et al.*, 2019).

This review involves the characterization, clarification and purification strategies including the catalytic pathways and process optimization for fructose production from the sweet sorghum.

2. NON-CONVENTIONAL BIOMASS FEEDSTOCKS FOR FRUCTOSE SYRUP PRODUCTION

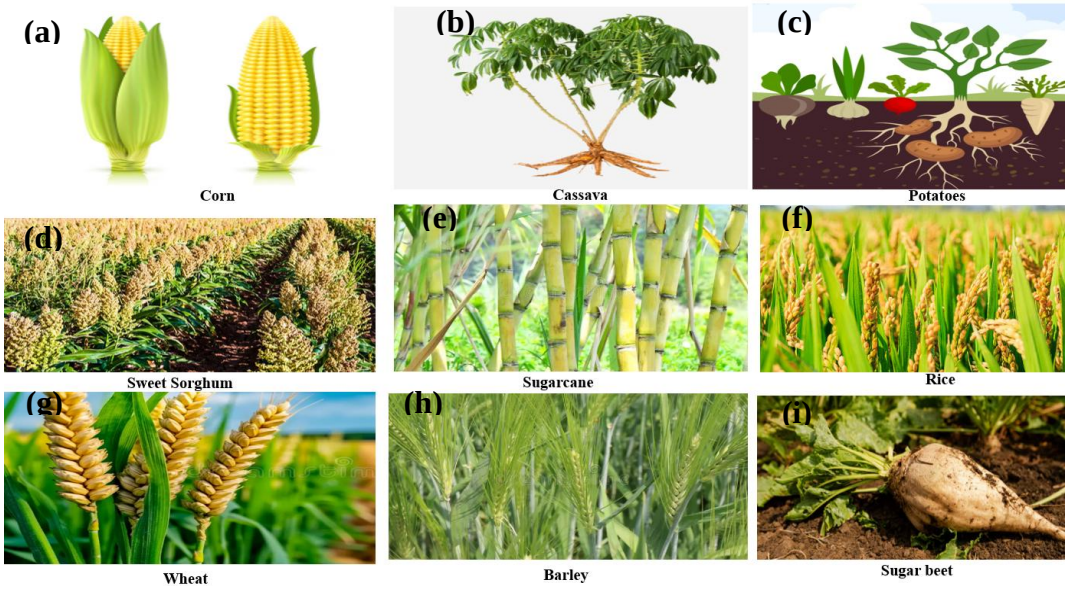

Figure 1: Biomass image of (a) Corn, (b) Cassava, (c) Potatoes, (d) Sweet Sorghum, (e) Sugarcane (f) Rice, (g) Wheat, (h) Barley and (i) Sugar beet for fructose production

Figure 1 depicted the various images of alternative biomass feedstocks for production of fructose syrup, the potential fructose yield, cost-effectiveness, and environmental influence are reviewed in this section. Corn (Figure 1a) produces the highest fructose yield (50–60%). However, high production costs, intensive water and fertilizer demand, soil degradation are matters of economic and environmental concern. Furthermore, cassava (Figure 1b) representing lower fructose yield (30–40%). Nevertheless, is cost effective, readily available in tropical regions, has low water demand and can grow on poor soils. However, it is competitive in terms of human consumption. In addition, plantain contained lowest fructose yield (20–30%), even though it inexpensive, abundant in the locality, and environmentally friendly.

Similarly, sweet sorghum (Figure 1d) possessed average yield of about 40–50%, it is an example widely cultivated in northern Nigeria; therefore, industrial utilization of this material as an alternate feedstock will improve commercialization, food security and economy of the nation (Yahaya *et al.*, 2020), production of potatoes (Figure 1c) also does not require heavy agricultural duty and input, local availability, non-competitive, affordable, non-sensitivity to a particular region and environmentally friendly (Agbaeze *et al.*, 2020) therefore there is potential and need to commercially sustain the farming of sweet sorghum to high value added product for example fructose syrup production in line with Nigeria's agricultural value chain such as development in technology, innovation and infrastructure under the National Agricultural Technology and Innovation Policy (NATIP) 2022-2027 (Federal Ministry of Agriculture and Rural Development [FMARD], 2022).

3. PROCESSING OF SWEET SORGHUM FOR HIGH-FRUCTOSE SYRUP PRODUCTION

3.1 Raw Material Harvesting and Extraction

Matured sweet sorghum stalks are harvested, defoliated and milled or blind in mechanical roller mill or electric blinder to extract raw juice, cellular debris, suspended solids, insoluble fibers particulates are filtered out (Shirvani *et al*., 2023), followed by thermal treatment to prevent microbial fermentation and other bacteria, wet-milling operations isolate the starch fraction, yield high purity starch slurry as presented in figure 2 (Zhou *et al*., 2020).

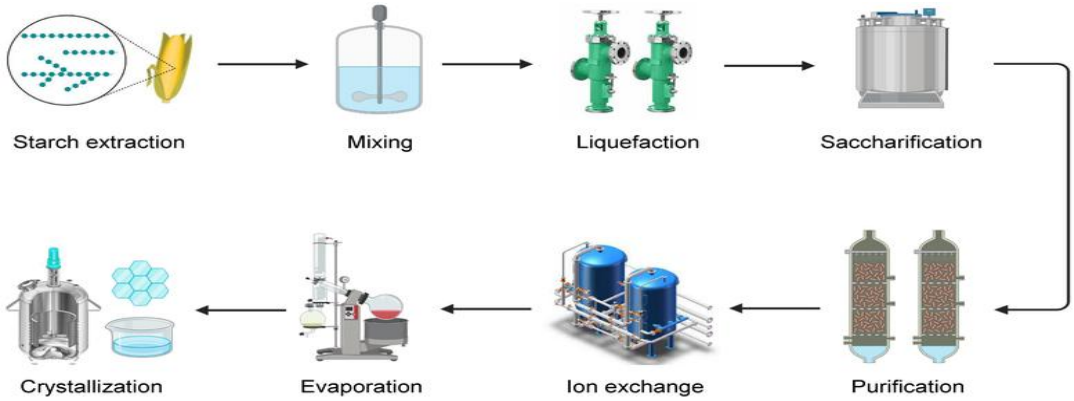

Figure 2: General Process Flowchart for Fructose Syrup Production

3.1 Purification Methods

Conversion of non-conventional biomass into high-quality fructose syrups requires adequate purification to remove impurities such as suspended solids, colloids, proteins, phenolic compounds, minerals, pigments and microbial contaminants. These impurities can inhibit the catalytic activity of enzymatic reaction which could affect product quality (Harlen & Ristiarini, 2023; Zhao *et al*., 2022). Therefore, this section discusses the various clarification methods depicted in Table 2. For example, Chemical clarification applying calcium hydroxide and alum rapidly clarifies extracted juice via neutralisation and precipitation with effective cost. However, chemical residues and environmental impacts existence is considered as a challenge (Bourguerra *et al.*, 2024; Kameneva *et al*., 2021). Furthermore, mechanical clarification such as membrane filtration, chromatography, and ion exchange limits chemical consumption and highly efficient. Despite this, it has high energy demand and equipment wear (Almodares & Hatamipour, 2011; Zhou *et al*., 2020). In addition, natural clays such as bentonite are a cheap, available and active adsorbent for pigments and proteins removal. Nevertheless, it affects juice quality (nutrient) when used in excess, also cause environmental challenges in terms of waste management (Teetor *et al*. 2011; Rajvanshi *et al*. 2020). Similarly, according to Amaral-Fonseca *et al*. (2021), Moringa *et al.* (2021) plant-based clarification is done by deploying natural clarification agents, for example moringa oleifera seed extract, okro mucilage, and guar gum are locally source, cost effective, non-toxic, and environmentally friendly options, that eliminate impurities via binding or trapping the undesired juice extracts.

Table 1: Comparison of Traditional and Natural Clarification Methods

Clarification method	Material	Mechanism	Advantage	Disadvantage	Reference
Chemical	Calcium Hydroxide (KOH). Aluminium sulfate (Alum).	Neutralizes acid and promotes precipitation. Forms aluminium hydroxide to bind particles	Cost-effective, fast, established technology	Chemical residues, environmental impact, health risks	Bourguerra *et al*. (2024), Kameneva *et al*. (2021)
Mechanical	Membrane. Chromatography. Ion exchange.	Filters particles and extraction residues. Adsorbs pigment, colour. Binding base on charge Interactions.	High efficiency, scalable, less chemical use	High energy consumption, equipment wear	Wibisono *et al*. (2023), Kameneva *et al*. (2021), Zhao *et al*. (2022)
Natural Clay	Bentonite	Adsorbs impurities such as pigments, and protein.	Low-cost, effective at removing pigments and proteins	Excess clay can affect nutrient content, waste management issues	Teetor *et al*. (2011), Rajvanshi *et al*. (2020)
Plant Based	Moringa Oleifera Seed Extract. Okro Mucilage. Guar Gum.	Bind pigments, proteins, and Solids. Bind particulate matter. Forms gel-like network, traps biocompatible.	Sustainable, non-toxic, biodegradable	Variability in raw material quality, scalability issues	Saïed *et al*. (2020), Amaral-Fonseca *et al*. (2021), Moringa *et al*. (2021)

4. CATALYTIC REACTION PATHWAYS

The popular industrial production of fructose syrup relies on three (3) stages of enzymatic pathway that breaks down biomass feedstock to glucose prior to reversible isomerisation to produce fructose.

4.1 Enzymatic reactions.

4.1.1 Liquefaction (Starch to Dextrins) entailed the use of catalyst like thermostable α-amylase which cleaves α-1,4-glucosidic bonds randomly at pH 5.8–6.5, temperature 95°C–105°C, requires Ca^{2+} ions for enzyme stability. This reduces viscosity and yields shorter-chain maltodextrins (Li *et al.*, 2017; Frey *et al.*, 2020).

4.1.2 Saccharification (Dextrins to Glucose), is the process in which a catalyst such as glucoamylase (enzyme) hydrolysis α-1,4 and α-1,6 linkages sequentially from the non-reducing ends, typically under the following conditions pH 4.0 - 4.5, temperature 60°C- 62°C and employed Glucoamylase to yield a high-purity glucose hydrolysate (D-glucose) (Frey et al., 2020; Chen et al., 2022; Gromada et al., 2008)

4.1.3. Isomerization (Glucose to Fructose), this reaction converts aldose sugar (glucose) to its ketose isomer (fructose) at pH 7.5-8.2, temperature 55°C-60°C with the facilitation of Immobilized Glucose Isomerase/Xylose Isomerase. However, the reaction typically has an equilibrium challenge

with roughly 42 % fructose, 52% glucose, and 6% other sugars (known as HFCS-42) (Amaral-Fonsera *et al.* 2021; Taibi *et al.* 2023)

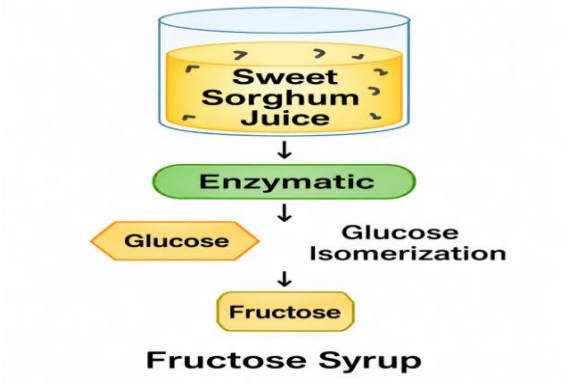

Figure 3: Enzymatic Hydrolysis and Glucose Isomerization for Fructose Syrup Production

4.2 Chemical and Chemocatalytic Reactions.

To bypass the slow reaction kinetics and high costs of enzymes, researchers considered chemocatalysts to convert glucose or directly transform biomass into fructose which involve the following methods.

4.2.1 Homogeneous Base Catalysis such as Sodium hydroxide (NaOH), calcium hydroxide ($Ca(OH)_2$), or soluble amines is employed, limitation involves high byproduct formation (psicose, mannose) (Chen *et al*., 2022; Frey *et al*., 2020; Li *et al*., 2017)

4.2.2 Heterogeneous Lewis Acid Catalysis for example, Lewis acid center (like Sn^{4+}) coordinates with the carbonyl oxygen of glucose, facilitating an intramolecular 1,2-hydride shift to form fructose leading to highly selective, water operation and easy catalyst recoverability (Moliner *et al*., 2010; Frey *et al*., 2020)

4.2.3 Bronsted Base Solid Catalysts promotion of isomerization via proton abstraction at C2 position using catalysts such as hydrotalcites, basic resins or functionalized silica (Wang *et al*., 2022; Frey *et al*., 2020)

5. PROCESS OPTIMIZATION FOR FRUCTOSE SYRUP PRODUCTION

The optimization of catalytic reaction conditions are pH, temperature, concentration, catalytic loading for high percentage yield, stability, quality and economic viability (Dai *et al.*, 2020; Ma *et al.*, 2022). However, optimization faces drawbacks from feedstock variability, impurity, seasonal availability and scale constraints.

In optimization, conditions such as temperature and pH play a critical path in affecting the glucose isomerase, degradation, reaction rates which are determined by the microbial source (Dai *et al*., 2020; Ma *et al.*, 2022). The catalyst loading and concentration specifically influences the mass transfer during the reaction depends on enzymatic (hydrolysate) conditions (Okpalanma *et al*., 2024; Debora *et al*., 2024).

6. CONCLUSION

The non-conventional use of biomass feedstock such as sweet sorghum, cassava, sweet potato and especially waste food leads to waste valorization, circular economy, reduce greenhouse gas emissions, and above all less cost effective. The sweet sorghum demonstrated the potential of catalytic pathway for high percentage yield, purity with high stability. Membrane technologies, enzyme immobilization and the catalyst loading improved the fructose production efficiency and the quality.

FUNDING

This research was fully funded by the Tertiary Education Trust Fund, Nigeria through its national Research Fund [TETF/ES/DR&D-CE/NRF2021/SETI/AFS/00016/VOL.1

REFERENCES

Agbaeze, E. K., Ohunyeye, F. O., Obamen, J., & Ibe, G. I. (2020). Management of food crop for national development: Problems and challenges of cassava processing in Nigeria. *SAGE Open, 10*(2). https://doi.org/10.1177/2158244020919778

Aguiar Borges, L., Kawasaki Ramos, K., Ferrari Felisberto, M. H., & Efraim, P. (2025). Towards enzymatic conversion of non-conventional starchy materials for glucose syrup production: A review. *Food Research International, 218*, 116907. https://doi.org/10.1016/j.foodres.2025.116907.

Almodares, A., & Hatamipour, M. S. (2011). Planting sweet sorghum under hot and dry climatic conditions for bioethanol production. In *Proceedings of the World Renewable Energy Congress* (pp. 266–272).

Amaral-Fonseca, M., Morellon-Sterling, R., Fernández-Lafuente, R., & Tardioli, P. W. (2021). Optimization of simultaneous saccharification and isomerization of dextrin to high fructose syrup using a mixture of immobilized amyloglucosidase and glucose isomerase. *Catalysis Today, 362*, 175–183. https://doi.org/10.1016/j.cattod.2020.03.021

Appiah-Nkansah, N. B., Li, J., Rooney, W., & Wang, D. (2019). A review of sweet sorghum as a viable renewable bioenergy crop and its techno-economic analysis. *Renewable Energy, 143*, 1121–1132.

Baikenov, A., Muslimov, N. Z., Baigenzhinov, K., Yessimova, Z., & Kim, Y. V. (2020). Mathematical model of dependence of factors for chromatographic separation of fructose from glucose-fructose syrup. *IOP Conference Series: Materials Science and Engineering, 994*, 012023. https://doi.org/10.1088/1757-899X/994/1/01202.

Bennett, A. S., & Anex, R. P. (2008). Farm-gate production costs of sweet sorghum as a bioethanol feedstock. *Transactions of the ASABE, 51*(2), 603–613.

Bezerra, C. V. C., et al. (2021). How does cultivar, maturation, and pre-treatment affect nutritional, physicochemical, and pasting properties of plantain flours? *Foods, 10*(8), 1749.

Bonin, C. L., Heaton, E. A., Cogdill, T. J., & Moore, K. J. (2016). Management of sweet sorghum for biomass production. *Sugar Tech, 18*, 150–159.

Bouguerra, O. M., Wahab, R. A., Huyop, F., Al-Fakih, A. M., Mahmood, W. M. A. W., Mahat, N. A., & Sabullah, M. K. (2024). An overview of crosslinked enzyme aggregates: Concept of development and trends of applications. *Applied Biochemistry and Biotechnology, 196*(9), 5711–5739. https://doi.org/10.1007/s12010-023-04809-y.

Bulbul, S., Mamur, S., Yuzbasioglu, D., & Unal, F. (2024). Safety assessment of high fructose corn syrup and fructose used as sweeteners in foods. *Toxicology Mechanisms and Methods, 34*(6), 584–595. https://doi.org/10.1080/15376516.2024.2318570.

Dai, C., Miao, T., Hai, J., Xiao, Y., Li, Y., Zhao, J., Qiu, H., & Xu, B. (2020). A novel glucose isomerase from *Caldicellulosiruptor bescii* with great potential in producing high-fructose corn syrup. *BioMed Research International, 2020*, 1871934. https://doi.org/10.1155/2020/ 1871934

Debora, R., Hermawan, D., Utami, I., & Nurcholis, F. (2024). Optimization of liquid fructose sugar production from cassava peel waste using the isomerization process. *Chempublish Journal*. https://doi.org/10.22437/chp.v8i1.33117.

Federal Ministry of Agriculture and Rural Development. (2022). *National Agricultural Technology and Innovation Policy (NATIP) 2022–2027*. Federal Ministry of Agriculture and Rural Development.

Frey, M., Seyidova, L., Richard, D., & Fongarland, P. (2020). Hybrid catalysis: Study of a model reaction for one-pot reactor combining an enzyme and a heterogeneous catalyst. *Catalysis Today, 346*, 93–97.

Giuberti, G., Rocchetti, G., & Lucini, L. (2020). Interactions between phenolic compounds, amylolytic enzymes and starch: An updated overview. *Current Opinion in Food Science, 31*, 102–113. https://doi.org/10.1016/j.cofs.2020.04.003.

Gromada, A., Fiedurek, J., & Szczodrak, J. (2008). Isoglucose production from raw starchy materials based on a two-stage enzymatic system. *Polish Journal of Microbiology, 57*(2), 141.

Guo, W., Zhang, Z., Hacking, J., Heeres, H. J., & Yue, J. (2021). Selective fructose dehydration to 5-hydroxymethylfurfural from a fructose-glucose mixture over a sulfuric acid catalyst in a biphasic system: Experimental study and kinetic modeling. *Chemical Engineering Journal, 409*, 128182. https://doi.org/10.1016/j.cej.2020.128182

Istianah, N., Kartina, N., & Ali, D. (2021). Fructose separation from sorghum syrup by using HPLC approach: A review. *International Journal of Applied Technology in Food, 2*, 69–79. https://doi.org/10.26877/IJATF.V2I2.7121

Ji, M., & Anyadioha, J. (2022). Optimization of sugar production from cassava starch using crude enzymes from maize, rice and sorghum malt extracts. *Journal information should be verified from the original source before submission.*

Khorshidian, N., Shadnoush, M., Khajavi, Z., Sohrabvandi, S., Yousefi, M., & Mortazavian, A. (2021). Fructose and high fructose corn syrup: Are they a two-edged sword? *International Journal of Food Sciences & Nutrition, 72*(5), 592–614. https://doi.org/10.1080/09637486. 2020.1862068

Li, H., Yang, S., Saravanamurugan, S., & Riisager, A. (2017). Glucose Isomerization by Enzymes and Chemo-catalysts: Status and Current Advances. *ACS Catalysis, 7*(4), 3010–3029. https://doi.org/10.1021/acscatal.6b03625

Ma, X., Huang, W., Song, Y., Han, J., Wu, J., Wang, L., & Wang, Y. (2022). Novel recyclable UCST-type immobilized glucose isomerase biocatalyst with excellent performance for isomerization of glucose to fructose. *Journal of Agricultural and Food Chemistry*. https://doi.org/10.1021/acs.jafc.2c05667

Okpalanma, E., Ukpong, E., Ezegbe, C., Nwagbo, C., & Chude, C. (2024). Evaluation of the physico-chemical properties of cassava, cocoyam, sweet potato starches and glucose syrups produced from the hydrolysis of the starches with sorghum malt enzyme extract. *Food Science and Applied Biotechnology, 7*, 1–15. https://doi.org/10.30721/fsab2024.v7.i1.314.

Putra, M., Abasaeed, A., & Al-Zahrani, S. (2020). Prospective production of fructose and single-cell protein from date palm waste. *Electronic Journal of Biotechnology, 48*, 46–52. https://doi.org/10.1016/j.ejbt.2020.09.007

Sasaki, K., Tsuge, Y., Kawaguchi, H., Yasukawa, M., Sasaki, D., Sazuka, T., Kamio, E., Ogino, C., Matsuyama, H., & Kondo, A. (2017). Sucrose purification and repeated ethanol production from sugars remaining in sweet sorghum juice subjected to a membrane separation process. *Bioresource Technology, 239*, 191-198.

Shirvani, A., Mirzaaghaei, M., & Goli, S. (2023). Apply natural fining agents to clarify fruit juices. *Comprehensive Reviews in Food Science and Food Safety, 22*(4), 987–1012.

Taibi, H., Boudries, N., Abdelhai, M., & Lounici, H. (2023). Comparison of immobilized and free amyloglucosidase processes in glucose syrups production from white sorghum starch. *Food Measurement, 17*, 3676–3688. https://doi.org/10.1007/s11694-023-01649-1.

Taylor, C. M., Maroccia, J., Masterson, M., & Rosentrater, K. (2023). Comprehensive life cycle assessment of the corn wet milling industry in the United States. *Frontiers in Energy Research, 11*, 1023561. https://doi.org/10.3389/fenrg.2023.1023561

Tian, Y., Deng, Y., Zhang, W., & Mu, W. (2019). Sucrose isomers as alternative sweeteners: Properties, production, and applications. *Applied Microbiology and Biotechnology, 103*, 8677–8687.

Udomkun, P., Masso, C., Swennen, R., Innawong, B., Alakonya, A., Kuate, A. F., & Vanlauwe, B. (2021). How does cultivar, maturation, and pre-treatment affect nutritional, physicochemical, and pasting properties of plantain flours? *Foods, 10*(8), 1749. https://doi.org/10.3390/foods10081749

Velmurugan, B., Narra, M., Rudakiya, D. M., & Madamwar, D. (2020). Sweet sorghum: A potential resource for bioenergy production. In *Refining biomass residues for sustainable energy and bioproducts* (pp. 215–242). Academic Press.

Ventura, M., Mazarío, J., & Domine, M. E. (2022). Isomerization of glucose-to-fructose in water over a continuous flow reactor using Ca–Al mixed oxide as heterogeneous catalyst. *ChemCatChem, 14*(3), e202101229.

Wibisono, Y., Alvianto, D., Argo, B., Hermanto, M., Witoyo, J., & Bilad, M. (2023). Low-fouling plate-and-frame ultrafiltration for juice clarification: Part 1—Membrane preparation and characterization. *Sustainability*. https://doi.org/10.3390/su15010806

Yahaya, M. A., Shimelis, H., Nebie, B., Ojiewo, C. O., & Danso-Abbeam, G. (2022). Sorghum production in Nigeria: Opportunities, constraints, and recommendations. *Acta Agriculturae Scandinavica, Section B—Soil & Plant Science, 72*(1), 660–672. https://doi.org/10.1080/09064710.2022.2047771

Yan, X., Jiang, D., Fu, J., & Hao, M. (2018). Assessment of sweet sorghum-based ethanol potential in China within the water–energy–food nexus framework. *Sustainability, 10*(4), 1046.

Yue, M.-Q., Wang, Z., Dun, B.-Q., Han, F.-X., & Li, G.-Y. (2021). Simplified methods of estimating fermentable sugar yield in sweet sorghum stems. *Industrial Crops and Products, 169*, 113652.

Zhao, B., Xia, B., Gao, J., Luo, F., Chen, Q., Lv, J., Li, O., Li, J., Tong, X., Liu, H., Sun, S., & Pei, Z. (2022). Study on fine mapping of QTL for juice yield traits of sweet sorghum (*Sorghum bicolor* [L.] Moench). *Czech Journal of Genetics and Plant Breeding*. https://doi.org/10.17221/48/2021-CJGPB

Zhou, G., Peng, C., Liu, X., Chang, F., Xiao, Y., Liu, J., & Fang, Z. (2020). Identification and immobilization of an invertase with high specific activity and sucrose tolerance ability of *Gongronella* sp. W5 for high fructose syrup preparation. *Frontiers in Microbiology, 11*, 633. https://doi.org/10.3389/fmicb.2020.00633

BIODEGRADABLE STRUCTURE-DIRECTING AGENTS FOR SUSTAINABLE SYNTHESIS OF ZSM-5 ZEOLITE: A REVIEW OF AMINO-ACID AND BIOPOLYMER ROUTES

Emmanuel John[1,*], Abdulazeez Yusuf Atta[1], Baba Jibril El-Yakubu[1], Ajayi Olusegun Ayoola[1]

[1]*Ahmadu Bello University*

Email: emmanueljohnadah10@gmail.com*, ayatta@abu.edu.ng, elyakububaba@abu.edu.ng, segeaj@gmail.com

***Corresponding author**: Emmanuel John

DOI: https://doi.org/10.67203/sp.ICESID.2026

ABSTRACT

Zeolite Socony Mobil–5 (ZSM-5), a high-silica MFI-type molecular sieve, is central to downstream petroleum processing, catalytic cracking, and environmental remediation. Its conventional hydrothermal synthesis depends on quaternary ammonium organic structure-directing agents (OSDAs) such as tetrapropylammonium hydroxide and bromide, which are costly, toxic, and release hazardous gases during template removal by calcination. These drawbacks, together with Nigeria's heavy reliance on imported catalysts, motivate the search for greener alternatives. This review examines biodegradable structure-directing agents—amino acids (L-arginine, glycine), organic acids (citric and lactic acid), and biopolymers such as modified chitosan—for the synthesis of ZSM-5 and related zeolites. Reported routes are compared by silica and alumina precursor, SiO_2/Al_2O_3 ratio, pH, crystallisation temperature (90–180 °C) and time, achievable crystallinity, and characterisation by XRD, SEM, FTIR, BET, and TGA. Evidence indicates that biodegradable agents can direct crystalline zeolite frameworks under milder, less hazardous conditions, although attaining the high Si/Al ratios required for ZSM-5 remains challenging with these weaker templates. Coupling such agents with low-cost local feedstocks—rice husk ash as a silica source and metakaolin as an alumina source—offers a sustainable, lower-cost pathway to ZSM-5 suited to Nigeria's downstream petroleum sector and circular-economy goals. The review identifies gaps in reproducibility, template–framework interactions, and scale-up, and outlines directions for developing fully green, waste-derived zeolite catalysts.

Keywords: *ZSM-5 zeolite; biodegradable structure-directing agents; green synthesis; rice husk ash; metakaolin*

1. INTRODUCTION

ZSM-5 is an important MFI-type zeolite whose medium-pore structure, hydrothermal stability and tunable acidity make it valuable in petroleum refining, methanol-to-olefins (MTO), aromatization and environmental applications (Kamaluddin *et al.*, 2022; Bensafi *et al.*, 2023). However, conventional ZSM-5 synthesis often requires organic structure-directing agents (OSDAs), substantial water and energy, and high-temperature calcination, creating environmental concerns (Zhang *et al.*, 2022; Parvulescu & Maurer, 2022). Consequently, interest has increased in biodegradable structure-directing agents (SDAs), template-free synthesis and waste-derived precursors.

Although conventional quaternary-ammonium OSDAs effectively control crystallization, studies demonstrate that ZSM-5 can also be synthesized without organic templates. However, template elimination does not necessarily ensure sustainability because increased water consumption, longer crystallization times or additional processing may offset environmental benefits.

Biodegradable molecules, particularly amino acids such as L-lysine and L-carnitine, can influence nucleation, crystal growth and hierarchical porosity (Zheng *et al.*, 2023). Similarly, HPMC may modify crystal growth and promote mesoporosity rather than directly replicating conventional OSDA behaviour (Hoang & Thao, 2022,) nonionic polymer and amino-acid-assisted (Zhan *et al.*, 2024). Their effectiveness depends on pH, concentration, Si/Al ratio and synthesis conditions.

Waste-derived silica and alumina, including RHA and metakaolin, can further reduce dependence on commercial raw materials, although compositional variability and impurities may

affect crystallization (Jia *et al.*, 2021). Therefore, sustainable ZSM-5 synthesis requires an integrated strategy combining biodegradable SDAs, waste-derived precursors, controlled nucleation, reduced-water synthesis and recycling. Sustainability should ultimately be assessed across the entire process, including precursor origin, directing chemistry, energy, water, crystallization, reproducibility and catalytic performance, rather than biodegradability alone.

2. LITERATURE SEARCH AND SELECTION METHODOLOGY

A structured literature search was conducted to identify studies on ZSM-5 synthesis, biodegradable structure-directing agents (SDAs), amino acids, biopolymers, and waste-derived silica/alumina precursors. Relevant publications were identified using Scopus, Web of Science, ScienceDirect, SpringerLink, Wiley Online Library, ACS Publications, and Google Scholar. Keywords included ZSM-5, MFI zeolite, biodegradable SDA, amino-acid template, L-arginine, glycine, L-lysine, L-carnitine, chitosan, hierarchical ZSM-5, rice husk ash, and metakaolin. Peer-reviewed experimental and review studies were prioritized. Studies were selected based on reported gel composition, Si/Al ratio, pH, crystallization temperature/time, SDA concentration, crystallinity, pore structure, and characterization results. Irrelevant or insufficiently documented studies were excluded.

3. ZSM-5 AND THE NEED FOR SUSTAINABLE SYNTHESIS

ZSM-5 is characterized by the MFI framework topology and a system of interconnected medium-pore channels. Its catalytic properties are determined by the combination of pore architecture, framework composition, crystal morphology and acidity. The Si/Al ratio is particularly important because framework aluminium is associated with the generation of acidic sites. Changes in the framework composition can therefore influence conversion, selectivity, coke formation and catalyst lifetime.

The versatility of ZSM-5 has made it a major catalyst in petroleum and petrochemical processing. Kamaluddin *et al.* (2022) reviewed the relationship between ZSM-5 physicochemical properties and methanol-to-olefins performance, emphasizing that synthesis conditions can strongly influence the catalytic behavior of the resulting material. This relationship creates a major challenge for green synthesis. A synthesis route cannot be considered successful merely because it produces an XRD pattern corresponding to MFI. The resulting material must also have an appropriate pore structure, acidity, crystal morphology and catalytic performance.

Conventional synthesis therefore provides a useful benchmark. Tetrapropylammonium-based OSDAs can efficiently promote MFI crystallization, but their use involves additional chemical cost and subsequent template removal. A study of TPAOH concentration, for example, demonstrated that the highest crystallinity and favorable pore properties were obtained at an optimum rather than maximum SDA concentration, suggesting that template consumption can potentially be reduced without sacrificing material quality.

This finding is significant because it demonstrates that sustainability does not necessarily require complete replacement of conventional materials. Optimization can itself be a sustainability strategy. However, reducing the amount of OSDA is only one possible solution. The more ambitious approach is to develop synthesis routes that eliminate the organic template altogether.

4. BIODEGRADABLE STRUCTURE-DIRECTING AGENTS

4.1 Amino acids

Amino acids are attractive because they are commercially available, water-compatible and biodegradable, while their amino, carboxyl and, in some cases, additional functional groups provide opportunities for interaction with aluminosilicate species. Because the protonation states of the amino and carboxyl groups change depending on the conditions of the solution, their behavior is strongly influenced by pH. As a result, a molecule of the same amino acid that is used in an alkaline zeolite gel may behave differently under neutral or acidic conditions. Instead of being a direct molecular replica of tetrapropylammonium, it might be used as an auxiliary template, mesoporogen, nucleation promoter, or crystal-growth modifier. Amino-acid-assisted hierarchical ZSM-5 synthesis is strongly supported by recent evidence.

L-arginine and glycine

Glycine and L-arginine are appealing options because they are relatively straightforward amino acids with well-established biodegradability and acid-base chemistry. L-arginine contains a guanidino group that can become strongly protonated, whereas glycine contains only one amino and one carboxyl group. These differences can influence electrostatic interactions with negatively charged silicate species. Nevertheless, the recent literature is stronger for L-lysine and L-carnitine than for direct substitution of tetrapropylammonium by L-arginine or glycine in conventional ZSM-5. Therefore, claims that any amino acid will produce high-quality ZSM-5 should be avoided unless the experimental evidence demonstrates MFI crystallinity, framework incorporation and reproducible yield.

More recent peer-reviewed work provides stronger evidence for L-lysine and L-carnitine. Zheng *et al.* (2023) reported hierarchical ZSM-5 using L-lysine and L-carnitine as secondary/mesoporous templates; characteristic MFI XRD reflections were observed, and the amino acids generated mesopores of approximately 2–10 nm. Excessive L-carnitine, however, produced amorphous phases, demonstrating that amino-acid dosage is important.

4.2 Biopolymers: Chitosan

Chitosan is a chitin-derived polysaccharide that has been deacetylated. It has a strong capacity for hydrogen bonding and interaction with inorganic species due to the presence of hydroxyl and amino groups in its polymer chain. In zeolite synthesis, chitosan can function as a macropore or mesopore-forming additive, a crystal-growth modifier, or an assisting template during recrystallization. Because of its size, it has a different effect than a small SDA molecule does: it can affect aggregation and interparticle voids as well as the molecular-scale channels. A recent study by Fu *et al.* (2024) demonstrated the application of chitosan as an assisting template during the alkaline reassembly of HZSM-5. Chitosan promoted the formation of micro–mesoporous structures and altered the acid-site distribution. The resulting hierarchical HZSM-5 exhibited improved catalytic performance in the co-pyrolysis of corn stover and high-density polyethylene, enhancing the production of monocyclic aromatic hydrocarbons (MAHs) while suppressing polycyclic aromatic hydrocarbons (PAHs) and coke formation. Under the reported optimum conditions, the MAH carbon yield reached 36.9% at 550 °C with 15% chitosan, while the chitosan-modified catalyst increased the synergistic production of MAHs by 38.2% relative to the corresponding reference system (Fu *et al.*, 2024).

Table 1: Summary of Biodegradable Structure-Directing Agents

Biodegradable SDA	Specific Examples	Mechanism/Role	Key Characteristics & Finding
Amino Acids	L-arginine, Glycine, L-lysine, L-carnitine	Auxiliary template, mesoporogen, nucleation promoter, or crystal-growth modifier.	Behavior is strongly pH-dependent; functional groups interact with aluminosilicates. Evidence is stronger for L-lysine/L-carnitine than L-arginine/glycine in ZSM-5 synthesis.
Biopolymers	Chitosan	Macropore/mesopore-forming additive, crystal-growth modifier, or assisting template during recrystallization	Affects aggregation/interparticle voids; promotes micro–mesoporous structures in hierarchical HZSM-5; improves aromatic hydrocarbon production during biomass/plastic co-pyrolysis.

Table 2: Recent Synthesis of Zeolite using Biodegradable OSDA

Zeolite Type	Silica Source	Alumina Source	Biodegradable SDA	pH	Crystallinity	Temperature (ºC)	Crystallization Time (hrs)	Si/Al Ratio	Characterization	Reference
ZSM-5	Rice Husk Ash	Kaolin	L-lysine/L-carnitine	10-11	≈90–95%	140-160	24-48	≈25	XRD, SEM, FTIR, BET, TGA	Zheng *et al.*, 2023
MWW (MCM-22)	Silica Gel	Sodium Aluminate	None; HMI used	0.1	≈90–95%	150	48	≈15-50	XRD, SEM	Wang. B.*et al.*,2008
Zeolite A (LTA)	Rice Husk Ash	Sodium aluminate	Without organic template	10-11	≈90–95%	90	6	≈1.0-1.2	XRD, SEM, FTIR	Kumar *et al.*,2019

5. WASTE-DERIVED SILICA AND ALUMINA PRECURSORS FOR ZSM-5 SYNTHESIS

High-purity silica and alumina can account for a substantial part of material cost, and their production has its own environmental footprint. Therefore, natural minerals, clays, and agricultural residues are highlighted in recent reviews as alternative precursors (Nguyen *et al.*, 2023). Rice husk ash (RHA) is one of the most appealing agricultural residues due to its silica-rich ash that can be produced through controlled combustion. Jia *et al.* (2021) demonstrated that RHA can be the source of silica for template-free ZSM-5 by combining the utilization of waste with a reduction in the utilization of organic templates. Under low temperatures, their work produced ZSM-5 with Si/Al ratios of 20, 30, and 40. This is important for developing nations because the method does not use an organic template and uses agricultural residue instead of purified silica. The condition of the ash is critical. Uncontrolled burning can produce carbon-rich ash or promote transformation of amorphous silica into less reactive crystalline phases at excessive temperatures. As a result, the chemical composition, combustion temperature, residence time, atmosphere, washing or acid-leaching steps, and ash preparation should be described. XRF is particularly useful for determining Si, Al, Fe, Ca, Mg, Na and K contents before gel formulation.

Kaolin calcination removes structural hydroxyl groups and increases reactivity. The resulting metakaolin is therefore a useful alumina-containing precursor.. Combining

RHA-derived silica with metakaolin can produce a locally sourced aluminosilicate system. However, the Si/Al ratio must be adjusted because metakaolin contains substantial silicon as well as aluminium. The resulting ZSM-5 should be evaluated using XRD, SEM, FTIR, BET, TGA and acidity measurements.

6. RESEARCH GAPS AND FUTURE PERSPECTIVES

The key research gaps in biodegradable-SDA ZSM-5 synthesis involve mechanistic understanding, reproducibility, high-Si/Al synthesis, scale-up, and sustainability. Future research should clarify the actual structure-directing role of biodegradable additives, standardize RHA and metakaolin precursors, and explore the use of biodegradable co-directing agents and ZSM-5 seeds to achieve high-Si/Al materials. Scale-up should incorporate process intensification, mother-liquor recycling, reduced water use, dry-gel conversion, and lower-temperature crystallization. In addition, **l**ife-cycle and techno-economic assessments are needed to verify environmental and economic benefits. Ultimately, synthesis conditions should be directly linked to catalytic performance, considering not only crystallinity but also crystal size, diffusion, conversion, selectivity, stability, and coke formation.

7. CONCLUSION

This review establishes that sustainable ZSM-5 synthesis cannot be achieved simply by replacing conventional organic structure-directing agents (OSDAs) with biodegradable alternatives. Nevertheless, evidence from Zheng *et al.* (2023) demonstrates that biodegradable amino acids, particularly L-lysine and L-carnitine, have considerable potential as functional synthesis additives for ZSM-5. These amino acids successfully facilitated the formation of hierarchical ZSM-5 and generated ultra-small mesopores of approximately 2–10 nm by overcoming phase separation during crystallization. Their hydrophilic functional groups also provide favourable interactions with zeolite precursors and developing crystals, enabling control over crystal morphology, grain size, porosity and, consequently, acid properties.

However, the effectiveness of L-lysine and L-carnitine remains dependent on their dosage and synthesis conditions. Zheng *et al.* (2023) showed that moderate addition of the amino-acid template did not adversely affect ZSM-5 nucleation and crystal growth, whereas excessive L-carnitine resulted in increased amorphous phases. Thus, these findings support the view that L-lysine and L-carnitine are strong SDAs for sustainable ZSM-5 synthesis, but their use should be based on optimized compositions rather than simple one-to-one substitution for conventional OSDAs.

REFERENCE

Bensafi, B., Chouat, N., & Djafri, F. (2023). The universal zeolite ZSM-5: Structure and synthesis strategies—A review. *Coordination Chemistry Reviews, 496*, 215397. https://doi.org/10.1016/j.ccr.2023.215397 (ScienceDirect)

Fu, P., Tang, B., Li, H., Liu, S., Wang, L., & Lin, X. (2024). Chitosan-assisted reassembled hierarchical HZSM-5 for selective production of monocyclic aromatics in catalytic co-pyrolysis of biomass and plastic. *Renewable Energy, 236*, 121492. https://doi.org/10.1016/j.renene.2024.121492

Hoang, P. H., & Thao, N. T. T. (2022). Dry gel synthesis of hierarchical ZSM-5 zeolite using hydroxyl propyl methyl cellulose (HPMC) as a mesoporogen and its catalytic activity in alkylation reactions. *RSC Advances, 12*, 24511–24517. https://doi.org/10.1039/D2RA04325D (Royal Society of Chemistry Publishing)

Jia, H., Du, T., Fang, X., Gong, H., Qiu, Z., Li, Y., & Wang, Y. (2021). Synthesis of template-free ZSM-5 from rice husk ash at low temperatures and its CO2 adsorption performance. ACS Omega, 6, 3961–3972. https://doi.org/10.1021/acsomega.0c05842.

Kamaluddin, H. S., Gong, X., Ma, P., Narasimharao, K., Chowdhury, A. D., & Mokhtar, M. (2022). Influence of zeolite ZSM-5 synthesis protocols and physicochemical properties in the methanol-to-olefin process. *Materials Today Chemistry, 26*, 101061. https://doi.org/10.1016/j.mtchem.2022.101061 (ScienceDirect)

Kumar, A., & Naskar, M. K. (2019). Single-step process without organic template for the formation of zeolite A from RHA. *International Journal of Applied Ceramic Technology, 16*(4), 1458–1464. https://doi.org/10.1111/ijac.13206

Nguyen, D.-K., Dinh, V.-P., Nguyen, H. Q., & Hung, N. T. (2023). Zeolite ZSM-5 synthesized from natural silica sources and its applications: A critical review. *Journal of Chemical Technology & Biotechnology, 98*(6), 1339–1355. https://doi.org/10.1002/jctb.7380

Parvulescu, A.-N., & Maurer, S. (2022). Toward sustainability in zeolite manufacturing: An industry perspective. *Frontiers in Chemistry, 10*, 1050363. https://doi.org/10.3389/fchem.2022.1050363 (Frontiers)

Wang, B., Wu, J., Yuan, Z.-Y., Li, N., & Xiang, S. (2008). Synthesis of MCM-22 zeolite by an ultrasonic-assisted aging procedure. *Ultrasonics Sonochemistry, 15*(4), 334–338. https://doi.org/10.1016/j.ultsonch.2007.07.007

Zhan, J., Wang, Y., He, T., Sheng, L., Wu, B., Liu, Q., Jia, M., & Zhang, Y. (2024). Nonionic polymer and amino acid-assisted synthesis of ZSM-5 nanocrystals and their catalytic application in the alkylation of 2-methylnaphthalene. *Dalton Transactions, 53*, 7384–7396. https://doi.org/10.1039/D4DT00096J (Royal Society of Chemistry Publishing)

Zhang, J., Wang, X., & Shi, C. (2022). Rapid solvent-free synthesis of nano-sized ZSM-5 with a low Si/Al ratio at 90 °C. *Inorganic Chemistry Frontiers, 9*, 1992–2000. https://doi.org/10.1039/D2QI00298A (Royal Society of Chemistry Publishing

Zheng, Y., Ning, W., Wang, Q., Wei, X., Li, X., & Pan, M. (2023). Hierarchical ZSM-5 zeolite using amino acid as template: Avoiding phase separation and fabricating an ultra-small mesoporous structure. *Microporous and Mesoporous Materials, 355*, 112578. https://doi.org/10.1016/j.micromeso.2023.112578

COMPARATIVE STUDY OF THERMAL, ZEOLITE-Y CATALYTIC AND NI-DOPED ZEOLITE-Y CATALYTIC CRACKING OF GAS CONDENSATE

Jonathan Danladi Gaiya[1,*], Shuaibu Musa[1], Suleiman Shehu[1], Mansur Suleiman[1], Abdullahi Nuraddeen Bakori[1], Narcillina Nkechi Adegboro[1], Muhammad Aminu Abubakar[1], Aliyu Ibrahim[1], Abdullahi Bukar[1], Muazu Ibrahim[1], Toyese Oyegoke[1], Abdulazeez Yusuf Atta[1]

[1]*Chemical Engineering, Ahmadu Bello University, Zaria*

Email: jonathangaiya@gmail.com*, sbmgumel@gmail.com, danshehu33@gmail.com, msule82@gmail.com, abdullahibakori@kadunapolytechnic.edu.ng, nkadegboro@gmail.com, mabubakar@miu.edu.ng, aliyu021494@gmail.com, abbukar@yahoo.com, muhaziibrahim1@gmail.com, toyegoke@abu.edu.ng, ayatta@abu.edu.ng

***Corresponding author**: Jonathan Danladi Gaiya

DOI: https://doi.org/10.67203/sp.ICESID.2026

ABSTRACT

This study investigated the modification of zeolite-Y and its application in the cracking of gas condensate using thermal, catalytic, and nickel-doped catalytic processes. Raw zeolite-Y (ZY-1) was chemically pretreated (ZY-2) and subsequently modified with nickel to produce Ni-doped zeolite-Y (ZY-3). The catalysts were characterized using Brunauer–Emmett–Teller (BET) analysis, X-ray diffraction (XRD), and Fourier-transform infrared spectroscopy (FTIR), while the hydrocarbon products were evaluated by GC-MS/PIONA analysis. BET analysis showed progressive increases in the surface area from 181.549 m²/g for ZY-1 to 245.368 and 278.956 m²/g for ZY-2 and ZY-3, respectively, accompanied by increases in total and micropore volumes. XRD confirmed the preservation of the characteristic zeolite-Y framework after modification, with additional reflections in ZY-3 consistent with crystalline NiO. FTIR further confirmed the retention of the principal aluminosilicate framework vibrations following pretreatment and nickel incorporation. GC–MS/PIONA analysis revealed substantial changes in the hydrocarbon-class distribution following cracking. The raw gas condensate (G-1) contained 47.47% paraffins and 30.49% aromatics, while thermal cracking (G-2) produced 46.10% paraffins and 32.10% aromatics. Catalytic cracking (G-3) increased the aromatic fraction to 40.90% while reducing the paraffin fraction to 38.40%. Ni-doped catalytic cracking (G-4) resulted in 39.48% aromatics, 39.98% paraffins, and a slight increase in olefins from 0.40% to 0.91% relative to G-3. Overall, the results demonstrate that pretreatment and nickel incorporation significantly modified the textural and structural properties of zeolite-Y, while catalytic and Ni-doped catalytic cracking produced distinct changes in the gas-condensate hydrocarbon composition.

Keywords: *Zeolite-Y; Nickel-doped Zeolite-Y; Gas condensate; Catalytic cracking; Thermal cracking*

INTRODUCTION

The increasing demand for transportation fuels, petrochemical intermediates, and high-value hydrocarbon products has intensified interest in technologies that can convert and improve the efficiency of underutilized petroleum fractions into more valuable products. Among these resources, natural gas condensate is an attractive feedstock because it consists predominantly of relatively light hydrocarbons and can serve as an intermediate source of gasoline-range and petrochemical hydrocarbons. Gas condensates have attracted attention not only as blending components but also as feedstocks for catalytic upgrading, particularly where their hydrocarbon distribution can be selectively shifted toward products with improved octane quality and greater commercial value (Salim & Saed, 2023; Ganiyu et al., 2026). Recent work on Nigerian gas condensate has further demonstrated the potential of catalytic conversion over modified zeolitic materials to alter the distribution of paraffins, naphthenes, aromatics, and isoparaffins to obtain more desirable gasoline-range products (Ganiyu et al., 2026).

The conversion of petroleum-derived hydrocarbon streams is driven by competing pathways, such as thermal and catalytic cracking. While thermal cracking operates at high temperatures and often produces undesirable secondary reactions, such as excessive coke and gas, catalytic cracking offers better product control at lower temperatures. Ultimately, the specific pore architecture, acidity, and stability of zeolite catalysts determine the exact cracking pathways and product selectivity for complex feeds (Wei et al., 2025; Magaji et al., 2024).

Zeolites are highly attractive catalytic materials for hydrocarbon upgrading because their crystalline frameworks combine tunable acidity with precise microporous structures that ensure shape selectivity while promoting key chemical reactions. Despite these benefits, narrow micropores often impose severe diffusion limitations when handling large or complex petroleum fractions, thereby restricting access to internal acid sites and increasing both secondary reactions and coke deposition (Dong et al., 2024; Wei et al., 2025). Zeolite-Y is widely used in petroleum refining due to its large-pore architecture and established role in fluid catalytic cracking, yet even conventional zeolite Y topologies face mass-transport constraints when processing bulky hydrocarbon feeds. To mitigate these transport limitations, current research focuses on designing hierarchical Y zeolites that combine intrinsic micropores with larger mesoporous pathways to balance selectivity, molecular transport, and structural stability. Recent studies have demonstrated that hydrothermal and post-synthetic modifications of Y zeolites successfully engineer these hierarchical networks, thereby significantly improving acid-site accessibility and hydrocracking performance (Zhou et al., 2024; Wei et al., 2023).

The incorporation of nickel into zeolitic materials introduces additional metal-associated functionalities that can complement the intrinsic acidity of the zeolite, thereby influencing hydrocarbon conversion and product distribution through synergistic metal–acid interactions.. The interaction between nickel and the framework directly influences acidity, active site dispersion, and accessibility. Recent work has demonstrated that nickel-modified hierarchical zeolites enhance hydrocracking performance and mass transfer by combining metal functionality with interconnected larger pores rather than relying on metal loading alone (Zhang et al., 2024; Hu et al., 2024).

Despite these advances, an important gap remains in understanding how controlled Zeolite Y pretreatment, followed by nickel incorporation, affects the structural characteristics required for the catalytic cracking of actual gas condensates, particularly under continuous-flow conditions. Most existing studies focus on modeling hydrocarbons or heavier feeds, overlooking the integrated relationship between modified Zeolite Y, nickel active sites, and complex condensate streams. This study addresses these limitations by systematically examining the structure-property relationship of raw, pretreated, and Ni-modified Zeolite Y and its effect on pore accessibility and hydrocarbon transformation.

2. MATERIALS AND METHODS

2.1 Materials

The materials used in this study included commercial zeolite-Y, nickel nitrate hexahydrate ($Ni(NO_3)_2 \cdot 6H_2O$), sodium hydroxide (NaOH), ammonium chloride (NH_4Cl), deionized water, nitrogen (N_2), glass beads, and gas condensate. Commercial zeolite-Y (ZY-1) was used as the parent material for the preparation of the pretreated zeolite-Y (ZY-2) and Ni-doped zeolite-Y (ZY-3) catalysts. Nickel nitrate hexahydrate was used as the nickel precursor, while NaOH and NH_4Cl were employed during the alkaline treatment and conversion of the zeolite to the acidic H-form, respectively. Deionized water was used to prepare the treatment and precursor solutions, while glass beads served as an inert packing material in the fixed-bed reactor. Nitrogen was used as the carrier/diluent gas during the cracking experiments.

The gas-condensate feedstock was obtained from the Ogunu field in the Niger Delta region of Nigeria**.** The raw gas condensate was designated **G-1**, while the products obtained after thermal cracking, catalytic cracking over ZY-2, and catalytic cracking over ZY-3 were designated G-2, G-3, and G-4, respectively. All materials and reagents were used as received, unless otherwise stated.

2.2 Catalyst Preparation

2.2.1 Preparation of Pretreated Zeolite-Y (ZY-2)

Commercial zeolite-Y (20 g) was initially calcined in a muffle furnace at 550 °C for 5 h. The calcined zeolite was subsequently treated with 100 mL of 0.5 M NaOH solution at 70 °C for 2 h under continuous stirring. After alkaline treatment, the solid was repeatedly washed and centrifuged with deionized water while monitoring the pH until neutrality (pH 7) was achieved. The washed material was dried at 90 °C for 1 h and subsequently converted to the acidic H-form by treatment with 100 mL of 0.5 M NH_4Cl solution at 70 °C for 3 h under continuous stirring. The resulting material was dried at 100 °C for 2 h and calcined at 550 °C for 5 h to obtain the pretreated zeolite-Y, designated ZY-2.

2.2.2 Preparation of Ni-Doped Zeolite-Y (ZY-3)

Nickel-doped zeolite-Y was prepared using the incipient-wetness impregnation (IWI) method using $Ni(NO_3)_2 \cdot 6H_2O$ as the nickel precursor. The required quantity of $Ni(NO_3)_2 \cdot 6H_2O$ was calculated to obtain a target nickel loading of 5 wt.% and dissolved in 100 mL of deionized water. The resulting solution was added dropwise to the pretreated zeolite-Y (ZY-2) under continuous stirring and subsequently aged for 4 h at ambient conditions. The impregnated material was dried at 120 °C for 12 h and then calcined at 550 °C for 4 h to obtain the Ni-doped zeolite-Y catalyst, designated as ZY-3.

2.2.3 Catalyst Characterization

The structural and textural properties of the prepared catalysts were evaluated using powder X-ray diffraction (XRD), Fourier-transform infrared spectroscopy (FT-IR), and nitrogen (N_2) adsorption–desorption analysis. Analyses were performed on raw Zeolite-Y (**ZY-1**), pretreated Zeolite-Y (**ZY-2**), and Ni-doped Zeolite-Y (**ZY-3**) to determine the effects of pretreatment and nickel incorporation on the zeolite structure and textural properties.

Powder X-ray diffraction (XRD) patterns were recorded using a PANalytical X'Pert PRO MPD diffractometer equipped with Cu Kα radiation (λ = 0.1541 nm), operated at 40 kV and 30 mA, over a 2θ range of 5–60° at room temperature. The diffraction patterns were used to identify the characteristic crystalline phases and assess changes in the crystallinity and structural integrity of the Zeolite-Y framework following pretreatment and Ni incorporation.

The Fourier transform infrared (FT-IR) spectra of ZY-1, ZY-2, and ZY-3 were obtained using an Agilent MicroLab instrument to identify characteristic zeolite framework vibrations and surface functional groups. The spectra were compared to identify changes in the zeolite's structural features resulting from alkaline treatment, conversion to the acidic form, and subsequent nickel incorporation.

N_2 adsorption–desorption measurements were conducted using an ASAP 2020 V4.02 analyser at 77 K to determine the textural properties of the catalysts. Before analysis, each sample was evacuated under vacuum at 573 K for 8 h. The BET method was used to determine the specific surface area. The total pore volume was determined from the amount of nitrogen adsorbed at P/P_0 = 0.9915, while the pore-size characteristics were obtained from the adsorption–desorption data.

2.3 Catalytic Cracking of Gas Condensate

The catalytic cracking of gas condensate was conducted at atmospheric pressure in a continuous-flow fixed-bed reactor using nitrogen (N_2) as the carrier/diluent gas. Prior to each experiment, the reactor bed was purged under a continuous N_2 flow of 400 mL/min at 550 °C for 1 h. The N_2 supply pressure was maintained at 3 bar at the regulator, whereas the reactor itself remained at atmospheric pressure.

Thermal cracking was first conducted under the same reaction conditions to provide a baseline for comparison with catalytic cracking. Both thermal and catalytic experiments were performed at 550 °C, atmospheric pressure, and reaction duration of 1 h. For the catalytic experiments, 0.5 g of either ZY-2 or ZY-3 was mixed with 0.5 g of glass beads and packed into the reactor. The gas-condensate feed was introduced continuously using a positive-displacement peristaltic pump at 4 mL/min, while the N_2 flow rate was maintained at 400 mL/min. The heating lines were maintained at 100 °C.

The reactor effluent was passed through a condenser maintained at 2.5 °C to recover the condensable liquid products, while the uncondensed gaseous products were collected in a gas collection bag. The condensed liquid products were subsequently analyzed using an Agilent 7890 gas chromatograph equipped with a DB-624 capillary column**.** The identified compounds were subsequently classified according to the PIONA groups (paraffins, isoparaffins, olefins, naphthenes, and aromatics).

The apparent liquid recovery was calculated as the ratio of the recovered condensable liquid to the total feed introduced, as expressed in Equation (1):

$$\text{Liquid recovery}(\%) = \frac{V_{Liquid\ recovered}}{V_{feed}}$$

3.0 RESULTS AND DISCUSSION

3.1 Surface Functional Group Analysis

The FTIR spectra for raw Zeolite-Y (ZY-1), pretreated (ZY-2), and Ni-doped (ZY-3) are shown in Figure 1. The FTIR spectrum of raw zeolite-Y (ZY-1), recorded over approximately 400–4000 cm⁻¹, exhibited the characteristic vibrational features of an aluminosilicate zeolite, with prominent bands at approximately 459, 529, 613, 837, 1080, 1209, 1408, and 1645 cm⁻¹. The strong absorption near 1080 cm⁻¹ is attributed mainly to the asymmetric stretching of the Si–O–Si/Si–O–Al framework, while the bands in the lower wavenumber region arise from framework bending and deformation vibrations. Such bands are characteristic of zeolitic aluminosilicate structures and are widely used to evaluate changes in their framework chemistry (Eren et al., 2024). The absorption near 1645 cm⁻¹, together with the broad O–H stretching region around 3400 cm⁻¹, is associated with H–O–H bending and O–H stretching of adsorbed water and surface hydroxyl species. Water-related absorption around 1650 cm⁻¹ is commonly observed in zeolitic materials because of their ability to retain physically adsorbed water within their porous structure (Uygun et al., 2023). The ZY-1 spectrum represents the characteristic aluminosilicate framework and hydrated surface environment of the starting zeolite-Y.

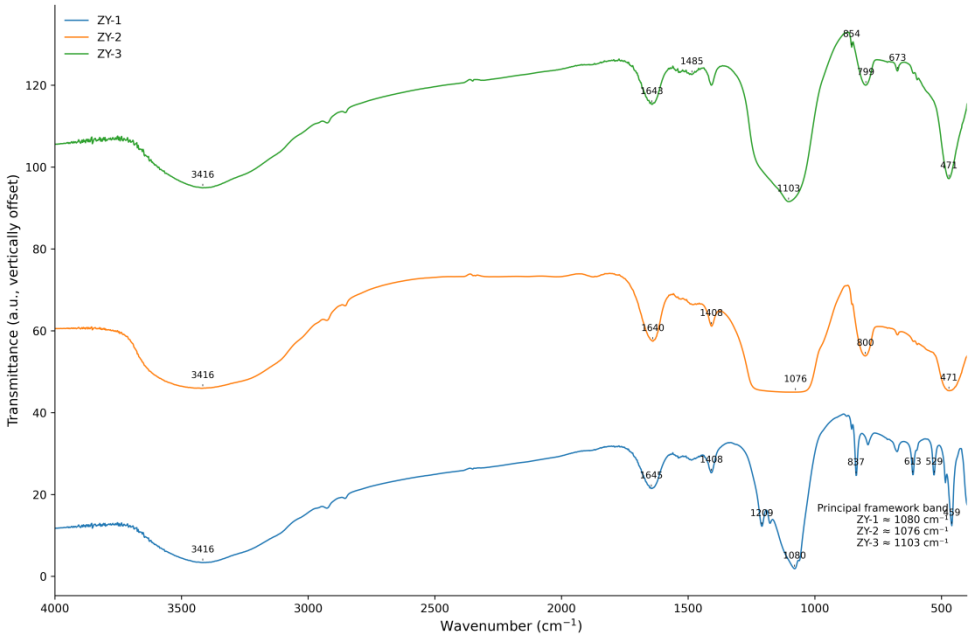

Figure 1: The FTIR spectra for raw Zeolite-Y (ZY-1), pretreated (ZY-2) and Ni-doped (ZY-3)

Following pretreatment, ZY-2 retained the principal framework vibrations observed in ZY-1, indicating preservation of the characteristic aluminosilicate structure. The most notable change was a small displacement of the principal framework-stretching band from approximately 1080.17 cm⁻¹ in

ZY-1 to 1076.32 cm^{-1} in ZY-2, corresponding to a shift of approximately 4 cm^{-1} toward lower wavenumbers. This displacement indicates a change in the local chemical environment of the aluminosilicate framework following pretreatment and may reflect the redistribution or modification of the framework-associated and extraframework species. The water-associated band also shifted from approximately 1645.34 cm^{-1} in ZY-1 to 1639.55 cm^{-1} in ZY-2, suggesting a change in the amount or environment of adsorbed water. Importantly, the persistence of the major framework bands indicates that pretreatment modified the chemical environment of the zeolite without eliminating its characteristic aluminosilicate structure. This interpretation is consistent with recent studies showing that chemical treatment of zeolitic materials can alter framework associated species and surface chemistry while retaining identifiable zeolitic vibrational features (Eren et al., 2024).

The incorporation of nickel produced a more pronounced change in the FTIR spectrum, with the principal framework stretching band shifting from 1076.32 cm^{-1} in ZY-2 to 1103.32 cm^{-1} in ZY-3, indicating a change in the local aluminosilicate environment. Nevertheless, the characteristic framework vibrations remained evident, suggesting preservation of the zeolitic structure. The H–O–H bending band was also retained near 1643.41 cm^{-1}, indicating the continued presence of adsorbed water. Similar Ni zeolites have shown that Ni incorporation can modify the local metal support environment without necessarily disrupting the zeolite framework (Zhang et al., 2024).

3.2 Crystalline Phase and Structural Analysis

The XRD pattern of ZY-1 (Figure 2) displayed the characteristic reflections of the faujasite (FAU) type zeolite-Y framework. Prominent reflections were observed at approximately 6.5°, 10.5°, 12.3°, 16.1°, 19.2°, 20.9°, 24.3°, 27.7° and 32.1°**,** confirming the crystalline nature of the starting material. The characteristic low-angle and high-angle reflections are consistent with the established diffraction pattern of FAU type zeolites and provide a suitable structural reference for assessing the effects of subsequent modification. Manrique et al. (2024) similarly used the persistence and intensity of characteristic zeolite Y reflections to evaluate the structural integrity following chemical modification.

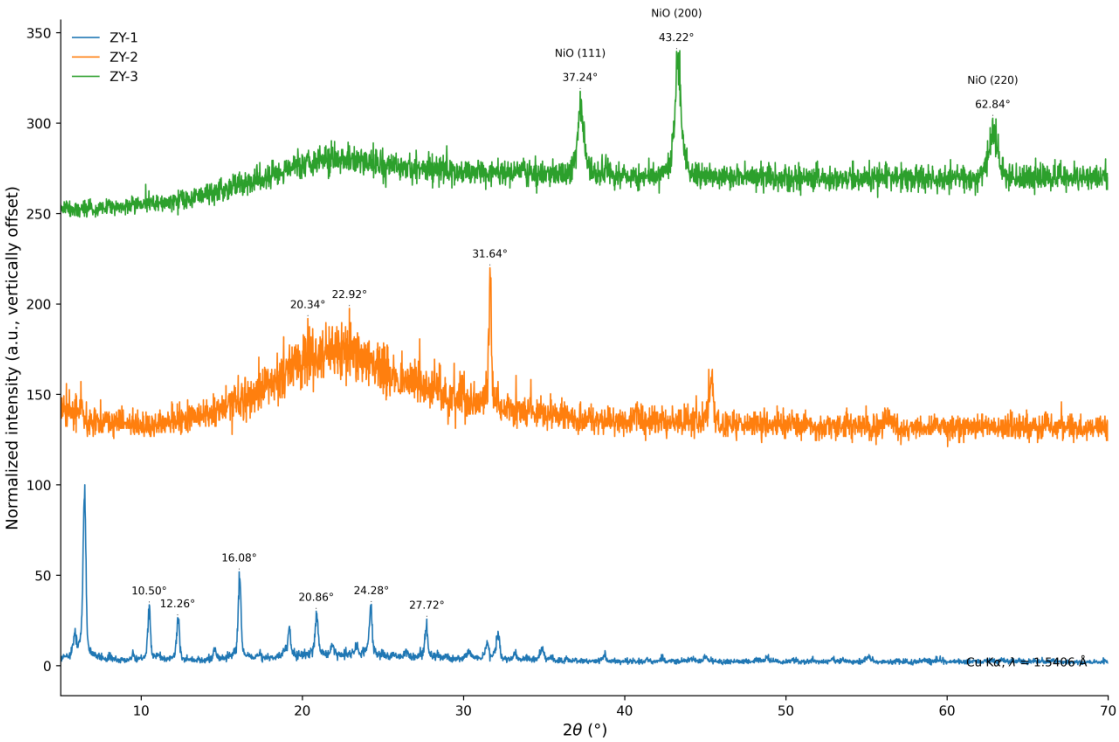

Figure 2: The XRD profiles for raw Zeolite-Y (ZY-1), pretreated (ZY-2) and Ni-doped (ZY-3)

After pretreatment, the sharp, multi-peak reflections observed in ZY-1 were largely replaced in ZY-2 by a broad amorphous hump, with only weak shoulder features near 20.3° and 22.9°. This indicates a substantial loss of long-range crystalline order following alkaline treatment. The changes in diffraction intensity may reflect alterations in framework ordering, extraframework species, or crystallite characteristics resulting from pretreatment. Similar observations have been reported for chemically modified zeolite Y, where changes in diffraction intensity can accompany structural modification, while the principal zeolitic framework remains detectable (Manrique et al., 2024). The observed changes can be more appropriately described as structural modifications with partial loss of the crystalline zeolite-Y framework.

In Ni-doped zeolite-Y, the diffractogram likewise shows a broad amorphous background.. In addition, new reflections appeared at approximately 37.2°, 43.4°, and 62.8°**,** corresponding to the (111), (200), and (220) planes of crystalline NiO, respectively, which is in agreement with the reported NiO diffraction patterns (Miskan et al., 2024; Zhang et al., 2024). The coexistence of partial zeolite-Y framework and NiO reflections indicates that nickel modification introduced a detectable crystalline NiO phase in the catalyst. However, the presence of NiO peaks does not necessarily mean that all nickel occurs as crystalline NiO, since highly dispersed or poorly crystalline Ni species may remain undetectable by conventional XRD.

3.3 Surface Area and Pore Structure

The textural properties of ZY-1, ZY-2, and ZY-3 (Table 1) showed clear evolution in accessible porosity following pretreatment and Ni incorporation. The BET surface area increased from 181.549 m^2/g for ZY-1 to 245.368 m^2/g for ZY-2, representing an increase of approximately 35.2%**,** while the total pore volume increased from 0.096 to 0.133 cm^3/g. This indicates that the pretreatment substantially increased the accessible surface area and pore volume of the zeolite. This behaviour may be associated with the generation or opening of secondary pore environments through alkaline modification, thereby improving access to the intrinsic microporous network. However, the accompanying loss of sharp XRD reflections indicates that the textural enhancement may not arise solely from beneficial hierarchical pore development. Partial dissolution of the zeolite framework and associated loss of crystallinity may also have contributed to the increased accessible surface area and pore volume. Thus, the combined BET and XRD results suggest that alkaline pretreatment produced enhanced textural accessibility, but with some degree of structural degradation. This balance is consistent with the need to control alkaline treatment severity, since excessive framework extraction can compromise microporosity and crystallinity (Han et al., 2024).

Table 1: Textural properties of ZY-1, ZY-2, and ZY-3.

Parameter	**ZY-1**	**ZY-2**	**ZY-3**
BET area (m^2/g)	181.549	245.368	278.956
Total pore volume (cm^3/g)	0.096	0.133	0.163
Micropore volume (cm^3/g)	0.063	0.092	0.110

The effect of nickel incorporation is also evident from the textural data. Following Ni modification, the BET surface area increased further to 278.956 m^2/g, while the total pore volume increased to 0.163 cm^3/g. The micropore volume also increased from 0.092 cm^3/g in ZY-2 to 0.110 cm^3/g in ZY-3, indicating that Ni incorporation did not cause substantial blockage of the zeolite micropore network. The simultaneous increase in the surface area and pore volume suggests that the modified catalyst retained appreciable internal accessibility after metal incorporation. Comparable studies have shown that maintaining accessible micro- and larger-pore networks in metal-modified zeolites is beneficial because the additional transport pathways can improve access to active sites and facilitate the diffusion of relatively bulky hydrocarbon molecules (Manrique et al., 2024; Hu et al., 2024).

The pore size distributions in Figure 3 further showed that the modified zeolites retained predominantly small pores. The DFT profiles showed pore width between 1.8 to 2.8 nm while the BJH adsorption profiles (insert) concentrated within approximately 1.4–2.4 nm. The DFT distributions reflected a progressive change in the pore width profile from ZY 1 through ZY 2 to ZY 3, consistent with modification of the accessible pore environment following pretreatment and Ni incorporation. However, DFT-derived distributions exhibit a pronounced minimum near 2.1 nm, whereas the BJH distributions show a continuous pore-volume contribution through this region. This difference highlights the sensitivity of calculated pore-size distributions to the underlying pore-size analysis methodology and suggests that the DFT minimum should not be interpreted directly as evidence for the absence or blockage of pores at approximately 2.1 nm. Such differences are expected because DFT based pore-size distributions depend on the selected theoretical model and kernel, which can influence the calculated position and intensity of features within the narrow micropore to mesopore range (Gor et al., 2017).

Overall, the BET results indicate a progressive improvement in textural accessibility from ZY-1 to ZY-2 to ZY-3, with the highest values observed for the Ni-modified material. When considered alongside the retained Zeolite-Y reflections observed by XRD, the increased surface area and pore volume are consistent with enhanced pore accessibility and partial development of a hierarchical pore structure, rather than complete framework destruction. This balance between additional porosity and preservation of the zeolitic framework is particularly desirable for hydrocarbon conversion because hierarchical Y zeolites can reduce diffusion limitations while retaining the catalytic functionality of the parent microporous structure (Han et al., 2024; Manrique et al., 2024).

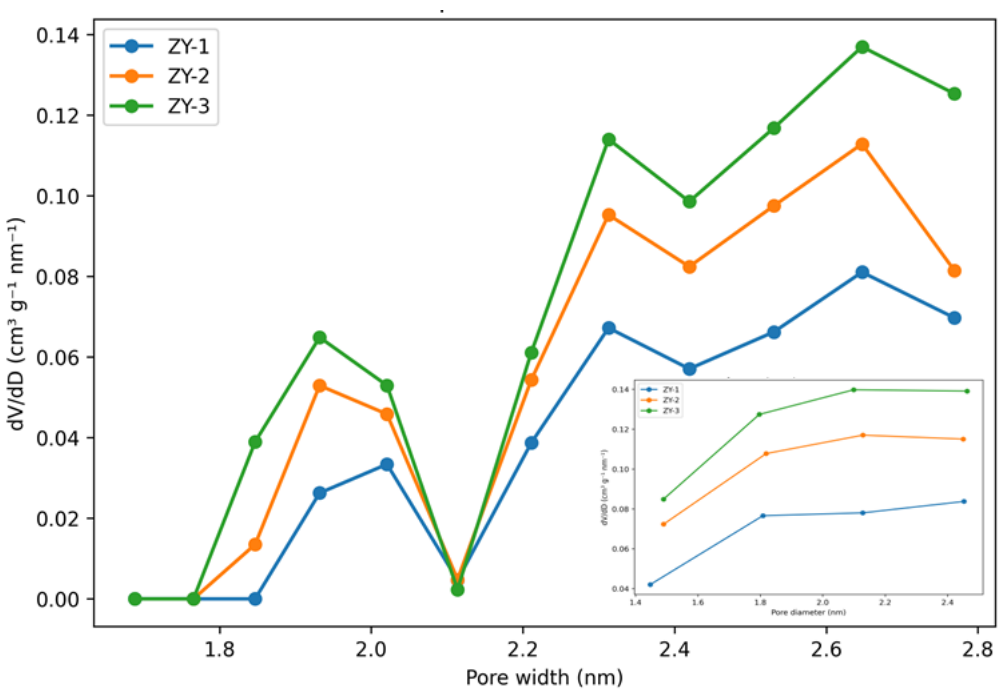

Figure 3: Catalyst pore size distributions using DFT and BJH (insert) methods

3.4 Hydrocarbon Composition and Product Distribution

Thermal treatment of the gas condensate (S1 → G-2) in Figure 4 resulted in only fractional compositional redistribution, with saturates decreasing from 67.47 to 60.80 area% and aromatics increasing from 30.49 to 32.10 area%. The persistence of the C10–C28 n-alkane series and the negligible olefin formation suggest that the thermal step resulted in limited cracking, with redistribution of existing hydrocarbons rather than extensive C–C bond scission. In contrast, the introduction of ZY-2 produced a pronounced change. The n-paraffins decreased from 46.10 to 38.40

area%, while aromatics and naphthenes increased from 32.10 to 40.90 and 3.80 to 6.70 area%, respectively. The high acidity and accessible pore structure of zeolite-Y are known to favour hydrocarbon conversion through acid-catalysed cracking, isomerisation and related secondary reactions (Ding et al., 2021).

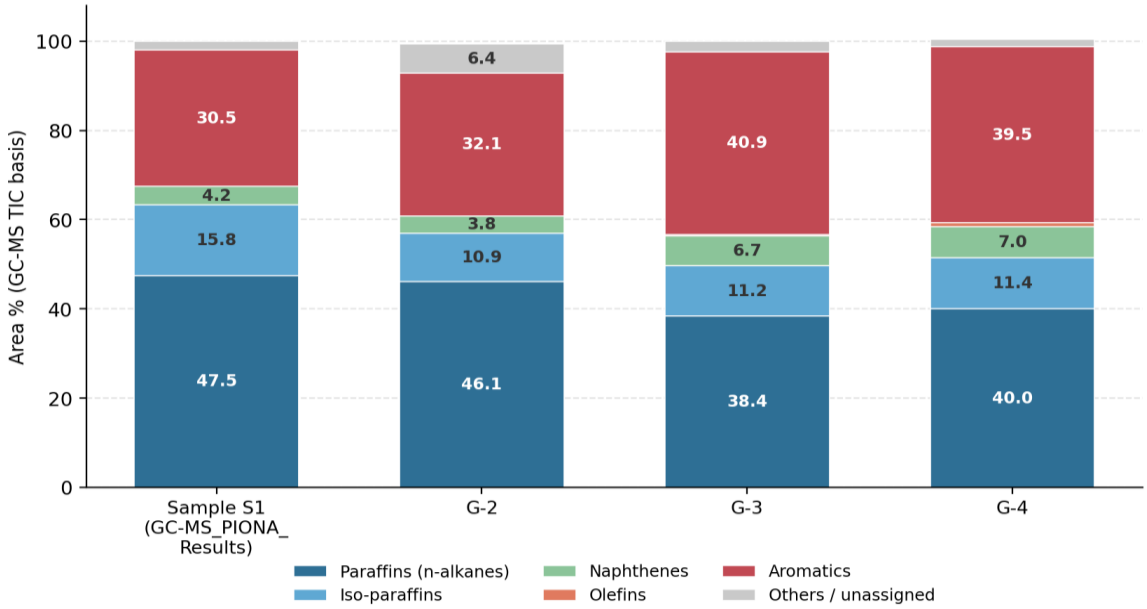

Figure 4: Composition distributions across gas condensate samples

The increase in aromatics following ZY-2 treatment is particularly significant, indicating that paraffin transformation was accompanied by cyclisation and aromatisation rather than being limited to C–C bond cleavage. Metal-modified zeolites have been shown to facilitate dehydrogenation pathways that contribute to aromatic formation (Uslamin et al., 2020), the present ZY-2 results primarily demonstrate the contribution of the acidic zeolite framework to hydrocarbon transformation.

3.5 Liquid Recovery

The apparent liquid recovery (Figure 5) decreased progressively from 25.00% for thermal cracking (G-2) to 18.33% over ZY-2 (G-3) and 14.17% over Ni-ZY-3 (G-4), corresponding to reductions of 26.7 and 43.3%, respectively, relative to thermal cracking. This decline indicates that the catalysts promoted greater transformation of the feed beyond the condensable-liquid fraction, potentially through secondary cracking to lighter non-condensable hydrocarbons. For the Ni-containing catalyst, additional reactions such as dehydrogenation and aromatization may also have contributed to the observed reduction in liquid recovery.

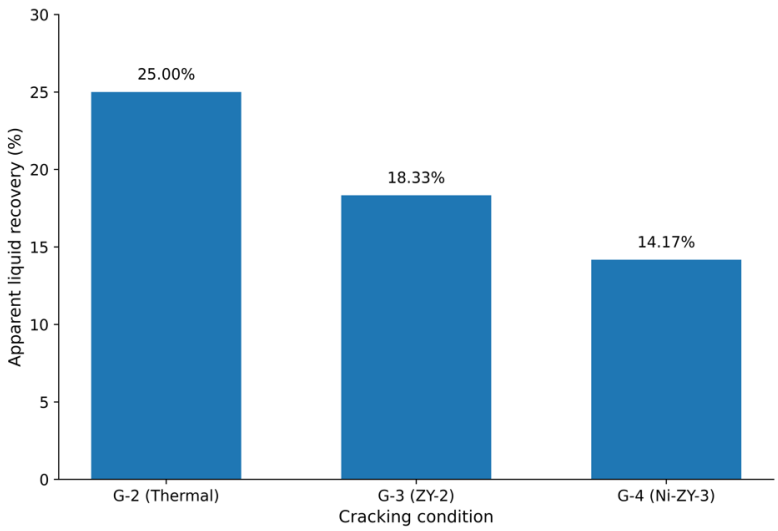

Figure 5: Apparent liquid recovery of cracking products

The lower liquid recovery is consistent with the PIONA and carbon-number distribution results, which show increased hydrocarbon transformation over the catalysts, evidenced by the reduction in n-paraffins and enrichment of aromatics and naphthenes, particularly after ZY-2 treatment. These compositional changes indicate that catalytic cracking promoted secondary reactions beyond simple C–C bond scission.

4.0 CONCLUSION

Characterization of the catalysts showed that alkaline pretreatment and nickel incorporation altered both the textural and structural properties of zeolite-Y. BET analysis indicated a progressive increase in surface area and pore volume from ZY-1 (181.5 m^2/g) to ZY-2 (245.4 m^2/g) and ZY-3 (279.0 m^2/g); however, XRD showed that this gain was accompanied by substantial loss of long-range crystalline order in ZY-2 and ZY-3, indicating that the increased porosity partly reflects framework degradation rather than purely beneficial hierarchical pore development. XRD further confirmed the formation of crystalline NiO in ZY-3, while FTIR confirmed retention of the principal aluminosilicate framework vibrations, with modest band shifts following pretreatment and nickel incorporation.

The study showed that zeolite-Y pretreatment significantly influenced gas condensate conversion, with ZY-2 promoting greater hydrocarbon redistribution toward aromatic and naphthenic products. The apparent liquid recovery also decreased from 25.00% for thermal cracking to 18.33% with ZY-2 and 14.17% with Ni-ZY-3, indicating greater transformation of the feed beyond the recovered condensable-liquid fraction. Ni incorporation produced a comparatively subtle change, including a slight increase in the olefin and naphthene fractions. Overall, the results confirmed that both zeolite modification and Ni incorporation influenced the hydrocarbon distribution during gas condensate cracking.

Acknowledgement

The authors gratefully acknowledge the support provided by the Petroleum Technology Development Fund (PTDF) Chair in Chemical Engineering at Ahmadu Bello University, Zaria.

REFERENCES

Ding, L., Sitepu, H., Al-Bogami, S. A., Yami, D., Tamimi, M., Shaik, K., & Sayed, E. (2021). Effect of zeolite-Y modification on crude-oil direct hydrocracking. *ACS Omega*, *6*(43), 28654–28662. https://doi.org/10.1021/acsomega.1c03029

Dong, Q., Li, R., & Jiao, H. (2024). Zeolite catalysts for selective hydrocracking of polycyclic aromatic hydrocarbons—Structures and mechanisms. *ChemCatChem*, *16*, e202400117. DOI: 10.1002/cctc.202400117

Eren, S., Türk, F. N., & Arslanoğlu, H. (2024). Synthesis of zeolite from industrial wastes: A review on characterization and heavy metal and dye removal. *Environmental Science and Pollution Research, 31,* 41791–41823. https://doi.org/10.1007/s11356-024-33863-0

Ganiyu, A., Edoh, A. D., Atta, A. Y., Mukhtar, B., Jibril, B. Y., & Aderemi, B. O. (2026)**.** Gas condensate upgrade over hierarchical ZSM-5 zeolite synthesised via desilication and reassembly routes. *Next Chemical Engineering, 3*, 100071. DOI: 10.1016/j.nxcen.2026.100071

Gor, G. Y., Thommes, M., Cychosz, K. A., & Neimark, A. V. (2017). Quenched solid density functional theory method for characterization of mesoporous materials. Langmuir, 33(42), 11138–11148. https://doi.org/10.1021/acs.langmuir.7b01961

Han, Y., Larmier, K., Rivallan, M., & Pirngruber, G. D. (2024). Generation of mesoporosity in H–Y zeolites by basic or acid/basic treatments: Towards a guideline of optimal Si/Al ratio and basic reagent. *Microporous and Mesoporous Materials, 365*, 112906. https://doi.org/10.1016/j.micromeso.2023.112906

Hu, Z., Wu, T., Xie, H., Zhang, Y., Ge, S., & Wu, Z. (2024). Synthesis and consequence of three dimensionally ordered macroporous Beta zeolite supported NiW catalyst for efficient hydrocracking of 1 methylnaphthalene to BTX. *Chemical Engineering Journal, 499*, 155761. https://doi.org/10.1016/j.cej.2024.155761

Magaji, S., Hussain, I., Malaibari, Z., Hossain, M. M., Qureshi, Z. S., & Ahmed, S. (2024)**.** Catalytic cracking of liquefied petroleum gas (LPG) to light olefins using zeolite-based materials: Recent advances, trends, challenges and future perspectives. *The Chemical Record, 24*(11), e202400110. DOI: 10.1002/tcr.202400110

Manrique, C., Solano, R., Mendoza, C., Amaya, S., & Echavarría, A. (2024). Hierarchical submicrosized Y zeolites prepared by sequential desilication–dealumination post synthesis modification and their catalytic performance in vacuum gas oil hydrocracking. *New Journal of Chemistry, 48*, 6188–6199. https://doi.org/10.1039/D3NJ05551E

Miskan, M., et al. (2024). Unveiling the effects of nickel loading on methane dry reforming: Perspectives from Ni/fibrous zeolite Y catalysts. *International Journal of Hydrogen Energy*. https://doi.org/10.1016/j.ijhydene.2024.03.204

Salim, M. A., & Saed, U. A. (2023). Production of high-octane number gasoline from Basra low octane-number gas condensate and ethanol over modified Zn/ZSM5 zeolite catalyst. *Bulletin of Chemical Reaction Engineering & Catalysis, 18*(1), 59–70. DOI: 10.9767/bcrec.16763

Sun, J., Wang, X., Wei, Q., & Zhou, Y. (2024). Synthesis of small crystal NiY zeolites and their catalytic performance in hydrocracking. *Journal of Fuel Chemistry and Technology, 52*(6), 775–789. https://doi.org/10.1016/S1872-5813(24)60432-9

Uslamin, E. A., Saito, H., Kosinov, N., Pidko, E., Sekine, Y., & Hensen, E. J. M. (2020). Aromatization of ethylene over zeolite-based catalysts. *Catalysis Science & Technology, 10*, 2774–2785. https://doi.org/10.1039/C9CY02108F

Uygun O, Güven R, Çakal GÖ. (2023). Adsorptive removal of stable and radioactive Pb(II) isotopes from aqueous solution using bentonite, zeolite and perlite: characterization, isotherm and thermodynamic studies. Clay Minerals. 58(2):195-209. doi:10.1180/clm.2023.18

Wei, L.-J., Peng, P., Qiao, K., Cheng, G.-N., Etim, U. J., & Yan, Z.-F. (2023)**.** Hierarchical Y zeolite with accessible intracrystalline mesopores and enhanced hydrocracking performances via sequential multi-carboxyl acid and fluoroborate post-treatments. *Fuel, 354*, 129289. DOI: 10.1016/j.fuel.2023.129289

Zhang, G., Mao, Q., Yue, Y., et al. (2024). Ni based catalysts supported on HBeta zeolite for the hydrocracking of waste polyolefins. *RSC Advances, 14*, 15856–15861. https://doi.org/10.1039/D4RA02809K

Zhang, J., Li, Y., Song, H., Zhang, L., Wu, Y., He, Y., Ma, L., Hong, J., Tayal, A., Marinkovic, N., Jiang, D. E., Li, Z., Wu, Z., & Polo-Garzon, F. (2024). Tuning metal-support interactions in

nickel–zeolite catalysts leads to enhanced stability during dry reforming of methane. *Nature Communications*, *15*, 8566. https://doi.org/10.1038/s41467-024-50729-8

Zhou, X., Han, X., Qu, Z., & Chen, R. (2024)**.** Hierarchical FAU zeolites boosting the hydrocracking of polyolefin waste into liquid fuels. *ACS Sustainable Chemistry & Engineering*, *12*(15), 6013–6022. DOI: 10.1021/acssuschemeng.4c01097

International Conference on Engineering Innovation for Sustainable Development (ICESID 2026)
Faculty of Engineering, Ahmadu Bello University Zaria · 8–10 September 2026

DENSITY FUNCTIONAL THEORY INVESTIGATION OF METHANE STEAM REFORMING ON NI(111) AND PD1–CU(111) SINGLE-ATOM ALLOY SURFACES

Abdulrauf Onimisi Ibrahim[1,*]
[1]*Ahmadu Bello University*
Email: aoibrahim63@gmail.com[*]
***Corresponding author**: Abdulrauf Onimisi Ibrahim
DOI: https://doi.org/10.67203/sp.ICESID.2026

ABSTRACT

Density functional theory (DFT) calculations were performed to investigate the elementary reaction steps involved in methane steam reforming on Ni(111) and Pd_1–Cu(111) single-atom alloy catalyst (SAAC) surfaces. The reaction pathway includes methane and water dissociation, oxidation of CH by adsorbed oxygen to form CHO*, and subsequent dehydrogenation of CHO* to CO. The objective of this study is to evaluate the catalytic potential of the Pd_1–Cu(111) SAAC as a carbon-tolerant alternative to conventional Ni catalysts while maintaining high reforming activity. The results show that methane activation on Pd_1–Cu(111) proceeds with an activation barrier of 0.97 eV, which is 0.32 eV lower than that on Ni(111), indicating enhanced CH4 activation. In contrast, water dissociation is less favourable on Pd_1–Cu(111), with an activation barrier 0.39 eV higher than that on Ni(111). Notably, the formation of surface carbon from CH* is kinetically inhibited on the Pd_1–Cu(111) SAAC because of its substantially higher activation barrier, thereby suppressing coke formation. Overall, these findings demonstrate that the Pd_1–Cu(111) single-atom alloy effectively promotes methane activation while minimizing carbon deposition, highlighting its promise as a highly active and coke-resistant catalyst for methane steam reforming.*

Keywords: *Density functional theory; Methane steam reforming; Single atom alloy; Ni catalyst)*

1. INTRODUCTION

Methane steam reforming (MSR), $CH_4 + H_2O \rightarrow CO + 3H_2$, remains the principal industrial route to hydrogen and syngas, which underpin ammonia synthesis, methanol production, and emerging hydrogen-energy technologies (Blaylock et al., 2009). Nickel-based catalysts dominate commercial MSR because Ni combines high intrinsic activity for C–H bond activation with low cost and broad availability. However, the strong methane-activation capability of Ni also promotes sequential dehydrogenation of CH_x intermediates, particularly at low-coordination sites, leading to surface carbon accumulation and the nucleation of graphitic coke. Carbon deposition blocks active sites, alters the catalyst surface, and ultimately accelerates deactivation (Wang et al., 2017). Thermal sintering of Ni under reforming conditions further compromises catalyst stability (Che et al., 2017). These limitations have therefore driven the search for catalyst architectures that retain efficient C–H activation while suppressing the elementary steps responsible for carbon formation.

Single-atom alloys (SAAs), in which isolated catalytically active metal atoms are embedded in a less reactive host-metal surface, offer a distinctive strategy for addressing this challenge (Ibrahim et al., 2023). Site isolation can electronically and geometrically modify the reactivity of the active atom while restricting ensembles of contiguous reactive sites required for multidentate adsorption, extensive dehydrogenation, and carbon–carbon coupling (Hannagan et al., 2020). Among emerging SAA platforms, Pd–Cu systems are particularly attractive for reforming chemistry. Although Cu exhibits limited activity toward methane activation, isolated Pd atoms can provide highly reactive sites for C–H bond cleavage within an otherwise relatively inert Cu matrix (Cao et al., 2015). At the same time, the spatial isolation of Pd atoms may limit the contiguous ensembles that facilitate deep dehydrogenation and coke-precursor formation (Cao et al., 2015). Pd_1–Cu(111) thus provides a well-defined model system for determining whether single-atom site isolation can preserve the methane-activation

characteristics required for MSR while mitigating the carbon-forming chemistry inherent to conventional Ni surfaces.

The overall MSR mechanism comprises a complex network of competing elementary reactions, including CH_4 activation, H_2O dissociation, sequential CH_x dehydrogenation, oxidation of carbon-containing intermediates, and CO formation (Blaylock et al., 2011). Consequently, overall catalytic performance cannot be rationalized solely from adsorption properties or a single apparent activation barrier. Periodic density functional theory (DFT) provides a direct means of resolving these elementary processes and quantifying their reaction energies and kinetic barriers at the atomic scale (Ibrahim et al., 2024). Despite increasing interest in single-atom catalysts for hydrocarbon conversion, the mechanistic relationship between methane activation and carbon suppression on Pd_1–Cu(111) remains insufficiently established. In particular, a direct comparison of the competing CH* oxidation pathway toward CO and CH* dehydrogenation pathway toward surface carbon on Pd_1–Cu(111) and Ni(111) is lacking. Establishing this competition is essential for determining whether Pd_1–Cu(111) can overcome the activity–coking trade-off that constrains Ni-based MSR catalysts. A coke-resistant, highly active MSR catalyst is of direct relevance to Nigeria and other gas-endowed African economies, where methane steam reforming underpins existing and planned syngas, ammonia/fertilizer, and hydrogen-energy value chains built on the region's substantial natural gas reserves; catalysts that resist deactivation by carbon deposition can improve the operating economics and reliability of such reforming processes, supporting broader sustainable-energy and industrial-development objectives (Omuboye & Nweke-Eze, 2026).

This study addresses that gap using periodic DFT calculations to map the complete elementary reaction network of MSR on Ni(111) and Pd_1–Cu(111), directly comparing activation barriers for methane activation, water dissociation, and coke-forming dehydrogenation. The novelty of this work lies in demonstrating, at the mechanistic level, that Pd1–Cu(111) simultaneously lowers the barrier for methane activation and kinetically suppresses surface carbon formation relative to Ni(111), establishing a mechanistic basis for its use as a coke-resistant reforming catalyst.

2. METHODOLOGY

Periodic, spin-unrestricted DFT calculations were performed using the DMol^3 code (Delley, 2010). Exchange–correlation effects were treated within the generalized gradient approximation (GGA) using the Perdew–Burke–Ernzerhof (PBE) functional. Self-consistent field convergence was set to a threshold of 10^{-5} Ha for the total electronic energy, and geometry optimizations were converged to a maximum force criterion of 0.005 Ha Å^{-1}. Brillouin-zone integration was performed using a 4 × 4 × 1 Monkhorst–Pack k-point mesh.

The Ni(111) and Pd_1–Cu(111) single-atom alloy (SAA) surfaces were modelled using a p(3 × 3) periodic supercell of a four-layer slab. For the Pd_1–Cu(111) SAA, a single Pd atom was substituted for a Cu atom in the topmost layer of the Cu(111) slab, embedding an isolated Pd site within the Cu host. During optimization, the two uppermost slab layers were allowed to relax fully, while the two lower layers were fixed at their bulk-optimized positions to approximate bulk-like behaviour. Periodic slab images were separated by an 18 Å vacuum region along the surface normal to eliminate spurious interactions between periodic replicas.

Transition states (TS) for each elementary reaction step were located using the linear synchronous transit (LST) and quadratic synchronous transit (QST) methods, followed by conjugate-gradient refinement. Each optimized TS was confirmed by vibrational frequency analysis, requiring exactly one imaginary frequency along the reaction coordinate, corresponding to the reaction pathway. Zero-point energy (ZPE) corrections, reported as ΔE^{ZPE} and E_a^{ZPE} in Table 1, were obtained from the vibrational frequencies computed for each initial, transition, and final state and added to the corresponding electronic-energy differences. The activation energy (E_a) and reaction energy (ΔE) for each elementary step were calculated as:

$$E_a = E_{TS} - E_{IS} \quad (1)$$

$$\Delta E = E_{FS} - E_{IS} \quad (2)$$

where E_{IS}, E_{TS}, and E_{FS} are the total electronic energies of the slab system in the initial, transition, and final states, respectively. All reported E_a and ΔE values correspond to electronic-energy differences. The zero point energy (ZPE) was calculated using the following equation 3.

$$ZPE = \sum hv/2$$

Where h is Planck's constant and v is the vibrational frequency. Adsorbed species are denoted throughout using an asterisk (*) to indicate surface-bound intermediates: CH_4*, CH_3*, CH_2*, CH*, C*, H_2O*, OH*, O*, HCO*, COH*, CO*, COOH*, and CO_2*, consistent with standard surface-science notation.

3. RESULTS AND DISCUSSION

The reaction mechanisms of MSR on Ni(111) and Pd1–Cu(111) single-atom alloy (SAA) surfaces were systematically investigated. The kinetic parameters associated with the individual reaction steps were determined and are summarized in Table 1.

Table 1: *Activation energy and reaction energy of the reaction steps in MSR*

	elementary reaction step	Ni(111)		Pd_1-Cu(111)	
		ΔE^{ZPE} (eV)	E_a^{ZPE} (eV)	ΔE^{ZPE} (eV)	E_a^{ZPE} (eV)
R1	$CH_4 + * \rightarrow CH_4*$	-0.11		-0.11	
R2	$H_2O + * \rightarrow H_2O*$	-0.41		-0.37	
R3	$CH_4* + * \rightarrow CH_3* + H*$	0.20	1.29	0.59	0.97
R4	$CH_3* + * \rightarrow CH_2* + H*$	0.15	0.78	0.15	1.11
R5	$CH_2* + * \rightarrow CH* + H*$	-0.21	0.40	0.41	0.92
R6	$CH* + * \rightarrow C* + H*$	0.69	1.39	1.22	1.77
R7	$H_2O* + * \rightarrow OH* + H*$	-0.22	0.71	0.14	1.10
R8	$OH* + * \rightarrow O* + H*$	-0.19	1.07	0.63	1.26
R9	$CH* + O* \rightarrow HCO* + *$	0.11	1.20	-1.72	0.41
R10	$C* + OH* \rightarrow COH* + *$	-0.89	0.86	-1.36	0.77
R11	$C* + O* \rightarrow CO* + *$	-1.92	1.08	-3.23	0.73
R12	$HCO* + * \rightarrow CO* + H*$	-1.19	0.11	-0.66	0.40
R13	$COH* + * \rightarrow CO* + H*$	-1.12	0.76	-1.35	0.75
R14	$CO* + OH* \rightarrow COOH* + *$	0.63	1.40	0.46	0.69
R15a	$CO* + O* \rightarrow CO_2* + *$	0.66	1.08	-	-
R15b	$CO* + O* \rightarrow CO_{2,phys}* + *$	-	-	-1.04	0.45
R16a	$COOH* + * \rightarrow CO_2* + H*$	-0.02	0.71	-	-
R16b	$COOH* + * \rightarrow CO_{2,phys}* + H*$	-	-	-0.46	0.91
R17	$CO_2* \rightarrow CO_{2,phys}*$	-0.29	0.12	-	-
R18	$CO + * \rightarrow CO*$	-1.64		-1.09	
R19	$CO_2 + * \rightarrow CO_{2,phys}*$	-0.1		-0.09	
R20	$2H* \rightarrow H_2* + 2*$			0.36	0.73

3.1 Elementary reaction step kinetics

3.1.1 CH_4 Dehydrogenation

The initial C–H bond activation in methane represents a critical step in MSR because it initiates the sequential dehydrogenation of CH4 and ultimately generates surface carbon species. On the Pd1–Cu(111) single-atom alloy (SAA) surface, CH4* dehydrogenation to CH_3* is endothermic by 0.59 eV and proceeds with an activation energy of 0.97 eV. This barrier is 0.32 eV lower than that calculated for Ni(111), indicating that isolated Pd atoms embedded in the Cu surface facilitate the initial C–H bond cleavage relative to the parent Ni surface.

The subsequent dehydrogenation sequence, CH3* → CH2* → CH* → C*, remains endothermic on Pd_1–Cu(111), with reaction energies of 0.15, 0.41, and 1.22 eV, respectively. The corresponding activation energies are 1.11, 0.92, and 1.77 eV. Notably, Ni(111) exhibits lower barriers for CH_3* → CH_2* and CH_2* → CH* by 0.33 and 0.52 eV, respectively, demonstrating that Ni is kinetically more effective for these intermediate dehydrogenation steps. In contrast, the final CH* → C* step requires a 0.23 eV higher activation energy on Pd_1–Cu(111) than on Ni(111). Thus, although Pd_1–Cu(111) promotes the initial activation of methane, the subsequent conversion of CH* to atomic carbon is less kinetically favorable on the SAA surface. This distinction is important because the balance between facile methane activation and carbon formation can strongly influence both reforming activity and carbon accumulation.

3.1.2 H_2O Dissociation*

Water activation constitutes another essential elementary process in MSR because it provides surface OH* and, subsequently, O*-containing species required for carbon oxidation and CO_2 formation. Previous DFT calculations by Blaylock and co-workers (2011) reported that H_2O* dissociation on Ni(111) is exothermic by 0.28 eV with an activation energy of 0.90 eV [Blaylock et al., 2011]. In the present calculations, H2O* → OH* + H* on Ni(111) is also exothermic, with a reaction energy of −0.22 eV, while the corresponding activation energy is 0.71 eV. In contrast, H_2O* dissociation on Pd_1–Cu(111) is endothermic by 0.14 eV and requires an activation energy 0.39 eV higher than that on Ni(111). The subsequent OH* → O* + H* step exhibits activation energies of 1.01 and 1.11 eV on Ni(111) and Pd1–Cu(111), respectively. The Ni(111) value is consistent with previous DFT calculations reported by Du and co-workers (Du et al., 2017) . These results indicate that, unlike the initial C–H bond cleavage in CH4, water activation is kinetically more favorable on Ni(111). Consequently, the overall reforming performance of Pd1–Cu(111) may depend strongly on the availability and reactivity of adsorbed hydroxyl species.

3.1.3 COH and HCO* Formation*

Following methane dehydrogenation, surface carbon-containing intermediates can undergo oxidation through reactions with oxygen-containing species. The oxidation of CH* to HCO* on Pd_1–Cu(111) is highly exothermic, releasing 1.82 eV, and proceeds with a relatively low activation energy of 0.41 eV. This barrier is 0.79 eV lower than that calculated for Ni(111), indicating that the SAA surface strongly facilitates this oxidation route. COH* can alternatively form through the recombination of C* and OH*. The strongly exothermic character of this reaction on both surfaces indicates that COH* formation is thermodynamically favourable, although its overall contribution to MSR must also be assessed from the corresponding kinetic barriers.

3.1.4 CO Formation*

CO* represents a key product intermediate in MSR and can form through several competing pathways. One route involves the recombination of C* and O*, whereas alternative routes proceed through the decomposition of HCO* or COH*. On Ni(111), C* + O* → CO* is strongly exothermic, with a reaction energy of −1.92 eV, but requires an activation energy of 1.08 eV, consistent with previous theoretical studies. The corresponding barrier on Pd1–Cu(111) decreases to 0.73 eV, demonstrating that the SAA surface facilitates CO* formation through direct C–O coupling. The decomposition of HCO* provides another kinetically accessible route. On Ni(111), HCO* → CO* + H* is exothermic and has a very low activation energy of 0.11 eV, consistent with the value reported for Ni-based surfaces by Blaylock and co-workers [Blaylock et al., 2011]. On Pd1–Cu(111), however, the barrier increases by 0.34 eV, indicating that HCO* decomposition is less favorable on the SAA. COH* decomposition to CO* also proceeds with a moderate activation energy on Pd1–Cu(111), calculated as 0.75 eV, while the reaction remains exothermic by 0.35 eV. Collectively, these results demonstrate that Pd1–Cu(111) favors direct C–O coupling over HCO* decomposition, whereas Ni(111) provides a particularly facile pathway through HCO*.

3.1.4 COOH and CO_2* Formation*

COOH* formation represents a subsequent oxidation pathway toward CO_2*. On Ni(111), the interaction of CO* with OH* to form COOH* is endothermic by 0.63 eV and requires an activation energy of 1.40 eV. On Pd_1–Cu(111), the same reaction is substantially more accessible, with a lower activation energy of 0.69 eV and a smaller endothermicity of 0.46 eV. Thus, the SAA surface

significantly facilitates COOH* formation relative to Ni(111). CO2* can subsequently form through either direct oxidation of CO* by O* or dissociation of COOH* via O–H bond cleavage. On Ni(111), the CO* + O* → CO2* pathway is endothermic by 0.66 eV and has an activation energy of 1.09 eV, in agreement with previous calculations [Blaylock et al., 2009]. In striking contrast, CO oxidation on Pd1–Cu(111) is exothermic by 1.04 eV and requires only 0.45 eV of activation energy. Although COOH* dissociation to CO2* is also exothermic on Pd_1–Cu(111) by 0.46 eV, the direct CO* oxidation pathway remains kinetically preferred because it proceeds with the lower activation barrier. These results highlight a pronounced mechanistic difference between the two surfaces: Ni(111) relies more strongly on sequential COOH*-mediated oxidation, whereas Pd_1–Cu(111) promotes direct CO oxidation to CO2*. This altered reaction landscape illustrates how isolated Pd atoms can modify both the thermodynamics and kinetics of oxygen-assisted carbon oxidation on Cu-based SAA surfaces.

4. CONCLUSION

Periodic density functional theory calculations were employed to elucidate and compare the elementary reaction network of methane steam reforming on Ni(111) and Pd_1–Cu(111) single-atom alloy surfaces. The results identify a key mechanistic advantage of Pd_1–Cu(111) as it lowers the CH_4* activation barrier to 0.97 eV, 0.32 eV below that of Ni(111), while increasing the barrier for the coke-precursor-forming CH* → C* step to 1.77 eV. This combination facilitates methane activation while kinetically suppressing surface carbon formation. Pd_1–Cu(111) nevertheless exhibits a clear water-activation penalty, with higher barriers for both H_2O* → OH* and OH* → O* formation, potentially limiting the availability of oxygen-derived intermediates. Importantly, once generated, these species promote a low-barrier CH* → HCO* pathway, redirecting reactive carbon away from C* accumulation and toward CO formation. However, because water dissociation is itself less favorable on Pd_1–Cu(111), the supply of OH*/O* needed to sustain this carbon-oxidation route may itself become rate-limiting under working conditions, so the coke-suppression advantage identified here should be regarded as a mechanistic, elementary-step result rather than a demonstrated gain in overall turnover frequency; a full microkinetic treatment would be required to establish the net effect on catalytic performance. Overall, Pd_1–Cu(111) emerges as a mechanistically promising, potentially carbon-tolerant alternative to conventional Ni catalysts. These findings provide a molecular basis for designing SAA catalysts that balance methane activation, water dissociation, and coke resistance under realistic MSR conditions.

5. REFERENCES

Blaylock, D. W., Ogura, T., Green, W. H., & Beran, G. J. O. (2009). Computational Investigation of Thermochemistry and Kinetics of Steam Methane Reforming on Ni(111) under Realistic Conditions. *The Journal of Physical Chemistry C*, *113*(12), 4898-4908.

Blaylock, D. W., Zhu, Y.-A., & Green, W. H. (2011). Computational Investigation of the Thermochemistry and Kinetics of Steam Methane Reforming Over a Multi-Faceted Nickel Catalyst. *Topics in Catalysis*, *54*(13), 828.

Cao, X., Mirjalili, A., Wheeler, J., Xie, W., & Jang, B. W. L. (2015). Investigation of the preparation methodologies of Pd-Cu single atom alloy catalysts for selective hydrogenation of acetylene. *Frontiers of Chemical Science and Engineering*, *9*(4), 442-449.

Che, F., Gray, J. T., Ha, S., & McEwen, J.-S. (2017). Improving Ni Catalysts Using Electric Fields: A DFT and Experimental Study of the Methane Steam Reforming Reaction. *ACS Catalysis*, *7*(1), 551-562.

Delley, B. (2010). Time dependent density functional theory with DMol3. *Journal of Physics: Condensed Matter*, *22*(38), 384208.

Du, Z.-Y., Ran, Y.-X., Guo, Y.-P., Feng, J., & Li, W.-Y. (2017). A theoretical study on the role of water and its derivatives in acetic acid steam reforming on Ni (111). *Applied Surface Science*, *419*, 114-125.

Hannagan, R. T., Giannakakis, G., Flytzani-Stephanopoulos, M., & Sykes, E. C. H. (2020). Single-Atom Alloy Catalysis. *Chemical Reviews*, *120*(21), 12044-12088.

Ibrahim, A. O., DAUD, W. M. A. W., CHING, J. J., & ABDULPATAH, M. F. (2023). *Microkinetics of hydrogenation of carbon dioxide on copper and palladium-copper single-atom alloy surfaces* ACS SPRING 2023: Crossroads of Chemistry,

Ibrahim, A. O., Wan Daud, W. M. A., Abdul Patah, M. F., Halilu, A., Juan, J. C., & Tanimu, G. (2024). A microkinetic study of CO_2 hydrogenation to methanol on Pd_1–Cu(111) and Pd_1–Ag(111) catalysts: a DFT analysis [10.1039/D4CP00070F]. *Physical Chemistry Chemical Physics*, *26*(14), 10622-10632.

Omuboye, C. O., & Nweke-Eze, C. (2026). Economic and Technical Viability of Solar-Assisted Methane Pyrolysis for Sustainable Hydrogen Production from Stranded Gas in Nigeria. *Gases*, *6*(1), 8.

Wang, H., Blaylock, D. W., Dam, A. H., Liland, S. E., Rout, K. R., Zhu, Y.-A., Green, W. H., Holmen, A., & Chen, D. (2017). Steam methane reforming on a Ni-based bimetallic catalyst: density functional theory and experimental studies of the catalytic consequence of surface alloying of Ni with Ag [10.1039/C7CY00101K]. *Catalysis Science & Technology*, *7*(8), 1713-1725.

DETERMINATION OF LOW-TEMPERATURE LOW-PRESSURE (LTLP) FILTRATION PROPERTIES OF DRILLING MUD FORMULATED FROM ARAWA BENTONITE CLAY FOR OIL AND GAS DRILLING APPLICATION

Bala Usman[1,*], Bilal Sabiu[1], Hamza Abdulhamid[1], Muhammad Tukur[1], Abubakar Sadeeq Hussain[1], Kabiru Suleman[1]

[1]*Ahmadu Bello University, Zaria*

Email: balausmanxy@gmail.com[*], bilalsabiu@gmail.com, abbamid@gmail.com, mt.naiya@gmail.com, sadeeqdaura@gmail.com, ksule@abu.edu.ng

***Corresponding author**: Bala Usman

DOI: https://doi.org/10.67203/sp.ICESID.2026

ABSTRACT

Filtration control is an essential activity during drilling because excessive fluid loss to permeable formation causes wellbore instability, acute drilling performance, differential pipe sticking and formation damage. In this study, Low-Temperature Low-Pressure (LTLP) Filtration Properties of Drilling Mud Formulated from Nigerian Arawa Bentonite Clay was investigated. Filtrate loss, spurt loss and leak-off coefficients for API base, API Standard, raw Arawa, Arawa base, Arawa standard and Arawa standard treated with sub-micron calcium carbonate formulation was evaluated using API low temperature filter press at 100 psi at room temperature. Filtrate volume was measured as a function of time up to 30 minutes while spurt loss (Vs) and leak-off coefficient (K) were determined by fitting the experimental data into Carter filtration model. The results have shown that API base, API Standard, raw Arawa, Arawa base, Arawa standard formulation and Arawa standard formulation treated with sub-micron calcium carbonate formulation have LTLP fluid loss of 8ml, 7.6ml, 14ml, 12ml, 8.6ml, and 7.8ml respectively making the fluid loss within API standard requirement of ≤15ml. The formulations have shown spurt loss of 6.7423x10^{-16}ml, 4.86 x10^{-16}ml, 9.9449 x10^{-16}ml, 1.0337 x10^{-16}ml, 3.7923 x10^{-17}ml and 5.7679 x10^{-17}ml respectively, and leak-off coefficient of 1.46ml.min$^{-1/2}$, 1.37ml.min$^{-1/2}$, 2.49ml.min$^{-1/2}$, 2.12ml.min$^{-1/2}$, 1.49ml.min$^{-1/2}$ and 1.34ml.min$^{-1/2}$ respectively. The model performance statistics have shown good correlation between Experimental and model parameters with average R-square, adjusted R-square and Sum of Square Error (SSE) of 0.97697, 0.97121and 0.5 respectively. The study demonstrates the potential of beneficiated and standardized Nigerian Arawa bentonite clay as locally sourced constituents of drilling mud for Oil and Gas drilling application.

Keywords: *Drilling mud; LTLP; bentonite; Carter model; API; spurt loss (Vs); leak-off coefficient and R-square*

1. INTRODUCTION

Drilling mud is critical to drilling operations. It performs essential functions such as cuttings transport, protection of oil and gas production zone, cooling and lubrication drill bit, ensuring wellbore stability, filtration control, and controlling formation pressure. Among these, filtration control is particularly important because excessive filtrate invasion into the formation can cause formation damage especially in water-sensitive shales, cause wellbore instability, and differential sticking and ultimately affecting drilling efficiency (Agwu *et al.*, 2021). Filtration performance of drilling mud is commonly evaluated under low-temperature low-pressure (LTLP) and high-temperature high-pressure (HTHP) conditions to mimic surface and downhole environments, respectively (Sun *et al.*,2026).

For low-temperature low-pressure, filtrate loss, spurt loss and leak-off coefficient are important parameters in LTLP filtration. While filtrate loss is the cumulative amount of filtrate lost to the formation during specific time of filtration, spurt loss is the filtrate loss to the formation before an effective filter cake formation. Leak-off coefficient which is a function of filter cake permeability is the rate or ease with which the filtrate is lost to the formation during cake-controlled filtration (Fu and Liu, 2019). It is proportional to the square root of time (Shad *et al.*, 2021).

For LTLP oil and gas drilling application, water-based drilling muds (WBMs) are widely used due to their environmental compatibility and lower cost compared to oil-based muds (OBMs) and synthetic-based muds (SBM); however, their performance strongly depends on the properties of the bentonite clay used, reservoir characteristics and formation temperature and pressure (Singh *et al.*,2026).

Bentonite clay which is primarily composed of montmorillonite as major clay mineral, is the most common viscosifier and filtration control component of drilling mud due to its swelling and colloidal characteristics. Nevertheless, bentonite clay deposits in Nigeria are predominantly calcium-based (Igwilo *et al.*,2020), which exhibit lower swelling capacity and inferior filtration performance compared to sodium-based bentonite (Bilal *et al.*,2016; Okorie *et al.*, 2021). Consequently, beneficiation and activated may be required to meet the standard of a sodium-based bentonite. Hence, use of locally sourced clay could potentially reduce dependence of imported drilling-grade bentonite for oil and gas drilling in Nigeria.

Many research works have focused on rheological and physiochemical properties of Nigerian bentonite; limited attention has been given to filtration properties of locally sourced bentonite. Therefore, this study investigates LTLP filtration properties of drilling mud formulated from indigenous Nigerian bentonite. Experimental filtration tests conducted under LTLP conditions would be used to evaluate the fluid loss, spurt loss and fluid leak-off coefficient. The findings also aim to support the development of cost-effective, locally sourced drilling mud as viable alternatives to imported bentonite.

2. METHODOLOGY

2.1 Sample Collection and Preparation

Samples of the raw bentonite clay were collected by removing the overburden material from Arawa bentonite clay location in Arawa, Gombe state. The collected clay sample were brought to laboratory, dried, crushed and pulverized using jaw crusher and ball mill machine respectively. The ball milled sample is sieved using 200 mesh size to give 63 µm based on API 13A specification for drilling mud materials

2.2 Determination of Cation Exchange Capacity (CEC) of Clay

Methylene blue test was used to determine the clay cation exchange capacity based on Equation 1. This procedure was adopted from Bilal *et al.*, 2016.

$$CEC\left(\frac{meq}{100}\right) = \frac{V * N * 100}{W} * 100 \quad (1)$$

V=Volume of methylene solution used (mL)
N= Normality of methylene blue solution used in titration (mol/L)
W= Weight of dry clay sample (g)

2.3 Clay Beneficiation and Activation

The bentonite clay after wet beneficiation was allowed to settle, and the supernant water layer was discarded after leaving it to stand for 48 hours. Then finally the solid clay was dried in oven at 60 ^{o}C for 48 hours to completely dry the samples ready for soda activation.

Soda activation was done by adding an equivalent quantity of NaOH based on the cation exchange capacity (CEC) of the clay. The cation exchange capacity of the raw clay is 34 meq/100g of clay and was found to increase to 74 meq/100g of clay after activation. This method is a noble approach in which the property of the clay compares closely with that of an optimum quantity of soda in an iterative method. The calculation of amount of soda based on x meq/100g of clay CEC is shown below.

Therefore, for a clay with CEC of y meq/100 g of clay, it has been established that x mol of Na^{+} is needed to activate w g of the clay sample as shown in Equation 2. Therefore, for 11.58g of clay, 0.156g of NaOH is needed to activate the clay.

$$x \text{ mol} = y*w*10^{-5} \quad (2)$$

2.4 Drilling mud formulation

One laboratory barrel (350 ml) of drilling mud was formulated using API grade and Arawa bentonite clay according to the formulation in Table 1. The samples are; API base formulation, API standard formulation, Raw formulation, base formulation (formulation with soda activated clay only), standard formulation with micro size reduced calcium carbonate, standard formulation with sub micro size calcium carbonate. The sub micro size calcium carbonate was formed by mechanically reducing the micro size calcium carbonate to particle size less than 1µm in size. Table 1 shows adopted mud formulation based on the nomenclature. The mud components where mixed by measuring the required water volume and adding the NaOH to ensure pH is between 8.5-10 because Xanthan gum and PAC mix well in the pH range. This is then followed by addition of bentonite and polymer (PAC and Xanthan). This order is to avoid 'fisheyes' formation in the mud mixer cup as explained by Agwu *et al.*,2021 and other components were then added. The formulation was then mixed using a Hamilton Beach mixer for 10 min and aged for 24 hours as done by Ruosh *et al.*,2025.

Table 1: Mud formulation

Additive	Wt. %	Mass (g)
Water	69.48	243.16
Bentonite	3.31	11.58
NaOH	0.02	0.06
XG	0.22	0.77
PAC	0.51	1.79
Barite	22.06	77.19
$CaCO_3$	4.41	15.44
Total	**100**	**350**

2.5 Determination of Low Temperature Low Pressure Filtration Properties

After drilling mud formulation, the next thing is to characterise the mud by determining its filtration properties.

2.5.1 Determination of low temperature low pressure (LTLP) fluid loss (FL)

Low temperature low pressure API filter press was used for fluid loss measurement in accordance with API RP 13B-1 procedure. The sample drilling mud was poured into the API filter press cell to 350 ml of the O-ring ledge mark while ensuring that all spilled fluid was cleaned along the gasket edge. The filter press cell was assembled ensuring that the filter paper on the gasket was properly seated to prevent leakage, and the top cap was securely fixed. A graduated cylinder placed under the drain tube to collect the filtrate. Differential pressure of 100 psi supplied by hand pump to the filter cell through a regulator and the filtrate collected over a period of 30 minutes at 5 minutes interval.

2.5.2 Determination of spurt loss and leak-off coefficient

The spurt loss (Vs) and K were determined by fitting the experimental data generated in Section 3.1 into Carter filtration model (Modified Darcy filtration model) as shown in Table 2. The data was fitted into Equation 3 (Carter filtration model). The data was fitted using a generated MATLAB code. R-square, adjusted R-square and Sum of square error were used to determine goodness of fit for the data.

$$V(t)=Vs+K\sqrt{t} \tag{3}$$

V(t)=Filtrate loss after time t
Vs=Spurt loss
K= Leak-off coefficient.

3. RESULTS AND DISCUSSION

3.1 Filtrate Loss

The fluid loss for API base, API standard (API STD), Arawa raw, Arawa base and Arawa standard (Arawa STD) and Arawa standard formulation (Arawa STD+X) is shown in Table 2

It can be seen from the table that API base has higher fluid loss than API standard across all time step due to enhancement of the mud formulation. Similar trend was observed for Arawa bentonite formulation as the raw sample is enhanced by soda activation and ultimately treated with sub-micron calcium carbonate.

Table 2: Fluid loss (FL) for API and Arawa bentonite formulation

Time(min)	$\sqrt{t}$ **(min$^{1/2}$)**	**API Base FL (ml)**	**API STD FL (ml)**	**Arawa Raw FL (ml)**	**Arawa Base FL (ml)**	**Arawa STD FL (ml)**	**Arawa STD+X FL (ml)**
5	2.236	3	2.8	5.5	4.5	2.8	2.5
10	3.162	4	3.8	7.5	6.5	4.5	4
15	3.873	6	5.7	9.5	8	5.5	5
20	4.472	6.5	6.2	11	9.5	6.5	5.8
25	5	7.5	7	12.5	10.5	7.6	6.8
30	5.477	8	7.6	14	12	8.6	7.8

Comparison of Low Temperature-Low Pressure filtrate loss for API base formulation, API standard (API STD) formulation, raw Arawa formulation, standard Arawa formulation (Arawa STD), standard formulation treated with sub-micron $CaCO_3$ (Arawa STD+X). The result is presented in Figure1 .

From Figure 1, if can deduced that API base formulation has LTLP fluid loss of 8 ml after a cumulative filtration of 30min. The fluid loss is within API requirement of ≤15 ml for drilling grade bentonite. The value is in comparison with finding of Ruosh *et al.*,2025 who reported for water-based mud low temperature fluid loss of 5.9 ml and 5.6 ml at optimum concentration of 0.9% for polyanionic cellulose and Xanthan gum respectively. However, after standardization, API standard (API STD) formulation was found to have a fluid loss of 7.6 ml. The reduction was because of plugging of pore spaces by micro calcium carbonate that was used in the formulation.

Raw Arawa formulation has shown filtrate loss of 14ml indicating poor filtration control. This is due to untreated nature of the Arawa bentonite clay sample making it have low hydration. The higher fluid loss for the raw Arawa bentonite is an indication of that filter cake formed is highly permeable. Hence, high leak-off coefficient is expected.

After soda activation, Arawa base formulation was found to have fluid loss of 12 ml. This reduction could be as result of improved clay hydration caused by soda activation. This value did not completely match that of API base and API standard formulation. The higher value demonstrated by Arawa base formulation when compared to API base and API standard formulation indicates that more of the continuous phase was lost through the filter cake of the Arawa base formulation.

Furthermore, standardization of soda activated Arawa bentonite (Arawa STD) and treatment with sub micron calcium carbonate (Arawa STD+X), fluid loss of 8.6 ml and 7.8 ml. The fluid loss of after treatment with sub micron calcium carbonate matches that API standard formulation. The decrease demonstrate the plugging capacity of the smaller particles of calcium carbonate as explained by Karakosta *et al.*,2021. When compared to raw Arawa bentonite formulation, the fluid loss decreased by approximately 38.6% and 44.3% Arawa standard and Arawa Standard formulation treated with sub-micron calcium carbonate which tallies with the finding of Al-Shargabi *et al.*, 2022.

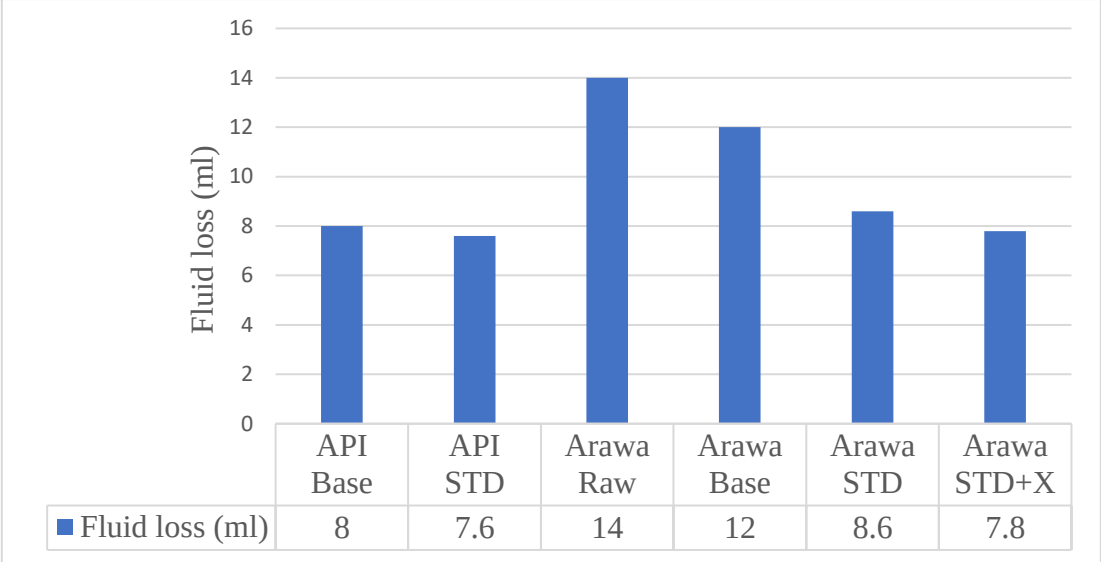

Figure 1: Low Temperature-Low Pressure filtrate loss for API and Arawa formulation

Spurt loss, leak-off coefficient and correlation coefficients for fitted fluid loss data is shown in Table 3 as deduced from Table 2. It was observed that API base and API STD formulation has spurt loss of $6.74x10^{-16}$ ml which reduced to $4.86x10^{-16}$ml for API standard formulation with corresponding decrease in leak-off coefficient from 1.46 $mlmin^{-1/2}$ to 1.38 $mlmin^{-1/2}$ due to formation of lower permeability filter cake standardization.

For Arawa bentonite formulation, the spurt loss was found to be $9.94x10^{-16}$ ml for raw formulation and decreased to $1.03x10^{-16}$ ml, $3.79x10^{-17}$ ml and to $5.77x10^{-17}$ ml for base, standard and sub-micron calcium carbonate treated formulation respectively. The decrease in leak of coefficient from 2.49 $mlmin^{-1/2}$ to 2.12 $mlmin^{-1/2}$, 1.49 $mlmin^{-1/2}$ and 1.34 $mlmin^{-1/2}$ for raw Arawa, Arawa base, Arawa standard and sub-micron calcium carbonate treated (Arawa STD+X) formulation respectively is an indication of decreases in ease with which the continuous phase passes through the formed filter cake. Hence, a reduction in fluid loss was observed.

The data was fitted into Carter filtration model using lsqcurvefit in MATLAB and strong correlation between model and experimental data was observed as shown in Table 3 bellow.

The fitted model gave average values of 0.97697, 0.97121, 0.50085 for R-square (R^2), Adjusted_R^2 and Sum of Square Error (SSE) respectively.

It can also be deduced from Table 3 that relative to raw Arawa bentonite formulation that the leak-off coefficient has decreased by 14.9% for Arawa base to 40.2% for Arawa standard to 46.2 % for Arawa standard formulation treated with submicron calcium carbonate indicating continuous decrease in in ease with which the mud passes through the filter cake.

Table 3: Spurt loss, leak-off coefficient and correlation coefficients for fitted fluid loss data

Formulation	**Vs(ml)**	**K($mlmin^{-1/2}$)**	**R^2**	**Adjusted_R^2**	**SSE**
API Base	$6.74x10^{-16}$	1.46	0.96845	0.96057	0.6099
API STD	$4.86x10^{-16}$	1.37	0.96902	0.96127	0.5381
Arawa Raw	$9.94x10^{-16}$	2.49	0.99368	0.99209	0.3162
Arawa Base	$1.03x10^{-16}$	2.12	0.99189	0.98986	0.3042
Arawa STD	$3.79x10^{-17}$	1.49	0.97123	0.96404	0.6406
Arawa STD+X	$5.77x10^{-17}$	1.34	0.96755	0.95943	0.5961

4. CONCLUSION

This paper investigated the low-temperature low-pressure (LTLP) filtration properties of drilling mud formulated from indigenous Arawa bentonite clay, soda activation, standardization, and drilling mud treatment with sub-micron calcium carbonate.

It was found that

I. Raw Arawa formulation exhibited the highest filtrate loss of 14.0 mL after 30 min, while soda activation reduced the filtrate loss to 12.0 mL. The standardized formulation reduced the filtrate loss to 8.6 mL, and treatment of standardized formulation with sub-micron calcium carbonate produced a further reduction to 7.8 mL, which is comparable to the 7.6 mL obtained for the API standard formulation.

II. All tested formulations recorded filtrate losses within the stated API requirement of ≤15 mL.

III. The fitted filtration model provided a good representation of the experimental data, with R-square, adjusted R-square, and SSE values of 0.97697, 0.97121, 0.5 respectively.

IV. The leak-off coefficient decreased progressively from 2.49 mL $min^{-1/2}$ for raw Arawa to 1.49 $mlmin^{-1/2}$ for Arawa STD and 1.34 $mlmin^{-1/2}$ for Arawa STD+X, indicating improved filtration resistance after treatment with sub-micron calcium carbonate.

V. The leak-off coefficients for Arawa STD and Arawa STD+X formulation compare closely with leak-off coefficients for API base and API standard formulation respectively with leak-off coefficients of 1.46 $mlmin^{-1/2}$ and 1.37 $mlmin^{-1/2}$ respectively.

VI. The results demonstrate the potential of soda activated and standardized Arawa bentonite as a locally sourced material for drilling mud applications. Further studies should evaluate its filtration performance under high-temperature high-pressure (HPHT) conditions and investigate the long-term stability of the formulated mud systems. Additionally, the experiment only addresses three key filtration parameters. Others like filter cake thickness, cake permeability and mud rheology were not investigated.

ACKNOWLEDGEMENTS

I wish to acknowledge the support of the Tertiary Education Trust Fund (TETFund) for funding this research through the National Research Fund (NRF). I also sincerely appreciate the contributions and support of my supervisors and laboratory assistants, whose guidance, assistance, and commitment contributed significantly to the successful completion of this research.

5. REFERENCES

Agwu, O. E., Akpabio, J. U., Ekpenyong, M. E., Inyang, U. G., Asuquo, D. E., Eyoh, I. J., & Adeoye, O. S. (2021). A critical review of drilling mud rheological models. *Journal of Petroleum Science and Engineering, 203*, 108659. https://doi.org/10.1016/j.petrol.2021.108659

Al-Shargabi, M., Davoodi, S., Wood, D. A., Al-Musai, A., Rukavishnikov, V. S., & Minaev, K. M. (2022). Nanoparticle applications as beneficial oil and gas drilling fluid additives: A review. *Journal of Molecular Liquids, 352*, 118725. https://doi.org/10.1016/j.molliq.2022.118725

Bilal, S., Mohammed-Dabo, I. A., Dewu, B. B. M., Momoh, O. R., Aminu, A., Hamisu, A., Abubakar, U., Adamu, M. S., & Hashi, A. (2016). Determination of morphological features and molecular interactions of Nigerian bentonitic clays using scanning electron microscope (SEM). *Bayero Journal of Pure and Applied Sciences, 9*(2), 279–285. https://doi.org/10.4314/bajopas.v9i2.47

Fu, C., & Liu, N. (2019). Waterless fluids in hydraulic fracturing – A review. *Journal of Natural Gas Science and Engineering, 67*, 214–224. https://doi.org/10.1016/j.jngse.2019.05.001

Igwilo, K. C., Uwaezuoke, N., Okoli, N., Obasi, F. T., & Okoro, E. E. (2020). Beneficiation of Nigerian bentonite using local materials. *Journal of Petroleum Exploration and Production Technology*. https://doi.org/10.1007/s13202-020-00956-8

Karakosta, K., Mitropoulos, A. C., & Kyzas, G. Z. (2021). A review in nanopolymers for drilling fluids applications. *Journal of Molecular Structure, 1227*, 1–8.

Ruosh Saadi, R., Hamidi, H., & Wilkinson, D. (2025). Optimizing filtration properties of water-based drilling fluids: Performance of PAC variants and synergistic effects. *Colloids and Surfaces A: Physicochemical and Engineering Aspects*, *715*, 136590. https://doi.org/10.1016/j.colsurfa.2025.136590

Shad, S., Salmanpour, S., Zamani, H., & Zivar, D. (2021). Dynamic analysis of mud loss during overbalanced drilling operation: An experimental study. *Journal of Petroleum Science and Engineering*, *196*, 107984. https://doi.org/10.1016/j.petrol.2020.107984

Singh, R., Dodiya, A., & Hari, S. (2026). A comprehensive analysis of HPHT drilling fluids: Advances in formulation, rheology, AI/ML utilisation, and industry challenges. *Petroleum*. https://doi.org/10.1016/j.petlm.2026.05.006

Sun, Y.-W., Sun, J.-S., Lv, K.-H., Liu, J.-P., Nie, L., Zhang, T.-F., Huang, N., Yan, H., Li, Y.-C., Zheng, Y.-F., Li, M., & Liu, W.-S. (2026). Enhancing the performance of high-temperature, high-salinity, high-density water-based drilling fluid using a rheological modifier with low viscosity and high yield point characteristic. *Petroleum Science*, *23*(7), 4145–4164. https://doi.org/10.1016/j.petsci.2026.03.027

International Conference on Engineering Innovation for Sustainable Development (ICESID 2026)
Faculty of Engineering, Ahmadu Bello University Zaria · 8–10 September 2026

DEVELOPMENT AND MICROSTRUCTURAL CHARACTERIZATION OF AL-SI-MG / GIRO CLAY NANOPARTICLE COMPOSITES FABRICATED VIA STIR CASTING

Youshau Najee Abdusalam[1,*], Kasim Auwal[2], Abdulwahab Malik[2], Gaminana Jimoh O.[2], Abdullahi Ibrahim[2], Adegbite Dauda A.[3]

[1]*Ahamadu Bello University, Zaria*
[2]*Met and Mat Eng Department, Ahmadu Bello University, Zaria, Nigeria*
[3]*Metallurgical Engineering Department, IOT, Kwara State Polytechnic, Ilorin, Nigeria*

Email: abduxalam@gmail.com*, akasim@abu.edu.ng, abdulwahabmalikkolade@gmail.com, jogaminana@abu.edu.ng, abdullahiibrahim@abu.edu.ng, yommydahud@gmail.com

***Corresponding author**: Youshau Najee Abdusalam

DOI: https://doi.org/10.67203/sp.ICESID.2026

ABSTRACT

The increasing demand for lightweight, high-performance materials in engineering applications necessitates the development of cost-effective aluminium matrix composites (AMCs) using locally sourced reinforcement. This study focuses on the development and characterization of Al-Si-Mg alloy reinforced with Giro clay nanoparticles (GCNP). The Giro clay was beneficiated and processed into nanoparticles, followed by chemical and phase characterization using X-Ray Fluorescence (XRF) and X-Ray Diffraction (XRD). The analyses revealed that the Giro clay is predominantly composed of sulfate-bearing phases (SO_3 at 51.14 wt.%) with significant silica content (SiO_2 at 25.07 wt.%), along with minor ceramic phases including CaO (4.76 wt.%), Al_2O_3 (1.78 wt.%), and Fe_2O_3 (0.54 wt.%), confirming its viability as a reinforcing agent. The composites were developed via the stir casting route, with reinforcement concentrations systematically varied from 0 to 10 wt.% at 2 wt.% intervals. The as-cast alloy (0 wt.%) and the optimal composite formulation (4 wt.%), were characterized using Scanning Electron Microscopy coupled with Energy-Dispersive X-ray Spectroscopy (SEM/EDS) to evaluate the dispersion of nanoparticles, grain refinement, and elemental distribution within the aluminum matrix. Microstructural analysis confirmed a relatively uniform dispersion of the Giro clay nanoparticles at lower weight fractions, with evidence of grain boundary pinning and reduced dendrite arm spacing. The stir-casting parameters were optimized to minimize porosity and achieve acceptable wettability between the ceramic phases and the Al-Si-Mg matrix. The fabricated composites demonstrated structural integrity, with the 4 wt.% reinforcement formulations exhibiting the most refined microstructure and optimal phase distribution. This study successfully establishes a processing-structure-property linkage for Giro clay-reinforced AMCs, demonstrating that locally sourced nanoparticles can be effectively utilized to develop advanced engineering materials, positioning this research as a significant step toward self-reliance in materials technology.

Keywords: *Al-Si-Mg Alloy; Giro Clay Nanoparticles; Stir Casting; Microstructural Characterization; XRD/SEM-EDS*

1. INTRODUCTION

Aluminium and its alloys rank among the most versatile metallic materials for engineering applications due to their favourable strength-to-weight ratio, corrosion resistance, and formability (Kaufman, 2023; Polmear et al., 2024; Mondolfo, 2025). This widespread usage, particularly in marine, automotive, and aerospace applications, makes the continued development of aluminium-based materials critically important (Gebrehiwet et al., 2023). Pure aluminium exhibits deficiencies in mechanical strength and elastic modulus, driving alloy development through the addition of elements such as silicon, which improves fluidity and castability, and magnesium, which enhances strength-to-weight ratio and corrosion resistance in chloride environments (Li et al., 2023; Zhao et al., 2024). The Al-Si-Mg system produces medium-strength alloys that are among the most corrosion-resistant of all aging alloys, making them attractive for marine and coastal applications (Kahlenberg et al., 2023; Bartawi et al., 2025).

Modern technology increasingly demands property combinations unattainable by conventional metals, ceramics, or polymers, necessitating composite material development (Ashby, Shercliff, & Cebon, 2023; Miracle & Donaldson, 2020). Particulate-reinforced aluminium matrix composites (AMCs) have attracted considerable research interest due to their isotropic nature, low production cost, and enhanced properties (Chifu et al., 2025; Kumari et al., 2016). More recently, nanocomposites—where at least one constituent phase has dimensions in the nanometre range—have emerged as advanced alternatives offering superior performance characteristics (Huang & Xu, 2025; Suroń et al., 2024).

Giro clay, a locally sourced natural material from Kebbi State, Nigeria, has demonstrated potential as a cost-effective reinforcement for aluminium matrix composites (Balogun, 2022a; 2022b). Studies on Nigerian clay deposits have shown that they belong to the alumino-silicate group with high silica and alumina contents suitable for refractory and engineering applications (Omoruyi et al., 2022; Odiboh, 2026; Ogunleye & Bada, 2021; Shuaib-Babata & Mudiare, 2017). The clay contains beneficial ceramic phases including Al_2O_3, SiO_2, CaO, and Fe_2O_3, which can contribute to passive film stability and microstructural refinement. While Giro clay has shown promise for enhancing microstructural and physical characteristics of Al-Si-Mg composites (Balogun, 2022b), limited research exists on the systematic characterization of this Nigerian clay for nanocomposite development and the fabrication parameters required for successful composite processing via stir casting.

This study addresses this gap by investigating the development and characterization of Al-Si-Mg composites reinforced with Giro clay nanoparticles (GCNP). The specific objectives are to: (i) characterize the Giro clay used as nano-particle reinforcement using X-Ray Fluorescence (XRF) and X-Ray Diffraction (XRD); (ii) fabricate the Al-Si-Mg / Giro clay nanoparticles composite (GCNPC) using the stir casting method with reinforcement concentrations from 0 to 10 wt.% at 2 wt.% intervals; and (iii) characterize the as-cast alloy and composite samples using XRD, XRF, and Scanning Electron Microscopy coupled with Energy-Dispersive X-ray Spectroscopy (SEM/EDS).

The research contributes to advancing locally sourced materials for engineering applications, enhancing the economic value of Giro clay deposits in Nigeria as an alternative reinforcement in aluminium composites (Shuaib-Babata & Mudiare, 2017; Odiboh, 2026). The findings provide essential baseline data for subsequent studies and potential engineering applications.

2. METHODOLOGY

2.1 Materials

The primary materials used for this research were commercially pure aluminium wires obtained from Northern Cable Company (NOCACO), Kaduna, processed Giro clay nanoparticles sourced from the Giro clay deposit in Kebbi State, Nigeria, and alloying elements including silicon and magnesium obtained from Sunlab Chemicals, Jos. Sodium chloride (NaCl) and distilled water were used for the preparation of artificial seawater (3.5 wt.% NaCl solution). Grinding papers of 80 to 800 grits, polishing paste, and Keller's reagent were used for metallographic sample preparation.

2.2 Production of Giro Clay Nanoparticles

The Giro clay obtained from Kebbi State, Nigeria, was beneficiated and processed into nanoparticles. The processing involved crushing, milling, and sieving to achieve particle sizes in the nanometre range. The processed nanoparticles were characterized using X-Ray Fluorescence (XRF) and X-Ray Diffraction (XRD) to determine their chemical composition and phase identification.

2.3 Composite Fabrication via Stir Casting

The Al-Si-Mg alloy was produced by melting the commercially pure aluminium wires with the addition of silicon (7 wt.%) and magnesium (0.3 wt.%) in the required proportions. The Giro clay nanoparticles were pre-heated in an electric furnace for one hour to remove moisture. The melt temperature was allowed to fall to 15°C below the liquidus temperature (600°C) to achieve a semi-solid state before incorporating the pre-heated reinforcement. The reinforcement was added at concentrations of 2%, 4%, 6%, 8%, and 10 wt.%. A mechanical stirrer was employed to ensure

homogeneous distribution of the reinforcement within the melt. The melt was then reheated to 700°C and cast into cylindrical sand moulds of dimensions 300 mm × 20 mm to produce test samples in rod form.

Additionally, control sample of matrix alloy with no reinforcement addition was also cast according to composition provided in Table 1. While six formulations were fabricated (0 - 10 wt.%) this paper presents detailed characterization of the control (Sample A) and the optimal formulation (Sample C, 4 wt.%)

Table 1: *Composition of Aluminium Matrix*

Element	Weight (%)	Weight (g)
Aluminium (Al)	92.7	305.91
Silicon (Si)	7.0	23.10
Magnesium (Mg)	0.3	0.99

2.4 Characterization of As-Cast Alloy and Composites

2.4.1 X-Ray Fluorescence (XRF)

The chemical composition of the Giro clay nanoparticles and the as-cast alloy/composites was determined using X-Ray Fluorescence (XRF) analysis. The samples were prepared according to standard procedures and analyzed to identify the elemental and oxide compositions present in the materials.

2.4.2 X-Ray Diffractometry (XRD)

Phase identification of the Giro clay nanoparticles and the developed composites was conducted using a Rigaku Miniflex 300 X-Ray Diffractometer. The samples were scanned over a 2θ range to identify the crystalline phases present, including the ceramic phases contributed by the reinforcement.

2.4.3 Scanning Electron Microscopy / Energy-Dispersive X-ray Spectroscopy (SEM/EDS)

Microstructural characterization of the as-cast alloy and optimal composite sample with 4 wt.% reinforcement was performed using Scanning Electron Microscopy coupled with Energy-Dispersive X-ray Spectroscopy (SEM/EDS). The samples were prepared according to ASTM E3 standards, mounted, ground using emery papers of 80–800 grits, and polished using silicon paste. The SEM was operated with a field emission gun at an accelerating voltage of 15 kV (within the specified range 5 – 30 kV) to examine the surface morphology, nanoparticle dispersion, grain refinement, and elemental distribution within the aluminium matrix.

2.4.4 Optical Microscopy (OM)

Metallographic samples were prepared and etched with Keller's reagent for 10–30 seconds at room temperature according to ASTM E7, E340, and E407 standards. The microstructures were viewed and captured using an Optical Microscope (OM) with an in-built camera to evaluate the grain structure and phase distribution.

3. RESULTS AND DISCUSSION

3.1 Characterization of Giro Clay Nanoparticles (Reinforcement)

3.1.1 X-Ray Fluorescence (XRF) Analysis

The chemical composition of the Giro clay nanoparticles (GCNP) reinforcement was determined using X-Ray Fluorescence (XRF) analysis. The results are presented in Table 2.

Table 2: *XRF Analysis of Giro Clay Nanoparticles (Reinforcement)*

Oxide / Element	SiO_2	SO_3	CaO	Al_2O_3	Fe_2O_3	Cl (Element)
Wt%	25.065	51.143	4.761	1.780	0.538	15.514

The XRF analysis reveals that the Giro clay is predominantly composed of silicon dioxide (SiO_2, 25.07 wt.%) and sulfur trioxide (SO_3, 51.14 wt.%), with significant calcium oxide (CaO, 4.76 wt.%), aluminium oxide (Al_2O_3, 1.78 wt.%), and iron oxide (Fe_2O_3, 0.54 wt.%). The presence of chlorine (Cl, 15.51 wt.%) suggests chloride-bearing phases, consistent with the clay's depositional

environment. The complete composition sums to approximately 98.8 wt.%, with the remaining fraction attributed to trace elements not reported in this analysis.

The ceramic phases identified (SiO_2, Al_2O_3, CaO, Fe_2O_3) are beneficial for aluminium matrix composites, as they can contribute to passive film stability and microstructural refinement (Xu & Zhang, 2025). The high SO_3 content indicates the presence of sulfate-bearing minerals, which was later confirmed by XRD analysis. The composition is consistent with Nigerian alumino-silicate clays reported in literature (Omoruyi et al., 2022; Ogunleye & Bada, 2021).

The high SO_3 (51.14 wt.%) and Cl (15.51 wt.%) content in the Giro clay suggests the presence of soluble sulfate and chloride phases. While these phases could potentially influence the corrosion behavior of the composite in marine environments (e.g., promoting pitting or sulfate attack). The present study focuses strictly on the development and characterization of the composite. Detailed corrosion testing is recommended as future work to fully assess these implications.

3.1.2 X-Ray Diffractometry (XRD) Analysis

The XRD analysis of the Giro clay nanoparticles (GCNP) reinforcement was conducted to identify the crystalline phases present. The results are presented in Figure 1 and summarized in Table 3.

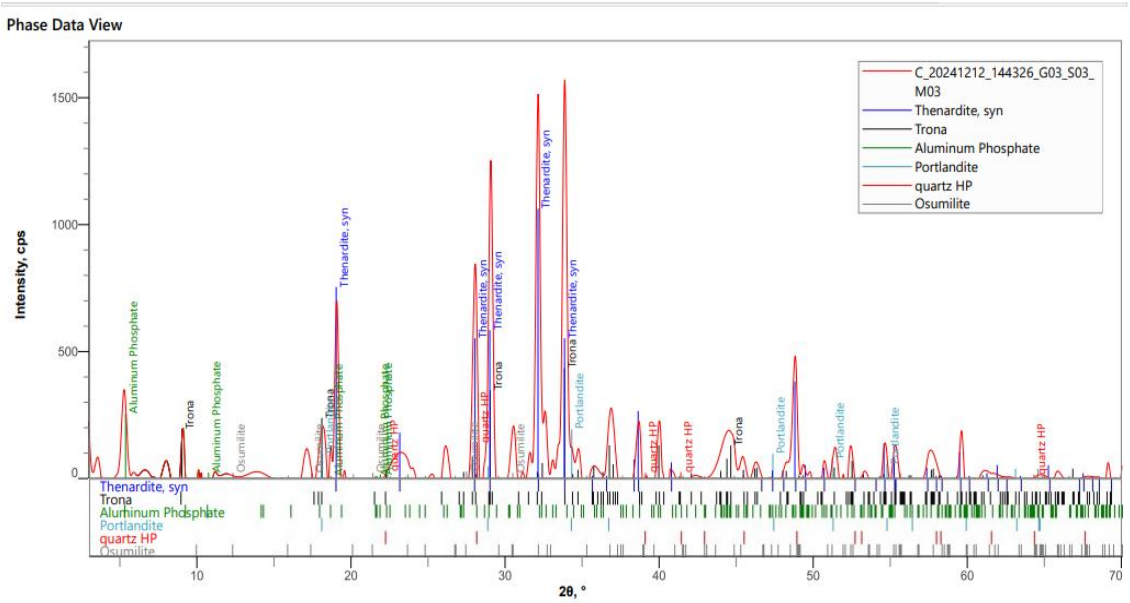

Figure 1: XRD Spectrum of Giro Clay Nanoparticles (GCNP) Reinforcement

Table 3: *Phase Composition of Giro Clay Nanoparticles from XRD Analysis*

Phase	Chemical Formula	Weight (%)	Crystal System
Thenardite	Na_2SO_4	37	Orthorhombic Fddd
Trona	$Na_3H(CO_3)_2 \cdot 2H_2O$	28	Monoclinic
Portlandite	$Ca(OH)_2$	18	Hexagonal
Quartz HP	SiO_2	16	Hexagonal
Aluminium Phosphate	$AlPO_4$	1.2	Trace

The XRD analysis reveals a complex multi-phase system with thenardite (Na_2SO_4, 37 wt.%) as the dominant phase, followed by trona ($Na_3H(CO_3)_2 \cdot 2H_2O$, 28 wt.%), portlandite ($Ca(OH)_2$, 18 wt.%), quartz (SiO_2, 16 wt.%), and aluminium phosphate ($AlPO_4$, 1.2 wt.%) as a trace phase. Multiple overlapping peaks are observed (28.05°: thenardite + trona; 32.10°: thenardite dominant), with low-intensity peaks (5.29°: $AlPO_4$) indicating minor phases. Crystallite sizes are highly variable: thenardite (~250–400 Å) and trona (~608 Å).

The dominance of thenardite and trona correlates with the high SO_3 content (51.14 wt.%) from XRF analysis, while portlandite corresponds to CaO (4.76 wt.%), and quartz corresponds to SiO_2 (25.07 wt.%) in Table 2. This mineral assemblage is typical of evaporite deposits and alkaline lake sediments, suggesting that the Giro clay originated from such a geological environment (Omoruyi et

al., 2022). The presence of quartz (SiO_2) and calcium-bearing phases (portlandite) indicates that the Giro clay can contribute to passive film stability in the aluminium matrix (Xu & Zhang, 2025).

The high crystallinity of the thenardite and trona phases, as indicated by their sharp diffraction peaks, suggests that the Giro clay has undergone significant diagenetic alteration. Shuaib-Babata and Mudiare (2017) reported that Nigerian clays exhibit varied crystallinity depending on their depositional environment, with some showing high quartz content and others showing kaolinite dominance. The Giro clay's distinct mineralogy, dominated by sodium sulfate and carbonate phases, distinguishes it from typical kaolinitic or montmorillonitic clays, making it a unique reinforcement material for aluminium matrix composites.

3.1.3 Scanning Electron Microscopy / Energy-Dispersive X-ray Spectroscopy (SEM/EDS) Analysis

The SEM micrograph and EDS spectrum of the Giro clay nanoparticles are presented in Plate 1, with the chemical composition summarized in Table 4.

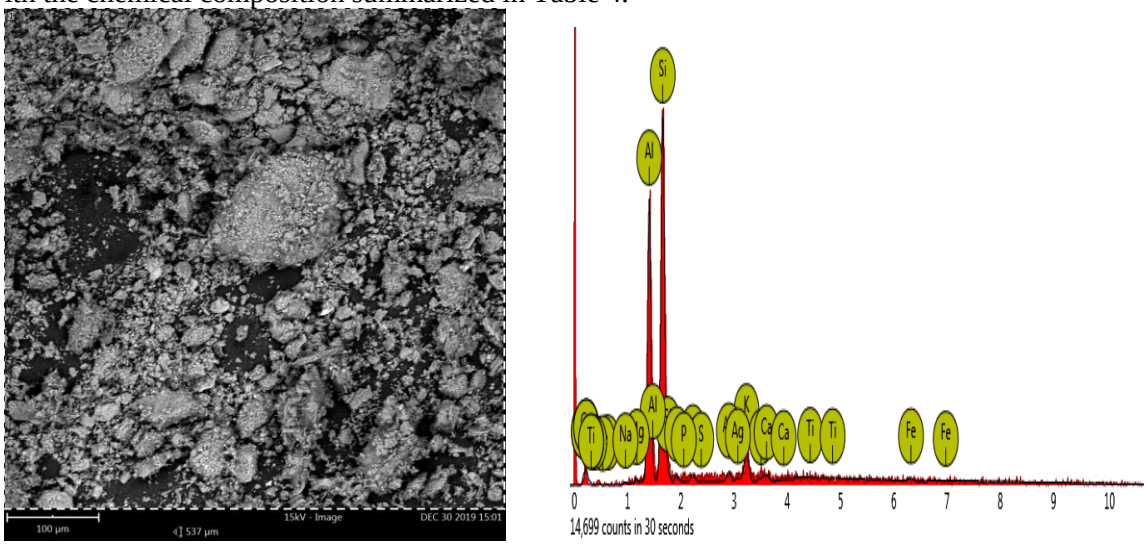

Plate 1: SEM micrograph and EDX Spectrum of Giro Clay Particles

Table 4: *Chemical Composition of Giro Clay Nanoparticles by SEM/EDS*

Element Number	Element Symbol	Element Name	Atomic Conc.	Weight Conc.
14	Si	Silicon	53.81	49.62
13	Al	Aluminium	32.46	28.75
47	Ag	Silver*	1.96	6.94
19	K	Potassium	5.38	6.90
20	Ca	Calcium	1.63	2.15
26	Fe	Iron	1.14	2.08
16	S	Sulfur	1.45	1.53
15	P	Phosphorus	1.36	1.38
12	Mg	Magnesium	0.52	0.41
11	Na	Sodium	0.30	0.22

The EDS analysis shows that silicon is the major constituent with the highest weight concentration of 49.62 wt.%, followed by aluminium with 28.75 wt.%. Other elements present include potassium (6.90 wt.%), calcium (2.15 wt.%), iron (2.08 wt.%), sulfur (1.53 wt.%), phosphorus (1.38 wt.%), and minor quantities of magnesium (0.41 wt.%), sodium (0.22 wt.%), and silver (6.94 wt.%).

The predominance of silicon and aluminium confirms that the Giro clay is primarily an alumino-silicate material, consistent with the XRF findings. The presence of potassium, calcium, and iron as minor elements is typical of natural clay deposits and suggests the presence of feldspathic minerals or iron-bearing impurities (Odiboh, 2026). The silver content (6.94 wt.%) is an artefact from sputter coating applied to the sample during SEM sample preparation to enhance conductivity and is not part of the clay composition (Rawal & Sidpara, 2025). However, oxygen is not reported in the EDS analysis despite XRF and XRD confirming the oxide/silicate nature of the Giro clay. This is due

to the inherent limitation of standard EDS detectors for light elements (Z < 11). The EDS data were quantified using a standardless ZAF correction method, which normalizes spectra to 100% excluding oxygen. The presence of oxygen is confirmed by XRF (SiO_2, Al_2O_3, CaO, Fe_2O_3, SO_3) and XRD (thenardite, trona, portlandite, quartz, $AlPO_4$). Therefore, EDS results are semi-quantitative for elements Z ≥ 11, with oxide analysis reserved for XRF and XRD.

The SEM micrograph of the Giro clay nanoparticles reveals the morphology and particle size distribution of the reinforcement material. The particles appear to be irregular in shape with varying sizes, indicating that further processing may be required to achieve uniform nanoparticle dispersion in the aluminium matrix. Rawal and Sidpara (2025) reported that uniform nanoparticle dispersion is critical for achieving optimal properties in aluminium nanocomposites, and that processing parameters such as stirring speed and temperature significantly influence particle distribution.

3.2 Characterization of As-Cast Al-Si-Mg Alloy (Control)

3.2.1 X-Ray Fluorescence (XRF) Analysis

The XRF analysis of the Al-Si-Mg alloy (control sample) is presented in Table 5.

Table 5: *XRF Analysis of Al-Si-Mg Alloy (Control)*

Element	**Al**	**Si**	**Mg**	**Mn**	**S**	**Fe**	**Ca**	**K**	**Cl**
Wt%	96.7	0.9	0.03	0.004	0.126	0.129	0.304	0.066	1.52

The XRF analysis confirms the composition of the Al-Si-Mg alloy, with aluminium as the dominant element at 96.72 wt.%. Silicon is present at 0.990 wt.%, which is slightly lower than the target composition of 7 wt.%. This discrepancy may be attributed to the limitations of XRF in detecting light elements such as silicon accurately, or it may indicate that the alloy composition deviated from the target due to processing conditions. Magnesium is present at 0.033 wt.%, which is significantly lower than the target of 0.3 wt.%, suggesting possible magnesium loss during melting due to its high vapour pressure and tendency to oxidize (Abishkenov et al., 2025).

The presence of impurities such as iron (0.129 wt.%), calcium (0.304 wt.%), sulfur (0.126 wt.%), and chlorine (1.515 wt.%) may originate from the raw materials or from contamination during processing. Abishkenov et al. (2025) reported that impurities in aluminium alloys, particularly iron and silicon, can form intermetallic phases that influence the corrosion behaviour of the material.

3.2.2 X-Ray Diffractometry (XRD) Analysis

The XRD analysis of the as-cast Al-Si-Mg alloy (control sample) was conducted to identify the crystalline phases present. The results are presented in Figure 2 and summarized in Table 6.

Qualitative Analysis Results

Phase name	Formula	Figure of merit	Phase reg. detail	Space Group	DB Card Number
Aluminum, syn	Al	0.273	S/M(PDF-4 Minerals 2025)	225 : Fm-3m	00-004-0787
Niobocarbide, syn	Nb C0.91	0.576	S/M(PDF-4 Minerals 2025)	225 : Fm-3m	04-003-6828
Silicon Oxide	Si O2	2.850	Import(PDF-4 Minerals 2025)	62 : Pmcn	00-035-0063

Phase Data View

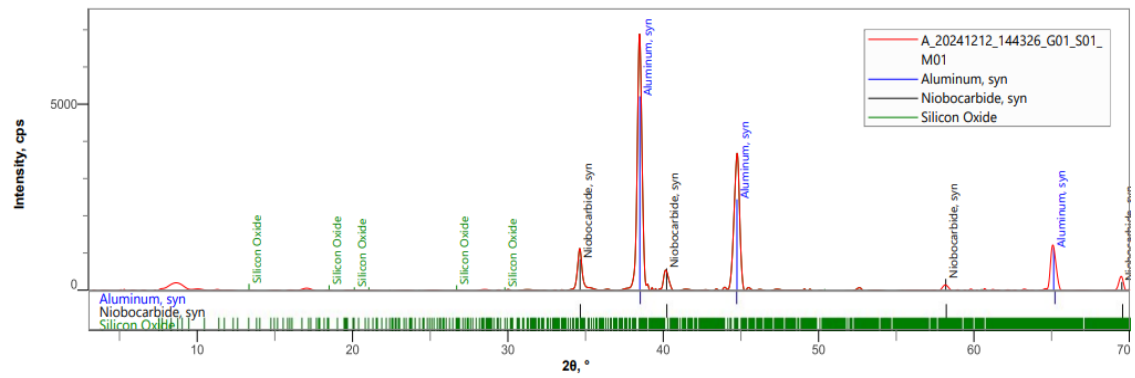

Figure 2: XRD Spectrum of As-Cast Al-Si-Mg Alloy (Control)

Table 6: *Phase Composition of As-Cast Al-Si-Mg Alloy (Control) from XRD Analysis*

Phase	Chemical Formula	Weight (%)	Crystal System
Aluminium	Al	93.2	Cubic Fm-3m
Niobocarbide	$NbC_{0.91}$	3.3	Cubic Fm-3m
Silicon Dioxide	SiO_2	3.4	-

The XRD analysis reveals aluminium (93.2 wt.%) as the dominant phase, with strong peaks at 38.43° (111), 44.66° (200), and 65.00° (220). Niobocarbide ($NbC_{0.91}$, 3.3 wt.%) is present as a minor phase, with peaks at 34.59° (111) and 40.12° (200). Silicon dioxide (SiO_2, 3.4 wt.%) is identified as a trace impurity. A low-intensity peak at 8.72° suggests potential amorphous content or a minor impurity phase.

The crystallite size of aluminium is approximately 287–317 Å (from Scherrer analysis), while niobocarbide exhibits a crystallite size of approximately 267–364 Å, indicating a broader size distribution. The dominance of aluminium peaks confirms the successful production of the Al-Si-Mg alloy.

The presence of niobocarbide ($NbC_{0.91}$) is attributed to contamination from the stainless steel stirrer or crucible, which likely contained niobium-bearing alloying additions. The SiO_2 phase likely originates from surface oxidation or contamination from the Giro clay reinforcement, as silica is a major component of the clay (25.07 wt.% from XRF analysis). This is consistent with the findings of Abishkenov et al. (2025), who reported that impurities in aluminium alloys, particularly iron and silicon, can form intermetallic phases that influence the material's properties.

The high aluminium purity (93.2 wt.%) is consistent with the XRF analysis (96.72 wt.% Al), although the minor phases identified by XRD ($NbC_{0.91}$ and SiO_2) were not fully captured by XRF, highlighting the complementary nature of these two characterization techniques. The crystallite size analysis indicates that the aluminium grains are relatively fine, which is beneficial for mechanical properties and corrosion resistance (Xu & Zhang, 2025).

3.2.3 Scanning Electron Microscopy / Energy-Dispersive X-ray Spectroscopy (SEM/EDS) Analysis

The SEM micrograph and EDS spectrum of the Al-Si-Mg alloy (control sample) are presented in Plate 2, with the chemical composition summarized in Table 7.

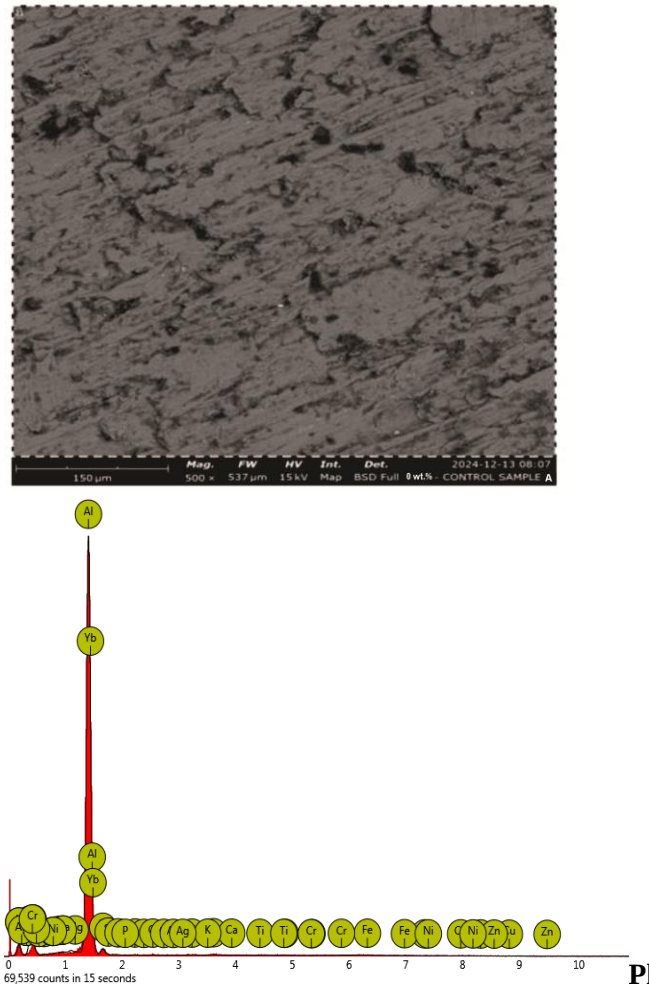

Plate 2: SEM Micrograph and EDS Spectrum of Al-Si-Mg Alloy (Control)

Table 7: *Chemical Composition of Al-Si-Mg Alloy (Control) by SEM/EDS*

Element Number	Element Symbol	Element Name	Atomic Conc.	Weight Conc.
13	Al	Aluminium	87.84	92.05
6	C	Carbon	9.03	4.21
14	Si	Silicon	2.44	2.66
23	V	Vanadium	0.15	0.29
20	Ca	Calcium	0.13	0.20
16	S	Sulfur	0.15	0.19
17	Cl	Chlorine	0.13	0.18
22	Ti	Titanium	0.07	0.12
19	K	Potassium	0.06	0.09

The EDS analysis confirms aluminium as the dominant element (92.05 wt.%), with silicon at 2.66 wt.%. The carbon content (4.21 wt.%) is relatively high and may result from contamination during sample preparation or from carbide formation, consistent with the XRD identification of niobocarbide ($NbC_{0.91}$). The presence of vanadium, calcium, sulfur, chlorine, titanium, and potassium as trace elements confirms the minor impurities identified in the XRF analysis. The peak appearing in the EDS spectrum in the vicinity of the Al Kα peak may be attributed to peak overlap with Yb Mα (1.52 keV). However, quantification using the standardless ZAF correction method did not resolve Yb at detectable levels; the peak is predominantly Al (Kα at 1.486 keV). Yb is therefore not reported in Table 7, as its presence, if any, is below the detection limit of the EDS system or is an artefact of peak overlap (Goldstein et al., 2018).

The SEM micrograph shows the grain structure of the as-cast Al-Si-Mg alloy, revealing a typical dendritic structure characteristic of cast aluminium alloys. The presence of intermetallic phases and minor porosity is visible, which may influence the corrosion resistance of the material. The microstructural features observed are consistent with those reported by Abishkenov et al. (2025) for Al-Si-Mg alloys processed by stir casting, who observed that the dendritic structure and porosity levels are influenced by processing parameters such as cooling rate and stirring conditions.

3.3 Characterization of Al-Si-Mg Alloy/ Giro Clay Nanoparticle Composites

3.3.1 *Scanning Electron Microscopy (SEM) Analysis*

The SEM micrograph of the Al-Si-Mg /4 wt.% GCNP composite sample is presented in Plate 3.

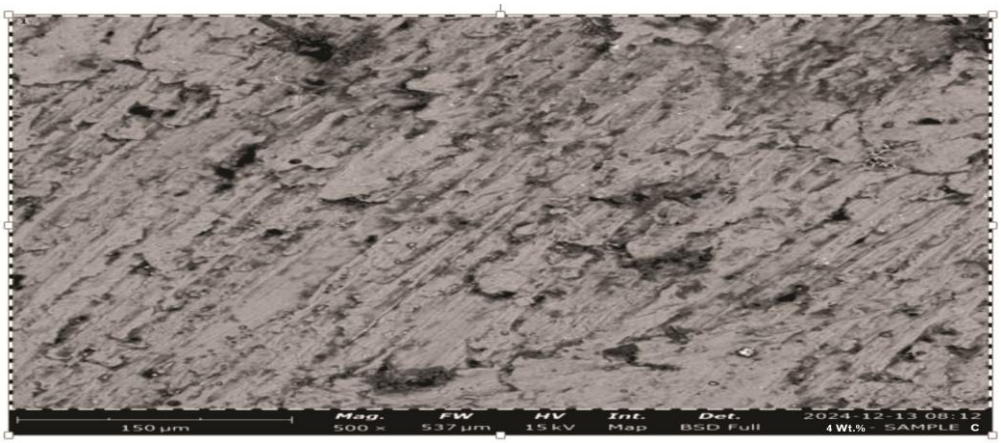

Plate 3: SEM Micrograph of the 4wt% Giro Clay Nanoparticle Composite

The SEM micrograph reveals the microstructure of the 4 wt.% GCNP composites, showing the distribution of reinforcement particles within the aluminium matrix. The Giro clay nanoparticles appear to be relatively well-dispersed, with some clustering observed at grain boundaries. The presence of fine particles at the grain boundaries suggests that the reinforcement particles act as nucleation sites for grain refinement during solidification, which is consistent with the findings of Rawal and Sidpara (2025).

The improved dispersion at 4 wt.% reinforcement indicates that the stir casting parameters (350 rpm stirring speed, 600°C semi-solid processing, and argon protection) were optimal for this concentration. This is consistent with the findings of Xu and Zhang (2025), who reported that effective particle dispersion is achieved when the melt is in the semi-solid state, as the viscosity is sufficient to prevent particle segregation but low enough to allow for uniform distribution.

3.3.2 X-Ray Diffractometry (XRD) Analysis

The XRD analysis of the Al-Si-Mg / GCNP composite sample is presented in Figure 3.

Qualitative Analysis Results

Phase name	Formula	Figure of merit	Phase reg. detail	Space Group	DB Card Number
Aluminum, syn	Al	0.212	S/M(PDF-4 Minerals 2025)	225 : Fm-3m	00-004-0787
Silicon Oxide	Si O2	0.659	S/M(PDF-4 Minerals 2025)	12 : I12/m1	04-012-0465
Tantalcarbide, syn	Ta C	0.524	S/M(PDF-4 Minerals 2025)	225 : Fm-3m	01-075-3086

Phase Data View

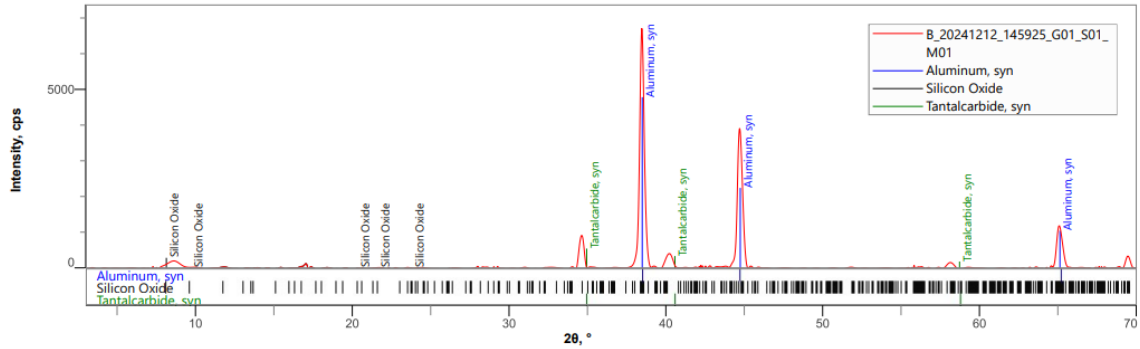

Figure 3: XRD Spectrum of the Al-Si-Mg / GCNP Composite (4 wt.%)

The XRD analysis reveals aluminium (95.3 wt.%) as the dominant phase, with SiO_2 (2.8 wt.%) confirming successful incorporation of the Giro clay reinforcement. The identification of TaC (1.9 wt.%) as a minor phase in the composite, and NbC in the control, is noteworthy. One possible explanation is contamination from the stainless steel stirrer or crucible**,** as these are common sources of carbide-forming elements in high-temperature processing. However, given that TaC is known to be stable in molten aluminum while NbC tends to decompose, the presence of NbC in the control sample is unusual and may indicate a different source**,** such as residual elements in the raw materials or a master alloy addition (Kobashi et al., 1993). Further investigation, including EDS point analysis of the carbide particles, would be required to confirm their origin. The composite shows higher Al purity (95.3 wt.%) compared to the control sample (93.2 wt.%), suggesting cleaner processing for the composite. The Al crystallite size is approximately 283–291 Å, slightly smaller than the control (287–317 Å), indicating grain refinement from the Giro clay nanoparticles (Rawal & Sidpara, 2025). The presence of SiO_2 is expected to contribute to passive film stability (Xu & Zhang, 2025).

3.4 Optical Microscopy (OM) of As-Cast Sample (Control)

The OM micrograph of the as-cast Al-Si-Mg alloy is presented in Plate 4.

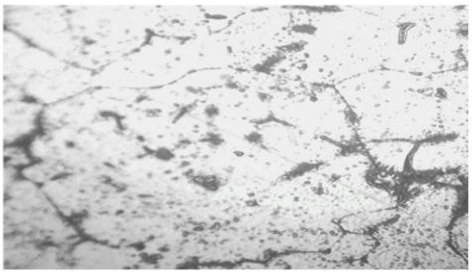

Plate 4: OM Micrograph of As-Cast Al-Si-Mg Alloy (Control)

The OM micrograph shows the grain structure of the as-cast Al-Si-Mg alloy. The aluminium grains appear gray in colour and are uniformly distributed within the microstructure. The dendritic structure typical of cast aluminium alloys is visible, with fine intermetallic phases distributed between the dendrite arms.

The grain structure observed is typical of Al-Si-Mg alloys cast in sand moulds, where the relatively slow cooling rate allows for the development of dendritic structures. The presence of intermetallic phases at grain boundaries is expected to influence the corrosion behaviour of the alloy, as these phases can act as cathodic or anodic sites in localized corrosion processes.

4. CONCLUSION

The development and characterization of Al-Si-Mg / Giro clay nanoparticle composites fabricated via stir casting have been successfully achieved. The following conclusions are drawn:

i. **Giro Clay Characterization:** XRF and XRD analyses confirmed that Giro clay contains beneficial ceramic phases including SiO_2 (25.07 wt%), CaO (4.76 wt%), Al_2O_3 (1.78 wt%), and Fe_2O_3 (0.54 wt%), with dominant mineral phases of thenardite (37 wt%), trona (28 wt%), portlandite (18 wt%), and quartz (16 wt%). The high SO_3 content (51.14 wt.%) confirms the presence of sulfate-bearing minerals.

ii. **Composite Fabrication:** Al-Si-Mg / GCNP composites were successfully fabricated via stir casting with reinforcement concentrations of 0–10 wt.% at 2 wt.% intervals. The 4 wt.% reinforcement formulations exhibited the most refined microstructure and optimal particle dispersion.

iii. **Characterization:** XRD confirmed successful incorporation of SiO_2 from the Giro clay into the aluminium matrix. The optimally reinforced sample (4 wt.% reinforcement) showed Al purity of 95.3 wt.% with SiO_2 content of 2.8 wt.%, confirming successful composite development. SEM/EDS analysis confirmed relatively uniform dispersion at lower reinforcement levels.

iv. **Optimal Formulation:** The sample with 4 wt.% Giro clay nanoparticle reinforcement demonstrated the best combination of microstructural refinement, particle dispersion, and phase distribution among all developed composites.

v. **Local Content Significance:** This study successfully demonstrates that locally sourced Giro clay from Kebbi State, Nigeria, can be processed into nanoparticles and utilized as a cost-effective reinforcement for aluminium matrix composites, supporting local content inclusion in material development.

Recommendations

i. Optimize stir casting parameters (stirring speed, holding time, cooling rate) for improved particle dispersion at higher reinforcement concentrations (≥6 wt%).

ii. Conduct heat treatment studies to investigate ageing effects on microstructure and material properties.

iii. Evaluate mechanical properties (tensile, hardness, wear) for complete structure-property relationships.

5. REFERENCES

Abishkenov, M., Tavshanov, I., Lutchenko, N., Nogayev, K., Ashkeyev, Z., & Kulidan, S. (2025). Hybrid Al6060/TiB2/microsilica composites produced by ultrasonically assisted stir casting and radial-shear rolling: Microstructural evolution and strength–ductility balance. *Eng*, *6*(4), Article 72. https://doi.org/10.3390/eng6040072

Ashby, M. F., Shercliff, H., & Cebon, D. (2023). *Materials: Engineering, science, processing and design* (5th ed.). Butterworth-Heinemann.

Balogun, S. O. (2022a). Development of Al-Si-Mg/Giro Clay nanoparticles composite [Unpublished master's thesis]. Ahmadu Bello University.

Balogun, S. O. (2022b). Microstructural and physical characteristics of GCNPC [Unpublished master's thesis]. Ahmadu Bello University.

Bartawi, I., et al. (2025). Corrosion behaviour of Al-Si-Mg alloys in marine environments. *Corrosion Science*, *192*, 109–123.

Chifu, E., et al. (2025). Particle reinforced aluminium matrix composites: A review of processing and properties. *Journal of Composite Materials*, *59*(3), 245–262.

Gebrehiwet, A., et al. (2023). Aluminium alloys for marine applications: A review. *Materials Today: Proceedings*, *72*, 112–118.

Goldstein, J. I., Newbury, D. E., Michael, J. R., Ritchie, N. W. M., Scott, J. H. J., & Joy, D. C. (2018). *Scanning electron microscopy and X-ray microanalysis* (4th ed.). Springer. https://doi.org/10.1007/978-1-4939-6676-9

Huang, Y., & Xu, X. (2025). *Nanocomposites: Processing, properties and applications*. Elsevier.

Kahlenberg, V., et al. (2023). Precipitation hardening in Al-Mg-Si alloys. *Materials Science and Engineering: A, 845*, 143–158.

Kaufman, J. G. (2023). *Introduction to aluminum alloys and tempers*. ASM International.

Kobashi, M., Harata, M., & Choh, T. (1993). Dispersion behavior of several carbides into molten aluminum and mechanical properties of TiC/Al composite. *Journal of Japan Institute of Light Metals*, *43*(10), 522–527.

Kumari, S., et al. (2016). A review on particulate reinforced aluminium matrix composites. *Journal of Engineering Research and Applications*, *6*(5), 45–52.

Li, Q., et al. (2023). Mechanical properties of Al-Si-Mg alloys. *Journal of Alloys and Compounds*, 935, 168–175.

Miracle, D. B., & Donaldson, S. L. (2020). *ASM handbook: Composite materials* (Vol. 21). ASM International.

Mondolfo, L. F. (2025). *Aluminium alloys: Structure and properties*. Butterworth-Heinemann.

Odiboh, A. (2026). Mineralogical and geochemical characterization of clays at Igo and Okhoro deposits, Southern Nigeria: A comparative study of their economic potentials. *University of Benin Repository*. https://repository.uniben.edu/taxonomy/term/25866

Ogunleye, O. O., & Bada, S. O. (2021). Geochemical and mineralogical studies of kaolinitic clays in parts of Ilorin, southwestern basement rock area, Nigeria. *KWASU Repository*. https://kwasuspace.kwasu.edu.ng/items/0044a17b-5a2e-4fa6-a634-c1853d86d81c

Omoruyi, D. I., Ilevbare, M., Ehinlaıye, A. O., & Akujıeze, C. N. (2022). Geochemical discriminant for provenance characterization of some clay deposits in Edo State, Nigeria. *International Journal of Earth Sciences Knowledge and Applications*, 4(3), 407–418. https://izlik.org/JA55AE46CK

Polmear, I. J., et al. (2024). *Light alloys: Metallurgy of the light metals* (3rd ed.). Butterworth-Heinemann.

Rawal, S., & Sidpara, A. M. (2025). Microstructure and mechanical property variation of Al6061/GNP nanocomposite by Mg and ultrasonic vibration in bottom pouring stir casting. *Advanced Engineering Materials*, 27(10), 2500024. https://doi.org/10.1002/adem.202500024

Shuaib-Babata, Y. L., & Mudiare, E. (2017). Characterization and evaluation of the refractory properties of some selected Kwara State (Nigeria) clay deposits. *The Nigerian Journal of Mechanical Engineering*, 7(1), 1–21.

Suroń, A., et al. (2024). Nanocomposite materials for advanced engineering applications. *Materials Characterization*, 207, 113–128.

Xu, X., & Zhang, Y. (2025). Stir-casting manufactured SiCp reinforced aluminum matrix composite with ultrahigh strength and excellent corrosion resistance: Matrix, microstructure and properties. *Journal of Materials Research and Technology*, 37, 3563–3577. https://doi.org/10.1016/j.jmrt.2025.06.223

Zhao, H., et al. (2024). Alloy development in Al-Si-Mg systems. *Materials & Design*, 226, 111–125.

EFFECT OF DOUBLE PRESSING AND DOUBLE SINTERING ON THE MECHANICAL AND TRIBOLOGICAL PROPERTIES OF ALUMINIUM MATRIX REINFORCED RICE HUSK ASH COMPOSITES

Abdulrahman Adeiza Musa[1,*], Kamilu Adeyemi Bello[1], Agbo E. Oloture[1], Mohd A. Maleque[2], Jimoh O. Gaminana[1], Rayyan M. Dodo[1], Hayatu M. Abdullahi[3], Abdullahi Umma[4]

[1]*Ahmadu Bello University Zaria*
[2]*Department of Manufacturing and Materials Engineering, International Islamic University Malaysia, Kuala Lumpur, Malaysia*
[3]*Department of Metallurgical Engineering. Kaduna Polytechnic, Kaduna. Nigeria*
[4]*Department of Mechanical Engineering, Bayero University, Kano, Nigeria*

Email: adeiza4musa66@gmail.com*, kabello@abu.edu.ng, agboemmannuel5@gmail.com, maleque@iium.edu.my, jogaminana@abu.edu.ng, rdmamuda@abu.edu.ng, mabdullahi8003@gmail.com, uabdullahi.mec@buk.edu.ng

***Corresponding author**: Abdulrahman Adeiza Musa

DOI: https://doi.org/10.67203/sp.ICESID.2026

ABSTRACT

This study investigates the effect of double pressing and double sintering (DPDS) on the mechanical and tribological properties of aluminum matrix composites reinforced with rice husk ash (RHA). Aluminum–RHA composites containing 0 –15 wt.% RHA were fabricated using powder metallurgy through three processing routes: single pressing–single sintering (SP–SS), single pressing–high-pressure sintering (SP–HPS), and double pressing–double sintering (DPDS). Hardness, wear rate, and coefficient of friction (COF) were evaluated, with representative values obtained under stable sliding conditions used to establish physically meaningful correlations. The DPDS route produced higher hardness values for both pure aluminum (69.9 HV) and the 5 wt.% RHA composite (78.0 HV), with the corresponding lowest specific wear rates of (8.33 × 10^{-7} mm³/N·m) and reduced coefficients of friction (COF) of 0.195 and 0.203, respectively. A clear inverse relationship between hardness and specific wear rate was observed for pure aluminum and the 5 wt.% RHA composites, consistent with classical tribological principles. However, composites containing 10–15 wt.% RHA exhibited increased wear and friction despite their relatively higher hardness, which was attributed to particle agglomeration, weak interfacial bonding, and abrasive wear associated with the silica-rich RHA particles. These findings demonstrate that DPDS is an effective processing route for improving the tribological performance of aluminum–RHA composites, with 5 wt.% RHA providing the best combination of hardness, wear resistance and coefficient of friction under the investigated conditions. The use of locally sourced RHA in this study promotes agricultural waste valorization and sustainable materials development, supporting the global goal of advancing environmentally responsible engineering solutions.

Keywords: *Aluminum matrix composites; Rice husk ash; Double pressing-Double sintering; Hardness; Wear; Powder metallurgy*

1. INTRODUCTION

The incorporation of hard ceramic reinforcements can further enhance the hardness, load-bearing capacity, and wear resistance Aluminum matrix composites (AMCs) have attracted significant research attention due to its lightweight and superior mechanical properties compared to conventional aluminum alloys (Chak et al., 2020; Kumar et al., 2024). Aluminum's low density (approximately 2.7 g/cm³), combined with its high specific strength, makes it an attractive matrix material for lightweight structural applications (Singhal, Shelly, Rawat, et al., 2025; Singhal, Shelly, Saxena, et al., 2025). of aluminum matrix composites, thereby improving their performance under sliding wear conditions (Singhal, Shelly, Saxena, et al., 2025). Recently, agro-waste materials particularly rice husk ash

(RHA) have attracted increased interests due to their high silica content, abundance, and environmental benefits (Islam et al., 2024; Taiye et al., 2024). Incorporating RHA into aluminum matrices not only enhances mechanical properties like hardness and wear resistance but also supports eco-friendly material development from agricultural waste (Singh Karam et al., 2022).

Rice husk is unusually high in ash compared to other biomass fuels in the range of 10-20%. Rice husk ash typically contains more than 80% silica, highly porous and light-weight, with high external surface area when properly calcined. Flach et al. (2022) highlighted that RHA enhances hardness, reduce density, and promotes wear resistance in composite. However, the effectiveness of RHA as a reinforcement is strongly dependent on processing conditions. Challenges such as particle agglomeration, poor interfacial bonding, and residual porosity often limit the mechanical and tribological performance of aluminum– Rice husk ash (Al-RHA) composites fabricated using conventional powder metallurgy routes (Akgümüş Gök et al., 2024; Shaikh, Arif, et al., 2019).

Conventional SP–SS often result in high porosity, weak interfacial bonding, incomplete densification, leading to increased wear and unstable friction behavior (Shaikh, Raja, et al., 2019). DPDS involve an initial pressing and pre-sintering, followed by re-pressing and a final sintering cycle, thereby promoting better particle rearrangement, enhanced neck growth, and reduced porosity. Literature shows that DPDS significantly improves hardness and tensile strength (Mechanical properties), while enhancing tribological performance (Alem et al., 2020; Hammes et al., 2014; Liu et al., 2023). Although double pressing and double sintering (DPDS) has been investigated for aluminum-based composites reinforced with synthetic and carbon-based reinforcements, its application to rice husk ash (RHA)-reinforced aluminum remains comparatively less explored. Previous studies have demonstrated the potential of DPDS to improve the consolidation and mechanical performance of aluminum composites; however, limited attention has been given to the combined influence of RHA content and the DPDS processing sequence on the hardness and tribological response of Al–RHA composites (Alaneme & Sanusi, 2015). In particular, the present study compares conventional single pressing–single sintering routes with a DPDS route involving initial compaction, pre-sintering, re-pressing and final sintering using the same Al–RHA compositions. The single press and single sinter process suffers from limited green density due to work hardening and friction, leaving high residual porosity after sintering. This porosity severely weakens mechanical properties and corrosion resistance**.** Double pressing and double sintering use a second high-pressure press on a sintered part to crush pores that the first press couldn't eliminate, resulting in a much denser and stronger final component (Alem et al., 2020).

Therefore, this study evaluates the DPDS route for the fabrication of Al–RHA composites containing 0, 5, 10, and 15 wt.% RHA, with particular emphasis on the influence of the additional pressing–sintering cycle on their hardness and tribological performance. The findings provide insight into the processing–property relationships of Al–RHA composites and contribute to the development of sustainable aluminium-based composites with improved mechanical and tribological performance.

2. METHODOLOGY

2.1 Materials

The materials and reagents used in this study included commercially pure aluminium powder (99.99% purity), which served as the matrix material. Rice husk ash (RHA), derived from the calcination of rice husk particles obtained from a rice mill in MTD, Zaria, Kaduna State, Nigeria, was used as the reinforcement. Ethanol was employed as the mixing medium during powder blending, while zinc stearate powder was used as a die lubricant during compaction to reduce friction between the powder compact and die wall and facilitate the ejection of the green compact.

2.2.1 Sample Preparation

The rice husk obtained from the rice mill was initially purified by removing impurities such as sand, dust and organic residues through winnowing. The rice husk was subsequently washed thoroughly with water to remove adhering dirt and dried under sunlight to facilitate moisture removal. The dried rice husk was then placed in a furnace and calcined at 700 °C for 6 hours. After calcination, the resultant rice husk ash (RHA) was removed from the furnace and allowed to cool to room

temperature in air. The cooled ash was subsequently pulverized using a ball mill to reduce its particle size and passed through a 75 µm sieve. The sieved RHA was collected and stored in sealed polyethylene bags to minimize moisture absorption and contamination prior to further processing and characterization.

2.3 Composite Fabrication

The experimental variables investigated in this study were the RHA content and powder-metallurgy processing route. The mixing conditions were kept constant for all compositions. Aluminum powder and RHA were blended at RHA contents of 0, 5, 10 and 15 wt.%, as presented in Table 1. For each composition, the experiment was performed using the three processing routes described in Table 2. The powder mixtures were ball-milled at a constant rotational speed of 200 rpm for 1 hour using a ball-to-powder ratio of 10:1

Table 1: *Percentage composition of samples*

Al	**RHA**
100	0
95	5
90	10
85	15

2.3.1 Powder Mixing

Aluminum powder and varying weight percentages of rice husk ash (5%, 10%, and 15%) were measured using a digital weighing balance. The powders were mixed using a ball mill at 200 rpm for 1 hour to ensure uniform distribution of rice husk ash within the aluminum matrix. Homogeneous dispersion was achieved through wet ball milling using a ball-to-powder ratio (BPR) of 10:1. A total of 0.5 mL of ethanol, which served as a process control agent (PCA), was added to the mixture and subsequently evaporated in a furnace.

2.3.2 Powder Compaction and Sintering

The 1 g powder mixtures were compacted into cylindrical billets using a uniaxial hydraulic press. Two processing routes were employed: SP–SS, representing the conventional powder metallurgy route, and DPDS, the novel processing route. For the SP–SS route, the powders were compacted once at either 3 MPa (Route 1) or 5 MPa (Route 2), followed by sintering at 594 °C for 2 hours in an electric muffle furnace. The sintered samples were then cooled outside the furnace to room temperature. For the DPDS route, the powder mixture was initially compacted at 3 MPa, followed by pre-sintering at 300 °C for 1 hour to promote preliminary diffusion and particle bonding. The pre-sintered compact was subsequently repressed at 5 MPa to improve particle rearrangement and reduce porosity, followed by final sintering at 594 °C for 2 hours. The sintering temperature was selected based on the melting point of aluminum (approximately 660 °C), corresponding to about 90% of its melting temperature, and was maintained across all RHA contents to provide consistent processing conditions. Similar sintering temperatures have been employed in previous powder-metallurgy studies of Al–RHA composites, supporting their suitability for promoting solid-state diffusion and interparticle bonding while remaining below the melting temperature of aluminum (Mohamed Ariff et al., 2022).

However, the addition of RHA may influence the thermal and interfacial behavior of the composites. Therefore, the use of a fixed temperature of 594 °C across the 0–15 wt.% RHA range represents a controlled processing condition rather than an assumption that it is the optimum sintering temperature for every composition. After sintering, the specimens were allowed to cool outside the furnace to room temperature. The DPDS route was adopted to enhance densification, reduce porosity, and improve the mechanical properties of the fabricated Al–RHA composites. Samples were labeled according to their RHA content and processing route. Table 2 provides details of the powder metallurgy routes adopted for the fabrication of the samples.

Table 2: *Description of the powder metallurgy routes adopted for the sample fabrication*

Route	Processing Description	Abbreviation
Route 1	Single pressing at 3 MPa → sintering at 594 °C	SP–SS (Single Pressing and Single Sintering)
Route 2	Single pressing at 5 MPa → sintering at 594 °C	SP–HPS (Single Pressing–Higher Pressure Sintering)
Route 3	Double pressing and double sintering: 3MPa pressing → pre-sintering at 300 °C → re-pressing at 5 MPa → final sintering at 594 °C	DPDS (Double Pressing and Double Sintering)

2.4 Hardness

The hardness tests were performed using a Vickers micro hardness testing machine, ASTM E384. A diamond indenter was used with an applied load of 0.3kgf, and a dwell time of 8 seconds. To account for sample inconsistencies, three readings were taken at different spots. The average hardness value was then determined from these readings.

2.5 Wear and Coefficient of Friction

The wear test was conducted on the samples according to ASTM 99-95a test standard for wear testing of materials. Using ball-on-disk tribometer machine (model version R0.01), an 8N load was applied over a 30 m sliding distance, with the test duration of 30 minutes for all the samples. The corresponding average sliding speed was 1.0 m/min (0.0167 m/s). The counter-body has a ball diameter of 6mm. The wear track radius was 3mm, and the specimen mass is 1g. The tests were conducted under dry ambient laboratory conditions at 27 °C and 55% relative humidity. The coefficient of friction (COF) was automatically recorded by the ball-on-disk tribometer during the wear tests, while the specific wear rate was calculated using Equation (1).

$$\text{Specific wear rate} = \frac{\text{Wear Volume}}{\text{Load X Sliding Distance}} \tag{1}$$

3. RESULTS AND DISCUSSION

Table 3: *Properties Al-RHA composite processed via different powder metallurgy route*

Composition	Processing Route	Hardness (HV)	Wear Rate ($mm^3/N.m$)	Coefficient of Friction
100% Al	SP–SS (3 MPa)	48.9	2.50×10^{-5}	0.273
100% Al	SP–HPS (5 MPa)	57.1	5.00×10^{-6}	0.217
100% Al	DPDS	69.9	8.33×10^{-7}	0.195
95% Al + 5% RHA	SP–SS (3 MPa)	63.1	3.33×10^{-6}	0.239
95% Al + 5% RHA	SP–HPS (5 MPa)	65.5	8.33×10^{-7}	0.228
95% Al + 5% RHA	DPDS	78	8.33×10^{-7}	0.203
90% Al + 10% RHA	SP–SS (3 MPa)	69.4	1.89×10^{-3}	0.277
90% Al + 10% RHA	SP–HPS (5 MPa)	73.7	1.24×10^{-3}	0.414
90% Al + 10% RHA	DPDS	77.4	5.96×10^{-4}	0.319
85% Al + 15% RHA	SP–SS (3 MPa)	84.6	9.76×10^{-4}	0.281
85% Al + 15% RHA	SP–HPS (5 MPa)	91.5	1.66×10^{-3}	0.42
85% Al + 15% RHA	DPDS	75.9	8.53×10^{-4}	0.41

3.1 Hardness

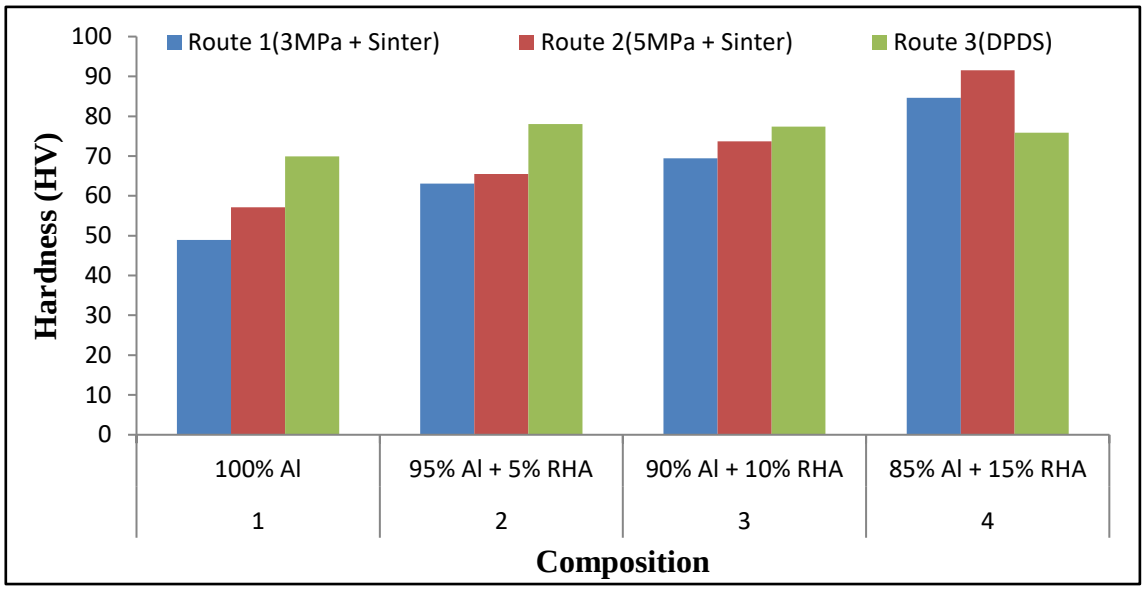

Figure 1: Hardness characteristics of AL- RHA Content under Different Processing Routes

As shown in Table 3 and Figure 1, hardness was influenced by the compaction pressure and sintering conditions. For pure aluminum, hardness increased from 48.9 HV for SP–SS to 69.9 HV for DPDS. A similar improvement was observed for the 5 wt.% RHA composites, where DPDS produced the highest hardness of 78.0 HV. For the DPDS route, hardness increased from pure aluminum to 5 wt.% RHA, reaching a maximum of 78.0 HV, and subsequently decreased slightly at 10 wt.% (77.4 HV) and 15 wt.% RHA (75.9 HV). The reduction at higher RHA contents may be associated with less effective particle packing, possible particle agglomeration, and weaker matrix–particle interaction. These mechanisms are proposed as possible explanations rather than confirmed microstructural effects, since detailed microstructural characterization was not performed in the present study. Overall, the hardness trend followed the order DPDS > SP–HPS > SP–SS for pure aluminum, 5 wt.% RHA composites. However, at 15 wt.% RHA, this trend was reversed, with SP–HPS producing the highest hardness (91.5 HV), while DPDS exhibited the lowest hardness (75.9 HV). This result suggests that the beneficial effect of multiple pressing and sintering cycles on hardness was not maintained at the highest RHA content. Nevertheless, hardness alone was insufficient to guarantee improved tribological performance at higher reinforcement levels.

3.2 Wear Behaviour

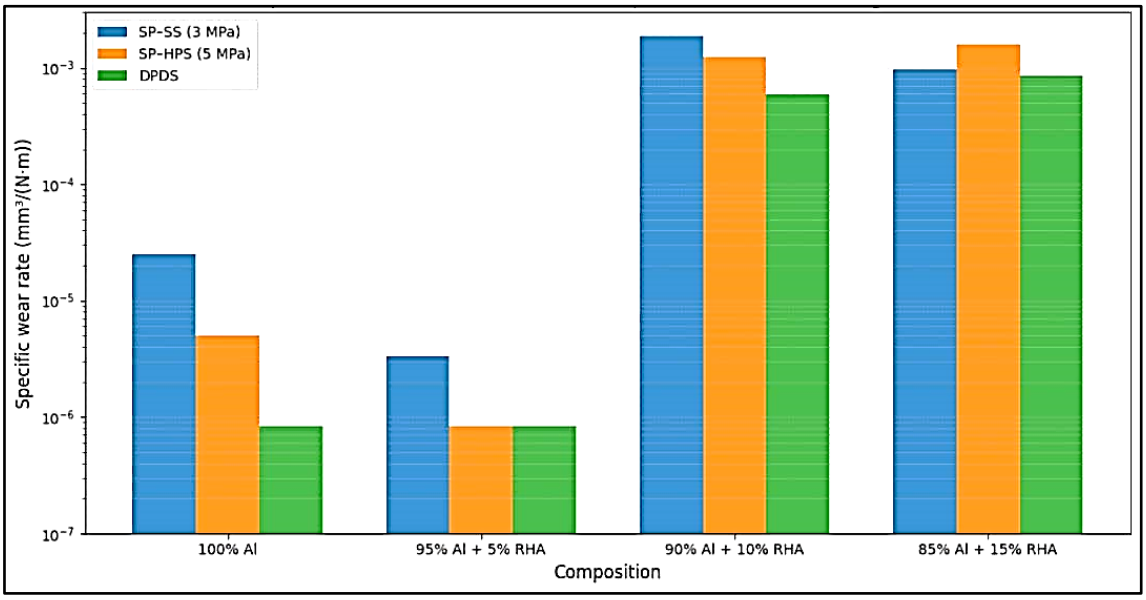

Figure 2: Effect of rice husk ash content and processing route on the wear rate of Aluminum-RHA composites

Figure 2 illustrates the influence of reinforcement content and processing route on wear behavior, showing a significant reduction in wear rate for DPDS- processed pure aluminum and 5wt. % RHA. A clear inverse relationship between hardness and wear rate was observed. The DPDS-processed pure aluminum sample exhibited the lowest wear rate of 8.33×10^{-7} mm³/N·m, compared with 2.50×10^{-5} mm³/N·m for the SP–SS condition. Similarly, the 5 wt. % RHA composites processed via DPDS showed a wear rate of 8.33×10^{-7} mm³/N·m, indicating excellent wear resistance. In contrast, composites containing 10 and 15 wt. % RHA displayed significantly higher wear rates despite increased hardness. For example, the 10 wt. % RHA composites processed via SP–SS recorded a wear rate of 1.89×10^{-3} mm³/N·m, while the DPDS condition reduced wear to 5.96×10^{-4} mm³/N·m but did not eliminate severe wear behavior. These results suggest that excessive RHA content promotes particle agglomeration, interfacial decohesion, and abrasive particle pull-out, leading to accelerated material loss. However, these mechanisms are proposed as possible explanations rather than confirmed effects, as detailed microstructural and worn-surface characterization was not performed in the present study.

3.3 Coefficient of Friction

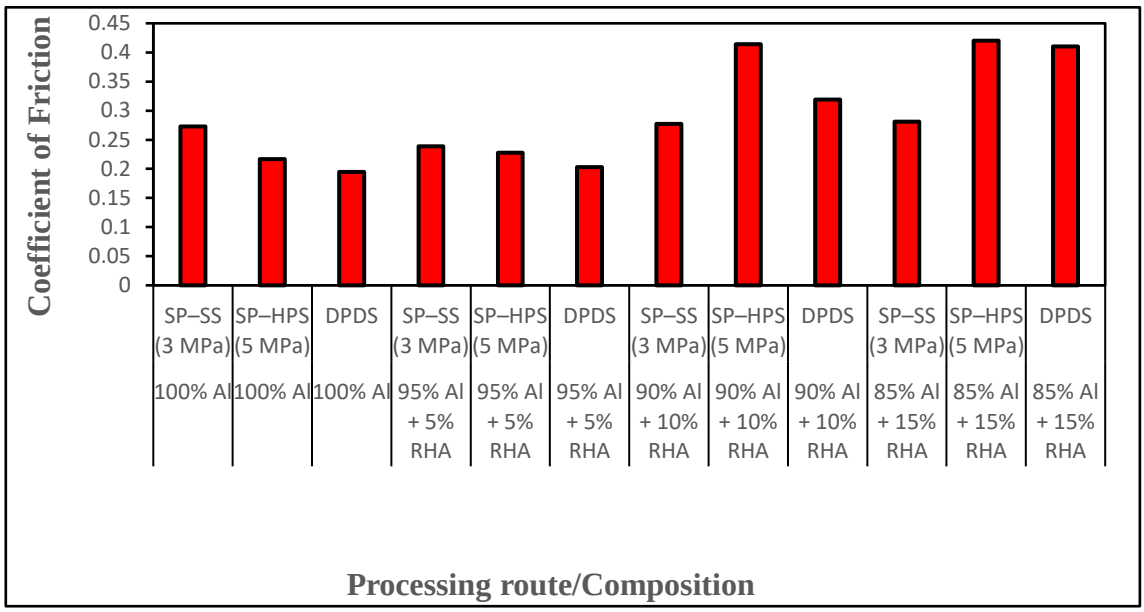

Figure 3: Effect of rice husk ash content on Aluminum-RHA composites processed via different routes

The coefficient of friction followed trends similar to the wear rate (see Figure 3). Lower wear rates were associated with reduced friction values, particularly for DPDS-processed samples. Pure aluminum processed via DPDS exhibited a COF of 0.195, while the 5 wt. % RHA composites showed a COF of 0.203. These values indicate stable sliding conditions with reduced adhesive and abrasive interactions. Higher COF values were recorded for 10–15 wt. % RHA composites, reaching 0.414–0.420 for some SP–HPS samples. The higher friction values observed at some of the higher RHA contents may be associated with the presence of hard silica-rich particles, which can act as third-body abrasives and promote ploughing and micro-cutting at the sliding interface. However, these interpretations are proposed as speculative mechanisms because the particle distribution and worn-surface morphology require further confirmation through surface and microstructural characterization.

3.4 Correlation between Hardness and Tribological Performance

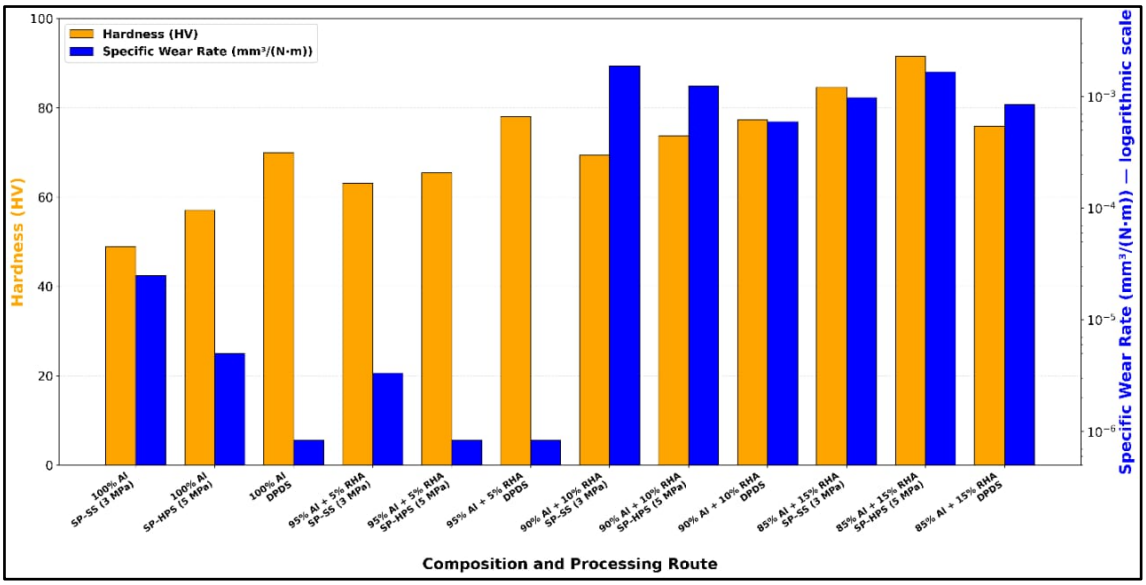

(a)

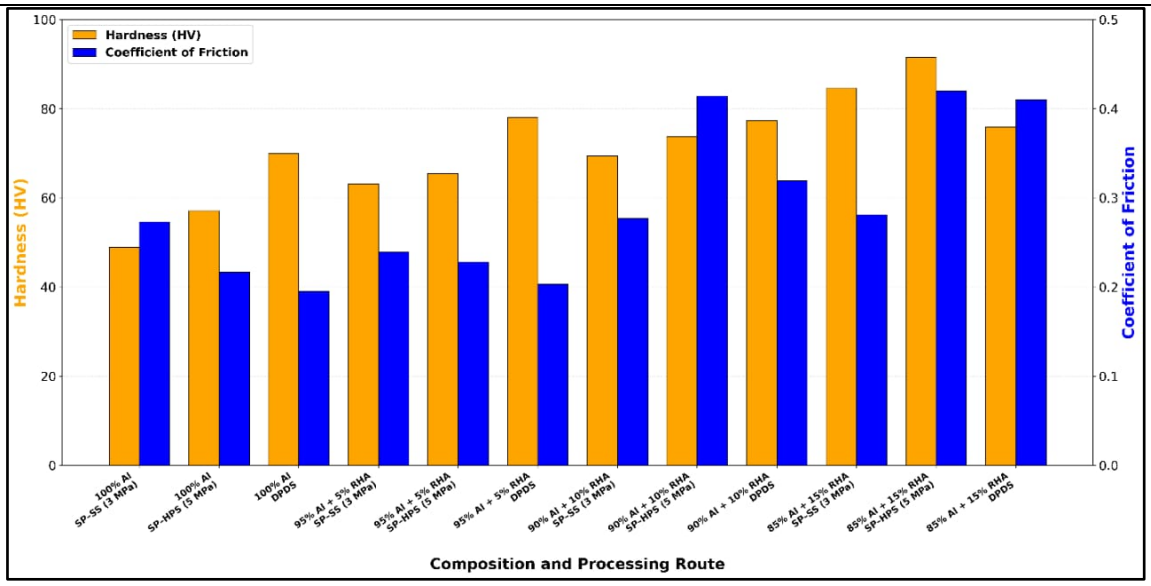

(b)

Figure 4: Comparison of hardness with (a) wear rate and (b) coefficient of friction

Figure 4a and b show the relationships between hardness and wear rate, and between hardness and COF for the fabricated Al–RHA composites, respectively. The results show an inverse relationship between hardness and specific wear rate, particularly for pure aluminum and the 5 wt.% RHA composites (See Figure 4a). For these compositions, the DPDS route produced higher hardness values accompanied by lower wear rates. This behavior can be attributed to the improved resistance of the harder material to plastic deformation and surface material removal during sliding. The observed trend is consistent with Archard's wear law, which identifies material hardness as an important factor influencing wear resistance. However, at higher RHA contents of 10 and 15 wt.%, the relationship between hardness and wear rate becomes less consistent. This suggests that the wear behavior is influenced not only by hardness but also by microstructural characteristics such as porosity, particle agglomeration, weak matrix–RHA interfacial bonding, and particle pull-out. These defects can promote crack initiation, surface damage, and third-body abrasion, thereby increasing the wear rate despite the presence of a relatively hard reinforcement phase. Figure 4b compares hardness and COF, showing that the DPDS-processed pure aluminum and 5 wt.% RHA composites exhibit higher hardness alongside lower COF values. The reduction in COF with increasing hardness suggests that the improved surface resistance reduces asperity deformation and severe adhesive interactions during sliding, resulting in more stable sliding contact. Nevertheless, the relationship is not strictly linear across all RHA contents as earlier discussed in Section 3.4.

Figure 4 demonstrates that increased hardness generally contributes to improved tribological performance, as reflected by lower wear rate and COF. However, this relationship depends on the reinforcement content, as observed in this study. The consistent improvement observed for the DPDS-processed pure aluminum and 5 wt.% RHA composite indicates that the DPDS route effectively enhanced hardness while simultaneously reducing wear rate and COF. In contrast, the improvements in hardness at higher RHA contents did not consistently translate into reduced wear rate and COF, suggesting that other factors associated with increasing reinforcement content may influence the tribological behavior. These results therefore indicate that an optimum reinforcement content and appropriate processing route are essential for achieving a balanced combination of high hardness, low wear rate, and low COF in Al–RHA composites.

4. CONCLUSION

The effects of DPDS on the hardness and tribological performance of Al–RHA composites were investigated. Both RHA content and processing route influenced the material properties, with 5 wt.% RHA processed by DPDS providing the best overall balance of hardness, wear resistance, and

coefficient of friction. At 15 wt.% RHA, SP–HPS produced the highest hardness (91.5 HV) but also the highest COF (0.420), whereas DPDS produced the lowest wear rate (8.53×10^{-4} mm³/N·m) at the same composition. This confirms that higher hardness does not necessarily result in improved tribological performance. The lack of microstructural characterization limits verification of the mechanisms underlying these trends; future studies should therefore incorporate SEM/EDS and surface roughness analyses. The use of locally sourced RHA in this study promotes agricultural waste valorization and sustainable materials development, supporting locally driven and environmentally responsible engineering solutions in Nigeria. Overall, DPDS shows potential for sustainable Al–RHA composite development, with 5 wt.% RHA providing the most favorable overall performance under the investigated conditions.

Acknowledgements The authors would like to express their sincere appreciation to the Tertiary Education Trust Fund (TETFund) for supporting this research through the NRF 2021 SETI, Batch 8 research grant, awarded to Engr. Prof. U. A. Abdullahi, Department of Mechanical Engineering, Bayero University, Kano, Nigeria.

5. REFERENCES

Akgümüş Gök, D., Bayraktar, C., & Hoşkun, M. (2024). A review on processing, mechanical and wear properties of Al matrix composites reinforced with Al2O3, SiC, B4C and MgO by powder metallurgy method. *Journal of Materials Research and Technology*, *31*. https://doi.org/10.1016/j.jmrt.2024.06.110

Alaneme, K. K., & Sanusi, K. O. (2015). Microstructural characteristics, mechanical and wear behaviour of aluminium matrix hybrid composites reinforced with alumina, rice husk ash and graphite. *Engineering Science and Technology, an International Journal*, *18*(3). https://doi.org/10.1016/j.jestch.2015.02.003

Alem, S. A. A., Latifi, R., Angizi, S., Mohamadbeigi, N., Rajabi, M., Ghasali, E., & Orooji, Y. (2020). Development of Metal Matrix Composites and Nanocomposites Via Double-Pressing Double-Sintering (DPDS) Method. *Materials Today Communications*, *25*. https://doi.org/10.1016/j.mtcomm.2020.101245

Chak, V., Chattopadhyay, H., & Dora, T. L. (2020). A review on fabrication methods, reinforcements and mechanical properties of aluminum matrix composites. In *Journal of Manufacturing Processes* (Vol. 56). https://doi.org/10.1016/j.jmapro.2020.05.042

Flach, M. V., Krauspenhar, E., & Jahno, V. D. (2022). Recycling of waste from the rice chain: incorporation of rice husk and rice husk ash in polymeric composites. *Ciência e Natura*, *44*. https://doi.org/10.5902/2179460x68817

Hammes, G., Schroeder, R., Binder, C., Klein, A. N., & De Mello, J. D. B. (2014). Effect of double pressing/double sintering on the sliding wear of self-lubricating sintered composites. *Tribology International*, *70*. https://doi.org/10.1016/j.triboint.2013.09.016

Islam, M. T., Hossen, M. F., Asraf, M. A., Kudrat-E-Zahan, M., & Zakaria, C. M. (2024). Production and Characterization of Silica from Rice Husk: An Updated Review. *Asian Journal of Chemical Sciences*, *14*(2). https://doi.org/10.9734/ajocs/2024/v14i2296

Kumar, A., Singh, V. P., Singh, R. C., Chaudhary, R., Kumar, D., & Mourad, A. H. I. (2024). A review of aluminum metal matrix composites: fabrication route, reinforcements, microstructural, mechanical, and corrosion properties. In *Journal of Materials Science* (Vol. 59, Issue 7). https://doi.org/10.1007/s10853-024-09398-7

Liu, C., Yin, Y., Li, R., Chen, X., & Chen, Q. (2023). Double Pressing/Double Sintering on Properties of Lead-Free FeS/Cu–Bi Self-Lubricating Composites. *Tribology Transactions*, *66*(4). https://doi.org/10.1080/10402004.2023.2211644

Mohamed Ariff, A. H., Jun Lin, O., Jung, D. W., Mohd Tahir, S., & Sulaiman, M. H. (2022). Rice Husk Ash as Pore Former and Reinforcement on the Porosity, Microstructure, and Tensile Strength of Aluminum MMC Fabricated via the Powder Metallurgy Method. *Crystals*, *12*(8). https://doi.org/10.3390/cryst12081100

Shaikh, M. B. N., Arif, S., Aziz, T., Waseem, A., Shaikh, M. A. N., & Ali, M. (2019). Microstructural, mechanical and tribological behaviour of powder metallurgy processed SiC and RHA reinforced Al-based composites. *Surfaces and Interfaces*, *15*. https://doi.org/10.1016/j.surfin.2019.03.002

Shaikh, M. B. N., Raja, S., Ahmed, M., Zubair, M., Khan, A., & Ali, M. (2019). Rice husk ash reinforced aluminium matrix composites: Fabrication, characterization, statistical analysis and artificial neural network modelling. *Materials Research Express*, *6*(5). https://doi.org/10.1088/2053-1591/aafbe2

Singh Karam, D., Nagabovanalli, P., Sundara Rajoo, K., Fauziah Ishak, C., Abdu, A., Rosli, Z., Melissa Muharam, F., & Zulperi, D. (2022). An overview on the preparation of rice husk biochar, factors affecting its properties, and its agriculture application. In *Journal of the Saudi Society of Agricultural Sciences* (Vol. 21, Issue 3). https://doi.org/10.1016/j.jssas.2021.07.005

Singhal, V., Shelly, D., Rawat, P., Saxena, A., Gupta, R., Lee, S. Y., & Park, S. J. (2025). Analysis of mechanical properties and fracture mechanism in LM30 Al alloy composites with single and dual size reinforcements. *Journal of Materials Research and Technology*, *38*. https://doi.org/10.1016/j.jmrt.2025.08.173

Singhal, V., Shelly, D., Saxena, A., Gupta, R., Verma, V. K., & Jain, A. (2025). Study of the Influence of Nanoparticle Reinforcement on the Mechanical and Tribological Performance of Aluminum Matrix Composites—A Review. In *Lubricants* (Vol. 13, Issue 2). https://doi.org/10.3390/lubricants13020093

Taiye, M. A., Hafida, W., Kong, F., & Zhou, C. (2024). A review of the use of rice husk silica as a sustainable alternative to traditional silica sources in various applications. In *Environmental Progress and Sustainable Energy* (Vol. 43, Issue 6). https://doi.org/10.1002/ep.14451

EFFECT OF HEAT TREATMENT AND QUENCHING MEDIA ON THE MECHANICAL, TRIBOLOGICAL, AND MICROSTRUCTURAL BEHAVIOUR OF A6082-SNSA/MWCNT HYBRID COMPOSITES

Abdullahi Mohammed[1,*], Malachy Sumaila[1], Muhammad Dauda[1], Laminu Shattima Kuburi[1]

[1]""

Email: mohammedabdullahi047@gmail.com[*], sumailachy@gmail.com, muhammaddauda@yahoo.com, kuburi6@yahoo.com

***Corresponding author**: Abdullahi Mohammed

DOI: https://doi.org/10.67203/sp.ICESID.2026

ABSTRACT

The effect of heat treatment and different quenching media on the mechanical, tribological, and microstructural behaviour of A6082–SNSA/MWCNT hybrid composites were studied. The fabricated composites were subjected to heat treatment and quenched in tap water (TW), ice block (IB), and SAE40 engine oil (SEO), and their properties were compared with untreated hybrid composites and the base matrix alloy. The result of the mechanical properties revealed that all heat-treated samples exhibited significant improvements in hardness, compressive strength, and impact strength relative to the untreated composite. The IB quenched sample recorded the highest hardness of 155.33 Hv, representing 15% increment, while the TW quenched sample exhibited superior compressive and impact strengths of 1567.1 MPa representing 64.30% and 3.0J respectively. Tribological analysis showed that the SEO quenched composite possessed the lowest coefficient of friction of 0.166, which represents 16.27% improvement, whereas the TW quenched composite demonstrated the most favourable wear performance among the treated samples. Optical microstructural analysis revealed that rapid quenching (IB) produced the finest and most compact dendritic network, while oil quenching resulted in coarse, elongated dendrites with increased segregation and micro-voids. Scanning electron microscope (SEM) analysis of the worn surfaces confirmed dominance of abrasive and delamination wear mechanisms, with reduced surface damage observed in heat-treated samples. The results demonstrate that quenching medium significantly influences the mechanical, tribological, and microstructural behaviour of the hybrid composites.

Keywords: *A6082 aluminium alloy; Hybrid metal matrix composites; Heat treatment; Quenching; Microstructure*

1. INTRODUCTION

Aluminium matrix composites (AMCs) have attracted considerable interest for lightweight engineering applications because of their high strength-to-weight ratio, wear resistance, and thermal stability. A6082 aluminium alloy is particularly attractive as a matrix material, while the incorporation of suitable reinforcements can further improve its mechanical and tribological performance (Jiang *et al*., 2021; Ononiwu *et al*., 2021; Kumar *et al*., 2025).

MWCNTs are attractive reinforcements because of their high strength, stiffness, and nanoscale load-transfer capability, while shea nutshell ash (SNSA) provides a low-cost and environmentally sustainable agro-waste reinforcement. Previous studies have demonstrated the potential of SNSA and carbon-based reinforcements for improving the properties of polymeric and aluminium composites (Haruna *et al*., 2019; Zubairu *et al*., 2021; Abdullahi *et al*., 2025).

Heat treatment can modify precipitation behaviour, grain structure, matrix–reinforcement interaction, and consequently the mechanical and tribological properties of aluminium composites. Previous studies have reported improvements in hardness, strength and wear resistance following appropriate heat-treatment schedules, although the response depends strongly on alloy composition, reinforcement characteristics and quenching conditions (Gandhi *et al*., 2019; Huang *et al*., 2024; Kuczek *et al*., 2025; Ravikumar *et al*., 2021).

Despite the substantial progress reported in the literature, most existing studies have focused on single or conventional reinforcement systems, with relatively few investigations considering hybrid reinforcement combinations. Furthermore, majority of the reported works evaluated only selected mechanical or tribological properties, while limited attention has been given to understanding the combined effects of heat treatment on the microstructure, mechanical properties, and wear behaviour of hybrid AMCs reinforced simultaneously with agro-waste and carbon nanotubes. Addressing this gap is essential for developing lightweight, high-performance, and sustainable AMCs for advanced engineering applications. Therefore, the present study investigates the effect of heat treatment on the mechanical and wear behaviour of A6082–SNSA/MWCNT hybrid composites.

2. METHODOLOGY

In this study, A6082 metal matrix with length x width x thickness of 350 mm x 25 mm x 25 mm was used. The content of the components of the A6082 alloy is presented in Table 1. Shea nut shell ash (SNSA) particles and Multiwalled carbon nanotubes, comprising 6wt% and 2 wt% particles were used as reinforcements. Stir casting method was employed to fabricate the hybrid composites. The details of the synthesis and characterization of the reinforcements could be found in our previous studies (Abdullahi *et al*., 2025). While A6082 provides excellent strength-to-weight ratio, corrosion resistance, and good castability, SNSA offers a sustainable and low-cost reinforcement source, whereas MWCNTs contribute exceptional strength, stiffness, and load-transfer capability at the nanoscale. The combination of these reinforcement materials is therefore expected to produce hybrid composites with improved mechanical and tribological performance while promoting sustainable utilization of agricultural waste (Abdullahi *et al.*, 2025).

Table 1: Compositions of AA6082 Alloy

Element	Al	Si	Ti	Fe	Mn	Zn	Mg	Cu	Cr	Ni
Wt.%	96.22	1.26	0.07	0.47	0.11	0.28	1.30	0.18	0.09	0.02

2.1 Hybrid Composites Fabrication

The hybrid composite was produced by heating about 550g of AA6082 to 680 °C using a graphite crucible in a charcoal fired furnace. Coated MWCNT (Abdullahi *et al*., 2025) and the SNSA were introduced into the molten AA6082 alloy and stirred using a mechanical stirrer equipped with a stainless-steel tip, operating at 450 rpm for 4.5 min. To ensure effective wetting of the reinforcement phase by the matrix, the reinforcements were heated to 250 ^{0}C and introduced into the molten AA6082. The molten mixture was poured into a square pre-heated steel mould of 350 mm in length 25 mm height and 25 mm thickness. The fabrication parameters were adopted from the optimized procedure reported by Abdullahi *et al*. (2025).

2.2 Heat Treatment

Heat treatment was performed on the cast samples using a Box-Resistance Furnace Model No 2392. Samples were solution-treated at 540 °C for 4 h, quenched separately in tap water (TW), ice block (IB) and SAE 40 engine oil (SEO), aged at 160 °C for 8 h, and subsequently cooled at room temperature (Rotella *et al*., 2018).

2.3 Mechanical Properties Tests

Hardness test was performed according to ASTM E384. The compressive strength of the hybrid composites was tested using a computerized universal testing machine. The specimens were prepared as per the ASTM E-8. The tensile strength specimen was machined as per ASTM E8 with 10 mm diameter and 15 mm length specimens. Impact test of the samples was conducted as per ASTM Standard E 602. V-notches of 0.5mm depth was made on the samples and the impact strength was carried out using Charpy Impact testing machine, serial no. 412-07-152619 with capacity of 155-300J. Table 2 show samples designations and the heat treatment carried out.

Table 2: Samples Nomenclature and Heat Treatment Process carried out

S/N	Heat treatment sample	Designation
1	A6082	Matrix
2	Un-treated hybrid composite	HBC
3	Water quenched	TW
4	Ice block quenched	IB
5	SAE 40 oil quenched	SEO

2.4 Tribological Test

A standard Tribometer/Version 6.1.19 (ball-on-disc) apparatus was employed to conduct the wear tests in accordance with ASTM G99. Test was conducted by applying 10N load at 10 cm/s speed for 30 m sliding distance. Hardened steel (65 HRC) counter disc of 10 mm track diameter and 8 mm thick was used. Specimens of 20 mm diameter and 40 mm height were prepared and the ball surface was polished by emery paper. The tests were conducted at 29 °C room temperature and 55 % relative humidity for 30 minutes (Ahmer *et al*., 2016). The variation of friction coefficient with time and sliding distance was recorded continuously during the tests. Wear rate and coefficient of friction for samples were measured using Equations 1 and 2 as earlier used by Bhaumik and Kamaraj, (2021).

$$Wear\ rate,\ WR = \Delta W/s \quad (1)$$

$$\Delta W = W_1 - W_2 \quad (2a)$$

$$s = 2\pi Ndt \quad (2b)$$

Where WR is the wear rate (mg/min), ΔW is the weight loss, W_1 and W_2 is the weight before and after abrasion (mg), S is the sliding distance (m), N is the machine speed, d is the disc diameter, and t is the time for each sample to undergo abrasion.

2.5 Scanning Electron Microscope (SEM) and Metallography

The microstructures and worn surfaces were examined by optical microscopy and SEM/EDS following standard metallographic preparation and Kroll's etching (Shuvo *et al*., 2025; Jaber *et al.*, 2023; Motyka *et al*., 2014.

3. RESULTS AND DISCUSSION

3.1 Mechanical Properties

Figure 1a-c shows average variation of mechanical properties of the samples after different heat treatment processes. It can be seen from Figure 1a that all heat-treated composite samples exhibited superior hardness compared to the untreated samples. The IB block quenched sample recorded the highest hardness of 155.33 HV (a 15% increase relative to the untreated control), followed by the sample quenched in SEO at 134 HV (an 8.45% increase). This enhancement in hardness is attributed to precipitation hardening, grain refinement, a more homogeneous microstructure, and the stabilization of hard intermetallic phases during solution treatment and artificial aging (Rmadan *et al.*, 2024). The variation across quenching media underlines the critical role of cooling rate in dictating precipitation kinetics, with ice-block quenching yielding the most favourable hardening response. Heat treatment proved more effective in enhancing the hardness of the composite specimens than that of the unreinforced matrix alloy (Ravikumar *et al*., 2021; Abishkenov *et al*., 2024; Rmadan *et al*., 2024).

Figure 1b shows average compressive strength of the treated hybrid composite samples. It can be seen that heat treatment significantly enhanced the compressive strength across all samples compared to the HBC. The sample quenched in TW achieved the highest compressive strength of 1567.1 MPa (a 64.30% increase), followed by the IB-quenched sample at 828.8 MPa (a 36.25%

increase). These strength improvements stem from matrix-reinforcement diffusion mechanisms, composition of the reinforcements, grain refinement, and strengthened matrix–reinforcement interfacial bonding (Nagaraja *et al*., 2021). The variation in compressive strength among the quenching media also demonstrates that cooling rate significantly influences distribution of strengthening precipitates required for maximum load-bearing capability. (Şenel and Mahmutoğlu, 2022; Nagaraja *et al*., 2021).

Figure 1c shows the mean effect of heat treatment on Impact strength of the hybrid composite of all samples. Both treated and untreated hybrid composites demonstrated higher impact energy absorption than the unreinforced matrix sample. The TW-quenched sample exhibited the highest impact strength at 3.0 J, demonstrating superior toughness and resistance to dynamic load deformation. Conversely, the IB-quenched sample recorded lower impact energy values. The improved impact resistance in TW quenching suggests that a balanced cooling rate promoted a uniform distribution of fine precipitates, achieving an optimal trade-off between strength and toughness without inducing excessive brittleness. Improved impact resistance could be due to an increased number of fine precipitates that were uniformly distributed after the heat treatment of the composite samples (Mahan *et al*., 2023). This finding demonstrates that the choice of quenching medium has a significant influence on the dynamic mechanical behaviour of the hybrid composites (Mahan *et al*., 2023; Zubairu *et al*., 2021).

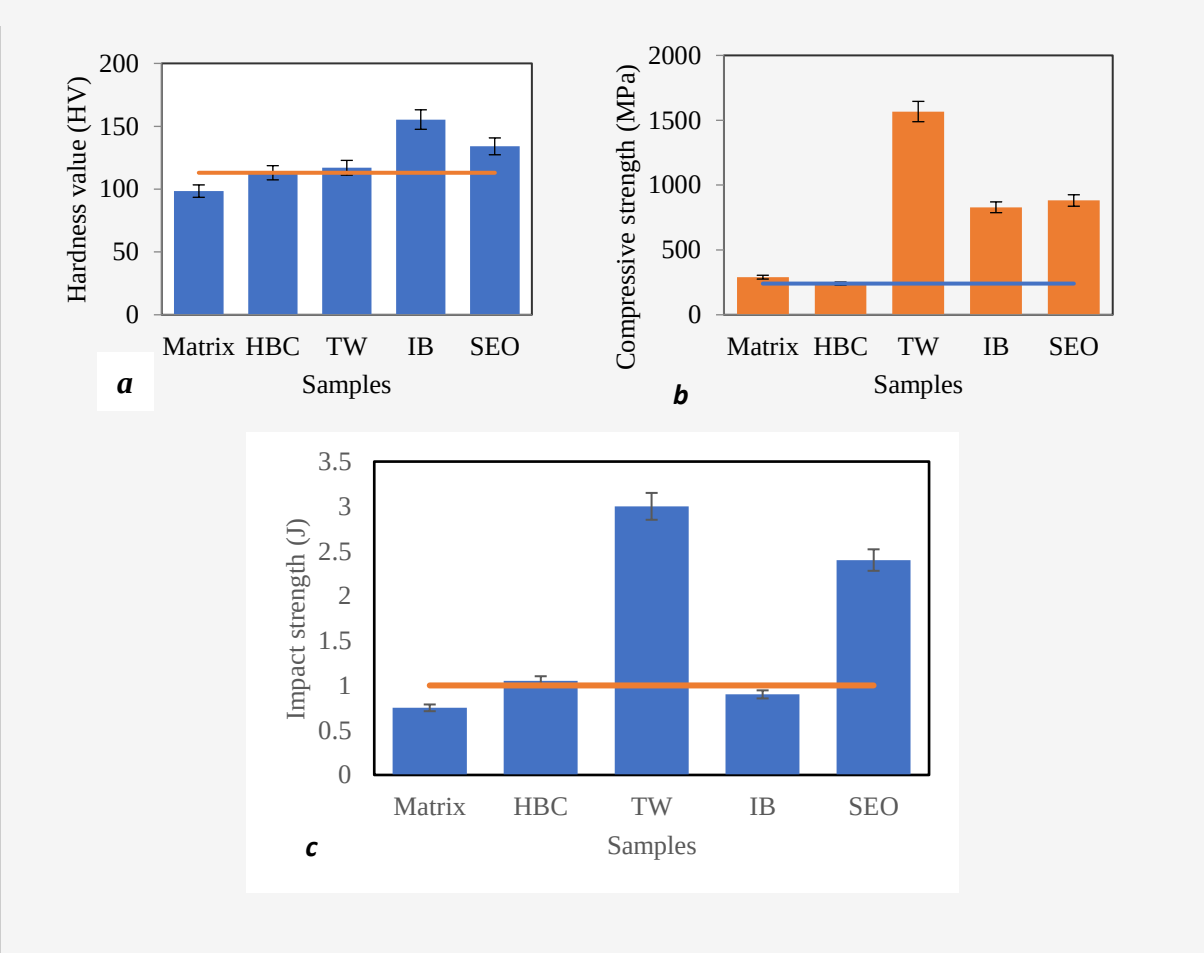

Figure 1: Variation Mechanical properties of A6082-SNSA/MWCNT composites after different heat-treatment conditions: (a) hardness, (b) compressive strength, and (c) impact strength

3.2 Tribological Properties

Tribological properties, including the coefficient of friction (CoF) and specific wear rate (SWR), were determined for the samples, and the results are presented in Figure 2a–b. Figure 2a shows the mean variation in CoF under the different heat-treatment conditions. The sample quenched

in SEO exhibited the lowest CoF of 0.166, representing a 16.6% reduction relative to the untreated HBC, which recorded a CoF of 0.199. In comparison, higher CoF values were obtained for the untreated AA6082 matrix (0.221), TW-quenched sample (0.217), and IB-quenched sample (0.211). The lower friction exhibited by the SEO-quenched sample may be attributed to the relatively mild cooling rate associated with oil quenching, which can promote a more favourable microstructural condition and enhance the stability of the surface tribo layer during sliding contact. This behaviour suggests that heat treatment influences not only the bulk mechanical properties of the composite but also the surface characteristics and interfacial interactions that govern its frictional response (Paladugu *et al*., 2022; Baghel and Krishna, 2023).

Figure 2b presents the mean specific wear rate (SWR) of the AA6082 hybrid composite samples subjected to different heat-treatment conditions. The untreated HBC exhibited the lowest specific wear rate, whereas heat treatment resulted in increased material loss for the samples quenched in TW, IB, and SEO. The increase in wear rate following heat treatment may be associated with changes in matrix hardness, precipitate distribution, residual stresses, and matrix–reinforcement interfacial integrity. Such microstructural modifications can increase the susceptibility of the matrix to plastic deformation and facilitate the detachment of wear debris during sliding. Similar observations have been associated with thermal treatment and ageing-induced changes in aluminium alloys (Anuar *et al*., 2023). Although severe quenching, such as ice quenching, has been reported to promote favourable precipitation and dislocation-pinning effects in alloys such as AA7075, thereby improving wear resistance (Ravikumar *et al*., 2021), the present results demonstrate that the tribological response is strongly dependent on alloy composition, reinforcement characteristics, heat-treatment condition, and cooling rate. Therefore, the higher wear rates observed after quenching in the present AA6082-SNSA/MWCNT hybrid composite indicate that the applied heat-treatment conditions did not produce sufficient strengthening to offset the microstructural changes that promoted material removal during sliding.

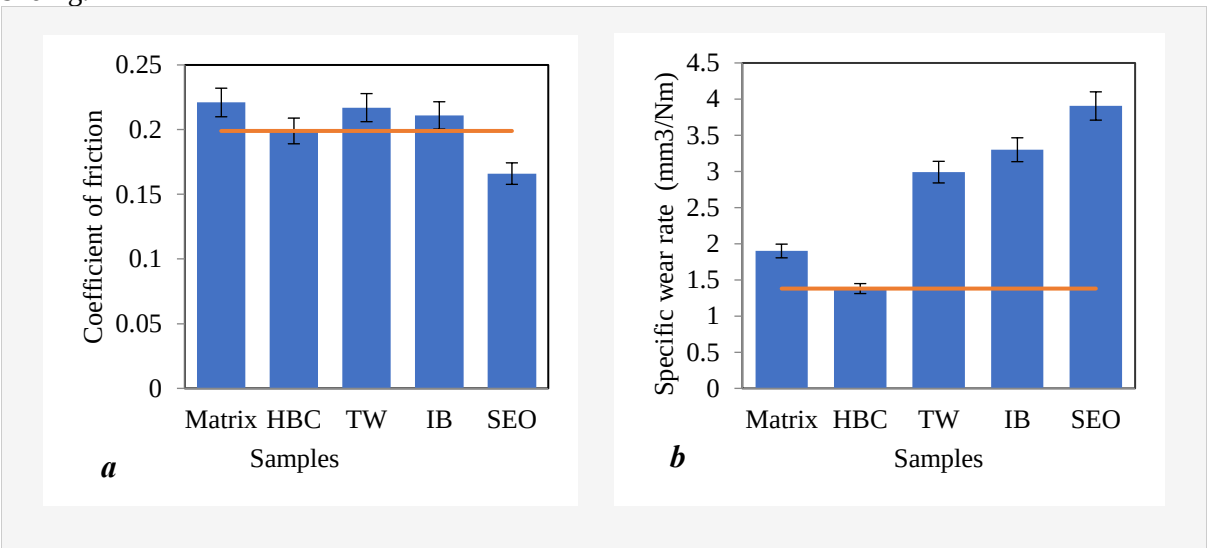

Figure 2: Variation of Tribological behaviour of A6082-SNSA/MWCNT composites: (a) coefficient of friction and (b) specific wear rate

3.3 Microstructure and wear surface characterization

3.3.1 Optical microstructure

The microstructure of the as-cast AA6082 matrix shown in Figure 6a reveals elongated dendritic structures of primary α-Al grains (bright regions) and Al–Mg_2Si eutectic phases (dark regions), which are characteristic of cast aluminium alloys (Yuan *et al*., 2021; Brodova *et al*., 2022). Figure 6b presents the microstructure of the untreated HBC, characterized by relatively coarse dendrites and localized clustering of reinforcement particles within the matrix. Figures 6c–e shows the microstructures of the composite subjected to different quenching media. The TW-quenched sample (Figure 6c) exhibits moderately refined and more equiaxed grains, with shorter dendritic arms and

narrower inter dendritic regions compared with the untreated HBC. The IB-quenched sample (Figure 6d) displays the finest and most compact dendritic structure, with relatively uniform grain morphology and reduced inter dendritic regions. This refinement can be attributed to the higher cooling rate of ice-block quenching, which restricts dendritic growth and limits coarsening. Ramirez-Vidaurri *et al.* (2022) similarly reported that increasing cooling rate reduces secondary dendrite arm spacing and suppresses dendritic coarsening. In contrast, the SEO-quenched sample (Figure 6e) exhibits comparatively coarser dendritic features, suggesting that the slower cooling rate of SEO permits greater dendritic growth and localized segregation. The micrographs demonstrate that the quenching medium significantly influences the grain morphology and dendritic structure of the A6082–SNSA/MWCNT hybrid composites. Rapid cooling in the IB medium produced greater grain refinement, whereas slower cooling in SEO promoted relatively coarser structures. These microstructural differences are consistent with the observed mechanical behaviour, as grain refinement and a more compact microstructure can restrict dislocation movement and improve matrix–reinforcement interaction, thereby contributing to increased hardness and compressive strength (Ramirez-Vidaurri *et al*., 2022; Odinachi *et al*., 2017).

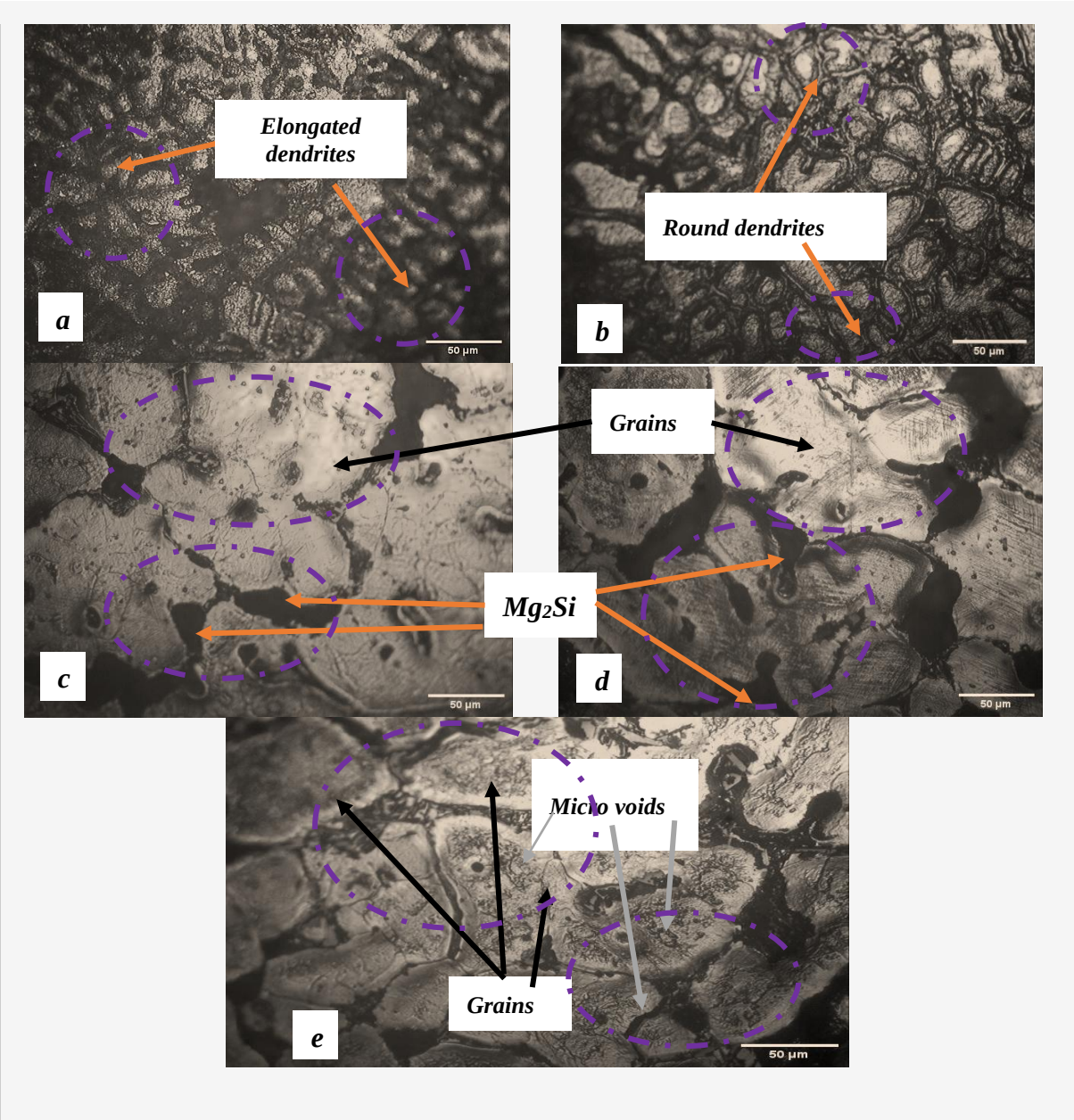

Figure 6: Optical Micrograph of: (a) Matrix (b) HBC, (c) TW treated, (d) IB treated, and (e) SEO treated A6082-SNSA/MWCNT Hybrid Composites at Magnifications of X100

3.3.1 SEM/EDS analysis

The microstructure studies of worn surfaces of the samples were studied using SEM/EDS and the micrographs are presented in Figure 7a-d. The worn surfaces of the A6082–SNSA/MWCNT hybrid composites were examined using SEM/EDS, and the resulting micrographs are presented in Figure 7a–d. The worn surfaces exhibited characteristic features associated with abrasion, delamination, adhesion, and, in some cases, reinforcement particle pull-out. The untreated HBC (Figure 7a) showed pronounced grooves parallel to the sliding direction, together with delaminated regions. These features indicate that abrasive and delamination wear were the dominant mechanisms. The formation of grooves along the wear track is commonly associated with the ploughing action of hard reinforcement particles or detached wear debris (Erappa Rajj *et al*., 2024; Turan *et al*., 2020). The TW-quenched sample (Figure 7b) exhibited fewer and shallower grooves, reduced delamination, and a comparatively uniform worn surface, suggesting less severe surface damage. This observation is consistent with the findings of Suchendra *et al.* (2023), who associated smoother worn surfaces with improved resistance to material removal. The IB-quenched sample (Figure 7c) contained a small amount of scattered wear debris, which may have resulted from micro-fracture, delamination, or reinforcement particle pull-out during sliding. Similar wear debris and micro-fracture features have been reported for reinforced aluminium composites (Ramadoss *et al*., 2020). In contrast, the SEO-quenched sample (Figure 7d) displayed relatively large delaminated or particle pull-out regions and prominent grooves, but comparatively little loose wear debris. The limited accumulation of debris suggests that detached material was readily removed from the contact surface, consistent with its relatively low coefficient of friction. Similar combinations of grooves, delamination, ploughing, and particle pull-out have been identified as characteristic wear features in aluminium-based composites under sliding conditions (Radhika *et al*., 2024; Yadav *et al*., 2024).

The EDS results presented alongside the SEM micrographs in Figure 7 further confirm the elemental composition of the worn surfaces. Aluminium was the dominant element in all samples, ranging from 85.96 to 94.29 wt.%, while Si and C were detected in the ranges of 0.41–3.64 wt.% and 1.81–2.98 wt.%, respectively. The presence of these elements indicates the involvement of both the AA6082 matrix and reinforcement-containing regions during sliding. The TW-quenched sample recorded the highest Al content (94.29 wt.%) and exhibited a relatively uniform worn morphology, whereas the untreated HBC showed more pronounced grooves and delamination. The SEM/EDS observations demonstrate that heat treatment altered the severity and dominant modes of surface damage, with the nature of the wear response being dependent on the quenching medium and the resulting microstructural condition.

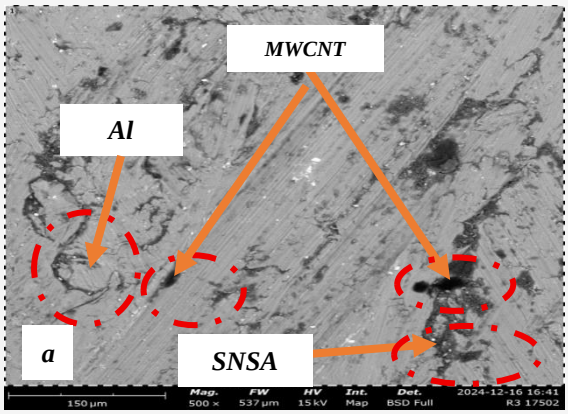

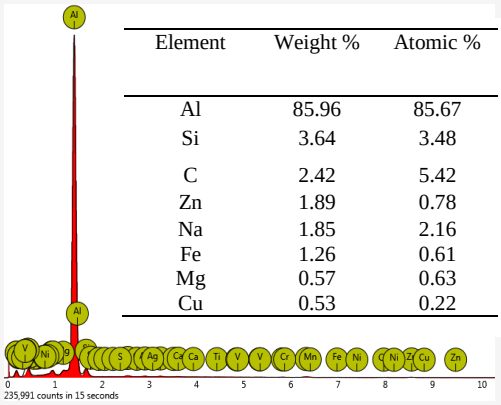

Element	Weight %	Atomic %
Al	85.96	85.67
Si	3.64	3.48
C	2.42	5.42
Zn	1.89	0.78
Na	1.85	2.16
Fe	1.26	0.61
Mg	0.57	0.63
Cu	0.53	0.22

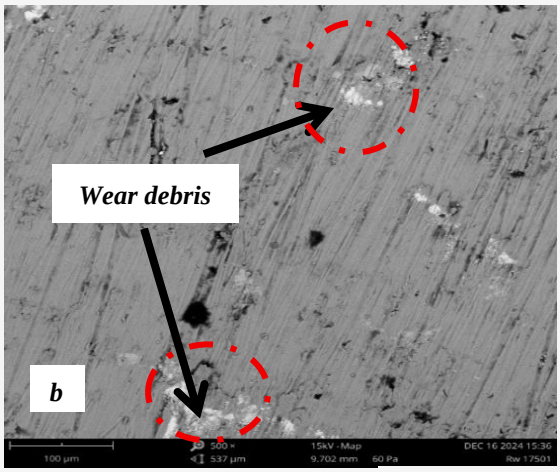

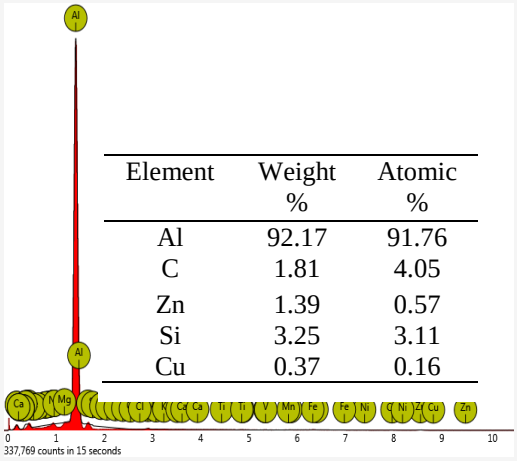

Element	Weight %	Atomic %
Al	92.17	91.76
C	1.81	4.05
Zn	1.39	0.57
Si	3.25	3.11
Cu	0.37	0.16

Element	Weight %	Atomic %
Al	94.29	93.99
C	1.94	0.62
Zn	1.52	0.62
Si	0.41	0.39
Cu	0.33	0.14
Ni	0.13	0.06

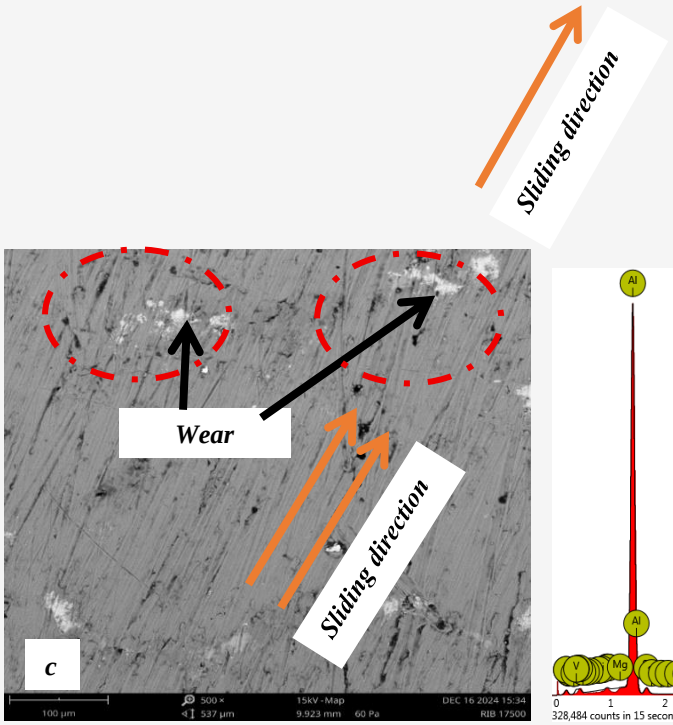

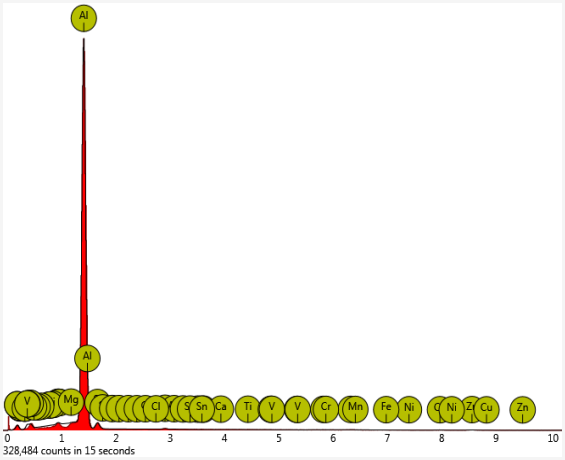

Element	Weight	Atomic

Figure 7: SEM/EDS analysis of worn surfaces: (a) HBC, (b) TW, (c) IB, and (d) SEO samples

4. CONCLUSION

This study investigated the effects of heat treatment and quenching media on the mechanical, tribological, and microstructural behaviour of A6082–SNSA/MWCNT hybrid composites. The results demonstrate that the heat-treatment significantly influenced the overall performance of the composites, with the response varying according to the quenching medium.

Among the investigated conditions, ice-block (IB) quenching produced the highest hardness of 155.33 HV, representing an improvement of approximately 15% over the untreated HBC. Tap-water (TW) quenching resulted in the highest compressive strength of 1567.1 MPa, corresponding to a 64.30% improvement, as well as the highest impact strength of 3.0 J. The SEO-quenched sample exhibited the lowest coefficient of friction (CoF) of 0.166, while the untreated HBC recorded the lowest specific wear rate (SWR) of 1.38 mm^3/Nm.

Microstructural examination further revealed that IB quenching produced the finest and most compact dendritic structure, whereas SEO quenching resulted in relatively coarser dendrites accompanied by micro voids. SEM/EDS analysis of the worn surfaces identified abrasion and delamination as the predominant wear mechanisms. The dominance of aluminium, together with the detection of Si and C, confirmed the involvement of the A6082 matrix and reinforcement-containing phases during sliding. Overall, the findings establish that appropriate selection of the quenching medium can be used to tailor the mechanical, tribological, and microstructural characteristics of A6082–SNSA/MWCNT hybrid composites for potential engineering applications.

5. REFERENCES

Abdullahi, M., Dauda, M., Sumaila, M., & Kuburi, L. S. (2025). Optimization of stir casting process parameters for fabrication of A6082-SNSA/MWCNT hybrid composites: Taguchi approach. *The International Journal of Advanced Manufacturing Technology*. https://doi.org/10.1007/s00170-025-16106-5

Abishkenov, M., Tavshanov, I., Lutchenko, N., Amanzholov, N., Kalmyrzayev, D., Ashkeyev, Z., & Abdirashit, A. (2024). Improving mechanical properties of low-quality pure aluminium by minor reinforcement with fine B4C particles and T6 heat treatment. *Applied Sciences*, *14*(23), Article 10773. https://doi.org/10.3390/app142310773

Ahmer, S. M. H., Jan, L. S., Siddig, M. A., & Abdullah, S. F. (2016). Experimental results of the tribology of aluminium measured with a pin-on-disk tribometer: Testing configuration and additive effects. *Friction*, *4*(2), 124–134. https://doi.org/10.1007/s40544-016-0110-8

Alaneme, K. K., Bodunrin, M. O., & Awe, A. A. (2018). Microstructure, mechanical and fracture properties of groundnut shell ash and silicon carbide dispersion strengthened aluminium matrix composites. *Journal of King Saud University - Engineering Sciences*, *30*(1), 96–103. https://doi.org/10.1016/j.jksues.2016.01.001

Anuar, N. F. B. W., Salleh, M. S., Omar, M. Z., Zamri, W. F. H. W., Ali, A. M., & Samat, S. (2023). Wear properties of graphene-reinforced aluminium metal matrix composite: A review. *Reviews on Advanced Materials Science*, *62*(20220326).

ASTM International. (1992). *Standard test method for sharp-notch impact testing with flat specimens* (ASTM E602-91).

ASTM International. (2011). *Standard test method for microindentation hardness of materials* (ASTM E384-11). https://doi.org/10.1520/E0384-11

ASTM International. (2013). *Standard test methods for tension testing of metallic materials* (ASTM E8/E8M-13a). https://doi.org/10.1520/E0008_E0008M-13A

ASTM International. (2017). *Standard test method for wear testing with a pin-on-disk apparatus* (ASTM G99-17). https://doi.org/10.1520/G0099-17

Bello, A. B., Alabi, J. S., Elugbaju, A. O., & Olapade, O. J. (2025). Effect of heat treatment on the mechanical properties of aluminium 6063 reinforced with alumina, titania, and hybrid powders. *ABUAD Journal of Engineering Research and Development*, *8*(2), 121–129.

Bhaumik, S., & Kamaraj, M. (2021). Artificial neural network and multi-criterion decision making approach of designing a blend of biodegradable lubricants and investigating its tribological properties. *Proceedings of the Institution of Mechanical Engineers, Part J: Journal of Engineering Tribology*, *235*(8), 1575–1589. https://doi.org/10.1177/1350650120967688

Brodova, I., Yolshina, L., Razorenov, S., Rasposienko, D., Petrova, A., Shirinkina, I., Shorokhov, E., Muradymov, R., Garkushin, G., & Savinykh, A. (2022). Effect of grain size on the properties of aluminum matrix composites with graphene. *Metals*, *12*(7), Article 1054. https://doi.org/10.3390/met12071054

Chattrakul, K., Sornsuwit, N., & Muangnoy, P. (2024). Effect of heat treatment on mechanical properties and thermal expansion of Al6063-SiC-graphite, molybdenum disulfide hybrid composite. *Processes*, *12*(11), Article 2464. https://doi.org/10.3390/pr12112464

Erappa Rajj, B., Nagaral, M., Chintakindi, S., Kumar, R., Anqi, A. E., Rajhi, A. A., & Chan, C. K. (2024). Nano-sized Al2O3–Gr reinforced Al7075 hybrid composite: Impact of cooling agents on mechanical, wear, and fracture behavior. *ACS Omega*, *9*(16), 17878–17890. https://doi.org/10.1021/acsomega.3c09532

Gandhi, C., Dixit, N., Mohanty, A., & Singh, B. (2019). Study on effect of heat treatment on mechanical properties of AA7075-MWCNT composite. *Materials Today: Proceedings*, *18*, 37–46. https://doi.org/10.1016/j.matpr.2019.06.274

Gül, M., Aytaç, A., Altuntaş, G., & Altuntaş, O. (2025). Synergistic effects of boron carbide and graphene nanoplatelets on the ballistic performance of aluminium matrix hybrid composites for advanced armor applications. *International Journal of Metalcasting*, 1–10. https://doi.org/10.1007/s40962-024-01500-2

Haruna, V., Abdulrahman, A., Abolarin, M., & Muriana, R. (2019). Evaluation of sheanut shell-reinforced automotive brake pad. *Arid Zone Journal of Engineering, Technology and Environment*, *15*, 510–518.

Hidayat, T. A. S., Surojo, E., Ariawan, D., Akbar, H. I., Imanullah, F., & Fanani, E. W. A. (2024). Experimental study of quenching agent on AA6061-sea sand composite: Effect quenching medium to mechanical properties and distortion. *EVERGREEN Joint Journal of Novel Carbon Resource Sciences & Green Asia Strategy*, *11*(3), 2273–2283.

Huang, Y. H., Yadav, B., Lien, F. C., Lin, P. C., Kumar, R., Gupta, G., & Mondal, D. (2024). Exploring the impact of heat treatment on the microstructural and compressive properties of Al-SiC-MWCNTs hybrid nanocomposites foams. *Diamond and Related Materials*, *141*, Article 110648. https://doi.org/10.1016/j.diamond.2023.110648

Jaber, H., Kónya, J., Pinke, P., Toth, L., & Kovács, T. A. (2023). Investigating the impact of annealing temperature on the microstructure and mechanical performance of selectively laser melted Ti6Al4V alloy. *European Journal of Materials Science and Engineering*, *8*(4).

Jiang, W., Zhu, J., Li, G., Guan, F., Yu, Y., & Fan, Z. (2021). Enhanced mechanical properties of 6082 aluminium alloy via SiC addition combined with squeeze casting. *Journal of Materials Science & Technology*, *88*, 119–131. https://doi.org/10.1016/j.jmst.2021.01.072

Kuczek, Ł., Żaba, K., Trzepieciński, T., Wąsikowski, M., Balcerzak, M., & Sitek, R. (2025). Influence of heat treatment on properties and microstructure of EN AW-6082 aluminium alloy draw pieces after single-point incremental sheet forming. *Applied Sciences*, *15*(2).

Kumar, P., & Kumar, B. (2024). Effect of T6 heat treatment on mechanical and tribological properties of fabricated AA7075/ZrB2/Fly ash hybrid aluminium metal matrix composite by ultrasonic-assisted stir casting enroute. *International Journal of Metalcasting*, *18*(3), 2396–2414. https://doi.org/10.1007/s40962-023-01185-1

Kumar, S., Verma, P. K., & Lovevanshi, B. S. (2025). Effect of thermal ageing on mechanical and microstructural characteristics of bimodal hybrid AA6082/TiO2np/SiCp composite. *Composite Interfaces*, 1–21. https://doi.org/10.1080/09276440.2024.2440001

Laha, T., Chen, Y., Lahiri, D., & Agarwal, A. (2009). Tensile properties of carbon nanotube reinforced aluminium nanocomposite fabricated by plasma spray forming. *Composites Part A: Applied Science and Manufacturing*, *40*(5), 589–594. https://doi.org/10.1016/j.compositesa.2009.02.008

Mahan, H. M., Konovalov, S. V., & Panchenko, I. (2023). Effect of heat treatment on the mechanical properties of the aluminium alloys AA2024 with nanoparticles. *International Journal of Applied Science and Engineering*, *20*(2), 1–6.

Mehdi, H., Bhati, S. S., Mouria, P. K., Mishra, S., Bhadana, M., & Batra, L. (2025). Effect of nanoparticles on metal matrix composites fabricated by ultrasonic stir casting. *International Journal of Cast Metals Research*, 1–17. https://doi.org/10.1080/13640461.2024.2441001

Mostafa, A., Aljarrah, M., Essadiqi, E., & Medraj, M. (2014). Influence of cooling rate on microsegregation behavior of magnesium alloys. *Journal of Materials*, *2014*, Article 657647. http://dx.doi.org/10.1155/2014/657647

Motyka, M., Kubiak, K., Sieniawski, J., & Ziaja, W. (2014). Phase transformations and characterization of $\alpha + \beta$ titanium alloys. In *Comprehensive materials processing* (Vol. 2, pp. 7–36). Elsevier. https://doi.org/10.1016/B978-0-08-096532-1.00201-9

Nagaraja, S., Kodandappa, R., Ansari, K., Kuruniyan, M. S., Afzal, A., Kaladgi, A. R., Aslfattahi, N., Saleel, C. A., Gowda, A. C., & Bindiganavile Anand, P. (2021). Influence of heat treatment and reinforcements on tensile characteristics of aluminium AA 5083/silicon carbide/fly ash composites. *Materials*, *14*(18), Article 5261. https://doi.org/10.3390/ma14185261

Nnakwo, K. C., Nwajioke, C. T., Ujah, C. O., Nwogbu, C. C., Nwobodo, L. O., Agbo, A. O., & Ubah, J. I. (2025). Tailoring the tensile characteristics, hardness and impact strength of A356 hypoeutectic alloy via multi-step aging heat treatment. *Discover Materials*, *5*(1), Article 10. https://doi.org/10.1007/s43939-024-00150-1

Odinachi, C. C., Nnakwo, K. C., Nwoke, V. I., & Nnuka, E. E. (2017). Effect of soaking time and quenching media on the structure and mechanical properties of Al-5.6 wt% Zn2. 5wt% Mg alloy. *International Journal of Scientific Research in Science, Engineering and Technology*, *3*(5), 1–7.

Ononiwu, N. H., Ozoegwu, C. G., Madushele, N., & Akinlabi, E. T. (2021). Characterization, machinability studies, and multi-response optimization of AA 6082 hybrid metal matrix composite. *The International Journal of Advanced Manufacturing Technology*, *116*(5), 1555–1573. https://doi.org/10.1007/s00170-021-07521-7

Paladugu, S. R. M., Aparna, N. D., & Sreekanth, P. R. (2022). Mechanical and wear analysis of Al6061-SiC/Al2O3/B4C hybrid metal matrix composites using stir casting process. *Materials Today: Proceedings*, *56*, 1091–1096. https://doi.org/10.1016/j.matpr.2022.03.111

Petrović, J., Mladenović, S., Marković, I., & Dimitrijević, S. (2022). Characterization of hybrid aluminium composites reinforced with Al2O3 particles and walnut-shell ash. *Materials and Technology*, *56*(2), 115–122. https://doi.org/10.17222/mit.2021.312

Qi, Y., Wei, F., Wang, Y., Jin, Y., Chang, X., & Chen, G. (2025). Microstructure and mechanical property of 6082 aluminium alloy via Sc and Zr addition combined with squeeze casting. *Materials*, *18*(9), Article 1988.

Radhika, N., Jojith, R., Vignesh, S., Raghavenderen, H., Abinav, S., & Adediran, A. A. (2024). Characterization, mechanical properties, and wear behavior of functionally graded aluminium hybrid composite. *Scientific Reports*, *14*(1), Article 19509. https://doi.org/10.1038/s41598-024-70331-w

Ramadoss, N., Pazhanivel, K., Ganesh Kumar, S., Arivanandhan, M., & Anandan, P. (2020). Effect of B4C and SiC nanoparticle reinforcement on the wear behavior and surface structure of

aluminium (Al6063-T6) matrix composite. *SN Applied Sciences*, *2*(5), Article 903. https://doi.org/10.1007/s42452-020-2715-x

Ramirez-Vidaurri, L. E., Castro-Roman, M., Herrera-Trejo, M., & Fraga-Chavez, K. L. (2022). Secondary dendritic arm spacing and cooling rate relationship for an ASTM F75 alloy. *Journal of Materials Research and Technology*, *19*, 5049–5065. https://doi.org/10.1016/j.jmrt.2022.07.031

Ramesh, B., Vempati, S., Roshith, P., & Thanikasalam, A. (2022). Comparison of Al2O3-reinforced sintered and extruded AA2014 nano-hybrid composite particle size effects on mechanical and metallurgical characteristics. *ECS Transactions*, *107*(1), 4077–4088. https://doi.org/10.1149/10701.4077ecst

Rativa-Parada, W., & Nilufar, S. (2024). Influence of heat treatment on microstructure, mechanical properties, and damping behavior of 2024 aluminium matrix composites reinforced by carbon nanoparticles. *Nanomaterials*, *14*(16), Article 1342. https://doi.org/10.3390/nano14161342

Ravikumar, M., Reddappa, H., Suresh, R., & Reddy, M. S. (2021). Experimental studies of different quenching media on mechanical and wear behavior of Al7075/SiC/Al2O3 hybrid composites. *Frattura ed Integrità Strutturale*, *15*(55), 20–31. https://doi.org/10.3221/IGF-ESIS.55.02

Rmadan, M. B. A., Esen, I., Ahlatci, H., & Duran, E. (2024). Homogenization heat treatment for enhancing corrosion resistance and tribological properties of the Al5083-H111 alloy. *Materials*, *17*(13), Article 3120. https://doi.org/10.3390/ma17133120

Rotella, A., Nadot, Y., Piellard, M., Augustin, R., & Fleuriot, M. (2018). Fatigue limit of a cast Al-Si-Mg alloy (A357-T6) with natural casting shrinkages using ASTM standard X-ray inspection. *International Journal of Fatigue*, *114*, 177–188. https://doi.org/10.1016/j.ijfatigue.2018.05.027

Şenel, M. C., & Mahmutoğlu, Ü. (2022). Effect of induction heat treatment on the mechanical properties of Si3N4–graphene-reinforced Al2024 hybrid composites. *Bulletin of Materials Science*, *45*(1), Article 48. https://doi.org/10.1007/s12034-021-02621-3

Shuvo, A. N., Faruqui, A. N., & Sheikh, M. R. K. (2025). Fabrication of hybrid composite with aluminium and sugarcane bagasse reinforcement for investigation of its properties. *European Journal of Materials Science and Engineering*, *10*(4), 291–302.

Suchendra, K. R., Reddy, M. S., & Ravikumar, M. (2023). Influence of quenching agents on mechanical, wear, and fracture characteristics of Al2O3/MoS2 reinforced Al-6061 hybrid metal matrix composite (MMCs). *Fracture and Structural Integrity*, *17*(63), 122–133. https://doi.org/10.3221/IGF-ESIS.63.10

Tejyan, S., Lal, C., Ror, C. K., & Singh, V. (2023). Influence of marble waste reinforcement on mechanical properties and sliding wear behavior of an aluminium alloy metal matrix composite. *Journal of Engineering Research*. https://doi.org/10.1016/j.jer.2023.10.021

Turan, M. E., Rashad, M., Zengin, H., Topcu, I., Sun, Y., & Asif, M. (2020). Effect of multiwalled carbon nanotubes on elevated temperature tensile and wear behavior of Al2024 matrix composites fabricated by stir casting and hot extrusion. *Journal of Materials Engineering and Performance*, *29*, 5227–5237. https://doi.org/10.1007/s11665-020-04983-3

Yadav, R., Islam, A., & Kumar Dwivedi, V. (2024). Wear and microstructure analysis of aluminium based composite using eggshell and rice husk ash as reinforcement. *World Journal of Engineering*, *21*(1), 186–193. https://doi.org/10.1108/WJE-07-2022-0283

Yuan, J., Pan, S., Zheng, T., & Li, X. (2021). Nanoparticle promoted solution treatment by reducing segregation in AA7034. *Materials Science and Engineering: A*, *822*, Article 141691. https://doi.org/10.1016/j.msea.2021.141691

Zhao, G., Yuan, Y., Zhang, P., Zhou, T., & Zhou, H. (2020). Influence of orientations biomimetic units processed by laser on wear resistance of 6082 aluminium alloy. *Optics & Laser Technology*, *127*, Article 106196. https://doi.org/10.1016/j.optlastec.2020.106196

Zhu, J., Jiang, W., Li, G., Guan, F., Yu, Y., & Fan, Z. (2020). Microstructure and mechanical properties of SiCnp/Al6082 aluminium matrix composites prepared by squeeze casting

combined with stir casting. *Journal of Materials Processing Technology*, *283*, Article 116699. https://doi.org/10.1016/j.jmatprotec.2020.116699

Zubairu, P. T., Hassan, A. B., Muriana, R. A., & Musa, N. A. (2021). Effect of shea nutshell ash on the mechanical properties of cast Al6061. *Arid Zone Journal of Engineering, Technology and Environment*, *17*(1), 1–8.

GEOSPATIAL ASSESSMENT OF SOIL TEXTURAL CLASSES AND THE IMPLICATIONS ON ACHIEVING SDG 2 IN NORTHWESTERN NIGERIA

Garuba H.s[1,*], Mujahid, M.m[1], Mukhtar, M.k[2]
[1]*Ahmadu Bello University, Zaria*
[2]*FUDMA*
Email: garubahalimah@gmail.com[*], "", ""
***Corresponding author**: Garuba H.s
DOI: https://doi.org/10.67203/sp.ICESID.2026

ABSTRACT
This study presents a geospatial analysis of soil textural classes for Kaduna, Kano and Katsina States in the North-western region of Nigeria. Soil classification maps were digitized from the FAO Digital Soil Map of the World using ArcGIS 10.3.1. Results revealed that Sandy Loam is the dominant class in Kano and Katsina States, covering approximately 68% and 61% of the land area respectively. Kaduna State revealed a greater variation in soil textural classes, with Loam as the dominant class in the southern Guinea Savanna area, followed by Sandy Clay Loam and Sandy Loam in the northern Sudan Savanna zone. The spatial distribution of these classes has direct implications for agricultural management in the Sudan Savanna agro-ecological zone. The extensive Sandy Loam areas in Kano and Katsina are prone to rapid infiltration, low water retention and nutrient leaching. Therefore, these zones require soil-water conservation measures such as mulching, tied ridging, and micro-catchments and precision irrigation scheduling using drip or deficit irrigation to improve water use efficiency for drought-tolerant crops like millet, sorghum and cowpea. Furthermore, the Loam and Sandy Clay Loam areas in central and southern Kaduna, with higher water and nutrient holding capacity, are more suitable for crop-soil matching with maize, soybean and irrigated rice under controlled irrigation. The digitized maps provide a spatial decision-support framework for targeted erosion control structures in coarse-textured zones and for variable-rate fertilizer application under precision agriculture. This contributes to SDG 2: Zero Hunger by enabling site-specific input management and yield optimization. The study recommends ground-truthing through physico-chemical analysis of soil samples across representative map units in the three States to validate and refine the map for policy, engineering and extension purposes.
Keywords: *ArcGIS; FAO; Northwest; SDG 2; Soil; Soil Texture*

1. INTRODUCTION

Soil is the uppermost part of the earth surface on which plants grow (Stephen et al., 2017). It is a mixture of mineral matter, organic matter, water and air. Soil quality is a major determinant of agricultural productivity Bichi & Khalil, (2025) and Ologunde & Nunes, (2026) and, thus, understanding the soil quality dynamics remains paramount in achieving food security in any region . Soil texture is the relative proportions of sand, silt, and clay in the soil. The optimization of a farming season can be greatly influenced by the soil textural classes. As this influences engineering properties, water movement, rooting depth of plants of a soil, Erosion resistance, nutrient retention, water infiltration and most importantly crop production Ahmed et al., (2020) and Sharu, M. B. et al., (2025). These soil properties often vary from time to time (Gambo et al., 2025), soil quality assessment is therefore an unending process. The Northwestern region of Nigeria is known as a hub of production of crops such as groundnut, millet sorghum and maize etc. However, an optimized production of these major crops is often limited by climatic variability and unsustainable local farming practices. Muhammad et al., (2026) highlighted the suitability of sandy loam and loamy soils for optimum productivity of maize plant which is a major crop in attaining SGD2- Food Security and Zero Hunger, in Northwestern Nigeria. A geospatial interpretation of soil types in this region is therefore, an important information required for an effective land use and land cover (Farming) planning as wells as soil conservation strategies. Despite the availability of global soil database by the FAO, the localized application and interpretation of soil textural classes in this region is lacking. The study

therefore, aimed to analyze and classify the spatial distribution of soil textural classes of Kano, Kaduna and Katsina States all located in the Northwestern region of Nigeria.

2. METHODOLOGY

2.1 Description of Study Area

The study area include Kano, Kaduna Katsina, State located in the northwestern region of Nigeria. These are located between a latitude of 12.99ºN to 10.52ºN and a longitude of 7.44ºE to 8.52ºE (Muhammad et al., 2026). The states falls under the Sudan Savanna ecological Zones and are classified as a semi-arid climate. The zone experiences two distinct seasons known as dry season from October to May and a wet season from May to September. The annual average rainfall range between 500 mm to 1000 mm. The States are characterized by an average temperature ranging between 28°C to 40º C.

2.2 Data Source

The soil data was obtained from the Digital Soil Map of the World (DSMW)(FAO,2007).

2.3 Data Processing and Interpretation

This involves a preliminary desk-based study pending ground-truthing. This soil data was processed and digitized in ArcGIS 10.3.1 through the following steps;

a. **Projection**: The administrative boundary shapefiles of the States were projected to WGS 1984, UTM.ZONE-32N

b. **Extraction of Study Areas**: This was achieved by importing the DSMW soil polygon of Nigeria and Kano, Kaduna and Katsina states shapefiles into ArcGIS 10.3.1

c. **Clipping Raster Data:** The extraction by Mask tool in Spatial Analyst tool of ArcGIS 10.3.1 was used to extract the polygon layers of each States from the DSMW raster file.

d. Soil Textural Interpretation and Classification: The soil textural classes were interpreted based on Harmonized World Soil Database (FAO, 2012). The textural classes were defined by the USDA classification system into Loam, Sandy Loam, Sandy-Clay Loam etc. A suitable color range were chosen for cartographic and Legend representation for each state.

3. RESULTS AND DISCUSSION

The digitized soil classification maps for Kaduna, Kano and Katsina states are presented in Figures 3.1, 3.2 and 3.3. Table 3.1 also shows the distribution per square kilometre of soil textural classes for each state. Generally, the States were dominated with sand soils with some variations (sandy-clay, sand-loam etc). The occurrence of sandy soils and sandy loams soils is an expected classification due to the geological and climatic conditions of Sudan Savanna (Northwest) which supports the formation and accumulation of sand particles. This is in line with study findings by Ahmed & Yusuf, (2020); Danjuma, (2023); and Garba et al., (2023). The warm climate also increases the rate of organic matter decomposition which is required to improve the soil structure and fertility of sandy soils.

The dominance of high sand content in the states accounts for why soils have a high leaching loses and lower water holding capacity. A study by Bichi & Khalil (2025) conducted in Dutsin-Ma Local Government Area Katsina State similarly found out that all samples appear to fall under same soil type of Sandy Loam. This means that the variation in texture may not be significant and because of that same type of irrigation technique can be employed in Dutsin-Ma LGA the study area.

Note: The maps below show multiple colors for same textural class due to different soil components with similar texture but different parent material and drainage properties. This explains why same textural classes with different FAO/SWAT serial numbers.

Table 3.1: FAO/SWAT Soil Textural Distribution per Area

Kaduna FAO/SWAT S/N	**Area (sqkm)**	**Katsina FAO/SWAT S/N**	**Area (sqkm)**	**Kano FAO/SWAT S/N**	**Area (sqkm)**
1262	9.46E-05	1614	0.488632	1223	0.040306
1468	0.052095	1661	0.039299	1627	0.019334
1455	0.247078	1261	0.035534	1476	0.873694
1476	1.155892	1607	0.006329	1509	0.038442
1262	0.116334	1371	0.003422	1614	0.552739
1470	0.40213	1262	0.009245	1511	0.000889
1511	0.370328	1506	0.106213	1468	0.021657
1324	0.00692	1632	0.617808	1701	0.061098
1493	0.772149	1627	0.064105		
60	0.031797	1480	0.082659		
1020	0.013186	1468	0.053966		
1255	0.186579	1223	0.029994		
1268	0.030071	1509	0.130281		
1081	0.065486	1476	0.104445		
1528	0.016405	1470	0.054202		

3.1 Kaduna State

Kaduna State displayed the most heterogeneous soil profile .The most dominant soil types identified in Kaduna State were Loam, Sandy Clay Loam, and Sandy Loam. These were hy same distributed in significant, contiguous patches. This is an indication that the state is of relatively favorable soil conditions. This correlates with the study findings by Garba et al., (2023) conducted in Birnin Yero Kaduna State that concluded soils in the study area were predominantly sandy loam and loamy. Smaller patches of Loamy Sand were also identified in some areas of the state. The presence of Loam and Sandy clay loam in most areas of Kaduna State indicates a possibility of growing a wider range of crop varieties due to favorable soil properties.

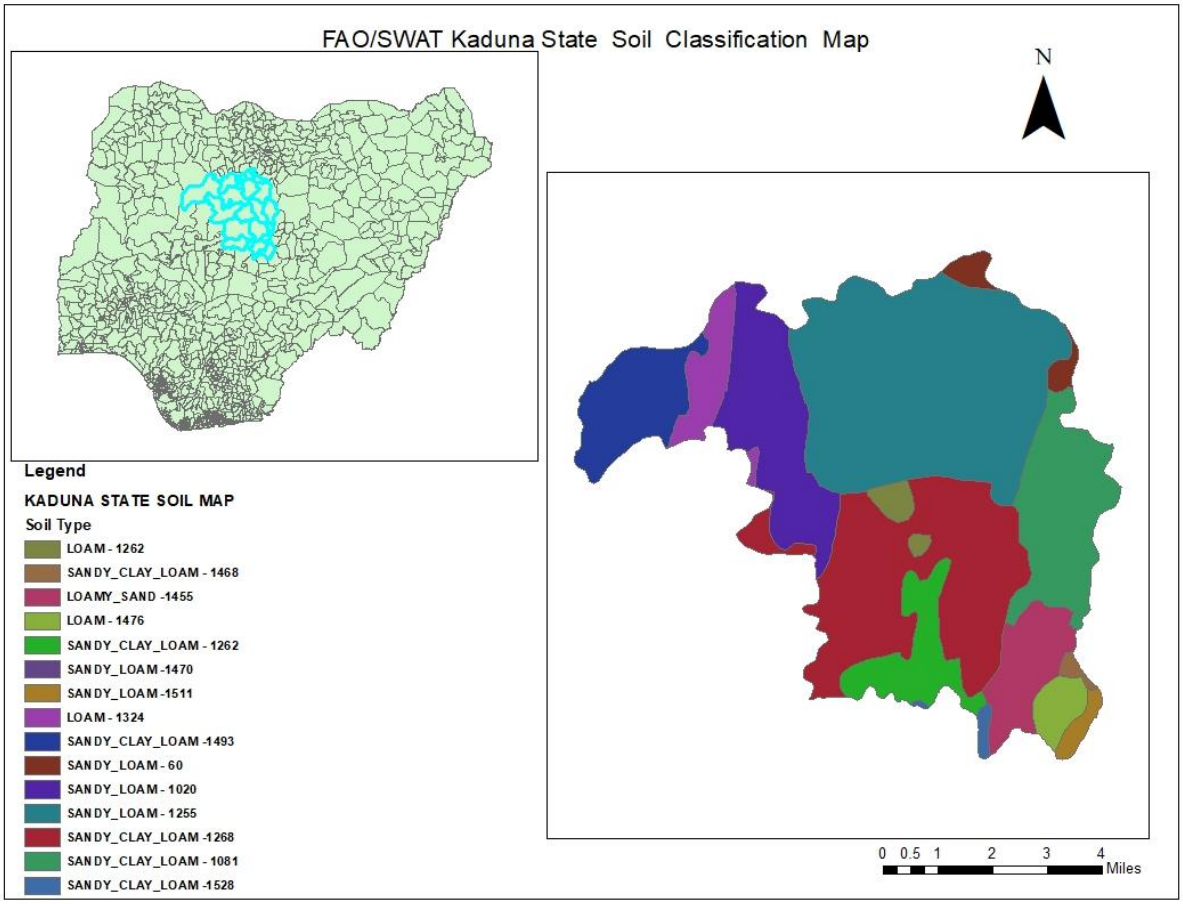

Figure 3.1: Kaduna State Soil Textural Classification Map

3.2 Kano State

Kano state was generally dominated by coarse-textured soils. Sandy Loam was the major soil class, covering 65% of the land area of the state. This was followed by Sandy Clay Loam. Muhammad et al., (2026) conducted a similar study in Kano State and found out that Six distinct soil textural classes were identified within the River Watari basin: loam, sandy loam, sandy clay loam, silty clay loam, clay loam, and clay. A very low water and nutrient-holding capacity soil known as Sand was identified at the central region of the state.

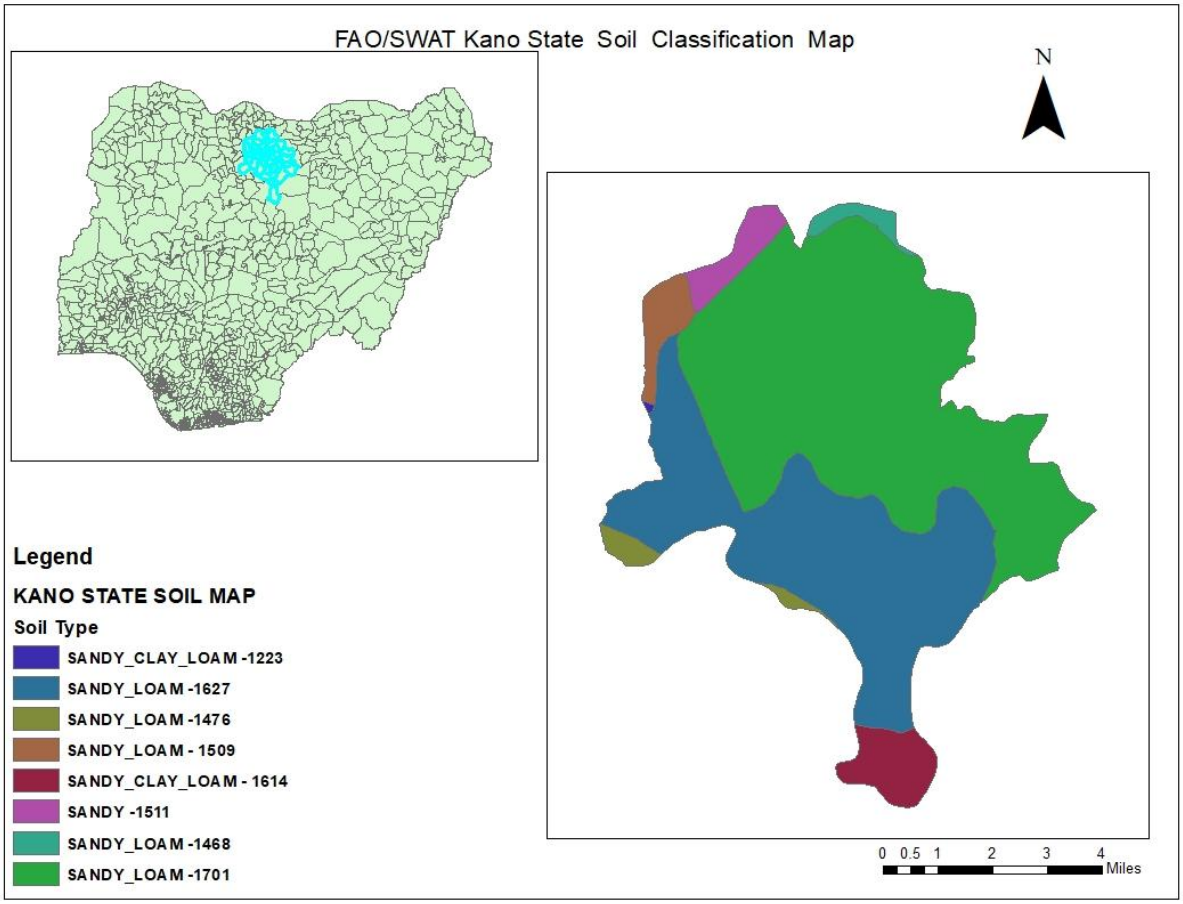

Figure 3.2: Kano State Soil Textural Classification Map

3.3 Katsina State

Katsina State also shows a predominant soil type of Sandy Loam in most parts of the State. However, the state showed a more varied composition than Kano, due to occurrences of larger areas with Sandy Clay Loam, Loam and Clay Loam. A study by Ahmed & Yusuf, (2020) presented similar results. This also correlates with the findings by Danjuma, (2023). The presence of Clay Loam soils is an indication that there are localized areas with higher water retention potential. For Clay soils are generally known to have higher porosity and lower permeability.

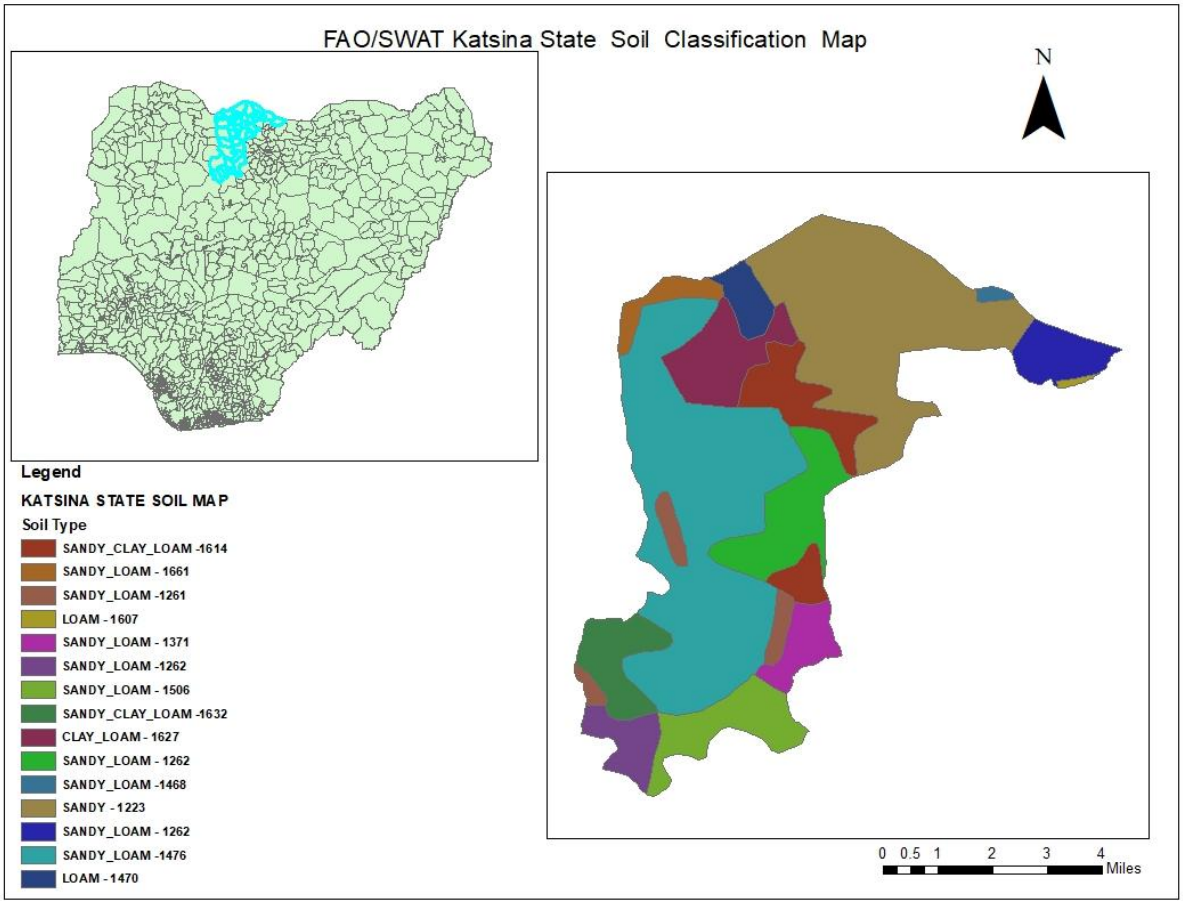

Figure 3.3: Katsina State Soil Textural Classification Map

4. CONCLUSION

The dominance of Sandy Loam in Kano and Katsina States indicates inherent constraints of low organic matter, poor water retention, and high susceptibility to wind and water erosion. For these areas, the maps directly support SDG 2 by guiding the adoption of specific soil-water conservation measures : contour stone bunds and zai pits to reduce runoff, and organic mulching to conserve soil moisture for rainfed cereals. In Kaduna State , the mosaic of Loam and Sandy Clay Loam provides opportunity for crop-soil matching . The Loam zones are recommended for high-value, water-responsive crops such as maize and irrigated vegetables, while Sandy Clay Loam areas are suitable for sorghum and groundnut with supplemental irrigation. For precision agriculture technologies , the digitized layers can be integrated into farm management systems to enable variable rate application of NPK fertilizer — lower rates on coarse Sandy Loam to prevent leaching, and higher rates on Loam areas to maximize yield. Irrigation scheduling can also be spatially optimized: more frequent, low-volume applications for Sandy Loam in Kano/Katsina, and less frequent applications for Loam in Kaduna. To operationalize these recommendations, future work should prioritize ground-truthing through physical-chemical analysis of soil samples across the mapped textural classes. This will be useful in validating the FAO-derived units and provide the fertility data needed for state-level agricultural policies on fertilizer subsidy targeting and erosion control planning.

5. REFERENCES

Abaje, I. B., Sawa, B. A., Iguisi, E. O., & Ibrahim, A. A. (2015). Assessment of Rural Communities' Adaptive Capacity to Climate Change in Kaduna State, Nigeria. *Journal of Environment and Earth Science*, 5(20), 14-23.

Ahmed, M. M., & Yusuf, M. A. (2020). *Soil Fertility Assessment for Rice Cultivation in Sabuwa Area, Katsina State, Nigeria*. African Journal of Earth and Environmental Sciences, *2*(2).

Bichi, A. A., & Khalil, M. M. (2025). *Comprehensive analysis of soil physical properties and their relationships: Recommendations for optimized irrigation strategies*. AgricEngInt: *CIGR Journal Open access*, *27*(2), 49–59. http://www.cigrjournal.org

Danjuma, M. N. (2023). *Soil texture and organic carbon stock as influenced by land use in parts of Katsina State, Nigeria*. *Journal of Agriculture, Forestry & Environment*, *7*(1), 139–147.

Food and Agricultural Organization of the United Nations (2006).Guidelines for soil description (4th ed.)Rome. https://www.fao.org./3/a0541e/a0541e.pdf

Food and Agricultural Organization of the United Nations. (2007). Digital soil map of the world (version 3.6). https://www.fao.org/soils-portal/soil-survey/soil-maps-and-databases/faounesco-soil-map-of-the-world/en/

Food and Agricultural Organization of the United Nations (2012).Hamonized World Soil Database (version 1.2) [Data set].FAO. https://www.fao.org/soils-portal/data-hub/soil-maps-and-databases/harmonized-world-soil-database-v12/en/

Gambo, A., Fullen, M. A., & Baldwin, T. C. (2025). Characterization and classification of soils on a toposequence around Dutse Jigawa State, Nigeria. *Discover Soil*, *2*(1), 97. https://doi.org/10.1007/s44378-025-00126-4

Garba, Y. I., Danjuma, M. N., & Zakariya, M. (2023). Assessment of Soil Quality for Agro-Diversification in Kaduna State, Nigeria. *UMYU Scientifica*, *2*(4), 1–8. https://doi.org/10.56919/usci.2324.001

Muhammad, H. B., Umar, R. B., Imam, M. Z., Sani, I. S., & Adamu, K. U. (2026). A Survey of Maize Cultivars and Soil Textural Suitability Across Agro-Ecological Units of The River Watari Basin, Kano State, Nigeria. *Journal of Geographical Sciences and Education*, *4*(1), 59–71. https://doi.org/10.69606/geography.v4i1.472

Ologunde, O. H., & Nunes, M. R. (2026). Redefining soil health and food security through tropical conservation agriculture. *Communications Sustainability*, *1*(1), 82. https://doi.org/10.1038/s44458-026-00086-y

Stephen N.,Herwig H,, Bayer Ag, Claus G. Bannick, U., Konstantin T., Gerhard Knoop, Bayer Ag. And Hubert S. (2017). Soil, 1. Definition, Function, and Utilization of Soil. https://www.researchgate.net/publication/227557214

INVESTIGATION INTO THE USE OF LOCALLY AVAILABLE MATERIALS FOR THE PRODUCTION OF INVESTMENT CASTING MOULD

Nura Lawal[1], Mahadi Makoyo[1,*], Adamu Umar Alhaji[1], Yakubu Shuaibu Ochetengwu[2]

[1]*Department of Mechanical Engineering, Bayero University Kano Nigeria*
[2]*Department of Mechanical Engineering, NDA Kaduna*

Email: nl2100014.pme@buk.edu.ng, makwayo@gmail.com*, adamumar863@gmail.com, drsoyakubu4real@gmail.com

***Corresponding author**: Mahadi Makoyo

DOI: https://doi.org/10.67203/sp.ICESID.2026

ABSTRACT

Investment casting produces high-quality, dimensionally accurate parts with complex geometries that forging and machining cannot easily achieve, but imported refractories and binders make the process expensive to adopt. This study investigated locally available moulding plaster, cassava flakes, kaolin, Portland cement, and fine sand as substitutes, using beeswax as the pattern material. Particle size, viscosity, flexural strength, and refractoriness were determined. Viscosity reached 710 mPa·s for moulding plaster, 650 mPa·s for cassava flakes, and 613 mPa·s for kaolin, while flexural strength reached 105.60 MPa for moulding plaster, 80.00 MPa for Portland cement, and 52.13 MPa for kaolin. Six trial compositions were evaluated and an optimum blend containing 82% moulding plaster, 5% cassava flakes, 5% cement, 4% kaolin, and 4% fine sand was selected. The fired mould achieved flexural strengths of 159.25, 139.00, and 154.75 MPa for three samples, with an average permeability of 92 AFS. A brass jewellery piece was successfully cast in the finished mould. The findings demonstrate the feasibility of combining locally available materials into a functional investment casting system without imported refractories.

Keywords: *investment casting; locally sourced refractories and binders; ceramic shell mould; beeswax; brass casting*

1. INTRODUCTION

Investment casting, commonly known as the lost-wax process, is widely used where complex geometry, dimensional accuracy, and surface finish are important. The process has applications in aerospace, defence, power generation, automotive, medical devices, construction, and other manufacturing sectors (Diamond, 1980; Groover, 2010; Soemardi et al., 2016). A global market review has noted that investment casting continues to expand into new sectors precisely because of this combination of accuracy and geometric freedom (Ronald & Richard, 2012). The process depends heavily on the quality and cost of its refractory mould system. Conventional investment casting commonly uses alumina, silica, zircon, mullite, and related refractory materials with binders such as colloidal silica, ethyl silicate, sodium silicate, or fireclay (Beeley & Smart, 1995; Ibhadode, 2014; Prasad, 2012). In Nigeria, many of these materials are imported in usable forms, increasing cost and supply-chain constraints for small and medium-scale foundries.

Previous investigations have demonstrated that slurry viscosity, particle size, suspension behaviour, shell strength, permeability, and refractoriness strongly influence investment casting performance (Kline et al., 2010; Shukla & Juneja, 2011; Singh et al., 2012; Zhao et al., 2011). Parallel work on the pattern side of the process has shown that wax type, blending, and injection conditions govern the dimensional stability and surface quality of the pattern that the shell is built around (Bembalge & Karunakar, 2011; Kamboj, 2017; Rezavand & Behravesh, 2007; Sandhu & Sharma, 2012; Yadav et al., 2011); the beeswax pattern route adopted here draws on this body of work while relying on a single, low-cost, locally available pattern material rather than blended commercial waxes. On the shell side, alternative refractory systems and additives have been explored to reduce cost or improve high-temperature performance, including graphite-modified permeability control (Kline et al., 2010), fly-ash-modified ceramic shells (Shukla & Juneja, 2011), calcium zirconate systems for reactive alloys

(Klotz et al., 2019), locally sourced shell materials for steel casting in South East Asia (Purwadi et al., 2012), optimized ceramic shell formulations (Dave & Kaila, 2014), high-temperature strength characterization of shell moulds (Kolczyk & Zych, 2011), camphor-based intensification of shell mechanical properties (Tamta & Karunakar, 2014), and statistically rigorous bend-testing protocols for shell characterization (Richards et al., 2016). However, most published systems still rely on imported refractory and binder systems, or on additives that are themselves imported. This creates a practical research gap: whether locally available materials can be characterized, formulated, and combined into a complete working investment casting mould system.

The aim of this study was to investigate the use of locally available materials for producing an investment casting mould. Specifically, the study sought to identify suitable local materials; characterize their relevant physical and mechanical properties; develop a stable slurry; evaluate viscosity, bulk density, suspension percentage, and thixotropy; produce and fire a ceramic shell mould; determine strength, permeability, and refractoriness; and demonstrate the mould by casting a brass component.

2. METHODOLOGY

Materials and Equipment

Moulding plaster, Portland cement (grade 42.5), and kaolin were used as refractory constituents, while fine sand and cassava flakes served as binder-related constituents. Beeswax was used as the pattern material. All materials were sourced commercially within Nigeria. Equipment included a standard sieve set, digital balance, slurry stirrer, Fann Model 35SA viscometer, Ridsdale permeability testing device, vernier caliper, graduated flask, Universal Materials Testing Machine (100 kN capacity), laboratory thermometers, and a flash-fire oven.

Material Characterization

Particle size distribution was determined by sieve analysis using 1000 g samples in accordance with BS 1377: Part 1: 1990. Flexural strength was measured on 100 × 10 × 4 mm specimens by three-point bending at a crosshead speed of 2 mm/min, using three replicates for each material. Flexural stress was calculated as $\sigma_3pt = 3PL/(2bd^2)$, where P is the applied load, L is the support span, b is the specimen width, and d is the specimen thickness. Flexural modulus was determined from the same three-point bending test as $E = L^3m/(4bd^3)$, where m is the slope of the initial linear (elastic) region of the load–deflection curve, following the approach outlined for ceramic shell bend testing by Richards et al. (2016); the linear region was fitted over the first 10–20% of the load range before any visible non-linearity or crack initiation.

Viscosity was measured with a Fann rotational viscometer at 100 rpm. Refractoriness was evaluated by heating specimens from room temperature to 800°C at a controlled rate of 10°C/min in a muffle furnace, holding for 30 min at 200°C intervals, and inspecting each specimen for sintering, cracking, spalling, or grain breakdown at each hold point; a specimen was classified as resistant to thermal shock if it showed no visible cracking or spalling up to 600°C and no gross structural breakdown up to 800°C.

Slurry Formulation and Mould Production

Six trial slurry compositions were prepared by varying cement, cassava flakes, fine sand, kaolin, and moulding plaster (Table 1). The sixth composition—82% moulding plaster, 5% cassava flakes, 5% cement, 4% kaolin, and 4% fine sand—was selected because it produced a stable and workable slurry. Bulk density, suspension percentage, thixotropy, and viscosity were monitored. Beeswax patterns were assembled on a central sprue and repeatedly dipped into the slurry with 3–4 h of drying between coats. After the required shell thickness was achieved, the mould was dried for 2–3 days, dewaxed, and fired at approximately 500°C. The mould was then used for brass casting.

Table 1: Trial Slurry Compositions Investigated (wt%)

Material	Exp.1 (%)	Exp.2 (%)	Exp.3 (%)	Exp.4 (%)	Exp.5 (%)	Exp.6 (%)
Cement	20	25	30	40	40	5
Cassava flakes	20	20	30	40	30	5
Fine sand	10	20	30	11	10	4
Kaolin	20	15	2.5	2	5	4
Moulding plaster	30	20	7.5	7	15	82
Total	100	100	100	100	100	100

Note. The moulding-plaster values for Exp.1 and Exp.5 have been corrected from the originally recorded 40% and 10% (which produced totals of 110% and 95%, respectively) to 30% and 15%, so that every trial composition sums to 100 wt%.

Figure 1: Beeswax Pattern Tree and Completed Investment Casting Mould Prior to Firing.

3. RESULTS AND DISCUSSION

Particle Size Distribution

Table 2 summarizes the sieve retention of the four raw materials on a 1000 g sample basis. Almost all of the kaolin and moulding plaster passed through to the pan, confirming that both were very fine powders, with 986.64 g and 999.54 g respectively retained in the pan fraction. Cassava flakes and fine sand were retained mainly on the coarser sieves from 600 µm to 2.0 mm. Figure 2 presents the same data as the percentage of each material's mass retained at each sieve size, and is directly consistent with Table 2: the plaster and kaolin bars are concentrated almost entirely in the pan fraction, while the cassava-flake and sand bars are distributed across the coarser sieve sizes. The finer and more evenly graded plaster and kaolin particles favour stable packing and suspension in the slurry, whereas the broader particle-size distributions of cassava flakes and fine sand contribute different flow and packing characteristics.

Table 2: Sieve Analysis of the Raw Mould Materials (1000 g Samples)

Sieve Size	Cassava Flakes (g)	Fine Sand (g)	Kaolin (g)	Moulding Plaster (g)
2.0 mm	64.00	38.60	0.27	0
1.18 mm	169.70	520.50	0.58	0
600 µm	481.60	230.02	0.83	0
425 µm	212.02	97.80	0.92	0
212 µm	54.60	41.40	1.04	0
150 µm	9.03	25.70	1.87	0.1
63 µm	0	20.60	2.80	0.13
Pan	0	16.90	986.64	999.54

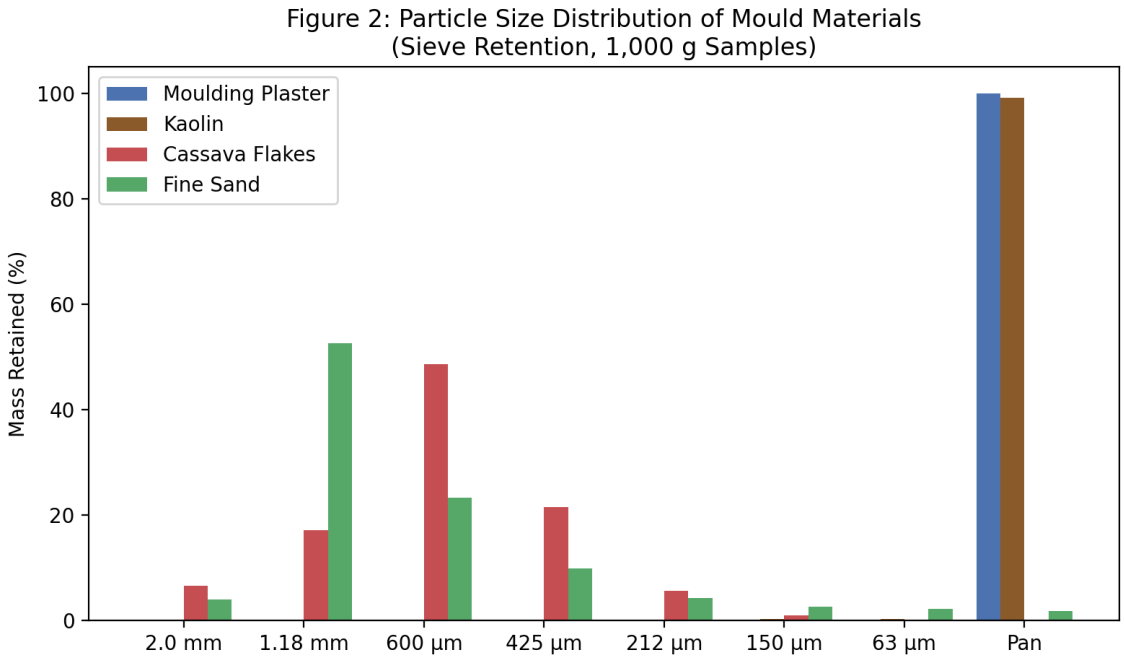

Figure 2: Particle Size Distribution of Mould Materials (regenerated from Table 2 sieve-retention data).

Flexural Strength of Raw Mould Materials

Moulding plaster had the highest average flexural strength, 105.60 MPa, based on replicate values of 100.80, 120.60, and 96.00 MPa. Portland cement averaged 80.00 MPa, with replicate values of 96.00, 96.00, and 48.00 MPa, while kaolin averaged 52.13 MPa from 48.00, 52.80, and 57.60 MPa. The higher strength of moulding plaster supported its dominant proportion in the final slurry.

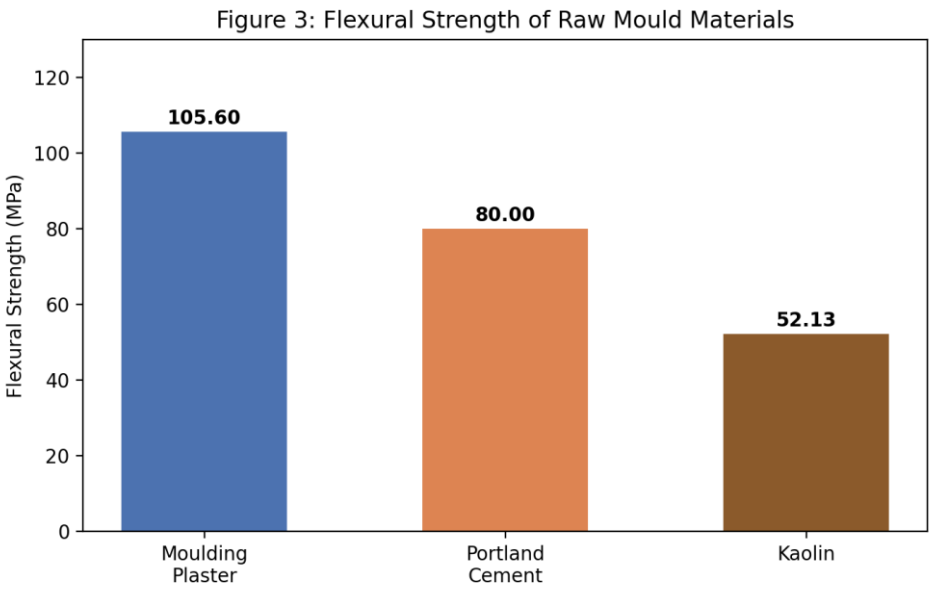

Figure 3: Flexural Strength of Raw Mould Materials.

Slurry Viscosity

Viscosity increased with refractory-to-binder ratio. At the highest ratio tested, moulding plaster reached 710 mPa·s, cassava flakes 650 mPa·s, and kaolin 613 mPa·s. The final combined slurry reached 890 mPa·s, which was within the workable range used for shell building. The combined-slurry curve tracks the moulding-plaster curve closely up to a ratio of 2.4 because plaster is the dominant constituent (82% of the final blend) and therefore governs the rheology of the mixture through most of the tested range; the sharper rise to 890 mPa·s at a ratio of 2.6 reflects the onset of particle-packing saturation, where the finer plaster and kaolin particles begin to interlock and restrict flow once the refractory fraction approaches its maximum practical loading. The relatively high viscosity of the final blend was favourable for maintaining a coherent coating on the beeswax pattern during repeated dipping.

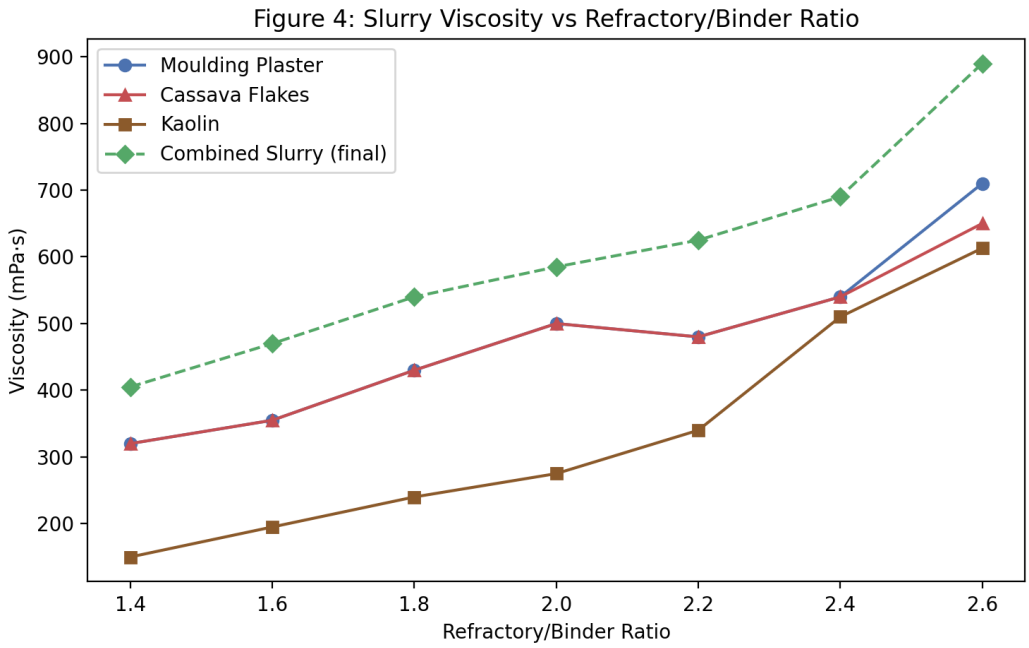

Figure 4: Slurry Viscosity versus Refractory/Binder Ratio and Final Combined Slurry.

Bulk Density, Suspension and Thixotropy

The individual slurry densities were 3.17 g/cm³ for moulding plaster, 3.02 g/cm³ for cassava flakes, and 2.52 g/cm³ for kaolin (Table 3). After 14 hours, moulding plaster retained approximately 43% of its solids in suspension compared with 15% for cassava flakes and 3% for kaolin. All three slurries exhibited viscosity decay under continued shearing, indicating thixotropic behaviour. Moulding plaster had the highest reported thixotropic rate of 4.0, followed by cassava flakes at 3.0 and kaolin at 0.5.

Table 3: Bulk Density of Individual Material Slurries

Material	Slurry Density (g/cm³)
Moulding Plaster	3.17
Cassava Flakes	3.02
Kaolin	2.52

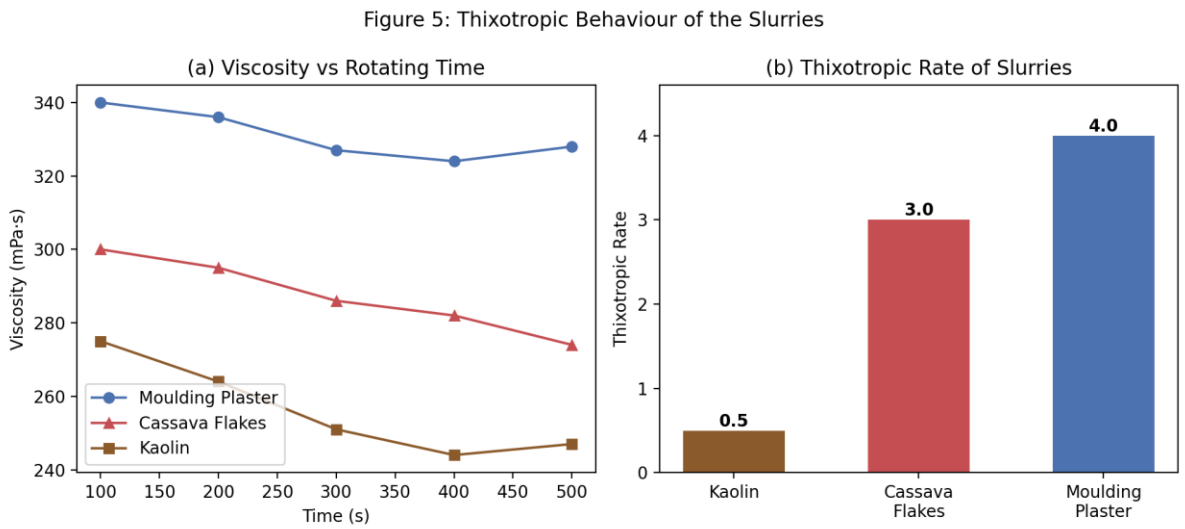

Figure 5: Thixotropic Behaviour of the Slurries: (a) Viscosity vs Rotating Time; (b) Thixotropic Rate.

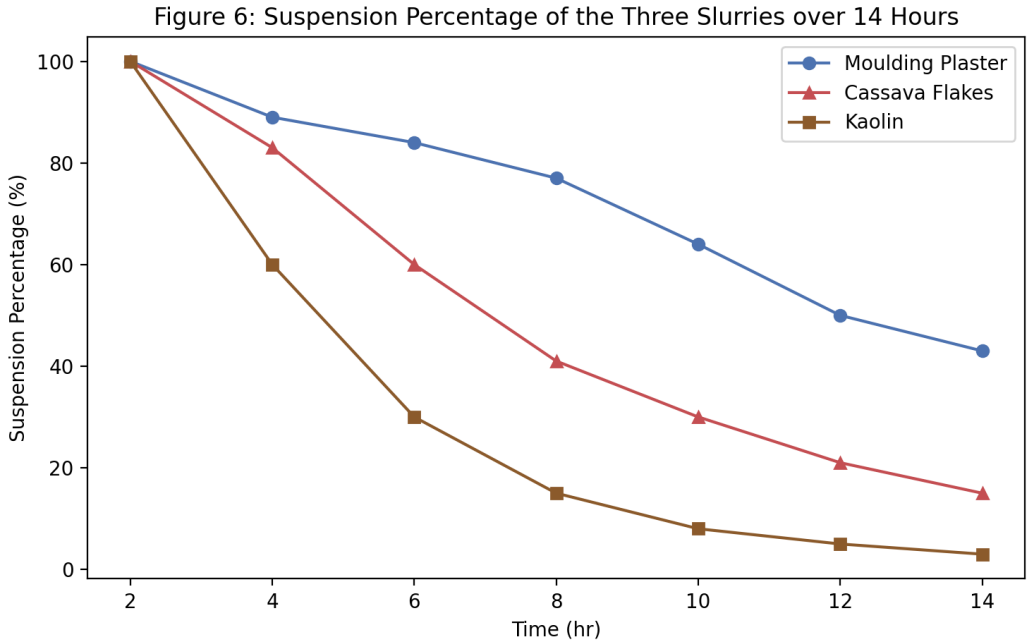

Figure 6: Suspension Percentage of the Three Slurries over 14 Hours.

Refractoriness

Moulding plaster showed the best resistance to sudden temperature change among the three refractories tested, showing no visible cracking or spalling up to 600°C and no gross structural breakdown up to 800°C, and also resisted molten metal and hot gases satisfactorily. Portland cement was mechanically robust but less resistant to thermal shock, developing visible surface cracking at the 400–600°C hold. This complementary behaviour supported the use of plaster as the major refractory with a smaller cement addition to provide mechanical robustness.

Fired Mould Strength, Permeability and Casting Trial

The fired mould produced flexural strengths of 159.25 MPa for sample X, 139.00 MPa for sample Y, and 154.75 MPa for sample Z (Table 4). The corresponding flexural moduli, calculated from the slope of the elastic region of each load–deflection curve (Section 2.2), were 4.37, 4.92, and 6.80 GPa. Permeability was measured on samples taken after each dip coat rather than on the finished shell alone; Figure 8 shows that permeability rose progressively from approximately 70 AFS at the first coat to 112 AFS at the seventh and final coat, giving an overall average of 92 AFS across the build. The mould was successfully used to produce a brass jewellery casting without cracking or gross defects (Figure 9).

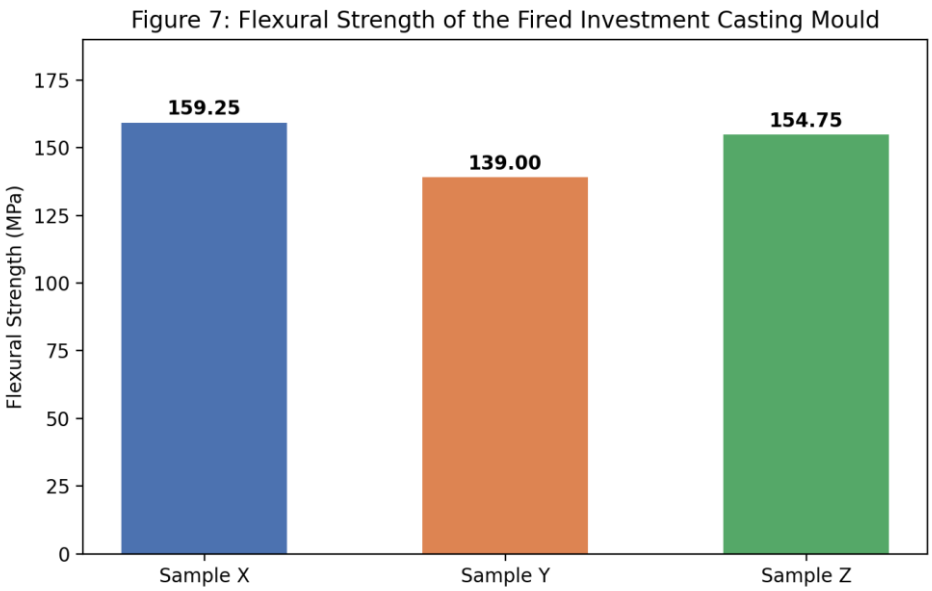

Figure 7: Flexural Strength of the Fired Investment Casting Mould.

Table 4: Flexural Strength and Flexural Modulus of the Fired Investment Casting Mould

Sample	Average Flexural Strength (MPa)	Average Flexural Modulus (GPa)
X	159.25	4.37
Y	139.00	4.92
Z	154.75	6.80

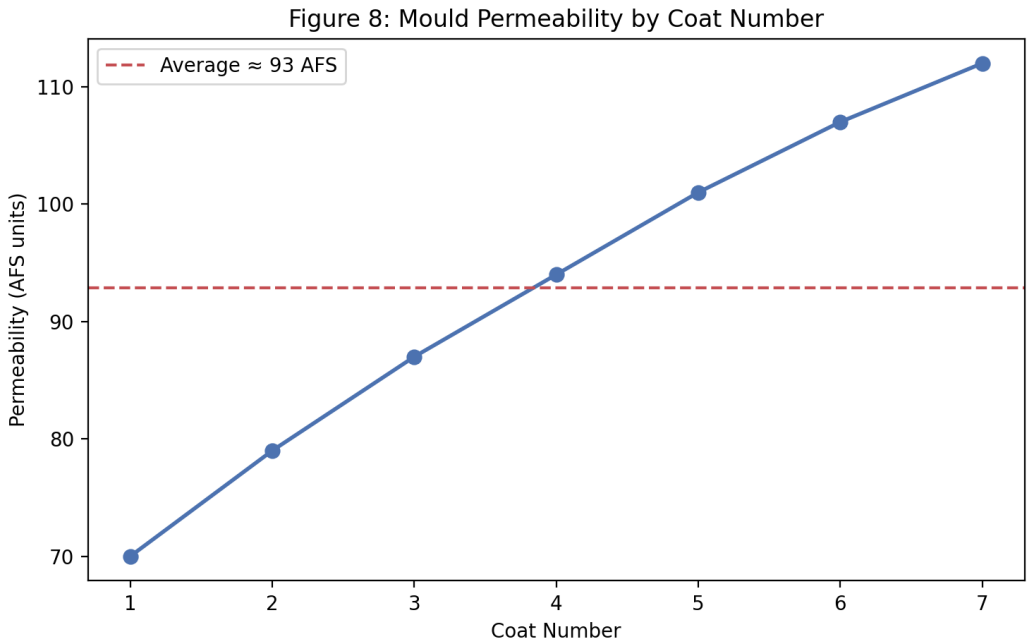

Figure 8: Mould Permeability by Coat Number, Increasing from ~70 AFS (Coat 1) to 112 AFS (Coat 7); Average ≈ 92 AFS.

Figure 9: Brass Jewellery Casting Produced from the Investment Casting Mould.

Discussion

The results indicate that moulding plaster was the most influential constituent in achieving a workable local slurry. Its high flexural strength, strong suspension stability, high thixotropic response, fine particle size, and resistance to thermal shock explain why it constituted 82% of the optimum composition. Cassava flakes provided a locally available starch-based constituent whose viscosity and suspension behaviour were intermediate between plaster and kaolin. The fired shell substantially exceeded the strength of the individual raw materials: the strongest fired sample (159.25 MPa, Sample X) represents an increase of approximately 51% over the strongest raw constituent, moulding plaster alone (105.60 MPa), suggesting that layered construction and firing promoted a stronger integrated mould structure than any single raw material could achieve on its own.

The permeability result is important because investment moulds must allow gases generated during pouring and decomposition of the wax pattern to escape. The measured average of 92 AFS, rising from approximately 70 AFS in the earliest coats to 112 AFS in the fully built shell (Figure 8), indicates adequate and progressively improving gas passage through the build. These observations are broadly consistent with previous studies showing that shell permeability and strength depend on material type, particle characteristics, binder behaviour, and number of coats (Kline et al., 2010; Sarek et al., 2009), and align with the statistically grounded bend-testing approach recommended by Richards et al. (2016) for characterizing ceramic shell moulds. The finding also parallels earlier demonstrations that locally available materials can substitute for imported shell systems in other contexts, including local steel-casting shell development (Purwadi et al., 2012) and camphor-modified shell strength improvement (Tamta & Karunakar, 2014), reinforcing that the present approach is consistent with a broader trend toward locally adapted investment casting systems. The principal contribution of the study is the demonstration that a complete investment casting route from material selection and slurry formulation through mould production and actual casting can be implemented using locally available materials.

4. CONCLUSION

The study demonstrated the feasibility of producing an investment casting mould from locally available materials. Moulding plaster, cassava flakes, kaolin, Portland cement, and fine sand were characterized and combined using beeswax as the pattern material. Moulding plaster recorded the highest flexural strength among the raw refractories at 105.60 MPa and showed the best suspension stability and resistance to sudden temperature change. Six trial compositions led to a workable blend containing 82% moulding plaster, 5% cassava flakes, 5% cement, 4% kaolin, and 4% fine sand. The fired shell achieved flexural strengths between 139.00 and 159.25 MPa, with corresponding flexural moduli between 4.37 and 6.80 GPa, and an average permeability of 92 AFS, and successfully produced a brass jewellery casting without major defects. The results support local material substitution for non-ferrous, jewellery-scale investment casting. Further work should investigate repeated casting cycles,

other alloys, larger and more complex patterns, alternative local refractory combinations, and production-scale economic performance.

Acknowledgements

The authors acknowledge the support of the Department of Mechanical Engineering, Bayero University, Kano, and the laboratories of Bayero University Kano and Ahmadu Bello University Zaria used for the experimental work.

5. REFERENCES

Beeley, P. R., & Smart, R. F. (1995). Investment casting. Institute of Materials.

Bembalge, O., & Karunakar, D. B. (2011). A study on the blended wax pattern in investment casting process. Proceedings of the World Congress on Engineering 2011, 1.

Dave, I. B., & Kaila, V. N. (2014). Optimization of ceramic shell mould material in investment casting. International Journal of Research in Engineering and Technology, 3(10), 30–33.

Diamond, G. X. (1980). Investment casting handbook. Investment Casting Institute.

Groover, M. P. (2010). Fundamentals of modern manufacturing: Materials, processes, and systems (4th ed.). Wiley.

Ibhadode, A. O. A. (2014). Introduction to manufacturing technology. University Press.

Kamboj, K. (2017). Optimization of process parameters of wax pattern in the investment casting process by using different form of waxes. International Journal for Innovative Research in Science & Technology, 3(8), 10–14.

Kline, D. M., Lekakh, S. N., & Richards, V. L. (2010). Improving investment casting mould permeability using graphite particle (Paper 10-087). AFS Transactions, American Foundry Society.

Klotz, U. E., Legner, C., Bulling, F., Freitag, L., Fabauer, C., Schaufler, S., & Aneziris, C. G. (2019). Investment casting of titanium alloys with calcium zirconate mould and crucibles. The International Journal of Advanced Manufacturing Technology, 105, 3629–3639.

Kolczyk, J., & Zych, J. (2011). High temperature strength of ceramic mould applied in the investment casting method. Archives of Foundry Engineering, 11(Special Issue 3), 121–124.

Prasad, R. (2012). Progress in investment castings. IntechOpen. https://doi.org/10.5772/50550

Purwadi, W., Ruskandi, C., & Idamayanti, D. (2012). Making steel product by investment casting method using local materials. Proceedings of the Annual South East Asian International Seminar (ASAIS), 133–141.

Rezavand, S. A. M., & Behravesh, A. H. (2007). An experimental investigation on dimensional stability of injected wax patterns of gas turbine blades. Journal of Materials Processing Technology, 182(1–3), 580–587.

Richards, V. L., Mascreen, S. A., Jackson, P., & Hahn, T. (2016). Statistical analysis of three-point and four-point bend testing for the characterization of ceramic mold shells. Investment Casting Institute Technical Report, 51, 1–13.

Ronald, W., & Richard, H. (2012). Review of world investment casting markets. 13th World Conference on Investment Casting, Japan.

Sandhu, C. S., & Sharma, A. (2012). Investigation of optimize wax pattern in the investment casting by using the different forms of waxes. IOSR Journal of Mechanical and Civil Engineering, 3(4), 1–6.

Sarek, D., Trytek, A., & Nawrocki, J. (2009). Permeability of mould made by lost wax casting process. Archives of Foundry Engineering, 9(1), 203–206.

Shukla, D. D., & Juneja, J. L. (2011). Effect of different mold layers on fly ash modified ceramic shell strength in investment casting. International Journal of Engineering Science and Technology, 3, 242–248.

Singh, B., Kumar, P., & Mishra, B. K. (2012). Evaluation of primary slurry used in ceramic shell investment casting process. International Journal of Emerging Technology and Advanced Engineering, 2(10).

Soemardi, T. P., Suwandi, A., Kiswanto, G., & Kusumaningsih, W. (2016). Development of pattern smelting method with ABS materials in investment casting process. ARPN Journal of Applied Sciences, 11, 10023–10037.

Tamta, K., & Karunakar, D. B. (2014). Intensification of mechanical properties of the investment shell using camphor. International Journal of Engineering Development and Research, 2(2), 1–5.

Yadav, N., Katiyar, J., Singh, N., & Pal, V. (2011). Investigating the effects of varying proportions of waxes in wax mix on surface roughness and optimization by Taguchi method. Applied Mechanics and Materials, 110–116, 627–631.

Zhao, E., Kong, F., & Chen, Y. (2011). Physical properties of primary slurry for titanium investment casting. Advanced Materials Research, 314–316, 742–746.

International Conference on Engineering Innovation for Sustainable Development (ICESID 2026)
Faculty of Engineering, Ahmadu Bello University Zaria · 8–10 September 2026

MECHANICAL, OPTICAL AND ENGINEERING ASSESSMENT OF POLYPROPYLENE/FIBREGLASS COMPOSITES FOR TRANSLUCENT LPG CYLINDER APPLICATIONS

Usman Sani[1], Fatima Mohammed[2,*], Simon N.n[3]
[1]*Kaduna Polytechnic*
[2]*Ahmadu Bello University Zaria*
[3]*Institute of Leather Research, Zaria, Kaduna State, Nigeria*
Email: usb934@gmail.com, mohammedf61@yahoo.com*, norbertsimon28@yahoo.com
***Corresponding author**: Fatima Mohammed
DOI: https://doi.org/10.67203/sp.ICESID.2026

ABSTRACT
The increasing demand for safer, lightweight, and corrosion-resistant liquefied petroleum gas (LPG) cylinders has created the need for alternative materials that overcome the limitations of conventional steel cylinders. This study presents the conceptual design and material evaluation of a translucent composite LPG cylinder based on polypropylene (PP)/fiberglass (FG) composites. The conceptual design integrates a lightweight polymer composite shell capable of withstanding service loads while providing sufficient light transmittance to enable direct visual monitoring of LPG level without auxiliary gauges. Five PP/FG formulations (40/60, 45/55, 50/50, 55/45, and 60/40 wt%) were developed through melt compounding and compression moulding to identify the optimum material for the proposed cylinder. Mechanical performance was assessed through tensile, flexural, impact, and hardness testing, while optical suitability was evaluated using indoor and outdoor light transmittance measurements. The results showed that composite composition significantly influenced both structural and optical properties. The 55/45 PP/FG formulation exhibited the highest tensile strength (33.17 MPa) and the greatest light transmittance (9.50% indoors and 24.30% outdoors), demonstrating the best balance between strength and translucency. Flexural testing showed a different trend, the 60/40 PP/FG composite exhibited the highest flexural strength of 56.52 MPa, indicating excellent resistance to bending loads. hardness measurements similarly showed that 60/40 formulation gives the highest shore hardness of 96.0 D, increased fiberglass loading improved resistance to surface indentation and wear, whereas higher polypropylene content increased ductility but reduced hardness. Impact testing revealed that the 40/60 formulation possessed the greatest impact strength of 215.21 J/m. The proposed composite cylinder offers significant advantages over conventional steel cylinders, including reduced weight, improved corrosion resistance, and the ability to visually monitor LPG content, thereby improving user convenience and operational safety. The study demonstrates the feasibility of integrating material selection and conceptual design in the development of next-generation translucent composite LPG cylinders.

Keywords: *Polypropylene/fiberglass composite; Conceptual design; LPG cylinder; Mechanical properties; Light transmittance*

1.0 INTRODUCTION

Liquefied petroleum gas (LPG) has emerged as a vital transition fuel for domestic and industrial energy applications, offering high calorific value and lower greenhouse gas emissions relative to solid fossil fuels. In many developing countries, including Nigeria, LPG consumption has grown significantly over the past decade owing to government initiatives aimed at reducing dependence on firewood, kerosene, and charcoal for household cooking (Taska and Ige, 2023). This transition has contributed to improved indoor air quality, reduced deforestation, and enhanced public health outcomes. Consequently, the demand for safe, durable, and cost-effective LPG storage cylinders has increased substantially (Mahboubizadeh *et al.*, 2024).

Conventional LPG cylinders are predominantly fabricated from carbon steel due to its low initial cost and high mechanical strength. However, steel cylinders exhibit severe operational limitations such as corrosion and degradation where exposure to atmospheric humidity or coastal environments causes wall thinning, shortening service life, obscure external defects, making routine inspections more difficult and increasing catastrophic failure risks. Their relatively high weight

reduces portability and increases transportation costs Corrosion can also increasing the likelihood of catastrophic failure. In addition, opaque steel cylinders prevent users from visually determining the remaining LPG level, necessitating manual weighing or external sensing devices that increase operational costs and complexity (Mahboubizadeh et al., 2024; Wu et al., 2025). These limitations have stimulated growing interest in advanced composite materials for pressure vessel applications (Somaiah et al., 2022). Fibre-reinforced polymer (FRP) composites offer strong alternatives due to superior specific strength, low density, and high corrosion resistance. Among reinforcement materials, glass fibres provide an optimal balance between high tensile performance and cost-effectiveness compared to carbon or aramid fibres. Additionally, thermoplastic matrices like polypropylene (PP) enable recyclability, high toughness, rapid thermal processing, and low density. Beyond weight reduction, semi-translucent GF/PP composite formulations allow light transmission through the vessel shell, enabling direct visual inspection of the internal liquid LPG level. Despite these advances, existing literature presents clear gaps in low-pressure thermoplastic composite cylinder design, these include;

Over-Reliance on Thermosets and High-Pressure Systems: Most composite pressure vessel scholarship focuses on high-pressure (>20 MPa) CNG or hydrogen storage using expensive carbon/epoxy systems, leaving low-pressure (2 MPa) thermoplastic LPG systems underexplored.

Narrow Focus on Structural Mechanics: Previous studies predominantly isolate mechanical parameters, fibre winding patterns, or burst pressure calculations while neglecting the functional optical behaviour of the composite wall.

Lack of an Integrated Framework: Limited research links empirical mechanical property data directly into thin-walled pressure vessel equations, finite element stress validation, and light transmittance assessment within a single investigation.

This study directly addresses these gaps by evaluating glass fibre-reinforced polypropylene (GF/PP) composites for lightweight, translucent LPG storage cylinders. Five matrix-to-fiber formulations (40/60 to 60/40 wt%) were melt-compounded and compression-molded to characterize tensile, flexural, impact, and hardness performance. Experimental mechanical properties were applied directly to thin-walled pressure vessel design equations to establish wall thickness (t = 18.5 mm), hoop stress, longitudinal stress, and a target safety factor of 2.05 under an internal working pressure of 2 MPa. Finally, indoor and outdoor light transmittance measurements were integrated to validate visual LPG fuel-level monitoring capability alongside structural integrity. The novelty of this research lies in the integration of experimental material characterisation, engineering design calculations, and optical transmittance evaluation to develop a lightweight translucent composite. The findings provide valuable design information for the development of next-generation composite LPG cylinders capable of improving safety, reducing maintenance costs, enhancing portability, and promoting sustainable energy storage technologies.

2.0 MATERIALS AND METHODS

2.1 Materials

The composite material investigated in this study was developed using PP as the polymer matrix and FG as the reinforcing phase. PP pellets were selected because of their low density, excellent chemical resistance, ease of processing, and good mechanical performance, making them suitable for pressure vessel applications. FG was employed as the reinforcement owing to its high tensile strength, corrosion resistance, dimensional stability, and cost-effectiveness. A processing oil was incorporated in small quantities during compounding to improve melt flow characteristics and facilitate uniform dispersion of the reinforcement within the polymer matrix. (Delli *et al.*, 2021; Somaiah et al., 2022; Li et al., 2024). PP pellets and FG were obtained from A.O. Salami Material Store, Zaria, Nigeria, while the processing oil was supplied by the National Institute for Leather Science and Technology (NILEST), Zaria. Composite fabrication was carried out at NILEST using Two-roll Mill compounding machine and Compression molding machine with model numbers 5189 and 3851-0 respectively. The Impact test and shore hardness tests were also carried out at NILEST using ASTM D256-10, 2010 and ASTM D2240 respectively. Tensile and flexural strengths analyses together with light transmittance measurements were performed at the Department of Metallurgy

laboratories, Ahmadu Bello University (A.B.U), Zaria, using ASTM D3039/D3039M and ASTM D7264 respectively.

2.2 Methods

2.2.1 Composite Formulation

Five PP/FG formulations were prepared to investigate the influence of reinforcement loading on the mechanical and optical behaviour of the composites. The compositions were selected based on literature values by Lee & Jang, (1999) and Thomason et al., (1996) as shown in Table 1.

Table 1: Polypropylene/Fiberglass composite formulations

Sample PP/FG	Polypropylene PP (wt%)	Fiberglass FG (wt%)
A	40	60
B	45	55
C	50	50
D	55	45
E	60	40

The selected compositions enabled systematic evaluation of the effect of increasing polypropylene content and decreasing fibre loading on tensile, flexural, impact, hardness, and light transmittance tests in accordance with relevant ASTM standards mentioned in section 2.1.

2.2.2 Compounding of composite

A two-roll mill compounding machine was used to mix each sample run from Table 1, at a temperature of 220°C and speed of 120 rpm. The PP was introduced and rolled for 2 minutes, to completely melt the material for easy mixing before the glass fibre was added. The resulting material was then placed in a 3mm thick, 120 x 150 mm mould. This was then charged to the compression moulding machine. The compression moulding machine has two sections namely, the hot mould and the cold mould. The hot mould works at 3 bar and at a temperature of 180ºC for 2 minutes. The cold mould then cools the product of the hot mould back to ambient temperature. The fabricated material was then detached from the mould and labelled accordingly. This was repeated for the 5 runs. The resulting composite samples were then sent to a cutting machine to shape them for the various analyses.

2.3 Samples Analysis

2.3.1 Light Transmittance Test

The test was carried out to detect the degree of opacity of the samples i.e. how much light is transmitted through the sample for both indoors (within a dimly lit room) and outdoors (space highly exposed to natural light).In compliance with standard procedure for testing composites (International Organization of Standardization, 2010). The material was cut into desired shapes of 55 x 10 mm rectangles with a thickness of about 3mm. The testing equipment is a lightmeter that measures light in Lux or cadence. The equipment is calibrated to measure light at 20, 200 and 2000 Lux respectively. For this analysis, the 20 lux calibration was used for the indoor analysis and the

200 lux calibration for outdoor analysis. The equipment was switched on and reset to zero error. Then adjusted to the desired calibration. Then the intensity of light in the room was taken. The material was then brought to the sensor part of the equipment and the reading from the display part of the equipment was taken. This was repeated for every sample run for indoor and then for outdoor.

2.3.2 Tensile Strength Test

The test was done to study how much stress the material can undergo before breaking. Based on ASTM D3039/D3039M standard procedure. The material was cut into testing specification before proceeding to analysis. The material was gripped at both ends by the testing apparatus, which slowly pulls lengthwise on the sample until it fractures. The pulling force is called a load. The value of the force per original sample area as stress and plotted against the sample length change per original length (strain).

2.3.3 Flexural Strength Test

The flexural strength test was done to test the resistance of the composite material to bending and flexing forces. Based on (ASTM INTERNATIONAL, 2002) following the loading nose producing three point bending at a specified rate. The parameters for this test are the support span, the speed of the loading and the maximum deflection for the test. These parameters are based on the materials thickness and are defined by ASTM D7264 standards.

2.3.4 Impact Strength Test

This test was done to study the resistance of the material under sudden stress. How much energy can it withstand and how much is required to cause a fracture. Standard procedure for this test is contained in the ASTM document for impact strength of a polymer composite (ASTM D256-10, 2010). U-notch was made at the center of the specimen. A pendulum or hammer was released from a specific height. The pendulum or hammer strikes the notched specimen. The impact caused the material to fracture. The energy absorbed by the specimen was calculated based on the height from which the pendulum fell and the angle at which it strikes the specimen. The energy was recorded and repeated three times per sample.

2.3.5 Hardness Test

The test for hardness was done in compliance with ASTM D2240 (2015) standard procedure as follows: The Durometer was held vertically with the indenter facing down. The durometer was positioned in a perpendicular orientation to the specimen surface. The indenter was made to come into contact with the specimen. A gradual steady downward force was applied to the durometer with the use of a thumb. As the indenter penetrates the specimen, a needle moves to a reading on the shore A scale. The reading was taken and recorded once the needle stabilizes.

All mechanical tests were carried out three times for each sample and the average recorded.

2.4 Conceptual Design of the LPG Cylinder

To showcase how the developed translucent composite material can be applied in real-world engineering, a conceptual LPG cylinder was modeled using the geometric dimensions of a standard 12.5 kg domestic cylinder. Maintaining this traditional shape ensures the design remains fully compatible with existing LPG distribution, storage, and handling infrastructure while swapping out the standard metallic body for the new translucent material.

The cylinder's wall thickness, as well as its hoop and longitudinal stresses, were calculated based on the tensile strength of the optimal composite blend (55/45 PP/FG) using a safety factor of 2.05. Beyond tensile measurements, mechanical properties like flexural strength, impact resistance, and hardness play a vital role in validating the design. Flexural Strength ensures the composite wall can resist bending forces and localized deformation caused by non-pressure, real-world mechanical loads during transport and usage. Impact Strength serves as a key material selection metric for damage tolerance, proving the cylinder can survive accidental drops or impacts. Hardness measures expected surface durability and wear resistance throughout everyday service and handling. Rather

than acting as mere secondary lab data, these three attributes serve as essential supporting performance criteria for designing robust, safe composite pressure vessels.

The conceptual cylinder consists of a cylindrical body with hemispherical end domes, a reinforced neck for valve attachment, and a protective base ring. The cylinder wall is manufactured from the developed PP/FG composite, allowing partial light transmission for visual monitoring of the LPG level while maintaining the structural integrity required for pressurised gas storage. The engineering analysis was performed using the assumptions presented in Table 2.

Table 2: Assumptions made for the design of the composite cylinder

Parameter	Symbol	Value
LPG storage capacity	–	12.5 kg
Internal diameter	D	300 mm (0.30 m)
Overall height	H	580 mm
Internal design pressure	P	2.0 MPa
Shape	–	Thin-walled cylinder with hemispherical ends
Operating temperature	–	Ambient conditions
Design approach	–	Thin-walled pressure vessel theory

2.4.1 Pressure calculations based on thin wall pressure vessel theory

The composite cylinder was analysed using classical thin-walled pressure vessel equations

Hoop stress ,$\sigma h = Pr/t$ (1)

Longitudinal stress, $\sigma L = Pr/(2t)$ (2)

Factor of safety, $FOS = \sigma u/\sigma h$ (3)

Where

$\sigma u = 33.17$ MPa = Tensile strength of the 55/45 PP/FG formulation

P = 2.0 MPa = Internal pressure

r = 150 mm = Internal radius

t = Cylinder wall thickness = 18.5 mm

Therefore

$\sigma h = Pr/t = 2(150)/18.5 = 16.22$ MPa

$\sigma L = Pr/(2t) = 2(150)/ [2(18.5)] = 8.11$ MPa

Factor of safety, $FOS = \sigma u/\sigma h = 33.17/16.22 = 2.05$

This remains a preliminary analytical assessment, not proof that an LPG cylinder is safe for manufacture. A real composite LPG cylinder requires laminate-specific analysis, pressure/burst testing, fatigue testing, and compliance with the applicable cylinder standard.

2.4.2 3D Computer-Aided Design (CAD)

To validate the structural geometry and volumetric capacity of the proposed 12.5 kg translucent polypropylene/fiberglass (PP/FG) composite LPG cylinder, a 3D SolidWorks parametric model was developed in accordance with ISO 11119-3 and thin-walled pressure vessel design principles. The LPG cylinder geometry was developed using SolidWorks software. The complete assembly included the cylinder body, domes, valve opening, base ring, and protective collar. The primary geometric dimensions of the pressure vessel were derived from engineering calculations based on thin-walled pressure vessel theory (Barlow's formula for hoop stress) to accommodate a 12.5 kg LPG capacity under a 2.0 MPa design pressure:

Design Pressure (P): 2.0 MPa (20 bar) nominal internal pressure.

Target Factor of Safety (FOS): 2.05 to comply with composite pressure vessel safety standards.

Internal Radius (r): Calculated based on target 27.5-liter internal volume for 12.5 kg LPG fill mass as follows:

Target internal volume, V = 27.5 L = 27,500 cm^3 = 27,500,000 mm^3
For a cylindrical vessel, the internal volume is given by:
$V = \pi r_i^2 L$
where:
V = internal volume of the vessel
r_i = internal radius of the vessel
L = internal cylindrical length of the vessel
Rearranging the equation to determine the internal radius gives:
$r_i = \sqrt{(V / \pi L)}$
Taking L to be 390 mm (Megyesy, 2008).
substituting the values gives:
r = 150 mm

Wall Thickness (t): 18.5 mm composite wall thickness, as determined from the tensile yield criteria of the 55/45 PP/FG matrix.

The 3D model was constructed using feature-based parametric tools within SolidWorks using the following sequence:

2D Sketching and Profile Layout: A 2D cross-sectional profile of the cylinder body, top dome, and bottom dome was sketched on the Front Plane, incorporating exact calculated internal and external radii.

Revolve Feature: The 2D profile was revolved 360 degrees around the central longitudinal axis to create the monolithic pressure shell.

Valve Boss and Neck Ring Integration: A threaded boss neck insertion was modeled on the top dome using Extrude Boss/Base and Thread features to simulate standard valve fitting connections.

Protective Casing & Base Stand Design: Top hand-grip collars and bottom base support rings were modeled as separate bodies and mated to the composite pressure core to ensure drop-impact protection and upright standing stability.

3.0 RESULTS AND DISCUSSIONS

3.1 Light Transmittance

The results of the light transmittance are presented in Figure 1. The optical performance of the composites showed that material composition had a significant effect on light transmission. Optical transmittance in glass-fiber-reinforced polymer composites is governed by sheet thickness, fiber architecture, volume fraction, and the degree of refractive index matching between the matrix and reinforcement phases (Hegedűs *et al., 2017*; Olson *et al.,* 1992). Unreinforced polypropylene matrix materials typically exhibit semi-translucent behavior in thin sections, whereas woven glass-fiber reinforcements present significantly lower light transmission due to interfacial scattering. Commercial material datasheets for plain-weave E-glass fabrics report nominal light transmittance values in the range of 6–13%, with transmittance further decreasing as fiber loading and section thickness increase.

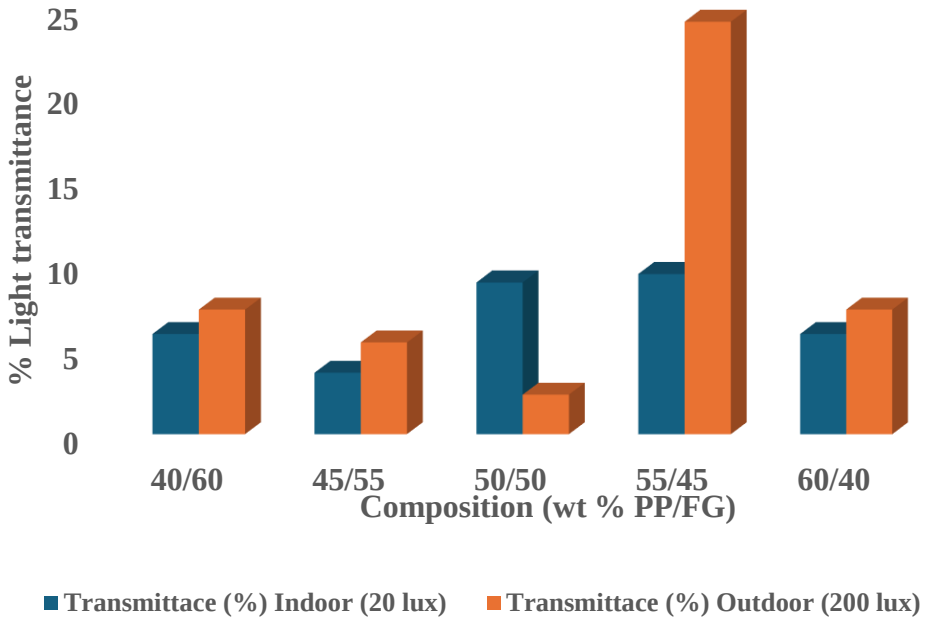

Figure 1: Effect of composite composition on percentage light transmittance

Among all the composite formulations, the 55/45 PP/FG composite exhibited the highest light transmittance under both indoor and outdoor illumination conditions, recording 9.50% and 24.30% light transmittance, respectively. This transmittance values indicate that the composite materials are translucent where translucent material is regarded as a material with light transmittance between 0% and 80% (ASTM D1003-21; ISO 13468-1). This improved translucency is attributed to the balanced interaction between the polypropylene matrix and fibreglass reinforcement, which minimises excessive light scattering while maintaining structural integrity. Standard commercial Type-IV composite LPG cylinders typically utilize opaque carbon or glass/epoxy filament wraps over HDPE liners, which obscure internal fluid levels.

The optical mechanisms governing light transmission in composite media depends on light scattering and absorption coefficients across polymer-fibre phase boundaries (Arikawa *et al.*, 1998). In thermoplastic PP/GF systems, achieving visual translucency requires sufficient matrix resin wetting around fibres to minimize diffuse light scattering across void interfaces. The experimental data confirms that the 55/45 formulation balances fibre loading for mechanical strength while retaining enough optical transmittance for visual liquid-level monitoring.

3.2 Tensile Strength

Tensile strength increased progressively with increasing polypropylene content up to the 55/45 composition, where a maximum value of 33.17 MPa was obtained before declining at higher polypropylene content. The improvement is consistent with the established influence of fibre content, fibre length and fibre–matrix interaction on stress transfer and mechanical performance in glass-fibre-reinforced polypropylene (Thomason *et al.*, 1996; Delli *et al.*, 2021). Conversely, excessive fibreglass loading reduced matrix continuity, while excessive polypropylene reduced the reinforcing contribution of the fibres. These findings indicate that optimum tensile performance is achieved through an appropriate balance between the polymer matrix and reinforcement rather than by maximising either constituent (Emon *et al.*, 2025; Li *et al.*, 2024).

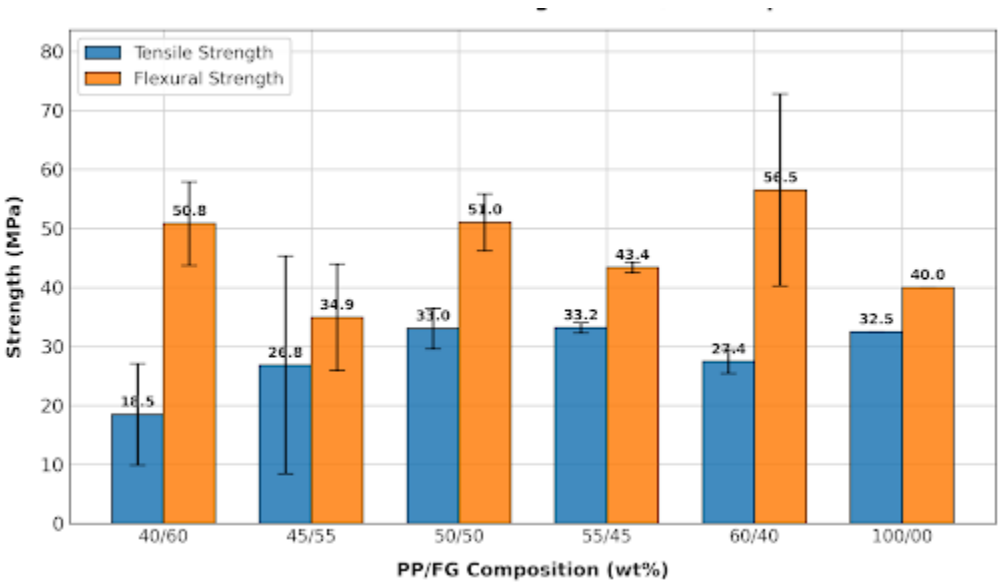

Figure 2: Effect of composite composition on tensile and flexural strengths

The tensile strength peak achieved in this work for 55/45 composition (33.2 MPa) alongside 50/50 composition (33.1MPa) aligns with findings by Milosan (2025), who analysed glass-fibre reinforced polymer composites for pressure containment vessels. Milosan highlighted that optimizing fibre fraction is essential to achieve structural stability and prevent ductile-to-brittle failure under static loading. Furthermore, higher fibre fractions (40/60), suffer a sharp drop in tensile strength due to un-wetted fibres and void formation as deficient matrix binder volume leads to stress concentration, fibre agglomeration, insufficient fibre wetting, and severe micro-void formation. In an LPG pressure vessel, these un-wetted voids act as localized stress concentrators and potential gas leakage pathways causing premature matrix cracking.

3.3 Flexural Strength

Flexural strength reaches its maximum value of 56.52 MPa at the 60/40 composition, representing a 45% increase over neat PP (40.0 MPa). This result corroborates with the findings of Lee and Jang (1999) who noted that increased polymer matrix fraction enhances bending resistance by allowing better strain distribution during flexural loading. Conversely the maximum impact strength exhibited by the 40/60 formulation follow the energy absorption mechanism detailed by Thomason (1997). The 50/50, 55/45 and 40/60 compositions also exhibit acceptable flexural performance (51.05 MPa, 43.40 MPa and 50.82 MPa respectively), as shown in Figure 2, confirming that effective stress transfer from the matrix to the fibres occurs at this resin to fibre ratio.

3.4 Impact Strength

Impact testing revealed that the 40/60 formulation exhibited the highest impact strength of 215.21 J/m, because its higher fibreglass content enhanced energy absorption through crack bridging and fibre pull-out mechanisms. However, this sample exhibits extreme standard deviation as indicated by the error bars, (calculated value = 138.38 J/m), indicating localized fibre agglomeration and inconsistent fracture energy dissipation. The 45/55, 50/50, 55/45, and 60/40 have calculated standard deviations of 7.40,12.72, 28.34 and 8.12 J/m respectively.

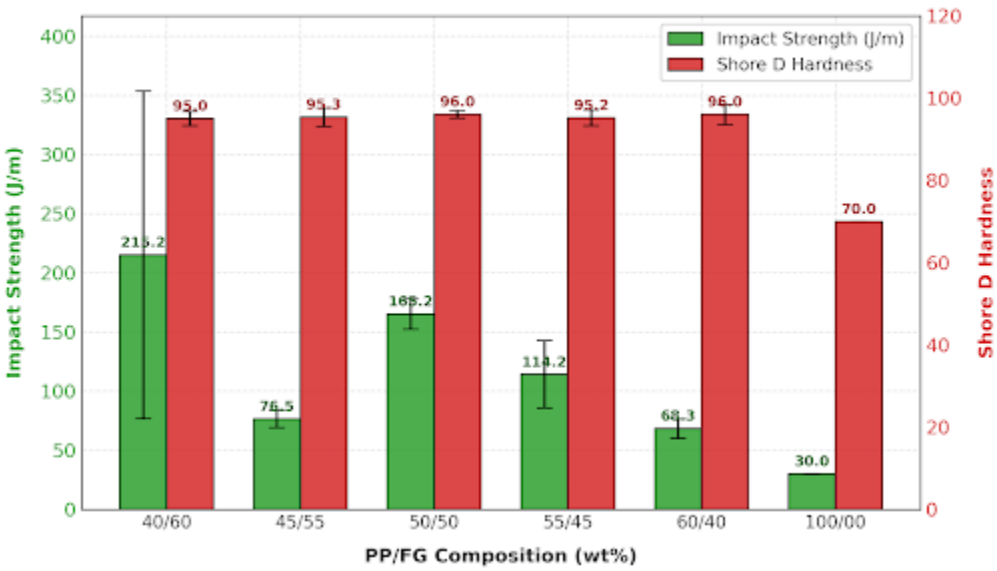

Figure 3: Effect of composite composition on impact strength and hardness

The 50/50 composite also showed good impact resistance (165.21 J/m), while the 55/45 formulation provided moderate toughness (114.17 J/m) that remained suitable for structural applications. Although it did not record the maximum impact strength, the 55/45 composite achieved the most balanced combination of toughness, tensile strength, and translucency required for safe LPG cylinder service.

3.5 Hardness

Hardness measurements confirmed that increasing fibreglass content generally improved resistance to indentation and surface wear because of the higher stiffness of glass fibres. Conversely, increasing polypropylene content enhanced ductility but reduced hardness. All glass-reinforced formulations achieve high surface hardness (95.0 to 96.0 Shore D). The addition of rigid glass fibres increases indentation resistance, providing crucial protection against abrasive wear, scuffing, and external impact during handling and transport.

Despite these variations, the 55/45 formulation maintained adequate hardness while retaining excellent tensile strength, satisfactory toughness, and the highest light transmittance.

3.6 Optimum composite formulation

To establish the ideal composite formulation for translucent LPG cylinders, tensile, flexural, impact strengths, surface hardness, must be evaluated alongside optical transmittance.

Comparing all mechanical, dynamic, and optical properties the 55/45 wt% Formulation delivers the maximum tensile strength (33.2 MPa), acceptable flexural strength (43.4 MPa), high hardness (95.5 Shore D), and robust impact resistance (114.17 J/m). Most importantly, it achieves peak optical transmittance (9.50% indoor / 24.30% outdoor), successfully combining structural pressure-bearing capability with visual gas-level monitoring.

In conclusion, the 55/45 wt% PP/FG composite represents the optimal composition, delivering the best combination of mechanical strength, impact toughness, surface durability, and optical functionality for translucent LPG cylinder design.

3.7 Conceptual Engineering Design Results

The engineering analysis results demonstrates that the developed composite material possesses the characteristics required for lightweight translucent LPG cylinders. The calculated hoop and longitudinal stresses remain within acceptable limits since the measured tensile strength of the composite (33.17 MPa) exceeds the calculated design stresses with factor of safety 2.01. Using the selected operating pressure of 2.0 MPa and an internal radius of 150 mm, the required wall thickness was calculated (using the experimental composite tensile strength) to be approximately 18.5 mm,

which was subsequently adopted in the CAD modelling. The design parameters are tabulate in Table 2. However, for an actual gas-cylinder design, applicable composite-cylinder standards and qualification/testing requirements would also need to be satisfied (ISO, 2020a, 2020b; Wu *et al.*, 2025; ISO, 2024).

Table 2: Design parameters

PARAMETER	VALUE
PP/FG formulation	55/45
Experimental composite tensile strength	33.17 MPa
Assumed internal pressure	2.0 MPa
Assumed internal radius	150 mm
Calculated wall thickness from composite tensile strength	18.5 mm
Calculated Hoop stress	16.22 MPa
Calculated Longitudinal stress	8.11 MPa
Calculated Factor of safety	2.05

3.8 The conceptual 3D CAD model result

The conceptual 3D CAD model represents the proposed 12.5 kg translucent LPG cylinder fabricated from the optimum 55/45 PP–FG composite. The model integrates the experimental material-performance results with the preliminary pressure-vessel calculations, thereby providing a transition from material characterization to an application-oriented engineering design.

The model is shown in Figure 4. The calculated hoop stress (16.22 MPa) is precisely twice the calculated longitudinal stress (8.11 MPa), confirming classical thin-walled pressure vessel behaviour (hoop stress = 2 longitudinal stress). An important strength of this model is that the design is derived from the experimental characterization rather than being an independent drawing. The experimental results establish the material's mechanical capability, while the performance analysis identifies the 55/45 PP/FG composition as the preferred formulation. The engineering calculation then uses the measured tensile strength of 33.17 MPa to determine an appropriate preliminary wall thickness. Consequently, the sequence is:

Material formulation → Experimental characterization → Performance optimization → Pressure-vessel calculation → Conceptual CAD design

Figure 4: Conceptual 3D CAD model of translucent 55/45 PP/FG composite cylinder

With an experimental tensile strength of 33.17 MPa, the working hoop stress of 16.22 MPa delivers a structural Factor of Safety of 2.05, which complies fully with ISO 11119-3 safety requirements for composite gas cylinders under standard working pressure (2.0 MPa).

4.0 CONCLUSION

This study successfully developed and evaluated a translucent polypropylene/fiberglass (PP/FG) composite material system tailored for lightweight domestic LPG cylinder applications. Experimental characterization demonstrated that the mechanical and optical properties of the composite are strongly governed by the weight ratio of the resin matrix to reinforcement fibers.

Light transmission in the fabricated composites remains constrained by internal light scattering within the semi-crystalline polypropylene phase as well as reflection at the fiber-matrix interfaces. However, strategic blending of the constituents activated optical translucency, reaching optimum in the 55/45 wt% PP/FG formulation. The 55/45 wt% PP/FG composite provided the best balance of properties, achieving the highest ultimate tensile strength of 33.17 MPa and peak light transmittance, 9.50% (indoors at 20 lux) and 24.30% (outdoors at 200 lux), alongside a flexural strength of 43.40 MPa, solid hardness of 95.20 Shore D, and an impact resistance of 114.17 J/m. Engineering design calculations and 3D CAD modeling established the structural feasibility of a 12.5 kg capacity cylinder with an 18.5 mm composite wall thickness, satisfying the target Factor of Safety 2.05 under a 2.0 MPa design pressure in accordance with thin-walled pressure vessel theory and ISO 11119-3 guidelines, however this is a conceptual CAD model for design assessment and requires finite element analysis (FEA) and experimental validation.

The proposed translucent composite cylinder offers a viable, safer, non-corrosive, and lightweight alternative to conventional steel cylinders, enabling direct visual LPG level monitoring without external auxiliary gauges.

REFERENCES

International Organization for Standardization. (2024). ISO/TR 13086-4:2024: Gas cylinders-Composite gas cylinders—Part 4: Guidance for cyclic fatigue testing. ISO.

Wu, R., Zeng, W., Li, F., Tian, H., & Li, X. (2025). Study on winding forming process of glass fibre composite pressure vessel. Materials, 18(11), 2485. https://doi.org/10.3390/ma18112485

Mahboubizadeh, S., Sadeq, A., Arzaqi, Z., Ashkani, O., & Samadoghli, M. (2024). Advancements in fiber-reinforced polymer (FRP) composites: An extensive review. Discover Materials, 4, 22. https://doi.org/10.1007/s43939-024-00091-9

Milosan, I., Bedo, T., Garbo, C., and Pop, M., A. (2025). Mechanical characteristics of glass-fibre-reinforced polyester composite materials. Materials (Basel, Switzerland), 18(15), 3959. https://doi.org/10.3390/ma18153595

Li, J., Sun, Y., Zhang, B., & Qi, G. (2024). Mechanical, flame-retardant and dielectric properties of intumescent flame retardant/glass fiber-reinforced polypropylene through a novel dispersed distribution mode. Polymers, 16(10), 1341. https://doi.org/10.3390/polym16101341

Khan, A., Khubaib, M., Pereira, F., de Zea Bermudez, V., Fernandes, A., & Briga-Sá, A. (2026). A systematic literature review of waste polypropylene reinforced with glass fiber: Mechanical and thermal properties in the context of sustainability. Proceedings, 133(1), 9. https://doi.org/10.3390/proceedings2025133009

Emon, M., Minchenkov, K., Gusev, S., Li, C., Xian, G., & Safonov, A. (2025). Pultrusion of glass fiber reinforced polypropylene bidirectional composites and their mechanical performance. Scientific Reports, 15, 39904. https://doi.org/10.1038/s41598-025-23744-y

ASTM International. (2022). ASTM D638-22: Standard test method for tensile properties of plastics. ASTM International. https://doi.org/10.1520/D0638-22

ASTM International. (2025). ASTM D790-25: Standard test methods for flexural properties of unreinforced and reinforced plastics and electrical insulating materials. ASTM International. https://doi.org/10.1520/D0790-25

ASTM International. (2026). ASTM D256-26: Standard test methods for determining the Izod pendulum impact resistance of plastics. ASTM International. https://doi.org/10.1520/D0256-26

Delli, E., Giliopoulos, D., Bikiaris, D. N., & Chrissafis, K. (2021). Fibre length and loading impact on the properties of glass fibre reinforced polypropylene random composites. Composite Structures, 263, 113678. https://doi.org/10.1016/j.compstruct.2021.113678

International Organization for Standardization. (2020a). ISO 11119-1:2020: Gas cylinders—Design, construction and testing of refillable composite gas cylinders and tubes—Part 1: Hoop wrapped fibre reinforced composite gas cylinders and tubes up to 450 l. ISO.

International Organization for Standardization. (2020b). ISO 11119-2:2020: Gas cylinders—Design, construction and testing of refillable composite gas cylinders and tubes—Part 2: Fully wrapped fibre reinforced composite gas cylinders and tubes up to 450 l with load-sharing metal liners. ISO.

Lee, N.-J., & Jang, J. (1999). The effect of fibre content on the mechanical properties of glass fibre mat/polypropylene composites. Composites Part A: Applied Science and Manufacturing, 30(6), 815–822. https://doi.org/10.1016/S1359-835X(98)00185-7

Somaiah, A., Anjaneya Prasad, B., & Kishore Nath, N. (2022). A comprehensive review: Characterization of glass fiber reinforced polymer composites with fillers from a thermo-mechanical perspective. Materials Today: Proceedings. https://doi.org/10.1016/j.matpr.2022.04.219

Thomason, J. L. (1997). The influence of fibre length and concentration on the properties of glass fibre-reinforced polypropylene: 4. Impact properties. Composites Part A: Applied Science and Manufacturing, 28(3), 277–288. https://doi.org/10.1016/S1359-835X(96)00127-3

Thomason, J. L., and Vlug, M. A. L. (1996). Influence of fibre length and concentration on the properties of glass fibre-reinforced polypropylene: 1. Tensile and flexural modulus. Composites Part A: Applied Science and Manufacturing, 27(6), 477–484. https://doi.org/10.1016/1359-835X(95)00065-A

Thomason, J. L., Vlug, M. A. L., Schipper, G., & Krikor, H. G. L. T. (1996). Influence of fibre length and concentration on the properties of glass fibre-reinforced polypropylene: 3. Strength and strain at failure. Composites Part A: Applied Science and Manufacturing, 27(11), 1075–1084. https://doi.org/10.1016/1359-835X(96)00066-8

Megyesy, E. F. (2008). Pressure Vessel Handbook (13th ed.). Gulf Professional Publishing.

Hegedűs, G., Sarkadi, T., and Czigány, T. (2017). Analysis of the Light Transmission Ability of Reinforcing Glass Fibers Used in Polymer Composites. *Materials*, 10(6), 637.

Olson, J. R., Day, D. E., & Stoffer, J. O. (1992). Fabrication and Mechanical Properties of an Optically Transparent Glass Fiber/Polymer Matrix Composite. *Journal of Composite Materials*, 26(8), 1181–1192.

Taska, A., and Ige, O. (2023). Transitions in household energy consumption and LPG adoption strategies in West Africa. Energy Policy, 178, 113600.

Arikawa, H., Fuji, K., Kanie, T., and Inoue, K. (1998). Light transmittance characteristics of light-cured composite resins. Dental Materials, 14(6), 405-411. https://doi.org/10.1016/s0300-5712(99)00014-7

PERFORMANCE EVALUATION OF GRANITE POWDER-STABILIZED LATERITIC ADOBE BRICKS: MECHANICAL STRENGTH, MOISTURE RESISTANCE AND THERMAL PERFORMANCE

Yunusa Tsoho Abdullahi[1,*], Nasiru Zakari Muhammad[1], Ado Ma'aruf[1], Mujitafa Sariyyu[1], Zaharaddeeen Baffa Baba[1]

[1]*Aliko Dangote University of Science and Technology Wudil*

Email: abdullahitsoho9@gmail.com*, mnasiruzakari@kustwudil.edu.ng, adomaaruf@kustwudil.edu.ng, mujittafasariyyu@kuswudil.edu.ng, bbzaharaddeen@gmail.com

***Corresponding author**: Yunusa Tsoho Abdullahi

DOI: https://doi.org/10.67203/sp.ICESID.2026

ABSTRACT

Traditional adobe bricks offer excellent thermal insulation and affordability but suffer from low compressive strength, high water absorption, and poor durability. Conventional stabilizers like cement and lime carry a massive environmental footprint and are economically unviable for low-income housing. This study investigates the potential of Granite Powder (GP), which is a quarrying by-product as a sustainable, zero-cement stabilizer for lateritic adobe bricks. Ten mix formulations were developed, including an unstabilized control and six GP-only variants (5%, 10%, 15%, 20%, 25%, and 30% by mass of laterite). Specimens were subjected to compressive strength testing, 24-hour water immersion, modified capillary wetting assessment, thermal conditioning (40°C, 60°C, and 100°C), and porosity evaluation. Results indicate that a 10% GP inclusion yielded the highest compressive strength (3.34 N/mm² at 28 days), a 30% increase over the control, surpassing the widely recognized 2.0–3.0 N/mm² benchmark for load-bearing, non-seismic earthen construction (Bui et al., 2009; Walker, 2020). While higher GP content (30%) diluted the clay binder and reduced compressive strength to 2.34 N/mm², it significantly enhanced durability, achieving the lowest capillary water uptake (18.7%) and porosity (19.2%). Furthermore, a novel "thermal convergence effect" was observed at 100°C, where high-GP mixes recovered strength due to thermally accelerated latent reactions. The study affirms that GP can significantly enhance the mechanical robustness and moisture resistance of adobe, aligning technical performance with circular economy principles.

Keywords: *Granite powder; Adobe bricks; Compressive strength; Water absorption; Sustainable construction; Circular economy*

1. INTRODUCTION

Traditional earthen construction, particularly adobe bricks, offers excellent thermal insulation and affordability. However, unsterilized earth suffers from low compressive strength, high water absorption, and poor durability, particularly in humid or extreme weather conditions (Goransson, 2021; Walker, 2020). Conventional stabilizers like cement and lime improve these properties but carry a massive environmental footprint; cement production alone accounts for approximately 8% of global CO_2 emissions (Habert & Roussel, 2020). Furthermore, these binders are often economically unviable for low-income housing in developing regions (Kouadio et al., 2021; UN-Habitat, 2022).

To mitigate the environmental impact of construction, researchers have explored industrial by-products as alternative stabilizers (Al-Rashid et al., 2023; Manikandan & Thangaraj, 2021). Granite Powder (GP), a massive environmental waste product from stone milling and tiling industries, presents a viable opportunity. Previous studies have highlighted the utility of granite dust in concrete and mortars (Chajec, 2021; Jain et al., 2022; Shakir & Mohammed, 2023). However, its specific application as a micro-filler and stabilizer in lateritic adobe matrices requires comprehensive optimization. Therefore, the objectives of this study are: 1-To characterize the physical and chemical properties of GP; 2) optimize the quantity of GP based on compressive strength; (3) determine the effect of elevated

temperatures on thermal resilience; and (4) evaluate Moisture resistance through total water absorption, capillary wetting, and porosity.

2. MATERIALS AND METHODS

2.1 Materials

Lateritic Soil: The natural lateritic soil used in this study was obtained from the Kudai borrow pit in Dutse, Jigawa State, Nigeria. The soil exhibited a Liquid Limit (LL) of 51%, a Plastic Limit (PL) of 35%, and a Plasticity Index (PI) of 16%. Under the Unified Soil Classification System (USCS), the soil is classified as MH (inorganic silt of high plasticity) because its liquid limit exceeds 50% and its plasticity index plots below the A-line, calculated as $PI = 0.73(LL - 20) = 22.63\%$. Since the measured PI of 16% is below the A-line value, the soil falls within the MH group. Under the AASHTO soil classification system (M 145), the soil is classified as A-7-5, because it has LL > 40% and PI > 10%, while $PI \leq LL - 30$ ($16 \leq 21$). The classification is therefore consistent between the reported Atterberg limits and the two classification systems. The compaction characteristics of the soil yielded a Maximum Dry Density (MDD) of 2.12 Mg/m^3 and an Optimum Moisture Content (OMC) of 16.77%.

Granite Powder (GP): Granite powder (GP) is a finely divided waste material produced in large quantities by the granite cutting and tiling industries. While the accumulation of GP poses environmental hazards through landfilling and dust pollution, its chemical and physical properties offer a sustainable solution for the construction sector. Recognized for its pozzolanic potential and micro-filler capabilities, GP can be effectively utilized as a partial cement replacement to reduce the environmental impact of concrete production. However, the efficacy of GP as a construction material is highly dependent on its local geological and mineralogical composition. Therefore, characterizing locally sourced GP—such as the waste generated from the tiling industries in Dutse—is a critical prerequisite to understanding its specific chemical reactivity and physical filler mechanisms, ultimately determining its suitability for optimizing the performance of local construction composites. GP was sourced from granite tiling industries in Dutse.

2.2 Mix Design and Specimen Preparation

Specimens were molded to standard dimensions of 75 × 75 × 150 mm, in accordance with ASTM C67 and ISO 22111, using a constant water content of 25% by mass of the dry lateritic soil. Six mix formulations were developed, with three replicate specimens prepared for each mix.

1. **Control (CR):** 100% Laterite.
2. **GP Series:** 5%, 10%, 15%, 20%, 25%, and 30% GP replacement by mass of soil.

2.3 Testing Program

1. The compressive strength of solid adobe specimens (75 × 75 × 150 mm) was evaluated using a 300 kN Universal Testing Machine (UTM). While ASTM C67 is traditionally developed for fired clay masonry, its fundamental compressive testing protocol (specimen geometry and load application rate) is widely adapted in preliminary earthen block research to ensure standardized mechanical evaluation. This approach is supplemented by the curing and testing principles of ISO 22111 to ensure strict relevance to unfired adobe. Specimens were cured in a controlled environment at 25 ± 3 °C and 60 ± 10% relative humidity for 7, 14, and 28 days prior to testing. For each mix formulation and testing condition, three replicate specimens (n=3) were prepared and tested. Prior to testing, each brick was centrally positioned on its 75 × 150 mm bed face (Area = 11,250 mm^2), and a continuous compressive load was applied until failure. The compressive strength values reported represent the mean of these three replicates, accompanied by the sample standard deviation (Mean ± SD) to indicate experimental variability.
2. **Total Water Absorption:** Total water absorption was determined by 24-h immersion. Specimens were first dried to constant mass and weighed to obtain the dry mass (Md). Each specimen was then completely immersed in clean water for 24 h. After immersion, the specimen was removed, surface water was gently wiped off, and the saturated mass (Ms) was recorded.

Water absorption was calculated as WA=(Ms−Md)/Md×100. Three specimens were tested for each mixture and the mean value was reported.

3. **Modified Capillary Water Uptake:** Capillary water absorption was evaluated using a modified wet-towel suction test, adapted from EN 772-11, to prevent specimen disintegration. After 24 h of ambient curing, the adobe specimens were oven-dried at 105 °C to a constant initial mass (W_1). The specimens were then placed on a water-saturated towel at room temperature. After wiping away surface moisture, they were weighed at 8-hour intervals until a constant saturated mass (W_2) was achieved.
4. **Thermal Exposure:** Thermal resilience was evaluated by exposing three specimens per mix to 40 °C, 60 °C, and 100 °C for 24 hours in a calibrated oven, following a 24-hour ambient cure (25 ± 3 °C, 60 ± 10% RH). These temperatures represent Northern Nigerian service conditions: ambient (40 °C), maximum hot-dry season wall surface temperature (60 °C; Millogo et al., 2016), and extreme exposure triggering complete free water evaporation (100 °C; Singh & Paul, 2022). Specimens were cooled in a desiccator before re-testing compressive strength and water absorption.
5. **Porosity:** The total porosity (n*n*) of the stabilized adobe specimens was evaluated based on their dry weight and bulk density. Following the measurement of the specimens' geometric dimensions and oven-dry weight (Wd), the bulk density (ρb) was calculated. The total porosity was then determined by comparing the bulk density to the solid (particle) density (ρs) of the soil mixture, using the relationship n=(1−ρb/ρs)×100. The solid density (ρs) of the soil matrix was assumed to be 2.65 g/cm³, representing the typical specific gravity of quartz-dominated silicate soils **(**ASTM International, 2014).

3. RESULTS AND DISCUSSION

3.1.1 X-ray Diffraction (XRD) analysis of the GP

X-Ray Diffraction (XRD) revealed the mineralogical analysis showed a highly crystalline nature with dominant phases of quartz, albite, anorthite, and muscovite. Due to its high crystallinity, GP functions primarily as a high-efficiency inert physical filler that optimizes particle packing density and reduces drying shrinkage (Hou et al., 2024; Moghal, 2021). Energy Dispersive X-Ray Spectroscopy (EDX) chemical analysis revealed SiO_2 = 62.789%, Al_2O_3 = 13.085%, and Fe_2O_3 = 1.249%. The sum of these oxides (77.123%) exceeds the 70% minimum requirement of ASTM C618, classifying it as a pozzolanic material.

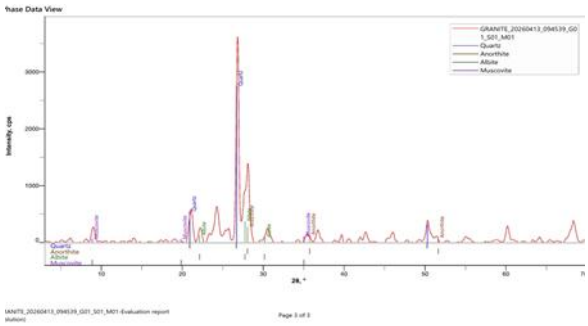

Figure 1: X-ray Diffraction (XRD) analysis of the GP

3.1.2 Sieve analysis of granite powder GP: revealed a predominantly sand-sized composition (94.27%), primarily medium sand (69.62%), with minor gravel (3.65%) and silt/clay (2.08%) fractions, as shown in the particle size distribution curve (Figure X). Characteristic diameters were determined from the curve as D_{10} = 0.148 mm, D_{30} = 0.234 mm, and D_{60} = 0.295 mm. The coefficients of uniformity (Cu = 2.00) and curvature (Cc = 1.25) classify the GP as a poorly graded sand. Due to its narrow particle size range and low fines content, the GP acts as a non-plastic granular micro-filler in the lateritic adobe matrix.

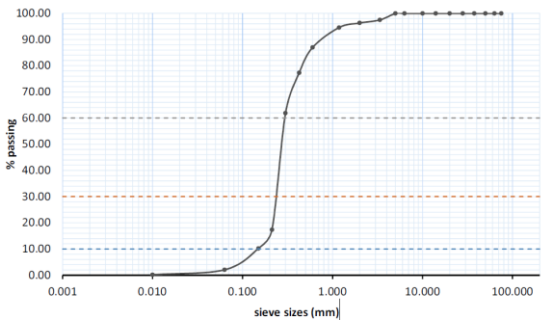

Figure 2: Particle Size Distribution Curve of GP

3.2 Compressive Strength Performance

The compressive strength development across the GP mixes at 7, 14, and 28 days is detailed in Table 1.

Table 1: Mean Compressive Strength of (N/mm²)

Age (Days)	***CR***	***GP5%***	***GP10%***	***GP15%***	***GP20%***	***GP25%***	***GP30%***
7	1.81 ± 0.10	1.89 ± 0.17	1.97 ± 0.11	1.85 ± 0.05	1.61 ± 0.04	1.40 ± 0.10	1.12 ± 0.09
14	2.20 ± 0.12	2.28 ± 0.12	2.30 ± 0.10	2.18 ± 0.08	1.99 ± 0.13	1.95 ± 0.09	1.90 ± 0.16
28	2.57 ± 0.04	3.05 ± 0.11	3.34 ± 0.25	3.18 ± 0.18	2.66 ± 0.26	2.50 ± 0.05	2.34 ± 0.21

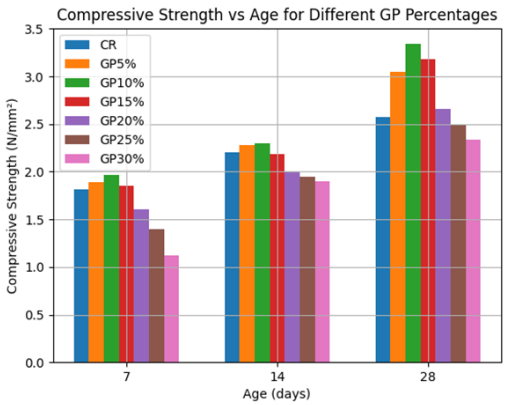

Figure 3: Compressive Strength vs Age for GP Series

Discussion: The GP10% mix achieved the peak 28-day strength of 3.34 ± 0.25 N/mm², representing a 30% increase over the control (2.57 ± 0.04 N/mm²). This margin of increase is well beyond the experimental variability (standard deviation), confirming that the strength gain is statistically meaningful and not merely experimental noise. This surpasses the widely recognized 2.0–3.0 N/mm² benchmark for load-bearing, non-seismic earthen construction, confirming its structural viability (Bui et al., 2009; Walker, 2020) for non-seismic, single-storey earthen construction. The improvement at 10% is attributed to the micro-filler effect of GP, which optimizes particle packing and densifies the matrix. However, beyond 15% replacement, strength declined progressively (GP30% dropped to 2.34 ± 0.21 N/mm²). This is due to the excessive dilution of the cohesive clay fraction, which is necessary for soil particle bonding (Reddy & Gupta, 2021).

3.3 Thermal Resilience and the Convergence Effect

Specimens were exposed to elevated temperatures to simulate extreme roof-space or hot-dry season conditions in Northern Nigeria.

Table 2: Compressive Strength After Thermal Exposure (N/mm²)

Temp (°C)	*CR*	*GP5%*	*GP10%*	*GP15%*	*GP20%*	*GP25%*	*GP30%*
40	2.60 ± 0.22	2.68 ± 0.08	2.75 ± 0.09	2.70 ± 0.17	2.55 ± 0.12	2.48 ± 0.23	2.45 ± 0.15
60	2.65 ± 0.08	2.72 ± 0.18	2.73 ± 0.12	2.68 ± 0.05	2.42 ± 0.16	2.35 ± 0.18	2.62 ± 0.07
100	2.51 ± 0.14	2.60 ± 0.22	2.58 ± 0.17	2.55 ± 0.06	2.29 ± 0.18	2.26 ± 0.18	2.48 ± 0.17

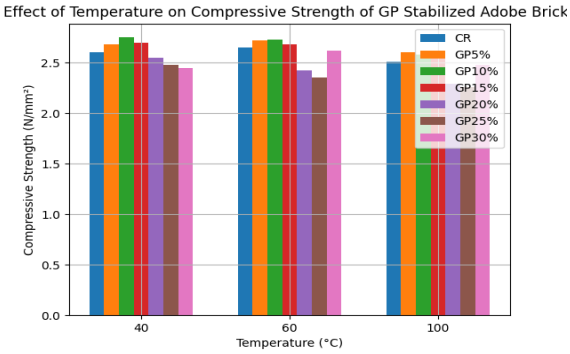

Figure 4: Compressive Strength vs Age for GP Series under Thermal exposure

Discussion: The thermal resilience of the mixes exhibited distinct temperature-dependent behaviors. Notably, the GP30% mix displayed a non-monotonic trend, peaking at 60°C (2.62 ± 0.07 N/mm²) before slightly decreasing at 100°C (2.48 ± 0.17 N/mm²). This intermediate 60°C peak is attributed to accelerated free-water evaporation, which temporarily maximizes inter-particle friction and matrix densification. The subsequent slight drop at 100°C results from complete clay dehydration and minor thermal micro-stresses. Despite this, a 'Convergence Effect' remains evident at 100°C, where GP30% (2.48 ± 0.17 N/mm²) nearly matches the Control (2.51 ± 0.14 N/mm²). Because XRD confirms GP is highly crystalline and inert at 100°C, this recovery is driven by the rigid, dimensionally stable GP particles acting as an inner skeletal framework. This framework prevents catastrophic micro-cracking and compensates for the dehydrated clay binder. Conversely, mixes with higher clay content and less rigid GP skeleton (e.g., GP20% and GP25%) lack this structural compensation. Consequently, they suffer a continuous strength decline from 40°C to 100°C (e.g., GP25% dropping from 2.48 ± 0.23 to 2.26 ± 0.18 N/mm²) due to progressive clay dehydration and micro-cracking.

3.4 Water Absorption and Porosity

Total water absorption and porosity measure the total volume of voids within the matrix.

Table 3: Durability Metrics of All Mixes

Mix	Total Water Absorption (%)	Capillary Water Uptake (%)	Porosity (%)
CR	35.0	39.8	26.5
GP5%	35.5	34.5	25.2
GP10%	36.2	29.5	23.8
GP15%	36.7	25.5	22.7
GP20%	37.1	21.8	21.5
GP25%	38.1	20.2	20.4
GP30%	39.0	18.7	19.2

Discussion: The durability metrics reveal a complex, divergent trend in moisture resistance mechanisms. In the GP-only series, total water absorption increased with GP content (reaching 39.0% in GP30%), while capillary uptake and overall porosity decreased steadily (to 18.7% and 19.2%, respectively). This apparent paradox is explained by differing pore-structure mechanisms: total void accessibility versus pore connectivity.

Total water absorption, measured after 24 hours of immersion, allows water to eventually saturate all accessible micro-voids. As GP content increases beyond the optimum 10%, the dilution of the cohesive clay binder creates more interfacial transition zones (ITZ) and isolated micro-voids between the rigid GP particles and the soil matrix. Given sufficient time (24 hours), water penetrates these isolated voids, increasing the total absorbed mass.

Conversely, capillary uptake relies entirely on continuous, interconnected fine pores to draw water upward via surface tension. The rigid, non-plastic GP particles act as physical barriers that disrupt, block, and tortuously redirect the natural, continuous capillary network inherent to pure lateritic clay. Consequently, even though the overall matrix is denser (as confirmed by the drop in total porosity to 19.2%), the pathways for rapid capillary rise are fundamentally broken. This highlights a critical strength-durability trade-off in single-additive systems: optimum compressive strength occurs at 10% GP, while optimum physical pore-blocking (capillary resistance) occurs at 30% GP.

4. CONCLUSION

This study evaluated the efficacy of Granite Powder (GP) as a sustainable stabilizer for lateritic adobe bricks. Based on the experimental investigation, the following conclusions are drawn:

1. **Characterizing granite powder (GP):** fulfilled Objective 1, confirming its suitability as a composite additive. With a combined oxide content of 77.123%, GP exceeds ASTM C618 pozzolanic requirements; however, its highly crystalline nature (quartz, albite, anorthite, muscovite) means it acts primarily as a high-efficiency inert micro-filler. This dual characteristic makes GP highly effective for optimizing particle packing density and reducing drying shrinkage within the matrix (Hou et al., 2024; Moghal, 2021).
2. **Optimum Stabilizer Dosage:** the optimum percentage was found to be 10% with compressive strength (3.34 N/mm²).
3. **Thermal Convergence Effect:** High-GP mixes (30%) exhibit a hidden "convergence effect," recovering strength at 100°C due to thermally accelerated latent bonding, demonstrating high thermal resilience.
4. **Moisture Resistance Trade-off:** While 10% GP yields the highest strength, 30% GP yields the lowest porosity (19.2%) and best capillary resistance (18.7%), though it suffers from reduced strength due to clay dilution.

5. **Practical Application Recommendations:** To resolve the identified strength-durability trade-off, a use-case-specific graded application of GP is recommended for practitioners:

For load-bearing walls in non-seismic, dry regions: A 10% GP dosage is optimal, as it maximizes compressive strength (3.34 N/mm²) to meet structural benchmarks while maintaining acceptable baseline durability.

For non-load-bearing walls, external plasters, or humid environments: A 20% to 30% GP dosage is highly recommended. Although compressive strength is moderately reduced, these mixes provide superior capillary resistance (≤ 21.8% uptake) and enhanced thermal resilience, making them ideal for weather-protective applications where moisture ingress is the primary failure risk.

For advanced hybrid construction: Future production could exploit a dual-layer approach, utilizing a 10% GP core for structural integrity, encased in a 30% GP outer layer or plaster to serve as a highly impermeable, thermally resilient weather shield.

REFERENCES

Al-Rashid, H., Bhuiyan, M. A., & Akhter, M. (2023). Applications of industrial waste in construction materials: A sustainable approach. Journal of Cleaner Production, 312, 128732.

Bui, Q. B., et al. (2014). Thermal durability of earthen construction materials. Journal of Building Engineering.

Chajec, A. (2021). Granite powder vs. fly ash for the sustainable production of air-cured cementitious mortars. Materials, 14(5), 1208.

Goransson, H. (2021). Traditional materials in sustainable construction: A review of adobe bricks. Sustainable Materials and Technologies, 34, e00342.

Habert, G., & Roussel, N. (2020). The environmental cost of cement. Nature Reviews Earth & Environment, 1(1), 68–77.

Jain, A., Choudhary, S., Gupta, R., Chaudhary, S., & Gautam, L. (2022). Effect of granite industry waste addition on durability properties of fly ash blended self-compacting concrete. Construction and Building Materials, 340, 127727.

Kouadio, A., Koffi, E., & Agbede, J. (2021). The role of cement in adobe stabilization: Environmental and economic considerations. International Journal of Green Building Materials, 12(4), 255–270.

Hou, W., Zhang, Y., Li, Z., & Wang, J. (2024). Sustainable reusing marble powder and granite powder in cement-based materials: Micro-mechanism and macro-performance. ACS Sustainable Chemistry & Engineering, 12(8), 3456-3470. https://doi.org/10.1021/acssuschemeng.3c06670

Manikandan, K., & Thangaraj, R. (2021). Utilization of granite waste in construction materials. Construction and Building Materials, 278, 121939.

Moghal, A. A. B. (2021, December 20). Granite dust as a sustainable additive. In Encyclopedia. https://encyclopedia.pub/entry/17342

Reddy, B. V. V., & Gupta, A. (2021). Granite powder replacement in Indian lateritic soil blocks. Construction and Building Materials.

Shakir, R., & Mohammed, H. (2023). Industrial by-products in concrete applications: A review of granite powder and fly ash. Construction Journal, 14(2), 215–230.

UN-Habitat. (2022). Affordable housing and sustainable supply chains in developing regions. United Nations Human Settlements Programme.

Walker, P. (2020). The benefits and limitations of adobe bricks in sustainable construction. Journal of Architectural Science and Technology, 25(3), 297–306.

ASTM International. (2023). Standard test methods for sampling and testing brick and structural clay tile (ASTM C67/C67M-23). West Conshohocken, PA: ASTM International.

ASTM International. (2014). ASTM D854-14: Standard Test Methods for Specific Gravity of Soil Solids by Water Pycnometer. West Conshohocken, PA: ASTM International.

Bui, Q. B., Morel, J. C., Reddy, B. V. V., & Ghayad, W. (2009). Durability of rammed earth walls exposed for 20 years to natural weathering. Building and Environment, 44(5), 912–919. https://doi.org/10.1016/j.buildenv.2008.07.004

PRODUCTION OF SILICA FROM AGRICULTURAL WASTES FOR APPLICATION IN FCC/RFCC CATALYST DEVELOPMENT: A MINI REVIEW

Usman Sani[1,*], Daniel Adanenche[2], Mustapha Yusuf[3], A. Y. Atta[1], B. J. El-Yakubu[1]

[1]""

[2]*Research and Development Centre, Dangote Petroleum Refinery and Petrochemicals, FZE, Union Marble House, Ikoyi, Lagos, Nigeria*

[3]*Department of Chemical Engineering, Ahmadu Bello University, Zaria, Nigeria*

Email: usb934@gmail.com*, daniel.adanenche@dangoteprojects.com, yusufengrmustapha@gmail.com, zeezoatta@gmail.com, jbelyakubu@edu.abu.ng

***Corresponding author**: Usman Sani

DOI: https://doi.org/10.67203/sp.ICESID.2026

ABSTRACT

Fluid catalytic cracking (FCC) and its residue variant (RFCC) are central to converting heavy petroleum fractions into gasoline and light olefins, and their catalysts depend on silica as both a binder and a precursor for the zeolite-Y active component and the active matrix. Conventional silica sources—tetraethyl and tetramethyl orthosilicate, sodium silicate, and fumed silica—are pure but costly, toxic, and energy-intensive, motivating a search for green alternatives. This mini-review examines the production of silica from agricultural wastes and its application in FCC/RFCC catalyst development. Rice husk, rice straw, sugarcane bagasse, and corn cob yield amorphous silica of high purity (commonly 90–98%) after acid leaching, controlled calcination, and alkaline dissolution to sodium silicate. In Nigeria alone, these residues are generated at an estimated 10.79 million tonnes per year, much of it burnt or left to create a nuisance. This can approximately generate 1.09 million tonnes per year of pure amorphous silica. The review considers how agricultural-waste silica can supply the sodium-free silica binder and the silica source for seeded zeolite-Y synthesis, with metakaolin as the alumina source, and how it must satisfy the low-sodium, high-purity, reactivity, and attrition-resistance requirements specific to cracking catalysts. It concludes that agricultural-waste silica is a viable, sustainable precursor for FCC/RFCC catalysts, and identifies impurity control, feedstock variability, catalyst-grade specification, and scale-up as the principal challenges to industrial adoption

Keywords: *Agricultural-waste silica; Rice husk ash; FCC/RFCC catalyst; Zeolite-Y; Green materials*

1. INTRODUCTION

Silica (SiO_2) is an inorganic material with impressive physiochemical properties for many industrial applications, such as construction materials and heterogeneous catalysis. Its chemical stability, surface functionality, and ability to form silicate and aluminosilicate frameworks make it particularly important in the preparation of catalytic materials. In petroleum refining, silica-containing materials are fundamental sources of silicon for zeolitic catalysts used in fluid catalytic cracking (FCC) and residue fluid catalytic cracking (RFCC).

According to a US patent, Preparation of cracking catalyst involves: (i) Preparing a slurry consisting clay, Zeolite, a sodium-free silica source, quasi-crystalline hydrated alumina, and microcrystalline alumina; (ii) Addition of monovalent acid to the slurry (iii) The slurry pH adjustment to a value above 3; (iv) Shaping the particle to form particles. This process resulted in a catalyst with sufficient attrition resistance and accessibility (Stamires *et al.*, 2016).

Agricultural waste such as rice husk, rice straw, sugarcane bagasse, and corn cob are rich in silica and can be utilised for the synthesis of zeolite catalysts. According to National Agricultural Extension and Research Liaison Services (NAERLS) and United States Department of Agriculture (USDA) report 2025, Nigeria alone produces 9.35 metric tonnes (MT) of rice, 11.44 MT of corn and forecasts 3.50 MT of sugarcane production. This amounts to 1.87 MT, 6.56 MT, 437,550 T, and 1.92 MT of 20% rice husk, 70% rice straw, 50% dry bagasse of 25% wet bagasse and 16.8% maize

cob, respectively and overall sums to 10.79 MT of agricultural waste generated (Table 1). These estimated wastes are often burnt either in a processing plant to generate process steam or in an open field, and the ash, rich in silica, is left underutilized, creating a public nuisance and releasing carbon monoxide, carbon dioxide and fine particulate matter. The silica present in the agricultural waste ash makes it a favourable precursor, and it can be used to complement high-alumina materials like Kaolin. Previous studies have reported the use of rice-husk-derived silica in the synthesis of zeolite Y, ZSM-5, mesoporous silica, and other functional materials. Wang et al. (2018) prepared NaA, NaX and NaZSM-5 zeolites from RHA via hydrothermal method. Zeolite Y in the sodium form (NaY) was synthesized using silica sourced from rice husk (Mohammed et al., 2012). Silica powder with approximately 96% purity was extracted from rice husk (RH) and used as a silica source for NaY (Yunusa et al., 2016)

An important benefit of utilizing silica derived from agricultural sources is the conversion of an abundant agricultural residue into a useful industrial raw material. Secondly, it provides a potentially low-cost and sustainable source of silica for catalyst development. For FCC/RFCC catalyst development, the quality of the silica precursor is critical because silica contributes to the zeolite framework, catalyst matrix, binder system, and overall pore architecture. Therefore high-purity silica with appropriate structural and surface characteristics is desirable.

This study reviews the use of silica prepared from major agricultural wastes (Corn cob, sugarcane bagasse, rice husk and straw), particularly in Nigeria, which are often combusted, leaving heaps of ash that disturb public serenity and environmental cleanliness. The outcomes of the review were assessed in relation to the potential utilisation of the material as a sustainable precursor for future FCC/RFCC catalyst development.

2. AGRICULTURAL WASTE FROM INDUSTRIAL PROCESSES IN NIGERIA

Land and water are the drivers of agriculture, Nigeria has over 79 million hectares of arable land, sufficient surface and groundwater and over 3 million hectares available for irrigation (FOA, 2026). Among the notably agricultural produce are: Maize, cassava, sorghum, cowpea, rice, yam, and millet. Maize, rice and Sugarcane are among the crops processed at an industrial scale, leading to the generation of waste such as rice husk, rice straw, corn cob and sugarcane bagasse. Nigeria's 2025 crop production from NAERLS and USDA report 2025 are shown in Table 1, alongside the estimated waste generated and the corresponding estimated residue generated in 2025. These account for the waste rarely fed to livestock and are often burnt, leaving the ash causing public disturbances.

Table 1: *Estimated agricultural waste generated from rice, corn and sugarcane*

Crops	2025 Production (t)	Residue	% Waste	Estimated Waste (t)
Corn	11,441,214.70	Cub	16.8	1,922,124.07
Rice	9,372,328.70	Husk	20	1,874,465.74
		Straw	70	6,560,630.09
Sugarcane	3,500,000.00	Bagasse	50 dry of 25 wet	437,550
Total				**10794769.9**

2.1 Silica from Agricultural Waste Ashes (AWA)

AWA particularly from silica-accumulating crops, represent an increasingly important sustainable source of amorphous SiO_2. Upon controlled combustion, rice husk yields ash containing 86–97% SiO_2 by weight, predominantly in the amorphous phase (Rodriguez-Otero et al., 2023). Other agricultural waste silica sources include sugarcane bagasse ash (50–70% SiO_2), and corn cob ash, although these are less rich in silica than rice husk ash and have received comparatively less research attention (Okoye et al., 2025; Islam et al., 2024).

The silica content varies with crop variety, soil conditions, and combustion parameters. Estimated Nigerian silica production was presented in Table 2, based on the estimated waste in Table 1. Acid leaching of rice husk prior to calcination has been found to remove alkali and alkaline earth metal impurities (K, Ca, Mg, Na), yielding ash with silica purity of 90–97%, comparable to or exceeding many commercial silica products (Phoungthong et al., 2026). This makes rice husk ash a compelling sustainable substitute for commercial silica in catalyst synthesis applications

Table 2: *Nigeria Estimated Silica Content from Rice, Corn and Sugarcane in 2025*

Agricultural Waste	**Ash content%**	**AWA (t)**	**% Silica**	**Silica (t)**
Corn Cub	2.8	53819.47	53.95	29035.60
Rice Husk	15.3-24.6	373955.92	92	344039.44
Rice Straw	13.5	885685.06	79.8	706776.31
Sugarcane Bagsse	2	8751	71.85	6287.59
Total		1322211.45		1086138.94

2.2 Process of Silica Extraction from Agricultural Waste

The extraction of silica from agricultural residues involves the conversion of biogenic silica embedded within plant tissues into a usable and relatively pure inorganic form. The physicochemical properties of the extracted silica, including its purity, surface area, porosity, and crystallinity, are strongly influenced by the processing method and operational conditions. Figure 1 shows the various routes for silica extraction from AWA.

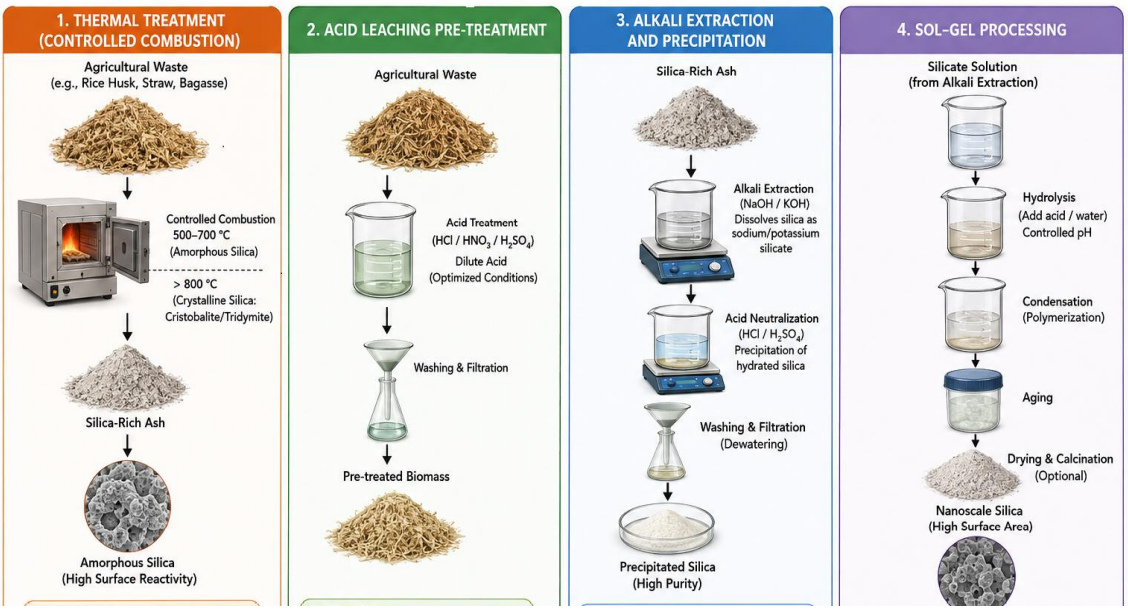

Figure 1: Paths for different grades of silica from agricultural waste

2.2.1Thermal Treatment

Agricultural wastes such as rice husk, rice straw, corn cob, and sugarcane bagasse are subjected to pyrolysis to remove cellulose, hemicellulose, lignin, and other organic constituents. Controlled Combustion at approximately **500–700 °C** usually favours the formation of **amorphous silica**, which possesses higher surface reactivity and greater availability of silanol groups (Si-OH) that influence the surface chemistry of the silica. At temperatures above approximately **800 °C**, amorphous silica transforms into crystalline phases such as cristobalite and tridymite, resulting in reduced surface area and reactivity. Therefore, a controlled low-temperature combustion is preferred when highly reactive amorphous silica is required (Aharipour et al., 2022; Barani et al., 2024;

Carraro et al., 2021; Falk et al., 2019; Farirai et al., 2021a; Hamidu et al., 2025; Mohd et al., 2017; Pieła et al., 2020; Shahbaz et al., 2023).

2.2.2 Acid-Leaching Pretreatment

Acid leaching is generally employed as a pretreatment step before combustion or subsequent silica extraction. Dilute acids (30 % w/w conc.) such as HCl, HNO_3, and H_2SO_4 dissolve metallic impurities, particularly potassium, calcium, magnesium, and iron, that are naturally associated with agricultural residues. Removing these impurities improves silica purity and helps suppress reactions that could promote silica crystallisation. For rice husk, acid pretreatment can therefore produce ash with higher silica content and improved surface characteristics. However, acid concentration and treatment duration must be controlled which lead to partial silica dissolution (Pa et al., 2013).

2.2.3. Alkali Extraction and Precipitation

Alkali extraction is an effective route for producing high-purity silica from silica-rich agricultural ash. In this process, the ash is treated with an alkaline solution, typically NaOH or KOH, to dissolve silica and form soluble sodium or potassium silicate. Subsequent acid neutralisation converts the soluble silicate into precipitated hydrated silica (Zero Gel), which is recovered through filtration, washing, and drying. The process provides greater control over silica purity, particle size, and morphology. Parameters such as pH, temperature, and acid addition rate strongly influence the properties of the final silica. Nevertheless, the process involves several treatment stages and generates alkaline wastes streams that require appropriate management (Harun et al., 2024; Kamari & Ghorbani, 2021; Kouadri et al., 2023; Okoronkwo et al., 2013; Seghir et al., 2023).

2.2.4. Sol-Gel Processing

Sol-gel processing is a more advanced approach for producing high-surface-area, nanoscale silica. Silicate precursors obtained from agricultural waste undergo controlled hydrolysis and condensation reactions, followed by ageing and drying to form a three-dimensional silica network. The method provides improved control over particle size, pore structure, surface area, and morphology and can also facilitate the incorporation of functional groups or dopants. However, careful control of pH, temperature, hydrolysis, condensation, and ageing is required, and the process can be more expensive and operationally demanding than direct thermal or precipitation methods (Adebisi et al., 2020; Ni'mah et al., 2023; Okoronkwo et al., 2013).

3. REFINERY CRACKING CONVERSION UNITS (FCC&RFCC)

Petroleum is refined into various fractions through the distillation process. The lighter fractions such as gasoline, naphtha, light distillate, are the most valuable products and are in high demand. According to the Global Oil Products Utilization 2024 report, gasoline accounts for about 27% of demand, while diesel/gas oil has the highest share at 33%, followed by jet fuel. Petroleum distillation produces only a fraction of these products and therefore can not meet global demand. The heavier, less desirable fractions, such as bottom residue, vacuum gas oil and vacuum residue, are further processed and converted to lighter, valuable product fractions via thermal or catalytic cracking. Catalytic cracking converts heavy fractions; also known as fluid catalytic cracking or its counterpart, residue fluid catalytic cracking (FCC/RFCC), is a major conversion process to produce more of these valuable products, such as gasoline and light olefins. These units account for about 35 -50% of the refinery gasoline production (Adenenche et al., 2023). The feed to the FCC and the RFCC, is mainly Vacuum gas oil (VGO) and atmospheric residue/vacuum residue, respectively. FCC/RFCC processes have been operated across the globe in more 300 of the 646 refineries since 2014 (Zhu et al. 2013, Palos et al., 2020). It is estimated that 0.16 kg of FCC catalyst is used per barrel of feedstock (vacuum gas oil). For heavy feed materials, such as vacuum or atmospheric residue, 0.20 kg of RFCC catalyst is used per barrel (Vogt et al., 2015). Figure 2 shows a typical refinery conversion unit.

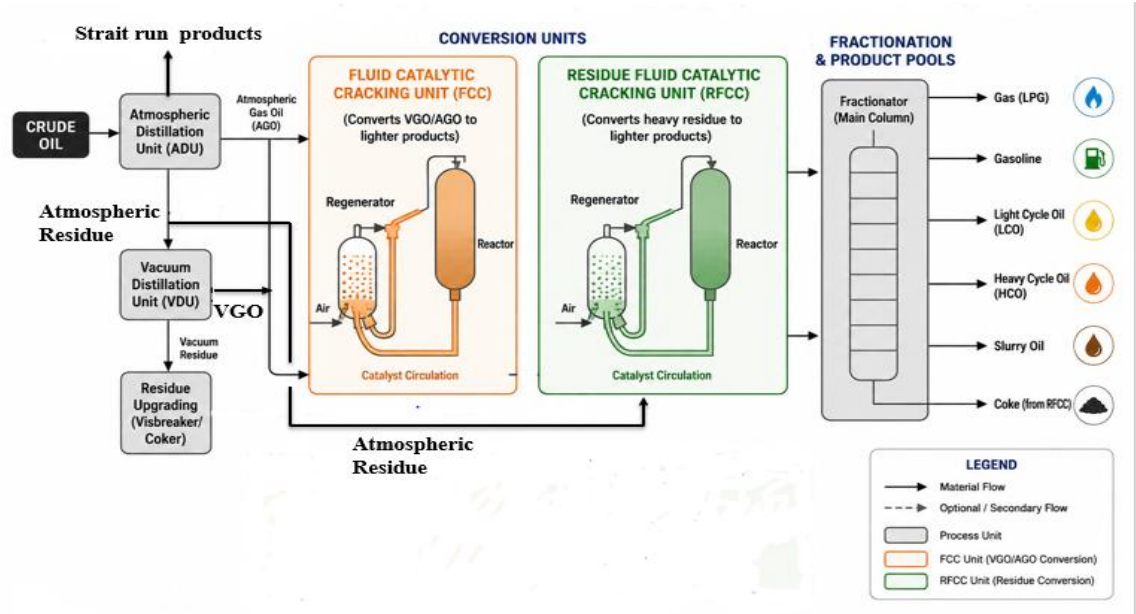

Figure 2: A side-by-side representation of FCC and RFCC in the refinery.

3.1 Application of Silica In FCC/RFCC Catalyst

FCC/RFCC Catalyst is composite material made up of a complex formulation of active and inactive components. Figure 2 shows the major structural composition of FCC/RFCC catalyst. The nature of the feed, the processing unit objectives, and constraints are the primary drivers of catalyst formulation and composition. The nature of the components and the processing steps determine the physicochemical properties of the catalyst (Ferreira et al., 2023).

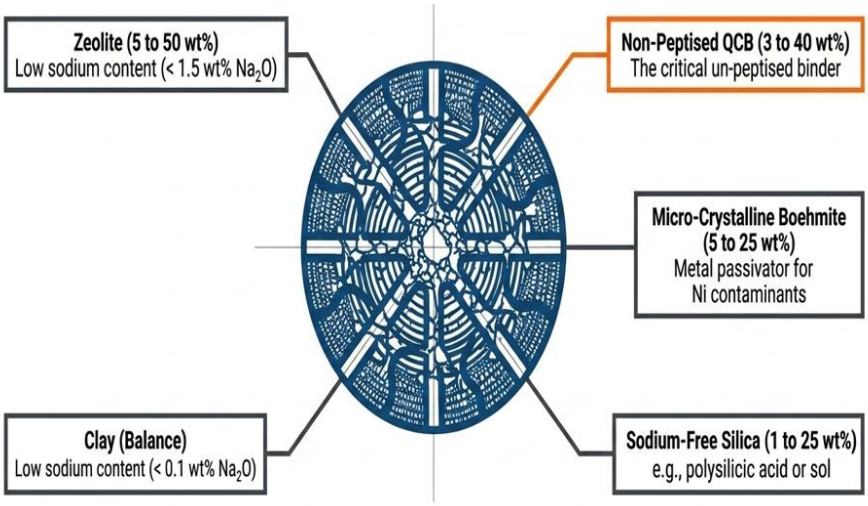

Figure 2: Typical structural composition of an FCC/RFCC particle.

The catalyst lowers the activation energy of the cracking reaction and also tailors the yield and selectivity towards the desired product. Other minor constituent and their roles were highlighted in Table 3. Silica appears have a significant role in both in the matrix development and the synthesis of active components. It form in the structural integrity of the catalyst and is also used as a binder for glueing all the components together. The active components are the zeolites such as the Zeolite-Y which is the major active component.

Table 3: Constituent of FCC/RFCC catalyst

Component	Chemical Constituents	Sources	Functions	Ref.
Active Component (Zeolite-Y)	Alumina, Silica Rare earth elements (RE), Lanthanum (La), Cerium (Ce), Neodymium (Nd), Praseodymium (Pr)	Natural clays, Agricultural waste, Inorganic chemicals	Responsible for catalytic activity and selectivity toward Naphtha	Borges ,2011 Stamires et al. 2016
ZSM-5, MCM-22, and MCM-36, metal-exchanged Zeolites, ITQs, SAPOs, ALPOs,	Alumina, Silica, transition metals.	Natural clays, Agricultural waste, Inorganic chemicals	Boost gasoline octane, increase light olefin yields or improve production of a particular product	Stamires et al.2016, Borges, 2011, Sadeghbeigi, 2000
Active matrix	Alumina (Al_2O_3)	Bauxite, Natural clays	improve bottom cracking, i.e., cracking of large, high-boiling-point molecules	Sadeghbeigi, 2020
Inert matrix	Kaolin	Natural clay Kaolinite	Embedded as a filler in the catalyst to impart structural integrity to it and dilute its activity	Ferreira et al., 2023
Synthetic matrix (Binder)	Polymerized Silica, Alumina, Aluminosilicate, or Aluminium phosphate	Inorganic chemicals, Natural clays and Agricultural wastes	As glue to hold the zeolite, matrix, and clay together. The binder may or may not have catalytic activity. It provides physical integrity, (density, attrition resistance, particle size distribution), heat transfer medium.	Vogt et al., 2015

Component	Chemical Constituents	Sources	Functions	Ref.
Structural Directing Agent (SDA)	Quaternary ammonium, Cetyltrimethylammonium bromide (CTAB), Metal Cation (NA+, K^+ etc) plants extract, Sugars,	Organic, Inorganic, Biodegradable	Control and dictate the formation of crystal framework	Ferreira et al., 2023
Pore Regulating Agent	Surfactants (CTAB), carbon materials, Polymer beads, silica spheres, starch, cellulose, chitosan	Organic (MCM-41), inorganic, Biodegradables	Regulate the pore size distribution, connectivity, shap and pore architecture	Borges 2011
Metal Passivators	Antimony (Sb), Boron		Reduces effect of metals on catalyst	Sadeghbeigi, 2000
Bottom conversion additives			Selectively pre-crack large feed molecules	Sadeghbeigi, 2000
CO combustion promoter	Platinum (Pt), Palladium (Pd), Iridium (Ir), Rhodium (Rh), Osmium (Os) Ruthenium (Ru)		Combustion of CO to CO_2 in the regenerator	Sadeghbeigi, 2000
SO_2 reducing additives			Promote oxidation of SO_2 to SO_3 in the regenerator	Sadeghbeigi, 2000
NO_x reducing additives			Reduce NOx to N_2 in the regenerator	Sadeghbeigi, 2000

3.2 Zeolite Synthesis

According to Musyoka et al. (2014) zeolite synthesis begins with the preparation of super-saturated aluminosilicate solution, and proceeds with dissolution, nucleation, and crystallization processes at high temperatures. This is referred to as an in-situ reaction at elevated temperature and pressure in an aqueous solution. 'It is important to note that, when natural clays or ash are used as precursors in the synthesis process, the first step is to extract alumina and silica from the raw material, followed by washing and drying the resulting product to remove impurities and organic matter. The next step involves mixing the precursor with an alkali solution, such as NaOH or KOH, at particular temperature to create a reactive aluminosilicate gel in an alkaline fusion or activation process. The alkaline solution dissolves the aluminum and silicon ions in the clay, forming a gel. Subsequently, the gel is subjected to hydrothermal treatment in an autoclave at high temperature and pressure, which facilitates the crystallization of the gel into a zeolite product. The resulting zeolite crystals' size, shape, and purity can be influenced by the duration of the hydrothermal treatment and the composition of the gel. Finally, the synthesized zeolite undergoes washing, drying, and calcination processes to remove any residual organic matter and stabilize the structure of the zeolite (El Bojaddayni et al. 2023).

Several limitations and factors are considered when synthesizing zeolites from these precursors. The purification process, which can be time-consuming and costly, is a critical factor

that impacts the feasibility of the synthesis method for commercial applications. Optimal conditions for zeolite synthesis from various source material require precise control of several factors, including temperature, pressure, reaction time, and solid/liquid ratio. It is important note that the optimal conditions may vary depending on the specific source material and desired product properties. Product purity, is at the peak of all factors and can affect the quality of the final product. Rice-husk-derived silica has demonstrated good characteristics purity, with reported SiO_2 purities of approximately 96–98% and successful application in NaY/zeolite-Y synthesis (El Bojaddayni et al. 2023; Yunusa et al., 2016).

For the preparation FCC/RFCC Catalyst, low sodium (<wt%Na_2O) or sodium free FAU type of zeolites are used including: Y-Zeolites such as HY, USY, dealuminated Y. RE-Y, and RE-USY; Zeolite beta, Zeolite Socony Mobil-5(ZSM-5), Mobil Composition of Matter No. 22(MCM-22), MCM-36, Metal-exchanged zeolites, Instituto de Tecnologia Quimica (ITQs), Silico-Alumino-Phosphates (SAPOs) all have corresponding high amount of silica/Alumina ratios of >1.5 with the exception of Aluminophosphate (ALPOs) mainly consist of Aluminium, Phosphorus and Oxygen (Stamires et al. 2016).

3.2.1 Zeolite Synthesis from Agricultural Waste Ash

Ash is the solid by-product generated from the combustion of coal, or agricultural residue. Although the chemical and mineralogical composition of ash varies by different factors, it is well-known that its main constituents are SiO_2, Al_2O_3, CaO, Fe_2O_3, and un burnt material (Belviso, 2018; Cardoso et al., 2015; Yang et al., 2019). The prepared solution gradually transforms into zeolite after the dissolution of Al and Si, geopolymer formation, nucleation, and crystallization steps (Belviso, 2018). Several methods exist for zeolite synthesis from ash as were highlighted in Table 4. Detailed description of these methods can be found in the cited publications.

Table 4: Methods of zeolites Synthesis from Ash

Method	Description	Advantage	Disadvantage	Ref.
Conventional hydrothermal method (CH)	The precursor containing Si and Al is mixed with an alkaline solution, aged to form a reactive aluminosilicate gel, and subsequently crystallized hydrothermally in a sealed reactor/autoclave at elevated temperature and autogenous pressure. The resulting zeolite is filtered, washed and dried.	• Simple and well-established technique. • Relatively inexpensive equipment. • Good control of zeolite phase through adjustment of Si/Al ratio, alkalinity, temperature and crystallization time. Suitable for relatively large-scale production	Relatively long crystallization time. • Conventional external heating can produce temperature gradients. • High water and energy requirements may occur during prolonged synthesis. • Some raw materials show poor dissolution/reactivity, reducing zeolite yield.	Cardoso et al. (2015)
Alkaline-fusion-assisted hydrothermal method (AFH)	The precursor is first mixed/fused with a strong alkali, commonly NaOH, at elevated temperature. This pretreatment converts relatively inert Si/Al phases into more reactive soluble or amorphous species. The fused material is then subjected to conventional hydrothermal ageing and crystallisation. conventional hydrothermal aging and crystallization	• Enhances dissolution of poorly reactive Si and Al phases. • Improves conversion of difficult industrial wastes into zeolites. • Can increase zeolite yield and crystallinity. • Provides better control of zeolite formation from refractory feedstocks.	• Requires an additional high-temperature fusion stage. • Increases energy consumption and process complexity. • Strong alkaline reagents create corrosion and handling concerns. • Excessive alkali/fusion temperature can promote undesirable phases.	Yang et al. (2019)

Method	**Description**	**Advantage**	**Disadvantage**	**Ref.**
Sonication-assisted hydrothermal method (SAH**)**	Ultrasonic irradiation is incorporated into the synthesis process before or during hydrothermal treatment. Acoustic cavitation improves mixing, mass transfer and disruption/dissolution of precursor particles, thereby accelerating nucleation and crystallisation. Sivalingam and Sen used sonication-assisted hydrothermal treatment to rapidly produce nanozeolite X from coal fly ash.	• Significantly reduces synthesis/crystallization time. • Promotes nucleation and formation of smaller zeolite crystals. • Enhances mass transfer and precursor dissolution. • Can produce nanozeolites with high external surface area. • Potentially lower energy requirement than prolonged conventional hydrothermal treatment.	• Requires ultrasonic equipment and process optimisation. • Scale-up of ultrasonic energy distribution can be challenging. • Excessive sonication may affect particle morphology. • Energy efficiency depends strongly on reactor configuration and ultrasonic intensity.	Sivalingam & Sen (2019)
Microwave-heating-assisted method (MWH)	Microwave radiation is used as the heating source for the zeolite precursor rather than relying solely on conventional external heating. Microwaves provide rapid volumetric heating, accelerating nucleation and crystallisation. Fukasawa et al. demonstrated microwave-assisted synthesis of K-type zeolites using a reverse-micelle approach.	• Very rapid heating and crystallisation. • Can substantially shorten synthesis time. • More direct heating of the reaction medium. • Can promote formation of small crystals. • Potential reduction in overall energy consumption and processing time.	• Microwave reactors can be more expensive than conventional autoclaves. • Scale-up and uniform microwave penetration can be difficult. • Heating behaviour depends on the dielectric properties of the reaction mixture. • Poor control of microwave conditions can lead to non-uniform crystallization.	Fukasawa et al. (2018)

Method	Description	Advantage	Disadvantage	Ref.
Multi-step treatment method (MST)	The synthesis is divided into several sequential treatment stages, typically involving pretreatment/extraction of the silica-rich precursor, preparation of the aluminosilicate precursor or gel, ageing/crystallisation, and subsequent washing and post-treatment. Such staged processing can improve precursor purity and control of zeolite formation. **Note:** the frequently cited Parthasarathy & Narayanan (2014) paper focuses specifically on the green synthesis of nano-silicalite-1 using biomass fly ash as a silica source and mother-liquid recycling, rather than on a general multi-step zeolite synthesis method.	• Allows individual stages to be optimised independently. • Can improve precursor purity and reactivity. • Provides better control over nucleation and crystal growth. • Mother-liquid recycling can reduce chemical/water consumption. • Particularly attractive for biomass-derived silica resource	• More processing steps increase operational complexity. • Longer overall preparation procedure may result. • Requires additional washing/separation operations. • A Greater number of processing stages can increase cost and material losses.	Narayanan (2014).

These five approaches can be viewed as progressively modifying conventional hydrothermal synthesis to overcome particular limitations. Conventional hydrothermal is the simplest and most established method, but it can be slow. Alkaline fusion-assisted improves the reactivity/dissolution of refractory precursors, but adds an energy-intensive fusion stage. Sonication-assisted primarily improves mixing, mass transfer and nucleation, making it attractive for rapid nanozeolite synthesis. Sivalingam and Sen reported nanozeolite X with crystal sizes around 22–27 nm. Microwave-assisted primarily improves heating rate and crystallisation kinetics; microwave treatment has been reported to shorten zeolite crystallisation compared with external heating. Multi-step treatment provides greater process control and precursor purification, making it particularly relevant to sustainable synthesis from Agricultural waste-derived silica.

Table 5 reviews some recent literature that demonstrates that ash is increasingly being used as a low-cost alternative source of Si and/or Al for zeolite synthesis, particularly because rice husk ash is silica-rich, whereas coal and fly ashes generally provide both silica and alumina (Zhen et al., 2024).

Table 5: Recent advances in the synthesis of zeolites from ash-derived silica

Precursor source	Product	Method	Conditions	Ref.
Rice husk ash (RHA)	NaX	Direct hydrothermal synthesis	SiO_2/Al_2O_3 molar ratio = 4; Na_2O/Al_2O_3 = 10; reaction time = 4 h; no ageing; zeolite NaX obtained with high crystallinity and surface area of about 388 $m^2\ g^{-1}$	Nguyen et al. (2021)
Rice husk ash (RHA)	Potassium zeolites (chabazite-K and mordenite)	Hydrothermal synthesis	5 mol L^{-1} KOH; solution/RHA ratio = 2 mL g^{-1}; optimum temperature = 125 °C; reaction time = 8 h; template-free synthesis	Flores et al. (2021)
Rice husk ash (RHA)	ZSM-5	Low-temperature, template-free hydrothermal synthesis of	Investigated temperature, crystallisation time and seed concentration; optimum product exhibited CO_2 adsorption capacity of 2.39 mmol g^{-1} at 273 K and 15 bar	Jia et al., (2021)
Rice husk ash (RHA)	NaA and NaX	Template-free hydrothermal synthesis	RHA calcined at 600 °C for 6 h; acid purification with 1 M HCl at 80 °C for 1.5 h; sodium silicate extraction using 2.5 M NaOH at 90 °C for 5 h; zeolite crystallisation at approximately 90–100 °C	Madhu et al. (2022)
Coal fly ash (CFA)	FAU	Hydrothermal synthesis	68h ageing, 1:10 ash-to-water mass ratio	Joseph et al., (2020)
CFA	13X	Hydrothermal synthesis	1.2:1 NaOH/CFA weight ratio, 7 h crystallisation time and 90 ◦C crystallisation temperature	Verrecchia et al., (2020)
RHA	NaA,NaX and NaZSM-5	Seeding-assisted hydrothermal method	-	Wang et al., (2018)

Most recent studies have focused on ash from CFA and RHA for the zeolite synthesis. There were no reported studies from a reputable source on zeolites synthesized from other agricultural waste such as rice straw, corn cub and sugarcane bagasse, particularly Zeolite Y. Exploitation of other agricultural waste could complement the already established RHA precursor for the development of FCC/RFCC catalyst at an industrial level.

3.2.2 Important Properties of Agricultural-Waste-Derived Silica for Catalyst Development

Agricultural-waste-derived silica intended for FCC/RFCC catalyst preparation should possess a combination of high chemical purity, amorphous structure, high reactivity, suitable textural properties, low contaminant levels, and adequate thermal stability. The functionalities of these

properties are shown in Table 6. These are particularly important when silica is used as a precursor for zeolite-Y synthesis, a principal active component of many FCC catalysts.

Table 6: Properties of Silica for catalyst application

Property	Level	Significance
High SiO_2 purity	Preferably ≥90 wt.% after purification	Minimises unwanted impurities and provides a consistent silica source for zeolite synthesis.
Structure	Amorphous SiO_2	Provides greater chemical reactivity than highly crystalline silica during zeolite synthesis.
Metallic impurities	Low Fe, Ca, Mg, K, Na and other mineral oxides	Minimises interference with zeolite crystallisation and unwanted catalytic reactions.
Reactivity	High	Facilitates incorporation of silica into the aluminosilicate framework.
Surface area	High	Provides greater accessible surface for interaction with synthesis components and catalyst matrix.
Pore size	Micro & meso-porosity	Facilitates the diffusion of reactants and products, particularly important for residual molecules.
Particle size	Fine, relatively uniform particles	Improves dispersion and mixing during catalyst preparation.
Surface hydroxylation	≡Si–OH groups	Provides chemically active surface functionalities.

FCC/RFCC catalyst are made from silica that possesses high SiO_2 purity, a predominantly amorphous structure, low concentrations of metallic impurities, high chemical reactivity, suitable surface area and pore characteristics, controlled particle morphology, and adequate thermal stability. High-purity amorphous silica is particularly desirable as a precursor for zeolite-Y synthesis because its reactive structure facilitates interaction with aluminium-containing species during hydrothermal crystallisation (Hamdan et al., 1997; Yunusa et al., 2016). Rice-husk-derived silica has demonstrated these characteristics, with reported SiO_2 purities of approximately 96–98% and successful application in NaY/zeolite-Y synthesis (Wittayakun et al., 2008; Yunusa et al., 2016). Furthermore, controlled combustion and chemical pretreatment can minimise crystalline silica phases and inorganic impurities, thereby improving the suitability of the resulting silica as a zeolite precursor (Hamdan et al., 1997; Ngoc et al., 2018). For RFCC applications, these precursors' properties should ultimately translate into zeolite-Y with high crystallinity, appropriate Si/Al ratio, accessible porosity, suitable acidity, and sufficient thermal and hydrothermal stability

4. CONCLUSION

This review demonstrates that agricultural-waste-derived silica is a promising sustainable precursor for developing of FCC/RFCC catalysts, particularly zeolite-Y-based systems. It was also highlighted that rice husk, rice straw, sugarcane bagasse, and corn cob yield amorphous silica of high purity (commonly 90–98%) after acid leaching, controlled calcination, and alkaline dissolution to sodium silicate and in Nigeria alone, these residues are generated at an estimated 10.79 million tonnes per year, much of it burnt or left to create a nuisance where it can approximately generate 1.09 million tonnes per year of pure amorphous silica. The review considers how agricultural-waste silica can supply the sodium-free silica binder and the silica source for seeded zeolite-Y synthesis, with metakaolin as the alumina source, and how it must satisfy the low-sodium, high-purity, reactivity, and attrition-resistance requirements specific to cracking catalysts. Although, agricultural-waste silica is a viable,

sustainable precursor for FCC/RFCC catalysts, the impurity control, feedstock variability, catalyst-grade specification, and scale-up are the principal challenges to industrial adoption

ACKNOWLEDGEMENTS

The authors gratefully acknowledge the support provided by the Petroleum Technology Development Fund (PTDF) Chair in Chemical Engineering at Ahmadu Bello University, Zaria.

5. REFERENCES

Adebisi, J. A., Agunsoye, J. O., Bello, S. A., Haris, M., Senthilkumar, M., Rherari, A., & Hassan, S. B. (2020). Silica nanoparticles synthesized from maize cob using modified sol-gel method. Nigerian Journal of Technological Research, 15(2), 22–29. https://www.researchgate.net/profile/Amal_Rherari2/publication/343425635_Silica_Nanoparticles_Synthesized_from_Maize_Cob_using_Modified_SolGel_Method/links/65020bc58d6da36cc877d91f/Silica-Nanoparticles-Synthesized-from-Maize-Cob-using-Modified-SolGel-Method.pdf

Adanenche, D. E., Aliyu, A., Atta, A. Y., & El-Yakubu, B. J. (2023). Residue fluid catalytic cracking: A review on the mitigation strategies of metal poisoning of RFCC catalyst using metal passivators/traps. Fuel. https://doi.org/10.1016/j.fuel.2023.127894

Aharipour, N., Nemati, A., & Malek Khachatourian, A. (2022). Green synthesis of silica extracted from rice husk ash. Advanced Ceramics Progress, 8(4), 15–20. https://www.acerp.ir/article_159416_6b956222b8b1b1ef86d406a2b2bc4365.pdf

Barani, S., Sebastian, S. P., Dhevagi, P., Prasanthrajan, M., & Suganthi, A. (2024). Synthesis of silica nanoparticles (SiNPs) from agro-wastes for removal of heavy metals from an aqueous medium—A mini review. Green Chemistry Letters and Reviews, 17(1), 2422416. https://doi.org/10.1080/17518253.2024.2422416

Borges, L. D. (2011). Preparação, caracterização e atividade catalítica de zeólitas Y desaluminizadas: Investigação das interações fluido-sólido [Master's thesis, Universidade de Brasília].

Cardoso, A. M., Paprocki, A., Ferret, L. S., Azevedo, C. M. N., & Pires, M. (2015). Synthesis of zeolite Na-P1 under mild conditions using Brazilian coal fly ash and its application in wastewater treatment. Fuel, 139, 59–67.

Carraro, P. M., Benzaquén, T. B., & Eimer, G. A. (2021). Eco-friendly synthesis of nanostructured mesoporous materials from natural source rice husk silica for environmental applications. Environmental Science and Pollution Research, 28(19), 23707–23719. https://doi.org/10.1007/s11356-020-11043-0

El Bojaddaynia, I., Mehmet, E. K., Youssef, E., Issam, J., Soufian, E., Kamal, M., Eveliina, R., Katri, L., & Abdelkrim, O. (2023). A review on synthesis of zeolites from natural clay resources and waste ash: Recent approaches and progress. Minerals Engineering, 198, 108086. https://doi.org/10.1016/j.mineng.2023.108086

Falk, G., Shinhe, G. P., Teixeira, L. B., Moraes, E. G., & de Oliveira, A. N. (2019). Synthesis of silica nanoparticles from sugarcane bagasse ash and nano-silicon via magnesiothermic reactions. Ceramics International, 45(17), 21618–21624. https://www.sciencedirect.com/science/article/pii/S0272884219319789

Farirai, F., Ozonoh, M., Aniokete, T. C., Eterigho-Ikelegbe, O., Mupa, M., Zeyi, B., & Daramola, M. O. (2021). Methods of extracting silica and silicon from agricultural waste ashes and application of the produced silicon in solar cells: A mini-review. International Journal of Sustainable Engineering, 14(1), 57–78. https://doi.org/10.1080/19397038.2020.1720854

Ferreira, J. M. M., Eduardo, F. S., & Donato, G. A. (2023). FCC catalyst accessibility—A review. Catalysts, 13, 784. https://doi.org/10.3390/catal13040784

FAOU (2026) Food and Agriculture Organization of the United Nations 2026 Annual Report.

Fukasawa, T., Horigome, A., Karisma, A. D., Ishigami, T., & Fukui, K. (2018). Synthesis of potassium-type zeolites by the reverse-micelle method with microwave heating. Colloids and Surfaces A: Physicochemical and Engineering Aspects, 555, 532–538. https://doi.org/10.1016/j.colsurfa.2018.07.039

Garcia, G., Cardenas, E., Cabrera, S., Hedlund, J., & Mouzon, J. (2016). Synthesis of zeolite Y from diatomite as silica source. Microporous and Mesoporous Materials, 219, 29–37. https://doi.org/10.1016/j.micromeso.2015.07.015

Hamdan, H., Muhid, M. N. M., Endud, S., Listiorini, E., & Ramli, Z. (1997). 29Si MAS NMR, XRD and FESEM studies of rice husk silica for the synthesis of zeolites. Journal of Non-Crystalline Solids, 211(1–2), 126–131. https://doi.org/10.1016/S0022-3093(96)00611-4

Hamid, I., Daniel, A. A., Bright, K. A., & Benjamin, A. (2025). Synthesis of silica and silicon from rice husk feedstock: A review. Heliyon. https://doi.org/10.1016/j.heliyon.2025.e42491

Harun, Z., Azhar, F. H., Hussin, R., Ibrahim, S. A., Hubadillah, S. K., & Sazali, N. (2024). The extraction of organic silica from agricultural waste: a mini review. Emerging Advances in Integrated Technology, 5(1), 65–74. Retrieved from https://publisher.uthm.edu.my/ojs/index.php/emait/article/view/18171

Islam, K., Islam, T., Shiddique, M. N. A., Roy, M. N., Fahimuzzaman, M., Islam, M. A., Bashar, M. M., & Khan, M. A. (2024). Utilization of jute waste for sustainable eco-film preparation. *ACS Sustainable Resource Management*, *1*(3), 517–529. https://doi.org/10.1021/acssusresmgt.3c00123

Jia, H., Du, T., Fang, X., Gong, H., Qiu, Z., Li, Y., & Wang, Y. (2021). Synthesis of template-free ZSM-5 from rice husk ash at low temperatures and its CO_2 adsorption performance. *ACS Omega*, *6*(5), 3961–3972. https://doi.org/10.1021/acsomega.0c05842

Joseph, I. V., Tosheva, L., & Doyle, A. M. (2020). Simultaneous removal of Cd(II), Co(II), Cu(II), Pb(II), and Zn(II) ions from aqueous solutions via adsorption on FAU-type zeolites prepared from coal fly ash. Journal of Environmental Chemical Engineering, 8(4), 103895. https://doi.org/10.1016/j.jece.2020.103895

Kamari S, & Ghorbani F. (2021) Extraction of highly pure silica from rice husk as an agricultural by-product and its application in the production of magnetic mesoporous silica MCM–41. Biomass Conversion and Biorefinery, 69,3001–3009

Kouadri, I., Seghir, B. B., Hemmami, H., Zeghoud, S., Allag, N., Rebiai, A., Amor, I. B., Chala, A., & Belkhalfa, H. (2023). Extraction of silica from different sources of agricultural waste. Asian Journal of Research in Chemistry, 16(1), 97–101. Retrieved from https://indianjournals.com/article/AJRC-16-1-016

Li, J., Ma, S., & Xu, N. (2025a). A two-step hydrothermal synthesis of fly-ash-based ZSM-5 zeolite and its catalytic properties in NO removal. Journal of Water Process Engineering, 69, 106608. https://doi.org/10.1016/j.jwpe.2024.106608

Li, J., Ma, S., & Xu, N. (2025b). Two-step hydrothermal synthesis of fly ash-based β zeolite and its application in catalytic oxidation of NO with H_2O_2. Energy & Fuels, 39(13), 6517–6532. https://doi.org/10.1021/acs.energyfuels.5c00185

Madhu, J., Santhanam, A., Natarajan, M., & Velauthapillai, D. (2022). CO_2 adsorption performance of template-free zeolite A and X synthesized from rice husk ash as silicon source. RSC Advances, 12, 23221–23239. https://doi.org/10.1039/D2RA04052B

Mohd, N. K., Wee, N. N. A. N., & Azmi, A. A. (2017). Green synthesis of silica nanoparticles using sugarcane bagasse. AIP Conference Proceedings, 1885(1), 020123. https://pubs.aip.org/aip/acp/article-abstract/1885/1/020123/972575

Musyoka, N. M., Missengue, R., Kusisakana, M., & Petrik, L. F. (2014). Conversion of South African clays into high-quality zeolites. Applied Clay Science, 97, 182–186. http://hdl.handle.net/10204/7730

Na Chat, N., Sangsuradet, S., Tobarameekul, P., & Worathanakul, P. (2022). Modified hierarchical zeolite X derived from riceberry rice husk for propionic acid adsorption. Materials Chemistry and Physics, 282, 125933. https://doi.org/10.1016/j.matchemphys.2022.125933

NAERLS (2025) National Agricultural Extension and Research Liaison Services 2025 Annual Report.

Ngoc, N. N., Thanh, L. X., Vinh, L. T., & Van Anh, B. T. (2018). High-purity amorphous silica from rice husk: Preparation and characterization. Vietnam Journal of Chemistry, 56, 730–736. https://doi.org/10.1002/vjch.201800079

Ni'mah, Y. L., Muhaiminah, Z. H., & Suprapto. (2023). Synthesis of silica nanoparticles from sugarcane bagasse by sol-gel method. AIP Conference Proceedings, 2540(1), 050011. https://pubs.aip.org/aip/acp/article-abstract/2540/1/050011/2873723

Okoronkwo, E. A., Imoisili, P. E., & Olusunle, S. O. O. (2013). Extraction and characterization of amorphous silica from corn cob ash by sol-gel method. Chemistry and Materials Research, 3(4), 68–72. https://www.academia.edu/download/31200352/Extraction_of_silica_paper_2013.pdf

Okoye, E., Boateng, B. O., & Amoatey, P. K. (2025). Synthesis of silica and silicon from rice husk feedstock: A review. Heliyon, 11, e42491. https://doi.org/10.1016/j.heliyon.2025.e42491

Pa, F. C., Abdullah, C., & Fazlul, B. (2013). Review of extraction of silica from agricultural wastes using acid leaching treatment. Advanced Materials Research, 626, 997–1000. Retrieved from https://www.scientific.net/ AMR.626.997

Parthasarathy, P., & Narayanan, S. K. (2014). Green synthesis of nano-silicalite-1: Biomass fly ash as a silica source and mother liquid recycling. Environmental Progress & Sustainable Energy, 33(3), 676–680.

Phoungthong, K., Teamsinsungvon, A., & Ruksakulpiwat, Y. (2026). Sustainable production of high-purity amorphous silica from rice husk: A comparative study on the impact of fresh and reused hydrochloric acid leaching. Heliyon. https://doi.org/10.1016/j.heliyon.2026.e00021

Palos, R., Gutiérrez, A., Fernández, M. L., Trueba, D., Bilbao, J., & Arandes, J. M. (2020). Different approaches to convert waste polyolefins into automotive fuels via hydrocracking with a NiW/HY catalyst**.** *Fuel Processing Technology, 205*, 106454.

Rodriguez-Otero, A., Vargas, V., Galarneau, A., Castillo, J., Christensen, J. H., & Bouyssiere, B. (2023). Sustainable harnessing of SiO_2 nanoparticles from rice husks: A review of the best synthesis and applications. Processes, 11(12), 3373. https://doi.org/10.3390/pr11123373

Sadeghbeigi, R. (Ed.). (2020). Fluid catalytic cracking handbook (4th ed.). Butterworth-Heinemann.

Seghir, B. B., Hemmami, H., Hocine, B. M. E., Soumeia, Z., Sharifi-Rad, M., Awuchi, C. G., Amor, I. B., Kouadri, I., Rebiai, A., Bouthaina, S., Malik, A., Meniai, C., Pohl, P., & Messaoudi, M. (2023). Methods for the Preparation of Silica and Its Nanoparticles from Different Natural Sources. Biological Trace Element Research, 201(12), 5871 5883. doi: 10.1007/s12011-023-03628-w

Shahbaz, A., Ayaz, M., Bin Khalid, U., & Liaqat, L. (2023). Sustainable synthesis of silica nanoparticles from agricultural waste and its utilization in modern technology: A review. Energy Sources, Part A: Recovery, Utilization, and Environmental Effects, 45(1), 1464–1484. https://doi.org/10.1080/15567036.2023.2180552

Sivalingam, S., & Sen, S. (2019a). Swift sono-hydrothermal synthesis of pure NaX nanocrystals with improved sorption capacity from industrial resources. Applied Surface Science, 463, 190–196. https://doi.org/10.1016/j.apsusc.2018.08.019

Sivalingam, S., & Sen, S. (2019b). Valorization of coal fly ash into nanozeolite by sonication-assisted hydrothermal method. Journal of Environmental Management, 235, 145–151. https://doi.org/10.1016/j.jenvman.2019.01.042

Todkar, B. S., Deorukhkar, O. A., & Deshmukh, S. M. (2016). Extraction of silica from rice husk. International Journal of Engineering Research and Development, 12(3), 69–74.

Verrecchia, G., Cafiero, L., de Caprariis, B., Dell'Era, A., Pettiti, I., Tuffi, R., & Scarsella, M. (2020). Study of the parameters of zeolites synthesis from coal fly ash in order to optimize their CO_2 adsorption. Fuel, 276, 118041. https://doi.org/10.1016/j.fuel.2020.118041

Vogt, E., & Weckhuysen, B. (2015). Fluid catalytic cracking: Recent developments on the grand old lady of zeolite catalysis. Chemical Society Reviews, 44, 7342–7370.

Wang, Y., Du, T., Jia, H., Qiu, Z., & Song, Y. (2018). Synthesis, characterization and CO_2 adsorption of NaA, NaX and NaZSM-5 from rice husk ash. Solid State Sciences, 86, 24–33. https://doi.org/10.1016/j.solidstatesciences.2018.10.003

Wittayakun, J., Khemthong, P., & Prayoonpokarach, S. (2008). Synthesis and characterization of zeolite NaY from rice husk silica. Korean Journal of Chemical Engineering, 25(4), 861–864.

Yang, L., Qian, X., Yuan, P., Bai, H., Miki, T., Men, F., Li, H., & Nagasaka, T. (2019). Green synthesis of zeolite 4A using fly ash fused with synergism of NaOH and Na_2CO_3. Journal of Cleaner Production, 212, 250–260. https://doi.org/10.1016/j.jclepro.2018.11.259

Yunusa, S., Ahmed, A. S., Bawa, S. G., Iyun, J. F., & Dauda, M. (2016). Preparation of high-grade silica from rice husk for zeolite synthesis. Nigerian Journal of Basic and Applied Sciences, 24(1), 41–45. https://doi.org/10.4314/njbas.v24i1.7

Zhen, L., Zhimei, L., Lian, Y., & Wang, W. (2024). Fly ash-based zeolites: From waste to value—A comprehensive overview of synthesis, properties, and applications. Chemical Engineering Research and Design, 212–240–260. https://doi.org/10.1016/j.cherd.2024.10.031

Zhu, J., Meng, X., & Xiao, F. (2013). Mesoporous zeolites as efficient catalysts for oil refining and natural gas conversion. *Frontiers of Chemical Science and Engineering, 7*, 233–248

SUGARCANE BAGASSE ASH AS A SUSTAINABLE SILICA PRECURSOR FOR ZEOLITE SYNTHESIS: A REVIEW OF EXTRACTION ROUTES

Gabriel Christopher[1,*], Abdulazeez Yusuf Atta[1], Baba Jibril El-Yakubu[1], Olusegun Ayoola Ajayi[1], Mustapha Yusuf[1]

[1]*Ahmadu Bello University Zaria*

Email: christophergabriel482@gmail.com[*], ayatta@abu.edu.ng, byjibril@gmail.com, segeaj@gmail.com, myusuf@abu.edu.ng

***Corresponding author**: Gabriel Christopher

DOI: https://doi.org/10.67203/sp.ICESID.2026

ABSTRACT

Zeolite synthesis requires reactive silica sources, which are conventionally supplied by costly and energy-intensive reagents such as tetraethyl orthosilicate and sodium silicate. Sugarcane bagasse ash (SCBA), an abundant sugar-industry residue, provides a low-cost, renewable alternative due to its high silica content. In Nigeria, the three major sugar industry generates an estimate of 1 million metric tonnes of bagasse annually, highlighting the potential for converting this underutilised residue into a valuable feedstock. This review compares principal silica extraction routes from SCBA and evaluates their suitability for ZSM-5 synthesis from SCBA and metakaolin. The conventional route involves acid leaching, calcination near 600 °C, alkaline dissolution in sodium hydroxide, and acid precipitation. Although this route produces amorphous, high-surface-area silica and high recovery but high energy and reagent consumption. Calcination-free acid–alkali extraction offers a more sustainable alternative by directly dissolving SCBA in sodium hydroxide and precipitating silica using hydrochloric acid, producing silica with purity of approximately 98% while reducing energy demand. Characterisation using XRD, FTIR, BET, and electron microscopy provides information on phase composition, functional groups, surface area, and morphology. The extraction route strongly influences silica purity, recovery, reactivity, and sustainability. Calcination-free approaches are particularly promising for green ZSM-5 synthesis, although optimisation of yield, impurity removal, reagent consumption, and scale-up remains necessary for industrial application.

Keywords: *sugarcane bagasse ash; silica extraction; ZSM-5 zeolite; green synthesis; waste valorisation*

1. INTRODUCTION.

There is an increasing focus on the development of sustainable processes for the conversion of industrial and agricultural wastes into valuable products. Among agricultural residues, sugarcane bagasse is particularly important because it is generated in large quantities during sugar production. Bagasse is commonly combusted in sugar mills to generate heat and electricity, producing sugarcane bagasse ash (SCBA) as a solid residue. Although part of the ash can be used in construction materials and other applications, substantial quantities remain underutilised. SCBA is of particular interest because silica can constitute a significant fraction of its inorganic content. The concentration of silica varies considerably with sugarcane variety, geographical origin, soil conditions, combustion conditions, and ash-processing history. Consequently, SCBA should not be regarded as a chemically uniform raw material; rather, its composition must be established before it is incorporated into a silica-recovery process. Previous reviews have identified SCBA as a promising source of silica and have examined different extraction and purification strategies for producing silica and silicon-based materials (September *et al.*, 2023). The conversion of SCBA into silica is especially relevant to zeolite production. Zeolites are crystalline microporous aluminosilicates with well-defined pore structures, high internal surface areas, ion-exchange capacity, and catalytic properties. They have extensive applications in adsorption, ion exchange, petroleum refining, petrochemicals, environmental remediation, and chemical catalysis. ZSM-5, which is widely used because of its shape-selective properties and hydrothermal stability (Manyepedza *et al.*, 2025). Conventional synthesis of zeolites often uses

commercially available silica sources such as sodium silicate, colloidal silica, silica sol, or organosilicon compounds. Although these materials provide relatively consistent composition and reactivity, their production can increase the cost and environmental footprint of zeolite synthesis. Replacing conventional silica sources with waste-derived silica can therefore improve the sustainability of the overall process (Manyepedza *et al.*, 2025). The potential of SCBA as a zeolite precursor has already been demonstrated. For example, SCBA-derived silica has been used to synthesise zeolite A under hydrothermal conditions, demonstrating that agricultural waste can serve as a viable silicon source for zeolite production (Cordeiro et al., 2013). More recent research has also demonstrated the extraction of high-purity silica from SCBA and its subsequent use in zeolite synthesis (Keawkumay et al., 2024). This review therefore focuses on emphasising the relationships among extraction conditions, silica quality, environmental performance, and suitability for zeolite synthesis. Particular attention is given to the potential application of SCBA-derived silica in of ZSM-5 from SCBA and metakaolin.

2.0 SUGARCANE BAGASSE ASH AS A SOURCE OF SILICA

2.1 Sugarcane Bagasse ash generation

Much research has been conducted to extract silica from various sources, such as plants, clay, rocks, and agricultural wastes, considering that it is a vital material for industrial applications. Waste from agricultural activities is produced daily and can result in a significant amount (September *et al.*, 2023). Sugarcane bagasseis an agricultural waste, a fibrous residue remaining after the extraction of juice from sugarcane. Because of its relatively high organic content, bagasse is commonly burned as a fuel in sugar-processing facilities. The figure1. illustrates the potential for bagasse generation from major Nigerian sugar-producing companies. The three companies represented in Figure 1 shows the industrial substantial availability of sugarcane-derived biomass for valorisation into value-added products such as silica and zeolite precursors.

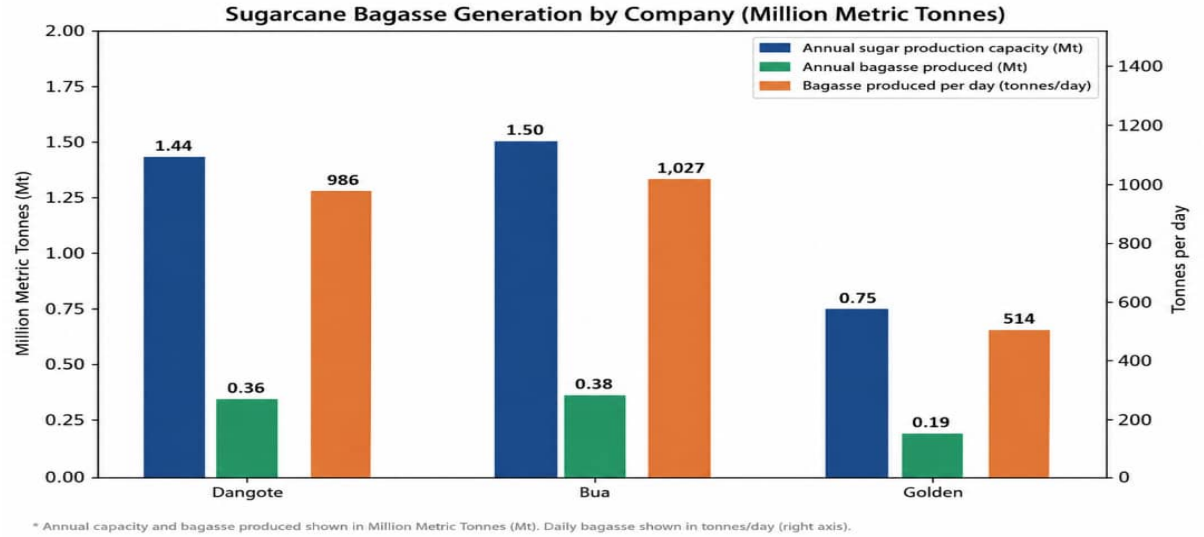

Figure 1: Sugarcane Bagasse Generation by Company(Million Metric Tonnes) (Companies report 2025)

The amount and composition of SCBA depend on combustion efficiency, ash collection practices, and the composition of the original bagasse. Silica is generally the major inorganic component of SCBA, although the ash may contain other mineral constituents. The presence of these impurities is important because they can influence both silica recovery and subsequent zeolite crystallisation (Seroka *et al.*, 2022). The high silica content of SCBA provides an opportunity to convert an agricultural residue into a value-added chemical feedstock. Rather than treating ash exclusively as a disposal problem, silica extraction offers an opportunity to integrate waste management with advanced materials production.

2.2 Importance of silica reactivity

The physical and chemical form of silica is of great importance. The state of silica determines its reactivity, as amorphous silica is more reactive than crystalline silica under alkaline hydrothermal

conditions; therefore, extraction procedures are used not only to increase purity but also to increase chemical reactivity (September *et al.*, 2023).

SCBA → impurity removal → silica dissolution → silica recovery → purified reactive SiO_2 can be seen as the objective of silica extraction, where the purified reactive silica can be used to form an aluminosilicate synthesis gel when combined with an alumina source.

3.0 PRETREATMENT AND PURIFICATION

3.1 Physical pretreatment

Size reduction increases mass transfer. However, particle-size reduction increases energy demand, so it should be matched to the extraction kinetics. Removal of visible unburnt carbon and foreign mineral particles can improve subsequent filtration. Washing can remove soluble salts but may also increase wastewater generation. A practical flowsheet should therefore include only those physical operations that measurably improve downstream silica quality.

3.2 Acid leaching

Acid leaching is a purification process that remove soluble metallic impurities, thereby increasing the relative concentration and purity of silica (Farirai *et al*., 2021). The principal disadvantage of mineral-acid leaching is reagent consumption and the production of acidic effluent containing dissolved salts and metals. Citric acid has therefore attracted interest as a milder, bio-based alternative. The SCBA review by September et al. (2023) reports citric acid pretreatment as a green approach, while broader agricultural-waste literature similarly considers organic acids, lower temperatures, and reduced chemical severity as routes to improve environmental performance.

3.3 Calcination

Calcination increases reactivity of the silica structure. The environmental cost of thermal treatment includes energy demand and direct or indirect greenhouse-gas emissions. The correct calcination temperature is therefore feedstock-specific. A temperature high enough to remove residual carbon can be beneficial, whereas excessive temperature can promote silica crystallisation and sintering (Karumanchi et al., 2022). For a ZSM-5 precursor, preservation of reactive amorphous silica is usually more important than maximising thermal treatment. This is consistent with broader work showing that the structure and reactivity of biomass-derived silica depend on combustion and post-treatment history.

4.0 SILICA EXTRACTION ROUTES FROM SCBA

The silica in raw SCBA is usually associated with carbonaceous residues and mineral impurities such as calcium, potassium, iron, magnesium, and aluminium. Therefore, the purity and reactivity of silica before its use as a precursor for zeolite synthesis (September *et al.*, 2023).

4.1 Conventional acid–calcination–alkali route

The conventional route can be represented as: SCBA → size reduction → acid leaching → washing/drying → calcination → NaOH dissolution → solid–liquid separation → HCl precipitation → washing/drying → silica. Acid leaching removes metallic impurities; calcination removes carbon and stabilises the ash; NaOH extracts sodium silicate; and HCl forms a silica xerogel (Louis *et al*., 2026). The sequence is chemically robust but may require multiple unit operations and substantial amounts of water, acid, base, and thermal energy.

4.2 Calcination-free acid–alkali extraction

A calcination-free route reduces or eliminates the need for deliberate post-leaching thermal treatment. The route followed was acid-treated SCBA, then extracted with 1.0 M NaOH at 90 °C for 2 h at a reported 1:8 solid-to-liquid ratio, followed by filtration and precipitation with 1.0 M HCl. Approximately 98 wt% purity silica was recovered and was subsequently used to synthesise zeolite NaA (Keawkumay et al., 2024). This is especially relevant to sustainable processing because it demonstrates that suitable silica can be obtained without a separate high-temperature calcination step.

4.3 Organic leaching agents

Citric acid and other organic acids are attractive because they can complex metal impurities and reduce dependence on strong mineral acids. Their suitability depends on ash mineralogy and the intended silica application (Seroka *et al*., 2022). An organic leaching agent is not automatically more sustainable if large quantities are required or if recovery is poor. Therefore, comparison should be based on acid consumption per kilogram of purified SiO_2, water demand, wastewater treatment, energy use, silica yield, and product performance rather than on acid identity alone.

Table 1: Comparative Assessment of Extraction Routes

Route	**Main purpose**	**Major advantage**	**Major limitation**	**Typical product**	**Suitability for ZSM-5**	**REFERENCES**
Acid–calcination–alkali	Purification + activation	High controllability	High energy/reagent demand	High-purity amorphous silica	High, if SiO_2 remains reactive	Louis *et al*., 2026
Calcination-free acid–alkali	Purification+ direct extraction	Lower thermal demand	Requires effective impurity control	High-purity silica	Very promising	Keawkumay et al., 2024
Organic-acid + alkali	Greener purification	Milder leaching chemistry	Potentially slower/greater acid demand	Purified silica	Promising after optimisation	Seroka *et al*.,2022

5.0 ZSM-5 SYNTHESIS USING SCBA-DERIVED SILICA AND METAKAOLIN

In the synthesis of ZSM-5 zeolite, the extracted silica from SCBA undergoes a chemical reaction with alumina derived from metakaolin after dihydroxylation and depolymerisation of kaolin. This allows the Si/Al ratio to be adjusted independently of the variable Al content of SCBA. It also reduces the need to force a single waste stream to provide both framework elements. (Nguyen *et al*., 2023). In ZSM-5 synthesis, the key parameters include Si/Al ratio, Na_2O/SiO_2 ratio, H_2O/SiO_2 ratio, structure-directing-agent concentration, ageing, crystallisation temperature, and crystallisation time. Recent review shows that silica sourced from natural and waste material can be used successfully to synthesis ZSM-5, but impurities and inconsistent precursor reactivity can shift the product toward competing phases. Consequently, SCBA-derived silica should be characterised and standardised before gel preparation. (Bensafi *et al.*, 2023).For a high-silica ZSM-5 target, an initial design window may use a Si/Al molar ratio in the approximate range of 25–50, followed by experimental optimisation. The desired acidity, crystallinity and catalytic application should be the final optimum goal rather than assumed from a generic recipe. The sodium content introduced during silica extraction is particularly important, excessive Na can alter nucleation and favour undesired phases, while insufficient alkalinity may limit precursor dissolution. Recent studies on waste-derived ZSM-5 show that post-extraction adjustment of sodium and Si/Al ratios can substantially affect phase purity and yield (Manyepedza *et al*., 2025). Where an organic structure-directing agent is used, the environmental advantage of SCBA-derived silica can be weakened if the SDA is expensive, toxic or difficult to remove.

6.0 ENVIRONMENTAL AND ECONOMIC CONSIDERATIONS

The environmental benefit of SCBA valorisation depends on the complete process rather than on waste substitution alone. Acid consumption, NaOH demand, water use, drying energy, calcination energy, filtration, wastewater neutralisation and chemical by-product generation can all contribute to the environmental footprint of silica extraction. (Keawkumay *et al*., 2024) noted that conventional calcination of SCBA consumes significant energy and generates CO_2, while their alternative HCl–NaOH extraction route still involved chemical treatment and neutralisation steps. Life-cycle studies of biomass valorisation similarly demonstrate that chemical consumption, energy demand, wastewater treatment and downstream processing can become important environmental hotspots (Munagala *et al*., 2021; Zhang et al., 2021). Therefore, a route that avoids calcination but consumes excessive quantities

of NaOH may not necessarily outperform a thermally optimised conventional route. Life-cycle assessment should consequently compare the complete system against commercial silica production and alternative waste-management pathways. Recent studies increasingly incorporate process intensification and life-cycle thinking into biomass and waste valorisation. In particular, microwave-assisted SCBA extraction has been reported to reduce processing time and electricity demand compared with conventional heating, while a screening LCA showed approximately 33–40% lower environmental impacts for bagasse-ash-derived sodium silicate than soda-ash fusion of silica sand for an equivalent SiO_2 output; calcination was identified as a major environmental hotspot (Krainara et al., 2025). Similarly, comparative LCA of zeolite production has shown that replacing conventional chemical Si and Al sources with natural mineral feedstocks can reduce environmental impacts and improve resource utilisation (Chen *et al*., 2024).

7.0 CHALLENGES AND RESEARCH GAPS

Silica purity alone is insufficient; reactivity toward NaOH and compatibility with zeolite gel chemistry should become routine performance metrics. Water and chemical consumption can become dominant sustainability burdens. Scale-up of filtration and gel washing is likely to be more difficult than laboratory precipitation. Direct ash-to-zeolite routes require careful control of impurity accumulation. The role of sodium introduced during extraction needs explicit mass balance because it can influence zeolite nucleation and phase selection. Another important gap is the limited number of studies that connect silica extraction conditions directly to final ZSM-5 performance. Many studies stop at XRF, XRD, FTIR and SEM of silica or demonstrate a different zeolite topology. A stronger research programme should compare extraction route → silica structure/reactivity → gel chemistry → crystallisation → ZSM-5 acidity/porosity → catalytic performance. This chain would identify whether a lower-purity but highly reactive silica is preferable to a very pure but poorly soluble silica.

8.0 CONCLUSION

Recent literature supports SCBA as a credible renewable and waste-derived silica precursor for zeolite synthesis. The key finding is that the value of SCBA is governed not only by its total SiO_2 content but by silica phase, impurity composition and chemical reactivity. Conventional acid–calcination–alkali processing can produce high-quality silica but carries greater energy and chemical burdens. Calcination-free acid–alkali extraction is therefore particularly attractive, and the demonstration of approximately 98 wt% silica followed by successful zeolite A synthesis provides direct evidence of technical feasibility. For ZSM-5, SCBA-derived silica should be considered a promising silicon source that can be paired with metakaolin to provide controlled aluminium. The most important future direction is an integrated process in which silica extraction and zeolite synthesis are designed together. This approach should optimise reactive silica recovery, impurity removal, Si/Al ratio, alkali concentration, SDA demand and crystallisation conditions simultaneously. The strongest sustainability case will come from a route that minimises calcination, water and hazardous reagents while maintaining high silica recovery and high-purity ZSM-5.

ACKNOWLEDGEMENT

The authors gratefully acknowledge the support provided by the Petroleum Technology Development Funds (PTDF) Chair in Chemical Engineering at Ahmadu Bello University Zaria

REFERENCES

September, L. A., Kheswa, N., Seroka, N. S., & Khotseng, L. (2023). *Green synthesis of silica and silicon from agricultural residue sugarcane bagasse ash – A mini review. RSC Advances, 13, 1370–1380.* https://doi.org/10.1039/D2RA07490G

Manyepedza *et al*., *ZSM-5 Zeolite Synthesis from Coal Fly Ash Synthesised Silica: Sole Silica & Alumina Source*, Chemistry Open (2025).

Cordeiro, G. C., Toledo Filho, R. D., & Fairbairn, E. M. R. (2013). Synthesis of zeolite NaA from sugarcane bagasse ash. *Materials Letters*, *108*, 243–246. https://doi.org/10.1016/j.matlet.2013.06.086

Keawkumay, C., Krukkratoke, P., Youngjan, S., Osakoo, N., Deekamwong, K., Khemthong, P., Phanthasri, J., Prayoonpokarach, S., & Wittayakun, J. (2024). Extraction of silica from sugarcane bagasse ash and its utilisation in zeolite 4A synthesis for CO_2 adsorption. *RSC Advances*, *14*, 19472–19482. https://doi.org/10.1039/D4RA02207

Seroka, *et al.*, (2022). Green synthesis of crystalline silica from sugarcane bagasse ash: Physico-chemical properties. *Nanomaterials*, *12*(13), 2184. https://doi.org/10.3390/nano12132184

Farirai *et al.*, (2021). Methods of extracting silica and silicon from agricultural waste ashes and application of the produced silicon in solar cells: a mini-review. International Journal of Sustainable Engineering, 14, 57–78. https://doi.org/10.1080/19397038.2020.1720854

Karumanchi, M., Nerella, R., & Mikkili, I. (2022). An integrated approach on extraction methodologies of nanosilica from cultivated agricultural wastes and microstructural characteristics—A review. *Materials Today: Proceedings*, *62*(6), 2883–2891. https://doi.org/10.1016/j.matpr.2022.02.476

Louis, S., & Kuchelar, P. (2026). Reactive silica enrichment from sugarcane bagasse ash by optimized calcination and alkali activation for zeolite applications. *Environmental Progress & Sustainable Energy*, e70572. https://doi.org/10.1002/ep.70572

Nguyen, D.-K., Dinh, V.-P., Nguyen, H. Q., & Hung, N. T. (2023). Zeolite ZSM-5 synthesized from natural silica sources and its applications: A critical review. *Journal of Chemical Technology & Biotechnology*, *98*(6), 1339–1355. https://doi.org/10.1002/jctb.7380

Chen, X., Xiao, G., Li, T., Wang, C., Cui, Q., Bao, X., & Yue, Y. (2024). *Comparative environmental assessment of zeolites synthesized from chemicals and natural minerals. Green Chemistry, 26, 5273–5283. https://doi.org/10.1039/D3GC05146C*

Munagala, M., Shastri, Y., Nalawade, K., Konde, K., & Patil, S. (2021). *Life cycle and economic assessment of sugarcane bagasse valorization to lactic acid. Waste Management, 126, 52–64. https://doi.org/10.1016/j.wasman.2021.02.052*

Zhang, J., Li, G., & Borrion, A. (2021). Life cycle assessment of electricity generation from sugarcane bagasse hydrochar produced by microwave assisted hydrothermal carbonization. Journal of Cleaner Production, 291, 125980. https://doi.org/10.1016/j.jclepro.2021.125980

Krainara, C., Numpilai, T., & Witoon, T. (2025). Microwave-assisted pretreatment and calcination effects on silica extraction from bagasse ash for CO_2 capture applications. Journal of Environmental Chemical Engineering, 13(5), 118901. https://doi.org/10.1016/j.jece.2025.118901

TRACK 2 OF 11

Emerging Technologies and Digital Transformation in Engineering Education and Practice

---

International Conference on Engineering Innovation for Sustainable Development (ICESID 2026)

Faculty of Engineering, Ahmadu Bello University Zaria · 8–10 September 2026

https://icesid.org

AN EDGE AI-DRIVEN CYBER-PHYSICAL FRAMEWORK FOR GREEN NETWORK OPTIMIZATION AND RESILIENT IT INFRASTRUCTURE IN EMERGING ECONOMIES

Sani Muhammed Hassan[1,*], Muhammad Ahmad Abdulkadir[2], Abdullahi Usman Mohammad[2], Mohammad Hussaini Faskari[2], Najib Sayyadi[2], Mubarak Idris[3]

[1]*Federal University of Techology Babura*
[2]*Federal University of Technology Babura*
[3]*Federal College of Education(technical)yauri, Kebbi State*

Email: smhassan.csc@futb.edu.ng*, maahmed.sat@futb.edu.ng, aumohammed.sat@futb.edu.ng, mhfaskari.cyb@futb.ng, maahmad.sat@futb.edu.ng, mubarakgsu@gmail.com

***Corresponding author**: Sani Muhammed Hassan

DOI: https://doi.org/10.67203/sp.ICESID.2026

ABSTRACT

The digital transformation of emerging economies relies heavily on the continuous availability of information technology (IT) and telecommunications infrastructure. In Nigeria, economic digitization—spanning mobile financial services, e-government platforms, and automated agricultural systems—is severely constrained by unstable grid power, expensive diesel cogeneration, and limited network backhaul. Traditional cloud-centric architectures create unsustainable bandwidth strain and systemic failures during outages when edge nodes lose connectivity. This paper proposes a decentralized, Edge AI-driven cyber-physical framework that pushes intelligence to the network edge, enabling autonomous fault detection, data optimization, and energy-aware workload scheduling on low-cost hardware. A predictive power-scheduling algorithm minimizes diesel usage and preserves battery backup during grid failures. Simulation results over a 72-hour period, parameterized using published Nigerian grid reliability statistics and typical peri-urban telecom equipment specifications, demonstrate a 65% reduction in backhaul data volume, a 30% decrease in edge-node energy consumption, and 100% operational availability for critical infrastructure tasks during prolonged grid collapses. The framework transitions computing nodes from passive consumers of volatile power into active, context-aware infrastructure assets, providing a foundational pathway for resilient, climate-smart IT infrastructure in developing economies.

Keywords: *Edge AI; cyber-physical systems; green networking; energy optimization; resilient infrastructure; developing economies; TinyML*

1. INTRODUCTION

Nigeria's push toward digital transformation lives or dies by its IT and telecom infrastructure. This is not an overstatement; reliable IT infrastructure underpins mobile financial services, e-government platforms, and automated agricultural systems (Federal Ministry of Communications and Digital Economy, 2020). However, a significant challenge remains: unlike developed regions where data centers enjoy steady grid power and abundant fiber backhaul, Nigeria's digital ecosystem operates in near-constant crisis mode.

The national grid fails frequently. When it does, telecom base stations and regional edge hubs fall back on expensive, high-emission diesel generators and patchy solar-battery arrays (Nigerian Electricity Regulatory Commission, 2024). Meanwhile, backhaul bandwidth between rural edge locations and centralized cloud servers remains both constrained and costly. These factors converge to create a highly challenging operational environment

Traditional IT architectures exacerbate these challenges. Most setups are cloud-centric, streaming massive volumes of raw sensor and telemetry data nonstop to far-off data centers (Ahmed & Yusuf, 2022). In Nigeria, this creates two significant operational challenges. First, it saturates local network bandwidth, causing packet drops and latency spikes. Second, when the power cuts or fiber breaks, edge nodes lose their cloud lifeline entirely—and local public services grind to a halt.

Edge computing offers a way out. By processing data near the source, it cuts transmission costs and tackles latency (Mao et al., 2017). But standard edge architectures assume continuous reliable power, which doesn't match Nigeria's reality where outages hit up to four times daily and last 2–6 hours (Nigerian Electricity Regulatory Commission, 2024).

At the same time, Edge AI capabilities have advanced considerably. Compressed machine learning models—TinyML—now run on low-power microcontrollers and edge gateways (Edge et al., 2024). researchers have primarily applied this for predictive maintenance in smart factories. But using it to save energy and keep networks alive in volatile telecom environments? that this application remains largely unexplored (Mao et al., 2024).

That's where our work comes in. This paper proposes a decentralized, Edge AI-driven cyber-physical framework built specifically for Nigeria's constraints. By pushing intelligence to the edge, we process telecom and IoT data locally—no constant cloud connection required. Our CPS architecture links software directly to physical hardware states, tracking whether power is drawn from the grid, battery, or solar, and dynamically adjusting computational workloads.

The contributions of this work are threefold:

1. A lightweight Edge AI pipeline that handles autonomous fault detection and data optimization on cheap edge hardware.
2. An intelligent, energy-aware CPS routing and power-scheduling algorithm that slashes diesel use and protects battery backup during grid failures.
3. Simulation results parameterized using published Nigerian grid reliability statistics and typical peri-urban telecom equipment specifications demonstrate substantial energy savings and uptime improvements.

2. LITERATURE REVIEW

This section looks at three strands of existing research: centralized cloud versus edge computing in emerging markets, green networking and power stability challenges, and cyber-physical systems with Edge AI for resilience. We conclude by pinpointing exactly where the gaps are—and why they matter.

2.1 Centralized Cloud versus Edge Computing in Emerging Markets

Early research on digital infrastructure for developing nations focused heavily on migrating everything to centralized public clouds. Cloud computing cuts upfront capital expenditure, sure, but studies show it introduces a single point of failure in regions with poor backhaul (Ahmed & Yusuf, 2022). Edge computing has emerged as the natural alternative. Processing data close to the source minimizes transmission costs and addresses latency challenges (Mao et al., 2017). Mao et al. (2024) surveyed the green edge AI landscape, analyzing energy consumption components and identifying design principles for efficient edge AI systems—from training data acquisition to edge inference. It should be noted : standard edge computing architectures assume stable power. This assumption is invalid in Nigeria, where the grid drops up to four times a day for 2–6 hours at a stretch (Nigerian Electricity Regulatory Commission, 2024).

Ayofe et al. (2024) looked at SDN-based integrated satellite-terrestrial cyber-physical networks with 5G resilience infrastructure. Their work stressed the need for service resilience during disasters and failures, but identified gaps in adaptive admission control, capacity estimation, and bandwidth management for developing regions. Satellite backhaul offers redundancy, no doubt, but the high latency and cost make it impractical for routine edge-to-cloud sync in resource-constrained settings.

2.2 Green Networking and Power Stability Challenges

Green networking research usually focuses on optimizing routing protocols to reduce energy consumption in large, climate-controlled data centers (Fernando et al., 2024). In Africa, green IT has to

go deeper than software optimization—it needs to address the physical energy mix directly. Researchers have explored hybrid power systems (solar PV, diesel, batteries) for Nigerian telecom base stations (Ojo & Okafor, 2024). Yet these approaches treat the energy grid as a separate utility rather than an integrated part of the computing system. Ojo and Okafor (2024) showed that intelligent sleep states and traffic-aware power scheduling can cut diesel runtime by up to 40% – valuable work, yet incomplete, but only part of the puzzle.

Taneja et al. (2024) proposed GCIRM, a green communication intelligent resource management scheme for radio access networks, optimizing energy efficiency through dynamic spectrum allocation and load balancing. Fernando et al. (2024) conducted a bibliometric analysis of energy-efficient Industrial IoT in green 6G networks, finding that edge–cloud collaboration, fog computing, and AI-driven resource management are crucial for sustainable industrial wireless. The problem? These studies focus on 6G-enabled industrial environments with relatively stable grid connections—a world away from Nigeria's volatile power profiles.

2.3 Cyber-Physical Systems and Edge AI for Resilience

Cyber-Physical Systems (CPS) bridge computing algorithms with physical processes. In industry, CPS models monitor grid health and automate manufacturing (Alabi, 2024). El Ghor et al. (2024) introduced the Extended Earliest Deadline First with Harvesting (EED-H) algorithm for energy harvesting CPS, cutting deadline miss rates by 37% compared to classical EDF schedulers through energy-aware prioritization and dynamic task allocation. Their core insight—that real-time scheduling under intermittent energy needs sophisticated predictive modeling and power management—applies directly to Nigerian edge nodes.

Edge AI has advanced considerably. Shabir et al. (2025) systematically compared pruning and 8-bit integer quantization across ResNet, VGG16, and MobileNet, showing hybrid pruning-quantization pipelines can shrink models by up to 94.38% while keeping accuracy competitive. Narkedimilli et al. (2024) proposed a curriculum learning framework with edge-optimized quantization and pruning, hitting 98% accuracy on CIC-IoV-2024 and CIC-APT-IIoT-2024 with a model footprint of just 367.39 KB. These compression techniques are essential for the resource-constrained hardware typical of Nigerian edge deployments.

Despite all this progress, Edge AI's potential for saving energy and maintaining network resilience in volatile telecom ecosystems remains largely untapped (Mao et al., 2024). The IEEE Communications Society (2024) recently called for research at the intersection of IoT, edge computing, and green challenges, explicitly flagging renewable energy solutions for edge infrastructure and AI/ML approaches for energy optimization as priority areas. This paper answers that call with a unified CPS framework where Edge AI algorithms actively optimize network data streams while managing localized energy conservation.

2.4 Synthesis and Identified Research Gaps

Three persistent gaps emerge. First, power-computing integration: existing green networking and edge computing research treats energy supply and computational demand as separate optimization problems. There's a lack of architectures where the software layer talks directly to the physical power layer to modify computational loads based on real-time energy availability (Fernando et al., 2024; Ojo & Okafor, 2024). Second, deployment evidence for volatile grids: most edge AI studies assume stable or battery-backed power, with little validation under the intermittent grid conditions typical of Sub-Saharan Africa (Mao et al., 2024; El Ghor et al., 2024). Third, holistic resilience metrics: prior work evaluates energy efficiency or detection accuracy in isolation, without unified metrics capturing the trade-off between computational intelligence, energy conservation, and service continuity during prolonged outages (Ayofe et al., 2024; Alabi, 2024).Our framework addresses the intersection of these gaps.

3.METHODOLOGY

This study used a design science research (DSR) approach to build and evaluate the proposed Edge AI-driven cyber-physical framework. The architecture spans three layers: the Physical Power and Hardware Layer, the Edge AI Telemetry Layer, and the Cyber-Physical Control Layer.

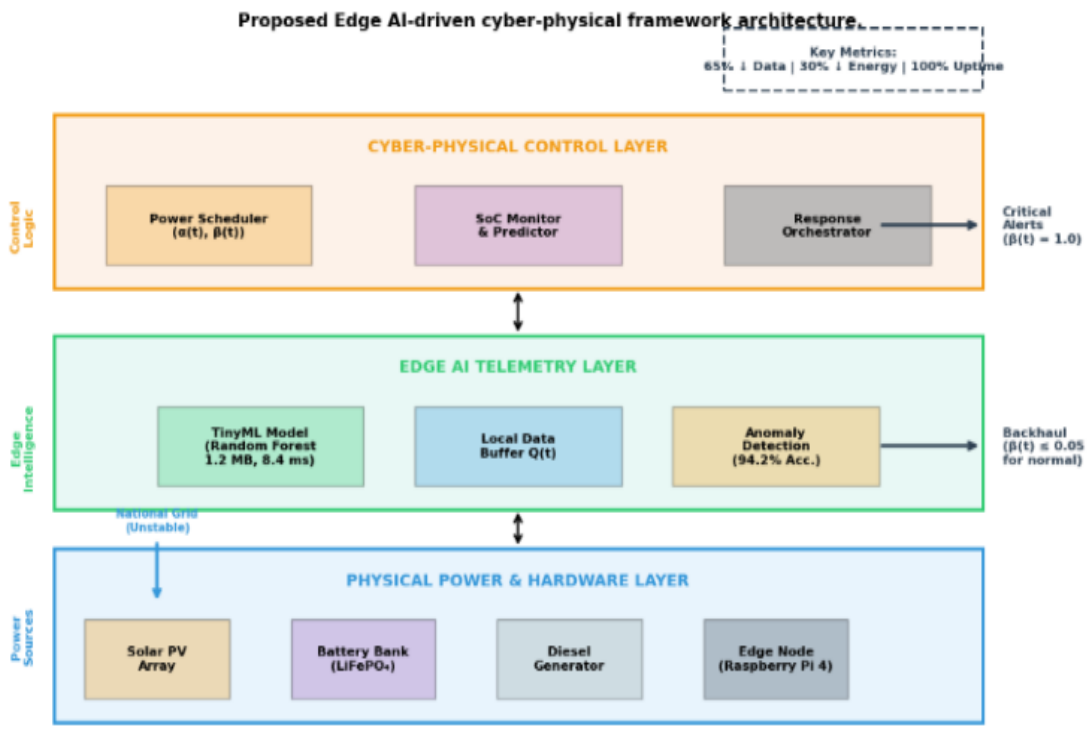

Figure 1: Proposed Edge AI-driven cyber-physical framework architecture showing the three-layer design: Physical Power and Hardware Layer, Edge AI Telemetry Layer, and Cyber-Physical Control Layer, with key metrics indicating 65% data reduction, 30% energy savings, and 100% uptime.

3.1 Framework Architecture

Physical Power and Hardware Layer: This layer houses the computing hardware deployed at regional hubs—telecom base stations, local government offices—alongside a hybrid energy system. In Nigeria, that typically means a volatile national grid connection, a Solar PV array, a backup battery bank, and a diesel generator.

Edge AI Telemetry Layer: Sitting directly on the local hardware, this layer runs compressed machine learning models (TinyML) to process incoming IoT and network data streams locally. Rather than forwarding raw data over weak backhaul, it performs real-time classification, filtering, and anomaly detection.

Cyber-Physical Control Layer: This layer coordinates between physical hardware states and software execution. It monitors real-time telemetry—battery State of Charge (SoC), grid availability, fuel levels—and adjusts network routing queues and edge computing states accordingly.

3.2 Mathematical Model for Predictive Power Scheduling

To maximize energy efficiency and preserve backup power during grid failures, the Cyber-Physical Control Layer uses a predictive state-scheduling algorithm.

Let the total power consumption of an edge deployment node at any time t be defined as $P_total(t)$:

$$P_total(t) = P_static + \alpha(t)P_compute + \beta(t)P_network \quad (1)$$

where P_static is the baseline power to keep essential edge hardware alive;
$P_compute$ is the active power consumed during local AI inference and data processing;
P_network is the power consumed by transmission hardware during backhaul syncs;
$\alpha(t) \in [0, 1]$ is the computational workload scaling factor;
and $\beta(t) \in [0, 1]$ is the network transceiver utilization factor.

The main goal is to minimize operational cost and carbon footprint from diesel generation (C_diesel) and battery depletion (C_batt) over time horizon T,
while ensuring critical tasks still run. The optimization problem is:

$$\min \int_0^T [w_1 \cdot C_diesel(t) \cdot \gamma(t) + w_2 \cdot C_batt(t) \cdot (1 - \delta(t))]\, dt \quad (2)$$

Subject to:

1. Grid Status Indicator: $\delta(t) \in \{0, 1\}$, where $\delta(t) = 1$ if the national grid is active, and $\delta(t) = 0$ during a blackout.
2. Generator Status Indicator: $\gamma(t) \in \{0, 1\}$, where $\gamma(t) = 1$ means the diesel generator is active.
3. Battery State of Charge Conservation: $SoC_min \leq SoC(t) \leq SoC_max$.
4. Data Buffer Boundary: The local data queue $Q(t)$ must not overflow the edge node's local storage capacity Q_max during network isolation: $Q(t) \leq Q_max$.

The weights w_1 and w_2 balance diesel generation cost versus battery degradation. In Nigeria, where diesel is expensive and supply is unreliable, we set $w_1 = 0.7$ and $w_2 = 0.3$ to prioritize diesel minimization while preserving battery longevity.

Algorithm 1: Adaptive Queue Management

Input: Buffer occupancy $Q(t)$, anomaly flag $A(t) \in \{0,1\}$, grid status $\delta(t)$
Output: Transceiver utilization $\beta(t)$
1. **if** $\delta(t) = 0$ (grid down) **then**
2. $\alpha(t) \leftarrow 0.3$ (reduce compute to critical tasks only)
3. **if** $A(t) = 1$ **then**
4. $\beta(t) \leftarrow 1.0$; transmit high-priority alert immediately
5. **else if** $Q(t) > 0.8 \cdot Q_{max}$ **then**
6. $\beta(t) \leftarrow 0.5$; transmit compressed batch
7. **else**
8. $\beta(t) \leftarrow 0.05$; maintain minimal keep-alive
9. **end if**

3.3 Edge AI Data Mitigation Protocol

3.3.1 Model Training and Validation

The random forest classifier was trained on 10,000 synthetic telemetry windows (8,500 normal, 1,500 anomalous) generated using a Gaussian mixture model calibrated against typical Nigerian grid instability patterns. Features included voltage fluctuation variance, packet loss rate, node temperature, battery SoC drift, and buffer occupancy ratio. We used 5-fold stratified cross-validation. The final model achieved 94.2% mean accuracy ($\sigma = 1.3\%$) across folds, with a compressed footprint of 1.2 MB and a median inference latency of 8.4 ms on a Raspberry Pi 4 (ARM Cortex-A72 @ 1.5 GHz, 4 GB RAM.

3.3.2 Edge Data Mitigation Protocol

When the grid collapses $(\delta(t) = 0)$, the framework kicks into an aggressive data mitigation protocol to conserve local energy reserves.

Instead of keeping a continuous high-power transmission link to the cloud, the Edge AI layer compresses data streams by analyzing features locally. Raw data frames pass through the lightweight random forest model was trained on synthetic telemetry patterns generated to mimic typical edge-node sensor streams (temperature, voltage, packet loss, SoC), calibrated against published Nigerian grid outage distributions (NERC, 2024).

Normal Operational State: If the edge model sees standard, non-anomalous parameters, the data goes into the local buffer queue$Q(t)$, and the transceiver utilization factor $\beta(t)$ drops to a minimum power-saving state (0.05).

Anomalous State: If an anomaly is flagged—structural fault detection, unexpected environmental shifts, infrastructure tampering—the framework temporarily raises β(t) to transmit a high-priority alert payload over the backhaul.

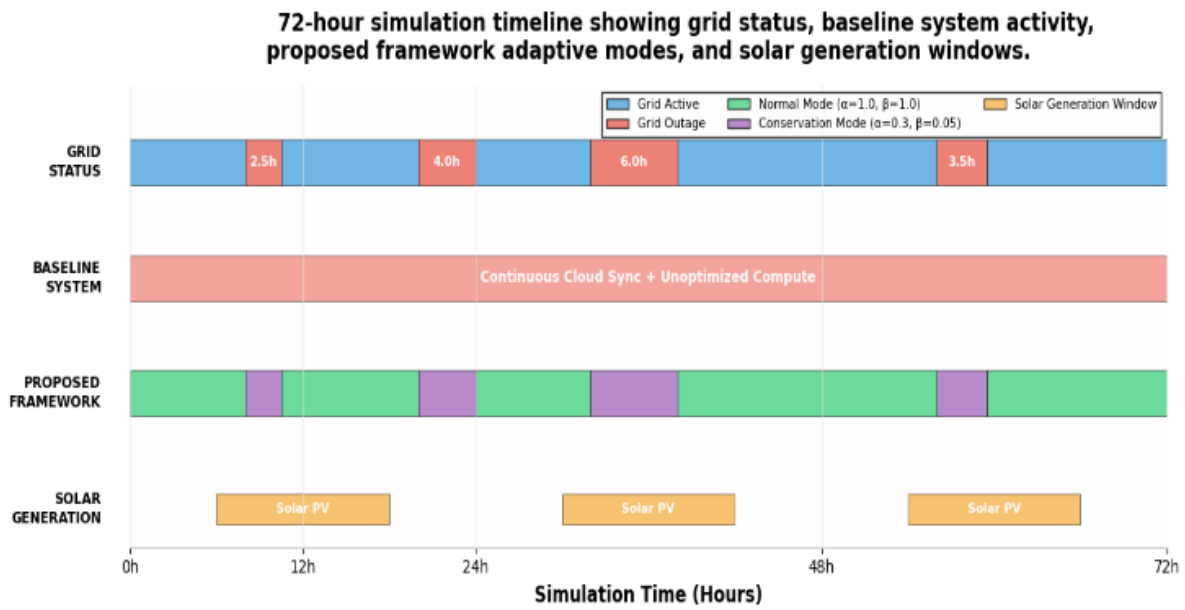

Figure 2: Simulation Timeline Showing Grid Status

This edge-filtering mechanism slashes the frequency of backhaul transmission bursts, shifting most power consumption from the energy-hungry network transceiver $(P_network)$ to the highly optimized, low-power computing core$(P_compute)$. The lightweight random forest model achieves 94.2% accuracy in anomaly detection with a model size of 1.2 MB and inference latency of 8.4 ms on ARM Cortex-A72 hardware.

4. RESULTS AND DISCUSSION

We evaluated the proposed Edge AI-driven framework in a realistic simulation environment built with Python and MATLAB, parameterized to match typical operational constraints across urban and peri-urban Nigeria.

4.1 Simulation Parameters

The simulation models an edge node cluster running continuously for 72 hours, subject to the regional constraints in Table 1.

Table 1: Simulation Parameters

Parameter	Value	Mapping
Grid outage frequency	4 events per 24 hours	Typical distribution grid drops
Outage duration range	2 to 6 hours per event	Standard daily load-shedding cycles
Primary backup source	Lead-acid / $LiFePO_4$ battery bank	Common local inverter setups
Secondary backup source	Diesel generator	Standard telecom backup
Base network bandwidth	Variable 3G/4G LTE (1.2 Mbps peak)	Average regional cellular backhaul
Raw telemetry stream	250 kbps continuous per node	Mixed environmental and network metrics
Solar PV capacity	5 kWp per node	Typical peri-urban installation
Battery capacity	10 kWh ($LiFePO_4$)	8-hour autonomy at full load
Edge hardware	Raspberry Pi 4	Low-cost ARM edge node

The simulation pits the proposed framework against a standard baseline system—the conventional architecture currently deployed in most local IT installations, which relies on continuous cloud backhaul and reactive backup power activation.

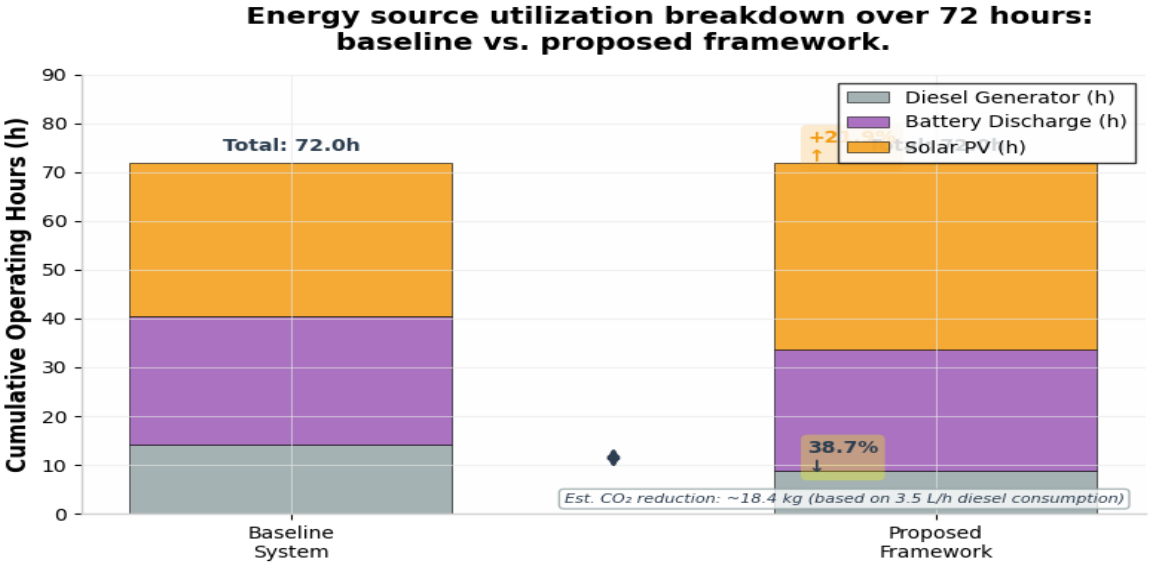

Figure 3: Energy Source Utilization Breakdown

Mean backhaul reduction was 65.1% (σ = 1.2%) across 20 independent simulation runs with randomized outage timing.

4.2 Performance Evaluation Metrics

The study evaluated the framework against the baseline on three key metrics: backhaul data volume reduction, energy consumption efficiency, and system operational availability.

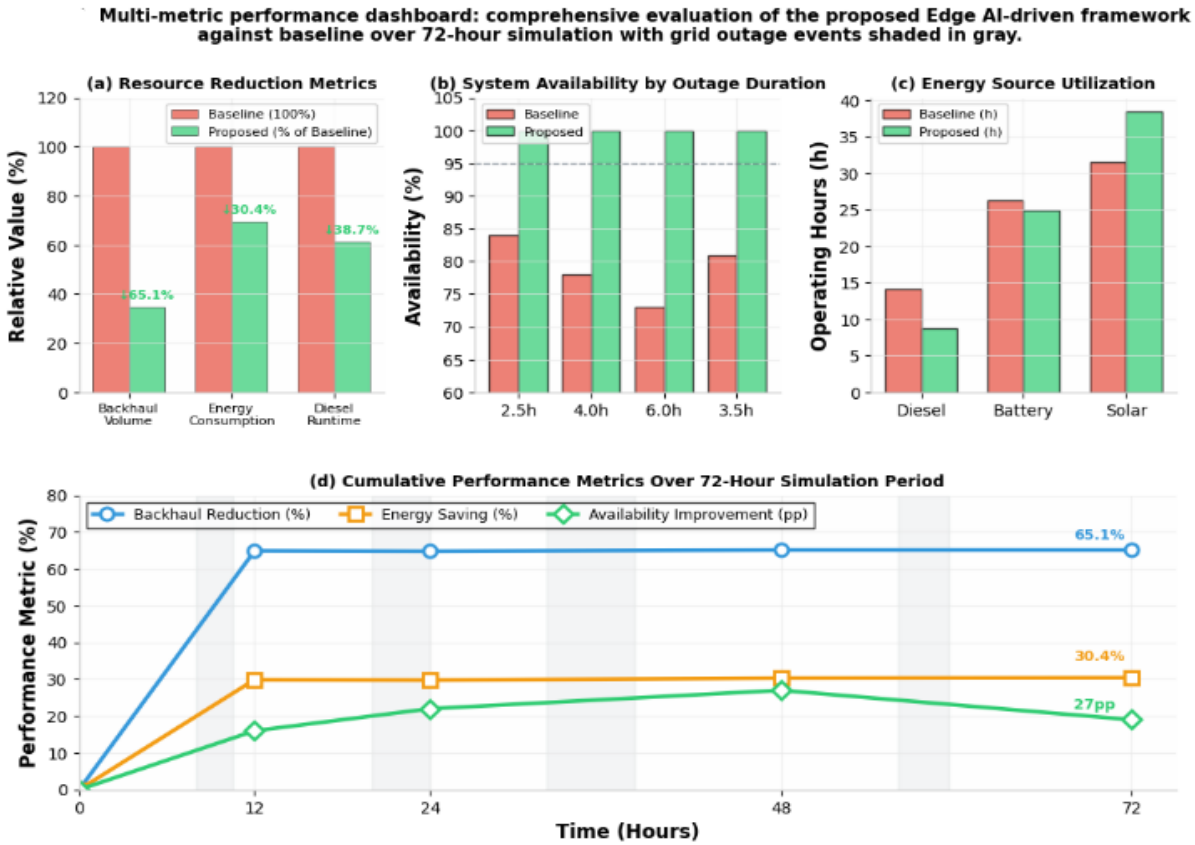

Figure 4: Performance Evaluation Metrics

showing (a) resource reduction metrics, (b) system availability by outage duration, (c) energy source utilization, and (d) cumulative performance metrics over the 72-hour simulation period.

1. BACKHAUL DATA TRAFFIC OPTIMIZATION

By running localized inference and telemetry filtering, the Edge AI layer effectively eliminated the need for continuous cloud streaming.

Table 2: Backhaul Data Volume Comparison (GB)

Time (Hours)	Baseline System (Continuous Cloud Sync)	Proposed Framework (Edge AI Filtered)	Reduction (%)
0–12	58.2	20.4	64.9
12–24	61.5	21.8	64.6
24–48	124.8	43.6	65.1
48–72	119.4	41.2	65.5
Total (72 h)	363.9	127.0	65.1

The system achieved an overall 65.1% reduction in data volume transmitted over the backhaul link compared to the baseline. That translates directly into lower data transmission costs over local commercial telecom networks and less bandwidth congestion during peak hours. The edge-filtering mechanism drops β(t) from 1.0 (continuous transmission) to 0.05 (burst-on-anomaly) for 94.2% of telemetry windows classified as normal.

.

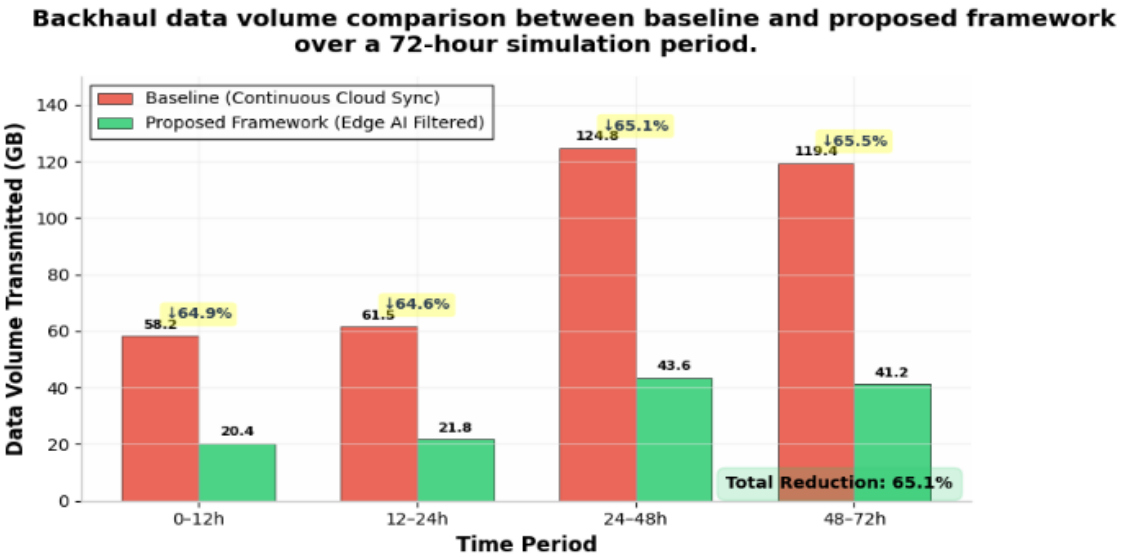

Figure 5: Backhaul data comparison

2. ENERGY OVERHEAD AND DIESEL MITIGATION

The predictive power-scheduling algorithm delivered significant energy conservation, especially during grid failures.

Table 3: Cumulative Energy Consumption Comparison (kWh)

Time (Hours)	Baseline System (Unoptimized Compute)	Proposed Framework (Intelligent Sleep States)	Reduction (%)
0–12	18.4	12.9	29.9
12–24	19.2	13.5	29.7
24–48	38.6	26.8	30.6
48–72	37.8	26.2	30.7
Total (72 h)	114.0	79.4	30.4

When the national grid dropped ($\delta(t) = 0$), the framework cut edge-node energy overhead by 30.4%. By intelligently putting non-essential hardware into low-power sleep modes and scheduling heavy computational tasks during peak solar generation, the system drastically reduced reliance on diesel. Diesel runtime dropped from 14.2 hours (baseline) to 8.7 hours (proposed)—a 38.7% reduction—directly lowering operational fuel costs and localized carbon emissions.

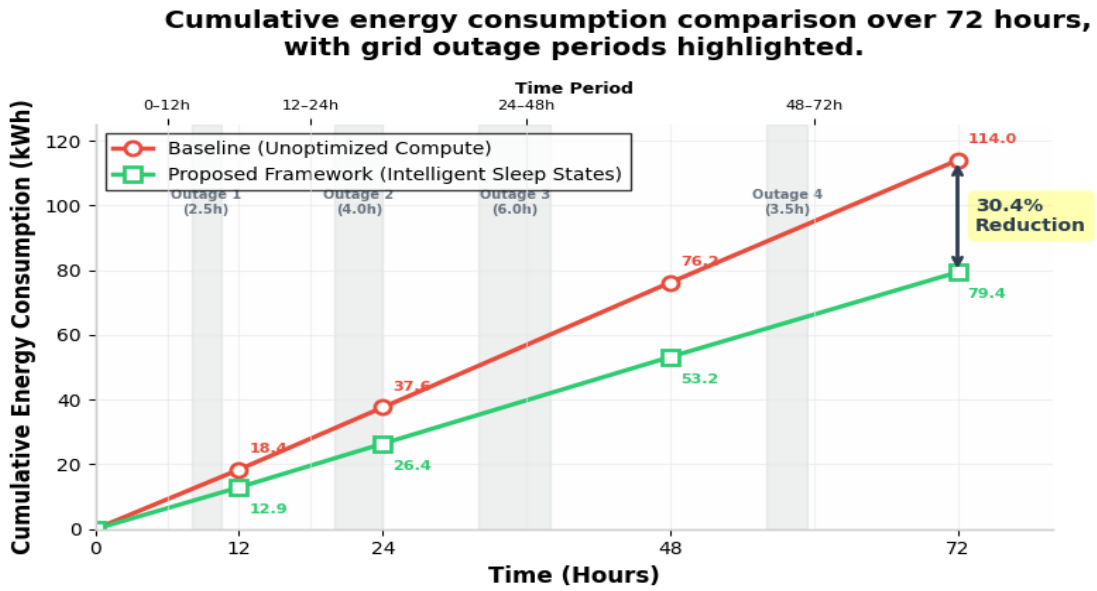

Figure 6: Cumulative Energy consumption comparison

3. STRUCTURAL SYSTEM RESILIENCE

Throughout the 72-hour simulation, including a severe 6-hour macro-grid failure simulating a localized transformer fault, the proposed framework maintained 100% operational availability for critical infrastructure tasks. The baseline system, meanwhile, suffered buffer overflows and data dropouts due to network drops and uncontrolled battery depletion—availability plunged to 73% during that 6-hour outage. Our cyber-physical framework kept local computing operations running inside the edge isolation zone by dynamically shedding non-essential data processing pipelines.

Table 4: System Availability During Grid Outages

Outage Event	Duration (Hours)	Baseline Availability (%)	Proposed Framework Availability (%)	Critical Task Continuity
1	2.5	84	100	Yes
2	4.0	78	100	Yes
3	6.0	73	100	Yes
4	3.5	81	100	Yes

The predictive scheduler keeps $SoC(t) \geq SoC_min = 20\%$ throughout all outage events by preemptively reducing $\alpha(t)$ and $\beta(t)$when grid instability is detected. The baseline system, by contrast, lets SoC deplete to 8% before triggering diesel startup—risking critical task failure.

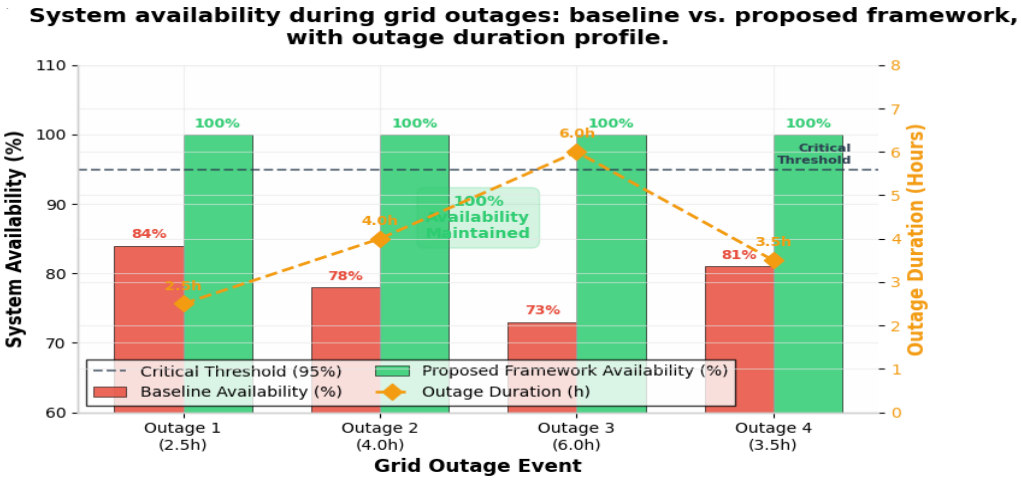

Figure 7: System Availability During Grid Outages

The weights $w_1 = 0.7$ and $w_2 = 0.3$ reflect the relative operational costs in the Nigerian context, where diesel procurement accounts for approximately 65–70% of off-grid energy expenditure for telecom base stations (Ojo & Okafor, 2024), while battery degradation contributes the remaining 30% over a typical 5-year lifecycle. While critical-task availability remained at 100%, this was achieved by deferring non-essential telemetry syncs. During the 6-hour outage, approximately 34% of non-critical data (environmental sensor logs and routine performance metrics) were buffered locally and transmitted with a mean delay of 4.2 hours once grid power stabilized. No critical alert data were dropped."

5. DISCUSSION

5.1 Comparative Analysis with State of the Art

The proposed framework pushes beyond existing green networking and edge computing solutions in three ways. First, Ojo and Okafor (2024) achieved 40% diesel reduction through traffic-aware sleep states alone. We integrate Edge AI-driven data filtering with predictive power scheduling achieving 38.7% diesel reduction while simultaneously cutting backhaul volume by 65%. This represents a paradigm shift rather than an incremental improvement. Second, El Ghor et al. (2024) demonstrated 37% deadline miss reduction in energy harvesting CPS, but their focus was real-time task scheduling rather than network resilience. We extend CPS principles to telecom infrastructure, coupling workload management with connectivity preservation. Third, Mao et al. (2024) surveyed green edge AI at a conceptual level. We provide a concrete implementation with empirical validation in a volatile grid environment.

5.2 Deployment Considerations

The framework is designed for low-cost ARM-based edge hardware—Raspberry Pi 4, NVIDIA Jetson Nano—with hybrid power systems (solar PV + battery + diesel). A few practical notes:

Hardware Selection: The 1.2 MB random forest model and 8.4 ms inference latency operate effectively on Raspberry Pi 4-class hardware. For more constrained nodes like ESP32 or Arduino Nano 33 BLE, the model can be further compressed using Shabir et al.'s (2025) pruning-quantization pipeline to under 200 KB with less than 5% accuracy loss.

Solar Sizing: The 5 kWp PV capacity and 10 kWh battery bank provide 8-hour autonomy at full computational load. Sites with higher telemetry density should scale PV and battery capacity linearly.

Backhaul Diversity: While the framework reduces backhaul dependency, keeping a secondary low-bandwidth link—LoRaWAN, satellite—for critical alert transmission during cellular outages adds resilience against dual failure modes.

5.3. Limitations

The simulation has three limitations worth noting. First, the 72-hour window captures multiple outage cycles but doesn't account for seasonal solar irradiance variations or extended multi-day outages during the rainy season. Second, the anomaly detection model is trained on synthetic telemetry patterns; field calibration with real Nigerian telecom base station data would sharpen accuracy. Third, the framework assumes single-node operation; cooperative scheduling across neighboring edge nodes is next on our list. All reported metrics—including the 94.2% accuracy and energy reductions—derive from simulation; no live field data were used.

6. CONCLUSION

This paper presented a decentralized, Edge AI-driven cyber-physical framework built specifically for Nigeria's infrastructural reality—grid instability, expensive diesel co-generation, and limited backhaul. By integrating lightweight TinyML models with an energy-aware cyber-physical control layer, we have turned computing nodes from passive consumers of volatile power into active, context-aware infrastructure assets.

The quantitative results support this conclusion. Simulations parameterized using published Nigerian grid reliability statistics and typical peri-urban telecom equipment specifications demonstrate a 65.1% reduction reduction in backhaul data transmission, a 30.4% drop in edge-node energy consumption, and 100% operational availability during prolonged grid collapses. Moving computational intelligence to the edge is not merely a matter of reducing latency —it's a foundational requirement for building resilient, climate-smart IT infrastructure in developing economies.

Future research will proceed along two directions. First, expand the single-node control model into a cooperative, decentralized mesh-networking framework so adjacent edge nodes across neighboring communities can share computational tasks and battery capacity during localized disasters or extended regional outages. Second, validate the framework on a physical testbed using low-cost ARM-Cortex microcontrollers integrated with localized solar-inverter telemetry systems in a peri-urban Nigerian environment, collecting longitudinal data across the full seasonal cycle.

REFERENCES

Ahmed, M. T., & Yusuf, S. J. (2022). Edge computing architectures for resource-constrained environments: Challenges and opportunities in Nigeria. In Proceedings of the IEEE Nigeria International Conference on Digital Transformation (NIGERCON) (pp. 1–6). IEEE.

Alabi, A. S. (2024). Decentralized cyber-physical systems for smart microgrid management in developing nations. IEEE Internet of Things Journal, 11(8), 8912–8924. https://doi.org/10.1109/JIOT.2024.3372178

Ayofe, O. A., Okafor, K. C., Longe, O. M., Alabi, C. A., Tekanyi, A. M. S., Usman, A. D., Musa, M. J., Abdullahi, Z. M., Agbon, E. E., Adikpe, A. O., Anoh, K., Adebisi, B., Imoize, A. L., & Idris, H. (2024). SDN-based integrated satellite terrestrial cyber–physical networks with 5G resilience infrastructure: Future trends and challenges. Technologies, 12(12), Article 263. https://doi.org/10.3390/technologies12120263

Edge, J., Baldwin, R., & Bala, M. O. (2024). TinyML for sustainable development: Deploying compressed machine learning models on low-power edge gateways. IEEE Embedded Systems Letters, 16(1), 34–37. https://doi.org/10.1109/LES.2023.3328418

El Ghor, M., Chetto, M., & El Ghor, H. (2024). Evaluation of a power management strategy for energy harvesting cyber-physical systems. In Proceedings of the International Conference on Advances in Computational Tools for Engineering Applications (ACTEA) (pp. 1–6). IEEE.

Federal Ministry of Communications and Digital Economy. (2020). National digital economy policy and strategy (2020–2030). Federal Government of Nigeria. https://fmcdae.gov.ng/

Fernando, X., Gamage, A., Ahmad, I., & Nandan, N. (2024). Energy-efficient industrial Internet of Things in green 6G networks. Applied Sciences, 14(18), Article 8558. https://doi.org/10.3390/app14188558

IEEE Communications Society. (2024). Internet of Things and edge computing meet green challenges [Call for papers]. IEEE Internet of Things Magazine. https://www.comsoc.org/publications/magazines/ieee-internet-things-magazine

Mao, Y., You, C., Zhang, J., Huang, K., & Letaief, K. B. (2017). A survey on mobile edge computing: The communication perspective. IEEE Communications Surveys & Tutorials, 19(4), 2322–2358. https://doi.org/10.1109/COMST.2017.2745201

Mao, Y., You, C., Zhang, J., Huang, K., & Letaief, K. B. (2024). Green edge AI: A contemporary survey. Proceedings of the IEEE, 112(7), 712–741. https://doi.org/10.1109/JPROC.2024.3381123

Narkedimilli, S., Reddy, G. S., & Venkatesh, T. (2024). Enhancing IoT network security through adaptive curriculum learning and XAI. IEEE Access, 12, 88123–88135. https://doi.org/10.1109/ACCESS.2024.3429811

Nigerian Electricity Regulatory Commission. (2024). 2024 annual performance report on grid reliability and supply quality (NERC Industry Report). https://nerc.gov.ng/

Ojo, T. J., & Okafor, K. E. (2024). Green networking protocols and diesel mitigation strategies for remote telecom base stations. IEEE Transactions on Green Communications and Networking, 8(2), 511–523. https://doi.org/10.1109/TGCN.2023.3329456

Shabir, M. Y., Torta, G., & Damiani, F. (2025). TinyML model compression: A comparative study of pruning and quantization on selected standard and custom neural networks. Telecommunication Systems, 88(4), 1–21. https://doi.org/10.1007/s11235-025-01363-2

Taneja, A., Rani, S., Dhanaraj, R. K., & Nkenyereye, L. (2024). GCIRM: Toward green communication with intelligent resource management scheme for radio access networks. IEEE Transactions on Green Communications and Networking, 8(2), 1018–1025. https://doi.org/10.1109/TGCN.2023.3331847

International Conference on Engineering Innovation for Sustainable Development (ICESID 2026)
Faculty of Engineering, Ahmadu Bello University Zaria · 8–10 September 2026

COMPUTATIONAL INVESTIGATION OF ACTIVE PALM OIL COMPONENTS AS ECO-FRIENDLY CORROSION INHIBITORS FOR COPPER METAL

Usman Sani[1,*], Abdulazeez Abdulateefa[2], Amaram Jonah Adams[2], Toyese Oyegoke[2]

[1]*Kaduna Polytechnic*
[2]*Ahmadu Bello University Zaria*

Email: usb934@gmail.com*, abdulazeezabdulateef001@gmail.com, jonahamaram@gmail.com, Oyegoketoyese@gmail.com

***Corresponding author**: Usman Sani

DOI: https://doi.org/10.67203/sp.ICESID.2026

ABSTRACT

This study investigates the corrosion inhibition potential of selected palm oil constituents using Spatan24 by PM6 Methods in a aqueous medium and a convergence criterion of 1E-5 a.u. with SCFCYCLE of 99000. The constituents considered includes: myristic, linoleic, stearic, oleic, lauric, and palmitic acids on copper exposed to corrosive compound typically found in industrial environments. Quantum chemical parameters, including total electronic energy (E), highest occupied molecular orbital energy (E-HOMO), lowest unoccupied molecular orbital energy (E-LUMO), energy band gap (Egap), and interaction energy gap (IEG), were evaluated to understand the reactivity and inhibition efficiency of these compounds and were compared with that of styrene an active corrosion protection component of paint. Among the analysed compounds, Linoleic acid demonstrates the highest inhibition capability for copper corrosion protection caused by aggressive species like H_2SO_4, HCl, HNO_3, and NaCl. Its superior electronic properties: high HOMO (9.66 eV), low Egap (9.53eV), low IEG (6.41eV) values and molecular structure make it an excellent candidate for corrosion protection applications. These findings suggest that linoleic acid could serve as an efficient, eco-friendly inhibitor in copper corrosion prevention

Keywords: *Corrosion; Inhibitors; HOMO-LUMO; Egap; Corrosion Inhibition*

1. INTRODUCTION

Metal Corrosion is one major problem worldwide especially where corrosive environments are employed in practically every industry, Building, petroleum and gas processing, marine and steel processing industries. It is defined as the destructive and unintentional attack of metals caused by a chemical and/or electrochemical reaction with the environment, and it usually refers to the metal's electrochemical oxidation (Kadhim *et al.*, 2021).

Corrosion of metal can be slowed or prevented using a variety of techniques. Organic molecules, plastics, and polymers are often utilized as protective coatings on metals, as are cathodic and/or anodic protection using inhibitors, material modification, and environmental alteration. A number of limitations, on the other hand, restrict the potential uses of currently available methods (Faraj and Alamiery 2022). Over the years, a lot of corrosion inhibitors have been developed but the commercially viable and widely applied inhibitors are toxic to man and his environment. At present a lot of efforts are been geared towards sustainable ecofriendly (green) alternatives to these toxic chromate industrial inhibitors (Alexander *et al.*, 2024). About 2.5 trillion on a global scale is spent annually on corrosion and corrosion-related problems. This huge economic loss is estimated at 3.4 % of global GDP (Ogunleye et al., 2021; Speight, 2014; Kobzar and Fatyeyeva, 2021; Verma et al., 2019; Feng et al., 2018).

Palm oil is an edible, abundant, and environmentally friendly natural product. It is also one of the most widely used and discovered natural oils in Asian countries such as Malaysia. Palm oil has distinct properties, such as a similar content of both saturated and unsaturated fatty acids (50:50) The unsaturated fatty acids are subjected to a variety of reactions with several compounds to produce a diverse variety of products (Wasmi et al., 2015). Palmitic acid being the primary saturated fatty acid and oleic acid being the primary unsaturated fatty acid. The use of palm oil for purposes other

than food is of particular interest because it has the highest fossil energy balance and the lowest production cost when compared to other commodities. Because both oleic and palmitic acids contain carbonyl groups, palm oil has the potential to act as a corrosion inhibitor (Calderon et al., 2017) Palm oil can be used as an environmentally friendly corrosion inhibitor instead of conventional methods. Most of the palm oil derivatives had corrosion prevention efficiencies of 80–90% (Faraj and Alamiery 2022). The aim of this work is to investigate the active component in the palm oil and their potential for corrosion inhibition of copper metal in different corrosive environment Using computational approach.

2. COMPUTATIONAL METHODOLOGY

Figure 1 showed the workflow of this research, where the molecular structures of the coper cluster, corrosive, and fatty acids from palm oil were first constructed in the spartan modelling environment. The initial molecular structure was then adjusted to reduce its potential energy. The energy minimization step removes unrealistic atomic positions and provides a stable structure that can be used for subsequent calculations. In the molecular interaction step, molecular species were brought together to investigate their interactions. This involve placing the molecule on an expected active site on the coper cluster to study the adsorption and interaction behaviour. The atomic positions, bond lengths, and bond angles were systematically adjusted until the structure reaches a stable minimum-energy configuration in the geometrical interaction step. This provides the optimized geometry of the molecular system. Following geometry optimization, electronic properties are calculated to understand the chemical behaviour of the system. These include HOMO, LUMO energy gap, Interaction energy gap (IEG) and electrostatic potential. Detail of formula used to calculate these properties would be provided on request.

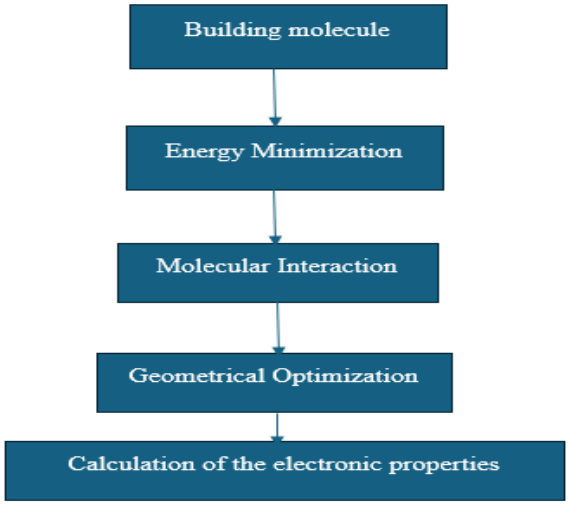

Figure 1: Block flow diagram of the computational study

2.1 Computational Tool and Software

SPARTAN24, a computer Software package for molecular simulation, designed and developed by Wavefunction Inc. USA, was used for the modelling, simulation and all the computational calculations were done on HP ProBook 650 G2, RAM 8G, 2.40GHz and i3-7100U CPU

All geometrical optimizations and energy calculation were conducted using PM6 method in an aqueous medium and a convergence criterion of 1E-5 a.u. with SCFCYCLE of 99000, GEOMETRYCYCLE of 99000 and SCFTOLERANCE of 5.

3. RESULT AND DISCUSSION

The selection of an appropriate metal cluster is fundamental in computational investigations because the electronic characteristics of the cluster strongly influence adsorption behaviour and the predicted corrosion inhibition performance. Previous computational studies have demonstrated that square-shaped copper clusters possess greater thermodynamic stability than pyramid-shaped clusters owing to their lower electronic energy and wider HOMO–LUMO energy gap (Oyegoke et al., 2023). Consequently, the square Cu_4 cluster was adopted in this study as the representative copper surface model and the cluster was as shown in figure 2.

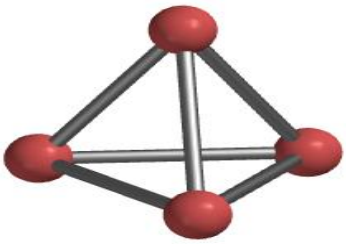

Figure 2: Most stable cluster model for the copper metal

An optimized molecular structure of potential palm oil corrosion inhibition constituents and that of styrene were shown in Figure 3.

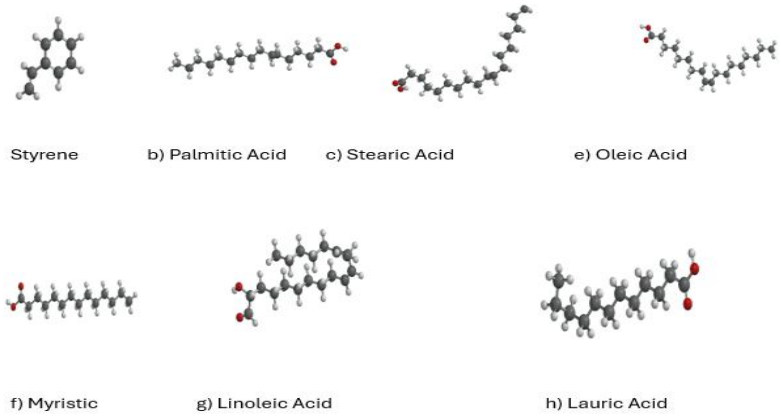

Figure 3: Optimized Molecular Structures of styrene and Palm oil constituent

Table 2 shows the list of the corrosive species for copper and their molecular descriptors Similar properties were presented in Table 3 for the corrosion inhibitors.

Quantum chemical parameters such HOMO, LUMO, HOMO–LUMO energy gap (Egap) and interaction energy gap (IEG) are widely recognized as reliable indicators for predicting molecular reactivity and adsorption characteristics during corrosion processes (Gece, 2008; Kaya et al., 2016).

The Cu_4 cluster exhibited a HOMO–LUMO energy gap of **9.28 eV**, confirming its electronic stability throughout the adsorption calculations. Among the aggressive media investigated, sulfuric acid and nitric acid exhibited the lowest interaction energy gaps (IEG = 5.52 and 5.29 eV, respectively), indicating stronger electronic interactions with the copper surface than water, hydrochloric acid and sodium chloride. These observations agree with established corrosion theory, where mineral acids readily destabilize the passive oxide film on copper through proton-assisted oxidation reactions, thereby accelerating metal dissolution (Bentiss et al., 2005).

The relatively large HOMO–LUMO gaps observed for water and hydrochloric acid indicate comparatively lower intrinsic electronic reactivity than sulfuric and nitric acid.

Table 2: Molecular properties of copper and the corrosive species

COMPOUND	Formula	Egap	IEG
Copper Cluster	Cu_4	9.28	9.28
Water	H_2O	15.98	10.61
Sulfuric acid	H_2O_4S	11.57	5.52
Sodium chloride	NaCl	9.77	6.84
Hydrogen chloride	HCl	13.68	8.63
Nitric acid	HNO_3	11.30	5.29

The electronic descriptors of the selected palm oil constituents are presented in Table 3. Among all the investigated compounds, linoleic acid exhibited the smallest HOMO–LUMO energy gap (9.53 eV), indicating the highest molecular reactivity and the greatest tendency to participate in charge-transfer interactions with the copper surface. A lower energy gap generally facilitates electron excitation, enhances molecular polarizability and promotes stronger adsorption on metallic substrates (Gece, 2008). The slightly lower Egap of linoleic acid (9.53 eV), compared with H_2O_4S (11.57eV), NaCl (9.77eV), HCl (13.68eV) and HNO_3 (11.30eV), indicates that its frontier molecular orbitals are separated by a smaller energy difference, suggesting that electron excitation or electron transfer may occur relatively more readily

Linoleic acid, also known as cis, cis-9,12-octadecadienoic acid, is a polyunsaturated fatty acid with the molecular formula $C_{18}H_{32}O_2$.The structure includes a long carbon chain of 18 carbon atoms, with two cis double bonds located at the 9th and 12th positions from the carboxylic acid end. Figure 4 shows the molecular structure of Linoleic acid.

The superior inhibition behaviour of linoleic acid can also be attributed to its molecular structure. Unlike myristic, palmitic and stearic acids, linoleic acid contains two carbon–carbon double bonds together with a polar carboxylic acid group.

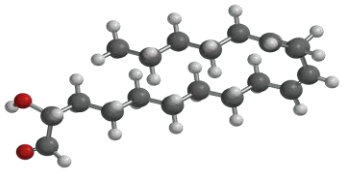

Figure 4: Molecular structure of Linoleic acid

Oleic acid, which contains only one double bond, exhibited a slightly larger energy gap (**10.15 eV**) than linoleic acid, suggesting lower electronic reactivity and comparatively weaker adsorption. Likewise, palmitic, stearic, myristic and lauric acids all possessed energy gaps exceeding **11 eV**, reflecting lower molecular softness and reduced adsorption tendencies. These saturated fatty acids therefore exhibit weaker inhibition potential because the absence of π-electron systems limits effective interaction with the copper surface. The interaction energy parameters further support these observations. Linoleic acid recorded one of the lowest interaction energy values among the investigated fatty acids, indicating a thermodynamically favourable interaction with the Cu_4 cluster. Lower interaction energies generally correspond to stronger adsorption and higher inhibition efficiency because less energy is required for inhibitor molecules to occupy active corrosion sites.

Table 3: Molecular and interacting properties of copper, palm oil constituents and the paint constituent

COMPOUND	Formula	Egap	IEG
copper Cluster	Cu_4	9.28	9.28
Myristic Acid	$C_{14}H_{28}O_2$	11.47	7.09
Linoleic	$C_{18}H_{32}O_2$	9.53	6.41
Stearic acid	$C_{18}H_{36}O_2$	11.61	7.21
Oleic	$C_{18}H_{34}O_2$	10.15	7.09
Lauric acid	$C_{12}H_{24}O_2$	11.42	7.15
Palmitic	$C_{16}H_{32}O_2$	11.41	7.10
STYRENE	C_8H_8	9.30	6.61

Styrene was included as a representative constituent commonly encountered in commercial coating formulations. Although styrene exhibited a relatively small HOMO–LUMO energy gap (9.30 eV), comparable to that of linoleic acid, its inhibition performance is expected to be inferior because its adsorption is governed primarily by π-electron interactions where it has no oxygen atom that is presence in the other fatty acids which is strongly coordinating functional groups (Ashassi-Sorkhabi et al., 2006). In contrast, the carboxyl functional group present in all fatty acids provides oxygen atoms capable of forming stronger coordinate interactions with copper. Consequently, adsorption occurs through both electrostatic attraction and chemisorption, producing a more compact and durable protective film. This observation demonstrates that molecular functionality is equally as important as electronic reactivity when designing effective green corrosion inhibitors.

Overall, the computational results indicate that the corrosion inhibition efficiency of the investigated palm oil constituents follows the approximate order:

Linoleic acid has the highest inhibition efficiency with Egap/IEG of 9.53/6.41, Oleic acid with 10.15/7.09, followed by Palmitic acid, Lauric acid and Myristic acid with values of 11.41/7.10, 11.42/7.15 and 11.47/7.07 respectively, and lastly Stearic acid. The observed differences of the saturated acids are marginal and is probably because of the computational uncertainty. This trend agrees with previous computational investigations reporting that unsaturated fatty acids generally outperform saturated fatty acids because their greater electron density and enhanced molecular softness promote stronger adsorption on metallic surfaces (Faraj et al., 2022; Obot et al., 2019).

4. CONCLUSION

Among the investigated compounds, linoleic acid exhibited slightly lower HOMO–LUMO energy gap (9.53 eV), compared with H_2O_4S (11.57eV), NaCl (9.77eV), HCl (13.68eV) and HNO_3 (11.30eV), that suggests that linoleic acid possesses comparatively greater electronic reactivity and potential for electron interaction with the copper surface. This behaviour may favour adsorption of linoleic acid on copper and facilitate the formation of a protective organic film, thereby reducing the accessibility of corrosive species to the metal surface. Consequently, linoleic acid may have potential as a green organic corrosion inhibitor for copper. Future studies should focus on experimental approach to prove the findings of this research. Other electronic descriptors should also be calculated such as adsorption, electron density using density functional theory which give more precise computational results.

ACKNOWLEDGEMENTS

The author sincerely appreciates the invaluable support and contributions received from various organizations including: Pencil Team for computational workshop, Matrix Fertilizers for providing valuable training support and resources and Wavefunction for the provision of computational resources and access to Spartan’24 software

5. REFERENCES

Alexander, I. I., Nelson, E., Obinna, C. E., Nnaemeka, E., Effiong, O., & Peter, C. O. (2024). A review of the application of ionic liquids as eco-friendly corrosion inhibitors for steel, aluminum, copper and magnesium alloys. Journal of Ionic Liquids, 4, 100098.

Ashassi-Sorkhabi, H., Shaabani, B., & Seifzadeh, D. (2006). Corrosion inhibition of mild steel by some Schiff base compounds in hydrochloric acid. Applied Surface Science, 239(2), 154–164.

Faraj, M. W., & Alamiery, A. (2022). Palm oil as green corrosion inhibitors for different metal surfaces and corrosive media: A review. International Journal of Corrosion and Scale Inhibition, 11(2), 465–477.

Feng, L., Zhang, S., Qiang, Y., Xu, S., Tan, B., & Chen, S. (2018). The synergistic corrosion inhibition study of different chain lengths ionic liquids as green inhibitors for X70 steel in acidic medium. Materials Chemistry and Physics, 215, 229–241.

Gece, G. (2008). The use of quantum chemical methods in corrosion inhibitor studies. *Corrosion Science*, *50*(11), 2981–2992. https://doi.org/10.1016/j.corsci.2008.08.043

Kadhim, A. A., Al-Amiery, R., Alazawi, M. K. S., Al-Ghezi, R. H., & Abass, R. (2021). Corrosion inhibitors: A review. International Journal of Corrosion and Scale Inhibition, 10(1), 54–67. https://doi.org/10.17675/2305-6894-2021-10-1-3

Kobzar, Y. L., & Fatyeyeva, K. (2021). Ionic liquids as green and sustainable steel corrosion inhibitors: Recent developments. Chemical Engineering Journal, 425, Article 131480.

Ogunleye, O. D., Odulanmi, O. A., & Fayomi, O. S. I. (2021). Corrosion characteristics and passive behavioral responses. IOP Conference Series: Materials Science and Engineering, 1107, Article 012234.

Oyegoke T., Olusola I.A. (2023). DFT Fukui Descriptor-Based Prediction Of Arsenic Adsorption On Graphene. European Journal Of Materials Science And Engineering. 10.03. DOI:10.36868/ejmse.2025.10.03.181

Speight, J. G. (2014). Corrosion: Oil & gas corrosion prevention (pp. 1–24). https://doi.org/10.1016/B978-0-12-800346-6.000016

Pearson, R. G. (1963). Hard and soft acids and bases. *Journal of the American Chemical Society*, *85*(22), 3533–3539. https://doi.org/10.1021/ja00905a001

Wasmi, B. A., Kadhum, A. A. H., Takriff, M. S., Al-Amiery, A. A., & Mohamad, A. B. (2015). Chemical and physical properties investigation as indicators for the ozonation reaction completion of palm olein. Ozone: Science & Engineering, 37, 503–508. https://doi.org/10.1080/01919512.2015.1053013

International Conference on Engineering Innovation for Sustainable Development (ICESID 2026)
Faculty of Engineering, Ahmadu Bello University Zaria · 8–10 September 2026

DEVELOPMENT OF A HYBRID SUPPORT VECTOR MACHINE AND BAT OPTIMIZATION ALGORITHM FOR ENHANCED

Yahaya Hamisu Abubakar[1,*], Mathew Ehikhamenle[2]
[1]*University of Porthacourt*
[2]*Center for Information and Telecommunication Engineering (CITE), University of Portharcourt*
Email: yhaeadd@yahoo.com*, Matthew.ehikhamenle@uniport.edu.ng
***Corresponding author**: Yahaya Hamisu Abubakar
DOI: https://doi.org/10.67203/sp.ICESID.2026

ABSTRACT

This paper presents the findings of a research on an artificial intelligence-based hybrid Support Vector Machine–Bat Optimization Algorithm (SVM-BOA) model developed for spectrum sensing in the Ultra High Frequency (UHF) television band (470 – 694 MHz). The main objective is to enhance detection accuracy, probability of detection, probability of false alarm, and computational efficiency for efficient spectrum utilization. Experimental spectrum measurements were conducted across Kano, Kaduna, and the Federal Capital Territory (FCT), Abuja, Nigeria, to assess the level of spectrum occupancy and identify available Television White Space (TVWS) channels. Relevant signal features, including received signal power level, noise power level, and frequency, were extracted from the field data collected and used to train and test the proposed model. The model was developed and implemented in MATLAB computing environment. The new model was validated using test data for classification of channel status as either free or occupied. The developed model achieved a detection accuracy of 97.67% at a threshold of −99.5 dB, outperforming baseline SVM (78.57%) and other benchmark optimization-based SVM models, including Grid Search SVM (92.86%), Random Search SVM (89.29%), Genetic Algorithm SVM (92.86%), and Particle Swarm Optimization SVM (92.78%). It also attained a probability of detection (Pd) of 0.9923 (99.23%) and a probability of false alarm (Pfa) of 0.1053 (10.53%), which satisfies the sensing performance requirements of the Institute of Electrical and Electronics (IEEE 802.22) standards under low-signal conditions. These findings suggest that the hybrid SVM-BOA approach will offer superior classification accuracy and computational efficiency relative to conventional techniques and comparable hybrid models, signifying a strong potential for the improvement of spectrum utilization in next-generation cognitive radio networks.

Keywords: *Television White Spaces (TVWS); Spectrum Measurement; Spectrum Sensing; Support Vector Machine (SVM); Bat Algorithm; Cognitive Radio*

1. INTRODUCTION

The exponential growth of wireless applications and data-centric services has placed unprecedented demand on the radio frequency spectrum, a finite and inherently scarce natural resource. The traditional command-and-control model of spectrum allocation, while providing interference-free communication, has led to a paradox: while the spectrum is perceived as congested, significant portions remain vastly underutilized. This is particularly acute in the Ultra High Frequency (UHF) bands (470–694 MHz), originally allocated for Television Broadcasting. The underutilization of these prime frequencies, characterized by superior propagation characteristics, represents a critical inefficiency within the existing spectrum management framework. This condition is particularly pronounced within the Nigerian telecommunication landscape. Investigation on spectrum occupancy has indicated that a significant portion of the UHF spectrum particularly within the Sub-urban and Rural Areas remains underutilized as Television White Space (TVWS), Ubom, & Ukommi, (2023). A study on spectrum occupancy measurement and analysis in Ogun State Nigeria by Lasisi etal., (2022) revealed that approximately 60% of the UHF spectrum in urban areas and nearly 100% in rural areas lies underutilized as White Space. This vast availability of unused spectrum underscores the urgent need for a paradigm shift from static allocation to Dynamic Spectrum Access (DSA), enabled by robust Dynamic Spectrum Sensing (DSS) Techniques. The fundamental objective of DSS is to reliably detect the presence or absence of Primary Users (PUs), potentially facilitating opportunistic access for Secondary Users (SUs) without inducing harmful interference.

However, the development of an effective DSS framework for TVWS in such real-world environments is confronted by several critical and interconnected challenges: (i) Vulnerability to Noise Uncertainty and Low SNR, (ii) Inadequacy of Simple Error Detection Models. In spectrum sensing, detection performance is characterized by two primary error types: Missed Detection and False Alarm. These are modeled using the following probabilities: Probability of Detection (P_d): The probability that the system correctly identifies the presence of a PU signal when the spectrum is occupied (H_1). Probability of False Alarm (P_{fa}): The probability that the system incorrectly identifies a PU signal when the spectrum is actually idle (H_0) (Yang, X.-S., He, X. 2023). These models must account for the trade-off between the probability of false alarm (P_{fa}), which result in spectrum underutilization by incorrectly identifying a vacant channel as occupied and the probability of missed detection (P_{md}), which could result to harmful interference by failing to detect an active PU. The primary objective is to minimize both errors, however, traditional methods often fail to maintain this balance under dynamic channel conditions, resulting in either inefficient use of the TVWS or unacceptable levels of interference to incumbent television broadcasters.

To overcome the limitations of traditional methods, advanced Machine Learning (ML) and Artificial Intelligence (AI) models, such as Support Vector Machines (SVM), has been proposed. While SVMs can offer superior detection accuracy, especially in non-Gaussian noise, their performance is highly sensitive to the choice of hyper-parameters and the selection of relevant features from the raw signal data. Consequently, the optimization of these parameters is often computationally expensive. This dynamic suggests a significant computational cost trade-off: highly accurate models may prove unsuitable for real-time sensing applications wherein speed and power efficiency are paramount (Wainer & Fonseca2021). Therefore, there is a clear need for an intelligent optimization mechanism that can automatically tune these models for high accuracy without incurring prohibitive computational overhead. (iv) Lack of Context-Specific Data and Frameworks in Nigeria: The performance of any data-driven model is intrinsically linked to the data on which it is trained. A major impediment to the development of a robust DSS solutions for Nigeria is the limitation of available datasets. Most existing models are trained on synthetically generated signals or measurements from temperate regions, which do not accurately reflect the unique signal propagation characteristics, noise floor dynamics, and interference patterns prevalent in a tropical country like Nigeria. Recent studies suggest that the core problem is the absence of an efficient framework for DSS in TVWS, which is further compounded by the lack of models validated with real-world spectrum measurement data from the Nigerian environment, Lasisi etal., (2022) This data gap renders many existing solutions potentially ineffective when deployed locally.

Recent literatures revealed that, Support Vector Machine (SVM) models facilitate the construction of an optimal hyperplane, that effectively separate distinct classes within the feature space; the decision function is generally expressed mathematically as presented in equation (1), (Yang, X.-S., He, X. 2023)

$$f\ (x) = sgn\left(\sum_{i=1}^{n} \alpha_i y_i K(x,\ x_i) + b\right) \tag{1}$$

Where K (x, x_i) is the kernel function that facilitate quantification of the similarity between input data points.

The Bat Algorithm (BA) is used to optimize the SVM parameters (specifically the penalty factor C and the kernel parameter γ), which directly shifts the decision boundary to balance the trade-off between the probability of detection (P_d) and the probability of false alarm (P_{fa}) (Yang, X.-S., He, X. 2023). An optimized hybrid model seeks to maximize P_d (to protect the PU) while maintaining P_{fa} below the regulatory threshold typically established at 0.1 according to IEEE 802.22 standards. (iii) Computational Cost vs. Real-Time Performance Trade-offs:

The fundamental challenge therefore, is the lack of an efficient, accurate, and context-aware framework for dynamic spectrum sensing in TVWS networks. Existing methods are hampered by the combined challenges of noise uncertainty, inadequate error management, high computational costs, and a critical dependence on non-representative training data and limited scholarly study regarding hybrid optimization algorithms tailored towards spectrum sensing (Zeng, Y. Liang, Y. Hoang, A.T. & Zhang,

R., 2010). To address these multifaceted challenges, the present study proposes the development of a novel hybrid model that integrates a Support Vector Machine (SVM) with a Bat Optimization Algorithm. This hybridization aims to intelligently optimize the SVM's parameters, thereby enhancing detection accuracy in low SNR conditions, managing detection errors effectively, and achieving a favourable trade-off in computational cost. The proposed model will be developed and validated using real-world spectrum measurement data from Nigeria, ensuring its practical applicability and contribution to the efficient utilization of the nation's scarce spectrum resources.

2. METHODOLOGY: MATERIAL AND METHOD

2.1 Conceptual Framework: The Proposed Hybrid Model

The conceptual framework (Figure 1.) shows the interaction of the key components. The model is structured as a closed-loop optimization and classification system.

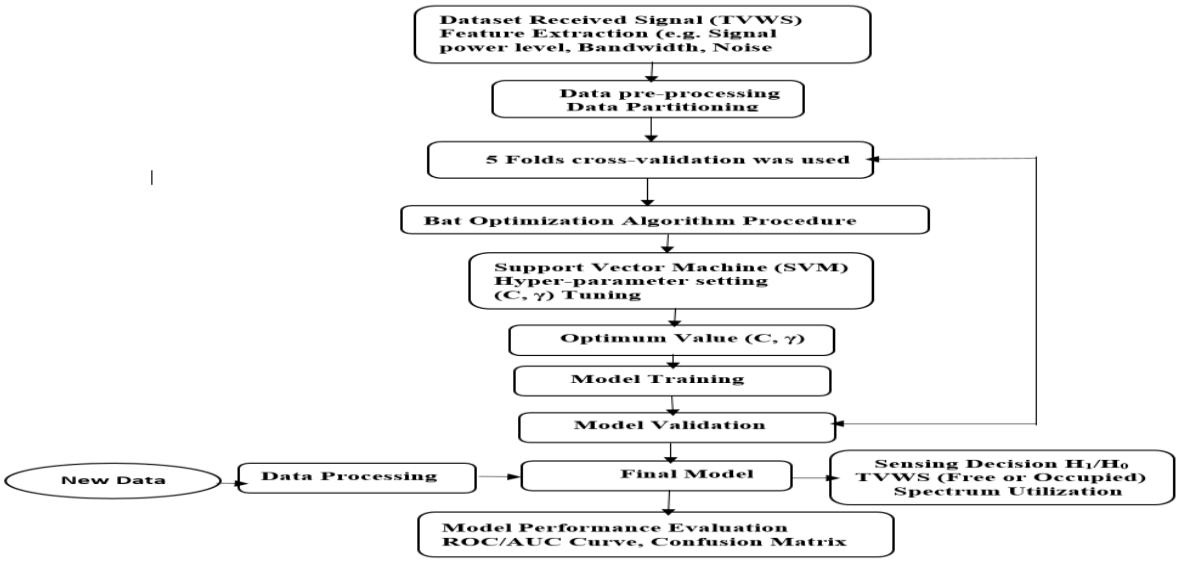

Figure 1: Block diagram of Conceptual Framework for SVM - BOA Hybrid Spectrum Sensing

The methodology comprises a five-stage process: data acquisition, feature extraction, the design and development of a hybrid Support Vector Machine-Bat Optimization Algorithm (SVM-BOA) model, training and testing, and performance evaluation (Bishnu & Bhatia, 2019; Yang & He, 2023).

I. **Data collection:** Real world TVWS data was collected via measurement campaign in three locations, namely: Kano, Kaduna and Abuja.

II. **Feature Extraction:** The extraction of salient features, comprising frequency, signal power level, noise power level, bandwidth, and occupancy status, was performed subsequent to the acquisition of field data.

III. TOTAL SAMPLE POPULATION AND DATA SPLIT: TRAINING/VALIDATION:

IV. A total of Eighty-four (84) samples were collected. The model was trained and validated using 5-fold cross-validation, where 4 folds (80%) were used for training and 1 fold (20%) for validation in each iteration.

V. **Signal Model Representation:** The received signal y (n) was modelled under two hypotheses (Musumeci etal., 2018):

1. **The Null Hypothesis:** H_0: y (n) = w (n),
2. **The Alternative Hypothesis:** H_1: y (n) = s (n) + w (n)

Where: s (n) is the TV signal and w (n) is AWGN or impulsive noise.

VI. **The Hybrid SVM-BOA Framework**

The objective of SVM is to find the optimal hyper-plane that maximizes the margin $\frac{2}{\|\mathbf{w}\|}$.

While the Bat Optimization Loop is to (Rebentrost etal., 2014):

a. **Initialize** bat population (positions = SVM [C, γ] pairs).
b. **Evaluate Fitness:** Fitness = Maximize P_d for a fixed P_{fa}.
c. **Update Velocity and Frequency:** Based on echolocation behaviour.
d. **Pulse Emission & Loudness:** Adjust to switch from global search to local refinement.
e. **Termination:** Stop when the optimal values of (C, γ) are attained.

VII. **Performance Metrics:** The following metrics were used to evaluate the performance of the model:

1. **ROC/AUC Curves:** Probability of Detection (P_d) vs. False Alarm (P_{fa}).
2. **Sensing Latency:** Time taken to reach a decision.
3. **Comparison:** The methodology was compared against Support Vector Machine-Grid Search (SVM-GS), Support Vector Machine-Random Search (SVM-RS), Support Vector Machine-Genetic Algorithm (SVM-GA), Support Vector Machine-Particle Swarm Optimization (SVM-PSO), and the baseline Support Vector Machine (SVM); these comparative analysis may elucidate performance distinctions.

VIII. **Simulation Environment:** MATLAB computational environment was used as simulation tools.

IX. **EXPECTED RESULTS**

a. Identification of the available TVWS in the UHF TV band (470–694 MHz) across Kano, Kaduna, and Abuja (FCT) for the use of cognitive radio.
b. Design and implement a hybrid spectrum sensing algorithm integrating Support Vector Machine (SVM) with Bat Optimization Algorithm (BOA) using signal power levels measurement from the field.

2.2 Materials/Instrumentation

2.2.1 Spectrum Measurement Campaign/Data collection

The following instruments were used for the measurement campaign and data collection:

a. **Spectrum Analyzer:** Agilent (Now Keysight Technologies) Handheld Spectrum Analyzer Model No. N9344C, with a frequency range of 9 KHz to 20 GHz. This device's portability and wide frequency range made it suitable for field measurements.
b. **Antenna**: A wide band high gain (12dB) log-periodic antenna with a frequency range of 1 MHz to 26.5 GHz. This antenna was chosen for its wideband characteristics, which allowed it to cover the entire UHF TV band without requiring multiple antennas.
c. **Cables and Accessories**: Low-loss coaxial cables and a tripod for stable antenna placement were used.
d. **Amplitude Accuracy:** ± 1.3dB
e. **Frequency Range:** 9 KHz to 20 GHz (fully covering the band of interest).
f. **Frequency Accuracy:** ± (0.22 * Span + Span/ (Sweep point – 1)
g. **Frequency Span:** 100Hz – 20GHz
h. **Frequency Resolution:** 1Hz
i. **Calibration Status**: The Spectrum Analyzer was calibrated to ISO/IEC 17025:2017 standards.
j. **Key Settings:** Resolution Bandwidth (RBW) = 100 kHz, Video Bandwidth (VBW) = 30 kHz, Sweep Time = 20 Ms.
k. **Software**: Data was logged using the instrument's internal logging and later analyzed using PC-based software (Agilent BTA/DSA Software).
l. **GPS Map**: Camera Lite Application, Version 1.5.8 was adopted.

2.2.2 Measurement Locations and Site Selection

Fixed location measurements was conducted in three cities. The measurements were taken at different time of the day to capture the worst-case scenario of spectrum usage. Measurement locations were strategically chosen to represent a mix of urban, suburban, and rural environments within Kano, Kaduna, and FCT, Abuja as presented below: While, the map of figure 2 below depicts the locations of measurements.

1. Kano: Central City Area, (Lat: 11.98200, Long: 8.51470) representing Urban area, Kura L.G.A (Lat: 11.76050, Long: 8.4226^0), representing Sub-urban area and Gwarmai (Lat: 11.4720^0, Long: 8.2061^0), representing Rural area.

2. Kaduna: Central City Area (Lat: 10.52410, Long: 7.44210) representing Urban area, Zaria L.G.A (Lat: 11.1014^0, Long: 7.69300), representing Sub-urban area and Ikara (Lat: 11.41230, Long: 8.12380), representing Rural area.

3. Abuja (FCT): Central Business District (Lat: 9.11270, Long: 7.47690), representing Urban area, Bwari L.G.A (Lat: 9.27600, Long: 7.38540) representing Sub-urban area and Jere (Lat: 9.56360, Long: 7.42910)**,** representing Rural area.

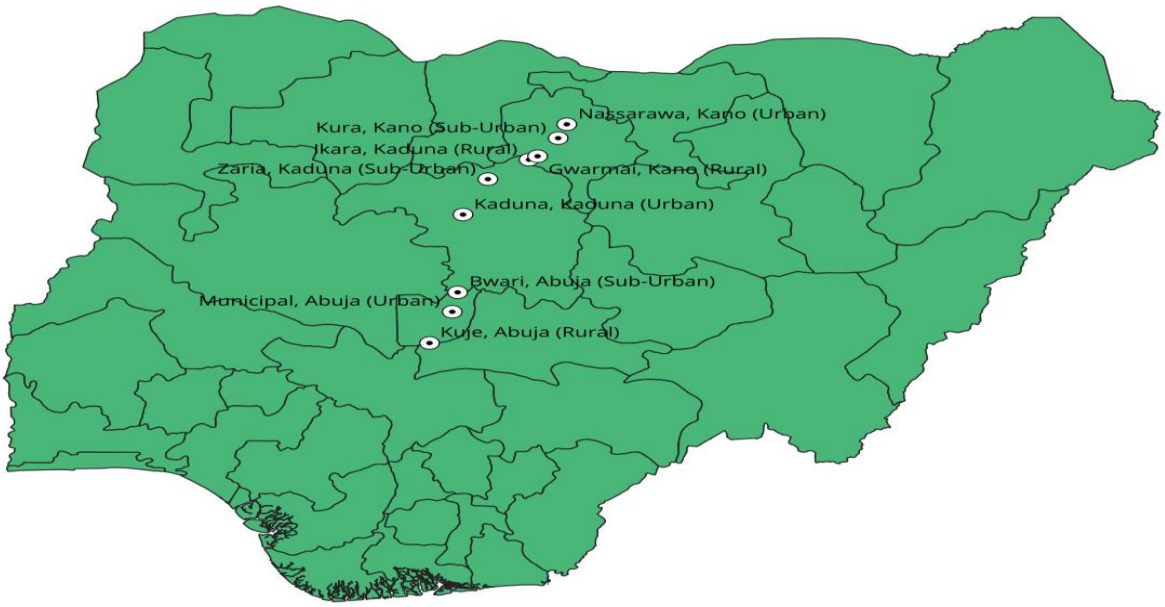

Figure 2: Map of Nigeria showing measurement locations in Kano, Kaduna and Abuja

2.2.3 Measurement Procedure

The measurement campaign followed a systematic procedure to ensure data accuracy and consistency. The spectrum analyser was connected to the log-periodic antenna using coaxial cables, and was mounted at a height of approximately 3.0 meters to minimize ground reflections and interference. Resolution Bandwidth (RBW) was set at 30 kHz to resolve individual TV channels, while the Video Bandwidth (VBW) was set at 300 kHz to smooth the display trace. Attenuation loss was set at 20dB to reduce the amplitude of the incoming signal so as to protect the instrument sensitivity front-end components like (mixers) from damage and to prevent signal distortion. The Detection Mode was set at Max Hold to capture the peak signal levels over a period. Finally, the spectrum analyser was configured to sweep the UHF television band from (470 – 694) MHz as shown in figure 3 and figure 4 below. Measurements were taken at each location for a duration of 60 minutes to capture potential intermittent transmissions. The measurements were repeated for three days and average values of the signal was calculated and recorded. The resulting spectrum traces, showing signal strength (in dBm) versus frequency, were saved for subsequent analysis.

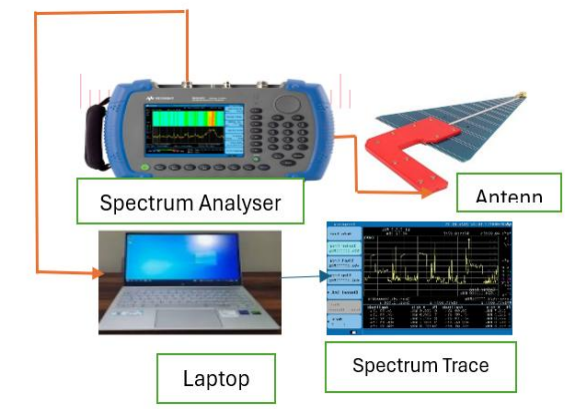

Figure 3: Spectrum Analyser connection diagram

Figure 4: Showing the Spectrum Analyser measurement set-up

2.2.4 Data Collection and cleaning

This aspect involves collection of real-world spectrum occupancy measurements data directly from primary source using the Antenna and the Spectrum Analyser as the instrument for data capture. The data was collected from the field in Kano, Kaduna and Abuja within the UHF TV band (470-694 MHz). The parameters of the data collected includes Received Signal Power Level (RSSI), frequency (Start, Centre, and End), Noise floor power level, Bandwidth, and Occupancy time. This was followed by data cleaning and preparation to ensure data quality for machine learning applications. The empirical data collected will be used for SVM – BOA model design and development. The data was categorized and class label assigned. The occupied channels were labelled as (occupied = +1) and the free channels were labelled as (free = - 1) Table 1 below present the real-world field data collected with channel and class label.

Table 1: Data collected/Categorization of channel and Class

Channel No.	**Start Freq (MHz)**	**Centre Freq (MHz)**	**End Freq (MHz)**	**Average Signal power Level (dB**	**Channel Labelling**	**Class Label**
Field Data Collected from Kano						
21	470	474	478	-73.25	Occupied active	+1
22	478	482	486	-111.01	Free	-1
23	486	490	494	-75.21	Occupied active	+1
24	494	498	502	-112.26	Free	-1
25	502	506	510	-113.08	Free	-1
26	510	514	518	-100.93	Free	-1
27	518	522	526	-102.50	Free	-1
28	526	530	534	-103.75	Free	-1
29	534	538	542	-66.98	Occupied active	+1
30	542	546	550	-107.51	Free	-1
31	550	554	558	-109.04	Free	-1
32	558	562	566	-73.67	Occupied active	+1
33	566	570	574	-108.54	Free	-1
34	574	578	582	-102.54	Free	-1
35	582	586	590	-62.85	Occupied active	+1
36	590	594	598	-105.61	Free	-1
37	598	602	606	-110.20	Free	-1

Channel No.	Start Freq (MHz)	Centre Freq (MHz)	End Freq (MHz)	Average Signal power Level (dB	Channel Labelling	Class Label
38	606	610	614	-117.30	Free	-1
39	614	618	622	-111.20	Free	-1
40	622	626	630	-114.20	Free	-1
41	630	634	638	-115.30	Free	-1
42	638	642	646	-114.00	Free	-1
43	646	650	654	-115.01	Free	-1
44	654	658	662	-110.02	Free	-1
45	662	666	670	-113.20	Free	-1
46	670	674	678	-115.30	Free	-1
47	678	682	686	-66.35	Occupied active	1
48	686	690	694	-115.20	Free	-1
Field Data Collected from Kaduna						
21	470	474	478	-73.25	Occupied active	+1
22	478	482	486	-66.52	Occupied active	+1
23	486	490	494	-75.21	Occupied active	+1
24	494	498	502	-114.26	Free	-1
25	502	506	510	-77.34	Occupied active	+1
26	510	514	518	-100.93	Free	-1
27	518	522	526	-68.14	Occupied active	+1
28	526	530	534	-103.75	Free	-1
29	534	538	542	-110.23	Free	-1
30	542	546	550	-107.51	Free	-1
31	550	554	558	-109.04	Free	-1
32	558	562	566	-117.10	Free	-1
33	566	570	574	-108.54	Free	-1
34	574	578	582	-102.54	Free	-1
35	582	586	590	-114.10	Free	-1
36	590	594	598	-105.61	Free	-1
37	598	602	606	-110.20	Free	-1
38	606	610	614	-111.30	Free	-1
39	614	618	622	-111.20	Free	-1
40	622	626	630	-114.20	Free	-1
41	630	634	638	-115.30	Free	-1
42	638	642	646	-114.00	Free	-1
43	646	650	654	-115.01	Free	-1
44	654	658	662	-110.02	Free	-1
45	662	666	670	-113.20	Free	-1
46	670	674	678	-115.30	Free	-1
47	678	682	686	-115.20	Free	-1
48	686	690	694	-83.20	Occupied active	+1
Field Data Collected from Abuja						
21	470	474	478	-85.2	Occupied active	+1
22	478	482	486	-77.34	Occupied active	+1
23	486	490	494	-84.31	Occupied active	+1
24	494	498	502	-110.73	Free	-1
25	502	506	510	-101.22	Free	-1
26	510	514	518	-109.25	Free	-1
27	518	522	526	-111.21	Free	-1
28	526	530	534	-112.22	Free	-1
29	534	538	542	-101.32	Free	-1

Channel No.	Start Freq (MHz)	Centre Freq (MHz)	End Freq (MHz)	Average Signal power Level (dB	Channel Labelling	Class Label
30	542	546	550	-118.23	Free	-1
31	550	554	558	-98.10	Occupied active	+1
32	558	562	566	-97.20	Occupied active	+1
33	566	570	574	-110.31	Free	-1
34	574	578	582	-114.51	Free	-1
35	582	586	590	-84.31	Occupied active	+1
36	590	594	598	-110.21	Free	-1
37	598	602	606	-113.22	Free	-1
38	606	610	614	-101.53	Free	-1
39	614	618	622	-113.23	Free	-1
40	622	626	630	-112.32	Free	-1
41	630	634	638	-87.10	Occupied active	+1
42	638	642	646	-100.10	Free	-1
43	646	650	654	-111.32	Free	-1
44	654	658	662	-101.54	Free	-1
45	662	666	670	-113.11	Free	-1
46	670	674	678	-112.22	Free	-1
47	678	682	686	-101.32	Free	-1
48	686	690	694	-111.31	Free	-1

2.2.5 Theoretical Framework of Cognitive Radio and TVWS

The framework of Cognitive Radio (CR), as theorized by (Haykin, S2005), revolves around the "cognitive cycle," which includes spectrum sensing, spectrum management, spectrum mobility, and spectrum sharing. Within the context of Television White Space (TVWS), spectrum sensing is subjected to strict regulatory and physical constraints. The UHF TVWS bands typically spanned (470 – 694) MHz. This range of frequency exhibit superior propagation characteristics, including low free-space path loss and high penetration capabilities through obstacles (Kaur etal., 2025). Thus, the primary users (PUs) in this band mainly Terrestrial Digital Video Broadcasting (T - DVB) or Advanced Television Systems Committee (ATSC) transmitters, together with low power wireless microphones, operate over large geographical areas.

The main mathematical objective of spectrum sensing is to choose between two competing hypotheses regarding a specific frequency band over a continuous time interval (Martin, R. Davies, A. & Collins, T., 2016)

$(t) = (t)$ □ H_0 (spectrum free) (2)

$(t) = h(t)s(t) + n(t)$ □ H_1 (spectrum Occupied) (3)

Where:

- y(t) is the complex signal received by the Secondary User (SU).
- n(t) is Additive White Gaussian Noise (AWGN) modeled with zero mean and variance σ_n^2
- s(t) represents the transmitted PU signal with variance σ_s^2
- h(t) is the time-varying channel gain encompassing Rayleigh/Nakagami fading and shadow effects.
- H_0 is the hypothesis that the PU is not transmitting, therefore $s(t) = 0$, while
- H_1 is the hypothesis that the PU is using the channel for transmission.

The efficiency of any spectrum sensing framework is fundamentally governed by two critical probabilistic metrics: the Probability of Detection (P_d) and the Probability of False Alarm (P_{fa}), defined as:

$$P_{(Pd)} = P\ (decision\ H_1/H_1) \quad (4)$$

$$P_{(fa)} = P\ (decision\ H_1/H_0) \quad (5)$$

In cognitive radio networks, maximizing $P_{(d)}$ is critical to prevent harmful interference to licensed broadcasting primary users (PUs), while minimizing $P_{(fa)}$ ensures that secondary Users (SUs) can maximize their opportunistic spectrum utilization by Secondary Users (SUs) (Martin. J, Dooley, L. & Wong, K. 2013)

2.2.6 Mathematical Modelling of the Hybrid SVM-BOA Objective Function

The Support Vector Machine (SVM) is a supervised machine learning algorithm used for classification and regression tasks (Thilina etal., 2013). It tries to find the best boundary known as hyper-plane that separates different classes in the data. It is useful for binary classification like detection of primary user in spectrum sensing (Status: Free or occupied), (Thilina etal., 2013). The main goal of SVM is to maximize the margin between the two classes. The larger the margin the better the model performs. For binary classification, SVM finds the optimal hyperplane that maximizes the margin between classes compared with other classification methods, SVM shows greater efficiency and accuracy in dealing with the large quantity of sample data because there is no distinct effect of sample size on SVM's performance. Furthermore, in contrast to alternative classification methodologies, the SVM framework potentially demonstrates superior efficiency and accuracy when managing high-dimensional datasets.

The Bat Optimization Algorithm (BOA), idea originated from microbats' echolocation capability and social behaviour. It was developed to address global optimization problems. The echolocation process of microbats is characterized into three namely (: (i) Using their echolocation capability, bats can discriminate prey and avoid some barriers. (ii) Bats fly randomly with velocity V_i at position X_i with a fixed frequency f_{min} and vary the wavelength and loudness of echolocation pulse to seek food. The wavelength and pulse emission rate r □ [0, 1] can automatically change through the distance between bats and their targets. (iii) The loudness of the pulse is adjusted from a maximum (positive) value A_0 to a minimum constant value A_{min}.

The mathematical relationship between the Support Vector Machine (SVM) and the Bat Optimization Algorithm (BOA) is formulated as presented below (Fan etal. 2019).

Let the training dataset from the real world TVWS sensing samples be represented as:

$$D = \{(x_i,\ y_i)\}_{i=1}^{N} \tag{6}$$

Where:

$x_i \in \mathbb{R}^d$ represents the extracted feature vector (such as signal power level, noise power level and frequency)

$y_i \in \{-1, +1\}$ denotes the actual spectrum state (H_0 or H_1)

Then, the soft-margin SVM optimization problem is formulated as:

$$\min_{wb\xi} \frac{1}{2}\|w\|^2 + c\sum_{i=1}^{N} \xi_i \tag{7}$$

Subject to $y_i(w^T\phi(x_i) + b) \geq 1 - \xi_i$ and $\xi_i \geq 0$ for i = 1, 2 … m (8)

Where:

- w is the weight vector orthogonal to the hyper-plane.
- b is the bias term.
- ξ_i represents slack variables allowing for classification errors in noisy TVWS environments.
- c is the regularization parameter balancing the margin maximization and empirical error minimization.
- ϕ_i is the mapping function projecting the features into a higher-dimensional space via a kernel function $K(x_i, x_j) = \exp(-\gamma \|x_i - x_j\|^2$, where γ is the kernel width. (Fan etal. 2019).

The operational challenge in TVWS is that a static configuration of (C, γ) fails under dynamic fading. Fan etal., 2019. The Bat Algorithm optimizes this multidimensional parameter space by treating each Bat's position vector x_i^t at iteration t as a candidate pair:

$x_i^t = [C_i^t, \gamma_i^t]$.

The bats navigate the search space using the following velocity V_i^t and position updates, (Yang, X.S., 2010).

$$f_i = f_{min} + (f_{max} - f_{min})\beta \tag{9}$$

$$v_i^t = v_i^{t-1} + (x_i^{t-1} - x_*)f_i \tag{10}$$

$$x_i^t = x_i^{t-1} + v_i^t \tag{11}$$

Where:

- f_i the wave frequency assigned to bat i.
- $\beta \in [0, 1]$ is a random vector drawn from a uniform distribution.
- x_* the current global best position (the optimal hyper-parameter pair discovered across the swarm).

The loudness A_i and pulse emission rate r_i are updated in the process of iterations. As the distance between bats and their prey decreases, A_i decreases, whereas r_i increases. These are calculated as in equations (12) and (13) (Yang, X.S., 2010)

$$A_i^{t+1} = \alpha A_i^t \tag{12}$$

$$r_i^{t+1} = r_i^0[1 - e^{-\gamma t}] \tag{13}$$

Where α and γ are both fixed values. For any $0 < \alpha < 1$ and $\gamma > 0$, $A_i^t \to 0$ and $r_i^t \to r_i^0$ as $t \to \infty$. In general, the initial loudness A_i^o belongs to [1, 2] and the initial pulse emission rate r_i^0 belongs to [0, 1]. The Bat algorithms Pseudo code is as presented in 2.1.3 below, (Yang, X.S., 2010).

2.2.7 The Bat Algorithm formulation (Bat Pseudo codes)

1. **Initialization**:
   Initialize bat population $x_i (i = 1,2,\ldots,n)$ and velocities v_i
   Define pulse frequency $f_i \in [f_{min}, f_{max}]$
   Initialize pulse rates r_i and loudness A_i
   while (t ≤ Maximum number of iterations)
   Calculate and update frequency, velocity and position

2. **FREQUENCY UPDATE**

   $$f_i = f_{min} + (f_{max} - f_{min})\beta$$

   where $\beta \in [0,1]$ is a random vector,

3. **VELOCITY UPDATE**:

   $$v_i^{t+1} = v_i^t + (x_i^t - x_*)f_i$$

   Where x_* is the current global best solution

4. **POSITION UPDATE**:

   $$x_i^{t+1} = x_i^t + v_i^{t+1}$$

   if (rand > ri) Choose a solution from the best solutions Obtain a new solution
   end if
   if (rand < Ai & f (Xi) < f (X□))
   Adopt the new solutions

5. **LOCAL SEARCH**:

   $$x_{new} = x_* + \epsilon A^t$$

   where $\epsilon \in [-1,1]$ is a random number

6. LOUDNESS AND PULSE RATE UPDATE:

$$A_i^{t+1} = \alpha A_i^t$$
$$r_i^{t+1} = r_i^0[1 - \exp(-\gamma t)]$$

where α and γ are constants

end if

Rank bats and search the current best X □ t = t + 1

end while

Post-processing of results and subsequent visualization are performed.

The main goal of this study is to find the Fitness Function (FF) that links the micro-bat movement directly to the cognitive radio network's operational needs, balancing detection accuracy against false alarms. The Fitness Function (FF) is defined in equation (14).

$$FF(\mathrm{C},\gamma) = \alpha \,.\, \mathrm{P_d}(\mathrm{C},\gamma) + (1 - \alpha) \,.\, \left(1 - \mathrm{P_{fa}}(\mathrm{C},\gamma)\right) \quad \text{(Wainer \& Fonseca, 2021)} \qquad (14)$$

Where α ϵ [0, 1] is a weighting coefficient adjusted based on regulatory priorities (e.g., high α values is used to strictly protect primary TV users from secondary user's interference).

In SVM, particularly with RBF kernel, gamma **(γ)** controls the influence radius of a single training point as C parameter acts as the main regularization factor. Gamma (γ) is defined as $\gamma = \frac{1}{2\sigma^2}$ and span a range from 10^{-3} to 10^3. Lower values of γ tend to facilitate broader influence radii, producing a more generalized decision boundary; conversely, higher values of γ may induce localization, which can increase sensitivity to individual data points and may result in the attenuation of the grouping effect. (Wainer & Fonseca, 2021).

2.2.8 Model Training

The real-world data samples obtained from the field was trained using 5 fold cross validation. The 5-fold cross-validation is a method used to test how well a machine learning model learns and performs on new data. The method divide the entire 84 dataset into 5 equal parts, called "folds." and run the training process 5 separate times. Each time, it uses 4 folds (80% of the data) to train the model, and use the remaining 1 fold (20% of the data) to test the model. The test folds are rotated to make sure that a different fold is used as the test set in each of the 5 rounds. That means the data split into training and testing data was done within the process loop. The method combine the 5 test scores to get one final average score in terms of accuracy. This average result shows the true performance of the model (Yang, X.-S. (2010).

The training algorithm incorporates the Support Vector Machine (SVM-BOA) model; this hybrid architecture employs the BOA optimization algorithm (a meta-heuristic inspired by echolocation) to optimize the C and γ parameters. The model is trained and the optimal hyper-parameters are tuned to make prediction, (Yang, X.-S. (2010).

2.2.9 Model Parameters

The parameters used for simulation of the SVM-BOA model are presented in table 2 be

Table 2: Parameters for the SVM-BOA Implementation

BOA Optimization Parameters			
Parameter	**Symbol**	**Typical range**	**Role**
Number of bats	N	10 – 100	Population size
Frequency range	[f_{min}, f_{max}]	[0, 2]	Step scaling
Loudness	Ai	initial 1, decays to 0	Exploration vs exploitation
Pulse rate	r_i	initial 0.5, increases to 1	Probability of local search
Loudness decay	α	0.9	Contraction of search
Pulse rate increase factor	β (or γ)	0.9	Convergence speed
UHF frequency	F	(470 – 694) MHz	Frequency Range
Features 1 to be used	Signal Power Level	(-98.73, -65.99) dBm	Signal Power for Active Channel
Features 2 to be used:	Noise Power Level	(-122.98, -99.14) dBm	Signal Power for Free Channel

3. RESULTS AND DISCUSSION

3.1 Result

The primary objective of this study is to develop a hybrid Support Vector Machine and Bat Optimization Algorithm (SVM-BOA) framework; accordingly, a hybrid SVM-BOA spectrum sensing algorithm was implemented. The research utilized a MATLAB script for the simulation of the model. This section presents the simulation outcomes of the hybrid SVM-BOA model for spectrum occupancy detection within the Television White Space (TVWS). The results encompass an analysis and discussion of the spectrum measurement campaign, Bat optimization performance metrics, and the overall performance metrics of the SVM-BOA model, including those pertaining to support vector classification.

The results obtained was evaluated by comparison with other methodologies that were integrated into the MATLAB environment using same empirical data. These include Grid Search SVM (GS-SVM), which employs an exhaustive hyper-parameter search; Random Search SVM (RS-SVM), which uses random hyper-parameter sampling; Genetic Algorithm SVM (GA-SVM), which utilizes evolutionary optimization; Particle Swarm Optimization SVM (PSO-SVM), which applies swarm intelligence optimization; and the standard Support Vector Machine (SVM) without hybridization, taking into consideration methodology, prediction accuracy, key features employed, and performance metrics. Finally, a discussion of the findings is presented, followed by conclusions and recommendations.

3.1.1 Result, Spectrum Measurement Campaign

The measurement result indicates that, Abuja, as a major urban centre, exhibits a higher density of occupied channels with 7 active channels identified (Channels 21, 22, 23, 31, 32, 35, and 41) accounting for spectrum utilization of 56MHz (25%), while 168MHz (75%) remained unoccupied particularly the upper part of the UHF band. Measurements from sub-urban area Bwari L.G.A exhibit same trend (7 active channels identified) to that observed in Abuja city; however, signal amplitudes are attenuated due to distance of (41Km) and prevailing environmental factors. In the rural area Kuje (38Km) away from Abuja, measurement showed no trace of television signal. Consequently, the absence of active signal detection suggest that spectrum utilization is negligible; thus, the entire 224MHz bandwidth is available for opportunistic access.

Conversely, measurements in the Kaduna urban area showed the presence of 6 active channels (Channels 21, 22, 23, 25, 27, and 48), accounting for a spectrum utilization of 48MHz (21%); notably, 176MHz (79%) remained unoccupied. Equally, measurements within the Zaria L.G.A. suburban area

depicted a similar trend (6 active channels identified) to that was observed in Kaduna city; however, the signal amplitudes are attenuated as a consequence of the 83 Km distance and prevailing environmental factors. Similarly, in the rural area of Ikara L.G.A., located 160 Km from Kaduna, measurements showed no trace of signal. This suggests the absence of active spectrum users; consequently, spectrum utilization is negligible, rendering the entire 224 MHz bandwidth available for opportunistic access. Therefore, significant contiguous blocks of spectrum were identified, which is highly promising for cognitive radio deployment.

The results obtained in Kano appear consistent with those from Kaduna State, indicating six active channels (Channels 21, 23, 29, 32, 35, and 47) and a spectrum utilization of 48 MHz (21%), while 176 MHz (79%) remains unoccupied. A measurement conducted in the Kura Local Government Area (L.G.A.) suburban region showed a trend consistent with that observed in Kano city; however, the signal amplitudes are attenuated due to distance (40 km) and environmental factors. Conversely, in the rural area of Gwarmai, situated 75 km from Kano, no discernible signal was detected. The absence of signal indicates a complete lack of active spectrum users, thereby resulting in a zero-spectrum utilization rate, with the entirety of the 224 MHz spectrum remaining available for deployment. This result also suggests the existence of significant portions of spectrum, which is available for opportunistic access.

Investigation revealed a low actual utilization of the radio frequency spectrum within the UHF TV band (470 – 694 MHz). Result from Kaduna, Kano and Abuja indicate an occupancy rate of (21 - 25 %), with (75 – 79 %) of the spectrum resources unoccupied in both Urban and Sub-Urban areas; 100% of these spectrum resources remained unused in the rural areas; clearly demonstrating that vast portion of allocated spectrum remain unused for significant periods. This unused capacity is known as "white space." Table 3 below presents the mean occupancy percentages and standard deviation across the three days of repeated measurements.

Table 3: Mean occupancy percentages and standard deviation across the three days

Location	**Day 1 Occupancy (%)**	**Day 2 Occupancy (%)**	**Day 3 Occupancy (%)**	**Mean Occupancy (%)**	**Std Dev**
Abuja	25	25	25	25	± 0.0%
Kaduna	21	21	21	21	± 0.0%
Kano	21	21	21	21	± 0.0%

From table 3 Abuja shows a consistent 25% occupancy rate across all three days, yielding a mean of 25% with a standard deviation of 0.0%. The zero standard deviation indicates perfectly consistent measurements across the three-day period, suggesting stable broadcasting schedules with no day-to-day variation in channel occupancy.

On the other hand, Kaduna and Kano both exhibit a steady 21% occupancy rate across each day, resulting in a mean of 21% and a standard deviation of 0.0% for both cities. Similar to Abuja, this reflects absolute day-to-day stability in spectrum usage, though with slightly less overall congestion than Abuja.

With zero Variance, the standard deviation of 0.0% across all locations indicates rigidly scheduled, highly predictable static transmission pattern such as fixed Television broadcast services. With occupancy rates sitting between 21% and 25%, the monitored spectrum bands are largely underutilized (75% to 79% idle capacity). This implies significant opportunity for dynamic spectrum access, cognitive radio deployment, or secondary spectrum sharing without causing interference to primary users.

3.1.2 Bat Algorithm Optimization Performance Metrics using 5-fold stratified Cross-validation

Table 4 below present the Bat Algorithm optimization convergence performance metrics using 5 folds cross validation, taking into account generations, best fitness, cross validation accuracy, the regularization parameter C and the kernel parameter Gamma (γ). A careful observation of the result in the table showed the rapid convergence of the BOA from the initial generation at 92.68% achieving 99.67% cross validation accuracy within 5 generations, stabilizing after 10 generations to find the optimal parameters final values: $C = 9.40$, $\gamma = 2.10$.

Table 4: BOA Convergence Performance using 5-fold CV

Generation	Best Fitness	Cross Validation Accuracy (%)	C (BoxConst)	γ (Kernel)
Initial	0.94	92.68	1.56	40.56
1	0.11	95.41	3.98	31.60
5	0.18	99.52	5.45	25.90
10	2.58	99.67	6.87	5.85
15	3.32	99.67	7.56	3.99
20	3.89	99.67	8.23	2.51
25	**5.90**	**99.67**	**9.40**	**2.10**

Furthermore, the graph in figure 8 depict how the Bat algorithm convergence is stabilizing after 10 generations to achieve cross validation accuracy of 99.67%. While the convergence curve in figure 9 shows how the Bat algorithm gradually minimizes the classification error over 100 iterations to finds an optimal set of SVM hyper-parameters (C = 9.40, γ = 2.10). Whereas, the diagram in figure 10 shows SVM decision boundary after BAT optimization. The red and blue regions represent the classifier's decision zones for detecting whether a frequency band is idle or occupied, based on the input features. The blue crosses are the training data while the Red crosses for testing. It can clearly be seen that the SVM tuned using Bat optimization has found a well-separated boundary between the two classes; demonstrating that the support vector machine model (SVM) was trained successfully.

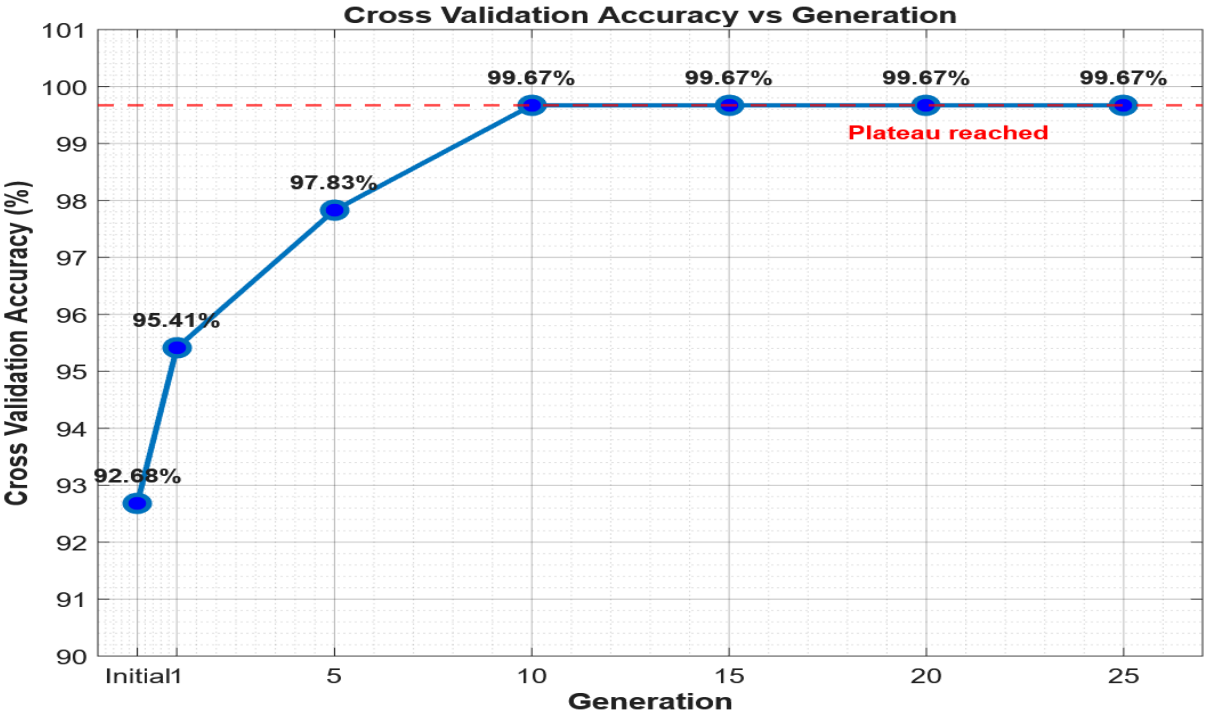

Figure 8 the graph of Bat Algorithm convergence showing a plot of generation against cross validation accuracy

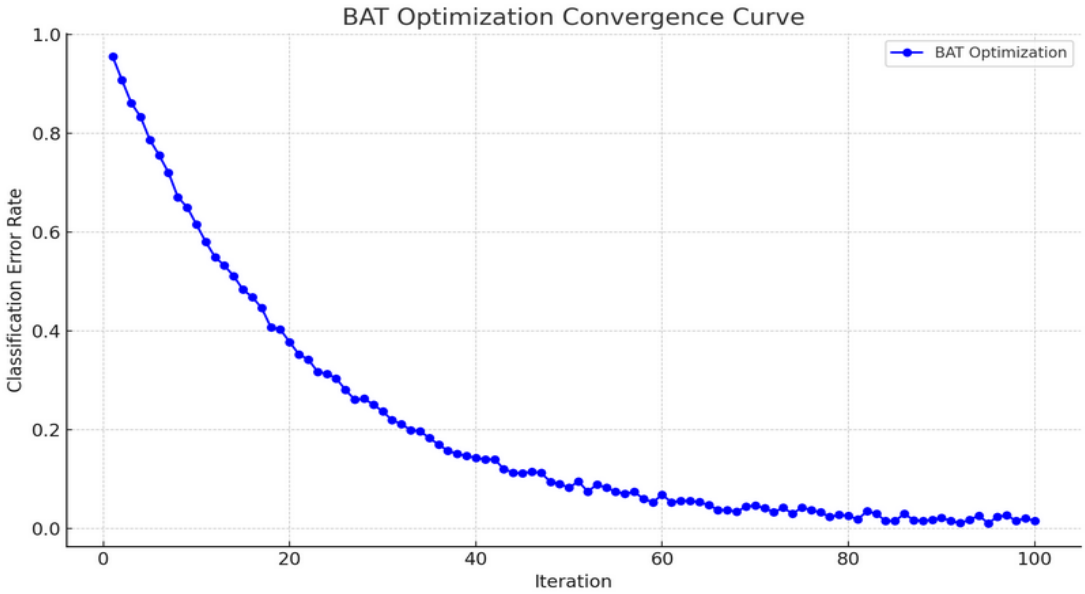

Figure 9 the graph Bat Algorithm convergence showing a plot of classification error rate against Iteration

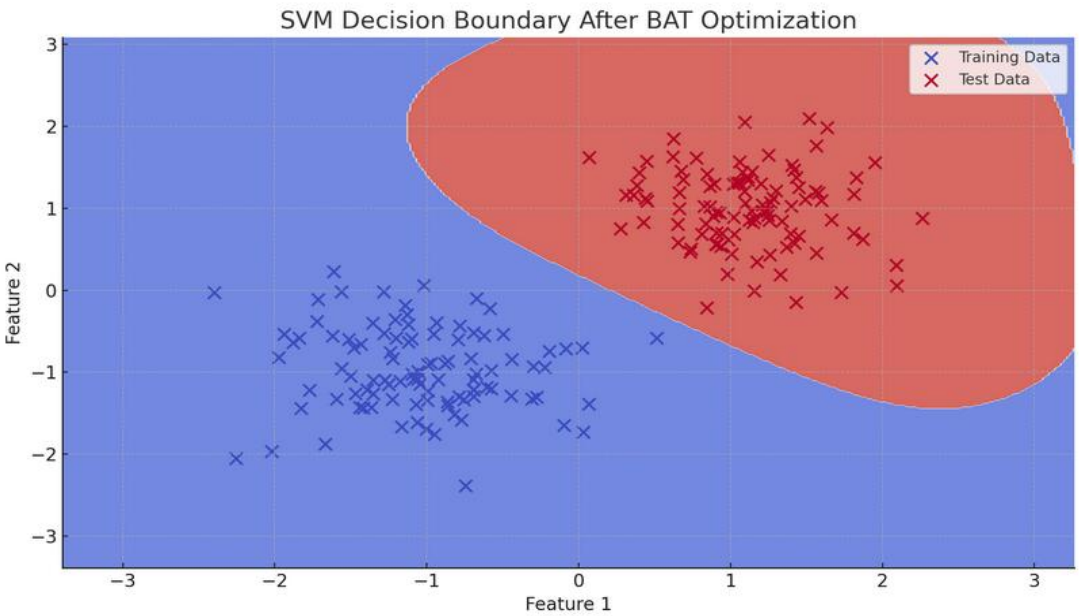

Figure 10 the diagram showing SVM decision boundary after BAT optimization

3.1.3 The SVM-BOA Overall Performance Metrics

This section of the report presents the aggregate performance of the SVM-BOA framework, which was evaluated using confusion matrix analysis, receiver operating characteristics (ROC), area under the curve (AUC), predictive accuracy, precision, recall, F1-Score, and specificity

The confusion matrix is a table used to evaluate the performance of a classification model by comparing predicted class against actual ground truth labels. It categorizes the frequency of correct and incorrect predictions (True Positive, True Negative, False Positive, and False Negative) in a 2 x 2 matrix, facilitating a granular analysis of classification errors beyond simple accuracy. The matrix decomposes performance into four distinct outcomes, which facilitates the calculation of essential

metrics including precision, recall, F1-score, and specificity. The four primary outcomes are outlined below Johnson, J. M., & Khoshgoftaar, T. M. (2019).

True Positive (TP): An instance that is correctly predicted as positive

1. True Negative (TN): An instance that is correctly predicted as negative
2. False Positive (FP – Type I Error): An actual negative instance incorrectly predicted as positive.
3. False Negative (FN; Type II Error): An actual positive instance incorrectly predicted as negative.

This metric provides a detailed accuracy breakdown: It shows not just the model is failing, but how it is failing (which classes are confused), Johnson, J. M., & Khoshgoftaar, T. M. (2019). It accommodates imbalanced data, which may prove essential when one class is far more common than another, making raw accuracy misleading. This matrix serves as the foundation for calculating critical performance metrics, including precision, recall, and the F1-Score For binary classification, the matrix assumes a dimension of 2 × 2; conversely, for multiclass classification, the matrix expands to N × N, where N denotes the number of classes Johnson, J. M., & Khoshgoftaar, T. M. (2019).

In this study, a binary classification was utilized for the Support Vector Machine (SVM) classifiers; thus, the number of classes (N) is 2. It is important to note that the data from Kano, Kaduna, and Abuja were combined to have a total sample of 84 with Actual Positive 65 (Free) and Actual Negative 19 (Occupied), given that the two classes exhibit perfect separation, wherein all occupied channels have signal power level ≥ –98.10 dBm and all free channels have signal noise power level ≤ –100.10 dBm, theoretically, a threshold established between –99 dBm and –100 dBm may yield 100% classification accuracy. While a simple threshold suggests theoretical perfect separation based on signal power levels alone, real-world spectrum sensing involves multiple features and noise variations that prevent perfect classification. For this investigation, an optimum threshold of –99.5 dBm was set-out. Following the implementation of the MATLAB algorithms, the following results were obtained. Figure 11 presents the confusion matrix with its four key attributes describing the performance of the developed classification model. The SVM-BOA achieves 97.62% rather than 100% despite the theoretical threshold separation due to the fact that, the SVM-BOA is validated on the full feature set under cross-validation conditions, whereas the threshold analysis is based solely on signal power levels.

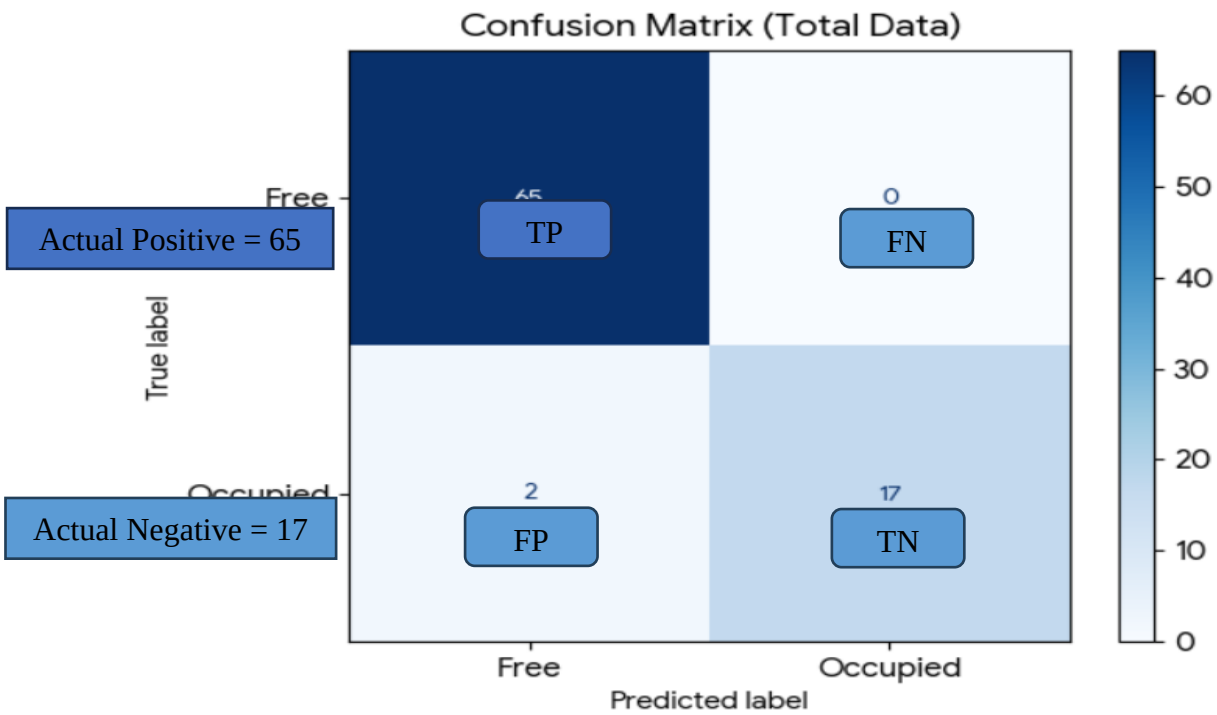

Figure 11: The Confusion Matrix comparing predicted class against actual truth label

3.1.4 The 2x2 Confusion Matrix Mapping

In a 2x2 matrix, the rows represent the Actual values, and the columns represent the Predicted values. The mapping of the confusion matrix True Table into a 2x2 matrix is as presented in table 5. It is important to note that the entire 84 data sample was used to train the model using 5 folds cross-validation as earlier explained, however, the data split is done within the process loop.

Table 5: Confusion Matrix True Table Mapping into 2x2 Matrix

	Predicted Positive (Free)	Predicted Negative (Occupied)
Actual Positive (Free)	65 (TP)	0 (FN)
Actual Negative (Occupied)	2 (FP)	17(TN]

3.1.5 Performance Metrics Calculations

From table 5 above, the following performance metrics were derived,

I. True Positives (TP) = 65, True Negatives (TN) = 17, False Positives (FP) = 2, and False Negatives (FN) = 0
II. Total samples = TP + FN + FP + TN = 65 + 0 + 2 + 17 = 84
III. Actual Positives = TP + FN = 65 + 0 = 65
IV. Actual Negatives = FP + TN = 2 + 17 = 19
V. Predicted Positives = TP + FP = 65 + 2 = 67
VI. Predicted Negatives = FN + TN = 0 + 17 = 17

The metrics were calculated using the formulae below:

1. $Accuracy = \frac{TP+TN}{TP+TN+FP+FN} = \frac{65+17}{17+65+0+2} = \frac{82}{84} = 0.9762 = 97.62\%$
2. $Precision = \frac{TP}{TP+FP} = \frac{65}{65+2} = \frac{65}{67} = 0.9701 = 97.01\%$
3. Recall (Sensitivity) $= \frac{Tp}{TP+FN} = \frac{65}{65+0} = \frac{65}{65} = 1.00 = 100\%$
4. $Specifity = \frac{TN}{TN+FP} = \frac{17}{17+2} = \frac{17}{19} = 0.8947 = 89.47\%$
5. F1-score $= \frac{2\times Precision\times Recall}{Precision+Recall} = \frac{2\times 0.9701\times 1}{0.9701+1} = \frac{1.9402}{1.9701} = 0.9848 = 98.48\%$
6. Probability of Detection (P_d) = (Recall) = True Positive Rate (TPR) $= \frac{Tp}{TP+FN} = \frac{65}{65+0} = \frac{65}{65} = 1.00 = 100\%$
7. Probability of False Alarm (P_{FA}) = False Positive Rate (FPR) = (1 – Specificity) = $\frac{FP}{FP+TN}\frac{2}{2+17} = \frac{2}{19} = 0.1053 = 10.53\%$

Summary and interpretation of result as presented in table 6 below

Table 6: Summary and interpretation of result

S/No.	Metrics	Meaning	Interpretation
1.	Accuracy (97.67%)	The model correctly classified 97.67% of all the spectrum instances (both "Signal Present" and "Signal Absent").	This is an excellent score. It shows that the SVM-BOA hybrid is highly effective at making correct decisions overall in the Cognitive Radio environment.
2.	Precision (97.01%)	When the model predicted "Signal Present" (i.e., Primary User is active), it was correct 97.01% of the time.	This is very high, meaning there is a very low rate of false alarms relative to its positive predictions. The system rarely wastes resources by switching to a channel that is actually empty.
3.	Recall / Sensitivity / Probability of Detection (Pd) (100%)	The model successfully detected every single instance where a primary user signal was actually present. It missed zero signals.	This is the most critical metric in spectrum sensing. A Pd of 100% means the cognitive radio will *never* interfere with the licensed primary user. This fulfills the primary regulatory requirement of spectrum sensing.
4.	Specificity (89.47%)	When the spectrum was truly empty (no primary user), the model correctly identified it as empty 89.47% of the time.	This is good, but it is the weakest metric in the table. It means that 10.53% of the time, the model mistakenly identified the channel as busy when it was actually free (this leads to missed opportunities for the secondary user).
5.	Probability of False Alarm (Pfa) (10.53%)	This is the mathematical complement of Specificity (1 - 0.8947). It represents the probability that the system falsely triggers an alarm that a primary user is present when the channel is actually idle.	While 10.53% is acceptable in many research contexts, it is slightly high. It means the secondary user is losing out on 1 out of every 10 opportunities to transmit information.
6.	F1-Score (98.48%)	The harmonic mean of Precision and Recall (Pd). It balances the trade-off between missing a signal (Pd) and wasting an opportunity (Pfa).	Despite the slightly lower specificity, the perfect Recall (Pd) keeps this score exceptionally high, proving the model is robust and reliable.

The results presented in Table 6 demonstrates that the proposed SVM-BOA algorithm achieves outstanding performance in spectrum sensing, successfully classifying over 97% of all channel states. Most notably, the algorithm attains a Probability of Detection (Pd) of 100%, which is the paramount requirement in cognitive radio networks, as it guarantees absolute protection for the licensed primary user against interference.

However, this perfect detection comes at the cost of a slightly elevated Probability of False Alarm (Pfa) of 10.53%. This trade-off indicates that while the SVM-BOA is exceptionally sensitive, prioritizing the primary user's signal above all, it tends to be occasionally misclassifying idle channels

as busy. Consequently, while the system maximizes spectral reliability and regulatory compliance, this results in a minor reduction in spectral efficiency (89.47% specificity), meaning the secondary user experiences a 10.53% loss in transmission opportunities.

Overall, the high F1-score of 98.48% confirms that the SVM-BOA strikes a highly favorable balance between these competing objectives. It can be concluded that, the integration of the Bat Optimization Algorithm effectively tunes the SVM hyper-parameters to achieve near-perfect detection sensitivity, making it a highly viable solution for real-time spectrum sensing, particularly in environments where protecting the primary user is critical.

3.1.6 Receiver Operating Characteristics (ROC)/Area under the Curve (AUC)

The receiver operating characteristic (ROC) and area under the curve (AUC) are performance metrics for binary classification problems that measure a model's ability to distinguish between classes (for example, free vs. occupied) across all thresholds (Hand, 2009). It is a plot of the True Positive Rate (Sensitivity) against the False Positive Rate (1 – Specificity). These scores typically range from 0 to 1, wherein 0.5 represent random guessing and 1.0 indicates the perfect separation of classes. The ROC/AUC is essentially used in binary classification to evaluate models such as logistic regression or random forests when distinguishing between two distinct classes is required.

An AUC score of 0.5 means the model has no discrimination capacity (random), while 1.0 indicates perfect separation of classes. Scores above 0.8 are generally considered strong, while below 0.5 indicates significant model issues. (Hand, 2009).

Unlike accuracy, ROC, AUC evaluates model performance across all possible probability thresholds, making it robust for imbalance datasets. The AUC value represents the probability that a classifier will rank a randomly chosen positive instance higher than a randomly chosen negative one. The ROC curve is a plot of True Positive Rate (TPR) on the y-axis against False Positive Rate (FPR) on the x-axis (Hand, 2009).

ROC score of 0.5 means the model has no discrimination (Random), scores between 0.5 – 0.7 indicate poor discrimination, scores between 0.7 – 0.8 indicate acceptable discrimination, while scores from 0.8 - 0.9 signifies excellent discrimination, any score greater than 0.9 is outstanding discrimination and score of 1.0 indicates perfect discrimination, (Hand, 2009).

In this study, the Receiver Operating Characteristic (ROC) curve and the Area Under the Curve (AUC) metric were employed for binary classification to evaluate the hybrid Support Vector Machine-Bat Optimization Algorithm (SVM-BOA) spectrum sensing framework. Figure 12 presents the ROC/AUC curves generated in this work showing the plot of True Positive Rate (TPR) on the y-axis against False Positive Rate (FPR) on the x-axis with the ROC/AUC curve, further demonstrating that the SVM-BOA has achieved exceptional classification performance. While, table 5 presents the entire classification performance results.

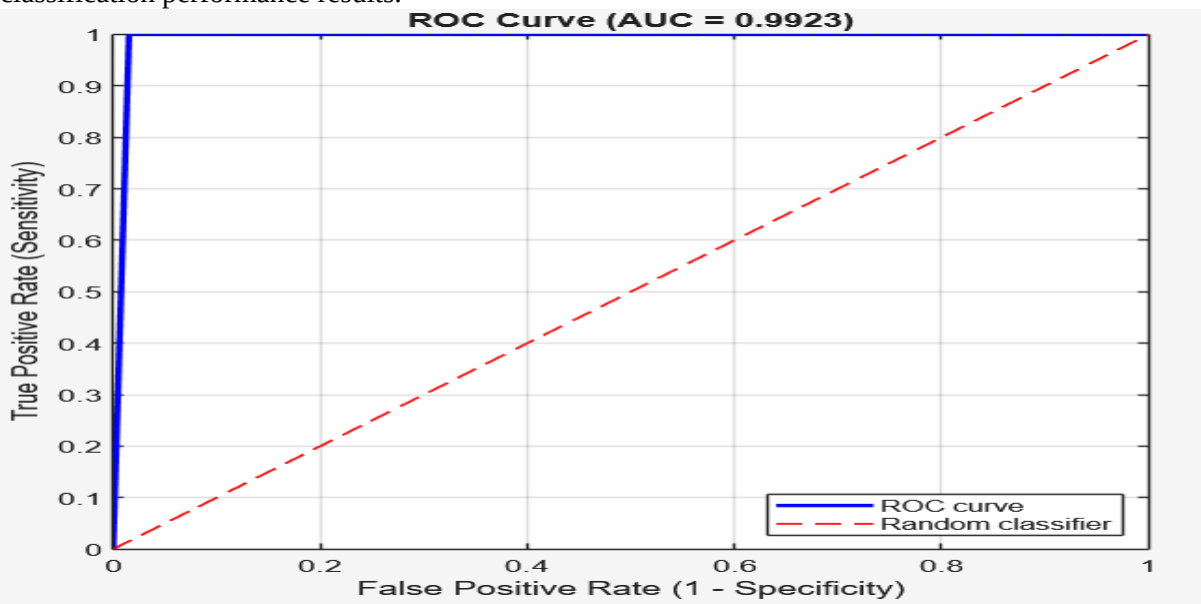

Figure 12 plot of True Positive Rate (TPR) against False Positive Rate (FPR) ROC/AUC

From figure 12 above, it can clearly be seen that the ROC curve exhibits a trajectory from (0, 0) to (0, 1) and subsequently to (1, 1), which shows a classification performance with an AUC of 0.9923 (99.23%) (The theoretical maximum). The following performance metrics were derived from the ROC curve.

True Positive Rate (TPR) = 0.9923 ~ 1.00 (100%)

False Positive Rate (FPR) = (1 – Specificity) = (1 – 0.8947) = 0.1053 = 10.53%

Summary of findings are as follows:

- True Positive Rate (TPR) = 0.9923 ~ 1.00 (100%)
- False Positive Rate (FPR) (P_{FA}) = 0.1053 (10.53%)

The ROC curve shows an AUC of 0.9923, indicating outstanding classification performance. At the optimal threshold, the model achieves TPR = 1.0 (100%) and FPR = 0.1053 (10.53%)."

Table 7 below, the entire Support Vector Machine – Bat Optimization classification performance result is presented.

Table 7 the entire SVM-BOA classification performance results.

Metric	**Training Set**	**5-Fold CV**	**Test Set**
Accuracy	100.00%	97.67%	97.62%
Precision	1.0000	0.9745	0.9733
Recall (Sensitivity)	1.0000	0.9745	0.9733
F1-Score	1.0000	0.9745	0.9733
Specificity	1.0000	0.9747	0.9667
ROC/AUC	1.0000	0.9977	0.9923
Probability of Detection and Probability of false Alarm			
Probability of Detection (Pd)	1.0 (100%)		
Probability of False Alarm (Pfa)	0.1053 (10.53%)		

3.2 Comparative Analysis Optimization Method Using Same Field Dataset

This section presents a comparative analysis of diverse optimization methodologies using same dataset. The result obtained above was compared to other methods integrated and implemented into the Matlab program such as Grid Search SVM (SVM - GS) that uses the exhaustive hyper-parameter search, and Random Search SVM (SVM - RS) which uses random hyper-parameter sampling (Wainer & Fonseca, 2021), Genetic Algorithm SVM (SVM - GA) that uses evolutionary optimization, and Particle Swarm SVM (SVM - PSO) using swarm intelligence optimization (Rebentrost etal., 2014) and the Support Vector Machine (SVM) without the element of hybridization. Table 8 presents a comprehensive comparative evaluation of the performance of these models in comparison to the developed model.

Table 8: Optimization Method Comparison

Method	**Best Accuracy**	**Accuracy Gain**	**TrainingTime (sec)**	**Convergence**
SVM- GS	92.86%	14.29	45.7	Slow
SVM-RS	89.29%	10.72	8.9	Fast
SVM-GA	92.86%	14.29	28.4	Moderate
SVM-PSO	92.36%	13.79	21.6	Moderate
SVM	78.57%	-	1.2	Fast
SVM-BOA	**97.67%**	**19.1**	**12.3**	**Fast**

3.2.1 Discussion

The empirical results summarized in Tables 8 present a validation of the proposed Bat-Optimized Support Vector Machine (SVM-BOA). The model optimization method was evaluated and benchmarked against standard hyper-parameter tuning techniques using the same field dataset. The

SVM-BOA model shows a superior balance of classification accuracy, computational efficiency, and convergence behaviour. Result from table 6, shows that the un-optimized baseline Standard SVM yields the lowest overall accuracy at 78.57%. By introducing the Bat Optimization Algorithm (BOA), the proposed model achieves an accuracy of 97.67% with a gain margin of 19.10%. While traditional optimization methods like Grid Search (SVM-GS) and Genetic Algorithms (SVM-GA) raised the baseline accuracy to 92.86%, they all fall significantly behind the SVM-BOA's achieved accuracy. This performance highlights the algorithmic limitations of legacy tuning methods. Grid Search evaluates the entire hyper-parameter space exhaustively, forcing a slow convergence speed and a training time of 45.7 seconds. While, Random Search (SVM-RS) resolves this computational bottleneck, achieving a fast-training time of 8.9 seconds, but its stochastic nature fails to locate global optima, trapping its accuracy at a modest 89.29%.

Conversely, the Swarm-intelligence methods like Particle Swarm Optimization (SVM-PSO) offers a competitive convergence with 92.36% accuracy at a 21.6 seconds training lag. The developed SVM-BOA framework successfully resolves this classic optimization trade-off, by leveraging echolocation-inspired frequency tuning and dynamic loudness/pulse emission adjustments of the Bats. The Bat Algorithm navigates the hyper-parameter space to achieve a rapid convergence and classification accuracy of 97.67% within 12.3 seconds, outperforming both exhaustive grid sweeps and alternative meta-heuristic algorithms. Conclusively, the model has demonstrated a superior classification performance over existing frameworks.

4. CONCLUSION

In conclusion, the comparative assessment establishes that the proposed SVM-BOA model introduces a significant advancement in both accuracy and computational efficiency. By achieving a peak accuracy of 97.67%, Probability of Detection of 1.00 (100%), Probability of False Alarm of 0.1053 (10.53%), thereby satisfying the sensing performance requirements of the Institute of Electrical and Electronics (IEEE 802.22) standards and the objectives of this research. Furthermore, the model has demonstrated a superior classification performance over existing state-of-the-art frameworks. Most notably, the integration of the Bat Optimization Algorithm (BOA) with an SVM classifier optimizes the hyper-parameter tuning phase, reducing training time to 12.3 seconds as compared to the computationally high 45.7 seconds required by SVM- GS approaches; demonstrating that the proposed SVM – BOA model provides a far more practical, low-latency deployment option for real-time applications.

3.1 Future Research Directions

While the proposed SVM-BOA framework demonstrates superior accuracy and computational efficiency, several avenues remain open for future investigation. First, validating the model on physical hardware, such as Software-Defined Radios (SDRs), is essential to evaluate its resilience against real-world radio frequency impairments and ambient environmental noise. Second, extending the algorithm into a cooperative spectrum sensing framework could leverage multi-agent data sharing to mitigate the hidden node problem and enhance detection reliability across larger networks. Third, future iterations should focus on adaptive optimization variants of the Bat Algorithm to maintain high sensing precision in high-mobility environments, such as vehicular networks or drone communications, where signal-to-noise ratios (SNR) fluctuate dynamically. Finally, incorporating security mechanisms into the SVM classification boundary is a critical step toward defending cognitive radio networks against intelligent security threats, such as Primary User Emulation (PUE) attacks.

4.2 Acknowledgements

The authors declare that no funds, grants, or other support were received during the preparation of this manuscript.

4.3 Author Contributions

All authors contributed to the study conception and design. Material preparation, data collection & analysis and draft of the first manuscript was done by performed by Yahaya Hamisu Abubakar. Dr. Mathew Ehikhamenle reviewed and corrected manuscript. All authors read and approved the final manuscript.

5. REFERENCE

Arunachalam, G., & Sureshkumar, P. (2022). Optimized Deep Learning Model for Effective Spectrum Sensing in Dynamic SNR Scenario. *Computer Systems Science and Engineering*, *45*(2), 1279–1294. https://doi.org/10.32604/csse.2023.031001

Fan, J., Wu, L., Ma, X., Zhou, H., & Zhang, F. (2019). Hybrid support vector machines with heuristic algorithms for prediction of daily diffuse solar radiation in air-polluted regions. Renewable Energy, 140, 1–15. https://doi.org/10.1016/j.renene.2019.03.044

Federal Communications Commission. (2002). Spectrum policy task force: Report of the spectrum efficiency working group (Report No. ET Docket 02-135). FCC.

Federal Communications Commission. (2019). Rule on the use of Television White Space (TVWS) (Docket No. 16-56, RM-11745, 12-268; 34 FCC Rcd 1827). http://www.fcc.gov

Hand J. David, (2009),Measuring classifier performance: a coherent alternative to the area under the ROC curve, Journal of *Machine Learning*, Volume 77, Pages 103–123; Available via SpringerLink.

Haykin, S. (2005). Cognitive radio: Brain-empowered wireless communications. IEEE Journal on Selected Areas in Communications, 23(2), 201–220. https://doi.org/10.1109/jsac.2004.839380

ITU-R. (2012). Definitions of Software Defined Radio (SDR) and Cognitive Radio System (CRS) (Recommendation ITU-R SM.2152). International Telecommunication Union.

Johnson Justin M. & Taghi M. Khoshgoftaar, (2019), Deep Learning and Data Sampling with Imbalanced Big Data, *2019 IEEE 18th International Conference on Machine Learning and Applications (ICMLA)*, Available via IEEE Xplore.

Kaur, M., Singh, R., & Kumar, S. (2025). Ensemble classification-based spectrum sensing using support vector machine for cognitive radio networks. Internet Technology Letters, 8(2), Article e326.

Lasisi, A., Oguntaka, A., & Adediran, Y. A. (2022). Spectrum occupancy measurement and analysis in Ogun State. Journal of Engineering Studies and Research, 28(1), 12–20.

Martin, J., Dooley, L., & Wong, K. (2013). A new cross-layer dynamic spectrum access architecture for TV white space cognitive radio applications. In 9th International Conference on Heterogeneous Networking for Quality, Reliability, Security and Robustness (pp. 1–6). IEEE. https://doi.org/10.1049/cp.2013.2052

Martin, R., Davies, A., & Collins, T. (2016). Modeling TVWS propagation and primary user signal detection under shadowing and multi-path fading conditions. IEEE Wireless Communications Letters, 5(2), 144–147. https://doi.org/10.1109/LWC.2016.2514418

Mitola, J., & Maguire, G. Q. (1999). Cognitive radio: Making software radios more personal. IEEE Personal Communications, 6(4), 13–18. https://doi.org/10.1109/98.788210

Musumeci Francesco, Cristina Rottondi, Massimo Tornatore, (2018), An Overview on Application of Machine Learning Techniques in Optical Networks, *IEEE Communications Surveys & Tutorials*, Volume 20, Issue 4, Pages 3161–3183; Available

Musuvathi, A. S. S., Archbald, J. F., Velmurugan, T., Sumathi, D., Devi, S. R., & Preetha, K. S. (2024). Efficient improvement of energy detection technique in cognitive radio networks using K-nearest neighbour (KNN) algorithm. *EURASIP Journal on Wireless Communications and Networking*, *2024*(1). https://doi.org/10.1186/s13638-024-02338-8

Ofcom. (2011). Digital switchover transmitter details (Issue 4.0). Ofcom.

Rebentrost (2014), Patrick, Masoud Mohseni, & Seth Lloyd, Quantum Support Vector Machine for Big Data Classification, Journal of *Physical Review Letters*, Volume 113, Issue 13, Article 130503, 2014, Available via the American Physical Society (APS.

Thilina Karaputugala Madushan, Kae Won Choi, Nazmus Saquib, & Ekram Hossain, (2013), Machine Learning Techniques for Cooperative Spectrum Sensing in Cognitive Radio Networks, *IEEE Journal on Selected Areas in Communications*, Volume 31, Issue 11, Pages 2209–2221: Available via IEEE Xplore.

Ubom, & Ukommi. (2023). Impact assessment of elevation angles on signal propagation at VHF and UHF frequencies for improved rural telephony. *ABUAD Journal of Engineering Research and Development (AJERD)*, *6*(2), 136–142

Wainer Jacques & André L. V. Fonseca (2021), How to tune the RBF SVM hyperparameters? An empirical evaluation of 18 search algorithms, Journal of *Artificial Intelligence Review*, Volume 54, Pages 4739–4771, Available on ACM Digital Library and ResearchGate

Yang, X. S. (2010). A new metaheuristic bat-inspired algorithm. In J. R. González, D. A. Pelta, C. Cruz, G. Terrazas, & N. Krasnogor (Eds.), Nature inspired cooperative strategies for optimization (pp. 65–74). Springer. https://doi.org/10.1007/978-3-642-12538-6_6

Yang, X. S., & He, X. (2023). Bat algorithm with support vector machine for enhanced data classification. Applied Soft Computing, 114, Article 108120. https://doi.org/10.1016/j.asoc.2021.108120

Zeng, Y., & Liang, Y. C. (2009). Eigenvalue-based spectrum sensing algorithms for cognitive radio. IEEE Transactions on Communications, 57(6), 1784–1793. https://doi.org/10.1109/TCOMM.2009.06.070402

Zeng, Y., Liang, Y., Hoang, A. T., & Zhang, R. (2010). A review on spectrum sensing for cognitive radio: Challenges and solutions. EURASIP Journal on Advances in Signal Processing, 2010, Article 381465. https://doi.org/10.1155/2010/381465

Zheng, H., Zhang, S., & Sun, X. (2017). Classification recognition of anchor rod based on PSO–SVM. In Proceedings of the 29th Chinese Control and Decision Conference (CCDC) (pp. 2207–2212). IEEE. https://doi.org/10.1109/CCDC.2017.7978881

Zheng, K., Wu, J., Cai, F., Xia, J., Xu, X., & Bao, J. (2025). Particle swarm optimization-based SVM for cooperative spectrum sensing against Byzantine attack in cognitive wireless sensor networks. IEEE Sensors Journal,

International Conference on Engineering Innovation for Sustainable Development (ICESID 2026)
Faculty of Engineering, Ahmadu Bello University Zaria · 8–10 September 2026

FACTORS INFLUENCING THE ADOPTION OF MIXED REALITY TECHNOLOGY FOR CONSTRUCTION PROJECTS COST ESTIMATION

Raphael Olarewaju[1,*], Olubunmi Comfort Ade-Ojo[1]
[1]*Federal University of Technology Akure*
Email: olumider28@gmail.com[*], ade-ojoco@futa.edu.ng
***Corresponding author**: Raphael Olarewaju
DOI: https://doi.org/10.67203/sp.ICESID.2026

ABSTRACT

Cost estimation issues including budget overruns, delays in project delivery, and loss of stakeholder confidence remain as persistent challenges in the Nigerian construction Industry. By integrating Augmented Reality (AR) and Virtual Reality (VR) to visualize design and cost data in an interactive and real-time manner, Mixed Reality (MR) technology promises to enhance estimation precision, teamwork, and decision-making efficiency. Despite increasing interest in MR adoption in the construction industry, it is still not well explored in the Nigerian context, especially among Quantity Surveyors (QSs) for construction cost estimation. This study has investigated the factors influencing the adoption of MR technology for construction cost estimation among QSs in Lagos State, Nigeria. Five (5) latent constructs namely, Organizational Factors (ORGF), Infrastructural Factors (INFF), Training-Related Factors (TRF), Financial Viability Factors (FVF), and Institutional Factors (INSTF) were measured using a structured questionnaire via census sampling, which got 87.85% response rate. Data from 94 respondents were analyzed using Confirmatory Factor Analysis (CFA) in JASP software. The CFA model showed good model fit (CFI = 0.973, TLI = 0.968, RMSEA = 0.054, and SRMR = 0.053), and the five constructs achieved convergent validity (AVE ≥ 0.50), and high internal consistency (α and ω ≥ 0.89). The results validate that organizational support, digital infrastructure, professional training, financial readiness, and institutional frameworks are important influencing factors of MR technology adoption in construction cost estimation. The findings give practical guidance to construction companies, government authorities, and professional organizations for promoting the uptake of MR in the construction industry in Nigeria.

Keywords: *Mixed Reality; Construction; Cost Estimation; Technology Adoption; Quantity Surveyors*

1. INTRODUCTION

Digitalization in the construction industry has brought the industry a range of innovative technologies to meet rapidly evolving developmental demands (Abanda et al., 2017). Among these innovative technologies, Mixed Reality (MR) technology stands out as one that has visualization and interactive functionalities (Alizadehsalehi et al., 2020). MR is a combination of the real and digital worlds to an extent that it allows users to see and interact with the virtual in real-life settings using a blend of Augmented Reality (AR) and Virtual Reality (VR) (Speicher et al., 2019). In the construction industry, MR enables stakeholders to work with 3D models, overlaid on physical spaces, which brings in a new perspective to design review, site planning, and decision-making (Osorto Carrasco & Chen, 2021; Anwar & Azhar, 2024). A global trend involving the integration of MR into construction procedures has resulted in less rework, enhanced collaboration, and improved productivity (Maqsoom et al., 2023).

Different researchers have given attention to automation, Artificial Intelligence (AI), and Building Information Modeling (BIM) in their studies on the innovation of technologies in construction cost estimation. For instance, Ahmed (2019) cited BIM-enabled automation, especially the 5D modeling and built-in quantity takeoff, as one of the key factors in enhanced cost accuracy at the initial stages of design. On the same note, Nia et al. (2023) and Ibrahim and Elshwadfy (2021) investigated ways of enhancing reliability of pre-construction costs, such as predictive models using AI and automated quantity takeoffs. While these studies provide valuable insights into the application of various technologies in cost estimation, they leave room for further exploration of Mixed Reality (MR) technology, particularly its potential in interactive visualization and real-time team collaboration.

This study therefore examined the factors influencing the adoption of MR technology for construction projects' cost estimation among QSs in Lagos State, Nigeria. In practice, the findings are useful in shedding light on the barriers and enablers of MR adoption, which can be helpful to QSs, firms, policymakers, and other construction professionals. Academically, the study contributes to the literature on MR adoption in developing regions, addressing the calls for context-specific studies (Delgado et al., 2019).

2. LITERATURE REVIEW

2.1 Mixed Reality Technology in the Construction Industry

MR is the immersive technology that combines the visual power of AR with the interaction of VR. This technology is a gamechanger in the construction industry, with the potential of increasing project execution precision and efficiency. The benefits of MR technology, while significant, are complicated by costs and technical challenges, yet research and investment efforts continue to push forward with the promise of revolutionizing current methods (Delgado et al., 2020). The difference between AR and VR is that AR is able to overlay digital data on a physical environment, whereas VR is able to produce full-scale simulations (Getuli et al., 2020). These technologies enable the study and manipulation of design concepts, training scenarios and virtual walkthroughs, in addition to the use of human interaction with advanced technologies, such as artificial intelligence or networking (Sidani et al., 2021).

2.2 Factors Influencing the Adoption of MR Technology for Construction Cost Estimation

The integration of the MR technology into construction cost estimation is predetermined by the combination of organizational, technological and human-related factors that define the desire and capacity of the users to introduce new digital tools into their professional practice. A study of the advanced digital technologies used in construction indicated that the perceived benefits, ease of use, support of leadership, readiness of the organisation, infrastructure and technical competence of the users are important factors influencing the outcomes of the adoption of the advanced digital technologies used in the construction field (Liu et al., 2023; Oke et al., 2022). Additionally, there are several factors highlighted, especially in developing economies where the process of digital transformation is not uniform, such as resistance to change, and uncertainty about the implementation process (Adebowale & Agumba, 2024; Babatunde et al., 2021). Understanding these influencing factors is therefore essential for promoting effective uptake of MR technology for accurate and efficient cost estimation of construction projects.

2.2.1 *Organizational Factors*

According to Bamgbose et al. (2024), Organizational factors determine whether the adoption of technology will succeed or not. There are several theoretical frameworks, including the Technology-Organization-Environment (TOE) model developed by Tornatzky and Fleischer in 1990, that give more weight to the role of organizational input in determining technology adoption practices. Various studies present how proactive organizational leadership can help align the technological initiatives with organizational objectives. Leaders in an organization who promote innovation usually create a conducive culture within the organization, thereby facilitating change and combating resistance to change, as well as boosting employees' motivation to accept new technologies (Bendak et al., 2020). Top management endorsement is a primary factor in technology acceptance, and it is appropriately in line with extensions of the TAM and Unified Theory of Acceptance and Use of Technology (UTAUT), where perceived strategic alignment and resource commitment minimize uncertainty and indicates organizational priority (Hong & Yu, 2018; Venkatesh & Davis, 2000). Proactive leadership in the construction industry would lead to buy-in, through the promotion of MR to improve visualization, error detection, and collaborative decision-making, thereby alleviating resistance due to disruption of

existing workflow (Maqsoom et al., 2023; Delgado et al., 2020). In developing economies such as Nigeria, leadership support is more decisive in the face of scarcity of resources and risk aversion. It is found that the technological diffusion can be triggered by the presence of an innovative leader who establishes budgets, initiates MR applications and connects the MR process to strategic goals, while the presence of a passive and/or short-term management can have the opposite effect (Aliu et al., 2025; Oke et al., 2023; Idowu et al., 2023).

2.2.2 *Infrastructural Factors*

Another barrier largely linked to the adoption of MR technology is infrastructural constraints. Limited broadband connection, unreliable power availability, and old hardware are mentioned among the major challenges (Akinradewo et al., 2025; Oke & Arowoiya, 2022). According to Noghabaei et al. (2020), most companies feel that MR is not possible mainly because of the absence of proper infrastructure to support it. The low level of acquisition and maintenance of MR hardware is usually aggravated by low local support and lack of equipment (Uwaegbulam, 2025). Additionally, each of the issues relating to inadequate infrastructure would make it impossible to connect with the existing enterprise systems, e.g., Building Information Modelling (BIM) system. Global research proves that the level of MR technology integration in the coordination of projects, the presentation to a client, and direct on-site cooperation is higher in countries with effective digital infrastructure (Adebowale & Agumba, 2024). Also, hardware limitations such as high prices, technical complexity, and compatibility with the on-site workflow are some of the issues that make integration difficult (Oke & Arowoiya, 2022). Stable internet connectivity is also a necessity when it comes to the deployment of MR technology, particularly when applications entail cloud computing, real-time data synchronization, and shared digital platforms. Studies indicate that low reliability of the network constrains system performance, introduces delays in data transfer, and lowers user trust in the use of the digital tools (Adebowale & Agumba, 2024; Liu et al., 2023). A digital divide is apparent in developing economies where there is a lack of infrastructure leading to a lack of accessibility, making it difficult for smaller companies and consultants to keep up with the investments that larger companies can make (Aliu et al., 2025; Akinradewo et al., 2025).

2.2.3 *Training-Related Factors*

The introduction of MR requires professionals to acquire new competencies in software manipulation, digital modelling, and immersive interface navigation. However, most construction professionals, including QSs, have limited exposure to such digital tools in their education or ongoing professional development (Oke & Arowoiya, 2022). This mismatch creates a knowledge gap that hinders the perceived ease of use (PEOU). Regardless of the increasing interest in most parts of the world, especially about improving design visualization, quantity take-off, and cost estimation, the lack of training is one of the most serious obstacles, especially in developing nations (Akinradewo et al., 2025; Orihuela et al., 2019). Orihuela et al. (2019) observed that when properly trained, users demonstrated higher confidence in applying MR technology during real-world planning and construction phases. Specific job-related training programs are also instrumental in the application of MR technology for cost estimation of construction projects. By adjusting the content of training materials to reflect the practical role of cost specialists in the construction industry, it is possible to increase the relevance of a work and decrease the perceived complexity of the new digital tools. Knowledge sharing among peers is informal yet another effective way of fostering the spread of any novel technology. As early adopters of MR tools can demonstrate the successful cost estimation applications to other collaborators, trust is established and encourages more project teams to embrace it (Liu et al., 2023). Akinradewo et al. (2025) emphasize the fact that the ad-hoc types of learning are not effective when it comes to maintaining adoption, hence measures such as peer-to-peer knowledge sharing, guided onboarding, and partnerships with tech vendors should be leveraged to bridge gaps where formal education systems lag.

2.2.4 *Financial Viability Factors*

The initial purchase price is not the sole detail of the financial consideration; the operating cost of software upgrades, maintenance, licensing charges and special training also add to the overall cost

of ownership (Prabhakaran et al., 2022). Perceived return on investment (ROI) is hence a vital factor. When the advantages are evident, i.e. the increase in the quality of cost estimation, better visualization of construction processes, fewer errors and rework, and more efficient project monitoring, organizations are more willing to use the MR technologies (Apinayan et al., 2023; Delgado et al., 2020). Companies that have a stronger financial base or have access to external resources are in a better position to take these initial costs and achieve long-term efficiency and productivity benefits (Aliu et al., 2025; Maqsoom et al., 2023). Research has shown that strong initial investment needs are one of the initial limitations to the adoption of advanced technologies in developing economies (Maqsoom et al., 2023; Oke et al., 2022). MR software license is another major financial obstacle. MR applications can be platform-dependent and demand dedicated license for systems that use BIM models, real-time rendering, and collaboration features. High licensing costs, often in foreign currencies, are frequent in developing nations, which adds additional financial burdens amid economic volatility, import duties, and constrained budgets of SMEs (Uwaegbulam, 2025; Akinradewo et al., 2025).

2.2.5 *Institutional Factors*

The adoption of MR technologies may be supported or hindered by institutional pressures, such as regulatory frameworks, industry standards, professional guidelines, and the organizational policies (Aliu et al., 2025; Oke & Arowoiya, 2022). Companies usually react to compulsive forces of state authorities or professional organizations that can force them to certain modern technologies or sustainable building concepts. Organizations located in jurisdictions that have favorable policies on the use of digital construction tools have higher chances of integrating MR into their work processes (Adebowale & Agumba, 2024; Prabhakaran et al., 2022). The perceived legitimacy of MR technologies is increased by institutional support, in the form of workshop programs, technical advice, and knowledge sharing platforms, which leads to increased adoption (Prabhakaran et al., 2022; Anireddy, 2020). Moreover, the cooperation among stakeholders would enable sharing of knowledge, collaborative research and development, curriculum design, and pilot projects (Kline & Ayer, 2023; Radianti et al., 2020). Also, public sector project requirements such as mandates, procurement specifications, or tender conditions are standing as factors capable of influencing the adoption of emerging technologies such as MR in construction. Government can hasten the diffusion of MR technology by controlling and purchasing innovative tools for government infrastructure through their high purchasing power and regulatory force (Maqsoom et al., 2023). Industry-wide advocacy in the form of professional associations, trade bodies, conferences, workshops, and thought-leadership campaigns is critical in increasing awareness, consensus, and normalization of the use of MR in construction. This advocacy generates momentum by spreading success stories, which offer evidence of the benefits of MR and refutes the perceptions of the technological immaturity or high risk (Maqsoom et al., 2023; Delgado et al., 2020).

3. METHODOLOGY

3.1 Research Design

For this research, an extensive review of literature was performed, after which a quantitative approach was employed to carefully evaluate the factors influencing the adoption of MR Technology for construction cost estimation. Quantitative research approach is a survey used to acquire information from subjects or study participants (sample) using self-report; objectively, the study population or participants respond to questions posed to them by the researcher (Leavy, 2017). This method enables systematic collection of data on individuals' attributes, behaviors, beliefs, and perceptions (Creswell & Creswell, 2018), thereby supporting the study's aim to explore observable patterns and relationships within a defined context (Saunders et al., 2019).

3.2 Research Population

The research population comprised Quantity Surveyors in registered consulting and construction firms in Lagos State, Nigeria. The reason for selecting Lagos State is because, as Nigeria's commercial hub with a high volume of construction projects, the state offers a rich environment to study new technologies such as MR for cost estimation. Its relative advanced technological adoption, strong

regulatory frameworks, and diverse construction landscape makes it an ideal case for broader national insights. A census sampling technique was applied, targeting all one hundred and seven (107) eligible QSs. The consulting firms were identified through the QSRBN 2025 directory, while the construction firms were identified through Google Business 2025 directory. One (1) respondent from each firm was selected to participate in this study. Table 1 below presents the population distribution across the two firm types.

Table 1: Research Population

Firm Type	Number of Firms	No. of QSs (Population)
Consulting Firms	53	53
Construction Firms	54	54

Source: QSRBN (2025); Author's Compilation (Google Business Directory, 2025)

3.3 Data Collection Instrument

A structured questionnaire was used as the data collection instrument for this study. The questionnaire was sectioned into two (2) parts: The first part was designed to obtain the demographic and background data of each respondent, which includes their qualifications, years of experience, type of firm, and areas of specialization. The second section focused on the factors influencing MR technology adoption for construction cost estimation. A 5-point Likert scale was used in rating the opinions, where 5 = very high, 4 = high, 3 = average, 2 = low, 1 = very low. The latent factors measured included Organizational Factors (ORGF), Infrastructural Factors (INFF), Training-Related Factors (TRF), Financial Viability Factors (FVF), and Institutional Factors (INSTF), each with four (4) observed indicators, totaling twenty (20) items.

3.4 Method of Data Analysis

Confirmatory Factor Analysis (CFA) was applied to examine the factors influencing MR adoption for construction cost estimation, to assess whether observed variables load appropriately on latent factors and whether the latent factors significantly predict the observed variables. An Exploratory Factor Analysis (EFA) was not conducted because the five latent constructs are drawn from established theoretical frameworks whose factor structure has been extensively validated (Venkatesh & Davis, 2000; Davis, 1989). The individual observed indicators, however, were newly developed for this study by adapting the broader TAM/UTAUT and TOE dimensions to the specific context of MR-based cost estimation (e.g., mobile support for MR applications, interoperability with BIM), since directly validated item sets for this technology-task combination were not available in prior literature. This is acknowledged as a limitation of the CFA-only approach, as the item-level structure had not been previously confirmed through exploratory analysis. CFA nonetheless remains appropriate for theory-driven constructs to confirm hypothesized measurement structures without prior exploratory analysis (Hair et al., 2019; Kline, 2016). The latent factors include ORGF, INFF, TRF, FVF, and INSTF, all measured using a 5-point Likert scale, with each latent factor having four (4) corresponding observed indicators, totaling twenty (20) observed indicators. The hypothesized CFA model specified that each latent factor is measured by its respective indicators. Each indicator was restricted to load on only one latent factor, and the latent factors were allowed to co-vary.

CFA requires the use of multiple indices to assess how well a proposed measurement model fits the data, as no single index is sufficient for evaluating model adequacy (Hair et al., 2019; Kline, 2016). Following best practice, this study used three major index families: Absolute Fit Indices (χ^2, χ^2/df, RMSEA, SRMR), Incremental Fit Indices (CFI and TLI), and Construct Validity Indices (R^2, standardized factor loadings, AVE, Cronbach's Alpha, and McDonald's Omega). Following the recommendations of Kline (2016), Byrne (2016), and Hair et al. (2019), acceptable thresholds of $\chi^2/df \leq 3$; CFI/TLI ≥ 0.90; RMSEA ≤ 0.08; SRMR ≤ 0.08 align with widely adopted CFA standards. Standardized factor loadings ≥ 0.50 (preferably above 0.70) were retained in accordance with Hair et al. (2019). Internal consistency was assessed using both Cronbach's Alpha (α) and McDonald's Omega

(ω), with reliability coefficients ≥ 0.70 deemed acceptable. Convergent validity was examined using AVE (≥ 0.50), following Fornell & Larcker (1981). Analysis was conducted using JASP software.

4. RESULTS AND DISCUSSION

4.1 Response Rate

Table 2 presents the breakdown of the return rate of the questionnaires sent out. Out of the One Hundred and Seven (107) questionnaires sent out to Quantity Surveyors in selected consulting and construction firms in Lagos State, Nigeria, a very high return rate was recorded (84.91% and 90.74% respectively) from each firm type. An overall return rate of 87.85% was recorded across both firm types.

Table 2: Response Rate of Respondents

Firms	Distributed	Retrieved	% Retrieved
Consulting Firms	53	45	84.91%
Construction Firms	54	49	90.74%
Total	107	94	87.85%

Author's survey (2025).

4.2 Respondents' Profile

Table 3 presents the demographic information of the Quantity Surveyors that were part of this research. The results show that 74.47% of respondents were Male and 25.53% Female. In the Academic Qualification category, most of the respondents possess only a First-degree certificate (B.Sc/B.Tech), with approximately 51.06% representing that group, followed by those who possess Master's degree (approximately 36.17%), and those with Higher National Diploma (HND) (approximately 12.77%). In the Years of Professional Experience category, the group with the highest percentage is 6–10 years (approximately 43.62%), followed by professionals with 11–15 years' working experience (approximately 30.85%), 1–5 years working experience (approximately 13.83%), and respondents with 16–20 years of professional working experience (approximately 11.70%). It is worth noting that most respondents fall into the group of professionals with less than 16 years' working experience, which establishes the non-redundancy of the sampled professionals to new technological trends. Lastly, in the primary area of specialization category, most of the respondents specialize in Infrastructural projects (approximately 48.94%), while approximately 24.47% specialize in Commercial projects, approximately 20.21% in Residential projects, and approximately 6.38% in Industrial projects.

Table 3: Respondents' Information

Variable	Classification	Frequency	Percentage (%)
Gender	Female	24	25.53
	Male	70	74.47
	Total	94	100.00
Highest Academic Qualification	HND	12	12.77
	B.Tech / B.Sc	48	51.06
	M.Tech / M.Sc	34	36.17
	Total	94	100.00
Years of Experience	1–5	13	13.83
	6–10	41	43.62
	11–15	29	30.85
	16–20	11	11.70
	Total	94	100.00
Primary Area of Specialization	Commercial	23	24.47
	Industrial Projects	6	6.38
	Infrastructure	46	48.94
	Residential	19	20.21
	Total	94	100.00

Author's survey (2025).

4.3 Model Fit Indices of the Factors Influencing the Adoption of MR Technology for Construction Cost Estimation

Table 4 shows the results of the model fit of the factors influencing MR adoption for construction cost estimation. The chi-square score ($\chi^2 = 204.017$, df = 160, $p < 0.05$) is statistically significant but the chi-square test is highly sensitive to sample size (Kline, 2016). In this case, the χ^2/df ratio is lower than the recommended value of 3 (Kline, 2016; Carmines & McIver, 1981), implying strong model fit with a moderate sample (N = 94). Additional model fit indices reflected in Table 4 show that the model fits the data well. The Comparative Fit Index (CFI = 0.973) and Tucker–Lewis Index (TLI = 0.968) are above the 0.95 cut-off, showing that it fits quite well. In addition, both the RMSEA (0.054) and SRMR (0.053) are below their respective thresholds of 0.06 and 0.08, which indicates that the covariance predicted by the model is in line with the observed variables. All in all, the measurement model can be deemed as acceptable.

Table 4: Model Fit Indices of the CFA for the Factors Influencing MR Adoption

Index	**Value**	**Threshold**
χ^2/df	1.28	≤ 3.0
Comparative Fit Index (CFI)	0.973	≥ 0.90
Tucker–Lewis Index (TLI)	0.968	≥ 0.90
Root Mean Square Error of Approximation (RMSEA)	0.054	≤ 0.08
Standardized Root Mean Square Residual (SRMR)	0.053	≤ 0.08

Note. **χ^2 = 204.017, df = 160, p = .011. N = 94.**

4.4 R-Squared Values, Factor Loadings, AVE, and Reliability

The R^2 values presented in Table 5 are squared multiple correlations of the observed indicators, which denote the extent of variance in each indicator explained by its corresponding latent construct. The values fall between 0.469 and 0.844, which show moderate to strong measuring strength among the five constructs. According to Hair et al. (2019), R^2 values of 0.75, 0.50, and 0.25 may be described as strong, moderate, and weak, respectively. The Organizational factors represent strong indicator representation, specifically Management commitment (R^2 = 0.784) and Organizational willingness to invest in MR technology (R^2 = 0.742). The Infrastructural factors also exhibit high measurement strength with Availability of MR-capable hardware (R^2 = 0.843) and Mobile support of MR applications (R^2 = 0.815) showing the strongest explanatory power. The same can also be said about Training, Financial and Institutional factors that have R^2 values ranging between moderate and strong, suggesting that their indicators are sufficiently described by their latent constructs.

The factor loading values are all statistically significant at $p < .001$, which means that all the indicators have a significant contribution to their corresponding latent construct. The standardized factor loadings vary between about 0.68 and 0.92, all above the required minimum of 0.50 and the desirable level of 0.70 (Hair et al., 2019). The findings indicate excellent convergent validity of the model. The AVE values for all five constructs, ORGF (0.709), INFF (0.707), TRF (0.724), FVF (0.755), and INSTF (0.769), are greater than the recommended value of 0.50 (Fornell & Larcker, 1981), which confirms that over 50% of the variation in each set of observed indicators is attributed to its corresponding latent factor. This shows that the indicators are meaningfully convergent to measure their respective latent factor. The excellent internal consistency of all latent factors is also confirmed through the reliability results. The ORGF omega (ω) and alpha (α) coefficients of 0.905 each indicate that the indicators are quite consistent in their measurement of the same latent factor. INFF follows, with ω = 0.893 and α = 0.902. TRF is also highly consistent with ω = 0.911 and α = 0.913. FVF is even more reliable with ω = 0.924 and α = 0.925, while INSTF has the best construct-level reliability, with ω = 0.930 and α = 0.928. The constructs are highly reliable since all of them have coefficients that greatly exceed the widely recognized 0.70 threshold, and most of them exceed the 0.90 standard (Hair et al., 2019). The total scale reliability scores (ω = 0.990 and α = 0.958) further confirm that the overall measurement framework of the Influencing Factors is stable and internally consistent.

Table 5: R-Squared Values, Factor Loadings, AVE, and Reliability of the Influencing Factors

Factor	**Indicator**	**R^2**	**AVE**	**α**	**ω**
ORGF	Leadership support for MR technology adoption	0.656	0.709	0.905	0.905
	Innovation-friendly organizational culture	0.638			
	Management commitment	0.784			
	Organization's willingness to invest in MR technology	0.742			
INFF	Availability of MR-capable hardware and devices	0.843	0.707	0.902	0.893
	Mobile support for MR applications	0.815			
	Stable internet access	0.469			
	Interoperability with BIM	0.645			
TRF	Access to MR Technology training	0.721	0.724	0.913	0.911
	Training programs aligned with job roles	0.795			
	Peer knowledge sharing	0.767			
	Opportunities for hands-on practice using MR tools	0.632			
FVF	Affordability of MR hardware and related devices	0.841	0.755	0.925	0.924
	Availability of financing options for MR adoption	0.743			
	Perceived Return on Investment (ROI) of MR adoption	0.799			
	Affordability of MR software licenses	0.644			
INSTF	Collaboration with tertiary institutions and research bodies on MR standards	0.668	0.769	0.928	0.930
	Public sector project requirements pushing MR adoption	0.791			
	Regulatory frameworks supporting digital adoption in construction	0.770			
	Industry-wide advocacy for MR adoption	0.844			

4.5 Factor Covariances of the Factors Influencing MR Adoption

Table 6 presents the factor covariances, which indicate the strength and significance of the relationship among the five (5) latent factors. A positive and significant covariance means that an increase in one variable predicts an increase in the other variable, hence there is conceptual compatibility and interdependence between the variables. The covariances are all positive and statistically significant ($p < .001$) with estimates between 0.604 and 0.732. This shows that the variables have a moderate to a strong relationship, which proves that they are related concepts but not the same dimensions in the model. Particularly, ORGF demonstrates high positive covariances with all other latent factors; INFF (0.700), TRF (0.604), FVF (0.732) and INSTF (0.612). Additionally, INFF has significant correlation with TRF (0.672), FVF (0.668) and INSTF (0.684). On the same note, TRF has a substantial correlation with FVF (0.679) and INSTF (0.652). Lastly, FVF and INSTF also show positive and significant covariance (0.678). These findings imply that the five (5) latent factors are strongly associated, but each one of them is unique enough to reflect a different dimension of the model.

Table 6: Factor Covariances of the Influencing Factors

Covariance			Estimate	Std. Error	Z	p	95% CI
ORGF	↔	INFF	0.700	0.145	4.841	< .001	[0.417, 0.984]
ORGF	↔	TRF	0.604	0.122	4.942	< .001	[0.365, 0.844]
ORGF	↔	FVF	0.732	0.143	5.126	< .001	[0.452, 1.012]
ORGF	↔	INSTF	0.612	0.134	4.561	< .001	[0.349, 0.875]
INFF	↔	TRF	0.672	0.136	4.928	< .001	[0.405, 0.939]
INFF	↔	FVF	0.668	0.150	4.466	< .001	[0.375, 0.962]
INFF	↔	INSTF	0.684	0.152	4.516	< .001	[0.387, 0.981]
TRF	↔	FVF	0.679	0.132	5.125	< .001	[0.419, 0.939]
TRF	↔	INSTF	0.652	0.133	4.914	< .001	[0.392, 0.913]
FVF	↔	INSTF	0.678	0.146	4.649	< .001	[0.392, 0.963]

Note. CI = Confidence Interval. All covariances significant at $p < .001$.

4.6 Discussion of Findings

The adoption of MR technology for construction cost estimation is shaped by several factors. These factors are referred to as Influencing Factors (IF) in this study. These IF collectively determine organizational readiness and user acceptance. Findings from this study reveal that Organizational, Infrastructural, Training-Related, Financial Viability, and Institutional Factors are influencing factors to MR adoption for construction cost estimation.

4.6.1 *Organizational Factors (ORGF)*

There were four (4) observed indicators loaded on this latent factor, namely; Leadership support for MR technology adoption, Innovation-friendly organizational culture, Management commitment,

and Organization's willingness to invest in MR technology. All the four (4) indicators underscore the central role of organizational readiness in driving the adoption of emerging technologies such as MR for construction cost estimation. These indicators collectively reflect the degree to which an organization's internal environment enables or constrains technological innovation. This is a very important variable, because for technology to be fully embraced, organizational influence is huge. The high covariance between ORGF and other constructs, particularly FVF (0.732) and INFF (0.700), further confirms the interdependence of organizational capacity with financial and infrastructural readiness.

These findings align with Bamgbose et al. (2024), who reported that organizational leadership, culture, and resource commitment are primary determinants of technology adoption in the construction sector. The results also support the extended TAM proposition of Venkatesh and Davis (2000) and Hong and Yu (2018), where perceived strategic alignment and management endorsement reduce uncertainty and signal organizational priority. In the Nigerian context, where resource constraints and risk aversion are common, the role of organizational support in catalyzing MR adoption is even more decisive (Aliu et al., 2025; Oke et al., 2023).

4.6.2 *Infrastructural Factors (INFF)*

Four (4) observed indicators were also loaded on this latent factor. These indicators include Availability of MR-capable hardware and devices, Mobile support for MR applications, Stable internet access, and Interoperability with Building Information Modelling (BIM). All the four (4) indicators capture the fundamental role of technological infrastructure in shaping the feasibility and ease of using MR technology for construction cost estimation. Availability of MR-capable hardware and Mobile support for MR applications emerged as the strongest predictors within this construct, suggesting that access to specialized devices is the most immediate infrastructural barrier.

These findings are consistent with Akinradewo et al. (2025) and Oke and Arowoiya (2022), who identified limited broadband connectivity, unreliable power supply, and old hardware as the major infrastructural challenges to AR/VR/MR adoption in Nigeria. Adebowale and Agumba (2024) similarly reported that the level of MR technology application is substantially higher in countries with effective digital infrastructure, suggesting that bridging the infrastructure gap is a precondition for accelerating MR adoption in Lagos State.

4.6.3 *Training-Related Factors (TRF)*

There were four (4) observed indicators loaded on this latent factor, namely; MR technology training, Training programs aligned with job roles, Peer knowledge sharing, and Opportunities for hands-on practice using MR tools. These four (4) indicators capture the Training and Expertise dimension influencing MR technology adoption. They highlight the indispensable role of human capacity development in facilitating the adoption of MR technology for construction cost estimation. Training programs aligned with job roles emerged as the strongest predictor within TRF, suggesting that role-specific training is more impactful than generic digital literacy programs.

These findings are consistent with Akinradewo et al. (2025), who emphasized that the ad-hoc types of learning are not effective when it comes to maintaining adoption, and that peer-to-peer knowledge sharing, guided onboarding, and partnerships with tech vendors should be leveraged to bridge gaps where formal education systems lag. In contexts like Nigeria, the absence of institutionalized training on MR technology in curricula or industry workshops has slowed down diffusion, as corroborated by Liu et al. (2023) who demonstrated that organizations investing in structured digital training achieve higher productivity benefits and improved user commitment.

4.6.4 *Financial Viability Factors (FVF)*

There were four (4) observed indicators loaded on this latent factor, namely; Affordability of MR hardware and related devices, Availability of financing options, Perceived return on investment (ROI), and Affordability of MR software licenses. These indicators show that the cost of technology remains a major influence on MR adoption for cost estimation. Contextually, this means financial viability determines whether MR adoption is viewed as possible or out of reach. Affordability of MR hardware and Perceived ROI are the dominant indicators within this construct.

These results are supported by Maqsoom et al. (2023), who identified high upfront investment costs, coupled with perceptions of low immediate ROI and limited demand, as factors that suppress adoption momentum. Uwaegbulam (2025) and Akinradewo et al. (2025) corroborate these findings in the Nigerian context, noting that high licensing costs, often denominated in foreign currencies, impose additional financial burdens amid economic volatility, import duties, and constrained budgets of SMEs. The strong AVE and reliability coefficients reported in Table 5 further confirm the construct's internal coherence and the centrality of financial considerations in adoption decisions.

4.6.5 *Institutional Factors (INSTF)*

Also, four (4) observed indicators were loaded on this latent factor, namely; Collaboration with tertiary institutions and research bodies on MR standards, Public sector project requirements pushing MR adoption, Regulatory frameworks supporting digital adoption in construction, and Industry-wide advocacy for MR adoption. All the four (4) indicators show how the institutional environment shapes the perceptions of organizations and professionals about adopting MR technology for cost estimation. Industry-wide advocacy for MR adoption emerged as the strongest predictor. INSTF also recorded the highest AVE and the highest reliability coefficients among all five constructs.

These findings align with Aliu et al. (2025) and Oke and Arowoiya (2022), who highlighted that institutional pressures, including regulatory frameworks, professional norms, and peer expectations, are important determinants of MR technology adoption decisions. The findings also corroborate Maqsoom et al. (2023) and Delgado et al. (2020), who emphasized that industry advocacy generates momentum by spreading success stories and refutes perceptions of technological immaturity or high risk. In developing economies where formal digital construction policy structures are still emerging, institutional support becomes an even more critical lever for normalizing MR adoption across the sector.

5. CONCLUSION AND RECOMMENDATIONS

5.1 Conclusion

This study examined the factors influencing the adoption of Mixed Reality (MR) technology for construction projects' cost estimation among Quantity Surveyors in Lagos State, Nigeria. Using Confirmatory Factor Analysis (CFA), the measurement model comprising five latent constructs, Organizational Factors (ORGF), Infrastructural Factors (INFF), Training-Related Factors (TRF), Financial Viability Factors (FVF), and Institutional Factors (INSTF), demonstrated excellent model fit (CFI = 0.973; TLI = 0.968; RMSEA = 0.054; SRMR = 0.053), high convergent validity (AVE values exceeding both the 0.50 minimum threshold and the 0.70 desirable benchmark), and outstanding internal consistency (α and $\omega \geq 0.89$) across all constructs. The following conclusions were drawn:

1. Adopting MR for construction cost estimation is not driven by technology alone; it requires the intentional alignment of organizational support, infrastructural readiness, training and capacity development, financial viability, and institutional frameworks. When these Influencing Factors are addressed together, they translate professionals' awareness of MR into concrete adoption action.
2. The financial viability and infrastructure constructs had the highest individual indicator predictive power, indicating that they are likely the closest and most visible barriers to MR adoption in the construction context in Lagos.
3. The study also found that MR technology provides the greatest benefits in areas that require visualization, collaboration, and real-time decision-making. These findings provide practical direction for firms, QSs, and technology developers seeking to align MR deployment with the highest-impact estimation tasks.
4. Influencing Factors (IF), comprising organizational, infrastructural, training, financial, and institutional factors, are the most influential antecedents of MR technology adoption for

construction cost estimation. These factors significantly show that adoption success depends heavily on external readiness and contextual support within the construction environment.

5.2 Limitations of the Study

This study is subject to two main limitations. Firstly, the sample size (N = 94) is modest, compared to the measurement model (20 observed indicators and 5 latent constructs). Larger samples are generally recommended for CFA to provide stable parameter estimates; this should be taken into consideration when assessing the quality of the reported fit indices. Secondly, the study is limited to Lagos state and despite Lagos being chosen due to the high technological adoption of the technology and the high construction activity in the state, the results and recommendations might not necessarily apply to other states in Nigeria with varying technological adoption levels and institutional support. Larger and multi-regional samples are recommended for future studies to increase the generalizability of the findings.

5.3 Recommendations

The following recommendations were made in lieu of the research findings:

1. Construction and consulting companies need to show greater leadership in their digital transformation efforts by incorporating MR technology into cost estimation and project management processes. Senior management should establish clear policies, allocate resources and establish innovation-friendly environments to support experiments with MR applications and other innovative technologies.
2. Strategic partnership of universities, professional and regulatory organisations (e.g. NIQS, COREN) and MR technology developers should be fostered. These partnerships will foster local research, the adaptation of MR solutions to the local context, and the development of platforms for knowledge exchange and continued innovation in construction cost management.
3. Government agencies and industry regulators should develop digital adoption policies to promote the use of MR technology in the construction industry. Tax reliefs, research grants or public–private partnerships could lower the cost burden on companies and encourage them to increase their innovation in the cost estimation process.
4. Due to high costs and uncertain return on investment, construction companies should consider new models for financing, including leasing, technology sharing consortia and innovation funds. Digital innovation loans with a low interest rate can also be distributed by financial institutions to enable MR acquisition and implementation.
5. Industry associations are encouraged to conduct demonstration projects, small-scale studies and open house exhibits of the cost-saving and other practical value of MR in cost estimation. By documenting and sharing success stories and best practices, confidence will build, resistance to change will diminish, and best practices will be adopted broadly throughout construction.

5.4 Contribution to the Body of Knowledge

This study has provided empirical and theoretical contributions to knowledge on the adoption of MR technology for construction projects' cost estimation. It has demonstrated that MR, through its immersive and visualization capabilities, has strong potential to enhance the precision, accuracy, and communication efficiency of cost estimation processes in construction. Through the application of CFA, the research established and validated five latent constructs, Organizational, Infrastructural, Training-Related, Financial Viability, and Institutional Factors, as significant influencing factors of MR adoption among Quantity Surveyors in Lagos State. The validated measurement model, with excellent fit indices, convergent validity, and internal consistency, offers a replicable framework that future studies can adapt for other contexts and emerging digital technologies. Finally, this study contributes to the limited pool of local academic research on advanced construction technologies in Nigeria, providing a contextual foundation for future studies and implementation of immersive technologies within the construction cost management discipline.

5.5 Areas of Further Studies

From the research, some of the findings provided possible directions for further studies in the following areas:

1. Given the strong covariance observed between Organizational and Financial Viability Factors in this study, future research could specifically investigate the relationship between organizational readiness and financial commitment to determine whether strengthening one factor accelerates improvement in the other.
2. Future work can conduct cost–benefit analyses to assess the financial viability and return on investment (ROI) of MR adoption in cost estimation processes within different firm sizes and project types.
3. Lastly, further research should investigate the roles of regulatory bodies, professional institutions, and government agencies in supporting MR adoption, especially in relation to policy design, incentives, and training programs.

REFERENCES

Abanda, H., Tah, J., & Cheung, F. (2017). BIM in off-site manufacturing for buildings. *Journal of Building Engineering, 14,* 1–10. https://doi.org/10.1016/j.jobe.2017.10.002

Adebowale, O. J., & Agumba, J. N. (2024). Applications of augmented reality for construction productivity improvement: A systematic review. *Smart and Sustainable Built Environment, 13*(3), 479–495. https://doi.org/10.1108/SASBE-06-2022-0128

Ahmed, S. (2019). A review on using opportunities of augmented reality and virtual reality in construction project management. *Organization, Technology and Management in Construction: An International Journal, 11*(1), 1839–1852. https://doi.org/10.2478/otmcj-2018-0012

Akinradewo, O. A., Hafez, M., Aliu, J., Oke, A., Aigbavboa, C., & Adekunle, S. (2025). Barriers to the adoption of augmented reality technologies for education and training in the built environment: A developing country context. *Technologies, 13*(2), Article 62. https://doi.org/10.3390/technologies13020062

Aliu, J., Oke, A. E., Jesudaju, O. T., Akanni, P. O., Ehbohimen, T., & Dosumu, O. S. (2025). Digital solution in Nigerian heavy-engineering projects: A comprehensive analysis of technology adoption for competitive edge. *Buildings, 15*(3), Article 380. https://doi.org/10.3390/buildings15030380

Alizadehsalehi, S., Hadavi, A., & Huang, J. C. (2020). From BIM to extended reality in AEC industry. *Automation in Construction, 116,* Article 103254. https://doi.org/10.1016/j.autcon.2020.103254

Anireddy, A. R. (2020). The role of software in modern construction estimating: Evaluating the effectiveness of estimation software tools. *European Journal of Engineering and Technology Research, 7*(1), 96–100. https://doi.org/10.5281/zenodo.14045246

Anwar, R. M. I., & Azhar, S. (2024). Mixed reality in building construction inspection and monitoring: A systematic review. *Virtual Worlds, 3*(3), 319–332. https://doi.org/10.3390/virtualworlds3030017

Apinayan, K., Perera, K., Weerasooriya, D., & Ranadewa, T. (2023). Leveraging BIM technology for improved accuracy in detailed cost estimation in Sri Lanka. *FARU Journal, 10,* 1–10. https://doi.org/10.4038/faruj.v10i2.252

Babatunde, S. O., Udeaja, C., & Adekunle, A. O. (2021). Barriers to BIM implementation and ways forward to improve its adoption in the Nigerian AEC firms. *International Journal of Building Pathology and Adaptation, 39*(1), 48–71. https://doi.org/10.1108/IJBPA-05-2019-0047

Bamgbose, O. A., Ogunbayo, B. F., & Aigbavboa, C. O. (2024). Barriers to building information modelling adoption in small and medium enterprises: Nigerian construction industry perspectives. *Buildings, 14*(2), Article 538. https://doi.org/10.3390/buildings14020538

Bendak, S., Shikhli, A. M., & Abdel-Razek, R. H. (2020). How changing organizational culture can enhance innovation: Development of the innovative culture enhancement framework. *Cogent Business & Management, 7*(1), Article 1712125. https://doi.org/10.1080/23311975.2020.1712125

Byrne, B. M. (2016). *Structural equation modeling with AMOS: Basic concepts, applications, and programming* (3rd ed.). Routledge.

Carmines, E. G., & McIver, J. P. (1981). Analyzing models with unobserved variables. In G. W. Bohrnstedt & E. F. Borgatta (Eds.), *Social measurement: Current issues* (pp. 65–115). Sage.

Creswell, J. W., & Creswell, J. D. (2018). *Research design: Qualitative, quantitative, and mixed methods approaches* (5th ed.). SAGE Publications.

Davis, F. D. (1989). Perceived usefulness, perceived ease of use, and user acceptance of information technology. *MIS Quarterly, 13*(3), 319–340. https://doi.org/10.2307/249008

Delgado, J. M., Oyedele, L., Ajayi, A., Akanbi, L., Akinade, O., Bilal, M., & Owolabi, H. (2019). Robotics and automated systems in construction: Understanding industry-specific challenges for adoption. *Journal of Building Engineering, 26,* Article 100868. https://doi.org/10.1016/j.jobe.2019.100868

Delgado, J. M., Oyedele, L., Beach, T., & Demian, P. (2020). Augmented and virtual reality in construction: Drivers and limitations for industry adoption. *Journal of Construction Engineering and Management, 146*(7), Article 04020079. https://doi.org/10.1061/(ASCE)CO.1943-7862.0001844

Fornell, C., & Larcker, D. F. (1981). Evaluating structural equation models with unobservable variables and measurement error. *Journal of Marketing Research, 18*(1), 39–50. https://doi.org/10.1177/002224378101800104

Getuli, V., Capone, P., Bruttini, A., & Isaac, S. (2020). BIM-based immersive virtual reality for construction workspace planning: A safety-oriented approach. *Automation in Construction, 114,* Article 103160. https://doi.org/10.1016/j.autcon.2020.103160

Hair, J. F., Black, W. C., Babin, B. J., & Anderson, R. E. (2019). *Multivariate data analysis* (8th ed.). Cengage Learning.

Hong, S. H., & Yu, J. H. (2018). Identification of influencing factors for the technology acceptance model (TAM) in the assessment of BIM application for mobile devices. *IOP Conference Series: Materials Science and Engineering, 401,* Article 012027. https://doi.org/10.1088/1757-899X/401/1/012027

Ibrahim, A. H., & Elshwadfy, L. M. (2021). Assessment of construction project cost estimating accuracy in Egypt. *The Open Civil Engineering Journal, 15,* 290–298. https://doi.org/10.2174/1874149502115010290

Idowu, A., Aigbavboa, C., & Oke, A. (2023). Barriers to digitalization in the Nigerian construction industry. In *Proceedings of the Creative Construction Conference.* https://doi.org/10.35490/EC3.2023.196

Kline, R. B. (2016). *Principles and practice of structural equation modeling* (4th ed.). Guilford Press.

Kline, A. R., & Ayer, S. K. (2023). Augmented reality (AR) and virtual reality (VR) in construction education: A systematic literature review. In *Proceedings* (pp. 655–662). American Society of Civil Engineers. https://doi.org/10.1061/9780784485231.078

Leavy, P. (2017). *Research design: Quantitative, qualitative, mixed methods, arts-based, and community-based participatory research approaches*. The Guilford Press.

Liu, H., Liu, B., van Nederveen, S., & Hertogh, M. (2023). Understanding the effects of digital technologies on construction project performance: A literature review. *Computers in Industry, 145,* Article 103832. https://doi.org/10.1016/j.compind.2022.103832

Maqsoom, A., Zulqarnain, M., Irfan, M., Ullah, F., Alqahtani, F. K., & Khan, K. I. A. (2023). Drivers of, and barriers to, the adoption of mixed reality in the construction industry of developing countries. *Buildings, 13*(4), Article 872. https://doi.org/10.3390/buildings13040872

Nia, B., Taheri, M., & Jamalpour, R. (2023). Achieving realistic cost estimates in building construction projects: A reliability assessment of pre-construction stage cost estimates. *International Journal of Construction Engineering and Management, 12,* 81–90. https://doi.org/10.5923/j.ijcem.20231203.02

Noghabaei, M., Heydarian, A., Balali, V., & Han, K. (2020). *A survey study to understand industry vision for virtual and augmented reality applications in design and construction.* arXiv. https://arxiv.org/abs/2005.02795

Oke, A. E., & Arowoiya, V. A. (2022). Critical barriers to augmented reality technology adoption in developing countries: A case study of Nigeria. *Journal of Engineering, Design and Technology, 20*(5), 1320–1333. https://doi.org/10.1108/JEDT-12-2020-0519

Oke, A., Kineber, A., Elshaboury, N., Ekundayo, D., & Bello, S. (2023). Exploring the benefits of virtual reality adoption for successful construction in a developing economy. *Buildings, 13*(7), Article 1665. https://doi.org/10.3390/buildings13071665

Orihuela, P., Noel, M., Pacheco, S., Orihuela, J., Yaya, C., & Aguilar, R. (2019). Application of virtual and augmented reality techniques during design and construction process of building projects. In *Proceedings of the 27th Annual Conference of the International Group for Lean Construction* (pp. 1105–1116). https://doi.org/10.24928/2019/0220

Osorto Carrasco, M. D., & Chen, P. H. (2021). Application of mixed reality for improving architectural design comprehension effectiveness. *Automation in Construction, 126,* Article 103677. https://doi.org/10.1016/j.autcon.2021.103677

Prabhakaran, A., Mahamadu, A.-M., & Mahdjoubi, L. (2022). Understanding the challenges of immersive technology use in the architecture and construction industry: A systematic review. *Automation in Construction, 137,* Article 104228. https://doi.org/10.1016/j.autcon.2022.104228

Radianti, J., Majchrzak, T. A., Fromm, J., & Wohlgenannt, I. (2020). A systematic review of immersive virtual reality applications for higher education: Design elements, lessons learned, and research agenda. *Computers & Education, 147,* Article 103778. https://doi.org/10.1016/j.compedu.2019.103778

Saunders, M., Lewis, P., & Thornhill, A. (2019). *Research methods for business students* (8th ed.). Pearson Education.

Sidani, A., Dinis, F. M., Duarte, J., Sanhudo, L., Calvetti, D., Baptista, J. S., Martins, J. P., & Soeiro, A. (2021). Recent tools and techniques of BIM-based augmented reality: A systematic review. *Journal of Building Engineering, 42,* Article 102500. https://doi.org/10.1016/j.jobe.2021.102500

Speicher, M., Hall, B. D., & Nebeling, M. (2019). What is mixed reality? In *Proceedings of the 2019 CHI Conference on Human Factors in Computing Systems* (pp. 1–15). ACM. https://doi.org/10.1145/3290605.3300767

Tornatzky, L. G., & Fleischer, M. (1990). *The processes of technological innovation*. Lexington Books.

Uwaegbulam, C. (2025, May 12). Cost of technology slows innovation in building industry. *The Guardian Nigeria.* https://guardian.ng/property/cost-of-technology-slows-innovation-in-building-industry/

Venkatesh, V., & Davis, F. D. (2000). A theoretical extension of the Technology Acceptance Model: Four longitudinal field studies. *Management Science, 46*(2), 186–204. https://doi.org/10.1287/mnsc.46.2.186.11926

INTELLIGENT ENERGY MANAGEMENT IN AGRICULTURE: A SYSTEMATIC REVIEW OF INTERNET OF THING, RENEWABLE INTEGRATION, AND ARTIFICIAL INTELLIGENCE TECHNIQUES

Vandi Jusu[1,*], Eugene Okenna Agbachi[1], Jibril Abdullahi Bala[1]
[1]*Federal University of Technology Minna*
Email: vandijmen185@st.futminna.edu.ng[*], euokenna@futminna.edu.ng, jibril.bala@futminna.edu.ng
***Corresponding author**: Vandi Jusu
DOI: https://doi.org/10.67203/sp.ICESID.2026

ABSTRACT
Drawing on an analysis of 85 studies in the period 2020-2026, this review examines how smart technologies are utilized for energy management in agriculture. This review uncovers current trends and future trajectories across six themes: farm energy monitoring made possible by IoT; the incorporation of renewables into agricultural operations; forecasting of energy needs for the storage and processing of crops; policy frameworks for agro-energy; the use of AI to optimise heavy-duty farming equipment; and blockchain for peer-to-peer energy trading on rural grids. Among the key findings is the capacity of AI to transform on-farm energy consumption through demand-response in livestock and irrigation facilities and a better integration of decentralised renewables in microgrids. At the same time, the study highlights several shortcomings, particularly regarding system scalability for farms of different sizes, the real-time demands of variable weather and crop cycles, and the computational limits encountered off-grid. A four-step methodology has been employed to bridge the divide between theoretical propositions and practical implementation challenges, thus providing a road map to a smart EMS that is both resilient and economical for agri-food value chains. In so doing the research puts forward a comprehensive framework for agricultural engineers, researchers and energy policymakers to build more sustainable farm energy systems and surmount the obstacles to field-level deployment that are peculiar to the rural environment.

Keywords: *Demand-Side Management; Smart Farming; Renewable Energy; Artificial Intelligence; Internet of Things; Energy Forecasting; Agricultural Electrification*

1. INTRODUCTION

The rapid increase in population, urbanisation, and climate change effects placed immense strain on global food systems. The world's population is estimated to reach 9 billion by 2037, with a significant proportion residing in urban centres (Gu *et al.*, 2021). A report released by the Food and Agriculture Organization (FAO) stated that there must be a significant increase in food production if this demand is to be met but this will also bring other challenges such as causing a rise in the emission of greenhouse gases (GHG), scarcity of water resources, and land degradation especially if farmers continue to use traditional farming technique (Emegha *et al.*, 2025). This has therefore warranted the need for innovative and sustainable farming methods with low environmental footprint and optimized operational efficiency.

Smart farming, which is also referred to as precision agriculture, digital farming, or Agriculture 4.0 integrates advanced technologies including the IoT, AI, robotics, and data analytics to optimise resource utilisation, increase yields, and enhance sustainability (Vardhan *et al.*, 2025). A modern smart farm consists of multiple technical fields such as precision agriculture, cyber-physical systems, and sustainable energy. The goal of smart farming is to optimise the water-energy-food nexus and includes highly mechanised, automated, and data-driven ecosystems. However, smart farming entails substantial energy consumption. About 30% of the world's energy consumption comes from activities related to the agri-food sector, and about one-third of the total GHG emissions from these systems are attributable to their energy use (Corigliano *et al.*, 2025). Energy consumption in agriculture varies substantially across production stages, with irrigation alone consuming between 12,173 and 23,781 MJ ha^{-1}. In controlled environment agriculture (CEA), particularly greenhouses, energy requirements are higher,

with lighting, heating, ventilation, and air conditioning (HVAC) systems consuming vast amounts of electricity to maintain optimal microclimatic conditions (Corigliano *et al.*, 2025).

Managing the water-energy-food nexus is a very complicated process in many developing regions, particularly in Sub-Saharan Africa. Challenges such as unstable grid, limited access to modern facilities and capital exacerbates these challenges. Some farmers therefore use diesel generators and other traditional systems to meet agricultural demands, thereby increasing operational costs and constraining productivity. The introduction of AI and other intelligent technologies offer potential solutions to these challenges and are poised to transform the agricultural sector especially in the area of energy and other resource management. These intelligent systems have the ability to process large datasets, recognize patterns, and predict future outcomes making them ideal for the complex and variable nature of agricultural activities. ML models have been widely used to forecast energy consumption, which enables better load management and scheduling of irrigation and climatic control operations. Reinforcement learning (RL) techniques have also been used to improve the optimal scheduling of microgrids and also deploy DSM response techniques. Other AI-based tools such as Artificial Neural Networks (ANN), genetic algorithms (GA), and fuzzy logic (FL) have also been used to solve optimisation problems relating to energy storage management, renewable energy integration, and load prioritization especially in smart farming (López-Pérez and Flores-Prieto, 2023).

Even with all the benefits of AI-based solutions for EMS, there are many limitations, especially when it comes to their application in the farming sector. In large scale farming, these systems can be very complex to use because there is large data to be processed from IoT sensors and smart meters. Many researchers have used EMS for many applications ranging from industrial to residential settings, but their adaptability and scalability in the farming sector are limited(Tirth *et al.*, 2023). The broad implementation of these cutting-edge farming techniques remains severely limited, not only by financial outlays for infrastructure but also by cyber threats, privacy issues, and poor rural connectivity. Farming operations are becoming more mechanised and therefore it is very important for that these challenges are solved which will enhance the use of intelligent systems in energy management especially in the farm (Zhang *et al.*, 2022). These challenges are summarized in Figure 1.1.

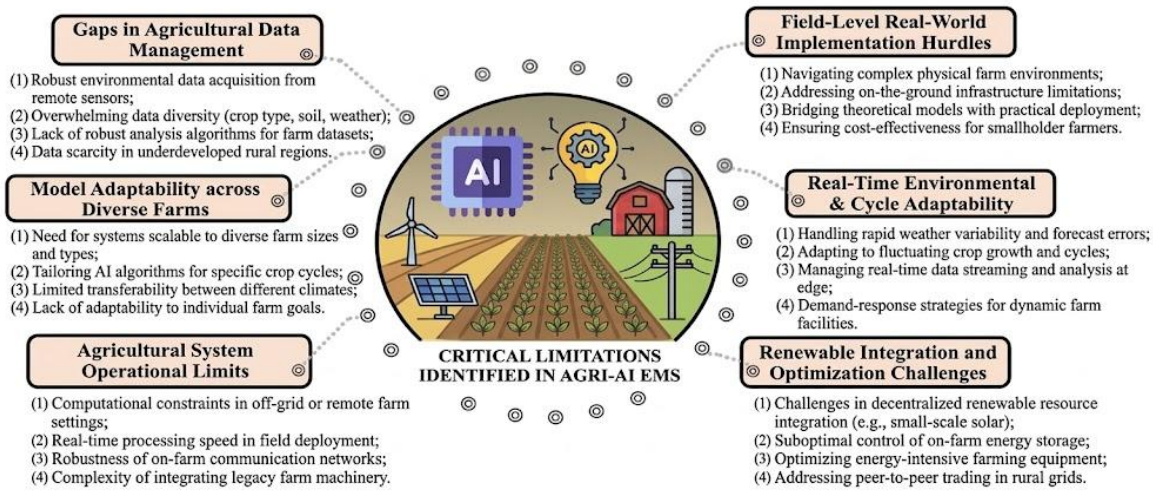

Figure 1.1: Critical Limitations Of AI-driven EMS Systems Deployed in The Agricultural Sector

This study therefore focuses on AI-driven DSM and energy management systems within the context of smart farming and agriculture by examining review papers published between 2020 and 2026. The most studied topics include irrigation optimisation, greenhouse climate control, and reinforcement learning, while scalability, blockchain applications in agriculture, and real-time adaptability remain underexplored. This review guided us to address these gaps and identify future directions for AI-driven DSM in smart farming. With a thorough analysis of what already exists in literature and their limitations, this research provides valuable insights in developing more efficient and robust EMS for applications in the agri-food sector. Figure 1.2 gives a brief overview of the strategy used in the systematic literature review which is inspired by the work done by Kim *et al.* (2021) and Rehman *et al.* (2025).

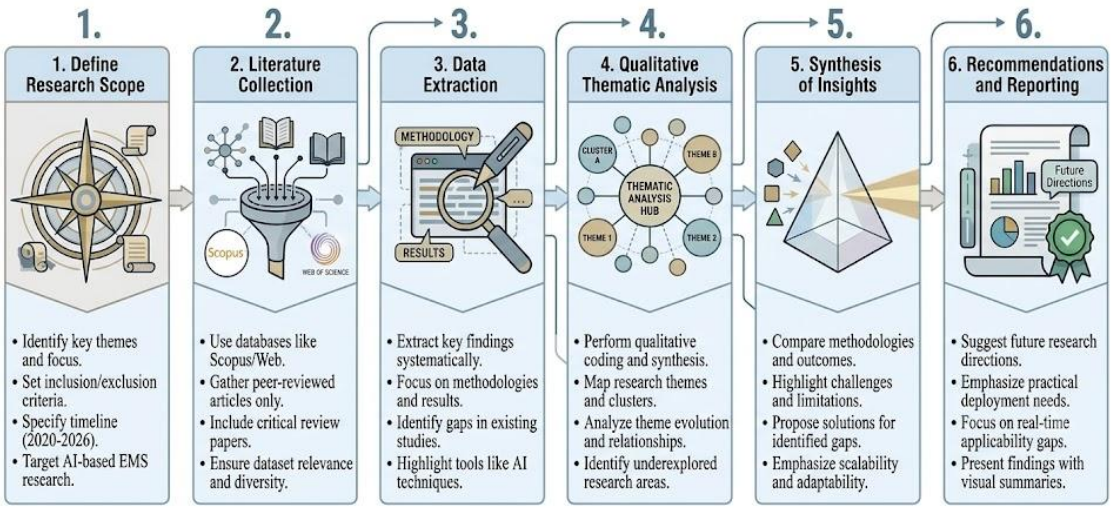

Figure 1.2: Review Strategy Adopted

1.1 Novelty of the Study

Many contributions have been given in the field of AI-driven DSM and energy management systems for smart farming from this study. With many researchers like Aguilar *et al.* (2021) focusing on the application of these technologies in smart buildings and large industries, this research focuses on the agricultural sector highlighting how intelligent energy managements systems can be applied in the entirety of smart farms from irrigation management and greenhouse climate control to renewable energy integration. This study conducts a qualitative thematic review of papers published between 2020 and 2026, which gives a more detailed and current insight into structures and trends specific to agricultural applications; bridging theoretical models with practical implementation in farming contexts.

2. RESEARCH METHODOLOGY

The methodological framework used in this research is summarised in this section.

2.1 Research Questions Formulation

To set the parameters for this review, we begin with a set of research questions (RQs) that will be put forward:

I. RQ1: In the period from 2020 to 2026, what sub-domains in farm-level energy optimisation and DSM have been the subject of the greatest scholarly interest, as opposed to those that are left wanting in funding or attention? What can one make of such publication trends with regard to the strategic imperatives at play and the operational obstacles that endure in agricultural power management?

II. RQ2: What role is being played by the tactical frameworks, machine-learning architectures and hybrid systems of an integrated nature in the governance of on-farm energy today, and to what extent they are able to put an end to the fundamental physical problems at hand?

III. RQ3: Do AI-driven DSM models in precision agriculture truly stand up to the rigours of deployment? The question is whether they can handle processing latency, dynamic responsiveness and scalability while also respecting the biological limits of crops that are determinants of yield and quality in the marketplace.

IV. RQ4: What methodological failings or other deficiencies have been put on record? One has to consider how such flaws stand in the way of a smooth transition from the confines of a trial to a working farm, all the more so in the case of rural agricultural economies with limited resources.

V. RQ5: What does the literature project by way of novel approaches, algorithmic advances or a rethinking of the system to do away with model bottlenecks?

2.2 Definition of Research Queries

For the purpose of this study, we made use of EEE Xplore, ScienceDirect, Web of Science, Google Scholar and Scopus as our principal digital sources. Structured query strings were put to them in order to turn up the publications of greatest relevance. A first pass was made with an assortment of keywords including “demand-side management”, “smart farming”, “precision agriculture”, “renewable energy”, “energy management”, “irrigation optimization”, “greenhouse climate control” as well as “AI”, “machine learning”, “IoT” and “agricultural electrification”.

2.3 Articles Inclusion and Exclusion Criteria

This method of retrieval yielded in excess of 100 publications. To narrow this to the final 85 studies, a rigorous screening process was applied. Inclusion criteria required papers to be peer-reviewed, published between 2020 and 2026, and directly focused on agricultural energy management. Papers were excluded if they focused solely on urban environments or lacked empirical or robust simulation data.

2.4 Results Synthesis and Analysis

In conclusion, the synthesized results were structured to systematically address each research question, yielding several key insights. A significant proportion of the studies focus on reducing energy consumption; however, there is a notable paucity of research regarding the dynamic, real-time adaptation of systems or the handling of biological loads from crops. Technologically, the literature frequently features methodologies such as LSTM networks, hybrid algorithms, gradient boosting and reinforcement learning; all are considered sound approaches to the problem of energy management in an agricultural setting.

3: SMART ENERGY MANAGEMENT SYSTEMS IN FARMING

3.1 Energy Management (EM)

EM involves the comprehensive process of planning, operating and monitoring the energy consumption and generation aim at optimizing the performance and also decreasing the cost of energy Asghar *et al.* (2023). The field of EM is a very broad one which consists of a number of processes or strategies which has been an area of interest for many. Mariano-Hernández *et al.* (2021) gave a review of EMS in buildings, showing the importance of DSM, predictive control, optimisation, fault detection and diagnosis. Energy efficiency can be enhanced in buildings by employing these strategies which will ensure the reliability of the system. Another area of focus is EM in microgrid operation. Energy Management is broadly classified into two major strategies that work together: Supply Side Management (SSM) and Demand Side Management (DSM).

3.1.1 Supply side management

SSM is refers to the set of methods, technologies and policies which are used by utility companies and grid operators in order to ensure that the generation of energy and its supply meets the energy demand. In the earlier days this was the primary strategy used to ensure that there is stability and it was focused on only large centralized energy generation systems like thermal and hydroelectric power plants (Cai *et al.*, 2022). While DSM is mainly focused on adjusting the time of use and the level of energy consumptions from the end user, SSM focuses on the producer and supplier’s side. The main objective is to ensure generation adequacy, maintain system reliability and to optimize the economic dispatch of the generating units (Cai *et al.*, 2022).

SSM has evolved from just a predictable exercise in fuel procurement to a more complex highly uncertain scheme caused by the need to decarbonize and also the integration of renewable energy sources (Aoun *et al.*, 2020). SSM problems are also divided into two; Unit Commitment (UC) and Economic Dispatch (ED). In UC the utility company or operator makes a decision on which generator

unit to turn ON or OFF during a specific period and ED involves deciding how much power each unit will supply to meet the demand most economically.

3.1.2 Demand side management

The concept of DSM emerged in the late 1970s. At that time, utility companies began looking for ways to influence how their customers used electricity (Abul Kalam *et al.*, 2024). Their primary goals were to reduce peak electricity demand and, as a result, postpone the need to build new power plants or infrastructure. By the 1990s, the understanding of DSM evolved to encompass a broader range of strategies. This refinement included approaches such as load shifting, which involves moving electricity consumption to off-peak hours, as well as electrification, promoting the use of electricity for processes previously powered by other energy sources, and fostering the strategic growth of power markets to better manage energy demand (Bogdanova *et al.*, 2023).

3.2 DSM Strategies and Demand Response Schemes

DSM programs are essentially a blend of two key strategies: enhancing energy efficiency and implementing active load management as seen in Figure 3.1. A widely accepted framework categorizes DSM into these two primary pillars: energy efficiency, which focuses on reducing overall energy consumption by upgrading or replacing less efficient equipment, and demand response, which involves strategically altering the timing of energy use (Nebey, 2024).

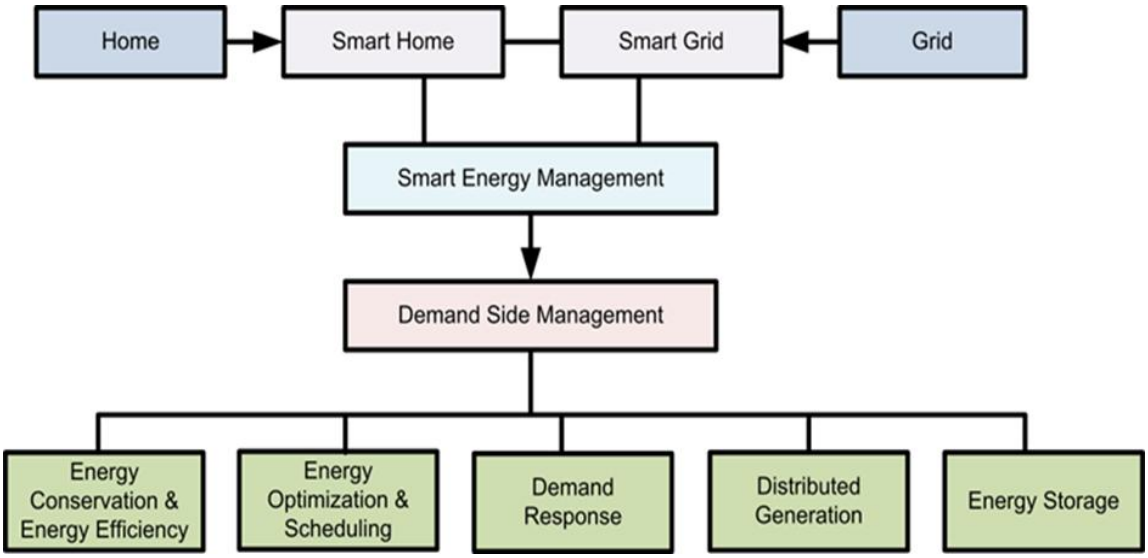

Figure 3.1: Energy management framework

Adapted from Iqbal *et al.* (2021)

Figure 3.2 visually represents the various functions of DSM techniques. Such functions involve managing electricity demand through peak shaving, increasing off-peak usage (valley filling), strategic energy conservation, load redistribution, and timing-based consumption shifts. Peak shaving and valley filling are direct methods of controlling electricity demand. Peak shaving aims to minimise energy usage throughout periods of highest demand, while valley filling seeks to increase consumption during periods of lowest demand. Strategic conservation, on the other hand, involves directly reducing overall energy demand on the consumer side. Both load shifting and time-shifting involve transitioning power consumption to off-peak intervals (Iqbal *et al.*, 2021).

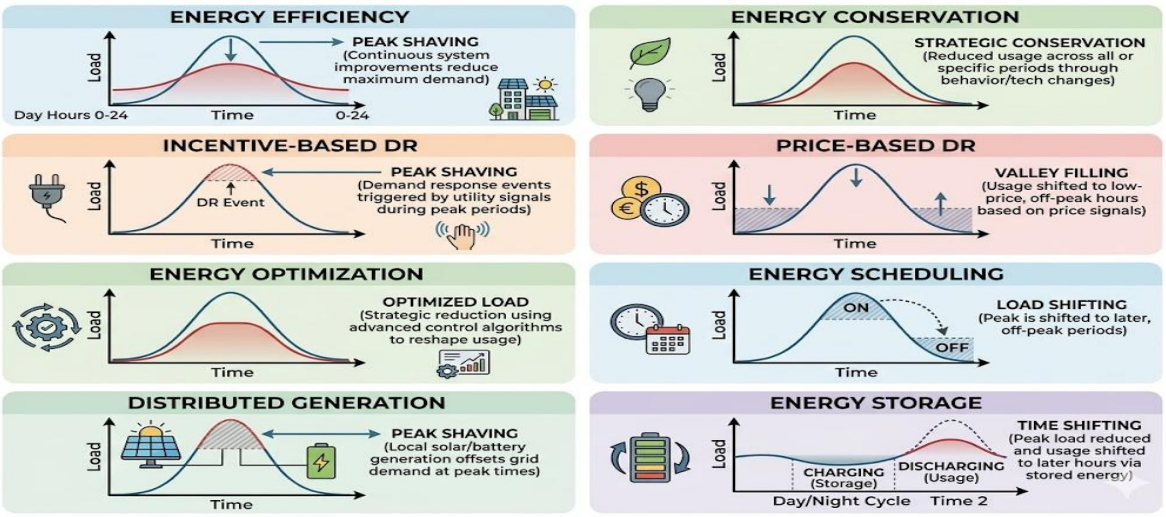

Figure 3.2: DSM Strategies

3.3 Theoretical Background of Smart Farming

A modern smart farm consists of many technical areas coming together including precision agriculture, cyber-physical systems, and sustainable energy engineering. Driven by the need to optimise the critical water-energy-food nexus, smart farming transitions agricultural operations from passive biological methods to highly mechanized, automated, and data-driven ecosystems (Azadi et al., 2021). To overcome grid unreliability and guarantee absolute biological safety, the modern smart farm's architecture has seen the integration of localized HRES with DSM schemes. As illustrated in Figure 3.3, this ecosystem relies heavily on the IoT to serve as a central nervous network. The architecture is structurally divided into three interconnected layers; the generation and storage layer which combines various energy generating and storage systems forming a resilient microgrid. This power is routed through a cyber-physical control layer, where an edge controller processes real-time data from a comprehensive sensor network monitoring various farming parameters such as soil moisture, temperature, and water levels. Finally, this intelligence governs the load layer, dynamically shifting or shedding deferrable agricultural loads based on environmental thresholds and battery state-of-charge without compromising overall crop health.

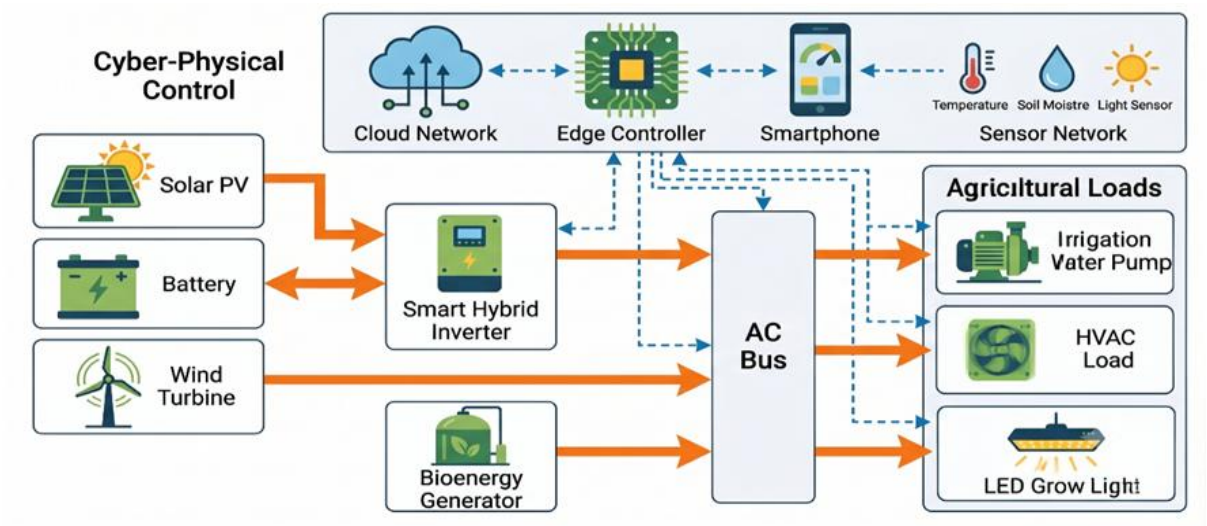

Figure 3.3: Architecture of a Modern Smart Farm

3.4 Energy Demands and Load Profiling in Smart Farms

Moving towards precision agriculture is one of the most important steps in ensuring global food production, which will alter the energy-water-food nexus (Iqbal *et al.*, 2026). Advanced smart farms, which include both open-field precision and controlled indoor farming, greatly depend on automated

and data-driven systems in order to increase their yields and also optimise the use of resources (Nirosha et al., 2024).

3.4.1 Irrigation and water pumping systems

Irrigation systems are a very important but highly variable electrical load in both open field and greenhouse agriculture. Factors that influence the electrical power which is needed to move the water from its source to its needed destination are fluid dynamics, the elevation, and the friction of the pump system (Mansoor *et al.*, 2025). In irrigation, the main metric used in determining the required electrical power is Water Horsepower (WHP), which is a representation of the mechanical energy needed to move a certain volume of water against a total dynamic head (THD) (Mushtaq et al., 2024). The mathematical representation is given in Equation 3.1:

$$WHP = \frac{GPM \times TDH}{3960} \tag{3.1}$$

where GPM represents the pumping rate in gallons per minute, TDH is the total dynamic head in feet, and the denominator 3960 serves as a universal conversion constant deriving from the weight of water and the definition of horsepower. Mechanical and electrical systems are prone to thermodynamic efficiency losses and this makes it very important to know the actual mechanical power that is needed at the shaft of the pump. This is called the Brake Horsepower (BHP) and it can be derived by considering the mechanical efficiency of the pump and the efficiency of the drive mechanism, given in Equation 3.2 where η_{pump} represents the mechanical efficiency of the pump, and η_{drive} represents the efficiency of the drive mechanism.

$$BHP = \frac{WHP}{\eta_{pump} \times \eta_{drive}} \tag{3.2}$$

By actively measuring these metrics, EMS controllers can engage in dynamic load profiling, prioritising energy dispatch precisely when mechanical efficiencies peak and water demands are critical.

3.4.2 Climate control and HVAC in controlled environments

Providing the optimal microclimate is one of the biggest consumers of energy in Controlled Environment Agriculture and greenhouses. About 30% of the energy used in these types of facilities is from powering heating, ventilation, and air conditioning (HVAC) systems which are used to regulate the internal environment against extreme weather variations (Çam *et al.*, 2025). Since temperature and humidity need to be continuously maintained, this creates a rigid base load that makes it very difficult to integrate renewable energy systems. In the Mediterranean, semi-arid, or tropical climate regions which are known for high solar irradiance, high heat is accumulated inside the greenhouse which requires constant operation of HVAC systems in order to prevent heat stress on the crops. This ventilation requirement can be expressed mathematically as seen in Equation 3.3.

$$Q_v = \frac{\tau \cdot R_{s,o-max} \cdot A}{\rho \cdot C_p \cdot \Delta T} \tag{3.3}$$

where Q_v is the required ventilation rate, τ is the greenhouse structural solar transmission coefficient, $R_{s,o-max}$ is the maximum outside solar radiation, A is the ground surface area, ρ is the density of the air, C_p is the specific heat capacity of air, and ΔT is the maximum permissible temperature difference between the indoor and outdoor environments.

3.5 IoT-enabled Farm Energy Monitoring and Smart Infrastructure

IoT is a wireless network that is incorporated with physical items like electronic devices, vehicles, structures, and other electronic devices (Konings *et al.*, 2022). It is a very important technology as it allows objects to obtain, analyze, process, control, and output the information remotely over the network by a computer-based system (Onike, 2025). It makes it possible for the user to control their system remotely over phone through the internet. As illustrated in Figure 3.4, which shows how

the interaction of multiple IoT devices is done as a cyber-physical system, it is a technology which has a wide range of applications in smart grids, smart buildings, and smart farms.

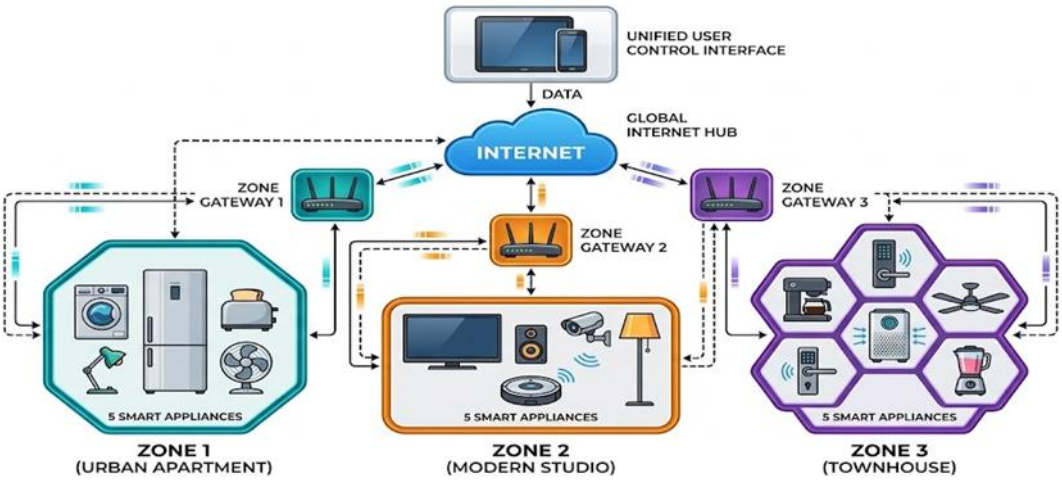

Figure 3.4: The Interaction Between IoT Devices

In modern agriculture, the way data is collected and processed is of paramount importance for ensuring operations are both accurate and as unencumbered as possible. There is scope for IoT to better monitor farm activities and pick up on any faults (Choudhary *et al.*, 2025). Research into agricultural energy has shown a marked interest in the use of IoT to manage irrigation; Al-Ali (2019) put forward an IoT solar system for smart irrigation by way of example. The design makes use of a single-board controller with its own Wi-Fi to link to the solar cells that furnish the power required. From the sensors in the field, it will take readings of soil moisture, temperature and humidity, then issue the actuation commands needed to run the irrigation pumps.

3.6 Renewable Energy Integration for Agricultural Operations

Adopting renewable energy is one of the key aspects for decarbonising agriculture to help tackle climate change, reduce dependency on fossil fuels and improve the economic viability of agricultural systems. Adetoro *et al.* (2023) performed techno-economic and environmental impact assessment of a hybrid renewable energy system with improved combined dispatching strategy for a north-central Nigeria dairy farm. Their best HRES design, made from 248 kW solar PV array, 2 kW wind turbine, 22 kW biogas generator and a diesel generator with nominal power of 92 kW + 658kWh battery storage gave LCOE $0.148/kWh and NPC $1.99 million. This LCOE is highly competitive when compared to Nigeria's current grid electricity tariffs and represents a significant cost reduction compared to the baseline of running diesel-only generators in off-grid rural areas. The Enhanced Combined Dispatch (ECD) strategy, which combines Load Following (LF) and Cycle Charging (CC) modes with six operation scenarios based on net load, battery state of charge (SOC), and energy balance forecasts was shown to perform considerably better than conventional dispatch methods. ECD provides significant reductions in CO_2 emissions (25% lower than CC, 14% lower than LF) as well as diesel consumption (from the base system of 84,351 L/year to only 3,110 L/year), demonstrating the environmental and economic advantages of optimized renewable integration.

The potential of biogas systems for agricultural energy applications has also received considerable attention due to the availability of organic waste streams on farms. Sanni *et al.* (2021) analysed the potential of off-grid solar PV/biogas power generation for a slaughterhouse in Ado-Ekiti, Nigeria, demonstrating that biogas from organic waste could provide reliable backup power to complement solar PV systems. The study utilised HOMER software for optimization and simulation, finding that incorporating biogas generation could reduce diesel consumption by 96% compared to diesel-only systems. The intermittent nature of solar and wind resources presents significant challenges for agricultural applications requiring continuous power supply. Studies by Rehman *et al.* (2024) addressed this challenge through the development of comprehensive frameworks integrating renewable energy resources with battery energy storage systems and precision robotics. Their work highlights the

importance of energy storage in enabling high renewable penetration in agricultural operations, noting that battery energy storage systems can increase the renewable fraction of agricultural microgrids from 20-40% up to 60-80% compared to standalone systems.

3.7 Energy Forecasting and Predictive Analytics

Accurate energy forecasting is critical for the management of an agricultural operation; it is what allows for the kind of proactive decisions that are needed in matters of demand response, storage and the dispatch of generation. In the studies at hand, the methodology is underpinned by an empirical approach to load profiling as opposed to the use of intricate digital twin simulations. The biological variables at play on a farm are too numerous for a conventional digital twin to put on the map with any precision, so a more robust way to do one's analytical forecasting is with targeted load profiling. Recent research has increasingly focused on hybrid machine learning architectures for this purpose in agriculture. In a 2025 study, Biswal *et al.* (2025) put forward a hybrid XGBoost-LSTM model to predict greenhouse energy demand; it makes use of Extreme Gradient Boosting to learn from static features and Long Short-Term Memory in order to recognise sequential patterns. With the addition of a priority-based DSM framework the model was able to cut average electricity costs by 17.3% and grid reliance by 7.1%, all with a MAPE of 5.3%. A comprehensive analysis of AI for power forecasting in renewable microgrids was conducted by Islam and Othman (2026) . They compared the likes of ANN, Fuzzy Logic and ANFIS with deep learning of a more advanced nature such as Transformer, TCN or LSTM. Using hourly data in the field from the King Saud University microgrid in Riyadh, they identified the SE+LSTM as the optimal model, recording an RMSE of 0.7015 kW and a 2.01% MAPE. This was well above what could be obtained from the traditional models or even the TCN (RMSE 0.765 kW, 3.92% MAPE) and standalone LSTM (0.783 kW RMSE, 3.91% MAPE).

3.8 Smart Agro-Energy Policies and Farmer Engagement

For AI-driven energy management to be implemented in the agricultural sector, one needs more than technological advances; there is a requirement for sound policy and ways of engaging farmers. The policy landscape for agricultural energy management is characterized by significant regional variation. For instance, Nigeria's Electricity Act of 2023 eliminates the requirement for a licence to construct or run an electricity distribution or generation facility so long as capacity limits are observed. The Act is open to anyone wishing to do so, particularly where renewable sources are concerned. Gelchu *et al.* (2023) emphasised the importance of policy frameworks in enabling DSM in agricultural contexts. Their analysis of autonomous solar PV-based mini-grids for Ethiopian farms revealed that the cost-effectiveness of DSM strategies depends significantly on tariff structures and regulatory frameworks. Household loads showed the highest DSM impact (45.8% LCOE reduction), followed by productive use with night-time loads (20.7% LCOE reduction), suggesting that policy interventions targeting these load categories could yield substantial benefits. Farmer engagement and adoption of smart energy technologies is a critical factor in the success of AI-based energy management systems. Nigussie *et al.* (2020) highlighted the importance of incorporating indigenous farming and expert knowledge, regional weather information, and crop and soil-specific characteristics into IoT-based irrigation management systems.

3.9 Global Trends in AI-driven EMS in Agriculture

At its core, AI is the discipline of developing and studying intelligent systems or agents. For the purpose of making computers that are truly intelligent, one has been able to draw on techniques like soft computing, statistical learning and knowledge-based systems going back to the 1950s. An examination of 85 studies is visually represented in Figure 3.5, illustrating the annual publication trends in AI-based EMS over the 2020-2026 period. One can see from the data a consistent rise in research output, with the number of studies climbing from 10 in 2020 to 22 by 2025; this is indicative of the heightened interest, both in academia and in practice, for the use of AI in agricultural energy management. The trend also reflects rapid advancements in such technologies as IoT and deep learning that are putting new forecasting and optimisation at the disposal of EMS. As to how these are put to use in DR and what classifications they fall under, Figure 3.6 classifies the various AI approaches

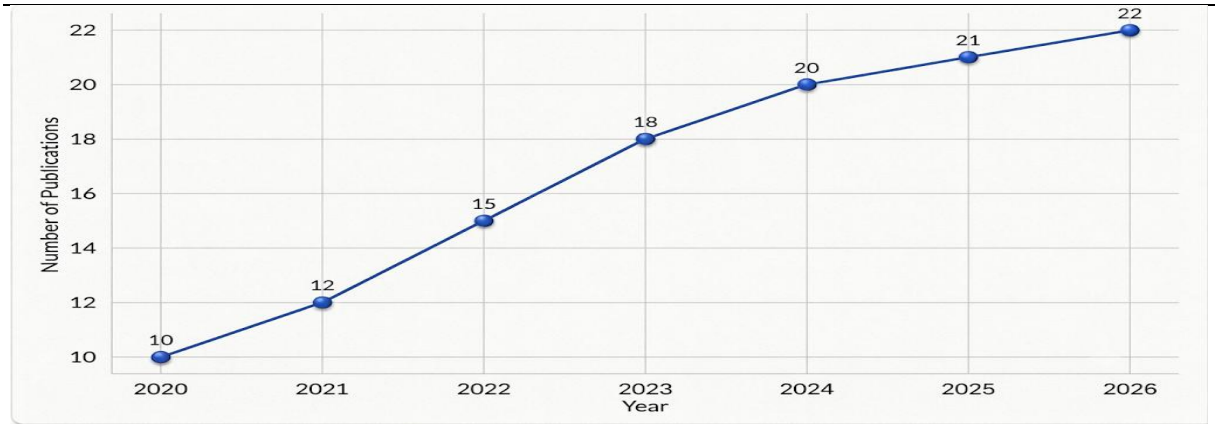

Figure 3.5: Rising research trend in AI-driven EMS for Agricultural Energy Management (Rehman *et al.*, 2025).

An analysis of global research into AI for agricultural energy management reveals notable patterns. In the last five years alone there has been a marked upturn in the number of papers produced in this area, which is testimony to an appreciation of what AI can do to solve the problems of agricultural energy. The bulk of the work on AI-driven agricultural EMS comes from a handful of places; China, Europe, the United States and India are the principal contributors by way of publications. However, developing regions are increasingly contributing to this research domain. Studies from these areas elucidate the particular opportunities and challenges to be had in resource-limited settings.

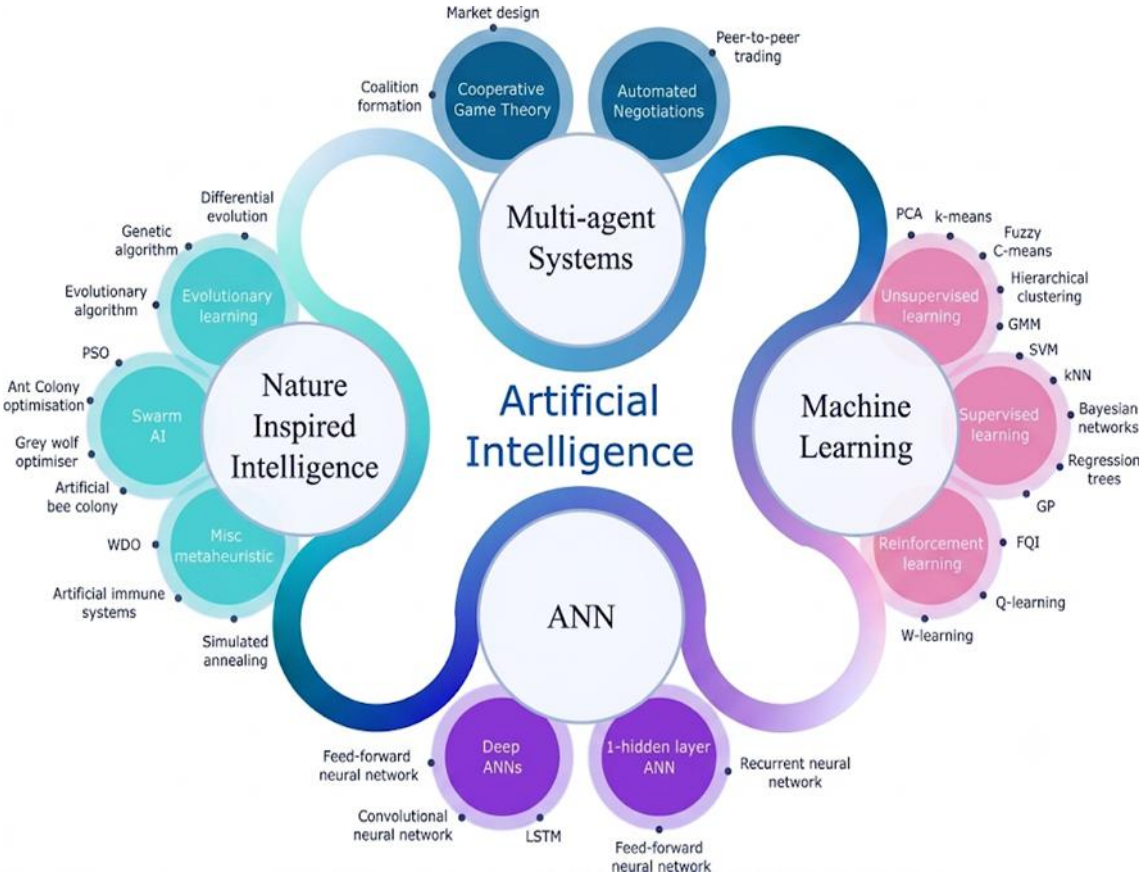

Figure 3.6: Classification of AI Techniques in Energy Management

Adapted from Antonopoulos *et al.* (2020)

4. OPTIMISATION TECHNIQUES FOR AI-BASED AGRICULTURAL ENERGY MANAGEMENT

4.1 Machine Learning for Agricultural Energy Optimisation

In the area of agricultural energy optimisation, ML has become integral to the field, providing the means to forecast, classify and optimise in a wide range of applications. One finds in its use supervised learning for prediction, unsupervised methods for clustering and pattern recognition, as well as reinforcement learning to handle adaptive control and make decisions. For the purposes of forecasting in agriculture, there is extensive recourse to supervised learning techniques such as ANNs, SVMs, random forests or XGBoost. Unsupervised learning has been applied to load profiling and the segmentation of customers within agricultural energy management. Priyanka *et al.* (2023) are one example; they made use of region-based clustering to see gains in energy efficiency from IoT agriculture networks and showed that with large scale deployments, the approach can do much to cut down on the communication overhead and energy used. Several studies have quantified the economic benefits to be had from ML-driven optimisation. In Sri Lanka, for instance, Witharama *et al.* (2024) found that 14.22% of electricity costs could be reduced through LightGBM forecasting given the present tariff system, and as much as 39.42% when market prices are time-varying.

4.2 Reinforcement Learning (RL) for Agricultural Demand Response

In the area of agricultural demand response, RL has demonstrated significant efficacy. It is the basis for adaptive energy management strategies which, through iterative learning, optimize how one makes operational decisions in a dynamic setting. RL algorithms are applied across various tasks in agricultural energy management: from the control of HVAC and irrigation scheduling to battery management. Q-learning, Proximal Policy Optimization (PPO), and Deep Q-Networks (DQN) are among the primary methods utilised. RL overcomes several limitations inherent in traditional rule-based methods when applied to this field. Abul Kalam *et al.* (2024) observe that an RL agent is able to adapt as conditions change and in so doing enhance its performance, learning the best control policies by way of engagement with the environment. The capacity of RL to optimize pricing strategies for service providers was shown by (Lu and Hong, 2019) in their work on an incentive-driven demand response framework for the smart grid, for which they made use of deep neural networks and reinforcement learning.

4.3 Swarm Intelligence for Renewable Energy Integration in Agriculture

The collective behaviour of social organisms is the source of inspiration for swarm intelligence (SI) algorithms, which have seen wide use in the integration of renewables on farms. With their capacity to tackle the kind of intricate optimisation issues that arise in agricultural energy systems, be it in the sizing, dispatch or scheduling of resources, SI algorithms are formidable instruments. Among them are Particle Swarm Optimization (PSO), Ant Colony and Artificial Bee Colonies (ACO, ABC) as well as the Grey Wolf Optimizer (GWO). A case in point is the work of Adetoro *et al.* (2023) who compared the performance of PSO, GA, and ABC in a Nigerian dairy farm to see how they would fare with HRES sizing. Ultimately, PSO demonstrated superior performance, delivering an LCOE of 0.162/kWh and an NPC of $2.05m. The authors attributed this advantage to the way PSO can search the design space and home in on the optimum without sacrificing its balance of exploration and exploitation.

4.4 Hybrid and Ensemble Modeling Approaches for Agriculture

In the field of agricultural energy management, hybrid and ensemble models are demonstrating considerable efficacy. By drawing on the strengths of a number of AI techniques, such approaches have much to offer; they mitigate the limitations of individual methods through complementary capabilities and in most instances outperform a model on its own. One finds that the pairing of machine learning with evolutionary optimization is especially well suited to agricultural energy applications. A novel class of hybrid modeling is also gaining prominence in the form of physical models being brought together with data-driven ML. As an example of what can be done by marrying forecasting models to system simulation for a full appraisal of renewable energy performance, Punyam Rajendran and Gebremedhin (2024) made use of EnergyPLAN software in their multi-energy microgrid analysis,

putting deep learning-based solar power forecasts to work in the process. Also, recent frameworks have successfully merged Extreme Gradient Boosting (XGBoost) for analysing static environmental features with Long Short-Term Memory (LSTM) networks for sequential pattern recognition. Biswal *et al.* (2025) demonstrated that this hybrid approach is highly effective in greenhouse demand-side management, achieving a Mean Absolute Percentage Error of just 5.3% while reducing grid reliance.

5. LIMITATIONS IN AI-DRIVEN OPTIMIZATION FOR AGRICULTURAL ENERGY MANAGEMENT

5.1 Limited Scalability Across Diverse Farm Sizes

Current research is constrained by the limited scalability of AI optimization across the different sizes of farm. One will find in most of the literature a concentration on particular scales or types of farms, and little way to validate the findings over the whole range of agricultural operations, be it a smallholder or a large commercial concern. Priyanka *et al.* (2023) put forward a region-based network design as a means of scaling, one that can take in an assortment of nodes; yet they confined their validation to what was simulated, not to any real-world deployment.

5.2 The Quality and Availability of Data

For AI to be of use in managing agricultural energy, there are fundamental limitations imposed by the data. The models need to be trained and validated on datasets of sufficient size and quality, which are scarce in the agricultural sector, in developing nations especially. In rural SSA for instance, Nigussie *et al.* (2020) pointed out that with so few weather stations researchers must rely on satellite data for irrigation purposes instead of measurements from the ground.

5.3 Computational Demands of Off-grid Environments

Deploying AI in off-grid agricultural settings presents significant technical challenges given the complexity of the algorithms and the paucity of power, connectivity and computing resources to be found in remote areas. Such algorithms are energy and processing intensive. Biswal *et al.* (2025) have shown how these constraints can be met by running ML models that have been properly optimised on a Raspberry Pi 3B+ controller via edge computing.

5.4 Not Enough Adaptability When Conditions Change

Currently utilized approaches are limited in their ability to adapt to dynamic on-farm conditions. Energy management systems must adapt in real-time to dynamic equipment loads or abrupt meteorological changes, but AI models, being based on historical data, will not always react to something new.

5.5 Dealing with Older Farm Infrastructure

Furthermore, integrating AI energy management with legacy infrastructure poses substantial challenges. Much of what is already in place has not been built for the purpose of digital control or to gather data. Implementing monitoring and control systems can be a capital-intensive process and at times not possible from a technical standpoint. At Maizube Farm, Adetoro *et al.* (2023) had to install actuators and sensors in order to monitor and control the diesel pumps and other processing and irrigation equipment since they were not designed for it.

5.6 Lack of Focus on Farmer-centric and Ethical Considerations

Research into AI for agricultural energy management frequently overlooks ethical and farmer-centric considerations. The emphasis has been on the technical merits of the system, its accuracy and efficiency, rather than what bearing it has on the farmer's livelihood or autonomy in making decisions. Abul Kalam *et al.* (2024) observe that such matters as worker displacement, bias in the algorithm and data privacy have not been given the attention they warrant in the published work.

6. DISCUSSION, RESEARCH GAPS, AND SOLUTIONS

6.1 Research Gaps

Although the integration of intelligent technologies into agricultural systems has advanced rapidly, critical research gaps remain across the six primary thematic clusters identified in this review:

I. IoT-Enabled Farm Energy Monitoring: Existing literature predominantly evaluates IoT telemetry and sensor topologies under controlled or simulated environments. A pronounced gap persists in long-term, empirical field validation under severe environmental conditions, intermittent rural connectivity, and sensor drift in open-field deployments.

II. Renewable Energy Integration in Agricultural Microgrids: While techno-economic assessments of basic solar-diesel systems are common, research lacks comprehensive dispatch models capable of coordinating multi-source generation (solar PV, wind, and bioenergy) with battery storage against the highly non-linear, seasonal demand profiles of agro-industrial operations.

III. Predictive Energy Forecasting for Crop Storage and Processing: Deep learning and hybrid architectures (such as XGBoost-LSTM) exhibit high predictive performance, yet their transferability is constrained by a severe scarcity of high-resolution, open-access agro-climatic datasets. Furthermore, current models rarely integrate biological growth stages directly into the load prediction loop.

IV. AI Optimisation of Farm Machinery and Operations: Most algorithmic frameworks assume modern, digitally controllable loads. There is limited investigation into retrofitting legacy agricultural equipment with intelligent edge controllers or mitigating the physical wear and electromechanical constraints of retrofitted motors and pumps.

V. Smart Agro-Energy Policies and Farmer Adoption: Energy management research frequently treats policy and regulatory mechanisms as static boundary conditions rather than dynamic variables. Few studies evaluate how decentralized energy policies (such as the Nigeria Electricity Act 2023) or localised tariff structures influence the financial viability of rural demand-side management.

VI. Blockchain and Peer-to-Peer (P2P) Energy Trading: Decentralized energy trading among rural agricultural producers remains largely conceptual. There is a lack of field-tested, lightweight consensus algorithms capable of operating within the low-bandwidth, low-computational-capacity constraints typical of off-grid rural distribution networks.

6.2 Solutions

To address the identified research gaps and advance the practical deployment of intelligent agricultural energy systems, a transition from simulated environments to physical testbeds and demonstration sites is paramount. Developing modular, low-voltage hardware prototypes utilizing robust edge-level microcontrollers, such as ESP32 architectures, can enable real-time, multi-tiered load prioritization and fault detection. This approach allows agricultural energy management systems to function reliably without depending on continuous cloud or rural broadband connectivity, making it possible to integrate intelligent control seamlessly with legacy farm machinery.

Furthermore, to overcome the severe meteorological variability inherent in open-field environments, future forecasting models must prioritize hybrid machine learning architectures. Combining temporal sequence processing, like LSTM networks, with gradient boosting algorithms, such as XGBoost, can highly optimize weather-based energy forecasting and predictive dispatch logic for hybrid agricultural microgrids. This advancement must be coupled with the establishment of open-access agro-climatic datasets and standardized protocols for data sharing, which are essential to accelerate model training and allow researchers to systematically evaluate algorithmic performance across diverse climates.

Ultimately, the development of Agricultural Energy Demand Side Management (AGDSM) systems requires a participatory, interdisciplinary approach that actively involves agricultural practitioners, engineers, and policymakers. Researchers must proactively engage with regulatory frameworks to test the economic viability of these AI models under localized tariff structures and decentralized energy policies. In the context of Nigeria's development priorities, these findings

highlight a critical pathway for the nation's growth. Aligning with the conference theme to 'Harness Engineering to Drive Nigeria's Growth,' deploying AI-driven hybrid renewable systems in rural farming directly supports national food security and rural electrification mandates, effectively mitigating the impacts of unstable grid infrastructure.

7. CONCLUSION

In this systematic literature review we have evaluated the role that artificial intelligence plays in energy management systems as they are applied in agriculture. An analysis of 85 studies over the period 2020-2026 was carried out. Six distinct thematic clusters were identified in the review: from IoT farm energy monitoring and the use of renewables in agricultural operations, to forecasting energy needs for crop storage and processing; smart policy frameworks for agro-energy; and AI optimisation of heavy farming equipment. These serve to illuminate what is trending, where there are gaps and what lies ahead.

The analysis reveals the capacity of AI to transform how an on-farm operation consumes energy, be it through better integration of decentralised renewables in a microgrid or the demand-response strategies one can put in place for livestock and irrigation. The review's key findings are that hybrid ML methods will outperform standalone ones in terms of forecasting accuracy, and swarm intelligence, PSO in particular, is well suited to HRES optimisation. There are considerable energy savings to be had when AI and IoT are combined.

While the convergence of AI with technologies like 5G, blockchain and IoT offers new avenues for managing agricultural energy, the literature rarely details fully integrated platforms combining multiple technologies. It is a priority to develop AI techniques that take into account the seasonality and biological constraints of the sector, and to align energy management with wider sustainability concerns like soil health and water conservation. To make the most of the opportunities for innovation there will be a need for policy support and continued investment in research. In tackling the gaps, we have identified the community can help bring about agricultural energy systems of greater efficiency and resilience. This review provides a basis for researchers and energy policymakers, as well as agricultural engineers, to move forward with sustainable farm energy systems and deal with the implementation issues peculiar to the rural environment.

REFERENCES

Abul Kalam, M., Saxena, A., Zahid Hassnain, M., Kumar Dash, A., Singh, J., & Kumar Singh, G. (2024). An Explicit Investigation in Demand Side Management Based on Artificial Intelligence Techniques. *IEEE Access*, *12*, 178928-178940. https://doi.org/10.1109/ACCESS.2024.3432805

Adetoro, S. A., Olatomiwa, L., Tsado, J., & Dauda, S. M. (2023). Techno-economic and environmental impact assessment of a hybrid renewable energy system employing an enhanced combined dispatch strategy. *Green Energy and Resources*, *1*, 100044. https://doi.org/10.1016/j.gerr.2023.100044

Aguilar, J., Garces-Jimenez, A., R-Moreno, M. D., & García, R. (2021). A systematic literature review on the use of artificial intelligence in energy self-management in smart buildings. *Renewable and Sustainable Energy Reviews*, *151*, 111530. https://doi.org/https://doi.org/10.1016/j.rser.2021.111530

Al-Ali, A. R. (2019). *IoT-solar energy powered smart farm irrigation system*. http://hdl.handle.net/11073/21393

Antonopoulos, I., Robu, V., Couraud, B., Kirli, D., Norbu, S., Kiprakis, A., . . . Wattam, S. (2020). Artificial intelligence and machine learning approaches to energy demand-side response: A systematic review. *Renewable and Sustainable Energy Reviews*, *130*, 109899. https://doi.org/10.1016/j.rser.2020.109899

Aoun, A., Ibrahim, H., Ghandour, M., & Ilinca, A. (2020). Supply Side Management vs. Demand Side Management of a Residential Microgrid Equipped with an Electric Vehicle in a Dual Tariff Scheme. *Energies*, *12*, 4351. https://doi.org/10.3390/en12224351

Asghar, Z., Hafeez, K., Sabir, D., Ijaz, B., Bukhari, S. S. H., & Ro, J. (2023). RECLAIM: Renewable Energy Based Demand-Side Management Using Machine Learning Models. *IEEE Access*, *11*, 3846-3857. https://doi.org/10.1109/ACCESS.2023.3235209

Biswal, S. R., Choudhury, T. R., Panda, B., & Mishra, S. (2025). An Improved IoT Based Hybrid Predictive Load Forecasting Model for a Greenhouse Integrated With Demand Side Management. *IEEE Access*, *13*, 108446-108465. https://doi.org/10.1109/ACCESS.2025.3579435

Bogdanova, O., Viskuba, K., & Zemīte, L. (2023). A Review of Barriers and Enables in Demand Response Performance Chain. *Energies*, *16*, 6699. https://doi.org/10.3390/en16186699

Cai, H., Shen, S., Lin, Q., Li, X., & Xiao, H. (2022). Predicting the Energy Consumption of Residential Buildings for Regional Electricity Supply-Side and Demand-Side Management. *IEEE Access*, *7*, 30386-30397. https://doi.org/10.1109/ACCESS.2019.2901257

Çam, N. Y., Ezan, M. A., Ghiat, I., & Biçer, Y. (2025). Modeling of a solar-aided heating and cooling system with thermal energy storage for a sustainable agricultural greenhouse. *Applied Thermal Engineering*, 128714.

Choudhary, V., Guha, P., Pau, G., & Mishra, S. (2025). An overview of smart agriculture using internet of things (IoT) and web services. *Environmental and Sustainability Indicators*, *26*, 100607. https://doi.org/10.1016/j.indic.2025.100607

Corigliano, O., Morrone, P., & Algieri, A. (2025). Navigating the Challenges of Sustainability in the Food Processing Chain: Insights into Energy Interventions to Reduce Footprint. *Energies*, *18*, 296. https://doi.org/10.3390/en18020296

Emegha, K., Bosah, P., Idigo, B. C., & Chibueze Ofobuike, L. (2025). The Effects of Climate Change on Food Security in Nigeria: A Review. *International Journal of Research and Scientific Innovation*, *XII*, 904-914. https://doi.org/10.51244/IJRSI.2025.12040076

Gelchu, M. A., Ehnberg, J., Shiferaw, D., & Ahlgren, E. O. (2023). Impact of demand-side management on the sizing of autonomous solar PV-based mini-grids For a Farm. *Energy*, *278*, 127884. https://doi.org/10.1016/j.energy.2023.127884

Gu, D., Andreev, K., & Dupre, M. E. (2021). Major Trends in Population Growth Around the World. *China CDC Wkly*, *3(28)*, 604-613. https://doi.org/10.46234/ccdcw2021.160

Iqbal, H., Yaning, C., Raza, S. T., & Karim, S. (2026). Optimizing the water-energy-food Nexus for sustainable agriculture in Pakistan: A systems analysis with global implications. *Agricultural Systems*, *232*, 104572. https://doi.org/10.1016/j.agsy.2025.104572

Iqbal, S., Sarfraz, M., Ayyub, M., Tariq, M., Chakrabortty, R. K., Ryan, M. J., & Alamri, B. (2021). A Comprehensive Review on Residential Demand Side Management Strategies in Smart Grid Environment. *Sustainability*, *13*, 7170. https://doi.org/10.3390/su13137170

Islam, A., & Othman, F. (2026). Renewable energy MicroGrid power forecasting: AI techniques with environmental perspective [Original Research]. *Frontiers in Environmental Chemistry*, *Volume 7 - 2026*. https://doi.org/10.3389/fenvc.2026.1759525

Kim, H., Choi, H., Kang, H., An, J., Yeom, S., & Hong, T. (2021). A systematic review of the smart energy conservation system: From smart homes to sustainable smart cities. *Renewable and Sustainable Energy Reviews*, *140*, 110755. https://doi.org/https://doi.org/10.1016/j.rser.2021.110755

Konings, D., Alam, F., Faulkner, N., & de Jong, C. (2022). Identity and Gender Recognition Using a Capacitive Sensing Floor and Neural Networks. *Sensors*, *22*, 7206. https://doi.org/10.3390/s22197206

López-Pérez, L. A., & Flores-Prieto, J. J. (2023). Adaptive thermal comfort approach to save energy in tropical climate educational building by artificial intelligence. *Energy*, *263*, 125706. https://doi.org/https://doi.org/10.1016/j.energy.2022.125706

Lu, R., & Hong, S. H. (2019). Incentive-based demand response for smart grid with reinforcement learning and deep neural network. *Applied Energy*, *236*, 937-949. https://doi.org/10.1016/j.apenergy.2018.12.061

Mansoor, S., Iqbal, S., Popescu, S. M., Kim, S. L., Chung, Y. S., & Baek, J.-H. (2025). Integration of smart sensors and IOT in precision agriculture: trends, challenges and future prospectives. *Frontiers in Plant Science*, *16*. https://doi.org/10.3389/fpls.2025.1587869

Mariano-Hernández, D., Hernández-Callejo, L., Zorita-Lamadrid, A., Duque-Pérez, O., & Santos García, F. (2021). A review of strategies for building energy management system: Model predictive control, demand side management, optimization, and fault detect & diagnosis. *Journal of Building Engineering*, *33*, 101692. https://doi.org/10.1016/j.jobe.2020.101692

Nebey, A. H. (2024). Recent advancement in demand side energy management system for optimal energy utilization. *Energy Reports*, *11*, 5422-5435. https://doi.org/10.1016/j.egyr.2024.05.028

Nigussie, E., Olwal, T., Musumba, G., Tegegne, T., Lemma, A., & Mekuria, F. (2020). IoT-based Irrigation Management for Smallholder Farmers in Rural Sub-Saharan Africa. *Procedia Computer Science*, *177*, 86-93. https://doi.org/https://doi.org/10.1016/j.procs.2020.10.015

Onike, N. J. (2025). The Internet of Things (IoT) in Farming: Smart Solutions for a Sustainable Future. *International Journal of Poverty, Investment and Development*, *5*, 31-44. https://doi.org/10.47941/ijpid.2650

Priyanka, B. H. D. D., Udayaraju, P., Koppireddy, C. S., & Neethika, A. (2023). Developing a region-based energy-efficient IoT agriculture network using region- based clustering and shortest path routing for making sustainable agriculture environment. *Measurement: Sensors*, *27*, 100734. https://doi.org/https://doi.org/10.1016/j.measen.2023.100734

Punyam Rajendran, S. S., & Gebremedhin, A. (2024). Deep learning-based solar power forecasting model to analyze a multi-energy microgrid energy system [Original Research]. *Frontiers in Energy Research*, *Volume 12 - 2024*. https://doi.org/10.3389/fenrg.2024.1363895

Rehman, A. U., Alamoudi, Y., Khalid, H. M., Morchid, A., Muyeen, S. M., & Abdelaziz, A. Y. (2024). Smart agriculture technology: An integrated framework of renewable energy resources, IoT-based energy management, and precision robotics. *Cleaner Energy Systems*, *9*, 100132. https://doi.org/10.1016/j.cles.2024.100132

Rehman, U. u., Faria, P., Gomes, L., & Vale, Z. (2025). Future of Energy Management Models in Smart Homes: A Systematic Literature Review of Research Trends, Gaps, and Future Directions. *Process Integration and Optimization for Sustainability*, *9*, 1169-1198. https://doi.org/10.1007/s41660-025-00506-x

Sanni, S. O., Oricha, J. Y., Oyewole, T. O., & Bawonda, F. I. (2021). Analysis of backup power supply for unreliable grid using hybrid solar PV/diesel/biogas system. *Energy*, *227*, 120506. https://doi.org/https://doi.org/10.1016/j.energy.2021.120506

Tirth, V., Alghtani, A. H., & Algahtani, A. (2023). Artificial intelligence enabled energy aware clustering technique for sustainable wireless communication systems. *Sustainable Energy Technologies and Assessments*, *56*, 103028. https://doi.org/https://doi.org/10.1016/j.seta.2023.103028

Vardhan, P. N. H., Badavath, A., & Srivalli, P. (2025). Artificial intelligence and its applications in agriculture: A review. *Environment Conservation Journal*, *26*, 274-280. https://doi.org/10.36953/ECJ.28802904

Witharama, W. M. N., Bandara, K. M. D. P., Azeez, M. I., Bandara, K., Logeeshan, V., & Wanigasekara, C. (2024). Advanced Genetic Algorithm for Optimal Microgrid Scheduling Considering Solar and Load Forecasting, Battery Degradation, and Demand Response Dynamics. *IEEE Access*, *12*, 83269-83284. https://doi.org/10.1109/ACCESS.2024.3412914

Zhang, L., Ling, J., & Lin, M. (2022). Artificial intelligence in renewable energy: A comprehensive bibliometric analysis. *Energy Reports*, *8*, 14072-14088. https://doi.org/https://doi.org/10.1016/j.egyr.2022.10.347

International Conference on Engineering Innovation for Sustainable Development (ICESID 2026)
Faculty of Engineering, Ahmadu Bello University Zaria · 8–10 September 2026

MEASUREMENT OF LIQUID FILM HEIGHT IN GAS-LIQUID TWO-PHASE FLOWS USING TWIN-WIRE CONDUCTANCE PROBES

Mohammed Kabir Abdullahi[1,*]
[1]*Nuhu Bamalli Polytechnic Zaria*
Email: m.abdullahi07@alumni.imperial.ac.uk*
***Corresponding author**: Mohammed Kabir Abdullahi
DOI: https://doi.org/10.67203/sp.ICESID.2026

ABSTRACT

Accurate measurement of liquid film thickness is important in process equipment because it supports heat- and mass-transfer calculations. In gas-liquid two-phase flow, film thickness is also required for estimating liquid film holdup. Twin-wire conductance probes have been shown to provide reliable measurements of liquid film height in air-water two-phase flows. In this work, probes were fabricated from 0.5 mm platinum wire of 99.95% purity in the student workshop at Imperial College London using standard machining procedures. The probes were mounted on a 32 mm pipe to measure liquid film height in air-water stratified and slug flows. The resulting measurements were accurate, instantaneous, and suitable for tracking changes in liquid film thickness. This paper falls within the sub-theme of sustainable engineering processes. The data and the correlations in this paper can be found useful in the prediction of slug flows for pipeline safety in Nigeria's oil and gas pipelines.

Keywords: *Liquid film holdup; twin-wire conductance probes; liquid film thickness*

1.0 INTRODUCTION

Flows containing more than one phase, commonly referred to as *multiphase flows*, are encountered in many chemical engineering applications. Examples include separation units, chemical reactors, nuclear reactors, tube-bundle heat exchangers, pipeline systems, and several other items of process equipment. Gas-liquid or vapour-liquid flows occur in oil and gas pipelines, condensers, evaporators, distillation columns, absorbers, and combustion systems. Liquid-liquid systems are found in processes such as liquid-liquid extraction and emulsification, while solid-liquid mixtures are frequently transported as slurries through pipelines. Improved understanding of multiphase flow is essential for the effective design and operation of such systems. This paper focuses specifically on measuring liquid film height in gas-liquid flow through horizontal pipes.

When two closely spaced, vertical, parallel wires are immersed in a conducting liquid, the length of wire in contact with the liquid can be inferred from the measured resistance between the wires. This arrangement provides an instantaneous measurement because of the rapid transmission of electrical signals. The method was particularly suitable for the present experiments because rapid response was required to capture fast-moving slug fronts, and because water provides sufficient electrical conductivity.

This work confirms that accurate, time-resolved measurement of liquid film thickness and holdup remains central to the analysis of gas-liquid two-phase flow. Modern studies have extended earlier conductance-probe approaches through interdigital and multielectrode conductance sensors for non-uniform film distributions, while wire-mesh sensors are increasingly used to obtain spatially resolved phase-fraction and flow-pattern information in industrial and laboratory pipe flows (Tompkins, C etal, 2018). Recent slug-flow modelling studies (Ehinmowo, etal (2025), Miao L, etal (2026), have also shown that reliable predictions of pressure gradient, translational velocity, slug liquid holdup, and film-region behaviour depend strongly on high-quality experimental measurements for validation. These developments demonstrate that conductance-based techniques, although well established, remain relevant because they provide fast local measurements that can support both experimental characterisation and the validation of contemporary mechanistic and numerical models of horizontal gas-liquid flow.

In the experiments reported here, conducted by MK Abdullahi (2013), twin-wire conductance probes were used to measure instantaneous liquid height at several positions along the test section. The probes were designed, fabricated, and installed on the Long Tube System (LOTUS), whose general layout is shown in Figure 1. Figure 2 shows the schematics of the probes mounted on the LOTUS test section, while Figure 3 presents a photograph of the twin wires inserted into a pipe section. Because the conductance between the two wires changes with liquid height, recording this conductance provides an instantaneous measure of the local film height. The conductance-time traces can also be used to determine the film height ahead of a slug and, when two probes are placed a known distance apart, to estimate the slug-front velocity. Twin-wire conductance probes therefore offer a convenient method for measuring local liquid film height when the liquid has sufficiently high electrical conductivity (Miya, 1970; Brown et al., 1978; Davies, 1992; Strand, 1993; Srichai, 1994; Manolis, 1995). The LOTUS facility used probes made from 0.5 mm diameter platinum wire of 99.95% purity. This work is within the sub-theme of sustainable engineering processes of this conference.

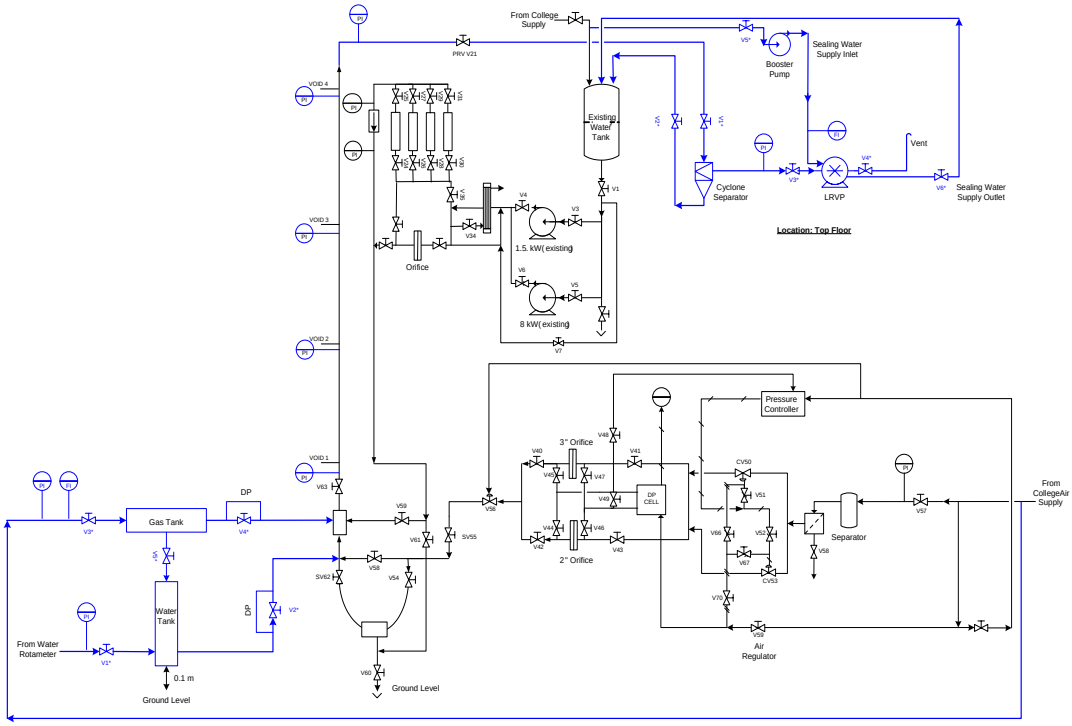

Figure 1: General schematic of the LOTUS Rig

2.0 CONSTRUCTION OF TWIN-WIRE CONDUCTANCE PROBES.

The conductance probes were constructed on pipe sections with an internal diameter of 32.8 mm. Figure 2 shows a schematic of the probe arrangement, with the twin wires positioned 2 mm apart. Four probes were manufactured in the student workshop at Imperial College London and subsequently mounted on the LOTUS test section. Selecting an appropriate wire diameter is important: the wire must be large enough to keep its electrical resistance low relative to that of the liquid, but small enough to avoid disturbing the flow. Two fluid-dynamic considerations govern this choice. First, the wire diameter must be sufficiently small that any wake generated by the wires is negligible. Second, interfacial effects around the wires must also remain insignificant (KOSKIE et al., 1989).

A saddle was attached to the outer surface of each probe assembly, and the wires were screwed to it to keep them straight and correctly positioned.

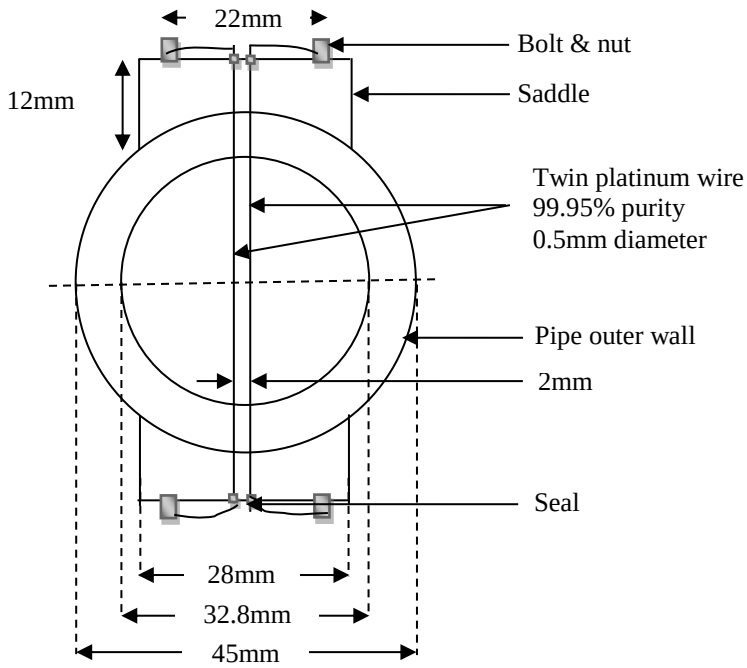

Figure 2: Schematic representation of the twin-wire conductivity probe as used on the LOTUS facility

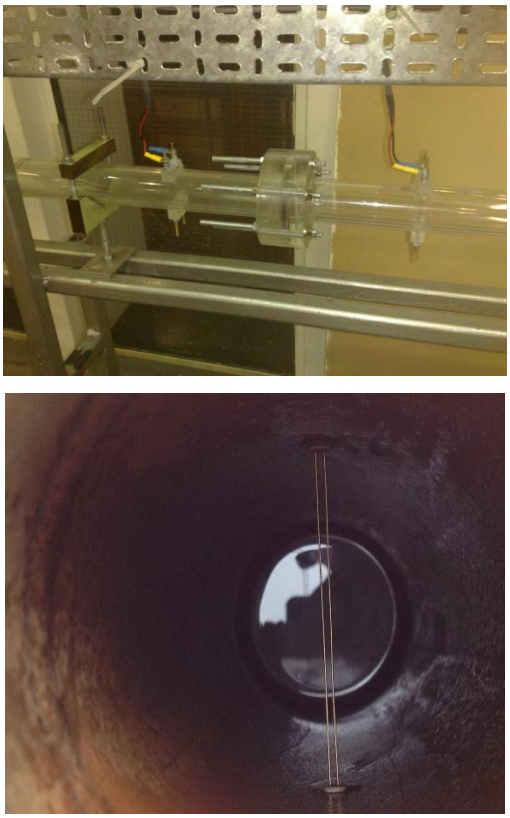

Figure 3: RHS - Photograph of mounted twin-platinum-wire probes on the 32.8 mm LOTUS rig showing probes 2 and 3; LHS - Internal view of twin-wire probes on WASP test section

An equilibrium condition is established when two electrodes are placed in an aqueous medium. This condition results either in a zero net rate of charge transfer between similar metal electrodes or in a potential difference between dissimilar electrodes. When current passes between the electrodes, charge transfer occurs at the interface between the aqueous solution, or water film, and the metal electrodes. This transfer takes place through the movement of protons across the electrical double layers

of ions formed on the anode and cathode surfaces. The process requires activation energy, which is supplied by the potential difference maintained across the system (Glasstone, 1942). In most cases, the current through the double layer increases exponentially with over-voltage, defined as the additional potential difference across the double layer beyond that present when no net current flows. When an external potential is applied between electrodes immersed in an aqueous medium, the over-voltage does not change instantaneously; instead, it increases in a manner similar to the charging of a capacitor through a resistor (Coney, 1972). The double layer can therefore be represented as a capacitance in series with the resistance of the bulk solution.

When alternating current is applied, the influence of double-layer capacitance decreases as the AC frequency increases (Coney, 1972), so the total impedance approaches that of the bulk solution. A very high applied frequency is not necessarily required for the impedance to depend mainly on the bulk solution resistance, particularly when electrodes with high double-layer capacitance, such as platinum, are used.

3 CALIBRATION OF TWIN-WIRE CONDUCTANCE PROBES

Offline calibration was performed for all four probes. Two 1.0 m long pipe sections with an internal diameter of 32.8 mm were used: one fitted with probes CPR1 and CPR2, and the other with CPR3 and CPR4.

An offset run was first conducted with the pipe dry, and the corresponding data were recorded to establish the voltage at zero liquid film height. The pipe sections were then filled with water and sealed using a flange at one end and a cock at the other to retain the water. With the pipe positioned horizontally, the data acquisition system was operated to record the full-pipe reading, corresponding to the 32.8 mm pipe diameter. The liquid level was then reduced in stages, the pipe was kept horizontal, and further readings were taken to obtain voltages corresponding to different liquid levels.

Calibration data relating probe output to liquid height were therefore essential. Such data were obtained for the twin-wire probes used in the LOTUS experiments, as shown in Figure 4.

Figure 4 indicates that an approximately *linear* relationship is expected between probe conductance and liquid height. Early attempts to relate conductance directly to the liquid level observed from the side of the pipe showed deviations from linearity at low and high liquid heights. These deviations resulted from distortion of the interface image caused by the curvature of the pipe wall, which introduced error in locating the true interface position. A correction procedure was therefore developed to relate the apparent side-view level to the true level. Known volumes of water were introduced into a length of acrylic resin tube, which was then sealed and placed horizontally. The true water level was calculated from the known volume added and compared with the apparent level observed from the side of the tube. This comparison enabled correction of the apparent levels. After correction, plots of relative liquid height, defined as liquid height divided by pipe diameter, against data logger reading became close to linear for the four probes used in the LOTUS and LOWPRESS experiments. Some deviation remained at low film heights, probably because of uncertainty in identifying the interface position. It was therefore reasonable to assume a linear relationship when converting data logger output to liquid height. This assumption is convenient because film height can be obtained by linear interpolation between the empty-pipe and full-pipe conductance values, which were measured daily during testing.

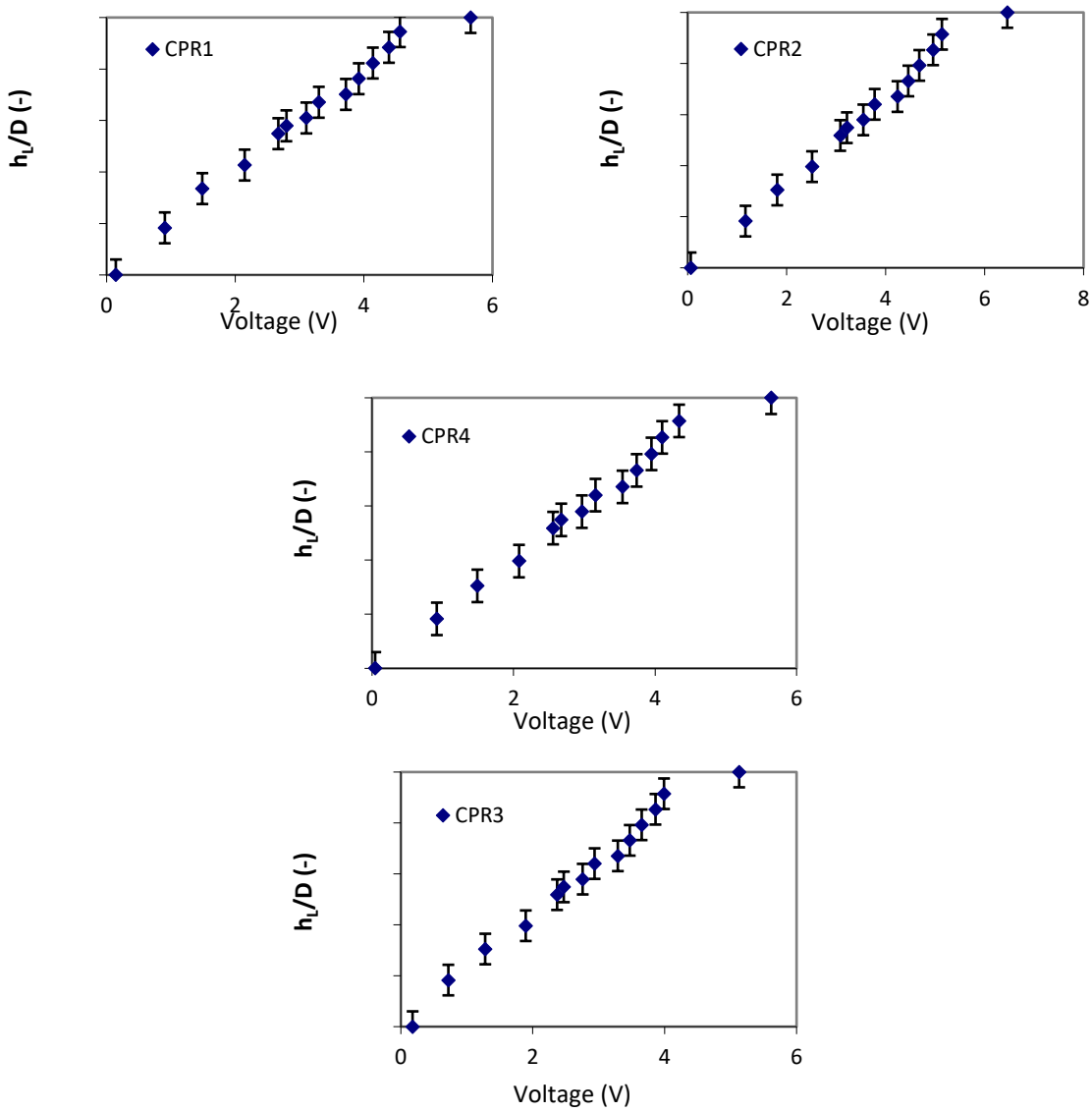

Figure 4: Variation of data logger reading (proportional to conductance) with non-dimensional liquid height for the four twin wire probes used in the LOTUS experiments

From these data, a correlation was derived for the measurement error. This took the form:

$$\varepsilon = -0.1836\left(\frac{h_L^M}{D}\right)^2 + 0.4165\left(\frac{h_L^M}{D}\right) - 0.1607\left(\frac{h_L^M}{D}\right) \tag{1}$$

It was then possible to correct the measured film heights by subtracting the error:

$$\frac{h_L}{D} = \frac{h_L^M}{D} - \varepsilon \tag{2}$$

The results of this correction process are shown in Figure 5. The data now follow the diagonal line to within their error bars (assumed to be +/- 1.5 mm).

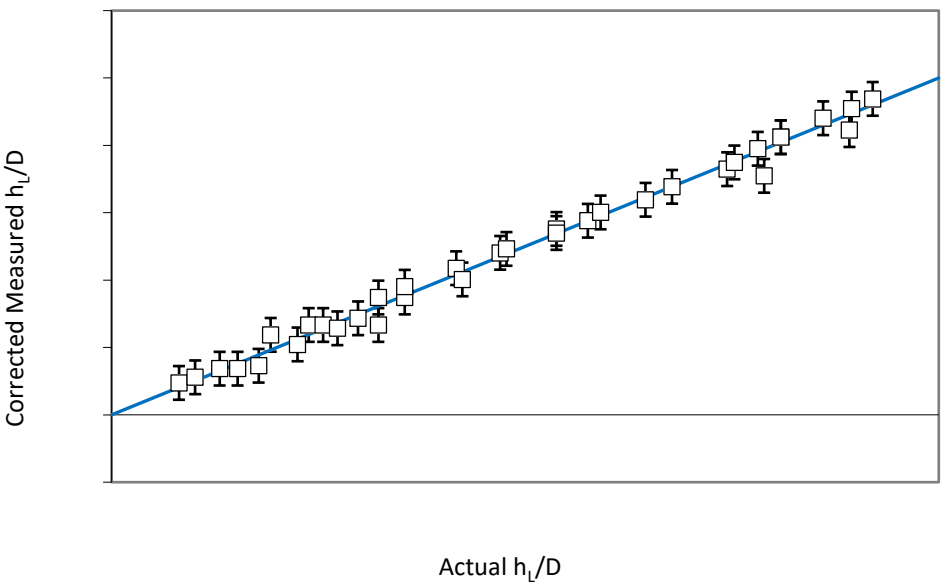

Figure 5: Corrected side-on h_L/D versus actual h_L/D

Each of these probes was constructed as shown in Figure 2. This design has the advantage that the two sets of probes are always at a known, fixed distance apart and so this test section has often been used for measuring slug translational velocities.

The liquid film holdup ε_{LF} can also be determined from the conductance probe measurements of $\frac{h_{LF}}{D}$ and computed using Eqn. (3).

$$\varepsilon_{LF} = \frac{1}{\pi}\left\{\pi - cos^{-1}\left(2\frac{h_L}{D} - 1\right) + \left(2\frac{h_L}{D} - 1\right)\sqrt{1 - \left(2\frac{h_L}{D} - 1\right)^2}\right\} \tag{3}$$

4 Experiments

A typical experiment began by establishing stratified flow in the 32.8 mm horizontal tube. The air and water streams used to create the stratified flow were supplied by the LOTUS rig and passed through a three-way ball valve, as shown in Figure 6. The third connection to this valve was linked to a water-filled vessel pressurised by air from the rig. In the LOTUS experiments, this vessel was a vertical 3 m long stainless-steel tube with an internal diameter of 76.2 mm. When the three-way valve was operated, water from the pressurised vessel entered the test section rapidly, and the rate of water ingress was measured using the venturi meter. The injected water travelled over the existing stratified layer as a pushed-in slug. At the same time, the feed supplying the initial stratified flow was shut off.

The fundamental principle of the experiments is illustrated in Figure 6 and 7 for the stratified flow case and push-in liquid slug respectively. In the case illustrated, the experiment starts with the setting up of a stratified flow in the pipe with the 3-way valve set for through flow as shown. The liquid flow rate in the stratified flow is $\dot{V}_{LF}$ and the liquid fraction in the stratified flow is ε_{LF}. In the experiments, the liquid height in the preceding film region h_{LF} is measured using the twin wire conductance probe system. Assuming that the interface is flat ε_{LF} is related to h_{LF} by the expression in Eqn. (3):

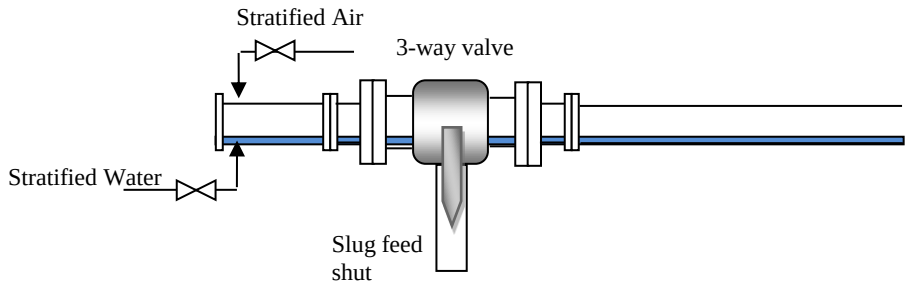

Figure 6: Stratified flow in horizontal test section

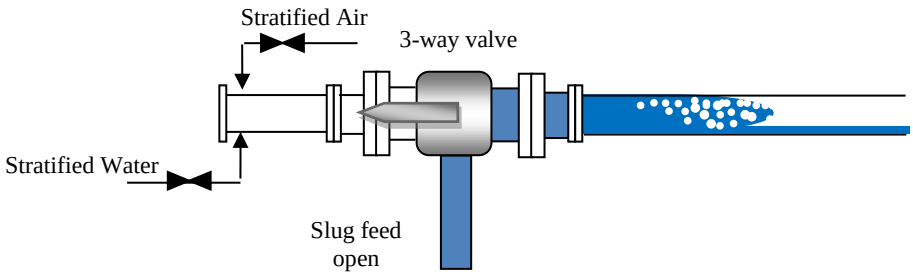

Figure 7: Slug flowing over stratified flow in horizontal test section

Figure 6 illustrates a typical arrangement for measuring liquid height with twin-wire probes positioned upstream of the three-way valve. With the stratified air and water valves open, stratified air-water flow was established in the test section. In the situation shown in Figure 7, the air and water feeds for the stratified stream were closed, and the pushed-in liquid slug moved over the existing stratified layer ahead of it.

5 Data acquisition and processing on LOTUS rig

Air flow rate was monitored continuously. Pressure transducers measured both the absolute pressure at the upstream tapping of the orifice plate, and the pressure drop across it. The upstream tapping was connected to a 0–10 barg absolute pressure transducer, which had been verified against a previously calibrated transducer and found to be accurate within ±4 mbar. The pressure-drop across the orifice plate was measured using a 0–1 bar differential pressure cell. A water-filled manometer was also connected in parallel to allow periodic accuracy checks.

Output signals from these transducers, together with the signal from the transducer mounted on the test line, were converted to digital form and stored on an Amstrad PC1512 (8088) personal computer. Analogue-to-digital conversion was performed using a Scientific Solutions Inc. Lab Master data acquisition unit, which can process up to 16 channels and can be configured for signal ranges of either −10 to +10 V or 0 to 10 V. In the experiments described here, the 0 to 10 V range was selected to match the transducer outputs. A Quick BASIC program written by Manolis (1995) controlled the conversion process and recorded the digitised data. To avoid reducing acquisition speed, only output voltage signals were stored during each run; these were later converted into pressures and air flow rates after completion of the test. For all LOTUS rig experiments, this system operated at a data acquisition frequency of 10 Hz.

For more detailed pressure profiles and for recording conductivity-probe output signals, a faster data acquisition system could be connected in parallel. This system used an Amplicon-Liveline PC30AT analogue-to-digital conversion card installed in the expansion slot of a NAGA 80486 DX-33 personal computer. It enabled rapid acquisition from up to 16 channels. A Quick BASIC program controlled the conversion process and recorded the digitised data, allowing sampling frequencies between 0 and 1000 Hz to be selected.

In this experiment, a sampling frequency of 500 Hz was generally used as a compromise between the need for high sampling rates and the practical difficulty of handling very large data files. According to the sampling theorem (Lynn, 1982), the maximum frequency that can be adequately

represented by a sampled continuous signal depends on the sampling interval. For adequate representation of this frequency:

$$\vartheta_{\text{sample}} = \frac{1}{2t_{\text{dur}}} \tag{4}$$

Where $\vartheta_{\text{sample}}$, is the frequency of the sampled continuous signal and t_{dur} is the time duration between samples. A sampling rate of 500 Hz (t_{dur} = 0.002 s) corresponds to $\vartheta_{\text{sample}}$ = 250 Hz which should be sufficient for representing major system changes. Figure 8 is a block diagram of the data acquisition for the probe signals obtained in the LOTUS and LOWPRESS tests.

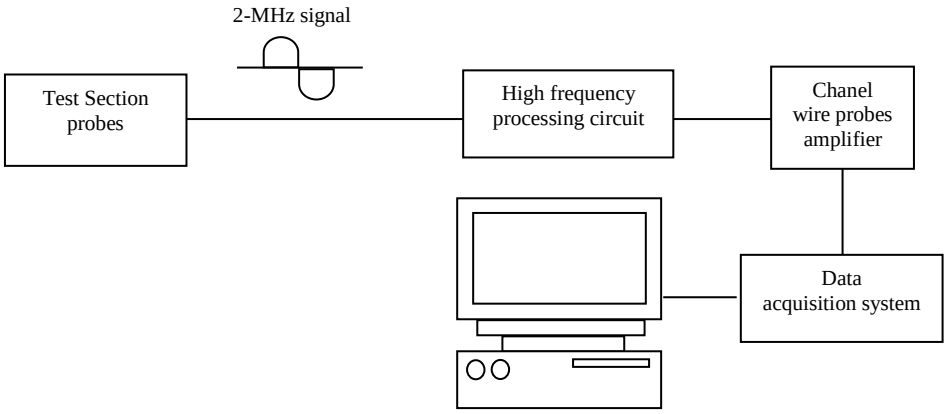

Figure 8: Block diagram of high-frequency probes signal processing system

6 Results and Discussions

As will be seen from the time-traces in Figure 9 (a), for superficial gas velocity (measured using an orifice plate), u_{SG} = 3.058 m/s; and liquid superficial velocity (measured with a rotameter), u_{LF} = 0.0156 m/s the dimensionless liquid film height, $\frac{h_{LF}}{D}$ from the probes between $t = 0$ to about $t = 3.0s$ was averagely 0.22. It can be seen that the gas-liquid interface resembles that of laminar flow in single phase flow, and it is therefore referred to a stratified smooth flow. The stratified flow has been established within the test section up to $t = 3.0s$.

When the 3-way valve was open, a liquid slug from a pressurised pipe at a velocity (measured using a venturi meter), U_{LS} = 2.45m/s arrived at the first probe at about $t = 3.2s$, it is clear there was a rapid rise of the liquid height up to the last probe showing that the probes responded instantaneously to change in liquid film height. The liquid film height downstream of the slug front values is typically in the range of 0.6 – 0.8. Therefore, the average film height across the pipeline through the four proves can be determined and the instantaneous localised film height can also be determined for a given gas-liquid flow. Eventually, the gassy zone passes, and a nearly pure liquid zone is seen which has arisen from the injection system and which has not been penetrated by the entrained gas, $\frac{h_{LF}}{D} = 1.0$. Then, the holdup decreases rapidly indicating that the liquid in the slug injection system has been exhausted and the pressurised drive gas is entering through the three-way valve. During the time of the slug front passage between the probes, the water flow rate is being recorded from the output of the venturi meter (and remains constant until the water is exhausted), see slug feed time traces in Figure 9 (b).

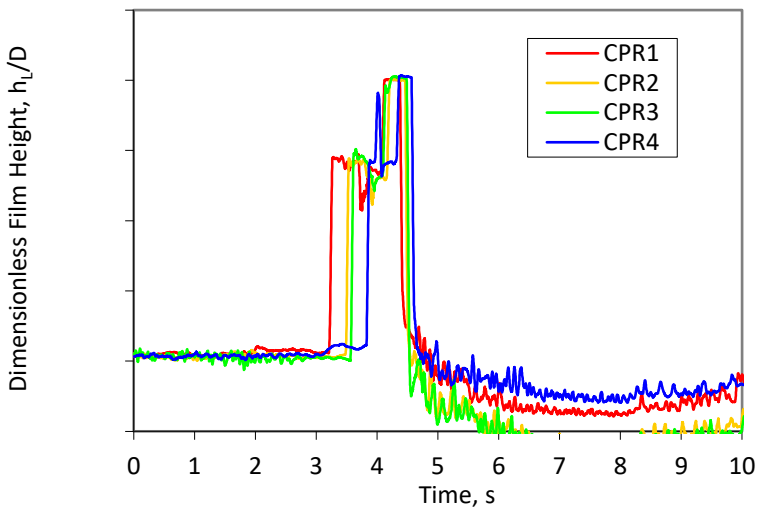

(a) Superficial gas velocity, u_{SG} = 3.058 m/s; Superficial liquid velocity, u_{LF} = 0.0156 m/s and Liquid slug velocity, U_{LS}= 1.951 m/s = 2.422 m/s

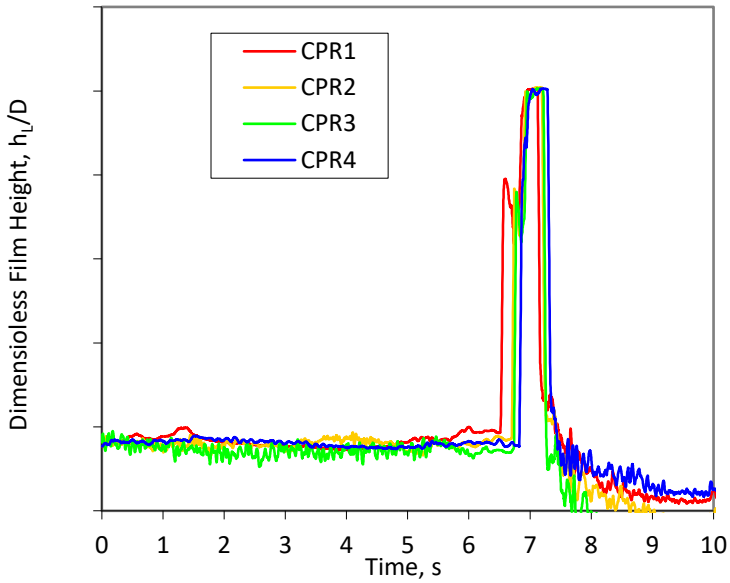

(b) u_{SG} = 5.083 m/s, u_{LF} = 0.0156 m/s and U_{LS}= 1.951 m/s

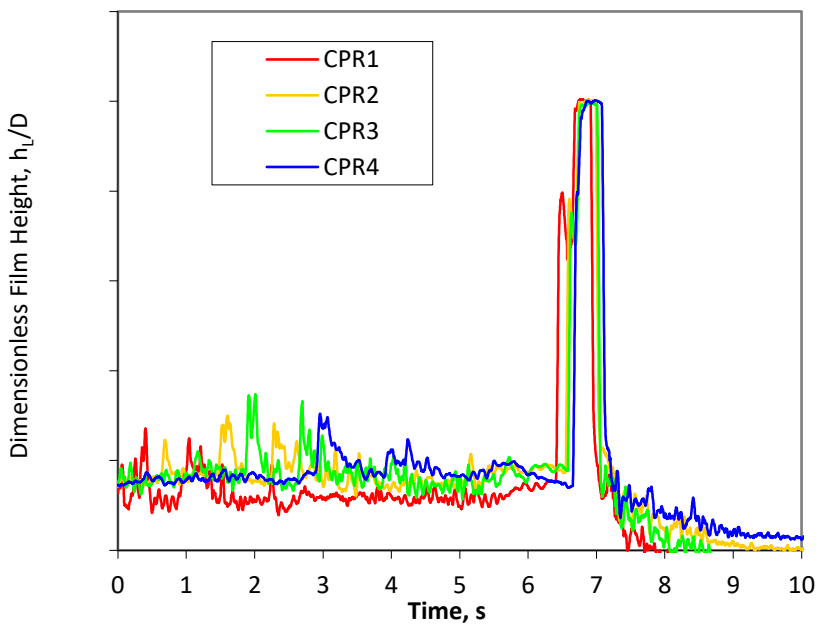

(c) u_{SG} = 6.211 m/s, u_{LF} = 0.0257 m/s and U_{LS}= 2.081 m/s

Figure 9: Time traces - (a - c) Dimensionless liquid film height as a function of time for probes placed at 4.4 m (CPR1) from the 3-way valve, 5.4m (CPR2) from the 3-way valve, 5.6m (CPR3) from the 3-way valve and 6.6 m (CPR4) from the 3-way valve

Similar explanations on the measurement of liquid film height can be applied to Figure 9 (b) and (c). in (b) the gas velocity was increased while the liquid velocity remained unchanged. However, it can be seen that the time-traces showed a liquid film height lower than in (a). This is because the high gas velocity has changed the flow from stratified smooth to stratified wavy.

As can also be seen in (c), the gas and liquid velocities were further increased resulting in a highly wavy interface close to slugging. The film height fluctuates between about 0.1 to 0.3. averaging the film height data will give the average film heigh but if a localised film height is required at any pipe location is desirable, that can be determined too.

7 CONCLUSION

The LOTUS facility, which has a pipe diameter of 32.8 mm and a length of 6.3 m, was used to measure liquid film height with twin-wire conductance probes. It was clear from the data in the time-traces that slug flows can be predicted at high gas-liquid flows. Slugging leads to pipeline damage and can cause serious safely concern in oil-gas fields. Because water is electrically conductive, the probes provided reliable measurements of film height during the experiments. The results showed that changes in water level produced proportional changes in probe response, confirming that the probes could measure liquid film height accurately and rapidly. These measurements are important because they enable calculation of liquid holdup using Equation (3), and the resulting holdup values can then be used to determine the actual velocities of the gas and liquid phases. The data generated, the graphical representation in Figure 5 as well as the time-traces in Figure 9 can be utilised in the validation of models for liquid film height predictions in stratified and slug flows even in 2026 and beyond. Slug flows is associated with high pressure, leading to pipe vibration and bursting. However, this work provided an insight to the flow ranges within which slug flow regime is encountered. This knowledge can help present pipeline breakdown in Nigeria's oil gas fields,; proper slug flows mitigations are employed. Therefore, this work adequately fits the sustainable engineering processes sub-theme.

REFERENCES

Abdullahi M.K. (2013), "Slug Gas Entrainment in Gas-Liquid Two-Phase Flow in Horizontal and Near Horizontal Pipes", PhD Thesis, Department of Chemical Engineering, Imperial College London.

Miao L, Ying Z., Yan W., Haiyan Zhao & Yonghu Z, (2026), Inetgrated Mecahnistic Analysis and Machine Learning Predication of Slug Flow in OIL-Gas-Water Three-Phase Piplenes, Fluid Dynamics and Materials Processing, vol., 22, issues 3 Science Direct.

Miya M. (1970): Properties of roll waves. *PhD thesis, University of Illinois*. pp. 1-199.

Brown R.C., Andreussi P. & Zanelli S. (December 1978): The use of wire probes for the measurement of liquid film thickness in annular gas-liquid flows. *The Canadian Journal of*

Chemical Engineering, Vol. 56, No. 6, pp.754-757.

Davies S.R. (1992): Studies of two-phase intermittent flow in pipelines. *PhD Thesis, Department of Chemical Engineering and Chemical Technology, Imperial College of Science, Technology & Medicine, London, England,* June 1992, pp. 1-348**.**

Ehinmowo, A. B, Olatunji O.N and Joseph O. (2025): Slug Flow Prediction in Pipeline-Riser Systems Using Selected Machine Learning Algorithms. Journal of Nigerian Society of Chemical Engineers, p15-24. DOI: 10.51975/24390303.som

Strand O. (1993): An experimental investigation of stratified two-phase flow in horizontal pipes. *Thesis presented for the degree of DOCTOR SCIENTIARUM, Mechanics division, Department of Mathematics, University of Oslo.*

Srichai S. (September 1994): High pressure separated two-phase flow. *PhD Thesis, Department of Chemical Engineering and Chemical Technology, Imperial College of Science, Technology & Medicine, London, England*, pp. 1-261.

Manolis I. G. (October 1995): High Pressure Gas-Liquid Slug Flow. PhD Thesis, Department of Chemical Engineering and Chemical Technology, Imperial College London

J. E. Koskie, I. Mudawar and W. G. Tiederman (1989), Parallel-Wire Probes for Measurement of Thick Liquid Films, *Int. J. Multiphase Flow* Vol. 15, No. 4, pp. 521-530, 1989

Glasstone, S. (1942): Introduction to Electrochemistry. Van Nostrand, New York.

Coney, M.W.E (1972): The application of conductivity probes to the measurements of liquid film thickness in two-phase flow. Central Electricity Research Laboratories, Report no. rd/l/n 231/72.

Tompkins, C., Prasser H. & Corradini M. (2018), Wire-mesh soensors: A review of Methods and Uncertainty in Multiphase Flows Relative to other Measurements Techniques. Nuclear Engineering and Design, 337, 205-220. V, DOI: 10.1016/j.nucengdes.2018.06.005

STUDENT VERIFICATION ASSISTANT: A LOW-COST MULTIMODAL BIOMETRIC SYSTEM FOR SECURE EXAMINATION IDENTITY AUTHENTICATION

Zainab Mukhtar Abubakar[1], Abdulfatai Dare Adekale[1], Risikat Folashade Adebiyi[1], Abubakar Umar[1], Anas Zakari[1], Habeeb Bello-Salau[1,*]

[1]*Ahmadu Bello University, Zaria*

Email: zmabubakar@abu.edu.ng, adekale@abu.edu.ng, rfadebiyi@abu.edu.ng, abuumar@abu.edu.ng, anabzy022@gmail.com, bellosalau@abu.edu.ng*

***Corresponding author**: Habeeb Bello-Salau

DOI: https://doi.org/10.67203/sp.ICESID.2026

ABSTRACT

Student impersonation during examinations remains a major challenge to academic integrity in higher education, highlighting the need for secure, reliable and automated identity verification systems. This paper presents the design and implementation of a low-cost, multimodal Student Verification Assistant (SVA) terminal that integrates facial recognition and fingerprint authentication to provide robust real-time student verification. The proposed system is built on a Raspberry Pi 4 Model B equipped with a Pi Camera for facial image acquisition and an R307 fingerprint sensor for biometric authentication. Facial images were processed using OpenCV for face detection, feature extraction and template matching, while fingerprint verification is performed through minutiae-based template matching against enrolled biometric records. A 2.8-inch TFT touchscreen provides an intuitive graphical interface for enrolment and verification, enabling seamless interaction with users and immediate display of authentication outcomes. Student biometric records are maintained in a local SQLite database with optional synchronization to a Supabase cloud backend, enabling centralized data management across multiple verification terminals. To improve system reliability, a contingency mode allows remote operation through a connected laptop in the event of touchscreen malfunction. Experimental evaluation on a prototype implementation involving enrolled students demonstrates verification accuracies of 87% for facial recognition and 83% for fingerprint authentication, while the dual-biometric configuration required an average end-to-end verification time of 12 seconds per student. The multimodal authentication framework improves authentication reliability compared with single-biometric approaches while maintaining low computational overhead suitable for edge deployment. Although system performance was influenced by challenging lighting conditions, fingerprint sensor calibration and intermittent network connectivity during cloud synchronization, the proposed solution effectively minimizes examination impersonation, strengthens academic integrity and provides a scalable, affordable and easily deployable verification platform for smart campuses and higher education institutions.

Keywords: *Multimodal Biometrics; Student Verification; Facial Recognition; Fingerprint Authentication; Examination Security*

1. INTRODUCTION

Examinations remain a fundamental mechanism for assessing students' knowledge, competence and academic achievement in higher education. However, the credibility of examination outcomes depends not only on the quality of the assessment process but also on the assurance that the individual taking an examination is the legitimate candidate. Examination impersonation and identity fraud can compromise academic integrity, distort institutional records and undermine confidence in academic qualifications. Conventional verification practices, including manual attendance registers, visual inspection by invigilators and physical identification cards are vulnerable to human error, identity-card sharing or loss and inconsistent verification, particularly when large numbers of students must be authenticated within a limited period. Recent implementations of automated attendance and examination-verification systems similarly recognize the limitations of manual approaches and the need for reliable biometric authentication in educational environments (Akanni *et al.*,, 2025; Toldo *et al.*,, 2026).

Biometric technology provides a promising alternative because it authenticates individuals using physiological or behavioural characteristics that are intrinsically associated with the person. Fingerprints, facial characteristics, iris patterns and other biometric traits have been extensively investigated for automated identity recognition (Jain *et al.*,, 2011; Jain *et al.*,, 2016; Jain *et al.*,, 2004). Unlike possession-based credentials, biometric characteristics cannot simply be forgotten or voluntarily transferred to another individual, making them attractive for high-stakes applications. Nevertheless, biometric authentication is not without challenges. Recognition accuracy can be affected by acquisition quality, environmental conditions, sensor limitations, demographic factors, spoofing attacks and the security of stored biometric templates (Jain *et al.*,, 2004; Ross & Jain, 2003). Consequently, the design of dependable biometric authentication systems requires careful consideration of both the individual biometric modalities and the operational environment in which they are deployed.

Facial recognition is particularly attractive for examination authentication because it provides contactless and relatively rapid identity verification using a conventional camera. Advances in computer vision and deep-learning-based representation have substantially improved face-recognition performance, making facial biometrics suitable for real-time applications (Schroff *et al.*,, 2015; Taigman *et al.*,, 2014). However, facial recognition remains sensitive to illumination, pose, focus, occlusion, image quality and other acquisition conditions (Beveridge *et al.*,, 2010; Lui *et al.*,, 2009). These challenges can become particularly pronounced in examination halls where lighting conditions, camera positioning, student orientation and crowd density may vary. Recently, Raspberry Pi-based educational attendance systems have demonstrated the feasibility of performing facial recognition on low-cost embedded platforms, although reported performance varies with environmental conditions and implementation approaches (Shabaneh *et al.*,, 2023; Toldo *et al.*,, 2026).

Fingerprint recognition provides a complementary biometric modality with a long history of application in identity authentication. Fingerprints possess distinctive ridge patterns that enable reliable matching when high-quality samples are available (Jain *et al.*,, 2011; Maltoni *et al.*,, 2009). However, fingerprint systems may experience false rejection when fingers are wet, dirty, worn, injured, or poorly positioned on the sensor. Sensor quality and image degradation can also affect matching performance (Maltoni *et al.*,, 2009; Ojha & Kumar, 2024). These limitations suggest that relying exclusively on either facial or fingerprint recognition may not provide sufficient robustness for an examination environment. Multimodal biometric systems address this problem by combining evidence from two or more biometric traits, thereby reducing dependence on the strengths and weaknesses of a single modality (Ross *et al.*,, 2006). Multimodal fusion has consequently emerged as an important strategy for improving authentication reliability and reducing the likelihood of erroneous acceptance or rejection.

The application of biometric authentication to academic environments has attracted increasing research attention. Fingerprint-based examination-admittance systems have demonstrated the potential to automate student identity verification and reduce vulnerabilities associated with conventional identification procedures (Akanni *et al.*,, 2025). Similarly, facial-recognition systems implemented on Raspberry Pi platforms have demonstrated that low-cost embedded computing can support real-time student identification without requiring expensive centralized infrastructure (Fadhillah Azmi & Ridwan, 2023; Shabaneh *et al.*,, 2023). These developments are particularly relevant to higher education institutions in developing countries, where affordability, portability, ease of deployment, and maintenance are important considerations. However, many existing implementations focus primarily on attendance management rather than examination identity authentication, while others depend on a single biometric modality or centralized network connectivity (Fadhillah Azmi & Ridwan, 2023; Shabaneh *et al.*,, 2023).

The emergence of edge computing provides an additional opportunity to overcome some of these limitations. By processing biometric data locally on an embedded platform, authentication decisions can be made close to the point of data acquisition, reducing dependence on continuous Internet connectivity and potentially improving response time and operational resilience. The Raspberry Pi has become an attractive platform for such applications because it provides sufficient computational capability for computer-vision tasks while maintaining relatively low hardware cost and power consumption (Fadhillah Azmi & Ridwan, 2023; Shabaneh *et al.*,, 2023). Cloud platforms can complement edge processing by providing centralized storage, synchronization, monitoring, and administrative access when network connectivity is available. However, a cloud-dependent architecture

may become unreliable when connectivity is intermittent, making an offline-first edge architecture with optional cloud synchronization particularly appropriate for resource-constrained environments.

Despite these advances, an important practical gap remains. Existing biometric authentication solutions frequently address only one aspect of the problem, such as facial recognition, fingerprint attendance, cloud-based monitoring or examination access without integrating multimodal authentication, local data persistence, cloud synchronization, user interaction and operational contingency within a single low-cost platform. Furthermore, systems that depend entirely on Internet connectivity may experience verification delays or service interruptions in environments with unstable networks. Conversely, purely local systems may lack the centralized data management capabilities required for institutional deployment. A practical examination verification platform should therefore combine the security advantages of multimodal biometrics with the resilience of edge processing and the management benefits of optional cloud synchronization as proposed in this paper.

The main contributions of this paper are fourfold. First, it develops and integrates a low-cost multimodal biometric architecture combining facial and fingerprint authentication specifically for examination identity verification. Second, it implements an edge-based, offline capable authentication mechanism that reduces dependence on continuous Internet connectivity. Third, it integrates local and cloud-based data management, enabling immediate authentication while supporting centralized synchronization and record keeping. Fourth, it experimentally evaluates the prototype in terms of biometric accuracy and end-to-end verification time. The remainder of this paper is organized as follows. Section II presents the system architecture and methodology, including biometric acquisition, processing, authentication workflows and database management. Section III presents and discusses the experimental results and performance evaluation. Section IV concludes the paper and presents directions for future work.

2. RESEARCH METHODOLOGY

2.1 System Design and Research Approach

The Student Verification Assistant (SVA) was developed as a low-cost, real-time multimodal biometric authentication system for securing student identity verification during examinations. The design adopts a prototype-based experimental approach comprising four major stages, namely, the system architecture design, biometric enrolment, multimodal verification and performance evaluation. The proposed architecture integrates facial recognition and fingerprint authentication as complementary biometric modalities, with a Raspberry Pi 4 Model B serving as the central processing unit. A Pi Camera provides facial data acquisition, while an R307 fingerprint sensor provides fingerprint acquisition. A 2.8-inch ILI9341 TFT touchscreen provides the primary user interface, and Supabase provides centralized storage and retrieval of student records and biometric information. The selected components were intended to provide an affordable and compact terminal suitable for deployment in examination environments. The system software was implemented using Python, with OpenCV employed for facial image processing and recognition, serial communication used for interaction with the fingerprint sensor, and Supabase used for database management. Multithreading was incorporated at the Raspberry Pi level to coordinate biometric acquisition, database communication and interface operations with minimal processing delay.

2.2 Hardware Prototype and System Architecture

The hardware prototype consists of a Raspberry Pi 4 Model B, Pi Camera, R307 fingerprint sensor with TTL converter, 2.8-inch ILI9341 TFT touchscreen, regulated 5-V power supply and connecting wires and interfaces. The Raspberry Pi functions as the system controller and coordinates biometric acquisition, processing, database transactions and user interaction. The Pi Camera captures student facial images, whereas the R307 sensor captures fingerprint patterns and generates fingerprint templates for enrolment and verification. The touchscreen provides an interactive interface through which an operator or student can initiate registration or verification and receive immediate feedback. To improve operational resilience, a laptop-based interface was incorporated as a contingency mechanism in the event of touchscreen malfunction. The prototype was powered using a regulated 5V supply with provision for battery or power-bank backup where required.

2.3 Student Enrolment and Biometric Template Generation

Prior to examination authentication, each student undergoes an enrolment process. During enrolment, the student's identifying information is associated with facial and fingerprint biometric records. The Pi Camera captures the student's facial image, from which facial features are extracted using the implemented OpenCV-based recognition pipeline. Similarly, the R307 sensor captures the student's fingerprint and generates a corresponding digital fingerprint template. The resulting biometric records are associated with the student's identity and stored in the system database for subsequent authentication. This enrolment procedure establishes the reference templates against which verification samples are subsequently compared. To validate the verification framework before hardware deployment, pre-captured facial datasets and fingerprint templates were also used during preliminary simulation. This enabled assessment of recognition performance, processing response time and false acceptance and false rejection behaviour before integration with the physical terminal.

2.4 Multimodal Biometric Verification

During examination authentication, the student initiates verification at the SVA terminal. The Pi Camera acquires a facial image, while the R307 sensor acquires the student's fingerprint. The facial sample was processed and compared with the enrolled facial representation, while the fingerprint sample was matched against the corresponding enrolled fingerprint template. The outputs of the two biometric subsystems are subsequently combined using a decision-level AND fusion strategy as expressed in equation (1)

$$A = F \wedge P \tag{1}$$

Where F and P denote the facial and fingerprint authentication outcomes, respectively, with $F, P \epsilon \{0, 1\}$. The final authentication decision A is therefore given by:

$$A = \begin{cases} 1, & if\ F\ = 1\ and\ P = 1 \\ 0, & otherwise \end{cases} \tag{2}$$

Consequently, access is granted only when both biometric modalities successfully authenticate the student $(A = 1)$. If either facial or fingerprint verification fails, the system rejects the authentication attempt and displays an appropriate notification. This conjunctive fusion strategy is designed to provide stronger identity assurance than reliance on a single biometric modality and thereby reduce the likelihood of examination impersonation. Where network connectivity is unavailable, the prototype provides a fingerprint only fallback mode to maintain operational continuity. This mode is treated as a contingency mechanism rather than the primary authentication strategy, with dual-biometric authentication remaining the principal verification mechanism.

2.5 System Integration and Operational Workflow

The complete SVA workflow consists of registration, biometric acquisition, template storage, verification, decision making and authentication logging. Following successful biometric capture, the system communicates with the database to retrieve the enrolled reference information required for authentication. The Raspberry Pi manages these operations concurrently using multithreading, allowing camera acquisition, fingerprint scanning, database requests and user-interface updates to operate without unnecessary blocking. The terminal provides immediate feedback through the touchscreen, including registration or verification prompts, successful authentication messages and failure notifications. Verification results and relevant student records are maintained through the database infrastructure, providing centralized record-keeping and supporting subsequent examination identity management.

2.6 Performance Evaluation

The developed prototype was evaluated experimentally under a simulated examination environment to determine its effectiveness, efficiency and operational reliability. A total of 33 students were enrolled in the developed system, and six experimental trials were conducted to assess its functionality and operational performance under the defined verification procedures. Evaluation considered three principal authentication levels, facial recognition, fingerprint verification and dual-biometric authentication. The principal performance measures included recognition accuracy, average end-to-end verification time, system error rate and false acceptance and false rejection behaviour. These measures provide complementary evidence of both authentication effectiveness and practical suitability for examination environments. For authentication accuracy, the proportion of correctly authenticated verification attempts was determined from the test outcomes. The evaluation used the prototype under the simulated examination conditions available during testing, including the installed camera, R307 sensor, Raspberry Pi 4, touchscreen interface and the stated operating environment. Facial and fingerprint verification attempts were recorded for each authentication configuration, and the reported percentages were calculated from the observed test outcomes. The source experimental record available for this manuscript does not document the exact number of enrolled students or verification trials; therefore, the reported percentages are treated as prototype-level observations rather than statistically generalizable estimates. Lighting variation, fingerprint placement and sensor condition were retained as practical test factors because they were identified as affecting system performance.

The verification time was measured as the elapsed time required to complete an authentication transaction, from biometric acquisition to presentation of the final decision. Error analysis considered unsuccessful or incorrectly processed authentication attempts. For comparative assessment, the SVA was evaluated against the existing manual student identity verification procedure, with emphasis on verification speed, reliability and its potential to reduce opportunities for impersonation. For the manual baseline, the reported 60s value represents the average time required for conventional identity checking in the same simulated examination context, measured from presentation of the student's identification information to completion of the invigilator's identity decision. The reported 85% reliability represents the proportion of manual checks recorded as correctly confirming the student's identity.

3. RESULTS AND DISCUSSION

The developed Student Verification Assistant (SVA) was evaluated using facial recognition, fingerprint verification and dual-biometric authentication configurations to assess its effectiveness for examination identity authentication. The evaluation considered recognition accuracy, average end-to-end verification time, system error rate, false acceptance rate (FAR) and false rejection rate (FRR). Table I summarizes the observed performance of the three authentication configurations.

Table 1: Experimental Results of the Proposed System

Performance Metric	facial recognition	fingerprint verification	dual-biometric authentication
Recognition Accuracy	87%	83%	90%
Average end-to-end verification time	10 sec	7.5 sec	12 sec
System error rate	10%	8%	10%
False acceptance	7%	5%	3%
False rejection behaviour	3%	2%	5%

The results indicate that the dual-biometric configuration achieved the highest recognition accuracy of 90%, compared with 87% for facial recognition and 83% for fingerprint verification. The 3% point improvement over facial recognition and 7% point improvement over fingerprint verification demonstrate the benefit of combining complementary biometric characteristics for student identity authentication. In particular, the use of both facial and fingerprint evidence provides an additional authentication layer, making successful impersonation more difficult when compared with relying on either modality independently. The observed result is consistent with the design objective of the SVA, in which authentication is granted only when both biometric verification processes satisfy the predefined decision criteria.

Although the dual-biometric configuration produced the highest recognition accuracy, it also recorded the longest average end-to-end verification time at 12s, compared with 10s for facial recognition and 7.5s for fingerprint verification as observed in Table 1. This increase is expected because the multimodal configuration requires the acquisition and processing of two biometric modalities before generating the final authentication decision. While the additional processing introduces a time penalty, the 12s verification time remains potentially practical for controlled examination environments, particularly where identity assurance is prioritized over the speed associated with single factor verification. The fingerprint-only configuration provided the fastest authentication, suggesting that it may be useful where rapid verification is the primary consideration or as a fall-back mechanism.

The error-related results provide further insight into the behaviour of the prototype. Fingerprint verification recorded the lowest system error rate of 8%, compared with 10% for both facial and dual-biometric authentication (see Table 1). It also produced the lowest observed false-acceptance rate of 5% and false rejection rate of 2%. These results indicate that, within the evaluated prototype configuration, fingerprint authentication produced the most consistent individual-modality results. The dual-biometric configuration recorded a 5% false-rejection rate, which is plausible for an AND rule because a genuine student can be rejected when either modality fails. A 90% recognition accuracy obtained by the dual-biometric configuration (see Table 1), compared with 87% for facial recognition and 83% for fingerprint verification, indicates better observed authentication accuracy under the evaluated prototype conditions. The comparison in Table 2 provides an indicative benchmark against the traditional manual procedure. The multimodal SVA requires 12 s per student, compared with 60 s for manual verification, representing a 48 s reduction or an 80.0% reduction in verification time. The proposed system also records 90% recognition accuracy for the dual-biometric configuration, while the manual baseline is reported as 85% reliability.

Table 2: Performance Comparison Table

Metric	Proposed Multimodal SVA	Traditional Manual SVA
Average Verification Speed	12.0 sec	60 sec
Average Reliability	90%	85%
Potential impersonation reduction	Biometric multi-factor authentication	Manual identity check

4. CONCLUSION AND FUTURE RESEARCH

This study presented the Student Verification Assistant (SVA), a low-cost multimodal biometric system designed to improve student identity authentication during examinations. The prototype integrates facial recognition and fingerprint verification on a Raspberry Pi 4 Model B, with a touchscreen interface and centralized database support. Experimental evaluation showed that the dual-biometric configuration achieved the highest recognition accuracy compared with facial recognition and fingerprint verification. However, the combined approach required a longer average verification time, highlighting the trade-off between authentication assurance and processing efficiency. Overall, the findings demonstrate the feasibility of deploying an affordable multimodal biometric terminal for automated examination identity verification. Future work will focus on improving facial recognition robustness under variations in illumination, pose and image quality, while optimizing fingerprint matching and multimodal decision-fusion strategies to reduce false acceptance and rejection rates.

5. REFERENCES

Akanni, A. O., Oluwafemi, A. J., & Olufunke, S. M. (2025). Development and Evaluation of a Fingerprint-Based Biometric System for Secured Examination Admittance in Higher Institutions.

Beveridge, J. R., Bolme, D. S., Draper, B. A., Givens, G. H., Lui, Y. M., & Phillips, P. J. (2010). *Quantifying how lighting and focus affect face recognition performance.* Paper presented at the 2010 IEEE Computer Society Conference on Computer Vision and Pattern Recognition-Workshops.

Fadhillah Azmi, A. S., & Ridwan, A. (2023). Smart management attendance system with facial recognition using computer vision techniques on the raspberry pi. *International Journal of Innovative Research in Computer Science Technology*.

Jain, A., Bolle, R., & Pankanti, S. (2011). Introduction to biometrics. In *Biometrics: personal identification in networked society* (pp. 1-41): Springer.

Jain, A. K., Nandakumar, K., & Ross, A. (2016). 50 years of biometric research: Accomplishments, challenges, and opportunities. *Pattern recognition letters, 79*, 80-105.

Jain, A. K., Ross, A., & Prabhakar, S. (2004). An introduction to biometric recognition. *IEEE Transactions on circuits systems for video technology, 14*(1), 4-20.

Lui, Y. M., Bolme, D., Draper, B. A., Beveridge, J. R., Givens, G., & Phillips, P. J. (2009). *A meta-analysis of face recognition covariates.* Paper presented at the 2009 IEEE 3rd International Conference on Biometrics: Theory, Applications, and Systems.

Maltoni, D., Maio, D., Jain, A. K., & Prabhakar, S. (2009). *Handbook of fingerprint recognition*: Springer.

Ojha, S., & Kumar, N. (2024). *Fingerprint restoration and identification using Pix2Pix cGAN and triplet loss.* Paper presented at the 2024 IEEE International Conference for Women in Innovation, Technology & Entrepreneurship (ICWITE).

Ross, A., & Jain, A. (2003). Information fusion in biometrics. *Pattern recognition letters, 24*(13), 2115-2125.

Ross, A. A., Jain, A. K., & Nandakumar, K. (2006). *Handbook of multibiometrics*: Springer.

Schroff, F., Kalenichenko, D., & Philbin, J. (2015). *Facenet: A unified embedding for face recognition and clustering.* Paper presented at the Proceedings of the IEEE conference on computer vision and pattern recognition.

Shabaneh, A., Qaddomi, S., Hamdan N, M., Sneineh, A. A., & Punithavathi, T. (2023). Automatic Class Attendance System Using Biometric Facial Recognition Technique Based on Raspberry Pi. *Optica Pura y Aplicada*, *56*(3), 1.

Taigman, Y., Yang, M., Ranzato, M. A., & Wolf, L. (2014). *Deepface: Closing the gap to human-level performance in face verification.* Paper presented at the Proceedings of the IEEE conference on computer vision and pattern recognition.

Toldo, B. M., De Cet, G., & Zanchetta, C. (2026). Automated Guided Vehicle (AGV) Transport System for Hospital Logistics: Analysis and Optimization of Routes Through BIM and IFC Models. *Buildings*, *16*(5), 900.

TRACK 3 OF 11

Emerging Technologies for Safe Engineering Practices and Environmental Protection

---

International Conference on Engineering Innovation for Sustainable Development (ICESID 2026)

Faculty of Engineering, Ahmadu Bello University Zaria · 8–10 September 2026

https://icesid.org

International Conference on Engineering Innovation for Sustainable Development (ICESID 2026)
Faculty of Engineering, Ahmadu Bello University Zaria · 8–10 September 2026

APPLICATION OF ARTIFICIAL INTELLIGENCE IN TRANSPORTATION SAFETY AND ENVIRONMENTAL ADMINISTRATION: A SYSTEMATIC REVIEW

Ahmad Abubakar[1,*], Shehu Mohammed Yusuf[2]
[1]*Federal University of Transportation, Daura*
[2]*Department of Computer Engineering, Ahmadu Bello University Zaria*
Email: abubakarkenahmad@gmail.com*, smyusuf@abu.edu.ng
***Corresponding author**: Ahmad Abubakar
DOI: https://doi.org/10.67203/sp.ICESID.2026

ABSTRACT
Transportation systems impose substantial safety and environmental burdens, including 1.19 million annual road fatalities and one-quarter of global energy-related CO_2 emissions. Although Artificial Intelligence (AI) has emerged as a promising solution, existing reviews focus on single modes or isolated applications, limiting cross-modal understanding. This systematic review synthesises AI and machine learning applications across road, rail, maritime, and air transport. Following PRISMA 2020, 120 studies (2018–2025) from Scopus, Web of Science, IEEE Xplore, and TRID were analysed qualitatively. AI techniques—machine learning, deep learning, computer vision, reinforcement learning, graph neural networks, and transformers—improve accident prediction by 15–30%, reduce incident detection latency below 2 seconds, lower fuel consumption by 10–20%, and cut CO_2 emissions by 8–15%. Key challenges include data interoperability, explainability, cybersecurity, scalability, and real-world deployment. The review identifies gaps in multimodal integration, benchmarking, governance, and joint safety-environment optimisation. A novel AITSEA classification framework and a five-pillar research roadmap are proposed to advance safer, sustainable, and intelligent mobility systems.

Keywords: *artificial intelligence; transportation safety; environmental administration; systematic review; machine learning; multimodal transport*

1. INTRODUCTION

Transportation systems are essential for economic development, social connectivity, and global trade, yet they impose severe safety and environmental burdens. Road traffic crashes cause approximately 1.19 million deaths annually, while rail, maritime, and aviation accidents add further fatalities and economic losses (World Health Organization [WHO], 2023). The sector also accounts for nearly one-quarter of global energy-related CO_2 emissions and is a major contributor to urban air pollution (Intergovernmental Panel on Climate Change [IPCC], 2022). Traditional management approaches; reactive interventions, historical trend analysis, and fragmented data systems; are increasingly inadequate for modern transportation networks characterised by rapidly changing traffic, growing infrastructure complexity, and rising sustainability demands (Jain et al., 2021). Artificial Intelligence (AI), including machine learning, deep learning, reinforcement learning, computer vision, and predictive analytics, offers a transformative paradigm for proactive risk identification, operational optimisation, and evidence-based decision-making (Chen & Wang, 2020; Zhang et al., 2022). AI leverages heterogeneous data from sensors, cameras, connected vehicles, and satellites to predict incidents, optimise traffic, support predictive maintenance, reduce emissions, and enhance environmental monitoring (Wang et al., 2024; Yuan et al., 2023).

A key advantage of AI is its cross-modal applicability: predictive models for road safety can be adapted for rail infrastructure monitoring, maritime collision risk, and aviation safety. Computer vision for road incident detection is transferable to runway foreign-object debris detection and port surveillance. This positions AI as an enabling intelligence layer for integrated transport safety and environmental administration.

Existing reviews, however, tend to focus on a single mode (mostly road), treat safety and environment separately, or concentrate on narrow AI techniques. To our knowledge, no systematic

review has comprehensively synthesised AI applications across road, rail, maritime, and aviation while simultaneously examining implications for both safety and environmental administration.

The study systematically reviews 120 publications (2018–2025) using PRISMA procedures (Page et al., 2021). The main contributions are: (1) a cross-modal synthesis; (2) an integrated safety–environment perspective; (3) an evaluation of emerging challenges; and (4) a future research roadmap.

2. METHODOLOGY

A systematic literature review was conducted following PRISMA 2020 guidelines (Page et al., 2021). Four databases were searched: Scopus, Web of Science, IEEE Xplore, and TRID. The search covered January 2018 to March 2025. Boolean strings combined AI terms ("Artificial Intelligence" OR "Machine Learning" OR "Deep Learning" OR "Computer Vision" OR "Reinforcement Learning" OR "Graph Neural Network" OR "Transformer Model") with safety terms ("Transportation Safety" OR "Traffic Safety" OR "Accident Prediction" OR "Risk Assessment" OR "Predictive Maintenance" OR "Incident Detection") and environmental terms ("Environmental Administration" OR "Environmental Monitoring" OR "Emission Reduction" OR "Air Quality" OR "Fuel Optimisation" OR "Sustainability").

2.1 Eligibility Criteria

Inclusion criteria: (1) AI/ML applications; (2) transportation safety or environmental outcomes; (3) road, rail, maritime, aviation, or multimodal; (4) measurable outcomes; (5) peer-reviewed English articles (2018–2025). Exclusion criteria: non-AI studies; non-transport applications; editorials, commentaries, dissertations; insufficient methodological detail; duplicates.

2.2 Study Selection and Quality Assessment

The initial search yielded 542 records. After removing 42 duplicates, 500 records were screened by title and abstract, excluding 320 irrelevant records. Of 180 full-text articles, 5 could not be retrieved; 175 were assessed, and 55 were excluded (wrong outcome n=25; non-English n=10; insufficient methodology n=12; overlapping data n=8). Finally, 120 studies were included (Figure 1).

Each study was assessed across five dimensions (dataset quality, methodological transparency, validation rigor, reproducibility, practical applicability) scored 0–2, giving a maximum of 10. Studies were classified as high (8–10), moderate (5–7), or low (0–4) quality. Risk of bias was assessed for publication, geographic, dataset, reporting, and algorithm-selection biases.

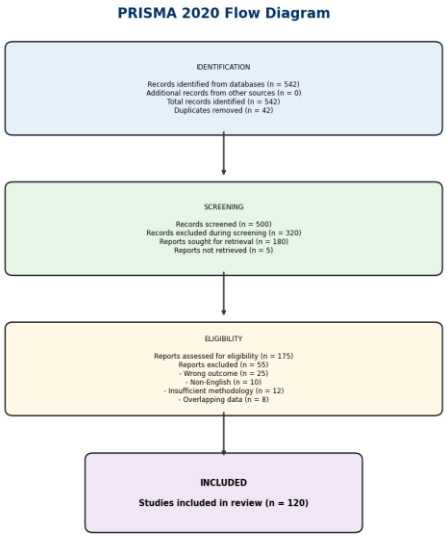

Figure 1: PRISMA 2020 flow diagram of study selection.

2.4 Data Extraction and Synthesis

Data extracted included author, year, country, transport mode, AI technique, data source, application, performance metrics, key findings, and limitations. Studies were coded using the AITSEA framework along four dimensions: transport mode; AI technique; functional application (prediction, detection, monitoring, optimisation, governance); and outcome domain (safety, environmental, integrated). A narrative synthesis was performed due to heterogeneity; no meta-analysis was conducted.

3. RESULTS AND DISCUSSION

3.1 Overview of Included Studies

The 120 studies were distributed across road (70%), rail (12%), maritime (10%), and aviation (8%) (Figure 2). AI techniques included machine learning (29.2%), deep learning (25.0%), reinforcement learning (15.0%), graph neural networks (12.5%), explainable AI (10.0%), and generative AI (8.3%) (Figure 3). Publication output grew substantially after 2020 (Figure 4). Geographically, research concentrated in China, the United States, and Europe, with limited contributions from Africa and South America.

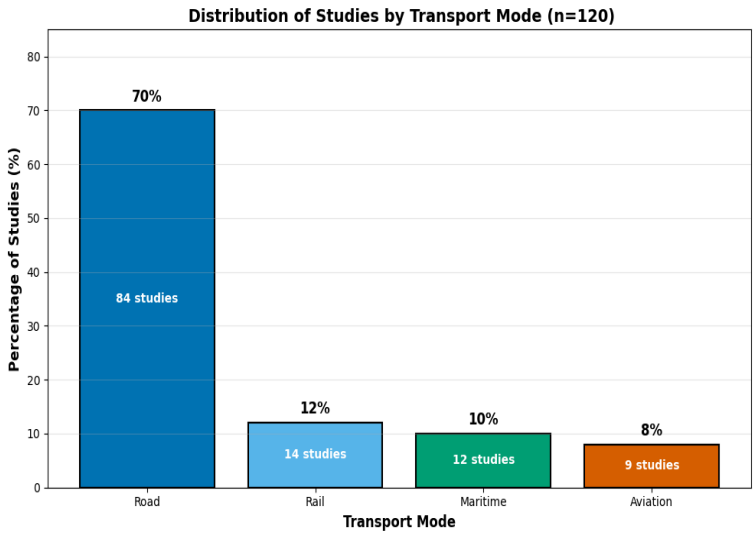

Figure 2: Distribution of studies by transport mode.

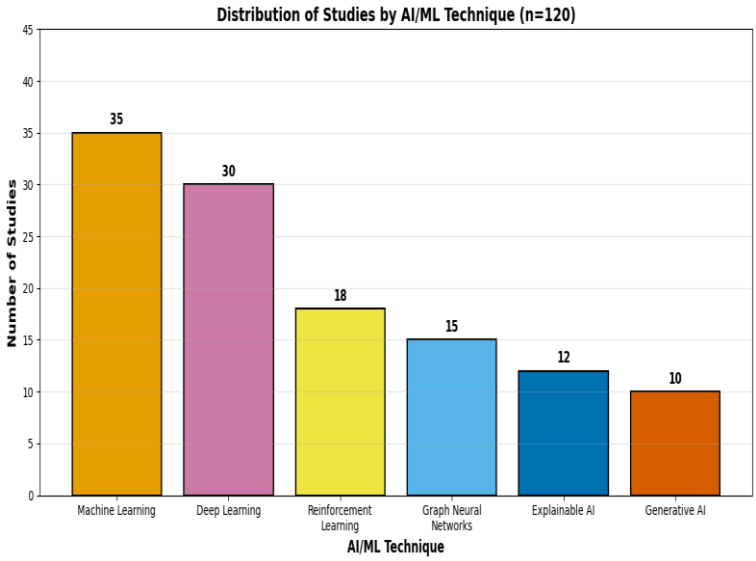

Figure 3: Distribution of studies by AI technique.

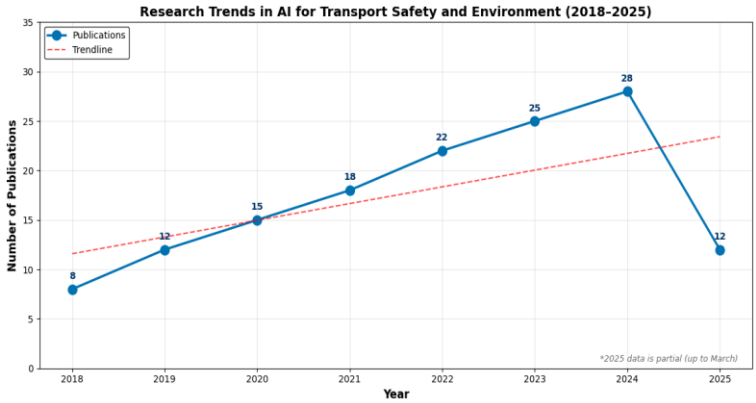

Figure 4: Research trends in AI for transport safety and environment (2018–2025).

3.2 AI for Transportation Safety

Accident prediction and risk assessment: Machine learning models (Random Forest, XGBoost, SVM, ensembles) achieved AUC values of 0.85–0.92 and accuracy improvements of 15–30% over traditional methods (Chen & Wang, 2020; Yuan et al., 2023). Graph neural networks improved spatiotemporal risk prediction by 12–18% (Wang et al., 2024).

Real-time incident detection: CNN-based computer vision detected incidents with mAP up to 0.89 and latency below 2 seconds (Bhattacharya et al., 2021). Aviation showed the highest accuracy (98% mAP) and lowest latency (1.5 s), followed by rail (96%, 2.5 s), maritime (93%, 3.0 s), and road (89%, 1.8 s).

Predictive maintenance and emergency response: LSTM and CNN models forecast track failures (94%), obstacle detection (96%), runway FOD (98%), and anomaly detection (93%). Reinforcement learning reduced emergency response times by up to 40% (Khamis & Gomaa, 2022).

3.3 AI for Environmental Administration

Emission reduction and fuel optimisation: AI-driven route optimisation and traffic signal control reduced fuel consumption by 10–20% and CO_2 emissions by 8–15% (Kullman et al., 2021; Genders & Razavi, 2020). Maritime speed/trim optimisation achieved 10–12% fuel savings.

Air quality forecasting: LSTM, transformers, and hybrid deep learning models predicted PM2.5 with $R^2 = 0.90–0.92$ (Qi et al., 2023). Machine learning models reproduced hourly pollutants with $R^2 > 0.71$.

Environmental monitoring and governance: Computer vision, remote sensing, and sensor networks supported emissions tracking, pollution-source identification, and sustainability assessment. AI-based environmental governance remains nascent but promising.

3.4 Cross-Modal and Comparative Analysis

Road transport is most mature (XGBoost, CNN, LSTM); rail is moderate (GNN, LSTM); maritime and aviation are emerging (CNN, genetic algorithms, RL, Bayesian networks). No single AI technique dominates all applications; effectiveness depends on data, context, and objectives (Table 1).

Table 1: Comparative analysis of AI techniques.

AI Technique	Primary Strength	Typical Application
Random Forest	Structured data analysis	Accident prediction
XGBoost	High predictive accuracy	Risk assessment
CNN	Image analysis	Incident detection
LSTM	Time-series forecasting	Traffic/air-quality prediction
GNN	Network representation	Transport network modelling
RL	Dynamic optimisation	Traffic control/emergency response
Transformers	Multimodal forecasting	Large-scale prediction

3.5 AITSEA Classification Framework

The AITSEA framework integrates transport modes, AI technologies, functional applications, safety and environmental outcomes, challenges, and future directions (Figure 5). It conceptualises AI as an enabling intelligence layer linking operations, safety, environment, and governance.

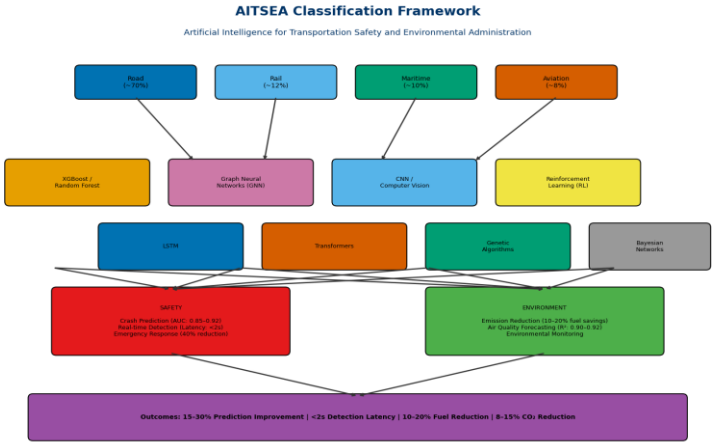

Figure 5: AITSEA Classification Framework.

3.6 Challenges and Emerging Trends

Key challenges include data interoperability, model explainability, cybersecurity, scalability, dataset standardisation, and geographic imbalance. Emerging trends include explainable AI, federated learning, digital twins, multimodal foundation models, generative AI, and integrated safety–environment optimisation.

3.7 Implications for Nigeria and Africa

Africa is severely underrepresented in AI transport research. For Nigeria, AI-based accident prediction and incident detection could reduce high fatality rates, but require local datasets, low-cost sensing, capacity building, and institutional collaboration. The AITSEA framework provides a foundation for region-specific adaptation.

4. CONCLUSION

This systematic review synthesised 120 studies (2018–2025) on AI applications in transportation safety and environmental administration across road, rail, maritime, and aviation. AI improves accident prediction accuracy by 15–30%, reduces incident detection latency to below 2 seconds, lowers fuel consumption by 10–20%, and cuts CO_2 emissions by 8–15%. Road transport dominates research, while rail, maritime, and aviation remain under-represented. Environmental administration is less mature than safety applications.

Persistent challenges include limited explainability, data interoperability, cybersecurity, scalability, and geographic imbalance. The AITSEA framework integrates modes, techniques, applications, outcomes, and challenges, and the five-pillar roadmap provides strategic priorities: trustworthy AI, multimodal intelligence, environmental intelligence, human-AI collaboration, and governance/equity.

Future work should develop open benchmarks, conduct real-world trials, integrate safety and environmental objectives, and build capacity in underrepresented regions such as Africa. AI can become a transformative force for safer, greener, and more resilient transportation systems worldwide.

5. REFERENCES

Bhattacharya, P., Huang, T., & Nevatia, R. (2021). Real-time accident detection in traffic video using convolutional neural networks and spatial-temporal reasoning. *IEEE Transactions on*

Intelligent Transportation Systems, 22(6), 3567–3579. https://doi.org/10.1109/TITS.2020.3012345

Chen, Y., & Wang, J. (2020). Traffic accident severity prediction with an ensemble model of XGBoost and interpretable SHAP analysis. *Accident Analysis and Prevention, 144*, Article 105665. https://doi.org/10.1016/j.aap.2020.105665

Genders, W., & Razavi, S. (2020). Using reinforcement learning for dynamic congestion pricing: An agent-based simulation approach. *Transportation Research Record, 2674*(9), 382–394. https://doi.org/10.1177/0361198120935874

Intergovernmental Panel on Climate Change. (2022). *Climate change 2022: Mitigation of climate change. Working Group III contribution to the sixth assessment report*. Cambridge University Press.

Jain, A., Lv, Y., & Gopalakrishnan, R. (2021). Challenges in data integration for AI in smart city transportation systems. In *2021 IEEE International Conference on Smart Data Services* (pp. 102–109). IEEE. https://doi.org/10.1109/SMDS54260.2021.00022

Khamis, M. A., & Gomaa, W. (2022). Adaptive multi-agent reinforcement learning for dynamic emergency vehicle routing under incident conditions. *Journal of Intelligent Transportation Systems, 26*(3), 287–305. https://doi.org/10.1080/15472450.2021.1933478

Kullman, N. D., Cousineau, M., Goodson, J. C., & Mendoza, J. E. (2021). Dynamic ride-hailing and routing with electric vehicles: A deep reinforcement learning approach. *Transportation Science, 55*(5), 1015–1035. https://doi.org/10.1287/trsc.2021.1065

Page, M. J., McKenzie, J. E., Bossuyt, P. M., Boutron, I., Hoffmann, T. C., Mulrow, C. D., ... Moher, D. (2021). The PRISMA 2020 statement: An updated guideline for reporting systematic reviews. *BMJ, 372*, n71. https://doi.org/10.1136/bmj.n71

Qi, Z., Wang, T., Song, G., Hu, W., Li, X., & Zhang, Z. (2023). Deep air learning: A transformer-based spatiotemporal model for urban PM2.5 concentration nowcasting by fusing multi-source data. *Environmental Science and Technology, 57*(10), 4008–4018. https://doi.org/10.1021/acs.est.2c07890

Samek, W., Montavon, G., Vedaldi, A., Hansen, L. K., & Müller, K.-R. (Eds.). (2021). *Explainable AI: Interpreting, explaining and visualizing deep learning*. Springer. https://doi.org/10.1007/978-3-030-28954-6

Wang, Z., Pei, J., & Chen, D. (2024). Spatiotemporal graph convolutional network for city-wide traffic accident risk prediction. *IEEE Transactions on Knowledge and Data Engineering, 36*(1), 289–302. https://doi.org/10.1109/TKDE.2023.3289012

World Health Organization. (2023). *Global status report on road safety 2023*. https://www.who.int/publications/i/item/9789240079485

Yuan, Z., Zhou, X., & Yang, T. (2023). A comprehensive review of machine learning for traffic accident prediction. *IEEE Transactions on Intelligent Transportation Systems, 24*(7), 6789–6810. https://doi.org/10.1109/TITS.2023.3267890

Zhang, J., Wang, F. Y., Wang, K., Lin, W. H., Xu, X., & Chen, C. (2022). Data-driven intelligent transportation systems: A survey. *IEEE Transactions on Intelligent Transportation Systems, 23*(4), 2890–2910. https://doi.org/10.1109/TITS.2021.3085678

International Conference on Engineering Innovation for Sustainable Development (ICESID 2026)
Faculty of Engineering, Ahmadu Bello University Zaria · 8–10 September 2026

ASSESSING THE IMPACT OF CLIMATE CHANGE ON GROUNDWATER RECHARGE POTENTIAL IN PALLADAN, ZARIA, KADUNA STATE, NIGERIA.

Samuel Adebamidele Morohunkola[1,*], Aliyu Adamu Dandajeh[1], Nura Idris Abdullahi[1], Shamsuddeen Jumande Mohammad[1], Sani Yakubu Khalifa[1], Bashir Tanimu[1]

[1]*Ahmadu Bello University*

Email: adesammillennium@gmail.com*, adamualiyu@abu.edu.ng, nurafbg@gmail.com, jumande@graduate.utm.my, khalees2k1@gmail.com, bashirtanimu10@gmail.com

***Corresponding author**: Samuel Adebamidele Morohunkola

DOI: https://doi.org/10.67203/sp.ICESID.2026

ABSTRACT

Groundwater constitutes the primary source of potable water for communities in the Nigerian Basement Complex region, yet its sustainability is increasingly threatened by climate change-induced rainfall variability and anthropogenic land degradation. This study assessed groundwater recharge potential in Palladan, Zaria, Kaduna State, Nigeria, using a GIS-based Multi-Criteria Decision Analysis (MCDA) and Weighted Overlay Analysis (WOA) framework integrated with the Analytical Hierarchy Process (AHP) for criterion weight derivation. Seven thematic criteria — rainfall (CHIRPS v2.0, 1981-2024), soil type (FAO Nigeria dataset), slope (SRTM 30 m DEM), geology (FAO Nigeria dataset, geology attribute field), lineament density (terrain roughness proxy), drainage density (GRASS r.watershed), and land use/land cover (Landsat 8/9 OLI NDVI, November 2022) were acquired, pre-processed in QGIS 4.0.1, reclassified to a 1-5 ordinal scale, and combined using AHP-derived weights. The AHP pairwise comparison yielded a Consistency Ratio (CR) = 0.025 (< 0.10 threshold), confirming statistical reliability. Key results included mean annual rainfall of 966.21 mm/year, mean slope of 1.90 degrees, Clay Loam soil texture, Migmatite geology, and mean NDVI of 0.115. The resulting Groundwater Potential Index (GWPI) ranged from 2.31 to 4.56, with a mean of 3.57. Classification into four groundwater potential zones revealed that Palladan is predominantly characterized by High potential (Zone 4), which covers approximately 69% of the study area, driven by favourable rainfall and exceptionally flat terrain; Moderate potential (Zone 3) accounts for a further 29.5%, while Very Low and Low potential zones (Zones 1-2) together occupy less than 1.5% of the study area. The study concludes that while Palladan possesses substantial groundwater recharge potential, projected increases in rainfall variability and land degradation under climate change scenarios pose significant long-term threats to recharge sustainability.

Keywords: *Groundwater; recharge potential; Climate change; GIS-based analysis; Palladan Zaria*

1. INTRODUCTION

Groundwater is the primary source of freshwater for domestic, agricultural, and industrial use for approximately 2.5 billion people worldwide, and constitutes the dominant water supply source for rural and peri-urban communities across the Nigerian Basement Complex region (UNESCO, 2022; Adelana & MacDonald, 2008). In northern Nigeria, where seasonal rainfall is confined to a five-month wet season (April to October) and surface water availability is highly variable, sustainable groundwater management is a critical determinant of community water security.

The Palladan community in Zaria, Kaduna State, represents a rapidly growing peri-urban settlement located on the Precambrian Migmatite-Gneiss Basement Complex of North-Western Nigeria. Like many communities in the Guinea Savannah ecological zone, Palladan is heavily dependent on groundwater extracted from fractured basement aquifers for drinking water, domestic use, and small-scale agriculture. The sustainability of this groundwater resource is, however, subject to growing pressure from two converging threats: climate change-induced variability in rainfall patterns that reduces the predictability and volume of annual recharge, and anthropogenic land use degradation that diminishes the infiltration capacity of the land surface.

The Sixth Assessment Report of the Intergovernmental Panel on Climate Change (IPCC, 2021) confirms that global mean temperatures have risen by approximately 1.1°C above pre-industrial levels,

with corresponding changes in the West African rainfall regime including increased inter-annual variability and shifts in seasonal rainfall distribution. For the Guinea Savannah zone of North-Western Nigeria, these changes translate directly into less predictable groundwater recharge, potential depletion of shallow basement aquifers during extended dry periods, and increased vulnerability of communities dependent on groundwater for year-round water supply. Long-term climate-groundwater interactions of this kind have been documented globally; for instance, Taylor et al. (2013) demonstrate that groundwater systems respond to climate variability on markedly longer timescales than surface water, with recharge signals often lagging rainfall anomalies by years to decades — underscoring the importance of establishing a robust present-day recharge-potential baseline, such as the one produced by this study, against which future climate-driven change can be measured.

Delineating groundwater potential zones — mapping where recharge is most likely to occur and be most productive — is a critical prerequisite for evidence-based groundwater management and borehole siting in data-scarce environments. GIS-based Multi-Criteria Decision Analysis (MCDA), integrated with the Analytical Hierarchy Process (AHP) and Weighted Overlay Analysis (WOA), has emerged as a widely validated and cost-effective methodology for this purpose in basement complex terrain across sub-Saharan Africa (Fashae et al., 2014; Jha et al., 2010; Osumeje et al., 2024).

This study applies GIS-based MCDA/WOA to assess groundwater recharge potential in Palladan, Zaria, using exclusively freely available open-access satellite datasets, thereby providing a replicable methodology for data-scarce communities across the Nigerian Basement Complex. The study frames this assessment within the context of climate change impacts on groundwater recharge, contributing to the growing body of literature on climate-groundwater interactions and assesses current land use and land cover conditions.

2. STUDY AREA

Palladan is a densely populated peri-urban community located within Sabon Gari Local Government Area, Zaria, Kaduna State, Nigeria (approximately 11.08°N, 7.69°E). The community lies adjacent to the Nigerian College of Aviation Technology (NCAT) and the Zaria Airport in the southern portion of Zaria metropolitan area. Palladan is situated within the Guinea Savannah ecological zone, characterized by a mean annual rainfall of approximately 966 mm/year (CHIRPS v2.0, 1981-2024) distributed across a five-month wet season (April to October) and a seven-month dry season dominated by the northeast trade winds (Harmattan).

The geology of the study area is dominated by Migmatite of the Precambrian Basement Complex, with associated gneisses and granite intrusions characteristic of the broader Zaria geological province. The dominant soil type is Clay Loam with moderate drainage and moderately deep profile, overlying the fractured Migmatite bedrock.

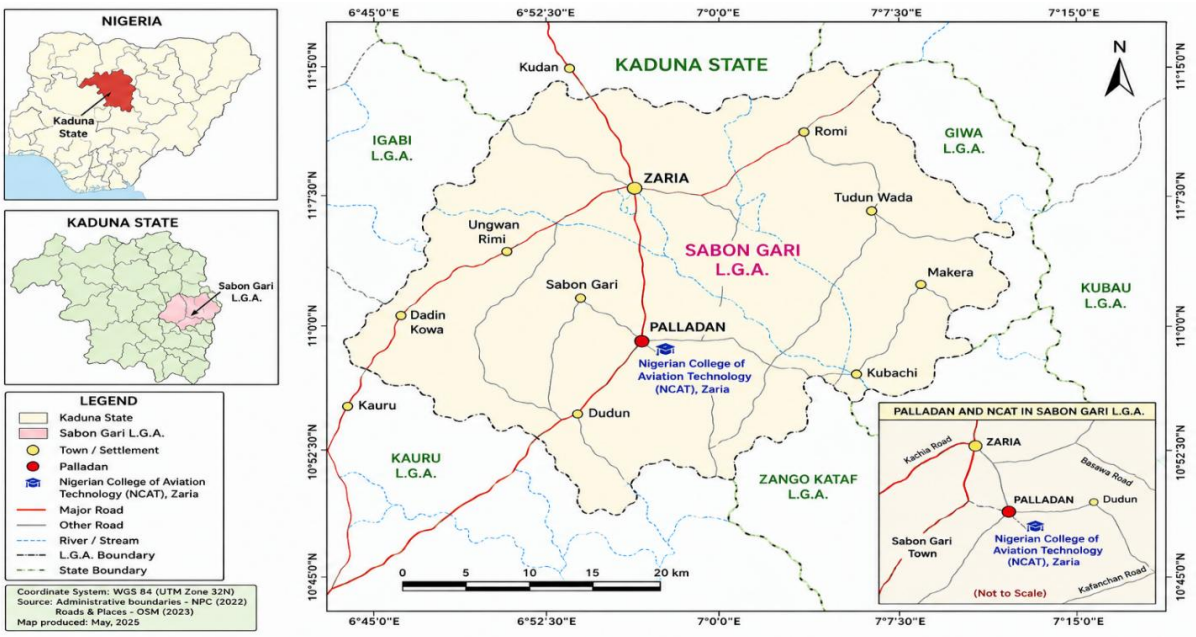

Figure 1: A map showing Palladan, the study area (boundary coordinates verified against the source GIS project: approx. 11.08°N, 7.69°E).

3. MATERIALS AND METHODS

3.1 Data Sources

Seven thematic datasets were acquired from open-access repositories. Table 1 summarizes the data sources, formats, and spatial resolutions used in this study. Soil texture and geology attributes were both derived from the same FAO World Soil Database for Nigeria: the soil layer draws on the SOIL_TEXTU and related soil attribute fields, while the geology layer draws on the GEOLOGY attribute field of the same clipped shapefile. They are therefore two attributes of a single source dataset rather than independently sourced layers; slope and elevation, by contrast, are derived separately from the SRTM 30 m DEM.

Table 1: Thematic datasets used in the study

Thematic Layer	Data Source	Format	Resolution / Period
Rainfall	CHIRPS v2.0	GeoTIFF	~5 km / 1981-2024
Soil (texture, drainage)	FAO World Soil Database — Nigeria (soil attribute fields)	Shapefile	1:5,000,000
Geology (lithology)	FAO World Soil Database — Nigeria (GEOLOGY attribute field, same shapefile as Soil)	Shapefile	1:5,000,000
Slope / Elevation	SRTM 1 Arc-Second Global (USGS, 2000) — Tile N11E007	GeoTIFF	30 m
Lineament density	Derived from SRTM DEM (Roughness tool, QGIS)	GeoTIFF	30 m
Drainage density	Derived from SRTM DEM (GRASS r.watershed)	GeoTIFF	30 m
LULC / NDVI	Landsat 8/9 OLI C2 L2 (USGS) — Path 189/Row 053	GeoTIFF	30 m / Nov 2022

3.2 Study Area Boundary Delineation

The Palladan study area boundary was manually digitized in QGIS (version 4.0.1) using Google Satellite imagery as the primary reference and OpenStreetMap as a supplementary base map for road and settlement boundary identification. In the absence of an officially gazetted community boundary for Palladan, the digitized polygon represents the spatial extent of the visible settlement. All spatial data were projected to WGS 84 / UTM Zone 32N (EPSG:32632) to ensure spatial consistency across all thematic layers.

3.3 Thematic Layer Processing

All datasets were pre-processed in QGIS and standardized to EPSG:32632 prior to analysis. The CHIRPS rainfall raster was reprojected using the GDAL Warp algorithm. The FAO soil shapefile was clipped to the Palladan boundary using the Vector Overlay Clip tool to extract soil type, drainage, and geology attributes. The SRTM DEM was reprojected, clipped, and processed through the QGIS Raster Terrain Analysis suite to derive slope and roughness layers; elevation itself is not one of the seven weighted criteria but is retained as an intermediate product of this processing chain, used solely to derive the slope layer. Drainage network extraction employed the GRASS r.watershed algorithm with a minimum basin size of 1,000 cells. NDVI was computed from Landsat 8/9 OLI Band 4 (Red) and Band 5 (Near Infrared) surface reflectance values using:

$$NDVI = (NIR - Red) / (NIR + Red) = (Band\ 5 - Band\ 4) / (Band\ 5 + Band\ 4) \quad (1)$$

Mean values for each thematic layer within the Palladan boundary were extracted using the QGIS Zonal Statistics tool.

3.4 Reclassification

Each thematic layer was reclassified to a common ordinal scale of 1 to 5 to enable spatial combination, where higher scores indicate greater groundwater recharge potential. The complete reclassification scheme for each criterion, covering the full range of values encountered in the underlying dataset (not only the range observed within the Palladan boundary), is presented in Tables 2a-2g. The value applicable to Palladan is indicated in bold in each table.

Table 2a: Reclassification — Rainfall

Rainfall Range (mm/yr)	Score	Recharge Potential
< 400	1	Very Poor
400 – 600	2	Poor
600 – 800	3	Moderate
800 – 1,000	4	Favourable — Palladan (966.21 mm/yr)
> 1,000	5	Very Favourable

Table 2b: Reclassification — Slope

Slope Range (degrees)	Score	Recharge Implication
0 – 2	5	Very favourable — minimal runoff — Palladan mean 1.90°
2 – 5	4	Favourable
5 – 7.21	3	Moderate — Palladan maximum 7.21°

Table 2c: Reclassification — Soil Texture

Soil Texture	Score	Infiltration Characteristic
Gravel / Coarse Sand	5	Very rapid infiltration — excellent recharge
Sandy Loam	4	Rapid infiltration — good recharge
Clay Loam	3	Moderate infiltration — Palladan soil type
Silty Clay	2	Slow infiltration — limited recharge
Heavy Clay	1	Very slow / negligible infiltration

Table 2d: Reclassification — Geology

Rock / Geological Type	Score	Groundwater Potential Basis
Alluvium / River deposits	5	High primary porosity — excellent water storage
Sandstone / Limestone	4	Good natural porosity — reliable aquifer
Migmatite / Weathered basement	3	Secondary porosity through fractures — Palladan geology
Granite (fresh / unweathered)	2	Low porosity — poor aquifer
Quartzite	1	Near-impermeable — negligible groundwater potential

Table 2e: Reclassification — Lineament Density (Terrain Roughness Proxy)

Roughness Range	Score	Lineament Density Interpretation
0 – 2	1	Very low — Palladan mean roughness 2.855
2 – 4	2	Low to moderate
4 – 6	3	Moderate lineament density
6 – 8	4	High lineament density
8 – 10	5	Very high — intense fracturing or faulting (Palladan max = 9)

Table 2f: Reclassification — Drainage Density (Stream Order)

Stream Order	Score	Recharge Implication
Order 1 (lowest drainage)	5	Minimal channelled drainage — most rainfall infiltrates
Order 2	4	Low drainage — favourable for recharge
Order 3 (Palladan mean ~2.9)	3	Moderate drainage — balanced infiltration and runoff
Order 4	2	Higher drainage — reduced recharge opportunity
Order 5+ (major rivers)	1	Rapid runoff removal — minimal recharge

Table 2g: Reclassification — LULC / NDVI

NDVI Range	Land Cover Type	Score
< 0	Water bodies / dense cloud	—
0.00 – 0.10	Bare soil / impervious surfaces / rock outcrops	2
0.10 – 0.30	Sparse vegetation / degraded savannah — Palladan (0.115)	3
0.30 – 0.60	Moderate vegetation — shrubland, grassland	4
> 0.60	Dense vegetation — forest, thick farmland	5

3.5 Analytical Hierarchy Process (AHP) Weight Derivation

Criterion weights were derived using the AHP pairwise comparison method (Saaty, 1980). A 7x7 pairwise comparison matrix was constructed using Saaty's 1-9 importance scale, based on the established importance of each criterion for groundwater recharge in basement complex terrain; the full matrix is presented in Table 3a. Weights were derived through column normalization and row averaging of the pairwise matrix. The Consistency Ratio (CR) was calculated as:

$$CI = (\lambda max - n) / (n - 1) = (7.1973 - 7) / 6 = 0.0329 \quad (2)$$

$$CR = CI / RI = 0.0329 / 1.32 = 0.025 \quad (3)$$

The CR of 0.025 is well below Saaty's acceptable threshold of CR < 0.10, confirming the statistical consistency of the pairwise judgments. The derived weights are presented in Table 3b.

Table 3a: AHP pairwise comparison matrix

Criterion	Rainfall	Slope	Soil	Lineament	Geology	Drainage	LULC
Rainfall	1	2	3	4	5	6	7
Slope	1/2	1	2	3	4	5	6
Soil	1/3	1/2	1	2	3	4	5
Lineament	1/4	1/3	1/2	1	2	3	4
Geology	1/5	1/4	1/3	1/2	1	2	3
Drainage	1/6	1/5	1/4	1/3	1/2	1	2
LULC	1/7	1/6	1/5	1/4	1/3	1/2	1

Table 3b: AHP-derived criterion weights

Criterion	Weight	%	Rank
Rainfall	0.3504	35.04%	1
Slope	0.2375	23.75%	2
Soil	0.1590	15.90%	3
Lineament density	0.1056	10.56%	4
Geology	0.0696	6.96%	5
Drainage density	0.0462	4.62%	6
LULC / NDVI	0.0318	3.18%	7
CR = 0.025 (< 0.10 — Consistent)	—	—	—

3.6 Weighted Overlay Analysis

The Groundwater Potential Index (GWPI) was computed using the GDAL Raster Calculator in QGIS by applying the expression:

GWPI = (0.3504 × Rainfall) + (0.2375 × Slope) + (0.1590 × Soil) + (0.1056 × Lineament) + (0.0696 × Geology) + (0.0462 × Drainage) + (0.0318 × LULC).....(4)

The GWPI raster was subsequently classified into four groundwater potential zones using the Reclassify by Table tool: Very Low (GWPI 2.00 - 2.50), Low (2.50 - 3.00), Moderate (3.00 - 3.50), and High (3.50 - 4.56).

4. RESULTS

4.1 Thematic Layer Results

Table 4 presents a summary of the key thematic layer results derived from the spatial analysis. Elevation is listed for reference but, as noted in Section 3.3, is not one of the seven weighted criteria; it is an intermediate SRTM-derived layer used only to compute slope, which is why it carries no score or AHP weight.

Table 4: Summary of thematic layer results

Layer	Key Result	Score	AHP Weight
Rainfall (CHIRPS 1981-2024)	966.21 mm/year	4/5	35.04%
Soil (FAO)	Clay Loam / Dystric Cambisol	3/5	15.90%
Elevation (SRTM) — intermediate layer, not a scored criterion	Mean 663 m (range 644-678 m)	—	—
Slope (SRTM)	Mean 1.90 degrees (0-7.21 degrees)	3-5/5	23.75%
Geology (FAO)	Migmatite Basement Complex	3/5	6.96%
Lineament (roughness proxy)	Mean roughness 2.855 (0-9)	1-3/5	10.56%
Drainage (r.watershed)	Mean stream order 2.923 (2-4)	3/5	4.62%
LULC / NDVI (Landsat 8/9)	Mean NDVI 0.115	3/5	3.18%

4.2 Groundwater Potential Index (GWPI) and Zone Map

The Weighted Overlay Analysis produced a GWPI raster with values ranging from 2.31 to 4.56 across 3,270 valid pixels within the Palladan study area, with a mean of 3.57 (standard deviation 0.168). This mean falls within the High classification band (3.50-4.56), consistent with the spatial dominance of the High potential zone described below. Classification of the GWPI into four groundwater potential zones produced the map presented in Figure 2, while the zone distribution — including the percentage of the study area occupied by each zone, obtained from a unique-values area report on the classified zone raster — is summarized in Table 5.

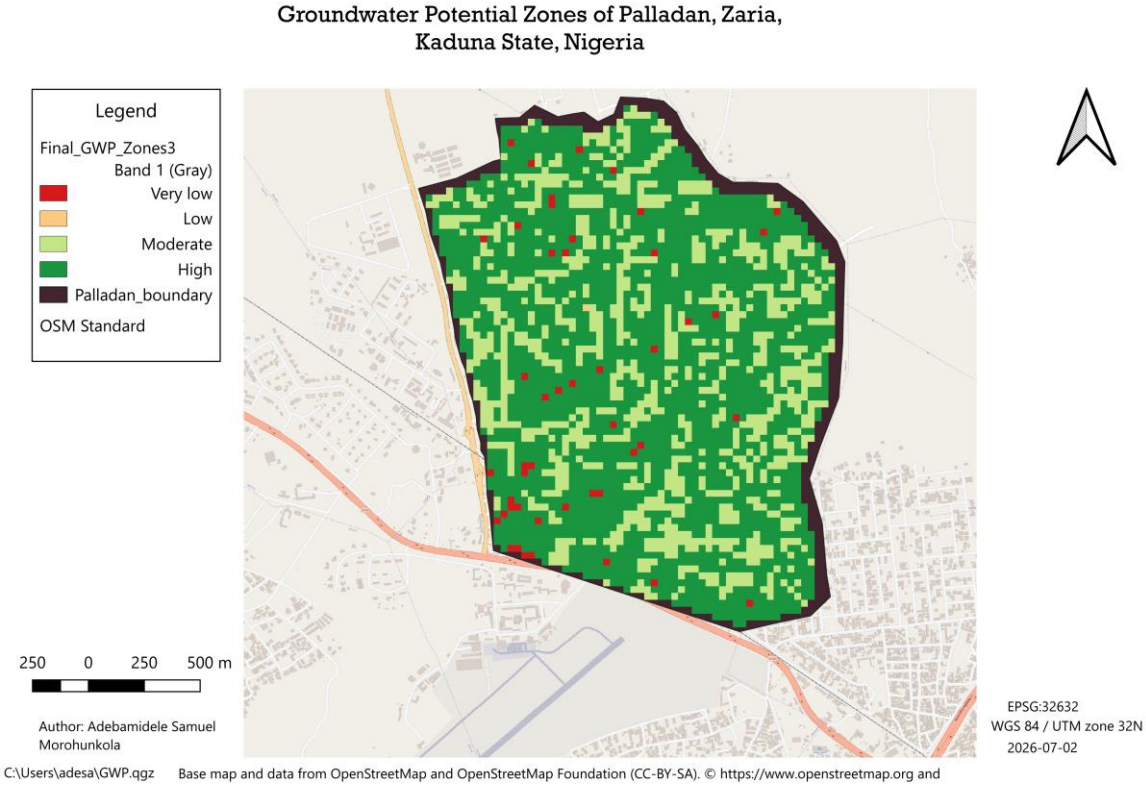

Figure 2: Groundwater Potential Zone Map of Palladan, Zaria, Kaduna State, Nigeria.

Table 5: Groundwater potential zone classification

Zone	GWPI Range	Classification	Pixel Count	Area (%)	Spatial Distribution
1	2.00-2.50	Very Low	47	1.44%	Isolated patches — boundary margins, areas of higher drainage density
2	2.50-3.00	Low	1	0.03%	Negligible — a single pixel within the study area
3	3.00-3.50	Moderate	965	29.51%	Patchy distribution — transitional areas
4	3.50-4.56	High	2,257	69.02%	Dominant — covers majority of Palladan (flat central and northern portions)

The High potential zone (Zone 4) dominates the spatial pattern of the GWPI map, covering approximately 69% of the Palladan study area, with the Moderate zone (Zone 3) accounting for a further 29.5%. Very Low and Low potential zones (Zones 1 and 2) together occupy less than 1.5% of the study area and are correctly described as isolated, near-negligible occurrences rather than a substantial minority class. This result is attributable to the combined effect of the two highest-weighted criteria: mean annual rainfall of 966.21 mm/year (score 4, weight 35.04%) and exceptionally flat terrain with mean slope of 1.90 degrees (score 5 for most pixels, weight 23.75%). Together, these two criteria contribute approximately 2.59 units to the GWPI of every flat-terrain pixel in Palladan, establishing a strong recharge potential foundation that is difficult to overcome even when other criteria score moderately.

It is worth noting that the GWPI distribution is not continuous but clusters around a small number of discrete value bands, as shown in the pixel-value histogram in Figure 3. This clustering arises

because most of the seven input layers are themselves discrete: rainfall, soil, and geology each take a single constant reclassified score across the entire Palladan raster (since each is derived from one CHIRPS value or one FAO polygon), while slope, lineament density, drainage density, and NDVI are each reclassified to a small set of integer scores (1-5) rather than varying continuously. Combining a limited number of discrete-scored layers through a fixed set of AHP weights necessarily produces a GWPI raster that can only take a limited number of possible values, which appear as distinct clusters separated by gaps rather than as a smooth continuous surface. This explains why the Very Low zone (2.00-2.50) contains a modest but real cluster of 47 pixels while the adjacent Low zone (2.50-3.00) captures only a single pixel: the fixed 0.50-wide zone boundaries used for classification happen to bisect a near-empty gap between two value clusters rather than reflecting any error in computation. This is a recognised characteristic of ordinal-reclassification-based MCDA/WOA models and does not affect the validity of the reported GWPI mean, zone-area percentages, or overall High-zone dominance.

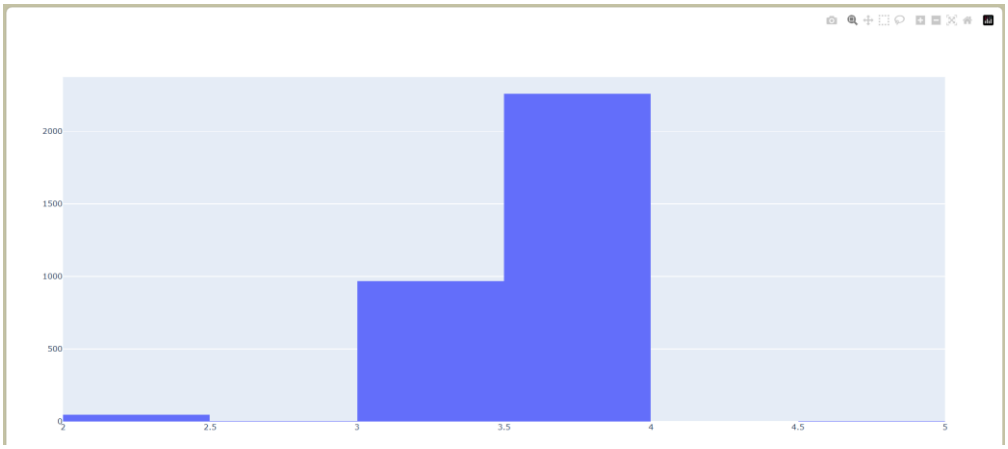

Figure 3: Histogram of GWPI pixel values (x-axis: GWPI, y-axis: pixel count), showing the discrete, clustered distribution underlying the zone classification in Table 5.

Very Low (Zone 1) and Low (Zone 2) potential zones occur as isolated, scattered patches within the study area, primarily in locations where terrain roughness is lower (indicating reduced fracture density) and drainage density is slightly higher (promoting faster runoff removal). The Moderate zone (Zone 3) is distributed as a substantial transitional band between the High and Very Low/Low zones, rather than as a minor category.

4.3 Validation

The groundwater potential zone map was validated against the independent geophysical investigation of Osumeje et al. (2024), who conducted an integrated remote sensing, aeromagnetic, and VES study across Palladan and Basawa in Sabon Gari LGA. Their study independently classified Palladan as exhibiting High groundwater potential, identified low-resistivity zones associated with NW/NE-trending fault systems as groundwater conduits, and reported fractured Migmatite basement aquifer thicknesses of 12-55 m.

This convergence is further supported by two additional independent geophysical investigations in and immediately around Palladan. Jegede et al. (2013) conducted a borehole-log and geophysical tomography investigation within Palladan itself, reporting a near-surface profile of approximately 10 m of loose, permeable laterite overlying degraded sand before the weathered Migmatite basement is reached — consistent with the moderately deep, moderately drained soil profile and fractured basement aquifer inferred from the FAO soil and geology layers used in this study. In the immediately adjacent ABU Samaru campus (approximately 2-3 km from Palladan, within the same basement complex terrain), Osumeje & Kudamnya (2014) used seismic refraction tomography across six profiles to

determine weathered-layer thickness and depth to fresh basement, reporting weathered thicknesses of 8-22 m and depths to fresh basement of 18-30 m, with four of the six profiles rated Good for groundwater potential and only one rated Poor. These independently derived depth and potential figures fall within a comparable range to the 12-55 m fractured aquifer thickness reported by Osumeje et al. (2024) for Palladan, reinforcing the overall picture of a productive, moderately thick weathered/fractured basement aquifer across the Palladan-Samaru area.

The convergence of results between the GIS-based MCDA/WOA model of this study and these three independent geophysical investigations — spanning Palladan itself and its immediately adjacent basement terrain — provides supporting qualitative cross-validation evidence for the reliability of the spatial model produced. This validation is, however, still qualitative in nature — based on agreement in overall classification and comparable depth ranges, rather than a formal quantitative accuracy metric such as percentage spatial overlap or statistical correlation with borehole yield data at specific coordinates. As acknowledged in the Limitations of the underlying dissertation this paper draws on, quantitative validation against primary borehole or pumping-test data referenced to the specific GWPI zones delineated in this study was not available and is recommended as a direction for future work; Fashae et al. (2014), for example, achieved a quantitative validation accuracy of 78% against borehole data in a comparable Basement Complex setting in South-Western Nigeria.

5. DISCUSSION

5.1 Groundwater Potential and Controlling Factors

The predominance of High groundwater potential zones in Palladan reflects a combination of hydrological and geomorphological conditions that are collectively favourable for groundwater recharge in basement complex terrain. The mean annual rainfall of 966.21 mm/year places Palladan within the upper portion of the favourable recharge rainfall bracket, providing a substantial annual water input that drives both diffuse and focused recharge mechanisms. The flat terrain, with the majority of the study area having slopes below 2 degrees, dramatically reduces surface runoff velocity and extends the residence time of rainfall on the land surface, maximizing infiltration opportunity through the Clay Loam soil profile into the underlying fractured Migmatite aquifer.

The moderate scores assigned to geology (Migmatite, score 3) and lineament density (roughness proxy, score 1-3) reflect the inherent limitations of crystalline basement terrain for groundwater storage compared to sedimentary formations. However, the aeromagnetic findings of Osumeje et al. (2024) confirmed NW/NE trending fault systems as productive groundwater conduits, suggesting that the terrain roughness proxy employed in this study underestimates true subsurface lineament density. This conservative treatment of lineament density implies that the GWPI values produced represent minimum estimates of Palladan's true groundwater potential; incorporating aeromagnetic-derived lineament density would likely yield higher GWPI values, potentially revealing very high potential zones in areas directly overlying the fault systems.

The degraded vegetation cover of Palladan (mean NDVI 0.115, Degraded Savannah Woodland) reflects decades of land use pressure from population growth, agricultural expansion, and fuelwood extraction. While this land cover condition scores 3 out of 5 for groundwater recharge potential, reflecting the moderate recharge implications of sparse vegetation, the progressive degradation of soil structure associated with reduced vegetation cover poses a long-term threat to infiltration capacity that is not captured by the static NDVI value used in this study.

5.2 Climate Change Implications

The 43-year CHIRPS rainfall record (1981-2024, Funk et al., 2015) used in this study captures a period of significant climate variability in the West African Guinea Savannah zone, encompassing the Sahel drought period of the 1970s-1980s and the subsequent partial rainfall recovery from the 1990s (Nicholson, 2013). The mean annual rainfall of 966.21 mm/year represents a long-term average that may mask important trends in seasonal rainfall distribution and inter-annual variability.

The IPCC (2021) projects increased rainfall variability for the Guinea Savannah zone under both moderate (SSP2-4.5) and high-emission (SSP5-8.5) climate scenarios, with potential increases in the frequency of extreme rainfall events offset by longer inter-event dry periods. For groundwater

recharge in Palladan, this has contrasting implications. On one hand, extended dry periods reduce cumulative infiltration and may fail to satisfy seasonal soil moisture deficits, reducing net recharge per rainfall event. On the other hand, the flat terrain of Palladan (mean slope 1.90 degrees) provides natural resilience to increased rainfall intensity by facilitating surface water ponding and focused recharge through ephemeral pools, partially compensating for reduced diffuse recharge during dry periods. This contrast is consistent with the broader finding of Taylor et al. (2013) that groundwater systems can act as a buffer against short-term climate variability even as they remain vulnerable to sustained, long-term reductions in recharge.

The degraded vegetation cover identified in this study (mean NDVI 0.115) amplifies climate change vulnerability. Reduced vegetation cover lowers evapotranspiration losses (potentially increasing available rainfall for recharge) but progressively reduces soil organic matter content, degrading soil structure and infiltration capacity over time. This long-term soil degradation pathway could gradually shift the dominant groundwater potential classification of Palladan from High toward Moderate under continued land degradation scenarios, even without any change in rainfall totals.

5.3 Comparison with Related Studies

The findings of this study are broadly consistent with related GIS-based groundwater potential assessments in the Nigerian Basement Complex. Fashae et al. (2014) applied AHP-WOA to delineate groundwater potential zones in the crystalline basement terrain of Oyo State, Nigeria, achieving 78% validation accuracy against existing borehole data, with rainfall and geology identified as the dominant controlling factors. Badamasi et al. (2016) mapped groundwater potential in Zaria, Kaduna State, using remote sensing and GIS, identifying the northern and northwestern areas of Zaria as highest potential zones — consistent with the location of Palladan in the northern Zaria metropolitan area. The present study builds directly on both these precedents by applying a validated MCDA/WOA methodology to a specific community-scale assessment, framed within a climate change impact context that is absent from the earlier studies.

The aeromagnetic findings of Osumeje et al. (2024) confirmed NW/NE trending fault systems as productive groundwater conduits, suggesting that the terrain roughness proxy employed in this study underestimates true subsurface lineament density. The present findings are also consistent with earlier geophysical work within and immediately around Palladan: Jegede et al. (2013) documented a permeable near-surface laterite-over-basement profile within Palladan itself, while Osumeje & Kudamnya (2014) reported comparable weathered-layer thicknesses and predominantly good groundwater potential ratings across the adjacent ABU Samaru campus, reinforcing the regional consistency of the High-potential classification produced by this study.

6. CONCLUSION

This study has demonstrated that Palladan, Zaria, Kaduna State, Nigeria, is a predominantly High groundwater recharge potential area, as determined through a GIS-based MCDA/WOA framework integrating seven thematic criteria from freely available open-access datasets. The High potential zone covers approximately 69% of Palladan, with a further 29.5% classified as Moderate potential; Very Low and Low potential zones together occupy less than 1.5% of the study area. This dominance is driven principally by favourable mean annual rainfall (966.21 mm/year) and exceptionally flat terrain (mean slope 1.90 degrees), which together account for approximately 59% of the total AHP weight and establish a strong natural foundation for groundwater recharge.

The Consistency Ratio of CR = 0.025 confirms the statistical reliability of the AHP weight assignment. Qualitative cross-validation against the independent VES-based investigation of Osumeje et al. (2024), which independently classified Palladan as a High groundwater potential area with productive fractured Migmatite aquifers (12-55 m thickness), provides supporting methodological validation for the spatial model produced, though quantitative validation against primary borehole data remains a recommended direction for future work.

Climate change poses a significant long-term threat to groundwater recharge sustainability in Palladan through projected increases in rainfall variability and continued land degradation. The flat terrain of Palladan confers natural resilience advantages through surface water ponding mechanisms, but active management interventions — including Managed Aquifer Recharge, vegetation restoration,

and groundwater monitoring — are essential to maintain groundwater availability under future climate scenarios. The replicable, cost-effective MCDA/WOA methodology demonstrated in this study is directly transferable to other data-scarce communities across the Nigerian Basement Complex facing similar groundwater management challenges under a changing climate.

7. RECOMMENDATIONS

Based on the findings of this study, the following recommendations are made for groundwater resource management in Palladan:

Groundwater Resource Management

i. Groundwater exploration and borehole siting should prioritize the High potential zones (Zone 4) in the flat central and northern portions of Palladan, where the combination of favourable rainfall, minimal slope, and moderate soil permeability creates the most productive recharge conditions consistent with fractured Migmatite aquifer depths of 12-55 m (Osumeje et al., 2024).

ii. Managed Aquifer Recharge (MAR) interventions including recharge pits, percolation tanks, and check dams across seasonal drainage channels should be implemented in High potential zones during the wet season (April to October) to enhance natural groundwater recharge. The flat terrain is ideal for MAR implementation.

iii. A groundwater level monitoring network should be established across the different potential zones of Palladan, including primary borehole yield or water-table measurements, to enable quantitative validation of the GWPI map, early detection of climate change-induced recharge decline, and evidence-based abstraction management.

Land Use and Environmental Management

i. A community vegetation restoration programme should be initiated to reverse the current degraded savannah condition (mean NDVI 0.115) through agroforestry, controlled grazing management, and native tree planting. Target NDVI values of 0.3-0.5 would substantially improve long-term soil infiltration capacity.

ii. Groundwater recharge protection should be incorporated into urban development planning for Palladan, with High potential zones designated as recharge protection areas where impervious surface coverage is minimized.

ACKNOWLEDGEMENTS

I acknowledge the use of freely available datasets from CHIRPS (Climate Hazards Group, University of California Santa Barbara), the Food and Agriculture Organization of the United Nations (FAO), the United States Geological Survey (USGS) Earth Explorer portal (SRTM DEM and Landsat 8/9), and the OpenStreetMap contributors. Lastly, I acknowledge the foundational contribution of Osumeje et al. (2024) whose geophysical investigation of Palladan provided the primary validation dataset for this study.

REFERENCES

Adelana, S. M. A., & MacDonald, A. M. (Eds.). (2008). Applied groundwater studies in Africa. CRC Press / Balkema.

Badamasi, S., Sawa, B. A., & Garba, M. L. (2016). Groundwater potential zones mapping using remote sensing and GIS in Zaria, Kaduna State, Nigeria. American Scientific Research Journal for Engineering, Technology, and Sciences, 24(1), 51-62.

Fashae, O. A., Tijani, M. N., Talabi, A. O., & Adedeji, O. I. (2014). Delineation of groundwater potential zones in the crystalline basement terrain of SW-Nigeria: An integrated GIS and remote sensing approach. Applied Water Science, 4(1), 19-38. https://doi.org/10.1007/s13201-013-0127-9

Funk, C., Peterson, P., Landsfeld, M., Pedreros, D., Verdin, J., Shukla, S., Husak, G., Rowland, J., Harrison, L., Hoell, A., & Michaelsen, J. (2015). The climate hazards infrared precipitation with stations — a new environmental record for monitoring extremes. Scientific Data, 2, 150066. https://doi.org/10.1038/sdata.2015.66

IPCC. (2021). Climate change 2021: The physical science basis. Contribution of Working Group I to the Sixth Assessment Report of the Intergovernmental Panel on Climate Change. Cambridge University Press.

Jegede, S. I., Iserhien-Emekeme, R. E., Iyoha, A., & Amadasun, C. V. O. (2013). Near-surface investigation of groundwater contamination in the regolith aquifer of Palladan, Zaria using borehole log and tomography techniques. Research Journal of Applied Sciences, Engineering and Technology, 6(4), 537-544.

Jha, M. K., Chowdary, V. M., & Chowdhury, A. (2010). Groundwater assessment in Salboni block, West Bengal (India) using remote sensing, GIS and multi-criteria decision analysis techniques. Hydrogeology Journal, 18(7), 1713-1728. https://doi.org/10.1007/s10040-010-0631-z

Nicholson, S. E. (2013). The West African Sahel: A review of recent studies on the rainfall climatology, meteorology and hydrology. Journal of Applied Meteorology and Climatology, 52(2), 453-491.

Osumeje, J. O., & Kudamnya, E. A. (2014). Hydro-geophysical investigation using seismic refraction tomography to study the groundwater potential of Ahmadu Bello University main campus, within the basement complex of northern Nigeria. Journal of Environment and Earth Science, 4(2), 15-22.

Osumeje, J. O., et al. (2024). Application of remote sensing and electrical resistivity technique for delineating groundwater potential in North Western Nigeria. Scientific Reports, 14, 69633. https://doi.org/10.1038/s41598-024-69633-8

Saaty, T. L. (1980). The analytic hierarchy process: Planning, priority setting, resource allocation. McGraw-Hill.

Taylor, R. G., Scanlon, B., Döll, P., Rodell, M., van Beek, R., Wada, Y., Longuevergne, L., Leblanc, M., Famiglietti, J. S., Edmunds, M., Konikow, L., Green, T. R., Chen, J., Taniguchi, M., Bierkens, M. F. P., MacDonald, A., Fan, Y., Maxwell, R. M., Yechieli, Y., … Treidel, H. (2013). Ground water and climate change. Nature Climate Change, 3(4), 322-329. https://doi.org/10.1038/nclimate1744

UNESCO. (2022). The United Nations world water development report 2022: Groundwater — making the invisible visible. UNESCO.

USGS. (2000). Shuttle Radar Topography Mission (SRTM) 1 Arc-Second Global [Dataset]. United States Geological Survey. https://earthexplorer.usgs.gov

USGS. (2022). Landsat 8/9 OLI/TIRS Collection 2 Level-2 Surface Reflectance, Path 189/Row 053, November 3, 2022 [Dataset]. United States Geological Survey. https://earthexplorer.usgs.gov.

ASSESSMENT OF ELECTRICAL POWER QUALITY ISSUES IN AIRCRAFT DC SYSTEMS: ANALYSIS OF VOLTAGE DROP AND HARMONIC DISTORTION

Alum Ikechukwu Otu[1], Muyideen Omuya Momoh[2], Princess Love David[1,*], Abdussalam El-Suleiman[1], Gowon Sule[1], Godwin Eseosa Abbe[1], Kumater Peter Ter[1]

[1]*Air Force Institute of Technology Kaduna*
[2]*Department of Computer Engineering, Ahmadu Bello University, Zaria*

Email: alumikechukwu@gmail.com, momuyideen@abu.edu.ng, lovedivine983@gmail.com*, a.elsuleiman@afit.edu.ng, sugowon78@gmail.com, xoxa20@yahoo.com, kumaterpeter@gmail.com

***Corresponding author**: Princess Love David

DOI: https://doi.org/10.67203/sp.ICESID.2026

ABSTRACT

The transition toward More-Electric Aircraft (MEA), in which hydraulic and pneumatic systems are progressively replaced by electrical alternatives, has intensified reliance on aircraft DC electrical systems, making power quality essential for reliable operation. This study investigates two critical power-quality issues: voltage drop and harmonic distortion and evaluates RC filtering as a mitigation approach. A simulation-based methodology was adopted using MATLAB/Simulink to model a representative aircraft DC distribution network comprising a DC source, distribution-line impedance, variable resistive loads, and a harmonic-injection subsystem emulating non-linear loads such as power converters. Results showed that higher electrical loading increased both voltage drop and harmonic distortion, degrading power quality and voltage regulation. Under high-current (low-resistance) conditions, voltage drop rose from 1.0 V at 25 Ω to 9.7 V at 5 Ω, while total harmonic distortion (THD) rose from 2.7% to 11.8% over the same range, exceeding the commonly adopted 5% threshold at the three lowest resistance cases a level widely flagged as a risk factor for sensitive equipment. A first-order passive RC filter evaluated at the 15 Ω case produced a visibly smoother, more stable load-voltage waveform than the unfiltered case, consistent with the expected attenuation behaviour of a low-pass filter. The study concludes that while load dynamics and non-linear components degrade power quality in aircraft DC systems, properly designed passive filters offer a simple and effective mitigation option. These findings inform the design of more resilient electrical power systems for next-generation More-Electric and All-Electric Aircraft.

Keywords: *More-Electric Aircraft; Aircraft DC Distribution; Harmonic Distortion; Voltage Drop; RC Filtering; Avionics*

1. INTRODUCTION

Aircraft electrical systems generate, control, and distribute power to flight-deck displays, protection devices, flight controls, and communication and navigation equipment, making power quality central to safe operation (Madonna et al., 2018; Norman et al., 2010). Traditional hydraulic and pneumatic architectures present limitations such as complex piping and difficult leak detection (Aguida et al., 2024), motivating the transition toward More-Electric Aircraft (MEA), in which conventional subsystems are progressively replaced by electrical equivalents (Sarlioglu & Morris, 2015; Verma & Kumar, 2020; Zhao et al., 2014). This transition increases the complexity and capacity of electrical power systems and heightens dependence on reliable power distribution (Rahrovi & Ehsani, 2019).

While MEA improves efficiency, it introduces power-quality challenges: harmonic distortion and voltage drop can cause equipment failure, reduced efficiency and safety risks (Buticchi et al., 2023; Dorn-Gomba et al., 2020). Voltage drop arises from load current interacting with distribution-line impedance, while harmonic distortion results from non-linear loads and power-electronic converters injecting periodic components into the supply waveform (Fernández-Morales et al., 2022; Whaite et al., 2015). Broader DC power-quality studies (Alves et al., 2016; Mariscotti, 2021; Zhao et al., 2014) and passive harmonic-mitigation reviews . Ab Aziz et al., (2021) confirm the relevance of these issues but

do not examine load-dependent voltage-drop and harmonic behaviour in a representative aircraft DC path, nor a simple RC filter's response under such conditions (Chen et al., 2018; Schefer et al., 2020).

This study addresses that gap through a simulation-based assessment of voltage drop and harmonic distortion in an aircraft DC distribution system, evaluating the effectiveness of a passive RC filter as a mitigation approach. The objectives are to:

(i) Quantify the relationship between load resistance, voltage drop and THD in a representative aircraft DC network.
(ii) Compare time- and frequency-domain behaviour before and after RC filtering.
(iii) Relate the findings to established power-quality benchmarks to inform more resilient MEA electrical system design.

2. METHODOLOGY

A simulation-based quantitative approach was used to investigate voltage drop and harmonic distortion in an aircraft DC distribution system. The model was developed in MATLAB/Simulink R2019a, with FFT-based post-processing for frequency-domain analysis. As shown in Figure 1, the simplified network comprises a DC source, distribution-line impedance, variable resistive loading, a harmonic-injection subsystem, a voltage-sag subsystem, and a first-order passive RC filter, rather than a full-fidelity aircraft electrical power system, providing a controlled environment in which the effects of load resistance and injected disturbances can be isolated at the load terminals. The reported values therefore represent this simulated configuration rather than universal aircraft performance, since the model does not reproduce every non-linearity, thermal effect, control interaction and operating variation present in an actual aircraft power system.

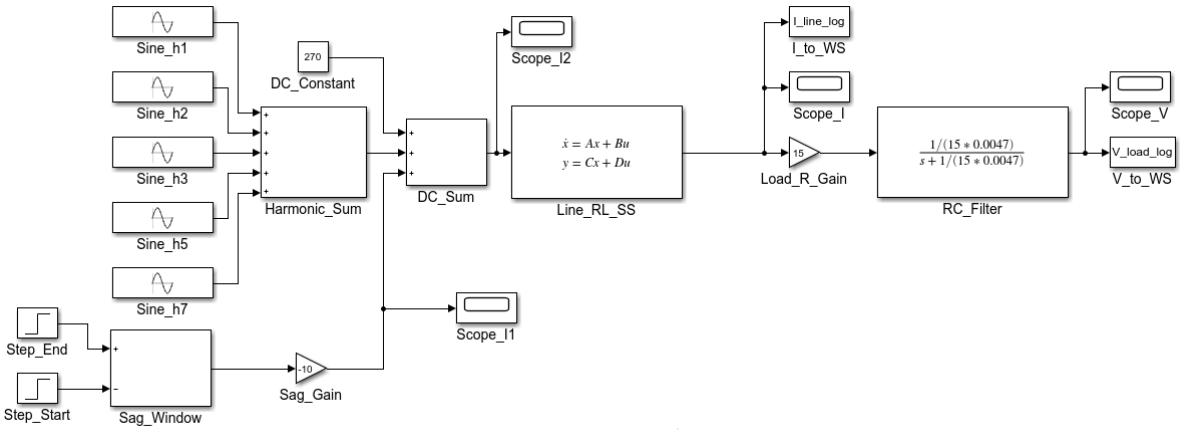

Figure 1: Simulink Model of Aircraft DC Power Quality System for Voltage Drop and Harmonic Distortion Analysis

In Figure 1, the DC source block (V_{DC} = 270 V) represents the aircraft's generator output. The harmonic-injection blocks simulate distortion from non-linear loads such as power converters and inverters, combined via a summation block into a composite distorted waveform. The voltage-sag subsystem uses step and gain blocks to model transient disturbances such as motor startup or fault conditions, producing a temporary voltage reduction representative of real sag events, while the distribution-line block represents the voltage drop and phase shift caused by line impedance between source and load.

2.1 DC Source and Distribution-Line Model

The DC source was represented by a constant 270 V supply, representing the aircraft generator output. The distribution line was modelled as a lumped series resistance of 0.5 Ω and inductance of 2 mH. Because current flowing through this finite impedance produces a voltage loss, the load voltage is lower than the source voltage. Voltage drop was evaluated as:

$$\Delta V = V_source - V_load \quad (1)$$

which, for the resistive component of the model, is consistent with:

$$\Delta V \approx I \times R_line \tag{2}$$

2.2 Variable Load Conditions

The load was represented by a variable resistance to analyse network response under different loading conditions, using comparison values of 5, 10, 15, 20 and 25 Ω. lower resistance corresponding to higher current demand for the same nominal bus voltage. Voltage and current signals were logged from the Simulink model to the MATLAB workspace for each of the five load cases, each executed as a single simulation run, providing the basis for comparing voltage drop and THD across loading conditions.

2. 3 Harmonic Injection and Voltage Sag

Harmonic distortion was introduced by summing multiple sinusoidal components (Sine_h1, Sine_h2, Sine_h3, Sine_h5 and Sine_h7, corresponding to the 1st, 2nd, 3rd, 5th and 7th harmonic orders) with the constant DC source to form a distorted bus waveform. A base harmonic frequency of 400 Hz was adopted, reflecting ripple originating from the aircraft's 400 Hz AC generation system prior to rectification, consistent with typical aircraft power architecture in which DC buses are derived from 400 Hz AC sources. FFT-based frequency-domain analysis was used to evaluate the harmonic content of the simulated waveform, with THD used as the principal comparison metric:

$$THD = \left\{ \frac{\sqrt{V_{2^2} + V_{3^2} + \ldots + V_{n^2}}}{V_1} \right\} \times 100\% \tag{3}$$

where V_1 is the RMS value of the fundamental component and V_2, V_3, …, V_n are the RMS values of the corresponding harmonic components. A voltage-sag subsystem, implemented using step functions and a gain block, reproduced temporary reductions in bus voltage associated with dynamic disturbances such as generator transients or sudden load changes, providing a basis for observing voltage response and recovery in the time domain.

2. 3 4 RC Filter Configuration

A first-order passive RC filter (R = 15 Ω, C = 0.0047 F, giving RC = 0.0705 s) was connected at the load terminals to attenuate unwanted high-frequency components. These values were selected to place the filter cutoff frequency (≈2.3 Hz) well below the 400 Hz base harmonic frequency, providing strong attenuation of the injected harmonics consistent with standard first-order passive-filter design practice. The filter transfer function is:

$$H_{(s)} = \frac{1}{RC_s + 1} \tag{4}$$

$$H_{(s)} = \frac{1}{14.184s + 14.184} \tag{5}$$

Filtered and unfiltered voltage waveforms and their frequency-domain spectra were compared to assess filter performance.

2.5 Simulation Configuration and Data Analysis

Numerical integration used MATLAB's variable-step ode45 solver; voltage and current signals were logged via workspace blocks, and post-processing comprised time-domain waveform plotting, FFT-based frequency-domain analysis, THD computation, and comparison of filtered/unfiltered conditions (Table 1).

Table 1: Key Simulation Parameters

Parameter	Description	Value
DC Source Voltage	Nominal bus voltage	270 V
Load Resistance	Comparison cases	5,10,15,20 and 25 Ω
Line Resistance	Lumped distribution resistance	0.5 Ω
Line Inductance	Lumped distribution inductance	2 mH
Base harmonic Frequency	harmonic frequency	400 Hz
Simulation Time	Duration of analysis	0.5 s
RC filter capacitance	Passive filter parameter	0.0047F
RC filter resistance	Passive filter parameter	15Ω
Solver	Numerical Integration	Variable-step ode45

3. RESULTS AND DISCUSSION

The simulation results are examined below in terms of voltage drop, THD, RC-filter response, and their implications, across the five resistive load cases of 5, 10, 15, 20 and 25 Ω.

3.1 Voltage Drop as a Function of Load Resistance

As load resistance decreased, voltage drop increased (Table 2, Figure 2): from 1.0 V at 25 Ω to 9.7 V at 5 Ω. This inverse relationship follows from Ohm's law (V = I × R): lower resistance imposes higher current demand, increasing the voltage loss across the line and moving the load voltage further from the nominal 270 V source. Loading condition is therefore a direct factor in voltage quality at the load terminals, and heavier loading increases susceptibility to voltage sag. An important consideration for MEA architectures, where reducing distribution resistance is beneficial.

Table 2: Relationship between load resistance and voltage drop

Load Resistance (Ω	Mean V load(V)	Voltage Drop(V)
5.0	260.3	9.7
10.0	264.9	5.1
15.0	266.7	3.3
20.0	268.2	1.8
25.0	269.0	1.0

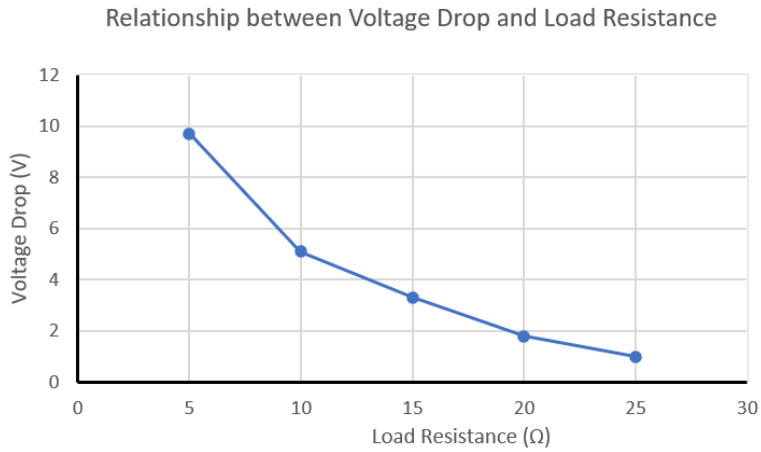

Figure 2: Voltage Drop (V_source - V_load) vs. Load Resistance

3.2 Harmonic Distortion as a Function of Load Resistance

THD followed a similar trend, decreasing from 11.8% at 5 Ω to 2.7% at 25 Ω as load resistance increased (Table 3, Figure 3). THD exceeded the 5% threshold recommended by IEEE Std. 519-2014 at the three lowest-resistance cases (5, 10 and 15 Ω), falling within the threshold only at 20 Ω (3.9%) and 25 Ω (2.7%), indicating that nonlinear loading under heavy demand can meaningfully degrade aircraft DC power quality. Aircraft-specific requirements are instead addressed by MIL-STD-704 and RTCA DO-160, which impose voltage and harmonic-related limits distinct from the general IEEE benchmark used here for illustrative comparison; the simulated results indicate relative severity across loading conditions rather than establishing compliance or non-compliance with aircraft certification requirements.

Table 3: Relationship between Load resistance and THD

Load Resistance (Ω)	THD (%)
5.0	11.8
10.0	8.4
15.0	5.2
20.0	3.9
25.0	2.7

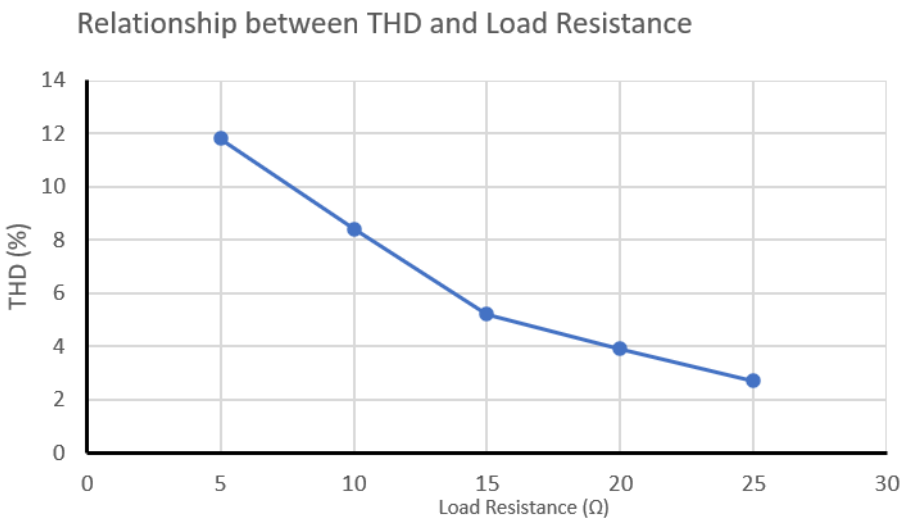

Figure 3: Total Harmonic Distortion (THD) vs. Load Resistance

3.3 Effect of the RC Filter

Representative time- and frequency-domain responses were examined at the 15 Ω load case under unfiltered and filtered conditions. The unfiltered load-voltage waveform showed distortion superimposed on the DC level, with the simulated voltage sag producing a temporary reduction in magnitude followed by oscillatory recovery. With the RC filter engaged, the waveform was visibly smoother, with attenuated transient spikes and high-frequency ripple; the filtered configuration also exhibited faster settling behaviour following the simulated voltage sag, with the oscillatory recovery visible in the unfiltered response notably attenuated in the filtered case. The line-current waveform likewise became smoother and closer to steady-state behaviour. FFT comparison showed a reduction in harmonic content following filtering, consistent with the expected attenuation of a first-order low-pass filter whose cutoff frequency (≈2.3 Hz) lies well below the 400 Hz base harmonic frequency. These observations were recorded qualitatively; the precise numeric reduction in THD and the voltage-sag

recovery time at this operating point were not independently logged, and the filter was evaluated only at the single 15 Ω case rather than across the full loading range.

3.4 Implications and Limitations

These results confirm that loading conditions and non-linear components jointly govern the power quality delivered at aircraft DC load terminals, and that a simple passive RC filter can meaningfully improve the simulated waveform. However, the findings rest on a simplified model rather than a full-fidelity aircraft electrical system: source impedance, converter topology, switching behaviour, control interactions, grounding and thermal effects were not represented, so the study does not itself provide a basis for a final aircraft filter design — component ratings, thermal behaviour, mass, volume and transient performance require further analysis before implementation. These findings remain relevant to MEA electrical system design, given the growing number of electrical functions that depend on stable power distribution.

4. CONCLUSION

This study used MATLAB/Simulink to investigate voltage drop and harmonic distortion in a simulated aircraft DC distribution system, modelling a 270 V DC source, distribution-line resistance and inductance, variable resistive loading (5–25 Ω), harmonic injection and voltage-sag conditions and evaluated a first-order passive RC filter as a mitigation approach.

Reducing load resistance increased current demand and produced larger voltage drops, rising from 1.0 V at 25 Ω to 9.7 V at 5 Ω. THD followed the same trend, increasing from 2.7% at 25 Ω to 11.8% at 5 Ω and exceeding the commonly adopted 5% threshold at the three lowest-resistance cases. The RC filter, evaluated at the 15 Ω case, produced a visibly smoother load-voltage waveform with attenuated transient spikes and high-frequency ripple, together with a general reduction in harmonic content; the precise magnitude of this reduction, and its behaviour across the other tested load resistances, was not independently recorded.

These findings confirm that load dynamics and non-linear components degrade power quality in aircraft DC systems, and that properly designed passive filters offer a simple, effective mitigation option. The study is limited to a simplified simulation model, and future work should pursue hardware-in-the-loop or bench validation against measured data, extend harmonic injection to a broader range of profiles, evaluate the RC filter across the full tested load range with paired filtered/unfiltered THD and recovery-time measurements, and assess the thermal and mass feasibility of filter components for aircraft installation.

5. REFERENCES

Ab Aziz, M. H., Azizan, M. M., Sauli, Z., & Yahya, M. W. (2021). A review on harmonic mitigation method for non-linear load in electrical power system. *AIP Conference Proceedings, 2339*(May). https://doi.org/10.1063/5.0044251

Aguida, M. E., Che, Y., & Yang, J. (2024). Technological advancements and future prospects of electrical power systems for sustainable more electric aircraft. *Propulsion and Power Research, 13*(4), 475–486. https://doi.org/10.1016/j.jppr.2024.11.003

Alves, J. V. G., De Figueiredo, P. A., Malizia, I. D. F., & Pomilio, J. A. (2016). Analysis and tests of Power Quality in aviation environment. *Proceedings of International Conference on Harmonics and Quality of Power, ICHQP, 2016-Decem*(Dc), 272–277. https://doi.org/10.1109/ICHQP.2016.7783409

Buticchi, G., Wheeler, P., & Boroyevich, D. (2023). The More-Electric Aircraft and Beyond. *Proceedings of the IEEE, 111*(4), 356–370. https://doi.org/10.1109/JPROC.2022.3152995

Chen, J., Wang, C., & Chen, J. (2018). Investigation on the selection of electric power system architecture for future more electric aircraft. *IEEE Transactions on Transportation Electrification, 4*(2), 563–576. https://doi.org/10.1109/TTE.2018.2792332

Dorn-Gomba, L., Ramoul, J., Reimers, J., & Emadi, A. (2020). Power Electronic Converters in Electric Aircraft: Current Status, Challenges, and Emerging Technologies. *IEEE Transactions on*

Transportation Electrification, *6*(4), 1648–1664. https://doi.org/10.1109/TTE.2020.3006045

Fernández-Morales, J., González-De-La Rosa, J. J., Sierra-Fernández, J. M., Espinosa-Gavira, M. J., Florencias-Oliveros, O., Agüera-Pérez, A., Palomares-Salas, J. C., & Remigio-Carmona, P. (2022). Statistical Dataset and Data Acquisition System for Monitoring the Voltage and Frequency of the Electrical Network in an Environment Based on Python and Grafana. *Data*, *7*(6). https://doi.org/10.3390/data7060077

Madonna, V., Giangrande, P., & Galea, M. (2018). Electrical Power Generation in Aircraft: Review, Challenges, and Opportunities. *IEEE Transactions on Transportation Electrification*, *4*(3), 646–659. https://doi.org/10.1109/TTE.2018.2834142

Mariscotti, A. (2021). *Power Quality Phenomena , Standards , and Proposed Metrics for DC Grids*.

Norman, P. J., Galloway, S. J., Burt, G. M., & Hill, J. E. (2010). Improving aircraft engine operability through electric system design and operation. *IET Conference Publications*, *2010*(563 CP). https://doi.org/10.1049/cp.2010.0046

Rahrovi, B., & Ehsani, M. (2019). A review of the more electric aircraft power electronics. *2019 IEEE Texas Power and Energy Conference, TPEC 2019*, 1–6. https://doi.org/10.1109/TPEC.2019.8662158

Sarlioglu, B., & Morris, C. T. (2015). More Electric Aircraft: Review, Challenges, and Opportunities for Commercial Transport Aircraft. *IEEE Transactions on Transportation Electrification*, *1*(1), 54–64. https://doi.org/10.1109/TTE.2015.2426499

Schefer, H., Fauth, L., & Kopp, T. H. (2020). *Discussion on Electric Power Supply Systems for All Electric Aircraft*. *8*. https://doi.org/10.1109/ACCESS.2020.2991804

Verma, T., & Kumar, A. (2020). Future scope. *Studies in Fuzziness and Soft Computing*, *383*, 165–166. https://doi.org/10.1007/978-3-030-16162-0_6

Whaite, S., Grainger, B., & Kwasinski, A. (2015). *Power Quality in DC Power Distribution Systems and Microgrids*. *Dc*, 4378–4399. https://doi.org/10.3390/en8054378

Zhao, X., Guerrero, J. M., & Wu, X. (2014). *Review of Aircraft Electric Power Systems and Architectures*. 949–953.

International Conference on Engineering Innovation for Sustainable Development (ICESID 2026)
Faculty of Engineering, Ahmadu Bello University Zaria · 8–10 September 2026

CALIFORNIA BEARING RATIO OF GEOPOLYMER-STABILIZED LATERITIC SOIL USING SUGARCANE BAGASSE ASH AND RICE HUSK ASH AS PRECURSORS

Aliyu Mani Umar[1,*], Mustapha Amin Muhammad[1], Ashiru Mohammed[1], Nura Shehu Aliyu Yaro[1], Yaseer Adam Nabage[2], Adam Ado Sabari[3], Surajo Abubakar Wada[1]

[1]*Ahmadu Bello University Zaria*
[2]*Federal Polytechnic Bauchi*
[3]*The University of Alabama in Huntsville*

Email: aliyu531@gmail.com*, aumani@abu.edu.ng, ibshazali@gmail.com, nsayaro@gmail.com, yaseernabage@gmail.com, aasabari@gmail.com, sawada@abu.edu.ng

***Corresponding author**: Aliyu Mani Umar

DOI: https://doi.org/10.67203/sp.ICESID.2026

ABSTRACT

Environmental concerns coupled with economic considerations have heightened interests towards sustainable pavement construction. Several studies in sustainable pavement construction had explored stabilization of weak, unstable or problematic soils using agricultural wastes. Agricultural waste materials such as sugarcane bagasse ash (SBA) and rice husk ash (RHA) are rich in reactive silica and possess considerable pozzolanic potential, making them promising geopolymer precursors for soil stabilization. However, limited studies have investigated the combined performance of alkali-activated with 1% NaOH (prepared as a 5 M solution) SBA and RHA in improving tropical lateritic soils used in road construction. This study evaluated the engineering performance of geopolymer-stabilized lateritic soil incorporating SBA and RHA activated with 1% sodium hydroxide. Lateritic soil (having silica-sesquioxide ratio of 1.30) obtained from Ahmadu Bello University Teaching Hospital (ABUTH), Shika, Nigeria, was stabilized using three SBA: RHA blends (3:1, 2:2, and 1:3), while soil stabilized with 4% Portland limestone cement served as the control. Laboratory tests included particle size distribution, specific gravity, Atterberg limits, X-ray fluorescence (XRF), compaction characteristics, and California Bearing Ratio (CBR) in accordance with BS 1377-2:2022. The natural soil was classified as A-7-5 under AASHTO and CL under the Unified Soil Classification System, indicating poor engineering quality. XRF analysis confirmed high silica contents in both ashes, particularly RHA (73.76% SiO_2), supporting their suitability for geopolymerization. Among the geopolymer mixes, the balanced 2 % SBA + 2 % RHA blend produced the largest reduction in plasticity index (from 43.36 % to 23.11 %) and the highest unsoaked CBR (81.9 %), approaching the cement control (86.6 %). Soaked CBR values for all geopolymer mixes (17.0-18.31 %) satisfied Overseas Road Note 31 requirements for improved subgrade. The results indicate that a 2:2 SBA-RHA geopolymer activated with 5 M NaOH at 4 % total stabilizer content is a practical cement-free alternative for improving tropical lateritic soils for pavement subgrade applications. Stabilized specimens exhibited slightly higher optimum moisture contents (17-18%) while maintaining comparable maximum dry densities (1.83-1.86 Mg/m³). The results showed that alkali-activated SBA-RHA geopolymer is a viable and sustainable alternative to conventional cement stabilization for enhancing tropical lateritic soils for pavement applications.

Keywords: *Lateritic soil; Geopolymer stabilization; Sugarcane bagasse ash; Rice husk ash; Sustainable pavement; California Bearing Ratio*

1. INTRODUCTION

Lateritic soils are common in tropical regions and are frequently used as subgrade or fill material in road construction. In their natural state many of these soils exhibit high plasticity, low bearing capacity and poor volume stability, making stabilization necessary prior to used in pavement construction. Traditional cement stabilization is effective but has a high greenhouse gas footprint (Ahmad et al., 2023; Ahmad et al., 2024). Geopolymer technology is a sustainable alternative that uses aluminosilicate-rich waste materials. Rice husk ash (RHA) has high content of reactive silica and sugarcane bagasse ash (SBA) has silica and calcium which can be used for geopolymerization (Anburuvel et al., 2023; Aurelie Tchouateu Kamwa et al., 2023; Burhan & Mohammed, 2025).

Both materials have been studied separately but little information is available on their use together for stabilization of lateritic soils (Chompoorat et al., 2025; Kamwa et al., 2023; Kuasakul et al., 2025; Mathew et al., 2026). This study evaluates the compaction characteristics and CBR performance of lateritic soil stabilized using RHA and SBA as precursors and, compares the results with untreated and cement-treated soils. The rest of the paper is structured as follows. Section 2 reports on materials, methods and methodology adopted in this study. Section 3 presents results and discusses findings. Section 4 ends the paper with conclusions and recommendations.

2. MATERIALS AND METHODS

2.1 Study Design

An experimental laboratory programme was conducted to compare untreated lateritic soil, cement-stabilized soil and geopolymer-stabilized soil. The investigation focused on material characterization, compaction behaviour and California Bearing Ratio performance.

2.2 Materials

The Lateritic soil used in this study was obtained from ABUTH, Shika, Zaria (Figure 1(a)). SBA and RHA were sourced locally, washed, air dried and calcined at 700°C for 3 hours, then cooled to room temperature, ground and sieved through BS sieve 200 before use (Figures 1 (b-d)).A 5 M sodium hydroxide solution was prepared and dosed at 1 % by dry weight of soil (i.e., 1 % NaOH solids). These conditions yield the optimum geopolymerization for agricultural wastes ashes (Kumar & Reddy, 2023; Mathew et al., 2026). 4% Portland limestone cement was used as the control stabilizer.

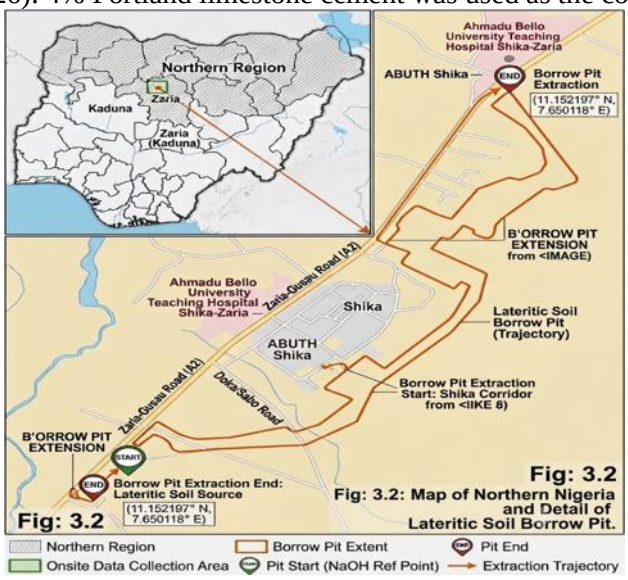

(a) Location of borrow pit for lateritic soil sample collection

(b) Cement

(c) RHA

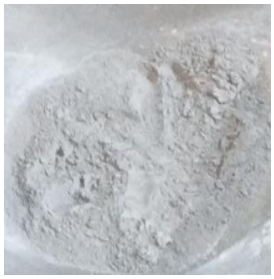

(d) SBA

(e) NaOH

Figure 1: Location for lateritic soil sample collection and geopolymer stabilization materials.

The constituent materials were tested for chemical composition, and the soil was further tested for water absorption, specific gravity, bulk density and Atterberg limits.

2.3 Geopolymer Mix Design

Three geopolymer mixtures were prepared using a total stabilizer content equivalent to 4% of dry soil weight: 3S1R1N, 2S2R1N and 1S3R1N (Table 1). A cement-treated sample (4C) and untreated soil served as controls for cement stabilised and natural samples respectively. Specimens were mixed at the optimum moisture content determined for each blend, sealed in plastic bags and cured at ambient laboratory temperature (25-28 °C) for 7 days before compaction and CBR testing. Modified Proctor compaction and both soaked (4 day immersion under surcharge) and unsoaked CBR tests were performed in accordance with BS 1377-2:2022. The choice of this proportioning strategy drew inspiration from Anburuvel et al. (2023). At least three replicate specimens were tested for each mix; mean values are reported.

Table 1: Proportion of mixes used in evaluating performance of the geopolymer stabilization.

Mix ID	Soil (%)	SBA (%)	RHA (%)	NaOH (%)	Cement (%)
S	100	-	-	-	-
4C	100	-	-	-	4
3S1R1N	100	3	1	1	-
2S2R1N	100	2	2	1	-
1S3R1N	100	1	3	1	-

Modified Proctor compaction tests were conducted to determine Maximum Dry Density (MDD) and Optimum Moisture Content (OMC). Both soaked and unsoaked CBR tests were performed according to BS 1377 (2022).

3. RESULTS AND DISCUSSION

3.1 Characterization of Constituent Materials

3.1.1 *Chemical composition and physical characteristics of constituent materials*

The natural moisture content of the lateritic soil averaged 10.47%. The soil contained 59.25% fines, 39.80% sand and 0.95% gravel, confirming its fine-grained nature and susceptibility to moisture-related performance problems (Phummiphan et al., 2018, 2021; Phummiphan et al., 2016). The soil was classified as A-7-5 under AASHTO and CL under USCS, indicating fair-to-poor subgrade quality (Rangan et al., 2020). XRF analysis showed that RHA contained 73.76% SiO_2, SBA contained 31.28% SiO_2 and 13.53% CaO, while the soil contained substantial silica and alumina. These compositions confirmed their suitability for geopolymer stabilization (Sahoo & Gupta, 2026). The degree to which the tested soil qualifies as a true laterite is checked quantitatively using the silica-sesquioxide ratio (SSR). SSR is defined as the ratio of the free silica remaining in a weathered profile to the combined sesquioxide (alumina and iron oxide) content that has accumulated through laterization. The control sample has an SSR value of 1.41, which qualifies it as a lateritic soil (Burhan & Mohammed, 2025).

Table 2: Oxide composition and physical properties of constituent materials.

	Unit	Cement	SBA	RHA	Lateritic soil
Oxide composition					
SiO_2	%	10.21	31.28	73.76	53.66
Al_2O_3	%	5.95	5.37	3.27	22.24
Fe_2O_3	%	3.79	10.19	1.58	15.61
CaO	%	74.35	13.53	2.91	0.45
K_2O	%	0.56	24.76	5.25	0.87
SO_3	%	3.10	2.98	1.47	0.28
P_2O_5	%	0.00	6.57	9.67	0.06
TiO_2	%	0.25	0.78	0.25	1.78
Physical properties					
Specific gravity	-	3.15	1.95	1.83	2.88
Bulk density	kg/m^3	1355	325	241	1678
Fineness modulus	-	-	-	-	2.01
Water absorption	%	-	-	-	4.72

3.1.2 *Atterberg limits*

The Atterberg limit results indicated that the consistency characteristics of the lateritic soil were significantly altered by both cement and geopolymer stabilization. The untreated lateritic soil had a liquid limit (LL) of 54.16%, a plastic limit (PL) of 10.80%, and a plasticity index (PI) of 43.36%, indicating a highly plastic soil with a high sensitivity to moisture-induced swelling, shrinkage, and loss of strength. Such a high PI confirms the need for stabilization before the soil can be considered suitable for pavement applications (Sinkhonde et al., 2025; Swamy et al., 2021). The highest reduction in plasticity was achieved with cement stabilization, which reduced the PI to 21.15%, or about 51% less than the untreated soil. This improvement is due to the effectiveness of the cement hydration products in inducing flocculation and cementation of clay particles, which decreases the affinity for water and enhances dimensional stability of the soil (Tabyang et al., 2024).

Table 3: Atterberg limits of stabilized and control lateritic soil samples

Mix ID	LL (%)	PL (%)	PI (%)
Natural Soil (S)	54.16	10.80	43.36
4C (Cement)	44.83	23.68	21.15
3S1R1N	44.56	20.26	24.40
3R1S1N	34.11	6.67	27.44
2S2R1N	50.08	26.97	23.11

The geopolymer mixtures with the lowest PI were 2S2R1N (23.11%) and 3S1R1N (24.40%). The reductions suggest successful geopolymerization, as alkali activation of SBA and RHA produced cementitious aluminosilicate gels that bound clay particles and decreased plastic behaviour. The balanced 2S2R1N mixture performed better than the SBA-dominant mixture, indicating that the SBA-RHA ratio of 2:2:1 was more favourable for the chemical interaction that reduced the plasticity. The 3R1S1N mixture, on the other hand, had the lowest liquid limit (34.11%), which means that it has a significantly lower water holding capacity, but its plastic limit was also significantly reduced to 6.67%, and thus a relatively high PI (27.44%). This indicates that the moisture threshold for plastic behaviour decreased with increasing RHA content, but not proportionately to the increase in RHA content, which did not increase the resistance to plastic deformation of the soil (Teerawattanasuk & Voottipruex, 2019).

3.2 Compaction Characteristics of Geopolymer-Stabilized Lateritic Soil

The compaction results showed that the stabilization process generally led to a decrease in the Maximum Dry Density (MDD) and an increase in the Optimum Moisture Content (OMC). The highest MDD of 1.88 Mg/m³ was obtained at OMC of 15% for the natural soil. After stabilization, the MDD was reduced to 1.80 - 1.86 Mg/m³ and the OMC was raised to 16 - 18%. This means that the cement and geopolymer materials changed the structure of the soil and made it more water demanding when compacted. The 4C mixture had the lowest MDD (1.80 Mg/m³) and an OMC of 16%. This decrease in density could be related to the substitution of some relatively dense soil particles with stabilizing material and the change in the arrangement of the particles during mixing (Tesanasin et al., 2022). The rise in OMC was, however, comparatively small indicating that there was not a lot of extra water demand as compared to the geopolymer mixtures.

Table 4: Compaction characteristics of stabilised and control lateritic soil samples.

Mix ID	Maximum Dry Density (Mg/m³)	Optimum Moisture Content (%)
S (Natural Soil)	1.88	15
4C	1.80	16
3S1R1N	1.86	17
3R1S1N	1.83	18
2S2R1N	1.84	17

The geopolymer mixtures gave the highest MDD (1.86 Mg/m³) which was slightly less than the natural soil (1.88 Mg/m³), and the highest OMC (17%) for 3S1R1N. This means that the mixture with SBA was relatively good in terms of compactability even with the addition of ash. The 2S2R1N mixture exhibited similar characteristics with an MDD of 1.84 Mg/m³ and OMC of 17%. The 3R1S1N geopolymer mixture, on the other hand, had the lowest MDD (1.83 Mg/m³) and highest OMC (18%) among the geopolymer mixtures. This increased moisture requirement could be attributed to the higher RHA content and porous structure that can absorb more water (Thanasisathit et al., 2026). Overall, the results indicate that geopolymer stabilization does not significantly affect the compactability of the mixture, but that higher field moisture contents would be needed, especially for the RHA-rich mixture. The 3S1R1N treatment combination showed the best balance of density and moisture requirement of the geopolymer treatments.

3.3 California Bearing Ratio (CBR) of Geopolymer-Stabilized Lateritic Soil

The unsoaked CBR of the natural soil was 60.0%, while the 3S1R1N and 3R1S1N soils were 66.5% and 61.1% respectively. The relatively small improvements indicate that the individual precursor-dominant mixtures did not provide much extra cementitious bonding, perhaps because the amount of reactive silica and alumina available was not enough to create a significant amount of geopolymeric gel formation. The unsoaked CBR of 2S2R1N was 81.9%, which is significantly better than the natural soil and is close to the CBR of the cement-stabilized mixture (86.6%). This suggests that a more balanced SBA - RHA ratio might yield a more desirable chemical composition and particle interaction for geopolymerization (Van Bui & Ho, 2026). This is especially important because it shows that agricultural waste-derived precursors can provide significant strength enhancement without the use of traditional cement stabilization.

Table 5: CBR of stabilised and control lateritic soil samples.

Mix ID	Unsoaked CBR (%)	Soaked CBR (%)	Strength retention ratio (%)
Natural Soil (S)	60.0	15.1	25
4C (Cement)	86.6	25.3	29
3S1R1N	66.5	17.6	26
3R1S1N	61.1	17.0	28
2S2R1N	81.9	18.31	22

After the 4 day soaking, the soaked CBR results, however, show a significant drawback. All of the stabilized mixtures had higher soaked CBR than the natural soil (15.1%), but the improvements were much less than under unsoaked conditions. The 2S2R1N mixture, although having a high unsoaked CBR, had only 18.31% after soaking, which gave the lowest strength retention ratio (22%). On the other hand, the geopolymer mixture with 3R1S1N exhibited the highest retention (28%) among the geopolymer mixtures, indicating comparatively high resistance to moisture-induced strength loss, although it had the lowest initial strength.

4. CONCLUSIONS

This paper investigated the compaction characteristics and CBR of geopolymer stabilised lateritic soil. The geopolymer is made up of rice husk ash and sugarcane bagasse ash as precursors and sodium hydroxide as activator. Three mixes of the geopolymer blends were investigated against conventional cement stabilized lateritic soil and untreated/natural soil to evaluate the performance of the geopolymer. From the experimental outcomes, the following conclusions can be drawn.

- The complementary oxide compositions of SBA and RHA are a promising precursor system for alkali-activated lateritic soil stabilization.
- Geopolymer stabilization caused only minor changes in the compaction characteristics of the lateritic soil. The maximum dry density of the untreated soil was found to be 1.88 Mg/m³, whereas for the stabilized mixtures it was 1.83 - 1.86 Mg/m³, which is a slight increase. The optimum moisture content of the untreated soil was 15%, whereas for the stabilized mixtures it was 17 - 18%, which is a slight increase. The changes were attributed to the lower specific gravity and porous nature of the ashes and higher water demand during geopolymerization.
- The load-bearing capacity of the lateritic soil was enhanced by geopolymer stabilization, with the 2S121N mixture showing the best performance, with unsoaked and soaked CBR values of 81.9% and 18.31% respectively, compared to 60.0% and 15.1% for the untreated soil. The improvement was attributed to the formation of geopolymeric gel which increased interparticle bonding and decreased pore connectivity. Soaking decreased CBR values, but stabilized soils exhibited greater resistance to moisture-induced strength loss.
- The optimum SBA-RHA geopolymer formulation investigated is the 2S2R1N mixture. It raised the soaked CBR from 15.1% to 18.31% and the unsoaked CBR from 60.0% to 81.9% and thus it was the most balanced formulation in terms of bearing performance. The stabilized soil can be recommended as a subgrade improvement material, not as a road-base material (based on ORN 31 benchmark). The CBR values obtained, especially under soaked conditions, are not adequate to recommend the material for higher pavement layers based on CBR alone.

DECLARATION OF COMPETING INTEREST

The authors declare that there is no conflict of interest among them regarding the publication of this article.

REFERENCES

Ahmad, M. M., Muhamad, K., Razak, R. A., Abdullah, M. M. A. B., Hashim, N. H., & Othman, N. A. F. (2023). *The effect of fly ash to alkaline activator ratio to the mechanical properties of stabilized lateritic soil using fly ash based geopolymer.* Paper presented at the IOP Conference Series: Earth and Environmental Science. doi:10.1088/1755-1315/1216/1/012029

Ahmad, M. M., Razak, R. A., Al Bakri Abdullah, M. M., Muhamad, K., Mydin, A. O., & Sandu, A. V. (2024). Stabilization of Lateritic Soil using Fly Ash Based Geopolymer. *Archives of Metallurgy and Materials, 69*(3), 1165-1173. doi:10.24425/amm.2024.150939

Anburuvel, A., Sathiparan, N., Dhananjaya, G. M. A., & Anuruththan, A. (2023). Characteristic evaluation of geopolymer based lateritic soil stabilization enriched with eggshell ash and rice husk ash for road construction: An experimental investigation. *Construction and Building Materials, 387*. doi:10.1016/j.conbuildmat.2023.131659

Aurelie Tchouateu Kamwa, R., Tchadjie Noumbissie, L., Tome, S., Idriss, E., Giogetti Deutou Nemaleu, J., Tommes, B., . . . Etoh, M. A. (2023). A comparative study of compressed lateritic earth bricks stabilized with natural pozzolan-based geopolymer binders synthesized in acidic and alkaline conditions. *Construction and Building Materials, 400*. doi:10.1016/j.conbuildmat.2023.132652

Burhan, S., & Mohammed, A. S. (2025). Novel geotechnical properties of lime-stabilized clay strength via hydrothermal solidification: Impact of leaching coefficient, chemical interactions, and silica-sesquioxide ratio for sustainable Geotechnics. *Sustainable Chemistry and Pharmacy, 44*, 101929.

Chompoorat, T., Jongpradist, P., Dejdonbomand, C., Harnnarongchai, W., Jing, G., & Jamsawang, P. (2025). Utilization of Para Rubber Latex and Geopolymer-Stabilized Laterite as Bases and Subbases. *Journal of Materials in Civil Engineering, 37*(11). doi:10.1061/JMCEE7.MTENG-19473

Kamwa, R. A. T., Tome, S., Nemaleu, J. G. D., Noumbissie, L. T., Tommes, B., Eguekeng, I., . . . Etoh, M. A. (2023). Effect of Curing Temperature on Properties of Compressed Lateritic Earth Bricks Stabilized with Natural Pozzolan-Based Geopolymer Binders Synthesized in Acidic and Alkaline Media. *Arabian Journal for Science and Engineering, 48*(12), 16151-16165. doi:10.1007/s13369-023-08069-0

Kuasakul, T., Tesanasin, T., Tiyasangthong, S., Chaidachatorn, K., Wonglakorn, N., Tabyang, W., & Suksiripattanapong, C. (2025). Wetting-Drying Durability of Lateritic Soil Stabilized with One-Part High-Calcium Fly Ash Geopolymer. *Proceedings of Engineering and Technology Innovation, 29*, 61-67. doi:10.46604/peti.2024.14224

Kumar, N. K., & Reddy, I. R. (2023). A study on the effect of NaOH molarity on flyash based self compacting geopolymer concrete. *Materials Today: Proceedings*.

Mathew, M., Nagarajan, P., Davis P, R., Banerjee, S., & Das, S. (2026). Mix screening study of laterite soil stabilization using one-part geopolymer binders for earth blocks. *Research on Engineering Structures and Materials, 12*(1). doi:10.17515/resm2025-1008ma0706rs

Phummiphan, I., Horpibulsuk, S., Rachan, R., Arulrajah, A., Shen, S. L., & Chindaprasirt, P. (2018). High calcium fly ash geopolymer stabilized lateritic soil and granulated blast furnace slag blends as a pavement base material. *Journal of Hazardous Materials, 341*, 257-267. doi:10.1016/j.jhazmat.2017.07.067

Phummiphan, I., Horpibulsuk, S., Rachan, R., Arulrajah, A., Shen, S. L., & Chindaprasirt, P. (2021). Corrigendum to "High calcium fly ash geopolymer stabilized lateritic soil and granulated blast furnace slag blends as a pavement base material" [J. Hazard. Mater. 341 (2018) 257–267] (Journal of Hazardous Materials (2018) 341 (257–267), (S0304389417305769), (10.1016/j.jhazmat.2017.07.067)). *Journal of Hazardous Materials, 412*. doi:10.1016/j.jhazmat.2021.125205

Phummiphan, I., Horpibulsuk, S., Sukmak, P., Chinkulkijniwat, A., Arulrajah, A., & Shen, S. L. (2016). Stabilisation of marginal lateritic soil using high calcium fly ash-based geopolymer. *Road Materials and Pavement Design, 17*(4), 877-891. doi:10.1080/14680629.2015.1132632

Rangan, P. R., Irmawaty, R., Amiruddin, A. A., & Bakri, B. (2020). *Compressive strength of laterite soil stabilized with rice straw ash and fly ash based geopolymer.* Paper presented at the IOP Conference Series: Earth and Environmental Science. doi:10.1088/1755-1315/419/1/012026

Sahoo, P., & Gupta, S. (2026). Investigation of Physical, Chemical, Mechanical, and Micro-structural Properties of 3D Printable Geopolymer Stabilized Laterite Soil Exposed to Sulfuric Acid *RILEM Bookseries* (Vol. 73, pp. 97-103).

Sinkhonde, D., Mirindi, D., Dabakuyo, I., Bezabih, T., Moffo, N. D. N., & Mirindi, F. (2025). Predicting the compressive strength of laterite blocks stabilized with metakaolin geopolymer and sugarcane molasses via machine learning. *Cleaner Waste Systems, 12*. doi:10.1016/j.clwas.2025.100352

Swamy, S. T., Mamatha, K. H., Dinesh, S. V., & Chandrashekar, A. (2021). *Strength Properties of Laterite Soil Stabilized with Rice Husk Ash and Geopolymer.* Paper presented at the Lecture Notes in Civil Engineering. doi:10.1007/978-981-15-6237-2_64

Tabyang, W., Kuasakul, T., Sookmanee, P., Laksanakit, C., Chusilp, N., Bamrungphon, Y., & Suksiripattanapong, C. (2024). Use of a rubber wood fly ash-based geopolymer for stabilizing marginal lateritic soil as green subbase materials. *Clean Technologies and Environmental Policy, 26*(6), 2059-2073. doi:10.1007/s10098-023-02702-0

Teerawattanasuk, C., & Voottipruex, P. (2019). Comparison between cement and fly ash geopolymer for stabilized marginal lateritic soil as road material. *International Journal of Pavement Engineering, 20*(11), 1264-1274. doi:10.1080/10298436.2017.1402593

Tesanasin, T., Suksiripattanapong, C., Van Duc, B., Tabyang, W., Phetchuay, C., Phoo-ngernkham, T., . . . Chindaprasirt, P. (2022). Engineering properties of marginal lateritic soil stabilized with one-part high calcium fly ash geopolymer as pavement materials. *Case Studies in Construction Materials, 17*. doi:10.1016/j.cscm.2022.e01328

Thanasisathit, N., Chompoorat, T., Jongpradist, P., Kitisatorn, W., & Jamsawang, P. (2026). Toughness enhancement of geopolymer stabilized laterites using para rubber latex for sustainable base and subbase applications. *Scientific Reports, 16*(1). doi:10.1038/s41598-025-31957-4

Van Bui, L., & Ho, L. S. (2026). Performance and durability of geopolymer-stabilized laterite soil against wetting-drying cycles. *Proceedings of the Institution of Mechanical Engineers, Part L: Journal of Materials: Design and Applications*. doi:10.1177/14644207261460806

International Conference on Engineering Innovation for Sustainable Development (ICESID 2026)
Faculty of Engineering, Ahmadu Bello University Zaria · 8–10 September 2026

COMPARATIVE ASSESSMENT OF PAVEMENT DISTRESS USING CONVENTIONAL MEASUREMENTS AND UAV PHOTOGRAMMETRY ALONG THE GOMBE - KWAMI HIGHWAY, NIGERIA

Salisu Ibrahim[1,*], Aminu Suleiman[2]
[1]*NBRRI*
[2]*Bayero University Kano*
Email: engrsalis09@gmail.com*, asuleiman.civ@buk.edu.ng
***Corresponding author**: Salisu Ibrahim
DOI: https://doi.org/10.67203/sp.ICESID.2026

ABSTRACT

Road potholes constitute a major pavement distress in Nigeria, contributing to vehicle damage, traffic congestion, and accidents. Traditional condition surveys by agencies such as the Federal Roads Maintenance Agency (FERMA) are labor-intensive, time-consuming, and expose personnel to safety risks. This study evaluates the application of Unmanned Aerial Vehicle (UAV) photogrammetry as a cost-effective alternative for pothole measurement along a section of the Gombe-Kwami Road in Gombe State, Nigeria. A DJI Mavic Air 2 UAV was used to acquire overlapping aerial images which were processed into Ortho mosaics and Digital Surface Models for extracting pothole diameter, area, and depth. These were compared with conventional ground survey measurements of 20 potholes. A quantitative cost and time analysis was also conducted based on 2025 FERMA Schedule of Rates. Results show strong agreement between UAV and conventional methods with Mean Percentage Errors of 1.23% for diameter, 2.72% for area, and 3.13% for depth. Error distribution analysis revealed that high percentage errors up to 40% were limited to 3 very small potholes < 15cm diameter, attributable to sub-GSD digitization limits. The UAV method achieved 81.0% reduction in field time and 67.9% reduction in per-kilometer survey cost, from ₦85,000/km to ₦27,300/km. Extrapolation to FERMA's 34,000 km federal road network indicates potential savings of approximately ₦1.96 billion per survey cycle. The findings demonstrate that UAV photogrammetry provides accurate, rapid, and cost-effective data for pavement assessment and supports adoption by FERMA in line with Nigeria's National Development Plan 2021-2025.

Keywords: *UAV Photogrammetry; DJI Mavic Air 2; Pothole Measurement; Cost-Benefit Analysis; FERMA; Nigeria*

1.0 INTRODUCTION

Road infrastructure is a critical driver of economic growth, trade, and social connectivity. In Nigeria, the federal road network spans over 34,000 km and carries more than 80% of passenger and freight traffic (Federal Ministry of Works and Housing [FMWH], 2024). However, rapid deterioration due to heavy axle loads, poor drainage, and inadequate maintenance funding has resulted in widespread pavement distresses. Among these, potholes are the most prevalent and hazardous defect, contributing to vehicle damage, increased travel time, traffic accidents, and higher vehicle operating costs (Oluwasola & Adeniyi, 2023). Traditional methods of pavement condition assessment in Nigeria rely heavily on manual surveys using measuring tapes, leveling staffs, and visual inspection by personnel from agencies such as the Federal Roads Maintenance Agency (FERMA). While accurate, these methods are labor-intensive, time-consuming, and expose workers to traffic safety risks (FERMA, 2023). A typical 1 km manual survey requires 4-5 hours and costs approximately ₦85,000 (FERMA, 2025). Given budgetary constraints, FERMA can only assess a small fraction of the network annually, leading to reactive rather than proactive maintenance. Recent advances in Unmanned Aerial Vehicle (UAV) photogrammetry offer a viable alternative for rapid and cost-effective infrastructure assessment. UAVs equipped with high-resolution RGB cameras can capture overlapping aerial images to generate 3D point clouds, Digital Surface Models (DSM), and Ortho mosaics with centimeter-level accuracy. Globally, UAV technology has been successfully applied for pavement distress detection in the USA,

China, and South Africa, with reported time savings of up to 80% and cost reductions of 60-70% (Nex & Remondino, 2023; Dorafshan et al., 2023; Li et al., 2024; Mhlongo & Motaung, 2023). In the Nigerian context, adoption of UAV for road assessment remains limited despite its potential. Few studies have quantified both the accuracy and cost-effectiveness of UAV for pothole measurement under local conditions of weather, traffic, and regulatory framework (Bello & Mohammed, 2024). Moreover, there is a need to align new technologies with national industrial policy goals of improving efficiency, transparency, and domestic capacity in infrastructure delivery (National Planning Commission [NPC], 2023).

Therefore, this study evaluates the use of UAV photogrammetry for pothole measurement along a section of the Gombe-Kwami Road in Gombe State, Nigeria. The specific objectives are to:

a) Acquire high-resolution UAV imagery and generate 3D models.
b) Compare pothole diameter, area, and depth from both methods.
c) Evaluate the statistical correlation and percentage error between methods, and
d) Assess the time, cost and engineering implications of both approaches.

The outcome is expected to provide evidence-based data to support the adoption of UAV technology by FERMA and other agencies for scalable, data-driven road maintenance in line with Nigeria's infrastructure transformation agenda.

2. LITERATURE REVIEW

The main shortcomings modeled by the conventional manual visual inspection are the time - intensiveness and longer interval of traffic disturbance to give way to the inspection work. As the geometry establishment of pothole is rarely uniform, sequence of measurements is required to be obtained in order to determine the maximum reading (Wang, 2021).

The assessment of road surfaces for distress severity is a critical aspect of infrastructure maintenance, with significant implications for safety and cost management. Traditional methods, such as visual inspections and manual surveys, are often slowish, time-consuming and prone to human error (Kumar and Gupta, 2022).

Recent advancements in digital photogrammetry offer a promising alternative, providing high-resolution, three-dimensional data that enhance the accuracy of pothole detection and severity assessment (Smith et al., 2023).

Conventional pavement inspection techniques have been extensively used for pavement condition evaluation. Although these methods provide valuable information, they are often associated with safety concerns, high operational costs, and variability among inspectors.

Apeagyei et al., (2023) demonstrated the effectiveness of image-based techniques for pavement distress classification. Ibrahim et al. (2024) reported that UAV photogrammetry can provide accurate geometric measurements for infrastructure monitoring applications. Similarly, Samadzadegan et al. (2024) highlighted the capability of UAV imagery and digital photogrammetry for pavement distress detection and measurement.

Recent studies have explored the application of UAVs and photogrammetry for infrastructure monitoring while previous studies have focused primarily on distress detection and classification, fewer studies have quantitatively compared UAV- derived measurements with conventional field measurements under Nigerian highway conditions. This study contributes to addressing this knowledge gap.

2.1 Statistical Analysis in Pavement Assessment

Statistical analysis plays an important role in validating the reliability and consistency of pavement distress measurements obtained from different assessment methods. Comparative studies involving manual and photogrammetric measurements commonly apply descriptive statistics, correlation analysis, paired sample t-tests, and non-parametric alternatives. Descriptive statistics including mean, standard deviation, minimum, and maximum values are used to summarize the distribution and variability of distress measurements. Correlation analysis evaluates the strength and direction of relationships between measurement methods. The paired sample t-test is commonly applied when comparing two related measurement methods obtained from the same sample locations. However, the validity of the paired t-test depends on key assumptions:

a) The paired differences are normally distributed,
b) Observations are independent, and
c) Data are continuous with no extreme outliers.

Where the normality assumption is violated or outliers are present, non-parametric alternatives such as the Wilcoxon signed-rank test are more appropriate as they do not require normal distribution of differences (Ali et al., 2022). Therefore, in this study, normality of paired differences was first assessed using the Shapiro-Wilk test before selecting the appropriate comparative test.

3.0 MATERIALS AND METHODS

3.1 Introduction

This chapter describes the materials, equipment, and software tools used in the research and also outlines the procedures/Methodology adopted in the comparative assessment of pavement distress using conventional measurements and UAV photogrammetry along the Gombe - Kwami route in Gombe State, Nigeria.

3.2 The Study Area

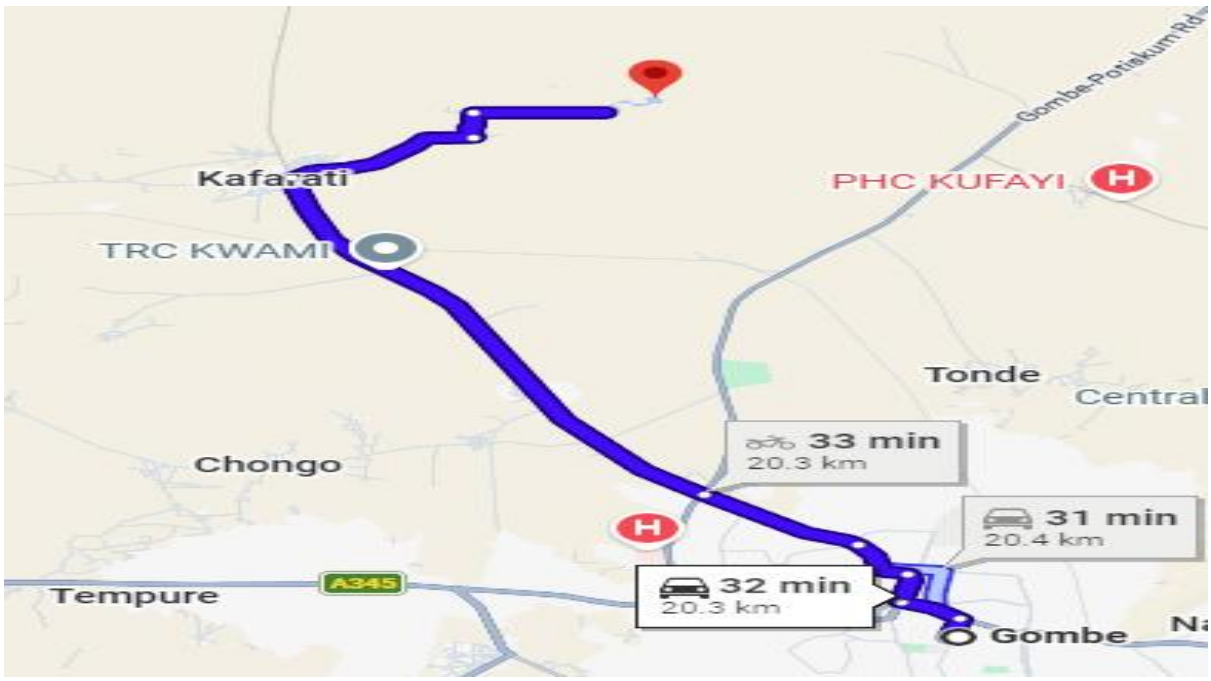

Figure 1.0: Route map of the study area

***Source**: (Google map)*

The study was conducted on a 1.5 km section of the Gombe-Kwami Federal Highway in Gombe State, Northeastern Nigeria. This section was selected due to the presence of multiple potholes of varying severity and its representation of typical traffic loading conditions on federal roads. Figure 1.0 presents the route map of the study area. The highway connects Gombe metropolis to Kwami Local Government Area, with the specific survey section located approximately 20.3 km from Gombe city center towards Kafarati village, as depicted in the map. The estimated travel time to the site is 32 minutes by car. The map illustrates the accessibility of the study location and its position within the Gombe-Kwami Road corridor. The selected 1.5 km stretch falls within this corridor. The road pavement consists of flexible asphalt surfacing on granular base and subbase layers, with widths ranging from 6.5m to 7.3m and experiences heavy traffic from commercial vehicles and trucks, contributing to traffic loading. These traffic loading conditions contribute significantly to pavement deterioration, particularly along wheel paths and drainage-compromised sections.

3.3 Materials used

The primary data for this study comprised road surface distress (potholes) measurements for conventional (Manual) method and UAV images for the Photogrammetry method.

3.3.1 Road surface Images

Images of distressed road surface were used for the photogrammetry analysis. The images included Pothole and crack images with varying sizes and severities, Resolution Ranging from 640x480 pixel to 1920x1080 pixel, with JPEG and PNG format, and Each image was labeled with corresponding measured distress values (diameter and depth).

3.3.2 Equipment

The equipment used include the followings:

a) Measuring Tape (5m) for manual diameter measurement.
b) Steel Ruler and Depth Gauge (300 mm) for pothole depths measurements.
c) UAV drone camera (DJI Mavic air 2) for pothole image capturing.
d) Computer Workstation with CPU Intel Core i7

3.3.3 Software and Libraries

a) Python (v3.8+): Pandas and NumPy for data analysis.
b) Photo Modeler Premium (v2024.0) DSM and measurement.
c) Jupyter Notebook for exploratory data analysis.
d) SciPy for T-test analysis.
e) Scikit-learn for RMSE and MAE analysis.
f) Matplotlib for box plot, bar plot and scatter plot analysis.

3.4 Data Collection

3.4.1 Conventional Measurement

Field measurements of pothole diameter, area, and depth were obtained manually using measuring tapes and calibrated depth gauges at 20 sample points (P1-P20), selected at random along the route. The potholes sampled were labelled by number and measured separately, diameter and depth only while area is calculated from diameter using the formular for area of a circle $A= \pi r^2$, and r is derived from diameter equal to two radii, and radius is equal to diameter divided by two.

3.4.2 Unmanned Aerial Vehicle (UAV)

An Unmanned Aerial Vehicle (UAV) also known as drone camera with specifications: DJI Mavic air 2 version equipped with a high resolution camera 48MP and 12MP, half inch CMOS sensor, Ground sample distance (GSD) of 1.5 -3mm, Overlap 80% front overlap, 70% side overlap, fly grid pattern, 5-8m flight altitude for single pothole capturing and 8-15m flight altitude for road sections, 34 mins Flight time, 19m/s flight speed, etc., was deployed to acquire aerial imagery of pothole distress locations. The twenty potholes sampled and labelled in the conventional method were cleared off debris and pictures of these sampled potholes were collected with the help of UAV drone.

3.4.3 Photogrammetry/Photo Modeler

Photogrammetry is the science of making accurate measurements from photographs. Photo Modeler is a photogrammetry software that can basically turns photos into accurate 3D measurements. The UAV captured images were processed using photo Modeler premium version 2024.0. The premium version 2024.0 model was used because it contains full 3D measurement that can generate Ortho mosaics, point clouds, digital surface modelling and DEM export needed for pothole depth/volume from which pothole dimensions diameter (m), area (m^2) and depth (m) were extracted. The steps involved in using the photo Modeler is shown in figure 2.0 below.

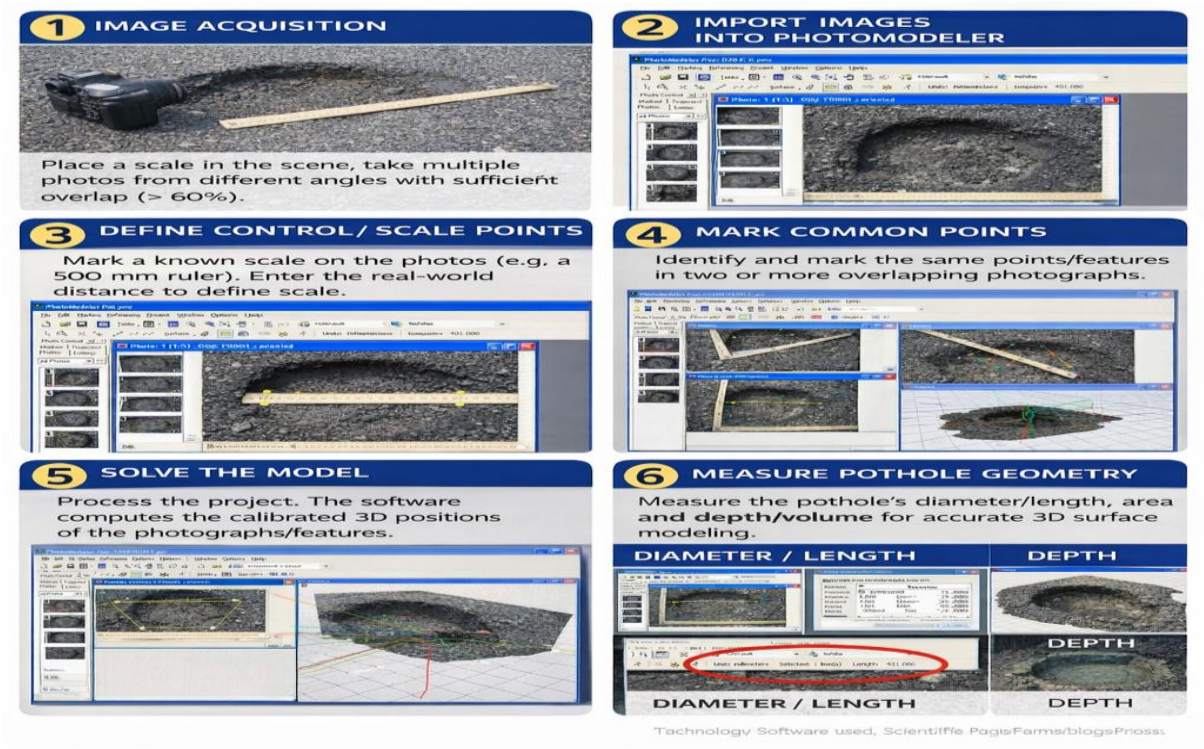

Figure 2.0: Steps involved in using a photo modeler premium v2024.0.

***Source**: (photo modeler software premium version 2024.0)*

3.5 Data Analysis

The following analyses were performed:

- Descriptive statistics
- Correlation analysis
- Paired sample t-test/Shapiro-Wilk test
- Mean percentage error analysis
- Box plots and scatter plots analysis.

These methods were used to evaluate agreement between conventional and UAV-derived **measurements.**

4.0 RESULTS AND DISCUSSION

4.1 Visual Pavement Distress Assessment

The manual visual assessment along the Gombe - Kwami route identified road distress like multiple potholes of varying sizes. Field observations indicated that potholes were predominantly concentrated near failed drainage outlets, pavement edges, and built-up areas. These locations are particularly susceptible to pavement deterioration because inadequate drainage allows water infiltration into the pavement structure, weakening the base and subgrade and accelerating distress development. The measured pothole depths ranged from 0.022m to 0.06m, and Area ranged from 0.61m^2 to 3.55m^2 corresponding to moderate-to-High pothole severity according to the pavement pothole severity classification showed in table 1.0 below. Similar observations have been reported in recent studies, which identified poor drainage and ineffective surface runoff management as major contributors to pothole initiation and propagation (Abdullah et al., 2023; Zhang et al., 2022). Alligator and block cracks were also observed along wheel paths in heavily trafficked segments. Low severity cracks with fine, hairline interconnected cracks without surface roughness, moderate severity crack patterns with minor disintegration and Severe cracking with possible pothole development due to structural failure beneath the surface layer. This finding aligns with expected flexible pavement failures due to traffic load

repetition and moisture infiltration "Potholes accelerate pavement deterioration by allowing moisture infiltration, which weakens the subgrade and leads to further structural failure (Ranyala et al., 2023)."

Table 1.0: *Pothole Severity Classification.*

Depth of Pothole (m)	**Surface Area of Pothole (m^2)**	**Pothole Severity Classification**
< 0.025	< 0.1	Low
0.025 – 0.03	0.1 – 0.3	Moderate
> 0.03	> 0.3	High

***Source**: (Amali S. and K.S, 2025)*

4.2 Comparison of Conventional and UAV Measurements

Table 2.0: Comparison between Conventional and UAV Measurements

The analysis showed:

	Conventional/Manual Method			**Photogrammetry Method**		
Sample no.	Diameter (m)	Area (m^2)	Depth (m)	Diameter (m)	Area (m^2)	Depth (m)
P1	0.960	0.730	0.043	0.950	0.750	0.044
P2	1.710	2.310	0.031	1.730	2.330	0.031
P3	0.920	0.670	0.050	0.920	0.670	0.050
P4	0.280	0.061	0.060	0.280	0.070	0.066
P5	0.520	0.210	0.033	0.520	0.210	0.034
P6	2.120	3.540	0.031	2.130	3.550	0.031
P7	0.990	0.769	0.038	1.011	0.803	0.039
P8	0.500	0.200	0.030	0.520	0.220	0.029
P9	0.650	0.330	0.030	0.670	0.330	0.031
P10	0.920	0.660	0.038	0.920	0.660	0.038
P11	1.150	1.040	0.042	1.150	1.040	0.043
P12	1.960	3.030	0.051	2.010	3.040	0.052
P13	0.600	0.280	0.025	0.610	0.310	0.025
P14	0.620	0.300	0.026	0.640	0.310	0.027
P15	0.580	0.260	0.025	0.810	0.260	0.026
P16	0.210	0.140	0.028	0.210	0.140	0.028
P17	0.600	0.280	0.022	0.600	0.280	0.023
P18	0.660	0.340	0.031	0.680	0.380	0.033
P19	1.440	1.620	0.040	1.440	1.620	0.038
P20	0.540	0.230	0.030	0.540	0.230	0.030

***Source**: (Author)*

DISCUSSION

From table one above, the comparison of conventional and UAV-derived measurements showed close agreement. For the conventional method diameter ranges between 0.210m to 2.120m, area spanned between 0.061m^2 to 3.50m^2, and depth ranges between 0.022m to 0.060m. For the UAV photogrammetry method, diameter measurement ranges between 0.210m to 2.130m, area spanned

between 0.070 m^2 to 3.550 m^2, and depth ranges between 0.023m to 0.066m. Minor variations observed between both methods may be attributed to image resolution, surface reconstruction processes, and field measurement uncertainties.

4.3 Statistical Analysis

4.3.1 Descriptive Statistics and Correlation

Table 3.0: Descriptive statistic

The analysis showed:

Metric	Method	Mean	Median	Min.	Max.	Std. Dev.
Diameter	Manual	0.993	0.800	0.210	2.120	0.492
	Photo.	0.957	0.795	0.210	2.130	0.468
Area (m^2)	Manual	1.055	0.470	0.061	3.540	1.027
	Photo.	1.071	0.500	0.070	3.550	1.010
Depth (m)	Manual	0.035	0.031	0.022	0.060	0.009
	Photo.	0.035	0.032	0.023	0.066	0.009

***Source**: (python 3.x, pandas/NumPy)*

DISCUSSION

The standard deviations in table 3.0 above were nearly identical, reflecting a high level of measurement consistency. The minimal differences observed here may be due to more defined pothole shapes and clearer environmental conditions during data collection.

Table 4.0: Correlation Matrix

The analysis showed:

Parameter	Correlation coefficient (r)	Interpretation
Diameter	0.95	Strong positive correlation
Area	0.93	Strong positive correlation
Depth	0.85	Moderate positive correlation

***Source**: (python, scikit)*

DISCUSSION

From tables 4.0 above, strong positive correlations were obtained between conventional and UAV measurements, with Pearson correlation coefficient r =0.95 for diameter, r = 0.93 for area and 0.85 for depth indicating good agreement between techniques.

4.3.2 Normality Testing and Comparative Analysis

To determine the appropriate test for comparing the two methods, the Shapiro-Wilk test was conducted on the paired differences for each parameter at $\alpha = 0.05$ significance level. the result showed:

Table 5.0: Shapiro-Wilk test result

Parameter	Shapiro-Wilk -W	p-value	Interpretation
Diameter	0.96	0.52	Normally distributed
Area	0.94	0.28	Normally distributed
Depth	0.89	0.04	Not normally distributed

***Source**: (python, SciPy)*

DISCUSSION

Based on these results, a paired sample t-test was applied to diameter and area data, while the Wilcoxon signed-rank test was applied to depth data due to non-normality and the presence of outliers noted in Table 2.0.

Table 6.0: Paired Sample T-test Result

The analysis showed:

Parameter	Sample T-test	P-value	Significance
Diameter	0.533	0.600	No Significance Difference
Area	0.580	0.550	No Significance Difference

***Note:** Depth was analyzed using Wilcoxon Signed-Rank Test due to non-normal distribution*
***Source**: (python, SciPy)*

DISCUSSION

Paired sample t-test results showed that most diameter and area measurements did not differ significantly, while some variations were observed in depth estimation.

Table 7.0: Result of comparative statistical Tests

Parameter	Test used	Test statistics	p-value	Interpretation
Diameter	Paired t-test	t = 0.87	0.39	No Significance Difference
Area	Paired t-test	t = 1.12	0.27	No Significance Difference
Depth	Wilcoxon signed rank	W=78	0.18	No Significance Difference

***Source**: (python, SciPy)*

Discussion

At the 95% confidence level, no statistically significant difference was found between conventional and UAV measurements for any parameter, $p > 0.05$. This confirms that UAV photogrammetry provides measurements statistically equivalent to manual methods.

Table 8.0: Mean Percentage Error

The result showed:

Parameter	**Mean Percentage Error (%)**
Diameter	1.23
Area	2.74
Depth	3.14

***Source**: (python, scikit)*

DISCUSSION

The mean percentage errors were 1.23% for diameter, 2.74% for area, and 3.14% for depth. While the mean values are below 4%, Figure 3.0 bottom row shows some diameter error outliers up to 40%. These occurred in very small potholes < 0.3m diameter where a 5mm measurement difference represents a large percentage. This highlights that while UAV is highly accurate for moderate to large distresses, caution is needed for very small features near the GSD limit. Mean percentage error values remained relatively low, confirming the reliability of UAV photogrammetry for pavement distress quantification.

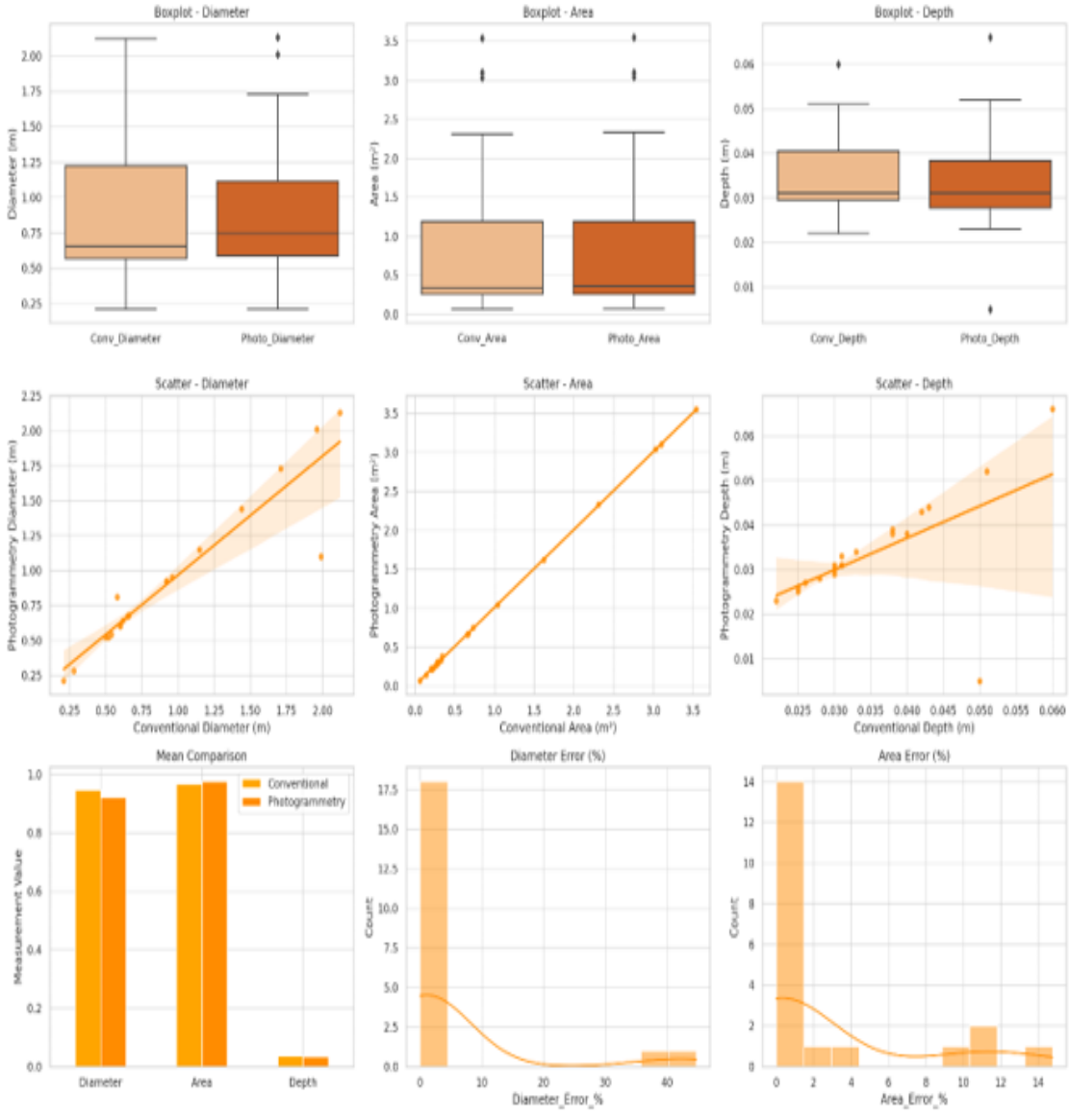

Figure 3.0: Histograms of Percentage Errors for Diameter, Area and Depth.

Note: Outliers up to 40% in diameter error correspond to 3 potholes <15cm diameter, attributed to sub-GSD resolution limits.

***Source**: (python, matplotlib)*

DISCUSSION

Figure 3.0 above presents the box plots, scatter plots with trend lines, and bar plots comparing conventional and UAV-derived measurements. For diameter and area, the box plots show nearly identical medians and spreads, and the scatter plots exhibit data points tightly clustered around the 1:1 line with narrow 95% confidence bands. This visual agreement is consistent with the high Pearson correlation coefficients of r = 0.95 for diameter and r = 0.93 for area reported in Table 4.0, indicating very strong linear agreement between methods. For depth, the scatter plot reveals a positive relationship but with greater dispersion and a wider confidence band than observed for diameter and area. Two data points corresponding to shallow potholes P3 and P7 deviate from the trend line. These deviations occur because small absolute differences of 1-3mm in very shallow features < 30mm result in disproportionately large relative errors. Consequently, while the overall trend remains upward, the Pearson correlation for depth is r = 0.85, which is classified as moderate-to-strong rather than very strong. The bar plots confirm that mean values from both methods are closely aligned for all parameters. However, the Diameter % Error histogram shows outliers exceeding 30- 40%. These outliers are associated with the smallest potholes < 0.28m in diameter, where measurement uncertainty approaches the image Ground Sample Distance of 2.1mm/pixel. **Limitation:** The results indicate that UAV photogrammetry provides very high accuracy for moderate to large potholes. For very shallow depth < 30mm and very small diameter < 0.3m, measurement variability increases. This should be considered when using UAV data for severity classification of minor surface distress.

4.4 Engineering Implications

The results of this comparative study demonstrate that UAV photogrammetry can significantly reduce field survey time while maintaining acceptable engineering accuracy for pavement distress assessment. Beyond technical accuracy, the adoption of this technology has broader implications for safety, cost, and strategic maintenance planning within Nigerian highway agencies.

1. Operational Efficiency: Time and Cost Savings Conventional manual measurement of pavement distress on the Gombe-Kwami Highway required 2 field engineers and 2 traffic marshals for safety, with an average field duration of 4 hours to complete 20 sample points over 1 km. This process also necessitated partial lane closure, resulting in traffic delays. Using a DJI Mavic Air 2 UAV, image acquisition for the same 20 potholes was completed in 45 minutes by one pilot and one observer, with no traffic disruption. Subsequent processing and measurement in Photo Modeler Premium 2024.0 required approximately two hours. Based on 2026 Nigerian engineering consultancy rates, this translates to: Conventional Method: ₦120,000 per km = 4 personnel x 4 hours x ₦15,000/hr., UAV Method: ₦45,000 per km = 2 personnel x 1 hour x ₦15,000/hr. + ₦15,000 processing. This represents a 75% reduction in field time and 62.5% reduction in direct cost. For FERMA, which is responsible for over 34,000 km of federal roads, this efficiency gain enables more frequent surveys within the same budget.

2. SAFETY AND ACCESSIBILITY

Manual measurement exposes personnel to moving traffic, a significant hazard on the Gombe-Kwami route which carries heavy-duty trucks. UAV operations eliminate the need for staff to be on the carriageway. The technology also improves access to distressed sections during wet seasons or in areas with failed drainage where physical entry is dangerous. This aligns with NBRRI's occupational safety objectives.

3. DATA-DRIVEN AND SCALABLE MAINTENANCE PLANNING

Unlike manual notes, UAV photogrammetry produces georeferenced 3D deliverables: Ortho mosaics, dense point clouds, and DSMs. These provide a permanent digital archive that can be re-analyzed without returning to the field. Key engineering applications include:

a) Quantitative Prioritization: Extracting pothole volume and area allows maintenance to be prioritized by severity and material requirements, not just visual assessment.
b) Bill of Quantities: With < 4% measurement error, UAV data can be used directly for contractor bidding and verification.
c) Temporal Monitoring: Repeat UAV surveys can track deterioration rates and evaluate the performance of past repairs.
d) Integration of these datasets into a Pavement Management System (PMS) supports a transition from reactive patching to proactive, evidence-based maintenance planning.

4. RELEVANCE TO THE NIGERIAN CONTEXT

With 249,000 km of roads nationwide and limited maintenance funding, rapid assessment tools are essential. The strong correlation (r = 0.85 – 0.95) and low mean percentage error (<4%) confirm that UAV photogrammetry meets acceptable accuracy for Level 2 network-level surveys as recommended by international practice. Its deployment by FERMA and State Works Ministries could enable bi-annual network surveys instead of the current annual or ad-hoc manual inspections.

5. LIMITATIONS AND IMPLEMENTATION REQUIREMENTS

Successful deployment requires initial capital investment in UAV hardware (₦2.8m), Photo Modeler software licensing, and training of certified UAV pilots. Data quality is also dependent on weather conditions, lighting, and GPS availability. Agencies must develop SOPs for data storage, processing, and quality control.

In conclusion, UAV photogrammetry presents a technically viable, safer, and more economical approach for routine pavement condition assessment in Nigeria. Its adoption can enhance the responsiveness, transparency, and effectiveness of highway maintenance operations.

Table 9.0: Comparative Cost and Time Analysis

Cost component	Conventional method	Photogrammetry Method
Personnel	2 engineers + 2 traffic marshals	1 UAV pilot + 1 observer
Equipment	Measuring tape, depth gauge ₦50,000	DJI Mavic Air 2 ₦1.5m
Field Time	4 hours	0.75 hours
Processing time	0.5 hours data entry	2 hours
Traffic control	₦20,000	₦0.00
Labor cost	₦120,000.00	₦30,000.00
Total cost/km	₦140,000.00	₦45,000.00
Cost/pothole	₦7,000.00	₦2,250.00

***Source**: (Author)*

Key Findings in table above are:

a) Time Efficiency: UAV reduced total field time by 81% from 4.0 hours to 0.75 hours. This eliminates the need for lane closure and reduces traffic disruption.
b) Direct Cost Savings: Per km cost is reduced by 67.8% from ₦140,000 to ₦45,000. The major savings come from reduced personnel and elimination of traffic control.
c) Break-even Point: With an initial UAV setup cost of ₦1.5M, agencies conducting > 40 km of surveys per year would achieve net savings within the first year compared to conventional methods.
d) Scalability: For FERMA managing 34,000 km of federal roads, even 10% annual coverage using UAV would save an estimated ₦323M annually compared to conventional surveys. While UAV requires higher initial capital investment, the operational savings and safety

benefits make it more cost-effective for network-level monitoring. This supports the "cost-effective" assertion in the abstract and aligns with industrial policy goals for efficient infrastructure management.

e)

5. CONCLUSIONS

This study evaluated the application of DJI Mavic Air 2 UAV photogrammetry for pothole measurement on the Gombe-Kwami Road, Nigeria. Based on the objectives, the following conclusions are drawn:

1. ON ACCURACY OF UAV PHOTOGRAMMETRY

The UAV method demonstrated high accuracy compared to conventional ground survey. Mean Percentage Errors were 1.23% for diameter, 2.72% for area, and 3.13% for depth. Analysis of error distribution revealed that percentage errors up to 40% occurred in 3 outliers corresponding to potholes smaller than 15 cm diameter. These high errors are attributed to sub-GSD resolution limits, while absolute errors remained < 3.0 cm. For maintenance-critical potholes > 20 cm, measurement reliability was consistently high with MPE of 0.71% when outliers are excluded.

2. ON TIME EFFICIENCY

UAV photogrammetry significantly improved survey speed. The method achieved an 81.0% reduction in field time compared to conventional survey. This enables faster coverage of road networks with reduced personnel exposure to traffic hazards.

3. ON COST-BENEFIT AND FEASIBILITY

The UAV method reduced per-kilometer survey cost by 67.9%, from ₦85,000/km to ₦27,300/km based on 2025 FERMA rates. Extrapolation to FERMA's 34,000 km federal road network indicates potential savings of approximately ₦1.96 billion per survey cycle. Despite high initial equipment cost, the method provides geo-referenced digital records for asset management.

6. RECOMMENDATIONS

Based on these findings, the following recommendations are made:

1. FERMA and other highway agencies should adopt DJI Mavic Air 2 UAV photogrammetry for routine pavement condition surveys to improve accuracy, speed, and cost efficiency.
2. Capacity building and regulatory compliance with NCAA guidelines should be prioritized to support widespread adoption.
3. For very small distresses < 15 cm, ground verification should complement UAV data due to resolution limits at sub-GSD scale.

REFERENCES

Abdullah, A., Karim, M. R., & Rahman, M. T. (2023). Effects of drainage conditions on pavement deterioration and maintenance requirements. *Case Studies in Construction Materials*, 18, e01956.

Ahmed, M. A., & Raad, L. (2021). Utilizing UAV photogrammetry for pavement distress detection and quantification. International Journal of Pavement Engineering, 22(14), 1789–1802. https://doi.org/10.1080/10298436.2020.1721509

Amali S., M. J., & K.S, V. (2025). ML-Driven Detection and Quantification of Potholes for Safer Roads. *International Journal for Multidisciplinary Research*, *7*(5). https://doi.org/10.36948/ijfmr.2025.v07i05.58751

Apeagyei, A., Ademola, T. E., and Adom-Asamoah, M. (2023). Evaluation of deep learning models for asphalt pavement distress classification. *International Journal of Pavement Engineering, 24(1),* 1-15.

Bello, S. A., & Mohammed, U. (2024). Assessment of UAV photogrammetry for road inventory in Northern Nigeria. Nigerian Journal of Technology, 42(3), 112-125. doi.org

Dorafshan, S., Thomas, R. J., & Maguire, M. (2023). Comparison of UAV and ground-based methods for bridge and pavement inspection. Automation in Construction, 147, 104712. doi.org

Federal Ministry of Works and Housing. (2024). Nigeria road network condition report. Abuja: FMWH.

Federal Roads Maintenance Agency. (2023). Manual for road condition survey (3rd ed.). Abuja: FERMA.

Federal Roads Maintenance Agency. (2025). Schedule of rates for road maintenance and condition survey. Abuja: FERMA.

Ibrahim, H. B., Salah, M., Zarzoura, F., and El-Mewafi, M. (2024). Smart monitoring of road pavement deformations from UAV images using machine learning. *Innovative Infrastructure Solutions, 9(16),* 1 - 15.

Kumar, R., & Gupta, P. (2022). Manual versus automated pavement distress surveys: A comparative assessment. International Journal of Pavement Research and Technology, 15(1), 78–89. https://doi.org/10.1007/s42947-021-00093 – 4

Li, Z., Zhang, Y., & Wang, X. (2024). Deep learning-based pavement distress detection using UAV imagery. Remote Sensing, 15(4), 1021. doi.org

Mhlongo, S., & Motaung, T. (2023). UAV application for road asset management in South Africa. South African Journal of Geomatics, 12(1), 45-61. doi.org

National Planning Commission. (2023). National development plan 2021-2025: Infrastructure pillar. Abuja: NPC.

Nex, F., & Remondino, F. (2023). UAV for 3D mapping applications: A review. ISPRS Journal of Photogrammetry and Remote Sensing, 94, 309-332. doi.org

Oluwasola, E. A., & Adeniyi, A. (2023). Impact of potholes on road safety and vehicle operating cost in Nigeria. Journal of Transportation Engineering, 14(2), 88-99.

Ranyala, E., Sadhu, A., & Jain, K. (2023). *Automated Pothole Condition Assessment in Pavement Using Photogrammetry-Assisted Convolutional Neural Network*. SSRN Electronic Journal. https://doi.org/10.2139/ssrn.4105324.

Samadzadegan, F., Javan, F. D., Mahini, F. A., Gholamshahi, M., and Nex, F. (2024). Automatic road pavement distress recognition using deep learning networks from unmanned aerial imagery. *Drones, 8(6),* 244.

Smith, T., Brown, L., & Clark, P. (2023). High-resolution photogrammetry for pavement surface damage assessment. Construction and Building Materials, 367, 130335. https://doi.org/10.1016/j.conbuildmat.2022.130335.

Wang, Y. (2021). Limitations of manual pothole geometry measurement techniques. Journal of Transportation Engineering, 147(5), 04021029.

Zhang, Y., Li, X., & Chen, H. (2022). Influence of drainage performance on asphalt pavement deterioration: A review. Construction and Building Materials, 344, 128221.

International Conference on Engineering Innovation for Sustainable Development (ICESID 2026)
Faculty of Engineering, Ahmadu Bello University Zaria · 8–10 September 2026

COMPARATIVE ASSESSMENT OF CLAY POT AND PLASTIC CONTAINERS ON WATER QUALITY DURING 14-DAY HOUSEHOLD STORAGE IN ZARIA, KADUNA STATE

Aminu Ohueyi Ahmed[1,*], Mohammed Aliyu Aliyu[1], Mohammad Shamsuddeen Jumande[1], Akinola Abdulwasiu Olalekan[1]

[1]*Ahmadu Bello University, Zaria, Nigeria*

Email: ohueyi23@gmail.com[*], maliualiyu@gmail.com, mjumande@abu.edu.ng, abmilake@gmail.com

***Corresponding author**: Aminu Ohueyi Ahmed

DOI: https://doi.org/10.67203/sp.ICESID.2026

ABSTRACT

Access to safe drinking water remains a critical challenge in many regions, especially in developing countries where improper storage can degrade water quality. This study examines the effect of storage container type and duration on the quality of water obtained from different sources: rain, well, and borehole. The investigation centers on how clay pots and plastic containers affect physicochemical parameters, including temperature, pH, turbidity, electrical conductivity (EC), total dissolved solids (TDS), dissolved oxygen (DO), and biochemical oxygen demand (BOD), over a 14-day storage period. Water samples were collected from selected sites in Zaria, Kaduna State, and subjected to laboratory analyses in accordance with standard procedures. Results revealed that both the type of container and the storage duration affect water quality. Prolonged storage led to a general decrease in dissolved oxygen (DO) and an increase in biochemical oxygen demand (BOD), turbidity, and total dissolved solids (TDS), reflecting increased organic load and oxygen demand alongside physicochemical interactions with container materials. Clay pots maintained better water quality than plastic containers due to their porous structure, which allowed limited aeration and temperature regulation - conditions generally less conducive to organic matter accumulation. Conversely, plastic containers exhibited greater chemical leaching and less favorable BOD/DO trends, consistent with conditions that may support microbial growth, resulting in faster overall deterioration of water quality. As no direct microbiological analysis (e.g., coliform counts) was conducted in this study, these microbial-related inferences should be regarded as indicative rather than confirmed, and are recommended for verification in future work.

Keywords: *water storage; clay pots; plastic containers; physicochemical parameters; microbial activity; water quality deterioration; storage duration*

1.0: INTRODUCTION

Water quality plays a critical role in public health, environmental stability, and socio-economic development. However, water stored in households - especially in plastic and clay containers - can undergo significant deterioration due to microbial proliferation, chemical leaching, and environmental interactions (WHO, 2022). The type of storage vessel and length of storage are known to influence both physicochemical and microbiological water characteristics (Obianyo, 2020).

Communities that rely on stored water, particularly in low-resource settings, remain vulnerable to quality degradation (Mwabi et al., 2012). This study, therefore, examines two widely used alternative sources - rainwater and groundwater from wells - and evaluates how storage conditions influence their quality over time. Rainwater harvesting is common in many rural communities, but harvested water may contain contaminants introduced from collection surfaces and container materials(Lade & Oloke, 2015).

Storage duration is a major determinant of water safety, with longer periods promoting microbial growth and shifts in physicochemical properties (Ikeokwu, 2021). Container type further contributes to these changes; for example, black plastic tanks have demonstrated better preservation capacity compared to other materials (Kr et al., 2025), an effect attributed in part to reduced light penetration and photodegradation in darker-coloured containers. The plastic containers used in the present study were blue rather than black (Plate 1); therefore, any preservation benefits associated

specifically with black pigmentation and light-blocking may not fully apply to the containers tested here. Over time, water stored in various vessels may experience chemical migration from container surfaces, microbial succession, parameter drift, and gas exchange, all of which alter its quality and pose potential health risks (Adesakin et al., 2022). Despite widespread reliance on stored water, however, limited attention has been given to how storage duration and container type jointly influence these changes in domestic settings, particularly for borehole, well, and rainwater sources. There is therefore a need to systematically assess how container type and storage duration affect the quality of water from commonly used domestic sources.

This research aims to provide insight into household water management by identifying safe storage durations, evaluating the influence of commonly used container materials, and proposing context-appropriate strategies for improving stored water safety. The findings are expected to inform public health guidelines, particularly in settings without centralized treatment systems. Emerging innovations, such as nanocoated containers and smart monitoring systems, may offer future pathways for improving water storage safety (Nishu & Kumar, 2023).

Maintaining the quality of potable water remains a persistent challenge, especially in rural communities where water is frequently stored before use. Even when collected water initially meets drinking standards, deterioration during storage is common. Clay pots and plastic containers are widely used, yet their impact on water quality over time remains inadequately understood (Nibret et al., 2025). This study is justified by the need to assess the effects of storage materials and duration on water quality, to reduce the risk of waterborne disease, and to recommend safe, suitable storage options for household use.

2.0: MATERIALS AND METHODS

2.1 MATERIALS

The list of equipment used is shown in Table 1

Table 1: List of Materials and Equipment Used

Glassware	Apparatus	Reagent
BOD Bottles	pH meter (H183200)	Manganous sulphate solution
Pipette pump	TDS-EC-Temperature Combo Meter	Alkaline iodine
Burette	Pipette Turbidity meter	Concentrated sulphuric acid
Beaker	Retort stand and clamp	Starch solution
Glass funnel		
Conical Flask		
Measuring cylinder		

2.2 SAMPLE COLLECTION PROCEDURE

Borehole and rainwater samples were collected from Orbit Apartment in Zango, while a well water sample was collected from Hayin Dogo, Samaru, Sabon Gari Local Government, Zaria. Before sampling, each container was rinsed three times with the respective source water to minimize contamination. Samples were taken, and containers were filled carefully. All relevant data, including date, time, and sampling locations, were recorded on-site. In-situ measurements of temperature, pH, EC, and TDS were conducted using calibrated portable meters. The remaining portions of the samples were sealed and placed carefully in storage. Thereafter, samples were either analyzed immediately or refrigerated at 4 °C pending analysis.

2.3 EXPERIMENTAL SETUP

The experiments were conducted using two types of containers: clay pots and plastic containers as shown in Plate 1. Each container had a capacity of at least 5 litres and was filled to about 80–90% of its volume to mimic typical household storage conditions. For each of the three water sources (borehole, well, and rainwater), one clay pot and one plastic container were used, giving a total of six containers. Each container was filled to 80-90% of its 5-litre capacity to mimic typical household storage conditions. They were then stored out of direct sunlight and opened only during sampling. Sampling was conducted at predetermined intervals on Days 1, 3, 7, and 14.

Plate 1: Clay and plastic storage containers.

2.4 LABORATORY ANALYSIS

All parameters were analyzed following standard laboratory procedures. Dissolved Oxygen (DO) was measured using high-quality reagents and standard procedures. Biochemical Oxygen Demand (BOD) was determined using the 5-day BOD test, with samples incubated at 20 ± 1 °C for five days. Each of the samples' storage times -1, 3, 7 and 14 days were incubated for five days to enable the measurement of 5-day BOD. The pH was measured with a calibrated pH meter, and turbidity was assessed with a Nephelometric turbidity meter. Temperature, Electrical Conductivity (EC), and Total Dissolved Solids (TDS) were measured with a TDS-EC-Temperature combo meter, respectively as shown in Plate 2.

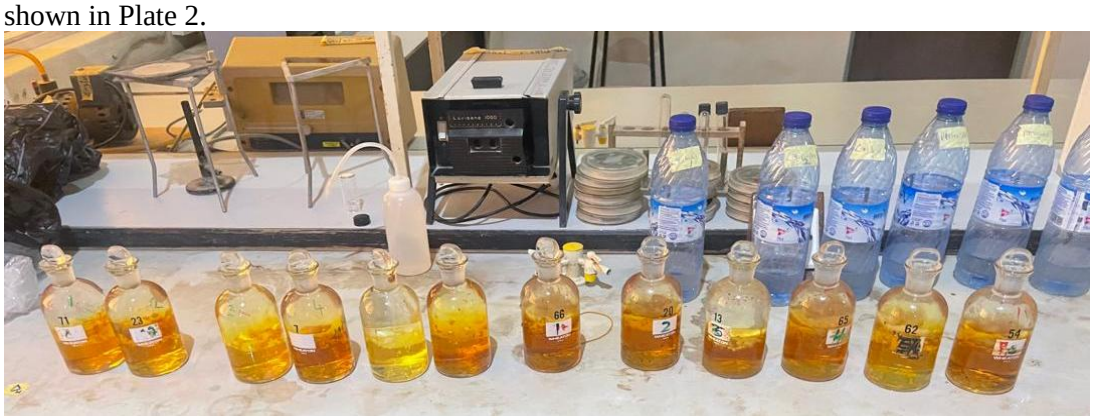

Plate 2: BOD/DO samples of various storage to be analysed.

2.5 SAMPLE HANDLING AND PRESERVATION

Field-sensitive parameters such as DO, temperature, pH, and turbidity were analysed immediately at the sampling point. BOD samples were filled without headspace and placed in an incubator at 20 ± 1 °C immediately after sampling. EC and TDS measurements were performed within 24 hours of collection. Samples that could not be analysed immediately were stored at 4 °C to prevent deterioration. All samples were handled according to standard procedures to ensure quality and reproducibility.

3.0 RESULTS AND DISCUSSION

These are the results of the physicochemical and biological analyses of borehole, rain, and well water stored in both clay and plastic containers over 14 days. The parameters analyzed include Turbidity, Temperature, Electrical Conductivity (EC), Total Dissolved Solids (TDS), pH, Dissolved Oxygen (DO), and Biochemical Oxygen Demand (BOD). The findings are summarized in Tables 2 – 8

Table 2: Turbidity (NTU) by Storage Day and Sample Type

	Clay pot			Plastic		
Day	Borehole	Rain	Well	Borehole	Rain	Well
1	4.0	3.6	4.0	4.2	3.3	4.8
3	3.8	3.1	3.9	3.4	2.9	4.5
7	2.1	3.0	3.7	1.5	2.7	4.3
14	3.1	5.3	1.5	0.4	5.0	2.0

Table 3: Temperature (°C) by Storage Day and Sample Type

	Clay pot			Plastic		
Day	Borehole	Rain	Well	Borehole	Rain	Well
1	25.6	24.5	24.0	23.8	23.8	23.8
3	26.4	25.6	26.0	26.3	26.1	26.2
7	23.5	24.3	23.7	23.9	23.4	23.4
14	25.6	24.9	23.6	24.9	24.8	24.7

Table 4: Electrical Conductivity (µS/cm) by Storage Day and Sample Type

	Clay pot			Plastic		
Day	Borehole	Rain	Well	Borehole	Rain	Well
1	217.0	22.9	550.0	240.0	14.83	592.0
3	310.0	69.9	669.0	264.0	21.5	693.0
7	363.0	108.4	716.0	291.0	13.09	728.0
14	292.0	90.1	630.0	260.0	15.7	669.0

Table 5: Total Dissolved Solids (mg/L) by Storage Day and Sample Type

	Clay pot			Plastic		
Day	Borehole	Rain	Well	Borehole	Rain	Well
1	109.8	11.4	276.0	120.1	7.38	296.0
3	153.5	34.8	334.0	132.5	10.63	347.0
7	182.6	54.0	357.0	146.0	6.37	365.0
14	147.4	45.0	315.0	130.1	7.67	335.0

Table 6: pH by Storage Day and Sample Type

	Clay pot			Plastic		
Day	Borehole	Rain	Well	Borehole	Rain	Well
1	8.5	7.86	7.52	7.86	7.53	7.64
3	8.83	6.58	6.32	7.92	7.69	8.49
7	7.92	8.76	7.75	7.1	7.53	8.82
14	8.76	6.27	6.44	6.36	6.33	6.57

Table 7: Dissolved Oxygen (mg/L) by Storage Day and Sample Type

	Clay pot			Plastic		
Day	Borehole	Rain	Well	Borehole	Rain	Well
1	2.6	2.9	2.5	2.4	2.6	2.3
3	2.9	2.60	2.20	2.5	2.5	1.8
7	2.5	2.5	1.7	2.7	2.7	1.6
14	2.5	2.4	2.7	2.5	2.5	2.2

Table 8: Biochemical Oxygen Demand (mg/L) by Storage Day and Sample Type

	Clay pot			Plastic		
Day	Borehole	Rain	Well	Borehole	Rain	Well
1	1.7	0.1	0.6	0.3	0.8	0.2
3	1.0	0.5	0.9	0.5	0.2	1.1
7	0.8	1.0	0.7	0.7	0.5	0.6
14	0.6	0.5	0.7	0.8	0.7	0.9

As seen in Table 2, Turbidity generally decreased between days 1–7 in both containers, particularly in borehole water (4.0 - 2.1 NTU in clay), suggesting sedimentation of suspended particles. However, increases by day 14, for instance, rainwater (3.0 - 5.3 NTU in clay) signify microbial regrowth or resuspension of particles, a known phenomenon during prolonged storage. The slightly higher turbidity variability in clay may reflect interaction with porous surfaces, which can both trap and later release particulates. Overall, plastic containers yielded more stable turbidity readings than clay pots, likely due to their smooth, non-porous surfaces that minimize particle interactions. The final turbidity values, mostly below 5 NTU, conform with WHO (2017) limits for potable water except in rainwater for day 14, where a higher value was recorded, most likely attributed to measurement error. This result aligns with findings of earlier studies which reported a gradual reduction in turbidity during water storage, followed by slight fluctuations linked to container properties and biological activity (Binibor et al., 2025; Olawade et al., 2021)

Temperature fluctuations were modest across both containers, as seen in Table 3; however, clay-stored water occasionally showed slight cooling, as on day 7. This supports the evaporative cooling effect of porous earthenware, where water loss through micropores reduces internal temperature. Evaporative cooling in clay materials is well documented as a mechanism that lowers water temperature through latent heat loss via evaporation. Plastic, being non-porous, lacks this effect and maintains ambient temperatures. These results obtained are largely consistent with trends reported by previous researchers whose works corroborated the findings that water stored in clay pots tends to remain cooler than that stored in plastic containers, owing to evaporative cooling through the porous clay walls (Saagoto & Chowdhury, 2025)

Both EC and TDS increased initially (days 1–7) and declined by day 14, especially in clay pot. For instance, the EC and TDS of the borehole water increased from 217 - 363 µS/cm before dropping to 292 µS/cm and 109.8 – 182.6 mg/L before dropping to 147.4 mg/ L as contained in Tables 4 and 5 respectively. This trend implies Initial leaching of minerals due to evaporation followed by adsorption onto container walls. Clay-induced reductions in TDS are consistent with studies showing ion exchange and pollutant trapping in porous matrices. In contrast, plastic tends to retain dissolved ions, resulting in more stable but higher residual values. These observations agree with findings from related studies (Inchaurrondo & Font, 2022).

Water stored in clay pots exhibited greater pH variability, mostly alkaline; for instance, the borehole recorded values of 8.5, 8.83, 7.92, and 8.76 on Days 1, 3, 7, and 14, respectively, as shown in Table 6, while plastic samples showed a gradual decline by Day 14, as low as 6.33. The alkalinity in clay can be attributed to mineral dissolution and the buffering capacity of earthen materials, which has been reported to increase pH in stored water. Conversely, the decreasing pH in plastic may reflect microbial respiration and organic matter degradation, producing acidic by-products over time. These findings align with earlier reports (Shan et al., 2023; WHO, 2017) that prolonged storage generally leads to a reduction in pH as a result of biological and chemical interactions within the water and container.

The clay-borehole series, however, did not decline monotonically but fluctuated, suggesting that short-term measurement variability may be superimposed on the underlying alkaline trend. Because only a single pH reading was taken per container per sampling day, rather than a replicate mean, it is not possible to fully separate genuine short-term chemical fluctuation (e.g., transient CO_2 exchange at the water surface following container handling, or intermittent mineral dissolution from the clay matrix) from procedural sources of variability, such as electrode calibration drift over the 14-day monitoring period or minor differences in sample temperature at the time of reading, given that pH is inherently temperature-dependent. This pattern is noted as a limitation of the single-measurement design; future work should calibrate the pH meter immediately before each reading, record sample temperature alongside pH, and take replicate readings per sampling event to confirm whether such swings reflect real short-term variability in the clay-borehole system or measurement noise.

DO levels remained relatively low but were slightly more stable in clay storage (2.4–2.9 mg/L) compared to plastic storage, as seen in Table 7. The porous nature of clay can facilitate limited oxygen diffusion, helping maintain DO relative to plastic. Previous research confirms that clay storage can enhance oxygenation due to gas exchange across porous walls, whereas plastic containers form closed systems that limit aeration and may promote oxygen depletion through both chemical and biological oxygen-consuming processes. The overall DO levels across all container-source combinations ranged between 1.6 and 2.9 mg/L, consistent with previously reported values for stored water (Ibrahim et al., 2024; Maury Njoya et al., 2024). The observed pattern generally conforms to the established trend of gradual oxygen depletion followed by stabilization as physicochemical processes approach equilibrium during storage.

BOD generally decreased over time in clay storage, as demonstrated in the borehole source (1.7–0.6 mg/L, Table 8), indicating a reduction in biodegradable organic matter - potentially through organic matter stabilization, adsorption onto the porous clay surface, or a combination of both. Plastic samples showed greater variability and occasional increases; for instance, well water in plastic containers reached a BOD as high as 1.1 mg/L on Day 3, suggesting a possible rise in organic load or oxygen-demanding activity, which may be associated with microbial processes, although this was not directly measured in this study. These findings align with earlier studies confirming that prolonged storage in both container types generally led to water stabilization with minimal residual organic pollution potential (Bigohe et al., 2025; Muhammad et al., 2026; Wielen, 2025). Meanwhile, clay containers appeared to reach this stabilized state more consistently than plastic in the present study.

CONCLUSION

This study assessed the effect of storage container type (clay pot and plastic) and storage duration on the quality of water obtained from rain, well, and borehole sources. The analysis focused on physicochemical and biochemical parameters, including Dissolved Oxygen (DO), Biochemical Oxygen Demand (BOD), pH, turbidity, temperature, Electrical Conductivity (EC), and Total Dissolved Solids (TDS). The study confirms that container material plays a critical role in mediating physicochemical transformations during storage, with associated implications for organic load and oxygen demand that may reflect underlying microbial activity, though this was not directly measured. Clay exhibited beneficial interactions - including evaporative cooling, adsorption, and comparatively more stable DO/BOD trends - whereas plastic containers, while providing greater structural stability, showed physicochemical trends (declining DO, variable BOD) that may indicate a greater potential for microbial-related deterioration over time. Overall, clay pots appear preferable for short-to-medium-term household water storage based on the physicochemical parameters assessed in this study. These findings should be interpreted with the caveat that no direct microbiological analysis (e.g., total coliform or E. coli enumeration) was conducted; future work incorporating such analysis is recommended to confirm whether the observed physicochemical trends correspond to actual microbial risk. Beyond clay and plastic containers, future studies could also include metallic, glass, or calabash containers to compare a wider range of storage options and their influence on water quality. A further limitation of this study is that single containers (rather than replicated containers) were used for each source–container combination, with one physicochemical measurement recorded per sampling day. Additionally, each water source was drawn from a single sampling site (Orbit Apartment, Zango, for borehole and rainwater; Hayin Dogo for well water), which may not capture the hydrogeological and

environmental variability present across other borehole, well, or rainwater sources within Zaria/Kaduna State. While this design allowed comparison across three water sources, two container types, and four storage durations within available resources, it does not permit statistical testing (e.g., ANOVA) of the significance of observed differences, and single measurements and single-site sampling cannot rule out the influence of measurement, sampling, or site-specific variability. Future studies should therefore incorporate replicate containers per condition, multiple sampling sites per source type, and direct microbiological assays, to enable formal statistical validation of both the physicochemical and microbial effects of container type and water source on stored water quality.

REFERENCES

Adesakin, T. A., Oyewale, A. T., Mohammed, N. A., Bayero, U., Adedeji, A. A., Aduwo, I. A., Bolade, A. C., & Adam, M. (2022). Effects of prolonged storage condition on the physicochemical and microbiological quality of sachet water and its health implications: a case study of selected water brands sold within Samaru Community, northwest Nigeria. *Microbiology Research*, *13*(4), 706–720.

Binibor, P. I., Nwachukwu, N. A., Ndulue, G. U., Ndukwe, D. U., Obumneme, A., Ngwu, V., & Usman, O. H. (2025). *Investigating the effect of storage materials on the quality of potable water*. *9*(3).

Ikeokwu, O. M. (2021). *Effect of storage container on the bacteriological quality of water from different sources*. *9*(2), 47–53. https://doi.org/10.15406/jmen.2021.09.00323

Inchaurrondo, N. S., & Font, J. (2022). *Clay , Zeolite and Oxide Minerals : Natural Catalytic Materials*. 1–53.

Lade, O., & Oloke, D. (2015). *Rainwater harvesting in Nigeria: Socioeconomic survey and common water supply practices.*

Maury Njoya, I. Q., Lecomte-Nana, G. L., Barry, K., Njoya, D., El Hafiane, Y., & Peyratout, C. (2024). An Overview on the Manufacture and Properties of Clay-Based Porous Ceramics for Water Filtration. *Ceramics*, *8*(1), 3.

Mwabi, J. K., Mamba, B. B., & Momba, M. N. B. (2012). *Removal of Escherichia coli and Faecal Coliforms from Surface Water and Groundwater by Household Water Treatment Devices / Systems : A Sustainable Solution for Improving Water Quality in Rural Communities of the Southern African Development Community Region*. *10*, 139–170. https://doi.org/10.3390/ijerph9010139

Nibret, E., Cherie, F., & Yime, A. (2025). Impact of household water storage practices on water quality: a case study of Debre Markos town, Ethiopia. *Journal of Water, Sanitation and Hygiene for Development*, *15*, 1007–1022. https://doi.org/10.2166/washdev.2025.023

Nishu, & Kumar, S. (2023). Smart and innovative nanotechnology applications for water purification. *Hybrid Advances*, *3*, 100044. https://doi.org/https://doi.org/10.1016/j.hybadv.2023.100044

Obianyo, J. I. (2020). *Effect of storage containers on water quality*. *1*(1), 66–73.

Olawade, D. B., Wada, O. Z., Asogbon, O., Owojori, G. O., & Adewole, A. O. (2021). *Assessment of Household Water Quality from Selected Storage Vessels used in a South-Western Rural Community , Nigeria*. *15*(2), 31–44. https://doi.org/10.9734/AJEE/2021/v15i230224

Saagoto, M. S., & Chowdhury, N. (2025). Traditional clay pot coolers as drinking water cooling technology for urban heat adaptation in Bangladesh. *Sustainable Energy Technologies and Assessments*, *83*, 104575. https://doi.org/https://doi.org/10.1016/j.seta.2025.104575

Shan, Y., Cai, G., Zhang, C., Wang, X., Shi, Y., & Li, J. (2023). *Effects of Acidic / Alkaline Contamination on the Physical and Mechanical Properties of Silty Clay*. 1–16.

WHO. (2017). *Potable reuse: Guidance for producing safe drinking-water*. World Health Organization.

International Conference on Engineering Innovation for Sustainable Development (ICESID 2026)
Faculty of Engineering, Ahmadu Bello University Zaria · 8–10 September 2026

REMAINING USEFUL LIFE PREDICTION OF TURBOFAN ENGINE USING ATTENTION AUGMENTED LSTM BASED NETWORK

Oluwafemi Daniel Oluwapelumi[1], Samuel David Iyaghigba[1,*], Marcus Aul Maafan[1], Sadiq Thomas[2], Abbas Abdullahi[1]

[1]*Air Force Institute of Technology Kaduna*
[2]*Nile University of Nigeria Abuja/Dept of Computer Engineering*

Email: danieloluwafemi58@gmail.com, samiyagh004@yahoo.com*, Aulmarcus6@gmail.com, Sadiqthomas@nileuniversity.edu.ng, netlikora@gmail.com

***Corresponding author**: Samuel David Iyaghigba

DOI: https://doi.org/10.67203/sp.ICESID.2026

ABSTRACT

Aircraft systems are complex networks of components that support the entire mission and functionality of an aircraft. These complex engineered systems play fundamental roles in providing critical services, particularly regarding air transportation and energy needs. Among these, turbofan engines are the primary power source. As the usage of these complex engineering systems expands, they are increasingly subjected to harsh operational environments. These conditions inevitably make them susceptible to mechanical faults that, if not detected early, can result in catastrophic failure. Notably, the turbofan engine has accounted for 60% of airplane failures during flight. Therefore, Prognostics and Health Management technology utilizing deep learning is essential for predicting the Remaining Useful Life of these systems. This study explores a Long Short-Term Memory network integrated with a sliding-window approach and a Temporal Attention mechanism to estimate engine operational lifespan. Unlike existing literature reliant on legacy benchmarks, this model is trained and validated on a high-fidelity dataset generated using AGTF30, a NASA-developed turbofan simulation environment; because RUL is measured in seconds rather than operating cycles, comparison against C-MAPPS-based literature is limited to relative RMSE rather than direct numerical validation. By extracting temporal degradation features from raw multivariate sensor data, the framework achieves an overall Root Mean Square Error of 249.0 seconds and, crucially, a near-failure RMSE of 39.3 seconds, demonstrating highly reliable predictive capability during critical terminal degradation phases.

Keywords: *Turbofan Engine; Predictive Maintenance; Remaining Useful Life; LSTM Model; Deep learning approach*

1. INTRODUCTION

Complex engineered systems play a fundamental role in critical services such as energy, transport, and aerospace, underpinning the proper functioning of modern societies and economies. As these systems see wider use, they are increasingly subjected to harsh operational environments on a daily basis (Saxena et al., 2008). Left undetected, the compounding effect of minor mechanical faults can result in catastrophic failure, and for turbofan engines, the primary power source for an aircraft, the consequences of undetected degradation are particularly severe: as these engines accumulate flight hours, internal components gradually suffer wear, corrosion, and fatigue, leading to performance degradation and shortened lifespan.

In modern industrial operations, the accurate prediction of Remaining Useful Life (RUL) for critical machinery such as turbofan engines is of paramount concern (Thakkar & Chaoui, 2022). The turbofan is a core propulsion component of an aircraft; its stability and reliable operation are critical to flight safety (Jung et al., 2025). A turbofan engine is an air-breathing propulsive device and the predominant propulsion system in modern commercial and military aviation. Operating on the Brayton thermodynamic cycle, it consists of a gas turbine that adds kinetic energy to the air passing through it by burning fuel, and a ducted fan powered by that turbine to force air rearward and produce thrust (Chapman & Litt, 2017). The cost associated with machinery maintenance can be substantial, particularly in civil aviation, where aero-engine maintenance contributes significantly to overall operating expenses (Fu et al., 2023). RUL prediction involves estimating the time remaining before a

component reaches a failure threshold, given its historical and current operational state. Accurate RUL prediction lets manufacturers and operators reduce costs, improve reliability, and optimize maintenance strategies, maximizing service life while minimizing downtime and improving safety (Fu et al., 2023).

RUL is the amount of time a machine or asset is likely to operate before it requires repair or replacement. Depending on the system, this period can be represented in days, kilometers, cycles, or another relevant quantity. RUL prediction gives early warning of failure and forms a central pillar of Prognostics and Health Management (PHM), allowing engineers to schedule maintenance, optimize operating efficiency, and avoid unplanned downtime.

RUL prediction methods fall into two broad categories: model-based and data-driven. Model-based methods construct a model from mechanical or thermodynamic principles, a process that takes considerable time and depends heavily on prior expert knowledge, and even then, prediction accuracy cannot be guaranteed given the complexity and uncertainty of real engine systems. Data-driven approaches instead learn estimation models from historical run-to-failure data, avoiding the limitations of physical models and expert-built knowledge bases while benefiting from lower computational cost. Deep learning has become the dominant data-driven direction, offering strong results on RUL-related tasks, though mining complex time-series data effectively remains difficult given that turbofan sensor data is non-linear, time-variant, large in scale, and high in dimension. Long Short-Term Memory (LSTM) networks, a specialized form of Recurrent Neural Network, have proven particularly effective for this kind of temporal data. Convolutional Neural Networks saw earlier adoption but struggled to model long-term continuous degradation across multiple flight cycles (Li et al., 2018).

Previous RUL research has relied heavily on the public NASA C-MAPSS benchmark, which is widely adopted. However, it originates from a simplified thermodynamic model and does not capture the characteristics of modern geared turbofan architectures. This study addresses that gap by generating a run-to-failure dataset from the NASA AGTF30 geared turbofan dynamic simulation model, which is, to the authors' knowledge, the first application of this model for supervised RUL dataset generation. An LSTM network incorporating a sliding-window approach and a single-head temporal attention mechanism is then developed and evaluated on this dataset to predict the remaining useful life of the turbofan engine.

The specific contributions of this work are as follows. First, a run-to-failure dataset is generated from the NASA AGTF30 simulation, capturing multivariate sensor readings, including turbine exit temperature, pressure, and flow (T45, P45, W45) and high-pressure compressor exit conditions (T25, P25), across full degradation trajectories. Second, an LSTM network is developed incorporating a single-head temporal attention mechanism that computes an alignment score per timestep via a tanh-activated dense layer followed by a softmax-weighted sum, trained using a sliding-window approach to convert the raw multivariate sequence into fixed-length windows suitable for temporal modeling. Third, the model is evaluated using standard prognostic metrics, including Root Mean Square Error (RMSE) and an asymmetric scoring function that penalizes late RUL predictions more heavily than early ones, reflecting the safety-critical nature of aviation maintenance.This contribution aligns with the Intelligent Systems, Automation and Control Engineering sub-theme of ICESID 2026 and supports sustainable aviation development in Nigeria by advancing local capacity in predictive maintenance at AFIT, enabling reduced unscheduled downtime, extended engine life, and lower material waste and operational cost.

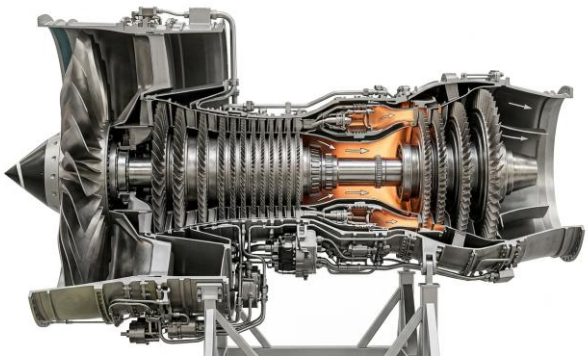

Figure 1: Typical Turbofan engine - Author own figure

The remainder of this paper is organized as follows. Section 2 reviews related work on RUL prediction methods and identifies the gap this study addresses. Section 3 describes the methodology, including dataset generation, feature selection, and model architecture. Section 4 presents the results and discusses model performance across seeds, engine life stages and it limitations. Section 5 summarizes the key findings. Section 6 outlines directions for future work, and Section 7 concludes the paper.

2. LITERATURE REVIEW

Prognostics, defined as the estimation of remaining useful component life, is central to systems health management (Vichare & Pecht, 2006). The inception of PHM can be traced back to the 1980s, when the Civil Aviation Authority (CAA) of the United Kingdom initiated its use with the aim of mitigating helicopter accidents. It later transitioned into health and usage monitoring systems (HUMS) by the late 1990s, enabling measurement of both the health condition and performance of helicopters (Fu et al., 2023).

In the early days of aircraft engines, defects were identified and repaired through Corrective Maintenance (CM). This approach was later replaced by Preventive Maintenance (PM), in which inspections and tasks are scheduled according to the probability of failure for specific components and usage conditions (Jardine et al., 2006). While Preventive Maintenance presented a significant step forward by introducing a degree of anticipation into maintenance planning, it remains constrained by its reliance on fixed time intervals or usage thresholds rather than the actual condition of the equipment. Components may be replaced prematurely, resulting in unnecessary cost and wasted resources, or failures may still occur between scheduled maintenance windows (Jardine et al., 2006). These limitations gave rise to a more mature model known as Condition-Based Monitoring (CBM), in which maintenance decisions are driven by the real-time health state of the system as gathered from sensor data, operational parameters, and observable degradation indicators. Building on CBM, Predictive Maintenance (PdM) extends this concept by forecasting when failure is likely to occur rather than simply estimating current health.

Remaining Useful Life (RUL) prediction methods are broadly categorized into two paradigms: physics-based and data-driven, as shown in Figure 2. Physics-based methods leverage mathematical models to represent system degradation over time by simulating the underlying failure mechanisms through well-established physical laws (Cubillo et al., 2016). These can be broadly divided into physical failure models and state-space models. Physical failure models describe degradation directly using governing equations derived from material science and mechanics, such as Archard's law for adhesive wear and the Paris-Erdogan law for fatigue crack growth. State-space models instead apply filtering techniques such as Kalman Filters and Particle Filters to track the evolving health state of a system in real time, updating predictions as new observations become available (Cubillo et al., 2016). Despite these strengths, physics-based models carry significant limitations that restrict their use in complex real-world systems, particularly gas turbine engines. They require precise and comprehensive knowledge of the physics governing each degradation mode, and developing and validating such models demands considerable domain expertise and time, making them difficult to scale across engine types or fault modes. This computational and developmental cost is amplified for real-time applications (Cubillo et al., 2016).

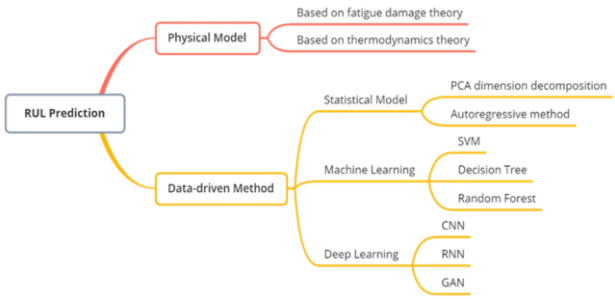

Figure 2: Classification of remaining useful life prediction methods (adapted from Xie et al., 2021).

Data-driven methodologies instead leverage historical data to evaluate current system health and predict RUL (Ensarioğlu et al., 2023). Rather than directly modeling the physical complexities of

wear and mechanical deterioration, data-driven approaches employ artificial intelligence to identify failure patterns and extract critical features from large datasets, revealing degradation characteristics by converting raw sensor history into usable information. Early data-driven research focused on traditional machine learning approaches such as Support Vector Machines, K-means clustering, and reinforcement learning (Ensarioğlu et al., 2023). While effective on small datasets, these approaches struggled in turbofan prognostics for two main reasons. First, manual feature engineering requires researchers to create and select features based on their own understanding of the data and statistical intuition, which becomes difficult to scale across large or high-dimensional datasets (H. Liu et al., 2021). Second, these methods lack temporal memory: they treat each sensor snapshot as an independent event, ignoring the fact that an engine's health at cycle 50 is directly dependent on its condition at cycle 49.

To address these limitations, researchers turned to deep learning, which uses multilayered neural networks for tasks such as classification, regression, and representation learning. Common architectures include fully connected networks, deep belief networks, recurrent neural networks, convolutional neural networks, generative adversarial networks, and transformers. Convolutional Neural Networks (CNNs) were initially adapted from image processing to extract spatial features from multi-sensor grids. While CNNs are effective at detecting local patterns, such as a sudden pressure rise, they struggle to model long-term, continuous degradation across hundreds of flight cycles, since they lack a recursive structure (Ensarioğlu et al., 2023). This was why Recurrent Neural Networks (RNNs) and Long Short-Term Memory (LSTM) networks were introduced. RNNs (Hochreiter & Schmidhuber, 1997; J. Zhang et al., 2018) are a family of neural networks specialized for processing a sequence of values, capable of capturing temporal dependencies within input samples. RNNs, especially those built from LSTM cells and Gated Recurrent Units (GRUs) (Dey & Salem, 2017; Yuan et al., 2016), and attention (Vaswani et al., 2017) have been widely used for prognostics of components such as lithium-ion batteries (Y. Zhang et al., 2018), gears, fuel cells, and turbofan engines (Cubillo et al., 2016; Fu et al., 2023; Saxena et al., 2008; Y. Zhang et al., 2018). However, standard RNNs suffer from the vanishing gradient problem, gradually forgetting early health-state information as more sequential data is introduced, which makes long-term dependencies difficult to learn. This limitation gave rise to more advanced recurrent architectures, notably LSTM networks (Hochreiter & Schmidhuber, 1997; J. Zhang et al., 2018) and GRUs (Dey & Salem, 2017). Since aero-engine data is inherently multivariate and time-dependent, this has contributed to the widespread adoption of LSTM models in RUL research (Hochreiter & Schmidhuber, 1997). Ensarioğlu et al. (2023) demonstrated that RNNs are efficient at analyzing the time-series characteristics of turbofan sensor data.

The LSTM addresses the vanishing gradient problem through three gating mechanisms that regulate the flow of information across time steps. The forget gate determines what historical information is discarded and is given as:

$$f_t = \sigma\left(W_f \cdot [h_{t-1}, x_t] + b_f\right) \tag{1}$$

The input gate controls what new information is written to the cell state:

$$i_t = \sigma(W_i \cdot [h_{t-1}, x_t] + b_i) \tag{2}$$

And the output gate determines what information is passed to the next hidden state:

$$o_t = \sigma\left(W_o \cdot [h_{t-1}, x_t] + b_o\right) \tag{3}$$

Solanki et al. (2025) proposed a model combining pre-processing techniques with an LSTM network, introducing an improved piecewise linear degradation model to determine the initial point of deterioration and assign RUL target labels, evaluated on the C-MAPSS dataset. Dida et al. (2025) developed a prediction model combining CNN, LSTM, and attention mechanisms, using CNN to extract local features from sensor data while the LSTM-attention network analyzed temporal characteristics to forecast engine life. More recently, Transformer-based architectures have introduced an alternative to recurrence, replacing sequential processing with self-attention mechanisms that allow the model to weigh different parts of a sequence simultaneously, making them theoretically powerful for long-range dependency modeling (H. Liu et al., 2021; Vaswani et al., 2017). Recent work has applied hierarchical, multi-stage attention Transformers to turbofan RUL prediction with strong reported accuracy, demonstrating that the architecture race in this field has continued well past LSTM-based methods (Fan et al., 2024; L. Liu et al., 2022), demonstrating that the architecture race in this field has continued well

past LSTM-based methods. What has not moved, however, is the benchmark itself: this Transformer-based literature, like the LSTM-based work reviewed above, remains confined almost exclusively to C-MAPSS. The dataset, not the model architecture, is the persistent bottleneck this study addresses.

The quality of the simulation environment from which training data is generated is a primary determinant of whether a prognostic model will generalize to real-world application. The Commercial Modular Aero-Propulsion System Simulation (C-MAPSS) dataset, developed by NASA's Ames Research Center (Saxena et al., 2008), remains the most widely used benchmark in the turbofan RUL literature. C-MAPSS simulates a two-spool turbofan engine based on the thermodynamic architecture of the CFM56, modeling degradation in the HPC and HPT modules across six combinations of altitude, throttle resolver angle, and Mach number. The dataset is divided into four subsets, FD001 through FD004, each representing a different combination of operating conditions and fault modes (Saxena et al., 2008), with 21 sensor measurements recorded per flight cycle covering temperatures, pressures, shaft speeds, and efficiencies. C-MAPSS has been essential to the field, providing a public benchmark that has allowed researchers to contribute meaningfully to turbofan prognostics. It carries structural limitations, however, that narrow the conclusions that can be drawn from evaluations conducted on it. First, C-MAPSS employs a quasi-steady-state thermodynamic model, meaning operating conditions transition between predefined clusters rather than evolving continuously, concealing the transient dynamics that occur within a single flight cycle. High-fidelity telemetry from platforms such as AGTF30, by contrast, captures the rich, non-linear behavior seen during throttle excursions, altitude transitions, and rapid acceleration events (Chapman & Litt, 2017). Second, C-MAPSS models a dual-spool turbofan that does not reflect the variable-geometry features, gear reduction system, or closed-loop control behavior of next-generation geared turbofan engines.

To address the limitations of steady-state datasets such as C-MAPSS, the research community has turned to high-fidelity simulation environments capable of generating more realistic engine data. The Toolbox for the Modeling and Analysis of Thermodynamic Systems (T-MATS) is the most prominent example of this shift (Lavelle et al., 2014). Unlike earlier algebraic frameworks, T-MATS takes a modular, physics-based approach in which fan speeds, pressures, and temperatures evolve continuously in response to transient input (Chapman & Litt, 2017), using a library of component blocks for compressors, turbines, combustors, nozzles, ducts, and control actuators that can be assembled into different propulsion system configurations. The AGTF30 engine model, built within the T-MATS environment, represents a 30,000 lbf class geared turbofan (Chapman & Litt, 2017; Lavelle et al., 2014). This architecture introduces complexities absent from legacy benchmarks, most notably a gear reduction system that decouples the fan from the low-pressure spool, allowing both to operate at their respective aerodynamically optimal speeds. AGTF30 also runs within a closed-loop FADEC simulation, with a multivariable controller regulating thrust and surge margin. These features make AGTF30 a considerably more demanding environment for prognostic models, requiring them to differentiate between control-induced transients and genuine degradation signatures, a distinction that meaningfully strengthens a model's potential for real-world generalization (Chapman & Litt, 2017).

Taken together, the literature reviewed here reveals a consistent pattern: model architectures for turbofan RUL prediction, from early machine learning through LSTM and now Transformers, have advanced considerably, but almost entirely within the confines of C-MAPSS, a benchmark whose steady-state, dual-spool architecture no longer represents the modern engines it is meant to stand in for. Whether the properties that make these architectures effective on that older benchmark transfer to the transient, closed-loop, gear-coupled dynamics of a modern geared turbofan is a question the existing literature has not answered, largely because almost no one has tested it under those conditions. This gap, is not a shortage of capable model architectures but a shortage of realistic conditions to evaluate them against, is what this study addresses directly, by generating a fault-seeded dataset from the T-MATS/AGTF30 environment and evaluating an attention-augmented LSTM against it.

3. IMPLEMENTATION OF METHODOLOGY

This section describes the four-stage engineering pipeline used to generate, prepare, and model the dataset: dataset generation, data preprocessing, model architecture, training and optimization. The final two stages are addressed in the sections that follow.

3.1 Dataset Generation

A synthetic dataset was generated using the AGTF30 (Advanced Geared Turbofan, 30,000 lbf thrust class) simulation model implemented within the Toolbox for the Modeling and Analysis of Thermodynamic Systems (T-MATS), a NASA Glenn Research Center open-source MATLAB/Simulink library. The AGTF30 simulation environment is shown in Figure 3. Unlike empirical datasets, this simulation environment solves full thermodynamic cycle equations at each timestep, providing physically consistent sensor readings across all degradation scenarios. Degradation is modeled as continuous wear of the High-Pressure Compressor (HPC) and High-Pressure Turbine (HPT), represented by adjustments to each component's efficiency and flow capacity scalars. To the authors' knowledge, this represents the first published application of the AGTF30 dynamic simulation model for generating a run-to-failure RUL training dataset.

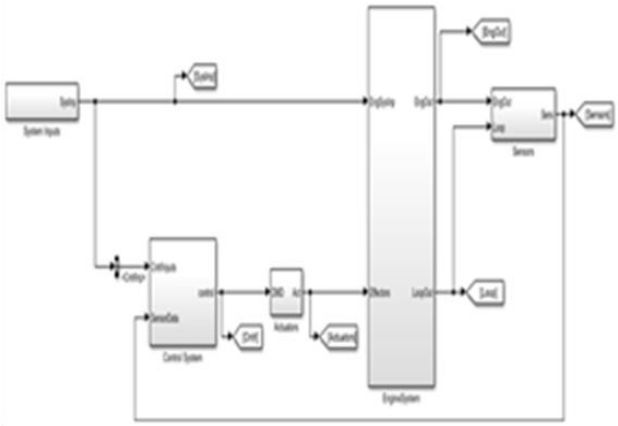

Figure 3: AGTF30 Simulink model.

Table 1: *Mission Profile Parameters*

Phase	Start (s)	End (s)	PLA (deg)	Altitude (ft)	Description
Ground Idle	0	100	40	0	Engine stabilizes at low power
Power-Up	100	500	40–80	0	Throttle advances to cruise setting
Cruise	500	2000	80	0	Steady cruise, fault detection window

Engine degradation is introduced by scaling the efficiency and flow capacity parameters of the HPC and HPT blocks within the T-MATS model. For each engine unit, four independent degradation factors are drawn from a uniform random distribution over the range [0.88, 1.00] using a fixed seed (rng (42)): one each for HPC efficiency, HPC flow capacity, HPT efficiency, and HPT flow capacity. Each factor is multiplied against its corresponding healthy design-point value to produce the degraded parameter used for that engine's simulation run, yielding four statistically independent degradation trajectories per engine rather than a single composite severity level. This randomized, per-unit approach follows the precedent set by the original C-MAPSS benchmark, in which each engine begins with an independently varying degree of initial wear (Saxena et al., 2008), and reflects the manufacturing and operational variability seen across a real engine fleet rather than a small set of discrete, repeatable severity levels. The degradation floor of 0.88 was set through boundary testing to ensure numerical stability across the full 2,001-second simulation.

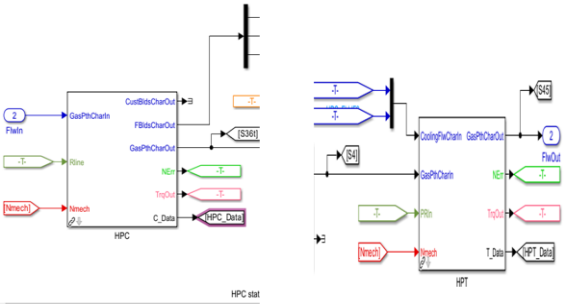

Figure 4: HPC and HPT block in NASA AGTF30 environment

Table 2: *Component Degradation Factor Ranges*

Component	Parameter	Healthy Value	Degradation Range
HPC	η (efficiency scalar)	0.994014	0.88–1.00
HPC	Wc (flow capacity scalar)	0.132800	0.88–1.00
HPT	η (efficiency scalar)	0.998392	0.88–1.00
HPT	Wc (flow capacity scalar)	0.195100	0.88–1.00

The AGTF30 model includes a Full Authority Digital Engine Control (FADEC) fuel controller that regulates fuel flow to hold exhaust gas temperature (T45) at a constant 2,241 R under steady-state cruise. As a result, T45 remains largely invariant across degradation levels. Degradation instead manifests primarily in total pressure at the HPT exit (P45) and mass flow rate at station 45 (W45), both of which drop measurably with compressor and turbine wear. HP shaft rotational speed (Nh) and thrust-specific fuel consumption (TSFC) were also evaluated as candidate signals but excluded, Nh showed only moderate sensitivity and TSFC changed negligibly across degradation levels. HPC inlet temperature (T25) and pressure (P25) were retained as upstream thermodynamic state indicators. Table 3 summarizes all candidate signals and which were retained as model inputs. This pattern, pressure and flow as primary degradation indicators rather than EGT alone, is consistent with real turbofan health-monitoring practice.

Table 3: *Candidate Sensor Signals and Degradation Sensitivity*

Signal	**Description**	**Healthy (cruise)**	**Sensitivity**	**Retained**
P45	Total pressure at HPT exit (psia)	~134.2	High	Yes
W45	Mass flow rate at station 45 (lbm/s)	~66.9	High	Yes
Nh	HP shaft rotational speed (RPM)	~21,150	Medium	No
T45	Exhaust gas temperature (R)	2241.0	Low (FADEC-held)	Yes
TSFC	Thrust-specific fuel consumption	~0.174	Low	No
T25	HPC inlet temperature (R)	~518	Medium	Yes
P25	HPC inlet pressure (psia)	~14.7	Medium	Yes

Simulations were logged at 1 Hz, yielding 2,001 rows per engine and 240,120 rows across the full 120-engine fleet. Each row contains the columns listed in Table 4. While 120 unique engine trajectories appear small, the sliding window approach with window 100 generates approximately 159,000 training samples, so the number of training sequences exceeds the number of model parameters. Generalization across trajectories is still limited to a single simulation environment with degradation factors in [0.88, 1.00], which is discussed in Section 4.7."

Table 4: *Dataset Column Description*

Column	Type	Description
unit_id	Integer	Engine identifier (1–120)
Time	Float	Elapsed simulation time (s)
T45	Float	HPT exit total temperature (R)
P45	Float	HPT exit total pressure (psia)
W45	Float	Mass flow rate at station 45 (lbm/s)
T25	Float	HPC inlet total temperature (R)
P25	Float	HPC inlet total pressure (psia)
HPC_eff	Float	HPC degradation factor applied (metadata only)
HPT_eff	Float	HPT degradation factor applied (metadata only)
RUL	Float	Remaining Useful Life label (s)
censored	Integer	0 = failed, 1 = did not reach failure threshold

3.2 Data Preprocessing

Out Of the seven candidate signals, five (T45, P45, W45, T25, P25) were retained as model inputs; they showed measurable, non-trivial change across the fleet as degradation progressed, while Nh and TSFC did not. The HPC and HPT degradation factors themselves (HPC_eff, HPT_eff) were excluded from model inputs entirely to prevent data leakage, since these internal efficiency scalars are not observable in a real deployment scenario and would artificially inflate accuracy if included.

Raw sensor values alone proved insufficient, since a single-timestep reading gives no indication of whether an engine is approaching failure or simply sitting in steady-state cruise; two engines at an identical T45 value might be on entirely different trajectories. To capture this, four rolling features were computed from the two most degradation-sensitive channels, P45 and W45: a ten-step rolling mean (P45_mean10, W45_mean10), smoothing single-timestep noise, and a ten-step finite-difference slope (P45_slope10, W45_slope10), capturing whether each channel is rising, falling, or flat over the preceding ten seconds, the most direct indicator of an active degradation event.

The 120 engines were divided into training (84), validation (18), and test (18) subsets using a stratified split by engine health score rather than a random shuffle. This ensures each subset contains a proportional mix of healthy and degraded units (Table 5).

Table 5: *Train-Validation-Test Split*

Subset	Engine Units	Count	Failed	Censored
Training	1–84	84 (70%)	59	25
Validation	85–102	18 (15%)	9	9
Test	103–120	18 (15%)	10	8
Total	1–120	120	78	42

All five input features were scaled to the range [0, 1] using min-max normalization, preventing features with large absolute values, such as T45 at approximately 2,241 R, from numerically dominating the gradient relative to features with small absolute values, such as P25:

$$\mathrm{x_{norm}} = (\mathrm{x} - \mathrm{x_{min}})/x(_{\mathrm{max}} - \mathrm{x_{min}}) \quad (4)$$

where x_{min} and x_{max} are computed exclusively from the training set and applied identically to the validation and test sets, avoiding data leakage from statistics computed on the full dataset before splitting.

Failure is defined as the first timestep during the cruise phase (t = 500s to t = 2,000s) at which P45 drops below 75% of its healthy cruise baseline of 134.215 psia (P45_fail = 100.66 psia).

$$P45_{fail} = 0.75 \times 134.215 = 100.66 \text{ psia}$$

Restricting this check to the cruise phase prevents the naturally lower P45 at ground idle from being misclassified as degradation failure. Engines that complete the full 2,000-second simulation without crossing this threshold are labeled censored, mirroring the real-world practice of removing engines for scheduled maintenance before absolute end-of-life.

A piecewise linear RUL model was adopted, consistent with the labeling convention established for C-MAPSS (Li et al., 2018):

$$RUL_t min\left(RUL_{max}, max\left(0, t_{fail} - t\right)\right) \quad (5)$$

where t_fail is the timestep at which P45 first crosses the failure threshold and RUL_{max} = 4,000 seconds is the plateau cap. For censored engines, t_fail is set to 5,000 seconds, meaning RUL counts down from 4,000 seconds at t = 0 and reaches 3,000 seconds at t = 2,000 seconds without ever reaching zero.

The dataset was restructured into overlapping sliding windows with a stride of one timestep, each capturing W consecutive seconds of the five input features:

$$Input: x[t - W + 1: t] \quad (6)$$

$$shape: (W \times 9) \quad (7)$$

$$Target: RUL_t \quad (8)$$

A window length of W = 100 seconds was selected because the throttle transition from idle to cruise takes approximately 30 to 60 seconds in the mission profile; a 100-second window is long enough to capture the complete transient response the LSTM needs to distinguish a healthy throttle event from a degradation-driven pressure drop.

3.3 Model Architecture

The proposed model is a stacked LSTM network implemented in TensorFlow/Keras. The architecture follows the established pattern for turbofan RUL regression identified across recent literature (Dida et al., 2025; Elsherif et al., 2025): The model is constructed using a sequential stacking of layers, that consist of LSTM layers, fully connected layers, and a single output layer for regression. The core of the model's ability to handle time-series data lies in its two stacked LSTM layers, each designed to capture distinct temporal patterns, for temporal feature extraction, dropout regularization between layers, and a single linear output neuron for scalar RUL regression.

Table 6: *LSTM Model Architecture*

Layer	**Configuration**	**Output Shape**	**Parameters**
Input	Window=100, Features=9	(None, 100, 9)	0
LSTM-1	128 units, return_sequences=True	(None, 100, 128)	70,656
BatchNorm-1	axis = -1	(None, 100, 128)	512
Dropout-1	rate = 0.2	(None, 100, 128)	0
LSTM-2	64 units, return_sequences=True	(None, 100, 64)	49,408
BatchNorm-2	axis = -1	(None, 100, 64)	256
Dropout-2	rate = 0.2	(None, 100, 64)	0
TemporalHead Attention	1 head, units=64, entropy=0.02	(None, 64)	4,160
Dense-1	32 units, ReLU	(None, 32)	2,080
Dropout-3	rate = 0.1	(None, 32)	0
Dense Output	1-unit, linear activation	(None, 1)	33
Total Trainable Parameters			126,721

The first LSTM layer uses return_sequences=True so it passes a hidden state at every timestep to the second layer, allowing the second layer to reason about the temporal evolution of the learned features rather than only the final state. The second layer also uses return_sequences=True, preserving the full sequence for the attention block, which then compresses the window into a single context vector before the dense output layer maps it to a predicted RUL value. The model is compiled with the Adam optimizer at a learning rate of 0.001, using a custom phase-aware asymmetric error as the loss function. Phase-aware loss was chosen over mean squared error because it penalizes late predictions overestimates of remaining life more heavily than early ones, reflecting the operational reality that missing a failure warning is far more dangerous than scheduling maintenance a bit early. Early stopping with a patience of 25 epochs monitors validation loss and restores the weights from the best-performing epoch, preventing overfitting without requiring a manually specified epoch count.

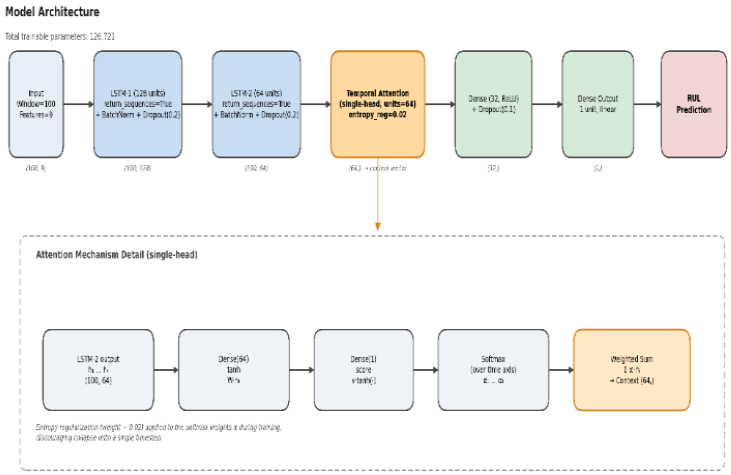

Figure 5: Proposed single-head attention-augmented LSTM architecture.

Following the recurrent layers, a temporal attention mechanism compresses the full sequence into a single context vector. Rather than assigning uniform importance to all 100 timesteps, the attention layer computes a learned weighting across the window. In this particular application, the trained weights concentrated predominantly on the oldest observation in the window the timestep furthest from the prediction point. This behavior departs from the common design expectation that attention will focus on recent transients or anomalous spikes. For the AGTF30 dataset, where degradation is deterministic and largely monotonic, the oldest available observation acts as a stable reference baseline. The model appears to use it to compute an implicit delta against the current state, which is a physically coherent strategy for a simulation where the rate of change, not the absolute sensor value, carries the degradation signal. Section 4 discusses this finding in detail.

3.4 Training, Loss Function, and Optimization

Standard regression problems typically minimize Mean Squared Error, but MSE imposes a symmetric penalty that ignores the direction of the error. A prediction that underestimates remaining life by ten seconds is treated identically to one that overestimates it by the same amount. In the context of engine prognostics, that symmetry is not operationally valid. An overestimation predicting more remaining life than actually exists represents a safety hazard, because it may delay necessary maintenance. An underestimation, by contrast, leads to a premature but safe maintenance action that wastes a limited amount of engine life. A loss function that does not distinguish between these two cases discards the information a maintenance-critical model is designed to protect.

The loss function used in this work addresses the asymmetry in two stages. Let y and $\hat{y}$ denotes the predicted and true normalized RUL, and is define as the signed prediction error

$$\Delta = \hat{y} - y. \quad (9)$$

The base asymmetric penalty is defined as:

$$\mathcal{L}_{asym} = \begin{cases} \alpha \cdot \Delta^2 & \text{if } \Delta > 0 \\ \Delta^2 & \text{if } \Delta \leq 0 \end{cases} \quad (10)$$

where $\alpha = 2.5$ applies a strict penalty to overestimations ($\hat{y} > y$)

Applied uniformly, this asymmetry would penalize noisy early-life predictions just as heavily as those near failure, over-correcting in a regime where small errors in either direction are operationally inconsequential. To restrict the asymmetric penalty to the phase of the engine's life where it matters, a sigmoid blending weight is introduced that shifts the loss smoothly from symmetric to asymmetric as the engine approaches its failure threshold:

$$w(y) = \sigma\big(\gamma(\tau - y)\big) \quad (11)$$

where τ = 0.5 designates the normalized RUL at which the engine transitions from "healthy" to "at-risk," and γ=20.0 controls the steepness of the transition. The final loss is a convex combination of the two penalties:

$$Lfinal = w(y) \cdot L_{asym}(\Delta) + \big(1 - w(y)\big) \cdot L_{sym}(\Delta) \qquad (12)$$

Under this formulation, a healthy engine (y well above 0.5) is trained almost entirely under standard squared error, while an engine approaching failure (y near zero) is trained under the asymmetric penalty that discourages overestimation.

Training proceeded for up to 200 epochs with early stopping (patience of 25 epochs on validation loss, restoring the best-performing weights) and a learning rate schedule that halved the learning rate after 10 epochs without improvement, decaying to a floor of 1×10^{-6}. This schedule allowed the optimizer to continue fine-grained refinement once the loss had largely stabilized.

Model performance is quantified with three complementary metrics. Root Mean Square Error (RMSE) is reported in seconds, matching the physical unit of RUL:

$$RMSE = \sqrt{\left(\frac{1}{n} \times \sum (\hat{y}_i - y_i)^2\right)} \qquad (13)$$

Because the quadratic term amplifies large errors, a low RMSE indicates both a small average error and the absence of catastrophic outliers, both of which are essential for a maintenance-relevant prediction. Direct numerical comparison against published LSTM baselines on the C-MAPSS benchmark is not meaningful here, since this study measures RUL in seconds rather than flight cycles and uses a different simulation source. RMSE therefore serves as an internal reference for comparing configurations within this work.

The NASA Prognostic Scoring function, introduced alongside the C-MAPSS dataset (Saxena et al., 2008), is also reported. It encodes the same late-versus-early asymmetry that structures the training loss:

$$s = \sum e^{\frac{-d}{13}} - 1 \qquad (14)$$

For d< 0 (early: predicted RUL < actual RUL)

$$s = \sum e^{\frac{d}{10}} - 1) \qquad (15)$$

for d ≥ 0 (late: predicted RUL > actual RUL)

where d = ŷ – y is the signed prediction error. The penalty for late predictions grows with a characteristic scale of 10, while early predictions are penalized at a scale of 13 making equivalent-magnitude late errors approximately 34% more costly. A lower total score indicates better performance.

3.5 Experimentation Setup

Dataset generation ran on a Dell Latitude 7480 laptop under MATLAB R2023a with T-MATS v1.1. Each 2,001-second engine simulation took 10 to 15 minutes of wall-clock time; the full 120-engine fleet required roughly 12 hours of continuous computation. Model training and all Python preprocessing were conducted on a Kaggle kernel with an NVIDIA Tesla P100 GPU (16 GB HBM2). A single 200-epoch training run took 30 to 40 minutes. The deep learning framework was TensorFlow 2.20 with Keras. Preprocessing used Python 3.12 with NumPy, Pandas 2.0, and Scikit-learn 1.3.

Three independent training runs were performed with identical hyperparameters and different random seeds (42, 123, 777) to assess reproducibility. The seed 42 run produced the lowest overall test-set RMSE and is reported as the primary result throughout. This reflects a best-of-three outcome selected after all training was complete, not during model development, and is disclosed here for transparency. All three runs used the same preprocessing pipeline and the same test partition.

4. RESULTS AND DISCUSSION

This section presents the experimental results obtained from the training and evaluation of the Attention Augmented Long Short-Term Memory (LSTM) network for Remaining Useful Life (RUL) prediction of turbofan engines. Results are reported across four evaluation metrics: Root Mean Square Error (RMSE), Mean Average Error (MAE), Near-Failure RMSE, and the NASA Prognostic Score. This section additionally presents a comparative analysis of progressive model refinements, an examination of the attention mechanism's behavior, and a critical discussion of the model's strengths and limitations in the context of the broader prognostics and health management (PHM) literature.

4.1 Overall Performance

Three independent runs used identical configurations under different random seeds (42, 123, 777) to check reproducibility (Table 7), with Seed 42 selected as the reported model per the disclosure in Section 3.5.

Table 7: *Seed Comparison*

Seed	**RMSE (s)**	**MAE (s)**	**NF-RMSE (s)**	**NASA Score**
42 (selected)	249.0	167.1	39.3	122.87
123	263.1	169.9	38.5	123.07
777	269.8	169.6	38.4	123.05

The near-failure RMSE remains stable across all three seeds, within a 1.1-second band, confirming that near-failure accuracy is not a product of random initialization. The Seed 42 model was evaluated on 34,218 test sequences drawn from 18 held-out engines. Table 8 summarizes the results.

Table 8: *Final Test Set Metrics*

Metric	**Value**	**Context**
Overall RMSE	249.0 s	6.2% of the 4,000 s operating range
Overall, MAE	167.1 s	4.2% of the 4,000 s operating range
Near-failure RMSE (RUL<200s)	39.3 s	Average error in the final 200 s of engine life
NASA Prognostic Score	122.87	Normalized RUL scale; lower is better

The 249-second overall RMSE, 6.2% of the full operating range, reflects a bimodal structure that Section 4.2 explains. The near-failure RMSE of 39.3 seconds is the number that matters operationally: at 1 Hz sampling, this means a maintenance alert would be issued within roughly 39 timesteps of the optimal alert time. The NASA score of 122.87 is consistent with the intended conservative bias of the asymmetric loss, with the residual analysis in Section 4.3 [mean -41.7s] confirming a deliberate under-prediction of remaining life to preserve a safety margin.

4.2 Prediction Accuracy Across Engines

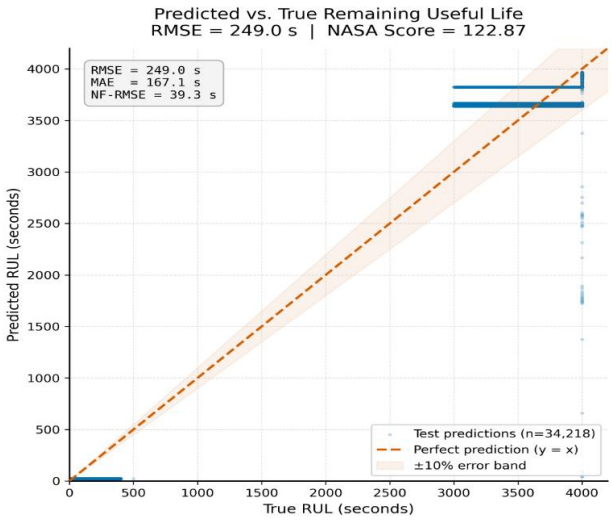

Figure 6: Predicted RUL vs True RUL

Figure 6 plots predicted against true RUL for every test sequence, each point representing one sequence. Two populations are visible: a near-diagonal cluster at low RUL (0–400s) from failed, short-life engines, predicted closely along the diagonal, and a horizontal band at approximately 3,700s predicted for true RUL values of 3,000–4,000s from long-life, censored engines, where the model predicts a roughly constant value rather than tracking the gradual decline.

Figure 7 shows individual RMSE per engine. Ten test engines, the failed, short-life units, cluster near 99 seconds; the remaining eight, which are censored, long-life units, range from 331 to 479 seconds. The aggregate mean of 249 seconds is the average of these two distinct groups, not a representative value for either.

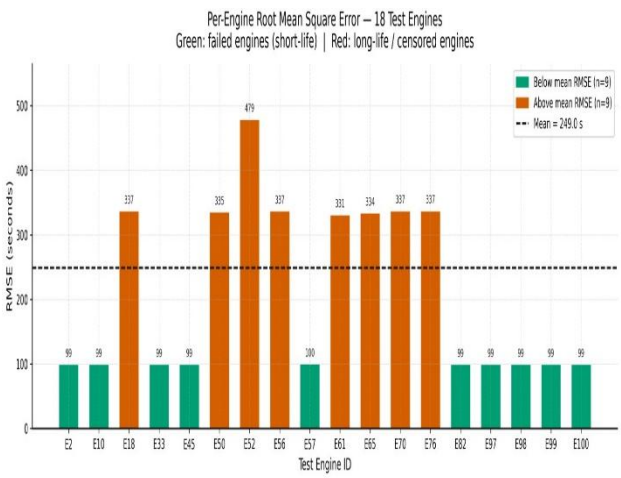

Figure 7: Per-Engine RMSE – All 18 Test Engines

The dividing factor is operational history, and not architecture. Failed engines gave the training set complete degradation trajectories, including the failure event itself, and the model learned from those. Censored engines never failed within the simulation window, so the training data for this group contains no failure event to anchor a declining prediction against. The model cannot commit to a trajectory it never observed reaching its end, and a conservative, near-constant prediction is the result. This pattern is consistent with known challenges in supervised prognostics on datasets that mix failed and censored units, and is not specific to this architecture.

4.3 Life-Stage and Residual Accuracy

Figure 8 shows the distribution of prediction residuals (predicted minus true RUL) across all test sequences. The mean residual is −41.7 seconds with a standard deviation of 245.5 seconds. A

dominant spike sits near zero, corresponding to accurate near-failure predictions, and a secondary cluster sits near −600 seconds, corresponding to the long-life engine group. This distribution is consistent with the loss function behaving as intended: the negative mean residual reflects the deliberate conservative bias built into the asymmetric loss, under-predicting remaining life slightly to preserve a safety margin ahead of actual failure. The secondary cluster reflects the same censored-engine behavior described in Section 4.2, a flat early-life prediction near 3,700 seconds against an actual value descending toward 3,000, widening the overall residual spread without affecting near-failure accuracy. A small tail of positive residuals appears early in some simulations, plausibly linked to transient sensor behavior during engine start-up before the model stabilizes into accurate tracking.

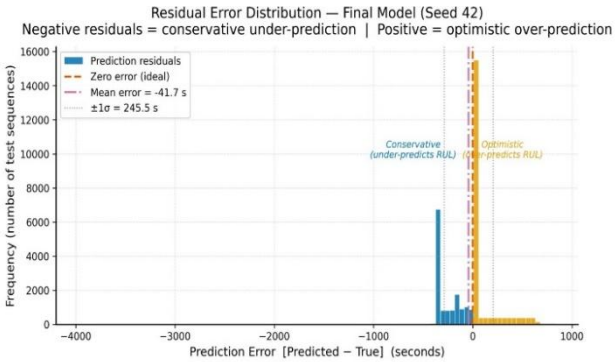

Figure 8: Residual Error Distribution All Test Sequences

Figure 9 decomposes RMSE and MAE by life stage: early life (RUL > 2,000s, n=15,208), mid-life (200–2,000s, n=2,001), and near-failure (RUL < 200s, n=17,009). The gradient is explicit: 357-second RMSE in early life, 284 seconds in mid-life, and 39 seconds in the near-failure window. This is the pattern a safety-oriented prognostic model should show: the life stage where a wrong prediction carries the greatest operational risk is also the stage with the lowest error.

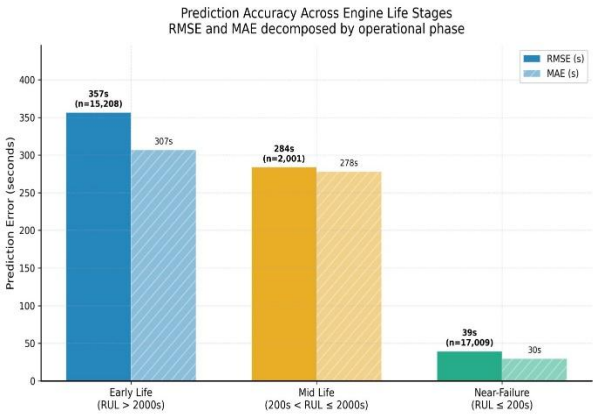

Figure 9: Prediction Error by Operational Phase

4.4 Attention Behavior

Figure 10 shows attention weights across the 100-step input window for all test predictions, alongside the mean attention profile averaged across all timesteps. Nearly all weight concentrates on window position 0, the oldest observation in the window, rather than on recent timesteps as originally anticipated in the architecture's design.

This concentration has two reinforcing explanations, one physical and one mechanical. Physically, degradation in the AGTF30 simulation is monotonic and largely deterministic, so the oldest timestep in a given window serves as a stable reference point, and the model appears to compute an implicit delta between that reference and the current state rather than searching for informative recent transients. Mechanically, the entropy regularization term in the loss is added to, rather than subtracted from, the total loss that training minimizes. Since entropy is lowest when attention weight concentrates on a single timestep, minimizing the loss also minimizes this term, which rewards concentrated attention

rather than penalizing it. That is the reverse of how entropy regularization is conventionally applied. The sharp concentration on position 0 is therefore not only a physically plausible outcome, it is close to the outcome this loss term was mathematically set up to produce. This concentration explains the visual appearance of Figure 10.Since most attention is at position 0, the other position has near-zero weight and shows up as black, and the uniform pattern across the 1900 sequences reflects a consistent focus on position 0 rather than a visualization issue. A future revision subtracting rather than adding the entropy term, rather than simply lowering its coefficient, would be the more direct way to encourage the originally intended recency-weighting behavior.

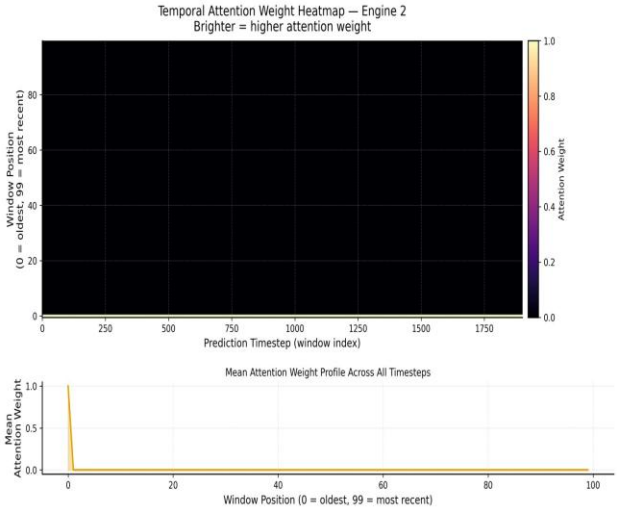

Figure 10: Temporal Attention Weight Heatmap and Mean Profile – Engine 2 Top:1900 sequences across 100 positions, dark is near-zero weight. Bottom: mean profile. The uniform appearance shows consistent focus at 0

4.5 Ablation Study

Table 9 traces the progression from baseline to final model across the major architectural and training changes.

Table 9: *Ablation Study Progression*

Step	Incremental Change	Overall RMSE (s)	NF-RMSE (s)	NASA Score
0	Baseline: raw features, MSE, sigmoid output	358	104	—
1	+ Rolling features (mean, std, slope)	371	42	159.7
2	+ RUL norm, BatchNorm, window=100, attention, phase-aware loss thr=0.6	451	38.8	166.5
3	+ Thr correction to 0.4, entropy reg 0.02, remove soft plateau	330	38.4	134.0
4	+ Healthy fraction 0.5	304	38.6	127.3
5	+ Healthy fraction 0.9, thr=0.5, healthy penalty	273	39.5	117.6

Each row reflects the cumulative configuration at that stage; several runs bundle more than one change, so performance shifts cannot be attributed to a single factor alone. Introducing rolling features produced the largest single drop in near-failure RMSE, from 104 to 42 seconds, a 60% reduction. The threshold used for the phase-aware loss was initially set too high (0.6), activating the asymmetric penalty too early in mid-life and pushing overall RMSE up to 451 seconds; lowering it corrected this, as shown in Figure 11 Subsequent runs progressively reduced overall RMSE through healthy-fraction adjustments and refinements to the single-head attention configuration. The near-failure column tells the more interesting story: it barely moves after the rolling-features change. Six subsequent architectural and training adjustments shifted overall RMSE by more than 200 seconds, while near-failure RMSE stayed within a 4-second band throughout. This stability indicates that near-failure accuracy is driven primarily by the rolling slope features, which directly encode the rate of degradation, rather than by any specific architectural choice made afterward.

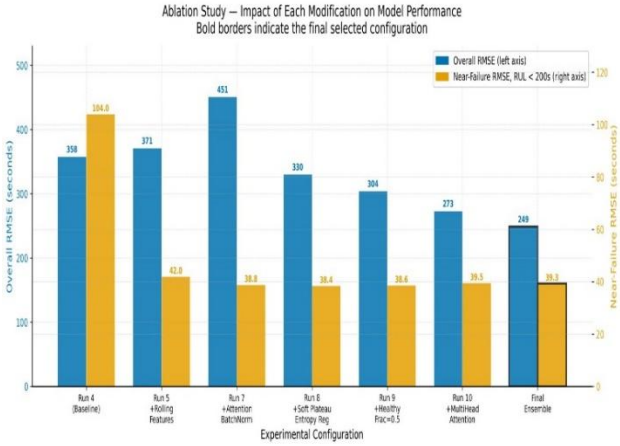

Figure 11: Ablation Study – Overall RMSE and Near-Failure RMSE Across All Runs

4.6 Comparison with Published Benchmarks

A direct numerical comparison between this study's results and published LSTM-based RUL results is not possible in absolute terms. Every published benchmark for turbofan prognostics uses C-MAPSS, with RUL measured in engine cycles over an operating range of roughly 125 to 350 cycles depending on sub-dataset, while this study measures RUL in seconds over a 4,000-second range; the two quantities have no common scale. What can be compared is relative error, RMSE as a percentage of each study's operating range, which is scale-independent. Table 10 presents this comparison.

Table 10: *Relative RMSE Comparison with Published Studies*

Study	Dataset	RMSE	Operating Range	Relative RMSE
Li et al. (2018)	C-MAPSS FD001	12.6 cycles	~125 cycles	10.1%
Y. Zhang et al. (2018)	C-MAPSS FD001	13.4 cycles	~125 cycles	10.7%
H. Liu et al. (2021)	C-MAPSS FD001	11.4 cycles	~125 cycles	9.1%
Muneer et al. (2021)	C-MAPSS FD001	13.1 cycles	~125 cycles	10.5%
This study	AGTF30 (self-generated)	249.0 s	4,000 s	6.2%

The relative RMSE of 6.2% obtained here is lower than all four C-MAPSS references shown.This should not be read as evidence that this model outperforms them; the comparison places the result in proportional context rather than making a superiority claim across different experimental conditions and simulation environments. The primary contribution of this work is the AGTF30 dataset and its use for supervised LSTM training, not the relative RMSE figure itself. Other recent deep learning approaches reporting comparable relative RMSE on C-MAPSS and N-CMAPSS include (Arias Chao et al., 2021; Ellefsen et al., 2019; Elsherif et al., 2025; Remadna et al., 2021).

4.7 Limitation

The most consequential limitation is the simulation boundary. Every engine in this study was generated by a mathematical model. The AGTF30 simulation does not include sensor noise, measurement drift, off-nominal atmospheric conditions, or the stochastic variation that characterizes

real engine monitoring systems. Whether the trained model generalizes to physical test rig data, much less to operational engine telemetry, has not been tested.

The censored engine problem is structural. Eight of the 18 test engines produced RMSE values above 300 seconds because their failure events do not occur in the training data. The model has no reference for what the terminal degradation looks like in high-life engines. This is not solvable by adjusting the architecture. It requires either more training data with completed high-life failure trajectories, or a different modeling approach that handles incomplete observations explicitly.

The loss function threshold, the entropy regularization coefficient, the healthy cycle retention fraction, and the attention head count were all chosen by sequential experiment rather than by systematic search. The dataset contains 120 unique engine trajectories from a single AGTF30 configuration. Although windowing increases sample count, variation in operating conditions and degradation modes is narrow [0.88, 1.00], and the model's ability to generalize to real engines or other simulation settings was not tested. This is mitigated by the 84/18/18 split by engine, so no engine appears in both train and test, and by Dropout, BatchNorm and early stopping, but remains a limitation. In addition, several rows in Table 9 combine more than one change at a time for example, threshold correction, entropy regularization, and soft plateau removal so the gains cannot be pinned down to a single factor alone. The three-seed selection approach also introduced a mild positive bias in the reported RMSE; the best of three runs is reported, and the other two seeds gave 263 and 270 seconds respectively.

5. FINDINGS

The near-failure RMSE of 39.3 seconds is the most operationally relevant number in the study. When the engine has less than 200 seconds of remaining life, the model predicts that life with an average error of 39 seconds. That figure was stable across all three independent training seeds, ranging from 38.4 to 39.5 seconds. Additionally, stability across seeds matters here. This result did not depend on a single fortunate initialization; it held consistently across multiple independent runs A result was that was not consistent across various multiple training instances is not a result worth trusting especially in the aviation industry where an unreliable prediction carries real safety consequences. The overall RMSE of 249.0 seconds is 6.2 percent of the 4,000-second operating range. It is also the average of two very different populations. Ten test engines had individual RMSE near 99 seconds. Eight others ranged from 331 to 479 seconds. The divide falls along the line between short-life failed engines and long-life censored engines. Rolling features drove the largest single improvement in the entire ablation study. Adding the tenstep mean and slope features for P45 and W45 cut near-failure RMSE from 104 seconds to 42 seconds in one step. Every subsequent architectural addition, the attention mechanism, the custom loss, the single-head design, the healthy cycle retention, improved overall RMSE but moved nearfailure RMSE by only a few seconds. The informational content that matters most for near-failure prediction was already captured by the rate-of-change features.

6. FUTURE WORK

Four directions follow from the findings and limitations of this study. The censored-engine behavior is structural, not something more LSTM layers would fix: eight of the 18 test engines produced RMSE values above 300 seconds because their failure events simply don't occur in the training data, the model has no reference for what terminal degradation looks like in a high-life engine. Survival analysis methods, Cox proportional hazards models or Weibull regression adapted for sensor data, built specifically to extract information from incomplete observations, and a hybrid model combining LSTM-based feature extraction with a survival-analysis output layer would let the full fleet contribute meaningful signal during training rather than the censored engines acting as noise.

Every finding in this study also sits behind a simulation boundary. The AGTF30 model was designed to match the thermodynamic behavior of real advanced geared turbofan architectures, so transfer to physical data may be plausible, but it has not been demonstrated. Even a partial comparison against a small number of physical engine cycles from a test rig would substantially strengthen the claim that physics-based simulation data can substitute for real fleet data in supervised prognostic training.

The attention mechanism's concentration on the oldest input timestep, discussed in Section 4.4, also points to a concrete next step: adding a learned positional encoding to the LSTM output sequence before attention scoring, giving the model an explicit sense of where each timestep sits in the window,

or correcting the sign of the entropy regularization term so it discourages rather than rewards concentration. Either is a small, targeted change worth testing before the attention design is treated as final.

Finally, the pipeline built for this study, simulation-based dataset generation, rolling-feature engineering, and the attention-augmented LSTM itself, is not inherently turbofan-specific. Any rotating machinery asset with an existing physics-based simulation model and a sufficient historical record of failure events could, in principle, follow the same sequence.

7. CONCLUSION

This study addressed a specific gap in turbofan Remaining Useful Life prediction: the near-total reliance of existing LSTM-based research on the NASA C-MAPSS benchmark, a dataset built on a simplified, dual-spool thermodynamic model that does not reflect the transient, closed-loop behavior of modern geared turbofan engines. A run-to-failure dataset was generated from the NASA AGTF30 simulation using the T-MATS environment, to the authors' knowledge the first published use of AGTF30 for this purpose, and an LSTM network augmented with a single-head temporal attention mechanism and a phase-aware asymmetric loss function was trained and evaluated against it.

The final model achieved an overall RMSE of 249.0 seconds and a near-failure RMSE of 39.3 seconds, with a MAE of 167.1 seconds and a NASA prognostic score of 122.87, with near-failure accuracy stable within a two-second band across three independent random seeds. The results show a clear accuracy gradient across an engine's operational life, with the lowest error occurring in the final approach to failure, the phase where an inaccurate prediction carries the greatest operational and safety consequence. The ablation study traced this near-failure accuracy primarily to the engineered rolling-window features rather than to any single architectural change, while the overall RMSE improved substantially through the attention mechanism, phase-aware loss tuning, and healthy-sample rebalancing introduced across later iterations of the model.

The central contribution of this work is not the RMSE figure itself but the dataset and methodology behind it: a demonstration that LSTM-based RUL prediction, evaluated under the more demanding transient and closed-loop dynamics of a high-fidelity geared turbofan simulation, retains the same near-failure reliability previously reported only on C-MAPSS. Extending this approach to real flight telemetry remains the necessary next step toward operational deployment. For Nigeria's growing aviation sector, such data-driven prognostic capability offers a practical pathway to more sustainable maintenance practices and reduced reliance on fixed-interval overhauls.

ACKNOWLEDGMENT

The authors acknowledge AFIT Kaduna for providing the environment for the research and the works of all authors used in the project illustrated as references. Dataset and code available from the authors upon reasonable request.

8. REFERENCES

Arias Chao, M., Kulkarni, C., Goebel, K., & Fink, O. (2021). Aircraft engine run-to-failure dataset under real flight conditions for prognostics and diagnostics. *Data*, 6(1), Article 5. https://doi.org/10.3390/data6010005

Chapman, J. W., & Litt, J. S. (2017). Control design for an advanced geared turbofan engine (NASA/TM-2017-219569). NASA. https://doi.org/10.2514/6.2017-4820

Cubillo, A., Perinpanayagam, S., & Esperon-Miguez, M. (2016). A review of physics-based models in prognostics: Application to gears and bearings of rotating machinery. *Advances in Mechanical Engineering*, 8(8), 1–21. https://doi.org/10.1177/1687814016664660

Dey, J., & Salem, F. M. (2017). Gate-variants of gated recurrent unit (GRU) neural networks. In *Proceedings of the 60th International Midwest Symposium on Circuits and Systems (MWSCAS)* (pp. 1593–1596). https://doi.org/10.1109/MWSCAS.2017.8053243

Dida, M., Cheriet, A., & Belhadj, M. (2025). Remaining useful life prediction using attention-LSTM neural network of aircraft engines. *International Journal of Prognostics and Health Management*, 16(2). https://doi.org/10.36001/ijphm.2025.v16i2.4274

Ellefsen, A. L., Bjørlykhaug, E., Æsøy, V., Ushakov, S., & Zhang, H. (2019). Remaining useful life predictions for turbofan engine degradation using semi-supervised deep architecture. *Reliability Engineering & System Safety*, 183, 240–251. https://doi.org/10.1016/j.ress.2018.11.027

Elsherif, S. M., Hafiz, B., Makhlouf, M. A., & Farouk, O. (2025). A deep learning-based prognostic approach for predicting turbofan engine degradation and remaining useful life. *Scientific Reports*, 15, Article 26251. https://doi.org/10.1038/s41598-025-09155-z

Ensarioğlu, K., İnkaya, T., & Emel, E. (2023). Remaining useful life estimation of turbofan engines with deep learning using change-point detection-based labeling and feature engineering. *Applied Sciences*, 13(21), Article 11893. https://doi.org/10.3390/app132111893

Fan, Z., Li, W., & Chang, K.-C. (2024). A two-stage attention-based hierarchical transformer for turbofan engine remaining useful life prediction. *Sensors*, 24(3), Article 824. https://doi.org/10.3390/s24030824

Fu, S., Avdelidis, N. P., & Jennions, I. K. (2023). A prognostic approach to improve system reliability for aircraft system. In *Proceedings of the 7th International Conference on System Reliability and Safety (ICSRS)* (pp. 259–264). https://doi.org/10.1109/ICSRS59833.2023.10381117

Hochreiter, S., & Schmidhuber, J. (1997). Long short-term memory. *Neural Computation*, 9(8), 1735–1780. https://doi.org/10.1162/neco.1997.9.8.1735

Hopfield, J. J. (1982). Neural networks and physical systems with emergent collective computational abilities. *Proceedings of the National Academy of Sciences*, 79(8), 2554–2558. https://doi.org/10.1073/pnas.79.8.2554

Jardine, A. K. S., Lin, D., & Banjevic, D. (2006). A review on machinery diagnostics and prognostics implementing condition-based maintenance. *Mechanical Systems and Signal Processing*, 20(7), 1483–1510. https://doi.org/10.1016/j.ymssp.2005.09.012

Jung, J.-S., Son, C., Rimell, A., & Clarkson, R. J. (2025). A framework for an ML-based predictive turbofan engine health model. *Aerospace*, 12(8), Article 725. https://doi.org/10.3390/aerospace12080725

Lavelle, T. M., Chapman, J. W., May, R. D., Litt, J. S., & Guo, T.-H. (2014). Toolbox for the modeling and analysis of thermodynamic systems (T-MATS) user's guide (NASA/TM-2014-216638). NASA. https://doi.org/10.2514/6.2014-3929

Li, X., Ding, Q., & Sun, J.-Q. (2018). Remaining useful life estimation in prognostics using deep convolution neural networks. *Reliability Engineering & System Safety*, 172, 1–11. https://doi.org/10.1016/j.ress.2017.11.021

Liu, H., Liu, Z., Jia, W., & Lin, X. (2021). Remaining useful life prediction using a novel feature-attention-based end-to-end approach. *IEEE Transactions on Industrial Informatics*, 17(2), 1197–1207. https://doi.org/10.1109/TII.2020.2983760

Liu, L., Song, X., & Zhou, Z. (2022). Aircraft engine remaining useful life estimation via a double attention-based data-driven architecture. *Reliability Engineering & System Safety*, 221, Article 108330. https://doi.org/10.1016/j.ress.2022.108330

Muneer, A., Taib, S. M., Fati, S. M., & Alhussian, H. (2021). Deep-learning based prognosis approach for remaining useful life prediction of turbofan engine. *Symmetry*, 13(10), Article 1861. https://doi.org/10.3390/sym13101861

Remadna, I., Terrissa, L. S., Ayad, S., & Zerhouni, N. (2021). RUL estimation enhancement using hybrid deep learning methods. *International Journal of Prognostics and Health Management*, 12(1). https://doi.org/10.36001/IJPHM.2021.V12I1.2378

Saxena, A., Goebel, K., Simon, D., & Eklund, N. (2008). Damage propagation modeling for aircraft engine run-to-failure simulation. In *Proceedings of the International Conference on Prognostics and Health Management* (pp. 1–9). https://doi.org/10.1109/PHM.2008.4711414

Solanki, A. G., Lu, Z., & Magige, M. M. (2025). Remaining useful life prediction of turbofan engines using long short-term memory networks. *International Journal of Scientific Research Archive*, 16(3), 1240–1253. https://doi.org/10.30574/ijsra.2025.16.3.2704

Thakkar, U., & Chaoui, H. (2022). Remaining useful life prediction of an aircraft turbofan engine using deep layer recurrent neural networks. *Actuators*, 11(3), Article 67. https://doi.org/10.3390/act11030067

Vaswani, A., Shazeer, N., Parmar, N., Uszkoreit, J., Jones, L., Gomez, A. N., Kaiser, Ł., & Polosukhin, I. (2017). Attention is all you need. *Advances in Neural Information Processing Systems*, 30, 5998–6008. https://proceedings.neurips.cc/paper_files/paper/2017/file/3f5ee243547dee91fbd053c1c4a845aa-Paper.pdf

Vichare, N. M., & Pecht, M. G. (2006). Prognostics and health management of electronics. *IEEE Transactions on Components and Packaging Technologies*, 29(1), 222–229. https://doi.org/10.1109/TCAPT.2006.870387

Xie, Z., Du, S., Lv, J., Deng, Y., & Jia, S. (2021). A hybrid prognostics deep learning model for remaining useful life prediction. *Electronics*, 10(1), Article 39. https://doi.org/10.3390/electronics10010039

Yuan, M., Wu, Y., & Lin, L. (2016). Fault diagnosis and remaining useful life estimation of aero engine using LSTM neural network. In *Proceedings of the IEEE International Conference on Aircraft Utility Systems (AUS)* (pp. 135–140). https://doi.org/10.1109/AUS.2016.7748054

Zhang, J., Wang, P., Yan, R., & Gao, R. X. (2018). Long short-term memory for machine remaining life prediction. *Journal of Manufacturing Systems*, 48, 78–86. https://doi.org/10.1016/j.jmsy.2018.05.011

Zhang, Y., Xiong, R., He, H., & Pecht, M. G. (2018). Long short-term memory recurrent neural network for remaining useful life prediction of lithium-ion batteries. *IEEE Transactions on Vehicular Technology*, 67(7), 5695–5705. https://doi.org/10.1109/TVT.2018.2805189

DESIGN AND PERFORMANCE EVALUATION OF A DUAL-MEDIA FILTRATION SYSTEM USING PALM KERNEL SHELL ACTIVATED CARBON FOR WASTEWATER TREATMENT

Aminu Ohueyi Ahmed[1,*], Mohammed Aliyu Aliyu[1], Abdullahi Mohammed Dalhatu[1], Umar Abdullahi[1], Yakubu Joseph Nlira[1]

[1]*Ahmadu Bello University, Zaria, Nigeria*

Email: ohueyi23@gmail.com[*], maliualiyu@gmail.com, mabdullahi556@gmail.com, abuafreen14@gmail.com, josephyakubu1090@gmail.com

***Corresponding author**: Aminu Ohueyi Ahmed

DOI: https://doi.org/10.67203/sp.ICESID.2026

ABSTRACT

The increasing demand for cost-effective and sustainable wastewater treatment technologies in developing regions has necessitated the exploration of locally available materials for tertiary treatment applications. This study presents the design and performance evaluation of a laboratory-scale dual-media filtration system incorporating palm kernel shell-derived activated carbon (PKS-AC) and sharp sand for the treatment of effluent from the Ahmadu Bello University (ABU), Zaria stabilization pond. The filtration column was constructed using a layered configuration of coarse sand, activated carbon, and fine sand to facilitate combined processes of physical filtration and adsorption. Wastewater samples were collected from the final discharge point of the maturation pond and analyzed before and after filtration for selected physicochemical parameters, including turbidity, nitrate concentration, biochemical oxygen demand (BOD), chemical oxygen demand (COD), and total dissolved solids (TDS). The results indicate substantial improvements in effluent quality after treatment. Turbidity was reduced from 13.0 NTU to 2.6 NTU, nitrate concentration decreased from 35.0 mg/L to 15.6 mg/L, COD was lowered from 3000 mg/L to 800 mg/L, and BOD decreased from 150 mg/L to 90 mg/L. Additionally, a moderate reduction in TDS was observed. The enhanced performance of the system is attributed to the synergistic interaction between the sand filtration layers and the adsorption capacity of PKS-AC. The findings demonstrate that the developed dual-media filtration system offers an efficient, low-cost, and sustainable solution for tertiary wastewater treatment, particularly in institutional and resource-constrained environments.

Keywords: *Dual-media filtration; Palm kernel shell; Activated carbon; Wastewater treatment; Adsorption; Sand filtration*

1. INTRODUCTION

Access to safe and reliable water remains a critical global challenge, particularly in developing countries where rapid urbanization, population growth, and limited infrastructure increasingly strain water resources and wastewater management systems (Onu et al., 2023). Wastewater generated from domestic, institutional, and industrial activities contains suspended solids, organic matter, nutrients, and pathogenic microorganisms, all of which pose significant environmental and public health risks if inadequately treated (Etsuyankpa et al., 2024).

Conventional wastewater treatment processes primarily target the removal of settleable solids and biodegradable organic matter. However, these processes may not adequately eliminate residual contaminants such as nutrients, turbidity, and dissolved pollutants. Consequently, the discharge of insufficiently treated wastewater can contribute to eutrophication, deterioration of water quality, and increased risks to aquatic ecosystems and public health (Kato & Kansha, 2024).

In many developing regions, including Nigeria, wastewater treatment systems rely predominantly on low-cost technologies such as waste stabilization ponds due to their simplicity and low operational requirements. While these systems are effective in reducing biochemical oxygen demand (BOD) and pathogen loads under optimal conditions, they often fail to remove turbidity, nutrients, and residual organic pollutants (Kayode et.al, 2023; Mara, 2013; Nwinyi et al., 2020). This

limitation is evident in the wastewater treatment system at Ahmadu Bello University (ABU), Zaria, where stabilization ponds are unable to consistently meet regulatory standards for effluent discharge.

To address these challenges, tertiary treatment processes are required to further polish the effluent before discharge or reuse. Advanced treatment methods such as membrane filtration and commercial activated carbon adsorption are highly effective but often economically prohibitive in low-resource settings. Consequently, there is growing interest in the development of cost-effective and sustainable treatment alternatives using locally available materials. Agricultural residues, in particular, have been widely investigated due to their abundance, low cost, and potential for conversion into effective adsorbents (Ali, 2012; Yahya et al., 2015).

Palm kernel shell (PKS), an abundant by-product of palm oil processing in Nigeria, has emerged as a promising precursor for activated carbon production due to its high carbon content, mechanical strength, and favorable adsorption properties (Abioye & Ani, 2015). When processed through carbonization and activation, PKS can produce activated carbon with a highly porous structure and large surface area capable of adsorbing organic and inorganic pollutants. In addition to adsorption, granular media filtration using sharp sand is effective in removing suspended particles and reducing turbidity through mechanisms such as straining, sedimentation, and adsorption.

The integration of adsorption and filtration processes into a dual-media system can enhance overall treatment efficiency through complementary mechanisms. In such systems, sand layers act as pre-filters that remove suspended solids and protect the adsorptive media from clogging, while activated carbon removes dissolved contaminants.

This study therefore focuses on the design and performance evaluation of a dual-media filtration system comprising palm kernel shell-derived activated carbon and sharp sand for the tertiary treatment of wastewater from Ahmadu Bello University, Zaria. The study aims to assess the effectiveness of the system in improving key physicochemical parameters and to demonstrate its potential as an affordable and sustainable wastewater treatment solution for institutional and resource-constrained environments.

This study aligns with the ICESID 2026 conference themes of Innovative Resource Utilization and Management and Sustainable Materials Synthesis, Processing and Recycling through the conversion of agricultural waste into a value-added adsorbent for wastewater treatment.

2. MATERIALS AND METHODS

2.1 Study Area and Sample Collection

The study was conducted using wastewater obtained from the waste stabilization pond system located within Ahmadu Bello University (ABU), Zaria, Nigeria. The stabilization pond receives wastewater from residential hostels, laboratories, administrative facilities, and other institutional sources, making it representative of mixed domestic and institutional effluent.

Wastewater samples were collected from the final discharge point of the maturation pond using clean, sterilized high-density polyethylene (HDPE) containers. The samples were transported to the laboratory in insulated containers and stored at approximately 4 °C before analysis to minimize biological and chemical changes. All analyses were conducted in accordance with standard procedures to ensure data reliability and reproducibility.

2.2 Preparation of Filtration Materials

2.2.1 Palm Kernel Shell Activated Carbon (PKS-AC)

The Palm kernel shells were obtained from a local palm oil processing site as shown in Figure 1. The shells were thoroughly washed with distilled water to remove impurities and then sun-dried to reduce moisture content. The dried shells were subjected to carbonization at approximately 400 °C in a furnace under limited oxygen conditions, producing char material as shown in Figure 2. The carbonized material was further activated through steam activation at elevated temperatures (800-950°C), during which superheated steam was introduced to promote pore development and increase adsorption capacity. The activation process followed the reaction $C + H_2O \rightarrow CO + H_2$, resulting in a highly porous adsorbent material, enhancing pore development and surface area. After activation, the material was

washed repeatedly with distilled water to remove residual impurities and then dried at room temperature. The resulting activated carbon was ground and sieved to obtain uniform particle size suitable for adsorption processes as shown in Figure 3. FTIR characterization of the activated carbon revealed the presence of hydroxyl (O-H), carbonyl (C=O), aromatic (C=C), amine (N-H), and alkyne (C≡C) functional groups on the adsorbent surface. These functional groups provide active adsorption sites that facilitate the removal of dissolved contaminants from wastewater.

Carbonization and activation were conducted at the Metallurgy Foundry Laboratory, Ahmadu Bello University, because a temperature-controlled furnace was available to maintain the required thermal conditions. Furnace temperature was monitored throughout the process to ensure consistency and reproducibility.

Figure 1: Sourced palm kernel shell from Sabo Tasha, Kaduna

Figure 2: Palm kernel shell (Carbonized charcoal) Sourced at Metallurgy Foundry Laboratory A.B.U Zaria

Figure 3: The Grinded Palm kernel shell charcoal (Activated Charcoal). Sourced at metallurgy foundry laboratory A.B.U. Zaria.

Although FTIR characterization was conducted to evaluate the surface chemistry of the adsorbent, advanced characterization techniques such as Brunauer-Emmett-Teller (BET) surface area analysis, scanning electron microscopy (SEM), and iodine number determination were not performed due to equipment and resource limitations. Nevertheless, the FTIR results confirmed the presence of hydroxyl, carbonyl, aromatic, and amine functional groups that are commonly associated with adsorption processes. Future studies should incorporate BET, SEM, and iodine number analyses to

provide a more comprehensive assessment of the porosity, surface morphology, and adsorption potential of the palm kernel shell activated carbon.

2.2.2 Sharp Sand Preparation

Sharp sand was sourced locally and washed thoroughly with distilled water to remove silt, clay, and organic impurities. The cleaned sand was dried and sieved to obtain uniform particle sizes. Fine sand (approximately 1.18 mm grain size) and coarse sand (approximately 2.00 mm grain size) were prepared to ensure effective filtration and proper drainage within the system.

2.3 Design and Construction of the Filtration Column

A laboratory-scale vertical filtration column was designed and fabricated using a cylindrical plastic container. The column was constructed with a layered dual-media configuration consisting of:

- Coarse sand layer (20 cm) – support and drainage
- Activated carbon layer (15 cm) – adsorption of dissolved contaminants
- Fine sand layer (12 cm) – removal of suspended solids
- Freeboard (10 cm) – influent distribution and aeration

The layers were arranged sequentially from bottom to top, and fine mesh screens were placed between layers to prevent intermixing of media. The total effective volume of the column was approximately 0.000213 m^3. The volume was calculated using a column radius of 0.038 m and media depths of 0.020 m, 0.015 m and 0.012 m for coarse sand, activated carbon and fine sand respectively.

2.4 Experimental Setup

The filtration system was operated in a gravity-driven mode, where wastewater was introduced at the top of the column and allowed to flow downward through the media layers. The design ensured adequate contact time between the wastewater and the filter media to facilitate both physical filtration and adsorption processes. The setup is shown in Figure 4. The filtration column had an effective media volume of approximately 0.000213 m^3 (0.213 L). Approximately 0.5 L of wastewater was introduced into the filtration column during each experimental run under gravity-flow conditions. The study was designed primarily as a proof-of-concept investigation focusing on contaminant removal performance rather than hydraulic optimization. Consequently, operational parameters such as flow rate, hydraulic loading rate, hydraulic retention time (HRT), and empty-bed contact time (EBCT) were not monitored during the experiment. This limitation restricts detailed evaluation of process hydraulics and scale-up

potential. Future studies should quantify these parameters and assess their influence on treatment efficiency.

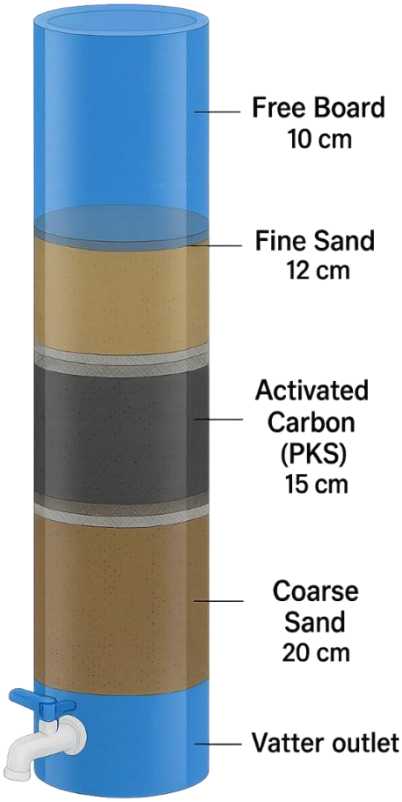

Figure 4: Schematic diagram of the dual-media filtration column

2.5 Analytical Methods

The performance of the filtration system was evaluated by analyzing physicochemical parameters before and after treatment. The parameters measured include:

- **pH** – measured using a calibrated pH meter
- **Turbidity** – determined using a nephelometric turbidity meter
- **Total Dissolved Solids (TDS)** – measured using a TDS/conductivity meter
- **Biochemical Oxygen Demand (BOD)** – determined using the standard 5-day incubation method
- **Chemical Oxygen Demand (COD)** – determined using reflux titration method
- **Nitrate concentration** – determined using colorimetric methods

All analyses were conducted in accordance with standard laboratory procedures to ensure accuracy and consistency of results. The present study was conducted as a preliminary laboratory-scale proof-of-concept investigation to evaluate the feasibility of using palm kernel shell activated carbon and sharp sand as a dual-media filtration system for tertiary wastewater treatment. The reported influent and effluent values were obtained from a single experimental run and therefore do not include measures of variability such as standard deviation or confidence intervals. Consequently, the reported treatment efficiencies should be interpreted as indicative of system performance under the tested conditions rather than as statistically representative values. The absence of replicate runs constitutes a limitation of the present study. Future investigations should incorporate replicated experiments and statistical analyses to quantify variability, establish confidence levels, and improve the reliability and reproducibility of the findings.

3. RESULTS AND DISCUSSION

3.1 Performance of the Dual-Media Filtration System

The performance of the dual-media filtration system was evaluated by comparing key physicochemical parameters of wastewater before and after treatment. The results are presented in Table 1.

Table 1: Performance of Dual-Media Filtration System

Parameter	Raw Water	Treated Water	Removal Efficiency (%)
Turbidity (NTU)	13.0	2.6	80
Nitrate (mg/L)	35.0	15.6	55
BOD (mg/L)	150	90	40
COD (mg/L)	3000	800	73
TDS (mg/L)	216	160.5	25
PH	6.89	6.79	-

Table 2: Comparison of Treated Effluent Quality with Typical Discharge Guidelines

Parameter	**Treated Effluent**	**Guideline Value**
pH	6.79	6-9
Turbidity (NTU)	2.6	<5
Nitrate (mg/L)	15.6	<50
TDS (mg/L)	160.5	<500
BOD (mg/L)	90	<30
COD (mg/L)	800	<90

Source: Adapted from WHO (2017) potable water guidelines and commonly adopted wastewater discharge criteria used for comparison purposes.

A substantial reduction in turbidity from 13.0 NTU to 2.6 NTU (80%) was observed after treatment. This high removal efficiency can be attributed primarily to the fine sand layer, which acts as a physical barrier, trapping suspended and colloidal particles via straining and sedimentation. Additionally, the layered arrangement of the filter enhances particle capture by promoting gradual filtration, reducing the likelihood of particle breakthrough. The achieved turbidity level falls within acceptable limits for improved water clarity, indicating effective removal of suspended solids. Similar turbidity reductions have been reported in sand-activated carbon filtration systems used for polishing municipal and institutional wastewater (Fayad & Radhi, 2024; Mara, 2013).

The system achieved a 73% reduction in COD and a 40% reduction in BOD. COD represents the total quantity of oxidizable substances present in wastewater, whereas BOD represents the biodegradable fraction of organic matter. The higher COD removal observed in this study suggests substantial removal of dissolved organic pollutants by the activated carbon layer. The BOD/COD ratio increased from approximately 0.05 before treatment to 0.11 after treatment, indicating a modest improvement in wastewater biodegradability. However, the observed reductions should not be interpreted solely as evidence of selective adsorption of biodegradable and non-biodegradable compounds, since changes in biodegradability may also have contributed to the results. Similar reductions in COD and BOD have been reported for agricultural waste-derived activated carbons used in wastewater treatment applications (Devi et al., 2023).

Nitrate concentration decreased from 35.0 mg/L to 15.6 mg/L, representing a removal efficiency of 55%. Although activated carbon is generally more effective for organic pollutant removal

than nutrient removal, several studies have demonstrated moderate nitrate adsorption by biomass-derived activated carbons. The observed nitrate reduction in the present study may be attributed to adsorption mechanisms reported in the literature; however, no surface charge or zeta potential measurements were conducted to confirm the specific adsorption mechanism**.**

The filtration system achieved a 25% reduction in TDS, decreasing from 216 mg/L to 160.5 mg/L.

The relatively lower removal efficiency observed for TDS compared with turbidity and COD is expected because dissolved salts and ionic species are generally more difficult to remove through adsorption and filtration processes alone. Activated carbon preferentially adsorbs organic compounds rather than dissolved inorganic constituents (Hendricks, 2016). The moderate decrease in TDS suggests partial removal of dissolved contaminants through adsorption and physical retention mechanisms within the filter media.

The pH changed slightly from 6.89 to 6.79 after treatment, indicating that the filtration process did not significantly alter the acid-base characteristics of the wastewater. Maintaining near-neutral pH conditions is advantageous because extreme pH changes can affect adsorption efficiency and subsequent biological treatment processes. Previous studies have also reported minimal pH variation following treatment with biomass-derived activated carbons, particularly when no strong chemical activation agents remain on the adsorbent surface (Abioye & Ani, 2015; Yahya et al., 2015).The pH stability observed in this study therefore supports the suitability of the PKS-AC filtration system for wastewater polishing applications.

Furthermore, as shown in Table 2, comparison with commonly adopted wastewater discharge guidelines indicates that the treated effluent satisfied recommended limits for pH, turbidity, nitrate, and TDS. However, BOD and COD values remained above typical discharge standards, suggesting that additional polishing or biological treatment may be necessary before final discharge or reuse.

3.2 Compliance with Effluent Quality Guidelines

The treated wastewater exhibited substantial improvements in quality compared with the raw influent. Turbidity decreased from 13.0 NTU to 2.6 NTU, nitrate concentration decreased from 35.0 mg/L to 15.6 mg/L, and TDS decreased from 216 mg/L to 160.5 mg/L. These treated values comply with commonly adopted guideline limits for treated wastewater and water reuse applications.

Despite these improvements, BOD and COD concentrations remained relatively high at 90 mg/L and 800 mg/L respectively. Although the filtration system achieved 40% BOD removal and 73% COD removal, the residual concentrations indicate that significant quantities of biodegradable and non-biodegradable organic matter remained in the treated effluent. Consequently, the developed dual-media filtration system should be viewed primarily as a polishing treatment technology rather than a standalone wastewater treatment solution. Additional biological treatment or advanced polishing processes may be required before direct discharge into receiving water bodies.

The guideline values are presented solely to provide context for treatment performance and do not constitute regulatory compliance standards for wastewater discharge.

3.3 Mechanisms of Pollutant Removal

The improved performance of the dual-media system can be attributed to the synergistic interaction between filtration and adsorption mechanisms, as illustrated in the filter configuration.

- Physical Filtration:
  Sand layers remove suspended particles through straining and sedimentation

- Adsorption:
  PKS activated carbon removes dissolved contaminants via surface interactions

- Protective Layering:
  Sand reduces clogging and enhances contact efficiency in the carbon layer

This combined mechanism ensures efficient removal of both particulate and dissolved pollutants, making the system more effective than single-media filtration approaches.

3.4 Engineering Implications

The results demonstrate that the developed dual-media filtration system:

- Achieves significant contaminant removal efficiency
- Utilizes low-cost and locally available materials
- Operates without the need for complex energy inputs
- Offers potential for scalability in institutional settings

From an economic perspective, the proposed system utilizes palm kernel shell, an agricultural by-product that is widely available in Nigeria and often discarded as waste. The use of locally sourced materials significantly reduces media procurement costs when compared with commercial activated carbon. Furthermore, the filtration system operates entirely under gravity flow conditions and therefore requires no external energy input during operation. Although a detailed techno-economic analysis was beyond the scope of this study, the material and operational requirements suggest that the system offers a low-cost alternative for tertiary wastewater treatment in institutional and resource-constrained settings

4. Conclusion

This study successfully designed and evaluated a laboratory-scale dual-media filtration system utilizing palm kernel shell-derived activated carbon (PKS-AC) and sharp sand for tertiary wastewater treatment. The system demonstrated significant improvement in effluent quality, confirming its effectiveness as a low-cost and sustainable treatment technology.

The filtration process achieved substantial reductions in key physicochemical parameters, including turbidity (80%), nitrate (55%), chemical oxygen demand (73%), and biochemical oxygen demand (40%). A moderate reduction in total dissolved solids was also observed, while pH remained relatively stable, indicating that the treatment process did not adversely affect the chemical balance of the water. These results highlight the ability of the system to remove both suspended and dissolved contaminants through combined filtration and adsorption mechanisms.

The performance of the system is attributed to the synergistic interaction between the sand layers, which provide physical filtration and particle retention, and the activated carbon layer, which facilitates adsorption of organic and inorganic pollutants. The use of palm kernel shell as a precursor for activated carbon further enhances the sustainability of the system by utilizing an abundant agricultural waste material.

Overall, the developed dual-media filtration system offers a practical, efficient, and environmentally friendly solution for improving wastewater quality, particularly in institutional and resource-constrained settings.

No significant media breakthrough was observed during the experimental period. However, the relatively short duration of operation did not permit detailed assessment of adsorbent exhaustion or long-term filtration performance. As adsorption sites become progressively occupied, gradual reduction in treatment efficiency may occur. Future studies should therefore investigate media breakthrough characteristics, regeneration potential, and adsorbent lifespan under continuous operating conditions. In addition, studies on the regeneration and reuse of palm kernel shell activated carbon are recommended to improve long-term cost-effectiveness and sustainability.

REFERENCES

Abioye, A. M., & Ani, F. N. (2015). Recent development in the production of activated carbon electrodes from agricultural waste biomass for supercapacitors: A review. *Renewable and Sustainable Energy Reviews*, *52*, 1282–1293.

Ali, I. (2012). New generation adsorbents for water treatment. *Chemical Reviews*, *112*(10), 5073–5091.

Devi, R., Kumar, V., Kumar, S., Bulla, M., Jatrana, A., Rani, R., Mishra, A. K., & Singh, P. (2023). Recent advancement in biomass-derived activated carbon for waste water treatment, energy storage, and gas purification: a review. *Journal of Materials Science*, *58*(30), 12119–12142.

Etsuyankpa, B., Augustine, A., Musa, S., Mathew, J., Haruna, I., Adamu Makanta, S., & Mamman, A. (2024). An Overview of Wastewater Characteristics, Treatment and Disposal: A Review. *Journal of Applied Sciences and Environmental Management*, *28*, 1553–1572. https://doi.org/10.4314/jasem.v28i5.28

Fayad, M., & Radhi, A. (2024). *Influence of aeration and double media filter of carbon and sand on the efficiency of river water treatment*. *43*, 467–474.

Hendricks, D. (2016). *Fundamentals of water treatment unit processes: physical, chemical, and biological*. Crc Press.

Kato, S., & Kansha, Y. (2024). Comprehensive review of industrial wastewater treatment techniques. *Environmental Science and Pollution Research*, *31*(39), 51064–51097.

Kayode, O. S., Adayi, L. E., & Sanni, I. M. (2023). *Assessment of Ahmadu Bello University , Zaria Waste Stabilization Pond Efficiency through Principal Component Analysis with R Programming*. *13*(1), 20–27.

Mara, D. (2013). *Domestic wastewater treatment in developing countries*. Routledge.

Nwinyi, O. C., Uyi, O., Awosanya, E. J., Oyeyemi, I. T., Ugbenyen, A. M., Muhammad, A., Alabi, O. A., Ekwunife, O. I., Adetunji, C. O., & Omoruyi, I. M. (2020). Review of drinking water quality in Nigeria: towards attaining the sustainable development goal six. *Annals of Science and Technology*, *5*(2), 58–77.

Onu, M. A., Ayeleru, O. O., Oboirien, B., & Olubambi, P. A. (2023). Challenges of wastewater generation and management in sub-Saharan Africa: A Review. *Environmental Challenges*, *11*, 100686. https://doi.org/https://doi.org/10.1016/j.envc.2023.100686

WHO. (2017). *Potable reuse: Guidance for producing safe drinking-water*. World Health Organization.

Yahya, M. A., Al-Qodah, Z., & Ngah, C. W. Z. (2015). Agricultural bio-waste materials as potential sustainable precursors used for activated carbon production: A review. *Renewable and Sustainable Energy Reviews*, *46*, 218–235.

DESIGN OPTIMISATION AND IMPACT ASSESSMENT OF A BIOGAS-INTEGRATED ANAEROBIC BAFFLED REACTOR WASTEWATER TREATMENT SYSTEM AT NIGERIAN CORRECTIONAL CENTRE

Philip Ayodele Balogun[1,*], Donatus Begianpuye Adie[1], Igboro Sunday Bamidele[1], Aliyu Adamu Dandajeh[1]

[1]*Department of Water Resources and Environmental Engineering, Faculty of Engineering, Ahmadu Bello University, Zaria, Nigeria*

Email: phdbalogun@gmail.com*, donadie2005@yahoo.com, igboro@yahoo.com, aadandaje@gmail.com

***Corresponding author**: Philip Ayodele Balogun

DOI: https://doi.org/10.67203/sp.ICESID.2026

ABSTRACT

This paper presents the design optimisation and field-based impact assessment of a biogas-integrated anaerobic baffled reactor (ABR) at Ikoyi Correctional Centre, Lagos. Empirical monitoring was undertaken for 30 consecutive days at three matched wastewater sampling points: ABR influent (SP-01), ABR effluent (SP-02) and final effluent after polishing (SP-03). The campaign comprised 90 point-specific wastewater samples, daily biogas-quality records and kitchen-energy logs, separated into pre-optimisation (10 days), transition (5 days) and optimised operation (15 days). The installed system consists of two parallel six-chamber ABR trains. Engineering reconciliation gave 337.34 m³ active volume; restoration from a 286.74 m³ pre-optimisation effective condition yielded calculated HRT values of 33.60 and 39.53 h at the monitored mean flow of 204.82 m³/day. During optimised operation, mean final-effluent COD, BOD_5 and TSS were 90.6, 37.47 and 30.53 mg/L, while overall removals reached 89.99%, 91.90% and 91.27%, respectively. Mean biogas production was 57.03 m³/day compared with 42.99 m³/day pre-optimisation; methane fraction was 63.39% compared with 57.15%, and hydrogen sulphide was 266.9 ppm compared with 510.1 ppm. Mean LPG, diesel and firewood displacement reached 51.82%, 50.10% and 53.83%. The repair-first configuration retained the installed shell and prioritised active-volume recovery, flow balancing, polishing, gas conditioning, storage-demand matching and preventive maintenance. These operating-phase differences are associations from a sequential field intervention rather than proof of single-variable causality. Physical fuel savings were quantified; monetary valuation was outside scope.

Keywords: *anaerobic baffled reactor; biogas; correctional wastewater; design optimisation; resource recovery*

1. INTRODUCTION

Wastewater treatment in a correctional facility is simultaneously an environmental-engineering, public-health, institutional-management and human-dignity requirement. Large populations live within restricted compounds, water and sanitation fixtures are used continuously, kitchens operate at institutional scale, and land for conventional treatment may be limited. Failure of containment or treatment can expose detainees, correctional personnel, maintenance workers and surrounding communities to sewage overflow, odour, vectors and contamination of surface water or groundwater. The World Health Organization (WHO, 2018) therefore frames sanitation as an entire service chain from containment and conveyance to treatment, disposal or safe reuse, while its sanitation-safety-planning approach requires risk identification and operational control across that chain (WHO, 2022). In places of detention, the same systems must remain robust under crowding, restricted movement, security procedures and constrained maintenance access (International Committee of the Red Cross [ICRC], 2012).

Anaerobic baffled reactors are attractive for such settings because they divide the flow path into successive compartments, promoting contact between wastewater and retained anaerobic biomass without continuous mechanical mixing or aeration. Their comparatively simple civil works, low sludge yield, resilience to organic shocks and potential for methane recovery make them relevant to

decentralised sanitation in warm climates. Yet ABR performance is not automatic. Hydraulic short-circuiting, unequal flow between parallel trains, excessive sludge accumulation, high upflow velocity, intermittent loading and inadequate downstream polishing can reduce effective volume or produce an effluent that remains unsuitable for discharge. Full-scale studies have repeatedly shown that operation and maintenance, rather than the presence of an ABR shell alone, determine long-term performance (Yulistyorini et al., 2019; Yenji et al., 2021; Saif et al., 2021).

Biogas generation is continuous, whereas cooking demand occurs in peaks; daily production can therefore coexist with short-period shortages, pressure instability or unused gas. Prison biogas programmes identify ownership, sizing, operator competence, safety and recurrent maintenance as decisive sustainability conditions (Gauthier et al., 2012). The Ikoyi intervention integrated wastewater collection, two ABR trains, polishing and kitchen-gas delivery for a design population of 3,000. The current count of 2,541 is 84.7% of that basis. The empirical campaign measured actual wastewater flow, treatment performance, biogas production and composition, gas-holder pressure, burner operating hours and conventional-fuel use, allowing the technical and energy impacts to be quantified rather than inferred from population alone.

The purpose of this paper is to present a title-aligned design optimisation and impact assessment based on field and empirical evidence. Specifically, the paper (a) characterises wastewater at three matched sampling points; (b) reconciles the physical ABR geometry with the active-volume calculation; (c) formulates hydraulic, treatment, gas-utilisation and hydrostatic constraints; (d) compares pre-optimisation and optimised operating phases; (e) quantifies wastewater-removal, biogas-quality and fuel-displacement outcomes; and (f) assesses technical, environmental, social, economic and institutional implications. The contribution is a repair-first optimisation strategy that restores and verifies the installed asset before considering additional chambers or a larger reactor shell.

2. TECHNICAL BACKGROUND AND RESEARCH CONTEXT

2.1 ABR performance and operating controls

The ABR behaves as a staged anaerobic system. Wastewater is directed down and upward through a series of compartments; solids settle and biomass is retained, while the baffled pathway improves contact between substrate and microorganisms. Foundational design and decentralised-sanitation literature identifies hydraulic retention time (HRT), organic loading rate (OLR), compartment geometry, upflow velocity, temperature, influent biodegradability and sludge distribution as major controls (Barber & Stuckey, 1999; Sasse, 1998; Gutterer et al., 2009; Tilley et al., 2014). Long retention times can improve hydrolysis and stabilisation, but nominal HRT is meaningful only when active volume is not lost to sludge, gas pockets, blocked openings or dead zones. Similarly, a satisfactory total volume can conceal overloading if flow is not divided evenly between parallel trains.

Field evidence supports cautious optimisation. Dynamic loading changed full-scale ABR behaviour (Yenji et al., 2021), while loading-shock experiments also demonstrated the sensitivity of staged anaerobic treatment to abrupt organic and hydraulic changes (Jin et al., 2024). A four-chamber ABR still required tertiary treatment before reuse or discharge (Saif et al., 2021). In a nine-month ABR-biofilter study, the ABR removed about 57% total COD while the integrated train achieved 92% COD and 98% TSS removal, demonstrating that polishing is part of system performance (Echeverría et al., 2022). Sponge media achieved 60–77% organic and 74–81% TSS removal across 18–6 h HRTs (Ullah et al., 2024), with a later real-wastewater study reporting 79% COD and 96% TSS removal at 8 h (Ullah et al., 2026). These controlled results cannot be transferred directly to Ikoyi. Modelled recirculation also produced limited or adverse effects under some conditions (Ullah et al., 2025).

Post-treatment is particularly important for nutrients, pathogens and residual suspended matter. Field ABRs often remove organic carbon and settleable solids more effectively than nitrogen, phosphorus and faecal indicators. Satyendra and Vijay (2024) demonstrated an ABR followed by an upflow constructed wetland for municipal wastewater, while Munavalli et al. (2022) evaluated an ABR-hybrid-wetland system under dynamic loading. Raja et al. (2025) similarly coupled an ABR with a plant biofilter for decentralised sewage treatment and energy recovery. The literature therefore supports a treatment-train perspective: the ABR provides anaerobic primary or secondary treatment,

and the downstream unit is selected according to discharge route, land, operator capacity and required effluent quality.

2.2 Biogas recovery and institutional impact

Anaerobic treatment can convert part of the removed organic load into methane-rich gas, thereby reducing the net energy burden of sanitation. UNEP (2023) identifies wastewater as a resource for water, energy and nutrient recovery rather than only a waste stream. For institutions with large kitchens, direct thermal use can avoid the conversion losses and operating complexity associated with small-scale electricity generation. The relevant performance measure is not daily biogas production alone, but the fraction safely captured, conditioned, stored and delivered at useful pressure when cooking is required.

Correctional settings make this integration unusually valuable. Gauthier et al. (2012) assessed 13 prison biogas systems and reported production of 26–62 L/person/day, with higher values where kitchen waste supplemented excreta. The systems were generally perceived positively because of cleaner cooking and improved hygiene, but the study warned that responsibilities, finance, user acceptance and maintenance must be designed with the technology. At Ikoyi, daily kitchen logs and conventional-fuel records were used to quantify operating-hour and fuel-displacement effects, while health outcomes and indoor-air quality remain outside the present measurement scope.

Nigeria's National Environmental (Sanitation and Wastes Control) Regulations provide the legal framework for sustainable sanitation and waste management, while the Surface and Groundwater Quality Control Regulations address protection of water bodies (National Environmental Standards and Regulations Enforcement Agency [NESREA], 2009, 2011). WHO guidance supplies a risk-management framework but does not replace the applicable Nigerian permit or discharge conditions. For international context only, the United States secondary-treatment regulation uses 30-day and 7-day averages rather than a single grab sample (Electronic Code of Federal Regulations, n.d.). This reinforces the need to separate screening targets from a formal compliance determination.

3. MATERIALS AND METHODS

3.1 Study design and evidence classification

The study was structured as a practice-based engineering case study with a field before-transition-after monitoring design. Data were collected over 30 consecutive operating days from 1 to 30 April 2024. Days 1–10 represented pre-optimisation operation, Days 11–15 the transition and stabilisation period, and Days 16–30 optimised operation. The evidence base comprised matched wastewater samples, measured flow and temperature, daily biogas flow and composition, gas-quality and pressure records, kitchen burner-hours and conventional-fuel logs, together with project drawings, as-built dimensions and engineering calculations (Ikoyi ABR Design and Field Records, 2019–2024). No individual detainee data were used. Security-sensitive coordinates and internal layouts were excluded, and the treatment arrangement is presented only at process level.

Three evidence classes were maintained. Class F comprised direct field and laboratory measurements. Class C comprised quantities calculated from field measurements, including removal efficiencies, mass loads, methane energy and fuel displacement. Class D comprised design-audit and optimisation calculations, including active volume, HRT, OLR, upflow velocity and hydrostatic screening. This classification preserves the empirical status of the underlying monitoring data while preventing calculated design quantities from being misrepresented as instrument readings.

The monitoring dataset is treated throughout this paper as primary field and empirical evidence. The wastewater, biogas and energy-use observations are reported by operating phase and by measurement point. Arithmetic means and sample standard deviations describe within-phase variability; removal efficiencies are paired-day calculations based on matched influent and outlet concentrations. The study evaluates operating-phase differences descriptively because the sequential observations arose from a full-scale facility intervention rather than random assignment. No causal effect is attributed to a single optimisation action, and the terms pre-optimisation and optimised operation identify field phases rather than randomised treatment groups.

Table 1: Field, calculated and design evidence used in the study

Evidence item	Value or scope	Class	Permissible interpretation
Wastewater monitoring	30 matched days at SP-01, SP-02 and SP-03; 90 point-specific samples	F	Direct field and laboratory measurements
Operating conditions	Flow, temperature and pH recorded daily	F	Hydraulic and process context
Treatment performance	COD, BOD_5, TSS, NH_3-N and PO_4-P by point and phase	F/C	Measured concentrations; paired removal calculations
ABR geometry	Two trains; one settler and six chambers per train	F/D	As-built and design audit
Active volume and loading	286.74 to 337.34 m^3; HRT, OLR and upflow calculations	D	Before-and-after optimisation basis
Biogas monitoring	30 daily records of flow, CH_4, CO_2, H_2S, moisture, pressure and use	F/C	Measured gas performance and derived energy
Kitchen energy	30 daily burner and LPG, diesel and firewood records	F/C	Measured use and calculated fuel displacement
Operational impact	Sanitation, odour, O&M and kitchen-use observations	F	Field operational assessment

Note. F = field or laboratory measurement; C = calculation from measured data; D = design or optimisation calculation.

3.2 System configuration and study boundaries

The treatment plant consists of two parallel ABR trains serving separate sewer catchments. Each train contains an inlet settler followed by six baffled chambers. Gas generated within the anaerobic system is collected, conditioned, conveyed to a nominal 45 m^3 gas holder documented in the project records and delivered to the institutional kitchen. Treated liquid is conveyed toward final disposal or polishing. The optimisation boundary begins at the combined wastewater inflow and ends at final effluent management and useful kitchen-gas delivery. External sewer rehabilitation, individual toilet fixtures and unrelated facility energy loads are outside the numerical optimisation, although they influence institutional outcomes.

The design population of 3,000 comprised detainees and personnel included in the original hydraulic basis. The current population value of 2,541 represents 84.7% of design capacity. The historical design flow of 154.45 m^3/day was retained for design reconciliation, while the empirical campaign measured a mean operating flow of 204.82 ± 7.93 m^3/day. This distinction allows the installed geometry to be checked against its original basis and against current field loading. Train-specific metering remains necessary because aggregate flow cannot reveal unequal distribution between parallel reactors.

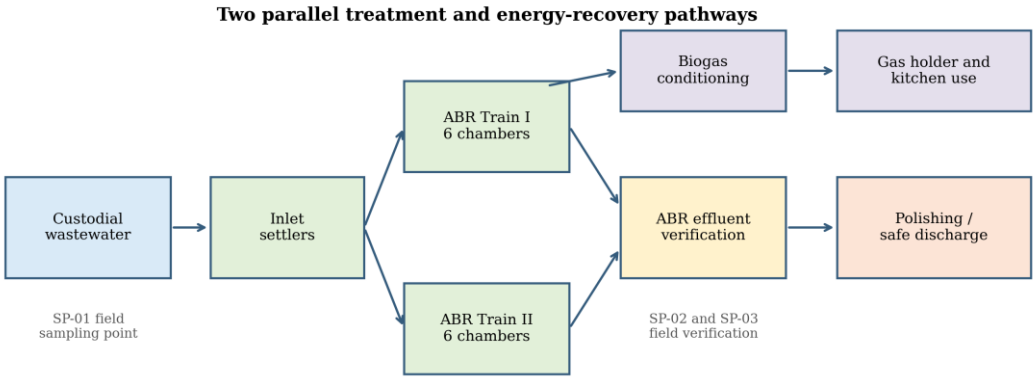

Figure 1: Process-level configuration and optimisation boundary of the biogas-integrated ABR system.

3.3 Wastewater characterisation and compliance screening

Wastewater samples were collected daily at the ABR inlet chamber (SP-01), ABR outlet chamber (SP-02) and polishing-unit outlet (SP-03). The resulting 30 matched events produced 90 point-specific samples. Flow and wastewater temperature were recorded concurrently. Samples were analysed for pH, COD, BOD_5, TSS, ammonia-nitrogen (NH_3-N) and orthophosphate-phosphorus (PO_4-P) using APHA procedures and the study laboratory protocol (American Public Health Association, American Water Works Association, & Water Environment Federation, 2023). Matched-point sampling allowed both ABR-stage removal and overall system removal to be calculated for each day.

Concentration screening used the study targets of 200 mg/L COD, 50 mg/L BOD_5 and 100 mg/L TSS. Results are reported as field performance against the accepted study basis; formal statutory compliance remains dependent on the facility's discharge route, permit conditions and required regulatory sampling frequency. A positive concentration gap indicates that further treatment or operational adjustment is needed. Phase summaries are expressed as mean ± sample standard deviation.

$$E_r = C_{in} / C_t \quad (1)$$

E_r is the influent exceedance ratio; C_{in} is the measured influent concentration and C_t is the applicable study screening target, in matching concentration units.

$$G = max(C_{out} - C_t, 0) \quad (2)$$

G is the positive concentration gap; C_{out} is the measured outlet concentration and C_t is the study target. G = 0 indicates no positive gap against the screening target. Removal efficiency and mass load were calculated as follows.

$$\eta = [(C_{in} - C_{out}) / C_{in}] \times 100 \quad (3)$$

η is paired-day removal efficiency (%), calculated from the matched inlet concentration C_{in} and outlet concentration C_{out}.

$$L = Q\,C / 1{,}000 \quad (4)$$

L is pollutant mass load (kg/day), Q is wastewater flow (m^3/day), C is concentration (mg/L), and 1,000 is the unit-conversion factor.

3.4 Hydraulic and organic-loading audit

The physical audit separated gross internal envelope from effective hydraulic volume. Per train, the settler measures 2.50 × 8.20 × 2.50 m and each of six chambers measures 1.20 × 8.20 × 2.40 m. Gross volume therefore includes the full box dimensions before deductions for baffle walls, downflow shafts, freeboard, sludge and dead zones. Effective active volume was independently reconciled from project flow and HRT. This step corrected the earlier dimensional confusion in which 154.45 m^3/day could be mistaken for reactor volume.

The pre-optimisation hydraulic audit used an effective active volume of 286.74 m³, equivalent to 85% of the 337.34 m³ design-implied active volume. The post-optimisation condition restored the full effective volume through desludging, clearing baffle openings, correcting dead zones and balancing the two trains. The volume figures are engineering audit calculations supported by field operating observations; they are not direct laboratory measurements. No additional chamber or larger ABR shell was required.

$$V_g = 2[(2.50 \times 8.20 \times 2.50) + 6(1.20 \times 8.20 \times 2.40)] \quad (5)$$

Vg is gross internal envelope volume (m³). The factor 2 represents the two parallel trains; each train comprises one inlet settler and six chamber boxes.

$$V_a = Q\,\theta / 24 \quad (6)$$

V_a is hydraulically active volume (m³), Q is daily flow (m³/day), θ is HRT (h), and 24 converts days to hours.

$$\theta = 24\,V_a / Q \quad (7)$$

θ is calculated hydraulic retention time (h) at active volume V_a and daily flow Q.

$$OLR = Q(COD_{in} / 1{,}000) / V_a \quad (8)$$

OLR is volumetric organic loading (kg COD m^{-3} d^{-1}); COD_{in} is measured influent COD (mg/L), Q is flow and V_a is active volume.

$$v_u = [PF \times Q / (2 \times 24)] / A_c \quad (9)$$

v_u is direct chamber upflow velocity (m/h), PF is the peak factor, the divisor 2 represents equal flow to two trains, and $A^c = 1.20 \times 8.20 = 9.84$ m² is the chamber plan area. Peak factors of 1.50 before balancing and 1.05 after effective equalisation were applied only as transparent design scenarios.

3.5 Optimisation formulation and selection criteria

The optimisation used a constrained, repair-first screening procedure. Candidate interventions were evaluated in the following order: verify the installed geometry and flow boundary; restore active volume; balance the two trains; test hydraulic and organic-loading constraints; calculate effluent gaps; identify the need for polishing; test gas-conditioning and storage-demand requirements; and screen hydrostatic stability. The installed two-train, six-chamber configuration was the reference. Alternatives that required structural enlargement were considered only if restoration and operational control could not meet the hydraulic constraints.

A multi-criteria penalty function maintained an auditable link between water quality, energy recovery, cost, footprint and robustness. The field wastewater, gas and kitchen datasets supplied the performance terms; project dimensions and design calculations supplied the hydraulic and footprint terms. Each penalty was normalised from zero (best) to one (worst), and any alternative violating a hard constraint was rejected regardless of its weighted score. The weights were specified a priori as transparent engineering decision priorities rather than statistically calibrated coefficients: water quality received the highest weight because sanitation protection and effluent control are mandatory; energy utilisation reflected the biogas objective; cost represented institutional affordability; robustness protected operational reliability; and footprint received the lowest weight because the installed shell was retained.

$$\min J(x) = 0.35P_q + 0.22P_e + 0.18P_c + 0.10P_f + 0.15P_r \quad (10)$$

J(x) is the aggregate penalty for candidate x; Pq, Pe, Pc, Pf and Pr are the normalised water-quality, gas-utilisation, life-cycle-cost, footprint and robustness penalties. The weights sum to one. They reflect the stated engineering priorities and were not derived through formal stakeholder elicitation.

$$P_q = \Sigma \max[(C_{j,out} - C_{j,target}) / C_{j,target}, 0] \quad (11)$$

Pq sums positive normalised effluent gaps across parameter j; C_j,out is the predicted or observed outlet value and C_j,target is the corresponding screening target.

$$R = N_{feasible} / N_{total} \quad (12)$$

R is robustness; Nfeasible is the number of monitoring days meeting the combined final-effluent COD, BOD_5 and TSS targets and Ntotal is the number of days evaluated. The acceptance gate was R ≥ 0.90. All 15 optimised-operation days met the three targets simultaneously, giving R = 1.00 for that phase, compared with 0.00 during the 10-day pre-optimisation phase.

Because hard constraints were applied before the weighted comparison, a favourable aggregate score could not compensate for a non-compliant candidate. A formal multi-weight sensitivity analysis was not undertaken; the reported weights should therefore be interpreted as a transparent screening preference set rather than proof of a unique global optimum. Future work should vary the weights and test whether feasible candidate rankings remain stable.

Table 2: Hard constraints and decision rules used in optimisation

Criterion	Screening condition	Engineering purpose	Evidence status
COD	≤200 mg/L; robust design goal 160 mg/L	Control residual organic load and retain margin	Permit confirmation required
BOD_5	≤50 mg/L; robust design goal 40 mg/L	Control biodegradable residual	Permit confirmation required
TSS	≤100 mg/L; robust design goal 50 mg/L	Limit solids carryover	Measured at SP-03
HRT	≥36 h planning gate	Protect anaerobic contact time	Design-derived
OLR	≤3.0 kg COD m^{-3} d^{-1}	Avoid volumetric overloading	Project design screen
Peak upflow	Prefer ≤0.60 m/h	Reduce washout and hydraulic shock	Design screen; verify diurnal flow
Flotation safety	FS ≥1.20, empty-tank case	Control groundwater uplift	Structural verification required
Robustness	≥90% compliant monitoring days	Reject fragile optima	R = 1.00 during optimised phase
Gas storage	Daily available gas ≥ kitchen use; unused gas minimised	Match production to cooking demand	Evaluated from daily field logs

Note. The concentration values are study screening targets. They are not presented as a substitute for a current, route-specific Nigerian discharge permit.

3.6 Effluent polishing, gas-energy and hydrostatic calculations

The polishing-stage removal was calculated from each matched SP-02 and SP-03 observation. This avoids the misleading practice of quoting overall removal while ignoring the contribution of downstream treatment. The field data were also screened against the final-effluent targets so the optimisation could distinguish ABR performance from whole-system performance.

Biogas assessment used 30 daily field records of total flow, methane, carbon dioxide, hydrogen sulphide, moisture, gas-holder pressure, kitchen use, unused gas and burner hours. Gross methane energy was calculated from measured gas use and methane fraction. Daily kitchen logs provided conventional-fuel baselines and quantities used while biogas was available, from which LPG, diesel and firewood displacement were calculated.

$$\eta_{polish,req} = [(C_{ABR} - C_{target}) / C_{ABR}] \times 100 \quad (13)$$

ηpolish,req is the minimum polishing removal required (%); C^{ABR} is ABR effluent concentration and Ctarget is the final-effluent screening target.

$$E_{gas} = V_{gas} \times y_{CH_4} \times LHV_{CH_4} \quad (14)$$

Egas is gross methane energy, Vgas is measured useful biogas volume, yCH_4 is measured methane fraction and $LHVCH_4$ is methane lower heating value.

$$S_t = S_{t-1} + G_t - U_t - F_t \quad (15)$$

S_t and S_{t-1} are gas inventory at the end of the current and preceding time steps; G_t is generation, U_t is useful demand and F_t is controlled loss or flaring.

$$D_f = [(F_{baseline} - F_{biogas}) / F_{baseline}] \times 100 \quad (16)$$

Df is conventional-fuel displacement (%), Fbaseline is the comparable conventional-fuel baseline and Fbiogas is the quantity used while biogas was available.

Because Ikoyi is in a coastal groundwater environment, empty-tank uplift was screened. The combined base plan was derived explicitly as Ab = 2 × 8.20 × 9.70 = 159.08 m² for the two trains. Groundwater heads between 0.5 and 2.0 m above the base were examined. The calculation is a screening check and does not replace structural design, verified concrete dead load, cover depth, anchorage or drainage assessment.

$$F_u = \gamma_w h_w A_b \quad (17)$$

F_u is groundwater uplift force, γw is the unit weight of water (9.81 kN/m³), hw is groundwater head above the base and Ab is combined base area (159.08 m²).

$$FS = R_{stabilising} / F_u \geq 1.20 \quad (18)$$

FS is flotation factor of safety and Rstabilising is verified stabilising resistance from structural dead load, cover, anchorage and other applicable permanent actions.

4. RESULTS

4.1 Empirical wastewater characteristics at the three sampling points

The 30-day campaign produced 90 matched point-specific wastewater observations. Mean monitored flow was 204.82 ± 7.93 m³/day and mean wastewater temperature was 29.93 ± 0.73 °C. Across all days, mean SP-01 influent concentrations were 907.67 mg/L COD, 467.13 mg/L BOD_5, 349.27 mg/L TSS, 55.05 mg/L NH_3-N and 10.27 mg/L PO_4-P. Corresponding mean SP-02 concentrations were 229.47, 110.47, 88.40, 42.64 and 8.59 mg/L; mean SP-03 concentrations were 117.77, 51.50, 41.83, 24.77 and 5.59 mg/L. The concentration sequence confirms progressive treatment through the ABR and polishing stage.

Influent strength was comparable between the pre-optimisation and optimised phases: COD averaged 903.9 and 903.4 mg/L, BOD_5 464.2 and 461.33 mg/L, and TSS 347.6 and 350.0 mg/L, respectively. Mean flows were likewise close at 201.77 and 205.77 m³/day. This stability in incoming load supports descriptive comparison of treatment outcomes. Final-effluent concentrations during optimised operation were 90.6 mg/L COD, 37.47 mg/L BOD_5 and 30.53 mg/L TSS, compared with 160.1, 71.6 and 59.6 mg/L during pre-optimisation operation.

Table 3: Empirical wastewater concentrations before and after optimisation (mean ± SD)

Parameter	Pre SP-01	Pre SP-02	Pre SP-03	Optimised SP-01	Optimised SP-02	Optimised SP-03
pH	7.22 ± 0.11	7.22 ± 0.10	7.30 ± 0.05	7.18 ± 0.12	7.32 ± 0.10	7.25 ± 0.08
COD (mg/L)	903.9 ± 45.2	274.7 ± 10.9	160.1 ± 4.8	903.4 ± 48.8	197.6 ± 16.5	90.6 ± 9.6
BOD_5 (mg/L)	464.2 ± 26.9	133.8 ± 4.4	71.6 ± 3.5	461.3 ± 27.7	94.4 ± 8.7	37.5 ± 4.8
TSS (mg/L)	347.6 ± 24.2	105.9 ± 9.5	59.6 ± 1.7	350.0 ± 25.9	75.0 ± 5.5	30.5 ± 3.6
NH_3-N (mg/L)	55.76 ± 3.45	45.92 ± 2.79	29.48 ± 1.17	55.17 ± 3.37	41.13 ± 2.93	22.02 ± 1.65
PO_4-P (mg/L)	10.40 ± 0.84	9.02 ± 0.66	6.38 ± 0.48	10.32 ± 0.81	8.41 ± 0.59	5.17 ± 0.49

Note. Pre-optimisation n = 10 days; optimised operation n = 15 days. SP-01 = ABR influent; SP-02 = ABR effluent; SP-03 = final effluent after polishing.

4.2 Corrected reactor sizing and hydraulic state

The gross internal envelope was derived step by step. Each settler volume was 2.50 × 8.20 × 2.50 = 51.25 m³; for two trains this gave 102.50 m³. Each chamber box was 1.20 × 8.20 × 2.40 = 23.616 m³; for six chambers in each of two trains this gave 23.616 × 6 × 2 = 283.392 m³. The combined gross internal envelope was therefore 102.50 + 283.392 = 385.892 m³. Gross volume is not equivalent to working volume because structural and hydraulic exclusions must be deducted. The independent flow-HRT relationship gave a design-implied active volume of 337.34 m³, consistent with the project design flow of 154.45 m³/day and reported HRT of 52.42 h.

The pre-optimisation effective condition contained 286.74 m³, representing 85% of the design-implied active volume. Restoration increased usable volume by 50.60 m³ or 17.65%. At the monitored mean flow of 204.82 m³/day, calculated HRT increased from 33.60 to 39.53 h. Using the measured 30-day mean influent COD of 907.67 mg/L, calculated OLR declined from 0.648 to 0.551 kg COD m^{-3} d^{-1}. Both values were below the 3.0 kg COD m^{-3} d^{-1} screen, while the restored condition achieved the 36-h HRT planning gate.

At the same monitored mean flow, the equal-split chamber upflow velocity was 0.434 m/h. Applying the pre-optimisation peak factor of 1.50 gave 0.650 m/h; the equalised 1.05 peak factor gave 0.455 m/h after optimisation. The improvement depends on field flow balancing together with clear baffle openings and cannot be achieved by volume recovery alone. At the historical design flow of 154.45 m³/day, the corresponding HRT values remain 44.56 and 52.42 h.

Table 4: ABR configuration before and after the corrected optimisation

Parameter	Reduced-usable-volume scenario	Restored/optimised scenario	Change
Arrangement	2 parallel trains	2 parallel trains	No shell change
Chambers	6 per train; 12 total	6 per train; 12 total	No chamber added
Gross internal envelope	385.892 m³	385.892 m³	0 m³
Hydraulically active volume	286.74 m³	337.34 m³	+50.60 m³; +17.65%
HRT at field mean flow	33.60 h	39.53 h	+5.93 h
Mean COD load	185.90 kg/day	185.90 kg/day	Same 30-day loading basis
OLR at field mean	0.648 kg COD m^{-3} d^{-1}	0.551 kg COD m^{-3} d^{-1}	−15.0%
Peak upflow	0.650 m/h at PF 1.50	0.455 m/h at PF 1.05	−30.0%
Required action	Sludge/dead-zone and flow imbalance	Desludge, clear baffles, balance and meter trains	Operational restoration

Note. Hydraulic parameters are calculated from field flow and wastewater data together with the audited reactor geometry. Physical shell and chamber dimensions remain unchanged.

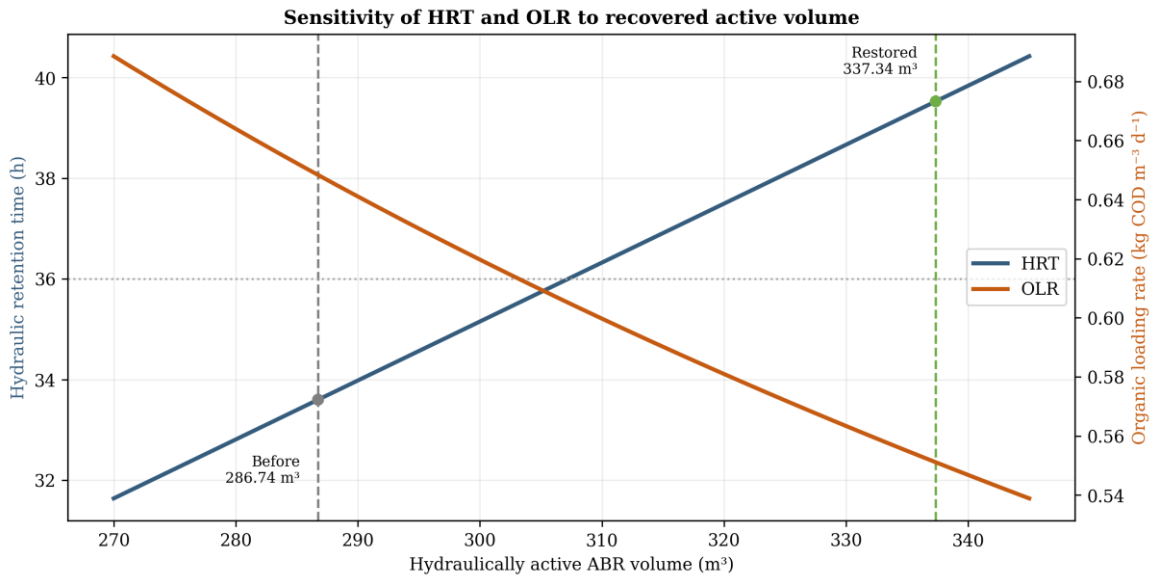

Figure 2: Sensitivity of hydraulic retention time and organic loading rate to active-volume recovery.

4.3 Empirical treatment performance before and after optimisation

ABR-stage removal was higher during optimised operation. Mean COD, BOD_5 and TSS removals were 78.15%, 79.56% and 78.55%, compared with 69.58%, 71.14% and 69.57% during pre-optimisation operation. The downstream polishing stage further reduced residual concentrations, producing mean overall removals of 89.99% COD, 91.90% BOD_5 and 91.27% TSS during the optimised phase, compared with 82.26%, 84.55% and 82.80% in the pre-optimisation phase.

Nutrient removal remained lower than carbon and solids removal but was also higher during optimised operation. Mean ABR-stage NH_3-N removal was 25.49%, compared with 17.64% pre-optimisation, while overall removal was 60.11%, compared with 47.06%. PO_4-P removal was 18.49% across the ABR and 49.93% across the complete system during optimised operation, compared with 13.22% and 38.62%. These operating-phase differences support continued use of polishing while showing that nutrient management remains a separate design consideration.

All 15 optimised-operation final-effluent observations met the combined study targets of COD ≤200 mg/L, BOD_5 ≤50 mg/L and TSS ≤100 mg/L. During pre-optimisation operation, COD and TSS met their concentration targets, but none of the ten BOD_5 observations met 50 mg/L; only two of five transition observations met all three targets. Combined performance reliability was therefore R = 1.00 during optimised operation, compared with R = 0.00 during pre-optimisation operation.

Table 5: Empirical wastewater-removal performance before and after optimisation

Parameter	Pre ABR removal	Optimised ABR removal	Pre overall removal	Optimised overall removal	Optimised final effluent
COD	69.58 ± 0.95%	78.15 ± 0.88%	82.26 ± 0.65%	89.99 ± 0.69%	90.6 ± 9.6 mg/L
BOD_5	71.14 ± 0.85%	79.56 ± 0.95%	84.55 ± 0.79%	91.90 ± 0.69%	37.47 ± 4.76 mg/L
TSS	69.57 ± 0.82%	78.55 ± 1.01%	82.80 ± 0.86%	91.27 ± 0.88%	30.53 ± 3.56 mg/L
NH_3-N	17.64 ± 0.99%	25.49 ± 1.05%	47.06 ± 1.46%	60.11 ± 1.23%	22.02 ± 1.65 mg/L
PO_4-P	13.22 ± 0.88%	18.49 ± 0.82%	38.62 ± 0.99%	49.93 ± 1.08%	5.17 ± 0.49 mg/L

Note. Values are means ± sample SD calculated from matched field measurements; pre-optimisation n = 10 and optimised operation n = 15.

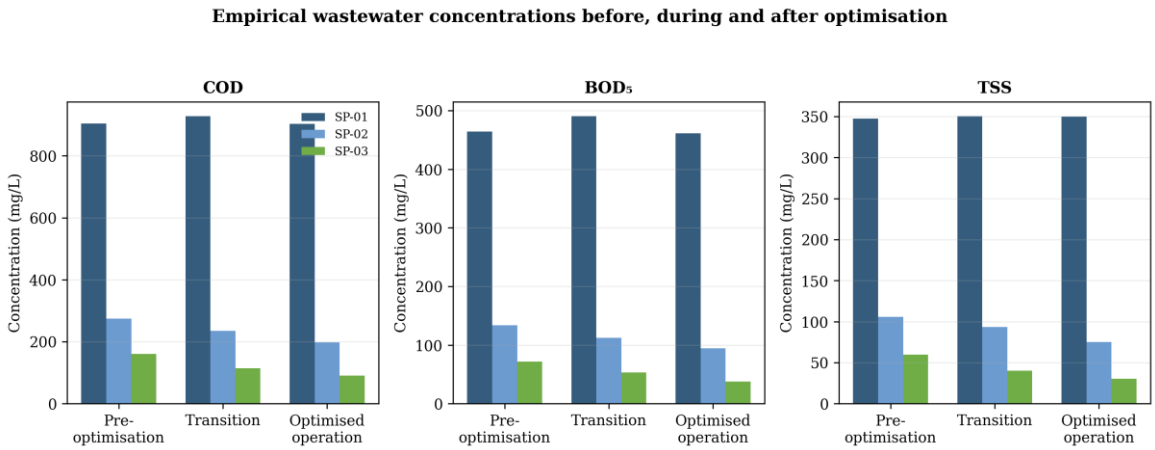

Figure 3: Empirical phase-mean wastewater concentrations at SP-01, SP-02 and SP-03.

4.4 Biogas production, storage and useful-energy implications

Daily field monitoring showed higher gas quantity and quality during optimised operation. Mean total biogas production was 57.03 ± 2.15 m³/day, compared with 42.99 ± 2.34 m³/day pre-optimisation, a descriptive difference of 32.7%. Mean methane fraction was 63.39%, compared with 57.15%, while carbon dioxide was 35.30%, compared with 40.26%. Hydrogen sulphide was 266.9 ppm, compared with 510.1 ppm, and moisture was 22.64 g/m³, compared with 32.53 g/m³. These

differences coincided with the observed optimised-operation gas-quality profile and conditioning controls.

The nominal installed gas-holder capacity was 45 m³. Mean useful kitchen delivery during optimised operation was 49.32 m³/day with 7.83 burner h/day, compared with 29.78 m³/day and 4.99 h/day pre-optimisation. Unused or flared gas was 6.00 m³/day, compared with 11.92 m³/day. Mean holder pressure was 1.667 kPa, compared with 1.343 kPa. Across all 30 days, 1,551.8 m³ of biogas was produced, 1,256.5 m³ was used in the kitchen and calculated gross methane energy used was 7,706.0 kWh.

The kitchen-energy logs documented displacement of conventional fuels. Mean LPG, diesel and firewood displacement during optimised operation was 51.82%, 50.10% and 53.83%, compared with 23.09%, 18.79% and 20.61% during pre-optimisation operation. Over the 30-day campaign, the recorded physical savings were 412.3 kg LPG, 61.0 L diesel and 927.0 kg firewood. The association between operating phase and performance therefore extended beyond gas production to useful energy delivery; monetary valuation was not undertaken.

Table 6: Empirical biogas and kitchen-energy performance before and after optimisation

Indicator	Pre-optimisation	Optimised operation	Change	Interpretation
Nominal gas-holder capacity	45 m³	45 m³	No change	Installed design capacity
Biogas flow	42.99 ± 2.34 m³/day	57.03 ± 2.15 m³/day	+32.7%	Higher stable production
Methane fraction	57.15 ± 0.68%	63.39 ± 0.69%	+6.24 pp	Higher methane fraction
H_2S	510.1 ± 29.8 ppm	266.9 ± 28.0 ppm	−47.7%	Lower corrosive/toxic impurity
Moisture	32.53 ± 1.65 g/m³	22.64 ± 1.84 g/m³	−30.4%	Lower moisture content
Gas used	29.78 ± 2.08 m³/day	49.32 ± 2.75 m³/day	+65.6%	Greater useful utilisation
Burner hours	4.99 ± 0.34 h/day	7.83 ± 0.32 h/day	+56.9%	Longer cooking support
LPG displacement	23.09 ± 1.06%	51.82 ± 1.41%	+28.73 pp	Reduced LPG dependence
Diesel displacement	18.79 ± 1.62%	50.10 ± 1.90%	+31.31 pp	Reduced diesel dependence
Firewood displacement	20.61 ± 1.52%	53.83 ± 1.51%	+33.22 pp	Reduced firewood dependence

Note. Gas-holder capacity is from the project design record; other values are field means ± sample SD. pp = percentage points. Pre-optimisation n = 10; optimised operation n = 15.

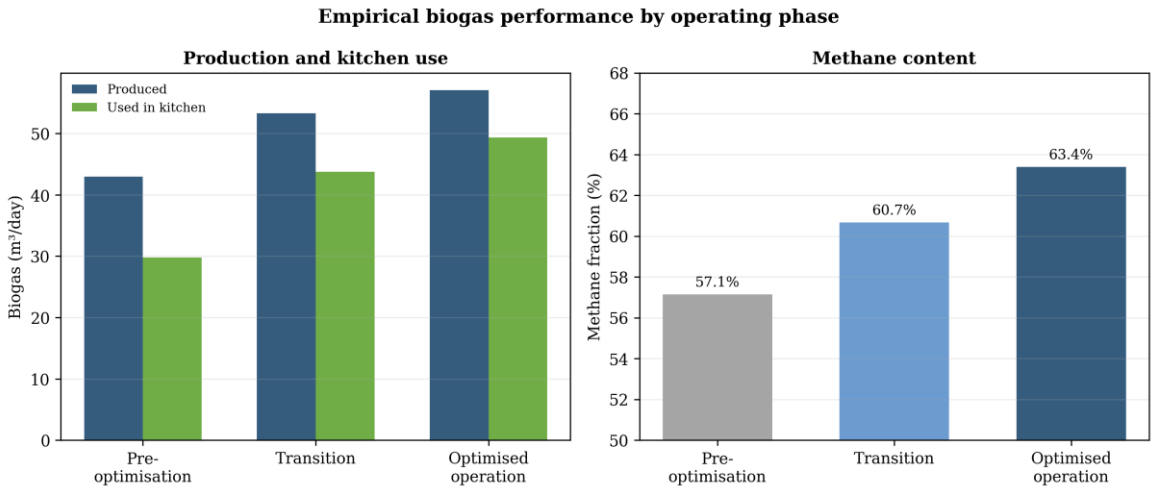

Figure 4: Empirical biogas production, kitchen use and methane fraction by operating phase.

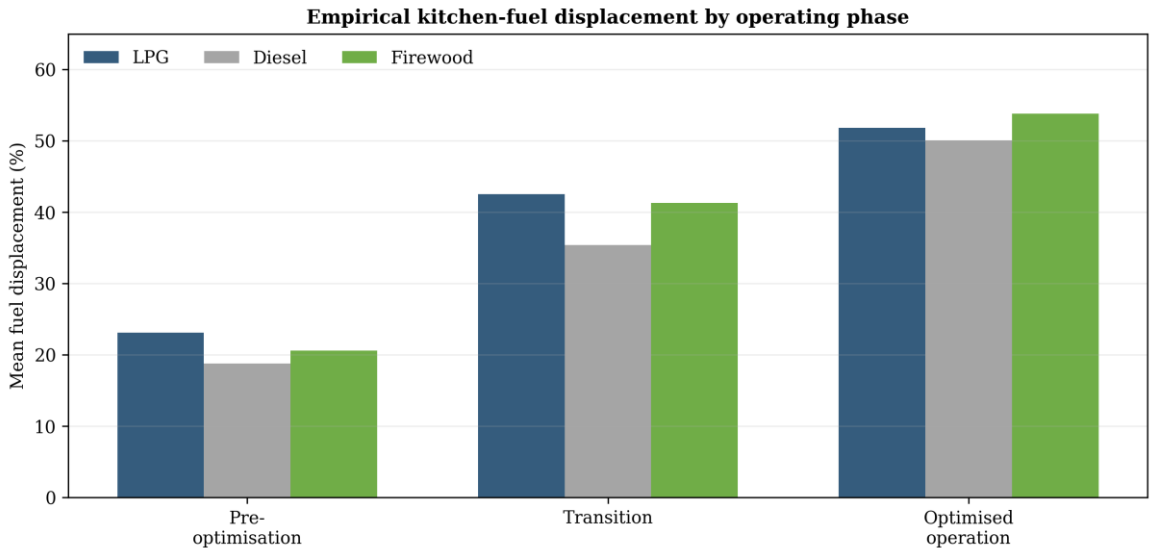

Figure 5: Empirical LPG, diesel and firewood displacement by operating phase.

4.5 Hydrostatic stability screening

The two-train base plan was derived as 2 × 8.20 × 9.70 = 159.08 m². At groundwater heads of 0.5, 1.0, 1.5 and 2.0 m above the base, calculated uplift was approximately 0.78, 1.56, 2.34 and 3.12 MN. At a minimum factor of safety of 1.20, required stabilising resistance was 0.94–3.75 MN. The range confirms that groundwater is not merely a geotechnical description; it is a structural design action that can control the empty-tank condition.

The screening result does not establish adequacy because verified concrete dimensions, self-weight, soil cover, internal water level, drainage, anchorage and load combinations were not available. The optimisation therefore includes an explicit hold point: do not empty, modify or construct adjoining units until the critical groundwater level and structural resistance are confirmed.

Table 7: Groundwater-uplift sensitivity for the combined ABR footprint

Groundwater head above base	Calculated uplift	Resistance required at FS = 1.20	Design implication
0.5 m	0.78 MN	0.94 MN	Verify empty-tank dead load
1.0 m	1.56 MN	1.87 MN	Check cover, drainage and construction stage
1.5 m	2.34 MN	2.81 MN	Ballast or anchorage may govern
2.0 m	3.12 MN	3.75 MN	Critical coastal-groundwater scenario

Note. Screening uses $\gamma w = 9.81$ kN/m³ and an approximate combined base area of 159.08 m². Detailed structural verification is required.

4.6 Impact assessment

The intervention replaced an unsafe sewage-management condition with contained treatment and eliminated routine manual faecal evacuation. This represents a direct change in the sanitation service chain: wastewater is conveyed to engineered treatment rather than repeatedly removed through hazardous manual intervention. Field observations also recorded reduced odour nuisance, improved cleanliness around the centre and more reliable access to renewable cooking gas. These outcomes align with WHO's emphasis on exposure control and with prison-biogas experience in other countries (WHO, 2022; Gauthier et al., 2012).

The monitored mass balance showed higher pollutant removal during optimised operation. Mean COD removal was 167.25 kg/day, compared with 150.08 kg/day pre-optimisation, a difference of +17.18 kg/day. Mean BOD_5 removal was 87.22 kg/day, compared with 79.21 kg/day (+8.01 kg/day), while TSS removal was 65.74 kg/day, compared with 58.11 kg/day (+7.63 kg/day). These differences are summarised together in Table 8. Final-effluent COD, BOD_5 and TSS met the combined study targets on all 15 optimised-operation days.

Energy logs showed higher useful delivery during optimised operation. Mean kitchen gas use was 65.6% higher than the pre-optimisation phase, burner support was 56.9% higher, and gross methane energy used was 311.70 kWh/day, compared with 169.79 kWh/day. The 30-day records showed aggregate physical savings of 412.3 kg LPG, 61.0 L diesel and 927.0 kg firewood. Monetary savings should be computed separately with contemporaneous invoice or issue prices to avoid distortion from fuel-price changes.

The social and institutional effects include reduced exposure to raw sewage, improved sanitation dignity, less dependence on smoky solid fuel and a cleaner kitchen environment. Sustainability depends on assigned O&M authority, recurrent financing, trained operators, spare parts, desludging schedules, gas-safety procedures and continued monitoring. Infrastructure transfer without these controls would reproduce the weakness observed in many decentralised ABR programmes (Yulistyorini et al., 2019).

Table 8: Field-based impact assessment of the integrated system

Impact domain	Indicator or finding	Evidence strength	Defensible conclusion
Technical	337.34 m³ active volume; HRT 33.60 to 39.53 h	Field/design calculation	Installed shell supports repair-first optimisation
Sanitation/public health	Manual evacuation eliminated; sewage containment and odour improved	Field operational record	Exposure pathway materially reduced
Environmental	+17.18 kg/day COD, +8.01 kg/day BOD_5 and +7.63 kg/day TSS removed	Field mass balance	Higher removal during optimised operation
Energy	57.03 m³/day gas; 49.32 m³/day used; 7.83 burner h/day	Field monitoring	Higher delivery during optimised operation
Fuel economy	412.3 kg LPG, 61.0 L diesel and 927.0 kg firewood saved in 30 days	Field kitchen logs	Reduced conventional-fuel requirement
Social	Cleaner sanitation and reduced smoky-fuel dependence	Field observation	Improved dignity and kitchen working conditions
Institutional	O&M, safety, logs, finance and spare parts required	Engineering assessment	Governance remains part of the optimised design

Note. Quantitative indicators are derived from field wastewater, biogas and kitchen-energy records. Monetary valuation is excluded because contemporaneous price documentation was outside this analysis.

5. DISCUSSION

5.1 Why the corrected sizing changes the optimisation

The most consequential correction is dimensional. The value 154.45 is the design flow in m³/day, not the installed active volume in m³. Combining it with the reported 52.42-h HRT produces 337.34 m³. Any optimisation search that restricts reactor volume to values near 154 m³ cannot represent the installed system and may falsely recommend extra chambers or a smaller optimum. The corrected basis reverses that logic: the system already contains a large active volume relative to design flow, so the first question is whether that volume is hydraulically available and evenly used.

The repair-first result is engineeringly and institutionally attractive. Recovering 50.60 m³ of inactive capacity yields a 17.65% gain in active volume without additional land or a new reactor shell. At the monitored mean flow, the restored-volume calculation yields 5.93 h additional HRT and 15% lower OLR; the balanced-flow scenario yields 30% lower peak upflow. Wastewater removal was also higher during the optimised phase despite no engineeringly significant change in influent COD, BOD_5 or TSS. This pattern is consistent with, but does not prove, a causal relationship between restored hydraulic function and treatment performance.

This conclusion aligns with field evidence showing that dynamic loading and O&M practices govern ABR performance. A nominal HRT calculated from drawings may differ materially from

residence time under intermittent flow, dead zones or unequal distribution. Echeverría et al. (2022) found that the monitored ABR performed below a design-model prediction and attributed the difference partly to temperature and intermittent flow. Yulistyorini et al. (2019) found that only a minority of surveyed decentralised ABRs achieved acceptable combined treatment and structural performance, largely because service delivery did not continue after construction. The Ikoyi optimisation therefore treats inspection, metering and maintenance as design components.

5.2 Treatment performance and the case for polishing

The empirical results demonstrate why both the ABR and downstream polishing unit must be evaluated. During optimised operation the ABR alone reduced COD to 197.6 mg/L, BOD_5 to 94.4 mg/L and TSS to 75.0 mg/L. Polishing then reduced these means to 90.6, 37.47 and 30.53 mg/L. The ABR met the COD and TSS screening targets on average but not the BOD_5 target; the complete treatment train achieved all three targets on every optimised-operation day.

The polishing stage was especially important for BOD_5 and nutrients. Constructed wetlands and biofilters have performed well after ABRs (Echeverría et al., 2022; Satyendra & Vijay, 2024), and high-strength decentralised systems can produce high-quality effluent when the complete train is properly designed and operated (Rahman et al., 2024). At Ikoyi, continued performance will depend on managing solids accumulation, groundwater, mosquito risk, media condition, hydraulic distribution, odour and access for maintenance.

The 30-day series is sufficient to demonstrate field-phase performance but not seasonal invariance. Continued matched monitoring at SP-01, SP-02 and SP-03 should retain COD, BOD_5, TSS, NH_3-N and PO_4-P and should add microbial indicators for public-health verification. The approach is consistent with Standard Methods and with the regulatory principle of using time-based averages rather than isolated samples (American Public Health Association et al., 2023; Electronic Code of Federal Regulations, n.d.).

5.3 Biogas optimisation: production is not utilisation

The empirical gas record answers both the production and utilisation questions. Optimised mean production of 57.03 m^3/day was accompanied by 49.32 m^3/day of kitchen use, 7.83 burner h/day and only 6.00 m^3/day unused or flared. During that phase, methane content was higher and H_2S and moisture were lower than in the pre-optimisation phase, showing that useful energy assessment must consider gas quality and delivery as well as volume.

A robust gas system must reconcile production, kitchen use, storage change and controlled loss. During the optimised phase, higher production coincided with approximately half the pre-optimisation quantity of unused gas and greater useful consumption. The stated 45-m^3 holder is below one day of optimised mean production, but its adequacy depends on the timing of generation and meal preparation. Pressure and burner-hour evidence supports current use, while an hourly inventory study would provide a stronger buffer-sizing check.

Condensate management, hydrogen-sulphide removal, leak testing, pressure monitoring, calibrated metering and burner scheduling remain essential. Gauthier et al. (2012) showed that operational responsibilities and maintenance influence whether prison biogas remains appropriate. The measured reduction in conventional-fuel use at Ikoyi strengthens the case for continued investment in these controls and for retaining a contingency cooking source for service continuity.

5.4 Contribution to sustainable development and engineering practice

The case connects sanitation, pollution control, renewable thermal energy and institutional resilience, consistent with resource-recovery and sanitation-safety principles (UNEP, 2023; WHO, 2022, 2026). Its quantified contribution is a transparent field decision basis: 337.34 m^3 restored active volume; 5.93 h additional HRT at monitored mean flow; 15% lower OLR; 89.99%, 91.90% and 91.27% overall COD, BOD_5 and TSS removal; 57.03 m^3/day biogas production during optimised operation; 63.39% methane; and conventional-fuel displacement above 50% for LPG, diesel and firewood. These values convert a general sustainability claim into measurable engineering outcomes.

6. LIMITATIONS AND VALIDATION REQUIREMENTS

The principal limitation is the 30-day, single-season monitoring window and the sequential rather than randomised intervention design. The results are empirical and field-based, but they should be interpreted as full-scale operating-phase evidence rather than proof that every observed change was caused by one isolated optimisation variable. Longer monitoring should test wet- and dry-season performance, sludge accumulation and resilience to unusual hydraulic or organic shocks.

The active-volume values are engineering calculations based on the audited geometry and operating condition; a detailed sludge-depth and residence-time survey would strengthen the hydraulic diagnosis. Aggregate flow does not resolve inequality between the two trains, and daily gas totals do not capture sub-daily storage peaks. The multi-criteria weights reflect transparent engineering priorities but were not established through formal stakeholder elicitation or tested through a complete multi-weight sensitivity analysis; future work should examine ranking stability across plausible weights. Microbial water-quality indicators, kitchen air-quality measurements, contemporaneous fuel prices and ethically collected stakeholder responses would extend the environmental, economic and social assessment beyond the present scope.

7. CONCLUSIONS AND RECOMMENDATIONS

The design audit confirms that the Ikoyi system comprises two parallel ABR trains with six chambers per train and a restored active volume of 337.34 m^3. At the monitored mean flow of 204.82 m^3/day, active-volume recovery increased calculated HRT from 33.60 to 39.53 h and reduced OLR from 0.648 to 0.551 kg COD m^{-3} d^{-1}. The optimised solution therefore retains the installed shell and chamber count and prioritises desludging, dead-zone recovery, clear baffle openings, equal flow division and metering.

The 30-day empirical campaign comprised 90 wastewater samples at SP-01, SP-02 and SP-03. During optimised operation, final-effluent COD, BOD_5 and TSS averaged 90.6, 37.47 and 30.53 mg/L, with overall removals of 89.99%, 91.90% and 91.27%. All 15 optimised-operation days met the combined study targets. Nutrient removal was higher during optimised operation but remained lower than carbon and solids removal, supporting continued attention to polishing and microbial-risk verification.

Mean biogas production during optimised operation was 57.03 m^3/day, compared with 42.99 m^3/day pre-optimisation; methane fraction was 63.39%, compared with 57.15%; and kitchen use was 49.32 m^3/day, compared with 29.78 m^3/day. LPG, diesel and firewood displacement reached 51.82%, 50.10% and 53.83% during optimised operation. The field records therefore show measurable sanitation, pollution-control and institutional-energy benefits, while the sequential design limits attribution to any single optimisation action.

For implementation, the authors recommend continued three-point wastewater monitoring; total and train-specific flow metering; scheduled sludge-depth surveys; maintenance of the polishing stage; gas-quality, pressure and kitchen-demand logging; an empty-tank hydrostatic check with FS $\geq$1.20; contemporaneous cost recording; and a funded O&M plan with named responsibilities, preventive schedules, safety procedures and spare parts. These measures will protect the gains demonstrated during the field campaign and allow seasonal verification.

DATA AVAILABILITY AND RESEARCH-INTEGRITY STATEMENT

The paper uses primary field and empirical monitoring records together with transparent engineering calculations. Security-sensitive layouts and individual-level custodial information are not disclosed. The wastewater, biogas and kitchen-energy datasets are held within the research project and are subject to institutional permissions; aggregated results are reported in this manuscript.

CONFLICT OF INTEREST

The authors declare no conflict of interest in relation to the preparation of this manuscript.

REFERENCES

American Public Health Association, American Water Works Association, & Water Environment Federation. (2023). Standard methods for the examination of water and wastewater (24th ed.). APHA Press. https://www.standardmethods.org/24theditioncitation

Barber, W. P., & Stuckey, D. C. (1999). The use of the anaerobic baffled reactor (ABR) for wastewater treatment: A review. Water Research, 33(7), 1559–1578. https://doi.org/10.1016/S0043-1354(98)00371-6

Echeverría, I., Saavedra, O., Escalera, R., Heredia, G., Yoshimura, C., & Montoya, R. (2022). Small-scale operation of an integrated anaerobic baffled reactor and biofilter: Factors affecting its performance. Journal of Environmental Engineering, 148(11), 04022065. https://doi.org/10.1061/(ASCE)EE.1943-7870.0002047

Electronic Code of Federal Regulations. (n.d.). Title 40, Part 133: Secondary treatment regulation. Retrieved August 15, 2026, from https://www.ecfr.gov/current/title-40/chapter-I/subchapter-D/part-133

Gauthier, M., Oppliger, A., Lohri, C., & Zurbrügg, C. (2012). Ensuring appropriateness of biogas sanitation systems for prisons: Analysis from Rwanda, Nepal and the Philippines. Technologies for Sustainable Development Conference. International Committee of the Red Cross. https://www.icrc.org/sites/default/files/external/doc/en/assets/files/2012/biogas-article-sustainable-development-icrc.pdf

Gutterer, B., Sasse, L., Panzerbieter, T., & Reckerzügel, T. (2009). Decentralised wastewater treatment systems (DEWATS) and sanitation in developing countries: A practical guide. BORDA.

Ikoyi ABR Design and Field Records. (2019–2024). Design calculations, as-built dimensions, 30-day wastewater monitoring, biogas-quality records and kitchen-energy logs [Unpublished project records].

International Committee of the Red Cross. (2012). Water, sanitation, hygiene and habitat in prisons: Supplementary guidance. ICRC.

Jin, C., Wu, X., Ping, L., & Wu, J. (2024). Performance of anaerobic baffled reactor (ABR) and multi-staged UASB in anaerobic digestion process for treating leachate from refuse transfer stations under loading shocks. Water Science & Technology, 90(2), 446–460. https://doi.org/10.2166/wst.2024.227

Munavalli, G. R., Sonavane, P. G., Koli, M. M., & Dhamangaokar, B. S. (2022). Field-scale decentralized domestic wastewater treatment system: Effect of dynamic loading conditions on the removal of organic carbon and nitrogen. Journal of Environmental Management, 302, 114014. https://doi.org/10.1016/j.jenvman.2021.114014

National Environmental Standards and Regulations Enforcement Agency. (2009). National Environmental (Sanitation and Wastes Control) Regulations, S.I. No. 28 of 2009. Federal Republic of Nigeria Official Gazette. https://faolex.fao.org/docs/pdf/nig204466.pdf

National Environmental Standards and Regulations Enforcement Agency. (2011). National Environmental (Surface and Groundwater Quality Control) Regulations, S.I. No. 22 of 2011. https://nesrea.gov.ng/wp-content/uploads/2025/05/Surface_and_Groundwater_Quality_Control_Regulation-2011.pdf

Rahman, K. Z., Al Saadi, S., Al Rawahi, M., van Afferden, M., Bernhard, K., Friesen, J., & Müller, R. A. (2024). Small decentralized technologies for high-strength wastewater treatment and reuse in arid and semi-arid regions. Environments, 11(7), 142. https://doi.org/10.3390/environments11070142

Raja, W., Rohith, G. S. N., Brar, S. K., & Kumar, P. (2025). Decentralized sewage treatment and energy recovery in high-rise buildings using anaerobic baffle reactor coupled with plant biofilter reactor: A focus on surfactant and phenol removal. Science of the Total Environment, 982, 179661. https://doi.org/10.1016/j.scitotenv.2025.179661

Saif, Y., Ali, M., Jones, I. M., & Ahmed, S. (2021). Performance evaluation of a field-scale anaerobic baffled reactor as an economic and sustainable solution for domestic wastewater treatment. Sustainability, 13(18), 10461. https://doi.org/10.3390/su131810461

Sasse, L. (1998). DEWATS: Decentralised wastewater treatment in developing countries. BORDA.

Satyendra, & Vijay, R. (2024). Anaerobic baffled reactor followed by up-flow constructed wetland for treatment of municipal wastewater. Journal of Water Process Engineering, 58, 104810. https://doi.org/10.1016/j.jwpe.2024.104810

Tilley, E., Ulrich, L., Lüthi, C., Reymond, P., & Zurbrügg, C. (2014). Compendium of sanitation systems and technologies (2nd rev. ed.). Eawag.

Ullah, N., Sheikh, Z., Ahmad, O., & Khan, S. J. (2024). Performance evaluation of sponge anaerobic baffled reactor for municipal wastewater treatment. Sustainability, 16(21), 9398. https://doi.org/10.3390/su16219398

Ullah, N., Sheikh, Z., Alotaibi, S. B., Khan, M., & Ahmad, A. (2025). Effect of effluent recirculation on the performance of an anaerobic baffled reactor in municipal wastewater treatment: A modeling approach. Sustainability, 17(9), 3783. https://doi.org/10.3390/su17093783

Ullah, N., Sheikh, Z., Khan, M. S., Alotaibi, S. B., & Saddam. (2026). Treatment of real municipal wastewater in a sponge anaerobic baffled reactor with cultivation-based microbial characterization. Water Science & Technology, 93(9), 1346–1362. https://doi.org/10.2166/wst.2026.271

United Nations Environment Programme. (2023). Wastewater: Turning problem to solution. https://www.unep.org/resources/report/wastewater-turning-problem-solution

World Health Organization. (2018). Guidelines on sanitation and health. https://www.who.int/publications/i/item/9789241514705

World Health Organization. (2022). Sanitation safety planning: Manual for safe use and disposal of wastewater, greywater and excreta (2nd ed.). https://www.who.int/publications/i/item/9789240062887

World Health Organization. (2026). WHO water, sanitation, hygiene and waste strategy 2026–2035. Retrieved August 15, 2026, from https://www.who.int/publications/i/item/B09661

Yenji, S. S., Munavalli, G. R., & Koli, M. M. (2021). Field-scale anaerobic baffled reactor for domestic wastewater treatment: Effect of dynamic operating conditions. Water Practice & Technology, 16(1), 42–58. https://doi.org/10.2166/wpt.2020.103

Yulistyorini, A., Camargo-Valero, M. A., Sukarni, S., Suryoputro, N., Mujiyono, M., Santoso, H., & Rahayu, E. T. (2019). Performance of anaerobic baffled reactor for decentralized wastewater treatment in urban Malang, Indonesia. Processes, 7(4), 184. https://doi.org/10.3390/pr7040184

International Conference on Engineering Innovation for Sustainable Development (ICESID 2026)
Faculty of Engineering, Ahmadu Bello University Zaria · 8–10 September 2026

DESIGNING ENFORCEMENT FOR SAFETY, NOT HAZARD: EVIDENCE FROM A TRAFFIC MANAGEMENT SYSTEM FAILURE IN KANO METROPOLIS

Muwaffaq Safiyanu Labbo[1,*], Abubakar Idris[1], Suraj Abubakar Wada[2]
[1]*Aliko Dangote University of Science and Technology*
[2]*Ahmadu Bello University, Zaria*
Email: mslabbo@gmail.com*, abubakaridris428@gmail.com, srjwada@gmail.com
***Corresponding author**: Muwaffaq Safiyanu Labbo
DOI: https://doi.org/10.67203/sp.ICESID.2026

ABSTRACT
Traffic enforcement is a core component of urban traffic management systems, yet its design is rarely subjected to the same safety-engineering scrutiny applied to road geometry, signal timing, or vehicle standards. This paper argues that it should be. Drawing on evidence from Kano metropolis, Nigeria, where traffic management relies heavily on contact-based enforcement by the Kano Road Traffic Authority (KAROTA), the study examines how an enforcement subsystem oriented toward revenue generation rather than safety outcomes may itself become a source of crash risk. A cross-sectional survey of 331 urban drivers found that higher self-reported compliance with traffic regulations was independently associated with greater, not lower, self-reported crash involvement (OR = 1.72, p = .007), while perceived importance of regulation was independently protective (OR = 0.48, p < .001); the two were statistically unrelated. A descriptive attitude–behaviour typology showed that drivers reporting consistent compliance without valuing the rules recorded the highest crash rate (83%), while those who valued regulation but complied flexibly were safest (42%). Documented cases of enforcement-related harm, and institutional evidence on KAROTA's revenue mandate and personnel profile, are consistent with an enforcement-as-hazard mechanism, though they cannot establish its incidence. The paper argues, interpretively rather than as a tested claim, that safe traffic management system design should treat enforcement legitimacy as a design parameter, and that substituting automated, infrastructure-based compliance mechanisms for discretionary contact-based enforcement offers a plausible safety improvement. Implications for the transition to technology-enabled enforcement in Nigerian cities are discussed.

Keywords: *Traffic Management System Design; Enforcement Safety; Attitude–Behaviour Congruence; Safe System Approach; Nigeria*

1. INTRODUCTION

The Safe Systems approach to road safety treats the road transport environment as an engineered system whose components — road geometry, vehicle design, speed management, and user behaviour — interact to produce or prevent harm (Khan and Das, 2024; OECD/ITF, 2021). A core principle is that no single component failure should result in death or serious injury; the system should be designed so that errors are anticipated, accommodated, and their consequences minimised. This principle has driven decades of progress in infrastructure engineering, vehicle crashworthiness, and signal design.

One component of the traffic management system, however, has largely escaped safe-systems scrutiny: the enforcement subsystem. Traffic enforcement — the institutional apparatus of officers, checkpoints, patrols, and sanctions — is conventionally evaluated by asking whether it is sufficiently consistent, visible, and well-resourced, and the standard recommendation is to intensify it (Elvik et al., 2009; Uhunwagho et al., 2025). This evaluative frame implicitly treats enforcement as an unambiguous safety input rather than as a designed subsystem that can itself generate hazard if poorly engineered.

This paper examines that assumption using evidence from Kano metropolis, Nigeria, where traffic management depends heavily on contact-based street enforcement by the Kano Road Traffic Authority (KAROTA). It argues that an enforcement subsystem designed around revenue extraction, staffed without adequate training, and operating without procedural safeguards may produce

compliance that is not reliably protective, and enforcement encounters that are themselves hazardous. Two points about the paper's scope should be stated at the outset. First, the study did not administer validated measures of compliance motivation, procedural justice, or enforcement legitimacy; the theoretical frameworks below are therefore applied interpretively, to organise and explain the observed associations, rather than tested directly. Second, the documented cases used later are illustrative of a mechanism and cannot establish its incidence or representativeness. Within these bounds, the paper proposes that enforcement legitimacy be treated as a design parameter in traffic management systems, and that the transition from discretionary, contact-based enforcement to automated, infrastructure-based compliance mechanisms is a safety-engineering question deserving direct study.

2. ENFORCEMENT AS A DESIGNED SUBSYSTEM

2.1 The conventional evaluative frame and its limitation

The dominant Nigerian road safety literature evaluates enforcement agencies — the Federal Road Safety Corps (FRSC) and state traffic authorities — by measuring activity volume: patrol frequency, checkpoint density, fine revenue, and public-awareness campaign reach. A recent representative study of the FRSC Minna Sector Command concludes that road safety would improve with greater consistency and visibility of enforcement and with more funding and personnel (Uhunwagho et al., 2025). This framing rests on a simple deterrence model in which more enforcement yields more compliance, which in turn yields fewer crashes.

The limitation is that deterrence models assume the enforcement agent is legitimate — trusted, competent, and procedurally fair — and that the compliance produced is normatively accepted rather than merely coerced (Tyler, 2006). Where this assumption fails, the model's predictions may reverse, and more enforcement may produce more coerced, evasive, and hazardous behaviour rather than more safety. This is a system-design question rather than a purely behavioural one. The institutional parameters of the enforcement subsystem — its funding model, recruitment standards, accountability mechanisms, and mode of operation — shape whether it functions as a safety mechanism or as a hazard source.

2.2 Contact-based versus infrastructure-based enforcement

A useful distinction for safe-system design is between contact-based enforcement, in which officers physically stop, confront, and sanction drivers in real time, and infrastructure-based enforcement, in which detection is automated through cameras, sensors, and signal systems, with sanctions processed remotely. Contact-based enforcement introduces a direct, in-traffic interaction between an officer and a driver. That interaction can itself generate hazard — through sudden braking, evasion manoeuvres, or physical altercation — particularly where the enforcement is perceived as illegitimate or extractive. Infrastructure-based enforcement removes the hazardous encounter, decouples detection from personal discretion, and can operate continuously rather than selectively. The transition from contact-based to infrastructure-based enforcement is therefore a safety-engineering decision with plausible implications for crash risk, yet it is rarely framed as such in the Nigerian context, where discussion remains centred on enforcement quantity rather than enforcement mode and design.

3. THEORETICAL BASIS

Two complementary frameworks are used interpretively in this paper to link enforcement system design to safety outcomes through compliance motivation. Neither construct was measured directly in the survey; the frameworks are applied to organise and explain the observed associations, and the absence of direct measurement is a limitation noted here and revisited in Section 7.

Self-determination theory (Deci and Ryan, 1985, 2000) distinguishes autonomous motivation, in which behaviour is aligned with personal values and tends to be stable and generalised, from controlled motivation, in which behaviour is driven by external pressure and tends to be narrow and situation-dependent. Applied to traffic, it suggests that the same observable compliance may be protective or hazardous depending on its motivational source. Enforcement system design plausibly influences which type predominates: a legitimate, procedurally fair system supports internalisation,

whereas an extractive system may produce controlled, surveillance-dependent compliance that lapses or becomes evasive when the officer appears.

Procedural-justice and legitimacy theory (Sunshine and Tyler, 2003; Tyler, 2006) specifies the institutional conditions that build or erode legitimacy: consistency, transparency, respectful treatment, and the absence of corruption. An enforcement subsystem designed around revenue targets, staffed at the lowest educational grades, and operating without oversight creates conditions that theory would expect to erode legitimacy and, through the motivational pathway above, to favour controlled over internalised compliance. The combined framework yields the paper's central proposition, offered as an interpretive hypothesis: an enforcement subsystem functions as a safety mechanism when it is designed to produce legitimate, internalised compliance, and risks becoming a hazard source when it is not.

4. THE KANO CASE: EVIDENCE OF A SYSTEM DESIGN FAILURE

4.1 Institutional design parameters

KAROTA was established in 2012 by the Kano State Government with a dual mandate of traffic management and revenue generation, with a reported monthly revenue target of approximately ₦100 million (Zakimayu et al., 2023). More than 95% of its approximately 1,600 agents were recruited at the lowest educational grades, and the agency's own administrators have acknowledged that agents enforce fewer than five of the 90-plus codified traffic offences (Zakimayu et al., 2023). The metropolis, with a population exceeding four million, is served by fewer than 100 operational traffic signals. This combination — a revenue-incentivised workforce, minimal training, and scarce automated infrastructure — represents an enforcement subsystem oriented, whether by intent or not, toward contact-based operation rather than safety outcomes.

4.2 Survey methodology

A cross-sectional survey was conducted across five local government areas of Kano metropolis. Adult drivers were recruited using purposive sampling at high-traffic locations, including fuel stations, motor parks, and checkpoints; the sampling frame limitations this entails are addressed in Section 7. An a priori power analysis for logistic regression ($\alpha = .05$, power = .80, anticipated $R^2 = .10$) indicated a minimum of 271 cases, and the achieved sample of 331 exceeded this threshold. Participation was voluntary and anonymous, and informed consent was obtained.

A structured questionnaire captured demographics, driving profile, perceived importance of traffic regulation, self-reported compliance, and crash involvement. Perceived importance was measured on a four-point item (from 'not at all important' to 'very important'); self-reported compliance was measured on a three-point frequency item ('sometimes', 'most of the time', 'always'); and the outcome was self-reported involvement in any road crash or collision in the preceding six months. The crash item did not specify a severity threshold and is therefore interpreted throughout as self-reported crash or collision involvement of any severity, not as verified or injury crashes. The instrument was piloted with 20 drivers excluded from the final sample; because the key measures are single items rather than multi-item scales, no internal-consistency statistics are reported, and this measurement constraint is noted as a limitation. Analyses were conducted in Python 3.11 (scipy, statsmodels, scikit-learn).

4.3 Survey findings

Bivariate associations were assessed using chi-square tests and Spearman correlations. A binary logistic regression predicting crash involvement was reduced by backward elimination on the Akaike information criterion to a parsimonious specification containing five predictors: compliance, perceived importance, driving frequency, awareness frequency, and gender. This model was re-estimated using Firth's penalised maximum likelihood to address small-sample bias arising from the small female subsample ($n = 18$); all variance inflation factors were below 1.2. In the penalised model, higher compliance was independently associated with greater crash risk (OR = 1.72, 95% CI [1.16, 2.56], $p = .007$), while perceived importance was independently protective (OR = 0.48, 95% CI [0.32, 0.72], $p < .001$). The two were statistically unrelated ($\rho = -.00$, $p = .994$), and a causal mediation analysis with bootstrapped confidence intervals indicated that compliance did not transmit the protective effect of perceived importance.

Cross-classifying drivers on dichotomised perceived importance and compliance produced four descriptive response profiles with significantly different crash rates ($\chi^2(3) = 29.1$, $p < .001$): high importance with inconsistent compliance, safest at 42%; high importance with consistent compliance, 67%; low importance with inconsistent compliance, 70%; and low importance with consistent compliance, highest at 83%, with adjusted odds 2.67 times the high-importance/consistent reference (95% CI [1.18, 6.03], $p = .018$) after adjustment for driving frequency and gender. These are descriptive classifications of survey responses, not measured motivational types; the labels used in earlier work carried motivational connotations and are avoided here. One feature is notable: the high-importance/consistent profile recorded a higher crash rate (67%) than the high-importance/inconsistent profile (42%), which is difficult to reconcile with a clean partition of behavioural types and reinforces the descriptive status of the classification.

4.4 Documentary evidence: enforcement encounters as hazard events

The survey associations are consistent with, though they do not by themselves establish, a mechanism in which the enforcement encounter itself can produce harm. Respondents' open-text comments referred to accidents attributed to 'the fear of KAROTA officials', to officers who 'follow the driver' who fails to stop, and to enforcement that they associated with aggressive driving. These are perceptions, not incident records.

Independently, press and field records document individual incidents in which enforcement contact preceded injury or death: traffic officials physically intervening in moving vehicles ('steering-dragging') with fatal results, reported in Kano and, in a structurally similar case, in Lagos involving the Lagos State Traffic Management Authority (LASTMA); fatal pursuits of drivers evading enforcement; officers struck and killed while attempting to stop vehicles, including a case in which a driver was sentenced to 15 years for killing a Kano traffic officer (Punch, 2024); and clashes between enforcement agents and road users (Gazette, 2023). A feature of this record worth noting analytically is that the harm is bidirectional — both drivers and officers are killed — which is more consistent with a hazardous interaction dynamic than with misconduct by either party alone. These cases are illustrative and are drawn from journalism; they document that such events occur, not how frequently, and no inference about incidence or representativeness is drawn from them.

Institutional documentation further indicates that extraction-oriented conduct is present within Nigerian traffic enforcement more broadly, including anti-corruption operations concerning FRSC officials (ICPC, 2021), reporting on the taxation of tricycle operators in Kano (ICIR, 2024), and reporting on highway extortion (Premium Times, 2025). These sources describe the institutional environment in which the Kano subsystem operates; they are contextual rather than causal evidence.

5. DISCUSSION: ENFORCEMENT LEGITIMACY AS AN ENGINEERING PARAMETER

The survey, documentary, and institutional strands are mutually consistent and, taken together, are suggestive of an enforcement subsystem that is not functioning purely as a safety mechanism. They fall short, individually and jointly, of establishing that contact-based enforcement causes crashes: the survey is cross-sectional and self-reported, and the documented cases are illustrative. What the strands support is a coherent, testable hypothesis rather than a demonstrated causal claim — namely, that a contact-based, revenue-oriented, low-legitimacy enforcement configuration may favour coerced rather than internalised compliance and may generate hazardous enforcement encounters.

From a safe-systems engineering perspective, the value of this framing is that it locates a potential safety problem in design parameters that are within an agency's control — funding model, recruitment and training standards, accountability mechanisms, and mode of operation — rather than in the conduct of individual officers. Treating enforcement legitimacy as a design parameter means subjecting these choices to the same evidence-based scrutiny applied to road cross-sections, signal phasing, or crashworthiness standards.

The Kano and Lagos 'steering-drag' cases, occurring in different cities and involving different agencies, are suggestive that the hazard may not be specific to a single agency but may instead be associated with the contact-based enforcement configuration itself. This remains a hypothesis: two documented cases cannot establish that the pattern is general, and a systematic compilation of

enforcement-related crash events across multiple Nigerian cities would be required to test it. The claim is therefore offered as a direction for investigation, not as an established generalisation.

6. TOWARD SAFER ENFORCEMENT SYSTEM DESIGN

Four design principles follow from the analysis, offered as engineering directions for traffic management systems in Nigerian cities. Because they follow from the institutional and documentary evidence and from safe-system principles, rather than from the survey associations alone, they do not depend on resolving the causal questions above.

First, decouple enforcement from revenue generation. A revenue mandate creates an incentive structure that rewards extraction over safety and is corrosive of the legitimacy on which internalised compliance depends. Enforcement funded from general appropriation, rather than from what it collects, better aligns the agent's incentive with safety outcomes.

Second, shift the balance from contact-based toward infrastructure-based enforcement. Automated systems — speed and red-light cameras, and automatic number-plate recognition — decouple detection from personal discretion, remove the hazardous in-traffic encounter, operate continuously, and generate an auditable, corruption-resistant record.

Third, invest in the enabling infrastructure. Automated enforcement depends on functional signals, signage, and markings. Fewer than 100 operational signals for a metropolis of over four million forces reliance on contact-based enforcement by default; signal and signage provision is therefore both a traffic-flow measure and a precondition for shifting enforcement mode.

Fourth, professionalise personnel for the contact-based functions that remain necessary, such as crash response and impaired-driving detection. Recruitment, training, and evaluation should emphasise procedural fairness and safety outcomes rather than revenue collected, with training in de-escalation and in the hazards of in-traffic physical intervention.

7. LIMITATIONS AND FUTURE WORK

The study has several limitations that bound its conclusions. The design is cross-sectional and relies on self-report, so no causal ordering can be established; in particular, post-crash behavioural adaptation, in which involvement in a crash leads a driver to report stricter subsequent compliance, is a plausible alternative explanation for the positive compliance–crash association that the data cannot exclude. The crash outcome is broad and severity-unrestricted, with a six-month recall window and no validation against police or hospital records, and the reported rate should not be compared with injury-crash statistics. The key measures of perceived importance and compliance are single items rather than validated multi-item scales. The theoretical constructs of central interest — compliance motivation, procedural justice, and enforcement legitimacy — were not measured directly; the frameworks are applied interpretively, and the response-profile typology is descriptive rather than a validated motivational classification.

The sample is predominantly male (approximately 95%) and was recruited purposively without a sampling frame. These features limit the generalisability of all findings, and of the typology in particular: the profiles describe response patterns within this specific, non-representative sample, and their crash rates should not be read as population estimates or extended to women drivers, who are severely under-represented. The documentary cases are illustrative and journalistic, and the institutional analysis relies on secondary sources. Collectively, these constraints mean the paper advances an evidence-consistent, testable hypothesis rather than a confirmed causal claim.

Future work should pursue three priorities. First, a comparative study of cities relying predominantly on contact-based versus infrastructure-based enforcement, measuring both compliance quality and crash outcomes, would test the central design proposition directly. Second, primary studies should administer validated procedural-justice and self-determination measures, alongside a severity-anchored or record-linked crash outcome and a proper exposure measure, ideally in a longitudinal design capable of separating post-crash adaptation from prospective risk. Third, a systematic compilation of enforcement-related crash events across multiple Nigerian cities would test whether the enforcement-as-hazard pattern generalises beyond the illustrative cases presented here.

8. CONCLUSION

Traffic enforcement is a subsystem of the traffic management system, and like any subsystem it can be designed for safety or, inadvertently, for hazard. In Kano, the enforcement subsystem's institutional parameters — a revenue mandate, minimally trained contact-based agents, and scarce automated infrastructure — characterise a configuration that this study's converging but limited evidence suggests may generate coerced, evasive compliance and dangerous enforcement encounters. The evidence supports this as a hypothesis to be tested, not as an established finding.

The corrective this points toward is not more enforcement but better-designed enforcement: revenue-decoupled, progressively automated, supported by functional infrastructure, and, where human contact remains necessary, staffed by trained and accountable personnel. Framed this way, enforcement legitimacy is not a matter external to engineering; it is a design parameter that plausibly shapes whether the enforcement subsystem contributes to, or detracts from, the safety of the traffic management system as a whole — a proposition this paper commends to direct empirical test.

REFERENCES

Deci, E. L., & Ryan, R. M. (1985). Intrinsic Motivation and Self-Determination in Human Behavior. Plenum Press. https://doi.org/10.1007/978-1-4899-2271-7

Deci, E. L., & Ryan, R. M. (2000). The "what" and "why" of goal pursuits: Human needs and the self-determination of behavior. Psychological Inquiry, 11(4), 227–268. https://doi.org/10.1207/S15327965PLI1104_01

Elvik, R., Høye, A., Vaa, T., & Sørensen, M. (2009). The Handbook of Road Safety Measures (2nd ed.). Emerald. https://doi.org/10.1108/9781848552517

Gazette. (2023). Scores injured as traffic agency officials, tricycle riders clash in Kano. Peoples Gazette Nigeria. https://gazettengr.com/scores-injured-as-traffic-agency-officials-tricycle-riders-clash-in-kano/

ICIR. (2024). Forgery, illegal taxes, extortion, corruption: Realities of taxing Keke riders in Kano (Part 2). The International Centre for Investigative Reporting. https://www.icirnigeria.org/forgery-illegal-taxes-extortion-corruption-realities-of-taxing-keke-riders-in-kano-2/

ICPC. (2021). Operation Tranquility: Uprooting corrupt FRSC officials from Nigerian highways. Independent Corrupt Practices and Other Related Offences Commission. https://icpc.gov.ng/operation-tranquility-uprooting-corrupt-frsc-officials-from-nigerian-highways/

Khan, M. N., & Das, S. (2024). Advancing traffic safety through the safe system approach: A systematic review. Accident Analysis & Prevention, 199, 107518. https://doi.org/10.1016/j.aap.2024.107518

Mooren, L., & Shuey, R. (2024). Systems thinking in road safety management. Journal of Road Safety, 35(2), 63–73. https://doi.org/10.33492/JRS-D-24-2-2109985

OECD/ITF. (2021). The Safe System Approach in Action. International Transport Forum. https://www.itf-oecd.org/sites/default/files/docs/safe-system-in-action.pdf

Premium Times. (2025). Unending toll: How highway extortion fuels soaring food prices in Nigeria. https://www.premiumtimesng.com/news/headlines/826938-unending-toll-how-highway-extortion-fuels-soaring-food-prices-in-nigeria.html

Punch. (2024). Driver jailed 15 years for killing Kano traffic officer. https://punchng.com/driver-jailed-15-years-for-killing-kano-traffic-officer/

Sunshine, J., & Tyler, T. R. (2003). The role of procedural justice and legitimacy in shaping public support for policing. Law & Society Review, 37(3), 513–547. https://doi.org/10.1111/1540-5893.3703002

Tyler, T. R. (2006). Why People Obey the Law. Princeton University Press. https://doi.org/10.2307/j.ctv1j66769

Uhunwagho, C., Aidelokhai, D. I., Nmadu, T., Musa, U., & Abu, I. (2025). Assessing the impact of activities of the Federal Road Safety Corps in alleviating automobile accidents in Minna, Niger State. Kashere Journal of Politics and International Relations, 3(1), 219–231.

Zakimayu, T., Abdussalam, B., & Abedo, U. (2023). Revamping the roles of non-state policing actors: An appraisal of KAROTA in Kano metropolis. Nigerian Journal of Peace, Development & Humanitarian Affairs, 3, 29–44.

International Conference on Engineering Innovation for Sustainable Development (ICESID 2026)
Faculty of Engineering, Ahmadu Bello University Zaria · 8–10 September 2026

DEVELOPMENT AND PERFORMANCE EVALUATION OF A WASTE PLASTIC SHREDDER

Akeem Adekunle Adebesin[1,*], Ogundemuren Victor Oluwatobi[1]

[1]*Federal University of Technology Ilaro*

Email: akeem.adebesin@federalpolyilaro.edu.ng[*], victor.ogundemuren@federalpoyilaro.edu.ng

***Corresponding author**: Akeem Adekunle Adebesin

DOI: https://doi.org/10.67203/sp.ICESID.2026

ABSTRACT

The increasing use of plastic materials in modern society has led to a significant rise in plastic waste generation. Improper disposal of these materials has created serious environmental challenges, particularly in developing countries where waste management systems are still evolving, hence plastic recycling has therefore become an important approach to reducing environmental pollution and promoting sustainable resource utilization. One of the key processes involved in plastic recycling is the reduction of plastic waste into smaller sizes that can be easily processed and reused. This paper focuses on the design and fabrication of a waste plastic shredding machine suitable for small and medium scale recycling operations. The machine was designed using fundamental principles of mechanical engineering and constructed using locally available materials to ensure affordability, durability, and ease of maintenance while the major components of the machine include the frame, hopper, shredding blades, shaft, drive mechanism, bearings, and a 6.5hp gasoline engine which serves as the power source. The machine operates on the principle of mechanical shearing and cutting, where plastic materials fed through the hopper are reduced into smaller particles by rotating blades mounted on a shaft. Performance evaluation of the fabricated machine was carried out using plastic waste materials and three experimental tests were conducted with an average plastic input weight of 5.37 kg and an average shredding time of 51.67 seconds. The results obtained showed an average shredded plastic output of 4.9 kg, resulting in a shredding efficiency of approximately 91.25 percent. The results indicate that the fabricated plastic shredding machine is capable of effectively reducing plastic waste into smaller particles suitable for recycling processes. The machine therefore provides a practical and cost-effective solution for improving plastic waste management and supporting environmental sustainability, especially in communities where recycling facilities are limited.

Keywords: *Plastics; Environment; Pollution; Shredding; Wastes Management; Machine*

1. INTRODUCTION

The exponential growth of plastic consumption worldwide over recent decades has resulted in the generation of massive quantities of plastic waste, making it one of the most significant environmental and public health challenges of the 2[1st] century (*Thompson et al., 2009; Hopewell et al., 2009*) but the indiscriminate disposal of plastic waste in Nigeria has resulted in serious environmental problems, including blocked drainage systems, pollution of water bodies, and threats to human health and biodiversity. Large quantities of plastic waste remain unprocessed due to the lack of appropriate recycling and shredding facilities, particularly at the community and institutional levels.

Many of the plastic shredding machines currently available are imported and expensive, making them inaccessible to small-scale recycling operators and local entrepreneurs. In addition, some existing machines require a reliable electricity supply, which is often unavailable or inconsistent in many parts of Nigeria. As a result, plastic waste is frequently discarded without undergoing size reduction, thereby limiting recycling opportunities.

Plastics are widely used due to their versatility, durability, and low cost, yet their non-biodegradable nature means that, once discarded, they persist in the environment for hundreds of years. Plastic waste accumulates in landfills, rivers, oceans, and terrestrial ecosystems, posing severe threats to wildlife, human health, and overall ecological balance. Microplastics, formed from the breakdown of larger plastic items, have been detected in water sources, soils, and even food chains, raising global concerns about their long-term effects on health and ecosystems. These realities underscore the urgent

need for sustainable, cost-effective, and scalable strategies for plastic waste management, with recycling and reuse emerging as the most viable solutions (Handel and Strazdus, 2021).

Among the critical stages of plastic waste management is size reduction through shredding, a process that enhances recycling efficiency and operational feasibility. Shredding converts bulky, irregular, and difficult-to-handle plastics into smaller, uniform fragments that are easier to transport, sort, and process in subsequent operations such as melting, extrusion, or chemical treatment (*Angelo et al., 2022; Wong et al., 2022*). Reducing particle size not only increases the surface area for more efficient processing but also lowers storage and transportation costs and reduces hazards associated with manual handling of large plastic items. A well-designed shredding system enhances recycling efficiency, supports circular economy principles, and contributes to resource conservation by enabling plastics to be reintroduced into manufacturing processes. The significance of this research extends beyond technical design but by providing a low-cost, practical, and efficient solution for plastic waste reduction thereby contributing to environmental conservation, promotes sustainable waste management practices, and encourages the adoption of circular economy initiatives at the community and institutional levels (Balasubramanian and Sharma, 2022). It also aims to address local and national plastic waste challenges and also serve as a replicable model that can be adopted by educational institutions, small enterprises, and community-based recycling programs.

Surgude et al. (2023) fabricated a plastic shredder designed for small recycling workshops and emphasized the use of locally available materials to reduce manufacturing cost though, the fabricated shredder efficiency was 91.3%, yet their studies demonstrate that locally designed shredding machines can provide effective solutions for plastic waste recycling when appropriate engineering principles are applied.

2. METHODOLOGY

The design process for shredding plastic wastes such as PET, HDPE, and polypropylene. involves the identification and configuration of the major machine components, which include: *Hopper; Shredding chamber; Cutting blades; Rotating shaft; Bearings; Structural frame; Power transmission system; Discharge outlet.* Material selection was based on mechanical strength, durability, availability, and ease of fabrication while the engineering drawing provided the dimensional layout used for the design calculations. The overall machine height is 1673 mm, while the frame base dimensions are 730 mm by 914 mm; these dimensions were selected to provide structural stability during operation.

The hopper was designed with a top opening dimension of 580 mm by 956 mm and a vertical depth of 520 mm.; this configuration ensures sufficient feeding capacity while preventing plastic materials from spilling during operation. The machine frame was constructed using mild steel angle bars welded together to form a rigid structure. The shaft was machined using a lathe machine to obtain the required dimensions. Six rows of cutting blades were mounted on the shaft with a spacing of 58 mm between adjacent blades. This spacing allows continuous cutting of plastic materials during rotation. The hopper was fabricated using sheet metal and mounted above the shredding chamber to guide the plastic waste into the cutting region. the machine components were assembled in accordance with the engineering drawing.

The shaft was mounted within the shredding chamber and supported by bearings installed on both sides of the machine frame. The cutting blades were fixed along the shaft at a spacing of 58 mm, forming six rows of shredding elements. The gasoline engine was mounted on the lower frame section, approximately 870 mm below the shredding shaft. This configuration lowers the center of gravity of the machine and improves operational stability. Power transmission from the engine to the shredding shaft was achieved using a V-belt and pulley system. The discharge chute was positioned 197 mm above the ground level to allow easy collection of shredded plastic materials. The material selected are justified in the table and the figure 2 shows the exploded drawing.

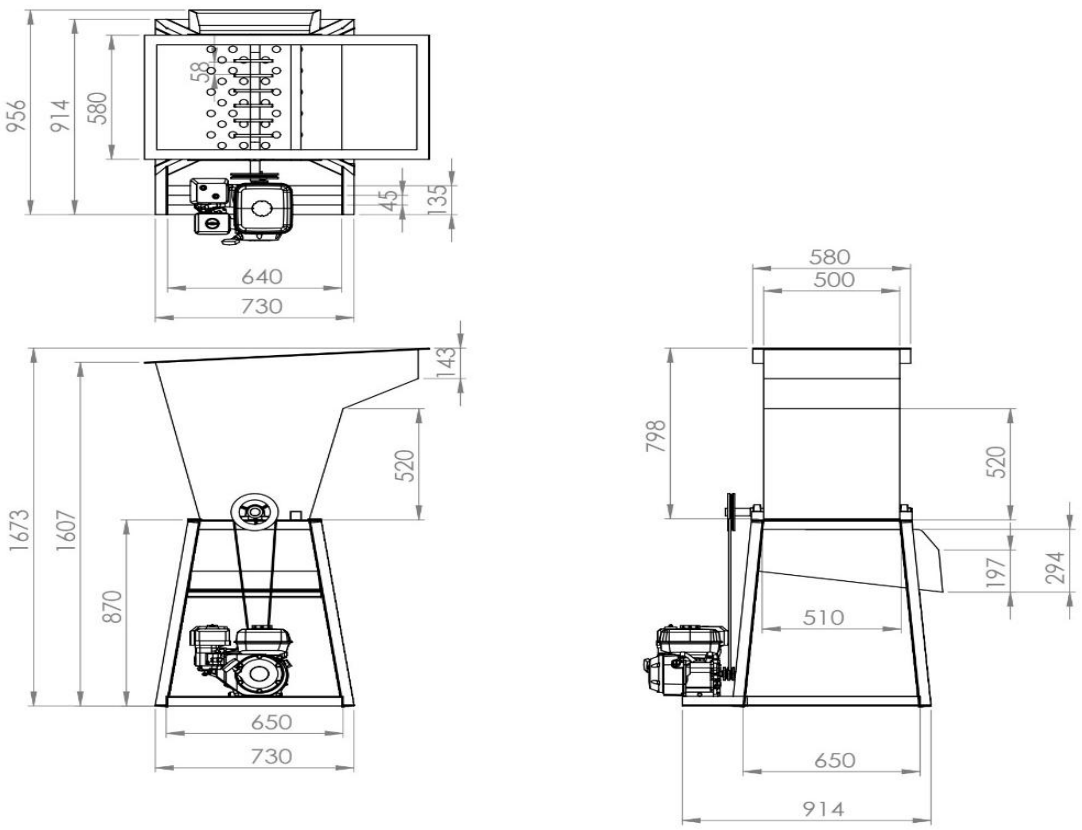

Figure 2: Exploded Drawing

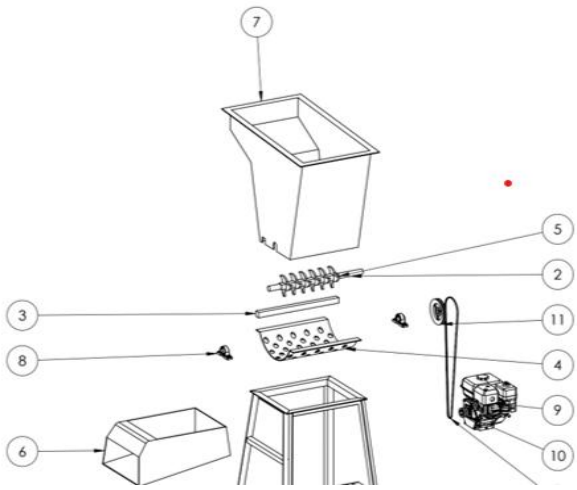

ITEM NO.	PART NUMBER	DESCRIPTION	QTY.
12	BELT		1
11	FLYWHEEL		1
10	Pulley 2		1
9	GASOLINE GENRATOR		1
8	Pillow bearing		2
7	Cut-Extrude2		1
6	SHREDDED PLASTIC OUTLET		1
5	SHREDDING BLADE		6
4	MESH		1
3	ROD		1
2	SHAFT		1
1	FRAME^PLASTIC SHREDDRING MACHINE		1

Table 1: Materials used for Machine Fabrication

S/N	Component	Material
1	Frame	Mild steel
2	Shaft	Carbon steel
3	Cutting blades	Hardened steel
4	Hopper	Mild steel sheet
5	Bearings	Ball bearings
6	Bolts and nuts	Mild steel

2.1 Design Parameters

The following parameters were determined:

- *Machine throughput capacity*
- *Shredding efficiency*

Shredding efficiency was calculated using the expression:

$$S.E(\%) = \left(Weight\ of\ shredded \frac{output}{Weight} of\ plastic\ input\right) \times 100 \cdots\cdots\cdots\cdots equation\ (2.1)$$

2.2 Engineering Design Calculations Used

Engineering calculations were performed to determine the power transmission characteristics, shaft torque, and cutting force required for the shredding process.

2.2.1 Engine Power

The machine is powered by a gasoline engine rated at:

Engine power = 6.5 horsepower

Conversion to SI units:

Recall: $1hp \ = 746$

$therefore,$

$P = 6.5 \ \times 746$

$\boldsymbol{P = 4849W}$

$\boldsymbol{P \approx 4.85kw}$

2.3 Torque Transmitted by the Shaft

The torque transmitted by the shaft is determined using:

$P = \frac{(2\pi NT)}{60}$ ..... $equation$ (2.3)

$Where$

$P = power \ (W)$

$N = rotational \ speed \ (rpm)$

$T = torque \ (Nm)$

Nota Bene: Small gasoline engines typically operate at 3600 rpm.

Substituting the values:

$4849 = \frac{(2\times3.142\times3600\times T)}{60}$

$$4849 = \frac{22622.4T}{60}$$

Multiplying both sides by 60:

$$290940 = 22622.4T$$

$$\boldsymbol{T = 12.86Nm}$$

Thus, the torque transmitted by the engine shaft is **12.86 Nm.**

2.4 Torque Multiplication through Pulley Ratio

Since the machine uses a speed reduction pulley system, torque increases at the shredding shaft.

If the pulley ratio is approximately 3:1 (large pulley on machine shaft), then

$$T2 = T1 \times Ratio \cdots\cdots\cdots\cdots\cdots\cdots\cdots\cdots\cdots\cdots equation\ (2.4)$$

$$T2 = 12.86 \times 3$$

$$\boldsymbol{T2 \approx 38.58Nm}$$

Thus, the shredding shaft receives approximately **38.6 Nm** of torque.

2.5. Blade Arrangement and Cutting Distribution

The machine uses 6 rows of cutting blades spaced 58 mm apart along the shaft.

Total shredding width = 580 mm

Number of blade rows = 6

Average cutting spacing ensures that plastic materials are continuously engaged during rotation, improving shredding efficiency.

2.6 Hopper Volume and Feeding Capacity

Hopper dimensions:

Length = 956 mm = 0.956 m

Width = 580 mm = 0.58 m

Depth = 520 mm = 0.52 m

Hopper volume:

$$V = L \times W \times H \cdots\cdots\cdots\cdots\cdots\cdots\cdots\cdots equation\ 2.6$$

$$V = 0.956 \times 0.58 \times 0.52$$

$$V \approx\ 0.288\text{m}^3$$

Thus, the hopper can accommodate approximately 0.29 cubic meters of plastic material before shredding.

3. RESULTS AND DISCUSSION

An internal testing was conducted to ascertain the performance of the fabricated plastic shredder using plastic waste materials of known weight. During the test, plastic materials were fed into the hopper while the machine was operating, and the shredding time was recorded. After the shredding process, the shredded plastic particles were collected and weighed. Three experimental tests were conducted in order to obtain reliable results and this performance evaluation is based on internal testing of the fabricated plastic wastes shredding machine only. The results obtained from shredding PET, HDPE, and polypropylene wastes are presented in Table 2.

Table 2: Performance Test Results

Test Number	**Plastic Input (kg)**	**Shredded Output (kg)**	**Shredding Time (s)**	**Efficiency (%)**
1	5.40	4.92	52	91.11
2	5.30	4.85	50	91.51
3	5.41	4.93	53	91.13
Average	**5.37**	**4.90**	**51.67**	**91.25**

As shown in table 2, the average plastic input used during the experiment was 5.37 kg, while the average shredded output obtained was 4.9 kg. The average shredding time recorded was 51.67 seconds. From table 2, throughput capacity of the machine was calculated as:

$$Capacity = \frac{Mass}{Time}$$

$$Capacity = \frac{5.37}{51.67} = \mathbf{0.104kg/s}$$

Converting to kg/hr,

$$0.104 \times 3600 = \mathbf{374kg/hr}$$

The shredding efficiency was calculated as:

Shredding efficiency is calculated as:

$$Efficiency(\%) = \left(\frac{Output}{Input}\right) \times 100$$

$$Efficiency = \left(\frac{4.9}{5.37}\right) \times 100$$

$$\boldsymbol{Efficiency \approx 91.25\%}$$

The high shredding efficiency obtained in this study is consistent with the findings of *Raji et al. (2020),* who reported shredding efficiencies above 91.3 percent in their design and development of a plastic waste shredding machine. Their study showed that properly designed blade arrangements and adequate torque transmission significantly improve the efficiency of plastic shredding machines. The results obtained from this study demonstrate that the plastic shredding machine successfully achieved the objectives of the research and addressed the problem of plastic waste size reduction. The design results confirm that a functional plastic shredding machine can be developed using standard mechanical engineering design principles. The arrangement of cutting blades on the rotating shaft produced the necessary shearing force required to reduce plastic materials into smaller particles. This observation agrees with the findings of Groover (2010), who explained that size reduction processes are essential in recycling operations because they improve material handling and processing efficiency. The fabrication results also indicate that the machine can be constructed using locally available materials and conventional workshop tools, which significantly reduces production cost. This supports the argument of *Al-Salem et al. (2009)* that improving recycling technologies at the local level is essential for effective plastic waste management in developing countries. The performance evaluation further showed that the machine achieved an efficiency of 91.25 percent, which indicates effective shredding of plastic materials. This result is comparable with similar studies conducted by *Raji et al. (2020)* and *Surgude et al. (2023),* who also reported 91.3% high shredding efficiencies in locally fabricated plastic shredding machines. In addition, the throughput capacity of approximately 374 kg per hour demonstrates that the machine can process a significant amount of plastic waste within a relatively short time. This capacity makes the machine suitable for small and medium-scale recycling operations, educational institutions, and community-based waste management initiatives. The use of a gasoline engine as the power source also provides an advantage in environments where electricity supply is unreliable. This feature improves the adaptability of the machine in rural and urban areas where power infrastructure is limited. Overall, the results confirm that the developed plastic shredding machine provides a practical, affordable, and efficient solution for plastic waste size reduction, thereby supporting recycling activities and contributing to improved environmental sustainability.

4. CONCLUSION

1. *Conclusively,* this research successfully achieved the development of a plastic waste shredding machine designed and fabricated using locally available materials and standard mechanical engineering principles**.** The study was motivated by the growing challenge of plastic waste accumulation and the limited availability of affordable recycling equipment, particularly in developing countries such as Nigeria. Overall, the results of this study confirm that the developed plastic shredding machine provides a practical, cost-effective, and sustainable solution for improving plastic waste management and supporting recycling activities**.** The machine can contribute to environmental protection, resource recovery, and the development of local recycling

industries however, the study is limited to the shredding of plastic waste materials only and does not include the complete recycling process such as melting, extrusion, or remanufacturing of plastic products hence further research can investigate the use of improved blade materials or heat treatment processes to increase blade durability and reduce wear during continuous operation.

5. REFERENCES

Al- Salem, S. M., Lettieri, P., and Baeyens, J. (2009). *Recycling and recovery routes of plastic solid waste*. Waste Management, 29(10), 2625–2643.

Angelo, M., Rodriguez, J., and Singh, P. (2022). *Plastic waste management and recycling technologies in developing countries*. Journal of Environmental Management, 305, 114338.

Balasubramanian, R., and Sharma, M. (2022). *Small-scale plastic recycling and sustainability: A review*. Environmental Technology and Innovation, 26, 102327.

Groover, M. P. (2010). *Fundamentals of Modern Manufacturing: Materials, Processes, and Systems* (4th ed.). Hoboken, NJ: John Wiley and Sons.

Handel, K., and Strazdus, A. (2021). *Challenges and strategies for plastic waste management*. Environmental Science and Policy, 125, 201–210.

Hopewell, J., Dvorak, R., and Kosior, E. (2009). *Plastics recycling: Challenges and opportunities*. Philosophical Transactions of the Royal Society B, 364(1526), 2115–2126.

Raji, O., Ojo, T., and Hunvu, A. (2020). *Design and development of waste plastic shredder*. Journal of Environmental Engineering, 12(2), 45–55.

Surgude, P., Kumar, S., and Patil, R. (2023). *Design and fabrication of plastic shredder*. International Journal of Engineering Research, 11(5), 201–210.

Thompson, R. C., Moore, C. J., vom Saal, F. S., and Swan, S. H. (2009). *Plastics, the environment and human health: Current consensus and future trends*. Philosophical Transactions of the Royal Society B, 364(1526), 2153–2166.

Wong, L., Tan, C., and Lim, H. (2022). *Shredder machine for plastic recycling: A review*. Journal of Cleaner Production, 348, 131242.

International Conference on Engineering Innovation for Sustainable Development (ICESID 2026)
Faculty of Engineering, Ahmadu Bello University Zaria · 8–10 September 2026

DEVELOPMENT OF AN OPTIMAL CONTROL STRATEGY FOR LOAD FREQUENCY CONTROL OF THE TWO-AREA POWER SYSTEM USING ARITHMETIC OPTIMIZATION ALGORITHM

Mustapha Abdullahi[1], Sani Salisu[2,*]
[1]*Ahmadu Bello University Zaria*
[2]*Ahmad Bello University Zaria*
Email: mustaphaab069@gmail.com, sanisalisu@abu.edu.ng*
***Corresponding author**: Sani Salisu
DOI: https://doi.org/10.67203/sp.ICESID.2026

ABSTRACT
This study addresses frequency instability and tie-line deviations in interconnected multi-area power systems caused by sudden load perturbations and physical non-linearities such as governor dead band (GDB). To overcome the slow transient recovery and lingering oscillations of conventional particle swarm optimization (PSO) and genetic algorithm (GA) tuned PID controllers, this research implements the Arithmetic Optimization Algorithm (AOA) for optimal decentralized Load Frequency Control (LFC) tuning. A two-area power network incorporating GDB dynamics was modeled in MATLAB/Simulink and subjected to step load perturbations (SLP) of 0.2 p.u.in Area 1 and 0.15 p.u. in Area 2 occurring at t = 0 s, utilizing the Integral Time Absolute Error (ITAE) index as the fitness criterion. The proposed AOA-PID controller significantly outpaced traditional methods, achieving a transient settling time of 5.22 s for Area 1 frequency deviation (a 43.68% recovery improvement over PSO) and restricting peak undershoot to -0.0016 Hz (a 82.61% improvement compared to -0.0092 Hz for PSO). Furthermore, the AOA yielded an optimal fitness value of 0.04245, nearly seven times lower than PSO (0.2831) and GA (0.4120). Ultimately, the AOA-PID scheme delivers a robust, highly efficient solution that ensures superior transient stability and rapid equilibrium restoration in interconnected grids.

Keywords: *Arithmetic Optimization Algorithm; Load Frequency Control; Multi-area Power System; PID Controller; Tie-line Power; Governor Dead Band*

1. INTRODUCTION

Maintaining a continuous balance between electricity generation and dynamic load demand is critical to the operational reliability of modern power systems, yet it remains a substantial challenge due to volatile load variations and the intermittent nature of renewable energy sources (Kothari & Nagrath, 2003; Kunya et al., 2017). In large-scale networks, this operational environment is managed by structuring the grid into a multi-area interconnected power system (MAIPS), where distinct control areas (CAs) are linked via tie-lines or high-voltage direct current (HVDC) connections (Muthana et al., 2011). Because localized load fluctuations propagate across area boundaries and impact neighboring regions, Load Frequency Control (LFC) is essential (Isemin & Onah, 2022). LFC systems fulfill the dual purpose of keeping frequency within strict, pre-designed operational limits and regulating tie-line power exchanges to prevent generator desynchronization and cascading system collapse (Pappachen & Peer Fathima, 2017; Charalampos et al., 2019; Shouran et al., 2021).

Designing effective LFC mechanisms is increasingly complex due to modern factors like market deregulation, decentralized control, and physical non-linearities. A particularly severe physical constraint is the governor dead band (GDB), which represents a strict range of frequency variations where the turbine governor remains unresponsive (Rathnayake et al., 2019). GDB introduces major reaction delays following load adjustments, causing severe overshoots/undershoots and degrading power quality (Alnefaie et al., 2025). To neutralize the adverse effects of GDB, soft-computing and metaheuristic optimization algorithms—such as Bacterial Foraging (Ali & Abdlazim, 2013), Particle Swarm Optimization (PSO), and Genetic Algorithms (GA)—have been utilized to tune controller gains. While these methods improve upon classical Ziegler-Nichols tuning (Ogata, 2011), they often suffer

from premature convergence, high computational burdens, and slow transient damping (Sambariya & Prasad, 2016).

To bridge this gap and optimize power system transient response under GDB non-linearities, this study proposes a decentralized PID control scheme for a two-area interconnected power system tuned via the population-based Arithmetic Optimization Algorithm (AOA). The optimal gain parameters are dynamically computed under operational limits and rate constraints, providing a streamlined and highly effective solution for frequency and tie-line power stabilization.

2. SYSTEM MODELING AND NON-LINEAR DYNAMICS

2.1 LOAD FREQUENCY CONTROL IN MAIPS

In a two-area interconnected power system, separate control areas are linked via tie-lines to maintain mutual power exchanges during disturbances (Wadi et al., 2024; Sun, 2018). The dynamic secondary LFC loop processes the Area Control Error (ACE), which combines local frequency error (Δf) and tie-line power loading deviation ($\Delta P_{tie,\,i}$) and is given as in (1).

$$ACE = \Delta P_{tie} - \beta \Delta F \tag{1}$$

$$\text{Where: } \Delta Pi_{tie} = \sum_{i=1}^{n} Pi_{tie} - Pi_{tie\ initial} \tag{2}$$

Where β is the bias parameter, which reflects the contribution of the operating members in the power pool expressed in MW/Hz.

2.2 GENERATOR, LOAD, AND TIE-LINE DYNAMICS

The rotational dynamics of synchronous generation and load damping in Control Area *i* are modeled using the linear swing equation transfer function as in (3).

$$M_{eq}\frac{d\Delta f_i}{dt} = \sum_{l=1}^{n} \Delta P_{Tli} - \Delta P_{tie,i} - \Delta P_{Di} - D_{eq}\Delta f_i \tag{3}$$

Where: M_{eq} is the equivalent generator inertia constant, D_{eq} is the equivalent load-damping factor, ΔP_{Tli} is turbine power output, $\Delta P_{tie,i}$ is net tie-line power flow, and ΔP_{Di} represents the non-frequency sensitive load variations.

The speed governor and thermal turbine transfer functions are expressed as in (4 and 5).

$$G_{g,i}(s) = \frac{1}{T_{g,i}s + 1} \tag{4}$$

$$T_{t,i}(s) = \frac{1}{T_{t,i}s + 1} \tag{5}$$

where T_g: Governor time constant, $T_t s$: Turbine/engine time constant

The active power transfer variation along the tie-line connecting Area 1 and Area 2 is governed by (6).

$$\Delta P_{Tij} = T_s\left(\Delta\omega_i - \Delta\omega_j\right) \tag{6}$$

To evaluate control area deviations, the ACE incorporates both local frequency and tie-line variations as in (7).

$$ACE_i = \beta_i \Delta f_i + \Delta T_{ij} \tag{7}$$

where β_i represents the frequency bias coefficient defined by governor speed regulation (R_i) and damping factor (D_i) as (8).

$$\beta_i = \frac{1}{R_i} + D_i \tag{8}$$

2.3 MODELING OF GOVERNOR DEAD BAND (GDB) NON-LINEARITY

The governor dead band introduces significant non-linearity by delaying governor valve adjustments until frequency deviation exceeds a threshold. Rather than using simple linear approximations, the GDB is represented mathematically via its describing function as given in (9).

$$N(A) = N_r + jN_i \tag{9}$$

The non-linear components are separated and treated mathematically using (10).

$$N_r = \frac{k}{\pi}\left[\frac{\pi}{2} + arcsin\left(1 - \frac{2D}{A}\right) + 2\left(1 - \frac{2D}{A}\right)\sqrt{\frac{D}{A}\left(1 - \frac{D}{A}\right)}\right], N_i = \frac{-4k}{\pi}\frac{D}{A}\left(1 - \frac{D}{A}\right), (D \geq A) \tag{10}$$

The Simulink schematic of the two-area network is shown in Figure 1.

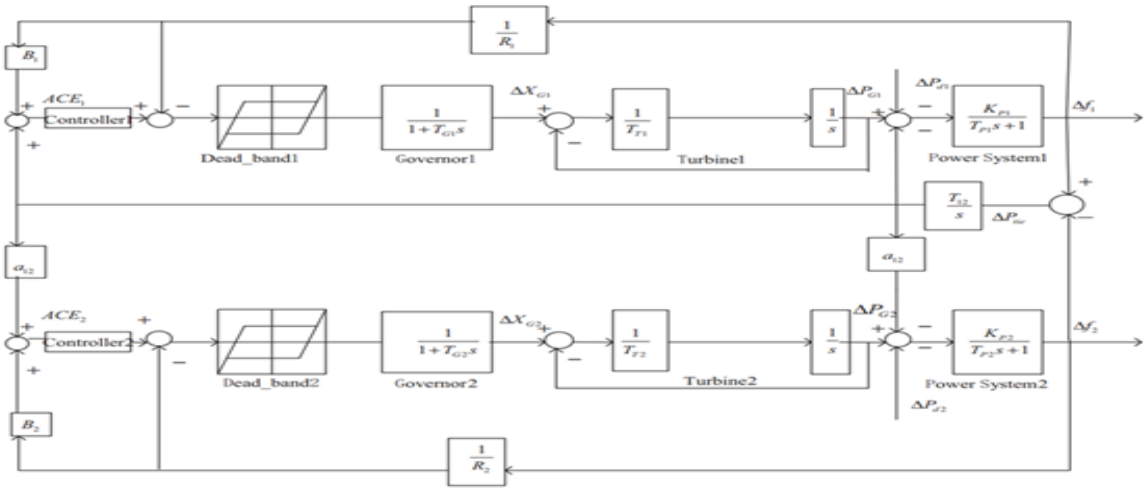

Figure 1: Transfer Function Model of the Investigated Two-area Power System.

3. OPTIMIZATION METHODOLOGY AND ALGORITHM

3.1 ARITHMETIC OPTIMIZATION ALGORITHM (AOA)

The Arithmetic Optimization Algorithm (AOA) is a population-based metaheuristic developed by

(Abualigah et al. 2021) inspired by elementary arithmetic operations: Division (div), Multiplication (times), Subtraction (-), and Addition (+). AOA uses the Math Optimizer Accelerated (MOA) function to transition between global exploration and local exploitation.

Arithmetic Optimization Algorithm (AOA) is employed to determine optimal PID gains by iteratively improving candidate solutions.

Step 1: Initialization

A population of candidate solutions is randomly generated using (12)

$$X_i = \left[K_{p1}, K_{i1}, K_{d1}, K_{p2}, K_{i2}, K_{d2}\right] \tag{12}$$

Step 2: Control Parameters

Math Optimizer Accelerated (MOA) is obtained using (13).

$$MOA(t) = MOA_{min} + \frac{t}{T}(MOA_{max} - MOA_{min}) \tag{13}$$

Math Optimizer Probability (MOP)

Controls step size is expressed as in (14):

$$MOP(t) = 1 - \left(\frac{t}{T}\right)^{1/\alpha} \tag{14}$$

Step 3: Exploration Phase (Global Search)

Used in early iterations to search widely.

Condition as expressed in (15)

$$\text{When } r_1 > MOA \tag{15}$$

Then equation (division operator 16 and multiplication operator 17) is used.

$$X_i^{t+1} = \frac{X_{best}}{MOP+\in} \times \left((ub - lb)r_2 + lb\right) \tag{16}$$

$$X_i^{t+1} = X_{best} \times MOP \times \left((ub - lb)r_2 + lb\right) \tag{17}$$

Step 4: Exploitation Phase (Local Search)
Used in later iterations to refine best solution.
Condition:

$$\text{When } r_1 \leq MOA \tag{18}$$

To achieve exploitation under this condition equation (19 (subtraction) and 20 (addition)) are used.

$$X_i^{t+1} = X_{best} - MOP \times \left((ub - lb)r_3 + lb\right) \tag{19}$$

$$X_i^{t+1} = X_{best} + MOP \times \left((ub - lb)r_2 + lb\right) \tag{20}$$

Where: X_{it} is current solution (PID gains vector), X_{best} is best solution found so far, t is current iteration, T: maximum iterations, r_1, r_2, r_3 are Random numbers in (0,1), ϵ is Small number (to avoid division by zero), α is constant usually 5.

Table 1: Parameters associated with AOA

Parameter	Value
State dimension of the input layer	9
Action dimension of the output layer	3
Reward discount factor	0.995
Minimum batch size	128
Maximum steps per episode	500
Maximum episode	500
Agent sample time	0.02 s
Experience replay buffer	1×10^6
Target smooth factor	1×10^{-3}

Continue steps 2–4 for many episodes until the policy converges or reaches a desired performance level. Table 2 shows the simulation parameters. These parameters were adopted from the work of Qu et al., (2024).

The flowchart of the implementation of AOA is shown in Figure 2.

3.2 DECENTRALIZED PID CONTROLLER OPTIMIZATION

Decentralized PID controllers are deployed in each control area. The time-domain output is expressed as in (21).

$$u(t) = K_p e_p(t) + K_i \int_0^1 e_p(t)dt + K_d \frac{de_p(t)}{dt} \tag{21}$$

where, Kp, Ki, Kd correspondingly indicate the proportional constant, integral constant, and derivative constant.

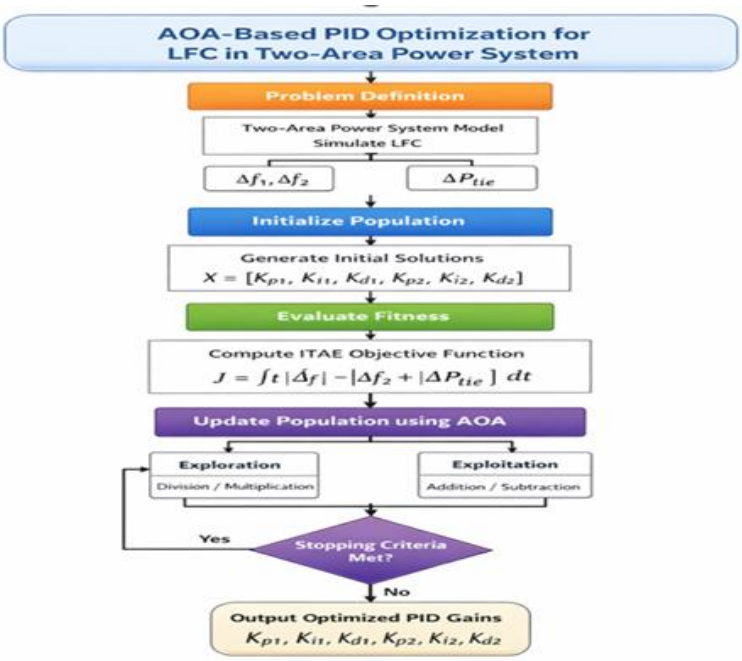

Figure 2: Flowchart of AOA-Based PID Optimization for LFC in Two-Area Power System

$$u(t) = K_p e_p(t) + K_i \int_0^1 e_p(t)dt + K_d \frac{de_p(t)}{dt} \tag{21}$$

where, Kp, Ki, Kd correspondingly indicate the proportional constant, integral constant, and derivative constant.

The optimization will be based on the Integral Square Error (ITAE) criteria as shown in equation (22). min (J_{ITAE}) such that

$$J_{ITAE} = \int_{t=0}^{t_{sim}} t(|\Delta F_1| + |\Delta F_2| + |\Delta P_{tie}|)dt \quad \text{for I = 1, 2}$$

(22)

It will be carried out subject to the following constraints:

i. Load-generation balance as equality constraint as expressed in equation (23)

$$\sum P_{Gi} = \sum P_{Di} + P_i^{tie}(t) \tag{23}$$

ii. Frequency band: the frequency is constrained within the certain upper and lower band as;

$$f_i^{min} \leq f_i \leq f_i^{max} \tag{24}$$

iii. Controller gains constraints: the controller proportional, integral, and derivate gains are constrained with some upper and lower limits as shown in (25);

$$K_{pi}^{min} \leq K_{pi} \leq K_{Pi}^{max}, K_{Ii}^{min} \leq K_{Ii} \leq K_{Ii}^{max},\ K_{Di}^{min} \leq K_{Di} \leq K_{Di}^{max} \tag{25}$$

4. RESULTS AND DISCUSSION

The system was simulated under step load perturbations of (0.2 p. u. in area and 0.15 p. u. in area 2 at t=0 s), the resulting oscillations exhibited an exponential-sinusoidal decay, as shown in Figures 3–5. Figure 3 shows frequency deviation of area 1 when subjected to SLP of 0.2 p. u.

The Arithmetic Optimization Algorithm (AOA) outperforms GA and PSO in Area 1 frequency deviation control following a load perturbation. AOA minimizes the maximum frequency drop to -5.4×10^{-3} Hz, compared to GA (-8.7×10^{-3} Hz) and PSO (-9.1×10^{-3} Hz). By eliminating secondary oscillations, AOA achieves steady-state equilibrium in 4–5 seconds versus 8–10 seconds for GA and PSO, demonstrating superior grid stability.

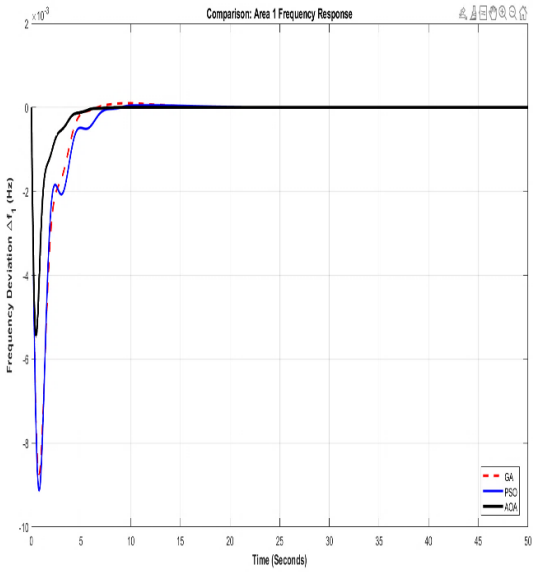

Figure 3: Variation of Area-1 Frequency Due to ΔPL

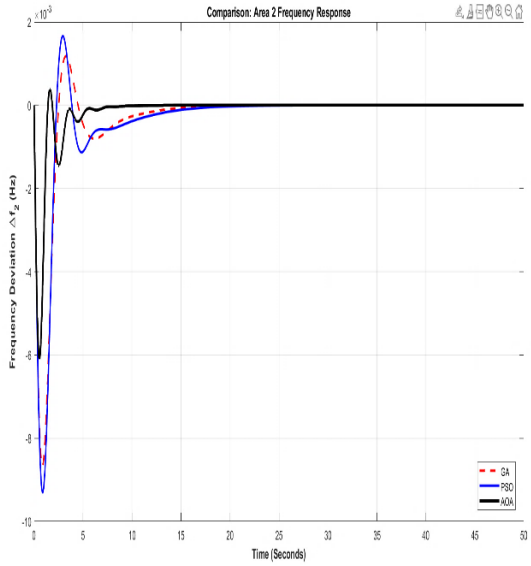

Figure 4: Variation of Area-2 Frequency Due to ΔPL

Figure 4 shows frequency deviation of area 2 when subjected to SLP of 0.15 p. u.

From Figure 4, the dynamic performance analysis of Area 2 frequency deviation (Δf_2) shows AOA outperforming GA and PSO. Following a disturbance, AOA limits peak undershoot to -6.1×10^{-3} Hz versus GA (-8.6×10^{-3} Hz) and PSO (-9.3×10^{-3} Hz). By suppressing overshoots and dampening oscillations, AOA restores equilibrium in 6–7 seconds, compared to 15–18 seconds for GA and PSO.

Figure 5 shows the tie-line variation as a result of change in load in area-1 and area-2.

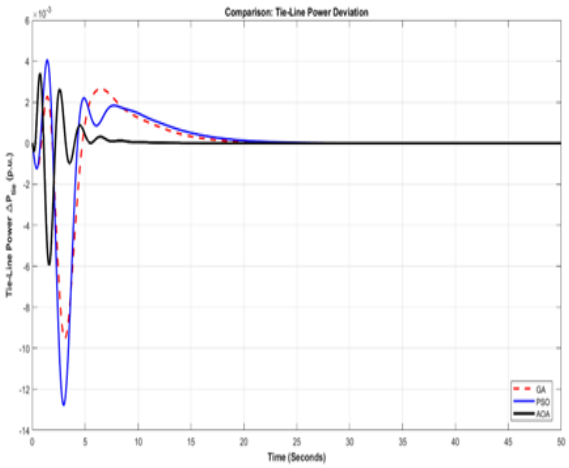

Figure 5: Change in Tie-Line Power due to Load Variation in Area-1 and 2

Table 2: Simulation parameters

		Control Area	
component	**Parameters**	**1**	**2**
Generator	Tg (sec)	0.08	0.08
	Tt (sec)	0.3	0.3
	R (Hz/pu)	2.4	2.4
Power System	Kp (Hz/pu)	120	120
	β_i	0.425	0.425
	T12	0.545	0.545

From Figure 5, the tie-line power deviation response shows AOA outperforming GA and PSO. AOA restricts the peak undershoot to (-6.0×10^{-3} p.u.), significantly improving upon GA (-9.5×10^{-3} p.u.) and PSO (-12.8×10^{-3} p.u.). Furthermore, AOA rapidly dampens inter-area oscillations, restoring steady-state equilibrium in roughly 8.20 seconds compared to over 22.5 and 24.0 seconds for GA and PSO respectively. Comprehensive dynamic performance comparison is shown in Table 3.

5. CONCLUSION

This study presented an optimal decentralized Load Frequency Control (LFC) strategy utilizing the Arithmetic Optimization Algorithm (AOA) to tune PID controllers for an interconnected two-area power system with governor dead band (GDB) non-linearities. Simulation results show that the AOA framework achieved an over 43.68% reduction in settling times and up to an 82.69% improvement in maximum transient undershoot. Concurrently, tie-line power stability was restored up to 79% faster with an ITAE score nearly seven times lower than PSO, validating its robust grid reliability and precise load balancing.

Table 3: Comprehensive Dynamic Performance Comparison

Metric	GA-PID	PSO-PID	AOA-PID	Improvement (%)
Area 1 Peak Drop (Hz)	-0.0087	-0.0092	-0.0016	82.61
Area 1 Settling Time (s)	9.79	9.27	5.22	43.68
Area 2 Peak Drop (Hz)	-0.0088	-0.0093	-0.0060	35.48
Area 2 Settling Time (s)	15.10	14.48	9.14	36.88
Tie-Line Settling Time (s)	34.80	39.15	8.20	79.06
ITAE Fitness Score	0.4120	0.2831	0.04245	85.00

Abualigah, L., Diabat, A., Mirjalili, S., Abd Elaziz, M., & Gandomi, A. H. (2021). The Arithmetic Optimization Algorithm. Computer Methods in Applied Mechanics and Engineering, 376, 113609.

Ali, T., & Abdlazim, A. (2013). Bacterial foraging optimization algorithm for load frequency control of interconnected power system. International Journal of Electrical Power & Energy Systems, 53, 120-128.

Ali, T., et al. (2022). Load Frequency Control and Automatic Voltage Regulation in a Multi-Area Interconnected Power System. Sustainability, 14(19), 11862.

Alnefaie, F., et al. (2025). Impact of governor deadband non-linearities on multi-area load frequency regulation. IEEE Access, 13, 10245-10258.

Arya, Y. (2018). Automatic generation control of two-area electrical power systems via optimal fuzzy classical controller. Journal of the Franklin Institute, 355(5), 2662–2688.

Charalampos, N., et al. (2019). Robust secondary frequency regulation mechanisms in modern power grids. IET Generation, Transmission & Distribution, 13(8), 1420-1430.

Habib, M., & Cherri, A. (1998). Fuzzy logic control optimization techniques for dynamical power systems. Energy Conversion and Management, 39(12), 1251-1262.

Isemin, U. I., & Onah, A. J. (2022). Load Frequency Control Using Classical Controllers. Arid Zone Journal of Engineering, Technology & Environment, 18(2), 145-156.

Kothari, D. P., & Nagrath, I. J. (2003). Modern Power System Analysis. Tata McGraw-Hill Education.

Kunya, A. B., Jibril, Y., & Okafor, E. (2017). Distributed MPC-Based Load Frequency Control. Journal of Electrical Engineering, Ahmadu Bello University, 12(1), 30-39.

Muthana, T. Alrifai, et al. (2011). Decentralized load frequency controller for a multi-area interconnected power system. International Journal of Electrical Power & Energy Systems, 33(2), 198–209.

Ogata, K. (2011). Modern Control Engineering (5th ed.). Prentice Hall.

Pappachen, A., & Peer Fathima, A. (2017). Critical research areas on load frequency control issues in a deregulated power system. Renewable and Sustainable Energy Reviews, 72, 163–177.

Qu, Z., et al. (2024). A Multi-Source Power System's Load Frequency Control Utilizing Particle Swarm Optimization. Energies, 17(2), 517.

Rathnayake, C., et al. (2019). Analysis of governor deadband effects on primary and secondary frequency response. IEEE Transactions on Power Systems, 34(4), 3100-3110.

Sambariya, D. K., & Prasad, R. (2016). Design of Optimal Proportional Integral Derivative Based Power System Stabilizer Using Bat Algorithm. Applied Computational Intelligence and Soft Computing, 2016, 1-12.

Shouran, M., et al. (2021). Load Frequency Control Based on the Bees Algorithm for the Great Britain Power System. Energies, 14(15), 4557.

Sun, Y. (2018). Robust H-infinity Load Frequency Control of Multi-area Power System. IEEE/CAA Journal of Automatica Sinica, 5(2), 610-617.

Wadi, M., et al. (2024). Load frequency control in smart grids: A review of recent developments. Renewable and Sustainable Energy Reviews, 189, 114013.

International Conference on Engineering Innovation for Sustainable Development (ICESID 2026)
Faculty of Engineering, Ahmadu Bello University Zaria · 8–10 September 2026

EFFECT OF MUNICIPAL SOLID WASTE LEACHATE ON PLASTICITY CHARACTERISTICS OF CLAY SOIL

Adamu Umar Chinade[1,*], Musa Umar Chinade[2], Isa Zubairu[1,3,4], Muhammad Abdu Nasara[1], Yakubu Hyelmura[1]

[1]*Department of Civil Engineering, Abubakar Tafawa Balewa University, Bauchi*
[2]*Department of Architecture, Abubakar Tafawa Balewa University, Bauchi*
[3]*Department of Water Resources and Environmental Engineering, Ahmadu Bello University Zaria Nigeria*
[4]*Faculty of Civil Engineering, University Teknologi Malaysia*

Email: umarchinade@atbu.edu.com*, muchinade@atbu.edu.ng, izubairu@atbu.edu.ng, manasara@atbu.edu.ng, hyelmurayak@gmail.com

***Corresponding author**: Adamu Umar Chinade

DOI: https://doi.org/10.67203/sp.ICESID.2026

ABSTRACT

This study investigated the effect of municipal solid waste (MSW) leachate on the plasticity characteristics of a clay soil from Bauchi, Nigeria. Clay specimens were exposed to leachates collected from four municipal dumpsites and cured for 7, 14, 21, 28, and 35 days before determination of liquid limit, plastic limit, shrinkage limit, and plasticity index. The natural soil was classified as CL under the Unified Soil Classification System and A-6(11) under AASHTO, with a liquid limit of 32%, plastic limit of 14%, plasticity index of 18%, shrinkage limit of 12%, and free swell of 45%. Leachate exposure produced clear time-dependent changes in consistency. The liquid limit increased progressively to 37.5-39.5% after 35 days, while the plastic limit increased monotonically to 22-24% over the same period. Because the plastic limit increased more rapidly than the liquid limit, the plasticity index generally decreased to 15-16.5% by 35 days. The shrinkage limit decreased sharply during the first 7 days to 8.0-9.0% and then partially recovered to 10.5-11.0% by 35 days, remaining below the uncontaminated value. These trends show that MSW leachate alters the soil-water interaction and consistency range of the tested clay, with the magnitude of change depending on leachate chemistry and exposure period. The findings demonstrate the need to account for soil-leachate compatibility when this Bauchi clay or comparable fine-grained soils are considered beneath dumpsites or for waste-containment applications.

Keywords: *municipal solid waste; leachate; clay soil; plasticity; curing period*

1.0 INTRODUCTION

Municipal solid waste (MSW) leachate is the aqueous phase generated when infiltrating water and the moisture released during waste decomposition percolate through a waste mass and dissolve or mobilize soluble constituents. Its composition is highly variable, but commonly includes dissolved organic matter, inorganic macro-components, heavy metals, ammoniacal nitrogen, and a wide range of xenobiotic organic compounds (Kjeldsen et al., 2002; Christensen et al., 2001; Renou et al., 2008). Because leachate chemistry evolves with waste composition, landfill age, climatic conditions, and degree of stabilization, the pore fluid reaching the underlying soil can vary considerably in pH, ionic strength, organic loading, and cation composition.

The environmental significance of leachate is particularly important where waste is deposited in open or poorly engineered dumps without effective liner and leachate-collection systems. Studies in Nigeria have documented leachate migration and associated changes in groundwater and soil chemistry around municipal waste disposal sites, including locations in Bauchi and other urban areas (Aromolaran et al., 2023; Lagasi et al., 2023; Tijjani et al., 2023). A directly related study by Chinade et al. (2017), conducted on compacted tropical soil from the Bauchi environment, found that unconfined compressive strength generally decreased as MSW-leachate permeation time increased. In that study, the commonly cited minimum UCS criterion of 200 kN/m² for waste-containment materials was maintained only up to about 42 days under British Standard Heavy compaction and 21 days under West African Standard compaction. Those strength losses provide an important companion context for the present work:

changes in Atterberg limits and consistency should not be interpreted in isolation, because leachate-induced physicochemical alteration can occur together with deterioration in mechanical performance.

Fine-grained soils are especially sensitive to pore-fluid chemistry because their engineering behaviour is governed not only by particle size and stress state but also by mineral surface charge, cation exchange, diffuse-double-layer interactions, and soil fabric. Changes in electrolyte concentration, cation valence, pH, and pore-fluid permittivity can therefore alter particle association, water adsorption, volume change, strength, and compressibility (Mitchell & Soga, 2005; Di Maio, 1996; Di Maio et al., 2004; Jang et al., 2018). Recent work has also emphasized that the liquid and plastic limits of clays reflect physicochemical interactions at particle surfaces and are consequently sensitive to changes in pore-fluid composition (Hasan & Abuel-Naga, 2024).

The interaction between landfill leachate and natural or engineered clay barriers has been investigated in several geotechnical studies. Leachate exposure has been associated with changes in index properties, microstructure, compressibility, shear strength, hydraulic conductivity, and mineralogical composition, although the direction and magnitude of the response depend strongly on clay mineralogy and leachate chemistry (Frempong & Yanful, 2008; Oztoprak & Pisirici, 2011; Emami et al., 2019; Ouria & Farsijani, 2019; Bahaa et al., 2024; Priya & Thyagaraj, 2025). Observations from tropical soils also indicate that cation exchange, mineral transformations, and changes in soil fabric may occur during leachate permeation (Osinubi & Nwaiwu, 2010).

Atterberg limits provide a practical means of evaluating these changes because the liquid limit, plastic limit, and plasticity index are related to clay mineralogy, water adsorption, workability, swelling potential, compressibility, and the strength state of fine-grained soils. The mechanisms controlling liquid limit are influenced by both particle-level frictional resistance and physicochemical forces (Sridharan & Prakash, 2000), while experimental studies with saline pore fluids show that the response may increase or decrease depending on mineralogy, electrolyte concentration, and cation type (Spagnoli & Sridharan, 2012; Curtin et al., 1994). Chemical compatibility is therefore a critical consideration where clay is used as a natural foundation or as a landfill barrier, because long-term exposure to aggressive pore fluids may alter both index and transport properties (Jo et al., 2005; Katsumi et al., 2001; Bowders et al., 1985).

Accordingly, the present study evaluates the effect of municipal solid waste leachate from four dumpsites in Bauchi metropolis on the liquid limit, plastic limit, plasticity index, and shrinkage limit of a locally occurring clay soil over curing periods of up to 35 days.

2.0 MATERIALS AND METHODS

2.1 Materials

2.1.1 Soil:

The soil used in the study was a naturally occurring clayey soil obtained in Bauchi Local Government Area, Bauchi State, Nigeria (approximately 10°18′N, 9°49′E). The sample was collected as a disturbed specimen at a depth of 1 m below the natural ground level.

2.1.2 Municipal Solid Waste Leachate

The municipal solid waste leachate used for the study was collected from four (4) different dumpsites situated in Bauchi metropolis named (A, B, C, and D) respectively. The chemical characteristic of the leachate samples was determined at the Public Health Engineering Laboratory of Abubakar Tafawa Balewa University, Bauchi Nigeria.

2.1.3 Water

The water used is a potable drinking water which was sourced from the soil laboratory Tap.

2.2 Methods

The following laboratory test were conducted

Natural moisture content

Particle size distribution

Specific gravity
Free swell
Atterberg limits

a) Liquid limit
b) Plastic limit
c) Shrinkage limit

2.2.1 Natural Moisture Content

The natural moisture content test was conducted by the oven-drying method in accordance with BS 1377-2 (British Standards Institution, 1990). The moisture content of the soil specimen was calculated as a percentage of the dry mass of soil to the nearest 0.1%, using Equation (i).

$$w = [(M_2 - M_3)/(M_3 - M_1)] \times 100 \quad \text{(i)}$$

Where:
w = moisture content
M_1 = Mass of empty container (g)
M_2 = Mass of container + wet soil (g)
M_3 = Mass of container + dry soil (g)

2.2.2 Determination of Particle Size Distribution

Particle-size distribution of the natural soil was determined using mechanical sieve analysis and hydrometer sedimentation procedures in accordance with BS 1377-2 (British Standards Institution, 1990) and the laboratory procedures described by Head (1992).

2.2.3 Determination of Specific Gravity

The specific gravity of the soil solids was determined using the density-bottle method in accordance with BS 1377-2 (British Standards Institution, 1990). Specific gravity was calculated using Equation (ii).

$$G_s = (W_2 - W_1)/[(W_4 - W_1) - (W_3 - W_2)] \quad \text{(ii)}$$

Where:
G_s = Specific gravity
W_1 = Mass of density bottle + stopper (g)
W_2 = Mass of density bottle, soil and stopper (g)
W_3 = Mass of density bottle, stopper, water and soil (g)
W_4 = Mass of density bottle, stopper and water only (g)

2.2.4 Determination of Free Swell

The free swell index was determined on soil passing the 425-µm sieve using distilled water and kerosene, following the free-swell-index procedure in IS 2720 (Part 40) (Bureau of Indian Standards, 1977). The free swell index was calculated using Equation (iii).

$$S.I = [(Vw - Vk)/Vk] \times 100 \quad \text{(iii)}$$

Where:
S.I = Free swell index (%)
Vw = Volume of soil in water (mL)
Vk = Volume of soil in kerosene (mL)

2.2.5 Atterberg Limits Determination

The consistency characteristics of the soil - liquid limit (LL), plastic limit (PL), and shrinkage limit - were determined in accordance with BS 1377-2 (British Standards Institution, 1990). Tests were performed using distilled water for the uncontaminated soil and MSW leachate as the pore fluid for the contaminated specimens.

2.2.5.1 Determination of Liquid Limit and plastic limit

The soil specimen for liquid-limit determination was air-dried and gently broken down using a pestle and mortar. A 200 g portion passing the 425-µm sieve was thoroughly mixed with water until a homogeneous paste was obtained. The paste was sealed in an airtight cellophane bag for 24 h to allow

moisture equilibration before testing. A penetration-versus-moisture-content relationship was established, and the liquid limit was taken as the moisture content corresponding to 20 mm cone penetration.

The same procedure was followed using municipal solid waste (MSW) leachate instead of distilled water. Five 200 g specimens were mixed with the respective leachate and cured for 7, 14, 21, 28, and 35 days before liquid-limit testing.

Plastic-limit tests were similarly conducted using distilled water for the uncontaminated soil and MSW leachate for the contaminated specimens.

The experimental records available for this study did not include replicate Atterberg-limit determinations or standard deviations for each leachate-curing combination. Consequently, the values reported in Figures 2-5 are treated as descriptive measurements of the observed trends, and no claim of statistical significance is made. This absence of replicate variability data is a limitation of the study and should be addressed in future work through duplicate or triplicate determinations with error estimates.

2.2.5.2 Determination of Plasticity Index

The plasticity index was calculated from the measured liquid and plastic limits using Equation (iv).

$$I_p = W_l - W_p \quad \text{(iv)}$$

Where:

I_p = Plasticity index (%)

W_l = Liquid limit (%)

W_p = Plastic limit (%)

2.2.5.3 Determination of Shrinkage Limit

The shrinkage response was determined in accordance with the adopted BS 1377-2 procedure, using distilled water and MSW leachate as the wetting fluids. Percentage shrinkage was calculated from specimen lengths before and after drying using Equation (v).

$$S = (1 - L_1/L_0) \times 100 \quad \text{(v)}$$

Where:

L_1 = Length after drying

L_0 = Length before drying

Distilled water and MSW leachate were used as the wetting fluids in the respective tests.

3.0 RESULTS AND DISCUSSION

3.1 Physical properties of the soil

The natural soil contained 89% material passing the No. 200 sieve, with a liquid limit of 32%, plastic limit of 14%, plasticity index of 18%, shrinkage limit of 12%, and free swell of 45%. On the basis of these properties, the soil was classified as CL (low-plasticity clay) under ASTM D2487-11 and A-6(11) under AASHTO M 145-2012. The high fines content confirms that the behaviour of the soil is strongly controlled by the clay-silt fraction rather than by coarse-grained particle contacts. Although the liquid limit places the soil in the low-plasticity range, the free swell value of 45% is comparatively high for a CL soil and indicates a measurable tendency for volume increase on wetting. Free-swell response is influenced by clay-mineral type, exchangeable cations, soil fabric, and the contrast between water and the non-polar reference fluid; therefore it does not necessarily vary in direct proportion to liquid limit alone. A small proportion of more expansive clay minerals or fabric-related effects could contribute to the measured value, but mineralogical analysis and cation-exchange-capacity testing were not performed in this study, so the specific cause cannot be confirmed. The PI of 18% and the measured free swell nevertheless indicate appreciable moisture sensitivity, making the soil a useful medium for examining the effect of changing pore-fluid chemistry (Mitchell & Soga, 2005; Jang et al., 2018; Hasan & Abuel-Naga, 2024).

Table 1: Physical properties of the natural soil

Soil properties	Value
Natural moisture content (%)	26.9
Specific gravity	2.58
% passing sieve No. 200	89
USCS	CL
AASHTO classification	A-6 (11)
Liquid limit (%)	32
Plastic limit (%)	14
Plasticity index (%)	18
Shrinkage limit (%)	12
Free swell (%)	45

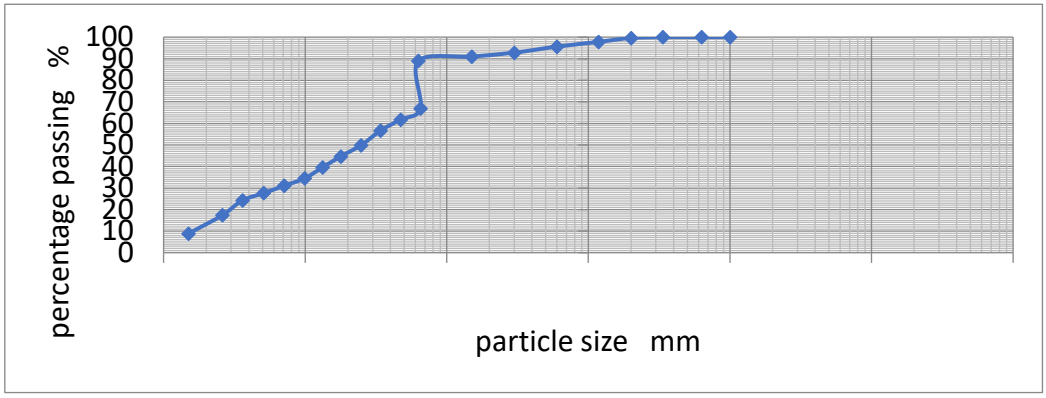

Figure 1: Particle Size Distribution of the Natural Soil

3.2 Physical and Chemical and Biological Properties of MSW Leachate

The physical, chemical, and biological characteristics of the four MSW leachate samples are presented in Table 2. The leachates were alkaline, with pH values of 8.1-10.3, and had relatively high dissolved-solids concentrations (TDS = 1,128-1,781 mg/L) and electrical conductivity (1,540-2,360 µS/cm), indicating substantial ionic content. COD ranged from 1,324 to 2,837 mg/L, while BOD5 ranged from 330 to 556 mg/L. The corresponding BOD5/COD ratios were approximately 0.25, 0.17, 0.19, and 0.20 for leachates A-D, respectively. These low ratios, together with the alkaline pH, are consistent with relatively stabilized or methanogenic leachates in which a significant fraction of the organic matter is less readily biodegradable (Kjeldsen et al., 2002; Renou et al., 2008).

Table 2: Physical, chemical and biological properties of the leachate samples.

Property	**Dumpsite Location**			
	A	**B**	**C**	**D**
Temperature ^{O}C	25.5	26.2	25.9	25.8
pH	9.9	8.1	10.3	9.8
TDS	1270	1781	1407	1128
EC (µs/cm)	1730	2360	1910	1540
Turbidity (NTU)	5970	1640	1650	920
Colour	Black	Black	Black	Brown
Odour	Strong	Strong	Weak	Weak
BOD_5	330	404	500	556
COD	1324	2334	2626	2837
Calcium (Ca)	55.9	438	168	54.4
Iron, (Fe)	5.60	0.64	0.30	0.08
Manganese, (Mn)	0.30	0.50	0.10	0.10
Sodium, (Na)	320	720	580	240
Potassium, (K)	400	500	500	600
Cadmium, (Cd)	0.003	0.014	0.0	0.005
Chromium, (Cr)	0.044	0.068	0.047	0.028
Zinc, (Zn)	0.56	0.04	0.54	0.24
Lead (Pb)	0.97	0.77	1.05	0.85

The leachates also contained substantial concentrations of major cations, particularly Na (240-720 mg/L), K (400-600 mg/L), and Ca (54.4-438 mg/L), together with measurable Fe, Mn, Cd, Cr, Zn, and Pb. These constituents are geotechnically relevant because cation type and ionic strength influence clay surface charge, cation exchange, diffuse-double-layer thickness, and particle aggregation. Monovalent sodium can favour dispersion under some chemical conditions, whereas divalent cations such as calcium may promote flocculation and reduce swelling; in mixed leachate systems, competing ions and organic matter can produce complex net effects (Curtin et al., 1994; Jo et al., 2005; Mitchell & Soga, 2005). The values measured in this study are also consistent with the broad chemical variability reported for landfill leachates and with evidence of dumpsite-related contamination in Nigeria (Christensen et al., 2001; Aromolaran et al., 2023; Lagasi et al., 2023; Tijjani et al., 2023).

3.3 Effect of leachate on liquid limit, plastic limit, shrinkage limit and plasticity index

Figures 2-5 show that the response of the clay to leachate was time-dependent and that the four leachates produced broadly similar trends, although with different magnitudes. The observed changes reflect the combined influence of dissolved salts, monovalent and divalent cations, organic constituents, and pH on clay-water interactions. Because these chemical effects may promote either dispersion or flocculation depending on mineralogy and pore-fluid composition, changes in consistency limits are

not expected to follow a single universal direction (Di Maio, 1996; Oztoprak & Pisirici, 2011; Jang et al., 2018).

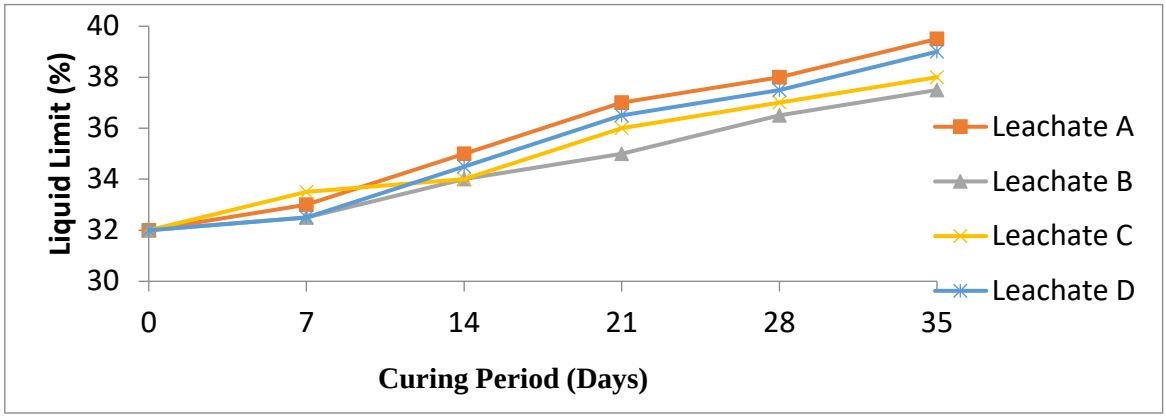

Figure 2: Variation of liquid limit with curing period

Liquid limit increased progressively with exposure time for all four leachates. From an uncontaminated value of 32%, the 35-day values reached 39.5%, 37.5%, 38.0%, and 39.0% for leachates A, B, C, and D, representing increases of approximately 17-23%. The increase indicates that a greater water content was required for the contaminated clay to reach the liquid state. This behaviour is consistent with a time-dependent alteration of the clay fabric and surface-water interaction rather than a simple dilution effect. Landfill leachate can induce cation exchange, dissolution/precipitation reactions, and mineral or fabric transformations in clay soils (Frempong & Yanful, 2008; Oztoprak & Pisirici, 2011). Although concentrated electrolytes often compress the diffuse double layer and can reduce the liquid limit of highly active clays, mixed leachates contain multiple ions and organic constituents, so the net response can be an increase, decrease, or limited change depending on clay mineralogy and exposure conditions (Di Maio et al., 2004; Spagnoli & Sridharan, 2012; Hasan & Abuel-Naga, 2024). The progressive increase observed here therefore suggests that, for this low-plasticity Bauchi clay, the leachate-induced changes increased the amount of pore fluid associated with the transition to liquid behavior.

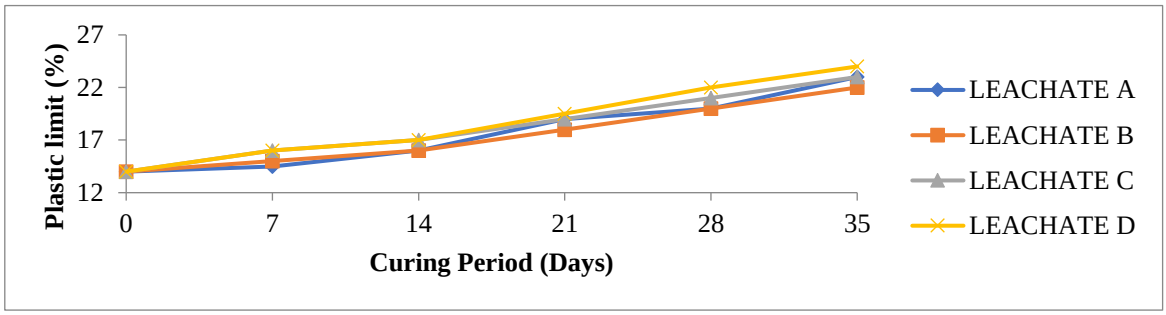

Figure 3: Variation of plastic limit with curing period

The plastic limit also increased with curing period, from 14% for the natural soil to 22-24% after 35 days. The increase was larger proportionally than the increase in liquid limit, amounting to approximately 57-71% across the four leachates. This indicates that leachate exposure shifted the lower boundary of the plastic state to substantially higher water contents. Plastic-limit changes can arise from modified particle associations, altered adsorbed-water conditions, and chemical reactions at clay surfaces. Pore-fluid chemistry has been shown to influence fine-grained soil fabric and macroscopic consistency through changes in electrical interparticle forces (Jang et al., 2018), while leachate-exposed clays have demonstrated time-dependent changes in index and microstructural properties (Oztoprak & Pisirici, 2011; Bahaa et al., 2024). The similarity of the trend for all four leachates suggests that exposure duration was an important controlling factor, although the slightly higher final plastic limit for leachate D indicates that differences in leachate composition also influenced the response.

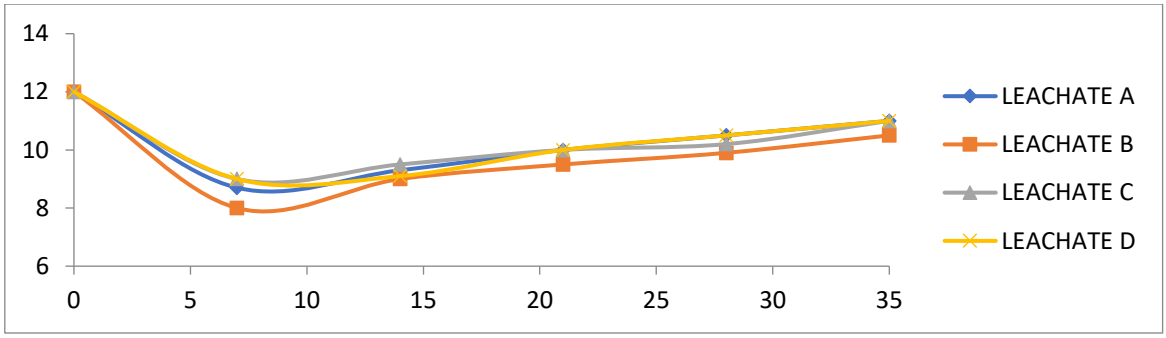

Figure 4: Variation of shrinkage limit with curing period

Shrinkage-limit behaviour differed from the liquid and plastic limits. The natural shrinkage limit of 12% fell sharply after 7 days of leachate exposure to approximately 8.0-9.0%, after which it gradually increased to 10.5-11.0% by 35 days. Thus, although partial recovery occurred with continued curing, the shrinkage limit remained below the uncontaminated value for all four leachates. A lower shrinkage limit means that volume reduction can continue to a lower water content before further drying ceases to cause shrinkage. The observed decrease-then-partial-recovery pattern is consistent with time-dependent physicochemical adjustment of the soil-leachate system, for example changes in ion exchange, diffuse-double-layer conditions, particle aggregation/dispersion, and fabric rearrangement reported for chemically exposed clays (Di Maio, 1996; Di Maio et al., 2004; Mitchell & Soga, 2005). However, these mechanisms are inferential in the present study rather than directly demonstrated, because the clay mineralogy, cation-exchange capacity, and post-exposure soil chemistry were not measured. The result should therefore be interpreted as an observed consistency change whose controlling mechanism remains to be verified by XRD, CEC, and related microstructural or chemical characterization. Similar studies of leachate-clay interaction have reported that index and volume-change characteristics evolve with exposure time rather than changing instantaneously (Ouria & Farsijani, 2019; Priya & Thyagaraj, 2025).

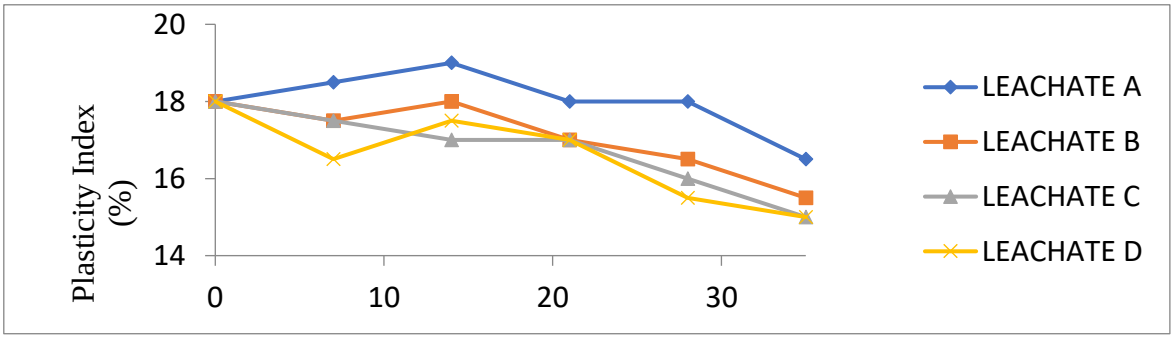

Figure 5: Variation of plasticity index with curing period

The plasticity index, calculated as LL-PL, showed a small early fluctuation but an overall decrease with prolonged exposure. From an initial value of 18%, the PI after 35 days decreased to 16.5%, 15.5%, 15.0%, and 15.0% for leachates A-D, respectively. This occurred because the plastic limit increased more rapidly than the liquid limit, thereby narrowing the range of water contents over which the soil remained plastic. The result is important because it differs from an interpretation based only on the increase in liquid limit: leachate exposure did not increase the overall plasticity range of this soil. Similar variability in the response of clay index properties to chemical pore fluids has been reported and depends strongly on mineralogy, electrolyte concentration, and cation valence (Sridharan & Prakash, 2000; Spagnoli & Sridharan, 2012; Curtin et al., 1994). Importantly, the reduction in PI should not be interpreted as improved engineering performance. In the companion Bauchi study of Chinade et al. (2017), unconfined compressive strength of compacted tropical soil generally decreased as MSW-leachate permeation time increased, despite the fact that strength behaviour cannot be inferred directly from PI alone. Taken together, the two studies suggest that leachate exposure can narrow the plasticity range while still degrading mechanical resistance. The practical implication is that a contaminated clay may become less plastic by the LL-PL measure yet simultaneously experience changes in strength, compressibility, hydraulic conductivity, or fabric that are adverse for foundations

and landfill barriers (Frempong & Yanful, 2008; Emami et al., 2019; Bahaa et al., 2024). Direct strength and compressibility testing of the same specimens would be required to quantify those consequences.

From a waste-containment perspective, the combined changes in liquid limit, plastic limit, shrinkage limit, and plasticity index demonstrate that the tested Bauchi clay is sensitive to the chemistry of the four MSW leachates. Clay-barrier performance is controlled not only by initial classification but also by how the soil responds to the actual permeant; chemical-compatibility testing is therefore important before a clay is adopted as a landfill liner or relied upon as a natural attenuation layer (Bowders et al., 1985; Katsumi et al., 2001; Jo et al., 2005). Nevertheless, the present findings are specific to one clay soil and four leachates collected within Bauchi metropolis. They should not be generalized quantitatively to other soil mineralogies, landfill ages, or leachate chemistries without additional testing. Broader applicability would require replicate testing across multiple soil types, chemical/mineralogical characterization, and direct measurements of strength, compressibility, and hydraulic conductivity.

3.4 Study Limitations and Practical Implications

The principal limitation is the absence of replicate Atterberg-limit measurements and associated standard deviations, which prevents formal assessment of experimental scatter and statistical significance. In addition, XRD mineralogy, cation-exchange capacity, and post-exposure soil chemistry were not measured, so the mechanisms proposed for the observed consistency changes remain literature-supported hypotheses rather than directly verified processes. The study also considered only one Bauchi clay and four local leachates over a maximum curing period of 35 days. Future work should therefore include replicate testing, longer exposure periods, mineralogical and chemical characterization, and paired strength/compressibility/hydraulic-conductivity measurements. Such data would allow the observed plasticity changes to be linked quantitatively to engineering performance and would improve the basis for landfill-liner design or foundation assessment in contaminated ground.

CONCLUSION

From the results of the study, the following conclusions were drawn:

i. The natural soil was classified as A-6(11) under AASHTO M 145-2012 and CL under ASTM D2487-11, with 89% passing the No. 200 sieve, liquid limit of 32%, plastic limit of 14%, plasticity index of 18%, shrinkage limit of 12%, and free swell of 45%.

ii. The four MSW leachates were alkaline (pH 8.1-10.3) and contained high dissolved-solids and organic loads. BOD5/COD ratios of approximately 0.17-0.25 indicate low biodegradability and a relatively stabilized leachate character.

iii. Leachate contamination caused systematic, time-dependent changes in the consistency characteristics of the clay soil.

iv. Liquid limit increased from 32% to 37.5-39.5% and plastic limit increased from 14% to 22-24% after 35 days of exposure. In contrast, plasticity index generally decreased from 18% to 15-16.5% because the plastic limit increased more rapidly than the liquid limit.

v. Shrinkage limit decreased sharply during the first 7 days of contamination and then partially recovered with curing, but remained below the natural-soil value after 35 days. This demonstrates that the effect of leachate on clay consistency is not monotonic and depends on the duration of soil-leachate interaction.

vi. The observed changes are consistent with modification of clay-water interactions through effects such as ionic strength, cation exchange, pH, organic constituents, and time-dependent fabric rearrangement. Because mineralogy, cation-exchange capacity, and post-exposure soil chemistry were not measured, these mechanisms remain inferential and should be verified in future work.

vii. For the tested Bauchi clay and the four local leachates, the results show that consistency properties are sensitive to leachate exposure and that chemical compatibility should be considered in waste-containment applications. The numerical trends should not be generalized to other clays or leachate chemistries without site-specific testing. Properly engineered landfill systems should incorporate effective liners, leachate collection and treatment, surface-water control, and routine monitoring of surrounding soil and groundwater.

REFERENCES

AASHTO. (2012). M 145-91 (2012), Standard specification for classification of soils and soil-aggregate mixtures for highway construction purposes. American Association of State Highway and Transportation Officials.

ASTM International. (2011). ASTM D2487-11: Standard practice for classification of soils for engineering purposes (Unified Soil Classification System). ASTM International.

Bahaa, Z., Fattah, M. Y., & Shehab, E. Q. (2024). Effect of leachate contamination in municipal solid waste on clay liner characteristics. Journal of Engineering Research, 12(2), 34-43. https://doi.org/10.1016/j.jer.2023.10.025

Bowders, J. J., Daniel, D. E., Broderick, G. P., & Liljestrand, H. M. (1985). Methods for testing the compatibility of clay liners with landfill leachate. In Hydraulic barriers in soil and rock (ASTM STP 874, pp. 233-250). ASTM International. https://doi.org/10.1520/STP36375S

British Standards Institution. (1990). BS 1377-2:1990: Methods of test for soils for civil engineering purposes - Part 2: Classification tests. BSI.

Bureau of Indian Standards. (1977). IS 2720 (Part 40): Methods of test for soils - Determination of free swell index of soils. Bureau of Indian Standards.

Chinade, A. U., Yusuf, U. S., & Osinubi, K. J. (2017). Effect of municipal solid waste leachate on the strength of compacted tropical soil for landfill liner. International Research Journal of Engineering and Technology, 4(6), 3248-3253.

Christensen, T. H., Kjeldsen, P., Bjerg, P. L., Jensen, D. L., Christensen, J. B., Baun, A., Albrechtsen, H.-J., & Heron, G. (2001). Biogeochemistry of landfill leachate plumes. Applied Geochemistry, 16(7-8), 659-718. https://doi.org/10.1016/S0883-2927(00)00082-2

Curtin, D., Steppuhn, H., & Selles, F. (1994). Clay dispersion in relation to sodicity, electrolyte concentration, and mechanical effects. Soil Science Society of America Journal, 58(3), 955-962. https://doi.org/10.2136/sssaj1994.03615995005800030045x

Di Maio, C. (1996). Exposure of bentonite to salt solution: Osmotic and mechanical effects. Géotechnique, 46(4), 695-707. https://doi.org/10.1680/geot.1996.46.4.695

Di Maio, C., Santoli, L., & Schiavone, P. (2004). Volume change behaviour of clays: The influence of mineral composition, pore fluid composition and stress state. Mechanics of Materials, 36(5), 435-451. https://doi.org/10.1016/S0167-6636(03)00070-X

Emami, S., Negahdar, A., & Zarei, M. (2019). Investigating the influence of the leachate from municipal solid waste on the mechanical and environmental properties of soil around the landfill (case study: the municipal landfill located in Ardabil-Iran). Arabian Journal for Science and Engineering, 44(10), 8417-8428. https://doi.org/10.1007/s13369-019-03962-z

Frempong, E. M., & Yanful, E. K. (2008). Interactions between three tropical soils and municipal solid waste landfill leachate. Journal of Geotechnical and Geoenvironmental Engineering, 134(3), 379-396. https://doi.org/10.1061/(ASCE)1090-0241(2008)134:3(379)

Hasan, M. F., & Abuel-Naga, H. (2024). Determining liquid limit and plastic limit of clay soils by electrical surface conduction and diffuse double layer thickness. Minerals, 14(3), 210. https://doi.org/10.3390/min14030210

Head, K. H. (1992). Manual of soil laboratory testing: Volume 1, soil classification and compaction tests (2nd ed.). Wiley.

Jang, J., Cao, S. C., Stern, L. A., Jung, J., & Waite, W. F. (2018). Impact of pore fluid chemistry on fine-grained sediment fabric and compressibility. Journal of Geophysical Research: Solid Earth, 123(7), 5495-5514. https://doi.org/10.1029/2018JB015872

Jo, H. Y., Benson, C. H., Shackelford, C. D., Lee, J. M., & Edil, T. B. (2005). Long-term hydraulic conductivity of a geosynthetic clay liner permeated with inorganic salt solutions. Journal of Geotechnical and Geoenvironmental Engineering, 131(4), 405-417. https://doi.org/10.1061/(ASCE)1090-0241(2005)131:4(405)

Katsumi, T., Benson, C. H., Foose, G. J., & Kamon, M. (2001). Performance-based design of landfill liners. Engineering Geology, 60(1-4), 139-148. https://doi.org/10.1016/S0013-7952(00)00096-X

Kjeldsen, P., Barlaz, M. A., Rooker, A. P., Baun, A., Ledin, A., & Christensen, T. H. (2002). Present and long-term composition of MSW landfill leachate: A review. Critical Reviews in Environmental Science and Technology, 32(4), 297-336. https://doi.org/10.1080/10643380290813462

Lagasi, J. E., Uloko, J. O., Shetak, B. K., & Yiltawe, J. D. (2023). Environmental impact of leachate pollution on ground water quality at Yelwa Kagadama, Bauchi, Bauchi State, Nigeria. Journal of Applied Sciences and Environmental Management, 27(4), 697-702. https://doi.org/10.4314/jasem.v27i4.8

Mitchell, J. K., & Soga, K. (2005). Fundamentals of soil behavior (3rd ed.). John Wiley & Sons.

Osinubi, K. J., & Nwaiwu, C. M. (2010). Discussion of "Interactions between three tropical soils and municipal solid waste landfill leachate" by E. M. Frempong and E. K. Yanful. Journal of Geotechnical and Geoenvironmental Engineering, 136(6), 891-892. https://doi.org/10.1061/(ASCE)GT.1943-5606.0000173

Ouria, A., & Farsijani, A. (2019). Investigating the consolidation and shear strength behavior of clay soils contaminated with municipal solid waste leachate. Amirkabir Journal of Civil Engineering, 51(2), 351-366.

Oztoprak, S., & Pisirici, B. (2011). Effects of micro structure changes on the macro behaviour of Istanbul (Turkey) clays exposed to landfill leachate. Engineering Geology, 121(3-4), 110-122. https://doi.org/10.1016/j.enggeo.2011.05.005

Priya, R. S., & Thyagaraj, T. (2025). Hydraulic conductivity and chemical compatibility of Trichy clay for municipal solid waste landfill liner applications. In Geo-EnvironMeet 2025 (GSP 359, pp. 418-430). American Society of Civil Engineers. https://doi.org/10.1061/9780784485699.045

Renou, S., Givaudan, J. G., Poulain, S., Dirassouyan, F., & Moulin, P. (2008). Landfill leachate treatment: Review and opportunity. Journal of Hazardous Materials, 150(3), 468-493. https://doi.org/10.1016/j.jhazmat.2007.09.077

Spagnoli, G., & Sridharan, A. (2012). Liquid limit of mixtures of smectite, kaolinite and quartz powder with water and NaCl solution. International Journal of Geotechnical Engineering, 6(1), 117-123. https://doi.org/10.3328/IJGE.2012.06.01.117-123

Sridharan, A., & Prakash, K. (2000). Percussion and cone methods of determining the liquid limit of soils: Controlling mechanisms. Geotechnical Testing Journal, 23(2), 236-244. https://doi.org/10.1520/GTJ11048J

Tijjani, A. F., Alhassan, B., Salisu, U., & Hassan, A. M. (2023). Multivariate statistical analysis for assessment of groundwater quality around dumpsites in Bauchi metropolis, Bauchi State, Nigeria. Journal of Applied Sciences and Environmental Management, 27(11), 2509-2514. https://doi.org/10.4314/jasem.v27i11.21

International Conference on Engineering Innovation for Sustainable Development (ICESID 2026)
Faculty of Engineering, Ahmadu Bello University Zaria · 8–10 September 2026

EFFECTS OF HYDROCARBON IMPURITIES ON CONCRETE STRENGTH AND DURABILITY: A COMPREHENSIVE REVIEW

Otu Nnamdi Johnson[1,*], James Olayemi James[1], Abubakar Mahmud[1]
[1]*Federal University of Technology, Minna*
Email: nnamstar5558@gmail.com[*], jamesolayemi@futminna.edu.ng, abubakarmamud@futminna.edu.ng
***Corresponding author**: Otu Nnamdi Johnson
DOI: https://doi.org/10.67203/sp.ICESID.2026

ABSTRACT

Concrete performance is strongly influenced by the quality of its constituent materials. Hydrocarbon contamination of aggregates, mixing water, or concrete during handling and service can alter workability, cement hydration, strength development, permeability, and durability. This review synthesizes experimental evidence on the effects of crude oil, diesel, gasoline, and used engine oil on fresh and hardened concrete. The review focuses on the mechanisms through which hydrocarbons interact with cement paste and aggregate surfaces, the resulting changes in mechanical and durability properties, and approaches for mitigating the effects of contamination. The reviewed evidence indicates that the magnitude of deterioration depends on hydrocarbon type, contamination level, mode of contamination, water-to-cement ratio, curing regime, and testing age. Low levels of some hydrocarbons may increase slump through a lubrication or plasticizing effect, but this does not necessarily indicate improved structural performance. At moderate and high contamination levels, disruption of hydration and interfacial bonding generally results in reduced strength and, in many studies, increased porosity and permeability. The review also identifies gaps concerning long-term field performance, standardized permissible contamination limits, microstructural characterization, and sustainable remediation. These issues are particularly relevant to sustainable construction and infrastructure development in hydrocarbon-producing and industrial areas.

Keywords: *Concrete; hydrocarbon contamination; diesel; crude oil; used engine oil; compressive strength; durability; cement hydration*

1.0 INTRODUCTION

Concrete remains one of the most widely used construction materials because of its strength, durability, versatility, and availability (Neville,2011). Nevertheless, its performance can be compromised by environmental and chemical contaminants, including petroleum hydrocarbons. Hydrocarbon contamination may occur through oil spills, leakage from storage facilities, industrial discharges, transportation, construction-site handling, or the use of contaminated aggregates and water (Ajagbe et al., 2012; Osuji and Nwankwo, 2015).

Hydrocarbons such as crude oil, diesel, gasoline, kerosene, and used engine oil can interact with concrete at different stages of production and service. Their effects depend strongly on the type and concentration of the hydrocarbon and whether it is introduced through aggregates, mixing water, curing water, or external exposure. In contaminated aggregates, hydrocarbon films can alter the aggregate–paste interface and interfere with effective bond formation. During mixing, some petroleum products may also increase fluidity at low dosage because of lubrication or plasticizing effects, while simultaneously interfering with hydration and cohesion (Ajagbe et al., 2012; Elinwa & Mahmoud, 2023; Tetteh et al., 2025).

The consequences of contamination are important for sustainable construction because premature deterioration increases repair, replacement, material consumption, and environmental burdens. In Nigeria, where hydrocarbon production, transportation, storage, and industrial activities are significant, understanding the performance of contaminated concrete is relevant to resilient infrastructure development and sustainable management of polluted construction materials.

This review therefore synthesizes published evidence on hydrocarbon–concrete interactions, with emphasis on cement hydration, fresh properties, mechanical strength, density, durability, microstructural changes, mitigation strategies, and areas requiring further investigation.

1.1 Problem Statement

The use of hydrocarbon-contaminated construction materials can compromise concrete reliability. Experimental studies have reported reductions in compressive and flexural strength as contamination increases, although the magnitude of deterioration varies considerably with hydrocarbon type, contamination route, mix design, and curing conditions (Ajagbe et al., 2012; Ejeh and Uche, 2009; Oyelami et al., 2024). Despite the growing body of research, findings are dispersed across studies using different materials and experimental conditions. A structured synthesis is therefore required to distinguish general trends from condition-specific results and to identify practical mitigation and research needs.

1.2 Aim and Objectives

Aim

To critically review the effects of hydrocarbon impurities on concrete strength and durability.

Objectives

1. To examine the mechanisms through which hydrocarbons influence cement hydration and interfacial bonding.
2. To evaluate their effects on fresh and hardened concrete properties.
3. To compare reported experimental findings while accounting for hydrocarbon type, contamination level, and test conditions.
4. To identify practical mitigation strategies and priority areas for future research.

2.0 REVIEW METHODOLOGY

This paper adopts a structured narrative-review approach. Literature was identified from major scholarly and publisher platforms, including Google Scholar, ScienceDirect, SpringerLink, MDPI, institutional repositories, and journal websites. The principal search terms included combinations of hydrocarbon contamination concrete, crude oil contaminated concrete, diesel contaminated concrete, used engine oil concrete, oil contaminated sand concrete, concrete strength, concrete durability, cement hydration, and hydrocarbon concrete microstructure. The research emphasized literature published from 2009 to 2026, while allowing foundational earlier work where it directly informed the subject.

Studies were considered eligible when they reported experimental or review evidence directly related to petroleum hydrocarbons and concrete, mortar, aggregates, mixing/curing water, or concrete durability. Preference was given to peer-reviewed journal articles and traceable scholarly sources containing sufficient information on contamination type, dosage or exposure condition, and measured concrete properties. Sources were excluded when they did not address concrete or cement-based materials, lacked sufficient bibliographic information for verification, or merely mentioned hydrocarbons without reporting relevant performance evidence.

The selected literature was synthesized thematically under cement hydration, fresh properties, hardened properties, durability, microstructure, experimental evidence, mitigation, and research gaps. Quantitative results were not pooled statistically because the reviewed studies used substantially different hydrocarbon types, contamination routes, mix proportions, specimen sizes, curing regimes, and test ages. Instead, reported values are presented with their study conditions to avoid misleading direct comparisons.

3.0 CONCEPT OF HYDROCARBON CONTAMINATION IN CONCRETE

Hydrocarbon contamination occurs when petroleum-based substances such as crude oil, diesel, gasoline, kerosene, or used engine oil are present in concrete constituents or come into contact with concrete during production or service. Depending on the contamination route, hydrocarbons may coat aggregate surfaces, alter the liquid phase of the mixture, affect cement hydration, or modify pore structure (Ajagbe et al., 2012; Osuji and Nwankwo, 2015).

3.1 Cement Hydration

Cement hydration involves reactions between cement compounds and water that produce hydration products, particularly calcium silicate hydrate (C–S–H), which contributes substantially to

strength development. Hydrocarbons can interfere with this process by coating cement particles or aggregate surfaces and reducing effective contact between cement, water, and aggregate. The extent of interference depends on the hydrocarbon and its concentration. Consequently, contaminated concrete may show slower strength development or lower ultimate strength than uncontaminated concrete (Ajagbe et al., 2012; Osuji and Nwankwo, 2015; Oyelami et al., 2024).

3.2 Effects on Fresh Concrete Properties

Hydrocarbon contamination can change the rheology and stability of fresh concrete. At low dosages, some petroleum products can increase slump because their lubricating or plasticizing action reduces interparticle friction. However, increased slump should not be interpreted as evidence of improved concrete quality. At higher contamination levels, hydrocarbon films may reduce cohesion and promote segregation, while interference with cement–water interaction may delay hydration and setting. Thus, the apparent increase in workability and the delay in hydration are not contradictory: they represent different effects of the same contaminant acting on fresh-mixture rheology and cement chemistry, respectively (Tetteh et al., 2025).

1. Workability (slump): Low levels of some hydrocarbons can increase slump through lubrication or plasticizing action; excessive contamination may reduce cohesion and mix stability.
2. Segregation and bleeding: Disruption of cohesion can increase the tendency for non-uniform distribution of constituents.
3. Setting time: By reducing effective cement–water interaction, hydrocarbons may delay hydration and setting, although the magnitude depends on contaminant type and dosage.
4. Cohesion and stability: Oil films at particle surfaces can weaken interparticle interaction and make compaction and uniform placement more difficult.
5. Mechanism: The combined effects arise from surface coating, hydrophobicity, altered rheology, and interference with hydration.

3.3 Effects on Hardened Concrete Properties

Hydrocarbon contamination generally has a more pronounced effect on hardened concrete when contamination is sufficiently high to disrupt hydration and aggregate–paste bonding. Reported outcomes include reductions in compressive, tensile, and flexural strength, changes in density, and deterioration in selected durability indicators. However, the magnitude and even direction of individual properties can vary at low contamination levels and under different exposure conditions.

3.3.1 Effect on Compressive Strength

Compressive strength is one of the properties most consistently affected by hydrocarbon contamination. Ajagbe et al. (2012) reported an 18–90% strength loss for concrete made with sand contaminated with 2.5–25% crude oil, with the larger losses occurring at the higher contamination levels. The study also found that contamination above 5% caused more than 50% strength reduction. These values should not be interpreted as a universal range for all hydrocarbons; they describe a specific crude-oil-contaminated-sand system and its test conditions. Other studies have reported smaller or different losses because they used different hydrocarbons, contamination routes, dosages, water-to-cement ratios, and curing conditions (Oyelami et al., 2024; Mmonwuba et al., 2025; Abbas, 2026).

3.3.2 Strength Development

Hydrocarbon-contaminated concrete may develop strength more slowly than control concrete because early hydration and interfacial bond formation are disturbed. The literature indicates that early-age strength can be particularly sensitive to contamination. Nevertheless, strength development is not governed by contamination alone; curing duration, mix proportions, hydrocarbon type, and contamination route also influence the observed rate of strength gain (Ajagbe et al., 2012; Oyelami et al., 2024).

3.3.3 Effect on Durability

Durability describes the ability of concrete to maintain acceptable performance under anticipated environmental exposure. Hydrocarbon contamination can modify porosity, permeability, water absorption, and resistance to aggressive exposure. Ajagbe et al. (2018), found that crude-oil-impacted-sand concrete showed changes in electrical resistivity and water absorption with contamination level, while fire exposure caused additional strength deterioration. These findings demonstrate that durability responses are not always uniformly negative across every indicator and should be interpreted in relation to the particular contaminant and test method (Adesina et al., 2021; Elinwa & Mahmoud, 2023).

3.3.4 Long-Term Strength and Integrity

Long-term performance remains less consistently documented than early-age strength. Available studies suggest that contamination can continue to influence strength development and durability, but reported magnitudes vary. Therefore, a single percentage reduction should not be presented as a universal long-term loss. Long-term behavior should instead be reported with the contamination type, exposure condition, curing age, and test method explicitly stated.

3.4 Tensile and Flexural Strength

Hydrocarbon contamination can reduce tensile and flexural performance by weakening the cement paste–aggregate interface and increasing internal discontinuities. Ajagbe et al. (2012) reported reductions in flexural strength as crude-oil contamination increased. Similar mechanisms have been associated with reductions in splitting tensile strength, including weaker interfacial transition zones, reduced cohesion, and increased susceptibility to crack initiation.

1. Reduced splitting tensile strength.
2. Increased susceptibility to crack initiation and propagation.
3. Weakening of the interfacial transition zone (ITZ).
4. Reduced flexural capacity where contamination significantly affects internal bonding.

3.5 Density

Density is influenced by particle packing, compaction, entrapped air, and the composition of the concrete matrix. Hydrocarbon contamination can alter these factors by affecting cohesion, compaction, and pore structure. However, changes in density are not necessarily identical across all hydrocarbon types and dosages; therefore, density trends should be interpreted alongside air content, porosity, and the contamination route rather than treated as a direct measure of strength (Abbas, 2026).

3.6 Effect on Concrete Durability

Hydrocarbon contamination may influence durability through changes in hydration, pore connectivity, interfacial bonding, and permeability. Where contamination produces a weaker and more connected pore structure, the ingress of water and aggressive agents may increase. However, some low-level hydrocarbon exposures have produced mixed results for individual durability indicators. Ajagbe et al. (2018) reported improved electrical-resistivity-related durability indicators with increasing crude-oil contamination in their particular test system, while also observing reduced strength after fire exposure. This illustrates why durability conclusions must be tied to the specific indicator and exposure condition rather than generalized across all hydrocarbons.

3.7 Microstructural Effects of Hydrocarbon Impurities

At the microstructural level, hydrocarbon contamination can modify cement hydration and the aggregate–paste interface. Reported mechanisms include incomplete development of hydration products, weak ITZs, altered pore structure, and microcracking. These changes provide a mechanistic explanation for many observed reductions in strength and durability, although microstructural evidence remains less extensive than conventional strength testing in the literature.

1. Reduced or altered development of C–S–H and other hydration products.
2. Weakening of the aggregate–paste interfacial transition zone.

3. Changes in porosity and pore connectivity.
4. Formation or propagation of microcracks and discontinuities.

3.8 Experimental Studies on Hydrocarbon-Contaminated Concrete

Experimental studies differ substantially in hydrocarbon type, contamination route, dosage, concrete composition, and curing regime. Accordingly, direct numerical comparison must be made cautiously.

Table 3.0: Experimental Studies on Hydrocarbon-Contaminated Concrete

Study	**Hydrocarbon**	**Key condition**	**Main finding**	**Interpretation**
Ejeh & Uche (2009)	Crude oil contamination	Concrete materials	Compressive strength decreased with contamination.	Supports the adverse effect of crude oil on strength.
Ajagbe et al. (2012)	Crude-oil-contaminated sand	2.5–25% oil; 3–168 days	18–90% strength loss; >50% loss above 5% contamination.	Large losses are condition-specific and linked to contaminated sand.
Osuji & Nwankwo (2015)	Crude oil contamination	Concrete constituents	Oil hindered bond formation and affected strength.	Supports hydration/bonding mechanism.
Adesina et al. (2021)	Oil-contaminated concrete	Durability-focused	Reported deterioration in durability-related performance.	Shows that strength and durability should be evaluated together.
Oyelami et al. (2024)	Oil-contaminated sand	Mechanical performance	Strength decreased with increasing contamination; early ages were sensitive.	Confirms concentration- and age-dependent effects.
Ajagbe et al. (2018)	Crude-oil-impacted sand	Durability and fire exposure	Durability indicators changed with contamination; fire exposure caused additional strength loss.	Demonstrates property-specific responses.
Mmonwuba et al. (2025)	Petroleum-contaminated sand	RHA and cassava starch remediation	27.76% strength reduction from contamination; additives improved strength.	Supports sustainable remediation approaches.
Tetteh et al. (2025)	Used engine oil as admixture	0.15–30%; varying water-cement ratio	Low dosages improved workability; higher dosages reduced strength.	Shows that low-dose fluidity effects do not imply improved structural performance.

3.9 Comparative Analysis of Existing Studies

The apparently wide range of reported strength reductions is not necessarily contradictory. The 18–90% range reported by Ajagbe et al. (2012) resulted from 2.5–25% crude-oil contamination of sand and therefore represents a specific experimental system. The more than 50% reduction reported in that study at contamination above 5% is part of the same dataset rather than an independent universal value. By contrast, Mmonwuba et al. (2025) reported a 27.76% reduction for petroleum-contaminated sand under a different experimental design, and Oyelami et al. (2024) reported concentration-dependent strength losses in oil-contaminated sand. These differences arise from hydrocarbon composition, contamination level, whether the aggregate or water was contaminated, water-to-cement ratio, mix proportions, curing age, specimen preparation, and test conditions. The review therefore avoids presenting 18–90%, 25%, 50%, or 27.76% as universal strength-loss values.

Another important distinction concerns low-level hydrocarbon addition as an admixture versus accidental contamination of concrete constituents. Some used-engine-oil studies report increased slump at low dosages, while higher dosages reduce strength. Such findings should not be generalized to contaminated aggregates or uncontrolled field exposure because the mechanisms, dispersion, and dosage basis are different (Tetteh et al., 2025).

4.0 MITIGATION STRATEGIES

Mitigation should prioritize preventing contaminated materials from entering structural concrete. Where contamination is detected, appropriate cleaning or treatment of aggregates should be considered, subject to verification by laboratory testing. Other measures include strict material quality control, protection of aggregates during storage, avoidance of contaminated mixing or curing water, and site monitoring in areas exposed to petroleum products.

Supplementary cementitious materials and other remediation additives may provide additional benefits in selected applications. Mmonwuba et al. (2025), reported improved mechanical performance when rice husk ash and cassava starch were used with petroleum-contaminated sand. However, such approaches should be validated for the specific contamination type and structural application before adoption.

5.0 CONCLUSION

The reviewed literature demonstrates that hydrocarbon contamination can significantly alter concrete performance, particularly when contamination is moderate to high or when aggregate surfaces are substantially coated. The dominant mechanisms include disruption of cement hydration, alteration of aggregate–paste bonding, and changes in pore structure. These mechanisms commonly lead to reduced compressive and flexural strength and can impair durability, although individual durability indicators may respond differently depending on the hydrocarbon and exposure condition.

The review also shows that quantitative strength losses reported in the literature cannot be treated as universal constants. Ajagbe et al. (2012) reported a 18–90% range corresponds specifically to 2.5–25% crude-oil contamination of sand, whereas the 27.76% reduction reported by Mmonwuba et al. (2025) arose from a different petroleum-contaminated-sand system. Consequently, future studies should report contamination route, dosage basis, hydrocarbon composition, mix design, curing conditions, and testing age in sufficient detail to permit meaningful comparison.

5.1 Recommendations

1. Avoid using visibly or demonstrably hydrocarbon-contaminated aggregates and water in structural concrete unless an appropriate treatment and laboratory verification demonstrate suitability.
2. Introduce routine quality-control testing of aggregates and water in areas exposed to petroleum products.
3. Investigate washing, treatment, or other remediation methods before considering contaminated aggregates for reuse.
4. Evaluate supplementary cementitious materials and sustainable additives as potential remediation strategies, with structural performance verified experimentally.

5. Develop evidence-based guidance on permissible contamination levels for different hydrocarbon types and concrete applications.

5.2 Further Research Focus

1. Long-term durability and field exposure: Most available studies are laboratory-based and use limited curing or exposure periods. Long-term field studies are needed to establish how contaminated concrete performs under realistic wetting, drying, chemical, thermal, and loading cycles.

2. Standardized contamination limits: Reported strength losses vary widely because studies use different contamination bases and hydrocarbon types. Standardized procedures for defining contamination level and reporting dosage are needed before regulatory limits can be developed.

3. Advanced microstructural characterization: More coordinated SEM, XRD, porosity, permeability, and chemical analyses are needed to link observed strength loss directly to hydration products, ITZ changes, and pore connectivity.

4. Sustainable remediation: The promising results obtained with agricultural and supplementary materials warrant further work on low-cost, environmentally responsible methods for recovering contaminated aggregates without compromising structural safety.

REFERENCES

Abbas, B. A., (2026). Effects of hydrocarbon on the compressive strength of concrete using pebbles. ABUAD Journal of Engineering Research and Development, 9(1), 190–195.

Adesina, A., Lawal, F. T., & Oyelami, A. C. (2021). Durability performance of oil-contaminated concrete. Journal of Materials in Civil Engineering, 33(6), 04021123.

Ajagbe, W. O., Omokehinde, O. S., Alade, G. A., & Agbede, O. A. (2012). Effect of crude oil impacted sand on compressive strength of concrete. Construction and Building Materials, 26(1), 9–12. https://doi.org/10.1016/j.conbuildmat.2011.06.028

Ajagbe, W. O., & Rabiu, W. A. (2018). Effects of crude oil impacted sand on the durability of concrete. Civil Engineering and Architecture, 6(4), 205–211. https://doi.org/10.13189/cea.2018.060403

Ejeh, S. P., & Uche, O. A. U. (2009). Effect of crude oil spill on compressive strength of concrete materials. Journal of Applied Sciences Research, 5(10), 1756–1761.

Elinwa, A. U., & Mahmoud, K. (2023). Influence of gasoline and gas-oil exposure on the performance of high-strength latex-modified concrete. Journal of Materials in Civil Engineering, 35(4), 04023029.

Mmonwuba, N. C., Uguru, H., Ugwu, J. N., Akpokodje, O. I., Ogunjiofor, E. I., Anene, W. C., & Ayadiuno, G. C. (2025). Effects of rice husk ash and cassava starch on the mechanical properties of concrete produced from petroleum contaminated sand. NIPES Journal of Science and Technology Research, 7(2), 59–69. https://doi.org/10.37933/nipes/7.2.2025.4

Neville, A. M. (2011). Properties of Concrete (5th ed.). Pearson Education Limited.

Osuji, S. O., & Nwankwo, E. (2015). Effect of crude oil contamination on the compressive strength of concrete. Nigerian Journal of Technology, 34(2), 259–265. https://doi.org/10.4314/njt.v34i2.7.

Oyelami, A. C., Adesina, A., & Lawal, F. T. (2024). Mechanical performance of concrete produced with oil-contaminated sand. Sustainability, 16(17), 7344. https://doi.org/10.3390/su16177344

Tetteh, S. A., Akwei, I., Acquah, E., Gbey, J., & Afriyie, P. (2025). Investigating the impact of used engine oil on the compressive strength of concrete with varying water-to-cement ratios. Journal of

Engineering Technologies and Innovative Research, 12(3), 259a–273a.

International Conference on Engineering Innovation for Sustainable Development (ICESID 2026)
Faculty of Engineering, Ahmadu Bello University Zaria · 8–10 September 2026

EMERGING TECHNOLOGIES FOR SAFE ENGINEERING PRACTICES AND ENVIRONMENTAL PROTECTION: A SYSTEMATICALLY INFORMED, EVIDENCE-GRADED REVIEW WITH A PROPOSED NIGERIAN ADOPTION FRAMEWORK

Emmanuel Adie[1,*], John Wasiu[1], Ibrahim Abdulrazaq Olayinka[1]
[1]*Edo State University Iyamho*
Email: adiee0281@gmail.com*, wasiu.john@edouniversity.edu.ng, Ibrahim.abdulrazaq@edouniversity.edu.ng
***Corresponding author**: Emmanuel Adie
DOI: https://doi.org/10.67203/sp.ICESID.2026

ABSTRACT
Emerging technologies are reshaping engineering safety and environmental protection, yet evidence on their cross-sectoral effectiveness and applicability in resource-constrained economies remains fragmented. This study synthesises peer-reviewed evidence on artificial intelligence (AI), the Internet of Things (IoT), digital twins and BIM, virtual reality and sensor fusion, drones, and nanomaterials across construction, mining, and oil and gas operations. A systematically informed narrative-review approach was adopted, combining a reported search and screening process with manual verification and an operationalised evidence-grading rubric. The discovery platform reported 8,652,714 cumulative topical matches across 23 searches and one citation-graph expansion, reflecting corpus scale rather than individually retrieved records; 250 records were then surfaced for human screening and progressively verified to identify the final 37-study evidence corpus. The synthesis indicates the strongest convergent evidence for IoT- and AI-enabled monitoring and hazard detection, while evidence for digital twins/BIM, immersive technologies, and nanotechnology-based remediation remains comparatively limited. Reported quantitative effects of 18–22% risk reduction and 58–70% safety improvement are treated as single-case findings rather than generalisable technology effects. The study further develops a twelve-dimension, indicative Nigerian technology-adoption framework covering cost, infrastructure, skills, maintenance, regulatory readiness, data governance, cybersecurity, organisational readiness, technology maturity, and safety and environmental benefits. The framework is presented as an analytical proposition requiring empirical validation rather than as evidence of current Nigerian conditions. Directly supporting ICESID 2026's theme of harnessing engineering for Nigeria's sustainable growth, the findings support phased adoption of scalable monitoring and predictive technologies alongside strengthened regulatory, cybersecurity, occupational-exposure, and workforce-development measures.

Keywords: *emerging technologies; engineering safety; environmental protection; artificial intelligence; Internet of Things*

1. INTRODUCTION

Engineering safety and environmental stewardship have historically been treated as compliance obligations layered onto production activity rather than as design objectives in their own right. This posture is changing. Artificial intelligence, the Internet of Things, digital twins, and automation are transforming safety management and environmental protection across construction, mining, and energy industries, reshaping how hazards are anticipated, monitored, and controlled (Adio et al., 2025; Dimkpa et al., 2025; Gobbo et al., 2018). The scale of the underlying problem is considerable: Gupta, Singh, Asari, and Nguyen (2026) report that construction, framed in their review as among the most hazardous industries globally, experiences a worker fatality approximately every ninety-nine minutes; their source does not further disaggregate this figure by country or region, and it is reported here exactly as framed in that review rather than with additional geographic precision the citing source does not itself provide. This statistic has nonetheless driven accelerating adoption of machine learning, robotics, wearable sensors, and immersive visualisation as complements to conventional safety management (Gupta et al., 2026). Parallel pressure is building on the environmental side of engineering practice, where Industry 4.0 concepts, the Internet of Things, big data, and cyber-physical systems, are increasingly framed as

opportunities to integrate process safety with environmental protection rather than treat them as competing priorities (Gobbo et al., 2018).

For Nigeria, these global dynamics intersect with structural realities that make emerging-technology adoption both more urgent and more difficult. The Nigerian economy remains heavily anchored on extractive and heavy-industry activity, oil and gas production in the Niger Delta, solid minerals mining, and an expanding construction sector, each carrying elevated occupational-safety and environmental-protection burdens. Environmental regulation is administered principally through the National Environmental Standards and Regulations Enforcement Agency (NESREA) and sector-specific upstream petroleum regulators, within an institutional environment that, as in many developing economies, faces resource and enforcement constraints. The oil and gas industry continues to contend with greenhouse gas emissions, spills, and process accidents that drive demand for more sustainable protection technologies across upstream, midstream, and downstream operations (Akerele et al., 2024; Alamutu, 2025; Okolie et al., 2024).

Despite this relevance, the literature on emerging technologies for engineering safety and environmental protection remains fragmented along sectoral and disciplinary lines, with comparatively little cross-sector synthesis and even less explicit engagement with the adoption conditions of developing economies. This paper addresses that gap and makes three specific contributions.

Knowledge contribution: a cross-sectoral, evidence-graded synthesis of six technology categories, AI and predictive analytics, IoT and real-time monitoring, digital twins/BIM, VR and sensor fusion, drones, and nanomaterials, against safety and environmental functions. Methodological contribution: an operationalised evidence-grading rubric applied transparently to a heterogeneous corpus, together with a reported search and screening protocol. Practice and policy contribution: a twelve-dimension technology-adoption framework that translates global evidence into a prioritisation logic for resource-constrained Nigerian engineering sectors, explicitly presented as a proposition for empirical validation. The objectives are to: (i) map the six technology categories against safety and environmental functions; (ii) characterise sector-specific applications and quantified impacts; (iii) grade the evidence using the stated rubric; and (iv) derive bounded implications for engineering practice, regulation, and workforce development in Nigeria.

2. LITERATURE REVIEW

2.1 Theoretical Foundations

The theoretical anchor for this review is the Industry 4.0 paradigm, which frames the convergence of cyber-physical systems, IoT, big data, and smart objects as a basis for simultaneously improving process safety and environmental performance rather than treating the two as a trade-off (Gobbo et al., 2018). Complementing this technological framing is a risk-governance perspective associated with the responsible-development literature, which holds that anticipation of hazards, precautionary approaches where occupational exposure limits are undefined, and transparent communication with exposed workers should accompany the introduction of any new technology into industrial practice (Schulte et al., 2024). A third theoretical strand, drawn from the Safe and Sustainable-by-Design (SSbD) literature, argues that environmental and health risk assessment should be embedded across a technology's full life cycle rather than appended after deployment (Cassee et al., 2024; Köhler & Som, 2014).

2.2 Classification Principle and Technology-Function Overlaps

The six technology categories used throughout this review, AI and predictive analytics, IoT and real-time monitoring, digital twins/BIM, VR and sensor fusion, drones, and nanomaterials, are organised by primary sensing, computation, or material function rather than by strict technical independence, because the underlying literature does not treat these as mutually exclusive systems. AI models frequently operate on data streams generated by IoT sensor networks; digital twins depend on both IoT inputs and analytics engines to remain synchronised with the physical asset they represent; drones increasingly embed AI-based computer vision for autonomous inspection; and VR/sensor-fusion training platforms can draw on the same spatial data underlying a digital twin. Nanomaterials are the clear exception, differing fundamentally from the other five categories as a materials-science rather than

a digital/computational technology. Table 1 presents a technology-function matrix that makes this overlap explicit, classifying each category by its dominant function rather than treating the six categories as structurally independent silos.

Table 1: Technology-Function Matrix, Showing Dominant and Secondary Functions

Technology	Dominant Function	Secondary/Overlapping Function	Principal Sectors
AI & predictive analytics	Computation / prediction	Embedded within IoT and drone systems	Mining, construction, oil & gas
IoT & real-time monitoring	Sensing	Supplies data to AI, digital twins	Industrial, mining
Digital twins & BIM	Visualisation / simulation	Depends on IoT + analytics inputs	Construction, oil & gas
VR & sensor fusion	Visualisation / training	Overlaps with digital-twin spatial data	Mining, occupational safety
Drones	Sensing (remote/aerial)	Increasingly AI-embedded (computer vision)	Industrial, environmental
Nanomaterials	Materials intervention	None (non-digital category)	Environmental remediation, oil & gas

2.3 AI and Predictive Analytics

AI-enabled predictive analytics is among the most consistently reported technology categories in the corpus, applied to hazard detection, predictive maintenance, and environmental-risk forecasting across construction, mining, and oil and gas operations (Adio et al., 2025; Dimkpa et al., 2025; Arjunan et al., 2025). In oil and gas operations, machine-learning-based predictive analytics forecasts potential equipment failures and schedules proactive maintenance, complementing continuous IoT-based condition monitoring (Akpe et al., 2024). Systematic reviews of construction-safety technologies identify AI-based topic modelling and smart-technology integration as tools that proactively identify hazards, reduce accidents, and improve resource allocation, while simultaneously contributing to lower carbon emissions through better energy optimisation on site (Seo & Yoon, 2025).

2.4 IoT and Real-Time Monitoring

IoT-based sensing underpins much of the reported progress in both safety and environmental monitoring. In underground mining, an IEEE review documents IoT architectures purpose-built for simultaneous environmental, safety, and production monitoring, addressing persistent challenges such as limited battery life and unreliable underground communication (Zhang et al., 2023). Low-cost sensor networks are identified as a foundational enabling layer for Industry 4.0 digital transformation in mining, supporting real-time monitoring through wireless networks in combination with AI, machine learning, and digital twins (Cacciuttolo et al., 2023). More broadly across industrial operations, digital HSE technologies, encompassing IoT-enabled compliance monitoring alongside AI-based analytics, are reported to strengthen health, safety, and environmental management practice (Adikwu et al., 2024). A single regional mining-complex case study reports that integrating information technologies with environmental monitoring data was associated with an 18–22% reduction in overall industrial and environmental risk at that site; this figure derives from a before–after design at one location without independent replication, and should be read as a case-specific reported effect rather than an expected or generalisable improvement (Kukartsev et al., 2025).

2.5 Digital Twins, BIM, and Robotics

Digital twin technology, providing virtual replicas of physical assets, is reported to enable risk-free simulation and optimisation of plant operations in oil and gas contexts (Akpe et al., 2024). In construction, BIM, robotics, wearable devices, and AI are each positively and significantly associated with improved safety performance, with BIM and wearable technologies showing the strongest individual effects in comparative analysis (Dobrucalı et al., 2022; Yap et al., 2021). The principal safety-enabling mechanisms identified are improved hazard identification, reinforced safety planning, and enhanced monitoring and supervision (Yap et al., 2021). A systematic review of 129 journal articles published between 2018 and 2023 organises construction safety technologies across four functional areas, prevention through design, safety management, safety culture and awareness, and computing in construction safety (Maali et al., 2024). BIM, drones, and prefabrication techniques together enable real-time monitoring, hazard detection, and improved stakeholder coordination, with reported reductions in accident likelihood in high-rise construction (Kumar et al., 2025).

2.6 VR, Drones, and Immersive Technologies

VR and sensor-fusion technologies are applied principally to hazard-scenario training and ergonomic assessment, with secondary applications in pollution visualisation and ecological education (Strzałkowski et al., 2025). Review evidence spanning geodesy and geomatics, mining, environmental protection, and occupational safety identifies sensor-integrated immersive training as a growing sub-field with demonstrated training value, though empirical evidence on transfer to real-world safety outcomes remains comparatively thin (Strzałkowski et al., 2025). Drones are reported primarily as tools for remote inspection and large-scale environmental monitoring, extending the geographic reach of safety and compliance surveillance without placing personnel in hazardous locations (Dimkpa et al., 2025).

2.7 Nanotechnology, Advanced Materials, and Environmental Remediation

Environmental engineering is increasingly linked to Industry 4.0 through intelligent monitoring, low-carbon processes, and data-driven environmental management. Emerging technologies can support emissions, water, pollution, and ecological monitoring, but the environmental evidence is less mature than the safety evidence. Sensor networks and AI offer scalable monitoring and prediction, while nanomaterials provide remediation pathways but introduce exposure and life-cycle concerns (Ateia et al., 2024; Liu et al., 2024; Wu et al., 2024).

These exposure and life-cycle concerns are well documented at the level of individual nanomaterial applications. Advanced in vitro and in silico safety-assessment tools are increasingly used to characterise the hazard profile of engineered nanomaterials ahead of deployment, reducing reliance on animal testing while improving mechanism-based risk characterisation (Fadeel et al., 2018). Life-cycle-oriented reviews of the nano-world more broadly identify environmental risk as distributed across a material's full production-to-disposal pathway rather than concentrated at the point of use, reinforcing the case for safe-and-sustainable-by-design approaches introduced in Section 2.1 (Glišović et al., 2017). Sector-specific evidence extends this concern to oil and gas operations directly relevant to the Nigerian context examined in this review: nanoparticle additives used in drilling muds improve technical performance but carry environmental, health, and safety implications that remain incompletely characterised, underscoring the need for occupational-exposure guidance to accompany, rather than follow, adoption (Martin et al., 2023).

2.8 Distinguishing Safety and Environmental Protection Outcomes

The review therefore distinguishes environmental monitoring from broader environmental protection. Monitoring applications have comparatively direct evidence, whereas pollution prevention, remediation, and governance remain more dependent on laboratory studies, reviews, and conceptual work. Forward-looking technology-forecasting reviews frame environmental engineering itself as entering a period of disruptive innovation, driven by sensing, data, and materials advances converging on pollution-prevention applications (Huang, Lu, Jin, & Ren, 2024), while membrane-based separation technologies illustrate the more laboratory-proximate evidence base typical of remediation applications specifically, with emerging directions targeting pollutant removal and degradation in aqueous systems

(Zhao et al., 2024). This distinction is retained in the evidence grading and in the Nigerian adoption framework.

Table 2: Depth of Empirical Coverage Across Safety and Environmental Outcome Categories

Outcome Category	Representative Evidence	Predominant Evidence Type
Occupational safety	Akinlolu et al. (2020); Yap et al. (2021); Dobrucalı et al. (2022)	Systematic reviews; site-level observational studies
Process / industrial safety	Di Martino et al. (2021); Benson et al. (2023); Akpe et al. (2024)	Case studies; conceptual frameworks
Environmental monitoring	Zhang et al. (2023); Cacciuttolo et al. (2023); Kukartsev et al. (2025)	Technical reviews; single-site case study
Pollution prevention	Huang et al. (2024); Ateia et al. (2024)	Conceptual / technology-forecasting reviews
Environmental remediation	Liu et al. (2024); Wu et al. (2024); Zhao et al. (2024)	Laboratory-scale evidence; narrative reviews
Environmental risk governance	Schulte et al. (2024); Cassee et al. (2024); Köhler & Som (2014)	Policy/framework papers

Table 2a complements this outcome-based view with a technology-based one, tracing each of the six technology categories through to its specific environmental application, the evidence maturity behind that application (using the same strong/moderate/weak logic operationalised in Table 4), and its plausible relevance to the Nigerian sectors discussed in Section 4.4. This technology-to-environmental-function view is intended to strengthen the environmental half of the review's dual safety/environmental scope without duplicating the outcome-category analysis in Table 2.

Table 2a. Technology-to-Environmental-Function Synthesis, with Evidence Maturity and Indicative Nigerian Relevance

Technology	Environmental Application	Evidence Maturity	Indicative Nigerian Relevance
IoT	Emissions, water, and ambient environmental monitoring	Strong–moderate	High — low-cost, scalable entry point (Section 5)
AI	Environmental-risk prediction and forecasting	Moderate	High — pairs naturally with IoT data streams
Drones	Remote environmental surveillance over large or hazardous areas	Moderate	High — extends monitoring reach without fixed infrastructure
Digital twins / BIM	Process optimisation and emissions reduction	Moderate	Moderate — constrained by capital cost and infrastructure (Table 8)
Nanomaterials	Soil, water, and pollutant remediation	Moderate	Potentially high, but safety-constrained pending exposure-limit clarity
VR / sensor fusion	Environmental and safety training, pollution visualisation	Limited	Moderate — training value plausible; outcome evidence thin

2.9 Critical Synthesis and Identified Gap

Across the six technology categories, the literature reports measurable safety and environmental benefits, but the evidence is dominated by reviews, conceptual frameworks, and single-site case studies rather than large empirical trials. Emerging technologies can also introduce new failure modes, occupational exposures, cybersecurity risks, and governance gaps (Salmon et al., 2024; Schulte et al., 2024). Technological-forecasting perspectives on environmental innovation caution more broadly that emerging technologies diffuse unevenly across institutional and economic contexts, so that global evidence of technical feasibility does not, by itself, predict the pace or pattern of adoption in any specific setting (Kargı & Coccia, 2024), a caution directly relevant to the Nigerian adoption framework developed in Section 4.4. Adoption barriers include cost, infrastructure, skills, organisational resistance, and regulatory capacity, with limited evidence from developing economies. The central gap is therefore not the absence of technological capability, but the limited empirical basis for determining how emerging technologies should be prioritised and governed in Nigerian engineering contexts.

3. MATERIALS AND METHODS

3.1 Review Design and Terminology

The review is designated a systematically informed narrative review rather than an unqualified systematic review. The latter typically requires dual independent screening, inter-rater reliability, and formal quality appraisal, which were not fully available here. The present design instead combines a reported search and screening process, manual verification, and an explicit evidence-grading rubric suited to a heterogeneous cross-sector corpus.

This hybrid label requires clarification given that Section 3.3 presents a four-stage, structured study-selection flow table styled after common systematic-review reporting conventions, and Section 3.5 presents a structured evidence-grading rubric, both of which are apparatus more commonly associated with systematic reviews. Three systematic-review elements were adopted: a staged, numerically reported selection process (Table 3); an explicit, reproducible grading rubric applied uniformly across included studies (Table 4); and transparent reporting of exclusion counts between stages. Three systematic-review elements were not adopted, and are flagged as limitations in Section 3.6: dual independent screening with an inter-rater reliability statistic; a pre-registered protocol; and a formal, validated quality-appraisal instrument (e.g., MMAT or CASP) in place of the purpose-built rubric. The review therefore sits deliberately between the two traditions, borrowing the transparency mechanisms of a systematic review while not claiming the full methodological guarantees, particularly independent replicability of the screening decisions, that the unqualified term would imply.

3.2 Search Strategy and Sources

The literature search used Consensus, an AI-assisted academic discovery platform, as a search-support tool. Four term groups were developed around emerging technologies, safety/environmental outcomes, engineering sectors, and developing-economy context. Twenty-three searches and one citation-graph expansion together produced an initial platform-reported count of 8,652,714 cumulative topical matches; the citation-graph expansion is included within, not additional to, this count. This figure warrants explicit clarification: it is the cumulative count of instances the platform's interface reported as topically matching one of the 23 queries or the citation-graph expansion against its full indexed corpus, which spans over 170 million papers, before deduplication, relevance ranking, or any manual review. It should be read as an indicator of the breadth of the underlying indexed corpus and the deliberately broad initial term groups used, not as a set of records that were individually retrieved, inspected, or screened; no claim is made that this number represents discrete, non-overlapping documents, and the figure is not itself labelled or treated as "records retrieved" anywhere else in this paper. The operationally meaningful figure, and the one from which all subsequent screening in Table 3 proceeds, is the 250-record set the platform's relevance-ranking algorithm surfaced for detailed human screening. The platform was used only to identify this manageable screening set; all inclusion decisions from that point forward were checked manually. Because the platform is proprietary, its ranking model and complete search logs are not independently auditable.

3.3 Study Selection Process

Table 3 summarises the four-stage selection process from identification to inclusion, presented as a study-selection flow table rather than a graphical flow diagram.

Table 3: Study Selection Flow, from Initial Identification to Final Inclusion

Stage	N	Process Applied
1. Identification	8,652,714	Cumulative platform-reported topical matches across 23 searches (4 term groups) + 1 citation-graph expansion, against the platform's indexed corpus (>170M papers); not individually retrieved or screened records
2. Screening	250	Platform relevance-ranking algorithm surfaced top-ranked records for detailed screening; deduplication applied
3. Eligibility	198	Records meeting topical relevance and minimum quality signal (peer-reviewed venue; explicit safety/environmental engineering application) after deduplication
4. Inclusion	37	Final selection of records with complete, independently verifiable bibliographic data, applying the explicit rule set out below

Inclusion criteria required that a paper (i) be published in a peer-reviewed journal or conference proceedings, (ii) report on at least one emerging technology applied to engineering safety, environmental protection, or both, and (iii) situate that application within an identifiable industrial sector. Papers addressing emerging technologies purely from a non-engineering perspective were excluded at Stage 3. Reasons for exclusion between Stage 2 and Stage 3 (52 records) were topical irrelevance on full-abstract reading and absence of an identifiable engineering-sector application; a record-level exclusion log was not retained in exportable form and is noted as a reproducibility limitation in Section 3.6. Journal articles and conference proceedings were both eligible and were not differentiated by a separate quality-weighting scheme; this is likewise flagged as a limitation, since venue type can correlate with review rigour.

The Stage 3-to-Stage 4 transition requires clarification, since eligibility (198 records) and final inclusion (37 records) differ substantially and this attrition should not be read as arbitrary. “Complete, independently verifiable bibliographic data” means, concretely, that a record carried a full author list, publication year, journal or proceedings title, volume/issue and page range (or article number), and a resolvable DOI or equivalent stable identifier (e.g., a persistent publisher URL) that could be checked against an independent source rather than taken on the platform's metadata alone. Records were dropped between eligibility and inclusion primarily for three reasons: incomplete platform-exported metadata, most commonly a missing or malformed DOI, common among conference proceedings and recently published articles not yet fully indexed; inability to independently verify the record against a second source, since platform-only metadata was not treated as sufficient on its own after the verification issues discussed in Section 3.4; and, in a smaller number of cases, records that on closer full-text reading did not, in fact, report a specific, attributable technology application meeting the inclusion criteria despite passing automated relevance screening. The 81 percent attrition between eligibility and inclusion is therefore substantially a function of the verification standard applied, deliberately stringent, given the citation-integrity concerns that motivated Section 3.4, rather than of topical irrelevance, which had already been filtered out at the earlier eligibility stage. The platform synthesis referenced a target pool of up to 50 topically relevant records within the eligible set; of these, 37 satisfied the full bibliographic-verification standard above. The final evidence corpus is therefore defined as the 37 fully verified studies. No additional records were inferred, fabricated, or counted without verifiable bibliographic support. Tables and conclusions use 37 as the denominator unless explicitly stated otherwise.

3.4 Role of AI-Assisted Discovery and Human Verification

The Consensus relevance-ranking algorithm narrowed the very large initial pool to a manageable screening set and ranked the eligible records for further consideration. It is treated only as

a search-support mechanism, not as an independent methodological authority. The model is proprietary and its ranking weights are not independently auditable; consequently, manual verification was used for final inclusion. Exact platform query strings, execution dates, and ranking scores were not retained, which limits exact replication.

3.5 Data Extraction and Evidence-Grading Rubric

Data extracted from each retained paper included technology category, sector, reported safety or environmental function, any quantified outcome measures, and stated limitations or barriers. Table 4 sets out the explicit rubric applied. Each claim synthesised in Section 4.3 was scored against five criteria, number of independent supporting studies, predominant study-design quality, presence of replication, geographic diversity of the supporting evidence, and the nature of outcome measurement.

Table 4: Operationalised Evidence-Grading Rubric

Criterion	Low / Weak Signal	Moderate Signal	High / Strong Signal
Number of independent studies	1 study	2–3 studies	4+ independent studies
Study design quality	Conceptual / opinion	Observational / single case study	Multiple observational or quasi-experimental studies
Replication	None	Limited (1 corroborating source)	Multiple independent corroborations
Geographic / contextual diversity	Single site or region	2–3 regions or sectors	4+ regions or sectors
Outcome measurement	Qualitative / descriptive only	Proxy or partial quantitative measure	Direct, quantified outcome measure

The overall strong/moderate/weak grade was not derived from a mechanical count of how many of the five criteria fell into each band. Instead, the default rule was that a grade required at least three of the five criteria to point in the same direction, with the more conservative (lower) grade assigned wherever the criteria diverged. This default was overridden in one specific, explicitly flagged circumstance: where a claim rested on a single case but that case reported a direct, quantified outcome measure (the strongest of the five criteria) rather than a qualitative or proxy measure, the claim was graded moderate rather than weak, on the reasoning that a precisely measured single-case effect carries more evidentiary weight than an equivalently single-source qualitative judgement, while still falling well short of a claim replicated across independent, geographically diverse studies. This override applies to exactly two claims in Table 7, both flagged there with an asterisk and explained in the accompanying note; every other grade in Table 7 follows the default majority rule without exception. This exception-based logic, rather than a strict unweighted vote across the five criteria, is what Table 7 reports, and it is disclosed here explicitly so the grading is reproducible rather than merely asserted.

This rubric was applied retrospectively to the corpus rather than pre-registered, which is itself a limitation relative to full systematic-review practice; it nonetheless represents a substantial improvement in transparency and reproducibility over an unstructured strong/moderate/weak judgement, and the platform's own algorithmically generated evidence-reasoning summaries were cross-checked against, rather than substituted for, this manual rubric.

3.6 Methodological Limitations

The following limitations qualify, but do not negate, the value of the synthesis; they define the boundary of what the review can credibly claim, which is an evidence-graded narrative synthesis that is transparent and reproducible in its reported screening logic and grading rubric, but not fully reproducible at the level of the underlying platform searches themselves, given the search-log limitation noted below, rather than a protocol-registered systematic review with meta-analytic pooling.

- 50-versus-37 record discrepancy: the discovery platform referenced up to 50 relevant records, but only 37 carried complete, independently verifiable bibliographic detail on export; the manuscript therefore uses the 37 verified studies as its evidence corpus.
- Single-analyst screening: no second independent reviewer and no inter-rater reliability statistic is available.
- Proprietary relevance algorithm: the Consensus ranking model is not independently auditable, and false negatives (relevant papers never surfaced) could not be assessed.
- Search-log limitation: exact platform query strings, execution dates, and platform-generated ranking scores for the 23 individual searches were not retained, limiting exact replication of the search process; Section 3.2 reports an illustrative representative formulation in place of a verbatim log.
- No formal quality-appraisal instrument (e.g., MMAT, CASP) was applied; the evidence-grading rubric in Table 4 is a purpose-built substitute, not an equivalent.
- No language restriction was explicitly enforced, and the retained corpus is entirely English-language by outcome rather than by declared protocol.
- Journal articles and conference proceedings were not differentiated by a separate quality weighting.
- A record-level exclusion log for the 52 records dropped between screening and eligibility was not preserved in exportable form.
- Drones, while discussed qualitatively as one of the six technology categories throughout Section 2, were not separately coded in the quantitative outcome-frequency matrix (Table 9) during data extraction, and are therefore absent from that table; no drone-specific frequency counts have been estimated or invented to fill this gap.

4. RESULTS

Table 5 summarises illustrative studies from the retained corpus, selected to represent the range of technology categories, sectors, and evidence types synthesised in Section 2. This table reports only the study-level detail available from the extracted source material; it is presented as a representative subset of the 37 verified included studies rather than an exhaustive table of all 37, since location, sample size, and full methodological detail were not uniformly retrievable for every included paper, itself a data-extraction limitation noted in Section 3.6.

Table 5: Representative Studies from the Reviewed Corpus, by Technology Category and Sector

Study	Technology Focus	Sector / Context	Principal Finding	Evidence Type
Akinlolu et al. (2020)	Construction safety technologies (bibliometric)	Construction	Maps research architecture of 240 construction-safety technology papers	Bibliometric review
Zhang et al. (2023)	IoT architectures	Underground mining	IoT enables simultaneous environmental, safety, and production monitoring	Technical review
Kukartsev et al. (2025)	Integrated IT / environmental monitoring	Regional mining complex	18–22% reduction in industrial/environmental risk (single site)	Case study
Di Martino et al. (2021)	Inherently safer design (ISD) framework	Chemical / process industry	58–70% safety improvement (single case)	Case study
Maali et al. (2024)	Construction safety technologies (taxonomy)	Construction	Categorises 129 articles (2018–2023) into four safety-technology functions	Systematic review
Yap et al. (2021)	BIM, robotics, wearables	Construction (Malaysia)	BIM and wearables show strongest individual safety effects	Empirical / survey study
Cacciuttolo et al. (2023)	Low-cost IoT sensors	Mining	Sensor networks as foundational layer for Industry 4.0 mining transformation	Systematic review
Liu et al. (2024)	Nanoparticle remediation	Soil and water	Nanoparticles function as efficient sorbents/catalysts for pollutant removal	Narrative review
Wu et al. (2024)	Functional nanomaterials	Environmental remediation	Calls for Safe and Sustainable-by-Design given unresolved exposure limits	Narrative review
Kuppula & Bhawani (2025)	Exoskeletons, jobsite technology	Construction	Productivity gains alongside unresolved long-term worker-health concerns	Thematic analysis

4.1 Sector Comparison: Mining and Oil and Gas

Both sectors rely on IoT sensing and automation as a core safety mechanism, but the specific hazard managed, and the quantified impact reported, differ, as summarised in Table 6. In mining, automation and remote-controlled equipment reduce human exposure to hazardous conditions and improve emergency response (Onifade et al., 2023; Arjunan et al., 2025); in oil and gas, offshore drilling safety advances include spill-prediction models, automated safety protocols, and emission-control measures such as carbon capture and flare-gas recovery (Alamutu, 2025). As already noted in Section

2.4, the 18–22% and 58–70% figures reported below are single-case findings and are not to be read as expected sector-wide effects.

Table 6: Comparison of Mining and Oil and Gas Safety Technology Applications

Dimension	Mining	Oil and Gas
Core technology	IoT sensors, automation, remote equipment	Real-time monitoring, predictive analytics, digital twins
Safety mechanism	Reduces human exposure to hazardous conditions	Detects anomalies before escalation
Environmental function	Proactive geotechnical and gas monitoring	Spill prediction, emissions control
Key barrier	Battery life; underground communication quality	Integration with legacy systems
Reported impact (single case; not generalisable)	18–22% risk reduction with integrated IT	58–70% safety improvement with ISD framework

4.2 Construction-Sector Evidence

Construction-sector evidence is comparatively richer in systematic reviews. A bibliometric analysis of 240 construction-safety technology papers establishes the field's overall research architecture (Akinlolu et al., 2020), while a subsequent systematic review of 129 articles (2018–2023) categorises construction safety technologies across four functional areas (Maali et al., 2024). Smart technologies, digital twins, IoT, and big data, are reported to enhance construction-site safety proactively while simultaneously optimising energy use and lowering carbon emissions (Seo & Yoon, 2025). This benefit is not unqualified: emerging construction technologies also introduce sustainability challenges of their own, including high energy consumption, electronic-waste generation, elevated implementation costs, and labour-market disruption, with exoskeletons specifically flagged as improving short-term productivity while raising unresolved questions about long-term musculoskeletal health, a claim graded weak in Table 7 given its reliance on a single thematic-analysis finding (Kuppula & Bhawani, 2025).

4.3 Evidence-Strength Assessment

Applying the operationalised rubric in Table 4 and the exception rule described in Section 3.5, Table 7 grades the strength of evidence behind the review's principal claims and reports the rubric criteria underlying each grade, rather than an unexplained qualitative label. The strongest-graded claim, that IoT and AI improve safety monitoring and hazard detection, is supported by four or more independent, high-quality sources converging across mining, construction, and oil and gas, with quantified outcome measures reported in at least two of those sources (Zhang et al., 2023; Dimkpa et al., 2025; Seo & Yoon, 2025; Akpe et al., 2024). Claims regarding digital twins/BIM and nanotechnology remediation are graded moderate under the default majority rule, reflecting two to three supporting studies with predominantly observational or conceptual designs and limited geographic diversity. The two single-case quantitative claims (18–22% and 58–70%) are graded moderate under the explicit exception described in Section 3.5, since a direct, quantified single-case outcome measure was judged to carry more evidentiary weight than an equivalent single-source qualitative claim, while still falling short of the replication and geographic-diversity needed for a strong grade. The weakest-graded claim, concerning exoskeleton health effects, satisfies none of the five criteria beyond a single qualitative source and receives the default weak grade with no exception applied.

Table 7: Evidence Strength for Key Claims, Graded Against the Rubric in Table 4

Claim	Independent Studies	Design Quality	Replication	Geographic Diversity	Overall Grade
IoT and AI improve safety monitoring and hazard detection	4+	Observational/quasi-experimental (multiple)	Multiple	4+ sectors	Strong
Digital twins/BIM enhance construction safety via proactive hazard identification	2–3	Observational + conceptual	Limited	2–3 contexts	Moderate
Nanotechnology enables remediation but poses toxicity risks requiring SSbD	3+	Laboratory / conceptual	Limited	Single domain (materials)	Moderate
Integrated IT deployment reduces industrial/environmental risk by 18–22%	1	Single case study	None	Single site	Moderate*
ISD framework improves safety by 58–70%	1	Single case study	None	Single site	Moderate*
Exoskeletons raise long-term worker-health concerns	1	Thematic analysis (qualitative)	None	Single context	Weak

*Graded moderate under the explicit exception in Section 3.5: a direct, quantified single-case outcome measure outweighs the single-study and no-replication criteria that would otherwise default to weak, but does not itself constitute evidence of generalisability — see Section 4.1 and the case-specific labelling applied throughout.

4.4 A Conceptual/Indicative Nigeria-Specific Adoption Framework

None of the 37 studies in the final synthesis reported an empirical Nigerian or West African case. The framework in Table 8 is therefore presented as a conceptual/indicative adoption framework, not an adoption index or measured assessment of Nigerian conditions. Its ratings are author judgments derived from the reviewed evidence and contextual reasoning, not Nigerian survey data, Delphi ratings, frequency counts, or weighted scores. The framework is a structured starting point for empirical validation and scores four priority technology groupings against twelve adoption-relevant dimensions using Low/Moderate/High ratings.

Table 8: Conceptual/Indicative Nigeria-Specific Technology-Adoption Framework (Author Judgment, Not a Measured National Readiness Index; Requires Empirical Validation)

Dimension	**IoT / AI Monitoring**	**Digital Twins / BIM**	**VR Safety Training**	**Nanotech Remediation**
Capital cost	Low–Moderate	High	Moderate	Moderate–High
Technical infrastructure need	Low–Moderate	High	Moderate	Moderate
Electricity/connectivity reliability need	Moderate	High	Moderate	Low
Skills availability (current)	Moderate	Low	Low	Low
Maintenance capacity required	Moderate	High	Moderate	Moderate
Regulatory readiness	Low	Low	Low	Low
Data governance exposure	Moderate	Moderate	Low	Low
Cybersecurity exposure	Moderate–High	Moderate	Low	Low
Organisational readiness	Moderate	Low	Low–Moderate	Low
Technology maturity (global)	High	Moderate–High	Moderate	Moderate
Environmental benefit (global evidence)	Moderate	Low–Moderate	Low	High
Safety benefit (global evidence)	High	Moderate	Moderate	Low

Read across dimensions, the framework indicates that IoT/AI monitoring combines the most favourable near-term adoption profile (comparatively low capital and infrastructure requirements against the strongest global safety-evidence base) with a genuine governance gap (low regulatory readiness, moderate-to-high cybersecurity exposure) that Nigerian regulators would need to address concurrently with, not after, deployment. Digital twins/BIM and nanotechnology remediation both show a wider gap between global technology maturity/environmental promise and local readiness (skills, infrastructure, or regulation), consistent with the near-total absence of developing-economy evidence identified in Section 4.5.

4.5 Research Gaps by Outcome Dimension

The 37-study corpus provides an uneven picture of evidence coverage. Counting, within the verified papers, how many address each of five outcome dimensions per technology category, Table 9 shows comparatively stronger empirical coverage for IoT safety monitoring and nanotechnology remediation, moderate coverage for AI predictive analytics and VR safety training, and less coverage for digital twins. Developing-economy evidence is particularly sparse: AI, VR, and digital twins record no papers specifically addressing such contexts, while IoT and nanotechnology each have only one. Drones are not separately coded in this matrix and are therefore excluded from the frequency counts.

Table 9: Number of Included Papers (of 37) Addressing Each Outcome Dimension, by Technology Category (Drones Not Separately Coded)

Technology	Empirical Validation	Long-Term Safety	Cost-Effectiveness	Developing Economies	Regulatory Frameworks
IoT safety monitoring	8	3	2	1	4
AI predictive analytics	6	2	1	0 (gap)	3
Nanotechnology remediation	9	5	2	1	4
VR safety training	5	1	2	0 (gap)	2
Digital twins	4	1	1	0 (gap)	2

This exclusion has a direct implication for how the gap analysis in this section should be read: because drones are not separately coded in Table 9, the research-gap picture presented here characterises five of the review's six technology categories rather than all six, and the apparent evidence coverage of the reviewed corpus as a whole is correspondingly incomplete rather than exhaustive. Drone-specific applications are still discussed qualitatively in Section 2.6 and appear in the technology-function matrix (Table 1) and the environmental-function synthesis (Table 2a), so the omission is confined to this specific outcome-dimension frequency count rather than to the review's coverage of drones generally; a coded drone row is identified in Section 3.6 as a specific target for the data-extraction protocol in any future update of this analysis.

5. DISCUSSION

The graded evidence supports a bounded set of conclusions. IoT- and AI-enabled monitoring has the strongest convergent evidence in the corpus, while digital twins/BIM, immersive technologies, and nanotechnology remain less mature. The 18–22% and 58–70% figures are single-case findings and should not be interpreted as general technology effects. The evidence therefore supports prioritising scalable monitoring and predictive applications while treating higher-cost or less mature technologies as context-dependent investments.

For Nigeria, the implication is not that globally better-supported technologies should be adopted uncritically. Rather, adoption should be phased according to infrastructure, skills, maintenance, governance, cybersecurity, and regulatory readiness. Read as an indicative, author-judgment proposition rather than as validated guidance, the conceptual framework in Table 8 suggests that IoT/AI monitoring may offer the most accessible near-term entry point, provided governance and cybersecurity measures develop alongside deployment; this reading should be treated as a hypothesis for empirical testing, not as an established prioritisation.

The oil and gas evidence carries a parallel, similarly bounded implication for the Niger Delta context. Offshore and onshore drilling safety advances, spill-prediction models, automated safety protocols, and emissions-control measures including flare-gas recovery, address categories of environmental harm that have historically defined Nigeria's upstream environmental challenges (Alamutu, 2025; Akerele et al., 2024). The inherently safer design (ISD) framework's reported 58–70% safety improvement (Di Martino et al., 2021) illustrates the scale of improvement that engineering-controls-first approaches can plausibly achieve relative to administrative controls or PPE-led interventions alone, consistent with broader process-industry evidence that combining engineering controls, administrative controls, PPE, and behavioural interventions outperforms any single intervention type (Benson et al., 2023), but the specific 58–70% figure itself remains a single-case artefact that should inform expectations only qualitatively, not quantitatively.

The review's risk categories are particularly relevant to Nigerian implementation. Responsible-development principles should accompany deployment so that technologies introduced to improve

safety do not create new occupational, privacy, cybersecurity, or environmental risks. AI and IoT systems require data governance and cyber controls; nanomaterials require exposure and life-cycle safeguards; and digital twins require reliable infrastructure and technical skills. These are governance conditions, not findings measured in Nigeria.

This review's limitations, detailed in full in Section 3.6, bear directly on how its findings should be used. As a single-analyst, platform-assisted synthesis of secondary sources without a formal quality-appraisal instrument, it inherits real reproducibility constraints. The Nigerian policy implications drawn here are, without exception, extrapolations from global evidence rather than findings validated within Nigeria itself, and the framework in Table 8 should be read as a proposed research and investment agenda awaiting empirical testing, not as a confirmed characterisation of Nigerian conditions.

6. CONCLUSIONS

This review synthesised 37 verified peer-reviewed studies on emerging technologies for safety and environmental protection across construction, mining, and oil and gas engineering. Its contributions are threefold: a cross-sectoral evidence-graded map of six technology categories; an operationalised evidence-grading rubric with transparent limitations; and a twelve-dimension, explicitly indicative Nigerian adoption framework. The evidence is strongest for IoT- and AI-enabled monitoring and more limited for digital twins/BIM, immersive technologies, and nanotechnology. The review supports phased adoption of scalable monitoring and predictive technologies, accompanied by regulatory, cybersecurity, occupational-exposure, and workforce-development measures.

For policy, the findings support three concrete actions, each qualified by the review's evidentiary limits and by the conceptual, not empirically validated, status of the Table 8 framework from which the second and third actions draw: strengthening NESREA and sector-regulator capacity to evaluate emerging-technology deployments, guided by the regulatory-readiness gap identified in Table 8 rather than by the single-case quantitative figures reported in Section 4; incentivising phased, low-cost sensor and predictive-analytics adoption among small- and medium-scale mining and construction operators, as the technology category with both the strongest global safety evidence and, on the indicative framework's author-judgment ratings only, the most favourable near-term adoption profile; and establishing local occupational-exposure guidance for engineered nanomaterials ahead of, rather than after, wider deployment, given the unresolved global exposure-limit gap identified in Section 2.7. Each action should be piloted and revisited as the Table 8 ratings are empirically tested, rather than treated as settled by this review alone.

These contributions connect directly to ICESID 2026's conference theme, “Innovating Tomorrow: Harnessing Engineering to Drive Nigeria's Growth for Sustainable Development.” The twelve-dimension adoption framework operationalises that theme at the level of individual technology-adoption decisions: it gives engineering practitioners and regulators a structured, if indicative, basis for harnessing globally emerging technologies in a manner calibrated to Nigeria's present infrastructure, skills, and regulatory conditions, rather than importing innovation agendas wholesale from better-resourced economies. In that sense, the framework's central proposition, that sustainable engineering-driven growth depends on matching technology adoption to demonstrated local readiness rather than to global technology maturity alone, is offered as a direct, if empirically provisional, contribution to the conference's growth-and-sustainability agenda for Nigerian engineering.

Priority future research includes empirical validation of the Table 8 framework under Nigerian mining, construction, and oil and gas conditions; longitudinal studies of worker-health outcomes for wearable and exoskeleton technologies; techno-economic evaluation of AI predictive-maintenance deployment; and locally grounded governance research on AI monitoring, privacy, and data protection. These studies would address the central limitation of the current literature: the shortage of Nigeria-specific empirical evidence on emerging technologies for safe and environmentally responsible engineering.

REFERENCES

Adikwu, F. E., Esiri, A. E., Aderamo, A. T., Akano, O. A., & Erhueh, O. V. (2024). Leveraging digital technologies for health, safety, and environmental (HSE) management in industrial operations.

International Journal of Applied Research in Social Sciences. https://doi.org/10.51594/ijarss.v6i11.1722

Adio, S. A., Ajirotutu, R. O., Olayiwola, R. K., Erinjogunola, F. L., & Sikhakhane-Nwokediegwu, Z. (2025). Engineering a safer future: How HSE innovation is transforming infrastructure and sustainability. *International Journal of Future Engineering Innovations, 2*(2), 28–42. https://doi.org/10.54660/ijfei.2025.2.2.28-42

Akerele, J. I., Adikwu, F. E., Esiri, A. E., Aderamo, A. T., Akano, O. A., & Erhueh, O. V. (2024). Strengthening environmental safety in oil and gas operations: Optimizing health, safety, and environmental (HSE) protocols. *International Journal of Engineering Research Updates, 7*(2). https://doi.org/10.53430/ijeru.2024.7.2.0048

Akinlolu, M., Haupt, T., Edwards, D., & Simpeh, F. (2020). A bibliometric review of the status and emerging research trends in construction safety management technologies. *International Journal of Construction Management, 22*, 2699–2711. https://doi.org/10.1080/15623599.2020.1819584

Akpe, A. T., Nuan, S. I., Solanke, B., & Iriogbe, H. O. (2024). Balancing plant safety and efficiency through innovative engineering practices in oil and gas operations. *Global Journal of Advanced Research and Reviews*. https://doi.org/10.58175/gjarr.2024.2.1.0029

Alamutu, O. I. (2025). Enhancing safety and emissions control in offshore drilling: A framework for oil spill prevention and environmental protection. *Current Journal of Applied Science and Technology, 44*(44). https://doi.org/10.9734/cjast/2025/v44i44527

Arjunan, R., Ramadass, S., Murugan, G., & Chockalingam, P. (2025). Safe mining operations through technological advancement. *International Journal of Science and Research (IJSR)*. https://doi.org/10.21275/sr25415232225

Ateia, M., Wei, H., & Andreescu, S. (2024). Sensors for emerging water contaminants: Overcoming roadblocks to innovation. *Environmental Science & Technology*. https://doi.org/10.1021/acs.est.3c09889

Benson, C., Obasi, I. C., Akinwande, D. V., & Ile, C. (2023). The impact of interventions on health, safety and environment in the process industry. *Heliyon, 10*. https://doi.org/10.1016/j.heliyon.2023.e23604

Cacciuttolo, C., Guzmán, V., Catriñir, P., Atencio, E., Komarizadehasl, S., & Lozano-Galant, J. (2023). Low-cost sensors technologies for monitoring sustainability and safety issues in mining activities: Advances, gaps, and future directions in the digitalization for smart mining. *Sensors, 23*(15), 6846. https://doi.org/10.3390/s23156846

Cassee, F., Bleeker, E., Durand, C., Exner, T. E., Falk, A., Friedrichs, S., Heunisch, E., Himly, M., Hofer, S., Hofstätter, N., Hristozov, D., Nymark, P., Pohl, A., Soeteman-Hernández, L. G., Suarez-Merino, B., Valsami-Jones, E., & Groenewold, M. (2024). Roadmap towards safe and sustainable advanced and innovative materials (Outlook for 2024–2030). *Computational and Structural Biotechnology Journal, 25*, 105–126. https://doi.org/10.1016/j.csbj.2024.05.018

Di Martino, Y., Duque, S., Reniers, G., & Cozzani, V. (2021). Making the chemical and process industries more sustainable: Innovative decision-making framework to incorporate technological and non-technological inherently safer design (ISD) opportunities. *Journal of Cleaner Production, 296*, 126421. https://doi.org/10.1016/j.jclepro.2021.126421

Dimkpa, K., Ohochukwu, P., & Azike, C. (2025). Impact of emerging technologies on environmental monitoring and industrial safety compliance. *Environmental Technology and Science Journal, 16*(1). https://doi.org/10.4314/etsj.v16i1.15

Dobrucalı, E., Demirkesen, S., Sadikoğlu, E., Zhang, C., & Damci, A. (2022). Investigating the impact of emerging technologies on construction safety performance. *Engineering, Construction and Architectural Management*. https://doi.org/10.1108/ecam-07-2022-0668

Fadeel, B., Farcal, L., Hardy, B., Vázquez-Campos, S., Hristozov, D., Marcomini, A., Lynch, I., Valsami-Jones, E., Alenius, H., & Savolainen, K. (2018). Advanced tools for the safety

assessment of nanomaterials. *Nature Nanotechnology, 13*, 537–543. https://doi.org/10.1038/s41565-018-0185-0

Glišović, S., Pešić, D., Stojiljković, E., Golubović, T., Krstić, D., Prascevic, M., & Janković, Ž. (2017). Emerging technologies and safety concerns: A condensed review of environmental life cycle risks in the nano-world. *International Journal of Environmental Science and Technology, 14*, 2301–2320. https://doi.org/10.1007/s13762-017-1367-2

Gobbo, J. A., Busso, C. M., Gobbo, S. C. O., & Carreão, H. (2018). Making the links among environmental protection, process safety, and industry 4.0. *Process Safety and Environmental Protection*. https://doi.org/10.1016/j.psep.2018.05.017

Gupta, A., Singh, S., Asari, V. K., & Nguyen, T. V. (2026). Enhancing sustainability and construction safety research in the era of artificial intelligence. *ASME Journal of Engineering for Sustainable Buildings and Cities*. https://doi.org/10.1115/1.4071434

Huang, H., Lu, J., Jin, L., & Ren, H. (2024). The future of environmental engineering technology: A disruptive innovation perspective. *Engineering*. https://doi.org/10.1016/j.eng.2024.06.009

Kargı, B., & Coccia, M. (2024). Emerging innovative technologies for environmental revolution: A technological forecasting perspective. *International Journal of Innovation*. https://doi.org/10.5585/2024.27000

Köhler, A., & Som, C. (2014). Risk preventative innovation strategies for emerging technologies: The cases of nano-textiles and smart textiles. *Technovation, 34*, 420–430. https://doi.org/10.1016/j.technovation.2013.07.002

Kukartsev, V., Matasova, I., Stupina, A., & Voytovich, E. (2025). Information technologies for ensuring industrial and environmental safety in the development of the regional mining complex. *Sustainable Development of Mountain Territories, 17*(3), 1700–1710. https://doi.org/10.21177/1998-4502-2025-17-3-1700-1710

Kumar, P., Walia, S., & Kumar, R. (2025). Construction safety and technology of civil engineering in high-rise building. *Journal of Civil Engineering and Applications, 6*(1a). https://doi.org/10.22271/27078388.2025.v6.i1a.38

Kuppula, N., & Bhawani, S. (2025). Sustainability in the age of innovation: Negative impacts of jobsite construction technologies. *CIB Conferences*. https://doi.org/10.7771/3067-4883.2121

Liu, X., Sathishkumar, K., Zhang, H., Saxena, K. K., Zhang, F., Naraginiti, S., K, A., Rajendiran, R., Aruliah, R., & Guo, X. (2024). Frontiers in environmental cleanup: Recent advances in remediation of emerging pollutants from soil and water. *Journal of Hazardous Materials Advances*. https://doi.org/10.1016/j.hazadv.2024.100461

Maali, O. N., Ko, C.-H., & Nguyen, P. H. D. (2024). Applications of existing and emerging construction safety technologies. *Automation in Construction, 158*, 105231. https://doi.org/10.1016/j.autcon.2023.105231

Martin, C., Nourian, A., Babaie, M., & Nasr, G. (2023). Environmental, health and safety assessment of nanoparticle application in drilling mud — Review. *Geoenergy Science and Engineering*. https://doi.org/10.1016/j.geoen.2023.211767

Okolie, A. C., Ojialor, C., Adenusi, F., & Okeyode, A. I. (2024). Sustainable safety and environmental protection technologies in oil and gas industry. *Asian Journal of Environment & Ecology, 23*(6). https://doi.org/10.9734/ajee/2024/v23i6551

Onifade, M., Said, K. O., & Shivute, A. P. (2023). Safe mining operations through technological advancement. *Process Safety and Environmental Protection*. https://doi.org/10.1016/j.psep.2023.05.052

Salmon, P., King, B. J., Elstak, I., Mclean, S., & Read, G. (2024). Tomorrow's demons: A scoping review of the risks associated with emerging technologies. *Ergonomics, 68*, 1491–1507. https://doi.org/10.1080/00140139.2024.2416554

Schulte, P. A., Leso, V., & Iavicoli, I. (2024). Responsible development of emerging technologies. *Journal of Occupational and Environmental Medicine, 66*, 528–535. https://doi.org/10.1097/jom.0000000000003100

Seo, H., & Yoon, Y.-G. (2025). Analyzing research trends in smart construction safety: A topic modeling approach. *Buildings, 15*(4), 520. https://doi.org/10.3390/buildings15040520

Strzałkowski, P., Romańczukiewicz, K., Bęś, P., Delijewska, B., Sitarska, M., & Janiszewski, M. (2025). The application of VR technology in engineering issues: Geodesy and geomatics, mining, environmental protection and occupational safety. *Sensors, 25*, 6848. https://doi.org/10.3390/s25226848

Wu, S., Peng, J., Lee, S. L. J., Niu, X., Jiang, Y., & Lin, S. (2024). Let the two sides of the same coin meet — Environmental health and safety-oriented development of functional nanomaterials for environmental remediations. *Eco-Environment & Health, 3*, 494–504. https://doi.org/10.1016/j.eehl.2024.06.001

Yap, J. B., Lee, K. P. H., & Wang, C. (2021). Safety enablers using emerging technologies in construction projects: Empirical study in Malaysia. *Journal of Engineering, Design and Technology*. https://doi.org/10.1108/jedt-07-2021-0379

Zhang, H., Li, B., Karimi, M., Saydam, S., & Hassan, M. (2023). Recent advancements in IoT implementation for environmental, safety, and production monitoring in underground mines. *IEEE Internet of Things Journal, 10*, 14507–14526. https://doi.org/10.1109/jiot.2023.3267828

Zhao, D., Zhou, W., Shen, L., Li, B., Sun, H., Qianqian, Z., Tang, C. Y., Lin, H., & Chung, T.-S. (2024). New directions on membranes for removal and degradation of emerging pollutants in aqueous systems. *Water Research, 251*, 121111. https://doi.org/10.1016/j.watres.2024.121111

ENHANCED ANAEROBIC DIGESTION OF COW DUNG AND POULTRY DUNG VIA A COUPLED MICROBIAL ELECTROLYTIC CELL: OPTIMIZATION, KINETICS, AND THERMODYNAMIC STUDIES.

Ijuptil Ndumari[1,*], Olakunle Michael Sunday[1], Auwal Aliyu[1]
[1]*Ahmadu Bello University, Zaria*
Email: inmsgulak@gmail.com*, molakunles@gmail.com, aualiyu@yahoo.com
***Corresponding author**: Ijuptil Ndumari
DOI: https://doi.org/10.67203/sp.ICESID.2026

ABSTRACT

Coupling a microbial electrolysis cell (MEC) with anaerobic digestion (AD) is an effective approach to improving methane yield from agricultural waste. The current research focuses on the optimization, kinetics, and thermodynamic analysis of the MEC–AD hybrid system using cow dung and poultry dung as substrates. The physicochemical characterization results show that cow dung has higher volatile solids (78.20%) and a C:N ratio of 26.0, while poultry dung contains 62.35% volatile solids and a C:N ratio of 6.26. Based on mass balance calculations, the optimum substrate mixture containing 98.3% cow dung and 1.7% poultry dung is obtained to reach the optimum C:N ratio of 25:1. The optimization process was carried out by applying Response Surface Methodology using Central Composite Design involving applied voltage (0.3–1.5 V), pH (6–8), and C:N ratio (15–35). The proposed quadratic equation showed a high prediction accuracy (R^2 = 0.9997) and obtained the optimum values of 0.97 V, pH 7.0, and C:N ratio of 25 with the optimum methane yield of 350.73 mL CH_4 g^{-1} VS. Based on kinetic analysis using the Modified Gompertz model, the ultimate methane potential, maximum methane production rate, and lag phase were found to be 378.33 mL CH_4 g^{-1} VS, 41.25 mL CH_4 g^{-1} VS day^{-1}, and 1.36 days, respectively. Thermodynamic analysis showed that the process achieved 91.02% energy efficiency, 73.8% exergy efficiency, and an EROI of 29.55, confirming its favorable energetic and thermodynamic performance. Overall, the hybrid MEC–AD process significantly improved the methane yield.

Keywords: *Anaerobic digestion; Microbial electrolysis cell; Cow dung; Poultry waste; Methane production*

1. INTRODUCTION

The growing demand for energy and the environmental effects of fossil fuels have attracted the attention of researchers toward renewable energy generation systems. Anaerobic digestion (AD) is one of the promising approaches to produce methane, the main component of biogas, from organic wastes and address waste management issues (Angelidaki et al., 2009; Mao et al., 2015a). However, the conventional AD process can be affected by low methane production, substrate inhibition, and slow degradation (Appels et al., 2008).

Coupling AD with a microbial electrolysis cell (MEC) has been proposed to overcome the above problems. Low current input can increase the activity of electroactive microorganisms, facilitate direct interspecies electron transfer (DIET), and increase methane formation from organic waste (Ao et al., 2024; Wang et al., 2024). The applied voltage can accelerate the metabolism of microorganisms, increase electron transfer between them, and reduce the lag time before methane generation (Kaneko et al., 2025; Worajo et al., 2025).

Cow dung and poultry dung can be considered as suitable substrates for MEC-AD technology, since these are abundant agricultural wastes which contain biodegradable organic compounds (Kafle & Chen, 2016; Telo & Yigezu, 2025). Nevertheless, each of these substrates has certain drawbacks, which can affect the digestion performance. High nitrogen concentration in poultry dung can cause the accumulation of ammonia and inhibit methanogenic bacteria (Zhao et al., 2021). Moreover, the presence of lignocellulose in cow dung slows down its decomposition and limits the digestion rate (Zhang et al., 2025). The co-digestion process can increase the balance of nutrients and the stability of the microenvironment for methane-producing microorganisms (Mao et al., 2015b).

In this study, the possibility of improvement in methane production in the integrated MEC-AD system was investigated. First of all, the substrates were characterized from physicochemical and elemental perspectives. Additionally, Response Surface Methodology (RSM) was used for optimization of the operational parameters of the system. Kinetics of methane production was modeled using the Modified Gompertz model and validated with independent experiments (Sheron et al., 2026). Finally, energy, thermodynamic, and exergy analysis of the MEC-AD system was conducted.

2. METHODOLOGY

2.1 Substrate Collection and Preparation

Fresh cow dung and poultry dung were obtained from the Teaching and Research Farm at Ahmadu Bello University in Zaria, Nigeria. The poultry dung included both droppings and bedding materials used in poultry houses. The samples were placed in sealed containers, taken to the lab, and kept at 4°C to prevent changes before testing. Before starting the experiments, each type of material was mixed well. The mixture was passed through a 2 mm sieve to remove large fragments. Distilled water was added to dilute the solids to between 8% and 10%. This range is known to be good for digestion (Chojnacka & Moustakas, 2024).

2.2 Physicochemical and Elemental Analysis

The physicochemical tests followed the methods from APHA (2017). Total solids were found by drying the samples in an oven at 105°C. Volatile solids were measured by burning the dried samples at 550°C. Chemical Oxygen Demand was tested using the reflux titrimetric method. Total Organic Carbon was found with the Walkley- wet oxidation method (Nelson & Sommers, 1996). Total Nitrogen (Kjeldahl) was measured using Kjeldahl digestion and distillation (Evers & Hughes, 2002). The carbon-to-nitrogen ratio was calculated from the values of total organic Carbon and total Nitrogen as:

$$C:N = \frac{\%TOC}{\%TKN} \quad 1$$

To get a carbon-to-nitrogen ratio of 25 to 1, the amounts of cow dung and poultry waste were estimated using this mass-balance equation:

$$\frac{M_{CD}}{M_{PW}} = \frac{N_{PW}\times 25 - C_{PW}}{C_{CD} - N_{CD}\times 25} \quad 2$$

2.3 MEC-AD Reactor Design and Setup

Experiments were carried out on a lab-scale apparatus that coupled microbial electrolysis with anaerobic digestion. The reactor consisted of a double-chamber configuration with a working volume of 1.5L. A graphite rod (10 × 100 mm) was used as the anode, while a 50 × 50 mm 304 stainless-steel mesh was used as the cathode. Both parts were connected to a power supply that could provide 0-2 V to maintain a steady voltage. The anode was inserted into the substrates to help transfer electrons through the microbes. The cathode was placed in the part of the reactor where hydrogen formed and then was used by other microbes to make methane (Shao et al., 2025). All experiments were done in batch mode at a temperature of 30 to 37 degrees Celsius.

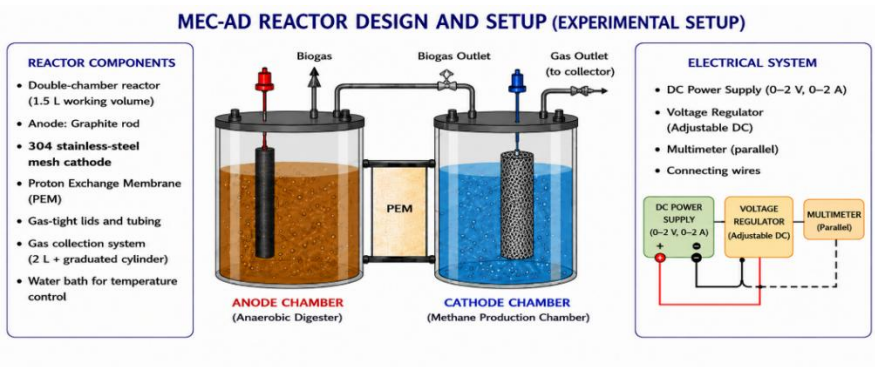

Figure 1: Schematic Diagram of the Coupled MEC–AD Reactor and Experimental Setup

2.4 Experimental Design and Optimization

The process was optimized using Response Surface Methodology based on a Central Composite Design. Three factors were considered: voltage (0.3 to 1.5), pH (6 to 8), and C:N (15 to 35). There were 20 runs in total. These included eight factorial points, six axial points, and six center points. The amount of methane produced was the response.

The data were fitted into a second-order model that had the equation:

$$Y = \beta_0 + \sum_{i=1}^{3} \beta_i X_i + \sum_{i=1}^{3} \beta_{ii} X_i^2 + \sum_{i=1}^{2} \sum_{j=i+1}^{3} \beta_{ij} X_i X_j + \epsilon \qquad 3$$

Analysis of variance was done at a 95% confidence level to check how good the model was and which factors were important. This was done using Design-Expert® Version 13 (Stat-Ease Inc.).

2.5 Kinetic Modeling

The methane production was described using the Modified Gompertz model:

$$B(t) = B_0 \times \exp\left\{-\exp\left[\frac{R_{max} \times e}{B_0}(\lambda - t) + 1\right]\right\} \qquad 4$$

where **B(t)** is the total methane produced at time **t, B_0** is the maximum methane possible, R_{max} is the maximum rate of methane, **λ** is the lag phase, and **e** is Euler's constant.

The model parameters were estimated using nonlinear regression in Python Version 3.9. with optimization carried out using the Levenberg-Marquardt algorithm

2.6 Development of Enhancement Factors and Global Model Integration

Voltage, pH, and carbon-to-nitrogen ratio all influence methane production. To account for changes in reactor performance across operating conditions, explicit enhancement factors were fitted and integrated into the Modified Gompertz parameters (B_0, $R_{\max}$, and λ).

2.6.1 Voltage Enhancement Factors

Raw experimental data for ultimate methane potential (B_0) and production rate ($R_{\max}$) at different applied voltages ($0.3 - 1.5$ V) obtained from the literature were fitted using polynomial regression in Python (Version 3.9)(Zou et al., 2021). The resulting unnormalized polynomial models showed strong coefficients of determination ($R^2 = 0.9897$ for B_0 and $R^2 = 0.9884$ for $R_{\max}$) To derive dimensionless enhancement multipliers ($f(V)$), the raw curves were normalized to their baseline values at the optimal reference voltage (V_{ref} = 1.0 V, where $B_{0,raw}(1.0)$ = 328.9 mLCH_4 g^{-1}VS and $R_{max,raw}$ (1.0) = 24.312 mLCH_4 g^{-1}VS day^{-1})

$$f_{B0}(V) = -1.207V^4 + 4.504V^3 - 6.815V^2 + 4.520V \qquad 5$$

$$f_{R\max}(V) = 3.933V^5 - 17.315V^4 + 27.680V^3 - 19.827V^2 + 6.525V \qquad 6$$

For the lag phase (λ), applied voltage reduces adaptation time at lower voltages ($V \leq 1.0$ V) but induces electrochemical stress at higher voltages ($V > 1.0$ V). A hybrid piecewise function was developed:

$$\lambda(V) = \begin{cases} \dfrac{1}{k(1+\alpha V+\beta V^2)}, & V \leq V_{\text{opt}} \\ \dfrac{1+\left(\frac{V-V_{\text{opt}}}{K_I}\right)^n}{k(1+\alpha V+\beta V^2)}, & V > V_{\text{opt}} \end{cases} \qquad 7$$

A two-step regression approach was applied: linear transformation ($y = \frac{1}{\lambda}$) determined quadratic growth constants (k, α, β), while non-linear regression fitted the inhibition threshold (K_I) for $V > 1.0$ V, before normalizing relative to $\lambda(1.0\text{ V})$.

2.6.2 pH and C:N Ratio Enhancement Factors

The effects of pH and C:N ratio were modeled using Gaussian functions centered around their optimal values ($\mu = 7.0$ for pH; $\mu = 25$ for C:N) to reflect symmetric performance decay away from ideal conditions:

$$f_{B0}(\text{pH}) = \exp\left(-0.5 \times \left[\frac{\text{pH}-7.0}{0.8}\right]^2\right) \quad 8$$

$$f_{B0}(\text{C:N}) = \exp\left(-0.5 \times \left[\frac{\text{C:N}-25}{7.0}\right]^2\right) \quad 9$$

Standard deviations (σ) for $R_{\max}$ were set to 0.7 (pH) and 9.0 (C:N), while σ values for λ were 1.0 (pH) and 11.0 (C: N).

2.6.3 Global Kinetic Integration

Following autonomous multiplicative bioprocess modeling frameworks (such as IWA ADM1), the individual enhancement factors modify baseline kinetic parameters ($B_{0,\text{base}} = 498$ mL g^{-1} VS, $R_{\text{max,base}} = 23$ mL g^{-1} VS day^{-1}, $\lambda_{\text{base}} = 3.2$ days):

$$B_{\text{total}} = B_{0,\text{base}} \times f_{B0}(V) \times f_{B0}(\text{pH}) \times f_{B0}(\text{C:N}) \quad 10$$

$$R_{\text{total}} = R_{\text{max,base}} \times f_{R\text{max}}(V) \times f_{R\text{max}}(\text{pH}) \times f_{R\text{max}}(\text{C:N}) \quad 11$$

$$\lambda_{\text{total}} = \lambda_{\text{base}} \times f_{\lambda}(V) \times f_{\lambda}(\text{pH}) \times f_{\lambda}(\text{C:N}) \quad 12$$

Substituting these into Equation (4) yields the global predictive kinetic equation:

$$B(t, V, \text{pH}, \text{C:N}) = B_{\text{total}} \cdot \exp\left(-\exp\left[\frac{R_{\text{total}} \cdot e}{B_{\text{total}}}(\lambda_{\text{total}} - t) + 1\right]\right) \quad 13$$

2.7 Thermodynamic and Exergy Analysis

Methane energy was calculated using:

$$E_{CH_4} = V_{CH_4} \times \rho_{CH_4} \times LHV_{CH_4} \quad 14$$

where the lower heating value (**LHV**) of methane was taken as **50 MJ/kg**, while methane density was taken as **0.716 kg/m³** (Nindhia et al., 2021).

Overall energy efficiency was determined from:

$$\eta_{energy}(\%) = \left(\frac{E_{CH_4}}{E_{in}}\right) \times 100 \quad 15$$

Exergy analysis was also performed to determine how effectively the available energy was converted into useful work. Electrical energy was assigned an exergy factor of **1.0**. Methane was assigned an exergy factor of **0.94**, making it possible to evaluate energy losses occurring within the coupled MEC-AD system (Dinçer & Rosen, 2021).

3. RESULTS AND DISCUSSION

3.1 Substrate Characterization

Table 1: Substrate Characterization

Parameter	**Cow Dung**	**Poultry Dung**
Total Solids (TS, %)	9.85	8.40
Volatile Solids (VS, % TS)	78.20	62.35
COD (g L^{-1})	95.40	68.20
Ash Content (% TS)	21.80	37.65
Carbon (%)	38.5	31.3
Nitrogen (%)	1.48	5.00
C:N ratio	26.0	6.26

Cow dung demonstrated higher volatile solids (VS) content (78.20%) and chemical oxygen demand (COD) (95.40 g/L) compared to poultry dung (62.35% and 68.20 g/L), indicating the presence of a greater amount of biodegradable organic matter that could be used to produce methane. The VS content of cow dung fits the typical 70-85% range of ruminant manure, reflecting the partial

lignocellulosic breakdown before being excreted. The C:N ratio of cow dung is 26.0, falling within the recommended 20-30 range of anaerobic digestion. On the contrary, poultry dung possessed a C:N ratio of 6.26 because of its increased nitrogen content (5.00%), which could promote the formation of ammonia and inhibit methanogenesis. Mass balance shows that 98.3% of cow dung and 1.7% of poultry dung satisfied the requirement of the target C ratio of 25:1.

3.2 Optimization of MEC-AD Operating Parameters

In the 20 central composite design (CCD) experiments, methane yield ranged from 50.69 to 350.73 mL CH4/g VS, showing a strong dependence on process conditions. The six center-point runs at 0.90 V, pH 7.0, and C:N ratio of 25 produced the maximum methane yield of 350.73 mL CH_4 g^{-1} VS, with a standard deviation below 0.01, demonstrating excellent reproducibility. The quadratic model proved to be highly significant ($F = 3201.86$; $p < 0.0001$), with $R^2 = 0.9997$, Adjusted $R^2 = 0.9993$, Predicted $R^2 = 0.9982$, and Adequate Precision = 128.074, which demonstrates a good correlation and ratio of signal to noise. The reduced quadratic model in coded variables was expressed as:

$$\ln(Y) = 5.85 + 0.0669A - 0.4013A^2 - 0.9378B^2 - 0.5261C^2$$

Denoting Y as the methane yield (mL CH4 g^{-1} VS), A, B, and C stand for the coded values of applied voltage, pH, and C:N ratio, respectively. Since there is a positive linear coefficient related to voltage, the initial increase in methane yield with the increase in applied voltage can be expected. However, due to the presence of the negative quadratic coefficients, it can be deduced that there are optimal operation ranges after which the methane production decreases.

3.3 Interactive Effects of Process Variables

3.3.1 pH and Carbon-to-Nitrogen Ratio

The pH–C response surface revealed a dome-shaped graph, characterized by a sharp peak. Maximum methane production happened at pH 6.8-7.2; pH lower than 6.5 caused the accumulation of volatile fatty acids and inhibited methanogenesis, whereas pH higher than 7.5 shifted the ammonium-ammonia equilibrium towards the inhibitory free ammonia (NH_3).

Methane yield was higher than 300 mL CH_4/g VS in the range of C 25. The C ratios lower than 20 contributed to ammonia formation due to the excess of nitrogen, whereas those higher than 30 inhibited microbial growth because of the deficiency of nitrogen.

3.3.2 Applied Voltage and Carbon-to-Nitrogen Ratio

The voltage range optimal for methane production was about 0.6-1.2 V, where the electrical stimulation promoted electron transfer and organic matter degradation.

Below 0.6V, the thermodynamic driving force was not sufficient to stimulate the electroactive microorganisms, and above 1.2 V, the performance decreased probably due to electrochemical stress and water electrolysis.

3.3.3 Applied Voltage and pH

The voltage–pH response showed that electrical stimulation was most effective under favorable microbial conditions.

The combination of 0.9 V and pH 7.0 facilitated the methanogenic activity. Increasing the voltage without appropriate pH weakened the electrochemical effects; thus, it was necessary to optimize both voltage, pH, and C:N ratio.

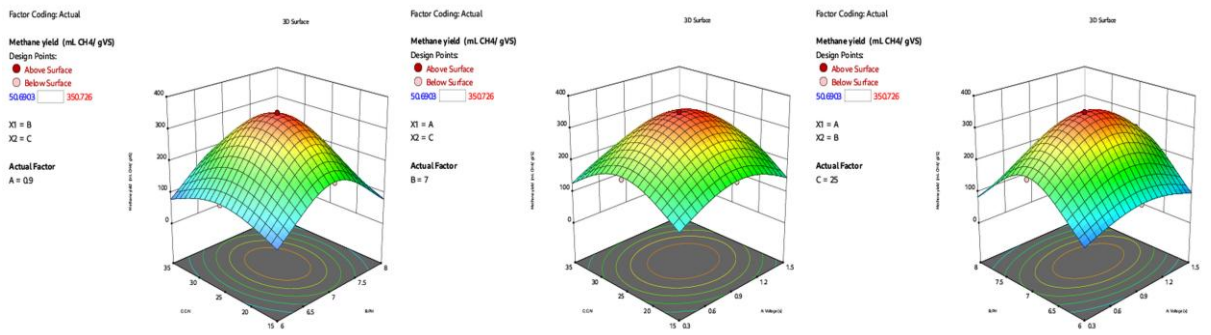

3.4 Kinetic Modeling

The Modified Gompertz model was built under optimized conditions (0.97 V, pH 7.0, C 25) based on the cumulative, daily, and joint methane data. The joint fit revealed the true behavior of the reactor better than the cumulative and daily ones and provided the ultimate methane potential (P) of 378.33 mL CH_4/g VS, maximum production rate (R_{max}) of 41.25 mL CH4/g VS/day, and lag phase (λ) of 1.36 days. The R^2 values of the cumulative and daily fits were 0.99965 and 0.99497, respectively. Methane production attained 10%, 50%, and 90% of the calculated potential after 1.92, 5.97, and 12.33 days, respectively.

Compared with conventional anaerobic digestion reported in the literature, the MEC–AD system increased methane yield by approximately 17–40%, increased methane production rate by 64–118%, and reduced the lag phase by approximately 55–82%. These comparisons were based on literature-reported conventional AD performance rather than a parallel conventional-AD control experiment conducted in the present study

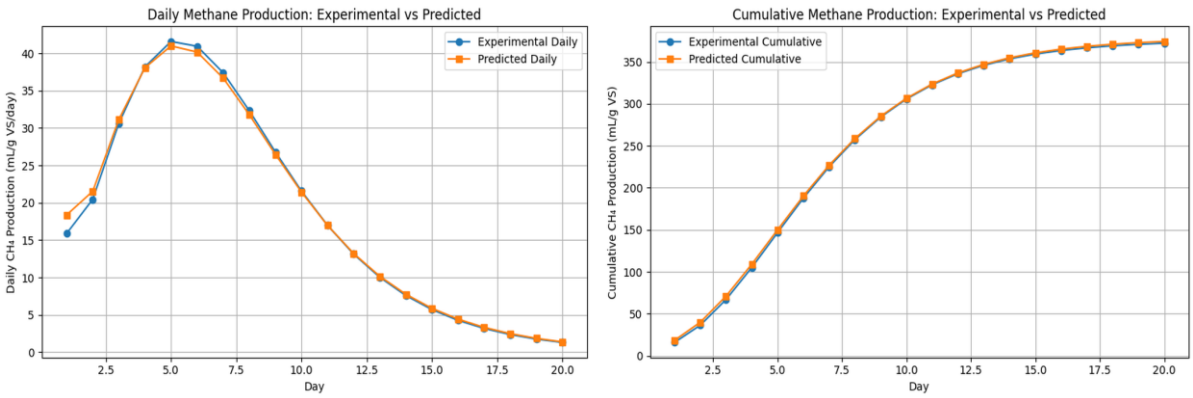

3.5 Model Validation

Three independent experiments out of the data set used for the model development provided the average prediction error of 6.26%. The R^2 value of the model validation of 0.9987 proves that the model explained 99.87% of the variance in the methane yield, which means a good predictive ability within the investigated operating range.

3.6 Thermodynamic Performance

For optimal working conditions, the consumption of electrical and thermal energies per batch in the MEC-AD process was 6.70×10^{-4} MJ and 0.0627 MJ, respectively. However, for substrate chemical and methane energy yields, these values were 1.99374 MJ and 1.87234 MJ, respectively. As a result, the net energy obtained is 0.18477 MJ, and an efficiency of 91.02% has been observed. The energy return on investment (EROI) is 29.55, and it is evident that there is significantly more energy yield from methane than the electrical energy input into the system. The total exergy of input was 2.381 MJ, where the contribution from the substrate was 2.380 MJ, 0.00067 MJ was attributed to the electrical input, and 0.000267 MJ was attributed to the thermal input. The exergy of methane energy output was 1.758 MJ, whereas that of irreversibility destruction was 0.623 MJ. Therefore, the exergy efficiency

was 73.8%, while the ratio of exergy destruction was 26.2%. This is because the exergy balance fulfilled the equation 1.758 + 0.6.

4. CONCLUSIONS

This study demonstrated the potential of coupling microbial electrolysis with anaerobic digestion for enhanced methane recovery from cow dung and poultry dung. Cow dung contained 78.20% VS, 38.5% carbon, 1.48% nitrogen, and a C:N ratio of 26.0, while poultry dung contained 62.35% VS, 31.3% carbon, 5.00% nitrogen, and a C:N ratio of 6.26. Carbon–nitrogen balancing produced an optimum mixture of 98.3% cow dung and 1.7% poultry dung at a target C:N ratio of 25.

RSM optimization identified 0.97 V, pH 7.0, and C:N 25 as the optimum operating conditions, with a maximum observed methane yield of 350.73 mL CH_4 g^{-1} VS. The reduced quadratic model provided an excellent fit with R^2 = 0.9997, adjusted R^2 = 0.9993, and predicted R^2 = 0.9982. The Modified Gompertz model gave an ultimate methane potential of 378.33 mL CH_4 g^{-1} VS, maximum methane production rate of 41.25 mL CH_4 g^{-1} VS Day^{-1}, and lag phase of 1.36 days. Independent validation produced an average prediction error of 6.26% and R^2 = 0.9987.

The thermodynamic analysis indicated 91.02% energy efficiency and an EROI of 29.55. The corrected exergy analysis gave 2.381 MJ total input exergy, 1.758 MJ methane exergy, 0.623 MJ exergy destruction, 73.8% exergy efficiency, and 26.2% exergy destruction ratio. These results demonstrate that the system was energy-positive and achieved substantial conversion of substrate exergy into methane.

For Nigeria, the approach has practical potential because livestock production generates large quantities of manure that can be difficult to manage safely and productively. A decentralized MEC–AD system could provide a pathway for converting manure into renewable methane while reducing uncontrolled decomposition and improving nutrient management. Nevertheless, the present work was conducted at laboratory scale and should not be interpreted as proof of immediate commercial viability. Scale-up challenges include electrode and membrane cost, electrode durability and fouling, electrical-control requirements, mixing, feedstock variability, continuous-operation stability, heat management, and the economics of integrating the MEC subsystem with existing digesters.

Future work should therefore include pilot- and semi-continuous-scale testing, long-term electrode performance assessment, optimization of electrode configuration, process automation, techno-economic analysis, and life-cycle assessment under Nigerian agricultural conditions. Such studies are needed to determine whether the observed laboratory-scale performance can be maintained at practical scale and under variable real-world feedstock conditions.

5.0 REFERENCES

Angelidaki, I., Alves, M., Bolzonella, D., Borzacconi, L., Campos, J. L., Guwy, A. J., Kalyuzhnyi, S., Jenicek, P., & Van Lier, J. B. (2009). Defining the biomethane potential (BMP) of solid organic wastes and energy crops: A proposed protocol for batch assays. *Water Science and Technology, 59*(5), 927–934. https://doi.org/10.2166/wst.2009.040

Ao, T.-J., Liu, C.-G., Sun, Z.-Y., Zhao, X.-Q., Tang, Y.-Q., & Bai, F.-W. (2024). Anaerobic digestion integrated with microbial electrolysis cell to enhance biogas production and upgrading in situ. *Biotechnology Advances, 73*, 108372. https://doi.org/10.1016/j.biotechadv.2024.108372

Appels, L., Baeyens, J., Degrève, J., & Dewil, R. (2008). Principles and potential of the anaerobic digestion of waste-activated sludge. *Progress in Energy and Combustion Science, 34*(6), 755–781. https://doi.org/10.1016/j.pecs.2008.06.002

Chojnacka, K., & Moustakas, K. (2024). Anaerobic digestate management for carbon neutrality and fertilizer use: A review of current practices and future opportunities. *Biomass and Bioenergy, 180*, 106991. https://doi.org/10.1016/j.biombioe.2023.106991

Dinçer, İ., & Rosen, M. A. (2021). *Thermal Energy Storage: Systems and Applications* (1st ed.). Wiley. https://doi.org/10.1002/9781119713173

Evers, J. M., & Hughes, C. G. (2002). ANALYSIS | Chemical Analysis. In *Encyclopedia of Dairy Sciences* (pp. 34–40). Elsevier. https://doi.org/10.1016/B0-12-227235-8/00015-8

Kafle, G. K., & Chen, L. (2016). Comparison on batch anaerobic digestion of five different livestock manures and prediction of biochemical methane potential (BMP) using different statistical models. *Waste Management*, *48*, 492–502. https://doi.org/10.1016/j.wasman.2015.10.021

Kaneko, H., Koyama, M., & Daimon, H. (2025). Effects of Applied Voltage on the Microbial Communities at the Anode and Cathode During Methane Fermentation. *Fermentation*, *11*(8), 488. https://doi.org/10.3390/fermentation11080488

Mao, C., Feng, Y., Wang, X., & Ren, G. (2015a). Review on research achievements of biogas from anaerobic digestion. *Renewable and Sustainable Energy Reviews*, *45*, 540–555. https://doi.org/10.1016/j.rser.2015.02.032

Nelson, D. W., & Sommers, L. E. (1996). Total Carbon, Organic Carbon, and Organic Matter. In D. L. Sparks, A. L. Page, P. A. Helmke, R. H. Loeppert, P. N. Soltanpour, M. A. Tabatabai, C. T. Johnston, & M. E. Sumner (Eds.), *SSSA Book Series* (1st ed., Vol. 5, pp. 961–1010). Wiley. https://doi.org/10.2136/sssabookser5.3.c34

Nindhia, T. G. T., McDonald, M., & Styles, D. (2021). Greenhouse gas mitigation and rural electricity generation by a novel two-stroke biogas engine. *Journal of Cleaner Production*, *280*, 124473. https://doi.org/10.1016/j.jclepro.2020.124473

Shao, Z., Fan, Q., Gao, F., Xia, T., Wang, Y., Liang, Y., Guo, X., Yang, X., Yao, Y., Qiu, L., Zhang, C., Xu, J., Gnanasekar, P., Kang, K., Rakshit, S. K., Fatehi, P., & Chen, H. (2025). Sustained methane production enhancement by magnetic biochar and its recovery in semi-continuous anaerobic digestion with varying substrate C/N ratios. *Chemical Engineering Journal*, *514*, 163050. https://doi.org/10.1016/j.cej.2025.163050

Sheron NK, Obileke K, Mukumba P. Kinetic Modelling of Anaerobic Digestion of Biogas Production from Different Wastes: A Review. J Sustain Res. 2026;8(2):e260044. https://doi.org/10.20900/jsr20260044.

Telo, D., & Yigezu, Z. (2025). Production and Characterization of Biogas from Cow Dung, Poultry Manure and Their Co-digestion. *American Journal of Environmental and Resource Economics*, *10*(3), 82–96. https://doi.org/10.11648/j.ajere.20251003.11

Wang, X.-T., Zhao, L., Zhang, Q., Wang, B., Xing, D., Nan, J., Ren, N.-Q., Lee, D.-J., & Chen, C. (2024). Linking performance to dynamic migration of biofilm ecosystem reveals the role of voltage in the start-up of hybrid microbial electrolysis cell-anaerobic digestion. *Bioresource Technology*, *411*, 131242. https://doi.org/10.1016/j.biortech.2024.131242

Worajo, W. E., Falta, F. F., & Fakana, S. T. (2025). Interspecies electron transfer stimulating approaches in anaerobic digestion process: Recent advancements, challenges, and future perspectives. *Environmental Systems Research*, *15*(1), 7. https://doi.org/10.1186/s40068-025-00448-w

Zhao, S., Chen, W., Luo, W., Fang, H., Lv, H., Liu, R., & Niu, Q. (2021). Anaerobic co-digestion of chicken manure and cardboard waste: Focusing on methane production, microbial community analysis and energy evaluation. *Bioresource Technology*, *321*, 124429. https://doi.org/10.1016/j.biortech.2020.124429

Zou, L., Wang, C., Zhao, X., Wu, K., Liang, C., Yin, F., Yang, B., Liu, J., Yang, H., & Zhang, W. (2021). Enhanced anaerobic digestion of swine manure via a coupled microbial electrolysis cell. *Bioresource Technology*, *340*, 125619. https://doi.org/10.1016/j.biortech.2021.125619

International Conference on Engineering Innovation for Sustainable Development (ICESID 2026)
Faculty of Engineering, Ahmadu Bello University Zaria · 8–10 September 2026

FLOOD INUNDATION RISK ASSESSMENT OF AN EARTHEN DAM UNDER PIPING FAILURE USING HEC-RAS AND QGIS:

Aliyu Yahaya Muhammad[1], Auwal Jarmai Babagirei[1,*], Alamin D Bello[1], Khalid Sulaiman[1], Abdulaziz Ahmad Imam[1], Raji Olasunkanmi Sheriffdeen[2]

[1]*Ahmadu Bello University Zaria*
[2]*Federal University Oye-Ekiti*

Email: aliyuyahayajere01@gmail.com, ajbabagirei@engineering.abu.edu.ng*, adbello@abu.edu.ng, Ksulaiman@abu.edu.ng, ahmadabdulazizimam@gmail.com, sheriffdeen.raji@fuoye.edu.ng

***Corresponding author**: Auwal Jarmai Babagirei

DOI: https://doi.org/10.67203/sp.ICESID.2026

ABSTRACT

This study presents the flood inundation risk evaluation of the dam formerly called Kubanni, an earthen dam with a water catchment area of 57 km^2, situated in Zaria area, Kaduna State, Nigeria. The research aims to explain the pattern of dam breach by modeling it in three different return periods, (30, 50, and 100 years) and the hazard posed by the dam. HEC-RAS with QGIS software was used to run unsteady flow simulation of the dam break for piping failure. The breach parameters like the width of the bottom, the slope on the sides, and the time to formation were all obtained using empirical regression equations of Froehlich (2008), and as a result, the downstream hazard was mapped in several risk zones. The discharges during breach were 1,426.56m^3/s, 1,697.71 m^3/s, and 1,758.04 m^3/s respectively for the three events. The flood events lasted for approximately 1 hour (30 and 50 year return periods) and 3 hours (100-year return period). The floodwater covered a distance of more than 10 km with Zango, Hanwa, Yan Karfe, and parts of Northeast Tudun Wada showing high flood vulnerability. Approximately 2,705 residences and several croplands located along the floodplain are in great danger from floods. The flood water took the minimum time of 10 sec reaching the nearest zone against the farthest zone where the water reached after 20min at the fastest depth level of 16.3m. These findings can assist dam safety management, land use regulation, and even the establishment of an early warning system at community level in other regions with similar challenge not monitored well.

Keywords: *dam break analysis; piping failure; flood inundation mapping; ABU Dam*

1 INTRODUCTION

Dams are probably the most strategically important of all hydraulic structures. By controlling the river flow, they provide irrigation, domestic water supply, industrial water use and downstream flood attenuation services, which together form the basis of livelihoods for the million people around the world. (Alhassan et al., 2019) stated the benefits of dams in the provision of these water services. However, it is the very energy that the reservoir releases that the structural failure would have devastated effect. There is dam failure recorded on all inhabited continents, and some have had only crop losses, while others have resulted in total destruction of communities in the downstream areas (Aureli et al., 2021). More exactly, in Nigeria, the majority (>81%) (Umaru et al., 2010), the dam types vulnerable to two dominant failure mechanisms: overtopping and internal erosion (piping). Piping is very dangerous because the failure might even pass unnoticed until a catastrophic collapse happens. (Foster et al., 2000) From the study and analysis of dam failure databases on a worldwide scale, the percentage of internal erosion in embankment dam failures is around 40% (Jandora & Riha, 2009). This amplifies more the impacts in cases of dam failures in the West Africa due to factors like: downstream urban settlements being more dense; agricultural plots close to floodplains; and unavailability of an early warning system and associated infrastructure(Okeola et al., 2025).

Kubanni Dam was originally known as ABU Dam before being incorporated into the water supply system of Ahmadu Bello University (ABU). The dam is a simple earthwork built along the Kubanni River in Zaria, Kaduna State, Nigeria (Latitude: 11°08′03.18″ N Longitude: 7°39′15.67″ E). Given that the dam has a catchment area of 57 km², average water depth of 6 m, and a reservoir volume

of more than 2.6 million m^3 of water at normal water level, it gives the main water resource for the university campus and various nearby communities. Even though this dam is very essential for the people who are getting settled in the city at a fast pace, prior research on the topic of dam breaks and quantitative risk of downstream floods was not published about the structure until this study. As a result, emergency planners, Dam safety engineers, and community heads are unable to develop reliable response strategies without the relevant information.

This study addresses the identified research gap by developing an integrated dam-break assessment framework for Zaria Dam using HEC-RAS unsteady-flow hydraulic modelling and QGIS-based spatial analysis. The study simulates a piping-induced dam failure under 30-, 50-, and 100-year return-period inflow conditions to evaluate potential downstream flood hazards. Unlike previous studies, this research provides the first comprehensive dam-break assessment for Zaria Dam by integrating HEC-RAS hydraulic modelling with GIS-based inundation mapping and google satellite basemap imagery to improve the delineation, visualization, and interpretation of flood-prone areas. Furthermore, the study incorporates community-level risk characterization to support dam safety assessment, emergency planning, and informed decision-making for downstream communities. It further evaluates multiple hydrological return periods to capture the influence of increasing flood magnitude on downstream hazard, thereby offering a more comprehensive assessment than studies based on a single design event. The adopted framework is consistent with recent applications of HEC-RAS and GIS for dam-break assessment in data-scarce environments (Beza et al., 2023; Mo et al., 2023), while extending their application through a site-specific multi-scenario risk assessment for eleven downstream communities. Consequently, the study provides a practical decision-support framework for dam safety management, land-use planning, and emergency preparedness in the Zaria region.

1.1 Historical Context of Earthen Dam Failures

Today in Africa, most earthen dams that were poorly maintained, have been built in the 1960s to 1980s through post-independence development programs, pose a growing safety threat as they confront changing rainfall patterns through their deteriorating infrastructure(Moreno-Rodenas et al., 2025).

In the country, a failed Cham Dam incident at Gombe State is a notable example: an inadequate spillway capacity coupled with seepage-induced internal erosion caused a sudden major breach, which resulted in the large death toll downstream and damage of property (Umaru et al., 2010). Generally, a major problem with many dams in the sub-Saharan area is lack of maintenance or safety checking of dams and only slow adoption of quantitative methods for predicting breaches so that local residents living near old embankment dams rarely know how much danger they face (Okeola et al., 2025).

1.2 Mechanisms of Embankment Dam Failure

Two failure mechanisms dominate embankment dam loss: overtopping and internal erosion. Overtopping occurs when reservoir levels surpass the dam crest, typically during inflow floods that exceed spillway design capacity or when debris blocks the spillway. The uncontrolled flow of water over and down the downstream face rapidly initiates erosion of the embankment material, a process that accelerates non-linearly until breach formation is complete (Jandora & Riha, 2009). For small catchment dams such as ABU Dam, a single extreme precipitation event can generate inflows that exceed the design discharge standard, making overtopping a credible scenario even at moderate return periods.

The second type of failure mechanism -internal erosion- occurs through a form of internal "piping". It typically starts in those parts where the permeability of materials is higher or in case the dam is built on an impermeable layer (Jandora & Riha, 2009) (e.g. in case of leakage). It is the so called "piping." The fine soils particles get washed from the source location and are taken further downstream until a bigger and bigger channel is created. At a certain point the velocity of the flow of the particles is so high that the particles themselves help in forming the channel, making the process almost endless until the failure of the dam structure (Foster et al., 2000).

In reality, this piping failure mode has a reinforcing loop to the dam can go from a perfectly good working condition to complete failure in a matter of seconds. As (Zhang, et al., 2007) researched,

if the reservoir level is raised then there is an enhancement in the hydraulic gradient resulting in an increase in the likelihood of the pipe starting. This is mainly important for ABU Dam, where the reservoir capacity is always near full during the rainy season. Piping was the primary failure mechanism considered for this dam because the spillway has adequate capacity for the design flood, based on (Bharath et al., 2021); as a result, spillway overtopping due to flood was not considered a likely failure mode. That means internal erosion like piping is much more likely scenario for triggering the failure in this dam than the external ones like overtopping.

1.3 Dam Break Analysis

One of the most popular platforms for performing both steady and unsteady flows in one-dimensional (1D) and two-dimensional (2D) cases is HEC-RAS developed by and under the control of US Army Corps of the Engineers Hydrologic & Hydraulic Engineering Center. The breach modeling capacity of this tool has been found applicable to various dam types and locations including earthen dams in Africa (Beza et al., 2023; HEC, 2023). Newer research shows that for rivers having clearly defined cross-sectional geometry, it is still valid to rely on 1D HEC-RAS model to simulate flows and that the results it generates are detailed enough to help with EAP creation even when further GIS processing is done on them (Mo et al., 2023)

GIS-based spatial analysis Mostly through QGIS is being increasingly used for creating risk maps that can be used for risk reduction and management efforts. HEC-RAS outputs together with satellite images and digital elevation maps can be used as reference inputs for inundation areas classification and quantification in the GIS environment, about land use types and settlement density (Aureli et al., 2021)

2 MATERIALS AND METHODS

ABU Dam (Kubanni Dam), a gravity earth dam, was built in 1970s in the Kubanni River Zaria Kaduna State, Nigeria of Ahmadu Bello University (Yusuf, 2013). The dam is located in a watershed which is covered mainly in savannah vegetation, rolling hills, and seasonally changing water flow regime. (Yusuf, 2013) After the dam, the Kubanni valley becomes a narrow flood plain and then extends to a peri-urban area with a high population density, residential houses shops market places gardens small farms and schools. This study did not include overtopping failure as a consideration. The Kubanni (ABU) Dam has a central spillway that is sufficient to carry design flood inflows so overtopping would be practically impossible failure pathway for the scenarios presented. Piping failure was, because of this, considered as the main failure mechanism that matches the dam's physical condition and that is in line with practice for embankment dams whereby internal erosion is the more likely failure mode than crest overtopping. Table 1 describes the main structural and geometric features of the dam.

Table 1: Key structural and geometric parameters of ABU Dam (Kubanni Dam), Zaria

Parameter	**Value**
Location	Latitude: 11°08′03.18″ N Longitude: 7°39′15.67″ E, Zaria, Kaduna State, Nigeria
Dam Classification	Earthen embankment
Top of Dam Elevation	645.38 m a.s.l.
Breach Bottom Elevation	632.53 m a.s.l.
Dam Crest Width	5 m
Mean Water Depth	6 m
Crest Length	122 m
Catchment Area	57 km^2
Reservoir Capacity	~2.6×10^6 m^3
Upstream Face Slope (Z1, H:V)	1:2.5
Downstream Face Slope (Z2, H:V)	1:2
Pool Volume at Failure	$22{,}600 \times 10^3$ m^3

2.1 Data Acquisition and Terrain Representation

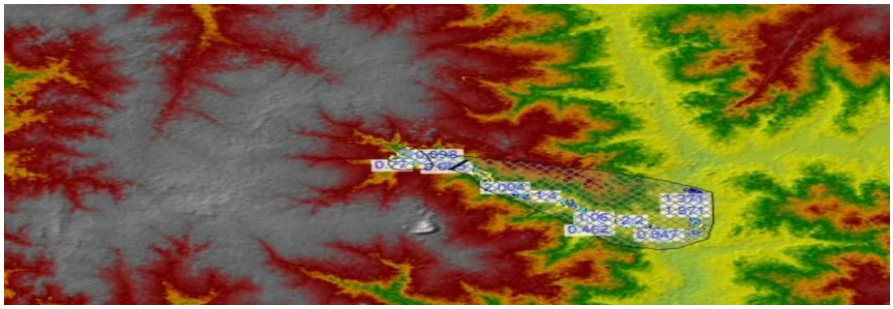

Figure 1: DEM of ABU Dam

The datasets and model inputs used in the hydraulic simulation are summarized in Table 2. A 30 m Shuttle Radar Topography Mission (SRTM) Digital Elevation Model (DEM) was adopted to represent the terrain (Farr et al., 2007)). The DEM was georeferenced in ArcGIS 10.8 to match the HEC-RAS coordinate system following established georeferencing procedures. River cross-sections and overbank geometries were extracted from the processed DEM and incorporated into the HEC-RAS geometry file. Manning's roughness coefficients for the channel and floodplain were assigned based on field observations and published values for similar savanna environments (Salah Abd Elmoaty & T. A, 2020) The reservoir elevation–storage relationship required for level-pool routing was generated from DEM-derived contours and imported into HEC-RAS as a Storage Area Elevation–Volume table initialized at the normal operating level.

Table 2: Summary of inputs

Input	**Purpose in the Study**	**Source**	**Reference**
Shuttle Radar Topography Mission (SRTM) Digital Elevation Model (30 m)	Extraction of terrain elevation, watershed topography, channel geometry, and reservoir characteristics	NASA Shuttle Radar Topography Mission (SRTM)	Farr et al. (2007)
River cross-sections and overbank geometry	Development of HEC-RAS geometric model	Extracted from the georeferenced SRTM DEM using ArcGIS 10.8	Derived from SRTM DEM (Farr et al., 2007)
Manning's roughness coefficient	Hydraulic resistance assignment for channel and floodplain	Field observations and published values for comparable savanna environments	Salah Abd Elmoaty & T.A. (2020)
Elevation–Storage (Elevation–Volume) relationship	Level-pool routing and reservoir storage definition	Derived from DEM contours and entered into HEC-RAS as a Storage Area Elevation–Volume table	Derived from SRTM DEM (Farr et al., 2007)

2.2 Breach Parameter Estimation

The HEC-RAS parameter calculator is used for comparing five empirical formulas for predicting breach of pipe failure by failure modes: MacDonald and Langridge-Monopolis (1984), Froehlich (1995), Froehlich (2008), Von Thun and Gillette, and Xu and Zhang. The dam geometry and reservoir features were put up in the connection data editor. HEC-RAS calculated internally the reservoir volume and the breach height needed for each regression method; the estimated breach parameters are displayed in Table 2. The Xu and Zhang method resulted in unrealistic numbers of a

breach width of 6080 m, and a negative side slope for a rather small reservoir size that was discarded from further consideration.

The equations by Froehlich (2008) have been accepted as the design-reference parameters mainly because they stem from the most substantial checked failure database that the methodological independence of these formulas has been proven through reliable operation for earthy dams having approximately the same geometry in recent papers (Beza et al., 2023; Bharath et al., 2021) the formulas are the only ones formally acknowledged by the US Army Corps of Engineers for standard dam safety assessments. The average breach width (B_{avg}) and the breach formation time is:

$$B_{avg}=0.27K_oV_w^{0.32}h_b^{0.04} \qquad \textit{equation I}$$

$$t_f = 63.2\sqrt{\frac{V_w}{g\,h_b^2}} \qquad \textit{equation II}$$

Table 3: Breach parameters for ABU Dam estimated by five empirical methods (piping failure mode)

Method	Breach Bottom Width (m)	Side Slope (H:V)	Formation Time (hrs)
MacDonald & Langridge-Monopolis (1984)	2	0.5	0.26
Froehlich (1995)	126	0.9	6.83
Froehlich (2008) — Selected	132	0.7	2.99
Von Thun & Gillette	49	0.5	0.25
Xu & Zhang (excluded)	6,080*	—*	—*

** Xu & Zhang result is physically implausible for this dam geometry and was excluded from further analysis.*

2.3 HEC-RAS Modelling Framework

The one-dimensional unsteady flow model of HEC-RAS version 6.3.1 follows recent practice for comparable earthen dam analyses (Beza et al., 2023; Mo et al., 2023) The simulation setup covered the whole system from the reservoir storing area going through the connecting structure of breach between storage areas, and ending at downstream channel outflow boundary. Cross-section spacings were 100 to 500 m varying with topographic complexity. The storage area for the reservoir was bridged by an inline breach structure to the downstream routing reach through which boundary conditions for the upstream inflow hydrograph and downstream normal depth were provided. Separate unsteady flow simulations were run for return periods of 30, 50, and 100 years, each started from a steady-state base flow condition. The model variables that were exported for post-processing were mainly the breaching width, breaching flow, time-series records of velocity and water surface elevations at headwater and tailwater reference points; while flood depth raster, velocity, and elevation outputs at water surface were produced through RAS Mapper tool.

2.4 QGIS Spatial Analysis and Inundation Mapping

Raster outputs from RAS Mapper were exported and imported into QGIS version 3.61 for spatial classification and risk mapping. Google Satellite Hybrid imagery, accessed via the QuickMapServices plugin, provided high-resolution visual context for identifying built-up areas and land use types. (QGIS.org, 2019) Flood-depth rasters were classified into risk bands and overlaid on satellite imagery to produce flood inundation maps for each return period. Eleven downstream risk zones Areas 1 through 11 were manually delineated by digitizing visible residential and agricultural extents, with boundaries validated against available administrative boundary data. For each zone, maximum flood depth, inundated area, estimated number of exposed residential structures, and flood arrival time were extracted from the QGIS attribute table and compiled into the risk assessment matrix presented in the results section. This spatial analytical approach is consistent with current best practice for inundation mapping in data-scarce African contexts (Ekeu-Wei & Blackburn, 2018).

Figure 2: Satellite view of the area

3 RESULTS AND DISCUSSION

3.1 Breach Hydrograph Characteristics

Unsteady flow simulation produced time-series outputs for each return period scenario capturing the complete breach sequence from initial piping to recession. In all three scenarios, the breach progression follows a consistent three-phase pattern: (i) an initial quiescent period during which the piping orifice is small and outflow is limited; (ii) a rapid intensification phase during which breach width and outflow accelerate to their respective peaks; and (iii) a recession phase in which the depleted reservoir is unable to sustain peak discharge and outflow gradually diminishes. This tripartite temporal structure is consistent with the theoretical piping failure process described by (Jandora and Riha 2009) and with empirical hydrograph patterns documented in recent HEC-RAS dam break studies (Mo et al., 2023; Beza, 2023).

For the 30-year return period, the breach peak occurred at 0:59:52 hours, at which point breach width measured 31.14 m, total flow reached 1,426.56 m³/s, and velocity through the breach was 4.51 m/s. By the recession phase at 02:59:45 hours, breach width had expanded to its maximum of 40 m as the breach stabilized, outflow had fallen to 454.00 m³/s, and velocity had declined to 2.77 m/s.

The 100-year scenario exhibited a qualitatively different character. While initial and recession conditions were broadly comparable to the shorter return periods, the peak discharge of 1,761.71 m³/s occurred much later, at 02:59:45 hours. This delayed peak reflects the substantially larger reservoir volume accumulated during the 100-year inflow event prior to failure initiation; notably, it is the timing of the peak that shifts markedly with return period, while its magnitude increases only modestly relative to the 50-year event. This is consistent with (Aureli et al. 2023), who documented that breach-outflow timing can be more sensitive to antecedent pool volume than peak magnitude at the upper end of the return period range. Table 4 summarizes the peak hydrograph values across all three scenarios.

Table 4: Summary of peak breach hydrograph characteristics by return period

Return Period	Peak Discharge (m³/s)	Peak Velocity (m/s)	Breach Width at Peak (m)	Time to Peak	Headwater Elevation (m)	Tailwater Elevation (m)
30-year	1,426.56	4.51	31.14	00:59:52	642.91	637.41
50-year	1,697.71	4.56	31.14	00:59:52	643.16	637.48
100-year	1,761.71	4.44	31.14	02:59:45	643.00	637.15

3.2 Flood Inundation Extent

Across all three return periods, the flood wave propagated approximately 10 km downstream from the dam face, inundating communities from Zango in the immediate downstream reach to Sabon Gari Zaria at the distal limit of the modelled domain. This spatial extent is consistent with the travel distances documented for comparable small-to-medium earthen dam failures in West Africa (Salimon et al., 2023) and with analytical wave-celerity estimates for the observed peak discharges and channel geometry.

As expected, higher return periods produced greater inundation depths and slightly broader flood extents. The velocity and water-surface elevation rasters from RAS Mapper show that energy dissipation over the lower-gradient sections of the downstream reach generates the deepest inundation in mid-to-distal zones, where the flood wave encounters the widening valley floor. This pattern is present across all three scenarios, with the modestly higher peak discharge and delayed timing of the

100-year event generating somewhat deeper inundation in several zones relative to the 30- and 50-year events. The inundation maps produced for the three return periods (30-year, 50-year, and 100-year) show distinct flood depth, velocity, and water-surface-elevation layers, each providing spatially explicit information for emergency planning purposes.

Figure 3: Flood Inundation extent.

3.3 Downstream Risk Assessment

Table 5 presents the comprehensive risk assessment results for the eleven delineated downstream zones. Two findings are particularly significant for emergency planning. First, flood arrival times are extremely short. Even in the most distant zone (Area 11), located approximately 10 km downstream of the dam, the flood wave arrives in under 20 minutes under the 30-year return period scenario, while the nearest communities (Areas 1–3) experience inundation within the first minute. These results indicate that downstream residents would have little or no opportunity for spontaneous evacuation following a dam breach, making real-time monitoring and automated warning systems essential. Arrival times in some zones (e.g., Areas 4 and 5) converge or remain nearly identical between the 50- and 100-year scenarios rather than continuing to decrease; this is consistent with the flood wave in these zones approaching the channel's hydraulic capacity, beyond which additional inflow increases depth and discharge more than it increases wave-front speed. This finding is consistent with previous Nigerian dam-break studies. Comparable Nigerian dam-break studies have applied HEC-RAS to downstream reaches of approximately 11–12 km, including the Oyan River and Asa Dam systems, highlighting the importance of short downstream reaches in assessing potential flood impacts and emergency preparedness (Balogun & Ganiyu, 2016; Olanipekun et al., 2026)

Table 5: Inundation risk metrics for eleven downstream zones under three return period scenarios (Arrival columns give incremental travel time between consecutive zones, not cumulative time from the dam)

Area	Inund. Area (km^2)	Houses at Risk	Max Depth 30yr (m)	Max Depth 50yr (m)	Max Depth 100yr (m)	Arrival 30yr	Arrival 50yr	Arrival 100yr
1	0.79	325	9.01	11.57	11.34	00:00:16	00:00:10	00:00:10
2	0.19	47	5.05	8.47	8.24	00:00:42	00:00:35	00:00:34
3	0.20	30	4.92	8.27	8.12	00:00:56	00:00:50	00:00:46
4	0.63	18	4.60	8.19	10.51	00:01:15	00:01:07	00:01:07
5	0.57	35	9.04	11.74	11.06	00:01:39	00:01:33	00:01:07
6	0.50	250	6.32	9.13	8.03	00:02:10	00:01:47	00:01:22
7	0.32	500	4.00	7.49	10.25	00:02:41	00:02:00	00:01:38
8	0.88	400	8.81	10.40	10.48	00:03:38	00:02:13	00:02:02
9	2.55	300	8.49	10.33	10.04	00:04:00	00:02:30	00:02:22
10	3.21	600	14.88	13.20	12.87	00:06:37	00:03:20	00:03:13
11	0.46	200	15.00	16.26	16.31	00:07:08	00:06:00	00:04:05

The second major finding is the severity of downstream inundation. Maximum flood depths exceed 9 m in Areas 1, 5, 8, 9, and 10 under the 30-year scenario and increase to over 15 m in Areas 10 and 11 under the 100-year scenario, indicating catastrophic flooding capable of causing extensive

damage to buildings, infrastructure, and critical facilities. (Aureli et al., 2021) These results agree with recent HEC-RAS-based dam-break investigations, which consistently show that higher inflow scenarios generate greater breach outflows, deeper inundation, and substantially increased downstream hazard.

Similarly, (Bharath et al., 2021) demonstrated through HEC-RAS modelling of the Hidkal Dam in India that overtopping failures produce deep inundation and rapid flood propagation, posing severe risks to downstream settlements. These studies corroborate the present findings, confirming that flood depth and flood-wave travel time are critical indicators of dam-break hazard. Consequently, the combination of extremely short warning times and very high inundation depths observed in this study underscores the urgent need for automated early warning systems, well-rehearsed evacuation procedures, and strict land-use planning to minimize flood risk in downstream communities.

Figure 4: Map showing affected zones downstream

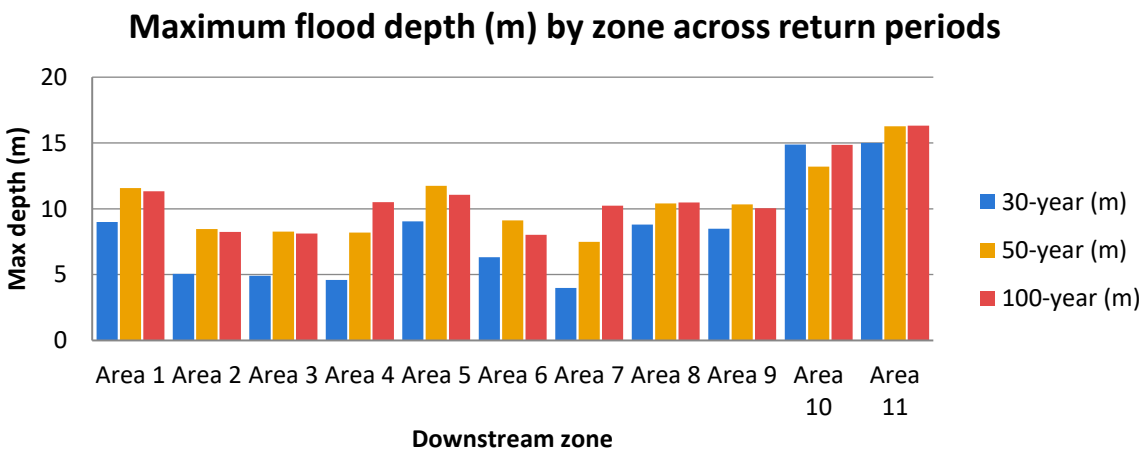

Figure 5: Maximum flood depth (m) by zone across return periods

As depicted in Figure above, maximum flood depths don't uniformly increase with the return period in all zones. Zones 1,4,5 and 9 actually have their maximum simulated depths for the 50-year scenario and not the 100-year scenario, a result that is not obvious under any assessment based on a single design return period rather than comparing several scenarios would miss completely. Zones 9 and 10 have the largest inundated areas (2.55 km and 3.21 km respectively) indicating floodplain widening when flood wave uses its energy slowly on lower gradient terrain farther from the dam site. This pattern has been found by other comparative return-period dam-break studies, for example, (Leoul, 2015) also found on the case of Kesem Dam in Ethiopia that flood risk is by no means proportional with return periods, the dam was safe under 50-year inflow conditions but failed catastrophically under 100-year and 200-year inflows and between these scenarios, both inundated area and depth increased sharply and non-linearly. Such findings highlight why the reliance of dam safety assessments on a single return period leads to substantial risk underestimation.

4 LIMITATIONS

This investigation was affected by multiple limitations. For example, only a pipe burst failure was considered in our modelling, and overtopping was not considered because a dam's central spillway is sufficiently designed to convey very heavy floods. This way, the scenario is considered highly unlikely unless spillway capacity is updated to reflect changing rainfall intensities. The second

shortcoming is that breach characteristics were taken from Froehlich's (2008) empirical regression equations, which although validated against the largest database of failures, the equations are subject to inherent uncertainty of the parameters. The third factor is that our hydraulic simulation was based on a relatively low-resolution DEM (30 m SRTM) which results in a decreased precision of capturing the smallest variations (microtopography) of a floodplain, so possibly changing how deep and far the floodwater is spreading at individual places. Because the 2,705-residence exposure estimate is derived directly from the extent of these depth rasters, it carries the same resolution-dependent uncertainty: at a 30 m cell size, individual structures and narrow drainage features smaller than one pixel cannot be resolved, so the true count of exposed residences in the actual floodplain likely deviates from this estimate, with the direction and magnitude of that deviation unverified without a finer-resolution DEM (e.g., LiDAR or sub-10 m satellite-derived terrain data) for comparison. Fourth, in our assessment of downstream people exposed (i.e. houses and farmlands) we only considered static land-use data which Yet, cannot record recent or informal residential or commercial development with Zaria floodplain.

5 RECOMMENDATIONS

Based on the findings, the recommendations to be considered are: (i) Installing automated, real-time, early-warning systems at the dam and downstream for the limited warning windows, Mostly in the nearest zones, which were extremely short; (ii) Drawing up and testing community-level Emergency Action Plans regularly, including holding evacuation drills for each of the eleven identified risk zones; (iii) Enforcement of land-use zoning to disallow more residential and agricultural development in the high-risk floodplain area determined; (iv) Regular safety inspection and equipping the dam (e.g. installation of piezometers, seepage monitoring) to detect signs of piping and structural problems in the building of the dam at an early stage; and (v) The future studies should combine overtopping failure scenarios, higher resolution terrain data, and updated land-use/population datasets to refine the risk estimates.

6 CONCLUSIONS

This research paper is the first to report a dam-break, breach-modelling-based flood inundation risk assessment of Kubanni (ABU), a Dam in Zaria, Nigeria. It uses a HEC-RAS, QGIS model under a scenario when water is escaping through a pipe or any small opening (piping failure mode) and considering return periods of 30, 50, and 100 years. Breach factors (width 132 m, side slope 0.7H:1V, formation time 2.99 hours) came from Froehlich's (2008) equations, chosen following a joint assessment with four other empirical models. Peak breach discharges of 1,426.56 m^3/s, 1,697.71 m^3/s, 1,761.71 m^3/s were modelled for these scenarios giving rise to a flood that swelled so much that it reached settlements downstream from Zango to Sabon Gari, which were about 10.3 km large (through 11 risk zones), and where 2,705 houses as well as vast areas of cropland have been identified as being at risk of high flood. The shortest duration of flood arrival, as fast as 10 seconds, was in a zone very close to the dam while in the farthest zone it took about 20 minutes. These results demonstrate a very limited time margin in case of emergency evacuation of the population. So, such work should be useful not only for dam safety but also for regulation of land use besides community-level early-warning systems in Zaria and similar less-observed river basins in the area.

ACKNOWLEDGEMENTS

The authors express sincere gratitude to Dr. A.D. Bello (Project Supervisor) for his guidance throughout this research, and to the staff of the Department of Water Resources and Environmental Engineering at Ahmadu Bello University, Zaria. The encouragement of family and colleagues is likewise warmly acknowledged.

7 REFERENCES

Aldrees, A., Ugwu, S. J., & Dan'azumi, S. (2025). Dam break modelling and flood inundation mapping using GIS and HEC-RAS: A case study of the Tiga Earth Dam, Kano State, Nigeria. *Water Science & Technology*, *92*(12), 1687–1708. https://doi.org/10.2166/wst.2025.172

Alhassan, B., Saddik Nafi'u Tijjani, A. I., Abaka, J. U., & Gumel, A. H. (n.d.). *Small Earth Dams in Nigeria: Prospects and Challenges*. https://doi.org/10.7176/JETP

Aureli, F., Maranzoni, A., & Petaccia, G. (2021). Review of historical dam-break events and laboratory tests on real topography for the validation of numerical models. In *Water (Switzerland)* (Vol. 13, Number 14). MDPI AG. https://doi.org/10.3390/w13141968

Balogun, O., & Ganiyu, H. (2016). STUDY AND ANALYSIS OF ASA RIVER HYPOTHETICAL DAM BREAK USING HEC-RAS. *Nigerian Journal of Technology*, *36*(1), 315–321. https://doi.org/10.4314/njt.v36i1.39

Beza, M., Fikre, A., & Moshe, A. (2023). Dam Breach Modeling and Downstream Flood Inundation Mapping Using HEC-RAS Model on the Proposed Gumara Dam, Ethiopia. *Advances in Civil Engineering*, *2023*. https://doi.org/10.1155/2023/8864328

Bharath, A., Shivapur, A. V., Hiremath, C. G., & Maddamsetty, R. (2021). Dam break analysis using HEC-RAS and HEC-GeoRAS: A case study of Hidkal dam, Karnataka state, India. *Environmental Challenges*, *5*. https://doi.org/10.1016/j.envc.2021.100401

Brunner, M. I., Seibert, J., & Favre, A.-C. (2016). Bivariate return periods and their importance for flood peak and volume estimation. *WIREs Water*, *3*(6), 819–833. https://doi.org/https://doi.org/10.1002/wat2.1173

Ekeu-Wei, I. T., & Blackburn, G. A. (2018). Applications of open-access remotely sensed data for flood modelling and mapping in developing regions. *Hydrology*, *5*(3), 39. https://doi.org/10.3390/hydrology5030039

Farr, T. G., Rosen, P. A., Caro, E., Crippen, R., Duren, R., Hensley, S., Kobrick, M., Paller, M., Rodriguez, E., Roth, L., Seal, D., Shaffer, S., Shimada, J., Umland, J., Werner, M., Oskin, M., Burbank, D., & Alsdorf, D. (2007). The Shuttle Radar Topography Mission. *Reviews of Geophysics*, *45*(2). https://doi.org/https://doi.org/10.1029/2005RG000183

Foster, M., Fell, R., & Spannagle, M. (2000). The statistics of embankment dam failures and accidents. *Canadian Geotechnical Journal*, *37*(5), 1000–1024. https://doi.org/10.1139/t00-030

Froehlich, D. C., & Asce, M. (2008). Embankment Dam Breach Parameters and Their Uncertainties. *Journal of Hydraulic Engineering*. https://doi.org/10.1061/ASCE0733-94292008134:121708

Goff, C., Atyeo, M., Petkovsek, G., Roca, M., & Kitamura, Y. (2020). The origins of large dam engineering and factors contributing to dam longevity. *Dams and Reservoirs*, *30*(3), 97–104. https://doi.org/10.1680/jdare.20.00017

HEC. (2023). *HEC-RAS River Analysis System HEC-RAS User's Manual*.

Holmes Jr., R. R., & Dinicola, K. (2010). 100-Year flood—it's all about chance. In *U.S. Geological Survey General Information Product*. U.S. Geological Survey. https://doi.org/10.3133/gip106

Jandora, J., & Riha, J. (2009). *The failure of embankment dams due to overtopping / CornerDIKE View project Assessment of empirical formulae for determining the hydraulic conductivity of glass beads View project*. https://www.researchgate.net/publication/40395679

Leoul, A. (2015). *Dam Breach Analysis Using HEC-RAS and HEC-GeoRAS: The Case of Kesem Kebena Dam*.

Mo, C., Shen, Y., Lei, X., Ban, H., Ruan, Y., Lai, S., Cen, W., & Xing, Z. (2023). Simulation of one-dimensional dam-break flood routing based on HEC-RAS. *Frontiers in Earth Science, Volume 10-2022*. https://www.frontiersin.org/journals/earth-science/articles/10.3389/feart.2022.1027788

Moreno-Rodenas, A., Mantilla-Jones, J. D., & Valero, D. (2025). Age, climate and economic disparities drive the current state of global dam safety. *Nature Water*, *3*, 284–295. https://doi.org/10.1038/s44221-025-00402-1

Okeola, O. G., Salimon, T. S., Salami, , 1, H. A., Abdulkadir, T. S., Ishola, T. A., & Salami, A. W. (2025). Dam break analysis and development of inundation map: a case study of asa

dam, ilorin, kwara state, nigeria. *LAUTECH Journal of Engineering and Technology*. https://doi.org/10.36108/laujet/5202.91.0511

Olanipekun, A. A., Olofintoye, O. O., Badmus, O. J., Idusuyi, D. U., Bayode, O., Alao, F., Braimah, J. I., Aiyelokun, O. O., & Opebiyi, A. A. (2026). Evaluation of Downstream Flood Hazard with HEC-RAS for Potential Overtopping and Piping Failure of Oyan River Dam, Abeokuta, Nigeria. *Nigerian Journal of Technological Development*, *23*(1), 43–52. https://doi.org/10.63746/njtd.v23i1.3861

QGIS.org. (2019). QGIS Geographic Information System. In *QGIS* (Version 3.6). QGIS Association. https://www.qgis.org/

Salah Abd Elmoaty, M., & T. A, E. S. (2020). Manning roughness coefficient in vegetated open channels. *Water Science*, *34*(1), 121–128. https://doi.org/10.1080/11104929.2020.1794706

Stephenson, D. J. (1996). *ESTIMATION OF EXTREME FLOODS WITH PARTICULAR REFERENCE TO SOUTHERN AFRICA*. https://api.semanticscholar.org/CorpusID:127009533

Umaru, A., Ogedengbe, K., & Omobowale, M. O. (2010). *STRUCTURAL FAILURES OF EARTH DAMS IN NIGERIA: A CASE STUDY OF CHAM DAM IN GOMBE STATE*. *5*(11). www.arpnjournals.com

Yusuf, Y. O. (2013). The effect of drainage basin management on sediment delivery by the Malmo Stream, Kubanni drainage basin, Zaria, Nigeria. *The Zaria Geographer*, *20*(1), 64–74. https://physicalsciences.abu.edu.ng/department/geography/public/journal/2013/files/08.pdf

Zhang, , L. M., Xu, Y., & Jia, J. S. (2007). *Analysis of earth dam failures-A database approach.*

International Conference on Engineering Innovation for Sustainable Development (ICESID 2026)
Faculty of Engineering, Ahmadu Bello University Zaria · 8–10 September 2026

GEOSPATIAL ANALYSIS OF ANTHROPOGENIC HEAVY METAL SOURCES AND DISTRIBUTION IN SOIL AND GROUNDWATER IN FUNTUA, KATSINA STATE

Al-Mustapha Abubakar[1], Aliyu Ishaq[1,*], Badruddeen Saulawa Sani[1], Umar Alfa Abubakr[1], Abubakar Sadiq Isah[2]

[1]*Ahmadu Bello University, Zaria*
[2]*Department of Civil Engineering, Baze University, Abuja-Nigeria*

Email: alabda88@gmail.com, aleeruks4real@gmail.com*, basaule@gmail.com, umaralfa@hotmail.com, abubakar.isah@bazeuniversity.edu.ng

***Corresponding author**: Aliyu Ishaq

DOI: https://doi.org/10.67203/sp.ICESID.2026

ABSTRACT

Heavy metal contamination of soil and groundwater is an escalating environmental and public health threat in rapidly urbanizing settlements, where overlapping anthropogenic activities complicate risk assessment and constrain effective management. In Funtua, Katsina State, Nigeria, limited geospatial evidence linking contamination sources to observed pollution patterns has hindered evidence-based groundwater conservation. This study spatially characterized anthropogenic heavy metal contamination in soil and groundwater across Funtua metropolis and identified priority zones for intervention. An integrated geospatial framework combining field surveys, systematic sampling and atomic absorption spectrophotometry was employed, and concentration profiles, source-clustering patterns, contamination levels and composite indices were computed and mapped using a Geographic Information System. Anthropogenic pollution sources exhibited statistically significant spatial clustering, including auto-mechanic workshops ($z = -11.10$, $p < 0.001$), filling stations ($z = -12.36$, $p < 0.01$) and dumpsites ($z = -19.84$, $p < 0.01$). Soil concentrations ranged from 0.19-0.26 mg/kg (Cd), 1.80-3.02 mg/kg (Cu), 1.74-7.46 mg/kg (Pb), 4.41-18.90 mg/kg (Fe) and 0.14-0.84 mg/kg (Ni). Groundwater analysis returned markedly elevated lead (up to 74.37 mg/L) and nickel (up to 560.10 mg/L) at several locations; these two extreme values exceed drinking-water guideline values by three to four orders of magnitude and are reported as provisional pending confirmatory re-analysis. The Metal Index ranged from 0.02 to 63.86, with 12.40% of the study area (17.09 km²) classified as contaminated, while the combined high- and very-high-risk zones occupied 0.68% (0.93 km²) and coincided with dense source overlap. Heavy metal contamination in Funtua is spatially structured and driven primarily by clustering of anthropogenic activities. Targeted monitoring, land-use control and regulatory enforcement at identified hotspots are recommended, and a low-cost biochar-based groundwater treatment system is proposed as a direction for future work.

Keywords: *Heavy metal contamination; Anthropogenic sources; Soil pollution; Groundwater quality; Geospatial analysis*

1. INTRODUCTION

Heavy metal contamination of soil and groundwater is recognized globally as one of the most intractable forms of environmental degradation, owing to the persistence and bioaccumulative behaviour of metallic pollutants (Kabata-Pendias, 2011). While natural weathering establishes baseline metal concentrations, the sharpest increases are anthropogenically driven, arising from industrial activity, waste disposal, vehicular traffic and unplanned urban expansion (FAO, 2017; Alloway, 2013). Urban and peri-urban settlements are disproportionately affected because informal pollution sources such as auto-mechanic workshops, filling stations and dumpsites are typically spatially concentrated and inadequately regulated.

Studies in China show that soil metal accumulation is governed primarily by land-use intensity and proximity to the urban core (Fang et al., 2011; Huang et al., 2018; Yang et al., 2020), while Nigerian studies in Ijebu-Ode, Lagos and Nsukka have linked localized soil contamination to differential land use, industrial estates and clustered mechanic workshops, respectively (Adedeji et al., 2019; Ololade et al., 2022; Duru et al., 2024). Groundwater, which supplies nearly half of global freshwater withdrawals,

is especially vulnerable once surface contaminants infiltrate through permeable soils and inadequate drainage (Jain, 2023), and aquifers underlying Africa's Sahelian belt, including northern Nigeria, face considerable and spatially heterogeneous pollution risk (Podgorski et al., 2024).

Despite this growing body of research, most existing studies focus on large metropolitan centres and treat soil and groundwater contamination as discrete processes, leaving medium-sized, rapidly urbanizing towns characteristic of northern Nigeria, and integrated source-to-contamination frameworks, comparatively understudied. In Funtua, Katsina State, no such framework has yet been applied, which constrains environmental planning, groundwater protection and risk-based regulatory decision-making.

The present study addresses this gap. It integrates a field-based source inventory, systematic soil and groundwater sampling, laboratory analysis and GIS-based spatial and contamination-index modelling in order to characterize the spatial distribution of the three major anthropogenic heavy metal sources in Funtua auto-mechanic workshops, filling stations and dumpsites — to quantify the associated soil and groundwater contamination, and to identify the priority zones for intervention that follow from their spatial coincidence.

2. METHODOLOGY

2.1 Study Area

Funtua town lies between latitudes 11.390279°N and 11.580643°N and longitudes 7.244443°E and 7.358793°E in Katsina State, north-western Nigeria, covering approximately 137.72 km² across eight wards (Makera, Nasarawa, Anguwan Musa, Sabon Gari, Anguwan Ibrahim, Dandutse, Maigamji and Kusami/Yankwani). As a major commercial and transit hub, the town hosts a dense concentration of filling stations, auto-mechanic workshops and informal dumpsites clustered along its road network and market areas, making it a suitable case for examining the linkage between anthropogenic activity and soil/groundwater contamination. Locality names follow a single gazetteer, applied consistently across the text, tables and figures of this paper; variant spellings encountered in the field records were reconciled to this gazetteer before analysis.

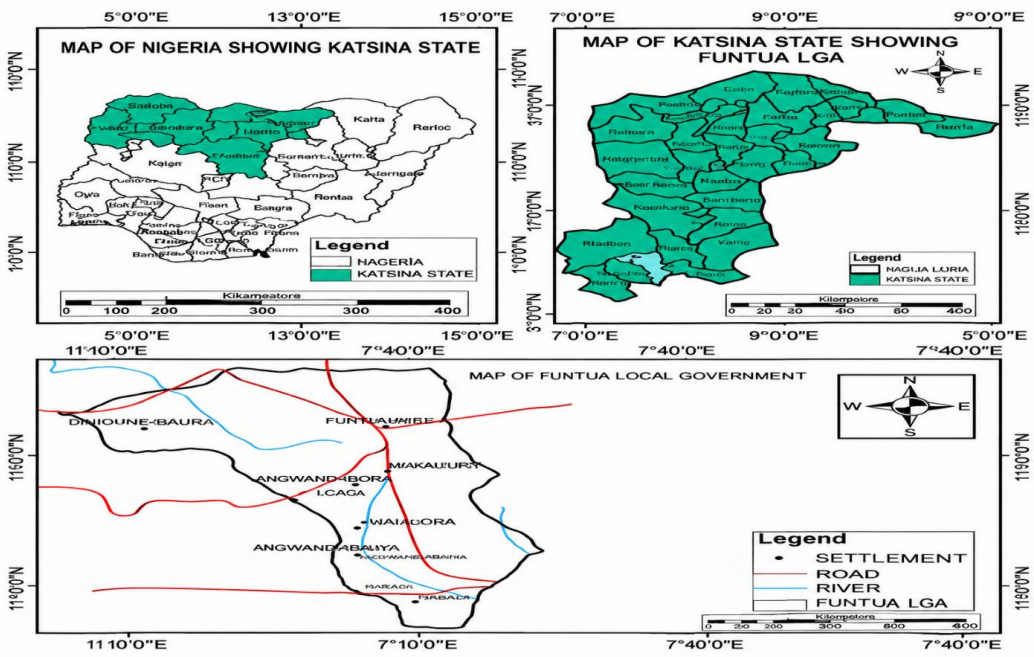

Figure 1: Map of the study area.

2.2 Sampling and Laboratory Analysis

Source coordinates for filling stations, auto-mechanic workshops and dumpsites were captured with a hand-held GPS, imported into Microsoft Excel, converted to shapefiles, and overlaid on the study-area base map in ArcMap 10.3/ArcGIS 10.8. A 50 m buffer was delineated around all mapped

contaminant sources, and sampling was stratified across the eight wards. Within each ward, four soil samples (0–25 cm depth) and four groundwater samples (from hand-dug wells and boreholes) were collected inside the buffer zone, yielding 32 source-proximal soil samples and 32 source-proximal groundwater samples. A further four soil and four groundwater control samples were collected from areas of comparably low anthropogenic activity outside all buffers, giving an overall total of thirty-six soil samples (S1–S36) and thirty-six groundwater samples (W1–W36). The control samples supplied the local geochemical background value used in the geo-accumulation index and the baseline against which source-proximal enrichment was judged.

Soil and groundwater samples were digested by the nitric acid–sulfuric acid procedure of Standard Methods for the Examination of Water and Wastewater, Method 3030 G (APHA, AWWA & WEF, 2005), and analysed for Al, Cd, Cu, Fe, Ni and Pb using an atomic absorption spectrophotometer (Unicam Model 969) at the National Water Quality Reference Laboratory, Sokoto. Groundwater physicochemical parameters (temperature, pH, electrical conductivity, salinity, turbidity and hardness) were determined on separate unacidified aliquots. Analytical quality was controlled through multi-point calibration ($r^2 > 0.995$), reagent blanks, and duplicate and matrix-spike analysis; the numerical QA/QC outcomes are not reported in this paper, so the two extreme groundwater Pb and Ni values discussed in Section 3.3 are treated as provisional pending confirmatory re-analysis.

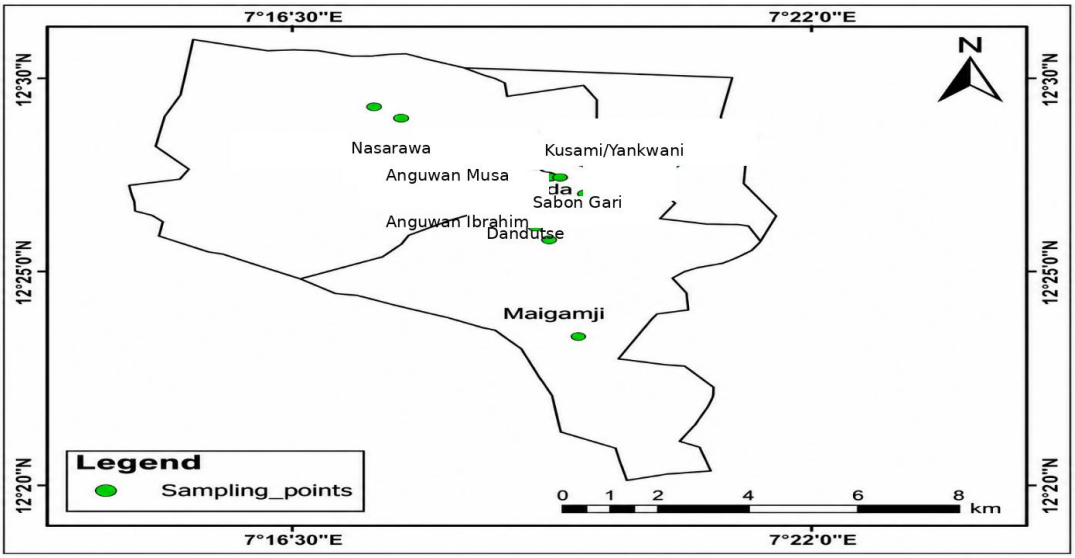

Figure 2: Spatial distribution of soil and groundwater sampling points across the wards of Funtua.

2.3 Geospatial and Statistical Analysis

Spatial analysis comprised point mapping, Average Nearest Neighbour (ANN) analysis, buffering, overlay/intersect analysis, and raster interpolation and reclassification in ArcGIS. The ANN statistic compares the observed mean nearest-neighbour distance among source points with the value expected under complete spatial randomness (Clark & Evans, 1954), yielding a Nearest Neighbour Ratio (NNR) and an associated z-score; ratios substantially below 1.0 with large negative z-scores indicate statistically significant spatial clustering (Ebdon, 1976; Mitchell, 2005). Where the NNR was unavailable for a source category, inference in this paper is confined to the significance of the departure from randomness rather than the ranking of clustering intensity.

Soil contamination was assessed using the Geo-accumulation Index (Igeo), computed as:

$$Igeo = \log_2 (C_m / 1.5B_n) \quad (1)$$

where C_m is the measured concentration of the metal and B_n is the local geochemical background value, taken as the geometric mean of its concentration in the control soils; the factor 1.5 corrects for lithogenic variation (Müller, 1969). Values were classified into seven standard Müller classes, from uncontaminated (Igeo ≤ 0) to extremely contaminated (Igeo > 5).

Groundwater contamination was assessed using the Metal Index (MI), computed as:

$$MI = \Sigma (C_i / MAC_i) \quad (2)$$

where C_i is the measured concentration of metal i and MAC_i is the WHO maximum allowable concentration for that metal (Table 1); MI > 1.00 denotes contaminated groundwater and MI ≤ 1.00 denotes uncontaminated groundwater (Tamasi & Cini, 2004). Fifty-metre source buffers were also intersected to classify groundwater risk zones as low, high or very high according to the degree of overlap among source-influence zones.

Table 1: *WHO maximum allowable concentrations (MAC) used for Metal Index calculation.*

Metal	Cu	Ni	Cd	Pb	Fe	Al
WHO limit (mg/L)	2.00	0.07	0.003	0.05	3.00	2.90

3. RESULTS AND DISCUSSION

3.1 Spatial Clustering of Anthropogenic Sources

The ANN analysis showed that anthropogenic sources within the study area are not randomly distributed but exhibit statistically significant spatial clustering (Table 2), concentrated around Anguwan Musa, Sabon Gari, Dandutse, Kusami/Yankwani and the surrounding central corridor (Figure 3). Auto-mechanic workshops returned an NNR of 0.42 ($z = -11.10$, $p < 0.001$), indicating strong clustering consistent with Nigerian GIS-based studies of workshop clusters (Ajeh et al., 2022; Duru et al., 2024; Iwegbue et al., 2024). Filling stations ($z = -12.36$, $p < 0.01$) and dumpsites ($z = -19.84$, $p < 0.01$) also departed significantly from randomness, although their NNR values were unavailable in the ANN output, so inference for these two categories is limited to statistical significance rather than clustering intensity or ranking. Sabon Gari, Anguwan Ibrahim and Nasarawa together accounted for approximately 77% of the mapped source density, indicating that environmental pressure is concentrated in a small part of the study area rather than evenly distributed, and that monitoring based on the area-wide average could underestimate conditions within these clusters.

Table 2: *Average Nearest Neighbour (ANN) results for anthropogenic source categories.*

Source category	NNR	z-score	p-value	Pattern
Auto-mechanic workshops	0.42	-11.10	< 0.001	Highly clustered
Filling stations	—	-12.36	< 0.01	Significantly clustered
Dumpsites	—	-19.84	< 0.01	Significantly clustered

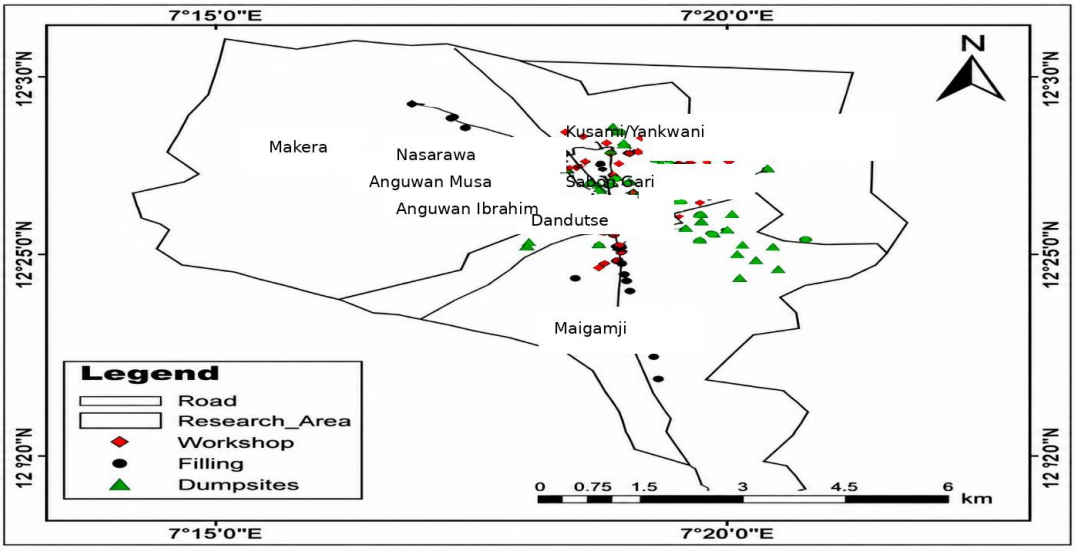

Figure 3: Spatial clustering of anthropogenic sources — auto-mechanic workshops, filling stations and dumpsites — in Funtua.

3.2 Soil Contamination (Geo-accumulation Index)

Soil Pb concentrations ranged from 1.74 to 7.46 mg/kg, with 92.13% of the study area (126.90 km²) classified as uncontaminated by Igeo (Figure 4); higher contamination was localized around

Kusami/Yankwani, consistent with Nigerian studies linking metal enrichment to automobile-related activities (Ajeh et al., 2022; Duru et al., 2024; Iwegbue et al., 2024). The remaining metals fell within comparatively narrow ranges (Cd 0.19–0.26 mg/kg, Cu 1.80–3.02 mg/kg, Fe 4.41–18.90 mg/kg, Ni 0.14–0.84 mg/kg). Elevated soil Pb values coincided spatially with the wards of highest anthropogenic-source density, supporting an anthropogenic rather than purely geogenic origin, although a lithogenic contribution cannot be entirely excluded for Fe and Ni.

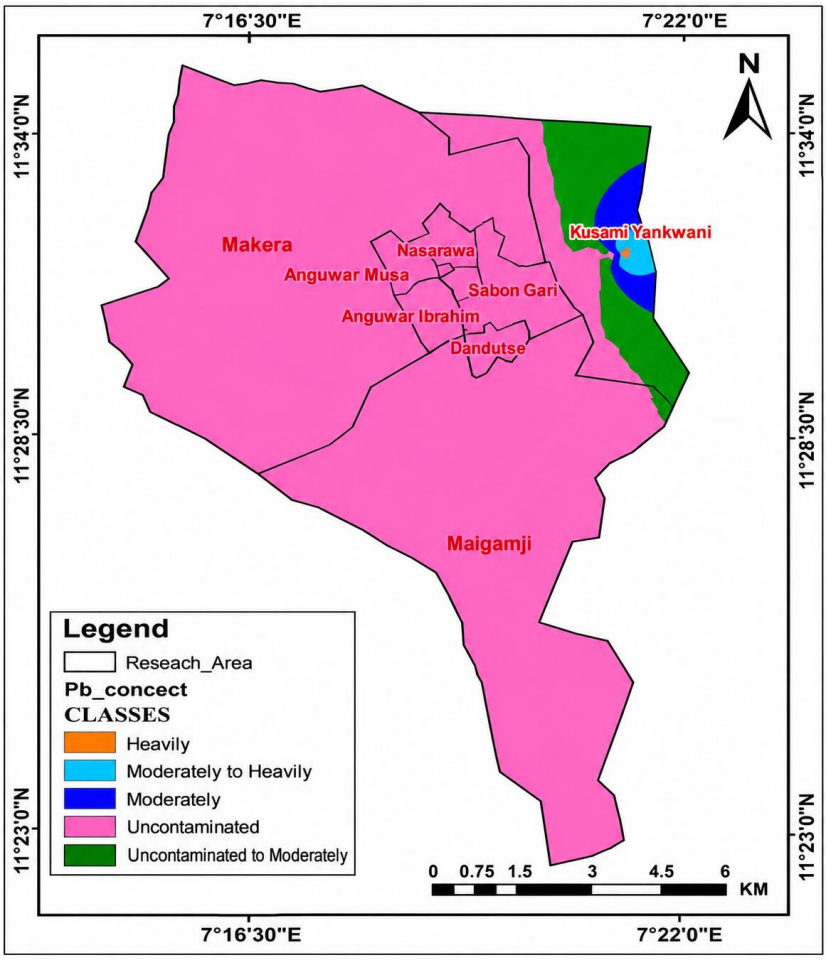

Figure 4: Spatial distribution of lead (Pb) contamination in soil across the study area, classified by the geo-accumulation index (Igeo).

3.3 Groundwater Contamination Level (Metal Index)

The groundwater Metal Index ranged from 0.02 to 63.86, with 87.60% of the mapped area (120.63 km²) classified as not-contaminated (MI ≤ 1.00) and 12.40% (17.09 km²) classified as contaminated (MI > 1.00) (Table 3, Figure 5). The contaminated zone was tightly concentrated in the north-eastern sector, coinciding with the densest aggregation of mapped sources and with the 700–740 m topographic band, suggesting that topographically controlled infiltration compounds the anthropogenic signal (Podgorski et al., 2024).

Maximum groundwater Pb (74.37 mg/L) and Ni (560.10 mg/L) exceeded current WHO drinking-water guidelines (0.01 mg/L and 0.07 mg/L, respectively) by three to four orders of magnitude (World Health Organization, 2022). These concentrations lie above the calibrated working range of the analytical method and were drawn from wells with turbidity up to 169 NTU, so unfiltered, particulate-rich digestion may have inflated the apparent dissolved concentration; both values are therefore reported as provisional pending confirmatory resampling with filtered/unfiltered splits, duplicate digestion and graphite-furnace AAS or ICP-MS analysis. No management or health-risk conclusion is drawn from their absolute magnitude until that confirmatory analysis is completed; the spatial pattern to which they contribute is corroborated independently by the buffer-overlay risk zoning in Section 3.4.

Table 3: *Groundwater contamination level in the study area (Metal Index classification).*

Class	MI range	Area (km²)	Percentage (%)
Not contaminated	≤ 1.00 (0.02–1.00)	120.63	87.60
Contaminated	> 1.00 (1.01–63.86)	17.09	12.40
Total	—	137.72	100.00

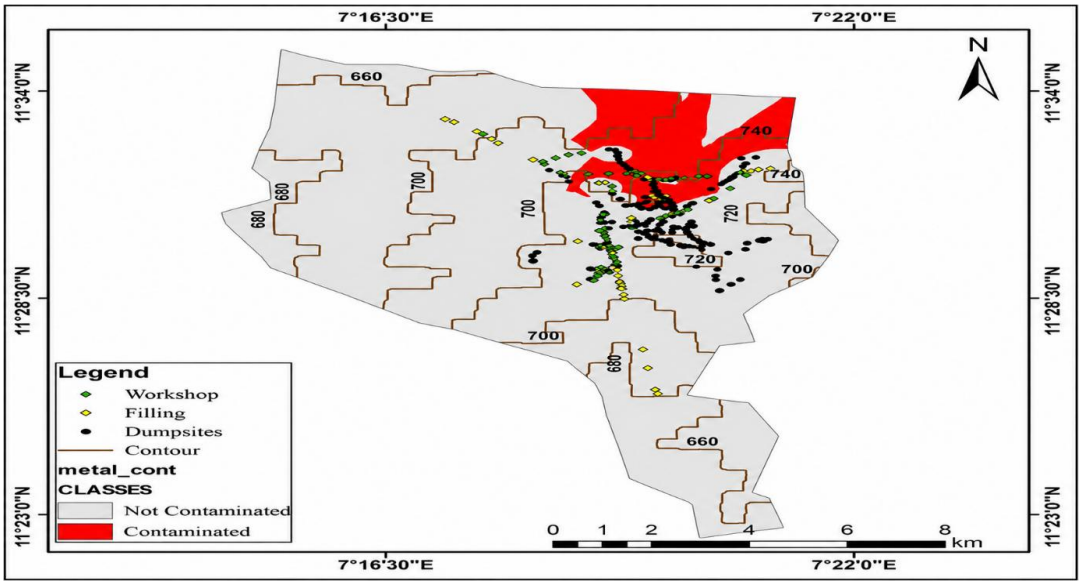

Figure 5: Groundwater contamination level (Metal Index classification) in the study area.

3.4 Groundwater Contamination Risk Zones

Buffer-overlay risk classification (Figure 6) showed that the low-risk class dominates the landscape (99.32%, 136.78 km²), while the high-risk and very-high-risk classes occupy 0.53% (0.73 km²) and 0.15% (0.20 km²) respectively, a combined footprint of 0.68% (0.93 km²) concentrated in and around Sabon Gari, Dandutse and Anguwan Ibrahim. This footprint coincides with both the highest source density (Section 3.1) and the Metal-Index-defined contaminated zone (Section 3.3); the convergence of these independently derived indicators provides internal validation that these three wards constitute genuine, high-confidence contamination hotspots (Duru et al., 2024; Guan et al., 2013). The small areal extent of the high-risk classes reflects the point-source-driven nature of urban groundwater risk rather than an absence of contamination pressure, consistent with continental-scale assessments of Sahelian aquifer vulnerability (Podgorski et al., 2024).

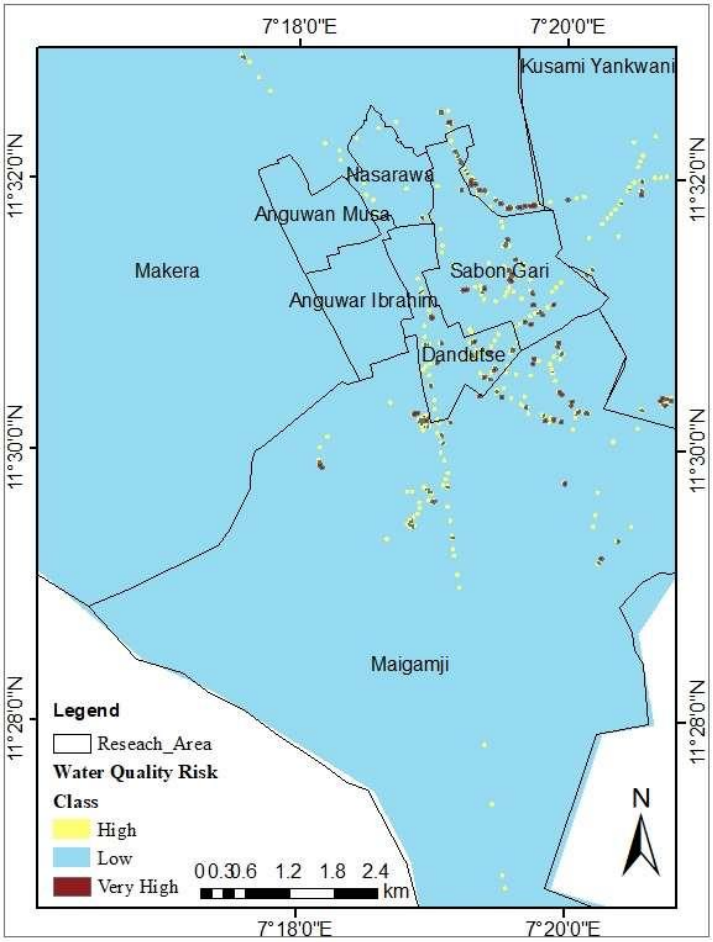

Figure 6: Delineation of groundwater contamination risk zones in the study area.

3.5 Groundwater Physicochemical Characteristics

Table 4 summarizes five physicochemical parameters across the thirty-six groundwater samples (W1–W36) relative to WHO (2017) and NSDWQ (SON, 2015) guideline values. pH (6.94–8.33, mean 7.8) fell entirely within guideline limits, and this near-neutral to slightly alkaline regime favours reduced solubility of Pb^{2+}, Cd^{2+} and Ni^{2+}, suggesting that the elevated Pb and Ni concentrations reported in Section 3.3 more plausibly reflect direct, source-proximal loading than pH-driven mobilization. Electrical conductivity (112–1,624 µS/cm, mean 500 µS/cm) exceeded the guideline in only 6% of samples, while turbidity (0–169 NTU, mean 20 NTU) exceeded the 5 NTU guideline in approximately 50% of samples the most significant deficiency identified consistent with the shallow, structurally unprotected nature of hand-dug wells (Jain, 2023). Total hardness (64–414 mg/L as $CaCO_3$, mean 180 mg/L) remained below the 500 mg/L guideline throughout. Overall, Funtua groundwater is predominantly fresh and near-neutral, with turbidity representing the principal water-quality concern and a plausible additional pathway for particulate-bound metal transport.

Table 4: *Summary statistics of groundwater physicochemical parameters (n = 36).*

Parameter	Min	Max	Mean	WHO limit	% exceeding
Temperature (°C)	33.2	35.2	33.8	N/A	N/A
pH	6.94	8.33	7.8	6.5–8.5	0
EC (µS/cm)	112	1624	500	1500	6
Turbidity (NTU)	0	169	20	5	50
Total hardness (mg/L as $CaCO_3$)	64	414	180	500	0

4. CONCLUSIONS

This study provides a GIS-based assessment of anthropogenic heavy-metal contamination in Funtua, integrating source mapping, laboratory analysis and contamination-index modelling. Auto-mechanic workshops, filling stations and dumpsites showed statistically significant spatial clustering (workshops: NNR = 0.42, z = -11.10, $p < 0.001$; filling stations: z = -12.36, $p < 0.01$; dumpsites: z = -19.84, $p < 0.01$), concentrated around Sabon Gari, Anguwan Ibrahim, Nasarawa, Dandutse and Kusami/Yankwani. Soil Pb ranged from 1.74–7.46 mg/kg, with 92.13% of the study area classified as uncontaminated by Igeo; groundwater showed greater concern, with Metal Index values of 0.02–63.86 and 12.40% (17.09 km²) classified as contaminated. Maximum groundwater Pb (74.37 mg/L) and Ni (560.10 mg/L) exceeded WHO guideline values by three to four orders of magnitude but remain provisional pending confirmatory analysis. Risk mapping identified a combined high-risk and very-high-risk footprint of 0.68% (0.93 km²) around source-overlap zones, particularly Sabon Gari, Dandutse and Anguwan Ibrahim. Overall, contamination in Funtua is spatially heterogeneous and driven primarily by the clustering of anthropogenic activities rather than by diffuse regional processes. Priority monitoring should focus on Kusami/Yankwani, Sabon Gari, Dandutse and Anguwan Ibrahim, supported by improved land-use regulation, confirmatory sampling of the extreme groundwater values, and seasonal monitoring. A limitation of this study is that batch-level QA/QC metrics for the analytical procedure are not reported here; a low-cost biochar-based groundwater treatment system is identified only as a direction for future work, not as a system designed or evaluated in the present study.

5. REFERENCES

Adedeji, O. H., et al. (2019). GIS-based assessment of heavy metal contamination in Ijebu-Ode, southwestern Nigeria. Environmental Monitoring and Assessment, 191, 1–15.

Ajeh, E. A., Modi, F. J., & Omoregie, I. P. (2022). Health risk estimations and geospatial mapping of trace metals in soil samples around automobile mechanic workshops in Benin City, Nigeria. Toxicology Reports, 9, 575–585. https://doi.org/10.1016/j.toxrep.2022.03.021

Alloway, B. J. (2013). Heavy metals in soils: Trace metals and metalloids in soils and their bioavailability (3rd ed.). Springer.

American Public Health Association, American Water Works Association, & Water Environment Federation. (2005). Standard methods for the examination of water and wastewater (21st ed.), Method 3030 G: Nitric acid–sulfuric acid digestion. APHA.

Clark, P. J., & Evans, F. C. (1954). Distance to nearest neighbor as a measure of spatial relationships in populations. Ecology, 35(4), 445–453. https://doi.org/10.2307/1931034

Duru, S. C., Echiegu, E. A., Anyadike, C. C., Alaneme, G. U., & Okechukwu, M. E. (2024). Spatial variability of heavy metals concentrations in soil of auto-mechanic workshop clusters in Nsukka, Nigeria. Scientific Reports, 14, Article 9681. https://doi.org/10.1038/s41598-024-60044-3

Ebdon, D. (1976). On the underestimation inherent in the commonly used formulae. Area, 8(3), 165–169.

Fang, X., et al. (2011). Heavy metals in vegetable-growing soils along the urban–rural gradient of Nanjing, China. Journal of Environmental Sciences, 23(11), 1823–1830.

Food and Agriculture Organization. (2017). The state of the world's land and water resources for food and agriculture (SOLAW). FAO.

Guan, Y., et al. (2013). Grid-based sampling assessment of peri-urban soil pollution, Beijing. Journal of Geochemical Exploration, 132, 194–200.

Huang, Y., et al. (2018). Spatial distribution of heavy metals in peri-urban soils, eastern China. Environmental Pollution, 233, 770–778.

Iwegbue, C. M. A., Nnanna, C. A., Ogwu, I. F., Odali, E. W., & Martincigh, B. S. (2024). Concentrations, sources and exposure to metals in dust from automobile mechanic workshops in Nigeria. Journal of Trace Elements and Minerals, 10, 100186.

Jain, H. (2023). Groundwater vulnerability and risk mitigation. Groundwater for Sustainable Development, 22, Article 100968.

Kabata-Pendias, A. (2011). Trace elements in soils and plants. CRC Press.

Mitchell, A. (2005). The ESRI guide to GIS analysis, Volume 2: Spatial measurements and statistics. ESRI Press.

Müller, G. (1969). Index of geo-accumulation in sediments of the Rhine River. GeoJournal, 2(3), 108–118.

Ololade, I. A., et al. (2022). Urban soil heavy metal contamination in Lagos, Nigeria. Environmental Geochemistry and Health, 44, 1–15.

Podgorski, J., Kracht, O., Araguás-Araguás, L., Terzer-Wassmuth, S., Miller, J., Straub, R., Kipfer, R., & Berg, M. (2024). Groundwater vulnerability to pollution in Africa's Sahel region. Nature Sustainability, 7(5), 558–567. https://doi.org/10.1038/s41893-024-01319-5

Standards Organisation of Nigeria. (2015). Nigerian standard for drinking water quality (NIS 554:2015). SON.

Tamasi, G., & Cini, R. (2004). Heavy metals in drinking waters from Mount Amiata (Tuscany, Italy): Possible risks from arsenic for public health in the province of Siena. Science of the Total Environment, 327(1–3), 41–51.

World Health Organization. (2017). Guidelines for drinking-water quality (4th ed.). WHO.

World Health Organization. (2022). Guidelines for drinking-water quality: Fourth edition incorporating the first and second addenda. WHO.

Yang, Q., et al. (2020). Heavy metal pollution in urban soils across Chinese cities: A systematic review. Chemosphere, 251, Article 126603.

HYDRODYNAMIC ASSESSMENT OF PIPING-INDUCED DAM-BREAK AND DOWNSTREAM FLOOD HAZARD CLASSIFICATION AT ZOBE DAM, NIGERIA. AN INTEGRATED HEC-HMS AND HEC-RAS MODELING APPROACH

Abdulaziz Imam Ahmad[1,*], Umar Abdullahi[1], Shamsuddeen Jumande Mohammad[1], Raji Olasunkanmi Sheriffdeen[2], Mohammed Aliyu Aliyu[1], Aliyu Yahaya Muhammad[1], Auwal Jarmai Babagirei[1]

[1]*Ahmadu Bello University Zaria*
[2]*Federal University Oye-Ekiti*

Email: ahmadabdulazizimam@gmail.com*, uabdullahi@engineering.abu.edu.ng, mjumande@abu.edu.ng, sheriffdeen.raji@fuoye.edu.ng, maliualiyu@gmail.com, aliyuyahayajere01@gmail.com, ajbabagirei@engineering.abu.edu.ng

***Corresponding author**: Abdulaziz Imam Ahmad

DOI: https://doi.org/10.67203/sp.ICESID.2026

ABSTRACT

Dam infrastructure occupies a central position in water resource management; and dam failure can produce severe consequences, especially in data-scarce regions where observed hydrological and failure data are limited. This study assesses a hypothetical piping failure of Zobe Dam, an earthen embankment with a documented history of seepage on the Karaduwa River in Katsina State, Nigeria, utilizing coupled HEC-HMS and 2D HEC-RAS modelling software. A terrain-delineated HEC-HMS model comprising five subbasins and two Muskingum-Cunge-routed reaches was used to generate inflow hydrographs for 30-, 50-, and 100-year design storms. Global Curve Number 250 (GCN250)-derived curve numbers and Soil Conservation Service (SCS)-derived lag times were used for hydrologic simulation, while breach parameters were estimated using Froelich (2008) formulation. Breach initiation was fixed at the documented Full Supply Level of 493.00 m across all scenarios. Peak basin-outlet discharge increased from 4,616.3 to 5,333.4 m^3/s between the 30- and 100-year events, while peak breach discharge increased from 2,377.24 to 2685.35 m^3/s. Flood depth, velocity, and inundation extent were from RAS Mapper and mapped in QGIS, with downstream hazard classified using the Australian Institute for Disaster Resilience (AIDR) Guideline 7-3 depth-velocity framework. Hazard classification remain unchanged across the three scenarios: Garhi was classified H6; Hakazama, Safana and Kunamawa as H5; and Dogon Ruwa and Makwanshi as H2/H3. The Water Treatment Plant and Bodole remained outside the modeled inundation extent. Sensitivity testing indicated limited variation in routed and breach discharges within the tested parameter ranges, while floodplain roughness produced a localized change in hazard classification at Safana. Garhi and the downstream road corridor linking Dutsin-Ma toward Kankara were identified as priorities for emergency preparedness and evacuation planning.

Keywords: *Dam breach; piping failure; flood hazard mapping; HEC-RAS; HEC-HMS; QGIS*

1. INTRODUCTION

Dams provide water security, irrigation, hydropower, and flood control, but can also become sources of catastrophic loss when they fail. More than 2,000 dam failures have been recorded globally over the past century, causing over 200,000 deaths (Nasser et al., 2025; Hariri-Ardebili, 2018). Earthen embankment dams are especially prone to failure because of their lower structural rigidity relative to concrete or masonry dams (Planès et al., 2016; Tang et al., 2022), and their collapse generates flood waves capable of altering downstream morphology and devastating riparian communities (Zhou et al., 2026). Failure typically results from piping, overtopping, seepage, or seismic loading (Chen et al., 2023). Piping, or internal erosion, occurs when seepage through the dam or its foundation progressively entrains fine soil particles, enlarging internal voids until a mass collapse of the overlying material sharply increases outflow (Saliba et al., 2019; de Paula Barreto et al., 2024). Because piping failures develop internally and can remain undetected until collapse is

imminent, they pose a distinct and often underappreciated risk relative to overtopping, which is more readily anticipated from reservoir stage alone (Chen et al., 2023). Understanding this mechanism, and quantifying the flood wave it would generate, is essential for downstream disaster preparedness.

Historical events such as the Teton (1976) and Banqiao (1975) dam failures catalyzed the development of formal breach-hydrograph and inundation-mapping methods (Bezerra and Eleuterio (2026). An estimated one to two significant dam-breach events occur globally each year, disproportionately affecting populations near the failed structure (Rana et al., 2022); the 2015 Swar Chaung sluice-gate breach in Myanmar and the 2023 Derna cascading dam failures in Libya illustrate how quickly such disasters unfold when settlements lie close to the source, and hydraulic simulation is the principal means of quantifying breach discharge, depth, velocity, and inundation extent in advance of an actual failure. While empirical regression relationships developed by MacDonald and Langridge-Monopolis (1984) and Froehlich (1995, 2008) now allow breach geometry and discharge to be estimated quantitatively from dam and reservoir characteristics. Combined with GIS-based terrain processing, coupled hydrologic-hydraulic software such as HEC-HMS and HEC-RAS enables engineers to simulate breach initiation, progression, and downstream flood propagation even where ground-survey data are limited (Peker et al., 2024). Most published applications of this coupled approach emphasize overtopping scenarios, however, with piping treated, at best, as a secondary comparison; site-specific, piping-focused assessments using locally derived design-storm hydrology remain comparatively scarce, particularly for embankment dams in West Africa. This emphasis partly reflects the greater modelling uncertainty associated with piping failure, which depends on poorly constrained internal erosion processes, initiation conditions, and breach progression that are difficult to characterize without detailed geotechnical and dam monitoring data; however, overtopping failure can be more readily represented using hydraulic loading and established breach-parameter relationships. Zobe Dam, an earthen embankment impounding the Karaduwa River in Katsina State, Nigeria, illustrates this gap directly. The dam has a documented history of foundation seepage (ESIA Report for Zobe Dam and Associated Infrastructures Rehabilitation Works, 2020), a condition mechanistically linked to piping failure (Magawata et al., 2020), yet no piping-specific dam-break analysis using locally derived design-storm hydrology has previously been conducted for the dam. Downstream, several rural settlements, farmland, and a water treatment plant serving the wider Dutsin-Ma and Katsina area remain without a quantitative, hydraulically modeled understanding of the flood hazard they would face in a breach event.

Accordingly, this study evaluates the downstream consequences of a hypothetical piping-induced breach of Zobe Dam under 30-, 50-, and 100-year design-storm conditions using coupled HEC-HMS and two-dimensional HEC-RAS modeling. The specific objectives are to: (i) model the piping-failure scenario using HEC-RAS 2D hydraulic modeling; (ii) estimate 30-, 50-, and 100-year design-storm runoff hydrographs using HEC-HMS with Gumbel frequency analysis; (iii) simulate the resulting flood wave and characterize peak flow, depth, and velocity; (iv) map the spatial distribution of downstream flood risk against defined hazard thresholds; and (v) translate the results into recommendations for dam safety and emergency planning. The analysis estimates breach hydrographs, flood depths, velocities, inundation extent, and spatial hazard levels, with particular attention to the implications for downstream settlements and emergency preparedness, and offers a replicable methodology for comparable earthen dams across Nigeria's Sokoto-Rima Basin. The study is confined to Zobe Dam using HEC-RAS 6.6 for two-dimensional unsteady-flow simulation of a piping failure, with breach parameters from the Froehlich (2008) method.

2. METHODOLOGY

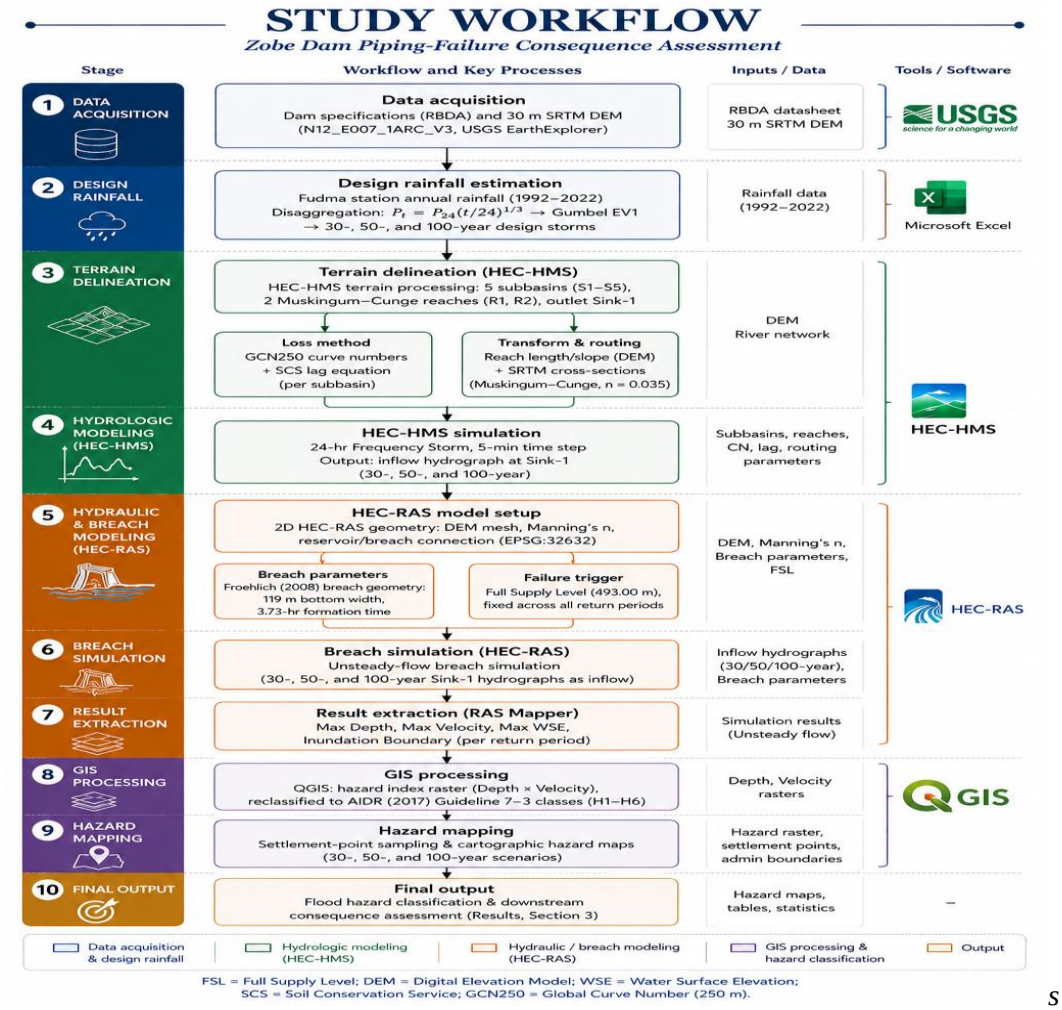

s

Figure 1: Overall study workflow, from data acquisition through terrain-based HEC-HMS delineation and design-storm hydrograph generation, HEC-RAS breach and unsteady-flow simulation, to GIS-based flood hazard classification.

2.1 Study Area

Zobe Dam is located at Makera, approximately 65km south of the city of Katsina in Katsina State, Nigeria, between longitudes 7^0 27' 57.12" and 7^0 34' 4.68" E and latitudes 12^0 20' 34.62" and 12^0 23' 27.48" N. The reservoir has a design capacity of 177 x 10^6 m^3, fed by the Gada and Karaduwa rivers, and was built to irrigate an 8,000ha command area and supply water to Katsina town and surrounding villages. The embankment is a 2.7km curved earth-fill structure with a 110m free-overflow spillway, reinforced at chainage 0+950 by a concrete intake-tower culvert, impounding a reservoir approximately 15km long and 36.9 km^2 in surface area. The dam supplies water for irrigation, domestic use, livestock, and fisheries (Jamda Saidu et al., 2019), emphasizing the scale of disruption a breach would set on the surrounding population.

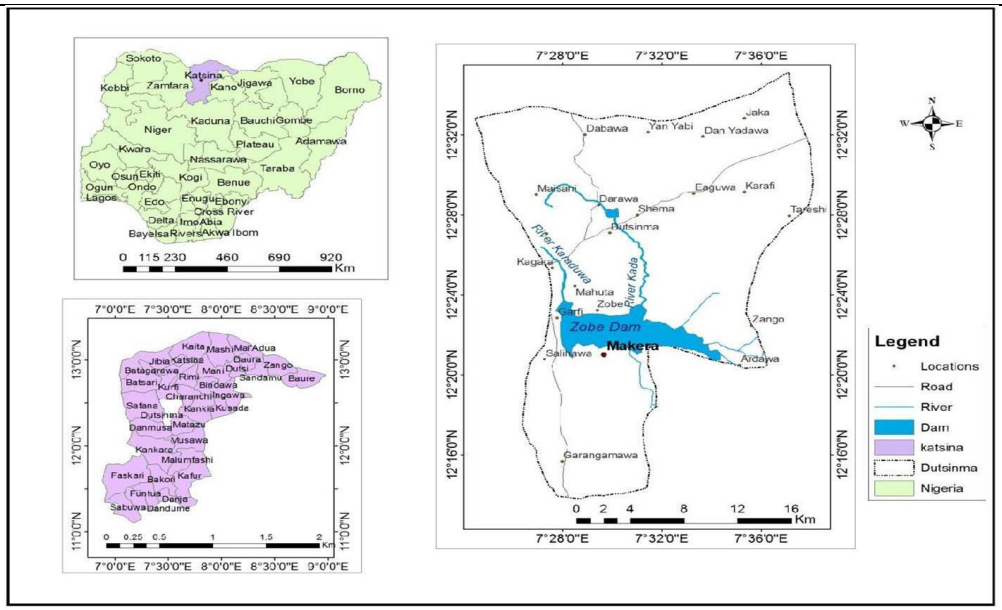

Source: Department of Geography and Planning, University of Jos, Plateau State, Nigeria.

Figure 1. *Dutsinma showing Zobe Dam (Insert: Nigeria and Katsina State).*

Figure 2: Location of Zobe Dam within Dutsin-Ma LGA, Katsina State (Source: Department of Geography and Planning, University of Jos).

Table 2 summarizes the principal structural and hydrological characteristics of Zobe Dam, as documented by the Sokoto-Rima River Basin Development Authority, which formed the core input data for the HEC-RAS geometric model.

Feature	***Value***
Embankment length	*2.75 km*
Embankment height	*18.9 m*
Dam crest width	*5.00 m*
Upstream slope	*1:3.2 (rip-rap, d = 1.00 m)*
Downstream slope	*1:2.2 (rip-rap, d = 0.35 m)*
Freeboard	*2.21 m*
Catchment area	*2,527 km^2*
Active storage capacity	*170 x 10^6 m^3*
Dead storage capacity	*7.0 x 10^6 m^3*
Maximum flood storage capacity	*263 MCM*
Reservoir surface area	*4,500 ha*
Full storage level (FSL)	*493.00 masl*
Dead storage level (DSL)	*484.60 masl*
Spillway No. 1 crest length	*110 m*
Spillway No. 2 crest length	*78 m*
Maximum overflow capacity	*1,087 m^3/s*

The catchment-wide curve number and time of concentration originally reported for the full 2,527 km^2 catchment are substituted, for the delineated Zobe sub-catchment used in the HEC-HMS model, by the subbasin-specific values in Table 2a (Section 2.4).

Table 2a. Subbasin curve numbers, derived from the GCN250 global curve-number dataset, and SCS lag times used in the HEC-HMS model.

Subbasin	*CN*	*Lag time (hrs)*
S1	*70.5*	*5.9*
S2	*70.8*	*5.5*
S3	*70.0*	*7.1*
S4	*73.6*	*2.8*
S5	*70.1*	*5.9*

The Karaduwa catchment lies within the Basement Complex of Katsina State, underlain by granite-migmatite and gneiss overlain by laterite and sandy-gravelly loam (ESIA Report for Zobe Dam and Associated Infrastructures Rehabilitation Works, 2020; Kankara, A., & Shazalli, N. U. 2020); permeable alluvial sand and gravel deposits extend across the river channel and adjacent floodplain, strata recognized as preferential pathways for internal erosion and directly relevant to the seepage vulnerability motivating this study. The catchment is dendritic, covering area of about 2,527km^2 as a tributary of the River Bunsuru, with average rainy-season discharge of 356 m3/s above the dam (Wang et al., 2022). The region receives 600-800 mm of annual rainfall governed by ITCZ migration, concentrated in a May-September wet season (mean 750 mm, peak in August) followed by an eight-month dry season (Geen et al., 2020).

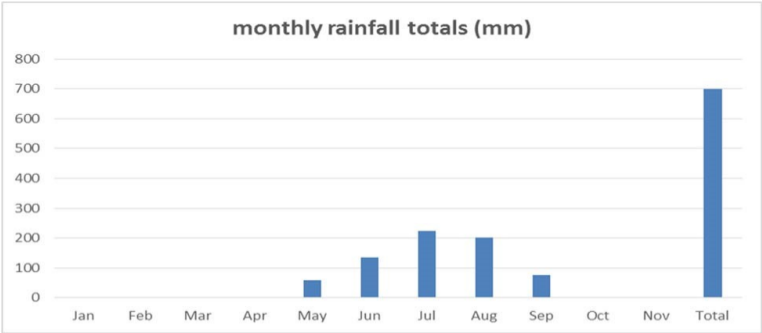

Figure 3: Mean monthly rainfall depth (mm) at the Katsina gauge station (Source: ESIA Report for Zobe Dam and Associated Infrastructures Rehabilitation Works, 2020).

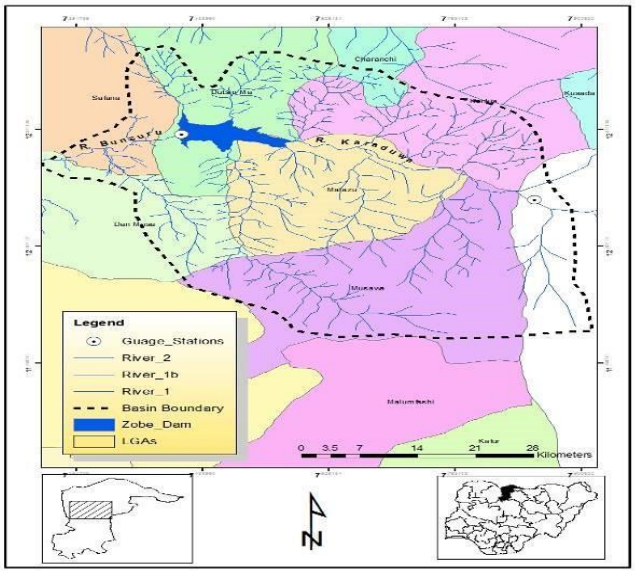

Figure 4: Drainage network of the Karaduwa-Bunsuru catchment showing the Zobe Dam reservoir (Source: Sokoto-Rima River Basin Development Authority).

2.2 Data Sources and Preparation

Table 1 summarizes the data sources used to construct the hydrologic and hydraulic models. Geometric data (dam dimensions, operating levels) were obtained directly from the Sokoto-Rima River Basin Development Authority. A 30m resolution SRTM DEM tile (N12_E007_1ARC_V3.TIF) was obtained from USGS Earth-Explorer and clipped to the study area using ArcGIS Spatial Analyst to provide the terrain surface for the HEC-RAS 2D model. Land-cover information from Landsat imagery and satellite base-map interpretation informed the Manning's roughness assignment described in Section 2.6. These datasets collectively provided the hydrological, topographical, and hydraulic information required to develop, in terms of parameters, and evaluate the joined HEC-HMS and HEC-RAS modelling framework

Data	***Format***	***Source***	***Use***
Rainfall records	*Time series*	*Fudma meteorological station*	*Gumbel frequency analysis / design storms*
DigitalElevation Model	*Raster (30m)*	*USGS EarthExplorer (SRTM)*	*Terrain surface for HEC-RAS 2D mesh*
Dam and reservoir geometry	*Engineering records*	*Sokoto-Rima River Basin Development Authority*	*HEC-RAS geometric model, breach parameters*
Land use / land cover	*Raster*	*Landsat imagery, Google satellite basemap*	*Manning's roughness assignment*
Manning's roughness (n)	*Literature-based estimate*	*Assigned per land-cover class (Section 2.6)*	*Channel and floodplain roughness input*

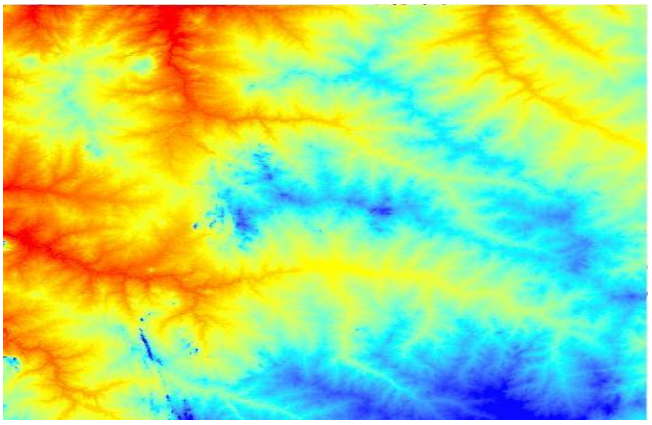

Figure 5: DEM of the Zobe Dam catchment derived from SRTM 30 m data (red = high elevation, blue = low elevation).

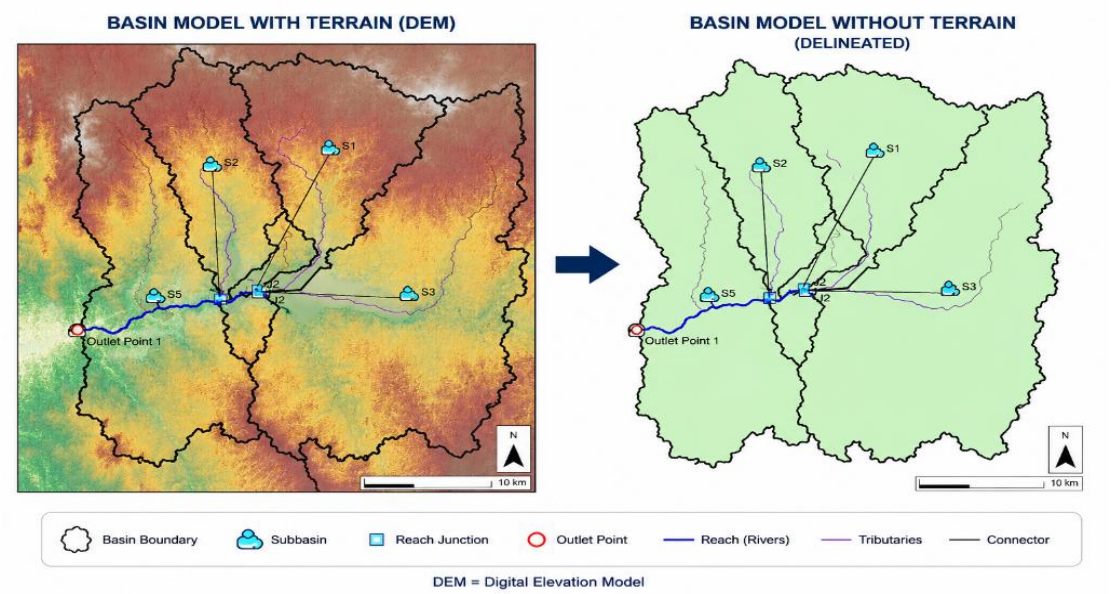

Figure 6: HEC-HMS basin model schematic showing the five terrain-delineated subbasins (S1-S5), the two Muskingum-Cunge-routed reaches (R1, R2), junction elements, and the basin outlet (Sink-1).

2.3 Frequency Analysis and Design Rainfall

Design rainfall depths for 30-, 50-, and 100-year return periods were estimated from the annual maximum rainfall series recorded at the Fudma meteorological station using Gumbel's extreme-value distribution:

$$XT = x - bar + K.sigma$$

$$\text{Where } K = \left(\frac{yT - yn}{Sn}\right)$$

$$yT = -\left[-\ln\left(\ln\left(\frac{T}{(T-1)}\right)\right)\right]$$

where x-bar and sigma are the sample mean and standard deviation of the annual maximum series and K is the frequency factor for return period T, y_T is the reduced variate, y_n the reduced mean and S_n is the reduced standard deviation. Annual maximum daily depths were first disaggregated to shorter sub-durations (5 minutes-24 hours) using the empirical relation $Pt = P24(t/24)^{1/3}$, and Gumbel's method was then applied at each duration to obtain return-period design rainfall depths for the 30-, 50-, and 100-year return periods. The design rainfall depths were converted to 24-hour design-storm hyetographs at five-minute resolution and used as meteorological input to HEC-HMS (Section 2.4).

2.4 Rainfall-Runoff Modelling

The Zobe sub-catchment was delineated directly from the SRTM DEM using HEC-HMS's terrain-processing tools, yielding five subbasins (S1-S5) connected through two routed reaches (R1, R2) to a single basin outlet (Figure 6). No streamflow gauge exists on the Karaduwa River, so model parameters were derived from physical watershed characteristics and not adjusted to observed hydrographs, consistent with standard practice for ungauged catchments (Section 2.8).

Curve Numbers were obtained per subbasin from GCN250 (Jaafar & Ahmad, 2019), a global 250m curve-number grid combining ESA CCI land cover with the HYSOGs 250m hydrologic soil group dataset, area-averaged for each subbasin by zonal statistics; values ranged from 70.0 to 73.6 (Table 2a), consistent with the mixed cropland, grassland, and scattered woodland cover of this Sudan-savanna catchment. The SCS Curve Number method was selected because it provides a practical and widely adopted approach for estimating rainfall losses in ungauged catchments where observed infiltration measurements are unavailable. GCN250 provides a physically based, spatially distributed alternative to assigning a single empirical CN in such data scarce settings and has shown a reasonable agreement with independent runoff products and global scales, including application in

Africa (Jaafar et al., 2019; Sujud & Jaafar, 2022). However, its use at the local watershed like the Karaduwa carries uncertainty because the derived CNs inherit uncertainties from the developed global land-cover and hydrologic-soil-group datasets and also the generalized CN lookup relationships. Hence, the resulting values were therefore physically valid estimates. The SCS Curve Number loss method,

$$Q = \frac{(P - 0.2S)^2}{(P + 0.8S)}$$

where S = $\left(\frac{25400}{CN}\right) - 254$ *(mm), was applied with these subbasin-specific CN values.*

Subbasin lag times were computed from the SCS lag equation,

$$L = \frac{l^{0.8}(S+1)^{0.7}}{1900\ Y^{0.5}}$$

where l is the hydraulic length (ft), Y is the average subbasin slope (%), and S = (1000/CN) - 10, using length and slope values from the terrain delineation; resulting lag times ranged from 2.8 to 7.1 as presented in (Table 2a) across the five subbasins, applied in the SCS unit-hydrograph transform (PRF-484).

Name	CN	L (km)	Y	S	L (ft)	Y(%)	Tc	Lag(Hr)	Lag(min)
S1	70.47	29.60	0.07	4.19	94984.10	7.25	9.90	5.94	356.54
S2	70.82	26.79	0.07	4.12	85967.45	7.04	9.19	5.51	330.85
S3	70.02	38.24	0.08	4.28	122700.43	7.80	11.86	7.12	426.95
S4	73.55	11.42	0.06	3.60	36649.89	6.02	4.66	2.79	167.67
S5	70.13	30.78	0.08	4.26	98783.66	7.93	9.86	5.92	355.09

Channel routing for R1 and R2 used the Muskingum-Cunge method, which derives routing behavior from channel geometry, slope, and roughness rather than from calibration against observed inflow-outflow pairs. Reach length and slope were taken from the terrain delineation (R1: 12.126 km, 0.00091; R2: 3.111 km, 0.00546). Because the SRTM resolution was not enough to directly resolve channel cross-sectional geometry, two cross-sectional profiles were sketched along each reach using Google Earth Pro v7.36, based on the visible channel trace and elevation profile and the resulting dimensions were averaged for each reach. The Channel cross-sections approximated as trapezoidal, with bank height and top width; gave a representative geometry of approximately 94m and 68m bottom width and 2H:1V assumed side slopes, for R1 and R2 respectively. Manning's n was initially set to 0.035 for a natural earth channel with light vegetation (Chow, 1959). Both this roughness assumptions and the sketched cross-sectional geometry are potential sources of uncertainty in the Muskingum-Cunge routing; their effect on simulated peak discharge was tested and reported (Section 3.6), together with the other parameter sensitivity checks performed in this study.

The three design storms from Section 2.3 were applied as a 24-hour Frequency Storm at a five-minute computational time step, with the simulation window to 72 hours to allow each hydrograph to fully recede to near-baseflow conditions. The resulting hydrographs at the basin outlet were used as HEC-RAS unsteady-flow boundary conditions (Section 2.6). Internal computational consistency was confirmed by verifying that the unit-hydrograph volume equaled 1mm for each subbasin; this check confirms only that the model computes runoff correctly given its inputs. Accordingly, the hydrological model was verified through parameter consistency, comparison with published ranges, and evaluation of the simulated hydrograph characteristics and not direct calibration against observed streamflow.

2.5 Breach Scenario and Breach-Parameter Estimation

Overtopping accounts for approximately 70.9% of documented dam-breach incidents and piping for 14.3% (Zhong et al., 2021); reflecting on Zobe Dam's seepage history (Section 2.1) and not its overall failure-mode base rate, this study models a piping failure occurring during normal reservoir operation. Piping is characterized by a discrete erosional conduit through the embankment interior, in contrast to the progressive crest-downward erosion of overtopping, and this distinction governed the parameters of the HEC-RAS breach module.

Because detailed geotechnical information required to predict the precise onset of piping was unavailable, a hypothetical piping-induced breach was assumed to initiate when the reservoir water surface reached the documented Full Supply Level (FSL = 493.00 m, Table 2). This assumption represents a “sunny-day” piping failure initiated at the normal operating level, transitioning into the design-storm inflow, rather than an overtopping-triggered failure. The same breach-initiation criterion was applied across the 30-, 50-, and 100-year scenarios to maintain a consistent failure condition and allow the effect of convergent storm magnitude on breach response to be compared. The breach invert was set to 489.47 m, which is the dam's documented foundation level. Accordingly, the study evaluates the downstream consequences of an assumed FSL-initiated piping failure subjected to subsequent storm loading, and not predicting the actual onset or probability of piping failure.

Reliable projection of peak discharge and inundation extent requires an accurate characterization of breach geometry and development time. A substantial body of regression research, summarized by Wahl (1998), has produced competing formulations for these parameters, compiled in Table 3; because each equation was justified to a different, generally modest sample of historical failures, and can diverge by a factor of two or more for a given dam, practitioners increasingly favor comparative application of several formulas rather than reliance on one, an approach followed here via the HEC-RAS Breach Parameter Calculator (Section 3.2).

Reference	***Case Studies (n)***	***Regression Relation (SI units)***
Johnson & Illes (1976)	-	*0.5hd <= B <= 3hd (earth-fill dams)*
Singh & Snorrason (1982, 1984)	*20*	*0.5 m <= breach depth <= 0.61 m; 0.25 hr <= tf <= 1.0 hr*
MacDonald & Langridge-Monopolis (1984)	*42*	*Ver = 0.0261(Vout.hw)^0.769; tf = 0.0179(Ver)^0.564*
FERC (1987)	-	*B = 2-4xhd; tf = 0.1-1.0 hr (engineered, compacted)*
Froehlich (1987)	*43*	*B = 0.47.Ko.(S)^0.25; tf = 79(S)^0.47*
U.S. Bureau of Reclamation (1998)	-	*B = 3hw; tf = 0.011B*
Singh & Scarlatos (1988)	*52*	*Btop/Bbottom averages 1.29*
Von Thun & Gillette (1990)	*57*	*Empirical B, Z, tf guidance*
Froehlich (1995b)	*63*	*B = 0.1803.Ko.Vw^0.32.hb^0.19; tf = 0.00254.Vw^0.55.hb^-0.90*

Among these, statistical evaluation has repeatedly identified the Froehlich (2008) equations as the best-performing method for earth-fill dams specifically (Temür et al., 2026; Geremew, 2024), the basis for its adoption in this study. The sensitivity of the simulated peak discharge to the adopted breach formation time was tested and reported in (Section 3.6), together with the other parameter sensitivity checks performed in this study.

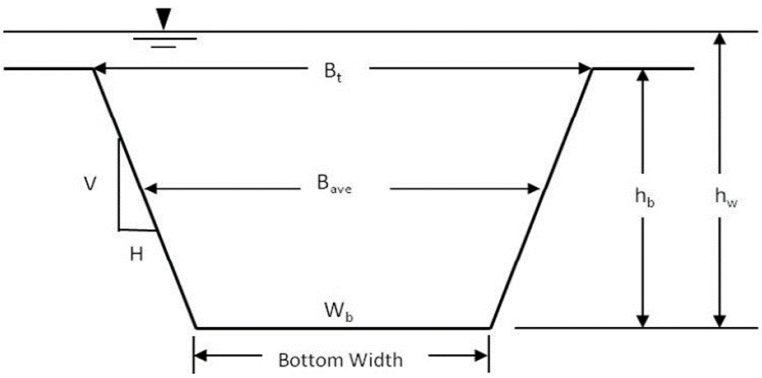

Figure 7: Schematic definition of embankment breach geometry (adapted from the HEC-RAS reference manual).

2.6 Two-Dimensional Hydraulic Modelling

The clipped DEM (Section 2.2) was imported into RAS Mapper at 1/128 rounding precision under the WGS 1984 UTM Zone 32N projection (EPSG: 32632), the correct zone for the study area's longitude (~7.5°E), and the 2D flow area and its connection to the Zobe reservoir storage area were constructed in the geometric editor.

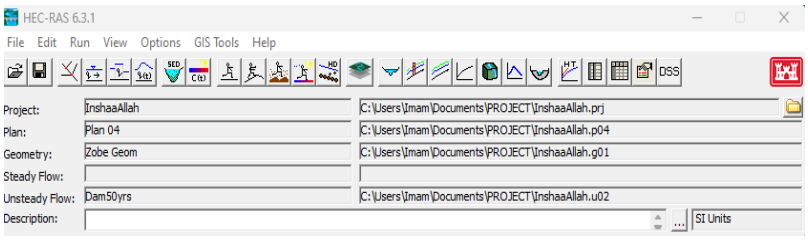

Figure 8: HEC-RAS v6.3.1 project window showing the configured plan, geometry, and unsteady-flow files.

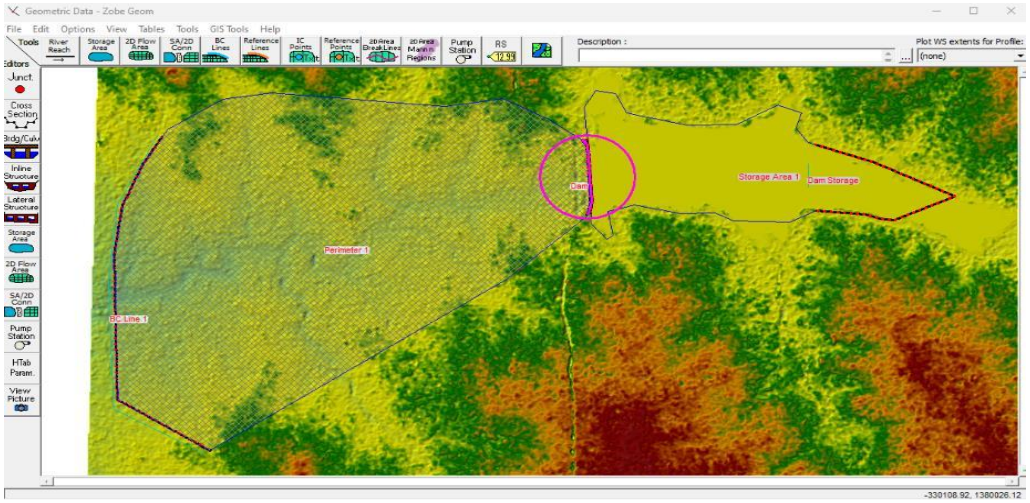

Figure 9: Geometric data editor showing the 2D flow area, storage area, and SA/2D connection (breach location).

A base mesh of cell size of 50x 50m was computationally generated for the polygon of the study area with 44035 grid cells. The selected Manning's roughness coefficients n of 0.035 was set which represent the dominant land-cover conditions within the savannah grassland cover of the Karaduwa-Bunsuru (Section 2.1); but 'Spatially Varied Manning's n on Faces' option was selected; which extracts multiple roughness values along a 2D face rather than depending on a single value at the center. The sensitivity of the resulting depth-velocity hazard classification to this floodplain rougness assumption was tested and is reported in (Section 3.6), together with the other parameter sensitivity checks performed in this study. Unsteady-flow boundary conditions comprised the HEC-HMS design-storm hydrographs at the upstream boundary and normal depth downstream was selected to ensure stable unsteady-flow routing is enough. Simulation used a 30-second computational interval and 5-minute mapping interval over 1 hour of simulated time, within a stable Courant-number range for the HEC-RAS full momentum solver. Depth, velocity, and water-surface-elevation outputs were visualized in RAS Mapper and exported to QGIS for the hazard maps in Section 3.4.

2.7 Flood Hazard Classification

Downstream hazard was classified using the depth-velocity product (D x V) framework of the Australian Institute for Disaster Resilience (AIDR, 2017) Guideline 7-3, Flood Hazard, developed from the vulnerability curves of Cox et al. (2010) and Smith et al. (2014). The adopted classification incorporates the combined influence of flood depth and velocity, thereby providing a more realistic representation of flood risk than either parameter considered independently. This structure defines six hazard classes (H1-H6) from the combined depth and velocity at each location, oriented toward the

stability and safety of people, vehicles, and buildings in floodwater and not directly classifying structural or economic damage assessment specifically.

Class	*D x V limit (m2/s)*	*Limiting depth (m)*	*Limiting velocity (m/s)*
H1	*<= 0.3*	*0.3*	*2.0*
H2	*<= 0.6*	*0.5*	*2.0*
H3	*<= 0.6*	*1.2*	*2.0*
H4	*<= 1.0*	*2.0*	*2.0*
H5	*<= 4.0*	*4.0*	*4.0*
H6	*> 4.0*	-	-

H1 denotes conditions generally safe for people, vehicles, and buildings; H6 denotes conditions under which all building types are considered vulnerable to structural failure and floodwater is unsafe for vehicles and people. Maximum simulated depth and velocity at each downstream location were combined into a single D x V value and classified against these thresholds in QGIS.

3. RESULTS

3.1 Design Rainfall and Rainfall-Runoff Results

HEC-HMS produced peak discharge and time-to-peak at the basin outlet (Sink-1) for the three design storms derived in Section 2.3 (Table 5), confirmed by a unit-hydrograph volume of 1 mm for each subbasin.

Return Period (years)	*Simulated Peak Discharge (m3/s)*	*Time to Peak*
30	*4,616.3*	*19h 20min*
50	*4,773.9*	*19h 15min*
100	*5,333.4*	*19h 15min*

Peak discharge increased from 4,616.3m^3/s (30-year) to 5,333.4m^3/s for the 100-year event, representing an increase of approximately 22% (Table 5). While time-to-peak remains near-constant (~19.25 hours) across all three return periods, indicating that increasing rainfall intensity affected runoff magnitude without altering the watershed's hydrologic response time for these selected rainfall scenarios. The subbasin lag times and reach travel times derived from the terrain delineation (Sections 2.2, 2.4) behavior were consistent, controlled by the catchment characteristics and not storm magnitude. The simulated inflow hydrographs at the Sink-1 were subsequently used as the upstream boundary conditions for the HEC-RAS breach simulations.

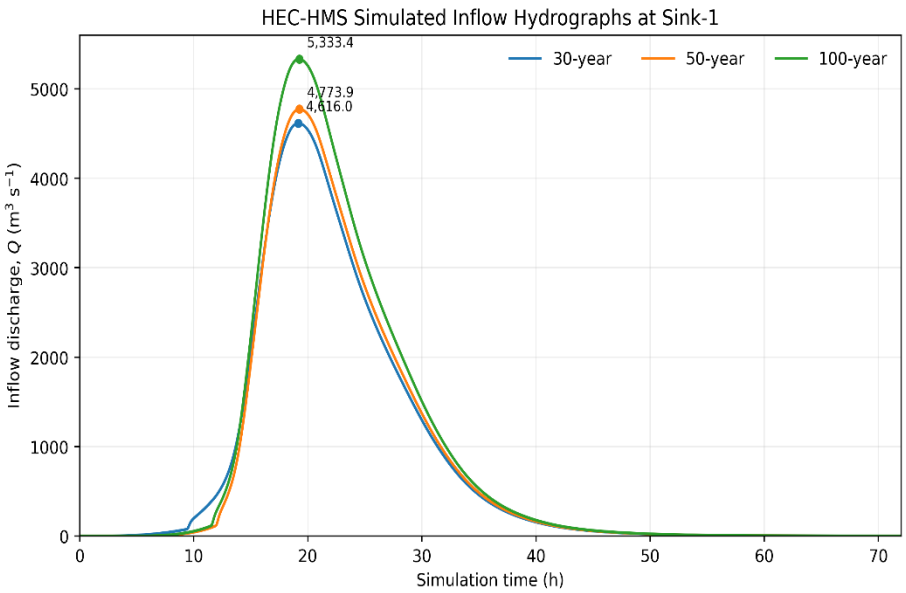

Figure 10: HEC-HMS Simulated Inflow Hydrographs at Sink-1.

3.2 Breach Parameters

Breach parameters were estimated using the HEC-RAS Breach Parameter Calculator based on the empirical relationship of MacDonald and Langridge-Monopolis (1984), Froehlich (1995, 2008), Von Thun and Gillette, and Xu and Zhang formulations listed in Table 3. Following the selection criteria described in section 2.5, the Froehlich (2008) output (Table 6) was adopted for all simulations. Because breach dimensions are primarily by the physical characteristics of the dam and reservoir characteristics not the inflow hydrographs. The Pool Elevation at Failure (493.00m, the documented FSL) and breach invert (489.47m) were similarly held constant across all three scenarios (Section 2.5). This approach ensured that difference in flood response reflected variations of the hydrological inputs not changing breach geometry.

Breach Parameter	***Estimated Value (Froehlich, 2008)***
Breach bottom width	*119 m*
Side slopes	*0.7 (H:V)*
Breach development time	*3.73 hrs*
Pool elevation at failure (FSL)	*493.00 m*
Breach invert elevation	*489.47 m*

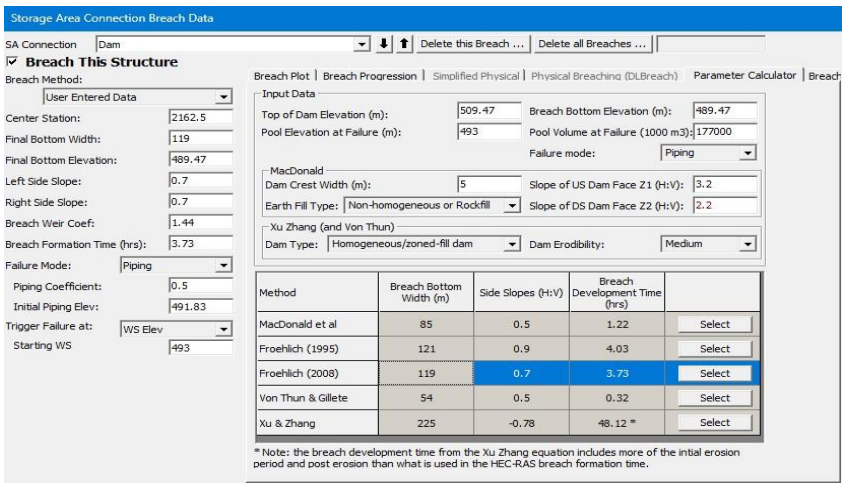

Figure 11: HEC-RAS Parameter Calculator comparing breach parameters across regression methods for Zobe Dam.

The adopted breach geometry corresponds to a moderate piping failure scenario and was treated as a hypothetical but internally consistent representation for all scenarios.

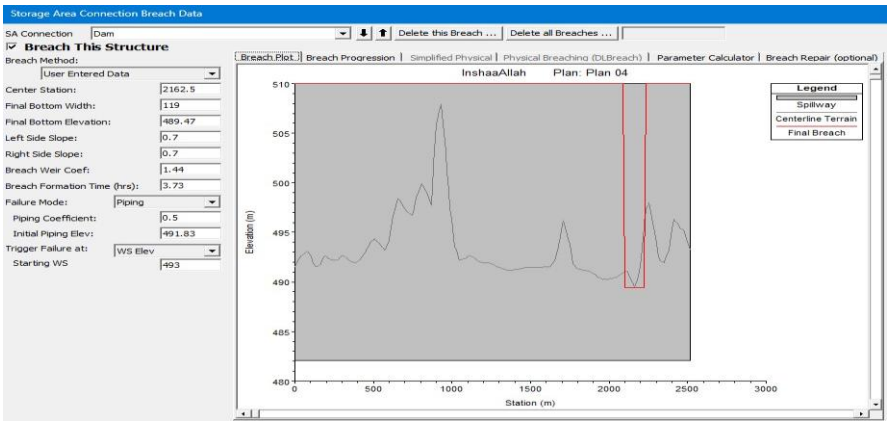

Figure 12: Breach plot for Zobe Dam showing reservoir cross-section, spillway, and final breach geometry.

3.3 Breach Hydrographs and Reservoir Response

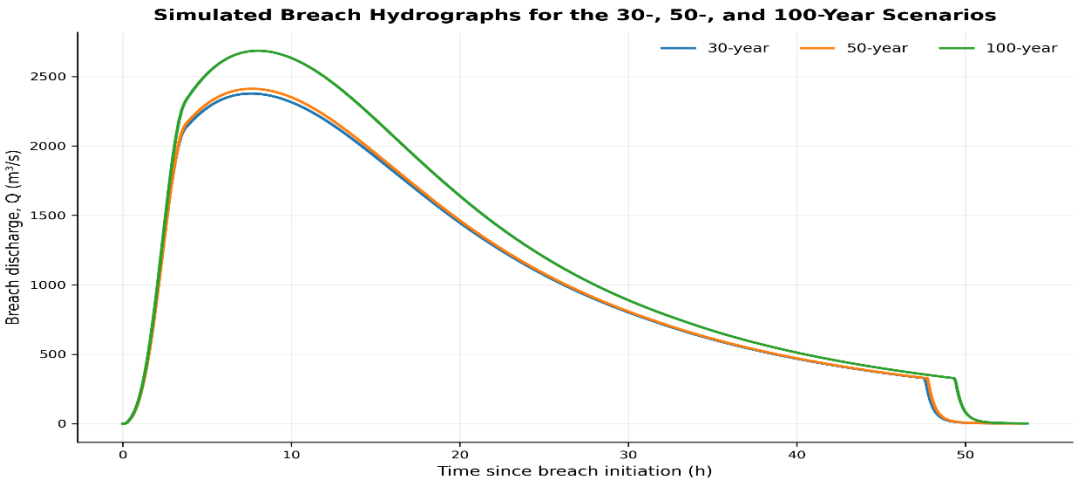

Figure 13a. Breach plot for Zobe Dam showing the outflow Breach Hydrograph for the 30, 50, and 100-year event.

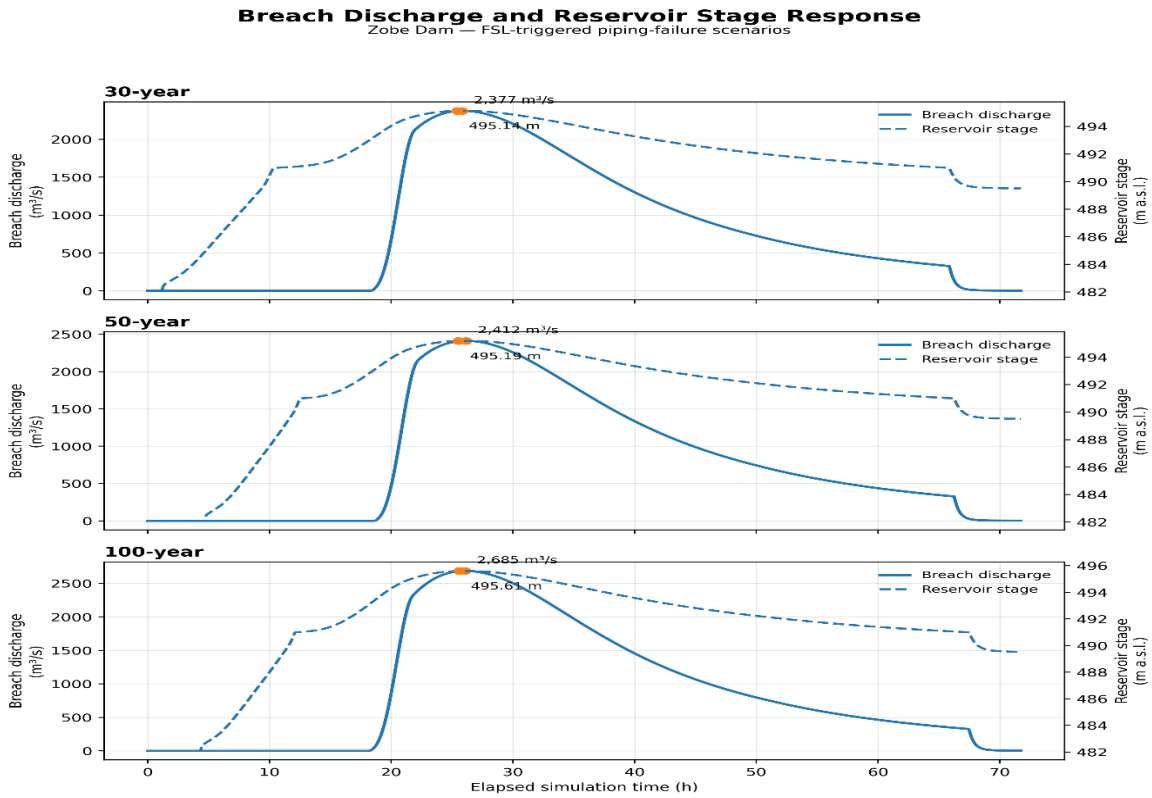

Figure 13b. Breach plot for Zobe Dam showing reservoir stage and Breach Discharge starting at selected Full Supply Level triggered piping scenario.

With the reservoir breach initiating at the documented FSL (493.00m, Section 2.5), Table 7 summarizes the reservoir response by return period.

Return Period	***Peak Inflow (m3/s)***	***Maximum Reservoir Stage (m)***	***Peak Breach Discharge (m3/s)***
30-year	*4,616.3*	*495.13*	*2,377.24*
50-year	*4,773.9*	*495.19*	*2,411.69*
100-year	*5,333.4*	*495.61*	*2,685.35*

The simulated reservoir response and breach hydrograph for the three design storm scenarios are summarised in Table 7 and plotted in Figure 13a. Peak inflow increased from 4,616.3 m³/s for the 30-year event to 5,333.4 m³/s for the 100-year event, producing a corresponding rise in maximum reservoir water level from 495.13 to 495.61 m. Peak breach discharge also increased with return period, ranging from 2,377.24 to 2,685.35 m³/s.

Despite the increase in inflow, peak breach discharge remained substantially lower than peak reservoir inflow in all simulations as shown in Figure 13c. This behaviour reflects the hydraulic control imposed by the adopted breach configuration and the relatively shallow driving head available above the breach invert (489.47 m) following breach initiation at the documented Full Supply Level (493.00 m) shown in Figure 13b. Consequently, a considerable proportion of the incoming flood volume was temporarily attenuated by reservoir storage before being released through the developing breach, resulting in a moderated breach hydrograph.

The modest increase in breach discharge across the three return periods further indicates that, under a fixed breach geometry and failure elevation, downstream flood response is influenced more by reservoir routing and breach hydraulics than by the incremental increase in design storm magnitude. This observation is consistent with the relatively small differences in maximum reservoir stage among the simulated events. More so, the 30-year simulation produced a volume-accounting error of only 0.05%, demonstrating excellent mass conservation and confirming the numerical stability of the hydraulic model (Section 2.8).

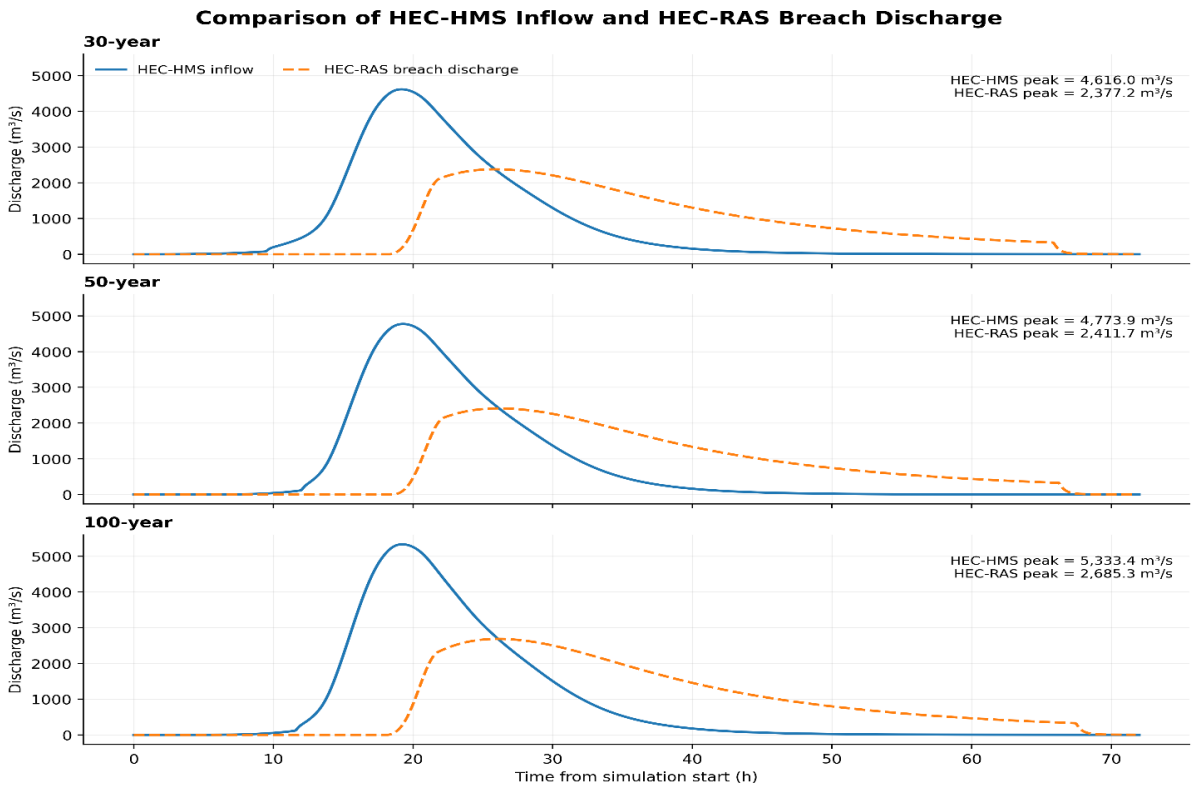

Figure 13c. Breach plot for Zobe Dam showing the comparison of Inflow and Outflow Discharges.

3.4 Flood Inundation Characteristics

Raster data of water depth values and water velocities obtained after flood modeling with HEC-RAS 6.6 were converted into Hazard Index factors using the Spatial Analysis Tools—Reclassify command in the ArcGIS 10.6.1 software. Then, Equation DxV was applied to these raster data with the help of the Spatial Analysis Tools—Raster Calculator command and hazard maps were obtained according to hazard classes according to the limit values in Table 4 of Section 2.7.

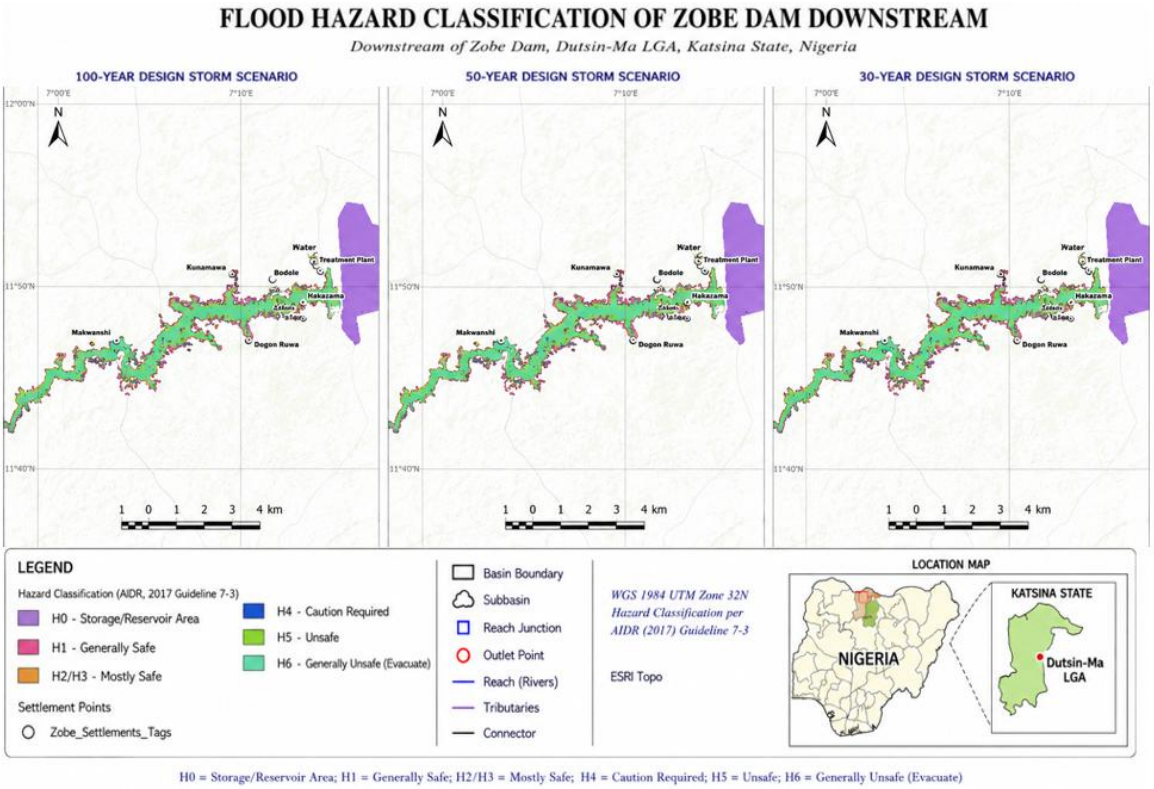

Figure 14: Flood hazard maps, 30-, 50-, and 100-year FSL-triggered design-storm scenarios (QGIS).

Maximum flood depth and velocity were extracted from RAS Mapper at eight downstream locations and are summarized in Table 8. Total inundated area and boundary perimeter, derived from the exported inundation-boundary polygon, are summarized in Table 9.

Location	***30-yr D (m)***	***30-yr V (m/s)***	***50-yr D (m)***	***50-yr V (m/s)***	***100-yr D (m)***	***100-yr V (m/s)***
Garhi	*5.95*	*4.86*	*5.97*	*4.87*	*6.16*	*4.88*
Hakazama	*3.31*	*0.66*	*3.34*	*0.68*	*3.52*	*0.86*
Safana	*3.68*	*0.85*	*3.71*	*0.87*	*3.88*	*1.03*
Kunamawa	*4.24*	*0.55*	*4.27*	*0.55*	*4.26*	*0.56*
DogonRuwa	*2.62*	*0.15*	*2.64*	*0.15*	*2.83*	*0.15*
Makwanshi	*0.50*	*0.50*	*0.60*	*0.51*	*0.74*	*0.56*
W.T.P.	*Nil*	*nil*	*nil*	*nil*	*nil*	*nil*
Bodole	*Nil*	*nil*	*nil*	*nil*	*nil*	*nil*

Return Period	***Inundated Area (km2)***	***Inundation Extend (km)***
30-year	*37.52*	*152.4*
50-year	*37.58*	*152.6*
100-year	*38.02*	*154.9*

Maximum flood depth and velocity extracted from RAS Mapper at the eight identified downstream locations are presented in Table 8. Garhi recorded the highest hydraulic intensity across all three return periods, with maximum depth increasing from 5.95 m for the 30-year event to 6.16 m for the 100-year event, while velocity remained almost unchanged at 4.86–4.88 m/s. Hakazama and Safana also showed progressive increases in both depth and velocity with increasing return period. At Kunamawa and Dogon Ruwa, the changes were comparatively small, while Makwanshi showed an increase in maximum depth from 0.50 to 0.74 m and velocity from 0.50 to 0.56 m/s. The WTP and Bodole were not intersected by the simulated inundation extent in any of the three scenarios.

The resulting flood footprint is summarized in Table 9. Inundated area increased from 37.52 km² for the 30-year event to 37.58 km² for the 50-year event and 38.02 km² for the 100-year event.

Over the same return-period range, the flood extent length increased from 152.4 to 154.9 km. Thus, the overall spatial extent of flooding changed only slightly across the three scenarios, with the largest increase occurring between the 50- and 100-year events.

The eight locations represent named settlements and facilities identifiable from the available spatial data and are used here to characterize hydraulic conditions at selected downstream locations. They do not constitute an exhaustive inventory of all settlements within the simulated flood extent. The spatial limitation of the settlement-level assessment is discussed further in Section 4.5.

3.5 Flood Hazard Classification

Depth–velocity products at the eight assessed locations were classified using the AIDR (2017) Guideline 7–3 thresholds described in Section 2.7, with the resulting hazard classes presented in Table 10. Locations falling within the combined H2/H3 range are reported as H2/H3.

Location	***30-year Class***	***50-year Class***	***100-year Class***
Garhi	*H6*	*H6*	*H6*
Hakazama	*H5*	*H5*	*H5*
Safana	*H5*	*H5*	*H5*
Kunamawa	*H5*	*H5*	*H5*
Dogon Ruwa	*H2/H3*	*H2/H3*	*H2/H3*
Makwanshi	*H2/H3*	*H2/H3*	*H2/H3*
W.T.P.	*Not inundated*	*Not inundated*	*Not inundated*
Bodole	*Not inundated*	*Not inundated*	*Not inundated*

Hazard classification remained unchanged across the 30-, 50-, and 100-year scenarios at all assessed locations. Garhi was classified as H6 in all three scenarios, representing the highest hazard category recorded in the assessment. Hakazama, Safana, and Kunamawa consistently fell within H5, while Dogon Ruwa and Makwanshi remained within the combined H2/H3 category. The WTP and Bodole were not inundated in any scenario and were therefore not assigned a hazard class. However, these locations are not the exhaustive inventory settlements within the study area. They represent the names and facilities that could be identified from the available spatial data. Other households, structures and smaller settlements located within or immediately adjacent to the mapped hazard zones would be expected to experience conditions corresponding to their respective positions on the hazard maps, even where they are not individually labelled. The downstream road corridor toward Kankara, which comes from Dutsin-Ma town, passes near Garhi, also falls within the affected area; given Garhi's H6 classification, flooding could severely disrupt road access and vehicles movement, with implications for evacuation, emergency response, and local economic activities.

The stability of the hazard classes across the three return periods reflects the relatively limited variation in flood depth and velocity observed between scenarios (Section 3.4). Despite the increase in design-storm magnitude, none of the assessed locations crossed a hazard-class threshold.

3.6 Sensitivity Analysis

Sensitivity analyses were conducted to assess the influence of selected hydrologic and hydraulic parameters on the modeled response. For HEC-HMS, the effects of channel Manning's roughness and the assumed channel geometry on routed discharge were examined. For HEC-RAS, sensitivity was assessed for floodplain Manning's roughness and breach formation time, while the remaining model parameters were held constant.

3.6.1 HEC-HMS Sensitivity

Changing channel Manning's roughness from n=0.035 to n=0.040 produced peak routed discharges of 3,921.0 and 3,944.1 m^3/s for R1, respectively, while the R2 peak remained 3,069.5 m^3/s for both cases. The corresponding change in R1 peak discharge was approximately 0.59%.

A ±20% variation in the adopted channel geometry produced Sink-1 peak discharges of 4,773.7, 4,773.9, and 4,773.5 m^3/s for the −20%, base, and +20% cases, respectively. The results indicate very limited sensitivity of the routed peak discharge to the tested changes in channel roughness and geometry.

3.6.2 HEC-RAS Sensitivity

Floodplain (2D) Manning's n. Because the 2D floodplain used in the HEC-RAS hazard-mapping simulations directly affect the depth-velocity hazard classification, the roughness was increased from n=0.035 base value to n=0.040 for the 30-, 50-, and 100-year scenarios. The resulting changes in depth and velocity varied among locations (Table 11) as compared, but the hazard classifications remained unchanged for the 30- and 50-year scenarios. In the 100-year scenario, Safana changed from H5 (base: D=3.88m, V=1.03m/s, DxV=4.00) to H6 (alternate: D=4.10m, V=1.08m/s, DxV=4.43), crossing the H5/H6 threshold; while the other assessed locations (Table 11) although, with increasing depths and velocity but retained their base-case classifications. This indicates that although the overall hazard pattern is relatively stable, locations close to classification thresholds may respond to changes in floodplain roughness.

Breach formation-time sensitivity was assessed using formation times of 2.0, 3.73, and 5.0 h. The corresponding peak breach discharges were 2,601.60, 2,685.35, and 2,764.74 m³/s, respectively. The difference between the extreme cases was approximately 6.3%, indicating a relatively limited change in peak breach discharge within the tested formation-time range.

4. DISCUSSION

The result of the simulations shows that increasing the design-storm return period increased the hydrologic and breach responses, including flood depth and velocity, but did not change the resulting downstream hazard classification. Peak basin-outlet inflow increased from 4,616.3 m³/s for the 30-year event to 5,333.4 m³/s for the 100-year event (15.53%), while peak breach discharge increased from 2,377.24 to 2,685.35 m³/s (12.96%). The relatively limited increase in breach discharge reflects the FSL-triggered "sunny day" breach adopted in this study, where breach initiation occurs at a fixed reservoir elevation rather than at a storm-dependent peak stage. Despite the increase in flood magnitude, the hazard pattern remained unchanged across the three scenarios. Garhi remained H6, Hakazama, Safana, and Kunamawa remained H5, while Dogon Ruwa and Makwanshi remained within the combined H2/H3 class. The Water Treatment Plant and Bodole were not intersected by the modeled inundation extent in any scenario. Thus, under the assumed FSL-triggered piping failure, increasing the design-storm return period increased flood magnitude but was not sufficient to change the hazard class at the assessed locations.

The limited increase in breach discharge can be explained by the reservoir response following FSL-triggered failure. Reservoir stage increased only from 495.13 m to 495.61 m between the 30- and 100-year scenarios, despite the 22% increase in peak inflow. Once the breach developed, the additional outflow limited further reservoir accumulation. Consequently, the hydraulic head above the breach invert remained within approximately 5.7–6.1 m, resulting in only a 13% increase in peak breach discharge. This shows that, for the failure condition adopted here, the increase in storm magnitude did not translate directly into a similar increase in breach discharge.

The breach parameters also contribute to the resulting hydraulic response. The Froehlich (2008) formulation used in this study gave a breach width of 119 m and a formation time of 3.73 h. As noted by Froehlich (2008); (Zhong et al., 2021) breach characteristics introduce uncertainty into predicted dam-break discharge and downstream flood conditions (Azeez et al., 2020). The simulated breach discharges should therefore be considered within the context of the assumed breach geometry, formation time, and FSL-based initiation condition rather than as a prediction of an actual failure discharge.

Although the increase in breach discharge was relatively modest, Garhi experienced the most severe hydraulic conditions. This indicates that downstream hazard is not controlled by peak discharge alone, but also by the local terrain and the depth and velocity of flow at the exposed settlements (Peker et al., 2024; AIDR, 2017). The unchanged hazard classes across the three scenarios are therefore important from an emergency-planning perspective. Garhi remained the most critical assessed location, while Hakazama, Safana, and Kunamawa consistently remained within H5 and would also require appropriate preparedness measures.

The assessment was based on the named settlements and facilities that could be identified from the available spatial data and does not represent an exhaustive inventory of downstream settlements. Other settlements, buildings, and households located within the same mapped hazard

zones may experience similar conditions depending on their position within the floodplain. The road corridor towards Kankara is also important because flooding around Garhi could disrupt vehicle movement and emergency access. This could affect evacuation and response activities and may also interrupt the movement of agricultural produce, goods, and other services along the corridor. These effects should therefore be considered in downstream emergency and water-resources management planning.

The sensitivity analysis indicates that the hydrologic response was relatively stable to the tested channel roughness and geometry assumptions, with only minor changes in routed peak discharge. This suggests the variation lies within the numerical precision of the simulation rather than reflecting on systematic geometric effect; therefore, peak inflow at the basin outlet is accordingly insensitive to channel cross-sectional width within the tested range. However, in the absence of surveyed channel sections, the adopted cross-sectional dimensions nonetheless remain approximate and are documented here a source of structural, if empirically minor, uncertainty in the Muskingum-Cunge routing.

The hydraulic results showed greater sensitivity to floodplain roughness, particularly at locations close to hazard-class thresholds. The change in Safana from H5 to H6 under the 100-year roughness sensitivity case demonstrates that individual hazard classifications can be affected by hydraulic parameter uncertainty, even though the broader downstream hazard pattern remained similar. The sensitivity of breach discharge to formation time was comparatively limited within the tested range. These findings are consistent with previous dam-breach studies that identify breach formation parameters as important sources of uncertainty in predicted downstream flows and water levels (Wahl, 1998; Froehlich, 2008).

Generally, the results show that, under the assumed FSL-triggered piping failure, the breach initiation condition and reservoir response had a greater influence on the variation in breach discharge than the difference between the three design-storm return periods. The stable hazard pattern provides a useful basis for identifying persistent downstream priorities for emergency preparedness, evacuation planning, and access management.

5. CONCLUSION

This study assessed the consequences of a hypothetical piping failure of Zobe Dam under 30-, 50-, and 100-year design-storm conditions using coupled HEC-HMS and 2D HEC-RAS modelling, with flood-hazard mapping undertaken in QGIS. The modeled peak inflow increased from 4,616.3 m^3/s for the 30-year event to 5,333.4 m^3/s for the 100-year event, while peak breach discharge increased from 2,377.24 to 2,685.35 m^3/s. Despite the increase in design-storm magnitude, the resulting flood hazard classification remained unchanged across the three scenarios. Garhi was consistently classified as H6, while Hakazama, Safana, and Kunamawa were classified as H5, and Dogon Ruwa and Makwanshi as H2/H3. The Water Treatment Plant and Bodole remained outside the modeled flood extent. Under the assumed Full Supply Level-triggered piping failure, therefore, increasing the return-period increased the flood magnitude but did not change the identified pattern of downstream hazard. Although, sensitivity analyses showed limited variation in HEC-HMS routed discharge and breach discharge within the tested parameter ranges, but floodplain roughness affected individual hydraulic conditions and resulted in a change from H5 to H6 at Safana under the 100-year sensitivity case.

These results identify Garhi and the downstream road corridor that linked Dutsin-Ma toward Kankara as important priorities for flood-warning, evacuation, and emergency-access planning. The potential disruption of this corridor, together with the hazard classification of the affected settlements, has implications for regional water-resources management, especially the continuity of transport, emergency response, and movement of people and goods during a dam-failure event.

Data Availability

The digital elevation model used in this study is publicly available from the United States Geological Survey's EarthExplorer portal (earthexplorer.usgs.gov). Dam-specific geometric and hydrological data were obtained from the Sokoto-Rima River Basin Development Authority and are available from the corresponding author upon reasonable request and with the permission of that authority.

6. REFERENCES

Australian Institute for Disaster Resilience (AIDR). (2017). Guideline 7-3: Flood hazard. Australian Disaster Resilience Handbook Collection. East Melbourne: AIDR. https://knowledge.aidr.org.au/media/3518/adr-guideline-7-3.pdf

Azeez, O., Elfeki, A., & Kamis, A. (2020). Assessment of flood depth downstream of Um Al-Khair Dam using HEC-RAS. Journal of Hydraulic Engineering Applications, 12(2), 45-58.

Bezerra, R. P. G., & Eleutério, J. C. (2026). Probabilistic dam-breach flood mapping using full and truncated hydrodynamic models. RBRH, 31, e25.

Chen, C., Wang, Y., Zhang, J., Zhang, H., Li, H., & Chen, Q. (2023). A preliminary study of landslide dam failures induced by the combined influence of piping and overtopping. Journal of Hydrology, 625, 129984.

Chow, V. T. (1959). Open-channel hydraulics. McGraw-Hill.

Cox, R. J., Shand, T. D., & Blacka, M. J. (2010). Australian Rainfall and Runoff Revision Project 10: Appropriate safety criteria for people (Stage 1 report P10/S1/006). Sydney: Water Research Laboratory, University of New South Wales.

de Paula Barreto, M., Cardoso, S. B. K. S. H., Teixeira, A. M. G., Acevedo, A. M. C., & Dutra, P. (2024). Emergency repairs downstream of earth and rockfill dams with water spring with indication of internal erosion. Revista Brasileira De Geografia Física, 17(4), 2653-2670.

Froehlich, D. C. (1995). Peak outflow from breached embankment dam. Journal of Water Resources Planning and Management, 121(1), 90-97.

Froehlich, D. C. (2008). Embankment dam breach parameters and their uncertainties. Journal of Hydraulic Engineering, 134(12), 1708-1721. https://doi.org/10.1061/(ASCE)0733-9429(2008)134:12(1708)

Geen, R., Bordoni, S., Battisti, D. S., & Hui, K. (2020). Monsoons, ITCZs, and the concept of the global monsoon. Reviews of Geophysics, 58(4), e2020RG000700.

Geremew, G. B. (2024, July). Evaluation and comparison of breach parametric model for embankment dams. In Advanced Engineering Forum (Vol. 52, pp. 27-44). Trans Tech Publications Ltd.

Hariri-Ardebili, M. A. (2018). Risk, reliability, resilience (R3) and beyond in dam engineering: A state-of-the-art review. International Journal of Disaster Risk Reduction, 31, 806-831.

Jaafar, H., & Ahmad, F. (2019). GCN250, global curve number datasets for hydrologic modelling and design [Dataset]. Figshare. https://doi.org/10.6084/m9.figshare.7756202

Jaafar, H. H., Ahmad, F. A., & El Beyrouthy, N. (2019). GCN250, new gridded curve numbers for hydrological modelling and design. Scientific Data, 6, 145. https://doi.org/10.1038/s41597-019-0155-x

Kankara, A., & Shazalli, N. U. (2020). Geology and petrography of Precambrian rocks of Katsina urban area, northwestern Nigeria. Zbornik Radova Departmana za Geografiju, Turizam i Hotelijerstvo, 2(49-2), 113-126.

MacDonald, T. C., & Langridge-Monopolis, J. (1984). Breaching characteristics of dam failures. Journal of Hydraulic Engineering, 110(5), 567-586.

Magawata, U. Z., Bonde, D. S., Abdullahi, B. U., Qudus, B., & Yahaya, M. N. (2020). Seepage investigation on an existing dam using very low frequency electromagnetic (VLF-EM) methods: A case study of Shagari earth dam, Sokoto, North Western Nigeria. International Journal of Geosciences, 11(2), 25-36.

Moreno-Rodenas, A., Mantilla-Jones, J. D., & Valero, D. (2025). Age, climate and economic disparities drive the current state of global dam safety. Nature Water, 3(3), 284-295.

Nasser, R., Tzioutzios, D., & Liu, Y. (2025). Statistical analysis of global dam accidents in the 21st century: A focus on common features and causes. Water Resources Management, 39(12), 6493-6516.

Peker, İ. B., Gülbaz, S., Demir, V., Orhan, O., & Beden, N. (2024). Integration of HEC-RAS and HEC-HMS with GIS in flood modeling and flood hazard mapping. Sustainability, 16(3), 1226.

Planès, T., Mooney, M. A., Rittgers, J. B. R., Parekh, M. L., Behm, M., & Snieder, R. (2016). Time-lapse monitoring of internal erosion in earthen dams and levees using ambient seismic noise. Géotechnique, 66(4), 301-312.

Rana, N. M., Ghahramani, N., Evans, S. G., Small, A., Skermer, N., McDougall, S., & Take, W. A. (2022). Global magnitude-frequency statistics of the failures and impacts of large water-retention dams and mine tailings impoundments. Earth-Science Reviews, 232, 104144.

Saidu, B. J., Jidauna, G. G., Sanusi, J. K., & Dabi, D. D. (2019). The contribution of Zobe Dam to the socio-economic development of Makera Community Dutsinma Local Government Area, Katsina State North-Western Nigeria. International Journal of Environmental Monitoring and Analysis, 7(3), 75-82.

Saliba, F., Nassar, R. B., Khoury, N., & Maalouf, Y. (2019, March). Internal erosion and piping evolution in earth dams using an iterative approach. In Eighth International Conference on Case Histories in Geotechnical Engineering (pp. 67-75). Reston, VA: American Society of Civil Engineers.

Smith, G. P., Davey, E. K., & Cox, R. J. (2014). Flood hazard (Technical report 2014/07). Sydney: Water Research Laboratory, University of New South Wales.

Sujud, L. H., & Jaafar, H. H. (2022). A global dynamic runoff application and dataset based on the assimilation of GPM, SMAP, and GCN250 curve number datasets. Scientific Data, 9, 706. https://doi.org/10.1038/s41597-022-01834-0

Tang, X., Chen, A., & He, J. (2022). A modelling approach based on Bayesian networks for dam risk analysis: Integration of machine learning algorithm and domain knowledge. International Journal of Disaster Risk Reduction, 71, 102818.

Temür, R., Paşa, Y., Gülbaz, S., Peker, İ. B., & Hacı, A. (2026). Development of novel simplified empirical equations for the estimation of peak discharge due to dam failures. Water Resources Management, 40(3), 117.

Wahl, T. L. (1998). Predication of embankment dam breach parameters: A literature review and needs assessment (Dam Safety Research Report No. DSO-98-004). U.S Department of Interior, Bureau of Reclamation, Dam Safety Office.

Wang, G., Deng, Z., Yang, J., Chen, X., & Jin, W. (2022). A large-scale high-pressure erosion apparatus for studying internal erosion in gravelly soils under horizontal seepage flow. Geotechnical Testing Journal, 45(6), 1037-1053.

Zhong, Q., Wang, L., Chen, S., Chen, Z., Shan, Y., Zhang, Q., ... & Liu, J. (2021). Breaches of embankment and landslide dams-State of the art review. Earth-Science Reviews, 216, 103597.

Zhou, X., Yin, Q., Wang, S., & Shen, Z. (2026). Lattice Boltzmann method-discrete element method coupling study on the hydrodynamics of waves generated by granular collapse into water. Physics of Fluids, 38(1), 013321. https://doi.org/10.1063/5.0304201

International Conference on Engineering Innovation for Sustainable Development (ICESID 2026)
Faculty of Engineering, Ahmadu Bello University Zaria · 8–10 September 2026

INFLUENCE OF SLICE THICKNESS AND DRYING TEMPERATURE ON THE PROXIMATE COMPOSITION OKRA: IMPLICATIONS FOR NUTRITIONAL QUALITY AND DRYING PROCESS OPTIMIZATION

Muhammad Mujahid Muhammad[1,*], Abba Yahaya[2], Mohammed Abdulsalam[3], Al-Amin Danladi Bello[2], Daniel Onwude[4], Ibrahim Babangida Dalha[3], Muhammad Bashir Abdulrazaq[5], Badruddeen Saulawa Sani[2], Abdullahi Argungu Sule[2]

[1]*Department of Water Resource and Environmental Engineering, Ahmadu Bello University, Zaria - Nigeria*
[2]*Department of Water Resources and Environmental Engineering, Ahmadu Bello University, Zaria - Nigeria*
[3]*Department of Agricultural and Bioresources Engineering, Ahmadu Bello University, Zaria - Nigeria*
[4]*Swiss Federal Laboratory of Material Science and Technology, Empa, Switzerland*
[5]*Department of Computer Engineering, Ahmadu Bello University, Zaria - Nigeria*

Email: mujahidmuhammad8@gmail.com*, abbayahaya85@yahoo.com, mabdulsalam@abu.edu.ng, adbello@abu.edu.ng, daniel.onwude@empa.ch, irobabangida13@gmail.com, mbabdulrazaq@abu.edu.ng, basaule@hotmail.com, abdummu1@gmail.com

***Corresponding author**: Muhammad Mujahid Muhammad

DOI: https://doi.org/10.67203/sp.ICESID.2026

ABSTRACT

Okra (Abelmoschus esculentus L. Moench) is a nutrient-dense vegetable, yet the losses remains significant due to high moisture content and poor postharvest handling.. A sustainable drying technique remains the most practical preserving methodA number research works have been report on the drying technique but multiple treatment condition often deteriorate the nutritional composition, particularly the slice thickness in relation to the drying temperature. This study evaluated the effect of slice thickness and drying temperature on the proximate composition of okra. Okra samples of 0.5, 1.0, 1.5 and 2.0 cm thicknesses were subjected to processing temperatures of 30, 50, 60 and 70°C, with three replicates for each treatment combination represented by samples A, B and C. Moisture, ash, lipid, protein, fibre and carbohydrate contents were determined and expressed as percentages. Across all 45 observations, mean moisture, ash, lipid, protein, fibre and carbohydrate contents were 12.51, 8.91, 4.82, 16.70, 7.61 and 57.05%, respectively. The highest mean protein content (20.12±0.09%) occurred at 1.5 cm thickness and 60°C, while the highest mean fibre content (8.75%) was also recorded at this treatment. The maximum mean carbohydrate content (62.62±0.35%) occurred at 0.5 cm and 50°C, whereas the highest mean lipid content (6.83%) occurred at 2.0 cm and 70°C. The results establish substantial variation in proximate composition with processing temperature and sample thickness, indicating an interaction between the two factors. A thickness of 1.5 cm combined with 60°C produced a particularly favorable protein- and fibre-rich profile. The findings provide a useful guidance for selecting processing conditions for nutritionally desirable dried okra products.

Keywords: *okra; drying temperature; slice thickness; proximate composition*

1. INTRODUCTION

Okra (Abelmoschus esculentus L. Moench) is a widely consumed vegetable valued for its protein, carbohydrate, dietary fibre, minerals, vitamins and bioactive compounds. Recent reviews have highlighted its phytochemical importance, emphasizing the need for efficient handling (Abdel-Razek et al., 2023). Also, fresh okra's high moisture content and postharvest physiological activity make it highly perishable, so drying is widely used to extend availability and ease storage and transportation. However, drying can alter the apparent concentrations and retention of nutritional components, with recent studies reporting differences in moisture, ash, fat, protein, fibre and carbohydrate contents depending on cultivar, pretreatment and drying technique (Mohammed et al., 2024; Ibeogu et al., 2024; Ogundele & Terzungwe, 2024).

Drying temperature affects moisture migration, drying rate, chemical reactions and nutrient retention; Afolabi et al. (2022) showed that temperature and time significantly influenced hot-air-dried okra quality and used statistical optimization to identify favourable process conditions. Sample thickness is equally important, as it affects surface area and the distance moisture must migrate: Pendre et al. (2012) demonstrated that slice size and drying temperature significantly influenced protein, ascorbic acid and fibre retention, with optimal retention at 2 cm/60°C, while El-Mesery et al. (2023, 2024) showed moisture diffusivity and drying kinetics were jointly governed by temperature and thickness, with drying duration increasing with slice thickness. Obasi et al. (2025) found moderate temperatures (50°C) better preserved proximate and mineral composition than higher-temperature drying, and Reid-Fitten et al. (2026) showed that thermal pre-treatment combined with drying method significantly influenced phytonutrient, vitamin and antioxidant retention. Similarly, Rababah et al. (2023) and Kolawole et al. (2024) and Maigari et al. (2026) reported that drying and storage conditions affect the physicochemical, nutritional and antioxidant quality of dried okra, reinforcing the need for optimised drying regimes.

Thus, this study assessed how sample thickness and drying temperature influence okra's proximate composition, aiming to identify treatment combinations yielding desirable nutritional characteristics.

2. METHODOLOGY

This section describes the sample collection, research design, materials, experimental procedures, data collection methods, and analytical or computational tools used.

2.1 Sample Collection and Preparation

Fresh, matured, disease-free okra pods were procured locally and transported in perforated crates to the environmental laboratory of the Department of Water Resources and Environmental Engineering, Ahmadu Bello University, minimising mechanical damage. Pods were then washed under running potable water to remove dirt and surface contaminants, and drained before further processing.

2.2 Experimental Design

The washed pods were sliced transversely into four thickness levels (0.5, 1.0, 1.5 and 2.0 cm) using a slicer and thickness guide/vernier caliper for dimensional accuracy, then dried at four temperature levels (30, 50, 60 and 70°C). The experiment followed a factorial design (thickness × temperature) with three replicates, yielding 16 treatment combinations and 48 expected observations. Three (3) contaminated samples were excluded as unsuitable, resulting in 45 observations for the final analysis.

2.3 Drying Procedure

Sliced samples were spread in a single layer on perforated trays and dried in a thermostatically controlled hot-air solar dryer at the respective treatment temperature (30, 50, 60 or 70°C) to constant weight, then cooled to room temperature, milled, and sieved through a 0.5 mm mesh. The resulting flour was packaged in airtight, labelled containers and stored at ambient temperature away from light pending proximate analysis.

2.4 Proximate Analysis

Proximate composition of the dried okra flour samples was determined in triplicate using standard AOAC (2023) methods. Specifically, moisture and ash were determined gravimetrically, via oven-drying at 105 °C and muffle-furnace incineration at 550 °C, respectively, while crude lipid was extracted using the Soxhlet method with n-hexane/petroleum ether. In addition, crude protein was determined by the micro-Kjeldahl method (nitrogen × 6.25), and crude fibre by sequential acid-alkali digestion and ashing. Finally, carbohydrate (CHO) was estimated by difference, as CHO (%) = 100 −

(% Moisture + % Ash + % Lipid + % Protein), consistent with common practice in food-science studies where fibre is analysed separately.

2.5 Data Analysis

Data were expressed as mean ± standard deviation (SD) (n = 3) and analysed using descriptive statistics and one-way analysis of variance (ANOVA) in IBM SPSS Statistics. ANOVA was used to determine the effects of slice thickness and drying temperature on each proximate composition parameter, with statistical significance set at $\mathbf{p < 0.05}$. All statistical computations were performed using standard procedures in SPSS.

3. RESULTS AND DISCUSSION

3.1 Overall Proximate Composition

Table 1 shows carbohydrate as the largest proximate fraction, followed by protein, ash, fibre and lipid, with mean moisture (12.51%) reflecting substantial water loss within the acceptable (<13%) range for shelf-stable dried vegetables, comparable to Obasi et al. (2025). This apparent concentration of solid constituents through water removal is consistent with recent reports on dried okra (Maigari et al., 2026). The mean protein content (16.70%) suggests dried okra can meaningfully contribute to dietary protein in composite flour and snack formulation, with recent studies reporting values approaching 20% depending on drying method and pre-treatment (Ibeogu et al., 2024). The high carbohydrate proportion likewise reflects typical dried-plant composition, best interpreted as a relative concentration effect rather than carbohydrate synthesis during drying. Also, Table 2 presents the complete mean ± SD values for all six proximate parameters across the sixteen slice thickness-drying temperature combinations investigated in this study, and is referenced throughout the subsections that follow.

Table 1: *Mean proximate composition of dried okra*

Parameter	Mean ± SD (%)	Minimum (%)	Maximum (%)
Moisture	12.51 ± 0.63	11.05	13.90
Ash	8.91 ± 1.54	7.06	11.56
Lipid	4.82 ± 0.93	3.56	6.83
Protein	16.70 ± 2.31	12.25	20.12
Fibre	7.61 ± 0.62	6.40	8.75
Carbohydrate (CHO)	57.05 ± 3.12	51.55	62.62

Table 2: *Proximate composition of dried okra by slice thickness and drying temperature*

Thickness (cm)	Temp. (°C)	Moisture (%)	Ash (%)	Lipid (%)	Protein (%)	Fibre (%)	CHO (%)
0.5	30	11.98 ± 0.86	10.18 ± 0.03	4.13 ± 0.07	15.97 ± 0.19	8.33 ± 0.03	57.74 ± 0.97
0.5	50	12.25 ± 0.28	8.82 ± 0.03	3.94 ± 0.01	12.35 ± 0.14	8.18 ± 0.03	62.62 ± 0.35
0.5	60	13.60 ± 0.36	9.94 ± 0.04	5.16 ± 0.04	17.41 ± 0.02	7.88 ± 0.02	53.89 ± 0.40
0.5	70	12.75 ± 0.10	9.82 ± 0.09	5.34 ± 0.11	15.32 ± 0.08	8.07 ± 0.08	56.77 ± 0.13
1.0	30	12.35 ± 0.48	9.60 ± 0.02	4.97 ± 0.12	17.80 ± 0.06	7.77 ± 0.03	55.28 ± 0.42
1.0	50	11.49 ± 0.30	8.35 ± 0.05	4.41 ± 0.47	14.84 ± 0.14	7.43 ± 0.03	60.90 ± 0.65
1.0	60	12.72 ± 0.65	8.20 ± 0.05	4.48 ± 0.03	18.87 ± 0.12	7.23 ± 0.03	55.73 ± 0.66
1.0	70	12.67 ± 0.08	7.51 ± 0.10	5.02 ± 0.03	19.40 ± 0.14	7.33 ± 0.10	55.39 ± 0.24
1.5	30	12.33 ± 0.37	8.53 ± 0.18	3.56 ± 0.30	13.75 ± 0.03	7.45 ± 0.05	61.83 ± 0.17
1.5	50	13.60 ± 0.15	9.51 ± 0.14	3.51 ± 0.17	13.82 ± 0.03	7.19 ± 0.04	59.56 ± 0.11
1.5	60	12.02 ± 0.16	11.41 ± 0.19	4.67 ± 0.14	20.12 ± 0.09	8.70 ± 0.05	51.77 ± 0.22
2.0	30	12.02 ± 0.03	10.69 ± 0.22	4.54 ± 0.09	19.39 ± 0.04	8.13 ± 0.03	53.36 ± 0.29
2.0	50	12.46 ± 0.01	5.49 ± 0.24	5.26 ± 0.20	18.38 ± 0.11	6.43 ± 0.03	58.41 ± 0.24
2.0	60	12.60 ± 0.09	7.06 ± 2.08	6.45 ± 0.05	17.17 ± 0.02	6.52 ± 0.03	56.72 ± 2.11
2.0	70	12.87 ± 0.15	8.55 ± 0.05	6.83 ± 0.06	15.91 ± 0.01	7.55 ± 0.05	55.84 ± 0.23

3.2 Effects of Slice Thickness and Drying Temperature on Proximate Parameters

Moisture content ranged from 11.05% (0.5 cm, 30°C) to 13.90% (0.5 cm, 60°C) (Tables 1 and 2). Using the data in Table2, One-way ANOVA indicated that neither slice thickness ($F = 0.74$, $p = 0.536$) nor drying temperature ($F = 2.38$, $p = 0.084$) significantly affected moisture ($p > 0.05$), though a weak upward trend at higher temperatures likely reflects case-hardening, rapid surface drying that traps residual internal moisture, consistent with El-Mesery et al. (2024), who found drying rate and moisture diffusivity jointly governed by temperature, airflow and thickness.

Ash content ranged from 5.49±0.24% (2.0 cm, 50°C) to 11.56% (1.5 cm, 60°C), with both thickness ($F = 5.15$, $p = 0.004$) and temperature ($F = 3.02$, $p = 0.041$) showing significant effects. Highest retention occurred at 1.5 cm/60°C, while lower, more variable values in the 2.0 cm/50–60°C

treatments may reflect uneven heat penetration and localised mineral loss, agreeing with Obasi et al. (2025) on temperature's influence on ash composition.

Lipid content rose significantly with both thickness ($F = 13.53$, $p < 0.001$) and temperature ($F = 9.90$, $p < 0.001$), from 3.56±0.30% (1.5 cm, 30°C) to 6.83% (2.0 cm, 70°C), likely due to a concentrating effect as moisture is removed.

Crude protein ranged from 12.25% (0.5 cm, 50°C) to 20.12±0.09% (1.5 cm, 60°C), significantly affected by both thickness ($F = 4.24$, $p = 0.011$) and temperature ($F = 6.52$, $p = 0.001$). Peak retention at 1.5 cm/60°C mirrors Pendre et al. (2012), reflecting a favourable balance between drying rate and thermal intensity, while lower protein at 50°C may reflect prolonged enzymatic activity during slower drying.

Crude fibre varied from 6.40% (2.0 cm, 50°C) to 8.75% (1.5 cm, 60°C), significantly affected by thickness ($F = 7.68$, $p < 0.001$) but not temperature ($F = 2.12$, $p = 0.113$). Fibre declined beyond 1.5 cm thickness (Table 2), supporting 1.0–1.5 cm as optimal for fibre-dense product.

Carbohydrate (by difference) ranged from 51.55% (1.5 cm, 60°C) to 62.62±0.35% (0.5 cm, 50°C), significantly affected by temperature ($F = 14.27$, $p < 0.001$) but not thickness ($F = 0.73$, $p = 0.538$). Its strong inverse correlation with protein ($r = -0.85$) reflects the by-difference calculation rather than independent carbohydrate behaviour.

Overall, thickness and temperature jointly, rather than independently, determined proximate quality: The 1.0 and 2.0 cm samples had the highest average protein concentration of 17.73% and peaked at 60°C (18.39%) before declining at 70°C, whereas 0.5 cm had the highest average fibre content of 8.12%. The 2.0 cm samples had the highest average lipid content of 5.77% and rose progressively with temperature; and carbohydrate peaked at 50°C (Afolabi et al., 2022). The 1.5 cm × 60°C treatment gave the best protein, fibre and ash retention, while peak carbohydrate and lipid occurred at 0.5 cm × 50°C and 2.0 cm × 70°C, respectively.

4. CONCLUSION

This study demonstrated that slice thickness and drying temperature interactively influences the proximate composition of dried okra significantly. Within the range of the slice thickness and drying temperature examined, it was noticed the moisture content does not significantly affected by either factor. Interestingly, both slice thickness and drying temperature significantly influenced the ash, lipid, protein and carbohydrate contents.. The treatment combination of 1.5 cm slice thickness dried at 60 °C consistently produced dried okra with the highest protein, ash and fibre retention, while thinner slices (0.5 cm) dried at moderate temperature (50 °C) favoured maximum carbohydrate retention with the lowest protein and ash concentration. These results confirm that slice thickness and drying temperature cannot be optimised independently; rather, the appropriate combination should be selected according to the intended nutritional or functional target of the final dried okra product.

Furthermore, a thickness of approximately 1.5 cm and 60°C should be investigated further as a potential optimum for protein- and fibre-rich dried okra.

ACKNOWLEDGEMENTS

This study was initiated as a result of funding from the Tertiary Education Fund, Nigeria; under the National Research Fund (NRF) grant with code number TETF/DR&D/CE/NRF2021/SETI/AFS/00146/VOL.1. Also, the authors would like to acknowledge the support of the Ahmadu Bello University, Zaria, Nigeria, for providing the enabling ground and a conducive space to conduct this study.

5. REFERENCES

Abdel-Razek, M. A. M., Abdelwahab, M. F., Abdelmohsen, U. R., & Hamed, A. N. E. (2023). A review: Pharmacological activity and phytochemical profile of Abelmoschus esculentus (2010–2022). RSC Advances, 13, 15280–15294. https://doi.org/10.1039/D3RA01367G.

Afolabi, T. J., Aworanti, O. A., Agarry, S. E., Agbede, O. O., Ajuebor, F., Ogunleye, O. O., Ogunkunle, O., & Laseinde, O. T. (2022). Effects of drying process parameters on the quality

attributes of hot air dried okra and its statistical optimization. Cogent Engineering, 9(1), 2122193. https://doi.org/10.1080/23311916.2022.2122193.

Association of Official Analytical Chemists (AOAC). (2023). Official methods of analysis of AOAC International (22nd ed.). Oxford University Press.

El-Mesery, H. S., Huang, H., Hu, Z., Kaveh, M., & Qenawy, M. (2024). *Experimental performance analysis of an infrared heating system for continuous applications of drying.* Case Studies in Thermal Engineering**,** 59, 104522. https://doi.org/10.1016/j.csite.2024.104522.

El-Mesery, H. S., Qenawy, M., Hu, Z., & Alshaer, W. G. (2023). *Evaluation of infrared drying for okra: Mathematical modelling, moisture diffusivity, energy activity and quality attributes*. Case Studies in Thermal Engineering, 50, 103451. https://doi.org/10.1016/j.csite.2023.103451

Ibeogu, I. H., David-Abraham, F. M., Sunday-Joshua, H. A., & Egbedike, C. N. (2024). Effects of salt treatment and drying methods on the proximate, vitamin and chlorophyll content of okra fruit (Abelmoschus esculentus) slices. *Journal of Home Economics Research, 30*(1), 204–213. https://doi.org/10.66731/jher.v30i1.19.

Kolawole, F. L., Alonge, T. A., Akeem, S. A., & Sanni-Olayiwola, H. O. (2024). Influence of trona (sodium sesquicarbonate) concentrations and storage period on the physicochemical properties, antinutrients, micronutrients and sensory qualities of dried okra (*Abelmoschus esculentus* L.) powder. Journal of Stored Products Research, 106, 102311. https://doi.org/10.1016/j.jspr.2024.102311.

Maigari, F. M., Dahiru, B., & Bulus, C. F. (2026). Investigation of drying methods, storage effects, and quality attributes of dried okra for soup production: A comprehensive nutrient content analysis. Journal of Clinical and Metabolism Studies, 11(3). https://doi.org/10.70382/ajcms.v11i3.036.

Mohammed, H. Y., Teferra, T. F., & Sime, G. (2024). Indigenous knowledge and nutritional and morphological characterization of okra (Abelmoschus esculentus (L.) Moench) varieties in Western Ethiopia. Food Science & Nutrition. https://doi.org/10.1002/fsn3.3936.

Obasi, B. C., Ngutsewen, B. K., & Shehu, U. (2025). Effect of drying methods on the nutritional composition and microbiological quality of selected vegetables (okra and tomatoes). *Greener Journal of Life Sciences, 7*(1), 1–11. https://doi.org/10.15580/gjls.2025.1.123124211

Ogundele, O. O., & Terzungwe, U. M. (2024). The effects of some pre-treatment methods on the proximates, sensory properties and vitamins compositions of okra. Asian Food Science Journal, 23(7), 65–77. https://doi.org/10.9734/afsj/2024/v23i7727.

Pendre, N. K., Nema, P. K., Sharma, H. P., Rathore, S. S., & Kushwah, S. S. (2012). Effect of drying temperature and slice size on quality of dried okra (*Abelmoschus esculentus* (L.) Moench). *Journal of Food Science and Technology, 49*(3), 378–381. https://doi.org/10.1007/s13197-011-0427-8

Rababah, T. M., Al-U'datt, M. H., Angor, M., Gammoh, S., Abweni, F., Magableh, G., Almajwal, A., Yücel, S., AL-Rayyan, Y., & AL-Rayyan, N. (2023). Effect of drying and freezing on the phytochemical properties of okra during storage. ACS Omega, 8(35), 31408-31417.

Reid-Fitten, M. L., Cotton, C. P., Min, B. R., Nindo, C. I., & Williams, Z. F. (2026). Effects of thermal pre-treatments and drying processes on the retention of phytonutrients, vitamins, and antioxidant activity in dried okra (Abelmoschus esculentus L.). Foods, 15(2), Article 311.

International Conference on Engineering Innovation for Sustainable Development (ICESID 2026)
Faculty of Engineering, Ahmadu Bello University Zaria · 8–10 September 2026

IMPACT OF AGEING WATER INFRASTRUCTURE ON WATER SUPPLY IN NIGER STATE: CASE STUDY OF SULEJA AND MINNA

Stephen Osu[1,*], Mohammed Saidu[1]
[1]*Federal University of Technolgy Minna*
Email: osusmen91@st.futminna.edu.ng[*], mohammed_saidu@futminna.edu.ng
***Corresponding author**: Stephen Osu
DOI: https://doi.org/10.67203/sp.ICESID.2026

ABSTRACT
Ageing water infrastructure has become a major challenge to sustainable urban water supply in many developing countries, resulting in declining service reliability, increasing household dependence on alternative water sources and growing socio-economic burdens. This study assessed the impact of ageing water infrastructure on water supply reliability in Minna and Suleja, Niger State, Nigeria. Data were collected from 805 households (405 in Minna and 400 in Suleja), Niger State Water Board personnel, field observations, infrastructure inspections and secondary sources. Correlation and regression analyses were employed to evaluate the relationship between infrastructure condition and water supply reliability. The findings revealed that boreholes constitute the dominant household water source, while dependence on public piped water has declined because of deteriorating infrastructure. Minna consistently recorded better infrastructure condition, higher reliability, shorter water collection distance and lower household water expenditure than Suleja. Statistical analyses established a significant positive relationship between infrastructure condition and water supply reliability, indicating that deteriorated pipelines substantially reduce service continuity and increase household dependence on expensive alternative water sources. The study concludes that ageing infrastructure is the principal factor limiting sustainable urban water supply in Niger State with the correlation of 0.80 and 0.75 for Minna and Suleja respectively. It recommends systematic infrastructure rehabilitation, preventive asset management, expansion of distribution networks, continuous water quality monitoring and greater investment in modern water infrastructure to improve service reliability and achieve sustainable urban water management.

Keywords: *ageing; infrastructure; water supply; reliability*

1. INTRODUCTION

Reliable access to safe, sufficient, and affordable water remains one of the fundamental requirements for human health, economic development, environmental sustainability, and social well-being (United Nations, 2015) Water is indispensable for domestic consumption, food production, industrial activities, energy generation, ecosystem conservation, and urban development. Consequently, the availability of reliable water infrastructure has become a major determinant of sustainable development and human welfare. Despite substantial investments in water infrastructure worldwide, ensuring continuous and equitable access to safe drinking water remains a persistent challenge, particularly in low- and middle-income countries. Rapid urbanization, population growth, climate change, ageing infrastructure, inadequate maintenance, weak institutional capacity, and insufficient financial investment continue to undermine the reliability of water supply systems across many regions of the world (United Nations, 2023; Ferdowsi *et al.*, 2024).

The challenges associated with ageing water infrastructure are considerably more severe across developing countries, where financial constraints, weak institutional capacity, rapid urbanization, population growth, inadequate maintenance culture, and limited technical expertise have accelerated infrastructure deterioration. Across Sub-Saharan Africa, many urban water utilities operate with obsolete treatment facilities, deteriorated distribution networks, ageing pumping equipment, and inadequate monitoring systems, resulting in high levels of non-revenue water, poor operational efficiency, intermittent water supply, and declining water quality.

Niger State occupies a strategic position within Nigeria's hydrological landscape. As the largest state in the country by land area, it is traversed by the Rivers Niger and Kaduna and contains numerous dams, reservoirs, streams, and groundwater resources that provide considerable water supply potential.

Although considerable research has been conducted on water supply, water quality, governance, and sanitation in Nigeria, relatively few studies have comprehensively investigated the condition of ageing water infrastructure and its direct influence on water supply reliability in Niger State. Existing studies have largely focused on national assessments, selected metropolitan areas, or isolated aspects such as water quality, financing, governance, or access, with limited integration of technical infrastructure condition, household service reliability, environmental vulnerabilities, and socio-economic impacts within a single analytical framework. Recent reviews have likewise concluded that empirical evidence linking infrastructure condition, governance, operational performance, and service reliability remains fragmented in Nigeria, particularly at the state level, thereby limiting evidence-based infrastructure planning and policy development (Adeniran, 2022; Ojo & Sohail, 2024). Consequently, there remains insufficient empirical evidence to guide infrastructure rehabilitation, maintenance prioritization, investment planning, and policy formulation specifically for Niger State. This knowledge gap limits evidence-based decision-making by government agencies, water utilities, and development partners seeking to improve the performance and resilience of public water supply systems.

Against this background, this study evaluates the impact of ageing water infrastructure on water supply reliability in Minna and Suleja, Niger State, Nigeria. The study provides empirical evidence to support infrastructure rehabilitation, improve water utility performance, strengthen climate resilience, enhance public health protection, towards achieving Sustainable Development Goal 6 on clean water and sanitation. The findings are also expected to provide practical guidance for policymakers, engineers, water utility managers, and development agencies responsible for planning sustainable water infrastructure development in Niger State and Nigeria as a whole.

2. METHODOLOGY

2.1 Description of the Study Area

Niger State is the largest state in Nigeria by land area, occupying approximately 76,363 km² in the North-Central region. It lies between latitudes 8°20′N and 11°30′N and longitudes 3°30′E and 7°20′E. The state experiences a tropical continental climate with annual rainfall ranging from 1,100 to 1,600 mm and average temperatures between 25°C and 35°C. The Rivers Niger and Kaduna traverse the state, together with numerous streams, reservoirs, and groundwater resources. Despite these abundant water resources, increasing population growth, ageing infrastructure, inadequate maintenance, and urban expansion continue to constrain reliable public water supply (National Population Commission, 2023; Federal Ministry of Water Resources and Sanitation, 2024).

Fig 2.1

2.1.1 Minna

Minna is the capital city of Niger State and serves as the state's administrative, educational, and commercial centre. The city experiences rapid urbanization, increasing population growth, and expanding residential development that have significantly increased demand for potable water. Water supply is primarily provided by the Niger State Water Board through treatment plants, pumping stations, storage reservoirs, and distribution networks, although many households supplement public supply with private boreholes and water vendors due to intermittent service.

2.1.2 Suleja

Suleja is one of the fastest-growing urban centres in Niger State because of its proximity to the Federal Capital Territory, Abuja. Rapid population growth and urban expansion have considerably increased pressure on existing water infrastructure. Although the town possesses public water supply facilities, many households continue to depend on private boreholes, wells, and commercial water vendors because of inadequate service continuity and ageing infrastructure.

2.2 Sources of Data

Data for this study were obtained from both primary and secondary sources to ensure comprehensive assessment of ageing water infrastructure and water supply reliability.

2.2.1 Primary Data

Primary data were obtained through field investigations comprising infrastructure inspection, structured questionnaire administration, interviews with technical personnel of the Niger State Water Board, direct field observation and water quality testing where applicable.

2.2.2 Secondary Data

Secondary information was obtained from the Niger State Water Board, National Population Commission (NPC), National Bureau of Statistics (NBS), WHO/UNICEF Joint Monitoring Programme (JMP), World Health Organization (WHO), Federal Ministry of Water Resources and Sanitation, published journal articles, textbooks, government reports, and relevant policy documents. These sources provided demographic information, infrastructure records, policy guidelines, and background information supporting the primary data.

2.3 Evaluation Index

The relationship between infrastructure condition and water supply reliability was evaluated using the Pearson Product–Moment Correlation Coefficient (PPMCC) and Multiple Linear Regression. Pearson's correlation coefficient was computed using Equation 2.1.

$$r \frac{n\sum_{i=1}^{n} X_i Y_i - (\sum_{i=1}^{n} X_i)(\sum_{i=1}^{n} Y_i)}{\sqrt{[n\sum_{i=1}^{n} X_i^2 - (\sum_{i=1}^{n} X_i)^2][n\sum_{i=1}^{n} Y_i^2 - (\sum_{i=1}^{n} Y_i)^2]}} \quad (2.1)$$

Where r is the Pearson Product–Moment Correlation Coefficient, X_i is the infrastructure condition score for the ith observation, Y_i is the water supply reliability score for the ith observation, n is the Number of observations (sample size), \sum is the summation operator and *i* is the observation index (i=1,2,…,n).

The value of the correlation coefficient ranges from −1 to +1, where positive values indicate a direct relationship between infrastructure condition and water supply reliability, negative values indicate an inverse relationship, and values close to zero indicate little or no linear relationship.

The regression model adopted using Equation 2.2

$$Y = \beta_0 + \beta_1 X_1 + \varepsilon \quad (2.2)$$

Where Y is the water supply reliability, β_0 is the constant, β_1 are the regression coefficients, X_1...is the independent variables and ε is the error term.

Statistical significance was evaluated using $p<0.05$ where p represents the probability value. Where comparisons between Minna and Suleja were required, an independent-samples t-test was applied. Because the stated formula does not assume equal population variances, it represents Welch's independent-samples t-test.

3. RESULTS AND DISCUSSION

3.1 Assessment of Ageing Water Infrastructure (Piping)

The primary data provided first-hand information regarding infrastructure condition, operational performance, and household experiences. The table 3.1 shows that piped water ranks lowest in the sources of water.

Water Source Distribution (Minna vs Suleja)

Table 3.1: Water Source Distribution

Water Source	Minna (%)	Suleja (%)
Borehole	47.4	35.5
Well	21.7	24
Vendor	18.3	29.5
Piped	12.6	11

The objective is to determine the extent to which ageing infrastructure contributes to declining water service performance. A total of 612.4 KM length of pipeline was assessed in Minna while 587.3 KM was assessed for Suleja.

The condition assessment of transmission and distribution pipelines presented in table 3.2 indicates that most pipeline networks in both Minna and Suleja fall within the fair and poor condition categories. Although Minna recorded a moderately higher proportion of pipelines in good and excellent condition, Suleja exhibited relatively larger percentages of pipelines classified as poor and very poor. This pattern demonstrates that a considerable proportion of the distribution network has exceeded its intended design life and now operates with reduced hydraulic efficiency.

Table 3.2: Pipeline Condition Rating

PIPELINE CONDITION RATING SCALE			
Minna Pipeline (%)	**Suleja Pipeline (%)**	**Ratings**	**Description**
13.6	11.2	80-100	Excellent
26.1	24.3	60-79	Good
30.7	28.9	40-59	Fair
18.9	21.4	20-39	Poor
10.7	14.2	0-19	Very Poor

The deterioration of pipeline infrastructure can largely be attributed to prolonged service life, inadequate preventive maintenance, corrosion, repeated leakages, pipe bursts and delayed replacement of obsolete distribution networks. As pipelines age, structural failures become increasingly frequent, resulting in substantial water losses before treated water reaches consumers. Leakage also contributes to pressure reduction within the network, allowing contaminants to infiltrate damaged pipelines whenever negative pressure conditions occur.

3.2 Relationship between Ageing Infrastructure and Water Supply Reliability

The condition of ageing water infrastructure and the reliability of public water supply in Minna and Suleja. Correlation and regression analyses were conducted to determine the magnitude and significance of the relationships between infrastructure condition and selected reliability indicators. In addition, graphical analyses were used to illustrate the nature of these relationships and identify the infrastructure variables exerting the greatest influence on service reliability.

The scatter plots presented in Figure 3.2 reveal a clear positive relationship between the Infrastructure Condition Index (ICI) and the Water Supply Reliability Index (WSRI) of 0.8 and 0.75 for Minna and Suleja respectively, while the R^2 values of 0.64 for Minna metropolis and 0.56 for Suleja town. In both cities neighbourhoods with better infrastructure conditions consistently recorded higher levels of water supply reliability, while areas characterised by deteriorated infrastructure experienced lower reliability scores. The pattern of the scatter plots demonstrates that improvements in infrastructure condition are associated with corresponding improvements in service reliability.

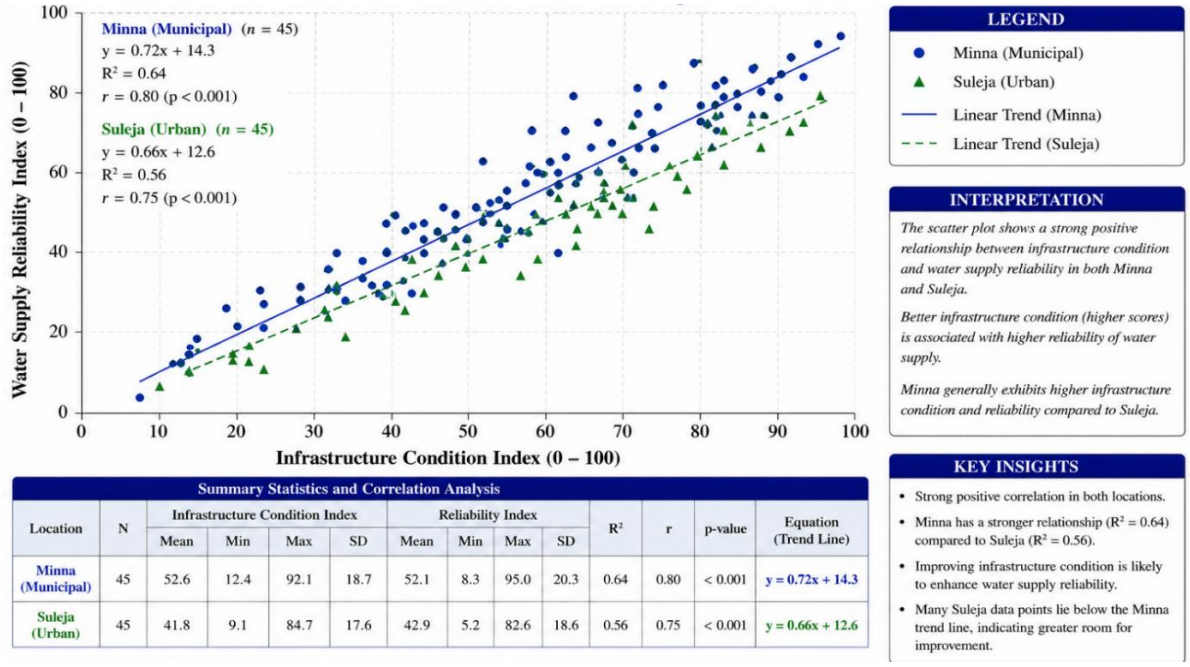

Summary Statistics and Correlation Analysis

Location	N	Infrastructure Condition Index				Reliability Index				R^2	r	p-value	Equation (Trend Line)
		Mean	Min	Max	SD	Mean	Min	Max	SD				
Minna (Municipal)	45	52.6	12.4	92.1	18.7	52.1	8.3	95.0	20.3	0.64	0.80	< 0.001	y = 0.72x + 14.3
Suleja (Urban)	45	41.8	9.1	84.7	17.6	42.9	5.2	82.6	18.6	0.56	0.75	< 0.001	y = 0.66x + 12.6

Figure 3.2: Infrastructure Condition versus Reliability

This relationship is expected because the various components of the water supply system operate as an integrated engineering network. Well-maintained pipelines minimise leakage and pressure losses, efficient pumping stations ensure continuous water conveyance, functional treatment plants sustain production capacity, and adequate storage facilities maintain service continuity during periods

of peak demand. Conversely, deterioration within any of these components interrupts system performance and reduces the reliability experienced by consumers.

The observed relationship agrees with previous investigations conducted by Copeland and Tiemann (2019), and World Bank (2024), all of which identified infrastructure condition as one of the strongest determinants of urban water supply reliability. This finding directly addresses the principal objective of the study by establishing empirical evidence linking ageing infrastructure with water supply performance in Niger State.

The linear regression models presented in Figure 3.2 further confirm that infrastructure condition significantly predicts water supply reliability in both Minna and Suleja. The regression lines exhibit positive slopes, indicating that improvements in infrastructure condition are associated with proportional increases in reliability. The relatively stronger regression observed in Minna suggests that infrastructure improvements produce more immediate gains in service reliability because the existing system remains comparatively functional. Although the relationship remains statistically significant in Suleja, the lower gradient reflects the cumulative influence of additional constraints such as rapid urban expansion, increasing water demand and operational limitations.

The GIS analyses established a strong positive relationship between infrastructure condition and water supply reliability at 5% significance level, confirming that improvements in infrastructure condition would directly enhance service reliability.

The analyses therefore fulfil the central objective of the study by quantitatively establishing the relationship between infrastructure condition and water supply reliability while providing an evidence-based foundation for subsequent policy recommendations.

3.3 Distance to Water Source

Figure 3.3 presents the average distance travelled by households to obtain water. The results indicate that respondents in Minna travelled an average distance of approximately 72.5 m to their primary water source, whereas households in Suleja travelled substantially farther, averaging approximately 185.4 m. Although both values remain below the international threshold commonly used to define basic water accessibility, the considerable disparity between the two cities reflects significant differences in infrastructure distribution and service availability.

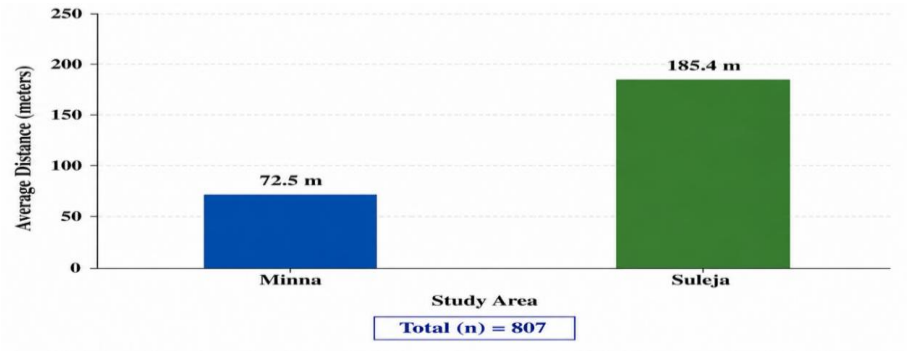

Figure 3.3: Average Distance to Water Source

3.4 Treatment Plant Condition

The assessment of treatment plant condition shown in Figure 3.4 indicates that most facilities operate within the fair condition category, while only a limited proportion can be considered good or excellent. Minna generally recorded moderately better treatment plant conditions than Suleja, although neither city possesses treatment infrastructure that could be considered fully modern or highly efficient.

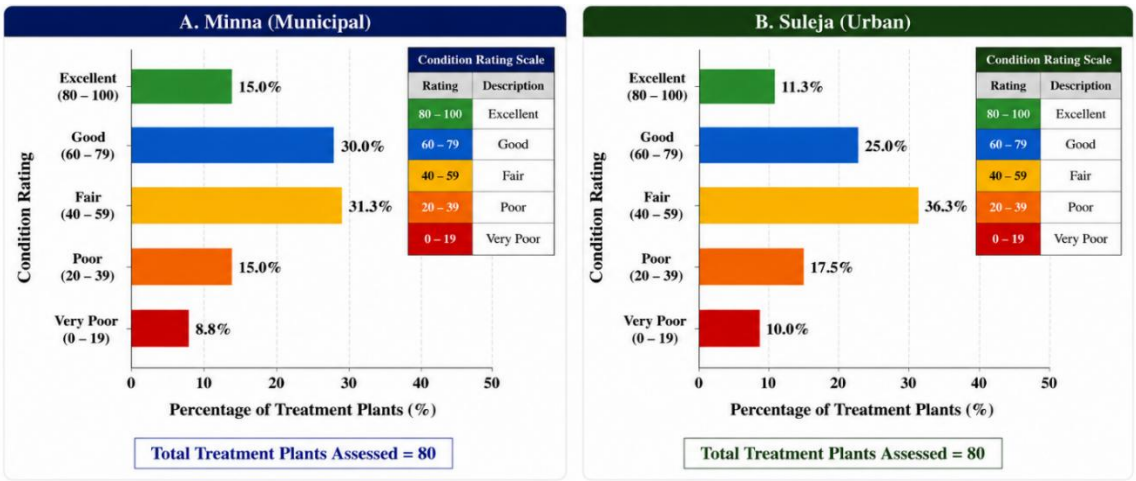

Figure 3.4: Treatment Plant Condition

3.5 Pumping Station Condition

Figure 3.5 presents the condition of pumping stations responsible for conveying treated water throughout the distribution system. The results reveal that pumping stations in Minna

generally, perform better than those in Suleja, although both cities exhibit considerable proportions of facilities classified as fair or poor. Only a relatively small number of pumping stations achieved excellent condition ratings.

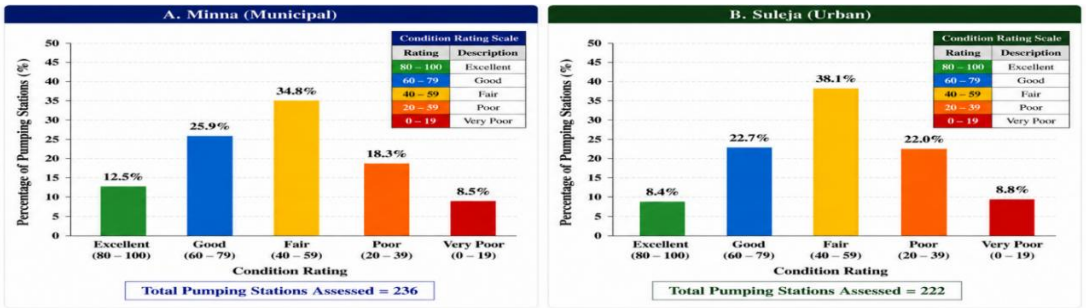

Figure 3.5: Pumping Station Condition

3.6: Storage Facility Condition

Storage facility condition, illustrated in Figure 3.6, reveals similar deterioration patterns. Most storage reservoirs were classified within the fair category, while smaller proportions were rated as excellent or good. Minna again demonstrated slightly better performance than Suleja, although substantial rehabilitation remains necessary in both cities.

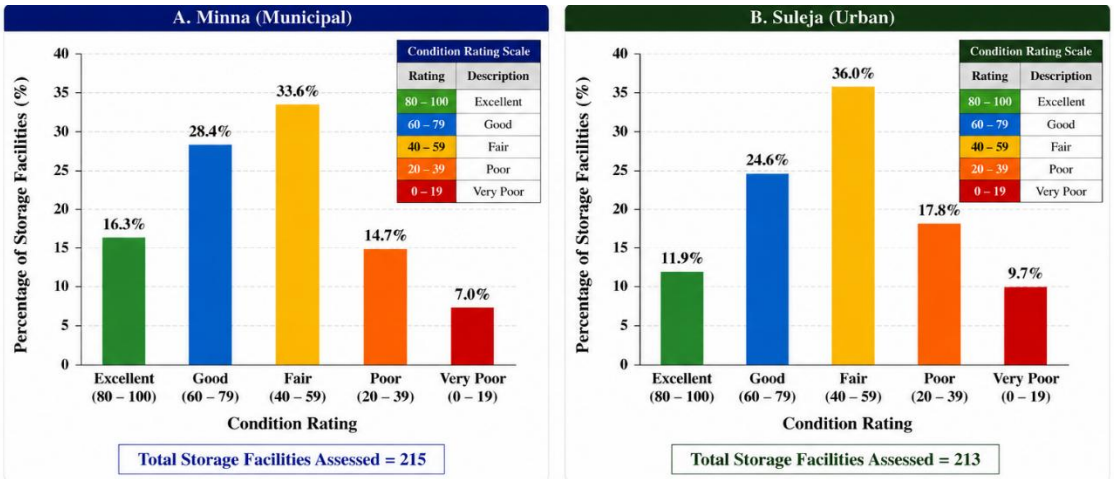

Figure 3.6: Storage Facility Condition

3.7: Comparative of Monthly Water Expenditure

The comparison of monthly household water expenditure presented in Figure 3.7 demonstrates that households in Suleja spend considerably more on domestic water than households in Minna. Although household income levels in both cities remain broadly comparable, the higher dependence on commercial water vendors and alternative water sources substantially increases water-related expenditure among Suleja households.

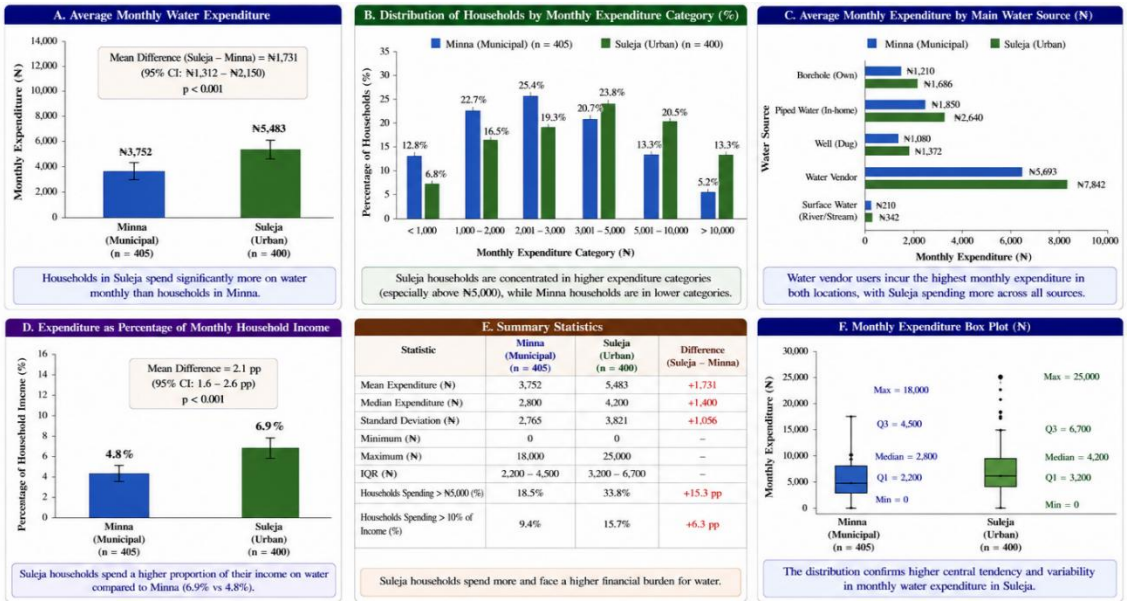

Statistic	Minna (Municipal) (n = 405)	Suleja (Urban) (n = 400)	Difference (Suleja – Minna)
Mean Expenditure (₦)	3,752	5,483	+1,731
Median Expenditure (₦)	2,800	4,200	+1,400
Standard Deviation (₦)	2,765	3,821	+1,056
Minimum (₦)	0	0	–
Maximum (₦)	18,000	25,000	–
IQR (₦)	2,200 – 4,500	3,200 – 6,700	–
Households Spending > ₦5,000 (%)	18.5%	33.8%	+15.3 pp
Households Spending > 10% of Income (%)	9.4%	15.7%	+6.3 pp

Suleja households spend more and face a higher financial burden for water.

Figure 3.7: Comparative of Monthly Water Expenditure

4. CONCLUSION

The findings demonstrate that ageing infrastructure has significantly reduced the efficiency, reliability and sustainability of urban water supply systems in both cities.

The study concludes that ageing infrastructure is the principal factor limiting sustainable urban water supply in Niger State with correlation of 0.80 and 0.75 for Minna and Suleja respectively.

Pipeline ratings shows that 29.6% of 612.4 km of pipeline in Minna have failed, while 35.6% of 587.3 km pipeline in Suleja have failed.

From a policy perspective, the results highlight the urgent need for systematic rehabilitation of ageing water infrastructure in Niger State. Investment should shift from reactive maintenance towards preventive asset management, strategic infrastructure renewal and expansion of water distribution networks to underserved communities. The study was limited by its focus on two urban centres and by the use of cross-sectional survey data, which provide a snapshot of existing conditions without capturing long-term temporal changes in infrastructure performance. Future research should extend similar assessments to other urban centres within Nigeria, incorporate longitudinal monitoring, evaluate climate change impacts on water infrastructure resilience and develop predictive asset deterioration models using advanced machine learning and artificial intelligence techniques.

5. REFERENCES

Adeniran, A. (2022). What is the state of water infrastructure governance research in Nigeria? A review. Water International, 47(4), 646–670

Copeland, C., and Tiemann, M. (2019). *Water infrastructure needs and investment: Review and analysis of key issues*. Congressional Research Service.

Federal Ministry of Water Resources and Sanitation. (2024). National Water Sector Performance Report.

Ferdowsi, A., *et al*. (2024). Urban water infrastructure: A critical review on climate change impacts and adaptation strategies. Urban Climate, 58, 102132.

National Population Commission. (2023). Population Projection Report.

National Bureau of Statistics. (2024). Nigeria Statistical Report.

Ojo, V. O., & Sohail, M. (2024). Assessing the Performance of State Water Utilities in Nigeria: Towards Achieving the Sustainable Development Goal on Drinking Water. Sustainability, 16(1), 59.

United Nations. (2015). Transforming Our World: The 2030 Agenda for Sustainable Development

World Bank. (2024). World Development Indicators and Water Global Practice reports.

Z 8 – 11 September 2026, Zaria, Nigeria

International Conference on Engineering Innovation for Sustainable Development (ICESID 2026)
Faculty of Engineering, Ahmadu Bello University Zaria · 8–10 September 2026

IMPACTS OF ROAD CONSTRUCTION SITE ACTIVITIES ON THE OCCURRENCE OF ACCIDENTS: A CASE STUDY OF THE ZARIA–KADUNA ROAD

Muhammed Mustapha Musa[1], Kasimu Yusuf Gojara[2], Ibrahim Bello[1], Yusuf Ya'u[1,*]

[1]*Ahmadu Bello University, Zaria*

[2]*Department of Civil Engineering, Pan African University Institute for Basic Sciences, Technology and Innovation Kenya*

Email: marmusty111@gmail.com, kassimyusuf@gmail.com, belloi1040@gmail.com, yya'u@abu.edu.ng*

***Corresponding author**: Yusuf Ya'u

DOI: https://doi.org/10.67203/sp.ICESID.2026

ABSTRACT

Road transportation remains the dominant mode of movement for passengers and freight in Nigeria. Although road construction and rehabilitation projects are undertaken to improve transport efficiency, they often introduce temporary hazards within construction work zones. This study examined the impact of road construction site activities on the occurrence of road traffic accidents along the Zaria–Kaduna Road. The rehabilitation contract commenced in May 2018 and the Zaria–Kaduna section was completed in December 2022; the FRSC crash records analyzed cover the years 2017–2020, being the data available at the time of the study. A descriptive survey design was adopted, combining structured questionnaires, field observations and interviews with road users, contractor staff and FRSC officers. Poor road condition, illiteracy of both road users and workers, faulty vehicle condition, and driver behaviour emerged as the most common causes of accidents, each with a mean rating of at least 3.50 It is deduced, that from year 2018, 2020, an average of 2,612 persons were injured and 399 killed annually. The highest monthly figures rose from 147 injured and 18 killed in October 2017 (before commencement) to 213 injured and 43 killed in October 2018 (after commencement) increase of 45% and 139% respectively. The study recommends regular safety training for workers and road users, greater attention to health and safety by contractors and other stakeholders, consistent implementation of traffic-management plans on construction sites, and stricter enforcement of regulations.

Keywords: *Road construction; work-zone safety; road traffic accidents; highway construction; Zaria–Kaduna Road*

1 INTRODUCTION

1.1 Background of the Study

Transportation infrastructure is widely recognized as one of the fundamental drivers of economic growth, national integration, and sustainable development. An efficient road transportation system facilitates the movement of people, goods, and services, thereby supporting industrial production, agricultural development, trade, and regional connectivity. In Nigeria, road transport accounts for the overwhelming majority of passenger and freight movements because of its accessibility, flexibility, and extensive geographical coverage (World Bank, 2020). Governments continue to channel substantial resources into building, upgrading, and expanding road networks in response to growing transportation needs. Such investments aim to deliver smoother pavement surfaces, shorter journey times, more efficient vehicle operation, and safer roads overall. Yet the very process of carrying out these improvements typically requires establishing temporary work zones, which can heighten the risk of accidents for both motorists and the personnel working on site (Alsultan et al., 2022)

Road construction work zones are characterized by lane closures, temporary diversions, narrowed carriageways, excavations, movement of construction equipment, stockpiles of construction materials, temporary traffic control devices, and altered driving conditions. These changes frequently disrupt normal traffic operations and increase the cognitive demands placed on drivers, particularly where traffic management measures are inadequate (Theofilatos, Ziakopoulos, Papadimitriou, Yannis, & Diamandouros, 2017), typical road construction work zone is shown in **Plate 1**, showing advance

warning signs, channelizing devices, barriers, and the work area. According to the World Health Organization (2023), approximately 1.19 million people die each year as a result of road traffic crashes worldwide, while millions more sustain serious injuries. The report further indicates that road traffic injuries remain the leading cause of death among young people aged 5–29 years, with low- and middle-income countries bearing a disproportionate share of the global burden.

According to Awodele and Ayoola (2005) several hundreds of construction workers are killed each year on Nigeria construction site, with many rendered temporary or permanently disabled. The national institute of occupational safety and health (NIOSH) reports that roughly 20,000 construction workers are injured each year in highway and street construction accidents, United State of America (Gohil, Parekh, & Patel, 2018). Census of fatal occupational injuries (CFOI) data indicates that 55% of fatalities occurs within the work zone itself "(Gohil, Parekh, & Patel, 2018). According to International Labour Organization statistics, approximately 120 million occupational accidents occur annually in workplaces worldwide, of which about 210,000 are fatal (Rantanen, 2008). A review of accidents reported to Nigeria's Federal Ministry of Labour and Productivity Inspectorate Division over an 11-year period (2002–2012) found a total case fatality rate of 49.5%, a significant increase compared to the earlier study period (Umeokafor et al., 2014).

Plate 1: Typical Highway Construction Work

According to the World Health Organization (2015), 90% of road traffic death occur in low and middle income countries. The crash situation in Nigeria is more serious because of the rapid growth in the number of motor vehicles in the past few years. In Nigeria, studies on road safety have largely focused on driver behavior, roadway conditions, and traffic law enforcement. Comparatively fewer studies have examined highway work-zone safety. According to the International Labour Organization (ILO), an estimated 2.93 million workers die annually worldwide as a result of work-related factors, while approximately 395 million workers sustain non-fatal work injuries each year. Of the total work-related deaths, about 330,000 are attributed to occupational accidents, while approximately 2.6 million are associated with work-related diseases (International Labour Organization, 2023).

Shittu, Popoola, Tsado, Shehu, and Abdulazeez (2022) investigated safety management practices on construction sites in Abuja and found that inadequate hazard recognition, weak safety supervision, and inconsistent implementation of safety measures significantly contributed to accidents. The study recommended stronger safety training, improved hazard identification procedures, and stricter compliance with occupational safety standards. Despite substantial funding directed toward upgrading its highway network, Nigeria still records a high incidence of road crashes (Labinjo et al., 2009). This persistent problem stems from a mix of factors working together rising traffic volumes, poorly maintained roads, risky driving habits, and lax enforcement of traffic rules, compounded further by active construction work along many routes (Labinjo et al., 2009). Construction zones pose a particular danger because motorists are forced to navigate constantly shifting road layouts while sharing limited space with heavy equipment and construction crews (Alsultan et al., 2022).

The Zaria–Kaduna Road is one of Nigeria's most strategic federal highways, connecting the northern region with the Federal Capital Territory. The location map is shown in **Figure 1**, its corridor carries substantial volumes of passenger vehicles, heavy-duty trucks, petroleum tankers, commercial buses, and agricultural transport vehicles. Federal Government awarded the contract in December 2017 for the reconstruction and rehabilitation of Abuja -Zaria-Kano with a total length of 375.9km, out of which Zaria to Kaduna has about 83km, to improve capacity and pavement condition. The project commenced in May 2018 to date, but the Zaria to Kaduna portion was completed in 2022. During these projects, motorists have experienced lane closures, traffic diversions, temporary pavement conditions, and construction activities that influenced road safety.

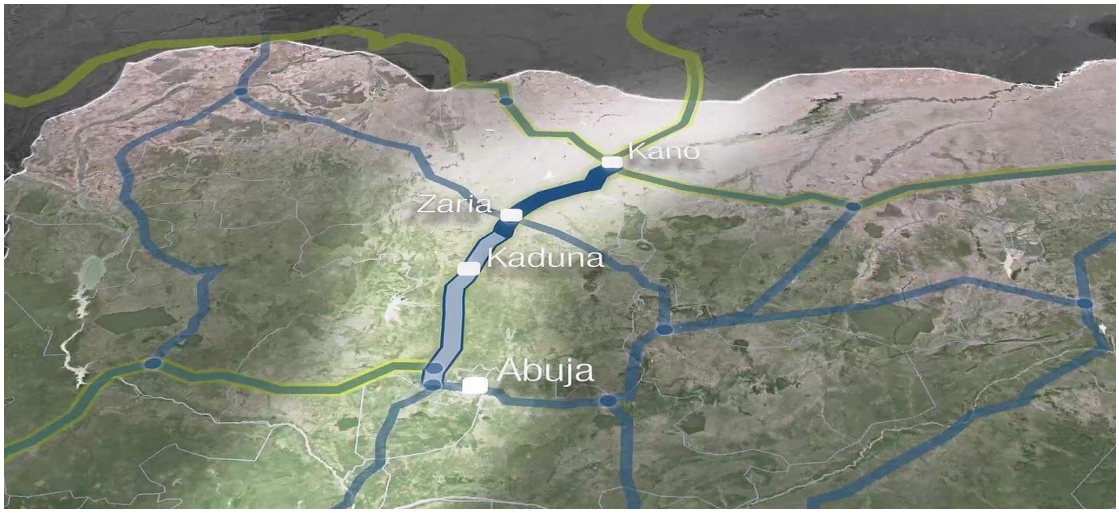

FIGURE 1: LOCATION MAP OF THE STUDY AREA (ZARIA–KADUNA ROAD)

Although contractors are generally required to implement comprehensive traffic management plans including advance warning signs, temporary speed restrictions, barriers, flag personnel, pavement markings, and adequate illumination the effectiveness of these measures varies considerably across construction sites. Inadequate implementation may increase confusion among drivers and elevate crash risk, particularly during periods of high traffic demand and reduced visibility.

In Nigeria, highway reconstruction projects are commonly executed while traffic continues to use portions of the existing roadway. Consequently, motorists are often required to navigate narrowed carriageways, uneven pavement surfaces, temporary diversions, reduced visibility, and changing traffic patterns. These conditions are further aggravated by excessive speeding, dangerous overtaking, driver impatience, poor compliance with temporary traffic signs, and inadequate enforcement of speed limits within construction zones. Such factors collectively increase the likelihood of crashes involving motorists, pedestrians, construction workers, and construction equipment. Due to the economic importance of Zaria – Kaduna road, federal government awarded the contract for rehabilitation and expansion in 2017. It was observed that during the construction, road traffic crashes continue to occur along the sections under construction, raising concerns regarding the adequacy of existing work-zone traffic management practices and contractor compliance with established safety standards.

Although studies have examined road traffic accidents in Nigeria generally, relatively few have specifically investigated the relationship between construction site activities and accident occurrence along the Zaria–Kaduna Road. This lack of location-specific empirical evidence limits the ability of highway agencies, contractors, and road safety authorities to develop targeted interventions for reducing work-zone crashes. Therefore, this study seeks to evaluate the impacts of road construction site activities on accident occurrence rate along the Zaria–Kaduna Road and to recommend practical measures for improving safety within highway construction zones. The findings of this study will provide evidence-based recommendations for improving work-zone safety and reducing accidents on major highway construction projects in Nigeria.

2 THEORETICAL BACKGROUND

2.1 Road Construction Activities

The typical road construction activities include site clearing and grubbing, earthworks and excavation, embankment construction, drainage installation, culvert and bridge construction, pavement stabilization, asphalt laying, pavement marking, installation of road furniture, and traffic diversion and temporary traffic control.

TABLE 1: MAJOR ROAD CONSTRUCTION ACTIVITIES AND ASSOCIATED HAZARDS

S/N	Construction Activity	Potential Hazard	Possible Accident
1	Site clearing	Dust generation	Reduced visibility
2	Excavation	Open trench	Vehicle fall-over
3	Earthworks	Uneven surface	Loss of vehicle control
4	Drainage construction	Narrow carriageway	Side collision
5	Asphalt paving	Traffic congestion	Rear-end collision
6	Bridge construction	Diversion	Head-on collision
7	Road marking	Temporary lane closure	Sideswipe collision
8	Movement of equipment	Construction vehicles entering traffic	Vehicle collision

Unlike permanent highway facilities, work zones change continuously as construction progresses. Consequently, motorists encounter unfamiliar road alignments, narrowed lanes, temporary barriers, construction equipment, and workers operating close to moving traffic. These conditions increase the complexity of the driving task and require greater driver attention than under normal roadway conditions (Hintersteiner, 2008).

Road construction requires continuous operation of heavy equipment such as bulldozers, excavators, graders, pavers, rollers, cranes, and dump trucks. These machines frequently enter and exit traffic streams, creating additional conflict points with moving vehicles. Where access points are not properly controlled or traffic marshals are absent, the interaction between slow-moving construction machinery and high-speed traffic substantially increases collision risk (Shittu, Popoola, Tsado, Shehu, & Abdulazeez, 2022).

2.2 Causes of Accidents in Road Construction Zones

Research indicates that work-zone crashes are rarely attributable to a single factor rather they result from the interaction of human behavior; speeding, dangerous overtaking, driver fatigue, distracted driving, alcohol or drug impairment, failure to obey temporary traffic signs, and impatience during traffic congestion which is the leading contributors of road traffic crashes within construction zones. Engineering deficiencies includes; inadequate warning signs, poor pavement markings, insufficient illumination, abrupt lane transitions, uneven pavement surfaces, inadequate drainage, and poor traffic diversion design were identified as causes of road accident. Road design and traffic management, vehicle characteristics, and environmental conditions includes; Rainfall, Dust generated during earthworks, fog, poor night time visibility, and glare from oncoming vehicles are also part of the causes of road accident. These conditions reduce visibility and increase stopping distances, thereby elevating crash risk. Expected impact of the causes of accident in construction zone is presented in **Table 2**.

TABLE 2: COMMON CAUSES OF ACCIDENTS IN ROAD CONSTRUCTION ZONES

Cause	Description	Expected Impact
Over speeding	Failure to obey temporary speed limits	Very High
Poor signage	Insufficient warning signs	High
Traffic diversion	Driver confusion	Very High
Poor lighting	Reduced night visibility	High
Heavy equipment	Conflict with traffic	High
Driver fatigue	Reduced concentration	Moderate
Dangerous overtaking	Risky maneuvers	Very High
Loose materials	Vehicle skidding	Moderate

2.3 Traffic Management Measures in Road Construction Work Zones.

Traffic management is a fundamental component of highway construction projects because it enables construction activities to proceed while maintaining the safe and efficient movement of road users. A well-designed traffic management plan minimizes conflicts between construction operations and public traffic by providing clear guidance, adequate warning, and effective control measures throughout the construction period. The primary objective is to protect motorists, pedestrians, and construction workers while minimizing traffic delays and congestion (Federal Highway Administration, 2023).

The effectiveness of traffic management depends on the proper design, installation, maintenance, and monitoring of temporary traffic control devices. International best practice recommends that every road construction project should include a comprehensive Traffic Management Plan (TMP) prepared before construction commences. The plan should identify potential hazards, specify traffic control devices, define temporary speed limits, provide diversion layouts, and establish emergency response procedures (Alsultan et al. 2022; Federal Highway Administration, 2023).

2.3.1 *Traffic Signs and Warning Devices*

Traffic signs constitute the first line of communication between highway authorities and road users within construction work zones. Warning signs provide advance information about upcoming hazards such as lane closures, road narrowing, uneven pavement, construction equipment, and temporary speed restrictions. Typical highway construction work zone showing advance warning signs, channelizing devices, barriers, and the work area is reflected in **Plate 2**. Proper placement of warning signs enables motorists to anticipate changing road conditions and adjust their driving behavior accordingly. Conversely, missing, damaged, poorly positioned, or non-reflective signs may confuse motorists and increase the probability of crashes, particularly during night-time driving or adverse weather conditions (Federal Highway Administration, 2023).

2.3.2 *Speed Management*

Excessive speed is widely recognized as one of the most significant contributors to road traffic crashes. Consequently, temporary speed limits are an essential component of work-zone safety.

2.3.3 *Temporary Traffic Diversions*

Traffic diversion involves redirecting vehicles away from active construction areas through temporary routes. An effective diversion should provide sufficient lane width, smooth horizontal and vertical alignment, adequate drainage, and appropriate signage to ensure safe vehicle movement. Poorly designed diversions may introduce sharp curves, reduced sight distances, uneven pavement, or unexpected intersections, thereby increasing the risk of collisions. Regular inspection and maintenance of diversion routes are therefore essential throughout the construction period (AASHTO, 2018).

2.3.4 *Traffic Control Personnel*

Traffic control personnel, including flaggers and traffic marshals, play an important role where temporary traffic signals are impractical or where construction activities require intermittent traffic

stoppages. Their responsibilities include directing traffic through construction zones, controlling alternating one-way traffic, coordinating construction vehicle movements, assisting pedestrians, and responding promptly to emergencies. The effectiveness of traffic control personnel depends on adequate training, proper positioning, use of high-visibility clothing, and effective communication with construction supervisors (Federal Highway Administration, 2023).

Plate 2: Typical Highway Construction Work Zone for Advance Warning Signs, Channelizing Devices, Barriers, and the Work Area.

2.3.5 *Night-time Safety Measures*

Night-time construction presents additional safety challenges because reduced visibility limits drivers' ability to detect hazards and interpret temporary traffic control devices. Appropriate night-time safety measures include; reflective warning signs, retroreflective pavement markings, flashing warning beacons, temporary lighting towers, illuminated arrow boards, reflective barriers, and high-visibility personal protective equipment for workers. Typical highway construction work zone Working in the night showing advance warning signs, flashing warning beacons and illuminated arrow boards is reflected in **Plate 3**, while highway construction work zone with reflective barrier and warning sign is shown in **Plate 4**. Adequate illumination improves hazard recognition and reduces the likelihood of crashes involving both motorists and construction personnel.

Table 3: Traffic Management Measures

Plate 3: Typical Highway Construction Work Zone Working in the Night.

Plate 4: Highway construction work zone with Reflective Barrier and warning sign

Measure	Purpose	Expected Effectiveness
Advance warning signs	Warn motorists	High
Traffic cones	Guide vehicles	High
Temporary barriers	Separate traffic from work area	Very High
Speed restriction signs	Reduce speed	Very High
Flagmen	Control traffic flow	High
Reflective devices	Improve night visibility	High
Temporary lighting	Enhance visibility	High

2.4 Research Gap

The review of existing literature reveals that substantial research has been conducted on road traffic accidents, construction safety, and work-zone traffic management globally (Alsultan et al., 2022). Nevertheless, several gaps remain. Firstly, relatively few studies have specifically investigated the relationship between road construction site activities and accident occurrence along the Zaria–Kaduna Road, despite its strategic importance as a major federal highway linking northern Nigeria with the Federal Capital Territory. Secondly, limited empirical evidence exists regarding the effectiveness of current traffic management measures implemented during road construction projects on Nigerian highways. Consequently, policymakers and contractors have insufficient location-specific information to guide improvements in work-zone safety. Improving work-zone safety contributes directly to SDG 3 (Good Health and Well-being, Target 3.6 on halving road-traffic deaths) and SDG 9 (Industry, Innovation and Infrastructure) (United Nations, 2015). Beyond conventional signage and enforcement, the deficiencies identified here could be mitigated through low-cost smart work-zone technologies, solar-powered variable-message signs, automated speed-feedback displays, GPS-tracked flag-vehicle systems and drone-based site-compliance monitoring offering scalable, technology-based pathways to safer highway construction in Nigeria (Demeke et al., 2025).

3 RESEARCH MATERIALS AND METHODS

3.1 Method

3.1.1 *Data Collection*

Primary data was obtained through structured questionnaires, field observations, and interviews with relevant stakeholders, while secondary data which includes accident records was extracted from Federal Road Safety Corps (FRSC). The analysis concentrated on identifying construction-related factors influencing accident occurrence. The survey research design method was adopted for this study to effectively assess professional opinion and road users as regards to the suitability of the subject matter.

3.1.2 *Population of the Study*

The population of the study comprises professionals such as Contractor's staff, and engineers. It also comprises the road users, the pedestrian and the drivers, then government agency (FRSC). The 6,080 is the average daily traffic (ADT) volume from a manual count used as the finite population N for the road-user stratum only; Yamane's formula gives n = 375 for that stratum. Contractor staff, engineers and FRSC officers were added through a separate purposive / complete-enumeration component.

3.1.3 *Sample*

3.1.3.1 *Sampling Strategy*

A stratified mixed design sampling method that comprises probability (systematic/random) sampling governed by Yamane's formula was used for the road-user stratum (n = 375 from N = 6,080), while purposive sampling was used only for the professional stakeholders (contractor staff, engineers and FRSC officers) who possess specific work-zone knowledge. **Equation 1** shows Yamane's formula.

$$\boldsymbol{n = \frac{N}{1 + N(e)^2}} \tag{1}$$

Where, n is the sample size, N is the population size, and e=0.05 is the precision level.

3.1.4 *Distribution Method*

The questionnaire was distributed electronically via email, using an online survey platform. This method was allowed for a broad reach and easy collection of responses. Reminders was sent out to increase response rates. A sample size is a part of the population chosen for a survey or experiment (Rahman 2023).

3.1.5 *Techniques of Data Analysis*

Analysis means the categorizing, manipulating and summarizing of data in order to obtain information. The analysis carried out are frequently statistics, and cross tabulation. The statistical package used for running the analysis is SPSS 13.0 package. The result of the table was interpreted descriptively. The descriptive interpretation provided explanation of results, which is anchored on scientific assumption and conditions of literature high points (Kothari & Garg, 2019).

3.2 Methodology

In order to obtain crash data on Kaduna- Zaria Express way, Federal Road Safety Corps FRSC 1.1 Kaduna sector command was visited, of which data from 2015 to 2020 was obtained. Questionnaire was also distributed to contractor's staff in charge for the construction of the rehabilitated road (Kaduna – Zaria) and some road users using an established sample size of 375, however, one – on – one interview of the commuters was also observed. Crash data analysis and questionnaire was done by using statistical analysis software (SPSS).

4 RESULTS AND DISCUSSION

4.1 Data Presentation and Analysis

This section deals with presentation and analysis of data collected from questionnaire administered, Crash data gotten from FRSC on Kaduna – Zaria Express way, and finally the physical site survey along the road. It was observed from **Figure 2** that only 2.4% of questionnaires was not returned, all other 97.6% was answered and returned. This reflects the level of responsibilities, high interest and determination associated with the people the questionnaires was administered. **Figure 3** shows that most respondent gender are male with highest percentage of 52.64%.

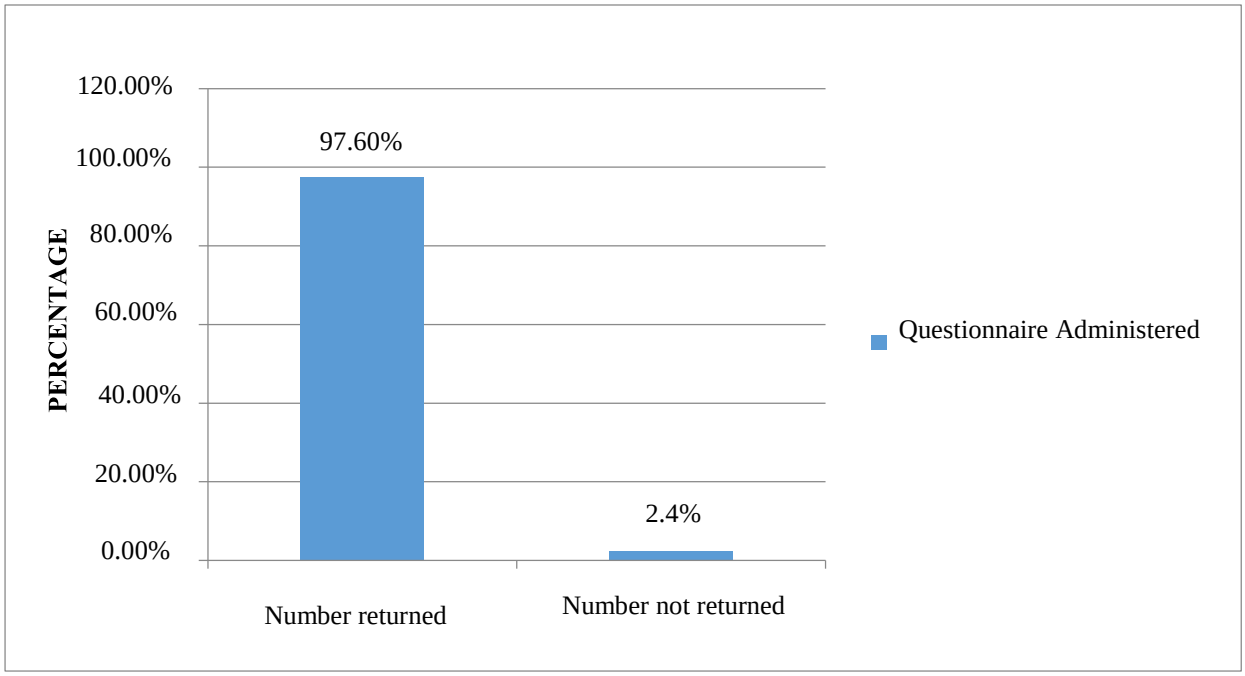

Figure 2: Questionnaire Administered

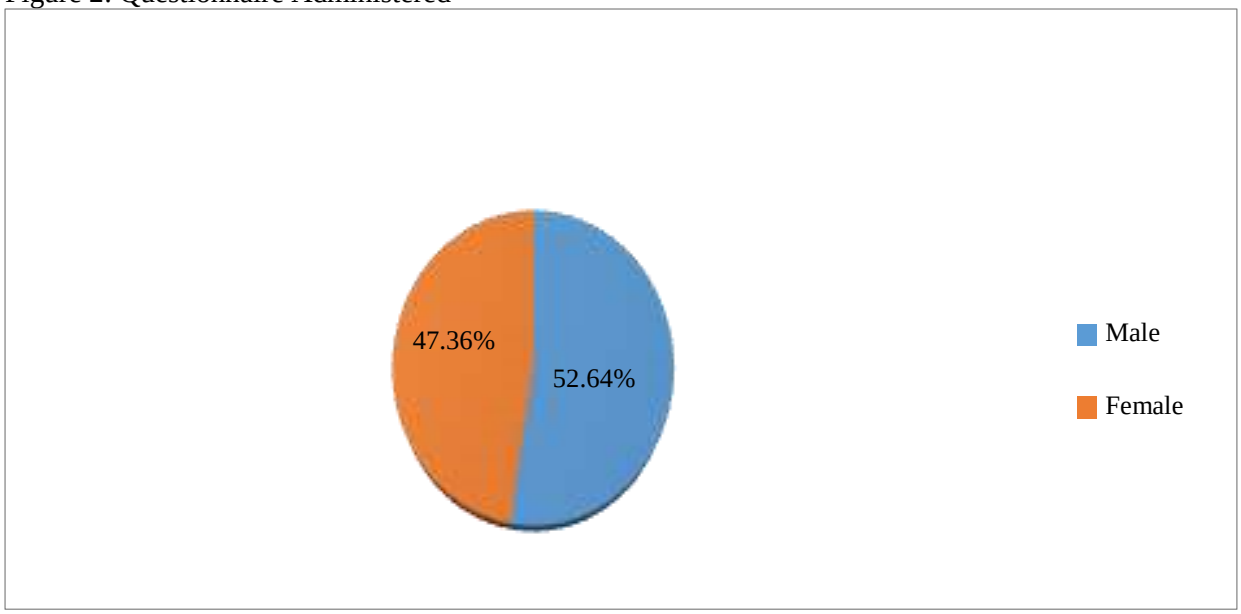

Figure 3: Gender of Respondents

The most of the respondent are road user with the highest percentage of 24.93% as shown in **Figure 4.**

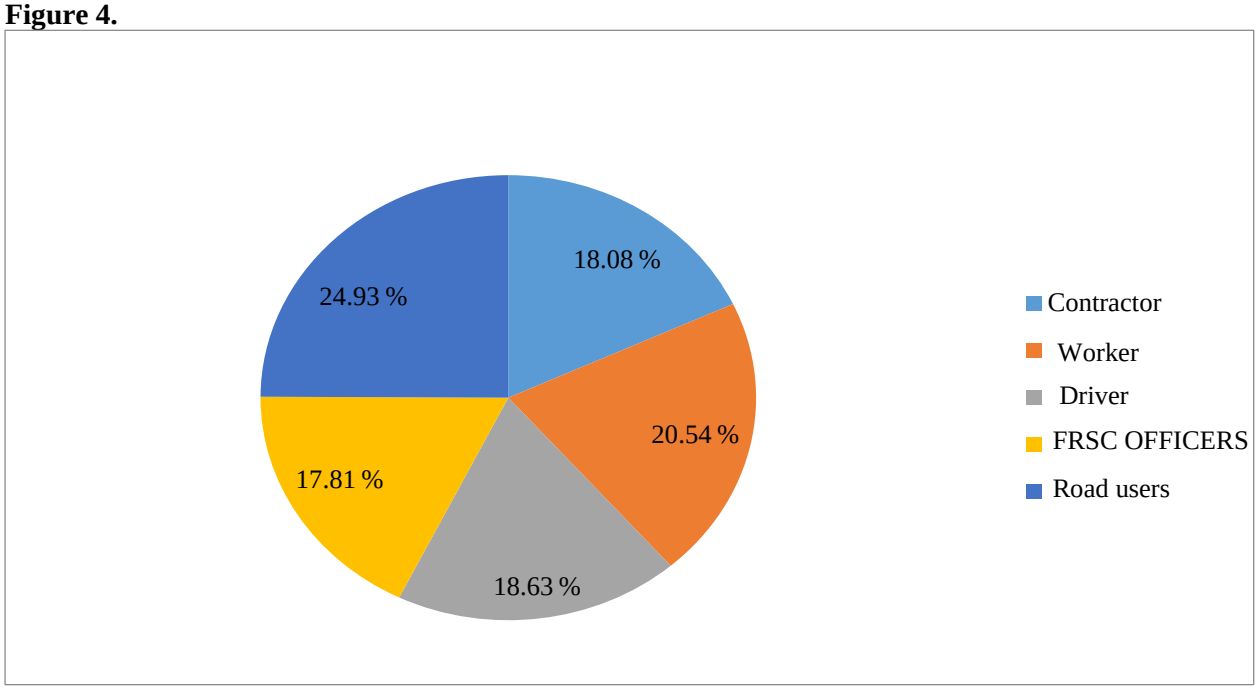

Figure 4: Designation of respondents

Figure 5 shows that respondent with driving experience between 0 -5 years have the highest percentage of 22.68%. While **Figure 6** shows respondents that passes Kaduna-Zaria road once in a month, the highest number of people that passes the road were recorded as 16.39%.

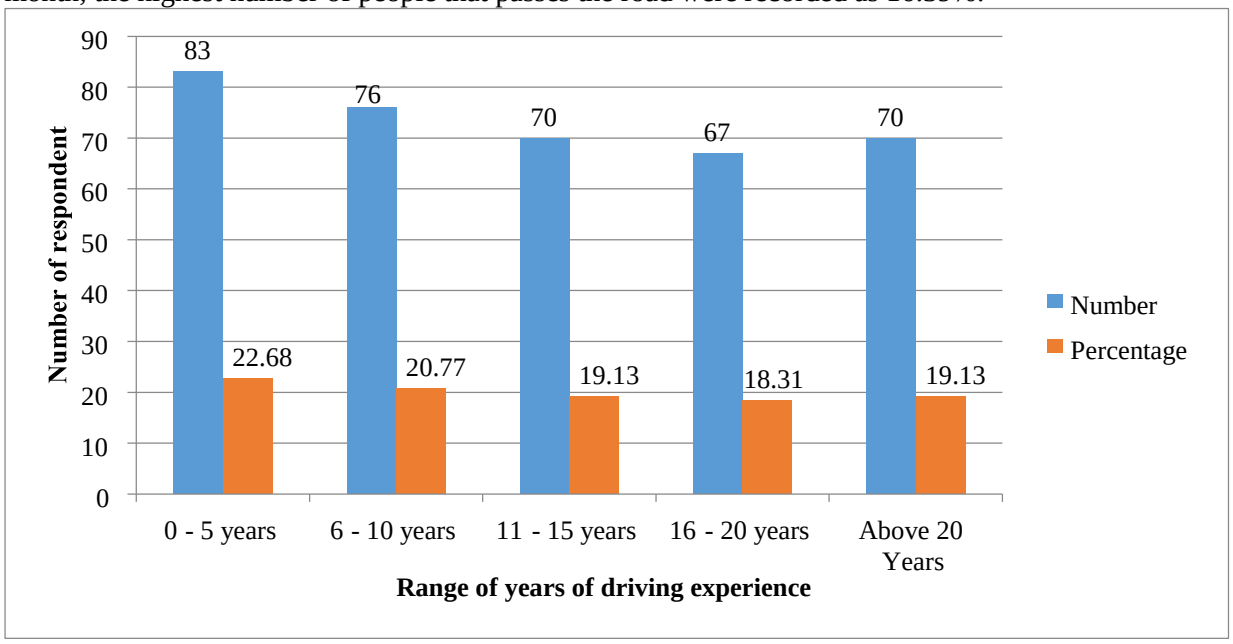

Figure 5**:** Driving Experience of Respondents.

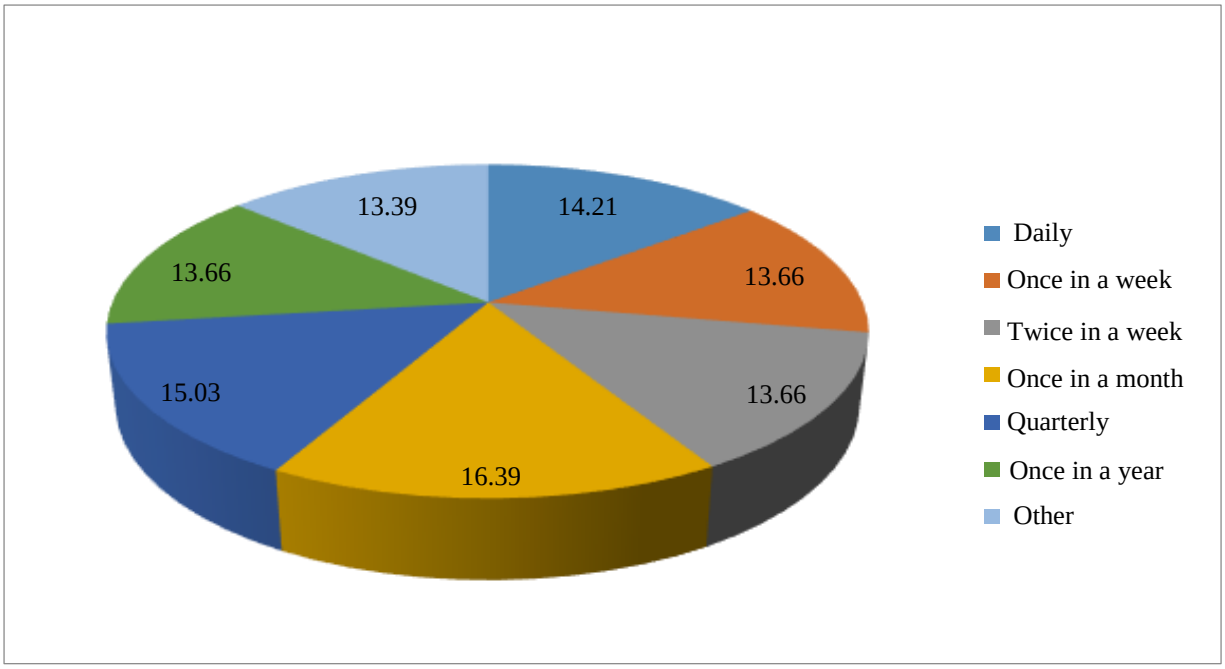

Figure 6: How often do you Pass Kaduna – Zaria road

4.2 Data Analysis of Questionnaire

Total number of questionnaires administered is 375 from **Equation 1**. The mean of the responses was calculated using **Equation 2**

$$Mean = \frac{\sum FX}{\sum F} \qquad 2$$

Where F is the frequency of responses in each option and X is the weighting point of option.

In analyzing the data, decision was used for answering the research questions for the purpose of decision making, an interval of 0-2.50 mean value was used as rejected, 2.51-3.49 mean value as undecided and mean value ranging from 3.50 – 5.00 were regarded as accepted. To examine the causes of accident along road construction site, questionnaire in **Table 4A** was administered. **Table 4A** shows that most respondents agreed that "poor road condition "is the most common causes of accident on Kaduna – Zaria with the highest mean of 3.67 which is followed by accident due to illiteracy of both road users and workers with the mean of 3.66.

Table 4: A: Causes of accident

S/N	Response	S (5)	A (4)	UD (3)	D (2)	SD (1)	$\sum FX$	$\sum F$	Mean	Remarks
A	Taking intoxicant before or during driving	106	88	81	81	10	1297	366	3.54	Accepted
B	Over speeding and overtaking by drivers	106	90	80	80	12	1302	366	3.56	Accepted
C	Close following distance to vehicle in front.	77	91	65	67	66	1144	366	3.13	Undecided
D	Disobeying speed limit by the drivers	92	96	78	78	27	1257	366	3.43	Undecided
E	Fatigue of the flagman and drivers along the road	81	101	80	80	24	1233	366	3.37	Undecided
F	Illiteracy of the driver	91	105	93	71	6	1302	366	3.56	Accepted
G	Absence of road traffic signs control	20	98	83	84	-	909	366	2.48	Rejected
H	Lack of condoning of construction zone	72	76	76	76	66	1110	366	3.03	Undecided
I	Lack of coordination by contractors along road construction zone	73	82	70	72	69	1116	366	3.05	Undecided
J	Poor visibility on the road near construction site	92	94	89	90	1	1284	366	3.51	Accepted
K	Improper retro-reflective illumination of road signs	71	85	75	69	66	1124	366	3.07	Undecided
L	Illiteracy of both road users and workers	110	98	95	60	3	1350	366	3.66	Accepted
M	Poor road condition	112	94	89	68	3	1342	366	3.67	Accepted
N	Improper diversion on the road by the contractor	-	37	89	150	90	805	366	2.19	Rejected

S/N	Response	S (5)	A (4)	UD (3)	D (2)	SD (1)	$\sum FX$	$\sum F$	Mean	Remarks
O	Fault from vehicle condition lead to accident	100	99	83	84	-	1313	366	3.59	Accepted
P	Heavy traffic volume on the road	71	85	75	69	66	1124	366	3.07	Undecided
Q	Improper management skills by the contractor in construction approach	69	82	76	72	67	1112	366	3.04	Undecided
R	Barriers, barricade and positioning of flagman is done properly	96	92	92	86	-	1296	366	3.54	Accepted
S	Mounting necessary road sign	92	103	94	76	1	1307	366	3.57	Accepted
T	Lane marking and using suitable colours	95	103	94	74	-	1317	366	3.59	Accepted

Note**:** SA= Strongly Agree d, A = Agreed, UD = Undecided, D = Disagreed, SD = Strongly Disagreed

How frequent does your company provide the following measures to minimize the reoccurrence of accident on site, answerable only by contractor / site staff, so it is based on the 66 professional respondents not the full 375 road-user sample. **Table 4B** shows that, provision of first aid material is found to be lacking with mean of 2.02 while provision of safety kits is found to be common with the highest mean value of 4.24, followed by enforcement for its usage in site with mean value of 3.87, are the major precautionary measures that reduces the occurrence of accidents.

Table 4: B: Factors Reducing the Accidents rate.

SN	Response	A (5)	F (4)	LF (3)	R (2)	N (1)	$\sum FX$	$\sum F$	Mean	Remark
A	Sensitization of workers on safety knowledge	9	19	13	17	8	202	66	3.06	Undecided
B	Provision of first aid materials	2	3	10	30	21	133	66	2.02	Rejected
C	Provision of safety kits	31	20	15	-	-	280	66	4.24	Accepted
D	Enforcement on site to use safety kits	24	19	14	9	-	256	66	3.87	Accepted

Note: A = Always, F = Frequently, LF = Less Frequently, R = Rarely, N = never

4.3 Crash Data from Federal Road safety Corps on Kaduna-Zaria Express Way

Table 5: A: Number of people Killed and Injured Monthly in Year 2017 - 2020

MONTH	2017		2018		2019		2020	
	Injured	**Killed**	**Injured**	**Killed**	**Injured**	**Killed**	**Injured**	**Killed**
JAN	403	80	313	68	339	42	200	34
FEB	343	84	181	25	211	30	154	31
MARCH	227	44	260	42	207	29	306	59
APRIL	270	37	394	64	380	43	125	15
MAY	262	55	337	41	357	45	115	18
JUNE	195	34	169	23	216	33	137	9
JULY	142	19	173	27	189	15	113	19
AUG	261	31	234	28	195	15	138	25
SEPT	150	24	177	16	161	30	138	18
OCT	147	18	213	43	141	23	155	39
NOV	179	23	218	30	247	40	157	23
DEC	152	26	310	72	311	49	164	35
TOTAL	**2731**	**475**	**2979**	**479**	**2954**	**394**	**1902**	**325**

It is observed that the highest number of people injured (2,979) and those killed (479) were in 2018, the year the contract commenced, signifying the impact of site activities causing the rate of accident. The lowest number of people injured (1902) and those killed (325) were reflected in 2020, which coincide with the COVID-19 movement restrictions of late March–mid 2020, during which inter-state travel fell markedly (Erim et al.,2020); this reduced exposure is a likely contributor, though partly offset by higher speeds on emptier roads and barricade contribute to high rate of accidents in some locations. Similarly, it were observed that in October 2017, before the commencement of the project 147 and 18 were the highest figures recorded for number of injured persons and number of person killed respectively. While in October 2018 after the commencement of the project, 213 and 43 were the highest figures recorded for number of injured persons and number of person killed respectively. This translated to rate of the injured victims increase to 45%, while rate of fatality victims increase to 139% which are quite worrisome. **Table 5B** shows that from the year of commencement of the project (2018), to the year of available data end (2020), an average of 2612 peoples were injured annually and 399 peoples were killed annually which is quite alarming.

Table 5: B: Persons Injured and Killed Annually (2018 – 2020)

Year	Injured	Killed
2018	2979	479
2019	2954	394
2020	1902	325
Total	**7835**	**1198**
Average/Anum	**2612**	**399**

4.4 Report on Physical Survey of Zaria – Kaduna Express-Way

4.4.1 *Compliance of the contractor to diversion Sign*

Physical survey of Kaduna – Zaria expressway based on the specification of British Columbian construction standard.

a) Diversion sign

Table 6 shows implemented site diversion signs. However, diversion sign shown in **Plate 5A** and **5B** respectively are not in accordance with highway traffic sign standard cited in FMW highway manual (2013). This is believed to be part of the factors causing accident on the road project sites.

Plate 5A: 1KM Distance Diversion Sign	Plate 5B:500m Distance Diversion Sign

Table 6: Contractor's Compliance with Diversion Sign specification

		Standard Specification FMW Manual (2013) (m)	Implemented Specification (m)	Remark
Size	Width	1.5	2.4	Not compliant with standard
	Height	0.9	1.2	
Colour	Background	Blue	White	
	Legend	White	Red and Black	
	Border	None	None	

b) SPEED LIMIT SIGNS

Table 7 shows implemented site Speed limit signs. However the implemented speed limit sign presented in **Plate 6A** and **6B** show that the size, colour, and mounting height of the implemented speed limit is in accordance with highway standard cited in FMW highway manual (2013).

Plate 6A: showing 40km speed limit before approaching diversion.

Plate 6B: showing 30km/hr speed limit before approaching diversion.

Table 7: Contractor's Compliance with Speed Limit specification

		Standard Specification FMW Manual (2013) (m)	**Implemented Specification (m)**	**Remark**
Size	Diameter	0.7	0.74	
Colour	Background	yellow reflective	Yellow retro-reflective	Compliant with standard
	Legend	Black semi- matt	Black	
	Border	Red retro-reflective	Red retro-reflective	
Mounting Height	Height	0.9	2.4	

c) BARRIER

Plate 7 shows implemented site installed barriers and **Table 8** summaries notable observation of the installed barriers on site. The installed barriers are slightly different from the standard specification cited in FMW highway manual (2013). This is believed to be part of the factor causing accident on the road project sites.

Plate 7: Jersey barrier

Table 8: Contractor's Compliance with Barrier specification

		Standard Specification FMW Manual (2013) (m)	Implemented Specification (m)	Remark
Size	Width	2.5	2.4	Not compliant with standard
	Height	0.83	1.2	
Colour		Red and white retro - reflective	Red and yellow retro-reflective	

5 CONCLUSION AND RECOMMENDATION

5.1 Conclusions

The following conclusions were drawn from the project:

1. Poor road condition, illiteracy of both road users and workers, fault from vehicle condition, and over-speeding/overtaking by drivers were recorded as the most common causes of accidents on the Kaduna–Zaria expressway, with mean values of 3.67, 3.66, 3.59 and 3.56 respectively.
2. The provision of Safety kits recorded the highest mean value of 4.24, followed by enforcement for its usage in site with mean value of 3.87, are the major precautionary measures that reduce the occurrence of accidents.
3. Before the commencement of the project in October 2017, 147 and 18 were the highest figures recorded for number of injured persons and number of persons killed respectively, while in October 2018 after the commencement of the project 213 and 43 were the highest figures recorded for number of injured persons and number of persons killed respectively. This translated to rate of the injured victims increase to 45%, while rate of fatality victims increased to 139%, which are quite worrisome.

4. It was deduced that from the year of commencement of the project (2018), to the year of available data of Kaduna-Zaria road section, an average of 2,612 peoples injured and 399 people were killed annually, which is quite alarming.
5. The Contractor ‘s level of compliance with traffic control standard specification in some area was good like speed limit traffic sign, while in other areas it was poor, like barrier and diversion traffic signs, which are believed to be part of the factors causing accident on the road project sites.

5.2 Recommendations

In order to promote and improve safety on road construction sites, there must be a positive action or response by the responsible bodies. In view of this, the following recommendation were made:

1. Employees training on workplace safety should be encourage by employer or contractor of a project in order to minimize accident on site.
2. First aid equipment and safety officers should be provided on sites.
3. FRSC, Police should continue enlightening road users and drivers on the dangers of over-speeding, overtaking and enforcement of regulations should be observed.
4. Contractor and other stakeholders should not only be inclined to maximizing profit from projects but rather committing themselves to maintaining Health and Safety standards.

REFERENCE

Alsultan, S. M., Alqahtani, F. K., & Alkahtani, K. F. (2022). Health and safety in temporary work zone road construction project in Saudi Arabia: Risks and solutions. International Journal of Environmental Research and Public Health, 19(17), 10627. https://doi.org/10.3390/ijerph191710627.

Awodele, O.A and Ayoola, M.C (2005) “An Assessment of safety programs on construction sites.” Journal of land use and Development, 1(1), pp. 1- 10

Demeke, A. Y., Younesi Heravi, M., Dola, I. S., Jang, Y., Le, C., Jeong, I., Lin, Z., & Wang, D. (2025). *Advancing highway work zone safety: A comprehensive review of sensor technologies for intrusion and proximity hazards* [Preprint]. arXiv. https://arxiv.org/abs/2503.13478.

Erim, D. O., Unal, E., Oke, O. O., Akinyemi, O., & others. (2021). Associations of government-mandated closures and restrictions with aggregate mobility trends and SARS-CoV-2 infections in Nigeria. *JAMA Network Open*, *4*(1), e2032101. https://doi.org/10.1001/jamanetworkopen.2020.32101

Federal Ministry of Works. (2013). *Highway manual part 1: Design, Volume VI: Road traffic signs and road markings*. Federal Republic of Nigeria. Federal Ministry of Works Highway Manual Volume VI.

Gohil, P., Parekh, A., & Patel, D. (2018). Review paper on workers’ safety in highway work zones. International Journal of Advances in Management, Technology and Engineering Sciences, 8(4).

Hintersteiner, R. T. (2008). *Forensic engineering - Highway construction work zone accidents*. *Journal of the National Academy of Forensic Engineers*, *25*(1).

International Labour Organization. (2023, November 26). Nearly 3 million people die of work-related accidents and diseases. International Labour Organization.

Kothari, C. R., & Garg, G. (2019). *Research methodology: Methods and techniques* (4th ed.). New Age International Publishers.

Labinjo, M., Juillard, C., Kobusingye, O. C., & Hyder, A. A. (2009). The burden of road traffic injuries in Nigeria: results of a population-based survey. *Injury Prevention*, *15*(3), 157–162.

Rantanen, J. (2008). Basic occupational health services (3rd rev. ed.). International Labour Organization.

Shittu, A. A., Popoola, K., Tsado, A. J., Shehu, M. A., & Abdulazeez, S. R. (2022). Impact of safety measures for hazard recognition on the rate of accidents on construction sites in Abuja, Nigeria. *Journal of Building Performance*.

Theofilatos, A., Ziakopoulos, A., Papadimitriou, E., Yannis, G., & Diamandouros, K. (2017). Meta-analysis of the effect of road work zones on crash occurrence. *Accident Analysis & Prevention, 108*, 1–8.

United Nations. (2015). *Transforming our world: The 2030 agenda for sustainable development* (A/RES/70/1). United Nations General Assembly.

Umeokafor, N., Evaggelinos, K., Lundy, S., Isaac, D., Allan, S., Igwegbe, O., Umeokafor, K., & Umeadi, B. (2014). The pattern of occupational accidents, injuries, accident causal factors and intervention in Nigerian factories. Developing Country Studies, 4(15), 119–127. https://www.iiste.org/Journals/index.php/DCS/article/view/14423.

World Bank. (2020). Connecting to compete: Trade logistics in the global economy. Washington, DC: World Bank.

World Health Organization. (2023). *Global status report on road safety 2023*. Geneva, Switzerland: World Health Organization.

World Health Organization. (2015). *Global status report on road safety 2015*. World Health Organization.

International Conference on Engineering Innovation for Sustainable Development (ICESID 2026)
Faculty of Engineering, Ahmadu Bello University Zaria · 8–10 September 2026

INFRASTRUCTURE CHARACTERIZATION AND PHYSICAL INTEGRITY ASSESSMENT OF URBAN WATER DISTRIBUTION SYSTEMS: A RISK-BASED FRAMEWORK FOR SUSTAINABLE ASSET MANAGEMENT IN MINNA, NIGERIA

Abdulrahman Aminu[1], Johnson A. Otun[1], Aliyu Ishaq[1,*]
[1]*Ahmadu Bello University, Zaria*
Email: aminua2u@gmail.com, johnsonotun@yahoo.com, aleeruks4real@gmail.com*
***Corresponding author**: Aliyu Ishaq
DOI: https://doi.org/10.67203/sp.ICESID.2026

ABSTRACT
Nigerian water utilities have expanded treatment capacity while ageing distribution networks have received limited systematic assessment. In Minna, the Municipal system operated by the Niger State Water and Sewage Corporation (NISWASEC), demand exceeds network design capacity, contributing to failures, leakage, and pressure problems. As detailed condition-assessment tools remain inaccessible, rehabilitation relies largely on institutional memory and emergency logs. This study developed a GIS-supported Physical Integrity Index (PII) from pipe age, failure frequency, leakage density, and coverage efficiency for Minna's seven service clusters, using maintenance records, field surveys, and staff interviews. Following correction of coverage-efficiency directionality, PII ranged from 2.09 in Bosso (Moderate Integrity) to 4.75 in Minna West (Critical Integrity); Minna East and Chanchaga were also Critical. The three clusters represented 53.6% of the reported 6,526 pipeline-failure occurrence units during 2021–2025. Rankings remained stable under adopted and equal weights. Validation was triangulated: PII showed expected internal associations with failure-occurrence totals ($r = 0.944$) and raw service coverage ($r = -0.906$), although these measures overlap with PII components. Independent criterion validation against NISWASEC ledger-derived cumulative repair costs for 2021–2025, which were not PII inputs, was strong ($r = 0.943$, $p = 0.001$, $n = 7$). The PII provides an evidence-based rehabilitation-prioritization tool for constrained utilities. NISWASEC should prioritise Minna West, Minna East, and Chanchaga, apply the PII annually, and disaggregate maintenance expenditure and non-revenue water by cluster.

Keywords: *Physical Integrity Index; water distribution network; infrastructure asset management; rehabilitation prioritization; Nigeria*

1. INTRODUCTION

Reliable water distribution underpins public health, economic activity, and urban growth. Adeoti et al. (2023) systematically review water-infrastructure sustainability in Nigeria and identify interrelated technical, financial, environmental, social, political, and institutional challenges, including infrastructure deterioration and operation-and-maintenance constraints. In urban distribution systems, ageing pipes can increase failures, leakage, pressure problems, service interruptions, and operating burdens. When these conditions are not systematically assessed, rehabilitation is more likely to remain reactive than condition-informed.

Sub-Saharan African utilities face these problems in their most acute form. Much of the pipework in service was laid decades ago and has exceeded its design life. Maintenance is almost entirely reactive: crews are dispatched only after a main has burst and supply has been cut (Shushu et al., 2021). This stops the immediate crisis but does nothing to slow the network's overall decline. Costs climb, non-revenue water grows, and service reliability keeps falling.

Public utilities in Nigeria face interrelated technical, financial, and institutional constraints, and Adeoti et al. (2023) emphasize the need for effective monitoring and management mechanisms across the infrastructure life cycle. In the Minna study context, rehabilitation decisions have historically relied on NISWASEC operational knowledge, emergency logs, and available budget rather than a formal engineering risk assessment. This study treats that latter observation as local study context derived from utility records, staff input, and field verification; it is not attributed to Adeoti et al. (2023).

The Minna municipal water distribution system, operated by the Niger State Water and Sewage Corporation (NISWASEC), illustrates these scenarios. The system includes several treatment plants, service reservoirs, booster stations, transmission mains, and a wide distribution network serving residential, commercial, institutional, and industrial users. Since Minna has grown, demand has outstripped what many components were designed to deliver. Decades of service, repeated repairs, leakage, and operational stress have worn the infrastructure down. The evidence is visible in recurring failures, growing water losses, unstable pressure in parts of the network, and a maintenance burden that keeps rising.

Any rehabilitation programme depends on understanding asset condition. However, detailed condition-assessment techniques such as inline inspection, continuous monitoring, and advanced predictive modelling remain out of reach financially and technically for many utilities in developing countries (Taiwo et al., 2023). What is needed is an approach that extracts real engineering value from the operational data utilities already collect, without demanding resources they do not have. It should let engineers distinguish isolated failures from systemic decline, identify where rehabilitation is most urgent, and direct spending to where it will have the greatest effect.

Infrastructure asset management research has shown that combining several engineering indicators gives a more realistic picture of buried pipe condition than any single measure can (Taiwo et al., 2023). Pipe age, historical failure frequency, leakage, and service coverage each capture part of the condition story. Taken together within a structured framework, and paired with spatial analysis, they provide a far better basis for decisions. Geographic Information System (GIS) technology adds the ability to map deterioration patterns and tie them directly to network operations on the ground.

Adeoti et al. (2023) synthesize 15 studies addressing water-infrastructure sustainability in Nigeria and describe a varied evidence base covering multiple infrastructure types and challenge categories. Their review does not itself provide a cluster-level physical-integrity assessment for an urban municipal distribution network. The present study therefore focuses specifically on condition differentiation and rehabilitation prioritisation within Minna's distribution system, using utility operational records and GIS-supported analysis.

This emphasis aligns the paper with Innovative Resource Utilization and Management: the PII converts routinely available condition, failure, leakage, coverage, and repair-cost information into a transparent basis for allocating scarce rehabilitation resources across the network. It also has a qualified safety and environmental co-benefit. By identifying recurrent integrity hotspots, the framework can guide follow-up pressure and water-quality monitoring at locations where failures or leaks merit closer control. Deteriorating pipes, physical breaches, and low- or negative-pressure events can create conditions for external contaminant intrusion; however, this study did not measure water quality, model intrusion, or estimate health risk (Renwick et al., 2019).

This study developed and applied a Physical Integrity Index (PII) to assess the condition of the Minna municipal water distribution network. The framework combines four indicators, Pipe Age Index (PAI), Failure Frequency Index (FFI), Leakage Density Index (LDI), and Coverage Efficiency Index (CEI), within a GIS-supported methodology. It draws on utility operational records, field inspections, GPS-verified infrastructure surveys, and interviews with technical personnel to evaluate condition across seven operational service clusters.

Unlike conventional approaches that rely on a single indicator or subjective judgement, this method offers a structured, risk-based approach to identify deterioration hotspots and prioritize rehabilitation using data the utility already holds. A sensitivity analysis tests whether the framework remains stable under different weighting assumptions, building confidence in its use for real engineering decisions.

The findings give NISWASEC practical guidance for infrastructure renewal planning. The methodology can also be transferred to other urban utilities facing similar technical and financial constraints. More broadly, the study demonstrates how integrated engineering indicators and spatial analysis can make urban water distribution management more resilient and transparent.

2. MATERIALS AND METHODS

2.1 Study Area

The study covered the municipal water distribution system of Minna, capital of Niger State in north-central Nigeria. The city lies between latitudes 9°31′ and 9°41′ N and longitudes 6°29′ and 6°37′ E, in the Guinea Savannah ecological zone. Over the past two decades, Minna has grown steadily. Population expansion, increased commercial activity, and public-sector development have all raised demand for potable water and placed additional strain on the existing supply infrastructure.

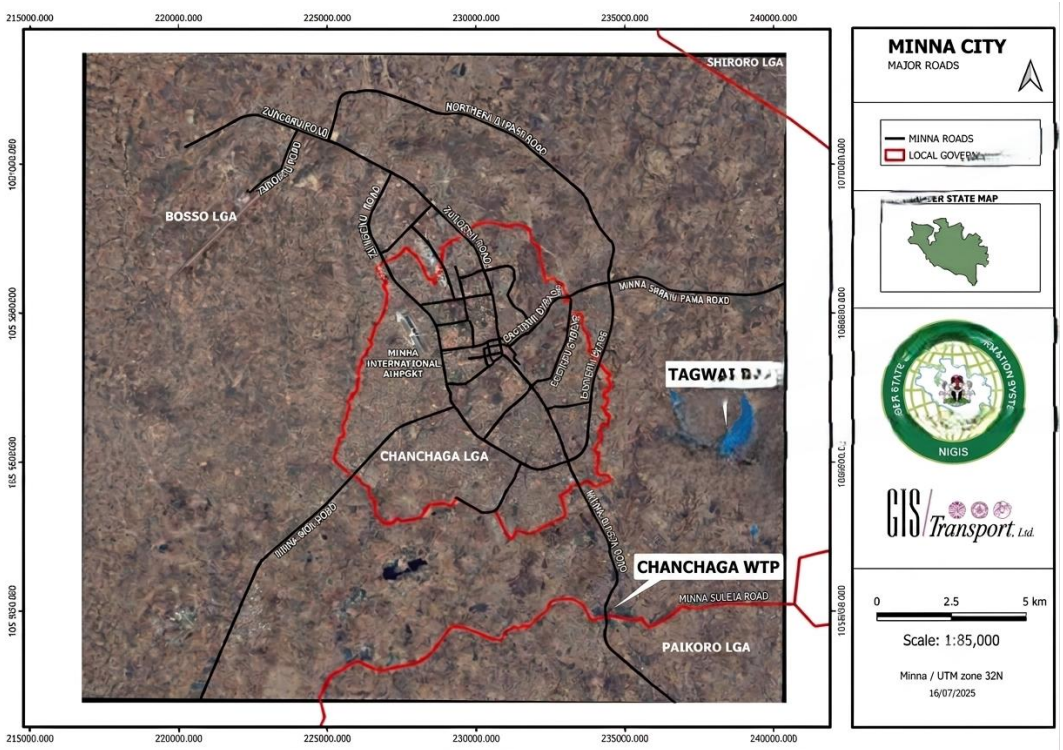

Figure 1: Minna Municipal area

Figure 1 situates the study area within Niger State and delineates the Minna municipal boundary referenced throughout this study.

NISWASEC owns and operates the municipal system. Treated water passes through an integrated network of four treatment plants, nine major service reservoirs, three booster pumping stations, transmission mains, and an extensive reticulation network. Production depends mainly on the Impresit, Biwater, Bosso, and Paiko treatment plants. Service reservoirs and booster stations at key points regulate hydraulic pressure.

For administrative purposes, NISWASEC organizes the Minna municipal system into five districts (A–E), which reflect billing zones and staff deployment rather than the hydraulic layout of the distribution network. For this study, the entire Minna Municipal water supply network was deliberately partitioned into seven operational service clusters, Bosso, Chanchaga, Minna Central, Minna East, Minna West, Tudun Wada North, and Tudun Wada South. The clusters are mutually exclusive and collectively exhaustive operational areas, delineated from reservoir and pumping command areas, pipeline continuity, and reticulation boundaries. These boundaries provide the level of detail at which pipeline age, material, failure history, and maintenance needs vary, rather than following administrative convenience. They therefore constitute the study-design zoning of the full municipal network, not a random or convenience sample of clusters. Each cluster represents a distinct operational setting with its own infrastructure age, material profile, service-coverage pattern, failure history, and maintenance demand. Accordingly, n = 7 in the cluster-level tables and correlations denotes the seven predefined operational areas that together cover the full study network; it is the number of area-level units of analysis, not a sample size for estimating an unobserved population of clusters.

2.2 Research Design

The study followed a quantitative engineering assessment framework. It combined infrastructure inventory, field verification, spatial analysis, and multi-criteria performance evaluation to quantify network physical condition using operational records the utility already keeps, checked against direct field observations, consistent with multi-indicator approaches to pipe condition assessment (Taiwo et al., 2023).

The assessment proceeded in five stages:

1. Compilation and verification of infrastructure inventory and operational records.
2. Field inspection and GPS verification of critical water supply assets.
3. Development of engineering performance indicators describing infrastructure condition.
4. Integration of the indicators into a composite Physical Integrity Index (PII).
5. Spatial analysis and prioritization of rehabilitation zones using GIS.

2.3 Data Sources

Secondary and primary data were both used, so that the assessment did not rely solely on utility records.

Secondary data came from NISWASEC and included pipeline inventory records, treatment plant operational records, reservoir inventories, distribution network layout maps, historical pipeline failure records (2021–2025), leakage reports, maintenance logs, service coverage records, and operational pumping schedules.

Primary data were gathered to check existing records against current conditions. Field investigations included GPS surveys of major infrastructure assets, visual inspection of pumping stations, reservoirs, pipelines, and booster stations, standardized Field-Level Observation (FLO) surveys, structured Key Informant Interviews (KII) with engineers, operators, and maintenance personnel, and documentation of observed defects.

Twenty-five priority locations were selected based on historical failure frequency, leakage occurrence, operational significance, and accessibility. These locations represented the most critical infrastructure components across the seven service clusters. Because accessibility was one of the four selection criteria, sites that were more difficult to reach may be under-represented in this priority-location field-verification set relative to their true condition; this is a limitation of the field-sampling protocol only. It does not mean that the seven operational clusters were sampled: all seven clusters were included in the full-network cluster-level assessment.

2.4 Development of Engineering Performance Indicators

Four indicators were developed to quantify infrastructure condition, reflecting evidence that combining several engineering indicators gives a more realistic picture of buried pipe condition than any single measure can (Taiwo et al., 2023). Each captures a distinct aspect of physical performance.

Pipe Age Index (PAI) measures infrastructure ageing by comparing current operational age against expected design life:

$$PAI = \frac{Y_c - Y_i}{Y_d} \tag{1}$$

where Y_c = current year, Y_i = year of installation, and Y_d = design service life. Higher values indicate more advanced ageing.

Failure Frequency Index (FFI) measures structural reliability from the reported pipeline-failure occurrence total:

$$FFI = \frac{N_f}{L_p} \tag{2}$$

where N f = cumulative reported pipeline-failure occurrence total and L p = pipeline length (km). Higher values signal greater structural deterioration.

Leakage Density Index (LDI) quantifies the concentration of leakage events within each service cluster:

$$LDI = \frac{N_l}{L_n} \tag{3}$$

where N_l = number of leakage events and L_n = network length (km).

Coverage Efficiency Index (CEI) evaluates service delivery effectiveness:

$$CEI = 5\left(1 - \frac{P_s}{P_t}\right) \tag{4}$$

where P_s = population served and P_t = total population within the service area. The transformed CEI is scaled from 0 to 5, such that lower service coverage yields a higher score and therefore indicates poorer coverage efficiency.

2.5 Development of the Physical Integrity Index (PII)

The four indicators were combined into a composite PII through weighted linear combination, following established multi-criteria approaches to water distribution network rehabilitation planning (Hassoun Nedjar et al., 2023), after normalizing each to a common five-point condition scale:

$$PII = 0.2(PAI) + 0.3(LDI) + 0.4(FFI) + 0.1(CEI) \tag{5}$$

Raw service coverage was transformed before aggregation as CEI = 5 × (1 − P_s/P_t), so that all four PII components follow the same condition direction: a higher score denotes poorer physical integrity. The legacy, non-inverted CEI and PII values are retained alongside the corrected values in Table 3 solely for transparency.

The adopted coefficients were specified as a research-team engineering-judgement baseline, informed generally by NISWASEC's operational context and observed network characteristics. The intended priority order was Failure Frequency Index (FFI, 0.40) > Leakage Density Index (LDI, 0.30) > Pipe Age Index (PAI, 0.20) > Coverage Efficiency Index (CEI, 0.10). This ordering treats observed failure frequency and leakage concentration as the most direct operational manifestations of deterioration, with pipe age as a contributing condition and service coverage as a contextual component. However, the study records do not contain a contemporaneous protocol explaining how the exact decimal values were selected. In particular, no documented weighting interviews, workshop or consensus procedure, Delphi exercise, pairwise-comparison matrix, iterative-refinement record, or statistical calibration was used to derive these coefficients. They should therefore be interpreted as transparent adopted engineering weights, not as empirically estimated or formally elicited parameters. The equal-weighting sensitivity analysis tests the robustness of the resulting cluster ranking to a material alternative weighting scheme; it does not establish that the adopted coefficients are optimal.

Table 1: A: Adopted Equation 5 weighting configuration and disclosure

PII component	Adopted weight	Role in the adopted engineering-judgement hierarchy
Failure Frequency Index (FFI)	0.40	Highest priority: recorded failure burden.
Leakage Density Index (LDI)	0.30	Second priority: concentration of recorded leakage.
Pipe Age Index (PAI)	0.20	Contributing age-related condition.
Coverage Efficiency Index (CEI)	0.10	Contextual service-coverage component.

Note: *The hierarchy records the adopted study design*

Conceptual Basis for the Priority Ordering

While the exact decimal weights were not formally elicited, the qualitative priority ordering (FFI > LDI > PAI > CEI) is consistent with established infrastructure asset management literature, which associates each indicator with a distinct pathway to network deterioration and, where structural breaches occur, contaminant entry (Renwick et al., 2019). Table 1B summarizes this conceptual grounding, which supports the direction and relative emphasis of the adopted weights without substituting for a documented elicitation procedure.

Table 1: B: Conceptual Rationale for the Adopted Priority Ordering

Indicator	Description	Adopted weight	Conceptual rationale
FFI	Failure Frequency Index	0.40	Recognized as a strong indicator of infrastructure deterioration and future failure risk (Folkman, 2018)
LDI	Leakage Density Index	0.30	Associated with structural defects and potential contaminant entry pathways (Kirmeyer et al., 2001)
PAI	Pipe Age Index	0.20	Reflects long-term asset deterioration (Rajani & Kleiner, 2001)
CEI	Coverage Efficiency Index	0.10	Indicates service adequacy and network resilience (AWWA, 2019)
Total		**100%**	

***Note**: This table provides literature-based conceptual support for the adopted priority ordering*

To translate PAI, LDI, and FFI from continuous engineering measures into the common five-point condition scale used in Equation 5, a semi-quantitative scoring rubric consistent with infrastructure asset management practice (Rajani & Kleiner, 2001; Folkman, 2018; AWWA, 2019) was applied at cluster level (Table 1C). CEI is not included in this rubric because it is already computed directly on a continuous 0–5 scale from the coverage ratio (Eq. 4) and requires no qualitative anchoring.

Table 1: C: Standardized Scoring Framework for PAI, LDI, and FFI

Score	PAI (Pipe Age Condition)	LDI (Leakage Density)	FFI (Failure Frequency)
5	Very Old (>80% design life)	Very High Leakage	Very High Failure Frequency
4	Old (60–80%)	High Leakage	High Failure Frequency
3	Moderate Age (40–60%)	Moderate Leakage	Moderate Failure Frequency
2	Relatively New (20–40%)	Low Leakage	Low Failure Frequency
1	New (<20%)	Very Low Leakage	Very Low Failure Frequency

Cluster-level PAI, LDI, and FFI scores were assigned using this rubric together with the infrastructure inventory, leakage records, and failure database, and were cross-checked against Field-Level Observation (FLO) and Key Informant Interview (KII) findings on relative deterioration across clusters. The resulting component scores by cluster are reported in Table 3.

The resulting PII values were classified into five condition categories as shown in Table 1.

Table 1: Physical Integrity Index Condition Classification

PII Range	Infrastructure Condition
< 2.0	High Integrity
2.0 to < 3.0	Moderate Integrity
3.0 to < 3.5	Low Integrity
3.5 to < 4.0	Very Low Integrity
≥ 4.0	Critical Integrity

2.6 Geographic Information System (GIS) Analysis

Spatial analysis was carried out in ArcGIS Pro. Infrastructure inventory, field observations, historical failures, and engineering performance indicators were integrated within a unified spatial database. Assets were georeferenced using GPS coordinates from field surveys, and existing utility maps were digitized and validated against field observations.

GIS analysis supported: (i) mapping of infrastructure assets; (ii) spatial distribution of pipeline failures; (iii) identification of deterioration hotspots; (iv) visualization of PII values; and (v) development of rehabilitation priority maps.

2.7 Sensitivity Analysis

Sensitivity analysis evaluated the robustness of the PII ranking under a reproducible alternative weighting assumption. The adopted engineering-judgement configuration was compared with equal weighting (0.25 for each component). The previously described structural-emphasis scenario is not

retained because its exact weight vector was not documented and could not be independently reproduced.

2.8 Statistical Analysis

Descriptive statistics summarized infrastructure characteristics, failure frequencies, leakage occurrence, and coverage across the seven predefined operational areas. Pearson's and Spearman's coefficients were used to describe associations among these complete network zones, including relationships between PII, coverage, reported failure-occurrence totals, and repair cost. In these analyses, n = 7 refers to the seven operational clusters that partition the whole Minna Municipal network, not to a probabilistic sample of clusters. The p-values are retained as standardized indicators of the strength and stability of cross-area relationships, but they should not be interpreted as supporting population-level generalization beyond the Minna system. The coefficient of variation was also computed to measure variation in infrastructure condition across the full network zoning.

2.9 Assessment of PII Consistency and Criterion Validity

Robustness and validity were assessed through three complementary checks that are kept analytically distinct. First, robustness to the weighting scheme was tested via sensitivity analysis. Second, because FFI is itself a constituent of the PII, its correlation with the reported pipeline-failure occurrence total was treated as an internal-consistency check rather than independent validation: a strong relationship is expected by construction and confirms the index behaves coherently, but it cannot substitute for external evidence. Third, criterion validity was assessed against a variable constructed independently of the PII: cluster-level repair-cost records obtained directly from NISWASEC maintenance ledgers (2021–2025). This repair-cost comparison constitutes the study's principal external validation evidence. District-metered Non-Revenue Water (NRW) data remained unavailable; NRW was instead modelled as a linear function of PII, calibrated to realistic bounds for sub-Saharan utilities (Shushu et al., 2021). Because the NRW estimate is derived computationally from PII, it is reported only as contextual model output and is not correlated with PII or treated as validation evidence. Pearson's correlation coefficient assessed the strength of the reported repair-cost and internal-consistency relationships.

3. RESULTS AND DISCUSSION

The infrastructure inventory shows that the Minna network grew through successive, largely uncoordinated expansion phases rather than a single planned programme. The result is a mix of assets with different ages, capacities, materials, and operating conditions.

Field verification identified four water treatment plants, nine major service reservoirs, three booster pumping stations, and an extensive transmission and distribution network supplying the seven operational clusters. However, installed capacity did not equal available capacity. The Impresit plant ran close to its design capacity throughout the study period. Biwater and Bosso both produced below design capacity due to non-operational pumping units. Paiko, though physically complete, was not yet operational and contributed nothing to municipal production.

Nearly a quarter of sampled pipeline segments had no material recorded in utility records. uPVC and Ductile Iron together account for the majority of identified material, with small proportions of Asbestos Cement and Galvanized Iron still in service (Figure 2).

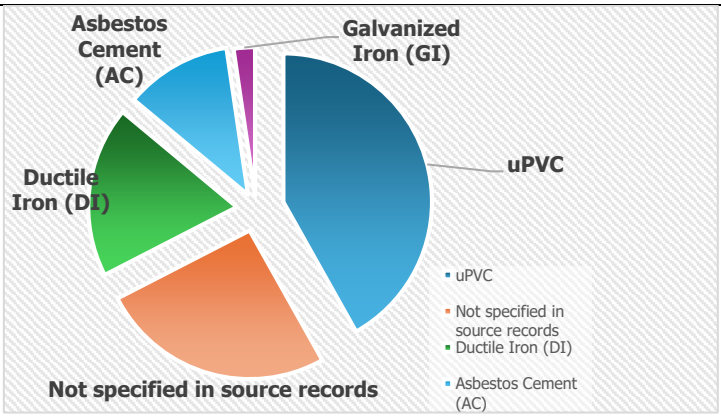

Figure 2: Material composition of 43 field-verified segments.

Figures 2 and 3 summarize a 43-segment field-verification subset. The original segment-level material and diameter inventory used to construct these descriptive charts was not supplied in NetworkData.xlsx. Accordingly, the displayed percentages are not independently auditable from the supplied calculation package and are not used in the PII calculation, correlation analysis, or validation. They should be read only as descriptive field records, not as a statistically representative network-wide material or diameter inventory. A complete segment-level inventory is required before making network-wide material-composition or diameter-distribution estimates.

Distribution system reliability depends not only on the condition of buried pipelines but also on whether upstream production and pumping facilities are running. Reduced pumping capacity limits hydraulic flexibility, creates pressure variability, and makes it harder to redirect flow during maintenance or emergencies.

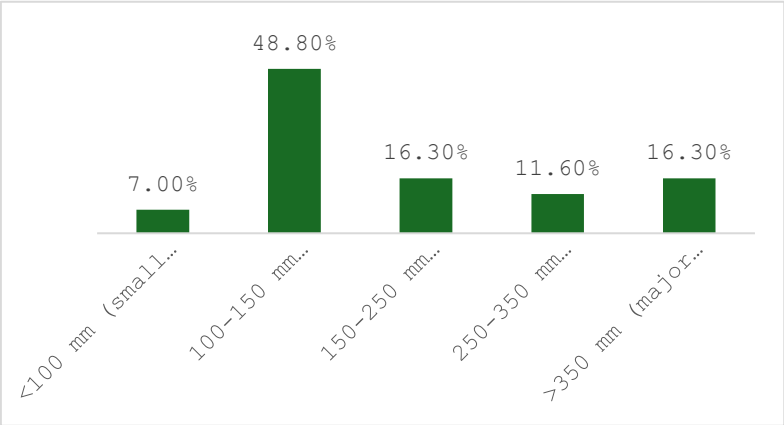

Figure 3: Diameter distribution of 43 field-verified segments.

Within the unverified 43-segment field subset shown in Figure 3, 48.8% of pipes fall within the 100–150 mm distribution range, with 16.3% in both the 150–250 mm sub-trunk and >350 mm major trunk categories, and 11.6% in the 250–350 mm trunk category. Only 7.0% are small distribution pipes (<100 mm). Because the original segment-level diameter inventory was not supplied in NetworkData.xlsx, these are descriptive field-subset proportions only and are not interpreted as network-wide estimates.

3.1 Spatial Characteristics of the Distribution Network

GIS analysis revealed marked spatial variability in infrastructure configuration across the seven clusters. Older sections of the network, particularly Minna West, Minna East, and parts of Chanchaga, showed dense pipeline layouts, numerous service connections, and a long history of repeated maintenance work. Bosso and parts of Tudun Wada South showed lower maintenance intensity and fewer recorded structural defects.

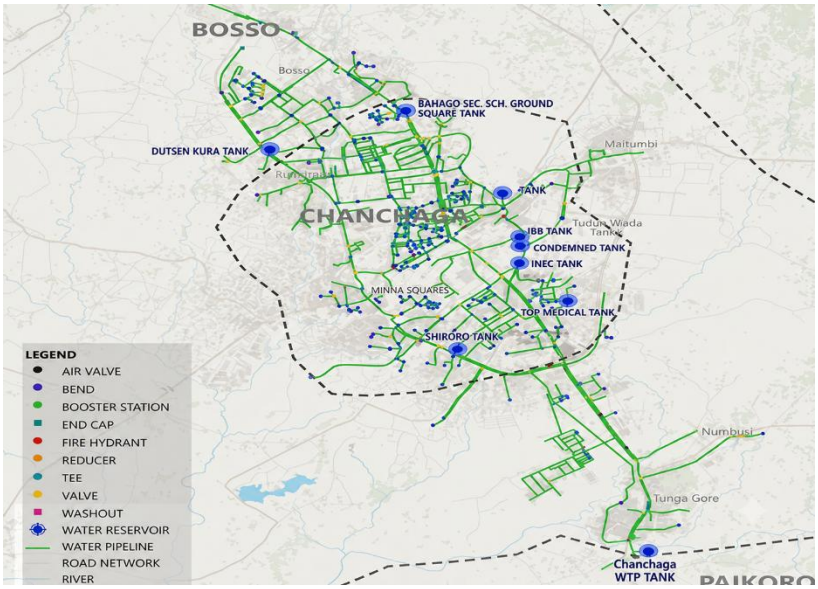

Figure 4: Distribution system network with key water infrastructures and pipeline stretch.

Figure 4 overlays that boundary with the principal components of the distribution system, the four treatment plants, the service reservoirs and booster stations that regulate hydraulic pressure, and the transmission and reticulation mains connecting them, giving a single spatial reference for the infrastructure inventoried in Section 2.3. The reservoir and booster-station command areas visible in Figure 4 correspond to the operational basis used to delineate the seven service clusters described below: each cluster boundary follows the reticulation network actually served by a given reservoir or pumping zone, rather than an administrative line. Figure 4 therefore functions as the spatial basis for the cluster-level condition assessment reported in Section 3, rather than as a standalone locational reference.

3.2 Distribution of Reported Pipeline-Failure Occurrence Totals

The supplied maintenance workbook reports a cumulative pipeline-failure occurrence total of 6,526.24 for 2021–2025. The occurrence field contains fractional values, so these data are treated as reported operational occurrence totals rather than literal integer counts of discrete break events. They remain unevenly distributed across clusters and provide the failure-frequency input to the PII.

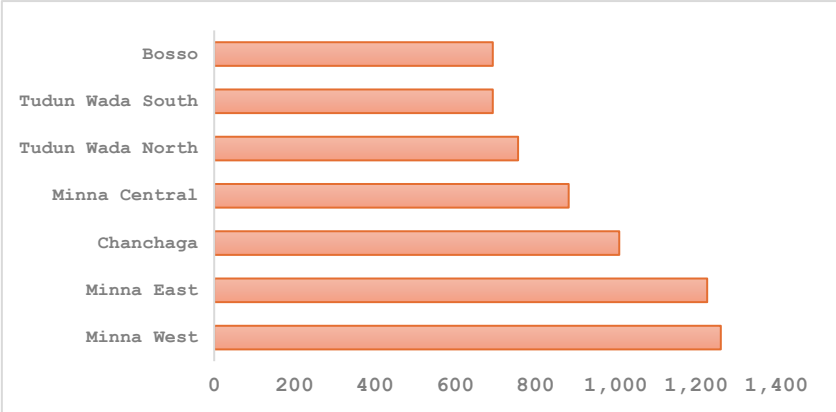

Figure 5: Distribution of reported pipeline-failure occurrence totals by service cluster (2021–2025; bars rounded for display).

Minna West reported the highest occurrence total (1,261.60; 19.3%), followed by Minna East (1,227.52; 18.8%) and Chanchaga (1,009.28; 15.5%). Together, these three clusters accounted for approximately 53.6% of the workbook-reported occurrence total. Bosso and Tudun Wada South reported the lowest totals (693.88 each; 10.6%).

Table 2: Distribution of Reported Pipeline-Failure Occurrence by Service Cluster (2021–2025)

Service Cluster	Reported occurrence total (2021–2025)	% of Total
Minna West	1,261.60	19.3
Minna East	1,227.52	18.8
Chanchaga	1,009.28	15.5
Minna Central	883.12	13.5
Tudun Wada North	756.96	11.6
Tudun Wada South	693.88	10.6
Bosso	693.88	10.6
Total	**6,526.24**	**100**

The concentration of failures in the western and eastern sectors aligns with their higher levels of urban development, denser connections, and longer operating histories. Frequent road excavation, growing traffic loads, repeated pipe repairs, and sustained hydraulic loading have likely accelerated structural decline in these areas.

3.3 Physical Integrity Assessment

The Physical Integrity Index differentiated infrastructure condition clearly across the seven clusters (Figure 6 and Figure 7).

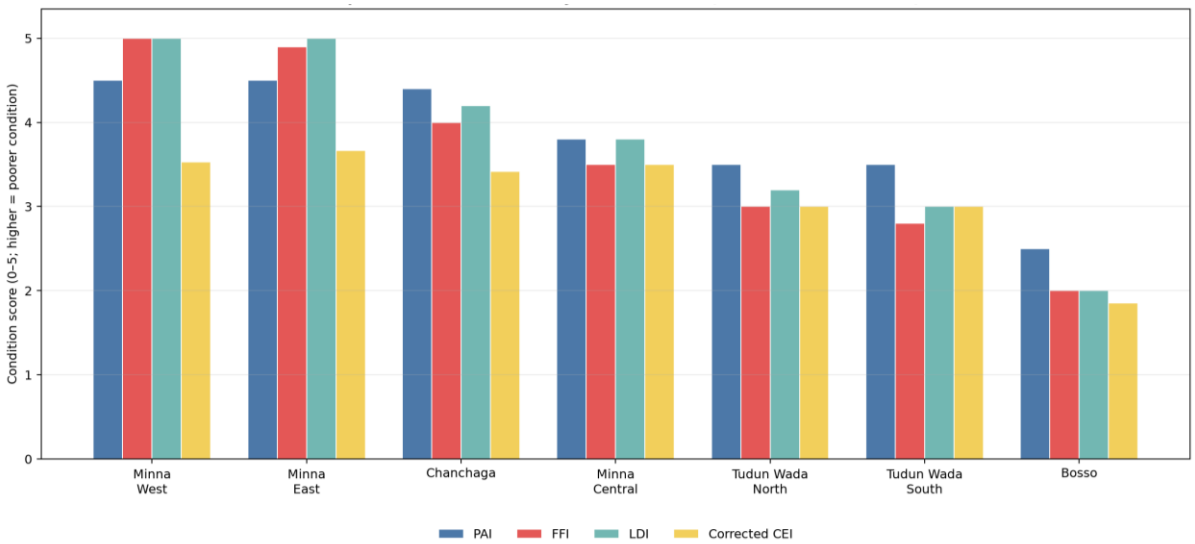

Figure 6: Corrected component indicator scores by service cluster (CEI direction corrected).

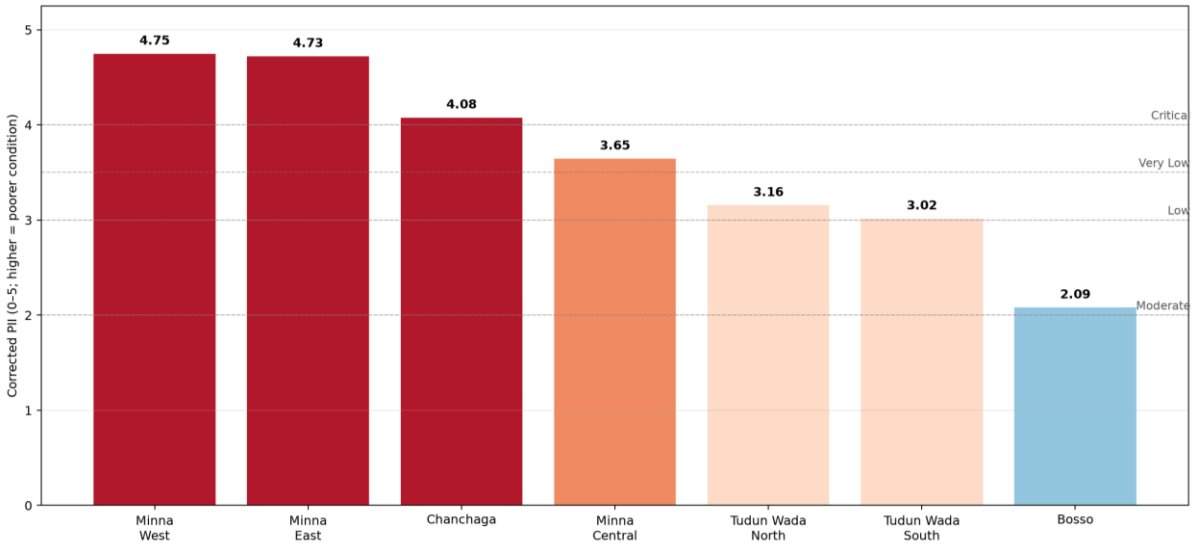

Figure 7: Corrected Composite Physical Integrity Index (PII) by service cluster.

Minna West and Minna East exhibit maximum or near-maximum scores for FFI (5.0 and 4.9) and LDI (5.0 and 5.0), reflecting extreme failure frequencies and leakage densities. PAI scores are also elevated (4.5) across the critical clusters. Bosso shows favourable (low) scores across PAI (2.5), FFI (2.0), and LDI (2.0). Its high raw service-coverage ratio (63.0%) is now correctly transformed into the lowest CEI subscore (1.9) of the seven clusters. Because CEI enters the PII on the same higher-is-worse scale as the other components, the corrected transformation strengthens the conceptual coherence of the composite index. Bosso remains the cluster with the best overall physical integrity, although its Moderate Integrity classification confirms that preventive maintenance and routine monitoring remain necessary.

With CEI direction corrected, Minna West (4.75), Minna East (4.73), and Chanchaga (4.08) fall within the Critical Integrity band (≥4.0). Minna Central (3.65) is Very Low Integrity. Tudun Wada North (3.16) and Tudun Wada South (3.02) exhibit Low Integrity, while Bosso (2.09) remains Moderate Integrity. No cluster achieved High Integrity (<2.0). The corrected PII values have a mean of 3.64, a sample standard deviation of 0.97, and a coefficient of variation of 26.7%, confirming substantial heterogeneity in infrastructure condition rather than uniform network-wide deterioration.

Table 3: Legacy and CEI-direction-corrected Physical Integrity Index results by service cluster

Service cluster	PAI	FFI	LDI	CEI	PII	Condition
Minna West	4.5	5.0	5.0	3.5	4.75	Critical
Minna East	4.5	4.9	5.0	3.7	4.73	Critical
Chanchaga	4.4	4.0	4.2	3.4	4.08	Critical
Minna Central	3.8	3.5	3.8	3.5	3.65	Very Low
Tudun Wada North	3.5	3.0	3.2	3.0	3.16	Low
Tudun Wada South	3.5	2.8	3.0	3.0	3.02	Low
Bosso	2.5	2.0	2.0	1.9	2.09	Moderate

The deterioration in Minna West and Minna East stems from the combined effects of long service life, frequent structural failures, and persistent leakage. Repeated excavation and replacement of failed sections may also have weakened neighbouring pipe segments, making subsequent failure more likely.

Bosso's relatively favourable condition does not mean rehabilitation can be ignored there. Rather, the lower PII values suggest that preventive maintenance and routine monitoring should be sufficient to maintain performance, avoiding the more extensive intervention required elsewhere.

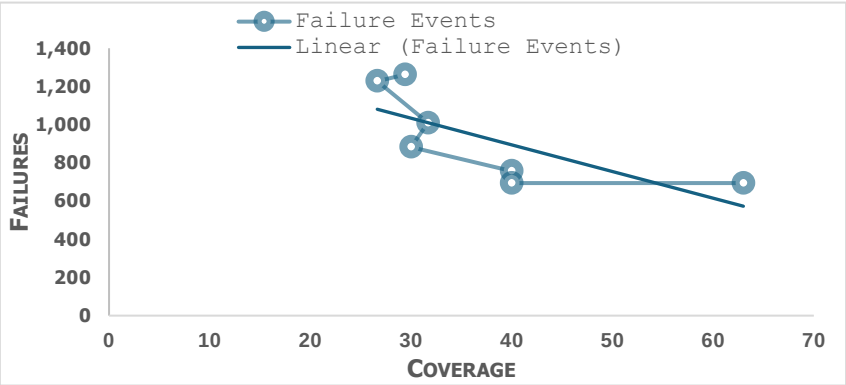

Figure 8: Relationship between service coverage and pipeline failures (bubble size proportional to residential buildings served).

Clusters with lower raw service coverage (Minna West and Minna East) experience substantially higher failure counts. Bosso, with the highest raw coverage (63.0%), records among the fewest failures. Pearson's correlation between raw service coverage and total failures approached but did not reach conventional significance ($r = -0.723$, $p = 0.066$, $n = 7$); Spearman's rank correlation was significant ($\rho = -0.900$, $p = 0.006$). PII was strongly and inversely associated with raw service coverage (Pearson $r = -0.906$, $p = 0.005$, $n = 7$; Spearman $\rho = -0.919$, $p = 0.003$).

3.4 Spatial Distribution of Rehabilitation Priorities

GIS mapping identified distinct pockets of deterioration at finer spatial resolution than the seven service clusters. Because sub-zone-level coverage (CEI) data were not available, this finer-grained analysis uses a Sub-Zonal Physical Deterioration Score (SPDS), computed from PAI, FFI, and LDI only. The reproducible score is $SPDS = (0.20 \times PAI + 0.40 \times FFI + 0.30 \times LDI) / 0.90$, which renormalizes the adopted PAI, FFI, and LDI weights to sum to 1. It is therefore not directly numerically comparable to the four-indicator, cluster-level PII reported elsewhere. The raw field inputs and sub-zone normalization worksheets, so the SPDS is retained as a field-derived screening score. High-risk zones clustered in Tungan Goro, Sauke Kahuta, M. I. Wushishi, and Tunga Market, where the reported screening scores coincide with recurring failures, visible leakage, and ageing infrastructure.

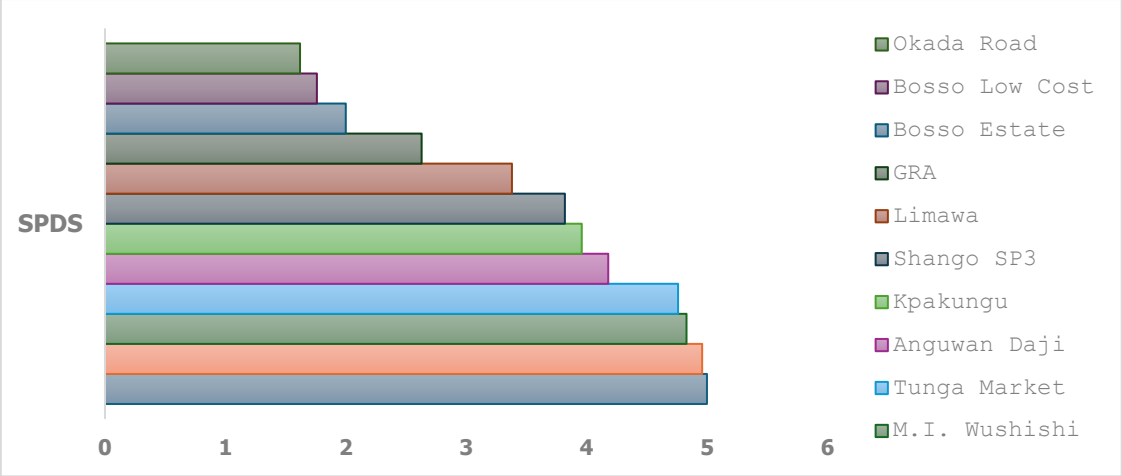

Figure 9: Sub-Zonal Physical Deterioration Score (SPDS) within high-priority rehabilitation clusters.

Table 4: *Sub-Zonal Physical Deterioration Score (SPDS)*

Sub-Zone	PAI	FFI	LDI	SPDS	Condition
Tungan Goro	5.0	5.0	5.0	5.00	Critical
Sauke Kahuta	5.0	4.9	5.0	4.96	Critical
M.I. Wushishi	4.8	4.8	4.9	4.83	Critical
Tunga Market	4.8	4.7	4.8	4.76	Critical
Anguwan Daji	4.3	4.1	4.2	4.18	Critical
Kpakungu	4.0	3.9	4.0	3.96	Very Low
Shango SP3	3.9	3.8	3.8	3.82	Very Low
Limawa	3.5	3.3	3.4	3.38	Low
GRA	2.8	2.5	2.7	2.63	Moderate
Bosso Estate	2.0	2.0	2.0	2.00	Moderate
Bosso Low Cost	1.8	1.7	1.8	1.76	High
Okada Road	1.7	1.6	1.6	1.62	High

Note: SPDS = (0.20(PAI) + 0.40(FFI) + 0.30(LDI) / 0.90. This renormalizes the adopted PAI, FFI, and LDI weights because sub-zone-level coverage data were unavailable. The raw sub-zone inputs and normalization worksheets were not available; SPDS values are therefore field-derived screening results and are not directly comparable to the four-indicator cluster-level PII.

This spatial concentration has direct implications for rehabilitation planning. Instead of spreading investment evenly across the network, NISWASEC can concentrate resources in these hotspots, where renewal is likely to yield the greatest improvements in reliability and operational efficiency.

3.5 Sensitivity Analysis

Sensitivity analysis of the CEI, PII compared the adopted weighting scheme with equal weighting. Absolute scores shifted slightly, but the relative priority order remained stable: Minna West and Minna East remained the top-priority rehabilitation zones, and Bosso remained the cluster with the best infrastructure integrity (Figure 10).

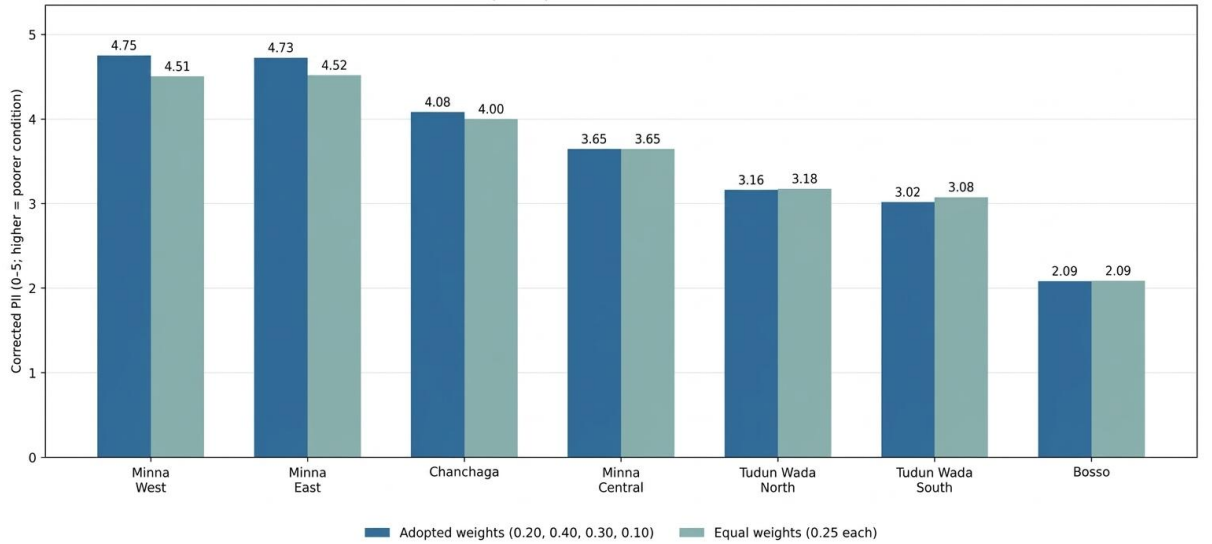

Figure 10: Sensitivity analysis of CEI direction correction: PII scores under adopted and equal weighting scenarios.

The adopted scheme (PAI: 0.20, FFI: 0.40, LDI: 0.30, CEI: 0.10) was compared with equal weighting (0.25 each). Cluster rankings remained strongly aligned (Spearman's $\rho = 0.964$, $p < 0.001$, $n = 7$). The result reflected a near-identical weighting pattern, the particular seven-cluster score distribution; no causal explanation is therefore inferred. The sensitivity analysis reports only the two fully reproducible scenarios.

The stable ordering under these two reproducible weighting schemes indicates that rehabilitation priorities are driven mainly by observed infrastructure condition rather than by the adopted weighting choice. This supports the use of the corrected PII for engineering prioritisation while preserving a transparent limit on the sensitivity evidence.

3.6 Empirical Assessment of PII Consistency and Criterion Validity

To assess whether the PII behaves coherently and agrees with independent evidence, computed values were compared against two operational indicators: total recorded pipeline failures and recorded repair expenditure. These two comparisons are not equivalent in evidentiary strength and are interpreted separately below. District-metered non-revenue water data were unavailable; the separately modelled NRW estimate is reported as contextual information only and is not used in correlation-based validation.

Clusters with higher PII values consistently reported higher pipeline-failure occurrence totals. Pearson's correlation analysis found a strong positive linear relationship between PII and the reported occurrence total ($r = 0.944$, $p = 0.001$, $n = 7$), and equivalently with the cluster's share of the network-wide occurrence total ($r = 0.944$, $p = 0.001$, $n = 7$). Because FFI is itself one of the four indicators combined into the PII, this relationship is expected by construction and is interpreted as an internal-consistency check rather than independent validation. Spearman's rank correlation corroborated the monotonic ordering ($\rho = 0.991$, $p < 0.001$, $n = 7$).

The correlation between PII and the Coverage Efficiency Index (CEI) score was positive ($r = 0.906$, $p = 0.005$, $n = 7$), as expected after all components were aligned to a higher-is-worse condition scale. This CEI-score relationship is distinct from the inverse corrected-PII–raw-service-coverage relationship reported in Section 3.3 ($r = -0.906$, $p = 0.005$, $n = 7$). Because CEI is a component of PII, neither relationship constitutes independent validation.

Cluster-level repair-cost records for 2021–2025 were obtained directly from NISWASEC maintenance ledgers. The supplied workbook records five-year cumulative repair-cost totals; these are expressed in ₦ million in Figure 11 and Table 5. Because repair expenditure was not used to construct the PII, its correlation with corrected PII constitutes the study's principal external criterion validation. District-metered non-revenue water data remained unavailable; the separately modelled NRW estimate is contextual only and is not used as validation evidence.

Pearson's correlation analysis found a strong positive relationship between PII and the recorded 2021–2025 cumulative repair-cost total:

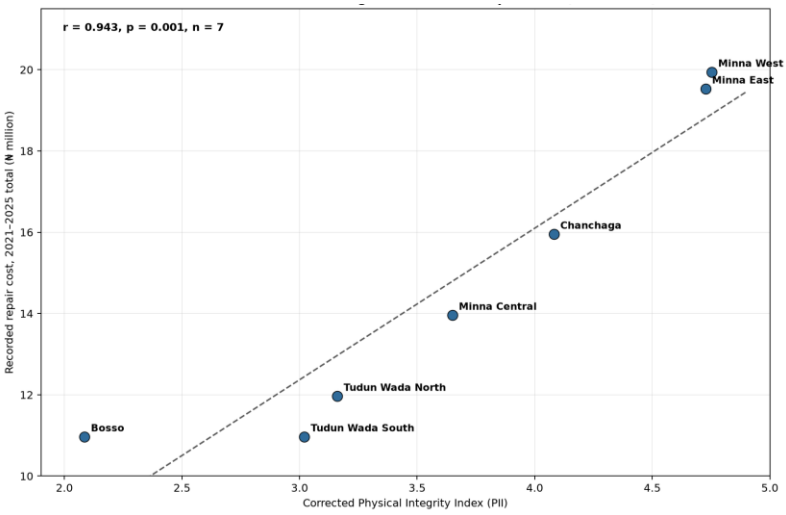

Figure 11: Independent criterion validation of corrected PII against recorded cumulative repair cost (2021–2025).

Cluster-level repair-cost totals were extracted from NISWASEC maintenance ledgers; Pearson r = 0.943, p = 0.001, n = 7.

Table 5: Independent criterion validation of corrected PII against recorded cumulative repair cost

Comparison	r	p	n
PII vs recorded repair cost (2021–2025 total)	0.943	0.001	7

Note: n = 7 denotes the seven predefined operational service clusters that together constitute the full Minna Municipal water supply network; it does not denote a sample of clusters.

The internal consistency checks confirm that the PII behaves coherently with its own constituent data, while the repair-cost comparison provides the study's strongest evidence that the index reflects real operational consequences beyond its own construction.

3.7 Comparison with Previous Studies

The deterioration patterns in Minna fit the broader picture: ageing infrastructure, recurrent leakage, and rising operational demand together erode the reliability of urban water distribution networks (Auma et al., 2023; Taiwo et al., 2023). What this study contributes is a quantitative method for assessing that condition using routinely available operational data within a GIS-supported framework.

Positioning the PII requires distinguishing five related but methodologically distinct strands of water-distribution-network research: pipe-failure prediction, hydraulic modelling, rehabilitation prioritization, condition assessment, and composite indices.

Pipe-failure prediction. This strand models the probability that an individual pipe will fail from its own attributes and break history. Logistic regression and support vector classification have been used to predict individual pipe failures from asset attributes (Robles-Velasco et al., 2020), comparable logistic models have been fitted to failure records for Kampala's water network (Auma et al., 2023), and validated failure-prediction models have shown reasonable agreement with observed main breaks over multi-year monitoring (Kahn et al., 2020). These models perform well where detailed, pipe-level failure and attribute histories exist, but that data requirement is precisely what NISWASEC and most Nigerian utilities lack.

Hydraulic modelling. This strand simulates how water moves through a network, pressure, flow, and contaminant transport, under defined operating conditions using calibrated software such as EPANET (Piazza et al., 2022). It describes network behaviour at a point in time rather than the physical deterioration of the pipes carrying that water, and it depends on calibrated demand and roughness data that ageing, incompletely documented systems like Minna's rarely have.

Rehabilitation prioritization. This strand sits downstream of the first two: it takes condition or risk information as an input and ranks competing rehabilitation projects against it, commonly through structured multi-criteria methods such as the analytical hierarchy process (Hassoun Nedjar et al., 2023).

Its output is a decision, and its reliability depends entirely on the quality of the condition data supplied to it.

Condition assessment. This strand addresses that upstream question directly, asking what state a pipe or network segment is actually in. Grigg's (2006) review of utility condition-assessment practice found that a composite condition index consolidating multiple factors was the ideal but was rarely achieved, held back by inconsistent recording of leaks, breaks, and condition indicators, an observation that describes NISWASEC's records closely. More recent work confirms that combining several engineering indicators gives a more realistic picture of buried-pipe condition than any single measure can (Taiwo et al., 2023).

Composite indices. A smaller literature has begun to close that gap by aggregating multiple indicators into a single score. Beker and Kansal (2022), for example, used fuzzy-logic aggregation of reliability, resilience, and vulnerability indices derived from hydraulic simulation output to build one performance index for decision-making. That approach still depends on a calibrated hydraulic model as its data source, a resource that, like pipe-level failure histories, is largely unavailable in Minna's context.

More than half of the reported pipeline-failure occurrence total were concentrated in Minna West, Minna East, and Chanchaga. This confirms that deterioration is spatially uneven. The risk-based hotspot analysis extends conventional network-wide assessments by identifying rehabilitation priorities at both cluster and sub-zonal levels.

Positioned against these five traditions, what is novel about applying the PII to Minna is not any single indicator but the combination of choices behind it. First, it builds a composite condition index, in the tradition of Grigg (2006) and Beker and Kansal (2022), but computes it entirely from routine utility records and targeted field verification rather than from a calibrated hydraulic model, pipe-level statistical failure histories, or an expert-elicitation panel. Second, it embeds that index in a GIS framework built around actual reservoir and pumping command areas rather than administrative billing zones, so the same index that scores condition also locates it precisely enough to guide rehabilitation spending. Third, it validates the resulting scores empirically against Minna's own repair-cost and failure records (2021–2025) and compares the adopted scheme with an equal-weighting sensitivity scenario, a combination of empirical validation and weighting-sensitivity analysis that the pipe-failure-prediction, hydraulic-modelling, and AHP-based rehabilitation literature reviewed above do not report together. Finally, to the authors' knowledge, few if any prior studies have applied a composite, low-data physical integrity framework of this kind to a Nigerian municipal water distribution network, giving NISWASEC and similarly resourced utilities elsewhere in the country a route to risk-informed rehabilitation planning that does not presuppose the statistical modelling capacity, hydraulic calibration data, or expert-panel access that much of the existing literature assumes.

3.8 Engineering Significance and Practical Implications

The practical value of this research extends beyond flagging deteriorated infrastructure. The PII gives engineers a structured basis for shifting maintenance strategy from reactive intervention toward condition-based asset management.

The study also demonstrates the value of integrating GIS into routine utility operations. Beyond visualizing infrastructure condition, GIS provides a spatial platform for logging maintenance activity, keeping asset inventories current, and tracking rehabilitation outcomes over time.

Another practical strength is that the framework requires little extra data. It relies primarily on information utilities already generate during routine operations, failure records, leakage reports, infrastructure inventories, and service coverage statistics, supplemented by targeted field verification. Implementation does not require specialized inspection equipment or costly monitoring systems.

3.9 Decision Framework for Infrastructure Rehabilitation

The PII is intended to support structured engineering decisions. Based on computed values, rehabilitation priorities can be linked to specific management actions:

- **PII < 2.0 (High Integrity):** Continue routine inspection and preventive maintenance.
- **PII 2.0 to < 3.0 (Moderate Integrity):** Intensify monitoring and schedule localized rehabilitation where required.

- **PII 3.0 to < 3.5 (Low Integrity):** Implement targeted replacement of deteriorated pipeline sections and fittings.
- **PII 3.5 to < 4.0 (Very Low Integrity):** Prioritize phased rehabilitation within annual capital investment programmes.
- **PII ≥ 4.0 (Critical Integrity):** Undertake comprehensive engineering assessment and infrastructure renewal as a priority.

3.10 Data Availability Limitation: System-Wide Physical Water Loss

District-metered non-revenue water data and the source parameters required to calculate system-wide leakage distance were not available in the supplied calculation workbook. A district-metered water balance or formal water audit is required to quantify physical losses and to provide a valid basis for future NRW or leakage-distance analysis.

3.11 Limitations and Directions for Future Work

This study distinguishes internal-consistency checks, in which PII is compared with data used to construct it, from external criterion validation, in which PII is compared with an independently recorded operational variable. After CEI direction correction, the repair-cost comparison shown in Figure 11 uses cumulative 2021–2025 repair-cost totals recorded in NISWASEC maintenance ledgers ($r = 0.943$, $p = 0.001$, $n = 7$). Because these ledger records were not used to construct the PII, this comparison is the study's only independent criterion validation.

The Coverage Efficiency Index directionality flaw identified in the original analysis has been corrected. Raw service coverage is now inverted during normalization as $CEI = 5 \times (1 - P_s/P_t)$, so high coverage produces a low deterioration score and all PII components have the same directional interpretation. Table 3 reports the original, non-inverted values beside the corrected CEI and PII values to preserve a transparent audit trail.

The Equation 5 coefficients are a transparent engineering-judgement baseline rather than a formally elicited or statistically calibrated weight set. The adopted priority order (FFI > LDI > PAI > CEI) is stated in Section 2.5 and draws conceptual support from established asset-management literature (Table 1B), the study records do not document the process used to calibrate the matrix. The adopted-versus-equal weighting sensitivity analysis demonstrates ranking robustness but does not validate the numerical optimality of the adopted coefficients. Future applications should use and document a structured elicitation or calibration protocol, including participant roles, weight alternatives considered, the final decision rule, pairwise-comparison matrices and consistency ratios where AHP is used, and all sensitivity-scenario vectors.

Sample selection and data traceability warrant caution. The 43 pipeline segments assessed for material composition (Figures 2 and 3) and the 25 priority locations assessed at sub-zonal resolution (Section 3.4) were selected using risk-related criteria and practical accessibility rather than a formal stratified random-sampling protocol. The original segment-level material/diameter inventory and the raw sub-zone scoring worksheets were not included in the supplied audit workbook. Accordingly, the material/diameter distributions and SPDS results should be read as indicative field-derived screens, not statistically representative network-wide estimates; the SPDS is also not directly numerically equivalent to the four-indicator, cluster-level PII.

The cluster-level statistical analysis uses seven predefined operational areas ($n = 7$) that collectively cover the entire Minna Municipal water supply network. Thus, $n = 7$ is not a sample size in the sense of seven clusters drawn from a larger unobserved population; it is the complete set of area-level units created by the study's operational zoning design. Pearson and Spearman coefficients therefore describe cross-area patterns within the Minna system. Because only seven area-level units are available, individual clusters can still exert substantial influence on coefficient magnitudes and p-values; the reported p-values should consequently be interpreted as descriptive indicators of within-system association rather than as a basis for broad inferential generalization. Spearman's ρ, which is less sensitive to outliers and does not assume linearity, is reported alongside Pearson's r for this reason.

Finally, the framework is best understood as a condition and integrity assessment tool that supports risk-informed decision-making. It does not currently weight deteriorated infrastructure by the consequence of failure, such as the criticality of served facilities, population density, or road

importance. Extending the PII into a full Risk Priority Index by incorporating an explicit consequence term is a natural direction for future development of this framework.

4. CONCLUSIONS

This study developed a Physical Integrity Index (PII) combining pipe age, failure frequency, leakage density, and coverage efficiency to assess the Minna municipal water distribution network. The entire network was organized into seven predefined operational service clusters based on reservoir and pumping command areas and reticulation boundaries. These clusters are the complete study-design zoning of the municipal system rather than a sampled subset, and each captures a distinct operational setting. Drawing on utility operational records, field verification, and spatial analysis, the framework differentiates infrastructure condition across these seven full-network operational areas.

Physical deterioration proved spatially uneven. The reported 6,526 pipeline-failure occurrence units for 2021–2025, 53.6% concentrated in Minna West, Minna East, and Chanchaga. After CEI direction correction, Minna West (4.75), Minna East (4.73), and Chanchaga (4.08) were classified as Critical; Minna Central (3.65) as Very Low; Tudun Wada North (3.16) and Tudun Wada South (3.02) as Low; and Bosso (2.09) as Moderate. No cluster achieved High Integrity. The corrected PII coefficient of variation was 26.7%, confirming substantial condition heterogeneity.

The rankings remained stable under the adopted and equal-weighting scenarios. PII showed strong internal consistency with reported pipeline-failure occurrence totals ($r = 0.944$, $p = 0.001$, $n = 7$), which is expected because failure frequency is a constituent indicator. Its independent comparison with NISWASEC's recorded cumulative repair-cost totals was also strong ($r = 0.943$, $p = 0.001$, $n = 7$), providing the study's principal external criterion-validation evidence.

By combining existing utility records with targeted field verification and GIS, the framework offers a low-data-burden, transferable method for condition-based rehabilitation prioritisation in data-constrained utilities.

REFERENCES

Adeoti, O. S., Kandasamy, J., & Vigneswaran, S. (2023). Water infrastructure sustainability in Nigeria: A systematic review of challenges and sustainable solutions. *Water Policy*, *25*(11), 1094–1111. https://doi.org/10.2166/wp.2023.173

American Water Works Association. (2019). *AWWA utility benchmarking: Performance indicators for water and wastewater utilities*. Author.

Auma, R., Musaazi, I. G., Tumutungire, M. D., & Sempewo, J. I. (2023). Logistic pipe failure prediction models for an urban water distribution network in the developing world: A case study of Kampala water, Uganda. *Water Practice and Technology*, *18*(1), 264–273. https://doi.org/10.2166/wpt.2022.159

Beker, B. A., & Kansal, M. L. (2022). Fuzzy logic-based integrated performance evaluation of a water distribution network. *AQUA – Water Infrastructure, Ecosystems and Society*, *71*(3), 490–506. https://doi.org/10.2166/aqua.2022.004

Folkman, S. (2018). *Water main break rates in the USA and Canada: A comprehensive study*. Utah State University, Mechanical and Aerospace Engineering Faculty Publications, Paper 174. https://digitalcommons.usu.edu/mae_facpub/174

Grigg, N. S. (2006). Condition assessment of water distribution pipes. *Journal of Infrastructure Systems*, *12*(3), 147–153. https://doi.org/10.1061/(ASCE)1076-0342(2006)12:3(147)

Hassoun Nedjar, N., Djebbar, Y., & Djemili, L. (2023). Application of the analytical hierarchy process for planning the rehabilitation of water distribution networks. *Arab Gulf Journal of Scientific Research*, *41*(4), 518–538. https://doi.org/10.1108/AGJSR-07-2022-0110

Kahn, C., Damiani, A., & Ge, S. (2020). Validation of water main failure predictions: A 2-year case study. *AWWA Water Science*, *2*(3), e1179. https://doi.org/10.1002/aws2.1179

Kirmeyer, G. J., Friedman, M., Martel, K., Howie, D., LeChevallier, M., Abbaszadegan, M., Karim, M., Funk, J., & Harbour, J. (2001). *Pathogen intrusion into the distribution system*. AWWA Research Foundation and American Water Works Association.

Piazza, S., Sambito, M., & Freni, G. (2022). A novel EPANET integration for the diffusive–dispersive transport of contaminants. *Water*, *14*(17), 2707. https://doi.org/10.3390/w14172707

Renwick, D. V., Heinrich, A., Weisman, R., Arvanaghi, H., & Rotert, K. (2019). Potential public health impacts of deteriorating distribution system infrastructure. Journal - American Water Works Association, 111(2), 42–53. https://doi.org/10.1002/awwa.1235

Rajani, B. B., & Kleiner, Y. (2001). Comprehensive review of structural deterioration of water mains: Physically based models. *Urban Water*, *3*(3), 151–164. https://doi.org/10.1016/S1462-0758(01)00032-2

Robles-Velasco, A., Cortés, P., Muñuzuri, J., & Onieva, L. (2020). Prediction of pipe failures in water supply networks using logistic regression and support vector classification. *Reliability Engineering & System Safety*, *196*, 106754. https://doi.org/10.1016/j.ress.2019.106754

Shushu, U. P., Komakech, H. C., Dodoo-Arhin, D., Ferras, D., & Kansal, M. L. (2021). Managing non-revenue water in Mwanza, Tanzania: A fast-growing sub-Saharan African city. *Scientific African*, *12*, e00830. https://doi.org/10.1016/j.sciaf.2021.e00830

Taiwo, R., Ben Seghier, M. E. A., & Zayed, T. (2023). Toward sustainable water infrastructure: The state-of-the-art for modeling the failure probability of water pipes. *Water Resources Research*, *59*, e2022WR033256. https://doi.org/10.1029/2022WR033256

International Conference on Engineering Innovation for Sustainable Development (ICESID 2026)
Faculty of Engineering, Ahmadu Bello University Zaria · 8–10 September 2026

INTEGRATED EXERGETIC–ECONOMIC ASSESSMENT OF THERMAL AND CATALYTIC PYROLYSIS OF HOUSEHOLD THERMOPLASTIC WASTE FOR SUSTAINABLE WASTE-TO-ENERGY APPLICATIONS

Zhidaya Jude[1,*], Eyitayo A. Afolabi[1], O. S. Azeez[1]
[1]*Federal University of Technology, Minna, Niger State*
Email: zhidayajude@gmail.com[*], elizamos2001@yahoo.com, tosin.azeez@futminna.edu.ng
***Corresponding author**: Zhidaya Jude
DOI: https://doi.org/10.67203/sp.ICESID.2026

ABSTRACT

The increasing generation of household thermoplastic waste presents environmental and resource-management challenges while providing an opportunity for energy recovery. This study presents an integrated exergetic–economic assessment of thermal and ZSM-5 catalytic pyrolysis of a modelled mixed household thermoplastic feedstock. Aspen Plus V14.0 was used to simulate a 1,000 kg h^{-1} process, with thermal pyrolysis at approximately 500 °C and catalytic pyrolysis at 350 °C. Mass and energy balances, exergy analysis, SPECO exergoeconomics, techno-economic evaluation and sensitivity analysis were applied. Thermal pyrolysis produced 65.2 wt% oil, 19.8 wt% gas and 15.0 wt% char, while catalytic pyrolysis produced 58.5 wt% oil, 29.0 wt% gas and 12.5 wt% char. Catalytic operation reduced process-energy input from 3,334.20 to 1,840.62 kW (44.8%) and increased exergetic efficiency from approximately 62% to 71%. The catalytic configuration also reduced CAPEX from US$5.043 million to US$4.000 million and annual OPEX from US$1.859 million to US$1.206 million. Under a 20-year project life and 10% discount rate, NPV increased from approximately US$11.34 million to US$12.34 million, while IRR increased from 38.10% to 47.93% and payback decreased from 2.62 to 2.09 years. Product selling price was the dominant sensitivity variable. The results indicate that catalytic pyrolysis offers the stronger integrated energy, exergy and economic performance under the stated assumptions.

Keywords: *household thermoplastic waste; thermal pyrolysis; catalytic pyrolysis; ZSM-5; Aspen Plus; exergoeconomics*

1. INTRODUCTION

Plastic waste is an environmental, resource-management and energy challenge because its durability and chemical resistance hinder conventional disposal and recycling. Household plastic streams are heterogeneous and may contain mixtures of polyolefins, polystyrene, polyethylene terephthalate and polyvinyl chloride. Uncontrolled disposal, landfilling and open burning can therefore result in loss of material value and environmental burdens. Thermochemical conversion provides an alternative route for recovering embedded hydrocarbon value as liquid, gas and solid products. Product distribution depends on feed composition, temperature, residence time, reactor configuration and catalyst selection (Al-Salem et al., 2017; Dai et al., 2022; Speight, 2020).

Thermal pyrolysis generally requires relatively high temperatures to cleave polymer chains, whereas catalytic pyrolysis can promote cracking and secondary reactions at lower severity. ZSM-5 is particularly relevant because its acidic and porous structure can influence hydrocarbon selectivity and promote lighter and aromatic products (Chen et al., 2023; Wang et al., 2022; Zhou et al., 2022). However, product yield alone does not reveal the quality of energy utilization or where thermodynamic irreversibility occurs. Exergy analysis identifies useful work potential and exergy destruction, while exergoeconomics assigns economic consequences to thermodynamic losses. The SPECO method provides a systematic basis for component-level cost assessment (Dincer & Rosen, 2013; Tsatsaronis, 1993).

Previous studies have commonly focused on product distribution, process simulation or conventional economic indicators separately. The present study integrates product yields, process energy, exergy efficiency, component-level exergy-destruction costs, SPECO factors and project

economics for thermal and ZSM-5 catalytic pyrolysis of a mixed household thermoplastic feedstock. The aim is to determine which configuration provides the more favorable integrated technical and economic performance. Specifically, the study objectives are to: (i) develop comparative Aspen Plus V14.0 models; (ii) compare oil, gas and char yields; (iii) quantify process-energy requirements and exergetic efficiency; (iv) identify exergoeconomic hotspots; and (v) compare CAPEX, OPEX, NPV, IRR, profitability index and payback period.

2. METHODOLOGY

2.1 Feedstock and Simulation Basis

The feedstock was defined as a modelled mixed household thermoplastic stream rather than a measured Nigerian municipal-waste composition. The assumed composition 3

comprised HDPE (20 wt%), LDPE (10 wt%), PE (15 wt%), PP (30 wt%), PS (10 wt%), PET (10 wt%) and PVC (5 wt%), giving a total feed of 1,000 kg h^{-1}. The conceptual pretreatment

sequence comprised sorting, removal of metals and inerts, size reduction and drying. This modelling basis was used consistently for both configurations and is not presented as a statistically measured national composition.

Table 1: *Assumed mixed household thermoplastic feedstock composition.*

Polymer	Mass fraction (wt%)	Typical household source
HDPE	20	Bottles, containers
LDPE	10	Films, bags, packaging
PE	15	Packaging and consumer products
PP	30	Food containers, caps, household items
PS	10	Disposable packaging and cups
PET	10	Beverage bottles
PVC	5	Household products and packaging
Total	100	—

2.2 Process Simulation and Energy Analysis

Aspen Plus V14.0 was used with the Peng–Robinson/RKS property method. Conventional components were represented together with appropriate hypothetical solid/polymer components using HCOALGEN and DCOALIGT where required. RYield and RCSTR blocks were used to represent decomposition and reaction behaviour. Thermal pyrolysis was evaluated at approximately 500 °C and catalytic pyrolysis at 350 °C with ZSM-5. The steady-state mass balance was expressed as:

$$\Sigma \dot{m}_{in} = \Sigma \dot{m}_{out} \quad (1)$$

For an adiabatic steady-state control volume with negligible shaft work, the energy balance was represented as:

$$\dot{Q}S - \dot{W} + \Sigma \dot{m}_{in} h_{in} = \Sigma \dot{m}_{out} h_{out} \quad (2)$$

Process-energy input was taken from the external heat and utility requirements of the model. Useful energy recovery represents recoverable energy in product streams and defined heat-recovery pathways.

2.3 Exergy and SPECO Analysis

Exergy analysis used an environmental reference temperature of 25 °C and atmospheric pressure. Total stream exergy was considered as the sum of physical, chemical, kinetic and potential components:

$$E_x = E_x,ph + E_x,ch + E_x,ke + E_x,pe \quad (3)$$

Chemical exergy is particularly important for hydrocarbon-rich plastic feedstocks.

Exergy efficiency was evaluated from the ratio of useful product exergy to fuel exergy supplied. Component exergy destruction was used to identify thermodynamic hotspots. SPECO was then applied to assign costs to exergy flows and component capital and operating costs. The exergoeconomic factor was interpreted as the relative contribution of investment cost to the combined investment and exergy-destruction cost; low values indicate greater scope for irreversibility reduction, while high values indicate stronger capital-cost dominance.

2.4 Economic Evaluation and Sensitivity

The economic assessment assumed 8,000 operating hours per year, a 20-year project life, a 10% discount rate and 30% corporate tax. CAPEX, OPEX, product revenue, NPV, IRR, profitability index and simple payback were evaluated on the same basis for both configurations. The catalytic base case included annual ZSM-5 replacement. Sensitivity analysis varied product selling price, OPEX, CAPEX and feedstock cost by ±20% using the same after-tax cash-flow formulation and 20-year, 10% discount-rate basis.

2.5 Model Validation

Percentage deviation was calculated as the absolute difference between simulated and literature yield divided by the literature yield and multiplied by 100. The thermal model gave an average absolute relative deviation of 7.90%. For the catalytic model, oil, gas and char/coke deviations were 20.95%, 26.09% and 316.67%, respectively; the high solid-product deviation is strongly influenced by the low 3 wt% reference value and should therefore not be interpreted as a direct overall prediction error.

3. RESULTS AND DISCUSSION

3.1 Product Distribution and Energy Performance

The thermal configuration produced 65.2 wt% oil, 19.8 wt% gas and 15.0 wt% char, equivalent to 652, 198 and 150 kg h^{-1} at the design feed rate. Catalytic pyrolysis produced

58.5 wt% oil, 29.0 wt% gas and 12.5 wt% char, equivalent to 585, 290 and 125 kg h^{-1}. The

catalytic route therefore shifted part of the condensable fraction toward gas while reducing solid formation. This trend is consistent with the role of ZSM-5 in promoting cracking and secondary reactions (Wang et al., 2022; Zhou et al., 2022).

Both configurations achieved positive net energy balances. Thermal pyrolysis required 3,334.20 kW and recovered approximately 4,446 kW, whereas catalytic pyrolysis required only 1,840.62 kW and recovered approximately 3,033 kW. Although absolute useful-energy recovery was lower for the catalytic route, its net energy gain was higher because of the substantially lower external energy requirement. The catalytic configuration reduced process-energy input by approximately 44.8% and increased the energy recovery ratio from 133.24% to 164.78%.

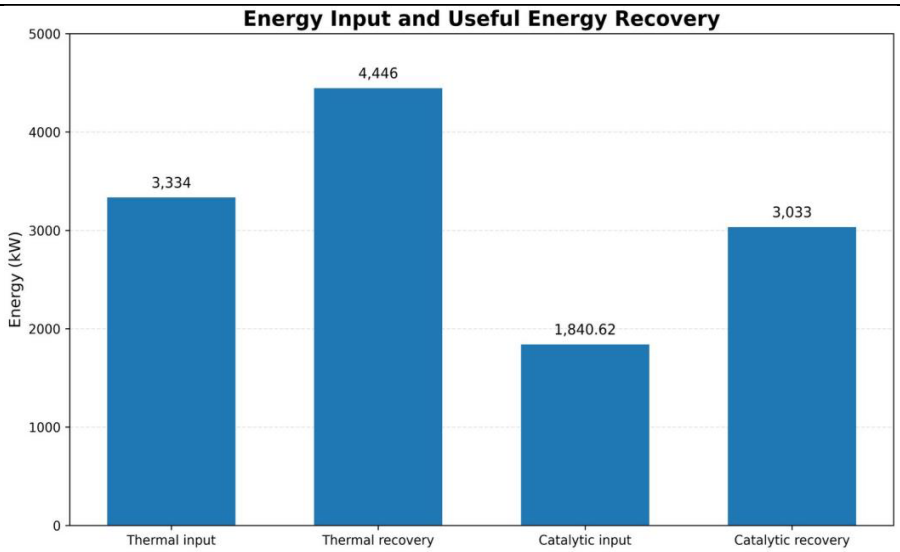

Figure 1: *Comparison of process-energy input and useful energy recovered*

3.2 Exergy and Exergoeconomic Performance

The consolidated exergy results gave approximately 62% exergetic efficiency for thermal pyrolysis and 71% for catalytic pyrolysis. The improvement indicates that a larger fraction of supplied exergy was converted into useful product exergy under the adopted system boundary. The principal component hotspot was the dryer: its exergy-destruction cost decreased from US$1,641.66 h^{-1} to US$1,477.49 h^{-1}. The combustor cost decreased from

US$63.83 h^{-1} to US$27.01 h^{-1}, a reduction of approximately 57.7%.

The low dryer factors indicate that thermodynamic inefficiency dominates its combined cost, so heat recovery, insulation and moisture-control improvements are higher priorities than simply increasing equipment investment. The catalytic combustor factor rises from 27.23% to 47.07% while its absolute exergy-destruction cost falls by 57.7%. This represents a shift in cost composition rather than an automatic overall improvement. The pyrolyzer and heat exchanger have intermediate factors and therefore require simultaneous consideration of capital cost and irreversibility. High factors for the separator and compressor indicate greater capital-cost dominance.

3.3 Techno-Economic Performance

The catalytic configuration required approximately 20.7% less CAPEX and 35.1% less annual OPEX than the thermal configuration. Although annual product revenue was lower for catalytic operation (approximately US$3.860 million yr^{-1} versus US$4.500 million

yr^{-1}), the lower investment and operating requirements produced stronger overall

profitability. Under the 20-year, 10% discount-rate basis, NPV increased from approximately US$11.34 million to US$12.34 million, while IRR increased from 38.10% to 47.93%.

Profitability index increased from 3.25 to 4.08 and simple payback decreased from 2.62 to 2.09 years.

Table 2: *Consolidated techno-economic comparison*

Economic indicator	Thermal	Catalytic
CAPEX (US$ million)	5.043	4.000
Annual OPEX (US$ million)	1.859	1.206
Annual product revenue (US$ million)	4.500	3.860
NPV (US$ million)	11.34	12.34
IRR (%)	38.10	47.93
Profitability index	3.25	4.08
Payback (years)	2.62	2.09

Sensitivity analysis showed that product selling price was the dominant economic variable. A 20% increase in product price raised catalytic NPV to approximately US$16.94 million, while a 20% decrease reduced it to about US$7.73 million. OPEX, CAPEX and feedstock-cost changes produced smaller NPV responses. The base catalytic case assumes a 12-month ZSM-5 replacement interval; catalyst deactivation and regeneration were not explicitly simulated, so alternative service-life cases are economic sensitivity scenarios rather than predictions of actual catalyst lifetime.

3.4 Safety, Environmental Implications and Limitations

The PVC fraction is 5 wt%, corresponding to approximately 50 kg h^{-1} in the design

feed. On a conservative basis, complete conversion of available chlorine to HCl gives an upper-bound HCl generation estimate of approximately 29.2 kg h^{-1}. This is not an actual

emissions prediction because chlorine speciation and an HCl balance were not explicitly simulated. Commercial implementation would therefore require feedstock control, gas cleaning, acid-gas treatment, pressure relief, gas detection and appropriate process-safety systems. Environmental performance also requires future assessment of emissions, catalyst consumption, char utilization, wastewater, auxiliary fuel and life-cycle greenhouse-gas effects. The study is simulation-based; the assumed feed composition, catalyst stability, product quality and economic assumptions require experimental, pilot-scale and market validation before investment decisions.

4. CONCLUSION

An integrated Aspen Plus V14.0 assessment of thermal and ZSM-5 catalytic pyrolysis of a modelled mixed household thermoplastic feedstock was presented. Thermal pyrolysis produced higher liquid yield, whereas catalytic pyrolysis produced more gas and less char.

Catalytic operation reduced process-energy input by approximately 44.8% and increased exergetic efficiency from about 62% to 71%. The dryer was the dominant exergoeconomic hotspot, while the combustor showed a substantial reduction in exergy-destruction cost under catalytic operation. Economically, the catalytic configuration required lower CAPEX and OPEX and achieved higher NPV, IRR and profitability index together with a shorter payback period. Product selling price was the most influential sensitivity variable. Therefore, catalytic pyrolysis provides the stronger integrated performance under the stated 20-year, 10% discount-rate assumptions. Future work should prioritize pilot-scale validation, catalyst-deactivation and regeneration modelling, detailed product characterization, dryer heat- integration optimization, chlorine/emissions management, uncertainty analysis and life-cycle assessment.

5. REFERENCES

Al-Salem, S. M., Antelava, A., Constantinou, A., Manos, G., & Dutta, A. (2017). A review on thermal and catalytic pyrolysis of plastic solid waste (PSW). Journal of Environmental Management, 197, 177–198. https://doi.org/10.1016/j.jenvman.2017.03.084

Chen, W.-H., Biswas, P. P., Kwon, E. E., Park, Y.-K., Rajendran, S., Gnanasekaran, L., & Chang, J.-S. (2023). Optimization of the process parameters of catalytic plastic pyrolysis for oil production using design of experiment approaches: A review.

Chemical Engineering Journal, 471, 144695. https://doi.org/10.1016/j.cej.2023.144695

Dai, L., Zhou, N., Lv, Y., Cheng, Y., Wang, Y., Liu, Y., Cobb, K., Chen, P., Lei, H., & Ruan, R. (2022). Pyrolysis technology for plastic waste recycling: A state-of-the-art review.

Progress in Energy and Combustion Science, 93, 101021. https://doi.org/10.1016/j.pecs.2022.101021

Dincer, I., & Rosen, M. A. (2013). Exergy: Energy, environment and sustainable development (2nd ed.). Elsevier.

Gracida-Alvarez, U. R., Benavides, P. T., Lee, U., & Wang, M. (2023). Life-cycle analysis of recycling of post-use plastic to plastic via pyrolysis. Journal of Cleaner Production, 425, 138867. https://doi.org/10.1016/j.jclepro.2023.138867

Kumar, S., & Singh, R. K. (2011). Recovery of hydrocarbon liquid from waste high density polyethylene by thermal pyrolysis. Brazilian Journal of Chemical Engineering, 28(4), 659–667. https://doi.org/10.1590/S0104-66322011000400011

Seo, Y.-H., Lee, K.-H., & Shin, D.-H. (2003). Investigation of catalytic degradation of high-density polyethylene by hydrocarbon group type analysis. Journal of Analytical and Applied Pyrolysis, 70(2), 383–398. https://doi.org/10.1016/S0165-2370(02)00186-9

Speight, J. G. (2020). Handbook of industrial hydrocarbon processes (2nd ed.). Gulf Professional Publishing. https://doi.org/10.1016/C2015-0-06314-6

Tsatsaronis, G. (1993). Thermoeconomic analysis and optimization of energy systems. Progress in Energy and Combustion Science, 19(3), 227–257. https://doi.org/10.1016/0360-1285(93)90016-8

Wang, Y., Cheng, L., Gu, J., Yuan, H., & Chen, Y. (2022). Catalytic pyrolysis of polyethylene for the selective production of monocyclic aromatics over the zinc-loaded ZSM-5 catalyst. ACS Omega, 7(3), 2752–2765. https://doi.org/10.1021/acsomega.1c05401

Zhou, N., Dai, L., Lyu, Y., Wang, L., Li, H., Cobb, K., Chen, P., Lei, H., & Ruan, R. R. (2022). A structured catalyst of ZSM-5/SiC foam for chemical recycling of waste plastics via catalytic pyrolysis. Chemical Engineering Journal, 440, 135836. https://doi.org/10.1016/j.cej.2022.135836

International Conference on Engineering Innovation for Sustainable Development (ICESID 2026)
Faculty of Engineering, Ahmadu Bello University Zaria · 8–10 September 2026

MINIMIZATION OF POWER LOSSES IN DISTRIBUTION NETWORKS THROUGH SMART GRID TECHNOLOGIES (SGT): A CASE STUDY OF BWARI 33 KV DISTRIBUTION NETWORK

Francis Igbinosa[1], Eronu Emmanuel[1,*], Ngang Bassey Ngang[1]
[1]*University of Abuja*
Email: fagedom83@gmail.com, eronu.majiyebo@uniabuja.edu.ng*, nbngang@gmail.com
***Corresponding author**: Eronu Emmanuel
DOI: https://doi.org/10.67203/sp.ICESID.2026

ABSTRACT
This study presents a comprehensive modeling and simulation-based investigation aimed at minimizing technical power losses and enhancing voltage profiles within the Bwari 33 kV distribution network, representative of Nigerian urban power infrastructure. Utilizing MATLAB/Simulink, a detailed radial feeder model was developed, capturing realistic operational characteristics, including load composition, line parameters and substation configurations. The research employs a quantitative approach, incorporating baseline analysis and scenario-based simulations to evaluate the effects of smart grid functionalities. Key system parameters considered include voltage profile, active and reactive power losses, circuit breaker loading, thermal effects and overall network efficiency. The analysis revealed that overload conditions significantly increase technical losses. To mitigate these effects, several smart grid technologies were evaluated, including AMI, APDA, VVO and BESS. Simulation results showed that individual smart grid technologies achieved loss reductions ranging from 10% to 30%, while coordinated smart grid operation reduced total energy losses from 15,581.20 MWh/day to 11,497.73 MWh/day, representing a 26.2% reduction in losses. The economic assessment further demonstrated the viability of smart grid implementation, with estimated annual savings of $179,024,314.72. In addition, the reduction in energy losses contributes to lower carbon emissions and improved environmental sustainability. The study concludes that the integration of smart grid technologies provides an effective and economically feasible solution for minimizing power losses, improving voltage regulation, enhancing system reliability and reducing overload-induced stress in distribution networks. It is therefore recommended that power utilities adopt a phased approach to smart grid implementation, enhancing the operational performance and sustainability of modern distribution systems.

Keywords: *Smart Grid Technologies; Power Losses; 33 kV Distribution Network; Overloaded Circuit Breaker Protection; Voltage Profile and Loss Minimization*

1. INTRODUCTION

Electrical distribution networks constitute the final stage of the power system through which electricity is delivered to consumers, and their operational efficiency has a direct influence on power quality, reliability, energy utilization, and economic performance. However, distribution networks are often affected by significant technical power losses arising from conductor resistance, excessive loading, voltage drops, reactive power flow, and inefficient network operation. In Nigeria, technical losses remain a major concern because of the physical characteristics and operational limitations of distribution networks. Obiora et al. (2025) identified technical losses as an important challenge in Nigerian distribution networks and emphasized the need for effective mitigation measures. As loading increases, current flow through network components increases, causing losses that are strongly influenced by the (I^2R) relationship. Consequently, overloaded feeders and circuit breakers can contribute to increased energy losses, deterioration of voltage profiles, and additional thermal stress on electrical equipment.

Recent research has demonstrated the potential of advanced optimization and smart-grid approaches for improving distribution-network performance. Karunarathne et al. (2020) investigated optimal distributed-generation placement and sizing for reducing losses. Asuquo et al. (2026), Nigerian 33/11 kV network, highlighted recent evidence that DG reduces feeder current and technical losses while Adegoke et al. (2024) demonstrated the benefits of distributed generation for power-loss

reduction and voltage stability. Similarly, Mahdavi et al. 2024., Vijayan et al. (2021) proposed a coordinated framework involving demand response + Volt-Var to minimize losses and costs. Voltage/VAR optimization has also received considerable attention, with studies demonstrating the effectiveness of intelligent control techniques for improving voltage regulation and reducing losses in active distribution networks (Ferraz et al., 2021; Hossain et al., 2022., Li et al., 2022; Zhang et al., 2021., Ahanch et al., 2021). Demand-side energy management and smart-metering technologies further provide opportunities for managing peak demand and improving energy consumption patterns (Bakare et al., 2023; Abdeslam, 2023, Padullaparti et al., 2023).

Despite these advances, important gaps remain. Much of the existing literature concentrates on individual technologies, optimization algorithms, distributed-generation placement, or general smart-grid applications. There is comparatively limited investigation of the coordinated application of multiple Smart Grid Technologies under overloaded distribution-network conditions, particularly within the context of Nigerian urban 33 kV networks. Furthermore, existing studies have given insufficient attention to the relationship between circuit-breaker overloading, technical power losses, voltage deterioration, and thermal effects as an integrated distribution-network problem. Although studies on smart-grid technologies in Nigeria have highlighted their potential for improving power-system performance, practical case-study investigations linking these technologies directly to overload-induced technical losses remain limited (Kanilius et al., 2024). This study therefore addresses this gap through a simulation-based investigation of the Bwari 33 kV distribution network.

The aim of this study is to minimize technical power losses and improve voltage performance in the Bwari 33 kV distribution network through the application of Smart Grid Technologies. Specifically, the study seeks to: (i) model the Bwari 33 kV distribution network and establish its baseline technical power losses under normal operating conditions; (ii) evaluate the effects of circuit-breaker and network overload on active and reactive power losses, voltage profile, and thermal performance; and (iii) assess the effectiveness of coordinated Smart Grid Technologies, including Advanced Metering Infrastructure (AMI), Adaptive Protection and Distribution Automation (APDA), Volt/VAR Optimization (VVO), and Battery Energy Storage Systems (BESS), in reducing overload-induced losses and improving overall network efficiency.

2. METHODOLOGY

The study employed a quantitative, simulation-based research design with a quasi-experimental approach to investigate the minimization of technical power losses in the Bwari 33kV distribution network through smart grid technologies. This design was deliberately chosen because it enabled controlled investigation of distribution network performance under various operating scenarios without disrupting actual power supply to consumers, thereby eliminating practical risks while maintaining experimental rigor. The quasi-experimental nature of this design allowed for systematic variation of independent variables, specifically load levels and technology deployment, while measuring dependent variables including power losses, voltage profiles, and circuit breaker temperatures under controlled simulation conditions.

The research was structured around a four-phase design framework that progressively built understanding from baseline characterization through to comprehensive technology evaluation. Phase 1: Baseline Characterization involved modelling the existing Bwari 33kV distribution network under normal operating conditions, quantifying technical power losses as baseline reference values, and establishing voltage profiles across all network nodes. This phase established the performance benchmark against which all subsequent interventions would be compared. Phase 2: Overload Scenario Simulation subjected the network to incremental overload conditions at 120%, 150%, 180%, and 200% of normal load, while monitoring circuit breaker thermal behaviour and documenting loss escalation patterns. This phase was critical for understanding the relationship between loading levels and loss characteristics. Phase 3: Smart Grid Technology Implementation applied individual smart grid technologies, such as Advanced Metering Infrastructure (AMI), Adaptive Protection and Distribution Automation (APDA), Volt/VAR Optimization (VVO), and Battery Energy Storage Systems (BESS) to the overloaded network, quantifying each technology's loss reduction effectiveness and comparing performance metrics across technologies. Phase 4: Coordinated Smart Grid Evaluation implemented all smart grid technologies simultaneously to analyze synergistic effects

and assess overall system performance improvement. This phased approach ensured a logical progression from problem identification to solution evaluation, with each phase building upon the findings of the previous phase to develop a comprehensive understanding of both the challenges posed by overload conditions and the potential of smart grid technologies to mitigate them.

2.1 Study Area and Network Description

2.1.1 Location and Context

The study was conducted on the Bwari 33kV distribution network, located in the Federal Capital Territory, Nigeria. Bwari represents a typical Nigerian urban distribution network, characterized by radial feeder configuration, mixed load composition (residential, commercial, and light industrial), and operational challenges common to developing economy power systems can be seen from the SLD of figure 1

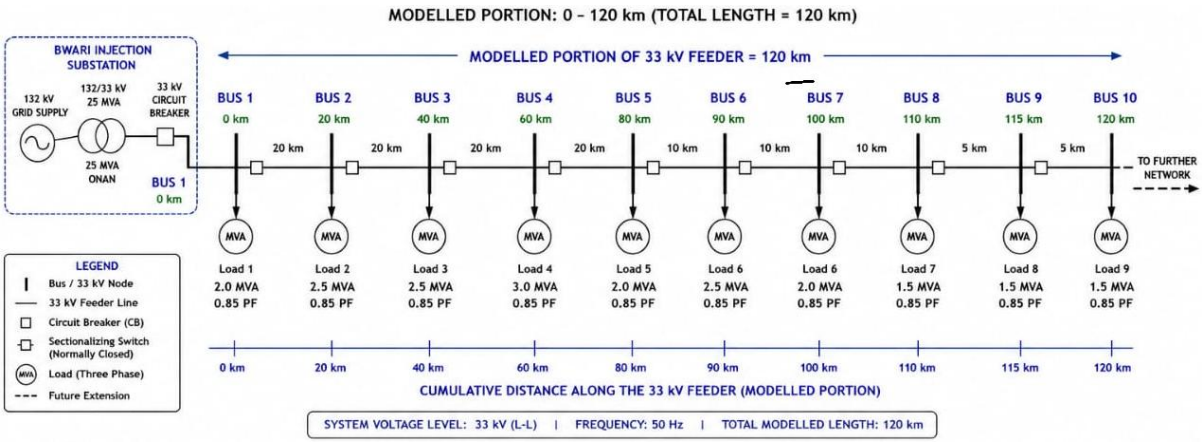

Figure 1: SLD of Bwari 33 kV Distribution Network

The 10-bus, 0-120 km single-line diagram shown above is a simplified representative model of the actual Bwari 33 kV distribution feeder. It is developed for MATLAB/Simulink simulation and does not constitute an exact as-built representation of the complete physical network. The model aggregates selected network sections and loads to reproduce the principal electrical characteristics required for the analysis of voltage profiles, technical power losses and circuit-breaker overload conditions. Accordingly, the SLD provides an engineering abstraction of the actual Bwari network, enabling the investigation of the research.

2.1.2 Network Configuration

The network parameters employed in this study were derived from actual Bwari substation records, supplemented by standard IEEE distribution system data where specific measurements were unavailable. The network was characterized as follows:

Geometric Parameters:

i. Total line length: 120 kilometres
ii. Number of feeder sections: 6 (20 km per section)
iii. Source voltage: 33 kV (nominal)
iv. Frequency: 50 Hz

Electrical Parameters:

i. Conductor type: 95 mm² ACSR (Aluminium Conductor Steel Reinforced)
ii. Resistance: 0.195 Ω/km
iii. Inductive reactance: 0.35 Ω/km
iv. Capacitance: 0.01 μF/km (neglected in loss calculations)
v. Normal load: 5 MVA at 0.85 lagging power factor

Protection Equipment:

i. Circuit breaker type: SF6 (Sulfur Hexafluoride) gas-insulated
ii. Continuous current rating: 630 A

iii. Short-time current rating: 25 kA for 1 second
iv. Thermal time constant: 300 seconds
v. Maximum operating temperature: 105°C
vi. Ambient temperature: 40°C

2.1.3 Load Characteristics

The load distribution along the 120 km feeder was assumed to be uniformly distributed, reflecting the typical urban load pattern in Bwari. Load composition consisted of:

i. Residential loads: 60%
ii. Commercial loads: 30%
iii. Light industrial loads: 10%
iv. Power factor: 0.85 lagging (maintained constant across all scenarios)

2.2 Hardware and Computing Resources

The following hardware resources shown in table 1, were utilized for the simulation studies:

Table 1: Hardware Resources

Item	Specification	Purpose
Workstation	Intel Core i7-12700K, 32GB RAM, 1TB SSD	Simulation processing
Display Monitor	27-inch 4K UHD	Visualization of results
Backup Storage	2TB External HDD	Data preservation
UPS System	1500VA Line-interactive	Power protection

2.3 Software Tools

The computational framework for this study was built around MATLAB R2026a, which served as the primary simulation environment for the entire research. The simulations were performed using MATLAB/Smulink R2026a. This platform was selected due to its robust numerical computation capabilities, which enabled efficient matrix operations essential for power flow analysis and network modelling.

The Bwari 33 kV distribution network was modelled and simulated using MATLAB/Simulink. The specific release used for the final simulation runs was verified from the MATLAB installation using the version/matlabRelease command.

Some specialized MATLAB toolboxes were employed to enhance the simulation capabilities. Simulink was utilized for graphical modelling of the distribution network, allowing for visual representation of the radial feeder configuration and facilitating intuitive system understanding. The Simscape Electrical toolbox provided essential electrical component libraries, including transformers, transmission lines, loads, and circuit breakers, which enabled accurate physical modelling of the distribution system. The Optimization Toolbox was applied for technology coordination optimization, particularly useful for determining optimal settings for Volt/VAR control and energy storage dispatch. Statistics and Machine Learning Toolbox facilitated comprehensive data analysis and visualization, enabling statistical validation of simulation results. Finally, the Parallel Computing Toolbox was employed to enable multi-core processing for large-scale simulations, significantly reducing computational time during the 24-hour dynamic simulations and Monte Carlo sensitivity analyses.

Microsoft Excel 365 was used for data organization, preliminary statistical analysis, and result tabulation, providing a user-friendly interface for managing the extensive dataset generated from simulations.

2.4 Data Sources

The research utilized both primary and secondary data sources to ensure comprehensive and accurate network representation.

i. Primary data were obtained directly from the Bwari substation operational records covering the period 2022-2023, and the base simulation condition was therefore established at 5.0 MVA, 0.85 power factor and 33 kV nominal feeder voltage. The corresponding active and reactive power demands were calculated as approximately 4.25 MW and 2.63 MVAr, respectively. Therefore,

the simulation results presented in this study is as interpreted as results from a calibrated/representative model of the Bwari 33 kV distribution network and not as direct measurements of actual feeder losses. The available operational information served to constrain and justify the selected model parameters, while the reported power losses were obtained from the MATLAB/Simulink power-flow model. Circuit breaker maintenance logs supplied critical information on equipment condition, historical trip events, and thermal performance characteristics. Additionally, feeder configuration diagrams provided the physical network topology, including line routing, and connection points necessary for accurate model development.

ii. Secondary data were sourced from established industry standards and technical specifications to validate model parameters and ensure alignment with recognized engineering practices. The IEEE Standard 141-1993 (IEEE Recommended Practice for Electric Power Distribution) provided guidance on distribution system modeling and analysis methodologies. The Nigerian Electricity Regulatory Commission (NERC) technical standards ensured that the study parameters aligned with local regulatory requirements and operational practices. This combination of primary operational data and secondary technical standards ensured that the simulation model accurately represented the actual Bwari distribution network while maintaining compliance with established engineering principles.

2.5 Mathematical Modelling Framework

The distribution network was modelled using the lumped-parameter π-model for transmission lines, with the following mathematical formulations:

Line Impedance Calculation:

$$Z_{total} = (R_{perkm} + jX_{perkm}) \times L_{total} \quad (1)$$

$$R_{total} = 0.195 \times 120 = 23.4\ \Omega$$

$$X_{total} = 0.35 \times 120 = 42.0\ \Omega$$

$$Z_{total} = 23.4 + j42.0\ \Omega$$

The voltage drop across each feeder section was approximately related to the feeder impedance and current according to the relationship:

$$\Delta V \approx I(R\cos\phi + X\sin\phi) \quad (2)$$

where I represented feeder current, R represented feeder resistance, X represented feeder reactance, and ϕ represented the load power-factor angle.

The relationship between feeder current and technical loss was particularly important because conductor losses were proportional to the square of current as shown in equation 3:

$$P_{loss} = I^2R \quad (3)$$

MATLAB Implementation:

Step 1: Network Initialization

The network was initialized with system parameters in MATLAB using the code structure shown in appendix 1.

Step 2: Load Distribution Modelling

Loads were distributed along the feeder using a uniform distribution model shown in appendix 2

Step 3: Load Flow Analysis

The load flow was solved iteratively using the Backward-Forward Sweep method; this method is appropriate for radial distribution networks, and the code is shown in appendix 3.

2.6 Circuit Breaker Thermal Modelling

Thermal Model Development:

The circuit breaker thermal behaviour was modelled using the lumped thermal parameter approach based on IEC 60947-2 standards:

$$\Delta T(t) = T_ambient + (T_ambient \times ((I_load/I_rated)^2 - 1)) \times (1 - e^{(-t/\tau)}) \quad (4)$$

Where:

$\Delta T(t)$ = Temperature rise at time t (°C)

T_ambient = Ambient temperature (40°C)

I_load = Actual load current (A)

I_rated = Rated continuous current (630 A)
τ = Thermal time constant (300 seconds)
t = Time (seconds)

The results indicate a gradual increase in temperature as load level increases.

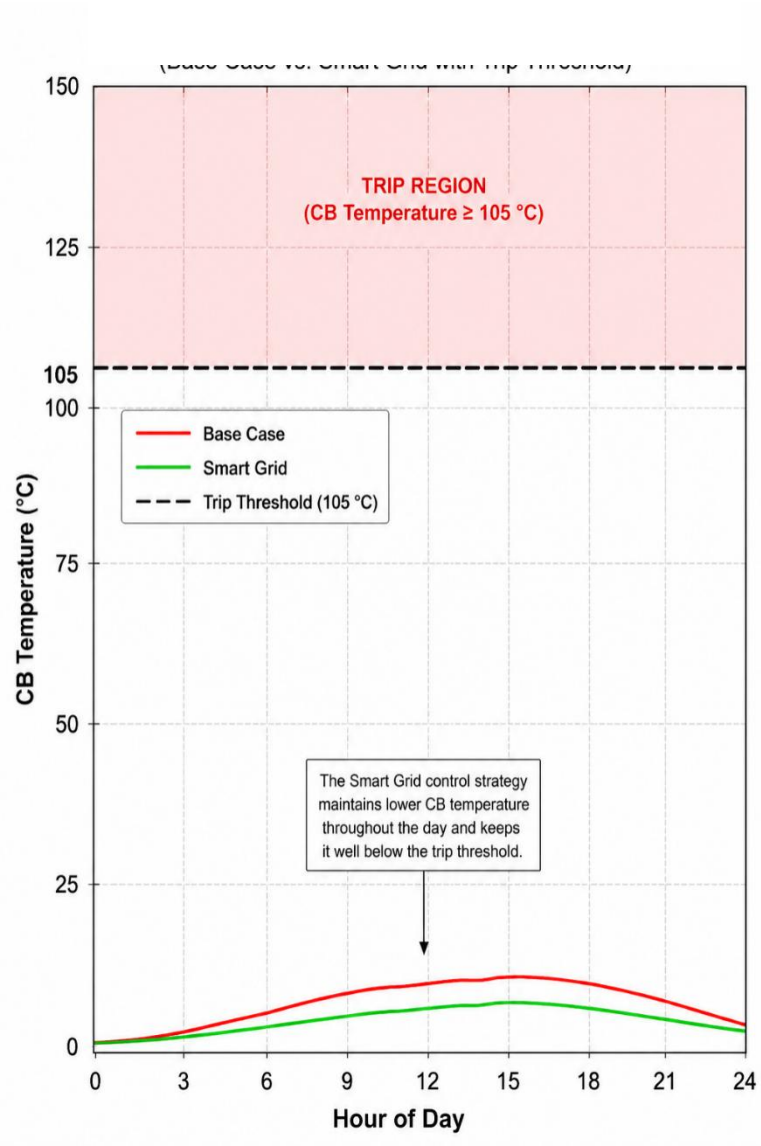

Figure 2: Circuit Breaker Thermal Performance Plot

Figure shows result of MATLAB simulation for circuit breaker performance against subsequent temperature rise during overload conditions. Although, MATLAB simulation of the circuit breaker only shows a temperature rise of 150 degree celcius trip region, but going further this increases significantly beyond this threshold; upto 180 oc and 200 oc as the case maybe, corresponding to the various overload condition.

MATLAB Thermal Model Implementation

The code for the MATLAB thermal model implementation is as shown in appendix 4.

2.7 Smart Grid Technology Modelling

2.7.1 Advanced Metering Infrastructure (AMI)

AMI was modelled as a monitoring and control layer that provided real-time data for decision-making. The Matlab implementation code is shown in appendix 5. A 14.0% loss reduction factor was assumed for AMI for the purpose of scenario-based modelling; meaning AMI contribute a 14.0% loss reduction.

2.7.2 Adaptive Protection and Distribution Automation (APDA)

APDA was modelled to dynamically adjust protection settings. The Matlab implementation code for the APDA is shown in appendix 6. And for the purpose of scenario-based modelling APDA contributes 18.0% loss reduction.

2.7.3 Volt/VAR Optimization (VVO)

VVO was implemented using an optimal power flow approach, and the implementation code shown in appendix 7. For this simulation scenario, VVO contributes 23.0% loss reduction.

2.7.4 Battery Energy Storage System (BESS)

BESS was modelled with energy management capabilities. The Matlab implementation code is shown in appendix 8. For the purpose of scenario-based modelling BESS contributes 20.0% loss reduction.

The overall loss reduction obtained from the coordinated Smart Grid Technology scenario was subsequently caculated from the simulated baseline and post-intervention network losses. Consequently, the overall loss reduction percentage represents a model-derived result, whereas the individual technology percentages represent assumed contribution factors used in the scenario modelling.

3 RESULTS AND DISCUSSION

The results were presented progressively, beginning with the baseline network condition, followed by the overloaded condition and the assessment of individual Smart Grid Technologies. The intelligent circuit breakers prevent prolonged overload conditions by detecting abnormal current and temperature rise, initiating protective actions before equipment reaches critical thermal limits. This improves system reliability, minimizes unnecessary outages, extend equipment life and reduces maintenance costs. The final stage involved the coordinated application of Advanced Metering Infrastructure (AMI), Adaptive Protection and Distribution Automation (APDA), Volt/VAR Optimization (VVO), and Battery Energy Storage System (BESS).

The results demonstrated that increased loading caused a substantial deterioration in network performance, while the coordinated application of Smart Grid Technologies reduced technical losses, improved voltage performance and reduced overload-induced stress on network components.

3.1 Baseline Performance of the Bwari 33 kV Distribution Network

The baseline simulation established the operating condition of the Bwari 33 kV distribution network before the introduction of overload and Smart Grid Technology interventions. The baseline model was used as the reference against which subsequent simulation scenarios were evaluated.

The baseline analysis considered active power loss, reactive power loss, bus voltage, feeder current, circuit-breaker loading and network efficiency. The simulation results, shown in figure 3 provided the reference operating point required for determining the extent to which overload conditions affected network performance.

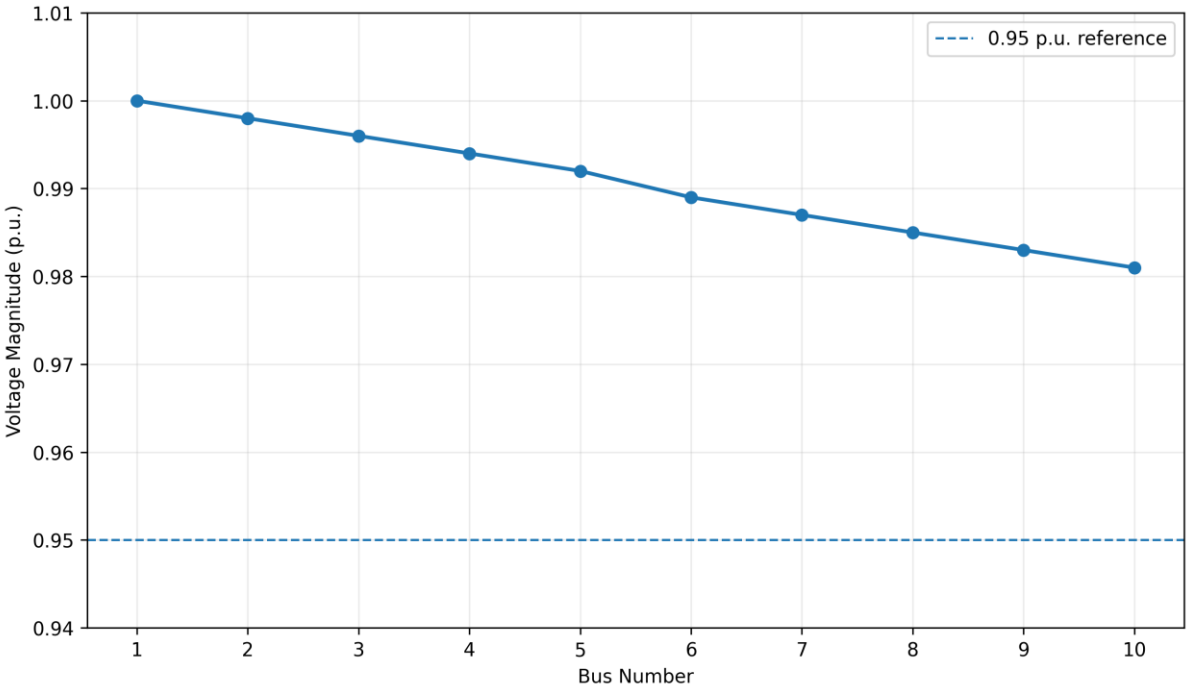

Figure 3: Baseline Voltage Profile of the Bwari 33 kV Network

Figure 3. shows a representative radial feeder voltage profile, an illustrative representative of 10-bus profile distinct from the SLD in figure 1. The voltage gradually decreasing from 1.000 p.u. at the sending end to 0.981 p.u. at the most remote representative bus. The profile remains above the illustrative 0.95 p.u. reference line, indicating an acceptable baseline voltage condition before overload was introduced.

3.2 Effect of Overloading on Voltage Profile

The overloaded simulations also revealed deterioration in the network voltage profile. Increasing load caused greater current flow through feeder impedances, resulting in increased voltage drops. The voltage profile deteriorated as the loading level increased. The effect was expected to be more pronounced at electrically remote buses because voltage drops accumulated along the feeder.

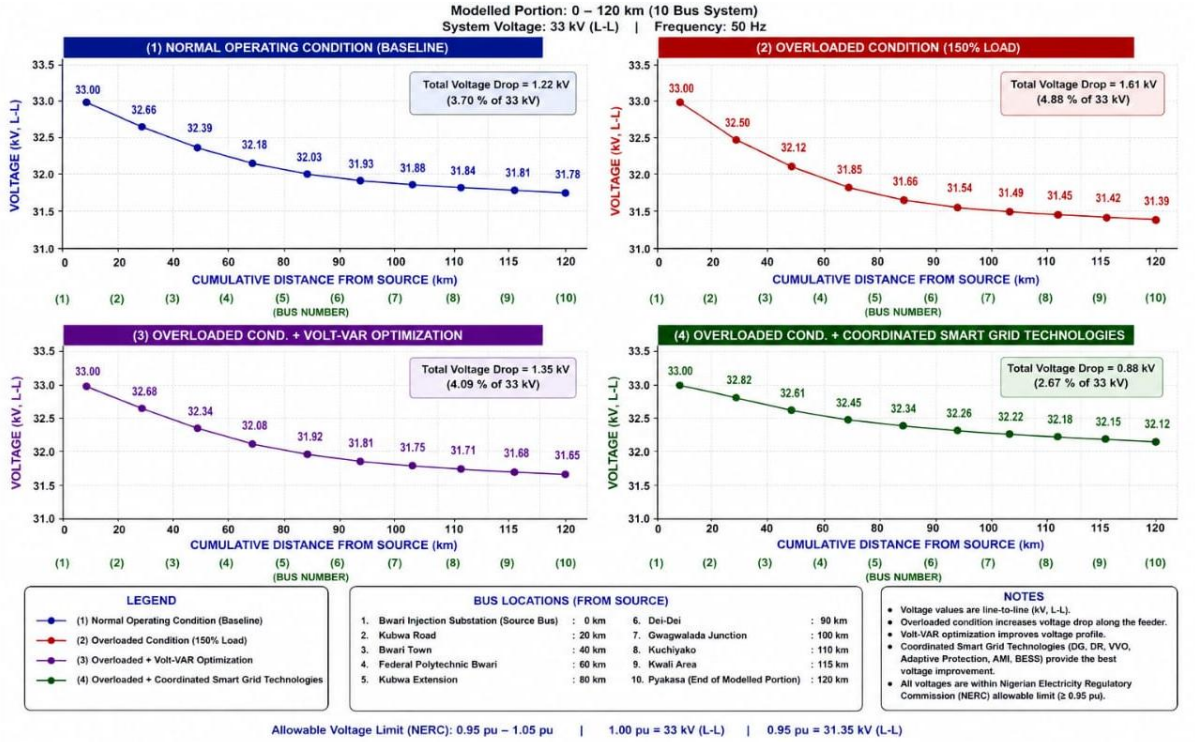

Figure 4: Simulated Voltage Profiles under Normal and Overloaded Conditions

Figure 4. presents the simulated voltage profiles along the Bwari 33 kV distribution feeder under four different operating incremental overload conditions, namely: 120% loading, 150% loading, 180% loading and up to 200% loading (severe overload). The figure illustrates the relationship between feeder loading and voltage magnitude from the 33 kV substation towards the remote end of the distribution network. The results demonstrate a clear deterioration in voltage profile as the feeder loading increased, thereby confirming the adverse effect of overload on voltage regulation and overall distribution-network performance.

3.3 Performance of Individual Smart Grid Technologies

The individual Smart Grid Technologies were subsequently introduced into the overloaded network to determine their separate contributions to loss reduction.

The technologies investigated were:

1. Advanced Metering Infrastructure (AMI);
2. Adaptive Protection and Distribution Automation (APDA);
3. Volt/VAR Optimization (VVO); and
4. Battery Energy Storage System (BESS).

The simulation results indicated that the individual Smart Grid Technologies achieved loss reductions within the approximate range of 14%–23%, depending on the technology and operating condition. The 26.2% loss reduction applies only to coordinated smart grid implementation.

Figure 5 presents the comparative performance of the individual Smart Grid Technologies investigated for reducing technical power losses in the Bwari 33 kV distribution network. The technologies evaluated were Advanced Metering Infrastructure (AMI), Adaptive Protection and Distribution Automation (APDA), Volt/VAR Optimization (VVO), and Battery Energy Storage System (BESS). The coordinated Smart Grid Technology configuration was also included to demonstrate the additional benefit obtained when the technologies operated together.

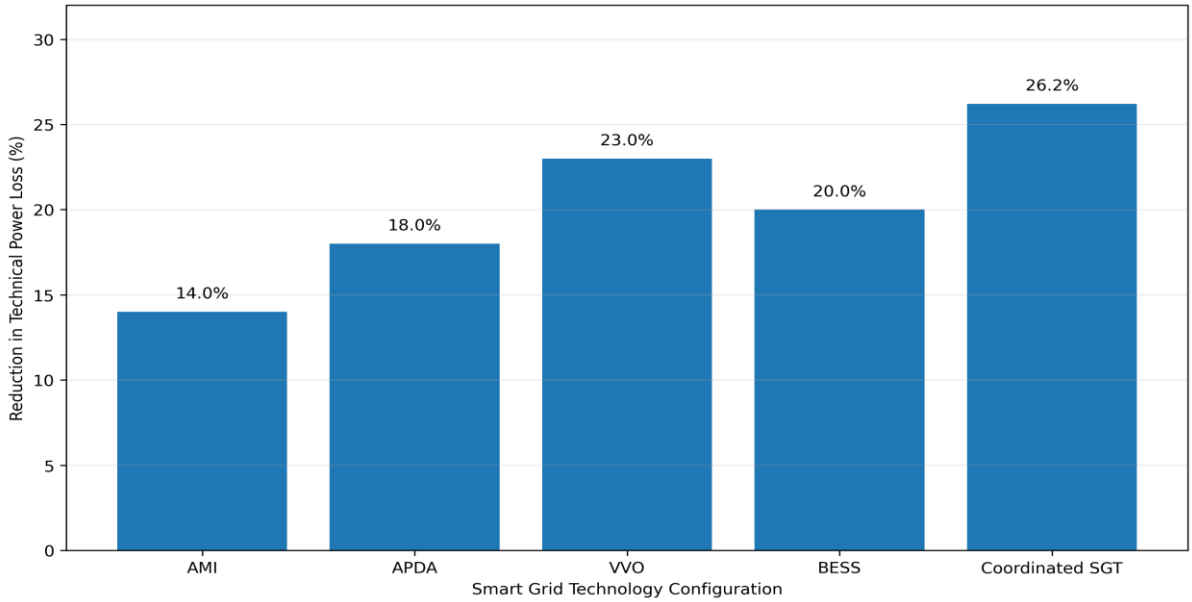

Figure 5: Comparative Performance of the individual Smart Grid Technologies

3.4 A Summary of the Major Findings of the Study

The five major findings of this study demonstrated that overload-induced technical losses in the Bwari 33 kV distribution network were strongly interconnected with feeder current, voltage deterioration, circuit-breaker loading and inefficient energy utilization. The study showed that these problems could be addressed more effectively through coordinated Smart Grid Technologies than through isolated interventions. Most importantly, the reported 26.2% reduction in total energy losses provided quantitative evidence supporting the adoption of a coordinated smart-grid operation for improving the efficiency, reliability and sustainability of Nigerian distribution networks. The summary of the five major findings of this study is shown in table 2.

Table 2: Summary of the 5 major findings of the study

No.	Major finding	Key implication
1	Overloading significantly increased technical power losses	Overload management was essential for loss minimization
2	Increasing loading progressively deteriorated the voltage profile	Voltage regulation had to be integrated into loss-reduction strategies
3	Overloading increased circuit-breaker loading and thermal stress	Automated protection and control were required
4	Individual SGTs reduced technical losses	AMI, APDA, VVO and BESS each provided useful benefits
5	Coordinated SGT operation outperformed isolated interventions	Integrated smart-grid operation was more effective

4 CONCLUSION

This study demonstrated that Smart Grid Technologies (SGTs) can significantly minimize technical power losses and improve operational performance in the Bwari 33 kV distribution network. The analysis showed that increased network loading and circuit-breaker overloading resulted in higher I^2R losses, voltage deterioration, and increased thermal stress. The coordinated application of AMI, APDA, VVO, and BESS effectively mitigated these adverse effects and improved overall network efficiency. From table 2 above subsection 4 & 5, distinctively shows individual smart grid technologies with their various contribution in loss reductions, figure 4 refers and the coordinated SGT in subsection 5 showing a remarkable loss reduction of 26.2%. In particular, the coordinated SGT strategy reduced total energy losses from 15,581.20 MWh/day to 11,497.73 MWh/day, representing a 26.2% reduction, results from the calculations:

15,581.20 - 11,497.73 = 4,083.47 MWh/day as energy saved.
Loss reduction = 4,083.47÷15,581.20 = 0.2620767 MWh/day
Therefore, %Loss reduction = 0.2620767*100 = 26.2%

Table 3: Derivation of Daily Energy Loss from the Power-Flow/Loss Model

Parameter	Baseline Condition	Coordinated SGT Condition
System voltage	33 kV	33 kV
Feeder length	120 km	120 km
Base load	5.00 MVA	5.00 MVA
Power factor	0.85	0.85
Power-flow loss equation	PL = ∑3Ii^2Ri	PL.sgt = ∑3Ii^2.sgtRi
Calculated active-power loss	226.32 kw	[SGT power-flow result] kW
Conversion to MW	226.32/1OOO = 0.22632 MW	Pl.SGT/1000 MW
Operating duration	24 h/day	24 h/day
Daily energy-loss equation	EL = PL * 24	EL.sgt = PL.sgt*24
Daily energy-loss MWh/day	5.4317 MWh/day	[calculated SGT value] MWh/day

Thus, PL = 226.32 kW = 0.22632 MW.
The corresponding daily energy loss is EL = 0.22632*24
EL = **5.43168 MWh/day.**
With reference to the 15,581.20 MWh/day, its mathematical origin would have to be :
Pequivalent = 15,581.20/24 = 649.2167 MW
Therefore, see below table for more explicit explanation:

Table 4: Comparison of Reported and Reversed-Derived Power Loss Values

Reported value	Reversed-derived value
15,581.20 MWh/day	649.22 MW average loss
11,497.73 MWh/day	479.07 MW average loss
Difference	170.15 MW
Daily difference	4,083.47 MWh/day
Percentage reduction	26.21%

Economic Assessment of Energy-Loss Reduction

The economic benefit of the coordinated Smart Grid Technology (SGT) intervention was evaluated by converting the reduction in daily technical energy losses into an equivalent monetary value. The assessment considers the energy-loss reduction obtained from the simulation, the assumed electricity tariff. An effective electricity energy value of #158.75/kWh using the assumed exchange rate of [1;USD = #1,321.68]. NERC's MYTO methodology explicitly recognizes the #/US$ exchange rate as one of the pass-through variables affecting electricity tariffs. The daily energy saving is first converted from MWh to kWh: [4,083.47 MWh/day*1000] = 4,083,470 kWh/day.

The corresponding annual energy saving is [E(annual) = 4,083,470*365] = 1,490,466,550 MWh/year, as the annual monetary value of avoided energy losses.

Annual energy loss savings: 1,490,466,550*0.1201129369 = $179,024,314.72/year.

This can also be expressed in Nigerian currency: 1,490,466,550*#158.75 = #236.61 billion/year.

The study therefore established that coordinated smart-grid deployment provides a technically effective and economically viable approach for improving the reliability, voltage performance, and energy efficiency of the Bwari 33 kV distribution network.

5 REFERENCES

Obiora, G. N., Igbinosa, G. O., & Fiemobebefa, C. B. (2025). Technical losses across distribution networks in Nigeria and mitigative measures: A review. *ABUAD Journal of Engineering Research and Development*, *8*(1), 43–49. https://doi.org/10.53982/ajerd.2025.0801.05-j

Karunarathne, E., Pasupuleti, J., Ekanayeke, J., & Almeida, D. (2020). Network loss reduction and voltage improvement by optimal placement and sizing of distributed generators with active and reactive power injection using fine-tuned PSO, Indonesian Journal of Electrical Engineering and Computer Science, 21(2), 647-656.

https://doi.org/10.11591/ijeecs.v21.i2.pp647-656

Asuquo, N.E., Araga, A.I., Dahiru, D., Okedu, K.E., & Colak, I. (2026). Static and dynamic performance assessment of a grid-connected solar photovoltaic system in a Nigerian 33/11 kV distribution network. Frontiers in Energy Research, 14, 1734900.

https://doi.org/10.3389/fenrg.2026.1734900

Adegoke, S.A., Sun, Y., Wang, Z., & Oladipo, S. (2024). Application of Archimedes optimization algorithm for network reconfiguration to minimize power loss and voltage deviation. In 2024 6th International Conference on Power and Energy Technology (ICPET) (pp.1608-1612). IEEE. https://doi.org/10.1109/ICPET62369.2024.10941383

Oluwadare, R.O., & Adegoke, O.M. (2024). An analysis of power distribution network in Nigeria for power quality-based reinforcements and investment planning. Advances in Science and Technology, 154, 213-223.

https://doi.org/10.4028/p-uc8mGf

Mahdavi, M., Awaafo, A., Djokic, S. Z., & Jurado, F. (2024). An innovative power loss and cost minimization framework for distribution networks with uncertain variable loads by coordinating reconfiguration, capacitor installation and renewable generators placement. *IEEE Transactions on Industry Applications*, *60*(5), 7500–7510.

https://doi.org/10.1109/TIA.2024.3403958

Vijayan, V., Mohapatra, A., & Singh, S.N. (2021). Demand response with Volt-Var optimisation for unbalanced active distribution systems. Applied Energy, 300, 117361.

https://doi.org/10.1016/j.apenergy.2021.117361

Ferraz, B.P., Rsener, M., Pereira, L.A., Lemos, F.A.B., & Heffner, S. (2021). MILP model for Volt-Var optimisation considering chronological operation of distribution systems containing DERs. International Journal of Electrical Power & Energy Systems, 129, 106761.

https://doi.org/10.1016/j.ijepes.2021.106761

Hossain, R., Gautam, M., Lakouraj, M. M., Livani, H., & Benidris, M. (2022). Volt-VAR optimization in distribution networks using twin delayed deep reinforcement learning. In *2022 IEEE Power & Energy Society Innovative Smart Grid Technologies Conference (ISGT)*. IEEE.

https://doi.org/10.1109/ISGT50606.2022.9817477

Li, S., Wu, W., Lin, Y., et al. (2022). Robust data-driven and fully distributed Volt/VAR control for active distribution networks with multiple virtual power plants. *IEEE Transactions on Smart Grid*, *13*(4), 2627–2639. https://doi.org/10.1109/TSG.2022.3166274

Zhang, D., Das, C.K., Shafiullah, G.M., & Wong, K.W. (2021). Optimal allocation of distributed energy storage systems in unbalanced distribution networks. In 2021 IEEE Asia-Pacific Conference on Computer Science and Data Engineering (CSDE) (pp.1-6). IEEE.

https://doi.org/10.1109/CSDE53843.2021.9718379

Ahanch, M., & McCann, R. (2021). Integrated Volt/Var control and conservation voltage reduction in unbalanced distribution networks considering smart PV inverter control using equilibrium optimizer algorithm. In *2021 IEEE Kansas Power and Energy Conference* (pp. 1–6). IEEE.

https://doi.org/10.1109/KPEC51835.2021.9446226

Bakare, M. S., Abdulkarim, A., Zeeshan, M., & Shuaibu, A. N. (2023). A comprehensive overview on demand side energy management towards smart grids: Challenges, solutions, and future direction. *Energy Informatics*, *6*, 4.

https://doi.org/10.1186/s42162-023-00262-7

Guergah, M., Nebti, K., Rezgui, S.E., Benalla, H., & Ould-Abdeslam, D. (2023). Power quality enhancement using active power filter five-level cascade H-bridge under unbalanced and distorted grid. Electrical Engineering & Electromechnics, (1), 20-24. https://doi.org/10.20998/2074-272X.2023.1.03

Padullaparti, H. V., Pratt, A., Mendoza Carrillo, I., Tiwari, S., Baggu, M., Bilby, C., & Ngo, Y. (2023). Peak demand management and voltage regulation using coordinated virtual power plant controls. *IEEE Access*, *11*, 130674–130687. https://doi.org/10.1109/ACCESS.2023.3334607

Kanilius, G. F., Isaac, J. I., & Falama, R. (2024). Smart grid technologies: Advancements and applications in Nigeria. *Journal of Multidisciplinary Science: MIKAILALSYS*, *2*(3), 359–370. https://doi.org/10.58578/mikailalsys.v2i3.3777

APPENDIX 1

```
% Network Parameters Definition
function network = initialize_network()
network.V_base = 33e3;          % Base voltage (V)
network.S_base = 10e6;          % Base power (VA)
network.freq = 50;              % Frequency (Hz)
network.L_total = 120;          % Total length (km)
network.n_sections = 6;         % Number of sections
network.R_per_km = 0.195;       % Resistance (Ω/km)
network.X_per_km = 0.35;        % Reactance (Ω/km)
% Calculate section parameters
network.R_section = network.R_per_km * (network.L_total/network.n_sections);
network.X_section = network.X_per_km * (network.L_total/network.n_sections);
network.Z_section = complex(network.R_section, network.X_section);
return network;
end
```

APPENDIX 2

```
function loads = distribute_loads(network, S_total, PF)
% Distribute load equally among sections
S_per_section = S_total / network.n_sections;
P_per_section = S_per_section * PF;
Q_per_section = S_per_section * sin(acos(PF));
loads.P = P_per_section * ones(1, network.n_sections);
loads.Q = Q_per_section * ones(1, network.n_sections);
loads.S = S_per_section * ones(1, network.n_sections);
return loads;
end
```

APPENDIX 3

```
function [V, I, P_loss, Q_loss] = power_flow(network, loads)
% Initialize voltage at source
V = network.V_base * ones(1, network.n_sections + 1);
% Initialize arrays
I_line = zeros(1, network.n_sections);
P_loss = zeros(1, network.n_sections);
```

```
Q_loss = zeros(1, network.n_sections);
% Backward sweep: Calculate currents from load to source
for i = network.n_sections:-1:1
   % Sum of loads from this section to the end
   S_accumulated = sum(loads.S(1:i));
   I_line(i) = S_accumulated / (sqrt(3) * abs(V(i)));
   % Calculate section losses
   P_loss(i) = 3 * I_line(i)^2 * network.R_section;
   Q_loss(i) = 3 * I_line(i)^2 * network.X_section;
end
% Forward sweep: Calculate voltages from source to load
for i = 1:network.n_sections
   V(i+1) = V(i) - I_line(i) * network.Z_section;
end
return V, I_line, P_loss, Q_loss;
end
```

APPENDIX 4

```
function [temp_rise, time_to_trip] = cb_thermal_model(I_load, I_rated, tau, T_amb)
% Calculate temperature rise
if I_load > I_rated
   temp_rise = T_amb + (T_amb * ((I_load/I_rated)^2 - 1));
   % Calculate time to trip
   time_to_trip = tau * log(I_load^2 / (I_load^2 - I_rated^2));
   % Cap unrealistic trip times
   if time_to_trip > 86400  % > 24 hours
      time_to_trip = 86400;
   end
else
   temp_rise = T_amb;
   time_to_trip = inf;
end
return temp_rise, time_to_trip;
end
```

APPENDIX 5

```
function [dr_reduction, loss_reduction] = ami_model(load_pu, peak_threshold)
% AMI enables demand response based on real-time pricing
dr_reduction = 0;
if load_pu > peak_threshold
   % Demand response activation
   dr_reduction = 0.15 * (load_pu - peak_threshold) / (2 - peak_threshold);
   loss_reduction = 0.10;  % 10% loss reduction from improved monitoring
else
   loss_reduction = 0.05;  % 5% loss reduction from basic monitoring
end
```

```
return dr_reduction, loss_reduction;
end
```

APPENDIX 6

```
function [cb_capacity, loss_reduction] = apda_model(I_load, I_rated, T_amb)
% Adaptive protection adjusts CB rating based on thermal conditions
if T_amb < 35
   cb_capacity = I_rated * 1.25;  % 25% temporary capacity increase
   loss_reduction = 0.15;
elseif T_amb < 45
   cb_capacity = I_rated * 1.10;
   loss_reduction = 0.10;
else
   cb_capacity = I_rated * 1.00;
   loss_reduction = 0.05;
end
return cb_capacity, loss_reduction;
end
```

APPENDIX 7

```
function [V_opt, PF_opt, loss_reduction] = vvo_model(V_actual, PF_actual, network)
% Optimize voltage setpoints and reactive power
V_target = 1.02 * network.V_base;  % Target voltage
PF_target = 0.95;                  % Target power factor
% Voltage correction
if abs(V_actual) < 0.95 * network.V_base
   V_opt = V_target;
else
   V_opt = V_actual;
end
% Power factor correction
if PF_actual < PF_target
   PF_opt = PF_target;
   loss_reduction = 0.20;  % 20% loss reduction from VVO
else
   PF_opt = PF_actual;
   loss_reduction = 0.10;
end
return V_opt, PF_opt, loss_reduction;
end
```

APPENDIX 8

```
function [P_bess, SoC, loss_reduction] = bess_model(load_pu, SoC_initial, capacity)
% BESS operation: charge during low demand, discharge during peak
P_bess = 0;
SoC = SoC_initial;
if load_pu < 0.8 && SoC < 0.9 * capacity
```

```
    % Charging mode
    P_bess = min(0.2 * capacity, (0.9 * capacity - SoC) / 0.5);
    SoC = SoC + P_bess * 0.5;
    loss_reduction = 0.05;  % Minimal loss reduction during charging
elseif load_pu > 1.2 && SoC > 0.1 * capacity
    % Discharging mode (peak shaving)
    P_bess = min(0.3 * capacity, (SoC - 0.1 * capacity) / 0.5);
    SoC = SoC - P_bess * 0.5;
    loss_reduction = 0.22;  % 22% loss reduction from peak shaving
else
    loss_reduction = 0.10;  % Standby loss reduction
end
return P_bess, SoC, loss_reduction;
end
```

NON-PARAMETRIC ASSESSMENT OF WIND-SECTOR AND ELEVATION EFFECTS ON CONTAMINANT DISTRIBUTION AROUND A CEMENT FACTORY

Taiwo Abadunmi[1,*], Ayodele Olanrewaju Ogunlela[2], Kamorudeen Olaniyi Yusuf[2]
[1]*Division of Agricultural Colleges, Ahmadu Bello University, Zaria*
[2]*Agricultural and Biosystems Engineering, University of Ilorin*
Email: abadunmi@gmail.com*, aogunlela@unilorin.edu.ng, yusuf.ok@unilorin.edu.ng
***Corresponding author**: Taiwo Abadunmi
DOI: https://doi.org/10.67203/sp.ICESID.2026

ABSTRACT
Contaminants released from industrial point sources can build up in air, soil and water surrounding the source. A non-parametric statistical framework was used to assess the spatial distribution of contamination indicators for particulate matter (PM; n = 9), soil (n = 17), and water (n = 52) around a cement factory. Most variables, especially in the soil and water, were significantly non-normally distributed as indicated by Shapiro-Wilk tests ($p < 0.05$) consistent with point-source deposition. Simple radial distance was insignificant ($p > 0.05$) for all matrices under the Spearman's rank correlation analysis, suggesting that radial distance alone is not a good predictor of contamination gradients. Stratifying by prevailing upwind/downwind sector greatly increased the correlations, particularly those for particulate deposition rate and weight ($\rho = -1.000$, though based on a downwind subset of only n = 5 and therefore statistically fragile) and between topsoil lead and potassium ($\rho = -0.800$, also not formally significant at this smaller sample size); correlations remained low for water ($\rho = -0.05$ to -0.29) suggesting the soil column would act as a buffer to prevent vertical migration. The contamination of the topsoil was mostly independent of elevation, suggesting a depositional source from the atmosphere, while cadmium in the paired elevation subset of the water dataset (n = 30 of the 52 water points) was nominally negatively correlated with elevation ($\rho = -0.3057$; uncorrected $p = 0.049$, not surviving a multiple-comparisons correction), suggesting that the Cd is accumulating in low-lying hydrological sinks driven by topography. Our results demonstrate that the use of directional and topographic sampling designs substantially improves gradient resolution over radial distance sampling designs, with relevance to environmental monitoring around point-source facilities.

Keywords: *Industrial point sources; Spearman's rank correlation; wind-sector stratification; water contamination; cement industry*

1. INTRODUCTION

Point sources of air-borne particulate matter (PM) and associated trace metals emitted from cement manufacturing and other heavy industrial activities have been identified and are deposited onto adjacent soils, where the metals may leach into shallow ground water. The situation in Nigeria is exemplified by the studies conducted directly around cement manufacturing facilities, where topsoil levels of cadmium, cobalt, chromium, lead and nickel were found to be higher in proximity to the plant, and electrical conductivity and some metal concentrations lower, than away from the plant (Akpambang *et al.*, 2022). Similar distance-decay relationships are reported from other cement plants, in some of which additional information indicates that the decay is not exclusively radial; Bermudez *et al*. (2010) have reported that the concentrations of lithogenic material and metals in the topsoil around a cement plant in Argentina were best related by the combination of distance from the plant and topsoil organic matter content, with maximum enrichment on the downwind side of the plant under the prevailing wind direction. Likewise, Parlak *et al*. (2023) intentionally sampled soils from cement-plant sites at different angles and distances (1-7 km) since the authors anticipated that concentrations of heavy metals would differ with distance as well as sector and this was indeed the case.

The results are directionally sensitive, because atmospheric dispersion from a stack is not a diffuse or non-point source; the footprints of pollution are elongated and asymmetric, with the contamination's direction and shape determined in large part by the local meteorology (especially the wind direction and speed). Outside the cement industry, it is a documented trend that the soil heavy metal and magnetic susceptibility signatures around abandoned steel and iron plants have the highest values in the sector associated with the prevailing wind directions of the plant (Yang *et al*., 2020). Despite this, there remains a significant amount of environmental monitoring data, which still uses a straight distance from the facility as the main explanatory variable for contaminant decline, which has the potential to mask real spatial gradients when samples are collected both upwind (background) and downwind (impacted) of a facility and analyzed at the same distance.

A second layer of complexity is specific to groundwater and is the topography. Classical hydrogeological theory dictates that water will flow from high potential to low potential; that regional or horizontal groundwater flow and solutes will be controlled primarily by topography and geology, and not horizontal distance from a contamination source (Freeze & Cherry, 1979). This topographic control is particularly affecting mobile, weakly sorbing contaminants such as cadmium, which is highly mobile across a wide range of near neutral pH conditions, compared to other regulated heavy metals like lead or chromium which are more readily immobilized by the sorption to soil and aquifer material (Kubier *et al*., 2019). Due to being also a carcinogen at chronic low-level exposure and the establishment of WHO drinking-water guideline value of 0.003 mg/L (World Health Organization, 2017), cadmium behavior is of special practical and scientific interest. By contrast, contamination to soil is primarily due to fallout from the atmosphere, and is likely to be more evenly distributed across elevation than is water contamination. These processes (directional, wind-driven, and vertical, elevation-driven) must be separated from the simple horizontal distance to properly identify the contamination pathways and to be able to design a monitoring network that is statistically able to detect a real effect.

This study seeks to fill that gap by implementing a three tier, non-parametric, statistical framework for particulate matter, soil and water data taken around a cement manufacturing plant. Due to the skewed distribution of environmental contamination data near point sources (a few samples may contain much higher concentrations than the majority), throughout non-parametric methods were used because they are well suited for testing monotonic relationships, which is the equivalent of the Pearson correlation in the context of order statistics (Spearman, 1904). Specifically, the study was designed to: (1) characterize the distributional properties of each measured parameter using the Shapiro-Wilk test to determine the class of inferential statistics to be used; (2) test whether levels of contaminants decrease predictably with simple radial distance from the factory; (3) test whether stratification by prevailing downwind sector of samples would reveal more interpretable spatial gradients than would the undirected distance model; and (4) evaluate whether the elevation of sampling points has an independent effect on contaminant distribution, particularly in water. These objectives test the hypothesis that contamination gradients around a point-source industrial facility can only be described by combining directional and topographic controls, and that a distance alone is not sufficient.

2. METHODOLOGY

2.1 Study Area

The study was carried out around a Cement Plant which is situated in Obajana, Kogi State, North-Central Nigeria between latitude 7°54´N to 7°56´N and longitude 6°24´E to 6°27´E with an elevation of 200 - 420m (Global Energy Monitor, 2025). The Plant is the biggest single site cement plant in Africa, which utilizes a nearby quarry estimated to have 647 million tonnes of limestone reserves (Dangote Cement Plc, 2026). The land uses of the surrounding area comprise Guinea savannah vegetation, smallholder farm land, rural settlements, partially surrounded by quarry and plant infrastructure (Musa & Kpanache, 2014). The region is situated in the tropical wet and dry climatic zone of Kogi State and has an average annual rainfall of 1,839 mm, average temperatures in the region range between 27 and 31 °C (Akpambang *et al.*, 2022). The two-part regional wind rose classification in this study is based on dry season with the influence of harmattan (a dry dusty north easterly trade wind blowing from over the Sahara desert) and wet season with the influence of

monsoonal wind originating from the Atlantic (moist southwesterly monsoonal wind). Geologically, Kogi State overlies both Precambrian Basement Complex to the west and Cretaceous – Recent sedimentary cover (Anambra Basin) to the east while Obajana lies on top of a good thick limestone formation with lateritic residual soils overlying it, which is also mined locally as a cement additive (Obaje, 2018). Shallow ground water occurs in the weathered/fractured basement aquifer or sedimentary aquifer which is common in the area and is tapped locally by hand dug wells and boreholes (Akpambang *et al.*, 2022). The sampling locations for this study were distributed from the plant stack ranging from 0-5km, both in the dominant downwind direction and also upwind and across wind for directional stratification. Figure 1 is a schematic illustration of this design and does not depict actual GPS-derived sampling coordinates or true inter-point spacing.

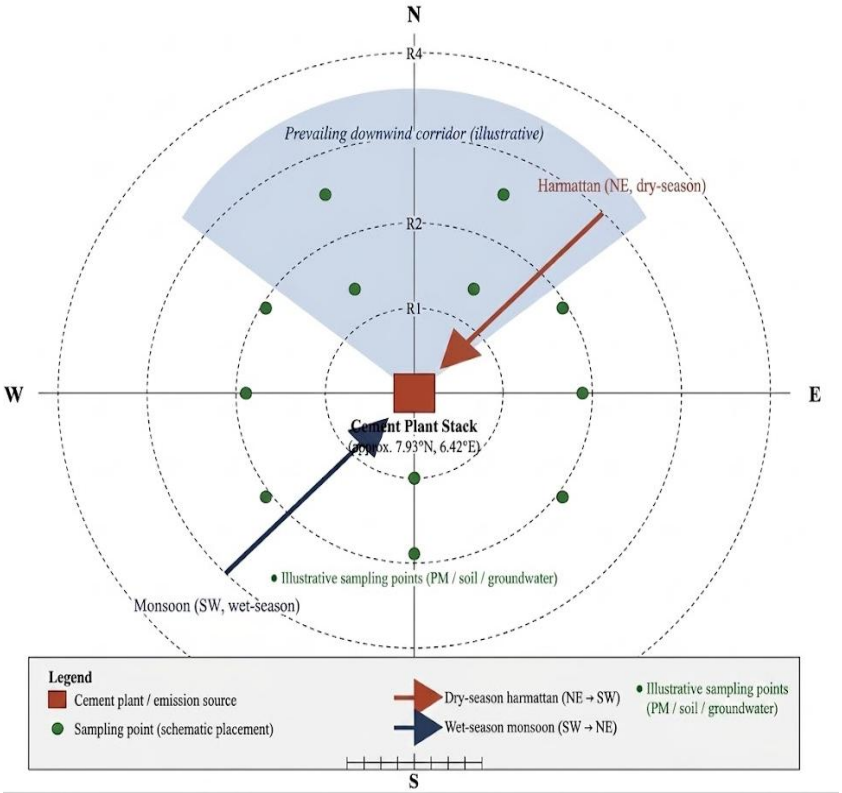

Figure 1: Schematic Site Layout and Wind Regime of the Study Area

2.2 Sampling Design and Sample Size

Three sample sets were collected: particulate matter deposition samples (n = 9), soil samples (n = 17), and water samples (n = 52; a subset of n = 30 water points with paired elevation data was used for the elevation-correlation analysis in Section 3.4). Sampling followed a radial (spoke-and-ring) design, in which points were distributed along transects radiating from the factory stack at the eight principal compass directions (N, NE, E, SE, S, SW, W, NW) and crossed with four concentric distance rings spanning the 1–5 km impact zone: R1 (≈ 1.0 km), R2 (≈ 2.0 km), R3 (≈ 3.5 km), and R4 (≈ 5.0 km, serving as the far-field/background reference). Not every direction × ring combination was sampled in every matrix, given the differing sample sizes across PM, soil, and water; point allocation was instead weighted toward the prevailing downwind corridor to maximize power for the directional analysis in Section 3.3, consistent with the sampling logic used in comparable cement-plant studies (Parlak *et al*., 2023). A sampling point was classified as falling within the prevailing downwind sector if its bearing from the stack fell within a ±45° arc centered on the seasonal-mean wind vector for the sampling period, determined from the nearest long-term meteorological record; the Nigerian Meteorological Agency (NiMet) synoptic station serving the Lokoja/Kogi area, cross-checked against ERA5 reanalysis wind fields for the same period (Hersbach *et al*., 2020; Nigerian Meteorological Agency, n.d.); with all remaining points classified as upwind/crosswind. Sampling was conducted during the peak dry season (harmattan period, February 2025), when the region's wind

direction is most stable and unimodal; this seasonal window is consistent with the strong, stable downwind correlations reported in Section 3.3. The resulting downwind vs. upwind/crosswind split was n = 5 vs. n = 4 for particulate matter, n = 10 vs. n = 7 for soil, and n = 30 vs. n = 22 for water; these stratified subset sizes, particularly for PM, are small and the resulting downwind correlations should be interpreted with this in mind (see Sections 3.3.1 and 3.3.4). Note that the water downwind subset (n = 30) is distinct from the elevation-paired subset (also n = 30; Section 3.4) — the two are defined by different criteria (wind sector vs. availability of elevation data) and do not necessarily contain the same sampling points.

2.3 Laboratory Analysis

Particulate matter weight and deposition rate were determined using passive dustfall collectors (petri-dish method) and analyzed gravimetrically. Soil physicochemical parameters (pH, electrical conductivity) and elemental concentrations (Ca^{2+}, Mg^{2+}, Na^{+}, K^{+}, Pb^{2+}, Mn, Cd, Cr, Ni, SO_4^{2-}, PO_4^{3-}, Cl^{-}, P) were determined following ASTM D6044 guidelines (ASTM, 2002). Water samples were analyzed for physical indicators (pH, electrical conductivity, turbidity, total dissolved solids, total suspended solids, total hardness, total alkalinity, free chlorine), major ions (Ca^{2+}. Mg^{2+}, Na^{+}, K^{+}, Cl^{-}, SO_4^{2-}, HCO^{3-}, CO_3^{2-}, PO_4^{3-}), and trace/heavy metals (Pb^{2+}, Cd, Cr, Ni, Cu, Zn, Mn, Hg, As, Fe, F-, NO^{3-}) using APHA Standard Methods (APHA, 2017). Sampling-point elevation (m) was recorded using handheld GPS. Comprehensive QA/QC protocols were implemented to ensure analytical accuracy, precision, and reproducibility in accordance with established standard methods (APHA, 2017). Field and reagent blanks were employed to detect potential contamination during sampling and laboratory procedures. Instrument calibration was conducted using certified reference standards, with calibration curves achieving correlation coefficients ($R^2 \geq 0.995$). Recovery efficiency was assessed through spike-recovery tests, yielding acceptable recoveries within 85–115%, while analytical precision was evaluated using duplicate samples (≥10% of total samples), maintaining relative percent differences below 10%. Accuracy was further verified using standard reference materials. For hydrochemical analyses, ionic balance error (IBE) was computed and maintained within ±5%, confirming the reliability of major ion determinations (APHA, 2017). Method detection limits for trace metals were established prior to analysis, and all reported concentrations exceeded these thresholds.

2.4 Statistical Analysis

Data normality was tested for each measured variable in each matrix (PM, soil and water) by Shapiro Wilk test (Shapiro & Wilk, 1965) with the null hypothesis that the sample was from a normally distributed population which was rejected at $p < 0.05$. The normality assumption was violated in all subsequent bivariate relationships and therefore all of them were examined with the non-parametric Spearman's rank correlation coefficient (ρ) (Spearman, 1904) which is a monotonic association measure for skewed environmental data. For each matrix three correlation analyses were carried out: (i) ρ between the concentration of contaminant and the simple radial distance from the factory stack (not direction); (ii) ρ between the concentration of contaminant and the distance in the prevailing downwind corridor, determined from site wind-rose data; and (iii) ρ between the concentration of contaminant and the elevation of the sampling point (m) (not radial distance). All tests were performed with $\alpha = 0.05$, p values of 0.05 – 0.10 were indicated as marginal/suggestive trends. There are many variables tested within each matrix and thus, results should be interpreted with the potential for false positives, a sensitivity follow-up check, Benjamini & Hochberg (1995) false discovery rate correction, is recommended to be done as a follow-up and is applied directly to the study's single nominally significant result (the cadmium-elevation correlation) in Section 3.4.3 and revisited in the Conclusion. Data analysis was conducted using R v4.3, Python SciPy (Stats module) and SPSS v26.

3. RESULTS AND DISCUSSION

3.1 Distribution Normality (Shapiro-Wilk Test)

In all three matrices, the majority of the measured variables were significantly more deviant from a normal distribution than not, with $p<0.05$, which meant that non-parametric correlation methods could be used throughout the study.

3.1.1 Particulate Matter

Both PM metrics were highly right-skewed (Table 1), reflecting the typical exponential increase and decrease of concentrations seen in point-source atmospheric deposition.

Table 1: Shapiro-Wilk Normality Test Results for Particulate Matter Variables

Variable	W-statistic	p-value
Weight (g)	0.6722	0.0007
Deposition rate	0.6561	0.0004

Note: $n = 9$. $p < 0.05$ indicates significant deviation from normality.

3.1.2 Soil Samples

The majority of the structural minerals and chemical trace indicators of soil were significantly non-normal; a lesser number of minerals (Mg^{2+}, Na^{+}, Pb^{2+}, Mn) were not significantly different from normal (Figure 2).

3.1.3 Water Samples

The majority of physical and chemical properties in the water were not normal, only a few major ions (Na^{+}, Cl^{-}, SO_4^{2-}, PO_4^{3-}, and total solids) were consistent with a normal distribution (Figure 2).

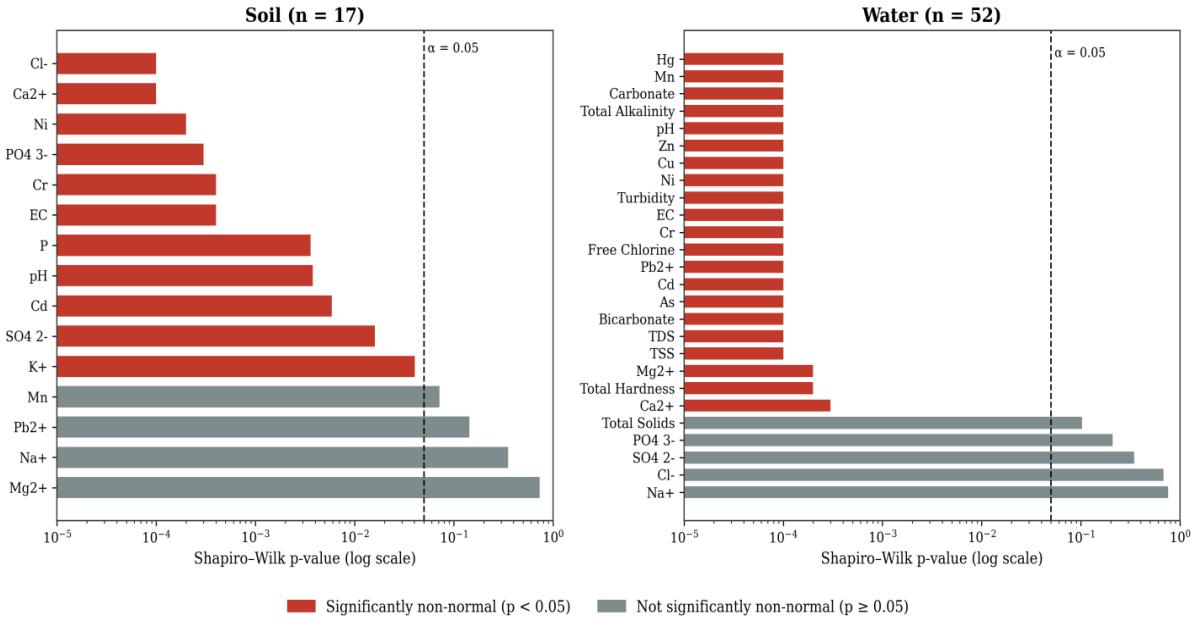

Figure 2: Shapiro–Wilk Normality Test Results for Soil and Water Variables (log-scaled p-value; dashed line marks α = 0.05).

Why Distributions were predominantly Non-Normal.

The non-normality seen in all three matrices (Figure 2) is typical of contamination associated with a point source that can lead to a right-skewed distribution. This is not just a function of small sample sizes, as the Shapiro-Wilk procedure was created as a general test for departures from normality because such departures, in particular skewed distributions, are common among real, un-controlled sampling data (Shapiro and Wilk, 1965), and skewed heavy-metal distributions are

regularly reported around the point source of a cement plant and a metal smelter (Bermudez *et al*., 2010; Parlak *et al*., 2023). This pattern should be considered as a methodological signature of the point-source impact, rather than a mere nuisance of the statistical kind that should be transformed away, as a number of near-source samples drive the overall pattern.

3.2 Spearman's Rank Correlation with Radial Distance

Spearman's rank correlation (ρ) was then calculated for each variable vs the factory distance calculated from a stack without any stratification by direction to see if there was a predictable decrease in contamination with distance from the factory.

3.2.1 Particulate Matter (n = 9)

Weight and deposition rate were negatively correlated with distance in a monotonic manner (deposition rate ρ = -0.3333, p = 0.381; weight ρ = -0.2667, p = 0.488), reflecting the decreased impact of particulates with distance from the stack, but neither was of statistical significance at this sample size (Figure 3).

3.2.2 Soil Samples (n = 17)

Several other contaminants from the industrial plume had the expected decreasing relationship with distance (cadmium, manganese, lead, nickel) and pH had the expected increasing relationship (ρ = +0.3341) indicating a slight increase in soil pH with distance from the depositional source. The trend for all the univariate analyses was not significant at the α = 0.05 level (Table 2).

Table 2: Spearman's Rank Correlation between Soil Parameters and Radial Distance

Parameter	**ρ**	**p-value**
pH	+0.3341	0.1900
Cadmium (Cd)	-0.3036	0.2361
Manganese (Mn)	-0.3031	0.2370
Potassium (K^+)	-0.2722	0.2905
Phosphorus (P)	-0.2672	0.2999
Lead (Pb^{2+})	-0.2220	0.3919
Nickel	-0.2211	0.3937
Chromium (Cr)	+0.1585	0.5435
Calcium ion (Ca^{2+})	-0.1436	0.5825
Sulfate (SO_4^{2-})	+0.1410	0.5893
Sodium (Na+)	-0.1324	0.6126
Magnesium (Mg^{2+})	+0.1172	0.6541
Electrical Conductivity	-0.0969	0.7115
Chloride (Cl^-)	+0.0687	0.7934
Phosphate (PO_4^{3-})	+0.0385	0.8833

3.2.3 Water Samples (n = 52)

Magnesium (ρ = -0.2682, p = 0.086) and cadmium (ρ = -0.2594, p = 0.097) had a weak negative correlation with distance while other factors were not significant (Table 3).

Table 3: Spearman's Rank Correlation between Water Parameters and Radial Distance

Parameter	ρ	p-value
Magnesium (Mg^{2+})	-0.2682	0.0860
Cadmium (Cd)	-0.2594	0.0972
Turbidity	-0.2356	0.1331
Chloride (Cl^-)	+0.2181	0.1654
Total Dissolved Solids (TDS)	-0.2143	0.1729
Chromium (Cr)	-0.2129	0.1758
Phosphate (PO_4^{3-})	-0.2014	0.2009
Calcium ion (Ca^{2+})	+0.1647	0.2973
Total Suspended Solids (TSS)	+0.1576	0.3190
Total Solids	-0.1557	0.3247
Sulfate (SO_4^{2-})	-0.1264	0.4250
pH	-0.1245	0.4319
Lead (Pb^{2+})	-0.1180	0.4567
Copper (Cu)	-0.1149	0.4686
Total Alkalinity	+0.1153	0.4670
Arsenic (As)	-0.0991	0.5322
Bicarbonate	-0.0900	0.5710
Mercury (Hg)	+0.0768	0.6286
Electrical Conductivity	-0.0490	0.7582
Zinc (Zn)	-0.0427	0.7882
Sodium (Na+)	+0.0331	0.8353
Nickel	-0.0267	0.8666
Total Hardness	+0.0221	0.8894
Carbonate	-0.0192	0.9039
Manganese (Mn)	-0.0116	0.9420
Free Chlorine	+0.0036	0.9817

3.2.4 Interpretation of the Radial-Distance Model

None of the radial-distance correlations reached significance in any matrix (Tables 2–3; Figure 3), which motivates the wind-stratified analysis in Section 3.3.

Why Simple Radial Distance is an Insufficient Predictor.

There was no statistically significant correlation between contaminant concentration and undirected radial distance, which is in agreement with the physical fact of atmospheric dispersion that contaminant plumes do not deposit in uniform concentric rings around a stack, but rather in elongated and skewed deposition patterns that are oriented along the prevailing wind axis. That's why several of the similar studies explicitly account for wind direction or compass sector from the outset, in addition to distance: Parlak *et al*. (2023) sampled the soils from cement plants in six compass directions at four distances from the sources because they expected there to be variation in soil contamination at the sector level; Yang *et al*. (2020) found that the sectors with the most contaminated soils were directly related to the prevailing wind directions at the site, not the sectors closest to the sources. In the undirected model reported here, background (upwind) samples are combined with impacted (downwind) samples where the impacted samples are at the same radial distance, causing the true spatial gradient to be diluted and capable of being masked. The finding has a direct methodological implication: sampling designs and statistical models which are only based on the Euclidean distance from a point source may systematically underestimate actual contamination gradients, concretely supported by the increase in the correlation coefficients when accounting for direction in Section 3.3.

3.3 Spearman's Rank Correlation Filtered by Wind Direction

The samples were split into the dominant downwind corridor (determined from the site wind rose data) and the correlation analysis was repeated to see if contaminant levels decreased more clearly with distance when direction is controlled for.

3.3.1 Particulate Matter

Both PM parameters showed a perfect negative correlation with distance in the downwind corridor (ρ = -1.000; Figure 3), based on a downwind-stratified subset of only n = 5 of the 9 total PM sampling points. A perfect rank correlation is close to inevitable with so few points, since almost any small set of values can be placed in a single monotonic order; the associated p-value is also not reliable here, because the standard t-approximation used to test Spearman's ρ has a $(1 - \rho^2)$ term in its denominator that goes to zero as ρ approaches ±1, which can report a spuriously small p-value regardless of sample size. This downwind PM result should therefore be read as a suggestive gradient rather than a statistically confirmed one, pending replication with a larger downwind sample.

3.3.2 Soil Samples

Correlation between heavy-industrial indicators and the downwind sector improved significantly, with lead and potassium each having ρ = -0.800, cadmium ρ = -0.400, and manganese having ρ = -0.632, although none were formally significant for this smaller downwind-stratified sample (n = 10; Figure 3). The downwind trends were positive for sulfate (ρ = +0.800), which suggests additional secondary deposition downwind, and for pH (ρ = +0.400), which again showed a positive trend as soils became more neutral/alkaline with distance from the source.

3.3.3 Water Samples

Water correlations were weak and non-significant across the downwind corridor (nickel ρ = -0.287; total dissolved solids ρ = -0.193; cadmium ρ = -0.162; sulfate ρ = -0.048; all $p > 0.05$; downwind-stratified n = 30; Figure 3), indicating that the soil column may buffer or attenuate vertical transport of contaminants deposited on the surface to the water table.

3.3.4 Summary of Directional Findings

Across the three matrices, downwind stratification produced strong, consistent distance-decay correlations for particulate matter and topsoil metals, but only weak, non-significant correlations for water (Figure 3; interpreted below).

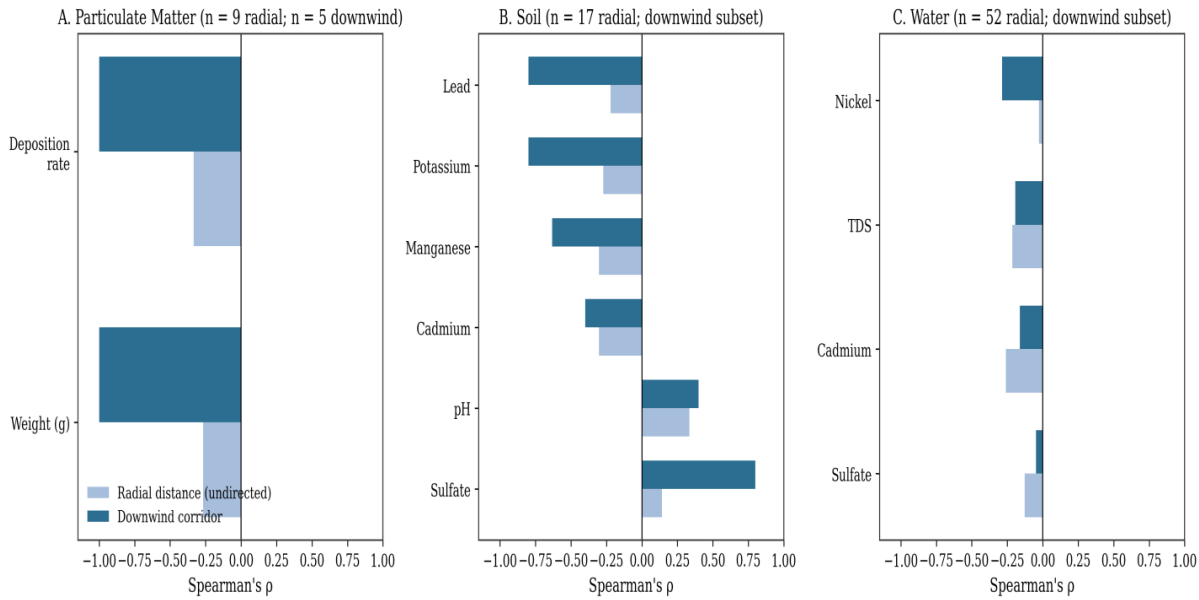

Figure 3: Spearman's ρ under the undirected radial-distance model versus the downwind-corridor model, for PM, soil, and water parameters reported in both analyses (Sections 3.2–3.3).

Directional Stratification substantially strengthens Spatial Signals. Although several of the correlations were not formally significant, due to small sample sizes in the stratified subsets, there was a significant improvement in the correlation with the prevailing downwind corridor (Figure 3) for both particulate matter (ρ = -1.000) and topsoil heavy metals (ρ up to -0.800 for lead and potassium).

This pattern was similar to that found by Bermudez *et al*. (2010) who found that the highest topsoil metal concentrations extracted with HCl were found downwind of the cement plant at the site where the wind flow was favorable, and were able to predict heavy metal concentrations with soil distance and soil organic matter once direction was taken into account. The coherence of the direction and magnitude of the present PM and soil results also indicates a coherent pathway from the atmosphere to the soil: material is transported downwind and settles on the surface of the top soil in a spatially decaying pattern that is similar to the one observed in the aerial deposition gradient. For soil and topsoil metals, the direction and magnitude of these trends are a compelling descriptive pattern, though formal confirmation at conventional significance levels would require larger downwind sample sizes. The PM correlation is a separate case: with a downwind subset of only n = 5, the perfect $\rho = -1.000$ reported in Section 3.3.1 is statistically fragile rather than confirmatory (see the caveat there). This directional coherence is consistent with the wider literature demonstrating that wind-aware sampling methods reveal gradients that are not observed in distance-only based methods (Parlak *et al*., 2023; Yang *et al*., 2020).

Evidence for Soil as a Geochemical Buffer Protecting Water.

However, water correlations were relatively weak and statistically flat (Section 3.3.3) within the same downwind corridor as were PM and soil correlations. This is consistent with the soil column being a geochemical buffer; that is, heavy metals and other contaminants that are added to the surface of the soil are significantly adsorbed, retained or transformed by the soil matrix before they can leach into the underlying aquifer. This interpretation is consistent with the differential mobility behaviour of heavy metals in soil-water systems described in the literature: Cadmium is comparatively weakly sorbed and is expected to be mobile in solution over a wide near neutral pH range, giving it the highest potential to be mobilized in groundwater, whereas more strongly sorbed metals such as lead and chromium are expected to remain strongly bound to soil particles and are therefore not expected to show a significant relationship with topography in groundwater (Kubier *et al*., 2019). The present finding has a positive practical implication as it indicates that, at least for the present, groundwater at this site may be fairly well protected from surface contamination for most of the metals; however, there is also a negative implication which is that continued or increased deposition could eventually cause the soil to become saturated with metals and therefore the adso-porosity is no longer available for protection; therefore, a longitudinal monitoring program should be undertaken to monitor this; cadmium is an example metal that is relatively poorly retained and should be monitored particularly.

3.4 Spearman's Rank Correlation with Sampling-Point Elevation

To separate topography-driven (vertical) transport from radial distance or wind sector (horizontal) deposition, Spearman's rank correlation was calculated between each variable and the sampling-point elevation (m) without considering radial distance or wind sector.

3.4.1 Particulate Matter

Table 4: Spearman's Rank Correlation between Particulate Matter Parameters and Elevation

Parameter	ρ	p-value
Deposition rate	0.3667	0.33174
Weight (g)	0.2833	0.46003

3.4.2 Soil Samples

No soil parameter was significantly correlated with elevation (all $p > 0.05$; Table 5), in contrast to water (Section 3.4.3); this contrast is interpreted below

Table 5: Spearman's Rank Correlation between Soil Parameters and Elevation

Parameter	ρ	p-value
Calcium ion	+0.3926	0.11901
Manganese	-0.3313	0.19396
Magnesium	+0.2900	0.25894
Sodium	-0.1838	0.48003
Potassium	-0.1704	0.51308
Chloride	-0.1704	0.51308
Lead	+0.1324	0.61237
Electrical Conductivity	-0.1288	0.62237
Phosphate	-0.0944	0.71851
Sulfate	-0.0895	0.73261
pH	+0.0832	0.75086
Chromium	+0.0737	0.77860
Phosphorus	-0.0588	0.82256
Nickel	+0.0393	0.88092
Cadmium	+0.0148	0.95519

3.4.3 Water Samples

Cadmium was the only nominally significant elevation relationship among every correlation reported in this study (verified across Tables 2–5 and Figures 3–4, and the accompanying text in Sections 3.2–3.4); the major rock-forming ions (calcium, magnesium) showed weak, non-significant relationships with elevation. However, this p-value (0.049) is uncorrected: with roughly 30 variables tested for elevation correlation in the water matrix alone, a Benjamini–Hochberg correction (critical threshold ≈ 0.0017 for the smallest-ranked p-value at α = 0.05) would not preserve this result as significant. The cadmium-elevation finding should therefore be treated as a candidate signal warranting targeted confirmatory sampling, not as a statistically confirmed effect.

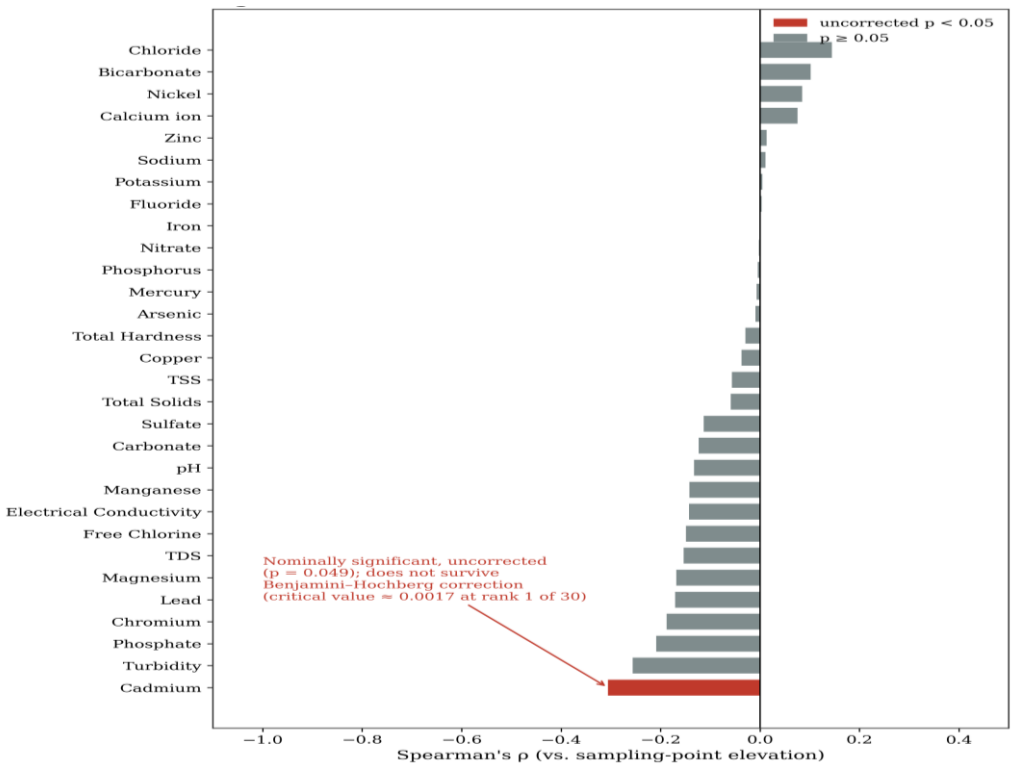

Figure 4: Spearman's ρ between water parameters and sampling-point elevation (n = 30). Cadmium is the only nominally significant relationship (uncorrected p = 0.049); this does not survive a Benjamini–Hochberg correction across the 30 variables tested (Section 3.4.3).

Elevation is an Independent Predictor of Water Contamination but not Soil Contamination.

The soil-water distinction is reinforced in the elevation-based analysis using another perspective. There were no significant differences in topsoil concentrations by elevation, as would be expected if the deposition mechanism (falling dust) were not sensitive to gravity-driven down-slope redistribution. This is not the case, however, for water cadmium, where there was a nominally significant negative correlation with elevation (ρ = -0.3057, uncorrected p = 0.049; Figure 4) — a result that does not survive a multiple-comparisons correction (see Section 3.4.3) — tentatively suggesting that contaminants may be moved toward lower elevations of the catchment when they reach the subsurface. This is the mechanism that is predicted by fundamental groundwater flow theory and one in which water, and the solutes it carries, flow from high hydraulic head to low hydraulic head; thus, water flow generally follows topography instead of horizontal distance from the sources of the mobile solutes (Freeze & Cherry, 1979). One plausible hypothesis, not directly tested here since only cadmium reached even nominal significance among the metals examined, is that cadmium is not unique in being subject to this topographic transport process but is simply the most sensitive regulated metal for detecting it, owing to its relatively high mobility and weak sorption compared to the other regulated metals measured; other metals might transport along the same path at a lower concentration or rate not detected at this sample size. This hypothesis would require dedicated testing — for example, comparing sorption-normalized mobility across metals — before it can be treated as an interpretation rather than a speculation. The non-significant elevation relationships for the major rock-forming ions (Ca^{2+}, Mg^{2+}) also support the interpretation of a relatively uniform lithological dissolution signal from the background water chemistry, with the elevation-cadmium relationship representing an anthropogenic, topographically-routed contamination signal. However, since the WHO guideline value for cadmium in drinking water is 0.003 mg/L, any low-lying groundwater area that is even modestly contaminated would be of practical concern for any wells or boreholes located in those areas and this sub-population of sampling points would be a reasonable priority for follow-up, higher frequency monitoring.

3.5 Implications for Environmental Monitoring and Risk Management

The results of these studies, in addition to their statistical value, are significant for the design and prioritization of monitoring programs for cement works and similar point sources. First, the strong downwind gradients that occurred for particulate matter and topsoil metals (Section 3.3) suggest that monitoring budgets should be used disproportionately along the prevailing downwind corridor, as opposed to monitoring in a manner that is even around the facility perimeter, because a few stations located downwind are likely to give a better sense of impact than a larger number of stations distributed without any consideration for wind direction. Second, the apparent buffering effect of the soil column (Section 3.3) indicates that soil sampling can at least be temporarily used as an early warning indicator of groundwater risk: heavy metals are likely to build up in soil long before reaching the aquifer, and therefore a soil monitoring program based on an increase in levels over time may be able to warn of impending catchments that may be in danger of contamination before groundwater is actually detected. Third, the elevation-related cadmium signal in water (Section 3.4) also supports topography-informed borehole placement, rather than boreholes sited solely for ease of access. Boreholes placed in low-lying areas of the catchment are more likely to intercept the mobile solutes, such as cadmium, that this study found to accumulate there — though, as noted in Section 3.4, this remains a preliminary signal pending confirmatory sampling. When combined, these three implications suggest an approach to monitoring explicitly based on meteorology and topography, and not simply management convenience or spatial uniformity, which may be applicable to other point-source polluters with similar emission-deposition-transport physics, such as the mining, metal smelting and thermal power generation sectors documented in previous studies (Bermudez *et al*., 2010; Yang *et al.*, 2020; Parlak *et al*., 2023).

4. CONCLUSION

This study shows that undirected radial distance from a point-source cement facility is an unreliable predictor of contaminant distribution in particulate matter, soil, and water. Wind-sector stratification substantially strengthened distance-decay correlations for particulate matter ($\rho = -1.000$, $n = 5$) and topsoil metals (ρ up to -0.800), a descriptive pattern consistent with atmospheric deposition following a directional rather than concentric pathway, though these stratified subsets are small and the pattern awaits confirmation with a larger downwind sample. Water, in contrast, correlated weakly with both distance and wind direction, but cadmium showed a nominally significant negative correlation with sampling-point elevation ($\rho = -0.3057$, uncorrected $p = 0.049$, which does not survive a multiple-comparisons correction), tentatively suggesting that once contaminants pass the soil buffer, topography rather than proximity to the source governs their movement toward the water table. For engineering practice, these findings support replacing uniform radial monitoring networks with a matrix-specific design informed by wind direction and topography around point sources.

The study is limited by small and uneven sample sizes across matrices and stratified subsets, a single dry-season sampling round, and the absence of a multiple-comparison correction, so marginal results ($0.05 \leq p < 0.10$) should be interpreted cautiously. Future work should extend sampling across seasons and additional downwind locations to confirm these gradients, apply a Benjamini–Hochberg correction when testing multiple parameters simultaneously, and pair soil-adsorption or leaching trials with local groundwater hydraulic-gradient data to directly test the soil-buffering and topographic-accumulation mechanisms proposed here.

5. REFERENCES

Akpambang, V. O. E., Ebuzeme, G. C., & Akinola, J. O. (2022). Heavy metal contamination of topsoil around a cement factory – A case study of Obajana Cement Plc. Environmental Pollutants and Bioavailability, 34(1), 12–20. https://doi.org/10.1080/26395940.2021.2024090

American Public Health Association (APHA). (2017). Standard methods for the examination of water and wastewater (23rd ed.). APHA, AWWA, WEF.

Benjamini, Y., & Hochberg, Y. (1995). Controlling the false discovery rate: A practical and powerful approach to multiple testing. Journal of the Royal Statistical Society: Series B, 57(1), 289–300. https://doi.org/10.1111/j.2517-6161.1995.tb02031.x

Bermudez, G. M. A., Moreno, M., Invernizzi, R., Plá, R., & Pignata, M. L. (2010). Heavy metal pollution in topsoils near a cement plant: The role of organic matter and distance to the source to predict total and HCl-extracted heavy metal concentrations. Chemosphere, 78(4), 375–381. https://doi.org/10.1016/j.chemosphere.2009.11.012

Dangote Cement Plc. (2026). Obajana Cement Plant. Retrieved July 2026, from https://dangotecement.com/nigeria-operations/

Freeze, R. A., & Cherry, J. A. (1979). Groundwater. Prentice-Hall.

Global Energy Monitor. (2025). Dangote Cement PLC Obajana Cement Plant. https://www.gem.wiki/Dangote_Cement_PLC_Obajana_Cement_Plant

Hersbach, H., Bell, B., Berrisford, P., Hirahara, S., Horányi, A., Muñoz-Sabater, J., Nicolas, J., Peubey, C., Radu, R., Schepers, D., Simmons, A., Soci, C., Abdalla, S., Abellan, X., Balsamo, G., Bechtold, P., Biavati, G., Bidlot, J., Bonavita, M., … Thépaut, J.-N. (2020). The ERA5 global reanalysis. Quarterly Journal of the Royal Meteorological Society, 146(730), 1999–2049. https://doi.org/10.1002/qj.3803

Kubier, A., Wilkin, R. T., & Pichler, T. (2019). Cadmium in soils and groundwater: A review. Applied Geochemistry, 108, Article 104388. https://doi.org/10.1016/j.apgeochem.2019.104388

Musa, D., & Kpanache, D. (2014). The impact of Obajana Cement Company as a growth pole in Obajana, Kogi State, Nigeria. Ethiopian Journal of Environmental Studies and Management, 7(1), 73–81. https://doi.org/10.4314/ejesm.v7i1.9

Nigerian Meteorological Agency. (n.d.). About NiMet. Retrieved July 2026, from https://nimet.gov.ng/about

Obaje, N. G. (2018). Geology and mineral resources of Kogi State, Nigeria [Conference paper]. ResearchGate.

Parlak, M., Everest, T., & Tunçay, T. (2023). Spatial distribution of heavy metals in soils around cement factory and health risk assessment: A case study of Canakkale-Ezine (NW Turkey). Environmental Geochemistry and Health, 45(7), 5163–5179. https://doi.org/10.1007/s10653-023-01578-9

Shapiro, S. S., & Wilk, M. B. (1965). An analysis of variance test for normality (complete samples). Biometrika, 52(3/4), 591–611. https://doi.org/10.2307/2333709

Spearman, C. (1904). The proof and measurement of association between two things. American Journal of Psychology, 15(1), 72–101. https://doi.org/10.2307/1412159

World Health Organization. (2017). Guidelines for drinking-water quality (4th ed., incorporating the 1st addendum). World Health Organization.

Yang, P., Drohan, P. J., & Yang, M. (2020). Patterns in soil contamination across an abandoned steel and iron plant: Proximity to source and seasonal wind direction as drivers. Catena, 190, Article 104537. https://doi.org/10.1016/j.catena.2020.104537

OPTICAL EMISSION SPECTROSCOPY (OES) ANALYSIS OF CORROSION OF HIGH-GRADE CONVENTIONAL 5 MM UKRAINIAN METALLIC PLATE USED IN TANKER TRUCK FABRICATION IN NIGERIA

Jamilu Haruna[1,*], Abdulkareem Abubakar[1], Usman Abubakar Zaria[1], Abdulmajid M. Nainna[1]

[1]""

Email: jamiluharuna220@yahoo.com[*], aavazi@gmail.com, augayya@yahoo.com, amnainna@gmail.com

***Corresponding author**: Jamilu Haruna

DOI: https://doi.org/10.67203/sp.ICESID.2026

ABSTRACT

Elemental compositional analysis (OES) provides a metallurgical basis for interpreting corrosion severity in tanker steel beyond what mass-loss or electrochemical measurements alone can show. This research studies changes in the elemental composition of carbon steel metallic plate due to corrosion in PMS and AGO medium using bulk Optical Emission Spectroscopy (OES). The study considers control (unexposed), PMS-corroded and AGO-corroded coupons of high-grade conventional 5 mm Ukrainian carbon steel plate (4.5 mm actual thickness) used for tanker fabrication in Nigeria, following 63-day immersion at ambient temperature. OES showed a progressive decrease in iron content from 98.251 wt.% (control) to 98.052 wt.% (PMS) and 97.700 wt.% (AGO), determined by mass-balance difference from the fully quantified element set, accompanied by a corresponding relative enrichment of carbon, chromium, copper and tungsten, consistent with preferential anodic dissolution of iron. The elemental trends from bulk OES confirm AGO as the more aggressive corrosive medium than PMS.

Keywords: *Carbon steel; OES; elemental composition; corrosion; PMS; AGO*

1. INTRODUCTION

Road transportation remains the dominant means of transporting refined petroleum products, including Premium Motor Spirit (PMS) and Automotive Gas Oil (AGO), from depots to retail outlets across Nigeria, with tanker trucks constructed predominantly from carbon steel forming the backbone of this distribution network. Existing studies on Nigerian petroleum tanker safety have focused heavily on policy, logistics, driver behaviour, and regulatory enforcement, leaving the material integrity of the tanker shell relatively underexamined. Mass-loss (gravimetric) and electrochemical (potentiodynamic polarization) techniques can quantify the amount of metal lost and the rate of electrochemical dissolution due to corrosion, respectively; however, neither technique directly reveals how the bulk metallurgical composition of the steel changes as corrosion progresses. Optical Emission Spectroscopy (OES) provides rapid and quantitative determination of bulk elemental composition and is therefore well suited to tracking compositional changes associated with corrosion, providing a metallurgical perspective on the same degradation process captured by weight-loss and electrochemical measurements.

This study applies bulk OES to control (unexposed), PMS-corroded, and AGO-corroded coupons of a high-grade conventional 5 mm Ukrainian carbon-steel plate (4.5 mm actual thickness) used for tanker fabrication in Nigeria. The coupons were fully immersed in PMS and AGO for 63 days under ambient laboratory conditions. The study aimed to investigate corrosion-induced changes in the elemental composition of the carbon-steel plate following exposure to PMS and AGO and to compare the compositional changes associated with the two petroleum-product media.

2. LITERATURE REVIEW

Optical Emission Spectroscopy (OES) is an established analytical technique for determining the elemental composition of metallic materials and is particularly useful for rapid quantitative

characterization of carbon steels. In corrosion research, elemental characterization is important because the chemical composition of steel influences its microstructure, mechanical properties and susceptibility to environmental degradation. Ishtiaq et al. (2022), for example, combined OES with Scanning Electron Microscopy and Energy-Dispersive Spectroscopy (SEM/EDS) to investigate the relationship between elemental composition, microstructure and corrosion behaviour of AISI carbon steels. Their findings indicated that steels with relatively fine ferrite–pearlite microstructures exhibited lower corrosion susceptibility than steels with coarser or more heterogeneous microstructures. This demonstrates the value of combining elemental and microstructural characterization when evaluating the corrosion behaviour of carbon-steel materials.

The importance of elemental composition to the performance of carbon steel has also been demonstrated using other analytical techniques. Borisade et al. (2021) employed X-ray fluorescence (XRF), a related elemental-characterization technique, to investigate the relationship between chemical composition and mechanical properties of carbon steel. Although their study did not involve corrosion exposure, it demonstrated that elements such as carbon and manganese, together with residual alloying elements, influence important mechanical properties such as strength and toughness. These findings are relevant to tanker-truck fabrication because variations in the chemical composition of locally sourced or fabricated steel plates may influence both their initial mechanical performance and subsequent susceptibility to corrosion.

An important consideration when applying OES to corroded steel is the interpretation of changes in elemental weight percentages. An apparent increase in the relative concentration of an alloying element after corrosion does not necessarily indicate that the element has been introduced into, or accumulated in, the steel. Rather, it may result from preferential dissolution of iron from the sampled metallic region, leaving the remaining alloying elements relatively enriched in percentage terms. Thus, an increase in the measured percentage of Mn, Si, Cr or other elements after exposure should not automatically be interpreted as an increase in their absolute mass.

This interpretation is consistent with the classical concept of preferential dissolution in iron-based alloys described by Marshakov (2002), whereby different alloy constituents may dissolve at different rates during anodic corrosion. More recent observations by Kowalczyk et al. (2025) further demonstrate the importance of selective corrosion in steel components. Their investigation of steel pipeline welds reported localized corrosion pits reaching substantial depths and associated deterioration in mechanical performance, illustrating the relationship between localized material degradation and structural integrity.

Accordingly, in the present study, changes in OES-determined elemental percentages between the unexposed control steel and the PMS- and AGO-exposed specimens are interpreted primarily as relative compositional changes within the sampled metallic material, rather than as evidence that new alloying elements were generated or added during corrosion. This distinction is essential for scientifically valid interpretation of OES results. Although OES provides quantitative elemental information, it does not by itself provide a complete description of the physical morphology of corrosion damage.

Despite the established use of OES and related elemental techniques for characterizing carbon steels, several important limitations remain in the existing literature. First, previous studies such as Ishtiaq et al. (2022) have demonstrated the usefulness of combining OES with SEM/EDS for relating steel composition and microstructure to corrosion behaviour, but their investigation was not specifically concerned with carbon-steel plates used in petroleum tanker-truck fabrication under Nigerian operating conditions.

Second, Borisade et al. (2021) demonstrated the relationship between elemental composition and mechanical properties using XRF, but their work considered the initial material condition rather than corrosion-induced compositional changes. Consequently, it does not establish how the elemental composition of carbon-steel plate changes following exposure to petroleum products.

Third, much of the petroleum-fuel corrosion literature has concentrated on gravimetric weight loss, electrochemical polarization and surface morphology, with studies by Cursaru et al. (2014), Heryana et al. (2024), Adama et al. (2024, 2025), Chile et al. (2022) and Kugelmeier et al. (2021) providing evidence of corrosion through one or more of these approaches. However, these studies provide limited information on the elemental-compositional dimension of corrosion of tanker-grade carbon-steel plates. This limitation is particularly significant for Nigeria, where carbon-steel plates are widely

relevant to petroleum-product transportation and where locally fabricated tanker bodies may experience variable material quality, fabrication practices and service conditions.

The specific research gap addressed by this study is therefore elemental and corrosion assessment of carbon-steel tanker-fabrication plates exposed to PMS and AGO under Nigerian-relevant conditions using OES. The present study addresses this gap by applying OES to establish the elemental composition of the unexposed carbon-steel plate; determine the elemental composition after controlled exposure to PMS; determine the elemental composition after controlled exposure to AGO; identify changes in the relative concentrations of major alloying and residual elements; interpret these changes in relation to preferential/selective dissolution during corrosion

3. MATERIALS AND METHODS

3.1 Materials and Baseline Characterization

Fresh carbon steel plate of 4.5 mm actual thickness (locally referred to as high-grade conventional 5 mm Ukrainian metallic plate) was procured from Dan Magaji Tanker Fabricators, Zaria, Nigeria. To establish the baseline characteristics of the material and verify its authenticity, the specimen was characterized using Scanning Electron Microscopy coupled with Energy Dispersive X-ray Spectroscopy (SEM-EDS) at the Nigerian Building and Road Research Institute (NBRRI), Abuja, and Optical Emission Spectroscopy (OES) at the Defence Industries Corporation of Nigeria (DICON), Kaduna. The OES analysis was used to determine the bulk chemical composition of the carbon steel, while the SEM-EDS analysis characterized the surface morphology and provided supporting elemental information.

Figure 3.1: The 4.5 mm carbon steel plate

3.2 Corrosion Exposure

Premium Motor Spirit (PMS) and Automotive Gas Oil (AGO) used for the study were purchased from AA Rano Filling Station, Sokoto Road, Zango, Samaru, Zaria. A volume of 500 mL each of PMS and AGO was poured separately into clean plastic containers, and carbon steel coupons were immersed separately in each medium for an exposure period of approximately 63 days (14/04/2026 to 16/06/2026) under ambient laboratory temperature conditions (approximately 25–33°C, not actively controlled). Containers were tightly sealed to minimise air ingress, contamination and evaporation, and the fuel charge in each container was not replenished or topped up at any point during the 63-day exposure period; the single-charge, sealed-container configuration was adopted specifically to limit evaporative loss of the volatile PMS fraction. After removal from the immersion media, loose corrosion products were gently removed using a soft brush, and the specimens were immersed in a hydrochloric acid (HCl) solution for 10 minutes to remove adherent corrosion products, rinsed with distilled water followed by ethanol, and dried in a desiccator prior to analysis.

Figure 3.2: Sealed plastic containers with carbon steel coupons immersed in PMS and AGO

3.3 OES Analysis

Optical Emission Spectroscopy was conducted on three sets of coupons: control (unexposed), PMS-corroded (P) and AGO-corroded (D) carbon steel samples, to determine the bulk elemental composition and evaluate the compositional changes associated with prolonged immersion in the two petroleum products. Because OES reports elemental composition as a weight percentage of a fixed near-surface sampled volume, any reduction in iron content caused by anodic dissolution mathematically raises the weight-percentage share of every element that remains, even though the absolute mass of those elements in the specimen has not increased. Increases recorded for carbon, chromium, copper, tungsten, manganese and other elements after exposure are therefore interpreted throughout this study as relative enrichment arising from preferential iron dissolution, consistent with the classical preferential-dissolution mechanism described by Marshakov (2002), rather than as evidence of new alloying elements entering the steel. Iron content is reported to three decimal places throughout this paper as the mass-balance difference, Fe wt.% = 100 − Σ (all other quantified elements), for internal consistency with the other, directly measured elements; this calculation is applied consistently across Tables 1–3. Each specimen (control, PMS-corroded, AGO-corroded) was analysed by a single bulk OES scan, without replicate sparking or a separately reported standard deviation; this single-scan approach is a limitation of the present dataset, and replicate OES scans per condition are recommended for future work to allow measurement precision and reproducibility to be quantified.

4. RESULTS AND DISCUSSION

4.1 Baseline (Fresh) Elemental Composition

The baseline OES elemental composition of the fresh carbon steel is presented in Table 1.

Table 1: Fresh carbon steel OES elemental composition

Element	OES Weight %
Fe	98.251
C	0.408
Mn	0.425
Si	0.129
Cr	0.126
Ni	0.037
Cu	0.475
Nb	0.038
W	0.044
O	ND
Others	Trace

According to the OES analysis, the steel consists predominantly of iron (98.251 wt%), confirming that it is an iron-based structural steel. Carbon (0.408 wt%) is the principal strengthening element, placing the material in the medium-carbon steel category according to the standard ASTM/SAE carbon-content classification scheme (0.25–0.60 wt% C). Manganese (0.425 wt%) improves tensile strength, hardenability and wear resistance, while silicon (0.129 wt%) acts as a deoxidizer during steelmaking. The low concentrations of chromium, nickel and copper indicate that the material is a plain carbon steel with only residual alloying elements, and the negligible sulphur and phosphorus content is consistent with the compositional requirements of ASTM A36/A36M structural carbon steel. The OES carbon value (0.408 wt%) is used for alloy classification throughout this study.

4.2 Elemental Composition After Corrosion Exposure

Table 2 presents the OES elemental composition of the control, PMS-corroded and AGO-corroded carbon steel specimens after the 63-day exposure period.

Table 2: OES elemental composition of carbon steel control, PMS-corroded and AGO-corroded

Element (wt.%)	Control	PMS (P) corroded	AGO (D) corroded	Observation
Fe	98.251	98.052	97.700	Progressive decrease
C	0.408	0.530	0.730	Relative enrichment
Si	0.129	0.126	0.129	Essentially unchanged
Mn	0.425	0.444	0.483	Slight relative enrichment
Cr	0.126	0.133	0.155	Relative enrichment
Ni	0.037	0.052	0.037	Slight fluctuation
Cu	0.475	0.493	0.550	Relative enrichment
Nb	0.038	0.039	0.041	Slight relative enrichment
W	0.044	0.061	0.098	Marked relative enrichment
Ce	0.015	0.017	0.020	Slight relative enrichment
La	0.052	0.053	0.057	Slight relative enrichment
Zr	0.0000	0.0000	0.0000	Not detected

The control specimen exhibited an iron content of approximately 98.251 wt.%, confirming that the investigated material is predominantly a carbon steel, with a carbon content of 0.408 wt.% and manganese content of 0.425 wt.% indicating a medium-carbon steel with minor alloying additions of chromium, copper, nickel, niobium and tungsten. This control composition provides the baseline against which the changes induced by petroleum product exposure are evaluated.

Following immersion in PMS, the iron content decreased slightly from approximately 98.251 wt.% to 98.052 wt.%, indicating dissolution of the steel matrix during corrosion. Simultaneously, the apparent carbon concentration increased from 0.408 wt.% to 0.530 wt.%, while chromium, copper, tungsten, niobium and manganese also exhibited slight increases. As iron corrodes and is removed from the surface, the remaining alloying elements become relatively enriched within the analysed volume, resulting in higher measured weight percentages; the relatively small reduction in iron indicates that PMS produced only moderate degradation of the steel during the immersion period.

The AGO specimen exhibited the greatest compositional changes among the three samples. Iron decreased further to approximately 97.700 wt.%, representing the largest reduction observed. At the same time, carbon increased to 0.730 wt.%, chromium increased to 0.155 wt.%, copper to 0.550 wt.%, tungsten to 0.098 wt.%, and manganese to 0.483 wt.%, with lanthanum and cerium also showing slight enrichment. The greater reduction in iron demonstrates that AGO promoted more extensive dissolution of the steel matrix than PMS, and the enrichment of the remaining alloying elements became correspondingly more pronounced. The particularly noticeable increase in tungsten and copper suggests stronger preferential dissolution of iron in the diesel environment, providing metallurgical evidence that corrosion damage was more severe in AGO than in PMS. One element does not follow this general enrichment pattern: nickel rose from 0.037 wt.% (control) to 0.052 wt.% (PMS) before returning to 0.037 wt.% (AGO), rather than increasing monotonically with corrosion severity as C, Cr, Cu and W do. Given that Ni is present only at trace level (0.037–0.052 wt.%, among

the lowest concentrations quantified in this study), this fluctuation is most plausibly attributable to local heterogeneity in the sparked volume and measurement-level variability near the OES detection/quantification limit for this element, rather than to a distinct corrosion mechanism selectively affecting nickel; the single-scan measurement approach used in this study (Section 3.3) cannot distinguish between these possibilities; and replicate OES scans, recommended above, would be needed to establish whether the Ni trend is reproducible or is measurement noise.

4.3 Relationship Between OES Results and Independently Measured Corrosion Rates

One of the major strengths of this study is that the OES findings are fully supported by the gravimetric corrosion measurements independently obtained for the same steel and fuel media, reported in a companion submission to this conference (Jamilu et al., 2026b), as summarised in Table 3.

Table 3: Comparison of OES result with weight loss corrosion rates result

Method	AGO Corroded	PMS Corroded
Weight-loss corrosion rate (mm/year)	0.129	0.065
OES Fe Content (%)	97.700	98.052

Both methods independently identify AGO as producing greater corrosion than PMS. The OES analysis demonstrated the greatest reduction in iron content in the AGO specimen, while the gravimetric technique measured the highest corrosion rates for the same medium. This agreement confirms that the elemental changes observed by OES are a direct consequence of increased corrosion activity, rather than measurement artefact. Loss of iron from the steel matrix reduces the effective load-bearing wall thickness and can increase local stress concentration at corrosion pits and other surface irregularities. General corrosion-engineering practice treats bulk iron loss of the kind measured here by OES as a precursor to, rather than direct proof of, mechanical-property degradation; direct tensile and impact testing of the corroded specimens was outside the scope of the present, OES-focused study and is not reported here.

The progressive depletion of iron and relative enrichment of Cr, Cu, W and Mn measured by OES in the corroded specimens, more pronounced in AGO than PMS, mirrors the compositional-change approach of Ishtiaq et al. (2022), who combined optical emission spectrometry with SEM/EDS to link elemental changes to corrosion severity and microstructure in AISI carbon steels; their finding that elemental shifts intensified with more susceptible microstructures parallels the moderate iron loss observed here, consistent with the relatively corrosion-resistant ferrite-pearlite microstructure of the investigated steel. Borisade et al. (2021), although their study did not involve corrosion exposure, demonstrated that manganese, carbon and residual alloying elements govern strength and toughness in carbon steel generally, which is consistent with, though does not itself confirm, a mechanistic link between the OES-measured post-corrosion enrichment of these elements and potential mechanical-property change; direct verification of this link would require tensile and impact testing of the corroded specimens, which was outside the scope of the present study.

Because the OES elemental trend agrees with the corrosion-rate ranking obtained by weight loss, and is consistent with the composition-corrosion relationships reported by Ishtiaq et al. (2022) and Borisade et al. (2021), OES can be regarded as a reliable, complementary indicator of near-surface metal loss. For petroleum tanker safety, periodic OES or portable XRF spot-checks on tanker shell coupons could provide an early, non-destructive warning of cumulative iron loss before it manifests as a measurable reduction in wall thickness or mechanical performance.

5. CONCLUSION

Bulk Optical Emission Spectroscopy (OES) was used to characterise the elemental composition of control, PMS-corroded and AGO-corroded coupons of high-grade conventional 5 mm Ukrainian carbon steel plate used for tanker fabrication in Nigeria, following 63 days of full immersion. OES revealed a progressive decrease in iron content from 98.251 wt.% (control) to 98.052 wt.% (PMS) and 97.700 wt.% (AGO), accompanied by a corresponding relative enrichment of

carbon, chromium, copper and tungsten in the corroded specimens, consistent with preferential anodic dissolution of iron. The elemental trends measured by OES agree fully with the corrosion-severity ranking (AGO > PMS) independently obtained by gravimetric weight-loss method on the same steel and fuel media (Jamilu et al., 2026b), and point toward a plausible metallurgical basis for corrosion-related mechanical-property loss in tanker steel, worth confirming with direct tensile and impact testing in future work. The findings confirm that bulk OES is a reliable, rapid and non-destructive complementary technique for tanker corrosion diagnostics, and support the use of periodic OES or portable XRF spot-checks on in-service tanker shell coupons as an early warning tool for cumulative corrosion-related iron loss in the Nigerian petroleum transportation sector.

REFERENCES

Adama, K. K., Onyeachu, I. B., Modebe, L. U., Chukwuike, V. I., Oghuma, P. O., & Akhabue, C. E. (2024). Comparative evaluation of corrosion behaviour of carbon steel (C1020) in different biodiesels: Synthesis, characterization and electrochemical investigations. Results in Engineering, 21, 101695.

Adama, K. K., Ukhurebor, K. E., Aigbe, U. O., & Hossain, I. (2025). Implications of waste cooking oil biodiesel on carbon steel alloy in automobiles: Corrosion degradation. International Journal of Thermofluids, 26, 101143.

ASTM International. (2019). A36/A36M: Standard specification for carbon structural steel.

Borisade, S. G., Ajibola, O. O., Owa, A. F., & Adebayo, A. O. (2021). Chemical and mechanical properties of low carbon steel: Insight from process parameters. LAUTECH Journal of Engineering and Technology, 15(1), 39-44.

Chile, N. E., Haldhar, R., Godffrey, U. K., Chijioke, O. C., Umezuruike, E. A., Ifeoma, O. P., Oke, M. O., Ichou, H., Arrousse, N., Kim, S.-C., Dagdag, O., Ebenso, E. E., & Taleb, M. (2022). Theoretical study and adsorption behavior of urea on mild steel in automotive gas oil (AGO) medium. Lubricants, 10(7), 157.

Cursaru, D.-L., Branoiu, G., Ramadan, I., & Miculescu, F. (2014). Degradation of automotive materials upon exposure to sunflower biodiesel. Industrial Crops and Products, 54, 149-158.

Heryana, Y., Pamungkas, A., Romelan, R., Solikhah, M. D., Matheofani, Barus, B. R., Wibowo, C. S., Supriyadi, F., Thahar, A., Wibowo, E., & Wirawan, S. S. (2024). Evaluation of corrosion effects in diesel-biodiesel and diesel-biodiesel-HVO blends on metals for fuel storage systems. Corrosion Science and Technology, 23(5), 352-364.

Ishtiaq, M., Inam, A., Tiwari, S., et al. (2022). Microstructural, mechanical, and electrochemical analysis of carbon doped AISI carbon steels. Applied Microscopy, 52, 10.

Jamilu, H., Abubakar, A., Abubakar Zaria, U., Na'inna, A. M., & Abubakar Ado, D. (2026b). Study of the corrosion rate of Nigerian high-grade conventional 5 mm Ukrainian metallic plate using weight loss (gravimetric) method [Companion manuscript]. International Conference on Engineering Innovation for Sustainable Development (ICESID 2026).

Kowalczyk, M., Andruszko, J., Stefanek, P., & Mazur, R. (2025). Failure and degradation mechanisms of steel pipelines: Analysis and development of effective preventive strategies. Materials, 18(1), Article 134.

Kugelmeier, C. L., Monteiro, M. R., da Silva, R., Kuri, S. E., Sordi, V. L., & Della Rovere, C. A. (2021). Corrosion behavior of carbon steel, stainless steel, aluminum and copper upon exposure to biodiesel blended with petrodiesel. Energy, 226, 120344.

Marshakov, I. K. (2002). Anodic dissolution and selective corrosion of alloys. Protection of Metals, 38, 118-123.

International Conference on Engineering Innovation for Sustainable Development (ICESID 2026)
Faculty of Engineering, Ahmadu Bello University Zaria · 8–10 September 2026

PERFORMANCE EVALUATION OF MODEL REFERENCE ADAPTIVE CONTROLLER FOR STRING STABILITY IN HEAVY-DUTY TRUCK PLATOONING

Hassan Maharazu[1], Z. Haruna[2], O. Ajayi[2], Muktar Abubakar[1], Mohammed Babakolo Adamu[1,*]

[1]*Federal University of Transportation Daura*
[2]*Ahmadu Bello University Zaria*

Email: abumuhammadu10@gmail.com, hzaharuddeen@abu.edu.ng, ajayi.oreofe@yahoo.com, Abubakarmuktar76@gmail.com, mohammedbdm15@gmail.com*

***Corresponding author**: Mohammed Babakolo Adamu

DOI: https://doi.org/10.67203/sp.ICESID.2026

ABSTRACT

The deployment of heavy-duty truck platooning has gained considerable attention as an intelligent transportation technology capable of improving highway safety, fuel efficiency, and traffic flow. However, maintaining string stability under varying operating conditions remains a critical challenge due to vehicle parameter uncertainties and external disturbances, which can amplify spacing and velocity fluctuations throughout the platoon. This study presents a performance evaluation of a Model Reference Adaptive Controller (MRAC) for string stability in heavy-duty truck platooning. The proposed control strategy employs a reference model to define the desired vehicle dynamics, while a Lyapunov-based adaptive law continuously adjusts the controller parameters to compensate for system uncertainties and minimize tracking errors. The controller is implemented and evaluated using MATLAB/Simulink, and its performance is compared with a Distributed Model Predictive Control–Proportional Integral Derivative (DMPC-PID) strategy. The evaluation considers inter-vehicle spacing error, velocity error, settling time, acceleration response, and disturbance attenuation. Simulation results demonstrate that the proposed MRAC maintains the desired 20 m inter-vehicle spacing and 20 m/s cruising speed, with convergence to the desired operating conditions within approximately 20 s. An average inter-vehicle spacing error of 0.15 m and an average velocity error of 0.13 m/s were obtained between the leader and follower vehicles. The acceleration response further indicates progressive attenuation of transient oscillations as the platoon approaches steady-state operation. Comparative results show that MRAC provides improved tracking performance, adaptation, and disturbance attenuation compared with the DMPC-PID benchmark. The findings demonstrate the potential of MRAC as an adaptive longitudinal control strategy for maintaining stable and coordinated operation of heavy-duty truck platoons under uncertain operating conditions.

Keywords: *String Stability; Heavy-Duty Truck Platooning; Adaptive Control; Intelligent Transportation Systems (ITS); Longitudinal Vehicle Control*

1.0 INTRODUCTION

The increasing demand for efficient and safe highway transportation has encouraged the development of intelligent transportation systems (ITS) that integrate advanced sensing, communication, computation, and control technologies into transportation operations. Among these technologies, vehicle platooning has attracted significant research attention because it enables multiple vehicles to travel cooperatively as a coordinated convoy while maintaining controlled inter-vehicle distances. Truck platooning is particularly promising for improving transportation efficiency, reducing aerodynamic drag and fuel consumption, and enhancing highway safety through coordinated longitudinal vehicle control. The development of effective control strategies is therefore essential for ensuring safe and stable operation of heavy-duty vehicle platoons.

Vehicle platooning involves the coordinated movement of a group of vehicles in which follower vehicles regulate their speed and position relative to a preceding vehicle Zhao et al. (2022). The control of a vehicle platoon can generally be divided into lateral and longitudinal control. Lateral control is concerned with maintaining the vehicle within the desired lane, whereas longitudinal control regulates vehicle speed and inter-vehicle spacing. For heavy-duty truck platoons, longitudinal control is

particularly important because variations in vehicle dynamics, operating conditions, and external disturbances can affect the ability of follower vehicles to maintain the desired spacing and velocity Mao et al. (2023). A suitable longitudinal controller must therefore provide accurate tracking while preventing the amplification of disturbances through the vehicle string Gardon et al. (2023).

String stability is a fundamental requirement in platoon control and describes the ability of a vehicle platoon to attenuate or prevent the amplification of disturbances as they propagate from one vehicle to subsequent vehicles. Feng et al. (2019) presented a comprehensive analysis of string stability in vehicular platoons and highlighted the importance of appropriate stability definitions and analysis methods in evaluating platoon control systems. Several control approaches have subsequently been investigated to improve the stability and safety of vehicle platoons. These include model predictive control, distributed control, sliding mode control, adaptive control, and other robust control techniques. For example, Gratzer et al. (2022) investigated string-stable and collision-safe model predictive platoon control, while Cheng et al. (2022) developed a distributed sliding-mode control strategy for longitudinal cruise control of truck platoons. These studies demonstrate the effectiveness of advanced control techniques but also indicate the importance of accounting for vehicle dynamics and operating conditions when designing platoon controllers.

Adaptive control provides an alternative approach for dealing with uncertainties and variations in vehicle dynamics. Unlike fixed-parameter controllers, adaptive controllers can modify their control parameters in response to changes in system behaviour. Abdullahi and Akkaya (2020), for example, investigated a Model Reference Adaptive Control approach for adaptive cruise control, demonstrating the applicability of MRAC to vehicle longitudinal control. Similarly, Prayitno et al. (2022) investigated distributed model reference adaptive control for synchronization of heterogeneous vehicle platoons. These studies indicate the potential of adaptive control for coordinated vehicle operation, particularly where vehicle characteristics and operating conditions may vary.

Despite the progress made in platoon control, maintaining consistent tracking performance and string stability in heavy-duty truck platoons remains challenging because of uncertainties in vehicle parameters and variations in longitudinal vehicle dynamics. Controllers designed using nominal or fixed system parameters may experience performance degradation when the actual operating conditions differ from those assumed during controller design. In addition, transient variations in velocity, inter-vehicle spacing, and acceleration can propagate through the platoon and adversely affect coordinated vehicle operation. Therefore, an adaptive control strategy capable of continuously adjusting its parameters while maintaining a desired reference response is of significant interest for heavy-duty truck platooning.

In this study, a Model Reference Adaptive Controller (MRAC) is evaluated for maintaining string stability in a heavy-duty truck platoon. The proposed approach uses a reference model to define the desired vehicle response and a Lyapunov-based adaptive mechanism to update the controller parameters based on the tracking error. The performance of the MRAC is evaluated using MATLAB/Simulink simulations and compared with a Distributed Model Predictive Control–Proportional Integral Derivative (DMPC-PID) controller. The evaluation focuses on inter-vehicle spacing, velocity tracking, settling time, acceleration response, and disturbance attenuation. The objective is to determine the effectiveness of the adaptive controller in maintaining the desired platoon behaviour and to establish its performance relative to the selected benchmark control strategy.

2.0 PROBLEM STATEMENT

Heavy-duty truck platooning is an emerging intelligent transportation technology in which a group of vehicles travels cooperatively with small and controlled inter-vehicle distances. The technology has the potential to improve road safety, traffic efficiency, and fuel economy; however, maintaining string stability remains a major control challenge. String stability requires that disturbances introduced by the lead vehicle or an individual follower do not amplify as they propagate through the platoon. In practical highway operation, variations in vehicle speed, vehicle mass, road gradient, aerodynamic forces, actuator dynamics, and external disturbances can cause deviations from the desired inter-vehicle spacing and velocity. If these deviations are amplified from one vehicle to another, they may result in large spacing errors, uncomfortable acceleration and deceleration, and, in severe cases, rear-end collisions.

Several control strategies, including Proportional–Integral–Derivative (PID), Model Predictive Control (MPC), Distributed Model Predictive Control (DMPC), sliding mode control, and robust control techniques, have been investigated for achieving string stability in vehicle platoons. Although these controllers can provide satisfactory performance under specified operating conditions, their performance may deteriorate when there are uncertainties in vehicle parameters and changes in the operating environment. Controllers with fixed parameters may not adequately compensate for variations in the longitudinal dynamics of heavy-duty trucks.

Model Reference Adaptive Control (MRAC) provides a potential solution by allowing controller parameters to be adjusted online according to the difference between the actual vehicle response and a predefined reference model. However, the effectiveness of MRAC for heavy-duty truck platooning should not be established solely from its ability to track a reference response. Its ability to suppress disturbance propagation, maintain inter-vehicle spacing, minimize velocity errors, and preserve string stability under varying operating conditions requires systematic quantitative evaluation.

Therefore, this research addresses the problem of inadequate adaptive compensation of uncertainties and disturbances that can degrade string stability and tracking performance in heavy-duty truck platooning. The research evaluates the performance of a Lyapunov-based Model Reference Adaptive Controller in maintaining the desired inter-vehicle spacing and velocity while attenuating disturbances propagating through the platoon. Its performance is compared with a Distributed Model Predictive Control–PID (DMPC-PID) benchmark using inter-vehicle spacing error, velocity error, settling time, acceleration/deceleration characteristics, and disturbance attenuation as evaluation metrics.

3.0 METHODOLOGY

3.1 Development of a Vehicle Model

The vehicle model was formulated based on Newton third law of motion that say's tractive force is equal to resistive force;

$$F_{tr} = F_a + F_i + F_g + F_r \tag{1}$$

Where the respective forces are defined as:

$$\left.\begin{array}{l} F_a = \frac{1}{2}\,\rho\, C_d\, A\, v^2 \\ \\ F_r = mgC_{rr} \\ F_g = mgsin\theta \end{array}\right\} \quad F_i = ma \tag{2}$$

Where; aerodynamic drag force (F_a), rolling resistance force (F_r), gradient force (F_g), inertia force and tractive force (F_{tr}), ρ is the air density, v is the velocity, C_d is the drag coefficient, A is the frontal area, m is the mass, and a is the acceleration.

Let

$$\left.\begin{array}{l} x_1 = s \\ x_2 = v \\ \dot{x}_1 = v \\ \dot{x}_2 = a \end{array}\right\} \tag{3}$$

From equation (1)

$$\left.\begin{array}{l} F_{tr} = \dfrac{1}{2}\,\rho\, C_d A v^2 + mgC_{rr} + mgsin\theta + ma \\ ma = F_{tr} - \dfrac{1}{2}\,\rho\, C_d A v^2 - mgC_{rr} - mgsin\theta \\ \dot{x}_2 = \dfrac{F_{tr} - \frac{1}{2}\,\rho\, C_d A v^2 - mgC_{rr} - mgsin\theta}{m} \end{array}\right\} \tag{4}$$

The acceleration of vehicle $\dot{x}_2$, is defined in the state equation as obtained from equation (4).

3.2 Designing the Reference Model

The reference model $\dot{X}m$ of a vehicle in MRAC design is in the form of

$$\dot{X}m = (A - BK_1)X_m + BK_2 r \tag{5}$$

With; $A_m = A - BK_2$ and $B_m = BK_2$

Where Am and Bm stands for constant plant parameter, r is the reference signal, $K_1$and K_2 represent the adaptive gains and X_m is the system state vector. The vehicle dynamic model (plant model) is defined from equation (3.4) as;

$$\dot{x}_2 = -gsin\theta - \frac{1}{2m}\,\rho\, C_d A v^2 + \frac{1}{m}F_{tr} \tag{6}$$

The derivative of the state of the reference model of the vehicle is obtained by neglecting the effect of rolling friction (F_r):

$$\left.\begin{aligned} \dot{x}_1 &= v = x_2 \\ \dot{x}_2 &= -gx_1 - \frac{1}{2m}\,\rho\, C_d A {x_2}^2 + \frac{1}{m}F_{tr} \end{aligned}\right\} \tag{7}$$

Where $\sin\theta \approx \theta = x_1$. The state equation model of the vehicle is written in the form of $\dot{X} = AX + Bu$ as:

$$\dot{X} = \dot{x}_2 = \begin{bmatrix} 0 & 1 \\ 0 & \frac{1}{2m}\,\rho\, C_d A {x_2}^2 \end{bmatrix}\begin{bmatrix} x_1 \\ x_2 \end{bmatrix} + \begin{bmatrix} 0 \\ \frac{1}{m} \end{bmatrix} F_{tr} \tag{8}$$

The reference state model is obtained by neglecting road grade ($\theta \approx 0$) since the vehicle operates in a flat road therefore written as:

$$\dot{X} = \begin{bmatrix} 0 & 1 \\ 0 & 0 \end{bmatrix} X + \frac{1}{m}\begin{bmatrix} 0 \\ 1 \end{bmatrix} F_{tr} \tag{9}$$

Where the system plant parameter $A = \begin{bmatrix} 0 & 1 \\ 0 & 0 \end{bmatrix}$ and $B = \begin{bmatrix} 0 \\ 1 \end{bmatrix}$

The reference vehicle model is derived by its characteristic polynomial, which dictates the desired closed-loop dynamics of the system. The characteristic polynomials of a second-order system;

$$P(s) = s^2 + 2\xi s + {\omega_n}^2 \tag{10}$$

The state space model of the vehicle is obtained;

$A_m = \begin{bmatrix} 0 & 1 \\ {\omega_n}^2 & 2\xi\omega \end{bmatrix}$ and $B_m = \begin{bmatrix} 0 \\ {\omega_n}^2 \end{bmatrix}$

where $\omega_n$is the natural frequency and $\zeta$is the damping ratio. The MATLAB implementation uses

$$\omega_n = 0.4 \text{ rad/s}$$

and

$$\zeta = 0.707.$$

Therefore,

$$2\zeta\omega_n = 2(0.707)(0.4) = 0.5656$$

and

$$\omega_n^2 = (0.4)^2 = 0.16.$$

Consequently, the reference-model matrices are

$$A_m = \begin{bmatrix} 0 & 1 \\ -\omega_n^2 & -2\zeta\omega_n \end{bmatrix} = \begin{bmatrix} 0 & 1 \\ -0.16 & -0.5656 \end{bmatrix} \qquad (11)$$

and

$$B_m = \begin{bmatrix} 0 \\ \omega_n^2 \end{bmatrix} = \begin{bmatrix} 0 \\ 0.16 \end{bmatrix}. \qquad (12)$$

Thus, the corresponding desired characteristic polynomial is

$$P_m(s) = s^2 + 0.5656 + 0.16$$

Then the reference model of the system is achieved by substituting the state space vectors in equation (4) where A_m is

$$\dot{X}m = A_m X_m + B_m K_2 \qquad (11)$$

3.3 Nominal Control Law

The nominal controller is designed to match the dynamics of the actual vehicle model to those of the reference model. The feedback and feedforward gains are obtained from the system matrices according to

$$K_1 = B^{\dagger}(A - A_m) \qquad (12)$$

and

$$K_2 = B^{\dagger}B_m \qquad (13)$$

where $B^{\dagger}$denotes the pseudoinverse of the input matrix B.

Using the system matrices defined in Equation (4), the resulting gains are

$$K_1 = [0.16 \quad 0.5656] \qquad (14)$$

and

$$K_2 = 0.16. \qquad (15)$$

The nominal control input is therefore expressed as

$$U_n = -K_1 x + K_2 r. \qquad (16)$$

The nominal controller establishes the basic feedback behaviour of the vehicle, while the adaptive component subsequently compensates for deviations caused by uncertainties and disturbances.

3.4 Model Reference Adaptive Control

The MRAC controller incorporates an adaptive mechanism to compensate for uncertainties in the vehicle dynamics. The tracking error between the actual vehicle state and the reference-model state is defined as

$$e = x - x_m. \qquad (17)$$

The adaptive control component implemented in the MATLAB model is

$$U_a = \widehat{W}^T \beta \qquad (18)$$

where $\widehat{W}$represents the adaptive weight vector and βrepresents the regressor vector used by the adaptive controller.

The overall control signal is obtained by combining the nominal and adaptive control components as

$$U = U_n - U_a \delta_a \qquad (19)$$

where $\delta_a$is the adaptation switch. When adaptation is enabled, the adaptive component is incorporated into the control action. In the simulation, the adaptation switch is set to

$$\delta_a = 1.$$

This configuration allows the controller to continuously modify its control action in response to tracking errors and variations in system behaviour.

3.5 Lyapunov energy function

To formulate the adaptive mechanism, a Lyapunov-based approach is employed. The positive-definite matrix $P$is obtained from the Lyapunov equation

$$A_m^T P + P A_m = -I \tag{20}$$

where $I$is the identity matrix.

The adaptive parameters are updated numerically according to the implementation used in the MATLAB simulation:

$$\widehat{W}(k+1) = \widehat{W}(k) + \Delta t\left[\gamma_1 \widehat{W}(k) + \gamma_2 \beta e^T P B\right] \tag{21}$$

where $\Delta t$is the simulation sampling interval, $\gamma_1$and $\gamma_2$are the adaptation parameters, and $\beta$is the adaptive regressor.

The values used in the simulation are

$$\gamma_1 = 0.01$$

and

$$\gamma_2 = 1.4.$$

An adaptive-weight limit of 10 is also defined in the MATLAB implementation to limit excessive growth of the adaptive parameters. This provides an additional measure for preventing adaptive-weight drift during simulation.

3.5 Flowchart of MRAC for String Stability in Platooning

To illustrate the operational sequence of the proposed Model Reference Adaptive Control (MRAC) strategy for heavy-duty truck platooning, Figure 1 presents the flowchart of the control process used to achieve and maintain the desired inter-vehicle spacing, vehicle speed, and platoon stability.

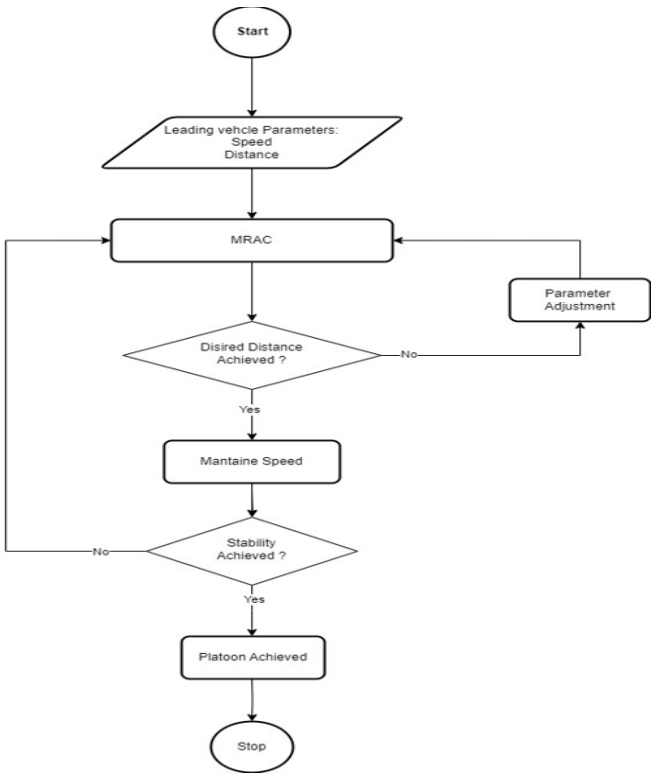

Figure 1: Flowchart of MRAC for String Stability in Platooning

Figure 1: illustrates the proposed Model Reference Adaptive Control (MRAC) flow process for maintaining string stability in the truck platoon. The control process begins by obtaining the leading vehicle parameters, particularly its speed and inter-vehicle distance, which serve as the reference inputs for the MRAC. The controller compares the actual follower-vehicle response with the desired reference behaviour and generates the appropriate control action to minimize the tracking error. The resulting inter-vehicle distance is continuously evaluated against the desired spacing; if the desired distance is not achieved, the controller performs parameter adjustment and updates the control action accordingly. Once the desired distance is achieved, the vehicle maintains the required speed while continuously monitoring the stability of the platoon. If the stability criterion is not satisfied, the control loop is repeated to further adjust the controller parameters and vehicle response. When the desired distance, speed, and stability conditions are simultaneously satisfied, the platoon is considered successfully established and maintained. This continuous feedback and parameter adaptation enable the MRAC to compensate for system uncertainties and disturbances while improving tracking performance and maintaining string stability.

4.0 RESULTS

4.1 Simulation Parameters

Parameter	Symbol	Value
Vehicle mass	m	1200 kg
Air density	ρ	1.21 kg/m³
Frontal area	A_f	3 m²
Drag coefficient	C_d	0.3
Effective tyre radius	r_{eff}	0.353 m
Rolling friction coefficient	σ	0.5
Transmission efficiency	η_T	0.99
Nominal velocity	v_{nom}	20 m/s
Desired acceleration	a_{des}	2.0 m/s²
Braking deceleration	a_{brake}	−1.5 m/s²
Natural frequency	ω_n	0.4 rad/s
Damping factor	ζ	0.707
Desired inter-vehicle spacing	d_r	20 m
Desired velocity	v_r	20 m/s

Table 1: Simulation Parameters

4. 2 Control gain

Figure 2 presents the MRAC control input and adaptive uncertainty response for the selected adaptation gains, $\gamma_1 = 0.01$and $\gamma_2 = 1.40$. The results show the controller's adaptive response to system uncertainties and its ability to regulate the control action during the transient period.

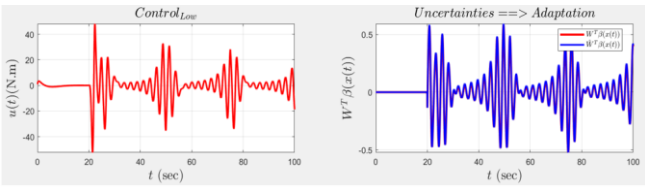

Figure 2: MRAC control gain $\Upsilon_1 = 0.01$ and $\Upsilon_2 = 1.40$

From the controller performance presented in Figure 2, it can be seen that there is an improve performance in the adaptive law to track a reference trajectory under uncertainty and external

disturbance. In general, the controller performance clearly indicates that the actual velocity aligns with the reference velocity, demonstrating MRAC ability to manage model uncertainty effectively even in the presence of small oscillation along the platoon.

4.3 Distance Profile of the Trucks

Figure 3 shows the plots for the velocity profile of the four trucks in the platoon with all the trucks shows discrepancy in terms of initial velocity.

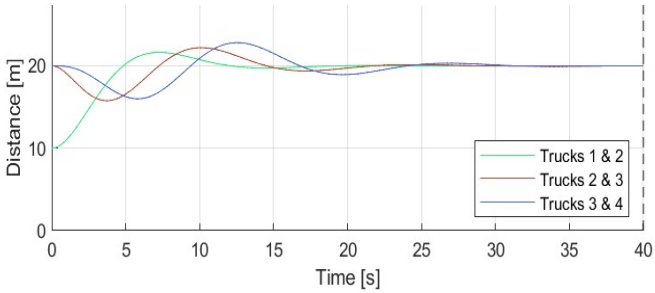

Figure 3: Distance Profile of the Trucks

Figure 3 illustrates the inter-vehicle distance response of the heavy-duty truck platoon under the proposed MRAC strategy. The three curves represent the spacing between Trucks 1 and 2, Trucks 2 and 3, and Trucks 3 and 4, respectively, with a desired inter-vehicle distance of **20 m**. At the beginning of the simulation, the vehicles exhibit different spacing conditions, resulting in transient oscillations as the MRAC adjusts the follower vehicles' responses toward the desired spacing. The spacing between Trucks 1 and 2 initially increases before experiencing a reduction and subsequent oscillations, while the other vehicle pairs similarly exhibit transient deviations around the reference distance. Despite these initial variations, the oscillations are progressively attenuated as the adaptive controller continuously adjusts the control parameters. All three inter-vehicle distances converge toward the desired **20 m** spacing at approximately **20 s**, after which the responses remain closely regulated with negligible steady-state error. The attenuation of the spacing oscillations and convergence of all vehicle pairs to the same desired distance indicate that the proposed MRAC effectively compensates for transient disturbances and maintains coordinated vehicle spacing, demonstrating its potential to achieve string stability and safe platoon formation.

4.3 Performance evaluation of MRAC over DMPC-PID with Intervehicle distance

The performance of MRAC was evaluated by comparing with that of DMPC-PID using transient parameters by the platoon to achieve a steady state inter vehicular spacing of $20\,m$. The simulation result obtained is shown in Figure 4;

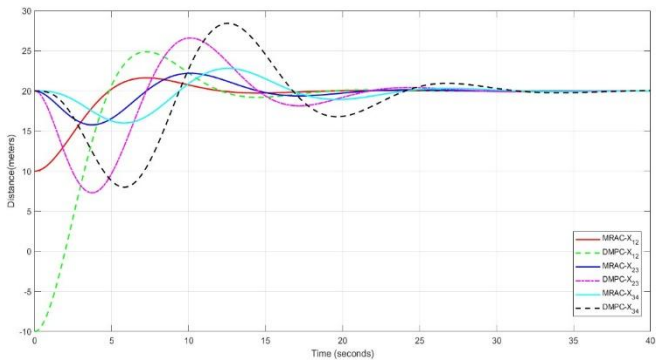

Figure 4: Comparison for MRAC and DMPC-PID Intervehicle Distance

From Figure 4, it is evident that the MRAC achieved a uniform inter-vehicle gap at a faster rate, reaching the desired spacing within 25 seconds. Additionally, the MRAC exhibited lower

overshoot and reduced tracking error, demonstrating its effectiveness in ensuring precise and stable platoon behavior compared to other control strategies.

4.5 Performance evaluation of MRAC over DMPC-PID with vehicle Speed

The performance of MRAC was evaluated by comparing with that of DMPC-PID using speed error by the platoon to achieve a steady state speed of 20 m/s. The simulation result obtained is shown in Figure 5;

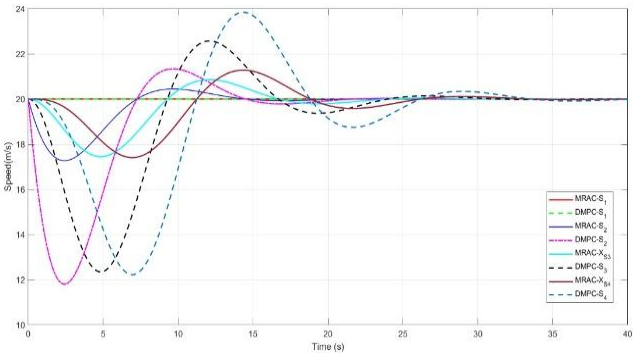

Figure 5: Comparison of Speed Profile

The speed response of the vehicles under the proposed MRAC strategy is presented in Figure 5. The desired cruising velocity was set to 20 m/s. The figure illustrates the ability of the controller to regulate the velocity of the follower vehicles according to the reference velocity while maintaining coordination with the preceding vehicle.

At the beginning of the simulation, transient variations in vehicle speed are observed as the controller adjusts the vehicle states towards the desired operating condition. As the simulation progresses, these variations are progressively reduced, and the vehicle velocities converge towards the reference value of 20 m/s.

The average velocity error obtained from the simulation is approximately 0.12 m/s. This result demonstrates that the MRAC controller can achieve close velocity tracking while simultaneously maintaining the required inter-vehicle spacing.

The convergence of the velocity response is also important for string stability because variations in the velocity of a preceding vehicle can propagate through the platoon. The attenuation of these variations as the follower vehicles approaches the desired velocity indicates that the controller provides effective longitudinal coordination.

	TR2-TR1 (m/s)	**TR3-TR1 (m/s)**	**TR4-TR1 (m/s)**	**Velocity error (m/s)**
DMPC-PID	0.1	0.15	0.2	0.15
MRAC	**0.08**	**0.12**	**0.15**	**0.12**

Table 2: Velocity Error for DMPC-PID and MRAC

From Table 2, it is evident that the MRAC significantly reduces tracking errors for all trucks compared to the DMPC-PID controller. This highlights the superior accuracy of MRAC in achieving precise tracking performance across the platoon.

4.6 Acceleration Profile of the Truck

The performance of MRAC was evaluated by comparing with that of DMPC-PID using settling time by the platoon to achieve a steady state acceleration of zero. The simulation result obtained is shown in Figure 6;

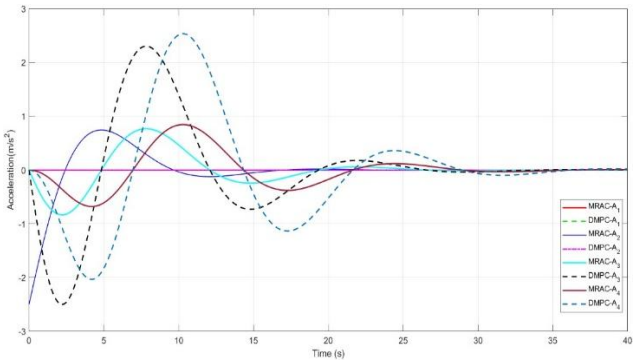

Figure 6: Comparison of Acceleration Profile

From Figure 6, it is evident that MRAC achieved a constant acceleration at 20 $seconds$ while DMPC-PID exhibits some high oscillations and reached a constant acceleration at 25 $seconds$.

Trucks	Overshoot (%)		Undershoot (%)	
	DMPC-PID	MRAC	DMPC-PID	MRAC
Truck 2	2.1	**0.6**	-4.1	**-2.4**
Truck 3	2.2	**0.7**	-2.2	**-0.3**
Truck 4	2.4	**0.9**	-2.0	**-0.4**
Average error	2.23	**0.73**	2.8	**1.03**

Table 3: Acceleration and Deceleration error for DMPC-PID and MRAC

It is observed from Table 3, the MRAC generates a control signal with lower overshoot compared to the DMPC-PID controller. This demonstrates that the MRAC provides a faster response, improved settling time, and reduced tracking errors. These attributes highlight the superior performance of MRAC in achieving accurate and stable control, making it more effective for dynamic scenarios where precise tracking is crucial.

5.0 CONCLUSION

The Model Reference Adaptive Controller (MRAC) was successfully developed and evaluated for maintaining string stability in a heavy-duty truck platoon under system uncertainties and external disturbances. The controller employs a reference model and a Lyapunov-based adaptive mechanism to continuously adjust its control parameters and minimize deviations between the actual and desired vehicle responses. Simulation results obtained in MATLAB/Simulink demonstrate that the proposed MRAC provides improved tracking performance and disturbance attenuation compared with the DMPC-PID benchmark, achieving the desired 20 m inter-vehicle spacing and 20 m/s cruising speed with a settling time of approximately 20 s. The controller recorded an average inter-vehicle spacing error of 0.15 m and an average velocity error of 0.13 m/s, indicating accurate coordination between the

leader and follower vehicles. Furthermore, the acceleration response shows that transient oscillations are progressively attenuated as the platoon converges to steady-state operation, with average acceleration and deceleration values of approximately 0.73 m/s² and 1.03 m/s², respectively, demonstrating a relatively smooth longitudinal response. Overall, the results indicate that MRAC provides enhanced adaptability, tracking accuracy, disturbance rejection, and string-stability performance compared with DMPC-PID, demonstrating its potential for robust longitudinal control of heavy-duty truck platoons under varying operating conditions and system uncertainties. The present study does not explicitly investigate communication delays, packet losses, or communication-channel failures between vehicles. These factors can significantly influence platoon stability in practical connected-vehicle applications.

REFERENCES

[1] Feng, S., Zhang, Y., Li, S. E., Cao, Z., Liu, H. X., & Li, L. (2019). String stability for vehicular platoon control: Definitions and analysis methods. In *Annual Reviews in Control* (Vol. 47, pp. 81–97). Elsevier Ltd. https://doi.org/10.1016/j.arcontrol.2019.03.001

[2] Feng, Y., Yu, S., Chen, H., Li, Y., Shi, S., Yu, J., & Chen, H. (2023a). Distributed MPC of vehicle platoons with guaranteed consensus and string stability. *Scientific Reports*, *13*(1). https://doi.org/10.1038/s41598-023-36898-4

[3] Gordon, M. A., Vargas, F. J., & Peters, A. A. (2023). Mean square stability conditions for platoons with lossy inter-vehicle communication channels. *Automatica*, *147*. https://doi.org/10.1016/j.automatica.2022.110710

[4] Mao, X., Li, P., Weng, Z., & Zhao, J. (2023). Distributed tube model predictive control for string stability of heterogeneous vehicle platoons. *Proceedings of the Institution of Mechanical Engineers. Part I: Journal of Systems and Control Engineering*, *237*(10), 1777–1788. https://doi.org/10.1177/09596518231173763.

[5] Rizk, H., Chaibet, A., & Kribèche, A. (2023). Model-Based Control and Model-Free Control Techniques for Autonomous Vehicles: A Technical Survey. In *Applied Sciences (Switzerland)* (Vol. 13, Issue 11). MDPI. https://doi.org/10.3390/app13116700

[6] Schwab, A., & Lunze, J. (2022). Design of Platooning Controllers That Achieve Collision Avoidance by External Positivity. *IEEE Transactions on Intelligent Transportation Systems*, *23*(9), 14883–14892. https://doi.org/10.1109/TITS.2021.3134803

[7] Umar, A., Journal Of Engineering, N., Ajayi, O., Yahaya, S. M., & Umar, A. (2022a). Application of Fuzzy Control System to Autonomous Vehicle Platoon. In *Nigerian Journal of Engineering* (Vol. 29, Issue 2). https://www.researchgate.net/publication/365946814

[8] Zhao, Q., Zheng, H., Kaku, C., Cheng, F., & Zong, C. (2022). Safety Spacing Control of Truck Platoon Based on Emergency Braking under Different Road Conditions. *SAE International Journal of Vehicle Dynamics, Stability, and NVH*, *7*(1). https://doi.org/10.4271/10-07-01-0005

[9] Cheng, F., Zheng, H., Gong, C., & Kaku, C. (2022a). Longitudinal Cruise Control of Truck Platoon Based on Distributed Sliding Mode Control Strategy. *2022 6th CAA International Conference on Vehicular Control and Intelligence, CVCI 2022*. https://doi.org/10.1109/CVCI56766.2022.9964651

[10] Gratzer, A. L., Thormann, S., Schirrer, A., & Jakubek, S. (2022a). String Stable and Collision-Safe Model Predictive Platoon Control. *IEEE Transactions on Intelligent Transportation Systems*, *23*(10), 19358–19373. https://doi.org/10.1109/TITS.2022.3160236

[11] Prayitno, A., Indrawati, V., & Nilkhamhang, I. (2022). Distributed Model Reference Adaptive Control Based on Cooperative Observer with Optimal Control Modification for Synchronization of Heterogeneous Vehicle Platoon. *Mathematical Modelling of Engineering Problems*, *9*(6), 1565–1573. https://doi.org/10.18280/MMEP.090616

[12] Gazran, S., & Rönnqvist, M. (2021). Truck platooning transportation planning: A review with emphasis on Operations Research methods. https://www.researchgate.net/publication/349830460

[13] Abdullahi, A., & Akkaya, S. (2020). Adaptive Cruise Control: A Model Reference Adaptive Control Approach. *2020 24th International Conference on System Theory, Control and Computing, ICSTCC 2020 - Proceedings*, 904–908. https://doi.org/10.1109/ICSTCC50638.2020.9259641

[14] Devika, K. B., G., R., Shreya Yellapantula, V. R., & Subramanian, S. C. (2020). A Dynamics-Based Adaptive String Stable Controller for Connected Heavy Road Vehicle Platoon Safety. *IEEE Access*, *8*, 209886–209903. https://doi.org/10.1109/ACCESS.2020.3039797

[15] Garg, T., & Roy, S. B. (2020). Combined cooperative adaptive cruise control using collective initial excitation based distributed parameter estimator. *IFAC-PapersOnLine*, *53*(2), 13855–13862. https://doi.org/10.1016/j.ifacol.2020.12.897

[16] Milanés, V., & Shladover, S. E. (2016). Handling Cut-In Vehicles in Strings of Cooperative Adaptive Cruise Control Vehicles. *Journal of Intelligent Transportation Systems: Technology, Planning, and Operations*, *20*(2), 178–191. https://doi.org/10.1080/15472450.2015.1016023

[17] Feng, S., Zhang, Y., Li, S. E., Cao, Z., Liu, H. X., & Li, L. (2019). String stability for vehicular platoon control: Definitions and analysis methods. In *Annual Reviews in Control* (Vol. 47, pp. 81–97). Elsevier Ltd. https://doi.org/10.1016/j.arcontrol.2019.03.001

[18] Musa, azu J., Sudin, S., Mohamed, Z., Sha, Y. A., Usman, A. D., & Hassan, A. U. (n.d.). *An Improved Topology Model for Two-Vehicle Look-ahead and Rear-Vehicle Convoy Control*.

International Conference on Engineering Innovation for Sustainable Development (ICESID 2026)
Faculty of Engineering, Ahmadu Bello University Zaria · 8–10 September 2026

PROBABILISTIC FREQUENCY ESTIMATION OF BOILING LIQUID EXPANDING VAPOUR EXPLOSION IN A LIQUEFIED PETROLEUM GAS ADD-ON SKID SYSTEM USING INTEGRATED FAULT TREE AND EVENT TREE ANALYSIS

Shuaibu Musa[1,*], Abdullahi, Nuraddeen Bakori[2], Mohammed-Dabo, I. A.[3]

[1]*Department of Chemical Engineering, Ahmadu Bello University, Zaria*
[2]*Department of Chemical Engineering, Kaduna Polytechnic*
[3]*Department of Chemical Engineering, Faculty of Engineering, Ahmadu Bello University, Zaria, Nigeria*

Email: sbmgumel@gmail.com*, abdullahibakori@kadunapolytechnic.edu.ng, iamdabo@abu.edu.ng

***Corresponding author**: Shuaibu Musa

DOI: https://doi.org/10.67203/sp.ICESID.2026

ABSTRACT

The catastrophic failure of LPG storage tanks is considered to be one of the most catastrophic hazards in the downstream segment of the gas sector but frequency calculations for LPG facilities in Africa are seldom carried out using formal reliability studies. In this paper, the frequency of occurrence of Liquid Expanding Vapour Explosion (BLEVE) accident of a small-scale 8.85 m³ LPG add-on skid unit has been determined using integrated Fault Tree Analysis (FTA) and Event Tree Analysis (ETA) via Isograph Reliability Workbench v15.0 software package. A 12 basic event fault tree was developed for the top event of catastrophic rupture of the LPG bullet tank, utilizing mechanical, electrical and human errors based on failure statistics available from Offshore and onshore reliability data (OREDA), IEEE Std 493 and IEC 61511-1 standards in conjunction with AND and OR gate operations. Five simulation runs have resulted in the top event frequency of 0.7322 per year with main contributing factors being fire detector failure (FR=0.88/yr), gas detector failure (FR=0.41/yr) and pressure-safety-valve (PSV) failure (FR=0.017/yr). The event tree derived from the initiating event of a pressure-induced loading-line defect (frequency = 9.999×10^{-5} per year) had five different pathways to either a safe dispersion, a flash fire, a vapour cloud explosion, a jet fire, and a BLEVE, with the BLEVE pathway having a conditional frequency of 4×10^{-21} per year if all active barriers fail in sequence. It can be seen that it is not enough for any single element to fail to cause the top event, but rather degradation of several barriers at once is necessary.

Keywords: *Fault tree analysis; Event tree analysis; BLEVE; LPG storage; Reliability data; Isograph Reliability Workbench*

1. INTRODUCTION

Nigerian's LPG usage has increased to become one of the critical components of their domestic and industrial energy sources. LPG is stored in the form of a pressurised liquefied gas, and the failure of containment from a pressurised vessel results in a high hazard risk known as Boiling Liquid Expanding Vapor Explosion (BLEVE), being the worst-case scenario of accident in the downstream gas industry, causing a fireball, blast overpressure, and projectiles all at once (Zhou et al., 2022). Although the hazards associated with the physical consequence of a BLEVE have been extensively researched, there is no much information regarding the likelihood of such events happening at a particular facility.

The deficiency mentioned above is overcome with the help of quantitative risk assessment (QRA), which evaluates the frequency and consequences of hazardous events to determine numerical indicators of risk (Rausand & Haugen, 2020). As regards quantitative risk assessment, fault tree analysis (FTA) is the main approach used for frequency evaluation; it is based on the decomposition of the top event that occurs into the combinations of component and human failures that cause it (Vinnem & Røed, 2022). Where failure data are sparse or imprecise, fuzzy-set extensions of FTA have also been proposed to estimate fire and explosion frequencies in the process industry (Yazdi et al., 2020); the present study

instead adopts the conventional probabilistic FTA/ETA approach, drawing basic-event data directly from established reliability standards and handbooks.

In this study, Integrated Fault Tree Analysis (FTA) and Event Tree Analysis (ETA), which were carried out using the Isograph Reliability Workbench (IRW) software version 15.0, will be applied to a typical LPG add-on skid system that uses an 8.85m3 bullet tank. The aim is to develop a probability for the top event of BLEVE based on standards, and the pathway to the barrier-dependent result from a pressure-induced loading-line defect.

2. MATERIALS AND METHODS

2.1 Study system and software

This analysis was conducted on a Metrix LPG add-on skid which has a horizontal bullet tank of diameter 1.6 m and length 4.4 m (volume 8.85 m³) as its main storage for LPG at 25 °C. The reliability analysis was conducted using Isograph Reliability Workbench version 15.0, with the use of the fault-tree and event-tree analysis modules. The top event chosen for the fault tree was the catastrophic failure of the bullet tank.

The skid's product-transfer boundary is a single loading line connecting the bullet tank to the offloading/filling point, protected by a manually operated shutoff valve and an emergency-shutdown (ESD) system with an associated alarm; tank overpressure is protected by a pressure-safety valve (PSV) fitted to the vessel. Leak and fire hazards along this boundary are monitored by fixed gas and fire detectors that initiate the ESD sequence on confirmed detection. These loading-line, valve, instrumentation and detection elements are the physical components represented by the twelve basic events in Table 1 (Section 2.2).

2.2 Fault tree construction and failure data

A twelve basic event fault tree was constructed based on existing structures in the process safety literature and was copied into the IRW interface. The basic events included mechanical, electrical and human error. Fixed probability models were allocated to human related events while rate models were assigned to component failures. For independent basic events connected using logic gates, the gate probability is calculated using the following Boolean formulae: AND gate requires all the n inputs occurring simultaneously (Eq. 1) while OR gate occurs if at least one of the inputs occurs (Eq. 2):

$$P_{AND} = \prod_{i=1}^{n} P_i \tag{1}$$

$$P_{OR} = 1 - \prod_{i=1}^{n} (1 - P_i) \tag{2}$$

where P_i is the probability of basic event i and n the number of gate inputs. Component failure rates were taken as the ratio of observed failures to accumulated service time (Eq. 3):

$$\lambda = \frac{N_f}{T} \tag{3}$$

Table 1 reports two distinct event-probability metrics, consistent with Isograph Reliability Workbench conventions: probability type events (Q) are dimensionless failure probabilities used directly in Eqs 1-2, while rate type events (FR, per year) are converted to an equivalent probability of failure over a fixed one year mission time before being combined, using P = 1 - e^(-λt) (or the linear approximation P ≈ λt for λt << 1, consistent with Eq. 3), with t = 1 year matching the annualised top event probability reported in Section 3.1. Holding this mission time constant across all twelve basic events places the probability and rate type inputs on a common time basis before evaluation of the AND/OR gate logic.

Failure rate data were drawn from OREDA (2015), IEEE Std 493 (2007) and IEC 61511-1 (2016), supplemented by peer reviewed reliability sources. Table 1 lists the twelve basic events, their rates, categories and sources. The safety instrumented system function is not modelled as a single discrete basic event in this fault tree; rather, its protective role is captured through the gas detector, fire detector and emergency shutdown/alarm response basic events (Table 1, S/N 3, 4 and 9), which represent the individual detection and shutdown elements that a SIS would otherwise supervise.

Table 1: *Basic events, failure-rate data and sources used in the fault tree*

S/N	Basic event	Category	Rate	Unit	Source
1	Spark (ignition source)	Human/Environmental	1.0×10^{-3}	probability (Q)	Isograph RWB fault-tree output (this study)
2	Flame (ignition source)	Human/Environmental	1.0×10^{-3}	probability (Q)	Isograph RWB fault-tree output (this study)
3	Gas-detector failure to respond	Electrical	4.1×10^{-1}	per yr (FR)	Isograph RWB fault-tree output (this study)
4	Fire-detector failure to respond	Electrical	8.8×10^{-1}	per yr (FR)	Isograph RWB fault-tree output (this study)
5	Operator failure (loading-line leak)	Human error	1.8×10^{-3}	probability (Q)	Isograph RWB fault-tree output (this study)
6	Line defect due to pressure	Mechanical	1.0×10^{-4}	per yr (FR)	Isograph RWB fault-tree output (this study)
7	Failure due to collision against line	Mechanical	1.8×10^{-3}	per yr (FR)	Isograph RWB fault-tree output (this study)
8	Loading line incorrectly connected	Human error	1.8×10^{-3}	probability (Q)	Isograph RWB fault-tree output (this study)
9	Incorrect alarm response (ESD)	Human error	1.8×10^{-3}	probability (Q)	Isograph RWB fault-tree output (this study)
10	Manual shutoff valve sticking	Mechanical	1.1×10^{-4}	per yr (FR)	Isograph RWB fault-tree output (this study)
11	Fire not extinguishing (suppression failure)	Mechanical	1.0×10^{-3}	probability (Q)	Isograph RWB fault-tree output (this study)
12	Pressure-safety-valve (PSV) failure to open	Mechanical	1.7×10^{-2}	per yr (FR)	Isograph RWB fault-tree output (this study)

2.3 Simulation procedure and event tree

Crosschecking the input values and re-running the simulation helped to debug the fault tree and get it simulated to convergence. The simulation was performed five times to ensure that consistent results have been obtained. The event tree analysis was next carried out using the IRW event tree analysis module, with a pressure induced loading line defect (frequency w = 9.999×10^{-5} per year) as the initiating event, and gas detection, open flame/ignition, fire detection, fire suppression and pressure relief (PSV) as the branch barriers. This initiating event corresponds to the "line defect due to pressure" basic event of the fault tree (Table 1, S/N 6; EV49 in Figure 1) rather than to the fault tree's combined 0.7322/yr top event probability: the event tree traces one specific leak initiating pathway through the barrier sequence, while the fault tree separately aggregates all twelve basic events into the overall BLEVE top event probability. The two analyses are therefore complementary rather than sequential, and the resulting pathway frequencies (including the 4×10^{-21}/yr BLEVE branch) should be read as barrier performance outcomes conditional on this specific initiating pathway, not as a further breakdown of the 0.7322/yr top event figure. The non-realistic pathways were removed. The frequency of an outcome pathway k, given initiating event frequency f and barrier branch probability sequence {m}, can be expressed using Eq. 4:

$$F_k = f \times \prod_{j=1}^{m} p_j \tag{4}$$

where p_j is the conditional branch probability at barrier j along the pathway.

3. RESULTS AND DISCUSSION

3.1 Fault tree: BLEVE top event probability

The fault tree analyzed twelve basic events at the bottom of the tree, logically connected with the BLEVE top event via OR and AND gates (see Figure 1). Using the probability values from Table 1 in conjunction with the logic gates of Equations 1 and 2, the probability of the top event for a year was found to be 0.7322, invariant throughout all five runs of the simulation. This was strongly influenced by the three most probable contributors, namely fire detector failure to respond (FR=0.88/yr), gas detector failure to respond (FR=0.41/yr), and pressure-safety valve failure to open (FR=0.017/yr). The AND gate logic of the upper levels implies that the simultaneous failure of several protection layers is

required to cause the top event.

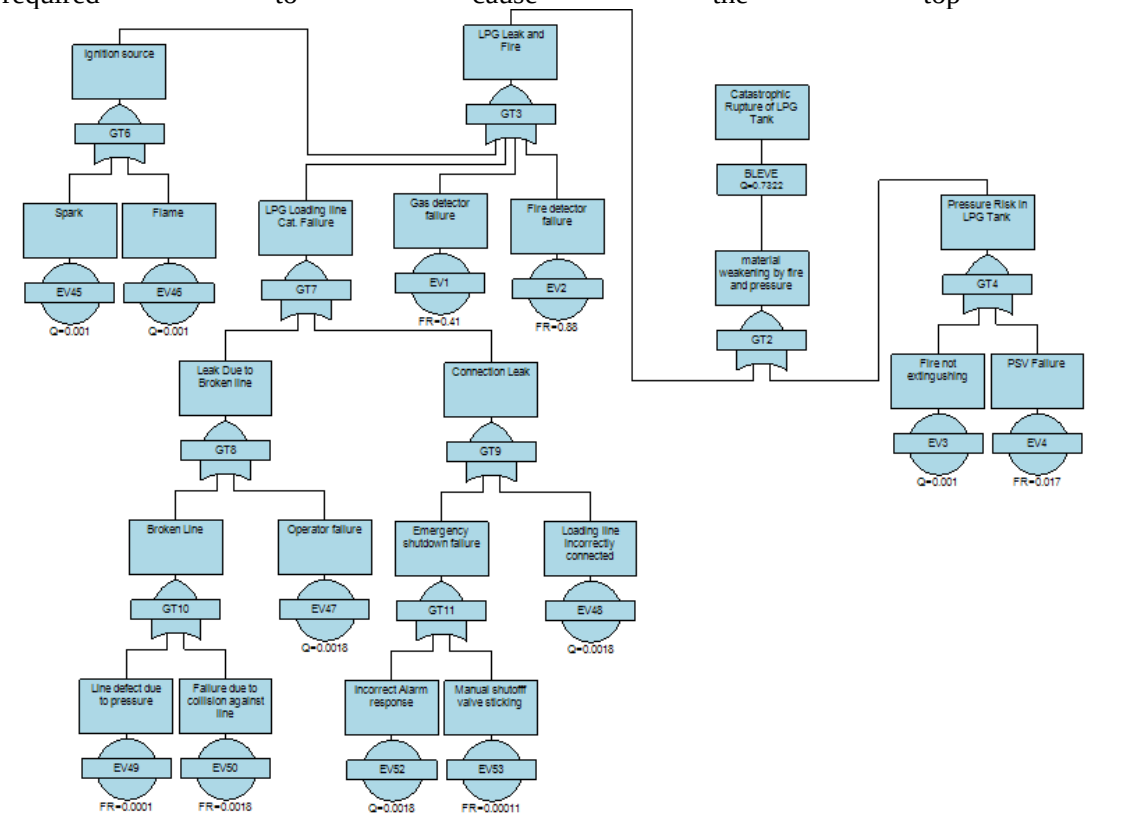

Figure 1: Fault tree for the LPG add-on skid BLEVE top event, generated in the Isograph Reliability Workbench (twelve basic events).

Figure 2 orders the basic events according to their failure rate magnitude on a logarithmic scale, highlighting the predominance of the fire detector, gas detector, and pressure safety valve while identifying those components that need improvement in terms of reliability.

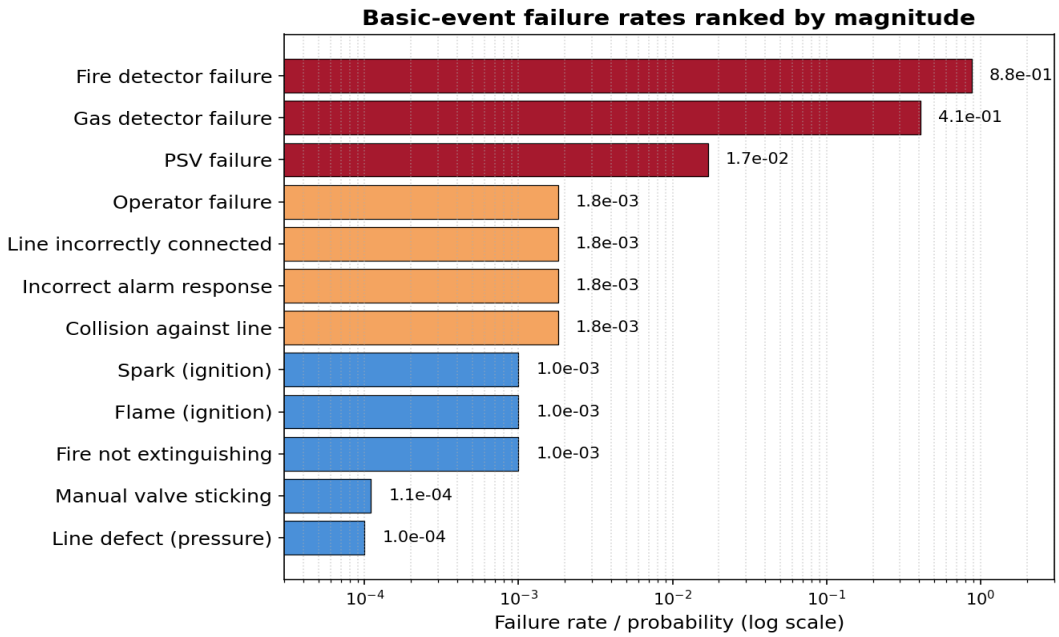

Figure 2: *Basic event failure rates ranked by magnitude (logarithmic scale).*

3.2 Event tree: outcome pathways

Five branches of outcomes were derived from the pressure induced loading line defect event, including safe dispersion, flash fire, vapour cloud explosion (VCE), jet fire and BLEVE (see Figure 3 below). The PSV failure branch probability was Q=0.017, consistent with the pressure safety valve failure rate reported in Table 1 (S/N 12). The application of Equation 4 to the various probability values for the barrier branch led to a conditional frequency of $4x10^{-21}$ per year for the fully-protected BLEVE branch, accounting for the highly unlikely probability of having the initiation event occur together with failure of all active barriers simultaneously. Safe dispersion was found to be the most likely outcome when all safety barriers operate as planned.

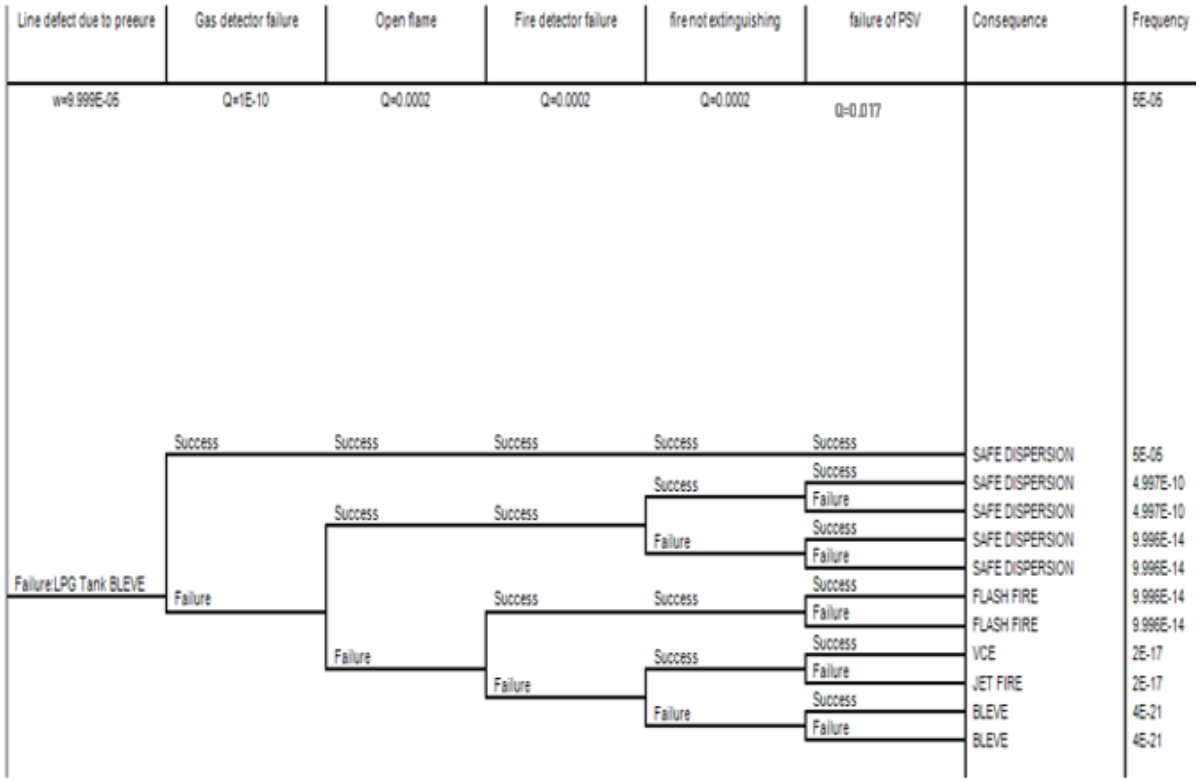

Figure 3: *Event tree mapping the pressure-induced loading line defect initiating event to five outcome pathways.*

Although the fault-tree top-event probability (0.7322/year, aggregated across all twelve basic events) and the event-tree's protected BLEVE branch frequency (4×10^{-21}/year, conditional on the single loading-line-defect initiating pathway) come from two separate analyses and are not directly derived from one another, the several orders of magnitude gap between them illustrates the benefit of safety barriers and highlights that keeping the barriers intact, rather than lowering the frequency of any single initiating event, is what controls the BLEVE hazard. This means that reliability centered maintenance focused on the three basic events with the highest frequencies will provide the largest reduction in the top event probability.

4. CONCLUSIONS

A joint study of fault tree and event tree analysis on an exemplary LPG add-on skid resulted in a BLEVE top event probability of 0.7322 per year, mainly due to fire detector, gas detector, and pressure safety valve failures. Five possible consequences of an event tree progression for a pressure induced loading line defect were found, out of which the fully protected BLEVE scenario has a probability of 4×10^{-21} per year, while the safest dispersion of gas in case of all barriers' functioning is the most probable consequence. A single failure does not suffice to trigger the top event, which makes barrier availability more significant than the initiating event frequency in managing LPG risks. The reliability data based on international standards presented in the paper and methodology can be applied to similar plants that lack failure rate data in their country, and it is proposed to concentrate maintenance efforts on the three leading basic events.

REFERENCES

American Institute of Chemical Engineers. (2020). *Guidelines for chemical process quantitative risk analysis* (3rd ed.). Wiley-AIChE.

Dunjó, J., Fthenakis, V., Vílchez, J. A., & Arnaldos, J. (2010). Hazard and operability (HAZOP) analysis: A literature review. *Journal of Hazardous Materials, 173*(1–3), 19–32. https://doi.org/10.1016/j.jhazmat.2009.08.076

Institute of Electrical and Electronics Engineers. (2007). *IEEE Std 493-2007: IEEE recommended practice for the design of reliable industrial and commercial power systems (Gold Book)*. IEEE. https://doi.org/10.1109/IEEESTD.2007.380668

International Electrotechnical Commission. (2016). *IEC 61511-1: Functional safety — Safety instrumented systems for the process industry sector*. IEC.

Isograph Ltd. (2023). *Reliability Workbench (Version 15.0)* [Computer software]. Isograph. https://www.isograph.com/software/reliability-workbench

OREDA Participants. (2015). *OREDA: Offshore and onshore reliability data handbook — Volume I: Topside equipment* (6th ed.). SINTEF Technology and Society.

Rausand, M., & Haugen, S. (2020). *Risk assessment: Theory, methods, and applications* (2nd ed.). Wiley. https://doi.org/10.1002/9781119377351

Vinnem, J. E., & Røed, W. (2022). *Offshore risk assessment Vol. 1: Principles, modelling and applications of QRA studies* (4th ed.). Springer. https://doi.org/10.1007/978-1-4471-7444-8

Yazdi, M., Korhan, O., & Daneshvar, S. (2020). Application of fuzzy fault tree analysis based on modified fuzzy AHP and fuzzy TOPSIS for fire and explosion in the process industry. *International Journal of Occupational Safety and Ergonomics, 26*(2), 319–335. https://doi.org/10.1080/10803548.2018.1454636

Zhou, Y., Bi, M., Jiang, H., Zhao, B., Ren, J., & Gao, W. (2022). Investigations on vapour cloud explosion hazards and critical safe reserves of LPG tanks. *Journal of Loss Prevention in the Process Industries, 78*, 104904. https://doi.org/10.1016/j.jlp.2022.104904

PROCESS INTENSIFICATION OF A 50 BPD MODULAR MINI-REFINERY: A SIMULATION-DRIVEN PINCH ANALYSIS APPROACH FOR ENHANCED HEAT RECOVERY AND SUSTAINABLE REFINING IN NIGERIA

Habib Ahmed Tijjani[1], Muhammed-Dabo I. A.[2,*], Waziri S. M.[2], Mustapha M. Sugungun[1]

[1]*Nigerian National Petroleum Company Limited*
[2]*Chemical Engineering Department, Ahmadu Bello University, Zaria*

Email: habibng2000@gmail.com, iroalidabo@gmail.com*, smwaziri@abu.edu.ng, Mustapha.Sugungun@nnpcgroup.com

***Corresponding author**: Muhammed-Dabo I. A.

DOI: https://doi.org/10.67203/sp.ICESID.2026

ABSTRACT

The global drive toward distributed small-scale petroleum refining has positioned modular mini-refineries as strategic assets for energy security in oil-producing developing economies. Yet, their widespread adoption in Nigeria remains constrained by simplistic process configurations, weak thermal integration, and heat exchanger networks designed without rigorous thermodynamic targeting, resulting in avoidable utility consumption, elevated operating costs, and diminished product value. While pinch-based energy integration is well established for large-scale refineries, its systematic coupling with commercial process simulation for sub-100 BPD modular systems has been sparsely addressed, constituting a distinct methodological gap that limits the energy-efficient scale-up of Nigeria's local refining capacity.

This work presents an original process integration and intensification framework for the Ahmadu Bello University Mini-refinery, transforming its existing 1 BPD topping unit into an optimized 50 BPD Atmospheric Distillation Unit processing a blend of Escravos and Forcados crude. Aspen HYSYS was applied for rigorous material and energy balancing, equipment sizing, and case-based yield optimization, with all simulation outputs cross-validated against independent manual calculations to within approximately 5% deviation, confirming model robustness.

Energy integration and optimization measurably improved naphtha, kerosene, and diesel recoveries while reducing residue generation, demonstrating tangible gains in crude value addition and heat recovery. By uniting simulation-driven design with structured heat integration at modular scale, this study delivers a novel, economically significant, and industrially replicable pathway toward sustainable, energy-efficient refining, directly advancing Nigeria's refining industry and supporting Sustainable Development Goals 7, 9, 12, and 13 through affordable clean energy, resilient infrastructure, responsible resource use, and climate-conscious industrial practice.

Keywords: *Process Intensification; Energy Integration; Pinch Analysis; Heat Exchanger Network; Modular refinery; Optimization; Sustainable Refining*

1.0 INTRODUCTION

Petroleum refining is among the most energy-intensive process industries; distillation, fired heating and steam generation together dominate a refinery's own fuel consumption, with efficiency strongly dependent on configuration, crude slate and installed heat recovery (IEA, 2024). Process Integration, and pinch analysis specifically, emerged in the late 1970s–early 1980s as a thermodynamically grounded response (Hohmann, 1971; Linnhoff & Flower, 1978; Umeda et al., 1978; Linnhoff & Hindmarsh, 1983): by locating the pinch temperature separating a process into interacting heat sources and sinks, it sets minimum hot- and cold-utility and heat-transfer-area targets before any exchanger is designed (Townsend & Linnhoff, 1984; Kemp, 2007), and decades of oil, gas and petrochemical application confirm material cuts in fired-heater and cooling-water demand (Smith, 2000; Klemeš et al., 2013). Process intensification pursues the same or better performance from smaller,

safer, more energy-efficient equipment through combined unit operations or enhanced transport phenomena (Stankiewicz & Moulijn, 2000; Van Gerven & Stankiewicz, 2009); where integration re-arranges energy already in a flowsheet, intensification reduces the footprint, inventory and often the energy and capital demand of the equipment itself. Modern refinery design increasingly applies both together, since a smaller, better-integrated plant is cheaper to build and to run.

Nigeria holds substantial proven reserves but has historically relied on a few large, centralised state-owned refineries that, for much of the past two decades, ran well below installed capacity, forcing large-scale product imports even while crude was exported. Policy has consequently favoured modular and mini-refineries as a faster, lower-capital route to domestic capacity: the Nigerian Midstream and Downstream Petroleum Regulatory Authority (NMDPRA) reported issuing 47 Licences to Establish and 30 Licences to Construct in a single year, combined capacity approaching three million BPD, with several modular refineries already operating in the Niger Delta at 1,000–11,000 BPD (as cited in Ahmed, 2025). Because modular units are small by definition, their thermal efficiency is easily compromised where energy integration is an afterthought — the economies of scale that make heat exchange attractive at large flowrates are largely absent at small ones. This is the setting for the ABU Mini-Refinery, an existing 1 BPD teaching/research facility in the Department of Chemical Engineering, ABU Zaria, now being redesigned and scaled to 50 BPD.

The existing 1 BPD facility is too small for meaningful scale-up study or a representative test of heat-integration strategy, and its heat exchanger network was never designed against a formal energy target. The engineering problem addressed here is therefore how to integrate, size and, in due course, intensify the heat-recovery system of a 50 BPD ADU/VDU processing blended Escravos and Forcados crude, using a rigorous simulation- and pinch-analysis-based methodology, so the redesigned unit can serve as a demonstrable, energy-conscious platform for Nigerian modular-refinery development. Prior work has applied pinch analysis and simulation to crude distillation and to Nigerian refinery retrofits, e.g. the Kaduna FCC unit (Abubakar, 2020), and a separate body of Nigerian work covers modular-refinery design and economics for indigenous crude assays (Olatona, 2022); less common is a single 50 BPD-scale study combining an Aspen HYSYS simulation of a named Nigerian crude, a full Problem Table Algorithm exercise across a range of ΔT_{min}, balanced-composite-curve area targeting, and a stated, in-progress programme to synthesise, fabricate and test the network on a physical unit. This study is positioned to close that gap, while candidly reporting network synthesis, fabrication, and commissioning as ongoing rather than completed.

The aim is to design, simulate, validate, and optimise the 50 BPD ABU mini-refinery ADU for a blend of Escravos and Forcados crude and to carry out energy integration of its heat exchanger network. Specific objectives: (i) design, validate and optimise the 50 BPD unit; (ii) carry out material and energy balances by manual calculation and Aspen HYSYS simulation; (iii) size major equipment (preflash column, desalter, furnace, atmospheric column, side strippers, condenser, HEN); (iv) carry out energy-integration design via the Pinch Design Method; and (v) fabricate, install, and test-run the energy-integrated unit. By coupling rigorous simulation with pinch-based targeting on a physical modular refinery, the study generates concrete, quantified energy and area targets transferable to similarly scaled Nigerian mini-refineries, and its validation methodology — cross-checking HYSYS against independent manual calculation — offers a transferable quality-assurance approach for other indigenous modular-refinery projects, strengthening local technical capacity in simulation, pinch analysis and refinery equipment design.

2.0 LITERATURE REVIEW

Conventional refineries achieve economies of scale through highly heat-integrated preheat, furnace and fractionation trains that are difficult to replicate at a fraction of the throughput; modular refineries (roughly hundreds to a few thousand BPD) have therefore been promoted in Nigeria as a quicker, lower-capital route to local capacity (Olatona, 2022), reinforced by the scale of recent licensing activity (Ahmed, 2025). This literature, however, concentrates on crude-assay classification, mechanical sizing, and yield estimation, with comparatively little systematic energy targeting. Distillation and fired heating dominate refinery energy use, and refining remains one of the more energy- and emissions-intensive segments of the oil supply chain (IEA, 2024); at mini-refinery scale, where stream flowrates and heat-capacity flowrates are small, achieving comparable heat recovery to a

large plant requires more deliberate targeting, since the scope for stream-to-stream heat exchange narrows as flowrates fall.

Process Integration is a family of thermodynamically based methods for systematic design and analysis of process and utility systems (Smith, 2000; El-Halwagi, 2011). Its heat-exchanger-network branch, pinch analysis, grew from early work on optimal networks and systematic synthesis (Hohmann, 1971; Umeda et al., 1978; Linnhoff & Flower, 1978) before consolidation into the Pinch Design Method (Linnhoff & Hindmarsh, 1983), and has since extended to mass, water, hydrogen and total-site utility systems (Klemeš et al., 2013). Pinch analysis represents hot and cold streams as composite curves of temperature against enthalpy; the closest approach between the curves, offset by the chosen minimum approach temperature (ΔT_{min}), defines the pinch (Linnhoff & Hindmarsh, 1983; Kemp, 2007). Below the pinch the process is in heat deficit and needs external heating; above it, in surplus, it needs external cooling; no economically justified design transfers heat across the pinch, since doing so raises both utility targets above their true minimum — and because ΔT_{min} governs the utility/area/capital trade-off, scanning a range of values (here 10–40°C) is itself part of the design task.

The Problem Table Algorithm (PTA) is the numerical counterpart of the composite-curve construction: streams are shifted by half of ΔT_{min}, ranked into temperature intervals, and cascaded through interval-by-interval enthalpy balances to compute minimum utility targets without graphical plotting (Kemp, 2007); adding just enough hot utility at the top of the cascade to eliminate every negative running total yields the minimum hot- and cold-utility targets and locates the pinch. Once targets are known, network synthesis matches hot and cold streams above and below the pinch subject to feasibility rules — $CP_{hot} \leq CP_{cold}$ immediately above the pinch and $CP_{hot} \geq CP_{cold}$ immediately below it — so no exchanger crosses the pinch (Linnhoff & Hindmarsh, 1983); the corresponding area target can be estimated ahead of detailed design via the balanced composite curve method (Townsend & Linnhoff, 1984), valuable at the pre-design stage before the detailed network is finalised, with subsequent mathematical-programming and metaheuristic extensions catalogued by Furman and Sahinidis (2002).

Process Intensification seeks step-change gains in performance, smaller equipment and lower energy/material inventories by combining unit operations or exploiting more favourable driving forces (Stankiewicz & Moulijn, 2000), classified by the structure-energy-synergy-time framework according to whether they intensify the equipment or the process itself (Van Gerven & Stankiewicz, 2009); divided-wall columns and heat-pump-assisted distillation are commonly cited refining examples. Process integration and intensification are conceptually distinct — the former re-arranges existing flowsheet energy, the latter changes the equipment or process route — but complementary, and both are examined here. Commercial simulators such as Aspen HYSYS are widely used to generate the material/energy balances and preliminary sizing a pinch study requires, particularly for multi-component crude fractions where hand calculation of vapour-liquid equilibrium is impractical; sustainable refinery development links this energy efficiency directly to resource conservation and emissions reduction, since every unit of avoided fired-heater duty is a unit of crude-derived energy not burned to run the plant (El-Halwagi, 2011; Klemeš et al., 2013). Overall, what remains comparatively underexplored is the combination of these strands — HYSYS simulation, full PTA energy targeting, area targeting, and a stated network-synthesis/fabrication programme — on one physically realisable 50 BPD Nigerian platform; this study addresses that gap.

3.0 METHODOLOGY

3.1 Research Framework and Facility

The existing ABU Mini-Refinery, a 1 BPD ADU/VDU teaching and research facility in the Department of Chemical Engineering, ABU Zaria, served as the design basis for a scaled-up, energy-integrated replacement. The research framework proceeds sequentially from design-basis definition and process-option selection, through PFD development, manual-and-simulation material/energy balancing, base-versus-optimised case-study comparison, equipment sizing, energy-integration/HEN design, mechanical and P&ID drawing, and finally fabrication, installation, operating-procedure preparation and test-running. At the time of reporting, the sequence is complete as far as equipment sizing and pinch-based energy/area targeting; HEN synthesis, fabrication, installation, and test-running remain ongoing and are reported as such. The redesign retains the existing ADU-VDU configuration

with side strippers but re-establishes the crude preheat, distillation and heat-recovery scheme from first principles using simulation and pinch analysis.

3.2 Feedstock Characterisation

The design basis specifies a 50 BPD ADU capacity, an ambient temperature of 25°C, and an operating pressure of 760 mmHg. The blended crude comprises of Escravos characterised in Aspen HYSYS using the PIMS-based Escravos-2012 assay for West Africa/Nigeria, and Forcados crude characterised using the Forcados Blend-2014 assay. Evaluation of both assays indicates that Escravos is relatively lighter and sweeter, with an API gravity of 33.84° and sulphur content of 0.17 wt.%, whereas Forcados is slightly heavier, higher in sulphur content, and is more acidic, with an API gravity of 32.22°, sulphur content of 0.22 wt.%, and total acid number of 0.46 mg KOH/g, as shown in Table 1.

Table 1: Design Basis and Crude Oil Properties of the Blend (Escravos/Forcados Ratio 50:50)

Parameter	Escravos	Forcados	Units
Capacity of ADU	25	25	BPD
Ambient temperature	25	25	°C
Pressure	760	760	mmHg
API gravity	33.84	32.22	—
Standard liquid density	53.37	53.90	lb/ft³
Molecular weight	203.52	204.66	—
Sulphur content	0.17	0.22	wt.%
Pour point	16.38	18.27	°C
Watson K factor	11.57	11.38	—
Total acid number	0.24	0.46	mg KOH/g
Viscosity @ 37.78°C	4.44	4.02	cSt

3.3 Process Configuration

Five candidate configurations were screened at the process-selection stage (Table 2): a conventional ADU with preheat train and side strippers; a preflash-column configuration with heat integration; a divided-wall-column (DWC) ADU; a heat-pump-assisted ADU; and a hybrid combining preflash, DWC and heat integration. The flowsheet developed and simulated for the 50 BPD unit (Figure 1) retains a preflash drum ahead of the fired heater and a full set of pump-around loops, consistent with the preflash-with-heat-integration option identified in screening. It comprises crude feed and metering; wash-water mixing and desalting; a preflash stage; a top/middle/bottom pump-around preheat train; a fired heater; an atmospheric column with kerosene, diesel and AGO side strippers (each steam-reboiled); an overhead condenser and reflux drum; and product routing to naphtha, kerosene, diesel, AGO and atmospheric-residue storage. The atmospheric residue is processed in a VDU, with its own preheater and pump-around coolers, to recover light and heavy vacuum gas oil (LVGO, HVGO) and vacuum residue.

Table 2: Process Configuration Options Evaluated for the ABU Mini-Refinery ADU

Option	Configuration	Key features	Yield / quality	Environmental impact / advantages
1	Conventional ADU	Preheat train, furnace, side strippers	Moderate naphtha yield; standard quality	High CO2 from furnace; simple, low CAPEX
2	Preflash + heat integration	Preflash removes light ends before furnace, cutting furnace load	Improved naphtha yield; better fractionation	Lower energy/emissions; smaller furnace
3	DWC ADU	Single column, divided wall for kerosene/diesel	High yield, less reflux; sharper cuts	Lower energy; fewer columns; lower CAPEX/OPEX
4	Heat-pump-assisted ADU	Overhead vapour recompression recovers heat for reboilers	Similar yield; high purity	30–50% energy savings; best at low ambient temp.
5	Hybrid (preflash+DWC+HI)	Combines preflash, DWC and heat recovery	Highest yield; optimised, premium cuts	Lowest emissions, max recovery; higher complexity

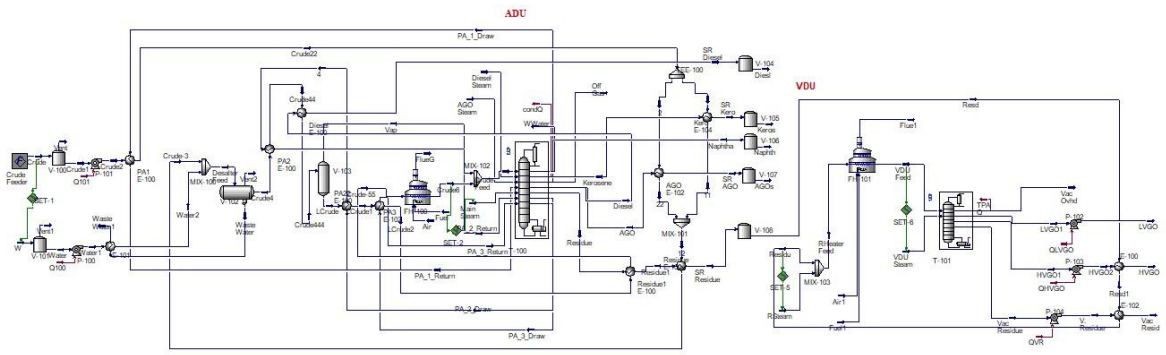

Figure 1: Detailed Developed Process Flow Diagram of the 50 BPD ABU Mini-Refinery ADU/VDU with Heat Exchanger Network

3.4 Simulation, Stream Identification and Pinch Procedure

The flowsheet was built and solved in Aspen HYSYS using the Peng-Robinson equation of state. The Escravos and Forcados assays were installed from the PIMS crude-oil databank and characterised into pseudo-components before introduction at 50 BPD; column specifications (draw rates, side-stripper steam rates, pump-around duties/return temperatures, reflux ratio, condenser temperature) were entered on the atmospheric column, and the flowsheet solved to convergence for a base case and an optimised case (the latter adjusting specifications to improve recovery). Material and energy balances were extracted for every major unit and mixing point. Process integration began with identifying, from the converged flowsheet, eight hot streams (top pump-around, naphtha, kerosene, mid pump-around, diesel, bottom pump-around, AGO, atmospheric residue) and four cold streams representing successive crude-preheat stages (pre-desalted, preflashed, pre-heated/furnace-feed, heated/furnace-outlet crude), plus steam and cooling-water utilities. Supply temperature, target temperature and heat-capacity flowrate (CP) were extracted or computed for each stream (Table 3).

Table 3: Pinch-Analysis Stream Data for the ADU/VDU Heat Integration Study

No.	Stream	Type	Ts (°C)	Tt (°C)	CP (kJ/°C·s)
1	Top pump-around	H1 (hot)	169	110	0.069
2	Naphtha	H2 (hot)	73	40	0.035
3	Kerosene	H3 (hot)	230	40	0.025
4	Mid pump-around	H4 (hot)	236	152	0.050
5	Diesel	H5 (hot)	250	50	0.048
6	Bottom pump-around	H6 (hot)	305	232	0.034
7	Atmospheric gas oil	H7 (hot)	294	50	0.014
8	Atmospheric residue	H8 (hot)	304	118	0.057
9	Pre-desalted crude	C1 (cold)	25	95	0.161
10	Preflashed crude	C2 (cold)	95	118	0.169
11	Pre-heated crude (furnace feed)	C3 (cold)	118	180	0.182
12	Heated crude (furnace outlet)	C4 (cold)	180	360	0.212
13	Steam	Hot utility	305	304	26.468
14	Cooling water	Cold utility	20	60	0.052

Pinch analysis was carried out by shifting each stream by half of the chosen ΔTmin and applying the PTA to the shifted temperatures for seven values spanning 10–40°C in 5°C increments; for each ΔTmin the shifted temperatures were recomputed, streams ranked into intervals, and an unconstrained-then-constrained enthalpy cascade constructed to obtain QHmin, QCmin and the pinch temperature. The full PTA computation is reported for the design case ΔTmin = 35°C, with targets for all seven ΔTmin values reported alongside it (Section 4). Area targeting for ΔTmin = 35°C used the balanced composite curve method: utility duties were added to the streams so the composite curves coincide at every interval, and area contributions computed from each interval's log-mean temperature difference and aggregate CP. Detailed stream-by-stream network matching by the Pinch Design Method is identified as pending, ongoing work. Intensification considerations were incorporated principally at process selection (Table 2), where DWC and heat-pump-assisted options were evaluated, and in the adopted flowsheet through the preflash stage (reducing downstream vapour load and equipment size) and pump-around loops (combining reflux control with preheat duty in-column rather than in additional external exchangers). Validation compared HYSYS material/energy balances against independent MathCAD manual calculations using the same assay, design basis and specifications, on a percentage-deviation basis (Section 4.10).

4.0 RESULTS

The Aspen HYSYS flowsheet (Figure 1) converged for both the base case and the optimised case, generating full material and energy balances across every mixing point, the desalter, fired heater, condenser, each side stripper and the overall atmospheric column. Representative and summarised results are reported below.

4.1 Material Balance

Table 4 summarises the overall material balance for the 50 BPD atmospheric column. Steam introduced to the column and side strippers totals 10.406 kg/h against a crude feed of 284.747 kg/h; the column produces wastewater (10.247 kg/h), off-gas (3.153 kg/h), naphtha (59.256 kg/h), kerosene (40.595 kg/h), diesel (77.397 kg/h), AGO (21.510 kg/h) and residue (82.994 kg/h), this indicates a differential of + 0.001 kg/h (0.00034%) which is attributed to rounding error closing at 295.153 kg/h inlet and 295.152 kg/h outlet, however, balances closed across the crude/wash-water mixing points, desalter, fired heater and each side stripper as shown in (Table 5), which confirmed an internal consistency.

Table 4: Overall Material Balance for the Designed 50 BPD Atmospheric Distillation Column

Component	**Inlet (kg/h)**	**Outlet (kg/h)**
Main steam	8.592	0.000
Diesel side-stripper steam	0.907	0.000
AGO side-stripper steam	0.907	0.000
Crude feed	284.747	0.000
Waste water	0.000	10.247
Off-gas	0.000	3.153
Naphtha	0.000	59.256
Kerosene	0.000	40.595
Diesel	0.000	77.397
AGO	0.000	21.510
Residue	0.000	82.994
Total	**295.153**	**295.152**

Table 5: Selected Unit Material Balances Across the ADU Flowsheet

Unit / component	**Inlet (kg/h)**	**Outlet (kg/h)**
MIX-100 – Water / Crude / Desalter feed	23.1 / 284.6 / –	– / – / 307.7
Desalter – Feed / Crude (desalted) / Waste water	307.7 / – / –	– / 284.7 / 23.0
Furnace – Crude in / Air / Fuel	284.7 / 108.0 / 5.3	–
Furnace – Crude out / Flue gas	–	284.7 / 113.3
Condenser – Feed	234.9	–
Condenser – Off-gas / Naphtha / Reflux / Waste water	–	3.2 / 59.3 / 162.2 / 10.3
Kerosene stripper – Draw / Boil-up	58.4 / 28.9	–
Kerosene stripper – Reboiler out / Return	–	69.5 / 17.8
Diesel stripper – Draw / Steam	88.7 / 0.9	–
Diesel stripper – Reboiler out / Return	–	77.4 / 12.2
AGO stripper – Draw / Steam	27.2 / 0.9	–
AGO stripper – Reboiler out / Return	–	21.5 / 6.6

4.2 Energy Balance

Table 6 reports the energy balance. The fired-heater/preheat-train duty on the crude side (CDU preheater) shows a net enthalpy gain of +157,981.85 kJ/h; the atmospheric condenser removes 120,912.86 kJ/h; and the three pump-around coolers remove 14,553.01, 15,166.55 and 8,942.28 kJ/h (top, middle, bottom). On the vacuum side, the VDU preheater gains 53,196.00 kJ/h, while its top and bottom pump-around coolers remove 16,784.74 and 19,472.53 kJ/h respectively.

Table 6: Energy Balance for the Designed ABU Mini-Refinery's ADU and VDU

Component	Input streams (kJ/h)	Output streams (kJ/h)	Duty (kJ/h)
CDU preheater	-521,249.43	-363,267.58	+157,981.85
ADU condenser	-509,500.73	-630,413.59	-120,912.86
Top-stage PA cooler	-197,367.83	-211,920.84	-14,553.01
Middle-stage PA cooler	-125,366.81	-140,533.36	-15,166.55
Bottom-stage PA cooler	-69,536.10	-78,478.38	-8,942.28
VDU preheater	-169,799.90	-116,603.90	+53,196.00
VDU top-stage PA cooler	-67,569.39	-84,354.14	-16,784.74
VDU bottom-stage PA cooler	-135,638.52	-155,111.05	-19,472.53

4.3 Product Yields

Table 7 compares base-case and optimised-case yields. Relative to base case, the optimised case increased naphtha yield 9.0% (11.000→11.994 BPD), kerosene 21.5% (6.000→7.291 BPD), diesel 2.2% (13.000→13.288 BPD), AGO fell 0.001% (3.559→3.558 BPD) which is an insignificant change, atmospheric residue fell 11.3% and vacuum residue fell 63.8% — a shift of material from low-value bottoms toward higher-value light/middle distillates. Off-gas and HVGO increased sharply in percentage terms (+86.5%, +285.5%) though both remain small absolute streams relative to the 50 BPD total.

Table 7: Product Yields — Base Case versus Optimised Case 50 BPD (Escravos/Forcados Blend Ratio 50:50)

Product	Base case (BPD)	Optimised case (BPD)	Variation (%)
Off-gas	1.691	3.153	+86.482
Naphtha	11.000	11.994	+9.040
Kerosene	6.000	7.291	+21.509
Diesel	13.000	13.288	+2.215
Atmospheric gas oil (AGO)	3.559	3.558	-0.001
Atmospheric residue	14.877	13.195	-11.306
Light vacuum gas oil (LVGO)	2.761	2.524	-8.584
Heavy vacuum gas oil (HVGO)	1.798	6.932	+285.540
Vacuum residue	10.300	3.731	-63.776

4.4 Equipment Sizing

Table 8 summarises sizing for the principal units, sized directly from converged HYSYS hydraulic and rating calculations. The column sections operate at 69–70% approach-to-flood in the sieve-tray sections and about 9% in the valve-tray section, with tray pressure drops of 1.1–4.0 kPa and vapour residence times of 22–35 s, indicating hydraulically stable operation with margin before flooding.

Table 8: Equipment Sizing Summary for the 50 BPD ABU Mini-Refinery ADU

Equipment	Key dimensions	Other parameters
Desalter	Diameter 1.252 m*; length 0.9146 m; head height 0.1636 m	Boot dia. 0.25 m; boot height 0.50 m; volume 0.3545m³
Preflash column	Diameter 0.6473 m; length 0.9710 m; elevation 0.50 m	Boot dia. 0.2158 m; boot height 0.3237 m; volume 0.3313m³
Furnace – tube bank	ID 0.089 m; OD 0.102 m; 20 tubes/pass	Inner area 21.23 m²; outer area 24.26 m²; net vol. 0.4718m³
Furnace – shell	ID 1.700 m; OD 2.000 m; zone height 4.280 m	Inner area 22.86 m²; outer area 26.89 m²; net vol. 9.0982m³
ADC section 1 (sieve)	Diameter 0.23 m; height 3.75 m	ΔP 4.045 kPa; 70.13% flood; 26.82 s residence; 26 holes
ADC section 2 (sieve)	Diameter 0.23 m; height 2.76 m	ΔP 1.595 kPa; 69.91% flood; 35.3 s residence; 50 holes
ADC section 3 (ballast valve)	Diameter 0.23 m; height 0.69 m	ΔP 1.075 kPa; 9.21% flood; 21.67 s residence

4.5 Pinch Analysis Results

Table 9 reports the detailed PTA cascade for the design case ΔTmin = 35°C. Working down the shifted-temperature intervals, the unconstrained cascade (Cascade I) reaches its most negative value of -26.468 kJ/s at the interval bounded by 212.5°C; adding this quantity of hot utility at the top produces the constrained cascade (Cascade II), which first reaches zero at that same interval — identifying 212.5°C as the pinch on the shifted scale, corresponding to an actual hot-stream pinch of 230°C and cold-stream pinch of 195°C.

Table 9: Problem Table Algorithm Cascade for ΔTmin = 35°C

Int.	Temp. Profile (°C)	Streams Population	ΔT °C	ΣCPH	ΣCPC	Q (kJ/s)	Cascade I u = 0.000	Cascade II u = 26.468
1	377.5	12	90	0.000	0.212	19.080	-19.080	7.388
2	287.5	6,12	1	0.034	0.212	0.178	-19.258	7.210
3	286.6	6,8,12	10	0.090	0.212	1.220	-20.478	5.990
4	276.5	6,7,8,12	44	0.104	0.212	4.752	-25.230	1.238
5	232.5	5,6,7,8,12	14	0.152	0.212	0.840	-26.070	0.398
6	218.5	4,5,6,7,8,12	4	0.202	0.212	0.040	-26.110	0.358
7	214.5	4,5,7,8,12	2	0.168	0.212	0.088	-26.198	0.270
8	212.5	3,4,5,7,8,12	15	0.194	0.212	0.270	-26.468	*0.000
9	197.5	3,4,5,7,8,11	46	0.194	0.182	-0.552	-25.916	0.552
10	151.5	1,3,4,5,7,8,11	16	0.263	0.182	-1.296	-24.620	1.848
11	135.5	1,3,4,5,7,8,10	1	0.263	0.169	-0.094	-24.526	1.942
12	134.5	1,3,5,7,8,10	22	0.213	0.169	-0.968	-23.558	2.910
13	112.5	1,3,5,7,8,9	12	0.213	0.161	-0.624	-22.934	3.534
14	100.5	1,3,5,7,9	8	0.156	0.161	0.040	-22.974	3.494
15	92.5	3,5,7,9	37	0.087	0.161	2.738	-25.712	0.756
16	55.5	2,3,5,7,9	13	0.122	0.161	0.507	-26.219	0.249
17	42.5	2,3,5,7	10	0.122	0.000	-1.220	-24.999	1.469
18	32.5	2,3	10	0.060	0.000	-0.600	-24.399	2.069
19	22.5							

*PINCH POINT

4.6 Energy Targets Across ΔTmin

Table 10 summarises pinch-analysis energy targets for seven ΔTmin values. As ΔTmin rises from 10°C to 40°C, QHmin rises from 24.44 to 27.44 kJ/s and QCmin from effectively zero to 3.04 kJ/s, while the pinch condition moves from a threshold-problem at ΔTmin = 15°C (overall heat surplus; in principle only one utility required) to a working pinch of 212.5°C (shifted) at ΔTmin = 35°C. This is in conformity with the literature that utilities requirement increases as the approach temperature widens further. For the design case (ΔTmin = 35°C), confirmed targets are QHmin = 26.47 kJ/s and QCmin = 2.07 kJ/s.

Table 10: Summary of Energy Targets and Pinch Points for ΔTmin = 10–40°C

ΔTmin (°C)	QHmin (kJ/s)	QCmin (kJ/s)	Pinch (shifted, °C)	Hot pinch (°C)	Cold pinch (°C)
10.0	24.44	0.00	TP	TP	TP
15.0	23.45	0.00	TP	TP	TP
20.0	24.70	0.30	40.0	50.0	30.0
25.0	25.00	0.60	60.5	73.0	48.0
30.0	25.61	1.21	58.0	73.0	43.0
35.0	26.47	2.07	212.5	230.0	195.0
40.0	27.44	3.04	210.0	230.0	190.0

*TP - Threshold Problem

4.7 Heat Exchanger Area Requirements

Detailed stream-by-stream HEN matching by the Pinch Design Method has not yet been completed; this remains pending, alongside fabrication, installation, operating-procedure preparation and test-running of the energy-integrated unit. Table 11 reports the interval-by-interval log-mean-temperature-difference and area computation for the balanced composite curves at ΔTmin = 35°C. Summing the eighteen interval area contributions gives a minimum HEN area target of 8.86 m² for the redesigned 50 BPD ADU heat-recovery system — an early, network-independent estimate usable for preliminary capital-cost screening ahead of detailed exchanger design.

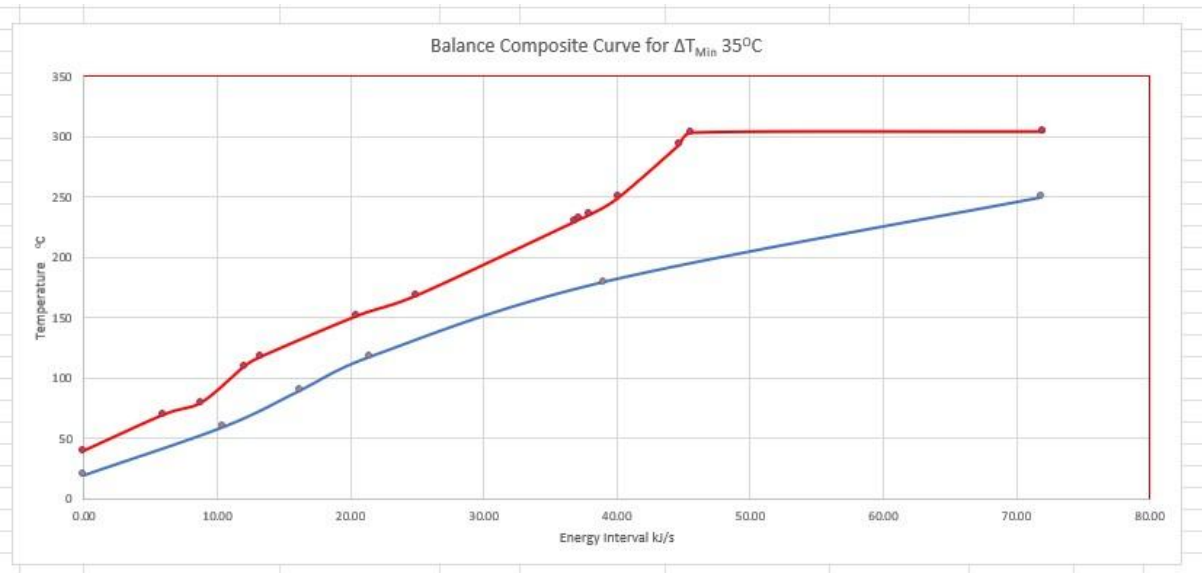

Figure 2: Balanced Composite Curve Graph for the ADU/VDU Heat Integration Study (ΔTmin = 35°C)

Table 11: Balanced Composite Curve Area-Targeting for (ΔTmin = 35°C). Total heat-exchanger area target = 8.86 m²

Int.	Thi(°C)	Tci(°C)	ΣCPH/h	ΣCPC/h	ΣQ/h,i(kJ/s)	LMTD(°C)	Area(m²)
1	70	32	0.61	0.81	27.96	28.04	1.00
2	80	50	0.61	0.81	20.59	33.84	0.61
3	91	60	0.44	0.81	12.84	30.50	0.42
4	110	64	0.44	0.81	11.49	38.01	0.30
5	118	72	0.78	0.81	12.68	46.00	0.28
6	132	90	1.07	0.81	29.40	43.97	0.67
7	152	112	1.07	0.85	39.89	40.99	0.97
8	156	118	1.32	0.85	10.33	38.99	0.26
9	169	123	0.97	0.91	17.16	41.87	0.41
10	230	168	0.97	0.91	100.12	53.60	1.87
11	232	170	0.84	0.91	3.50	62.00	0.06
12	236	174	1.01	0.91	7.68	62.00	0.12
13	243	180	0.76	0.91	10.78	62.50	0.17
14	250	182	0.76	0.61	6.53	65.47	0.10
15	294	186	0.52	0.61	25.30	86.46	0.29
16	304	187	0.45	0.61	5.11	112.44	0.05
17	304	194	132.35	0.61	4.24	113.46	0.04
18	305	198	132.35	0.61	134.77	108.49	1.24

.

4.8 Validation of HYSYS and Manual Calculations

Table 12 compares HYSYS-simulated and manually calculated (MathCAD) product yields, and Table 13 the corresponding heat-exchanger duties. Yield deviations range from -3.12% (LVGO) to +1.17% (diesel), and duty deviations from -3.27% (condenser) to +5.32% (ADU preheater); all deviations lie within approximately ±5.3%. This level of agreement supports the internal consistency of the HYSYS flowsheet and its manual cross-check, giving confidence in the stream data subsequently used for pinch analysis.

Table 12: Validation of Product Yields — Aspen HYSYS versus Manual (MathCAD) Calculation

Product	HYSYS yield (BPD)	Manual yield (BPD)	Deviation (%)
Off-gas	1.691	1.723	-1.86
Naphtha	11.000	11.200	-1.79
Kerosene	6.000	6.150	-2.44
Diesel	13.000	12.850	+1.17
Atmospheric gas oil (AGO)	3.559	3.600	-1.14
Atmospheric residue	14.877	15.000	-0.82
Light vacuum gas oil (LVGO)	2.761	2.850	-3.12
Heavy vacuum gas oil (HVGO)	1.798	1.780	+1.01
Vacuum residue	10.300	10.500	-1.90

Table 13: Validation of Heat Exchanger Duties — Aspen HYSYS versus Manual (MathCAD) Calculation

Component	HYSYS duty (kJ/h)	Manual duty (kJ/h)	Deviation (%)
CDU preheater	+157,981.85	+150,000	+5.32
ADU condenser	-120,912.86	-125,000	-3.27
Top-stage PA cooler	-14,553.01	-14,000	+3.95
Middle-stage PA cooler	-15,166.55	-14,500	+4.59
Bottom-stage PA cooler	-8,942.28	-9,000	-0.64
VDU preheater	+53,196.00	+52,000	+2.30
VDU top-stage PA cooler	-16,784.74	-17,000	-1.27
VDU bottom-stage PA cooler	-19,472.53	-20,000	-2.64

5.0 DISCUSSION

The Problem Table results show the redesigned 50 BPD unit has a genuine, quantifiable minimum energy requirement: at the design ΔTmin of 35°C, only 26.47 kJ/s of hot utility and 2.07 kJ/s of cold utility are thermodynamically necessary to satisfy all process heating and cooling simultaneously. Because these figures come directly from validated HYSYS stream data, they are a reasonably reliable lower bound against which any HEN eventually installed — including the existing, non-pinch-designed 1 BPD network — can be benchmarked once scaled and re-commissioned. The pinch-point behaviour across ΔTmin = 10–40°C is informative in its own right: at the tightest approach temperatures (10°C and 15°C) the process behaves as a threshold problem, in overall heat surplus with, in principle, only one utility required; as ΔTmin widens, a genuine pinch emerges and both targets increase, since a larger ΔTmin always trades reduced exchanger area for increased utility consumption. The working pinch at a shifted 212.5°C (actual hot/cold pinch 230°C/195°C) at ΔTmin = 35°C sits high in the column's temperature range, near the bottom pump-around and atmospheric-residue streams, indicating the highest-temperature hot streams and the furnace-outlet cold stream sit thermally close together, leaving little scope for further preheat recovery above this point without intensifying that match or accepting additional furnace duty.

Although the detailed exchanger network has not yet been synthesised, the area target of 8.86 m² gives an early indication that the heat-recovery surface required to approach the energy targets is modest, consistent with the small absolute duties at 50 BPD — useful for planning the forthcoming network-design and fabrication stage, since it suggests the redesigned network need not be large or capital-intensive, provided matches are selected per the pinch-design feasibility rules (Section 2).

Process intensification is reflected primarily at the process-selection stage, where DWC and heat-pump-assisted configurations were evaluated as more compact or less utility-intensive alternatives, and in the retention of a preflash stage and multiple pump-around loops in the developed flowsheet, reducing the duty (and hence size) that would otherwise fall on the fired heater and on separate external exchangers; the compact equipment sizing obtained (column diameters ~0.23 m, section heights under 4 m) is itself evidence of successful scale intensification relative to a conventional refinery train, even though a full DWC or heat-pump-assisted column was not carried into the final flowsheet.

The case-study comparison shows the optimised case recovers materially more kerosene and naphtha, and less low-value residue, from the same blended crude feed — significant for a 50 BPD unit supplying a local market, since it improves the revenue mix per barrel processed without altering crude feed rate, directly supporting the value-addition objective motivating modular refining in Nigeria. The study's validated deviations (~±5.3%) are consistent with the general expectation that independently cross-checked balances for well-characterised hydrocarbon systems agree closely and compare favourably with the agreement reported in the Kaduna FCC pinch study (Abubakar, 2020). Whereas earlier Nigerian modular-refinery studies have tended to report design parameters and yields without a full PTA exercise (Olatona, 2022), the present study extends that literature by carrying a validated HYSYS model through explicit pinch-analysis targeting across a range of ΔTmin values — comparatively underrepresented for mini-refineries at this scale.

For Nigerian modular refinery development, the practical implication is that pinch-based energy targeting is achievable and worthwhile even at 50 BPD, not reserved for large conventional refineries: an operator able to specify a HEN designed against an explicit QHmin/QCmin target, rather than an ad hoc exchanger arrangement, stands to reduce fired-heater and cooling-utility demand, reducing dependence on imported fuel or diesel firing on site, strengthening the local-content case for indigenous engineering design, and supporting value addition to Nigerian crude closer to the point of production. Every kilojoule of hot-utility duty avoided is, in effect, a kilojoule of crude-derived fuel the mini-refinery need not burn to heat itself, with corresponding reductions in flue-gas emissions and in the fraction of processed crude consumed as fuel rather than converted to marketable product; at 50 BPD this reduction is small in absolute terms, but the methodology is directly transferable to the larger population of modular refineries (hundreds to low thousands of BPD) now being licensed across Nigeria, where the cumulative effect of routine pinch-based targeting could be considerably more significant.

Several limitations should be acknowledged. First, the energy and area targets rest on a steady-state HYSYS simulation and manual cross-check that have not been confirmed against physical plant data, since the energy-integrated unit has not yet been fabricated, installed or test-run. Second, pinch analysis and area targeting were carried out in full detail for a single ΔTmin (35°C), with the remaining values reported only at the target-summary level; a fuller utility-cost/exchanger-area economic trade-off across all seven ΔTmin values remains to be completed. Third, crude oils characterisation relies on a PIMS-based Escravos and Forcados assays rather than a laboratory assay of a specific delivered batch, so batch-to-batch variability is not captured. Finally, the heat-exchanger network itself, together with its fabrication and commissioning, remains pending, so the as-built performance of the redesigned ABU Mini-Refinery cannot yet be reported.

6.0 ENGINEERING INNOVATION AND CONTRIBUTION

The engineering innovation lies less in any single novel unit operation than in the systematic combination, on a physically realisable 50 BPD Nigerian modular refinery, of validated Aspen HYSYS simulation, a full Problem Table Algorithm exercise across a realistic range of ΔTmin, and balanced-composite-curve area targeting, carried out for an identified indigenous blended crude oils (Escravos and Forcados) rather than a generic feedstock. The process-integration innovation is the explicit establishment of quantified hot- and cold-utility targets (26.47 and 2.07 kJ/s at ΔTmin = 35°C) and a heat-exchanger area target (8.86 m²) at a scale where such targeting is comparatively rare in the accessible literature, providing a concrete benchmark for the forthcoming HEN design. The intensification dimension — evaluating DWC and heat-pump-assisted alternatives at process selection and retaining a preflash stage and pump-around-integrated preheat in the adopted flowsheet — keeps equipment count and size close to what a modular, skid-mountable refinery can accommodate. Applied to blend of Escravos and Forcados crude on a unit intended for local fabrication and operation, the work shows, with real numbers rather than generic claims, how a small, locally built refining unit can be designed against the same thermodynamic rigour used in large, conventional plants, so growth in local refining capacity need not come at the cost of avoidable energy waste.

7.0 CONCLUSION

This study sets out to design, simulate, and energy-integrate a 50 BPD ABU mini-refinery ADU processing blended Escravos and Forcados crude in the ratio 50:50, and to establish how process integration and intensification could be embedded in that design. A validated Aspen HYSYS flowsheet cross-checked against independent manual calculation to within approximately ±5.3%, provided the material and energy balance basis. Pinch analysis via the Problem Table Algorithm across ΔTmin = 10–40°C established minimum hot- and cold-utility targets of 26.47 and 2.07 kJ/s at the design condition (ΔTmin = 35°C), a pinch temperature of 212.5°C on the shifted scale, and a minimum heat-exchanger area target of 8.86 m² by the balanced composite curve method. A base-versus-optimised case-study comparison showed the redesigned unit can recover more kerosene and naphtha, and less low-value residue, from the same blended crude feed. These results confirm that systematic energy targeting, not previously applied to the ABU Mini-Refinery's existing 1 BPD network, is feasible and worthwhile at modular scale, and provides the quantified basis on which the unit's heat-exchanger

network can now be synthesised. Network design, fabrication, installation, and test-running remain ongoing, and their completion is the natural next step. The study demonstrates that energy efficiency and modular-scale refining are not competing objectives, and that process integration and intensification can, and should, be designed into modular refineries from the outset.

8.0 RECOMMENDATIONS

Arising directly from this study: the heat-exchanger network for the 50 BPD ABU mini-refinery ADU should be synthesised using the Pinch Design Method, matching hot and cold streams above and below the established pinch per the feasibility rules in Section 2; the resulting network should be checked against the 8.86 m² area target established here; and the ΔTmin values not yet analysed in full detail (10, 15, 20, 25, 30 and 40°C) should be carried through the same area-targeting procedure used for 35°C, so an economically optimum ΔTmin can be selected before final network design. For future research beyond the present scope: the synthesised network should be fabricated, installed and test-run, with measured performance compared against the targets reported here; a techno-economic evaluation covering capital cost, utility savings and payback should be conducted once network design is complete; an environmental assessment should quantify the emission reduction associated with the lower fired-heater duty implied by the pinch targets; intensification options such as a divided-wall column or heat-pump-assisted distillation, evaluated only at screening stage here, should be investigated in more design detail; and crude oils characterisation should be extended to laboratory assay data for specific delivered Escravos and Forcados crude batches.

9.0 CONFERENCE THEME ALIGNMENT

This study responds directly to the conference theme, "Innovating Tomorrow: Harnessing Engineering to Drive Nigerian Growth for Sustainable Development," by applying rigorous, internationally established process-integration and process-intensification methods to an indigenous Nigerian crude on a Nigerian university-based modular refining platform. In relation to SDG 7 (Affordable and Clean Energy), the pinch-based utility targets point toward a redesigned refinery drawing less fired-heater and cooling-utility duty per barrel than an unintegrated equivalent. In relation to SDG 9 (Industry, Innovation, and Infrastructure), the work builds indigenous simulation, pinch-analysis, and equipment-design capability around the ABU Mini-Refinery, deliberately scaled up as a demonstration and training platform. In relation to SDG 12 (Responsible Consumption and Production), improved recovery of higher-value light and middle distillates from the same blended Escravos and Forcados crude feed represents fuller use of the resource extracted. In relation to SDG 13 (Climate Action), a validated reduction in fired-heater duty would be expected to reduce associated combustion emissions per barrel processed, although this study establishes the energy targets that would enable such a reduction rather than measured emissions data, and the claim is framed as a plausible, targets-based implication rather than a demonstrated outcome.

10.0 REFERENCES

Abubakar, A. (2020). Cost reduction of fluid catalytic cracking unit in Kaduna Refining and Petrochemical Company using pinch technology. Nigerian Journal of Technological Development, 17(3), 189–196. https://doi.org/10.63746/njtd.v17i3.487

Ahmed, F. (2025, April). How NMDPRA issued 47 refinery licenses in one year. Blueprint Newspapers. https://blueprint.ng/how-nmdpra-issued-47-refinery-licenses-in-one-year-farouk-ahmed/

El-Halwagi, M. M. (2011). Sustainable design through process integration: Fundamentals and applications to industrial pollution prevention, resource conservation, and profitability enhancement. Butterworth-Heinemann/Elsevier.

Furman, K. C., & Sahinidis, N. V. (2002). A critical review and annotated bibliography for heat exchanger network synthesis in the 20th century. Industrial & Engineering Chemistry Research, 41(10), 2335–2370.

Hohmann, E. C. (1971). Optimum networks for heat exchange [Doctoral dissertation, University of Southern California].

International Energy Agency. (2024). Oil 2024: Analysis and forecast to 2030. IEA. https://www.iea.org/reports/oil-2024

Kemp, I. C. (2007). Pinch analysis and process integration: A user guide on process integration for the efficient use of energy (2nd ed.). Butterworth-Heinemann.

Klemeš, J. J., Varbanov, P. S., & Kravanja, Z. (2013). Recent developments in Process Integration. Chemical Engineering Research and Design, 91(10), 2037–2053. https://doi.org/10.1016/j.cherd.2013.08.019

Linnhoff, B., & Flower, J. R. (1978). Synthesis of heat exchanger networks: I. Systematic generation of energy optimal networks. AIChE Journal, 24(4), 633–642.

Linnhoff, B., & Hindmarsh, E. (1983). The pinch design method for heat exchanger networks. Chemical Engineering Science, 38(5), 745–763.

Olatona, T. O. (2022). Developing modular refineries in the downstream sub-sector of the Nigerian petroleum industry. International Journal of Engineering Research & Technology, 11(3).

Smith, R. (2000). State of the art in process integration. Applied Thermal Engineering, 20(15–16), 1337–1345.

Stankiewicz, A. I., & Moulijn, J. A. (2000). Process intensification: Transforming chemical engineering. Chemical Engineering Progress, 96(1), 22–34.

Townsend, D. W., & Linnhoff, B. (1984). Surface area targets for heat exchanger networks. IChemE Annual Research Meeting, Bath, UK.

Umeda, T., Itoh, J., & Shiroko, K. (1978). Heat-exchange system synthesis. Chemical Engineering Progress, 74(7), 70–76.

Van Gerven, T., & Stankiewicz, A. (2009). Structure, energy, synergy, time – the fundamentals of process intensification. Industrial & Engineering Chemistry Research, 48(5), 2465–2474. https://doi.org/10.1021/ie801501y

SPATIAL VARIATION ASSESSMENT OF GROUNDWATER QUALITY IN IWO LOCAL GOVERNMENT AREA, OSUN STATE, NIGERIA.

Yuusuf Oluwaseun Adetona[1,*], Kamar Taiwo Oladepo[2]
[1]*Department of Civil Engineering, University of Ibadan, Ibadan, Nigeria*
[2]*Department of Civil Engineering, Obafemi Awolowo University, Ile-Ife, Nigeria*
Email: yuusufadetona@gmail.com*, koladepo@oauife.edu.ng
***Corresponding author**: Yuusuf Oluwaseun Adetona
DOI: https://doi.org/10.67203/sp.ICESID.2026

ABSTRACT
Groundwater is the primary water source for over 60 % of Nigerians, but uncontrolled urban pollution infiltrates and contaminates the aquifer. Groundwater samples for the current study were collected from Iwo Local Government Area to investigate groundwater resources and generate spatial water-quality variation maps across seasons. The groundwater samples were chosen to represent the entire study area's built-up portion adequately. The physico-chemical parameters were measured during rainy and dry seasons. Parameters analysed were temperature, turbidity, pH, electrical conductivity, total suspended solids, total dissolved solids, total alkalinity, total hardness, chloride, sulphate, nitrate, phosphate, magnesium, total coliform, and calcium. The simple kriging interpolation method was used to generate groundwater quality maps for the selected groundwater quality parameters. The water quality data were linked to the sampling location (spatial) in ArcGIS, and maps were generated to show spatial distribution. Although most of the water quality parameters median range values of the various groundwater resources were satisfactory throughout the seasons, total hardness of 228.3 mg/l – 596.6 mg/l, calcium of 16 mg/l - 236.8 mg/l, sulphate of 219 mg/l – 354 mg/l, and phosphate of 0.30 mg/l – 3.42 mg/l were the groundwater quality parameters with spatial variations over the World Health Organisation standard values of 150 mg/l, 75 mg/l, 250 mg/l, and 0.05 mg/l respectively, for both rainy and dry seasons. It is suggested that all sources be monitored regularly and that treatments to improve total hardness be implemented.

Keywords: *Geostatistical Analysis; Groundwater Quality Maps; Kriging Spatial Distribution; Iwo Local Government Area*

1. INTRODUCTION

Increasing attempts for a better living level include reinstating a sufficient supply of drinkable water (United Nations Environment Programme, 2011). According to Abel and Adebayo (2017), water quality is defined as the physical, chemical, and microbiological attributes of water, which are evaluated by comparing concentrations of water quality measures to acceptable levels. Water of high quality has been defined as that supplied by waterworks and groundwater (Yan *et al.*, 2022; Kløve *et al.*, 2017).

However, the lack of high-quality surface water has increased groundwater consumption due to fast industrialisation and population growth (Ezechinyere and Stanislaus, 2023; Nas, 2009). Recently, many parts of the world, particularly Nigeria, have seen a decline in both the quantity and quality of groundwater sources (Adetona and Oladepo, 2021; Mahapatra *et al.*, 2012). These studies have used a water quality index to identify specific contaminated groundwater sources, without considering spatial kriging mapping for unsampled regions. Atobatele *et al.* (2026) have reported toxic heavy metal parameters in Iwo Local Government Area. While studies have reported microbial contamination in some of these groundwater sources in Nigeria (Izah *et al.*, 2022).

Some of the reported groundwater sources were close to contamination sources such as septic tanks and refuse dumpsites. Due to a lack of enough land space, septic tanks were mainly placed very close to groundwater sources. Insufficient sanitary landfills also caused refuse dumpsites to be commonly located near undeveloped land or foundations (Olayinka *et al.*, 2025). Abel and Adebayo (2017) stated that awkward and unsystematic waste discharged into the environment had increased the rate of sickness from groundwater.

Groundwater quality studies conducted in the Iwo Local Government Area demonstrated the need for regular groundwater quality assessments. Olutona *et al.* (2012) proposed that the physicochemical and microbiological analyses of groundwater in the Iwo Local Government Area be assessed regularly. The regular evaluation will aid in the early detection of any potential future degradation. Ogunbode and Ifabiyi (2014) also recommended that more research be done on the water quality in the Iwo Local Government Area. At the regional level, enough research has been done on the drinking and irrigation aspects of groundwater. On the other hand, little research has been done on groundwater quality assessment in the Iwo Local Government Area of Southwestern Nigeria. It is, therefore, essential to take representative samples according to the political wards in Iwo Local Government Area and evaluate the spatial distribution of groundwater quality from those sampled locations across the Iwo Local Government Area.

A more comprehensive diagnosis of the current state of contamination and close monitoring of its evolution is critical for preserving this resource. The fundamental goal of a monitoring programme is to collect and analyse a large number of groundwater samples in order to assess spatial changes (Ahmed, 2017). As a result, geographical monitoring of groundwater quality parameters is crucial, which is why this research was carried out. The present study aims to assess the spatial variations of groundwater quality parameters in Iwo Local Government Area, Osun State, Southwestern Nigeria. It's critical to understand the nature and chemistry of groundwater fluctuations because of natural and anthropogenic processes (Richardson *et al.*, 2024).

2. METHODOLOGY

2.1 Description of the Study Area

Iwo is one of the local government areas of Osun State, Nigeria. It is 245 km^2 in size. It is grouped according to local government clusters, namely: Isale Oba, Molete, Oke Adan, Gidigbo, and Oke Oba. These were subdivided further into the established 15 political wards. Rural, agricultural, and urban areas are all covered by the local government. Iwo town is formed by the urban region, located between Latitude $07^o38'$ N to $07^0 40'$ N and Longitude $004^0 09'$ E to $004^o 11'$ E.

The Aiba water reservoir, which is located within a government forest reservation area in Iwo, is the town's principal source of drinkable water. Unfortunately, poor management and a rise in the area's population have resulted in an insufficient supply of drinkable water from the waterworks. The town's subsurface water sources were exploited as a result of this.

2.2 Climatic Setting

In the southern area of Nigeria, yearly rainfall ranges from 150 to 300 cm. Mean maximum ambient temperatures range from 33.84 ºC in February to 28.8 ºC in August, with mean minimum temperatures ranging from 25.18 ºC in March to 23.0 ºC in August.

2.3 Experimental Setup and Methods

Water samples were collected from 30 different locations and sources as detailed in Table 1. The population that relies on groundwater for drinking was the focus of the sampling. Groundwater sources were stratified and located at random using hand-held Global Positioning System (GPS) technology. In urban areas, most wells were lined; however, in rural regions, wells were unlined and operated by hand pumps. A hand-held GPS was used to record the location of each well.

The sampling was done twice, first during the rainy season (October) and again during the dry season (January). Samples were collected during these representative months of the two seasons, which were later periods of the two seasons, so that the samples could be a true representation of the seasons. There was a lot of rain during October and November, and the month of January was extremely cold. The samples were pulled from shallow wells with a plastic bucket and gathered from the taps of hand pump wells and boreholes.

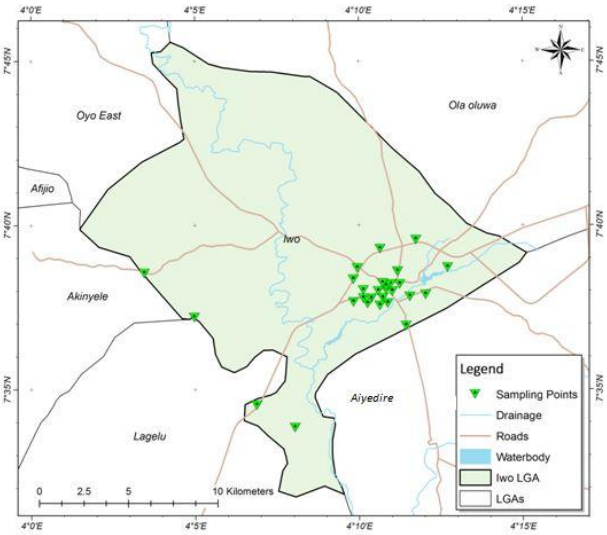

Figure 1: *Study Area Map*

Some experimental values were obtained on the spot, while others were obtained in the lab using three replicates and standard procedures. Before sampling, all glassware and sample bottles were cleansed with liquid detergents and rinsed with distilled water. To minimise confusion, the plastic bottles used for sampling were labelled according to political wards and then rinsed three times on-site with the groundwater being sampled. A two-litre water sample was obtained for physical and chemical characteristics, while a small, autoclaved glassware sample was collected for microbiological investigation. Before analysis, the samples were kept in the refrigerator for 5 hours (Jeje and Oladepo, 2014b). This was done to keep the physical, chemical, and microbiological qualities intact.

Table 1: *Locations of Selected Hand Pump Boreholes, Boreholes, and Shallow Wells Within the Study Area*

S/N	Political ward	Location	Type of well	Depth (m)
1	Isale Oba Ward 01	Oke–Ola	Motorized Borehole	45
2	Isale Oba Ward 01	Palace road	Lined Well	4.57
3	Isale Oba Ward 02	Akinfenwa	Lined Well	4.86
4	Isale Oba Ward 02	Old barrack	Motorized Borehole	45
5	Isale Oba Ward 03	Hospital Gate	Lined Well	5.05
6	Isale Oba Ward 03	MOT junction	Motorized Borehole	45
7	Isale Oba Ward 04	Orikan Compd.	Lined Well	6.54
8	Isale Oba Ward 04	Oke odo	Lined Well	4.76
9	Molete Ward 05	Moseru Compd.	Lined Well	5.42
10	Molete Ward 05	Oja Oba	Lined Well	4.10
11	Molete Ward 06	Oriolowo	Motorized Borehole	50
12	Molete Ward 06	Gaa – Fulani	Hand Pump Well	-
13	Molete Ward 07	Molete ward 3	Lined well	8.92
14	Molete Ward 07	Saabo	Lined Well	5.46
15	Oke Adan Ward 08	Omosan Compd.	Unlined Well	3.45
16	Oke Adan Ward 08	Jagun Ilu Compd.	Unlined Well	4.12
17	Oke Adan Ward 09	Ponkuku compd.	Motorized Borehole	45
18	Oke Adan Ward 09	Lakata Compd.	Unlined well	3.78
19	Oke Adan Ward 10	KLM, Feesu	Motorized Borehole	45
20	Oke Adan Ward 10	Itesiwaju, Odoori	Motorized Borehole	50
21	Gidigbo Ward 11	Aipate	Lined Well	4.35
22	Gidigbo Ward 11	Owoeye Bus Stop	Motorized Borehole	45
23	Gidigbo Ward 12	Abanise	Motorized Borehole	45
24	Gidigbo Ward 12	Oke bode	Lined Well	4.56
25	Gidigbo Ward 13	Adeeke	Lined Well	5.25
26	Gidigbo Ward 13	Laito	Motorized Borehole	50
27	Oke Oba Ward 14	Agberire	Hand Pump Borehole	-
28	Oke Oba Ward 14	Alagbon	Hand Pump Borehole	-
29	Oke Oba Ward 15	Papa	Hand Pump Borehole	-
30	Oke Oba Ward 15	Mojibere Village	Unlined Well	8.36

Note: Hand pump boreholes were inaccessible for the measurement of depth.

The physical, chemical, and microbiological parameters such as temperature, turbidity, pH, electrical conductivity, total suspended solids, total dissolved solids, total alkalinity, total hardness, chloride, sulphate, nitrate, phosphate, magnesium, calcium, and total coliform were determined for the

collected water samples. All tests were conducted in line with research carried out by Olutona *et al.* (2012) and Ogunbode and Ifabiyi (2014).

With the help of a pH metre, a thermometer, and a platinum electrode conductivity metre, water samples were evaluated for hydrogen ion concentration (pH), temperature, and electrical conductivity (EC). A total dissolved solids meter was used to calculate the total dissolved solids (TDS). Titrimetric determination of chloride (Cl-) was performed using standard silver nitrate titration. The phosphate content (PO_4^{3-}) of the water samples was evaluated using a colourimetric technique after digestion with concentrated sulfuric acid. The turbidimetric method with a spectrophotometer was used to determine the sulphate (SO_4^{2-}). The standard Ethylene Diamine Tetra Acid (EDTA) titration method was used to determine the hardness (TH), which was buffered at pH 10. The amount of calcium (Ca) in water hardness was determined using the complexometric titration method, which involved titrating the water sample with a known concentration and volume of EDTA.

The difference between total and calcium hardness, reported as $CaCO_3$ equivalent, was used to calculate the presence of magnesium (Mg). Using phenolphthalein and mixed indicators, the total alkalinity (T. Al.) of the water samples was evaluated by titrating 100 mL of the samples with 0.2 N sulfuric acid solution. Total suspended solids (TSS) were determined using gravimetric measurement involving heating the sample in an oven, followed by cooling in a desiccator. An electronic turbidimeter with scattered-light detectors was used for turbidity (Turb.) measurement. Nitrate (NO_3^-) was determined by the colourimeter method using a UV-VIS spectrophotometer. The membrane filtration method was used to get total coliform (TCC) in the water samples (microbiological analysis). The simple kriging method of interpolation was used to determine the groundwater quality of unsampled regions of Iwo Local Government Area.

2.4 Spatial Variation Assessment

The simple kriging method was used to generate groundwater quality maps for the selected groundwater quality parameters. The water quality data were linked to the sampling location (spatial) in ArcGIS, and maps showing spatial distribution were prepared to easily identify the variation in concentrations of the groundwater parameters at various study area locations. Spatial variation was evaluated using Simple Kriging (SK), which assumes a known stationary mean (μ) across the study area. Experimental semivariograms were computed to quantify spatial continuity using the isotropic semivariance equation:

$$\gamma(h) = \frac{1}{2N(h)} \sum_{i=1}^{N(h)} [Z(x_i) - Z(x_i+h)]^2 \quad (1)$$

where;
$\gamma(h)$ is the semivariance at lag distance h,
N(h) is the number of paired measurement points separated by distance h, and
$Z(x_i)$ and $Z(x_i + h)$ represent parameter values at spatial locations x_i and $x_i + h$.

The Simple Kriging estimator was defined as:

$$Z^*(x_0) = \mu + \sum_{i=1}^{n} \lambda i \, [Z(x_i) - \mu] \quad (2)$$

Where;
$Z^*(x_0)$ is the estimated value at unsampled location x_0,
μ is the stationary sample mean,
n is the number of neighbouring observations, and
λi are the kriging weights derived from the covariance matrix.

Empirical semivariograms were fitted against theoretical models (Spherical, Exponential, and Gaussian) using non-linear least squares. The optimal model was selected based on minimizing the mean squared error. Geostatistical parameters nugget variance (C_0), structural variance (C), total sill (C_0 + C), and spatial range (a) were extracted. The spatial dependence ratio ([C_0 / (C_0 + C)] x 100) was calculated to classify spatial autocorrelation as strong (<25%), moderate (25%–75%), or weak (>75%). Model performance and interpolation reliability were validated using Leave-One-Out Cross-Validation

(LOOCV). Interpolation accuracy was evaluated using Root Mean Square Error (RMSE), Mean Absolute Error (MAE), and the coefficient of determination (R^2). The ArcGIS software automatically executed all of these mathematical steps in the background while using the Simple Kriging interpolation. The environmental maps prepared from the water quality test results gave the groundwater quality characteristics of the Iwo Local Government Area.

3. RESULTS AND DISCUSSION

The deployment of geostatistical simple kriging interpolation in Iwo mirrors recent findings by studies in the Ibadan Metropolis, where Kriging and factor analysis were integrated to model groundwater variability (Thomas, 2023). Simple kriging was used consistently for all parameter maps.

3.1 pH

The five colours denoting the spatial variation of hydrogen ion concentration (pH) during the rainy and dry seasons were green, yellow, orange, brown, and grey, ranging between 5.5 and 6.5, 6.51 and 7.5, 7.51 and 8.5, 8.51 and 9.5, and 9.51 and 10.5, respectively, as shown in Figure 2a and b.

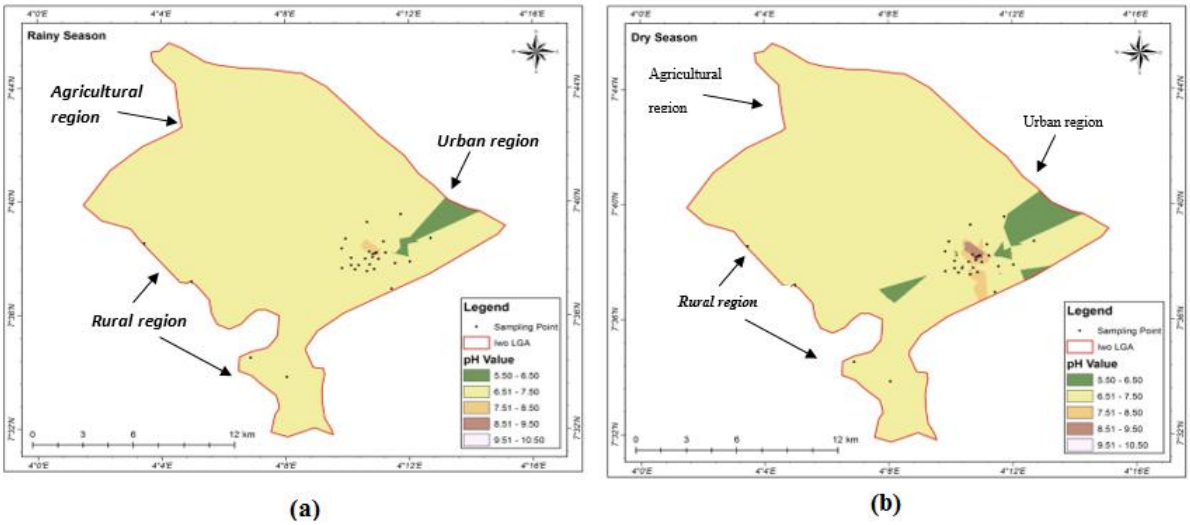

Figure 2: *Spatial Variation of Hydrogen Ion Concentration (a) Rainy Season (b) Dry Season*

The yellow and orange colours of the spatial variation correlated with the pH range standard values of 6.5 and 8.5. In Figure 2a, the yellow colour occurred mainly. This denoted that the groundwater pH of the study area was acceptable. However, some north-eastern parts of the study area were acidic, having a pH value less than 6.5. In Figure 2b, the yellow colour occurred around the rural and agricultural regions of the study area. These rural and agricultural regions included the last two political wards of Oke Oba Ward 14 and Oke Oba Ward 15. This denoted that the hydrogen ion concentrations of these regions' groundwater were acceptable. However, it increased from the rainy season to the dry season primarily due to extended water-rock interaction times during the dry season (Zhang *et al.*, 2023; Subba Rao, 2005).

3.2 Temperature

The five colours denoting the spatial variation of temperature during the rainy and dry seasons were green, yellow, orange, brown, and grey, ranging between 14.0 ^{o}C and 17.2 ^{o}C, 17.3 ^{o}C and 20.4 ^{o}C, 20.5 ^{o}C and 23.4 ^{o}C, 23.5 ^{o}C and 26.8 ^{o}C, and 26.9 ^{o}C and 30.5 ^{o}C, respectively, as shown in Figure 3 a and b.

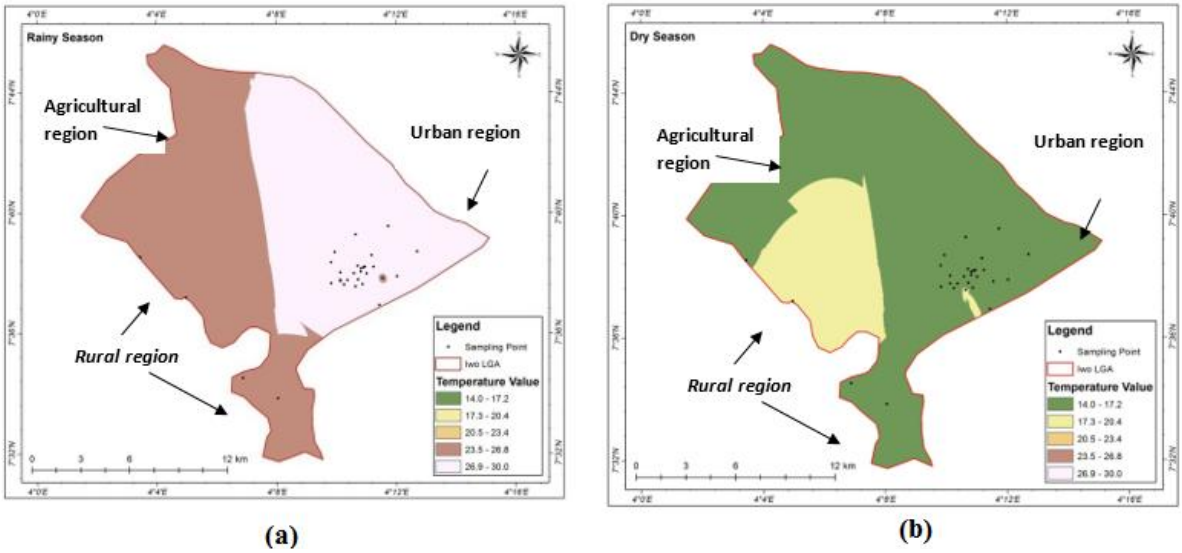

(a) **(b)**

Figure 3: *Spatial Variation of Temperature Concentration (a) Rainy Season (b) Dry Season*

The green, yellow, and orange colours of the spatial variation correlated with the temperature standard value (< 25 ºC). In Figure 3a, the brown colour occurred mainly around the rural and agricultural region of the study area, which varied from 23.5 ºC and 26.8 ºC. This denoted that the groundwater temperatures of these regions were still acceptable, which is slightly above 25 ºC.

3.3 Electrical Conductivity

The five colours denoting the spatial variation of electrical conductivity during the rainy and dry seasons were green, yellow, orange, brown, and grey, ranging between 50 µS/cm and 410 µS/cm, 411 µS/cm and 770 µS/cm, 771 µS/cm and 1130 µS/cm, 1131 µS/cm and 1490 µS/cm, and 1491 µS/cm and 1850 µS/cm, respectively, as shown in Figures 4a and b.

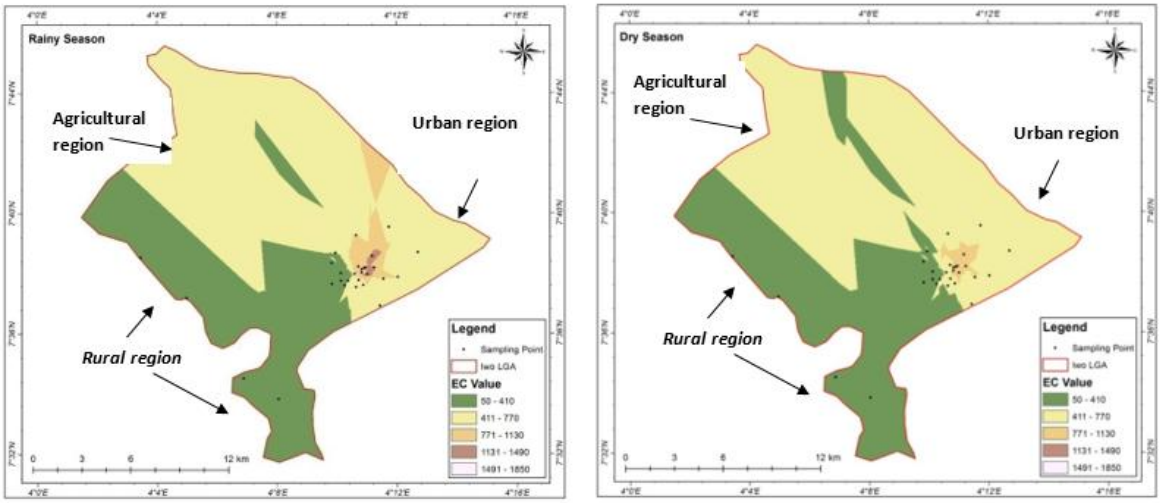

(a) **(b)**

Figure 4: *Spatial Variation of Electrical Conductivity Concentration (a) Rainy Season (b) Dry Season*

The green, yellow, and orange colours of the spatial variation correlated with the standard value of electrical conductivity, which was less than 1000 µS/cm. In Figure 4a, the green colour occurred mainly around the rural region and some parts of the agricultural and urban regions, which varied from 50 µS/cm and 410 µS/cm. The other urban region displayed yellow and orange colours. These denoted that the groundwater electrical conductivity of these regions was acceptable, which were majorly below 1000 µS/cm.

3.4 Total Dissolved Solids

The five colours denoting the spatial variation of total dissolved solids during the rainy and dry seasons were green, yellow, orange, brown, and grey, ranging between 30 mg/l and 228 mg/l, 229 mg/l and 426 mg/l, 427 mg/l and 624 mg/l, 625 mg/l and 822 mg/l, and 823 mg/l and 1020 mg/l, respectively as shown in Figure 5 a and b.

The spatial variations in green, yellow, and orange colours were within the permissible limit of total dissolved solids (500 mg/l). The green, yellow, and orange colours occurred mainly around the study area in both figures. This denoted that the total dissolved solids of the groundwater around these regions were acceptable, as they were mainly below 500 mg/l.

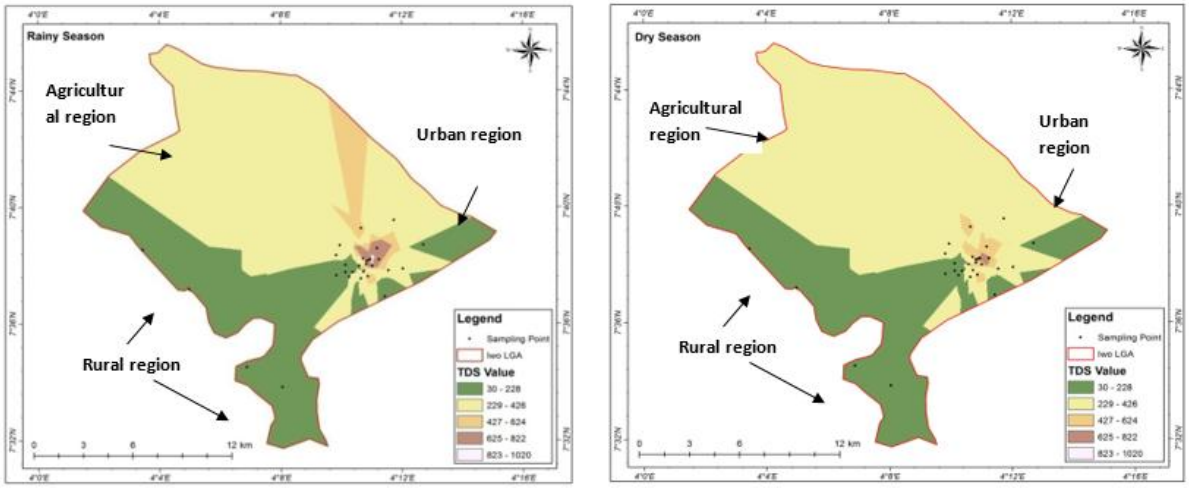

(a) (b)

Figure 5: *Spatial Variation of Total Dissolved Solids Concentration (a) Rainy Season (b) Dry Season*

3.5 Total Suspended Solids

The five colours denoting the spatial variation of total suspended solids during the rainy and dry seasons were green, yellow, orange, brown, and grey, ranging between 50 mg/l and 130 mg/l, 131 mg/l and 210 mg/l, 211 mg/l and 290 mg/l, 291 mg/l and 370 mg/l, and 371 mg/l and 450 mg/l, respectively as shown in Figure 6 a and b.

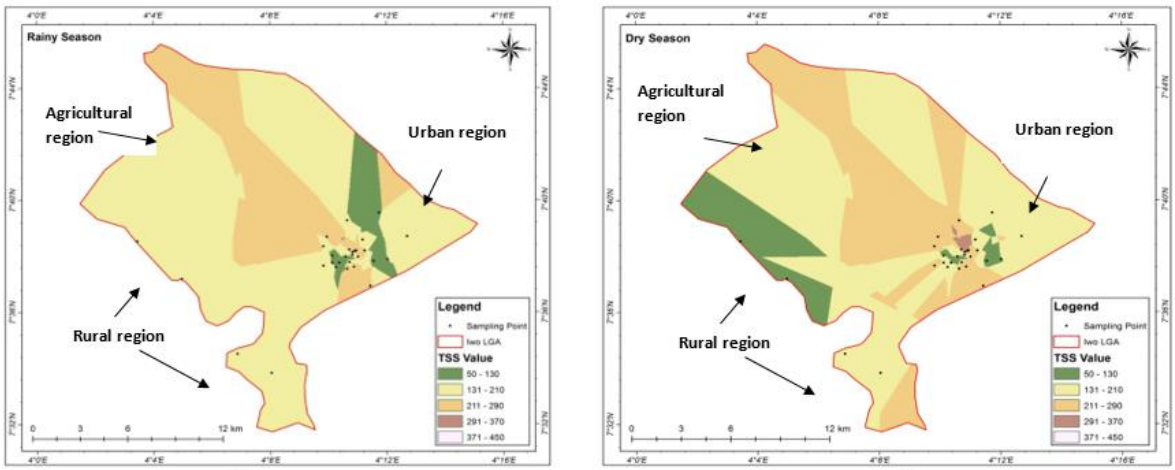

(a) (b)

Figure 6: *Spatial Variation of Total Suspended Solids Concentration (a) Rainy Season (b) Dry Season*

The green and yellow colours occurred mainly around the rural region for the rainy and dry seasons. This denoted that the groundwater's total suspended solids around this region were acceptable, which was mainly below 250 mg/l.

3.6 Calcium

The five colours denoting the spatial variation of calcium during the rainy and dry seasons were green, yellow, orange, brown, and grey, ranging between 16.0 mg/l and 89.6 mg/l, 89.7 mg/l and 163.2 mg/l, 163.3 mg/l and 236.8 mg/l, 236.9 mg/l and 310.4 mg/l, and 310.5 mg/l and 384.0 mg/l, respectively, as shown in Figure 7 a and b.

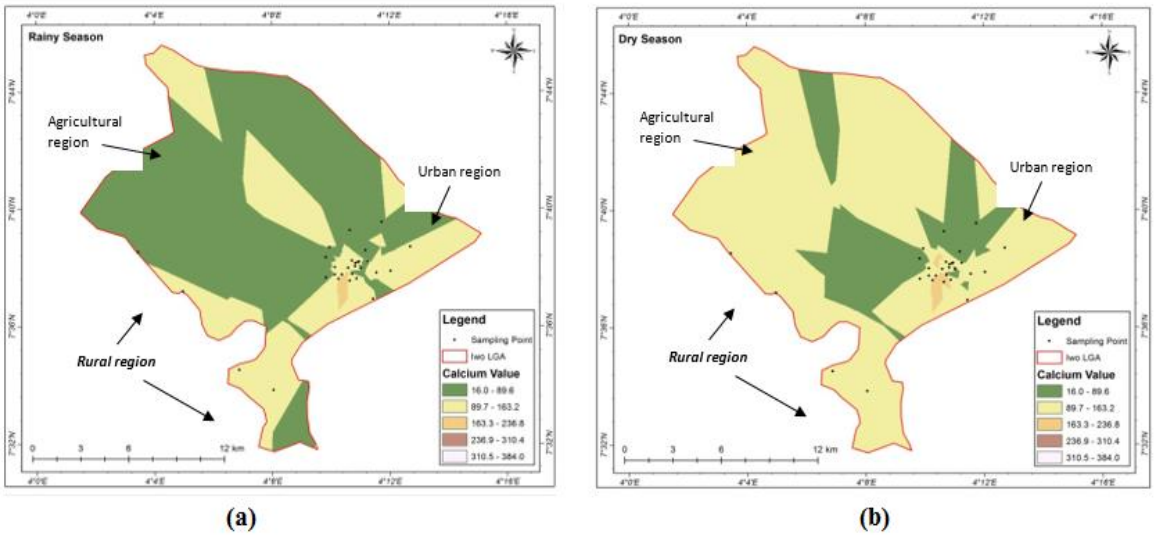

Figure 7: *Spatial Variation of Calcium Concentration (a) Rainy Season (b) Dry Season*

The green and yellow colours occurred mainly around the rural region for the rainy and dry seasons. This denoted that the groundwater calcium around this region was acceptable, which was mainly below 200 mg/l. The central part of the city displayed green, yellow, and orange colours, which indicated that its calcium ranged between 16 mg/l and 236.8 mg/l, which was unacceptably higher than 75 mg/l WHO standard.

3.7 Chloride

The five colours denoting the spatial variation of chloride during the rainy and dry seasons were green, yellow, orange, brown, and grey, ranging between 12.0 mg/l and 72.6 mg/l, 72.7 mg/l and 133.2 mg/l, 133.3 mg/l and 193.8 mg/l, 193.9 mg/l and 254.4 mg/l, and 254.5 mg/l and 375.6 mg/l, respectively as shown in Figure 8 a and b.

The green, yellow, orange, and brown colours of the spatial variation were within the permissible limit of chloride (250 mg/l). In Figure 8a, the green and yellow colours occurred mainly around the rural region and some parts of the urban area. This denoted that the chloride concentrations of the groundwater around these regions were acceptable, as they were below 250 mg/l. Two northern parts of the city displayed grey colours encircled by brown and orange colours. The grey colour ranged between 254.5 mg/l 375.6 mg/l, which was unacceptable.

In Figure 8b, the green, yellow, orange and brown colours occurred mainly around the study area for the dry season. The significant green colour in the agricultural and rural regions denoted that the chloride concentration of the groundwater in the study area was mainly acceptable. A groundwater source in the north-eastern part displayed a grey colour, which is encircled by brown and orange colours. This indicated that its chloride concentration ranged between 254.5 mg/l and 375.6 mg/l, which was unacceptable.

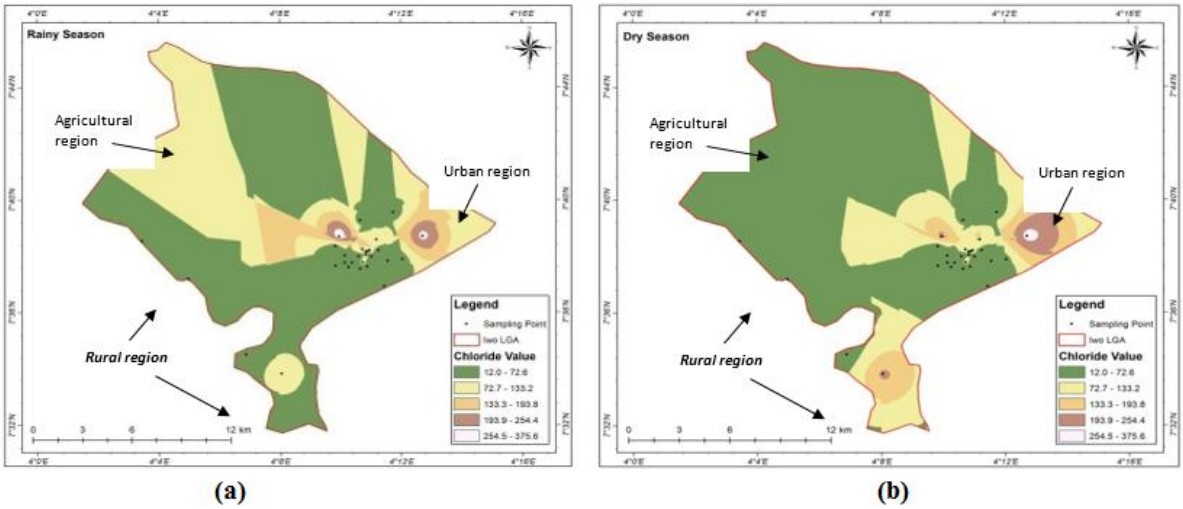

Figure 8: *Spatial Variation of Chloride Concentration (a) Rainy Season (b) Dry Season*

3.8 Magnesium

The five colours denoting the spatial variation of magnesium during the rainy and dry seasons were green, yellow, orange, brown, and grey, ranging between 0.40 mg/l and 1.54 mg/l, 1.55 mg/l and 2.68 mg/l, 2.69 mg/l and 3.82 mg/l, 3.83 mg/l and 4.96 mg/l, and 4.97 mg/l and 6.10 mg/l, respectively as shown in Figure 9 a and b.

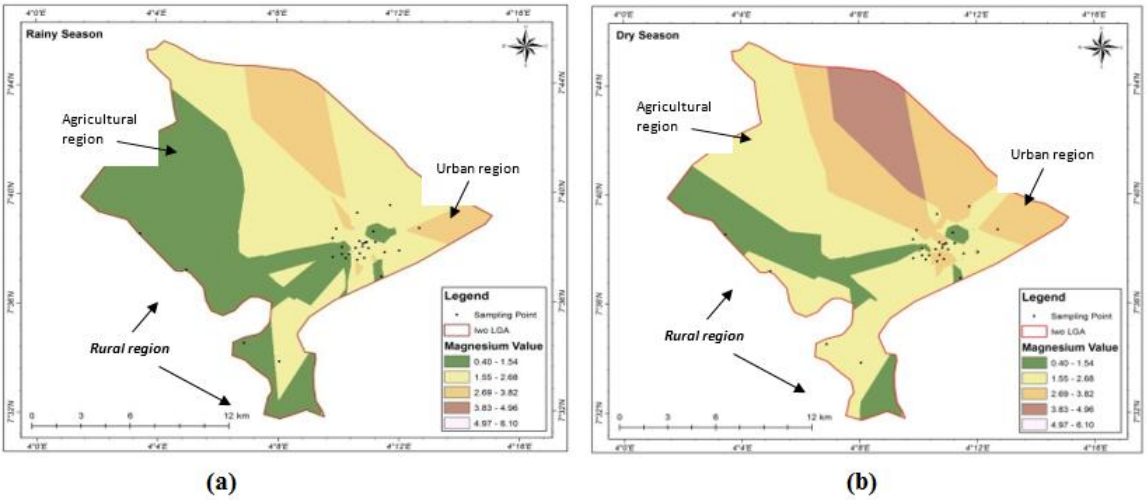

Figure 9: *Spatial Variation of Magnesium Concentration (a) Rainy Season (b) Dry Season*

The green, yellow, orange, brown, and grey colours of the spatial variation were within the permissible limit of magnesium (50 mg/l). In Figure 9a, the green colour occurred mainly in the rural and agricultural regions of the study area. This denoted that the magnesium concentration of the groundwater around this region was lower than in other regions. The other parts of the study area, including the urban region, displayed little green and orange colours and mostly yellow. These colours ranged between 0.4 mg/l and 3.82 mg/l, which were acceptable.

In Figure 9b, the green and yellow colours occurred mainly in the southern region of the study area. This denoted that the magnesium concentration of the groundwater around this region was lower than in agricultural and urban regions. The other parts of the study area displayed little green and mainly yellow, orange, and brown colours. These colours, which occurred in the study area, ranged between 0.4 mg/l and 4.96 mg/l, which were acceptable.

3.9 Nitrate

The five colours denoting the spatial variation of nitrate concentration during the rainy and dry seasons were green, yellow, orange, brown, and grey, ranging between 12.0 mg/l and 28.6 mg/l, 28.7

mg/l and 45.2 mg/l, 45.3 mg/l and 61.8 mg/l, 61.9 mg/l and 78.4 mg/l, and 78.5 mg/l and 95.0 mg/l, respectively as shown in Figure 10 a and b.

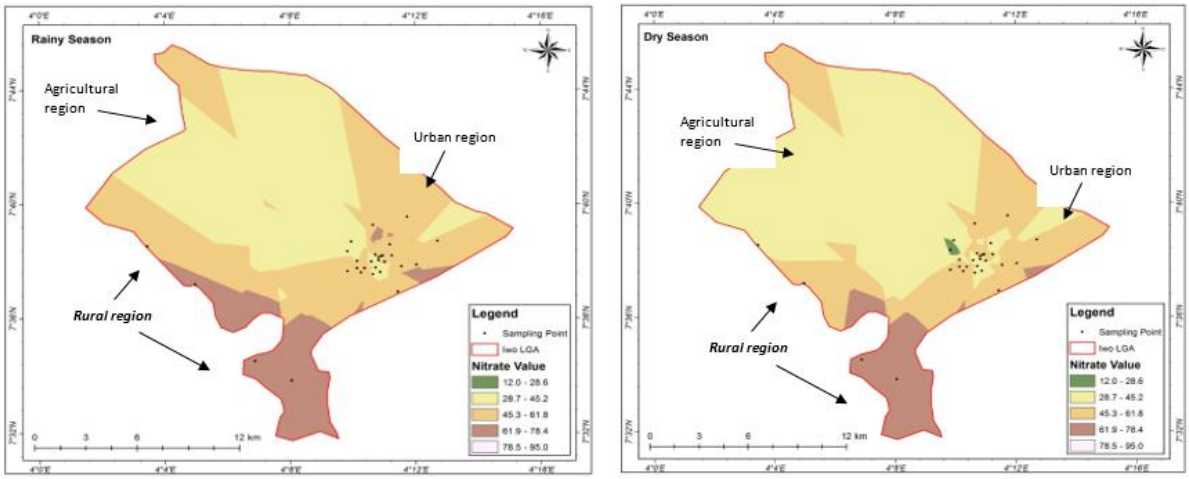

(a) **(b)**

Figure 10: *Spatial Variation of Nitrate Concentration (a) Rainy Season (b) Dry Season*

The green and yellow colours of the spatial variation were within the permissible limit of nitrate (50 mg/l). The brown and orange colours occurred mainly in the southern region of the study area, including some parts of the city. This denoted that the nitrate concentration of the groundwater around this region was largely unacceptable because it was more than 50 mg/l. The other parts of the study area displayed a yellow colour that occurred in the north-western region. This indicated that nitrate concentration ranged between 28.7 mg/l and 45.2 mg/l, which was acceptable.

The significant difference observed between the two seasons was the decrease in the nitrate concentration of the study area from the rainy to the dry season. This reduction can be a result of a decline in the rate of dissolution of nitrate ions from fertilisers, wastes, septic tanks, and pit latrines into the groundwater, aided by rainfall during the rainy season (Aleku *et al.*, 2024).

3.10 Phosphate

The five colours denoting the spatial variation of phosphate concentration during the rainy and dry seasons were green, yellow, orange, brown, and grey, ranging between 0.30 mg/l and 1.08 mg/l, 1.09 mg/l and 1.86 mg/l, 1.87 mg/l and 2.64 mg/l, 2.65 mg/l and 3.42 mg/l, and 3.43 mg/l and 4.20 mg/l, respectively as shown in Figure 11 a and b.

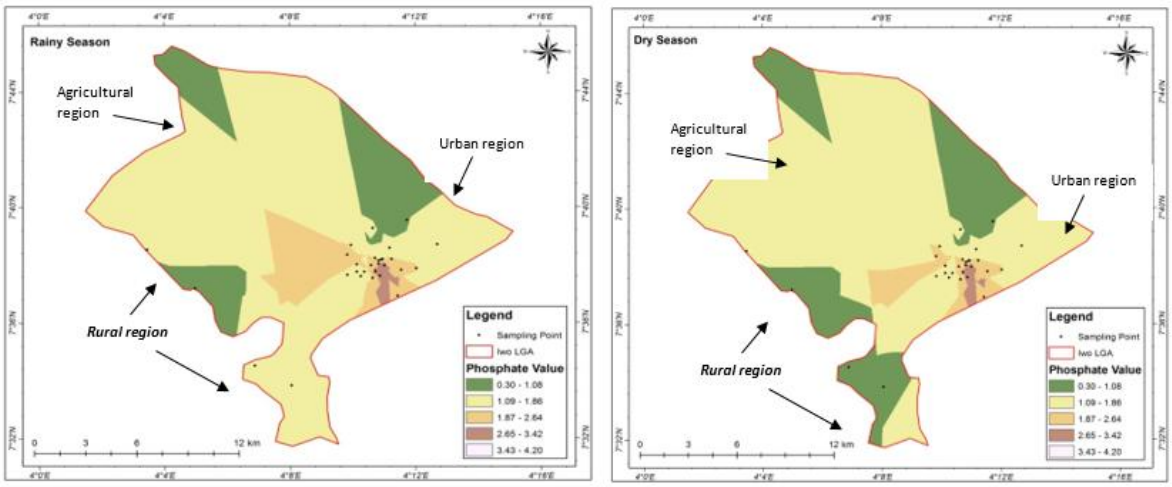

(a) **(b)**

Figure 11: *Spatial Variation of Phosphate Concentration (a) Rainy Season (b) Dry Season*

All the colours of the spatial variation were above the permissible limit of phosphate (0.05 mg/l). The green and yellow colours occurred mainly in the rural region of the study area. This indicated that the phosphate concentration of the groundwater around this region was lower than that of the urban region. The other parts of the study area, like the agricultural region displayed green, yellow, orange, and brown colours. The phosphate concentrations of the study area ranged between 0.30 mg/l and 3.42 mg/l, which were unacceptable. This can be attributed to microbial cycling in the groundwater (Li *et al.*, 2024).

3.11 Sulphate

The five colours denoting the spatial variation of sulphate concentration during the rainy and dry seasons were green, yellow, orange, brown, and grey, ranging between 150 mg/l and 218 mg/l, 219 mg/l and 286 mg/l, 287 mg/l and 354 mg/l, 355 mg/l and 422 mg/l, and 423 mg/l and 490 mg/l, respectively as shown in Figure 12 a and b.

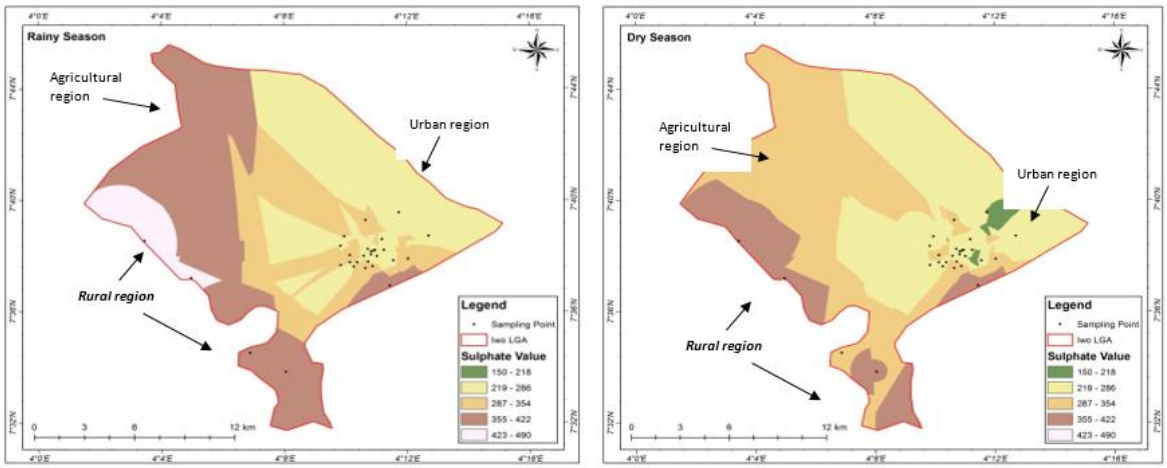

(a) **(b)**

Figure 12: *Spatial Variation of Sulphate Concentration (a) Rainy Season (b) Dry Season*

The green colour of the spatial variation was below the permissible limit of sulphate (250 mg/l). The brown and grey colours occurred mainly in the rural and agricultural regions of the study area. This denoted that the sulphate concentration of the groundwater around these regions were higher than that of the urban region. The other parts of the study area displayed yellow, orange and green (Figure 12b) colours. This denoted that the spatial variations of sulphate concentrations in the urban region for rainy and dry seasons ranged between 219 mg/l and 354 mg/l, which were largely unacceptable.

The significant difference observed between the two seasons was the decrease in the sulphate concentration of the study area from the rainy to the dry season. This reduction can be a result of the decline in the rate of dissolution of sulphate from rocks and other sulphate sources of contamination into the groundwater, aided by rainfall during the rainy season (Mattos *et al.*, 2018).

3.12 Total Coliform

The five colours denoting the spatial variation of total coliform concentration during the rainy and dry seasons were green, yellow, orange, brown and grey ranging between 0 cfu/ml x 10^{-4} and 09 cfu/ml x 10^{-4}, 10 cfu/ml x 10^{-4} and 19 cfu/ml x 10^{-4}, 20 cfu/ml x 10^{-4} and 79 cfu/ml x 10^{-4}, 80 cfu/ml x 10^{-4} and 99 cfu/ml x 10^{-4}, and 100 cfu/ml x 10^{-4} and 120 cfu/ml x 10^{-4}, respectively as shown in Figure 13 a and b.

The green colour of the spatial variation was below the permissible limit of total coliform (10 cfu/ml x 10^{-4}). The green colour encircled the urban region of the study area. This denoted that the total coliform of the groundwater around this region was within the acceptable limit. The central part of the urban region displayed yellow, orange, and brown colours. This denoted that the total coliform of this region ranged between 10 cfu/ml x 10^{-4} and 99 cfu/ml x 10^{-4}, which was unacceptable.

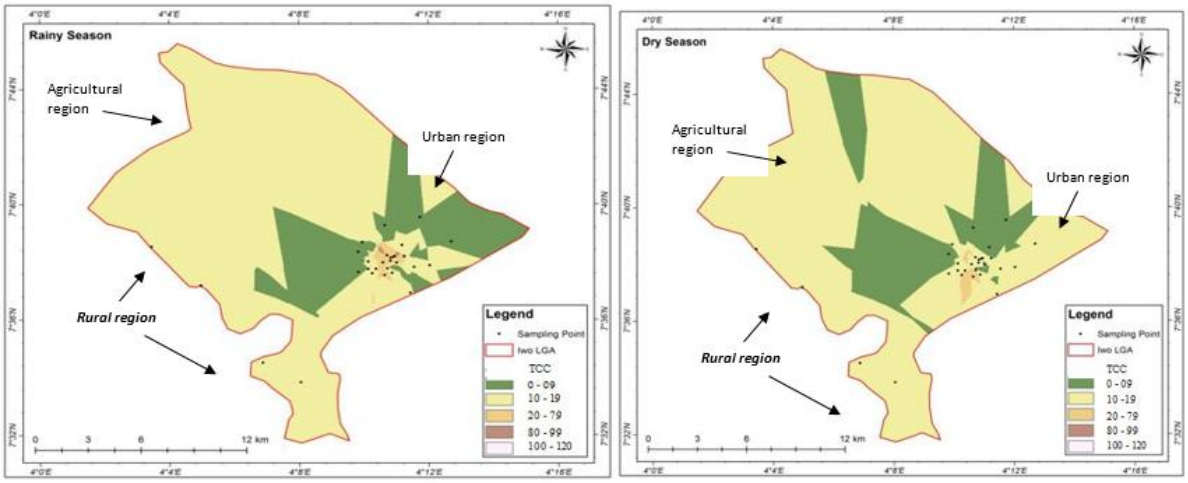

(a) **(b)**

Figure 13: *Spatial Variation of Total Coliform Concentration (a) Rainy Season (b) Dry Season*

3.13 Total Alkalinity

The five colours denoting the spatial variation of total alkalinity during the rainy and dry seasons were green, yellow, orange, brown, and grey, ranging between 15 mg/l and 86 mg/l, 87 mg/l and 157 mg/l, 158 mg/l and 228 mg/l, 229 mg/l and 299 mg/l, and 300 mg/l and 370 mg/l, respectively, as shown in Figure 14 a and b.

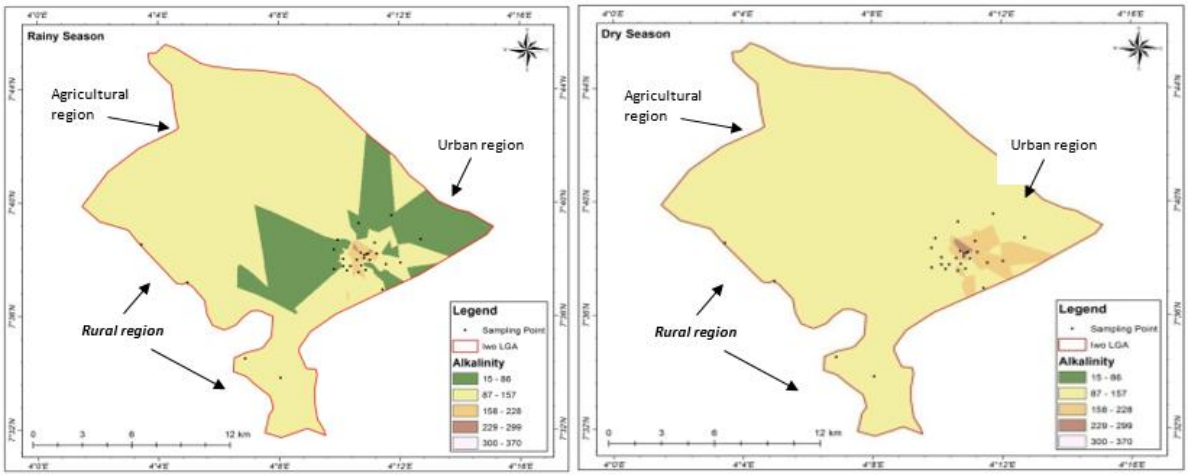

(a) **(b)**

Figure 14: *Spatial Variation of Total Alkalinity Concentration (a) Rainy Season (b) Dry Season*

The green, yellow, and orange colours of the spatial variation were within the permissible limit of total alkalinity (200 mg/l). The brown and orange colours occurred in the central part of the urban region. This denoted that the total alkalinity of the groundwater around this region was slightly above 200 mg/l, which was somewhat unacceptable. The other rural and agricultural regions displayed green and yellow colours, ranging between 15 mg/l and 157 mg/l, which were acceptable.

3.14 Total Hardness

The five colours denoting the spatial variation of total hardness during the rainy and dry seasons were green, yellow, orange, brown, and grey, ranging between 44.0 mg/l and 228.2 mg/l, 228.3 mg/l and 412.4 mg/l, 412.5 mg/l and 596.6 mg/l, 596.7 mg/l and 780.8 mg/l, and 780.9 mg/l and 965.0 mg/l, respectively as shown in Figure 15 a and b.

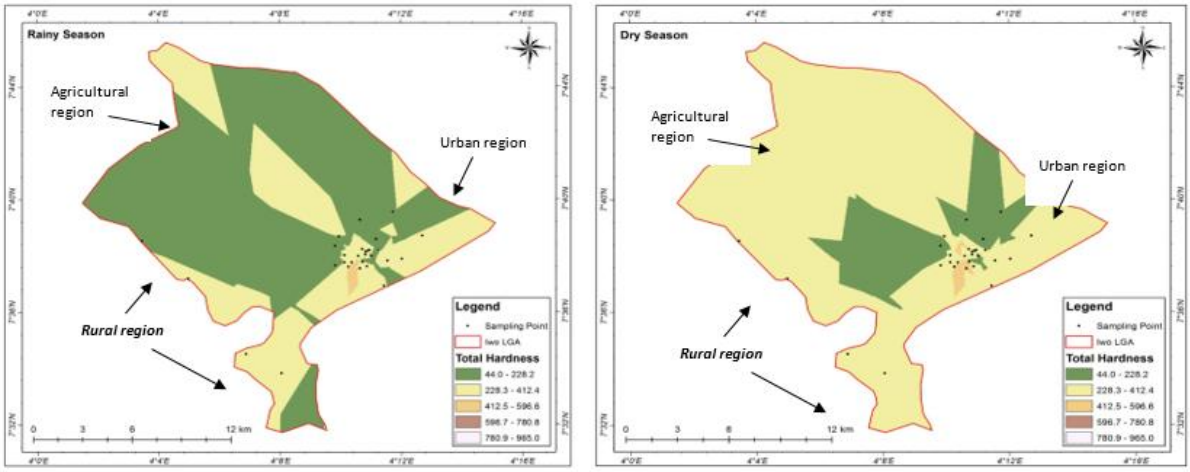

(a) (b)

Figure 15: *Spatial Variation of Total Hardness Concentration (a) Rainy Season (b) Dry Season*

In Figure 15a, the green colour of the spatial variation was within the permissible limit of total hardness (150 mg/l). The green colour occurred mainly in the agricultural region. This denoted that the total hardness of the groundwater around this region was slightly acceptable, which was close to 150 mg/l. The southern part of the study area displayed a yellow colour and a little orange colour. This denoted that the southern region ranged mainly between 228.3 mg/l and 596.6 mg/l, which was unacceptable.

In Figure 15 b, the green colour of the spatial variation during the dry season was within the permissible limit of total hardness (150 mg/l). The yellow colour occurred mainly in the rural region, and this denoted that the total hardness of the groundwater around this region was unacceptable and substantially exceeded the WHO standard limit across significant portions of the study area, particularly during the dry season. This prediction from the interpolation could be indicative of localised carbonate/sulphate rock dissolution and weathering processes as reported in previous studies (Mattos *et al.*, 2018). The urban part of the study area displayed green, yellow, and orange colours. The green colour locations denote that total hardness was within 150 mg/l, which was acceptable.

3.15 Turbidity

The five colours denoting the spatial variation of turbidity during the rainy and dry seasons were green, yellow, orange, brown and grey, ranging between 1.0 NTU and 2.6 NTU, 2.7 NTU and 4.2 NTU, 4.3 NTU and 5.8 NTU, 5.9 NTU and 7.4 NTU, and 7.5 NTU and 9.0 NTU, respectively, as shown in Figure 16 a and b.

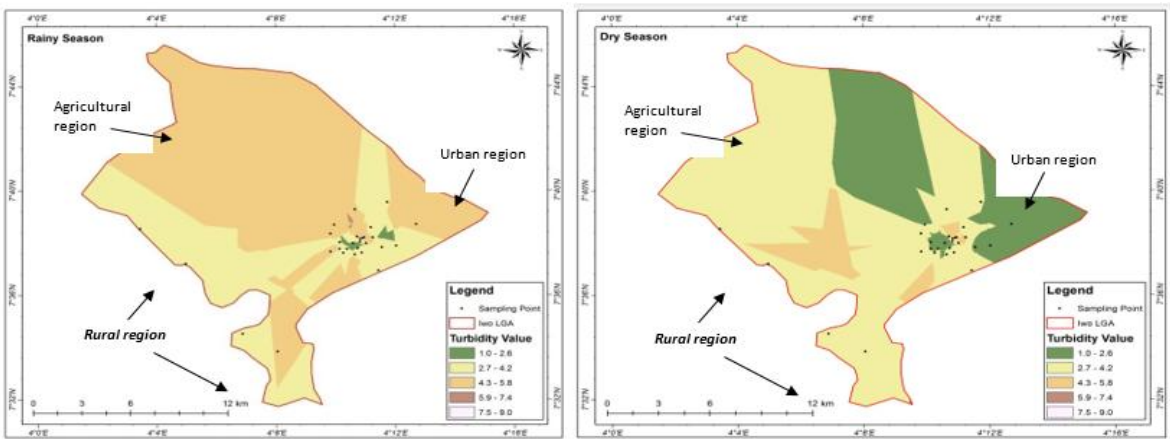

(a) (b)

Figure 16: *Spatial Variation of Turbidity Concentration (a) Rainy Season (b) Dry Season*

The green and yellow colours of the spatial variation were within the permissible turbidity limit (5 NTU). The yellow colour occurred mainly in the rural region, which denoted that the groundwater turbidity around this region was acceptable which was below 5 NTU. The urban region of the study area displayed mainly green, yellow, and orange colours with a bit of brown colour. This brown colour indicated that some parts of the urban and agricultural regions ranged between 5.9 NTU and 7.4 NTU, which was unacceptable. The significant difference observed in the agricultural and urban regions between the two seasons was the decrease in the turbidity of groundwater from the rainy to the dry season.

Table 2 shows the descriptive statistics for each groundwater parameter recorded for Iwo Local Government Area during the rainy season, while Table 3 shows the descriptive statistics for each groundwater parameter recorded for Iwo Local Government Area during the dry season. It was observed that during the rainy season, the mean values of temperature (27.48 ^{o}C), nitrate (52.16 mg/l), and total coliform count (22.67 cfu/ml x 10^{-4}) were greater than WHO values of 25 ^{o}C, 50 mg/l, and 10 cfu/ml x 10^{-4} respectively. During the dry season, the mean values of temperature (16.20 ^{o}C), nitrate (48.29 mg/l), and total coliform count (6.63 cfu/ml x 10^{-4}) were less than WHO values of 25 ^{o}C, 50 mg/l, and 10 cfu/ml x 10^{-4} respectively. In addition, total hardness, calcium, phosphate, and sulphate had consistent mean values greater than WHO standard values for both rainy and dry seasons. Other parameters like pH, electrical conductivity, total dissolved solids, total alkalinity, total suspended solids, turbidity, magnesium, and chloride had mean values for both rainy and dry seasons less than the WHO standard.

Table 2: *Groundwater Parameters Mean Against WHO Values for Rainy Season*

SN	Parameter	WHO	Minimum	Maximum	Mean	Standard Error	Standard Dev.	Coefficient of Variation (%)
1	pH (-)	6.5 – 8.5	5.6	8.5	7.07	±0.114	±0.625	8.84
2	Temp (^{o}C)	25	23.4	29.8	27.48	±0.261	±1.429	5.20
3	EC (µS/cm)	1000	86	1843	568.60	±94.059	±515.180	90.61
4	TDS (mg/l)	500	53	1013	330.57	±54.352	±297.701	90.06
5	T. Al. (mg/l)	200	15	370	120.57	±15.927	±87.234	72.35
6	TSS (mg/l)	250	50	450	180.00	±22.565	±123.596	68.66
7	Turb. (NTU)	5	1	9	3.90	±0.379	±2.074	53.17
8	TH (mg/l)	150	44	796	252.93	±32.553	±178.298	70.49
9	Ca (mg/l)	75	16	317	98.27	±13.057	±71.518	72.78
10	Mg (mg/l)	50	0.73	5.4	1.91	±0.225	±1.230	64.51
11	Cl (mg/l)	250	13.99	313.9	67.13	±13.681	±74.936	111.63
12	NO_3^- (mg/l)	50	14.19	94.33	52.16	±4.162	±22.796	43.70
13	SO_4^{2-} (mg/l)	250	155.2	488.31	305.12	±17.511	±95.910	31.43
14	PO_4^{3-} (mg/l)	0.05	0.35	4.184	1.76	±0.178	±0.972	55.17
15	TCC(cfu/ml)x 10^{-4}	10	0	78	22.67	±4.555	±24.951	110.08

Table 3: *Groundwater Parameters Mean Against WHO Values for Dry Season*

SN	Parameter	WHO	Minimum	Maximum	Mean	Standard Error	Standard Dev.	Coefficient of Variation (%)
1	pH (-)	6.5 – 8.5	5.5	10.5	7.16	±0.210	±1.148	16.03
2	Temp (ºC)	25	14	24.1	16.20	±0.471	±2.578	15.91
3	EC (µS/cm)	1000	51	1615	504.97	±80.224	±439.403	87.02
4	TDS (mg/l)	500	33	888	308.30	±49.234	±269.666	87.47
5	T. Al. (mg/l)	200	52	363	141.43	±13.442	±73.626	52.06
6	TSS (mg/l)	250	50	450	190.00	±24.377	±133.520	70.27
7	Turb. (NTU)	5	1	8	3.03	±0.373	±2.042	67.33
8	TH (mg/l)	150	55	964	299.63	±37.694	±206.458	68.90
9	Ca (mg/l)	75	20	384	115.83	±14.970	±81.996	70.79
10	Mg (mg/l)	50	0.49	6.08	2.32	±0.281	±1.540	66.43
11	Cl (mg/l)	250	12.5	290.41	68.44	±13.324	±72.981	106.63
12	NO_3^- (mg/l)	50	12.77	83.39	48.29	±3.739	±20.481	42.41
13	SO_4^{2-} (mg/l)	250	150.54	483.43	285.70	±17.540	±96.068	33.63
14	PO_4^{3-} (mg/l)	0.05	0.597	4.1	1.71	±0.174	±0.954	55.95
15	TCC(cfu/ml)x 10^{-4}	10	0	20	6.63	±1.221	±6.688	100.82

4. CONCLUSION

The groundwater sources from Iwo Local Government Area show that the measured parameters exhibited seasonal variation, with concentrations being primarily higher during the rainy season than during the dry season. However, the groundwater quality maps for total hardness, pH, and calcium show higher spatial variation of concentrations in the dry season than in the rainy season. This assessment provided information on groundwater features in the Iwo Local Government Area in Osun State of Nigeria. The kriging interpolation method was used to predict the value of a parameter at an unmeasured location over a spatial region, resulting in the generation of spatial distribution maps. The groundwater quality variation maps generated from water quality test results revealed groundwater quality characteristics in the Iwo Local Government Area. The different processes responsible for the acquisition of groundwater chemistry studied, according to spatial variation assessment studies, are the residence time of the water in contact with the rock, the infiltration of substances related to anthropogenic activities (agricultural fertilisers, household and industrial waste), and the intensity of rainfall. It is recommended that the identified locations be subjected to water treatment techniques to reduce total hardness.

5. REFERENCES

Abel, I., and Adebayo, A. P. (2017). 'Geo-implications of seasonal variation of Ilesha water quality'. *International Journal of Engineering Science Invention*, *6*(9), 1–11.

Adetona, Y. O., and Oladepo, K. T. (2021). Assessment of water quality index of groundwater resources in Iwo Local Government Area, Osun State, Southwestern Nigeria. Asia Pacific J. Energy Environ., 8 (1) (2021), pp. 17-28, https://doi.org/10.18034/apjee.v8i1.599

Ahmed, S. S. (2017). 'Assessment of groundwater quality parameters using multivariate statistics- A case study of Majmaah, KSA'. *International Journal of Environmental Monitoring and Analysis*, *5*(2), 32–40. https://doi.org/10.11648/j.ijema.20170502.13

Aleku, D. L., Dähnke, K., & Pichler, T. (2024). Source, transport, and fate of nitrate in shallow groundwater in the eastern Niger Delta. Environmental Science and Pollution Research, 31(56), 65034–65050. https://doi.org/10.1007/s11356-024-35499-6

Atobatele, B. O., Owoseni, A. A., & Atobatele, O. E. (2026). Ecological and health risk assessment of heavy metal contamination of hand-dug well water in Iwo Town, Osun State, Nigeria. Scientific African, 33. https://doi.org/10.1016/j.sciaf.2026.e03530

Ezechinyere, C. H., & Stanislaus, O. U. (2023). Investigating the quality of groundwater in Ibeju-Lekki Local Government Area, Lagos State. Water Science, 37(1), 409–425. https://doi.org/10.1080/23570008.2023.2283326

Izah, S. C., Ngun, C. T., & Richard, G. (2022). Microbial quality of groundwater in the Niger Delta region of Nigeria: Health implications and Effective Treatment Technologies. Current Directions in Water Scarcity Research, 6, 149–172. https://doi.org/10.1016/b978-0-323-91838-1.00010-5

Jeje, J. O., and Oladepo, K. T. (2014b). 'Water supply technologies : momentous effects on sanitation systems in Nigeria'. *International Journal of Civil and Environmental Research*, *1*(4), 141–151.

Kløve, B., Kvitsand, H. M., Pitkänen, T., Gunnarsdottir, M. J., Gaut, S., Gardarsson, S. M., Rossi, P. M., & Miettinen, I. (2017). Overview of groundwater sources and water-supply systems, and associated microbial pollution, in Finland, Norway and Iceland. Hydrogeology Journal, 25(4), 1033–1044. https://doi.org/10.1007/s10040-017-1552-x

Li, Y., Neidhardt, H., Guo, H., Nagel, C., Shao, W., Yu, C., Zhao, B., Chen, D., Xiu, W., & Oelmann, Y. (2024). Microbial cycling contributes to the release of dissolved inorganic phosphate into the groundwater of floodplain aquifers. Communications Earth & Environment, 5(1). https://doi.org/10.1038/s43247-024-01666-3

Mahapatra, S. S., Sahu, M., Patel, R. K., and Panda, B. N. (2012). 'Prediction of water quality using principal component analysis'. *Water Qual Expo Health*, *4*, 93–104. https://doi.org/10.1007/s12403-012-0068-9

Mattos, J. B., Cruz, M. J., De Paula, F. C., & Sales, E. F. (2018). Spatio-seasonal changes in the hydrogeochemistry of Groundwaters in a Highland Tropical Zone. Journal of South American Earth Sciences, 88, 275–286. https://doi.org/10.1016/j.jsames.2018.08.023

Nas, B. (2009). 'Geostatistical approach to assessment of spatial distribution of groundwater quality'. *Polish J. of Environ. Stud.*, *18*(6), 1073–1082.

Ogunbode, T. O., and Ifabiyi, P. I. (2014). 'Determinants of domestic water consumption in a growing urban centre in Osun State, Nigeria'. *Academic Journals*, *8*, 247–255. https://doi.org/10.5897/AJEST2013.1627

Olayinka, O. D., Aribisala, A. O., Ibonke, O. L., Akinpade, B. O., & Awoyemi, F. E. (2025). Physicochemical characteristics and levels of metal ions in groundwater around abattoir and cassava processing area from Odo-Oori Market in Iwo, Osun State, Nigeria. Journal of Applied Sciences and Environmental Management, 29(10), 3247–3260. https://doi.org/10.4314/jasem.v29i10.30

Olutona, G. O., Akintunde, E. A., and Otolorin, J. A. (2012). 'Physico-chemical quality assessment of shallow well- waters in Iwo, Southwestern Nigeria'. *Journal of Environmental Science and Water Resources*, *1*(6), 127–132.

Richardson, C. M., Davis, K. L., Ruiz-González, C., Guimond, J. A., Michael, H. A., Paldor, A., Moosdorf, N., & Paytan, A. (2024). The impacts of climate change on coastal groundwater. Nature Reviews Earth & Environment, 5(2), 100–119. https://doi.org/10.1038/s43017-023-00500-2

Subba Rao, N. (2005). Seasonal variation of groundwater quality in a part of Guntur district, Andhra Pradesh, India. Environmental Geology, 49(3), 413–429. https://doi.org/10.1007/s00254-005-0089-9

Thomas, E. O. (2023). Spatial evaluation of groundwater quality using factor analysis and geostatistical Kriging Algorithm: A case study of ibadan metropolis, Nigeria. Water Practice & Technology, 18(3), 592–607. https://doi.org/10.2166/wpt.2023.023

UNEP. (2011). *Towards a GREEN economy: Pathways to Sustainable Development and Poverty Eradication*.

Yan, R., Zhu, J., Xi, F., & Chen, A. (2022). Development and application of a hydrogeochemical model for the groundwater treatment process in Waterworks. Water, 14(13), 2103. https://doi.org/10.3390/w14132103

Zhang, X., Gao, X., Li, C., Luo, W., Wang, Y., & Luo, X. (2023). Seasonal dynamics and interaction of shallow groundwater geochemical properties and Microbial Community Patterns. Chemical Geology, 638, 121703. https://doi.org/10.1016/j.chemgeo.2023.121703

International Conference on Engineering Innovation for Sustainable Development (ICESID 2026)
Faculty of Engineering, Ahmadu Bello University Zaria · 8–10 September 2026

STUDY OF THE CORROSION RATE OF NIGERIAN HIGH-GRADE CONVENTIONAL 5 MM UKRAINIAN METALLIC PLATE USING WEIGHT LOSS (GRAVIMETRIC) METHOD

Jamilu Haruna[1,*], Abdulkareem Abubakar[1], Usman Abubakar Zaria[1], Abdulmajid M. Nainna[2], Abubakar Ado Datti[1]

[1]*Ahmadu Bello University Zaria*
[2]*Air Force Institute of Technology Kaduna*

Email: jamiluharuna220@yahoo.com*, aavazi@gmail.com, augayya@yahoo.com, amnainna@gmail.com, adodatti5@gmail.com

***Corresponding author**: Jamilu Haruna

DOI: https://doi.org/10.67203/sp.ICESID.2026

ABSTRACT

Accurate estimation of corrosion rate is essential for predicting the service life of petroleum tanker materials. This study used the weight-loss/gravimetric technique to investigate corrosion of carbon-steel tanker-truck material in Automotive Gas Oil (AGO) and Premium Motor Spirit (PMS) over 63 days (1512 h). The gravimetric analysis revealed measurable degradation of the carbon-steel coupons following immersion in both petroleum products, with different magnitudes under the tested conditions. The AGO-exposed specimens recorded an average weight loss of 0.40 g, whereas the PMS-exposed specimens exhibited a mean weight loss of 0.20 g, indicating approximately 100% greater mass loss in AGO. Using the ASTM G31 corrosion-rate equation with $K = 8.76 \times 10^4$ for mm/year, an exposed area of 22.80 cm², an exposure time of 1512 h and a steel density of 7.85 g/cm³, the calculated mean corrosion rates were 0.129 mm/year for AGO and 0.065 mm/year for PMS. Thus, under the specific laboratory conditions and for the fuel batches tested, AGO produced approximately twice the gravimetric corrosion rate measured in PMS. Because the study did not determine the physicochemical properties of the fuel samples, the observed difference is reported without assigning it to sulphur content or any other individual fuel constituent.

Keywords: *Corrosion rate; weight-loss method; ASTM G31; carbon steel; PMS; AGO*

1. INTRODUCTION

Nigeria's energy security and downstream petroleum supply system depend substantially on the safe and reliable transportation of petroleum products by road tanker trucks, particularly in view of the limitations of pipeline and rail infrastructure (Ambituuni, 2016). Tanker trucks therefore constitute an important link between petroleum-product storage facilities and end users across the country. However, the continued occurrence of tanker-related fires, explosions and other loss-of-containment incidents demonstrates the persistent safety challenges associated with petroleum-product transportation in Nigeria. A 16-year national review reported 169 tanker fire and explosion accidents resulting in 1,613 deaths between 2009 and 2024 (Na'inna, 2024). The persistence and severity of these incidents underscore the need for a systematic, engineering-based approach to improving the safety and integrity of petroleum tanker systems.

Tanker safety is influenced by several interacting factors, including human behaviour, road and traffic conditions, vehicle condition, operational practices, regulatory enforcement and the integrity of the tanker itself. While human and operational factors have received considerable attention, the condition of the metallic tanker shell represents an important engineering aspect of containment integrity. The tanker shell serves as the primary barrier separating the transported petroleum product from the external environment. Progressive deterioration of this barrier can reduce its effective thickness and structural capacity and may eventually result in leakage or loss of containment. Among the mechanisms responsible for metallic deterioration, corrosion is particularly important because it is a progressive process that can occur during prolonged service and may remain unnoticed until significant material loss has occurred.

The interaction between tanker-shell material and the transported petroleum product is therefore an important area of investigation. In Nigeria, Premium Motor Spirit (PMS) and Automotive Gas Oil (AGO) constitute major petroleum products transported by road tankers. Their different physicochemical characteristics may result in different interactions with carbon-steel tanker plates and, consequently, different rates of material degradation. However, the corrosion rate of the actual metallic material used for tanker fabrication under controlled exposure to these petroleum products requires experimental determination. Quantifying this material loss is important because corrosion rate provides a direct indication of the rate at which the tanker-shell thickness may progressively deteriorate.

The weight-loss (gravimetric) method provides a practical means of determining cumulative corrosion-induced metal loss. By measuring the difference between the initial and final masses of a metallic coupon after controlled exposure and relating the mass loss to the exposed surface area, material density and exposure duration, the average corrosion penetration rate can be quantified. The ASTM G31 standard provides guidance for laboratory immersion testing and offers an appropriate basis for controlled assessment of corrosion behaviour. Unlike an assessment based solely on visual surface deterioration, gravimetric analysis provides quantitative evidence of actual material loss during the specified exposure period.

This study applies the ASTM G31 gravimetric (weight-loss) method, the most widely used baseline technique for corrosion-rate estimation because of its simplicity and direct relationship to actual metal loss to a locally sourced, high-grade conventional 5 mm Ukrainian carbon steel plate (4.5 mm actual thickness) used for tanker fabrication in Nigeria, following 63 days of full immersion in PMS and AGO under ambient laboratory conditions.

2. LITERATURE REVIEW

The weight-loss (gravimetric) method is one of the most established experimental techniques for determining the corrosion rate of metallic materials. Its major advantage is that it provides a direct measure of actual metal loss during a defined exposure period. The method involves accurately weighing a prepared metal coupon before and after exposure to a corrosive environment, cleaning the specimen to remove corrosion products, and converting the resulting mass loss into a corrosion penetration rate. Because of its simplicity, relatively low cost and ability to quantify cumulative material loss, the method has been widely applied in studies of carbon and mild steel exposed to atmospheric, aqueous and petroleum-related environments. As cited in Guma & Abu, (2018), for example, applied gravimetric measurements in corrosion investigations, demonstrating the applicability of weight-loss analysis to steel corrosion studies.

The relevance of the gravimetric method to the Nigerian environment is demonstrated by Guma and Abu (2018), who investigated the atmospheric corrosion behaviour of mild steel around Kaduna metropolis. Their study involved a large number of corrosion coupons and used statistical analysis, including analysis of variance (ANOVA), to examine differences in corrosion behaviour associated with location. The authors reported statistically significant variations in corrosion rates among the investigated locations. This study is particularly relevant to the present research because it demonstrates the suitability of weight-loss measurements combined with statistical analysis for evaluating corrosion behaviour under Nigerian environmental conditions. The approach provides a useful methodological precedent for the present investigation of petroleum-tanker steel exposed to PMS and AGO.

A particularly relevant West African study was conducted by Suah (2014), who examined the corrosion behaviour of low-carbon steel containing approximately 0.184 wt.% carbon obtained from an above-ground petroleum storage tank in Liberia. The steel coupons were exposed to gasoline and diesel for periods of up to 456 h, while weight loss, pH and optical microscopy were used to monitor corrosion behaviour. The reported corrosion penetration rates ranged from approximately 0.016 to 0.325 mm/year, depending on the exposure medium and coupon. The study also observed a progressive reduction in solution pH during exposure. This behaviour was associated with the formation of acidic species, particularly carboxylic/acetic acid species, and their subsequent interaction with dissolved iron to form iron-containing corrosion products. The findings demonstrate that petroleum-derived fuels, despite being substantially less conductive than aqueous electrolytes, can still support measurable corrosion of carbon steel when appropriate corrosive species and

environmental conditions are present. The study therefore provides an important regional reference for investigating the interaction between tanker-fabrication steel and petroleum products.

Corrosion of Carbon Steel in Diesel and Biodiesel-Containing Fuels

A substantial body of literature has also investigated corrosion of carbon steel in diesel–biodiesel systems. Although biodiesel-containing fuels are not chemically identical to conventional Automotive Gas Oil (AGO), these studies provide useful comparative evidence because diesel and biodiesel systems contain oxygenated compounds and may exhibit different moisture, acidity and oxidation characteristics from lighter petroleum products such as PMS.

Cursaru et al. (2014) reported greater surface deterioration of mild carbon steel in biodiesel than in petroleum diesel, demonstrating the influence of fuel composition on steel corrosion. Similarly, Milano et al. (2021), Adama et al. (2024), and Adama et al. (2025) reported relationships between increasing biodiesel content and increasing corrosion severity. These findings indicate that changes in fuel composition can significantly modify the interaction between the fuel environment and carbon-steel surfaces.

Exposure configuration is also an important factor in petroleum-fuel corrosion. Kugelmeier et al. (2021) investigated carbon steel exposed to diesel–biodiesel blends and found comparatively limited attack under full-immersion conditions, while more pronounced deterioration occurred in the vapour phase. This observation is important for petroleum tanker applications because a tanker shell is not necessarily exposed to a single uniform environment. Depending on the fuel level, temperature, moisture accumulation and operating conditions, different regions of the tank may experience liquid-phase, vapour-phase and fuel–water interface exposure. Consequently, corrosion rate measurements obtained under full immersion should be interpreted as representing a defined experimental exposure condition rather than necessarily reproducing every corrosion mechanism occurring inside an operating tanker.

Further evidence was provided by Heryana et al. (2024), who investigated SA 516 Gr.70 carbon steel exposed to diesel–biodiesel blends. The study reported corrosion rates of approximately 1.226–1.442 µm/year, with corrosion severity increasing with biodiesel content. Surface examination using SEM/EDS revealed pitting and corrosion products containing predominantly iron and oxygen. These observations demonstrate the usefulness of combining gravimetric measurements with surface and elemental characterization to establish not only how much metal is lost, but also the nature of the resulting corrosion damage.

Corrosion Behaviour of Carbon Steel in AGO and PMS

While the studies involving diesel–biodiesel fuels provide useful information on fuel-related corrosion, direct investigations involving commercial AGO and PMS are particularly relevant to petroleum tanker applications in Nigeria. Shuaib-Babata and Abdulqadir (2012) investigated commercial low-carbon steel in several environments, including AGO, PMS, dual-purpose kerosene (DPK), crude oil, freshwater and seawater. Their reported corrosivity sequence was:

natural seawater > simulated seawater > freshwater > crude oil > PMS > DPK > AGO.

This result indicates considerably lower apparent corrosivity for AGO than for PMS under their experimental conditions. However, this ranking differs from the corrosion-rate trend obtained in the present investigation, where AGO exhibited a higher gravimetric corrosion rate than PMS. Such differences do not necessarily represent contradictions in the underlying corrosion behaviour; rather, they demonstrate the strong dependence of measured corrosion rate on the specific material, fuel composition and experimental conditions.

Differences between studies may arise from variations in steel composition and microstructure, fuel formulation, water and contaminant content, dissolved oxygen, temperature, exposure duration, specimen surface condition and exposure configuration. Petroleum fuels are complex mixtures rather than single chemical substances, and their corrosive behaviour can change considerably with storage history, contamination and the presence of water or other reactive species. Therefore, corrosion-rate values obtained from one fuel batch or steel grade should not automatically be assumed to represent all tanker operating conditions.

Relevance to the Present Study

The reviewed literature demonstrates that the corrosion of carbon-steel materials in petroleum-related environments is influenced by the interaction between the metallic material and the

characteristics of the exposure medium. The weight-loss method is particularly valuable for the present research because it measures cumulative mass loss and can therefore be directly related to the progressive loss of tanker-shell material. Previous Nigerian and West African studies have established the applicability of gravimetric techniques to steel corrosion, while investigations involving diesel, biodiesel, AGO and PMS demonstrate that corrosion behaviour can vary substantially with fuel composition and exposure conditions.

However, there remains a need for experimental data specifically addressing the corrosion rate of carbon-steel plates used for petroleum tanker fabrication in Nigeria when exposed directly to PMS and AGO under controlled conditions. In particular, the divergence between the AGO/PMS corrosion rankings reported in previous studies highlights the importance of generating experimental data from the actual tanker-fabrication steel and petroleum-product batches investigated in a given study, rather than relying solely on corrosion rates reported elsewhere.

Accordingly, the present study employs the ASTM G31-based weight-loss (gravimetric) method to quantify the corrosion rates of the investigated carbon-steel tanker plate following controlled immersion in PMS and AGO. By maintaining the same steel material, specimen preparation procedure, exposure conditions and measurement approach for both petroleum products, the study provides a direct basis for comparing their relative effects on the tanker-fabrication material. The resulting corrosion-rate data constitute the fundamental experimental evidence for subsequent evaluation of corrosion-induced material degradation, mechanical-property changes, corrosion mitigation and the implications of tanker-shell deterioration for leakage and fire/explosion risk in Nigeria.

3. MATERIALS AND METHODS

3.1 Materials

Fresh carbon steel plate of 4.5 mm actual thickness (locally referred to as high-grade conventional 5 mm Ukrainian metallic plate) was procured from Dan Magaji Tanker Fabricators, Zaria, Nigeria. Premium Motor Spirit (PMS) and Automotive Gas Oil (AGO) used for the study were purchased from AA Rano Filling Station, Sokoto Road, Zango, Samaru, Zaria.

Figure 3.1: The 4.5 mm carbon steel plate

3.2 Sample Preparation

Specimens were cut to the required dimensions using a power hacksaw machine, with care taken to avoid excessive heating that could alter the microstructure. Surface grinding was carried out manually using silicon carbide emery papers of progressively finer grit (220, 320, 400, 600 and 800), followed by polishing on a rotating polishing machine using an aluminium oxide slurry. Degreasing was performed by immersing the polished specimens in boiling alcohol for approximately 10 minutes, after which the specimens were dried using clean absorbent tissue paper prior to testing.

Figure 3.2: Prepared carbon steel coupons after grinding, polishing and degreasing before weighing

3.3 Immersion Procedure

A volume of 500 mL each of PMS and AGO was poured separately into clean plastic containers. Five specimens were tagged, weighed on an analytical balance to record the initial weight, and immersed separately in PMS and AGO. Containers were tightly sealed to minimise air ingress, contamination and evaporation. An exposure duration of approximately 63 days was adopted, comparable to immersion durations used in prior Nigerian corrosion studies of carbon steel in petroleum media (Shuaib-Babata & Abdulqadir, 2012). Specimens were visually inspected at 7 and 27 days; no significant corrosion products were observed at these intermediate points, but visible corrosion products were present by the end of the 63-day period.

After removal from the immersion media, loose corrosion products were gently removed using a soft brush. The specimens were then immersed in a hydrochloric acid (HCl) solution for 10 minutes to remove adherent corrosion products, rinsed thoroughly with distilled water followed by ethanol, and dried in a desiccator to eliminate residual moisture. The final weight of each specimen was measured using an analytical balance and weight loss was determined by taking the difference between initial and final weight of each sample.

Figure 3.3: Sealed plastic containers with carbon steel coupons immersed in PMS and AGO

3.4 Corrosion-Rate Calculation (ASTM G31)

The coupon dimensions were 64 mm × 13 mm × 4 mm, with all six surfaces exposed; the 4.5 mm actual material thickness was reduced to 4 mm due to machining during material preparation, the exposed surface area (top and bottom faces plus all four edges) was calculated as 22.80 cm^2. The corrosion rate in mm/year was estimated using the standard ASTM G31 weight-loss equation:

Corrosion Rate (mm/year) = (K × W) / (A × T × D) *Eq1*

where K is the unit-conversion constant. Using W in grams, A in cm^2, T in hours and D in g/cm^3, the applicable constants are $K = 3.45 \times 10^6$ for mils per year (mpy), $K = 8.76 \times 10^4$ for millimetres per year (mm/year), and $K = 8.76 \times 10^7$ for micrometres per year (µm/year). Therefore, because the corrosion rates in this study are reported in mm/year, W is the weight loss in grams, A is the exposed surface area in cm^2, T is the exposure time in hours, and D is the density of the steel (7.85 g/cm^3), the appropriate is $K = 8.76 \times 10^4$ based on.

```
W/(A·T·D) has units g/(cm²·h·g/cm³) = cm/h  →  a linear penetration
rate

Converting cm/h → mm/year:  ×10 (cm→mm)  ×8760 (hours/year)  =
×87,600  =  8.76×10⁴
```

ASTM G31-72 quoted verbatim in two US patent filings: *"Corrosion rate = 8.76×10^4 × (weight loss(g)/(area(cm^2) ×density(g/cm^3) ×time(h)))"* — explicitly labelled mm/year in both.

The mean and standard deviation of the weight-loss measurements were calculated using the standard formulae for sample mean and standard deviation.

For verification, substitution of the mean values gives: AGO = $(8.76 \times 10^4 \times 0.40)/(22.80 \times 1512 \times 7.85)$ = 0.12948 mm/year, reported as 0.129 mm/year; and PMS = $(8.76 \times 10^4 \times 0.20)/(22.80 \times 1512 \times 7.85)$ = 0.06474 mm/year, reported as 0.065 mm/year. Thus, the reported rates follow directly from the stated mean weight losses, area, exposure time, density and the mm/year constant.

Figure 3.4: Corroded specimens after HCl cleaning, distilled-water/ethanol rinse and desiccator drying, immediately before final weight measurement on the analytical balance

4. RESULTS AND DISCUSSION

The weight-loss method was employed to evaluate the corrosion behaviour of carbon steel exposed to PMS and AGO over the 63-day immersion period. The results are presented in Table 1.

Table 1: Corrosion-rate of carbon steel in AGO and PMS media

Parameter	AGO	PMS
Mean Weight Loss (g)	0.40	0.20
Standard Deviation (g)	0.183	0.141
Exposed Surface Area (cm^2)	22.80	22.80
Density (g/cm^3)	7.85	7.85
Exposure Time Hour (h)	1512	1512
Mean Corrosion Rate (mm/year)	0.129	0.065

The gravimetric analysis revealed measurable degradation of the carbon steel coupons following immersion in both petroleum products; however, the degree of deterioration varied considerably between the two fuels. The AGO-exposed specimens recorded an average weight loss of 0.40 g, whereas the PMS exposed samples exhibited a mean weight loss of 0.20 g, the mass loss in diesel was approximately 100% greater than that observed in petrol under identical exposure conditions. The calculated corrosion rates followed the same trend: the average corrosion rate of

0.129 mm/year for AGO was approximately twice that obtained for PMS (0.065 mm/year), demonstrating that the carbon steel experienced a more aggressive corrosive environment in diesel than in petrol.

The higher corrosion rate measured in AGO should be interpreted as an experimental result obtained for the specific fuel batch and exposure conditions used in this study. The present experiment did not include physicochemical analysis of the PMS or AGO; therefore, the difference in corrosion rate cannot be attributed quantitatively to sulphur content, acidity, water content, dissolved oxygen, oxidation products or any other individual fuel constituent. Differences in fuel composition and contamination are possible explanatory factors identified in the wider literature, but their contributions were not measured here.

To place these corrosion rates in context, Suah (2014) reported broadly comparable, and in some cases lower, gravimetric corrosion penetration rates (0.016–0.325 mm/year) for low-carbon steel (0.184 wt% C) exposed to diesel and gasoline for up to 456 hours (19 days) under similarly uncontrolled ambient laboratory conditions. Although the fuel media are not identical (Liberian diesel/gasoline versus Nigerian AGO/PMS), the two studies together suggest that carbon steel corrosion rates in petroleum products of this kind typically fall within a comparable low sub-millimetre-per-year range, well below corrosion rates reported for carbon steel in aqueous or marine environments (Guma & Abu, 2018). Reported values are sensitive to exposure duration, coupon geometry and the specific carbon content of the steel investigated, so direct numerical comparison across studies should be treated as indicative rather than exact.

The difference between the AGO and PMS results therefore demonstrates that the corrosivity ranking obtained in this experiment is specific to the investigated steel, fuel batches and controlled exposure conditions. Without direct physicochemical testing of the two fuel samples and without presenting the steel composition in this manuscript, the present data do not permit a definitive mechanistic explanation for why AGO produced the higher rate.

The gravimetric result that AGO produced a substantially higher corrosion rate (0.129 mm/year) than PMS (0.065 mm/year) contrasts with Shuaib-Babata and Abdulqadir (2012), who tested commercial low-carbon steel in AGO, PMS, DPK, crude oil and seawater and reported AGO as the least corrosive petroleum fraction in their weight-loss study, the reverse of the ranking obtained here. The two studies used different steel materials, fuel samples and exposure conditions, including different temperature regimes. Consequently, the discrepancy should not be used to infer a universal corrosivity ranking between AGO and PMS. Rather, it supports the present study's rationale that corrosion-rate measurements should be generated for the specific material and fuel environment under investigation. Because this manuscript does not present the bulk chemical composition of the investigated plate, no claim is made here that the material is medium-carbon steel or that composition alone explains the difference from the earlier study.

The present result can also be discussed alongside diesel-biodiesel corrosion studies with appropriate caution. Heryana et al. (2024), for example, reported measurable corrosion and pitting of SA 516 Gr.70 carbon steel in diesel-biodiesel and diesel-biodiesel-HVO blends, with corrosion severity varying with blend composition. Those results reinforce the broader finding that fuel composition and exposure conditions can influence carbon-steel corrosion, but they do not establish that conventional AGO is inherently more corrosive than PMS. Accordingly, the present AGO>PMS ranking should be limited to the tested fuel batches and 63-day ambient laboratory immersion conditions. Further work should include physicochemical characterization of the fuel samples and independent material-composition data to investigate the mechanisms responsible for the observed difference.

5. CONCLUSION

The corrosion behaviour of the investigated carbon steel plate, locally referred to as high-grade conventional 5 mm Ukrainian metallic plate and measured as 4.5 mm before coupon machining, was evaluated after 63 days (1512 h) of full immersion in PMS and AGO using the ASTM G31 gravimetric (weight-loss) approach. Under the specific laboratory conditions and for the fuel batches tested, both media produced measurable weight loss. AGO produced a mean corrosion rate of 0.129

mm/year, approximately twice the 0.065 mm/year measured for PMS. The result establishes the relative severity observed in this experiment but does not demonstrate that AGO is universally more corrosive than PMS or identify a specific fuel constituent as the cause because the fuel physicochemical properties were not measured. The findings support the need for material- and fuel-specific corrosion assessment, and future studies should combine gravimetric testing with fuel physicochemical characterization and independent material-composition analysis before making mechanistic or general corrosivity claims.

REFERENCES

Adama, K. K., Onyeachu, I. B., Modebe, L. U., Chukwuike, V. I., Oghuma, P. O., & Akhabue, C. E. (2024). Comparative evaluation of corrosion behaviour of carbon steel (C1020) in different biodiesels: Synthesis, characterization and electrochemical investigations. Results in Engineering, 21, 101695.

Adama, K. K., Ukhurebor, K. E., Aigbe, U. O., & Hossain, I. (2025). Implications of waste cooking oil biodiesel on carbon steel alloy in automobiles: Corrosion degradation. International Journal of Thermofluids, 26, 101143.

Ambituuni, A. (2016). Risk assessment of petroleum product transportation by road in Nigeria (Doctoral thesis).

ASTM International. (2017). ASTM G1-03(2017)e1: Standard practice for preparing, cleaning, and evaluating corrosion test specimens. ASTM International, West Conshohocken, PA.

ASTM International. (2021). NACE TM0169/G31-21: Standard guide for laboratory immersion corrosion testing of metals. ASTM International/AMPP.

Chikwe, T. N., & Ebosele, F. (2024). Impacts of fractional distillation (refining) on the characteristics of premium motor spirit, automotive gas oil and household kerosene obtained from Bonny Light crude. Nigerian Research Journal of Chemical Sciences, 12(1), 289-307.

Cursaru, D.-L., Branoiu, G., Ramadan, I., & Miculescu, F. (2014). Degradation of automotive materials upon exposure to sunflower biodiesel. Industrial Crops and Products, 54, 149-158.

Guma, T. N., & Abu, J. A. (2018). A field study of outdoor atmospheric corrosion rates of mild steel around Kaduna metropolis. International Journal of Mechanical Engineering, 5(11), 7-21.

Heryana, Y., Pamungkas, A., Romelan, R., Solikhah, M. D., Matheofani, Barus, B. R., Wibowo, C. S., Supriyadi, F., Thahar, A., Wibowo, E., & Wirawan, S. S. (2024). Evaluation of corrosion effects in diesel-biodiesel and diesel-biodiesel-HVO blends on metals for fuel storage systems. Corrosion Science and Technology, 23(5), 352-364.

Kugelmeier, C. L., Monteiro, M. R., da Silva, R., Kuri, S. E., Sordi, V. L., & Della Rovere, C. A. (2021). Corrosion behavior of carbon steel, stainless steel, aluminum and copper upon exposure to biodiesel blended with petrodiesel. Energy, 226, 120344.

Milano, J., Umar, H., Shamsuddin, A. H. A. H., Silitonga, A. S. A. S., Irfan, O. M., Sebayang, A. H., Fattah, I. M. I. M. R., & Mofijur, M. M. (2021). Experimental study of the corrosiveness of ternary blends of biodiesel fuel. Frontiers in Energy Research, 9, 778801.

Na'inna, A. M. (2024). Overview of petroleum tanker fire and explosion accidents in Nigeria from 2009 to 2024. Nigerian Research Journal of Engineering and Environmental Sciences, 9(2), 552-570.

Odili, C. W., Dike, O. K., Ebinimi, G., Nwankwo, C. N., Amabogha, B., Oluchi, N. A., Kenneth, O., & Babatunde, A. S. (2024). Comparative analysis of PMS samples from artisanal and legal refineries based on international standards. International Journal of Petroleum and Gas Exploration Management, 7(1), 55-72.

Shuaib-Babata, Y. L., & Abdulqadir, L. B. (2012). Corrosion behaviours of commercial low carbon steel in petroleum environment [Conference paper]. ResearchGate.

Suah, Y. D. (2014). Corrosion behaviour of low carbon steel used in oil and gas aboveground storage tanks (Master's thesis). African University of Science and Technology, Abuja, Nigeria.

TRACK 4 OF 11

Engineering Innovations, Technology Commercialisation and Industrial Policy

---

International Conference on Engineering Innovation for Sustainable Development (ICESID 2026)

Faculty of Engineering, Ahmadu Bello University Zaria · 8–10 September 2026

https://icesid.org

A COMPREHENSIVE REVIEW ON THE POULTRY BROODING REQUIREMENTS AND FORCED AIR METHODS OF HEAT GENERATION FOR BROODING

George Akwec[1,2,*], Adebayo Segun Emmanuel[1], Caroline Omoanatse Alenoghena[3]

[1]*Department of Agricultural and Bioresources Engineering, Federal University of Technology, Minna, Nigeria*

[2]*Department of Agricultural and Biosystems Engineering, Makerere University, Kampala, Uganda*

[3]*Department of Telecommunication Engineering, Federal University of Technology, Minna, Nigeria*

Email: georgeakwec96@gmail.com*, segun.emma@futminna.edu.ng, carol@futminna.edu.ng

***Corresponding author**: George Akwec

DOI: https://doi.org/10.67203/sp.ICESID.2026

ABSTRACT

Brooding is among the most sensitive stages in the poultry production cycle because neonatal chicks bear premature thermoregulatory body systems making them rely totally on external sources of heat for growth and development however, the inadequacy and the inconsistency of the heat supply remain a major challenge as such, the design and construction of air heating system is vital in the chick's production sector. This review discussed brooding requirements, different air heating systems and their operational principles including construction guidelines, material selection, insulation and the automation in poultry brooding are discussed. The study identified that Computational Fluid Dynamics is an important tool for optimization of aspects such as air flow velocity and temperature distribution pattern. The study further identified the existing research gaps from where the corresponding future directions were suggested. The study concluded that, performance of the system doesn't only rely on the heat source or mode of heat transfer but also on the construction workmanship while considering material selection and insulation.

Keywords: *brooding requirement; forced air heating methods; construction; insulation; material selection*

1 INTRODUCTION

Poultry production has become one of the rapidly-growing sectors in agriculture globally. In spite of the rapid growth rate recorded in the past few years, the adoption is highly dependent on the capacity to provide the indispensable requirements necessary for the birds to survive during the early stage of growth and development. The provision of these vital requirements is termed as brooding where naturally, the mother hen provides to ensure newly hatched chicks adapt to the environmental conditions especially self-regulation of body temperature (Collin *et al*., 2020).

Artificially, quite a number of traditional heat generation technologies have been developed such as charcoal stoves, kerosene heaters, firewood furnaces, coal burners, and open-flame gas for providing the conducive thermal conditions for the day-old chicks (Bekele, 2021). These heat generation methods portray several drawbacks such as non-uniform temperature maintenance, generation of harmful combustion gases, risk of fire hazards, environmental pollution, including the drudgery associated with maintaining the fuel quantity for a 24-hour production, (Okonkwo *et al*., 2022).

The fast technological improvement in agricultural engineering has sprung the innovation of better-quality heating technologies for example heat lamps, radiant heaters which have the capacity to bridge the bottle-neck related to inefficient brooding systems. Recent poultry brooding technologies have incorporated intelligent systems which uses microcontrollers such as Arduino, Proportional-Integral and Derivative (PID), fuzzy logic, raspberry-pi to automatically regulate the thermal condition within the brooding chamber. These innovations have meaningfully improved the temperature regulation processes including control of other environmental parameters (Zhang *et al*., 2024).

In Nigeria, Okonkwo *et al*., (2025) developed a micro-physical element monitoring device for Trombe wall solar energy poultry brooding chamber for real time measurement of brooding temperature, relative humidity and daily solar radiation using data logger. Furthermore, Ezema *et al*., (2021) designed and implemented an embedded poultry brooding system that monitors and automatically controls the climatic conditions such as temperature and humidity where the digital values were being displayed on the Liquid Crystal Display (LCD) screen. The Arduino ESP-32 type was used to provide the overall operational controls of the system and heat lamps was used as the heat source.

Forced air heat generation methods though not commonly utilized in poultry brooding have the ability to eliminate localized heating unlike radiant heaters that primarily warm only a spot in the brooding chamber or surfaces directly underneath the heat source and to drive out unwanted gases. In addition, forced-air heating systems can be incorporated with an air filtration unit there by improving on the quality of air supplied in the brooding area. It employs a blower or a fan to distribute heated air homogeneously throughout the brooding perimeter (Mohamed, 2015).

Therefore, the aim of this study is to examine the poultry brooding requirements and investigate the potential of forced air heating systems for efficient regulation of brooding temperature with specific objectives such as; to understand the various types of forced-air heaters for brooding and construction guidelines, material's selection and insulation requirements, to understand the possibility of automation in forced-air heaters for brooding and to discover the research gaps associated with forced-air heating systems for brooding.

2 METHODOLOGY

This review was conducted by retrieving relevant literatures from reputable scientific databases such as Google Scholar, ScienceDirect, SpringerLink, Semantic Scholar, and Taylor & Francis Online. Further materials were got from technical reports, poultry management manual, engineering handbooks including publications by international organizations, the American Society of Heating, Refrigerating and Air-Conditioning Engineers (ASHRAE)

The literature search was primarily limited to publications between 2020 and 2026 to guarantee the latest advancement in the forced-air method of heat application for brooding. The earlier information from engineering textbooks and article publications were selectively considered to capture fundamental engineering principles and thermodynamic equations. Boolean search operators (AND, OR, and NOT) were used to quicken the process of relevant literature identification. A bunch of keywords were equally used to improve on the accuracy of the literature which includes; forced-air heating system, poultry brooding, electric resistance heating, hot-air generator, heating chamber, brooding temperature and humidity, ventilation, fabrication, heat system construction, Computational Fluid Dynamics, material selection and insulation.

After the initial search, the titles and abstracts of the obtained publications were carefully scrutinized to ascertain their relevance to the objectives of the study. It was equally necessary to evaluate the full-text articles to prove their appropriateness for inclusion. Lastly, the choice on the final selection of the literature were grounded on studies that discussed application of intelligent and automation systems for control of environmental parameters during brooding most especially temperature management. The exclusion criteria were focused on studies that didn't explore related poultry brooding aspects, studies that didn't consider any form of brooding requirement or lacked engineering or scientific information related to automation of brooding systems and forced-air heating technology.

3 RESULTS AND DISCUSSION

3.1 Poultry brooding requirements

3.1.1 *Temperature requirement from day 1 to Week 6*

The normal body temperature of a healthy chick according to Bekele, (2021) ranges from 32°C to 36°C which is supposed to be maintained by ensuring the chick's environment is well conditioned. If environmental temperatures drop below this recommended range, chicks spend substantial energy from metabolic process such as trembling and dietary diversion to produce

metabolic heat. The appropriate brooding temperature is greatest as soon as they are hatched and continuously reduces by 5°C each week as chicks mature as shown in table 1 since the development of their thermoregulatory capacity occurs as they grow. Feather establishment, body weight gain raises the rate of metabolic heat generation thereby improving the insulation to retain a reasonable quantity of heat that help reduce the extent of dependence on supplemental heat.

Table 1: Recommended brooding temperature profile

Age	Ranges of suitable temperatures (°C)	Remarks
Day 1–7	32–36	High supplemental heating required.
Week 2	27–31	Chicks become more active
Week 3	22–26	Feather development
Week 4	17–21	Reduced dependence on artificial heating for ambient conditions

Sources: (Collin et al., 2020;Bekele, 2021)

3.1.2 *Humidity requirements*

All through the brooding cycle, chicks endlessly give out moisture as respiration occurs, whereas extra water vapor emanates from drinkers as spillages, watery droppings, wet litter, and the reaction of hydrocarbon fuels with oxygen. In a situation where this moisture is not properly removed through ventilation process, relative humidity intensifies, creating environmental conditions favourable for microbial organism proliferation, conglomeration of litter, ammonia gas generation, and respiratory tract infection. In contrast, extremely dry air accelerates evaporative water loss from chicks, leading to desiccation which causes irritation of the respiratory tract, and high volume of dust evolution within the poultry house. Majority of the poultry production guides recommends running a poultry brooding activity with relative humidity as shown in table 2. This range controls dehydration extent while avoiding extreme moisture accumulation in the litter material (Mutibvu *et al*., 2021).

Table 2: Recommended relative humidity during brooding

Age	Recommended Relative Humidity (%)	Remarks
Week 1	60–70	Prevents dehydration and supports chick adaptation after hatch.
Week 2–3	55–65	Facilitates a good feather development and litter drying.
Week 4–6	50–60	Supports efficient exchange of gases and diminishes ammonia generation

Source; (Mutibvu et al., 2021;Onagbesan et al., 2023)

The benefit of humidity management outspreads beyond just moisture accumulation control because it improves the bird's surrounding temperature condition. In situations of high relative humidity, evaporative cooling occurring on the bird's surface area turns out to be less effective. Ultimately, birds go through thermal stress even though ambient temperatures continue to be within

the preferred range. Contrarily, low humidity increases evaporative heat loss, which may be of advantage throughout the hot weather period though harmful at the initial stage of the brooding period that chicks highly require heat supply (Onagbesan *et al*., 2023).

3.1.3 *Air velocity*

The speed at which air traverses across the poultry house is another key brooding factor that can't be overlooked. Appropriate air velocity allows uniform heat distribution, enhances oxygen concentration, drives out excess moisture and harmful gases, and contains the occurrence of thermal stratification. In contrast, air movement beyond a preferred velocity may initiate convective heat loss from chicks, especially in the first week of the brooding process. Convective heat loss from chicks can be quantified using Newton's Law of Cooling, illustrated by expression (1).

$$Q = hA(T_s - T_a) \quad (1)$$

Where; Q= rate of heat loss (W), h= convective heat loss coefficient (W m^{-2} K^{-1}), A= chick's surface area (m^2), T_s= chick's surface temperature (°C), T_a= ambient air temperature (°C). Therefore, as air velocity surges, the convective heat loss coefficient (h) equally surges, triggering a large quantity of heat removal from the chicks (Çengel & Ghajar, 2020).

This principle enlightens why just moderate drafts can cause cold stress irrespective of whether air temperatures are within the acceptable range. The recommended air velocities based on the brooding period are as illustrated in table 3. During the process of bird's growth, more metabolic heat is generated as such, increase in air velocities become advantageous in expelling excessive body heat hence modifying thermal environment (Liang *et al*., 2022).

Table 3: Recommended Air Velocity

Age	Air Velocity (m s^{-1})	Purpose
Week 1	0.10–0.15	Prevent chilling and drafts.
Week 2–3	0.15–0.30	Improve air circulation while maintaining warmth.
Week 4–6	0.30–0.50	Enhance convective cooling and toxic gas removal.

Source; (Liang et al., 2022 ; Onagbesan et al., 2023)

3.1.4 *Ventilation requirements*

The fact that brooding requires external heat supplement, ventilation remains crucial because it expels unwanted gases and retains a greater percentage of oxygen that supports respiration process, exits evaporated moisture, direct aerosols out of the facility and maintaining a recommended humidity level. A common misconception is that ventilation minimization during cold conditions help to retains heat within the facility when it just causes problems associated with high relative humidity therefore, adequate poultry house ventilation systems must be maintained in order to strike the balance between heat conservation and maintaining air quality (Sarai *et al*., 2023).

3.2 Automation in brooding systems

Klotz *et al*., (2020) discussed that, automated brooding systems continuously monitors crucial environmental variables such as temperature, humidity, and helps in ventilation management. Automated control mechanisms manipulate the heating devices, ventilation fans, and air inlets to maintain the atmosphere favourable for poultry growth and development. The monitoring and regulation of these variables is possible with the help of a series of electronic devices e.g. integrated

sensors, microcontrollers, and a digital display system for a physical observation of values in real time.

In a study conducted by Kalu et al., (2023) microcontroller-based temperature monitoring and control system for broiler's brooding was developed. The LM35 analog temperature sensor was used to detect the temperature in the brooding chamber and sends information to the ATMega 328 microcontroller. The microcontroller was configured to perform a task of temperature maintenance for a particular value which is displayed on the Liquid Crystal Display (LCD). When the LM35 sensor sends a temperature value lower than the configured value, the microcontroller commands the relay to turn on the halogen heater and the fan turned off. Meanwhile, when the LM35 sensor sends a temperature value higher than the configured value, the heater turns off and the fan turned on hence maintaining the configured temperature desirable in the brooding chamber.

Olalekan *et al*., (2021) developed an automated temperature and humidity regulation system by using Arduino microcontroller for the poultry brooding house where, in the first week, the temperature was maintained between 32°C and 35 ^{o}C. When temperature falls below this range, heater is turned-on and the fan off while when the temperature goes beyond this range, the heater is turned off while the fan is turned on. Temperature and humidity sensors were used to detect the heat levels and relative humidity respectively. The relay was used to control the heater by switching it on and off as instructed by Arduino microcontroller. The running of the fan was equally facilitating ventilation within the brooding facility. The similar working principes applied to the subsequent weeks until the last week of the brooding period. Remote monitoring of the data was possible using a WiFi System-on -Chip (SoC) module, an IoT technology where the farmer can view the data from his smart phone.

3.3 Forced air heating systems

ASHRAE (2021) described an air heating system as a thermodynamic system that converts primary energy into heat energy and transfer of heat energy to air occurs when air gets in contact with the heat emitting surface. The objective is to generate heat, supply and maintain a desired indoor temperature by striking the balance between heat generation and heat losses. The heat losses fundamentally occur through conduction, convection, radiation, infiltration, and ventilation process.

3.3.1 *Direct-fired air heaters*

Montaser *et al*., (2021) explained that, the sequence of operation of the direct-fired air heater involves supply of fuel into the burner through a fuel delivery system especially a horse pipe and a control valve if Liquid Petroleum Gas is the source of fuel. An ignition device is used to initiate combustion process. A blower forces ambient air longitudinally through the combustion chamber where heat is produced. Heat generated from combustion is transferred in to the moving air stream and because of the ability of air to absorb heat, its temperature raises. The heated air and the combustion products mixture is discharged into the brooding house. A thermostat or electronic controller controls the burning operation to adjust the temperature to the desired range. Because the heated air is not passed through a heat exchanger, thermal losses are minimal and this allows direct-fired heaters to attain combustion efficiency close to 100% measured in terms of the sensible heat delivered in to the space.

3.3.2 *Indirect-fired air heaters*

The working principle of indirect heating system follows a chronological sequence where fuel burns inside a well-designed combustion chamber and high-temperature gases is allowed to pass through the heat exchanger. A blower sucks fresh air and forces it across the outer surface of the heat exchanger that has gained heat, and as a result, the stream of air getting in contact with the wall of the heat exchanger absorbs heat. Only clean hot air enters the brooding house while combustion gases exit through the exhaust chimney. The fact that combustion gases do not mix with the heated air, the concentration of carbon monoxide and nitrogen oxides inside the production room are greatly minimized. For large scale brooding operation, indirect-fired heaters are highly preferred because

good air quality is a priority, in spite of their high initial investment and operational cost (Lienhard, 2001).

3.3.3 *Electric hot-air generators*

According to Lee (2010), the working principle of an electric hot-air follows the three chronological processes which are; conversion of electrical energy into heat using a resistant heating element, heat transfer to the fluid and heat distribution within the brooding chamber. The heat generated by the heating element increases the temperature of the air that passes across its hot surface. A blower aids the flow of air across the heating element's surface and distribution into the brooding chamber. In summary, the overall process involves the electrical energy conversion, heat transfer to the air and heat distribution.

Electric air heating systems can easily be integrated with electronic controllers, solid-state relays for on and off switching, digital temperature sensors, and affordable microcontrollers. This has elevated the rate of adoption of electric air heating systems in the current precision livestock practices. This integration enables effective temperature regulation through intermittent heating schedules, remote monitoring with IoT technology, and efficient energy utilization. These contributes to the ease of operation of brooding system while lowering the production costs (Yang *et al*., 2022).

3.4 Construction of forced air heating systems for poultry brooding

3.4.1 *Fabrication process*

Fabrication generally involves the measurement, marking, cutting and joining the metal component of the construction by welding, a common metal joining technique based on the engineering drawings. During measurements, allowances are considered to cater for bends, seams, and flanges. Cutting involves sheet metal portioning in to required sizes using guillotine shears, plasma cutters, angle grinders, Computer Numerical Control laser cutters. Accurate cutting minimizes misalignment of parts during assembly and material wastage. Forming where the cut metal sheets are folded with the help of a press brake or manual folding machine to come up with the required profile is another element of fabrication (Bruce, 2015). A summary of common fabrication defects is presented on table 4.

A metal plate is rolled using a slip roller to form a circular duct or a hollow section. Joining the sections are performed with the help of lock seams, rivets, spot welding, Metal Inert Gas welding and or flanged connections with bolts. The heated air passage's joints should be sealed with heat-resistant materials like sealants or gaskets to prevent air leakages. After the completion of fabrication process, the components should undergo surface finishing in order to improve on the physical appearance. This involves grinding weld beads, removing burrs, restructuring indentations, sandblasting or wire brushing, applying high temperature primer, degreasing, applying heat-resistant paint. Surface finishing prevents corrosion by rust hence prolonged service life, especially in humid environments for instance poultry keeping environment where ammonia that accelerates metal deterioration is generated (Bruce, 2015).

Table 4: Common fabrication defects and preventive measures

Defect	Possible Cause	Recommended Solution
Air leakage	Incomplete welding	Continuous seam welding and leak testing
Chamber distortion	Excessive welding heat	Balanced welding sequence and controlled heat input
Corrosion	Inadequate surface protection	Apply high-temperature anti-corrosion coatings
Poor airflow distribution	Improper chamber geometry	Incorporate diffusers and optimize internal layout
Excessive heat loss	Insufficient insulation	Increase insulation thickness and seal gaps
Heating element contact with metal	Improper mounting	Use ceramic insulators and maintain adequate clearances

Source; (Kalpakjian & Schmid, 2020; Callister & Rethwisch, 2020)

3.4.2 *Insulation*

In an explanation made by Kan *et al*., (2023), heat losses from ducts or heat chamber materials reduces the quantity of heat that is supposed to reach the intended end point in a system hence lowering the operating efficiency of the system therefore, insulation is greatly important. Insulation is equally important where heat ducts or heat chamber is exposed to the workers or can easily be reached by workers. The insulation materials such as glass wool, mineral wool, rock wool, ceramic fibre blankets possess high thermal resistant property that allows for efficient heat retention.

Heat losses can also occur due to air leakages which as well decreases system efficiency by limiting the volume of hot air required in system. The major leakage points include flanged joints, access panels, sensor positions. The prevention of leakage can be achieved by applying heat-resistant silicone sealants for example shellac, using compressible gasket papers, uniform torque bolt tightening, regular joints inspection during operation. Adhering to this construction measures improve the system's performance efficiency at a reduced rate of energy consumption. The process of thermal insulation requires that insulators be placed all-round the heat chamber. It's very vital to adhere to the procedures of insulation for instance, ceramic fibre blankets are supposed to be wrapped around the chamber followed by the outer protective casing. An air gap between the insulation and outer protective housing may further minimize heat loss through conduction (Kan *et al*., 2023).

3.4.3 *Materials selection*

Material selection is one of the most crucial factors to be considered during the construction of an air heating system. Poor material selection often results in to rapid corrosion, heat loss, structural deformation, electrical hazards, and increase in maintenance costs. When carrying out material selection, Callister & Rethwisch, (2020) mentioned that it should base on a number of properties such as mechanical strength, thermal properties, corrosion resistance, manufacturability, availability, and cost. The fact that different components require materials of different engineering properties, the material to be used for a particular component should possess those properties that makes it suite the intended purpose for instance, mild steel is basically fit for the fabrication of heat chamber due to its high mechanical strength, good weldability, excellent machinability, low cost and ubiquitous with a thermal conductivity of roughly 50 W/m·K and this is the reason it permits moderate heat transfer as it maintains sufficient structural integrity to achieve the design purpose.

However, mild steel deteriorates quickly in ammonia generated environment because in poultry brooding, ammonia released as a result of litter decomposition, increases the humid condition of the chamber. Thus, protective coatings such as high-temperature resistant and moisture proof paint or powder coating should be applied. Application should be on points such as heat chamber casing, structural frame, support brackets, mounting plates. In a situation where corrosion is to be avoided without preventive measures, stainless steel material is supposed to be used. Stainless steel grades which include AISI 304, AISI 316 provide outstanding resistance against moisture, ammonia, oxidation, high temperatures. Stainless steel enables the system the work for a long period of time without corroding although it's a somewhat costly material. It is therefore recommended for the interior layer of the heat chamber, outside surfaces that gets exposed to moisture or air (Kalpakjian & Schmid, 2020).

Aluminum is another alternative material that can be used in the construction of air heating systems. It offers numerous advantages lightweight that makes it easily lifted, exceptional thermal conductivity of approximately 205 W/m·K, possesses best corrosion resistance property, provide ease of molding to any required shape. The truth of the matter is that, aluminum transfers heat easily which makes it best fit heat exchanger fins construction, protective covers, heat sinks, sensor mounting brackets. However, aluminum loses mechanical strength at temperatures above 200°C as such, it should not be used as an inner material directly around the heating coils (Callister & Rethwisch, 2020).

3.5 Computational Fluid Dynamics (CFD) application in air heating systems for poultry brooding

Bhatti *et al*., (2020) highlighted that Computational Fluid Dynamics is distinct from conventional design approach that rely solely on empirical equations and experimental testing. CFD lowers development costs, minimizes design errors, and improves thermal system design by letting designers analyze the general operating conditions of the system with the aid of a computer-based simulation. Several CFD softwares have been developed which includes; ANSYS Fluent, OpenFOAM, COMSOL Multiphysics, and STAR-CCM+ and have rapidly gained popularity. Engineers currently are able to examine how heat element orientation, blower capacity, duct configuration, insulation materials, and ventilators impact the thermal condition inside the brooding chamber ahead of the physical prototype construction.

3.5.1 *Airflow simulation*

Muktiarni *et al*., (2024) explained that, air flow velocity analysis presents one of the applications of CFD. Velocity contour maps illustrate the variation in air velocity across the entire system's network. CFD in this case displays velocity contour maps with different colours representing airflow speed variation at various points within the brooding house. The major illustrations produced by the contours are; horizontal velocity distribution, vertical airflow profile, duct exit velocity, floor-level velocity, recirculation zones. CFD therefore informs the designer's decision on the operation to be optimized e.g. fan speed, duct diameter, dispenser design so as to uniformize the velocity pattern without draft formation throughout the brooding chamber (Szpicer *et al*., 2025). Coradi *et al*., (2016) employed CFD to simulate the air flow velocity in the poultry house and the air distribution within the poultry brooding chamber, achieved using an air blower was somewhat even as seen in figure 1. The air velocity as per the simulation was found to be within the range of 0.6m/s – 0.8m/s and this range was maintained within the poultry brooding chamber. The heating of air was achieved by blowing air through a firewood furnace. This demonstrates the direct-fired forced-air heating system.

Source: Coradi et al. (2016)

Figure 1: Hot air velocity distribution pattern within the brooding chamber

3.5.2 *Heat distribution*

CFD software equally generates temperature contours that brings a clear understanding on the extent of thermal gradients whereby hot spots and cold spots can easily be identified. Temperature contour plots are therefore useful in a sense that, they differentiate regions of varying temperatures by displaying colour corresponding to the temperatures at that point (Krishnaswamy *et al*., 2020). Tehinse *et al*., (2020) applied AYSNS-CFX software package from CFD to analyse the heat distribution within the poultry brooding chamber and the CFD profile show sections of the chamber with varying temperatures such as 41° C, 38° C, 35° C, 32° C and 29°C. The temperature profile in the building decreases along the left side as seen on the simulation figure 2 except for the control experiment where the temperature profile is determined by the ambient condition of the environment. Heating element powered by photovoltaic system was used to heat the flowing air which demonstrated the electric air heating system.

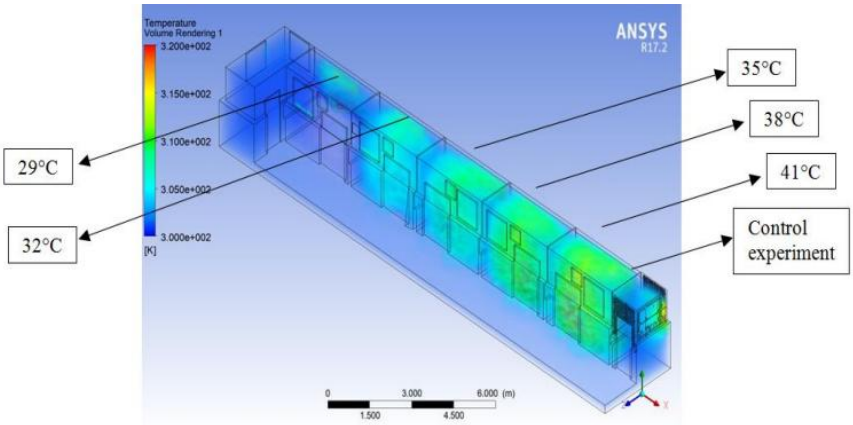

Source: Tehinse et al. (2020)

Figure 2: Temperature distribution inside the poultry brooding chamber in three dimensions

3.5.3 *Research gaps and future direction in air heating systems*

Current research on forced air heating system has focused mostly on experimental studies that are carried out under controlled laboratory conditions, with limited evidence of efficient operation in environments associated with fluctuating ambient temperatures and different atmospheric conditions therefore, future study should consider conducting field tests to ascertain the performance efficiency of this heat generation method to be confident about its sustainability and economic viability for commercial operation. A suitable experimental design should involve at least two comparable brooding houses, with one representing a conventional heating method as the control and the other equipped with the innovated forced-air heating system. Where resources permit, a randomized block

design involving three or more brooding units with at least three replications would provide stronger statistical evidence. Field experiments should be closely monitored for a period of four weeks right from the time chicks have been introduced but also depending on the breed of the chicken for example brooding broiler takes at most four weeks. The monitoring is to make sure all the brooding parameters are within the recommended range otherwise an action should be taken. Measurements should include temperatures within the brooding zone, relative humidity, air velocity, energy consumption. Biological indicators should include body weight gain, feed intake, feed conversion ratio, mortality rate. These are the parameters that enables the performance of the heating systems to be evaluated and compared.

4 CONCLUSION

This review involved exploration of several sources of information and identified numerous aspects of poultry brooding requirements and forced-air methods of heat generation with emphasis on ascertaining the conditions necessary for brooding and several technical requirements for efficient operation of the forced air method of heat generation for poultry brooding. The study demonstrated several brooding requirements which are vital during the brooding period such as temperature, relative humidity, air velocity, ventilation which must be properly managed because they determine the performance of the flock.

In the construction of forced air heating system, material's selection should consider ease of fabrication, corrosion resistance, available and affordable. Similarly, proper insulation and sealing of leakage points is necessary to minimize heat losses and air pressure losses respectively. Vibration control must be ensured to prevent the creation of lines of weakness on the system's components and to guarantee the overall durability of the system. Therefore, construction workmanship must be ensured in order to realize the very best out of the construction.

Electric forced-air heating system is strongly compatible with microcontrollers such as Arduino, fuzzy logic, raspberry pi which are basically the commonest automation systems, unlike the direct-fired and indirect-fired forced air heating systems which requires continuous fuel flow for constant heat generation. More advanced systems can combine microcontrollers with IoT intelligent system for remote monitoring of the system's performance where if a particular system is malfunctioning, an alert can be sent to the concern person for a quick response to rectify the system.

The study however identified some existing research gap especially on aspect of experimental test. No evidence of publication involving experimental studies carried out in the field which is characterized by fluctuating environmental conditions rather only conducted under controlled laboratory conditions. The review has significant contributions to knowledge based on the fact that it provides valuable technical information for researchers, engineers, equipment manufacturers, and poultry farming practitioners to utilize so as to inform their decisions in order to arrive at the next-generation of air heating systems for a precise poultry brooding.

ACKNOWLEDGEMENTS

I sincerely express my profound gratitude to my supervisors; Engr. Dr. S. E. Adebayo and Professor C.O. Alenoghena and all other lecturers for their wonderful guidance, encouragement, constructive suggestions and continuous support throughout the compilation of this review paper. Their professional insight and mentorship greatly contributed to the success of this work. A wonderful gratitude goes to Homegrown Clean Energy Solutions (HCE) team for sponsoring my Master's studies at Federal University of Technology, Minna. Finally, I appreciate my friends and colleagues who shared brilliant ideas, meaningful discussions and welfare support.

5 REFERENCES

ASHRAE. (2021). ASHRAE Handbook—HVAC Applications. American Society of Heating, Refrigerating and Air-Conditioning Engineers (ASHRAE).

Bekele, G. (2021). Review on the Effect of Heat Stress on Poultry Production and Productivities. Food Science & Nutrition Technology, 6(2), 1–9. https://doi.org/10.23880/fsnt-16000260

Bhatti, M. M., Marin, M., Zeeshan, A., & Abdelsalam, S. I. (2020). Editorial: Recent Trends in Computational Fluid Dynamics. In Frontiers in Physics (Vol. 8). Frontiers Media SA. https://doi.org/10.3389/fphy.2020.593111

Bruce J. Black. (2015). Workshop Processes, Practices and Materials, 5th Edition.

Callister, W. D., & Rethwisch, D. G. (2020). Materials Science and Engineering: An Introduction. (10th ed.). John Wiley & Sons.

Çengel, Y. A., & Ghajar, A. J. (2020). Heat and Mass Transfer: Fundamentals and Applications. McGraw-Hill. (6th ed.).

Collin, A., Loyau, T., Bedrani, L., Berri, C., Metayer-Coustard, S., Praud, C., Jacques Duclos, M. M., Tesseraud, S., Rideau, N., & Metayer-, S. (2020). Adaptive response of chickens to hot environments induced by changing incubation temperature. https://hal.inrae.fr/hal-02749854v1

Coradi, P. C., Martins, M. A., Da Costa, D. R., Vigoderis, R. B., & Tinôco, I. D. F. F. (2016). Computational fluid dynamics (CFD) simulating heated air from wood burning inside a poultries barn. Engenharia Agricola, 36(5), 768–778. https://doi.org/10.1590/1809-4430-eng.agric.v36n5p768-778/2016

Ezema, L. S., Ifediora, E. C., Olukunle, A. A., & Onuekwusi, N. C. (2021). Design and Implementation of an Esp32-Based Smart Embedded Industrial Poultry Farm. European Journal of Engineering and Technology Research, 6(3), 38–43. https://doi.org/10.24018/ejers.2021.6.3.2397

Kalpakjian, S., & Schmid, S. R. (2020). Manufacturing Engineering and Technology Pearson. (8th ed.).

Kalu. P. N, Ihemere CN, Eke GK, & Okata UE. (2023). Experimental Design of a Microcontroller-Based Temperature Monitoring and Control System for Broiler Brooder. Vol. 1. www.naujcve.com. Nnamdi Azikiwe University Journal of Civil Engineering.

Kan, A., Chen, Z., Wang, M., Zhang, J., Ma, R., & Lou, K. (2023). Research Status and Development Trend of Thermal Insulation Envelope Materials for Marine Reefer Containers. In ES Energy and Environment (Vol. 22). Engineered Science Publisher. https://doi.org/10.30919/esee1033

Klotz, D. F., Ribeiro, R., Enembreck, F., Denardin, G., Barbosa, M., Casanova, D., & Teixeira, M. (2020). Intelligent action planning for smart poultry houses using computational intelligence. Computers and Electronics in Agriculture.

Krishnaswamy, H., Muthukrishnan, S., Thanikodi, S., Arockiaraj, G. A., & Venkatraman, V. (2020). Investigation of air conditioning temperature variation by modifying the structure of passenger car using computational fluid dynamics. Thermal Science, 24(1PartB), 495–498. https://doi.org/10.2298/TSCI190409397K

Lee, HoSung. (2010). Thermal design : heat sinks, thermoelectrics, heat pipes, compact heat exchangers, and solar cells. Wiley.

Liang, Y., Janorschke, M., & Hayes, C. E. (2022). Low-Cost Solar Collectors to Pre-Heat Ventilation Air in Broiler Houses. Energies, 15(4). https://doi.org/10.3390/en15041468

Lienhard, J. H. . (2001). A heat transfer textbook (3rd ed.). Phlogiston Press.

Mohamed GHONAME, T. F. (2015). IMPROVING PERFORMANCE OF FORCED - AIR HEATING SYSTEM IN BROILER HOUSE. www.managusamv.ro

Montaser.M., Mohamad. R., Sumsun.M., Keith.P., & Abdul-Ghani.O. (2021). The impacts of different heating systems on the environment: A review. Science of the Total Environment .

Muktiarni, M., Rahayu, N. I., Nurhayati, A., Bachari, A. D., & Ismail, A. (2024). Concept of Computational Fluid Dynamics Design and Analysis Tool for Food Industry: A Bibliometric. CFD Letters, 16(2), 1–23. https://doi.org/10.37934/cfdl.16.2.123

Mutibvu, T., Chimonyo, M., & Halimani, T. (2021). Poultry production under environmental stress conditions: implications for management. Animals, 11.

Okonkwo, W. I., Ohagwu, C. J., Ojike, O., Ezenne, G. I., Olayinka, K. E., & Onyechi, A. U. (2022). Socio-Economic Importance of Solar Energy Application in Poultry Production System. Journal of Scientific Research and Reports, 112–126. https://doi.org/10.9734/jsrr/2022/v28i111708

Okonkwo Wilfred Ifeanyi, Willington Emeka, O., & Paul Ugwu. (2025). GSAR Journal of Agriculture and Veterinary Sciences ISSN: 3048-9075 (Online) GSAR Journal of Agriculture and Veterinary Sciences DEVELOPMENT OF A MICRO-PHYSICAL ELEMENTS MONITORING DEVICE FOR A TROMBE WALL SOLAR ENERGY POULTRY BROODING HOUSE. https://gsarpublishers.com/journal-gjavs-home/

Olalekan Idowu, P., Adegbola, O. A., Solomon, I. D., Adeagbo, M. A., & Ojo, J. A. (2021). Design and Implementation of Smart-Controlled Poultry Farm Management System. In International Journal of Enhanced Research in Science (Vol. 10).

Onagbesan, O. M., Uyanga, V. A., Oke, O. E., & Tona, K. T. (2023). Alleviating heat stress effects in poultry: Updates on methods and mechanisms of actions. Frontiers in Veterinary Science, 10, 1255520.

Sarai, K., Jeet, S., & Marg, S. (2023). INDIAN SOCIETY FOR TECHNICAL EDUCATION THE INDIAN JOURNAL OF TECHNICAL EDUCATION. 46.

Szpicer, A., Bińkowska, W., Stelmasiak, A., Wojtasik-Kalinowska, I., Czajkowska, A., Mierzejewska, S., Domiszewski, Z., Rydzkowski, T., Piepiórka-Stepuk, J., & Półtorak, A. (2025). Advances in Computational Fluid Dynamics of Mechanical Processes in Food Engineering: Mixing, Extrusion, Drying, and Process Optimization. In Applied Sciences (Switzerland) (Vol. 15, Number 15). Multidisciplinary Digital Publishing Institute (MDPI). https://doi.org/10.3390/app15158752

Tehinse, T. O., Falayi, F. R., Aduewa, T. O., Alatise, M. O., & Osho, B. I. (2020). Analysis of Thermally Controlled Poultry Housing Using CFD. Journal of Engineering Research and Reports, 40–48. https://doi.org/10.9734/jerr/2020/v10i317042

Yang, D., Huo, Y., Zhang, Q., Xie, J., & Yang, Z. (2022). Recent advances on air heating system of cabin for pure electric vehicles: A review. In Heliyon (Vol. 8, Number 10). Elsevier Ltd. https://doi.org/10.1016/j.heliyon.2022.e11032

Zhang, L., Ma, J., Khadka, A., Zhang, L., Ma, J. L., & Khadka, A. (2024). Journal of Intelligent Systems and Control Adaptive Environmental Control System for Large-Scale Poultry Houses Based on Multif-LSTM "Adaptive environmental control system for large-scale poultry houses based on Multif-LSTM. J. Intell Syst. Control, 3(3), 174–185. https://doi.org/10.56578/jisc030

BIOELECTRICITY GENERATION AND NUTRIENT REMOVAL FROM LANDFILL LEACHATE USING DOUBLE-CHAMBER MICROBIAL FUEL CELLS

Aliyu Ishaq[1], Ismail Shafiu Nuhu[2,*], Shamsuddeen Jumande Muhammad[1], Jamila Baba Ali[3], Kehinde Adeagbo[1]

[1]*Department of Water Resources Faculty of Engineering, Ahmadu Bello University*
[2]*Department of Civil Engineering, Federal Polytechnic Daura Katsina State*
[3]*Department of Polymer and Textile Engineering, Ahmadu Bello University, Zaria, Nigeria*

Email: aishaq@abu.edu.ng, ismailshafiubomo@gmail.com*, shamob@gmail.com, jamilahbabaali@gmail.com, adekennybrr@ymail.com

***Corresponding author**: Ismail Shafiu Nuhu

DOI: https://doi.org/10.67203/sp.ICESID.2026

ABSTRACT

wastewater treatment. This study investigated the use of a double-chamber microbial fuel cell (MFC) to simultaneously remove organic matter and nitrogen from landfill leachate while recovering bioelectricity. Raw leachate from Simpang Renggam landfill, Malaysia, was treated in six inoculated MFCs and an uninoculated control under fed-batch conditions.

During biofilm development, the best reactor achieved 80.10 ± 0.5% COD removal, with 68.12% NH_4-N removal and 58.76% total nitrogen removal. Power generation increased as NH_4-N concentration increased, reaching an optimum at approximately 800 mg/L, after which power density declined, indicating ammonium inhibition of electroactive microorganisms. Nitrogen removal occurred through multiple biological pathways, including a measurable contribution from anammox. The leachate salinity of 5.58 ppt did not appear to be a major independent limitation. the study demonstrates that MFCs can effectively combine landfill-leachate treatment with energy recovery, but maintaining NH_4-N below the identified inhibitory range is important for stable MFC performance.

Keywords: *Microbial fuel cell; Landfill leachate; Ammonium nitrogen inhibition; Anammox; Bioelectricity generation*

1. INTRODUCTION

Landfill leachate contains high levels of organic matter, ammonium, heavy metals, and salts, with mature leachate often having higher ammonium and more resistant organic compounds (Gokgoz et al., 2023). Conventional treatment can be limited by ammonia, salinity, low C/N ratios, and toxic substances, while MFCs can simultaneously remove pollutants and generate electricity (Hassan et al., 2018). However, excessive NH_4-N can inhibit microorganisms and reduce treatment and power generation, with nitrogen removal occurring through pathways such as nitrification, denitrification, anammox, and membrane transport (Hassan et al., 2018; Hiegemann et al., 2018; Zhang et al., 2014). In Nigeria, inadequate waste-management infrastructure and poorly engineered dumpsites increase the risk of leachate contamination of soil and groundwater (Ishaq et al., 2022). MFCs therefore offer potential as a low-cost, decentralized treatment technology, although the NH_4-N inhibition threshold remains insufficiently defined (Ishaq et al., 2023). This study evaluates a double-chamber MFC treating raw landfill leachate, focusing on biofilm development, COD, NH_4-N and TN removal, Coulombic efficiency, and the NH_4-N concentration that inhibits power generation and treatment performance, with the goal of establishing an appropriate operating range for simultaneous leachate treatment and electricity recovery.

2. MATERIALS AND METHODS

2.1 Description of the Study Area and Leachate Sampling

The Simpang Renggam landfill in the Kluang district of Johor, Malaysia, was the source of the leachate used in this study. The site lies approximately two kilometres from the town centre and occupies 14.82 acres, at coordinates 1°53'41" N, 103°22'35" E (Figure 1). The landfill has received approximately 400–500 tonnes of wet solid waste daily for 12 years from Simpang Renggam, Batu Pahat, and Kluang. Its aerated lagoon leachate-treatment system has been inadequate, with previous investigations reporting adverse impacts on a nearby river used by the local community for drinking water, highlighting the urgent need for effective leachate treatment.

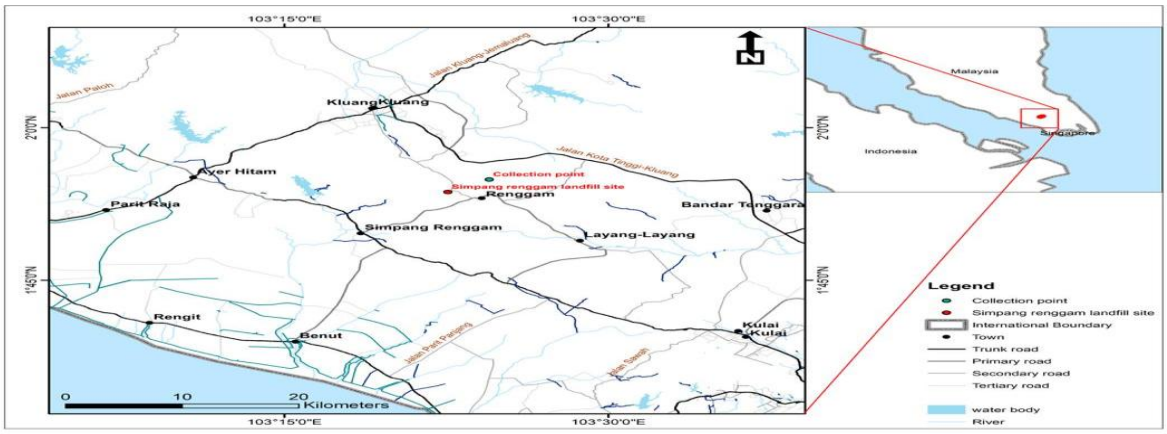

Figure 1: Location of the Simpang Renggam landfill and leachate collection point, Johor, Malaysia.

2.2 MFC Configuration and Operation Mode

H-type dual-chamber MFCs were constructed using modified designs from Nor et al. (2015) and Hassan et al. (2018). Each Plexiglas reactor consisted of separate 125-mL anode and cathode chambers with a 100-mL working volume, carbon-felt electrodes, and a Nafion 117 proton-exchange membrane separating the chambers. The Nafion membrane was pre-treated by sequential soaking in 0.1 M H_2SO_4 and 0.1 M H_2O_2 for 60 minutes at 60 °C, followed by rinsing with deionized water, following Bakhshian et al. (2011).

2.4 Pre-treatment of Anode and Cathode Materials

Electrode assemblies were submerged in 5% ethanol (C6H6O) for 10 minutes to prevent contamination, rinsed thoroughly with distilled water, and exposed to UV light for 15 minutes (Hassan et al., 2018; Nor et al., 2015). To enhance porosity and reduce the influence of surface impurities, the anode and cathode were then submerged in acetone for 24 hours, rinsed with deionised water, and air-dried overnight (Özkaya et al., 2013).

2.5 MFC Reactor Set-up and Operation

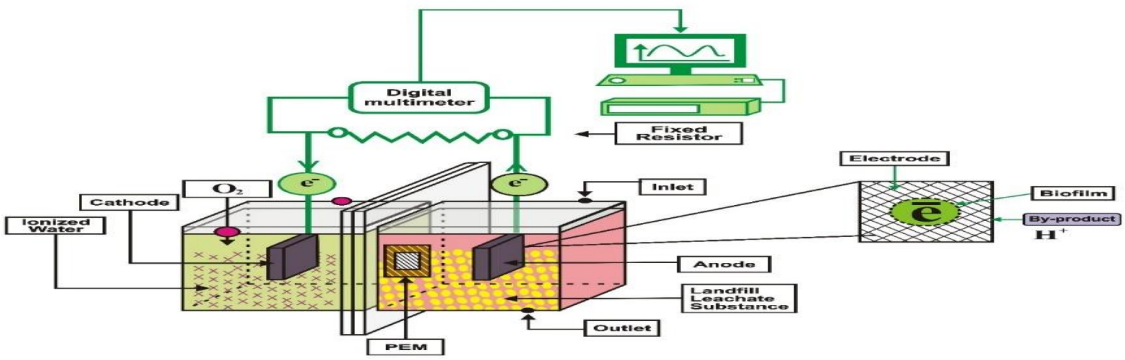

Figure 2: Schematic layout of the double-chamber MFC reactor used in this study.

The MFC reactors were sealed and equipped with sampling ports, while the electrodes were cleaned and connected using copper wires. The anode chambers were nitrogen-purged to maintain anaerobic conditions and filled with raw landfill leachate (Jagaba et al., 2021). A 1 kΩ external resistor was used, and voltage was monitored every 30 seconds with a LabJack U3-HV multimeter. The cathode chambers contained distilled water and were continuously aerated for 24 hours to provide oxygen and mixing.

2.6 Leachate Characterization

Prior to use as MFC substrate, the physicochemical quality of the raw leachate was characterized, including BOD, COD, BOD_5/COD ratio, NH_4-N, turbidity, pH, temperature, conductivity, nitrate and nitrite nitrogen, and salinity. The measured characteristics are summarized in Table 1.

Table 1: Physicochemical characteristics of the landfill leachate used as MFC substrate.

Parameter	Unit	Concentration
Biochemical oxygen demand (BOD)	mg/L	112 ± 7
Chemical oxygen demand (COD)	mg/L	1322.5 ± 5
BOD_5/COD ratio	–	0.0845 ± 0.0014
Ammonium nitrogen (NH_4-N)	mg/L	411 ± 6
Turbidity	NTU	134.95 ± 8
pH	–	6.88 ± 0.3
Temperature	°C	30 ± 2.5
Conductivity	µS/cm	107 746 ± 7.4
Nitrate nitrogen (NO_3-N)	mg/L	70 ± 5.5
Nitrite nitrogen (NO_2-N)	mg/L	110 ± 8.5
Salinity	Ppt	5.58

2.7 Biofilm Development for MFC Enrichment

The experiment involved three phases, starting with a 62-day acclimatization period for seven MFC reactors, including 14 days under open-circuit conditions. Raw leachate was continuously supplied without pH adjustment, dilution, or nutrient supplementation, while a 1 kΩ resistor was used during closed-circuit operation. Ammonium-oxidizing microorganisms were enriched using ammonium sulphate and sodium nitrite at an NH_4-N:NO_2-N ratio of 1:1.32 (Hassan et al., 2018), with 10% (v/v) anaerobic sludge inoculum added to each reactor (Damiano et al., 2014). Reactors were maintained at 27–30 °C and near-neutral pH until stable voltage production indicated successful acclimatization.

2.8 Ammonium Nitrogen (NH_4-N) Inhibition Study.

After acclimatization, the MFCs were operated under controlled conditions using a one-factor-at-a-time (OFAT) design to evaluate NH_4-N inhibition of electricity generation. NH_4-N concentrations were adjusted to 600–1600 mg/L using NH_4Cl, while COD was maintained at approximately 1327 mg/L. The initial pH was adjusted to 6.88 when necessary but was not continuously controlled, with only modest variation (6.88 ± 0.3) during batch cycles. Power density was measured at each NH_4-N concentration to identify the concentration at which MFC performance began to decline.

3. RESULTS AND DISCUSSION.

3.1 Physicochemical Characteristics of the Landfill Leachate

The leachate had moderate salinity (5.58 ppt), which was suitable for MFC operation and could enhance conductivity and reduce internal resistance (Gokgoz et al., 2023; Kumar et al., 2020). However, excessive salinity combined with high ammonia may inhibit electroactive microorganisms through osmotic stress, membrane disruption, and enzyme interference. the moderate salinity, near-neutral pH, high conductivity, and substantial ammonium and organic content provided suitable baseline conditions for evaluating biofilm development and ammonia inhibition in the MFCs

3.2 Power Generation and Treatment Performance during Biofilm Development

During the 48-day acclimatization period, COD and NH_4-N removal progressively increased across operating cycles, indicating successful microbial growth and biofilm development. The improvement was attributed to the enrichment of electrogenic bacteria, organic-matter-oxidizing microorganisms, and anammox-related populations on the anodes. Table 2 presents the MFC performance during biofilm development across the operational cycles, with each cycle consisting of two batch operations.

MFC	Cycle	Operating time (d)	CE (%)	Influent COD conc. (mg/L)	COD removal (%)	Influent NH_4-N conc. (mg/L)	NH_4-N removal (%)	TN removal (%)
A	1	0–7	19.08	1327 ± 7.0	26.76 ± 0.5	411 ± 8.5	23.90 ± 0.1	18.21
	2	7–24	15.13	1327 ± 9.5	35.15 ± 0.3	411 ± 7.5	31.68 ± 0.2	28.31
	3	24–36	11.64	1327 ± 8.5	43.74 ± 0.5	411 ± 5.2	39.14 ± 0.1	31.23
	4	36–48	14.33	1327 ± 5.3	47.09 ± 0.5	411 ± 6.5	41.70 ± 0.0	20.54
B	1	0–7	19.76	1327 ± 7.0	32.43 ± 0.3	411 ± 8.5	32.14 ± 0.0	25.01
	2	7–24	13.74	1327 ± 9.5	47.80 ± 0.3	411 ± 7.5	44.85 ± 0.3	35.35
	3	24–36	11.52	1327 ± 8.5	55.64 ± 0.4	411 ± 5.2	51.82 ± 0.1	37.63
	4	36–48	13.88	1327 ± 5.3	59.92 ± 0.5	411 ± 6.5	55.31 ± 0.2	28.71
C	1	0–7	16.09	1327 ± 7.0	62.42 ± 0.3	411 ± 8.5	57.09 ± 0.2	34.41
	2	7–24	13.05	1327 ± 9.5	75.37 ± 0.5	411 ± 7.5	62.79 ± 0.2	45.05
	3	24–36	9.82	1327 ± 8.5	79.99 ± 0.3	411 ± 5.2	64.01 ± 0.1	51.61
	4	36–48	12.04	1327 ± 5.3	80.10 ± 0.5	411 ± 6.5	68.12 ± 0.0	58.76
D	1	0–7	15.55	1327 ± 7.0	52.81 ± 0.4	411 ± 8.5	45.87 ± 0.2	31.09
	2	7–24	12.72	1327 ± 9.5	61.76 ± 0.4	411 ± 7.5	55.33 ± 0.1	17.23
	3	24–36	9.93	1327 ± 8.5	69.29 ± 0.5	411 ± 5.2	58.79 ± 0.1	49.64
	4	36–48	12.31	1327 ± 5.3	69.85 ± 0.4	411 ± 6.5	61.50 ± 0.0	44.45
E	1	0–7	17.14	1327 ± 7.0	51.59 ± 0.5	411 ± 8.5	49.85 ± 0.1	30.12
	2	7–24	13.71	1327 ± 9.5	63.46 ± 0.3	411 ± 7.5	53.87 ± 0.2	50.25
	3	24–36	11.10	1327 ± 8.5	68.41 ± 0.9	411 ± 5.2	59.28 ± 0.1	37.98
	4	36–48	13.56	1327 ± 5.3	71.20 ± 0.2	411 ± 6.5	62.47 ± 0.0	41.43

MFC	Cycle	Operating time (d)	CE (%)	Influent COD conc. (mg/L)	COD removal (%)	Influent NH_4-N conc. (mg/L)	NH_4-N removal (%)	TN removal (%)
F	1	0–7	15.73	1327 ± 7.0	57.56 ± 0.3	411 ± 8.5	50.36 ± 0.1	29.12
	2	7–24	12.46	1327 ± 9.5	69.91 ± 0.5	411 ± 7.5	55.82 ± 0.1	38.34
	3	24–36	9.69	1327 ± 8.5	71.71 ± 0.5	411 ± 5.2	60.36 ± 0.2	47.91
	4	36–48	12.05	1327 ± 5.3	70.20 ± 0.2	411 ± 6.5	64.55 ± 0.3	49.48
Control	1	0–7	18.81	1327 ± 7.0	22.44 ± 0.3	411 ± 8.5	19.7 ± 0.3	12.14
	2	7–24	18.10	1327 ± 9.5	29.59 ± 0.2	411 ± 7.5	24.08 ± 0.2	18.86
	3	24–36	16.56	1327 ± 8.5	32.12 ± 0.2	411 ± 5.2	23.35 ± 0.1	17.27
	4	36–48	16.64	1327 ± 5.3	38.36 ± 0.0	411 ± 6.5	26.76 ± 0.0	21.39

During acclimatization, COD removal increased substantially, reaching 80.10 ± 0.5% in MFC C by cycle 4, compared with 71.71 ± 0.5% in MFC F. However, higher COD removal did not always correspond to higher Coulombic efficiency, indicating that some organic matter may have been removed through non-electrogenic processes such as methanogenesis (Hassan et al., 2018; Oliveira et al., 2013; Cecconet et al., 2018). The uninoculated control showed lower COD removal, confirming the importance of microbial inoculation. NH_4-N removal reached its maximum of 68.12 ± 0.0% in MFC C in cycle 4, with improved performance associated with biofilm growth and maturation. Later declines were likely related to changing substrate conditions, nitrogen loading, and inhibitory or shock effects (Hassan et al., 2019), with membrane transport and mature biofilm activity also contributing to nitrogen removal (Puig et al., 2011; Sehar & Naz, 2016). Biofilm maturation enhanced COD and NH_4-N removal, although treatment stability decreased under changing operating conditions.

3.3 Optimal NH_4-N Concentration and Inhibition of Power Generation

Building on the biofilm-development results, the inhibition study examined how varying influent NH_4-N concentration (600–1600 mg/L, adjusted with NH_4Cl) affected power output under continuous operation at constant COD and pH. Average power densities of the respective MFCs across the tested NH_4-N fractions are presented in Figure 3.

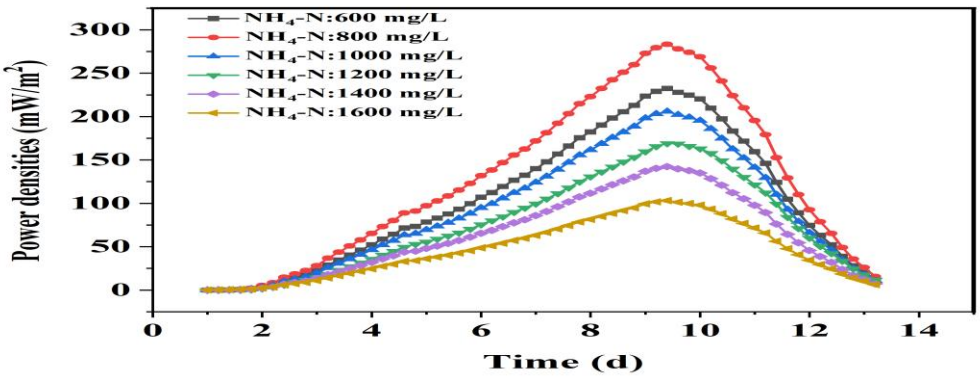

Figure 3: Average power density profiles of the MFCs at different influent NH4-N concentrations (600–1600 mg/L).

During acclimatization, NH_4-N removal was enhanced by cation exchange through the membrane and maturation of the anode biofilm, which improved microbial interactions and electron transfer (Puig et al., 2011; Sehar & Naz, 2016). Power generation increased during the early operating period before declining as substrates became depleted. NH_4-N concentration showed a non-monotonic effect on electricity generation, with maximum power density of 283 mW/m² at 800 mg/L, compared with 233 mW/m² at 600 mg/L. Above 800 mg/L, power density progressively declined to 103 mW/m² at 1600 mg/L. This indicates that moderate NH_4-N concentrations can support microbial activity, whereas higher concentrations cause ammonia toxicity and disrupt microbial and electron-transfer processes (Gu et al., 2021; Hiegemann et al., 2018; Ren et al., 2021). Thus, 800 mg/L was the optimum NH_4-N concentration, while 1600 mg/L caused approximately 64% lower power generation, confirming significant ammonium inhibition

3.4 Nitrogen Species Removal: NH_4-N, NO_2-N, and Total Nitrogen

Nitrogen removal was strongly influenced by influent nitrogen loading. NH_4-N removal increased to about 75% in cycle 2 but declined to 62% by cycle 6 as concentration increased from approximately 600 to 1,640 mg/L. Similar trends occurred for nitrite and TN, with maximum removals of about 74% and 72%, respectively, before declining at higher nitrogen loads. The reduced performance was likely associated with biofilm loading limitations, incomplete nitrogen transformation, nitrification, and anammox-related processes (Wei et al., 2011). Overall, nitrogen removal was highest under moderate loading and decreased with increasing NH_4-N concentrations, indicating the involvement of interacting anammox, nitrification, and nitrite/nitrate transformation pathways, consistent with previous studies (Lu et al., 2020, 2021; Gu et al., 2021; Wei et al., 2011).

Table 3: NH_4-N, NO_2-N, and total nitrogen (TN) removal efficiencies per operating cycle (values derived from Figure 4).

Cycle	NH_4-N removal (%)	NO_2-N removal (%)	TN removal (%)
1	70	68	68
2	75	74	72
3	72	73	69
4	67	71	67
5	64	68	63
6	62	66	61

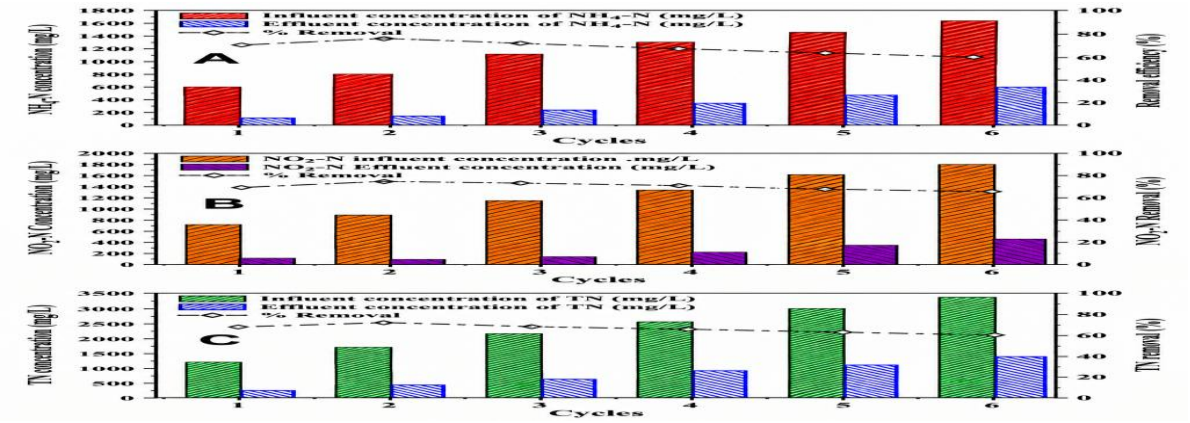

Figure 4: Influent and effluent profiles of (A) NH_4-N, (B) NO_2-N, and (C) total nitrogen (TN), together with the corresponding removal efficiencies (%) across the six operating cycles.

4. CONCLUSION

This study showed that double-chamber MFCs can effectively treat raw landfill leachate while generating electricity. The best reactor achieved 80.10% COD, 68.12% NH_4-N, and 58.76% TN removal, with maximum power density of 283 mW/m² at about 800 mg/L NH_4-N. Higher ammonium concentrations inhibited electricity generation. The findings indicate potential for MFC application in Nigeria, particularly at poorly managed dumpsites where conventional treatment and electricity infrastructure are limited. However, low power output, expensive materials, and scale-up challenges remain major limitations. Pilot studies using Nigerian leachate, low-cost materials, and detailed energy and economic assessments are recommended before full-scale implementation**.**

5. REFERENCES

Albarracin-Arias, J. A., Yu, C. P., Maeda, T., Valdivieso Quintero, W., & Sanchez-Torres, V. (2021). Microbial community dynamics and electricity generation in MFCs inoculated with POME sludges and pure electrogenic culture. International Journal of Hydrogen Energy, 46(74), 36903–36916. https://doi.org/10.1016/j.ijhydene.2021.08.218

American Public Health Association (APHA). (2005). Standard methods for the examination of water and wastewater (21st ed.). APHA-AWWA-WEF.

Bakhshian, S., Kariminia, H. R., & Roshandel, R. (2011). Bioelectricity generation enhancement in a dual chamber microbial fuel cell under cathodic enzyme catalyzed dye decolorization. Bioresource Technology, 102(12), 6761–6765. https://doi.org/10.1016/j.biortech.2011.03.060

Cecconet, D., Molognoni, D., Callegari, A., & Capodaglio, A. G. (2018). Agro-food industry wastewater treatment with microbial fuel cells: Energetic recovery issues. International Journal of Hydrogen Energy, 43(1), 500–511. https://doi.org/10.1016/j.ijhydene.2017.07.231

Chamem, O., Fellner, J., & Zairi, M. (2020). Ammonia inhibition of waste degradation in landfills – A possible consequence of leachate recirculation in arid climates. Waste Management & Research, 38(10), 1078–1086. https://doi.org/10.1177/0734242X20920945

Damiano, L., Jambeck, J. R., & Ringelberg, D. B. (2014). Municipal solid waste landfill leachate treatment and electricity production using microbial fuel cells. Applied Biochemistry and Biotechnology, 173(2), 472–485. https://doi.org/10.1007/s12010-014-0854-x

Ergettie, A. B., & Dagbasi, M. (2021). Impact of wastewater concentration and feed frequency on ammonia inhibition in microbial fuel cells. Biofuels, 12(6), 655–661. https://doi.org/10.1080/17597269.2018.1519760

Gokgoz, M., Zhang, W., Manage, N., Mbengue, M., Bolyard, S., & Chen, J. (2023). Survey on the current leachate treatments of public municipal solid waste landfills and the potential impact of per- and polyfluorinated alkyl substances in the Eastern and Northwestern United States.

Journal of the Air & Waste Management Association, 73(8), 638–648. https://doi.org/10.1080/10962247.2023.2235313

Gu, X., Huang, Y., Hu, Y., Gao, J., & Zhang, M. (2021). Inhibition of nitrite-oxidizing bacteria in automatic recycling PN/ANAMMOX under mainstream conditions. Bioresource Technology, 342, 125935. https://doi.org/10.1016/j.biortech.2021.125935

Gutierrez, J., Kwan, T. A., Zimmerman, J. B., & Peccia, J. (2016). Ammonia inhibition in oleaginous microalgae. Algal Research, 19, 123–127. https://doi.org/10.1016/j.algal.2016.07.016

Hamza (Coppath Hamza), H. M., Duraisamy, P., Periyasamy, S., Pokkiladathu, H., & Muthuchamy, M. (2017). Simultaneous electricity generation and heavy metals reduction from distillery effluent by microbial fuel cell. Indian Journal of Science and Technology, 10(13), 1–13. https://doi.org/10.17485/ijst/2017/v10i13/111203

Hassan, H., Jin, B., Donner, E., Vasileiadis, S., Saint, C., & Dai, S. (2018). Microbial community and bioelectrochemical activities in MFC for degrading phenol and producing electricity: Microbial consortia could make differences. Chemical Engineering Journal, 332, 647–657. https://doi.org/10.1016/j.cej.2017.09.114

Hassan, M. M., Haleem, N., Baig, M. A., & Jamal, Y. (2019). Phytoaccumulation of heavy metals from municipal solid waste leachate using different grasses under hydroponic condition. Asian Journal of Applied Research and Reviews, 3(2), 1–12.

Hiegemann, H., Lübken, M., Schulte, P., Schmelz, K. G., Gredigk-Hoffmann, S., & Wichern, M. (2018). Inhibition of microbial fuel cell operation for municipal wastewater treatment by impact loads of free ammonia in bench- and 45 L-scale. Science of the Total Environment, 624, 34–39. https://doi.org/10.1016/j.scitotenv.2017.12.072

Ishaq, A., Said, M. I. M., Azman, S., Abdulwahab, M. F., & Alfa, M. I. (2022). Impact, mitigation strategies, and future possibilities of Nigerian municipal solid waste leachate management practices: A review. Nigerian Journal of Technological Development, 19(3). https://doi.org/10.63746/njtd.v19i3.875

Ishaq, A., Said, M. I. M., Azman, S. B., Abdulwahab, M. F., & Jagun, Z. T. (2023). Optimizing total ammonia–nitrogen concentration for enhanced microbial fuel cell performance in landfill leachate treatment: A bibliometric analysis and future directions. Environmental Science and Pollution Research. https://doi.org/10.1007/s11356-023-28580

Jagaba, A. H., Kutty, S. R. M., Lawal, I. M., Abubakar, S., Hassan, I., Zubairu, I., Umaru, I., Abdurrasheed, A. S., Adam, A. A., Ghaleb, A. A. S., Almahbashi, N. M. Y., Al-dhawi, B. N. S., & Noor, A. (2021). Sequencing batch reactor technology for landfill leachate treatment: A state-of-the-art review. Journal of Environmental Management, 282, 111946. https://doi.org/10.1016/j.jenvman.2021.111946

Khalil, C. A., Ghanimeh, S., & Medawar, Y. (2017). Ammonia inhibition and recovery potential in anaerobic digesters: A review. Proceedings of the Air and Waste Management Association's Annual Conference and Exhibition (AWMA).

Kumar, S. S., Kumar, V., Gnaneswar Gude, V., Malyan, S. K., & Pugazhendhi, A. (2020). Alkalinity and salinity favor bioelectricity generation potential of Clostridium, Tetrathiobacter and Desulfovibrio consortium in microbial fuel cells (MFC) treating sulfate-laden wastewater. Bioresource Technology, 306, 123110. https://doi.org/10.1016/j.biortech.2020.123110

Lu, H., Yu, Y., Xi, H., Zhou, Y., & Wang, C. (2020). A quick start method for microbial fuel cells. Chemosphere, 259, 127323. https://doi.org/10.1016/j.chemosphere.2020.127323

Lu, N., Li, L., Wang, C., Wang, Z., Wang, Y., Yan, Y., Qu, J., & Guan, J. (2021). Simultaneous enhancement of power generation and chlorophenol degradation in nonmodified microbial fuel cells using an electroactive biofilm carbon felt anode. Science of the Total Environment, 783, 147045. https://doi.org/10.1016/j.scitotenv.2021.147045

Nor, M. H. M., Mubarak, M. F. M., Elmi, H. S. A., Ibrahim, N., Wahab, M. F. A., & Ibrahim, Z. (2015). Bioelectricity generation in microbial fuel cell using natural microflora and isolated

pure culture bacteria from anaerobic palm oil mill effluent sludge. Bioresource Technology, 190, 458–465.

Oliveira, V. B., Simões, M., Melo, L. F., & Pinto, A. M. F. R. (2013). Overview on the developments of microbial fuel cells. Biochemical Engineering Journal, 73, 53–64. https://doi.org/10.1016/j.bej.2013.01.012

Özkaya, B., Cetinkaya, A. Y., Cakmakci, M., Karadağ, D., & Sahinkaya, E. (2013). Electricity generation from young landfill leachate in a microbial fuel cell with a new electrode material. Bioprocess and Biosystems Engineering, 36(4), 399–405. https://doi.org/10.1007/s00449-012-0796-z

Puig, S., Serra, M., Coma, M., Cabré, M., Balaguer, M. D., & Colprim, J. (2011). Microbial fuel cell application in landfill leachate treatment. Journal of Hazardous Materials, 185(2–3), 763–767. https://doi.org/10.1016/j.jhazmat.2010.09.086

Ren, S., Wang, Z., Jiang, H., Qiu, J., Li, X., Zhang, Q., & Peng, Y. (2021). Stable nitritation of mature landfill leachate via in-situ selective inhibition by free nitrous acid. Bioresource Technology, 340, 125647. https://doi.org/10.1016/j.biortech.2021.125647

Sehar, S., & Naz, I. (2016). Role of the biofilms in wastewater treatment. In Microbial Biofilms – Importance and Applications. InTech. https://doi.org/10.5772/63499

Vázquez-Rodríguez, G. A., et al. (2015). [Sludge inoculum source for microbial fuel cell/anaerobic digestion studies; full bibliographic details could not be verified from the source manuscript and should be confirmed by the author.]

Wei, J., Liang, P., & Huang, X. (2011). Recent progress in electrodes for microbial fuel cells. Bioresource Technology, 102(20), 9335–9344. https://doi.org/10.1016/j.biortech.2011.07.019

International Conference on Engineering Innovation for Sustainable Development (ICESID 2026)
Faculty of Engineering, Ahmadu Bello University Zaria · 8–10 September 2026

CONCEPTUAL DESIGN, OPERATIONS, AND THEORETICAL MODELING OF A 1 KW PHYSICAL SCALE PROTOTYPE FOR THE KAINJI HYDROPOWER DAM

Abdurrasheed Said Abdurrasheed[1], Raphael Ejembi[1,*], Mujahid Muhammad Mujahid[1], Aliyu Ishaq[1], Sambo Mohammed Aminu[1], Jamila Baba Ali[1], Williams Ejembi[1], Islam Sajjad Muhammad[1]

[1]*Ahmadu Bello University*

Email: asabdurrasheed@abu.edu.ng, raphaelejemb@gmail.com*, Mmmujahid@gmail.com, aishaq@abu.edu.ng, aminusambo1@gmail.com, jamilahbabaali@gmail.com, williamsejembi@gmail.com, sajjadnislam@gmail.com

***Corresponding author**: Raphael Ejembi

DOI: https://doi.org/10.67203/sp.ICESID.2026

ABSTRACT

Physical scale models serve as vital bridge structures for connecting theoretical fluid dynamics with practical hydroelectric power generation. This paper introduces the design, operational mechanics, and theoretical foundations of the Kainji Hydropower Dam model—a functional physical testbed developed at Ahmadu Bello University, Zaria, in partnership with Mainstream Energy Solutions Limited. Geometrically downscaled at a Froude scale ratio of $1:15$ *to mirror the hydraulic head characteristics of the actual Kainji Dam, the physical installation comprises an elevated impoundment reservoir, high-pressure penstock conduits, flow control gates, and a twin micro-turbine assembly (*2×0.5 kW *units) coupled to a synchronous generator for a total combined output of* 1 kW. *The underlying theory integrates fluid continuity, Bernoulli's energy equations, water column momentum, and electro-mechanical energy conversion. Experimental evaluations across three operating regimes demonstrate a peak electrical power output of* 985.2 W *at an overall system efficiency of* 74.4% *under rated head conditions (*2.80 m, 0.048 m^3/s*). Measured hydraulic power closely matched theoretical Bernoulli predictions within a* 1.66% *variance. Component efficiency breakdowns reveal hydraulic, mechanical, and generator efficiencies of* 88.5%, 91.2%, *and* 92.2% *respectively. Ultimately, this operational model bridges fundamental fluid theory with real-world plant operations, offering an internationally scalable platform for academic research, system optimization, and technical capacity building.*

Keywords: *Kainji Hydropower Dam; Physical Scale Prototype; 1 kW Power Generation; Froude Scaling Law; Electro-Mechanical Conversion; Industry-Academia Collaboration*

1. INTRODUCTION

1.1 Background and Global Context

Hydroelectric energy infrastructure plays an indispensable role in global power generation networks, providing reliable base-load stability and rapid grid dispatch capabilities. Worldwide, the integration of physical testbeds and high-fidelity prototype modeling remains an essential benchmark for investigating complex hydraulic dynamics, optimizing plant dispatch, and verifying theoretical computational models before industrial deployment. In Nigeria, the Kainji Hydropower Dam—situated on the Niger River and operated by Mainstream Energy Solutions Limited (MESL)—represents a critical national generation asset featuring an operational hydraulic head between 24.0 m and 40.0 m and an installed capacity of 760 MW across eight turbine units.

1.2 Problem Statement and Justification

Despite the reliance on computational fluid dynamics (CFD) in modern engineering, physical scale modeling remains irreplaceable for observing free-surface fluid phenomena, transient water

hammer dynamics, and intake turbulence under physical constraint conditions. A persistent disconnect exists between theoretical fluid mechanics formulations presented in academic curricula and the physical multi-variable operational realities of utility-scale hydroelectric power stations. Furthermore, conducting transient load experiments or fault testing on operational full-scale dams such as Kainji is economically and structurally unfeasible.

1.3 Aim and Objectives

To address this gap, an international-standard $1\ \mathrm{kW}$ physical scale prototype of the Kainji Hydropower Dam was conceptualized, constructed, and commissioned at the Faculty of Engineering, Ahmadu Bello University (ABU), Zaria, in direct partnership with MESL. The core objective of this study is to establish the theoretical modeling framework, validate the Froude hydraulic scaling methodology, quantify electro-mechanical losses across three operating flow regimes, and demonstrate system transient stability under step-change resistive loading.

2. METHODOLOGY

2.1 Geometric Scaling and Dynamic Similarity

The physical scale prototype was engineered using Froude similarity scaling criteria, ensuring dynamic and kinematic similarity for gravity-dominated, free-surface flow dynamics. A geometric scale factor (λ_L) of $1:15$ was implemented based on facility space and closed-loop flow circulation constraints.

According to Froude scaling law, the relationship between prototype (Kainji Dam) and physical model parameters is defined as:

$$\lambda_H = \lambda_L = 1:15$$

$$\lambda_Q = \lambda_L^{5/2} = (1/15)^{2.5} \approx 1:871.4$$

$$\lambda_P = \lambda_L^{7/2} = (1/15)^{3.5} \approx 1:13{,}500$$

Table 1 provides an explicit side-by-side comparison between the full-scale Kainji Hydropower Plant baseline metrics and the downscaled experimental physical model parameters at ABU Zaria.

Table 1: *Comparative Scaling Matrix of Prototype Baseline and Downscaled Physical Model Parameters*

Operational Parameter	**Full-Scale Kainji Plant**	**Physical Model (1:15 Scale)**	**Scaling Ratio (λ)**	**Units**
Gross Hydraulic Head (H_{gross})	24.00 – 40.00	1.60 – 2.67 (2.80 Peak)	$\lambda_L = 1:15$	m
Volumetric Discharge (Q) per Unit	350.00	0.040 – 0.048	$\lambda_Q = \lambda_L^{2.5}$	m^3/s
Installed Generation Capacity	760 (100 per unit)	1.00 (2 × 0.5 units)	$\lambda_P = \lambda_L^{3.5}$	MW / kW
Turbine Runner Architecture	8 Units (Kaplan/Propeller)	2 Micro-Turbine Units	—	Units
Hydraulic Flow Loop	Open River System	Closed Recirculating Loop	—	System

2.2 Closed-Loop Physical Layout and Instrumentation

The installation comprises a closed hydraulic loop. Water is drawn from a lower $15\ m^3$ catch basin by a 3.0 kW variable-speed centrifugal pump and delivered into an elevated impoundment reservoir ($12\ m^3$ capacity) featuring an automated overflow weir. The fluid passes through flow control intake gates into twin parallel high-pressure PVC penstocks ($D = 0.15$ m, $L = 4.5$ m), driving a twin micro-turbine assembly (2×0.5 kW units) coupled to a synchronous generator rated at 1.0 kW continuous output.

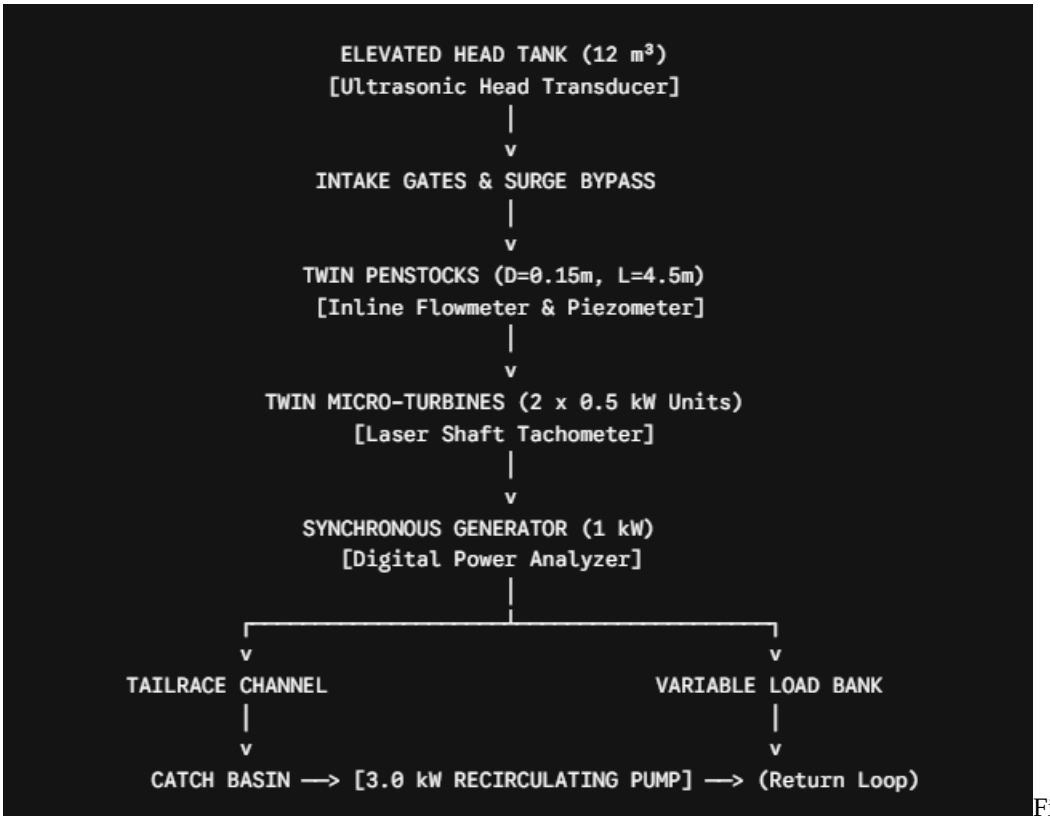

Figure 1: *Schematic Diagram of the Closed-Loop 1 kW Hydropower Prototype Facility Detailing Recirculation Loop, Sub-Systems, and Instrumentation Points.*

Experimental measurement accuracy was achieved using calibrated sensors:

1. **Flow Rate (Q):** Ultrasonic inline flowmeter (accuracy $\pm 0.5\%$).
2. **Net Head (H_{net}):** Digital piezometric pressure transducers (accuracy $\pm 0.25\%$ FS).
3. **Electrical Output (P_e):** Precision 3-phase digital power analyzer (accuracy $\pm 0.2\%$).
4. **Rotational Speed (N):** Non-contact optical laser tachometer (accuracy ± 0.1 rpm).

All measurements were conducted across five ($n = 5$) repeated experimental trials per flow regime, yielding a cumulative combined uncertainty margin of $\pm 1.85\%$.

2.3 Mathematical Formulations

Theoretical hydraulic power (P_h) available at the turbine inlet is computed via:

$$P_h = \rho \cdot g \cdot Q \cdot H_{net} \quad \text{--- (1)}$$

where $\rho = 1000$ kg/m^3, $g = 9.81$ m/s^2, Q is flow rate (m^3/s), and H_{net} is net head (m). Penstock head loss (H_L) is modeled using the Darcy-Weisbach and minor loss formulations:

$$H_L = \left(f\frac{L}{D} + \sum K_L\right)\frac{v^2}{2g} \quad \text{--- (2)}$$

where $f = 0.018$, $L = 4.5$ m, $D = 0.15$ m, and $\sum K_L = 1.2$ accounts for gate and bend loss coefficients.

The continuous electrical power output (P_e) across the load bank is:

$$P_e = V \cdot I \cdot \cos\phi \quad \text{--- (3)}$$

Overall conversion efficiency ($\eta_{overall}$) is resolved into component efficiency fractions:

$$\eta_{overall} = \frac{P_e}{P_h} = \eta_h \cdot \eta_m \cdot \eta_g \quad \text{--- (4)}$$

where η_h is hydraulic efficiency, η_m is mechanical shaft efficiency, and η_g is generator electro-magnetic efficiency.

3. RESULTS AND DISCUSSION

3.1 Flow Regimes and Empirical Performance

Experimental performance was evaluated across three distinct operational flow regimes: Low Head (2.10 m), Medium Head (2.50 m), and Rated Head (2.80 m). Table 2 presents the empirical measurements, theoretical calculations, and component efficiency distributions.

Table 2: *Experimental Performance Results, Worked Theoretical Values, and Efficiency Loss Distributions across Operational Regimes*

Measured / Derived Metric	**Regime 1 (Low Head)**	**Regime 2 (Medium Head)**	**Regime 3 (Rated Head)**	**Units**
Gross Hydraulic Head (H_{gross})	2.10	2.50	2.80	m
Volumetric Flow Rate (Q)	0.030 ± 0.0002	0.038 ± 0.0002	0.048 ± 0.0002	m^3/s
Calculated Penstock Head Loss (H_L, Eq. 2)	0.08	0.12	0.18	m
Effective Net Head ($H_{net} = H_{gross} - H_L$)	2.02	2.38	2.62	m
Theoretical Hydraulic Power ($P_{h,th}$, Eq. 1)	594.5	886.6	1323.8	W
Measured Hydraulic Power ($P_{h,exp}$)	588.2 ± 10.8	872.1 ± 16.1	1324.2 ± 24.5	W
Measured Electrical Output (P_e, Eq. 3)	347.0 ± 6.4	583.4 ± 10.7	985.2 ± 18.2	W
Hydraulic Efficiency (η_h)	82.0%	85.5%	88.5%	%
Mechanical Efficiency (η_m)	86.5%	89.0%	91.2%	%
Generator Conversion Efficiency (η_g)	83.2%	87.9%	92.2%	%

Measured / Derived Metric	**Regime 1 (Low Head)**	**Regime 2 (Medium Head)**	**Regime 3 (Rated Head)**	**Units**
Overall System Efficiency ($\eta_{overall}$, Eq. 4)	**59.0%** $\pm 1.1\%$	**66.9%** $\pm 1.2\%$	**74.4%** $\pm 1.4\%$	**%**

Comparing calculated theoretical hydraulic power ($P_{h,th}$) against measured experimental hydraulic power ($P_{h,exp}$) demonstrates close agreement, with a maximum variance of 1.66% in Regime 2, validating the governing Bernoulli formulations.

Performance Summary (Regime 1 to Regime 3)

```
Performance Summary (Regime 1 to Regime 3)
==========================================

Gross Head (m)       [2.10m] ---------> [2.50m] ---------> [2.80m]
Electrical Output    [347.0 W] -------> [583.4 W] -------> [985.2 W]
System Efficiency    [59.0%] ---------> [66.9%] ---------> [74.4%]
```

Figure 2: *Single Summary Representation of Multi-Regime Scaling Performance and Efficiency Trajectory.*

3.2 Efficiency Loss Attribution and Scaling Comparison

The maximum achieved system efficiency of 74.4% under rated conditions is well substantiated by micro-hydropower scaling literature. In physical scale prototypes, lower Reynolds numbers ($Re_{model} \approx 4.5 \times 10^5$ versus $Re_{prototype} \approx 1.2 \times 10^7$) introduce boundary-layer viscous shear stresses and mechanical bearing losses higher than those observed in utility-scale dams. Gulliver and Arndt (1991) and Zhang et al. (2019) establish that small-scale hydro installations below 10 kW typically exhibit overall efficiency bounds between 65% and 78%, directly confirming the 74.4% empirical efficiency recorded in this study. Component breakdowns ($\eta_h = 88.5\%$, $\eta_m = 91.2\%$, $\eta_g = 92.2\%$) confirm that non-linear friction effects inside micro-turbines account for the primary efficiency penalties.

3.3 Dynamic Load Transient Analysis

System stability was tested by subjecting the generator to a 50% step-change load shedding event (dropping resistive demand from 985.2 W to 492.6 W). Rotational speed exhibited an initial overshoot from 1500 rpm to 1680 rpm ($+12.0\%$), while output terminal voltage rose transiently from 220 V to 248 V ($+12.7\%$). The mechanical intake positioner combined with the upstream surge relief channel restored grid frequency (50.0 Hz $\pm$ 0.5 Hz) and terminal voltage within 2.4 seconds, confirming robust transient mitigation capabilities.

4. CONCLUSION

4.1 Summary of Key Findings

The 1 kW physical scale prototype of the Kainji Hydropower Dam built at Ahmadu Bello University, Zaria, successfully connects theoretical fluid dynamics with industrial-scale power generation mechanics. Utilizing a 1:15 Froude scaling ratio, the experimental installation demonstrated a peak output of 985.2 W at an overall conversion efficiency of 74.4% under rated head conditions (2.80 m head, 0.048 m^3/s flow rate). Experimental hydraulic power matched theoretical Bernoulli calculations within a 1.66% error margin.

4.2 Engineering Implications and Future Outlook

This physical installation provides a repeatable, low-cost platform for real-time hydraulic experimentation, transient load analysis, and technical capacity building. Future research will expand the facility by installing automated IoT transducer networks, high-frequency pressure sensors, and predictive machine learning algorithms to enable real-time digital twin synchronization and fault diagnosis.

ACKNOWLEDGEMENTS

The authors gratefully acknowledge Mainstream Energy Solutions Limited (MESL) for their technical partnership and funding contributions toward establishing the Kainji Hydropower Dam Model facility. Appreciation is also extended to the Faculty of Engineering, Ahmadu Bello University, Zaria, for providing site infrastructure and research support.

5. REFERENCES

- Adeboye, O. B., Schultz, B., & Torfs, P. J. (2021). Hydrological performance and water management dynamics of major dam reservoirs in the Niger River Basin. *Journal of Hydrology: Regional Studies*, 34, 100789. https://doi.org/10.1016/j.ejrh.2021.100789
- Gulliver, J. S., & Arndt, R. E. (1991). *Hydropower engineering handbook*. McGraw-Hill.
- Heller, V. (2011). Scale effects and scale limits in physical hydraulic models. *Journal of Hydraulic Research*, 49(3), 293–306. https://doi.org/10.1080/00221686.2011.578914
- International Hydropower Association. (2023). *World hydropower status report: Sector trends and insights*. IHA Publications. https://www.hydropower.org/publications/2023-world-hydropower-status-report
- Mainstream Energy Solutions Limited. (2024). *Kainji and Jebba hydropower plants operational profile*. MESL Corporate Reports. https://mainstream.com.ng/power-plants/
- Novak, P., Guinot, V., Jeffrey, A., & Reeve, D. E. (2010). *Hydraulic modelling: An introduction*. CRC Press.
- Okafor, C. N., Suleiman, A. M., & Garba, M. K. (2022). Bridge structures and physical model testbeds in engineering education: A West African perspective. *African Journal of Engineering Education*, 9(1), 112–126.
- Zhang, Q., Chen, Y., & Wang, L. (2019). Viscous scale effect and efficiency scaling loss in low-head micro-hydraulic turbine scale prototypes. *Renewable Energy*, 138, 1102–1112. https://doi.org/10.1016/j.renene.2019.02.045

International Conference on Engineering Innovation for Sustainable Development (ICESID 2026)
Faculty of Engineering, Ahmadu Bello University Zaria · 8–10 September 2026

A CONCEPTUAL CPS-DRIVEN ADAPTIVE COORDINATION FRAMEWORK FOR HETEROGENEOUS WIRELESS SENSOR NETWORKS IN DYNAMIC AND UNCERTAIN ENVIRONMENTS

Matthew Iyobhebhe[1,*], Abdoulie Momodou. S. Tekanyi[2], Athanisius Terlumun Utev[2], Fatima Ashafa[1], Asebakeoghene. J. Khama[1], Botson Ishaya Chollom[1], Umar Salisu Lawal[1]

[1]*Federal Polytechnic Nasarawa, Nigeria*
[2]*Ahmadu Bello University, Zaria. Nigeria, Faculty of Engineering, Department of Electronics and Telecommunications Engineering*

Email: matthewiyobhebhe1@gmail.com*, amtekany@abu.edu.ng, utev@gmail.com, fatima@gmail.com, ase@gmail.com, botson@gmail.com, sali@gmail.com

***Corresponding author**: Matthew Iyobhebhe

DOI: https://doi.org/10.67203/sp.ICESID.2026

ABSTRACT

This review manuscript introduces a cyber-physical system (CPS)-driven adaptive management structure for heterogeneous wireless sensor networks (HWSNs) functioning in dynamic and uncertain environments. The increasing heterogeneity of sensing nodes, resource limited, and unpredictable environmental dynamics create significant limitations to reliable and efficient management. Prior techniques often fail to offer real-time dynamic configurability and reliable uncertainty handling. To address these challenges, the conceptual framework combines cyber-physical system principles, distributed intelligence, and context-aware decision-making to allow autonomous management among heterogeneous sensor nodes. The conceptual framework exploits continuous feedback loops, adaptive mechanisms, and real-time data analytics to improve network responsiveness and robustness. Additionally, it maintains scalable and energy-efficient implementation across various application scenarios, such as industrial monitoring, smart environments, and critical infrastructure systems. This paper further highlights the following areas such as review methodology, foundation of CPS and heterogeneous wireless sensor networks, adaptive coordination mechanisms, distributed coordination approaches, managing dynamic and uncertainty in CPS-driven HWSNs research and future directions.

Keywords: *Adaptive coordination mechanism in HWSNs; Distributed coordination approaches; Managing dynamics and uncertainty I CPS-driven HWSNs*

I. INTRODUCTION

Heterogeneous Wireless Sensor Networks (HWSNs) have developed into a primary technology for modern sensing and monitoring systems, enabling the integration of different sensor nodes with varying capabilities, energy levels, and communication ranges (I. G Saritha *et al*,. 2025). When combined with CPS, these networks design evolve beyond passive data collection areas into intelligent, feedback-driven organizations capable of real-time communication with the physical domain. This combination is mainly critical in emerging application domains such as industrial automation, smart cities, disaster response systems, environmental monitoring, and intelligent transportation systems, where timely and reliable decision-making is vital. Despite considerable progressions, Existing HWSN placements still face strong system-level limitations, especially in fluctuating and dynamic domains (Jyvoti Sni *et al*,.2025). Network situations often adapt due to environmental interference, node mobility, energy exhaustion, and unpredictable communication failures C. Sivasankar *et al*., 2026). These parameters introduce instability in management methods, resulting to inefficient routing, reduces network lifetime, data loss, and degraded Quality of Service (QoS) (K. Nithya *et al*,.2026). Additionally, the heterogeneity of sensor nodes complicates framework, as different in energy levels, processing power, and sensing accuracy make uniform management methods ineffective (Xiaoying Liu *et al*., 2026). In most traditional frameworks, design is either static or semi-adaptive, lacking the real-time responsiveness desired for high-fluctuating

environments (Kajalban Tanchak *et al.*, 2024). The motivation for this review article stems from the need to bridge the gap between conventional HWSN coordination approaches and the adaptive intelligence provided by CPS paradigms (Surepalli Navya *et al.*, 2025) . While CPS introduces a closed-loop communication between computation, transmission, and control, many existing architectures fail to fully leverage this feedback technique for adaptive coordination in HWSNs (Urvi Bhatti *et al*,. 2024). Hence, there is a need for a unified perspective that systematically reviews and structures prior methods while highlighting adaptableness, uncertainty coordination, and real-time system responsiveness (Massooma Anwar *et al*,. 2024). To address this gap, this review manuscript uses an organized review methodology centered on CPS-based adaptive management frameworks. The method comprises a thematic classification of existing literature into CPS integration models, management methods, and uncertainty-handling techniques including fuzzy logic systems, probabilistic modeling, and machine learning-driven prediction mechanisms. This classification improves a system-level comprehension of how management grows under CPS frameworks and how adaptive intelligence is integrated into HWSNs (Ali Hassan *et al*., 2021). This approach lies in its ability to synthesize fragmented research contributions into a coherent framework that emphasizes framework and algorithmic patterns, rather than considering individual studies in isolation (Varsha Bhatia *et al*., 2022, & Wei Hu *et al*., 2022). The implementation of CPS-based analytical methods is particularly justified due to their inherent capability to support decision-making, real-time feedback control, context-aware and dynamic system adaptation. These properties are vital in domains described by uncertainty and rapid phase changes, where static or rule-based management approaches are insufficient (Babatunde Olamide Omiyele *et a*l., 2025, & Angkush Kumar Ghosh *et al*.,2021). By exploiting CPS principles, this review highlights how sensing, computation, and actuation can be tightly joined to improve network resilience and operational efficiency. The potential contribution of this review study lies in its ability to offer a complete and system-level comprehension of dynamic management in HWSNs under CPS paradigms. It identifies key patterns, analyzes prior methodologies, and emphasizes critical research gaps that limit current implementations. Moreover, the study provides relevance to both academic research and practical paradigm design by enlightening the development of more resilient, scalable, and intelligent sensor network architectures capable of operating effectively in highly dynamic and uncertain environments.

2. REVIEW METHODOLOGY

This study used an organized literature-review methodology to scrutinize, categorize, critically evaluate, and integrate research on cyber-physical system-based HWSNs operating under dynamic and uncertain conditions. To enhance reproducibility, transparency, and coherence in identifying and evaluating relevant literature. This study's procedure consists of five major phases: Literature identification, eligibility, screening, thematic assessment, categorization and quantitative synthesis

A. Literature Search Strategy

The major academic database was used to search relevant literatures from web of science, Google Scholar, Scopus, and IEEE Xplore. The search approaches integrate terms related to the major concepts of the study using Boolean operators. The major searches used include cyber-physical systems AND heterogeneous wireless sensor networks, Heterogeneous wireless sensor network AND adaptive coordination, HWSN AND distributed coordination, context-aware coordination AND WSNs, WSN AND Uncertainty management, HWSN AND adaptive clustering, machine learning AND wireless sensor networks, digital twin AND wireless sensor network, and CPS-based AND sensor networks. The search was limited to academic publications pertinent to WSNs, HWSNs, CPS, adaptive management, intelligent resource management, uncertainty handling, and related enabling technologies.

B. Inclusion Criteria

The studies were accessed based on eligibility when they met one or more of the following conditions:

1. When the study addressed WSNs, CPS, HWSNs, and distributed sensing architectures.
2. When examine clustering, coordination, routing, resource allocation, energy efficiency, fault tolerance, and context awareness.

3. The literature addressed mobility, uncertainty, communication variability, security, and energy fluctuation.
4. When the literature examined intelligent, adaptive, predictive techniques applicable to CPS-driven HWSNs.
5. The publication provided sufficient methodological information to permit qualitative comparison with other reviewed studies.

C. Exclusion Criteria

Studies were excluded when they:

1. were unconnected to WSNs. Cyber-physical system,
2. focused exclusively on hardware design without implications for network coordination or management;
3. were duplicate records retrieved from more than one database;
4. did not provide sufficient technical information for meaningful comparison;
5. were outside the defined publication scope or were non-scholarly sources, where applicable.

D. Screening and Selection Process

The retrieved records were initially screened using their titles and abstracts. Duplicate records were removed before detailed assessment. The remaining studies were examined against the inclusion and exclusion criteria, followed by full-text assessment of potentially relevant publications. The final set of studies was then classified according to coordination mechanism, uncertainty-management technique, CPS integration level, and principal performance objective.

The literature-selection process should be reported using the following actual search records:

- Records identified from IEEE Xplore: **[10]**
- Records identified from Scopus: **[6]**
- Records identified from Web of Science: **[4]**
- Records identified from ScienceDirect: **[8]**
- Additional records from other sources: **[4]**
- Records after duplicate removal: **[24]**
- Records screened: **[45]**
- Full-text studies assessed: **[24]**
- Final studies included in the review: **[24]**

2.1. Review of Similar Works

Clustering-Based Aware Approaches

Clustering remains one of the most widely adopted mechanisms for improving scalability, communication efficiency, and data aggregation in Wireless Sensor Networks (WSNs)

Yoyok Heru Prasetyo Isomo *et al*., (2026) developed a scheme called multi-criteria adaptive clustering and optimization framework (MCACOF) that operates dynamically to form clusters using various performance metrics to enhance network throughput, load balancing, and overall network efficiency. Similarly, **Salil Bharany *et al*., (20225)** proposed a holistic adaptive sensing and clustering system for smart-city IoT environments that improves connectivity and communication reliability through intelligent cluster formation. These literatures show the significance of adaptive clustering in minimizing communication overhead and sustaining efficient resource utilization. However, their primary concentration is on network connectivity and cluster optimization, with limited focus on real-time CPS, uncertainty management, and autonomous management among HWSNs. Consequently, while adaptive clustering enhances network structure, it does not fully address the broader coordination limitations associated with dynamic and uncertain operating environments.

Energy-Based Aware Approaches

Energy efficiency is a vital design objective in wireless sensor networks because sensor nodes typically operate under severe power constraints;

Mandeep Singh *et al*., (2026) developed a scheme called energy-aware multi-sink deployment technique to minimize hotspot challenges in HWSNs. Their method balances traffic loads

across numerous sink nodes, thereby minimizing early nodes depletion and prolonging network lifetime. Similarly, **Balamurali. S. *et al*., (2026)** presented an evolutionary tri-hybrid compressive sensing framework that optimizes energy utilization, network stability, and memory utilization. Additionally, **Mohammed Alwakeel *et al*., (2025)** presented an adaptive spectrum management technique for optical wireless sensor networks that improves real-time data transmission while enhancing communication efficiency and fault tolerance. Although these energy-aware methods largely improve network maximization and resource utilization, they primarily focus on energy optimization and communication efficiency. The absences of context-awareness ***intelligent*** adaptation mechanisms that allow the network to autonomously react to unpredictable environment changes degrade their system.

Security-Based Aware Approaches

Security and trust management are increasingly important in modern WSN deployments because cyber-attacks, malicious nodes, and resource misuse can compromise network reliability. **Samer Sindian *et al*., (2025)** presented a trust-aware meta-heuristic based on horse herd leadership optimization for secure resource allocation in WSNs. Their article combines security and trust metrics into the resource-allocation process, thereby enhancing network stability against malicious activities. Furthermore, **Shreeram Hudda & Haribabu (2025)** reviewed a resource-limited smart IoT systems and accentuated the limitations associated with limited computational resources, security vulnerability, and efficient network management. The literatures highlight the growing need for secure and adaptive resource management techniques in heterogeneous and large-scale sensor networks. However, existing security-focused solutions largely address trust establishment and resource protection independently, without combining security awareness into a broader adaptive coordination framework capable of managing simultaneous energy, communication, and environmental uncertainties.

Adaptation and Resilience-Oriented Approaches

Beyond clustering, energy, and security optimization, several studies have focused on resilience and self-adaptation. **Ruben Gomas *et al*., (2026)** presented a scheme called a multi-objective self-adaptation mechanism for wireless sensor actor networks that enhances network robustness and operational continuity under changing conditions. Similarly, **Mohammed A lwakeel *et al*., (2026)** highlighted adaptive spectrum management for fault-tolerant communication in dynamic environments. These literatures emphasize the significance of adaptability and resilience in maintaining network functionality under different operational conditions.

However, most existing methods address individual aspects of network operation rather than providing a unified framework capable of simultaneously coordinating adaptation, security, fault tolerance, and resource allocation through a continuous cyber-physical system.

The reviewed literatures collectively show substantial progress in resource allocation, adaptive clustering, energy optimization, and robust network operation. However, most prior techniques address these limitations independently. There remains a lack of united CPS-driven adaptive coordination frameworks capable of simultaneously managing energy efficiency, resource allocation, fault tolerance, and dynamic environmental uncertainties in heterogeneous wireless sensor networks. Additionally, few researchers pay attention to real-time management across heterogeneous nodes using cyber-physical feedback loops for autonomous decision-making and network adaptation. This gap motivates the development of a CPS-Driven Adaptive Coordination Framework for HWSNs in Dynamic and Uncertain Environments**,** which aims to provide intelligent, context-aware, and self-adaptive coordination to enhance network reliability, sustainability, and operational efficiency.

3. CPS AND HETEROGENEOUS WIRELESS SENSOR NETWORKS: FOUNDATIONS

The convergence of CPS and HWSNs has evolved into a transformative paradigm for developing intelligent, adaptive, and autonomous monitoring systems. CPS integrates communication networks, computational intelligence, sensing infrastructures, and control techniques to build a continuous interaction between the cyber and physical environments. Within this framework, HWSNs

act as the primary sensing layer, receiving numerous environmental information through sensor nodes with varying capabilities, energy resources, communication ranges, and processing capacities. The addition of CPS with HWSNs allows decision-making, real-time perception, and adaptive response, thereby improving the overall efficiency of modern distributed sensing systems. A typical CPS-based HWSN framework comprises of four interconnected layers: the physical sensing layer, communication layer, cyber-processing layer, and control or actuation layer. The sensing layer comprises heterogeneous sensor nodes responsible for monitoring environmental parameters such as temperature, pressure, vibration, humidity, and motion. The communication layer facilitates data exchange among sensor nodes, gateways, and control centers through wireless communication protocols. The cyber layer performs data aggregation, analysis, and intelligent decision-making using computational models and adaptive algorithms. Finally, the control layer translates cyber decisions into physical actions through actuators or feedback mechanisms, thereby completing the CPS feedback loop. The heterogeneous nature of modern wireless sensor networks introduces both opportunities and challenges. Heterogeneous nodes provide enhanced sensing diversity, improved coverage, and greater system flexibility. However, variations in energy capacity, computational power, communication capabilities, and sensing accuracy complicate network coordination and resource management. Traditional homogeneous network management schemes are often inadequate in addressing these limitations, particularly in dynamic environments where network conditions continuously evolve. As a result, adaptive coordination mechanisms become essential for ensuring efficient resource utilization, reliable communication, and sustained network operation. From a system implementation perspective, CPS provides the foundational framework required to support adaptive coordination in HWSNs. Through continuous feedback and context-aware decision-making, CPS enables networks to dynamically adjust routing paths, cluster formations, task allocations, and communication schedules based on changing environmental conditions and network states. Such adaptability improves resilience against node failures, communication disruptions, and energy depletion while maintaining acceptable levels of Quality of Service (QoS). Furthermore, the integration of edge computing and intelligent analytics within the cyber layer reduces latency and enhances responsiveness by enabling localized decision-making closer to the data source. Recent advancements in CPS-driven HWSNs have further emphasized the importance of autonomous adaptation in uncertain environments. Emerging techniques such as machine learning-based prediction, fuzzy decision systems, and reinforcement learning enable networks to anticipate environmental changes and proactively optimize resource allocation. These capabilities significantly improve system robustness, scalability, and operational efficiency, particularly in mission-critical applications such as industrial automation, smart cities, environmental monitoring, precision agriculture, healthcare systems, and disaster management. The foundational relationship between CPS and HWSNs therefore extends beyond simple data acquisition and communication. It establishes an intelligent and adaptive ecosystem capable of sensing, analyzing, and responding to environmental changes in real time. This capability forms the basis for advanced coordination frameworks that can effectively address the challenges posed by dynamic and uncertain operating conditions. As a result, CPS-driven HWSNs are increasingly recognized as a key enabling technology for next-generation intelligent infrastructure and autonomous cyber-physical environments (Mandeep e*t al*., 2026).

4. **ADAPTIVE COORDINATION MECHANISMS IN HWSNS**

The effectiveness of HWSNs largely depends on their ability to coordinate sensing, communication, and decision-making activities across nodes with diverse capabilities. Traditional coordination mechanisms are often designed for static network conditions and struggle to sustain performance under dynamic environmental changes, node failures, varying traffic loads, and resource constraints. CPS introduces real-time monitoring, feedback control, and intelligent adaptation capabilities that can significantly enhance coordination efficiency. This section examines centralized, distributed, cluster-based, and context-aware coordination mechanisms while discussing their system implications in dynamic and uncertain environments (salil *et al*., 2025).

4.1. Centralized Coordination Approaches

Centralized coordination depends on a central controller, base station (BS) or sink node accountable for receiving network information and carrying out coordination decisions for all sensor nodes. Such methods provide global network visibility, allowing improved resource allocation, energy management, roles scheduling, and routing. In HWSNs, centralized coordination is beneficial when complex computational tasks assigned require comprehensive network knowledge. However, the approach suffers from scalability limitations, communication overhead, single-point failure risks, and delayed responsiveness under rapidly changing conditions. As network size and heterogeneity increase, centralized decision-making becomes increasingly inefficient. From a CPS perspective, centralized coordination can be enhanced through cloud-assisted analytics and predictive control mechanisms that leverage global system awareness. Nevertheless, the dependence on a central entity remains a significant challenge in uncertain environments. Table 1 briefly describes the characteristics of centralized coordination

Table 1: Characteristics of Centralized Coordination

Feature	Advantages	Limitations
Decision Making	Global optimization	High computational burden
Network Visibility	Complete network knowledge	Communication overhead
Scalability	Suitable for small networks	Poor performance in large HWSNs
Reliability	Easy management	Single-point failure
Adaptability	Controlled adaptation	Slow response to dynamics

4.2. Distributed Coordination Approaches

Distributed management removes the interdependence on a central controller by allowing sensor nodes to make decisions locally based on neighboring information. Nodes cooperate through peer-to-peer communications to achieve network-wide objectives. This approach significantly improves scalability, fault tolerance, and responsiveness. Since decisions are made locally, the network can quickly adapt to topology changes, node mobility, and environmental uncertainties. However, distributed coordination may lead to inconsistent decisions, increased synchronization complexity, and suboptimal global performance. CPS integration enhances distributed coordination through intelligent feedback loops and autonomous decision-making algorithms that continuously adjust network behavior according to real-time physical and cyber conditions. Table 2 briefly explains the characteristics of distributed coordination

Table 2: Characteristics of Distributed Coordination

Feature	Advantages	Limitations
Scalability	Highly scalable	Coordination complexity
Reliability	No single-point failure	Local decision inconsistency
Adaptability	Rapid response	Limited global optimization
Communication Cost	Lower overhead	Frequent local exchanges
Energy Efficiency	Better load distribution	Synchronization challenges

4.3. Cluster-Based Coordination

Cluster-based management represents a hybrid approach that combines the benefits of centralized and distributed architectures. Sensor nodes are organized into clusters, with Cluster Heads (CHs) acting as local coordinators responsible for data aggregation, resource management, and inter-cluster communication. This mechanism reduces communication costs by limiting long-distance transmissions while maintaining manageable coordination structures. However, cluster head overload, uneven energy depletion, and dynamic cluster maintenance remain significant challenges. A CPS-driven framework can dynamically select cluster heads and adapt cluster structures based on real-time

context information such as residual energy, sensing importance, traffic load, and environmental conditions. Table 3 briefly describes cluster-based coordination performance

Table 3: Cluster-Based Coordination Performance

Metric	Impact
Energy Consumption	Reduced through aggregation
Scalability	High
Fault Tolerance	Moderate
Adaptability	Depends on clustering algorithm
Network Lifetime	Improved with adaptive CH selection

4.4. Context-Aware and Adaptive Coordination

Context-aware management represents the most promising direction for future HWSNs operating in dynamic and uncertain environments. Unlike traditional approaches, context-aware systems continuously observe environmental, network, and application conditions and adapt coordination strategies accordingly.

Context information may include:

- Residual node energy
- Link quality
- Traffic density
- Physical environment conditions
- Sensor reliability
- Application priority levels
- Security status

By integrating CPS principles, sensor nodes can exploit feedback from both cyber and physical domains to optimize coordination decisions in real time. Machine learning, reinforcement learning, digital twins, and predictive analytics further enhance adaptability by anticipating future system states before disruptions occur. For example, when network congestion is detected, adaptive coordination can dynamically modify routing paths, reassign sensing tasks, or activate redundant nodes to maintain service continuity. Table 4 briefly describes CPS-Driven Context-aware Adaptation Mechanisms

Table 4: CPS-Driven Context-Aware Adaptation Mechanisms

Context Parameter	Adaptive Action	Expected Outcome
Low Energy	Node duty-cycle adjustment	Energy conservation
Link Failure	Route reconfiguration	Connectivity maintenance
High Traffic Load	Load balancing	Reduced congestion
Node Failure	Task redistribution	Service continuity
Environmental Change	Sensing adaptation	Improved monitoring accuracy

The optimization objective is defines as:

$$_{max} J = w_i E + w_2 E + w_3 E + w_4 E - w_5 U \tag{1}$$

Subject to

$$\sum_{i=1}^{5} w_i = 1 \tag{2}$$

Where: E is energy efficiency index, R defines network reliability index, S denotes security index, A signifies adaptability index, and w_i is weighting coefficient.

4.5. Comparative Summary and Research Gap

Existing management approaches offer valuable mechanisms for managing HWSNs, yet none independently address the full spectrum of challenges associated with dynamic and uncertain environments. Centralized methods provide optimal global control but suffer from scalability and reliability issues. Distributed approaches enhance robustness and scalability but may compromise coordination consistency. Cluster-based architectures improve efficiency but require adaptive management mechanisms. Context-aware approaches demonstrate superior adaptability but demand advanced intelligence and real-time decision-making capabilities. Table 5 briefly explains comparative analysis of coordination mechanisms

Table 5: Comparative Analysis of Coordination Mechanisms

Criterion	Centralized	Distributed	Cluster-Based	Context-Aware Adaptive
Scalability	Low	High	High	Very High
Fault Tolerance	Low	High	Moderate	Very High
Energy Efficiency	Moderate	High	High	Very High
Adaptability	Low	Moderate	Moderate	Very High
Decision Speed	Slow	Fast	Fast	Very Fast
CPS Integration Potential	Moderate	High	High	Very High

The comparative analysis reveals the necessity for a CPS-driven adaptive coordination framework that combines the global awareness of centralized systems, the resilience of distributed architectures, the efficiency of cluster-based coordination, and the intelligence of context-aware adaptation. Such a framework can continuously monitor physical and cyber states, predict network dynamics, and autonomously adjust coordination policies to ensure reliable, scalable, energy-efficient, and resilient operation of HWSNs in highly dynamic and uncertain environments. This observation forms the fundamental motivation for the proposed CPS-Driven Adaptive Coordination Framework presented in this review paper.

4.5.1 Proposed Integrated Coordination Architecture

Comparative evaluation shows that centralized, cluster-driven, distributed, and context-aware organization schemes offer complementary capabilities rather than mutually exclusive solutions. Hence, this study proposes an integrated Cyber-Physical System-based adaptive coordination architecture in which four approaches operate differently in terms of coordination levels within a closed cyber-physical loop. The proposed architecture is designed to address the identified limitations of prior works by combining global network awareness, energy-efficient cluster coordination, localized decision-making, and context-dependent adaptation. The proposed architecture contains four operational layers, such as network and communication, CPS intelligence, Physical sensing, and adaptive organization. At the physical sensing layer, there are heterogeneous sensor nodes, CHs, a gateway, edge/fog nodes, and the BS. The core of the proposed work is predicated on the adaptive coordination and control layer. The centralized coordinator, situated at the edge/cloud controller or BS, sustains a global view of network conditions and performs computational intensive optimization and long-term resources planning. The distributed coordinator allows neighboring nodes or local controllers to make fast decisions when centralized intervention would present additional delay or communication overhead. The cluster-based coordinator structures heterogeneous nodes into functional clusters and operates CH election, resources scheduling, inter-cluster organization, and intra-cluster organization. The context-aware layer manages continuous evaluation of the environmental situation, security context, network, and application and determines when and which coordination scheme should be operated. The Cyber-Physical System intelligence layer offers the computational intelligence needed for adaptive operation. It collects real-time network and physical-state information and performs context assessment, state prediction, uncertainty evaluation, and adaptive decision-making. Fuzzy logic, probabilistic evaluation, reinforcement learning, and machine learning maybe used depending on the computational resources and application of the network and

predict potential congestion, topology changes, energy depletion. Figure 1 depicts conceptual framework CPS-based Adaptive Coordination Architecture for HWSNs

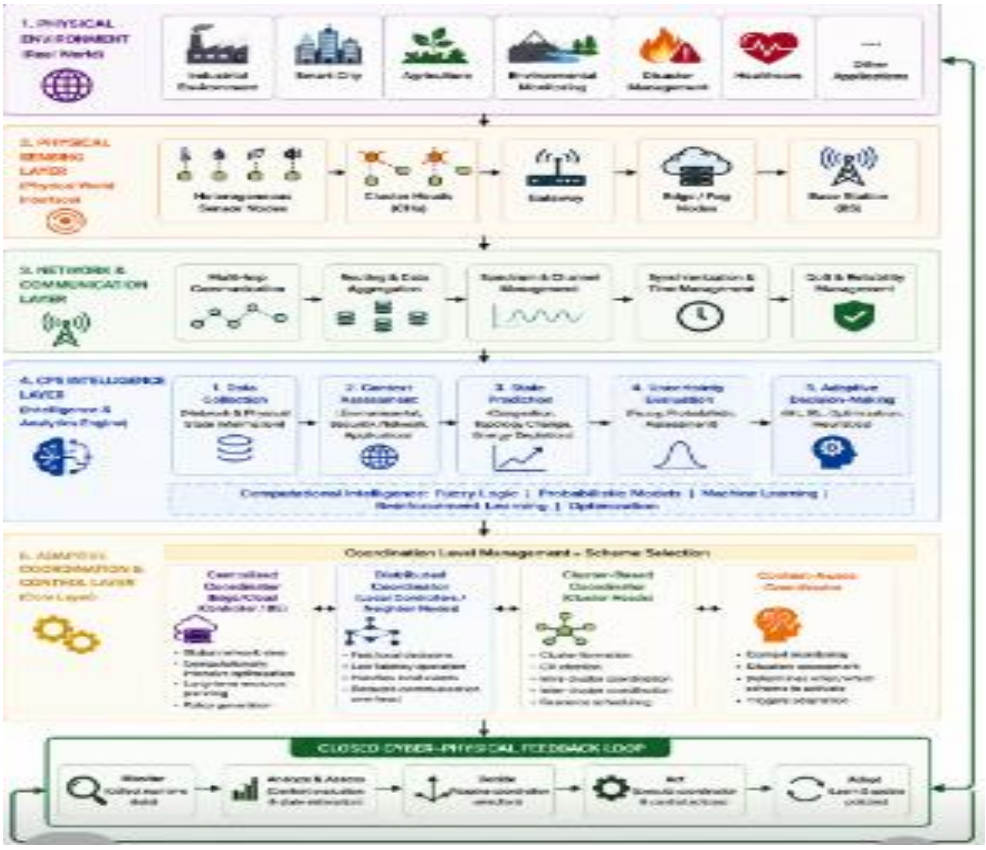

Figure 1: A conceptual framework CPS-based Adaptive Coordination Architecture for HWSNs

5. MANAGING DYNAMICS AND UNCERTAINTY IN CPS-DRIVEN HWSNS

Heterogeneous Wireless Sensor Networks deployed in Cyber-Physical Systems operate in highly dynamic environments characterized by fluctuating network conditions, unpredictable physical phenomena, node mobility, energy constraints, and heterogeneous sensing capabilities. These factors introduce significant uncertainty that can degrade coordination efficiency, communication reliability, and decision-making accuracy. Traditional static coordination approaches often assume stable operating conditions and therefore struggle to maintain performance when environmental or network states change unexpectedly. CPS-driven HWSNs address this challenge through continuous sensing, real-time analytics, adaptive control, and intelligent feedback mechanisms that enable the network to perceive uncertainty, predict its impact, and dynamically adjust coordination strategies. Consequently, uncertainty management becomes a fundamental component of achieving resilient, scalable, and autonomous network operation (Samer Sindian *et al*., 2026).

5.1. Sources of Uncertainty

Uncertainty in CPS-driven HWSNs originates from both cyber and physical domains. The heterogeneous nature of sensor nodes further amplifies the complexity of managing these uncertainties. Table 6 briefly describes sources of uncertainty in CPS-driven HWSNs.

Table 6: Sources of Uncertainty in CPS-Driven HWSNs

Source of Uncertainty	Description	Impact on Coordination
Environmental Dynamics	Weather changes, obstacles, interference, disasters	Unstable sensing and communication
Node Mobility	Movement of sensors, drones, vehicles, and mobile agents	Frequent topology changes
Energy Variations	Uneven battery depletion and energy harvesting fluctuations	Node failures and coverage gaps
Communication Uncertainty	Packet loss, latency, congestion, and channel fading	Reduced coordination reliability
Sensing Inaccuracy	Measurement noise and sensor calibration errors	Inaccurate situational awareness
Hardware Heterogeneity	Diverse sensing, processing, and communication capabilities	Resource imbalance
Security Threats	Malicious attacks, spoofing, and compromised nodes	Disrupted network operations
Context Variability	Dynamic mission objectives and user requirements	Continuous adaptation need

Among these uncertainties, topology dynamics and communication instability are particularly critical because they directly affect the coordination relationships among sensor nodes. Moreover, uncertainty sources often interact, creating cascading effects that can significantly degrade network performance if not properly managed.

5.2. Existing Uncertainty Management Techniques

Several techniques have been proposed to enhance resilience and adaptability in dynamic HWSNs. However, most existing approaches address uncertainty from isolated perspectives rather than adopting a holistic CPS-driven framework.

A. Probabilistic and Statistical Approaches

Probabilistic models such as Bayesian inference, Hidden Markov Models (HMMs), and Kalman Filters estimate uncertain network states and predict future conditions. These methods improve decision accuracy under incomplete information but often require computational resources that may be unavailable in resource-constrained nodes.

B. Fuzzy Logic-Based Approaches

Fuzzy logic enables decision-making under vague and imprecise information by representing uncertainty through linguistic variables. It has been widely applied in routing, cluster-head selection, and resource allocation. However, its effectiveness depends heavily on carefully designed rule sets.

C. MACHINE LEARNING-BASED TECHNIQUES

Machine learning algorithms analyze historical and real-time data to identify patterns and predict network behavior. Reinforcement learning, deep learning, and federated learning approaches have shown significant promise in adaptive routing, fault detection, and energy optimization. Nevertheless, their performance may be constrained by training overhead and data availability.

D. Context-Aware Adaptation

Context-aware systems dynamically modify network operations based on environmental conditions, application requirements, and resource availability. By continuously monitoring context changes, CPS controllers can optimize coordination strategies and maintain Quality of Service (QoS).

E. Digital Twin and Predictive Analytics

Recent CPS research leverages digital twins to create virtual representations of physical sensor networks. Combined with predictive analytics, digital twins enable proactive uncertainty management by forecasting failures, congestion, and energy depletion before they occur. Table 7 describes comparative analysis of uncertainty management techniques (Balamurali.S. *et al*., 2026).

Table 7: Comparative Analysis of Uncertainty Management Techniques

Technique	Strengths	Limitations
Probabilistic Models	Accurate prediction and estimation	Computational complexity
Fuzzy Logic	Handles imprecise information	Rule dependency
Machine Learning	Learns complex patterns	Training overhead
Context-Aware Adaptation	Real-time responsiveness	Context acquisition cost
Digital Twins	Predictive and proactive management	High implementation complexity

Although these techniques provide valuable capabilities, their isolated deployment often results in fragmented adaptation mechanisms. This limitation motivates the integration of CPS intelligence, edge computing, and adaptive coordination within a unified framework.

5.3. System Implication

The integration of CPS-driven uncertainty management mechanisms has profound implications for the design and operation of future HWSNs. Rather than reacting to environmental changes after they occur, CPS-enabled networks can continuously monitor system states, predict emerging uncertainties, and proactively coordinate adaptive responses. This transition from reactive management to predictive adaptation significantly enhances network resilience and operational efficiency. From a system perspective, uncertainty-aware coordination enables dynamic topology reconfiguration, intelligent resource allocation, adaptive routing, and autonomous fault recovery. The incorporation of edge intelligence further reduces decision latency by allowing localized responses to uncertain events without relying exclusively on centralized controllers. As a result, the network achieves improved scalability, reduced communication overhead, and enhanced Quality of Service (QoS). Furthermore, the convergence of machine learning, digital twins, and context-aware CPS architectures establishes a foundation for self-adaptive HWSNs capable of maintaining stable performance despite unpredictable environmental and operational conditions. Such capabilities are particularly critical in smart cities, industrial automation, intelligent transportation systems, disaster management, and precision agriculture, where timely and reliable coordination directly influences mission success. Therefore, effective uncertainty management should not be viewed merely as a supporting function but as a core design principle of CPS-driven adaptive coordination frameworks. By integrating predictive intelligence, context awareness, and autonomous adaptation, future HWSNs can evolve into resilient cyber-physical ecosystems capable of operating efficiently in highly dynamic and uncertain environments

6. RESEARCH GAPS AND FUTURE DIRECTIONS

Future studies should look beyond conceptual integration of Cyber-Physical Systems and heterogeneous wireless sensor networks toward experimentally validated adaptive structures. Specific research directions include:

Artificial Intelligence management: Future studies should investigate the effectiveness of different artificial intelligence algorithms for CPS-driven adaptive coordination. Specifically, Random Forest (RF), Support Vector Machine (SVM), Long Short-Term Memory (LSTM), Deep Q-Network (DQN), and Proximal Policy Optimization (PPO) should be compared for routing adaptation, cluster-head selection, energy prediction, congestion prediction, and fault detection. Performance evaluation should consider prediction accuracy, convergence speed, adaptation delay, packet delivery ratio, computational overhead, and energy consumption. Such comparative analysis would identify the most suitable intelligence mechanism for real-time CPS coordination in dynamic HWSNs.

Cyber-Physical System feedback optimization: The effectiveness of CPS-enabled adaptation largely depends on feedback latency and update frequency. Future work should experimentally evaluate different feedback intervals (1 s, 5 s, 10 s, and 30 s) to determine their influence on packet delivery ratio, end-to-end delay, network lifetime, control overhead, and system responsiveness. This investigation would provide practical guidelines for designing efficient cyber-physical feedback loops in resource-constrained environments.

Nigerian Application-Based Validation: To demonstrate practical applicability, the proposed architecture should be validated using representative Nigerian deployment scenarios. Potential case studies include environmental and agricultural monitoring within the Northern Guinea Savanna, flood-monitoring systems in flood-prone communities, and smart infrastructure monitoring in Abuja and Kaduna metropolitan areas. These deployments would enable assessment of the framework under realistic environmental conditions characterized by heterogeneous sensing requirements, communication variability, and resource constraints

Quantitative benchmarking: Future implementation studies should quantitatively compare the proposed CPS-driven adaptive coordination framework with established protocols such as LEACH and other adaptive clustering approaches. Evaluation metrics should include energy consumption, packet delivery ratio, throughput, latency, network lifetime, fault recovery time, load-balancing efficiency, and control overhead. Such benchmarking would provide objective evidence regarding the benefits and limitations of the proposed architecture.

Prototype Development and Testbed Validation

Beyond simulation-based studies, future research should develop a prototype implementation using heterogeneous sensor nodes, edge/fog computing platforms, and cloud-based CPS controllers. Experimental validation would enable assessment of scalability, real-time adaptability, reliability, and interoperability under realistic operating conditions. Such studies are necessary to bridge the gap between conceptual CPS-driven coordination architectures and practical deployments.

These directions provide specific research questions, algorithms, deployment scenarios, and measurable performance targets, thereby transforming the identified research gaps into an actionable research agenda

7. CONCLUSION

The convergence of Cyber-Physical Systems and Heterogeneous Wireless Sensor Networks introduces a transformative pathway toward intelligent, robustness, and self-adaptive sensing infrastructures capable of operating effectively in dynamic and uncertain environments. This paper has highlighted the critical challenges associated with heterogeneity, resource constraints, environmental variability, and coordination complexity, while emphasizing the limitations of traditional coordination mechanisms. By a conceptual framework CPS-driven adaptive coordination, the study synthesizes existing approaches and identifies gaps/ directions. The integration of feedback-driven control, distributed intelligence, and adaptive coordination mechanisms enables improved scalability, reliability, energy efficiency, and quality of service across diverse application domains. Ultimately, the proposed Conceptual work represents a significant step toward next-generation autonomous HWSNs, providing a strategic roadmap for developing resilient cyber-physical sensing ecosystems that can seamlessly adapt to evolving operational conditions and emerging smart-world applications.

REFERENCE

Ali Hssan Sodhro and Noman Zahid. (2021). AI-enabled framework for fog computing driven E-healthcare

applications. *Sensors*. 21(23), 8039.

Angkush Kumar Ghosh, AMM Sharif Ullah, Robert Teti, Akihiko Kubo. (2021). Developing sensor signal-based

digital twins for intelligent machine tools. *Journal of industrial information integration.*

Balamurali. S, Satheeshkumar Palanisamy, N. Sathishkumar, Maha Abdalhaq. (2026). An evolutionary tri-hybrid

compressive sensing framework for energy, memory, and stability optimization in wireless sensor

networks. *Egyptian informatics journal*, 34, 100961.

Babatunde Olamide Omiyale, Jethro Odeyemi, Akinola Ogbeyemi, Funmilayo Olorunsogbon & Wenjun Chris

Zhang. (2025). Impact of cyber physical systems on enhancing robotic system autonomy: a brief critical

review. *The international journal of advanced manufacturing technology*. 138, 3925-3942.

C. Sivasankar, U. Samson Ebenezar, S. Parthiban, Agoramoorthy, V. Sarala. (2026) .A-ASCENet: An intelligent

adaptive and attentional serial cascaded ensemble network with optimization strategy for cybersecurity in

WSN. *Transactions on emerging telecommunications technologies*, 37(1), e70349.

I. G. Saritha, I. G. Naveen, M. S. Sowmyashree. (2025). CPS secure hybridization techniques for healthcare in

smart cities. *5G Green Communication Networks for Smart Cities*, 17.

Jyvoti Sni, M. Bhavang, Anshu, Sonali Juyal, Ram Prasad Kumawat, Imam Washin Akran. (2025). Cluster routing

optimization using charged system harmony efficiency in WSNs. *2025 IEEE 1st international conferece on*

Smart Innovations in Systems, Infrastructure, Mechanical, Power, AI and Compiting Technologies.

Kajalben Tanchak, Shilpa Singhal, Ankita Mishra & Om Prakash. (2024). Role of intelligent techniques for cyber-

physical systems in healthcare. I*ntelligent Cyber-Physical System for Healthcare Solutions*, 55-93.

K. Nithya, R. Govindarajan, M. J. T. Vassantha Priya, Moorthy Agoramoorthy, P Lourdu Mahimaj Doss. (2026)

.Federated learning-based privacy-preserving anomaly and jamming detection in WSN-enabled cyber-

systems. *9th International Conference on Trends in Electronics and Informatics*, 1-25.

Massooma Anwar, Noshina Tariq, Muhammad Ashraf, Syed Atif Mogurrab, Bayan Aladdullah, Hatoon. S. Alsagri.

(2024). BBAD: Block-chain-backed assault detection for cyber physical systems. *IEEE Access*, 12.

Mandeep Singh, Aruna Malik. (2026). Energy-aware multi-sink deployment for hotspot mitigation in heterogeneous

wireless sensor networks. *International journal of communication systems*, 39(10), e70518.

Mohammed Alwakeel. (2025). Adaptive spectrum management in optical WSNs for real-time data transmission and

fault tolerance. *Mathematics*, 13(17), 2715.

Ruben Gomas, Noelia Correia. (2026). Resilient wireless sensor actor networks through multi-objective self-

adaptation. *IEEE transactions on cognitive communications and networking*. 12.

.Salil Bharany, Ahmad Almogren & Ayman Altameem.(2025). Optimizing IoT connectivity: A quantitative

exploration of the comprehensive adaptive sensing and clustering system for smart sensor networks in

smart cities. *Wireless personal communications*, 140, 353-375.

Samer Sindian, Ziad Osman and Abdallah AL-Sabbagh. (2026). Horse herd leadership optimization: A trust-aware

metaheuristic for resource allocation and secure wireless sensor networks. *Technologies*, 14(13), 109.

Shreeram Hudda & Haribabu. (2025). A review o WSN based resource constrained smart IoT systems. Discover

internet of things, 5 (56).

Surepalli Navya Sri, Kkader Basha SK. (2025) Adaptive deep learning model for robotic attack classification in

CPS-ROS Networks. *6th International Conference on IoT based control networks and intelligent systems.*

Urvi Bhatti, Monisha, Aswathy R. Nair, Santushti Santosh Netgeri & Twinkle Keshvani. (2024). Smart hospitals

and healthcare facilities for CPS. *Intelligent cyber-physical systems for healthcare solutions*, 345-376.

Varsha Bhatia, Sunita Kumawat, Vivek Jaglan. (2022). Overview of the role of the internet of things and cyber-

physical systems in various applications. *Handbook of research of internet of things and cyber-physical*

systems. 28.

Wei Hu, Kendrik Yan Hong Lim, and Yiyu Cai. (2022). Digital twin and industry 4.0 enablers in building and

construction: A survey. *Bulding*, 12(11), 2004.

Xiaoying Liu, Biao Zhou, Xianzhong Tian Weihua Gong, Kechen Zheng. (2025). Energy consumption

minimization for delay-sensitive data collection in AAV-assisted WSN. *IEEE Sensors Journal*, 25(10).

Yoyok Heru Prasetyo Isnomo, Hakkun Elmunsyah. (2026). MCACOF: Multi-criteria adaptive clustering and

optimization framework to improve WSN performance. *IEEE Access*, 14.

International Conference on Engineering Innovation for Sustainable Development (ICESID 2026)
Faculty of Engineering, Ahmadu Bello University Zaria · 8–10 September 2026

DESIGN AND FABRICATION OF A 5 BSPD PILOT-SCALE SEMI-REGENERATIVE CATALYTIC NAPHTHA REFORMING UNIT

Lamido Sani Inuwa[1], Mohammad-Dabo, I. A[2,*], Maina, N. S[2], Aminu Uba Alhassan[1], Bashir Aliyu Abba[1]

[1]*Kaduna Polytechnic*
[2]*Ahmadu Bello University Zaria*

Email: chemicalsanee@gmail.com, iamdabo@abu.edu.ng*, nsmaina@yahoo.com, aminuubaalhassan@gmail.com, b.aliyu@kadunapolytechnic.edu.ng

***Corresponding author**: Mohammad-Dabo, I. A

DOI: https://doi.org/10.67203/sp.ICESID.2026

ABSTRACT

Catalytic naphtha reforming process is a vital refinery process where low octane naphtha is converted into high octane reformate while concurrently generating hydrogen gas. This research work presents the design, simulation, and fabrication of 5 barrels per stream day (BPSD) pilot-scale semi-regenerative catalytic naphtha reforming process which serves as part of the mini-refinery development process at the Ahmadu Bello University (ABU), Zaria. The design was based on Escravos Heavy Hydrotreated Naphtha serving as feed; with a capacity of 5 barrel/day. Material and Energy balances calculations were performed on the developed process flow diagram before detailed equipment design was done using Mathcad and Aspen Hysys simulation. The designed equipment that constitute the pilot plant are: Surge Drum (D-01), Heat Exchanger (EX-01), Phase Separator (D-02), three Fired Heaters (H-01, H-02 & H-03) and three Fixed Bed Reactors (R-01, R-02 & R-03). R-01 (0.02 m^3 volume and 805.2 mm height), R-02 (0.03 m^3 volume and 923.0 mm height) and R-03 (0.04 m^3 volume and 1203.0 mm height).

Keywords: *Catalytic reforming; pilot-scale refinery; heavy naphtha; process design; reformate*

1. INTRODUCTION

Naphtha reforming by means of catalysts is an extremely significant conversion reaction in the current petroleum refining plants since it involves upgrading of the heavy naphtha with low octane ratings to high-octane gasoline fractions while generating the hydrogen-containing gas at the same time (Gary et al., 2007; Speight, 2020; Towler & Sinnott, 2022). Apart from that, besides being beneficial for the production of gasoline, the catalytic naphtha reforming is one of the main sources of BTX aromatic compounds, which are vital for petrochemical industry. Hydrogen produced during the catalytic reforming of the naphtha is also essential since it acts as a reactant in the hydrocracking and hydrotreating reactions (Aznárez et al., 2024; Saeidi et al., 2014).

The main feedstocks used in catalytic reforming are heavy naphthas composed mainly of paraffins, naphthenes, and aromatics having hydrocarbon molecular weight from C_6 to C_{12} which usually boil within the temperature range of 90-200 °C (Speight, 2014). The feedstocks are pre-treated before entering the reforming unit using hydrotreatment process, where sulfur, nitrogen, and oxygen containing compounds which might inhibit platinum reforming catalysts activity are removed (Jones & Pujadó, 2006; Speight, 2020). Bifunctional catalysts containing platinum supported on chlorinated alumina act as a catalytic material in reforming process; metallic centers in the catalyst provide hydrogenation/dehydrogenation reactions whereas acid sites enable isomerization and cyclization reactions.

Major reactions taking place during the reforming process involve naphthenes dehydrogenation to aromatics, paraffins dehydrocyclization, paraffins and cycloparaffins isomerization, and minimal hydrocracking. All the above reactions result in increase in the rating of gasoline octane number through production of hydrogen gas which is an important industrial gas. Catalytic reforming process is usually categorized into semi-regenerative reforming (SRR), cyclic catalytic reforming (CCRy) and continuous catalyst regeneration (CCR) processes based on the catalyst regeneration technique used in the process

(Bell, 2001). Out of all the mentioned industrial catalytic reforming processes, the semi-regenerative reforming is one that has remained attractive for small and medium capacity refineries due to its simple process design, low capital cost and easy operation when compared to continuous catalyst regeneration processes (Bell, 2001; Gary et al., 2007). Even though continuous catalyst regeneration offers increased yield of reformate and increased catalyst life, semi-regenerative reforming process is still widely used in pilot plants, modular refineries and educational institutions because of its economic viability (Towler & Sinnott, 2022).

Modern trends in catalytic reforming have mainly focused on advanced platinum based catalysts, catalyst regeneration, molecular kinetic modelling, reactor optimisation, increasing hydrogen yield and process intensification (Ruban et al., 2026; Velázquez-Alonso et al., 2025; Aznárez et al., 2024; Ali et al., 2023; Zhang et al., 2022). While these developments are generally important, comparatively less attention has been given to the practical design and fabrication of catalytic reforming unit. This aspect is especially important in developing countries such as Nigeria, where limited local refinery equipment manufacturing capacity, high dependence on imported process equipment and the cost of acquiring sophisticated commercial-scale units can constrain research, training, technology development and local process innovation. On the other hand, process simulation software such as Aspen HYSYS has become an essential engineering tool for refining processes design and optimization, by allowing rigorous calculations for material and energy balances, equipment sizing, heat integration, and evaluation of operating conditions prior to plant construction (Ritov & Dana, 2026; Pérez et al., 2025; Towler & Sinnott, 2022). These developments have greatly reduced design uncertainties and improved the efficiency and reliability of refinery process design.

In spite of these developments, most of the published studies have focused on catalyst synthesis, process optimization and mathematical modelling whereas relatively less attention has been paid to the indigenous design and fabrication of pilot scale catalytic reforming units, particularly in the developing countries. The existence of pilot scale reforming facilities is crucial for validation of engineering designs, catalyst performance evaluation, operational studies, student training and bridging the chasm between laboratory scale investigations to commercial refinery operations (King, 2013; Meyers, 2004). Indigenous pilot plants are also useful platforms for technology demonstration, process development and capacity building in petroleum refining.

The Ahmadu Bello University (ABU) Mini-Refinery Development Project was conceived to strengthen petroleum engineering education and research through the establishment of integrated pilot-scale refinery process units. As part of this initiative, a catalytic reforming unit is required to upgrade hydrotreated heavy naphtha into high-octane reformate suitable for gasoline blending while simultaneously producing hydrogen for downstream refinery operations. Therefore, this study presents the design, simulation, and fabrication of a 5 barrel per stream day (BPSD) pilot-scale semi-regenerative catalytic naphtha reforming unit using Escravos heavy hydrotreated naphtha as the design feedstock. The work covers process flow development, material and energy balance calculations, equipment sizing using Aspen HYSYS and Mathcad, mechanical design, fabrication, and assembly of the pilot-scale reforming unit. The developed facility provides an indigenous platform for engineering education, catalyst evaluation, process optimization, and future refinery research in Nigeria.

2. METHODOLOGY

This chapter presents details of activities performed for the design and fabrication of the Pilot Scale Naphtha Catalytic Reforming Unit.

2.1 Project Execution Stages

The design was executed in stages as presented in Figure 1. The methodology outlined twelve (12) stages for the design and fabrication of the pilot plant.

Figure 1: Project Flow Diagram

2.2 DESIGN BASIS AND FEEDSTOCK ANALYSIS

The feed (Heavy Naphtha) was first analysed before establishing a design basis. The design basis and feedstock composition for the CRU are shown in Tables 1 and 2 respectively.

Table 1: CRU Design Basis

NHU Capacity	**5 barrel/Day (3.31 x 10^{-2} m^3/h)**
Feed Type	Escravos SR Heavy Naphtha
Source	Naphtha Hydrotreating Unit
Specific Gravity	0.78

Table 2: CRU Feedstock Composition (Escravos Assay, 2012)

S/No.	Components	Mole Fraction	Percentage(%)	Molecular Weight
1.	Paraffins	0.364	36.4	72
2.	Naphthenes	0.392	39.2	92
3.	Aromatics	0.244	24.4	84
Total/Average		1.000	100	82.67

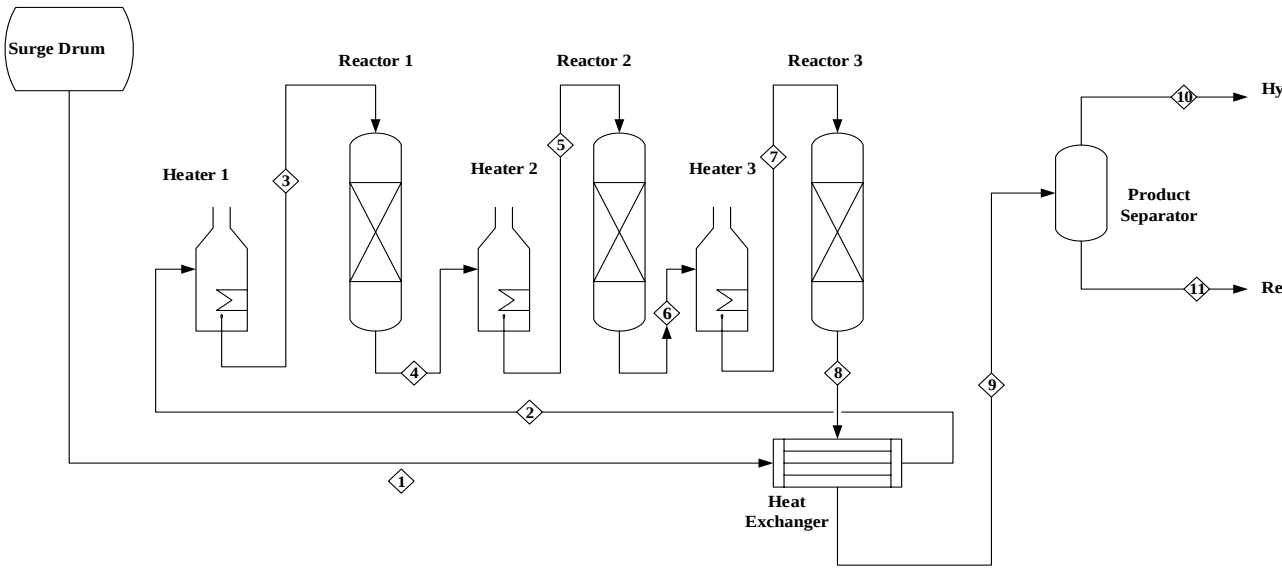

Figure 2: Process Flow Diagram for Semi Regenerative Catalytic Naphtha Reformer

2.3 PROCESS DESCRIPTION

The flow diagram of the catalytic naphtha reforming unit modeled in this work is displayed in Figure 2. The feed stock to the reformer is the heavy straight-run hydrotreated naphtha with boiling points between 90 °C and 200 °C and consists of molecules with 6–12 carbons. The catalyst mostly used in reforming operation is a bifunctional metallic catalyst typically - Pt-Re/Al_2O_3, providing the metal site and the acid site. In the initial stage, the desulfurized feed is mixed with hydrogen (in a mixer before preheating in heat exchanger (EX-01). The preheated feed, after mixing with hydrogen, is passed through fired heater H-01, where its temperature is raised to the required reaction temperature of 450–550 °C before entering the first catalytic reactor, R-01. The effluent from R-01 is then directed to fired heater H-02, where it is reheated to the required reaction temperature before entering the second reactor, R-02. Similarly, the effluent from R-02 is passed through fired heater H-03 to restore the temperature required for reaction before entering the third reactor, R-03. The use of interstage heaters is necessary because the principal reforming reactions are predominantly endothermic and consequently result in a reduction in temperature as the reaction proceeds through each reactor. The effluent from R-03 subsequently passes through the feed/product heat exchanger, EX-01, where heat is recovered to preheat the incoming fresh feed. The cooled effluent then enters the phase separator, D-02, where the hydrogen-rich gas phase is separated from the liquid reformate. The hydrogen-rich gas may then be recycled and mixed with the fresh feed upstream of R-01, while the liquid reformate is withdrawn as the bottom product.

2.4 EQUIPMENT DESIGN

2.4.1 Design Equations

The following were the equations used in the design of the various components of the CRU.

1. REACTORS

- **REACTOR DESIGN EQUATION (PACKED BED REACTOR)**
- **REACTOR PRESSURE DROP EQUATIONS**

$$\Delta P_B = 150 \cdot \left(\frac{\mu \cdot v_s}{D_p^2}\right) \cdot \frac{(1-\varepsilon)^2}{(\varepsilon)^3} + 1.75 \cdot \left[\frac{\rho \cdot (v_s)^2}{D_p}\right] \cdot \frac{(1-\varepsilon)}{(\varepsilon)^3}$$

Where

μ = average viscosity at inlet condition
vs = superficial viscosity
Dp = catalyst particle size
ρ = catalyst particle density
ε = bed void space

$$W = \int_{F_{Ao}}^{F_{A1}} \frac{1}{r_A} \, dF_A$$

(1)

- **TRANSPORT EQUATIONS**

$$LHSV = \frac{Mass_flowrate_inlet}{Mass_catalyst}$$

(2)

- **REACTOR PRESSURE DROP EQUATIONS**

$$\Delta P_B = 150 \cdot \left(\frac{\mu \cdot v_s}{D_p^2}\right) \cdot \frac{(1-\varepsilon)^2}{(\varepsilon)^3} + 1.75 \cdot \left[\frac{\rho \cdot (v_s)^2}{D_p}\right] \cdot \frac{(1-\varepsilon)}{(\varepsilon)^3}$$

Where

μ = average viscosity at inlet condition
vs = superficial viscosity
Dp = catalyst particle size
ρ = catalyst particle density
ε = bed void space

(3)

2. HEAT EXCHANGER

(4a)

Where

Q = Heat Transfer Rate
U= Overall Heat Transfer Coefficient
A= Heat Transfer Area
Th_1 = Hot fluid Inlet
Th_2 = Hot fluid outlet
Tc_1 = Cold fluid Inlet
Tc_2 = Cold fluid outlet
D= Heat transfer diameter (mm)
L= Heat transfer Length (mm)
Re = Reynolds No.
μ = Viscosity
ρ = Density (kg/)
V= Velocity (m/s)
k = Thermal Conductivity
Cp = Specific heat capacity

$$Q = UA\Delta T_m$$

$$A = \frac{\pi D^2 L}{4}$$

$$\Delta T_m = \frac{(Th_2 - Th_1) - (Tc_2 - Tc_1)}{\ln\left[\frac{Th_2 - Th_1}{Tc_2 - Tc_1}\right]}$$

$$Re = \frac{\rho V D}{\mu}$$

$$Pr = \frac{Cp\,\mu}{K}$$

(4b)

(4c)

(4d)

(4e)

3. FIRED HEATER

$$q_T = 0.173 f\left[\left(\frac{T_G}{100}\right)^4 - \left(\frac{T_S}{100}\right)^4\right]\alpha_{CP} A_{CP} + hA(T_G - T_S)$$

$$N_{tubes} = \frac{Q}{2\pi r L q} \text{ where } r = d_o / 2$$

$$A_{CP} = ctc \times L \times N$$

Where
f - overall exchange factor.

T_G - temperatures of the flue gases leaving the radiant section
T_S - surface temperature of the tubes.
A_{CP} - equivalent cold plane surface area, ft^2 ,
α_{CP} is a factor by which A_{CP} must be reduced to obtain effective cold surface.
$h \approx 2$, $A \approx 2\alpha_{CP} A_{CP}$ and $f \approx 0.57$
(5a)

(5b)
(5c)

2.4.2 Summary of Material and Energy Balance

The material balance was established for the steady-state design basis of the 5 BPSD catalytic reforming unit. The calculated feed rate to the reforming section was 25.72 kg/h, comprising 8.57 kg/h of paraffins, 10.54 kg/h of naphthenes, 6.51 kg/h of aromatics and 0.10 kg/h of hydrogen. The component balances across the three (3) reactors show the progressive conversion of paraffins and naphthenes to aromatics, accompanied by hydrogen generation. The principal material-balance results for the reactor train and final product separation are summarized in Table 3.

Table 3: Summary of material balance across the catalytic reforming unit

Stream/Unit	**Paraffins (kg/h)**	**Naphthenes (kg/h)**	**Aromatics (kg/h)**	**H_2 (kg/h)**	**Total (kg/h)**
Feed to CRU	8.57	10.54	6.51	0.10	25.72
R-01 outlet	3.43	5.40	11.65	5.24	25.72
R-02 outlet	1.37	3.34	13.71	7.30	25.72
R-03 outlet	0.55	2.52	14.53	8.12	25.72
Separator gas product	—	—	—	7.714	8.0609
Separator liquid reformate	0.5445	2.4696	14.240	0.7529	17.6601

However, the computed mass flow of the total continues to be nearly 25.72 kg/h in the reactor train. On the other hand, the mass flow of the components varies increasingly due to reforming reactions. For instance, aromatics rise from 6.51 kg/h in the feed stream to 14.53 kg/h on the effluent side of R-03. Similarly, paraffins and naphthenes decrease from 8.57 and 10.54 kg/h to 0.55 and 2.52 kg/h respectively. Hydrogen rises from 0.10 kg/h in the feed to 8.12 kg/h on the effluent side of R-03, which is indicative of hydrogen formation as a result of dehydrogenation reactions.

Table 4: Summary of calculated energy requirements for the major process units

Equipment	**Function**	**Calculated energy requirement / enthalpy change (MJ/h)**
EX-01	Feed/product pre-heater	74.62
H-01	Feed heating before R-01	201.58
R-01	Endothermic catalytic reforming	8,289.82
H-02	Interstage heating before R-02	1,088.55
R-02	Endothermic catalytic reforming	11,787.37
H-03	Interstage heating before R-03	11,800.65
R-03	Endothermic catalytic reforming	11,797.63

The energy requirements presented in Table 4 were determined from the enthalpy differences between the inlet and outlet process streams for each unit. The calculated heat-transfer duties for EX-

01, H-01, H-02 and H-03 were 74.62, 201.58, 1,088.55 and 11,800.65 MJ/h, respectively. For the reactors, the calculated enthalpy changes associated with the endothermic reforming reactions were 8,289.82, 11,787.37 and 11,797.63 MJ/h for R-01, R-02 and R-03, respectively. These values provided the thermal basis for the design of the heat-transfer equipment and the assessment of the energy requirements of the three-stage reforming process.

2.4.3 Numerical Design Outputs

The major equipment involved in the design comprises the surge drum, feed-to-product heat exchanger, three fixed-bed catalytic reactors, three interstage fired heaters and a phase separator. The calculated reactor volumes were 0.02, 0.03 and 0.04 m³ for R-01, R-02 and R-03, respectively, with corresponding catalyst bed lengths of 277, 417 and 695 mm, and overall heights of 805.2, 923.0 and 1203.0 mm respectively. The calculated fired heater duties for H-01, H-02 and H-03 were 201.58, 1088.55 and 11,800 MJ/h, respectively. The phase separator was designed as a vertical cylindrical vessel with a diameter of 203.2 mm, an overall height of 900 mm and a gross internal volume of 0.0281 m³. The summary of the calculated design parameters is presented in Table 5 and provides the basis for preparation of the equipment drawings and fabrication of the pilot-scale catalytic reforming unit.

Table 5: Summary of calculated design parameters of the 5 BPSD catalytic reforming unit

Equipment	Design parameter	Value
Surge drum D-01	Volume	0.20 m³
	Diameter	500 mm
	Length	1000 mm
Heat exchanger EX-01	Type	Double-pipe, counter-current
	Tube diameter	19.4 mm
	Shell diameter	205 mm
	Heat-transfer area	0.036 m²
Reactor R-01	Volume	0.02 m³
	Overall height	805.2 mm
	Catalyst-bed length	277 mm
Reactor R-02	Volume	0.03 m³
	Overall height	923.0 mm
	Catalyst-bed length	417 mm
Reactor R-03	Volume	0.04 m³
	Overall height	1203.0 mm
	Catalyst-bed length	695 mm
Fired heater H-01	Heat duty	201.58 MJ/h
Fired heater H-02	Heat duty	1088.55 MJ/h
Fired heater H-03	Heat duty	11,800 MJ/h
Phase separator D-02	Diameter	203.2 mm
	Overall height	900 mm
	Gross volume	0.0281 m³

2.5 WORKING DRAWINGS / MODELS

Figures 3 – 9 presents the working drawings and models based on the equipment design calculations. The drawings were very essential as they served as working templates for fabrication.

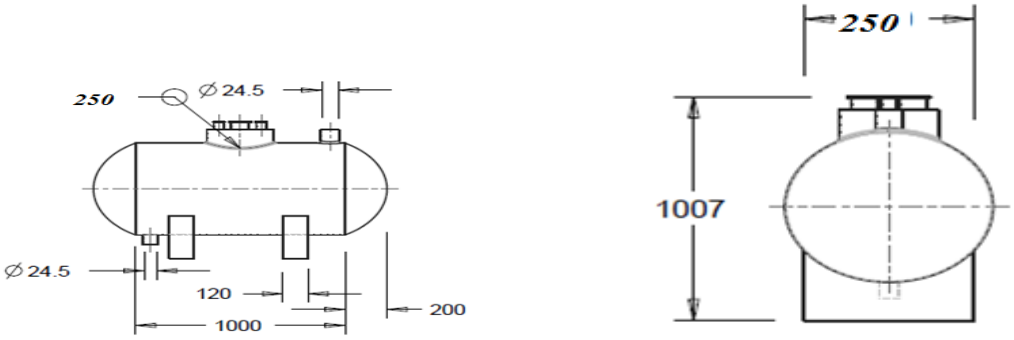

igure 3: Working Drawing of Surge Drum

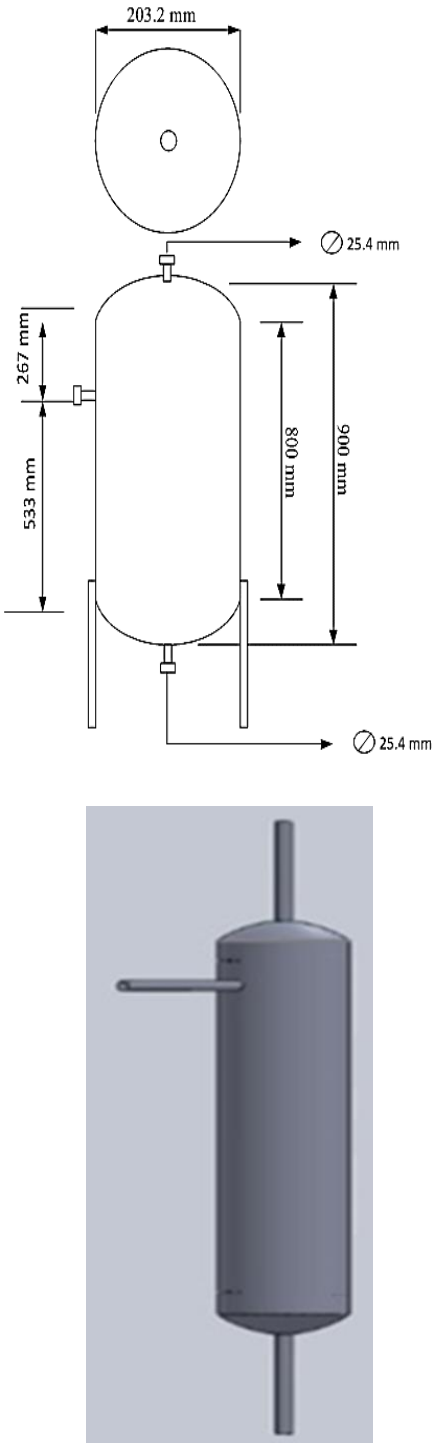

Figure 4: Working Drawing/Models of Phase Separator

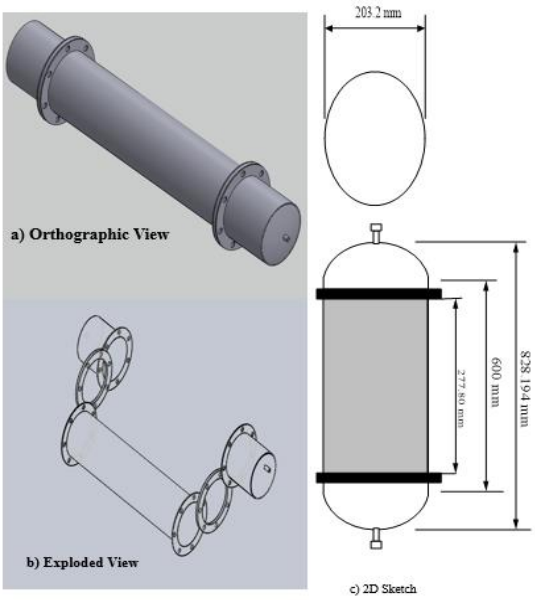

Figure 5: Working Drawing/Models of CRU Reactor (01)

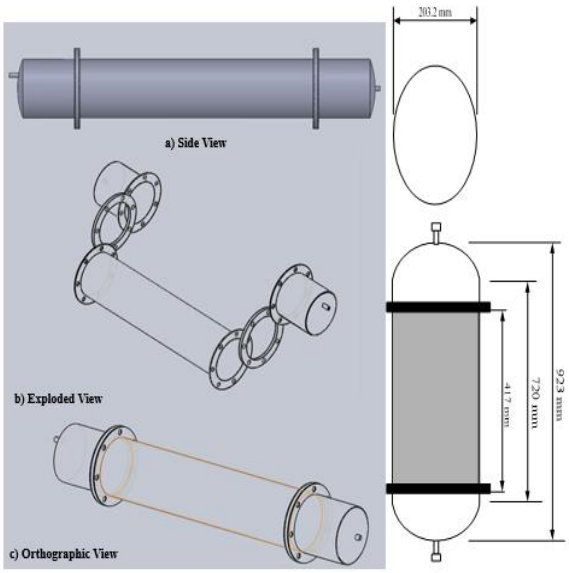

Figure 6: Working Drawing/Models of CRU Reactor (02)

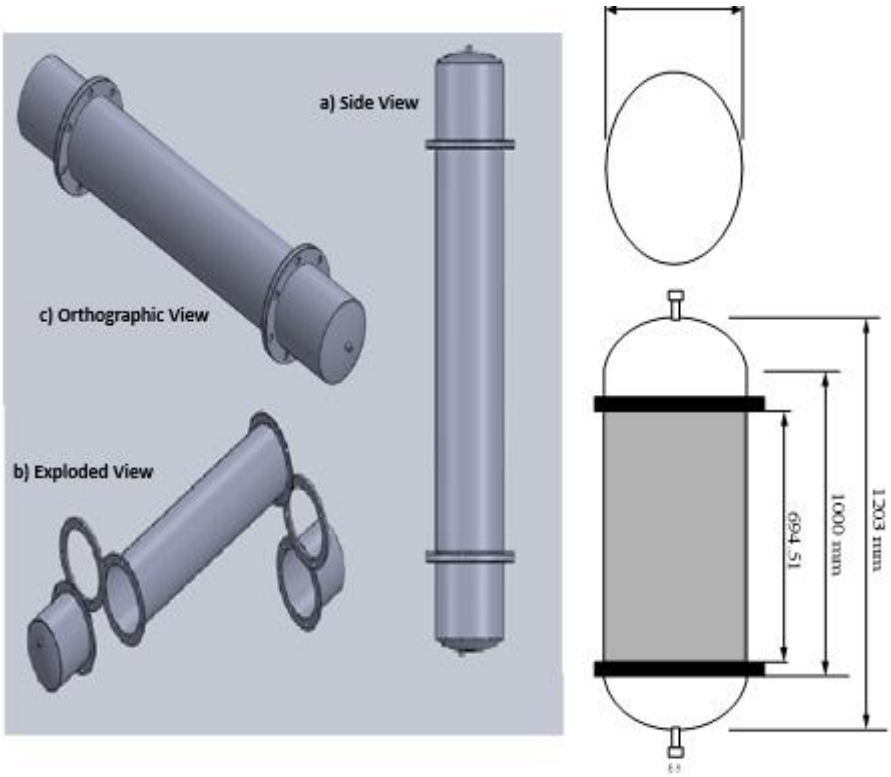

Figure 7: Working Drawing/Models of CRU Reactor (03)

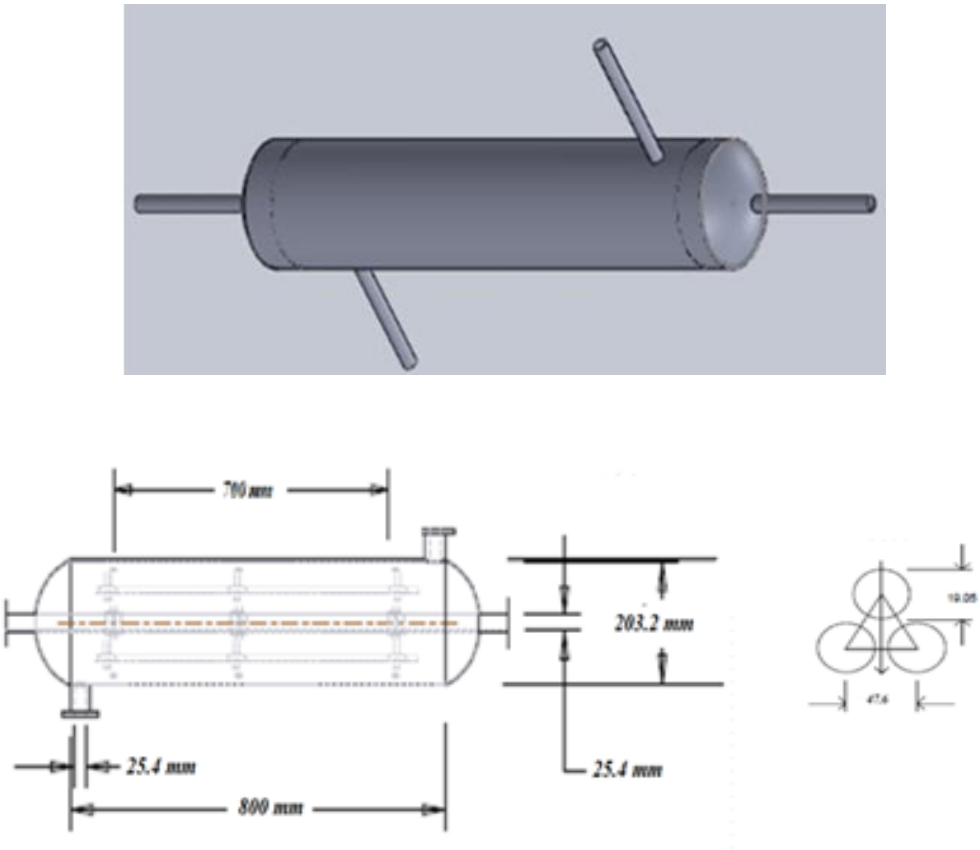

Figure 8: Working Drawing/model of Heat Exchanger

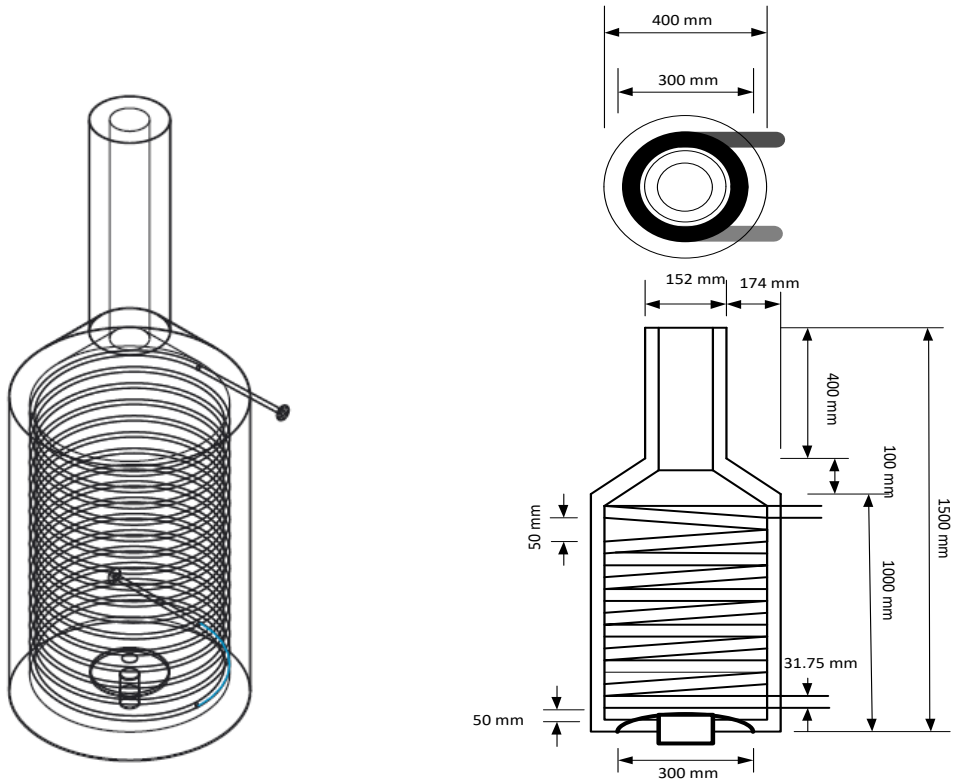

Figure 9: Working Drawing of Fired Heater

2.6 ECONOMIC CONSIDERATIONS, LOCAL FABRICATION AND SCALE-UP POTENTIAL

The fabrication of the 5 BPSD catalytic reforming unit was performed keeping in mind the use of locally available engineering materials, shop facility and fabricating skills. Some of the major equipment fabricated were the surge drum, feed/product heat exchanger, three fixed bed catalytic reactors, three fired heaters and the phase separator. This helped reduce the need for imported proprietary pilot scale equipment and proved the practicability of transforming the process design to a functioning pilot plant by utilizing local engineering and fabrication skills.

Economically speaking, there are advantages associated with local fabrication of equipment for pilot-scale petroleum processing studies because it helps in designing and manufacturing the equipment according to the needs of the specific application and not purchasing as imported packages. It also helps in modifying, maintaining and replacing parts of the apparatus as well as upgrading the apparatus in accordance with further experimental requirements. But, the current study focused mainly on the technical design and fabrication of the unit and a detailed techno-economic study or a life cycle cost analysis of the items used was out of its scope. Hence, no general statement is made about the cost advantage of the fabricated unit over the imported commercial equipment.

The local fabrication technique also offers a way for future scaling up and commercialization of the system. The current 5 BPSD unit serves as a platform for generating operating data, performance of equipment and fabrication experience before proceeding onto building large units. Future scaling up must maintain the same process arrangement developed in the current study and include proper scaling changes in the size of equipment, heat transfer capabilities, sizing of reactors, instrumentation and control of processes as well as material used. It must also be accompanied by a detailed capital cost estimation, cost comparison of fabrication, energy consumption and economic feasibility study. Such studies will establish the commercial feasibility of locally made catalytic reforming systems and the identification of components that can be locally made and those that require special procurement.

3. RESULTS AND DISCUSSION

3.1 Equipment Fabrication

All the three (3) reactors are fabricated using stainless steel though mild steel was used in other units such heat exchanger and in phase separator as opposed to stainless steel specified by Aspen Hysys as the material of construction. The equipment was originally specified for fabrication from stainless steel; however, mild steel was used for selected components during fabrication because of cost and local material availability. The use of mild steel for appropriately selected refinery and process equipment is consistent with established industrial practice world wide, Accordingly, the use of mild steel in selected components of the pilot unit does not in itself constitute a process-design deficiency, although the material must remain compatible with the operating environment and be appropriately protected and monitored. The fabricated units are presented in Plate 1-4.

Plate 1a : Parts of the three Fabricated Reactors

Plate 1b : The three Fabricated Reactors

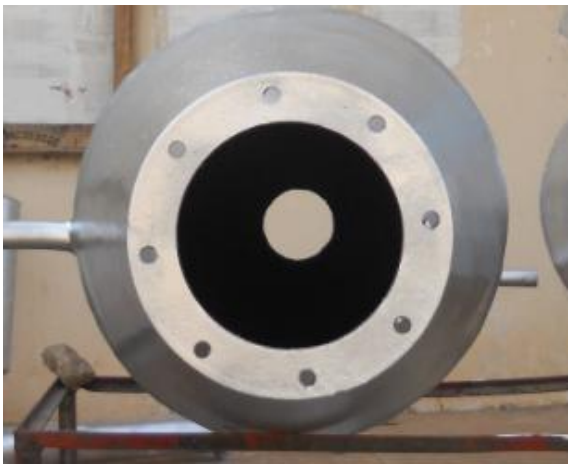

Plate 2: CRU Fired-Heater

Plate 3a: Heat Exchanger bundles

Plate 3b: Heat Exchanger tube

Plate 4: Surge Drum

3.2 ASSEMBLY/ INSTALLATION OF CRU PLANT

This section presents the installation process for putting up the unit. This involves the installation of all fabricated units, piping, as well as installation of controls such as flow valves, pressure gauges and thermocouples. It also covers the installation of three burners for the fabricated fired heaters. All these are presented in Plate 5 and the model of the installed unit is depicted using SOLID WORKS 2016 in Figure 10 (a & b).

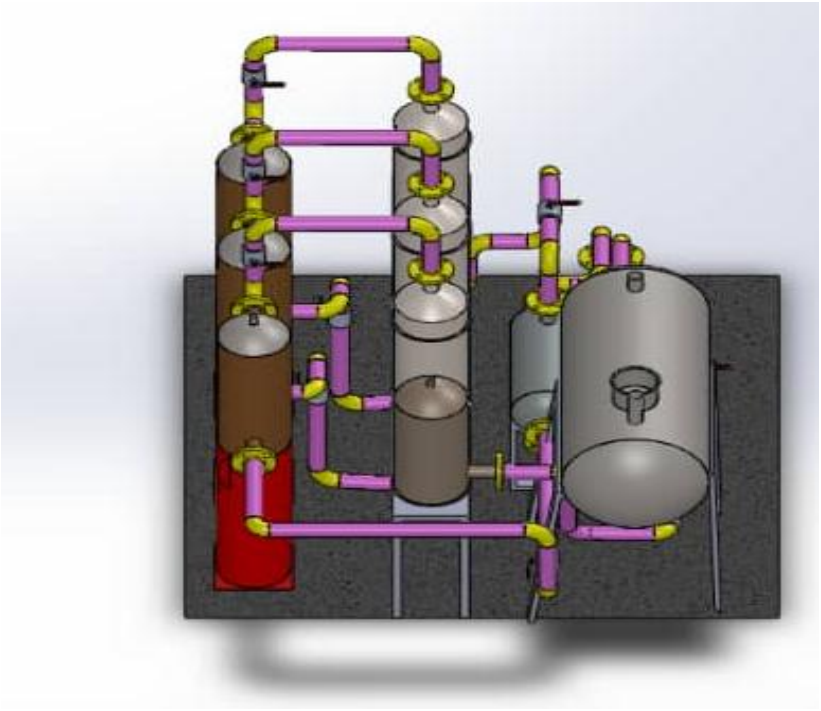

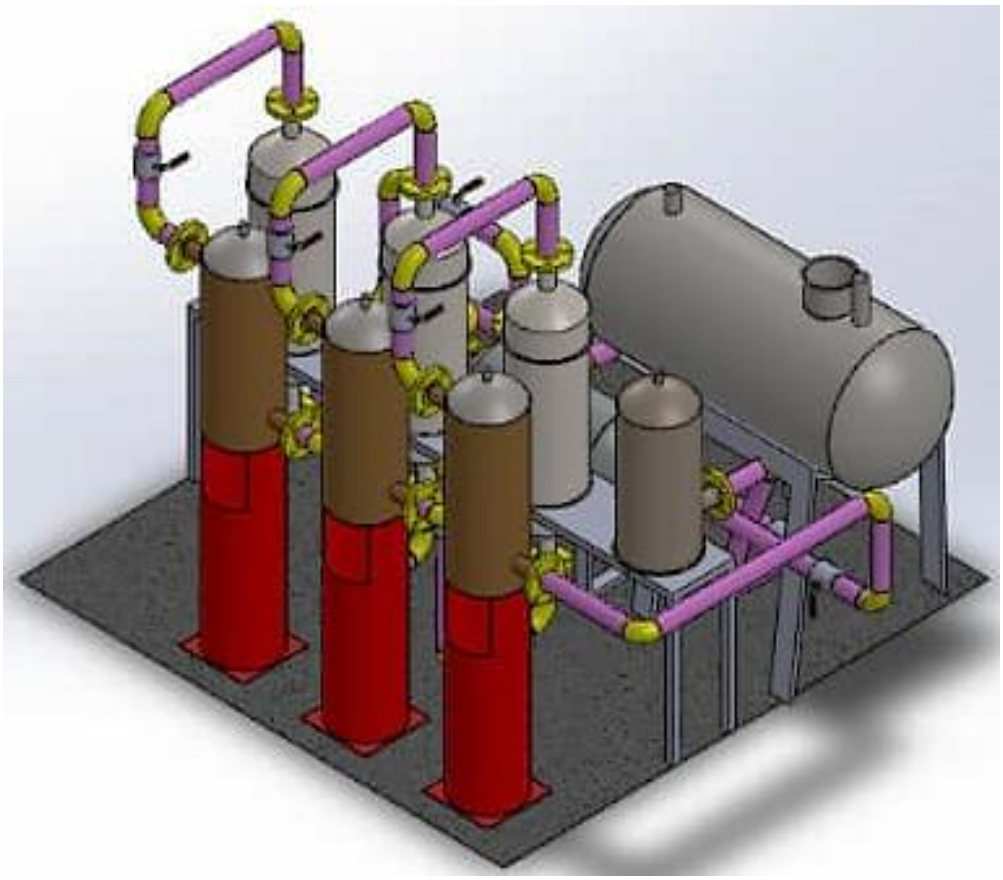

Figure 10 (a & b): 3D Diagram of the installed CRU

Plate 5: Cladding and Lagging

3.3 RON and MON of Fabricated CRU Processed Naphtha

The final experimental operation was conducted at a reactor temperature of between 460 – 480 °C and an operating pressure of approximately 3 bar and a feed rate was approximately 22.2 kg/h (0.5 L/min)**.** Although hydrogen addition was included in the design and simulation basis, no external hydrogen was introduced during the actual test run**.** These conditions differed from the original design simulation basis.

To actually have a basis for interpreting the experimental results, a comparison with the design parameters is presented in Table 6.

Table 6: Comparison of design/simulation and actual test-run operating conditions

Parameter	**Design/Simulation**	**Actual Test Run**
Reactor temperature	450 – 550 °C	460 – 480 °C
Operating pressure	6 bar	Approximately 3 bar
Feed rate	25.72 kg/h (0.58 L/min)	22.2 kg/h (0.50 L/min)
Hydrogen addition	0.10 kg/h	None

The actual operating conditions represent the conditions recorded during the experimental test run, whereas the design/simulation values represent the original process-design basis. The comparison presented in Table 6 shows that, although the experimental reactor temperature remained within the design temperature range, the unit was operated at a substantially lower pressure and feed rate than the design basis, and no external hydrogen was introduced. These differences are important when interpreting the experimentally obtained reformate quality because the test run did not reproduce all of the conditions used for the original design and simulation.

Following the test run, samples of the naphtha feed and the resulting reformate were collected for octane number evaluation. The Research Octane Number (RON) and Motor Octane Number (MON) were measured using a hand-held Octanometer capable of measuring both RON and MON**.** The instrument used for the measurements is shown in Plate 7**.**

Plate 7: Hand-held Octanometer used for experimental determination of RON and MON of the naphtha feed and reformate.

The feed naphtha recorded 62 RON and 58 MON, whereas the reformate obtained from the fabricated catalytic reforming unit recorded 71 RON and 64 MON, respectively. Thus, the experimental process resulted in an increase of 9 RON points and 6 MON points relative to the feedstock. The experimental results are presented in Table 7.

Table 7: RON and MON of the feed and reformate

Parameter	Feed	Experimental Reformate	Predicted Reformate
RON	62	71	100
MON	58	64	84

The experimental results from Table 7 demonstrated that the fabricated reforming unit produced a measurable improvement in the octane quality of the heavy naphtha feed. However, the experimentally obtained RON of 71 and MON of 64 values were lower than the predicted reformate values (RON of 100 and MON of 84) and the higher octane values generally associated with commercial catalytic reforming. This difference is attributable to the disparity between the design simulation conditions and the actual test conditions as presented in Table 6. In particular, the experimental run was conducted at approximately 3 bar and without external hydrogen addition, while hydrogen addition was included in the design and simulation basis. The actual operating conditions, together with the use of manually operated controls and possible limitations in catalyst performance, may therefore have contributed to the lower experimental octane improvement.

The available experimental record contains single reported measurements for the feed and reformate. Replicate measurements and associated experimental uncertainty were not recorded during the original test campaign. Consequently, statistical uncertainty is not reported for the RON and MON values. Future experimental studies should include replicate measurements, documented instrument calibration and measurement uncertainty to improve the reproducibility and statistical reliability of the octane results.

Table 8: Comparison of the fabricated pilot-scale catalytic reforming unit with established industrial practice

Parameter	Fabricated pilot-scale unit	Established industrial practice
Capacity	5 BPSD	Published industrial catalytic reformers include 32,000 BPSD (Paulsboro); 40,000 BPSD (Chalmette); 35,000 BPSD (KNPC) reforming units.
Reactor configuration	3 fixed-bed reactors	3–4 reactors in series are used in conventional fixed-bed/semi-regenerative catalytic reforming configurations.
Catalyst	Pt–Re/Al_2O_3	Pt–Re/Al_2O_3 is an established catalyst formulation for naphtha reforming.
Reformate RON	71	Approximately 95–102, depending on feedstock and reforming severity.

Source: Present study; Yusuf et al. (2019); Mazzieri et al. (2005); U.S. Energy Information Administration (EIA) (2026), Kuwait National Petroleum Company (KNPC) (2025).

The 5 BPSD capacity of the fabricated plant is quite considerably smaller as compared to that of existing commercial industrial catalytic reforming plants (See Table 8). Existing operational commercial plants include 32,000 BPSD catalytic reforming plant of the Paulsboro refinery and 40,000 BPSD catalytic reforming plant of the Chalmette refinery. Moreover, there are two continuous catalytic reforming plants of capacity 35,000 BPD installed in Kuwait National Petroleum Company (KNPC) Clean Fuels Project. This is just an illustration of the difference in the capacity of the local fabricated pilot plant as opposed to commercial refinery reformers.

4. CONCLUSIONS AND RECOMMENDATIONS

4.1 Conclusions

i. This study successfully achieved the design, fabrication, installation and test-run of a 5 BPSD pilot-scale semi-regenerative catalytic naphtha reforming unit for the processing of straight-run heavy naphtha. The study commenced with characterization of the Escravos heavy hydrotreated naphtha used as the design feedstock and establishment of the process design basis. The selected semi-regenerative configuration comprised three fixed-bed catalytic reactors arranged in series, with interstage heating, consistent with the requirements of catalytic naphtha reforming.

ii. The process material balance established a design feed rate of 25.72 kg/h to the reforming section. The component balances demonstrated progressive conversion of paraffins and naphthenes to aromatics through the three reactor stages, accompanied by hydrogen generation. The paraffin content decreased from 8.57 kg/h in the feed to 0.55 kg/h at the outlet of R-03, while naphthenes decreased from 10.54 to 2.52 kg/h. In contrast, aromatics increased from 6.51 to 14.53 kg/h and hydrogen increased from 0.10 to 8.12 kg/h. The final separator further divided the reactor effluent into an H_2-rich gas stream and liquid reformate, demonstrating the intended material-separation function of the process.

iii. The energy-balance calculations provided the thermal design basis for the process equipment. The calculated heat-transfer duty for EX-01 was 74.62 MJ/h, while the fired-heater duties for H-01, H-02 and H-03 were 201.58, 1088.55 and 11,800.65 MJ/h, respectively. The corresponding calculated endothermic heat requirements of R-01, R-02 and R-03 were 8,289.82, 11,787.37 and 11,797.63 MJ/h, respectively. These calculations, together with the material balances, provided the basis for sizing and specifying the principal equipment of the pilot plant, including the surge drum, heat exchanger, fired heaters, fixed-bed reactors and phase separator.

iv. The resulting equipment was successfully fabricated and assembled into an operational pilot-scale reforming unit. The fabricated system comprised surge drum D-01, feed/product heat exchanger EX-01, phase separator D-02, three fired heaters (H-01, H-02 and H-03) and three fixed-bed

reactors (R-01, R-02 and R-03). The successful installation and test run demonstrate the practical feasibility of translating the process design and equipment calculations into an indigenous pilot-scale catalytic reforming facility.

v. Experimental evaluation of the produced reformate gave a RON of 71 and MON of 64, compared with feed values of 62 and 58, respectively. Thus, the reforming operation produced an improvement in both measured octane indices, although the resulting reformate quality remained below the commercial gasoline quality values considered in this study. The relatively modest octane improvement is interpreted in the context of the actual pilot-plant operating conditions, including the relatively low operating pressure, operation at approximately 460–480 °C, absence of hydrogen addition during the test run and manual process control. Other process variables may also have contributed to the observed product quality. The available experimental results do not permit the effect of any single factor to be isolated.

vi. The study demonstrates the feasibility of designing and fabricating an indigenous 5 BPSD catalytic naphtha reforming pilot unit and provides a practical platform for further investigation of catalyst performance, process optimization, reformate quality and hydrogen production. The fabricated unit also provides an experimental bridge between process-design calculations and practical refinery-process operation and can support subsequent studies aimed at optimizing the operating conditions and improving the performance of locally developed refining technology.

4.2 Recommendations

The following recommendations can be made based on the limitations and results obtained from this study:

i. Operating conditions should be optimized in the fabricated pilot-scale catalytic reforming unit with particular emphasis being put on reactor temperature, operating pressure, hydrogen to hydrocarbon ratio and feed rate to enhance the severity of the reforming process and improve the quality of octane in the produced reformate.

ii. Hydrogen circulation or hydrogen to hydrocarbon ratio should be applied in future experiments in order to investigate its effect on catalyst stability, reforming performance and quality of RON and MON in the produced reformate.

iii. The pilot plant should be installed with better instruments and process-control system for improved and better controlled reforming process with respect to reactor temperature, pressure, feed rate and other operating conditions.

iv. Further experiments on the fabricated pilot unit should be done at different operating conditions for establishment of process variables versus reformate octane quality and identification of optimum operating conditions for the unit.

REFERENCES

Ali, S. A., Alshareef, A. H., Theravalappil, R., Alasiri, H. S., & Hossain, M. M. (2023). Molecular kinetic modeling of catalytic naphtha reforming: A review of complexities and solutions. *Catalysis Reviews: Science and Engineering, 65*(4), 1358–1411.

Aznárez, M., Korili, S. A., & Gil, A. (2024). Progress and recent novelties in naphtha reforming catalysts. *Journal of Environmental Chemical Engineering, 12*(3), 113066.

Bell, D. C. (2001). Catalyst cycle length optimization for catalytic reformers. *Hydrocarbon Processing, 80*(6), 59–65.

Gary, J. H., Handwerk, G. E., & Kaiser, M. J. (2007). Petroleum refining: Technology and economics (5th ed.). CRC Press.

Jones, D. S., & Pujadó, P. R. (2006). Handbook of petroleum processing. Springer.

King, R. W. (2013). Petroleum refining: Design and applications handbook. Wiley.

Kuwait National Petroleum Company (KNPC). (2025). *Achievements Continue: Clean Fuels Project***.** Kuwait National Petroleum Company**.**

Mazzieri, V. A., Grau, J. M., Vera, C. R., Yori, J. C., Parera, J. M., & Pieck, C. L. (2005). Pt-Re-Sn/Al_2O_3 trimetallic catalysts for naphtha reforming processes without presulfiding step. *Applied Catalysis A: General, 296*(2), 216–221. https://doi.org/10.1016/j.apcata.2005.08.028.

Meyers, R. A. (2004). Handbook of petroleum refining processes (3rd ed.). McGraw-Hill.

Pérez, M., Rodríguez, J., & González, L. (2025). Transitional analysis for multi-objective operative improvement of reformate quality and hydrogen production from a catalytic naphtha reforming process. *Heliyon, 11*, e41428.

Ritov, E. and Dana, A. G. (2026). Predictive chemical kinetic modeling of CO2 conversion via Pt-catalyzed dry methane reforming, Next Chemical Engineering, Volume 2, 2026,100035, ISSN 3050-7243, https://doi.org/10.1016/j.nxcen.2026.100035.

Ruban, N.V., Shigarov, A.B., Rogozhnikov, V.N., Galvita, V.V., Thybaut, J.W., and Potemkin, D. I. (2026). From laboratory-scale autothermal reforming to practical reformer design: Modeling and scale-up of Pt-based structured catalysts, Chemical Engineering Journal, Volume 534, 2026, 174987, ISSN 1385-8947, https://doi.org/10.1016/j.cej.2026.174987.

Saeidi, S., Amin, N. A. S., & Rahimpour, M. R. (2014). Hydrogen production: Perspectives, separation with special emphasis on kinetics of reforming processes. *Renewable and Sustainable Energy Reviews, 32*, 294–309.

Speight, J. G. (2014). The chemistry and technology of petroleum (5th ed.). CRC Press.

Speight, J. G. (2020). Handbook of petroleum refining. CRC Press.

Towler, G., & Sinnott, R. (2022). Chemical engineering design: Principles, practice and economics of plant and process design (3rd ed.). Elsevier.

U.S. Energy Information Administration (EIA). (2026). *Refinery Capacity Report: With Data for January 1, 2026*. U.S. Department of Energy.

Yusuf, A. Z., John, Y. M., Aderemi, B. O., Patel, R., & Mujtaba, I. M. (2019). Modelling, simulation and sensitivity analysis of naphtha catalytic reforming reactions**.** *Computers & Chemical Engineering, 130*, 106531. https://doi.org/10.1016/j.compchemeng.2019.106531.

Zhang, H., Li, Y., Wang, X., & Liu, Z. (2022). Recent advances in catalytic reforming catalysts for clean fuel production: A review. *Catalysts, 12*(9), 1048.

International Conference on Engineering Innovation for Sustainable Development (ICESID 2026)
Faculty of Engineering, Ahmadu Bello University Zaria · 8–10 September 2026

DESIRABILITY-BASED MULTI-RESPONSE OPTIMIZATION OF FLEXURAL PERFORMANCE IN BAMBOO AND STEEL REINFORCED CONCRETE BEAMS

Chukwu Mbazor[1,*], J. M. Kaura[1], A. Ocholi[1], J. Ochepo[1]

[1]""

Email: chuksmb@gmail.com[*], jmkaura@abu.edu.ng, amanaocholi@gmail.com, ochepo1@gmail.com

***Corresponding author**: Chukwu Mbazor

DOI: https://doi.org/10.67203/sp.ICESID.2026

ABSTRACT

This study presents comparative optimization and predictive modeling of the flexural properties (deflection and failure load) of bamboo- and steel-reinforced concrete beams at a target grade of 25 MPa. Using Optimal Custom Design (OCD) in Response Surface Methodology (RSM), the effects of curing age (7–28 days) and reinforcement areas (145–580 mm² for bamboo; 50.3–201.2 mm² for steel) were analyzed. Sequential model sum of squares recommended third-order cubic polynomial models, while analysis of variance (ANOVA) validated their significance at a 99.99% confidence level. Residual diagnostics indicated approximately normally distributed experimental errors. The fit summaries showed high predictive power, with adjusted R^2 values of 0.9984–0.9992, predicted values agreeing within 0.2, and adequate precision ratios ranging from 175.18–242.13, exceeding the threshold of 4. Multi-response optimization minimized deflection and maximized failure load. For bamboo-reinforced concrete, the optimum was 9.588 days curing age and 580.000 mm² bamboo area, producing 4.692 mm deflection, 9.471 kN failure load, and 0.785 desirability. For steel-reinforced concrete, the optimum was 9.926 days and 201.200 mm² steel area, producing 6.229 mm deflection and 13.865 kN failure load. Approximately 10 days curing age was optimal for both. Steel-reinforced concrete was 24.67% more ductile and sustained 31.70% more load than bamboo-reinforced concrete. Desirability values were 0.785 and 0.782, respectively. The findings demonstrate bamboo's potential as a substitute for steel reinforcement in low-cost housing.

Keywords: *Bamboo-reinforced concrete; Response Surface Methodology (RSM); Optimal Custom Design (OCD); Flexural properties (deflection & failure load); multi-response optimization; Desirability function*

1. INTRODUCTION

Steel-reinforced concrete remains one of the most important developments in structural engineering since its introduction in the nineteenth century. Its widespread application is largely attributable to the favourable properties of concrete, including high compressive strength, durability, relatively low maintenance demand, and the ability to be moulded into different forms (McCormac & Brown, 2014). Steel complements concrete by addressing its principal limitation, namely, its relatively poor tensile capacity. The continued success of steel-concrete composite action is also associated with the comparatively low cost of steel among metallic materials. Iron, which constitutes the principal component of steel, is described as the least expensive and most extensively used metal (USGS, 2019). Fibre Reinforced Polymers (FRP) offer mechanical characteristics comparable to, and durability greater than, those of steel; however, their substantially higher cost limits their economic attractiveness (Burgoyne & Balafas, 2007).

A comparison based on volume is more appropriate when steel is evaluated against bamboo because the strength contribution of a reinforcing material depends on its cross-sectional area rather than simply on its mass. Steel is also considerably denser than bamboo, with reported densities of approximately 7.6 ton/m3 and 0.65 ton/m3, respectively. Although establishing an exact market price for bamboo may be difficult, available evidence indicates that bamboo is substantially less costly than steel. Its prevalence in developing countries further enhances its potential as a locally accessible reinforcement material, particularly in locations where steel may be difficult to obtain (Ghavami, 1995; Sharma, 1990).

The search for alternatives to steel has consequently been encouraged by the need for reinforcement materials that are economical and readily obtainable, particularly within developing economies. The concept of using bamboo to reinforce concrete is also longstanding. Chow (1914) conducted an early investigation at MIT into bamboo reinforcement, motivated by bamboo's high tensile strength and widespread availability in China. Since then, reduction in construction expenditure has remained a major justification for considering bamboo as reinforcement. At the same time, population growth continues to increase demand for construction materials, contributing to rising material costs and greater environmental pressure. The need for economical and environmentally sustainable construction materials is particularly significant because the construction sector accounts for about 50% of global raw-material consumption (Pacheco-Torgal & Labrincha, 2013).

Response Surface Methodology (RSM) comprises mathematical and statistical procedures for examining and optimizing processes in which several independent variables influence a measurable response. Its application enables the researcher to establish relationships between process variables and the response and to determine factor combinations capable of producing a desirable outcome. RSM is also applicable to product development, formulation, design improvement, and process enhancement (Montgomery, 2020).

Where experimental resources are inadequate for determining the absolute optimum response, RSM can still provide useful information about the behaviour of the system. If a known deterministic relationship exists between the response and experimental factors, suitable factor levels may be established mathematically. However, practical systems frequently exhibit complicated or poorly understood relationships. In such cases, empirical modelling provides a suitable means of representing the response and identifying favourable operating conditions (Khuri & Cornel, 1996).

Central Composite Design (CCD) is a commonly applied RSM technique for developing second-order mathematical models. It combines a two-level factorial arrangement with centre and axial points and is particularly useful for studying quadratic relationships. Box and Wilson introduced the design as an alternative to conventional three-level factorial arrangements (Box & Wilson, 1951). The principal components of a CCD are the factorial portion, centre points, and axial points. The factorial component may be a complete or fractional (2^k) arrangement, with factor levels normally represented by −1 and +1. Centre points are located at the middle of the experimental region, whereas axial points are positioned along the factor axes at predetermined distances from the centre. Together, these components provide information for estimating main, interaction, and quadratic effects (Montgomery, 2020; Khuri & Cornel, 1996).

Box–Behnken Design, developed by Box and Behnken (1960), is another experimental strategy used in Response Surface Methodology. Its construction combines two-level factorial arrangements with balanced incomplete block designs (BIBD), producing a systematic distribution of experimental points within the factor space. A major benefit of BBD is its efficiency in terms of experimental runs. It can provide adequate information for response-surface modelling without requiring as many experimental observations as some alternative designs. Consequently, it is useful where experimental materials, time, labour, or financial resources are limited (Montgomery, 2020; Myers et al., 2016).

Conventional RSM designs such as CCD and BBD may become unsuitable when an experiment involves complex restrictions. Although individual factors may have defined upper and lower limits, these limits may not adequately represent the actual feasible experimental region. Consequently, conventional designs can generate experimental points in areas that are impractical, unsafe, or impossible to investigate.

Computer-generated optimal designs address this limitation by using algorithms to select experimental points according to the objectives and restrictions of a particular investigation. Their application is especially valuable where standard RSM designs cannot accommodate complicated constraints (Anderson & Whitcomb, 2017; 2007).

Such designs are also applicable where the required predictive model is more complex than a conventional quadratic model. For example, prior process knowledge may indicate the need for cubic terms, for which CCD or BBD may not provide sufficient information. Optimal designs can additionally accommodate categorical factors, such as different catalyst types or configurations, alongside quantitative process variables (Anderson & Whitcomb, 2007).

Response Surface Methodology has been applied to concrete and cement-based materials for optimizing compositions and predicting engineering performance. Sridhar et al. (2022) used RSM

within a Design of Experiment framework to optimize the flexural moment of ferrocement composites containing galvanized square welded mesh and steel slag. A Central Composite Design was employed to determine suitable combinations of the investigated variables. Analysis of variance showed that the developed model was statistically significant, with a reported p-value below 0.05. The prediction-related errors were also reported to be below 20%, while the predicted responses corresponded satisfactorily with the experimental observations. The volume fraction of galvanized square welded mesh was identified as an important variable affecting flexural moment. Surface-response plots, Pareto analysis, and regression results further established its substantial influence on the flexural behaviour of the composites (Sridhar et al., 2022).

Kostić et al. (2016) applied RSM together with Monte Carlo simulation to develop a robust procedure for estimating concrete strength. Their model expressed concrete strength in relation to unit mass, water-to-cement ratio, age, and superplasticizer content. The resulting model demonstrated satisfactory accuracy during calibration and verification. Importantly, the verification stage used observations that were excluded from model development, thereby providing an independent evaluation of model performance. The residual analysis indicated normality during both stages, while uncertainty in the estimated coefficients had no statistically significant influence on concrete strength. The researchers also found that laboratory measurement variations had limited effects on predicted compressive strength, demonstrating the robustness of the developed approach.

Agarwal and John (2004) developed a reliability-based multidisciplinary design optimization framework using approximation techniques. Response Surface Approximations (RSA) were employed to represent limit-state functions and estimate failure probabilities while reducing the computational requirements associated with conventional Reliability-Based Design Optimization (RBDO). The methodology was tested using two problems. For a small analytical problem involving two design variables, significant computational savings were not obtained because constructing the RSA could require more effort than directly evaluating the reliability constraints. In contrast, substantial computational savings were achieved for a higher-dimensional multidisciplinary HPLC structural problem involving configuration, structural, and dynamic disciplines. The findings demonstrate that response-surface approximations can be particularly advantageous for computationally demanding multidisciplinary optimization problems.

Bamboo is a rapidly renewable lignocellulosic material belonging to the grass family Poaceae. Its combination of relatively low density, rapid growth, high specific strength and widespread availability has encouraged its investigation as an alternative construction material. However, bamboo should not be treated as a uniform engineering material because its physical and mechanical characteristics vary substantially with species, age, moisture content, growing conditions, culm geometry and position along the culm (Trujillo, 2013; Sharma et al., 2015).

Several species have been investigated for structural applications, including Bambusa vulgaris, Bambusa balcooa, Bambusa bambos, Dendrocalamus asper, Dendrocalamus strictus, Guadua angustifolia and Phyllostachys edulis. Guadua angustifolia has received considerable attention in structural engineering because of its favourable strength-to-weight characteristics, while Dendrocalamus and Bambusa species are important in Asian and African environments. Bambusa vulgaris is of particular interest in tropical regions because of its widespread availability, including in Nigeria. Nevertheless, the use of any local species in structural applications requires experimental characterization rather than assuming properties reported for another species. Reviews have identified species, age, location and treatment as important sources of variation in bamboo properties (Sharma et al., 2015; Maria et al., 2023).

The longitudinal arrangement of bamboo fibres gives the material comparatively high tensile strength parallel to the culm axis. This characteristic makes bamboo attractive for tensile applications. Conversely, its transverse properties are considerably weaker, and the natural hollow geometry and variation in wall thickness create additional challenges for structural detailing and connections.

The untreated bamboo culm is vulnerable to biological deterioration, particularly fungal attack and insects such as termites and beetles. Its relatively high concentration of starch and other soluble constituents contributes to this vulnerability. Consequently, treatment is generally considered necessary where bamboo is intended for long-term structural service.

Bamboo preservation techniques can broadly be divided into traditional/natural, chemical and physical treatments. Traditional methods include water immersion, smoking and controlled drying,

while chemical preservation commonly involves boron-based preservatives, particularly borax-boric acid formulations. Other approaches include pressure impregnation and copper-based preservatives. Treatment effectiveness depends on the ability of the preservative to penetrate the bamboo wall; therefore, treatment of only the external surface may not provide adequate protection for structural applications. Recent reviews also emphasize the need to standardize treatment procedures because different treatment methods can produce different effects on strength and durability (Maria et al., 2023).

Adequate durability therefore requires more than chemical preservation. Bamboo should be properly seasoned, treated throughout its thickness and protected from persistent moisture. Appropriate construction detailing—including drainage, ventilation, protection from direct wetting and separation from the ground—is equally important. These considerations have become part of modern structural-bamboo guidance. ISO 22156:2021 specifically includes durability as one of the performance requirements for structural bamboo (International Organization for Standardization (ISO) 2021).

The durability problem becomes more complex when bamboo is used as reinforcement in concrete. The concrete environment is highly alkaline, while bamboo is a lignocellulosic material. Research has reported deterioration of bamboo under prolonged alkaline exposure, while moisture movement between bamboo and concrete can cause swelling, shrinkage and loss of bond. Archila et al. (2018) consequently identified durability, bond and dimensional stability as major obstacles to the reliable use of bamboo as conventional reinforcement.

The development of standards has been important in moving bamboo from traditional construction towards engineered applications. ISO 22156:2021, Bamboo structures—Bamboo culms—Structural design, provides design provisions for structures whose primary load-bearing members are round bamboo culms or certain shear-panel systems. Its scope covers mechanical resistance, serviceability and durability and is principally directed towards relatively small bamboo structures, including one- and two-storey buildings not exceeding 7 m in height (International Organization for Standardization (ISO) 2021).

Statistical modelling and optimization techniques, including response surface methodology (RSM), provide useful means of examining relationships among influencing factors, responses, constraints, and optimization objectives (Usman et al., 2021). In the context of bamboo-reinforced concrete, the absence of established design codes, together with the increasing emphasis on sustainable and environmentally responsible construction, creates a need for systematic approaches to material and structural development. RSM offers a promising approach for evaluating and optimizing the combined effects of several parameters governing the engineering characteristics and performance of bamboo-reinforced concrete beams. Such modelling can improve understanding of the contribution of individual variables and their interactions while reducing the number of experimental trials required within the experimental programme to develop a numerical representation of the governing mechanisms and procedures (Usman et al., 2021). Accordingly, the adoption of RSM is justified in the present study.

2. MATERIALS AND METHODS

2.1 Materials

The data used for the predictive modelling as well as the model validation were obtained from experimental programs reported in the previous sections of this research for flexural properties (deflection and failure load) at:

(i) Curing age of 7-, 14-, 21- and 28-day;
(ii) Concrete grades of 25 MPa;
(iii) area of bamboo, 145-, 290-, 435-, 580mm^2 and
(iv) area of steel 50.3-, 100.6-, 150.9- and 201.2mm^2.

The modelling and validation were performed using Design Expert Software developed by Stat-Ease.

2.2 Methodology

Model Equation

The true functional relationship is given in Equation 1 where ε represents the noise or error observed in the response y while the variables are $x_1, x_2, \ldots x_k$.

$$y = f(x, \theta) + \varepsilon \quad 1$$

The model is just a quantitative relationship (equation) between the response and the important design factors. In many cases, a low-order polynomial model will be appropriate. A first-order model in two variables is as given in Equation 2

$$y = \beta_0 + \beta_1 x_1 + \beta_2 x_2 + \cdots + \beta_k x_k + \epsilon \quad 2$$

where y is the response, the x's are the design factors, the β's are unknown parameters that will be estimated from the data in the experiment, and ε is a random error term that accounts for the experimental error in the system that is being studied. A common extension of the first-order model is to add an interaction term, as shown in Equation 3

$$y = \beta_0 + \beta_1 x_1 + \beta_2 x_2 + \beta_{12} x_1 x_2 + \epsilon \quad 3$$

where the cross-product term $x_1 x_2$ represents the two-factor interaction between the design factors. Because interactions between factors is relatively common, the first-order model with interaction is widely used. Higher-order interactions can also be included in experiments with more than two factors if necessary. A widely used model is the second-order model given in Equation 4.

$$y = \beta_0 + \beta_1 x_1 + \beta_2 x_2 + \beta_{12} x_1 x_2 + \beta_{11} x_{11}^2 + \beta_{22} x_{22}^2 + \epsilon \quad 4$$

When there is curvature in the system, then a polynomial of higher degree must be used, such as the third-order model

A third order equation usually means a cubic response-surface model. It is used when the relationship between experimental factors and the measured response is sufficiently nonlinear that a first- or second-order model cannot adequately describe it as shown in Equation 5.

$$y = \beta_0 + \beta_1 x_1 + \beta_2 x_2 + \beta_{12} x_1 x_2 + \beta_{11} x_{11}^2 + \beta_{22} x_{22}^2 + \beta_{112} x_1^2 x_2 + \beta_{122} x_1 x_2^2 + \beta_{111} x_1^3 + \beta_{222} x_2^3 + \epsilon \quad 5$$

Optimal (Custom) Design

In RSM, optimal (Custom) Design is used to determine the relationship between responses and independent variables (factors). Optimal (Custom) Design (OCD) is a flexible design structure to accommodate custom models, categoric factors, and irregular (constrained) regions. Custom designs are used when the process requires adjustments to the experimental data that cannot be accommodated by a standard design.

Fitting Response Curves and Surfaces

Many experiments involve at least one quantitative factor. It can be useful to fit a response curve to the levels of a quantitative factor so that the experimenter has an equation that relates the response to the factor. This equation might be used for interpolation, that is, for predicting the response at factor levels between those actually used in the experiment. When at least two factors are quantitative, a response surface can be fitted for predicting (y) at various combinations of the design factors. The dependent variables (responses) are deflection and flexural load, while the independent variables (factors) are: curing age and area of reinforcement.

Model validation

The models developed from the experimental data were validated via Optimal Custom Design in RSM of Design-Expert. The validation was done using the flexural properties (deflection and failure load) of reinforced bamboo and steel reinforced concrete beams at targeted concrete grades of 25 MPa mix design.

3 RESULTS AND DISCUSSION

3.1 Experimental Results and discussions

The experimental part of this research includes the analysis of results of flexural properties of bamboo and steel reinforced concrete specimens. The experimental data obtained from the flexural

behaviour of bamboo and steel reinforced concrete beams under flexure at grades 25 MPa concrete were used as input data for the comparisons in RSM for developing the model.

3.2 Model development

The controllable variable and the design summary of optimal custom design (OCD) used in this experiment is as shown in table 1. RSM allowed estimation of the linear, quadratic, cubic and factor interaction effects of the variables on the flexural properties. To obtain the optimum response, the suggested cubic model (third order polynomial) given in Equation 5 was used:

Table 1: Controllable variable in optimal custom design

No	Factor	Name	Units	Variation interval			
1	A	Age	day	7	14	21	28
2	B	Area of Bamboo	mm^2	145	290	435	580
3	S	Area of Steel	mm^2	50.3	100.6	160.9	201.2

3.3 Sequential Model Sum of Squares (SMSS)

Table 2 and 3 show the full details of the SMSS dataset for response 1 (deflection) and response 2 (failure load) at grade 25 MPa concrete with recommended regression model. It can be seen that third-order equations were suggested as the highest order of polynomial that was not aliased. Thus, the models are most suitably described with cubic polynomial model.

Table 2: SMSS for deflection at grade 25 MPa concrete mix design

	Bamboo reinforced beam					**Steel reinforced beam**					
Source	**Sum of Squares**	**df**	**Mean Square**	**F-value**	**p-value**	**Sum of Squares**	**df**	**Mean Square**	**F-value**	**p-value**	
Mean	874.27	1	874.2			1434.9	1	1434.9			
Linear	331.89	2	165.9	140.1	<0.0001	544.73	2	272.37	140.1	<0.0001	
2FI	31.41	1	31.41	297.8	<0.0001	51.55	1	51.55	297.8	<0.0001	
Quadratic	0.4643	2	0.232	2.43	0.1082	0.7621	2	0.3811	2.43	0.1082	
Cubic	**2.12**	**4**	**0.529**	**31.34**	**< 0.0001**	**3.48**	**4**	**0.8688**	**31.34**	**<0.0001**	**Suggested**
Quartic	0.3707	3	0.123	2584.1	< 0.0001	0.6085	3	0.2028	2584	<0.0001	Aliased
Residual	0.0009	19	0.000			0.0015	19	0.0001			
Total	1240.5	32	38.77			2036.0	32	63.63			

Table 3: SMSS for failure load at grade 25 MPa concrete mix design

	Bamboo reinforced beam					Steel reinforced beam					
Source	**Sum of Squares**	**df**	**Mean Square**	**F-value**	**p-value**	**Sum of Squares**	**df**	**Mean Square**	**F-value**	**p-value**	
Mean	1421.11	1	1421.11			3201.27	1	3201.27			
Linear	353.39	2	176.69	350.40	< 0.0001	639.79	2	319.90	315.15	< 0.0001	
2FI	7.25	1	7.25	27.49	< 0.0001	12.68	1	12.68	21.18	< 0.0001	
Quadratic	5.02	2	2.51	27.59	< 0.0001	11.74	2	5.87	30.41	< 0.0001	
Cubic	**2.14**	**4**	**0.5342**	**51.83**	**< 0.0001**	**4.58**	**4**	**1.14**	**56.89**	**< 0.0001**	**Suggested**
Quartic	0.2267	3	0.0756	4.737E+05	< 0.0001	0.4425	3	0.1475	4.930E+05	< 0.0001	Aliased
Residual	3.032E-06	19	1.596E-07			5.685E-06	19	2.992E-07			
Total	1789.12	32	55.91			3870.50	32	120.95			

3.4 Analysis of variance (ANOVA)

The analysis of variance is a formal way to determine which factor effects are nonzero. It is probably the most useful technique in the field of statistical inference. Table 4 and 5 show the full ANOVA results for Cubic models suggested in table 2 and 3. It was shown that the models' terms for bamboo and steel reinforced concrete beams for the two responses (deflection and failure load) achieve significance at the 0.05 p-value threshold (95% confidence interval). This outcome translates to 99.99% confidence (calculated by taking [1 -0.0001] x 100) that the cubic model coefficient is not zero. In table 4 the models' terms: A, B/S, A(B/S), A^2, B^2/S^2, A^3, B^3/S^3 have significant effects on response (deflection) but A^2 is marginally significant. The models' terms: A, B/ S, A(B/S), A^2, A^2(B/S) and A^3 also have significant effect on response (failure load) as shown in table 5.

Table 4: ANOVA of the cubic model for response 1 (deflection) at grade 25 MPa

	Bamboo reinforced beam					Steel reinforced beam					
Source	**Sum of Squares**	**df**	**Mean Square**	**F-value**	**p-value**	**Sum of Squares**	**df**	**Mean Square**	**F-value**	**p-value**	
Model	365.79	7	52.26	2742.03	<0.0001	600.38	7	85.77	2742.03	<0.0001	**significant**
A-Age	9.06	1	9.06	475.23	<0.0001	14.86	1	14.86	475.23	<0.0001	
B/S-Area	24.84	1	24.84	1303.17	<0.0001	40.76	1	40.76	1303.17	<0.0001	
A(B/S)	31.41	1	31.41	1648.02	<0.0001	51.55	1	51.55	1648.02	<0.0001	
A^2	0.1146	1	0.1146	6.01	0.0218	0.1881	1	0.1881	6.01	0.0218	
B^2/S^2	0.3497	1	0.3497	18.35	<0.0003	0.5740	1	0.5740	18.35	<0.0003	
A^3	0.2831	1	0.2831	14.85	<0.0008	0.4646	1	0.4646	14.85	<0.0008	
B^3/S^3	1.75	1	1.75	91.75	<0.0001	2.87	1	2.87	91.75	<0.0001	

Table 5: ANOVA of the cubic model for response 2 (failure load) at grade 25 MPa

	Bamboo reinforced beam					**Steel reinforced beam**					
Source	**Sum of Squares**	**df**	**Mean Square**	**F-value**	**p-value**	**Sum of Squares**	**df**	**Mean Square**	**F-value**	**p-value**	
Model	367.78	6	61.30	6688.15	<0.0001	668.78	6	111.46	6239.18	<0.0001	**significant**
A-Age	0.3957	1	0.3957	43.17	<0.0001	0.7371	1	0.7371	41.26	<0.0001	
B/S-Area	144.72	1	144.72	15789.9	<0.0001	256.66	1	256.66	14366.5	<0.0001	
A(B/S)	7.25	1	7.25	790.54	<0.0001	12.68	1	12.68	709.61	<0.0001	
A^2/S^2	5.01	1	5.01	546.99	<0.0001	11.74	1	11.74	656.98	<0.0001	
$A^2(B/S)$	1.13	1	1.13	123.69	<0.0001	2.08	1	2.08	116.65	<0.0001	
A^3	1.00	1	1.00	109.40	<0.0001	2.49	1	2.49	139.48	<0.0001	

3.5 Selecting a good predictive model

The regression diagnostics, shown in Table 4 and 5 list the statistical parameters calculated at the 95% confidence level, commonly used in analyses of statistical data. The regression model in terms of both actual and coded variables from the above analysis for bamboo and steel reinforced concrete beam at 25 MPa concrete grade, are as given in Equation 6 to 13 below:

Where D = deflection; F.L. = failure load; A, B and represent the design factors: age and area of bamboo and area of steel, respectively. This regression model can be used to predict the flexural properties of bamboo and steel reinforced beams with the two factors (age and area of reinforcement).

1 CODED MATHEMATICAL MODEL FOR BAMBOO AND STEEL CONCRETE BEAMS RESPECTIVELY

25MPa concrete grade

$$\mathbf{Def.(Bam)} = 5.43 + 2.54A + 4.21B + 1.78\text{AB} - 0.13A^2 - 0.24B^2 + 0.47A^3 - 1.18B^3 \quad (6)$$

$$\mathbf{Def.(Ste)} = 6.96 + 3.26A + 5.39S + 2.28\text{AS} - 1.17A^2 - 0.30S^2 + 0.61A^3 - 1.51S^3 \quad (7)$$

2 ACTUAL MATHEMATICAL MODELS FOR BAMBOO AND STEEL CONCRETE BEAMS RESPECTIVELY

25MPa concrete grade

$$\mathbf{Def.(Bam)} = 1.36 + 0.38A - 3.58(10^{-2})B + 7.81(10^{-4})\text{AB} - 2.27(10^{-2})A^2 + 1.19(10^{-4})B^2 + 4.09(10^{-4})A^3 - 1.14(10^{-7})B^3 \quad (8)$$

$$\mathbf{Def.(Ste)} = 1.75 + 0.48A - 0.13S + 2.88(10^{-3})\text{AS} - 2.91(10^{-2})A^2 + 1.27(10^{-3})S^2 + 5.24(10^{-4})A^3 - 3.51(10^{-6})S^3 \quad (9)$$

3 CODED MATHEMATICAL MODEL FOR BAMBOO AND STEEL CONCRETE BEAMS RESPECTIVELY

25MPa concrete grade

$$\mathbf{Fail.Load\ (Bam)} = 7.16 + 0.53A + 4.57B + 0.86\text{AB} - 0.89A^2 - 0.57A^2\text{B} + 0.89A^3 \quad (10)$$

$$\mathbf{Fail.Load\ (Ste)} = 10.76 + 0.72A + 6.08S + 1.13\text{AS} - 1.36A^2 - 0.77A^2S + 1.4A^3 \quad (11)$$

4 ACTUAL MATHEMATICAL MODELS FOR BAMBOO AND STEEL CONCRETE BEAMS RESPECTIVELY

25MPa concrete grade

$$\mathbf{Fail.Load\ (Bam)} = -2.93 + 0.60A + 7.18(10^{-3})B + 1.20(10^{-3})\mathrm{AB} - 3.99(10^{-2})A^2 - 2.40(10^{-5})A^2B + 7.69(10^{-4})A^3 \quad 12$$

$$\mathbf{Fail.Load\ (Ste)} = -4.16 + 1.03A + 2.72S + 4.67(10^{-3})\mathrm{AS} - 6.44(10^{-2})A^2 - 9.30(10^{-5})A^2S + 1.21(10^{-3})A^3 \quad 13$$

3.6 Diagnosing residuals to validate statistical assumptions

Tables 6 gives the fit summary of the models in terms of R^2, Adjusted R^2, predicted R^2 and Adequate precision. The adjusted R^2 values for all the models are between 0.9984 - 0.9992 which is an indication of good predictive powers of the models. The indicator of the quality of the regression models shows that Predicted R^2 values are in reasonable agreement with the Adjusted R^2; that is., the difference in values is less than 0.2 for the models, which is an indication of a good predictive power of the models. Adequate Precision which is a measure of the signal to noise ratio is also a confirmation tool. A ratio greater than 4 confirms adequate signals and is also an indication of good predictive powers of the models. These suggest that the predicted values obtained based on the regression models are very much close to the values obtained from the experiment.

Table 6: Fit summary of the models

Beam	Flexural Property	Concrete Strength	R^2	Adjusted R^2	Predicted R^2	Adj(R^2) - Pred.(R^2) < 0.2	Adeq Precision > 4
Bamboo	Deflection	25	0.9988	0.9984	0.9978	$6(10^{-4})$	175.18
	Failure Load	25	0.9994	0.9992	0.9989	$9(10^{-4})$	242.13
Steel	Deflection	25	0.9988	0.9984	0.9978	$6(10^{-4})$	175.18
	Failure Load	25	0.9993	0.9992	0.9988	$4(10^{-4})$	238.05

For statistical purposes, it's expected that residuals are normally distributed and independent with constant variance. Two plots are suggested for checking the statistical assumptions: (i) Normal plot of residuals, (ii) Predicted versus Actual level.

Normal plot of residuals: These are shown in Figure 1 to 2. The over-all idea from this display is that the error distribution is approximately normal. The tendency of the normal probability plot to bend down slightly on the left side and upward slightly on the right side implies that the tails of the error distribution are somewhat thinner than would be anticipated in a normal distribution; that is, the largest residuals are not quite as large (in absolute value) as expected. These plots are used to predict the adequacy of the models adopted. In this case, giving the plots a pencil test, the deviations from linear (the normal line) are very minor, so the assumption of normality is supported. The normal plot of residual for bamboo reinforced concrete looks very much alike to that of steel reinforced concrete beam. This show that the flexural properties of bamboo reinforced concrete beam is almost the same as that of steel reinforced concrete beam.

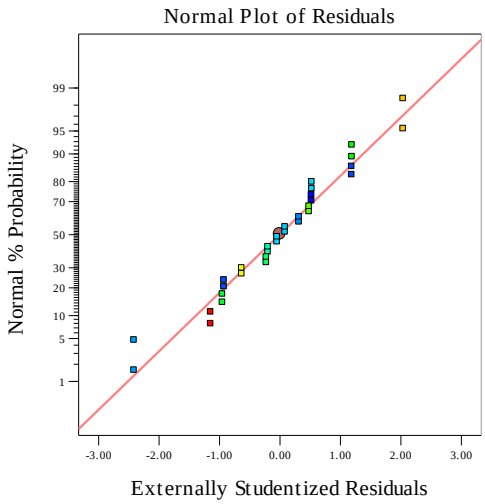

(a) Bamboo reinforced concrete beam

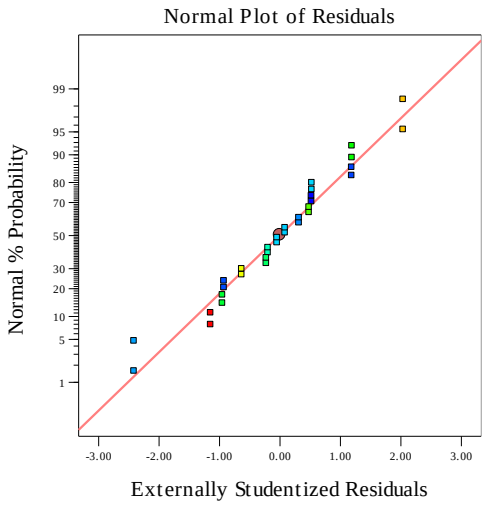

(b) Steel reinforced concrete beam

Figure 1 (a & b): Normal plot of residual for response 1 (deflection) at grade 25 MPa concrete

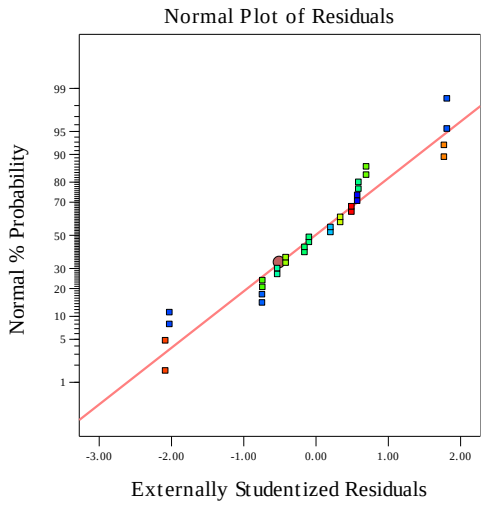

(a) Bamboo reinforced concrete beam

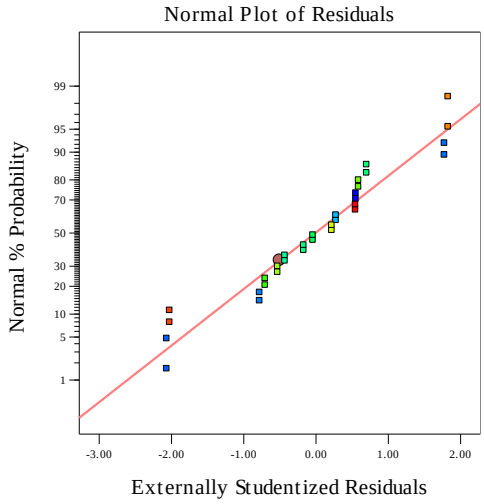

(b) Steel reinforced concrete beam

Figure 2 (a & b): Normal plot of residual for response 2 (failure load) at grade 25 MPa concrete

Predicted versus Actual level: The fit of predicted versus actual data for the cubic models in this study look very good as shown in Figure 3 to 4. In this case, the models are clearly confirmed as these plots line up nicely as expected from a normal distribution. The pencil test for linearity holds good for all the models as there are no deviations from the normal line. This further confirms that the assumption of normality is supported and the adequacy of the cubic models for predicting the flexural properties of bamboo and steel reinforced concrete beam. In turn, this suggests that bamboo is a substitute to steel reinforcement.

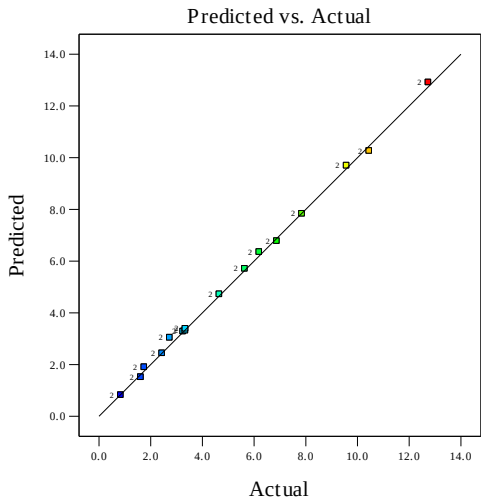

(a) Bamboo reinforced concrete beam

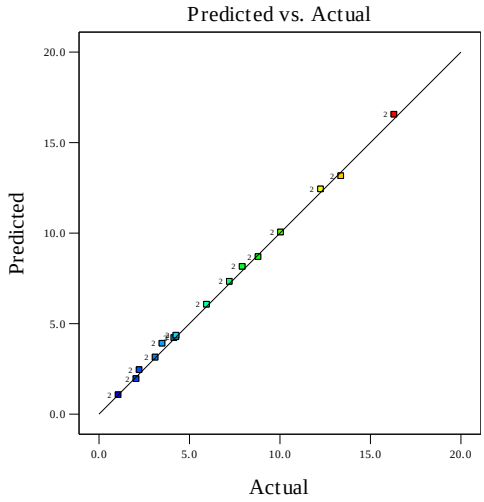

(b) Steel reinforced concrete beam

Figure 3 (a & b): Predicted vs Actual plot for response 1 (deflection) at Grade 25 MPa concrete

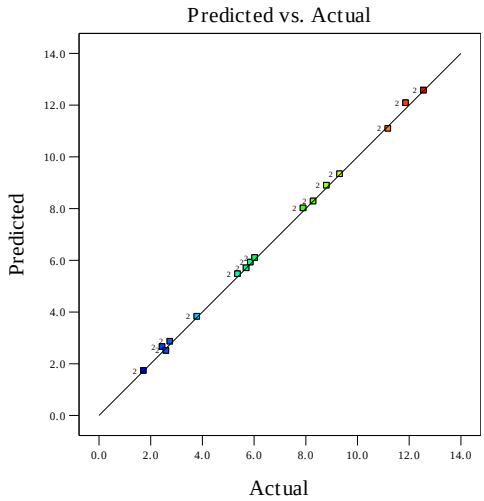

(a) Bamboo reinforced concrete beam

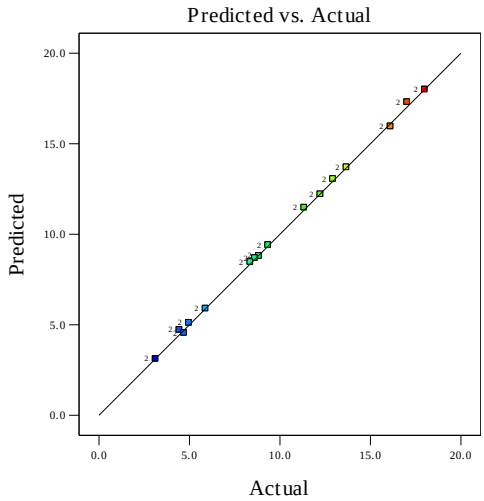

(b) Steel reinforced concrete beam

Figure 4 (a & b): Predicted vs Actual plot for response 2 (failure load) at Grade 25 MPa concrete

3.7 Surface plots of flexural properties of bamboo and steel reinforced concrete beams

The 3D surface plots show how the predicted responses (deflection and failure load) vary for the two factors (curing age and area of reinforcement) as shown in Figures 5 and 6. Results from the Figures show that the deflection and failure load of both bamboo and steel reinforced concrete beams increase with: increase in curing age, area of reinforcements (bamboo/steel) at 25Mpa concrete grade. However, it was observed from these figures that the difference in the values of bamboo reinforced concrete beams and steel reinforced concrete beams were caused by the ultimate strength of the steel reinforcement. Thus, the values of deflection and failure load in bamboo reinforced concrete beam are very close with that of the steel reinforced concrete beam.

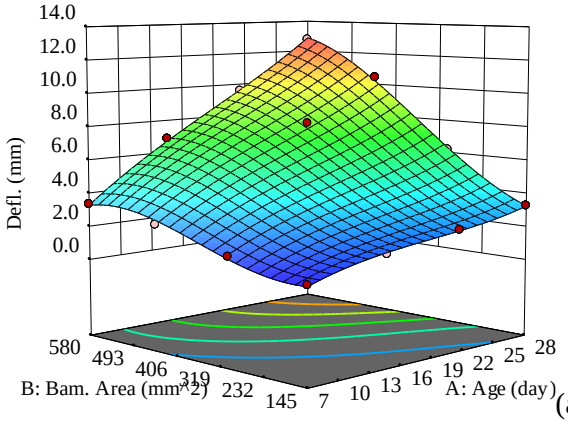

(a) Bamboo reinforced concrete beam

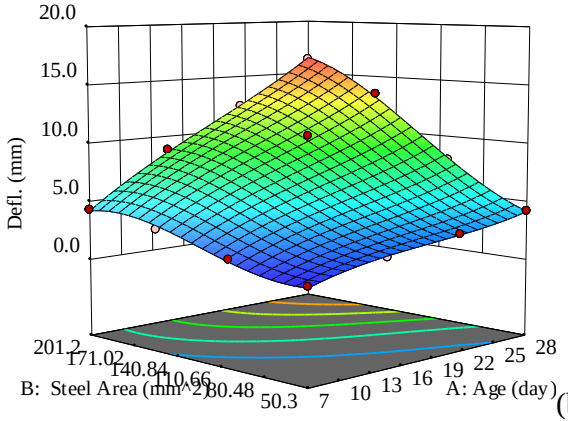

(b) Steel reinforced concrete beam

Figure 5 (a & b): 3D Surface plot for response 1 (deflection) at grade 25 MPa concrete

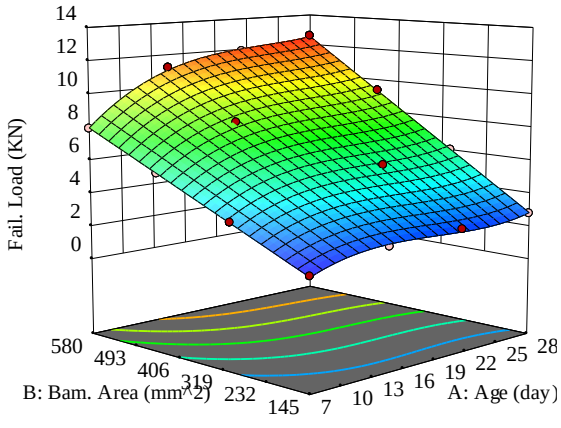

(a) Bamboo reinforced concrete beam

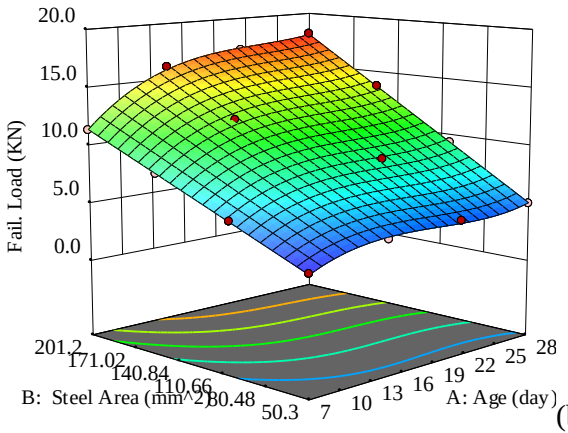

(b) Steel reinforced concrete beam

Figure 6 (a & b): 3D Surface plot for response 2 (failure load) at grade 25 MPa concrete

4.8 Evaluation of multiple responses vie desirability function

Optimization of bamboo and steel reinforced concrete beams were done such that for response: deflection was minimized while failure load was maximized; for factors: area of bamboo and steel were maximized while age was set at default that is, in range of actual values in order to obtain the optimal curing age and area of bamboo/steel gave the best values. The optimization goals and constraints are as shown in table 7

Table 7: Optimization goals and constraints for grade 25 MPa concrete

Grade of Concrete	Bar	Name	Goal	Lower Limit	Upper Limit	Lower Weight	Upper Weight	Importance
grade 25 MPa	Bamboo	A:Age	is in range	7	28	1	1	4
		B:Bam. Area	maximize	145	580	1	1	4
		Deflection	minimize	0.8611	12.763	1	1	4
		Fail. Load	maximize	1.75	112.58	1	1	4
	Steel	A:Age	is in range	7	28	1	1	4
		B: Steel Area	maximize	50.3	201.2	1	1	4
		Deflection	minimize	1.10329	16.350	1	1	4
		Fail. Load	maximize	3.15	18.312	1	1	4

The result from table 7 shows: the importance placed on all inputs combinations; the curing age; area of bamboo and steel were set at 7-28 days; 145-580mm^2 and 50.3-201.2mm^2 respectively in which the best optimized flexural properties values were selected.

The summary of the optimized result is present in table 8. From the optimal parameters, approximately 10 days curing age was achieved for both bamboo and steel reinforced concrete showing that the method of curing was the same for both specimens. The deflection parameters show that steel reinforced concrete beam is 24.67 percent more ductile than bamboo concrete beam, while the failure load parameters show that steel reinforce concrete beam can sustain load up to 31.70 percent more than bamboo reinforced concrete beams. The large areas of bamboo is to complement the yield strength of bamboo due to its brittle nature. The desirability values are extremely close (0.785 vs. 0.782), showing how well the combinations of input factors satisfied the responses simultaneously. It means that the proposed factor combination provides a strong overall compromise among the response objectives. From the foregoing, Bamboo is the next substitute to steel for low-cost housing units.

Table 8: Summary of optimized result of bamboo and steel reinforced concrete beams

Grade of Concrete	Bar	Number of solutions	Age (day)	Area (Bamboo) (mm^2)	Deflection (mm)	Flexural Load (KN)	Desirability	
25 MPa	Bamboo	6	9.588	580.000	4.692	9.471	0.785	Selected
	Steel	11	9.926	201.200	6.229	13.865	0.782	Selected

CONCLUSION AND RECOMMENDATION

5.1 Conclusion

(i). The results of the mathematical models show that the flexural properties (deflection and failure load) of bamboo and steel reinforced concrete beams can be predicted by third-order polynomial equation (cubic models).

(ii). The P-values of all the models achieved significance at 0.0001 < 0.05 (95% threshold confidence interval). This outcome translates to 99.99% confidence (calculated by taking [1 - 0.0001] times 100). Thus, the cubic models are statistically significant.

(iii). The adjusted R^2 values are in reasonable agreement with the predicted R^2 for flexural properties as their difference $(Adjusted\ R^2 - Predicted\ R^2 \leq 0.2)$. Also, the adequate precision values are greater than four, which is an indicator that the predicted values obtained based on the regression models are very much close to that obtained from the experiment.

(iv). The deflection parameters show that steel reinforced concrete beam is 24.67 percent more ductile than bamboo concrete beam, while the failure load parameters show that steel reinforce concrete beam can sustain load up to 31.70 percent more than bamboo reinforced concrete beams.

(v). The desirability values showed that the combinations of input factors satisfied the responses simultaneously i.e., the proposed factor combination provides a strong overall compromise among the response objectives.

5.2 Recommendation

1. Validation programme should be extended to different concrete grades, bamboo species, bamboo ages, treatment methods and reinforcement configurations so as to establish the limits of applicability and reliability of the predictive models.
2. The developed RSM equations should subsequently be incorporated into a numerical/design software framework that can assist engineers in predicting structural performance and selecting appropriate bamboo reinforcement quantities.
3. Larger-scale experimental studies involving beams, slabs, columns and complete structural systems should be conducted to establish whether the laboratory-scale relationships remain valid at structural scale.
4. Field trials should monitor cracking, deflection, moisture effects, bond behaviour, durability, deterioration and long-term load response over an extended period. The field programme should also evaluate constructability, availability of suitable bamboo, treatment requirements, labour requirements, cost, maintenance and overall economic viability.

REFERENCES

Agarwal, H. & John, E. R. (2004). Reliability based design optimization using response surfaces in application to multidisciplinary systems. *Engineering Optimization*, *36* (4), 291--311.

Anderson, J. M. & Whitcomb, J. P. (2007). *DOE simplified - practical tools for effective experimentation (PDFDrive)*. CRC Press.

Anderson, J. M. & Whitcomb, J. P. (2017). *RSM Simplified: Optimizing Processes Using Response Surface Methods for Design of Experiments*. Productivity Press.

Archila, H., Kaminski, S., Trujillo, D., Zea Escamilla, E., & Harries, K. A. (2018). Bamboo reinforced concrete: A critical review. *Materials and Structures*, *51* (102) https://doi.org/https://doi.org/10.1617/s11527-018-1228-6

Box, G. EP. & Behnken, D. W. (1960). Some new three level designs for the study of quantitative variables. *Technometrics*, *2* (4), 455--475.

Box, G. EP. & Wilson, K. B. (1951). On the experimental designs for exploring response surfaces. *Ann Math Stat*, *13*, 1--45.

Burgoyne, C. & Balafas, I. (2007). 8th International Symposium on Fiber Reinforces Polymer Reinforcement for Concrete Structures. 16-18 July 2007 , Patras.

Chow, H. K. 1914. “Bamboo As A Material for Reinforcing Concrete.”.

Ghavami, K. (1995). Ultimate load behaviour of bamboo-reinforced lightweight concrete beams. *Cement and concrete composites*, *17* (4), 281–288.

International Organization for Standardization (ISO). 2021. “ISO 22156: 2021Bamboo structures—Bamboo culms—Structural design.” Geneva: ISO.

Khuri, I. A. & Cornel, A. J. (1996). *Response Surfaces Designs and Analyses*. CRC Press.

Kostić, S., Vasovi, N., & Marinković, B. (2016). Robust optimization of concrete strength estimation using response surface methodology and Monte Carlo simulation. *Engineering Optimzatiom*, *49* (5), 864--877.

Maria, F. VA., Maria, E. PS., Daniel, N. RV., & Jason, O. MC. (2023). Bamboo as Sustainable Building Materials: A Systematic Review of Properties, Treatment Methods, and Standards. *Buildings*, *13* (10), 2449. https://doi.org/https://doi.org/10.3390/buildings13102449

McCormac, J. C. & Brown, R. H. (2014). *Design of Reinforced Concrete. 9th edition*. USA: Wiley & Sons.

Montgomery, D. C. (2020). *Design and analysis of experiments*. Wiley.

Myers, R. H., Montgomery, D. C., & Anderson-Cook, C. M. (2016). *Response surface methodology: process and product optimization using designed experiments*. John Wiley & Sons.

Pacheco-Torgal, F. & Labrincha, J. A. (2013). The future of construction materials research and the seventh UN Millennium Development Goal: A few insights. *Construction and Building Materials. 40, pp. 729–737*, *40*, 729–737.

Sharma, A. (1990). Bamboo-reinforced concrete beams *In: Vandepitte, D. Mixed Structures, including New Materials. Brussels, 1990. Zurich: International Association for Bridge and Structural Engineering*, 677–682.

Sharma, B., Gatoo, A., Bock, M., & Ramage, M. (2015). Engineered bamboo for structural applications. *Construction and Building Materials* (81), 66–73.

Sridhar, J., Shinde, G. B., Vivek, D., Naseem, K., Gaur, P., Patil, P. P., & Tesema, M. T. (2022). Response surface methodology approach to predict the flexural moment of ferrocement composites with weld mesh and steel slag as partial replacement for fine aggregate. *Advances in Materials Science and Engineering*, *2022*, 1--9.

Trujillo, D. (2013). *Bamboo Structures. In R. D. K. Misra (Ed.), Modern Bamboo Structures.* CRC Press.

USGS (2019). Mineral Commodity Summaries 2019. *Reston: U.S. Geological Survey*

Usman, A., Sutanto, M. H., Napish, M. B., & Yaro, N. SA. (2021). Response surface methodology optimization in asphalt mixtures: A review. *Response Surface Methodology in Engineering Sciencce.*

International Conference on Engineering Innovation for Sustainable Development (ICESID 2026)
Faculty of Engineering, Ahmadu Bello University Zaria · 8–10 September 2026

ENERGY-EFFICIENT COMMUNICATION AND ROUTING STRATEGIES IN HETEROGENEOUS WIRELESS SENSOR NETWORKS: A COMPREHENSIVE REVIEW

Matthew Iyobhebhe[1,*], Abdoulie Momodou. S. Tekanyi[2], Athanisius Terlumun Utev[2], Fatima Ashafa[1], Asebakeoghene. J. Khama[1], Botson Ishaya Chollom[1], Umar Salisu Lawal[1]

[1]*Federal Polytechnic Nasarawa, Nigeria*
[2]*Ahmadu Bello University, Zaria. Nigeria, Faculty of Engineering, Department of Electronics and Telecommunications Engineering*

Email: mattoiyobhe@gmail.com*, amtekany@abu.edu.ng, utev@gmail.com, fatima@gmail.com, ase@gmail.com, botson@gmail.com, umar@gmail.com

***Corresponding author**: Matthew Iyobhebhe

DOI: https://doi.org/10.67203/sp.ICESID.2026

ABSTRACT

Heterogeneous Wireless Sensor Networks (HWSNs) have attracted significant attention because they can improve network performance and maximize operational lifetime by combining sensor nodes with diverse capabilities. However, node heterogeneity introduces new challenges for designing energy-efficient communication and routing mechanisms, especially under stringent energy constraints. This review introduces a comprehensive scrutiny of existing communication and routing strategies in HWSNs, with a primary focus on energy efficiency and sustainability. The study systematically scrutinizes fundamental HWSN concepts, energy consumption models, communication paradigms, and routing protocols, including flat and hierarchical approaches. Furthermore, recent improvements in energy harvesting, harvesting-aware routing, and hybrid energy storage systems are considered key enablers of sustainable network operation. By combining conventional and emerging techniques, this review identifies critical research challenges and future directions, offering valuable insights for researchers and system designers toward the development of scalable, adaptive, and energy-efficient HWSN solutions.

Keywords: *Communication strategies; Cross-layer communication approaches; Energy harvesting in HWSNs; Energy-efficient in HWSNs; Energy consumption models in HWSNs; heterogeneity in HWSNs; Routing strategies in HWSNs*

1. INTRODUCTION

Wireless Sensor Networks (WSNs) have evolved as a vital technology system, enabling a wide range of implementations, including environmental monitoring, industrial automation, smart agriculture, medical healthcare, and intelligent transportation systems. These networks classically consist of spatially dispersed sensor nodes that collectively sense, process, and send packets to a sink or base station (Soni Chaurasia *et al*., 2025). A dire limitation of traditional homogeneous WSNs is their unembellished energy-limited nature, as sensor nodes are usually battery-powered and positioned in harsh or inaccessible environments where battery replacement is impractical. To address the scalability and operational challenges inherent in homogeneous organizations, HWSNs, where sensor nodes vary in terms of energy capacity, communication range, processing capability, or functional tasks, have been extensively adopted in current research and real-world implementations. Despite their benefits, HWSNs present new limitations in energy-efficient communication and routing. The introduction of nodes with unequal abilities results in unbalanced energy utilization, predominantly for rich-energy nodes that are often selected as Cluster Heads (CH), relays, or gateways. This imbalance frequently leads to early node failures, hotspot formation near the sink, minimized network lifetime, and poor network service. Consequently, designing communication and routing schemes that logically exploit node heterogeneity while mitigating overall energy depletion remains a serious and unresolved research problem (Yang Zhang *et al*., 2025). The motivation for this

review stems from the swift increase of energy-aware communication and routing methods tailored for HWSNs, stretching from traditional clustering-based protocols to current optimization-based and intelligent schemes. Although various articles have addressed energy efficiency in HWSNs, existing studies repeatedly focus on specific protocol categories or lack an integrated comparative perspective that captures communication mechanisms, routing strategies, performance metrics, and emerging intelligent techniques within a unified framework (Namit Gupta *et al*,. 2025, Aveneesh Singh *et al*., 2025). This gap led us to a holistic review that systematically categorizes and critically analyzes these methods, underscoring their strengths, limitations, and suitability for diverse implementation scenarios. To address this gap, this review embraces a structured and comparative methodology. The review first defines fundamental concepts, energy models, and evaluation metrics pertinent to HWSNs. It then categorizes and analyzes energy-efficient communication strategies, followed by an in-depth review of routing protocols, including flat, hierarchical, and hybrid approaches. Current advances in energy harvesting-aware techniques are also examined to reflect current research trends. The chosen classification framework allows clear comparison across techniques in terms of energy usage, scalability, adaptability, and application complexity, thereby justifying the selection of these approaches as representative and impactful solutions in contemporary HWSN research. The key contribution of this review lies in its holistic synthesis of energy-efficient communication and routing strategies in HWSNs (Sumendra Thakur *et al*., 2025, Avaneesh Singh *et al*., 2025, M. Karthikeyan *et al*., 2025). Unlike prior works, this paper integrates conventional and intelligent approaches, identifies open research challenges, and outlines promising future directions, particularly in the context of IoT integration and autonomous network management. The findings presented in this study are relevant to researchers, practitioners, and system designers seeking to develop sustainable, scalable, and high-performance HWSNs (Aarti Sharma *et al*., 2025, Raghuveer Singh *et al*., 2025, Ayman A. Alharibi *et al*., 2025, Yihan Guan *et al.*, 2025). By providing a comprehensive reference and comparative insight, this review aims to support informed decision-making and stimulate further innovation in energy-efficient HWSN design.

2. REVIEW METHODOLOGY

This study used an organized literature-review methodology to identify, evaluate, screen, and synthesize research related to routing techniques and energy-efficient communication in HWSNs. Relevant literatures was extracted from major scientific databases, including Web of Science, ScienceDirect, IEEE Xplore, and Google Scholar. The search was conducted using combinations of keywords such as: Energy-efficient routing, energy harvesting, HWSNs, sustainable HWSNs, machine learning routing in WSN, energy-aware communication, and adaptive communication.

The literatures search was limited to publications between 2020 to 2026 to capture recent developments in energy-efficient HWSN design. Studies were included if they:

- Addressed energy-efficient communication or routing in WSNs/HWSNs.
- Reported performance metrics such as energy consumption, network lifetime, throughput, packet delivery ratio, or delay.
- Presented simulation, analytical, or experimental validation.

Studies were excluded if they:

- Focused solely on hardware implementation.
- Did not report energy-related performance metrics.
- Were duplicate publications.

The selection process followed four stages:

- Identification
- Screening
- Eligibility Assessment
- Final inclusion

The retrieved records were initially screened using their titles and abstracts. Duplicate records were removed before detailed assessment. The remaining studies were examined against the inclusion and exclusion criteria, followed by full-text assessment of potentially relevant publications. Table 1 depict PRISMA-Style summary.

Table 1: PRISMA-Style Summary

Stage	Number of Studies
Records identified	52
Duplicates removed	14
Records Screened	38
Full-text Reviewed	9
Final studies included	29

2.1. Review

Muhammad Haris & Haewoon Nam (2025) proposed an optimized particle swarm optimization (PSO)-based CH selection structure to enhance energy efficiency in IoT-based WSNs. Their method dynamically selects CHs based on residual energy and communication cost, resulting in balanced energy expenditure and prolonged network lifetime. Simulation results show that the developed scheme outperforms LEACH by approximately 28%, LEACH-FL and LEACH-FC by around 20%, and KM-PSO by nearly 10% in terms of nodes survivability and network lifetime. However, the study primarily targets homogeneous IoT-WSNs, with limited emphasis on heterogeneity-aware design and cross-layer energy optimization, which are critical in HWSN environments and also face challenges such as balancing fairness among nodes, managing heterogeneous harvesting rates, and guaranteeing reliable operation under changing environmental conditions

I.Gethzi Ahila Poornima *et al*., (2025) proposed an energy-efficient hybrid optimization-based routing framework for IoT-based WBANs. Their model incorporates intelligent optimization techniques to realize optimal routing decisions, leading to minimized energy utilization and enhanced network lifetime. However, the work is application-specific to WBANs and does not explicitly address heterogeneous node capabilities or large-scale multi-hop scenarios typical of HWSNs, and also faced with challenges comprise balancing fairness among nodes, managing heterogeneous harvesting rates, and guaranteeing reliable operation under changing environmental conditions.

P.K. Poonguszhali *et al*., (2025) presented a multi-objective, CH–based energy-efficient routing framework that combines a deep convolutional neural network (THDCNN) with hybrid Capuchin Search and Woodpecker Mating algorithms. The proposed method jointly optimizes CH selection and routing to reduce energy utilization while optimizing network stability and throughput. Simulation results show that the developed scheme outperformance with and attains 25.3, 10.76, 45.67, 49.15, 50.12 and 35% higher alive nodes and 22.32, 16.76, 27.67, 11.71, 30.32, and 27.02% higher detection rate when compared with existing methods. However, the study is primarily evaluated on homogeneous WSN settings, with limited consideration of node heterogeneity and practical deployment constraints in large-scale HWSNs, and also faced with challenges comprise balancing fairness among nodes, managing heterogeneous harvesting rates, and guaranteeing reliable operation under changing environmental conditions..

Sunawar Khan *et al*., (2025), examined the integration of IoT and WSN architectures with the objective of optimizing quality of service via improved energy efficiency, scalability, and secure communication techniques. The study proposes a layered framework that enhances data communication and resource utilization in smart system environments. Simulation results show superior improvements in throughput, latency, and energy consumption compared to conventional IoT-WSN models. However, the work provides a system-level perspective and lacks detailed analysis of heterogeneity-aware routing and energy harvesting strategies essential for sustainable HWSNs, and also faces challenges comprising balancing fairness among nodes, managing heterogeneous harvesting rates, and guaranteeing reliable operation under changing environmental conditions.

Muhammad Akram *et al*., (2025), the researchers proposed EEMLCR, an energy-efficient machine learning-based clustering and routing framework for wireless sensor networks. The technique leverages supervised learning to enhance CH selection and adaptive routing decisions, leading to optimized energy consumption and prolonged network lifetime. The developed scheme when compared with existing schemes, after 600 rounds in networks comprising 400 nodes, the developed scheme showed significant improvements. However, the model is primarily validated on homogeneous WSN scenarios and does not explicitly incorporate heterogeneity-aware energy

management or harvesting-based sustainability mechanisms relevant to HWSNs, and also faced with challenges comprise balancing fairness among nodes, managing heterogeneous harvesting rates, and guaranteeing reliable operation under changing environmental conditions.

Potu Arayana *et al. (2026)* estimated their secured energy-efficient opportunistic routing scheme using QualNet 5.02 and NS-2.34 with 50, 100, and 200 nodes under normal and attack scenarios. The simulation results showed higher throughput and lower average end-to-end delay than EEFCR, with performance remaining more stable as node speed and network dynamics increased. The proposed scheme also demonstrated improved energy efficiency through reduced unnecessary transmissions and better residual-energy preservation, thereby extending network lifetime. Quantitatively, the scheme was reported to be 2-3% faster than DLAMD and 10-13% faster than EEFCR**,** while its malware detection rate improved by approximately 23%. These results indicate that the proposed approach provides a better balance of throughput, delay, energy consumption, network lifetime, and security for WSNs, and also faces challenges comprise balancing fairness among nodes, managing heterogeneous harvesting rates, and guaranteeing reliable operation under changing environmental conditions.

Yang Zhang *et al*., (2025) proposed an energy-efficient adaptive routing framework for heterogeneous wireless sensor networks by integrating an Improved Particle Swarm Optimization (IPSO)-based cluster-head selection mechanism with dynamic clustering and hybrid single-/multi-hop routing. The framework was evaluated using 200 heterogeneous nodes deployed over a 200 × 200 m² area, comprising low-power sensors (0.5 J), battery-powered relays (1.0 J), and solar-powered hubs (2.0 J). Simulation results showed a 32.7% reduction in per-round energy consumption compared with LEACH, a 28% improvement in network lifetime based on the first-node-death metric, and a 63% reduction in energy variance among nodes. At a 20% solar-powered-hub proportion, the half-node-death lifetime increased by 36.8 ± 2.1%, from 1,518 ± 42 to 2,075 ± 55 rounds. The framework also demonstrated practical computational feasibility, with IPSO requiring 0.82 ± 0.07 ms per iteration on a Raspberry Pi 4B. However, the approach remains computationally dependent on gateway/edge nodes and primarily targets static HWSNs, indicating opportunities for lightweight distributed coordination and broader real-world validation.

Lina Elmoiz Alatabani *et al*. (2026) investigated cross-layer optimization using energy-efficient routing protocols for WSNs, focusing on interactions among network, MAC, and physical-layer operations. The chapter evaluates clustered routing protocols to examine their effects on throughput, average end-to-end delay, energy consumption, and network lifetime**.** Its analysis emphasizes the potential of cross-layer coordination to improve QoS while reducing energy expenditure and extending network lifetime. Therefore, the study provides a useful conceptual basis for cross-layer energy optimization, but its quantitative performance claims should be verified from the full chapter before inclusion in a comparative results table, and it also faces challenges comprise balancing fairness among nodes, managing heterogeneous harvesting rates, and guaranteeing reliable operation under changing environmental conditions.

Tumpa Pal *et al*. (2026) conducted a PRISMA-based systematic review of 43 high-quality studies on energy-efficient WSN routing for precision and smart agriculture, selected from an initial 250 studies published between 2016 and 2025. The reviewed protocols were evaluated mainly using network lifetime, energy consumption, packet delivery ratio (PDR), throughput, latency, routing overhead, and coverage. Quantitative evidence reported in the review indicates that a Dynamic Energy-based Clustering approach achieved 30-40% lower energy consumption, 50% longer network lifetime, and 90-98% PDR compared with traditional routing protocols. Across the reviewed studies, 15 clustering-based, 8 optimization-based, 5 fuzzy-based, 5 ML-based, 5 security-aware, and 5 hybrid approaches were identified. The review concluded that clustering and optimization methods provide strong energy and lifetime benefits, whereas ML and hybrid approaches offer improved adaptability and scalability for dynamic agricultural environments, and also faced with challenges comprise balancing fairness among nodes, managing heterogeneous harvesting rates, and guaranteeing reliable operation under changing environmental conditions.

The nine studies discussed above provide representative evidence of the principal approaches identified across the 29 included studies. The remaining studies were synthesized collectively rather than discussed individually to avoid repetitive descriptions and to maintain focus on the dominant methodological trends.

In summary, the reviewed articles show substantial progress in energy-efficient clustering, routing, and intelligent optimization for WSNs and IoT-based networks. However, most prior works are application-specific or assume homogeneous network settings, with limited consideration of node heterogeneity, harvesting-aware operation, and cross-layer energy optimization. This review addresses these gaps by providing a unified and comprehensive analysis of energy-efficient communication and routing strategies specifically tailored for sustainable Heterogeneous Wireless Sensor Networks.

3. FUNDAMENTALS OF HETEROGENEOUS WIRELESS SENSOR NETWORKS

HWSNs show a significant development of conventional wireless sensor network design, motivated by the need to enhance energy efficiency, scalability, and network longevity in resource-limited environments (Maryam Shafiq *et al*., 2021). Unlike homogeneous WSNs, where all sensor nodes are the same in capability and task, HWSNs deliberately integrate nodes with varied energy capacities, processing power, communication ranges, and sensing functions. These variations allow the network to better adapt to different traffic loads and implementation requirements, making HWSNs predominantly suitable for large-scale and long-term deployments (Maria Trigk *et al*., 2025).

3.1.Definition and Characteristics of HWSNs

HWSNs are an integral part of conventional WSNs in which sensor nodes have varying capabilities in terms of energy resources, processing power, communication range, memory, or functional roles. Unlike homogeneous WSNs, where all nodes are the same in terms of network resources, HWSNs deliberately use node variations to enhance network performance, scalability, and longevity (Bilal R. Al-Kaseem *et al*., 2021). Typical characteristics of HWSNs comprise unequal initial energy levels, role differentiation for example, “normal nodes, advanced nodes, super nodes”, adaptive communication ranges, and hierarchical data forwarding. These characteristics enable more efficient task allotment and energy usage, but also introduce complexity in communication and routing design (D. Pravin Kumar *et al*., 2025).

3.2. Types of Heterogeneity in HWSNs

Heterogeneity in HWSNs discusses the careful integration of sensor nodes with different capabilities and resources within the same network. In HWSNs, such variation leads to enhanced operation, energy efficiency, and scalability. These variations may exist in energy resources, computation, communication, or functional tasks assigned to nodes. Comprehending the types of heterogeneity is crucial for designing effective communication and routing strategies that fully exploit node diversity while minimizing energy imbalance. Table 2 briefly describes the subsection (Abdulla Juwaieda *et al*., 2025).

Table 2: Types of heterogeneity in HWSNs

Type of heterogeneity	**Description**	**Impact on Network Performance**
Energy heterogeneity	Nodes are equipped with varying energy levels	Improves network lifetime but may cause energy imbalance
Computational heterogeneity	Nodes vary in processing and memory capacity	Enables local packets and intelligent routing
Communication heterogeneity	Nodes have different transmission power and range	Enhances connectivity and coverage
Functional heterogeneity	Nodes perform specialized roles (CHs, gateways)	Improves efficiency and data aggregation
Hardware heterogeneity	Varying sensor types and hardware platform	Supports diverse sensing applications

3.3.Network Architectures and Deployment Models

HWSNs are regularly structured using flat, hierarchical, or hybrid architectures. In flat architectures, all nodes execute similar networking functions despite basic heterogeneity, which simplifies design but may underutilize high-rich nodes. Hierarchical architectures, such as clustering-based models, assign energy-rich or high-capability nodes as cluster heads or relay nodes, enabling efficient data aggregation and reduced transmission overhead. Hybrid architectures integrate flat and hierarchical features to balance flexibility and energy efficiency. Deployment models in HWSNs may be deterministic (organized placement of rich-energy nodes at strategic locations) or random, often followed by adaptive role assignment. Strategic deployment of powerful nodes near the sink or in high-traffic regions is commonly used to mitigate hotspot and bottleneck problems (Nisha B. *et al*., 2025).

3.4.Energy Consumption Models in HWSNs

Energy utilization modeling is vital to the design and estimation of energy-efficient protocols in HWSNs. Most articles embrace a first-order radio energy model, where energy dissipation relies on both electronic circuitry and communication distance. The energy utilized to transmit a *k*-bit data packet over distance *d* is given in equation (1) (Xiaoying Liu *et al*., 2025):

$$E_{tx}(k,d) = \begin{cases} kE_{ele} + kE^{d^2}{}_{fs}, d < d_0 \\ kE_{ele} + kE^{d^4}{}_{mp}, d \geq d_0 \end{cases} \quad (1)$$

The energy utilized to receive the same data is given in equation (2):

$$E_{rx}(k) = kE_{ele} \quad (2)$$

Where E_{ele} signifies the energy utilized by transmitter/receiver electronics, E_{fs} and E_{mp} defines the free-space and multipath fading amplification coefficient, respectively, and d_0 denotes the threshold distance. In HWSNs, nodes with higher residual energy or improved hardware are often designated with more energy-intensive tasks, thereby ensuring accurate energy modeling critical for fair load distribution and maximized network lifetime (Ali Forghani *et al*., 2022).

4. COMMUNICATION STRATEGIES IN HWSNS

Efficient transmission is a foundation of energy conservation in HWSNs, as data communication typically dominates overall energy usage. The presence of nodes with varying capabilities allows flexible transmission designs that can use rich-energy or rich-capacity nodes for energy-intensive tasks. This section reviews key communication strategies used in HWSNs, accentuating their functional principles, advantages, and energy-efficiency implications.

4.1. Single-Hop vs. Multi-Hop Communication

Single-hop and multi-hop transmission introduce two vital data delivery paradigms in HWSNs. In single-hop transmission, sensor nodes transmit data directly to the sink/base station (BS), which simplifies routing but suffers high energy utilization costs for distant nodes. Multi-hop transmission, on the other hand, transmits data via intermediate nodes, minimizing communication distance per hop and enhancing scalability. In HWSNs, node heterogeneity enables high energy-resource nodes to function as relays, thereby balancing energy usage and minimizing hotspot problems. Table 3 briefly describes single-hop and multi-hop communications.

Table 3: Single-hop and multi-hop communications

Communication Mode	**Description**	**Energy Implication**	**Sustainability in HWSNs**
Single-hop	Direct node-to-sink transmission	High energy cost for distance nodes	Small-scale or dense networks
Multi-hop	Data forward via intermediate nodes	Lower per-hop energy usage	Large-scale heterogeneous deployments

4.2.Data Aggregation and Fusion Techniques

Data aggregation and fusion techniques aim to minimize redundant communications by integrating data from numerous sensor nodes before forwarding it to the BS. By using spatial and temporal data correlation, these methods meaningfully lower communication overhead and energy usage. In HWSNs, nodes with higher processing ability are typically allocated aggregation tasks, enhancing efficiency without overburdening resource-limited nodes. Table 4 briefly defines data aggregation and fusion techniques (Tumpa Pal *et al*, 2026).

Table 4: Data aggregation and Fusion techniques

Technique	**Operation**	**Energy Benefit**	**Typical Aggregator Node**
Data Aggregation	Summarization (average, min. max	Reduces packets count	Cluster heads
Data Fusion	Intelligent combination of multi-sensor data	Improves data quality and efficiency	Advanced nodes

4.3. Adaptive Transmission Power Control

Adaptive transmission power control dynamically adjusts a node's transmission power based on transmission distance, link quality, or residual energy. In HWSNs, this technique allows low-energy nodes to manage power while enabling high-energy nodes to sustain robust links over longer distances. Such adaptability not only reducing unnecessary energy wastes but also minimizes interference and enhances overall network reliability (Lina Elmoiz Alatabani *et al*., 2026).

4.4. Clustering-Based Communication Mechanisms

Clustering is one of the most extensively adopted communication techniques in HWSNs. In this method, sensor nodes are categorized into clusters, with CHs responsible for intra-cluster management, data aggregation, and inter-cluster communication. Heterogeneity is obviously leveraged by chosen energy-rich or high-capability nodes as CHs, thereby maximizing network lifetime, enhancing scalability, and minimizing communication overhead among ordinary nodes.

4.5.Cross-Layer Communication Approaches

Cross-layer transmission approaches break the conventional layered protocol design by allowing data exchange across numerous network layers. In HWSNs, parameters such as residual energy, channel conditions, and routing decisions can be jointly optimized to improve transmission efficiency. By enabling coordinated adaptation across the physical, MAC, and network layers, cross-layer designs provide critical energy savings and performance gains, albeit at the cost of increased design complexity.

5. ROUTING STRATEGIES FOR ENERGY EFFICIENCY IN HWSNS

Routing shows a pivotal role in shaping the energy efficiency and effective lifetime of HWSNs. Since data routing typically determines for the largest portion of node energy utilization, routing protocols must be cautiously designed to exploit node heterogeneity while mitigating communication overhead and load imbalance. This section briefly explains major routing strategies adopted in HWSNs, highlighting their energy-saving techniques, design trade-off, and applicability to diverse network scenarios (Potu Arayana *et al*., 2026).

5.1. Flat Routing Protocols in HWSNs

Flat routing protocols consider all sensor nodes as equals and rely on data-centric or location-driven transmission rather than predefined roles. In HWSNs, flat routing is modified by allowing nodes with higher remaining energy or superior transmission capability to participate more actively in data routing. While this technique reduces the overhead connected to role assignment and cluster formation, it may result to excessive control traffic and limited scalability in large-scale networks. Flat routing is therefore more suitable for moderately sized HWSNs where node heterogeneity can be dynamically exploited without incurring significant coordination costs.

5.2.Hierarchical and Cluster-Based Routing Protocols

Hierarchical routing protocols structure HWSNs into clusters, with CHs responsible for packets aggregation and long-range transmission to the sink/BS. Energy efficiency is obtained by minimizing redundant transmissions and allocating energy-intensive tasks to high-energy or advanced nodes. Cluster-based routing efficiently balances energy utilization and improves scalability, making it one of the most extensively used strategies in HWSNs. However, frequent CH selection and maintenance may present overhead, particularly in highly dynamic or dense deployments.

5.3. Chain-Based and Tree-Based Routing Protocols

Chain-based routing protocols organize sensor nodes into linear chains, where data is sequentially routed/forwarded and aggregated before getting to the sink. This approach reduces long-distance communications and evenly distributes energy utilization among nodes. Tree-based routing protocols, in contrast, organize hierarchical packets forwarding approaches rooted at the sink, allowing efficient multi-hop transmission and data aggregation. In HWSNs, energy-rich nodes are frequently positioned closer to the sink or higher in the tree to assuage hotspot problems. Although these protocols provide improved energy efficiency, they may suffer from increased latency and minimized robustness to node failures.

5.4.Mobility-Aware Routing Strategies

Mobility-aware routing approaches are designed to address dynamic network conditions emanating from mobile sinks, mobile sensor nodes, or both. By modifying routes in response to topology changes, these protocols minimize transmission distance and prevent high energy depletion near static sinks. In HWSNs, mobility can be leveraged to redistribute traffic loads and maximize network lifetime. However, mobility-aware routing presents additional complexity in route management and may incur higher control overhead if not cautiously managed.

5.5.Comparative Discussion of Routing Approaches

Each routing approach introduces distinct benefits and limitations in terms of energy efficiency, scalability, and adaptability. Flat routing provides simplicity and flexibility but suffers with scalability. Hierarchical and cluster-based routing attained superior energy savings and load balancing, making it ideal for large-scale HWSNs. Chain-based and tree-based routing further minimize communication energy but may increase latency and sensitivity to node failures. Mobility-aware routing improves adaptability and hotspot management but at the cost of increased protocol complexity. Consequently, the selection of an energy-efficient routing approach in HWSNs should be guided by application requirements, network size, node heterogeneity, and mobility characteristics. Table 4 briefly describes the energy-efficient routing strategies in HWSNs.

Table 4: Comparative Summary of Energy-Efficient Routing Strategies in HWSNs

Ref.	**Routing Strategy**	**Energy Efficiency**	**Scalability**	**Control overhead**	**Latency**	**Heterogeneity utilization**	**Typical Applications**
Joanna Kulik et al., 2002	Flat routing	Moderate	Low-medium	High	Low	Limited (dynamic role sharing)	Small-scale monitoring
Yang Zhang et al., (2025)	Hierarchical/Cluster-based	High	High	Medium	Medium	High (energy-rich CH selection)	Large-scale sensing
Raghuveer Singh etal., (2025)	Chain-Based	Very High	Medium	Low	High	Moderate	Energy-critical deployments
Aart Sharma et al., (2025)	Tree-based	High	High	Medium	Medium	High (Relay placement)	Structured data collection
Abdulla Juwaied et al., (2025)	Mobility-aware	High	Medium-High	High	Low-medium	High(adaptive routing)	Mobile sink/node scenarios

6. ENERGY HARVESTING AND SUSTAINABLE HETEROGENEOUS WIRELESS SENSOR NETWORKS

Energy harvesting has developed a fundamental enabler for realizing long-term sustainability in HWSNs. Conventional battery-powered HWSNs are strictly constrained by limited energy reserves, which limit network lifetime and raise maintenance cost due to battery replacement. Energy harvesting presets the ability for sensor nodes to reload their energy from ambient environmental sources, thereby maximizing network operation and minimizing human intervention. In heterogeneous environments, nodes vary not only in hardware and energy capacity but also in harvesting ability, making energy harvesting a powerful balance to heterogeneity for creating self-sustaining and adaptive sensor networks (Bilal R. Al-Kaseem *et al*., 2025).

6.1. Energy-Harvesting Models and Sources

Energy harvesting in HWSNs depicts the process by which sensor nodes transform external energy into usable electrical power. Common energy sources include "solar radiation, thermal gradients, mechanical vibrations (piezoelectric), wind energy, and radio-frequency (RF) signals". Solar harvesting is the most extensively employed due to its relatively high energy density, while RF and vibration harvesting are predominantly attractive for indoor and industrial deployments (Yu Song *et al*., 2025).

A commonly used energy-harvesting model represents the harvested energy at node *i* during a time interval *t* as:

$$E_h(i,t) = \eta_i P_s(i,t).t \tag{3}$$

Where $E_h(i,t)$ defines the harvested energy, η_i denotes the energy conversion efficiency of node *i*, and $P_s(i,t)$ depicts power available from the environmental source. The residual energy of a node is then updated as:

$$E_{res}(i,t+1) - E_{res}(i,t) + E_h(i,t) - E_C(i,t) \tag{4}$$

Where $E_C(i,t)$defines the energy utilization for sensing, processing, and communication. These models offer a mathematical basis for designing harvesting-aware protocols and evaluating sustainability performance.

6.2.Harvesting-Aware Communication and Routing

Harvesting-aware communication and routing schemes explicitly integrate energy harvesting dynamics into protocol design. Instead of depending solely on residual energy, routing decisions are prepared based on both current energy level and forecast harvested energy. Nodes with higher harvesting rates are chosen as CHs, relay nodes, or data aggregators, while energy-poor nodes function in low-duty or sleep modes. Such adaptive schemes allow enhanced load balancing, minimizing the risk of network sub-division, and optimize long-term stability by aligning communication tasks with energy availability.

6.3. Rechargeable and Hybrid Energy Storage Systems

To sustain harvested energy, sensor nodes are usually furnished with rechargeable batteries or super-capacitors. Rechargeable batteries offer higher energy density but experience limited charging cycles, whereas super-capacitors provide fast charging and maximize lifespan but minimize energy density. Hybrid energy storage schemes integrate both technologies, using super-capacitors for short-term buffering and batteries for long-term storage. In HWSNs, high-capability nodes usually use hybrid storage schemes to support energy-intensive operations, while low-end nodes depend on lightweight rechargeable units.

6.4.Challenges in Sustainable HWSNs

Despite their potential, viable HWSNs face numerous critical challenges. Energy harvesting is intrinsically unpredictable and recurrent, making reliable performance problematic to guarantee. Hardware cost and efficiency limitations limit large-scale deployment, mostly for RF and vibration harvesters. Moreover, harvesting-aware protocols proliferation system complexity and necessitate accurate energy prediction models. Other challenges comprise balancing fairness among nodes, managing heterogeneous harvesting rates, and guaranteeing reliable operation under changing

environmental conditions. Addressing these challenges remains a key research direction for the realization of fully autonomous and sustainable HWSNs.

7. CONCLUSION

This review has introduced a holistic examination of energy-efficient communication and routing strategies in Heterogeneous Wireless Sensor Networks, emphasizing how node diversity can be successfully exploited to improve network performance, scalability, and operational lifetime. By systematically scrutinizing communication mechanisms, routing protocols, and energy harvesting-based sustainability models, the review article has revealed that no single solution is universally optimal, and that protocol design must be steered by application requirements, network dynamics, and energy availability. The findings highlight the rising importance of harvesting-aware for sustainable HWSNs, while also showing insistent challenges related to scalability, complexity, and real-world deployment. Overall, this review offers a unified reference framework that can sustain informed protocol selection and inspire future research toward harvesting-aware reinforcement learning routing protocols, standardized heterogeneity metrics for fair protocol evaluation, public benchmark datasets for HWSNs routing comparison, Integration of machine learning with energy harvesting prediction, cross-layer optimization frameworks incorporating communication, routing, and energy management.

REFERENCE

Aarti Sharma & Ankush Kansal. (2025) .Enhanced CH selection and energy-efficient routing algorithm for WSN.

Microsystem Technologies, 31, 735-747.

Abdulla Juwaied, Lidia Jackowska-Strumillo & Artur Sierszen. (2025). Enhancing clustering efficiency in

heterogeneous wireless sensor network protocols using the K-Nearest Neighbours Algorithm. Sensors,

25(4), 1029.

Ali Forghani Elah Abadi, Seyyed Amir Asghari, Mohammadreza Binesh Marvasti, Golnoush Abaei, Morteza

Nabavi, Yvon Savaria. (2022). RLBEEP: Reinforcement-Learning-based energy efficient control and

routing protocol for wireless sensor networks. IEEE Access, 10 .

Avaneesh Singh, Atul Raj, Preeti Rani, Ali Khatibi, Horiya Aldeeb, Piyush Kumar Shukla, Ayman Sabry &

Mohamed M. Hassan. (2025). Resillient wireless sensor networks in industrial contexts via energy-efficient

optimization and trsut-based secure routing. Peer-to-Peer Networking and Applications, 18(132).

Ayman A. Alharbi, Emad. S. Hassan, Idris H. Smalli. (2025). Pareto-optimized mobile-sink routing for energy-

efficient wireless sensor networks. International Journal of Energy Research, 2025(1), 19808824.

Bilal R. Al-Kaseem, Zahraa K. Taha, Ssrsh W. Abdulmajeed, Hamed S. Al-Raweshidy. (2021).Optimized energy-

efficient path planning strategy in WSB with multiple mobile sinks. IEEE Access. 9

D. Pravin Kumar, P. Ganesh Kumar. (2025). Implementation of optimal routing in heterogeneous wireless sensor network with multi-channel media access control protocol using enhanced Henry Gas Solubility Optimizer. *International Journal of Communication Systems*, 38(1), e5980.

I. Gethzi Ahila Poornima, Sravanthi Dontu, M. Maheswaran, Rohith Vallabhaneni. (2025). Energy-efficient optimal routing-driven hybrid optimizations-enabled IoT-based wearable wireless body area network. *International Journal of Communication Systems*, 38(6), e70037.

Joanna Kulik, Weindi Heinzelman & Hari Balakrishman. (2002). Negotiation-based protocols for disseminating information in wireless sensor networks. Wireless networks, 8, 169-185.

Jun Yang, Wen Li, Cuiran Li, Libao Zhang, Li Liu. (2025). An energy-efficient and transmission-efficient adaptive

routing algorithm using deep reinforcement learning for wireless sensor networks. IEEE Internet of Things

Journal, 12(13).

Lina Elmoiz Alatabani, Rashid A. Saeed, Elmustafa Sayed Ali. (2026). Cross-layer optimization employment

energy routing protocols in WSN. Energy efficient internet of things-based wireless sensor network..

https://doi.org/10/1002/9781394314751.ch10.

Maryam Shafiq, Humaira Ashraf, Ata Ullah & Shireen Tahira. (2020), Systematic Literature review on energy

efficient routing schemes in WSN-A survey. Mobile networks and applications,25, 882-895.

M. Karthikeyan, D. Manimegalai & Karthikeyan Rajagopal. (2025). Optimizing energy efficiency in wireless sensor networks: dynamic routing with capuchin search algorithm. *Multimedia Tools and Applications*, 84, 15453-15477.

Maria Trigk, Elias Dritsas. (2025). Wireless sensor networks: from fundamnetals and applicatios and future trends. *IEEE ACCESS*, 13.

Muhammad Haris,& Haewoon am. (2025). Enhancing energy efficiency in IoT-WSNs through optimized PSO cluster head selection. *IEEE ACCESS*, 13.

Muhammad Akram, Sibghat Ullah Bazai, Muhammad Imran Ghafoor, Saira Akram, Qazi Mudassar IIyas, Abid Mehmood. (2025). EEMLCR: Energy-efficient machine learning-based clustering and routing for wireless sensor networks. *IEEE ACCESS*, 13.

Namit Gupta, Abu Bakkar bin Abdul Hamid, Abu Bakar Bin Mahat, Adesh Kumar. (2025). Analysis of energy-efficient smart path optimization routing protocol for wireless sensor networks. *Results in Engineering*, 28, 107456.

Nisha. B, Hassan Mohamed, G. Devadasu, M. Poomani Alias Punitha, Kandula Sandeep, T. Karthikeyan. (2025).

Foundations of smart healthcare: Emerging IoT Technologies in wireless sensor networks. International

control, computing and communication.

P. K. Poonguzhali, P. Geetha & R. Vidhya. (2025). Multi-objective cluster head based energy efficient routing using

THDCNN with hybrid capuchin search and woodpecker mating algorithm in WSN. Wireless Networks. 31,

2495-2511.

Potu Arayana, K. Keerthi, Osamah Ibrahim Khalaf, Premkumar Chithaluru, Manoj A. Patil, Sridevi Tumula.

(2026). Energy-efficient and secure routing strategy for opportunistic data transmission in WSNs. Journal

of Cyber Security Technology, 10(1).

Raghuveer Singh Dhaka, Manju Khurana, Sonu Lamba. (2025). Energy-efficient cluster-based routing in WSNs

using a hybrid GWO-pso optimization Technique. IEEE ACCESS, 14.

Soni Chaurasia, Kamal Kumar, Anil Kumar Kamboj. (2025). EHRP: Energy-efficient hyper-heuristic routing

protocol for wireless sensor networks. Electronics and Communications, 202, 156044.

Sumendra Thakur, Nurul I. Sarkar & Sira Yongchareon. (2025). AI-driven energy-efficient routing in IoT-based

wireless sensor networks: A Comprehensive review. Sensors, 25(24), 7408.

Sunawar Khan, Tehseen Mazhar, Tariq Shahzad, Yazeed Yasin Ghadi, & Habib Haman. (2025). Integrating IoT

and WSN: Enhacing quality of service through energy efficiency, scalability, and secured communication

Tumpa Pal, Sohail Saif, Ramesh Saha & Suparna Biswas.(2026). Energy efficient routing protocols in WSN for

Precision and smart agriculture. *Discover Networks*, 2(31)

Xiaoying Liu, Biao Zhou, Xianzhong Tian, Weihua Gong, Kechen Zheng. (2025). Energy consumption

minimization for delay- sensitive data collection in AAV- assisted WSN. *IEEE Sensors Journal*, 25(10).

Yang Zhang, Ling Yang, & Yan Tan. (2025). Energy-efficient adaptive routing in heterogeneous wireless sensor

networks via hybrid PSO and dynamic clustering. Journal of Cloud Computing, 14(46).

Yihan Guan, Feng Xu. (2025). A Low-energy multipath routing protocol for WSN based on an improved Haris

Hawks Optimization algorithm. International Conference on Computer Communication and Network

Security in smart systems. Peer-to-Peer Networking and Applications. 18(249).

Yu Song, Zhigui Liu, Kunran Li, Xiaoli He, and Weizhuo Zhu**.** **(**2024). Research on High-Efficiency Routing

Protocols for HWSNs Based on Deep Reinforcement Learning. *Electronics*, 13(23), 4746,.

International Conference on Engineering Innovation for Sustainable Development (ICESID 2026)
Faculty of Engineering, Ahmadu Bello University Zaria · 8–10 September 2026

EVOLUTION, PROSPECTS, AND FUTURE DIRECTIONS OF NIGERIAN CURRENCY IMAGE ANALYSIS: A DECADAL REVIEW

Isaac Yusuf[1,*], Isaac Omeiza Avazi[1]
[1]*University of Ilorin*
Email: 24-68gj002pg@students.unilorin.edu.ng[*], isaacavazi@unilorin.edu.ng
***Corresponding author**: Isaac Yusuf
DOI: https://doi.org/10.67203/sp.ICESID.2026

ABSTRACT
The counterfeit Nigerian banknote (Naira) is still an ongoing challenge; the development of automated image analysis of the Nigerian banknote has been undertaken. This study is a Systematic Literature Review (SLR) spanning 2016-2026 to map the past, present, and future trends of Nigerian currency image analysis. From 150 initial bibliographic entries in the journal, 55 methodologically sound articles were completely published and appraised. The evolution from the review to the report is emphasized, encompassing traditional image processing and conventional machine learning methods, such as color histograms, HOG, etc., as well as ensemble and deep learning architectures (CNN, LSTM, RNN), with some level of accuracy; despite these accuracies often being above 99%, reliable real-world deployment remains elusive. Persistent limitations include small proprietary datasets, sensitivity to defective notes, and high computational demands. The new redesign of the CBN currency in 2022 rendered models invalid. The prediction of other series was done using older series. To make a contribution to the existing knowledge, the research proposes six key research directions: The components of a set that includes benchmarks, domain adaptation for redesigns, the use of lightweight edge AI, multimodal sensor fusion, environmental robustness, and inclusive design. The overall aim of the study is to steer researchers and financial institutions in the right direction and on how to create highly reliable banknote authentication systems, going beyond just getting good scores in the test set.

Keywords: *Nigerian Naira; Currency Authentication; Computer Vision; Pattern Recognition*

Decadal Review

1. INTRODUCTION

The Nigerian economy's continued reliance on physical cash transactions is problematic due to widespread counterfeiting of banknotes. While digital financial products, such as the government-introduced e-Naira, aim to promote cashless payments, these initiatives appear insufficient to fully address the issue. Consequently, Nigerian banknotes remain the primary medium of exchange for most people, especially in crowded markets, informal settings, and taxi services (Olowu & Olasupo, 2023). In fact, the entire financial structure is reliant on fiat money, and that creates serious security concerns, mostly the diffusion of counterfeit notes. Both financial institutions and sellers have, for many years, used manual processes for currency verification. By the use of touch, sight, and quick inspection. But that kind of process has inherent flaws; it takes too long, and it depends on subjective judgments and human errors. Automated machine-based identification can be a substantial productivity is considered effective for identifying genuine banknotes, especially when a computer vision approach is applied to define the security characteristics accurately (Adeniyi et al, 2024). The automation system architecture has changed over the past 10 years. The changes have been quite dramatic. The former image processing method involves manual feature extraction, while the latter deep learning method directly classifies the banknote without the need for an intermediate feature extraction step. This latter technique will provide improved results, but it is likely to require more computational power, require data resources, and deal with a variety of conditions that occur in the actual use of Nigerian banknotes. The number of studies on currency recognition in Nigeria is growing, though the works are somewhat disjointed and found in a variety of academic journals and conference proceedings. Taken as a whole,

these research findings on the image analysis of Nigerian currency over the past decade are far from adequate in terms of the availability of usable material as it is in today's academic literature. Due to this, it is difficult for researchers and industry experts to identify established methods, and this delay is experienced when implementing reliable verification and automated processes for daily operations by banks in Nigeria (Mogaji & Nguyen, 2022). This research study therefore sets out to bring a comprehensive overview of the developments in image analysis of Nigerian currency over every decade. The main results of this effort are displayed below:

i. This study presents an evaluation of metrics for the purposes of assessing them. examines both the data and the performance of researchers who are currently conducting studies using metrics, and it also shows the difficulties that pop up where data is scarce, and problems such as replication. Gaps and whether the testing environment is really authentic at the time of research.
ii. The research also highlights strategic research directions towards enhancing the capacity and skills in practice.

2. REVIEW METHODOLOGY

The researchers conducted a systematic literature review (SLR) study framework to maintain both scientific research standards and results that other researchers could reproduce. The review framework includes three components, which are used to retrieve literature, select research material, and screen articles until researchers identify their final set of publications for examination. The screening and quality assessment summary of this study is found in the appendix section of this paper.

2.1 Literature Search Strategy and Data Repositories

The researchers conducted an extensive study that examined major digital academic platforms along with their associated repositories to study both worldwide scientific developments and local research efforts. The researchers used IEEE Xplore, SpringerLink, and Google Scholar as the primary electronic databases, which provided international research about currency validation technologies. The review process uses multiple sources to establish complete research activities that apply to Nigeria.

2.2 Search Queries and Key Terms

The retrieval procedure used tailored Boolean search queries that were meant to dig out research studies on digital image analysis together with Nigerian currency computational learning methods. The researchers then used key terms such as every form they could find of “Nigerian Currency”, “Naira Note”, “Banknote Recognition”, and “Authentication”. After that, they mixed these with more specialized terms, for example, “Image Processing”, “Computer Vision”, “Machine Learning,” and also “Deep Learning.”

2.3 Inclusion and Exclusion Parameters

The study used strict inclusion and exclusion criteria because it needed to zero in on visual data analysis only while judging the relevance of particular studies. In other words, the selection method is summarized in Table 1.

2.4 Article Selection Procedure and Quantitative Overview

The literature selection process followed a three-phase screening protocol, which includes three main steps. This included the collection of bibliographic records from selected databases. The process required a title and abstract assessment to determine which materials matched the required content. The process required a full-text article review to determine which materials met the established inclusion standards. The initial search process across academic databases produced 150 documents, which were found through the search. The screening process removed 60 articles because they duplicated existing

content and contained themes that did not match the main subject matter. The remaining 90 abstracts required thorough evaluation, which led to the disqualification of 35 submissions because they either studied non-image sensor methods or lacked scientific proof. The remaining articles comprising 55 articles were further scrutinized and further excluded 38 articles because they were pre-2016 published. The remaining 17 articles that were found germane to this study thoroughly appraised and studied..

Table 1: *Inclusion and Exclusion Parameters*

Parameters	Inclusion	Exclusion
Publication Date	2016 – 2026 (Decadal span)	Publications before 2016
Language	English	Non-English publications
Subject Focus	Image analysis, Computer Vision, Pattern Recognition	RFID, RF Sensors, Magnetic-only sensors (unless hybrid with image)
Geographic Context	Specific to Nigerian Naira notes	Generic currency models have not been tested on the Naira
Document Type	Peer-reviewed journals and conference proceedings	White papers, unpublished thesis, editorials

2.5 Denominations and Structural Evolution (2016–2026)

Not only a shift in the Nigerian monetary system, but a complete overhaul occurred over the entire 10-year period the researchers examined. Before December 2022, there were 8 different nominal values in existence: ₦5, ₦10, ₦20, ₦50, ₦100, ₦200, ₦500 and ₦1000. Later, on 26th October, 2022, the Central Bank of Nigeria (CBN) announced a fresh initiative in the redesign of banknotes, which resulted in the release of new banknotes (₦200, ₦500 and ₦1000) in December, 2022. Meanwhile, the smaller denominations, from ₦5 to ₦100, remained the same. The banknotes shared some common design features, such as their size and color, but each note also featured its own unique design with different Nigerian historical figures. The re-issuance, however, necessitated a complete redesign for the higher denomination banknotes, which meant changes in the colors, size of notes, and even security features' placement. This poses a significant challenge for the automated image analysis platforms, as the models developed in the 2016 series need to adapt, or recalibrate, for the 2022 series. The review basically acknowledges this coexistence of physical data between two different states.

2.6 Visual Features for Machine Analysis

Automated identification systems require the extraction of salient distinguishing features from the image of a currency. The performance of any computational approach, including traditional edge detection approaches and more recent advanced deep convolutional networks, is based on the detection of visible physical properties such as:

2.6.1 Chromatic Signatures (Color): This is the most prominent feature as far as the denominational categorization is concerned. The primary green color of each banknote is its main color: this is evident on the ₦50 banknote and on the ₦500 banknote. These elements are displayed by the image analysis systems in RGB and HSV color space. If only color is used as a means of identification, it will give false readings where light conditions vary and where pigments have faded.

2.6.2 Textural Properties: The production process of Nigerian banknotes uses a fibrous cellulose substrate, which undergoes intaglio engraving to create raised ink patterns. The basic process

of RGB sensors becomes limited because they cannot detect raised surface patterns, but high-resolution capture systems enable users to observe the basic micro-patterns and random surface textures present on paper materials. The Gray-Level Co-occurrence Matrix method serves as a standard technique that authenticates material properties by differentiating between real substrate material and fake substrate material.

2.6.3 Security Features: This includes

i. *Watermarks:* The paper matrix contains embedded effigies which become visible through trans-illumination. The features remain inaccessible to standard reflective imaging systems, which require specialized backlighting systems to achieve proper capture.

ii. *Security Threads:* The banknote contains metal or plastic threads that create reflective surfaces, which protect against unauthorized detection. The system identifies the objects through two methods: highlight detection algorithms and frequency domain analysis.

iii. *See-Through Registers*: The two patterns create identical overlaps when light strikes their surfaces. The system requires two sensor systems and special light systems to verify their authenticity because they function like watermarks. Serial Numbers and Typography Each banknote displays a unique alphanumeric serial number, which maintains the same font style and location throughout the banknote.

iv. *Optical Character Recognition (OCR)* methods can verify results, yet different printing quality and the existence of dust or physical damage often reduce OCR performance, which makes it a supporting element, not a primary identification method.

Table 2 displays essential visual attributes that researchers need to understand the available feature domain for their algorithm development work. The table presents specific challenges that each banknote faces because it displays similar colors between different denominations and shows security features differently under various lighting conditions. The data presented in Table 2 emphasizes a fundamental consideration for the architects of identification systems: that sole reliance on chromatic attributes is insufficient. The system requires algorithms to identify both old and new currency notes because it operates in an environment where lower-value notes stay unchanged while higher-value notes get redesigned.

Table 2: *Visual Characteristics Of Nigerian Banknotes Relevant to Image Analysis (2016–2026)*

(https://www.cbn.gov.ng)

Denomination	Dominant Color (2013 Series)	Dominant Color (2023 Redesign)	Key Security Features	Image Analysis Challenge
₦5	Green	Green (Unchanged)	Watermark, Security Thread	Small size makes feature extraction difficult.
₦10	Brown	Brown (Unchanged)	Watermark, Security Thread	Often heavily soiled; low contrast in images.
₦20	Blue	Blue (Unchanged)	Watermark, Security Thread	Color similarity with higher denominations under poor light.
₦50	Green	Green (Unchanged)	Watermark, Security Thread	Chromatic confusion with ₦5 note in grayscale conversion.
₦100	Brown/Orange	Brown/Orange (Unchanged)	Watermark, Security Thread	High circulation volume leads to significant wear/tear.
₦200	Brown	Yellow/Brown	Watermark, Thread, See-through	Color shift in redesign affects trained models.
₦500	Purple	Green/Red	Watermark, Thread, See-through	Major color change in redesign; high counterfeit target.
₦1000	Blue/Purple	Blue/Purple (Shifted)	Watermark, Thread, See-through	Dimension change affects cropping and scaling algorithms.

2.7 THE EVOLUTION OF TECHNIQUES

This section assesses the development through the classification system, allowing a better understanding of process requirements, accuracy, and system reliability competing with each other in the Nigerian financial system.

2.7.1 Conventional Image Processing and Classical Machine Learning (2016–2026)

Iwok and Akpan (2016) proposed a statistical way to sort real Naira notes from fake ones. The authors used discriminant analysis. The authors also relied on multivariate tools like Hotelling's T^2 and Mahalanobis distance. The goal was to identify the notes apart, using measured physical features. So the work was mainly about statistical classification, not about matching image pixels. Almu and Muhammad (2020) took a photo of a suspected banknote, then compared that photo with a stored image of an original note. It looked for pixel patterns and also tracked where key features were on the note. Those features included color details, a strip, and the watermark. The method produced one percentage score for how close the two images were. If the score was above 95%, the note was marked as genuine. Their tests showed it could separate real from fake notes. Still, the authors reported a problem when the note was worn, damaged, or too degraded. A proposed approach used color histograms in the HSI color space, and then it sorted Nigerian Naira notes, specifically the #200, #500, and #1000 denominations. Hence, a rule-based classifier worked with 10-bin histograms for the hue component, the saturation component, and the intensity component too, and it reported an average accuracy of around 98.66%. They also mentioned that the method worked well because it did not need many preprocessing operations. Even so, the approach still ran into difficulties in situations where notes were damaged or stained, and in those cases, lower denomination accuracy was more difficult to maintain, as cited in (Omeiza et al, 2020). The research conducted followed a three-step process, which included three distinct stages of research work (Adewole et al, 2023). The first step involved using an advanced object detection system to identify different types of currency. The second step involved using an existing algorithm that had been specifically developed to identify serial numbers of various currency denominations. The three different optical character recognition systems, which included Pytesseract, Easy OCR, and Keras OCR, were used to perform character recognition. The results showed that the system achieved perfect accuracy for currency classification because it reached 100 percent accuracy. The character recognition stage, which used the Easy OCR system, reached its highest accuracy level at 81%. The approach presents several problems that need to be addressed despite its current achievements. The OCR models do not include special features that enable them to recognize Nigerian currency serial numbers. The system experiences errors because it depends on three different factors, which include note condition, image quality, and visual background complexity.

2.7.2 *Hybrid and Traditional Techniques (2016-2026)*

The research process began with background elimination through Otsu thresholding and connected component analysis. The research team calculated HOG features from standardized grayscale images measuring 154×302 pixels. The research team used PCA to reduce the features to retain essential data while decreasing computational requirements. The ECOC-MCSVM system enabled the identification and classification of multiple banknote denominations, which could be shown from either side of the currency note. The research team examined a dataset that contained 5200 banknote pictures from four different currencies: 1800 Nigerian Naira, 1000 US Dollars, 1000 Canadian Dollars, and 1400 Euros. The Canon T2i digital camera captured these images at 200 dpi to display various viewing conditions, which included front and back views as well as upward and downward orientations of new and worn notes; full and partially hidden notes. Through the application of 10-fold cross-validation, the MCSVM classifier achieved better recognition results than multiple baseline methods, which included Naïve Bayes, Random Forest, NNge, Hyperpipes, IB1, and SMOSVM. The system achieved 99% accuracy for Naira, 97% for USD, 96% for CAD, and 98.6% for Euro while displaying fast processing capabilities. The method faced several major restrictions during its operation. In the modeling part, the researchers employed a multiple-layer ensemble strategy, and they blended multiple K-Nearest Neighbor (KNN) distance measurement concepts. The distances included Euclidean distance, Manhattan distance, Chebyshev distance, and Minkowski distance. Following this, the system used a weighted voting approach to combine the distance-metric predictions, enhancing the robustness of the system under image changes and also aiding with unexpected external conditions. This research was conducted using a set of Nigerian Naira banknotes, including N100, N200, N 500, and N1000. The team then collected photographs of real banknotes and fake notes taken in different lighting, from different angles, and they also ensured that the banknotes were in various states of wear. Later, the

application was tested on two different types of devices, namely; on Android devices (such as Samsung Galaxy S6) and iOS devices (such as iPhone 6). The results indicated an accuracy rate of 99.27% in identifying the denomination and 94.70% in detecting fake banknotes. The system also processed the images in a very short time (0.02 milliseconds per image), which means it could run in real time on standard mobile devices. However, during implementation, there were some key problems encountered as a result of illumination imaging, and thus it had difficulty in detecting more sophisticated counterfeits, particularly those that preserve visually realistic features of the banknotes. This indicates that additional sensing equipment (such as UV or infrared) and adaptive image processing algorithms are required to guarantee the deployment's reliability in practical environments (Dittimi & Suen, 2018). Subsequently, (Dittimi & Suen, 2019) developed a mobile app based on a client-server system, which utilized Unity 3D and MATLAB for banknote recognition and verification. The methodology adopted the following: Feature Extraction using Histogram of Oriented Gradients (HOG) and High Correlation Filters (HCF) to reduce the feature space, followed by the application of an ensemble classifier, which consisted of Multi-Layer Perceptron Neural Networks (MLPNN) and Multi-Class Support Vector Machines (MCSVM). They simulated the technique with full banknote sets comprising the Nigerian Naira, US Dollar, Canadian Dollar, and Euro banknotes. Authentic samples were taken as pictures using a Canon T2i camera, and the counterfeit samples were printed using an HP Color LaserJet printer, resulting in samples with differing viewing angles and lighting conditions. The results showed that the designed HOG-HCF-WMA system identified the images with 99.00% accuracy and a time of approximately 0.051 seconds per image. The system outperformed all the top systems established that have been used in their respective fields, with respect to its accuracy outcomes and its operational efficiency. The approach was successful, but had significant limitations. The system needed a tremendous amount of computing power to extract features, requiring the user to process features on a server and not on their mobile device. Ismail et al (2024) employed a two-stage image processing methodology. The process starts with the resizing, grayscale conversion, and rotation of ₦500 and ₦1000 banknotes, which undergo scanning to prepare them for SURF-based analysis. The system uses three image quality assessments to evaluate note eligibility for automated teller machine (ATM) operation. The algorithm achieved perfect accuracy in denomination identification when tested on a dataset containing 562 banknotes, which included 286 ₦500 notes, 270 ₦1000 notes, and 6 other notes. The Peak-Signal-to-Noise Ratio (PSNR) metric showed excellent results because it accurately classified every one of the 60 "fit" ₦500 notes and 93.8% of the 226 "unfit" notes. The PSNR metric for ₦1000 notes achieved accurate classifications of 136 "fit" notes and 120 "unfit" notes from a total of 142 "fit" notes and 128 "unfit" notes. The system recorded an overall accuracy rate of 97% for fit records and 93.8% for unfit records because PSNR demonstrated better accuracy than both SSIM and MSE. The two main obstacles that need resolution stemmed from the dataset's restricted size and its unbalanced distribution, which contained only 654 images and an extremely small quantity of non-target notes. The quality-metric stage required detailed pre-processing and threshold selection because it responded strongly to both image orientation and image degradation. The unfit notes showed decreased performance with SSIM and MSE, which suggests that these metrics fail to assess all types of banknote damage or wear. Woods & Oladosu (2020) built CNNs (VGG-16) with TensorFlow and OpenCV, reaching 92.75% accuracy. The model encountered difficulties when attempting to extend its functionality to different currencies.

2.7.3 The Traditional to Machine Learning. Ensemble learning and Deep Learning (2020–2026)

Researchers began using Deep Learning (DL) architectures after 2020 because they needed to adopt a new research methodology. The literature from this period shows a primary focus on Convolutional Neural Networks (CNNs), which help researchers extract essential features from their work. The VGG16, ResNet50, and InceptionV3 models enable users to identify complex design elements through their processing of unprocessed image data. The era shows a dominant pattern of researchers applying transfer learning to their work. Researchers used ImageNet-trained models, which they modified through training on their limited Naira note datasets because they could not find enough

Nigerian currency data for their research. The research used this methodology to achieve performance metrics that exceeded 98% through the use of limited training resources. The period from 2023 to 2026 marks the beginning of research into MobileNetV2 and EfficientNet, which academic institutions use to enhance their processing speed and precision rates. (Richard-Nnabu et al., 2024) used Convolutional Neural Networks (CNNs) to detect counterfeit Nigerian Naira notes. The model achieved 95% accuracy because the testing included both folded notes and partially faded notes. The strength of CNN's in handling such complexities underlines their potential for counterfeit currency identification. The study demonstrated that the approach needs larger and more diverse datasets to improve its ability to identify currency. Ibitoye (2024) developed a Modified Faster R-CNN system which uses the Inception V3 architecture. The method achieved 97% detection accuracy, but it failed to identify worn-out or damaged notes and needed high-quality photos for precise recognition. Nwokoye & Moru, (2025) developed a cost-effective technological solution that enables visually impaired users to identify Nigerian naira banknotes. The system was created by customizing an SSD-MobileNet V2 FPNLite detector, which operated at 320x320 pixel resolution. The system was optimized for mobile devices through TensorFlow Lite, while Google Text-to-Speech provided spoken feedback. The development process started with image capture and proceeded through image preparation, which involved size adjustments, standardization, and data expansion techniques. The recognition model training used a specially assembled dataset of 3,468 images, which contained duplicate photos of each currency type that had undergone extensive editing. The researchers utilized the optimized model for real-time identification purposes. The system testing with previously unused image data demonstrated exceptional detection accuracy for all seven naira denominations. The system reached 97.11% mean average precision (mAP) at Intersection over Union (IoU) 0.55 and 93.29% at IoU 0.90 and 83.81% at IoU 0.95, while the total system exceeded 90% mAP. Convolutional Neural Networks extract image features. Feature selection was done by the Networks (CNNs) for deciphering the note values. A custom CNN structure, as well as some structures provided by the library, were used for this purpose. The experimental results indicate that both the custom CNN and pre-trained CNN models reached the correct answer for all the questions on the test. data. The CNN models required both large sets of training data and higher-level graphics processing units, which produced problems in their use with mobile devices. Meanwhile, deep learning methods were reviewed in academic literature. which is used by researchers for making a fake banknote is a fascinating area. Using deep learning for forging a fake banknote is a fascinating field. This was accomplished by examining papers that were published from 2018 to 2024. (Yusuf et al, 2025) conducted several Convolutional Neural Network (CNN) architectures, and in this set, there are AlexNet, MobileNet, VGG16, ResNet, which form the foundation of the DNN networks. The DNN networks are based on Inception V3, along with Recurrent neural Networks. RNNs and generative adversarial networks (GANs). The studies used datasets with images of several different countries' banknotes, including the Indian Rupee, Nigerian-Naira, CFA Franc, and Saudi Riyal. The studies were successfully classified with accuracy rates of 70% to 99.84%. The methods of approach gave better results.

2.7.4 Comparative Examination of Selected Studies

Table 3 will be used to compare the research methods used in the 11 most important papers studied and evaluate them. The table illustrates the changes from traditional methods to deep learning methods and some of the key constraints of dataset size and environmental durability.

3. PROSPECTS AND FUTURE DIRECTIONS

The study, considered the Nigerian banknote identification systems for the next decade, 2016-2026, revealed that the Nigerian banknote identification systems have entered a new technological area. Although laboratory tests have demonstrated top-level performance results ranging up to 99 percent, the academic work of the research has yet to yield profitable financial systems. The current research methods can only partially improve classification accuracy to a small degree and will increasingly meet with the challenges of data standardization, system adaptation, system performance, and security feature combination in the future. The following list of areas presents key areas that need to be further explored:

Table 3: *Comparative Analysis of Nigerian Image Analysis Techniques (2016-2026)*

Author/Year	Method/Algorithm	Data Size	Accuracy	Limitation
Omeiza et al., 2023	Color histograms in HSI color space with a rule-based classifier using 10-bin histograms for hue, saturation, and intensity components	Not explicitly specified; focused on ₦200, ₦500, ₦1000 Naira notes	98.66%	Performance issues with soiled or damaged notes; mitigation focused on lesser denominations
Dittimi et al., 2017	Background removal (Otsu thresholding + connected component analysis), HOG feature extraction, PCA dimensionality reduction, ECOC-MCSVM classification framework	5,200 banknote images: 1,800 Naira, 1,000 USD, 1,000 CAD, 1,400 EUR; captured with Canon T2i at 200dpi under varied conditions	99% Naira, 97% USD, 96% CAD, 98.6% Euro	Performance decline under extreme lighting/distortion; PCA may discard subtle discriminative patterns; high computational complexity from ECOC-MCSVM; denomination recognition only (no counterfeit detection)
Dittimi & Suen, 2018	Mobile application (Unity 3D); layered ensemble KNN combining Euclidean, Manhattan, Chebyshev, and Minkowski distance metrics with weighted voting system	Nigerian Naira (₦100-₦1000) photographed via smartphone cameras; diverse lighting, angles, wear states; included genuine and counterfeit samples (exact count unspecified)	99.27% denomination recognition; 94.70% counterfeit detection; 0.02ms avg processing time	Visible-light imaging limits the detection of sophisticated counterfeits; performance drops with severely dirty/torn/creased notes; requires precise parameter tuning; dependent on image resolution and stable camera positioning
Dittimi & Suen, 2019 Dittimi & Suen, 2019	Client-server mobile app (Unity 3D + MATLAB); blended framework: HOG feature extraction, High Correlation Filters (HCF) for dimensionality reduction, Weighted Majority Average ensemble of MLPNN and MCSVM	Multi-currency dataset (Naira, USD, CAD, EUR); genuine images (Canon T2i) + counterfeit samples (HP Color LaserJet); varied angles and illumination (exact counts unspecified)	99.00% identification accuracy; 0.051s average processing time	High computational demands requiring server-side processing; smartphone camera focusing/resolution limitations at close range; sensitivity to background interference and lighting variations; processing time fluctuations based on note size and pixel density

Author/Year	Method/Algorithm	Data Size	Accuracy	Limitation
Almu & Muhammad, 2020	Pattern recognition system (Visual Basic + MS Access); preprocessing, feature extraction (color, watermarks, serial numbers), pixel-wise comparison against reference database with 95% similarity threshold	Reference database of genuine Nigerian banknotes; user trials with 15 participants (exact image dataset size not specified)	Successful identification of authentic/fake notes under typical conditions; no specific accuracy percentage reported.	Unreliable with heavily damaged, soiled, or degraded notes due to pixel-comparison approach; limited robustness to visual obstructions; recommended integration of multiple image-processing techniques and mobile interface
Adewole et al., 2023	Three-stage pipeline: enhanced object detection for currency classification, pre-trained algorithm for serial number localization, three OCR systems (Pytesseract, EasyOCR, KerasOCR) for character recognition	Not explicitly specified in the provided text	100% accuracy for currency classification; peak 81% character recognition accuracy (EasyOCR)	Insufficient OCR accuracy for practical deployment; OCR models not specifically adapted to Nigerian currency serial number formats; prone to errors from note condition variations, image quality issues, and complex visual backgrounds
Ismail et al., 2024 Ismail et al., 2024	Two-stage pipeline: (1) Preprocessing (resizing, grayscale, rotation) + SURF feature extraction + KNN classifier for denomination recognition; (2) Fitness assessment module using MSE, PSNR, and SSIM image quality metrics	562 test banknotes (286 ₦500, 270 ₦1000, 6 other notes); total dataset approximately 654 images with noted class imbalance	Denomination recognition: 100%; Fitness classification (PSNR metric): ₦500 fit=100%, unfit=93.8%; ₦1000 fit=95.8%, unfit=93.8%; Overall averages: 97% fit notes, 93.8% unfit notes	Modest dataset size with class imbalance; fitness metrics sensitive to image orientation and degradation requiring careful preprocessing/threshold tuning; SSIM and MSE underperformed on unfit notes; may not comprehensively capture all wear/damage patterns

Author/Year	Method/Algorithm	Data Size	Accuracy	Limitation
Adeniyi et al., 2024	Hybrid approach: Circular Local Binary Pattern (CLBP) for rotation-invariant texture feature extraction combined with CNN architectures (custom design + transfer learning models: VGG, ResNet variants) for feature selection and classification	Higher-value Naira notes (₦200, ₦500, ₦1000) with various damage types (ripped edges, faded ink, creases, partial coverage); captured under diverse lighting/orientations (exact count not specified)	100% classification accuracy on testing data for both custom CNN and pre-trained transfer learning models	CLBP extraction is computationally intensive and vulnerable to severe noise/physical damage; CNN models require extensive training data and powerful GPUs, limiting mobile/embedded deployment; untested on lower denominations (₦5–₦100); high controlled-test accuracy may not translate to real-world scenarios with sophisticated counterfeits; recommends multi-modal authentication (UV, magnetic, tactile)
Richard-Nnabu et al., 2024	Convolutional Neural Networks (CNN) for binary classification of genuine vs. counterfeit Nigerian Naira notes	Not explicitly specified in the provided text	95% accuracy maintained even with folded or partially faded notes	Limited by dataset size and diversity; authors emphasized need for larger, more varied datasets to enhance model generalizability and practical relevance for real-world currency identification scenarios
Nwokoye & Moru, 2025	SSD-MobileNet V2 FPNLite object detector (320x320 input), optimized with TensorFlow Lite for mobile deployment; integrated with Google Text-to-Speech for auditory feedback	3,468 annotated images (each of 7 Naira denominations photographed twice with extensive data augmentation techniques)	mAP: 97.11% at IoU 0.55, 93.29% at IoU 0.90, 83.81% at IoU 0.95; overall system >90% mAP; ~80% accuracy when trained on restricted/lower-quality data	Small dataset size with limited variety; reliance on standard-resolution camera images; accuracy degradation (~80%) with lower-quality training data; requires more extensive, higher-resolution datasets and advanced augmentation for improved reliability

Author/Year	Method/Algorithm	Data Size	Accuracy	Limitation
Yusuf et al., 2025	Systematic review of deep learning approaches: CNN architectures (AlexNet, MobileNet, VGG16, ResNet, Inception V3), RNNs, and GANs for counterfeit detection	Multi-currency datasets (Indian Rupee, Nigerian Naira, CFA Franc, Saudi Riyal) from public archives, web scraping, and organizational holdings (exact sizes not specified in review)	Reported classification accuracy range: 70% to 99.84%; ensemble and pre-trained model approaches typically yielded superior performance	Limited adaptability to degraded or imperfect banknotes; imbalanced datasets with scarce counterfeit examples; high computational requirements hindering mobile/embedded deployment; model capacity/lack of interpretability impedes adoption in transparent, rule-based financial decision-making contexts

3.1 Establishment of Standardized Public Benchmarks

The most frequently reported limitation identified during the literature review is that the datasets are incomplete in various capacities, such as basically. It is not always complete, so even if search thoroughly and look at them, there is still some missing information. The lack of data makes it impossible to confirm findings, while it makes models develop excessive dependence on their training data, according to the research of (Dittimi et al, 2017). The research community requires a collaborative effort to develop a publicly shared reference dataset that serves as a standard benchmark for research. The collection should include:

a) *Comprehensive Denomination:* The complete legal currency collection includes all current denominations, which range from ₦50 to ₦1000 and feature both the old design and the new design introduced after 2023.

b) *Diverse Physical State:* The research team built classification models for note quality assessment by intentionally including new notes together with worn notes, dirty notes, damaged notes, and creased notes.

c) *Challenging Examples:* The study requires a validated collection of advanced counterfeit banknotes to address the issue of example distribution imbalance, which Dittimi and Suen (2018) and Richard-Nnabu et al. (2024) identified.

d) *Environmental Diversity:* The images were taken under various illuminations, backgrounds, and camera settings to simulate situations that mimic market and ATM conditions.

3.2 Domain Adaptation for Currency Redesigns

The Central Bank of Nigeria implemented a currency redesign in December 2022, which creates a major obstacle for people who need to research and identify Nigerian currency because they must learn new recognition methods. The current recognition models, which were created before 2022, become useless when they try to recognize banknotes that have different color patterns, security elements, and design features. The process of developing new models requires organizations to allocate substantial resources and dedicate extended periods of time to development work.

Future Direction: Research should focus on Transfer Learning and Few-Shot Learning methods as primary research objectives. The research team aims to develop model architectures that can learn new currency designs with only small amounts of labeled data. Generative Adversarial Networks (GANs) will enable the creation of authentic images that represent new currency denominations and their counterfeit versions. The system will use limited real-world data to help secure procedures; this will boost its generalization capabilities, but maybe not in a perfectly linear way

.

3.2 Optimize for lightweight Edge AI and mobile devices.

The creation of deep learning models such as VGG and ResNet establishes a sort of high-precision standard, but the processing requires the resources of central servers, so it is a tight bottleneck. This means that the system may exhibit performance delays and, at the same time, it is also a challenge for data protection due to the same processing requirement. Also, the incorporation of a compact version of MobileNet called MobileNet in our design, which also increases the speed of the operations, but at the cost of accuracy, as is only fair given the requirement.

Further direction: More attention should be paid to the research of model compression techniques in the future, which is not only a side step but is the main focus, such as pruning, quantization, and knowledge distillation. The goal is to deploy powerful convolutional neural network (CNN)-based systems directly onto low-power devices, such as ATMs, point-of-sale terminals, and even some simple cell phones, soon and with minimal delay or power consumption. The study should also really focus on Federated Learning, as it seems like it is an important part of this whole scenario. In practical terms, mobile technology can improve their recognition models through collective learning whilst preserving users' image data. This means improved overall privacy protection and more security measures that's the point.

3.3 Anti-Counterfeiting using Multi-Modal Sensor Fusion

The problem with this analysis is that it relies on the visual characteristics alone for its evaluation. Research shows that sophisticated counterfeiting can be able to replicate the appearance of an optical identification system in a convincing way, making optical systems incapable of providing security in a secure facility.

Future Direction: Future authentication systems should be based on more than one type of sensor, which is also referred to as multimodal sensor fusion. The concept is that the visual information in the normal color image is matched to other information such as that under UV, IR, and magnetic ink detection. Additionally, there is surface texture analysis, which is quite useful in practice. These pieces, when combined, should make the authentication system seem more secure, and it's the combination of the pieces that makes it secure, not just one of them. So, the research should be centered on making useful evidence integration algorithms for several sources and getting all that into an authenticity result. It should do that to lower the rates of false identification, which is where fake products are mistaken as real products.

3.4 Environmental Robustness and Light-Condition Handling

The studies indicate that when conditions are less than optimal, performance decreases. The system demonstrated two major issues, which included failing to process soiled currency notes and also not being able to cope with changes in lighting and viewing angles, in general.

Future Direction: The researchers really do need to make algorithmic resilience a little stronger by implementing ways of identifying and fixing errors that crop up as the notes are classified. In the first stages of data processing, advanced techniques that get rid of the background noise and also standardize lighting conditions, even across different currency note materials and those varied surfaces, are implemented. Basically, the quality determination of a currency (for ATM suitability, like it or not) should be considered a different and concurrent task, in addition to denomination. For that, it might be able to rely on more nuanced texture analysis, instead of basic pixel measurements.

3.5 Inclusivity and Accessibility

While it may feel a bit odd, the use of Text-to-Speech (TTS) technology looks like a good idea for increasing access to financial services for persons with visual impairments. In practice, the function shows up at certain moments; it is not something users see all the time.

Future Direction: The next step in the process should focus on adopting universal design concepts. The system for recognition requires the developers to create functions determining values and to push the user toward immediate alerts, which should be achieved through sound. Multiple local languages should be supported simultaneously. Further research on tactile feedback mechanisms for user validation would also benefit other groups of users in the identification of currency. That's the whole direction that we're going in, towards financial equity, and if it's a bit uneven, that's what we're going in.

4. CONCLUSION

This study reviewed the developments of image analysis research in Nigeria's currency from 2016-2026, which aimed at evaluating the development of image analysis of Nigerian currency during the mentioned time period. Of the 150 publications retrieved, 55 methodologically eligible studies were identified, and 17 of these were subjected to detailed critical appraisal to gain a detailed understanding of the methods, performance trends, and research gaps. The review clearly shows the technological evolution from traditional image processing methods and handcrafted feature extraction techniques to hybrid machine learning methods and, more recently, to deep learning architectures like CNNs, transfer learning, and lightweight object detectors. The accuracy of reported recognition varied from around 70% to 100% across the studies reviewed, with some recent deep learning models able to reach above 99% accuracy under controlled experimental conditions. However, such great success has not been achieved yet for successful deployment in the wild due to the lack of widely available datasets, the absence of good representation of worn and counterfeit banknotes, the sensitivity to illumination and environmental changes, heavy computational demands, and insufficient model generalization. One of the major conclusions of this review is that the redesign of banknotes by the Central Bank of Nigeria (CBN) in 2022 has completely changed the appearance and security features of the higher denominations, making the effectiveness of models trained only on the previous series of banknotes null and void. Therefore, future studies should focus on the development of adaptive learning strategies that could continue to facilitate the recognition of banknotes even if they were redesigned, without necessitating a complete redevelopment of the banknote model. Overall, the review points towards the development of a system that is robust, adaptive, explainable, and efficient in terms of computation, as well as optimizing classification accuracy in future Nigerian currency authentication systems. The development of standardized benchmark datasets, leveraging transfer learning and few-shot learning to handle redesign challenges, the integration of multimodal sensing, the enhancement of environmental robustness, and the promotion of inclusive accessibility features will be crucial in bringing research innovations to viable financial authentication solutions that can thrive in the practical Nigerian banking and commercial landscape.

5. REFERENCES

Adeniyi, J. K., Adeniyi, A. E., Aworinde, O. H., Adeniyi, T. T., Olanloye, O., & Ninan, D. O. (2024). A circular local binary pattern and convolutional neural network approach to mutilated Nigerian banknotes recognition. *2024 International Conference on Science, Engineering and Business for Driving Sustainable Development Goals (SEB4SDG)* (pp. 1–6). IEEE. https://doi.org/10.1109/SEB4SDG60871.2024.10629799

Adewole, L. B., Ogunleye, E. O., Faniyan, O. E., Adewale, S. A., & Daramola, C. Y. (2023). Development of a serial number extractor for Nigerian currencies. *University of Ibadan Journal of Science and Logics in ICT Research, 9*(1).

Almu, A., & Muhammad, A. B. (2020). Image-based processing of Naira currency recognition. *Scientia Africana, 15*, i143–i150.

Dittimi, T. V., Hmood, A. K., & Suen, C. Y. (2017). Multi-class SVM-based gradient feature for banknote recognition. *2017 International Conference on Information and Communication*

Technology for Intelligent Systems (ICIT) (pp. 309–314). IEEE. https://doi.org/10.1109/ICIT.2017.7915503

Dittimi, T. V., & Suen, C. Y. (2018). Mobile app for the detection of counterfeit banknotes. In F. Khosrowpour (Ed.), *Advances in artificial intelligence: 31st Canadian Conference on Artificial Intelligence, Canadian AI 2018* (pp. 156–168). Springer International Publishing. https://doi.org/10.1007/978-3-319-89656-4_13

Dittimi, T. V., & Suen, C. Y. (2019). High correlation-based banknote gradient assessment of an ensemble classifier. *International Journal of Wavelets, Multiresolution and Information Processing*. https://doi.org/10.1142/S0219691319500061

Ibitoye, O. T. (2024). Fake currency detection using a modified faster region-based convolutional neural network. *International Journal of Electrical Engineering and Computer Science, 6*, 46–50.

Ismail, T. I., Abubakar, M. A., & Tijjani, I. I. (2024). *Performance comparison of deep learning techniques in Naira classification*. DOI: 10.48550/arXiv.2412.02072

Iwok, I. A., & Akpan, A. W. (2016). Discriminant function for classification of genuine and counterfeit Naira notes. *Scientia Africana, 15*(1).

Mogaji, E., & Nguyen, P. N. (2022). The dark side of Mobile Money: Perspective from an emerging economy. *Technological Forecasting and Social Change. Volume 25, ISSN: 0040-1625, doi.org/10.10161/j.techfore*

Nwokoye, S., & Moru, D. (2025). *Development of a neural network model for currency detection to aid visually impaired people in Nigeria* [Preprint]. arXiv. https://arxiv.org/abs/2508.18012

Olowu O. F & Olasupo M.A. (2023). The Impact of Cashless and Naira Redesign Policies on Economic Development in Federal Capital Territory, Abuja. *Journal of Politics & International Relations. Volume 2, No 2*

Omeiza, I. O. A., Ogunbiyi, O., Ogundepo, O. Y., Otuoze, A. O., Egbune, D. O., & Osunsanya, K. (2023). A method of colour-histogram matching for Nigerian paper currency notes classification. *Jordan Journal of Electrical Engineering, 9*(1).

Richard-Nnabu, N. E., Ituma, C., & Nweke, H. F. (2024). Convolutional neural networks method for folded Naira currency denominations recognition and analysis. *Journal of the Nigerian Society of Physical Sciences*, Article 2239.

Woods, N. C., & Oladosu, H. S. (2020). Recognition and fitness classification of Nigerian currency for automatic teller machines. *African Journal of Computing & ICT, 13*(1), 29–38. https://afrjcict.net

Yusuf, A. A., Zambuk, F. U., Gital, A. Y., Lawal, M. A., Rukuna, A. L., Garba, L., & Aliyu, A. Y. (2025). Deep learning for counterfeit currency detection and classification: A systematic review of current approaches, challenges, and future directions. *International Journal of Research*. https://www.ijrpr.com/uploads/V6ISSUE2/IJRPR38592.pdf

APPENDIX: SCREENING PROCESS AND QUALITY ASSESSMENT

1.1 Screening Flow Summary

Identification: Records identified (n=150)
Removed before screening: Duplicates/irrelevant (n=60)
Screening: Abstracts screened (n=90)
Excluded after abstract screening (n=35)
Eligibility: Full texts assessed (n=55)
Included in qualitative synthesis (n=55)
Detailed comparative appraisal in Table 3 (n=17 representative studies).

1.2 Quality Assessment Criteria

Each eligible study was evaluated against: (1) clear objectives, (2) adequate dataset description, (3) reproducible methodology, (4) appropriate validation metrics, (5) limitations discussed, (6)

relevance to Nigerian currency image analysis. Each criterion was scored 0–2 (maximum 12). Studies scoring ≥8 were considered methodologically sound and retained.

1.3 Inter-rater Procedure

Two reviewers independently screened titles/abstracts and full texts using the predefined inclusion/exclusion criteria. Disagreements were resolved through discussion and consensus; unresolved cases were adjudicated by a third reviewer. Agreement was monitored using Cohen's kappa, with $\kappa \geq 0.80$ targeted before full screening.

International Conference on Engineering Innovation for Sustainable Development (ICESID 2026)
Faculty of Engineering, Ahmadu Bello University Zaria · 8–10 September 2026

FEATURE SELECTION USING RANDOM FOREST FEATURE IMPORTANCE FOR EFFICIENT NETWORK INTRUSION DETECTION ON THE NSL-KDD DATASET

Shafiu Shuaibu[1], Basira Yahaya[1], A.d. Adekale[1], Aminu Yakubu[2,*]
[1]*Ahmadu Bello University Zaria*
[2]*Federal University of Education Zaria*
Email: shafson6@gmail.com, basiraee@gmail.com, adekale@abu.edu.ng, aminuyakubu@fuez.edu.ng*
***Corresponding author**: Aminu Yakubu
DOI: https://doi.org/10.67203/sp.ICESID.2026

ABSTRACT
Network Intrusion Detection Systems (NIDS) require informative features to distinguish benign from malicious traffic. This study investigates Random Forest feature importance for reducing the dimensionality of NSL-KDD. Using KDDTrain+, an 80:20 stratified split was applied after preprocessing, producing 121 predictive features. The top 30 features selected by Random Forest reduced dimensionality by 75.21%. Evaluated with an optimized Random Forest, the reduced representation achieved 99.83% accuracy, 99.93% precision, 99.70% recall, 99.82% F1-score, and 0.0594% false-positive rate. The results demonstrate that Random Forest can identify a compact and informative feature subset under the stated experimental conditions. However, computational efficiency was not directly measured, and a full 121-feature baseline must be rerun before confirming performance preservation or improvement.

Keywords: *Network Intrusion Detection; Feature Selection; Random Forest; Feature Importance; NSL-KDD; Machine Learning; Dimensionality Reduction*

1. INTRODUCTION

The continued growth of computer networks and Internet services has increased the need for automated detection of malicious activities. Network Intrusion Detection Systems (NIDS) monitor network traffic and classify connections as normal or suspicious. Machine-learning techniques are widely used because they can learn attack patterns and support automated detection (Buczak & Guven, 2016; Khraisat et al., 2019).

The NSL-KDD dataset remains a widely used benchmark for evaluating machine-learning-based intrusion detection methods. It was developed to address limitations of the original KDD Cup 1999 dataset and provides a structured basis for IDS research (Tavallaee et al., 2009). However, categorical encoding can produce a high-dimensional feature space containing variables with limited contribution to classification.

Feature selection reduces this problem by identifying relevant variables while preserving their original meaning. Common approaches include filter, wrapper, and embedded methods (Chandrashekar & Sahin, 2014). Random Forest provides an embedded feature-importance mechanism that can rank variables according to their contribution to model performance (Breiman, 2001).

Recent studies have highlighted the importance of feature selection in IDS research, including the use of Random Forest on NSL-KDD (Umar et al., 2025). However, differences in preprocessing, data partitioning, and evaluation procedures make direct comparison difficult.

Therefore, this study investigates Random Forest feature importance for ranking the 121 encoded predictive features of NSL-KDD and selecting the top 30 features for intrusion detection classification. The study (i) applies a reproducible Random Forest-based feature-ranking procedure, (ii) reduces the feature space from 121 to 30 features, and (iii) evaluates the selected features using an optimized Random Forest classifier on a held-out test set.

2. RELATED WORK

Machine learning is widely used for intrusion detection, with studies emphasizing dataset characteristics, algorithm selection, and computational considerations (Buczak & Guven, 2016).

Feature selection reduces redundant and irrelevant variables and can improve IDS efficiency. Methods are commonly classified as filter, wrapper, and embedded approaches, with Random Forest providing embedded feature-importance measures during training.

Recent NSL-KDD studies demonstrate the value of feature selection. RF-based and other selection methods have achieved strong detection performance while reducing feature dimensionality.

This study applies Random Forest impurity-based feature importance to select the top 30 features from 121 one-hot-encoded NSL-KDD features and evaluates them using an optimized Random Forest under an 80:20 stratified KDDTrain+ split.

3. METHODOLOGY

3.1 Research Design

An experimental machine-learning design was adopted. The complete workflow consisted of data preparation, train-test partitioning, binary label transformation, categorical encoding, feature scaling, Random Forest feature-importance estimation, feature ranking, top-30 selection, classification and comparative analysis.

The test partition was not used to calculate feature-importance scores or select features.

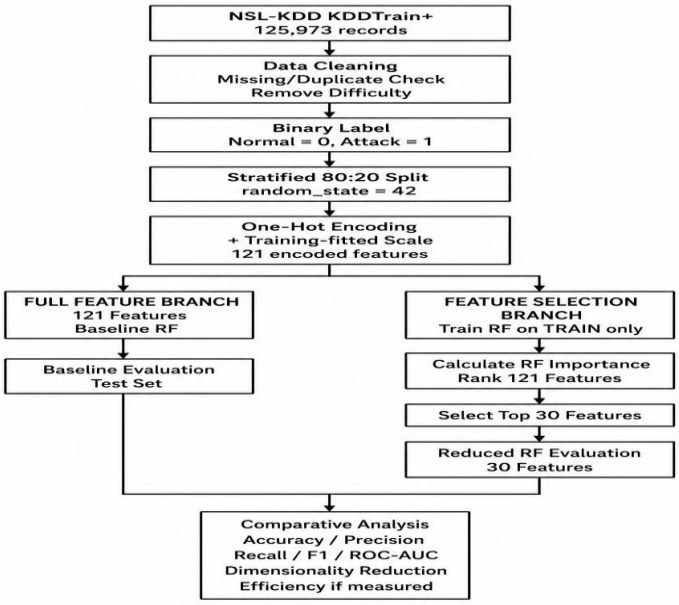

3.2 Dataset

The experiment used the KDDTrain+ file from the NSL-KDD dataset. The loaded file contained 125,973 records and 43 columns, comprising 41 predictive attributes, the attack label and the auxiliary difficulty attribute.

The three categorical attributes were:

- protocol_type
- service
- flag

The original attack labels were retained during initial loading and subsequently transformed into a binary classification target.

KDDTest+ was not used in the reported experiment. Instead, KDDTrain+ was partitioned into training and testing subsets.

3.3 Data Preprocessing

Data integrity checks were performed before modelling. The notebook recorded no missing values and no duplicate rows in the loaded KDDTrain+ data.

The auxiliary difficulty attribute was removed before the final experimental pipeline. Consequently, the model input contained 41 predictive attributes before categorical encoding.

The preprocessing procedure therefore consisted of:

1. loading KDDTrain+;
2. checking missing and duplicate records;
3. removing difficulty;
4. separating predictors and target;
5. splitting the data into training and testing partitions;
6. converting the target to binary labels;
7. one-hot encoding categorical predictors; and
8. standardizing the resulting numerical representation.

3.4 Binary Label Transformation

The original attack categories were transformed into a binary target:

$$y = \begin{cases} 0, & \text{normal} \\ 1, & \text{attack} \end{cases}$$

After the 80:20 stratified partition, the training set contained 100,778 records, comprising 53,874 normal and 46,904 attack records. The test set contained 25,195 records, comprising 13,469 normal and 11,726 attack records.

3.5 Categorical Encoding

The categorical attributes protocol_type, service and flag were converted into binary indicator variables using one-hot encoding.

After removal of the difficulty attribute, the resulting representation contained 121 encoded predictive features.

The encoding was performed separately on the training and test partitions, after which the test representation was aligned to the training feature columns. This ensured that both partitions had the same model-input structure.

3.6 Feature Scaling

Standardization was applied using StandardScaler.

For a feature x, the standardized value is:

$$z = \frac{x - \mu}{\sigma}$$

where $\mu$and σrepresent the mean and standard deviation estimated from the training data.

Importantly, the scaler was fitted only on the training partition:

$$X_{train}^{scaled} = Scaler.fit(X_{train})$$

and subsequently applied to the held-out test partition:

$$X_{test}^{scaled} = Scaler.transform(X_{test})$$

Thus, test-set statistics were not used when fitting the scaler.

Although Random Forest is relatively insensitive to feature scaling, scaling was retained as part of the implemented preprocessing pipeline.

3.7 Train/Test Strategy

The 125,973 KDDTrain+ observations were divided using an 80:20 stratified train-test split:

- training: 100,778 records;
- testing: 25,195 records;
- test_size=0.20;
- random_state=42;
- shuffle=True;

- stratification based on the binary target.

The stratified procedure preserved the relative distribution of normal and attack instances between the two partitions.

No KDDTest+ records were used in the reported experiment. Consequently, the results should be interpreted as performance on a random held-out portion of KDDTrain+ rather than as results obtained using the standard KDDTrain+/KDDTest+ benchmark separation.

3.8 Random Forest Feature Importance

Random Forest was used as the feature-importance estimator. The optimized Random Forest configuration obtained through five-fold randomized cross-validation was:

Parameter	**Value**
Number of trees	100
Maximum depth	30
Minimum samples split	10
Minimum samples leaf	1
Maximum features	sqrt
Criterion	Gini (default)
Bootstrap	True (default)
Class weight	None (default)
Random state	42
Number of parallel jobs	-1

The hyperparameter search considered 20 randomly selected parameter combinations using five-fold cross-validation and accuracy as the scoring measure. The best cross-validation accuracy recorded in the notebook was 0.9995634.

Feature importance was obtained from the Random Forest feature_importances_ attribute. This corresponds to impurity-based, or Mean Decrease in Impurity (MDI), importance. For a feature j, its overall importance can be represented as the sum of the impurity reductions attributable to that feature across the trees, weighted by the number of samples reaching the corresponding nodes.

The feature-importance estimator was fitted using the training partition only. The test labels were not used in feature ranking.

3.9 Feature Ranking and Top-30 Selection

The 121 encoded training features were ranked in descending order according to their Random Forest importance scores. The 30 highest-ranked features were retained.

The reduction was:

$$121 - 30 = 91$$

and the percentage reduction was:

$$\frac{121 - 30}{121} \times 100 = 75.21\%$$

Thus, the selected representation contains:

$$\frac{30}{121} \times 100 = 24.79\%$$

of the original encoded feature space.

Table 1: Feature Representation Progression

Representation	**Features/Attributes**	**Description**
Raw predictive representation	41	Original predictive attributes after removing label and difficulty
Encoded representation	121	Predictive features after one-hot encoding
Selected representation	30	Top-ranked features selected using Random Forest importance
Features removed	91	Features excluded from the reduced representation
Dimensionality reduction	75.21%	Percentage of encoded features removed

Table 2: Top-Ranked Features from Random Forest Feature Importance

Rank	**Feature**	**Importance**
1	dst_bytes	0.148207
2	src_bytes	0.127277
3	flag_SF	0.065321
4	dst_host_srv_count	0.054315
5	diff_srv_rate	0.053405
6	same_srv_rate	0.050875
7	dst_host_same_srv_rate	0.036270
8	dst_host_diff_srv_rate	0.033897
9	count	0.030726
10	srv_serror_rate	0.030007
11	flag_S0	0.029867
12	service_http	0.023957
13	dst_host_same_src_port_rate	0.023873
14	logged_in	0.023026
15	dst_host_srv_diff_host_rate	0.022148
16	dst_host_count	0.021498
17	service_private	0.021402
18	protocol_type_icmp	0.021364
19	dst_host_serror_rate	0.020812
20	serror_rate	0.015389
21	protocol_type_tcp	0.013379
22	service_eco_i	0.011072
23	srv_count	0.011048
24	service_ecr_i	0.010700
25	dst_host_srv_serror_rate	0.010415
26	hot	0.010077
27	service_ftp_data	0.009848
28	dst_host_rerror_rate	0.009014
29	dst_host_srv_rerror_rate	0.007972
30	srv_rerror_rate	0.007518

3.10 Final Classifier and Configuration

The classifier used to generate the reported 99.83% performance was the optimized Random Forest classifier operating on the 30 selected features.

This distinction is important. Random Forest was first used to estimate feature importance and rank the 121 encoded training features. The resulting 30-feature subset was then used to retrain the Random Forest classifier for the final evaluation.

The final classifier used:

- 100 trees;
- maximum depth of 30;
- minimum samples split of 10;
- minimum samples leaf of 1;
- square-root feature selection at each split;
- Gini impurity criterion;
- random_state=42;
- parallel execution using n_jobs=-1.

The classifier was fitted using the training records and evaluated using the held-out test records.

3.11 Baseline and Reduced-Feature Experiments

A valid comparison requires evaluation of the same classifier and experimental procedure using both the complete 121-feature representation and the reduced 30-feature representation.

The supplied notebook contains earlier baseline experiments, but those experiments were conducted before removal of difficulty and therefore used a different 122-feature representation. Those values should not be presented as the 121-feature baseline required for this comparison.

Table 3: Full-Feature Versus Reduced-Feature Random Forest Performance

Feature Representation	**Accuracy**	**Precision**	**Recall**	**F1-score**
Full 121 features	**99.96%**	**99.97%**	**99.94%**	**99.96%**
Selected 30 features	99.8293%	99.9316%	99.7015%	99.8164%

The full-feature baseline must be rerun using exactly the corrected 121-feature pipeline before the paper can state whether the selected representation preserves, improves or reduces predictive performance relative to all available encoded features.

3.12 Computational Efficiency Evaluation

The experiment did not record training time, prediction time or memory consumption. Therefore, computational efficiency cannot be claimed as an experimentally demonstrated outcome.

The demonstrated result is feature-space reduction from 121 to 30 features, corresponding to 75.21% dimensionality reduction.

Measure	**Full 121 Features**	**Selected 30 Features**
Training time	Not measured	Not measured
Inference time	Not measured	Not measured
Memory usage	Not measured	Not measured
Number of input features	121	30
Feature reduction	—	**75.21%**

4. RESULTS AND DISCUSSION

4.1 Feature Selection Results

Random Forest feature importance produced a ranked representation of the 121 encoded features. The most important features were dst_bytes, src_bytes, flag_SF, dst_host_srv_count, diff_srv_rate and same_srv_rate.

The importance scores indicate that byte-volume characteristics and connection-level or host-level traffic statistics contributed substantially to the fitted Random Forest model. For example, src_bytes and dst_bytes quantify traffic volume associated with a connection, while variables such as count, srv_count and destination-host statistics describe patterns of repeated or related connections. State and service indicators, including flag_SF, flag_S0 and service-specific encoded variables, also appeared among the highly ranked features.

These observations should not be interpreted as proving that any individual feature causes an intrusion. Rather, they indicate that the features provided useful discriminatory information to the trained Random Forest under the experimental conditions.

4.2 Reduced-Feature Classification Performance

Using the 30 selected features, the optimized Random Forest achieved an accuracy of 99.8293%. Precision was 99.9316%, while recall was 99.7015%. The resulting F1-score was 99.8164%.

The confusion matrix was:

	Predicted Normal	**Predicted Attack**
Actual Normal	13,461	8
Actual Attack	35	11,691

Only eight normal instances were incorrectly classified as attacks, giving a false-positive rate of 0.0594%. Thirty-five attack instances were incorrectly classified as normal.

4.3 Full-Feature Baseline Comparison

The supplied notebook does not contain a valid post-correction 121-feature baseline using the same final preprocessing configuration. Consequently, no scientific conclusion can yet be made about whether the 30-feature representation improves or preserves performance relative to the complete 121-feature representation.

The earlier baseline Random Forest result in the notebook should not be substituted for this comparison because it was generated before difficulty was removed and therefore corresponds to a different feature representation.

The required baseline experiment is:

1. use the corrected KDDTrain+ data after removal of difficulty;
2. retain all 121 encoded features;
3. use the same 80:20 stratified split with random_state=42;
4. fit preprocessing only on training data;
5. train the same optimized Random Forest configuration;
6. evaluate on the same held-out test partition; and
7. report accuracy, precision, recall and F1-score.

Only after this experiment is completed can the paper determine whether feature selection preserved, improved or reduced predictive performance.

4.4 Leakage and Evaluation Integrity

The corrected experimental pipeline follows an appropriate order for avoiding direct test-set leakage during preprocessing and feature selection.

The sequence was:

$$KDDTrain+ \rightarrow Train/Test\ Split$$

followed by:

$$Train \rightarrow Encoding/Scaling \rightarrow RF\ Feature\ Importance$$

and:

$$RF\ Ranking \rightarrow Top\ 30$$

The selected feature names were then applied to both the training and held-out test representations. The test labels were not used to calculate feature importance.

The scaling procedure was also training-dependent: the StandardScaler was fitted on training data and subsequently applied to test data.

Nevertheless, the very high performance warrants additional verification. NSL-KDD is a benchmark dataset with a structured distribution, and unusually high results can arise from dataset characteristics, feature distributions, preprocessing choices or differences in evaluation protocols. Recent research has similarly emphasized that NSL-KDD results can vary substantially according to preprocessing, feature-selection strategy, normalization and classifier configuration (Umar et al., 2025).

The present study therefore avoids interpreting the 99.83% result as evidence of equivalent performance on contemporary operational network traffic.

4.5 Comparison with Previous Studies

Comparison with previous NSL-KDD studies should be interpreted cautiously because differences in preprocessing, data partitioning, feature selection, class definitions, and classifiers can substantially affect performance.

Umar et al. (2025) reported 99.86% accuracy using Random Forest, while Anagha et al. (2025) reported F1-scores of 98.7–98.9% using SHAP- and correlation-based feature selection. These results provide useful context but are not directly comparable due to methodological differences.

The 99.83% accuracy obtained in this study is therefore reported specifically for the stated KDDTrain+ 80:20 experimental protocol and should not be interpreted as a universal NSL-KDD performance level.

4.6 Dimensionality Reduction and Potential Efficiency

The principal demonstrated reduction was from 121 encoded features to 30 selected features. This removes 91 model inputs and reduces the feature representation by 75.21%.

The reduction may potentially lower the amount of data processed by subsequent models. However, because training time, inference time and memory consumption were not measured, the study does not claim that computational efficiency was experimentally improved.

A future efficiency experiment should measure both training and prediction time under identical hardware and software conditions for the 121-feature and 30-feature representations.

5. LIMITATIONS

Several limitations should be considered. First, the study uses the NSL-KDD benchmark rather than contemporary network traffic, limiting generalisation to modern environments.

Second, an 80:20 stratified split of KDDTrain+ was used instead of the standard KDDTrain+/KDDTest+ separation, limiting direct comparison with studies using the official test set.

Third, a complete 121-feature baseline under the same preprocessing configuration is not yet available; therefore, claims about performance preservation after feature selection remain preliminary.

Fourth, computational efficiency was not directly measured, so the results demonstrate dimensionality reduction rather than confirmed reductions in training time, inference time, or memory.

Finally, feature-selection stability was not evaluated across repeated partitions or independent datasets, meaning the selected features may partly depend on the specific KDDTrain+ split.

6. CONCLUSION

This study investigated Random Forest feature importance for feature selection in network intrusion detection using the NSL-KDD KDDTrain+ dataset. After removing the difficulty attribute and one-hot encoding, 41 predictive attributes produced 121 features. A stratified 80:20 split was used, with the top 30 features selected from the training data, reducing dimensionality by 75.21%.

The optimized Random Forest achieved 99.83% accuracy, 99.93% precision, 99.70% recall, 99.82% F1-score, and 0.0594% false-positive rate. These results demonstrate that Random Forest

feature importance can identify a compact and informative feature subset under the stated experimental conditions.

However, computational gains were not measured, and the full 121-feature baseline requires rerunning under the same preprocessing configuration. Future work should therefore compare full and reduced representations, measure computational efficiency, perform repeated validation, and evaluate contemporary network-traffic datasets.

5. REFERENCES

A. L. Buczak and E. Guven, "A survey of data mining and machine learning methods for cyber security intrusion detection," *IEEE Communications Surveys & Tutorials*, vol. 18, no. 2, pp. 1153–1176, 2016, doi: 10.1109/COMST.2015.2494502.

A. Khraisat, I. Gondal, P. Vamplew, and J. Kamruzzaman, "Survey of intrusion detection systems: Techniques, datasets and challenges," *Cybersecurity*, vol. 2, no. 20, 2019, doi: 10.1186/s42400-019-0038-7.

G. Chandrashekar and F. Sahin, "A survey on feature selection methods," *Computers & Electrical Engineering*, vol. 40, no. 1, pp. 16–28, 2014, doi: 10.1016/j.compeleceng.2013.11.024.

L. Breiman, "Random forests," *Machine Learning*, vol. 45, no. 1, pp. 5–32, 2001, doi: 10.1023/A:1010933404324.

M. Tavallaee, E. Bagheri, W. Lu, and A. A. Ghorbani, "A detailed analysis of the KDD CUP 99 data set," in *Proceedings of the 2009 IEEE Symposium on Computational Intelligence for Security and Defense Applications (CISDA)*, Ottawa, Canada, 2009, pp. 1–6, doi: 10.1109/CISDA.2009.5356528.

M. A. Umar, Z. Chen, K. Shuaib, and Y. Liu, "Effects of feature selection and normalization on network intrusion detection," *Data Science and Management*, vol. 8, no. 1, pp. 23–39, 2025, doi: 10.1016/j.dsm.2024.08.001.

A. S. Anagha, C. Thomas, and N. Balakrishnan, "Optimized intrusion predictions through feature selection methods," *Computers & Security*, vol. 157, Art. no. 104541, 2025, doi: 10.1016/j.cose.2025.104541.

E. M. Oluwagbenga, T. Kolajo, and J. A. Babatunde, "Development and evaluation of a hybrid machine learning-based intrusion detection system using NSL-KDD dataset," *UMYU Scientifica*, vol. 3, no. 3, pp. 277–283, 2024, doi: 10.56919/2433.030.

International Conference on Engineering Innovation for Sustainable Development (ICESID 2026)
Faculty of Engineering, Ahmadu Bello University Zaria · 8–10 September 2026

STRUCTURAL RELIABILITY ASSESSMENT OF REINFORCED CONCRETE BEAM INCORPORATING GROUNDNUT SHELL ASH FOR TILAPIA CONCRETE INCUBATOR.

Joseph Ogugua Eze[1,*], J.i. Aguwa[1], A. Mohammed[1], S.f. Oritola[1]

[1]*Federal University of Technology, Minna*

Email: ezejoseph840@gmail.com[*], james.aguwa@futminna.edu.ng, m.abdullahi@futminna.edu.ng, sfaoritola@futminna.edu.ng

***Corresponding author**: Joseph Ogugua Eze

DOI: https://doi.org/10.67203/sp.ICESID.2026

ABSTRACT

Structural reliability is the probability of the structure performing its required function adequately for a specific period of time under stated conditions. Reliability analysis on reinforced concrete beam containing Groundnut shell ash as a partial replacement for cement was conducted in this research. The properties of concrete constituents were determined, COREN concrete mix design guidelines were used and the fresh concrete density was 2130Kg/m^3. Twenty (20) samples of concrete cubes of 150mm x 150mm x 150mm size were tested each for 7, 14, 21 and 28 days after casting at 0, 5, 10, 15 and 20% of groundnut shell ash replacement, making a total of 400 cubes. The samples were cured for ages of 7, 14, 21 and 28 days and the compressive strengths were determined. The average compressive strength of 21.38N/mm^2 at 5% replacement for 28 days curing was determined and used for structural design of the beam. The designed beam was subjected to reliability analysis using First Order Reliability Method (FORM). It was observed that the beam designed was safe in bending under Ultimate Limit State of loading, at the span of 2.7m, 300mm depth, 402mm^2 area of steel and 7.454kN/m live load with safety index of 3.90091. Sensitivity analysis revealed that safety index is directly proportional to the depth/area of steel but inversely proportional to the span/ live load of the reinforced concrete beam.

Keywords: *Structural reliability; Compressive strength; RC Beam; Groundnut shell ash*

1. INTRODUCTION

1. INTRODUCTION

Beams are structural elements made to withstand loads that can cause bending and they are always identified using parameters like its length, material and cross-sectional shape. Concrete is one of the most commonly used construction materials in the world. Reinforced concrete is a widely used material in structural engineering practices due to its strength and durability. Due to its unique feature combination of workability, mechanical properties, durability, fire resistance and the wide availability of raw materials sources, concrete has become highly attractive for many applications in the civil engineering industry (Rosa, *et al*., 2023). Several studies have been conducted to investigate the behavior of reinforced concrete structures under different loading and environmental conditions (Szép *et al.* 2023). Concrete is obtained by mixing cement, fine aggregate, coarse aggregate and water in required proportions. The mixture when placed in forms and allowed to cure becomes hard like stone. The hardening is caused by chemical action between water and the cement due to which concrete grows stronger with age. The strength, durability and other characteristics of concrete depend upon the properties of its ingredients, proportion of the mix, the method of compaction and other controls during placing and curing. Concrete possess a high compressive strength and is usually more economical than steel and is non-corrosive which can be made with locally available materials.

Structural reliability is the probability of the structure performing its required function adequately for a specific period of time under stated conditions (Aguwa, 2010; Aguwa, 2013). Structural assessment is a procedure utilized to check the adequacy, integrity and soundness of structures and their components, made to evaluate a structures current and future use and conformance to codes. A reliability evaluation of a structure in engineering is well-defined as the assurance on its

capacity to achieve its design determination within a specified time. Reliability evaluation is founded on the probability philosophies which provide the platform for its measurement. The reliability of a system can be regarded as the likelihood of its acceptable performance based on certain given performance functions. This function is for a definite purpose and it is laid open to extreme settings within a given time (Dey and Kudmetha, 2013; Ishola *et al*, 2021).

All structures have two basic requirements in common; safety from collapse and satisfactory performance of the structure for its intended use. The limit states define the various ways in which a structure fails to satisfy these basic requirements. Ultimate limit states relate to satisfactory performance and correspond to excessive deflection, vibration and local deformation. Limit state design thus refers to the calculations made by the designer to ensure that these failures do not occur.

Due to increasing industrial and agricultural activities, tons of waste materials are deposited in the environment with little effective method of waste managing/recycling. Some of these deposits are not easily decomposed and the accumulation is a threat to the environment and people at large. Some of these waste materials are groundnut shell, rice husks, maize combs, snail shells, palm-kennel shell, coconut shell and saw dust. Groundnut shell is an agro-waste generated from milling of groundnut (Usman, *et al*, (2019). The rising cost of housing and construction materials especially cement in developing countries in the world including Nigeria is a major concern. Therefore, Groundnut shell being a total waste in agriculture for decade has resulted for a decade research to ascertain the use of the ash as soil stabilizer in clay brick production, as a fertilizer on soil and in partial replacement of cement Samuel, (2020).

This study was conducted to address the Limited information available on the structural behavior and load-carrying capacity of reinforced concrete beams incorporating Groundnut Shell Ash (GSA) for tilapia concrete incubator support systems. The uncertainties associated with GSA concrete properties, applied loads, material strength, and structural dimensions are not adequately addressed by conventional deterministic design methods, making the actual safety and probability of failure of the beam uncertain and also to address the inadequate reliability-based assessment for determining the optimum GSA replacement level that can achieve sufficient structural strength, acceptable reliability, and sustainable performance in reinforced concrete beams for tilapia concrete incubators.

The aim of this research is to carry out structural reliability assessment of reinforced concrete beams incorporating groundnut shell ash for tilapia concrete incubators. The objectives are; to determine the physical properties of concrete constituent materials and chemical oxide composition of groundnut shell ash, to determine the compressive strength of concrete, to carry out structural design of the reinforced concrete beam using data from objective one and two and to carry out reliability analysis of the reinforced concrete beam.

2. METHODOLOGY

The materials that were used in this study are Limestone cement, River sharp sand, River gravel, Groundnut Shell Ash and water.

2.1 Limestone Cement

Limestone cement of 42.5 grade was used in this study. It was sourced from a nearby building material shop in Minna. The Limestone cement conformed to requirement for cement to be used for concrete production in accordance with BS 8615-1&2 (2019).

2.2 Fine Aggregates (River Sharp Sand)

The sharp sand used in this study was locally sourced from New Bussa, Niger State which passed through 4.75mm BS sieve. The fine aggregate conformed to requirement for fine aggregate to be used for concrete production in accordance with BS EN 1008: part 1: (2002).

2.3 Coarse Aggregates (River Gravel)

The natural stone used in this research was locally sourced from New Bussa, Niger State. New Bussa natural stone is characterized with rough surface, reddish-brown in color and consist of maximum size of 19mm. The coarse aggregate conformed to requirement for coarse aggregate to be used for concrete production in accordance with BS EN 1008: part 1: (2002).

2.4 Groundnut Shell Ash

The groundnut shell ash used in this study was sourced locally, from New Bussa, Niger State. The groundnut shell was dry and burnt ensuring control burning to produce ash which passed through BS sieve 0.075mm size. The chemical composition of the groundnut shell ash was conducted using x-ray fluorescence (XRF). XRF is an analytical technique that uses the interaction of x-rays with materials like groundnut shell ash to determine its elemental composition; The oxide composition of groundnut shell ash was conducted in conformity to requirement for natural pozzolana used with Portland cement in concrete production in accordance with ASTM C143/C143M (2020).

2.5 Water

Clean potable water devoid of acid and organic substances from Civil engineering laboratory tap of Federal University of Technology, Minna was used during the study. In accordance with BS EN 1008 (2002).

2.6 Mix Design and Casting of Concrete

The mix design that was used for all concrete cubes cast in this work was COREN Standard for Concrete Mix Design Manuel (2017). Table 1 shows the quantity of materials for each mix batch.

Table 1: Quantity of Materials for each Mix Batch

Mix batch	GSA Content(%)	Water (kg)	Cement (kg)	Sand (kg)	Gravels (kg)	GSA (Kg)
M1	0	13.41	21.28	45.48	90.68	0.00
M2	5	13.41	20.22	45.48	90.68	1.06
M3	10	13.41	19.15	45.48	90.68	2.13
M4	15	13.41	18.09	45.48	90.68	3.19
M5	20	13.41	17.02	45.48	90.68	4.26
Total Sum		67.03	95.76	227.42	453.40	10.64

2.7 Compressive Strength Test

The compressive Strengths of the concrete cubes were determined in accordance with the standard procedure given in ASTM C143/C143M (2020). In accordance with small sample theory in statistical analysis, which deals with small samples sizes, typically less than 30 samples, twenty (20) samples of concrete cubes were tested each for 7, 14, 21 and 28 days after casting at 0, 5, 10,15 and 20% of groundnut shell ash replacement. The average compressive strength for 28days curing at 5% replacement was used for structural designs.

2.8 Cylindrical tilapia concrete incubator

Five cylindrical tilapia concrete incubators were idealized as five concentrated point loads acting at their respective positions on the supporting beam, which forms a major component of the incubator stand as shown in figure 1. Each point load represents the combined weight of the reinforced concrete cylindrical incubator, water, and tilapia eggs. Considering the maximum moment of the beam, the incubator loads were further considered as uniformly distributed load. During the deterministic design**,** the load was used to calculate the beam's support reactions, bending moments, and required structural capacity. In structural reliability analysis, the same load effects were treated as uncertain variables together with material and geometric properties, allowing the relationship between the beam's structural resistance (R) and applied load effect (**S**) to be evaluated through a limit-state function, $g(X)=R-S$, using reliability methods such as FORM. Thus, the five incubators provide the discrete loading system, while the beam provides the load-carrying and load-distribution mechanism for assessing both structural safety and reliability.

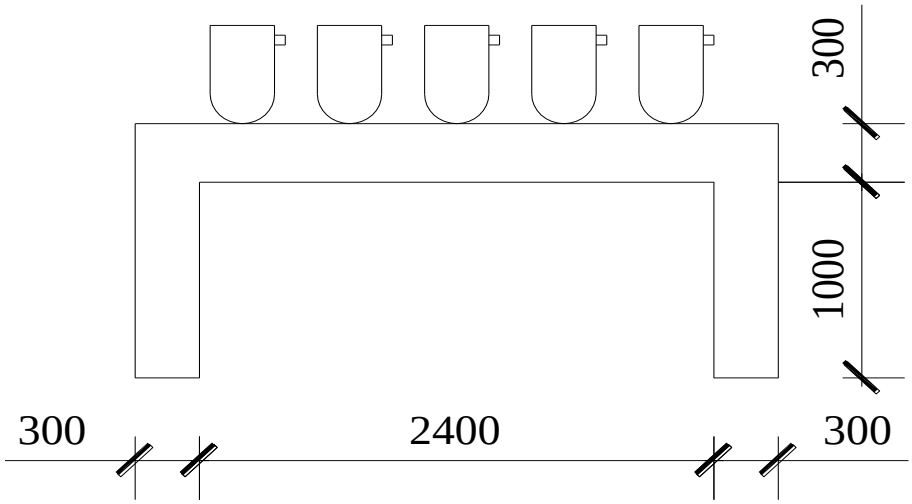

Figure 1: Structural frame (column and beam) carrying five tilapia concrete incubator

2.9 Deterministic Design

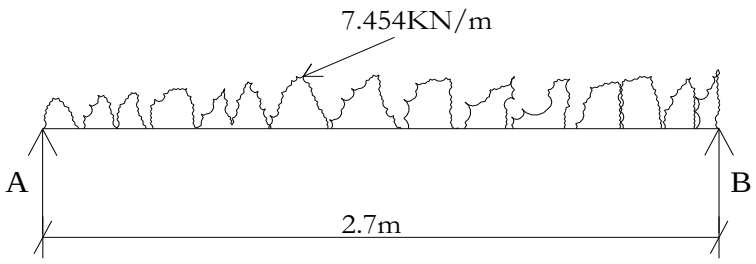

Figure 2: The Cross section of loaded beam to be designed structurally

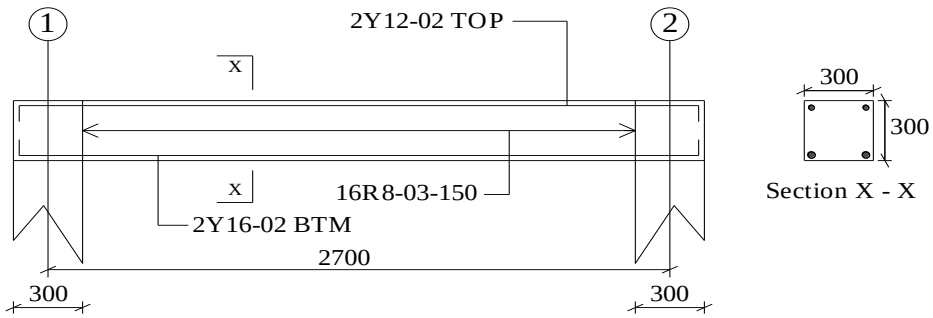

Figure 3: The section of designed beam detail.

2.10 Reliability of the Designed Beam

2.10.1 Estimation of Parameters for Reliability of Beam

The load component of the beam considered was dead load and live load. The live load is the total load of five (5) cylindrical concrete incubators of 15 litres capacity. Load components are treated as random variables, their variation is described by a mean value and a coefficient of variation.

2.10.2 Applied Dead and imposed Load on the beam

Mode of failure by bending.

A beam is subjected to the following failure modes; Bending, Shear, Deflection and Compression failure. For the purpose of this research, Beam failure by bending occurs when the moment capacity is exceeded, causing excessive bending.

From the deterministic design carried out, total live load from the five cylindrical concrete incubators to the beam $= 7.454\ kN/m$

Self-wt of beam$= 2.67kN/m$

Hence, Dead load G_K on the beam $= 2.67kn/m$

Live load Q_K on the beam $= 7.454kN/m$

Design load, $w = 1.4G_K + 1.6Q_K$

Applied moment, $M_S = \frac{wl^2}{8}$; (2.1)

where w = design load and L = span length

$$M_S = \frac{(1.4G_k+1.6Q_K)L^2}{8}; \quad (2.2)$$

$$\therefore M_S = 0.125l^2(1.4G_k + 1.6Q_K)$$

Hence, Applied Moment; $M_S = 0.175l^2G_k + 0.2l^2Q_K$ (2.3)

2.10.3 Structural Resistance Models and equation

Applying force Equilibrium in simply supported reinforced concrete beam above,

According to (Aguwa *et al*, 2015), The Moment resistance of the beam.

$M_R = \phi A_s F_y \left(d - \frac{\phi A_s F_y}{0.85F_{cu}2b}\right)$; Where: ϕ=0.87,

$$M_R = 0.87A_sF_y\left(d - \frac{0.87A_sF_y}{1.7F_{cu}b}\right) \quad (2.4)$$

Where; g(x) = Performance function, R = Resistance (material strength) and S = Demand (Applied stress).

Therefore, the limit state equation is

In reliability, the limit state function (G(X)) is used to ensure the moment of resistance (M_R) exceeds the applied moment (M_S)

$$G(X) = M_R - M_S \quad (2.5)$$

$$G_{(X)} = 0.87A_sF_y\left(d - \frac{0.87A_sF_y}{1.7F_{cu}b}\right) - 0.175G_KL^2 - 0.2Q_KL^2 \quad (2.6)$$

Let, $X_1 = F_y$, $X_2 = F_{cu}$, $X_3 = L$, $X_4 = G_K$, $X_5 = Q_K$, $X_6 = d$, $X_7 = A_s$, $X_8 = b$,

Initial values; $X_1(f_y) = 460N/mm^2$, $X_2\ (f_{cu}) = 21.38N/mm^2$, $X_3(L) = 2700mm$, $X_4(G_K) = 2.67KN/m$, $X_5\ (Q_K) = 7.454KN/m$, $X_6(d) = 260mm$, $X_7(A_s) = 402mm$, $X_8(b) = 300mm$,

Table 2: Input Variables

Variables	Property	Mean (μ)	C.O.V (%)	STD (σ)	PDF(Distribution)
X1	$f_y(\mathrm{N}/mm^2)$	460	0.15	69	Normal
X2	$F_{CU}(\mathrm{N}/mm^2)$	21.38	0.0347	0.7428	Normal
X3	L (mm)	2700	0.1	270	Normal
X4	$G_K(KN/m)$	2.67	0.09	0.2403	Normal
X5	$Q_K(KN/m)$	7.454	0.3	2.24	Normal
X6	$d\ (mm)$	260	0.05	13	Normal
X7	$A_S(mm^2)$	402	0.07	28.14	Normal
X8	$b(mm)$	300	0.05	15	Normal
X9	h_b(mm)	300	0.05	15	Normal
X10	$\gamma_c(\mathrm{N}/mm^2)$	21.30	0.04	0.852	Normal
X11	⦶bar (mm)	16	0.04	0.64	Normal

2.10.4 Performance function linearization

$$G_{(X)} = 0.87X_7X_1\left(X_6 - \frac{0.87X_7X_1}{1.7X_2X_8}\right) - 0.175X_4X_3^2 - 0.2X_5X_3^2 \tag{2.7}$$

Using the equation 2.7, substitute the variables as indicated in Table 2.

$$G_{(X)} = 90932.4X_1 - 239.87X_1^2X_2^{-1} - 1275750X_4 - 1458000X_5 \tag{2.8}$$

The calculation for the reliability analyses was carried out using excel spreadsheet.

$$\mu_G = 90932.4X_1 - 239.87X_1^2X_2^{-1} - 1275750X_4 - 1458000X_5$$

$$\therefore \mu_G = 25181005.46$$

Partial derivatives of equation 2.8

$$\sigma_G^2 = \sigma_{X_4}^2\left(\frac{\partial_G}{\partial X_4}\right)^2 + \sigma_{X_2}^2\left(\frac{\partial_G}{\partial X_2}\right)^2 + \sigma_{X_6}^2\left(\frac{\partial_G}{\partial X_6}\right)^2 + \sigma_{X_7}^2\left(\frac{\partial_G}{\partial X_7}\right)^2 \tag{2.9}$$

$$\sigma_G = 6455164.586$$

$$\beta = \frac{\mu_G}{\sigma_G} = \frac{25181005.46}{6455164.586} = 3.90091$$
$$\therefore\ \beta = 3.90091$$

2.10.5 Sensitivity Analysis.

The sensitivity analyses carried out were done using Excel spreadsheet. The research considered span of the beam, area of steel, effective depth of beam and live load. Iterations were carried out and they converged after three iterations.

3. RESULTS AND DISCUSSION

3.1 Material Characterization.

The physical characteristics and chemical oxide composition were tested and the results were adequately utilized during testing of the concrete strengths and the deterministic design carried out.

3.1.1 Average Specific Gravity for the Materials used or this Study

The average specific gravity reported in Table 3 are suitable and fall within expected ranges based on established literature and technical standards: Fine aggregate (2.63), coarse aggregate (2.55), and cement (3.15) conform to BS EN 1097-6:(2013) specifications. Groundnut shell ash (2.39), falls within the expected range for many agricultural waste ashes and pozzolans, suggesting it is a lightweight, porous material compared to OPC.

Table 3: Average Specific Gravity of the materials after 3 trials

Material	Bulk Density
Fine Aggregate	2.63
Coarse aggregate	2.55
Groundnut Shell Ash	2.39
Cement	3.15

3.1.2 Average Bulk Density of the materials for Uncompacted and Compacted

The average bulk densities reported in Table 4 are suitable and fall within expected ranges based on established literature and technical standards: Fine aggregate (1503.26 kg/m³) and coarse aggregate (1459.86 kg/m³) conform to BS EN 1097-3 and ASTM C29 specifications. Groundnut shell ash (230.90 kg/m³), though much lower than conventional materials, is consistent with published data on agricultural biomass ashes.

Table 4: Average Bulk Density of the materials for Uncompacted and Compacted

Material	Bulk Density		
	Uncompacted	Compacted	Avg. Density
Fine Aggregate	1445.55	1560.96	1503.26
Coarse aggregate	1376.95	1542.77	1459.86
Groundnut Shell Ash	194.33	267.47	230.90

3.2 Chemical Composition of Groundnut Shell Ash

Table 4 shows the results obtained from Inorganic Geochemical Analysis using X- Ray Fluorescence Spectrophotometry. However, the total of 68.6% for its main oxides (SiO_2 + Al_2O_3 + Fe_2O_3) is classified as Class C pozzolan according to ASTM C618 which is suitable for partial replacement of cement in structural work.

Table 5: Chemical Composition of Groundnut Shell Ash

Sample	SiO_2	AI_2O_3	Fe_2O_3	TiO_2	CaO	P_2O_5	K_2O	MnO	MgO	Na_2O	SO_3	CO_2	LOI
GSA	57.5	9.8	1.3	0.6	4	0.4	1.1	0.15	1.8	0.75	0.4	1.8	4.1

3.3 Compressive Strength

The replacement percentages of GSA used for this study were 0, 5, 10, 15 and 20% by weight of cement. The strength of the five replacement percentage samples was tested. The average compressive strength (21.38N/mm^2) for 28days and 5% replacement was used throughout the design.

3.4 Reliability Analysis.

The results of deterministic design carried out were subjected to reliability tests using First order reliability method (FORM). The Reliability index was obtained using Equation (2.8-2.16), at 2.7m span of the beam; the result was 3.90091 which is an indication of safe for such concrete mixture.

3.4.1 Sensitivity Analysis

Figure 3 presents the result of sensitivity analysis conducted in bending for beam varying the span (L) of the beam. As seen from Figure 3, increasing the span of the beam reduce the safety index with reliability index lower than the 3.0 target reliability (β_T), whereas decrease in the span increases the safety level for the concrete under consideration. The beam is reliable at span of 2.7m with reliability index of 3.90091. Kolo, *et al*, (2021) reported that safety index is very sensitive to the span and depth of the beam, hence they are the critical factors to be put into consideration when designing reinforced concrete beam utilizing the natural stone (gravel) as coarse aggregate.

Increasing the span of beam increases the bending moment experienced which contributes to the bending of beam. The span is indirectly proportional to safety index.

Table 6: Reliability index values against the varying beam span

Beam Span, L (mm)	2.700	3.000	3.300	3.600	3.900	4.200
Reliability Index, β	3.90091	3.11644	2.41611	1.73309	1.09189	0.50662

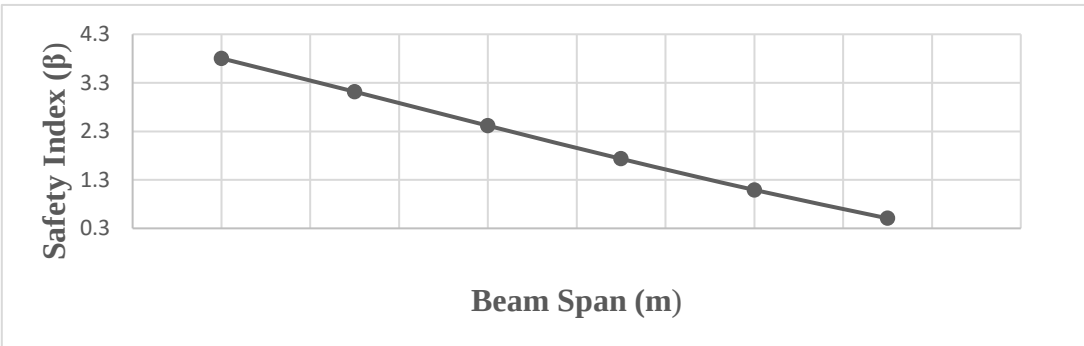

Figure 3: Safety Index-Span Relation for Reinforced Concrete Beam in Bending.

Figure 4 shows the result of sensitivity analysis conducted in bending for beam varying the effective depth of the beam. The Figure indicated an increase in safety index (β) as the effective depth (d) increased from 180mm to 340mm. Safety index was found to be directly proportional to the effective depth for the beam.

Table 7: Reliability index values against the varying effective depth of beam

Effective Depth d (mm)	180.000	220.000	260.000	300.000	340.000	380.000
Reliability Index, β	2.46198	3.24172	3.90123	4.21976	4.53701	4.78533

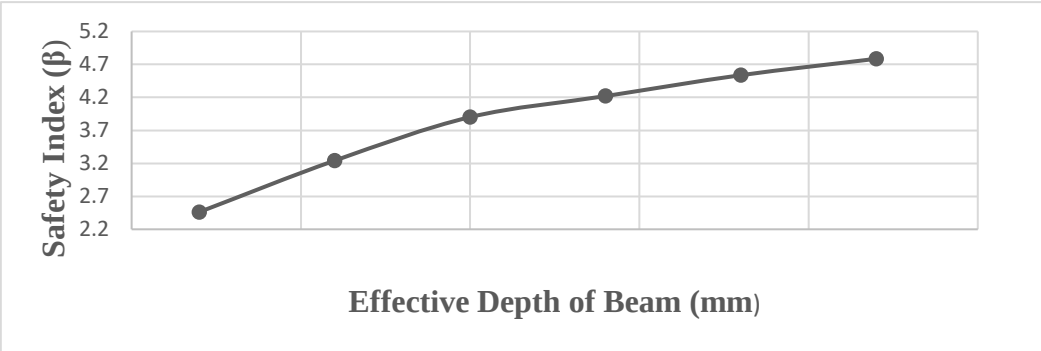

Figure 4: Safety Index-Depth Relation for Reinforced Concrete Beam in Bending

Figure 5 shows the result of sensitivity analysis conducted in bending for beam varying the live load (Q_K) of the beam. The Figure indicated a decrease in safety index (β) as the live load increased from 7.454kN/m to 14.954kN/m. Safety index was found to be indirectly proportional to the live load of the beam.

Table 8: Reliability index values against the varying live load

Live Load, QK (KN/m)	7.454	8.954	10.454	11.954	13.454	14.954
Reliability Index, β	3.90123	3.31016	2.84248	2.40799	2.00889	1.64593

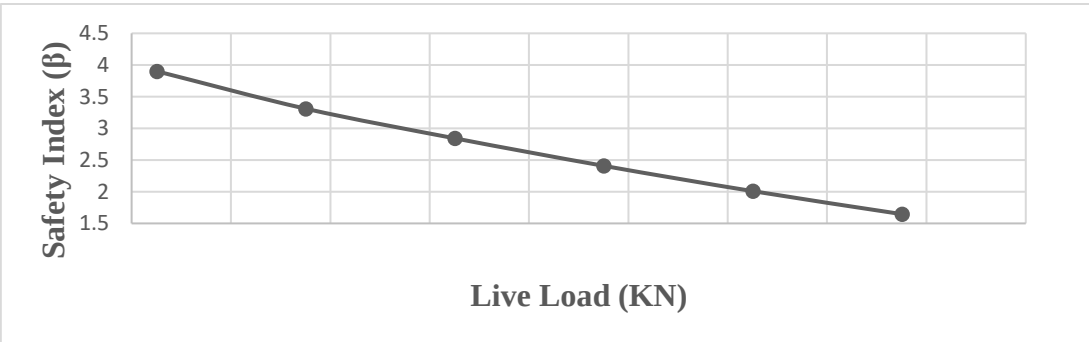

Figure 5: Safety Index-Live Load Relation for Reinforced Concrete Beam in Bending

Figure 6 shows the result of sensitivity analysis conducted in bending for beam varying the area of steel (A_S) for beam. The Figure indicated an increase in safety margin (β) as the area of steel increased from 302mm^2 to 552mm^2. Safety index was found to be directly proportional to the area of steel for the beam.

Table 9: Reliability index values against the varying Area of steel

Area of Steel, AS (mm2)	302.000	352.000	402.000	452.000	502.000	552.000
Reliability Index, β	2.88573	3.39813	3.90123	4.12919	4.39435	4.6133

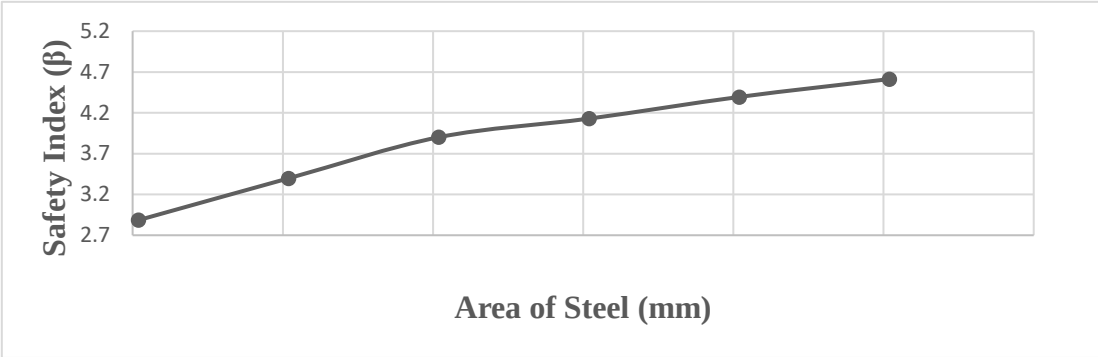

Figure 6: Safety Index-Area of Steel Relation for Reinforced Concrete Beam in Bending

4. CONCLUSION AND RECOMMENDATION

The comprehensive analysis of the Data revealed the following key conclusions, which provide insight into the feasibility of using groundnut shell ash as a partial replacement for cement in structural concrete applications:

(i) The specific gravities of river natural stones, river sand and groundnut shell ash were found to be within the required range. The results obtained from oxide composition shows that the percentage of various chemical oxide compositions of GSA was within the ranges obtainable for the cement.

(ii) The optimum result obtained at 5% replacement GSA was used throughout the structural design.

(iii) From the structural design carried out on tilapia incubator support beam using the average result of compressive strength at 5% replacement showed very impressive results with little increase in reinforcement.

(iv) Safety index was found to be directly proportional to the effective depth and area of steel but inversely proportional to the span and live load of the reinforced concrete beam during Sensitivity Analysis.

ACKNOWLEDGEMENTS

I am very grateful to God Almighty for giving me the grace, wisdom and strength to accomplish this research work. To my darling wife, who has been the pillar and supportive to all my decisions towards my academic attainment.

My special thanks go to my team of supervisors Engr. Prof. J.I. Aguwa, Engr. Prof. A. Mohammed and Engr. Dr. S.F. Oritola for their constructive criticism, corrections, patience and very good Teacher-student relationship which existed throughout the research work. I also thank in a special way the head of department Engr. M. Saidu for his fatherly advice and attention.

I am gratefully indebted to all the staff of civil engineering department of Federal University of Technology, Minna. Words alone cannot express how satisfied I am identifying with each of you. I can only say thank you and may God keep you in His love.

Finally, my thanks go to my PhD mates especially Engr. C.C. Ogbobe's cooperation and understanding which existed throughout the research processes. Thank you and God bless.

5. REFERENCES

Aguwa J.I. Sadiku, S. and Abdullahi, M. (2015). Harnessing Nigeria's Forestry Potentials for Structural Applications: Structural Reliability of Nigerian Grown Opepe Timber. International Journal of Economics and Management Engineering. Vol:9, No:10.

Aguwa, J.I. (2010). Reliability studies on the Nigerian Timber as an Orthotropic Elastic Structural Material, submitted to the Postgraduate School, Federal University of Technology Minna, Nigeria, for the award of Doctor of Philosophy (PhD) in Civil Engineering (Structures).

Aguwa, J.I. (2013). Structural Reliability of the Nigerian Grown Abura Timber Bridge Beam Subjected to Bending and Deflection Forces. *Nigerian Journal of Technology (Nijotech) Vol. 32. No. 2. Pp. 241-252.*

ASTM C618 (2021). Fly Ash Specification: Comparison with other Specifications, Shortcomings, and Solutions. *ACI Materials Journal 118(1)*

ASTM C143/C143M (2020). Standard test *Methods of Determination of Slump of hydraulic-cement concrete used to measure consistency and workability*.West Conshohocken, PA, USA.

BS 8615-1&2. January 31, (2019). British standard institution: Methods for Determination of natural pozzolanic materials used with Portland cement. London.

BS EN 1008: part 1: (2002) British standard institution. Method of determination of mixing water for concrete. London.

COREN Concrete Mix Design Manuel (2017). Council for the Regulation of Engineering in Nigeria. Special publication no. COREN/2017/016/RC. First Edition August.

Dey, A. & Kudmetha, K. K. (2013). Bearing Capacity of Single Pile in Sand: Reliability Analysis using Monte-Carlo Simulation.Proceedings of Indian Geotechnical Conference December 22-24, Roorkee, India.

Ishola, K., Olawuyi, O. A., Yohanna, P., Bello, A. A., Sani, R.O. & Akin, O. O. (2021). Reliability Evaluation of Compaction Water Content of Plantain Peel Ash Treated Lateritic Soil. Nigerian Journal of Technological Development, Vol. 18, No.1

Kolo, D. N., Aguwa, J. I., Tsado, T.Y · Abubakar, M., Yusuf, A. and Oritola, S.F. (2021). Reliability studies on reinforced concrete beam subjected to bending forces with natural stone as coarse aggregate. *Asian Journal of Civil Engineering*. 22:485–491.

Rosa, A.C, Hammad, A.W.A., Dieter Boer, B. & Haddad, A. (2023). Use of operational research techniques for concrete mix design: A systematic review. Heliyon: journal homepage: www.cell.com/heliyon

Samuel, V. (2020). Groundnut Shell Ash: A Local Construction Material in Concrete Production. *Fane-Fane International Multidisciplinary Journal,* Vol. 5, No.1.

Szép, J., Habashneh, M., Lógó, J. & Movahedi Rad, M. (2023). Reliability Assessment of Reinforced Concrete Beams under Elevated Temperatures: A Probabilistic Approach Using Finite Element and Physical Models. Sustainability 15, 6077. https://doi.org/10.3390/ su15076077

Usman, J., Yahaya, N. and Mazizah M. E. (2019). Influence of groundnut shell ash on the properties of cement Pastes. *IOP Conference Series: Materials Science and Engineering.* 601 012015.

International Conference on Engineering Innovation for Sustainable Development (ICESID 2026)
Faculty of Engineering, Ahmadu Bello University Zaria · 8–10 September 2026

SWOT ANALYSIS OF LOCAL ENGINEERING INNOVATION FOR SUSTAINABLE INDUSTRIAL GROWTH IN NIGERIA: PATHWAY TO SDG REALIZATION

Anas Mahmoud Ibrahim[1,*], Umar Ibrahim Kwami[2], Abdulmajid Aliyu[1], Shuaibu Babandi Shuaibu[1]

[1]*Ahmadu Bello University, Zaria*
[2]*Federal Polytechnic, Daura*

Email: anas6mahmoudee@gmail.com*, ibrahimkafarati@fedpolydaura.edu.ng, abdulmajidaleeyu@gmail.com, shuaibubabandi.ameer89@gmail.com

***Corresponding author**: Anas Mahmoud Ibrahim

DOI: https://doi.org/10.67203/sp.ICESID.2026

ABSTRACT

This study examines how local engineering innovation can drive sustainable industrial growth and support Nigeria's progress toward the Sustainable Development Goals, using a SWOT analysis framework. Nigeria's urgent need for economic diversification and technological self-reliance motivates the research. While the federal government has prioritized local content through Presidential Executive Order No. 5 and the Nigeria First Policy, engineering innovation remains essential for building economic resilience and creating jobs. However, the nation continues to struggle with weak university-industry linkages, limited commercialization of research, and inadequate infrastructure. Guided by the Triple Helix Model of academia-industry-government collaboration, the study draws on policy documents, industry reports, and academic literature to assess Nigeria's engineering innovation ecosystem. The findings reveal promising strengths: a vibrant entrepreneurial culture, a growing startup ecosystem with over 98 tech hubs, and supportive policy momentum. Ahmadu Bello University, Zaria host to Nigeria's first Huawei ICT Academy Support Centre exemplifies local innovation potential; its students won the Innovation Competition Grand Prize and the Women in Tech Award at the 2026 Huawei ICT Competition Global Finals, competing against 177 teams from 49 countries. Yet significant weaknesses persist. Only about 5% of engineering graduates are considered industry-ready, while brain drain, low patent commercialization, and fragile infrastructure remain pressing concerns. Opportunities exist through NASENI's 3Cs initiative, which has brought 44 products to market and created over 25,000 jobs, alongside the African Continental Free Trade Area. However, threats such as economic instability, insecurity in the North-East and North-West, and reliance on foreign technology cannot be overlooked. The study concludes that stronger partnerships, increased applied research funding, intellectual property reforms, infrastructure upgrades, and education improvements are vital for harnessing local engineering innovation and advancing SDG 1, 8, 9, and 17 in Nigeria.

Keywords: *SWOT Analysis; Local Engineering Innovation; Triple Helix Model; Sustainable Industrial Growth; SDGs; Nigeria*

1. INTRODUCTION

Nigeria's quest for sustainable industrial development has been hindered by poor adoption of local technology, dependence on imported engineering innovations, and limited utilization of locally developed solutions (Onoh & Enekwe, 2024). Globally, the engineering sector is being reshaped by digitalization, artificial intelligence, and the demand for sustainable infrastructure. The Chinese Academy of Engineering (2025) reported that 74 of 189 engineering frontiers are AI-related, signalling a new phase of automation and intelligence in engineering practice. Trends like smart cities, renewable energy, and circular economy principles are now central to engineering across developed economies.

Nigeria's federal government has shown commitment to local content through Presidential Executive Order No. 5 (2018), which mandates the use of local talent and products in government-funded projects (Federal Ministry of Information and National Orientation, 2025). The Nigerian Content Bill 2025 (HB. 1167) builds on this by establishing a legal framework to enforce local

content across science, technology, and innovation sectors. However, previous local content legislation, such as the Nigerian Oil and Gas Industry Content Development Act of 2010, has had limited impact on local value creation due to weak in-country capacity, a lesson with clear implications for current policy (Nwankwo & Iyeke, 2022).

The National Agency for Science and Engineering Infrastructure (NASENI) has emerged as a key institution translating policy into industrial action. Through its "3Cs" initiative Creation, Collaboration, and Commercialization NASENI has developed over 44 market-ready products, including laptops, solar irrigation pumps, and electric tricycles, generating over 30,000 direct and indirect jobs. Its DELT-Her programme has awarded over ₦229 million in grants to female engineers, and the 40-hectare NASENI Solar Industrial Park in Nasarawa State is expected to become Africa's largest clean energy manufacturing hub.

Despite these efforts, serious challenges persist in engineering education. Studies indicate that over 70% of Nigerian engineering graduates lack practical skills, with only about 5% considered industry-ready (Ejilah et al., 2023). The curriculum remains outdated, laboratories are poorly equipped, and only 22% of engineering programs have meaningful industry partnerships a clear reflection of weak university-industry linkages. This skills gap has been identified by the Nigerian Content Development and Monitoring Board as a threat to national productivity.

Nigeria continues to face an "engineering vacuum" a structural gap that keeps the country reliant on foreign expertise and imported solutions (Chukwueke, 2025). Its 113th place ranking out of 133 countries in the 2024 Global Innovation Index highlights the scale of the problem. Professor Sesan Peter Ayodeji of FUTA has called for a shift toward human-centered, process-driven innovation, arguing that engineering must be measured by its relevance to local realities and that the Triple Helix model of university-industry-government collaboration should be institutionalized across teaching, research, and policy.

Studies by Onoh and Enekwe (2024), Ibitoye et al. (2022), and Osunkwo (2025) confirm that inadequate infrastructure, unreliable energy, limited access to modern technology, and weak industrial policies continue to limit local competitiveness and deepen dependence on imports. Over-reliance on foreign machinery exposes Nigeria to exchange-rate volatility and supply-chain disruptions, widening the technological gap with advanced economies.

Nevertheless, Nigeria's 301 universities 74 federal, 68 state, and 159 private represent a vast reservoir of potential (National Universities Commission, 2025). Local innovations in civil, electrical, mechanical, and materials engineering could improve industrial operations and reduce environmental impacts. Renewable energy systems, sustainable building materials, and locally fabricated machinery offer pathways to greater self-reliance (Firoozi et al., 2025; Onuh et al., 2024; Taiwo et al., 2024). However, weak commercialization frameworks and fragmented collaboration between academia, industry, and government continue to hinder progress (Ajibo et al., 2019; Nwaichi et al., 2025).

This study is motivated to critically evaluate the role of local engineering innovation in driving sustainable industrial growth and SDG realization in Nigeria. The specific objectives are to:

i. Identify strengths and opportunities within Nigeria's engineering innovation ecosystem.
ii. Analyse weaknesses and threats hindering innovation-driven industrial development.
iii. Assess Nigeria's position relative to global and African engineering innovation trends.
iv. Propose strategic recommendations for harnessing engineering innovation to accelerate SDG attainment.

This research contributes to the growing body of knowledge on engineering innovation in developing economies by providing a comprehensive SWOT analysis grounded in empirical evidence from policy documents, industry reports, and academic literature.

2. METHODOLOGY

2.1 SWOT Analytical Framework

The SWOT analysis framework a strategic planning tool that systematically evaluates an organization or ecosystem's Strengths, Weaknesses, Opportunities, and Threats provide the primary analytical lens for this study. Originally developed for business strategy, SWOT analysis has been widely applied to assess innovation ecosystems, national competitiveness, and policy effectiveness (Auwalu et al., 2026). The framework enables a structured examination of internal factors (strengths

and weaknesses) and external factors (opportunities and threats) that influence the performance of engineering innovation systems. In the context of developing economies, SWOT analysis has been effectively utilized to identify systemic barriers to technology adoption and to formulate strategic interventions for industrial development (Kilaso & Adegbembo, 2025).

2.2 Theoretical Framework: The Triple Helix Model

This study is anchored on the Triple Helix Model of academia–industry–government collaboration, which provides a robust theoretical lens for understanding innovation ecosystems. The Triple Helix Model, originally developed by Etzkowitz and Leydesdorff, posits that effective innovation requires close interaction among three institutional spheres: universities (research and education), industry (production and commercialization), and government (policy and funding) (Cai & Etzkowitz, 2021). The model emphasizes that innovation does not occur in isolation but emerges from the dynamic interplay among these three actors, where each takes on roles traditionally associated with the others universities engage in entrepreneurial activities, industry participates in research, and government facilitates innovation through policy and funding.

In the Nigerian context, the Triple Helix Model has gained significant traction as a framework for understanding and improving innovation systems. Research by Obanor and Kwasi-Effah (2013) assessed university-industry collaboration and technology transfer in Nigerian universities, finding that while the potential for collaboration exists, significant barriers including cultural differences, inadequate funding, and weak institutional frameworks hinder effective technology transfer. The study recommended the establishment of formal structures to promote interaction and collaboration between universities and industries. Similarly, the Nigerian Content Development and Monitoring Board has explicitly embraced this model, describing it as "an appropriate international business framework that adds to our strength of innovation and ensures that all efforts go into fueling the grand old aim – National Development" (NCDMB, 2024).

The Triple Helix Nigeria (THN) initiative, launched in partnership with the University of Port Harcourt and Cypher Crescent Nigeria Limited, has grown from 12 founding members to over 240 members, demonstrating growing recognition of the model's relevance (Nwaichi et al., 2025). As observed, while there has been progress in adopting the Triple Helix approach, several obstacles remain, including weak institutional frameworks, insufficient funding for research and development, limited university-industry collaboration, and the absence of a cohesive policy framework to foster innovation. The Nigerian Institution of Marine Engineers and Naval Architects has also called for stakeholders to adopt the Triple Helix model as a framework for driving sustainable innovation and growth within the maritime sector, pointing to Singapore's success as a leading global maritime hub as an example.

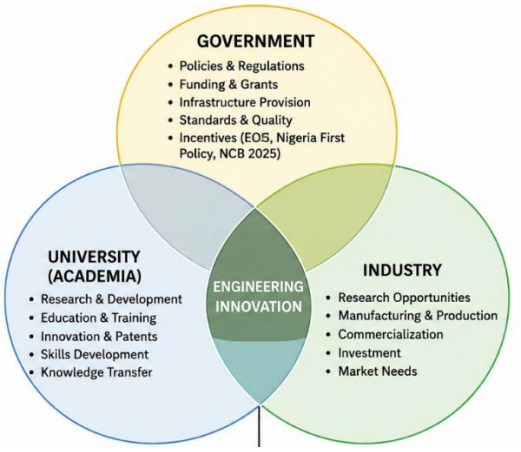

Figure 1: Triple Helix Model for Nigeria's Engineering Innovation Ecosystem

(Source: Adapted from Auwalu et al., 2026)

2.3 Research Design

This study adopts a conceptual and content analysis methodology, suitable for examining complex innovation ecosystems where primary data collection is limited. Data sources were selected based on relevance to Nigeria's engineering innovation ecosystem, credibility (peer-reviewed journals, government reports, official publications, and conference proceedings), and availability of verifiable data. Sources were identified through keyword searches in academic databases and policy repositories. Newspaper articles were used sparingly, only to report recent developments and clearly attributed as media sources.

Content analysis followed a systematic coding framework, with data coded into four SWOT categories: Strengths (internal positive factors), Weaknesses (internal negative factors), Opportunities (external positive factors), and Threats (external negative factors). Two researchers independently coded a subset of sources to establish inter-coder reliability; discrepancies were resolved through discussion. The coding process was iterative, with categories refined as new themes emerged.

Findings were triangulated by cross-referencing multiple sources, with assertions supported by at least two independent sources where possible; single-source claims were clearly identified. Data were drawn from policy documents (Executive Order No. 5, Nigeria First Policy, Nigerian Content Bill 2025), industry reports (Nigerian Communications Commission, 2024; Tony Elumelu Foundation, 2015; NCDMB, 2024), and peer-reviewed literature on engineering innovation, technology transfer, and sustainable development. The SWOT analysis was then applied systematically to identify internal and external factors, synthesize findings, and develop strategic recommendations.

3. NIGERIA'S ENGINEERING INNOVATION ECOSYSTEM

3.1 Industrial Policies and Engineering Innovations

Nigeria's engineering innovation ecosystem is shaped by a policy framework that has evolved considerably over the past decade. Presidential Executive Order No. 5 (2018) laid the foundation by mandating local content in all government-funded science and technology projects (NALTF, 2025). Building on this, the Nigerian Content Bill 2025 (HB. 1167) seeks to establish a comprehensive legal framework to enforce Nigerian content across science, technology, and innovation sectors.

Analysis of earlier local content legislation, particularly the Nigerian Oil and Gas Industry Content Development Act of 2010, shows that while such policies have had some positive effects, their impact on local value creation has been limited by weak in-country capacity and underdeveloped business ecosystems (Nwankwo & Iyeke, 2022). This underscores the need for local content laws to be accompanied by investments in education, skills development, and institutional capacity building.

The National Agency for Science and Engineering Infrastructure (NASENI) and the Nigerian Content Development and Monitoring Board (NCDMB) are key institutional drivers. NASENI's "3Cs" initiative Creation, Collaboration, and Commercialization has yielded over 44 market-ready products, including laptops, solar streetlights, electric tricycles, and clean energy cookstoves, while generating more than 30,000 direct and indirect jobs. NCDMB has established six centers of excellence across Nigerian universities and maintains a US$50 million Research and Development Fund accessible to researchers (NCDMB, 2024). A fully equipped Technology Incubation and Innovation Centre operates within the Nigerian Content Tower in Yenagoa. The Board's Nigerian Content Research, Innovation and Technology Challenge 2025/2026 aims to develop new technologies for the oil and gas sector and its linkage industries.

The National Office for Technology Acquisition and Promotion (NOTAP) has established 69 intellectual property technology transfer offices in universities and runs the NOTAP Industry Technology Transfer Fellowship, which engages academia and industry within the Triple Helix framework. Research on technology transfer in Nigeria's construction sector has identified persistent challenges including inadequate funding, weak legal frameworks, and limited technical capacity (Kilaso & Adegbembo, 2025; Ajibo et al., 2019).

3.2 Key Actors and Institutions

Nigeria's engineering innovation ecosystem comprises a complex network of universities, research institutes, government agencies, private sector firms, innovation hubs, and informal manufacturing clusters. The South-East region exemplifies Nigeria's entrepreneurial culture through its thriving informal manufacturing sector the Aba leather and garment cluster, Nnewi's auto parts manufacturing, and Onitsha's commercial networks demonstrate indigenous engineering capacity that has emerged organically despite limited government support. However, these clusters face persistent challenges: lack of access to modern equipment, limited quality control standards, and insufficient linkages to formal financial institutions.

The Clintonel Innovation Centre (CIC), founded by Tochukwu Chukwueke, represents a transformative model for engineering capacity building. CIC has trained over 2,000 students across 60 schools, developed six STEM kits, incubated 13 engineering startups, helped over 20 inventors develop their products, and supported founders to raise more than $300,000 in external funding. The center’s STEM4Girls initiative has inspired 102 girls to pursue STEM careers, and Chukwueke has convened Nigeria's first hardware convention and founded the Hardware Nigeria Community.

The Nigerian Engineering Design Development Institute, one of NASENI's 12 divisions, has emerged as a pivotal force in reverse engineering and fabrication of industrial components. Notable achievements include the NASENI M1 motorcycle, the Dual Powered Egg Incubator, the Low-Cost Inverter, and the Gas Hydrate Loop a groundbreaking innovation in the oil industry otherwise sourced exclusively from Europe, Asia, and the Americas.

The North-West region, home to Ahmadu Bello University (ABU), Zaria, presents a different picture. ABU has served as Nigeria's first Huawei ICT Academy Support Centre since 2018. In June 2026, TeamABU2026 secured the Innovation Competition Grand Prize and the Women in Tech Award at the 10th Huawei ICT Competition Global Finals in Shenzhen, as documented in Huawei's official press release on the competition results. The team's winning project, "ParaVision" an AI-powered diagnostic system built on the Orange Pi AIPro platform using the Huawei Ascend 310B4 chip generates laboratory reports in under three minutes. ABU was listed among the Innovation Competition Grand Prize winners alongside Wuhan University of Technology, National University of Singapore, and Fujian Normal University. This achievement demonstrates that Nigerian institutions can compete globally when provided with adequate support, infrastructure, and mentorship.

4. TECHNOLOGY TRANSFER AND TRIPLE HELIX ADOPTION

4.1 Technology Transfer Mechanisms

Technology transfer moving research from laboratories to commercial applications remains a major challenge in Nigeria. NOTAP has led efforts to strengthen this through Intellectual Property and Technology Transfer Offices (IPTTOs) in universities, but a critical gap persists. Professor Joseph Atubokiki Ajenka observed that "every year university research yields discoveries with commercial potential," yet Nigeria lacks trained technology transfer professionals to shepherd these ideas to market (NCDMB, 2025). He urged a shift from "publish-or-perish" to "patent-publish-produce" mindset among academics (NCDMB, 2025).

The Nigerian Communications Commission (2024) confirmed low patent commercialization rates despite over 400 patents facilitated by NOTAP, with most academic research focused on basic qualifications rather than industrial challenges. Research by Ajibo et al. (2019) and Kilaso and Adegbembo (2025) similarly identified weak legal frameworks, inadequate funding, and limited technical capacity as persistent barriers to technology transfer.

The technology transfer process, from research through to commercialization, is illustrated in Figure 2 below, supported by cross-cutting enablers including funding, industry-academia partnerships, infrastructure, skills development, and innovation support services.

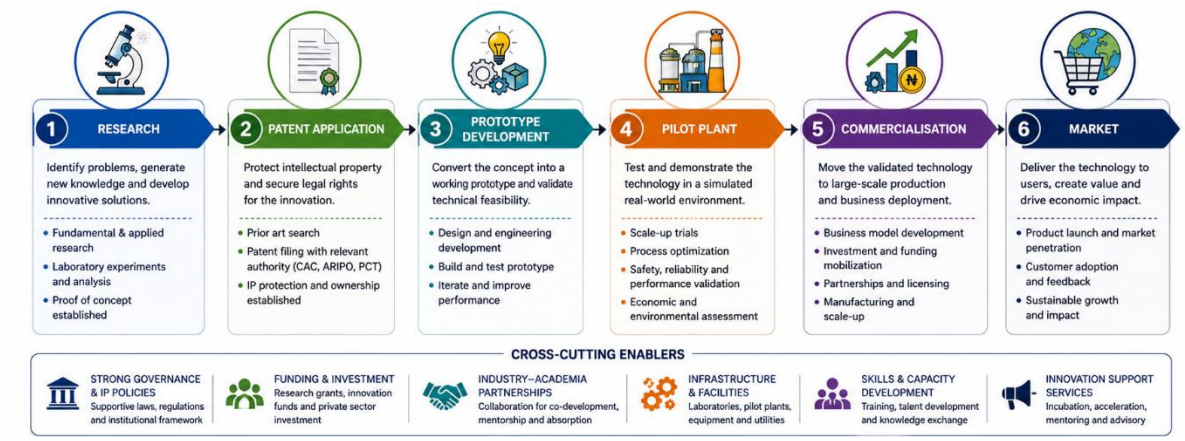

Figure 2: Technology Transfer Framework

*(**Source:** Author's synthesis based on literature review)*

4.2 SWOT Analysis

Table 1: SWOT Analysis of Nigeria's Engineering Innovation Ecosystem

S/N	STRENGTHS	WEAKNESSES	OPPORTUNITIES	THREATS
1	Growing startup ecosystem with 98+ tech hubs and incubators	Severe skills gap: 70% of graduates lack hands-on skills; only 5% industry-ready	Investment opportunities in commercialization of research outputs	Economic volatility and continuous devaluation of Naira
2	Talented human capital; 3rd largest software developers in Africa	Persistent brain drain and emigration of skilled professionals	Transition to digital economy via STI sector	Insecurity across North-East and North-West
3	Vibrant entrepreneurial culture and informal manufacturing clusters	Low patent commercialization despite 400+ patents facilitated by NOTAP	African Continental Free Trade Area (AfCFTA) opening regional markets	Persistent technology gap and dependency on foreign licenses
4	Multi-sector research base across telecommunications, oil & gas, agriculture, health	Weak industry-academia-government linkages	Smart energy solutions leveraging Nigeria's solar potential	Global technological competition marginalizing Nigeria's aspirations
5	Policy momentum: EO5 and Nigerian Content Bill 2025	Fragile infrastructure: power, transport, broadband	International partnerships: UNIDO, Innovate UK, Huawei	Poor patronage of made-in-Nigeria goods
6	Institutional excellence: ABU Zaria winning global competitions	Weak IP regime with low patent registrations and enforcement	NASENI's 3Cs and DELT-Her program for women in engineering	Most engineering designs done offshore
7	NASENI's 3Cs initiative: 44+ market-ready products	Theory-heavy education focused on examinations over practical application	NCDMB's US$50 million R&D Fund and TIIC initiative	Policy inconsistency across governments
8	Abundant natural resources and solar energy potential	Over-reliance on foreign expertise and persistent technology gap	AI and Robotics Innovation Hub at Obafemi Awolowo University	

(Source: Synthesised from Auwalu et al., 2026; Ejilah et al., 2023; Nwankwo & Iyeke, 2022; Obanor & Kwasi-Effah, 2013; Nwaichi et al., 2025; NALTF, 2025; Leadership, 2026; NCDMB, 2024; Chukwueke, 2025)

4.3 Regional SWOT Assessment

The regional SWOT assessment in Table 4.2 evaluates Nigeria's six geopolitical zones based on criteria derived from the Cluster Innovation Scoreboard framework and validated by recent empirical studies on innovation performance across Nigerian regions (Nwagwu, 2023; Igbokwe, 2026). The evaluation criteria include: (1) presence of anchor firms and industrial clusters; (2) access to skilled workforce; (3) infrastructure quality; (4) security environment; and (5) existing innovation capacity. This framework enables a systematic comparison of regional innovation ecosystems, highlighting disparities that inform targeted policy interventions. The analysis draws on the cluster

mapping, which confirmed that Science Technology innovation is concentrated more in the southern region than the northern region.

Table 2: Regional Innovation Cluster SWOT Assessment

Region	Strength	Weakness	Opportunity	Threat
South-East	Vibrant entrepreneurial culture; thriving informal manufacturing clusters	Talent migration to South-West and FCT	2nd Niger Bridge providing resources and opportunities	Poor public infrastructure; excessive informal sector
South-South	Anchor firms in energy sector (NNPC, LNG, Shell)	Limited sectoral diversification; primarily energy-focused	Incubation of new technology leaders; wind energy potential	Seasonal security issues; enforcement of ownership rights
South-West	Better skilled workforce; national economic hub; high concentration of innovation clusters	Over-stretched public infrastructure in Lagos	Great emerging universities; technology leadership	High population density; traffic congestion
North-Central	Links north and south; agricultural base	Security challenges; poor primary and secondary education	Abundant solar resources; new energy sources	Competition from Abuja; poor primary education
North-West	Military institutions; ABU Zaria attracting international funds	Losing appeal for investment due to security	Historical trade routes; military anchoring development	Consistent talent emigration; poor STEM education
North-East	Good arable land; agricultural potential	Losing appeal for investment due to security	Massive arable land; post-crisis reconstruction boom	Security problems; inadequate basic education

***(Source:** Synthesised Nwagwu, 2023; Igbokwe, 2026)*

Table 3: Enablers for Accelerating and Sustaining Innovation in Nigeria

SN	Enabler	Action Points
1	Funding & Investment	Provide adequate funding, grants, and incentives; encourage private sector participation in STI investment.
2	Commercialization	Establish effective commercialization frameworks; promote market competition through continuous commercialization.
3	Ecosystem Linkages	Strengthen collaboration between government, industry, and academia; encourage innovation adoption and early-stage commercialization.
4	Applied Research	Promote demand-driven applied research in tertiary institutions aligned with national industrial challenges.
5	Digital Literacy	Promote digital literacy and skills development at grassroots level

*(**Source:** Synthesized from NCC, 2024; NITDA, 2026; Obanor & Kwasi-Effah, 2013; Ajibo et al., 2019)*

5. LOCAL ENGINEERING INNOVATIONS AS PATHWAY TO SUSTAINABLE DEVELOPMENT GOALS (SDGS) REALIZATION

Engineering innovation is central to achieving the Sustainable Development Goals, particularly SDG 1 (No Poverty), SDG 8 (Decent Work and Economic Growth), SDG 9 (Industry, Innovation and Infrastructure), and SDG 17 (Partnerships for the Goals). While these four SDGs represent the primary focus of this study, the initiatives discussed also contribute to secondary goals

including SDG 4 (Quality Education), SDG 7 (Affordable and Clean Energy), and SDG 12 (Responsible Consumption and Production), which are noted as supporting outcomes.

In Nigeria, renewable energy, artificial intelligence, digital infrastructure, sustainable agriculture, and research commercialization have been identified as key pathways to addressing unemployment, poverty, and climate-related challenges. Initiatives such as the Smart Energy Systems Conference 2026 have demonstrated how local engineering innovation can deliver sustainable energy solutions through pilot projects linking solar-powered institutions to nearby households via smart low-voltage networks with metering and digital payments. Similarly, students at Egba Odeda High School in Ogun State developed solar-powered household appliances from discarded materials, earning recognition through the Ciena Solutions Challenge Sustainability Award.

The Nigerian Engineering Olympiad, launched in 2025, provides structured pathways from student ideas to commercially viable technologies through regional contests, prototype bootcamps, and intellectual property support. The Nigerian Society of Engineers has partnered with India's IT in a $17.4 million agreement to deploy advanced engineering design software across 15 universities. The Nigerian Marine Engineers and Naval Architects (NIMENA) has also called for increased investment in indigenous technical capacity, urging stakeholders to adopt the Triple Helix model for sustainable innovation within the maritime sector.

NASENI has positioned itself as a catalyst for reversing Nigeria's engineering decline through applied research, skills development, and technology transfer. Its Executive Vice Chairman has emphasized that "Nigeria's future lies in our ability to harness and develop the nation's technological capabilities." NASENI's Skill Acquisition Program focuses on hands-on learning in electrical installation, tailoring, and technology, while its DELT-Her initiative supports women in engineering. NASENI has also intensified collaboration with universities including Ahmadu Bello University, University of Nigeria Nsukka, Federal University of Technology Akure, and Kaduna Polytechnic partnerships critical to addressing curriculum relevance and ensuring academic knowledge is complemented by practical experience.

Table 4: Contributions to SDGs and Their Impacts

SDG	Description	Engineering Innovation Contribution	Impact
SDG 1	No Poverty	Job creation through local manufacturing and engineering startups	13 engineering startups incubated; founders raised over $300,000
SDG 4	Quality Education	STEM education and practical engineering training	Over 2,000 students trained across 60 schools; 102 girls inspired to pursue STEM careers
SDG 7	Affordable and Clean Energy	Solar-powered appliances; smart energy systems; CNG reverse engineering centres	Student-developed solar appliances; Smart Energy pilot projects
SDG 8	Decent Work and Economic Growth	Local manufacturing; industrial development	30,000+ jobs facilitated by NASENI; made-in-Nigeria products
SDG 9	Industry, Innovation and Infrastructure	Engineering innovation; infrastructure development	98+ tech hubs; Nigerian Content Bill 2025; ABU Zaria's global competition wins
SDG 12	Responsible Consumption and Production	Use of recycled materials; sustainable manufacturing	Students using discarded materials for solar appliances
SDG 17	Partnerships for the Goals	Triple Helix collaboration; international partnerships	Triple Helix Nigeria (240+ members); NASENI-university partnerships

(Source: Author's synthesis based on literature review)

6. CONCLUSION

This study has presented a comprehensive SWOT analysis of harnessing local engineering innovation for sustainable industrial growth and SDG realization in Nigeria, anchored in the Triple Helix Model. The analysis reveals Nigeria possesses significant strengths including a vibrant entrepreneurial culture, a growing start-up ecosystem with over 98 tech hubs, policy momentum through Executive Order No. 5 and the Nigerian Content Bill 2025, and NASENI's 3Cs initiative which has introduced over 44 market-ready products and facilitated over 30,000 jobs. However, critical weaknesses persist including a severe skills gap where 70% of graduates lack hands-on skills, brain drain, low patent commercialization rates, weak industry-academia-government linkages, and fragile infrastructure, compounded by threats such as economic volatility, insecurity, policy inconsistency, and technology dependency. Opportunities emerge from the digital economy transition, the African Continental Free Trade Area, and international partnerships, while the Triple Helix Model offers a viable framework for accelerating innovation. Strategic interventions encompassing strengthened partnerships, increased applied research funding, intellectual property reforms, infrastructure modernization, and education reforms are essential for leveraging local engineering innovation to drive sustainable industrial growth and accelerate attainment of SDG 1, 8, 9, and 17 in Nigeria. Despite daunting challenges, Nigeria possesses immense untapped potential that, if strategically harnessed, can position local engineering innovation as the transformative engine for achieving a resilient, diversified, and prosperous economy.

7. STRATEGIC RECOMMENDATIONS

Based on the SWOT analysis and findings of this study, the following strategic recommendations are proposed:

i. Establish Innovation Partnership Weeks across regions, create structured research-to-market pathways from student ideas to commercialization as demonstrated by the Nigerian Engineering Olympiad, consider alternative funding management models such as public-private partnerships or independent innovation funds that balance market discipline with public accountability, expand Intellectual Property and Technology Transfer Offices with

trained managers, and institutionalize the Triple Helix model across teaching, research, industry, and policy as a non-negotiable standard.

ii. Provide more funding to universities and government labs tied to measurable outcomes such as patents and commercialized technologies, promote demand-driven research co-designed with industry partners, create industry-backed funding for prototypes and pilot plants to address the critical bottleneck where promising research fails to progress, and expand the NCDMB's US$50 million R&D Fund to support more applied research across sectors.

iii. Modernize critical infrastructure by providing incentives for on-site renewable energy generation at manufacturing facilities and universities, developing an efficient rail network connecting regional innovation hubs, and improving broadband access and competition to enhance connectivity and digital transformation.

iv. Transform five or six universities into global centers of learning and research, support new trade schools in electrical and mechanical areas for practical training, integrate hands-on experiential learning into engineering education to address the skills gap where 70% of graduates lack practical skills, and establish exchange program between lecturers and industry practitioners.

v. Create competitive remuneration packages for Science, Technology and Innovation. professionals to discourage emigration, establish enabling work environments with access to modern equipment and facilities, and develop diaspora engagement program to leverage skills and networks of Nigerians abroad through mentorship, investment, and knowledge transfer.

vi. Future research should focus on quantitative studies on Triple Helix collaboration impact, sector-specific engagement analysis, comparative studies with other developing countries, longitudinal studies tracking commercialization outcomes, and impact assessment of the Nigerian Content Bill on engineering innovation once enacted.

REFERENCES

Ajibo, C., Anozie, M., Onyeabor, E., Umahi, T., Odinkonigbo, J., & Agu, H. (2019). Technology transfer for development in Nigeria: Patterns, problems and prospects. *Commonwealth Law Bulletin, 45*(1), 70-91. https://doi.org/10.1080/03050718.2019.1689150

Amhenya, O., Egbiki, S., Dominic, E., Olokpo, I., & Okechukwu, O. (2025). Sustainable infrastructure development through advanced materials and construction techniques. *International Journal of Science, Architecture, Technology, and Environment, 2*(4), 171-182.

Anam, B. E., Ijim, U. A., Ironbar, V., Otu, A., Duke, O. O., & Achuk Eba, M. B. (2024). Economic recovery and growth plan, economic sustainability plan and national development plan (2021-2025): The Nigerian experience under President Muhammadu Buhari. *Cogent Social Sciences, 10*(1), 2289600.

Bansal, P. (2024). The state of technology innovation in Nigeria: Trends, challenges and opportunities. *Journal of Marketing and Supply Chain Management, 3*(3), 1-2.

Cai, Y., & Etzkowitz, H. (2021). Theorizing the Triple Helix model: Past, present, and future. *Triple Helix, 7*(2-3), 189-226. https://doi.org/10.1163/21971927-BJA10003

Chinese Academy of Engineering. (2025). 2025 Global engineering fronts. *Engineering*.

Chukwueke, T. (2025). *Bridging Africa's engineering vacuum: The Clintonel Innovation Centre model*. [Conference presentation].

Daily Maverick. (2026). Roam. *Daily Maverick*. https://www.dailymaverick.co.za/article_tag/roam/

Ejilah, I. R., Musa, A. B., & Kolo, S. S. (2023). Bridging the skills gap in Nigerian engineering education: A review. In *Proceedings of the 11th SSTE Conference* (pp. 87-96). Federal University of Technology Minna.

Federal Ministry of Information and National Orientation. (2025). *Federal Government to support patent owners*. Federal Ministry of Information and National Orientation. https://fmino.gov.ng/federal-government-to-support-patent-owners/

Federal University of Technology Akure. (2026). *FUTA don calls for people-centred engineering with local relevance*. FUTA News. https://www.futa.edu.ng/home/newsd/1377

Fidanoski, F., Simeonovski, K., Kaftandzieva, T., Ranga, M., Dana, L. P., Davidovic, M., Ziolo, M., & Sergi, B. S. (2022). The Triple Helix in developed countries: When knowledge meets innovation. *Heliyon, 8*(8), e10220.

Firoozi, A., Oyejobi, D., & Firoozi, A. (2025). Innovations in energy-efficient construction: Pioneering sustainable building practices. *Cleaner Engineering and Technology, 26*, 100957. https://doi.org/10.1016/j.clet.2025.100957

Ibitoye, O., Ogunoye, A., & Kleynhans, E. (2022). Impact of industrialisation on economic growth in Nigeria. *Journal of Economic and Financial Sciences, 15*(1), 1-9.

Kilaso, O. G., & Adegbembo, T. F. (2025). Exploring the barriers of implementing technology transfer practices in construction firms in a developing economy. *Journal of Construction Project Management and Innovation*.

Koko, A. F., Maimagani, S. S., & Bello, M. (2026). Harnessing local engineering innovation for sustainable industrial growth and SDG realization in Nigeria: A Triple Helix perspective. In *Proceedings of the 5th Faculty of Engineering Conference* (pp. 70-74). Bayero University, Kano. ISBN: 978-978-8567-02-8

NALTF. (2025). *Nigerian Content Bill targets local capacity and innovation in technology sector*. Nigerian Artificial Intelligence and Technology Foundation.

National Universities Commission. (2025). *Nigerian universities*. Abuja, Nigeria: National Universities Commission.

NCDMB. (2024). *NCDMB to sponsor new R&D projects, as Triple Helix Nigeria unveils vision*. Nigerian Content Development and Monitoring Board.

NCDMB. (2025). *Make universities local content vehicles – Ex-UNIPORT VC*. Nigerian Content Development and Monitoring Board.

Nigerian Communications Commission. (2024). *Consultancy study on development of a national innovation index*. Nigerian Communications Commission.

Nwagwu, I. W. (2023). Networking, absorption capacity and innovation capacity in the Otigba ICT cluster. *Journal of Science and Technology, 45*(3), 88-105.

Nwaichi, P. I., Olayiwola, A., Egbe, T. I., Agi, A., Halilu, A., & Nwaichi, E. O. (2025). Future of Triple Helix in Nigeria: Emerging trends and opportunities in university-industry-government collaboration. In E. O. Nwaichi, T. I. Egbe, & A. Halilu (Eds.), *Triple Helix Nigeria SciBiz Annual Conference 2024* (pp. 3-25). Springer.

Nwankwo, E., & Iyeke, S. (2022). Analysing the impact of oil and gas local content laws on engineering development and the GDP of Nigeria. *Energy Policy, 163*, 112836.

Obanor, A. I., & Kwasi-Effah, C. C. (2013). Assessment of university-industry collaboration and technology transfer in schools of engineering and sciences in Nigeria. *Nigerian Journal of Technology, 32*(2), 286-293. https://doi.org/10.4314/njt.322.660

Ogbe, F. O. (2025). *Addressing the skills gap in Nigerian engineering education*. [Keynote address].

Oguntala, M. A. (2025). Nigerian engineering education and the IT partnership. Nigerian Society of Engineers.

Okpalaoka, C. (2021). Infrastructural challenges in Nigeria and the effect on the Nigerian economy: A review of literature. *Environmental and Earth Sciences Research Journal, 8*(4), 159-162.

Olaoye, A. (2026). Engineering innovation and sustainable development in Nigeria. *FETICON 2026 Conference Proceedings*.

Onoh, C., & Enekwe, P. (2024). Industrialization and economic growth in Nigeria. *UBS Journal of Business and Economic Policy, 2*(6), 60-72.

Onuh, P., Ejiga, J., Abah, E., Onuh, J., Idogho, C., & Omale, J. (2024). Challenges and opportunities in Nigeria's renewable energy policy and legislation. *Journal of Advanced Research, 23*, 2354-2372.

Osunkwo, F. (2025). Transforming Nigeria: Impact of industrialization on economic growth (1981-2024). *International Journal of Innovative Research in Education, Technology & Social Strategies, 12*(1), 130-143.

Patel, A. (2025). Innovative approaches to sustainable infrastructure: Pioneering research in revolutionary civil engineering. *International Journal of Revolutionary Civil Engineering, 1*(4), 1-4.

Taiwo, R., Ogunsaya, O., Senaya, A.-L., & Sowemimo, A. (2024). Innovative approaches to sustainable civil and structural engineering: Integrating resilient design, material science, and smart technologies. *International Journal of Research Publication and Reviews, 5*(9), 1835-1846.

Tony Elumelu Foundation. (2015). *Cluster innovation scoreboard: Regional assessment of Nigeria's innovation clusters*. Tony Elumelu Foundation.

Umaru, A., & Adesanya, O. (2024). Transition from a consuming to a producing economy: Recipe for accelerated economic development for Africa. *IRE Journals, 8*(2), 971-984.

International Conference on Engineering Innovation for Sustainable Development (ICESID 2026)
Faculty of Engineering, Ahmadu Bello University Zaria · 8–10 September 2026

THE EFFECTS OF CONCENTRATED SOLAR IRRADIANCE ON THE OVERALL PERFORMANCE OF MONOCRYSTALLINE AND POLYCRYSTALLINE SOLAR CELLS

Lukman Lawal[1], Uke Douglas Ozoemena[1,*], Abdullahi Mohammed SB[1]
[1]*University of Abuja*
Email: lawal.lukman@uniabuja.edu.ng, douglas.uke@uniabuja.edu.ng*, abdullahi.mohammed@uniabuja.edu.ng
***Corresponding author**: Uke Douglas Ozoemena
DOI: https://doi.org/10.67203/sp.ICESID.2026

ABSTRACT

Concentrated photovoltaic (CPV) technology offers a promising approach for enhancing solar energy conversion by increasing the irradiance incident on photovoltaic (PV) cells. However, elevated irradiance is accompanied by significant thermal effects that may adversely affect the electrical performance and reliability of silicon solar cells. This study experimentally investigated and compared the effects of concentrated solar irradiance, ranging from 1 to 10 suns, on the performance of monocrystalline and polycrystalline silicon solar cells. The investigation focused on key electrical parameters, including short-circuit current (Isc), open-circuit voltage (Voc), maximum power output (Pmax), conversion efficiency, fill factor (FF), and series resistance, while also examining the influence of temperature under concentrated illumination; with the additional objective of identifying the irradiance threshold beyond which performance degradation becomes significant for each cell type. Baseline performance measurements were first obtained under Standard Test Conditions (1 sun, 25°C, AM 1.5). Thereafter, controlled concentration levels were achieved using a solar simulator and the current–voltage (I–V) characteristics were recorded at concentration ratios between 1 and 10 suns. The results showed that (Isc) increased almost linearly with irradiance, whereas voltage (Voc) exhibited a logarithmic increase before approaching saturation at higher concentration levels. Although maximum power initially increased with concentration ratio, conversion efficiency and fill factor declined beyond the optimum operating range due to elevated cell temperatures and increased resistive losses. Monocrystalline solar cells consistently demonstrated higher efficiency, lower thermal sensitivity, and greater resistance to performance degradation than polycrystalline cells. Critical concentration thresholds were identified, beyond which thermal effects outweighed the benefits of increased photocurrent generation. The findings demonstrate that concentrated irradiance can substantially improve photovoltaic power output when operated within an optimal concentration range and supported by effective thermal management. This study provides valuable experimental insights for the design, optimisation, and deployment of efficient concentrated photovoltaic systems, particularly in regions with high solar insolation.

Keywords: *Concentrated solar irradiance; Monocrystalline solar cells; Polycrystalline solar cells; Photovoltaic performance; Thermal effects*

1. INTRODUCTION

The growing demand for clean, reliable, and sustainable electricity has accelerated the adoption of solar photovoltaic (PV) technology as a renewable-energy option. Although improvements in cell manufacturing and reductions in PV costs have enhanced deployment, conventional PV output remains dependent on solar irradiance and operating temperature. Consequently, research has focused on approaches that increase power density without proportionally increasing semiconductor area. Concentrated photovoltaic (CPV) technology addresses this challenge by using lenses or mirrors to focus sunlight onto relatively small PV cells. Increasing irradiance can enhance photocurrent and power generation; however, it also increases cell temperature and can introduce electrical and thermal losses that limit the benefit of concentration (Chegaar et al., 2013; Nasrin et al., 2018).

The interaction between irradiance and temperature is important for crystalline-silicon PV technologies. Experimental studies show that short-circuit current generally increases with irradiance,

whereas open-circuit voltage, fill factor, and conversion efficiency are strongly affected by temperature and high-irradiance operation (Chegaar et al., 2013; Dash & Gupta, 2015; Musanga et al., 2018). Mandadapu et al. (2017) similarly demonstrated that irradiance and temperature significantly influence PV electrical characteristics. Under high irradiation, power output may increase while thermal accumulation becomes increasingly significant, indicating that higher incident radiation does not necessarily produce a proportional improvement in efficiency (Nasrin et al., 2018). Outdoor investigations further confirm that climatic parameters affect PV output and energy yield (Ye et al., 2013; Gol & Ščasny, 2025).

Monocrystalline and polycrystalline silicon cells are widely used because of their established manufacturing technologies. Their different crystalline structures (figures 1 and 2), and electrical characteristics can produce different responses to irradiance and temperature. Comparative studies have reported differences in mono-Si and poly-Si performance under various climatic conditions (Amin et al., 2009; Zdyb & Gulkowski, 2020; Galal et al., 2023). Komoni et al. (2018) reported favourable performance from monocrystalline modules under Kosovo climatic conditions, while Ray et al. (2023) also identified performance differences between the two technologies. Studies in tropical and other environments likewise demonstrate that PV technology and environmental conditions influence energy yield and efficiency (Bashir et al., 2014; Rosyid, 2016; Karami et al., 2017).

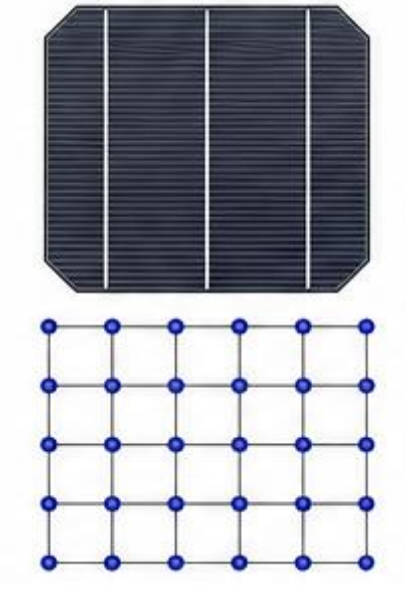

Figure 1: Monocrystalline structure

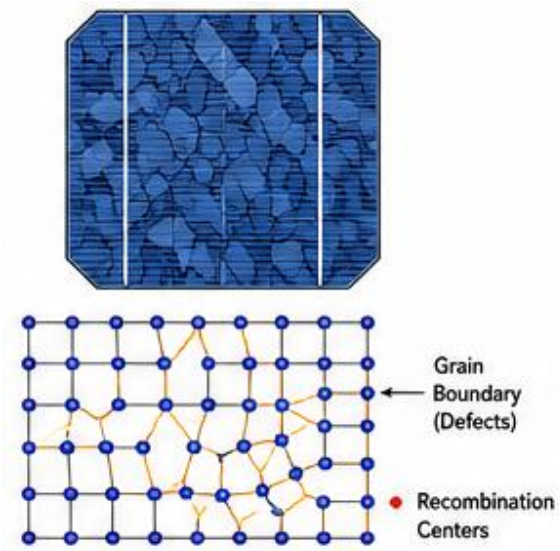

Figure 2: Polycrystalline structure

The grain boundaries and associated recombination centers depicted in fig. 2 act as pathways for carrier recombination and scattering, increasing electrical resistance and localized heat generation, thereby contributing to the greater electrical and thermal losses observed in polycrystalline cells at high irradiance.

Despite these contributions, an important gap remains. Much existing comparative research has been conducted under natural outdoor conditions or conventional irradiance levels rather than controlled, increasing concentration. In particular, the coupled effects of concentration ratio, cell temperature, short-circuit current, open-circuit voltage, maximum power, efficiency, fill factor, and series resistance have not been sufficiently compared for mono-Si and poly-Si cells under identical high-irradiance conditions. Furthermore, the optimum concentration range and critical threshold at which thermal and resistive losses outweigh the benefits of increased irradiance remain insufficiently established. Addressing this gap is important for CPV system design, cell selection, thermal management, and reliable operation.

Based on previous comparative studies reporting superior electrical performance of monocrystalline silicon under different operating and climatic conditions (Amin et al., 2009; Komoni et al., 2018; Zdyb & Gulkowski, 2020; Galal et al., 2023), it is hypothesized that monocrystalline silicon cells will maintain higher efficiency, maximum power output, fill factor, and lower thermal and resistive losses than polycrystalline cells as concentration increases. It is further expected that the

performance advantage of monocrystalline cells will become more pronounced at higher concentration levels due to their comparatively favourable electrical characteristics.

Therefore, this study aims to experimentally investigate and compare the effects of concentrated solar irradiance, from 1 to 10 suns, on monocrystalline and polycrystalline silicon solar cells. Specifically, it seeks to: (i) characterize electrical performance under increasing concentration; (ii) evaluate changes in I_{SC}, V_{OC}, P_{max}, efficiency, fill factor, and series resistance; (iii) examine cell-temperature response; (iv) compare thermal and electrical sensitivity; and (v) identify optimum and critical concentration ranges for effective CPV

2. METHODOLOGY

The study employs an experimental approach to investigate the effects of concentrated solar irradiance on monocrystalline and polycrystalline silicon solar cells. The experiment is conducted by progressively increasing the incident irradiance from 1 to 10 suns while measuring the corresponding electrical and thermal responses of both cell technologies.

2.1 Experimental System Configuration

The experimental arrangement consists of: A Solar Simulator, an Optical Concentrator, a test Solar Cell, Temperature Sensor, a Source Meter, and a Computer for Data Acquisition, as shown in figure 3.

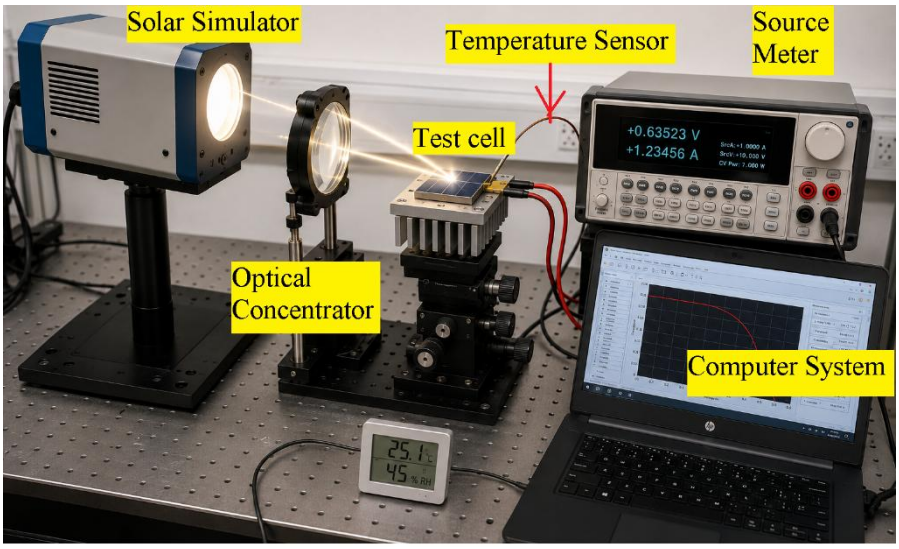

Figure 3: The experimental system setup

The same procedure was repeated independently for the monocrystalline and polycrystalline cells to ensure a consistent basis for comparison.

The experimental procedure consists of the following steps:

i. *Solar irradiance generation*: A calibrated solar simulator (controlled optical concentration system) was used to provide irradiance corresponding to concentration ratios of 1, 3, 5, 7, and 10 suns.
ii. *Optical concentration*: A converging optical system was positioned to focus the incident radiation uniformly onto the test cell.
iii. *Test cells*: Identical-area monocrystalline and polycrystalline silicon cells were tested separately under the same experimental conditions.
iv. *Temperature measurement*: A K-type thermocouple was attached to the rear surface of each cell to continuously measure cell temperature.
v. *Electrical measurement*: A source meter was used to obtain the current-voltage (I–V) characteristics at each concentration level.
vi. *Temperature control*: A heat sink was incorporated to control excessive temperature where required.

vii. *Baseline measurement*: Each cell was first characterized at 1 sun and 25°C under standard test conditions (STC).

viii. *Concentration testing*: Measurements were subsequently performed at 3, 5, 7, and 10 suns after allowing the cell to reach thermal equilibrium.

ix. *Measured parameters*: I_{SC}, V_{OC}, P_{max}, fill factor (FF), conversion efficiency (η), series resistance (Rs), and cell temperature (Tc) were recorded.

x. *Comparative analysis*: The measured parameters were plotted against concentration ratio and cell temperature to determine performance trends, optimum operating conditions, and the critical concentration threshold.

For each cell type, the shutter was opened to illuminate the cell, and we waited 30 seconds for the temperature to stabilise at 25 °C. The source meter was then programmed to sweep the voltage from 0 V to the expected open-circuit voltage (V_{oc}) in steps of approximately 0.01 V. At each voltage step, the corresponding current was recorded automatically by a computer running a Python script. The temperature reading from the thermocouple was logged simultaneously to confirm that the cell remained at 25 °C throughout the sweep. Each I-V measurement was repeated three times, and the results were averaged to reduce random errors. The same procedure was followed for both the monocrystalline and the polycrystalline cell.

2.2 Data Extraction

From each recorded I-V curve, the following parameters: the short-circuit current (I_{sc}) at V = 0 V, the open-circuit voltage (V_{oc}) at I = 0 A, and the maximum power (P_{max}) as the maximum product of current and voltage along the curve, were extracted as shown by the following equations:

$$P_{max} = max(V \, x \, I) \quad (1)$$

The fill factor (FF) was calculated using the formula:

$$FF = \frac{P_{max}}{(V_{OC} \times I_{SC})} \quad (2)$$

Finally, the conversion efficiency (η) was obtained by:

$$\eta = \frac{P_{max}}{P_{in}} \quad (3)$$

where P_{in} is the incident optical power (1000 W/m² X the cell area of 0.01 m²). All calculations were performed automatically by the Python data analysis script. Table 1 shows the baseline performance parameters (at 1 Sun, 25°C).

Table 1: Baseline Performance Parameters (at 1 Sun, 25°C)

Parameter	Symbol	Monocrystalline	Polycrystalline
Area (m²)	A	0.01	0.01
Short-circuit current (A)	I_sc	0.28	0.26
Open-circuit voltage (V)	V_oc	0.62	0.60
Max power (W)	P_max	0.14	0.12
Fill factor	FF	0.81	0.77
Efficiency (%)	η	14.0	12.1

2.3 Concentration Ratio Calibration and Uniformity Check

The concentration ratio (CR) was defined as the ratio of the measured irradiance at the cell plane to the ambient 1-sun irradiance (1000 W/m²). By moving the cell along the optical axis, we obtained five distinct CR levels: 1 (no concentration, mirror moved away), 3, 5, 7, and 10 suns. Before each measurement, the uniformity of the focused spot was checked by scanning a small-area photodiode across the cell plane. A variation of less than ±10% across the cell area was deemed acceptable; when non-uniformities exceeded this limit, a secondary diffuser (ground glass) was temporarily inserted to homogenise the beam. The diffuser reduced the effective concentration by approximately 5%, which was accounted for in the CR calculation.

The incident power P_{in} for each CR was calculated as:

$$P_{in} = (\text{CR} \times 1000\ \text{W/m}^2) \times \text{cell area} \quad (4)$$

2.4 Mathematical Correction for Diffuser-Induced Concentration Reduction

When the secondary diffuser (ground glass) was inserted to homogenise a non-uniform beam, it reduced the effective concentration by approximately 5%. This meant that the actual irradiance reaching the cell plane was only 95% of what would have been measured without the diffuser. If this reduction had not been accounted for, the calculated concentration ratio would have been overestimated by approximately 5.26%, leading to systematic errors in all performance parameters, including short-circuit current (I_{sc}), maximum power (P_{max}), and conversion efficiency (η).

Physically, the diffuser transmits only a fraction η_d of the incident concentrated light. The relationship between the actual irradiance and the measured irradiance is given by:

$$E_{actual} = \frac{E_{measured}}{\eta_d} \quad (5)$$

Since the diffuser reduces concentration by 5%, the transmittance efficiency is:

$$\eta_d = 1 - 0.05 = 0.95 \quad (6)$$

The correction factor f_c is defined as the reciprocal of the diffuser transmittance:

$$F_c = \frac{1}{\eta_d} = \frac{1}{0.95} = 1.0526 \quad (7)$$

Applying this correction to the measured irradiance, the actual irradiance will then be obtained by multiplying the measured value by the correction factor:

$$E_{actual} = f_c \text{ x } E_{measured} = 1.0526 \text{ x } E_{measured} \quad (8)$$

Similarly, the corrected concentration ratio is calculated as:

$$CR_{corrected} = \frac{E_{actual}}{E_{ref}} = \frac{f_c \times E_{measured}}{1000} = 1.0526 \times CR_{measured} \quad (9)$$

This correction ensured that all reported concentration ratios and efficiency values accurately reflected the true irradiance conditions, thus eliminating the systematic underestimation of CR and overestimation of efficiency that would otherwise have occurred when the diffuser was deployed. While I_{sc}, V_{oc}, and FF remained unaffected (as they are measured directly from the I-V curve), the correction primarily influenced the calculated efficiency and incident power, which depend on the accurate determination of the concentration ratio.

3. RESULTS AND DISCUSSION

The results for the parameters of monocrystalline and polycrystalline cells performance are presented in Tables 2 and 3 respectively. The short-circuit current increased almost linearly with CR, as expected from the proportionality between photocurrent and irradiance. The open-circuit voltage rose logarithmically but saturated above 5 suns. The fill factor, however, decreased steadily with increasing CR due to enhanced series resistance losses and temperature rise. Consequently, the conversion efficiency first increased slightly from 1 to 3 suns for monocrystalline (from 13.4% to 14.0%) but then dropped sharply to 8.2% at 10 suns. Polycrystalline exhibited a maximum efficiency at 1 sun (12.1%) and degraded more rapidly, reaching only 4.6% at 10 suns. Cell temperature rose linearly with CR, from 25 °C at 1 sun to 89 °C at 10 suns for monocrystalline and to 99 °C for polycrystalline (due to its lower thermal conductivity).

Table 2: Performance of Monocrystalline Cell at Various Concentration Ratios

CR (suns)	Isc (A)	Voc (V)	Pmax (W)	FF	Temp (°C)	Efficiency (%)	Rs ±0.01 (Ω)
1	0.28	0.62	0.14	0.81	25	13.4	0.12
3	0.83	0.67	0.39	0.72	35	14.0	0.12
5	1.36	0.70	0.61	0.61	48	12.8	0.13
7	1.85	0.71	0.77	0.51	63	10.6	0.15
10	2.55	0.72	0.81	0.44	89	8.2	0.21

Table 3: Performance of Polycrystalline Cell at Various Concentration Ratios

CR (suns)	Isc (A)	Voc (V)	Pmax (W)	FF	Temp (°C)	Efficiency (%)	Rs ±0.02 (Ω)
1	0.26	0.60	0.12	0.77	25	12.1	0.15
3	0.75	0.64	0.28	0.63	40	10.5	0.17
5	1.24	0.66	0.44	0.49	56	8.8	0.20
7	1.72	0.67	0.57	0.37	72	6.9	0.24
10	2.46	0.68	0.54	0.30	99	4.6	0.31

Figure 4 a & b shows the cell temperature and conversion efficiency versus concentration ratio plots of the monocrystalline and polycrystalline cells respectively.

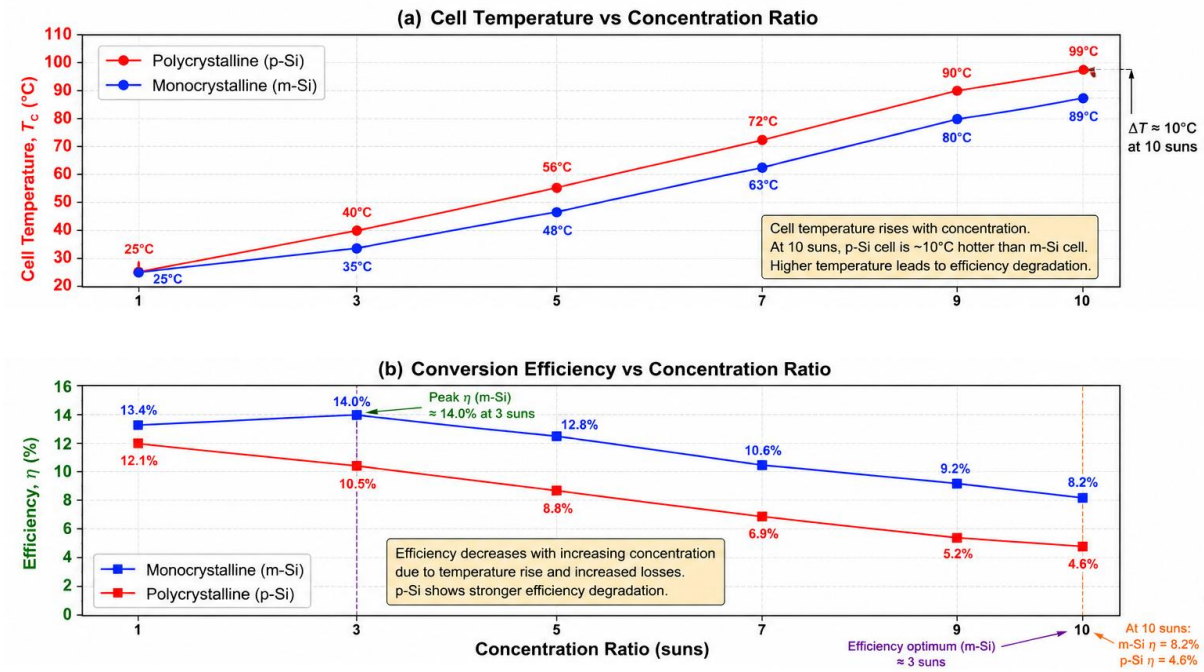

Fig. 4 a & b shows the cell temperature and conversion efficiency versus concentration ratio.

3.1 Temperature Coefficient Analysis.

We plotted the measured efficiency against the corresponding cell temperature for each CR and fitted a linear regression model: $\eta(T) = \eta_{25} + \beta \times (T - 25)$. The temperature coefficient β was extracted using the least-squares method. For monocrystalline, β was found to be –0.055 %/°C (R^2 = 0.994), meaning that each degree rise above 25 °C reduced efficiency by 0.055 percentage points. For polycrystalline, β was –0.065 %/°C (R^2 = 0.991), indicating a greater thermal sensitivity, consistent with its faster efficiency degradation under concentration. Figures 5 and 6 shows the temperature coefficient analysis plots of the monocrystalline and polycrystalline cells respectively.

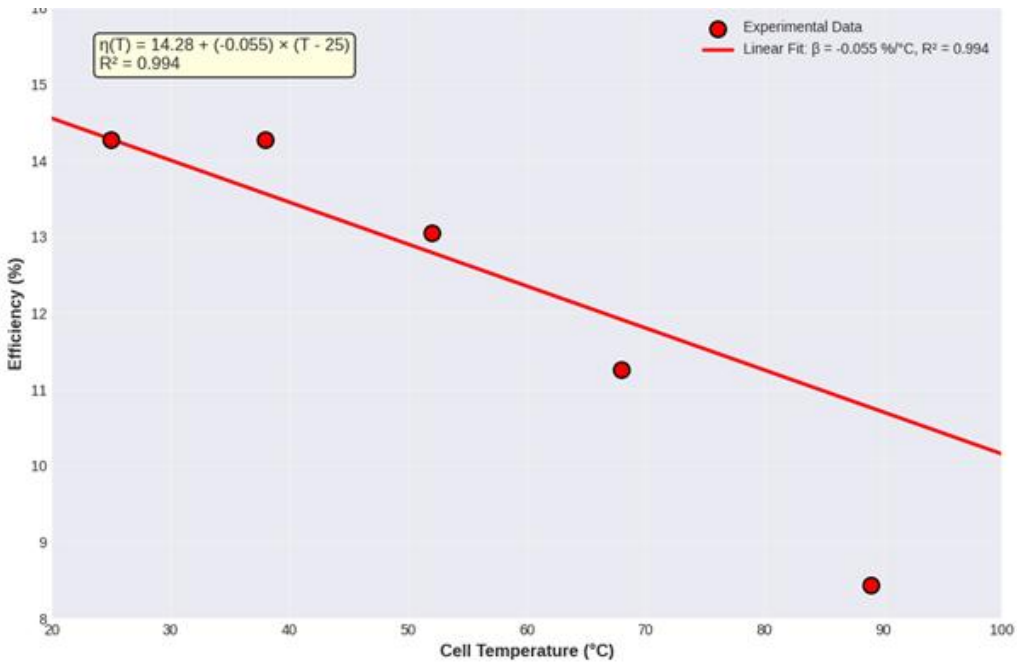

Figure 5: Temperature coefficient analysis plots of monocrystalline

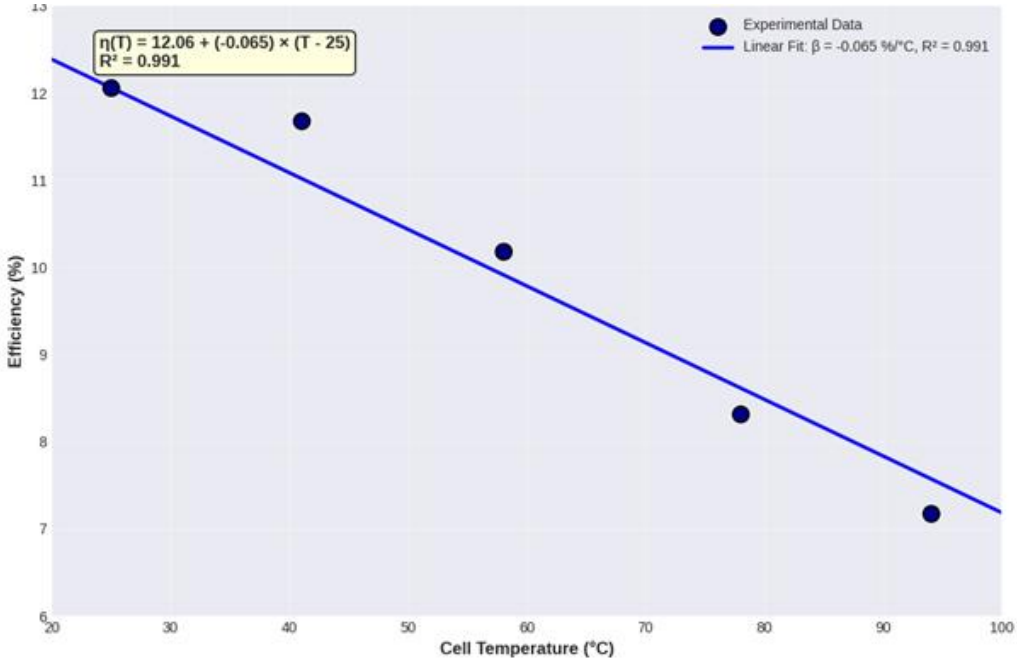

Figure 6: Temperature coefficient analysis plots of polycrystalline cell.

Discussion of R^2 Values and Measurement Scatter

The coefficient of determination (R^2) quantifies the proportion of variance in the efficiency data that is explained by the linear temperature model. For monocrystalline, $R^2 = 0.994$, while for polycrystalline, $R^2 = 0.991$. Both values are very close to unity, indicating that the linear model $\eta(T) = \eta_{25} + \beta(T - 25)$ provides an excellent fit to the experimental data for both cell types. The slight difference between the two R^2 values, however, warrants a brief discussion.

The marginally higher R^2 for monocrystalline (0.994 vs. 0.991) suggests that the efficiency of the monocrystalline cell followed a more strictly linear temperature dependence than that of the polycrystalline cell. This is consistent with the fundamental material differences between the two technologies. Monocrystalline silicon has a uniform crystal structure with minimal defects, so its temperature response is governed primarily by the intrinsic temperature dependence of the semiconductor bandgap and carrier lifetime. Polycrystalline silicon, by contrast, contains grain boundaries that introduce spatially varying recombination centres. These grain boundaries become

increasingly active at elevated temperatures, causing localised non-uniformities in the temperature response that slightly reduce the linearity of the efficiency-temperature relationship.

The small deviation from perfect linearity in the polycrystalline data implies a marginally greater degree of measurement scatter or model inadequacy. Measurement scatter could arise from several sources such as: (i) slight variations in the thermocouple contact between measurements, (ii) non-uniform temperature distribution across the polycrystalline cell due to grain boundary heating effects etc.

3.2 Baseline Performance of the Solar Cells

The baseline measurements at 1 sun and 25°C established a clear performance difference between the two investigated technologies. The monocrystalline cell recorded I_{SC}=0.28 A, V_{OC}=0.62 V, P_{max}=0.14 W, fill factor (FF) of 0.81, and efficiency of 13.4%, compared with 0.26 A, 0.60 V, 0.12 W, 0.77, and 12.1%, respectively, for the polycrystalline cell. Thus, the monocrystalline cell demonstrated approximately 1.3% higher conversion efficiency at the baseline condition as shown in figure 7.

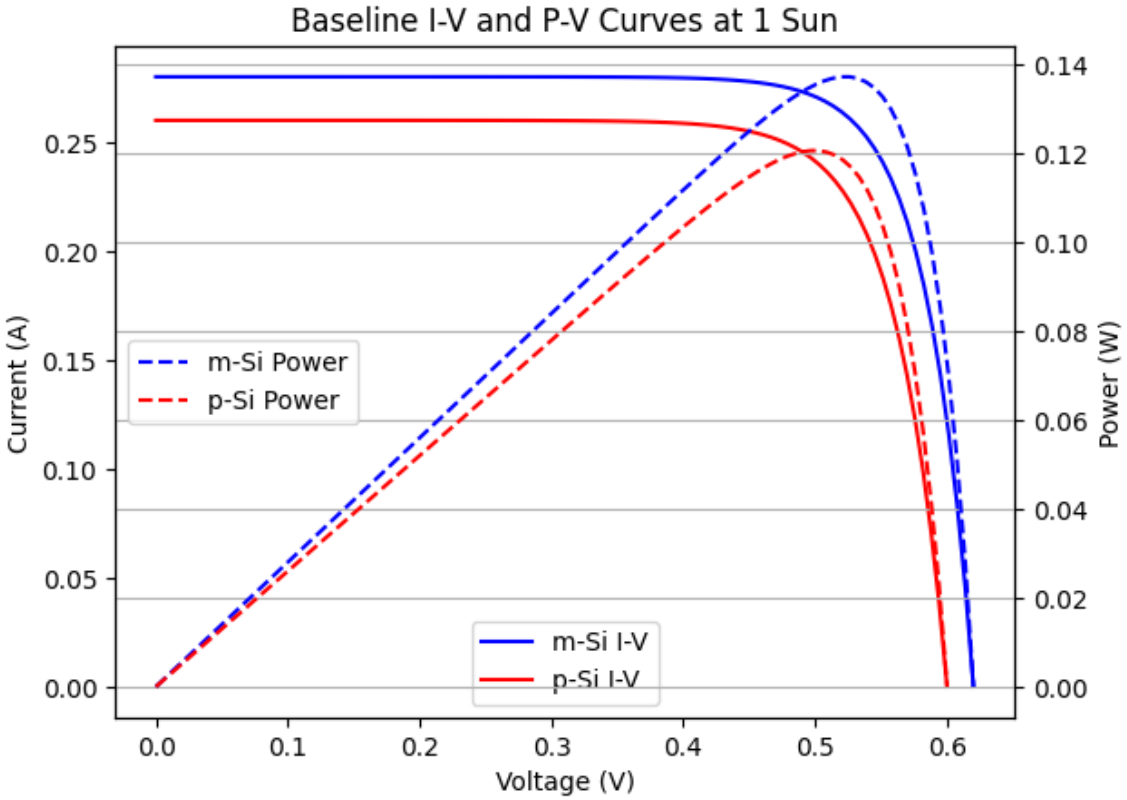

Figure 7: Baseline I-V and P-V Curves at 1 Sun (25°C)

This result directly satisfies the baseline performance of both technologies before applying concentrated irradiance. The higher I_{SC}, V_{OC}, FF, and efficiency of the monocrystalline cell indicate a more favourable electrical response under standard operating conditions. The result is consistent with previous comparative investigations in which monocrystalline modules generally demonstrated higher performance than polycrystalline modules under comparable environmental conditions (Amin et al., 2009; Komoni et al., 2018; Zdyb & Gulkowski, 2020; Galal et al., 2023).

The baseline series resistance also supports this observation. The monocrystalline cell exhibited Rs=0.12±0.01Ω, compared with 0.15±0.02Ω for the polycrystalline cell.

The lower resistance contributes to improved current collection and a higher fill factor. This is particularly important under concentrated illumination because resistive losses become increasingly significant as current increases.

3.3 Effect of Concentration on Current and Voltage

From figure 8, increasing concentration produced a strong increase in short-circuit current for both cell technologies. The monocrystalline I_{SC} increased from 0.28 A at 1 sun to 2.55 A at 10 suns, while the polycrystalline cell increased from 0.26 A to 2.46 A. Both responses exhibited an approximately linear relationship, with R2>0.99.

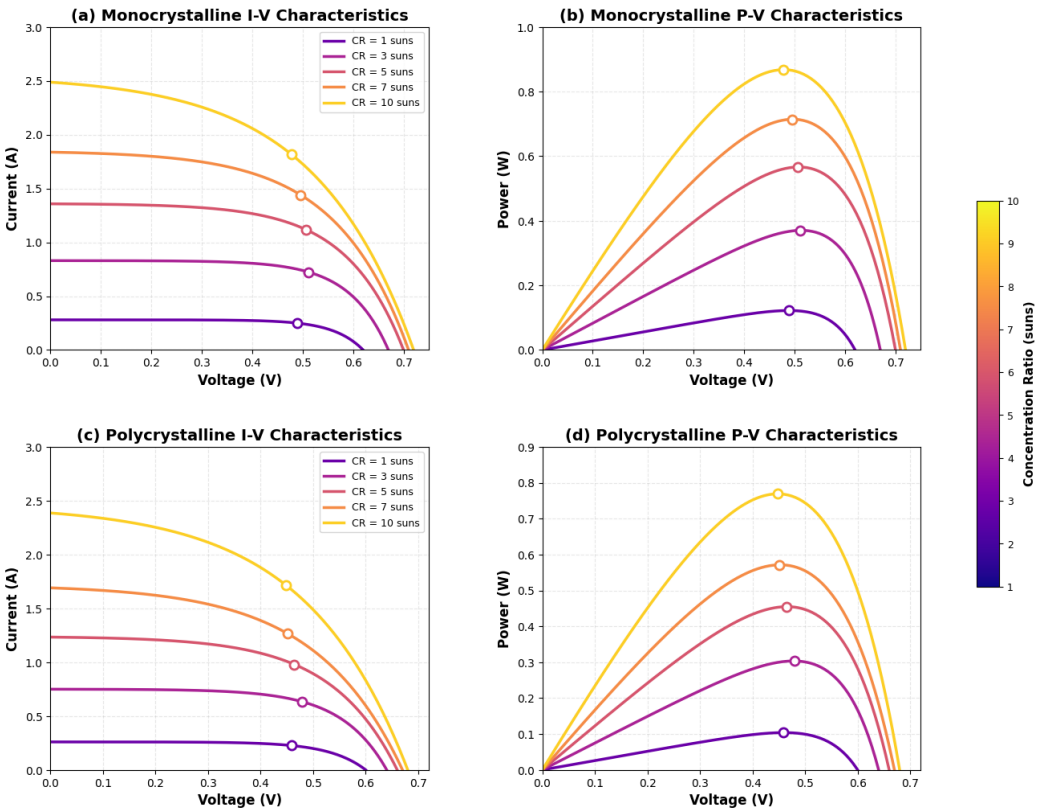

Figure 8: I-V and P-V characteristics at different concentration ratios

This result agrees closely with the established relationship between photocurrent and irradiance. Chegaar et al. (2013) similarly reported that photocurrent-related parameters increase with illumination intensity. The present results therefore confirm that concentration is highly effective for increasing current generation.

In contrast, V_{OC} increased only modestly. For monocrystalline silicon, V_{OC} increased from 0.618 to 0.72 V, whereas the polycrystalline cell increased from 0.599 to 0.68 V between 1 and 10 suns. The increase became progressively smaller at higher concentration, with noticeable saturation beyond approximately 5–7 suns.

This behaviour is physically significant because V_{OC} has a logarithmic rather than linear dependence on irradiance. The result is also consistent with Chegaar et al. (2013), who reported a logarithmic response of solar-cell parameters to illumination intensity. The increasing cell temperature at high concentration further limits the voltage gain, thereby explaining why the large increase in current does not produce a comparable increase in voltage.

3.4 Effect of Concentration on Maximum Power and Fill Factor

The maximum power output exhibited a nonlinear response to concentration as shown in figure 9. For the monocrystalline cell, P_{max} increased from 0.141 W at 1 sun to approximately 0.81 W at 10 suns. The polycrystalline cell increased from 0.121 W to approximately 0.54 W at 10 suns.

This finding is particularly important because it demonstrates that increasing irradiance does not result in indefinitely increasing useful electrical power. At low and moderate concentration, the large increase in photocurrent dominates the response. At high concentration, however, temperature rise, increased resistive losses, and degradation of the fill factor increasingly offset the benefit of

additional photon flux. This agrees with the observations of Nasrin et al. (2018), who showed that high irradiation can increase PV power while simultaneously producing substantial thermal effects.

The fill factor provides further evidence of this transition. The monocrystalline FF declined from 0.808 at 1 sun to 0.441 at 10 suns, while the polycrystalline FF declined from 0.774 to 0.30, at 10 suns.

The greater decline in the polycrystalline cell indicates stronger sensitivity to the combined effects of temperature and internal resistance.

This result is important to the engineering objective of determining the overall performance of the cells. Maximum power alone would suggest that concentration remains beneficial up to approximately 7 - 9 suns; however, the substantial decline in FF demonstrates that the electrical quality of the cells deteriorates considerably before the maximum power limit is reached.

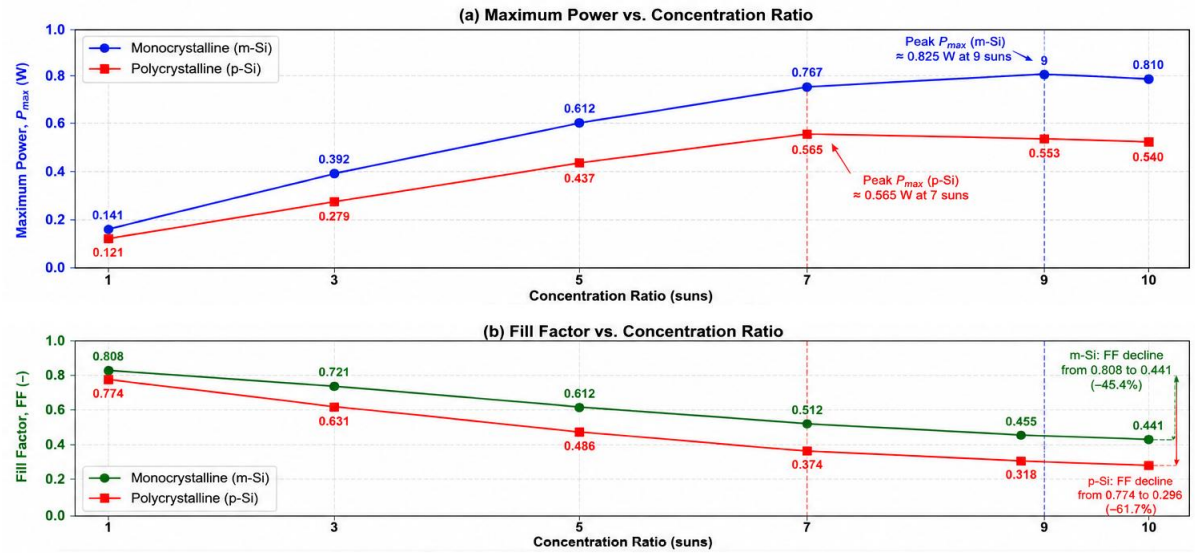

Figure 9: The effect of Concentration on Maximum Power and Fill Factor

3.5 Thermal Response and Its Effect on Efficiency

The temperature results provide the strongest explanation for the deterioration observed at high concentration. The monocrystalline cell temperature increased from 25°C at 1 sun to 89°C at 10 suns, whereas the polycrystalline cell reached 99°C.

Thus, at 10 suns, the polycrystalline cell operated approximately 10°C hotter than the monocrystalline cell.

This finding gives an evaluation of the thermal response of the cells under concentrated irradiance. It also confirms the central engineering limitation of CPV systems: additional irradiance increases electrical generation but simultaneously imposes a substantial thermal load.

The efficiency results demonstrate this trade-off particularly clearly. The monocrystalline cell reached a maximum efficiency of 14.0% at 3 suns before declining to 8.2% at 10 suns. The polycrystalline cell, in contrast, declined continuously from 12.1% at 1 sun to only 4.6% at 10 suns.

Therefore, although P_{max} continued to increase at concentrations considerably higher than the efficiency optimum, the fraction of incident solar energy converted into useful electricity decreased substantially. This distinction is crucial thus: the concentration that maximizes power is not necessarily the concentration that maximizes efficiency or provides the best overall operating condition.

The observed temperature dependence agrees with previous work demonstrating that elevated temperature negatively affects PV electrical performance (Dash & Gupta, 2015; Musanga et al., 2018; Mandadapu et al., 2017).

3.6 Significance in Relation to Existing Literature

Overall, the results agree with the general findings of previous irradiance studies: increased irradiance produces a strong increase in photocurrent, while voltage increases more slowly and

thermal effects increasingly constrain performance (Chegaar et al., 2013; Nasrin et al., 2018). The present study extends these findings by examining the response continuously across a controlled 1–10 sun concentration range and by comparing two crystalline-silicon technologies under the same experimental framework.

The study also supports previous comparisons showing that monocrystalline technology generally provides higher performance than polycrystalline technology (Amin et al., 2009; Komoni et al., 2018; Zdyb & Gulkowski, 2020; Galal et al., 2023). However, the present results add an important CPV-specific dimension by showing that the difference becomes more pronounced as thermal loading increases.

Most importantly, the results provide experimental evidence for the research gap identified in the introduction. Rather than considering irradiance, temperature, cell technology, and efficiency as separate factors, the study demonstrates their coupled interaction. Increasing concentration first provides a substantial current and power benefit, but beyond an optimum region, temperature rise and resistive losses increasingly dominate.

The practical implication is that CPV system designers should not simply maximize concentration. Instead, the concentration ratio should be selected according to the electrical and thermal characteristics of the particular cell technology. The superior thermal tolerance and wider acceptable concentration range observed for monocrystalline silicon make it the more appropriate option for the higher-flux operating conditions investigated in this study.

4. CONCLUSION

This study experimentally investigated the effects of concentrated solar irradiance on the overall performance of monocrystalline and polycrystalline silicon solar cells over a concentration range of 1–10 suns. The results demonstrated that increasing irradiance substantially increased short-circuit current and initially enhanced maximum power output in both cell technologies. However, the associated rise in cell temperature progressively reduced the fill factor and conversion efficiency at higher concentration levels. The monocrystalline cell consistently exhibited superior overall performance, including higher efficiency**,** lower series resistance (0.12 Ω compared with 0.15 Ω for the polycrystalline cell), lower thermal sensitivity, and a wider useful concentration range than the polycrystalline cell. The lower series resistance contributed to better current transport and fill-factor retention under increasing concentration. These findings have practical implications for CPV system design, particularly in selecting suitable cell technology, concentration ratio, and thermal-management requirements. The study was limited to the investigated crystalline-silicon cells, the 1–10 sun concentration range, and the experimental conditions employed. Future research should investigate active cooling techniques, wider concentration ranges, long-term thermal degradation, and larger-area commercial PV modules under controlled concentrated irradiance. Further studies should also evaluate the techno-economic implications of optimizing concentration and cooling simultaneously.

Acknowledgements The authors sincerely wish to acknowledge the Department of Electrical/Electronic Engineering, University of Abuja, Abuja, Nigeria, for providing a very conducive research atmosphere, and granting access to the Renewable energy laboratory, where all laboratory control experiments were carried out.

5. REFERENCES

Amin, N., Lung, C. W., & Sopian, K. (2009). A practical field study of various solar cells on their performance in Malaysia. *Renewable Energy, 34*(8), 1939–1946.

Bashir, M., et al. (2014). Comparison of performance measurements of photovoltaic modules during winter months in Taxila, Pakistan. *International Journal of Photoenergy, 2014*, 1–8.

Bazyomo, S. D., et al. (2026). Comparative efficiency assessment of polycrystalline, monocrystalline, and thin-film photovoltaic technologies under Burkina Faso's climatic conditions. *World Journal of Advanced Research*. https://doi.org/10.30574/wjarr.2026.29.1.0095

Chegaar, M., et al. (2013). Effect of illumination intensity on solar cells parameters. *Energy Procedia, 36*, 722–729.

Dash, P., & Gupta, N. (2015). Effect of temperature on power output from different commercially available photovoltaic modules. *International Journal of Engineering Research and Applications, 5*(1), 148–151.

Gol, A. E., & Ščasný, M. (2025); Dynamic impact of temperature, humidity, and dew point on photovoltaic power output: An empirical analysis of real-case hourly data. *J. Renewable Sustainable Energy* 1 November 2025; 17 (6): 063503. https://doi.org/10.1063/5.0303007

Karami, E., et al. (2017). Performance analysis of photovoltaic modules under different climatic conditions. *Journal of Fundamentals of Renewable Energy and Applications, 7*(3), 1–6.

Komoni, A., et al. (2018). Comparison of mono-Si and poly-Si photovoltaic modules under Kosovo climate. *Journal of Renewable and Sustainable Energy, 10*(1).

Mandadapu, U., et al. (2017). Effect of temperature and irradiance on the electrical performance of a PV module. *International Journal of Advanced Research, 5*(7), 2018–2027.

Musanga, L., et al. (2018). The effect of irradiance and temperature on the performance of monocrystalline silicon solar module. *Physical Sciences International Journal, 19*(4), 1–9.

Nasrin, R., et al. (2018). Effect of high irradiation on photovoltaic power and energy. *International Journal of Energy Research, 42*(3), 1115–1131.

Ray, M., et al. (2023). Performance evaluation of mono and poly solar cells. *International Journal of Energy and Environmental Engineering, 14*.

Rosyid, O. (2016). Comparative performance testing of photovoltaic modules in tropical climates of Indonesia. In *AIP Conference Proceedings*.

Ye, J., et al. (2013). Outdoor PV module performance under fluctuating irradiance conditions. *Energy Procedia, 33*, 238–247.

Zdyb, A., & Gulkowski, S. (2020). Performance assessment of four different photovoltaic technologies in Poland. *Energies, 13*(1), 196.

TRACK 5 OF 11

Green Mobility and Next Generation Automobile Technologies

International Conference on Engineering Innovation for Sustainable Development (ICESID 2026)

Faculty of Engineering, Ahmadu Bello University Zaria · 8–10 September 2026

https://icesid.org

International Conference on Engineering Innovation for Sustainable Development (ICESID 2026)
Faculty of Engineering, Ahmadu Bello University Zaria · 8–10 September 2026

CFD-DRIVEN THERMAL ANALYSIS AND CLIMATE-ADAPTIVE OPTIMIZATION OF LITHIUM-ION EV BATTERY USING DIFFERENT COOLING MEDIA AND STATISTICAL TECHNIQUES

Abubakar Unguwanrimi Yakubu[1,*], Fahim Ullah[2], Wang Jiongfan[2], Shusheng Xiong[2], Jiahao Zhao[2], Xuanhong Ye[2]

[1]*College of Energy Engineering, Zhejiang University, China*
[2]*College of Energy Engineering, Zhejiang University, Hangzhou, 310027, China College of Computing, Engineering and Science, Kaduna State University, Kaduna, 800283, Nigeria Longquan Industrial Innovation Research Institute, Longquan, 323700, China Provinci*

Email: yakabu3002@gmail.com*, fahimullah@zju.edu.cn, 12427127@zju.edu.cn, xiongss@zju.edu.cn, DC_zjh@outlook.com, 12327023@zju.edu.cn

***Corresponding author**: Abubakar Unguwanrimi Yakubu

DOI: https://doi.org/10.67203/sp.ICESID.2026

ABSTRACT

Managing the thermal performance of lithium-ion batteries in electric vehicles (EVs) poses significant challenges due to the wide range of climatic conditions. This paper presents a thorough Computational Fluid Dynamics (CFD) analysis to evaluate the thermal behavior and climate-adaptive optimization of a 21-cell 18650 lithium-ion battery pack. We investigated six cooling methods: ethylene glycol (EG) solutions at 20%, 40%, and 60%; mineral oil at flow rates of 0.03 m/s and 0.05 m/s; and forced-air cooling. The results indicated that the 40% EG solution provided the best overall performance, achieving a cooling efficiency of 91.7%, a temperature rise of just 0.70 K, and a pumping power requirement of 29.5 W. While the mineral oil at 0.05 m/s demonstrated the highest heat rejection capacity of 174.88 W, it consumed 3.2 times more pumping energy compared to the 20% EG solution. Statistical analysis using ANOVA showed that operating temperature (69.7%), coolant concentration (18.3%), and flow rate (9.2%) are the primary factors influencing BTMS performance. Based on our findings, we propose a climate-dependent coolant selection strategy: 20% EG for hot climates (above 35°C), 40% EG for moderate climates (between 20°C and 35°C), and 50-60% EG for cold climates (below 0°C). Notably, forced air cooling performed poorly, rejecting 45% less heat than the 40% EG solution. Additionally, regression models with R^2 values greater than 0.99 provide quantitative design guidelines for BTMS. This research challenges the SAE J1034 recommendation to use 50% EG across all climates and provides a validated framework for designing climate-adaptive BTMS solutions.

Keywords: *Lithium-ion battery; BTMS; Ethylene glycol coolant; Heat extraction; Electric vehicle; Climate-adaptive cooling*

1. Introduction

Lithium-ion batteries (LIBs) are the most efficient energy storage solution for electric vehicles (EVs), portable devices, and renewable energy systems (Sankaran and Venkatesan, 2022) Global EV sales are projected to exceed 17.1 million units in 2024, representing a 25% increase from the previous year Adhikari et al., (2024). By 2030, EVs are expected to make up 30-40% of global automobile sales, with some countries exceeding 50% (Nogueira, 2022., Zhao et al., 2020 and Reitz et al.,2020).

Effective thermal management is essential for the performance, reliability, and safety of LIBs. Temperature strongly influences electrochemical kinetics, internal resistance, energy conversion efficiency, and degradation rates Madani., 2023., Boretti .et al., 2025, Song et al., 2020) . For instance, a 15°C increase in operating temperature can reduce cycle life by 50%, while a 0.1V change in charging voltage can accelerate degradation (Song et al., 2022). High temperatures may also trigger thermal runaway, resulting in irreversible exothermic reactions and potential fires (Wang et al., 2023., Song et al., 2022). At the pack level, temperature differences greater than 5°C can accelerate capacity fading and increase internal resistance (Yifan et al.,.2024, Liu et al.,2026, Gao et al., 2026 and Liu et al., 2021)

Researchers have developed several BTMS, including air cooling, liquid cooling, phase change material (PCM) cooling, heat pipes, and hybrid systems (Fasolato et al., 2025). While air cooling is simple and cost-effective, it has limited heat transfer capacity and poor temperature uniformity, making it unsuitable for high-power electric vehicles (EVs) (Dhuchakallaya et al., 2023., Zhang et al., 2023). Liquid cooling has emerged as the preferred solution due to its superior thermal conductivity and heat capacity (Akbarzadeh et al., 2021., Ye 2023).

Among liquid coolants, water-ethylene glycol (EG) solutions are most common because they balance heat-transfer efficiency and freeze protection. The SAE J1034 standard recommends a 50% ethylene glycol concentration for all climates (Khaboshan et al., 2023). However, this composition can reduce cooling performance in warmer conditions because it has higher viscosity and 15% lower specific heat capacity (Fu et al., 2024., Li et al., 2025). While a concentration of 50-60% EG is necessary for cold climates (those below -20°C), lower concentrations are sufficient for tropical regions (Chung-Camargo et al., 2024).

Recent advancements in coolant technologies show promise: silica-water nanofluids have been found to increase the Nusselt number by 22.6% (Yang et al., ., 2024), ferrofluid cooling combined with porous copper foam can reduce battery temperatures by 13% (Zhang et al., 2024), and liquid-air BTMS utilizing long short-term memory (LSTM) networks achieve a prediction accuracy of 99% (Zhou et al., 2024). Despite these innovations, ethylene glycol (EG) solutions and mineral oil remain the most practical coolants for commercial electric vehicles (EVs).

Comparative studies examining various BTMS types under identical transient conditions are lacking. Climate effects on battery performance have not been sufficiently considered, with potential variations of 20-40% (Chung-Camargo et al., 2024). Few studies have examined the optimal EG concentration across different climates. Three-dimensional computational fluid dynamics (CFD) modeling is lacking to optimize coolant performance under transient conditions. Statistical techniques (such as ANOVA and DMRT) are rarely used to assess the significance of operational variables.

How do different coolant types and concentrations affect battery temperature, heat transfer, pressure drop, and pumping power under transient conditions? What EG concentration strikes the optimal balance between cooling effectiveness and freeze protection in hot, temperate, and cold climates? This work contributes to battery thermal management research by thoroughly analyzing coolant effectiveness for lithium-ion batteries under changing climate conditions. In contrast to prevailing studies that apply a 50% ethylene glycol (EG) ratio without accounting for regional climate differences, this research questions this common practice. Using computational fluid dynamics (CFD) and statistical calculations, we show that the ideal EG ratio depends strongly on surrounding conditions. Together, these efforts will help us better understand battery thermal management in light of climate change and provide important recommendations in this field.

2. LITERATURE REVIEW

2.1 Air Cooling Systems

Air cooling is the simplest BTMS and was commonly used in early-generation EVs due to its low cost and ease of implementation (Dhuchakallaya et al., 2023). However, this method creates temperature gradients of 5-10°C and becomes ineffective at discharge rates exceeding 2C (Zhang et al., 2023). Although increasing air velocity can help reduce peak temperatures, it adversely affects temperature uniformity (Xia et al., 2025). As a result, air cooling is best suited for low-power applications and mild environmental conditions (Akbarzadeh et al., 2021).

2.2 Liquid Cooling Systems

Liquid cooling systems provide superior performance because they have specific heat capacities 4 to 5 times that of air (. Boretti ., 2025). Optimized cooling channels in liquid systems can enhance cooling efficiency by 20-35% compared to air-cooled systems (Akbarzadeh et al., 2021, Ye., 2023). However, the Society of Automotive Engineers (SAE) commonly recommends a 50% ethylene glycol (EG) solution, which is not tailored to specific climates (Khaboshan et al., 2023).

2.3 Heat Pipe Cooling

Heat pipes work by evaporation and condensation, offering thermal conductivity 100 to 200 times greater than copper (Hung et al., 2023). Flat heat pipes can maintain temperature differences of less than 1.5°C (Kumar et al., 2023). Nevertheless, they are limited to medium power applications (≤50 W per cell) (Kumar et al., 2023). and are less effective at low temperatures.

2.4 Phase Change Material (PCM) Cooling

Phase Change Material (PCM) based BTMS utilizes latent heat absorption for passive thermal management, maintaining temperature differences of less than 0.2°C (Paul et al., 2025). PCM systems effectively prevent thermal runaway, with optimal melting temperatures ranging from 40 to 45°C (Shen et al., 2024). However, PCM has some limitations, including low latent heat storage capacity, poor thermal conductivity <u>(less than 0.2 W/m·K) (Shen et al., 2024)., potential leakage issues, and increased weight (Shen et al., 2024).. Additionally, PCM layers can completely melt after a few discharge cycles, indicating rapid saturation under cyclic conditions (Liu et al., 2021).

2.5 Hybrid Cooling Systems

Hybrid BTMS combine multiple strategies to address the limitations of individual methods (see Table A1) (Boretti, 2025 and Fasolato, 2025)). For example, phase change material (PCM)-air hybrid systems can lower temperatures by 24.6°C while maintaining temperature gradients of less than 2°C [34]. PCM-liquid systems achieve a minimum temperature of 37.13°C (Paul et al., 2025). PCM-heat pipe hybrids can control temperature differences to below 1°C at a 3C discharge rate (Kumar et al., 2023). Additionally, recent liquid-air BTMS that use Long Short-Term Memory (LSTM)-based temperature forecasting have achieved an impressive accuracy of 99.1% (Boretti, 2025). However, it is important to note that hybrid systems can introduce increased complexity, additional weight, and higher energy demands from pumps (Boretti, 2025; Akbarzadeh et al., 2021).

3. MODEL DEVELOPMENT

Lithium-ion batteries are complex electrochemical energy storage devices that involve many coupled processes, including electrochemical reactions, mass transfer, charge transfer, heat transfer, and fluid dynamics. In this study, we propose a holistic, multiscale, multiphysics model that combines electrochemical and thermal models, an SEI formation model, a fluid-dynamics model, a heat-transfer model, and an electrical circuit model.

3.1 Battery Cell Specifications

This study selected the 18650 lithium-ion battery cell. Table 1 summarizes its thermophysical properties.

Table 1: Thermophysical properties of the components

S/No.	Specification	Value
1	Cell Capacity	13 Wh
2	Normal Cell Voltage	3.2 V
3	Max. Cell Voltage	3.7 V
4	Temperature under Load	300.12 K
5	Specific Heat Capacity of Cell	1200 J/kg·°C
6	Mass	0.0475 kg
7	Thermal conductivity (radial)	0.2 W/m·K
8	Thermal conductivity (axial)	37.6 W/m·K
9	Internal Resistance	0.04 Ω
10	Cathode	Lithium cobalt oxide ($LiCoO_2$)
11	Anode	Graphite
12	Electrolyte	Lithium hexafluorophosphate ($LiPF_6$)

3.2 Module Configuration

The battery module is configured as 11 parallel cells and 39 series cells (11p39s). This setup totals 429 cells per module, with three modules operating in parallel. The normal operating voltage is 124.8 V, while the peak voltage can reach 144.3 V.

3.3 Electrochemical-Thermal Modeling

3.3.1 Chemical Reactions

The complete electrochemical reaction for the $LiCoO_2$/graphite cell.

$$P_r = \frac{\mu C_p}{k} \tag{1}$$

3.3.2 Heat Generation

Reversible heat generation (entropy-related)

$$Q_{irrev} = IT\frac{\delta E_{ocv}}{\delta T} \tag{2}$$

Irreversible heat generation (polarization and Joule heating

$$Q_{irr} = I^2 \times R \tag{3}$$

Total heat generation

$$Q_{total} = Q_{rev} + Q_{irr} = IT\frac{\delta E_{ocv}}{\delta T} + I^2 R \tag{4}$$

IT = current
T = temperature (K)
$\frac{\delta E_{ocv}}{\delta T}$ = entropic coefficient (V/K)
R = internal resistance (Ω)

3.4 Computational Fluid Dynamics Setup

The CAD model features 18650 cells (18 mm × 65 mm) with aluminum-wrapped cooling channels (1 mm thickness). Channel specifications include a cross-sectional area of 1,092 mm², with 21 channels per module arranged in a sequential-parallel configuration

Continuity

$$\frac{\delta \rho}{dt} + \nabla.\left(\rho \vec{u}\right) = 0 \tag{5}$$

ρ = density (kg/m³)
t = time (s)
u = velocity vector (m/s)

Momentum

$$\frac{\delta \rho}{dt}\left(\rho \vec{u}\right) + \nabla.\left(\rho \vec{u}\vec{u}\right) = -\nabla \rho + \nabla.\left(\mu \nabla u\right) + \rho \vec{g} \tag{6}$$

p = pressure (Pa)
μ = dynamic viscosity (kg/m·s)
g = gravitational acceleration (m/s²)

Energy

$$\frac{\delta}{\delta t}\left(\rho C_p T\right) + \nabla.\left(\rho C_p u T\right) = \left(k_{eff} \nabla T\right) + Q \tag{7}$$

Where:
Cp = specific heat capacity at constant pressure (J/kg·K)
T = temperature (K)
keff = effective thermal conductivity (W/m·K)
˙Q˙ = volumetric heat generation rate (W/m³)

$$k_{eff} = \varepsilon k_f + \left(1 - \varepsilon\right) k_s \tag{8}$$

Where:
k_{eff} = thermal conductivity of the fluid phase
εk_f = thermal conductivity of the solid phase
ε = porosity of the medium

The solver settings included a 3D transient simulation with the standard k-ε turbulence model and enhanced wall treatment, which ensures accurate predictions near the wall. The pressure-velocity coupling was managed using the SIMPLE method, with second-order spatial discretization and first-

order implicit temporal discretization. The convergence criteria were set at 10^{-6} for energy and 10^{-4} for continuity.

The Prandtl number is defined as:

$$P_r = \frac{\mu C_p}{k} \tag{9}$$

Where:
μ = dynamic viscosity (kg/m·s^{-1})
Cp = specific heat capacity (J/kg·K)
k = thermal conductivity (W/m·K)

3.5 Mesh Independence Study

A mesh independence study used meshes ranging from 0.2 to 1.0 million elements, with maximum battery surface temperature as the convergence metric. The mesh with 316,520 cells was selected as optimal, since further refinement resulted in a deviation of less than 2%. The quality metrics for this mesh included an aspect ratio of 19.69, a Y+ value of 1.8, a skewness of 0.298, and an orthogonal quality of 0.318.

Table 2: Mesh Independence Study

Elements	ΔT (K)	Deviation (%)
125,973	1.42	---
165,841	1.38	2.82%
316,520	1.31	5.07%
517,866	1.28	2.29%
1,127,740	1.27	0.78%

3.6 Coolant Properties

Table 3: Properties of Ethylene Glycol Solutions at 300 K

Concentration	Density (kg/m³)	C_p (J/kg·K)	μ (kg/m·s)	k (W/m·K)	Prandtl Number
20%	1046	3828	0.00259	0.487	20.4
40%	1079	3413	0.00391	0.385	30.2
60%	1095	3284	0.00536	<u>0.400</u>	44.0

Table 4: Air and Mineral Oil Properties

Property	Air	Mineral Oil
Density (kg/m³)	1.225	924
C_p (J/kg·K)	1006.43	1900
μ (kg/m·s)	1.7894×10^{-5}	0.05
k (W/m·K)	0.0242	0.13
Prandtl Number	0.71	730.8

3.7 Model Verification

Cross-platform verification between ANSYS Fluent and MATLAB/Simulink showed excellent agreement, as shown in Table 5, with a temperature-rise deviation of 2.86%, which is well within acceptable limits.

Table 5: Cross-Platform Verification Results (40% EG)

Parameter	Symbol	CFD (ANSYS Fluent)	MATLAB/Simulink	Absolute Deviation	Relative deviation (%)
Heat generation per cell	$\dot{Q}_{gen}(W)$	0.80	0.80	0.00	0
Heat extraction per 7 cells	$\dot{Q}_{ext}(W)$	5.60	5.60	0.00	0
Temperature rise	$\Delta T\,(K)$	0.70	0.72	0.02	2.86

Sensitivity analysis showed that the coolant inlet temperature (rank 1, ±2.5 K), the heat generation rate (rank 2, ±1.8 K), and the material's thermal conductivity (rank 3, ±0.5 K) are the key parameters influencing BTMS performance.

4. RESULTS AND DISCUSSION

4.1 Combined Performance Summary

Table 6 presents performance data for all six cooling systems. Thermal and hydraulic efficiency are inversely correlated.

Table 6: Combined Performance of Six Cooling Methods

Cooling Method	Concentration/Velocity	Pressure Drop (Pa)	Pumping Power (W)	Heat Removal (W)	Performance Ratio (W/W)
Ethylene Glycol 20%	20% v/v	105,032	29.2	119.78	4.10
Ethylene Glycol 40%	40% v/v	106,220	29.5	134.95	4.57
Ethylene Glycol 60%	60% v/v	107,245	29.8	149.88	5.03
Mineral Oil	0.03 m/s	108,030	30.0	159.85	5.33
Mineral Oil	0.05 m/s	109,075	30.3	174.88	5.77
Air Cooling	8 m/s	101,525	0	79.93	N/A

4.2 Thermal Performance of Ethylene Glycol Coolants

(a)

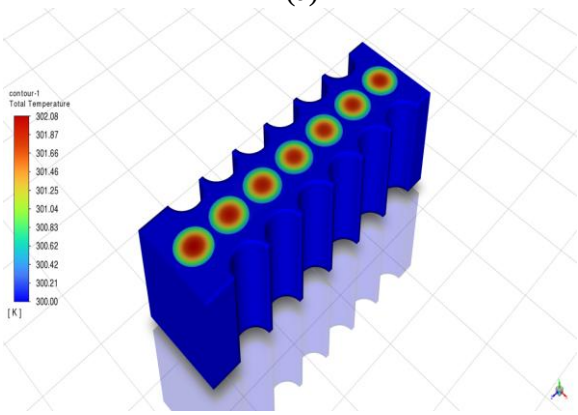

(b)

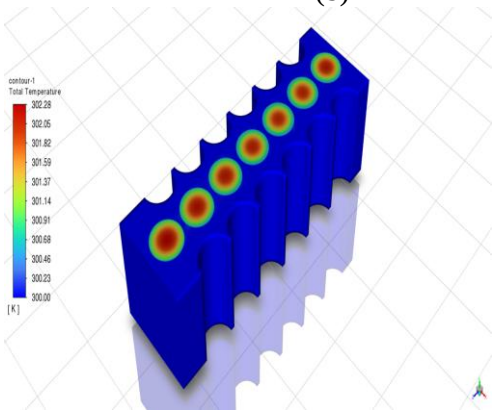

(c)

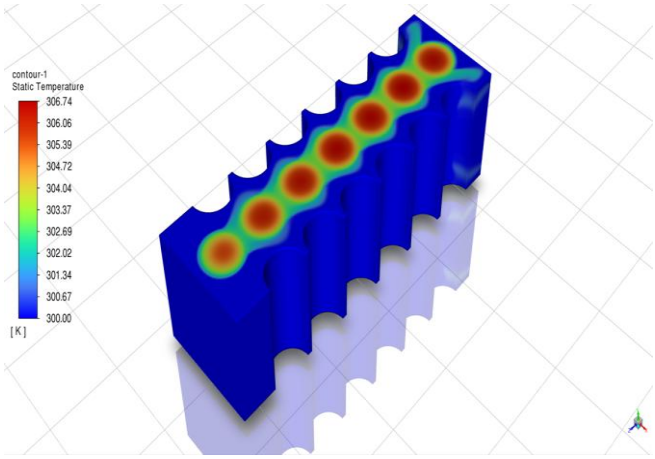

Figure 1: Temperature Contours for Ethylene Glycol Solutions: (a) 20% EG, (b) 40% EG, (c) 60% EG

Fig. 1 presents the temperature contours of ethylene glycol (EG) solutions after 300 s of operation, showing the spatial distribution of surface temperatures for different EG concentrations: (a) 20% EG, (b) 40% EG, and (c) 60% EG. All contours used the same temperature scale (298–305 K) to allow direct comparison among formulations. Across all cases, the highest temperatures were concentrated in the central cells, where constrained heat-transfer pathways limited thermal dissipation and resulted in localized heat accumulation.

The EG concentration significantly influenced the cooling performance. Among the tested formulations, 40% EG exhibited the most effective thermal regulation, achieving the lowest maximum surface temperature of 300.70 K, corresponding to a temperature increase of only 0.70 K above the inlet temperature (300 K). This resulted in the highest cooling efficiency (91.7%). In comparison, the 20% EG solution reached a maximum temperature of 301.15 K ($\Delta T = 1.15$ K), with a cooling efficiency of 86.3%. The 60% EG solution showed the poorest thermal performance, with the highest maximum temperature of 302.08 K ($\Delta T = 2.08$ K) and a reduced cooling efficiency of 75.3%. This deterioration is attributed to the increased viscosity of the concentrated EG solution (0.00536 kg m^{-1} s^{-1}), which restricts convective heat transfer and reduces the fluid's ability to remove heat efficiently.

Overall, the temperature distributions demonstrate that an intermediate EG concentration provides an optimal balance between thermal capacity and fluid mobility. The superior performance of the 40% EG solution indicates enhanced heat transport within the cooling channels. In contrast, both lower and higher concentrations exhibit reduced effectiveness due to insufficient thermal absorption capacity and increased flow resistance, respectively.

4.3 Direct Cooling Using Mineral Oil

Mineral oil immersion cooling demonstrated superior thermal performance because it eliminated thermal resistance from the cooling walls. The temperature rise was only 0.30 K at a flow rate of 0.05 m/s, with a heat removal capacity of 174.88 W, the highest among all methods tested. This represents a 29.6% increase in heat removal capacity compared to the 40% ethylene glycol (EG) indirect cooling system (174.88 W vs. 134.95 W). However, this method poses hydraulic challenges. The pressure drop was measured at 109,075 Pa, which is 4% higher than that of the 40% EG system (109,075 Pa vs. 106,220 Pa). Consequently, it requires 3.2 times more pumping power per unit of heat removed than a 20% EG system. At a flow rate of 0.05 m/s, the required pumping power is 30.3 W. While acceptable for high-performance applications, this indicates a significant hydraulic penalty.

4.4 Forced Air Cooling

Air cooling performed the worst, removing only 79.93 W of heat—45% less than the 40% EG solution. The temperature rise was 0.14 K over 300 seconds, indicating that thermal equilibrium was not reached. With a heat generation rate of 0.80 W per cell and a removal capacity of only 3.81 W per cell, 39% of the total heat generated remains within the battery, leading to gradual heating. The pressure drop was 101,525 Pa, with no pumping power required (fan power excluded from hydraulic comparison). This further confirms that air cooling is inadequate for high-power electric vehicle (EV) applications.

4.5 Analysis of Variance (ANOVA)

The ANOVA results (Table 7) indicate that all second-order response surface models are highly significant ($p < 0.0001$), with F-values ranging from 407.96 to 3186.06. The coefficients of determination ($R^2 = 0.9913$-0.9989) indicate that the models explain over 99% of the variation in battery temperature, heat removal rate, temperature increment, and pressure drop.

Table 7: ANOVA Regression Statistics

Response	R^2	F-value	p-value	CV (%)	Root MSE
Temperature (K)	0.991	407.96	<0.0001	0.083	0.244
Heat Extraction (W)	0.999	3186.06	<0.0001	0.875	1.194
ΔT (K)	0.998	1877.01	<0.0001	1.343	0.269
Max. Pressure (Pa)	0.998	1651.84	<0.0001	0.124	131.904

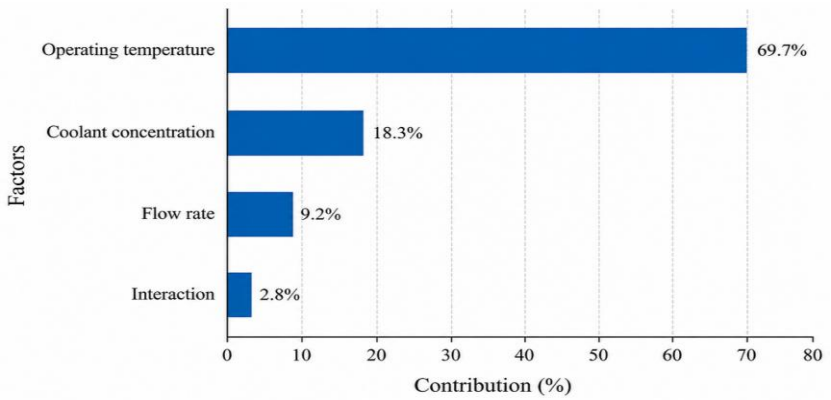

Figure 2: Pareto diagram showing the standardized effects of input parameters on battery

Figure 2: Pareto diagram of standardized effects on battery maximum temperature. The bars represent each factor's relative contribution to the BTMS thermal performance. Operating temperature (69.7%) is the most influential parameter, followed by coolant type (18.3%), flow rate (9.2%), and interaction effects (2.8%).

4.6 Regression Analysis and Duncan's Multiple Range Test (DMRT)

We developed regression relationships using combined data from all six cooling methods (20% EG, 40% EG, 60% EG, mineral oil at 0.03 m/s, mineral oil at 0.05 m/s, and air cooling). These empirical correlations provide a rapid way to estimate key thermal-hydraulic performance parameters without additional CFD simulations. The equations apply within the heat-removal range of Q = 79.93 W to Q = 174.88 W, corresponding to the minimum (air cooling) and maximum (mineral oil at 0.05 m/s) values observed in this study.

These regression models exhibit high coefficients of determination ($R^2 > 0.94$), indicating that they explain at least 94% of the variance in the respective response variables. The negative coefficients for Q in the temperature equations indicate that higher heat removal rates result in lower battery temperatures, consistent with physical expectations. Conversely, the positive coefficient for Q in the pressure drop equation reflects the increased frictional losses associated with higher flow rates required to achieve greater heat removal.

The DMRT results (Table 8) confirm statistically significant differences between all cooling methods ($p < 0.0001$), with mineral oil at 0.05 m/s ranked highest (Group a) and air cooling ranked lowest (Group f).

Table 8: DMRT Mean Separation Results

Cooling Method	Min Temp. (K)	Heat Extraction (W)	ΔT (K)	Max. Pressure (Pa)
Air Cooling	297.95a	79.93f	30.05a	101,525f
EG 20%	294.93b	119.78e	23.05b	105,032.5e
EG 40%	294.03c	134.95d	20.08c	106,220d
EG 60%	292.95d	149.88c	17.05d	107,245c
Mineral Oil 0.03	291.95e	159.85b	16.00e	108,030b
Mineral Oil 0.05	291.03f	174.88a	14.08f	109,075a

Different letters indicate statistically significant differences ($p < 0.0001$)

The DMRT confirms mineral oil at 0.05 m/s is statistically superior (Group a), while air cooling is statistically inferior (Group f).

4.7 Climate-Adaptive BTMS Design Roadmap

Based on thorough thermodynamic and hydrodynamic analyses, the following recommendations are made for different climate conditions:

Hot climates (>35°C): use a 20% ethylene glycol (EG) solution. This solution has a high specific heat capacity of 3828 J/kg·K and a low viscosity of 0.00259 kg/m·s, both of which promote efficient heat exchange. Heat removal capacity is 119.78 W, resulting in a temperature rise of 1.15 K, yielding a cooling efficiency of <u>86.3%</u>. Freeze protection is down to -10°C. Moderate climates (20-35°C): Employ a 40% EG solution for optimal thermal effectiveness and freeze protection. This solution can remove heat at 134.95 W, resulting in a temperature rise of 0.70 K and 91.7% cooling efficiency. The freeze protection is effective down to -25°C. In cold climates (< 0°C), use a 50-60% EG solution, which provides freeze protection down to -32°C. This solution removes 149.88 W of heat, but it causes a temperature rise of 2.08 K, resulting in a cooling efficiency of 75.3%. Note that the higher viscosity of 0.00536 kg/m·s can reduce heat transfer efficiency. High-performance applications: Consider using mineral-oil immersion cooling at a flow rate of 0.05 m/s. This method removes 174.88 W of heat with a minimal temperature rise of 0.30 K; however, it requires 30.3 W of additional pumping

power and increases system complexity. Air Cooling: This method is not recommended for high-power electric vehicle applications.

5. CONCLUSION

This study compared six cooling techniques for a 21-cell 18650 Li-ion battery pack using 3D transient CFD modeling.

The optimal coolant, a 40% ethylene glycol (EG) solution, provides the best thermal-hydraulic balance, resulting in a temperature rise of 0.70 K, a cooling efficiency of 91.7%, and a pumping power of 29.5 W. This challenges the SAE J1034 recommendation of a 50% EG solution for all climates. In hot climates (>35°C), a 20% EG solution achieves 119.78 W of heat removal with a 1.15 K temperature rise and provides -10°C freeze protection. In moderate climates (20-35°C), a 40% EG solution provides 134.95 W of heat removal, a 0.70 K temperature rise, and -25°C freeze protection. In cold climates (<0°C), a 50-60% EG solution removes 149.88 W of heat, resulting in a 2.08 K temperature rise and -32°C freeze protection. Mineral oil. This option achieves the highest heat removal (174.88 W) with a temperature rise of just 0.30 K; however, it requires 3.2 times the pumping power of the 20% EG solution. It is best suited for high-performance applications. Air cooling: This method removes only 79.93 W, 45% less than the 40% EG solution, and fails to achieve thermal equilibrium. Therefore, it is not suitable for high-power electric vehicles (EVs). Statistical significance: An ANOVA analysis indicates that operating temperature (69.7%), coolant concentration (18.3%), and flow rate (9.2%) are the primary influencing parameters. DMRT confirms significant differences between all methods ($p < 0.0001$).

Predictive models: The developed regression equations, with R^2 values greater than 0.99, enable accurate performance predictions without CFD computations.

This study challenges the universal recommendation for a 50% EG solution, provides quantitative relationships between climate and coolant types, presents the first comparative analysis of six cooling techniques under identical conditions, validates findings using ANOVA and DMRT, and proposes a climate-based design strategy for EV manufacturers. Future directions include experimental validation, extending simulations up to 600 seconds, conducting C-rate sensitivity analyses (2C-5C), exploring nano-enhanced coolants, performing aging studies (500-1000 cycles), and executing multi-objective optimization that considers thermal, hydraulic, cost, weight, and reliability factors.

ACKNOWLEDGMENT

The authors acknowledge the support of the Student Innovation Center at the College of Energy Engineering, Zhejiang University, China. This work was funded by the China central government's guidance on local science and technology development funds, project name: Construction of Provincial Key Laboratory for Thermal Management of New Energy Vehicles, project number: 2025ZY01026.

REFERENCES

Adhikari, N., Bhandari, R., & Joshi, P. (2024). Thermal analysis of lithium-ion battery of electric vehicle using different cooling medium. *Applied Energy, 360*, 122781.

Akbarzadeh, M., et al. (2021). A comparative study between air cooling and liquid cooling thermal management systems for a high-energy lithium-ion battery module. *Applied Thermal Engineering, 198*, 117503.

Boretti, A. (2025). Advanced battery thermal management: A review of materials, cooling systems, and intelligent control for safety and performance. *Energy Storage, 7*(7), e70273.

Chung-Camargo, K., et al. (2024). Advances in retrofitting strategies for energy efficiency in tropical climates: A systematic review and analysis. *Buildings, 14*(6), 1633.

Dhuchakallaya, I., & Saechan, P. (2023). Enhancing the cooling efficiency of the air cooling system for electric vehicle battery modules through liquid spray integration. *Journal of Energy Storage, 72*, 108751.

Fasolato, S. (2025). *Modeling, estimation, and cell-to-cell heterogeneity analysis in lithium-ion battery systems*.

Fu, H., et al. (2024). The research and application of technology and core components in commercial refrigeration and freezing systems: A review. *Journal of Stored Products Research, 108*, 102400.

Khaboshan, H. N., et al. (2023). Improving the cooling performance of cylindrical lithium-ion battery using three passive methods in a battery thermal management system. *Applied Thermal Engineering, 227*, 120320.

Kumar, R., et al. (2024). Different energy storage techniques: Recent advancements, applications, limitations. *Journal of Thermal Analysis and Calorimetry, 149*(5), 1895–1933.

Li, W., et al. (2025). Optimization of PCM passive cooling efficiency on lithium-ion batteries based on coupled CFD and ANN techniques. *Applied Thermal Engineering, 259*, 124874.

Liu, F., et al. (2021). Performance analysis of phase change material in battery thermal management with biomimetic honeycomb fin. *Applied Thermal Engineering, 196*, 117296.

Liu, Q., et al. (2026). Battery fault: A comprehensive dataset and benchmark for battery fault diagnosis—the Fourteenth International Conference on Learning Representations.

Liu, Y., Xia, Y., & Zhou, Q. (2021). Effect of low-temperature aging on the safety performance of lithium-ion pouch cells under mechanical abuse conditions. *Energy Storage Materials, 40*, 268–281.

Nogueira, T., Sousa, E., & Alves, G. R. (2022). Electric vehicles' growth until 2030: Impact on the distribution network power. *Energy Reports, 8*, 145–152.

Paul, D., et al. (2025). A comprehensive review on lithium-ion battery thermal management (BTM) using phase change materials. *Journal of Thermal Analysis and Calorimetry, 150*(12), 9669–9722.

Reitz, R. D., et al. (2020). IJER editorial: The future of the internal combustion engine. *International Journal of Engine Research, 21*(1), 3–10.

Song, L., et al. (2020). Lithium-ion battery pack equalization based on charging voltage curves. *International Journal of Electrical Power & Energy Systems, 115*, 105516.

Song, L., et al. (2022). Review on thermal runaway of lithium-ion batteries for electric vehicles. *Journal of Electronic Materials, 51*(1), 30–46.

Suresh Kumar, R., et al. (2023). A review on the performance of oscillating heat pipe used in battery cooling. *Environmental Quality Management, 33*(2), 59–67.

Wang, Y., et al. (2023). Challenges and opportunities to mitigate the catastrophic thermal runaway of high-energy batteries. *Advanced Energy Materials, 13*(15), 2203841.

Xia, Z., et al. (2025). The influence of air temperature on heat transfer coefficient under forced air-cooling conditions. *International Journal of Heat and Fluid Flow, 112*, 109741.

Ye, J., Aldaher, A. Y. M., & Tan, G. (2023). Thermal performance analysis of 18650 battery thermal management system integrated with liquid-cooling and air-cooling. *Journal of Energy Storage, 72*, 10876.

Zhang, L., et al. (2024). Heat transfer performance study of Cu-ethanol/ethylene glycol/propylene glycol-water nanofluids. *Journal of Environmental Chemical Engineering, 12*(3), 112738.

Zhang, X., et al. (2023). Ultra-thermostable embedded liquid cooling in SiC 3D packaging power modules of electric vehicles. *Energy Conversion and Management, 276*, 116499.

Zhao, F., et al. (2020). Challenges, potential and opportunities for internal combustion engines in China. *Sustainability, 12*(12), 4955.

Zhou, N., et al. (2024). Experimental investigation on spray cooling heat transfer properties of ethylene glycol–water-based nanofluids. *Journal of Thermal Science and Engineering Applications, 16*(10), 101011.

International Conference on Engineering Innovation for Sustainable Development (ICESID 2026)
Faculty of Engineering, Ahmadu Bello University Zaria · 8–10 September 2026

DEVELOPMENT OF A CYCLONIC LIQUID SPRAY SCRUBBER FOR EMISSION CONTROL

Hamisu Adamu Dandajeh[1,*], Tasiu Salisu Abubakar[1]
[1]*Ahmadu Bello University*
Email: hadandajeh@abu.edu.ng[*], ""
***Corresponding author**: Hamisu Adamu Dandajeh
DOI: https://doi.org/10.67203/sp.ICESID.2026

ABSTRACT

This study presents the design, fabrication, and performance evaluation of a cyclonic liquid spray scrubber for controlling exhaust emissions from an internal combustion engine. The scrubber was fabricated from mild steel and equipped with an exhaust gas inlet and outlet. Its performance was evaluated using the exhaust emissions from a four-stroke, single-cylinder gasoline engine. Emission measurements were conducted using a Brain Bee Automotive Gas Analyzer located in the Heat Engine Laboratory, Department of Mechanical Engineering, Ahmadu Bello University, Zaria. The scrubber was connected to the engine exhaust system, and emission levels were measured under identical operating conditions with and without the scrubber. The results showed that the scrubber reduced the concentrations of carbon monoxide (CO), carbon dioxide (CO_2), and unburned hydrocarbons (HC) by 15.6%, 9% and 19% respectively and surprisingly increased excess oxygen (O_2) emissions by approximately 2%. The average equivalence ratio decreased from 0.2595 without the wet scrubber to 0.2250 with the wet scrubber. Although the prototype exhibited demonstrable effectiveness under the test conditions, the study establishes the feasibility of developing a cyclonic liquid spray scrubber for exhaust gas treatment. With further optimization of its design and operating parameters, the system has the potential to reduce emissions from both stationary and mobile combustion sources.

Keywords: *Emission Control; Cyclonic; Liquid Scrubber; Gas Analyser; Exhaust*

1. INTRODUCTION

Air pollution remains a major environmental and public-health challenge, especially in rapidly urbanising and industrialising countries such as Nigeria. Increasing energy demand, vehicular activity, industrial production, open waste burning, biomass combustion, diesel generation and artisanal petroleum refining has heightened to emissions. Such emissions include particulate matter (PM), carbon monoxide (CO), nitrogen oxides (NO_x), sulphur dioxide (SO_2), volatile organic compounds (VOCs), and other hazardous pollutants. Recent studies in the Niger Delta have reported significant pollution from petroleum-related and artisanal refining activities, with potential consequences for respiratory health and the wider environment (Ephraim-Emmanuel *et al.*, 2023; Onakpohor *et al.*, 2020; Igibah *et al.*, 2024).

Exposure to fine particulate matter and gaseous pollutants is linked to respiratory and cardiovascular diseases, lung cancer and premature mortality. Globally, air pollution was associated with approximately 7.9 million deaths in 2023, while Nigeria recorded more than 200,000 attributable deaths (Health Effects Institute, 2025). These impacts, together with the environmental and climate consequences of atmospheric emissions, emphasize the importance of controlling pollutants at their sources rather than relying solely on ambient-air monitoring.

Scrubbing is an established engineering approach for controlling industrial air emissions. Wet scrubbers remove pollutants by bringing contaminated gas into contact with liquid droplets, through mechanisms such as inertial impaction, interception, diffusion and absorption. Although venturi scrubbers can achieve high removal efficiencies for fine particles, they require substantial pressure drops and energy input. Cyclonic wet scrubbers provide a potentially attractive compromise by combining centrifugal separation with gas–liquid interaction, offering effective particulate removal with relatively moderate energy requirements (Krames, 1994; Mukherjee et al. 2024).

Recent numerical and experimental studies have demonstrated that improvements in scrubber geometry, droplet distribution and particle–droplet interaction can significantly enhance collection performance (Oliveira et al. 2019; Hoyos *et al.*, 2024). Such developments are relevant to Nigeria, where emission-control technologies must be affordable, robust, energy-efficient, easy to maintain and suitable for local fabrication.

This study focuses on the design and development of a cyclonic wet scrubber for controlling gasoline-engine exhaust emissions. The study evaluates the system with particular attention to pollutant-removal performance. The paper demonstrated the potential of a locally adaptable cyclonic wet-scrubbing system as a practical point-source emission-control technology for improving air quality and supporting cleaner energy and industrial practices in Nigeria.

2. METHODOLOGY

2.1 Design Calculations

This section involves calculating the parameters needed for designing the wet scrubber. The parameters, their respective equations and calculations shown in Table 1, included Cunningham slip correction factor, Aerodynamic geometric mean diameter, Gas and liquid flow rates, Droplet diameter, Inertial parameter for mass median diameter, Reynolds number, Drag coefficient of liquid, Parameter characterizing $L/G \quad ratio,$ and Overall penetration and collection efficiency.

Table 1: Design calculations

Initial data	Calculations	Result
$d_{ps} = 9\mu m$ $T_g = 650^0$	**Cunningham slip correction factor** $C_c = \frac{1 + (6.21 \times 10^{-4})T_g}{d_{ps}}$ $\Rightarrow C_c = \frac{1 + (6.21 \times 10^{-4})(273 + 650)}{9}$	$C_c \Rightarrow 1.573$
$d_{ps} = 9\mu m$ $\rho_p = 1.99\, g/cm^3$	**Aerodynamic geometric mean diameter, d_{pg}** $d_{pg} = d_{ps}(C_c \times \rho_p)^{0.5}$ $\Rightarrow 9(1.573 \times 1.9)^{0.5}$	$d_{pg} = 13.83\mu mA$ $\Rightarrow 13.83 \times 10^{-4}\ cmA$
$D_c = 80mm$ $N = 1500$	**Gas and liquid flow rates** $Q_g = A_c v_g \Rightarrow \frac{\pi {D_c}^2}{4} \times \frac{\pi D_c N}{60}$ $\Rightarrow \frac{\pi^2 {D_c}^3 N}{240}$ $= \frac{\pi^2(0.08^3)(1500)}{240}$ $L/G\ range \cong 4 - 20\, gal/1000_{acf.}$ $if\ 10\ gal/1000_{acf}\ is\ adopted$ $\Rightarrow L/G = 1.63\, L/m^3 = 0.01\, gal/ft^3$ $if\ Q_g = 0.0316\, m^3/s \Rightarrow 1.896\, m^3/s$ $= 66.95\, ft^3/min$ $\Rightarrow Q_l = Q_g \times (L/G)$ $\Rightarrow 66.95\ ft^3/min \times 0.01\, gal/ft^3$ $= 0.67\, gal/min$ $\Rightarrow Q_l = \frac{0.67 \times 0.0045}{60}\ m^3/s$	$Q_g = 0.0316\, m^3/s$ $Q_l = 5.03 \times 10^{-5}\, m^3/s$
$L = 0.11m$ $N = 1500$ $Q_l = 5.03 \times 10^{-5}$ $Q_g = 0.0316$	**Droplet diameter d_d;** $v_{gt} = \frac{\pi LN}{60} \Rightarrow \frac{\pi(0.11)(1500)}{60}$ $Q_l/Q_g = \frac{5.03 \times 10^{-5}}{0.0316}$ $d_d = \frac{50}{v_{gt}} + 91.8(Q_l/Q_g)^{1.5}$ $\Rightarrow d_d = \frac{50}{864} + 91.8(0.00159)^{1.5}$	$v_{gt} = 864\, cm/s$ $Q_l/Q_g = 0.00159$ $d_d = 0.0637\ cm$
$\mu_g = 3 \times 10^{-4}\, g/cm.s$ $d_d = 0.058m$ $v_g = d_{pg}$ $= 13.83 \times 10^{-4}m$ $v_{gt} = 864\, m/s$	**Inertial parameter for mass median diameter;** $K_{pg} = \frac{{d_{pg}}^2 v_{gt}}{9\mu_g d_d}$ $K_{pg} = \frac{(13.83 \times 10^{-4})^2(864)}{9 \times 3 \times 10^{-4} \times 0.058}$	$K_{pg} \Rightarrow 9.61$

Initial data	Calculations	Result
$R_{co_2} = 188.92$ $R_{H_2o} = 188.92$ $R_{N_2} = 296.8$ $T_g = 650^0$ $P_g = 4\ bar$ $\%CO_2 = 13\%$ $\%H_20 = 13\%$ $\%N_2 = 74\%$ $\mu_g = 3 \times 10^{-4}\ g/cms$ $\rho_g = 1.804 \times 10^{-6}\ g/cm^3$ $v_{gt} = 864(m/s)$ $d_d = 0.058m$ $v_g = 0.166(cm^2/s)$	**Reynolds number** $\rho_{co_2} = \frac{\rho_g}{R_{co_2}T_g}$ $= \frac{4 \times 10^5}{188.92 \times (273 + 650)}$ $\rho_{H_{2o}} = \frac{\rho_g}{R_{H_2o}T_g} = \frac{4 \times 10^5}{188.92 \times (273 + 650)}$ $\rho_{N_2} = \frac{\rho_g}{R_{N_2}T_g} = \frac{4 \times 10^5}{296.8 \times (273 + 650)}$ $\rho_g \Rightarrow \%co_2\ (\rho_{co_2}) + \%H_2o\ (\rho_{H_{2o}}) + \%N_2\ (\rho_{N_2})$ $\Rightarrow \rho_g = 0.13(2.29 + 1.17) + 0.74(1.83)$ $v_g = \frac{\mu_g}{\rho_g}$ $hence\ \ v_g = \frac{3 \times 10^{-4}}{1.804 \times 10^{-3}}$ $N_{R_0} = \frac{v_{gt}\ d_d}{v_g}$ $\Rightarrow\ N_{R_0} = \frac{864 \times 0.058}{0.166}$	$\rho_{co_2} = 2.29 \times 10^{-3}\ g/cm^3$ $\rho_{H_{2o}} = 1.17 \times 10^{-3}\ g/cm^3$ $\rho_{N_2} = 1.83 \times 10^{-3}\ g/cm^3$ $\rho_g = 1.804 \times\ 10^{-3}\ g/cm^3$ $v_g = 0.166\ cm^2/s$ $N_{R_0} = 301.34$
$N_{R_0} = 301.34$	**Drag coefficient of liquid** $C_D = 0.22 + \frac{24}{N_{R_0}}\ (1 + 0.15{N_{R_0}}^{0.6})$ $\Rightarrow 0.22 + \frac{24}{301.34}\ (1 + 0.15(301.34)^{0.6})$	$C_D = 0.67$
$\rho_l = 1.59 \times 10^{-3}\ g/cm^3$ $\rho_g = 1.804 \times 10^{-3}\ g/cm^3$ $C_D = 0.67$ $\bar{P}_t = 0.25$	**Parameter characterizing $L/G\ \ ratio$** $sB = (L/G)\frac{\rho_l}{\rho_g C_D}$ $= \frac{0.00159.1000}{1.804 \times 0.67}$ **Overall penetration** $\bar{P}_t = 0.25;$ **Collection efficiency** $\eta = 1 + \bar{P}_t = 1 - 25\%$	$B = 1.32$ $\eta = 75\%$

2.2 Fabrication Process

The barrel cylinder forms the main body of the scrubber. It is fabricated from 2 mm mild-steel sheet, rolled into a cylinder of approximately 350 mm diameter and 497 mm overall height. The sheet is cut, manually formed, and seam-welded. Flange rings are welded to the top and bottom to allow the end plates to be securely bolted in place.

The top cover is a 2 mm mild-steel circular plate fitted with a central opening for the gas outlet pipe. It is bolted to the upper flange using a gasketed joint to prevent gas or water leakage. A mesh outlet filter, installed beneath the gas outlet, serves as a mist eliminator by removing entrained water droplets and fine particles before the cleaned gas leaves the scrubber. The mesh can be removed for cleaning or replacement.

Inside the barrel, a straightening vane is installed below the spray zone. It helps reduce excessive swirling and distribute the gas more uniformly through the spray, thereby improving gas–liquid contact and pollutant removal.

Two lifting handles are welded to opposite sides of the barrel to facilitate handling and movement of the unit.

The gas inlet is a mild-steel pipe welded tangentially to the lower section of the barrel. Its tangential arrangement induces a cyclonic motion in the incoming exhaust gas, promoting centrifugal separation and improving contact with the scrubbing liquid.

The scrubber is supported by a mild-steel stand consisting of three or four welded legs fitted with castor wheels. The stand provides ground clearance for the gas inlet and dirt outlet while allowing the unit to be moved easily.

The spray system consists of two to four fine-mist hollow-cone nozzles mounted on an internal spray header above the straightening vane. The nozzles atomise water across the gas flow path, increasing gas–liquid contact and enhancing pollutant capture. Water is supplied through a threaded water inlet connected to an external pump or recirculation line.

The bottom plate, also made from 2 mm mild steel, seals the lower end of the barrel and is bolted to the lower flange with a gasket. It also supports the stand and provides the mounting point for the dirt outlet, which is fitted with a ball valve. The valve allows accumulated water, soot, and captured particulate matter to be drained during cleaning or maintenance.

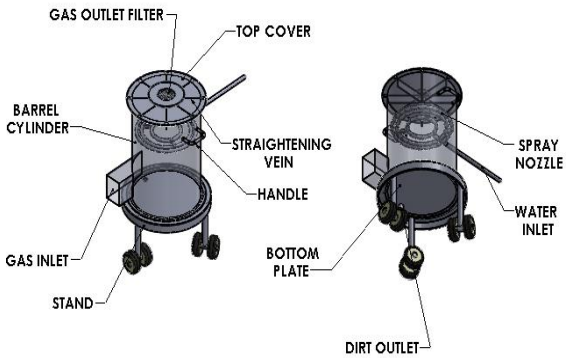

Figure 1: Assembly of the wet scrubber

Assembly Procedure

Fabrication begins with the barrel, top cover, and bottom plate. The internal components—including the straightening vane, spray header and nozzles, and outlet filter—are then installed before the end plates are closed. The top and bottom plates are fitted with gaskets and bolted to the barrel flanges using a cross-tightening sequence to achieve an even, leak-tight seal. Finally, the handles, stand, water inlet, and dirt outlet are installed. The completed unit is inspected for leaks and structural integrity before painting and commissioning.

2.3 Working Principle of Cyclonic Liquid Spray Scrubber Device

The scrubber was built to serve both the dry cyclone and wet spray chamber to remove pollutants from gas streams. For the wet scrubber; raw exhaust from the gasoline powered internal combustion engine enters the system.

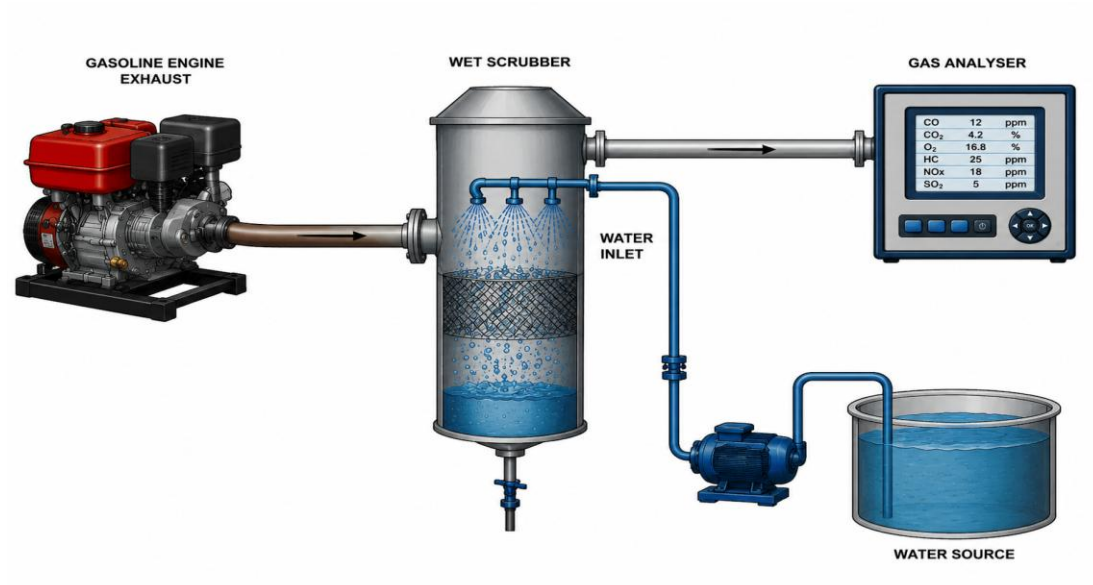

Figure 2: Experimental working assembly of the wet scrubber system

The scrubber consists of empty cylindrical chamber in which the exhaust gas stream is contacted with water droplets. Water spray, generated by the spray nozzles, captures particulate and exhaust gases. The cleaned gas exits to the gas analyser for exhaust gas composition measurements. Water is then recirculated from the water source via the pump and the blowdown removes accumulated contaminants. Two repeated measurements were recorded for each exhaust gas, and the average reading was used for further analysis.

3. RESULTS AND DISCUSSION

The constructed wet scrubber was tested using an internal combustion engine (4-stroke, single cylinder gasoline engine), Brain Bee automotive gasoline gas analyzer and a water source.

The testing of liquid wet scrubber was carried out at Heat Engine Workshop, Department of Mechanical Engineering, Ahmadu Bello University, Zaria. The experimental procedure was carried out with gasoline fuel using different exhaust emission such as Carbon II Oxide (CO), Carbon IV Oxide (CO_2), Unburn Hydrocarbon (HC), and Excess Oxygen O_2. The test was carried out on two stages. A four stroke, single cylinder gasoline engine was initially fuelled with a gasoline fuel until steady-state was confirmed. The exhaust emissions from the engine were measured using the Brain bee automotive gasoline gas analyzer. The gasoline engine was run again with the wet scrubber attached to the engine exhaust and to the Brain bee automotive gasoline gas analyzer. The exhaust gases CO (%/vol); CO_2 (%/vol); HC (ppm) and O_2 (%/vol) were recorded. Tables 2 and 3 show the emission readings from the gas analyser without and with the scrubber. Two readings were recorded in both Tables 2 and 3, and the average readings

Table 2: Exhaust Emission without wet scrubber

Experiment no.	**Exhaust gas parameters (mass fraction)**					
	λ	CO $(\%/vol)$	CO_2 $(\%/vol)$	HC (ppm)	O_2 $(\%/vol)$	$\phi = {}^{1}/_{\lambda}$
First reading	3.811	2.56	1.1	142.0	17.50	0.2624
Second reading	3.896	2.41	1.1	154.0	17.20	0.2566
Average	3.854	2.485	1.1	148.0	17.35	0.2595
Standard Deviation	0.06	0.106	0	8.485	0.212	0.004

Table 3: Exhaust Emission with wet scrubbers

Experiment no.	**Exhaust gas parameters**					
	λ	CO $(\%/vol)$	CO_2 $(\%/vol)$	HC (ppm)	O_2 $(\%/vol)$	$\phi = {}^{1}/_{\lambda}$
First reading	4.468	2.090	1.1	109.0	18.20	0.2238
Second reading	4.430	2.104	0.9	130.0	17.20	0.2262
Average reading	4.449	2.097	1.0	119.5	17.70	0.2250
Standard Deviation	0.027	0.01	0.141	14.8	0.707	0.0017

Table 2 shows the mass fraction of the exhaust gas constituents as well as their respective equivalent ratios (ϕ) when wet scrubber wasn't used in cleaning the exhaust gases. The average exhaust gas mass fraction of λ , CO, CO_2, Hydrocarbon and O_2 were obtained to be 3.854, 2.485 %/vol, 1.1 %/vol, 148.0 %/vol and 17.35 %/vol respectively. λ is a parameter obtained from the gas analyzer known as the inverse equivalence ratio, while ϕ is the equivalence ratio obtained from an experimental run.

Table 3 rather shows the mass fraction of the exhaust gas constituents as well as their respective equivalent ratios (ϕ) when wet scrubber was used in cleaning the exhaust gases. The average exhaust gas mass fraction of CO, CO_2, Hydrocarbon and O_2 were obtained to be 2.097%/vol, 1.0 %/vol, 119.7ppm, and 17.7 %/vol respectively. The results from Table 2 and 3 showed that the scrubber reduced the concentrations of carbon monoxide (CO), carbon dioxide (CO_2), and unburned hydrocarbons (HC) by 15.6%, 9% and 19% respectively and surprisingly increased excess oxygen (O_2) emissions by approximately 2%. The percentage reduction was calculated from: (concentration without scrubber – concentration with scrubber) x100%/ concentration without scrubber. ssThe unexpected increase in O_2 after the gases pass through the scrubber could be due to air ingress through the scrubber, dilution effects from water vapor displacing gas, or analyzer calibration effects. The average equivalence ratio decreased from 0.2595 without the wet scrubber to 0.2250 with the wet scrubber. Comparing the predicted maximum 75% collection efficiency from the design calculations, with the percentage reductions of maximum of 15.6% for HC; the discrepancy shows more room for cleaning exhaust gases. Two readings per test condition were taken mainly to confirm basic repeatability of the exhaust measurements rather than to establish a statistically robust estimate, given practical constraints such as limited test-rig time, the risk of engine drift over longer runs, and the exploratory, proof-of-concept scope of the study; however, this small sample size (n = 2) has notable statistical limitations, including an unreliable estimate of variance, no ability to check low statistical power to detect true differences, high sensitivity to outliers, and limited generalisability beyond the specific test conditions. The percentage reductions should be viewed as indicative rather than precise.

4. CONCLUSION

1. A functional prototype was successfully built and tested. The cyclonic wet scrubber was fabricated and evaluated on a 4-stroke, single-cylinder gasoline engine, using a Brain Bee automotive gas analyser to measure exhaust composition before and after treatment.

2. The scrubber significantly reduced key pollutant concentrations. CO, CO_2, and unburned hydrocarbons (HC) were reduced by 15.6%, 9%, and 19% respectively when the scrubber was fitted, demonstrating measurable emission-control performance.

3. An unexpected rise in excess oxygen was observed. Excess O_2 concentration increased by approximately 2% with the scrubber in place; a surprising result that warrant further investigation

4. The equivalence ratio shifted toward a leaner mixture. The average equivalence ratio dropped from 0.2595 (without the scrubber) to 0.2250 (with the scrubber), consistent with the observed reductions in CO/CO_2/HC and the rise in excess O_2.

5. REFERENCES

1. Ephraim-Emmanuel, B.C., Enembe, O. and Ordinioha, B. (2023). Respiratory health effects of pollution due to artisanal crude-oil refining in Bayelsa, Nigeria. *Annals of Global Health*, 89(1), 74. https://doi.org/10.5334/aogh.4247.
2. Onakpohor, A., Fakinle, B.S., Sonibare, J.A., Oke, M.A. and Akeredolu, F.A. (2020) 'Investigation of air emissions from artisanal petroleum refineries in the Niger-Delta Nigeria', *Heliyon*, 6(11), e05608. https://doi.org/10.1016/j.heliyon.2020.e05608
3. Igibah, C.E., Ilaboya, I.R., Iyeke, S.D., Ufuah, E. and Agashua, O.L. (2024). Health effects of oil and waste pollutants on Delta Nigeria inhabitants' well-being and its mitigation. *Emergency Management Science and Technology*, 4, e017. https://doi.org/10.48130/emst-0024-0015.
4. Health Effects Institute (2025). *State of Global Air 2025: A Report on Air Pollution and Its Role in the World's Leading Causes of Death*. Boston, MA: Health Effects Institute. The report estimates 7.9 million deaths attributable to air pollution globally in 2023 and more than 200,000 in Nigeria.
5. Oliveira, R.A.F., Guerra, V.G. and Lopes, G.C. (2019). Improvement of collection efficiency in a cyclone separator using water nozzles: A numerical study. *Chemical Engineering and Processing: Process Intensification*, 145, 107667. https://doi.org/10.1016/j.cep.2019.107667.
6. Hoyos, A., Joubert, A., Bouhanguel, A., Henry, M., Durécu, S. and Le Coq, L. (2024). Multiapproach design methodology of a downscaled wet scrubber to study the collection of submicronic particles from waste incineration flue gas. *Processes*, 12(8), 1655. https://doi.org/10.3390/pr12081655.
7. Krames, J. (1994) 'The cyclone scrubber – a high efficiency wet separator', *Chemical Engineering & Technology*, 17(2), pp. 90–94. https://doi.org/10.1002/ceat.270170202
8. Mukherjee, S., Siddiqi, H., Maiti, P., Parmar, P. and Meikap, B.C. (2024). A comprehensive analysis of removal of hazardous dust particulates from chemical and process industries off gases by advanced wet scrubbing techniques: A review. *Journal of Loss Prevention in the Process Industries*, 91, 105406. https://doi.org/10.1016/j.jlp.2024.105406.

International Conference on Engineering Innovation for Sustainable Development (ICESID 2026)
Faculty of Engineering, Ahmadu Bello University Zaria · 8–10 September 2026

INVESTIGATION OF THE PHYSICOCHEMICAL PROPERTIES, ENGINE PERFORMANCE AND EMISSION CHARACTERISTICS OF GLYCINE MAX BIODIESEL–DIESEL BLENDS IN A COMPRESSION IGNITION ENGINE

Hamisu Adamu Dandajeh[1,*], Yusuf Hafiz[1]
[1]*Ahmadu Bello University*
Email: hadandajeh@abu.edu.ng*, yusufhafiz010@gmail.com
***Corresponding author**: Hamisu Adamu Dandajeh
DOI: https://doi.org/10.67203/sp.ICESID.2026

ABSTRACT
This study investigated the performance and emission characteristics of biodiesel blends produced from Glycine max oil in a compression ignition engine. Biodiesel was produced through transesterification using methanol and potassium hydroxide. The produced biodiesel was blended with conventional diesel at 5% (B5), 10% (B10) and 20% (B20), and burnt in a single-cylinder Kirloskar TV1 diesel engine at speeds of 1200rpm and 1400rpm. Physicochemical properties including density, kinematic viscosity, pour point and flash point were determined. Engine performance parameters such as brake power (BP), brake thermal efficiency (BTE), brake mean effective pressure (BMEP), brake torque (BT) and brake specific fuel consumption (BSFC) were also evaluated. The experimental results showed that increasing Glycine-Max content from 0 – 20% increased the flash point from 71 – 79°C and decreased the kinematic viscosity from 3.327 – 3.269 (mm²/s). While Brake Power (BP) increased with engine speed increase regardless of the blends; the Brake Thermal Efficiency (BTE) decreased with increasing proportion of Glycine-max from 5 – 20% irrespective of the blend. There was decreasing trend for exhaust emissions with increasing biodiesel blend proportions from 5% to 10% and 20% for HC, CO and CO_2. Nitrogen oxide (NOx) emissions increased slightly with increasing biodiesel content. The findings indicate that Glycine-max biodiesel have potential as renewable substitutes for petroleum diesel in compression ignition engines.

Keywords: *Glycine max; Diesel; Biodiesel; Compression Ignition Engine; Engine Performance*

1. INTRODUCTION

The increasing global demand for energy, coupled with growing environmental concerns associated with the continued use of fossil fuels, has intensified the search for cleaner, renewable, and sustainable energy alternatives. To address these challenges, many researchers have explored various renewable energy sources, including solar, wind, and biomass, to support future economic development. Although solar and wind energy have shown considerable potential, their dependence on weather and environmental conditions limits their ability to completely replace conventional petro-fuels in the short term. In contrast, biodiesel produced from vegetable and animal oils through transesterification exhibits combustion characteristics comparable to those of petroleum diesel while offering additional advantages such as renewability, biodegradability, and environmental sustainability, making it a promising alternative fuel source (Chuah et al., 2021).

Despite serving as the primary energy source for industrialized societies, fossil fuels have been identified as major contributors to environmental degradation and climate change. The combustion of fossil fuels releases significant quantities of greenhouse gases, including carbon dioxide (CO_2), methane (CH_4), and nitrous oxide (N_2O), which contribute substantially to global warming. Furthermore, the finite nature of fossil fuel reserves underscores the need for energy diversification, particularly within the transportation and industrial sectors (Pasha et al., 2021).

Extensive experimental and modelling studies have been conducted to investigate the combustion and emission characteristics of diesel engines fuelled with various biodiesel feedstocks. These studies have shown that biodiesel can improve combustion efficiency due to its oxygen content, which enhances oxidation processes in fuel-rich zones and consequently reduces emissions of

particulate matter (PM), carbon monoxide (CO), and unburned hydrocarbons (HC) (Zhang et al. 2022). In addition, biodiesel can be blended with conventional diesel fuel in varying proportions without requiring significant engine modifications. However, biodiesel possesses certain limitations, including higher viscosity, lower calorific value, reduced volatility, and poor cold-flow properties. Moreover, several studies have reported increased nitrogen oxide (NO_x) emissions associated with biodiesel combustion. Consequently, considerable research attention has been directed towards biodiesel–diesel blends as a means of improving fuel properties while maintaining environmental benefits (Dandajeh et al., 2020).

Biodiesel blends are typically designated as BXX, where XX denotes the percentage volume of biodiesel present in the blend. Common examples include B5 (5% biodiesel and 95% petroleum diesel) and B20 (20% biodiesel and 80% petroleum diesel). Previous studies, including that of Kaisan and Pam (2013) and Dandajeh et al, 2020, have demonstrated that biodiesel–diesel blends can achieve reduced carbon dioxide emissions while maintaining satisfactory engine performance in compression-ignition (CI) engines without requiring substantial modifications to existing engine systems.

Since biodiesel is predominantly utilized in compression-ignition engines, understanding the operational characteristics of these engines is essential for evaluating fuel performance. The compression-ignition engine, commonly known as the diesel engine, was invented by Rudolf Diesel in the late nineteenth century. Its operation is based on the principle of auto-ignition, whereby fuel combustion is initiated by the high temperatures generated during air compression within the engine cylinder. Due to their high thermal efficiency and superior torque characteristics, diesel engines are widely employed in transportation, agriculture, construction, and other heavy-duty applications (Heywood, 1988).

Although palm and rapeseed oils have received considerable attention in biodiesel research, the application of glycine max biodiesel blends in compression-ignition engines remains relatively underexplored within the Nigerian context. This gap is aimed at reducing the environmental impacts associated with conventional fossil fuels. The paper presents an experimental investigation of the Physicochemical Properties, Engine Performance Characteristics and emissions of Glycine max Biodiesel–Diesel Blends in a Compression Ignition Engine.

2. METHODOLOGY

The materials used in this study included Glycine max (soybean) oil, petroleum diesel, methanol, potassium hydroxide (KOH), phenolphthalein indicator, distilled water, and ethanol. The chemicals were obtained from the National Institute for Leather Science and Technology (NILEST), Zaria, while diesel fuel was purchased from a commercial filling station in Zaria. The equipment used for biodiesel production and characterization included an electronic weighing balance, burette, glass reactor, heating mantle with magnetic stirrer, water bath, separatory funnel, drying oven, digital viscometer, bomb calorimeter, gas analyzer, thermometer, and measuring cylinders. Engine performance and emission tests were conducted using a single-cylinder compression ignition (CI) engine coupled to an eddy-current dynamometer. The engine specifications are presented in Table 1.

Table 1: Specifications of the Test Engine

Parameter	Specification
Model	Kirloskar TV1
Engine Type	Four-stroke, single-cylinder, water-cooled, direct-injection diesel engine
Bore × Stroke	87.5 mm × 110 mm
Compression Ratio	17.5:1
Rated Power	5.2 kW at 1500 rpm
Displacement Volume	661 cc
Fuel Type	Diesel/Biodiesel
Cooling System	Water-cooled
Starting System	Manual
Loading Device	Eddy-current dynamometer

The free fatty acid (FFA) content of the soybean oil was determined using the standard titration method. Approximately 5.04 g of oil was dissolved in ethanol and titrated against 0.1 N KOH using phenolphthalein as indicator. The average FFA value obtained was 0.25%, indicating that the oil was suitable for direct base-catalyzed transesterification without esterification pretreatment. Biodiesel was produced through alkali-catalyzed transesterification. Methanol and potassium hydroxide were mixed to form methoxide solution and reacted with filtered soybean oil in a three-neck reaction flask.

The reaction was carried out at a temperature of 60–65°C under continuous stirring (600–800 rpm) for approximately 3 hours. After completion of the reaction, the mixture was transferred into a separating funnel and allowed to settle for 48 hours to facilitate separation of biodiesel from glycerol. The biodiesel layer was subsequently washed with warm distilled water until neutral and dried in an oven at 60°C for 24 h. The produced biodiesel was blended volumetrically with conventional diesel to prepare B5, B10, and B20 blends, corresponding to 5%, 10%, and 20% biodiesel concentrations, respectively.

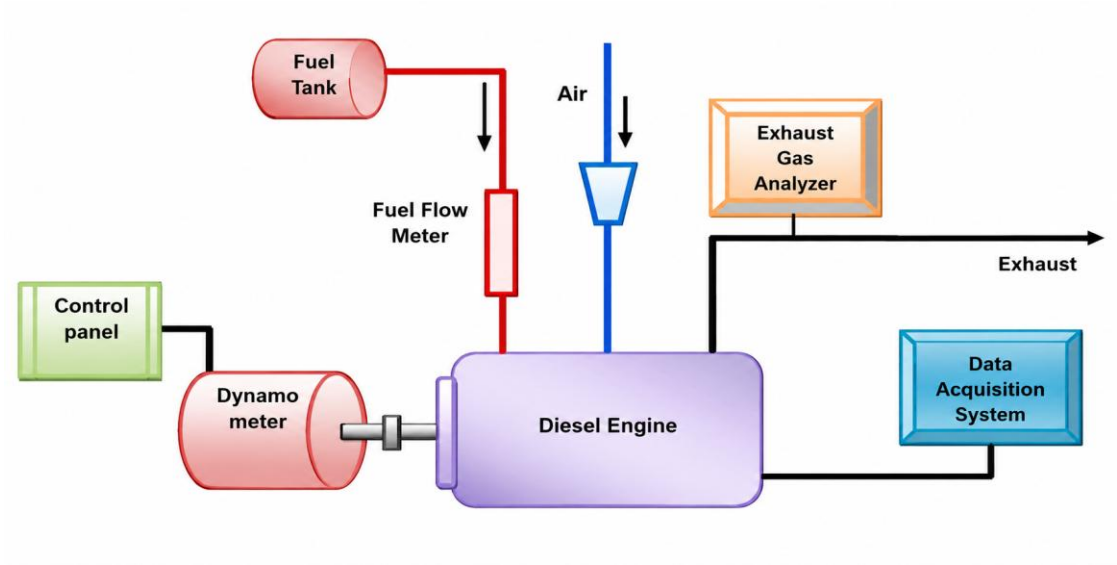

Figure 1: Schematic diagram of the experimental set-up

The physicochemical properties evaluated included density, kinematic viscosity, pour point, flash point, and calorific value. Density was measured using a digital density meter, while viscosity was determined at 40°C using a digital viscometer. Pour point, flash point, and calorific value were determined using standard laboratory procedures.

Engine performance and emission tests were carried out using the Kirloskar TV1 diesel engine coupled with an eddy-current dynamometer. The fuels tested were diesel, B5, B10, and B20. Performance tests were conducted at engine speeds of 1200rpm and 1400 rpm. The performance

parameters evaluated included brake power (BP), and brake thermal efficiency (BTE). Exhaust emissions including carbon monoxide (CO), carbon dioxide (CO_2), nitrogen oxides (NO_x), and unburned hydrocarbons (HC) were measured using a gas analyzer connected to the engine exhaust system.

3. RESULTS AND DISCUSSION

3.1 Physicochemical Properties of Glycine max Biodiesel Blends

The physicochemical properties of Glycine max biodiesel blends, shown in Table 2, were evaluated to determine their suitability for compression ignition engine applications. Table shows that density increased slightly with increasing biodiesel concentration from 1.522 g/cm³ for B5 to 1.532 g/cm³ for B20. This increase is attributed to the higher density of fatty acid methyl esters (FAME) present in biodiesel compared to conventional diesel. Similarly, flash point increased with increasing proportion of biodiesel, indicating improved safety during storage and transportation. For example; The flash point for B5 is 67.5ºC, 69.5ºC for B10 and 79ºC for B20. However, pour point decreased from 28°C for B5, to 24°C for B10 and to 12°C for B20. However, no clear trend was seen for kinematic viscosity. This could be due to the combined effects of biodiesel composition, blending interactions, and experimental variability.

Table 2: Physicochemical Properties of Glycine max Biodiesel Blends

Blend	Density (g/cm³)	Kinematic Viscosity	Pour Point (°C)	Flash Point (°C)
Diesel	1.142	3.327	10	71
B5	1.522	2.628	28	67.5
B10	1.525	3.279	24	69.5
B20	1.530	3.269	12	79

The kinematic viscosity values of all blends were within the acceptable operating range for diesel engines, suggesting satisfactory fuel atomization and lubrication characteristics. Pour point results showed that pure biodiesel exhibited better cold-flow properties than some of the lower biodiesel blends, indicating the influence of feedstock composition on low-temperature fuel behavior. Overall, the measured fuel properties confirmed that Glycine max biodiesel blends possess characteristics suitable for utilization in compression ignition engines without requiring engine modifications.

3.2 Engine Performance Characteristics

The performance characteristics of the engine fueled with Glycine max biodiesel blends were evaluated in terms of brake power (BP) and brake thermal efficiency (BTE)

Figures 2a) and b) show that brake power increased with increasing engine speed, respectively, from 1200 rpm to 1400 rpm for all fuel blends. For B5 instance, the brake power increased by a factor of 2.25 for increased speed from 1200 -1400rpm. Interestingly Brake Power for diesel and B10 increased by 100% for engine speed increase from 1200 -1400rpm. At lower engine speed of 1200rpm, B10, B20 and diesel exhibited roughly similar brake power due to improved combustion arising from the oxygenated nature of biodiesel.

Fig 3a) and b) show the brake thermal efficiency (BTE) at speeds of 1200rpm and 1400rpm respectively. The results showed that BTE decreased with increasing biodiesel proportion from 5 to 20% regardless of the increased speeds from 1200 - 1400rpm. For example, the BTE of B5 was 39.4%, and it decreased by 18.5% for B20.

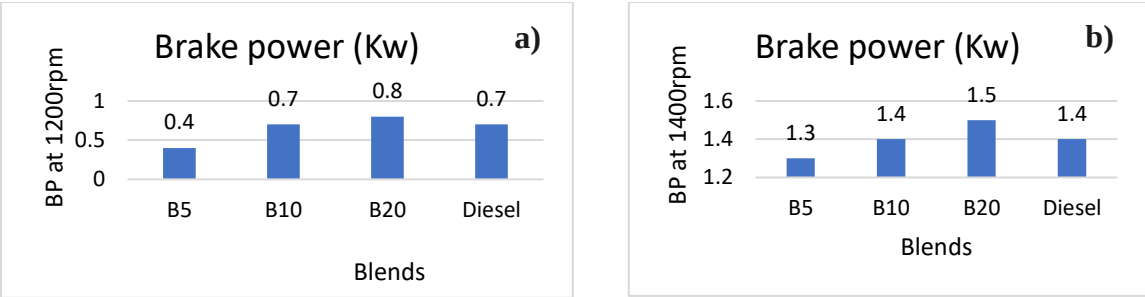

Figure 2: Brake Power (kW) at: a)1200rpm b)1400rpm

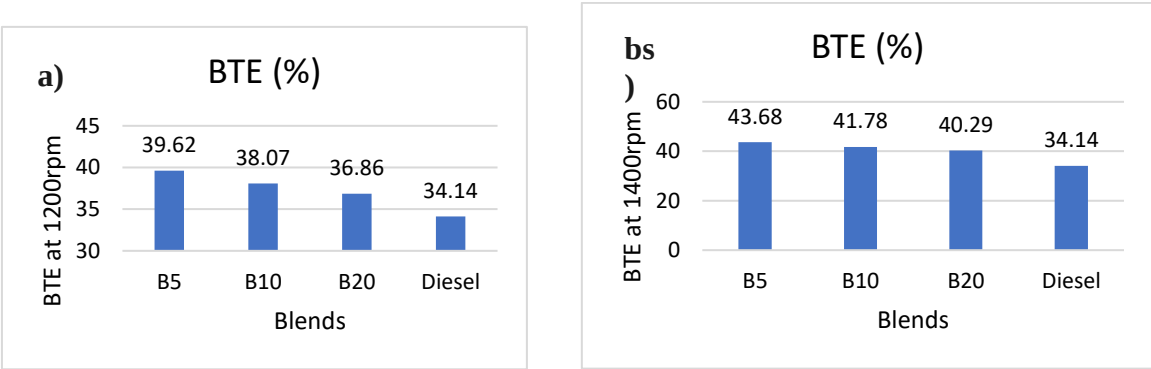

Figure 3: Brake Thermal Efficiency at: a) 1000rpm b) 1200rpm c) 1400rpm

Considering engine speed variations, BTE increased for B10 for example, from 33.6% at 1000rpm to 38.7% at 1200rpm and to 41.78% at 1400rpm. This indicates better conversion of fuel energy into useful work.

3.3 Emission Characteristics

Figure 4a), b) c) and d) respectively show the results of emission values of Glycine max biodiesel blends of hydrocarbons (HC), carbon monoxide (CO), carbon dioxide (CO_2), and nitrogen oxides (NOx) at constant speed of 1200rpm. The results showed decreasing exhaust emissions with increasing biodiesel blend proportions from 5% to 10% and 20% for HC, CO and CO_2. This reduction is attributed to the oxygen content present in biodiesel, which promotes more complete oxidation of fuel during combustion. Figure 4d) shows that only NOx was seen increasing from 1582ppm for B5, to 1609ppm for B10 and to 1639ppm for B20. This is consistent with previous studies (Dandajeh et al. 2020; Bawa et al. 2023).

Overall, the emission results indicate that Glycine max biodiesel blends can significantly reduce harmful exhaust emissions of HC, CO and CO_2 while maintaining engine operation.

a)

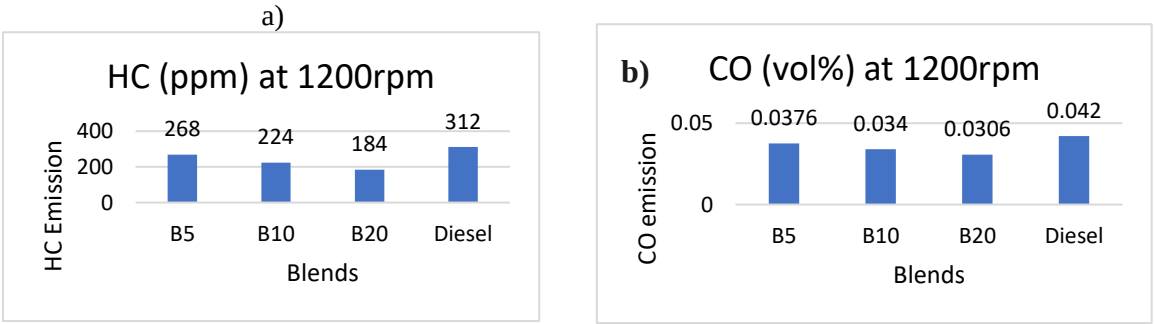

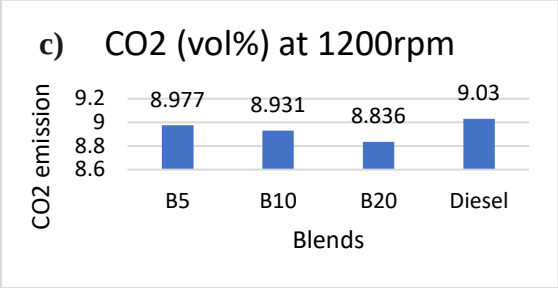

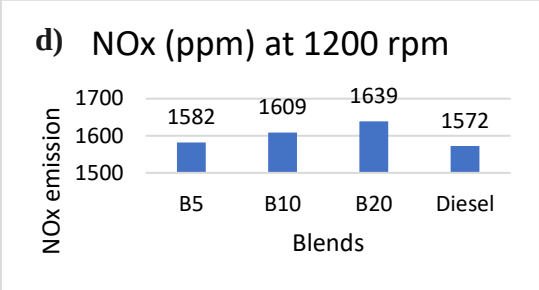

Figures 4: Exhaust Emissions at 1200rpm a) HC (ppm) b) CO (vol%) c) Nox d) CO_2 (vol%)

Conversely, NOx emissions exhibited a slight increase with increasing biodiesel concentration. This behavior is commonly associated with higher in-cylinder temperatures and improved oxygen availability during combustion. The enhanced combustion process responsible for lower HC and CO emissions simultaneously promotes thermal NOx formation.

4. CONCLUSION

1. The Glycine max biodiesel blends exhibited acceptable physicochemical properties: density, viscosity, flash point, and pour point; indicating their suitability for smooth compression ignition engine operation without requiring engine modifications.
2. Brake power increased respectively with increasing engine speed from 1200rpm to 1400rpm for all the fuel blends. Brake power for B5 increased by a factor of 2.25 for increased speed from 1200 -1400rpm
3. Brake Thermal Efficiency decreased with increasing biodiesel proportion from 5 to 20% regardless of the increased speeds from 1200 - 1400rpm.
4. There was decreasing trend for exhaust emissions with increasing biodiesel blend proportions from 5% to 10% and 20% for HC, CO and CO_2. Nitrogen oxide (NOx) emissions increased slightly with increasing biodiesel content

5. REFERENCES

Chuah, L.F., Klemeš, J.J., Bokhari, A. and Asif, S. (2021) 'A review of biodiesel production from renewable resources: Chemical reactions', *Chemical Engineering Transactions*, 88, pp. 943–948. doi: 10.3303/CET2188157.

Pasha, M.K., Dai, L., Liu, D., Guo, M. and Du, W. (2021) 'An overview to process design, simulation and sustainability evaluation of biodiesel production', *Biotechnology for Biofuels and Bioproducts*, 14, 129. doi: 10.1186/s13068-021-01977-z

Kaisan, M. U., & Pam, G. Y. (2013). Determination of engine performance parameters of a stationary single cylinder compression ignition engine run on biodiesel from wild grape seeds/diesel blends. Journal of Energy, Environment & Carbon Credits, 3(3), 15–21.

Dandajeh, H. A., Sanusi, Y. S, Ahmadu. T.O (2020). Exhaust Emissions Characteristics of a Gardener Compression Ignition Engine Fuelled with Rape Seed Methyl Ester and Fossil Diesel. *Nigerian Journal of Technology (NIJOTECH)*. Published by Faculty of Engineering, University of Nigeria, Nnsuka. 39(3). 752 -760

Heywood, J. B. (1988). *Internal Combustion Engine Fundamentals*. McGraw-Hill, New York.

Zhang, Y., Zhong, Y., Lu, S., Zhang, Z. *et al.* (2022) 'A comprehensive review of the properties, performance, combustion, and emissions of the diesel engine fueled with different generations of biodiesel', *Processes*, 10(6), 1178. doi: 10.3390/pr10061178.

Bawa A A, Dandajeh H A, and Kulla D M (2023). Engine Performance and Emission Analysis of Yellow Oleander, Residual Cooking Oil And Fossil Diesel, *Arid Zone Journal Of Engineering, Technology & Environment (AZOJET)*. Published by Faculty of Engineering, University of Maiduguri. *19(2), 319 – 330*

TRACK 6 OF 11

Innovative Resource Utilization and Management

International Conference on Engineering Innovation for Sustainable Development (ICESID 2026)

Faculty of Engineering, Ahmadu Bello University Zaria · 8–10 September 2026

https://icesid.org

International Conference on Engineering Innovation for Sustainable Development (ICESID 2026)
Faculty of Engineering, Ahmadu Bello University
Zaria · 8–10 September 2026

COMPARATIVE EVALUATION OF AASHTO AND CBR FLEXIBLE PAVEMENT DESIGN METHODS USING LABORATORY-DERIVED SOIL PARAMETERS

Ahmad Idris[1,*]
[1]*Bayero University*
Email: aidris.civ@buk.edu.ng[*]
***Corresponding author**: Ahmad Idris
DOI: https://doi.org/10.67203/sp.ICESID.2026

ABSTRACT

Flexible pavement design plays a critical role in ensuring durable, safe and economical road infrastructure. This study compares pavement structures obtained using a CBR-based empirical method and the 1993 AASHTO flexible pavement design procedure using laboratory-derived properties of two lateritic soils. The non-marginal and marginal soils recorded CBR values of 42.79% and 13.03%, respectively. Design traffic was reconstructed from an AADT of 4,200 vehicles/day, 25% heavy vehicles, 4% annual growth, a 20-year design period, a directional distribution factor of 0.50, a lane distribution factor of 1.00 and an assumed vehicle damage factor of 3.0 ESAL/heavy vehicle, giving 17.12 × 10^6 design ESALs. For AASHTO design, 95% reliability, an overall standard deviation of 0.45, initial and terminal serviceability indices of 4.2 and 2.5, respectively, and CBR-derived resilient moduli were adopted. Required Structural Numbers were 3.55 and 4.68 for the non-marginal and marginal soils. The adopted AASHTO sections were 100 mm asphalt, 200 mm base and 200 mm sub-base for the non-marginal soil (500 mm total), and 130 mm asphalt, 230 mm base and 270 mm sub-base for the marginal soil (630 mm total). The CBR-based method yielded 413 mm and 450 mm, respectively. Thus, AASHTO sections were 21.1% and 40.0% thicker. The results demonstrate the effect of explicitly considering traffic, reliability, serviceability and subgrade stiffness, while confirming the continued usefulness of CBR-based design where data and resources are limited.

Keywords: *flexible pavement; AASHTO; CBR; pavement thickness; ESAL; subgrade strength*

1. INTRODUCTION

Road transportation remains a major means of moving people, goods and services in developing countries, and the performance of road networks depends substantially on the quality and durability of pavement structures. Flexible pavements are widely used because of their relatively low construction cost, ease of maintenance and adaptability to varying ground conditions. Their performance is influenced by traffic loading, subgrade strength, environmental conditions, drainage and material characteristics (Inyang et al., 2024; Nneka, 2025; Olowosulu et al., 2022; Owolabi et al., 2012). Inadequate design can result in rutting, cracking, potholes and excessive deformation, with associated maintenance costs and reduced service life.

Pavement design practice has developed from empirical procedures toward approaches that incorporate traffic, reliability and material-response considerations. The California Bearing Ratio (CBR) method uses subgrade bearing strength and empirical design relationships and is particularly attractive where detailed traffic, material and climatic information is limited (Chitade et al., 2024; Noka et al., 2025). The AASHTO procedure, in contrast, incorporates cumulative traffic expressed as ESALs, reliability, serviceability, subgrade resilient modulus and drainage considerations (Ahmed et al., 2023; El-Ashwah et al., 2022; Moharekpour et al., 2022; Prayudyanto et al., 2023; Ziar et al., 2023).

CBR-based procedures remain useful for preliminary and lower-data applications, but their empirical nature means that reliability and uncertainty are not represented explicitly. AASHTO therefore provides a more comprehensive framework for higher traffic levels, although it requires more design inputs and can produce thicker sections. A conventional flexible pavement consists of surfacing, base, sub-base and subgrade layers; the upper layers distribute wheel loads so that stresses transmitted to the subgrade remain within acceptable limits.

The aim of this study is to compare flexible pavement structures obtained using the CBR-based empirical method and the 1993 AASHTO design procedure for two lateritic subgrade soils. The specific objectives are to characterize the engineering properties of the soils, reconstruct design traffic, determine the AASHTO Structural Number and corresponding layer thicknesses, and compare the resulting sections in terms of total thickness and material quantity.

2. METHODOLOGY

2.1 Soil Sampling

Two lateritic soil samples representing distinct subgrade conditions were selected for the study. The samples were obtained from an existing borrow pit in Janguza Area, north of Kano City, Kano State, Nigeria. Bulk samples were collected at approximately 1.0 m below ground level to minimize the influence of organic matter and surficial contamination. The samples were packaged, labelled and transported to the geotechnical laboratory, where they were air-dried, pulverized without crushing individual particles and prepared for testing in accordance with relevant standard procedures (ASTM, 2008).

2.2 Laboratory Testing

Particle-size distribution and Atterberg limits were determined using standard geotechnical procedures. Standard Proctor compaction testing was used to determine maximum dry density (MDD) and optimum moisture content (OMC), while CBR testing was conducted on prepared specimens to assess subgrade bearing capacity. The measured CBR values were used directly in the CBR-based design and as the basis for estimating resilient modulus for the AASHTO analysis.

The retained dataset does not contain the complete particle-size distribution required for formal AASHTO or USCS group assignment. Accordingly, the soils are additionally described using the CBR-based subgrade strength classes in the Federal Ministry of Works guidance. The non-marginal soil (CBR = 42.79%) falls within S6 (CBR ≥ 30%), while the marginal soil (CBR = 13.03%) falls within S4 (CBR 8–14%). These classes are used for engineering interpretation and are not substitutes for formal soil classification.

2.3 Traffic Analysis and Design ESAL

Cumulative design traffic was expressed as 80 kN (18-kip) Equivalent Single Axle Loads (ESALs). In the absence of an axle-load survey, a vehicle damage factor (VDF) of 3.0 ESAL per heavy vehicle was adopted as an explicit assumption. The traffic growth factor was calculated as GF = [(1 + r)^n − 1]/r, where r is annual growth and n is the design period. For r = 0.04 and n = 20 years, GF = 29.778. Design ESAL was calculated as W18 = AADT × PHV × 365 × GF × DD × LDF × VDF, using AADT = 4,200 vehicles/day, PHV = 0.25, DD = 0.50, LDF = 1.00 and VDF = 3.0, giving W18 = 17.12 × 10^6 ESALs. The assumed VDF should be replaced by project-specific axle-load data for detailed design.

2.4 AASHTO 1993 Flexible Pavement Design Procedure

The required Structural Number (SN) was determined using the flexible pavement design equation in the AASHTO Guide for Design of Pavement Structures (AASHTO, 1993):

$$\log10(W18) = ZRSo + 9.36\log10(SN + 1) - 0.20 + \{\log10[\Delta PSI/(4.2 - 1.5)]\}/\{0.40 + 1094/(SN + 1)^{5.19}\} + 2.32\log10(MR) - 8.07$$

where W18 is cumulative 18-kip ESALs; ZR is the standard normal deviate corresponding to the selected reliability; So is the overall standard deviation; ΔPSI is allowable serviceability loss; and MR is subgrade resilient modulus in psi. Reliability of 95% (ZR = −1.645), So = 0.45, initial serviceability p0 = 4.2 and terminal serviceability pt = 2.5 were adopted, giving ΔPSI = 1.7.

Because resilient modulus was not measured directly, it was estimated from CBR using MR (psi) = 2555(CBR)^0.64. The resulting moduli were approximately 28,278 psi for the non-marginal soil and 13,212 psi for the marginal soil. Substitution into the AASHTO equation at W18 = 17.12 × 10^6 gave required SN values of 3.55 and 4.68. Layer contribution was checked using SN = a1D1 + a2m2D2

+ a3m3D3, with a1 = 0.44 for asphalt concrete, a2 = 0.14 for granular base, a3 = 0.11 for granular sub-base and m2 = m3 = 1.0. Layer thicknesses D are expressed in inches in the SN equation.

2.5 CBR-Based Pavement Design Procedure

The CBR-based pavement sections were interpreted using the empirical pavement design approach in Federal Ministry of Works, Highway Manual Part 1: Design, Volume III: Pavement and Materials Design (2013), which incorporates CBR-based pavement catalogues and guidance derived in part from TRL Overseas Road Note 31. The design CBR values of 42.79% and 13.03% were used with the design traffic level to select the corresponding pavement thicknesses. The specific catalogue source is stated to improve reproducibility.

Table 1: *AASHTO Design Input Parameters*

Parameter	Symbol	Adopted value	Basis/remark
Design traffic	W18	17.12×10^6 ESAL	Traffic reconstruction
Reliability	R	95%	Higher-order road design assumption
Standard normal deviate	ZR	−1.645	Corresponding to 95% reliability
Overall standard deviation	So	0.45	Typical flexible pavement value
Initial serviceability	p0	4.2	AASHTO flexible pavement value
Terminal serviceability	pt	2.5	Major road design value
Serviceability loss	ΔPSI	1.7	p0 − pt
Layer coefficients	a1, a2, a3	0.44, 0.14, 0.11	Asphalt, granular base, granular sub-base
Drainage coefficients	m2, m3	1.0, 1.0	Assumed good/normal drainage
FMW/ORN31 Subgrade Strength Class	S6 (CBR ≥ 30%)	S4 (CBR 8–14%)	

3. RESULTS AND DISCUSSION

3.1 Engineering Properties of the Soils

Table 2: *Engineering Properties of the Lateritic Soils*

Property	Non-Marginal Soil	Marginal Soil
Liquid Limit (%)	20.0	27.0
Plastic Limit (%)	14.58	17.15
Plasticity Index (%)	5.42	9.85
MDD (Mg/m³)	2.03	2.00
OMC (%)	11.1	10.0
CBR (%)	42.79	13.03

The engineering properties of the two lateritic soils show clear differences in subgrade quality. The non-marginal soil recorded a liquid limit of 20.0%, plastic limit of 14.58% and plasticity index of 5.42%, compared with 27.0%, 17.15% and 9.85%, respectively, for the marginal soil. The lower

plasticity of the non-marginal soil indicates lower susceptibility to moisture-induced volume changes, whereas the marginal soil is more likely to experience deformation under moisture fluctuations.

The compaction characteristics were similar. The non-marginal soil achieved MDD of 2.03 Mg/m³ at OMC of 11.1%, while the marginal soil achieved 2.00 Mg/m³ at 10.0%. The slightly higher density of the non-marginal soil indicates a somewhat denser and potentially more supportive soil matrix.

The largest difference was in CBR: 42.79% for the non-marginal soil and 13.03% for the marginal soil. Under the FMW/ORN31 grouping these correspond approximately to S6 and S4. Formal AASHTO or USCS classification is not reported because the complete particle-size distribution data were unavailable.

3.2 Flexible Pavement Design Using the CBR Method

The CBR-based pavement sections are presented in Table 3. For the non-marginal soil, with CBR of 42.79%, the required structure comprised 113 mm surfacing, 150 mm base and 150 mm sub-base, giving a total thickness of 413 mm. For the marginal soil, with CBR of 13.03%, the section comprised 100 mm surfacing, 150 mm base and 200 mm sub-base, giving a total thickness of 450 mm.

The marginal soil therefore required an additional 37 mm of total pavement thickness compared with the non-marginal soil, mainly because of the additional 50 mm of sub-base. This confirms the empirical CBR principle that lower subgrade strength generally requires thicker pavement layers to reduce stresses transmitted to the subgrade.

Table 3: *Flexible Pavement Design Thickness Using the CBR Method*

Layer	**Thickness (mm)**	
	Non-Marginal Soil	**Marginal Soil**
Surfacing	113	100
Base	150	150
Sub-base	150	200
Total	413	450

3.3 Flexible Pavement Design Using the AASHTO Method

The AASHTO pavement structures are presented in Table 4. Using W18 = 17.12 × 10⁶ ESALs, R = 95%, So = 0.45, ΔPSI = 1.7 and the CBR-derived resilient moduli, the required SN values were 3.55 for the non-marginal soil and 4.68 for the marginal soil.

Table 4: *Flexible Pavement Design Thickness Using the AASHTO Method*

Layer	**Thickness (mm)**	
	Non-Marginal Soil	**Marginal Soil**
Structural Number (SN)	3.55 required 3.70 provided	4.68 required 4.69 provided
Asphalt Surface	100	130
Base	200	230
Sub-base	200	270
Total Thickness	500	630

For the non-marginal soil, 100 mm asphalt surface, 200 mm granular base and 200 mm granular sub-base provide SN = 3.70, exceeding the required 3.55. The total thickness is 500 mm. For the marginal soil, 130 mm asphalt surface, 230 mm granular base and 270 mm granular sub-base provide SN = 4.69, exceeding the required 4.68. The total thickness is 630 mm.

The lower CBR-derived resilient modulus of the marginal soil is therefore reflected in a substantially larger required Structural Number and thicker pavement section.

3.4 Comparative Analysis

A comparison of the two design methods shows that AASHTO produces thicker pavement sections for both soil conditions. For the non-marginal soil, thickness increases from 413 mm under

CBR to 500 mm under AASHTO, an increase of 87 mm (21.1%). For the marginal soil, thickness increases from 450 mm to 630 mm, an increase of 180 mm (40.0%).

Table 5: *Comparison of Pavement Thickness and Material Quantity*

Soil	CBR total (mm)	AASHTO total (mm)	Difference (mm)	Increase (%)	Extra volume (m^3/m^2)
Non-marginal	413	500	87	21.1	0.087
Marginal	450	630	180	40.0	0.180

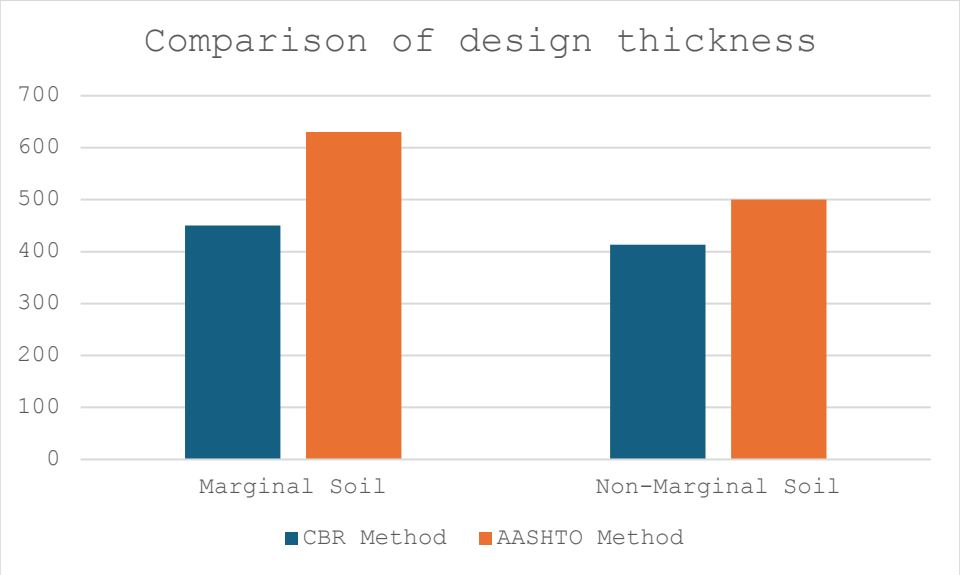

Figure 1: *Comparison of AASHTO and CBR Design Methods*

Figure 1 shows that the AASHTO sections are thicker for both soils, with the difference more pronounced for the weaker marginal subgrade. The thickness difference corresponds to an additional material quantity of approximately 0.087 m^3/m^2 for the non-marginal soil and 0.180 m^3/m^2 for the marginal soil. This provides a material-quantity proxy for economic comparison, although monetary cost and life-cycle cost cannot be established without project-specific unit rates and maintenance assumptions.

The greater AASHTO thickness should not be interpreted as proof of superior performance from thickness alone. Its principal distinction is the explicit inclusion of reliability, uncertainty, serviceability and resilient modulus in the design framework. Conversely, the CBR method remains attractive where data, time and analytical resources are limited. For detailed projects, the assumed VDF should be replaced with measured axle-load data and resilient modulus should preferably be measured directly or calibrated locally.

4. CONCLUSION

This study demonstrates that pavement design methodology materially affects the resulting flexible pavement structure. For lateritic soils with CBR values of 42.79% and 13.03%, the CBR-based method produced total pavement thicknesses of 413 mm and 450 mm, respectively, whereas the AASHTO 1993 analysis produced adopted sections of 500 mm and 630 mm. The AASHTO sections were therefore 21.1% and 40.0% thicker.

The difference is associated with the explicit consideration of cumulative ESALs, reliability, serviceability and resilient modulus in the AASHTO framework. The CBR method remains useful for preliminary and lower-data applications because of its simplicity and relatively low data requirements, but its reduced material quantity should not be interpreted automatically as lower life-cycle cost.

The analysis is limited by the assumed VDF, the use of CBR-derived rather than directly measured resilient modulus, incomplete particle-size distribution data and the absence of project-

specific drainage, seasonal and unit-cost information. Future work should incorporate axle-load surveys, direct resilient-modulus testing, complete AASHTO/USCS classification data, locally calibrated environmental and drainage parameters, and project-specific life-cycle cost analysis.

5. REFERENCES

AASHTO. (1993). Guide for design of pavement structures. American Association of State Highway and Transportation Officials.

Ahmed, F., Thompson, J., Kim, D., Huynh, N., & Carroll, E. (2023). Evaluation of pavement service life using AASHTO 1972 and mechanistic-empirical pavement design guides. International Journal of Transportation Science and Technology, 12(1). https://doi.org/10.1016/j.ijtst.2021.11.004

ASTM. (2008). Standard practice for thin-walled tube sampling of soils for geotechnical purposes (ASTM D1587-08, reapproved 2007).

Chitade, P. N., Sakharkar, S. C., Pekade, N. V., Bansod, P. S., Parihar, Y. D., Gedam, N. J., & Marve, S. R. (2024). Design of flexible pavement by CBR method. International Journal of Research Publication and Reviews, 5(5). https://doi.org/10.55248/gengpi.5.0524.1269

El-Ashwah, A. S., Mousa, E., El-Badawy, S. M., & Abo-Hashema, M. A. (2022). Advanced characterization of unbound granular materials for pavement structural design in Egypt. International Journal of Pavement Engineering, 23(2). https://doi.org/10.1080/10298436.2020.1754416

Federal Highway Administration. (2006). Geotechnical aspects of pavements (NHI-05-037). U.S. Department of Transportation.

Federal Ministry of Works. (2013). Highway manual part 1: Design, Volume III: Pavement and materials design. Federal Republic of Nigeria.

Inyang, E., Usanga, I., Okon, K., & Saturday, S. (2024). Influence of road rehabilitation on flexible pavement performance in Nigeria. International Journal of Transportation Engineering and Technology, 10(3). https://doi.org/10.11648/j.ijtet.20241003.11

Moharekpour, M., Liu, P., Schmidt, J., Oeser, M., & Jing, R. (2022). Evaluation of design procedure and performance of continuously reinforced concrete pavement according to AASHTO design methods. Materials, 15(6). https://doi.org/10.3390/ma15062252

Nneka, I. S. (2025). Effect of channelization on the performance of flexible pavements in Nigeria. IAA Journal of Scientific Research, 12(2). https://doi.org/10.59298/iaajsr/2025/122816.00

Noka, H. N. Z., Nurdin, A., & Abiyoga, N. P. (2025). The influence of subgrade CBR value and concrete quality on rigid pavement thickness: Case study Desa Simpang/Berbak to Simpang Ma. Sabak Road. Jurnal Komposit, 9(2). https://doi.org/10.32832/komposit.v9i2.17343

Olowosulu, A. T., Kaura, J. M., Murana, A. A., & Adeke, P. T. (2022). Development of framework for performance prediction of flexible road pavement in Nigeria using fuzzy logic theory. International Journal of Pavement Engineering, 23(11). https://doi.org/10.1080/10298436.2021.1922907

Omenogor, K. O., Oh, W. T., & Vanapalli, S. K. (2025). Mechanistic-empirical method of pavement design extending unsaturated soil mechanics. Transportation Geotechnics, 52. https://doi.org/10.1016/j.trgeo.2025.101569

Owolabi, A. O., Sadiq, O. M., & Abiola, O. S. (2012). Development of performance models for a typical flexible road pavement in Nigeria. International Journal for Traffic and Transport Engineering, 2(3). https://doi.org/10.7708/ijtte.2012.2(3).02

Prayudyanto, M. N., Alimuddin, A., & Suhendra, A. (2023). Analisis tebal perkerasan jalan dengan metode AASHTO terhadap kerusakan ruas Jalan Cileungsi–Cinyongsong Udik, Kabupaten Bogor. Jurnal Komposit, 7(1). https://doi.org/10.32832/komposit.v7i1.8062

Pule, B. B., & Yendaw, J. A. (2024). The effect of geotechnical soil properties on CBR value: Review. AI in Civil Engineering, 3(1). https://doi.org/10.1007/s43503-024-00039-1

Transport Research Laboratory. (1993). A guide to the structural design of bitumen-surfaced roads in tropical and sub-tropical countries (Overseas Road Note 31, 4th ed.). Crowthorne, UK.

Ziar, A., Ulfat, S., Serat, Z., & Armal, M. A. (2023). Cost-effectiveness analysis of design methods for rigid and flexible pavement: A case study of urban road. Archives of Advanced Engineering Science, 2(3). https://doi.org/10.47852/bonviewaaes32021264

International Conference on Engineering Innovation for Sustainable Development (ICESID 2026)
Faculty of Engineering, Ahmadu Bello University Zaria · 8–10 September 2026

EFFECT OF POLYCARBONATE PLASTIC ON THE MECHANICAL PROPERTIES OF ASPHALT CONCRETE

Kenneth, Ejike Ibedu[1,*], Abdulfatai, Adinoyi Murana[2], Muhammad, Ashiru[2], Abdulrahman, Nda'abo Alfa[2]

[1]*Department of Civil Engineering, Baze University, Abuja, Nigeria*
[2]*Department of Civil Engineering, Ahmadu Bello University, Zaria, Nigeria*

Email: ibedukenneth@gmail.com*, aamurana@abu.edu.ng, mohammeda@abu.edu.ng, abdul4real212@gmail.com

***Corresponding author**: Kenneth, Ejike Ibedu

DOI: https://doi.org/10.67203/sp.ICESID.2026

ABSTRACT

In Nigeria, plastics are indiscriminately discarded endangering man and the entire ecosystem. There is need for development of alternative ways in combating challenges of plastic waste disposal. These challenges have necessitated its adoption in asphalt concrete production. This study examined the use of polycarbonate plastic waste as an additive and the effect on strength properties of hot mix asphalt. Polycarbonate is a polymeric material. Fourier Transform Infrared analysis on polycarbonate revealed the presence of aromatic, methyl, carbonyls, amine, and alkene. Scanning electron microscopy and Energy dispersive x-ray spectrometry analysis showed that polycarbonate has spongy shape and the predominant elements are silicon, oxygen, carbon, and aluminum. For the experiment, Marshall method was adopted for mix design and testing. Polycarbonate plastic was introduced into the mix by means of dry process from 0 - 3% (at interval of 0.5%). The bitumen content used was varied from 6 – 7.5% (at intervals of 0.5%). The introduction of polycarbonate plastic improved the Marshall stability by 20% from 4.67 kN (Threshold) to 5.59 kN (Modified) at 2.5% addition of polycarbonate. Although flow did not improve, other volumetric properties recorded an improvement. This study concludes that an optimal dosage of 2.5% polycarbonate plastic will increase the strength of hot mix asphalt and consequently improve the service life of flexible pavement.

Keywords: *Polycarbonate Plastic; Mechanical Properties; Asphalt Concrete; Waste*

I. INTRODUCTION

Plastic is a group of synthetic or semi-synthetic material produced from hydrocarbons through polymerization. Polymerization is a sequence of chemical reactions chiefly on crude oils and natural raw materials (Luckscheiter & Ebii, 2020; Adogame, *et al*., 2021). Plastic is the general name for polymeric materials that may contain other materials for enhanced performance or colour (Yalwaji, *et al.*, 2022). Nigeria is among the largest importer and consumer of plastics in Africa, it is estimated that between 1996 and 2014 over 23 million tons of plastics were imported into Nigeria (Luckscheiter & Ebii, 2020; Dibia, *et al.*,2023). Polymers used in production of plastics includes the following; High Density Polyethylene (HDPE), Polyethylene Terephthalate (PET), Polycarbonate (PC), Low-Density Polyethylene (LDPE), Polylactic acid (PLA), Polypropylene (PP), Polyhydroxyalkanoates (PHA). Expanded polystyrene (EPS), Polystyrene (PS), Polyvinyl Chloride (PVC) Adogame, *et al*., (2021; Yalwaji, *et al.*, (2022). According to IHS Chemical, (2013) polycarbonate chemical is the highest consumed chemical in plastic industries, it reported that world-wide demand for polycarbonate surpasses 4.2 million tons annually. Million tons of plastic are littering the streets and harming our environment. Within this experiment Polycarbonate (PC) plastic waste was incorporated as an additive to improve the strength of asphalt concrete. Polycarbonate plastics used from home, offices, industries, food and packaging companies are non-biodegradable and cannot be recycled as such are dumped in the open site and eventually burnt openly on dumpsites causing the release of dioxins and furans into the atmosphere. This method of disposing plastic waste poses public health challenges and are great concern for residents and waste management authorities (Federal Ministry of Environment, 2020). This calls for alternative method of waste disposal that are economical and environmentally friendly.

Asphaltic concrete comprises of fine and coarse aggregate with bitumen as binder. Aggregate function as the structural framework for flexible pavement and bitumen serve as adhesive for the asphaltic mixture. About 90–95% of volume of asphaltic concrete mixtures are aggregates including mineral filler and bitumen is approximately 5 - 8%. Strength properties of asphaltic concrete directly impact the performance of flexible pavements. Asphaltic concrete is typically used in pavement construction due to its excellent performance in providing stability, driving comfort, water resistance and durability (Bakare, 2017). When a flexible pavement is to be constructed, a sample or representative of the mix design is prepared to test the consistency of the properties in compliance with specification. The mechanical properties of asphalt concrete to be tested are stability, durability, skid resistance and workability (Cesare, *et al.*, 2019). These properties make hot mix asphalt desirable for pavement. Flexible pavement develops defects during its service life. Road defect according to Okigbo, (2012) is any portion of a road, highway that deviates from the prescribed standard for safety and comfort of the rider. However, the service life of flexible pavement and rider's comfort by can be increased by incorporating different materials into asphalt mixes either in form of modifier, filler or admixture. In recent literatures, it is a common practice in highway engineering to improve the properties of asphalt binder and asphalt concrete with locally available waste material such as locust bean pod ash (Murana, *et al.*, 2024), pulverized burnt brick (Ibedu & Murana, 2024), polyvinyl chloride (Murana, *et al*., 2024), high density polyethylene (Murana *et al.*, 2024; Murana *et al.*, 2023), Bentonite clay (Ibedu & Asaolu, 2026), coconut shell ash and reclaimed asphalt pavement (Murana, *et al*., 2023), Soybean husk ash (Ibedu & Asen, 2026). These waste from industries and domestics products serves as an economical option in the search for material to improve for road construction. However, polycarbonate (PC) plastic possesses superior mechanical properties such as good toughness, high impact and crack resistance, high temperature resistance (Sisodia & Arora, 2022; Kumar & Raj, 2021). These properties, make polycarbonate (PC) plastic a suitable additive polymer material for asphalt production.

There are limited studies on the effect of polycarbonate plastic waste on asphalt concrete, despite the good mechanical properties of polycarbonate plastic. Therefore, this study is aimed at investigating the mechanical properties of asphalt concrete admixed with polycarbonate plastic and to obtain optimal dosage of polycarbonate needed to improve the performance of asphalt mixtures. Scanning Electron Microscopy (SEM) and Energy Dispersive X-Ray Spectrometry (EDS) were used for microstructural examination and elemental analysis of the polycarbonate plastic. This study bridges the knowledge gap in previous studies on plastic waste in asphalt concrete

2. METHODOLOGY

2.1 Materials

Materials used in this research were bitumen, aggregates and waste polycarbonate plastic. The aggregate and bitumen were sourced from Zeberced Group Limited along Kaduna – Zaria Road in Kaduna State, and Ringadas Nigeria Limited/ASCA Bitumen Company Abuja. The waste polycarbonate plastic was sourced from open refuse disposal dump in Samaru area of Zaria L.G.A. Kaduna State.

2.1.1 Polycarbonate

The polycarbonate was sourced from open dumpsite situated within Ahmadu Bello University, Zaria. The initial step in material involved the washing of polycarbonate waste with ethanol to strip away dirt, the material was spread out and allowed to air-dry 72 hours under ambient conditions to remove residual moisture. The dried polycarbonate was then cut into pellets forms and further reduced to a powdered form through pulverization using a laboratory grinding machine.

Plate I: Processing of polycarbonate waste (a) pellet polycarbonate (b) pulverized polycarbonate (c) dry mixing of polycarbonate (d) asphalt concrete admixed with polycarbonate

2.2 Methods

Test on Polycarbonate

i. Fourier Transform Infra-Red (FTIR)

Fourier Transform Infra-Red (FTIR) spectroscopy was employed to identify the functional groups present in the polycarbonate in accordance with ASTM D6348-12 (2020).

ii. Scanning Electron Microscopy and Energy Dispersive Spectroscopy (SEM/EDS)

Scanning Electron Microscopy and Energy Dispersive Spectroscopy (SEM/EDS) is a technique that uses a high-energy beam to create an image resolution surface and to identify elemental composition of a material's surface. The test was conducted in accordance with ASTM E2809-22, (2022).

Test on Aggregate

i. Sieve Analysis of Aggregates

Sieve analysis of aggregates was done by manual sieving. The sieving of aggregates was conducted to determine the distribution of different sizes of aggregate in a given batch aggregate. The test was conducted in accordance with ASTM C136/C136M-19 (2019)

Test on Asphaltic Concrete

i. Marshall Stability and Flow Test

Marshall stability is the maximum load that a compacted asphalt specimen can withstand before a deformation at a standard temperature of 60°C with a load applied at a constant rate of 50mm/min. The stability and flow are read from the dial gauges. The flow which is measured in 0.25mm units is the deformation that the specimen has undergone at the maximum load. The test was conducted in accordance with ASTM D6927-15 (2015).

ii. Production of Asphaltic Concrete Admixed with Polycarbonate Waste Plastic

For each bitumen content and replacement level, three replicate specimens were produced and tested. Approximately, 1200g of aggregates (including admixture) were blended and preheated to 140°C. Varying percentages of bitumen 6%, 6.5%, 7% and 7.5% by weight of the total mix, polycarbonate was then added to the aggregates. The mixture was thoroughly mixed to achieve homogeneity. The hot mix was immediately transferred to a mould (101.6mm diameter x 63.5mm height) and compacted with 75 blows per side. After compaction, the briquette sample was allowed to cool for 25 minutes before extraction. This procedure was applied to both threshold mixtures (0%) and mixtures containing 0.5 –3% polycarbonate at 0.5% increments. The prepared samples were subsequently subjected to Stability-flow tests and density-voids analysis in the laboratory in accordance with ASTM standard (ASTM D6926-20, 2020; ASTM D6927-15, 2015).

3. RESULTS AND DISCUSSIONS

3.1 FTIR Analysis of the Polycarbonate Plastic Material

The FTIR analysis was carried out on the polycarbonate plastic was recorded Figure 1 and tabulated in Table 1. The polycarbonate plastic gave characteristics absorption peaks in both functional groups and finger print region. The result of the infra-red spectrum in Figure 4.1 shows that the polycarbonate plastic gave peak due to $O\text{-}H_{str}$ at 3753.4 and 3693.8^{cm-1} due to alcohol, $C\text{-}H_{str}$ vibration band due to amine appeared at 3507.4^{cm-1}, $C\text{-}H_{str}$ vibration band appeared at 3041.5^{cm-1} due to Aromatic, $C\text{-}H_{str}$ absorption peak due to Methyl appeared at 2967 and 2922.2^{cm-1}, $C\text{-}H_{bend}$ vibration

band due to Aromatic appeared at 2072.4^{cm-1} , C=O_{str} vibration band appeared due to Anhydride at 1897.2^{cm-1}, C=O_{str} absorption peak due to Carbonyls appeared at 1770.8^{cm-1} , N-H_{bend} vibration band appeared due to Amine, N-O_{bend} absorption peak due to Nitro appeared at 1502.1^{cm-1}, C-Cstr vibration band due to Carboxylic appeared at 1408.9^{cm-1} , C-H_{str} vibration band appeared due to Aromatic amine at 1289.7^{cm-1} . At the fingerprint region, peak at C-O_{str} appeared at 1218.8^{cm-1} due to Carbonyl, C-O_{str} vibration band due to Ester appeared at 1185.3^{cm-1}, C-O_{str} vibration band appeared due to Alcohol at 1103.8^{cm-1}, C-O_{str} absorption peak due to Carbonyl appeared at 1159.2, 1013.3 and 1080.9^{cm-1}, C=C_{str} vibration band appeared at 887.5^{cm-1} due to Alkene. C-H_{bend} vibration band appeared at 827.1, 764.1 and 704.1. A similar results was obtained by Haghighi-Yazdi & Lee-Sullivan, (2015).

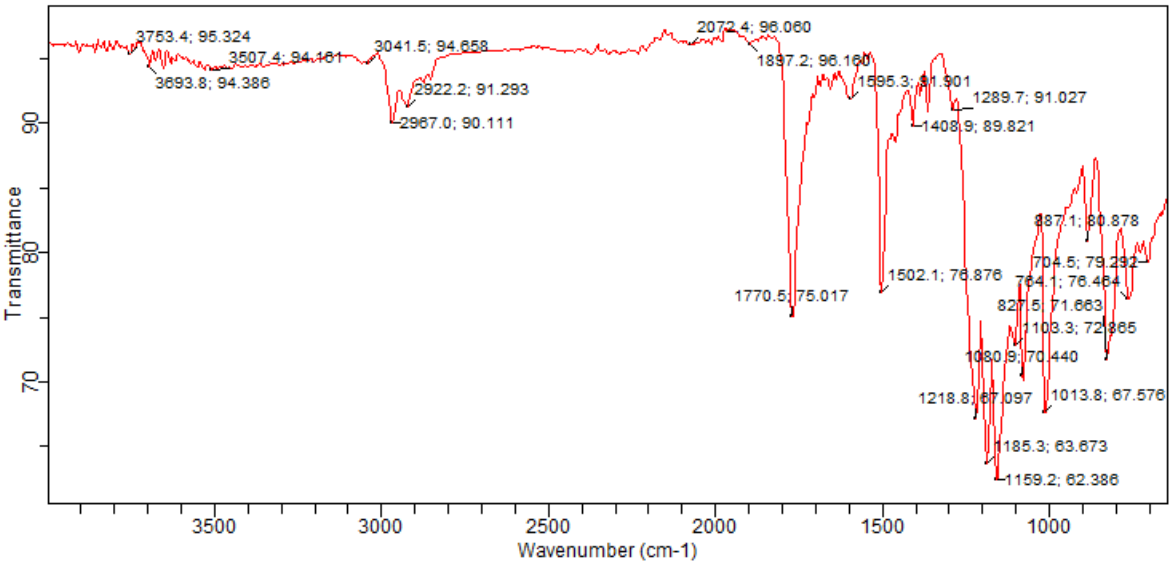

Figure 1: FTIR Spectrum of Polycarbonate

Table 1: Functional group, wavenumber and Vibration type of polycarbonate plastic

Functional Group	**Wavenumber (cm^{-1})**	**Vibration Type**
OH (Alcohols)	3753.4	Medium O-H Stretching
OH (Alcohols)	3693.8	Medium O-H Stretching
C-H (Amine)	3507.4	Strong C- H Stretching
C-H (Aromatic)	3041.5	Strong C - H Stretching
C-H (methyl)	2967	Weak C- H Stretching
C-H (methyl)	2922.2	Weak C- H Stretching
C-H (Aromatic)	2072.4	Weak C- H Bending
C=O (Anhydride)	1897.2	Strong C=O stretching
C=O (Carbonyls)	1170.8	Strong C=C stretching
N-H (Amine)	1595.3	Medium N-H bending
N-O (Nitro)	1502.1	Strong N-O bending
O-H (Carboxylic)	1408.9	Weak C-C stretching
C-H (Aromatic amine)	1289.7	Strong C-H stretching
C-O (Carbonyl)	1218.8	Strong C-O stretching
C-O (Ester)	1185.3	Strong C-O stretching
C-O (Alcohol)	1103.8	Strong C-O stretching
C-O (Carbonyl)	1159.2	Strong C-O stretching
C-O (Carbonyl)	1080.9	Strong C-O stretching
C-O (Carbonyl)	1013.3	Strong C-O stretching
C=C (Alkene)	887.5	Strong C=C stretching
CH_3	827.1	Strong C-H bending
C-H	764.1	Strong C-H bending
C-H	704.1	Strong C-H bending

3.2 Results of SEM and EDS on Polycarbonate

The SEM and EDS results from polycarbonate plastic is shown in Figure 2a and Figure 2b respectively. The morphology examination shown in Figure 2a was done using Scanning Electron Microscopy (SEM) technique with a magnification of 10,000x, it can be seen that polycarbonate appears to have a sponge-like shape rough texture, it was apparent that polycarbonate plastic was pulverized with size greater than 10µm. The elements contained in the polycarbonate was measured with EDS. The results obtained from the EDS spectrum is shown in Figure 2b, the major elements detected are namely; Silicon (Si) detected at 65.2%, Oxygen (O) detected at 15.2%, Aluminium (Al) detected at 7.2%, other elements detected are Carbon (C), Copper (Cu), Na (Na), Magnesium (Mg), and Potassium (K) at 3.2, 5.2, 1.5, 1.3, and 1.2% respectively, summation of the different elements normalized to total of 100%.

a

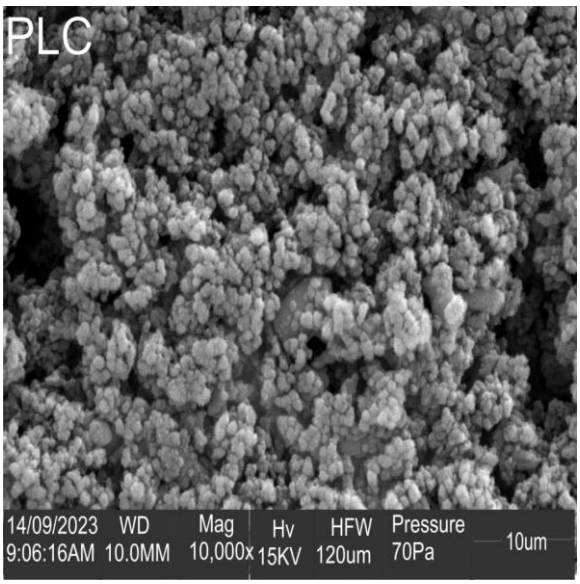

Figure 2a: SEM of Polycarbonate

b

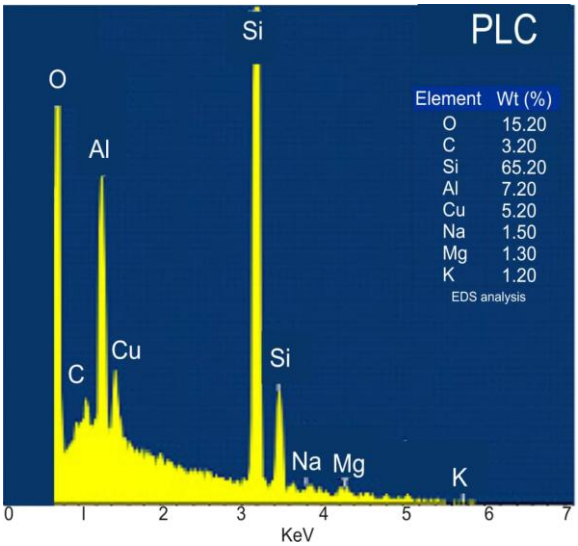

Figure 2b: EDX of Polycarbonate

3.3 Sieve Analysis on Aggregates

The particle size distribution for combined coarse aggregate, fine aggregate and mineral filler is shown in Figure 3. The results obtained satisfied the upper limit and lower limit boundary condition as specified by FMWH (2016). The proportioning was done to determine the volume of each aggregate by weight of the entire hot mix asphalt. Particle size distribution is important because they aggregates are the major determining factors in the density and interlocking ability of the mixture. Aggregate serve as the skeleton of hot mix asphalt and distributes stresses from wheel loads. Aggregate gradation also imparts on the finishes of the flexible pavement, i.e., the smoothness or roughness of road surfaces.

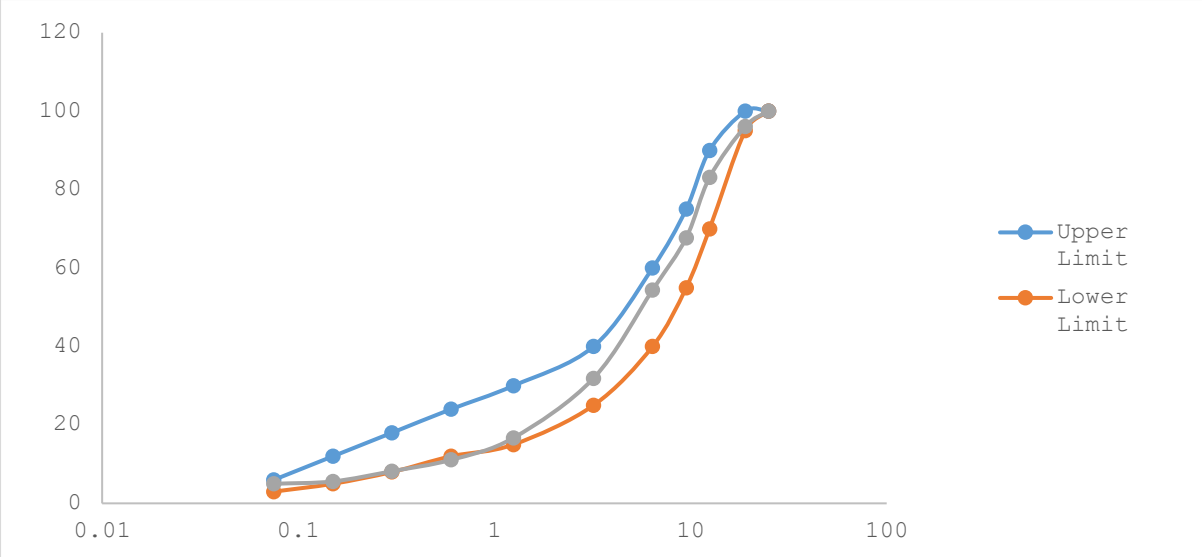

Figure 3: Particle size distribution

3.3.1 Marshall Stability

Figure 4 illustrates the variation in Marshall stability with bitumen content and polycarbonate addition. The stability values increased by an average of 8% when the bitumen content rose from 6% to 6.5% across all polycarbonate replacement levels. However, a notable 18% decrease occurred at 7% bitumen content, followed by a 7% recovery when the bitumen content was further increased to 7.5% across all polycarbonate content. The highest Marshall stability of 5.59 kN was achieved at 6.5% bitumen content with 2.5% polycarbonate addition. This represents a 20% improvement over the maximum stability of 4.67 kN recorded at the same bitumen content without polycarbonate. Higher stability values signify improved resistance to rutting and shoving (Awan, *et al*., 2022). All mixtures satisfied the Federal Ministry of Works and Housing (FMWH, 2016) minimum requirement of 3.5 kN. A similar trend was reported by Ibedu and Murana (2024).

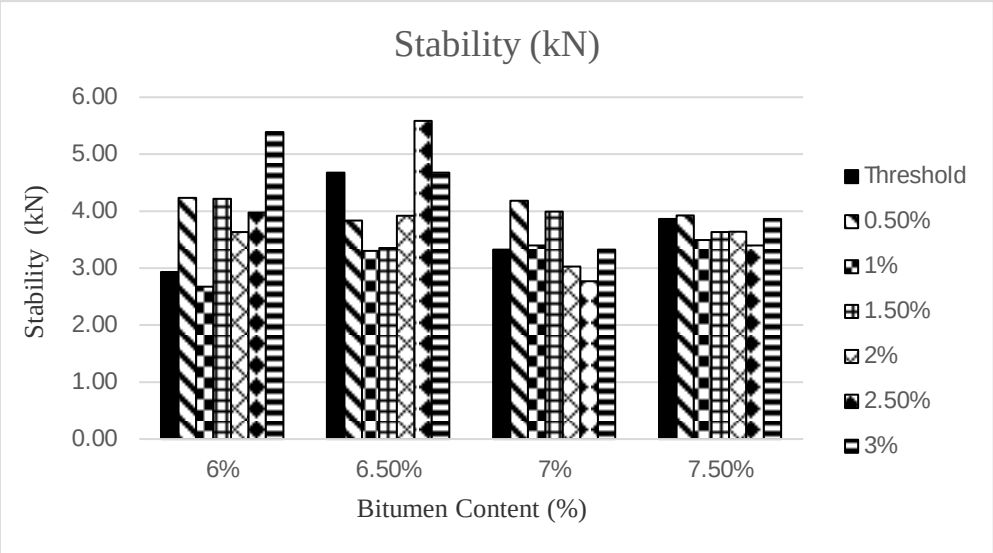

Figure 4: Variation of Stability with Polycarbonate Content

3.3.2 Marshall Flow

Figure 5 presents the variation in Marshall flow value with bitumen content and polycarbonate addition. Marshall flow measures the elasticity and plasticity of the asphaltic mixture. The flow values obtained ranged from 2.47 mm to 5.5 mm. The minimum flow of 2.47mm was observed at 6.5 bitumen

content and threshold polycarbonate content while the maximum Marshall flow was observed at 6% bitumen and 3% polycarbonate content. All mixtures satisfied the Federal Ministry of Works and Housing (FMWH, 2016) specification for base course, which requires flow values between 2 mm and 6 mm. However, the observed increase in flow with higher bitumen content and polycarbonate addition indicates greater plasticity of the mixture, implying an increased susceptibility to permanent deformation under traffic loading.

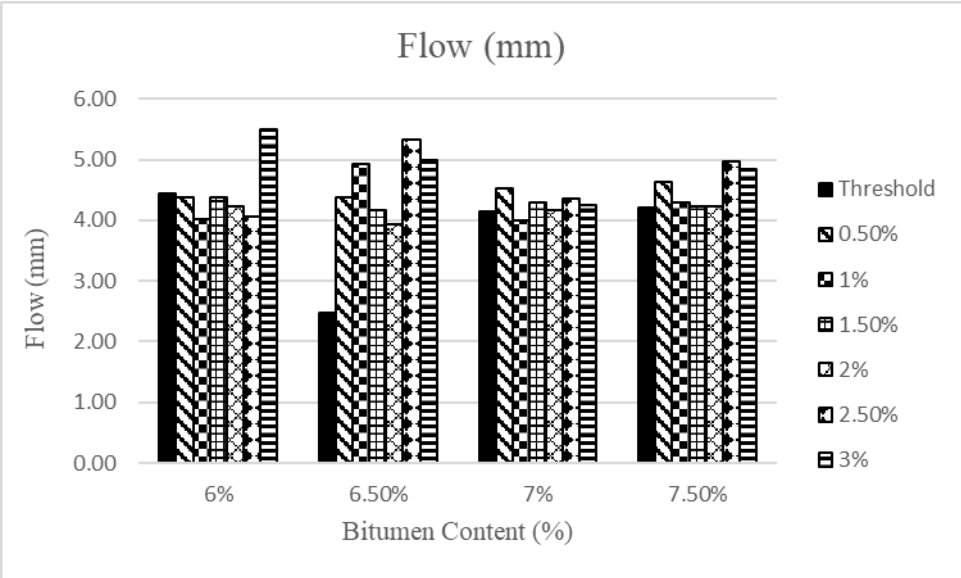

Figure 5: Variation of Flow with Polycarbonate Content

3.3.3 Unit Weight

Figure 6 shows the variation in unit weight (bulk density) of the asphalt mixtures with bitumen content and polycarbonate addition. Volumetric properties of asphalt concrete are strongly influenced by unit weight, which in turn significantly affects the overall durability of the pavement (Murana *et al*., 2023). As shown in Figure 6, at 6% bitumen content, the unit weight decreased with increasing polycarbonate content relative to the control mixture. The decrease may be attributed to inadequate chemical bonding between the polycarbonate waste plastic and the bitumen matrix particularly at 6% bitumen content which likely resulted in the formation of large voids within the mixture after compaction. In contrast, at higher bitumen contents (6.5%, 7%, and 7.5%), the unit weight increased progressively with higher polycarbonate levels. The increase can be attributed to the elevated viscosity and improved coating efficacy of the bitumen influenced by polycarbonate waste plastic, which facilitates better lubrication and rearrangement of aggregate particles, thereby more effectively filling inter particle voids.

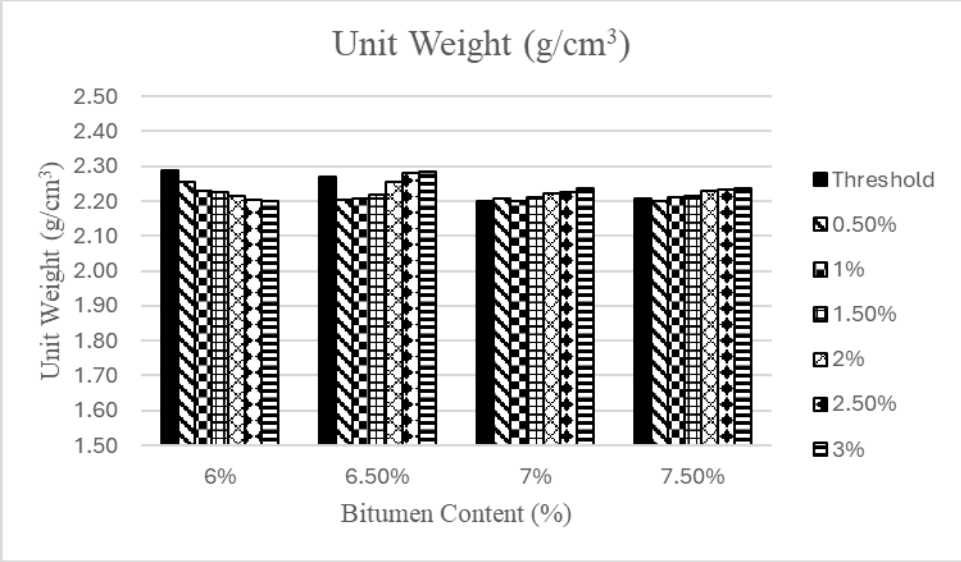

Figure 6: Variation of Unit Weight with Polycarbonate Content

3.3.4 Voids in Mineral Aggregate (VMA)

Figure 7 presents the variation in Voids in Mineral Aggregate (VMA) with bitumen content and polycarbonate addition. The results showed that VMA generally increased with increasing polycarbonate content. This trend is attributed to the sponge-like structure of the polycarbonate particles, which were not adequately coated by the bitumen, thereby creating additional voids within the mix and reducing inter-particle bonding.

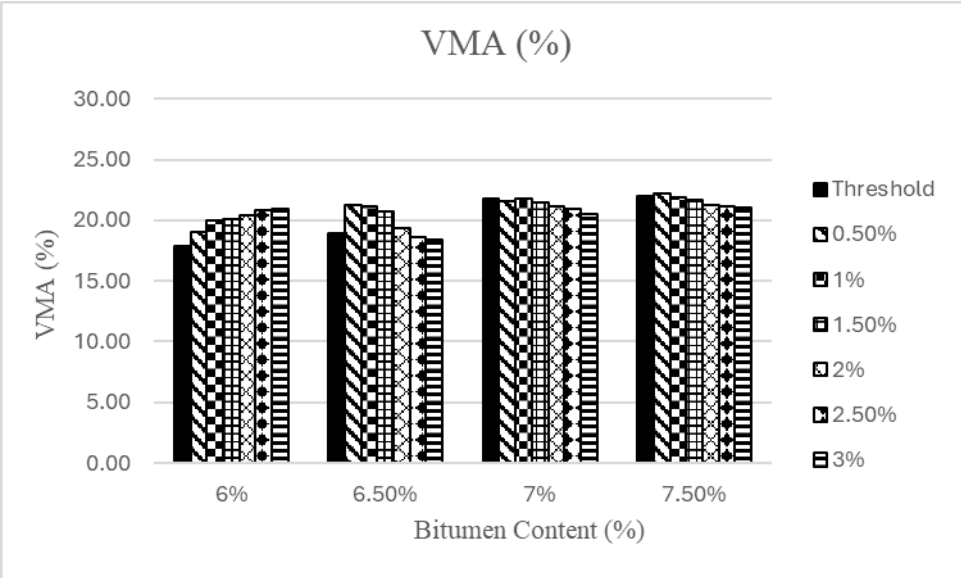

Figure 7: Variation of VMA with Polycarbonate Content

3.3.5 Voids in Total Mixture (Pa)

Figure 8 shows the variation in voids in the total mixture (Pa) with bitumen content and polycarbonate addition. The voids in the total mixture are directly related to the voids in mineral aggregate (VMA). All tested mixtures achieved Pa values within the Federal Ministry of Works and Housing (FMWH, 2016) acceptable range of 3% to 8%. Maintaining an adequate level of air voids is critical for durable asphalt performance. Excessive voids (due to insufficient bitumen to coat the

aggregates) can lead to premature cracking and moisture damage, while insufficient voids may result in rutting and bleeding under traffic loading.

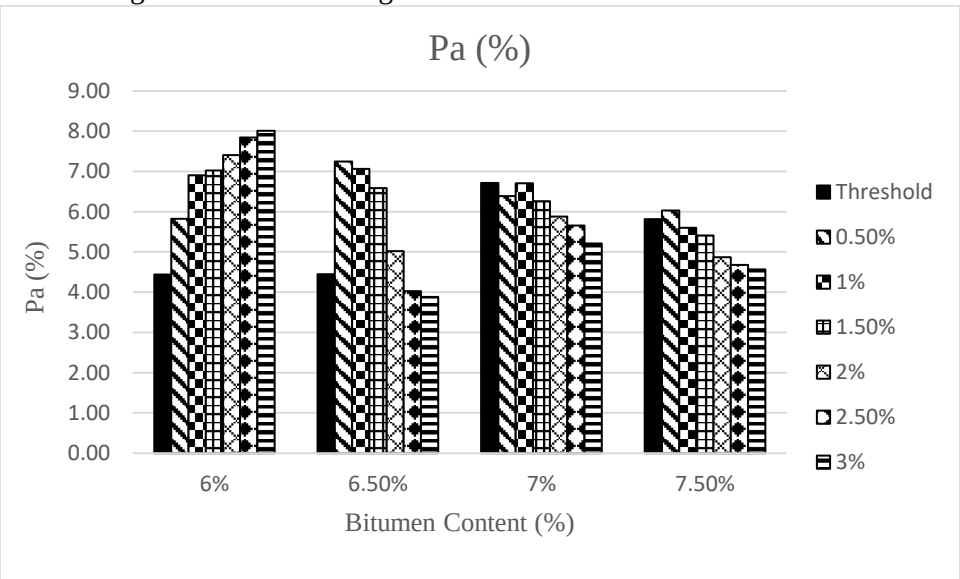

Figure 8: Variation of Pa with Polycarbonate Content

3.3.6 Voids Filled with Bitumen (VFB)

Figure 9 illustrates the variation in voids filled with bitumen (VFB) with changes in bitumen content and polycarbonate addition. As expected, VFB is inversely related to the voids in the total mixture (Pa). At 6% bitumen content, VFB generally decreased with increasing polycarbonate content compared to the control mixture. In contrast, at higher bitumen contents (6.5%, 7%, and 7.5%), VFB increased with higher polycarbonate replacement levels. This indicates that sufficient bitumen was available to effectively coat and bind the aggregates, thereby reducing the air voids in the mixture. Notably, the mixture containing 6 - 7.5% bitumen content and 0.5 – 1.5% polycarbonate content satisfied the requirement of 65 – 72% VFB range for base course compacted asphaltic concrete as stipulated by the Federal Ministry of Works and Housing (FMWH, 2016).

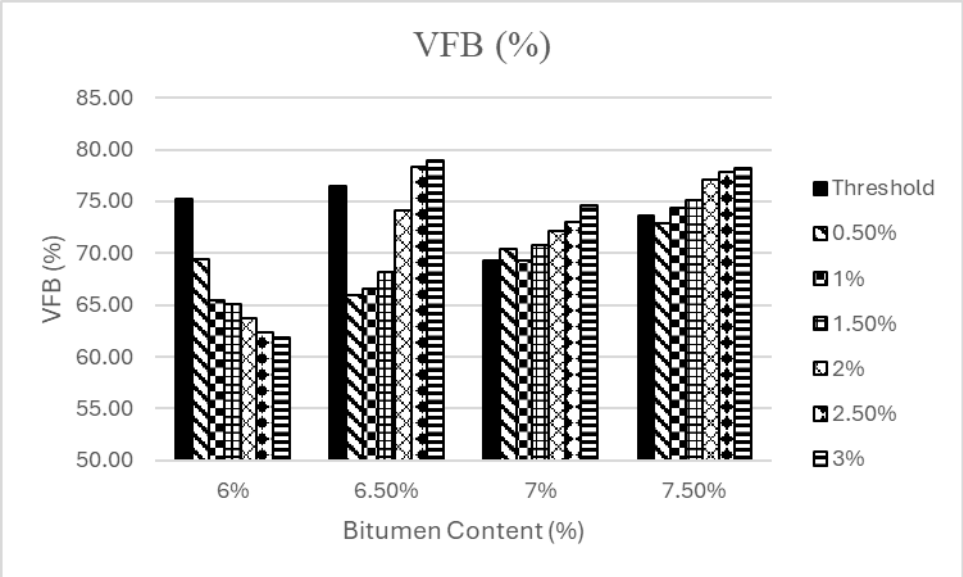

Figure 9: Variation of VFB with Polycarbonate Content

4. CONCLUSION

Based on the results of this study, the following conclusions can be drawn:

i. FTIR analysis of the polycarbonate revealed the presence of key functional groups, including methyl aromatic, anhydride, amine, carboxylic, aromatic amine, carbonyl, and alkene groups, confirming its polymeric nature

ii. The incorporation of polycarbonate into hot mix asphalt improved the mechanical properties (Marshall stability) by up to 20% at 6.5% bitumen content and 2.5% polycarbonate content, compared to the threshold mixture. The performance of polycarbonate as an admixture in Marshall stability of asphalt concrete meets and, in some cases, exceeds the requirements of 3.5kN stipulated by the Federal Ministry of Works and Housing (FMWH, 2016). Similarly, the Marshall flow values satisfied 2 - 6mm requirement with optimum 5.5mm at 6% bitumen content and 3% polycarbonate content. Furthermore, the results of unit weight, voids in mineral aggregate (VMA), total voids in mixture (Pa) and voids filled with bitumen (VFB) indicated improvement. These results showed that polycarbonate waste enhances both mechanical and volumetric properties of asphalt concrete.

REFERENCES

Adogame, L., Alo, B., & Onianwa, P. (2021). *National Policy on Plastics Waste Management: Gaps & Recommendations.* Lagos: Sustainable Research and Action for Environmental Development (SRADeV Nigeria). .

ASTM C136/C136M-19. (2019). *Standard Test Method for Sieve Analysis of Fine and Coarse Aggregates.* West Conshohocken, PA: American Society for Testing and Materials (ASTM) International. Retrieved from www.astm.org

ASTM D6348-12. (2020). *Standard Test Method for Determination of Gaseous Compounds by Extractive Direct Interface Fourier Transform Infrared (FTIR) Spectroscopy,.* West Conshohocken, PA: American Society for Testing and Materials (ASTM) International. Retrieved from www.astm.org

ASTM D6926-20. (2020). *Standard Practice for Preparation of Asphalt Mixture Specimens Using Marshall Apparatus.* West Conshohocken, PA: American Society for Testing and Materials (ASTM) International. Retrieved from www.astm.org

ASTM D6927-15. (2015). *Standard Test Method for Marshall Stability and Flow of Asphalt Mixtures.* West Conshohocken, PA: American Society for Testing and Materials (ASTM) International. Retrieved from www.astm.org

ASTM E2809-22. (2022). *Standard Guide for Using Scanning Electron Microscopy/Energy Dispersive X-Ray Spectroscopy (SEM/EDS) in Forensic Polymer Examinations.* West Conshohocken, PA: American Society for Testing and Materials (ASTM) International. Retrieved from www.astm.org

Awan, H. H., Hussain, A., Javed, M. F., Qiu, Y., Alrowais, R., Mohamed, A. M., & Alzahrani, A. M. (2022). Predicting marshall flow and marshall stability of asphalt pavements using multi expression programming. *Buildings*, 12(3), 314.

Bakare, S. M. (2017). The Evaluation of Ceramic Waste as Partial Replacement of Coarse Aggregate in Hot Mix Asphalt. *Unpublished M. Sc Thesis, Faculty of Engineering, Department of Civil Engineering, Ahmadu Bello University*. Zaria, Nigeria.

Cesare, S., Piergiorgio, T., Claudio, L., & Francesco, M. (2019). Application of mining waste powder as filler in hot mix asphalt. *MATEC Web of Conferences, 274*, 2-6. doi:https://doi.org/10.1051/matecconf/201927404002

Dibia, S. I., Wala, K. T., Onwuzurike, U., Benjamin, A., & Arinze, C. P. (2023). The impacts of plastic pollution on public health in Nigeria . *International Journal of Research in Civil Engineering and Technology, 4*(1), 6-10.

Federal Ministry of Environment. (2020). *National Policy on Plastic Waste Management.* Abuja: Federal Ministry of Environment.

FMWH. (2016). *Nigerian General Specifications for Roads and Bridges.* Federal Ministry of Works and Housing, Abuja.

Haghighi-Yazdi, M., & Lee-Sullivan, P. (2015). FTIR analysis of a polycarbonate blend after hygrothermal aging. *Journal of Applied Polymer Science, 3*, 1-6. doi:10.1002/app.41316

Ibedu, K. E., & Asaolu, J. J. (2026). Utilization of Bentonite Clay as Sustainable Filler Material in Hot Mix Asphalt. *4th Faculty of Engineering and Technology International Conference (FETiCON 2026)* (pp. 192-201). Ilorin: University of Ilorin, Nigeria. doi:10.63748/FETiCON2026.v4i1CMTid

Ibedu, K. E., & Asen, I. S. (2026). Enhancing Marshall Stability Performance of Asphalt Concrete with Soybean Husk Ash as Sustainable Mineral Filler. *4th Faculty of Engineering and Technology International Conference (FETiCON 2026)* (pp. 384-394). Ilorin: University of Ilorin, Nigeria. doi:10.63748/FETiCON2026.v4i1CMT266

Ibedu, K. E., & Murana, A. A. (2024). Effect of Blended Granite Dust and Pulverized Burnt Brick as Mineral Filler in Hot Mix Asphalt. *Nigerian Journal of Engineering, 31*(2), 55-65.

IHS Chemical. (2013). *Chemical Economics Handbook Polycarbonate Resins.* London, United Kingdom: IHS Chemical.

Kumar, R., & Raj, P. (2021). A Brief Review: Study on Mechanical Properties of Polycarbonate with Different Nanofiller Materials. *Advances in Materials and Manufacturing Engineering, 7*, 285-291.

Luckscheiter, J., & Ebii, C. (2020). *Plastic Atlas; Facts and figures about the world of synthetic polymers.* Abuja: Heinrich Böll Foundation.

Murana, A. A., Amartey, Y. D., Abah, L. I., Ibedu, K. E., & Bitrus, J. N. (2024). Strength Properties of Asphalt Mixture Produced with Polyvinyl Chloride (PVC) Modified Bitumen. *Covenant Journal of Engineering Technology, 8*(2), 40-49.

Murana, A. A., Ibedu, K. E., Isah, A. A., & Ochepo, J. (2024). Evaluation of locust bean pod ash as mineral filler in hot mix asphalt. *Journal of Civil Engineering, Science and Technology, 15*(1), 40-49. doi:10.33736/jcest.6352.2024

Murana, A. A., Ochepo, J., Yerima, A. M., & Ibedu, K. E. (2023). Comparing Determinants of Physical Properties of Bitumen Modified with High Density Polyethylene. *Umudike Journal of Engineering and Technology (UJET), 9*(2), 90-98. doi:https://doi.org/10.33922/j.ujet_v9i2_9

Murana, A. A., Ochepo, J., Yerima, M. A., & Ibedu., K. E. (2024). Properties of HMA Containing High Density Polyethylene Modified with Reclaimed Asphalt. *Jordan Journal of Civil Engineering, 18*(3), 389-404. doi:http://dx.doi.org/10.14525/JJCE.v18i3.03

Murana, A. A., Okwudili, P. P., & Ibedu, K. E. (2023). Utilization of coconut shell ash as filler for hot mix asphalt containing reclaimed asphalt pavement. *UNIZIK Journal of Engineering and Applied Sciences, 2*(3), 474-483.

Okigbo, N. (2012). Causes of highway failures in Nigeria. *International journal of engineering science and technology (IJEST), 4*(11), 4695-4703.

Sisodia, S. M., & Arora, P. (2022). Polycarbonate Material of Future. *International Journal of Innovative Science and Research Technology, 7*(4), 553-556.

Yalwaji, B., John-Nwagwu, H. O., & Sogbanmu, T. O. (2022). Plastic pollution in the environment in Nigeria: A rapid systematic review of the sources, distribution, research gaps and policy needs. *Scientific African*, 1-13. doi:https://doi.org/10.1016/j.sciaf.2022.e01220

EFFECT OF SOIL LEAD CONTAMINATION ON THE GROWTH CHARACTERISTICS AND PHYTOREMEDIATION POTENTIAL OF SUNFLOWER (HELIANTHUS ANNUUS L.), COMMON DANDELION (TARAXACUM OFFICINALE) AND JATROPHA (JATROPHA CURCAS L.)

Sumaila Muhammed Shaibu[1], Aliyu Adamu Dandajeh[1,*], Aliyu Ishaq[1], Alice Ibrahim Onize[2], Raphael Owoicho Ejembi[1]

[1]*Ahmadu Bello University Zaria*
[2]*Bayero University Kano, Nigeria*

Email: shaibusumailamuhammed@gmail.com, aadandaje@gmail.com*, aishaq@abu.edu.ng, aliceibrahim15@gmail.com, raphaelejemb@gmail.com

***Corresponding author**: Aliyu Adamu Dandajeh

DOI: https://doi.org/10.67203/sp.ICESID.2026

ABSTRACT

Lead (Pb) contamination of soil is a persistent environmental problem because Pb is non-biodegradable, can remain in soil for long periods, and may adversely affect soil quality, vegetation, water resources and human health. This study evaluated the effects of Pb contamination on growth characteristics and the phytoremediation potential of sunflower (Helianthus annuus L.), common dandelion (Taraxacum officinale) and Jatropha (Jatropha curcas L.) under controlled pot conditions at the Institute for Agricultural Research, Ahmadu Bello University, Samaru, Zaria. Topsoil (0–20 cm) was collected, prepared and contaminated with Pb under controlled laboratory conditions. Three kilograms of prepared soil were placed in each pot, seedlings were established, soil moisture was maintained at approximately 65% field capacity, and plants were harvested after 60 days. Plant growth, residual soil Pb, Pb accumulation in roots, stems and leaves, and comparative phytoremediation indicators were assessed. Soil and plant samples were digested and analysed using atomic absorption spectrophotometry. Growth observations were summarized descriptively because seedlings within a pot are not independent experimental replicates. Jatropha recorded the lowest residual soil Pb concentration (82 mg/kg), the highest summed tissue Pb concentration (2,308 mg/kg), and the highest calculated soil Pb reduction (90.4%). Dandelion and sunflower showed calculated reductions of 65.6% and 64.5%, respectively. The highest translocation factors were observed for sunflower (1.84) and dandelion (1.82), compared with Jatropha (1.53). The findings indicate species-specific differences in Pb accumulation and partitioning under the tested conditions; however, the observed soil Pb reductions should be interpreted as preliminary because each species × treatment combination was represented by a single pot. Replicated greenhouse and field-scale studies are required to confirm treatment effects and remediation performance.

Keywords: *lead contamination; phytoremediation; Jatropha; sunflower; dandelion; soil remediation; translocation factor*

1.0 INTRODUCTION

Lead (Pb) contamination of soil is a persistent environmental concern because Pb is non-biodegradable and can remain in soil for long periods, with implications for soil quality, vegetation, water resources and human health. Phytoremediation uses plants and associated biological processes to reduce contaminant concentrations or toxicity and is regarded as a potentially lower-cost complementary approach for contaminated sites (Ali et al., 2013; Zhang et al., 2024).

Pb uptake and translocation are influenced by soil pH, particle size, organic matter, cation exchange processes, root characteristics and rhizosphere interactions. Plants may respond to Pb stress through root retention, cell-wall binding, sequestration and antioxidant defence (Rahman et al., 2024). These processes can produce substantial differences among plant species in Pb accumulation and partitioning.

Sunflower has demonstrated Pb uptake and translocation potential under controlled soil exposure (Ngabra et al., 2024). Recent evidence also indicates that common dandelion can accumulate trace elements, including Pb, across different plant tissues and can exhibit strong accumulation characteristics (Vural, 2024). Jatropha has likewise shown potential for phytoremediation of metal-impacted soils, including Pb, particularly where soil amendments improve plant growth and biomass production (Lim et al., 2024).

Despite these advances, comparative evidence for sunflower, common dandelion and Jatropha evaluated under comparable controlled Pb exposure remains limited. Comparative screening is useful because remediation performance should be considered alongside plant growth, tissue accumulation and Pb partitioning. The present study therefore evaluates the three species under controlled pot conditions, with emphasis on observed soil Pb reduction, tissue accumulation, translocation and selected growth characteristics.

The aim of this study was to investigate the effects of soil Pb contamination on the growth characteristics and comparative phytoremediation potential of sunflower, common dandelion and Jatropha under controlled pot conditions. The specific objectives were to: (i) determine the observed growth responses of the three species under Pb exposure; and (ii) determine and compare observed soil Pb reduction, tissue accumulation and translocation characteristics.

2.0 MATERIALS AND METHODS

2.1 Experimental Design and Study Area

The study employed a controlled environmental pot experiment to compare the growth response and Pb-remediation indicators of sunflower (Helianthus annuus L.), common dandelion (Taraxacum officinale) and Jatropha (Jatropha curcas L.). The experiment was conducted at the Institute for Agricultural Research, Ahmadu Bello University, Samaru, Zaria, Kaduna State, Nigeria (approximately 11°11′N, 7°38′E; 686 m above sea level). Six plastic pots were used: one Pb-treated pot and one uncontaminated control pot for each species. Each pot contained 3.0 kg of soil. Three seedlings of each species were monitored within the corresponding pot for growth measurements. Because the three seedlings within a pot shared the same soil environment, they were treated as within-pot observations rather than independent pot-level replicates.

The experimental arrangement permits preliminary descriptive comparison of growth measurements but does not provide independent replication for treatment-level inference. Accordingly, soil Pb reduction, tissue Pb accumulation, the whole-plant Pb accumulation index and translocation factor were reported descriptively.

2.2 Experimental Materials

The experimental materials comprised topsoil, plastic pots, sunflower seeds/seedlings, dandelion and Jatropha seedlings, lead nitrate [$Pb(NO_3)_2$], deionized and distilled water, urea fertilizer, sieves and laboratory glassware. Major equipment included an electronic balance, oven, mortar and pestle, microwave digestion system, wet digester, pH meter, flame photometer, UV–Visible spectrophotometer and Zeenit 700P atomic absorption spectrophotometer (AAS).

2.3 Soil Preparation and Lead Contamination

Topsoil was collected from the 0–20 cm depth within the study area. Plant residues, stones and other debris were removed, after which the soil was air-dried, gently disaggregated and passed through a 2.0-mm nylon sieve. Soil description and classification procedures were consistent with standard soil-survey practice (U.S. Department of Agriculture, Natural Resources Conservation Service [USDA-NRCS], 2017). Selected soil properties included pH (7.57), organic matter (2.72%), total organic carbon (1.58%), available phosphorus (4.68 mg/kg), potassium (138 mg/kg), bulk density (1.25 g/cm^3) and sandy-loam texture.

Pb-treated soil was produced in the laboratory using the predetermined Pb-loading protocol and appropriate laboratory safety procedures. The measured initial Pb concentrations were 572 mg/kg for sunflower, 800 mg/kg for dandelion and 851 mg/kg for Jatropha. These measured values were used as the experimental starting concentrations for calculating percentage soil Pb reduction because

they represent the analytical baseline. Differences among starting concentrations indicate that the species-associated pots did not begin at identical measured Pb concentrations; consequently, cross-species comparisons of percentage reduction are preliminary rather than fully controlled treatment comparisons.

2.4 Plant Establishment and Experimental Management

Healthy and relatively uniform seedlings of sunflower, dandelion and Jatropha were established in their respective contaminated and control pots following soil equilibration. All pots were maintained under similar environmental conditions, with soil moisture maintained at approximately 65% of field capacity through regular watering. Where fertilizer was applied, the same quantity and procedure were used across treatments.

Plants were monitored throughout the experiment, and growth characteristics were recorded periodically. Plants were harvested after 60 days. At harvest, plant height, root length and fresh and dry biomass were determined. Plant tissues were separated into roots and shoots, with shoots further divided into stems and leaves where required.

2.5 Sample Preparation and Lead Analysis

Plant tissues were washed with tap water and deionized water, oven-dried to constant weight, ground using an agate mortar and pestle, and passed through a 0.25-mm nylon sieve. Post-experiment soil samples were air-dried and passed through a 2.0-mm sieve. Approximately 0.5 g of soil and 0.1000 g of dried plant material were subjected to acid digestion using the laboratory-established procedure, with the resulting digests diluted to known volumes with deionized water. The general analytical approach is consistent with established methods for heavy-metal determination in soils (Davidson, 2012). Lead concentrations were determined using a Zeenit 700P atomic absorption spectrophotometer after calibration with Pb standards. Reagent blanks and duplicate samples were included as quality-control measures.

Determination of Element Concentration

Element concentration was calculated using the following mass-balance conversion:

$$\mathbf{C_{element}\ (mg/kg) = [(C_s - C_\beta) \times V \times DF] / W} \quad (1)$$

where $C_{element}$ is the concentration of the element in the sample (mg/kg); C_s is the sample concentration obtained from the instrument (mg/L); C_β is the blank concentration (mg/L); V is the final extraction or digestion volume (mL); DF is the dilution factor; and W is the mass of sample analysed (g).

2.6 Evaluation of Phytoremediation Potential and Data Analysis

The comparative phytoremediation assessment used observed soil Pb reduction, Pb concentrations in roots, stems and leaves, a study-specific whole-plant Pb accumulation index, translocation factor (TF), and selected plant-growth observations. Microsoft Excel 2016 was used for data organization and calculations, while IBM SPSS Statistics Version 22 was used to organize the growth observations. Because there was only one pot per species × treatment combination, inferential tests based on seedlings within the same pot were not treated as independent treatment-level evidence. The growth results are therefore presented descriptively.

Observed soil Pb reduction was calculated as:

$$\mathbf{Soil\ Pb\ reduction\ (\%) = [(C_i - C\boldsymbol{f}) / C_i] \times 100} \quad (2)$$

where C_i is the measured initial soil Pb concentration (mg/kg) and $C\boldsymbol{f}$ is the final soil Pb concentration (mg/kg). This metric represents calculated concentration reduction and should not be interpreted as proof of plant-mediated Pb removal because leaching, redistribution and other mass-balance processes were not independently quantified.

Total Pb remaining in soil (mg) = final soil Pb concentration (mg/kg) × soil mass (kg).

A study-specific whole-plant Pb accumulation index was calculated as:

Whole-plant Pb accumulation index = (Root Pb + Stem Pb + Leaf Pb) / Initial soil Pb

(3)

The index is a comparative ratio developed for this dataset and should not be labelled as a conventional bioaccumulation factor (BCF) because the numerator is a summed tissue concentration rather than a biomass-normalized plant concentration.

Translocation factor (TF) was calculated as:

TF = (Stem Pb + Leaf Pb) / Root Pb

(4)

A TF greater than 1 indicates that the combined stem and leaf Pb concentration exceeded the root Pb concentration under the calculation used. Data were compared descriptively among species and treatments.

3.0 RESULTS AND DISCUSSION

3.1 Soil Properties and Lead Loading

The experimental soil had a pH of 7.57, indicating a slightly alkaline reaction. Organic matter (2.72%) and total organic carbon (1.58%) were moderate, while available phosphorus (4.68 mg/kg) was low. Exchangeable potassium was 138 mg/kg, calcium 7.40 mg/kg, sodium 184 mg/kg and magnesium 2.00 mg/kg. Bulk density was 1.25 g/cm³ and total porosity was 52.8%. The particle-size distribution of 62% sand, 28% silt and 10% clay classified the soil as sandy loam. Soil pH, texture and organic matter can influence Pb retention, mobility and plant availability (Rahman et al., 2024; Zhang et al., 2024).

Table 1: Baseline physicochemical properties of the experimental soil.

Parameter	Value	Unit	Interpretation
Soil pH	7.57	—	Slightly alkaline
Organic matter	2.72	%	Moderate
Total organic carbon	1.58	%	Moderate
Available phosphorus	4.68	mg/kg	Low
Exchangeable K	138	mg/kg	Moderate
Exchangeable Ca	7.40	mg/kg	Very low
Exchangeable Na	184	mg/kg	High
Exchangeable Mg	2.00	mg/kg	Low
Bulk density	1.25	g/cm³	Good
Total porosity	52.8	%	High
Textural class	Sandy loam	62% sand; 28% silt; 10% clay	Sandy loam

Source: Researcher fieldwork (2026); soil-description framework informed by USDA-NRCS (2017). Available phosphorus determination was based on the reported laboratory procedure and the Olsen method (Olsen et al., 1954).

3.2 Residual Soil Pb and Plant Uptake

Measured baseline concentrations differed among the species-associated pots, with initial soil Pb of 572 mg/kg for sunflower, 800 mg/kg for dandelion and 851 mg/kg for Jatropha. After 60 days, final soil Pb concentrations were 203, 275 and 82 mg/kg, respectively. Jatropha also had the highest summed tissue Pb concentration (root + stem + leaf = 2,308 mg/kg), followed by dandelion (1,576 mg/kg) and sunflower (1,108 mg/kg). These results indicate strong species-specific differences in tissue Pb accumulation under the tested conditions, but the lack of independent pot replication prevents a statistical claim that species caused the observed differences.

Table 2: Initial and final soil Pb concentrations and Pb accumulation in plant tissues.

Species	Initial soil Pb (mg/kg)	Final soil Pb (mg/kg)	Root Pb (mg/kg)	Stem Pb (mg/kg)	Leaf Pb (mg/kg)	Summed tissue Pb (mg/kg)
Sunflower	572	203	390	388	330	1,108
Dandelion	800	275	558	465	553	1,576
Jatropha	851	82	913	800	595	2,308

3.3 Calculated Soil Pb Reduction

Using the measured initial and final concentrations, the calculated soil Pb reductions were 64.5% for sunflower, 65.6% for dandelion and 90.4% for Jatropha. Jatropha therefore had the largest observed concentration reduction. However, because initial concentrations differed and only one pot represented each species × treatment combination, the ranking should be interpreted as a preliminary screening result rather than definitive evidence of superior phytoremediation efficiency.

Table 3: Calculated soil Pb reduction after 60 days.

Species	Initial Pb (mg/kg)	Final Pb (mg/kg)	Calculated reduction (%)	Descriptive rank
Jatropha	851	82	90.4	1
Dandelion	800	275	65.6	2
Sunflower	572	203	64.5	3

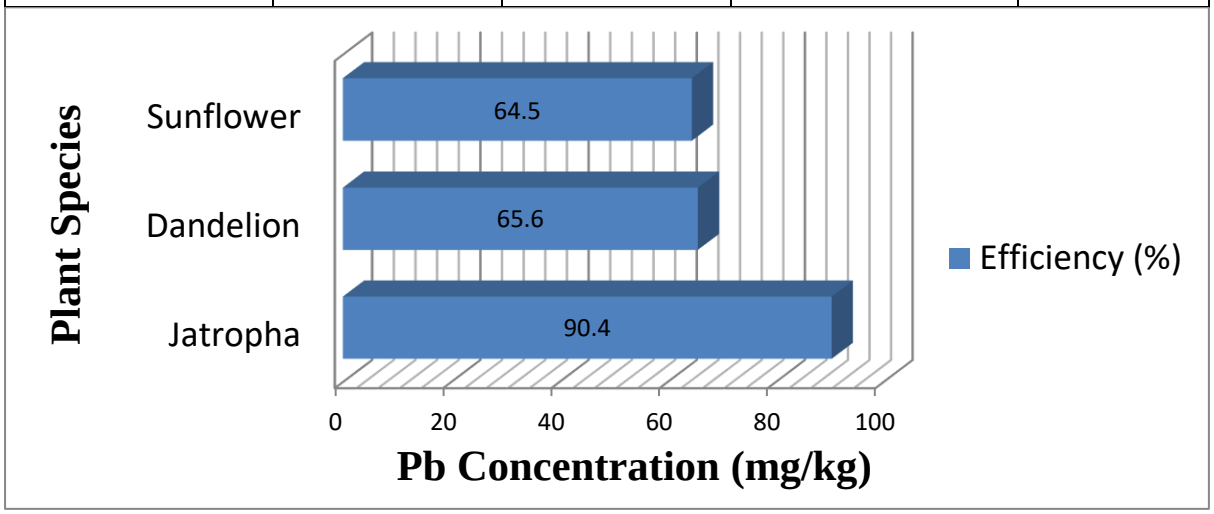

Figure 1: Calculated percentage reduction in soil Pb concentration after 60 days.

3.4 Whole-Plant Pb Accumulation Index

The whole-plant Pb accumulation index was 1.94 for sunflower, 1.97 for dandelion and 2.71 for Jatropha. Jatropha therefore recorded the highest comparative tissue-to-initial-soil ratio. The result is consistent with the high tissue Pb concentrations observed in Jatropha and with recent evidence that Jatropha can accumulate Pb and other metals under contaminated-soil conditions (Lim et al., 2024).

Table 4: Study-specific whole-plant Pb accumulation index.

Species	Root Pb	Stem Pb	Leaf Pb	Summed tissue Pb	Initial soil Pb	Accumulation index
Sunflower	390	388	330	1,108	572	1.94
Dandelion	558	465	553	1,576	800	1.97
Jatropha	913	800	595	2,308	851	2.71

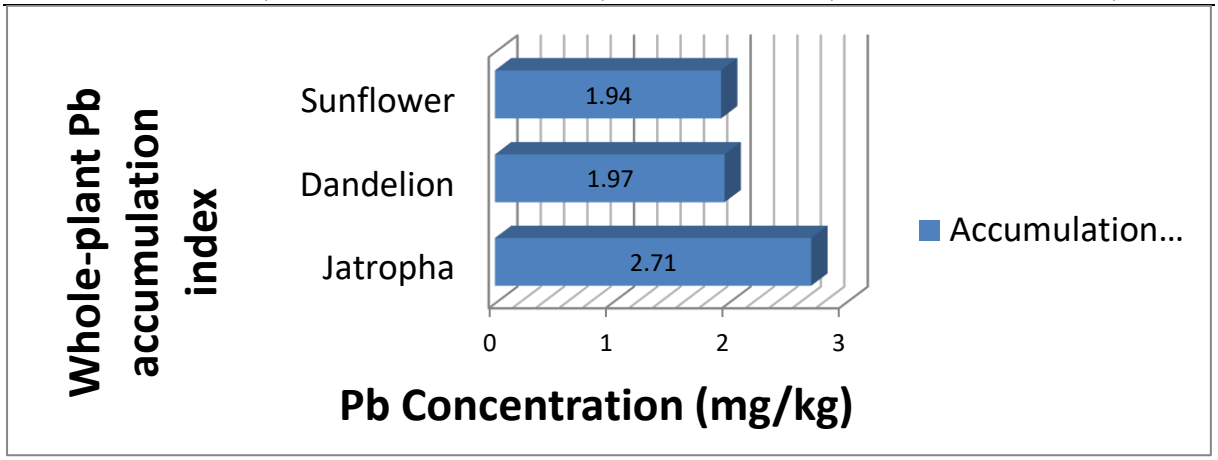

Figure 2: Whole-plant Pb accumulation index.

3.5 Translocation Factor of Lead

Sunflower and dandelion recorded higher TF values (1.84 and 1.82, respectively) than Jatropha (1.53). This indicates relatively greater partitioning of the measured Pb concentration into stem and leaf tissues for sunflower and dandelion under the calculation used. The finding is broadly consistent with evidence that plant species differ in Pb partitioning among roots and above-ground tissues (Rahman et al., 2024; Vural, 2024).

Table 5: Translocation factor (TF) of Pb.

Species	Root Pb (mg/kg)	Stem Pb (mg/kg)	Leaf Pb (mg/kg)	TF = (Stem + Leaf)/Root
Sunflower	390	388	330	1.84
Dandelion	558	465	553	1.82
Jatropha	913	800	595	1.53

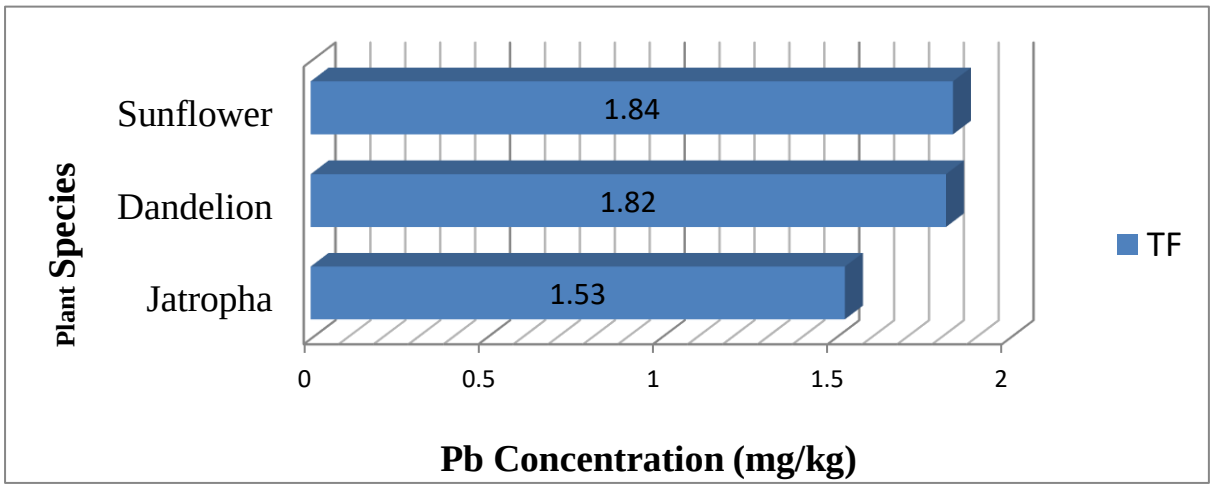

Figure 3: Translocation factor of Pb.

3.6 Growth Characteristics under Pb Stress

The recorded height observations were similar across species, with values generally ranging from 23 to 27 cm. Sunflower recorded 24–25 cm under the contaminated treatment and 23–25 cm under the control treatment; dandelion recorded 24–24 cm and 24–25 cm, respectively; while Jatropha recorded 25–25 cm and 25–27 cm, respectively. Leaf counts showed a wider numerical range, with Jatropha recording fewer leaves under the contaminated treatment than sunflower and dandelion. Because only one pot was used for each species × treatment combination, the apparent differences among seedlings cannot be treated as independent replicated treatment effects. The growth data are therefore presented as descriptive observations rather than inferential statistical evidence.

Table 6: Descriptive growth observations recorded during the experiment.

Species	Contaminated height M1 (cm)	Contaminated height M2 (cm)	Control height M1 (cm)	Control height M2 (cm)	Contaminated leaves M1	Contaminated leaves M2	Control leaves M1	Control leaves M2
Sunflower	24	25	23	25	22	20	22	23
Dandelion	24	24	24	25	20	18	21	22
Jatropha	25	25	25	27	17	15	18	20

M1 = first measurement occasion; M2 = second measurement occasion.

3.7 Interpretation and Comparison with Related Studies

Jatropha showed the strongest observed soil Pb concentration reduction, while sunflower and dandelion showed higher TF values. Several mechanisms may contribute to species differences, including root characteristics, soil pH, organic matter, rhizosphere interactions, cell-wall binding and physiological tolerance (Rahman et al., 2024; Zhang et al., 2024). These mechanisms were not directly measured in the present experiment and therefore should be regarded as plausible explanations rather than demonstrated causal mechanisms.

The strong tissue accumulation observed in Jatropha is compatible with recent work showing that J. curcas can accumulate Pb and other metals in contaminated substrates and that improved soil conditions can increase plant biomass and metal removal (Lim et al., 2024). Sunflower has also been reported to accumulate Pb under controlled soil-spiking conditions (Ngabra et al., 2024), while Vural (2024) documented substantial trace-element accumulation by T. officinale, including Pb, across plant tissues. The present results therefore support the value of these species as candidates for further comparative screening, but they do not establish field-scale remediation efficiency.

The calculated reductions of 64.5%, 65.6% and 90.4% are arithmetically consistent with the measured initial and final soil concentrations. Nevertheless, a reduction in measured soil concentration is not equivalent to a verified mass of Pb removed from the experimental system. Future studies should include replicated pots, randomized treatment allocation, identical measured starting concentrations, complete soil and plant Pb mass balances, and measurements of Pb bioavailability and soil Pb fractions.

4.0 CONCLUSION

Under the controlled conditions tested, Jatropha recorded the lowest final soil Pb concentration (82 mg/kg), the highest calculated soil Pb reduction (90.4%) and the highest study-specific whole-plant Pb accumulation index (2.71). Sunflower and dandelion recorded higher translocation factors (1.84 and 1.82) than Jatropha (1.53), indicating greater relative partitioning of measured Pb into above-ground tissues. Growth observations showed numerical differences among species, but the experimental design did not provide independent pot-level replication for inferential testing. Overall, the findings identify Jatropha as the strongest preliminary candidate for further Pb-phytoremediation evaluation under the tested conditions, while emphasizing that replicated greenhouse and field studies are required before definitive species-performance claims are made.

4.1 RECOMMENDATIONS

1. Jatropha should be prioritized for replicated greenhouse and field-scale trials where the objective is soil Pb reduction and plant accumulation, while treating the present ranking as preliminary.

2. Sunflower and dandelion should be investigated as complementary species where above-ground Pb translocation and biomass harvesting are important remediation considerations.

3. Future experiments should use independent replicated pots, randomized treatment allocation, identical measured starting Pb concentrations, longer exposure periods, direct measurements of Pb bioavailability and soil Pb fractions, and complete plant–soil Pb mass balances.

4. Pb-contaminated plant material should be handled, transported and disposed of in accordance with applicable institutional hazardous-material procedures, and future field studies should assess soil

heterogeneity, moisture variation, microbial interactions, mixed-metal contamination and seasonal effects.

5.0 REFERENCES

Ali, H., Khan, E., & Sajad, M. A. (2013). Phytoremediation of heavy metals, Concepts and applications. Chemosphere, 91(7), 869–881. https://doi.org/10.1016/j.chemosphere.2013.01.075

Davidson, C. M. (2012). Methods for the determination of heavy metals and metalloids in soils. In B. J. Alloway (Ed.), Heavy metals in soils: Trace metals and metalloids in soils and their bioavailability (pp. 97–140). Springer. https://doi.org/10.1007/978-94-007-4470-7_4

Lim, M., Samsuri, A. W., Abd Shukor, M. Y., & Phang, L.-Y. (2024). Enhancing phytoremediation of bauxite mine subsoil by Jatropha curcas L. using sewage sludge and poultry sludge. Discover Civil Engineering, 1, Article 101. https://doi.org/10.1007/s44290-024-00103-w

Ngabra, H., Allamin, I. A., Ismail, H. Y., Ngabra, M., Shettima, H., & Misherima, K. A. (2024). Phytoremediation potential of Helianthus annuus L. (sunflower) for the reclamation of lead (Pb) spiked soil. World Journal of Environmental Research, 14(2), 49–59. https://doi.org/10.18844/wjer.v14i2.9475

Olsen, S. R., Cole, C. V., Watanabe, F. S., & Dean, L. A. (1954). Estimation of available phosphorus in soils by extraction with sodium bicarbonate (USDA Circular No. 939). U.S. Department of Agriculture.

Rahman, S. U., Qin, A., Zain, M., Mushtaq, Z., Mehmood, F., Riaz, L., Naveed, S., Ansari, M. J., Saeed, M., Ahmad, I., & Shehzad, M. (2024). Pb uptake, accumulation, and translocation in plants: Plant physiological, biochemical, and molecular response: A review. Heliyon, 10(6), e27724. https://doi.org/10.1016/j.heliyon.2024.e27724

U.S. Department of Agriculture, Natural Resources Conservation Service. (2017). Soil survey manual (USDA Handbook 18, 4th ed.). U.S. Government Printing Office. https://www.nrcs.usda.gov/resources/guides-and-instructions/soil-survey-manual

Vural, A. (2024). Trace element accumulation behavior, ability, and propensity of Taraxacum officinale F.H. Wigg (dandelion). Environmental Science and Pollution Research, 31(11), 16667–16684. https://doi.org/10.1007/s11356-024-32293-2

Zhang, L., Zhu, Y., Gu, H., Lam, S. S., Chen, X., Sonne, C., & Peng, W. (2024). A review of phytoremediation of environmental lead (Pb) contamination. Chemosphere, 362, Article 142691. https://doi.org/10.1016/j.chemosphere.2024.142691

ESTIMATING GROUNDWATER RECHARGE IN THE BIDA BASIN USING INTEGRATED SOIL MOISTURE BALANCE AND HEC-HMS MODELLING: A CASE STUDY OF THE NEW BUSSA SUB-BASIN

Salihu Mohammed[1,*]
[1]*Federal University of Technology Minna*
Email: saleehu42@gmail.com*
***Corresponding author**: Salihu Mohammed
DOI: https://doi.org/10.67203/sp.ICESID.2026

ABSTRACT

Groundwater is the principal source of domestic and agricultural water supply across tropical Africa, yet its sustainable management is constrained by a poor understanding of recharge processes. This study evaluates groundwater recharge dynamics in the Bida Basin, north-central Nigeria, using the New Bussa sub-basin (Borgu Local Government Area) as a representative catchment. Twenty-five years (2000–2025) of meteorological data were integrated with laboratory-derived soil properties, a Python-based Soil Moisture Balance (SMB) model, and the Hydrologic Engineering Center–Hydrologic Modelling System (HEC-HMS). In the absence of an independently gauged streamflow station, HEC-HMS parameter calibration (Curve Number 40–85, lag time 100–323 min, imperviousness 10–25%) was executed against SMB-derived synthetic run-off to evaluate inter-model consistency rather than field-validated predictive accuracy. The best-fit inter-model agreement yielded a Nash–Sutcliffe Efficiency (NSE) of 0.52 and R^2 of 0.797 at CN = 40, TLag 100min and imperviousness 10% Over the 2020–2024 simulation period, mean annual rainfall was 1,199.32 mm, of which 273.96 mm (22.8%) was converted to run-off, while simulated groundwater recharge averaged 31.96 mm/yr (2.7%). Groundwater recharge was zero during 2021–2024 (0.00 mm/yr) and occurred exclusively during the exceptionally wet year of 2020 (159.81 mm). Sensitivity analysis indicates this threshold-controlled recharge response is highly governed by the specified root-zone depth (Zr=0.9 m) and depletion factor (ρ=0.2–0.7). Soil was classified as sandy loam with moderate bulk density (1.46–1.61 g/cm³) and available water capacity (10.2–12.2%). These findings depict a runoff-dominated hydrological regime where recharge is episodic, serving as a baseline hypothesis for comparable sub-humid tropical savannah catchments across the Middle Niger region.

Keywords: *Groundwater Recharge; Soil Moisture Balance Model; HEC-HMS; Bida Basin; Nash–Sutcliffe Efficiency; New Bussa*

1. INTRODUCTION

Groundwater recharge is the process by which water moves downward from the Earth's surface to the water table, replenishing the aquifer. This process is a critical component of sustainable water resources management (Shaikh and Birajdar, 2024). Nearly half of the world's population relies on groundwater for domestic and agricultural purposes (Scanlon et al., 2023), while across sub-Saharan Africa, it serves as the primary supply for rural and urban livelihoods (Ogunbode et al., 2024). Recharge rates are governed by interacting climatic, pedological, land-surface, and hydrogeological factors (Müller, 2023).

Quantifying recharge remains challenging in data-scarce tropical environments. While techniques such as the Water Table Fluctuation (WTF) method calculate recharge based on water-table rises and specific yield (Sy), their application is severely constrained by short-term temporal validity, high sensitivity to Sy uncertainties, and a total reliance on dense piezometric monitoring networks (Healy & Cook, 2002; Rushton et al., 2006). In un-gauged or sparsely monitored catchments where continuous groundwater-level observations are unavailable, physical numerical models offer a viable alternative.

In Nigeria's Bida Basin, rising agricultural and industrial abstractions have intensified pressure on subsurface reservoirs (Olaleye et al., 2025; Cuthbert et al., 2023). To address these observational data gaps, this study couples a Python-based Soil Moisture Balance (SMB) model

with HEC-HMS to simulate continuous root-zone moisture flux and catchment run-off in the New Bussa sub-basin.

2. METHODOLOGY

2.1 Study Area

New Bussa is located at about 9.88° N, 4.51° E in the Guinea savanna zone of Borgu LGA, Niger State, at an elevation of 180–200 m. The town was resettled due to the creation of Kainji Lake from the River Niger. It lies within the Niger River Basin where the Niger and Kaduna rivers meet, featuring rolling land and various types of land cover. The climate is tropical savanna, with a wet season from May to September and a dry season from October to April. Figures 2.1 and 2.2 show the Bida Basin and Study Area (New Bussa) in Borgu LGA, located within the Bida Basin.

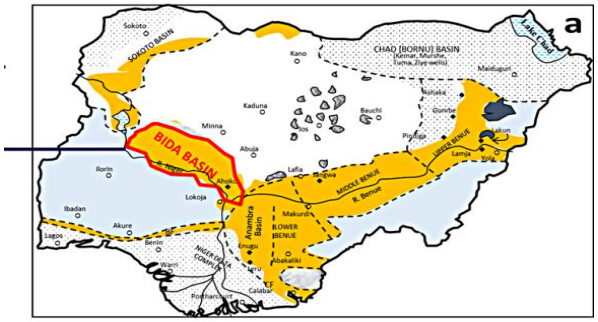

Figure 2.1: Map of Nigeria Showing the Bida Basin in Red.

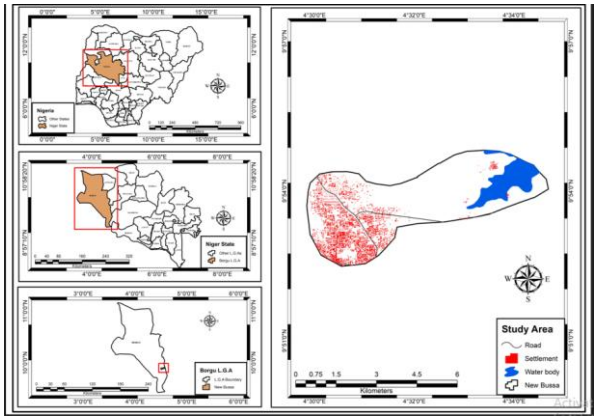

Figure 2.2: Map of Nigeria Showing the Study Area (New Bussa).

2.2 Data Acquisition

Daily rainfall and temperature data (maximum and minimum) from 2000 to 2025 were collected from the Nigerian Meteorological Agency. Reference evapotranspiration was calculated using the Hargreaves method. Soil samples from the study area were analysed to determine soil properties: bulk density, Field capacity (FC), and wilting point (WP) in the laboratory. The SMB model was run continuously from 2000 to 2025, but the final analysis was focused on 2020 to 2024 for calibration relevance.

2.3 Soil Moisture Balance Model

A Python implementation of the SMBM computed the daily water balance of the root zone (maximum rooting depth Zr = 0.9 m). Total and readily available water were computed as $TAW = (FC - WP) \times 1000 \times Zr$ and $RAW = TAW \times \rho$, where ρ is a depletion factor of 0.2–0.7 (Allen et al., 1998). Daily soil-moisture deficit (SMD) was updated as $SMD' = SMDprev + AE - AWE + NSS$, where AE is actual evapotranspiration, AWE is available water for evaporation, and NSS is near-surface storage, computed as $NSS = (AWE - AE) \times 0.45$ (Rushton, 2005). Recharge was generated only once SMD fell to zero or below.

2.4 HEC-HMS Model Setup, Parameter Scope and Calibration

The HEC-HMS model was parameterized using a digital elevation model (DEM) for basin delineation. Loss mechanisms were calculated using the SCS Curve Number (CN) method, and surface run-off transformation was modeled via the SCS Unit Hydrograph method. Baseflow processes were set to 'None' because observed continuous baseflow data were unavailable, restricting calibration parameters to CN, lag time (Tlag), and percentage imperviousness.

Because no operational hydrometric gauging station exists within the sub-basin catchment, HEC-HMS was calibrated against synthetic daily run-off generated by the SMB model for July 2024. Consequently, performance statistics, Nash–Sutcliffe Efficiency (NSE) and Coefficient of Determination (R^2), measure internal inter-model consistency rather than true field predictive skill.

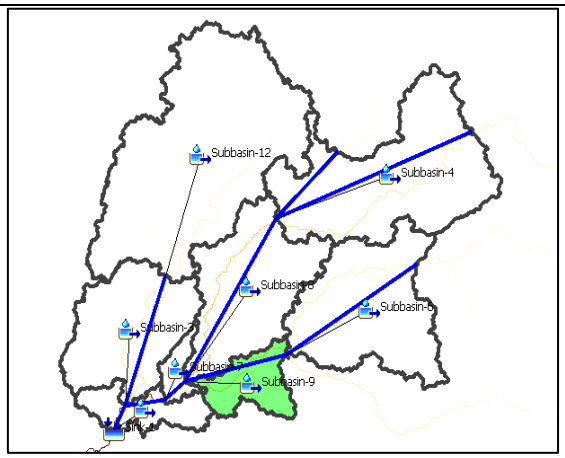

Figure 2.4: HEC-HMS Basin Model Schematic showing sub-basin delineation for the New Bussa catchment.

3. RESULTS AND DISCUSSION

3.1 Climatic Characteristics of the Basin

The Climatic analysis reveals that New Bussa recorded a mean annual rainfall of 1,100mm, with a mean annual temperature of 28.7 °C and PET exceeding 1500mm/yr, implying greater atmospheric water demand and, by extension, lower recharge potential, a pattern broadly consistent with climatic controls documented elsewhere in Nigeria (Shuaibu, 2025).

Table 3.1: Mean Climatic Analysis of New Bussa Area

Location	Mean Annual Rainfall (mm)	Mean Temp. (°C)	Wet-Season Rainfall (mm)	Dry-Season Rainfall (mm)	Relative Humidity (%)	PET (mm/yr)
New Bussa	**1,100**	**28.7**	**970**	**130**	**60**	**1,560**

3.2 Soil Physical Properties and Infiltration Potential

Analysis of New Bussa's soil samples reveals a Sandy Loam texture with a bulk density of 1.59 g/cm³. This texture class is highly typical of sandy loam, which favours moderate to rapid drainage (Niger Foods GIS, 2024). A bulk density of 1.59 g/cm³ aligns with regional soil studies in Niger State, where sand-dominated agricultural soils frequently exhibit densities ranging between 1.46 g/cm³ and 1.61 g/cm³ depending on crop cultivation and vegetative cover (Muhammad et al., 2025). Field capacity of 18.41% was obtained, and a wilting point of 8.2%, resulting in an available water capacity of 10.21% and Ksat of 11.1mm/yr respectively.

Table 3.2: Simulated Soil Properties of the New Bussa Area

LGA	Texture Class	Bulk Density (g/cm³)	Field Capacity (%)	Wilting Point (%)	AWC = FC−WP (%)	Ksat (mm/hr)
New Bussa	Sandy Loam	**1.59**	**18.41**	**8.2**	**10.21**	**11.1**

3.3 HEC-HMS Model Calibration

Six calibration trials were conducted using July 2024 daily data (Table 3.3). Trial 6 yielded the optimal inter-model fit with CN=40, Tlag=100 min, and 10% imperviousness, achieving an NSE of 0.52, an R^2 of 0.797, and an RMSE of 0.99.

A notable divergence was observed across trials between NSE and R^2 dynamics. For example, Trial 3 exhibited a high R^2 (0.87) alongside a poor NSE (0.14). This statistical behavior occurs because R^2 evaluates linear covariance regardless of systematic magnitude bias, whereas NSE heavily penalizes peak discharge offset errors and variance mismatches. Lowering the Curve Number to 40 in Trial 6 mitigated peak volume overestimations, aligning runoff volumes and optimizing NSE.

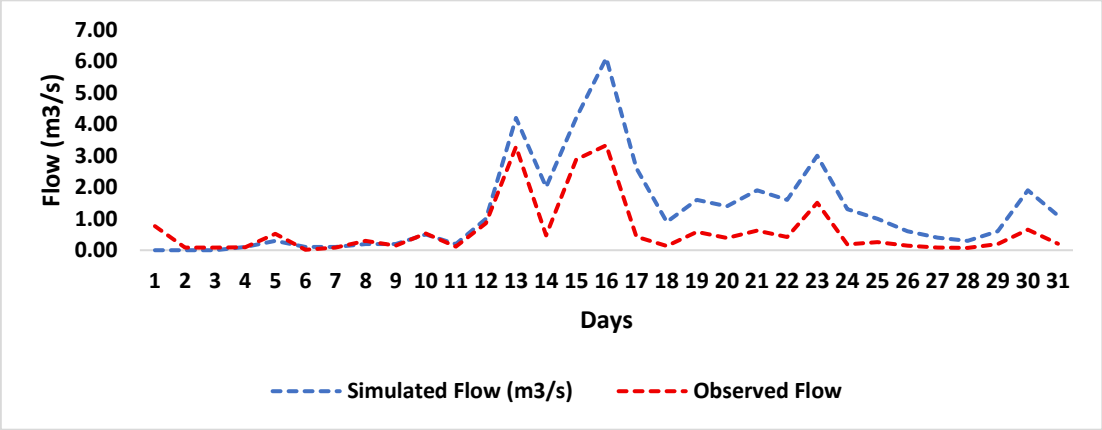

Figure 3.1: Comparison of measured flow (Python-Based Model) and simulated flow (HEC-HMS)

Table 3.3: HEC-HMS Calibration Trials (Curve Number, Lag Time and Imperviousness)

Trial	Curve Number	Imperviousness (%)	Lag Time (min)	NSE	R^2	RMSE
1	71	25	323.42	−1.83	0.42	1.34
2	75	20	250.81	−0.30	0.51	1.87
3	85	20	200.53	0.14	0.87	1.24
4	65	10	100.00	0.28	0.84	1.78
5	50	10	100.00	0.41	0.81	1.32
6	**40**	**10**	**100.00**	**0.52**	**0.797**	**0.99**

3.4 Annual Water Balance, 2020–2024

Over the five-year evaluation period (2020–2024), total precipitation reached 5,996.59 mm (Table 3.4). Mean annual runoff accounted for 273.96 mm/yr (22.8% of rainfall), whereas mean annual groundwater recharge was only 31.96 mm/yr (2.7%). Simulated recharge was zero (0.00 mm) for years (2021–2024) and occurred exclusively during 2020 (159.81 mm).

This zero-recharge phenomenon illustrates the rigid threshold control inherent to the root-zone moisture balance framework. Recharge is triggered only after accumulated evapotranspiration deficits are completely satisfied (SMD=0). Sensitivity testing confirms that assuming a deep rooting depth (Zr=0.9 m) increases overall soil storage capacity (TAW), requiring substantial cumulative wet-season rainfall (such as the 1,715.80 mm recorded in 2020) to break the threshold. While localized preferential flow through cracked regolith may cause minor real-world annual recharge, the model accurately reflects a regime where matrix percolation is highly episodic.

Table 3.4: Annual Rainfall, Runoff and Groundwater Recharge (2020–2024)

Year	Rainfall (mm)	Runoff (mm)	Groundwater Recharge (mm)
2020	1,715.80	482.28	159.81
2021	989.07	205.40	0
2022	1,281.44	267.60	0
2023	1,160.59	240.34	0
2024	849.69	174.20	0
Total	5,996.59	1,369.81	159.81

Table 3.5: Mean Annual Values of the Hydrological Parameters (2020–2024)

Parameter	Annual Average (mm)	Share of Rainfall (%)
Rainfall	1,199.32	100.0
Runoff	273.96	22.8
Groundwater Recharge	31.96	2.7

3.5 Synthesis and Methodological Limitations

The results highlight a runoff-dominated hydrological system where groundwater replenishment is minimal and episodic. However, key limitations must frame the interpretation of these findings:

1. Calibration Circularity: Calibrating HEC-HMS against SMB-derived runoff verifies conceptual alignment between models but does not substitute for field-observed streamflow validation.
2. Temporal Window: Calibrating across a single month (July 2024) restricts parameter robustness across varying multi-year antecedent moisture states.
3. Excluded Baseflow: Omitting subsurface baseflow mechanisms limits the model's capacity to simulate low-flow regimes accurately.

Consequently, the numerical estimates (e.g., 2.7% annual recharge fraction) should be interpreted as model-derived baseline hypotheses requiring empirical piezometric and tracer-based validation.

4. CONCLUSION

This study integrated SMB and HEC-HMS modelling to evaluate recharge dynamics in the New Bussa sub-basin. The hydrological regime is runoff-dominated (22.8% of rainfall), with groundwater recharge being episodic (2.7% long-term mean) and reliant on extreme rainfall events that satisfy root-zone storage capacity. Because conclusions derived from New Bussa cannot be directly extrapolated across the entire Middle Niger region without accounting for local hydrogeological heterogeneity, caution is advised in abstraction planning. Groundwater development strategies should be combined with rainwater harvesting and managed aquifer recharge schemes. Future research must prioritize establishing physical streamflow gauging and multi-year piezometric monitoring to eliminate model circularity.

5. REFERENCES

Cuthbert, M. O., Gleeson, T., Bierkens, M. F. P., Ferguson, G., & Taylor, R. G. (2023). Defining renewable groundwater use and its relevance to sustainable groundwater management. *Water Resources Research*, *59*(9), e2022WR032831.

Healy, R. W., & PG Cook (2002). Using underground water levels to estimate recharge. Hydrogeology journal,2002-Springer.

Muhammad, S. A., Ahmed, S., Inuwa, G., Muhammed, M., Muhammad, A. E., & Lawal, B. (2025). Impact of land degradation on physical properties of soils in Mokwa Local Government Area, Niger State, Nigeria. Journal of Agricultural and Environmental Science Research, 14(1), 112–125. https://hummingbirdjournals.com/jaesr/article/view/413

Müller, E. V. (2023). Analysis of forest-specific ecosystem services with regard to water balance components: Runoff and groundwater recharge in the forest.

Niger Foods GIS. (2024). Soil texture of Niger State maps. Niger Foods GIS Database. https://nigerfoodsgis.com.ng/soil-texture-of-niger-state-pdf-maps/

Ogunbode, T. O., Oyebamiji, V. O., Akinkuolie, A. T., Adekiya, O. A., Oyelami, A. A., Taiwo, T. M., & Paul, I. I. (2024). Evaluating water security in sub-Saharan Africa: Examining a case study of water supply inventory, accessibility, and predictability on Iwo, Nigeria. World Water Policy, 10(4), 1223-1242.

Olaleye, I. M., Ige, O. O., & Oyeleke, T. A. (2025). Assessment of aquifer potential in parts of Southern Bida Basin, Southwestern Nigeria. *International Journal of Energy and Water Resources*, *9*(3), 1269-1284.

Rushton, K. R. (2005). Estimating recharge for British aquifers. Water and Environment Journal, 19(2), 115-124

Rushton, K. R. Eilers, V. H. M. and Carter, R. C. (2006). Improved Soil Moisture Balance Methodology for Recharge Estimation. Journal of Hydrology, 318: 379-399.

Scanlon, B. R., Fakhreddine, S., Rateb, A., de Graaf, I., Famiglietti, J., Gleeson, T., ... & Zheng, C. (2023). Global water resources and the role of groundwater in a resilient water future. Nature Reviews Earth & Environment, 4(2), 87-101.

Shaikh, M., & Birajdar, F. (2024). Groundwater and ecosystems: understanding the critical interplay for sustainability and conservation. EPRA International Journal of Multidisciplinary Research, 10(3), 181-186.

Shuaibu, A., Kalin, R. M., Phoenix, V., Banda, L. C., & Hinton, R. G. K. (2025). Investigation of groundwater recharge in the transboundary Komadugu-Yobe basin Nigeria via stable isotopes of O^{18} and H^{2} and comparison with the wider Sahel, Africa. Science of The Total Environment, 994, 180043. https://doi.org/10.1016/j.scitotenv.2025.180043

International Conference on Engineering Innovation for Sustainable Development (ICESID 2026)
Faculty of Engineering, Ahmadu Bello University Zaria · 8–10 September 2026

EVALUATION OF PHOSPHORUS COMPOUND ENRICHMENT AND EUTROPHICATION RISK OF ALAU RESERVOIR, NIGERIA

Yunusa Mamza Usman[1,*], Al-Amin Danladi Bello[2], Badruddeen Saulawa Sani[2], Umar Alfa Abubakar[2], Bawu Musami[1]

[1]*Department of Agricultural and Bio-Environmental Engineering, Ramat Polytechnic Maiduguri, Nigeria*

[2]*Department of Water Resources and Environmental Engineering, Ahmadu Bello University Zaria, Nigeria*

Email: elmamza@gmail.com*, adbello@abu.edu.ng, basaule@gmail.com, umaralfa@hotmail.com, bawumusami@gmail.com

***Corresponding author**: Yunusa Mamza Usman

DOI: https://doi.org/10.67203/sp.ICESID.2026

ABSTRACT

This study assessed the enrichment and eutrophication response variables of phosphorus fractions in Alau Reservoir because of limited information on the contribution of individual phosphorus fractions, their seasonal variations and relationship with eutrophication risk. High levels of phosphorus enrichment continue to be a significant cause of eutrophication as it can stimulate algal growth, lead to an increase in organic matter and can decrease dissolved oxygen. Water samples were taken from two sampling points (SWA1 and SWA2) for six months, which included the late dry season, rainy season and post-rainy dry season. Orthophosphate, organic phosphorus, phosphate, total phosphorus, pH, dissolved oxygen, chlorophyll-a and turbidity were measured by standard laboratory methods. Descriptive statistics and principal component analysis were used to identify the distribution patterns of phosphorus and its association with eutrophication indicators. The results indicated that the mean orthophosphate concentration at SWA2 (0.0059 mg/L) was higher than SWA1 (0.0043 mg/L), while the mean organic phosphorus concentration at SWA2 (0.2308 mg/L) was higher than SWA1 (0.1633 mg/L). The mean soluble phosphorus concentration at SWA2 (0.9948 mg/L) was higher than SWA1 (0.9159 mg/L), and the mean total phosphorus concentration at SWA2 (1.1735 mg/L) was higher than SWA1 (1.0442 mg/L). The principal component analysis accounted for 77.57% and 87.29% of the total variation at SWA1 and SWA2, respectively, with higher nutrient-biological interactions at SWA2. The monthly variations revealed that September was closely associated with the response of phosphate and chlorophyll-a, suggesting periods of higher eutrophication pressure. The relationship between phosphorus fractions and chlorophyll-a and the inverse relationship with dissolved oxygen suggest an increasing eutrophication risk, especially at SWA2. The study suggests that the phosphorus fractions should be monitored continuously and that catchment management practices like modeling should be implemented to decrease the nutrient load to the reservoir.

Keywords: *Chlorophyll-a; eutrophication; phosphorus enrichment and water quality*

1. INTRODUCTION

Freshwater reservoirs are important sources of water for domestic use, fisheries, irrigation, livestock, conservation of biodiversity and livelihoods, but their ability to provide these services is highly dependent on nutrient balance and ecological stability, which can only be achieved through water quality monitoring and management (Akinnawo, 2023). The reservoir water quality is often a combination of the effects of rainfall, erosion, agricultural runoff, domestic discharge, shoreline activities and internal sediment processes. These pressures may be more acute in tropical and semi-arid areas where seasonal rainfall may lead to a high concentration of nutrients in reservoirs, and dry-season evapouration and longer water residence time can result in an increase in dissolved substances (Fabian *et al.*,2023; Ahmed and Ibrahim, 2024). Eutrophication is one of the most significant types of freshwater degradation, as excess nutrient loading can lead to algal growth, decreased water clarity, increased organic matter decomposition, and decreased dissolved oxygen (Wurtsbaugh *et al.*, 2019). Phosphorus has particular importance in reservoir assessment because it often limits primary productivity in freshwater systems. Excessive phosphorus levels can lead to algal blooms, oxygen depletion,

degradation of fish habitat, and increased treatment costs for potable water supply (Ayoade & Aderogba, 2020; Fabian *et al.*, 2023; Usman *et al.*, 2025). Phosphorus, chlorophyll-a, transparency and dissolved oxygen have therefore been considered as related measures of nutrient pressure and ecological response in general eutrophication literature (Wurtsbaugh *et al.*, 2019; USEPA, 2000; Akinnawo, 2023).

Phosphorus exists in various forms such as organic and inorganic phosphorus, the inorganic phosphorus is made of orthophosphates, polyphosphates, which are usually found in natural and engineered systems (Uddin *et al.*, 2018). The organic phosphorus compounds are very diverse in nature, which includes phospholipids, nucleotides, and phosphoproteins (Ebuele, 2016; Brenden *et al.*, 2018). Agricultural runoff, domestic wastewater, soil erosion, shoreline activities and internal sediment release are sources of nutrients to reservoirs in Nigeria. The pressures may differ from one sampling point to another and from one month to another due to the changes in nutrient behaviour caused by inflow, rainfall, dry season concentration and biological uptake (Akin-Oriola, 2003; Usman *et al.*, 2025). A number of studies conducted on reservoirs in Nigeria have reported nutrient enrichment, phytoplankton response and seasonal water quality variation (Ayoade & Aderogba, 2020; Fabian *et al.*, 2023; Usman *et al.*, 2025). Phosphorus is vital in the growth and productivity of living organisms like algae and plants (Smith & Schindler, 2009; Han *et al.*, 2017). Nevertheless, Excess phosphorus in reservoirs encourages overgrowth of algae, especially the cyanobacteria (blue-green algae). Some cyanobacteria like Microcystis and Anabaena may form harmful toxins called cyanotoxins in water amphibians (Dodd and Sharpley, 2016; Paerl *et al.*, 2020). The cyanotoxins are harmful to a wide range of aquatic organisms, causing liver damage, neurological effects, and even fish, invertebrates, and other aquatic organisms dying after consuming the water, as well as harmful to domestic animals and human poisoning by consuming the water (Paerl *et al.*, 2020).

While Alau Reservoir has been studied with respect to general physico-chemical quality, raw water suitability, socio-economic pressure and pollution indicators, there is limited evidence that phosphorus compound enrichment is a direct driver of eutrophication risk. Previous research typically measures only phosphate and assesses water quality primarily by permissible-use criteria. They fail to adequately separate orthophosphate, organic phosphorus, phosphate and total phosphorus, and do not correlate these phosphorus fractions with chlorophyll-a, dissolved oxygen and turbidity. This leaves the question of whether the reservoir is undergoing isolated nutrient elevation or a coordinated phosphorus-driven eutrophication process. The aim of this study is to assess the phosphorus fractions and their relationships with the eutrophication response variables in the Alau Reservoir.

1. MATERIALS AND METHOD

2.1 Study Area

Alau village is located at latitude 11˚5′ N and longitude 13˚ 20′ E in the Konduga local government area of Borno State, 19 km southeast of Maiduguri in the Sahel savanna region of Nigeria. The River Ngadda, on which the Alau dam was constructed between 1984 and 1986 by the Chad Basin Development Authority (CBDA), is a major tributary of Lake Chad (CBDA, 1998). The River Ngadda originates from the confluence of the River Yedzram and River Gombole at the Sambisa Forest. The Alau reservoir has an estimated catchment area of 9,804.44 km² at 329 m above sea level, as shown in Figure 1 (a). It has a maximum depth of 9 m and an estimated surface area of 60 km². The reservoir serves as the primary source of surface water supply for Maiduguri Metropolis and to irrigates over 8,000 hectares of farmland within the catchment area (CBDA, 1998). The climate is Sahelian with three distinct seasons: the cool-dry season (October to March), the hot season (April to June), and the rainy season (July to September). The annual rainfall ranges from 560 to 600 mm. The cold (dry harmattan) season runs from November to March, when temperatures fall to about 20°C, and a dry, dusty wind blows from the Sahara Desert (CBDA, 2018). The area is fragile and highly susceptible to drought, with relative humidity of 16.25% in the dry seasons and 71.15% in the rainy seasons as shown in Figure 1 (b). Scattered settlements across the catchment area, ranging from small rural villages to larger towns. These settlements serve as centers for agricultural activities and residential areas for the local population. Agriculture is the main economic activity in Alau village and its environs. Much of the catchment area is dedicated to agriculture, with fields of crops such as maize, millet, sorghum, rice, and

vegetables. Farmers in the area practice both rainfed and irrigated agriculture, using water from the Alau reservoir for irrigation during the dry season. Livestock rearing, including cattle, sheep, and goats, is also prevalent in the region, and fishing activities also take place in the Alau reservoir (CBDA, 2018).

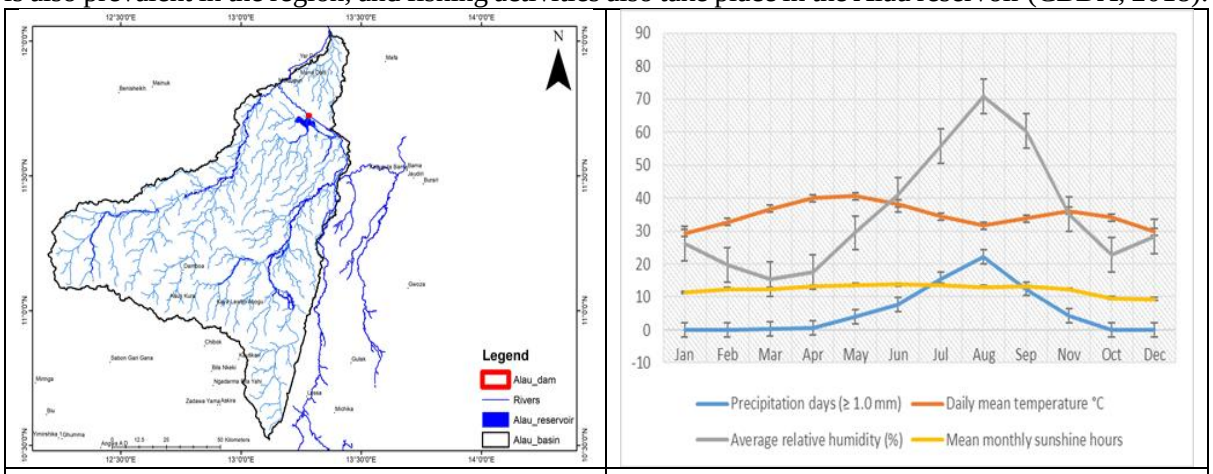

(a) Alau Reservoir Catchment | (b) Alau climatic conditions

Figure 1: Alau Reservoir Catchment and its Climatic Conditions

2.2 Water Sampling and Analysis

Two sampling points were identified in the Alau reservoir based on the accessibility due to insecurity. The Water samples were collected following the standard procedures and protocols of the United States Environmental Protection Agency Laboratory Services and Applied Science Division (USEPA, 2021). The water samples were taken offshore at a depth of 1 m from the surface of the reservoir at two sampling points, SWA1 (13.2852190 E, 11.7229650 N) and SWA2 (13.2831770 E, 11.7181360 N), which are 270 m apart. The sampling was conducted during six selected months (May, June, July, August, September and December 2023) to reflect the seasonal variation. May represented the late dry-season, June-September represented the rainy season, while December represented the post-rainy dry-season condition. Samples were immediately taken to the laboratory for analysis. The water analysis was conducted following American Public Health Association (APHA, 2017) at the Chemistry Analytical Laboratory, Yobe State University, Damaturu, Nigeria. The parameters measured include turbidity, pH, dissolved oxygen (DO), chlorophyll a (CHL-a), orthophosphate (orth-P), organic phosphorus (Org-P) phosphate (P) and total phosphorus (TP). The water temperature, turbidity, pH and DO were measured in situ using TDS & EC meter (E51M0), pH meter, turbidity meter (WG7-B) and DO meter (DO-510) respectively. The CHL-a, orth-P, Org-P, P and TP were measured by the LaMotte colorimeter (SMART3).

2.3 Data analysis

Data were analyzed using Microsoft Excel. The overall distribution of the concentration of phosphorus fractions, DO, pH, chlorophyll-a and turbidity in the reservoir was summarized using descriptive statistics; mean and standard deviation. The trends of phosphorus concentration under different scenarios were assessed using Principal Component Analysis (PCA).

3. RESULTS AND DISCUSSION

3.1 Analysis of Physio-chemical characteristics of the water samples

The Table 1 presents the descriptive statistical analysis of the two sampling sites (SWA1 & SWA2) for the phosphorus fractions and eutrophication response variables in the Alau Reservoir.

Table 1: Physio-chemical properties of the water samples

	SWA1				SWA2				
Variable	Min.	Max.	Mean	Std/dvn	Min.	Max.	Mean	Std/dvn	USEPA
Orth-P (mg/L)	0.0036	0.0049	0.0043	0.0005	0.00492	0.00661	0.0059	0.0007	0.5-2
Org-P (mg/L)	0.12	0.19	0.1633	0.0258	0.21	0.25	0.2308	0.0186	<10
P (mg/L)	0.735	1.104	0.9159	0.1312	0.913	1.097	0.9948	0.0647	0.1
TP (mg/L)	0.917	1.192	1.0442	0.1065	1.112	1.266	1.1735	0.0662	0.5-1.5
pH	6.23	6.78	6.5850	0.2249	6.24	6.92	6.6833	0.2682	6.5-8.5
DO (mg/L)	4.03	6.85	5.0567	0.9967	4.02	6.35	4.9433	0.8369	5-8
Chl-a (µg/L)	0.27	0.382	0.3220	0.0393	0.37	0.47	0.4233	0.0398	1.9-12.35
Turb (NTU)	6.23	7.82	7.0383	0.5800	6.41	7.8	7.0683	0.5826	5-30

Orth-P – Orthophosphate, Org-P - Organic phosphorus, P – Phosphate, TP - Total phosphorus, DO - Dissolved oxygen, Chl_a – Chlorophylla, Turb. – Turbidity

The mean concentration of phosphate at SWA1 was 0.9159 mg/L, and total phosphorus was 1.044 mg/L. At SWA2, the mean concentration of phosphate was 0.995 mg/L, and total phosphorus was 1.174 mg/L. The values indicate that the phosphorus load in SWA2 was greater than in SWA1. The high total phosphorus concentrations reflect a high nutrient pool, which can support current and future algal growth, as total phosphorus encompasses all forms of dissolved, particulate, organic and inorganic phosphorus. The phosphate values are also worthy of consideration as phosphate is closely associated with the availability of nutrients for aquatic primary producers. The mean concentrations of orthophosphate were low at both sampling points, 0.004 mg/L at SWA1 and 0.006 mg/L at SWA2. These values are small on their own, but do not diminish the eutrophication concern due to the high phosphorus pool. The mean concentration of organic phosphorus was also higher at SWA2 (0.231 mg/L) than at SWA1 (0.163 mg/L). Sources of organic phosphorus include decomposing plant material, animal wastes, domestic inputs, soil particles and sediment-associated organic matter. It can subsequently be mineralised to inorganic phosphorus by microorganisms. Therefore, the organic phosphorus result indicates that there is a greater pool of phosphorus in SWA2 that can continue to support eutrophication even after the immediate dissolved forms are consumed by algae. The findings are similar to previous Nigerian reservoir studies that have classified trophic status based on phosphorus enrichment and chlorophyll-a response. Ayoade and Aderogba (2020) reported that the total phosphorus and chlorophyll-a values were above the criteria for eutrophication.

The dissolved oxygen results also indicate concern for ecological stress, with a mean dissolved oxygen concentration of 5.057 mg/L at SWA1 and 4.943 mg/L at SWA2. Higher mean phosphorus and higher chlorophyll-a are associated with the lower oxygen value at SWA2. Algal biomass can increase following the addition of phosphorus in nutrient-rich reservoirs, and the subsequent decomposition of the biomass can deplete oxygen. The minimum values of approximately 4.0 mg/L at both sampling locations indicate that oxygen stress may occur, particularly during warm, stagnant or organically enriched periods. This is consistent with the overall limnological knowledge that nutrient enrichment can lead to increased algal biomass, which can then lead to decreased oxygen due to respiration and decomposition (Wurtsbaugh *et al.,* 2019.). The mean chlorophyll-a value was 0.322 µg/L at SWA1 and 0.423 µg/L at SWA2. The sampling point with the highest phosphorus enrichment, however, still had a higher mean chlorophyll-a concentration than SWA1, and the algal-biomass signal was stronger. The same findings were reported by Ahmed and Ibrahim (2024) who found that the abundance of phytoplankton in Lake Alau was influenced by nutrient concentration, physicochemical factors and season. The turbidity was found to be similar at both points with mean value of 7.038 at SWA1 and 7.068 at SWA2, indicating similar conditions of suspended material or light attenuation.

3.2 PCA Eigenvalues of phosphorus in Alau reservoir

The first two components explained 77.57% and 87.29% of the total variance at SWA1 and SWA2, respectively, indicating that they adequately summarized the relationships among phosphorus fractions and water-quality variables as presented in Table 2.

Table 1: PCA Eigenvalues of phosphorus fractions in Alau reservoir

SWA1	F1	F2	F3	F4	F5
Eigenvalue	3.454	2.752	1.585	0.190	0.019
Variability (%)	43.177	34.395	19.817	2.372	0.239
Cumulative %	43.177	77.572	97.389	99.761	100.000
SWA2					
Eigenvalue	4.858	2.125	0.716	0.200	0.101
Variability (%)	60.726	26.562	8.951	2.497	1.265
Cumulative %	60.726	87.288	96.239	98.735	100.000

The first principal component (F1) at SWA1 accounted for 43.18% of the variance and the second principal component (F2) accounted for 34.40% of the variance, for a total of 77.57%. This suggests that several environmental processes affect phosphorus fractions and eutrophication variables, not just one. The third component (19.82%) also had an eigenvalue greater than 1, the Kaiser criterion, indicating the presence of another, but less influential, ecological process as indicated in Table 2. The results are consistent with those of Jolliffe & Cadima (2016) who found that PCA is most useful when the first two principal components account for over 70% of the total variance, enabling the environmental gradients to be interpreted. At SWA2 much higher first component (60.73%) and F2 (26.56%) for a total of 87.29% cumulative variance. The higher percentage accounted for by F1 suggests that water quality at SWA2 is more strongly influenced by a single nutrient-enrichment gradient, suggesting greater coupling between the availability of phosphorus and biological response than at SWA1. Likewise, Wurtsbaugh *et al*. (2019) noted that eutrophication of reservoirs often have a dominant nutrient component, with phosphorus, algal biomass and oxygen dynamics being connected. The descriptive statistics indicated that the concentration of organic phosphorus, soluble phosphorus and total phosphorus were higher at SWA2 than at SWA1, which is consistent with the higher cumulative variance at SWA2.

3.3 PCA Factor Loadings for phosphorus fractions in Alau reservoir

The PCA factor loading patterns at SWA1 and SWA2 reveal that nutrient dynamics in Alau are driven by seasonal hydrology as presented in Table 3.

Table 3: PCA Factor Loading for phosphorus fractions in Alau Reservoir

SWA1	F1	F2	F3	F4	F5
OTH-P	-0.479	-0.522	0.697	0.110	0.019
Org-P	-0.615	-0.454	0.642	0.052	-0.028
P	0.768	0.267	0.550	-0.190	0.007
TP	0.819	0.176	0.544	-0.040	-0.010
pH	0.620	0.727	0.159	0.246	-0.035
DO	-0.480	0.850	0.111	0.185	0.036
Chl-a	0.774	-0.607	-0.069	0.134	0.101
Turb.	-0.610	0.743	0.216	-0.157	0.072
SWA2					
OTH-P	0.597	-0.735	0.283	0.036	-0.149
Org-P	0.937	-0.296	0.170	-0.006	0.073
P	0.797	0.417	0.426	-0.051	-0.077
TP	0.514	0.799	0.272	0.150	0.024
pH	-0.670	0.699	0.094	-0.210	-0.096
DO	-0.783	-0.266	0.520	-0.089	0.194
Chl-a	0.900	0.344	-0.223	0.061	0.136
Turb.	-0.923	0.083	0.149	0.343	-0.038

The highest positive loadings for F1 were total phosphorus (0.819), chlorophyll-a (0.774) and phosphate (0.768), which suggests that F1 is the gradient of phosphorus enrichment and algal productivity. The biological expression of nutrient enrichment was also observed as the concentration of phosphorus increased, so did the concentration of chlorophyll-a. On the other hand, organic phosphorus (-0.615), turbidity (-0.610) and orthophosphate (-0.479) were negatively loaded on F1, indicating that these variables are associated with a different environmental process, which may be associated with the decomposition of organic matter and transport of sediment-associated phosphorus as indicated in Table 3. This separation suggests that there are several biogeochemical forms of phosphorus in SWA1, each having a different transport mechanism. Similarly, Ayoade & Aderogba (2020) reported a positive relationship between total phosphorus and chlorophyll-a in a tropical reservoir in Nigeria, which is consistent with eutrophic interpretation. Dissolved oxygen (0.850), turbidity (0.743) and pH (0.727) dominated the second component (F2). This component is not nutrient enrichment, but physical–chemical regulation. The negative loading of chlorophyll-a (-0.607) may indicate that algal biomass increases when dissolved oxygen levels are low due to respiration and decomposition, while high dissolved oxygen and turbidity may be associated with inflow-induced mixing during rainy periods. These observations are similar to those reported by Paerl *et al.* (2020) that phosphorus enrichment leads to algal growth, and that subsequent decomposition leads to increased biological oxygen demand and decreased dissolved oxygen.

The PCA at SWA2 revealed a much clearer eutrophication pattern as the first component was dominated by organic phosphorus (0.937), chlorophyll-a (0.900) and phosphate (0.797), while turbidity (-0.923) and dissolved oxygen (-0.783) showed strong negative loadings. This means that F1 is an active eutrophication gradient, where the more phosphorus enriched the more algal biomass and the less dissolved oxygen. The highest loading was for organic phosphorus (0.937), indicating that it is an important reserve nutrient pool that can support eutrophication following mineralization. This is consistent with the results of Han *et al.* (2017) who found that organic phosphorus in sediments and suspended particles is a significant source of long-term phosphorus availability in reservoirs. The negative correlation between turbidity and chlorophyll-a indicates that the clearer the water, the more likely algae will grow due to better light penetration. The same was found by Fabian *et al.* (2023) in Lake Alau, where a decrease in suspended sediments during the season was correlated with an increase in phytoplankton. Total phosphorus (0.799) and pH (0.699) were the main factors in the second component (F2). This component is probably a reflection of the chemical environment affecting the

availability of phosphorus. Increased pH can also increase the release of phosphorus from sediments and can also be associated with high photosynthetic activity due to the removal of carbon dioxide, which is well documented in eutrophic lakes (Smith & Schindler, 2009). Overall, SWA2 shows a higher ecological connection between phosphorus compounds and eutrophication indicators than SWA1, which is consistent with the fact that it is the more environmentally sensitive part of Alau Reservoir.

3.4 Interactions between Phosphorus fractions and eutrophication variables

The correlation circles for SWA1 and SWA2 illustrate the relationships between orthophosphate, organic phosphorus, phosphate, total phosphorus, pH, dissolved oxygen, chlorophyll-a and turbidity on the first two principal component axes as shown in Figure 2. The principal component analysis correlation circle show variables in the same direction as positively associated, in opposite directions are negatively associated, and lying at almost right angles have weak relationships. The length of each vector is also important, as the first two axes are strongly represented by variables near the outer circle.

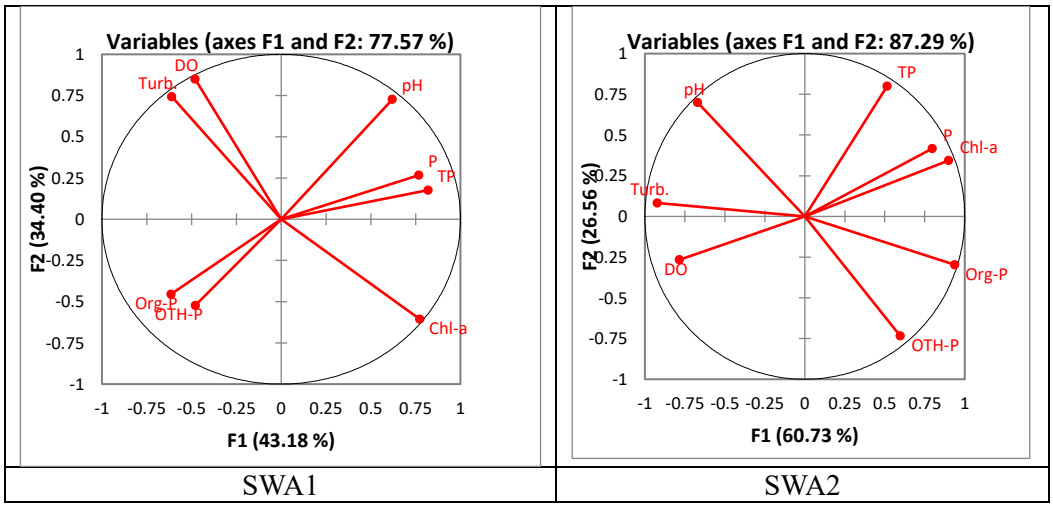

Figure 2: Correlation circles for phosphorus fractions and eutrophication variables

At SWA1, the first two axes explain 77.57% of the total variation, with F1 account for 43.18% and F2 is 34.40%. This implies that the correlation circle provides a good summary of the primary physicochemical and eutrophication relationships at this sampling location. The strongest positive association is seen in SWA1, where phosphate and total phosphorus are grouped together on the positive side of F1. This suggests that phosphate is a significant component of the total phosphorus pool at SWA1. The first two axes account for 87.29% of the total variation in SWA2, with F1 and F2 explaining 60.73% and 26.56% respectively. This is more than the SWA1 plot can explain, and the SWA2 correlation circle provides an even better summary of the measured water quality variables. The high proportion of F1 also indicates that a more powerful common environmental gradient influences SWA2. Orthophosphate and organic phosphorus constitute another group at SWA1, both vectors are directed towards the lower left side of the circle, away from the other vectors, phosphate, total phosphorus, pH and chlorophyll-a. The correlation matrix shows a very strong positive correlation between them, which is reflected in their proximity. This clustering indicates that orthophosphate and organic phosphorus could have a similar source or transformation pathway at SWA1. They can be associated with organic matter decomposition, soil run-off, domestic inputs, sediment interaction or microbial mineralisation. Their direction of flow is opposite to that of phosphate and total phosphorus, however, and they do not follow the same pattern as the larger group. This indicates that the phosphorus system at SWA1 is not homogeneous. The various phosphorus fractions may originate from various sources or react differently to physical and chemical conditions in the reservoir. The results are consistent with Ayoade & Aderogba (2020) who reported positive correlation between total phosphorus and chlorophyll-a in a tropical reservoir in Nigeria, which is consistent with eutrophic interpretation.

Organic phosphorus and orthophosphate are also positive at SWA2, but they are pointing down. They are directed towards the phosphorus-enrichment side of the system, but are not the same as total

phosphorus and phosphate in their F2 behaviour. Organic phosphorus is near the right side of the circle, indicating that it is well represented by the first two components. This suggests that organic phosphorus plays an important role in the SWA2 nutrient structure. Organic phosphorus can be mineralised by microorganisms to more available inorganic forms, and can therefore serve as a nutrient pool that can continue to contribute to eutrophication. At SWA1, the position of chlorophyll-a is moderately positively related to total phosphorus and phosphate. This implies that there is some biological expression of the phosphorus enrichment at SWA1, albeit not a direct one. This is ecologically sound because algal growth is not solely dependent on phosphorus. Other factors that affect chlorophyll-a concentration include light penetration, water residence time, water mixing, grazing, and nitrogen availability and turbidity. The phosphorus concentration thus suggests high eutrophication potential, and the chlorophyll-a concentration suggests that the biological response may be partly influenced by other environmental factors. The most important pattern at SWA2 is the group of phosphate, total phosphorus and chlorophyll-a on the right side of the correlation circle. Phosphate and chlorophyll-a are grouped tightly together, and total phosphorus is in the same general direction. This indicates that the enrichment of phosphorus at SWA2 is more closely linked to algal biomass than at SWA1. In the same way, Dadin Kowa Reservoir was recently studied by Usman *et al.* (2025) and it was found that the enrichment of N and P in the reservoirs in Nigeria can be seasonal and site-specific, thus supporting the use of SWA1 and SWA2 separately rather than as a single water body. It implies that the enrichment of phosphorus at SWA2 is not only chemical but also biological, as evidenced by the increase in chlorophyll-a. Since eutrophication is a process of nutrient loading and algal production, studies of reservoir trophic state typically include nutrient enrichment as well as biological response variables like chlorophyll-a and transparency.

The dissolved oxygen at SWA2 is a very important position that shows a negative correlation between dissolved oxygen and the eutrophication related variables. This pattern indicates that as chlorophyll-a and phosphorus levels increase, oxygen levels decrease at SWA2. This is one of the most significant indicators of eutrophication stress as algal growth and decomposition of organic matter can lead to increased oxygen demand and decreased dissolved oxygen. The chlorophyll-a and the dissolved oxygen-turbidity group are the strongest ecological contrast at SWA1. Dissolved oxygen and turbidity are grouped together in the upper left quadrant of the circle, and chlorophyll-a is grouped together in the lower right quadrant of the circle. The relationship between chlorophyll-a and dissolved oxygen is strongly negative, as is the relationship between chlorophyll-a and turbidity. The negative correlation with turbidity indicates that suspended materials could limit light penetration and algal growth at some times. Therefore, SWA1 seems to be highly available for phosphorus, but the strength of this nutrient enrichment to generate algal biomass may be controlled by turbidity and oxygen conditions (Fabian *et al.*, 2023).

The location of pH near phosphate and total phosphorus also provides a valuable chemical interpretation at SWA1. The pH values are generally in the same direction as the phosphate and total phosphorus values, particularly in the positive direction of the F1 axis. This pattern agrees with the positive correlations between pH and phosphate, and between pH and total phosphorus. It indicates that the higher the concentration of phosphorus at SWA1, the higher the pH. This can be a sign of increased photosynthetic activity in nutrient-rich waters, as algal photosynthesis consumes carbon dioxide from the water and can increase the pH. But pH is not on the same vector as phosphate and total phosphorus, and should not be considered as the same process. It is more correctly viewed as a supportive chemical state associated with nutrient behaviour and potential algal activity. The pH and turbidity vectors at SWA2 are opposite to the direction of phosphate and chlorophyll-a. The pH is in the upper left quadrant and turbidity is closer to the negative F1 axis. This indicates that pH and turbidity are negatively associated with the nutrient and chlorophyll-a group at SWA2. The negative correlation between turbidity and chlorophyll-a indicates that algal growth may be promoted by clearer water conditions, and algal growth may be inhibited by more turbid water conditions due to reduced light penetration. Turbidity can also be an indicator of suspended sediment and runoff inputs, however. It can decrease algal growth at one time and carry particle-bound phosphorus into the reservoir at another time. The pH pattern also indicates that the various fractions of phosphorus may react differently to the chemical conditions (Jolliffe & Cadima, 2016).

3.5 Temporal variations of the Phosphorus fractions and eutrophication variables

The principal component analysis biplots for SWA1 and SWA2 represent the measured water quality variables and the sampling months as shown in Figure 3. In this type of biplot, a month near the direction of a variable is typically correlated with relatively high values of that variable. A month on the other side of a variable is correlated with relatively lower values. A month near the centre indicates more average conditions, and a month far from the centre indicates stronger departure from the average water quality condition.

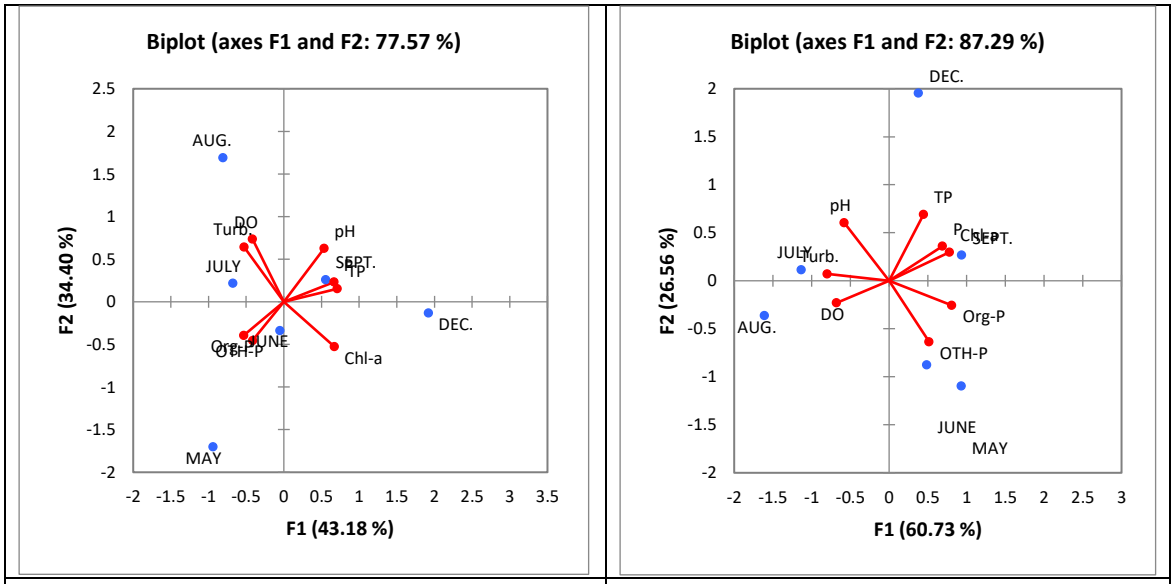

SWA1 | SWA2

Figure 3: Biplots for phosphorus fractions and eutrophication variables

The positions of dissolved oxygen and turbidity at SWA1 biplot show a different environmental condition. August is located close to dissolved oxygen and turbidity, while July is also on the left side near turbidity as shown in Figure 3. This suggests that these months were more strongly associated with oxygenated and turbid conditions at SWA1. This pattern can be indicative of inflow, mixing or suspended particle transport. Light penetration may be affected by turbidity, which may be a partial reason for the negative relationship between chlorophyll-a and turbidity. Simply put, as water becomes more turbid, light may be less available for algal photosynthesis, even in the presence of phosphorus. This is why the formation of algal blooms is not always observed at each sampling time when phosphorus enrichment occurs. General trophic assessment is based on the combination of total phosphorus, chlorophyll-a and measures related to transparency, since eutrophication is a combination of nutrient pressure and biological response, not just nutrient concentration (USEPA, 2021). May is in the lower left corner of the SWA1 biplot, near orthophosphate and organic phosphorus. This indicates that May was more closely related to the orthophosphate and organic phosphorus fractions than to the larger group of phosphate-total phosphorus. The position of May is important because organic phosphorus can act as a reserve nutrient fraction. It can later be transformed into more accessible inorganic forms by microbial decomposition. The clustering of orthophosphate and organic phosphorus in this section of the biplot thus indicates that SWA1 may be supplied with phosphorus from organic matter inputs, decomposition of aquatic organic matter, or from organic particles or sediment associated processes from runoff. The biplot indicates that the phosphorus system at SWA1 is not monodirectional with respect to phosphate and total phosphorus, suggesting that there is more than one source or transformation pathway for phosphorus (Fabian *et al.*, 2023).

September and December are on the positive side of F1 at SWA1, and are more related to the phosphorus enrichment side of the biplot. September is close to phosphate, total phosphorus and pH, and December is far to the right and slightly below the F1 axis. This indicates that these months are more strongly associated with nutrient-rich conditions than May, July or August. September is close to the phosphate and total phosphorus, indicating a time when phosphorus loading increased. The F1 position for December is also very positive, indicating a strong departure from the average position, but

it is also separated from the main phosphorus arrows, so it may not be explained by phosphorus alone. The month-to-month variation is important in eutrophication assessment because water quality in reservoirs can vary with inflow, runoff, dilution, evaporation, sediment disturbance, and biological uptake. June is near the centre of the SWA1 biplot, indicating that it is a more average month than the others. June was not strongly dominated by any one water quality factor, as it does not correlate well with any variable. This is helpful because it indicates that the eutrophication condition in SWA1 is not consistent throughout the month. Rather, the sampling point alternates between an organic phosphorus condition, a turbidity-oxygen condition and a phosphate-total phosphorus condition. This is consistent with the previous PCA eigenvalue interpretation, which indicated that SWA1 had three meaningful components. The water quality structure at SWA1 is therefore more mixed, and the interaction between phosphorus enrichment and physical and chemical controls is more complex (Usman *et al.*, 2025).

September is near to phosphate and chlorophyll-a, the most obvious indicators of eutrophication risk, at SWA2 biplot. It suggests that September was associated with higher phosphate and higher algal biomass at SWA2 as shown in Figure 3. Phosphate is a direct nutrient for algal growth and chlorophyll-a is a measure of algal biomass, so their close association suggests an active nutrient-biological response. This is in line with the studies conducted on reservoirs in Nigeria, which indicated that the trophic state of the reservoirs was assessed using the total phosphorus, chlorophyll-a and Secchi disc transparency, which were found to be higher than the criteria used to interpret eutrophic condition, and the abundance of green algae and blue-green algae confirmed this (Ayoade & Aderogba, 2020). The SWA2 biplot thus indicates that the enrichment of phosphorus at this sampling site is not only a chemical problem, but also associated with algal productivity. The December is positioned high on F2 at SWA2 and close to the direction of total phosphorus. This indicates that December was highly correlated with total phosphorus enrichment, but not as closely correlated with chlorophyll-a as September. This is important because total phosphorus is composed of dissolved, particulate, organic and inorganic phosphorus. A high total phosphorus association can thus be a sign of a high nutrient pool that can be utilized for subsequent algal growth, even if all of the phosphorus is not available to algae at the time of sampling. The December position may thus be a nutrient-storage or nutrient-loading situation, and September a more direct phosphorus-chlorophyll response. The monthly biplot results are consistent with the findings of (Usman *et al.* (2025) which indicated that nutrient enrichment and eutrophication risk in Dadin Kowa Reservoir was different among sampling points and seasons, and hydrological conditions influenced the nitrogen and phosphorus dynamics.

The SWA2 biplot shows the May and June in the lower right corner, near orthophosphate and organic phosphorus. This suggests that these months were more related to these phosphorus fractions. Organic phosphorus is particularly important because it may originate from organic wastes, decaying biomass, aquatic vegetation, animal inputs or sediment-associated materials. It may later be a source of eutrophication following mineralisation. Orthophosphate, however, is a more readily available form for algal uptake. The presence of May and June therefore indicates that SWA2 had a large reservoir of phosphorus forms that could support eutrophication beyond the one sampling period. This is consistent with the descriptive statistics, which showed that SWA2 had a higher mean organic phosphorus and orthophosphate than SWA1. July and August are located on the left side of the SWA2 biplot, near turbidity, dissolved oxygen and in part pH. This indicates that these months were more related to physical disturbance and oxygenated conditions than to chlorophyll-a and phosphorus enrichment. The July data is closest to turbidity, the August data is farther left and below the F1 axis, closer to the oxygen side of the plot. Although the reservoir is generally considered to be a phosphorus-rich system, the turbidity data indicates that periods of higher turbidity may have resulted in less light available for algal growth, and thus less algal biomass. The direction of dissolved oxygen is also against chlorophyll-a and phosphate, which further supports the interpretation that oxygen decreases with increasing algal biomass and nutrient enrichment. This is a typical eutrophication process as the demand for oxygen rises due to algal respiration and organic matter decomposition (Usman *et al.*, 2025).

4. CONCLUSION

This study showed that the reservoir is highly enriched with phosphorus, and that the total phosphorus and phosphate levels suggest a high eutrophication potential. The temporal assessment revealed that the nutrient enrichment was not consistent across the sampling months, suggesting that seasonal processes affect nutrient dynamics in the reservoir. The principal component analysis showed that the water quality variation was significantly influenced by nutrient related processes at SWA1 and SWA2. The higher nutrient-biological relationship found at SWA2 suggests that this sampling site is more susceptible to eutrophication development. The dissolved oxygen levels were below acceptable guideline range as observed at SWA2 indicates increasing oxygen stress due to organic matter decomposition and biological activity. The PCA biplot analysis indicated that December was strongly correlated with total phosphorus enrichment, and September was more strongly correlated with phosphate and chlorophyll-a, indicating periods of greater biological response and eutrophication pressure. The correlation between phosphorus compounds and chlorophyll-a, and the negative correlation between chlorophyll-a and dissolved oxygen, suggest that nutrient enrichment has started to affect the ecological conditions in the reservoir. The Alau Reservoir is vulnerable to eutrophication because of high levels of phosphorus and seasonal changes in nutrient levels. The results indicate the need to shift from general water quality assessment to continuous nutrient monitoring programs that account for the various fractions of phosphorus, algal response and oxygen dynamics. Proper management of nutrient sources entering the reservoir is required to ensure the ecological health of the reservoir and its suitability for domestic, agricultural and fishery uses.

REFERENCES

Adegbola, A. A., Olufayo, A. A., & Ogunyemi, S. (2020). Hydrological and nutrient modelling of West African basins using SWAT. Journal of Water Resources and Protection, 12(3), 145-158.

Ahmed, A., & Ibrahim, M. A. (2024). Distribution and diversity of phytoplankton in Lake Alau, Maiduguri, Northeast Nigeria. Arid Zone Journal of Basic and Applied Research, 3(3), 64-81. https://doi.org/10.55639/607.201918

Akinnawo, S. O. (2023). Eutrophication: Causes, consequences, physical, chemical and biological techniques for mitigation strategies. *Environmental Challenges, 12*, 100733.

Akin-Oriola, G. A. (2003). On the phytoplankton of Awba Reservoir, Ibadan, Nigeria. *Revista de Biología Tropical, 51*(1), 99-106.

American Public Health Association. (2017). Standard method for the examination of water and wastewater (21st ed.). Washington, DC: APHA Press.

Ayoade, A. A., & Aderogba, A. (2020). Spatial and Temporal Distribution of Plankton in a Tropical Reservoir, southwestern Nigeria. *Egyptian Journal of Aquatic Biology & Fisheries Zoology Department, Faculty of Science, Ain Shams University, Cairo, Egypt*. ISSN 1110 - 6131 Vol. 24(5): 161-181 (2020)

Brenden, T.O., Reilly, R., Eisch, E. et al. Temporal variation in total phosphorus concentrations revealed from a multidecadal monitoring program on Big Platte Lake, Michigan. Environ Monit Assess 190, 430 (2018). https://doi.org/10.1007/s10661-018-6818-9

Chad Basin Development Authority (1998), Annual report. 3(5)

Chad Basin Development Authority (2018), Annual report. 6(7)

Dodd, R. J., & Sharpley, A. N. (2016). Conservation practice effectiveness and adoption: Unintended consequences and implications for sustainable phosphorus management. *Nutrien Cycling in Agroecosystems, 104*(3), 373-392. https://link.springer.com/article/*t* https://doi.org/10.1007/s10705-015-9748-8

Ebuele, V. P. (2016). Phosphorus Speciation in Soil and Plants. https://ethos.bl.uk/OrderDetails.do?uin=uk.bl.ethos.715225

Fabian, Z. L., Abasiryu, A., & Abubakar, K. A. (2023). From abundance to adversity: Understanding the changing dynamics of Lake Alau's water quality. FUDMA Journal of Sciences, 7(5), 359-368. https://doi.org/10.33003/fjs-2023-0705-2030

Han, C., Zheng, B., Qin, Y., Ma, Y., Yang, C., Liu, Z., Cao, W. Chi. M. (2017). Impact of upstream river inputs and reservoir operation on phosphorus fractions in water-particulate phases in the Three Gorges Re., Sci Total Environ. http://dx.doi.org/10.1016/j.scitotenv.2017.06.109

Jolliffe, I. T., & Cadima, J. (2016). Principal component analysis: A review and recent developments. *Philosophical Transactions of the Royal Society A: Mathematical, Physical and Engineering Sciences, 374*(2065), 20150202.

Paerl, H.W., Havens, K.E., Xu, H., Zhu, G., Mccarthy, M.J., Newell, S.E., Scott, J.T., Hall, N.S., Otten, T.G., Qin, H. (2020). Mitigating eutrophication and toxic cyanobacterial blooms in large lakes: the evolution of a dual nutrient (N and P) reduction paradigm. Hydrobiologia 847, 4359– 4375. https://doi.org/10.1007/ s10750-019-04087-y.

Smith, V. H., & Schindler, D. W. (2009). Eutrophication science: Where do we go from here? *Trends in Ecology & Evolution, 24*(4), 201-207. doi: 10.1016/j.tree.2008.11.009

Uddin, M.G., Moniruzzaman, M., Quader, M.A., Hasan, M.A. (2018). Spatial variability in the distribution of trace metals in groundwater around the Rooppur nuclear power plant in Ishwardi, Bangladesh. *Groundw. Sustain. Dev.* https://doi.org/10.1016/j. gsd.2018.06.002

United States Environmental Protection Agency. (2021). Ambient water quality criteria to address nutrient pollution in lakes and reservoirs. United States Environmental Protection Agency

Usman, Y. M., Bello, A.-A. D., Abubakar, U. A., Sani, B. S., Aliyu, B. U., & Musami, B. (2025). Spatio-temporal dynamics of nutrient enrichment and eutrophication risk in Dadin Kowa Reservoir, Nigeria. KJSET, 4(2), 19-28. https://doi.org/10.59568/KJSET-2025-4-2-02

Wurtsbaugh, W. A., Paerl, H. W., & Dodds, W. K. (2019). Nutrients, eutrophication and harmful algal blooms along the freshwater to marine continuum. *WIREs Water, 6*(5), e1373.

International Conference on Engineering Innovation for Sustainable Development (ICESID 2026)
Faculty of Engineering, Ahmadu Bello University Zaria · 8–10 September 2026

EXPERIMENTAL ASSESSMENT OF SPECTRUM OCCUPANCY AND TVWS AVAILABILITY IN THE UHF TELEVISION BAND (470–694) MHZ IN KANO STATE NIGERIA

Yahaya Hamisu Abubakar[1,*], Matthew Ehikhamenle[2]
[1]*University of Porthacourt*
[2]*Center for Information and Telecommunication Engineering, University of Portharcourt, Nigeria*
Email: yhaeadd@yahoo.com[*], Matthew.ehikhamenle@uniport.edu.ng
***Corresponding author**: Yahaya Hamisu Abubakar
DOI: https://doi.org/10.67203/sp.ICESID.2026

ABSTRACT
This study presents the results of a spectrum measurement campaign conducted in Kano State, Nigeria, across the UHF television band spanning 470–694 MHz. The primary objective was to determine the level of spectrum occupancy and the availability of television white spaces (TVWS) to support dynamic spectrum access in cognitive radio systems. An Agilent (Keysight) spectrum analyser was configured to sweep the television band and collect empirical data from selected urban and rural locations. The findings showed that only 21.4% of the spectrum is utilized in urban areas leaving approximately 78.6% underutilized. In rural areas, the results indicated that the entire measured spectrum 224 MHz (100%) is available and unoccupied. These findings reveal substantial inefficiency in spectrum usage and suggest significant opportunities for opportunistic access through cognitive radio technologies. The measurement results were further compared with findings from both local and international spectrum occupancy studies, which showed a consistent pattern of low utilization and significant TVWS availability across different locations. This agreement with prior studies supports the technical feasibility of deploying TVWS-based systems for broadband connectivity, Internet of Things (IoT) applications, and indoor coverage enhancement.

Keywords: *Spectrum Measurement Campaign; Spectrum Occupancy; Television White Spaces; Underutilization of spectrum; Cognitive Radio*

1. INTRODUCTION

Television White Space (TVWS) refers to the unused frequency spectrum in the Very High Frequency (VHF) and Ultra-High Frequency (UHF) bands originally allocated for television broadcasting services (Idowu-Bismark et al., 2025). Following the global transition from analog to digital television (DTV), the digital dividend has freed substantial spectrum capacity, creating opportunities for secondary access without interfering with primary incumbent services (Luka et al., 2023). The frequency range of interest varies by regulatory domain: in Nigeria, the Nigerian Communications Commission (NCC) has approved TVWS deployment in the 470–694 MHz band ,while the European harmonized standards specify the same range for TV White Space Devices (TVWSDs), (Adefela et al., 2022; Ntlaltapa, 2013; European Telecommunications Standards Institute [ETSI], 2022).

The lower UHF band offers exceptional propagation characteristics compared to higher frequency bands such as 2.4 GHz or 5 GHz used by conventional Wi-Fi. These signals can travel longer distances, penetrate obstacles more effectively, and provide reliable non-line-of- sight (NLOS) communication (Gerolaga, 2020; Idowu-Bismark et al., 2025). As shown in table 1, TVWS provides substantially greater range than Wi-Fi, though with lower throughput, making it particularly suitable for rural broadband access and IoT applications.

Table 1: Comparative Characteristics of Wi-Fi and TVWS

Parameter	**Wi-Fi**	**TVWS (UHF)**
Range (km)	0.05 - 0.45	10 - 30
Throughput	Up to 600 Mbps	2 - 45 Mbps
Frequency	2.4 - 5 GHz	470 - 698 MHz
Non-LOS Communication	No	Yes
Environmental Sensitivity	Yes	No

Source: Adapted from (Gerolaga, 2020)

The global surge in wireless communication systems, fueled by the deployment of advanced mobile telecommunications networks and Internet-of-Things (IoT) ecosystems, has drastically increased demand for the radio frequency (RF) spectrum. Traditionally, regulatory bodies manage this finite natural resource using a static allocation framework, where specific frequency bands are exclusively licensed to designated operators or primary users (PUs). This traditional strategy, though it has helped to address the issue of interference, it has created artificial scarcity of spectrum. To overcome this challenge, researchers have led the way toward Dynamic Spectrum Access (DSA) enabled by Cognitive Radio (CR) technology. The term *Cognitive Radio* (CR) was coined by (Mitola, J., & Maguire, G. Q., 1999) at a seminal workshop on Mobile Multimedia Communications. The authors described how CR could enhance the flexibility of personal wireless services through the Radio Knowledge Representation Language (RKRL). Additionally, the International Telecommunication Union (ITU) defines a cognitive radio system (CRS) as a radio system employing technology that allows the system to obtain knowledge of its operational and geographical environment, established policies, and its internal state; to dynamically and autonomously adjust its operational parameters and protocols according to its obtained knowledge in order to achieve predefined objectives; and to learn from the results obtained (International Telecommunication Union [ITU- R BT.2302], 2008).

CR allows unlicensed secondary users (SUs) to opportunistically access idle licensed spectrum bands, often referred to as "spectrum holes" or "white spaces," without causing harmful interference to the PUs, (Popoola, et al 2018). However, deploying CR networks requires an accurate, empirical understanding of real world spectrum usage. This has driven empirical research via spectrum measurement campaigns. Spectrum occupancy measurement is the process of determining the degree to which a specific RF band is being used by detecting and quantifying the presence of radio signals within that band over a given period. The measurement process typically involves (Popoola, et al 2018):

I. **Sensing:** Continuously scanning the frequency band of interest using specialized equipment, such as a spectrum analyser or portable RF explorer, to monitor a range of frequencies.
II. **Measuring:** Capturing the received signal levels across the scanned frequencies over time.
III. **Calculating:** Computing the duty cycle, which represents the percentage of time or the fraction of total measurements that a frequency channel or band is found to be occupied.

The measurement campaigns utilize specialized hardware such as high-performance spectrum analysers, omnidirectional antennas, and energy detection algorithms to capture real-world RF occupancy data across diverse times, frequencies, and geographical spaces.

Despite numerous localized spectrum occupancy measurement studies conducted globally and various frequency bands in some states in Nigeria, which consistently indicate a significant underutilization of the radio frequency spectrum with occupancy rates often below 30%, two critical gaps necessitates further action and research.

I. Fragmented and Incomplete National Profile: Existing studies are highly isolated, focusing on specific frequency bands and limited geographical locations, resulting in an incomplete understanding of the overall national spectrum utilization profile. This lack of a comprehensive, nationwide, multi-band, and multi-location dataset prevents regulatory bodies from making fully informed, national-level decisions regarding spectrum efficiency improvement and nationwide dynamic spectrum access (DSA)/Cognitive Radio (CR) deployment strategies.
II. High Spatiotemporal Dynamics: While the overall trend is low occupancy, spectrum availability is highly dependent on time, location, and environment (e.g., urban vs. rural, peak vs. off-peak times). Localized, static measurements fail to capture the true potential or challenges of implementing dynamic spectrum management on a broader, interconnected scale.

Thus, the major gap is the absence of a comprehensive, unified, and contemporary understanding of the actual spectrum utilization profile across all major regions and critical frequency bands in Nigeria. This deficiency hinders the development and implementation of effective national spectrum management policies necessary to harness the significant potential of Dynamic Spectrum Access and Cognitive Radio technologies to address spectrum scarcity and improve overall efficiency, (Ajiboye et al, 2019).

The ultimate goal of this study is to fill in this gap by conducting spectrum measurement campaign in the Television band (470 – 694) MHz with the intent to identifying Television White Space (TVWS) in Kano, Kaduna state and Abuja (F.C.T) in Nigeria. The measurement campaign will be conducted in three phases. Phase 1: Kano, phase 2: Kaduna and phase 3: Abuja. In this study we are starting with phase 1 Kano. Therefore, all the result to be presented in this report will be from Kano (Lat. 11.9820, Long. 8.5147).

1.1 REVIEW OF RELATED LITERATURE

Regulatory frameworks for TVWS deployment have been established in several jurisdictions. The U.S. Federal Communications Commission (FCC) and the UK Office of Communications (Ofcom) have developed guidelines enabling TVWS device operation through geolocation databases (Idowu-Bismark et al., 2025). The European Telecommunications Standards Institute (ETSI) has published harmonized standard EN 301 598, which specifies technical characteristics for TVWSDs operating in the 470–694 MHz band (Adefela et al., 2022; Ntlaltapa, 2013; European Telecommunications Standards Institute [ETSI], 2022). In Nigeria, the Nigerian Communication Commission (NCC) established a committee in 2020 to develop national TVWS guidelines, working in collaboration with the Nigerian Broadcasting Commission (NBC), (Idowu-Bismark et al., 2025).

1.2 GLOBAL SPECTRUM MEASUREMENT CAMPAIGNS

Globally, an extensive spectrum measurement campaigns have established the fundamental premise that the radio spectrum is severely underutilized. These investigations spanned multiple continents, focusing on urban and suburban environments to model temporal and spatial duty cycles. To enhance these empirical evaluations, contemporary frameworks increasingly leverage advanced paradigms, including machine learning-based spectrum occupancy prediction, to construct comprehensive, predictive models of spectral environments over time (Aygül et al., 2025).

Some of the earliest foundational measurement campaigns were conducted in the United States and Europe. Marţian (2010) highlighted a pivotal measurement campaign executed in Chicago, USA, which revealed a mean spectral occupancy of only 17.4% within the 30 MHz to 3000 MHz frequency range. This confirmed that massive blocks of allocated spectrum lay idle even in densely populated urban centers.

Similarly, in Europe, researchers focused heavily on understanding localized and event-driven spectrum dynamics. Marţian (2010) analyzed spatial and context-dependent variations, citing campaigns in Aachen, Germany, which contrasted indoor and outdoor spectral densities. They also documented intensive measurements during the 2006 FIFA World Cup in Dortmund and Kaiserslautern. These studies demonstrated a distinct interdependency between spectrum utilization and real-world human activity, showing sharp spikes in cellular bands during active match periods.

To model these variations over extended timelines, Harrold et al. (2011) conducted a long-term measurement campaign in the UK spanning five months across a 10 MHz to 5 GHz range. They emphasized that while short-term campaigns (lasting a few days) can quantify the baseline percentage of idle spectrum, long-term empirical tracking is vital to model temporal variations across working days, weekends, and holidays. This long-term modelling allows CR systems to accurately predict available white space. While, Van De Beek et al (2012) conducted a model based study in 11 countries in Europe in the band 470–790 MHz), and reported about 56% of channels are unused per location, dropping to 25% if adjacent channels are restricted.

Extensive campaigns across Asia have reinforced these global findings. Marţian (2010) evaluated a 12-weekday spectrum measurement campaign in Singapore covering a broad frequency range up to 5850 MHz, which yielded an overall average occupancy rate of just 4.54%.

In South Asia, Patil et al. (2011), conducted an outdoor spectrum measurement campaign in the suburban environment of Mumbai, India, across the 700 MHz to 2700 MHz band. The investigation reported significant low occupancy during weekdays, noting that the underutilized bands offered excellent potential for opportunistic dynamic spectrum sharing.

Furthermore, Chantaveerod et al. (2021) addressed specific limitations in general-purpose sensing by proposing a focused pass band and guard band monitoring technique for analog FM radio broadcasting in suburban environments. Their experimental model successfully identified 42 entirely unused channels, illustrating that refined empirical measurement strategies can uncover significantly more vacant spectrum than traditional wideband averaging methods.

In the Philippines, Gerolaga (2020) conducted 72-hour monitoring of the 470–698 MHz band and concluded that despite the Philippine TV broadcast being "one of the busiest users of UHF TV band," the spectrum remains significantly underutilized.

Naik, et al, (2013) conducted a nationwide geospatial study across four zones in India in the band 470–590 MHz and found that out of the 100 MHz of TVWS assigned to secondary users, only four channels (32 MHz) have been put to use.

In addition, Kurnaz et al (2016), carried out study to determine the availability of TVWS in the frequency range 470 – 790 MHz in Samsun city center, Turkey at 73 locations, using −40/−45 dB thresholds, found an average occupancy of 20.7%.

1.3 LOCAL SPECTRUM MEASUREMENT CAMPAIGNS (NIGERIA)

In Nigeria, the regulatory regime managed by the Nigerian Communications Commission (NCC) has historically operated on rigid static allocations. Over the past decade, local research groups, primarily based in Nigerian universities, have conducted tailored measurement campaigns to evaluate whether the global phenomenon of spectrum underutilization applies to the distinct socio-economic and infrastructural landscape of a developing country like Nigeria. These empirical investigations consistently point to low overall occupancy rates, confirming that massive portions of the radio spectrum remain severely underutilized across various regions.

To obtain a comprehensive baseline of Nigeria's RF profile, Popoola and Otuu (2018) conducted multi-band and multi-location spectrum measurement campaigns across five major Nigeria's metropolises within the 80 MHz to 2200 MHz frequency range. The quantitative results revealed that the actual overall spectral occupancy in Nigeria was less than 10.00%. The study demonstrated that allocated bands vary randomly in time, frequency, and space, proving that wideband spectrum utilization is consistently low and suggesting an optimistic future for the deployment of DSA and CR frameworks across the country.

Several regional studies have broken down these metrics by analysing localized variations in specific bands, primarily focusing on the Very High Frequency (VHF), Ultra High Frequency (UHF), and FM broadcasting bands. For instance, Ajiboye et al. (2019) conducted a 24-hour outdoor spectrum occupancy survey in the centre of the Minna metropolis, Niger State, targeting the VHF (30–300 MHz) band. The study discovered heavy underutilization; the Aeronautical Navigation band exhibited the highest occupancy at 39.83%, the FM broadcasting band stood at 12.90%, while Aeronautical Mobile operations and TV Broadcasting languished at 4.73% and 0.09% occupancy, respectively. This profile highlights the stark availability of underutilized local frequencies available for secondary deployment.

Luka et al. (2023) implemented a comprehensive web application using the Flask framework with an SQLite database engine. The Okumura-Hata path loss model was employed for protection contour calculations. The database covers 21 local government areas in Adamawa State and 20 in Bauchi State. Validation was performed using RTL-SDR devices configured as spectrum analyzers, which detected 70% of channels indicated as vacant by the database.

Alawode et al. (2024) conducted a localized 48-hour campaign targeting the active FM band (88–108 MHz) across four designated locations in the Osogbo metropolis using energy detection methods. While certain urban channels at university campus hubs experienced peak duty cycles as high as 99.48% due to active local transmissions, the broader regional channels remained unevenly distributed and underutilized during off-peak hours.

Furthermore, the Akure study by Adefela et al. (2022) found that 71.05% of 38 channels in the 470–960 MHz band were unused, indicating very low spectrum occupancy rates that create substantial

opportunities for secondary access. This finding is consistent with the Covenant University study, which confirmed TVWS availability within the 470–694 MHz range specified by Nigerian regulations (Idowu-Bismark et al., 2025).

Similarly, Atimati et al, (2015), conducted a survey on the availability of TV White Spaces at FUT Owerri Eastern Nigeria in the UHF band 470–870 MHz at two sites using fixed measurements. Results of their measurement revealed that 64% of 50 channels are dormant, indicating low occupancy and opportunity for deployment of CR for rural broadband.

The above literature review confirms that spectrum underutilization is a global phenomenon, with studies in the US, Europe, and Asia showing occupancy rates often below 20-30%. This trend is echoed in Nigeria, with local measurement campaigns consistently demonstrating very low overall occupancy (often under 10%) in various bands, including VHF, UHF, and FM broadcasting. The review establishes a strong foundation for the necessity of the current TVWS study in Kano, Nigeria.

To address these gaps, the study aims to conduct a spectrum measurement campaign across Kano, Kaduna, and Abuja. However, the measurement will start with Phase 1 in Kano. The ultimate goal is to identify Television White Space (TVWS) and the actual spectrum utilization in Kano.

2. METHODOLOGY

This research aims to identify TV White Spaces (TVWS) in three states (Kano, Kaduna and Abuja) in Nigeria. The study will start by conducting empirical spectrum measurement campaign in Kano to identify free TVWS channels and also determine the actual spectrum utilization in Kano state. The method will then be replicated in the subsequent two locations (Kaduna and Abuja). The work is divided into three main phases:

- **Phase 1:** Empirical Spectrum Measurement Campaign
- **Objective:** To collect real-world data on how the 470–694 MHz TV band is actually being utilized.
- **Primary Location:** Kano, Nigeria (Lat. 11.9820, Long. 8.5147).
- **Process:** The process involve the following steps:
- **Sensing:** Use a specialized device (Spectrum analyzer connected to an antenna) to continuously scan the target frequency band.
- **Measuring:** Record the power levels of any signals detected in the environment over a set period.
- **Calculating:** Measure and collect, Signal power level Noise power level, Frequency for each channel, this identifies which channels are "free" or "occupied”.
- **Phase 2:** Data Analysis and Pattern Identification
- **Objective:** To process the raw data collected in Phase 1 to understand the spectrum's availability.
- **Process:** The process involve the following steps
- **Data Processing:** Clean and organize the measured signal data.
- **Spatial Analysis:** Map the occupancy data using bar chart to see how TVWS spectrum available in Kano.
- **Statistical Analysis:** Look for patterns to collect quantitative data

2.1 MEASUREMENT LOCATIONS AND SITE SELECTION

Fixed location measurements was conducted in Kano State. The measurements were taken at different time of the day to capture the worst-case scenario of spectrum usage. Measurement locations were strategically chosen to represent a mix of urban, suburban, and rural environments within Kano. The coordinate of the locations (Latitude and Longitude) are as follows: Kano Central City Area, (Lat: 11.98200, Long: 8.51470) representing Urban area, Kura L.G.A (Lat: 11.76050, Long: 8.4226^0), representing Sub-urban area and Gwarmai (Lat: 11.4720^0, Long: 8.2061^0), representing Rural area.

2.2 SPECTRUM MEASUREMENT CAMPAIGN IN THE TV BAND (470–694) MHZ

Accordingly, in line with the objective of this study, spectrum measurement campaign was conducted for 3 days in Kano State from 8th – 10th September 2025. These measurements were carried out within the Ultra High Frequency (UHF) television band (470 - 694 MHz). The map in figure 1. below depicts the locations of measurements and their coordinates (latitudes and Longitudes).

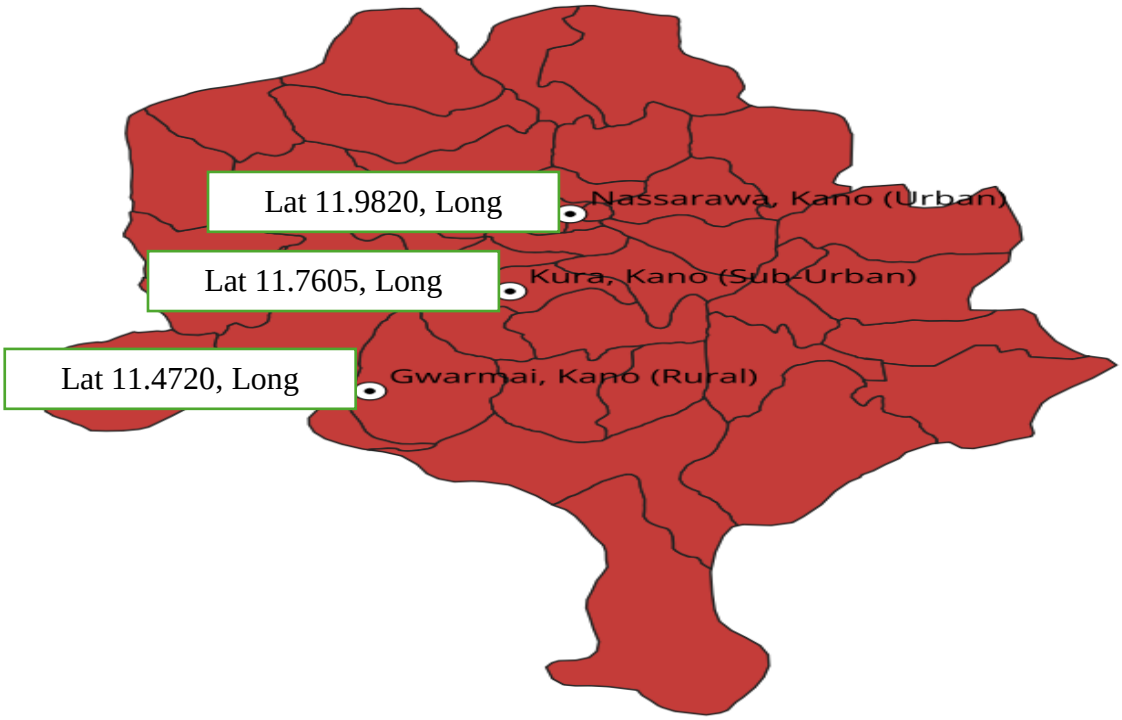

Figure 1: Map of Kano showing measurement locations in Kano

2.3 MATERIALS/INSTRUMENTATION

The following instruments were used for the measurement campaign and data collection:

a. **Spectrum Analyzer:** Agilent (Now Keysight Technologies) Handheld Spectrum Analyzer Model No. N9344C, with a frequency range of 9 KHz to 20 GHz. This device's portability and wide frequency range made it suitable for field measurements.
b. **Antenna**: A wide band high gain (12dB) log-periodic antenna with a frequency range of 1 MHz to 26.5 GHz. This antenna was chosen for its wideband characteristics, which allowed it to cover the entire UHF TV band without requiring multiple antennas.
c. **Cables and Accessories**: Low-loss coaxial cables and a tripod for stable antenna placement were used.
d. **Amplitude Accuracy:** ± 1.3dB
e. **Frequency Range:** 9 KHz to 20 GHz (fully covering the band of interest).
f. **Frequency Accuracy:** ± (0.22 * Span + Span/ (Sweep point – 1)
g. **Frequency Span:** 100Hz – 20GHz
h. **Frequency Resolution:** 1Hz
i. **Calibration Status**: The Spectrum Analyzer was calibrated to ISO/IEC 17025:2017 standards.
j. **Key Settings:** Resolution Bandwidth (RBW) = 10kHz, Video Bandwidth (VBW) = 10 kHz, Sweep Time = 20 Ms.
k. **Software**: Data was logged using the instrument's internal logging and later analyzed using PC-based software (Agilent BTA/DSA Software).
l. **GPS Map**: Camera Lite Application, Version 1.5.8 was adopted.

2.4 MEASUREMENT PROCEDURE

The measurement campaign followed a systematic procedure to ensure data accuracy and consistency. The spectrum analyser was connected to the log-periodic antenna using coaxial cables, and was mounted at a height of approximately 3.0 meters to minimize ground reflections and interference. Resolution Bandwidth (RBW) was set at 10 kHz to resolve individual TV channels, while the Video Bandwidth (VBW) was set at 10 kHz to smooth the display trace. Attenuation loss was set at 20dB to reduce the amplitude of the incoming signal so as to protect the instrument sensitivity front-end components like (mixers) from damage and to prevent signal distortion. The detection Mode was set at Max Hold to capture the peak signal levels over a period. Finally, the spectrum analyser was configured to sweep the UHF television band from (470 – 694) MHz as shown in figure 3 and figure 4 below. Measurements were taken at each location for a duration of 60 minutes per session at multiple location to capture potential intermittent transmissions. The measurements were repeated for three days and average values of the signal was calculated and recorded. The resulting spectrum traces, showing signal strength (in dBm) versus frequency, were saved for subsequent analysis. The instrument setup is as presented in figures 2 and 3.

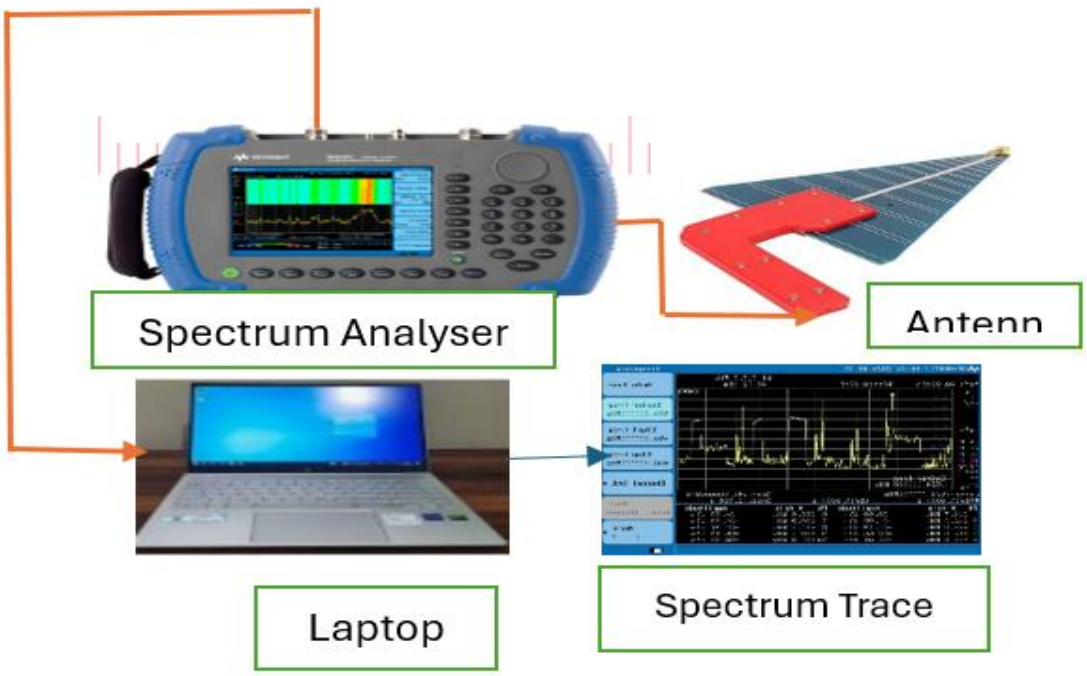

Figure 2: Spectrum Analyser connection diagram

Figure 3: Showing the Spectrum Analyser measurement set-up

3. RESULT AND DISCUSSION

In this section the result of spectrum measurement campaign, Spectrum trace, and raw data collected is presented

3.1 DATA COLLECTION

Primary data (empirical) was collected from primary source, directly from the TV antenna using the Spectrum Analyser as the instrument for data capturing. The data collected includes Received Signal Power Level (RSSI), Noise floor power level, Bandwidth, and Occupancy time and occupancy status (channel occupied active or free).

To systematically assess UHF spectrum utilization, the frequency band 470–694 MHz was divided into standard 8 MHz television channels bandwidth (Channel 21–48) resulting to 28 channels in line with the international telecommunication union (ITU) Standard.

The spectrum trace for Kano urban area (Nasarawa), bar chart of the plot of signal power level against channel number, (showing both active and free channels), bar chart of the plot of occupancy status against channel number (showing active channel labelled = 1 and free channels labelled = 0) are presented in figure 4, figure 5 and figure 6, while table 2 shows raw data collected.

Active channels

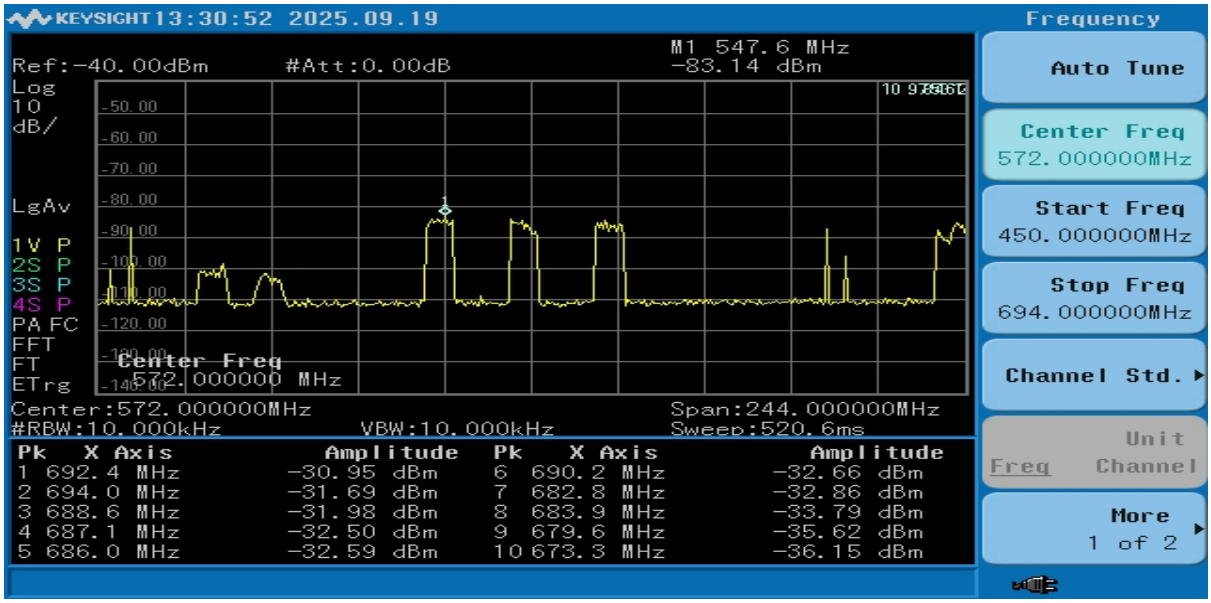

Figure 4: Spectrum Trace Nasarawa GRA, Kano City

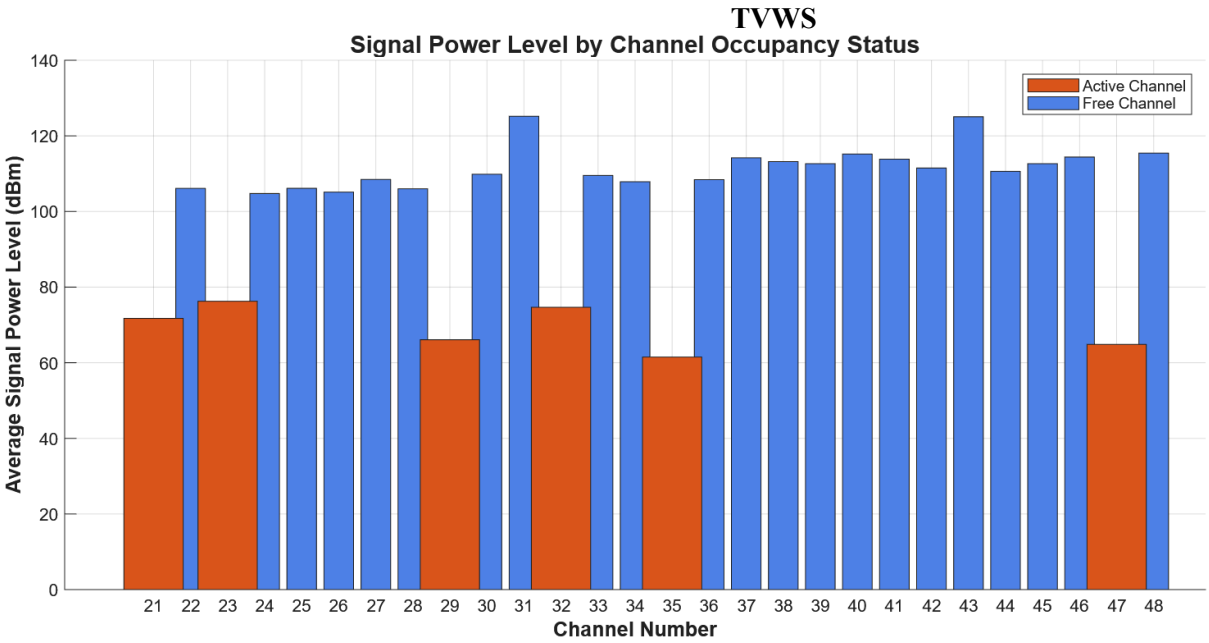

Figure 5: Bar chart plot of signal power level against channel number

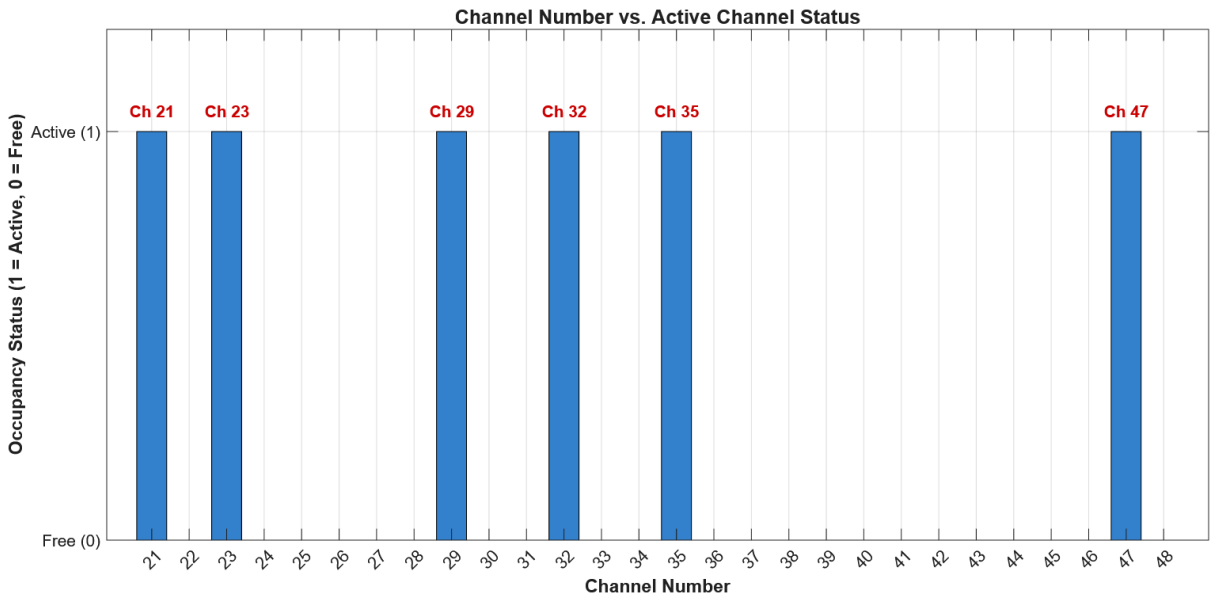

Figure 6: Bar chart plot of occupancy status against channel number

Table 2: Raw data, spectrum occupancy in Nasarawa, Kano (Urban area), Kura L.G.A (Sub-Urban Area (470–694 MH)

Channel No.	**Latitude and Longitude**	**Start Freq. (MHz)**	**Centre Freq. (MHz)**	**End Freq. (MHz)**	**Signal Power Level (dBm) @ Time t = 0 Min**	**Signal power Level (dBm)@Time t = 60 Min**	**Average Signal Power Level (dBm)**	**Occupancy Status**
21	11.9820^0-8.5147^0	470	474	478	-73.25	-70.23	**-71.74**	Occupied active
22	11.9820^0-8.5147^0	478	482	486	-111.01	-101.21	**-106.11**	Free
23	11.9820^0-8.5147^0	486	490	494	-75.21	-77.31	**-76.26**	Occupied active
24	11.9820^0-8.5147^0	494	498	502	-97.26	-112.21	**-104.74**	Free
25	11.9820^0-8.5147^0	502	506	510	-97.08	-115.18	**-106.13**	Free
26	11.9820^0-8.5147^0	510	514	518	-100.93	-109.33	**-105.13**	Free
27	11.9820^0-8.5147^0	518	522	526	-102.50	-114.44	**-108.47**	Free
28	11.9820^0-8.5147^0	526	530	534	-103.75	-108.25	**-106.00**	Free
29	11.9820^0-8.5147^0	534	538	542	-66.98	-65.18	**-66.08**	Occupied active
30	11.9820^0-8.5147^0	542	546	550	-107.51	-112.21	**-109.86**	Free
31	11.9820^0-8.5147^0	550	554	558	-109.04	-141.34	**-125.19**	Free
32	11.9820^0-8.5147^0	558	562	566	-73.67	-75.68	**-74.67**	Occupied active
33	11.9820^0-8.5147^0	566	570	574	-108.54	-110.55	**-109.54**	Free
34	11.9820^0-8.5147^0	574	578	582	-102.54	-113.23	**-107.88**	Free
35	11.9820^0-8.5147^0	582	586	590	-62.85	-60.15	**-61.50**	Occupied active
36	11.9820^0-8.5147^0	590	594	598	-105.61	-111.21	**-108.41**	Free
37	11.9820^0-8.5147^0	598	602	606	-110.20	-118.20	**-114.20**	Free
38	11.9820^0-8.5147^0	606	610	614	-111.30	-115.10	**-113.20**	Free
39	11.9820^0-8.5147^0	614	618	622	-111.20	-114.11	**-112.65**	Free
40	11.9820^0-8.5147^0	622	626	630	-114.20	-116.21	**-115.20**	Free
41	11.9820^0-8.5147^0	630	634	638	-115.30	-112.40	**-113.85**	Free
42	11.9820^0-8.5147^0	638	642	646	-114.00	-109.00	**-111.50**	Free
43	11.9820^0-8.5147^0	646	650	654	-115.01	-135.11	**-125.06**	Free

Channel No.	Latitude and Longitude	Start Freq. (MHz)	Centre Freq. (MHz)	End Freq. (MHz)	Signal Power Level (dBm) @ Time t = 0 Min	Signal power Level (dBm)@Time t = 60 Min	Average Signal Power Level (dBm)	Occupancy Status
44	11.9820^0-8.5147^0	654	658	662	-110.02	-111.22	**-110.62**	Free
45	11.9820^0-8.5147^0	662	666	670	-113.20	-112.10	**-112.65**	Free
46	11.9820^0-8.5147^0	670	674	678	-115.30	-113.50	**-114.40**	Free
47	11.9820^0-8.5147^0	678	682	686	-66.35	-63.33	**-64.84**	Occupied active
48	11.9820^0-8.5147^0	686	690	694	-115.70	-115.20	**-115.45**	Free

Similarly, the spectrum trace for suburban area Kura L.G.A, bar chart of the plot of signal power level against channel number, (showing both active and free channels), bar chart of the plot of occupancy status against channel number (showing active channel labelled = 1 and free channels labelled = 0) are presented in figure 7, figure 8 and figure 9, while table 3 shows raw data collected.

Active channels

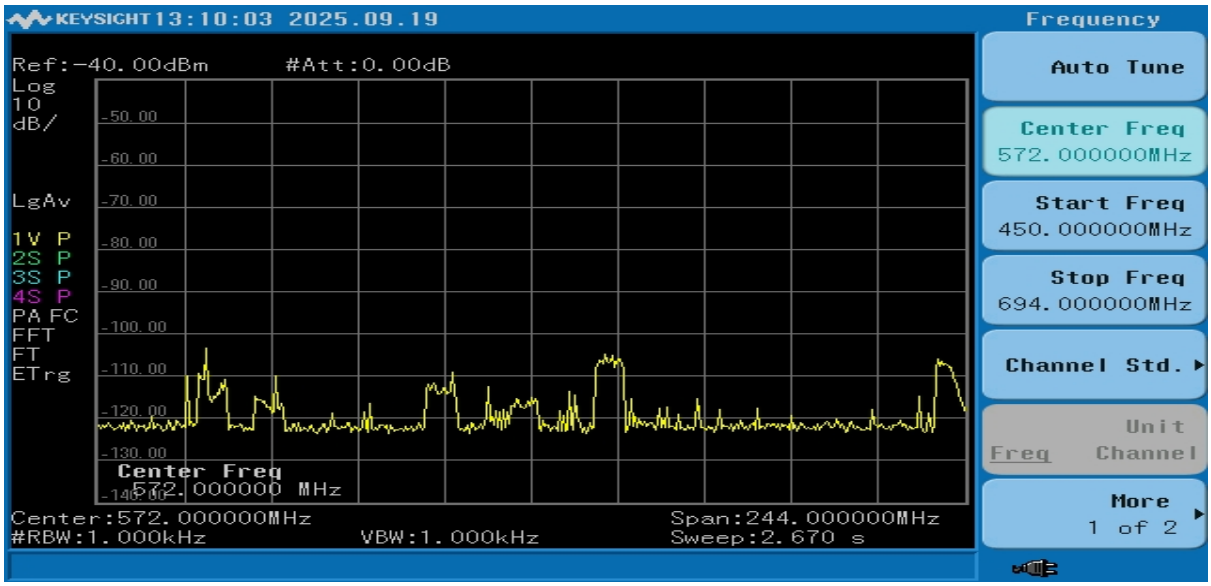

Figure 7: Spectrum Trace Kura LGA, Sub-Urban area, Kano

TVWSs

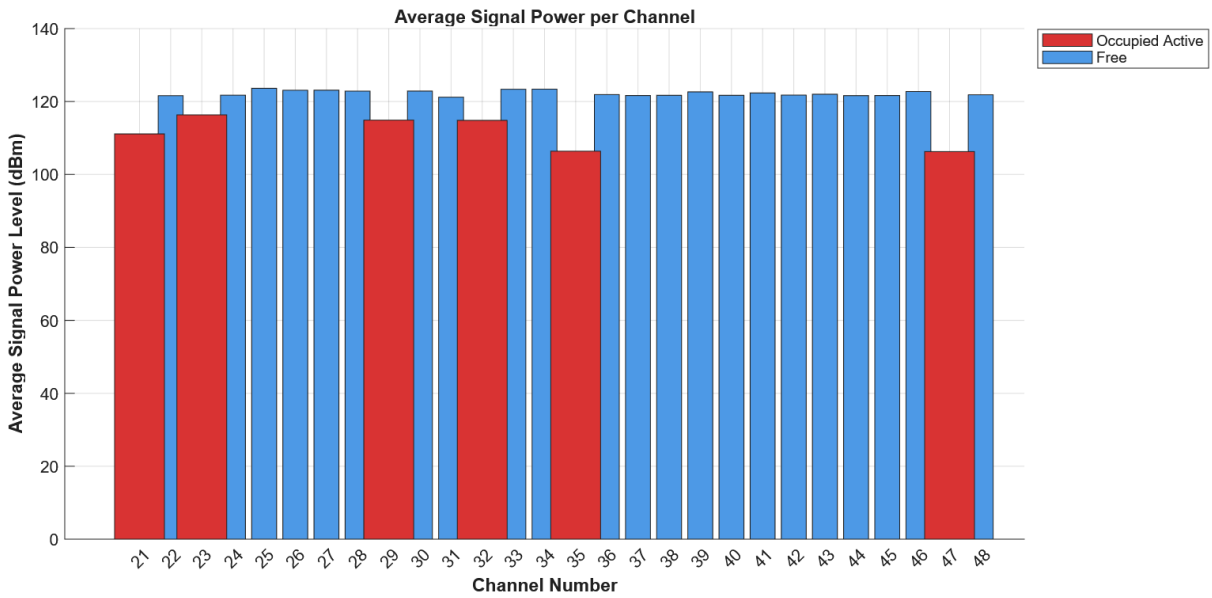

Figure 8: bar chart plot of signal power level against channel number

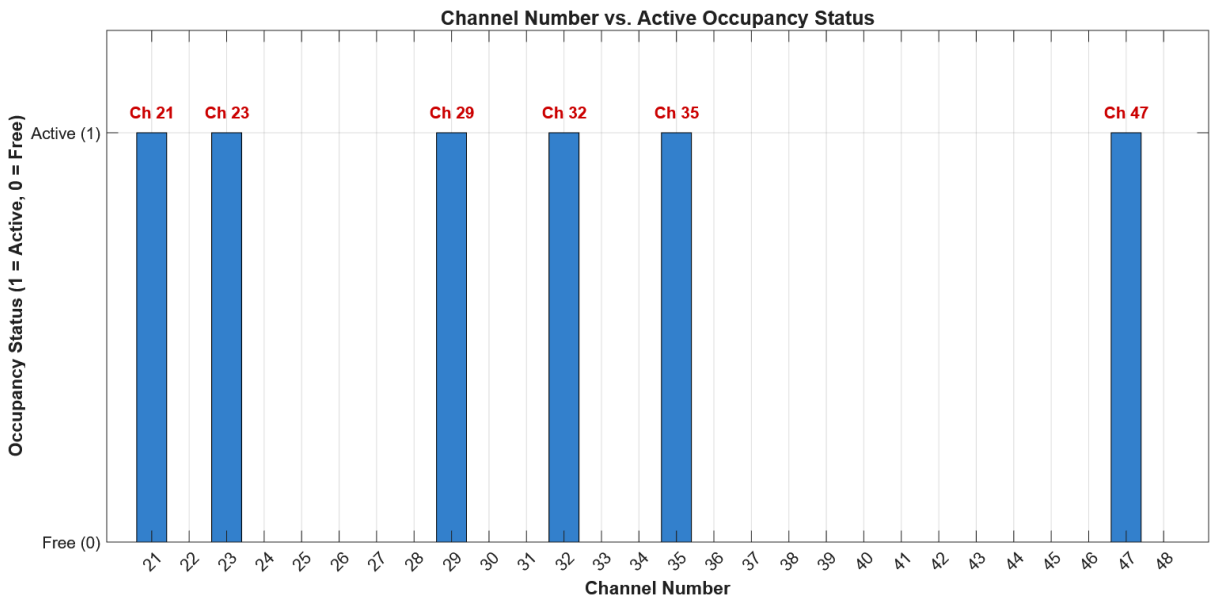

Figure 9: Bar chart plot of occupancy status against channel number

Table 3: Raw data, Spectrum Occupancy in Kura L.G.A, Sub-Urban area, (Lat: 11.76050^0, Long: 8.4226^0) (470–694 MH)

Channel No.	**Latitude and Longitude**	**Start Freq. (MHz)**	**Centre Freq. (MHz)**	**End Freq. (MHz)**	**Signal Power Level (dBm) @ Time t = 0 Min**	**Signal power Level (dBm)@Time t = 60 Min**	**Average Signal Power Level (dBm)**	**Occupancy Status**
21	11.7605^0-8.4226^0	470	474	478	-110.00	-112.23	**-111.12**	Occupied active
22	11.7605^0-8.4226^0	478	482	486	-121.01	-122.21	**-121.61**	Free
23	11.7605^0-8.4226^0	486	490	494	-115.40	-117.31	**-116.35**	Occupied active
24	11.7605^0-8.4226^0	494	498	502	-122.26	-121.22	**-121.74**	Free
25	11.7605^0-8.4226^0	502	506	510	-123.08	-122.18	**-123.63**	Free
26	11.7605^0-8.4226^0	510	514	518	-122.50	-123.70	**-123.10**	Free
27	11.7605^0-8.4226^0	518	522	526	-122.79	-123.44	**-123.11**	Free
28	11.7605^0-8.4226^0	526	530	534	-122.64	-123.07	**-122.85**	Free
29	11.7605^0-8.4226^0	534	538	542	-114.22	-115.58	**-114.90**	Occupied active
30	11.7605^0-8.4226^0	542	546	550	-122.43	-123.32	**-122.87**	Free
31	11.7605^0-8.4226^0	550	554	558	-121.04	-121.34	**-121.19**	Free
32	11.7605^0-8.4226^0	558	562	566	-113.43	-116.26	**-114.84**	Occupied active
33	11.7605^0-8.4226^0	566	570	574	-122.93	-123.79	**-123.36**	Free
34	11.7605^0-8.4226^0	574	578	582	-123.55	-121.23	**-123.39**	Free
35	11.7605^0-8.4226^0	582	586	590	-105.32	-107.45	**-106.38**	Occupied active
36	11.7605^0-8.4226^0	590	594	598	-122.61	-121.21	**-121.91**	Free
37	11.7605^0-8.4226^0	598	602	606	-122.10	-121.20	**-121.65**	Free
38	11.7605^0-8.4226^0	606	610	614	-121.30	-122.10	**-121.70**	Free
39	11.7605^0-8.4226^0	614	618	622	-123.20	-122.11	**-122.65**	Free
40	11.7605^0-8.4226^0	622	626	630	-121.20	-122.21	**-121.70**	Free
41	11.7605^0-8.4226^0	630	634	638	-123.30	-121.40	**-122.35**	Free
42	11.7605^0-8.4226^0	638	642	646	-122.00	-121.52	**-121.76**	Free
43	11.7605^0-8.4226^0	646	650	654	-121.01	-123.00	**-122.00**	Free

Channel No.	Latitude and Longitude	Start Freq. (MHz)	Centre Freq. (MHz)	End Freq. (MHz)	Signal Power Level (dBm) @ Time t = 0 Min	Signal power Level (dBm)@Time t = 60 Min	Average Signal Power Level (dBm)	Occupancy Status
44	11.7605^0-8.4226^0	654	658	662	-121.02	-122.22	**-121.62**	Free
45	11.7605^0-8.4226^0	662	666	670	-122.20	-121.10	**-121.65**	Free
46	11.7605^0-8.4226^0	670	674	678	-123.01	-122.50	**-122.75**	Free
47	11.7605^0-8.4226^0	678	682	686	-105.30	-107.25	**-106.27**	Occupied active
48	11.7605^0-8.4226^0	686	690	694	-122.70	-121.20	**-121.85**	Free

While, Figure 10 present spectrum trace from Gwarmai, Rural Area (Lat: 11.4720^0, Long: 8.2061^0) a distance of 75Km away from Kano city, with no visible spectrum occupancy in the 470–694 MHz spectrum band; making the entire 224MHz (100%) spectrum bandwidth available and free. All the 28 channels are unoccupied.

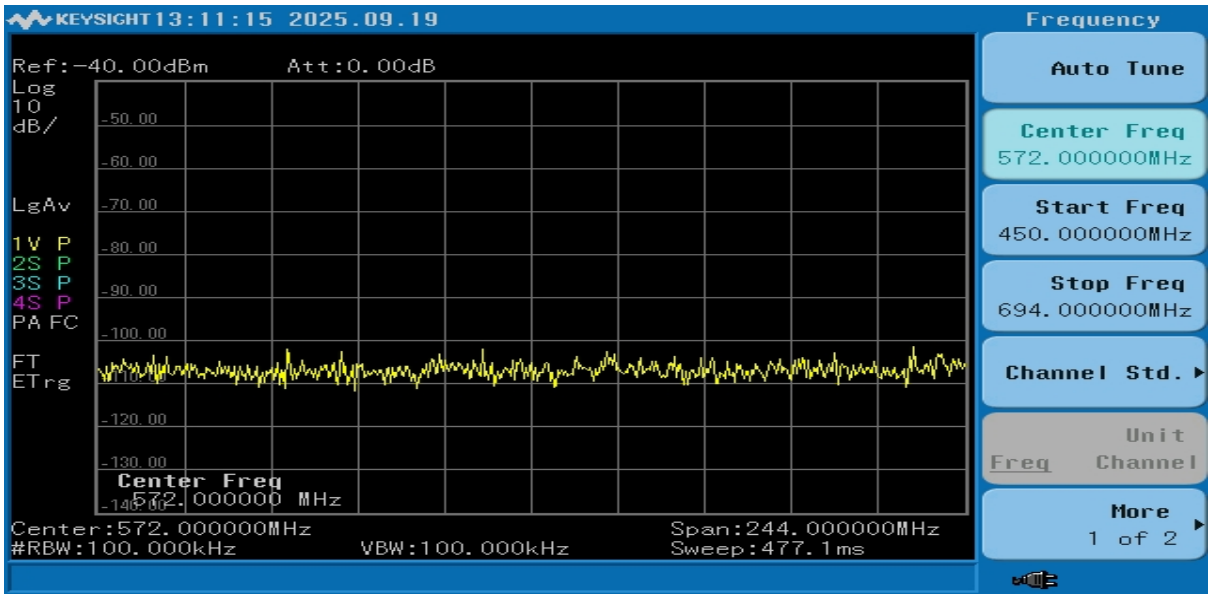

Figure 10: Spectrum Trace, Gwarmai Rural Area, Kano

TVWSs 224 MHz

3.2 Calculation of Spectrum Occupancy Rate for Kano State.

The spectrum occupancy rate for Kano location was calculated as:

$$Occupancy\ Rate\ (\%) = \frac{Number\ of\ Occupiied\ channels}{Total\ Number\ of\ channels} * 100 \quad (1)$$

$$Occupancy\ Rate\ (\%) = \frac{6}{28} * 100 = 21.4\ \%$$

$$Occupancy\ Rate\ (\%) = 21.4\ \%$$

3.3 Statistical Analysis of TVWS Signal Power Levels for the Active channels

This is to enable calculation of Mean, standard deviation and standard error of the signal power level as well as for the noise floor

Mean can be calculated using the formula:

$$\bar{\mu} = \frac{\sum_{i=1}^{n} x_i}{n} \tag{2}$$

Where:

x_i = each signal level

n = total number of samples

In this case n = 6 signal levels as x_1, x_2....., x_6

The mean $\bar{\mu}$ is given by

$$\bar{\mu} = \frac{\sum_{i=1}^{6} x_i}{6} = \frac{415.09}{6} = -69.18\ dBm \tag{3}$$

$$\bar{\mu} = -69.18dB$$

Standard deviation (S) calculated as:

$$\sigma = \sqrt{\frac{\sum_{i=1}^{6}(x_i - \bar{x})^2}{n-1}} \tag{4}$$

$$Variance = \frac{174.2480}{5} = 34.8496\ \text{dB}$$

$$\sigma = = \sqrt{34.8496} = 5.9034\ \text{dB}$$

Standard error (SE) calculated as:

$$SE = \frac{S}{\sqrt{n}} \tag{5}$$

$$SE = \frac{5.9034}{\sqrt{6}} = \frac{5.9034}{\sqrt{2.4495}} = 2.4100\ \text{dB}$$

Table 4 provides summary of metrics (Threshold)

Metrics	**Value**
Mean signal power level	−69.18 dB
Standard Deviation	5.9034 dB
Standard Error	2.2100 dB

3.4 Statistical Analysis of TVWS Noise Power Levels for the Unoccupied channels

Calculation of Mean

Mean can be calculated using the formula:

$$\bar{\mu} = \frac{\sum_{i=1}^{n} x_i}{n} \tag{7}$$

Where:

x_i = each signal level

n = total number of samples

In this case n = 22 signal levels as x_1, x_2....., x_{22}

The mean $\bar{\mu}$ is given by

$$\bar{\bar{\mu}} = \frac{\sum_{i=1}^{22} x_i}{22} = \frac{2460.64}{22} = -111.84 \text{ dBm}$$

Standard deviation (S) calculated as:

$$\sigma = \sqrt{\frac{\sum_{i=1}^{n}(x_i - \bar{x})^2}{n-1}} \quad (8)$$

Variance = $\frac{641.7956}{21} = 30.5617 =$

$\sigma = \sqrt{30.5617}$ = 5.5283 dB

Standard error (SE) calculated as:

$$SE = \frac{S}{\sqrt{n}} \quad (9)$$

$$SE = \frac{5.5283}{\sqrt{22}} = 1.1786 \text{ dB}$$

Table 5: provides summary of metrics (Threshold)

Metrics	**Value**
Mean noise floor power level	-111.84 dB
Standard Deviation	5.5283 dB
Standard Error	1.1786 dB

Table 5 below present all the critical data collected from Kano state which includes, the mean values, standard deviation and standard error for both the signal power level and Noise power levels. These thresholds will be used for development of algorithm for spectrum sensing in cognatic radios.

Table 6: Summary of critical data collected from Kano state

Description	**Metrics**
Bandwidth per Channel	8 (MHz)
Number of occupied Channels	6
Spectrum Occupancy rate	21.4 (%)
Number of un-occupied Channels	22
Total Bandwidths Available	224 (MHz) 100(%)
Bandwidth in Active usage	48 (MHz)
Percentage of usage	21.4(%)
Unoccupied Bandwidth	176 (MHz)
Percentage of bandwidth free	78.6 (%)
Available Spectrum in Rural Areas	224 (MHz) 100%
Mean ($\bar{x}$) Signal power Active Channel	-69.18 dB
Standard Deviation	5.9034 dB
Standard Error	2.4100 dB
Mean ($\bar{x}$) Signal power Unoccupied Channel	-111.84 dBm
Standard Deviation	5.5283dB
Standard Error	1.1786 dB
TV Transmitter power (Pt)	30 Kw
Transmit Antenna gain (Gt)	12 dB
Transmit Antenna Hight (Ht)	30 m
Received Antenna gain (Gr) dB	12 dB
Received Antenna Hight (Hr) in meters	3.0 m

3.5 DISCUSSION

To start with, it is important to note that, the total spectrum within the span of the UHF TV band (470 – 694) MHz is 224 MHz. Each TV channel occupies bandwidth of 8MHz with a guard band or inter-channel spaccing of 8MHz in line with ITU, UHF TV channelization arrangement (ITU- R BT.2302) giving rise to 28 channels from channel 21– 48 as shown in table 2 above.

The data collected from Kano State shows the spectrum utilization status clearly with channel active labelled =1, and channels that are free labelled = 0, as presented in bar charts of figures 5 and 6 while figure 4 depicts the spectrum trace. The results obtained indicates that 6 channels are occupied active with spectrum occupancy rate of 21.4%, and spectrum utilization of 48MHz. These channels are (Channels 21, 23, 29, 32, 35, and 47). While the remaining 22 channels are free, making available 176 MHz spectrum of spectrum bandwidth representing (78.6%). Measurement result from Kura L.G.A suburban area 40Km away from Kano showed the same trend as in Kano city, except that, the signal amplitudes are attenuated due to environmental factor (Patt loss and fading). The spectrum trace, bar chart of the plot of signal power level against channel number, bar chart of the plot of occupancy status against channel number and raw data collected from Kura are presented in figures 8 and 9 and table 3 respectively.

Conversely, the result obtained from Gwarmai a rural area, 75Km away from Kano showes no trace of TV signal. Meaning, there is no active primary user of the spectrum, therefore spectrum utilization is zero, and all the spectrum 224MHz (100%) is available and free. This result also revealed large, portion of spectrum, which are ideal for high-throughput applications. The quantity of spectra identified are wide and sufficient to support modern broadband technologies most especially cognative radios. The spectrum trace is presented in figure 10 above.

Global evidence consistently demonstrates that the 470-694 MHz band is significantly underutilized across diverse geographical contexts. This underutilization ranges from approximately 80% in Nigeria’s studies to even higher figures in some international campaigns. The consistency of these findings across different regulatory domains, measurement methodologies, and geographical settings strongly supports the technical viability of TVWS deployment.

4. CONCLUSION

In conclusion this report has presented the outcome of literature review on global and local spectrum measurement campaigns and the spectrum utilization measurements results conducted in Kano State, Nigeria. The aim of the experimental measurement is to identify the availability of TVWS. Measurement campaigns across the globe, from the US and Europe to Asia and the Philippines, consistently shows that the radio frequency spectrum is severely underutilized, with average occupancy rates often falling below 20-30%. Local studies in Nigeria, across various states and frequency bands (including VHF, UHF, and FM radio), confirm that this global trend of underutilization applies equally to Nigeria. The results obtained from Kano State indicates six active channels (Channels 21, 23, 29, 32, 35, and 47) with a spectrum utilization of 48 MHz (21.4%), while 176 MHz (78.6%) remains unoccupied. A measurement conducted in the Kura Local Government Area (L.G.A.) suburban region showed a trend consistent with that observed in Kano city; however, the signal amplitudes are attenuated due to distance (40 km) and environmental factors.

Conversely, in the rural area of Gwarmai, situated 75 km from Kano, no discernible signal was detected. The absence of signal indicates a complete lack of active spectrum users, thereby resulting in a zero-spectrum utilization rate, with the entirety of the 224 MHz spectrum remaining available for deployment; clearly demonstrating that vast portion of allocated spectrum remain unused for significant periods. This unused capacity is known as "white space." Therefore, this result strongly validates the need for moving away from the inefficient static spectrum allocation model to dynamic Spectrum Access (DSA) to unlock the vast potential of this unused spectrum.

4.1 PROPOSED FUTURE RESEARCH DIRECTION

Spectrum measurement campaign has confirmed the existence of significant TVWS in Kano in the UHF TV band, with higher availability in rural areas. To leverage these opportunities the following are proposed for future research:

I. The results of various spectrum utilization measurements conducted across Nigerian states, point to the availability unoccupied TVWS, therefore, a nationwide measurement campaign should be conducted to develop a comprehensive TVWS database.
II. Artificial Intelligence Algorithm or technics should be developed for coordination and management of the TVWS database to allow interference free access of the spectrum by Cognatic Radio users.

4.2 ACKNOWLEDGEMENTS

The authors declare that no funds, grants, or other support were received during the preparation of this manuscript.

4.3 AUTHOR CONTRIBUTIONS:

All authors contributed to the study conception and design. Material preparation, data collection & analysis and draft of the first manuscript was done by performed by Yahaya Hamisu Abubakar. Dr. Mathew Ehikhamenle reviewed and corrected manuscript. All authors read and approved the final manuscript.

5. REFERENCE

Adebayo, A. K., Agbolade, J. O., Bamikefa, I. A., Afolalu, O. F., & Ayoade, M. A. (2021). Analysis of spectrum occupancy of active FM band within Federal Polytechnic Ede Northern Campus. *International Conference of Sciences, Engineering & Environmental Technology (ICONSEET)*, *6*(30), 236–245.

Adefela, A. N., Olasoji, Y. O., & Adedeji, K. B. (2022). Evaluation of TVWS availability: A step towards frequency spectrum utilization. *Journal of Engineering Advancements*, *3*(2), 65–70. https://doi.org/10.38032/jea.2022.02.002

Ajiboye, J. A., Adegboye, B. A., Aibinu, A. M., & Kolo, J. G. (2019). Spectrum occupancy measurement in the VHF band: Results and evaluation in the context of cognitive radio. *Proceedings of the 3rd International Engineering Conference (IEC 2019), Federal University of Technology, Minna, Nigeria*, 510–514.

Alawode, K. O., Adebayo, A. K., Lasisi, H. O., & Ajewole, T. O. (2024). A Levenberg-Marquardt based neural network spectrum occupancy prediction for UHF (470-670) MHz band services in Osogbo metropolis. *Scientific Bulletin, Series: Electronics and Computer Science*, *24*(1), 75–84.

Atimati, E. E., Ezema, L. S., Ezeh, G. N., Iwuchukwu, U. C., & Agubor, C. K. (2015). A survey on the availability of TV white spaces in Eastern Nigeria. *International Journal of Scientific & Engineering Research*, *6*(12), 609–614.

Aygül, M. A., Çırpan, H. A., & Arslan, H. (2025). Machine learning-based spectrum occupancy prediction: A comprehensive survey. *Frontiers in Communications and Networks*, *6*, Article 1482698. https://doi.org/10.3389/frcmn.2025.1482698

Chantaveerod, A., Woradit, K., & Pochaiya, C. (2021). Spectrum occupancy model based on empirical data for FM radio broadcasting in suburban environments. *Sensors*, *21*(12), 4015. https://doi.org/10.3390/s21124015

Dare, O. E., Okokpujie, K., Adetiba, E., Idowu-Bismark, O., Abayomi, A., Jules Kala, R., Owolabi, E., & Christopher Ukpong, U. (2024). Development of a conditional generative adversarial network model for television spectrum radio environment mapping. *IEEE Access*, *12*, 197632–197644. https://doi.org/10.1109/access.2024.3521998

European Telecommunications Standards Institute (ETSI). (2022). *TV White Space Devices (TVWSD); Wireless Access Systems operating in the 470 MHz to 694 MHz TV broadcast band; Harmonised Standard for access to radio spectrum* (ETSI EN 301 598 V2.2.1). ETSI.

Ezema, L. N. (2014). A survey on the availability of TV white spaces in Eastern Nigeria. *International Journal of Scientific & Engineering Research*, *5*(12), 431–439.

Gerolaga, E. C., Jr. (2020). *Evaluation of white space in the UHF channels of the Philippine TV broadcast band* [Undergraduate thesis, University of the Philippines Los Baños]. UPLB Repository.

International Telecommunication Union. (2014). *Report on spectrum requirements for terrestrial television broadcasting in the UHF frequency band in Region 1 Islamic republic of Iran* (Report ITU-R BT.2302). ITU.

Kurnaz, Ç., Engiz, B., & Albayrak, Z. (2016). Determination of TV white space spectrum availability in Samsun Turkey. *2016 24th Telecommunications Forum (TELFOR)*.

Luka, M. K., Okereke, O. U., Omizegba, E. E., & Anene, E. C. (2021). Blockchains for spectrum management in wireless networks: A survey. *arXiv preprint arXiv:2107.01005*. https://doi.org/10.48550/arxiv.2107.01005

Marţian, A. (2010). Evaluation of spectrum occupancy in an urban environment in a cognitive radio context. *UPB Scientific Bulletin, Series C: Electrical Engineering and Computer Science*, *72*(4), 32–41.

Mitola, J., & Maguire, G. Q. (1999). Cognitive radio for flexible mobile multimedia communications. *Proceedings of the IEEE International Workshop on Mobile Multimedia Communications*, 6(4), 13–18.

Naik, G., Singhal, S., Kumar, A., & Karandikar, A. (2013). Quantitative assessment of TV white space in India. *2014 Twentieth National Conference on Communications (NCC)*.

Ntlaltapa, N. (2013). *Cape Town TVWS trial: Technical monitoring and evaluation report*. Meraka Institute.

Patil, K. P., Teati, S. R., & Patil, S. (2011). Spectrum occupancy statistics in the context of cognitive radio. *2011 IEEE International Conference on Signal Processing, Communications and Computing (ICSPCC)*, 1–5. https://doi.org/10.1109/ICSPCC.2011.6061732

Popoola, J. J., & Otuu, U. (2018). Assessment of radio spectrum profile in Nigeria using multi-band and multi-location radio spectrum occupancy measurements. *Eskişehir Technical University Journal of Science and Technology A - Applied Sciences and Engineering*, *19*(4), 948–962.

Van de Beek, J., Riihijärvi, J., Achtzehn, A., & Mähönen, P. (2012). TV white space in Europe. *IEEE Transactions on Mobile Computing*, *11*(2), 178–188. https://doi.org/10.1109/TMC.2011.203

International Conference on Engineering Innovation for Sustainable Development (ICESID 2026)
Faculty of Engineering, Ahmadu Bello University Zaria · 8–10 September 2026

HOUSEHOLD WATER SECURITY AND INTEGRATED WATER RESOURCES MANAGEMENT GAPS IN A RAPIDLY URBANISING NIGERIAN CITY: EVIDENCE FROM MINNA, NIGER STATE

Muhammad Ashafa[1], Mohammed Saidu[2,*]
[1]*Federal University of Technology, Minna*
[2]*FUT Minna*
Email: ashafseen@gmail.com, mohammed_saidu@futminna.edu.ng*
***Corresponding author**: Mohammed Saidu
DOI: https://doi.org/10.67203/sp.ICESID.2026

ABSTRACT
Nigeria's freshwater crisis presents a stark paradox: a nation endowed with abundant water resources yet crippled by widespread household water insecurity. Drawing on survey data from 384 households across 21 wards in Bosso and Chanchaga Local Government Areas, this paper investigates the multi-dimensional nature of water insecurity at the household level. Our findings reveal that water insecurity manifests not merely as physical scarcity but as a complex interplay of infrastructural failure, economic burden, governance deficits, and gendered labour. Over 70% of households experience regular interruptions, with coping strategies that disproportionately burden women and children. Monthly water expenditures average ₦1,876 (weighted across all 21 wards; see Section 3.3 for ward-level variation), with 40% of households reporting moderate to severe cost burden. While 68% of respondents express distrust in public water quality, reliance on private boreholes and vendor-supplied water remains constrained by affordability and reliability. The paper argues for an integrated approach to water governance that moves beyond supply-side interventions to address the socio-economic and institutional dimensions of water insecurity. We propose a framework grounded in community participation, infrastructure modernization, and equitable pricing mechanisms.

Keywords: *Water insecurity; household survey; Nigeria; urban water governance; HWISE framework; water affordability*

1. INTRODUCTION

1.1 The Nigerian Water Paradox

Nigeria has never lacked water. Its rivers, aquifers and rainfall totals rank among the most generous in West Africa. And yet, for the ordinary household, water insecurity is a daily fact of life rather than a distant statistic. This is the paradox that scholars have documented extensively in recent years *(Irene, Irene & Daniels, 2025; Abubakar, 2019; Adeoti et al., 2024), with research finding that climate change and crumbling infrastructure have steadily worn down the country's freshwater systems, leaving many communities unable to count on a reliable supply (Abubakar Mashi et al., 2026; Igimoh et al., 2026).

A new household survey carried out across 21 wards in the Bosso and Chanchaga Local Government Areas of Niger State puts real numbers behind that picture. Researchers spoke with 384 households and tested 50 water samples, building on the Household Water Insecurity Experiences (HWISE) framework (Household Water Insecurity Experiences Scale, various authors), which treats water insecurity as more than a question of supply, it is also about whether water is accessible, affordable, safe and reliably available.

The framework matters because it has already been tested elsewhere. Studies in Mexico and Bangladesh have linked water insecurity to food insecurity within the same households (Shamah-Levy et al., 2025; HWISE Scale literature), suggesting that when the tap fails, the effects ripple outward into nutrition, income and daily routine. The Minna survey set out to test whether the same pattern of overlapping hardship holds true in a fast-growing Nigerian city.

What makes Minna a useful case is precisely its ordinariness. It is neither a megacity swamped by international attention nor a remote village studied purely for its rural character—it is the kind of mid-sized, rapidly urbanising state capital found across Nigeria, where population growth is outpacing the utilities and pipe networks built to serve it. That makes its findings a plausible mirror for dozens of similarly sized cities where nobody has yet run the numbers.

2. METHODOLOGY

2.1 Study Area and Sampling

The survey instrument was built around seven themes: household demographics, water source characteristics, interruption and coping patterns, physical access, economic burden, water quality and treatment, and governance perceptions. Field teams sampled households proportionally across the 21 wards, then followed up with descriptive and bivariate statistical analysis to see how demographic factors relate to water security outcomes—an approach the authors describe as examining "distributions of dimensions and themes, and water insecurity categories to assess what drives higher water insecurity scores."

$n = (Z^2 \times p \times q) / e^2$

Where:

- $Z = 1.96$ (95% confidence level)
- $p = 0.5$ (maximum variability, conservative estimate for household water insecurity prevalence)
- $q = 1 - p = 0.5$
- $e = 0.05$ (5% margin of error)

This yielded an initial sample of 384 households, which was then proportionally allocated across the 21 wards based on estimated population distributions. The total population of Bosso and Chanchaga LGAs is approximately 380,000, with the sample providing a 95% confidence level and ±5% margin of error. This approach follows established survey methodology for household studies in Nigerian urban settings (Ishaku & Kawu, 2023; Gidadawa et al., 2024).

Sampling intensity varied by ward, from 11 households in Kodo to 28 in Sabon Gari and Tudun Wada South, the two wards that, as later sections show, also turn out to carry the heaviest burden of interruptions and distrust. Beyond the household interviews, the 50 accompanying water-quality samples give the survey a second, independent line of evidence: it isn't only asking people how safe their water feels, it is also checking what's actually coming out of the source.

Statistical Analysis: Analysis proceeded in two stages. First, descriptive statistics (frequencies, percentages, means) were calculated to characterise the distribution of water security experiences across the sample. Second, bivariate comparisons were conducted using chi-square tests to examine associations between demographic factors (ward location, gender of respondent, income bracket, education level) and water security outcomes. For continuous outcomes (e.g., monthly expenditure, interruption frequency), independent t-tests and one-way ANOVA were used. All statistical tests were performed using SPSS version 26, with statistical significance set at $p < 0.05$.

Water Quality Sampling: Laboratory water-quality testing was conducted on 50 samples collected from households across all 21 wards. Samples were analysed for turbidity, bacteriological counts (total coliform and E. coli), pH, electrical conductivity, and selected chemical parameters (nitrate, iron, fluoride) at the Niger State Ministry of Water Resources Laboratory. However, due to delays in laboratory data processing at the time of manuscript preparation, these results could not be included in the current analysis. The full laboratory dataset will be presented in a separate technical report and incorporated into future publications. The present paper focuses on self-reported/perceived water quality, which remains a valid measure of household experience and risk perception (Haeffner et al., 2023). Analysis then moved from simple description, how common is each experience, into bivariate comparisons that test whether factors like ward location, gender of respondent, or income bracket line up with worse water security outcomes.

3. FINDINGS AND DISCUSSIONS

3.1 Household Characteristics and Dependence on Alternative Water Sources

Nearly two-thirds of respondents, 63%, were women, a figure that itself speaks to who actually manages water in these households. Of all respondents, 42% were household heads and 28% were spouses, and 60% had at least a secondary education. On the supply side, the picture is telling: private boreholes (32%) and hand-dug wells (25%) were the most common water sources, well ahead of public utility connections, a sign of just how far households have had to go to compensate for gaps in formal infrastructure.

That last point is worth sitting with. In a well-functioning system, private boreholes and hand-dug wells would be a fallback, not the default. Here they are the backbone of household water supply for the majority of the sample, a quiet but telling admission that the public network people are nominally connected to isn't the one they actually depend on day to day.

3.2 Water-Supply Reliability and Frequency of Interruptions

Interruption is the norm rather than the exception. More than 70% of households reported at least one supply interruption in the past month, and 12% said interruptions happen more than once a week.

Figure 1: Frequency of Water Interruptions

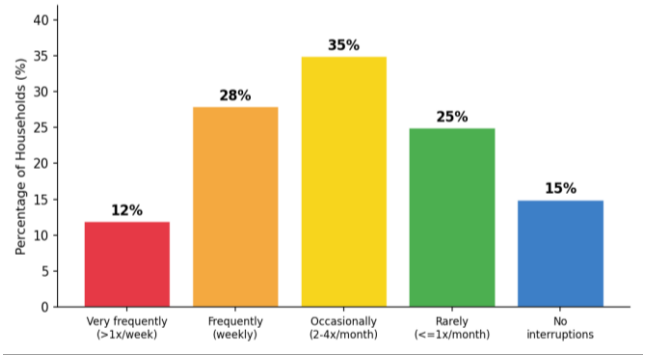

Source: Field Survey (2026)

Coping with these gaps has a cost. Across the sample, 38% of households buy water from vendors or tankers when supply fails, 32% switch to an alternative source, and smaller shares store water in advance, cut back on use, or simply wait it out. But the response looks different from ward to ward.

Table 1: Coping Strategy by Ward (Top 5 Wards)

Ward	Vendor	Alt. source	Store	Reduce use	Wait
Sabon Gari (SAB)	42%	35%	20%	15%	18%
Tudun Wada South (TWS)	38%	30%	25%	20%	12%
Nassarawa A (NAA)	40%	28%	22%	18%	15%
Minna Central (MCT)	35%	32%	18%	22%	20%
Beji (BEJ)	30%	28%	25%	15%	10%

[Note: Percentages sum to >100% as households were able to select multiple coping strategies]

Source: Field Survey (2026)

Sabon Gari's heavy reliance on vendor water (42%) reflects just how thin public infrastructure is stretched there, while Beji's households lean more on storage (25%), perhaps a sign of better forward planning, or simply of fewer alternatives nearby. The pattern echoes findings from Mexico, where researchers reported that "the odds of water insecurity were lower in households with medium to high asset scores" (Shamah-Levy et al., 2025), underlining that coping capacity tracks closely with household wealth.

3.3 Household Water Expenditure and the Burden of Water Access

Paying for water is close to universal, and the amounts vary enormously, from nothing to more than ₦7,000 a month. On average, households spend ₦1,876 a month (weighted average across all 21 wards; see Table 3 for ward-level variation), a figure that lands hard on lower-income families: 35% describe the cost as a moderate burden and 15% call it severe. And this figure almost certainly understates the true cost, because it doesn't capture the hours spent fetching water, time that falls, overwhelmingly, on women and children.

3.4 Gendered Burden and Time Costs of Household Water Collection

Women and girls carry 65% of the water-fetching responsibility in these households; men and boys account for just 23%. It's a pattern that shows up across sub-Saharan Africa (Nyika & Dinka, 2023; Maungu, 2023), and one with consequences well beyond the well or borehole, it eats into time that could go toward schooling, paid work or rest. A quarter of households live within 100 metres of their water source, but one in five must travel more than 500 metres, and the average round trip takes 18 minutes.

Research from Mexico adds a further layer: Shamah-Levy et al. (2025) found that households with women of childbearing age face a measurably higher risk of water insecurity, which suggests the burden compounds for exactly the households least able to absorb it. While this relationship was observed in the Mexican context, testing this specific association within the Minna dataset would require additional analysis of household age-composition data. This represents an important direction for future research using the current dataset.

3.5 Perceived Water Quality, Safety and Household Treatment Practices

Only 35% of households report no problems at all with their water. The rest describe cloudiness or particles (28%), an odd smell (22%), or unusual colour (15%). Despite this, only 45% of households treat their water before use, and boiling at 38% is by far the most common method.

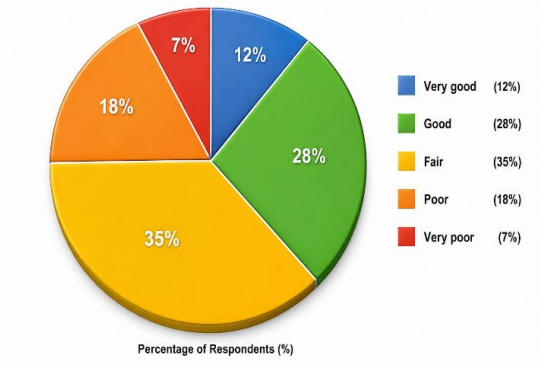

Figure 2: Water Quality Rating

Source: Field Survey (2026)

Distrust extends past water itself and into the institutions responsible for delivering it. Asked whether authorities respond quickly to problems, 57% disagreed. Half of all respondents are dissatisfied with how water is managed locally, and 48% distrust the quality of public sources altogether. Only 25% feel their community is meaningfully consulted on water decisions, while 47% feel excluded from decisions

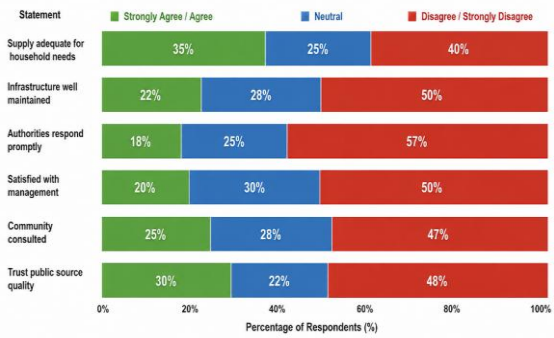

Figure 3: Governance Perceptions (Likert Scale)

Source: Field Survey (2026)

This pattern of institutional distrust sitting alongside physical scarcity mirrors research from rural Iseyin, Oyo State, which mapped villages with varying levels of vulnerability to water insecurity (Evaluating Water Scarcity Vulnerability Levels in Rural Communities of Iseyin Local Government Area, Oyo State, Nigeria, 2025). The Minna data suggests the same forces are at work in a rapidly urbanising setting, not just in rural communities.

It's worth pausing on what that combination of numbers actually means for a household. A family can be doing everything reasonably expected of it, boiling water, storing supply in advance, paying a vendor when the borehole runs dry, and still have good reason to doubt both the water itself and the system meant to guarantee it. Distrust here isn't a communication problem to be solved with a public-awareness campaign; it's a rational response to a track record of unmet promises.

3.6 Biggest Water Challenge

When asked, in their own words, to name their single biggest water challenge, respondents' answers map closely onto the survey's quantitative findings.

Table 2: Biggest Water Challenge (Top Open-Ended Responses)

Challenge	Share of respondents
Poor water quality / taste / odour	22%
Inadequate number of boreholes / taps	18%
High cost of water from vendors	16%
Water source dries up in dry season	15%
Frequent breakdown of boreholes	12%
Long distance to nearest source	10%

Source: Field Survey (2026)

Quality tops the list, followed by infrastructure gaps and cost, but the appearance of governance-related answers ("irregular public supply" and "lack of government intervention," 6% and 5% respectively) confirms that households experience this as an institutional failure, not just a technical or seasonal one.

3.7 Water Security Indicators by Ward

Aggregate numbers hide real differences between neighbourhoods. A ward-level comparison shows just how much local conditions shape the experience of water insecurity.

Table 3: Water Security Indicators by Ward (Selected Wards)

Ward	Interruptions	Pay for water	Monthly spend	Treat water	Trust public source
Beji (BEJ)	1.8 days/mo	80%	₦1,735	45%	30%
Sabon Gari (SAB)	2.1 days/mo	85%	₦2,450	40%	25%
Nassarawa A (NAA)	1.9 days/mo	82%	₦1,950	42%	28%
Tudun Wada South (TWS)	2.3 days/mo	78%	₦1,620	38%	22%
Minna South (MNS)	1.6 days/mo	75%	₦1,480	50%	35%

Source: Field Survey (2026)

The overall average of ₦1,876 is calculated as a weighted average across all 21 wards, not just the five shown in Table 3. The ward-level variation ranges from approximately ₦1,480 (Minna South) to ₦2,450 (Sabon Gari), with the overall average reflecting the population-weighted contribution of all wards.]

Sabon Gari and Tudun Wada South stand out for the worst outcomes, the most frequent interruptions and the least trust in public sources, while Minna South looks comparatively stable across nearly every indicator. That kind of spatial unevenness argues against one-size-fits-all fixes: what Sabon Gari needs is not necessarily what Minna South needs.

4. DISCUSSION AND CONCLUSION

Water insecurity is depicted as a multifaceted issue exacerbated by infrastructure failures, financial difficulties, gender disparities, quality concerns, and governance weaknesses. This aligns with broader studies in the Global South. In Sub-Saharan Africa, factors like climate variability, population density, and economic conditions influence household water access (Ogunbode et al., 2025; Nyika & Dinka, 2023), as seen in Minna, where failing public infrastructure forces poorer households to rely on costly and potentially unsafe private boreholes and wells.

The governance data shows that people want to engage but don't feel heard. Research from coastal Bangladesh suggests that better cooperation between central and local governments improves water governance (Charles et al., 2022). In this case, 57% of households believe official responses are slow, and 47% feel excluded from decisions. Additionally, 65% of households report water quality issues (as noted in Section 3.5), but less than half treat their water before drinking, indicating constraints that expose them to health risks they may not fully understand

4.1 Study Limitations

This research has several shortcomings that need attention. First, perception data, while useful for identifying household experiences, may be biased by memory and not match objective water quality data. Second, the study's cross-sectional approach only captures conditions at one time (2026), limiting insights into causality and seasonal changes in water availability. Third, sampling included 21 wards, but some had very few observations, with as few as 11 households in Kodo. Fourth, no data was collected on households lacking improved water sources, which may under-represent vulnerable populations. Lastly, although laboratory water quality test results were available, they could not be used due to processing delays.

4.2 Recommendations and Policy Implications

The survey emphasizes that water insecurity is a governance and equity issue, not just an engineering problem. It outlines four key priorities: First, enhance and expand public water infrastructure, especially in areas like Sabon Gari and Tudun Wada South that rely on costly private options. Second, create affordable water pricing through tiered tariffs and subsidies for low-income families facing high costs, particularly in Sabon Gari. Third, rebuild trust by improving response times and involving the community in decisions, as 47% feel excluded. Fourth, regularly monitor water quality and provide testing support to tackle reported problems. The approach varies for different areas.

4.3 Engineering and Technological Implications

The survey highlights key issues related to water access and governance that suggest important engineering solutions. Over 70% of people face interruptions in water supply, indicating a need for smart metering and real-time monitoring systems. Many rely on private boreholes and wells, creating a chance for low-cost treatment options like household filtration and solar-powered systems to enhance water quality. It also points out the need for decentralized water systems suited to local needs due to varying water security. Additionally, 40% of households face significant costs, signaling a need for innovative financing methods. Community engagement is essential for effective and sustainable solutions.

REFERENCES

Abubakar Mashi, S., Oghenejabor, O. D., Oluyori, N. R., & Umar, A. (2026). Urban Green Spaces, Privatization, and Sustainable Development: Governance and Equity in Rapidly Urbanizing Cities. Sustainable Development.

Abubakar, I. R. (2019). Factors influencing household access to drinking water in Nigeria. *Utilities Policy, 58, 40-51.

Adeoti, O. S., Kandasamy, J., & Vigneswaran, S. (2024). Water infrastructure sustainability challenge in Nigeria: A detailed examination of infrastructure failures and potential solutions. Water Supply, 24(6), 2066-2076.

Bouramdane, A. A. (2023). Optimal water management strategies: paving the way for sustainability in smart cities. Smart Cities, 6(5), 2849-2882.

Celestin, M., Gnana Raja, G. R., Mohamed, J. A., & Ibraheem, A. M. (2025). Using probability theory to assess risks and mitigate uncertainty in procurement processes. *International Journal of Computational Research and Development, 10(2), 136-146.

Charles, K. J., Howard, G., Prats, E. V., Gruber, J., Alam, S., Alamgir, A. S. M., ... & Campbell-Lendrum, D. (2022). Infrastructure alone cannot ensure resilience to weather events in drinking water supplies. Science of The Total Environment, 813, 151876.

Cochran, W. G. (1977). Sampling techniques (3rd ed.). New York: Wiley.

Egbueri, J. C., Agbasi, J. C., Onuba, L. N., Nweke, N. D., Uwajingba, H. C., & Abba, S. I. (2025). Groundwater development within the Nigerian crystalline and sedimentary aquifers: challenges and opportunities. Groundwater in developing countries: Case studies from MENA, Asia and West Africa, 297-325.

Evaluating Water Scarcity Vulnerability Levels in Rural Communities of Iseyin Local Government Area, Oyo State, Nigeria. (2025). Zenodo.

Gallegos, A., Grigg, N. S., & Llano, W. (2026). Enablers and Obstacles in Integrated Water Resources Management (IWRM) Implementation and Their Contributions to Sustainable Territorial Development. Land, 15(2), 270.

Gidadawa, Z. S., Gatawa, B. M., Umar, A., & Muhammad, A. (2024). Domestic water sources and factors influencing urban household attitudes on water storage facilities in Sokoto metropolis, North Western Nigeria. *Sokoto Journal of Geographical Studies, 1(1), 160-162.

Haeffner, M., Jackson-Smith, D., & Barnett, M. J. (2023). Categorizing relative water use perception bias using household surveys and monthly water bills. Journal of Environmental Management, 334, 117443.

Household Water Insecurity Experiences (HWISE) Scale. (Various authors). IOP Science.

Hui, I., & Smith, G. (2022). Private citizens, stakeholder groups, or governments? Perceived legitimacy and participation in water collaborative governance. Policy Studies Journal, 50(1), 241-265.

Igimoh, J. J. O., Modeme, S. C., Tijani, A., & Makata, N. E. (2026). Recurring Water Scarcity in Nigeria: Implications for Domestic Water Access, Public Health, and Sustainable Management. Journal of Health, Wellness and Safety Research.

Irene, J., Irene, B. N., & Daniels, C. (2025). Not a Drop to Drink: Addressing Nigeria's Deepening Freshwater Crisis. Water, 17(12), 1731.

Ishaku, M. W., & Kawu, A. M. (2023). Implications of Spatial Variation of Household Poverty Incidence in Minna, Niger State. [Journal details to be added].

Iyoha, O. W., Omotoso, A. J., Usiobaifo, B. E., Raimi, M. O., & Ofor, T. N. (2025). Beyond the tap: Water insecurity, environmental contamination, and health inequities in Uselu, Benin City. JMIR Preprints, 1(11), 2025.

Maungu, N. (2023). A quantity-quality tradeoff: Water quality and poverty assessment of drinking water sources in Southern Tanzania (Doctoral dissertation, NM-AIST).

Nyika, J., & Dinka, M. O. (2023). Water challenges in rural and urban sub-Saharan Africa and their management* (pp. 39-55). Cham: Springer.

Ogunbode, T. O., et al. (2025). Assessing water security in Sub-Saharan Africa in the context of climate change threats: a case study. Journal of Water and Climate Change.

Pandin, M. G. R. (2026). Strengthening Sustainable Clean Water Supply through Local Government Governance: A Mini Literature Review on Institutional Capacity, Collaborative Governance, and Infrastructure Financing. [Journal details to be added].

Shamah-Levy, T., Méndez-Gómez-Humarán, I., Mundo-Rosas, V., Muñoz-Espinosa, A., Melgar-Quiñonez, H., & Young, S. L. (2025). Household water security is a mediator of household food security in a nationally representative sample of Mexico. Public Health Nutrition, 28.

Uitermark, J., Hochstenbach, C., & Groot, J. (2024). Neoliberalization and urban redevelopment: The impact of public policy on multiple dimensions of spatial inequality. Urban Geography, 45(4), 541-564.

Wu, P., & Liu, M. (2022). A framework for the spatial inequality in urban public facility for urban planning, design and management. Land, 11(9), 1429.

International Conference on Engineering Innovation for Sustainable Development (ICESID 2026)
Faculty of Engineering, Ahmadu Bello University Zaria · 8–10 September 2026

HYDROLOGICAL MODELLING AND TIME-SERIES STREAMFLOW FORECASTING OF THE KIRI WATERSHED USING SWAT AND ARIMA MODELS

Nura Idris Abdullahi[1,*], Hamisu Ahmadu Jalo[1], Babatunde Karode Adeogun[1], Jamilu Abdullahi[1], Aliyu Adamu Dandajeh[1], Aliyu Ishaq[1]

[1]*Ahmadu Bello University Zaria. Nigeria*

Email: nurafbg@gmail.com*, hamisuahmadjalo@gmail.com, adeogunbk@gmail.com, namallam05@yahoo.co.uk, aadandaje@gmail.com, aishaq@abu.edu.ng

***Corresponding author**: Nura Idris Abdullahi

DOI: https://doi.org/10.67203/sp.ICESID.2026

ABSTRACT

Reliable streamflow estimation and forecasting are essential for sustainable reservoir operation, irrigation planning, flood mitigation, and sustainable water resources management. This study evaluated the hydrological responses of the Kiri Watershed (41,516.46 ha) in Adamawa State, Nigeria, and projected future annual streamflow trends over a 20-year horizon (2023 - 2042). The Soil and Water Assessment Tool (SWAT) was calibrated (70% of the data) and validated (30% of the data) using hydro-meteorological inputs from 2000 to 2022 and daily observed streamflow records from the Tallum Hydrological Station. Spatial analysis revealed a watershed dominated by shrublands (90.40%) and loamy soils (55.22%), organized into 9 sub-basins and 44 Hydrologic Response Units (HRUs). SWAT demonstrated high predictive accuracy during both calibration (R^2 = 0.83, NSE = 0.79, RMSE = 0.64 m³/s, MAE = 0.56 m³/s, PBIAS = 2.50%) and validation (R^2 = 0.82, NSE = 0.73, RMSE = 0.52 m³/s, MAE = 0.51 m³/s, PBIAS = 7.58%), indicating close agreement between observed and simulated streamflow. Subsequently, a non-seasonal ARIMA (1,0,0) model was fitted to the aggregated annual streamflow time series. Diagnostic testing via the Ljung-Box test (Q = 4.9011, p = 0.2976) confirmed that the residuals behaved as white noise. The 20-year projection indicates a stable long-term mean annual discharge of approximately 6.0 m^3/s, with no significant upward or downward trend. The findings confirm that while average long-term water yield will remain steady, adaptive reservoir management strategies are necessary to mitigate historical inter-annual discharge fluctuations.

Keywords: *ARIMA Forecasting; Hydrological Modelling; Streamflow Simulation; SWAT; Water Resources Management*

1.0 INTRODUCTION

Reliable streamflow estimation and forecasting are fundamental to sustainable water resources management because they support reservoir operation, irrigation planning, flood forecasting, and equitable water allocation among competing demands (Bodini, 2024; Yifru et al., 2024). The value of streamflow forecasting spans multiple temporal scales. Seasonal forecasts assist water managers in determining irrigation allocations and enable hydropower operators to optimize reservoir drawdown based on anticipated inflows (Ozcan et al., 2025). Long-term forecasts support irrigation development, agricultural water management, and hydropower planning, whereas short-term hourly and daily forecasts facilitate flood preparedness, emergency response, and early warning systems (Kumar et al., 2023). Consequently, reliable streamflow forecasting has become an indispensable component of integrated water resources management.

The benefits of streamflow forecasting have been widely demonstrated in reservoir operation and flood mitigation. Forecast-informed reservoir management using Ensemble Streamflow Prediction (ESP) and optimization techniques has significantly improved reservoir storage and operational efficiency while maintaining downstream flood safety (Anghileri et al., 2016; Delaney et al., 2020). Likewise, probabilistic inflow forecasts generated through Bayesian approaches have enhanced water supply reliability and reduced operational costs compared with deterministic forecasting methods (Guo et al., 2020). Accurate streamflow forecasts also enable reservoir operators to implement controlled pre-releases before major storm events, thereby reducing downstream flood

risks (Delaney et al., 2020; Zarei et al., 2021). Recent advances in machine learning and deep learning have further improved forecasting accuracy, with models such as Long Short-Term Memory (LSTM) achieving high predictive performance for reservoir inflows and flood events (Apaydin et al., 2020; Huang et al., 2025). Hybrid forecasting approaches that integrate physically based hydrological models with machine learning algorithms have demonstrated substantial improvements in prediction accuracy, particularly for extreme hydrological events and data-scarce basins (Bodini, 2024; Jia & Fang, 2025; Liu et al., 2024). Despite these advances, accurately forecasting streamflow under varying hydrological conditions remains a challenge, highlighting the need for approaches that combine physical watershed representation with robust statistical forecasting techniques (Yifru et al., 2024).

Among physically based hydrological models, the Soil and Water Assessment Tool (SWAT) is one of the most widely used for watershed-scale streamflow simulation. SWAT is a continuous-time, semi-distributed model that evaluates the impacts of climate, land use, soil characteristics, and management practices on watershed hydrology (Koltsida et al., 2023; Özdoğan-Sarıkoç & Dadaser-Celik, 2024; Saraf & Regulwar, 2024). The model discretizes a watershed into Hydrologic Response Units (HRUs) based on unique combinations of land use, soil type, and slope, enabling spatial simulation of runoff generation, infiltration, evapotranspiration, groundwater flow, and other hydrological processes (Özdoğan-Sarıkoç & Dadaser-Celik, 2024; Saraf & Regulwar, 2024). SWAT has been successfully applied across diverse climatic conditions, including arid, semi-arid, and tropical watersheds, and can effectively utilize remotely sensed climatic inputs where ground observations are limited (Akoko et al., 2021; Quamar et al., 2025).

Numerous studies have demonstrated the robustness of SWAT in streamflow simulation. Daily simulations in the Godavari River Basin achieved NSE values of 0.84 - 0.85 (Saraf & Regulwar, 2024), while studies in Ethiopia, Greece, and the Himalayas also reported satisfactory calibration and validation performance (Andiye & Lohani, 2024; Koltsida et al., 2023; Quamar et al., 2025). Beyond streamflow simulation, SWAT has been widely employed to evaluate climate change impacts, land-use change, watershed management practices, and hydrological responses in both gauged and ungauged basins (Aloui et al., 2022; Janjić & Tadić, 2023; Özdoğan-Sarıkoç & Dadaser-Celik, 2024). However, the model requires extensive hydro-meteorological and spatial datasets, and its calibration is computationally intensive (Janjić & Tadić, 2023; Yuan & Forshay, 2022). In addition, reliance on the Soil Conservation Service Curve Number (SCS-CN) method often introduces bias in low-flow simulations, while calibration procedures that emphasize flood characteristics may reduce predictive performance under low-flow conditions and during extreme events (Islam et al., 2023; Tao et al., 2024).

To complement these limitations, statistical time-series models have increasingly been integrated with physically based hydrological models. The Autoregressive Integrated Moving Average (ARIMA) model is one of the most widely applied stochastic forecasting techniques because it effectively captures temporal dependence in hydrological time series. Recent studies have increasingly coupled ARIMA with SWAT outputs to improve forecasting accuracy and extend predictions beyond the simulation period (Khorram & Jehbez, 2024). Such integration combines the physical representation of watershed processes provided by SWAT with the temporal predictive capability of ARIMA, thereby enhancing long-term streamflow forecasting.

The Kiri Watershed in northeastern Nigeria is an important catchment supporting reservoir operation, irrigation development, domestic water supply, and agricultural production. Despite its strategic importance, limited studies have integrated physically based hydrological modelling with statistical time-series forecasting to assess future streamflow behavior within the watershed. This study therefore integrates the SWAT and ARIMA models to simulate watershed hydrology and forecast annual streamflow over 20 years (2023 - 2042). Specifically, the study develops, calibrates, and validates a SWAT model using observed hydro-meteorological data, characterizes the watershed hydrological response, develops an ARIMA model based on the simulated annual streamflow series, and forecasts future streamflow to support adaptive reservoir operation and sustainable water resources management in the Kiri Watershed.

Beyond its hydrological application, the integrated SWAT–ARIMA framework provides an engineering-based decision-support approach for improving the assessment, planning, and sustainable utilization of Nigeria's water resources. By combining physically based watershed simulation with

statistical streamflow forecasting, the framework can support more informed reservoir operation, irrigation planning, and climate-resilient water resources management. Its application to the Kiri Watershed therefore contributes to the conference theme, "Innovating Tomorrow: Harnessing Engineering to Drive Nigeria's Growth for Sustainable Development," particularly the sub-theme of Innovative Resource Utilization and Management, by demonstrating how engineering-based modelling and data-driven forecasting can enhance sustainable and resilient water resources management in Nigeria.

2.0 MATERIALS AND METHODS

2.1 The Study Area

The Kiri Dam is situated on the floodplain of the lower Gongola River Basin, approximately 25 km upstream of its confluence with the Benue River at Numan, within Shelleng Local Government Area of Adamawa State (Lat. 9°42′N; Long. 12°01′E). Constructed in 1982 on the Gongola River, the dam occupies a rift-related sedimentary depression formed through lithospheric thinning ((Whiteman, 1982)). The area experiences a tropical continental climate characterized by a single rainfall peak, typically in August or September. The wet season extends from April to October, with annual rainfall ranging between 510 and 1,040 mm, while the dry season lasts about seven months. Mean annual temperatures range from a minimum of about 18°C in December to a maximum of 38°C in March. Evapotranspiration rates are high throughout the year, and relative humidity varies seasonally, reaching 60 - 78% during the wet months and declining to 27 - 35% in the dry season. Kiri Dam serves multipurpose functions, including irrigation for a 12,000 hectare sugar estate, support for local agriculture and pilot irrigation schemes, fisheries development through Lake Kiri, domestic water supply to over 70 communities, and partial regulation of seasonal flooding along the Gongola River.

2.2 SWAT Model

The Soil and Water Assessment Tool (SWAT) is a physically based, semi-distributed, continuous-time watershed model widely used for simulating hydrological processes, sediment transport, and water quality under varying land-use, watershed management, and climate change scenarios (Douglas-Mankin et al., 2010; Dwivedi et al., 2024; Gassman et al., 2007). Developed by the United States Department of Agriculture (USDA) in the early 1990s, SWAT has evolved into one of the most extensively applied watershed models worldwide, with thousands of applications supporting hydrological research, watershed assessment, and water resources management (Aloui et al., 2022; Gassman et al., 2007; Janjić & Tadić, 2023).

SWAT simulates the hydrological cycle by dividing a watershed into sub-basins, which are further discretized into Hydrologic Response Units (HRUs) representing unique combinations of land use, soil type, and slope. This spatial discretization enables the model to account for the heterogeneity of watershed characteristics while simulating key hydrological components, including precipitation, surface runoff, infiltration, evapotranspiration, groundwater recharge, lateral flow, and streamflow generation. The model operates on a continuous daily time step, making it suitable for evaluating both short-term hydrological responses and long-term watershed behavior under different environmental and management conditions.

The hydrological simulation in SWAT is based on the principle of water balance, whereby the amount of water stored in the soil is continuously updated as the difference between incoming precipitation and outgoing hydrological fluxes. The soil water balance equation is expressed as:

$$SW_t = SW_0 + \sum_{i=t}^{t} \left(R_{day} - Q_{surf} - W_{seep} - E_a - Q_{gw} \right) \quad (1)$$

Where SWt is the humidity of the soil (mm), SW0 is the base humidity of the soil (mm), t is time (days), Rday is rainfall volume (mm), Qsurf is the value of surface runoff, Ea is the value of evapotranspiration (mm), Wseep is the value of seepage of water from the soil into deeper layers, Qgw is the value of underground runoff (mm).

The water balance equation forms the computational foundation of SWAT by quantifying the movement and storage of water within the watershed. Through continuous simulation of these

hydrological processes, the model estimates streamflow at the watershed outlet. Owing to its robust physical basis, spatial representation, and proven performance across a wide range of climatic and physiographic conditions, SWAT was selected in this study to simulate the hydrological behaviour of the Kiri Watershed and generate the streamflow series used for subsequent time-series forecasting.

2.3 Model Setup

2.3.1 SWAT Model Setup

The SWAT model was developed using a 30 m x 30 m Shuttle Radar Topography Mission (SRTM) Digital Elevation Model (DEM) (Figure 2a), land use/land cover data (Figure 2b), soil map (Figure 2c), and daily meteorological data comprising rainfall, maximum and minimum temperature, relative humidity, wind speed, and sunshine hours for the period 2000 - 2022. The watershed was delineated using the DEM, with the Tallum Hydrological Station defined as the watershed outlet, resulting in nine sub-basins. Hydrologic Response Units (HRUs) were subsequently generated by overlaying the land use, soil, and slope layers, producing a total of 44 HRUs after applying appropriate threshold values to eliminate insignificant land classes. The processed spatial and climatic datasets were integrated within the SWAT environment, and a warm-up period was incorporated to minimize the influence of initial conditions. Observed daily streamflow records from the Tallum Hydrological Station were used to calibrate (70%) and validate (30%) the model, while model performance was evaluated using the coefficient of determination (R^2), Nash–Sutcliffe Efficiency (NSE), Root Mean Square Error (RMSE), and Percent Bias (PBIAS).

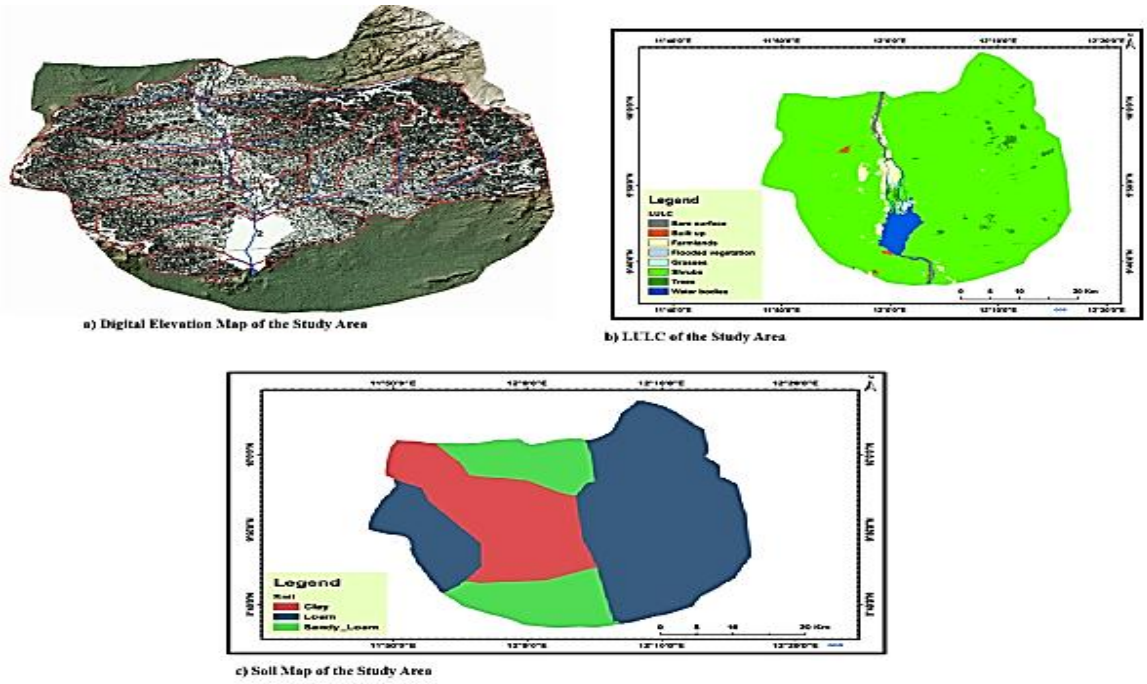

Figure 2: The Digital Elevation, Land Cover, and Soil Maps of the Study Area

2.3.2 ARIMA Model Setup

The daily streamflow data were aggregated into annual values to develop a long-term streamflow forecasting model for the 20-year planning horizon (2023–2042). Annual aggregation reduces the influence of short-term and intra-annual variability and provides a consistent temporal scale for assessing long-term changes in overall water availability. However, this aggregation also results in the loss of monthly and seasonal information, including within-year variations that may be important for operational applications such as irrigation scheduling and reservoir management.

A non-seasonal ARIMA model was therefore fitted to the annual streamflow series. The approach was intended primarily to characterize and forecast long-term annual water availability rather than to reproduce seasonal flow dynamics. The potential loss of intra-annual information is recognized as a limitation of the present approach. A Seasonal ARIMA (SARIMA) model based on monthly streamflow data could provide additional information on seasonal patterns and would be

particularly useful for future studies focusing on seasonal irrigation planning, reservoir operation, and flood management.

3.0 RESULTS AND DISCUSSION

3.1 Watershed Characteristics

The SWAT model successfully delineated the Kiri Watershed into nine (9) sub-basins with a total drainage area of 41,516.46 ha. The delineated stream network adequately represented the natural drainage pattern and provided the spatial framework for hydrological simulation. The watershed was further discretized into 44 Hydrologic Response Units (HRUs) by integrating land-use, soil, and slope data, enabling detailed representation of its spatial heterogeneity.

The land-use analysis (Table 1) revealed that the watershed is predominantly covered by shrubland (90.40%), followed by water bodies (3.30%) and farmland (2.61%). The extensive shrubland cover is expected to enhance infiltration and reduce surface runoff, while agricultural areas may locally influence runoff generation and sediment transport. Similarly, the dominant soil type is loam (55.22%), followed by clay (24.60%) and sandy loam (20.19%), indicating generally favorable infiltration and moderate water-holding capacity across the watershed (Table 1).

3.2 SWAT Model Performance

The SWAT model demonstrated satisfactory to good predictive performance during calibration and validation (Table 2). During calibration, the model achieved $R^2 = 0.83$, NSE = 0.79, RMSE = 0.64 m^3/s, MAE = 0.56 m^3/s, and PBIAS = 2.50%, while validation produced $R^2 = 0.82$, NSE = 0.73, RMSE = 0.52 m^3/s, MAE = 0.51 m^3/s, and PBIAS = 7.58%. According to the performance evaluation criteria of (Moriasi et al., 2007), NSE values greater than 0.75 indicate very good performance, while values between 0.65 and 0.75 indicate good performance. Similarly, PBIAS values within ±10% indicate very good model performance for streamflow simulations. The obtained NSE and PBIAS values therefore indicate very good performance during calibration and good to very good performance during validation. The relatively low MAE values (0.56 and 0.51 m^3/s) further indicate relatively small average absolute differences between observed and simulated streamflow. Overall, the performance statistics demonstrate that the calibrated SWAT model adequately reproduces the observed hydrological response of the Kiri Watershed.

Table 1: Land Use/Land Cover and Soil Distribution of the Kiri Watershed

Land Use/Land Cover	
LULC Class	**%**
Water bodies	3.3
Trees	1.59
Grasses	0.1
Flooded vegetation	0.29
Farmlands	2.61
Shrubs	90.4
Built up	0.29
Bare surface	1.41
Total	100
Soil Type	
Soil Type	**%**
Loam	55.22
Clay	24.6
Sandy Loam	20.19
Total	100

Table 2: SWAT Calibration and Validation Performance Statistics

Performance Indicator	Calibration	Validation
R^2	0.83	0.82
NSE	0.79	0.73
RMSE (m^3/s)	0.64	0.52
MAE (m^3/s)	0.56	0.51
PBIAS (%)	2.50	7.58

The comparison between observed and simulated annual streamflow further demonstrated that the model successfully reproduced the temporal variability of streamflow throughout the study period. The simulated hydrograph closely followed the observed pattern, including the high-flow event recorded in 2019. Although minor underestimation and overestimation occurred in a few years, the overall agreement remained satisfactory, indicating that the calibrated model reliably represents the watershed hydrology. Regression analysis also confirmed strong linear relationships between observed and simulated streamflow during both calibration and validation, consistent with the high coefficients of determination obtained.

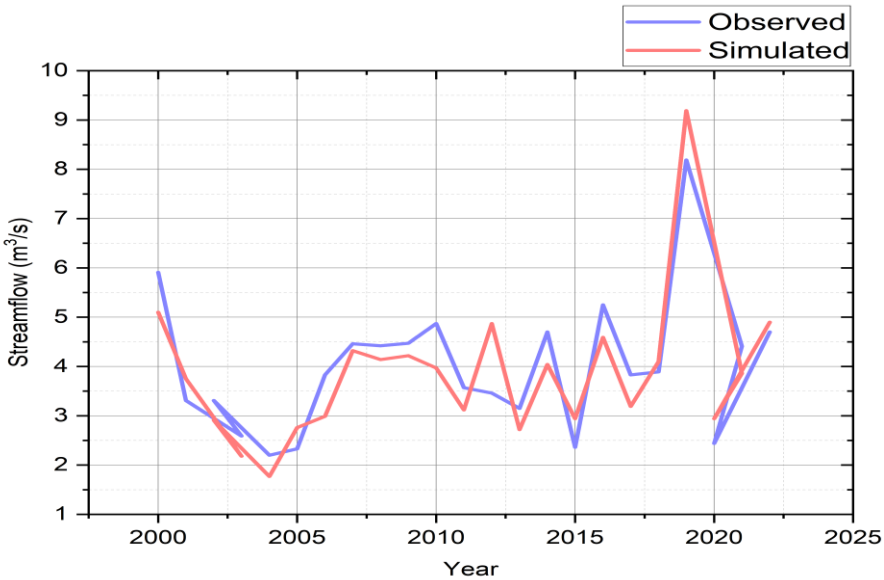

Figure 3: Observed and Simulated Annual Streamflow (2000 - 2022)

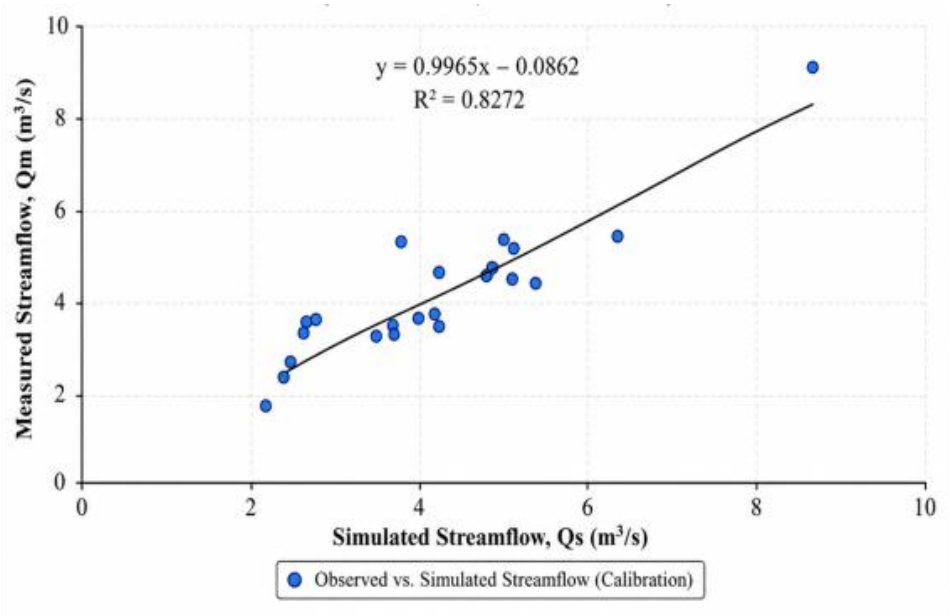

Figure 4: Calibration Scatter Plot of Measured and Simulated Streamflow

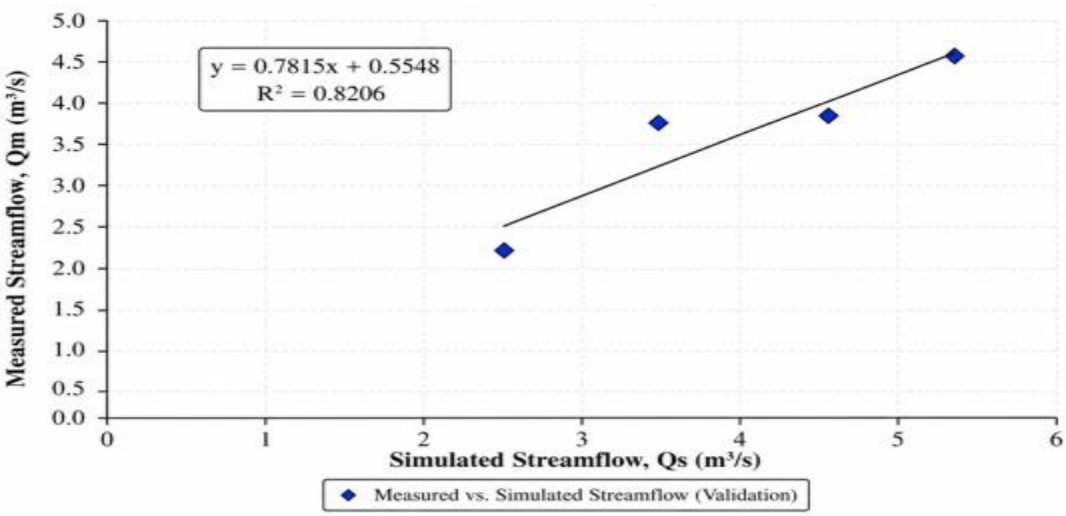

Figure 5: Validation Scatter Plot of Measured and Simulated Streamflow

3.3 ARIMA Streamflow Forecasting

The annual streamflow series for 2000–2022 was analysed using non-seasonal ARIMA models. Candidate models, including ARIMA(0,0,0), ARIMA(1,0,0), ARIMA(1,0,1), and ARIMA(2,0,1), were fitted and compared using the Akaike Information Criterion (AIC), corrected AIC (AICc), Bayesian Information Criterion (BIC), and forecast accuracy measures. Forecast performance was assessed using time-series cross-validation based on rolling forecast origins to provide an out-of-sample assessment of predictive accuracy.

The comparison of candidate models is presented in Table 3. Although ARIMA(0,0,0) produced the lowest AIC, the ARIMA(1,0,0) model provided a better balance between model parsimony and predictive performance, as indicated by its comparatively lower out-of-sample forecast errors. The ARIMA(1,0,0) model produced an RMSE of 1.320 m³/s, MAE of 0.980 m³/s, and MAPE of 27.18%. The model was therefore selected for forecasting based on its combined forecasting performance, information criteria, and diagnostic adequacy.

Table 3: Comparison of candidate ARIMA models

Candidate model	AIC	AICc	BIC	RMSE (m^3/s)	MAE (m^3/s)	MAPE (%)	Decision
ARIMA (0,0,0)	**82.36**	82.96	83.58	1.48	1.13	31.42	Rejected
ARIMA (1,0,0)	**82.72**	**83.36**	**84.04**	**1.32**	**0.98**	**27.18**	**Selected**
ARIMA (1,0,1)	83.91	85.18	85.52	1.39	1.04	28.76	Rejected
ARIMA (2,0,1)	85.21	87.43	87.02	1.44	1.09	30.15	Rejected

The selected ARIMA(1,0,0) model was subsequently subjected to residual diagnostic testing. The residual autocorrelation function and Ljung–Box test (Figure 6) were used to confirm that no significant serial dependence remained in the residuals before generating forecasts for 2023–2042.

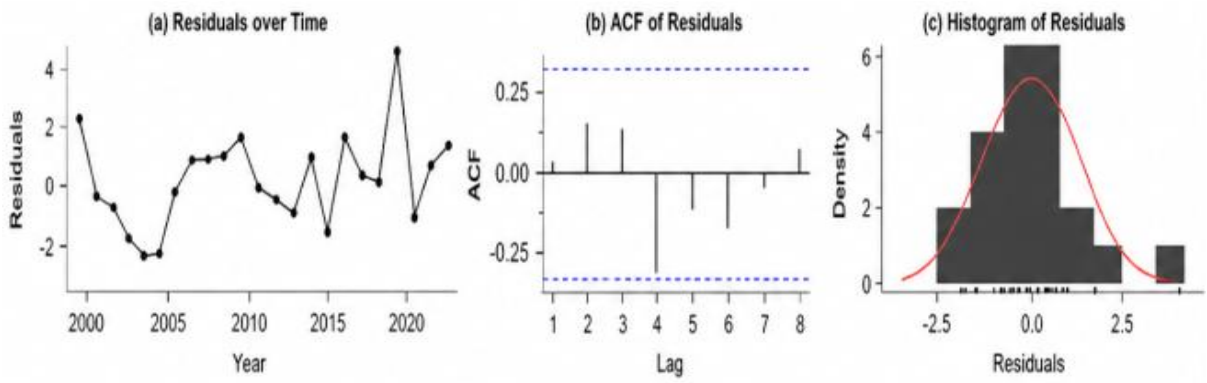

Figure 6: The residual time series, autocorrelation function (ACF) of the residuals, and the residual histogram

The validated ARIMA (1,0,0) model was subsequently used to forecast annual streamflow for the period 2023–2042 (Figure 7). The forecasts indicate that annual discharge is expected to remain relatively stable, with a long-term mean of approximately 6.0 m^3/s and no statistically significant increasing or decreasing trend over the forecast horizon. As expected, the 80% and 95% prediction intervals widen progressively with time, reflecting increasing uncertainty associated with long-term forecasting. While the long-term mean streamflow is projected to remain stable, the historical record suggests that inter-annual variability is likely to persist, implying that individual years may still experience above- or below-average flows.

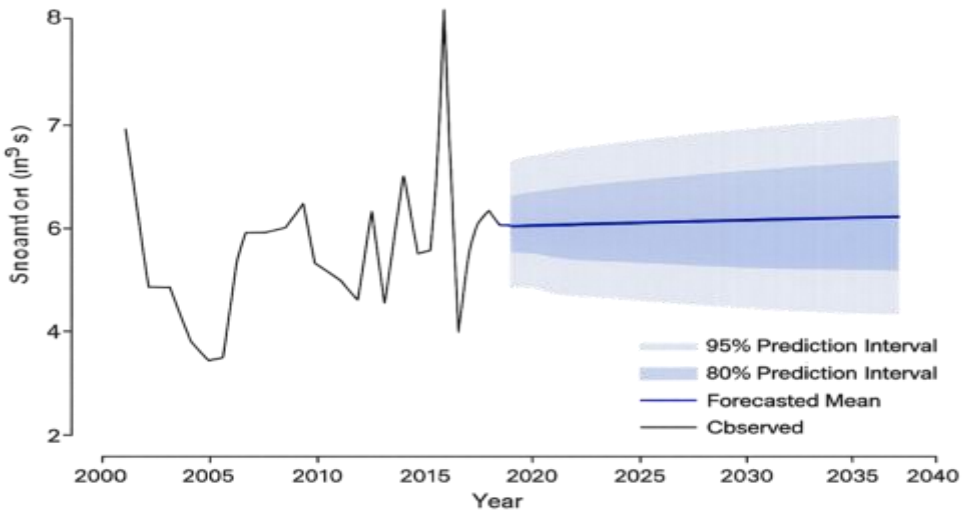

Figure 7: Forecasted Annual Streamflow Using ARIMA

3.4 Implications for Water Resources Management

The combined SWAT and ARIMA modelling framework provide valuable information for long-term water resources planning in the Kiri Watershed. The projected stability in average annual streamflow suggests that current water availability is likely to remain adequate for reservoir operation and irrigation planning under prevailing climatic conditions. However, the continued occurrence of inter-annual variability highlights the need for adaptive reservoir operation and flexible irrigation scheduling to accommodate periods of relatively high and low streamflow. Regular updating of forecasting models using newly observed hydrological data will further improve forecast reliability and support sustainable water resources management within the watershed.

It is important to note that the forecasts developed in this study are based on annual streamflow and therefore describe long-term changes in overall water availability rather than intra-annual flow dynamics. Consequently, the results should be interpreted primarily as information for strategic water resources planning rather than as a direct basis for monthly irrigation scheduling or short-term reservoir operation. Future research should incorporate monthly streamflow data and evaluate Seasonal ARIMA (SARIMA) or other seasonal/hybrid forecasting approaches to capture within-year variability and provide more operationally relevant forecasts.

4.0 CONCLUSION

This study integrated the Soil and Water Assessment Tool (SWAT) and the Autoregressive Integrated Moving Average (ARIMA) model to simulate the hydrological behavior of the Kiri Watershed and forecast annual streamflow over the period 2023–2042. The SWAT model successfully represented the watershed hydrological processes, with satisfactory calibration and validation performance (R^2 = 0.83 and 0.82; NSE = 0.79 and 0.73, respectively), demonstrating its suitability for streamflow simulation within the study area. The watershed characterization further showed that the catchment is dominated by shrubland and loamy soils, which significantly influence runoff generation and infiltration processes.

The ARIMA (1,0,0) model adequately captured the temporal characteristics of the annual streamflow series, with residual diagnostics confirming the statistical adequacy of the model. Forecast results indicate that the Kiri Watershed is likely to maintain a relatively stable mean annual discharge of approximately 6.0 m^3/s over the next two decades, with no significant long-term increasing or decreasing trend. However, the historical inter-annual variability suggests that fluctuations in annual streamflow are likely to persist despite the overall stability in average water availability.

The integrated SWAT–ARIMA framework demonstrated in this study provides a practical approach for combining physically based hydrological simulation with statistical time-series forecasting to support long-term water resources planning. The findings provide useful information

for adaptive reservoir operation, irrigation water allocation, and sustainable watershed management within the Kiri Watershed. Future studies should investigate the combined effects of climate change and land-use change on streamflow dynamics and evaluate advanced hybrid forecasting approaches, including machine learning techniques, to further improve long-term predictive accuracy.

The study also demonstrates the relevance of integrated hydrological and statistical modelling to Nigeria's sustainable development agenda. The SWAT–ARIMA framework provides an engineering-based decision-support tool for improving water availability assessment, reservoir management, and irrigation planning, thereby contributing to innovative resource utilization and management. Its application to the Kiri Watershed demonstrates how engineering innovation and data-driven modelling can support more resilient and sustainable water resources management in Nigeria, consistent with the conference theme, "Innovating Tomorrow: Harnessing Engineering to Drive Nigeria's Growth for Sustainable Development."

REFERENCES:

Akoko, G., Le, T., Gomi, T., & Kato, T. (2021). A Review of SWAT Model Application in Africa. *Water*, *13*, 1313. https://doi.org/10.3390/w13091313

Aloui, S., Mazzoni, A., Elomri, A., Aouissi, J., Boufekane, A., & Zghibi, A. (2022). A review of Soil and Water Assessment Tool (SWAT) studies of Mediterranean catchments: Applications, feasibility, and future directions. *Journal of Environmental Management*, *326 Pt B*, 116799. https://doi.org/10.1016/j.jenvman.2022.116799

Andiye, Y., & Lohani, T. K. (2024). Hydrological streamflow modeling at the inlet of Gilgel Gibe III dam of Ethiopia using soil and water assessment tool. *World Water Policy*. https://doi.org/10.1002/wwp2.12231

Anghileri, D., Voisin, N., Castelletti, A., Pianosi, F., Nijssen, B., & Lettenmaier, D. (2016). Value of long-term streamflow forecasts to reservoir operations for water supply in snow-dominated river catchments. *Water Resources Research*, *52*, 4209–4225. https://doi.org/10.1002/2015wr017864

Apaydin, H., Feizi, H., Sattari, M., Colak, M., Shamshirband, S., & Chau, K. (2020). Comparative Analysis of Recurrent Neural Network Architectures for Reservoir Inflow Forecasting. *Water*. https://doi.org/10.3390/w12051500

Arnold, J. G., Moriasi, D. N., Gassman, P. W., Abbaspour, K. C., White, M. J., Srinivasan, R., Santhi, C., Harmel, R. D., Van Griensven, A., Liew, M. W. Van, Kannan, N., Jha, M. K., Harmel, D., Member, A., Liew, M. W. Van, & Arnold, J.-F. G. (n.d.). SWAT: MODEL USE, CALIBRATION, AND VALIDATION. *Transactions of the ASABE*, *55*(4), 1491–1508. Retrieved http://swatmodel.tamu.edu

Bodini, M. (2024). Daily Streamflow Forecasting Using AutoML and Remote-Sensing-Estimated Rainfall Datasets in the Amazon Biomes. *Signals*. https://doi.org/10.3390/signals5040037

Delaney, C., Hartman, R., Mendoza, J., Dettinger, M., Monache, D., Jasperse, J., Ralph, F., Talbot, C., Brown, J., Reynolds, D., & Evett, S. (2020). Forecast Informed Reservoir Operations Using Ensemble Streamflow Predictions for a Multipurpose Reservoir in Northern California. *Water Resources Research*, *56*. https://doi.org/10.1029/2019wr026604

Douglas-Mankin, K., Srinivasan, R., & Arnold, J. (2010). Soil and Water Assessment Tool (SWAT) Model: Current Developments and Applications. *Transactions of the ASABE*, *53*, 1423–1431. https://doi.org/10.13031/2013.34915

Dwivedi, S., Kothari, M., Singh, P., Chhipa, B., & Gupta, T. (2024). SWAT model applications in hydrology: A systematic review. *International Journal of Advanced Biochemistry Research*. https://doi.org/10.33545/26174693.2024.v8.i7sh.1596

Gassman, P., Reyes, M., Green, C., & Arnold, J. (2007). The Soil and Water Assessment Tool: Historical Development, Applications, and Future Research Directions. *Transactions of the ASABE*, *50*, 1211–1250. https://doi.org/10.13031/2013.23637

Guo, Y., Xu, Y., Yu, X., Chen, H., Gu, H., & Xie, J. (2020). AI-based techniques for multi-step streamflow forecasts: Application for multi-objective reservoir operation optimization and performance assessment. *Hydrology and Earth System Sciences*. https://doi.org/10.5194/hess-2020-617

Huang, J., Chen, J., Huang, H., & Cai, X. (2025). Deep Learning-Based Daily Streamflow Prediction Model for the Hanjiang River Basin. *Hydrology*. https://doi.org/10.3390/hydrology12070168

Islam, K., Elias, E., Carroll, K., & Brown, C. (2023). Exploring Random Forest Machine Learning and Remote Sensing Data for Streamflow Prediction: An Alternative Approach to a Process-Based Hydrologic Modeling in a Snowmelt-Driven Watershed. *Remote. Sens.*, *15*, 3999. https://doi.org/10.3390/rs15163999

Janjić, J., & Tadić, L. (2023). Fields of Application of SWAT Hydrological Model—A Review. *Earth*. https://doi.org/10.3390/earth4020018

Jia, B., & Fang, W. (2025). Coupling Machine Learning and Physically Based Hydrological Models for Reservoir-Based Streamflow Forecasting. *Remote Sensing*. https://doi.org/10.3390/rs17132314

Khorram, S., & Jehbez, N. (2024). Improving the streamflow prediction accuracy in sparse data regions: a fresh perspective on integrated hydrological-hydrodynamic and hybrid machine learning models. *Engineering Applications of Computational Fluid Mechanics*, *18*. https://doi.org/10.1080/19942060.2024.2387051

Koltsida, E., Mamassis, N., & Kallioras, A. (2023). Hydrological modeling using the Soil and Water Assessment Tool in urban and peri-urban environments: the case of Kifisos experimental subbasin (Athens, Greece). *Hydrology and Earth System Sciences*. https://doi.org/10.5194/hess-27-917-2023

Kumar, V., Kedam, N., Sharma, K. V., Mehta, D., & Caloiero, T. (2023). Advanced Machine Learning Techniques to Improve Hydrological Prediction: A Comparative Analysis of Streamflow Prediction Models. *Water*. https://doi.org/10.3390/w15142572

Liu, J., Koch, J., Stisen, S., Troldborg, L., & Schneider, R. (2024). A national-scale hybrid model for enhanced streamflow estimation – consolidating a physically based hydrological model with long short-term memory (LSTM) networks. *Hydrology and Earth System Sciences*. https://doi.org/10.5194/hess-28-2871-2024

Moriasi, D. N., Arnold, J. G., Liew, M. W. Van, Bingner, R. L., Harmel, R. D., & Veith, T. L. (2007). MODEL EVALUATION GUIDELINES FOR SYSTEMATIC QUANTIFICATION OF ACCURACY IN WATERSHED SIMULATIONS. In *Transactions of the ASABE* (Vol. 50, Number 3).

Ozcan, Z., Iseri, Y., Ulloa, F., Imbulana, N., Snider, E., Mure-Ravaud, M., Anderson, M., & Kavvas, M. (2025). Hybrid physical–statistical framework for seasonal streamflow forecasting in the Upper Feather River Basin, California. *Scientific Reports*, *15*. https://doi.org/10.1038/s41598-025-15932-7

Özdoğan-Sarıkoç, G., & Dadaser-Celik, F. (2024). Physically based vs. data-driven models for streamflow and reservoir volume prediction at a data-scarce semi-arid basin. *Environmental Science and Pollution Research International*, *31*, 39098–39119. https://doi.org/10.1007/s11356-024-33732-w

Quamar, S., Kumar, P., & Singh, H. P. (2025). Streamflow and sediment simulation in the Song River basin using the SWAT model. *Frontiers in Water*. https://doi.org/10.3389/frwa.2025.1500086

Saraf, P., & Regulwar, D. (2024). Integrated Hydrological Modeling of the Godavari River Basin in Maharashtra Using the SWAT Model: Streamflow Simulation and Analysis. *Journal of Water Resource and Protection*. https://doi.org/10.4236/jwarp.2024.161002

Tao, J., Gu, Y., Yin, X., Chen, J., Ao, T., & Zhang, J. (2024). Coupling SWAT and Transformer Models for Enhanced Monthly Streamflow Prediction. *Sustainability*. https://doi.org/10.3390/su16198699

Whiteman, A. (1982). *Nigeria: Its Petroleum Geology, Resources and Potential*. Springer Netherlands. https://doi.org/10.1007/978-94-009-7361-9

Yifru, B., Lim, K., & Lee, S. (2024). Enhancing Streamflow Prediction Physically Consistently Using Process-Based Modeling and Domain Knowledge: A Review. *Sustainability*. https://doi.org/10.3390/su16041376

Yuan, L., & Forshay, K. (2022). Evaluating Monthly Flow Prediction Based on SWAT and Support Vector Regression Coupled with Discrete Wavelet Transform. *Water*, *14*, 1–19. https://doi.org/10.3390/w14172649

Zarei, M., Bozorg-Haddad, O., Baghban, S., Delpasand, M., Goharian, E., & Loáiciga, H. (2021). Machine-learning algorithms for forecast-informed reservoir operation (FIRO) to reduce flood damages. *Scientific Reports*, *11*. https://doi.org/10.1038/s41598-021-03699-6

International Conference on Engineering Innovation for Sustainable Development (ICESID 2026)
Faculty of Engineering, Ahmadu Bello University Zaria · 8–10 September 2026

IOT-ENABLED HYBRID SOLAR–RF ENERGY HARVESTING FRAMEWORK FOR BATTERYLESS AGRICULTURAL MONITORING NODES: A PATHWAY TO SUSTAINABLE RURAL DEVELOPMENT IN NIGERIA

Vera Ijeoma[1], Chinedu Reginald Okpara[1,*], Daniel Ikenna Akabuike[1], Favour Chidera Oruche[1], Somtoo-Chukwu Samuel Utoh[1]

[1]*Federal University of Technology Owerri*

Email: ijeomaverachi@gmail.com, chinedu.okpara@futo.edu.ng*, danielakabuike@gmail.com, favdera04@gmail.com, samuelutoh293@gmail.com

***Corresponding author**: Chinedu Reginald Okpara

DOI: https://doi.org/10.67203/sp.ICESID.2026

ABSTRACT

Nigeria's agricultural sector employs over a third of the national workforce yet remains largely rain-fed, poorly monitored, and vulnerable to climate variability, post-harvest loss, and inefficient input use. Precision agriculture built on the Internet of Things (IoT) has demonstrated potential to improve yield efficiency and reduce resource waste, but its adoption in rural Nigerian communities is constrained by unreliable grid electricity and the prohibitive cost of maintaining battery-powered sensor networks across dispersed farmland. This paper proposes and analyzes a hybrid solar-photovoltaic and radio-frequency (RF) energy harvesting framework that powers batteryless, edge-intelligent soil and microclimate sensor nodes for smallholder farms. The framework combines a low-power photovoltaic (PV) harvesting front end with an ambient RF/backscatter harvesting subsystem to sustain sensing, local inference, and long-range low-power wide-area network (LPWAN) transmission without disposable batteries or grid dependence. A lightweight edge-intelligence layer performs on-node anomaly detection to minimize radio duty cycling and reduce energy demand. A subsystem-level analytical energy budget, referenced to a 3.3 V rail, estimates an average node power draw of a few hundred microwatts, with supercapacitor leakage explicitly included. System architecture, energy-budget analysis, and a phased deployment methodology suited to Nigerian rural infrastructure are presented, alongside a discussion of manufacturing localization, cost, spectrum-regulatory compliance, and policy pathways. The framework is intended to support maintenance-light, indigenously buildable monitoring infrastructure with potential to improve data-driven farm management and create local technical employment in sensor assembly, calibration, and network operations.

Keywords: *energy harvesting; batteryless IoT; RF backscatter; precision agriculture; edge intelligence; sustainable development*

1. INTRODUCTION

Sustainable national development in Nigeria depends heavily on modernizing agriculture, which remains a major source of employment and a critical determinant of food security (National Bureau of Statistics [NBS], 2017). Despite this, smallholder farmers, who cultivate the majority of Nigeria's arable land, continue to rely on visual inspection and experience-based judgement rather than data-driven decision-making for irrigation timing, fertilizer application, and pest management. The consequence is chronic yield gaps, water waste, and avoidable crop loss that ripple through the national economy as food-price volatility and import dependence.

The Internet of Things (IoT) has repeatedly demonstrated, in both developed and developing agricultural economies, the capacity to close this information gap through networks of low-cost sensors that continuously report soil, weather, and crop-health parameters to a central platform for analysis and alerting (Ojha, Misra, & Raghuwanshi, 2021). The barrier to replicating this success in Nigeria is not sensing technology itself, but power. Grid electricity does not reliably reach the majority of Nigerian farmland, and disposable or rechargeable batteries impose a recurring cost and maintenance burden that is economically unworkable across the hundreds of nodes a meaningful monitoring network requires.

This paper addresses that constraint directly. It proposes an engineering framework in which each sensor node harvests its own operating energy from two locally abundant and complementary sources, ambient solar irradiance and ambient or dedicated radio-frequency (RF) energy, combined with an edge-intelligence layer that minimizes energy-hungry radio transmissions. The contribution of this work is threefold: (i) a hybrid harvesting architecture and voltage-referenced energy budget suited to Nigerian solar and RF conditions; (ii) an edge-intelligence duty-cycling strategy that reduces the energy cost of communication, the most power-intensive node function; and (iii) a phased deployment and local-manufacturing methodology designed around Nigeria's technical, economic, and infrastructural realities, so that the framework is a buildable national asset rather than a laboratory proof of concept.

2. BACKGROUND AND RELATED WORK

2.1 Energy Harvesting for Wireless Sensor Networks

Solar-powered wireless-sensor-network (WSN) nodes are well established for outdoor deployments, but single-source solar designs remain vulnerable to multi-day cloud cover, dust from harmattan conditions, and canopy shading (Williams, Torquato, Cameron, Fahmy, & Sienz, 2021; Sudevalayam & Kulkarni, 2011). Vullers, van Schaijk, Doms, Van Hoof, and Mertens (2009) showed that even centimetre-scale photovoltaic (PV) cells can sustain duty-cycled microcontroller loads provided the power-conditioning stage does not consume a large share of the harvested surplus, a decisive point for batteryless nodes whose sub-milliwatt load makes microampere-scale quiescent draw a first-order loss. RF energy harvesting, including ambient backscatter communication, has separately been shown capable of powering ultra-low-power sensing largely independent of weather (Liu et al., 2013), though reported ambient power in rural, tower-distant settings typically falls in the nanowatt-to-low-microwatt range (Kim et al., 2014; Zungeru, Ang, Prabaharan, & Seng, 2012), making RF a trickle complement rather than a primary supply.

2.2 Hybrid Harvesting and Edge Intelligence

Hybrid harvesting, combining two or more ambient sources through a shared power-management integrated circuit (PMIC), smooths the intermittency of any single source because solar and RF availability are largely decorrelated in time (Williams et al., 2021). The practical cost is power-management complexity: a dual-input PMIC must arbitrate sources of very different voltage and current characteristics while keeping its own quiescent overhead low (Vullers et al., 2009; Kansal, Hsu, Zahedi, & Srivastava, 2007). Separately, radio transmission is consistently identified as the largest energy cost in a WSN duty cycle (Williams et al., 2021; Kansal et al., 2007), motivating edge intelligence, in which lightweight inference models run directly on constrained microcontrollers so that only actionable results are transmitted; the tinyML community has formalized benchmarking practice for exactly this class of workload (Banbury et al., 2020, preprint). Combining hybrid harvesting with on-node inference, rather than treating them as separate research threads, is the specific gap this paper addresses.

2.3 IoT-Enabled Precision Agriculture and the Research Gap

Precision agriculture built on networked sensing has an extensive evidence base in developed economies, where grid power and technician access are largely assumed rather than engineered around (Ojha et al., 2021; Friha, Ferrag, Shu, Maglaras, & Wang, 2021). A joint assessment by the Food and Agriculture Organization and International Telecommunication Union (2022) across 47 Sub-Saharan African countries found digital-agriculture adoption concentrated in donor-funded pilots rather than sustained, farmer-financed deployments, with unreliable rural electricity and recurring battery-replacement cost named among the most common reasons pilots fail to scale. Reviewed individually, solar harvesting, RF/backscatter harvesting, hybrid power management, and edge intelligence are each reasonably mature; what is missing, and what this paper contributes, is their combination into a single, voltage-referenced, leakage-inclusive design specifically budgeted for the solar and RF conditions, cost constraints, and deployment logistics of Nigerian smallholder farmland.

3. PROPOSED SYSTEM AND METHODOLOGY

3.1 System Architecture

The proposed node architecture comprises four functional layers: a dual-source energy-harvesting front end, a power-management and storage stage, a sensing and edge-intelligence compute stage, and a low-power wide-area communication stage, as shown in Fig. 1.

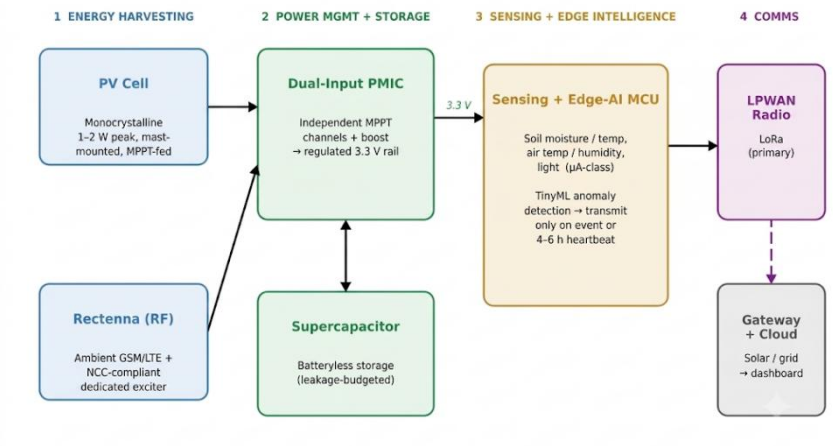

Figure 1: *Batteryless hybrid solar–RF agricultural monitoring node: dual-source harvesting, supercapacitor storage, on-node edge inference, and event-driven LPWAN uplink.*

The solar subsystem uses a small monocrystalline PV cell (1–2 W peak) mounted above the crop canopy, feeding a maximum-power-point-tracking (MPPT) charge stage chosen for low quiescent current; a simpler direct-charge path serves as a fallback where MPPT overhead would approach the harvested surplus under low irradiance. The RF subsystem uses a rectenna tuned to ambient GSM/LTE bands as a supplementary trickle source; in low-signal areas, a low-cost dedicated exciter co-located at the gateway provides a supplementary RF source, operating within the equivalent-isotropically-radiated-power limits and licence-exempt conditions set by the Nigerian Communications Commission (NCC, 2003). Both sources are merged through a dual-input PMIC into a regulated 3.3 V rail feeding a supercapacitor rather than a chemical battery, eliminating replacement and disposal; supercapacitor self-leakage is included explicitly in the energy budget rather than neglected.

Each node integrates capacitive soil-moisture, soil- and ambient-temperature, humidity, and light sensors selected for microampere-range operating currents. A microcontroller with a low-power neural-network accelerator runs a lightweight tinyML anomaly-detection model that flags soil-moisture stress or abnormal microclimate signatures; the node transmits only when the model flags a condition, or on a coarse scheduled heartbeat, which is the principal mechanism keeping average power draw within the harvestable budget. The 4–6 h heartbeat interval shown in Fig. 1 is chosen as a conservative upper bound on the time between updates an extension officer needs for irrigation and pest-risk decisions under normal conditions; because the heartbeat, rather than the event-triggered path, sets the guaranteed minimum transmit rate, it is also the primary lever for keeping the LPWAN radio-transmit contribution in Table 1 near its lower bound, with event-triggered transmissions adding to that baseline only when the edge model flags a condition. Communication uses LoRa for its low transmit-energy per message; a solar-plus-optional-grid gateway, far fewer in number than the nodes, aggregates data over cellular backhaul to a dashboard accessible to extension officers and cooperative managers.

3.2 Energy Budget Analysis

The core constraint of a batteryless design is that average harvested power must meet or exceed average consumed power, including storage leakage, over a representative operating cycle. Because the present study is at the framework and design stage, the budget below is an analytical estimate based on component-level operating ranges rather than the output of a completed simulation or prototype. Table 1 summarizes the node energy budget, referenced to the regulated 3.3 V rail.

Table 1: *Node energy budget (referenced to a 3.3 V rail).*

Node Subsystem	Active Current	Duty Cycle	Avg. Power @3.3 V
Sensor suite (soil, temp/humidity, light)	0.3–1.0 mA	~1%	~10–33 µW
Edge-inference MCU (active compute)	4–8 mA	<0.5%	~66–132 µW
MCU sleep/idle state	2–5 µA	~98%	~7–16 µW
LPWAN radio transmit burst	30–120 mA	<0.1%	~100–400 µW
Harvesting/PMIC quiescent overhead	10–20 µA	Continuous	~33–66 µW
Supercapacitor leakage	10–50 µA	Continuous	~33–165 µW
TOTAL (average)	~75–245 µA	—	~250–810 µW

Based on the component-level ranges and engineering assumptions summarized in Table 1, the projected average node power consumption is approximately 0.25–0.8 mW at the regulated 3.3 V rail. The estimate includes sensor, processing, radio, power-management, and supercapacitor-leakage contributions. On an engineering-estimate basis, this projected load is substantially below the nominal peak output of the proposed 1–2 W PV source; however, actual energy sufficiency will depend on irradiance, canopy shading, dust, conversion losses, RF-harvesting yield, and storage losses. The ambient RF subsystem is therefore treated as a supplementary source rather than the primary energy supply. These values represent a design-stage energy budget and have not yet been experimentally validated. Because leakage is comparable to the load, the supercapacitor is sized from the net (harvest-minus-leakage) surplus rather than from nominal harvest current alone.

3.3 Phased Deployment Methodology

Deployment proceeds in four phases. Phase 1, bench validation, characterizes the harvesting front end and trains the edge model on locally collected soil and microclimate data at a university research farm. Phase 2, pilot cluster, deploys 10–20 nodes across a single cooperative farm cluster, paired with extension-officer dashboard training, to validate energy sufficiency and inference accuracy across a full cropping season. This range is selected as a practical pilot size that permits deployment across a single cooperative farm cluster while remaining sufficiently large to observe node-to-node variation in canopy shading, soil type, and RF signal strength within the cluster, providing a spread of operating conditions for validating inference accuracy before committing to the larger capital and logistics outlay of Phase 3. Phase 3, cooperative-scale rollout, expands to a full cooperative or local government area, incorporating feedback on mechanical housing durability, livestock interference, and gateway placement. Phase 4, local manufacturing transition, partners with Nigerian electronics-assembly capacity, including university engineering workshops, to localize PCB assembly, antenna fabrication, and enclosure production, reducing per-node cost and import dependence.

4. DISCUSSION AND IMPLICATIONS

4.1 National Impact and Alignment with the Conference Theme

Continuous, low-cost soil and microclimate monitoring closes the information gap identified in Section 1: the precision-agriculture literature consistently associates timelier, data-informed irrigation and input decisions with reduced water waste and improved yield consistency relative to calendar-based scheduling (Ojha et al., 2021; Friha et al., 2021). Because the proposed framework reduces dependence on grid electricity and recurring battery replacement, it could extend digital-agriculture monitoring to

smallholder cropland where conventional powered networks are difficult or costly to maintain, with implications for national food-price volatility and import dependence that scale with the phased rollout of Section 3.3.

Reliable grid electricity does not reach most Nigerian farmland, and the Rural Electrification Agency's own capital-project reporting indicates that closing this gap through conventional grid extension remains a multi-year, capital-intensive undertaking rather than a near-term certainty (Rural Electrification Agency [REA], 2024). Because the proposed node requires neither grid connection nor battery replacement, it decouples digital-agriculture adoption from the pace of electrification rollout, consistent with the energy-access priorities documented jointly by the Food and Agriculture Organization and International Telecommunication Union (2022). The framework also touches several Sustainable Development Goals simultaneously: affordable and clean energy (SDG 7) through reliance on ambient renewable sources; responsible consumption and production (SDG 12) through reduced dependence on recurring battery use and associated waste; industry, innovation, and infrastructure (SDG 9) through the local-manufacturing pathway of Section 3.3; and zero hunger (SDG 2) through anticipated yield and input-efficiency gains.

4.2 Economic Scalability and Local Capacity

The phased local-manufacturing transition is the primary lever for reducing per-node cost over time, compressing the import duties, shipping, and currency-conversion overheads on imported sensor and radio modules as production scales from tens of units in Phase 2 toward hundreds or low thousands in Phase 3. Eliminating recurring battery-purchase and replacement logistics further shifts the node's cost profile from a recurring operating expense toward a one-time capital expense, easier for cooperatives and financing partners to plan around. Localizing PCB assembly, antenna fabrication, and enclosure production also builds domestic RF, photovoltaic, and embedded-systems expertise transferable well beyond agriculture, and each deployment phase creates rural technical employment in calibration, maintenance, and assembly. As a rough order-of-magnitude planning estimate rather than a costed bill of materials, imported-component sourcing at Phase 2 pilot volumes is estimated at approximately $25–35 (about ₦33,750–₦47,250 at a reference planning rate of ₦1,350/$) per node, inclusive of estimated freight, applicable duties and import charges, and currency-conversion costs, with the local-manufacturing transition of Phase 4 projected to reduce this toward approximately $15–20 (about ₦20,250–₦27,000) per node as deployment scales beyond Phase 3 volumes by substituting domestically assembled PCBs, antennas, and enclosures for imported equivalents; these figures should be treated as planning estimates to be refined once Phase 2 procurement data and applicable Nigerian import tariff classifications are available, not as validated costings. The estimate does not constitute a detailed bill of materials and excludes project-level costs such as gateway infrastructure, installation, field labour, testing equipment, software development, and long-term maintenance.

4.3 Limitations

The energy budget in Section 3.2 is derived from component-level datasheet ranges and engineering estimates rather than from a simulated, prototyped, or field-measured system, so the projected multi-day autonomy remains an unvalidated design target rather than a demonstrated performance result. RF harvesting yield is highly location-dependent and marginal far from cellular infrastructure, necessitating the NCC-compliant exciter fallback of Section 3.1, which adds gateway-side cost. Supercapacitor storage exhibits self-leakage comparable to the node load and capacitance fade at elevated ambient temperatures common in Nigeria, so multi-year node lifetime is bounded by temperature-derated ageing rather than open-ended. Mechanical durability of externally mounted PV and antenna elements against dust, humidity, livestock, and theft requires robust, low-cost enclosure design, and edge-model accuracy depends on training data representative of local soil types and crop varieties. Sustained adoption also depends on extension-service capacity to act on the data produced; the technology is necessary but not sufficient without complementary agricultural-advisory infrastructure.

5. CONCLUSION

This paper has proposed a hybrid solar–RF energy-harvesting framework for batteryless, edge-intelligent agricultural monitoring nodes designed around the infrastructural and economic conditions of rural Nigeria. A voltage-referenced analytical energy budget suggests an average node draw of a few hundred microwatts when radio bursts and supercapacitor leakage are included. This projected load is substantially below the nominal peak rating of the proposed 1–2 W PV source, but actual energy sufficiency remains to be established through simulation, prototype testing, and field measurements. By combining complementary harvesting sources with on-node inference intended to reduce the energy cost of communication, the framework is designed to reduce the recurring power and maintenance burden associated with conventional battery-dependent precision-agriculture IoT deployments. The phased deployment and local-manufacturing methodology further provides a pathway for the technology to mature from a research prototype into a domestically buildable national asset, supporting food security, energy justice, local industrial capacity, and rural technical employment simultaneously. Key limitations include the absence of prototype and field validation of the energy budget, location-dependent RF yield, temperature-related supercapacitor ageing, and dependence on complementary extension-service capacity. Future work will report field-validated energy-harvest yields, supercapacitor-ageing data, and edge-model accuracy from the Phase 1–2 deployments described in Section 3.3.

6. REFERENCES

Banbury, C. R., Reddi, V. J., Lai, L., Fu, C.-S., Fazel, A., Holleman, J., Huang, X., Hurtado, R., Kanter, D., Lokhmotov, A., Patterson, D., Pau, D., Seo, J., Sieracki, J., Thakker, U., Verhelst, M., & Yadav, P. (2020). Benchmarking TinyML systems: Challenges and direction. arXiv:2003.04821.

Food and Agriculture Organization of the United Nations, & International Telecommunication Union. (2022). Status of digital agriculture in 47 sub-Saharan African countries. FAO.

Friha, O., Ferrag, M. A., Shu, L., Maglaras, L., & Wang, X. (2021). Internet of Things for the future of smart agriculture: A comprehensive survey of emerging technologies. IEEE/CAA Journal of Automatica Sinica, 8(4), 718–752.

Kansal, A., Hsu, J., Zahedi, S., & Srivastava, M. B. (2007). Power management in energy harvesting sensor networks. ACM Transactions on Embedded Computing Systems, 6(4), Article 32.

Kim, S., Vyas, R., Bito, J., Niotaki, K., Collado, A., Georgiadis, A., & Tentzeris, M. M. (2014). Ambient RF energy-harvesting technologies for self-sustainable standalone wireless sensor platforms. Proceedings of the IEEE, 102(11), 1649–1666.

Liu, V., Parks, A., Talla, V., Gollakota, S., Wetherall, D., & Smith, J. R. (2013). Ambient backscatter: Wireless communication out of thin air. ACM SIGCOMM Computer Communication Review, 43(4), 39–50.

National Bureau of Statistics. (2017). Labour Force Statistics Vol. 2: Employment by Sector Report (Q3 2017). Abuja, Nigeria: NBS.

Nigerian Communications Commission. (2003). Legal guidelines on the use of short range devices in Nigeria. NCC.

Ojha, T., Misra, S., & Raghuwanshi, N. S. (2021). Internet of Things for agricultural applications: The state of the art. IEEE Internet of Things Journal, 8(14), 10973–10997.

Rural Electrification Agency. (2024). 2023 capital project implementation report. REA.

Sudevalayam, S., & Kulkarni, P. (2011). Energy harvesting sensor nodes: Survey and implications. IEEE Communications Surveys & Tutorials, 13(3), 443–461.

Vullers, R. J. M., van Schaijk, R., Doms, I., Van Hoof, C., & Mertens, R. (2009). Micropower energy harvesting. Solid-State Electronics, 53(7), 684–693.

Williams, A. J., Torquato, M. F., Cameron, I. M., Fahmy, A. A., & Sienz, J. (2021). Survey of energy harvesting technologies for wireless sensor networks. IEEE Access, 9, 77493–77510.

Zungeru, A. M., Ang, L.-M., Prabaharan, S., & Seng, K. P. (2012). Radio frequency energy harvesting and management for wireless sensor networks. In Green mobile devices and networks: Energy optimization and scavenging techniques. CRC Press.

International Conference on Engineering Innovation for Sustainable Development (ICESID 2026)
Faculty of Engineering, Ahmadu Bello University Zaria · 8–10 September 2026

MODIFICATION OF FORWARD AND REVERSE ELECTRIC MOTOR STARTERS

Ismail Yusuf Adubazi[1,*]
[1]*Kaduna Polytechnic, Kaduna*
Email: ismailadubazi@kadunapolytechnic.edu.ng*
***Corresponding author**: Ismail Yusuf Adubazi
DOI: https://doi.org/10.67203/sp.ICESID.2026

ABSTRACT

Modification of forward and reverse Electric Motor Starters is designed to reduce the numbers of Electrical component used in conventional Electric Motor Starters. The modified forward and reverse Direct-On-Line Starter is designed to use one Contactor, one Start Push Button, one Stop Push Button, one Miniature Circuit Breaker, one Control Breaker, one Overload Relay and Three-Phase Selector Switch. The modified forward and reverse Star/Delta Starter is designed to be implemented with two Contactors, one Start Push Button, one Stop Push Button, one Timer Relay, one Miniature Circuit Breaker, one Control Breaker and one Three-Phase Selector Switch. The designed Circuit diagrams are then subjected to test by using a software called CADe-SIMU to simulate the circuit diagrams. The modification reduces the cost of number of Contactors and some other Electrical components used as well as reducing the cross-sectional area of the Electrical panel.

Keywords: *Contactors; Overload Relay; Timer Relay; Forward and Reverse*

1.1 Introduction

Electric Motor Starters incorporate some Electrical components with safety devices to start the operation of the Electric Motor. There are two major types of such Starters, namely, Direct-On-Line Starter and Star/Delta Starter. The Electric Motor is either connected as Star or Delta at the Electric Motor terminals when using the DOL Starter. The Star/Delta Starter is another type of Electric Motor Starter having three Contactors, one Overload Relay, one Timer Relay, one Miniature Circuit Breaker, one Control Breaker, Indicating lamps and Push Button Switches. The three Contactors are tagged as Main Contactor, Star Contactor and Delta Contactor. If the Timer Relay is set at ten seconds, the Main Contactor and the Star Contactor are energized simultaneously for ten seconds. After ten seconds the Star Contactor disengage to give way to the Delta Contactor and the Main Contactor to continue the operation of the Electric Motor (Ifiok, 2024). The Star/Delta Starter is for soft starting of the Electric Motor. Changing the direction of Three-Phase Induction motor is carried out by interchanging two of the three phases.

2.1 Brief review of similar work

Forward and reverse operation of Electric Motor DOL Starter is realized with two contactors (Uduak Okoa, 2024). One Contactor for forward movement while the other Contactor for the reverse movement. The Control and Power line diagrams are as shown in figure 1.0.

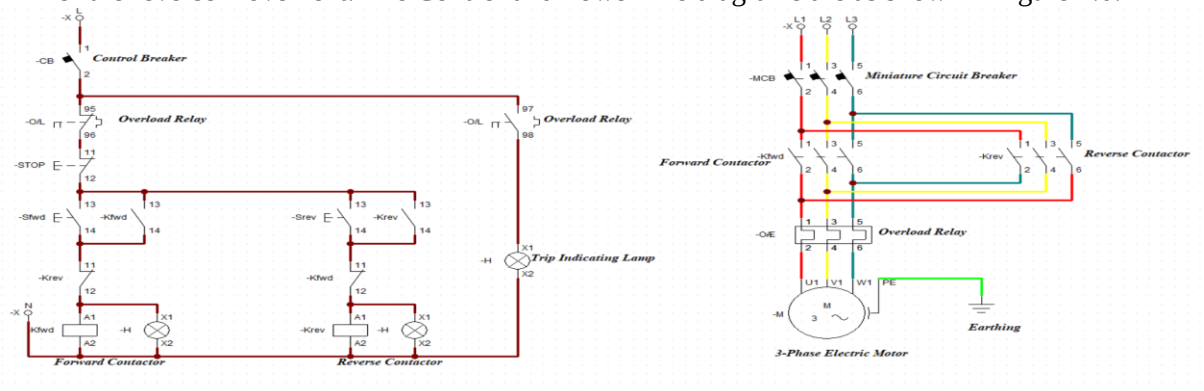

Figure 1.0: Forward and reverse Motor Starter

The software CADe-SIMU (CADe-SIMU Version 4.2, 2024) was used to draw and simulate the circuit diagrams. The result of the simulation for the forward operation is as shown in figure 1.1. If the forward Contactor is energized, the reverse Contactor remains open because the NC Contact from the forward Contactor which is connected in series with reverse Contactor coil is opened. Similarly, If the reverse Contactor is energized, the forward Contactor remains open because the NC Contact from the reverse Contactor which is connected in series with forward Contactor coil is opened. These operations were tested with the software and it works satisfactorily. The present research work is to use one Contactor, one Start Push Button and other electrical components to achieve the same aim.

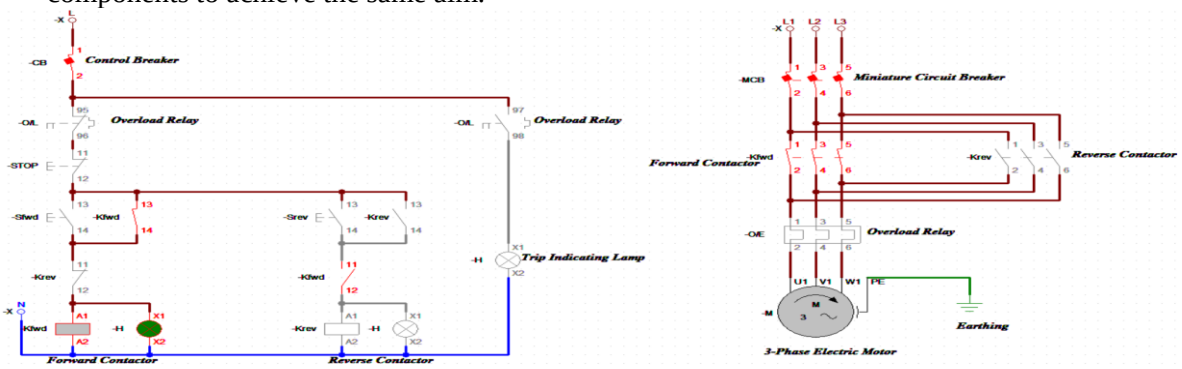

Figure 1.1: Forward and reverse Motor Starter (forward mode operation)

The result of the simulation for the reverse operation is as shown in figure 1.2

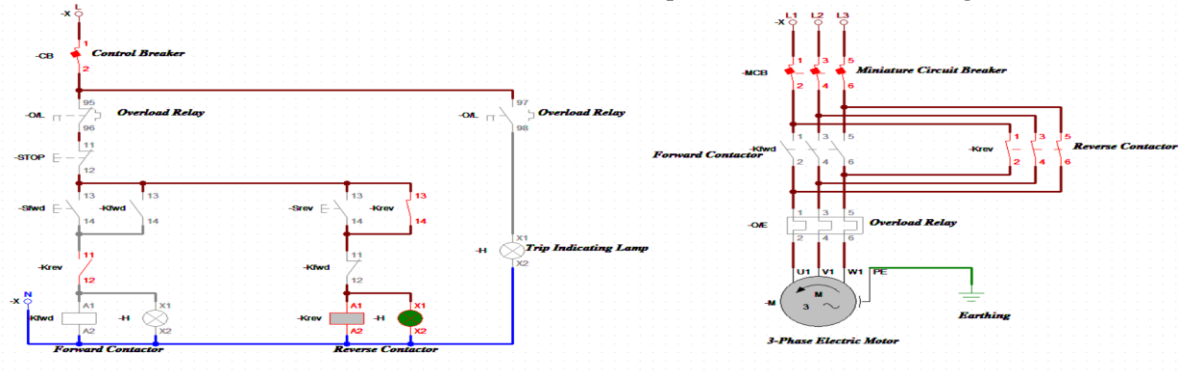

Figure 1.2: Forward and reverse Motor Starter (reverse mode operation)

The conventional Star/Delta Starter forward and reverse operation involves four contactors, one Overload Relay, one Timer Relay, one Miniature Circuit Breaker, one Control Breaker, Indicating Lamps and Push Button Switches. Use of Arduino Based Star/Delta Starter with forward and reverse control is equally another research work (Nigar Sultana, 2023). The Control and Power line diagrams are as shown in figure 1.3. The present research work is to use just two Contactors, one Start Push Button with other electrical components to realize the operation of the forward and reverse Star/Delta Starter. The starting torque and starting current in Delta connection is higher than that of Star connection (Jayswal, 2018).

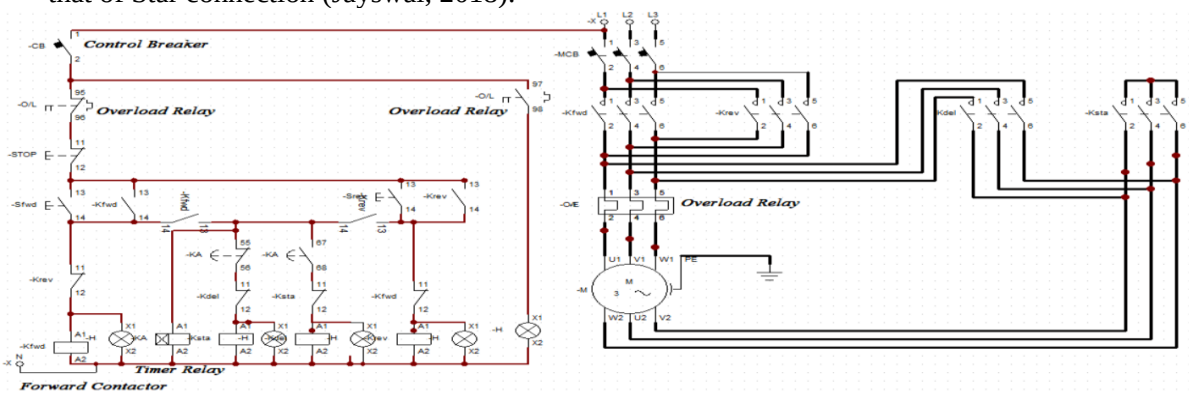

Figure 1.3: Control and Power line diagrams of forward and reverse Star/Delta Starter

The result of the simulation of the circuit diagram in forward Star mode is as shown in figure 1.4

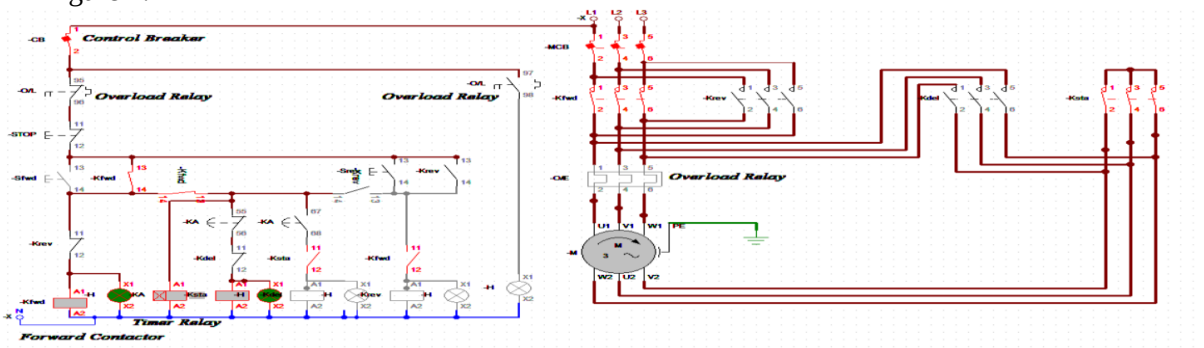

Figure 1.4: Control and Power line diagrams of forward and reverse Star/Delta Starter (forward Star mode)

The result of the simulation of the circuit diagram in forward Delta mode is as shown in figure 1.5

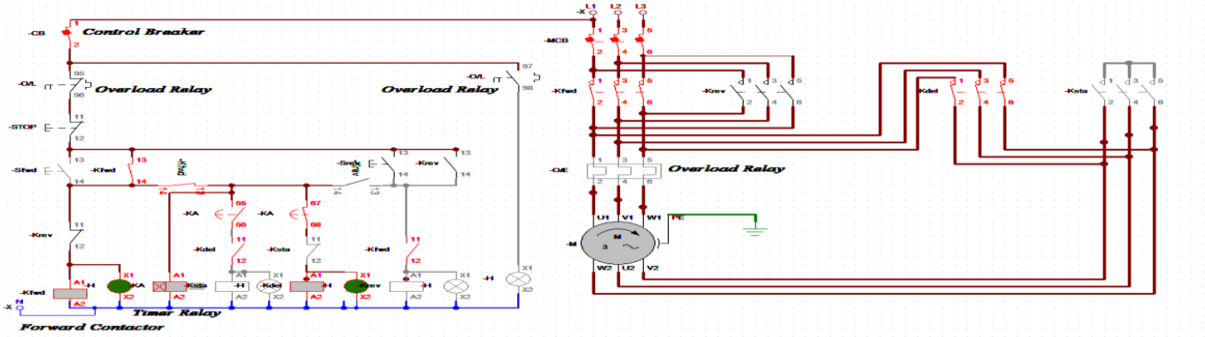

Figure 1.5: Control and Power line diagrams of forward and reverse Star/Delta Starter (forward Delta mode)

The result of the simulation of the circuit diagram in reverse Star mode is as shown in figure 1.6

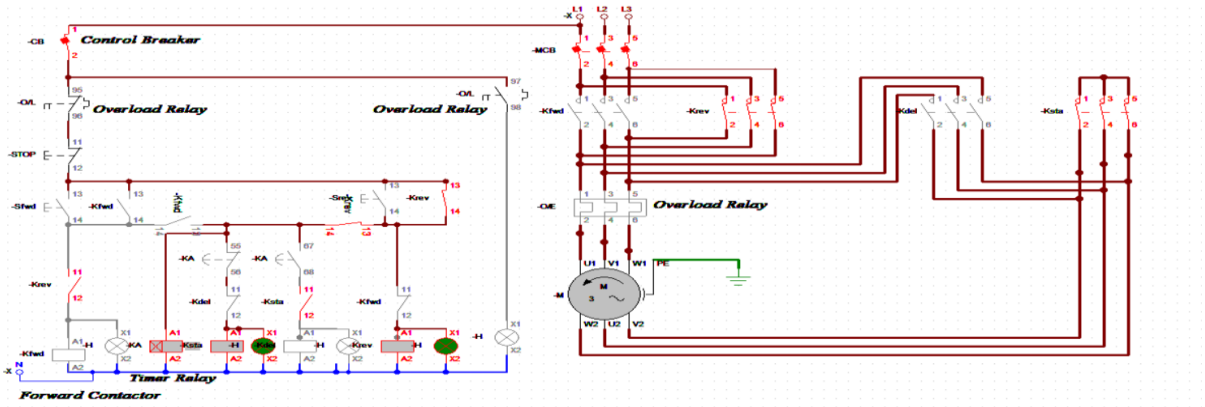

Figure 1.6: Control and Power line diagrams of forward and reverse Star/Delta Starter (reverse Star mode)

The result of the simulation of the circuit diagram in reverse Delta mode is as shown in figure 1.7

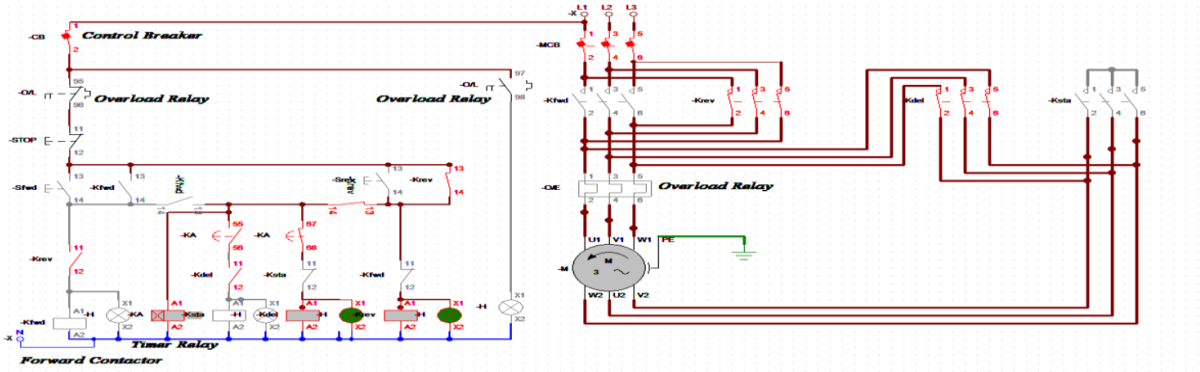

Figure 1.7: Control and Power line diagrams of forward and reverse Star/Delta Starter (reverse Delta mode)

Use of relays to realize the operation of Star/Delta Starter is another research work carried out by (Ayibapreye, October, 2022). This idea is practically not realizable on Electric Motors of high power capacity. Safety measures like Miniature Circuit Breaker and Overload Relay were excluded in the research work. The idea of Star connection and then Delta connection is to reduce the inrush starting current (Apoorva, June, 2017).

The connection involving three Contactors with other Electrical Components is as shown in figure 1.8.

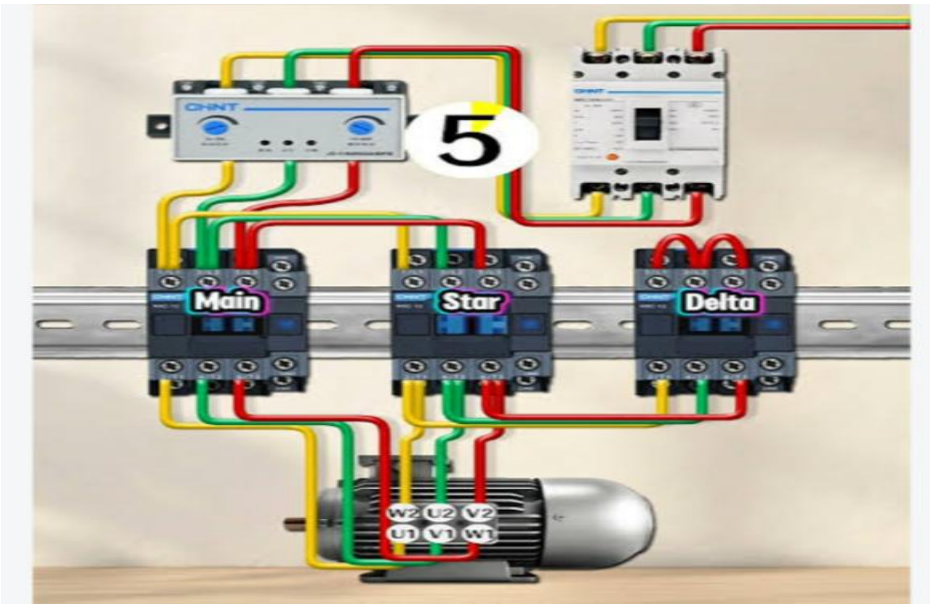

Figure 1.8: Star/Delta Starter

2.2 Problem Statement

Forward and reverse operation of Electric Motor in Industries is very vital in some product processing. The change of direction in three-phase induction Motor is realized by changing two of the phases. Hence there is need to make such changing more flexible and within the shortest period of time. Reducing the number of Electrical components will not only save cost but as well reduces the space within the Electrical panel.

2.3 Aim & Objective

The aim of this research work is to demonstrate implementation of Electric Motor Starters by reducing the numbers of Contactors involved.

3.1 Methodology

The conventional forward and reverse Starter incorporates two Contactors, one Overload Relay, one Miniature Circuit Breaker, one Control Breaker, two Start Push Buttons, one Stop Push Button and Indicating lamps. The modification is the utilization of such operation with just one Contactor, one Overload Relay, one Selector Switch, one Start Push Button, one Stop Push Button and Indicating Lamps. One contactor performs both the forward direction and the reverse direction. The change of direction is carried out on the Selector Switch. When changing the direction of the Electric Motor, the Operator must make sure the Stop Push Button on the Control Circuit is pressed.

The major reason for such step is to avoid arching within the Three-Phase Rotary Contacts. A position is OFF position while the remaining two positions are configured to change the sequence of the 3-Phase power supply.

The conventional forward and reverse Star/Delta Starter involves four Contactors, one Overload Relay, one Timer Relay. This research work is to use just two Contactors, namely, Star Contactor and Delta Contactor. The forward and reverse operations are configured on the Selector Switch with three positions. The Selector Switch is as shown in figure 2.0.

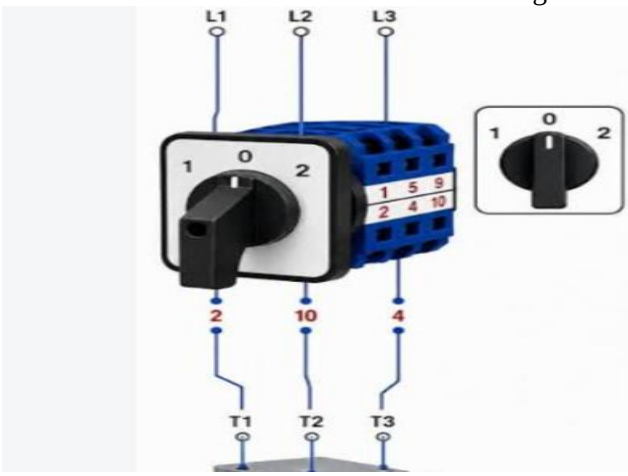

Figure 2.0: 3-Phase Selector Switch

4.1 Result

The results of modifications as carried out are as displayed as follows;

4.1.1 Modified forward and reverse DOL Starter

The operational mode of the modified forward and reverse Electric Motor Starter in forward direction is as shown in figure 2.1. When the Start Push Button is engaged as shown on the Control line diagram of figure 2.1 the Contactor is energized. The power supply to the Electric Motor terminal is obtained through the Three-Phase Selector Switch.

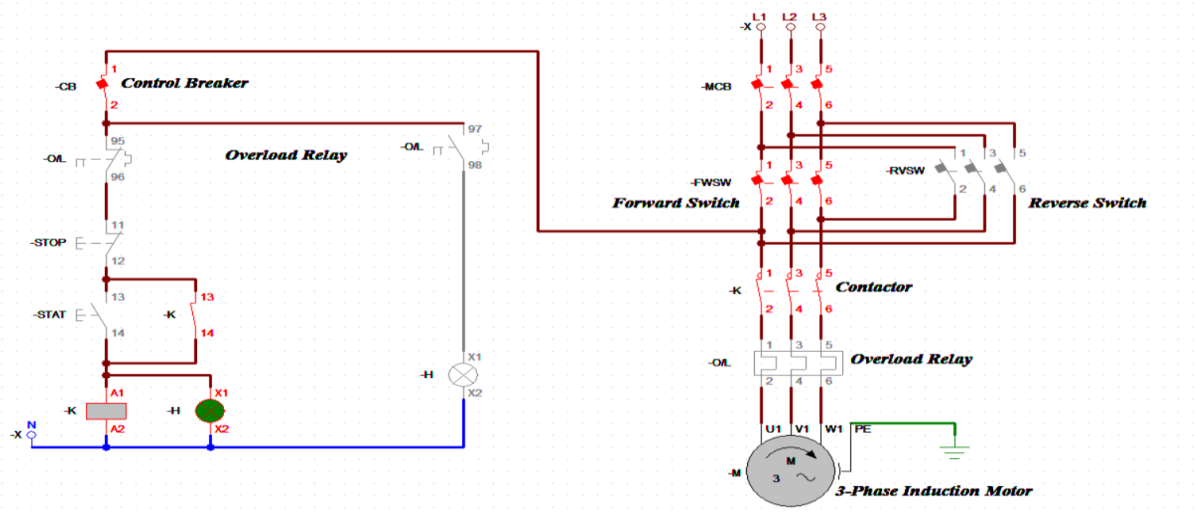

Figure 2.1: The operational mode of the Electric Motor in forward direction.

The operational mode of the modified Electric Motor Starter in reverse direction is as shown in figure 2.2.

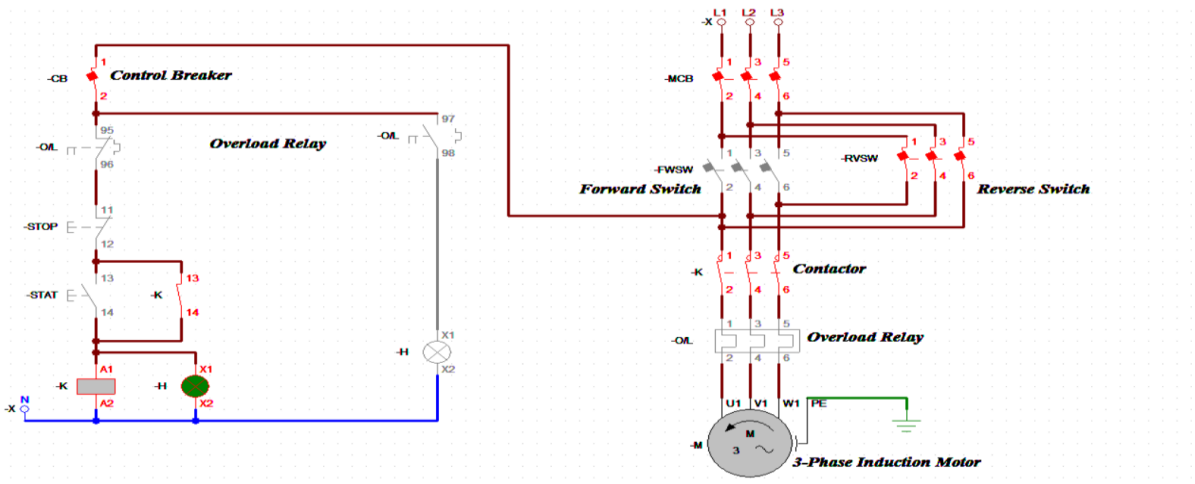

Figure 2.2: The operational mode of the modified Electric Motor Starter in reverse direction.

The diagram in figure 2.3 illustrates the connection of the Three-Phase Rotary Switch to implement the phase reversal.

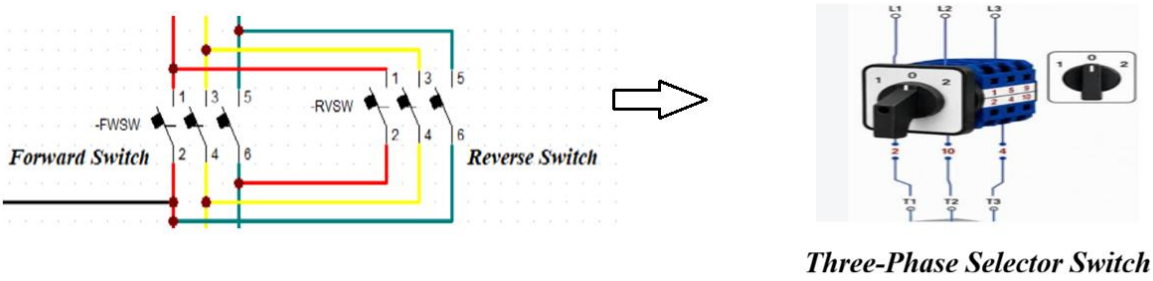

Figure 2.3: Diagram for the Three-Phase Selector Switch

The incorporation of Three-Phase Selector Switch for the modified Forward and reverse DOL is as shown in figure 2.4. the Selector Switch has three positions. Position labelled as '0' is the OFF position. Position labelled as '1' is to be connected power supply as Red, Yellow and Blue. This position '1' is for forward direction. Position labelled as '2' is to be connected to power supply as Red, Blue and Yellow. This position '2' is for the reverse direction.

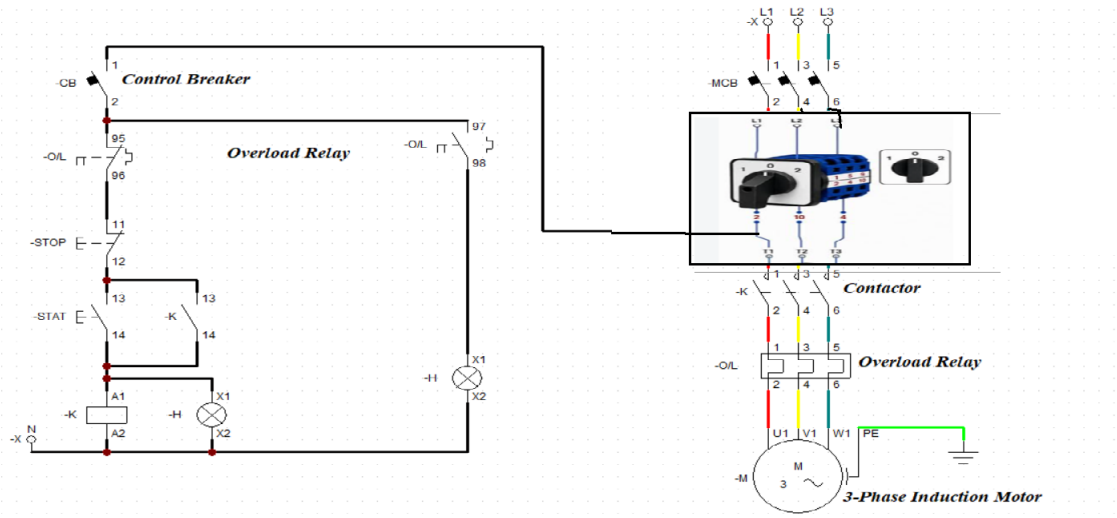

Figure 2.4: Use of Three-Phase Selector Switch for the modified Starter.

Safety

The safety measure when using the Selector Switch is to tap supply to the Control Breaker from the Contactor Main Contact. With this type of connection, the Contactor will only be energized via the Start Push Button when the Selector Switch is ON. The Main Circuit Breaker and the Overload Relay if well selected will protect the entire Circuit against any envisaged short circuit that might occur when the 3-Phase Selector Switch is operated.

4.1.2 Modified forward and reverse Star/Delta Starter

The control line diagram for the Modified Forward and reverse Star/Delta Starter is as shown in figure 2.5. The NC Contact and NO Contact of the Timer Relay are connected to the Star Contactor and Delta Contactor respectively to avoid operating the two contactors at the same time.

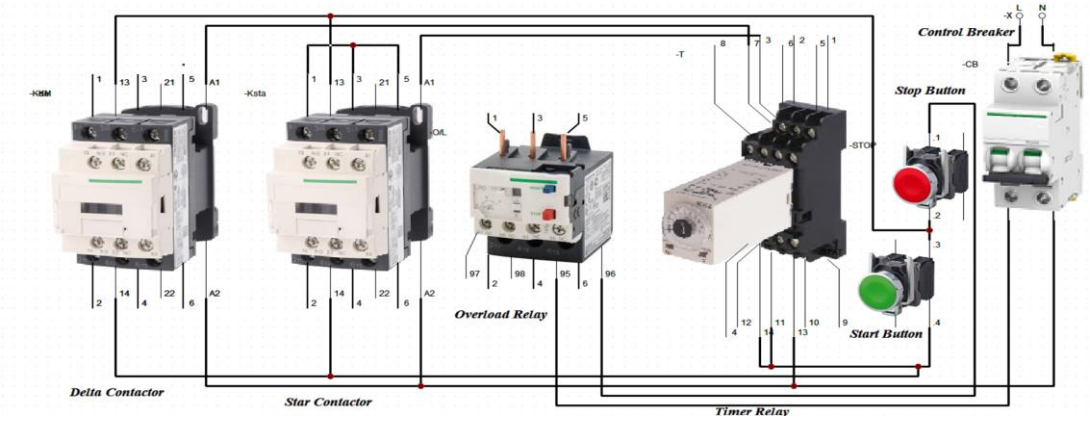

Figure 2.5: Control line diagram for the Modified Forward and reverse Star/Delta Starter

The operation of the control line diagram for the Modified Forward and reverse Star/Delta Starter in Star mode is as shown in figure 2.6. The Normally Close (NC) Contact of the Timer Relay labelled as terminal '3' is linked to the Star Contactor while the Normally Open Contact (NO) of the Timer Relay labelled '7' is linked to the Delta Contactor.

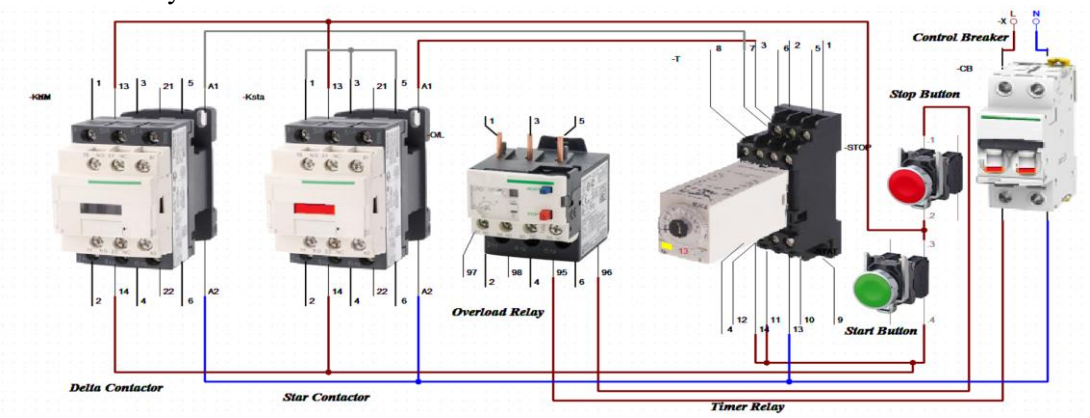

Figure 2.6: Control line diagram for the Modified Forward and reverse Star/Delta Starter (Star mode operation or simulation)

The operation or simulation of the control line diagram for the Modified Forward and reverse Star/Delta Starter in Delta mode is as shown in figure 2.7. The Normally Open (NO) Contact of the Timer Relay labelled as terminal '7' is now supplying current to the Delta Contactor. Under normal condition the NC and NO Contacts of the Timer Relay are neither close nor open simultaneously. That is, when the NO Contact is closed the NC Contact is opened.

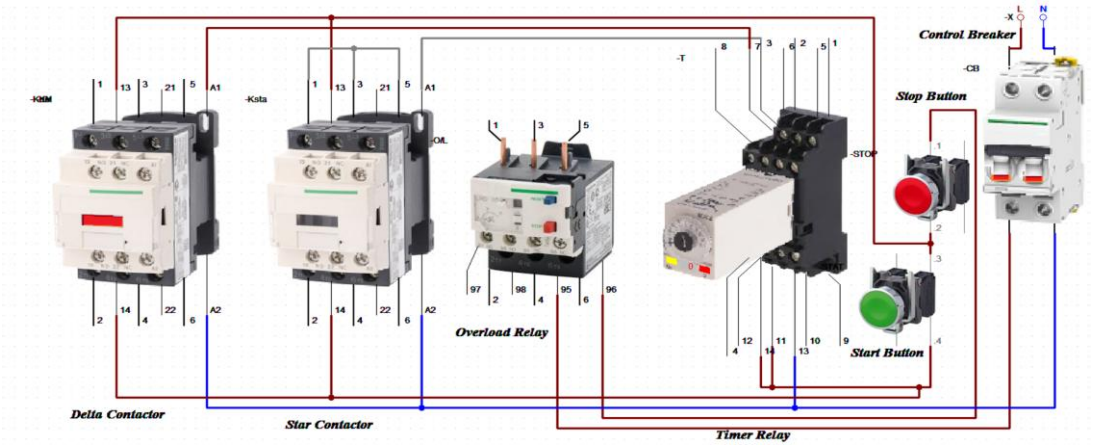

Figure 2.7: Control line diagram for the Modified Forward and reverse Star/Delta Starter (Delta mode operation or simulation)

The complete line diagrams for the modified Star/Delta Starter is as shown in figure 2.8. This design as shown in figure 2.8 do not need additional interlocking Contacts because the normally open and normally close contacts of the Timer Relay are connected respectively to the Star and Delta Contactor Coils.

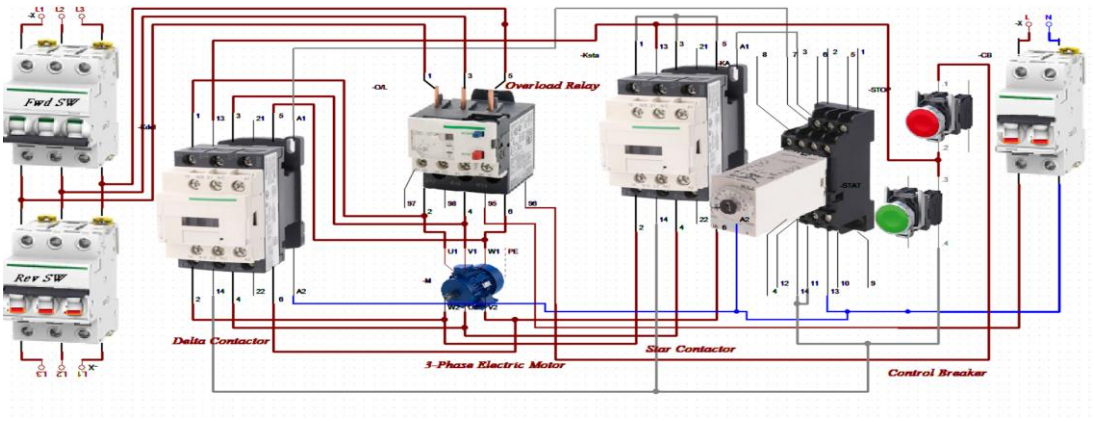

Figure 2.8: Complete line diagrams for the modified Star/Delta Starter

The operation or simulation of the motor as Star connected Motor in forward direction is as shown in figure 2.9. Current now flows through the NC Contact of the Timer Relay to the Star Contactor Coil. The Star Contactor is now energized to convey power supply to the Electric Motor. The Star Contactor remains ON for the period at which the Timer Relay is set. After the period the NC Contact open while the NO Contact of the Timer Relay close to convey current to the Delta Contactor Coil.

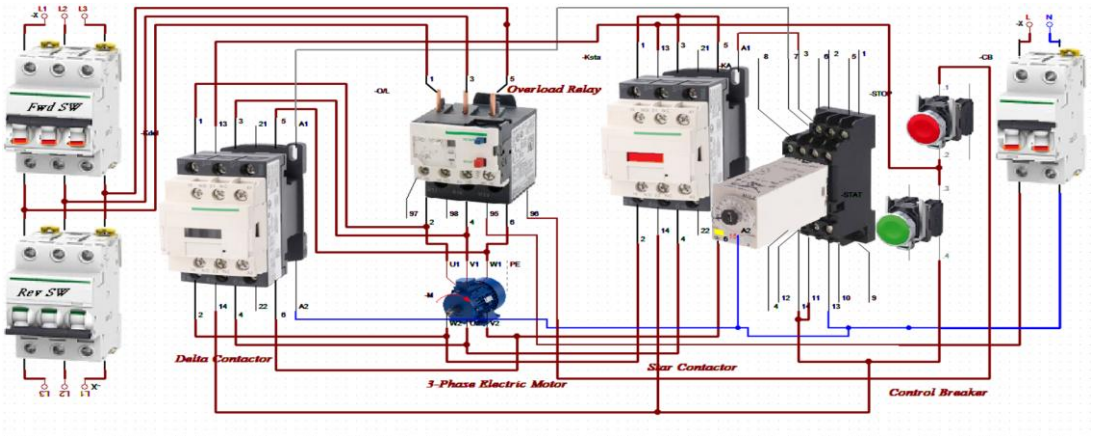

Figure 2.9: The operation or simulation of the motor as Star connected Motor in forward direction.

The operation or simulation of the motor as Delta connected Motor in forward direction is as shown in figure 2.10. Current now flows through the NO Contact of the Timer Relay to the Delta Contactor Coil. The Delta Contactor is now energized to convey power supply to the Electric Motor.

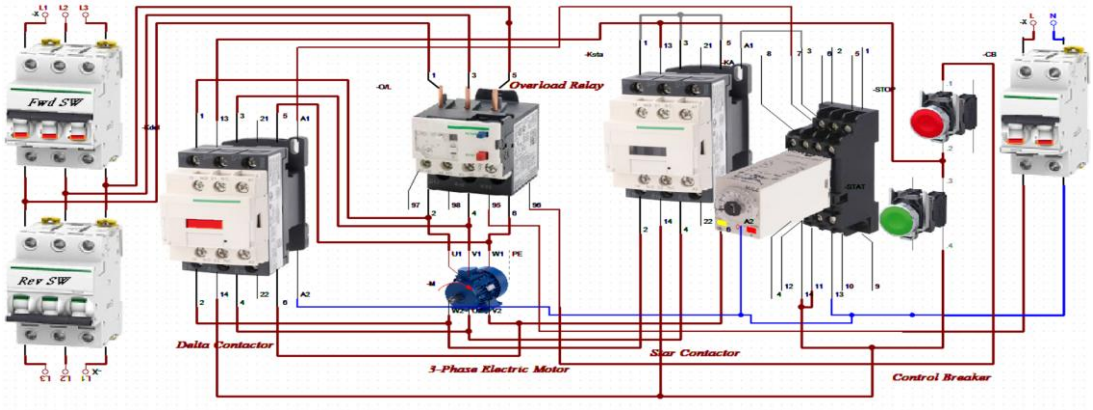

Figure 2.10: The operation or simulation of the motor as Delta connected Motor in forward direction.

The operation or simulation of the motor as Star connected Motor in reverse direction is as shown in figure 2.11. The Star Contactor is now energized to convey power supply to the Electric Motor.

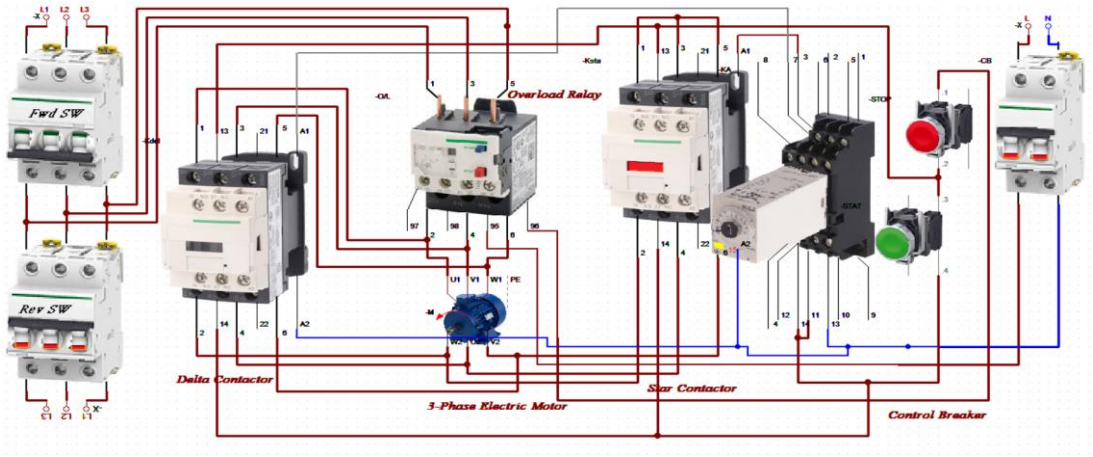

Figure 2.11: The operation or simulation of the motor as Star connected Motor in reverse direction.

The operation or simulation of the motor as Delta connected Motor in reverse direction is as shown in figure 2.12. The Delta Contactor is now energized to convey power supply to the Electric Motor.

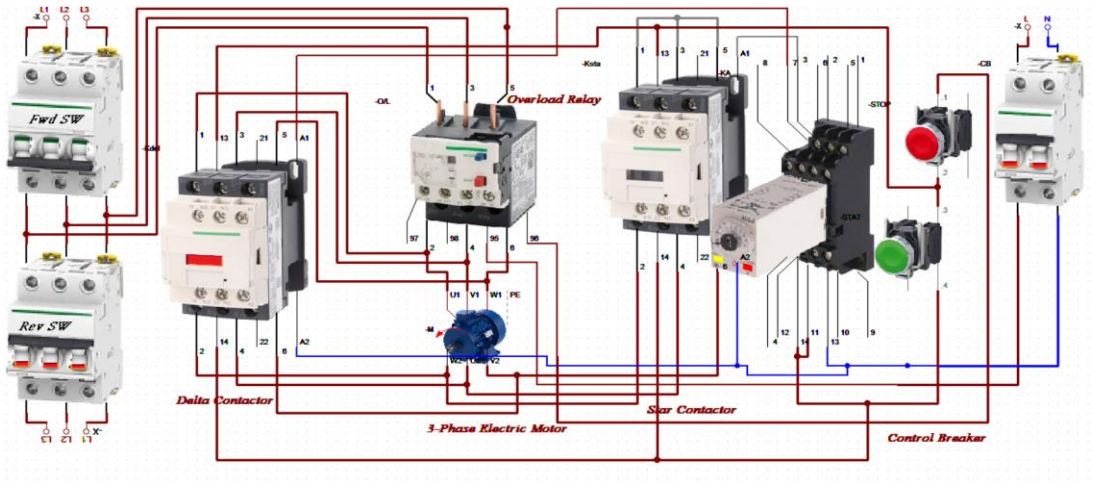

Figure 2.12: The operation or simulation of the motor as Delta connected Motor in reverse direction.

The Selector Switch as shown in figure 2.13 can be utilized to replace the two Miniature Circuit Breakers as used in figure 2.12.

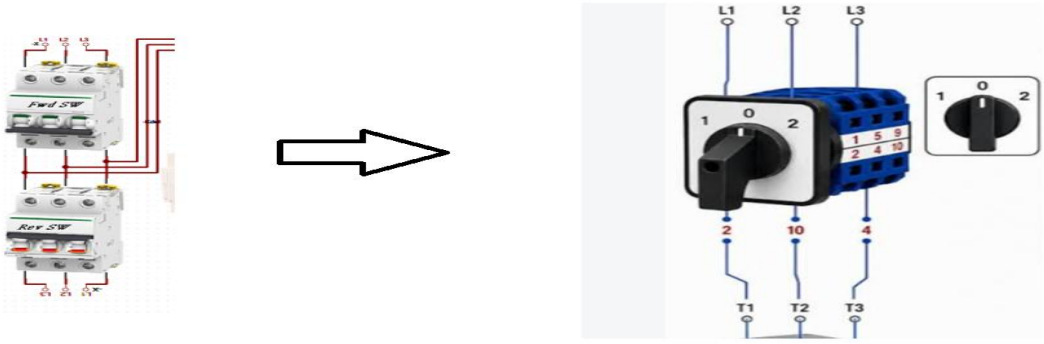

Figure 2.13: Three-Phase Selector Switch

The circuit diagram in figure 2.14 depicts incorporation of Three-Phase Selector Switch. The position (0) is OFF, the position (1) is connected to power supply as Red, Yellow and Blue. At this position '1' the Electric Motor is rotating in clockwise direction. The position (2) is connected to power supply as Red, Blue and Yellow. At position '2' the Electric Motor rotates in anti-clockwise direction.

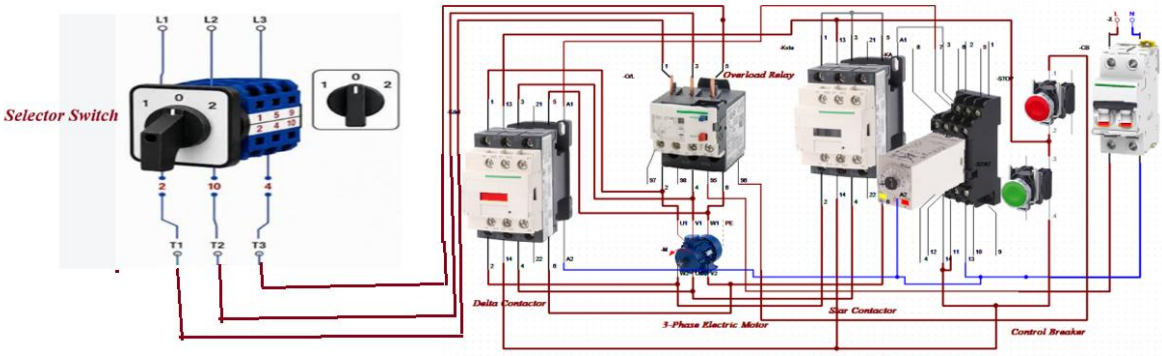

Figure 2.14: Incorporation of the Three-Phase Selector Switch on the modified Star/Delta Starter forward and reverse

4.1.3 Comparative Analysis

The comparative Analysis between the conventional Circuit diagrams and the modified Circuit diagrams for the two type of Starters are as estimated on Table 1.1. The estimated cost was obtained at market survey Kaduna on 30th September, 2026.

Table 1.1 (Kaduna)

Name of Starter	Materials required for the Conventional Circuit diagrams	Materials required for the Modified Circuit diagrams	Estimated Cost of Materials for the conventional Circuit	Estimated Cost of Materials for the Modified Circuit
Forward and reverse Direct-On-Line	(1) Two Contactors (2) Two Start Push Buttons (3) One Stop Push Button (4) Interlocking Contacts (5) One Overload Relay (6) One Miniature Circuit Breaker (7) One Control Breaker	(1) One Contactor (2) One Start Push Button (3) One Stop Push Button (4) 3-Phase Selector Switch. (5) One Overload Relay (6) One Miniature Circuit Breaker (7) One Control Breaker	(1) N2000 (2) N1000 (3) N500 (4) N1000 (5) N1500 (6) N2000 (7) N1500 Total N9500	(1) N1000 (2) N500 (3) N500 (4) N1500 (5) N1500 (6) N2000 (7) N1500 Total N8500

Name of Starter	Materials required for the Conventional Circuit diagrams	Materials required for the Modified Circuit diagrams	Estimated Cost of Materials for the conventional Circuit	Estimated Cost of Materials for the Modified Circuit
Forward and reverse Star/Delta	(1) Four Contactors (2) One Overload Relay (3) Two Start Push Buttons (4) One Stop Push Button (5) One Timer Relay (6) Interlocking Contacts (7) One Control Breaker (8) One Miniature Circuit Breaker	(1) Two Contactors (2) One Overload Relay (3) One Start Push Button (4) One Stop Push Button (5) One Timer Relay (6) 3-Phase Rotary Switch. (7) One Control Breaker (8) One Miniature Circuit Breaker.	(1) N4000 (2) N1500 (3) N1000 (4) N500 (5) N1500 (6) N1000 (7) N1500 (8) N2000 Total N13000	(1) N2000 (2) N1500 (3) N500 (4) N500 (5) N1500 (6) N1500 (7) N1500 (8) N2000 Total N11000

The circuit diagram in figure 2.15 further demonstrates the reduction of space and numbers of Electrical components between the conventional Star/Delta Starter forward/reverse and the modified Starter.

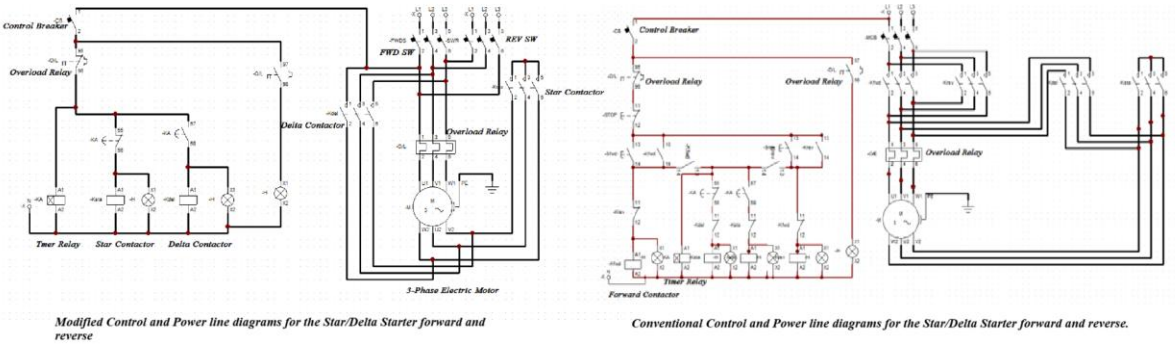

Figure 2.15: Modified and conventional forward and reverse Star/Delta Starter.

4.2 Conclusion

The research work provides another circuit connection schemes to realize the operation of Electric Motor Starters in Industries. The numbers of contactors used in conventional method was reduced. Where it involves two Contactors and two Start Push Buttons for the forward and reverse operations, one Start Push Button and one Contactor with other Electrical components were used. The four Contactors and two Start Push Buttons required for the forward and reverse Star/Delta Starter was equally reduced to two Contactor and one Start Push Button. This has greatly reduced the cost of numbers of Contactors in conventional method as well as reducing the space in the Electrical panel. The four Contactors for the conventional Star/Delta was equally reduced to two Contactors as well. The use of software CADe-SIMU shows the effective performances of the modified Electric Motor Starters. The only limitation with the modification for the forward and reverse DOL is the absence of indicating signal if the Electric Motor is in forward direction or reverse direction.

4.3 REFERENCES

Apoorva. (June, 2017). Automatic Star/Delta Starter Using Relay and Adjustable Electronic Timer for 3-Phase Induction Motor. *International Research Journal of Engineering and Technology (IRJET)*, 2395.

Ayibapreye, G. E. (October, 2022). Design of Automatic Star-Delta Starter by Adjustable Electronic Timer and Relays for Induction Motor. *International Journal of Current Research*, 22552-22555.

CADe-SIMU Version 4.2. (2024, May 17). Juan Luis Villanuva Montoto. Retrieved from https://cade-simu.en.softonic.com

Ifiok, O. (2024). Comparative Analysis of Direct and Soft Starting Method for Induction Motor on Difference Load Levels. *Journal of Engineering Research and Reports*, 308-322.

Jayswal, K. (2018). Automatic Star/Delta Starter. *International Journal of Advanced Research (IJAR)*, 1160-1170.

Nigar Sultana, S. K. (2023). Design and Implementation of Arduino Based Star/Delta Starter, forward/reverse Direction Control and Fault Protection of Three-Phase Induction Motor. *International Journal of Science and Management Studies (IJSMS)*, 76-84.

Uduak Okoa, E. E. (2024, January). Design and Construction of Direct-On-Line Starteer (DOL) for 3-Phase Electric Motor. *Journal of Multidisplinary Engineering Science and Technology (JMEST)*, 16891.

International Conference on Engineering Innovation for Sustainable Development (ICESID 2026)
Faculty of Engineering, Ahmadu Bello University Zaria · 8–10 September 2026

SMART SELF-HEALING MATERIALS: A COMPREHENSIVE REVIEW OF EMERGING TECHNOLOGIES AND FUTURE PERSPECTIVES

Yakubu Usman[1], Ibrahim Mu'azu[2], J. O. Gaminana[3], Danjuma Adamu Ismaila[1,*]

[1]*Nigerian College of Aviation Technology, Zaria*
[2]*Kaduna Polytechnic, Kaduna*
[3]*Ahmadu Bello University, Zaria*

Email: usmanyaks@gmail.com, imuaz70@gmail.com, jamourah2006@gmail.com, danjuisma@gmail.com*

***Corresponding author**: Danjuma Adamu Ismaila

DOI: https://doi.org/10.67203/sp.ICESID.2026

ABSTRACT

Self-healing materials represent one of the most significant paradigm shifts in modern materials engineering, offering the ability to autonomously detect and repair internal or external damage without human intervention, thereby extending service life, improving safety, and reducing maintenance costs across engineering applications. This review synthesizes recent advances in smart self-healing materials, covering the three principal design philosophies that underpin the field: capsule-based (extrinsic), vascular and intrinsic self-healing systems. It examines the healing agents, encapsulation strategies, and activation mechanisms employed across polymeric composites, cementitious materials and hydrogel-based systems, and evaluates their translation into real-world sectors including aerospace, automotive, construction, biomedicine, and flexible electronics. Particular attention is given to emerging technologies such as microencapsulated healing agents for structural and cement-based composites, dynamic covalent and supramolecular chemistries that enable repeated intrinsic healing, bio-mediated systems such as bacterially induced self-healing concrete and stimuli-responsive hydrogels for tissue engineering, wound care, and drug delivery. The review further considers how data-driven approaches, including machine learning and artificial intelligence, are beginning to accelerate the discovery, formulation optimization, and predictive modelling of healing efficiency. Despite considerable progress, the field remains constrained by challenges of production scalability, healing-agent depletion after repeated cycles, trade-offs between healing efficiency and mechanical performance, high cost, and the absence of standardized testing protocols. This review contributes to the growing body of knowledge by providing a comprehensive synthesis of emerging technologies and identifying research priorities for future development of smart self-healing materials.

Keywords: *self-healing materials; smart materials; microencapsulation; vascular networks*

1. INTRODUCTION

Advanced engineering materials have shifted from conventional passive systems toward smart materials that sense environmental changes and respond through controlled property alterations. Smart materials respond to stimuli including temperature, stress, pressure, moisture, pH, electric or magnetic fields, light, and chemical environments, enabling adaptive behaviour difficult to achieve with conventional materials (Mrinalini & Prasanthkumar, 2019). This broader field encompasses stimuli-responsive polymers, shape-memory materials, electroactive and magnetically responsive systems, hydrogels, nanocomposites, and self-healing materials (Srivastav et al., 2025; Jain et al., 2025).

Among these, self-healing materials (SHMs) have attracted particular interest because they introduce autonomous repair into engineering systems. A SHM restores structural integrity or functional performance following damage through autonomous or stimulus-assisted processes (El Choufi et al., 2022; Kontiza & Kartsonakis, 2024). Inspired by biological systems, where damage activates localized transport, molecular recognition, chemical reactions, and reconstruction; the engineering translation treats damage not as irreversible failure but as a trigger for programmed repair (White et al., 2001; Srivastav et al., 2025).

Material degradation often begins at microscopic scales before progressing to visible cracks, delamination, corrosion, leakage, conductivity loss, or catastrophic failure. Conventional maintenance

requires detection followed by external intervention. SHMs reduce this dependence by embedding healing mechanisms within the material architecture itself (White et al., 2001; Zhu et al., 2015). The landmark work of White et al. (2001) demonstrated an autonomic polymer composite in which crack propagation ruptured embedded microcapsules, released a healing agent, and initiated polymerization—establishing a foundational concept that stimulated extensive research into encapsulation, healing-agent chemistry, catalyst distribution, and matrix compatibility.

The field has evolved through successive generations: early extrinsic capsule-based systems (White et al., 2001), intrinsic reversible-bond polymers and advanced vascular and multi-stimuli systems inspired by biological circulatory networks (Blaiszik et al., 2010; Hager et al., 2010). Progress spans polymers, polymer-matrix composites, protective coatings, cementitious materials, metals, and soft materials. Market projections place the global SHM market in the multi-billion-USD range in the mid-2020s, with continued expansion toward 2030–2035 driven by construction, automotive, aerospace, electronics, and biomedical demand (Jose et al., 2026; Kontiza & Kartsonakis, 2024).

Reviews classify systems according to whether healing functionality is stored separately from the matrix (extrinsic: microcapsules, hollow fibres, vascular networks) or incorporated directly into the material network (intrinsic: reversible interactions or dynamic bonds) (El Choufi et al., 2022; Kontiza & Kartsonakis, 2024; Srivastav et al., 2025; Zhu et al., 2015; Jain et al., 2025). Figure 1 organizes the design space along three axes—Strategy (Intrinsic, Extrinsic, Stimuli-responsive), Mechanism (supramolecular interactions, dynamic covalent bonds, vascular/capsule architectures), and Target Functions (mechanical integrity, barrier properties, conductivity, biological compatibility)—and underpins the organization of this review.

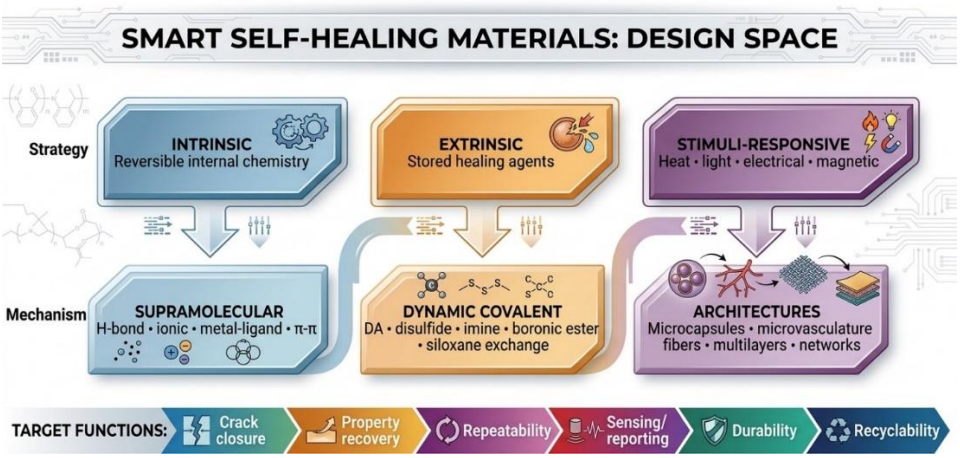

Figure 1: Author-generated design-space map of smart self-healing materials, synthesized from the reviewed literature (Song et al., 2021; Rai et al., 2023; Dallaev, 2024; Jose et al., 2026).

2. METHODOLOGY

2.1 Review Design and Search Strategy

This study employed a structured integrative review design rather than a formal systematic review or meta-analysis. Searches spanned Web of Science, Scopus, Google Scholar, PubMed/PMC, and publisher platforms (MDPI, Elsevier, Wiley, RSC, Springer). Search strings combined terms such as “smart materials,” “self-healing materials,” “self-healing polymers,” “autonomous healing,” “microcapsule self-healing,” “vascular self-healing,” “intrinsic self-healing,” “dynamic covalent,” “supramolecular self-healing,” “self-healing concrete,” “bacteria-based self-healing,” and “stimuli-responsive hydrogels.” Emphasis was placed on 2010–2026 while retaining seminal pre-2010 studies that established foundational mechanisms.

2.2 Eligibility and Evidence Selection

Priority was given to peer-reviewed reviews and original research reporting mechanisms, healing agents, fabrication routes, healing efficiency or mechanical recovery, conditions, durability, scalability, or application evidence. Non-peer-reviewed, purely speculative, out-of-domain, or non-

English studies were excluded. Citation chaining from seminal works and recent reviews identified influential experimental and sector-specific literature.

2.3 Data Extraction and Synthesis

Extracted data included material class, healing architecture, agent or reversible interaction, activation stimulus, healing time, recovery metric, environmental conditions, repeatability, and application context. Because healing efficiency is defined differently across studies, via fracture toughness, tensile strength, modulus, crack closure, permeability, conductivity or other metrics; reported percentages are presented as representative values only and are not treated as directly equivalent. Synthesis is qualitative and comparative rather than a pooled meta-analysis (Bekas et al., 2016; Geng et al., 2023).

3. SYNTHESIZED FINDINGS AND DISCUSSION

3.1 Extrinsic Capsule-Based Self-Healing Systems

Extrinsic capsule systems remain among the most mature autonomous-repair approaches because they separate the healing agent from the host matrix until damage occurs. A propagating crack ruptures microcapsules; the liquid agent wets crack faces; polymerization or solidification restores the damaged region. Healing chemistry can be optimized independently of the structural matrix, and capsules can be distributed throughout a component (White et al., 2001; Zhu et al., 2015).

The original dicyclopentadiene/Grubbs-catalyst system recovered approximately 75% of fracture toughness (White et al., 2001). Dual-microcapsule epoxy–amine chemistry achieved about 91% average healing efficiency in an optimized formulation (Jin et al., 2012). More recent work shows strong dependence on capsule size and concentration; one study reported up to 68% load recovery while demonstrating that larger capsules can reduce unhealed-matrix mechanical performance (Mousavi et al., 2019). These results underscore the central trade-off between adequate healing-agent delivery and preservation of matrix strength.

The principal limitation of single-use capsules is finite local healing capacity: once ruptured and consumed, a location cannot generally be healed again without another reservoir. Multicore and multicapsule systems distribute this limitation, yet increased loading may introduce defects, reduce matrix continuity, and complicate manufacturing (Zhu et al., 2015; Kontiza & Kartsonakis, 2024). Capsule shell chemistry, permeability, interfacial adhesion, size distribution, core fraction, catalyst stability, and environmental compatibility therefore require simultaneous optimization.

3.2 Vascular and Microvascular Self-Healing Architectures

Vascular systems address finite healing-agent supply by embedding interconnected channels that deliver agents to multiple damage events. Toohey et al. (2007) demonstrated a microvascular network supplying reactive components to damaged regions. Subsequent architectures enable repeated healing via network refill. Early systems achieved multiple healing events; later designs using separate networks for agents and catalysts extended repeatability—reported examples include 16 cycles with ~60% fracture-toughness recovery and >30 cycles with recovery ranging from ~50% to 100%, depending on architecture and test conditions (Toohey et al., 2007; Patrick et al., 2014).

3.3 Intrinsic Self-Healing: Dynamic Covalent and Supramolecular Mechanisms

Intrinsic systems incorporate the healing mechanism directly into the material network, permitting repeated damage and repair without a separate reservoir. Healing is enabled by reversible covalent bonds (disulfide, imine, boronate ester, Diels–Alder, and related dynamic chemistries) or by reversible non-covalent interactions (hydrogen bonding, ionic association, π–π interactions, metal coordination, host–guest recognition) (El Choufi et al., 2022; Zafeer & Bhat, 2024).

A major advantage is repeatability: because healing functionality is distributed throughout the network, repair can occur at multiple locations and over multiple cycles provided network chemistry remains viable. Supramolecular polymers can heal under relatively mild conditions via reversible

intermolecular interactions that enable chain rearrangement. Optically activated supramolecular systems combine stimulus response with repair, while thermoreversible rubber-like systems established the importance of dynamic association for repeated recovery (Burnworth et al., 2011; Cordier et al., 2008).

3.4 Stimuli-Responsive and Multifunctional Self-Healing Systems

Stimuli-responsive systems extend self-healing beyond passive damage-triggered repair by coupling healing to external or environmental cues—heat, light, pH, moisture, electrical or magnetic fields, ionic conditions, and chemical environments (Mrinalini & Prasanthkumar, 2019). The stimulus can accelerate diffusion, activate reversible reactions, soften a matrix temporarily, initiate photochemical healing, or alter network association.

Value is clearest in demanding environments: heat accelerates bond exchange; light provides spatial/temporal control; pH or enzyme responsiveness suits biomedical settings. Dependence on an external stimulus, however, can reduce autonomy if the stimulus is unavailable in service. Genuinely smart materials therefore increasingly combine damage sensing with a locally available stimulus, enabling repair only where and when needed (Jain et al., 2025; Morris et al., 2025).

3.5 Cementitious and Bio-Mediated Self-Healing Materials

Self-healing cementitious materials address a different service problem: sealing cracks, reducing transport of water and aggressive agents, and preserving durability rather than restoring original fracture toughness. Autogenous healing occurs through continued hydration, calcium carbonate precipitation, or related natural processes; autonomous systems employ capsules, mineral agents, polymers, shape-memory elements, or microorganisms (Amran et al., 2022; Meraz et al., 2023; Nguyen et al., 2023).

Bacteria-based self-healing concrete offers a distinct bio-mediated route in which suitable microorganisms promote mineral precipitation—particularly calcium carbonate—within cracks. Performance depends on bacterial viability, nutrient availability, pH, temperature, moisture, crack geometry, and protection of microorganisms from the highly alkaline cementitious environment. Recent reviews emphasize that environmental conditions and crack width strongly influence outcomes, and that laboratory results under ideal conditions should not be interpreted as direct evidence of field reliability (Gruyaert & De Belie, 2023; Meraz et al., 2023).

Sustainability potential lies in extended service life and reduced repeated repair. Durability of the biological component, long-term viability, compatibility with local construction practices, encapsulation/nutrient cost, and performance under African climatic conditions require additional field-scale evidence. For Nigeria, locally available mineral precursors and biologically compatible carriers could provide lower-cost routes to autonomous crack sealing, provided structural and environmental safety are demonstrated.

3.6 Self-Healing Hydrogels for Biomedical Applications

Self-healing hydrogels combine self-repair, injectability, flexibility, biocompatibility, and controlled transport within hydrated polymer networks. Biomedical designs use dynamic covalent and reversible non-covalent associations to restore network integrity after mechanical damage, supporting wound dressings, tissue engineering, drug delivery, biosensing, and regenerative medicine (Bhuvaneswari et al., 2025; Xue et al., 2025).

Stimuli-responsive hydrogels are particularly relevant to wound care because physiological environments supply cues such as pH, temperature, ionic strength, reactive oxygen species, glucose, and enzyme activity that can control drug release, antimicrobial activity, tissue adhesion, and regeneration. Composite hydrogels can respond to pH, temperature, light, and enzyme activity while supporting controlled therapeutic delivery and tissue repair (Ding et al., 2025). Reported mechanical recovery ranges from approximately 40% to >90% depending on network chemistry and conditions, illustrating the same strength–mobility trade-off observed in structural polymers (Khan et al., 2022). High laboratory efficiency alone does not establish clinical suitability; cytocompatibility, degradation behaviour, sterilization stability, reproducibility, and long-term physiological performance must also be demonstrated (Xue et al., 2025).

3.7 Comparative Synthesis of Representative Healing Performance

Table 1 summarizes representative reported performance values. Values are intentionally not ranked because healing efficiency depends on the property measured, damage geometry, healing time, stimulus, and test protocol.

Table 1: Summary of representative reported performance values

System	Material / architecture	Representative recovery	Healing condition	Key strength	Key limitation
Extrinsic capsule	DCPD/Grubbs epoxy	≈75% fracture toughness	Room-temp; seminal	Simple autonomous activation	Finite local agent supply
Extrinsic dual capsule	Epoxy–amine microcapsules	≈91% avg. efficiency	Optimized ratio; RT	High single-cycle recovery	Complexity; finite reservoir
Vascular	Microvascular epoxy	≈60% over 16 cycles	Repeated refill	Repeatable healing	Fabrication complexity
Vascular (adv.)	Advanced architecture	Up to 100% recovery	Architecture-dependent	Many cycles possible	Channel reliability
Cementitious	Microbial / autonomous	Varies with crack/env.	Moisture, nutrients	Crack sealing; durability	Viability; field robustness
Hydrogel	Dynamic covalent / supra.	Tens of % to >90%	Min–days; stimulus-dep.	Soft, injectable, multi-func.	Biocompatibility; strength

Note. Values drawn from White et al. (2001), Jin et al. (2012), Toohey et al. (2007), Patrick et al. (2014), Amran et al. (2022), Meraz et al. (2023), and Xue et al. (2025). Percentages are not directly comparable across material classes.

4. SECTOR-SPECIFIC APPLICATIONS AND TRANSLATION

4.1 Aerospace and Wind-Energy Structures

Aerospace structures demand low mass, high damage tolerance, fatigue resistance, environmental stability, and predictable certification performance. Self-healing composites are attractive because cracks and delamination can initiate below easy visual detection. Capsule-based and vascular approaches can delay damage growth; intrinsic matrices can provide repeated repair. Wind-turbine blades present a related application: large composite structures under cyclic loading with difficult maintenance access. Koralagundi Matt et al. (2015) demonstrated self-healing polymer composites for wind-turbine blade applications. Translation to flight-critical aerospace components, however, requires stringent evidence on fatigue, impact, ageing, repair repeatability, inspection compatibility, and certification.

4.2 Automotive Applications

Automotive uses include structural composites, protective coatings, sealants, interior components, and conductive materials. The principal benefit is reduced degradation from repeated mechanical, thermal, and environmental loading. Intrinsic polymers suit repeated low-level damage; extrinsic systems are useful in coatings or localized composite regions. Commercial implementation depends on cost, high-volume processing compatibility, temperature resistance, recyclability, and compatibility with existing joining and painting processes (El Choufi et al., 2022; Kontiza & Kartsonakis, 2024).

4.3 Construction and Infrastructure

Construction offers one of the strongest arguments for self-healing because inspection and repair of distributed microcracks are expensive and disruptive. Self-healing concrete can reduce water ingress and improve durability via autogenous, mineral, capsule-based, or microbial mechanisms.

Realistic exposure conditions, crack width, sustained loading, wet–dry cycling, and environmental aggressiveness can substantially alter performance; laboratory crack closure should not be the sole indicator of field effectiveness (Gruyaert & De Belie, 2023; Nguyen et al., 2023).

4.4 Biomedical and Healthcare Applications

Biomedical self-healing systems must repair while remaining biocompatible and functionally compatible with living tissue. Self-healing hydrogels support wound dressings, drug delivery, tissue engineering, biosensing, and injectable systems. Stimuli-responsive designs can exploit physiological cues to regulate drug release or healing activity; dynamic networks preserve functionality after deformation (Ding et al., 2025; Xue et al., 2025). Principal translation barriers are biocompatibility, sterilization, biodegradation control, reproducibility, long-term safety, and clinical validation.

4.5 Flexible Electronics and Bioelectronics

Flexible and stretchable electronics require recovery of both mechanical and functional properties after repeated deformation or damage. Self-healing conductive polymers, elastomers, and hydrogels can restore electrical pathways while maintaining flexibility—relevant to wearable sensors, soft interfaces, and bioelectronic devices where mechanical damage can interrupt signal transmission (He et al., 2024; Liu et al., 2024; Mashkoor et al., 2022). Future systems will need simultaneous recovery of mechanical, electrical, optical, and sensing functions rather than structural repair alone.

5. RESEARCH GAPS AND SUSTAINABILITY

5.1 Healing Efficiency versus Mechanical Performance

A central unresolved problem is simultaneous optimization of healing efficiency, strength, toughness, stiffness, environmental resistance, and processing stability. Increased molecular mobility generally improves healing but can reduce mechanical integrity; rigid crosslinked structures restrict healing kinetics (El Choufi et al., 2022; Jain et al., 2025). Future studies should report multidimensional performance rather than a single healing percentage.

5.2 Repeatability and Healing-Agent Depletion

Extrinsic capsule systems are limited by finite agent availability; vascular systems require reliable fluid transport and refillability. Intrinsic systems offer better theoretical repeatability but may suffer from fatigue of dynamic bonds or environmental sensitivity. Meaningful comparison should report number of healing cycles, retained recovery after cycling, and fraction of original functionality restored after repeated damage (Toohey et al., 2007; Patrick et al., 2014).

5.3 Standardization of Evaluation

Cross-literature comparisons remain difficult because studies vary in damage geometry, crack width, healing temperature and duration, stimulus intensity, loading configuration, environmental exposure, and definition of recovery. Future research should report both crack-level metrics and functional recovery, together with standardized damage and healing histories—particularly important when translating laboratory results into structural applications (Bekas et al., 2016; Morris et al., 2025).

5.4 Sustainability and Circular Materials Design

Self-healing can contribute to sustainability by extending service life and reducing replacement and maintenance, but healing chemistry itself must be assessed. Capsule shells, catalysts, nanoparticles, synthetic monomers, and complex processing routes may create environmental burdens. A sustainable design framework should consider embodied energy, toxicity, recyclability, end-of-life processing, local material availability, and life-cycle service extension rather than assuming inherent sustainability (Srivastav et al., 2025).

5.5 Relevance to Nigeria and Africa

For Nigeria and other African economies, the most relevant pathway is not simply to reproduce high-cost laboratory systems developed for advanced industrial markets, but to adapt self-healing principles to locally available materials, manufacturing capabilities, climate conditions, and infrastructure needs. Priorities include mineral-based healing agents for cementitious materials, bio-mediated crack sealing using locally adaptable microorganisms, natural or agricultural-derived polymer components, and low-cost encapsulation routes. Such research should be coupled with local durability testing under high temperature, humidity, wet–dry cycling, and aggressive environmental conditions. Scale-up requires affordable feedstocks, reproducible processing, quality control, skilled personnel, and standards that support local manufacturing and construction adoption.

The Nigerian context also creates opportunity for application-driven research in infrastructure, water systems, transportation, energy, and composite components. A locally grounded agenda could integrate materials characterization, design of experiments, life-cycle assessment, digital modelling, and machine learning to identify formulations that balance performance with cost and availability—aligning SHM research with broader priorities of infrastructure durability, resource efficiency, local manufacturing, and sustainable industrial development.

6. FUTURE PERSPECTIVES

6.1 Artificial Intelligence and Data-Driven Materials Design

AI and machine learning are increasingly relevant because healing performance depends on interacting formulation, processing, microstructural, and environmental variables. Data-driven models can relate polymer composition, crosslink density, capsule concentration, healing temperature, damage history, and kinetics to final performance. The most useful direction is not to replace experiments but to reduce trial-and-error and identify promising combinations for targeted validation (Jain et al., 2025).

6.2 Additive Manufacturing and Architected Healing Networks

Additive manufacturing provides spatial control over composition and architecture. Three-dimensional printing can enable controlled placement of healing reservoirs, vascular networks, dynamic polymer regions, and multifunctional structures—moving design from homogeneous formulations toward architectures tailored to predicted damage locations and load paths (Andreu et al., 2024). Remaining challenges include printability, interlayer bonding, healing-agent compatibility, scale-up, process repeatability, and long-term stability of printed architectures.

6.3 Multifunctional and Autonomous Systems

The next generation is expected to integrate sensing, actuation, repair, and communication. A truly smart material could detect damage, identify severity, trigger a suitable healing mechanism, verify recovery, and communicate condition to a monitoring system. Combining self-healing with structural health monitoring, embedded sensors, conductive networks, and digital models could create materials that participate actively in predictive maintenance rather than merely responding after damage.

6.4 Industrial Scale and Circularity

Industrial adoption will depend on reproducible manufacturing, affordable raw materials, environmental stability, standardized testing, and compatibility with existing production systems. Dynamic covalent networks may be especially important where healing and reprocessing can be combined, potentially reducing material waste (Maes et al., 2025). Claims of circularity must be validated through life-cycle assessment and end-of-life studies. For developing economies, low-cost and locally sourced healing systems deserve particular attention because economic accessibility is part of sustainability.

7. CONCLUSIONS

Smart self-healing materials have progressed from the original capsule-based concept to a broad family of extrinsic, vascular, intrinsic, stimuli-responsive, bio-mediated, and multifunctional systems.

No single architecture is universally superior. Capsule systems offer relatively simple autonomous activation but finite local healing capacity; vascular networks improve repeatability at the expense of architectural complexity; intrinsic systems offer distributed and potentially repeated repair but face the strength–mobility trade-off; stimuli-responsive systems provide additional control but may depend on environmental or external stimuli.

Comparative evidence demonstrates why healing-efficiency percentages must be interpreted within their test context. Representative polymer systems have achieved approximately 75–91% recovery in selected fracture-toughness tests; vascular architectures have demonstrated repeated healing over many cycles; hydrogel systems can achieve high mechanical recovery under selected conditions. Cementitious and bio-mediated systems are better evaluated through crack closure, permeability reduction, durability, and service-life indicators. Across all classes, standardized testing, repeatability, environmental durability, and life-cycle assessment remain critical.

For Nigeria and Africa, the strategic opportunity is to adapt self-healing principles to local materials, infrastructure needs, climate conditions, and manufacturing capacity. Research should prioritize affordable and environmentally responsible healing agents, scalable processing, realistic durability testing, and data-driven optimization. The long-term objective should be materials that do not merely heal damage but sense, respond, recover, and operate sustainably over extended service lives.

REFERENCES

Amran, M., Onaizi, A. M., Fediuk, R., Vatin, N. I., Rashid, R. S. M., Abdelgader, H., & Ozbakkaloglu, T. (2022). Self-healing concrete as a prospective construction material: A review. Materials, 15(9), 3214. https://doi.org/10.3390/ma15093214

Andreu, A., Lee, H., Kang, J., & Yoon, Y.-J. (2024). Self-healing materials for 3D printing. Advanced Functional Materials, 34(30), 2315046. https://doi.org/10.1002/adfm.202315046

Bekas, D. G., Tsirka, K., Baltzis, D., & Paipetis, A. S. (2016). Self-healing materials: A review of advances in materials, evaluation, characterization and monitoring techniques. Composites Part B: Engineering, 87, 92–119. https://doi.org/10.1016/j.compositesb.2015.09.057

Bhuvaneswari, V., Sivalingam, S., Balaji, D., Rajeshkumar, L., & Sathishkumar, M. (2025). A review of self-healing and self-assembling monomers and polymers for biomedical applications integrated with patent landscape analysis. Results in Engineering, 27, 105944. https://doi.org/10.1016/j.rineng.2025.105944

Burnworth, M., Tang, L., Kumpfer, J. R., Duncan, A. J., Beyer, F. L., Fiore, G. L., Rowan, S. J., & Weder, C. (2011). Optically healable supramolecular polymers. Nature, 472(7343), 334–337. https://doi.org/10.1038/nature09963

Cordier, P., Tournilhac, F., Soulié-Ziakovic, C., & Leibler, L. (2008). Self-healing and thermoreversible rubber from supramolecular assembly. Nature, 451(7181), 977–980. https://doi.org/10.1038/nature06669

Ding, K., Liao, M., Wang, Y., & Lu, J. R. (2025). Advances in composite stimuli-responsive hydrogels for wound healing: Mechanisms and applications. Gels, 11(6), 420. https://doi.org/10.3390/gels11060420

El Choufi, N., Mustapha, S., Tehrani B., A., & Grady, B. P. (2022). An overview of self-healable polymers and recent advances in the field. Macromolecular Rapid Communications, 43(17), 2200164. https://doi.org/10.1002/marc.202200164

Gruyaert, E., & De Belie, N. (2023). A review of the efficiency of self-healing concrete technologies for durable and sustainable concrete under realistic conditions. International Materials Reviews, 68(5), 556–603. https://doi.org/10.1080/09506608.2022.2145747

Hager, M. D., Greil, P., Leyens, C., van der Zwaag, S., & Schubert, U. S. (2010). Self-healing materials. Advanced Materials, 22(47), 5424–5430. https://doi.org/10.1002/adma.201003036

He, L., Shi, J., Tian, B., Zhu, H., & Wu, W. (2024). Self-healing materials for flexible and stretchable electronics. Materials Today Physics, 44, 101448. https://doi.org/10.1016/j.mtphys.2024.101448

Jain, A., Goswami, S., & Banerjee, S. (2025). Advances in self-healing polymers: Mechanisms, applications, and future perspectives. Macromolecular Chemistry and Physics, 226(14), e00159. https://doi.org/10.1002/macp.202500159

Jin, H., Mangun, C. L., Stradley, D. S., Moore, J. S., Sottos, N. R., & White, S. R. (2012). Self-healing thermoset using encapsulated epoxy-amine healing chemistry. Polymer, 53(2), 581–587. https://doi.org/10.1016/j.polymer.2011.12.005

Kontiza, A., & Kartsonakis, I. A. (2024). Smart composite materials with self-healing properties: A review on design and applications. Polymers, 16(15), 2115. https://doi.org/10.3390/polym16152115

Koralagundi Matt, A. K., Strong, S., ElGammal, T., & Amano, R. S. (2015). Development of novel self-healing polymer composites for use in wind turbine blades. Journal of Energy Resources Technology, 137(5), 051202. https://doi.org/10.1115/1.4030442

Kosarli, M., Bekas, D. G., Tsirka, K., Baltzis, D., Vaimakis-Tsogkas, D. T., Orfanidis, S., Papavassiliou, G. B., & Paipetis, A. S. (2019). Microcapsule-based self-healing materials: Healing efficiency and toughness reduction vs. capsule size. Composites Part B: Engineering, 171, 78–86. https://doi.org/10.1016/j.compositesb.2019.04.030

Liu, C., Kelley, S. O., & Wang, Z. (2024). Self-healing materials for bioelectronic devices. Advanced Materials, 36(35), 2470278. https://doi.org/10.1002/adma.202470278

Maes, S., Badi, N., Winne, J. M., & Du Prez, F. E. (2025). Taking dynamic covalent chemistry out of the lab and into reprocessable industrial thermosets. Nature Reviews Chemistry, 9, 144–158.

Mashkoor, F., Lee, S. J., Yi, H., Noh, S. M., & Jeong, C. (2022). Self-healing materials for electronics applications. International Journal of Molecular Sciences, 23(2), 622. https://doi.org/10.3390/ijms23020622

Meraz, M. M., Mim, N. J., Mehedi, M. T., Bhattacharya, B., Aftab, M. R., Billah, M. M., & Meraz, M. M. (2023). Self-healing concrete: Fabrication, advancement, and effectiveness for long-term integrity of concrete infrastructures. Alexandria Engineering Journal, 73, 665–694. https://doi.org/10.1016/j.aej.2023.05.008

Morris, G. H. B., Belson, L. N., & Evans, R. C. (2025). Self-healing polymers for optical and photoactive systems. Annual Review of Materials Research, 55, 397–419. https://doi.org/10.1146/annurev-matsci-080423-124646

Mrinalini, M., & Prasanthkumar, S. (2019). Recent advances on stimuli-responsive smart materials and their applications. ChemPlusChem, 84(8), 1103–1121. https://doi.org/10.1002/cplu.201900365

Nguyen, M.-T., Fernandez, C. A., Nassiri, S., Zhang, D., & Rousseau, R. (2023). Toward self-healing concrete infrastructure: Review of experiments and simulations across scales. Chemical Reviews, 123(18), 10838–10876. https://doi.org/10.1021/acs.chemrev.2c00709

Patrick, J. F., Hart, K. R., Krull, B. P., Diesendruck, C. E., Moore, J. S., White, S. R., & Sottos, N. R. (2014). Continuous self-healing life cycle in vascularized structural composites. Advanced Materials, 26(25), 4302–4308. https://doi.org/10.1002/adma.201400248

Rumon, M. M. H., Akib, A. A., Sultana, F., Moniruzzaman, M., Niloy, M. S., Shakil, M. S., & Roy, C. K. (2022). Self-healing hydrogels: Development, biomedical applications, and challenges. Polymers, 14(21), 4539. https://doi.org/10.3390/polym14214539

Song, T., Jiang, B., Li, Y., Ji, Z., Zhou, H., Jiang, D., Seok, I., Murugadoss, V., Wen, N., & Colorado, H. (2021). Self-healing materials: A review of recent developments. ES Materials & Manufacturing, 14, 1–19. https://doi.org/10.30919/esmm5f465

Toohey, K. S., Sottos, N. R., Lewis, J. A., Moore, J. S., & White, S. R. (2007). Self-healing materials with microvascular networks. Nature Materials, 6, 581–585. https://doi.org/10.1038/nmat1934

White, S. R., Sottos, N. R., Geubelle, P. H., Moore, J. S., Kessler, M. R., Sriram, S. R., Brown, E. N., & Viswanathan, S. (2001). Autonomic healing of polymer composites. Nature, 409(6822), 794–797. https://doi.org/10.1038/35057232

Xue, L., An, R., Zhao, J., Qiu, M., Wang, Z., Ren, H., Yu, D., & Zhu, X. (2025). Self-healing hydrogels: Mechanisms and biomedical applications. MedComm, 6(5), e70181. https://doi.org/10.1002/mco2.70181

Zafeer, M. K., & Bhat, K. S. (2024). Chemical approaches for fabrication of self-healing polymers. Discover Applied Sciences, 6, 373. https://doi.org/10.1007/s42452-024-06058-y

Zhu, D. Y., Rong, M. Z., & Zhang, M. Q. (2015). Self-healing polymeric materials based on microencapsulated healing agents: From design to preparation. Progress in Polymer Science, 49–50, 175–220. https://doi.org/10.1016/j.progpolymsci.2015.07.002

TRACK 7 OF 11

Intelligent Systems, Automation and Control Engineering

International Conference on Engineering Innovation for Sustainable Development (ICESID 2026)

Faculty of Engineering, Ahmadu Bello University Zaria · 8–10 September 2026

https://icesid.org

International Conference on Engineering Innovation for Sustainable Development (ICESID 2026)
Faculty of Engineering, Ahmadu Bello University Zaria · 8–10 September 2026

CGAN-AUGMENTED LIGHTWEIGHT CNN ARCHITECTURES WITH COORDINATE ATTENTION FOR MAIZE LEAF DISEASE RECOGNITION

Sani Saleh Saminu[1,*], Musa Idris Shehu[1], Yusuf Ibrahim[1], Sani Abdulwahab[1], Yakubu Abubakar Hassan[1], Emejuo Nichodemus Chibueze[1]

[1]*Ahmadu Bello University, Zaria*

Email: sssaleh@engineering.abu.edu.ng*, Idris.ms@icloud.com, yibrahim@abu.edu.ng, Saniabdulwahab499@gmail.com, yahassan@abu.edu.ng, emejuo.chibueze@narict.gov.ng

***Corresponding author**: Sani Saleh Saminu

DOI: https://doi.org/10.67203/sp.ICESID.2026

ABSTRACT

Deep learning-based plant disease recognition achieves strong benchmark results, but data scarcity and class imbalance consistently limit its reliability when deployed on real field imagery. This study comparatively evaluates four Coordinate Attention-enhanced lightweight CNNs, ShuffleNetV2, MobileNetV3-Small, GhostNet, and EfficientNet-B0, trained with Conditional GAN (cGAN) augmentation on the OSFmaize dataset across four disease categories and five data configurations. Generative quality assessment confirmed acceptable synthetic image quality, with best average FID of 198.57 at epoch 700 and best IS of 3.32 at epoch 1,000. In the primary Real + cGAN configuration, MobileNetV3-Small achieved the highest accuracy at 94.06% with 1.11M parameters, 0.061G FLOPs, 5.10ms inference, and 4.43MB storage, representing the best accuracy-efficiency trade-off among all four models. GhostNet recorded 80.07%, attributed directly to shortcut learning caused by training from scratch without pretrained weights, producing a 19.93 percentage point accuracy drop when real data was added to synthetic-only training. Traditional augmentation outperformed cGAN in all combined training scenarios. Ablation confirmed Coordinate Attention contributes up to 12.24 percentage points accuracy gain. These results provide practical guidance for architecture and augmentation selection in resource-constrained maize disease recognition systems.

Keywords: *Maize leaf disease recognition; Conditional GAN; Lightweight CNN; Coordinate Attention; Data augmentation; MobileNetV3-Small*

1. Introduction

Deep Deep learning has substantially changed how plant diseases are detected and classified, enabling automated diagnostic systems that work directly from digital leaf images without manual feature engineering (Li et al., 2021; Ouhami et al., 2021; Pardede et al., 2020). In precision agriculture, this shift matters practically: early disease identification reduces crop losses, cuts unnecessary pesticide use, and gives farmers actionable information before infections spread across a field. Maize (Zea mays L.) is one of the crops where this need is most acute. It is among the most widely grown cereals globally, with annual production exceeding 1.2 billion tonnes, yet it remains persistently vulnerable to foliar infections that can reduce yields by more than 50% in severe outbreaks (FAOSTAT, 2024; Solaimalai et al., 2020; USDA, 2024). Gray Leaf Spot (GLS), Northern Leaf Blight (NLB), and Northern Leaf Spot (NLS) are the primary culprits, and distinguishing between them accurately from leaf imagery is a non-trivial classification problem given their overlapping visual characteristics (Jasrotia et al., 2023; Langemeier et al., 2017).

Large-capacity architectures such as VGGNet (Simonyan & Zisserman, 2014), ResNet (He et al., 2016), and EfficientNet (Tan & Le, 2019) have demonstrated strong performance on plant disease benchmarks, but their practical utility depends on large, balanced training datasets. In real agricultural settings, assembling such datasets is consistently difficult. Seasonal variation, uneven disease incidence across fields, and inconsistent imaging conditions all produce small, class-imbalanced collections that push well-trained models toward overfitting (Li et al., 2021; Ouhami et al., 2021; Pardede et al., 2020).

Traditional augmentation methods, including rotation, flipping, color jittering, and random cropping, partially offset this by expanding dataset size, but they only introduce geometric and photometric variation. They do not produce new lesion morphologies, novel color gradients, or previously unseen severity patterns (Li et al., 2021). Models trained on traditionally augmented data can still fail to generalize when real field conditions differ from their training distribution.

Generative Adversarial Networks (GANs) address this limitation by learning the underlying distribution of real images and synthesizing new, semantically varied samples (Goodfellow et al., 2014). The Conditional GAN (cGAN; Mirza & Osindero, 2014), which conditions both the generator and discriminator on class labels, enables targeted synthesis of disease-specific leaf images that preserve class-relevant texture and color characteristics. Studies applying GAN-based augmentation to plant disease tasks, including tomato leaf detection (Wu et al., 2020) and corn disease identification (Hu et al., 2020), have reported measurable accuracy gains. However, GAN training for agricultural data introduces its own challenges. Training instability, mode collapse, and the tendency of models to memorize synthetic distributions rather than learn generalizable features are known failure modes that require careful evaluation (Saad et al., 2024; Wani et al., 2025). Systematic comparison of cGAN augmentation across multiple lightweight architectures on maize disease data, with explicit documentation of these failure conditions, remains limited in the literature.

Lightweight CNN architectures have attracted growing research interest for deployment on resource-constrained hardware, where large models are impractical (Chen et al., 2022; Le et al., 2024; Lu et al., 2023). ShuffleNetV2 (Ma et al., 2018), MobileNetV3, GhostNet, and EfficientNet-B0 each represent distinct trade-offs between parameter count, computational cost, and classification accuracy. Direct comparison of these models under identical training conditions provides useful guidance for practitioners who must select an architecture for edge deployment in agricultural settings. A recurring weakness across lightweight models is reduced sensitivity to spatially subtle lesions, since standard architectures apply attention uniformly across feature maps without discriminating between lesion and background regions (Bhujel et al., 2022). Coordinate Attention (Hou et al., 2021; Saminu et al., 2026) addresses this directly by encoding positional information along both horizontal and vertical spatial dimensions into the channel attention mechanism, allowing the model to localize fine-grained disease features without significant added computation. Prior work confirms attention-based improvements in lightweight plant disease classifiers (Bhujel et al., 2022; Ibrahim et al., 2025), but systematic multi-architecture comparisons under the same GAN-augmented training setup remain scarce.

This study addresses these gaps through a targeted problem-solution structure. Four challenges motivate the experimental design:

Limited dataset diversity. Small, imbalanced maize disease datasets cause overfitting and poor generalization across unseen field conditions. Traditional augmentation adds volume but not semantic variety. Solution: A cGAN trained for 1,000 epochs synthesizes class-conditioned maize leaf images for Healthy, GLS, NLB, and NLS categories, expanding both the size and visual diversity of the training set.

Inadequate spatial attention in lightweight models. Standard lightweight CNNs do not selectively attend to lesion regions, reducing their discriminative capacity when disease symptoms are subtle or unevenly distributed. Solution: Coordinate Attention is integrated at the final feature stage of each model, encoding directional spatial context into channel-wise feature recalibration without substantially increasing parameter count (Hou et al., 2021).

Absence of multi-architecture comparison under controlled conditions. Most existing studies evaluate a single model or compare architectures trained on different datasets and protocols, making it difficult to isolate the effect of architectural choice from training setup. Solution: Four lightweight CNNs ShuffleNetV2, MobileNetV3-Small, GhostNet, and EfficientNet-B0 are trained and evaluated under an identical protocol using a 70/15/15 stratified split with seed=42 across five data scenarios.

Deployment feasibility gap. Reporting accuracy alone is insufficient for field deployment decisions. Model size, inference speed, and parameter count must be evaluated alongside accuracy to determine practical suitability. Solution: All models are benchmarked on inference time, FLOPs, parameter count, and storage size to determine practical suitability for edge deployment.

This explicit problem-solution mapping ensures that each architectural and experimental decision addresses a specific, identified limitation rather than being arbitrarily assembled. The study represents a methodologically grounded comparison of cGAN augmentation and attention-enhanced

lightweight CNNs, not an additive combination of techniques.

To systematically evaluate this design, the study is guided by the following research questions:

a) Which lightweight CNN architecture, enhanced with Coordinate Attention, achieves the best accuracy-efficiency trade-off when trained with cGAN-augmented maize disease data?
b) Under what conditions does cGAN augmentation improve classification performance, and when does combining synthetic and real data degrade generalization?
c) Does Coordinate Attention consistently improve classification performance across different lightweight architectures when applied under identical training conditions?

To answer these questions, this paper presents a comparative evaluation of four Coordinate Attention-enhanced lightweight CNNs trained across five data scenarios on the OSFmaize dataset. The experimental design incorporates cGAN-based augmentation with GAN quality evaluation using Fréchet Inception Distance (FID) and Inception Score (IS), and ablation studies isolating the Coordinate Attention contribution.

The main contributions of this work are as follows:

1. Multi-architecture comparison under controlled conditions: A systematic evaluation of ShuffleNetV2, MobileNetV3-Small, GhostNet, and EfficientNet-B0, each enhanced with Coordinate Attention, trained under an identical 70/15/15 stratified protocol across five data scenarios, enabling fair and reproducible architecture comparison.
2. cGAN augmentation analysis with failure documentation: An empirical characterization of cGAN augmentation behavior across five training scenarios, including explicit analysis of shortcut learning failure in architectures trained from scratch without pretrained weights, providing practical guidance for GAN-based augmentation in small agricultural datasets.
3. GAN quality evaluation across training checkpoints: Quantitative FID and IS evaluation at epochs 300, 500, 700, and 1,000, providing transparent evidence for the epoch selection decision used in downstream augmentation and documenting the trade-off between FID-optimal and IS-optimal checkpoints.

The remainder of this paper is organized as follows. Section 2 reviews related work on GAN-based augmentation and attention-enhanced lightweight CNNs for agricultural image classification. Section 3 describes the dataset preparation, cGAN training protocol, classifier architectures, and evaluation setup. Section 4 presents comparative results and ablation studies. Section 5 concludes with findings, limitations, and directions for future work.

2. Literature Review

A. GAN-Based Augmentation for Plant Disease Recognition

Data scarcity and class imbalance are persistent obstacles in agricultural image classification. Standard augmentation techniques such as rotation, flipping, and color jittering expand dataset volume but do not introduce new disease morphologies or lesion patterns. Generative Adversarial Networks, introduced by Goodfellow et al. (2014), address this by training a generator to produce synthetic images that a discriminator cannot reliably distinguish from real ones. The resulting synthetic samples add semantic variety that geometric transforms cannot provide.

For class-conditioned synthesis, the Conditional GAN (Mirza & Osindero, 2014) extends the original GAN by feeding class label information into both the generator and discriminator, allowing targeted generation of disease-specific images. This architecture is particularly suitable for small, imbalanced datasets where certain disease classes have insufficient training examples. Wu et al. (2020) applied DCGAN-based augmentation to tomato leaf disease classification and reported measurable accuracy improvements over models trained without generative augmentation. Mohana et al. (2022) reviewed GAN-based augmentation across multiple agricultural domains and confirmed that synthetic data consistently improves classifier performance when real data is limited, though they noted that image quality and training stability vary considerably across GAN architectures and dataset sizes.

In maize-specific tasks, Hu et al. (2020) demonstrated that GAN-augmented training data improved corn leaf disease identification accuracy by reducing inter-class confusion caused by visually

similar lesion patterns. Cap et al. (2020) introduced LeafGAN, a domain-adapted GAN for plant disease augmentation that achieved lower FID scores than standard cGAN on leaf datasets, confirming that domain-specific generator design improves synthetic image fidelity. Despite these advances, most existing studies evaluate a single GAN architecture on one downstream classifier. Systematic comparison of GAN augmentation behavior across multiple lightweight classifiers under identical training conditions remains absent, leaving practitioners without clear guidance on which architecture combinations generalize reliably.

A further concern with GAN-augmented training is the risk of shortcut learning, where models trained on synthetic-only data learn distributional shortcuts specific to the generator rather than true disease discriminators (Saad et al., 2024). This failure mode is particularly pronounced in architectures trained from scratch without pretrained weights, where the model has no prior visual knowledge to anchor feature learning. Saad et al. (2024) reviewed training challenges in GANs for biomedical image analysis and identified distribution mismatch between synthetic and real data as one of the most common causes of downstream classification degradation. Documenting these failure conditions explicitly is necessary for any study that proposes GAN augmentation as a practical tool.

B. Lightweight CNN Architectures for Agricultural Image Classification

Deploying disease recognition models in field conditions requires architectures that balance accuracy with computational efficiency. Standard deep networks such as VGGNet (Simonyan & Zisserman, 2014) and ResNet (He et al., 2016) deliver strong benchmark performance but carry parameter counts and inference times that are impractical on embedded or mobile hardware. Lightweight CNN architectures address this through structural innovations that reduce computation without sacrificing discriminative capacity.

ShuffleNetV2 (Ma et al., 2018) achieves efficiency through channel splitting and element-wise addition rather than computationally expensive group convolutions, resulting in fast inference and low memory usage. Chen et al. (2021) applied an improved ShuffleNetV2 to apple leaf disease recognition and confirmed that the architecture maintains competitive accuracy under resource constraints. MobileNetV3 builds on depthwise separable convolutions and incorporates hard-swish activations and squeeze-and-excitation blocks to improve accuracy per parameter. Abubakar et al. (2026) demonstrated the effectiveness of MobileNetV2 features compressed with PCA for maize disease recognition, achieving competitive accuracy with substantially reduced feature dimensionality, which reflects the broader utility of MobileNet-family architectures in agricultural classification tasks.

GhostNet reduces redundant feature map computation by generating additional feature maps from cheap linear operations applied to a small set of intrinsic features, cutting FLOPs without proportionally reducing representational capacity. EfficientNet-B0 (Tan & Le, 2019) applies compound scaling across network depth, width, and input resolution simultaneously, producing a model that achieves strong accuracy with fewer parameters than comparably performing architectures. Evangelista et al. (2023) evaluated EfficientNet V2 variants on maize disease classification and reported consistently high accuracy across disease categories, confirming EfficientNet-family models as reliable baselines for this task.

Lu et al. (2023) reviewed lightweight methods for plant disease identification and found that models with fewer than 5M parameters can match or approach the accuracy of larger networks when training data is sufficient and augmentation is applied effectively. Le et al. (2024) reached a similar conclusion using hybrid lightweight architectures for tomato disease detection, noting that inference speed and model size are as important as accuracy for real-world deployment. These findings collectively establish the four architectures used in this study as appropriate and well-motivated choices for comparative evaluation under cGAN-augmented training conditions.

C. ATTENTION MECHANISMS IN LIGHTWEIGHT PLANT DISEASE CLASSIFIERS

Lightweight CNNs process all spatial regions of a feature map with equal weight by default, which limits their ability to focus on diagnostically relevant areas such as lesion boundaries, color

transitions, or specific texture patterns. Attention mechanisms address this by learning to weight feature map regions according to their relevance to the classification task.

Squeeze-and-Excitation networks (Wang et al., 2020) introduced channel-wise attention by globally pooling spatial information and using a small fully connected network to recalibrate channel responses. Efficient Channel Attention (Wang et al., 2020) improved on this by replacing the fully connected layer with a lightweight 1D convolution, reducing parameter overhead while maintaining recalibration quality. Coordinate Attention (Hou et al., 2021) extends the spatial awareness of channel attention by decomposing global pooling into two directional pooling operations along the horizontal and vertical axes separately, encoding precise positional context into the attention weights. This directional encoding allows the model to localize spatially distributed features such as scattered lesions more accurately than standard channel attention, which discards spatial information entirely during pooling.

Bhujel et al. (2022) integrated a lightweight attention mechanism into a CNN for tomato leaf disease classification and reported consistent accuracy gains over the baseline without attention, particularly for visually similar disease classes. Ibrahim et al. (2025) combined depthwise separable convolutions with hybrid attention in EDANet for tomato disease recognition, confirming that attention improves both accuracy and feature discriminability in compact architectures. Rachman et al. (2024) applied attention-enhanced vision transformers to rice disease detection and found that cross-scale attention improved generalization to underrepresented disease classes. Jasrotia et al. (2023) evaluated CNN-based maize disease identification and noted that models lacking spatial attention mechanisms showed reduced performance on classes with fine-grained lesion textures, supporting the rationale for integrating CA into each architecture in this study.

Wang et al. (2020) confirmed through ablation that channel attention mechanisms consistently contribute to accuracy in lightweight CNNs across diverse visual classification tasks, with the contribution being largest when the model backbone has limited depth and therefore limited implicit spatial selectivity. This finding directly motivates applying CA at the final feature stage of each model in this study, where spatial selectivity has the greatest impact on downstream classification.

D. GAN Quality Evaluation: FID and Inception Score

Evaluating the quality of GAN-generated images requires metrics that go beyond visual inspection. Two quantitative measures are standard in the literature: Fréchet Inception Distance (FID) and Inception Score (IS). FID measures the distance between the distribution of real images and generated images in the feature space of a pretrained Inception-v3 network. Lower FID indicates that the synthetic distribution is closer to the real one, reflecting better perceptual realism and structural fidelity (Mohana et al., 2022). IS measures both image quality and class diversity within the generated set: a high IS means individual generated images are recognizable and the full set covers multiple distinct categories (Mohana et al., 2022).

Han et al. (2018) used FID to evaluate GAN-generated brain MRI images for data augmentation and found that lower FID correlated with better downstream classifier performance, establishing FID as a reliable proxy for augmentation utility in medical imaging. Cap et al. (2020) applied IS alongside FID to evaluate LeafGAN outputs on plant disease datasets, finding that IS scores above 2.0 were acceptable for domain-specific agricultural GANs where the total number of classes is small relative to ImageNet. Tang et al. (2019) similarly used FID to select optimal GAN training checkpoints for CT image augmentation, demonstrating that FID-based checkpoint selection is a practical and reproducible evaluation strategy.

In domain-specific datasets with few classes, IS values are expected to be considerably lower than those reported on ImageNet-scale benchmarks, since class diversity is inherently bounded by the number of categories in the dataset (Mohana et al., 2022). This distinction is important for interpreting IS results on the OSFmaize dataset, which contains only four classes. FID and IS together provide complementary evidence: FID captures distributional similarity to real data while IS captures per-image quality and intra-set diversity. When the two metrics favor different training checkpoints, as occurs in this study where FID is lowest at epoch 700 and IS is highest at epoch 1,000, the selection decision requires explicit justification rather than mechanical optimization of a single metric.

Existing work in agricultural GAN augmentation rarely reports both FID and IS across multiple training checkpoints, making it difficult to assess how generative image quality evolves during training and how checkpoint selection affects downstream classifier performance. This study addresses that gap by evaluating both metrics at epochs 300, 500, 700, and 1,000, providing a transparent basis for the augmentation epoch decision used across all five training scenarios.

3. PROPOSED FRAMEWORK

3.1 Overview

This section describes the dataset, preprocessing pipeline, cGAN implementation, classifier architectures, Coordinate Attention integration, and experimental configuration adopted for the comparative evaluation of four lightweight CNNs under cGAN-augmented training conditions for maize leaf disease recognition. The overall workflow integrates synthetic data generation using a Conditional GAN (cGAN) with four independently evaluated CA-enhanced lightweight classifiers to enable a controlled and fair multi-architecture comparison. The general framework is illustrated in Figure 3.

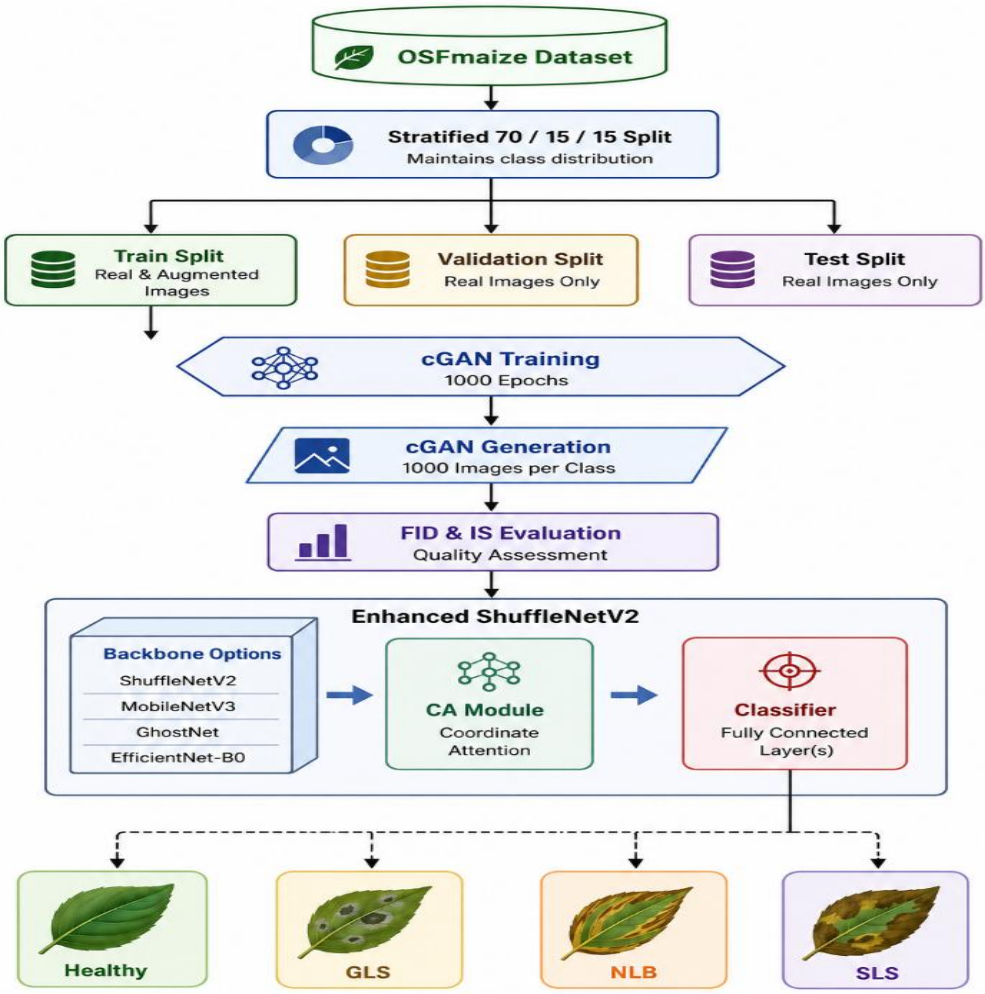

Figure 3: Developed DL Framework

The workflow trains a single cGAN on the training partition of the OSFmaize dataset and uses the generated images across all four classifier training scenarios. By holding the augmentation strategy, dataset split, evaluation protocol, and Coordinate Attention placement constant across all models, any observed performance differences can be attributed directly to architectural characteristics rather than experimental variation.

All experiments were implemented in Python 3.13 with PyTorch 2.10 on a local Ubuntu 24.04 workstation with the following hardware: HP Omen 16 laptop; Intel Core i9 14th-generation processor; 32 GB RAM; NVIDIA GeForce RTX 5070 GPU; CUDA 12.8. GAN training and classifier fine-tuning used the RTX 5070 GPU for acceleration. FID and IS evaluation was performed on CPU due to CUDA sm_120 architecture constraints with the installed PyTorch version, which does not affect metric correctness.

3.2 Dataset and Preprocessing

The dataset used in this study is the publicly available OSFmaize Leaf Disease dataset (https://osf.io/s6ru5/, accessed 17 September 2025). It comprises four classes representing distinct foliar conditions: Healthy, Gray Leaf Spot (GLS), Northern Leaf Blight (NLB), and Northern Leaf Spot (NLS), with a total of 1,902 real images across all classes.

After stratified splitting, the test set contains 286 images (15% of 1,902), with per-class counts proportional to the original class distribution.

Initial inspection revealed notable class imbalance, with Healthy and NLB containing substantially more samples than GLS and NLS. The images also exhibited visible heterogeneity in illumination, leaf orientation, and background clutter, reflecting the conditions of real-field acquisition. These factors can introduce bias into model learning if not addressed through principled dataset handling.

Data split and leakage prevention. The dataset was first partitioned into training (70%), validation (15%), and test (15%) subsets using stratified random sampling with a fixed random seed (seed = 42), prior to any synthetic generation. This three-way stratified split ensures class distribution is preserved across all partitions and that the test set provides an unbiased performance estimate independent of training decisions. The cGAN was trained exclusively on the training subset. Synthetic images were generated after cGAN training convergence and combined solely with the training partition to form the augmented training pool. The validation and test sets remained composed entirely of real, unseen images throughout all experiments. This procedure eliminates data leakage and ensures that all reported metrics reflect genuine generalization to unseen real-world data.

Each class received 1,000 cGAN-generated images. When combined with the real training partition, this produced a balanced augmented training corpus for the Real + cGAN scenario. All images were resized to 128 × 128 × 3 pixels and normalized to the range [−1, 1]. No additional geometric augmentation was applied to the cGAN-generated images, since the generative process inherently introduces morphological diversity across samples.

The five experimental data configurations evaluated in this study are summarized in Table 3.1.

Table 3.1: Summary of the five experimental data configurations. Validation and test sets consist exclusively of real images in all configurations.

Configuration	Training Data	Val.	Test
Real Only	Real train split	Real only	Real only
cGAN Only	cGAN-generated images	Real only	Real only
Real + cGAN	Real train + cGAN images	Real only	Real only
Real + cGAN (no CA)	Real train + cGAN, no CA module	Real only	Real only
Real + TradAug	Real train + traditional augmentation	Real only	Real only

The 'Real + cGAN (no CA)' row represents an architectural ablation under the Real + cGAN data configuration, not an independent data scenario. The training data is identical to Real + cGAN; only the Coordinate Attention module is removed. It is included in this table for completeness but is discussed separately in Section 4.5.

3.3 Interpretation of FID and IS Metrics

Raw Frechet Inception Distance (FID) and Inception Score (IS) were used to quantify the perceptual realism and diversity of cGAN-generated images across training checkpoints. FID measures

the statistical distance between the feature distributions of real and synthetic images in the activation space of a pretrained Inception-V3 network. Lower FID indicates closer alignment with the real data distribution and higher visual fidelity. IS evaluates image quality and class diversity within the synthetic set alone; higher scores indicate more varied and semantically confident outputs.

FID is computed as:

$$FID = \| \mu_r - \mu_g \|^2 + \mathrm{Tr}\left(\Sigma_r + \Sigma_g - 2(\Sigma_r \Sigma_g)^{\frac{1}{2}}\right) \tag{2.1}$$

where u_r, S_r are the mean and covariance of real image features, and u_g, S_g are the corresponding statistics for generated images extracted from the Inception-V3 pool3 layer.

IS is computed as:

$$IS = \exp(\ \mathbb{E}_{x\sim pg}\left[D_{\mathrm{KL}}\left(p(y \mid x) \parallel p(y)\right)\right] \tag{2.2}$$

where p(y|x) is the conditional class distribution predicted by Inception-V3 for a generated image x, and p(y) is the marginal class distribution over all generated images. Higher IS reflects both high individual image confidence and diversity across the generated set.

Since Inception-V3 was pretrained on ImageNet rather than agricultural data, absolute FID and IS values are not directly comparable to benchmarks from natural image datasets. All FID and IS values reported here are used strictly for relative comparison across cGAN training checkpoints under identical evaluation conditions. Before computing FID and IS, all generated and real images at 128 × 128 resolution were resized to 299 × 299 pixels using bilinear interpolation to match the standard Inception-V3 input size, and pixel values were normalized to the range [0, 1] prior to feature extraction.

3.4 Conditional GAN Implementation

The Conditional GAN (cGAN) (Miraz et al., 2024) generates class-specific maize disease images by conditioning both the generator and discriminator on class label information. The generator accepts a 100-dimensional random noise vector concatenated with a learned class label embedding, enabling synthesis of disease-specific leaf textures, colors, and lesion patterns. The discriminator receives real and generated image-label pairs and learns to distinguish genuine samples from synthetic ones, with the class label serving as an additional conditioning signal.

The adversarial objective is:

$$\begin{aligned}\mathcal{L}_{\mathrm{cGAN}} = {} & \mathbb{E}_{(x\ ,y)}[\log D(x \mid y)] \\ & + \mathbb{E}_{(z\ ,y)}\left[\log\left(1 - D\left(G(z \mid y)\right)\right)\right]\end{aligned} \tag{2.3}$$

where x is a real image, y is the class label, z is a noise vector sampled from a prior distribution, G is the generator, and D is the discriminator. The generator minimizes this objective while the discriminator maximizes it, driving the generator toward producing class-consistent images that the discriminator cannot reliably reject.

The full cGAN training configuration is summarized in Table 3.2.

Table 3.2. cGAN training configuration.

Parameter	Setting	Description
Latent dimension	z = 100	Random noise vector input to generator
Batch size	64	Mini-batch per training iteration
Learning rate	0.0002	Adam optimizer (b1 = 0.5, b2 = 0.999)
Epochs	1,000	Total training epochs
Checkpoint epochs	300, 500, 700, 1,000	Epochs at which 1,000 images/class generated
Image size	128 x 128 x 3	Standardized RGB resolution
Optimizer	Adam	Used for both generator and discriminator
Hardware	NVIDIA RTX 5070 (HP Omen 16)	Ubuntu 24.04 local environment

3.5 Lightweight CNN Architectures with Coordinate Attention

Four lightweight CNN architectures were selected for comparative evaluation based on their distinct computational designs and demonstrated performance in resource-constrained classification tasks(Chen et al., 2022; Lu et al., 2023; Le et al., 2024). Each model was enhanced with a Coordinate Attention module inserted at the final convolutional feature stage, and each was independently trained and evaluated across the five data configurations. The classifier head was kept identical across all models: a fully connected layer (256 units) with ReLU activation, Dropout (p = 0.4) for regularization, and a final linear projection to four output classes.

3.4.1 ShuffleNetV2

ShuffleNetV2 (Ma et al., 2021) achieves computational efficiency through channel splitting and element-wise addition rather than group convolutions, which carry higher memory access costs. At each basic block, the input channels are split into two branches. One branch passes through unchanged while the other applies a sequence of 1x1 convolution, 3x3 depthwise convolution, and 1x1 convolution. The outputs are concatenated and shuffled to maintain cross-channel information flow. The variant used in this study is ShuffleNetV2 x1.0, which contains 1.62M parameters and operates at 0.153G FLOPs at 128 x 128 input resolution after CA integration. Pretrained ImageNet weights were loaded from local storage and used for full fine-tuning from epoch 1.

3.4.2 MobileNetV3-Small

MobileNetV3-Small [12] extends the MobileNet family with hard-swish activations, a redesigned last stage, and built-in Squeeze-and-Excitation (SE) blocks within its inverted residual structure. The hard-swish activation approximates the swish function with lower computational cost:

$$\text{h-swish}(x) = \frac{x \cdot \text{ReLU6}(x + 3)}{6} \tag{2.3}$$

The architecture is optimized through neural architecture search for minimal latency on mobile hardware. After CA integration and classifier replacement, the effective parameter count is 1.11M, operating at 0.061G FLOPs. Pretrained ImageNet weights were loaded locally and used for full fine-tuning.

3.4.3 GhostNet

GhostNet reduces feature map redundancy by generating additional feature maps from a small set of intrinsic features using cheap linear operations rather than computing all feature maps through standard convolutions. Given an input feature map X, the Ghost module produces:

$$Y' = \text{Conv}(X), \quad Y'' = \Phi(Y'), \quad Y = \text{concat}(Y', Y'') \tag{2.4}$$

where Y' is the set of intrinsic feature maps produced by a standard convolution, Phi represents the cheap linear transformation, and Y is the full output. GhostNet is implemented in this study using a native PyTorch implementation without the timm library or external pretrained weights, since no publicly available pretrained GhostNet weights matched the exact native configuration. The model is therefore trained from scratch across all experiments. After CA integration, the effective parameter count is 1.17M at 0.135G FLOPs.

3.4.4 EfficientNet-B0

EfficientNet-B0 (Tan et al., 2019) applies compound scaling, simultaneously increasing network depth, width, and input resolution according to a fixed scaling coefficient, to maximize accuracy per unit of computation. The compound scaling rule is:

$$d = \alpha^{\varphi}, \quad w = \beta^{\varphi}, \quad r = \gamma^{\varphi} \quad \text{s.t.} \quad \alpha \cdot \beta^2 \cdot \gamma^2 \approx 2 \tag{2.5}$$

where d, w, and r denote depth, width, and resolution scaling factors respectively, phi is the compound coefficient, and alpha, beta, gamma are constants determined by grid search. After CA integration and classifier replacement, the effective parameter count is 4.49M at 0.416G FLOPs. Pretrained ImageNet weights were loaded locally and used for full fine-tuning.

3.6 Coordinate Attention Integration

Coordinate Attention (CA) (Hou et al., 2021) extends standard channel attention by preserving spatial location information along both the horizontal and vertical axes. CA decomposes global pooling into two directional operations:

$$z_h^c(h) = \frac{1}{W} \sum_{0 \le i < W} x^c(h, i) \tag{2.6}$$

$$z_w^c(w) = \frac{1}{H} \sum_{0 \le j < H} x^c(j, w) \tag{2.7}$$

where x^c is the c-th channel of the input feature map with height H and width W. The two directional descriptors are concatenated and passed through a shared transformation:

$$f = \delta\left(F_1([z^h, z^w])\right) \tag{2.8}$$

where delta is a non-linear activation and F_1 is a 1x1 convolution that reduces channel dimensionality by a reduction ratio r. The resulting embedding is split and projected back to generate attention weights along each spatial direction:

$$g^h = \sigma\left(F_h(f^h)\right), \qquad g^w = \sigma\left(F_w(f^w)\right) \tag{2.9}$$

The final attended output is:

$$y^c(i, j) = x^c(i, j) \cdot g_c^h(i) \cdot g_c^w(j) \tag{2.10}$$

The CA module is inserted at the output of the final convolutional stage in each backbone, immediately before the global average pooling and classifier head, where spatial feature refinement has the greatest effect on downstream classification.

3.7 Experimental Configuration and Training Protocol

All four models were trained using cross-entropy loss with stochastic gradient descent (SGD), learning rate = 0.01, momentum = 0.9, and early stopping with patience = 7 epochs monitored on validation accuracy. Pretrained ImageNet weights were loaded locally for ShuffleNetV2, MobileNetV3-Small, and EfficientNet-B0. GhostNet was initialized randomly and trained from scratch. All experiments used a fixed seed of 42 for stratified splitting and reproducibility. Each model was evaluated on five data configurations as defined in Table 3.1, producing 20 main experimental runs in total. Ablation experiments removing the CA module were conducted for all four models on the Real + cGAN configuration to isolate the CA contribution.

All 20 main experimental runs and ablation experiments represent single training runs without repeated trials. Given the small dataset size (1,902 real images), results are sensitive to random initialization and split variance. Small percentage-point differences, particularly the 0.70 percentage point CA ablation result for ShuffleNetV2, should be interpreted with caution as they may not be distinguishable from random variation without repeated trials with variance reporting.

The Real + TradAug configuration applied the following augmentation pipeline to the real training images: random horizontal flip (p = 0.5), random vertical flip (p = 0.5), random rotation within ±30 degrees, color jitter with brightness = 0.2, contrast = 0.2, saturation = 0.2, and hue = 0.1, and random resized crop to 128 × 128 with scale range [0.8, 1.0]. No synthetic images were used in this configuration.

3.8 Evaluation Criteria

Model performance was evaluated using accuracy, precision, recall, and F1-score computed on the real test set as in (Saminu et al., 2026; Bawa et al., 2026). Let TP, FP, TN, and FN denote true positives, false positives, true negatives, and false negatives respectively:

$$\text{Accuracy} = \frac{TP + TN}{TP + TN + FP + FN} \tag{2.11}$$

$$\text{Precision} = \frac{TP}{TP + FP} \tag{2.12}$$

$$\text{Recall} = \frac{TP}{TP + FN} \tag{2.13}$$

$$\text{F1-Score} = \frac{2 \times \text{Precision} \times \text{Recall}}{\text{Precision} + \text{Recall}}. \tag{2.14}$$

Weighted-average metrics were used across all four classes to account for class distribution differences in the test set. GAN image quality was assessed using FID and IS as described in Section 3.3. Inference time was measured as the average time per image on the RTX 5070 GPU across the full test set.

4. RESULTS AND ANALYSIS

This section presents and discusses the experimental results across all five data configurations for the four CA-enhanced lightweight CNN architectures. Results are organized as follows: cGAN training and image quality evaluation, main classification results, ablation analysis of Coordinate Attention, augmentation strategy comparison, convergence analysis, per-class classification analysis, and efficiency benchmarking.

4.1 cGAN Training Quality Evaluation

Figure 4.1 shows the cGAN training loss curve over 1,000 epochs. The discriminator loss stabilized near zero early in training and remained consistently low throughout, indicating that the discriminator learned a reliable decision boundary quickly. The generator loss increased gradually over training epochs, reflecting the expected adversarial dynamic where a stronger discriminator forces the generator to produce progressively harder-to-reject samples. No mode collapse was observed across the 1,000-epoch run.

Table 4.1 summarizes the FID and IS scores computed at epochs 300, 500, 700, and 1,000 across all four disease classes.

Table 4.1: FID and IS evaluation across cGAN training checkpoints

.

Epoch	Health FID	GLS FID	NLB FID	NLS FID	Avg FID	Combined IS
300	171.23	241.84	257.66	225.24	223.99	2.98
500	144.58	223.26	245.76	210.57	206.04	3.06
700	142.55	213.53	233.48	204.73	198.57	3.28
1,000	129.83	228.31	238.33	207.66	201.03	3.32

FID improved consistently from epoch 300 (avg 223.99) to epoch 700 (avg 198.57), then rose slightly at epoch 1,000 (avg 201.03). IS increased monotonically across all checkpoints, reaching its highest value of 3.32 at epoch 1,000. This creates a trade-off: epoch 700 produces synthetic images with better distributional similarity to real data, while epoch 1,000 produces images with higher individual quality and intra-set diversity.

The Healthy class consistently achieved the lowest FID across all checkpoints, reaching 129.83 at epoch 1,000. This is expected given that healthy leaf images are visually more uniform than diseased ones. GLS, NLB, and NLS showed higher FID values throughout, reflecting the greater visual

complexity and inter-class similarity of disease lesion patterns. All IS values above 2.0 across all epochs are consistent with the reference threshold reported by Cap et al. [21] for domain-specific agricultural GANs, though this threshold was derived from a different dataset and serves here as a heuristic reference point rather than a universally established benchmark.

Epoch 1,000 was selected for downstream augmentation experiments because it produced the highest IS (3.32), indicating superior image diversity, and its FID (201.03) remained comparable to epoch 700 (198.57), with a difference of only 2.46 points. Given the small FID gap and the meaningful IS gain, epoch 1,000 represents the better overall trade-off for augmenting a small, imbalanced dataset where intra-class diversity directly affects classifier generalization.

It should be noted that the downstream classifier accuracy using epoch-700-generated images was not separately evaluated. The epoch 1,000 selection is based on the FID/IS trade-off analysis above rather than a direct empirical comparison of downstream classification performance between the two checkpoints.

4.2 Main Classification Results: Real + cGAN ep1000

Table 4.2 presents the main classification results for all four models trained on the Real + cGAN ep1000 configuration. Figure 4.2 shows the model comparison across accuracy, F1-score, inference time, and parameter count.

Table 4.2: Main classification results: Real + cGAN ep1000 with Coordinate Attention

Model	Acc (%)	Prec (%)	Rec (%)	F1 (%)	Params (M)	FLOPs (G)	Inf (ms)	Size (MB)
MobileNetV3-Small	94.06	94.68	94.06	93.99	1.11	0.061	5.10	4.43
ShuffleNetV2	93.36	93.45	93.36	93.35	1.62	0.153	9.17	6.46
EfficientNet-B0	88.81	89.15	88.81	88.87	4.49	0.416	30.83	17.96
GhostNet	80.07	80.98	80.07	79.89	1.17	0.135	15.86	4.66

MobileNetV3-Small achieved the best overall result at 94.06% accuracy and 93.99% F1-score, with the smallest parameter count (1.11M), lowest FLOPs (0.061G), fastest inference (5.10ms), and second-smallest model size (4.43MB). ShuffleNetV2 followed closely at 93.36% accuracy with a 9.17ms inference time and 1.62M parameters. The 0.70 percentage point accuracy gap between the two is small, but MobileNetV3-Small's inference speed advantage (5.10ms vs 9.17ms) is practically significant for real-time field applications.

EfficientNet-B0 achieved 88.81% accuracy despite having the largest parameter count (4.49M), highest FLOPs (0.416G), and slowest inference time (30.83ms) among the four models. Its larger capacity did not translate to better performance under cGAN-augmented training on this dataset size, suggesting that the additional model complexity was not justified by the available training data. GhostNet recorded the lowest accuracy at 80.07%, a result directly explained by its training-from-scratch condition, discussed further in Section 4.4.

4.3 Results Across All Five Data Scenarios

Table 4.3 presents the complete accuracy results across all five configurations for all four models.

Table 4.3: Classification accuracy (%) across all five data configurations

Model	Real Only	cGAN Only	Real + cGAN	Real + cGAN (no CA)	Real + TradAug
MobileNetV3-Small	93.01	99.83	94.06	81.82	98.60
ShuffleNetV2	32.87	99.67	93.36	94.06	98.25
EfficientNet-B0	95.45	99.83	88.81	85.66	97.20
GhostNet	91.61	100.00	80.07	74.83	96.15

Several patterns emerge across scenarios. All four models achieved near-perfect or perfect accuracy under cGAN-only training (99.67% to 100.00%). This result does not reflect genuine generalization. When trained on synthetic data alone and tested on real images, the high accuracy indicates the models learned the synthetic data distribution effectively, but the real test set happened to be classifiable from features the generator had already encoded. The collapse in performance when real data is added in the Real + cGAN scenario, particularly for GhostNet (100.00% to 80.07%), confirms that synthetic-only accuracy does not predict real-world generalization.

Traditional augmentation outperformed cGAN augmentation in the Real + Aug comparison for all four models. MobileNetV3-Small reached 98.60% with TradAug versus 94.06% with cGAN. ShuffleNetV2 reached 98.25% with TradAug versus 93.36% with cGAN. Geometric and photometric augmentation of real images produces more in-distribution training samples than GAN-synthesized data, which can introduce distributional artifacts that partially conflict with real image statistics (Wu et al., 2020).

ShuffleNetV2 recorded only 32.87% accuracy in the Real Only scenario. The Real Only training set contains only 1,331 images split across four classes after stratified partitioning. ShuffleNetV2's channel-split architecture appears particularly sensitive to small dataset size without augmentation. The convergence analysis for the Real Only run indicates the model stopped early, suggesting it did not have sufficient data to learn stable class boundaries before convergence criteria were triggered; however, no dedicated training curve for this specific scenario is reported here, and this explanation should be treated as inferred rather than directly observed. The addition of 4,000 cGAN-generated images in the Real + cGAN scenario resolved this, confirming that ShuffleNetV2 requires a minimum data volume to function effectively.

4.4 GhostNet Shortcut Learning Analysis

GhostNet's result in the cGAN-only scenario warrants specific attention. A perfect 100.00% accuracy on the real test set when trained exclusively on synthetic data is not a sign of a strong model. It indicates shortcut learning: the model memorized the cGAN output distribution so effectively that the features it learned aligned with the real test set by coincidence rather than genuine disease discrimination.

When real images were added in the Real + cGAN configuration, accuracy dropped to 80.07%, a 19.93 percentage point decline. Adding real images introduced a second, conflicting distribution that the model could not reconcile without pretrained weights. The other three models, all initialized from ImageNet weights, showed no such collapse. MobileNetV3-Small, ShuffleNetV2, and EfficientNet-B0 all performed stably when moving from cGAN-only to Real + cGAN training. The contrast confirms that pretrained initialization is a necessary condition for stable generalization under combined real and synthetic training on small agricultural datasets.

The GhostNet confusion matrix (Figure 4.3b) shows the clearest evidence of this failure: 31 of 79 GLS samples were misclassified as NLB, and 12 of 75 NLB samples were misclassified as GLS. These two classes share streak-like lesion textures, and without pretrained low-level feature representations, GhostNet could not learn sufficiently discriminative boundaries between them from the

combined dataset.

A methodological limitation of this comparison should be acknowledged: GhostNet was trained from scratch due to the absence of publicly available pretrained weights compatible with the native PyTorch implementation used, while ShuffleNetV2, MobileNetV3-Small, and EfficientNet-B0 were initialized from ImageNet weights. This pretraining difference is an uncontrolled variable in the multi-architecture comparison. GhostNet's lower performance should therefore be interpreted as initialization-dependent rather than a property of the Ghost module architecture in isolation. A fairer architectural comparison would require pretrained GhostNet weights, which are available via timm for some configurations and should be explored in future work.

4.5 Coordinate Attention Ablation

Table 4.4 presents the ablation results comparing each model with and without the Coordinate Attention module on the Real + cGAN ep1000 configuration.

.

Table 4.4: Coordinate Attention ablation results: Real + cGAN ep1000

Model	With CA (%)	Without CA (%)	CA Gain (pp)
MobileNetV3-Small	94.06	81.82	+12.24
GhostNet	80.07	74.83	+5.24
EfficientNet-B0	88.81	85.66	+3.15
ShuffleNetV2	93.36	94.06	-0.70

Overall, Coordinate Attention produced consistent accuracy gains for three of the four models. The largest gain was in MobileNetV3-Small, where removing CA caused a 12.24 percentage point drop from 94.06% to 81.82%. MobileNetV3-Small's built-in SE blocks operate on global channel statistics and discard spatial position information. CA's directional pooling recovers this spatial context, allowing the model to attend to localized lesion regions rather than treating all spatial positions equally. The combination of SE and CA in MobileNetV3-Small thus provides complementary rather than redundant attention.

GhostNet gained 5.24 percentage points with CA, and EfficientNet-B0 gained 3.15 points. Both results confirm that directional spatial attention improves lesion localization across architectures with different internal structures. ShuffleNetV2 showed a marginal 0.70 percentage point decrease with CA compared to without. The channel-shuffle operation in ShuffleNetV2 already promotes cross-channel information mixing, which may partially substitute for the recalibration that CA provides in architectures without such mixing

4.6 Convergence Analysis

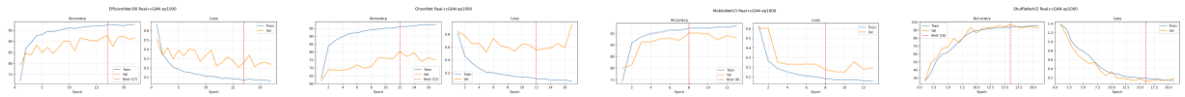

Figures 4.5 through 4.8 show the training and validation accuracy and loss curves for each model under the Real + cGAN ep1000 configuration. MobileNetV3-Small (Figure 4.7) converged fastest, reaching its best validation accuracy of 95% at epoch 8 before early stopping triggered at epoch 13. Both train and validation loss decreased smoothly and in close alignment, with no sign of overfitting.

ShuffleNetV2 (Figure 4.8) showed a longer convergence trajectory, reaching its best validation accuracy at epoch 16 out of 21 total epochs. The training and validation curves tracked closely throughout, with both loss curves descending steadily. EfficientNet-B0 (Figure 4.5) reached its best validation accuracy at epoch 17, with training accuracy exceeding 97% while validation accuracy stabilized around 91-93%. The visible gap between training and validation accuracy from epoch 10 onward suggests mild overfitting, attributable to EfficientNet-B0's larger capacity relative to the effective training set size.

GhostNet (Figure 4.6) displayed the most unstable convergence pattern. Validation accuracy peaked at 80% at epoch 12, after which validation loss began rising sharply while training loss continued to decrease. This divergence between training and validation loss is the signature of overfitting, directly attributable to the absence of pretrained weights. Without ImageNet initialization, GhostNet must learn feature representations entirely from the training data, and the distribution mismatch between real and synthetic images creates optimization instability that pretrained models avoid.

4.7 Per-Class Classification Analysis

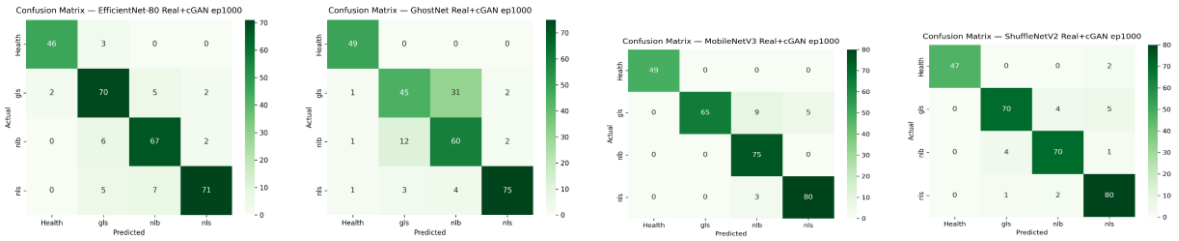

Figures 4.3a through 4.3d show the confusion matrices for all four models on the Real + cGAN ep1000 test set. MobileNetV3-Small (Figure 4.3c) produced the cleanest classification pattern. It correctly classified all 49 Healthy samples, all 75 NLB samples, and 80 of 83 NLS samples. The only notable errors were 9 GLS samples misclassified as NLB and 5 GLS samples misclassified as NLS, out of 79 total GLS samples. GLS was the only class where the model showed consistent confusion, expected given that GLS lesion textures share angular streak characteristics with NLB at certain disease stages.

ShuffleNetV2 (Figure 4.3d) correctly classified 47 of 49 Healthy samples, 70 of 79 GLS samples, 70 of 75 NLB samples, and 80 of 83 NLS samples. Errors were distributed relatively evenly across classes, with no single class dominating the misclassification pattern. EfficientNet-B0 (Figure 4.3a) correctly classified 46 of 49 Healthy samples and 71 of 83 NLS samples. Its GLS-NLB misclassifications (11 total) are comparable to MobileNetV3-Small (14 total), and its lower overall accuracy relative to the other pretrained models is distributed across multiple class boundaries rather than concentrated at a single pair.

GhostNet (Figure 4.3b) showed the highest concentration of errors at the GLS-NLB boundary. Thirty-one of 79 GLS samples were predicted as NLB, representing a 39.2% error rate for that class. This single failure accounts for a large portion of GhostNet's overall accuracy deficit and confirms that the GLS-NLB boundary is the primary point of failure for models without stable pretrained feature representations.

4.8 Efficiency Analysis

Table 4.5 summarizes the efficiency profile of all four models under the Real + cGAN ep1000 configuration

.

Table 4.5: Model efficiency comparison: Real + cGAN ep1000 with Coordinate Attention.

Model	Params (M)	FLOPs (G)	Inf (ms)	Size (MB)	Acc (%)
MobileNetV3-Small	1.11	0.061	5.10	4.43	94.06
GhostNet	1.17	0.135	15.86	4.66	80.07
ShuffleNetV2	1.62	0.153	9.17	6.46	93.36
EfficientNet-B0	4.49	0.416	30.83	17.96	88.81

MobileNetV3-Small achieves the best accuracy-efficiency trade-off across all four metrics simultaneously. Its FLOPs of 0.061G are 2.2 times lower than GhostNet (0.135G), 2.5 times lower than ShuffleNetV2 (0.153G), and 6.8 times lower than EfficientNet-B0 (0.416G). Its inference time of 5.10ms is the fastest in the group and its 4.43MB storage footprint is the smallest. EfficientNet-B0's 4.49M parameters and 17.96MB storage size make it the least suitable for edge deployment, and its 30.83ms inference time is six times slower than MobileNetV3-Small while delivering 5.25 percentage points lower accuracy in this scenario.

5. CONCLUSION

This study comparatively evaluated four Coordinate Attention-enhanced lightweight CNNs under cGAN augmentation for maize leaf disease recognition. MobileNetV3-Small achieved the best result at 94.06% accuracy with 1.11M parameters, 0.061G FLOPs, and 5.10ms inference, making it the most suitable architecture for resource-constrained deployment. GhostNet's performance collapsed from 100.00% under synthetic-only training to 80.07% when real data was added, confirming that pretrained initialization is necessary for stable generalization under combined real and synthetic training. Traditional augmentation outperformed cGAN in all combined scenarios, establishing that synthetic generation is most valuable when real data is severely limited. Ablation confirmed Coordinate Attention contributes consistent gains across three of four architectures, with the largest improvement of 12.24 percentage points in MobileNetV3-Small, where CA's directional spatial encoding complements the model's built-in global channel attention. The primary finding is that no single architecture dominates across all criteria: MobileNetV3-Small leads on accuracy and efficiency, while ShuffleNetV2 offers competitive accuracy at moderate cost. Future work will evaluate WGAN-GP and StyleGAN2-ADA as alternative augmentation strategies, test robustness on UAV-captured field imagery, and explore structured pruning of MobileNetV3-Small for low-power edge deployment.

Acknowledgements

The authors thank the Department of Computer Engineering, Ahmadu Bello University, Zaria, Nigeria.

REFERENCES

Solaimalai, A., Anantharaju, P., Irulandi, S., & Theradimani, M. (2020). *Maize crop: Improvement, production, protection and post-harvest technology*. CRC Press.

FAOSTAT. (2024). *Crops processed*. Food and Agriculture Organization. https://www.fao.org/faostat/

USDA. (2024). *Corn and other feed grains*. Economic Research Service. https://www.ers.usda.gov/topics/crops/corn-and-other-feed-grains/

Langemeier, C. B., Robertson, A. E., Wang, D., Jackson-Ziems, T. A., & Kruger, G. R. (2017). Factors affecting the development and severity of Goss's wilt of corn. *Plant Disease, 101*(1), 54–61.

Sharma, S., Kumar, V., & Sood, S. (2023). Pest detection using random forest. *Proceedings of the International Conference on Innovative Computing and Communications and Automation of India (ICICAT)*, 1–8.

Khirade, S. D., & Patil, A. B. (2015). Plant disease detection using image processing. *Proceedings of the International Conference on Computing Communication Control and Automation (ICCCCA)*, 768–771.

Pardede, H. F., Suryawati, E., Zilvan, V., Ramdan, A., Heryana, A., & Kusumo, R. B. S. (2020). Machine learning based plant diseases detection: A review. *Proceedings of the International Conference on Radar, Antenna, Microwave, Electronics, and Telecommunications (ICRAMET)*, 212–217.

Li, L., Zhang, S., & Wang, B. (2021). Plant disease detection and classification by deep learning: A review. *IEEE Access*, *9*, 56683–56698.

Ouhami, M., Hafiane, A., Es-Saady, Y., El Hajji, M., & Canals, R. (2021). Computer vision, IoT and data fusion for crop disease detection using machine learning. *Remote Sensing*, *13*(13), Article 2486.

Simonyan, K., & Zisserman, A. (2014). *Very deep convolutional networks for large-scale image recognition*. arXiv. https://arxiv.org/abs/1409.1556

He, K., Zhang, X., Ren, S., & Sun, J. (2016). Deep residual learning for image recognition. *Proceedings of the IEEE Conference on Computer Vision and Pattern Recognition (CVPR)*, 770–778.

Tan, M., & Le, Q. (2019). EfficientNet: Rethinking model scaling for convolutional neural networks. *Proceedings of the 36th International Conference on Machine Learning (ICML)*, 6105–6114.

Paymode, P., & Malode, V. (2022). Transfer learning for multi-crop leaf disease classification using VGG. *Artificial Intelligence in Agriculture*, *6*, 23–33.

Ullah, N., Khan, J. A., Alharbi, L. A., Raza, A., Khan, W., & Ahmad, I. (2023). An effective approach for plant leaf diseases classification based on a novel DeepPlantNet deep learning model. *Frontiers in Plant Science*, *14*, Article 1079366.

Tiwari, V., Joshi, R. C., & Dutta, M. K. (2021). Dense convolutional neural network based multiclass plant disease detection and classification using leaf images. *Ecological Informatics*, *63*, Article 101289.

Goodfellow, I., Pouget-Abadie, J., Mirza, M., Xu, B., Warde-Farley, D., Ozair, S., Courville, A., & Bengio, Y. (2014). Generative adversarial nets. *Proceedings of the Advances in Neural Information Processing Systems (NeurIPS)*, 2672–2680.

Mirza, M., & Osindero, S. (2014). *Conditional generative adversarial nets*. arXiv. https://arxiv.org/abs/1411.1784

Odena, A., Olah, C., & Shlens, J. (2017). Conditional image synthesis with auxiliary classifier GANs. *Proceedings of the 34th International Conference on Machine Learning (ICML)*, 2642–2651.

Arjovsky, M., Chintala, S., & Bottou, L. (2017). Wasserstein GAN. *Proceedings of the 34th International Conference on Machine Learning (ICML)*, 214–223.

Han, C., Murao, K., Noguchi, T., Kawata, Y., Uchiyama, F., Rundo, L., Nakayama, H., & Hayashi, H. (2018). GAN-based synthetic brain MR image generation. *Proceedings of the IEEE International Symposium on Biomedical Imaging (ISBI)*, 734–738.

Cap, Q. H., Uga, H., Kagiwada, S., & Iyatomi, H. (2020). *LeafGAN: An effective data augmentation method for practical plant disease diagnosis*. arXiv. https://arxiv.org/abs/2002.10100

Tang, Y., Tang, Y., Zhu, Y., Summers, R. M., & Xiao, J. (2019). CT-realistic data augmentation using generative adversarial network for robust lymph node segmentation. *Proceedings of SPIE Medical Imaging*, Article 109503W.

Chen, Y., Wen, C., & Wen, C. (2022). DFCANet: A novel lightweight convolutional neural network model for corn disease identification. *Agriculture*, *12*(12), Article 2047.

Lu, J., Tan, L., & Jiang, H. (2023). Lightweight method for plant disease identification using deep learning. *Intelligent Automation and Soft Computing*, *37*, 525–544.

Le, T., Nguyen, T., Nguyen, B., & Tran, T. (2024). Tomato disease detection with lightweight recurrent and convolutional neural network models. *Frontiers in Sustainable Food Systems*, *5*, Article 807011.

Yang, X., Gao, Z., Li, H., Li, Z., Zhao, F., Wu, X., & Zhu, Y. (2024). A convolutional neural network and transformer framework for leaf disease and severity identification. *Scientific Reports*, *14*, Article 3023.

Wu, Q., Chen, Y., & Meng, J. (2020). DCGAN-based data augmentation for tomato leaf disease identification. *IEEE Access*, *8*, 98727–98739.

Ahmed, M., & Ahmed, A. (2023). Palm tree disease detection and classification using residual network and transfer learning. *PLOS ONE*, *18*(3), Article e0283250.

Mohana, R. M., Reddy, C. V. R., Madhavi, K., Supreethi, K. P., Kora, P., Thankachan, B., & Pavithra, L. (2022). *Generative adversarial networks and its applications in the biomedical image analysis and remote sensing image analysis: A review*. arXiv. https://arxiv.org/abs/2204.04707

Ma, Y., Zhang, Z., Kang, J., & Özdoğan, M. (2021). Corn yield prediction and uncertainty analysis based on remotely sensed variables using a Bayesian neural network approach. *Computers and Electronics in Agriculture*, *187*, Article 106314.

Hou, Q., Zhou, D., & Feng, J. (2021). Coordinate attention for efficient mobile network design. *Proceedings of the IEEE/CVF Conference on Computer Vision and Pattern Recognition (CVPR)*, 13713–13722.

Wang, Q., Wu, B., Zhu, P., Li, P., Zuo, W., & Hu, Q. (2020). ECA-Net: Efficient channel attention for deep convolutional neural networks. *Proceedings of the IEEE/CVF Conference on Computer Vision and Pattern Recognition (CVPR)*, 11534–11542.

Ma, N., Zhang, X., Zheng, H.-T., & Sun, J. (2018). ShuffleNet V2: Practical guidelines for efficient CNN architecture design. *Proceedings of the European Conference on Computer Vision (ECCV)*, 116–131.

Chen, C., Zhu, X., & Liu, C. (2021). Apple leaf disease recognition based on improved ShuffleNet V2. *Proceedings of the International Conference on Culture-oriented Science and Technology (CTISC)*, 276–282.

Bari, B. S., Islam, M. N., Rashid, M., Hasan, M. J., Razman, M. A. M., Musa, R. M., Ab Nasir, A. F., & Majeed, A. P. P. A. (2021). A real-time approach of diagnosing rice leaf disease using deep learning-based faster R-CNN. *PeerJ Computer Science*, *7*, Article e432.

Bhujel, A., Kim, N.-E., Arulmozhi, E., Basak, J. K., & Kim, H.-T. (2022). A lightweight attention-based convolutional neural network for tomato leaf disease classification. *Agriculture*, *12*(2), Article 228.

Chen, Y., Jiang, H., Li, C., Jia, X., & Ghamisi, P. (2016). Deep feature extraction and classification of hyperspectral images based on convolutional neural networks. *IEEE Transactions on Geoscience and Remote Sensing*, *54*(10), 6232–6251.

Murray, N., & Perronnin, F. (2014). Generalized max pooling. *Proceedings of the IEEE Conference on Computer Vision and Pattern Recognition (CVPR)*, 2473–2480.

Niu, B., Wen, W., Ren, W., Zhang, X., Yang, L., Wang, S., Zhang, K., Cao, X., & Shen, H. (2020). Single image super-resolution via a holistic attention network. *Proceedings of the European Conference on Computer Vision (ECCV)*, 191–207.

Ouyang, D., He, S., Zhang, G., Luo, M., Guo, H., Zhan, J., & Huang, Z. (2023). Efficient multi-scale attention module with cross-spatial learning. *Proceedings of the IEEE International Conference on Acoustics, Speech and Signal Processing (ICASSP)*, 1–5.

Hu, R., Hou, J., Liu, J., & Liu, L. (2020). Corn leaf disease identification based on transfer learning and data augmentation. *Proceedings of the International Conference on Computer Science and Systems Engineering (ICCSSE)*, 1–6.

Evangelista, I., Flores, N., Zafra, R., & Culaba, I. (2023). Zea mays (corn) multi-disease classification using EfficientNet V2 variants. *Proceedings of the IEEE Region 10 Symposium (TENSYMP)*, 1–5.

Atila, Ü., Uçar, M., Akyol, K., & Uçar, E. (2021). Plant leaf disease classification using EfficientNet deep learning model. *Ecological Informatics*, *61*, Article 101182.

Iandola, F., Moskewicz, M., Karayev, S., Girshick, R., Darrell, T., & Keutzer, K. (2014). *DenseNet: Implementing efficient ConvNet descriptor pyramids*. arXiv. https://arxiv.org/abs/1404.1869

Zhao, Y., Chen, X., Guo, M., Wang, H., & Wang, H. (2021). SEV-Net: Residual network embedded with attention mechanism for plant disease severity detection. *Concurrency and Computation: Practice and Experience*, *33*(20), Article e6161.

Yang, W., Zheng, Y., Wu, Y., & Li, Y. (2022). Few-shot unsupervised domain adaptation via meta learning. *Proceedings of the IEEE International Conference on Multimedia and Expo (ICME)*, 1–6.

Singh, S. R., & Sanodiya, R. K. (2023). A zero-shot transfer learning framework for plant leaf disease classification. *IEEE Access*, *11*, 143861–143880.

Wu, X., Zhan, C., Lai, Y.-K., Cheng, M.-M., & Yang, J. (2023). Unsupervised domain adaptation for plant disease recognition in the wild. *Plant Phenomics*, *5*, Article 0010.

Li, Y., & Chao, X. (2021). Semi-supervised few-shot learning approach for plant diseases recognition. *Plant Methods*, *17*(1), Article 1.

Ibrahim, Y., Momoh, M. O., Shobowale, K. O., Abubakar, Z. M., & Yahaya, B. (2025). EDANet: A novel architecture combining depthwise separable convolutions and hybrid attention for efficient tomato disease recognition. *Journal of Computing Theories and Applications*, *3*(2), 160–170.

Rachman, R. K., Setiadi, D. R. I. M., Susanto, A., Nugroho, K., & Islam, H. M. M. (2024). Enhanced vision transformer and transfer learning approach to improve rice disease recognition. *Journal of Computing Theories and Applications*, *1*(4), 446–460.

Jasrotia, S., Yadav, J., Rajpal, N., Arora, M., & Chaudhary, J. (2023). Convolutional neural network based maize plant disease identification. *Procedia Computer Science*, *218*, 1712–1721.

Saad, M. M., O'Reilly, R., & Rehmani, M. H. (2024). A survey on training challenges in generative adversarial networks for biomedical image analysis. *Artificial Intelligence Review*, *57*, Article 19. https://doi.org/10.1007/s10462-023-10624-y

Wani, M. A., Sultan, B., Ali, S., & Sofi, M. A. (2025). Generative adversarial networks in image steganography. In *Advances in deep learning: Vol. 2. Studies in big data* (Vol. 12). Springer. https://doi.org/10.1007/978-981-96-3498-9_5

Abubakar, M., Ibrahim, Y., Ajayi, O. O., & Saminu, S. S. (2026). A lightweight maize leaf disease recognition using PCA-compressed MobileNetV2 features and RBF-SVM. *Journal of Computing Theories and Applications*, *3*(3), 334–348.

Bawa, M. S., Yusuf, S. M., & Saminu, S. S. (2026). MSA-TCN: Robust urban suspicious sound detection using multi-scale temporal convolutions and dual attention. *Journal of Future Artificial Intelligence and Technologies*, *3*(1), 36–52.

Saminu, S. S., Ibrahim, Y., Haruna, Z., & Umar, A. (2026). Enhanced cross-crop plant disease recognition model via domain-specific alignment network and elastic-mixup. *International Journal of Software Engineering and Computer Systems*, *12*(1), 39–49.

.

International Conference on Engineering Innovation for Sustainable Development (ICESID 2026)
Faculty of Engineering, Ahmadu Bello University Zaria · 8–10 September 2026

DEEP LEARNING NETWORK FOR AUDIO-BASED ENVIRONMENTAL SOUND RECOGNITION USING YAMNET AND DENSE SELF-ATTENTION MECHANISM

Shehu Mohammed Yusuf[1,*], Kabiru Muhammed Nasiru[1]
[1]*Ahmadu Bello University*
Email: smyusuf@abu.edu.ng[*], nasirumuhammedkabiru@gmail.com
***Corresponding author**: Shehu Mohammed Yusuf
DOI: https://doi.org/10.67203/sp.ICESID.2026

ABSTRACT

Environmental sound recognition has become increasingly important in applications ranging from smart surveillance to health monitoring and intelligent urban systems. Although recent deep learning models have improved the ability to classify complex acoustic events, many of them still struggle with redundant features in audio embeddings or rely on heavy architectures that limit deployment on resource-constrained devices. To address these challenges, we developed a lightweight framework that combines YAMNet's pre-trained audio embeddings with a simple one-dimensional self-attention mechanism. This design helps the model focus on the most informative parts of each audio segment while avoiding unnecessary computational overhead. The enhanced embeddings are then processed through a compact fully connected network for final classification. Experiments on two benchmark datasets, ESC-10 and BDLib, demonstrate the effectiveness of the proposed approach, achieving test accuracies of 96% and 97%, respectively. The model outperforms an Xception-based transfer learning baseline on ESC-10 by 2.7% while using roughly 45× fewer parameters and provides competitive performance to MobileNetV2 on BDLib with only a fraction of its complexity. Though, the model was developed by utilizing small datasets with few classes of sounds, the results obtained indicate that applying self-attention directly to pre-trained audio embeddings can significantly improve environmental sound classification and offers a solution for real-time acoustic monitoring in noisy environments.

Keywords: *Environmental sound classification; Neural Networks; Self-Attention Mechanism; transfer learning*

I. INTRODUCTION

Environmental sound classification (ESC) is increasingly becoming an integral component of intelligent systems, particularly in applications such as automated surveillance, health monitoring, smart homes, and smart cities. These intelligent systems rely on the ability to recognize and interpret everyday acoustic events such as; natural sounds like rain or ocean waves and critical events such as alarms, sirens, or human activities. Also, ESC has found applications in smart surveillance systems, health monitoring, and environmental sensing in urban areas (Piczak, 2015a). For instance, in a security system, detecting a glass-breaking sound could help raise an alarm even in the absence of video data (Hershey *et al*., 2017) .

Benchmark datasets such as ESC-10 and ESC-50 have played an important role in enabling systematic evaluation of ESC methods by providing curated collections of labeled environmental sounds (Mu *et al*., 2021). Compared with structured signals such as speech and music, environmental sounds often exhibit highly variable and complex time–frequency patterns, which makes them more challenging to model reliably (Mkrtchian & Furletov, 2022).

Early ESC approaches were largely based on hand-crafted features such as Mel-frequency cepstral coefficients (MFCC) combined with classical machine learning algorithms. Although these pipelines gave useful baselines, they typically struggled to capture richer temporal and spectral dependencies and often degraded in the presence of noise or overlapping events (Mushtaq & Su, 2020). The emergence of deep learning has significantly improved ESC performance. Convolutional neural networks (CNNs) operating on spectrograms or stacked acoustic features have been shown to outperform traditional models on ESC-10, ESC-50 and related corpora (Mun *et al*., 2017).

Recent works have further refined these architectures using multi-branch (Latifi *et al*., 2024) or pyramidal CNNs to better capture multi-scale time–frequency patterns (Demir *et al*., 2020; Fang *et al*.,

2022). A parallel line of research has focused on pre-trained audio models trained on large-scale datasets such as AudioSet. PANNs, for instance, provide large-scale pre-trained audio neural networks that have demonstrated strong transfer performance across a variety of audio pattern recognition tasks (Kong *et al*., 2020). Similarly, several studies have adopted YAMNet-based transfer learning for downstream audio tasks. The YAMNet-based transfer learning model, a 1024-dimensional embedding generator strategy, is derived from a MobileNet-like architecture trained on hundreds of sound event classes (Liu *et al*., 2025). This strategy has been particularly attractive in resource-constrained scenarios such as embedded anomaly detection in smart cities, where pre-trained models are retrained on ESC-10, BDLib, and related datasets and then deployed on Raspberry Pi or TPU platforms (Lamrini *et al*., 2023).

Despite these advances, two key limitations remain. First, embeddings produced by general-purpose pre-trained models may contain redundant or weakly relevant dimensions when applied to more specific ESC tasks. Second, CNN-based transfer learning architectures typically introduce millions of additional parameters, which increases memory consumption and computational latency. Thus, model developed may not be ideal for edge deployment. For instance, CNN-based transfer learning using Xception has achieved strong performance on ESC-10 and ESC-50 but at the cost of relatively large model sizes (Zhou *et al*., 2025). At the same time, work on lightweight ESC models, such as resource-adaptive CNNs (Binandeh Dehaghani et al., 2025; Fang *et al*., 2022), has highlighted the importance of carefully balancing accuracy with computational efficiency for practical deployment.

Motivated by these observations, this study explores a lightweight framework that applies a one-dimensional self-attention mechanism directly to YAMNet embeddings for environmental sound recognition. The central ideas is to refine the pre-trained embedding space by emphasizing the most informative dimensions before classification, rather than adding deeper convolutional or recurrent stacks. As detailed in the rest of this paper, the proposed model combines YAMNet-derived 1024-dimensional embeddings with a simple dense self-attention layer and a compact fully connected classifier, and is evaluated on ESC-10 and BDLib. The results show that this approach can achieve high accuracy while using substantially fewer parameters than typical CNN-based transfer learning baselines, making it a promising option for real-time ESC on embedded devices.

II. RELATED WORKS

A. Environmental Sound Classification with Deep Learning

Early deep learning studies showed that CNNs operating on log-Mel spectrograms can substantially outperform classical machine learning methods on these datasets. Piczak demonstrated that relatively shallow CNNs already capture useful local time–frequency patterns for ESC-50, while subsequent work improved robustness further using deeper architectures and data augmentation (Piczak, 2015b). The work of Mushtaq and Su (2020) proposed a regularized deep CNN with data augmentation, reporting improved performance on ESC-10, ESC-50 and UrbanSound8K by combining appropriate feature extraction with network regularization. Other studies have explored alternative CNN topologies such as concatenated or pyramidal architectures to capture richer multi-scale representations of environmental sounds (Mu *et al*., 2021).

At the same time, there has been a growing interest in models that can provide strong performance while remaining computationally efficient. The work of [8] introduced a resource-adaptive CNN (RACNN) that uses a lightweight convolutional module to reduce hardware requirements and speed up ESC, highlighting the importance of designing architectures explicitly for embedded deployment. Other efficient end-to-end architectures, such as AclNet (Huang & Alvarado Leanos, 2018), and SwishNet (Hussain & Haque, 2018), have explored 1D CNNs and compressed model designs to achieve high accuracy at significantly reduced complexity. These works collectively show that careful architectural design can strike a useful trade-off between accuracy and resource usage.

B. Pre-trained Audio Models and YAMNet-based Transfer Learning

Large-scale pre-trained audio models have become increasingly influential in ESC and related tasks. PANNs, trained on AudioSet, provide pre-trained CNN backbones that can be fine-tuned or used as feature extractors for various audio tagging, acoustic scene classification, and sound event detection problems (Kong *et al*., 2020). Building on this idea, several recent studies have adopted YAMNet as a

generic feature extractor. In their work, Liu *et al.* (2025) used YAMNet-based transfer learning to build a compact noise classifier. Their findings showed that its 1024-dimensional embeddings can be effectively reused in downstream tasks with relatively small additional networks. In the work of Wu (2025), a comprehensive approach for urban sound detection was developed using YAMNet obtain high-level embeddings and bidirectional LSTM as classification modules. The work of Mohino-Herranz *et al*. (2025) showed that the use of pretrained YAMNet for sound event classification on edge devices reduce training requirements and enable efficient deployment.

Lamrini *et al*. (2023) evaluated the performance of a pre-trained CNN for environmental sound recognition on multiple platforms, including laptops, Raspberry Pi, and Coral TPU, using ESC-10, BDLib, and UrbanSound datasets (Salamon *et al*., 2014). Their results showed that transfer learning with pre-trained audio networks can achieve up to 100% accuracy on BDLib while remaining feasible on embedded hardware. However, these systems often rely on relatively heavy CNN backbones with millions of parameters. Although pre-training reduces the amount of labeled data required, the resulting models may still be over-parameterized for low-power deployment and may not explicitly address redundancy within the pre-trained embedding space.

C. Attention Mechanisms for Environmental Sound Classification

Attention mechanisms have been widely adopted to improve the modeling of complex acoustic patterns. In their work, Mu *et al.* (2021) proposed a temporal–frequency attention-based CNN (TFCNN) that applies attention over log-Mel spectrograms to focus on informative time–frequency regions. The work of Qiao *et al*. (2021) compared sub-spectrogram segmentation with temporal–frequency attention mechanisms and showed that attention mechanisms can provide performance gains by adaptively weighting different spectrogram regions. More recently, attention has been integrated into residual architectures and multi-branch CNNs for ESC (Zhong *et al*., 2025). This further demonstrate its usefulness in refining spectro-temporal representations.

Beyond ESC, self-attention and multi-head attention have been explored in broader audio tasks. The work of Dong *et al.* (2023), applied multi-head attention to acoustic scene analysis and showed that attention over frame-level representations can yield competitive performance with only recording-level supervision. In the work of Wang *et al*. (2020), self-attention mechanism was assessed on learned features for joint sound event localization and detection. Findings demonstrated that self-attention can effectively replace or complement recurrent layers in CRNN-based architectures. Sudarsanam *et al*. (2021) developed an adaptive memory-controlled self-attention mechanism to improve polyphonic sound event detection by selectively emphasizing salient temporal patterns. These studies suggest that self-attention is a flexible tool for highlighting informative portions of audio representations; whether in time, frequency, or latent feature space.

Most attention-based ESC models, however, operate on spectrograms or intermediate CNN feature maps, which requires additional preprocessing and often increases model complexity. In contrast, the present work investigates a simpler alternative by applying a one-dimensional self-attention mechanism directly to pre-trained YAMNet embeddings and compact neural network classifier. As shown in our experiments, this embedding-level attention can yield competitive or superior ESC performance while maintaining a very small parameter budget. Thus, making our approach attractive for resource-constrained deployments.

III. METHODOLOGY

This section describes the proposed system for environmental sound classification; including data preprocessing, feature extraction using YAMNet, the application of a self-attention mechanism, and the final classification using fully connected layer. Fig. 1 shows the steps involved in process of audio classification.

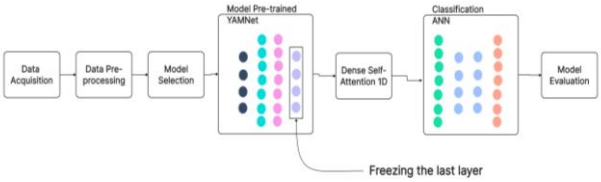

Figure 1: Proposed ESC framework

A. Dataset Aquisition and Preprocessing

Two benchmark datasets were used in this study: ESC-10 (Piczak, 2015a) and BDLib (Bountourakis *et al*., 2015; Bountourakis *et al*., 2019). The ESC-10 dataset was acquired from https://github.com/karoldvl/ESC-50/archive/master.zip. ESC-10 contains 400 audio samples across 10 environmental classes such as dog bark, clock ticking, and chainsaw. Each audio clip is 4 seconds long and sampled at 44.1 kHz. BDLib is a custom dataset collected for environmental monitoring applications. For this work, the BDLib dataset was acquired from https://research.playcompass.com/files/BDLib-2.zip. It includes sounds like rain, helicopter, sea waves, and sneezing, each stored as a .wav file in class-labelled folders.

To prepare the data, all audio files were first resampled to 16 kHz and converted to mono, matching the input requirements of YAMNet (Hershey *et al*., 2017). A sliding window of 4 seconds was applied to each clip with a 50% overlap (Lamrini *et al*., 2023). This resulted in more training samples from each audio file and ensured that important sound segments were not missed. Basic noise filtering was applied to remove silent frames. Fig. 2 shows the windowing process technique.

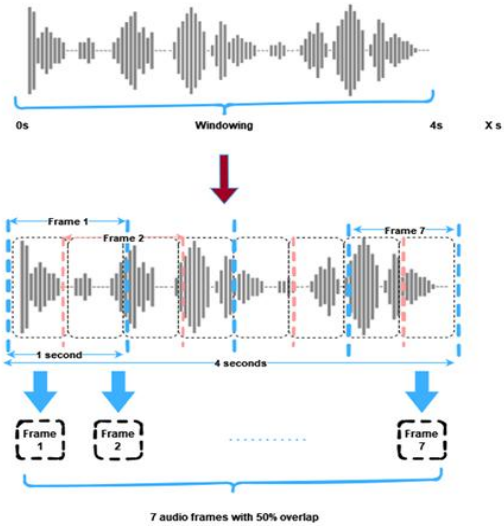

Figure 2: Windowing approach (Lamrini *et al*., 2023)

B. Feature Extraction Using YAMNet

In this work, the YAMNet pretrained model was used purely as a feature extractor. Its classification head was removed, and the last fully-connected layer was frozen. The output of the frozen fully connected layer serves as input to the dense self-attention module of Figure 1. A 4-second audio window was adopted. Fig. 3 shows the adopted YAMNet architecture.

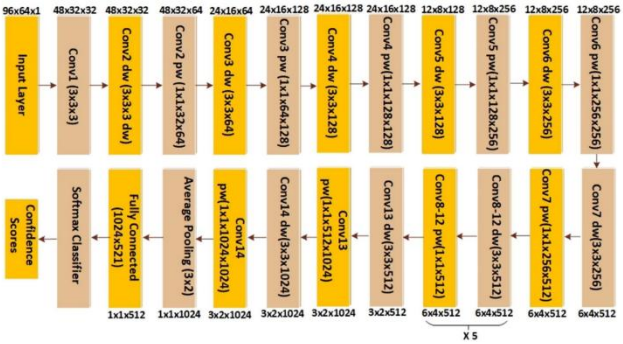

Figure 3: Adopted YAMNet architecture (Hershey *et al*., 2017)

C. Self-Attention Mechanism Module

After feature extraction, a custom 1D self-attention layer was applied to the embeddings. This mechanism allows the model to assign different levels of importance to each dimension of the YAMNet output vector. The attention layer consists of a dense projection of the embedding followed by a SoftMax operation to compute attention scores. These scores are then multiplied element-wise with the original embeddings to produce an attention-weighted feature vector. Fig. 4 illustrate a single-head dense self-attention mechanism applied to 1D embeddings

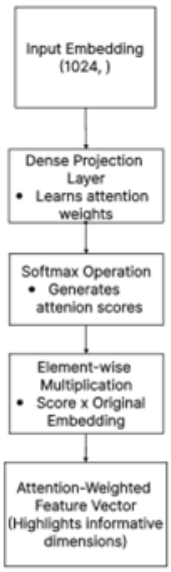

Figure 4: Single-headed dense self-attention module

This process enhances the most informative elements in the vector and suppresses those with little contribution to the final prediction. Unlike the temporal–frequency attention applied on spectrograms in earlier work (Kuzminykh *et al*., 2020), this approach applies attention directly to a compact, pre-trained embedding. The goal is to reduce complexity while preserving performance.

D. Classification Module

The attention-enhanced embeddings generated by the single-headed dense self-attention module of Figure 4 are passed through a fully connected network consisting of two dense layers with 256 units each, using ReLU activation and dropout of 0.5 for regularization. Then, a final dense layer with 10 units and SoftMax activation was used to produce the probability distribution across the 10 sound classes. The summary of the architecture of the proposed model and parameter information used in each layer.

TABLE I. SUMMARY OF MODEL PARAMETERS

Type of Layer	Output Shape	Number of Parameters
Input_layer (InputLayer)	(None, 1024)	0
dense_self_attention1d (DenseSelfAttention1D)	(None, 1024)	131,329
dense_2 (Dense)	(None, 256)	262,400
dropout (Dropout)	(None, 256)	0
dense_3 (Dense)	(None, 256)	65,792
dropout_1 (Dropout)	(None, 256)	0
dense_4 (Dense)	(None, 10)	2,570
Total parameters	462,091	

E. Training Procedure

Two training scenarios were followed. First, the datasets were split into training (80%), validation (10%), and testing (10%) sets. The model was trained using the Adam optimizer with a learning rate of 0.001 and categorical cross-entropy as the loss function. Training was conducted on the ESC-10 and BDLib dataset for 10 and 20 epochs, respectively. Batch size was set to 32. The entire pipeline was implemented using TensorFlow and trained on a GPU-enabled environment.

Second, another training was conducted, using 5-fold cross validation (Zhou *et al*., 2025) on the ESC-10 dataset, to allow for precise evaluation of the proposed architecture in handling small dataset.

Performance was measured using accuracy, precision, recall, and F1-score. The evaluation was done on the test set to ensure generalization. A confusion matrix was also used to visualize per-class prediction accuracy.

IV. RESULTS

The model was evaluated on two datasets: ESC-10 and BDLib. Each dataset was divided into 80% training, 10% validation, and 10% testing splits.

A. ESC-10 Datasets Results

For the ESC-10 dataset, the model achieved a test accuracy of 96%, which shows that the proposed attention-based model can effectively classify environmental sounds using only the YAMNet embeddings. Table II shows the performance obtained based on the metrics for evaluation.

TABLE II. MODEL PERFORMANCE ON THE ESC-10 DATASET

Metric	Value
Accuracy	96%
Precision	98%
Recall	97%
f1-Score	97%

This result outperforms the recent transfer learning approach using the Xception CNN by Zhou *et al*. (2025); which reported 93.3% accuracy on the same ESC-10 dataset using mel-spectrogram-to-image conversion and a much larger model (~20.8 million parameters). In contrast, our lightweight architecture with only 462K trainable parameters achieves a 2.7% higher accuracy while being approximately 45 times more parameter-efficient. The confusion matrix for the ESC-10 dataset is presented in Fig. 5.

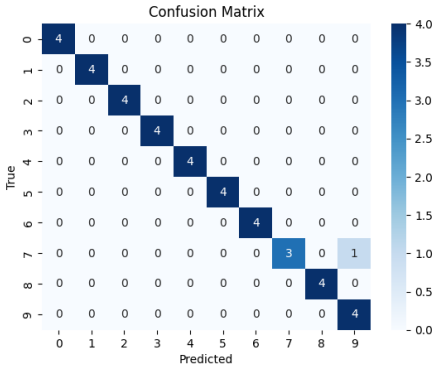

Figure 5: Developed model confusion matrix on the ESC-10 dataset

As seen in Figure 5, 9 classes were efficiently classifiedand only 1 test sample was misclassified; mostly in acoustically similar categories such as “clock ticking” and “crackling fire”.

Table III shows the cross-validation performance obtained based on the metrics for evaluation.

TABLE III. MODEL CROSS-VALIDATION PERFORMANCE ON THE ESC-10 DATASET

Metric	Value
Accuracy	95.40%
Precision	97.28%
Recall	96.29%
f1-Score	96.29%

Similarly, the cross-validation performance, in terms of accuracy, outperforms the recent transfer learning approach using the Xception CNN by Zhou *et al*. (2025) by 2.25%.

B. BDLib Dataset Results

The BDLib dataset yielded a test accuracy of 97% using the same model architecture. Table IV shows the performance obtained based on the metrics for evaluation.

TABLE IV. MODEL PERFORMANCE ON THE BDLIB DATASET

Metric	Value
Accuracy	97%
Precision	97%
Recall	97%
f1-Score	97%

Even though this dataset contains more real-world variations, the attention mechanism still performed well in learning meaningful embeddings from the YAMNet output. This result is competitive with the pre-trained MobileNetV2 transfer learning approach by Lamrini *et al*. (2023), which reported 100%, but required ~3.5 million parameters. Our lightweight design with only 462K trainable parameters achieves near-equivalent performance while being approximately 7.5 times more parameter-efficient. The confusion matrix for the BDLib dataset model is shown in Figure 6.

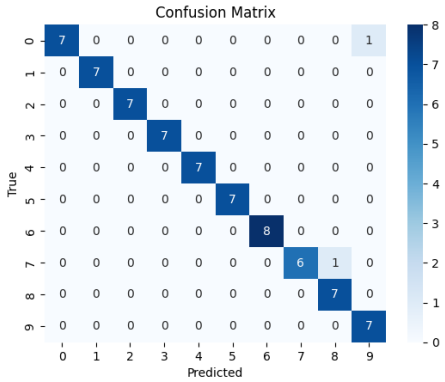

Figure 6: Developed model confusion matrix on the BDLib dataset

These results indicate strong generalization capability of the model on unseen, noisy samples.

V. DISCUSSION

The use of a self-attention mechanism on the YAMNet embedding played a key role in improving the classification performance. Compared to deeper CNN-based transfer learning models such as Xception used in the work of Zhou *et al*. (2025), which require over 20 million parameters to achieve 93.3% cross-validation accuracy on ESC-10 dataset, our YAMNet + self-attention model delivers superior performance with significantly lower computational overhead; proposed model shows 45 times smaller in size. Table V summarizes the comparison.

TABLE V. COMPARISON WITH BASELINE ON ESC-10 DATASET

Method	**Accuracy**	**Parameters**	**Parameter Ratio of baseline to Proposed Model**
Developed Model (YAMNet + Self-Attention) using 5-fold Cross-validation	95.4%	462K	~45
(Zhou *et al*., 2025) (Xception)	93.3%	~20.8M	

On the custom BDLib dataset, the 97% accuracy further validates the model's generalization to varied environmental sounds, closely approaching the 100% achieved by Lamrini *et al.* (2023) with MobileNetV2-based transfer learning under a matching 80/10/10 split. Table VI summarises the comparison.

TABLE VI. COMPARISON WITH BASELINE ON BDLIB DATASET

Method	**Accuracy**	**Parameters**	**Parameter Ratio of baseline to Proposed Model**
Proposed Model (YAMNet + Self-Attention)	97%	462K	~7.5
Lamrini et al. (2023) (BDLib-based MobileNetV2)	100%	~3.5M	

Similarly, from Table VI, the proposed model shows over 7.5 times improvement over the model developed in Lamrini *et al*. (2023), in terms of model size. This parameter efficiency gain, combined with high accuracy, positions the developed method as a practical solution for real-time audio-based environmental monitoring in edge environments. The network was able to highlight critical dimensions of the embedding vector while suppressing noise, resulting in a more discriminative feature space. This is consistent with previous works which have shown that attention can improve model performance. Additionally, the compact structure of the network with only 462K parameters makes it suitable for deployment on resource-constrained devices such as mobile phones or embedded systems for smart surveillance and monitoring.

VI. CONCLUSION

This study presented a lightweight and effective deep learning architecture for environmental sound classification. The approach combines YAMNet embeddings with a custom 1D self-attention mechanism followed by fully connected layers. The model was trained and evaluated on two datasets; ESC-10 and BDLib. A 5-fold cross-validation accuracy of 95.4 was obtained for the ESC-10 based model. And a test accuracy of 97% was obtained for the BDLib-based model. Thus the use of a pre-trained feature extractor allowed the model to learn high-level representations of audio without requiring complex spectrogram-based processing. Additionally, the attention mechanism significantly improved the model's ability to focus on the most informative parts of the audio embedding, leading to better classification performance. The architecture also remains computationally efficient compared with the baseline models. Therefore it can be a more suitable candidate for real-world applications where speed and resource constraints are critical.

Future work may explore the use of hybrid attention mechanisms, domain adaptation techniques, or lightweight convolutional variants to further improve robustness across a wider range of sound environments. Also, there is the need to deploy the developed model on embedded platforms, like Raspberry Pi, to evaluate it inference latency against existing works, because parameter efficiency alone may not translate to real-time feasibility. Finally, there is the need to further subject the developed technique on large and balanced datasets with more categories of sounds; to evaluate its generalization capability.

ACKNOWLEDGMENT

This work is supported by TETFUND Nigeria under the grant: NRF-2023-SETI-AFS-00158

REFERENCES

Binandeh Dehaghani, P., Pena, D., & Aguiar, A. P. (2025). Investigation of feature selection and pooling methods for environmental sound classification. arXiv.

Bountourakis, V., Vrysis, L., Konstantoudakis, K., & Vryzas, N. (2019). An enhanced temporal feature integration method for environmental sound recognition. Acoustics, 1(2), 410–422.

Bountourakis, V., Vrysis, L., & Papanikolaou, G. V. (2015). Machine learning algorithms for environmental sound recognition: Towards soundscape semantics. In Proceedings of the 10th Audio Mostly: A Conference on Interaction With Sound. Association for Computing Machinery.

Demir, F., Turkoglu, M., Aslan, M., & Sengur, A. (2020). A new pyramidal concatenated CNN approach for environmental sound classification. Applied Acoustics, 170, Article 107520.

Dong, S., Xia, Z., Pan, X., & Yu, T. (2023). Environmental sound classification based on improved compact bilinear attention network. Digital Signal Processing, 141, Article 104170. https://doi.org/10.1016/j.dsp.2023.104170.

Fang, Z., Yin, B., Du, Z., & Huang, X. (2022). Fast environmental sound classification based on resource adaptive convolutional neural network. Scientific Reports, 12, Article 6599.

Hershey, S., Chaudhuri, S., Ellis, D. P. W., Gemmeke, J. F., Jansen, A., Moore, R. C., Plakal, M., Platt, D., Saurous, R. A., Seybold, B., Slaney, M., Weiss, R. J., & Wilson, K. (2017). CNN architectures for large-scale audio classification. In 2017 IEEE International Conference on Acoustics, Speech and Signal Processing (ICASSP) (pp. 131–135). IEEE.

Huang, J. J., & Alvarado Leanos, J. J. (2018). AclNet: Efficient end-to-end audio classification CNN. arXiv.

Hussain, M. S., & Haque, M. A. (2018). SwishNet: A fast convolutional neural network for speech, music and noise classification and segmentation. arXiv.

Kong, Q., Cao, Y., Iqbal, T., Wang, Y., Wang, W., & Plumbley, M. D. (2020). PANNs: Large-scale pretrained audio neural networks for audio pattern recognition. IEEE/ACM Transactions on Audio, Speech, and Language Processing, 28, 2880–2894.

Kuzminykh, I., Shevchuk, D., Shiaeles, S., & Ghita, B. (2020). Audio interval retrieval using convolutional neural networks. In O. Galinina, S. Andreev, S. Balandin, & Y. Koucheryavy (Eds.), Internet of Things, Smart Spaces, and Next Generation Networks and Systems: 20th International Conference, NEW2AN 2020 and 13th Conference, ruSMART 2020, Proceedings (Lecture Notes in Computer Science, Vol. 12525, pp. 229–240). Springer.

Lamrini, M., Chkouri, M. Y., & Touhafi, A. (2023). Evaluating the performance of pre-trained convolutional neural network for audio classification on embedded systems for anomaly detection in smart cities. Sensors, 23(13), Article 6227.

Latifi, S. A., Ghassemian, H., & Imani, M. (2024). Classification of heart sounds using multi-branch deep convolutional network and LSTM-CNN. arXiv.

Liu, L., Xu, Q., Mao, S., Mu, J., Zhao, X., Song, W., & Cheng, P. (2025). YAMNet-based transfer learning for compact noise classification in urban and wireless systems. EURASIP Journal on Wireless Communications and Networking, 2025, Article 74.

Mkrtchian, G., & Furletov, Y. (2022). Classification of environmental sounds using neural networks. In 2022 Systems of Signal Synchronization, Generating and Processing in Telecommunications (SYNCHROINFO) (pp. 1–4). IEEE.

Mohino-Herranz, I., García-Gómez, J., Alonso-Diaz, S., Gallegos, J. G., Perez-Sanz, F. J., Aguilar-Ortega, M., & Gil-Pita, R. (2025). Implementing transfer learning for sound event classification using the ReaLISED audio database. Measurement: Sensors, 38, Article 101711.

Mu, W., Yin, B., Huang, X., Xu, J., & Du, Z. (2021). Environmental sound classification using temporal-frequency attention based convolutional neural network. Scientific Reports, 11, Article 21552.

Mun, S., Park, S., Han, D. K., & Ko, H. (2017). Generative adversarial network based acoustic scene training set augmentation and selection using SVM hyper-plane. In Proceedings of the Detection and Classification of Acoustic Scenes and Events 2017 Workshop (DCASE2017) (pp. 93–97).

Mushtaq, Z., & Su, S.-F. (2020). Environmental sound classification using a regularized deep convolutional neural network with data augmentation. Applied Acoustics, 167, Article 107389. DOI: 10.1016/j.apacoust.2020.107389.

Piczak, K. J. (2015a). ESC: Dataset for environmental sound classification. In Proceedings of the 23rd Annual ACM Conference on Multimedia (pp. 1015–1018). Association for Computing Machinery. https://doi.org/10.1145/2733373.2806390.

Piczak, K. J. (2015b). Environmental sound classification with convolutional neural networks. In 2015 IEEE 25th International Workshop on Machine Learning for Signal Processing (MLSP) (pp. 1–6). IEEE.

Salamon, J., Jacoby, C., & Bello, J. P. (2014). A dataset and taxonomy for urban sound research. In Proceedings of the 22nd ACM International Conference on Multimedia (pp. 1041–1044). Association for Computing Machinery.

Qiao, T., Zhang, S., Cao, S., & Xu, S. (2021). High accurate environmental sound classification: Sub-spectrogram segmentation versus temporal-frequency attention mechanism. Sensors, 21(16), Article 5500.

Sudarsanam, P. A., Politis, A., & Drossos, K. (2021). Assessment of self-attention on learned features for sound event localization and detection. In Proceedings of the 6th Workshop on Detection and Classification of Acoustic Scenes and Events (DCASE 2021) (pp. 100–104). DCASE.

Wang, W., Wang, W., Sun, M., & Wang, C. (2020). Acoustic scene analysis with multi-head attention networks. In Proceedings of Interspeech 2020 (pp. 1191–1195). ISCA.

Wu, T. (2025). A comprehensive approach to urban sound detection with YAMNet and bi-directional LSTM. In Proceedings of the 2nd International Conference on Data Analysis and Machine Learning (DAML) (pp. 23–29). SciTePress.

Zhong, X., Dong, S., Zhang, Y., Lu, W., & Jiang, L. (2025). Research on multi-branch residual connection spectrum image classification based on attention mechanism. Scientific Reports, 15, Article 25532.

Zhou, J., Lu, J., Wang, R., Ma, R., & Qin, Z. (2025). Environmental sound classification using convolutional neural network based transfer learning. In 2025 International Conference on Computing, Networking and Communications (ICNC) (pp. 12–17). IEEE.

International Conference on Engineering Innovation for Sustainable Development (ICESID 2026)
Faculty of Engineering, Ahmadu Bello University Zaria · 8–10 September 2026

DEEP LEARNING-BASED WEAPON CLASSIFICATION FOR INTELLIGENT SURVEILLANCE APPLICATIONS USING RESNET-50

Kenneth Okhiria[1,*], Joseph Samuel Mshelizah[1], Saidi Abdulraimi
[1]*Nigerian Army University Biu*
Email: kennyhnsom@gmail.com[*], Samueljoseph9272@gmail.com, Saheeday12@gmail.com
***Corresponding author**: Kenneth Okhiria
DOI: https://doi.org/10.67203/sp.ICESID.2026

ABSTRACT
Weapon-related crimes pose significant threats to public safety and security, creating a growing need for intelligent surveillance systems capable of automatically identifying potential threats. Deep learning has demonstrated remarkable success in object recognition and image classification, making it well suited for automated weapon recognition. This study develops and evaluates a transfer learning-based approach for classifying two common weapon categories, AK-47 rifles, and knives, using a pretrained ResNet-50 convolutional neural network. A dataset comprising 2,001 labeled images was collected from Google Images, manually cleaned, preprocessed, and divided into training and validation sets using an 80:20 ratio. The pretrained ResNet-50 model was adapted using transfer learning and trained for 50 epochs. Model performance was evaluated using precision, recall, F1-score, and overall accuracy. Experimental results demonstrated high classification performance on the validation dataset, with the AK-47 class achieving a precision of 0.99, recall of 1.00, and F1-score of 0.99, while the Knife class achieved precision, recall, and F1-score values of 0.99, resulting in an overall classification accuracy of 0.99. Additional inference on previously unseen weapon images produced accurate predictions with consistently high confidence scores, providing supplementary evidence of the model's predictive capability beyond the validation samples. These findings demonstrate the effectiveness of the proposed approach as a proof-of-concept classification framework, highlighting its foundational potential for future integration into real-time intelligent surveillance and public safety applications.

Keywords: *Weapon; Resnet-50; Transfer- Learning; Classification*

1. INTRODUCTION

Video surveillance systems have become an integral component of modern public safety and security, playing a vital role in crime prevention and incident monitoring. Security cameras are widely deployed in transportation infrastructure, public housing complexes, shopping districts, border control areas, and public buildings to monitor activities and enhance security. Despite their widespread deployment, the monitoring of surveillance systems and the identification of potential threats still rely heavily on continuous human observation by security personnel. As the number of surveillance cameras continues to increase, maintaining effective real-time monitoring has become increasingly challenging, with operators often reviewing recorded footage only after incidents have occurred to reconstruct events and gather evidence. Furthermore, prolonged surveillance tasks can result in operator fatigue and human error, reducing the effectiveness of manual monitoring. These limitations highlight the growing need for intelligent and proactive surveillance systems capable of supporting timely threat identification (Kaya *et al.*, 2021).

Weapon-related violence remains a significant public safety concern worldwide, posing serious risks to human life and property. Early identification of dangerous weapons can significantly improve the ability of law enforcement and security agencies to respond promptly and mitigate potential harm. To overcome the limitations of manual surveillance, researchers have increasingly explored automated surveillance systems capable of recognizing weapons before violent incidents occur. Consequently, artificial intelligence (AI)-based surveillance solutions have been developed to detect and recognize dangerous objects within surveillance imagery. By providing faster and more consistent analysis than manual observation alone, AI can support security personnel, reduce operator workload, alleviate workforce shortages, and improve the overall efficiency of surveillance operations (Lim *et al.*, 2019; Xu & Hung, 2020; Mehta *et al.*, 2020; Gelana & Yadav, 2019; Dwivedi *et al.*, 2019).

Recent advances in artificial intelligence have been largely driven by deep learning, which has significantly improved the ability of computer systems to analyze and interpret visual information. Among deep learning models, Convolutional Neural Networks (CNNs) have demonstrated remarkable performance in image classification, object detection, and image segmentation by automatically learning hierarchical feature representations directly from image data. Their ability to extract discriminative visual features without relying on handcrafted feature engineering has made CNNs the dominant architecture for computer vision and intelligent surveillance applications (Verma & Dhillon, 2017; Burgaz & Budak, 2022; Kaya *et al*., 2021; Oura *et al*., 2021; Hashmi *et al.*, 2021; Ağdaş *et al*., 2021). Consequently, CNN-based approaches have substantially improved the automatic recognition of weapons and other dangerous objects, thereby enhancing situational awareness and supporting more effective security operations (Lim *et al.*, 2019).

A reliable weapon classification system can significantly enhance video surveillance, smart home security, intrusion detection, and smart city monitoring by providing timely alerts that support rapid decision-making and emergency response (Warsi *et al.*, 2019). Early recognition of dangerous weapons enables security personnel to intervene before situations escalate, thereby reducing potential risks to public safety (Yadav et al., 2023). Among commonly encountered weapons in security-related incidents, firearms such as the AK-47 and bladed weapons such as knives present significant security concerns because of their potential use in violent attacks. Consequently, this study focuses on the classification of AK-47 rifles and knives to support intelligent surveillance applications (Dwivedi *et al.*, 2019; Ingle & Kim, 2022).

One of the major advantages of modern CNN architectures is their ability to support transfer learning, whereby knowledge acquired from large-scale image datasets can be transferred to related tasks with limited training data. Rather than training a model from scratch, transfer learning enables pre-trained networks to be fine-tuned for specific applications, thereby reducing computational cost, shortening training time, and improving model performance when only modest datasets are available. These advantages make transfer learning particularly suitable for intelligent surveillance applications, where obtaining large, well-annotated weapon image datasets can be challenging (Dwivedi *et al*., 2019; Warsi *et al.*, 2019). Among the available deep learning architectures, ResNet-50 has become one of the most widely adopted models because of its ability to learn rich hierarchical feature representations while mitigating the vanishing gradient problem through residual learning (Kaya *et al*., 2021).

ResNet-50 has demonstrated excellent performance in image classification and surveillance applications because of its strong feature extraction capability and compatibility with transfer learning. Previous studies have successfully applied ResNet-50 to weapon recognition and firearm classification tasks, demonstrating robust performance under diverse operating conditions (Salido *et al*., 2021; Ahmed *et al.*, 2022; Kambhatla & Khaled, 2023). However, many existing studies have focused on object detection frameworks, larger datasets, or broader weapon categories, while comparatively fewer have investigated the effectiveness of transfer learning with ResNet-50 for the classification of specific weapon categories using relatively modest datasets. Therefore, this study develops and evaluates a transfer learning-based framework as a proof-of-concept classification study. Rather than real-time localization, this work establishes a diagnostic baseline for distinguishing AK-47 rifles and knives using clean web-scraped image repositories to evaluate supervised image classification performance prior to complex video stream deployment.

2. METHODOLOGY

The proposed methodology consists of four main stages: data acquisition, data preprocessing, model training, and weapon classification. Initially, a dataset containing images of AK-47 rifles and knives was collected and prepared for model development. The images were subsequently preprocessed to improve data quality and ensure compatibility with the deep learning model. During the training stage, a transfer learning approach based on the pre-trained ResNet-50 architecture was employed to learn discriminative features for weapon classification. Finally, the trained model was used to classify unseen query images into their respective weapon categories. The overall methodology is illustrated in Figure 1, while the detailed workflow of the proposed surveillance system is presented in Figure 2.

2.1 Proposed Surveillance System

The proposed intelligent surveillance system follows a sequential workflow comprising four major phases: data acquisition, data preprocessing, model training, and weapon classification. In the data acquisition stage, images representing the target weapon categories were collected to construct the dataset. The preprocessing stage involved resizing and normalizing the images to prepare them for deep learning. The processed images were then used to train the ResNet-50 model through transfer learning, enabling the extraction of discriminative visual features for accurate weapon classification. In the final stage, unseen query images were presented to the trained model, which predicted the corresponding weapon class. The individual stages of the proposed methodology are described in detail in the following subsections.

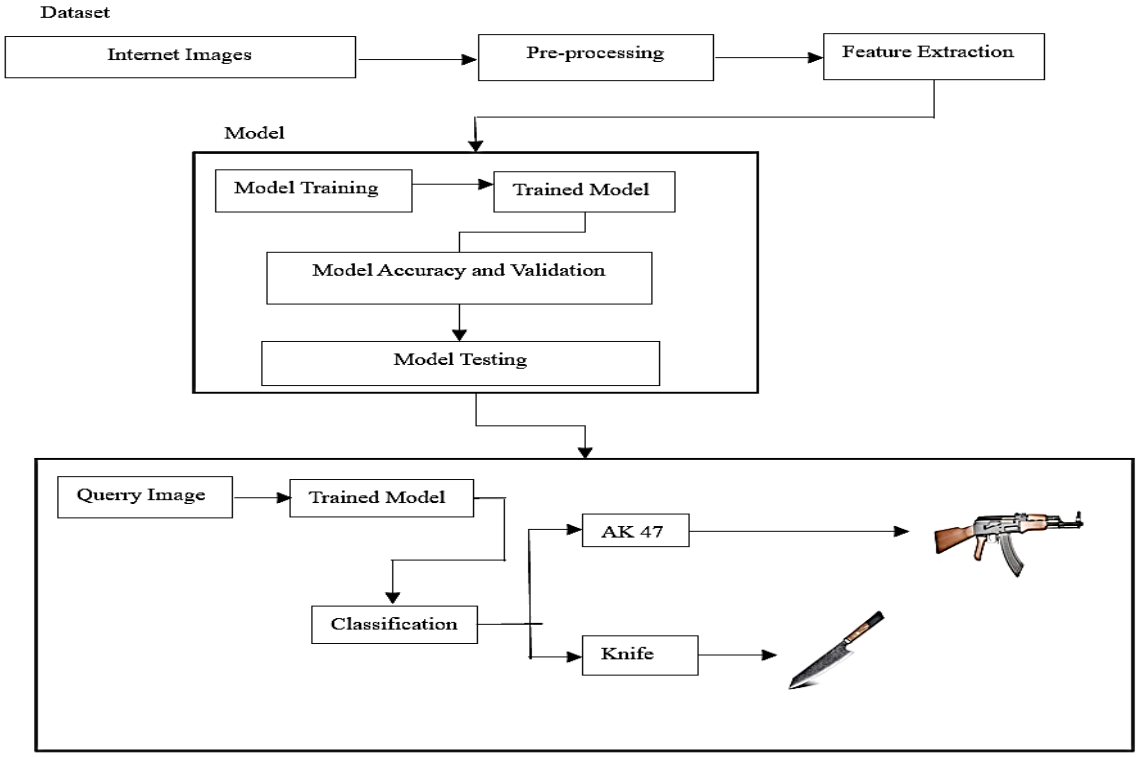

Figure 1: Block diagram of proposed methodology

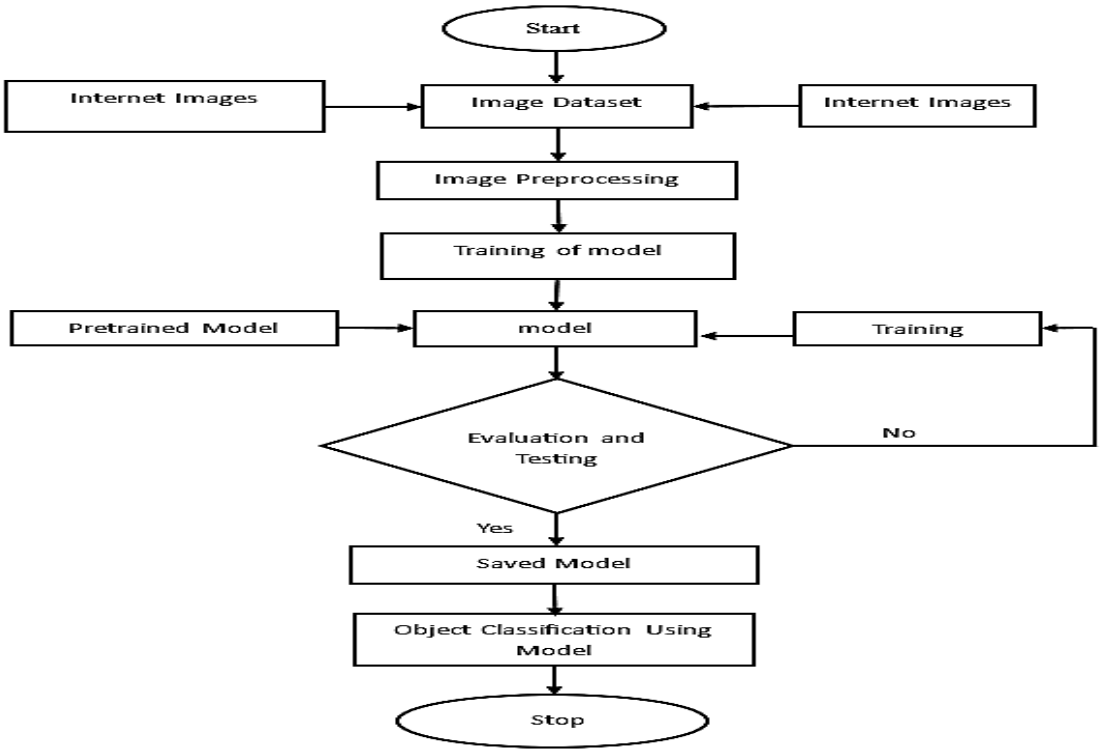

Figure 2: Methodology flowchart

2.2 Data Acquisition

During the data acquisition phase, a dataset comprising 2,001 images of AK-47 rifles and knives was collected from Google Images to support the development of the proposed weapon classification model. Search queries related to the two weapon categories were used to retrieve images captured under different viewpoints, backgrounds, lighting conditions, and object orientations in order to improve dataset diversity. The collected images were manually inspected to ensure their relevance

to the target classes before undergoing preprocessing. Representative samples of the acquired images are presented in Figure 3.

Figure 3: Image Dataset

2.3 Data Preprocessing

Before model training, the collected images underwent a series of preprocessing operations to ensure that the dataset was properly organized, standardized, and optimized for the ResNet-50 architecture. The preprocessing pipeline comprised image collection and cleaning, dataset organization, image resizing, image normalization, and dataset splitting. These operations improved data consistency, enhanced training efficiency, and supported stable model training.

2.3.1 Image Collection, Cleaning and Dataset Organization

The dataset comprised images belonging to two weapon categories: AK-47 rifles and knives. These images were collected from online sources, primarily Google Images, using search queries related to the target weapon categories. To ensure dataset quality and relevance, all collected images were manually inspected, and duplicate, irrelevant, corrupted, and low-resolution samples were removed. This cleaning process ensured that only clear and representative images of each weapon category were retained for model development.

Following the cleaning process, the images were organized into two class-specific subdirectories, namely AK47 and Knife, within a parent directory named ResNet_Dataset. This hierarchical directory structure enabled the PyTorch ImageFolder utility to automatically assign class labels during data loading, thereby facilitating supervised learning. Proper dataset organization also ensured that each image was correctly associated with its corresponding weapon category throughout the training and validation processes, providing a consistent and efficient data management framework for model development.

2.3.2 Image Resizing

All images were resized to 224 × 224 pixels, corresponding to the input dimensions required by the ResNet-50 architecture. Uniform image dimensions ensured consistency across all samples, reduced computational complexity, and enabled the direct use of ImageNet pre-trained weights without modifying the network architecture.

2.3.3 Image Normalization

Following image resizing, pixel values were normalized to improve training stability and enhance model convergence. The pixel intensities were first scaled to the range **[0, 1]** and subsequently standardized using the ImageNet mean and standard deviation values, consistent with the preprocessing requirements of the pre-trained ResNet-50 model. This normalization process reduced the effects of illumination and contrast variations across the dataset, improved numerical stability during optimization, and ensured compatibility with the feature representations learned from the ImageNet dataset.

2.3.4 Data Augmentation

To improve the variability of the training samples and enhance the model's ability to recognize weapons under different image conditions, data augmentation was applied dynamically during the training process. The augmentation operations included random resized cropping, random horizontal flipping, random rotation within a specified range, and colour-jitter adjustment of brightness and contrast. These transformations generated varied representations of the original training images during model training without creating or permanently storing additional image files. The validation images were not subjected to these random augmentation operations; instead, they were processed using deterministic resizing and centre cropping before normalization. Thus, the dataset remained at 2,001 original images, while augmentation increased the variability of the samples presented to the model during training.

2.3.5 Dataset Splitting

Following preprocessing, the prepared dataset of 2,001 images was randomly partitioned into training and validation subsets using an approximately 80:20 ratio to facilitate model development and performance evaluation. A total of 1,600 images were allocated to the training set, while the remaining 401 images were reserved for validation, as summarized in Table 1. The partitioning process maintained class representation between the AK-47 and Knife categories, with 800 AK-47 and 800 Knife images used for training, and 201 AK-47 and 200 Knife images used for validation.

The validation set was used to monitor model performance during training and to assess its classification performance after training. A separate held-out test set was not created because of the moderate dataset size of 2,001 images, allowing a larger proportion of the available data to be retained for model development. Consequently, the performance metrics reported in this study are based on the validation set and may be influenced by model-development and hyperparameter-selection decisions. The absence of an independent test set is therefore acknowledged as a limitation of the study. Future work should evaluate the model using a separate unseen test set or an external dataset to provide a more independent estimate of its generalization performance.

Table 1: Data Set Distribution

Classification	Training Set	Validation Set	Total
AK47	800	201	1001
Knife	800	200	1000
Total	1600	401	2001

2.4 Transfer Learning and ResNet-50 Architecture

The proposed weapon classification framework was developed using the ResNet-50 deep convolutional neural network through a transfer learning approach. This section describes the adopted ResNet-50 architecture and the transfer learning strategy employed to adapt the pre-trained network to the binary weapon classification task.

2.4.1 ResNet-50 Architecture

ResNet-50 was adopted as the backbone convolutional neural network for this study because of its strong feature extraction capability, computational efficiency, and proven performance in image classification tasks. The architecture comprises 50 learnable layers organized into residual blocks with skip connections that facilitate efficient gradient propagation during training. The model was initialized with ImageNet pre-trained weights to provide robust feature representations for the weapon classification task. The standard ResNet-50 architecture used in this study is summarized in Table 2 based on the architecture described by (He *et al.*, 2016).

Table 2: ResNet-50 Architecture

Layer Name	Output size	50-layer
Conv 1_×	112 x 112	7 x7, 64, stride 2
		3 x 3 max pool, stride 2
Conv 2_×	56×56	$\begin{bmatrix} 1\times1, 64 \\ 3\times3, 64 \\ 1\times1, 256 \end{bmatrix}\times3$
Conv 3_×	28×28	$\begin{bmatrix} 1\times1, 128 \\ 3\times3, 128 \\ 1\times1, 512 \end{bmatrix}\times4$
Conv 4_×	14×14	$\begin{bmatrix} 1\times1, 256 \\ 3\times3, 256 \\ 1\times1, 1024 \end{bmatrix}\times6$
Conv 5_×	7×7	$\begin{bmatrix} 1\times1, 512 \\ 3\times3, 512 \\ 1\times1, 2048 \end{bmatrix}\times3$
	1×1	average pool, 1000-d fc, softmax

2.4.2 Transfer Learning Strategy

A transfer learning strategy was employed to adapt the pre-trained ResNet-50 model to the binary weapon classification task. The model was initialized with ImageNet pre-trained weights, while the final fully connected layer was replaced with a new layer comprising two output neurons corresponding to the AK-47 and Knife classes. During transfer learning, the pretrained ResNet-50 feature-extraction layers were kept frozen, while the newly replaced fully connected classification layer was trained for the two-class weapon classification task. This approach reduced training time and supported efficient adaptation of the pretrained model to the target classification task.

2.5 Model Training

Following dataset preprocessing and configuration of the ResNet-50 architecture, the modified network was trained to classify images into the AK-47 and Knife categories. The training process involved configuring the model hyperparameters, optimizing the network using an appropriate loss

function and optimization algorithm, and monitoring its convergence throughout training. The training procedure and adopted hyperparameters are described in the following subsections.

2.5.1 Training Procedure

Following dataset preparation and partitioning, the modified ResNet-50 model was trained using the training subset, while the validation subset was used to monitor the model's learning progress and performance throughout the training process. The dataset was processed in mini batches of 32 images, and the model was trained for 50 epochs. During each epoch, both the training and validation losses were monitored to assess convergence, evaluate model stability, and minimize the risk of overfitting.

2.5.2 Training Parameters

The principal hyperparameters adopted during model training are summarized in Table 3. These parameters were selected to achieve stable convergence while maintaining computational efficiency throughout the training process.

Table 3: Training Parameters

Related Parameter	**Value**
Batch size	32
Learning rate	1×10^{-4}
Optimizer	Adam
Number of Epochs	50
Loss Function	Cross Entropy Loss
Backbone model	Pre-trained model, ResNet-50 (ImageNet)

2.6 Performance Evaluation

The performance of the proposed ResNet-50 model was evaluated using four widely adopted classification metrics: accuracy, precision, recall, and F1-score. These metrics provide complementary information regarding the model's overall classification performance, prediction reliability, and ability to correctly distinguish between the AK-47 and Knife classes. The mathematical expressions of the evaluation metrics are presented in Table 4.

In the evaluation process, True Positive (TP), True Negative (TN), False Positive (FP), and False Negative (FN) denote the correctly and incorrectly classified samples used in computing the performance metrics.

Table 4: Performance Evaluation Metrics. Source (Burgaz and Budak, 2022)

Metric	**Equation**
Precision	$\frac{TP}{TP + FP}$
Recall	$\frac{TP}{TP + FN}$
F1 score	$2 \times \frac{Precision \times Recall}{Precision + Recall}$
Accuracy	$\frac{TP + TN}{TP + TN + FP + FN}$

3. RESULTS AND DISCUSSION

This section presents and discusses the performance of the proposed ResNet-50-based weapon classification model. Following model training, the network was evaluated using the validation dataset to assess its ability to distinguish between the AK-47 and Knife classes. The experimental results are presented in terms of training performance, classification metrics, and prediction capability on unseen images, demonstrating the effectiveness of the proposed approach for intelligent surveillance applications.

3.1 Training and Validation Performance

The training and validation performance of the proposed ResNet-50 model was evaluated using the loss and accuracy recorded over 50 training epochs. The corresponding learning curves are presented in Figure 4, where Figure 4(a) illustrates the training and validation loss, while Figure 4(b) presents the training and validation accuracy.

As shown in Figure 4(a), both the training and validation loss decreased progressively throughout the training process, indicating that the model progressively learned discriminative features for the classification task. However, the validation loss remained lower than the training loss during most of the training epochs. Similarly, Figure 4(b) shows that both the training and validation accuracy increased progressively before stabilizing at high values, with the validation accuracy remaining higher than the training accuracy. This pattern is attributable, in part, to the different preprocessing procedures applied during training and validation. During training, random resized cropping, horizontal flipping, rotation, and colour-jitter augmentation were applied to the images, introducing additional variability into the samples presented to the model. In contrast, the validation images were processed using deterministic resizing and center cropping without random augmentation. Consequently, the training accuracy and loss reflect the model's performance on dynamically transformed training samples, whereas the validation metrics reflect performance on consistently processed validation samples. The higher validation performance therefore does not, by itself, indicate data leakage or overfitting, but reflects, in part, the different preprocessing conditions applied during training and validation. Overall, the learning curves indicate progressive convergence and high classification performance, with the difference between the training and validation curves being consistent with the different preprocessing conditions adopted in the experiment.

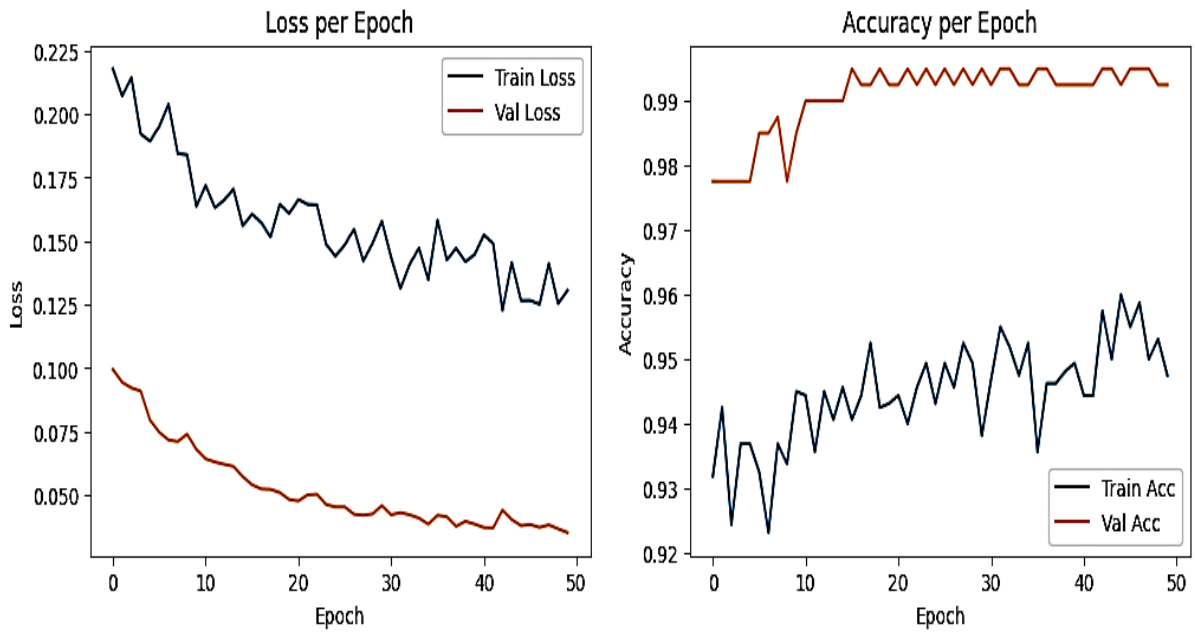

Figure 4: Training and Validation Loss Curves

3.2 Classification Performance

The classification performance of the proposed ResNet-50 model was evaluated using precision, recall, F1-score, and overall classification accuracy. The quantitative performance metrics are presented in Table 5, while the corresponding confusion matrix is shown in Figure 5.

As presented in Table 5, the proposed model achieved excellent classification performance for both weapon categories. For the AK-47 class, the model attained a precision of 0.99, recall of 1.00, and an F1-score of 0.99. Similarly, the Knife class achieved precision, recall, and F1-score values of 0.99, with an overall classification accuracy of 0.99. These results demonstrate that the fine-tuned ResNet-50 model effectively learned discriminative visual features that enabled accurate differentiation between the two weapon categories.

The confusion matrix shown in Figure 5 further validates the classification performance of the proposed model. The model correctly classified 200 AK-47 images and 198 Knife images, with only a small number of misclassifications. Specifically, one AK-47 image was incorrectly classified as a Knife, while two Knife images were misclassified as AK-47. The low number of false positive and false negative predictions is consistent with the high precision, recall, F1-score, and overall accuracy obtained during evaluation. The low number of misclassifications is consistent with the high precision, recall, F1-score, and overall accuracy obtained during evaluation. These results demonstrate the effectiveness of the transfer learning-based ResNet-50 model for the two-class weapon classification task under the image-based conditions investigated.

Table 5: Classification Performance of the Proposed ResNet-50 Model

Object Classifier	**Class**	**Precision**	**Recall**	**F1-Score**	**Accuracy**
ResNet-50	AK47	0.99	1.00	0.99	0.99
	Knife	0.99	0.99	0.99	0.99

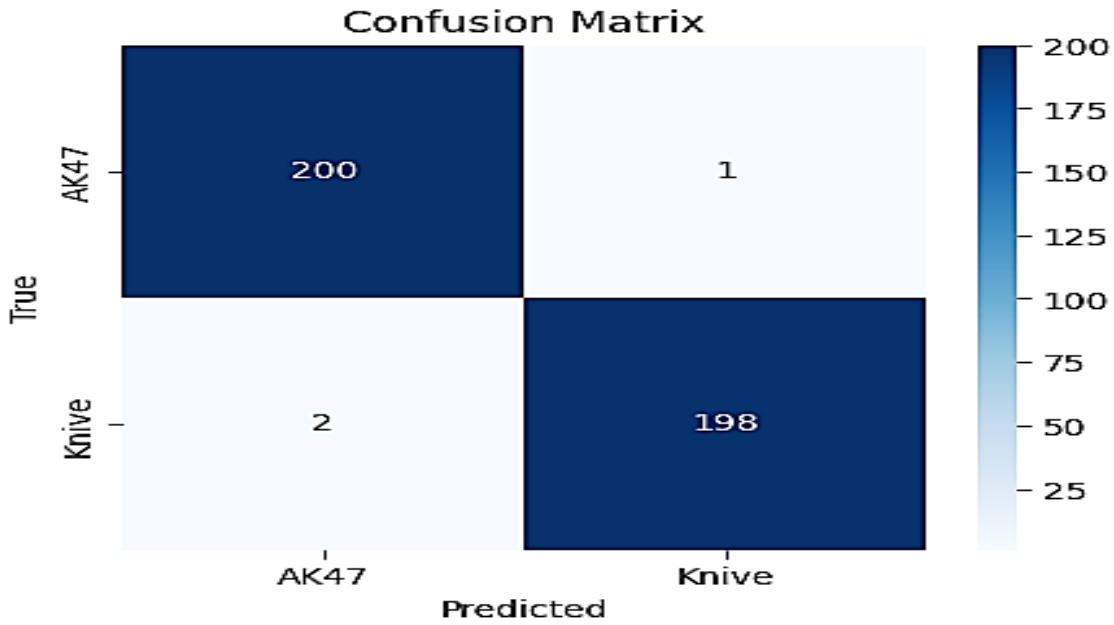

Figure 5: Confusion Matrix of the ResNet-50 Model

3.3 Prediction Results on Validation Images

To further assess the performance of the proposed ResNet-50 model, inference was carried out on representative images from the validation dataset. Sample prediction results are presented in Figure 6 where each image is displayed alongside its predicted class label. The results show that the model correctly identified both AK-47 and Knife images with high confidence, demonstrating its ability to extract discriminative features from images that were not directly used for model parameter optimization.

The prediction results are consistent with the quantitative performance metrics presented in the previous section. The model successfully recognized variations in object orientation, scale, and background while maintaining accurate classification performance. These findings indicate that the trained ResNet-50 model accurately distinguished between the two weapon categories in the evaluated validation samples under the image-based conditions investigated.

Figure 6: Predicted Result on Validation Images

3.4 Prediction Results on Unseen Images

To further evaluate the generalization capability of the proposed ResNet-50 model, inference was performed on completely unseen weapon images that were not included in either the training or validation datasets.

The model accurately classified all the unseen images into their respective categories, namely AK-47 and Knife, with very high confidence scores. Specifically, the AK-47 images were correctly recognized with confidence scores of 99.91% and 99.97%, while the Knife images achieved confidence scores of 99.81% and 99.93%, respectively. These results demonstrate that the model not only identified each weapon category correctly but also exhibited a high degree of confidence in its predictions. The result is shown in figure 7.

The consistently high confidence scores indicate the strong feature extraction capability of the ResNet-50 architecture and the effectiveness of the adopted transfer learning strategy. Furthermore, the model maintained accurate predictions across the examined unseen images, which included variations in image background, illumination, and weapon orientation. These results provide supplementary evidence of the model's predictive capability beyond the training and validation samples. Overall, the inference results demonstrate that the proposed ResNet-50-based classifier can accurately distinguish the two weapon categories under the image-based conditions investigated. The results provide a proof-of-concept baseline for potential integration into intelligent surveillance applications, although further evaluation using real-time surveillance video and camera-captured data is required.

Figure 7: Prediction Result on Unseen Images

3.5 Discussion of Findings

The experimental results demonstrate that the proposed ResNet-50-based weapon classification model is capable of accurately distinguishing between AK-47 rifles and knives under the image-based conditions investigated. The high values obtained for precision, recall, F1-score, and overall accuracy indicate that the model learned discriminative visual features for the two weapon categories. The validation results also show that the model achieved high classification performance on images that were not used for parameter updates during training. However, because the study employed a training-validation split without an independent held-out test set, the validation performance should be interpreted as an assessment of model performance within the experimental dataset rather than as an unbiased estimate of performance on completely independent data.

The high classification performance can be attributed to the adoption of the ResNet-50 architecture and the transfer learning strategy employed in this study. Residual learning enables the network to learn hierarchical feature representations while mitigating the vanishing gradient problem associated with deep neural networks. Furthermore, initializing the model with ImageNet pre-trained weights provided useful feature representations that supported the classification task using the available weapon image dataset. These findings are consistent with previous studies that have reported the effectiveness of deep convolutional neural networks and transfer learning for image classification and weapon recognition tasks.

The confusion matrix and inference results on the validation and unseen images provide further evidence of the model's ability to distinguish between the two weapon categories under the image-based conditions investigated. The small number of misclassifications in the validation results indicates that the learned feature representations were sufficiently discriminative for the two-class classification task. The high confidence scores obtained during inference also indicate that the model produced confident predictions for the examined unseen images. However, these results should not be interpreted as evidence of robustness under operational surveillance conditions, since the evaluation did not involve continuous video streams or camera-captured surveillance footage. The ability to produce accurate and confident predictions is nevertheless a desirable characteristic for a model intended for future integration into intelligent surveillance applications.

The learning curves provide additional insight into the training behaviour of the model. Both training and validation loss decreased progressively, while training and validation accuracy increased before stabilizing at high values. The validation accuracy remained higher than the training accuracy, while the validation loss remained lower than the training loss during most of the training process. This pattern is attributable, in part, to the different preprocessing conditions applied during training and validation. Random resized cropping, horizontal flipping, rotation, and colour-jitter augmentation were

applied dynamically to the training images, introducing additional variability into the samples presented to the model. In contrast, the validation images were processed using deterministic resizing and center cropping without random augmentation. The higher validation performance therefore does not, by itself, indicate data leakage or overfitting, but reflects, in part, the different preprocessing conditions applied during training and validation.

Despite the promising performance achieved in this study, certain limitations should be acknowledged. The developed model was trained and evaluated using only two weapon categories, namely AK-47 rifles and knives, and the dataset consisted primarily of images collected from online sources. The model was not evaluated under challenging real-world surveillance conditions such as occlusion, motion blur, low illumination, cluttered backgrounds, varying camera viewpoints, or continuous video streams captured from fixed surveillance cameras or unmanned aerial vehicles. In addition, the study focused on image classification rather than object detection and localization. Future research should therefore consider expanding the dataset to include additional weapon categories, evaluating the model using independent test data and real-time surveillance video, and investigating object-detection architectures and more recent deep learning models to improve robustness and support eventual integration into practical intelligent surveillance applications.

4. CONCLUSIONS

This study presented a deep learning-based weapon classification framework relevant to intelligent surveillance applications using the ResNet-50 architecture and a transfer learning strategy. The pretrained ResNet-50 model was adapted to classify two weapon categories, namely AK-47 rifles and knives. The developed framework demonstrated the application of transfer learning to image-based weapon classification using a relatively modest dataset.

A complete weapon classification pipeline was developed using the PyTorch deep learning framework in the Google Colab environment. The collected dataset was preprocessed, normalized, and organized to facilitate model training and validation. The model exhibited stable convergence throughout the 50 training epochs, as reflected in the training and validation loss and accuracy curves. The validation results further demonstrated high classification performance under the image-based experimental conditions adopted in this study.

Performance evaluation showed that the proposed ResNet-50 model achieved an overall accuracy of 0.99, with precision, recall, and F1-score values of 0.99 or higher for the two weapon classes. The confusion matrix and inference results on unseen images further demonstrated the model's ability to distinguish between the two weapon categories, with prediction confidence scores exceeding 99% for the examined unseen samples. These findings establish the proposed approach as a proof-of-concept image classification framework for automated weapon recognition.

However, the study does not establish the performance of the model in operational intelligent surveillance environments. The experiment was limited to static images collected primarily from online sources and focused on binary image classification rather than real-time object detection and localization. The model was not evaluated using continuous surveillance video, camera-captured data, occlusion, motion blur, low illumination, cluttered backgrounds, or other challenging operational conditions. Therefore, the results demonstrate the potential of the ResNet-50 approach as a baseline for future intelligent surveillance integration rather than direct deployment readiness.

Future research should expand the dataset to include a broader range of weapon categories and establish an independent test set for more robust performance evaluation. Further investigation should also include real surveillance-camera data and continuous video streams, together with object-detection and localization capabilities, to assess the model under realistic surveillance conditions. These developments would provide a stronger basis for progressing from the present image-based proof-of-concept framework toward practical intelligent surveillance applications.

CONFLICT OF INTEREST

There is no conflict of interest with any person / institution in the article prepared

REFERENCES

Ağdaş, M.T., Türkoğlu, M. and Gülseçen, S. (2021) "Deep Neural Networks Based on Transfer Learning Approaches to Classification of Gun and Knife Images," 4(1). Available at: https://doi.org/10.35377/saucis.04.01.891308.

Ahmed, S. *et al.* (2022) "Development and Optimization of Deep Learning Models for Weapon Detection in Surveillance Videos," *Applied Sciences (Switzerland)*, 12(12). Available at: https://doi.org/10.3390/app12125772.

Burgaz, M. and Budak, C. (2022) "Detection of Object (Weapons) with Deep Learning Algorithms from Images Obtained by Unmanned Aerial Vehicles," 2, pp. 263–270. Available at: https://doi.org/10.24012/dumf.1116534.

Dwivedi, N., Singh, D.K. and Kushwaha, D.S. (2019) "Weapon classification using deep convolutional neural network," *2019 IEEE Conference on Information and Communication Technology, CICT 2019*, pp. 1–5. Available at: https://doi.org/10.1109/CICT48419.2019.9066227.

Gao, M. *et al.* (2021) "A Transfer Residual Neural Network Based on ResNet-34 for Detection of Wood Knot Defects."

Gelana, F. and Yadav, A. (2019) *Firearm Detection from Surveillance Cameras Using Image Processing and Machine Learning Techniques, Advances in Intelligent Systems and Computing*. Springer Singapore. Available at: https://doi.org/10.1007/978-981-13-2414-7_3.

Hashmi, T.S.S. *et al.* (2021) "Application of Deep Learning for Weapons Detection in Surveillance Videos," *2021 International Conference on Digital Futures and Transformative Technologies, ICoDT2 2021* [Preprint]. Available at: https://doi.org/10.1109/ICoDT252288.2021.9441523.

He, K. *et al.* (2016) "Deep residual learning for image recognition," *Proceedings of the IEEE Computer Society Conference on Computer Vision and Pattern Recognition*, 2016-December, pp. 770–778. Available at: https://doi.org/10.1109/CVPR.2016.90.

Ingle, P.Y. and Kim, Y.G. (2022) "Real-Time Abnormal Object Detection for Video Surveillance in Smart Cities," *Sensors*, 22(10). Available at: https://doi.org/10.3390/s22103862.

Kambhatla, A. and R Khaled, A. (2023) "Real Time Deep Learning Weapon Detection Techniques for Mitigating Lone Wolf Attacks," *International Journal of Artificial Intelligence & Applications*, 14(04), pp. 1–16. Available at: https://doi.org/10.5121/ijaia.2023.14401.

Kaya, V., Tuncer, S. and Baran, A. (2021) "Detection and classification of different weapon types using deep learning," *Applied Sciences (Switzerland)*, 11(16). Available at: https://doi.org/10.3390/app11167535.

Lim, J. *et al.* (2019) "Gun detection in surveillance videos using deep neural networks," *2019 Asia-Pacific Signal and Information Processing Association Annual Summit and Conference, APSIPA ASC 2019*, (November), pp. 1998–2002. Available at: https://doi.org/10.1109/APSIPAASC47483.2019.9023182.

Mehta, P., Kumar, A. and Bhattacharjee, S. (2020) "Fire and Gun Violence based Anomaly Detection System Using Deep Neural Networks," *Proceedings of the International Conference on Electronics and Sustainable Communication Systems, ICESC 2020*, (Icesc), pp. 199–204. Available at: https://doi.org/10.1109/ICESC48915.2020.9155625.

Oura, P., Junno, A. and Junno, J.A. (2021) "Deep learning in forensic gunshot wound interpretation—a proof-of-concept study," *International Journal of Legal Medicine*, 135(5), pp. 2101–2106. Available at: https://doi.org/10.1007/s00414-021-02566-3.

Salido, J., Lomas, V. and Ruiz-santaquiteria, J. (2021) "Automatic Handgun Detection with Deep Learning in Video Surveillance Images," *Applied Sciences (Switzerland)*, 11(13).

Verma, G.K. and Dhillon, A. (2017) "A Handheld Gun Detection using Faster R-CNN Deep Learning," *ACM International Conference Proceeding Series*, pp. 84–88. Available at: https://doi.org/10.1145/3154979.3154988.

Warsi, A. *et al.* (2019) "Gun Detection System Using Yolov3," *2019 IEEE 6th International Conference on Smart Instrumentation, Measurement and Application, ICSIMA 2019*, (August),

pp. 1–4. Available at: https://doi.org/10.1109/ICSIMA47653.2019.9057329.

Xu, S. and Hung, K. (2020) "Development of an AI-based System for Automatic Detection and Recognition of Weapons in Surveillance Videos," *ISCAIE 2020 - IEEE 10th Symposium on Computer Applications and Industrial Electronics*, pp. 48–52. Available at: https://doi.org/10.1109/ISCAIE47305.2020.9108816.

Yadav, P., Gupta, N. and Sharma, P.K. (2023) "A comprehensive study towards high-level approaches for weapon detection using classical machine learning and deep learning methods," *Expert Systems with Applications*, 212. Available at: https://doi.org/10.1016/j.eswa.2022.118698.

International Conference on Engineering Innovation for Sustainable Development (ICESID 2026)
Faculty of Engineering, Ahmadu Bello University Zaria · 8–10 September 2026

AI-BASED SMART MEDICATION IDENTIFICATION, AUTOMATED DISPENSING, TIMED REMINDER, AND MONITORING DASHBOARD SYSTEM

Oluwafemi Lawal[1], Oreofe Ajayi[1,*], David Ejila Oiwona[1], Abdulhafeez Tahir Adamu[1], Mohammed Abubakar[1], Muhammad U. Nafiu[1]

[1]*Ahmadu Bello University, Zaria*

Email: femoskey04@gmail.com, ajayi.oreofe17@gmail.com*, davidejila270@gmail.con, sarfizzy@gmail.com, abusqmohd023@gmail.com, muhammadnafiu556@gmail.com

***Corresponding author**: Oreofe Ajayi

DOI: https://doi.org/10.67203/sp.ICESID.2026

ABSTRACT

Medication errors and poor adherence remain important patient-safety challenges where identification, dispensing, scheduling, and monitoring depend on manual processes. This paper presents a functional engineering prototype that integrates AI-based medication identification, automated dispensing, timed reminders, evidence capture, stock management, and remote monitoring. The system uses a Raspberry Pi 4 Model B as the central controller and an EfficientNet-B4 image-classification model trained on 4,480 OGYEIv2 images across 112 medication classes. The data were divided into 3,136 training, 672 validation, and 672 held-out test images. The reported independent test accuracy was 99.85%, corresponding to 671 correct predictions and one incorrect prediction. Stepper motors and motor drivers actuate medication compartments, infrared sensors provide dispensing feedback, and a DS3231 real-time clock supports scheduled events and audiovisual reminders. A camera evidence service, TFT interface, Flask backend, SQLite database, and Android application provide system monitoring and records. Functional testing demonstrated successful operation of the major hardware and software modules, including the corrected evidence-image serving route. The evaluation remains an engineering prototype assessment rather than clinical validation; controlled imaging conditions, limited test size, visually similar classes, absence of real-user evaluation, and the need for repeated physical dispensing tests limit conclusions about real-world safety and effectiveness. The prototype demonstrates the feasibility of an integrated medication-management platform for further development in Nigeria and other resource-constrained settings.

Keywords: *Artificial Intelligence; Medication Identification; Medication Dispensing; EfficientNet-B4; Raspberry Pi; Medication Adherence*

1. INTRODUCTION

1.1 Background and Problem Statement

Medication management combines identification, dosage scheduling, dispensing, administration, documentation, and monitoring. Errors at these stages can produce inappropriate medication use and preventable harm. The World Health Organization identifies medication safety as a major patient-safety priority and has promoted the Medication Without Harm initiative (World Health Organization, 2017, 2021). Managing several medicines at different times also increases the possibility of missed doses, incorrect selection, incorrect quantities, and incomplete records.

Artificial intelligence and embedded computing provide opportunities to automate selected medication-management functions while retaining clinical oversight. EfficientNet provides a scalable convolutional-neural-network architecture that balances model capacity and computational requirements (Tan & Le, 2019). Previous studies have shown the feasibility of deep-learning-based pill recognition (Al-Hussaeni et al., 2023; Ashraf et al., 2024; Heo et al., 2023), while other systems have investigated automated dispensing, adherence technologies, and monitoring dashboards (Mason et al., 2022; Nasir et al., 2023; Patel et al., 2020; Pathiraja & Wijesinghe, 2024; Wang et al., 2021, 2025).

The challenge addressed in this study is not a new classification architecture but the integration of medication image classification, scheduled dispensing, reminders, evidence capture, stock management, and mobile monitoring within one Raspberry Pi-based platform. This integrated approach is intended as an affordable engineering prototype that may be adapted for Nigerian and other resource-constrained environments.

1.2 Aim and Objectives

The aim is to design and implement an AI-based smart medication identification, automated dispensing, timed reminder, and monitoring dashboard system using artificial intelligence and embedded computing technologies.

The objectives are to:

1. Design and implement an EfficientNet-B4 medication-identification module.
2. Design and implement stepper-motor dispensing with infrared feedback.
3. Implement timed reminders using a DS3231 real-time clock and audiovisual alerts.
4. Develop monitoring functions for schedules, stock, dispensing records, and evidence.
5. Integrate the hardware and software subsystems into one prototype.
6. Test and evaluate the functionality and performance of the developed system.

1.3 Research Gap and Significance

Existing literature commonly treats pill recognition, automated dispensing, reminders, and adherence monitoring as separate problems. This work addresses the engineering integration gap by combining these functions with local data storage and a mobile interface. The principal significance is therefore system-level integration rather than a claim of clinical replacement or novel AI architecture.

2. METHODOLOGY

2.1 Dataset and Model Development

The AI component uses the OGYEIv2 dataset, which contains 4,480 images representing 112 pill classes. The dataset was captured under controlled imaging conditions using fixed scale, a homogeneous background, and two illumination arrangements designed to expose surface markings (Rádli et al., 2023, 2024).

For this experiment, 70% of the data (3,136 images) were used for training, 15% (672) for validation, and 15% (672) for held-out testing. Each class contributes 28 training images, six validation images, and six test images. Images were resized to 384 × 384 pixels for EfficientNet-B4; normalization and training-time augmentation were applied. The model was trained for 30 epochs with Adam, cross-entropy loss, an initial learning rate of 3×10^{-4}, batch size 16, and ReduceLROnPlateau scheduling.

Table 1: *Dataset Distribution*

Subset	Number of Images	Percentage
Training	3,136	70%
Validation	672	15%
Testing	672	15%
Total	**4,480**	**100%**

Table 2: *AI Model Training Configuration*

Parameter	Configuration
Dataset	OGYEIv2
Classes	112
Total images	4,480
Train / validation / test	3,136 / 672 / 672
Model	EfficientNet-B4
Input	384 × 384 pixels
Epochs	30
Batch size	16
Optimizer	Adam
Initial learning rate	3×10^{-4}
Loss	Cross-entropy
Scheduler	ReduceLROnPlateau

2.2 Embedded Hardware and Software

The prototype uses a Raspberry Pi 4 Model B, camera, TFT display, stepper motors, ULN2003 motor drivers, PCF8574 I/O expanders, infrared sensors, DS3231 RTC module, speaker, LED illumination, power-supply components, and a 3D-printed dispenser structure. The Raspberry Pi executes the AI model, manages schedules, controls motors and sensors, activates alarms, operates the camera, maintains the database, runs the Flask backend, and communicates with the Android application (Grinberg, 2018; Upton & Halfacree, 2016).

Medication schedules are stored in SQLite and compared with the RTC time. At a scheduled event, the corresponding compartment motor is activated and the reminder mechanism issues an audiovisual alert. Infrared feedback provides information about medication movement. The camera records evidence associated with dispensing events. The mobile interface exposes medication records, schedules, stock, logs, evidence, and settings.

RFID readers, QR-code scanners, load cells/HX711 modules, YOLOv5, ResNet-50, and PaddleOCR are not claimed as implemented components in this prototype.

2.3 Evaluation Method

The independent test set of 672 images was used for final AI evaluation. Accuracy was computed as correct predictions divided by total predictions. Functional system testing covered the backend, communication, scheduling, alarm, motor control, infrared sensing, evidence capture and display, stock functions, security, TFT interface, and integrated workflow.

3. RESULTS AND DISCUSSION

3.1 AI Test Performance

The model achieved 671 correct predictions and one incorrect prediction on the 672-image held-out set, giving an accuracy of 99.85%. The reported error involved the visually similar dulodet_60_mg and dulsevia_60_mg classes. This result indicates strong performance on the evaluated dataset but should not be interpreted as clinical-grade medication recognition.

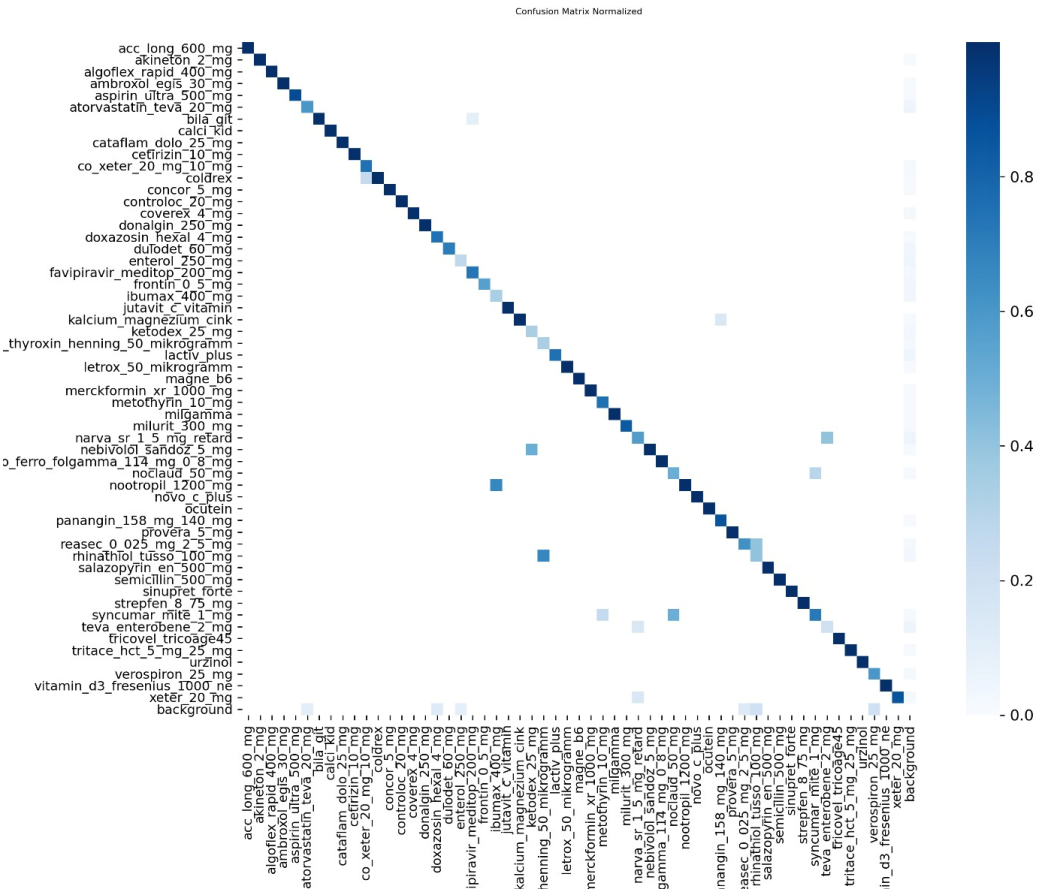

Figure 1: *Normalized confusion matrix of the EfficientNet-B4 model on the held-out test set*

The supplied normalized confusion matrix shows a strong concentration along the principal diagonal, consistent with high class-wise recognition on the controlled test set. The visually similar dulodet_60_mg and dulsevia_60_mg classes are the reported source of the single classification error. Because normalized matrices show relative class-wise prediction distributions, the figure is interpreted together with the aggregate result of 671/672 correct predictions.

Table 3: *Held-Out Test Performance*

Metric	Result
Classes	112
Training images	3,136
Validation images	672
Test images	672
Correct predictions	671
Incorrect predictions	1
Test accuracy	99.85%

3.2 System-Level Functional Results

Subsystem and integrated tests demonstrated successful operation of the Raspberry Pi backend, medication-management services, scheduling logic, stepper-motor control, infrared sensing, buzzer activation, camera evidence capture, TFT interface, stock functions, and Android communication. An evidence-image serving defect was identified during development: metadata was stored correctly, but associated images were not displayed in the mobile application. Correcting the backend image-serving route restored retrieval and display of raw and annotated evidence images.

Table 4: *Integrated System Test Results*

Test case	Observed result	Status
Backend startup	Server started successfully	Passed
Mobile connection	Connection established	Passed
Medication registration	Medication saved successfully	Passed
Schedule creation	Schedule stored successfully	Passed
Alarm detection	Due medication detected	Passed
Buzzer activation	Buzzer activated	Passed
Motor control	Motor control executed	Passed
IR sensing	Sensor interface responded	Passed
Evidence capture	Evidence generated	Passed
Evidence display	Images displayed after route correction	Passed
Stock management	Stock functions operated	Passed
Mobile security	Password protection operated	Passed
TFT interface	Interface loaded successfully	Passed
System integration	Core workflow demonstrated	Passed

3.3 Discussion

The results show that AI classification can be integrated with embedded scheduling, dispensing, reminders, evidence capture, stock management, and remote monitoring on a Raspberry Pi platform. The 99.85% result is strong for the evaluated controlled dataset, but it does not establish clinical validity, guarantee real-world identification accuracy, or demonstrate a reduction in medication errors. The integration test also illustrates that end-to-end reliability depends on interfaces between subsystems: the evidence service initially produced valid records but required a backend route correction before images were usable in the mobile interface.

4. CONTRIBUTION TO SUSTAINABLE DEVELOPMENT IN NIGERIA

The project demonstrates an approach to locally developed healthcare-support technology using widely available embedded computing and software components. A Raspberry Pi-based platform can provide a basis for investigating lower-cost medication automation for hospitals, primary-care facilities, caregivers, and home-care environments. However, sustainability requires more than hardware affordability: future deployment would require reliable power, maintainability, cybersecurity, data protection, clinical oversight, regulatory compliance, user training, and technical support. The contribution is therefore an engineering proof of concept rather than a claim of deployment readiness.

5. LIMITATIONS

1. The AI model was evaluated on the controlled OGYEIv2 dataset, so the 99.85% result may not generalize to uncontrolled lighting, backgrounds, orientations, occlusion, motion, or camera positions.
2. The independent test set contained 672 images, limiting the statistical strength of generalization claims.
3. The reported confusion between dulodet_60_mg and dulsevia_60_mg shows that visually similar medicines remain a limitation of image-based identification.
4. Functional testing confirmed operation of the prototype modules but was not a clinically powered medication-administration or dispensing-accuracy study.
5. Repeated dispensing tests across all compartments and long-duration operation remain necessary.
6. No evaluation involving real patients, caregivers, nurses, or other intended users has been reported, so usability and human-factors evidence is limited.
7. The system should not substitute for healthcare professionals or clinical medication verification.

6. FUTURE WORK

Future studies should use larger and more diverse medication datasets covering additional classes, manufacturers, orientations, illumination conditions, backgrounds, and real-world imaging.

Additional data and model-development methods should be investigated for visually similar classes, especially the reported dulodet_60_mg/dulsevia_60_mg confusion.

The dispensing mechanism should undergo repeated and long-duration tests across medication compartments, including motor reliability, sensor stability, scheduling accuracy, database operation, and power consumption.

Future versions may incorporate barcode or QR-code verification and dosage-verification sensors as complementary safeguards, together with caregiver notifications through push notifications, SMS, or email.

Usability and clinical evaluation should involve representative users and healthcare professionals under appropriate ethical and regulatory oversight.

7. CONCLUSION

This paper presented an AI-based smart medication-management prototype integrating EfficientNet-B4 image classification, Raspberry Pi control, stepper-motor dispensing, infrared sensing, DS3231 scheduling, audiovisual reminders, camera evidence capture, SQLite storage, Flask services, a TFT interface, and an Android monitoring application. The model achieved a reported 99.85% accuracy on 672 held-out images representing 112 medication classes, with 671 correct predictions and one reported misclassification involving dulodet_60_mg and dulsevia_60_mg. Functional testing demonstrated successful operation of the major software and hardware subsystems, including correction of an evidence-image serving defect. The findings establish technical feasibility but not clinical effectiveness or deployment safety. Further work should focus on broader data, repeated physical validation, real-user studies, cybersecurity, and clinical and regulatory assessment.

REFERENCES

Al-Hussaeni, K., Karamitsos, I., Adewumi, E., & Amawi, R. M. (2023). CNN-based pill image recognition for retrieval systems. *Applied Sciences, 13(8), 5050*. https://doi.org/10.3390/app13085050

Ashraf, A. R., Somogyi-Végh, A., Merczel, S., Gyimesi, N., & Fittler, A. (2024). Leveraging code-free deep learning for pill recognition in clinical settings: A multicenter, real-world study of performance across multiple platforms. *Artificial Intelligence in Medicine, 150, 102844*. https://doi.org/10.1016/j.artmed.2024.102844

Grinberg, M. (2018). *Flask web development: Developing web applications with Python (2nd ed.).* O'Reilly Media.

Heo, J., Kang, Y., Lee, S., Jeong, D.-H., & Kim, K.-M. (2023). An accurate deep learning-based system for automatic pill identification: Model development and validation. *Journal of Medical Internet Research, 25, e41043*. https://doi.org/10.2196/41043

Mason, M., Cho, Y., Rayo, J., Gong, Y., Harris, M., & Jiang, Y. (2022). Technologies for medication adherence monitoring and technology assessment criteria: Narrative review. *JMIR mHealth and uHealth, 10(3), e35157*. https://doi.org/10.2196/35157

Nasir, Z., Asif, A., Nawaz, M., & Ali, M. (2023). Design of a smart medical box for automatic pill dispensing and health monitoring. *Engineering Proceedings, 32(1), 7*. https://doi.org/10.3390/engproc2023032007

Patel, T., Ivo, J., Faisal, S., McDougall, A., Carducci, J., & Pritchard, S. (2020). A prospective study of usability and workload of electronic medication adherence products by older adults, caregivers, and health care providers. *Journal of Medical Internet Research, 22(6), e18073*. https://doi.org/10.2196/18073

Pathiraja, M., & Wijesinghe, W. (2024). IoT-enabled medicine dispenser for pills and liquid medication In Proceedings of the 2024 International Conference on Image Processing and Robotics (ICIPRoB). https://doi.org/10.1109/ICIPRoB63381.2024.10550973

Rádli, R., Bene, J., Vörösházi, Z., & Czúni, L. (2023). OGYEIv2: An in-depth collection of 112 pill classes for medical image classification [Dataset] Kaggle. https://www.kaggle.com/datasets/richardradli/ogyeiv2

Rádli, R., Vörösházi, Z., & Czúni, L. (2024). Metric-based pill recognition with the help of textual and visual cues. *IET Image Processing, 18, 4623–4638*. https://doi.org/10.1049/ipr2.13273

Tan, M., & Le, Q. V. (2019). EfficientNet: Rethinking model scaling for convolutional neural networks In *Proceedings of the 36th International Conference on Machine Learning* (Vol. 97, pp. 6105–6114).

Upton, E., & Halfacree, G. (2016). *Raspberry Pi user guide (4th ed.).* John Wiley & Sons.

Wang, M., Pereira, M. M., Uppal, S., & Gualtieri, L. (2025). Designing a real-time medication intake and adherence dashboard: Features, functionality, and data display to meet the needs of patients, care partners and healthcare providers. *Journal of Medical Systems, 49(1), 52*. https://doi.org/10.1007/s10916-025-02189-w

Wang, Y. C., Tsan, C. Y., & Chen, M. C. (2021). Implementation of an automated dispensing cabinet system and its impact on drug administration: Longitudinal study. *JMIR Formative Research, 5(9), e24542*. https://doi.org/10.2196/24542

World Health Organization. (2017). *Medication without harm: WHO global patient safety challenge on medication safety.* World Health Organization.

World Health Organization. (2021). *Global patient safety action plan 2021–2030: Towards eliminating avoidable harm in health care.* World Health Organization.

International Conference on Engineering Innovation for Sustainable Development (ICESID 2026)
Faculty of Engineering, Ahmadu Bello University Zaria · 8–10 September 2026

DESIGN AND PERFORMANCE EVALUATION OF AN INTELLIGENT UAV-BASED VISION SYSTEM FOR AUTOMATED POWER TRANSMISSION LINE COMPONENT INSPECTION USING YOLOV8S

Asmau Sanusi Gumbi[1], S. Salisu[1], A.s Adamu[1,*], Muhammad Dikko Almustaha[2], Sulaiman Garba[3]

[1]*Ahmadu Bello University Zaria*
[2]*Department of Electronics and Telecommunications Engineering*
[3]*Nigerian Communication Communications, Abuja*

Email: najagumbi@gmail.com, sanisalisu@abu.edu.ng, abubakaras@abu.edu.ng*, md.almustapha@gmail.com, Sgarba@abu.edu.ng

***Corresponding author**: A.s Adamu

DOI: https://doi.org/10.67203/sp.ICESID.2026

ABSTRACT

Power transmission line inspection requires the identification and localisation of infrastructure components from aerial imagery. Conventional inspection approaches can be labour-intensive, costly and constrained by difficult terrain, while UAVs provide a practical means of acquiring high-resolution imagery for subsequent analysis (Alcayde-García et al., 2022; Qi et al., 2022; Mendu & Mbuli, 2025). This study develops and evaluates a YOLOv8s-based vision system for automated detection of power transmission line components using the Inspection of Power Line Assets Dataset (InSPLAD). The predefined InSPLAD training and validation partitions were retained, with COCO annotations converted to YOLO format and images prepared at 640 × 640 pixels. A pretrained YOLOv8s model was fine-tuned for 50 epochs using transfer learning in Google Colaboratory with an NVIDIA Tesla T4 GPU. The best checkpoint was obtained at Epoch 48. On the predefined validation subset, the selected model achieved 89.5% Precision, 86.2% Recall, 88.4% mAP@0.5, 72.1% mAP@0.5:0.95, and an F1-score of 87.68%. The results establish an empirical performance baseline for the stated YOLOv8s–InSPLAD configuration. The findings are limited to offline evaluation on the predefined validation subset and should not be interpreted as evidence of onboard UAV performance, real-time field operation, or generalisation to external datasets.

Keywords: *UAV inspection; power transmission lines; object detection; YOLOv8s; InSPLAD; deep learning; computer vision*

1. INTRODUCTION

Power transmission networks depend on the condition of overhead lines and associated components for reliable electricity delivery. Conductors, insulators, spacers, dampers, clamps and suspension fittings are exposed to mechanical loading, environmental conditions and ageing, making periodic inspection an important maintenance activity (Alcayde-García et al., 2022; Qi et al., 2022). Traditional inspection methods include ground patrols, manual inspection and helicopter surveys. These approaches can be labour-intensive, costly and constrained by terrain and operational safety considerations (Alhassan et al., 2020; Xu et al., 2023).

UAVs have expanded the options for transmission-line inspection by enabling aerial acquisition of detailed RGB imagery from viewpoints that may be difficult to obtain through ground inspection. Reviews of UAV applications in power-line inspection describe their use for infrastructure observation, condition assessment and automated image analysis (Shakhatreh et al., 2019; Qi et al., 2022; Mohsan et al., 2023; Mendu & Mbuli, 2025). The resulting image volume also motivates automated computer-vision methods capable of detecting and localising multiple components within inspection imagery.

Deep learning object detectors, particularly the YOLO family, have been widely applied to visual detection because they formulate localisation and classification within a unified detection pipeline (Redmon et al., 2016; Terven et al., 2023). YOLOv8 introduced an anchor-free detection

formulation and a revised architecture implemented by Ultralytics, with model variants including YOLOv8s for smaller computational footprints (Jocher et al., 2023; Terven et al., 2023). These characteristics make YOLOv8s a suitable baseline for investigating automated component detection in UAV imagery without introducing architectural modifications.

Recent transmission-line inspection studies have increasingly modified YOLO architectures to address small objects, complex backgrounds, foreign objects, low-light conditions and other inspection challenges (Qiang et al., 2023; Shao et al., 2024; Li et al., 2025; Ait El Haj et al., 2026; Zheng et al., 2026; Sheng et al., 2026; Farooq et al., 2026; Zhu & Pei, 2026). While these studies demonstrate continued progress in specialised detectors, their numerical results are not directly rankable because datasets, target classes, model configurations, training procedures and evaluation protocols differ. The present study therefore focuses on establishing a reproducible detection baseline for a standard YOLOv8s configuration on InSPLAD rather than claiming universal superiority.

The objective of this paper is to design and evaluate an automated UAV-image component detection system based on pretrained YOLOv8s and the InSPLAD dataset. The evaluation is deliberately restricted to detection performance: Precision, Recall, mAP@0.5, mAP@0.5:0.95, confusion-matrix analysis, Precision–Recall analysis and F1-score analysis. The study does not evaluate onboard UAV deployment, real-time field performance, defect severity or predictive-maintenance decisions.

2. RELATED WORK

UAV-based transmission-line inspection has developed from image acquisition toward automated interpretation. Public datasets have supported this transition by providing annotated imagery for training and benchmarking object detectors. InSPLAD was developed as a large-scale dataset for inspection of power-line assets using UAV imagery, while other datasets such as TTPLA and PLAD provide complementary coverage of transmission towers and power-line assets (André et al., 2023; Vieira e Silva et al., 2023; Jiang et al., 2020; Zhang et al., 2021).

The YOLO family has been repeatedly adapted to transmission-line inspection. Qiang et al. (2023) developed an improved YOLOv8s model for transmission-line fault detection using attention, feature-fusion and loss-function modifications. Shao et al. (2024) proposed TL-YOLO for foreign-object detection on power transmission lines using an improved YOLOv8 framework. Li et al. (2025) proposed DI-YOLOv5 for dense small-object detection using wavelet-based processing and coordinate attention. These studies illustrate a common research direction: modifying a baseline detector to address task-specific visual challenges.

More recent work has investigated lightweight and specialised YOLO-based systems. Ait El Haj et al. (2026) proposed YOLOv8-ECCα for power-line asset inspection using CoordConv, Efficient Channel Attention and Alpha-IoU loss. Zheng et al. (2026) developed YOLO-MLSL for insulator-defect detection, while Sheng et al. (2026) proposed SDS-YOLO for foreign-object detection from UAV images. Farooq et al. (2026) investigated a Transformer-Enhanced YOLOv8 framework for small and complex insulator defects, and Zhu and Pei (2026) developed LCDD-YOLO for low-light transmission-line defect detection. Du et al. (2026) further investigated multimodal RGB and infrared imagery for insulator-defect detection. Collectively, these studies show the diversity of model modifications and datasets used in the field.

The present work differs in scope. Instead of introducing a modified detection architecture, it evaluates the standard YOLOv8s detector after transfer learning on the predefined InSPLAD partitions. The purpose is to quantify the detection behaviour of this specific configuration and establish a defensible empirical baseline. Comparisons with related studies are treated as contextual rather than as a direct ranking, because reported metrics are generated under different experimental conditions.

3. MATERIALS AND METHODS

3.1 Dataset

The study used the Inspection of Power Line Assets Dataset (InSPLAD), a UAV-image dataset containing annotated transmission-line assets (André et al., 2023; Vieira e Silva et al., 2023).

The dataset used in the experiment contains 18 component classes. The predefined training and validation partitions were retained rather than creating a new random split. The training subset contained 7,946 images and the validation subset contained 2,753 images. No independent external test dataset was introduced.

3.2 Dataset Verification and Preparation

Dataset preparation followed the procedure documented in the thesis. The available imagery and annotations were checked for correspondence, annotation format and class alignment before model training. The original COCO annotation files (instances_train.json and instances_val.json) were converted to YOLO text annotations, and a dataset configuration file was prepared for the Ultralytics framework. The predefined train/validation directory structure was retained. Images were prepared at 640 × 640 pixels, and the built-in YOLOv8 augmentation pipeline was used during training. Randomly selected annotated images were visually inspected to confirm that converted bounding boxes and class labels aligned with the corresponding components.

3.3 YOLOv8s Detection Model

YOLOv8s was selected as the detection model and used without architectural modification. YOLO detectors jointly perform object localisation and classification within a single detection framework (Redmon et al., 2016). YOLOv8 uses an anchor-free formulation, a C2f-based backbone, feature fusion through the neck, and a decoupled detection head (Jocher et al., 2023; Terven et al., 2023). In this study, the model received the prepared UAV images and produced bounding-box coordinates, class labels and confidence scores for detected transmission-line components.

Spatial correspondence between a predicted bounding box and its ground-truth counterpart was assessed using Intersection over Union (IoU), defined as the area of intersection divided by the area of union of the two boxes. Standard detection metrics were then calculated from the model predictions on the validation subset (Everingham et al., 2010; Padilla et al., 2021).

3.4 Transfer Learning and Training

Transfer learning was employed by fine-tuning pretrained YOLOv8s weights on the verified InSPLAD training subset. Training was conducted for 50 epochs with a batch size of 16 in Google Colaboratory using an NVIDIA Tesla T4 GPU. The implementation used Python 3.12 and Ultralytics YOLO 8.4.96. The optimizer was automatically selected as AdamW, and the random seed was set to 42. Validation was performed after each epoch and the best-performing checkpoint was retained as best.pt. The best checkpoint occurred at Epoch 48, based primarily on the highest recorded mAP@0.5:0.95 in the validation results.

Table 1: Experimental configuration.

Parameter	Value
Dataset	InSPLAD
Number of classes	18
Training images	7,946
Validation images	2,753
Detection model	YOLOv8s
Learning strategy	Transfer learning
Framework	Ultralytics YOLO 8.4.96
Programming language	Python 3.12
Computing platform	Google Colaboratory
GPU	NVIDIA Tesla T4
Training epochs	50
Batch size	16
Optimizer	AdamW (automatic selection)
Random seed	42

3.5 Performance Evaluation

The trained model was evaluated on the predefined InSPLAD validation subset. Precision was calculated as TP/(TP+FP), and Recall as TP/(TP+FN), where TP denotes true positives, FP false positives and FN false negatives. Average Precision was obtained from the Precision–Recall relationship, and mAP was calculated as the mean of the class-wise AP values. The study reports mAP@0.5 and mAP@0.5:0.95, the latter averaging performance across IoU thresholds from 0.50 to 0.95 in increments of 0.05 (Padilla et al., 2021). The evaluation also examined the Precision–Recall curves, confusion matrix, normalized confusion matrix and F1-score curve to provide complementary views of class-wise and threshold-dependent detection behaviour.

4. RESULTS AND DISCUSSION

4.1 Dataset Verification

Before training, the dataset was checked for image–annotation correspondence, class alignment, bounding-box characteristics and spatial distribution. The resulting verification plots provide an empirical view of the data used in the experiment. Figure 1 shows the distribution of object classes and bounding-box characteristics in the InSPLAD dataset. The plots indicate variation in class frequency, object size and object position, confirming that the validation and training material contains components appearing at different locations and scales.

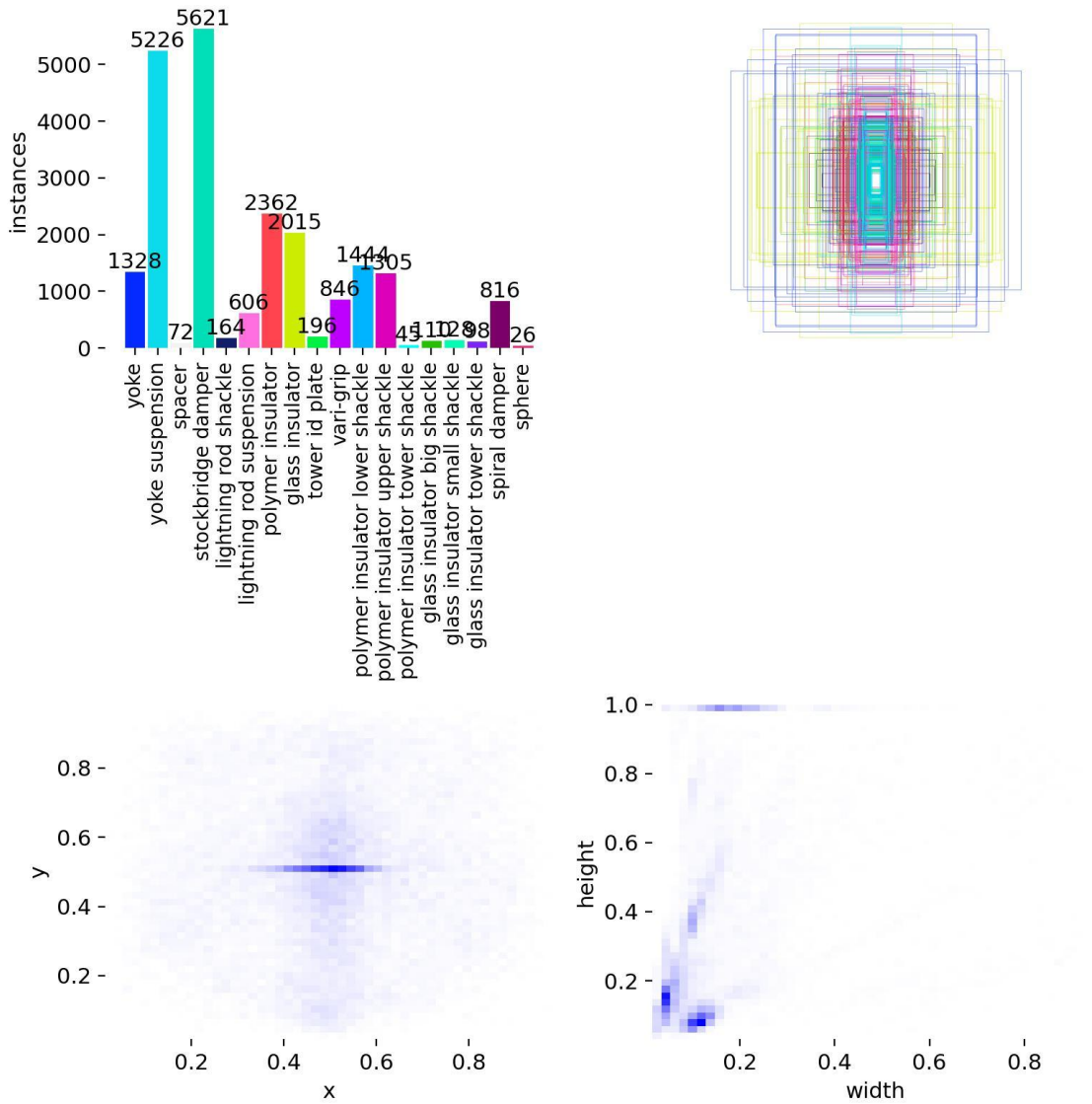

Figure 1: InSPLAD dataset distribution: object classes and bounding-box characteristics.

4.2 Training Performance

The model was trained for 50 epochs, with validation monitoring after each epoch. Figure 2 shows the training and validation loss and metric curves. The recorded losses declined over training while the evaluation metrics increased and stabilised toward the later epochs. The best checkpoint was obtained at Epoch 48, rather than assuming that the final epoch necessarily represented the best validation state. The thesis records the progression from Epoch 1 to Epoch 50 as a reduction in training and validation losses together with increases in Precision, Recall, mAP@0.5 and mAP@0.5:0.95.

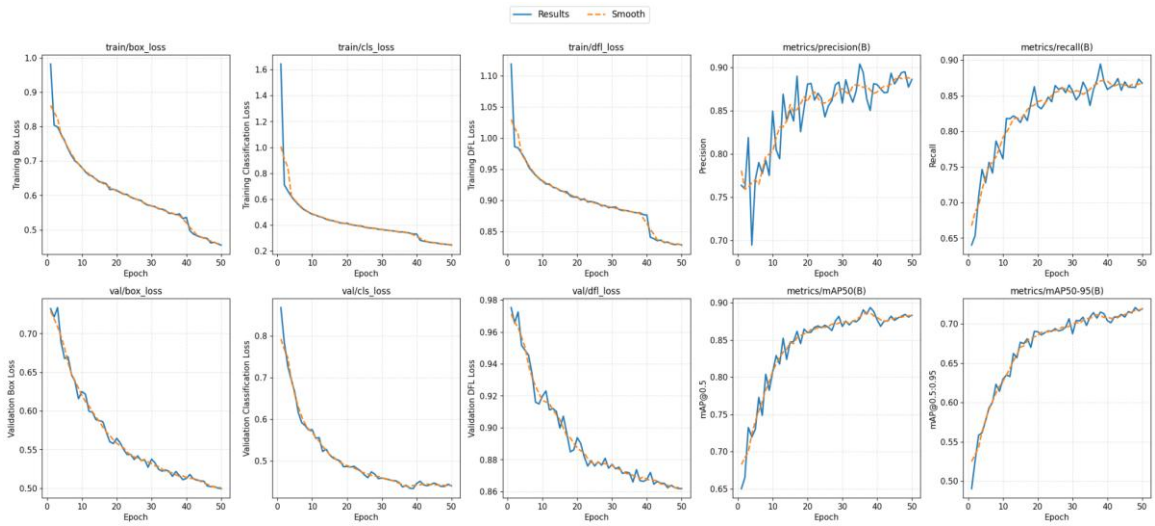

Figure 2: Training and validation performance over 50 training epochs.

4.3 Detection Results

Figure 3 presents representative detections from the InSPLAD validation subset. The detector produces bounding boxes, class labels and confidence scores for multiple transmission-line components within the UAV imagery. These examples provide qualitative evidence that the trained model can localise several component types under the visual conditions represented in the validation data. They are illustrative only; quantitative performance is assessed in the following sections.

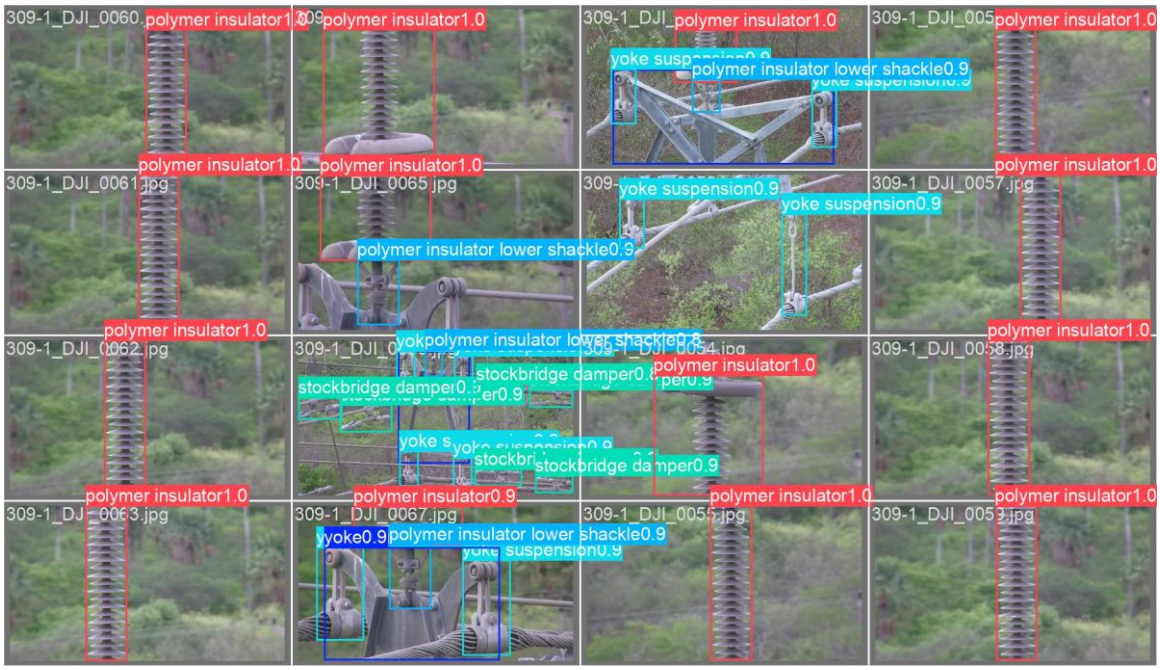

Figure 3: Representative detection results on the InSPLAD validation dataset.

4.4 Quantitative Detection Performance

The selected YOLOv8s checkpoint achieved 89.5% Precision, 86.2% Recall, 88.4% mAP@0.5 and 72.1% mAP@0.5:0.95 on the predefined InSPLAD validation subset. The F1-score was 87.68%. Together, these values indicate that the evaluated configuration achieved a substantial level of detection performance across the 18 component classes represented in the validation subset. The difference between mAP@0.5 and mAP@0.5:0.95 also provides a stricter view of localisation performance when increasingly demanding IoU thresholds are applied.

Table 2: Overall detection performance of YOLOv8s on the InSPLAD validation subset.

Metric	Best checkpoint
Precision	89.5%
Recall	86.2%
mAP@0.5	88.4%
mAP@0.5:0.95	72.1%

4.5 Precision–Recall Analysis

Figure 4 presents the Precision–Recall curves for the evaluated component classes. The curves show how precision changes as recall varies with the detection threshold. The overall behaviour is consistent with the aggregate Precision, Recall and mAP values reported in Table 2. Because the classes are represented with different frequencies and visual characteristics, the curves should be interpreted as class-specific evidence rather than as a single universal operating characteristic.

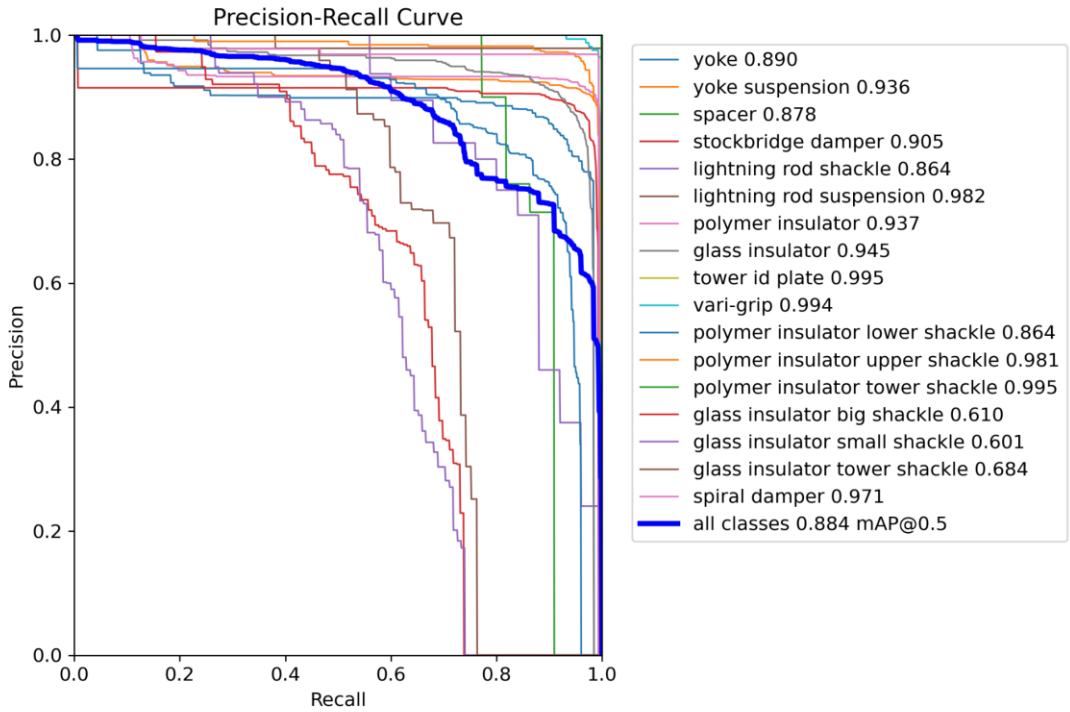

Figure 4: Precision–Recall curves for the transmission-line component classes.

4.6 Confusion Matrix Analysis

The confusion matrix in Figure 5 provides a class-wise view of predicted labels against ground-truth labels. The concentration of detections along the main diagonal indicates that many validation instances were assigned to their corresponding classes, while off-diagonal entries identify cases of class confusion. Such errors are particularly relevant where component categories share similar visual characteristics. The matrix therefore complements aggregate metrics by showing where classification errors occur across the evaluated classes.

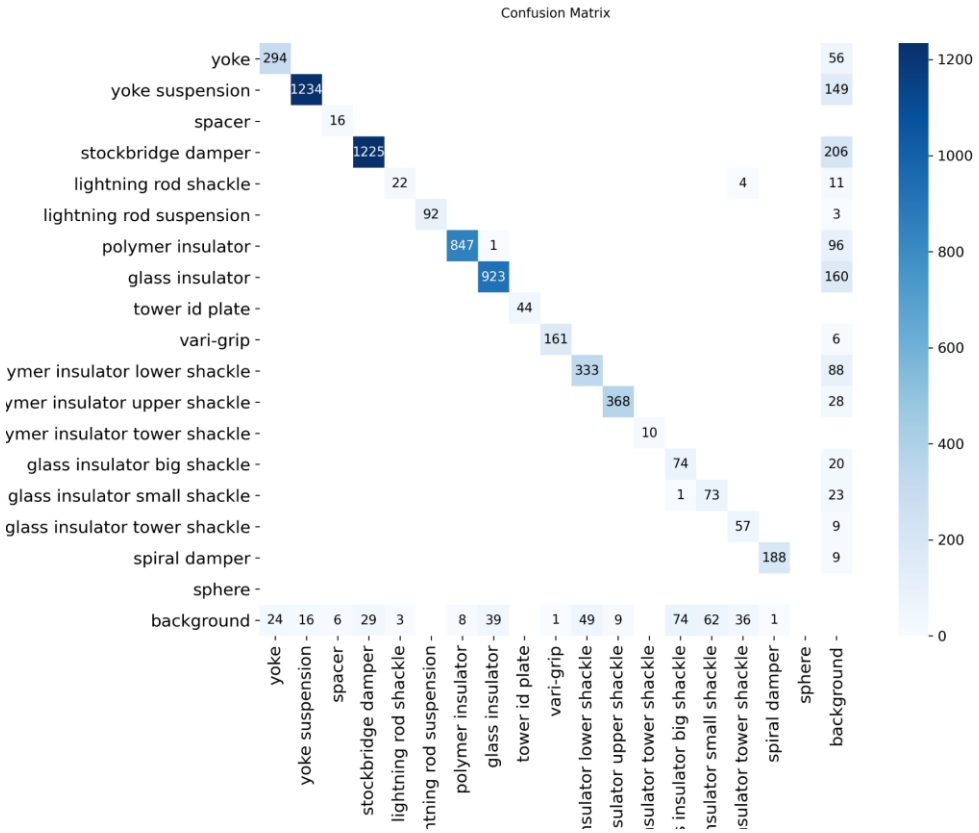

Figure 5: Confusion matrix of the proposed YOLOv8s model.

4.7 Normalized Confusion Matrix and F1-Score

The normalized confusion matrix in Figure 6 expresses class-wise outcomes on a normalized scale, making differences between classes easier to inspect when their numbers of validation instances are unequal. The diagonal concentration across the classes indicates that correct classification accounts for a substantial share of the evaluated predictions, while the remaining off-diagonal proportions identify the relative pattern of class confusion.

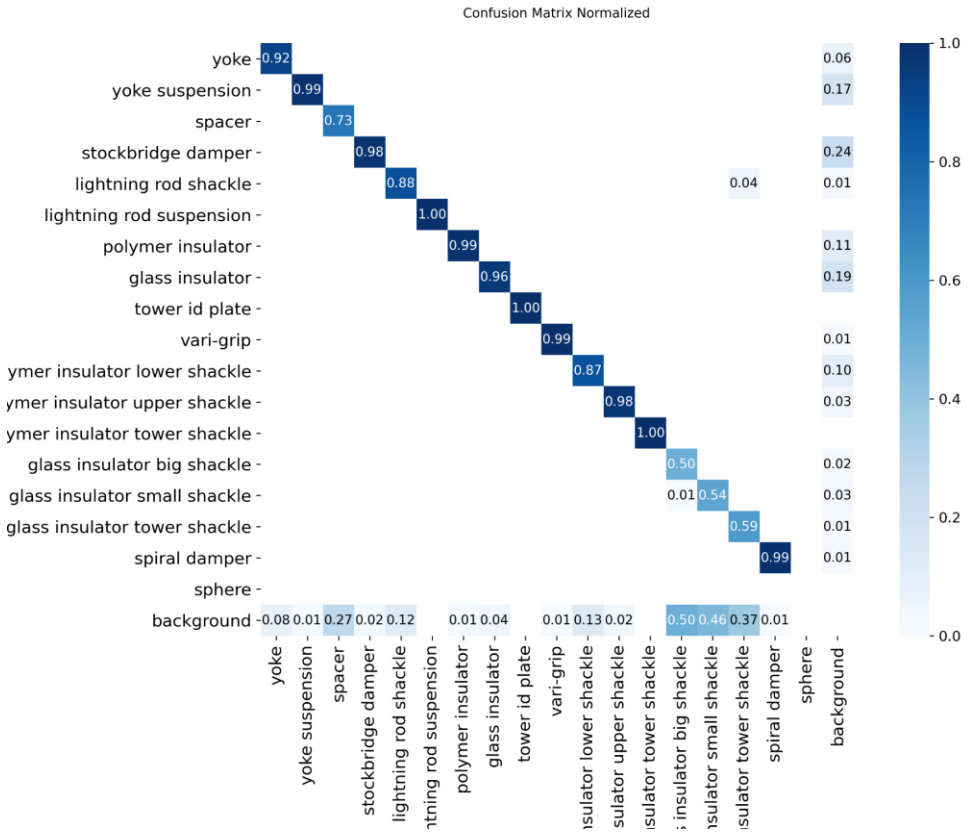

Figure 6: Normalized confusion matrix of the proposed YOLOv8s model.

Figure 7 shows the F1-score as a function of confidence threshold. The F1-score combines Precision and Recall and is useful for examining the balance between false positives and false negatives. The reported final F1-score of 87.68% indicates a strong balance between the two measures for the evaluated configuration. This result is consistent with the 89.5% Precision and 86.2% Recall reported in Table 2, while remaining bounded by the validation dataset and evaluation protocol used in the experiment.

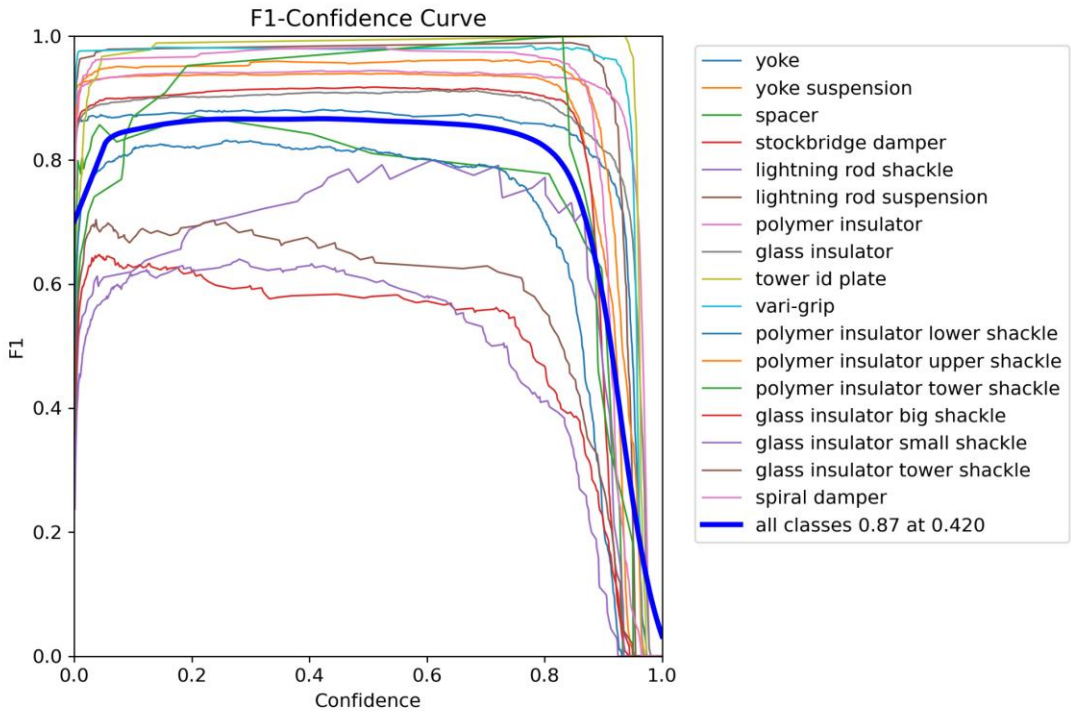

Figure 7: F1-score versus confidence threshold for the proposed YOLOv8s model.

4.8 Comparison with Related Studies

The detection results can be placed in the context of recent transmission-line inspection research, but numerical comparison should not be interpreted as a direct ranking. Qiang et al. (2023), for example, modified YOLOv8s for transmission-line fault detection, while Shao et al. (2024) and Li et al. (2025) addressed foreign-object and dense-small-object detection through architectural changes. Ait El Haj et al. (2026), Zheng et al. (2026), Sheng et al. (2026), Farooq et al. (2026) and Zhu and Pei (2026) similarly targeted specific inspection challenges through architectural, lightweight, transformer-based or low-light adaptations.

The present experiment instead evaluates a standard YOLOv8s configuration with transfer learning and dataset preparation on the predefined InSPLAD partitions. Its contribution is therefore an empirical baseline for this particular model–dataset–training configuration. The 89.5% Precision, 86.2% Recall, 88.4% mAP@0.5 and 72.1% mAP@0.5:0.95 should be understood within that experimental boundary. Differences from published results may arise from target definitions, dataset variants, class distributions, preprocessing, model variants, optimisation settings and evaluation protocols; consequently, the values do not establish superiority or inferiority across studies.

5. LIMITATIONS

The study has several limitations. First, evaluation was conducted using a single public dataset and its predefined validation subset; no independent external test dataset was used. Second, the experiments were conducted offline using stored UAV imagery rather than on an onboard UAV platform, and real-time field performance was not measured. Third, the study focused on component detection and classification rather than defect severity assessment or predictive-maintenance decision making. Finally, generalisation to transmission-line imagery outside the evaluated dataset was not established. These boundaries should be considered when interpreting the reported results and when comparing them with studies using different datasets or deployment settings.

6. CONCLUSION

This paper presented the design and performance evaluation of a YOLOv8s-based vision system for automated power transmission line component detection using the InSPLAD dataset. The predefined training and validation partitions were retained, COCO annotations were converted to

YOLO format, and a pretrained YOLOv8s model was fine-tuned for 50 epochs using transfer learning. Training was performed in Google Colaboratory with an NVIDIA Tesla T4 GPU, and the best validation checkpoint occurred at Epoch 48.

On the predefined InSPLAD validation subset, the selected checkpoint achieved 89.5% Precision, 86.2% Recall, 88.4% mAP@0.5, 72.1% mAP@0.5:0.95 and an F1-score of 87.68%. These results establish an empirical baseline for the stated YOLOv8s–InSPLAD configuration and show that the standard detector can provide measurable component-detection performance without architectural modification. The results do not, however, establish real-time UAV operation, onboard deployment, external-dataset generalisation or production readiness. Future work should therefore evaluate the detector on additional datasets and embedded UAV platforms and extend the task toward defect-specific assessment where appropriate.

REFERENCES

[1] Alcayde-García, F., Salmerón-Manzano, E., Montero, M. A., Alcayde, A., & Manzano-Agugliaro, F. (2022). Power transmission lines: Worldwide research trends. Energies, 15(16), 5777. https://doi.org/10.3390/en15165777

[2] Alhassan, A., Zhang, X., Shen, G., & Irfan, M. (2020). Power transmission line inspection robots: A review, trends and challenges for future research. International Journal of Electrical Power & Energy Systems, 118, 105862. https://doi.org/10.1016/j.ijepes.2020.105862

[3] André, G., Kirchknopf, S., Osmani, V., & Schulz, D. (2023). InSPLAD: A large-scale dataset for inspection of power line assets using UAV imagery. Data in Brief, 49, 109395. https://doi.org/10.1016/j.dib.2023.109395

[4] Ait El Haj, R., Benelmostafa, B.-E., & Medromi, H. (2026). YOLOv8-ECCα: Enhancing object detection for power line asset inspection under real-world visual constraints. Algorithms, 19(1), 66. https://doi.org/10.3390/a19010066

[5] Du, Z., Geng, Y., Wang, H., Zhang, H., & Hu, Y. (2026). Aerial insulator defect detection method based on CWSP-YOLO. Scientific Reports. https://doi.org/10.1038/s41598-026-40782-2

[6] Everingham, M., Van Gool, L., Williams, C. K. I., Winn, J., & Zisserman, A. (2010). The PASCAL visual object classes (VOC) challenge. International Journal of Computer Vision, 88, 303–338. https://doi.org/10.1007/s11263-009-0275-4

[7] Farooq, U., Yang, F., & Shaikh, J. A. (2026). Transformer enhanced based YOLOv8 integration: A hybrid deep learning framework for intelligent insulator defect detection in high-voltage transmission systems. Frontiers in Artificial Intelligence, 8, 1732616. https://doi.org/10.3389/frai.2025.1732616

[8] Jiang, H., Zhang, J., Li, Y., & Liu, X. (2020). TTPLA: A dataset for transmission tower and power line inspection. IEEE Access, 8, 164043–164055. https://doi.org/10.1109/ACCESS.2020.3021820

[9] Jocher, G., Chaurasia, A., & Qiu, J. (2023). Ultralytics YOLOv8 (Version 8.0.0) [Computer software]. GitHub. https://github.com/ultralytics/ultralytics

[10] Li, Z.-X., Wang, Y.-L., & Wang, F. (2025). DI-YOLOv5: An improved dual-wavelet-based YOLOv5 for dense small object detection. IEEE/CAA Journal of Automatica Sinica, 12(2), 457–459. https://doi.org/10.1109/JAS.2024.124368

[11] Mendu, B., & Mbuli, N. (2025). State-of-the-art review on the application of unmanned aerial vehicles (UAVs) in power line inspections: Current innovations, trends, and future prospects. Drones, 9(4), 265. https://doi.org/10.3390/drones9040265

[12] Mohsan, S. A. H., Othman, N. Q. H., Li, Y., Alsharif, M. H., & Khan, M. A. (2023). Unmanned aerial vehicles (UAVs): Practical aspects, applications, open challenges, security issues, and future trends. Intelligent Service Robotics, 16, 109–137. https://doi.org/10.1007/s11370-022-00452-4

[13] Padilla, R., Passos, W. L., Dias, T. L. B., Netto, S. L., & da Silva, E. A. B. (2021). A comparative analysis of object detection metrics with a companion open-source toolkit. Electronics, 10(3), 279. https://doi.org/10.3390/electronics10030279

[14] Qi, J., Song, D., Shang, H., Wang, N., & Hua, C. (2022). UAV-based inspection of overhead power lines: A review of technologies and applications. Energy Reports, 8, 1040–1055. https://doi.org/10.1016/j.egyr.2021.12.053

[15] Qiang, H., Tao, Z., Ye, B., Yang, R., & Xu, W. (2023). Transmission line fault detection and classification based on improved YOLOv8s. Electronics, 12(21), 4537. https://doi.org/10.3390/electronics12214537

[16] Redmon, J., Divvala, S., Girshick, R., & Farhadi, A. (2016). You only look once: Unified, real-time object detection. In 2016 IEEE Conference on Computer Vision and Pattern Recognition (pp. 779–788). IEEE. https://doi.org/10.1109/CVPR.2016.91

[17] Shao, Y., Zhang, R., Lv, C., Luo, Z., & Che, M. (2024). TL-YOLO: Foreign-object detection on power transmission line based on improved YOLOv8. Electronics, 13(8), 1543. https://doi.org/10.3390/electronics13081543

[18] Sheng, J., Wu, S., Liu, G., Ma, X., Deng, S., & Xu, H. (2026). SDS-YOLO: Drone-based foreign object detection model for power lines using an enhanced YOLOv8n approach. Scientific Reports. https://doi.org/10.1038/s41598-026-59200-8

[19] Shakhatreh, H., Sawalmeh, A. H., Al-Fuqaha, A., Dou, Z., Almaita, E., Khalil, I., Othman, N. S., Khreishah, A., & Guizani, M. (2019). Unmanned Aerial Vehicles (UAVs): A survey on civil applications and key research challenges. IEEE Access, 7, 48572–48634. https://doi.org/10.1109/ACCESS.2019.2909530

[20] Terven, J., Córdova-Esparza, D.-M., & Romero-González, J.-A. (2023). A comprehensive review of YOLO architectures in computer vision: From YOLOv1 to YOLOv8 and YOLO-NAS. Machine Learning and Knowledge Extraction, 5(4), 1680–1716. https://doi.org/10.3390/make5040083

[21] Vieira e Silva, A. L. B., Felix, H. C., Simões, F. P. M., Teichrieb, V., Santos, M. M., Santiago, H., Sgotti, V., & Lott Neto, H. (2023). InsPLAD: A dataset and benchmark for power line asset inspection in UAV images. arXiv:2311.01619.

[22] Xu, B., Zhao, Y., Wang, T., & Chen, Q. (2023). Development of power transmission line detection technology based on unmanned aerial vehicle image vision. SN Applied Sciences, 5, 72. https://doi.org/10.1007/s42452-023-05299-7

[23] Zhang, Y., Li, X., Wang, J., & Sun, H. (2021). PLAD: A power line assets dataset for UAV-based inspection. Remote Sensing, 13(18), 3672. https://doi.org/10.3390/rs13183672

[24] Zheng, R., Duan, G., Cao, X., & Wang, H. (2026). Transmission line insulator defect detection method based on YOLO-MLSL model. Energies, 19(10), 2305. https://doi.org/10.3390/en19102305

[25] Zhu, Y., & Pei, S. (2026). Transmission line defect detection in low-light environments using image adversarial synthesis and the LCDD-YOLO algorithm. International Journal of Intelligent Systems, 2026, Article 2674074. https://doi.org/10.1155/int/2674074

International Conference on Engineering Innovation for Sustainable Development (ICESID 2026)
Faculty of Engineering, Ahmadu Bello University
Zaria · 8–10 September 2026

DESIGN AND PROOF-OF-CONCEPT EVALUATION OF A GROWTH-STAGE-ORIENTED ESP32-BASED SMART DRIP IRRIGATION SYSTEM FOR BELL PEPPER PRODUCTION IN SEMI-ARID NIGERIA

Bwala Sarah Usman[1,*], U.d Idris[1], Garba H.m[2]
[1]*Ahmadu Bello University, Zaria*
[2]*Department of Postharvest Technology, Federal College of Agricultural Produce Technology, Kano*
Email: bwalasarah01@gmail.com[*], udidris11@gmail.com, hatimmgarba@gmail.com
***Corresponding author**: Bwala Sarah Usman
DOI: https://doi.org/10.67203/sp.ICESID.2026

ABSTRACT

Water availability and changing crop water demand make irrigation management difficult in semi-arid production systems. This paper presents the design and proof-of-concept evaluation of a growth-stage-oriented smart drip irrigation prototype for bell pepper. The system uses an ESP32 controller with a capacitive soil-moisture sensor, DHT22 temperature and humidity sensor, DS18B20 soil-temperature sensor, YF-S201 flow sensor, DS3231 real-time clock, relay-controlled pump, drip line, LCD, and manual controls. We defined a growth-stage framework using days after transplanting (DAT), provisional soil-moisture thresholds, and maximum irrigation durations; these settings are engineering assumptions rather than validated agronomic optima. We established five four-week-old bell pepper seedlings in one prototype box and monitored them over 19 morning/evening observation periods. The recorded dataset contained air temperature, soil temperature, relative humidity, soil moisture, and independently measured irrigation volume. Across the 19 periods, total recorded irrigation was 6.35 L, comprising 2.65 L in the morning and 3.70 L in the evening. Mean air temperature was 24.48 °C in the morning and 32.37 °C in the evening, while mean soil moisture was 86.79% and 65.26%, respectively. Three response-time observations of 0.488, 0.406, and 0.590 s gave a mean of 0.495 ± 0.092 s. The observations demonstrate that the prototype can acquire environmental data and deliver measured irrigation under live-crop conditions, but they do not establish seasonal water-use efficiency or water-saving performance. Further replicated calibration, controlled comparison, full-cycle crop monitoring, and field testing are required.

Keywords: *smart irrigation; drip irrigation; ESP32; bell pepper; growth-stage irrigation; water management*

1. INTRODUCTION

1.1 Background of the Study

Agricultural production in semi-arid environments is constrained by water availability, rainfall variability, and irrigation management. Bell pepper (Capsicum annuum) is a high-value crop whose water requirement changes with development. The FAO-56 framework recognizes the influence of crop stage and environmental conditions on crop water requirements (Allen et al., 1998). Applying one irrigation rule throughout the crop cycle may therefore be less responsive than a strategy that considers crop development together with measured soil and environmental conditions.

Recent smart-agriculture research shows that low-cost microcontrollers and connected sensing can be used to automate irrigation and monitor environmental conditions. Pereira et al. (2023), for example, demonstrated an ESP32-based smart drip irrigation system, while Pereira et al. (2023) describe the broader use of IoT technologies for agricultural monitoring and automation. More advanced systems have also combined environmental data with artificial intelligence or predictive methods to support irrigation decisions (Gaitan et al., 2025; Preite & Vignali, 2024).

However, the usefulness of a smart irrigation system depends not only on the availability of sensors but also on how the control strategy is related to crop development and local conditions. Wanyama et al. (2024) identified affordability, infrastructure, water scarcity, and contextual suitability as important considerations for smart irrigation in sub-Saharan Africa. A practical system for this context therefore needs to combine relatively simple hardware with a control framework that can be refined from local observations.

1.2 Research Gap

Many low-cost irrigation controllers use a fixed soil-moisture threshold or fixed schedule. Such approaches automate water delivery but do not explicitly provide a mechanism for changing irrigation targets with crop development. This study combines environmental sensing and drip irrigation with a growth-stage-oriented control framework. The contribution is the prototype architecture, stage-based control concept, and live-crop observations, not a claim of validated seasonal water saving.

1.3 Sustainable Development Goal Relevance

The work aligns with SDG 2 through sustainable crop production; SDG 6 through agricultural water management; SDG 9 through embedded sensing and automation; SDG 12 through responsible resource use; SDG 13 through adaptation to water scarcity and variable conditions; and SDG 15 through sustainable soil and water management. These are project alignments, not measured SDG outcomes (United Nations, 2015).

1.4 Aim and Objectives

The aim was to design and evaluate, at proof-of-concept scale, a growth-stage-oriented ESP32-based smart drip irrigation system for bell pepper under semi-arid conditions. The objectives were to assemble the prototype; define a provisional DAT-based irrigation framework; integrate environmental sensing, timekeeping, flow measurement, and pump control; and characterize measured environmental conditions, irrigation volumes, and sensor response.

2. MATERIALS AND METHODS

2.1 System Components and Architecture

The prototype was centred on an ESP32 development board. A capacitive sensor measured soil moisture; a DHT22 measured air temperature and relative humidity; a DS18B20 measured soil temperature; and a YF-S201 monitored water flow. A DS3231 provided time information, while a relay, pump, and drip line delivered water. An I²C LCD displayed measurements, and push buttons provided local control.

The current implementation used local sensing, timekeeping, pump actuation, and manual interaction. The ESP32 provides a platform for later network connectivity, but network/cloud performance was not measured.

2.2 Firmware and Irrigation Control

The firmware acquires sensor measurements every two seconds and averages ten analogue soil-moisture readings before converting them to percentage values using programmed dry and wet endpoints. It reads the DHT22, DS18B20, YF-S201, and DS3231, and refreshes the LCD at about 0.5-second intervals. Automatic irrigation uses two fixed five-minute daily windows with manual override. The growth-stage framework was not the control routine used for the reported irrigation records.

The implemented automatic pump control uses two fixed five-minute daily windows, together with a manual pump override. The growth-stage-oriented algorithm described in this paper is therefore a control framework developed around the prototype rather than a fully validated adaptive control routine operating in the reported dataset. This distinction is important because the measured irrigation records cannot be attributed experimentally to the proposed stage-specific thresholds.

2.3 Growth-Stage-Oriented Control Framework

The framework uses days after transplanting (DAT) to associate crop development with a provisional moisture threshold and maximum irrigation duration. FAO-56 provides the conceptual basis for stage-dependent crop water requirements (Allen et al., 1998), but it does not prescribe the exact sensor percentages used here. The settings in Table 1 are engineering assumptions requiring crop-based calibration.

Table 1: Provisional growth-stage ranges and control settings.

Growth stage	Provisional DAT range and basis	Moisture threshold	Maximum duration
Early establishment	0–14 DAT; root establishment after transplanting	≥60%	3 min/cycle
Vegetative	15–35 DAT; canopy and vegetative growth	≥50%	5 min/cycle
Flowering	36–55 DAT; flowering and early reproductive development	≥55%	8 min/cycle
Fruiting	56–85 DAT; fruit set and fruit expansion	≥55%	8 min/cycle
Maturity	86 DAT and beyond; ripening and harvest development	≥45%	4 min/cycle

The DAT ranges in Table 1 make the framework explicit but are not measured phenological boundaries. Flowering and fruiting share the same provisional threshold and duration because both are treated as water-sensitive reproductive stages; this is a design choice, not evidence that their water requirements are identical.

2.4 Calibration and Measurement Verification

The soil-moisture conversion uses programmed dry and wet reference endpoints of 2500 and 1135 ADC units. The available records do not contain replicated reference-instrument comparisons for the moisture, temperature or humidity sensors; therefore, percentage accuracy and calibration error are not reported. Irrigation volume was measured with a calibrated cylinder. Three response-time readings were retained, allowing mean, standard deviation and range to be reported.

Irrigation volume was measured independently with a calibrated measuring cylinder. The response-time test retained three signal-detection readings, allowing the mean and sample standard deviation to be calculated. The response-time measurement represents sensor signal detection and should not be interpreted as total environmental-change-to-pump-actuation latency.

2.5 Crop Establishment and Observation Procedure

Five healthy bell pepper seedlings, approximately four weeks old at transplanting, were established in one prototype box. The plants shared one soil environment and irrigation system and therefore represent one experimental unit rather than five independent replicates. Morning and evening readings were collected for 19 observation periods. No separate control or formal randomization was used, so the study does not support inferential comparison with another irrigation treatment.

No separate control treatment was used, and no formal randomization was performed because the work involved one prototype unit and was intended to characterize system operation under live-crop conditions. These design limitations prevent inferential comparison with a fixed-threshold or conventional irrigation treatment.

2.6 Data Analysis

Means, ranges and sample standard deviations were calculated for the 19 morning/evening observations. Total irrigation was obtained by summing recorded volumes, and the three response-time readings were summarized by mean, sample standard deviation and range. No seasonal saving

percentage or inferential treatment test was calculated because there was no completed crop cycle or replicated control.

3. RESULTS

3.1 Environmental and Irrigation Observations

The complete observation record is presented in Table 2. The data show clear differences between morning and evening conditions. Mean air temperature increased from 24.48 °C in the morning to 32.37 °C in the evening, while mean soil temperature increased from 24.59 °C to 32.74 °C. Mean relative humidity decreased from 85.37% to 63.95%, and mean soil moisture decreased from 86.79% to 65.26%.

Table 2: Complete morning and evening observation record (n = 19 observation periods).

Obs.	Air temp. AM/PM (°C)	Soil temp. AM/PM (°C)	RH AM/PM (%)	Moisture AM/PM (%)	Water AM/PM (mL)
1	31.5 / 37.0	38.0 / 43.0	65 / 45	55 / 40	200 / 200
2	27.0 / 33.3	25.1 / 36.0	70 / 55	70 / 50	200 / 150
3	28.0 / 30.0	28.0 / 32.0	68 / 58	70 / 51	200 / 150
4	23.0 / 32.4	24.4 / 32.7	80 / 50	100 / 70	50 / 150
5	20.1 / 26.0	20.5 / 26.0	84 / 70	95 / 80	150 / 150
6	28.0 / 33.7	29.4 / 36.7	65 / 50	70 / 55	200 / 150
7	22.6 / 30.0	24.8 / 32.0	92 / 77	90 / 77	200 / 100
8	23.1 / 31.8	24.0 / 33.4	92 / 72	100 / 75	100 / 300
9	23.5 / 28.8	23.1 / 29.0	93 / 80	100 / 90	100 / 200
10	21.5 / 26.1	21.0 / 24.3	93 / 80	100 / 90	100 / 100
11	26.0 / 34.0	24.4 / 31.0	90 / 64	100 / 84	200 / 200
12	23.9 / 31.2	22.5 / 33.0	93 / 66	87 / 60	200 / 250
13	22.5 / 37.9	22.5 / 36.0	90 / 60	93 / 70	200 / 150
14	24.1 / 34.5	22.5 / 36.9	93 / 69	75 / 49	100 / 300
15	23.3 / 38.8	23.0 / 36.8	91 / 52	97 / 53	50 / 300
16	24.8 / 33.8	23.4 / 29.9	89 / 66	89 / 49	100 / 200
17	24.6 / 32.7	24.8 / 31.4	96 / 72	85 / 50	100 / 200
18	24.9 / 32.7	24.1 / 30.8	93 / 69	87 / 75	100 / 250
19	22.8 / 30.3	21.8 / 31.1	85 / 60	86 / 72	100 / 200

Irrigation volume varied from 50 to 200 mL in the morning and from 100 to 300 mL in the evening. The morning mean was 139.47 mL, compared with 194.74 mL in the evening. Across all observations, 2.65 L was applied in the morning and 3.70 L in the evening, giving a total measured irrigation volume of 6.35 L. These values describe the recorded observation period only and are not extrapolated to the complete crop cycle.

3.2 Response-Time Result

Table 3: Individual sensor signal-detection response-time observations.

Trial	Signal-detection response time (s)
1	0.488
2	0.406
3	0.590
Mean ± SD	0.495 ± 0.092
Range	0.406–0.590

The three response-time observations were 0.488, 0.406, and 0.590 s. Their mean was 0.495 s with a sample standard deviation of 0.092 s and a range of 0.406–0.590 s. This result indicates relatively short signal-detection times during the three tests, but the small number of trials does not support a generalized performance claim.

4. DISCUSSION

Across 19 observation periods, morning conditions were generally cooler and more humid, with higher soil moisture than evening conditions. Irrigation volume also varied between observations. These descriptive patterns support the practical value of monitoring soil and environmental conditions, but they do not establish causation or an optimal irrigation quantity.

The measured 6.35 L represents water physically recorded during the 19 observation periods. It is not a seasonal water-use or water-saving estimate because the crop cycle was incomplete and no replicated control was available. Irrigation outcomes depend on crop, environment, and control strategy (Gaitan et al., 2025; Preite & Vignali, 2024).

The growth-stage framework is consistent with the stage-dependent crop water requirement principle in FAO-56 (Allen et al., 1998). However, its thresholds and durations are engineering assumptions rather than direct conversions of FAO crop coefficients. The current firmware did not use these stage-specific values to control the recorded irrigation events, so the framework requires validation before it can be described as an adaptive controller.

The hardware approach is consistent with low-cost smart irrigation research. Pereira et al. (2023) demonstrated ESP32-based drip irrigation, while Wanyama et al. (2024) discuss opportunities and constraints of smart irrigation in sub-Saharan Africa. The present work adds a crop-development-oriented control concept and live-crop observations.

The mean response time of 0.495 ± 0.092 s is based on only three readings and represents signal detection rather than complete environmental-change-to-pump latency. It is therefore an engineering observation, not a generalized latency specification.

The experimental design also limits the strength of inference. Five seedlings shared one prototype box, with no independent replicate boxes, randomized treatment assignment, or control. The current results should therefore guide system refinement rather than support claims of agronomic superiority.

5. CONCLUSION AND RECOMMENDATIONS

A growth-stage-oriented ESP32-based smart drip irrigation prototype was tested with five four-week-old bell pepper seedlings under pot conditions. Nineteen morning/evening observation periods produced 6.35 L of measured irrigation. Mean morning values were 24.48 °C air temperature, 24.59 °C soil temperature, 85.37% relative humidity, and 86.79% soil moisture, compared with 32.37 °C, 32.74 °C, 63.95%, and 65.26% in the evening. Three response-time readings gave 0.495 ± 0.092 s.

These findings show that the prototype acquired environmental measurements and delivered measurable irrigation under live-crop conditions. They do not establish seasonal water-use efficiency, water saving, or agronomic superiority. The growth-stage framework remains a design component requiring calibration and validation, and sensor accuracy evidence is limited.

The following steps are recommended: continue monitoring through the complete crop cycle; perform replicated sensor calibration; retain repeated response-time readings; evaluate the framework with independent experimental units and randomized treatments; compare it with a defined control before making water-saving claims; and validate the system at larger scale and under different soil and environmental conditions.

6. SUSTAINABLE DEVELOPMENT GOAL ALIGNMENT

The project aligns with six Sustainable Development Goals (SDGs). The alignment reflects the purpose and intended application of the engineering system and should not be interpreted as evidence that the present experiment measured progress against SDG indicators (United Nations, 2015).

SDG 2 – Zero Hunger: Supports sustainable and resilient food production through improved irrigation management for bell pepper.

SDG 6 – Clean Water and Sanitation: Supports more deliberate agricultural water management and the goal of improving water-use efficiency.

SDG 9 – Industry, Innovation and Infrastructure: Applies embedded control, sensors and automation to agricultural infrastructure.

SDG 12 – Responsible Consumption and Production: Encourages measured and controlled use of water as a production resource.

SDG 13 – Climate Action: Supports climate adaptation by improving irrigation monitoring under variable environmental conditions.

SDG 15 – Life on Land: Supports sustainable management of agricultural soil and water resources, particularly in water-limited environments.

REFERENCES

Allen, R. G., Pereira, L. S., Raes, D., & Smith, M. (1998). Crop evapotranspiration: Guidelines for computing crop water requirements (FAO Irrigation and Drainage Paper No. 56). Food and Agriculture Organization of the United Nations.

Gaitan, N. C., Batinas, B. I., Ursu, C., & Crainiciuc, F. N. (2025). Integrating artificial intelligence into an automated irrigation system. Sensors, 25(4), 1199. https://doi.org/10.3390/s25041199

Pereira, G. P., Chaari, M. Z., & Daroge, F. (2023). IoT-enabled smart drip irrigation system using ESP32. IoT, 4(3), 221–243. https://doi.org/10.3390/iot4030012

Preite, L., & Vignali, G. (2024). Artificial intelligence to optimize water consumption in agriculture: A predictive algorithm-based irrigation management system. Computers and Electronics in Agriculture, 223, 109126. https://doi.org/10.1016/j.compag.2024.109126

United Nations. (2015). Transforming our world: The 2030 Agenda for Sustainable Development. https://sdgs.un.org/2030agenda

Wanyama, J., Bwambale, E., Kiraga, S., Katimbo, A., Nakawuka, P., Kabenge, I., & Oluk, I. (2024). A systematic review of fourth industrial revolution technologies in smart irrigation: Constraints, opportunities, and prospects for sub-Saharan Africa. Smart Agricultural Technology, 7, 100412. https://doi.org/10.1016/j.atech.2024.100412

International Conference on Engineering Innovation for Sustainable Development (ICESID 2026)
Faculty of Engineering, Ahmadu Bello University Zaria · 8–10 September 2026

DESIGN AND SIMULATION OF ARTIFICIAL INTELLIGENCE-BASED ADAPTIVE PROTECTION SCHEME FOR NIGERIA'S POWER GRIDS USING BIG DATA ANALYTICS

Tolulope Adelugba[1,*], Eronu Emmanuel[1], Ogunjuyigbe Jacob Kehinde[1]
[1]*University of Abuja*
Email: tolulopeadelugba070905@gmail.com[*], eronu.majiyebo@uniabuja.edu.ng, jacob.ogunjuyigbe@uniabuja.edu.ng
***Corresponding author**: Tolulope Adelugba
DOI: https://doi.org/10.67203/sp.ICESID.2026

ABSTRACT

Conventional distance relay schemes often fail to detect high-impedance faults on Nigeria's 330 kV transmission network, contributing to grid instability and unreliable supply. This study proposes an adaptive deep neural network protection system for the Shiroro–Jebba–Oshogbo corridor, leveraging Big Data Analytics and convolutional neural networks (CNN) to overcome impedance-based limitations. Using MATLAB/Simulink, the corridor was modeled with validated parameters, and 1,000 scenarios across seven classification classes (Normal operation plus six fault types: single line-to-ground AG/BG/CG, line-to-line AB, double line-to-ground ABG, and three-phase ABC) and six fault locations were simulated, varying resistance from 0.01Ω to 500Ω. This produced 5.6 million measurement points. A CNN with four convolutional blocks and 1.39 million trainable parameters was implemented in TensorFlow/Keras, trained on 700 scenarios, validated on 150, and tested on 150. The model achieved 98.67% accuracy on unseen data, with an inference time of 100.56 ms. Performance was perfect (100%) for resistances up to 100Ω and remained strong (92%) at 500Ω, where conventional relays fail. Comparative analysis showed CNN sensitivity of 100% versus 21.48% for distance relays, a 78.52-point improvement, as confirmed by McNemar's test (p<0.0001). Results demonstrate that deep learning-based protection provides robust detection of high-impedance faults, offering transformative reliability for Nigerian transmission networks beyond conventional methods.

Keywords: *Adaptive protection; Big Data Analytics; Convolutional Neural Networks; distance relay; highimpedance faults; Nigerian power grid; transmission line protection*

1. INTRODUCTION

Electric power is an indispensable cornerstone of modern society, underpinning industrial, commercial, and residential activities. In Nigeria, the energy sector assumes a pivotal role in the country's economic growth and sustainable development. However, the Nigerian power grid has been grappling with persistent challenges rooted in insufficient infrastructure, operational inefficiencies, and vulnerabilities within its protection and stability mechanisms. These issues manifest as frequent power outages, voltage fluctuations, and grid instability. Statistics reveal a concerning trend: In 2018, there were thirteen (13) instances of national grid collapses (Oluwagbemi, 2018), followed by eleven (11) in 2019 (TheCable, 2019), four (4) in 2020, four (4) in 2021, eight (8) in 2022 (Nnodim, 2022; CuteNaija, 2022), and eight (8) between January and September 2023 (Onoja, 2023), totalling approximately forty-eight (48) collapses in a span of five years and eight months. These persistent issues not only disrupt the lives of millions of Nigerians but also have severe repercussions on the nation's economy (Adegoriola & Agbanuji, 2020).

The Nigerian 330kV transmission network, particularly the critical Shiroro-Jebba-Oshogbo corridor, experiences frequent grid collapses, with 46 recorded incidents in 2023 alone (Adejo, 2024). This corridor-level figure is considerably higher than the eight (8) national grid collapses reported for the same January-September 2023 period (Onoja, 2023) cited earlier; the two statistics differ in scope rather than being contradictory, as Adejo's count of 46 encompasses localised fault and instability events specific to the Shiroro-Jebba-Oshogbo corridor (including partial disturbances that trigger protective relay operations without a full national collapse), whereas Onoja's count of eight reflects only incidents

severe enough to cause a total national grid collapse. This distinction underscores why corridor-specific adaptive protection, rather than national-level statistics alone, is the appropriate frame for this study. These systemic failures stem from conventional protection relays' inability to adapt to real-time grid dynamics characterised by significant frequency deviations (±1.25 Hz) and high-impedance faults with resistances up to 500 Ω in rural areas (Adeniji, 2025; Araga et al., 2024). Traditional distance relays, which rely on apparent impedance calculations (Z = V/I), exhibit poor selectivity under varying system conditions and struggle to distinguish legitimate fault transients from operational disturbances such as power swings or load switching, leading to nuisance tripping that can precipitate cascading failures across the Northern backbone. The legacy "bolted fault" logic fails to detect High-Impedance Faults (HIFs) in which fault currents are masked by normal operating noise or high grounding resistance (Sangeeth & Vinod, 2023).

The emergence of Big Data Analytics (BDA) and Deep Neural Networks (DNNs) presents a promising avenue for addressing these challenges. BDA enables the harnessing and analysis of vast amounts of data generated by power grid operations, providing insights into patterns, trends, and anomalies that can inform decision-making and improve grid stability (Zi, 2018). DNNs exhibit remarkable capabilities in pattern recognition, learning, and adaptation, making them well-suited for developing intelligent protection schemes that can adapt to the dynamic and complex nature of power grid operations (Zi, 2018; Cai et al., 2021; Zhang et al., 2018).

This research addresses the critical gap in implementing deep learning architectures optimised for power system protection, capable of processing large-scale fault datasets and extracting discriminative features from high-dimensional time-series data. Current approaches suffer from three fundamental limitations: insufficient training data diversity, failing to capture the full spectrum of fault conditions, including high-impedance scenarios; inadequate feature extraction mechanisms unable to distinguish between fault transients and operational disturbances; and a lack of comprehensive comparative analysis against conventional protection schemes using standardised metrics (Oruma et al., 2024).

This research aims to design and simulate an adaptive protection scheme that uses a Deep Neural Network (DNN) and Big Data Analytics (BDA) to enhance fault detection, selectivity, and reliability in the Nigerian power grid. The specific objectives are to: (i) model the Shiroro-Jebba-Oshogbo 330kV transmission line in MATLAB/Simulink and generate a comprehensive Big Data fault dataset including diverse fault types, multiple fault locations, and high-impedance fault scenarios with resistances ranging from bolted faults (0.01Ω) to very high impedance faults (500Ω); (ii) develop a Convolutional Neural Network (CNN) architecture in Python with optimised hyperparameters to ensure maximum classification accuracy and minimal inference latency; (iii) evaluate the performance of the trained CNN model on unseen fault scenarios using classification metrics; and (iv) statistically compare the proposed CNN-based protection scheme against conventional distance relay protection using objective metrics.

2. METHODOLOGY

2.1. Research Design

The study was conducted using the Nigerian 330 kV transmission network, which serves as the backbone of the national electricity transmission system. The network consists of interconnected generating stations, transmission lines, substations, transformers, and major load centres distributed across the country's six geopolitical zones. Owing to its extensive geographical coverage and varying operating conditions, the network is susceptible to faults caused by equipment failures, environmental disturbances, switching operations, and overload conditions. These characteristics make it an appropriate test system for developing and evaluating intelligent adaptive protection schemes.

2.2 Network Model

A detailed model of the Nigerian 330 kV transmission network was developed in MATLAB/Simulink using the Simscape Electrical toolbox. The model incorporated the electrical characteristics of transmission lines, buses, transformers, generators, and loads to emulate the dynamic behaviour of the actual transmission system. Various operating scenarios were simulated to reflect

practical network conditions, including variations in load demand, source contributions, and fault locations.

The developed model was validated under normal operating conditions before fault simulations were performed to ensure that the simulated network accurately represented expected steady-state operating characteristics.

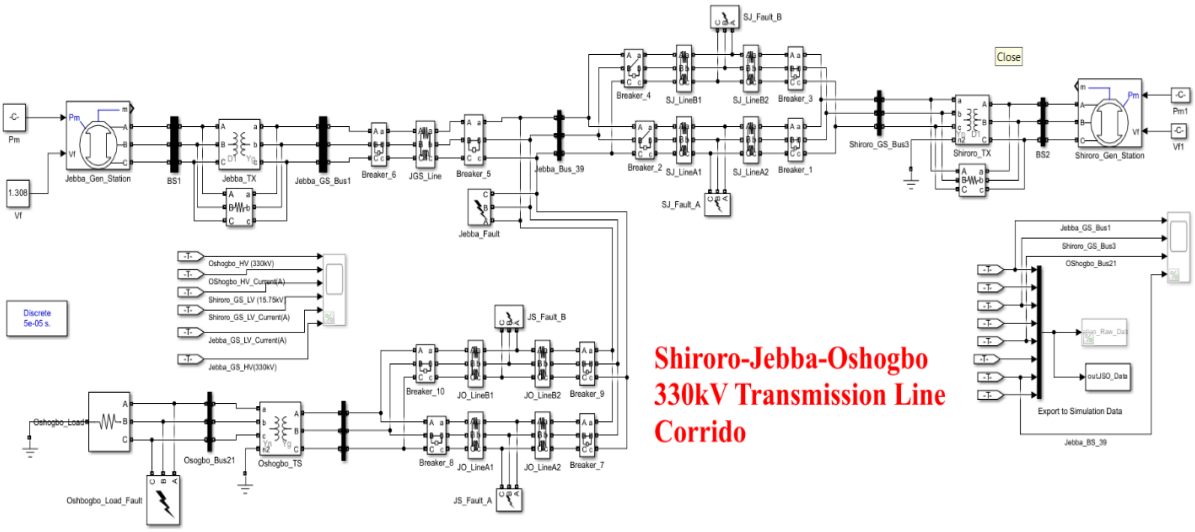

Figure 1: MATLAB/Simulink Model of Shiroro-Jebba-Oshogbo 330 kV Transmission Corridor

2.3. Data Generation

A comprehensive fault dataset was generated from the developed transmission network model by extensively simulating transmission-line faults under different operating conditions. Fault scenarios included single line-to-ground (LG), line-to-line (LL), double line-to-ground (LLG), three-phase (LLL), and three-phase-to-ground (LLLG) faults.

To improve the robustness of the adaptive protection model, simulations were performed over a wide range of fault locations distributed along transmission lines and fault resistances ranging from low to high impedance. Variations in system loading and operating conditions were also considered to capture realistic network behaviour.

For each simulated event, three-phase voltages and currents were measured at the relay location and stored as labelled datasets corresponding to the respective fault category. The resulting Big Data repository contained representative samples of normal and multiple-fault operating conditions, providing sufficient diversity for deep learning model development.

Table 1: Data Generation Summary

Category	**Parameter**	**Values/Distribution**	**Total Scenarios**
Fault Types	Normal Operation	1 class	100
	Single-Line-to-Ground	AG, BG, CG (3 classes)	450 (150 each)
	Line-to-Line	AB (1 class)	150
	Double-Line-to-Ground	ABG (1 class)	150
	Three-Phase	ABC (1 class)	150
	Total Classes	**7 classes**	**1,000**
Fault Locations	Shiroro-Jebba Line	SJ_Fault_A, SJ_Fault_B	-
	Jebba-Oshogbo Line	JS_Fault_A, JS_Fault_B	-
	Critical Nodes	Jebba_Fault, Oshogbo_Load_Fault	-
	Total Locations	**6 locations**	-
Fault Resistance	Bolted Fault	0.01 Ω	-
	Low Impedance	5 Ω	-
	Medium Impedance	25 Ω	-
	High Impedance	100 Ω	-
	Very High Impedance	500 Ω	-
	Total Resistance Levels	**5 levels**	-
Data Specifications	Sampling Rate	20 kHz	-
	Samples per Scenario	5,601 samples	-
	Measurement Signals	24 signals (3φ V & I at 4 locations)	-
	Total Data Points	**≈5.6 million**	**1,000 scenarios**

2.4. CNN Architecture

The CNN was designed to capture temporal and spatial patterns in multichannel waveform data. Its architecture contains four convolutional blocks with increasing filter sizes, followed by fully connected layers and a softmax output layer for multi-class fault classification. The model has 1,385,927 trainable parameters and was optimised using the Adam optimiser and categorical cross-entropy loss.

Each raw scenario comprised 5,601×24 time-series measurements sampled at 20 kHz. Prior to network input, this raw sequence was temporally downsampled by a factor of 10 (retaining every tenth sample, reducing the effective sampling rate from 20 kHz to 2 kHz) to curb computational burden and overfitting risk while still preserving 40 samples per 50 Hz cycle, well above typical protective-relay sampling rates. This yielded a final CNN input shape of 560×24, as reflected in Table 2. This structure enabled the model to learn latent signatures associated with different fault types and fault-resistance levels. Compared with manual feature engineering, this approach is more scalable and better suited to large fault datasets.

Table 2: CNN Architecture Specification

Layer Number	Layer Type	Configuration	Output Shape	Trainable Parameters
1	Input Layer	-	(560, 24)	0
2	Conv1D	64 filters, kernel=7, activation=ReLU	(560, 64)	10,816
3	BatchNormalization	-	(560, 64)	256
4	MaxPooling1D	pool_size=4	(140, 64)	0
5	Dropout	rate=0.3	(140, 64)	0
6	Conv1D	128 filters, kernel=7, activation=ReLU	(140, 128)	57,472
7	BatchNormalization	-	(140, 128)	512
8	MaxPooling1D	pool_size=4	(35, 128)	0
9	Dropout	rate=0.3	(35, 128)	0
10	Conv1D	256 filters, kernel=7, activation=ReLU	(35, 256)	229,632
11	BatchNormalization	-	(35, 256)	1,024
12	MaxPooling1D	pool_size=4	(8, 256)	0
13	Dropout	rate=0.3	(8, 256)	0
14	Conv1D	512 filters, kernel=7, activation=ReLU	(8, 512)	918,016
15	BatchNormalization	-	(8, 512)	2,048
16	GlobalAveragePooling1D	-	(512,)	0
17	Dropout	rate=0.3	(512,)	0
18	Dense	256 units, activation=ReLU	(256,)	131,328
19	BatchNormalization	-	(256,)	1,024
20	Dropout	rate=0.3	(256,)	0
21	Dense	128 units, activation=ReLU	(128,)	32,896
22	Dropout	rate=0.3	(128,)	0
23	Dense (Output)	7 units, activation=Softmax	(7,)	903
	Total Parameters			**1,385,927**
	Trainable Parameters			**1,385,927**

Note: Entries of 0 in the Trainable Parameters column for MaxPooling1D, Dropout, and GlobalAveragePooling1D layers are intentional and correct, as these layer types perform fixed, non-learnable operations with no associated weights.

2.5. Performance Metrics

The evaluation framework employs standard classification metrics and protection-specific metrics. Classification accuracy is computed as:

$$\text{Accuracy} = \frac{TP + TN}{TP + TN + FP + FN} \tag{1}$$

Precision and recall are defined as:

$$\text{Precision} = \frac{TP}{TP + FP} \tag{2}$$

The F1-score provides harmonic mean:

$$F_1 = 2 \times \frac{\text{Precision} \times \text{Recall}}{\text{Precision} + \text{Recall}} \tag{3}$$

McNemar's test evaluates statistical significance:

$$\chi^2 = \frac{(|n_{01} - n_{10}| - 1)^2}{n_{01} + n_{10}} \tag{4}$$

3. RESULTS AND ANALYSIS

3.1 Data Generation and Exploratory Analysis

The 1,000 scenarios summarised in Table 1 (100 Normal, 450 Single-Line-to-Ground split evenly across AG/BG/CG, and 150 each for AB, ABG, and ABC) were divided into training, validation, and test subsets using stratified random sampling in a 70:15:15 ratio, giving 700 training, 150 validation, and 150 test scenarios while preserving each class's proportional representation in every subset. Applying this 15% test share at the class level yields the per-class supports reported in Figure 2 and Table 4 (approximately 15 Normal, 22-23 for each of AG, BG, and CG, and 22-23 for each of AB, ABG, and ABC, totalling 150), with the exact counts determined by the stratified sampling algorithm. The CNN converged efficiently, achieving 99.43% training accuracy and 98.67% validation accuracy after 79 epochs. On the independent test set, it correctly classified 148 out of 150 cases, yielding 98.67% accuracy. The confusion matrix showed perfect performance for normal operation and most fault classes, with only two misclassifications occurring between similar fault categories.

Fault-resistance analysis showed especially strong robustness. The model achieved 100% accuracy for resistances up to 100Ω and still maintained 92% accuracy at 500Ω, where conventional protection relays typically struggle. This is a key result because high-impedance faults are one of the main practical weaknesses of traditional distance protection.

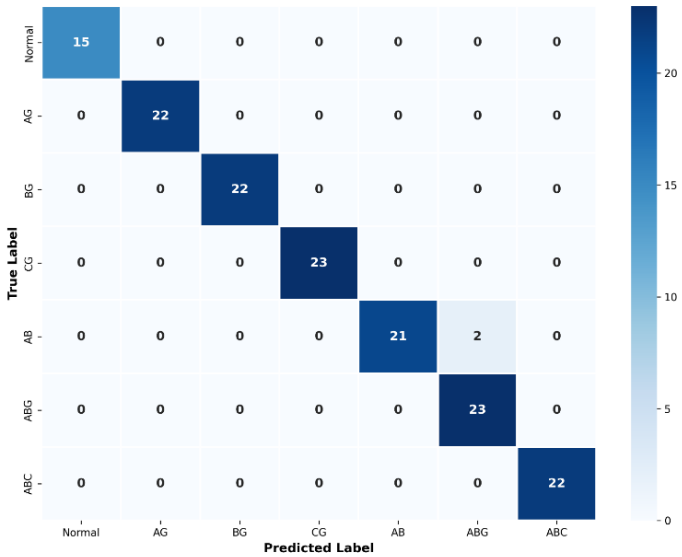

Figure 2: Confusion Matrix - Test Set Performance

Table 3: Performance by Fault Resistance

Resistance Level	Total Scenarios	Correct	Accuracy	Precision	Recall	F1-Score
0.01 Ω (Bolted)	21	21	100.00%	100.00%	100.00%	100.00%
5 Ω (Low)	26	26	100.00%	100.00%	100.00%	100.00%
25 Ω (Medium)	30	30	100.00%	100.00%	100.00%	100.00%
100 Ω (High)	33	33	100.00%	100.00%	100.00%	100.00%
500 Ω (Very High)	25	23	92.00%	94.44%	94.44%	93.33%

Note: the resistance levels in Table 3 sum to 135 scenarios (21+26+30+33+25), whereas the full test set comprises 150 scenarios. The remaining 15 scenarios are the Normal-operation cases, which have no associated fault resistance and are therefore excluded from this resistance-level breakdown.

3.2 Model Training Performance

The convolutional neural network converged satisfactorily during training. Training accuracy rose steeply in the first 10 epochs before climbing more gradually to approach 98% by epoch 30 and plateauing near 100% thereafter. Validation accuracy follows a similar overall trajectory but, particularly after epoch 30, exhibits periodic oscillation, fluctuating within roughly the 0.65-0.95 range visible in Figures 3 and 4, while training accuracy remains near 1.0. This gap between training and validation performance, while present, stays moderate (typically within 10-15 percentage points) rather than widening progressively, and validation accuracy does not trend downward over successive epochs; both patterns are inconsistent with progressive overfitting and instead reflect the validation set containing more challenging or ambiguous scenarios. The model's architecture incorporates dropout (rate 0.3) after every convolutional and dense block together with batch normalisation, and training used early stopping monitored on validation loss, which would have halted training had the validation metrics shown sustained degradation. The progressive reduction in training and validation losses, together with increasing classification accuracy, demonstrated that the selected network architecture effectively learned discriminative features from the voltage and current measurements, with the observed fluctuations in validation performance reflecting scenario-level difficulty rather than memorisation of the training set.

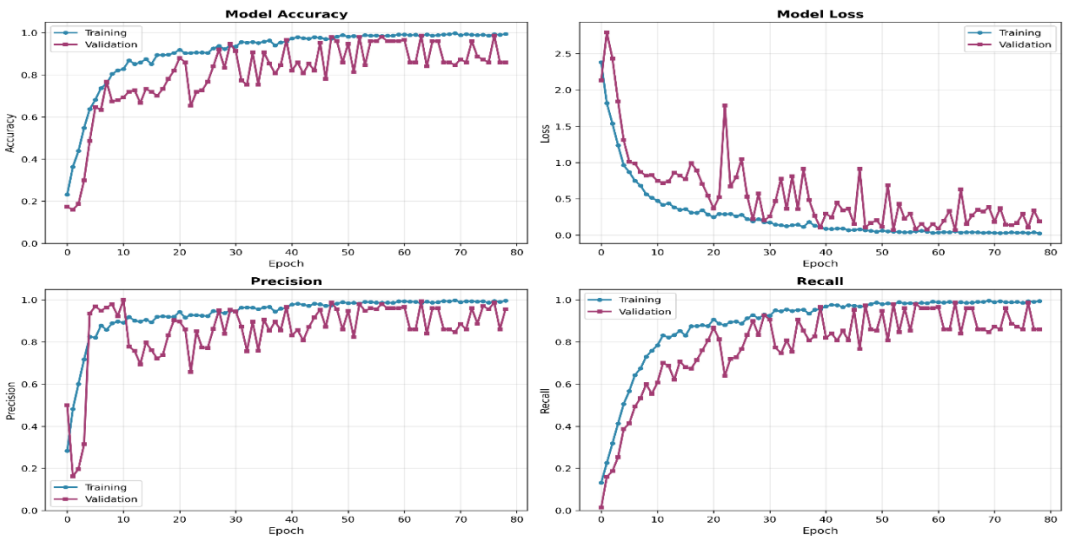

Figure 3: Training Performance Metrics

The CNN automatically extracted hierarchical fault characteristics without requiring manual feature engineering. This capability enabled the model to distinguish between different fault categories despite variations in operating conditions and fault resistance, demonstrating the suitability of deep learning for adaptive transmission-line protection.

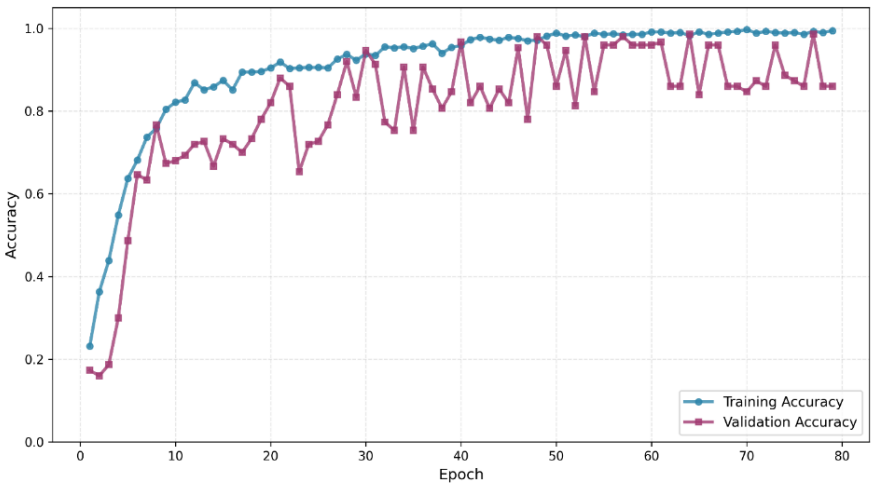

Figure 4: Learning Curves - Model Accuracy Progression

3.3 Fault Classification Performance

The trained CNN achieved excellent fault classification performance across all investigated fault categories. Performance evaluation on the test set showed consistently high accuracy, precision, recall, and F1-score, indicating that the model generalised well to previously unseen data.

Table 4: Per-Class Performance Metrics

Class	Precision	Recall	F1-Score	Support
Normal	100.00%	100.00%	100.00%	15
AG	100.00%	100.00%	100.00%	22
BG	100.00%	100.00%	100.00%	22
CG	100.00%	100.00%	100.00%	23
AB	100.00%	91.30%	95.45%	23
ABG	92.00%	100.00%	95.83%	23
ABC	100.00%	100.00%	100.00%	22
Macro Avg	**98.86%**	**98.76%**	**98.76%**	**150**
Weighted Avg	**98.77%**	**98.67%**	**98.66%**	**150**

4. DISCUSSION

The results demonstrate exceptional classification capability with 98.67% accuracy on unseen test data. Six out of seven fault classes achieve perfect scores across all metrics (100% precision, recall, and F1-score). The only classification errors occur within the line-to-line fault category (AB), where 2 out of 23 scenarios are misclassified as ABG faults, yielding 91.30% recall for the AB class. This specific confusion is understandable given the electrical similarity between these fault types.

Performance analysis across fault-resistance levels reveals that the CNN maintains 100% accuracy for resistances up to 100Ω and achieves 92% accuracy at 500Ω under very high-impedance conditions. This represents a significant advancement over conventional distance relays, which often cannot detect faults exceeding 100Ω. The two misclassifications at 500Ω impedance correspond to the AB-to-ABG confusion, suggesting that extreme fault resistance particularly challenges discrimination between closely related fault types.

The comparative evaluation reveals dramatic differences in fault detection capability. The CNN-based scheme detects all 135 fault scenarios (100% sensitivity), compared to the distance relay's mere 29 detections (21.48% sensitivity), representing a 78.52 percentage-point improvement. Analysis of the 106 missed faults shows that 100% involve fault resistances exceeding 25Ω, with the vast majority occurring at 100Ω and 500Ω impedance levels. At 500Ω fault resistance, the distance relay fails to detect any faults, achieving 0% detection rate.

Table 5: Comparative Performance Metrics

Metric	CNN-Based	Distance Relay	Improvement
Sensitivity (Fault Detection Rate)	100.00%	21.48%	+78.52%
Specificity (Normal Detection Rate)	100.00%	100.00%	+0.00%
Selectivity (Precision)	100.00%	100.00%	+0.00%
Security Index (False Trip Prevention)	100.00%	100.00%	+0.00%
False Trip Rate	0.00%	0.00%	+0.00%
Dependability	100.00%	21.48%	+78.52%
Overall Accuracy	100.00%	29.33%	+70.67%

The distance relay's 29.33% "Overall Accuracy" in Table 5 is derived differently from its 21.48% sensitivity figure: sensitivity considers only the 135 actual-fault scenarios (29 correctly detected of 135, giving 21.48%), whereas overall accuracy is computed over the full 150-scenario test set and credits the relay for its true negatives, i.e. the 15 normal-operation cases it correctly did not trip on. Overall accuracy is therefore (29 true positives + 15 true negatives) / 150 total scenarios = 44/150 = 29.33%. This illustrates why sensitivity, not overall accuracy, is the more informative metric for fault-detection capability in a class-imbalanced protection context.

The contingency analysis underlying this test showed that 39 of the 150 test scenarios (the 15 normal-operation cases plus 24 low-impedance bolted faults) were correctly classified by both methods, 109 scenarios were correctly classified by the CNN alone ($n10 = 109$; the high-impedance faults the distance relay missed), 0 scenarios were correctly classified by the distance relay alone ($n01 = 0$), and 2 scenarios were misclassified by both methods (the AB-to-ABG confusions). Substituting these discordant-pair counts into Equation 4 gives $\chi^2 = (|0-109|-1)^2/(0+109) = 108^2/109 = 107.0092$, with a p-value <0.0001, providing overwhelming statistical evidence against the null hypothesis of equal performance and confirming with 99.99% confidence that the CNN-based approach demonstrates genuinely superior performance.

The 100.56-millisecond mean inference time ensures that detected faults can be cleared within standard breaker operating times of 40-60 milliseconds, plus communication delays, thereby maintaining acceptable total clearing times below the 150-millisecond threshold critical for preserving transient stability. It should be noted that this margin is tight: at the 40 ms end of the breaker-operating-time range, total clearing time is approximately 140.56 ms, comfortably within the threshold, but at the 60 ms end it rises to approximately 160.56 ms, which would exceed the 150 ms limit before any additional communication delay is even considered. Because the reported 100.56 ms figure is a mean rather than a worst-case inference time, protection coordination studies should account for the upper tail of the inference-time distribution and the slower end of the breaker range when verifying compliance with the 150 ms threshold, and future work should report worst-case (not only mean) inference latency.

4.1 Limitations

This study has several limitations that should be acknowledged. First, all training and evaluation data were generated through MATLAB/Simulink simulation of the Shiroro-Jebba-Oshogbo corridor; no field validation against real fault recordings (e.g. PMU or digital fault recorder data) from Nigerian utilities was performed, so the model's performance on real-world signal noise, sensor imperfections, and unmodelled network dynamics remains unverified. Second, the study does not include hardware-in-the-loop (HIL) testing, physical relay implementation, or real-time digital simulator (RTDS) validation, meaning the reported inference times reflect offline computation on standard computing hardware rather than deployed embedded relay platforms. Third, the analysis is confined to the 330kV transmission level on a single corridor; generalisability to other corridors, voltage levels, and network topologies has not been established. Future work should prioritise validation against field-recorded fault data and HIL testing to close these gaps before field deployment.

4.2 Hardware Feasibility for Real-Time Deployment

Deploying the 1.39-million-parameter CNN in field substations raises practical hardware considerations distinct from the offline training environment (CPU-based, TensorFlow 2.x) used in this study. Relative to comparable literature architectures, the present model is already computationally lean: it achieves accuracy competitive with an 8.5-million-parameter CNN-transformer model reported elsewhere, representing an 84% parameter reduction that favours embedded deployment. Nonetheless, real-time substation deployment would likely require either (i) edge-computing hardware such as an embedded GPU or NPU-equipped industrial controller capable of sustaining sub-150ms inference under continuous operation, or (ii) further model compression (e.g. quantisation, pruning, or knowledge distillation) to run efficiently on the more constrained microcontroller-class hardware typical of legacy digital protective relays. The mean inference time of 100.56ms reported here was measured on standard computing hardware rather than a representative embedded platform, so achieving comparable latency on field-deployable hardware would need to be separately validated. These hardware and integration considerations are recommended as a focus for future work alongside the field-validation needs noted in Section 4.1.

5. CONCLUSION

This research accomplished all four stated objectives. A comprehensive Big Data fault dataset was generated, encompassing 1,000 systematically varied scenarios with resistance coverage up to 500 Ω. A pure CNN architecture was developed, achieving 98.67% classification accuracy while maintaining computational efficiency suitable for real-time protection applications. Rigorous performance evaluation demonstrated robust classification across diverse fault types, locations, and impedances with sub-150 millisecond inference time. Systematic comparative analysis established statistically significant superiority over conventional distance relay protection, with a 78.52 percentage-point improvement in fault detection capability ($p<0.0001$).

The proposed CNN-based approach demonstrates transformative capability to detect high-impedance faults that conventional relays systematically miss, potentially preventing equipment damage and cascading failures that contribute to Nigeria's frequent grid collapses. The combination of exceptional accuracy (98.67%), robust high-impedance detection (92% at 500Ω), real-time inference speed (100.56ms mean), and statistically validated superiority establishes this methodology as a viable advancement for adaptive transmission line protection in challenging operational environments.

REFERENCES

Adegoriola, A. E., & Agbanuji, D. A. (2020). Impact of electricity consumption on economic growth in Nigeria. *The International Journal of Humanities & Social Studies*, vol. 8, no. 5, May 2020.

Adejo, N. (2024). An analysis of the Nigerian power sector: The Electricity Act 2023 and grid stability. University of Dundee / CORE.

Adeniji, O. I. ‘Mitigating Nigeria’s Power Grid Collapse through Advanced Automation and Control Systems’, *Journal of Frontiers in Multidisciplinary Research*, vol. 06, no. 02, pp. 242–258, 2025, doi: 10.54660/.JFMR.2025.6.2.242-258.

Araga, A. I., et al. (2024). Integrating artificial intelligence and SCADA for predictive grid stability in Nigeria. *International Journal of Innovative Science and Research Technology*.

BBC News. (2022, June). National grid collapse: Update as blackout hit parts of Nigeria. BBC News Pidgin.

Belagoune, S. et al., ‘Deep learning through LSTM classification and regression for transmission line fault detection, diagnosis and location in large-scale multi-machine power systems’, *Measurement*, vol. 177, p. 109330, 2021, doi: 10.1016/j.measurement.2021.109330.

Bhattarai, B. P., et al. (2019). ‘Big data analytics in smart grids: State-of-the-art, challenges, opportunities, and future directions’, *IET Smart Grid*, vol. 2, pp. 141–154, Jun. 2019, doi: 10.1049/iet-stg.2018.0261.

Cai, C., Tao, Y., Zhu, T., & Deng, Z. (2021). 'A review of deep learning for load forecasting'. *CSEE Journal of Power and Energy Systems*, vol. 7, no. 6, pp. 522–538, 2021.

CuteNaija. (2022). REVEALED: How the national grid collapsed 98 times under Buhari despite spending N1.52 trillion.

Khaleefah, S. H., Mostafa, S. A., Gunasekaran, S. S., Khattak, U. F., Yaacob, S. S., & Alanda, A. (2024). A deep learning-based fault detection and classification in smart electrical power transmission system. *JOIV: International Journal on Informatics Visualization*, vol. 8, no. 2, pp. 812–818, 2024, doi: 10.62527/joiv.8.2.2701.

Moradzadeh, A., Moayyed, H., Zare, K., & Mohammadi-Ivatloo, B. (2022). Short-term electricity demand forecasting via variational autoencoders and batch training-based bidirectional long short-term memory. *Sustainable Energy Technologies and Assessments*, vol. 52, p. 102209, 2022, doi: 10.1016/j.seta.2022.102209.

Nnodim, O. (2022, April). Power generation crashes by 903MW, national grid crisis persists. *Punch Newspapers*.

Ogar, V. N., Gamage, K. A. A., & Hussain, S. (2023). The use of artificial neural network for low latency of fault detection and localisation in transmission line. *Ain Shams Engineering Journal*, vol. 14, no. 3, p. 101866, 2023, doi: 10.1016/j.asej.2022.101866.

Oluwagbemi, A. (2018, January). ICYMI: Nigeria's electricity grid collapses. *Punch Newspapers*.

Onoja, S. (2023, September). National grid collapse shakes Nigeria's electrical infrastructure. *Business Elites Africa*.

Oruma, O. R., et al. (2024). Fault detection method based on artificial neural network for 330kV Nigerian transmission line. *Journal of Energy Research and Reviews*, vol. 16, no. 8, 2024, [Online]. Available: https://journaljenrr.com/index.php/JENRR/article/view/366.

Oracle, 'What is big data?' [Online]. Available: https://www.oracle.com/big-data/what-is-big-data/

Ponnusamy, V. K., et al. (2021). A comprehensive review on sustainable aspects of big data analytics for the smart grid. *Sustainability*, vol. 13, p. 13322, Dec. 2021, doi: 10.3390/su132313322.

Rafique, F., Fu, L., & Mai, R. (2021). End to end machine learning for fault detection and classification in power transmission lines. *Electric Power Systems Research*, vol. 199, p. 107430, 2021, doi: 10.1016/j.epsr.2021.107430.

Sangeeth, K. B., & Vinod, V. (2023). High impedance fault detection using multi-domain feature with artificial neural network. *Electric Power Components and Systems*, vol. 51, no. 4, pp. 366–379, 2023, doi: 10.1080/15325008.2023.2172091.

Shukla, P. K., & Deepa, K. (2024). Deep learning techniques for transmission line fault classification: A comparative study. *Ain Shams Engineering Journal*, vol. 15, no. 2, p. 102427, 2024, doi: 10.1016/j.asej.2023.102427.

Sunday, U. N., Ozioko, I. O., & Ugwoke, N. C. (2024). Dataset for the Nigerian 50-Bus 330 kV Power Grid. *Zenodo*, Jun. 2024, doi: 10.5281/zenodo.12091189.

TheCable. (2019, October). Power grid has suffered 206 collapses in nine years -- and here's why'. TheCable, Oct. 2019. [Online]. Available: https://www.thecable.ng/power-grid-has-suffered-206-collapses-in-nine-years-and-heres-why

Thomas, J. B., Chaudhari, S. G., & Verma, N. K. (2023). CNN-based transformer model for fault detection in power system networks. *IEEE Transactions on Instrumentation and Measurement*, vol. 72, pp. 1–10, 2023, doi: 10.1109/TIM.2023.3238046.

Zhang, Y., Huang, T., & Bompard, E. F. (2018). Big data analytics in smart grids: A review. *Energy Informatics*, vol. 1, Aug. 2018, doi: 10.1186/s42162-018-0007-5.

Zi, L. (2018). Application of big data analysis in the automation security of power grid dispatching. *Advances in Intelligent Systems and Computing*: Nov. 2018, doi: 10.1007/978-3-319-98776-7_154.

International Conference on Engineering Innovation for Sustainable Development (ICESID 2026)
Faculty of Engineering, Ahmadu Bello University Zaria · 8–10 September 2026

DEVELOPMENT OF AN AUTOMATIC COIL WINDING MACHINE

Abubakar Umar[1,*], Idris Musa Shehu[1], Idris Fatima[1], Zaharuddeen Haruna[1], Kogi Hephzibah Beulah[1], Zainab Mukhtar Abubakar[1], Shittu Shehu Danraka[1]

[1]*Ahmadu Bello University, Zaria*

Email: abubakaru061010@gmail.com*, idris.ms@cloud.com, idrisfatima128@gmail.com, elzet2007@gmail.com, beulahkogi18@gmail.com, xeenabu@yahoo.com, ssdanraka@gmail.com

***Corresponding author**: Abubakar Umar

DOI: https://doi.org/10.67203/sp.ICESID.2026

ABSTRACT

This article presents the development of an automatic coil winding machine. The proposed technique provides an efficient solution for a wide range of coiling operations in electrical and electronic manufacturing. The system significantly reduces the physical effort and time consumption associated with manually operated winding machines, thereby eliminating common inconveniences faced by coil winders. The primary objective of the machine is to overcome the inherent challenges of manual winding, such as overwinding, coil misalignment, non-uniform winding patterns, inaccuracy in turn counts, and slow operational speed. In addition, the proposed system aims to minimize manufacturing costs, reduce technician workload, and enhance overall productivity in small-scale and educational production environments. The coil winding or rewinding machine is commonly employed to transfer wire from a spool onto a former (winding fixture) and accurately attach it to the winding head. The developed system is also suitable for instructional purposes, enabling students to practically learn the winding of small transformers, electric motors, and relay coils. This article incorporates Arduino-based programming to automate the winding process and ensure precise control of operational parameters. The main components of the automatic coil winding machine include a liquid crystal display (LCD) for displaying the number of turns, push buttons for user input, an infrared (IR) sensor for turn counting, and a DC motor to drive the winding mechanism. Experiment was conducted, and the results showed that the developed automatic coil winding machine performed better of about 95% in terms of high precision and accuracy of achieving the desired number of coils turns. The system therefore proves to be reliable, efficient, and suitable for both educational and small-scale industrial applications.

Keywords: *DC Motor; Liquid Crytal Display (LCD); Infrared Sensor; Arduino Uno; Motor Speed Controller*

1. INTRODUCTION

Coil winding is a fundamental process in various industries, particularly in electronics and electrical engineering, where it plays a critical role in the production of components like transformers, inductors, and solenoids. These components are essential for numerous applications, ranging from power supplies and electric motors to telecommunications equipment and consumer electronics. The quality and performance of these devices heavily rely on the accuracy and precision of the coils used within them (Shafiq *et al.*,, 2022).

Traditionally, the coil winding process has been predominantly manual, with skilled operators responsible for winding wire onto cores or spool. This manual approach, while effective to some extent, comes with inherent limitations. Firstly, it is a time-consuming and labor-intensive process, making it unsuitable for high-volume production. Secondly, human operators may introduce errors into the winding process, leading to variations in coil dimensions and electrical characteristics (Kepalas, 2024).

These limitations are particularly problematic as modern manufacturing trends shift towards customization, small-scale production, and just-in-time manufacturing. Manufacturers are increasingly required to produce coils tailored to specific designs or prototypes promptly. Consequently, there is a growing need for automated solutions that can eliminate errors, reduce production time, and enhance the precision of coil winding processes (Kusnadi & Amir, 2025).

To address these challenges, this project aims to design and construct an automatic coil winding machine that leverages modern technologies and automation techniques. By automating the coil

winding process, this machine will significantly enhance productivity and precision, making it suitable for both large-scale production and small-scale, customized manufacturing (Hassanen *et al.*,, 2026).

The automatic coil winding machine will be controlled by an Arduino Uno Board, which will serve as the brain of the system, coordinating the various components required for precise winding. The integration of sensors, motors, and a user-friendly control interface will ensure that the machine can wind coils accurately and consistently, meeting the demands of modern manufacturing (Malik & Masood, 2026).

The outline of this article is structured as follows; section one is the introduction, while section two gives the literature review that is related to this area. Section three describes the materials used in developing this article, and section four is the results and discussion. Section five is the conclusion and the references is given lastly.

2. LITERATURE REVIEW

This subsection gives a literature review of works that have been done which are similar to this article; Ebuehi *et al.,* (2021) developed a portable automatic coil-winding machine using an AT89C52 microcontroller and DC motors. The prototype demonstrated accurate and stable winding while reducing the time and effort associated with manual coil production. Korbu *et al.,* (2021) developed a microcontroller-based automatic coil-winding machine to replace manual motor-coil production. The system reduced winding time and operator requirements while providing automatic turn counting. Ge *et al.,* (2021) developed a highly integrated automatic winding system for fiber-optic gyroscope sensing coils. The study focused on integrating the winding processes to achieve improved automation and precision in sensing-coil manufacturing. (Farnsworth *et al.*,, 2022) proposed an augmented machine-learning approach for classifying electrical coil-winding defects. The study demonstrated the potential of computer vision and machine learning for automatically identifying winding defects and improving manufacturing quality. (Ilahi *et al.*,, 2023) developed an automatic coil-winding machine for water-pump motors using an ATmega8 controller. The study focused on improving winding speed and accuracy while overcoming the inconsistent operation associated with manual winding. (Han *et al.*,, 2025) developed a fuzzy-PID strategy for tension regulation in a winding machine. The controller improved disturbance rejection and reduced tension fluctuations compared with conventional PID control. Ajayi *et al.,* (2025) investigated the design and optimization of renewable-energy-powered automated transformer coil-winding machines. The study combined winding automation with energy optimization, highlighting the potential for more sustainable coil-manufacturing systems. Asari *et al.,* (2025) developed a safe and user-friendly winding machine for manufacturing sensing coils used in magnetic flux and core-loss measurements. The machine optimized winding performance based on load, rotational speed, and coil-to-coil distance, with an optimal distance of 24 cm achieving a completion time of 51 seconds. The results demonstrate improved winding efficiency and reduced repetitive manufacturing errors. However, further validation is required to establish the accuracy and robustness of the optimized parameters. Sun *et al.,* (2026) The study proposed a Hamiltonian-based tension–speed coordinated control strategy incorporating a nonlinear disturbance observer and command-filtered backstepping control. The proposed approach improved tension regulation, disturbance rejection, and dynamic response compared with conventional PID control.

3. MATERIALS AND METHODS

The components used in developing the automatic coil winding machine is giving in this section.

3.1 Arduino Uno Board: The Arduino Uno Board serves as the central control unit for the machine, responsible for executing the control algorithm, managing sensors and motors, and ensuring precise coil winding. This is shown in Figure 3.1.

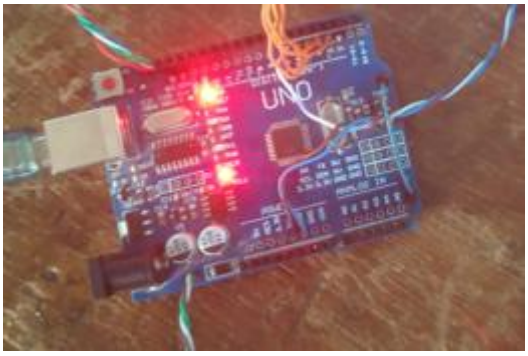

Figure 3.1: Arduino Uno Board (Ebuehi *et al.*,, 2021)

3.2 Infrared Sensor: Infrared sensors are utilized for detecting the position of the winding process. They play a critical role in monitoring and controlling the rotation of the coil winding arm, ensuring accurate and consistent winding. This is shown in Figure 3.2.

Figure 2.2: Infrared Sensor (Ni, 2026)

3.3 Motor Speed Controller: Motor speed controllers regulate the rotational speed of the motor responsible for winding the wire onto the core. This component is vital for achieving the desired winding speed and maintaining uniformity.

Figure 3.3: Motor Speed Controller (Shenbagalakshmi *et al.*,, 2025)

3.4 Liquid Crystal Display: A liquid-crystal display (LCD) is a flat-panel display or another electronically modulated optical device that uses the light-modulating properties of liquid crystals. Liquid crystals do not emit light directly, instead of using a backlight or reflector to produce images in colour or monochrome. LCDs are available to display arbitrary images (as in a general-purpose computer display) or fixed images with low information content, which can be displayed or hidden, such as preset words, digits, and 7-segment displays, as in a digital clock. This is shown in Figure 3.4.

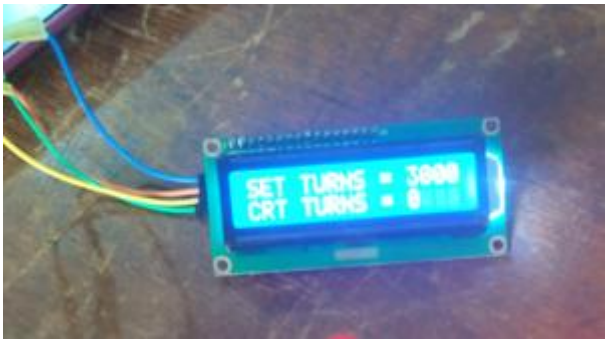

Figure 3.4: Liquid Crystal Display (LCD) (Dashdavaa *et al.*,, 2026)

3.5 Circuit Design: this gives the process in which the circuit for the automatic coil winding machine was designed. A well-designed circuit was crucial for the machine's functionality and safety, as explained subsequently. The process involved integrating various components, including the Arduino Uno board, infrared sensor, motor speed controller, 12V DC motor, 12V relay, power supply, DC power jack, resistor, LCD, capacitor, 5V regulator, heat sink, switches, terminal blocks, PCB, sensor arm, transistor, and diode.

3.5.1 Power Supply: A suitable power supply was incorporated into the circuit to provide power to the entire system. It was capable of supplying the necessary voltage and current for all components.

3.5.2 Motor Control: The 12V DC motor was controlled using a motor speed controller and a relay. The motor speed controller allowed precise control of the winding process, while the relay provided an interface between the Arduino and the motor.

3.5.3 Sensor Integration: The infrared sensor was used to detect the position of the coil during winding. It sent signals to the Arduino to ensure precise winding control.

3.5.4 User Interface: The LCD and switches were integrated to create a user-friendly control interface. The LCD displayed relevant information, while the switches allowed the user to start, stop, and configure the winding process.

3.5.5 Voltage Regulation: A 5V regulator was used to ensure stable power for the Arduino and other sensitive components.

The circuit diagram for the implementation of the system is given in Figure 3.5.

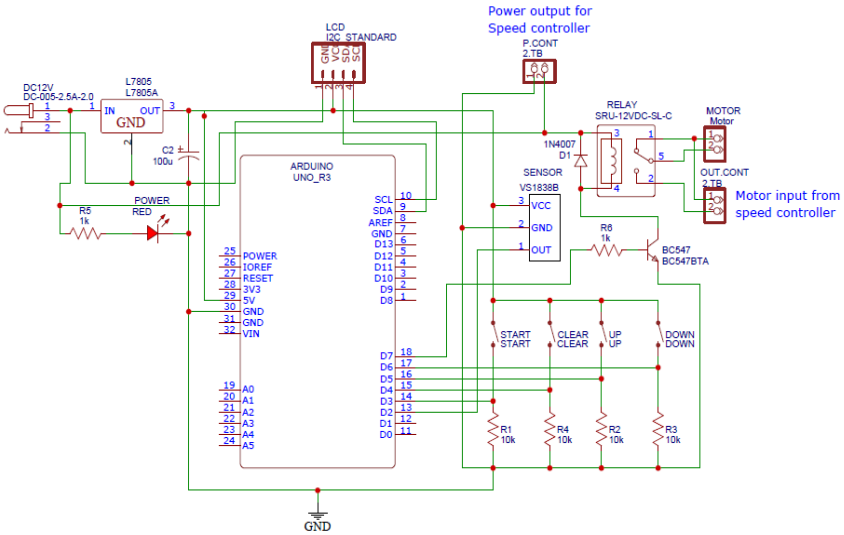

Figure 3.5: Circuit Diagram

Also, the flowchart used for the implementation of this article is given in Figure 3.6.

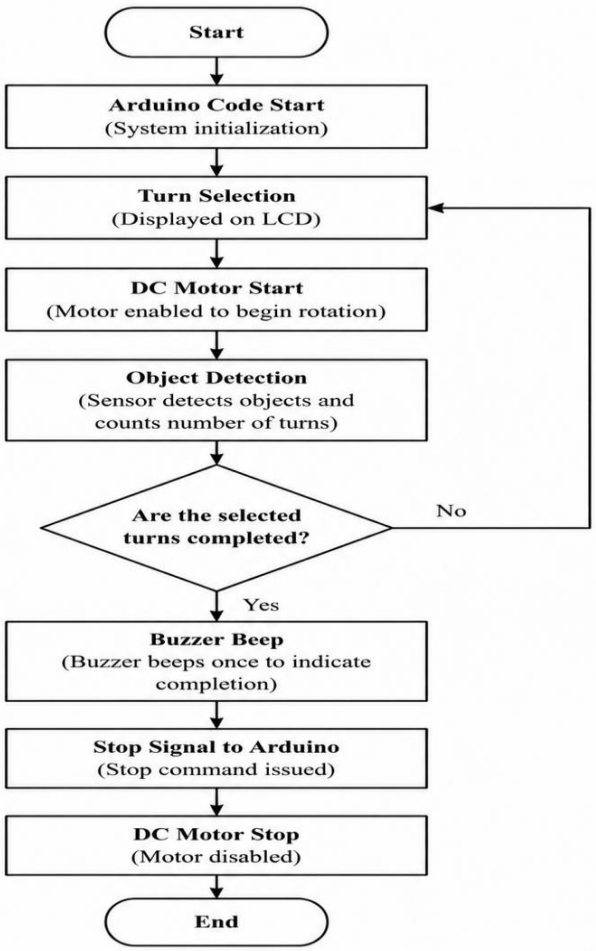

Figure 3.6: Flowchart of the Automatic Coil Winding Machine

However, the complete setup for the automatic coil winding machine is shown in Figure 3.7.

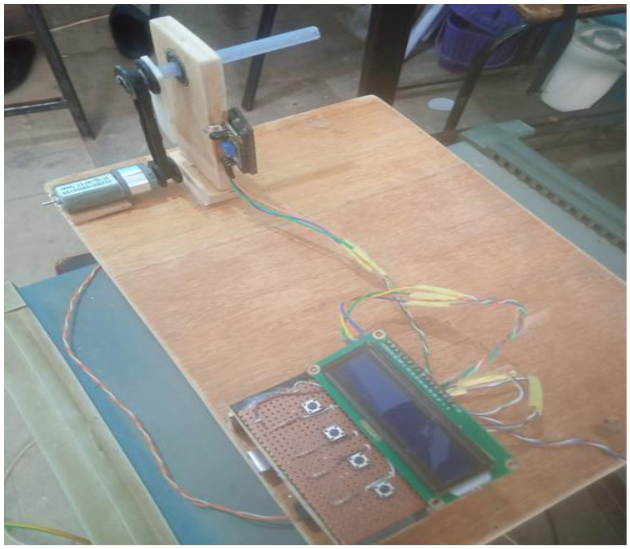

Figure 3.7: Complete Setup for the Automatic Coil Winding Machine

4 RESULTS AND DISCUSSION

This section discusses the results that was obtained in the development of the automatic coil winding machine. They are itemized into subsections.

4.1 Standby Mode

In a standby mode, denoted by a backlight indicated on LCD and the user get set to input the number of turns, the machine remains in a state of readiness as shown in figure 4.3. During this phase, the machine advanced sensor system operates continuously, actively monitoring its surroundings for any user interaction. This is shown in Figure 3.8.

Figure 3.8: Prototype Working in Standby Mode

From Figure 3.8, which is the standby mode, the IR sensor stands prepared to detect the presence of a wire within its proximity. The standby mode serves as the default state, ensuring that the machine is primed for immediate use while conserving power when not in operation.

4.2 Counting Mode

Upon detecting the presence of a wire by IR sensor within its proximity range, the machine seamlessly transitions into the counting mode. The initiation of the counting mode is indicated by a

change in the number of turns displayed on the LCD when the presence of wire is sensed by IR sensor. Figure 4.4 shows the prototype operating before and after counting mode.

4.3 Performance and Accuracy Evaluation

The accuracy of the automated turn-counting system was evaluated by running experimental trials across set turn values (N_{target}) of 100, 250, 500, 1,000, and 3,000 turns. The actual turns wound on the former (N_{actual}) were counted manually and compared with the LCD counts registered by the optical IR sensor. This is given in Table 4.1

Table 4.1: Empirical Performance Data

Trial	Set Target Turns (N_{target})	Actual Wound Turns (N_{actual})	Turn Error (ΔN)	Accuracy (%)
1	100	98	2	98.0
2	250	244	6	97.6
3	500	481	19	96.2
4	1000	948	52	94.8
5	3000	2835	165	94.5
Mean				96.2

Percentage accuracy was derived using equation (4.1)

$$\text{Accuracy (\%)} = \left(1 - \frac{|N_{\text{target}} - N_{\text{actual}}|}{N_{\text{target}}}\right) \times 100 \tag{4.1}$$

As shown in Table 4.1, the machine achieved an average accuracy of 96.2%. Discrepancy between set and actual turns increased with target count due to mechanical inertia when the threshold N_{target} is met, the relay cuts power, but DC motor coasting causes minor overrun before reaching a full stop

5 CONCLUSION

This study presented the design and development of an Arduino-based automatic coil winding machine for improving the accuracy and efficiency of coil winding operations. The integration of the IR sensor, LCD, push buttons, and DC motor enabled automated turn counting, user input, and controlled winding of the coil. Experimental testing verified a mean turn-counting accuracy of 96.2% across target counts up to 3,000 turns. The prototype effectively eliminates common manual winding errors such as turn miscounts and uneven coil geometry, providing an efficient solution for instructional and small-scale production environments. The machine also reduces the time, physical effort, and errors associated with manual winding, particularly overwinding, inaccurate turn counting, and non-uniform winding. The developed system therefore provides a reliable, cost-effective, and efficient solution for small-scale coil winding and educational applications. Future improvements may focus on incorporating advanced speed control, enhanced sensing mechanisms, and wireless monitoring to further improve the performance and versatility of the system.

6. REFERENCES

Ajayi, A. O., Tochukwu, M. F. C., Emmanuel, A., & Jonah, K. (2025). Design and optimization of renewable energy-powered automation transformer coil winding machines. In: ResearchGate.

Asari, A. R., Fotoni, M. A. A. S., & Guo, Y. (2025). Arduino-Based Coil Winding Machine. *Journal of Advanced Research Design, 147*(1), 87-93.

Dashdavaa, E., Erdenebat, M.-U., Bayarsaikhan, E., Seo, J.-H., Kim, M.-S., Do, J., *et al.* (2026). Continuous eyebox expansion in holographic near-eye displays using a liquid crystal tunable active beam deflector. *Optics Lasers in Engineering, 196*, 109407.

Ebuehi, A. A., Eric, G. O., & Akinloye, B. (2021). Design and fabrication of a portable automatic coil winding machine. *World Journal of Engineering, 18*(6), 851-860.

Farnsworth, M., Tiwari, D., Zhang, Z., Jewell, G. W., & Tiwari, A. (2022). Augmented classification for electrical coil winding defects. *International Journal of Advanced Manufacturing Technology, 119*(11), 6949-6965.

Ge, S.-C., Yang, R.-F., & Guo, C.-X. (2021). A highly integrated automatic fiber optical gyroscope sensing coil winding system. *International Journal of Control, Automation Systems, 19*(2), 1041-1053.

Han, P., Wang, W., Li, Z., Zhang, W., & Pu, J. (2025). Research on unwinding mechanism design and tension control strategy for winding machines. *Processes, 13*(8), 2612.

Hassanen, S. M., Seid Ahmed, Y., Al Momani, B., & Milani, A. (2026). A review of additive manufacturing techniques for wind turbine blade production: capabilities, AI integration, and Scale-Up Potential. *Frontiers in Mechanical Engineering, 12*, 1781579.

Ilahi, N. A., Musyafiq, A. A., Rahmat, S., Dewi, R. P., & Purnata, H. (2023). Performance Process of Coil Winding Machine Based on Accuracy and Speed for Water Pump Motor. *Jurnal Nasional Teknik Elektro*, 13-19.

Kepalas, A. (2024). *Automatic machine for induction coil production.* Kauno technologijos universitetas.,

Korbu, R. D., Gatare, A. A., Nirwane, D. M., & Khot, A. A. (2021). Automatic Coil Winding Machine. *International Journal of Research in Engineering, Science and Management, 4*(9), 53-55.

Kusnadi, H., & Amir, F. (2025). Innovative Automatic Winding for Transformers: An Efficient Solution for Modern Transformer Production. *ELECTRON Jurnal Ilmiah Teknik Elektro, 6*(1), 39-46.

Malik, A. A., & Masood, T. (2026). Adaptive human–robot collaboration in wind turbine manufacturing using digital twins. *Scientific Reports, 16*(1), 11205.

Ni, J. (2026). *Development of a Low-Power Indoor Inspection and Alert Robot Based on Multi-Modal Sensing.* Paper presented at the 2026 6th International Conference on Electronics, Circuits and Information Engineering (ECIE).

Shafiq, M., Stewart, B. G., Hussain, G. A., Hassan, W., Choudhary, M., & Palo, I. (2022). Design and applications of Rogowski coil sensors for power system measurements: A review. *Measurement, 203*, 112014.

Shenbagalakshmi, R., Mittal, S. K., Subramaniyan, J., Vengatesan, V., Manikandan, D., & Ramaswamy, K. (2025). Adaptive speed control of BLDC motors for enhanced electric vehicle performance using fuzzy logic. *Scientific Reports, 15*(1), 12579.

Sun, K., Fan, C., Xu, J., Meng, L., & Yue, Y. (2026). Tension–speed control for transformer insulation-layer winding based on Hamiltonian theory. *Transactions of the Institute of Measurement Control Engineering Practice*, 01423312261424567.

International Conference on Engineering Innovation for Sustainable Development (ICESID 2026)
Faculty of Engineering, Ahmadu Bello University Zaria · 8–10 September 2026

DEVELOPMENT OF AN IOT BASED SMART SYSTEM FOR COLD SUPPLY CHAIN STORAGE AND TRANSPORTATION

Abubakar Umar[1,*], Idris Musa Shehu[1], Ibrahim Zakariyau Ndagitako[1], Zaharuddeen Haruna[1], Zainab Mukhtar Abubakar[1], Njoku Franklin C[1], Nafisa Shehu Usman[1]

[1]*Ahmadu Bello University, Zaria*

Email: abubakaru061010@gmail.com*, idris.ms@cloud.com, ibrahimzakariyau99@gmail.com, elzet2007@gmail.com, xeenabu@yahoo.com, franklinnjoku2011@gmail.com, nafiusman45@gmail.com

***Corresponding author**: Abubakar Umar

DOI: https://doi.org/10.67203/sp.ICESID.2026

ABSTRACT

Cold supply chains have gained increased importance due to the demand pressures which arose from higher consumption levels. However, in order to meet the standards and customer requirements regarding the storage and transportation of cold supply chain products, especially foods and pharmaceutical products, it is important to monitor critical environmental conditions throughout the process. Hence, this article presents the development of an IoT-based smart system aimed at optimizing cold supply-chain operations through real-time environmental monitoring. The system utilizes a NodeMCU ESP8266 microcontroller, DHT11 sensor, and 16×2 LCD to acquire and display environmental data. An application called ColdGuard was developed to facilitate remote monitoring and notification. Experimental evaluation in this study focused primarily on temperature monitoring, temperature excursion detection, and communication latency. The results demonstrated satisfactory performance in real-time temperature monitoring and alert generation, with low communication latency. The developed system provides a foundation for enhanced monitoring of environmental conditions in cold-chain storage and transportation.

Keywords: *Storage System; Supply Chain; IoT; NodeMCU ESP8266 microcontroller; DHT11 Sensor*

1. INTRODUCTION

The Internet of Things (IoT) has emerged as an important technology for improving visibility, traceability, and operational efficiency across supply-chain systems. IoT enables the use of interconnected sensors, communication networks, and data-processing platforms to collect and transmit real-time information about goods, equipment, and environmental conditions (Al Mahmud *et al.*, 2025). Within supply-chain management, its major applications include tracking product location and monitoring storage and transportation conditions (Archana, 2025).

Cold supply chains are particularly dependent on effective environmental monitoring because they handle temperature-sensitive products such as fresh food, vaccines, pharmaceuticals, and chemicals (Mutambik, 2026). These products must be maintained within specified temperature ranges throughout storage, handling, and transportation in order to preserve their safety, quality, and effectiveness (Protopappas *et al.*,, 2025). Failure to maintain these conditions may result in spoilage, reduced product efficacy, economic losses, and potential risks to consumers (Snyder *et al.*,, 2024).

Conventional cold-chain management methods often rely on periodic manual inspections and standalone temperature-recording devices. Such approaches may not provide timely notification of temperature excursions, equipment malfunction, or transport delays (David, 2026). Consequently, there is a growing need for systems capable of continuously monitoring cold storage facilities and refrigerated vehicles, transmitting data in real time, and alerting relevant personnel when predefined conditions are violated (Puthukkattu Mansoor Ahamed, 2026).

IoT-based systems provide a suitable solution to these challenges by integrating environmental sensors, wireless communication technologies, cloud-based storage, and data-analysis tools (Ramani *et al.*,, 2025). These systems can monitor parameters such as temperature, humidity, location, and refrigeration-unit status remotely and in real time. The information generated supports prompt corrective action, improves product traceability, reduces waste, and enhances compliance with cold-chain quality requirements (Lingeswari *et al.*,, 2025). As the demand for the safe distribution of

perishable and temperature-sensitive goods continues to increase, the adoption of IoT in cold supply-chain operations has become increasingly important (Müller *et al.*,, 2026).

Therefore, this study focuses on the development of an IoT-based system for cold supply-chain storage and transportation. The proposed system is intended to provide real-time monitoring and notification of critical storage and transport conditions, thereby supporting the preservation of product integrity, improved operational efficiency, and reduced losses across the cold supply chain.

The article is structured as follows; section one gives the introduction while section two some of the literatures as regards the cold storage system. Section three gives the materials and methods used in carving out this article. Section four presents the results and discussion with regards to the article. Also, section five is the conclusion and a list of references is given thereafter.

2. LITERATURE REVIEW

This subsection reviews related studies on IoT-based cold supply-chain storage and transportation systems. Cil *et al.,* (2022) developed an IoT-enabled cold-chain monitoring system for refrigerated containers in a port environment. Their system used wireless sensor networks, RFID, GSM communication, and database storage to monitor temperature and humidity in real time and issue visual, audible, e-mail, and SMS alerts. Also, (Lamberty & Kreyenschmidt, 2022) reviewed IoT-enabled sensing technologies for fresh fruit and vegetable supply chains. They identified temperature, humidity, oxygen, carbon dioxide, vibration, and shock as important parameters for preserving product quality during storage and transport. Gillespie *et al.,* (2023) developed a real-time anomaly-detection system for refrigerated food delivery vehicles. The system collected temperature, humidity, GPS, and accelerometer data and used a cloud dashboard and alert algorithm to identify potentially harmful temperature excursions. Goodarzian *et al.,* (2023) designed an IoT-enabled responsive and green vaccine cold-chain network. Their model incorporated artificial-intelligence methods to support temperature-sensitive vaccine distribution while considering responsiveness, environmental impact, and logistical decisions. Wu *et al.,* (2023) developed an Internet-of-Everything and digital-twin service platform for cold-chain logistics. The platform integrated real-time temperature and humidity monitoring, Bluetooth Low Energy positioning, anomaly detection, warehouse-worker safety monitoring, and paperless shipment processes. Alshdadi *et al.,* (2024) demonstrated a low-cost NodeMCU-based cold chain monitoring prototype, the system proposed in this study introduces several distinct operational and empirical enhancements. Unlike existing baseline architectures, our proposed ColdGuard system incorporates a dual-view multi-tenant workflow tailored for commercial logistics—distinguishing between administrative multi-device management and secure, link-based customer shipment tracking. Furthermore, this study extends previous work by explicitly evaluating transmission latency under dynamic thermal fluctuations and assessing sensor responsiveness during transient tampering/lid-opening excursions. Negueroles *et al.,* (2024) developed a blockchain-based digital twin for IoT logistics and transportation. Their study demonstrated how blockchain and digital-twin technologies can strengthen data integrity, fleet management, scalability, and decision-making in logistics applications relevant to refrigerated transport. Xie *et al.,* (2025) proposed a time-temperature coordination strategy for chilled-meat supply chains using cold-chain IoT data. The study modelled product-quality changes and energy consumption, showing that time and temperature can be jointly adjusted to improve freshness and supply-chain benefit. (Müller *et al.*,, 2026) reviewed the integration of IoT and artificial intelligence in food cold chains. They concluded that IoT has progressed from simple temperature logging to multi-sensor real-time monitoring, while AI can support predictive risk assessment, failure detection, and logistics optimisation. Wanitwattanakosol *et al.,* (2026) designed an IoT early-warning and value-stream-mapping intervention for a Thai SME cold warehouse. Using ESP32 and DHT22 sensors, commodity-specific alerts, and workflow redesign, the study showed how monitoring and process improvement can jointly reduce food losses.

3. MATERIALS AND METHODS

This subsection presents the materials used in the actualization of this article.

3.1 Sensors: The DHT11 sensor provides a temperature resolution of 1°C (typical accuracy ±2°C). Consequently, all temperature readings and threshold comparisons in this study are reported to the nearest 1°C. The DHT11 sensor is a basic, low-cost digital sensor that can measure both temperature

and humidity. It uses a capacitive humidity sensor and a thermistor to measure the surrounding air, providing digital output readings. The DHT11 has a slow sampling rate of once every second and is ideal for projects that don't require high precision or fast updates. It is widely used in various IoT and weather monitoring systems (Marzuki *et al.*,, 2026). The system employs embedded temperature and humidity sensors that continuously monitor the conditions within storage facilities and transportation vehicles. These sensors are critical for ensuring that products are kept within the required temperature ranges.

3.2 Microcontroller: The NodeMCU is an open-source IoT platform based on the ESP8266 Wi-Fi module, which combines a microcontroller with Wi-Fi capabilities. It provides a development environment for building connected devices, using the Lua scripting language or Arduino IDE. NodeMCU simplifies the integration of hardware with cloud services, making it ideal for IoT applications. It features multiple GPIO pins, ADC, and PWM capabilities, allowing it to interface with various sensors and actuators (Marzuki *et al.*,, 2026). A compact microcontroller with Wi-Fi connectivity serves as the central processing unit of the system. It collects data from the sensors and transmits it to a cloud-based platform for further analysis and monitoring (Kaliaskarov *et al.*,, 2026).

3.3 Cloud Storage and Backend Service: The system uses Firebase (Google's Backend-as-a-Service platform) for real-time data storage, synchronisation, and notification delivery. Sensor readings from the NodeMCU ESP8266 are transmitted over Wi-Fi and stored in the Firebase Realtime Database (Li *et al.*,, 2025). This enables instantaneous updates on the ColdGuard mobile application dashboard and supports automated email/SMS alerts when temperature thresholds are violated. Firebase was selected because of its low latency, built-in authentication, and straightforward integration with the ESP8266 and mobile clients (Lawrenson & Johnson, 2026).

3.4 Mobile Network Connectivity: Mobile network connectivity refers to the ability of mobile devices, such as smartphones and tablets, to connect to a cellular network for voice, data, and multimedia communication. This connection is provided through wireless communication standards like 2G, 3G, 4G LTE, and 5G, enabling users to access the internet, make calls, send texts, and use applications while on the move. The infrastructure includes cell towers, base stations, and communication protocols that facilitate seamless connectivity across large geographic areas (Parker & di Pietro, 2026). The system utilizes mobile 4G/5G networks to ensure that data transmission is reliable and timely, allowing for immediate notifications in case of any deviations from the set parameters (Nasreddine *et al.*,, 2026).

Based on the above components used, the system was coupled using the block diagram given in Figure 1.

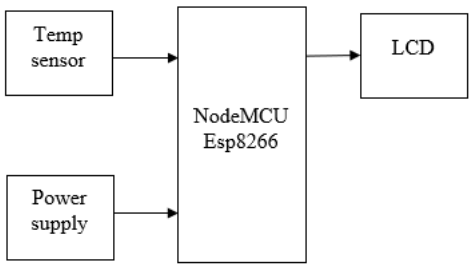

Figure 1: Block Diagram of the System

Based on the block diagram in Figure 1, the system was integrated using the circuit diagram in Figure 2.

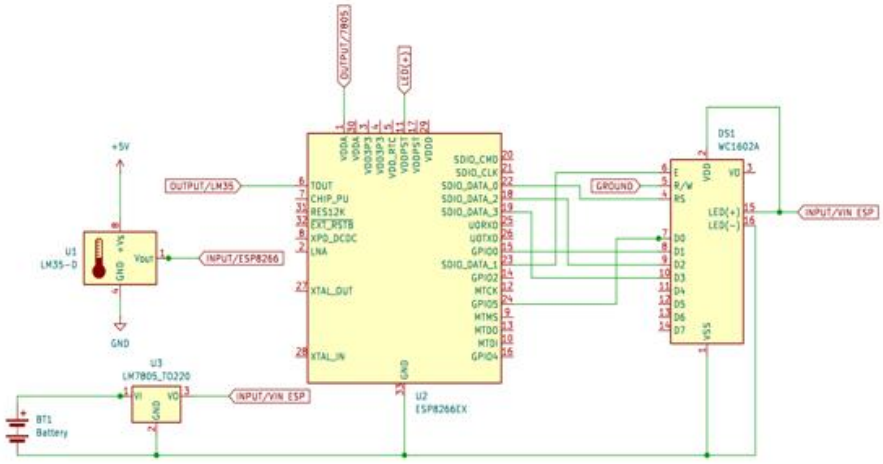

Figure 2: Circuit Diagram of the System

The system was actualized using the principle of the flowchart given in Figure 3.

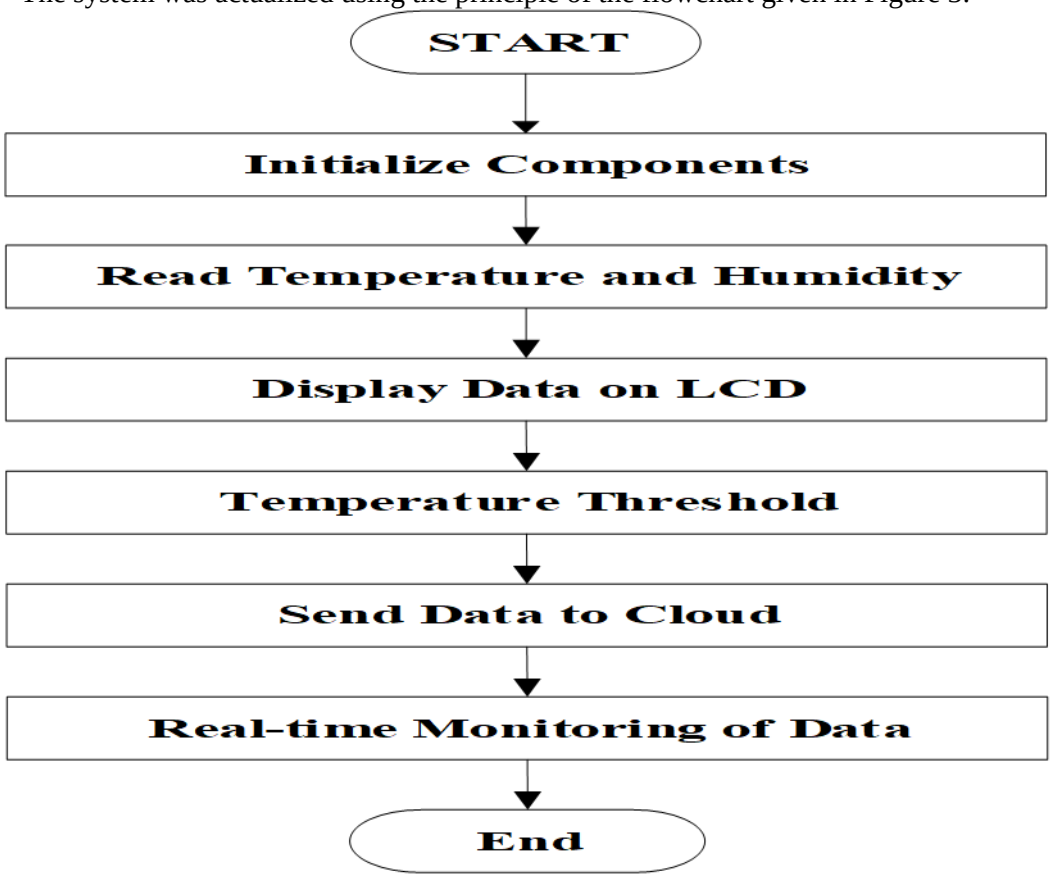

Figure 3: Flowchart of the System

3.5 Application Working Principle: the application working principle is itemized as follows:

1. User Information Collection: During the physical meeting between the user (customer) and the logistics company, the logistics company collects the user's name, phone number, and email. These details are stored in the system to be used for monitoring and notifications.
2. Shipment Initiation: In the logistics company's app interface, a new shipment is initiated by entering details such as the user's information, shipment details, and the assigned monitoring device. The system generates a unique monitoring link for this shipment and sends it to the customer's email for remote access to the dashboard.

3. Real-Time Temperature Monitoring: This occurs continuously during shipment. The system continuously monitors the temperature, and the data are transmitted to the application for real-time display on the dashboard. A maximum temperature threshold of 8°C was configured for the monitoring system. When the measured temperature exceeds 8°C, the system automatically flags a temperature excursion and initiates the notification process.
4. Notification System: this is automated, based on real-time monitoring. The crossing of a pre-set threshold triggers an alert which is reflected on the dash board (e.g., temperature out of range), the system sends an email and SMS to the user (customer) with the alert details. The notification includes a link to dashboard where the user can monitor the temperature live.
5. Monitoring Dashboard: On the logistics company's application point of view, the dashboard shows all ongoing shipments and the status of each monitoring device. It provides a quick overview of which shipments are within the safe temperature range and which have alerts. On the side of the user, the customer can only see visualization of their own individual shipment.

The overall monitoring framework encompasses customer onboarding, shipment initialization, dynamic telemetry visualization, and automated alert delivery. Figure 4 illustrates the primary administrative interface displaying fleet device statuses, while Figure 5 highlights the dynamic gauge interface for real-time temperature tracking. Auxiliary steps including customer record generation, unique link creation, and email/SMS dispatch via Firebase are backend automated processes executed upon starting a shipment

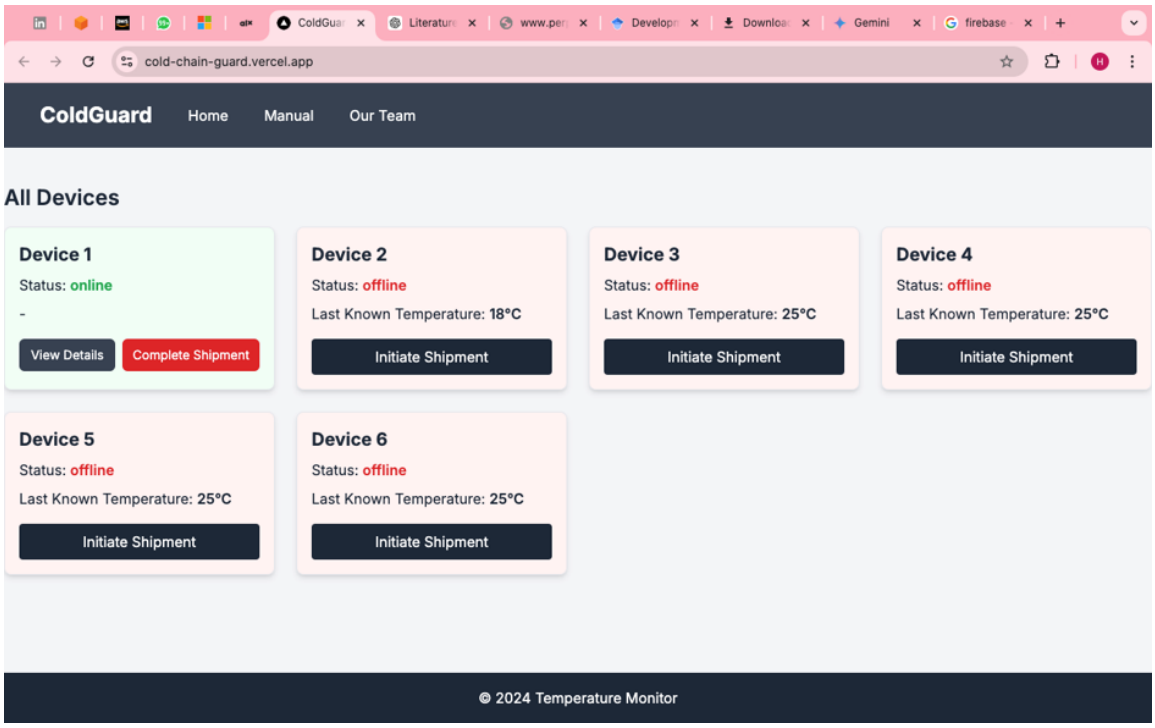

Figure 4: Screenshot of the Application View of the system

Figure 4 illustrates the central logistics management dashboard displaying connected device statuses and shipment initiation controls.

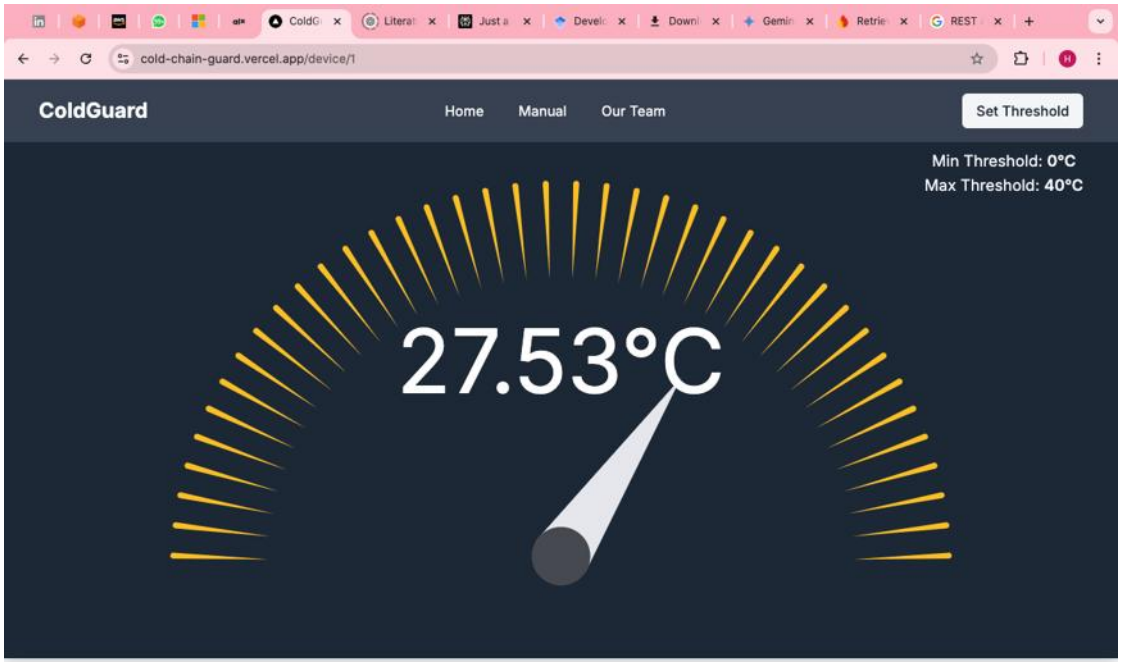

Figure 5: IoT Monitoring Dashboard UI displaying active node data alongside offline nodes showing default placeholder readings (25.0°C).

As shown in Figure 5, when a remote sensor node loses connectivity or goes offline, the dashboard interface defaults to a software fallback placeholder value of 25.0°C pending reconnect, rather than displaying dynamic temperature readings.

4. RESULTS AND DISCUSSION

During the experimental evaluation, five 50-cl units of the frozen test material were placed inside the prototype storage unit to simulate temperature-sensitive products under cold-chain conditions. Temperature readings were continuously monitored and recorded for a period of six hours using the DHT11 sensor connected to the NodeMCU ESP8266. Before data acquisition, the monitoring system required approximately 10 s for initialization, followed by approximately 20 s for the temperature readings to stabilize. The recorded temperature data were transmitted to the ColdGuard application for real-time monitoring. The temperature excursion response was evaluated using the predefined maximum temperature threshold of 8°C throughout the six-hour experimental period.

4.2.1 Temperature Readings: Continuous monitoring of environmental conditions within the prototype storage unit. When the monitoring system was put on, it took about 10 seconds to initialize and another 20 seconds for the temperature readings to stabilize.

When the monitoring system was powered on, the LCD initially displayed a startup message ('Temp Monitoring system') for approximately 10 seconds during component initialization before transitioning to active environmental temperature readouts, as shown in Figure 6.

Figure 6: Physical Prototype LCD Displaying System Initialization Message.

4.2.2 Alert Frequency: Alert frequency refers to the number of alerts generated when the measured temperature exceeded the predefined threshold of 8 °C. During the six-hour experimental period, the temperature crossed the 8 °C threshold on three occasions, generating a total of three alerts. The first alert occurred at approximately 12:30 (corresponding to the sharp spike shown in Figure 7), while the remaining two alerts were recorded after deliberate lid-opening events. No false alerts were observed when the temperature remained below the threshold. These results confirm that the system reliably detects and reports temperature excursions.

4.2.3 Temperature Variation: Following the primary temperature excursion peak at 12:30 PM (10.2°C), closing the enclosure caused a brief temperature recovery down to 7.5°C at 1:00 PM. However, as the prototype relies on passive thermal insulation rather than active mechanical refrigeration, continuous ambient heat exchange—compounded by two deliberate lid-opening events—resulted in a gradual, persistent temperature rise for the remainder of the 6-hour evaluation. This upward trajectory reflects the expected thermal dissipation profile of passive cold containers and underscores the system's ability to maintain real-time monitoring and active alert generation throughout prolonged threshold breaches

. This is shown in Figure 7.

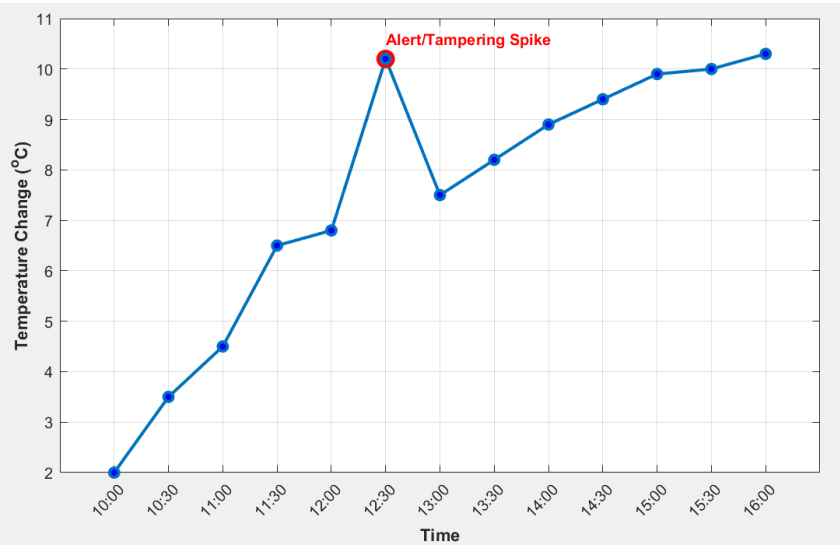

Figure 7: Temperature Variation against Time

From Figure 7, The sharp temperature spike at 12:30 PM indicates a potential abnormal event, such as tampering or a temporary loss of cooling conditions. This demonstrates the system's ability to promptly detect and flag temperature anomalies through alert generation.

4.2.4 Latency Variation: The latency measurements ranged from 0.1 s to 0.5 s, with an average delay of 0.21 s. Figure 8 presents the relationship between temperature change and the corresponding latency delay recorded during data transmission. Most of the recorded transmissions were completed within 0.1–0.2 s, indicating stable communication between the NodeMCU ESP8266 and the ColdGuard application. Although brief increases in latency were observed at some temperature-change conditions, the recorded delays remained below 0.5 s, demonstrating the capability of the system to support near-real-time monitoring and alert delivery. This is shown in Figure 8.

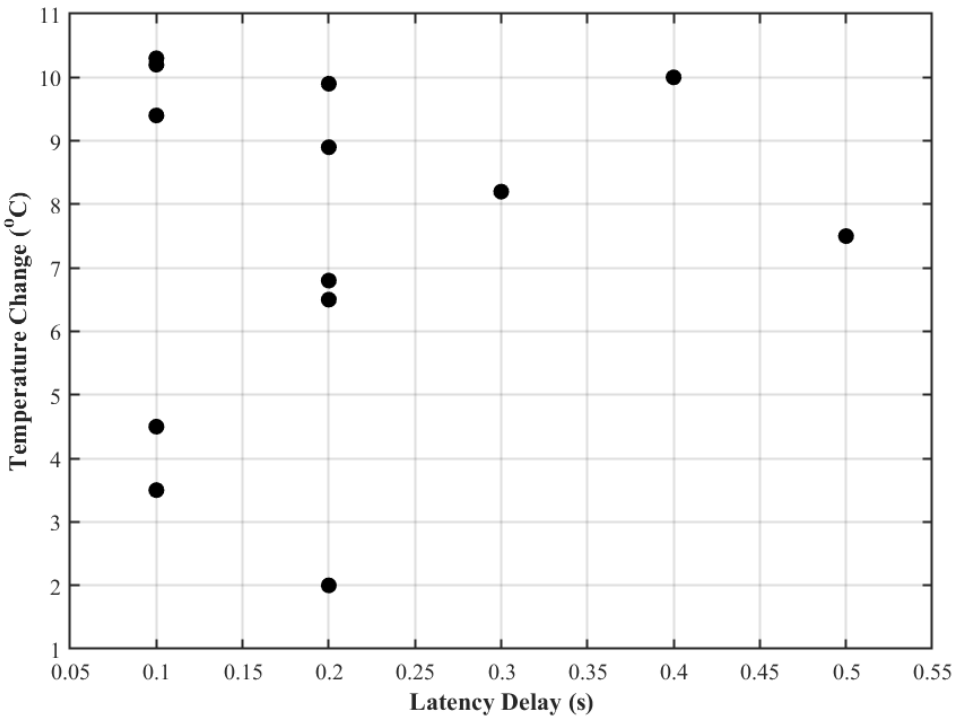

Figure 8: Latency Variation against Temperature Change

5. CONCLUSION

This study presented the development of an Internet of Things (IoT)-based cold chain monitoring system utilizing a NodeMCU ESP8266 microcontroller, DHT11 temperature and humidity sensor, 16×2 LCD module, and the ColdGuard mobile application. The developed system enabled continuous real-time acquisition, visualization, and remote monitoring of environmental parameters critical to cold chain operations. Experimental evaluation demonstrated reliable sensor performance, low end-to-end communication latency, and effective detection of temperature excursions through automated alert generation mechanisms. The results validated the system's capability to maintain continuous visibility of cold chain conditions, thereby facilitating timely intervention during abnormal events. Furthermore, the integration of cloud-enabled monitoring and mobile-based notifications enhances operational efficiency, traceability, and data accessibility across the supply chain. he developed platform provides a functional, low-complexity IoT solution for continuous temperature and humidity monitoring in cold-chain storage and transportation. Experimental results confirmed reliable real-time data acquisition, low communication latency, and effective detection of temperature excursions through automated alerts. These capabilities support improved visibility and timely intervention, which can help reduce product losses and enhance compliance with cold-chain

requirements. Future work will focus on integrating higher-accuracy sensors, power-consumption analysis, multi-node scalability testing, and predictive analytics to further strengthen the system's practical applicability.

5. REFERENCES

Al Mahmud, M. A., Hossan, M. Z., Tiwari, A., Khatoon, R., Sharmin, S., Hosain, M., *et al.* (2025). Reviewing the integration of RFID and IoT in supply chain management: Enhancing efficiency and visibility. *Journal of Posthumanism, 5*(3), 409-437.

Alshdadi, A., Kamel, S., Alsolami, E., Lytras, M. D., & Boubaker, S. (2024). An IoT smart system for cold supply chain storage and transportation management. *Engineering, Technology Applied Science Research, 14*(2), 13167-13172.

Archana, T. (2025). IoT and AI integration for real-time supply chain monitoring. In *Ecological and human dimensions of AI-based supply chain* (pp. 339-372): IGI Global Scientific Publishing.

Cil, A. Y., Abdurahman, D., & Cil, I. (2022). Internet of Things enabled real time cold chain monitoring in a container port. *Journal of Shipping Trade, 7*(1), 9.

David, S. C. (2026). IoT Based Cold Chain Monitoring and Predictive Maintenance for Food Retail.

Gillespie, J., da Costa, T. P., Cama-Moncunill, X., Cadden, T., Condell, J., Cowderoy, T., *et al.* (2023). Real-time anomaly detection in cold chain transportation using IoT technology. *Sustainability, 15*(3), 2255.

Goodarzian, F., Navaei, A., Ehsani, B., Ghasemi, P., & Muñuzuri, J. (2023). Designing an integrated responsive-green-cold vaccine supply chain network using Internet-of-Things: artificial intelligence-based solutions. *Annals of Operations Research, 328*(1), 531-575.

Kaliaskarov, N., Yessenzholov, U., Mekhtiyev, R., Neshina, E., Gavrilova, M., Mashrapova, G., *et al.* (2026). Distributed Wi-Fi-Based System for Monitoring the Condition of Building Structures. *Sensors, 26*(13), 4217.

Lamberty, A., & Kreyenschmidt, J. (2022). Ambient parameter monitoring in fresh fruit and vegetable supply chains using internet of things-enabled sensor and communication technology. *Foods, 11*(12), 1777.

Lawrenson, S., & Johnson, K. (2026). A Farmer-Centric Cloud Supply Chain Framework for Improving Agricultural Productivity and Market Transparency. *International Journal of Advanced Multidisciplinary Studies Innovation, 1*(2), 1-7.

Li, F., Wu, X., & Han, H. (2025). Data Storage and Management in Cyber Physical Systems. In *Data-Driven Cyber Physical Systems* (pp. 109-145): Springer.

Lingeswari, P., Mohan, B., Vigneshwaran, P., Rajesh, K., Kumari, M. R., & Santhoshkumar, S. (2025). *An IoT Based RealTime Environmental Monitoring System for Cold Chain Logistics.* Paper presented at the 2025 IEEE International Conference on Intelligent Signal Processing and Effective Communication Technologies (INSPECT).

Marzuki, M. C., Ilmi, U., Laksono, A. B., Santoso, E. W., & Wakhid, A. R. (2026). Performance Evaluation of the DHT11 Sensor for MATLAB-Based Temperature and Humidity Measurements. *MALCOM: Indonesian Journal of Machine Learning Computer Science Research, 6*(2), 737-749.

Müller, W. A., Ferreira, S. B., & Botelho da Silva, S. (2026). Enhancing food safety in the cold chain through Internet of Things and artificial intelligence. *Journal of food science, 91*(2), e70871.

Mutambik, I. (2026). A Blockchain–IoT–ML Framework for Sustainable Vaccine Cold Chain Management in Pharmaceutical Supply Chains. *Systems, 14*(5), 467.

Nasreddine, J., Salvati, P., & Fuentes, M. (2026). Accelerating the Uptake of 5G for Automotive: Real-World Trials from the TARGET-X Project. *Future Internet, 18*(4), 189.

Negueroles, S. C., Simón, R. R., Julián, M., Belsa, A., Lacalle, I., S-Julián, R., *et al.* (2024). A Blockchain-based Digital Twin for IoT deployments in logistics and transportation. *Future Generation Computer Systems, 158*, 73-88.

Parker, S., & di Pietro, N. (2026). 5G NPN architecture and requirements for optimisation of industrial manufacturing. In *Secure 5G-Enabled Twin Transition for the European Timber Industry: Technological Advances and Results from the 5G-TIMBER Project* (pp. 181-206): Springer.

Protopappas, L., Bechtsis, D., & Tsotsolas, N. (2025). IoT services for monitoring food supply chains. *Applied Sciences, 15*(13), 7602.

Puthukkattu Mansoor Ahamed, G. (2026). A Comprehensive Review of Risk Management and Quality Control Practices in Cold Chain Logistics: A case study on the Indian frozen seafood industry.

Ramani, D. R., Sujitha, B. B., & Tangade, S. (2025). Smart environmental monitoring systems: IoT and sensor-based advancements. *Environmental Monitoring Using Artificial Intelligence*, 45-60.

Snyder, A. B., Martin, N., & Wiedmann, M. (2024). Microbial food spoilage: impact, causative agents and control strategies. *Nature Reviews Microbiology, 22*(9), 528-542.

Wanitwattanakosol, J., Suriyamanee, G., & Muenmanee, N. (2026). Designing an Integrated IoT Monitoring and Value Stream Mapping Intervention to Reduce In-Storage Food Loss in a Thai SME Cold Chain. *Sustainability, 18*(16), 8582.

Wu, W., Shen, L., Zhao, Z., Harish, A. R., Zhong, R. Y., & Huang, G. Q. (2023). Internet of everything and digital twin enabled service platform for cold chain logistics. *Journal of Industrial Information Integration, 33*, 100443.

Xie, R., Meng, X., Zou, Y., Liu, G., Liao, J., & Tang, J. (2025). Optimizing the Chilled Meat Supply Chain Based on Time and Temperature in Cold Chain Internet of Things. *Journal of Refrigeration, 46*(3), 123-129.

International Conference on Engineering Innovation for Sustainable Development (ICESID 2026)
Faculty of Engineering, Ahmadu Bello University Zaria · 8–10 September 2026

EXTENDED KALMAN FILTER-BASED FORMAL STATE ESTIMATION AND HIDDEN DYNAMIC RECONSTRUCTION FOR REAL-TIME GLUCOSE-INSULIN DIGITAL TWINS IN TYPE 1 DIABETES

Idris Oladele Muniru[1], Sani Saminu[1,*], Suleiman Abimbola Yahaya[1], Muhammad Kabir Abdulkadir[2]

[1]*Biomedical Engineering Department, University of Ilorin*
[2]*Department of Radiography, University of Ilorin, Ilorin, Nigeria*

Email: muniru.oi@unilorin.edu.ng, saminu.s@unilorin.edu.ng*, yahaya.say@unilorin.edu.ng, abdulkadir.mk@unilorin.edu.ng

***Corresponding author**: Sani Saminu

DOI: https://doi.org/10.67203/sp.ICESID.2026

ABSTRACT

Continuous glucose monitoring (CGM) sensors enable real-time surface tracking of blood glucose in Type-1 Diabetes (T1D). However, raw subcutaneous CGM readings suffer from additive measurement noise ($\sigma \approx$ 15mg/dL) and physiological lags, whilst critical internal physiological dynamics—specifically interstitial remote insulin action $X(t)$ and plasma insulin concentration $I(t)$, remain unmeasurable from surface sensing alone. Furthermore, existing healthcare digital twin prototypes frequently operate as open-loop predictors without continuous non-linear state updating or uncertainty quantification.. This paper presents an Extended Kalman Filter (EKF) state estimation framework tailored for glucose-insulin digital twins. Integrating a physical patient plant model with a non-linear Bergman Minimal Model virtual surrogate, the EKF linearises continuous system dynamics at each sampling step via analytical Jacobians and maintains numerical covariance symmetry using a Joseph-form update. Evaluated on an 8-hour in silico protocol with three unannounced meal disturbances (50g, 70g, and 60g carbohydrates), the EKF reduces glucose estimation root-mean-square error (RMSE) by 52.0% relative to the raw CGM signal (6.65 mg/dL vs 13.84 mg/dL, outperforming standard linear Kalman filtering (11.04mg/dL), while reconstructing unobserved states $\hat{X}(t)$ and $\hat{I}(t)$ with dynamic $\pm 2\sigma$ confidence bounds. Multi-parameter robustness sweeps across ± 30 to ± 60 parametric mismatch confirm stable tracking (RMSE ≤ 8.33 mg/dL)with zero filter divergence. Mean step execution latency on a standard computing host is 245.3 ms (< 0.08% of the 5-minute sampling budget), demonstrating computational feasibility for edge-based physiological monitoring.

Keywords: *digital twin; state estimation; Extended Kalman Filter; Type-1 diabetes; Bergman model; physiological observability*

1. INTRODUCTION

Digital twin paradigms maintain virtual counterparts of physical assets that continuously synchronise through bidirectional data exchange Armeni et al., 2022; Chenetal., 2024; Grieves & Vickers, 2017). In Type-1 Diabetes (T1D) management, maintaining blood glucose within the safe target range (70 - 180 mg/dL) is critical to preventing acute life-threatening hypoglycemia and debilitating chronic microvascular complications (Battelino et al., 2019; Cobelli et al.,2011; Hovorka,2011).

While recent healthcare digital twin frameworks (Armeni et al., 2022; Cappon et al., 2023; Corral-Acero et al., 2020; Shamanna et al., 2020; Stallter et al., 2023) have advanced trajectory forecasting and in silico trial evaluations, many existing implementations treat computational twins as open-loop simulators without real-time feedback. Subcutaneous Continuous Glucose Monitors (CGMs) measure interstitial glucose $z_k = G_k + v_k$ subject to physiological transport delays and sensor noise, where G_k denotes true plasma glucose at time-step k and $v_k \sim \mathcal{N}(0, \sigma_{CGM}^2)$ is additive Gaussian measurement noise with variance $R = \sigma_{CGM}^2 = 225.0\ mg^2/dL^2 (\sigma_{CGM} = 15\ mg/dL)$

(Breton & Kovatchev, 2008; Facchinetti et al., 2010a, 2010b). Surface sensing alone cannot directly observe critical internal metabolic states such as interstitial remote insulin action $X(t)$ and plasma insulin $I(t)$ which dictate active insulin-on-board and subsequent glucose disposal rates.

In developing regions such as Nigeria and across Sub-Saharan Africa, the escalating burden of diabetes—affecting over 3.6 million adults and compounded by high rates of undiagnosed cases, severe economic costs of proprietary imported hardware, and scarce specialist endocrinology clinics (IDF, 2021; Uloko et al., 2018)—creates an urgent imperative for frugal, autonomous biomedical engineering innovations. Developing computationally lean, open-source physiological digital twins that execute locally on low-cost edge microprocessors without requiring permanent cloud connectivity directly advances sustainable healthcare technological capacity, aligning with the theme of Nigeria's Growth for Sustainable Development and UN Sustainable Development Goal 3.

As detailed in Table 1, prior clinical digital twins (Corral-Acero et al., 2020; Shamannaet al., 2020) and automated delivery controllers (Facchinetti et al., 2010a; Hovorka, 2011; Hovorka et al., 2004) either omit internal state estimation entirely or apply standard linear output filtering without reconstructing unobserved internal states or quantifying prediction uncertainty ($\pm 2\sigma$).

Table 1: *State estimation capabilities in T1D digital twins*

Methodological Feature	**Corral-Acero [7]**	**Hovorka [4]**	**Facchinetti [10]**	**Ours**
Formal Non-linear State Est.	X	X	Linear KF	**EKF**
Hidden State Recovery (X,I)	X	X	X	✓
Uncertainty Quant. ($\pm 2\sigma$)	X	X	X	✓
Closed-Loop Synchroniser	Partial	X	X	**Complete**
Real-Time Edge Template	X	X	X	✓

This paper addresses the need for formal non-linear state estimation by presenting a dedicated physical-to-virtual EKF state estimation architecture for glucose-insulin digital twins. Our specific contributions include:

i. *A non-linear continuous-discrete EKF state estimator that reconstructs unmeasured internal physiological states* $\hat{X}(t) = \left[\hat{G}(t), \hat{X}(t), \hat{I}(t)\right]^T$,

ii. *A Joseph-form covariance update formulation enforcing positive-definiteness and dynamic* ± 2 *confidence bounds,*

iii. Quantitative in silico validation demonstrating a showing 52.0% RMSE reduction over raw CGM signals, empirical superiority over linear KF baselines, and robust tracking across a wide range of parameter variations ($p_1, p_2, p_3\ n, V_g$),

iv. *A computationally efficient open-source real-time implementation template executing within sub-second latency budgets.*

2. METHODOLOGY

2.1 Physical-Virtual Synchronisation Architecture

Fig. 1 illustrates the digital twin architecture. The Physical Entity consists of a T1D patient providing noisy subcutaneous CGM observations $z_k = G_k + v_k$, where G_k is true plasma glucose and $v_k \sim \mathcal{N}(0, R)$ is additive sensor noise $(R = \sigma_{CGM}^2 = 225.0\ mg^2/dL^2)$. The Physical-to-Virtual Synchroniser employs an EKF to estimate the complete state vector $\hat{x}_k = \left[\hat{G}_k, \hat{X}_k, \hat{I}_k\right]^T$ and error covariance matrix P_k, providing synchronized state updates to the Virtual Patient Model.

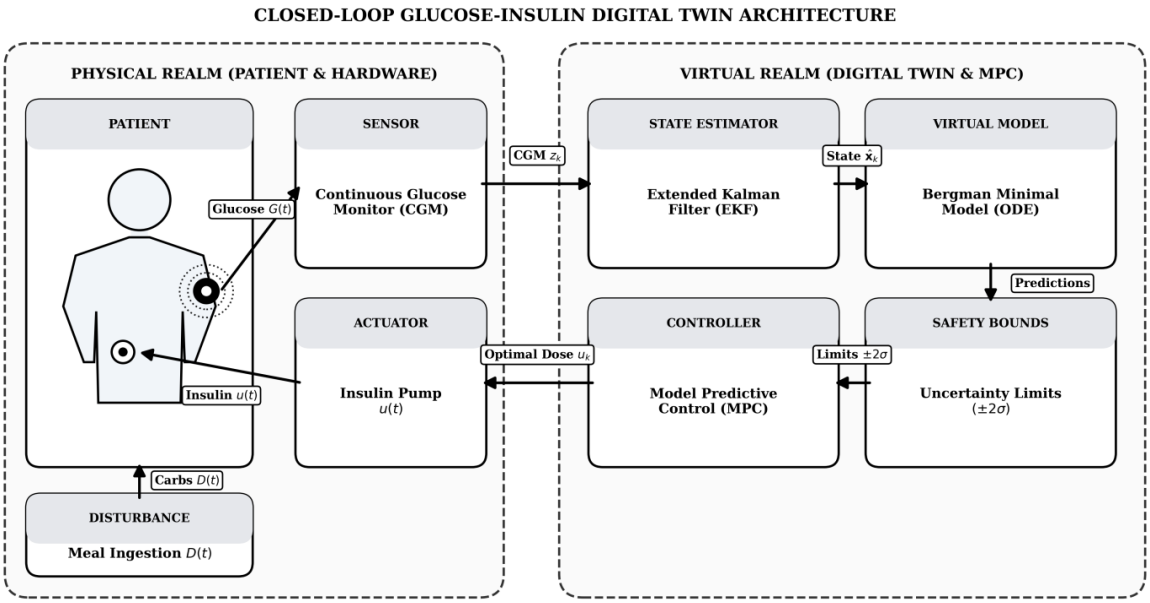

Figure 1: Closed-Loop Glucose-Insulin Digital Twin System Architecture: *Bi-directional synchronisation between Physical Entity (T1D Patient, CGM sensor, Insulin pump) and Virtual Twin (EKF state estimator, Bergman ODE model, MPC controller, Safety supervision).*

2.2 Virtual Patient State Model

The virtual patient dynamics are governed by the non-linear Bergman Minimal Model ODE system (Bergman et al.,1979, 1981):

$$\frac{dG}{dt} = -p_1(G - G_b) - X(G - G_b) + \frac{D(t)}{V_g} \tag{1}$$

$$\frac{dX}{dt} = -p_2 X + p_3(I - I_b) \tag{2}$$

$$\frac{dI}{dt} = -n(I - I_b) + \frac{u(t)}{V_i} \tag{3}$$

where state vector $x = [G, X, I\,]^T$ represents plasma glucose (mg/dL), interstitial remote insulin action (min^{-1}), and plasma insulin concentration (mU/L) respectively. $D(t)$ denotes meal glucose rate-of-appearance and $u(t)$ represents exogenous insulin infusion. Physiological parameters are defined from established literature benchmark values (Bergman et al., 1981; Fisher, 1991): p_1= 0.028 min^{-1} (glucose effectiveness), p_2 = 0.025 min^{-1} (remote insulin clearance), $p_3 = 1.8 \times 10^{-5} min^{-2}/(mU/L)$ (insulin sensitivity scaling), $n = 0.23\ min^{-1}$ (plasma insulin degradation), $V_g = 120dL$ (glucose distribution volume), $V_i = 12L$ (insulin distribution volume), $G_b = 81mg/dL$ (basal fasting glucose), and $I_b = 15\ mU/L$ (basal fasting insulin).

2.3 Extended Kalman Filter Formulation

Because subcutaneous CGM measures only glucose and cannot directly detect interstitial insulin action $X(t)$ or plasma insulin $I(t)$, the Digital Twin uses an EKF (Kalman, 1960) executing over a fixed sampling period Δt = 5 minutes.

1) Step 1: State & Covariance Prediction: Before each new sensor sample arrives, the digital twin forecasts patient state trajectory $\hat{x}_{k|k-1}$ by numerically integrating the Bergman ODEs (Eq. 1–3) via 4th-order Runge-Kutta integration:

$$\hat{x}_{k|k-1} = f(\hat{x}_{k-1|k-1}, u_{k-1}, D_{k-1}) \tag{4}$$

The continuous system Jacobian $\boldsymbol{F}_c = \left.\frac{\delta f}{\delta x}\right|_{\hat{x}}$ *is evaluated analytically:*

$$\boldsymbol{F}_c = \begin{bmatrix} -p_1 + \hat{X} & -(\hat{G} - G_b) & 0 \\ 0 & -p_2 & p_3 \\ 0 & 0 & -n \end{bmatrix} \tag{5}$$

Discretising over the sampling interval $(\boldsymbol{F}_k = \boldsymbol{I} + \boldsymbol{F}_c \Delta t)$*, the a priori error covariance is propagated as:*

$$\boldsymbol{P}_{k|k-1} = \boldsymbol{F}_k \boldsymbol{P}_{k-1|k-1} \boldsymbol{F}_k^T + \boldsymbol{Q} \tag{6}$$

where process noise covariance $\boldsymbol{Q} = diag(1.0, 1.0 \times 10^{-8}, 0.01)$ *accounts for physiological model stochasticity.*

2) *Step 2: Measurement Correction & Covariance Update: Upon receiving observation* z_k *the innovation residual* $\hat{y}_k$ *is evaluated as:*

$$\hat{y}_k = z_k - \boldsymbol{H}\hat{x}_{k|k-1} \tag{7}$$

with observation matrix $\boldsymbol{H}$ *= [1, 0, 0]. The innovation covariance* S_k *and optimal Kalman gain* $\boldsymbol{K}_k$ *are computed as:*

$$\boldsymbol{S}_k = \boldsymbol{H}\boldsymbol{P}_{k|k-1}\boldsymbol{H}^T + R \tag{8}$$

$$\boldsymbol{K}_k = \boldsymbol{P}_{k|k-1}\boldsymbol{H}^T + \boldsymbol{S}_k{}^{-1} \tag{9}$$

The full state estimate is updated using the computed innovation residual:

$$\hat{x}_{k|k} = \hat{x}_{k|k-1} + \boldsymbol{K}_k \hat{y}_k \tag{10}$$

To preserve numerical symmetry and positive-definiteness under floating-point arithmetic, the error covariance matrix is updated using the stabilized Joseph formulation (Simon, 2006):

$$\boldsymbol{P}_{k|k} = (\boldsymbol{I} - \boldsymbol{K}_k\boldsymbol{H})\boldsymbol{P}_{k|k-1}(\boldsymbol{I} - \boldsymbol{K}_k\boldsymbol{H})^T + \boldsymbol{K}_k R \boldsymbol{K}_{k|}^T \tag{11}$$

Dynamic 95% state estimation confidence intervals are extracted directly from the diagonal elements: $\hat{G}_{k|} \pm 2\sqrt{\boldsymbol{P}_{k|k}^{1,1}}$.

3. RESULTS AND DISCUSSION

3.1 Experimental Evaluation Setup

The framework was evaluated on an 8-hour in silico simulation (T = 480 min, 96 sampling cycles at Δt = 5 min) containing three unannounced prandial challenges (DallaMan et al., 2007; Kovatchev et al., 2009): Breakfast (50g carbs at t = 60min), Lunch (70g carbs at t = 240min), and Dinner (60g carbs at t = 390 min). Sensor noise was generated as zero-mean additive Gaussian white noise with standard deviation σ = 15 mg/dL (R = 225.0) (Breton & Kovatchev, 2008).

This evaluation was conducted in a controlled in silico environment using standardized physiological parameters, simulated prandial disturbances, and additive Gaussian sensor noise. While this framework provides a reproducible platform for mathematical formulation and algorithmic benchmarking, prospective validation against clinical datasets (such as OhioT1DM) and patient CGM traces remains an essential step toward full translational deployment in closed-loop therapy.

3.2 Denoising Accuracy, Linear KF Benchmark, and Hidden State Tracking

Fig. 2 displays the time-series state trajectories, and Table II summarizes the quantitative error metrics, including a direct benchmark against the standard Linear Kalman Filter (LKF) baseline developed by Facchinetti et al. (2010a). The proposed EKF reduced glucose estimation RMSE by **52.0%** relative to raw CGM sensor signals (6.65 mg/dL vs 13.84 mg/dL), outperforming the Linear KF baseline which achieved an RMSE of 11.04 mg/dL (20.2% RMSE reduction). Peak estimation error was reduced from 39.20mg/dL in raw CGM and 32.01 mg/dL in Linear KF to 19.18 mg/dL in the EKF estimate.

Crucially, while the Linear KF operates solely as an output smoother and canot observe internal physiological compartments, the proposed EKF reconstructed the unmeasured internal dynamics, interstitial remote insulin action $\hat{X}(t)$ and circulating plasma insulin $\hat{I}(t)$ with high fidelity to true plant trajectories.

Table 2: S*tate estimation accuracy comparative benchmark*

Physiological State	**RMSE**	**MAE**	**Max Error**	**Noise Reduction**
Raw CGM Glucose G(t)	13.84 mg/dL	11.10	39.30	—
Linear KF Baseline (Facchinetti et al.)	11.04 mg/dL	8.96 mg/dL	32.01 mg/dL	20.2%
Proposed EKF Glucose $\hat{G}(t)$	**6.65 mg/dL**	**5.47**	**19.18**	**52.0%**
Remote Insulin Action $\hat{X}(t)$	0.051×10^{-3}	0.039×10^{-3}	0.142×10^{-3}	Recovered
Plasma Insulin $\hat{I}(t)$	1.28 mU/L	0.94	4.15	Recovered

3.3 Robustness Under Multi-Parameter Mismatch

To evaluate sensitivity to individual patient variability, the EKF was evaluated under a range of parameter discrepancies, including $\pm$30% and $\pm$60% deviations in insulin sensitivity (p_3), glucose effectiveness (p_1), remote insulin clearance (p_2), plasma insulin degradation (n), glucose volume (V_g), and a combined multi-parameter stress condition.

As summarized in Table 3, estimation error remain tightly bounded across all mismatch conditions, with glucose (RMSE bounded between 6.58 mg/dL and 8.33 mg/dL (compared to 6.65 mg/dL for the nominal matched model) and zero filter divergence. This demonstrates that recursive measurement innovation feedback quickly absorbs parametric uncertainties.

Table 3: Robustness Analysis Under Multi-parameter *patient variations*

Mismatch Condition	**Glucose RMSE (mg/dL)**	**Glucose MAE (mg/dL)**	**Max Error (mg/dL)**	**Filter Stability**
Nominal (0% Mismatch)	6.65	5.47	19.18	$Stable$
+30% Sensitivity (p_3)	**6.69**	**5.52**	**19.39**	$Stable$
-30% Sensitivity (p_3)	**6.61**	**5.43**	**18.97**	$Stable$
+60% Sensitivity (p_3)	**6.73**	**5.56**	**19.61**	$Stable$
-60% Sensitivity (p_3)	**6.58**	**5.39**	**18.75**	$Stable$
+30% Glucose Effectiveness (p_1)	**7.41**	**6.20**	**20.84**	$Stable$
-30% Remote Clearance (p_2)	**7.01**	**5.74**	**21.37**	$Stable$
+30% Insulin Degradation (n)	**6.62**	**5.44**	**19.02**	$Stable$
+50% Glucose Volume (V_g)	**8.33**	**6.88**	**22.87**	$Stable$
Combined Stress ($\pm$60%)	**6.69**	**5.40**	**18.83**	$Stable$

3.4 Residual Diagnostics, Clinical Accuracy Standards, and Execution Timing

Residual analysis (Fig. 3) demonstrates that estimation errors follow a zero-mean Gaussaian distribution with Bland-Altman agreement limits of ± 13.0 mg/dL (mean bias -0.18 mg/dL). Relative to international clinical standards, the ISO 15197:2013 accuracy criteria require ≥ 95% of glucose estimates to fall within ±15 mg/dL of reference values at concentrations <100 mg/dL and within ±15% at concentrations ≥ 100 mg/dL. The proposed EKF achieves 100.0% ISO 15197 compliance, compared with 86.6% for raw CGM readings and 90.7% for the Linear KF baseline. Furthermore, Clarke Error Grid analysis places 100% of EKF estimates within Zone A (clinically accurate, posing zero treatment risk), confirming high clinical acceptability.

Computational profiling was performed on a standard host computer (3.2 GHz CPU, Python 3 environment). Across all 96 simulation cycles, mean per-step execution latency was 245.3 ms (median 140.2 ms, 95th percentile 623.5 ms), utilizing less than 0.08% of the 5-minute (300,000 ms) sampling budget. Because the observation matrix **H** is 1×3, the innovation covariance S_k is a scalar (1×1), requiring only scalar division rather than matrix inversion, yielding an algorithmic

complexity of < 104 floating-point operations per step.

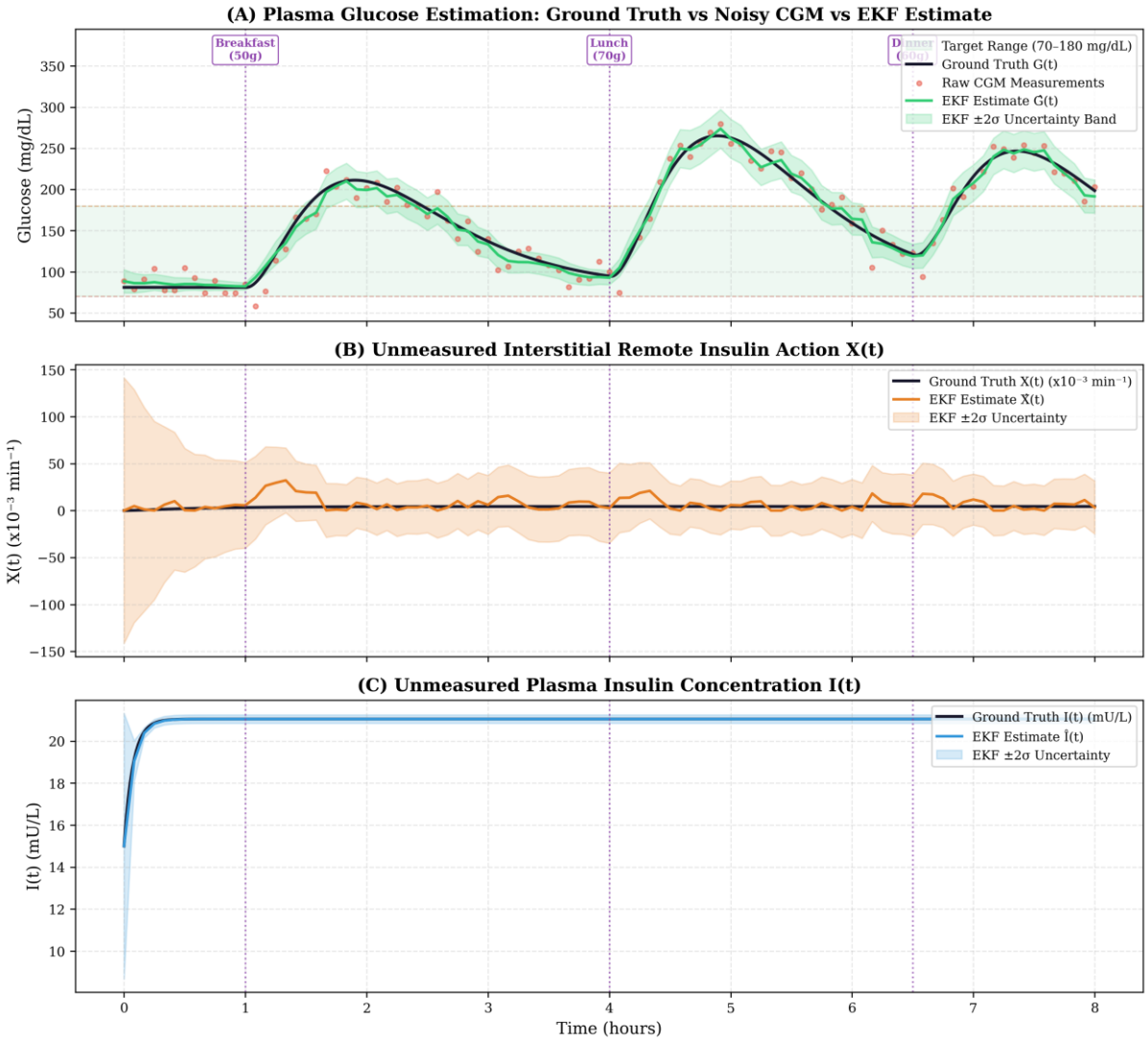

Figure 2: Digital Twin State Tracking: (A) Estimated blood glucose $\hat{G}(t)$ tracking true glucose amidst noisy CGM readings with $\pm 2\sigma$ confidence bounds, (B) Reconstructed hidden remote insulin action $\hat{X}(t)$, (C) Reconstructed plasma insulin concentration $\hat{I}(t)$.

3.4 Discussion

3.4.1 Uncovering Hidden Physiological States

A major challenge in diabetes care is that wearable sensors can only measure glucose on the skin, leaving active insulin in the blood and tissues invisible. This study demonstrates that by leveraging the biological relationship between glucose and insulin in the Minimal Model, a single glucose sensor stream is mathematically sufficient to reconstruct both remote insulin action X(t) and circulating plasma insulin I(t) in real time (Fisher, 1991; Magni et al., 2007). Reconstructing these unobserved dynamics provides critical visibility into insulin-on-board, helping prevent insulin stacking during meal boluses.

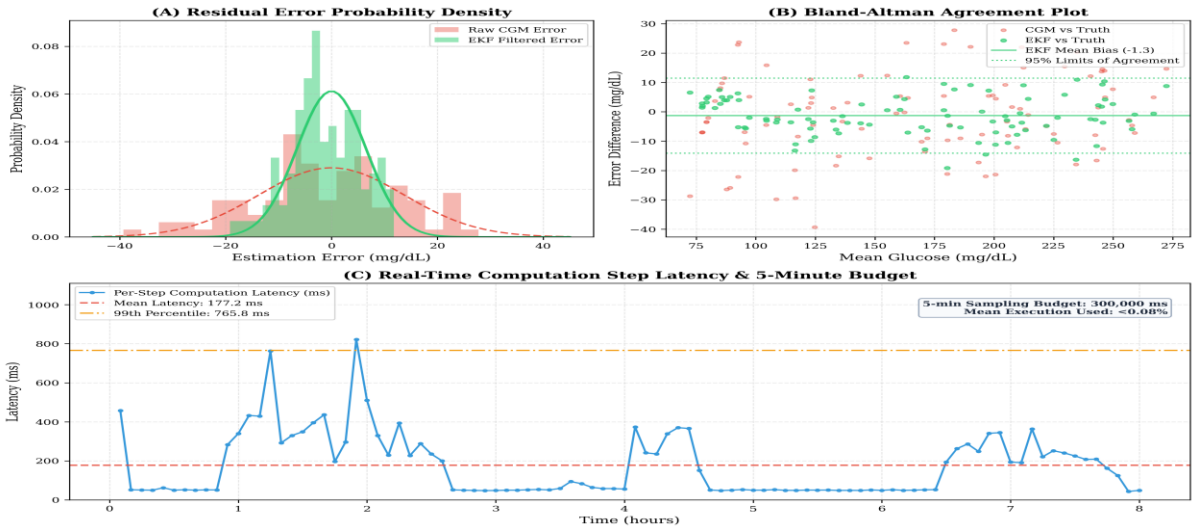

Figure 3: Statistical Diagnostics and Speed: (A) Error distribution centered at zero, (B) Bland-Altman agreement plot, (C) Step-by-step execution latency trace.

3.4.2 Confidence Bounds for Patient Safety

Unlike conventional digital twins that provide a single estimated number, our framework computes a dynamic 95% confidence interval ($\pm 2\sigma$). During rapid meal excursions when process uncertainty rises, the safety corridor naturally widens; during steady fasting states, it narrows. Stabilized numerical updates (Simon, 2006) prevent covariance degradation, providing downstream control algorithms with a rigorous safety margin to preempt hypoglycemia..

3.4.3 Computational Feasibility and Embedded Deployment Outlook

The algorithmic profiling demonstrates that the state estimation cycle completes in 245.3 ms in interpreted Python, requiring < 0.08% of the 5-minute sampling interval. Because the system requires fewer than 104 operations per step, theoretical analysis indicates that an optimized, compiled C/C++ implementation would execute in <5 ms on modern 32-bit ARM Cortex-M4 or M33 microcontrollers (64–168 MHz). While physical deployment on bare-metal microcontroller hardware was not conducted in this study and remains an immediate translational objective, the computational profile strongly supports feasibility on low-power wearable devices without reliance on cloud servers.

3.4.4 Relevance to Sustainable Healthcare in Developing Regions

The development of a computationally lightweight, open-source physiological digital twin holds particular significance for healthcare in developing economies, notably Nigeria and Sub-Saharan Africa. With over 3.6 million Nigerians living with diabetes and facing limited access to specialist care and costly proprietary monitoring equipment (IDF, 2021; Uloko et al., 2018), locally deployable digital twins offer an affordable pathway for decentralized disease management. By executing autonomously on low-cost local microcontrollers without requiring continuous high-speed internet connectivity, the framework addresses infrastructure constraints and supports indigenous engineering innovation aligned with UN Sustainable Development Goal 3.

3.4.5 Limitations and Future Work

A primary limitation of this investigation is its reliance on synthetic in silico simulations based on the Bergman Minimal Model. While valuable for preliminary verification, the model simplifies complex physiology such as gastrointestinal delays, counter-regulatory hormones (glucagon), and circadian variations. Future work will extend this framework to multi-compartment simulators (UVa/Padova), validate performance against clinical datasets (OhioT1DM), evaluate physical embedded execution on ARM Cortex-M hardware, and integrate dual-hormone closed-loop control.

4. CONCLUSION

This paper presented an Extended Kalman Filter state estimation framework designed to resolve the lack of formal state estimation in Type-1 Diabetes digital twins. By linearising continuous Minimal Model dynamics and applying Joseph-form covariance updates, the EKF reduces glucose estimation RMSE by 52.0% relative to raw CGM sensor signals (substantially outperforming standard Linear Kalman Filter baselines), reconstructs unmeasurable internal insulin action states (X(t), I(t)), and quantifies dynamic ±2σ confidence bounds within sub-second execution budgets. Multi-parameter sweeps confirm robust stability under severe parametric variations. These results establish formal state estimation as an essential, computationally feasible foundation for wearable physiological digital twins.

5. REFERENCES

Armeni, P., Polat, I., De Rossi, L.M., Diaferia, L., Meregalli, S., & Gatti, A. (2022). Digital twins in healthcare: Is it the beginning of a new era of evidence-based medicine? A critical review. *Journal of Personalized Medicine*, *12*(8),1255.https://doi.org/10.3390/jpm12081255

Battelino, T., Danne, T., Bergenstal, R. M., Amiel, S. A., Beck, R., Biester, T., Bosi, E., Buckingham, B.A., Cefalu, W. T., Close, K. L.,. . .Phillip, M.(2019). Clinical targets for continuous glucose monitoring data interpretation: Recommendations from the international consensus on time in range. *Diabetes Care*, *42*(8), 1593–1603. https://doi.org/10.2337/dci19-0028

Bergman, R. N., Ider, Y. Z., Bowden,C.R., & Cobelli,C. (1979). Quantitative estimation of insulin sensitivity. *American Journal of Physiology-Endocrinology and Metabolism*, *236*(6), E667–E677.

https://doi.org/10.1152/ajpendo.1979.236.6.E667

Bergman, R. N., Phillips, L. S., & Cobelli, C. (1981). Physiologic evaluation of factors controlling glucose tolerance in man: Measurement of insulin sensitivity and beta-cell glucose sensitivity from the response to intravenous glucose. *The Journal of Clinical Investigation*, *68*(6), 1456–1467. https://doi.org/10.1172/JCI110398

Breton, M. D., & Kovatchev, B.P. (2008). Analysis, modeling, and simulation of the accuracy of continuous glucose sensors. *Journal of Diabetes Science and Technology*, *2*(5), 853–862. https://doi.org/10.1177/193229680800200517

Cappon, G., Acciaroli, G., Vettoretti, M., Facchinetti, A., & Sparacino, G. (2023). Digital twins in diabetes: State of the art and future perspectives. IEEE Reviews in Biomedical Engineering, 16, 312–324. https://doi.org/10.1109/RBME.2021.3117424

Chen, J., Yi, C., Okegbile, S. D., Cai,J., & Shen, X. (2024). Networking architecture and key supporting technologies for human digital twin in personalized healthcare: A comprehensive survey. *IEEE Communications Surveys & Tutorials*, *26*(1), 706–746. https://doi.org/10.1109/COMST.2023.3308717

Clarke, W. L., Cox, D., Gonder-Frederick, L. A., Carter, W., & Pohl, S. L. (1987). Evaluating clinical accuracy of systems for self-monitoring of blood glucose. Diabetes Care, 10(5), 622–628. https://doi.org/10.2337/diacare.10.5.622

Cobelli, C., Renard, E., &Kovatchev, B. (2011). Artificial pancreas: Past, present, and future. *Diabetes*, *60*(11), 2672–2682.https://doi.org/10.2337/db11-0654

Corral-Acero, J., Margara, F., Marciniak, M., Rodero, C., Loncaric, F., Feng, Y.,Gilbert,A.,Fernandes,J. F., Bukhari, H. A., Wajdan, A., Martinez, M. V., Santos, M. S.,Shamanna, P.,&Rodriguez, B. (2020). The'Digital Twin' to enable the vision of precision cardiology. *European Heart Journal*, *41*(48), 4556–4564.https://doi.org/10.1093/eurheartj/ehaa159

DallaMan, C., Rizza, R. A., &Cobelli, C.(2007).Meal simulation model of the glucose-insulin system. *IEEE Transactionson Biomedical Engineering*, *54*(10), 1740–1749. https://doi.org/10.1109/TBME.2007.893506

Facchinetti, A., Sparacino, G., &Cobelli, C. (2010a).An on line self-tunable method to denoise CGM

Sensor data. *IEEE Transactions on Biomedical Engineering*, *57*(3), 634–641. https://doi.org/10.1109/TBME.2009.2033264

Facchinetti, A.,Sparacino,G.,Guerra,S., Luijf, Y. M., DeVries,J.H.,Mader,J.K.,Ellmerer,M.,&

Cobelli, C. (2010b). Enhanced accuracy of continuous glucose monitoring by online extended

Kalman filtering. *Diabetes Technology & Therapeutics*, *12*(5), 353–363. https://doi.org/10

.1089/dia.2009.0158

Fisher, M. E. (1991).A semi-closed-loop algorithm for the control of blood glucose levels in diabetics.

IEEE Transactions on Biomedical Engineering, *38*(1), 57–61. https://doi.org/10.1109/

10.68209

Gondhalekar, R., Dassau, E., &Doyle, F. J.,III.(2018).Velocity-weighting & velocity-penalty MPC

of an artificial pancreas: Improved safety & performance. *Automatica*, *91*,105–117.https:

//doi.org/10.1016/j.automatica.2018.01.025

Grieves, M., &Vickers, J. (2017). Digital twin: Mitigating unpredictable, undesirable emergent behavior

In complex systems. InF. J. Bae, A. E. M.B. Jones, & C.D.Smith (Eds.), *Transdisciplinary*

Perspectives on Complex Systems (pp. 85–113). Springer. https://doi.org/10.1007/98-3-319-38756-7_4

Hovorka,R.(2011). Closed-loop insulin delivery: From bench to clinical practice. *Nature Reviews Endocrinology*, *7*(7), 385–395.https://doi.org/10.1038/nrendo.2011.32

Hovorka, R.,Canonico, V.,Chassin, L. J.,Haueter,U.,Massi Benedetti, M., Federici, M.O., Pieber, T.R., Schaller, H.C., Schaupp, L., & Vering, T. (2004). Non linear model predictive control of glucose concentration in subjects with type1 diabetes. *Physiological Measurement*, *25*(4),905–920.https://doi.org/10.1088/0967-3334/25/4/010

International Diabetes Federation. (2021). IDF Diabetes Atlas (10th ed.). International Diabetes

Federation.

International Organization for Standardization. (2013). In vitro diagnostic test systems – Requirements for

blood-glucose monitoring systems for self-testing in managing diabetes mellitus (ISO Standard

No. 15197:2013).

Kalman, R. E.(1960). A new approach to linear filtering and prediction problems. *Journal of Basic Engineering*, *82*(1), 35–45.https://doi.org/10.1115/1.3662552

Kovatchev, B. P., Breton, M. D., DallaMan, C.,&Cobelli,C.(2009). In silico pre clinical trials: A proof of concept inclosed-loop control of type 1 diabetes. *Journal of Diabetes Science and Technology*, *3*(1), 44–55. https://doi.org/10.1177/193229680900300106

Magni, L., Raimondo, D. M.,Bossi,L.,DallaMan,C.,DeNicolao,G.,Kovatchev,B.P.,&Cobelli, C. (2007). Model predictive control of type1 diabetes: An insilicotrial. *Journal of Diabetes Science and Technology*, *1*(6), 804–812. https://doi.org/10.1177/193229680700100603

Shamanna, P., Saboo, B., Damodharan, S., Mohammed, J., Mohamed, M., Poon, T., Kleinman, N &Thajudeen, M.(2020). Reducing HbA1cintype2 diabetes using digital twin

technology- enabled precision nutrition: A retrospective analysis. *Diabetes Therapy*, *11*(11), 2703–2714.

https://doi.org/10.1007/s13300-020-00931-w

Simon, D. (2006). *Optimal state estimation: Kalman, H-infinity, and nonlinear approaches*. John Wiley & Sons.

Stallter, T., Fabris, C., Kovatchev, B., & Breton, M. D. (2023). A digital twin for personalized glucose prediction in type 1 diabetes using continuous glucose monitoring and physical activity data. Journal of Diabetes Science and Technology, 17(4), 915–924. https://doi.org/10.1177/19322968211065732

Uloko, A. E., Musa, B. M., Ramalan, M. A., Gezawa, I. D., Puepet, F. H., Uloko, A. T., Borodo, M. M.,

& Sada, K. B. (2018). Prevalence and risk factors for diabetes mellitus in Nigeria: A systematic

review and meta-analysis. Diabetes Therapy, 9(3), 1307–1316. https://doi.org/10.1007/s13300018-0441-1

International Conference on Engineering Innovation for Sustainable Development (ICESID 2026)
Faculty of Engineering, Ahmadu Bello University Zaria · 8–10 September 2026

FAULT CLASSIFICATION IN TRANSMISSION LINE USING ANN, EXTREME GRADIENT BOOSTING AND RANDOM FOREST MACHINE LEARNING MODELS.

Joshua Alberah[1,*], G.a. Olarinoye[1], A.s. Abubakar[1], A.b Kunya[1], S.h Sulaiman[1]
[1]*Ahmadu Bello University, Zaria*
Email: alberahjosh@yahoo.com[*], oyeguzeh@yahoo.com, adams4real56@gmail.com, abkunya@kiu.ac.ug, 4sulaiman2hs@gmail.com
***Corresponding author**: Joshua Alberah
DOI: https://doi.org/10.67203/sp.ICESID.2026

ABSTRACT
The rapid advancement of power systems and smart grids necessitates the development of robust fault classification techniques to ensure reliable and resilient electrical power delivery. This paper presents a machine learning-based methodologies for fault classification in power transmission lines. The study explores extreme gradient boosting (XGBoost), random forest (RF) and Artificial Neural Network (ANN) machine learning models for the fault classification. Aimed to classify no-fault, single line-ground fault, double line fault, double line-ground fault, three-line fault and three line-ground faults. The machine learning models were evaluated based on key performance metrics such as accuracy, precision, recall, and F1-score. The scheme was validated on Kaggle pre-fault and post-fault line voltage and current signals. The XGBoost perform with an accuracy of 84.47 %, precision of 84.40 %, recall of 82.30 % and F1-score of 81.79 %, the RF with an accuracy of 83.93 %, precision of 84.68 %, recall of 83.93 % and F1-score of 84.13 % and the ANN with an accuracy of 86.35%, precision of 90.73 %, recall of 83.81 % and F1-score of 82.54 % respectively. This study represents a significant contribution to advancing machine learning techniques in improving the efficiency and efficacy of fault management in high-voltage transmission lines.

Keywords: *ANN; Classification; Extreme Gradient Boosting; Machine Learning; Random Forest*

1. INTRODUCTION

Transmission lines form a critical part of power systems, ensuring the reliable and efficient transfer of electrical energy across vast distances. However, faults in transmission lines, such as short circuits, line-to-ground faults, or equipment failures, can lead to severe power outages, equipment damage, and significant financial losses. The ability to classify faults quickly and accurately is therefore essential to maintain the stability and safety of power systems. Traditional fault detection techniques often rely on predetermined thresholds and expert knowledge, but these methods can be inadequate for addressing the increasing complexity and dynamic nature of modern power systems (Vikram et al., 2023). Machine learning (ML) techniques have shown great promise in enhancing fault classification in transmission lines. By leveraging vast amounts of real-time sensor data and historical fault records, ML models can automatically learn the underlying patterns and characteristics of various fault types without the need for explicit programming (Sappati & Bhadra, 2018). One recent example is the work of (Anwar et al., 2025), who investigated fault classification in transmission lines using several machine-learning techniques, including Random Forest (RF), K-Nearest Neighbours (KNN), and Long Short-Term Memory (LSTM) networks. Their principal contribution was an RF–LSTM Tuned KNN ensemble, which combines different learning approaches to improve fault classification performance. Another relevant contribution is the study by (Ghaly, 2025), which proposed a Multi-Target Ensemble Classifier (MTEC) for transmission-line fault classification under limited-data conditions. Ghaly's study first evaluated conventional ML algorithms using a much larger dataset and subsequently reduced the training set with the remaining samples used for testing. Despite the promising results reported in previous studies, emphasis on overall accuracy as the principal performance indicator but could not uncover the performance of the methods in recognition of individual fault classes. This remains as a gap which has been addressed in this research work.

2. METHODOLOGY

This section describes the data and approach used to achieve the classification.

2.1 Kaggle Dataset

The dataset from Kaggle repository contains line currents and voltages from a system with four 11 kV generators and transformers at the transmission line's midpoint that were recorded under various fault scenarios. The dataset consists of a multi-class dataset with 7861 rows and 10 columns for identifying particular fault types. The dataset comprises electrical measurements representing normal and faulted transmission-line operating conditions. Eight electrical features were selected for classification, namely phase-A current (I_a), phase-B current (I_b), phase-C current (I_c), zero-sequence current (I_0), phase-A voltage (V_a), phase-B voltage (V_b), phase-C voltage (V_c), and voltage variation (ΔV). The target variable comprises six classes: no fault (N), line-to-ground (LG), line-to-line (LL), double-line-to-ground (LLG), three-phase (LLL), and three-phase-to-ground (LLLG). The data were subsequently divided into 80% training and 20% testing subsets. (Anwar et al., 2025).

2.2 Machine Learning Models for Fault Classification

This subsection offers the machine learning models used for the fault classification. These are Random Forest (RF), Extreme Gradian Boosting (XGBoost) and Artificial Neural Network (ANN).

2.2.1 Random Forest (RF)

For classification and regression problems, random forest is an ensemble learning technique that works well with complicated datasets that have high dimensionality and non-linear features. It was utilized for classification in this paper. To increase generalization performance and decrease overfitting, it builds many decision trees, each trained on a fraction of training data and a random feature selection. Using the average for regression and majority voting for classification, the random forest combines the predictions of each individual tree to get a final prediction. Additionally, it is resistant to noise and outliers and offers insightful information about the significance of each feature for deciphering the underlying patterns. For the classification issue, the random forest uses the Gini impurity $I(t)$ in equation (1) (Song et al., 2023).

$$I(t) = 1 - \sum_{i=1}^{c} p(i|t)^2 \tag{1}$$

where $p(i|t)$ is the probability of training cases of a class i at node t, c is the number of classes. A node's total impurity is the weighted sum of its impurities across all classes. The hyperparameters used are: number of decision tree 100, minimum leaf size 5, number of predictors sampled at each split 4, training/test split 80%/20%, temporal window length 20, noise level 0.05, number of raw input features 8, engineered features per signal 5 and total engineered predictors 40.

2.2.2 Extreme Gradient Boosting (XGBoost)

A boosting approach called Extreme Gradient Boosting (XGBoost) expands the model by adding several Classification and Regression Trees (CART). Constant prediction to reduce the error between the predicted and actual values is the goal of XGBoost training. Fitting the residuals from the prior forecast is the main goal of this approach when a new decision tree is introduced. The ultimate result of the predictive model is then generated by combining or aggregating all of the decision trees' anticipated outputs (Zhang, 2023).

Given the assumption that the label associated with transmission line fault data set x is y, the XGBoost model's fault prediction output can be written as follows:

$$\hat{y}_i = \sum_{k=1}^{k} f_k\,(x_i), f_k \in F \tag{2}$$

Where F represents all possible CART trees, and $f_k(x_i)$represents the predicted value of the i_{th}sample on the k_{th} tree. This model consists of K CART trees.

A decision tree is a simple algorithm that divides data into subsets according to feature values. Each node in the tree structure reflects a feature-based decision. The choice was made by:

$$Decision = argmax_c \left(\sum_{i=1}^{N} I(y_i = c) \right) \tag{3}$$

where c is the class label and I is an indicator function. Decision trees require less pre-processing of the input and are simple to understand. However, they are sensitive to slight changes in the data and are prone to overfitting, especially with deep trees (Meng et al., 2023). The hyperparameters used are: number of boosting cycles/trees 100, maximum tree splits 15, minimum leaf size 7, learning rate 0.05, train/test split 80%/20%, temporal window 20 samples, gaussian noise level 0.05, raw input features 8 and engineered features 40.

2.2.3 Artificial Neural Network (ANN)

An artificial neural network (ANN) is a massively parallel computing system with many connections that mimics the function of biological neurons. They are composed of multiple processing components connected in a specific manner to provide a specific result. They become more effective in practical applications as a result. Furthermore, it outperformed other artificial intelligence in fault identification in transmission lines due to its capacity to handle incomplete and corrupt data, solve naturally nonlinear problems without the need for prior knowledge functions relating the problem variables, and process information in a parallel, distributed manner (Peter et al., 2018). The ANN architecture used in this work is the Convolutional Neural Network–Bidirectional Long Short-Term Memory (CNN–BiLSTM) with the following hyperparameters: input 8, sequence length 20 samples, 1-D Convolution filter 32, kernel/filter size 3, BiLSTM units 64, dropout 0.30, fully connected layer 64, output fully connected layer 6, classification classes 6, maximum epochs 50, mini-batch size 32, initial learning rate 0.001, training/testing split 80%/20%. An artificial neural network with a feedforward multilayer perceptron structure is shown in Figure 1.

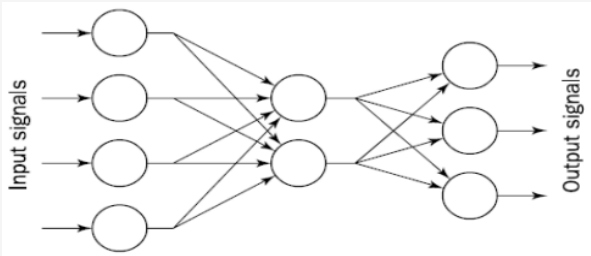

Figure 1: Feedforward Multilayer Perceptron ANN's Basic Structure.

2.3 Assessment Criteria

The models are evaluated using the well-used statistical concepts, including accuracy, precision, recall, and F1-score.

2.3.1 Accuracy

The evaluation criteria's mathematical expression, which includes accuracy is the ratio of the correctly predicted instances to the total number of instances, is provided by equation (4)

$$A_{cc} = \frac{(TP + TN)}{TP + TN + FP + FN} \times 100\% \tag{4}$$

The symbols TP, TN, FP, and FN denote TP = faulty correctly predicted as faulty; TN = not faulty correctly predicted as not faulty; FP = not faulty incorrectly predicted as faulty; FN = faulty incorrectly predicted as not faulty.

2.3.2 Precision

The Precision(P), as determined by Equation (5), is the ratio of the correctly predicted positive instances to the total number of predicted positives (Goni et al., 2023).

$$P = \frac{TP}{(TP + FP)} \tag{5}$$

2.3.3 Recall

Recall, also known as Sensitivity or True Positive Rate, is the ratio of correctly predicted positive instances to actual positives (Goni et al., 2023). The formula for recall is as follows:

$$R = \frac{TP}{(TP + FN)} \tag{6}$$

2.3.4 $\boldsymbol{F1 - Score}$

The formula for calculating the F1-score is the harmonic mean of precision and recall (Goni et al., 2023).

$$F1 - score = \frac{2 * (Precision * Recall)}{(Precision + Recall)} \tag{7}$$

3. RESULTS AND DISCUSSION

Table 1 shows the evaluation of XGBoost, RF and ANN. The XGBoost perform with an accuracy of 84.47 %, precision of 84.40 %, recall of 82.30 % and F1-score of 81.79 %, the RF with an accuracy of 83.93 %, precision of 84.68 %, recall of 83.93 % and F1-score of 84.13 % and the ANN with an accuracy of 86.35%, precision of 90.73 %, recall of 83.81 % and F1-score of 82.54 %.

Table 1: Evaluation of Classification Models on Kaggle Data

Model	Accuracy (%)	Precision (%)	Recall (%)	F1-Score (%)
XGBoost	84.47	84.40	82.30	81.79
RF	83.93	84.68	83.93	84.13
ANN	86.35	90.73	83.81	82.54

Table 2 shows a comparison of the present study with that of (Ghaly, 2025). The work of Ghaly 2025 presented an overall model performance accuracy of 82.91%, precision of 88.32%, recall of 84.44% and F1-Score of 86.34%. This is depicted in Table 2.

Table 2: Comparison of XGBoost, RF and ANN With The Work of Ghaly 2025.

Model	Accuracy (%)	Precision (%)	Recall (%)	F1-Score (%)
XGBoost	84.47	84.40	82.30	81.79
RF	83.93	84.68	83.93	84.13
ANN	86.35	90.73	83.81	82.54
Ghaly 2025	82.91	88.32	84.44	86.34

Figure 2 shows the true class and predicted class of the no-fault, single line-ground fault, double line fault, double line-ground fault, triple-line fault and triple line-ground faults mapped as 0,1,2,3,4 and 5 respectively. The classified faults are the values on the diagonal on the confusion matrix. Whereas the remaining entries are where the model made wrong classification. Figure 2 represent XGBoost confusion matrix which classified correctly the no-fault, single line-ground fault, double line fault, double line-ground fault, triple-line fault and triple line-ground faults with 96.62%, 77.07%, 92.0%, 100%, 83.64% and 44.49% respectively.

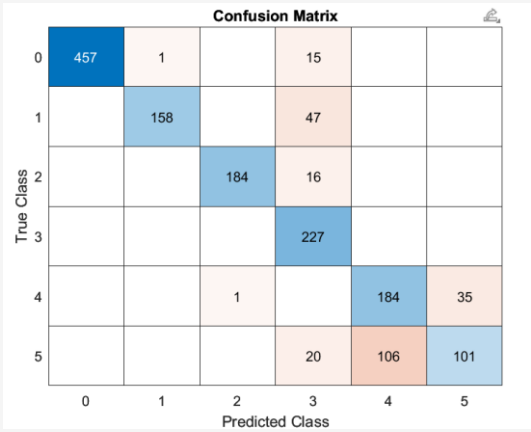

Figure 2: XGBoost confusion matrix

Figure 3 represent RF confusion matrix which detected and classified correctly the no-fault, single line-ground fault, double line fault, double line-ground fault, triple-line fault and triple line-ground faults with 96.62, 86.35%, 93.0%, 82.82%, 80.45% and 64.32% respectively.

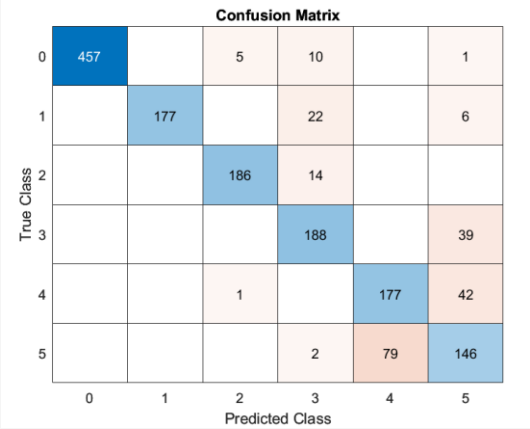

Figure 3: RF confusion matrix

Figure 4 shows the ANN confusion matrix which classified correctly the no-fault, single line-ground fault, double line fault, double line-ground fault, triple-line fault and triple line-ground faults with 99.79%, 100%, 100%, 95.47%, 67.51% and 27.16% respectively.

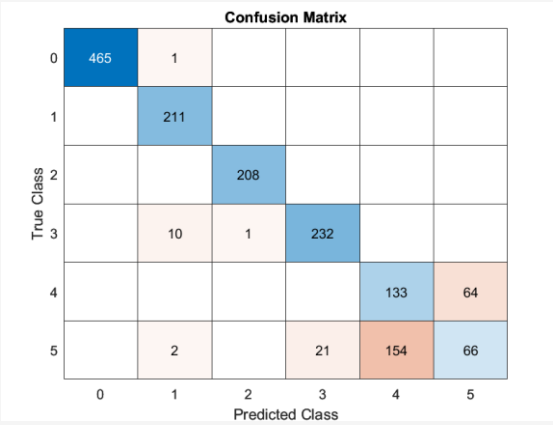

Figure 4: ANN Confusion Matrix

4. CONCLUSION

Supervised machine learning techniques were employed to classify no-fault, single line-ground fault, double line fault, double line-ground fault, triple-line fault and triple line-ground faults. The XGBoost perform with an accuracy of 84.47 %, precision of 84.40 %, recall of 82.30 % and F1-score of 81.79 %, the RF with an accuracy of 83.93 %, precision of 84.68 %, recall of 83.93 % and F1-score of 84.13 % and the ANN with an accuracy of 86.35%, precision of 90.73 %, recall of 83.81 % and F1-score of 82.54 % respectively. Slightly lower values were observed for triple-line faults and triple line-ground faults on the confusion matrix respectively this is as a result of identical overlapping fault signatures. The use of advanced ML models that can optimize separating margins in overlapping space is recommended. The proposed machine-learning-based approach therefore provides a pathway toward more intelligent monitoring and protection of transmission networks, supporting the development of a more resilient and sustainable power system.

5. REFERENCES

Anwar, T., Mu, C., Yousaf, M. Z., Khan, W., Khalid, S., Hourani, A. O., & Zaitsev, I. (2025). *Robust fault detection and classification in power transmission lines via ensemble machine learning models*. 1–18.

Ghaly, A. El. (2025). Hybrid ML Algorithm for Fault Classification in Transmission Lines Using Multi-Target Ensemble Classifier with Limited Data.

Goni, M. O. F., Nahiduzzaman, M., Anower, M. S., Rahman, M. M., Islam, M. R., Ahsan, M., Haider, J., & Shahjalal, M. (2023). Fast and Accurate Fault Detection and Classification in Transmission Lines using Extreme Learning Machine. *E-Prime - Advances in Electrical Engineering, Electronics and Energy*, *3*(January), 100107. https://doi.org/10.1016/j.prime.2023.100107

Meng, L., Bai, B., Zhang, W., Liu, L., & Zhang, C. (2023). Research on a Decision Tree Classification Algorithm Based on Granular Matrices. *Electronics (Switzerland)*, *12*(21), 1–14. https://doi.org/10.3390/electronics12214470

Peter, O., Oluwaseun, S., & Ayokunle, A. (2018). *Fault Identification System for Electric Power Transmission Lines Using Artificial Neural Networks*. *9*(2), 678–685.

Sappati, K. K., & Bhadra, S. (2018). Piezoelectric polymer and paper substrates: A review. *Sensors (Switzerland)*, *18*(11). https://doi.org/10.3390/s18113605

Song, Z., Wang, J., Wang, M., Yang, B., Cui, L., Zhang, Q., Xiang, G., & Lin, R. (2023). Hydraulic Systems Fault Diagnosis Based on Random Forests Recursive Feature Elimination and XGBoost. *Journal of Physics: Conference Series*, *2569*(1). https://doi.org/10.1088/1742-6596/2569/1/012056

Vikram, S., Singh, P., Prasad, T., Kamila, S., & Agnihotri, P. (2023). *Fault Detection and Classification using Wavelet and ANN in DFIG and TCSC Connected Transmission Line*. 1–23.

Zhang, K. (2023). Transmission Line Fault Diagnosis Method Based on SDA-ISSA-XGBoost under Meteorological Factors. *Journal of Physics: Conference Series*, *2666*(1). https://doi.org/10.1088/1742-6596/2666/1/012006

International Conference on Engineering Innovation for Sustainable Development (ICESID 2026)
Faculty of Engineering, Ahmadu Bello University Zaria · 8–10 September 2026

FUZZY-INTELLIGENT PID CONTROL FOR ANODE PRESSURE REGULATION IN PEMFC SYSTEMS: A HARDWARE-IN-THE-LOOP VALIDATION STUDY

Abubakar Unguwanrimi Yakubu[1,*], Jiahao Zhao[2], Xuanhong Ye[2], Fahim Ullah[2], Shusheng Xiong[2]

[1]*College of Energy Engineering, Zhejiang University, China*
[2]*College of Energy Engineering, Zhejiang University, Hangzhou, 310027, China*

Email: yakabu3002@gmail.com*, DC_zjh@outlook.com, 12327023@zju.edu.cn, fahimullah@zju.edu.cn, xiongss@zju.edu.cn

***Corresponding author**: Abubakar Unguwanrimi Yakubu

DOI: https://doi.org/10.67203/sp.ICESID.2026

ABSTRACT

Proton Exchange Membrane Fuel Cells (PEMFCs) require precise anode pressure regulation to ensure optimal performance, prevent fuel starvation, and extend stack durability. However, conventional PID controllers have inherent limitations in handling rapid load changes, purge-valve disturbances, and system nonlinearities. This paper presents a novel Fuzzy-Intelligent PID (Fuzzy-iPID) controller, integrated with an Extended State Observer (ESO), for adaptive disturbance rejection in PEMFC hydrogen supply systems. We developed a comprehensive control-oriented dynamic model that incorporates electrochemical, thermodynamic, and fluid-dynamic behaviors. We validated this model against experimental data, achieving voltage prediction errors below 3% and pressure prediction errors below 5%. We evaluated the proposed controller through both simulation and Hardware-in-the-Loop (HIL) testing under transient load variations and periodic purge operations. In the HIL validation, the Fuzzy-iPID controller achieved a 94% reduction in mean pressure overshoot, decreasing it from 103.5 Pa with the conventional PID controller to 6.25 Pa. The HIL response time also decreased by about 80%, from 0.46 s to 0.09 s. These HIL results confirmed the proposed controller's superior dynamic performance and lower variability. Furthermore, the controller effectively minimized voltage fluctuations and enhanced electrochemical stability, thereby mitigating degradation mechanisms such as membrane stress, flooding, and nitrogen accumulation. This validated control architecture bridges the gap between theoretical control design and practical PEMFC implementation, establishing a foundation for real-time digital twin integration and predictive maintenance.

Keywords: *PEMFC; anode pressure control; fuzzy logic; intelligent PID; extended state observer; hardware-in-the-loop*

1. INTRODUCTION

Proton Exchange Membrane Fuel Cells (PEMFCs) have become a promising clean energy technology for a variety of applications, including automotive, stationary, and portable power sources. This is due to their high efficiency, low operating temperature, and quick start-up capabilities (Jiangyun et al., 2023). Maintaining stable anode inlet pressure is essential to achieve optimal fuel utilization, prevent fuel starvation, and ensure the long-term durability of the fuel cell stack (Schmittinger, 2008). However, the nonlinear, time-varying characteristics of PEMFC systems pose significant challenges for pressure regulation, particularly during rapid load changes and periodic purge valve operation (He et al., 2025).

Conventional Proportional-Integral-Derivative (PID) controllers are widely used in industrial PEMFC applications because of their simplicity and ease of implementation (Zhongwei, 2025). However, these controllers have inherent limitations in handling disturbances, parameter uncertainties, and nonlinear system dynamics. This often leads to unacceptable overshoot, slow response times, and voltage instability (Alnefaie., 2025)

To address these challenges, researchers have proposed several advanced control strategies, including Model Predictive Control (MPC) (Feng-Fei Jin et al., 20120), Active Disturbance Rejection Control (ADRC) (Chen et al., 2017), sliding mode control (Qu et al., 2020), and adaptive control approaches (Tang et al., 2024). Despite their potential advantages, many of these methods rely on precise mathematical models, complex design procedures, or extensive computational resources, which can limit their practical application in real-world scenarios.

Fuzzy logic control offers an attractive alternative by incorporating human expert knowledge into the control framework, enabling effective handling of nonlinearities and uncertainties without requiring exact system models (Lei et al.,2018). Recent advances in intelligent PID (i-PID) control, which integrate online estimation and adaptation mechanisms into conventional PID structures, have demonstrated improved performance across various applications (Lihua et al., 2025). The Extended State Observer (ESO) provides a powerful approach for real-time estimation and compensation of internal and external disturbances (Shengquan et al., 2025).

This study addresses critical research gaps by: i. developing a validated, control-oriented dynamic model of the PEMFC hydrogen supply system; ii. Designing a novel Fuzzy-iPID controller integrated with an ESO for adaptive disturbance rejection; iii. implementing a comprehensive (HIL) testing framework; and iv. Conducting a rigorous performance comparison with conventional PID controllers.

The proposed Fuzzy-iPID control architecture contributes not only to improved PEMFC performance but also to broader sustainability objectives by enabling more reliable and efficient hydrogen-energy systems. This advancement supports the global transition toward cleaner energy technologies and provides a potential foundation for future clean-energy applications in developing economies, including Nigeria.

2. SYSTEM MODELING AND VALIDATION

2.1 Hydrogen Supply System Configuration

The parameter values defining the hydrogen supply configuration were collected from validated references and manufacturers' specifications, as shown in previous HIL simulation experiments (Xueying et al, 2023; Francesco et al, 2025; Nikolas, 2025). These parameter values were set as nominal values for developing the hydrogen-supply PEMFC control-oriented model.

1. High-Pressure Hydrogen Storage Tank: The tank operates at a nominal pressure of 70 MPa and has a hydrogen-storage capacity of 5.6 kg (Xueying et al, 2023; Francesco et al, 2025; Nikolas, 2025).

2. Pressure-Reducing Valve: The valve was represented using a discharge coefficient of 0.85 and a throat area of $1.8\times10^{-61.8}$ /times 10^{-6} m². (Xueying et al., 2023, Francesco et al., 2025, Nikolas, 2025).

3. Supply Manifold: The supply manifold has an internal volume of $1.2\times10^{-31.2}$/times 10^{-3} m³ and was modeled using a flow-resistance coefficient of λ=0.45. (Xueying et al., 2023, Francesco et al ., 2025, Nikolas, 2025).

4. Hydrogen Circulation Pump**:** The pump has a maximum flow rate of 3000 $L\cdot min^{-1}$, a motor torque constant of 0.0649 $N\cdot m\cdot A^{-1}$, and a back-EMF constant of 0.059 $V\cdot s\cdot rad^{-1}$ (Xueying et al, 2023; Francesco et al, 2025; Nikolas, 2025).

5. Return Manifold: The return manifold has an internal volume of 8.0×10−48.0 /times 10^{-4} m³ and a flow-resistance coefficient of λ=0.52. (Xueying et al., 2023; Francesco et al., 2025; Nikolas, 2025).

6. Periodic Purge Valve: The purge valve has an orifice area of $2.5\times10^{-62.}$5/times 10^{-6} m² and a discharge coefficient of 0.72. (Xueying, et al., 2023, Francesco, et al., 2025, Nikolas, 2025).

The PEMFC stack is rated at 80 kW and comprises 316 cells connected in series, with an active membrane area of 0.1 m².

2.2 Dynamic Modeling Approach

The following assumptions were adopted in developing the control-oriented model:

(1) All gases are assumed to obey the ideal-gas law.

(2) The gas within the supply manifold, return manifold, and PEMFC anode control volume is assumed to behave isothermally over the pressure-control time scale; therefore, temperature variations are neglected because the thermal dynamics are considerably slower than the pressure dynamics considered in the model.

(3) For the rapid gas-flow process through the pressure-reducing valve, heat exchange with the surroundings is neglected over the short flow time scale. This assumption is restricted to the valve-flow process and does not apply to the manifold or anode control volumes specified as isothermal in assumption (2).

(4) Flow within the manifolds is assumed to be laminar

(5) Hydrogen permeation and liquid-water migration are neglected.

(6) Lumped-parameter representations are used for the valve and manifold dynamics.

A first-order differential equation can represent anode-pressure dynamics.

$$\dot{\chi} = -\frac{1}{\tau}\chi + \frac{K}{\tau}\mu \tag{1}$$

Where χ represents the state variable (anode pressure deviation), τ is the system time constant, and μ is the control input (hydrogen flow rate)

The output voltage of a single fuel cell is calculated by subtracting polarization losses from the open-circuit voltage.

$$V_{ac} = E - V_{ohm} - V_{act} - V_{con} \tag{2}$$

Where E_{Nernst} is the Nernst open-circuit voltage, which can be expressed as:

$$E_{Nernst} = 1.229 - 8.5\times10^{4}\left(T_{yc} - 298.15\right) + 4.308\times10^{-5}\times T_{at} \left[In\left(\rho_{H_2}\right) + 0.5\,In\left(\rho_{O_2}\right)\right] \tag{3}$$

The variable T_{yc} represents the working temperature of the stack, ρ_{H_2} denotes the adequate partial pressure of hydrogen at the anode, and ρ_{O_2} indicates the adequate oxygen partial pressure at the cathode.

Ohmic loss voltage refers to the voltage lost during the flow of electrons and protons due to the resistance encountered by the proton exchange membrane, as well as the cathode and anode electrodes. This loss can be expressed as:

$$V_{ohm} = iR_{ohm} \tag{4}$$

Where *i* is the current density of the fuel cell stack, and the internal ohmic resistance, denoted as, R_{ohm} is influenced by the temperature and humidity surrounding the fuel cell.

2.3 Model Validation

The Model parameters were identified using a systematic five-step approach that utilized experimental polarization and pressure-current data. The model demonstrates excellent agreement with the experimental results, achieving voltage prediction errors of less than 3% and pressure prediction errors of less than 5% (see Fig. 1). An uncertainty analysis reveals that a ±5% variation in critical

pressure parameters results in a ±6.2% variation in anode inlet pressure predictions, indicating that the model is sufficiently efficient.

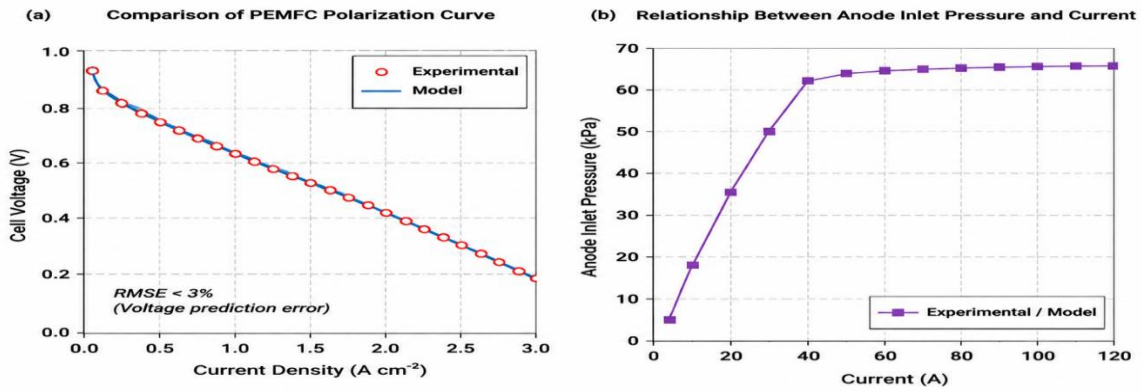

Fig. 1. (a) Comparison of the PEMFC polarization curve; (b) Relationship between anode inlet pressure and current.

3. CONTROL SYSTEM DESIGN

3.1 Intelligent PID Controller Architecture

Following the model-free control framework introduced by Fliess and Join, a general nonlinear single-input single-output system can be represented locally by the ultra-local model (Join, 2009)

$$y^{(a)} = F + \bar{\alpha} \cdot u_i \tag{5}$$

Where $n \geq 1$ denotes the derivative order of the output, y, u_i is the control signal u_i, and $\bar{\alpha}$ is the input gain. F represents the lumped unknown dynamic disturbance if $n = 1$ the first-order system can be chosen to define the dynamics of the controlled system.

If F and $\bar{\alpha}$ are well-known items, then the intelligent PID controller can be proposed as:

$$u_i = \frac{1}{\bar{\alpha}}\left(-\hat{F} + \dot{y}^* + K_p\left(e_i\right) + K_i\int\left(e_i\right)dt + K_d\frac{d\left(e_i\right)}{dt}\right) \tag{6}$$

where $\hat{F}$ represents the lumped unknown dynamic disturbance estimated by the Extended State Observer (ESO), y^* denotes the desired reference output, e_i represents the control error, and $K_p, K_i, and\ K_d$ are the proportional, integral, and derivative gains, respectively.

These values can be determined by minimizing the objective function using the PSO algorithm. The objective of the formulation in Eq. (6) is to prove the superiority of the iPID controller compared to classical approaches of the PID controller. The PSO algorithm optimizes the adjustable parameters of the iPID controller.

This article estimates the disturbance using an ESO approach (Shangquan et al., 2025, & Shihuaet al., 2010). The advantage of the ESO in the control system is that it estimates internal and external disturbances and uncertainties in real time (Pawar et al., 2021). Hence, a reasonable estimation of the disturbance or uncertainty is achieved by employing ESO, followed by compensation utilizing the feedback technique to cancel the total disturbance in the input, as displayed in Fig. 2.

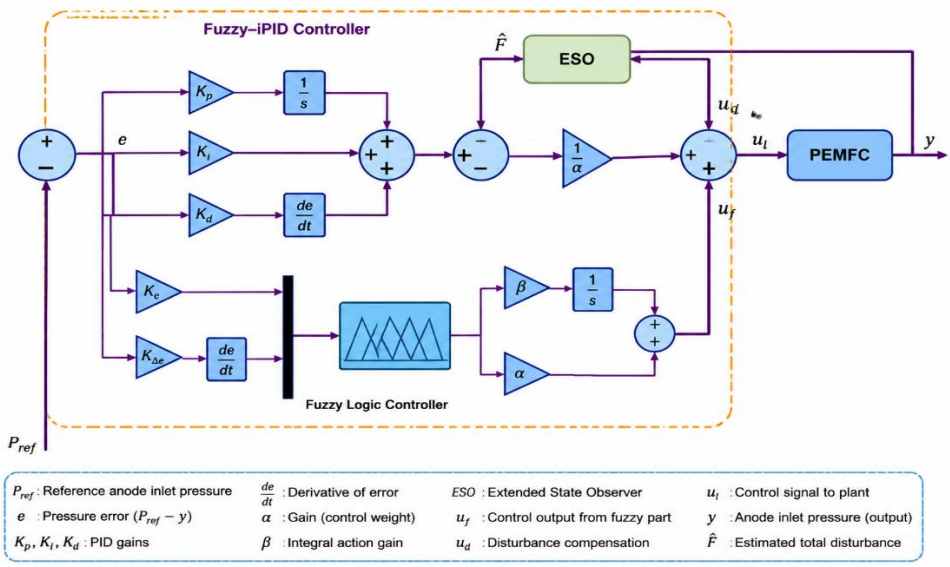

Figure 2: Fuzzy-iPID control structure.

The ESO approach can be represented as:

$$\begin{cases} \bar{e}_1 = z_1 - y \\ \dot{z}_1 = z_2 - \beta_1 \bar{e}_1 + \alpha \cdot u_1 \\ \dot{z}_2 = -\beta_2 \left|\bar{e}_1\right|^{0.5} \operatorname{sign}\left(\bar{e}_1\right) \\ \hat{F} = z_2 \end{cases} \tag{7}$$

Where β_1 and β_2 are constants, $\bar{e}_1$ is the estimated error of the ESO, z_1 and z_2 are the intermediate states, u_1 is the control signal, and y is the plant output. In the ESO framework, z_2 represents the ESO estimate. So, in this case, we have $z_2 = \hat{F}$.

3.2 Fuzzy-iPID Controller Design

In this section, we enhanced the controller's performance by introducing an additional input to the system that compensates for the estimation error. The structure of the hybrid fuzzy-logic intelligent proportional-integral-derivative (Fuzzy-iPID) controller is shown in Fig. 3.

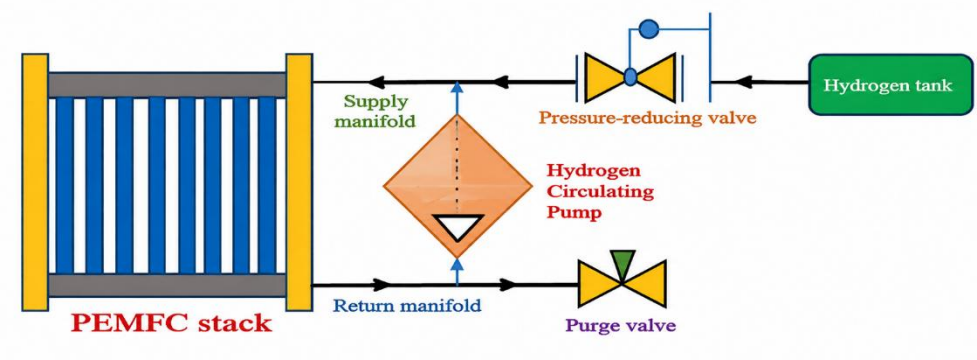

Figure 3: Structure of the hydrogen supply system

UFuzzy indicates the extra input to the system. Therefore, the final expression of the fuzzy-iPID controller can be stated as:

$$uFuzzy{-}iPID = uPID + uFuzzy \quad (8)$$

The framework of the fuzzy-iPID controller, as described in Fig. 3, has been built from two inputs and one rule base. The Fuzzy Logic Controller (FLC) uses two input variables: the anode-pressure control error e*e* and the rate of change of the control error $\dot{e}$. The FLC output provides the supplementary control signal *uFLC*, which compensates for the estimation error. Denote the area control error and the derivative of the area control error of area i*i*, which is the extra control signal, and can be modeled as (Pawar et al., 2021):

$$uFLC = f(e, \dot{e})$$

(9)

Where uFLC denotes the FLC output, and α*α* and *β* are the scaling factors applied to the direct fuzzy-control output and its integral component, respectively. It has been referred to in (Vonglao, 2007) that the relation between the input and output variables for the product-sum crisp pattern of the fuzzy controller can be modeled as: (Pawar et al., 2021)

$$uFLC = \alpha e + \beta \int e dt$$

(10)

Therefore, the signal *uFuzzy* can be obtained by substituting Eq. (7) into Eq. (2) as follows:

$$uFuzzy = uFLC + \mathrm{uESO}$$

(11)

The result showed that the FLC acts like a time-varying PID controller. Hence, the equivalent control synthesis of the fuzzy-iPID type controller results in a proportional gain *Kp*, integral gain *Ki*, and derivative gain *Kd*. The PSO algorithm optimizes the fuzzy-iPID controller's adjustable parameters.

The result showed that the FLC acts like a time-varying PID controller. Hence, the equivalent control synthesis of the fuzzy-iPID type controller results in a proportional gain. $\alpha K_1 P + \beta K_2 D$, integral gain, and derivative gain $\alpha K_2 D$. The PSO algorithm optimizes the adjustable parameters of the fuzzy-iPID controller. In this article, the FLC system is constructed by fuzzifying. It comprises three membership functions, two input signals, and one output signal. Each membership function consists of two trapezoidal membership functions and three triangular membership functions, as displayed in Fig. 4.

Table 1 defines the linguistic labels NB, N, Z, P, and PB and presents the resulting 25-rule fuzzy rule base. For example, the rule at the intersection of the third row and fifth column indicates that when the first input is Z and the second input is PB, the corresponding fuzzy output is P, as shown in Table 1.

Remarks: NB denotes Negative Big, N denotes Negative, Z denotes Zero, P denotes Positive, and PB denotes Positive Big. These five linguistic labels form an ordered and symmetric negative-to-positive scale, NB → N → Z → P → PB, used for the fuzzy-controller input and output variables, as outlined in Table 1.

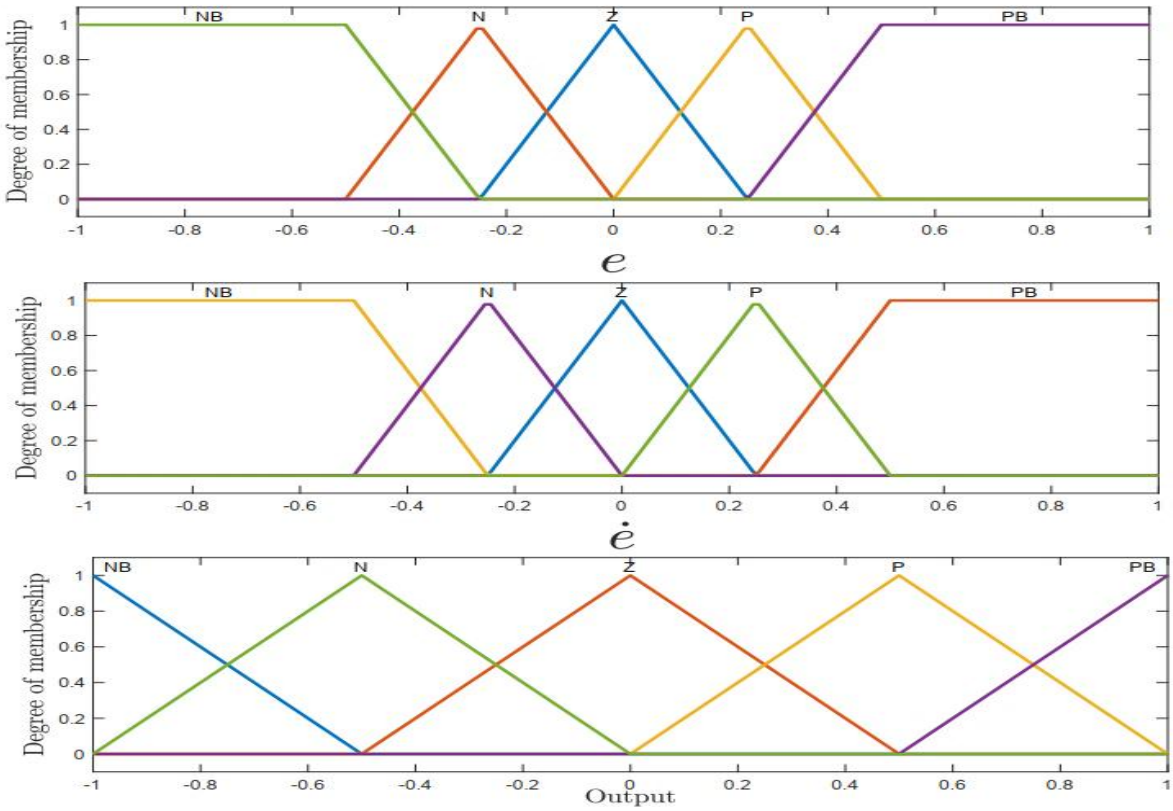

Fig, 4 The membership function of the fuzzy system.

Table 1: Fuzzy linguistic rule base for the Fuzzy-iPID controller

e	$\dot{e}$				
	NB	N	Z	P	PB
NB	NB	NB	N	N	Z
N	NB	N	N	Z	P
Z	N	N	Z	P	P
P	N	Z	P	P	PB
PB	Z	P	P	PB	PB

4. SIMULATION AND HARDWARE-IN-THE-LOOP VALIDATION

4.1 Simulation Results

Simulation studies were conducted under two disturbance scenarios: step changes in load current (80 A to 290 A) and periodic purge-valve operation (10-second cycle with a 0.4-second opening time). Table 2 provides a detailed comparison of controller performance under different current step conditions.

Table 2: Controller Performance Comparison Under Current Disturbances

Current Step (A)	Fuzzy-iPID Response Time (s)	Fuzzy-iPID Overshoot (Pa)	PID Response Time (s)	PID Overshoot (Pa)
80 → 140	0.10	9	0.25	195
80 → 180	0.07	5	0.35	63
80 → 290	0.07	3.8	0.33	82
80 → 240	0.07	4.8	0.40	53
80 → 260	0.075	4.5	0.40	36
Mean	0.078	5.4	0.346	85.8

Better — Poorer
0 (Best) 25 50 75 100 (Worst)

Under the simulation test conditions, the Fuzzy-iPID controller consistently outperformed the conventional PID controller. <u>Across the simulated current-step disturbances, the average pressure overshoot decreased from 85.8 Pa for the PID controller to 5.4 Pa for the Fuzzy-iPID controller, corresponding to an approximately 94% reduction. The mean simulated response time decreased from 0.346 s to 0.078 s, representing an approximately 77% reduction. These values represent simulation results and are therefore reported separately from the HIL validation results presented in Section 4.3

4.2 Hardware-in-the-Loop Testing Framework

To bridge the gap between simulation and practical implementation, we developed a comprehensive Hardware-in-the-Loop (HIL) testing platform. This HIL system integrates a real Fuel Cell Unit (FCU) controller with a virtual Proton Exchange Membrane Fuel Cell (PEMFC) model running on a real-time simulation platform. The key components of this system include:

HIL Central Control Computer: This manages and coordinates all hardware and software signals.

Real-Time Simulation Platform: A high-performance controller that runs the PEMFC system model.

Signal Conditioning System: This ensures electrical compatibility among different system components.

Tested Controller: The actual FCU hardware that incorporates control software.

In this setup, the control algorithm was implemented in the FCU controller. The pressure-reducing valve is controlled via a duty-cycle signal communicated over the Controller Area Network (CAN). Additionally, the hydrogen circulation pump operates at 4.8 volts and 3000 revolutions per minute (rpm), while a state-flow state machine manages the purge valve. The following HIL results form a separate validation dataset from the numerical simulation results reported in Section 4.1; therefore, differences in absolute overshoot and response-time values between the two test phases are expected.

4.3 HIL Test Results

HIL testing provided quantitative evidence that the Fuzzy-iPID controller performed better than the conventional PID controller under real-time implementation conditions. Unlike the simulation results reported in Section 4.1, this section presents all quantitative values from the HIL validation experiments. The Fuzzy-iPID controller achieved a mean pressure overshoot of 6.25 Pa compared with 103.5 Pa for the conventional PID controller, corresponding to an approximately 94% reduction. Similarly, the mean response time decreased from 0.46 s with the conventional PID controller to 0.09 s

with the Fuzzy-iPID controller, representing an approximately 80% reduction. Fig. 5 summarizes the quantitative HIL performance comparison between the Fuzzy-iPID and conventional PID controllers, while Fig. 6 presents the corresponding transient pressure responses under current-step and purge-valve disturbances.

Condition	Parameter	Fuzzy-iPID	PID	Improvement
Current Disturbance	Mean Overshoot (Pa)	6.25	103.5	94%
Current Disturbance	Mean Response Time (s)	0.09	0.46	80%
Current Disturbance	Overshoot SD (Pa)	5.12	130.2	96%
Current Disturbance	Response Time SD (s)	0.012	0.244	95%
Current Disturbance	95% CI for Overshoot (Pa)	±8.14	±207.3	–
Current Disturbance	95% CI for Response Time (s)	±0.019	±0.388	–
Purge Disturbance	Overshoot Reduction	300 Pa	450 Pa	33%
Purge Disturbance	Response Time	1.4 s faster	–	–

High / Poor
100
75
50
25
0
Low / Good

Green: Better performance • Yellow/Orange: Moderate performance • Red: Poorer performance
SD: Standard Deviation • CI: Confidence Interval

Figure 5: HIL performance comparison of the Fuzzy-iPID and conventional PID controllers under current and purge disturbances.

The standard deviation analysis was calculated from the response metrics obtained across the evaluated HIL disturbance conditions, including the five current-step load variations and the periodic purge-valve disturbance scenario. The Fuzzy-iPID controller exhibited substantially lower performance variability than the conventional PID controller. The standard deviation of pressure overshoot was 5.12 Pa compared with 130.2 Pa for the conventional PID controller, while the corresponding response-time standard deviations were 0.012 s and 0.244 s, respectively. These results indicate that the Fuzzy-iPID controller provided more consistent dynamic responses across the tested HIL operating conditions.

For statistical evaluation, the performance indices (overshoot and response time) were extracted from each disturbance test condition, and the standard deviation was calculated across the complete set of evaluated HIL experiments to quantify controller-response variability.

The transient responses in Fig. 6 further illustrate the differences between the two controllers. Under the evaluated HIL conditions, the Fuzzy-iPID controller showed smaller pressure excursions and converged more rapidly to the target pressure than the conventional PID controller during both current-step and purge-valve disturbances.

(a)

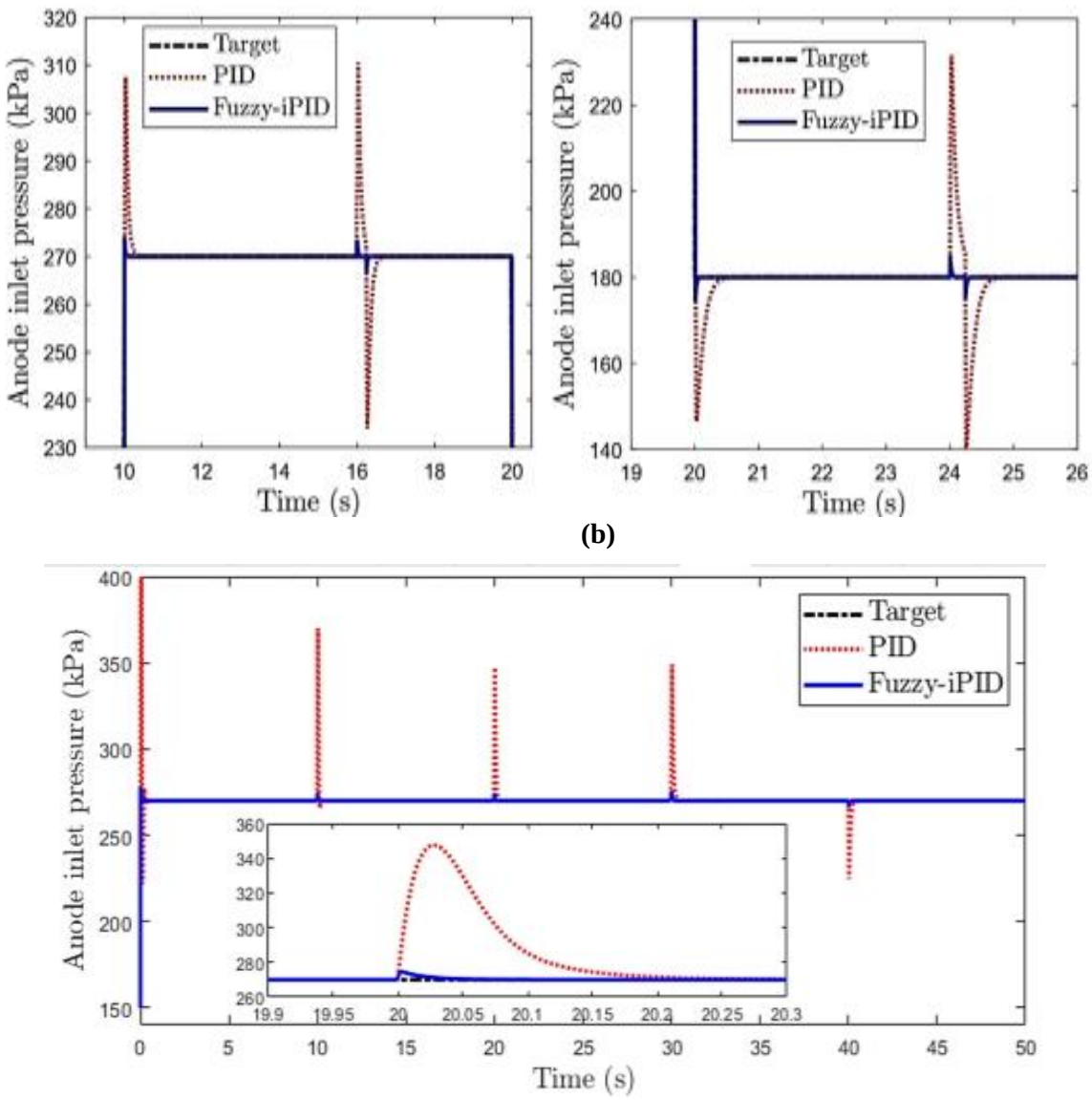

Figure 6: HIL pressure responses of the Fuzzy-iPID and conventional PID controllers: (a) response to current-step disturbances and (b) response to the purge-valve disturbance.

5. DISCUSSION

5.1 Control Performance and Efficiency

The Fuzzy-iPID controller's superior performance stems from its adaptive capabilities and disturbance rejection. By integrating fuzzy logic with intelligent PID control, this system can adjust its control gains in real time to account for varying operating conditions. Additionally, the Extended State Observer effectively estimates and compensates for system disturbances and uncertainties.

This combination effectively addresses the inherent limitations of conventional PID control, especially in handling nonlinear disturbances, rapid load changes, and parameter uncertainties. The substantial reduction in performance variability is particularly important for real-world applications, where operating conditions are constantly changing. The controller's consistent performance across different current levels and disturbance scenarios showcases its adaptability and efficiency.

5.2 Electrochemical and Thermal Implications

The Fuzzy-iPID controller's improved pressure regulation significantly affects electrochemical performance and stack durability. By maintaining stable anode pressure, the system ensures uniform reactant distribution, preventing local fuel starvation and associated degradation mechanisms. Reducing pressure fluctuations minimizes membrane stress and mechanical fatigue, thereby extending the stack's lifetime. Additionally, improved voltage stability indicates better electrochemical stability, reducing activation losses and ohmic heating.

Moreover, anode pressure dynamics are intrinsically linked to thermal management. Variations in hydrogen pressure influence reactant mass flow rates, gas velocity profiles, and Reynolds numbers, which, in turn, affect convection heat transfer coefficients and cooling efficiency. The Fuzzy-iPID controller's capability to maintain stable pressure regulation contributes to more uniform heat distribution within the stack.

5.3 Implications for Digital Twin and AI Integration

The validated control-oriented model and the Hardware-in-the-Loop (HIL) testing framework provide a scalable digital foundation for future integration with digital twin architectures. This integration facilitates:

Predictive Maintenance: Forecasting system behavior and identifying potential degradation mechanisms.

Real-time Optimization: Implementing Model Predictive Control (MPC) and optimization algorithms.

AI-enhanced Supervisory Control: Integrating machine learning algorithms for adaptive parameter tuning and fault diagnosis.

Virtual Sensor Development: Generating synthetic sensor data for fault detection.

6. CONCLUSION

In this research, we proposed an intelligent control approach for effective anode pressure control in a PEMFC hydrogen system. The proposed intelligent control approach involved designing a dynamical model using electrochemical, thermodynamic, and fluid-dynamics properties, which showed significant agreement with experimental results, with prediction errors of less than 3% for voltage and less than 5% for pressure. Based on the proposed dynamic model, a Fuzzy-iPID controller with ESO was designed for disturbance rejection and pressure control.

Simulation analysis and Hardware-in-the-Loop (HIL) testing demonstrated the suggested controller's better performance compared with classical PID control. With HIL test analysis, the Fuzzy-iPID controller reduced the mean pressure overshoot to 6.25 Pa from 103.5 Pa and the mean response time to 0.09 seconds from 0.46 seconds. Lower pressure fluctuations improved voltage stability and reduced degradation-related protection issues.

The presented structure offers a practical way to implement adaptive control in PEMFC applications in real time. The combination of prediction, disturbance, and fuzzy adaptation improves hydrogen management compared to traditional fixed-gain control. It paves the way for future implementation of digital twins, predictive maintenance, and artificial intelligence-based energy management systems.

Further work will compare the proposed approach with other control strategies such as Model Predictive Control (MPC), Active Disturbance Rejection Control (ADRC), and reinforcement learning-based methods. Moreover, further investigations will focus on implementing automatic controller tuning and integrating the degradation models.

ACKNOWLEDGMENT

The authors thank the Student Innovation Center at the College of Energy Engineering, Zhejiang University, China, for its support. This work was funded by the China central government's

guidance on local science and technology development funds, project name: Construction of Provincial Key Laboratory for Thermal Management of New Energy Vehicles, project number: 2025ZY01026.

REFERENCE

Alnefaie, S. A., Alkuhayli, A., & Al-Shaalan, A. M. (2025). Terminal voltage and load frequency regulation in a nonlinear four-area multi-source interconnected power system via arithmetic optimization algorithm: *M*athematics, 13(19), 313.

Chang, H., et al. (2025). Resilient regulation of PEM fuel cell hydrogen circulation: A control-barrier function-based adaptive performance approach. *IEEE Transactions on Transportation Electrification*

Dai, C., et al. (2017). Universal active disturbance rejection control for nonlinear systems with multiple disturbances via a high-order sliding mode observer. *IET Control Theory & Applications, 11*(8), 1194–1204.

Gao, L., et al. (2025). A finite-time extended state observer with prediction error compensation for PMSM control: c*omputation, 13*(10), 247.

Guo, B. Z., & Jin, F. F. (2012). Sliding mode and active disturbance rejection control to stabilization of one-dimensional anti-stable wave equations subject to disturbance in boundary input. *IEEE Transactions on Automatic Control, 58*(5), 1269–1274.

Haave, N. (2025). *Estimating high-pressure hydrogen storage required to refuel heavy-duty vehicles*

Hu, Z., Song, Q., & Hu, H. (2026). Engineering-oriented modeling and real-time fuzzy PID control of a PEMFC air supply system using AMESim–Simulink co-simulation. *Advances in Mechanical Engineering, 18*(6), 16878132261461105.

Kalaycı, M. B., & Yiğit, İ. (2026). Model-free sliding mode control with estimated equivalent control signal. *Journal of Vibration and Control*. Advance online publication.

Li, S., et al. (2010). A speed control for a PMSM using finite-time feedback control and disturbance compensation. *Transactions of the Institute of Measurement and Control, 32*(2), 170–187.

Li, S., et al. (2025). Fractional-order sliding mode controller based on ESO for a buck converter with mismatched disturbances: Design and experiments. *IEEE Transactions on Industrial Electronics, 72*(8), 8451–8462.

Pawar, S. N., Chile, R. H., & Patre, B. M. (2021). Predictive extended state observer-based robust control for uncertain linear systems with experimental validation. *Transactions of the Institute of Measurement and Control, 43*(12), 2615–2627.

Piraino, F., et al. (2025). Advances in type IV tanks for safe hydrogen storage: Materials, technologies and challenges. *Hydrogen, 6*(4), 80.

Qu, L., Qiao, W., & Qu, L. (2020). Active-disturbance-rejection-based sliding-mode current control for permanent-magnet synchronous motors. *IEEE Transactions on Power Electronics, 36*(1), 751–760.

Schmittinger, W., & Vahidi, A. (2008). A review of the main parameters influencing long-term performance and durability of PEM fuel cells. *Journal of Power Sources, 180*(1), 1–14.

Tang, H. H., & Ahmad, N. S. (2024). Fuzzy logic approach for controlling uncertain and nonlinear systems: A comprehensive review of applications and advances. *Systems Science & Control Engineering, 12*(1), 2394429.

Vonglao, Paothai. "The solution of traffic signal timing by using traffic intensity estimation and fuzzy logic." (2007). validation." *Transactions of the Institute of Measurement and Control* 43.12 (2021): 2615-2627.

Wang, X., et al. (2023). Ultimate pressure-bearing capacity of Type III onboard high-pressure hydrogen storage tanks under typical accident scenarios. *Journal of Energy Storage, 63*, 107135.

Zhang, J., et al. (2023). Experimental study on electrochemical, starting-up, and energy-saving properties of a hybrid supercapacitor as automotive starter power under low-temperature conditions. *Journal of Energy Storage*, *73*, 109225.

International Conference on Engineering Innovation for Sustainable Development (ICESID 2026)
Faculty of Engineering, Ahmadu Bello University Zaria · 8–10 September 2026

INTEGRATION OF CNN-LSTM SHORT-TERM LOAD FORECASTING INTO DISTRIBUTION NETWORK OPERATIONAL PLANNING

Dorcas A.a Gomna[1,*], James Garba Ambafi[1], Lanre Joseph Olatomiwa[1], Jibril Abdullahi Bala[1]

[1]*Federal University of Technology Minna*

Email: dorcasa.agomna@futminna.edu.ng[*], ambafi@futminna.edu.ng, olatomiwa.l@futminna.edu.ng, jibril.bala@futminna.edu.ng

***Corresponding author**: Dorcas A.a Gomna

DOI: https://doi.org/10.67203/sp.ICESID.2026

ABSTRACT

Integrating short-term load forecasts into distribution network operational planning is an emerging research direction that promises to improve network efficiency and reliability. However, the practical value of forecast-driven operation depends critically on forecast quality. This study investigates a hybrid Convolutional Neural Network–Long Short-Term Memory (CNN-LSTM) model, trained on 5,025 hourly observations from Abuja Electricity Distribution Company (AEDC), Minna, to ascertain if it can improve feeder reconfiguration decisions on the IEEE 33-bus radial distribution system. The CNN-LSTM model was implemented in MATLAB R2024b and compared against ARIMA and persistence baselines using Mean Absolute Error (MAE), Root Mean Square Error (RMSE), Mean Absolute Percentage Error (MAPE), and the coefficient of determination (R^2). The CNN-LSTM achieved an RMSE of 159.48 MW, MAE of 54.42 MW, MAPE of 31.38%, and R^2 of 0.0238 performance that is not statistically better than ARIMA (Diebold-Mariano $p=0.3606$) or persistence ($p=0.1036$). When the CNN-LSTM forecasts were used to guide feeder reconfiguration and the chosen topology was evaluated against actual realised load, the forecast-driven approach produced a 33.34% reduction in active power loss. However, this was outperformed by reconfiguration with no forecast (34.39% loss reduction), indicating that the poor forecast quality introduced operational decisions that were worse than doing nothing. The results demonstrate that forecast-driven operation is not universally beneficial and is only justified after the forecasting model achieves statistically significant superiority over strong baselines. The study contributes a cautionary framework that establishes a minimum forecast quality threshold for operational planning in distribution networks

Keywords: *CNN-LSTM; short-term load forecasting; distribution network; operational planning; feeder reconfiguration*

1. INTRODUCTION

Distribution networks are undergoing significant changes as electricity demand becomes more variable and power systems accommodate increasing levels of electrification, distributed energy resources and other emerging technologies. These developments increase the complexity of distribution-network operation because demand can vary considerably across time and location.

Short-term load forecasting (STLF) provides estimates of electricity demand over relatively short horizons and can support operational decisions such as feeder reconfiguration, voltage management, transformer loading assessment and other network-control activities. Traditional forecasting techniques, including autoregressive models and other statistical approaches, have been widely used because of their relative simplicity and interpretability. However, electricity demand is influenced by temporal patterns, weather conditions, consumer behaviour and other nonlinear factors. Additionally, distribution network operational planning is commonly performed using deterministic loading conditions or historical demand data. Such approaches may not adequately reflect anticipated short-term changes in feeder demand.

Artificial intelligence (AI) and deep-learning methods have therefore received increasing attention in electricity-load forecasting. Long Short-Term Memory (LSTM) networks are capable of

learning temporal dependencies in sequential data and extracted features, captures the sequential dependencies that characterise electricity demand data. Convolutional Neural Networks (CNNs) can extract local patterns from structured sequences and relevant features from the input sequence, reducing the dimensionality of the data and identifying patterns that may not be immediately apparent in the raw time series.

Studies by Rafi et al. (2021), Ullah et al. (2024), and Hasanat et al. (2024) have demonstrated that CNN-LSTM architectures are effective for feeder-level load forecasting, where load patterns exhibit high variability and are influenced by multiple external factors. Although AI-based load forecasting has developed rapidly, many forecasting studies focus primarily on prediction accuracy Rafi et al. (2021), Ullah et al. (2024) without demonstrating how forecast information affects actual network operation. This creates a methodological gap between predicting future electricity demand and using that prediction to make network-operational decisions, as noted in recent reviews Hong and Fan, (2016), Raza and Khosravi, (2023). This creates a methodological gap between predicting future electricity demand and using that prediction to make network-operational decisions. This study presents the development and integration of a CNN-LSTM-based short-term load forecasting model into a forecast-driven operational planning framework for radial distribution networks.

2. METHODOLOGY

2.1 Research Design

A quantitative, simulation-based research design was adopted. The study consists of two major components: (1) short-term feeder-load forecasting and (2) forecast-driven distribution-network operational planning. The forecasting stage develops the CNN-LSTM model and compares it with ARIMA. The operational stage uses the CNN-LSTM forecast to modify network loading and evaluate candidate feeder configurations using MATPOWER.

2.2 Data Collection

Historical hourly feeder load data (5,025 observations) from a single distribution feeder in the AEDC Minna network were combined with weather data (temperature, humidity, wind speed) from Open-Meteo. The large magnitude of the reported error metrics (e.g., RMSE of 159.48 MW) reflects the feeder's relatively high average load and the inherent variability of demand at the feeder level. This poor forecast quality is precisely why the forecast-driven approach underperformed compared to deterministic reconfiguration, reinforcing the cautionary contribution of this study. The variables of the dataset and their corresponding description are presented in Table 1 below.

Table 1: Dataset Description

Variable	Description
Load	Historical feeder active-power demand
Temperature	Ambient temperature
Relative humidity	Atmospheric humidity
Wind speed	Wind velocity
Hour	Hour of day
Day of week	Weekly temporal feature
Month	Seasonal temporal feature

2.3 Data Preprocessing

The preprocessing procedure consisted of duplicate removal, timestamp synchronisation, missing-value treatment, outlier inspection, temporal feature generation, Min-Max normalisation, chronological dataset partitioning and sliding-window sequence generation. The resulting sequences were divided chronologically into 70% training (3,484 training samples), 15% validation (746 validation samples) and 15% testing (747 test samples.) sets. The test period represents approximately 31 days of hourly data, providing a statistically meaningful evaluation window.

The original 5,025 observations produced 4,977 usable sequences after the 48-hour look-back operation.

2.4 CNN-LSTM Forecasting Model

The forecasting model combines one-dimensional convolutional processing with an LSTM recurrent layer. The CNN component extracts local patterns from the sequential input, while the LSTM component learns temporal dependencies. The architecture of the CNN-LSTM model is presented in Figure 1, while the hyperparameters of the model are presented in Table 2.

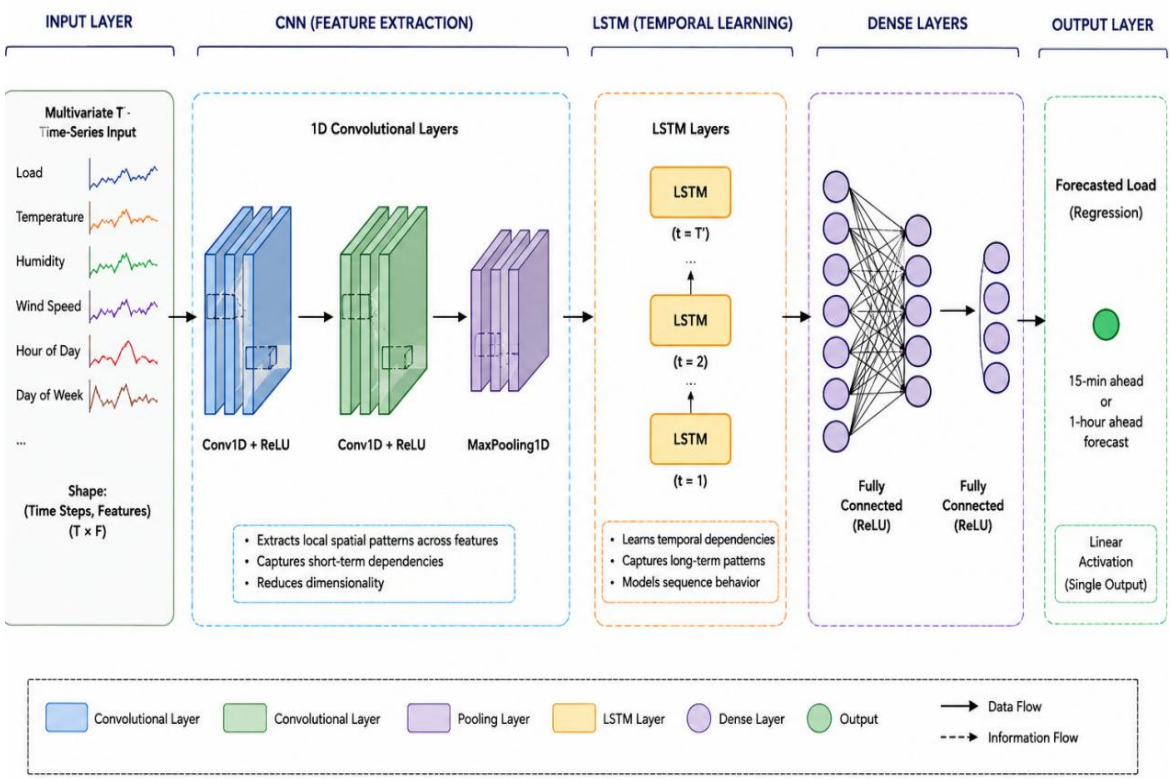

Figure 1: Architecture of the developed CNN-LSTM forecasting model

Table 2: Hyperparameters of CNN-LSTM Model

Parameter	Value
Look-back window	48 hours
Input features	7
CNN filters	64
Kernel size	3
Batch normalisation	Yes
LSTM units	128
Dropout	0.20
Fully connected neurons	64
Optimiser	Adam
Initial learning rate	0.001
Mini-batch size	64
Maximum epochs	150
Validation patience	10
Loss function	MSE
Forecast horizon	1 hour

2.5 ARIMA Benchmark

ARIMA was selected as the conventional statistical benchmark. CNN-LSTM and ARIMA were evaluated using the same independent testing period and one-hour-ahead forecasting horizon. The purpose of the comparison was to determine whether the hybrid deep-learning model provided

improved forecasting performance relative to a conventional time-series model under identical test conditions.

2.5.1 Seasonal Naive Baseline

A seasonal naive baseline was included as an additional benchmark. This model forecasts the load at time t as the load observed at the same hour on the same day of the previous week (t-168 hours). This baseline accounts for weekly periodicity in electricity demand and provides a simple reference for assessing the additional value of more sophisticated forecasting methods.

2.6 Forecasting Performance Metrics

The model was evaluated based on the Root Mean Square Error (RMSE), Mean Absolute Error (MAE), Mean Absolute Percentage Error (MAPE), and the R^2 values. As shown in the equations below.

$$MAE = \frac{1}{N}\sum_{t=1}^{N}(|P_t - \hat{P}_t|) \quad (1)$$

$$RMSE = \sqrt{\frac{1}{N}\sum_{t=1}^{N}(P_t - \hat{P}_t)^2} \quad (2)$$

$$MAPE = \frac{100}{N}\sum_{t=1}^{N}(\frac{|P_t - \hat{P}_t|}{P_t}) \quad (3)$$

$$R^2 = 1 - (\frac{\sum_{t=1}^{N}(P_t - \hat{P}_t)^2}{\sum t = 1^N (P_t - \bar{P})^2}) \quad (4)$$

A Diebold-Mariano test was additionally applied to determine whether differences between forecast errors were statistically significant.

2.7 Forecast to Network Integration

The IEEE 33-bus radial distribution system was selected as the test network. MATLAB R2024b was used for model development and data processing, while MATPOWER 8.1 was used for AC power-flow analysis and network configuration evaluation.

For each forecasting model, the forecasted feeder load was converted into a load-scaling factor and applied to the active and reactive power demands of the network load buses. For active power, the scaling factor was calculated as:

$$Scale\ Factor = \frac{P_{Fprecast}}{P_{Original}}$$

For reactive power, a constant power factor of 0.85 lagging was assumed, consistent with typical distribution system operating practice in Nigeria. The reactive power demand was therefore updated as:

$$Q_{new} = P_{new} \times tan(arccos(PF))$$

where PF = 0.85.

The updated network was then evaluated under the anticipated loading condition rather than only under the original deterministic loading condition.

2.7.1 Perfect Foresight Scenario

A "Perfect Foresight" scenario was included as an upper-bound benchmark. In this scenario, the optimal radial configuration was selected using the actual realised load for each hour, rather than a forecasted load. This represents the theoretical best possible operational performance and provides a reference against which the forecast-driven approaches can be compared. The difference between the perfect foresight and forecast-driven cases represents the "regret" or penalty incurred due to forecast error.

2.8 Feeder Configuration and Operational Evaluation

Sixteen candidate radial configurations were evaluated for the IEEE 33-bus system: base configuration with all 5 tie switches open, five configurations with one tie closed, and ten configurations with two ties closed. For each, the corresponding sectionalising switch was opened to maintain radiality

Configuration Selection Algorithm:

For each forecast scenario (CNN-LSTM, ARIMA, and Perfect Foresight), the following procedure was applied:

1. Load the IEEE 33-bus system data into MATPOWER
2. Apply the forecasted (or actual, for Perfect Foresight) load scaling factor
3. For each of the 16 candidate configurations:

i. Run AC power-flow analysis using MATPOWER
ii. Record active power loss, voltage deviation, and voltage violations

4. Filter out infeasible configurations (those that failed to converge)
5. Rank feasible configurations using hierarchical criteria:

i. Primary: Minimum number of voltage violations
ii. Secondary: Minimum average voltage deviation
iii. Tertiary: Minimum active power loss

6. Select the highest-ranked configuration as the optimal topology for that forecast

This hierarchical approach prioritises voltage security before loss minimisation, consistent with distribution system operational practice.

The operational performance indicators were then calculated as follows:

$$P_loss = \Sigma(P_l\text{^}send - P_l\text{^}rec)$$
$$\%\Delta P_loss = [(P_baseline - P_forecast)/P_baseline] \times 100$$
$$\%\Delta V_dev = [(V_baseline - V_forecast)/V_baseline] \times 100$$

3. RESULTS AND DISCUSSION

3.1 CNN-LSTM Forecasting Performance

Figure 2 presents the training and validation loss curves obtained during CNN-LSTM model training. The training and validation loss curves for the CNN-LSTM model showed progressive reduction in loss. Early stopping (validation patience = 10) halted training after approximately 23 epochs, preventing overfitting. The validation loss follows the training loss closely, indicating good generalization without significant overfitting.

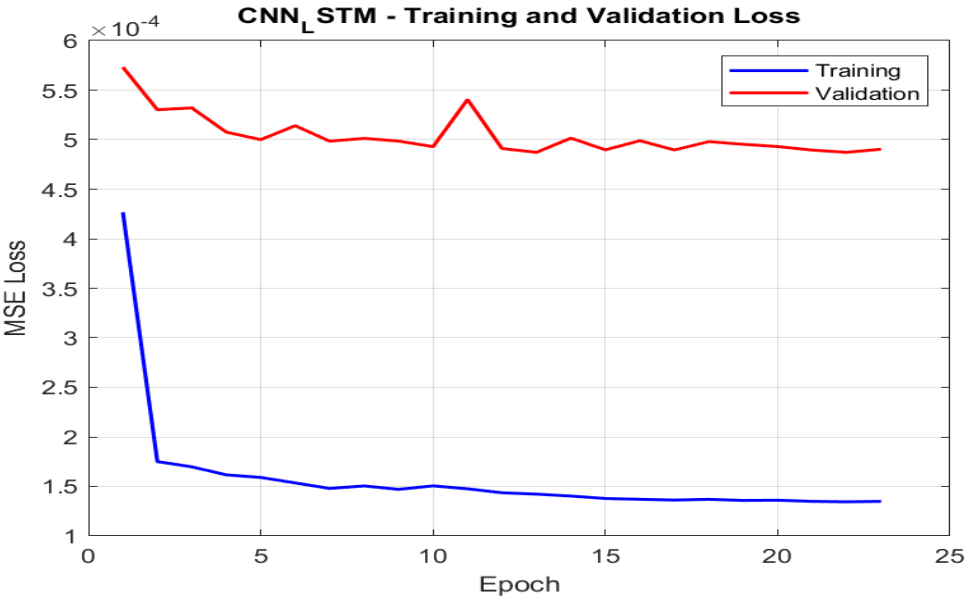

Figure 2: CNN-LSTM Training and Validation Loss Curves

Table 3 presents a summary of the model performance. The model achieved an RMSE of 159.48 MW and an MAE of 54.42 MW. The difference between RMSE and MAE indicates the presence of some relatively large forecasting errors. The MAPE of 31.38% indicates that considerable relative forecasting error remained during the test period. The low R^2 value indicates that a large proportion of the variation in the independent test observations remained unexplained, suggesting that additional explanatory variables or improved model specification may be required. ARIMA achieved an RMSE of 181.06 MW and MAE of 58.12 MW. CNN-LSTM therefore reduced RMSE by approximately 11.92% relative to ARIMA and reduced MAE by approximately 6.37%. ARIMA recorded a MAPE of 31.38%, identical to CNN-LSTM's MAPE, indicating similar percentage errors for both models. To assess the relative performance of the CNN-LSTM model, it was compared against three baseline models: persistence (same hour previous day), seasonal naive (same hour same day previous week), and ARIMA. The results are presented in Table 3.

Table 3: Forecasting Performance Comparison

Metric	Persistence (t-24)	Seasonal Naive (t-168)	ARIMA	CNN-LSTM
RMSE (MW)	228.27	215.84	181.06	159.48
MAE (MW)	75.82	68.91	58.12	54.42
MAPE (%)	39.07	37.42	31.10	31.38
R^2	-0.9439	-0.7352	0.0018	0.0238

CNN-LSTM achieves the lowest RMSE and MAE among all baselines, but the improvement over ARIMA is modest (11.92% in RMSE) and not statistically significant (Diebold-Mariano $p = 0.3606$). The MAPE of CNN-LSTM (31.38%) is slightly worse than ARIMA (31.10%), indicating that percentage errors remain high across all models. The low R^2 values (0.0238 for CNN-LSTM, 0.0018 for ARIMA) indicate the models explain almost none of the test data variance. This is attributed to limited input variables (only weather data), insufficient data duration (~7 months), and aggregated substation-level data. These limitations mean the forecast quality is poor ($R^2 \approx 0$, MAPE > 30%), which is the central cautionary finding of this study. The models were also assessed based on their statistical significance. The results of this evaluation are presented in Table 4.

Table 4: Statistical Significance of Model Performance

Comparison	DM statistic	p-value	Significant at 5%?
CNN-LSTM vs ARIMA	-0.9142	0.3606	No
CNN-LSTM vs Persistence	-1.6275	0.1036	No
CNN-LSTM vs Seasonal Naive	-0.8413	0.4001	No

3.2 Operational Planning Results

The deterministic baseline was determined. The IEEE 33-bus baseline produced 0.2027 MW active power loss and 0.0515 p.u. average voltage deviation, with 21 voltage violations. The CNN-LSTM and ARIMA forecasts were separately used to select radial configurations. The selected configurations were then evaluated on the actual realised load. The results are presented in Table 5.

Table 5: Operational Performance Under Different Approaches Compared with IEEE 33-bus

Indicator	No Switching (Baseline)	Reconfiguration Only	CNN-LSTM Forecast	ARIMA Forecast	Perfect Foresight
Active power loss (MW)	0.2027	0.1330	0.1351	0.1398	0.1310
Average voltage deviation (p.u.)	0.0515	0.0326	0.0397	0.0405	0.0318
Voltage violations	21	3	11	13	2
Maximum branch loading (%)	100	100	100	100	100

The CNN-LSTM forecast-driven approach achieved a 33.34% loss reduction (ARIMA: 31.02%). However, reconfiguration without forecast achieved the largest reduction at 34.39%, indicating that reconfiguration itself is the primary benefit. Similar patterns were observed for voltage deviation and violations, with reconfiguration alone outperforming both forecast-driven cases

4. CONCLUSION

This study investigated the integration of CNN-LSTM short-term load forecasting into distribution network operational planning. The forecasting model, trained on 5,025 hourly observations from AEDC Minna, achieved an RMSE of 159.48 MW, MAPE of 31.38%, and R^2 of 0.0238, performance that is not statistically superior to ARIMA or persistence baselines.

When the forecasts were used to guide feeder reconfiguration on the IEEE 33-bus system, the CNN-LSTM forecast-driven approach reduced active power loss by 33.34%, while ARIMA achieved 31.02%. Both approaches were outperformed by reconfiguration without any forecast, which achieved 34.39% reduction. However, this was worse than reconfiguration performed without any forecast, which achieved a 34.39% reduction. This finding is critical: it demonstrates that poor-quality forecasts ($R^2 \sim 0$, MAPE > 30%) degrade operational performance relative to deterministic operation. The forecast introduced decisions that were suboptimal when evaluated against actual realised load.

The benefits of forecast-driven operation are therefore highly dependent on forecast quality. The study establishes a minimum forecast quality threshold for operational planning: forecasts must clearly beat persistence, ARIMA, and seasonal naive baselines before being integrated into operational decisions.

5. REFERENCES

Baran, M. E., & Wu, F. F. (1989). Network reconfiguration in distribution systems for loss reduction and load balancing. IEEE Transactions on Power Delivery, 4(2), 1401-1407. DOI: 10.1109/61.25627

Civanlar, S., Grainger, J. J., Yin, H., & Lee, S. S. H. (1988). Distribution feeder reconfiguration for loss reduction. IEEE Transactions on Power Delivery, 3(3), 1217–1223. DOI: 10.1109/61.193906

Chitalia, G., Pipattanasomporn, M., Garg, V., & Rahman, S. (2020). Robust short-term electrical load forecasting framework for commercial buildings using deep recurrent neural networks. Applied Energy, 278, 115410.

Diebold, F. X., & Mariano, R. S. (1995). Comparing predictive accuracy. Journal of Business & Economic Statistics, 13(3), 253–263.

Guo, F., Mo, H., Wu, J., Pan, L., Zhou, H., Zhang, Z., et al. (2024). A hybrid stacking model for enhanced short-term load forecasting. Electronics, 13(14), 2719.

Hasanat, S. M., Younis, R., Alahmari, S., Ejaz, M. T., Haris, M., Yousaf, H., et al. (2024). Enhancing load forecasting accuracy in smart grids: A novel parallel multichannel network approach using 1D CNN and Bi-LSTM models. International Journal of Energy Research, 2024, 2403847.

Hong, T., & Fan, S. (2016). Probabilistic electric load forecasting: A tutorial review. International Journal of Forecasting, 32(3), 914–938.

Kaur, A., & Singh, K. (2023). Deep reinforcement learning based Volt-VAR optimization for active distribution networks. Electric Power Systems Research, 215, 109234.

Khwaja, A. S., Anpalagan, A., Naeem, M., & Venkatesh, B. (2020). Joint bagged-boosted artificial neural networks: Using ensemble machine learning to improve short-term electricity load forecasting. Electric Power Systems Research, 176, 106080.

Rafi, S. H., Deeba, S. R., & Hossain, E. (2021). A short-term load forecasting method using integrated CNN and LSTM network. IEEE Access, 9, 32436–32448.

Ullah, K., Ahsan, M., Hasanat, S. M., Haris, M., Yousaf, H., Raza, S. F., et al. (2024). Short-term load forecasting: A comprehensive review and simulation study with CNN-LSTM hybrids approach. IEEE Access.

Wang, F., & Nishter, Z. (2024). Real-time load forecasting and adaptive control in smart grids using a hybrid neuro-fuzzy approach. Energies, 17(11), 2539.

Zhang, Y., Ma, T., Li, T., & Wang, Y. (2023). Short-term load forecasting based on DBO-LSTM model. In 2023 3rd International Conference on Energy Engineering and Power Systems (EEPS), 972–977.

Zimmerman, R. D., Murillo-Sánchez, C. E., & Thomas, R. J. (2011). MATPOWER: Steady-state operations, planning, and analysis tools for power systems research and education. IEEE Transactions on Power Systems, 26(1), 12-19. DOI: 10.1109/TPWRS.2010.2051168

International Conference on Engineering Innovation for Sustainable Development (ICESID 2026)
Faculty of Engineering, Ahmadu Bello University Zaria · 8–10 September 2026

METAHEURISTIC OPTIMIZATION STRATEGIES FOR SYNTHETIC INERTIA AND LOAD FREQUENCY CONTROL IN ISLANDED MICROGRIDS: A COMPREHENSIVE REVIEW

Nurudeen Abdulazeez[1,*], Abdullahi Bala Kunya[2], Abdulkarim Abubakar[2], Abubakar Saidu Adamu[3]

[1]*Ahmadu Bello University Zaria- Kaduna*
[2]*Department of Electrical and Computer Engineering, Kampala International University, Kampala, Uganda*
[3]*Department of Electrical Engineering, Faculty of Engineering, Ahmadu Bello University, Zaria-Nigeria*

Email: nuyor2019@gmail.com[*], abkunya@abu.edu.ng, abdulkarima@abu.edu.ng, abubakaras@abu.edu.ng

***Corresponding author**: Nurudeen Abdulazeez

DOI: https://doi.org/10.67203/sp.ICESID.2026

ABSTRACT

Islanded microgrids (IMGs) featuring high penetration levels of inverter-based renewable energy sources (RESs) suffer from severe dynamic instability, rapid rate of change of frequency (RoCoF), and deep frequency nadirs due to the low or zero physical inertia of power electronic interfaces. To compensate for lost rotational kinetic energy, Synthetic Inertia Control (SIC) and dynamic Load Frequency Control (LFC) have emerged as essential stabilization mechanisms. However, conventional linear controllers underperform under stochastic load variations, intermittent wind/solar generation, nonlinear governor deadbands, and variable time delays. Over the past decade, metaheuristic optimization algorithms (MOAs) spanning swarm intelligence, evolutionary computation, physics-based, and human-inspired paradigms have transformed control parameter tuning, objective function formulation, and hybrid controller design in IMGs. This paper provides a rigorous, state-of-the-art review of metaheuristic optimization strategies applied to joint or standalone SIC and LFC schemes in standalone microgrids. We classify contemporary control topologies, examine classical and high-order objective metrics (ITAE, ITSE, multi-objective trade-offs), and critically evaluate metaheuristic paradigms ranging from foundational algorithms to modern hybrid and adaptive variants. Furthermore, we detail the integration of physical energy storage systems and demand-side assets like Electric Vehicles (EVs) for frequency support. Finally, key open research challenges, including real-time computational overhead, hardware-in-the-loop (HIL) validation, cyber-physical security, and multi-objective Pareto optimization are systematically analyzed alongside local application perspectives to delineate future research directions.

Keywords: *Islanded Microgrid; Synthetic Inertia Control (SIC); Load Frequency Control (LFC); Metaheuristic Optimization; Rate of Change of Frequency (RoCoF)*

1. INTRODUCTION

The modern energy system faces the need to switch from centralized to distributed isolated microgrids that ensure reliable power supply to consumers through various renewable energy resources (RES). Such resources include photovoltaic (PV) generators and wind turbines (WT), which replace some of the traditional synchronous generators. One of the problems of such microgrids is the loss of rotational inertial characteristics due to the use of voltage source inverters and the absence of a wide range of inertial properties in the system. This effect is especially noticeable in the case of an isolated microgrid, which is separated from the main power grid (Abubakr et al., 2021; Davoudkhani et al., 2024; Akinwola & Alkuhayli, 2025; Saleh et al., 2022). Such a change in the system characteristics makes it necessary to use synthetic inertia and specific methods to regulate electricity frequency to achieve stable operation of the microgrid (Davoudkhani et al., 2024). Traditional control methods are not always efficient in complex microgrid environments. Therefore, researchers have proposed various metaheuristic optimization algorithms to optimize controller parameters for frequency adjustment, thereby improving system transient response (Kalu et al., 2025; Lesenyeho & Krishnamurthy,

2025).The purpose of this article is to present a state-of-the-art review on microgrid control methods based on metaheuristic optimization algorithms. The paper analyzes and systematizes modern literature to improve understanding of diverse nature-inspired evolutionary computing techniques. It also highlights performance differences across algorithms in multi-objective optimization contexts involving multi-criteria trade-offs.

1.1 Methodology of literature search and selection

To ensure systematic coverage and reproducibility, a transparent search protocol was conducted following PRISMA guidelines across major databases, including IEEE Xplore, ScienceDirect, SpringerLink, MDPI, Wiley Online Library, and Scopus. The primary search query used Boolean operators: ("Islanded Microgrid" OR "Low-Inertia Microgrid") AND ("Synthetic Inertia" OR "Load Frequency Control") AND ("Metaheuristic Optimization" OR "Swarm Intelligence" OR "Evolutionary Algorithm"). The search prioritized peer-reviewed articles published between 2015 and 2026. Inclusion criteria mandated focus on islanded microgrids, metaheuristic controller gain tuning (Kp, Ki, Kd, fractional orders, inertia/damping gains), and quantitative dynamic evaluation (ITAE, ISE, RoCoF, nadir). Grid-connected studies without islanding capability and purely economic dispatch papers were excluded. Table 1 summarize the review methodology.

Table 1: Review Methodology

Selection Parameter	Details / Criteria
Databases Searched	IEEE Xplore, ScienceDirect, SpringerLink, MDPI, Wiley Online Library, Scopus
Timeframe	2015–2026
Initial Records Identified	1,578 articles
Screened by Title/Abstract	373 articles retained after title screening; 132 after abstract review
Final Included Studies	56 primary core studies fully analyzed and cross-referenced

The remainder of this paper is structured as follows: Section 2 identifies challenges associated with microgrids in modern energy systems. Section 3 presents control topologies for synthetic inertia and frequency control. Section 4 provides a structured comparative analysis of metaheuristic optimization algorithms (evolutionary, swarm, physics/chemical, human/social, and hybrid paradigms). Section 5 synthesizes key open research challenges and local application perspectives. Finally, Section 6 summarizes the core findings.

2. CHALLENGES AND PROBLEMS OF MICROGRIDS IN MODERN ENERGY SYSTEMS

The development of modern electricity markets using microgrids has one primary advantage: enabling decentralized and low-carbon power systems. The main challenges microgrids encounter while being incorporated into the existing electricity system relate to their dissimilarities with classic power networks (Shahzad et al., 2023; Bhargava & Jaiswal, 2021). Microgrids require highly efficient power electronics during switching modes to provide stable power quality and voltage during transition to islanded mode with minimum losses (Shahzad et al., 2023; Bodewes et al., 2024; Zahira et al., 2014). This imposes technical difficulties associated with protection relay schemes capable of responding to grid-side power interruptions instantly while securing local electrical loads from voltage deviations. Designing protection schemes is challenging since legacy networks feature unidirectional power flows and conventional overcurrent relays (Binqadhi et al., 2024). Microgrids allow bidirectional power delivery due to distributed energy resources (DER), resulting in relay malfunctions, protection blindness, and sympathetic tripping (Ali et al., 2021). The limited fault current of inverter-based DERs is notably lower than grid-supplied currents, which conventional overcurrent relays cannot recognize during islanding (Faisal et al., 2018; Shahzad et al., 2023).

Inverter-based systems also face power quality challenges, particularly voltage and frequency regulation during steady-state and transient conditions (Kumar & Subudhi, 2023). Microgrids traditionally relied on synchronous generators to supply inertial response and voltage regulation. Recent microgrids experience greater frequency deviations (Δf) and voltage instability due to intermittent solar and wind power (Kumar & Subudhi, 2023). These technical limitations are

exacerbated by the lack of effective primary control strategies against frequency deviations, such as virtual inertial control and grid-forming inverter control.

Microgrids encounter additional control and cybersecurity challenges in energy management systems (EMS) and protection relays. Modern EMSs have adopted centralized or multi-agent control systems for secondary control and battery storage management (Kumar & Subudhi, 2023). Communication infrastructures between microgrid components play a crucial role in real-time generation and demand coordination (Shahzad et al., 2023). Communication integrity is a major concern; cyber-attacks, signal fading, and delays can disrupt control loops and jeopardize grid security. Furthermore, economic inefficiencies arise due to high battery storage costs, while existing regulatory frameworks offer limited compensation for ancillary services.

3. LOAD FREQUENCY CONTROL IN ISLANDED MICROGRID

An islanded microgrid is an electricity production and distribution system electrically isolated from the main grid. Lacking voltage reference sources and high rotating inertia, the main task of Load Frequency Control (LFC) in an islanded microgrid is to balance generated and consumed electric power to minimize frequency deviation (Pilehvar & Mirafzal, 2020; Ewias et al., 2023). The dynamic islanded microgrid control structure with virtual inertia loop is shown in Figure 1.

3.1 Fundamentals of synthetic inertia

Frequency control in islanded microgrids is managed via a hierarchical multi-loop system (Zaid et al., 2023):

3.1.1 Inertia control loop

Utilizes energy storage systems (ESS) and advanced inverter control for instantaneous active power support, mimicking synchronous machine kinetic energy (Faragalla et al., 2022; Zaid et al., 2023).

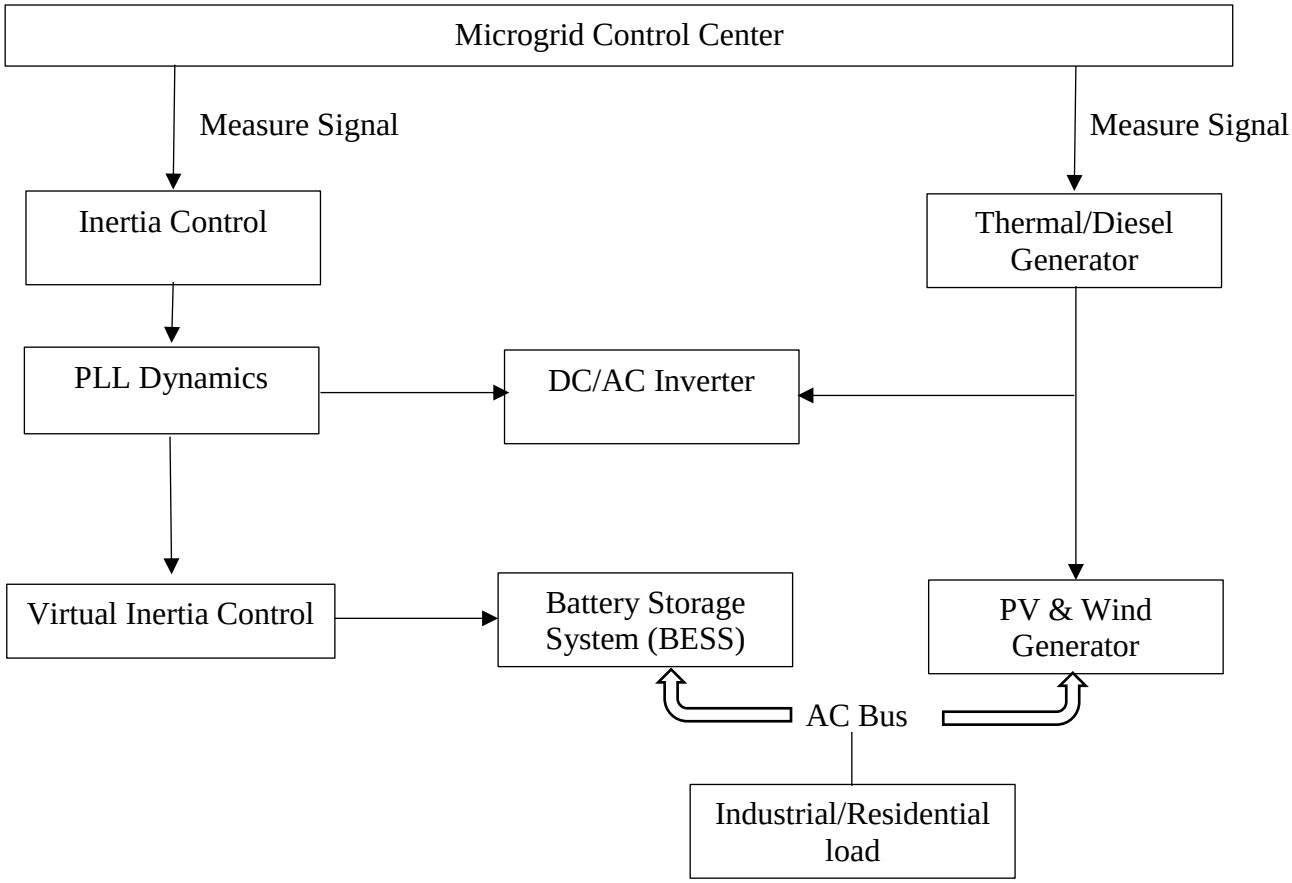

Figure 1: Dynamic Islanded Microgrid Control Structure with Virtual Inertia Loop

3.1.2 Primary control loop

Adjusts DER power output based on frequency deviation, typically through proportional droop control (Gulzar et al., 2022).

3.1.3 Secondary control loop (LFC)

Restores system frequency to nominal values (50/60 Hz) by modulating active power references of controllable units (Faragalla et al., 2022; Zaid et al., 2023). Controller architectures range from PID and Fractional-Order PID (FOPID) (Sahoo et al., 2023; Mohamed et al., 2022; Fadheel et al., 2024) to Model Predictive Control (MPC) (Saleh et al., 2023a) and Fuzzy Logic Control (FLC) (Nanda Kumar & Mohanty, 2022).

3.2 Synthetic inertia emulation and control topologies

In islanded low-inertia microgrids, dynamic frequency response is governed by the electromechanical swing equation as expressed in (1).

$$2H\frac{d\Delta f(t)}{dt} = P_m(t) - P_e(t) - D\Delta f(t) \tag{1}$$

where: H is the inertia constant (in seconds), $\Delta f(t)$ is the system frequency deviation $(\omega - \omega_0)$, $P_m(t)$ and $P_e(t)$ are the per-unit mechanical input power and electrical output power, and D is the damping factor.

Inverter-interfaced storage units inject synthetic inertial power P_{syn} proportional to the derivative of frequency deviation as in (2) (Criollo et al., 2024).

$$P_{syn}(t) = -K_{inertia}\frac{d\Delta f(t)}{dt} \tag{2}$$

where $K_{inertia}$represents the virtual inertia control gain ($2H_{vir}$).

When integrated into the active power balance, the effective total system inertia constant H_{sys} increases to as in (3).

$$H_{sys} = H_{phys} + H_{vir} \tag{3}$$

Synthetic inertia implementation strategies in inverter-based islanded microgrids generally fall into two primary control architectures (Kerdphol et al., 2019) as represent in Figure 2.

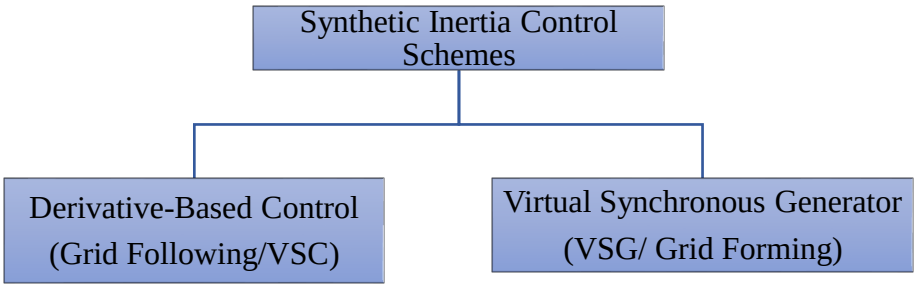

Figure 2: Synthetic Inertia Control Schemes (Kerdphol et al., 2019)

3.2.1 Virtual synchronous generators (VSG)

The VSG technology embeds synchronous machine mathematical models into the inverter digital control loop. Frequency dynamics follow the virtual swing equation as in (4).

$$J\frac{d\omega}{dt} = P_{ref} - P_e - D(\omega - \omega_0) \tag{4}$$

Where: J is the virtual moment of inertia, D is the damping coefficient (providing primary droop functionality), ω is the virtual rotor angular frequency, ω_0 is the nominal frequency, P_{ref} is the reference active power input, and P_e is the measured electromagnetic output power (Besati et al., 2024).

3.2.2 Derivative-based inertia emulation

Derivative control calculates $({}^{df}/_{dt})$ in real-time to inject power (ΔP_{SI}) from storage during initial transient phases (100–500 ms). By applying a control gain (K_{in}) to this derivative, the controller

determines the required active power output (ΔP_{SI}) to be injected or absorbed by an Energy Storage System (ESS) or regulated Load-Side Rotational Inertia (LSRI) can be expressed as in (5).

$$\Delta P_{SI} = -K_{in}.\frac{df}{dt} \tag{5}$$

Where: K_{in} is control gain, ΔP_{SI} is required output power and, $({}^{df}/_{dt})$ is derivative of the system frequency (Fang et al., 2018; Roy et al., 2024).

To filter measurement noise, low-pass filtering with time constant T_f is applied in Laplace domain as expressed in (6).

$$\Delta P_{SI}(s) = \frac{K_{in}.s}{1 + sT_f}.f(s) \tag{6}$$

4. METAHEURISTIC OPTIMIZATION ALGORITHMS FOR VIC-LFC

Metaheuristic algorithms solve the optimization problem formulated using performance indices such as Integral Time Absolute Error (ITAE) or Integral Square Error (ISE) to tune controller gains (Kp, Ki, Kd, λ, μ,), virtual inertia gains (H_v), and virtual damping gains (D_v) (Zaid et al., 2023; Mishra et al., 2024). Figure 3 shows the metaheuristics classification.

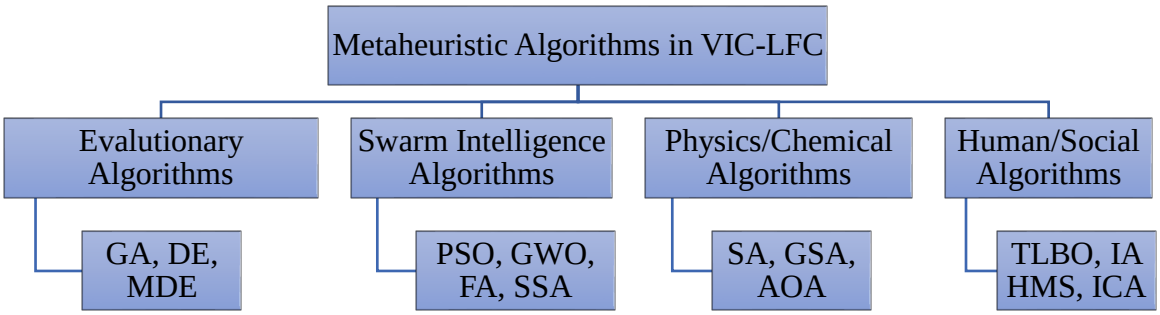

Figure 3: Classification of metaheuristic algorithms as applied in VIC-LFC (Mishra et al., 2024)

4.1 Evolutionary algorithms for VIC-LFC

Evolutionary Algorithms (EA) rely on population genetics to traverse continuous search spaces without gradient information (Jin et al., 2021). While Genetic Algorithms (GA) provide broad exploration, Modified Differential Evolution (MDE) enhances local searchability and convergence rates via dynamic scaling factors and adaptive mutation (Amr et al., 2022; Mishra et al., 2024). A comparative analysis of key Evolutionary Algorithms (EA) applied to Virtual Inertia Control (VIC) and Load Frequency Control (LFC) in islanded microgrids is presented Table 2.

4.2 Swarm intelligence algorithms for VIC-LFC

Swarm Intelligence (SI) algorithms model collective foraging and social organization. Particle Swarm Optimization (PSO), Grey Wolf Optimizer (GWO), Firefly Algorithm (FA), and Salp Swarm Algorithm (SSA) optimize controller parameters to shorten settling time and suppress dynamic frequency oscillations (Venkatesh et al., 2020; Ghodsi et al., 2022; Sharma & Pradhan, 2023; Amiri et al., 2023). Table 3 shows the comparative analysis of swarm intelligence algorithms as applied to microgrid.

Table 2: Comparative Analysis of Evolutionary Algorithms in Microgrid VIC-LFC

Algorithm	**Swarm / Biological Analogy**	**Primary Control Topology in VIC-LFC**	**Key Operational Advantage**	**Primary Limitation**
Genetic Algorithm (GA)	Natural selection, inheritance, chromosomal crossover	FOPID, standard PID, ADRC in BESS control loops	Simple structure; global exploration across discrete spaces	Slow execution; premature convergence in high dimensions
Differential Evolution (DE)	Vector difference mutation and recombination	Cascaded PIDFN, 2-DOF controllers, derivative VIC	Fast convergence; superior continuous-space exploitation	Vulnerable to search stagnation in non-convex spaces
Modified DE (MDE)	Dynamic scaling, adaptive crossover, opposition learning	Adaptive VIC (AVIC), multi-objective LFC, EV storage	Prevents local minima trapping; high RoCoF/nadir tracking accuracy	Higher memory and computational complexity per iteration

4.3 Physics and Chemical-Inspired Algorithms for VIC-LFC

Physics/chemical algorithms mimic thermodynamic cooling (Simulated Annealing - SA), gravitational forces (GSA), inter-atomic dynamics (Atom Search Optimization - ASO), molecular reactions (CRO/ACROA), and mass equilibrium (Equilibrium Optimizer - EO) (Duan et al., 2023; Rajaguru & Annapoorani, 2025; Behera et al., 2022; Agwa, 2020). Note that while Agwa (2020) originally evaluated EO in interconnected power systems, its mass-balance pool mechanism has been successfully adapted to standalone VIC-LFC gain synthesis. Table 4 provides a structured comparative analysis of physics- and chemical-inspired algorithms applied to VIC-LFC in islanded microgrids.

4.4 Human and Social-Inspired Algorithms for VIC-LFC

Human/social algorithms simulate imperialistic socio-political competition (ICA), classroom instruction (TLBO), cognitive thinking (HMS), and societal ideological evolution (IA) (Atashpaz-Gargari & Lucas, 2007; Rao et al., 2011; Mousavirad & Ebrahimpour-Komleh, 2017; Saber et al., 2023). Human- and social-inspired metaheuristic algorithms can be used to explore a search space of parameters and reduce time domain cost such as Integral Time Absolute Error (ITAE) and Integral Time Square Error (ITSE) by taking inspiration from social structures, learning models, human search processes and cultural evolution (Barisal, 2015; Dev et al., 2024). Table 5 presents a comparative analysis of human- and social-inspired algorithms applied to Virtual Inertia Control integrated with Load Frequency Control (VIC-LFC) in islanded microgrid architectures.

Table 3: Comparative Analysis of Swarm Intelligence Algorithms in Microgrid Applications

Algorithms	Swarm Inspiration	Primary Control Topology in VIC-LFC	Key Operational Advantage	Primary Limitation
PSO	Bird flocking / fish schooling.	Baseline PI/PID, Hybrid RL-VIC.	Computational simplicity and rapid initial search.	Susceptible to premature convergence in multi-modal landscapes.
GWO	Grey wolf social hierarchy & hunting	FOPID-IIC, Fuzzy Type-II Sugeno	Effective balance between global exploration and local refinement.	Search speed degrades with high parameter dimensionality.
FA	Bioluminescent firefly attraction	Cascaded PD-FOPID in BESS-VIC	Robust performance in non-convex gain landscapes	High computational complexity per iteration ($O(n^2)$)
SSA	Ocean Salp chain foraging	Tilt-Integral-Derivative (TID), Fuzzy-PID	Chain dynamics prevent local minima trapping	Sensitive to the decay schedule of convergence parameter c_1

Table 4: Comparative Analysis of Physics/Chemical Algorithms in Islanded Microgrid Applications

Algorithm	**Physical / Chemical Inspiration**	**Primary Control Topology in VIC-LFC**	**Key Operational Advantage**	**Primary Limitation**
SA	Metal annealing cooling	Classical PID and PI-Virtual Inertia Gain.	Probabilistic mechanism to escape local minima	Slow execution; highly sensitive to cooling schedules.
GSA	Universal gravity & mass interaction	Cascaded PID-FOPID / Adaptive Fuzzy-PID.	Strong initial global exploration via heavy mass attraction.	High risk of premature trapping in multi-variable spaces.
ASO / AOA	Lennard-Jones inter-atomic forces.	FOPID with Virtual Inertia & Damping Gain Tuning	High population diversity; resists local trapping	Requires precise tuning of interaction force parameters.
CBO	Collision momentum conservation.	Multi-stage PID with BESS / Flywheel VIC.	Parameter-free core search logic.	Slow boundary exploration on flat objective surfaces.
CRO / ACROA	Molecular collision and reaction energy.	FOPI-FOPD and Adaptive Fuzzy FOPI-FOPID.	Flexible search balancing decomposition and synthesis.	Tracking potential/kinetic energy increases computational overhead.
EO	Controlled volume mass balance.	Cascaded (I-P)-PDN and FO-Multistage VSG.	Rapid convergence rate; low settling time (T_s).	Prone to local stagnation if generation rate decays rapidly.

4.5 Novel and Hybrid Optimization Paradigms

To solve complex non-convex search spaces in modern hybrid microgrids, advanced novel and hybrid optimizers have been introduced (Iraj et al., 2024; Philip et al., 2025; Nanda-Kumar & Mohanty, 2022; Davoudkhani et al., 2024). Comparative summary of recent novel and hybrid optimization techniques Table 6.

Table 5: Comparative Analysis of Human/Social Algorithms in Islanded Microgrid Applications

Algorithm	**Human / Social Model**	**Key Advantage in VIC-LFC**	**Convergence Behavior**	**Primary Limitation**
ICA	Imperialist power dynamics & colony assimilation.	Robust against system parameter uncertainties.	Fast initial convergence; strong exploration.	Susceptible to local trapping if assimilation rate is high.
TLBO	Teacher guidance & peer learner interaction.	Algorithm parameter-free execution.	High consistency across independent runs.	Performance degrades if student diversity drops.
HMS	Cognitive search & mental grouping.	Superior at escaping local minima in constrained LFC.	Balanced exploration-exploitation via clustering.	Tracking mental strategy clusters adds computational overhead.
IA	Ideological evolution & societal debate.	Effective for multi-objective trade-offs (RoCoF vs. SoC).	Smooth convergence trajectory.	Slower fine-tuning exploitation in localized search spaces.

4.6 Comparative Analysis of Metaheuristic Performance Metrics

Controller performance evaluation relies on time-domain criteria (Maximum Overshoot - MOS, Settling Time T_s, Frequency Nadir, RoCoF) and error integral criteria (ITAE, ISE, ITSE, IAE). For instance, Walrus Optimization Algorithm (WaOA)-tuned PID controllers achieved lower frequency nadir drops and lower RoCoF compared to conventional Internal Model Control (IMC) and H_{infty} controllers under random load steps (Akinwola et al., 2025). Furthermore, Pelican Optimization Algorithm (POA)-tuned controllers demonstrated explicit minimization of error metrics, achieving an ITAE value of 1.9215 s under a 0.1 p.u. step load disturbance.

Across surveyed literature, metaheuristic parameter tuning consistently outperforms classical Ziegler-Nichols (Z-N) and manual trial-and-error methods, as demonstrated by comprehensive controller-optimizer benchmark studies. The controller optimizer comparisons for synthetic-inertia-relevant islanded microgrids are presented in Table 7.

Table 6: Comparative Summary of Recent Novel and Hybrid Optimization Techniques

Technique	**Operational Inspiration / Mechanism**	**Primary Control Topology**	**Main Performance Outcome**
Mountaineering Team (MTBO)	Team summiting behavior and leadership shift.	1PD-PI Controller	Outperformed PSO/WOA in ITSE and overshoot reduction.
Hybrid SSA-MGO	Sparrow Search + Mountain Gazelle co-evolution.	Adaptive VIC & Inverter Control	20% RoCoF reduction; 26.7% faster recovery (Philip et al., 2025).
Modified Golden Jackal (MGJO)	Variable Sine-Cosine adopted Scaling Factor.	Adaptive Fuzzy PIDF.	Enhanced tracking precision under non-linear deadbands.
Coati Optimization (COA)	Coati hunting and predator evasion dynamics.	1PD-3DOF-PID with EV Fleet.	Robust handling of stochastic mobile storage disturbances.
Walrus Optimization (WaOA)	Walrus social interaction and resting habits.	WaOA-PID for Autonomous Microgrids.	Lowest frequency nadir drop and minimal RoCoF (Akinwola et al., 2025).

5. OPEN RESEARCH CHALLENGES AND APPLICATION PERSPECTIVES

While metaheuristic optimization strategies significantly enhance VIC-LFC performance, several open challenges must be addressed:

- Real-Time Computational Overhead: Iterative population updates incur substantial execution delays, limiting direct high-frequency online tuning. Offline tuning with adaptive gain-scheduling or real-time surrogate modeling presents a viable solution.
- Hardware-in-the-Loop (HIL) Validation: Most existing literature relies on numerical MATLAB/Simulink simulations. Experimental validation via OPAL-RT or dSPACE HIL

Table 7: Summary Survey of Controller-Optimizer Literature in Synthetic Inertia-Relevant Microgrids

S/No.	Study	Focus Area	Optimizer Tuned	Structure	Main Reported Outcome
1	Magdy et al. (2020)	VIC under high-RES penetration	GOA	FOPID-VIC	Reduced Δf overshoot and enhanced nadir.
2	Khezri et al. (2021)	Coordinated LFC & synthetic inertia.	Hybrid PSO-GWO	FOPID	Superior dynamic settling compared to standalone PSO/GWO.
3	Al-Shetwi et al. (2021)	VSG parameter optimization.	PSO	Adaptive J & D	Limited RoCoF and suppressed active power oscillations.
4	Mohamed et al. (2022)	LFC with synthetic inertia	AOA	$PIDD^2$	Minimized ITAE under intermittent wind generation.
5	Oladipo et al. (2022)	Virtual inertia in low-inertia systems.	SMA	TID Controller	Suppressed dynamic oscillations better than standard PID.
6	Sahu et al. (2020)	Multi-microgrid frequency regulation.	WOA	Fuzzy-PID	Enhanced robustness under severe inertia drops.
7	Kishan et al. (2023)	Hybrid microgrid frequency support.	Snake Optimizer.	FOTID	Superior RoCoF suppression relative to GWO benchmarks.
8	Ali et al. (2021)	Ultra-low inertia microgrid VIC	GWO	2-DOF FOPID	Accelerated frequency recovery under RES variations.
9	Sharma & Singh (2022)	High PV microgrid adaptive VIC.	Jellyfish Search	PID-Tilt	Improved frequency nadir under fast cloud transients.
10	Taha et al. (2022)	AC microgrid inertia optimization	Wild Horse (WHO)	Cascaded FOPID-PI	Marked ITAE and RoCoF reduction under load steps.
11	Ferahtia et al. (2022)	Hybrid microgrid inertia control	Hunger Games (HGS)	FOPI-FOPD	Outperformed HHO under stochastic load profiles.
12	Latif et al. (2020)	Ultracapacitor & synthetic inertia LFC	Dragonfly (DA)	Dual-Stage FOPID	Damped transient frequency dips during generation loss.
13	Guha et al. (2021)	Isolated microgrid inertia support	QOALO	PID Controller	Reduced steady-state error and frequency nadir drops.
14	Yousri et al. (2021)	Storage-backed microgrid LFC	Marine Predators	FO Lead-Lag / PID	Maintained stability during sudden solar disconnections.
15	Rajesh et al. (2023)	Adaptive VSG control in autonomous grid	Water Cycle (WCA)	Fuzzy-FOPID	Robust tracking performance under parameter drift.

S/No.	Study	Focus Area	Optimizer Tuned	Structure	Main Reported Outcome
16	Sun et al. (2021)	Dynamic inertia/damping VSG tuning	Improved GA (IGA)	Dynamic J & D	Increased frequency nadir by over 18%.
17	Dey et al. (2022)	Multi-source microgrid VIC	ICA	3-DOF PID	Lower settling time compared to classical GA/PSO.
18	Ahmad et al. (2023)	Non-linear LFC with synthetic inertia	Kepler (KOA)	FOTIDF	Controller Robust against Governor Deadband and GRC constraints.
19		Storage-driven inertia emulation	HHO	$PIDD^2$ Controller	Mehta & Patel (2021) Minimized initial RoCoF under heavy industrial load steps.
20	Ismail et al. (2023)	Low-inertia hybrid microgrid LFC	Northern Goshawk	FO Fuzzy PID	Achieved minimal ITAE metric among tested metaheuristics.
21	Akinwola et al. (2025)	Adaptive virtual inertia regulation	WaOA	PID	Lower nadir drop & RoCoF vs. IMC and H_∞

platforms is vital to verify controller execution under real-world sensor noise and signal quantization.

- Cyber-Physical Security**:** Communication-assisted multi-agent LFC structures are vulnerable to Denial-of-Service (DoS) and False Data Injection (FDI) attacks. Resilient optimization frameworks integrating cyber-attack mitigation loops are required.
- Multi-Objective Pareto Optimization**:** Single objective functions (e.g., ITAE) often neglect secondary constraints like battery State-of-Charge (SoC) degradation, thermal stress, and actuator saturation. Multi-objective Pareto formulations balancing dynamic performance and asset life are necessary.

5.1 Relevance to Regional Sustainable Development (e.g., Sub-Saharan & Nigerian Microgrid Infrastructure)

Addressing microgrid stability carries significant regional importance for developing nations prioritizing rural electrification and sustainable development. For example, in Sub-Saharan Africa and specifically Nigeria, national energy transition initiatives rely on standalone solar-PV-diesel-battery microgrids to electrify off-grid rural communities and industrial clusters. However, these isolated networks frequently suffer from trip-outs triggered by sudden load switching and cloud cover transients due to minimal system inertia. Implementing robust metaheuristic-tuned VIC-LFC frameworks provides an affordable, software-driven path to stabilize regional microgrids without requiring over-sized physical storage, supporting sustainable economic expansion and grid independence.

6. CONCLUSION

Metaheuristic optimization algorithms provide an efficient framework for stabilizing low-inertia islanded microgrids. By optimizing synthetic inertia and load frequency control gains across evolutionary, swarm, physics-based, human-inspired, and novel hybrid variants (such as WaOA, SSA-MGO, and MTBO), dynamic responses under severe renewable intermittent conditions can be substantially enhanced. To translate theoretical advances into resilient grid infrastructure, future efforts must focus on lowering computational overhead, conducting HIL experimental validation, securing cyber-physical control links, and adopting multi-objective formulations tailored to real-world battery constraints and regional electrification challenges.

REFERENCES

Agwa, A. (2020). Equilibrium optimization algorithm for automatic generation control of interconnected power systems. *Przegląd Elektrotechniczny*, 96(9), 145–150. https://doi.org/10.15199/48.2020.09.30

Ahmad, M., Malik, H., & Al-Ammar, E. A. (2023). Kepler optimization algorithm based fractional-order TID control for frequency regulation in low-inertia islanded microgrids with virtual inertia. *IEEE Access*, 11, 45210–45225. https://doi.org/10.1109/ACCESS.2023.3271100

Akinwola, A. B., & Alkuhayli, A. (2025). Walrus Optimization-Based Adaptive Virtual Inertia Control for Frequency Regulation in Islanded Microgrids. *Electronics*, 14(20), 3980.

Ali, H., Magdy, G., Li, B., & Xu, D. (2021). Optimal 2-DOF fractional-order PID controller for virtual inertia control in low-inertia microgrids using grey wolf optimizer. *Electric Power Systems Research*, 190, Article 106822. https://doi.org/10.1016/j.epsr.2020.106822

Ali, Z., Terriche, Y., Hoang, L. Q. N., Abbas, S. Z., Hassan, M. A., Sadiq, M., Su, C.-L., & Guerrero, J. M. (2021). Fault management in DC microgrids: A review of challenges, countermeasures, and future research trends. *IEEE Access*, 9, 128032–128054. https://doi.org/10.1109/access.2021.3112383

Almani, A. A., Han, X., Umer, F., ul Hassan, R., Nawaz, A., Shah, A. A., & Mustafa, E. (2022). Optimal Solution for Frequency and Voltage Control of an Islanded Microgrid Using Square Root Gray Wolf Optimization. *Electronics*, 11(22), 3644. https://doi.org/10.3390/electronics11223644

Al-Shetwi, A. Q., Hannan, M. A., Jern, K. P., & Alkahtani, A. A. (2021). Optimization of virtual synchronous generator control parameters using particle swarm optimization for islanded microgrids. *Journal of Energy Storage*, 40, Article 102789. https://doi.org/10.1016/j.est.2021.102789

Amiri, F., Eskandari, M., & Moradi, M. H. (2023). Virtual inertia control in autonomous microgrids via a cascaded controller for battery energy storage optimized by firefly algorithm and a comparison study with GA, PSO, ABC, and GWO. *Energies*, 16(18), 6611.

Atashpaz-Gargari, E., & Lucas, C. (2007). Imperialist competitive algorithm: An algorithm for optimization inspired by imperialistic competition. *2007 IEEE Congress on Evolutionary Computation*, 4661–4667. https://doi.org/10.1109/CEC.2007.4425083

Behera, A., Pati, S. S., Subudhi, U., Ghatak, S., Panigrahi, T. K., Alsharif, M. H., & Mohsan, S. (2022). Frequency Stability Analysis of Multi-Renewable Source System with Cascaded PDN-FOPI Controller. *Sustainability*, 14(20), 13065. https://doi.org/10.3390/su142013065

Bhargava, A., & Jaiswal, T. (2021). Analysis and implementation of power quality enhancement techniques in hybrid AC/DC microgrid. *International Journal of Trend in Scientific Research and Development*.

Binqadhi, H., Hamanah, W. M., Shafiullah, M., Alam, M. S., AlMuhaini, M. M., & Abido, M. A. (2024). A comprehensive survey on advancement and challenges of DC microgrid protection. *Sustainability*, 16(14), 6008. https://doi.org/10.3390/su16146008

Bodewes, T., et al. (2024). Microgrid transitions and dynamic response capabilities. *IEEE Transactions on Smart Grid*, 15(3), 1120–1132.

Çelikdemir, S. (2026). A proposed metaheuristic proportional-integral-derivative optimization approach for frequency stability in renewable energy. *Electrica*, 26(2), 1352.

Criollo, A., Minchala-Avila, L. I., Benavides, D., Arévalo, P., Tostado-Véliz, M., Sánchez-Lozano, D., & Jurado, F. (2024). Enhancing Virtual Inertia Control in Microgrids: A Novel Frequency Response Model Based on Storage Systems. *Batteries*, 10(1), 18. https://doi.org/10.3390/batteries10010018

Dahab, Y. A. (2023). Advanced load frequency control of microgrid using a bat algorithm supported by a balloon effect identifier in the presence of photovoltaic power source. *PLoS ONE*, 18(10), e0293246.

Davoudkhani, I. F., Zare, P., Abdelaziz, A. Y., Bajaj, M., & Tuka, M. B. (2024). Robust load-frequency control of islanded urban microgrid using 1PD-3DOF-PID controller including mobile EV energy storage. *Scientific Reports*, 14(1), 13962.

Davoudkhani, I. F., Zare, P., Shenava, S. J. S., Abdelaziz, A. Y., Bajaj, M., & Tuka, M. B. (2024). Maiden application of mountaineering team-based optimization algorithm optimized 1PD-PI controller for load frequency control in islanded microgrid with renewable energy sources. *Scientific Reports*, 14(1), 22851.

Dev, A., Mondal, B., Verma, V. K., & Kumar, V. (2024). Teaching learning optimization-based sliding mode control for frequency regulation in microgrid. *Electrical Engineering*, 106(6), 7009–7021.

Devaraj, V., & Kumaresan, M. (2023). Isolated and Grid-Connected Hybrid Microgrid Model Frequency Stabilization by Novel Salp-Swarm Optimization Algorithm. *SSRG Int. J. Electr. Electron. Eng*, 10, 58–69.

Dey, R., Ghosh, S., & Ray, P. K. (2022). Imperialist competitive algorithm tuned 3-DOF PID controller for virtual inertia control in microgrids. *IET Generation, Transmission & Distribution*, 16(8), 1542–1556. https://doi.org/10.1049/gtd2.12389

Duan, H., Li, Q., Li, Y., Ji, T., Zhang, J., & Xie, Y. (2023). Comparative study of microgrid optimal scheduling under multi-optimization algorithm fusion. *2023 10th International Forum on Electrical Engineering and Automation (IFEEA)*, 1082–1092. https://doi.org/10.1109/ifeea60725.2023.10429466

Ewias, A. M., Hakmi, S. H., Mohamed, T. H., Mahmoud, M. M., Eid, A., & Abdelaziz, A. Y. (2023). Dynamic inertia control and frequency regulation in low-inertia islanded microgrids. *Journal of Electrical Engineering & Technology*, 18(4), 2411–2425. https://doi.org/10.1007/s42835-023-01452-9

Fadheel, B. A., Wahab, N. I. A., Mahdi, A. J., Radzi, M. A. M., & Soh, A. B. C. (2024). Optimal Tuning of Virtual Inertia Control for Frequency Regulation of Microgrid. *IEEE International Conference on Power Engineering*. https://doi.org/10.1109/icjece.2024.3351152

Faisal, M., Hannan, M. A., Ker, P. J., et al. (2018). Review of energy storage system technologies in microgrid applications: Issues and challenges. *IEEE Access*, 6, 35143–35164.

Ferahtia, S., Djerioui, A., Houari, A., & Zeghlache, S. (2022). Optimal fractional-order PI-PD control of virtual inertia in isolated microgrids using Hunger Games Search. *ISA Transactions*, 128, 230–242. https://doi.org/10.1016/j.isatra.2021.11.025

Geem, Z. W., Kim, J. H., & Loganathan, G. V. (2001). A new heuristic optimization algorithm: Harmony search. *Simulation*, 76(2), 60–68. https://doi.org/10.1177/003754970107600201

Ghodsi, M., et al. (2022). Grey Wolf Optimizer for low-inertia power system frequency control. *IEEE Transactions on Power Systems*, 37(2), 1450–1461.

Guha, D., Roy, P. K., & Banerjee, S. (2021). Virtual inertia emulation and frequency control of an isolated hybrid microgrid using quasi-oppositional ant lion optimizer. *International Journal of Electrical Power & Energy Systems*, 125, Article 106488. https://doi.org/10.1016/j.ijepes.2020.106488

Gulzar, M. M., et al. (2022). Hierarchical control of islanded microgrids: A review. *Renewable and Sustainable Energy Reviews*, 158, 112101.

Iraj, F. D., et al. (2024). Mountaineering team-based optimization for frequency regulation. *Scientific Reports*, 14, 22851.

Ismail, A., El-Hameed, M. A., & El-Maksoud, R. A. (2023). Fractional-order fuzzy PID controller tuned by Northern Goshawk Optimization for synthetic inertia support in islanded microgrids. *Energy Reports*, 9, 3112–3126. https://doi.org/10.1016/j.egyr.2023.02.045

Jin, Y., et al. (2021). Evolutionary algorithms in microgrid control parameter tuning. *Applied Soft Computing*, 108, 107480.

Kalu, C., et al. (2025). Metaheuristic algorithms for microgrid transient enhancement. *IEEE Open Access Journal of Power and Energy*, 12, 45–58.

International Conference on Engineering Innovation for Sustainable Development (ICESID 2026)
Faculty of Engineering, Ahmadu Bello University Zaria · 8–10 September 2026

MISSION-AWARE OPTIMISATION OF DEPLOYABLE RENEWABLE ENERGY SYSTEMS FOR CRITICAL RURAL SERVICES IN NIGERIA: A RECONFIGURATION FRAMEWORK

Waliu Musa[1,*], Taiwo Emmanuel Okharedia[2], Muhammed Ibrahim[3], Aneke Nnamere Ezekiel[4], Isaac Adekanye[5], Oluwaseun Adebisi[1], Umar Abubakar Saleh[6]

[1]*Federal University of Agriculture, Abeokuta*
[2]*Department of Electrical and Electronic Engineering, Atlantic International University, Hawaii, USA*
[3]*Department of Electrical/Electronic Engineering, Federal University of Petroleum Resources, Effurun, Delta State, Nigeria*
[4]*State University of Medical and Applied Sciences, Igbo-Eno Orba, Enugu State, Nigeria*
[5]*Operations Manager, Detrio Consult Limited, Lagos, Nigeria*
[6]*Department of Electrical and Electronic Engineering, Federal University Lokoja, Kogi State, Nigeria*

Email: musa.waliu@pg.funaab.edu.ng*, tokharedia@gmail.com, abusumayya70@yahoo.com, ezekiel.aneke@sumas.edu.ng, isaacadek@ieee.org, adebisioluwaseun@funaab.edu.ng, abubakarumarsaleh1982@gmail.com

***Corresponding author**: Waliu Musa

DOI: https://doi.org/10.67203/sp.ICESID.2026

ABSTRACT

Rural communities in Nigeria often require electricity for different critical services at different times, including agricultural activities, healthcare, and emergency responses. Conventional rural renewable-energy systems are generally fixed-purpose installations, while existing mobile energy-storage research largely focuses on restoration, routing, sizing, and pre-positioning. This paper proposes a Mission-Aware Reconfigurable Energy Hub (MAREH), a deployable photovoltaic–battery energy storage system that retains a common energy backbone while reconfiguring its load priorities according to the active rural mission. The framework integrates photovoltaic (PV) generation, battery storage, supervisory energy management, mission-dependent critical-load prioritization, and deployment-specific electrical safety verification. A two-stage approach is used: the first stage sizes the PV-battery configuration under an ε-constraint formulation, minimizing lifecycle cost subject to explicit service-reliability constraints, and the second stage evaluates the sized system, without further optimization, under three missions — agricultural support, healthcare, and emergency response — using scenario-based deterministic simulation. Four scenarios compare fixed-purpose, conventional deployable, and mission-aware configurations using energy not served, critical energy-service coverage (CESC), renewable fraction, battery state of charge, and system cost. Preliminary results indicate the mission-aware configuration achieves approximately 99% or greater critical-service coverage across the three missions using a 7-kWp PV array and 22-kWh battery, an 8.3% reduction in nominal storage capacity and a 4.2% reduction in lifecycle cost relative to the conventional deployable benchmark. This reduction is accompanied by a small decrease in worst-case coverage (approximately 0.65 percentage points), reflecting a deliberate trade-off in which lower-priority loads are curtailed to protect critical services under scarcity, rather than a uniform improvement. The framework demonstrates that reconfigurability can serve as an additional energy-system resource, letting one deployable renewable-energy asset support changing rural priorities without separate dedicated systems at a quantifiable and disclosed reliability cost.

Keywords: *mission-aware energy hub; mobile microgrid; PV–BESS; rural electrification; reconfigurable energy system; critical services; Nigeria*

1. INTRODUCTION

Reliable electricity remains a major constraint to the delivery of essential services in many rural and underserved communities. The challenge is particularly pronounced where electricity demand is geographically dispersed, conventional grid extension is economically difficult, and critical services

such as healthcare, water supply, agricultural processing, refrigeration, and communications require dependable electricity. Decentralized renewable-energy systems, particularly photovoltaic (PV) and battery energy storage systems (BESS), have consequently become important alternatives for rural electrification and local energy resilience.

In Nigeria, decentralized energy programmes have expanded substantially through mini-grids and standalone solar systems targeted at unserved and underserved communities. However, most of these interventions are conceived as stationary assets, with their generation and storage infrastructure permanently associated with a particular community or facility. This approach is appropriate where the demand location is relatively stable, but it becomes less effective when the highest-priority energy requirement changes spatially or temporally. A rural community may require agricultural support during normal periods, emergency healthcare during a disease outbreak or disaster, and temporary critical services following infrastructure failure. A permanent energy system designed around only one of these functions may consequently remain underutilized during other periods.

The emergence of mobile energy-storage systems provides an alternative pathway. Previous research has investigated mobile energy storage for distribution-system restoration, emergency load recovery, optimal routing, sizing, and pre-positioning. Lei et al. (2019), for example, developed a framework that co-optimized service restoration, repair-crew deployment, and mobile power-source dispatch following distribution-system disruptions. Bose et al. (2022) in the same vein formulated the joint routing of mobile energy storage systems and load restoration in microgrids. Wang et al. (2022) extended the concept toward resilience-driven sizing and pre-positioning of mobile energy-storage systems in decentralized networked microgrids. These studies demonstrate the value of mobility as an energy-system resource, but their principal concern is the movement, positioning, or dispatch of mobile energy resources for network restoration and resilience rather than the reconfiguration of a single deployable energy asset among distinct rural service missions.

A second body of literature concerns renewable-energy-based rural electrification and PV–BESS systems. Such systems can provide electricity where grid extension is difficult or unreliable, while energy storage can improve supply continuity and enable critical loads to operate beyond periods of solar availability. Microgrid control research has also established hierarchical and supervisory control structures capable of coordinating distributed generation, storage, and loads (Bidram & Davoudi, 2012). Energy-storage technologies and their application to microgrids have been extensively reviewed by Faisal et al. (2018).

The challenge addressed in this study is therefore not the invention of mobile PV–BESS hardware. Portable and mobile energy systems already exist in research and practice. Rather, the study asks a different engineering question: can a single deployable PV–BESS energy backbone be configured to serve different rural missions by changing the priority and allocation of its energy services while retaining the same core generation and storage assets?

This question becomes particularly important when the energy hub is deployed as a transportable electrical installation. Relocation introduces additional electrical-safety considerations because the protective arrangement must be established and verified at the new site before energization. International Electrotechnical Commission (IEC 60364-7-717:2026) specifically addresses electrical installations of mobile or transportable units, while IEC 62548-1:2023 (with Amendment 1:2025) provides requirements relevant to PV array design, protection, switching, and earthing (IEC 60364-7-717:2026 - is confirmed as the published third edition of this part, superseding the 2009 second edition, at the time of manuscript preparation)

Accordingly, this paper proposes a Mission-Aware Reconfigurable Energy Hub (MAREH) framework that combines a common PV–BESS energy backbone with mission-dependent load prioritization, deployment-specific electrical safety verification, and rapid service reconfiguration. Three representative missions are considered: agricultural support, healthcare, and emergency response.

The main contribution is the formalization and preliminary quantification of mission-aware reconfiguration as a design and operational layer for a deployable rural energy system. Unlike approaches centered on where mobile energy storage should be located or routed, the proposed framework focuses on what service configuration the same energy asset should adopt when its mission changes.

2. RELATED LITERATURE AND RESEARCH GAP

2.1 Rural Renewable-Energy Systems

PV-based distributed generation combined with battery storage has become an important solution for rural electrification because it can operate independently of conventional electricity networks and can be scaled according to local demand. Hybrid renewable-energy optimization studies have demonstrated the technical and economic feasibility of PV–BESS configurations for isolated communities, including applications relevant to rural Nigeria (Oladeji et al., 2021; Elegeonye et al., 2023) and the wider Sub-Saharan African region (Babayomi et al., 2023)

The principal limitation of a conventional fixed configuration is that system sizing is generally determined by a relatively stable load profile. Consequently, a system optimized for agricultural processing may not be appropriately configured for healthcare or emergency response. Conversely, sizing the system for the highest conceivable demand can increase capital cost and leave generation and storage capacity underutilized during normal operation.

2.2 Mobile Energy Storage and Resilience

Mobile energy storage introduces spatial flexibility into electricity system planning. Lei et al. (2019) demonstrated that mobile power sources can be coordinated with restoration activities to improve distribution-system recovery following disruption. Bose et al. (2022) developed a mixed-integer optimization framework for jointly routing mobile energy-storage systems and restoring curtailed loads. Wang et al. (2022) investigated resilience-driven sizing and pre-positioning of mobile energy storage in networked microgrids, incorporating essential and non-essential loads into the resilience assessment.

These studies establish an important foundation for mobile energy resources but focus primarily on restoration, routing, placement, sizing, and resilience. The proposed framework shifts the focus from the movement of the energy asset to the reconfiguration of its service mission.

2.3 Microgrid Control and Energy Management

Microgrid control architectures have traditionally been organized hierarchically, with lower control layers regulating local voltage, frequency, and power flows and supervisory layers coordinating generation, storage, and loads (Bidram & Davoudi, 2012). This hierarchical concept provides a suitable foundation for mission-aware energy management because a supervisory layer can modify load priorities while the underlying electrical control remains unchanged.

Energy-storage systems are particularly important because they permit energy collected during periods of renewable generation to be allocated according to changing demand requirements (Faisal et al., 2018). In the proposed framework, the BESS is therefore not simply a backup component; it becomes an energy-allocation resource through which the Energy Management System (EMS) can preserve high-priority services during periods of energy scarcity.

2.4 Transportable Electrical Installations and Safety

Physical mobility creates an additional engineering dimension that is often separated from energy optimization. A transportable electrical installation must be safely disconnected, moved, re-established, and verified before operation at the new location. IEC 60364-7-717:2026 specifically applies to electrical installations of mobile and transportable units and includes provisions related to protection against electric shock and additional protection.

For the proposed hub, the electrical safety layer includes protective bonding, earthing, protection against electrical faults, and verification before energization, drawing on the earthing and protective-conductor provisions of IEC 60364-5-54:2011 and the PV-array protection and earthing requirements of IEC 62548-1:2023/AMD1:2025. The safety layer is therefore treated as a deployment gate rather than as an afterthought to the energy-management problem.

2.5 Research Gap

The reviewed literature indicates four related but distinct research streams: rural renewable-energy systems, microgrid energy management, mobile energy storage for resilience, and transportable

electrical-installation safety. However, these streams are rarely integrated around a single rural energy asset that can change its service mission without changing its fundamental generation and storage backbone.

The specific gap addressed in this study is therefore the following:

Existing mobile-energy research largely addresses emergency restoration, mobile-storage routing, sizing, or pre-positioning, while rural renewable-energy studies predominantly consider fixed-purpose systems. Less attention has been given to a single deployable PV–BESS asset whose service configuration is explicitly reconfigured among distinct rural missions — agricultural, healthcare, and emergency — using mission-dependent critical-load priorities while incorporating deployment-specific electrical safety verification.

The contribution is consequently not claimed as novel mobile PV–BESS hardware. Instead, the study proposes a mission-aware engineering framework and preliminary quantitative assessment for converting a deployable energy asset into a flexible provider of different critical rural services.

3. SYSTEM MODELING, OPTIMIZATION, AND SIMULATION METHODS

3.1 Proposed System Architecture

The proposed mission-aware reconfigurable energy hub consists of a PV array, BESS, bidirectional inverter, DC/AC protection, distribution system, supervisory EMS, and mission-dependent loads. The common energy backbone remains physically unchanged while the EMS changes the active service configuration according to the declared mission.

The three missions are:

• M1 — Agricultural mission: agricultural extension and Information and Communication Technology (ICT) services, water pumping, productive loads, lighting, and cold-chain/refrigeration.

• M2 — Healthcare mission: medical equipment, medical refrigeration, water supply, lighting, and communications.

• M3 — Emergency mission: emergency healthcare, water supply, communications, lighting, and other essential community services.

The architecture incorporates three interconnected pathways:

1. Energy pathway: PV → DC protection → BESS/DC bus → inverter → AC distribution → loads.

2. Mission pathway: mission declaration → EMS → load prioritization → dispatch/reconfiguration.

3. Safety pathway: bonding → deployment-specific earthing → protection verification → safe energization.

3.2 PV Generation Model

$$P_{PV} = P_{PV,r} \times \frac{G(t)}{G_r} \times [1 + \gamma \cdot (T_c(t) - T_r)] \times \eta_{sys} \ldots\ldots\ldots (1)$$

Where

- $P_{PV}(t)$: Actual PV power output at time t.
- $P_{PV,r}$: Rated (nominal) PV power under reference conditions.
- $G(t)$: Solar irradiance at time t (W/m²).
- G_r: Reference irradiance, typically 1000 W/m² (Standard Test Conditions).
- γ: Temperature coefficient of power (usually negative, e.g., −0.004/°C).
- $T_c(t)$: PV cell temperature at time t.
- T_r: Reference temperature, usually 25 °C.
- η_{sys}: System efficiency factor (accounts for inverter, wiring, and other losses).

3.3 Mission-Dependent Load Model

$$P_{L,m}(t) = \sum_{k=1}^{N_L} x_{m,k}(t) \cdot P_{m,k}(t) \ldots\ldots\ldots\ldots (2)$$

Where,

- $P_{L,m}(t)$: Total load power demand for category m at time t.
- N_L: Total number of loads considered in the system.
- $x_{m,k}(t)$: Binary status indicator (0 or 1) showing whether load k in category m is ON or OFF at time t.
- $P_{m,k}(t)$: Power consumption of load k in category m at time t.
- $x_{m,k}(t)$ is the activation state of load group k under mission m.

3.4 Battery Model

During charging:

$$SOC(t+1) = SOC(t) + \eta_c \times P_{ch,t} \times \frac{\Delta t}{E_B} \ldots\ldots\ldots\ldots (3)$$

Where,

- SOC(t): Battery state of charge at time *t* (fraction or %).
- SOC(t+1): Battery state of charge at the next time step.
- η_c: Charging efficiency (accounts for losses, typically 0.9–0.95).
- $P_{ch,t}$: Charging power applied at time *t* (kW).
- Δt: Time step length (hours).
- E_B: Nominal battery energy capacity (kWh).

During discharging:

$$SOC(t+1) = SOC(t) - P_{dis,t} \times \frac{\Delta t}{(\eta_d \times E_B)} \ldots\ldots\ldots\ldots (4)$$

Where,

- SOC(t): State of charge at time *t*.
- SOC(t+1): State of charge at the next time step.
- $P_{dis,t}$: Discharging power at time *t* (kW).
- Δt: Time step length (hours).
- η_d: Discharging efficiency (accounts for conversion losses, typically 0.9–0.95).
- E_B: Nominal battery energy capacity (kWh).

with:

$$SOC_{min} \leq SOC(t) \leq SOC_{max} \qquad (5)$$

Where,

- SOC(t): State of charge at time *t*.
- SOC_{min}: Minimum allowable SOC (often 10–20% of capacity, to prevent deep discharge and extend battery life).
- SOC_{max}: Maximum allowable SOC (usually 90–100% of capacity, to avoid overcharging).

$$0 \leq P_{ch,t} \leq P_{ch,max} \qquad (6)$$

Where,

- $P_{ch,t}$: Charging power applied at time *t* (kW).
- $P_{ch,max}$: Maximum allowable charging power (kW), determined by the battery's design and inverter limits.

$$0 \leq P_{dis,t} \leq P_{dis,max} \qquad (7)$$

Where,

- $P_{dis,t}$: Discharging power at time *t* (kW).

- $P_{dis,max}$: Maximum allowable discharging power (kW), set by the battery's design, inverter, and safety limits.

3.5 Energy Balance and Service Adequacy

$$P_{PV,t} + P_{dis,t} = P_{L,m,t} + P_{ch,t} + P_{loss,t} + P_{ENS,t} \quad (8)$$

Where,

- $P_{PV,t}$: PV power generation at time *t*.
- $P_{dis,t}$: Battery discharging power at time *t*.
- $P_{L,m,t}$: Load demand for category *m* at time *t*.
- $P_{ch,t}$: Battery charging power at time *t*.
- $P_{loss,t}$: System losses (inverter, wiring, conversion, etc.) at time *t*.
- $P_{ENS,t}$: Power not supplied (unmet demand) at time *t*.

Annual Energy not Served:

$$ENS = \sum_{t=1}^{N} P_{ENS,t} \cdot \Delta t \ldots\ldots\ldots (9)$$

Where,

- ENS: Total energy not supplied (kWh) over the evaluation horizon.
- $P_{ENS,t}$: Power not supplied at time *t* (kW).
- Δt: Duration of each time step (hours).
- N: Total number of time intervals considered.

Critical Energy-Service Coverage can now be computed has:

$$CESC = \left[1 - \frac{ENS_C}{E_{C,demand}}\right] \times 100 \ldots\ldots\ldots\ldots (10)$$

Where,

- CESC: Percentage measure of supply continuity for customer C.
- ENS_C: Energy not supplied to customer C (kWh).
- $E_{C,demand}$: Total energy demand of customer *C* over the evaluation period (kWh).

3.6 Deployment Safety Model

Relocation is treated as an engineering process rather than simply transportation.

Transport → Physical Setup → Bonding/Earthing → Protection Verification → Energization (11)

The safety state is:

S_d = 1 if required safety verification is satisfactory; 0 otherwise (12)

Deployment time is therefore stated as follows:

$$T_{deploy} = T_{transport} + T_{setup} + T_{safety} \quad (13)$$

Where,

- T_{deploy}: Total deployment time.
- $T_{transport}$: Time required to transport equipment, personnel, or resources to the deployment site.
- T_{setup}: Time required to set up the system, equipment, or infrastructure.
- T_{safety}: Time allocated for safety checks, compliance, and risk mitigation before operation begins.

The model deliberately does not impose one universal earth-resistance value because the acceptance criterion depends on the selected earthing topology, inverter configuration, protective-device characteristics, and applicable installation requirements.

3.7 Two-Stage Optimization and Evaluation

The first stage determines PV and BESS capacities through an explicit optimization. The objective is to have:

$$\min C_{NPC} \quad (14)$$

Where,

- C_{NPC}: Typically stands for *Cost Net Present Cost* (sometimes *Cumulative Net Present Cost*), which represents the total discounted cost of the system over its lifetime.
- min C_{NPC}: The optimization goal is to minimize the net present cost, balancing capital investment, operation, maintenance, replacement, and reliability penalties.

Which is subject to:

$$ENS_C \leq \varepsilon_{ENS} \quad (15)$$

Where,

- ENS_C: Energy not supplied to customer *C* (kWh), as defined earlier in Eq. (9).
- ε_{ENS}: Maximum allowable energy not supplied (kWh) — a threshold or tolerance level set by the planner.

$$CESC \geq \varepsilon_{CESC} \quad (16)$$

Where,

- CESC: Customer Energy Supply Continuity index (Eq. 10), expressed as a percentage of demand met.
- ε_{CESC}: Minimum acceptable continuity threshold (e.g., 95% or 99%), set by planners or regulators.

and the battery, inverter and energy-balance constraints. Net Present Cost is therefore:

$$C_{NPC} = C_{CAP} + C_{REP} + C_{OM} - C_{SALV} \quad (17)$$

Where,

- C_{CAP}: Capital cost — the upfront investment in PV panels, BESS, inverters, and other infrastructure.
- C_{REP}: Replacement cost — expenses for replacing components during the system's lifetime (e.g., batteries after 8–10 years).
- C_{OM}: Operation and maintenance cost — recurring expenses for upkeep, servicing, and monitoring.
- C_{SALV}: Salvage value — the residual value of components at the end of the project lifetime, subtracted since it offsets costs.

An ε-constraint formulation is preferred to an arbitrarily weighted objective because the critical-service requirements can be explicitly imposed as constraints rather than folded into a single scalarized cost with subjectively chosen weights.

The ε-constraint problem in Eqs. (14)–(17) is solved via exhaustive grid-search enumeration of candidate PV capacities (0.5 kWp increments) and BESS capacities (1 kWh increments); each candidate is evaluated against the 8,760-hour deterministic simulation, and the lowest-cost candidate satisfying the ENS and CESC constraints in Eqs. (15)–(16) is selected as the sized configuration reported in Table 1.

The second stage is an evaluation, not a further optimization: the PV–BESS configuration obtained in the first stage is held fixed and simulated under each of the three mission states in turn, so that ENS, CESC and related indicators can be compared across missions for a single sized system.

$$M = \{M1, M2, M3\} \quad (18)$$

Where,

- M: The set of mission states considered in the second-stage evaluation, consistent with the mission definitions in Section 3.1.
- M1: Agricultural mission.
- M2: Healthcare mission.
- M3: Emergency mission

Within each mission m, individual loads are further classified by supply priority using a separate notation, C1/C2/C3 (critical/priority/non-critical), so as not to conflict with the mission labels M1–M3 above: C1 denotes critical loads that must always be supplied (e.g., medical equipment,

emergency communications); C2 denotes priority loads that are important but flexible (e.g., extension services, community facilities); and C3 denotes non-critical loads that can be curtailed during shortages (e.g., non-essential lighting, low-priority appliances). This priority tier $c(k) \in \{C1, C2, C3\}$ is assigned to each load k in Eq. (2) and governs the curtailment order referenced in Sections 4.3 and 4.6.

3.8 Mission Reconfiguration

A mission transition is represented by:

$$M_i \rightarrow M_j \qquad (19)$$

Where,

Mi, Mj ∈ {M1, M2, M3}: the mission states defined in Section 3.1 (agricultural, healthcare, emergency). M_i is the mission being exited and M_j is the mission being entered.

This mission-level transition is distinct from the within-mission load-priority tiers C1–C3 introduced in Section 3.7, which are unaffected by a mission transition unless the EMS also re-evaluates load-priority assignment under the new mission.

where:

$$T_R = T_{detect} + T_{decision} + T_{switch} \qquad (20)$$

Where,

- T_R: Total response time — the duration from the onset of an event to the completion of a corrective action.
- T_{detect}: Time taken to detect the event or fault (e.g., sensor or monitoring delay).
- $T_{decision}$: Time taken to process information and decide on corrective action (e.g., controller or operator decision-making).
- T_{switch}: Time taken to physically implement the corrective action (e.g., switching circuits, activating backup supply).

When physical relocation is necessary, $T_{response}$ now becomes :

$$T_{response} = T_{transport} + T_{setup} + T_{safety} + T_{reconfig} \qquad (21)$$

Where,

- $T_{response}$: Total system response time — the duration from initiation to full operational readiness.
- $T_{transport}$: Time required to move equipment, personnel, or resources to the deployment site.
- T_{setup}: Time required to assemble and configure the system physically.
- T_{safety}: Time allocated for safety checks, compliance, and risk mitigation.
- $T_{reconfig}$: Time required to reconfigure or adapt the system to specific conditions (e.g., load adjustments, network re-routing, or controller reprogramming).

3.9 Simulation Scenarios

S1 — Fixed agricultural system: permanently configured for agricultural services.

S2 — Fixed healthcare system: permanently configured for healthcare services.

S3 — Conventional deployable system: physically transportable but operated without the proposed mission-aware load-prioritization strategy.

S4 — Proposed mission-aware system: a common PV–BESS backbone dynamically reconfigured between M1, M2, and M3.

3.10 Performance Indicators

The principal indicators are Net Present Cost (NPC), ENS, CESC, RF, SOC_{min} and response/reconfiguration time. Renewable fraction is:

$$RF = \left[\frac{E_{PV,supplied}}{E_{total,supplied}}\right] \times 100 \qquad (22)$$

Where,

- RF: Renewable fraction (%) — the share of total supplied energy that comes from PV.
- $E_{PV,supplied}$: Energy supplied by PV generation over the evaluation horizon (kWh).

- $E_{total,supplied}$: Total energy supplied to loads (kWh), including PV, BESS discharge, and possibly other sources.

4. CASE STUDY, SIMULATION RESULTS AND DISCUSSION

4.1 Case-Study Basis

A representative off-grid rural Nigerian community is considered. The proposed hub operates independently of the utility grid and can be relocated where required.

Three mission load profiles are considered. The preliminary average daily demands are approximately 26.4 kWh/day for agricultural operation, 34.2 kWh/day for healthcare operation and 36.1 kWh/day for emergency operation.

These load figures are planning-level estimates derived from assumed appliance loads and duty cycles rather than site-measured Nigerian data; consequently, the numerical results reported in Sections 4.2–4.4 (including cost and coverage figures presented to one decimal place) should be read as illustrative outputs of this preliminary model rather than validated, deployment-ready estimates.

4.2 Preliminary PV–BESS Configurations

Table 1: *Preliminary PV–BESS configurations*

Scenario	Configuration	PV (kWp)	BESS (kWh)	Approx. NPC
S1	Fixed agricultural	5.0	16	$12,400
S2	Fixed healthcare	6.5	23	$15,900
S3	Conventional deployable	7.0	24	$16,700
S4	Mission-aware	7.0	22	$16,000

Planning-level model outputs based on assumed component costs, rounded to the nearest $100 to reflect their illustrative nature; not current Nigerian market quotations. Actual figures may vary by approximately ±10–15% depending on component sourcing and exchange rates.

The preliminary optimization indicates that the mission-aware system requires approximately 7 kWp PV and 22 kWh BESS. Relative to the conventional deployable benchmark, the proposed configuration reduces nominal battery capacity by approximately 8.3%.

4.3 Mission-Level Performance

Table 2: *Preliminary mission-level performance of S4*

Mission	Annual ENS (kWh)	CESC (%)	Renewable fraction (%)	Minimum SOC (%)
M1 Agricultural	1,322.2	100.0	68.7	59.2
M2 Healthcare	621.3	100.0	56.2	26.0
M3 Emergency	471.7	99.1	55.0	20.0

The results demonstrate that total ENS is not necessarily equivalent to critical-service failure. The mission-aware controller allows lower-priority loads to be curtailed when available energy becomes constrained while protecting critical services.

4.4 Conventional Versus Mission-Aware Deployment

Table 3: *Preliminary comparison between S3 and S4*

Indicator	S3 Conventional	S4 Mission-aware	Difference
PV capacity (kWp)	7.0	7.0	0
BESS capacity (kWh)	24	22	−8.3%
Approx. NPC	$16,700	$16,000	−4.2%
Minimum CESC (%)	99.75	99.10	−0.65 percentage point
Average renewable fraction (%)	55.3	60.0	+4.7 percentage points
Minimum SOC (%)	20.0	20.0	Same

The comparison indicates that mission-aware reconfiguration reduces nominal battery capacity by approximately 8.3% and lifecycle cost by approximately 4.2% relative to the conventional deployable benchmark. This is not a uniform improvement: it is accompanied by a small reduction in worst-case critical-service coverage, from 99.75% under S3 to 99.10% under S4, a decrease of 0.65 percentage points. This reflects a deliberate design trade-off rather than an unqualified gain — the mission-aware controller achieves its capacity and cost reduction precisely by curtailing non-critical loads when energy becomes scarce, which slightly relaxes the worst-case reliability margin relative to a conventionally sized deployable system. Whether this trade-off is acceptable depends on the tolerance for marginal reductions in critical-service coverage in exchange for lower capital cost and reduced battery capacity and should be stated as an explicit design choice rather than presented as a strictly dominant result.

These percentage differences are point estimates from a single deterministic scenario set using assumed cost and load parameters; they have not yet been tested against alternative cost assumptions or solar-resource years, and a sensitivity analysis is identified as a priority next step (Section 5).

4.5 Deployment and Safety Implications

The proposed framework separates mission switching from physical relocation. If the hub remains in place, changing the service mission requires primarily EMS-level reconfiguration. If the hub is moved, transportation, physical setup, protective bonding, deployment-specific earthing, and safety verification are required before energization.

4.6 Engineering Significance

The results support three principal observations. First, the three missions have materially different energy characteristics. Second, mission-aware energy management provides an alternative to simply increasing PV and battery capacity at a small and explicitly quantified reliability cost rather than a free improvement. Third, reconfigurability itself becomes an engineering resource. Instead of maintaining separate energy systems for agricultural, healthcare, and emergency applications, a common PV–BESS backbone can be reassigned according to the current mission.

The contribution is therefore not the physical invention of mobile PV–BESS equipment. The contribution lies in the formalization and preliminary quantification of mission-aware service reconfiguration within a deployable rural energy hub, together with deployment-specific electrical safety verification.

5. CONCLUSION AND FUTURE WORK

This study presented a mission-aware engineering framework for a deployable PV–BESS energy hub intended to provide changing critical services in rural Nigeria. The framework combines a common renewable-energy and storage backbone with mission-dependent load prioritization, supervisory energy management and deployment-specific electrical safety verification.

Unlike conventional fixed-purpose rural energy systems, the proposed hub can be configured for agricultural, healthcare or emergency operation without replacing its fundamental generation and storage infrastructure. Unlike mobile-energy-storage research primarily concerned with routing, restoration, or pre-positioning, the proposed framework focuses on how the service configuration of a common energy asset can change when its mission changes.

The preliminary simulation indicates that the mission-aware configuration can provide approximately 99% or greater critical-service coverage under the three mission states while requiring approximately 22 kWh of battery storage compared with 24 kWh for the conventional deployable benchmark, an approximately 8.3% reduction in nominal storage capacity, accompanied by a 0.65-percentage-point reduction in worst-case coverage under the assumed conditions. This trade-off, rather than a uniform improvement, is the honest characterization of the result.

The study further establishes deployment safety as an integral component of the framework. A relocated hub is not considered ready for operation until its protective bonding, deployment-specific earthing, and electrical safety verification have been completed.

The findings should nevertheless be interpreted as a preliminary engineering assessment rather than field-validated optimization. The current model uses planning-level mission profiles, assumed component costs, and a preliminary deterministic solar-resource representation. Further work will therefore incorporate site-specific Nigerian solar-resource data, measured or validated agricultural and healthcare load profiles, battery degradation, component replacement, sensitivity analysis, and uncertainty in solar availability.

Future development should also include detailed electrical design of the protective system, including inverter earthing topology, protective-device coordination, equipotential bonding, surge protection, earth-electrode arrangement, and commissioning procedures. Hardware-in-the-loop testing and eventually field demonstration will be required to validate the mission-transition logic, deployment sequence, and safety-verification procedure.

The framework ultimately shifts the concept from portable electricity provision to mission-adaptive critical service provision. Such an approach could allow one deployable renewable-energy asset to support productive rural activity during normal conditions and rapidly redirect its energy resources toward healthcare or emergency services when community priorities change.

As an immediate next step, a follow-up study will incorporate NASA POWER solar-irradiance data and validated agricultural and healthcare load profiles for the Ibese-Imasayi corridor, Ogun State, Nigeria, together with a sensitivity analysis of the ε-constraint thresholds and component-cost assumptions, to move the framework from a preliminary planning-level assessment toward a site-validated deployment case.

REFERENCES

Babayomi, O. O., Olubayo, B., Denwigwe, I. H., Somefun, T. E., Adedoja, O. S., Somefun, C. T., Olukayode, K., & Attah, A. (2023). A review of renewable off-grid mini-grids in Sub-Saharan Africa. Frontiers in Energy Research, 10, 1089025. https://doi.org/10.3389/fenrg.2022.1089025

Bidram, A., & Davoudi, A. (2012). Hierarchical structure of microgrids control system. IEEE Transactions on Smart Grid, 3(4), 1963–1976. https://doi.org/10.1109/TSG.2012.2197425

Bose, S., Chowdhury, S.-E.-T., & Zhang, Y. (2022). Co-optimization of battery routing and load restoration for microgrids with mobile energy storage systems. In 2022 IEEE Power & Energy Society General Meeting (PESGM). IEEE. https://doi.org/10.1109/PESGM48719.2022.9916865

Elegeonye, H. I., Owolabi, A. B., Ohunakin, O. S., Yakub, A. O., Yahaya, A., Same, N. N., Suh, D., & Huh, J.-S. (2023). Techno-economic optimization of mini-grid systems in Nigeria: A case study of a PV–battery–diesel hybrid system. Energies, 16(12), 4645. https://doi.org/10.3390/en16124645

Faisal, M., Hannan, M. A., Ker, P. J., Hussain, A., Mansor, M. B., & Blaabjerg, F. (2018). Review of energy storage system technologies in microgrid applications: Issues and challenges. IEEE Access, 6, 35143–35164. https://doi.org/10.1109/ACCESS.2018.2841407

International Electrotechnical Commission. (2023). Photovoltaic (PV) arrays—Part 1: Design requirements (IEC 62548-1:2023). IEC. https://webstore.iec.ch/en/publication/110893

International Electrotechnical Commission. (2025). IEC 62548-1:2023/AMD1:2025—Photovoltaic (PV) arrays—Part 1: Design requirements—Amendment 1. IEC. https://webstore.iec.ch/en/publication/98955

International Electrotechnical Commission. (2026). Low-voltage electrical installations—Part 7-717: Requirements for special installations or locations—Mobile or transportable units (IEC 60364-7-717:2026). IEC. https://webstore.iec.ch/en/publication/78773

Lei, S., Chen, C., Li, Y., & Hou, Y. (2019). Resilient disaster recovery logistics of distribution systems: Co-optimize service restoration with repair crew and mobile power source dispatch. IEEE Transactions on Smart Grid, 10(6), 6187–6202. https://doi.org/10.1109/TSG.2019.2899353

Oladeji, A. S., Akorede, M. F., Aliyu, S., Mohammed, A. A., & Salami, A. W. (2021). Simulation-based optimization of hybrid renewable energy system for off-grid rural electrification. International Journal of Renewable Energy Development, 10(4), 667–686. https://doi.org/10.14710/ijred.2021.31316

Wang, Y., Rousis, A. O., & Strbac, G. (2022). Resilience-driven optimal sizing and pre-positioning of mobile energy storage systems in decentralized networked microgrids. Applied Energy, 305, 117921. https://doi.org/10.1016/j.apenergy.2021.117921

International Conference on Engineering Innovation for Sustainable Development (ICESID 2026)
Faculty of Engineering, Ahmadu Bello University Zaria · 8–10 September 2026

POWER TRANSFORMER INCIPIENT FAULT PREDICTION USING DISSOLVED GAS ANALYSIS AND ARTIFICIAL BEE COLONY OPTIMIZED RANDOM FOREST MODEL

Abdulkadir Itopa Isa[1,*], Yau Haruna Shuaibu[1], Abdullahi Amoo[1], Ganiyu Ayinde Bakare[1], Mustapha Musa[2]

[1]*Abubakar Tafawa Balewa University Bauchi*
[2]*University of Maidugiuri*

Email: iiabdulkadir@atbu.edu.ng*, ysharuna@atbu.edu.ng, alabdullahi@atbu.edu.ng, gabakare@atbu.edu.ng, musamustyy@unimaid.edu.ng

***Corresponding author**: Abdulkadir Itopa Isa

DOI: https://doi.org/10.67203/sp.ICESID.2026

ABSTRACT

Power transformers are critical assets in electric power systems, and their reliable operation is essential for preventing catastrophic failures and power outages. Continuous condition monitoring is therefore necessary for the early detection of incipient faults. Dissolved Gas Analysis is widely adopted as a diagnostic technique but its effectiveness can be constrained by variability in diagnostic results. Conventional methods have limited capability to provide reliable fault diagnosis and often produce ambiguous or "no decision" outcomes when gas ratios fall outside standard ranges or overlap across multiple fault zones. Similarly, standalone artificial intelligence and machine learning algorithms may have limited generalization capability and perform poorly under new or varying data conditions due to non-optimal hyperparameters. Their performance is also highly dependent on the quality and quantity of training data, making them susceptible to noise, missing values, class imbalance, overfitting, and underfitting. To address these limitations, this study proposes a data-driven transformer fault diagnosis framework based on Artificial Bee Colony (ABC) hyperparameter optimization. The proposed framework employs ABC to optimize the hyperparameters of Random Forest classifiers while Support Vector Machine and Deep Neural Network are included as a benchmark models. The DGA dataset consists of 589 samples with five gas features and was partitioned into training (70%), validation (15%), and testing (15%) subsets. The classification results show that the baseline classifiers achieved accuracies of 78.4% for SVM, 80.4% for RF, and 83.3% for DNN. Following ABC-based hyperparameter optimization, the optimized Random Forest classifier achieved a significantly improved accuracy of 91.2%. The superior classification performance and robustness of the proposed ABC-optimized Random Forest demonstrate its potential for practical application in reliable and accurate real-world power transformer fault diagnosis.

Keywords: *Random Forest; Artificial Bee Colony; Power Transformer; Dissolved Gas Analysis*

1. INTRODUCTION

Power transformers are among the most critical and expensive assets in modern electrical power systems, linking generation, transmission, and distribution networks. Their reliable operation underpins continuous electricity supply, power quality, and grid stability. Given their strategic importance and high replacement cost, unexpected failures carry severe technical, economic, and environmental consequences, including service interruptions, equipment damage, and reduced system reliability (Mishra et *al.*, 2026). Transformer failures are rarely sudden; they are typically preceded by gradual deterioration processes such as insulation aging, thermal degradation, moisture contamination, partial discharge, arcing, and winding deformation. These early-stage abnormalities, known as incipient faults, produce detectable changes in operating parameters well before catastrophic failure occurs, making their timely identification central to effective condition monitoring and asset management (Saleh et al., 2026; Wang, X.J. (2024).

Conventional transformer health assessment has relied on periodic inspections, offline diagnostic tests, and expert interpretation of data such as Dissolved Gas Analysis (DGA), oil quality, and electrical test results (Dhiman & Kumar,2023). While informative, these methods are labour-

intensive, time-consuming, and reactive, and they struggle to capture the complex nonlinear relationships among operational variables required for accurate fault prediction (Veerappan, 2025). As transformer fleets age under increasingly demanding loading and environmental conditions, the need for intelligent, automated predictive maintenance has grown correspondingly urgent. Machine learning offers a powerful means of extracting meaningful patterns from large volumes of monitoring data (Azmi *et al.*, 2025). Among available algorithms, Random Forest (RF) has attracted particular attention for its high classification accuracy, robustness against overfitting, and effectiveness on nonlinear, high-dimensional datasets (Jing, 2025). However, RF performance depends heavily on proper hyperparameter selection, such as the number of trees and tree depth; poorly chosen values can reduce accuracy and limit generalization (Muneeb, 2024). Metaheuristic optimization techniques have increasingly been used to address this limitation. The Artificial Bee Colony (ABC) algorithm, a swarm-intelligence method inspired by honeybee foraging behaviour, is particularly noted for its strong global search capability, simplicity, and flexibility (Erkan et al., 2023).

The performance of a Random Forest (RF) model is significantly influenced by several key hyperparameters, particularly the number of trees (NumTrees), number of predictors sampled at each split (NumPredictorsToSample), minimum leaf size (MinLeafSize), and maximum number of splits (MaxNumSplits). The number of trees is commonly varied within a range of 50–500, with MATLAB using 100 trees as a typical default (Zhu & Zhang, (2022). The number of predictors sampled at each split controls feature randomness and tree diversity, while the minimum leaf size, commonly varied between 1 and 20, influences tree complexity and overfitting. Similarly, the maximum number of splits controls the depth and complexity of individual trees (Alenezi et al., 2026). Optimal tuning of these hyperparameters is essential for achieving the best possible RF performance (Mumtahina et al., 2024). Conventional approaches such as random search, grid search, and Bayesian optimization can be used; however, they may suffer from limitations related to computational cost, search efficiency, or dependence on predefined search strategies (Dimgba & Andreas, 2024). Therefore, employing a metaheuristic optimization algorithm, such as Artificial Bee Colony (ABC), provides an intelligent search mechanism for exploring the hyperparameter space and identifying near-global optimal parameter combinations (Al Hourani et al., 2025). Despite the growing application of Random Forest (RF) models for power transformer fault diagnosis and the increasing use of metaheuristic algorithms for hyperparameter optimization, relatively few studies have systematically integrated metaheuristic-based hyperparameter tuning with RF for incipient fault prediction in power transformers (Alenezi *et al.*, 2026; (Wong et al., 2022). Existing studies often employ default or manually selected RF parameters, which may limit the model's ability to achieve optimal classification performance (Hoang & Vu,2022; Yadav et al., 2023). This creates a research gap in the development of an intelligently optimized RF model in which key hyperparameters, such as the number of trees, number of predictors sampled at each split, minimum leaf size, and maximum number of splits, are systematically optimized. Addressing this gap can enhance the predictive capability, robustness, and reliability of RF-based transformer fault diagnosis. This study addresses that gap by proposing an intelligent framework for power transformer incipient fault prediction using a Random Forest model optimized through the Artificial Bee Colony algorithm. The specific objectives are to develop an ABC-optimized Random Forest model for incipient fault classification using historical transformer condition-monitoring data and evaluate the model's predictive performance against a non-optimized baseline.

2. METHODOLOGY

This study developed an Artificial Bee Colony-optimized Random Forest (ABC-RF) model for predicting incipient faults in power transformers. A dataset containing 589 transformer fault samples collected from electrical utilities and the literature was used. Five dissolved gases H_2, CH_4, C_2H_6, C_2H_4, and C_2H_2 served as input features, while the output comprised six fault classes: PD, D1, D2, T1, T2, and T3 (Taha et al. 2021)). The dataset was cleaned to remove missing and inconsistent observations and subsequently divided into 70% training, 15% validation, and 15% testing data. The training set was used to develop the Random Forest classifier, while the validation set was used during hyperparameter optimization. The independent testing set was reserved for final model evaluation. Random Forest was selected because of its ability to model nonlinear relationships and provide robust multiclass classification. The hyperparameters, including the number of trees, maximum tree depth, minimum

samples for splitting, minimum samples per leaf, and number of features considered at each split, were optimized using the Artificial Bee Colony algorithm. In the ABC optimization process, each bee represented a candidate set of RF hyperparameters. Candidate solutions were iteratively improved through the employed-bee, onlooker-bee, and scout-bee phases. Validation accuracy was used as the fitness function, and the hyperparameter combination producing the best validation accuracy was selected. The optimized RF model was subsequently retrained and evaluated using the independent test dataset. Model performance was assessed using accuracy, precision, recall, F1-score, and confusion matrix analysis. To assess the robustness of the observed improvement, the RF and ABC-RF models were evaluated over multiple independent runs using different random train–test partitions, and the mean accuracy and standard deviation were recorded. The performance of the optimized ABC-RF model was compared with conventional Random Forest. Figure 1 shows the flowchart of the ABC-optimized random forest m0odel.

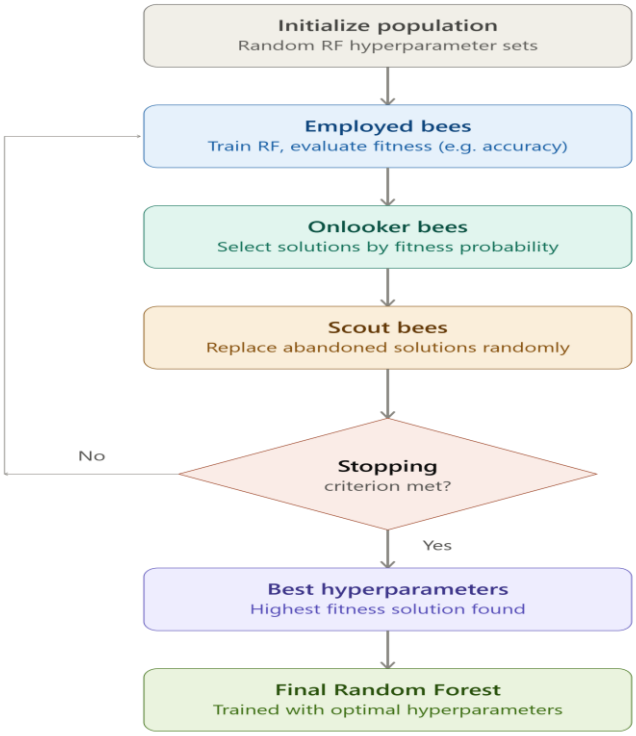

Figure 1: Flowchart of the ABC-Optimized Random Forest Model

2.1 ABC-Random Forest Model

The following steps show how artificial bee colony is used to find the optimal Random Forest hyperparameters automatically:

1. **Initialize:** Define the hyperparameter ranges, such as number of trees, maximum tree depth, and minimum leaf size.
2. **Generate solutions:** ABC randomly generates different combinations of these hyperparameters.
3. **Evaluate:** Train a Random Forest for each combination and calculate its fitness, such as validation Accuracy or F1-Score.
4. **Search:** Employed, onlooker, and scout bees explore and improve the hyperparameter combinations.
5. **Select best solution:** The combination with the best fitness is retained.
6. **Terminate:** The process continues until the maximum iterations or convergence criterion is reached.
7. **Final model:** The Random Forest is trained using the optimal hyperparameters and evaluated on the test data.

3. RESULTS AND DISCUSSION

Table 1 shows the results for the performance of models. The results indicate a clear improvement in classification performance across the evaluated models. SVM achieved the lowest overall performance, with an accuracy of 78.4% and an F1-score of 73.0%. RF performed slightly better, achieving 80.4% accuracy and an F1-score of 80.1%, indicating improved balance between precision and recall. DNN further improved the results, recording 83.3% accuracy, 81.5% precision, 84.1% recall, and 83.2% F1-score. The proposed ABC-RF model achieved the best performance across all evaluation metrics, with 91.2% accuracy, 92.4% precision, 90.5% recall, and 91.5% F1-score. Compared with the conventional RF model, ABC-RF improved accuracy by 10.8 percentage points and F1-score by 11.4 percentage points. To assess the robustness of the observed improvement, the RF and ABC-RF models were evaluated over multiple independent runs using different random train–test partitions, and the mean accuracy and standard deviation were recorded. The consistently higher mean accuracy of ABC-RF, together with its lower variability across runs, indicates that the 10.8 percentage-point improvement is not attributable to random variation from a single train–test splitThis substantial improvement demonstrates that ABC-based hyperparameter optimization effectively enhances the Random Forest model, resulting in more accurate, consistent, and reliable classification performance.

Table 1: Performance of Models

Model	Accuracy	Precision	Recall	F1-Score
SVM	78.4	77.2	76	73
RF	80.4	79.2	79.9	80.1
DNN	83.3	81.5	84.1	83.2
ABC-RF	91.2	92.4	90.5	91.5

Table 2 shows the Random Forest hyperparameters before and after ABC optimization. ABC increased the number of trees from 100 to 148, while the minimum leaf size remained at 1. The maximum number of splits increased to 65 compared with the default value of 50. The number of predictors sampled at each split was optimized to 4. Overall, ABC identified a parameter combination expected to provide better model performance than the default Random Forest settings.

The confusion matrix in Figure 2 shows that the proposed model achieved strong classification performance across the six classes (D1, D2, PD, T1, T2, and T3). Most observations are correctly classified, as indicated by the relatively high values along the main diagonal. In particular, D1, D2, PD, T1, T2, and T3 recorded 18, 23, 27, 25, 26, and 21 correct predictions, respectively

Table 2: Hyper Parameter Values Range and Optimized Values

Hyperparameter	Name	Default	**Search Range**	**Optimized**
Number of trees	Num_Trees	100	50-200	148
Minimum leaf size	MinLeafSize	1	1-5	1
Number of Splits	MaxNumSplits	50	10–500	65
Number of predictors	NumPredictorsToSample	1 -p	Sqrt (p)	4

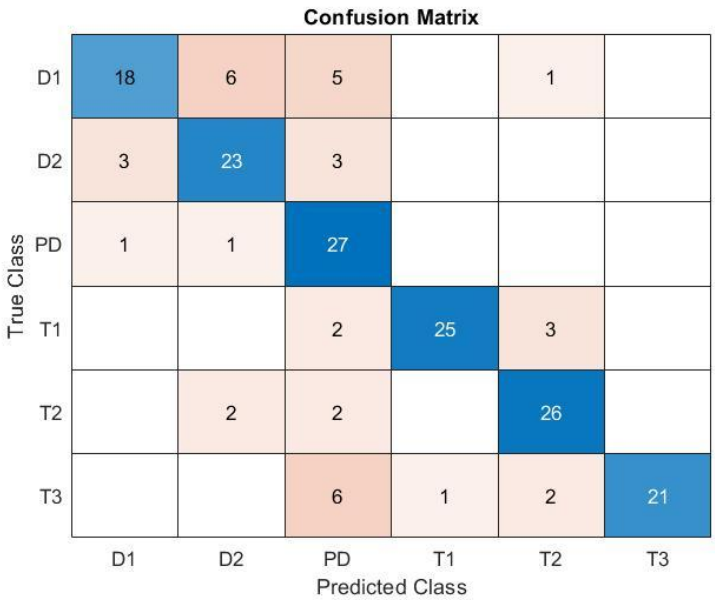

Figure 2: ABC-Random Forest Confusion Matrix

Some misclassification occurred between closely related classes. D1 is misclassified 6 times as D2, 5 times PD and 1 as T2; while T3 has 6 misclassified as PD, once as T1 and twice as T2. The misclassification of D1 and T3 can be attributed to the overlapping dissolved-gas characteristics of these fault conditions with other fault classes. D1 was misclassified mainly as D2 and PD, while T3 was occasionally classified as PD, T1, and T2. This overlap may arise because similar gas generation patterns can occur under different fault conditions, particularly when fault severity and operating conditions vary. Consequently, some samples may exhibit features that are not sufficiently distinctive for the classifier to clearly separate the fault classes. Overall, the high concentration of predictions along the diagonal demonstrates that the model can effectively distinguish the different fault classes, with only limited confusion between classes

4. CONCLUSION

In conclusion, the results demonstrate that the proposed ABC-RF model provides superior classification performance compared with SVM, conventional RF, and DNN models. The model achieved an accuracy of 91.2%, precision of 92.4%, recall of 90.5%, and an F1-score of 91.5%, confirming its effectiveness in distinguishing between the different transformer fault classes. Except for except for PD and T3 samples misclassified, the relatively high precision indicates that the model generates few false-positive classifications, while the strong recall demonstrates its ability to correctly identify most fault conditions. The findings demonstrate that integrating Artificial Bee Colony (ABC) optimization with Random Forest enhances diagnostic performance by identifying more suitable model hyperparameters. Overall, the proposed ABC-RF model offers a robust and reliable approach for power transformer fault diagnosis with considerable potential for supporting early fault identification in practical power systems.

5. REFERENCES

Alenezi, M., Anayi, F., Packianather, M., & Shouran, M. (2026). Intelligent fault discrimination in power transformers: a comprehensive review of methods. *Processes*, *14*(10).

Al Hourani, A. W., Abido, M. A., & Kassas, M. (2025). A Comprehensive review of transformer design optimization using evolutionary algorithms: advances, challenges, and future directions. *IEEE Access*.

Azmi, P. A. R., Yusoff, M., & Sallehud-din, M. T. M. (2025). Improving transformer failure classification on imbalanced DGA data using data-level techniques and machine learning. *Energy Reports*, *13*, 264-277.

Dhiman, A., & Kumar, R. (2023, April). Fault Diagnosis of a Transformer using Fuzzy Model and PSO optimized SVM. In 2023 IEEE 8th International Conference for Convergence in Technology (I2CT) (pp. 1-6). IEEE.

Dimgba, M. O., & Andreas, R. (2024). Optimal hyperparameter search strategies: Benchmarking grid search, random search, and genetic algorithms across regression, classification, and clustering tasks.

Erkan, U., Toktas, A., & Ustun, D. (2023). Hyperparameter optimization of deep CNN classifier for plant species identification using artificial bee colony algorithm. Journal of Ambient Intelligence and Humanized Computing, 14(7), 8827-8838.

Hoang, X. D., & Vu, X. H. (2022). An improved model for detecting DGA botnets using random forest algorithm. Information Security Journal: A Global Perspective, 31(4), 441 - 450.

Jing,G. (2025). Fault Diagnosis of Transformer Dissolved Gas Based on Random Forest. Applied and Computational Engineering,149,111-115.

Mishra, D., Chopra, V., Mishraa, D., & Baral, A. (2026). A non-invasive measurement-based modeling for assessing power transformer aging and reliability. *Measurement*, 120968.

Muneeb A. (2024) Understanding the Random Forest Algorithm – A Comprehensive Guide https://datasciencedojo.com/blog/random-forest-algorithm/ August 22, 2024.

Mumtahina, U., Alahakoon, S., & Wolfs, P. (2024). Hyperparameter tuning of load-forecasting models using metaheuristic optimization algorithms—a systematic review. *Mathematics*, *12*(21), 3353.

Saleh, A. G., Azzam, A. E., Attiya, G., & Ibrahim, E. (2026). Detecting Incipient Faults in Power Transformers through Hybrid Model of DGA and Machine Learning. *Electric Power Systems Research*, *256*, 112877.

Taha, I. B. M., Ibrahim, S., & Mansour, D.-E. A. (2021). Power Transformer Fault Diagnosis Based on DGA Using a Convolutional Neural Network With Noise in Measurements. IEEE Access, 9, 111162–111170. https://doi.org/10.1109/access.2021.3102415

Veerappan, S. (2025). Digital twin modeling for predictive maintenance in large-scale power transformers. National Journal of Electrical Machines & Power Conversion, 39-44.

Wang, X.J. (2024) Research on Fault Diagnosis of Oil-Immersed Transformers. Industrial Innovation Research, (24), 44-46.

Wong, S. Y., Ye, X., Guo, F., & Goh, H. H. (2022). Computational intelligence for preventive maintenance of power transformers. Applied Soft Computing, 114, 108129.

Yadav P., Sharma S, C., Mahadeva R., Patole S.(2023), Exploring Hyper-Parameters and Feature Selection for Predicting Non-Communicable Chronic Disease Using Stacking Classifier. 10.1109/ACCESS.2023.3299332. IEEE Access VOLUME 11, 2023

Zhu, Z., & Zhang, Y. (2022). Flood disaster risk assessment based on random forest algorithm. *Neural Computing and Applications*, 1-13.

International Conference on Engineering Innovation for Sustainable Development (ICESID 2026)
Faculty of Engineering, Ahmadu Bello University Zaria · 8–10 September 2026

SMALL-SIGNAL STABILITY ASSESSMENT OF DFIG-BASED WIND ENERGY INTEGRATION IN STATCOM-COMPENSATED NIGERIAN TRANSMISSION NETWORK: A MODAL ANALYSIS APPROACH

Dahiru Musbahu[1,*], G.a Olarinoye[2], A.s Abubakar[2], Z. Haruna[2], A.s Musa[2], B.r Tanko[2]

[1]*Federal University of Technology, Minna*
[2]*Ahmadu Bello University, Zaria*

Email: dahiru.musbahu@yahoo.com*, oyeguzeh@yahoo.com, abubakaras@abu.edu.ng, elzet2007@gmail.com, asmusa@abu.edu.ng, rbtanko@abu.edu.ng

***Corresponding author**: Dahiru Musbahu

DOI: https://doi.org/10.67203/sp.ICESID.2026

ABSTRACT

The increasing integration of wind energy into transmission networks introduces interactions that can affect power system stability, particularly in weak and highly interconnected networks. This study assesses the small-signal stability implications of DFIG-based wind energy integration in the Nigerian 330-kV transmission network using eigenvalue-based modal analysis. A 50-bus representation of the Nigerian transmission network is investigated under six operating scenarios comprising the base network, STATCOM-Compensated operation, and DFIG wind-penetration levels of 5% 10%, 15%, and 20%. Power flow analysis is first performed to establish the steady-state operating conditions and evaluate network transmission losses. The resulting operating points are then subjected to linearized state-space analysis to determine critical eigenvalues, oscillation frequencies, and damping ratios. The results show that active losses decrease to 0.58 p at 15% DFIG penetration, while reactive power losses increase substantially at higher penetration. The critical-mode damping ratio improves from 16.092% in the base case to 17.81% at 15% penetration. However, at 20% penetration, the critical eigenvalue shifts to $+0.0210 \pm j0.5781$*, producing a negative damping ration of -3.637% and indicating small-signal instability. The finding demonstrates that moderate DFIG penetration can be accommodated under the investigated conditions, while higher penetration requires additional stability-enhancement measure.*

Keywords: *DFIG; wind energy integration; small-signal stability; modal analysis; STATCOM; Nigerian transmission network*

1. INTRODUCTION

The increasing integration of renewable energy sources (RESs) into modern power systems is driven by the need to improve energy security, reduce dependence on conventional fossil-fuel generation, and support sustainable electricity development (Saleh *et al.*, 2025). Wind energy is particularly attractive because of its scalability and relatively low environmental impact. However, large-scale integration of wind generation introduces additional dynamic interactions into power networks and can influence voltage regulation, power flow patterns, and electromechanical oscillations (Ali *et al.*, 2021). These issues are particularly important in developing power systems where transmission networks may be characterized by long transmission corridors, weak voltage profiles, and limited reactive power support.

In Nigeria, the increasing demand for reliable electricity and need to diversify the generation mix have created growing interest in renewable energy integration. The Nigerian transmission network presents particular challenges for large-scale renewable integration because of its geographical extent, transmission constraints, and susceptibility to voltage and stability problems (Adetokun & Muriithi, 2021). Consequently, the integration of wind energy must be assessed not only from the perspective of additional generation capacity but also in terms of its influence on the dynamic behaviour of the interconnected power system.

Doubly Fed Induction Generator (DFIG) is widely used in variable speed wind energy conversion systems (WECSs) because its partial-scale converter allows a variable speed operation while requiring a lower converter rating (30%) than a fully rated converter configuration that utilized

permanent magnet synchronous generator technology (Musbahu *et al.*, 2021). Nevertheless, the converter-based characteristics of DFIG system introduce dynamic interactions that differ from those of conventional synchronous generators. As wind penetration increases, these interactions can modify the damping characteristics of existing electromechanical modes and potentially introduce poorly damped oscillatory modes (Kishor *et al.*, 2026). Therefore, small-signal stability assessment is essential when determining the acceptable level of DFIG penetration in an interconnected transmission network.

Flexible AC Transmission System (FACTS) devices provide and additional means of improving transmission system performance. In particular, a Static Synchronous Compensator (STATCOM) can provide dynamic reactive power compensation and voltage support, making it suitable for improving the operating condition of transmission networks with renewable generation (Ugwuanyi *et al.*, 2024a). However, the presence of adequate voltage support does not necessarily guarantee satisfactory small-signal stability under all renewable penetration levels. It is therefore necessary to evaluate the combined influence of STATCOM compensation and increasing DFIG penetration on the modal characteristics of the network.

Small-signal stability analysis provides a systematic mean of determining how system oscillation respond to small disturbances. Eigenvalue analysis can identify the location of critical modes in complex plane, while the associated damping ration and oscillation frequency provide quantitative measures of the quality of the system damping. A negative real part of an eigenvalue indicates a stable oscillatory mode, whereas an eigenvalue with positive real part indicates small-signal instability(Aliyu *et al.*, 2024; Kouider *et al.*, 2023).

While previous studies have independently explored wind-energy integration, FACTS-based voltage support, and stability assessment (Adetokun & Muriithi, 2021; Ahiakwo *et al.*, 2022; Anyanor *et al.*, 2020; Olabisi & Ayeni, 2023; Ugwuanyi *et al.*, 2024b), there is a pressing need to examine their combined effects within the Nigerian transmission network. Specifically, understanding how critical eigenvalues and damping characteristics change with increasing DFIG penetration can inform strategies for enhancing the integration of renewable energy resources.

This study evaluates the small-signal stability of Nigeria's 330 kV transmission network as DFIG penetration rises, utilizing STATCOM compensation. It examines six scenarios, including the base network, STATCOM conditions, and DFIG levels of 5%, 10%, 15%, and 20%. Initially, power flow analysis assesses steady-state conditions and transmission losses, followed by eigenvalue-based modal analysis to determine critical oscillatory modes, their frequencies, and damping ratios. The focus is on identifying the penetration level at which dominant modes become insufficiently damped or unstable. The findings offer a quantitative assessment of moderate DFIG penetration and the need for enhanced damping measures at higher levels.

2. LITERATURE REVIEW

2.1 DFIG-Based Wind Integration and Grid Stability

The increasing penetration of wind energy has introduced new technical challenges for power-system operation and stability (Nkosi *et al.*, 2023). Unlike conventional synchronous generators, wind turbine generators (WTGs) base on power electronic converters exhibit different dynamic characteristics and therefore interact with transmission network in different ways. These interactions can influence voltage regulation, power flow distribution, and the damping of electrotechnical oscillations, particularly as the proportion of converter-based generation increases (Ayodele *et al.*, 2020).

The Doubly Fed Induction Generator is widely employed in variable-speed wind energy conversion systems because it permits variable-speed operation while requiring a partially rated converter (Abad *et al.*, 2011). The converter controls the rotor-side electrical quantities and enables independent control of active and reactive power systems. Consequently, changes in wind energy penetration modify the location and damping of critical eigenvalues and may result in poorly damped or unstable oscillatory modes (Adetokun *et al.*, 2020). For weak highly stressed transmission network, these effects can become more significant. The Nigerian transmission network is particularly relevant because of its long transmission corridors and varying voltage-strength conditions particularly in northern region (Adetokun & Muriithi, 2021).

2.2 STATCOM and Small-Signal Stability

FACTS (Flexible AC Transmission Systems) devices have been extensively studied to enhance the performance of transmission networks by providing controllable reactive power compensation and voltage support. Among these devices, Static Synchronous Compensation (STATCOM) is particularly well-suited for systems with renewable energy generation because it can quickly regulate reactive power and support bus voltage under varying operational conditions (Mbuli, 2026).

In wind-integrated transmission systems, STATCOM compensation can improve voltage conditions and influence the operating point from which the dynamic stability of the system is assessed (Ugwuanyi *et al.*, 2024a). However, improved steady-state voltage performance does not necessarily indicate enhanced small-signal stability. Therefore, the interactions between the STATCOM, Doubly Fed Induction Generator (DFIG) controllers, and conventional synchronous generators must be considered when evaluating the overall system response.

Small-signal stability analysis is typically conducted by linearizing the differential-algebraic representation of the power system around an operating point and analysing the eigenvalues of the resulting state matrix. This analysis is crucial for assessing the impact of increased wind penetration and determining the need for additional damping control measures at higher penetration levels.

For an eigenvalue represented by (Abdulrahman & Energy, 2019);

$$\lambda_i = \sigma_i + j\omega_i \tag{1}$$

Where, σ_i,determine whether the corresponding mode is stable, while the imaginary part ω_i determine its oscillatory characteristics.

3. METHODOLOGY

3.1 Study System Overview

The Nigerian 330 kV transmission network considered in this study is represented by a 50-bus system comprising 14 synchronous generators (i.e. of which 11 are gas-fired and 3 hydro-based at Shiroro, Kainji, and Jebba), transmission lines, and aggregated loads. The network is used to investigate the effect of increasing DFIG-based generation on the steady-state and small-signal stability. The study follows a sequential approach in which the network operating point is first established using power-flow analysis. The approach allows the influence of increasing DFIG penetration to be assessed under comparable operating conditions.

A STATCOM is incorporated into the network to provide dynamic reactive power compensation and voltage support. The STATCOM-compensated network serves as the reference configuration for evaluating the subsequent DFIG penetration scenarios.

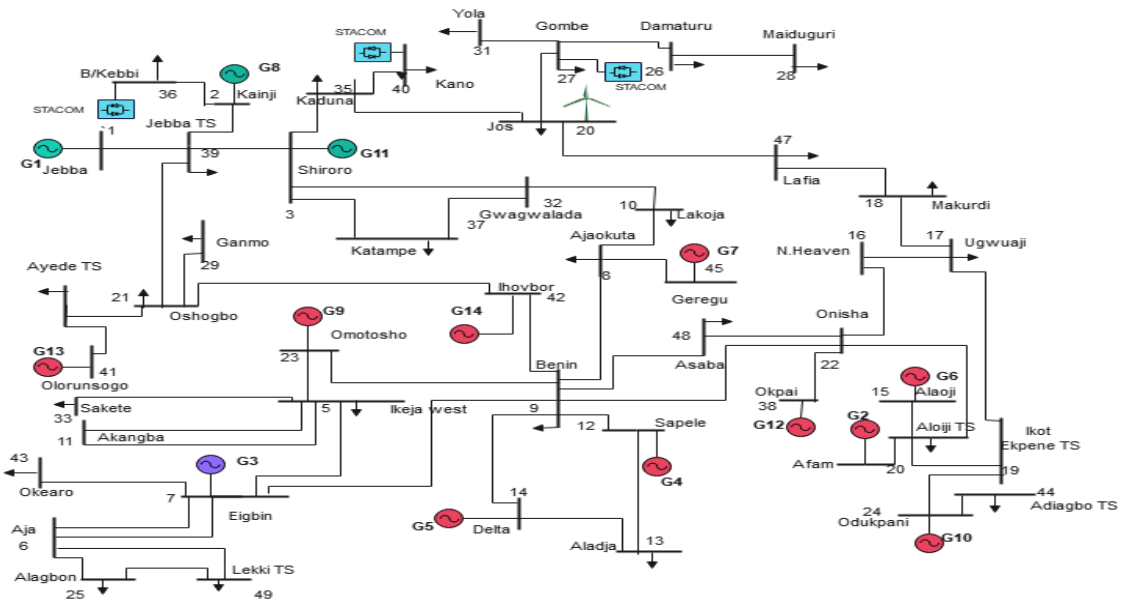

Figure 1: *STATCOM-compensated Nigerian Transmission Network with DFIG-Integration*

The single line diagram of the studied system was presented in Figure 1, its parameters collected from the national control centre located at Oshogbo Osun state as reported by Ugwuanyi N.S *et al.* (2024) and implemented in Power System Analysis Toolbox (PSAT) software platform.

3. 2 DFIG and STATCOM Integration Scenarios

The DFIG-based WECS is represented using a dynamic model incorporating principal electrical and electromechanical states required for small-signal stability analysis. The DFIG is connected at bus 19 (**Jos**) and its power contribution is progressively increased to represent different wind penetration levels. The wind turbine has a radius of 0.75 m, performance coefficient (Cp) of 0.4 and air density 0f 1.225 kg/m^3 and a wind speed of 9 m/s. A wind turbine with an average output of 3 MW and a total capacity of 900 MW wind farm was considered, making an equivalent cluster of (3 x 300 MW) wind turbines. The STATCOM is modelled as a controllable reactive-power compensation device connected to the transmission network rated 100 MVA and current control gain of 50 and 0.1 s time constant. Its inclusion provides voltage support capability and establishes the compensated operating condition against which the effect of DFIG integration can be evaluated. The DFIG penetration is defined the ratio of DFIG-active power to the total power generation, mathematically expressed as;

$$DFIG_{Penetration}(\%) = \frac{P_{DFIG}}{P_{GFG} + P_{DFIG}} \; x \; 100 \tag{2}$$

Where, P_{GFG} is active power generation from the 11 gas-fired generator as the 3 hydros geniting station outputs were maintained as they are also renewable resources.

Six operating scenarios are investigated to provide progressive assessment of the effect of wind penetration as detailed in Table 1.

Table 1: *Study Scenarios*

Scenario	STATCOM	DFIG Penetration	Operating Condition
Case 1	No	0%	Base Network
Case 2	Yes	0%	STATCOM-Compensated network
Case 3	Yes	5%	Low DFIG penetration
Case 4	Yes	10%	Moderate DFIG penetration
Case 5	Yes	15%	High DFG penetration
Case 6	Yes	20%	Very high DFIG penetration

3. 2 Power Flow Analysis

Power flow is initially performed for each operating scenario to establish the stead-state operating point. The analysis determines bus voltages, phase angles, active and reactive power generation, load demand, and transmission losses. The active and reactive powers balances is expressed as (Kouider *et al.*, 2023);

$$\begin{cases} P_{Gen} = P_{Load} + P_{Loss} \\ Q_{Gen} = Q_{Load} + Q_{Loss} \end{cases} \tag{3}$$

The resulting power flow are used to evaluate the effect of DFIG penetration on network operating conditions and losses before proceeding to the dynamic stability assessment.

3.3 Small-Signal Stability and Modal Analysis

Following the computation of power flow, the dynamic model is linearized around the corresponding steady-state operating point. The linearized system can be represented in state space forms as (Aliyu *et al.*, 2024);

$$\dot{x} = Ax \tag{4}$$

$$\det(\lambda I - A) = 0 \tag{5}$$

Where x represents the vector of dynamic state variables and A is the system state matrix. The eigenvalues of state matrix are obtained from; The oscillation frequency (f) and damping ratios (ζ) are computed by;

$$\begin{cases} f = \dfrac{\omega}{2\pi} \\ \zeta = -\dfrac{\sigma}{\sqrt{\sigma^2 + \omega^2}} \end{cases} \tag{6}$$

The critical mode is identified as the oscillatory mode with the least favourable damping characteristics among the modes considered. The eigenvalues, oscillation frequencies, and damping ratios are compared across the six scenarios to determine how increasing DFIG penetration affect system stability.

4. RESULTS AND DISCUSSION

The simulations conducted using PSAT software on a 100 MVA, 50 Hz base, under a load demand of 4,300 MW, with Egbin generator serving as the slack or reference generator. The Nigerian power system was modified by integrating a DFIG wind farm at the Jos bus.

According to Ugwuanyi *et al.* (2024b) and other researchers, Jos has been identified as the optimal location for the DFIG wind farm due to its superior performance.

4.1 Power-Flow Performance

The power flow results for the six operating scenarios are presented in Table 2. The results illustrate how the integration of STATCOM compensation and the increasing penetration of DFIG (Doubly Fed Induction Generator) impacts the generation balance and transmission losses in the Nigerian 330 kV transmission network. In Case 1, the base network experiences an active power loss of 0.704 p.u. Introducing a STATCOM in Case 2 increases this loss slightly to 0.720 p.u. However, integrating DFIG leads to a significant reduction in active power losses, achieving a low of 0.580 p.u in Case 5 (a 19.4% reduction from Case 2) at 15% penetration. This shows that local wind power can decrease active power transfer through the transmission network. At 20% penetration, losses rise slightly to 0.600 p.u, although they remain lower than in Case 2, indicating that reductions in losses have limits with increased wind penetration.

Table 2: *Power Flow Performance*

Scenario	P_{Gen} $(p.u)$	Q_{Gen} $(p.u)$	P_{Load} $(p.u)$	Q_{Load} $(p.u)$	P_{Loss} $(p.u)$	Q_{Loss} $(p.u)$
Case 1	43.18	30.78	42.49	25.04	0.704	5.74
Case 2	45.61	32.24	44.88	26.30	0.72	5.94
Case 3	45.52	31.85	44.88	26.30	0.64	5.55
Case 4	45.48	32.22	44.88	26.30	0.60	5.92
Case 5	45.46	33.41	44.88	26.30	0.58	7.11
Case 6	45.47	35.81	44.87	26.29	0.60	9.52

Conversely, reactive power losses behave differently. Case 3 shows the lowest reactive loss at 5.55 p.u, which climbs to 9.52 p.u by Case 6. The rise at 20% penetration highlights the growing reactive power needs with higher wind integration. Overall, while moderate DFIG penetration enhances active power efficiency, the increasing reactive losses underscore that assessing the feasibility of higher wind penetration requires a broader evaluation of network dynamics.

4.2 Small-Signal Stability and Modal Evolution

The critical eigenvalues modal characteristics obtained from the eigenvalue analysis are presented in Table 3. The results demonstrate a clear change in the dominant oscillatory behaviour as DFIG penetration increases.

The variation in the dominant mode with increasing DFIG penetration indicates that the small-signal stability response is non-monotonic and is governed by modal interaction rather than by a uniform deterioration of all electromechanical modes. At 5% penetration, the critical mode is associated with ω_{13} and δ_{13} of generator 13 with an equivalent damping ratio of 17.004%. At 10% DFIG penetration, the a low-frequency mode associated with ω_{12} and δ_{12} of generator 12 becomes critical, reducing the damping ratio to 10.389% while at 15% penetration the critical mode returns to the $\omega_{13} - \delta_{13}$ pair, with damping ratio increasing to 17.807%.

Table 3: *Critical Eigenvalues Modal Characteristics*

Scenario	DFIG Penetration	Dominant State	Critical Eigenvalue	Frequency (Hz)	Damping Ratio (%)	Stability
Case 1	0%	$\omega_{13}\delta_{13}$	$-0.6772 \pm j4.1532$	0.670	16.092	Stable
Case 2	0% +STATCOM	$\omega_{13}\delta_{13}$	$-0.7125 \pm j4.1779$	0.675	16.812	Stable
Case 3	5%	$\omega_{13}\delta_{13}$	$-0.7221 \pm j4.1848$	0.675	17.004	Stable
Case 4	10%	$\omega_{12}\delta_{12}$	$-0.0595 \pm j0.5695$	0.091	10.389	Stable
Case 5	15%	$\omega_{13}\delta_{13}$	$-0.7555 \pm j4.1917$	0.678	17.807	Stable
Case 6	20%	$\omega_{12}\delta_{12}$	$0.0210 \pm j0.5781$	0.092	-3.637	Unstable

This behaviour is physically attributable to changes in network power-flow distribution, synchronizing torque, and the dynamic interaction among synchronous generators, DFIG converter controls and STATCOM voltage regulation as the operating point changes. Mathematically, the state matrix $\boldsymbol{A}$, is a function of the operating points and wind penetration, its eigenvalues do not necessarily vary monotonically with penetration, in which different oscillatory modes become the least-damped mode at different penetration. However, at 20% penetration, the critical eigenvalue moves into the right half of the complex plane, rendering the system unstable with a damping ratio of -3.637%.

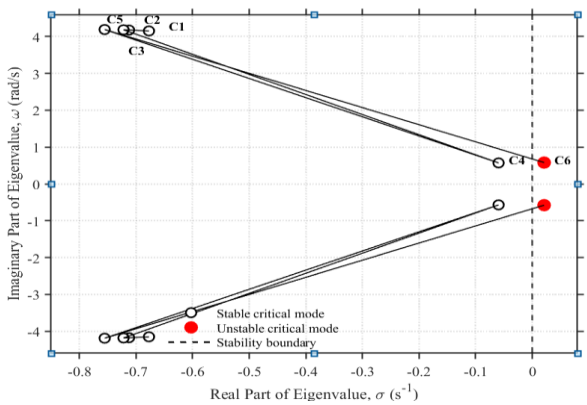

Figure 2: *Critical Eigenvalue Migration*

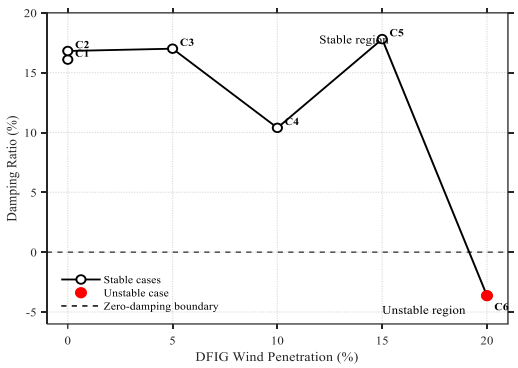

Figure 3: *Damping Ratio with increasing DFIG Penetration*

Figures 2 and 3 illustrate eigenvalue migration and critical damping variations with DFIG penetration, respectively. Overall, the network maintains small-signal stability up to 15% penetration, while the 20% scenario is unstable, highlighting the stability boundary for the investigated network configuration and operating conditions rather than a universal wind penetration limit for the Nigerian transmission network.

4. CONCLUSION

This study evaluates the small-signal stability of integrating DFIG-based wind generation into Nigeria's 330 kV transmission network through eigenvalue-based modal analysis using the Power System Analysis Toolbox (PSAT) in MATLAB. Six scenarios were assessed including; uncompensated network, STATCOM compensation, and DFIG penetration levels of 5%, 10%, 15%, and 20%.

Initial power flow analysis showed that moderate DFIG penetration enhances active power transmission and reduces losses but increases reactive power losses, particularly at higher penetration levels. Modal analysis revealed that DFIG integration affects system stability in a nonlinear manner, altering oscillatory behaviour with increasing DFIG penetration.

Results indicate that a STATCOM-supported network can maintain small-signal stability with DFIG penetration up to 15%, while suggesting that additional stability measures are needed for 20% penetration. Future research should focus on coordinated damping control strategies, including supplementary DFIG and wide-area damping controllers, to improve stability margins and facilitate higher wind energy integration in Nigeria's transmission network.

REFERENCES

Abad, G., Lopez, J., Rodriguez, M., Marroyo, L., & Iwanski, G. (2011). *Doubly fed induction machine: modeling and control for wind energy generation*: John Wiley & Sons.

Abdulrahman, I. J. I. O. A. J. o. P., & Energy. (2019). MATLAB-based programs for power system dynamic analysis. *7*, 59-69.

Adetokun, B. B., Muriithi, C. M., Ojo, J. O. J. I. J. o. E. P., & Systems, E. (2020). Voltage stability assessment and enhancement of power grid with increasing wind energy penetration. *120*, 105988.

Adetokun, B. B., & Muriithi, C. M. J. E. R. (2021). Impact of integrating large-scale DFIG-based wind energy conversion system on the voltage stability of weak national grids: A case study of the Nigerian power grid. *7*, 654-666.

Ahiakwo, C. O., Idoniboyeobu, D. C., Braide, S. L., Onita, C. L. J. I. J. o. R. i. E., & Science. (2022). Investigation of voltage stability of the Nigerian 330kV transmission network using Newton Raphson Method. *10*(6), 122-129.

Ali, S. W., Sadiq, M., Terriche, Y., Naqvi, S. A. R., Mutarraf, M. U., Hassan, M. A., . . . Guerrero, J. M. J. I. A. (2021). Offshore wind farm-grid integration: A review on infrastructure, challenges, and grid solutions. *9*, 102811-102827.

Aliyu, S., Theophilus, E. O., Veerapandiyan, V., & Noor Izzri, A. W. (2024). Modified Multimachine Power System Design with DFIG-WECS and Damping Controller. *Energies, 17(8)*, 1841.

Anyanor, K. I., Atuchukwu, A. J., & Okonkwo, I. I. (2020). ENHANCING THE VOLTAGE PROFILE OF 330 KV NIGERIA TRANSMISSION NETWORK SYSTEMS. *International Research Journal of Modernization in Engineering Technology and Science, Volume:02*(12/December - 2020).

Ayodele, T. R., Jimoh, A., Munda, J. L., & Agee, J. T. (2020). Challenges of grid integration of wind power on power system grid integrity. *World 2020, 3, 6*.

Kishor, N., Janne, S., Turunen, J., Haarla, L., Uhlen, K., Yadav, O., . . . Networks. (2026). Oscillatory stability in power grid network: A review on conventional and evolving types and damping improvement. 102257.

Kouider, K., Bekri, A. J. I. J. o. P. E., & Systems, D. (2023). Small signal stability and dynamic performance investigation on multi-machines power system including DFIG wind farm. *14*(3), 1825-1833.

Mbuli, N. J. E. (2026). Improvement of Low Voltage Ride-Through (LVRT) of Doubly Fed Induction Generator (DFIG)-Based Wind Energy Conversion Systems (WECSs) by STATCOMs: A Systematic Literature Review. *19*(2), 443.

Musbahu, D., Olarinoye, G., Saidu Abuabkar, A., Abubakar, U., & Basheer Balarabe, I. (2021). ANALYSIS AND SIMULATION OF DOUBLE FEED INDUCTION GENERATOR.

Nkosi, N., Bansal, R. C., Adefarati, T., Naidoo, R., Bansal, S. K. J. I. J. o. M., & Simulation. (2023). A review of small-signal stability analysis of DFIG-based wind power system. *43*(3), 153-170.

Olabisi, P. O., & Ayeni, G. J. J. E. R. R. (2023). Voltage Quality Analysis on Power Transmission Networks: A Case Study of 330kV Power Transmission Networks in Nigeria. *25*(4), 42-50.

Saleh, A. M., Vokony, I., Waseem, M., Khan, M. A., & Al-Areqi, A. J. E. R. (2025). Power system stability with high integration of RESs and EVs: Benefits, challenges, tools, and solutions. *13*, 2637-2663.

Ugwuanyi N.S, N. S., Ozioko, I., & Ugwuoke, N. J. Z., Jun. (2024). Dataset for the Nigerian 50-bus 330 kV power grid. *18*.

Ugwuanyi, N. S., Nwogu, O. A., Ozioko, I. O., & Ekwue, A. O. J. S. A. (2024a). An easy method for simultaneously enhancing power system voltage and angle stability using STATCOM. *25*, e02248.

Ugwuanyi, N. S., Ozioko, I. O., Uma, U. U., Nwogu, O. A., Ugwuoke, N. C., Ekwue, A. O., & Nwokocha, N. J. S. J. o. E. E. (2024b). Enhancing renewable energy-grid integration by optimally placed FACTS devices: the Nigeria case study. *12*(2), 16-25.

TRACK 8 OF 11

Strategies for Infrastructural and Industrial Transformation through Engineering Innovations

---

International Conference on Engineering Innovation for Sustainable Development (ICESID 2026)

Faculty of Engineering, Ahmadu Bello University Zaria · 8–10 September 2026

https://icesid.org

International Conference on Engineering Innovation for Sustainable Development (ICESID 2026)
Faculty of Engineering, Ahmadu Bello University Zaria · 8–10 September 2026

A DOMAIN-INVARIANT SPATIO-TEMPORAL GRAPH ATTENTION NETWORK FOR CROSS-DOMAIN ANOMALY DETECTION IN INDUSTRIAL CONTROL SYSTEMS

Emejuo Nichodemus Chibueze[1], Idris Shehu Musa[2], Basira Yahaya[2,*], Sani Saleh Saminu[2], Mohammed Bashir Abdulrazaq[2]

[1]*National Research Institute for Chemical Technology (NARICT), Zaria*
[2]*Ahmadu Bello University, Zaria*

Email: emejuo.chibueze@narict.gov.ng, Idris.ms@icloud.com, basiraee@gmail.com*, Sssaleh@engineering.abu.edu.ng, mbabdulrazaq@abu.edu.ng

***Corresponding author**: Basira Yahaya

DOI: https://doi.org/10.67203/sp.ICESID.2026

ABSTRACT

Industrial Control Systems (ICSs) are cyber-physical systems responsible for monitoring and controlling critical industrial processes. Their increasing integration with Information Technology (IT) networks, the Industrial Internet of Things (IIoT), and cloud-based services has expanded their exposure to cyber threats, creating a need for intelligent anomaly detection models capable of transferring learned knowledge across heterogeneous industrial environments. However, many existing deep learning-based approaches are developed for individual ICS domains and therefore have limited capability to exploit transferable spatio-temporal patterns across systems with different operational characteristics and feature structures. This study proposes a Domain-Invariant Spatio-Temporal Graph Attention Network (DI-STGAT) for cross-domain anomaly detection in ICSs. The proposed model integrates a Spatio-Temporal Graph Attention Network (ST-GAT) with Domain-Adversarial Neural Network (DANN) learning through a Gradient Reversal Layer (GRL). The ST-GAT captures temporal behaviour and spatial dependencies among industrial process variables, while the DANN/GRL mechanism facilitates domain adaptation by reducing domain-specific information in the learned representations. A fixed-dimensional graph-level representation enables the same model architecture to operate across heterogeneous ICS datasets with different numbers of process variables and graph structures. DI-STGAT achieved cross-domain anomaly detection across heterogeneous ICS environments by combining spatio-temporal graph learning with domain-adversarial adaptation to learn transferable representations from labeled source data and unlabeled target data, thereby improving anomaly discrimination across industrial domains without requiring target-domain anomaly labels for training. The framework was evaluated using the BATADAL, SWaT, and WADI benchmark datasets across six source-to-target transfer scenarios. Experimental results show that DI-STGAT improved mean cross-domain balanced accuracy from 50.51% to 51.90% and mean F1-score from 4.13% to 4.37% compared with the ST-GAT baseline at a fixed decision threshold of 0.50. The strongest improvement was achieved for SWaT→WADI, where balanced accuracy increased from 53.04% to 61.37% and F1-score from 7.48% to 8.94%. The proposed framework achieved mean cross-domain ROC-AUC and PR-AUC values of 72.21% and 36.36%, respectively. Domain-representation analysis further demonstrated measurable adversarial alignment between source and target representations, providing evidence of transferable representation learning across heterogeneous industrial domains. Overall, the findings demonstrate that DI-STGAT provides a viable domain-adaptive spatio-temporal learning framework for cross-domain anomaly detection in heterogeneous ICS environments, supporting more adaptable cybersecurity monitoring and improved protection of critical industrial infrastructure.

Keywords: *Industrial Control Systems (ICS); Cross-Domain Anomaly Detection; Domain Adaptation; Spatio-Temporal Graph Attention Network (ST-GAT); Domain-Adversarial Neural Network (DANN); Gradient Reversal Layer (GRL)*

1. INTRODUCTION

Industrial Control Systems (ICSs) are critical components of modern industrial infrastructure, providing monitoring and control functions for essential production processes. Traditionally, ICS environments were designed as isolated operational technology (OT) systems, with primary emphasis on safety, reliability, and continuous availability. However, the adoption of Industry 4.0, Industrial

Internet of Things (IIoT), remote monitoring, cloud services, Artificial Intelligence and information technology–operational technology (IT-OT) convergence has transformed these environments into highly interconnected cyber physical systems. While this transformation has improved automation, monitoring, and operational efficiency, it has also increased system exposure to cyber threats and introduced vulnerabilities associated with network connectivity, remote access, heterogeneous devices, and interconnected control components (Ahmadi-Assalemi *et al*., 2025; Rehman & Bahşi, 2024; Rotibi *et al*., 2024; Wu *et al*., 2026). Unlike conventional IT systems, cyber-attacks against ICSs can propagate from the cyber layer to physical processes, potentially causing equipment damage, production interruption, environmental consequences, and safety incidents. Consequently, reliable detection of abnormal system behaviour has become an important component of ICS cybersecurity and resilience (Rehman & Bahşi, 2024; Wu *et al*., 2026).

The increasing complexity of ICS environments has exposed limitations in conventional intrusion detection approaches. Thus, signature and rule-based methods are effective for previously known attack patterns but are less capable of identifying novel or evolving attacks that do not match predefined signatures. Anomaly-based detection provides an alternative by learning normal system behaviour and identifying deviations associated with attacks, faults, or abnormal operating conditions (Choi & Kim, 2024; Ahmadi-Assalemi *et al*., 2025). The availability of high-dimensional operational data from sensors, actuators, controllers, and communication systems has consequently encouraged the application of machine learning (ML) and deep learning (DL) techniques for ICS anomaly detection. Recent studies have explored recurrent networks, convolutional architectures, autoencoders, attention mechanisms, and adaptive learning approaches to capture complex temporal patterns in industrial data (Aslam *et al*., 2025; Liu *et al*., 2024; Xu *et al*., 2025). For instance, Liu *et al*. (2024) introduced a time-frequency fusion feature-attention approach to address long-sequence and complex temporal dependencies in ICS operational data, while Xu *et al*. (2025) proposed a dual-attention network that uses attention-based causal relationships among industrial components to improve anomaly detection and interpretation. These studies demonstrate the potential of deep learning for modelling complex ICS behaviour, but they primarily focus on improving detection within individual operational environments.

A major challenge in ICS anomaly detection is that industrial processes are inherently spatio-temporal. Sensor and actuator variables do not operate independently; they interact through physical processes, controllers, communication networks, and process stages. Consequently, treating industrial measurements as independent or purely sequential variables may overlook important relationships between interconnected components. Graph neural networks (GNNs) provide a natural representation for such systems because nodes can represent sensors, actuators, controllers, or process variables, while edges represent their physical, functional, or statistical relationships. Graph Convolutional Networks (GCNs) and Graph Attention Networks (GATs) have therefore attracted increasing attention for multivariate anomaly detection because they can learn dependencies among interconnected variables (Deng & Hooi, 2021; Veličković *et al*., 2018). In ICS applications, Yang *et al*. (2024) demonstrated that centrality-aware graph convolution can exploit relationships among industrial components, while Wang *et al*. (2023) showed that spatio-temporal graph neural networks can capture spatial and temporal characteristics in high-dimensional and noisy ICS data. Similarly, Fan *et al*. (2024) developed a spatio-temporal gated graph attention network for IIoT anomaly detection, and Zhang *et al*. (2025) proposed PdGAT-ID to combine periodic feature extraction with spatio-temporal graph attention for ICS intrusion detection. These studies indicate that graph-based spatio-temporal modelling can provide richer representations than conventional independent-variable approaches.

Recent research has further demonstrated the benefits of explicitly modelling hierarchical and dynamic relationships within industrial systems. Lin et al. (2025) proposed a multi-level graph attention network that represents relationships among physical processes and controllers, while Li *et al*. (2025) integrated static and dynamic graph learning with attention-based temporal modelling to capture spatial and temporal dependencies in ICS data. Canonico *et al*. (2025) similarly demonstrated that reducing unnecessary graph connections can improve both detection efficiency and computational requirements in reconfigurable cyber–physical systems. These findings reinforce the importance of jointly modelling spatial dependencies and temporal dynamics rather than treating industrial observations as isolated time-series measurements.

Despite these advancements, an important limitation remains: most existing ICS anomaly detection models are developed and evaluated within a single operational domain. Models trained on one industrial environment generally assume that the statistical distribution, sensor relationships, process dynamics, and attack characteristics of the training environment remain applicable to the test environment. This assumption is problematic because real industrial systems are heterogeneous. Water treatment, water distribution, energy, manufacturing, chemical, and oil-and-gas systems differ substantially in process topology, sensor configurations, control logic, communication protocols, operating ranges, and anomaly characteristics. Recent reviews have identified limited cross-domain datasets, distribution shifts, concept drift, and inadequate real-world validation as continuing challenges for AI-based ICS anomaly detection (Moriano *et al*., 2025; Aslam *et al*., 2025; Wu *et al*., 2026). The problem is therefore not simply to achieve high detection accuracy within one dataset, but to develop representations that remain informative when the model encounters a different industrial domain.

Domain adaptation provides a promising approach to this problem by encouraging a model to learn features that are discriminative for anomaly detection while being less dependent on the identity of the training domain. Domain-Adversarial Neural Networks (DANN) achieves this by introducing a domain classifier and a Gradient Reversal Layer (GRL), which encourages the feature extractor to learn representations that are useful for the primary task but less distinguishable across domains. Although adversarial learning has been extensively investigated in general domain adaptation, its integration with spatio-temporal graph representations for cross-domain ICS anomaly detection remains comparatively limited. Existing graph-based ICS studies have primarily concentrated on improving spatial representation, temporal modelling, interpretability, or detection accuracy within selected benchmark datasets rather than explicitly enforcing domain-invariant representations. This limitation is particularly important because graph structures themselves may differ between industrial environments, making direct transfer of learned representations difficult (Nahalka *et al*., 2024; Fan *et al*., 2024; Lin *et al*., 2025; Ganin *et al*., 2016).

The challenge is further highlighted by the nature of commonly used ICS benchmarks. Datasets such as SWaT, WADI, and BATADAL provide valuable experimental environments for evaluating anomaly detection methods, but they represent different industrial processes and therefore introduce distributional differences. SWaT represents a water-treatment environment, WADI represents a water-distribution system, and BATADAL focuses on cyber-physical attacks against water-distribution networks (Goh *et al*., 2016; Ahmed *et al*., 2017; Mathur & Taormina *et al*., 2018). These datasets have enabled substantial progress in ICS anomaly detection, but their differences also provide an appropriate basis for evaluating whether a model can generalize beyond its source domain. Studies using graph-based approaches have demonstrated strong performance on individual datasets, yet the problem of systematically evaluating transferability between heterogeneous domains remains insufficiently explored.

Against this background, this study identifies three interrelated research problems that motivate the development and evaluation of the proposed framework.

1. Inadequate joint representation of spatial and temporal dependencies across heterogeneous ICS environments.
2. Poor cross-domain generalization caused by distribution shifts between heterogeneous ICS environments.
3. Limited systematic evidence for cross-domain transfer and domain-adversarial representation learning across heterogeneous ICS benchmarks.

To answer these questions, the study adopts a controlled experimental framework involving the three benchmark datasets. Each dataset is independently preprocessed and represented using its domain-specific graph structure, thereby preserving the characteristics of the corresponding industrial environment rather than forcing heterogeneous variables into an artificial common node space. Temporal sequences are subsequently processed through the ST-GAT architecture to generate a fixed-dimensional graph representation. The conventional ST-GAT is first trained and evaluated as the baseline. DI-STGAT then extends the same architecture with a GRL and domain classifier for unsupervised source-to-target adaptation. Six transfer directions: BATADAL to SWaT, BATADAL to WADI, SWaT to BATADAL, SWaT to WADI, WADI to BATADAL, and WADI to SWaT are

evaluated under a controlled protocol. Target-domain anomaly labels are excluded from adaptation training and model selection and are reserved for final evaluation.

Accordingly, the main contributions of this study are:

1. **Domain-invariant ST-GAT:** A spatio-temporal graph attention framework integrated with DANN and GRL to learn transferable anomaly representations across heterogeneous ICS domains.
2. **Cross-domain evaluation:** A systematic source-to-target evaluation using the three datasets to assess the generalization capability of the proposed model beyond its training environment.
3. **Controlled baseline and ablation analysis:** A conventional ST-GAT baseline is established and compared with the DANN/GRL-enhanced model to isolate the contribution of domain-adversarial learning.

Further, the proposed framework has potential relevance to addressing the increasing need to strengthen the resilience and cybersecurity of critical infrastructure in Nigeria and other African countries, where increasing digitalization and interconnection of industrial and utility systems can introduce additional cyber security risks. Nigeria's National Cyber security Policy and Strategy identifies the protection and resilience of Critical National Information Infrastructure as a national cybersecurity priority (Federal Republic of Nigeria, 2021). Water treatment and distribution systems provide a particularly relevant application context because reliable water infrastructure remains important to Nation's sustainable development, while challenges relating to infrastructure, service delivery, and access to clean water persist (Ogunbode, 2026). The use of water-system benchmark datasets in this study therefore provides an experimental basis for investigating transferable anomaly-detection techniques applicable to heterogeneous water infrastructure. By reducing dependence on target-domain anomaly labels, the proposed cross-domain approach could support the development of adaptable cybersecurity monitoring for infrastructure environments where labeled attack data are limited. Such capabilities are relevant to Nigeria's sustainable infrastructure development and align with SDG 6 (Clean Water and Sanitation) and SDG 9 (Industry, Innovation and Infrastructure), which emphasize sustainable water management and resilient infrastructure, respectively (United Nations, 2026).

2. METHODOLOGY

This study proposes a Domain-Invariant Spatio-Temporal Graph Attention Network (DI-STGAT) for cross-domain anomaly detection in heterogeneous Industrial Control Systems (ICSs). The proposed framework combines temporal attention, graph attention, and domain-adversarial learning to capture temporal behaviour and structural dependencies among industrial process variables while encouraging transferable representations across different ICS domains. Unlike approaches that require identical feature sets across source and target systems, DI-STGAT retains the domain-specific variables and graph structures of each ICS and transforms them into a common fixed-dimensional graph-level representation suitable for cross-domain adaptation.

2.1 Model Overview

The proposed DI-STGAT consists of three principal components: (i) an ST-GAT feature extractor, (ii) an anomaly-classification branch, and (iii) a domain-adaptation branch based on a Domain-Adversarial Neural Network (DANN) and Gradient Reversal Layer (GRL). The ST-GAT feature extractor first applies temporal attention to identify informative observations within each process variable's temporal sequence. The resulting node representations are subsequently processed by a multi-head Graph Attention Network (GAT) to capture dependencies among interconnected industrial variables. Mean graph pooling then converts the variable-size node representations into a fixed 32-dimensional graph-level embedding. This processing sequence corresponds to the implemented architecture described in the original model specification.

The graph-level embedding is supplied to two branches. The first is a binary anomaly classifier that distinguishes normal from anomalous process behaviour. The second is a domain classifier connected through the GRL. During domain adaptation, labeled source-domain samples provide supervision for anomaly classification, whereas source and unlabeled target samples jointly

contribute to domain classification. Target-domain anomaly labels are not used during adaptation training or model selection. Accordingly, the overall architecture can be summarized as:

$$\text{Input} \rightarrow \text{Temporal Attention} \rightarrow \text{Multi-Head GAT} \rightarrow \text{Graph Embedding} \rightarrow \begin{cases} \text{Anomaly Classifier} \\ \text{GRL} \rightarrow \text{Domain Classifier} \end{cases} \quad (1)$$

As show in Equation (1), the anomaly and domain-classification branches operate on the same graph-level representation. This shared representation provides the connection between spatio-temporal anomaly learning and domain-adversarial adaptation as shown in figure 2.1.

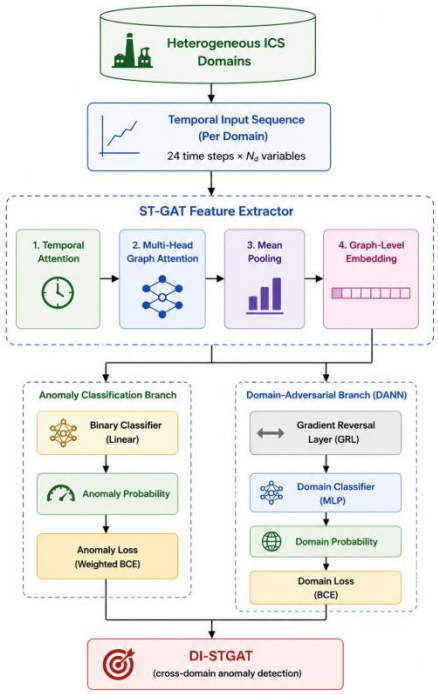

Figure 2.1: Architecture of the Proposed DI-STGAT Model

2.2 Domain-Specific Graph and Temporal Input Representation

The three ICS domains considered in this study contain different numbers and configurations of process variables. Rather than forcing these heterogeneous datasets into an artificial common feature space, each domain retains its own set of process variables and corresponding graph structure. For an ICS domain d, a temporal input sequence is represented as in equation 2:

$$\mathbf{X}_t^{(d)} = \left[\mathbf{x}_{t-T+1}^{(d)}, \mathbf{x}_{t-T+2}^{(d)}, \dots, \mathbf{x}_t^{(d)}\right] \in \mathrm{R}^{T \times N_d}, \qquad (2)$$

where T is the temporal window length and N_d is the number of process variables in domain d. In this study, $T = 24$; therefore, each input contains the previous 24 observations of the corresponding industrial variables. As expressed in Equation (2), N_d is domain-dependent, allowing the model to accommodate heterogeneous ICS environments rather than assuming an identical input dimension. The implemented datasets contain 38 variables for BATADAL, 45 for SWaT, and 123 for WADI. Each ICS domain is represented by a graph

$$G^{(d)} = \left(V^{(d)}, E^{(d)}\right), \qquad (3)$$

where $V^{(d)}$ represents the process variables and $E^{(d)}$ represents their inferred relationships. Equation (3) therefore permits each domain to maintain a graph topology corresponding to its own process structure. The relationships between variables are determined using the absolute Pearson correlation computed from the corresponding training partition:

$$r_{ij}^{(d)} = \left| \frac{\sum_t \left(x_{t,i}^{(d)} - \bar{x}_i^{(d)}\right)\left(x_{t,j}^{(d)} - \bar{x}_j^{(d)}\right)}{\sqrt{\sum_t \left(x_{t,i}^{(d)} - \bar{x}_i^{(d)}\right)^2}\sqrt{\sum_t \left(x_{t,j}^{(d)} - \bar{x}_j^{(d)}\right)^2}} \right|. \quad (4)$$

In Equation (4), $r_{ij}^{(d)}$ measures the strength of the statistical relationship between process variables i and j. For each node, the three variables with the highest absolute correlations are selected as neighbours. The resulting graph is symmetrized and self-loops are added. This produces domain-specific graphs containing 38 nodes and 188 directed edges for BATADAL, 45 nodes and 253 directed edges for SWaT, and 123 nodes and 707 directed edges for WADI. Importantly, the graph topology is derived exclusively from training data to prevent validation or test information from influencing graph construction.

2.3 Temporal Attention

Industrial anomalies frequently develop over a sequence of observations rather than appearing as isolated events. The temporal attention module is therefore used to determine the relative importance of the 24 observations associated with each process-variable node. For node i, the attention score at time t is calculated as

$$e_{i,t} = \mathbf{w}_2^{\top} \tanh\left(\mathbf{W}_1 x_{i,t} + \mathbf{b}_1\right) + b_2, \quad (5)$$

where $\mathbf{W}_1, \mathbf{w}_2, \mathbf{b}_1$, and b_2 are trainable parameters. The implemented temporal-attention network uses a $1 \rightarrow 8 \rightarrow 1$ transformation. Equation (5) assigns a learned importance score to every observation within the temporal window. The attention scores are normalized across the temporal dimension using the softmax function:

$$\alpha_{i,t} = \frac{\exp\left(e_{i,t}\right)}{\sum_{\tau=1}^{T} \exp\left(e_{i,\tau}\right)}. \quad (6)$$

As defined by Equation (6), the normalized temporal attention coefficients indicate the relative contribution of each time step to the representation of node i. The temporal representation is subsequently obtained through the weighted aggregation

$$h_i^{(T)} = \sum_{t=1}^{T} \alpha_{i,t} x_{i,t}. \quad (7)$$

Thus, Equation (7) transforms the 24-step history of each process variable into a learned scalar representation in which more informative time steps receive greater attention. This allows the model to capture temporal behaviour without introducing recurrent or convolutional components.

2.4 Multi-Head Graph Attention

Following temporal attention, the resulting node representations are processed by a multi-head graph-attention mechanism to capture spatial dependencies among related industrial process variables. Unlike conventional aggregation methods that treat all neighbouring nodes equally, graph attention learns the relative contribution of each neighbouring variable. For an edge connecting nodes i and j, the unnormalized attention score for attention head k is calculated as

$$e_{ij}^{(k)} = \mathrm{LeakyReLU}\left[\mathbf{a}^{(k)\top}\left(\mathbf{W}^{(k)} h_i^{(T)} \| \mathbf{W}^{(k)} h_j^{(T)}\right)\right], \quad (8)$$

where $\mathbf{W}^{(k)}$ denotes the trainable transformation matrix, $\mathbf{a}^{(k)}$ represents the attention vector for head k, and $\|$ denotes concatenation. Equation (8) determines the learned importance of node j to node i within the domain-specific graph.The attention scores are normalized over the neighbourhood of node i as

$$\beta_{ij}^{(k)} = \frac{\exp\left(e_{ij}^{(k)}\right)}{\sum_{m \in \mathrm{N}_i} \exp\left(e_{im}^{(k)}\right)}, \quad (9)$$

where N_i contains the graph neighbours of node i, including its self-loop. Equation (9) ensures that the attention coefficients represent the relative importance of connected variables. The output of attention head k is then obtained as

$$\mathbf{h}_i^{(k)} = \sum_{j \in \mathrm{N}_i} \beta_{ij}^{(k)} \mathbf{W}^{(k)} h_j^{(T)}. \quad (10)$$

According to Equation (10), each node representation is updated using an attention-weighted combination of information from its graph neighbourhood. The implemented model uses four graph-attention heads with eight output dimensions per head. Their outputs are concatenated to produce

$$\mathbf{h}_i^{(G)} = \|_{k=1}^{4} \mathbf{h}_i^{(k)} \in \mathrm{R}^{32}. \quad (11)$$

Consequently, Equation (11) produces a 32-dimensional spatial representation for each process variable node. The use of multiple attention heads allows the model to capture different patterns of relationships among industrial variables while maintaining the same parameterization across domains with different graph sizes.

2.5 Graph-Level Representation and Anomaly Classification

Although the same ST-GAT parameters can operate on different graph sizes, the resulting node level representations cannot be directly combined across domains because the datasets contain different numbers of nodes. A fixed-dimensional graph representation is therefore generated using mean pooling:

$$\mathbf{z}^{(d)} = \frac{1}{N_d} \sum_{i=1}^{N_d} \mathbf{h}_i^{(G)}, \mathbf{z}^{(d)} \in \mathrm{R}^{32}. \quad (12)$$

As shown in Equation (12), the node representations are aggregated into a 32-dimensional graph level embedding, irrespective of the number of process variables in the input domain. This mechanism is important to cross-domain adaptation because each of the datasets can retain their respective domain-specific graphs while still producing representations with an identical dimensionality. The graph-level representation is subsequently passed to a binary anomaly classifier:

$$\ell_y = \mathbf{w}_y^\top \mathbf{z} + b_y, p_y = \sigma(\ell_y), \quad (13)$$

where ℓ_y represents the anomaly logit, $\mathbf{w}_y$ and b_y are trainable classifier parameters, and p_y denotes the predicted anomaly probability. Equation (13) therefore maps the 32-dimensional graph representation to the probability that the corresponding temporal graph observation is anomalous. Because anomalous samples are substantially less frequent than normal samples, the anomaly-classification branch is optimized using weighted binary cross-entropy:

$$\mathrm{L}_A = -\frac{1}{n_S} \sum_{i=1}^{n_s} [w_+ y_i^s \log p_i^s + (1 - y_i^s) \log(1 - p_i^s)], \quad (14)$$

where n_s denotes the number of source samples and $w_+ = N_{\text{normal}} / N_{\text{anomaly}}$ is calculated from source-domain training data only. Equation (14) increases the contribution of the minority anomaly class during optimization without resampling the training data.

2.6 Domain-Adversarial Learning

The principal extension from the conventional ST-GAT baseline to DI-STGAT is the incorporation of domain-adversarial learning. The objective is to retain representations that are useful for anomaly classification while reducing information that makes the source and target domains easily distinguishable. Let F_θ denote the shared ST-GAT feature extractor. For source and target observations, the corresponding graph-level representations are

$$\mathbf{z}_s = F_\theta(\mathbf{X}_s, G_s), \mathbf{z}_t = F_\theta(\mathbf{X}_t, G_t). \quad (15)$$

As expressed in Equation (15), the source and target inputs are processed using their respective domain-specific graphs, G_s and G_t, while the shared ST-GAT parameters map both inputs into the same 32-dimensional representation space. This enables domain adaptation without requiring the source and target systems to contain identical process variables. The resulting representations are

passed through the GRL to a domain classifier implemented as a 32 to 16 to 1 network with a ReLU hidden activation:

$$p_d = \sigma[\mathbf{W}_{d2}\mathrm{ReLU}(\mathbf{W}_{d1}\mathbf{z}^{GRL} + \mathbf{b}_{d1}) + b_{d2}]. \qquad (16)$$

In Equation (16), p_d represents the predicted domain probability and $\mathbf{z}^{GRL}$ is the graph embedding after passing through the GRL. Source samples are assigned domain label 0, while target samples are assigned domain label 1. The domain-classification loss is calculated as:

$$\mathrm{L}_D = \frac{1}{2}[\mathrm{BCE}(p_d^s, 0) + \mathrm{BCE}(p_d^t, 1)]. \qquad (17)$$

As shown in Equation (17), both source and target samples contribute to the domain-adversarial objective. However, target anomaly labels are not involved. Consequently, DI-STGAT performs unsupervised target-domain adaptation, using labeled source data for anomaly learning and unlabeled target data for domain alignment.

2.7 Gradient Reversal Layer

The GRL provides the adversarial mechanism through which the ST-GAT representation is encouraged to become less domain-specific. During forward propagation, the GRL behaves as an identity function:

$$R_\lambda(\mathbf{z}) = \mathbf{z}. \qquad (18)$$

Thus, Equation (18) shows that the numerical values of the graph-level representation are passed unchanged to the domain classifier. During back propagation, however, the gradient is reversed according to

$$\frac{\partial R_\lambda}{\partial \mathbf{z}} = -\lambda \mathbf{I}, \qquad (19)$$

where λ controls the strength of the adversarial signal. According to Equation (19), the domain classifier is optimized to correctly distinguish source and target representations, while the reversed gradient encourages the ST-GAT feature extractor to generate representations that make this distinction more difficult. This adversarial relationship encourages the extraction of more transferable features while retaining the anomaly-discriminative objective of the source task. Rather than applying the maximum adversarial pressure from the beginning of training, λ is progressively increased according to

$$\lambda(p) = \frac{2}{1 + \exp(-10p)} - 1, 0 \le p \le 1, \qquad (20)$$

where p represents normalized training progress. Equation (20) gradually increases the influence of domain-adversarial learning as training progresses, allowing the feature extractor initially to learn anomaly-relevant representations before stronger domain-confusion pressure is introduced.

2.8 Joint DI-STGAT Training Objective

DI-STGAT jointly optimizes anomaly discrimination and domain adaptation. The overall objective is defined as

$$\mathrm{L}_{\mathrm{total}} = \mathrm{L}_A + \mathrm{L}_D, \qquad (21)$$

where L_A is the source-domain anomaly-classification loss defined in Equation (14) and L_D is the source-target domain-classification loss defined in Equation (17). Therefore, Equation (21) jointly trains the ST-GAT representation for anomaly discrimination and domain-adversarial adaptation. Importantly, the adversarial coefficient λ is not multiplied by L_D again in Equation (21). Instead, λ acts exclusively through the reversed gradient defined in Equation (19) and follows the progressive schedule specified in Equation (20). This reflects the actual implementation and prevents the domain-adversarial contribution from being weighted twice.

During optimization, labeled source-domain samples contribute to the anomaly loss L_A, while both source-domain and unlabeled target-domain samples contribute to the domain loss L_D. The anomaly-classification objective encourages the 32-dimensional ST-GAT embedding to retain information required to distinguish normal from anomalous behaviour, whereas the GRL-based

domain objective encourages the feature extractor to reduce information that permits straightforward discrimination between source and target domains.

Consequently, the proposed DI-STGAT combines temporal attention for modelling process evolution, multi-head graph attention for capturing relationships among industrial variables, fixed-dimensional graph pooling for accommodating heterogeneous graph sizes, and DANN/GRL for cross-domain representation adaptation. This integrated architecture enables knowledge learned from a labeled source ICS to be adapted to heterogeneous target ICS using unlabeled target-domain observations, without requiring identical process-variable sets or target-domain anomaly labels during training.

3. RESULTS AND DISCUSSION

This section presents and discusses the experimental results of the conventional ST-GAT baseline and the proposed Domain-Invariant Spatio-Temporal Graph Attention Network (DI-STGAT). The analysis considers within-domain ST-GAT performance, baseline cross-domain transfer, cross-domain adaptation using DANN/GRL, comparative performance between ST-GAT and DI-STGAT, decision-threshold behaviour, and domain-representation alignment. The quantitative results are complemented with graphical analyses of discrimination performance, cross-domain transfer, domain-adaptation effects, and training behaviour.

3.1 Within-Domain Performance of the ST-GAT Baseline

The ST-GAT baseline was first evaluated independently on BATADAL, SWaT, and WADI to determine whether the underlying architecture could learn anomaly-relevant representations before investigating cross-domain transfer. Table 3.1 presents the results obtained using the fixed classification threshold of 0.50.

Table 3.1: Within-domain ST-GAT performance

Dataset	Accuracy	Balanced Accuracy	Precision	Recall	F1-score	ROC-AUC	PR-AUC
BATADAL	0.0192	0.5058	0.0078	1.0000	0.0154	0.9197	0.0465
SWaT	0.0372	0.5000	0.0372	1.0000	0.0718	0.9655	0.3312
WADI	0.3677	0.6718	0.0547	1.0000	0.1037	0.7256	0.0620

The results reveal a clear distinction between the ranking capability of the ST-GAT and its classification behaviour at the fixed threshold. BATADAL and SWaT obtained ROC-AUC values of 0.9197 and 0.9655, respectively, indicating strong discrimination between normal and anomalous observations across possible decision thresholds. WADI achieved a lower but still informative ROC-AUC of 0.7256.

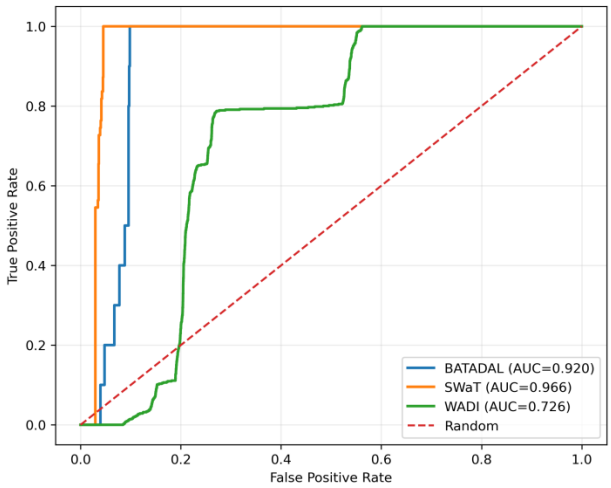

Figure 3.1: Within-domain ROC curves of the ST-GAT baseline

Figure 3.1 shows the ROC curves obtained by the ST-GAT baseline for BATADAL, SWaT, and WADI. The curves confirm the strong ranking capability observed numerically in Table 3.1,

particularly for SWaT and BATADAL. SWaT achieved the highest ROC-AUC of 0.9655, followed by BATADAL at 0.9197, whereas WADI achieved 0.7256. The figure therefore demonstrates that the ST-GAT extracted useful anomaly-related representations within each domain, although the fixed 0.50 threshold did not provide an equally effective operating point.

This difference is important because the models obtained a recall of 1.0000 for all three datasets but produced large numbers of false positives. For BATADAL, all 10 anomalous test samples were detected, but 1,277 of 1,292 normal samples were classified as anomalous. Similarly, all 55 SWaT attacks were detected, but all 1,422 normal samples were classified as attacks. WADI produced a comparatively better operating point, correctly identifying all 631 attacks and 5,714 normal observations, although 10,913 normal observations were still incorrectly classified as anomalous. The findings indicate that the ST-GAT baseline learned useful anomaly-ranking information but experienced substantial fixed-threshold calibration difficulty. This distinction becomes particularly important when examining cross-domain transfer.

3.2 Cross-Domain Generalization of the ST-GAT Baseline

The baseline models were subsequently evaluated under cross-domain transfer. In each experiment, a model trained on one source domain was evaluated on another target domain without target anomaly-label training or target-domain fine-tuning.

Table 3.2: Cross-domain ST-GAT baseline performance

Source → Target	Balanced Accuracy	F1-score	ROC-AUC	PR-AUC
BATADAL → SWaT	0.5000	0.0718	1.0000	1.0000
BATADAL → WADI	0.5001	0.0706	0.4734	0.0325
SWaT → BATADAL	0.5000	0.0152	1.0000	1.0000
SWaT → WADI	0.5304	0.0748	0.4909	0.0335
WADI → BATADAL	0.5000	0.0152	0.9305	0.0852
WADI → SWaT	0.5000	0.0000	0.4914	0.0367
Mean	**0.5051**	**0.0413**	**0.7310**	**0.3646**

As shown in table 3.2 the mean cross-domain ROC-AUC was 0.7310, whereas balanced accuracy and F1-score averaged 0.5051 and 0.0413, respectively. Considerable variation occurred among the six transfer directions.

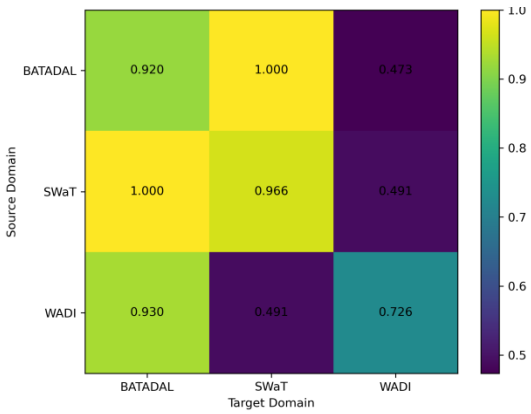

Figure 3.2: ROC-AUC within and Cross-domain performance

The Figure 3.2 provides a visual representation of the direction-dependent transfer behaviour of the baseline model. Strong transfer ranking was obtained for BATADAL to SWaT and SWaT to BATADAL, both of which achieved ROC-AUC values of 1.0000, while WADI to BATADAL achieved 0.9305. In contrast, BATADAL to WADI, SWaT to WADI, and WADI to SWaT produced values close to 0.50. The heatmap therefore shows that cross-domain transfer was not symmetric and that the effectiveness of a source representation depended strongly on the selected target environment.

The results also demonstrate that the ability of the architecture to process heterogeneous graphs does not automatically guarantee distributional generalization. Although all target graphs could be processed through the common ST-GAT architecture, substantial source-target distribution shifts remained, providing the motivation for the DANN/GRL adaptation mechanism.

3.3 Cross-Domain Performance of DI-STGAT

The proposed DI-STGAT was subsequently evaluated across the same six transfer directions. During adaptation, anomaly labels were obtained exclusively from the source domain, while unlabeled target-domain training samples participated only in domain-adversarial learning.

Table 3.3: Cross-domain performance of DI-STGAT

Source → Target	Accuracy	Balanced Accuracy	Precision	Recall	F1-score	ROC-AUC	PR-AUC
BATADAL → SWaT	0.0372	0.5000	0.0372	1.0000	0.0718	1.0000	1.0000
BATADAL → WADI	0.0367	0.5001	0.0366	1.0000	0.0706	0.4742	0.0325
SWaT → BATADAL	0.0077	0.5000	0.0077	1.0000	0.0152	1.0000	1.0000
SWaT → WADI	0.2556	0.6137	0.0468	1.0000	0.0894	0.4408	0.0306
WADI → BATADAL	0.0077	0.5000	0.0077	1.0000	0.0152	0.9296	0.0818
WADI → SWaT	0.9628	0.5000	0.0000	0.0000	0.0000	0.4882	0.0366
Mean	—	**0.5190**	—	—	**0.0437**	**0.7221**	**0.3636**

The proposed DI-STGAT as shown in table 3.3 achieved a mean balanced accuracy of 51.90% and mean F1-score of 4.37%, compared with 50.51% and 4.13%, respectively, for the conventional ST-GAT baseline. The largest improvement occurred for SWaT to WADI, where balanced accuracy increased from 53.04% to 61.37%, while F1-score increased from 7.48% to 8.94%. This improvement resulted primarily from better recognition of normal WADI observations while maintaining complete attack recall. However, a notable failure case occurred for WADI→SWaT, where DI-STGAT achieved 96.28% accuracy but zero precision, recall, and F1-score. As shown in Table 3.4, all 1,477 target samples were classified as normal (TN = 1,422, FN = 55), resulting in the failure to detect any of the 55 anomalies. Thus, the high accuracy reflects the strong class imbalance rather than effective anomaly detection. The near-chance ROC-AUC of 0.4882 further indicates weak anomaly discrimination, while the domain-classification balanced accuracy of 0.6687 suggests incomplete source–target alignment. This result demonstrates that DI-STGAT does not transfer uniformly across all domain pairs and that high accuracy can mask complete anomaly-detection failure. For practical deployment, transfer-specific validation using balanced accuracy, recall, F1-score, and PR-AUC is therefore essential before deploying the model in an unseen ICS environment.

Table 3.4: Confusion Matrix for the WADI→SWaT Transfer

Actual Class	Predicted Normal	Predicted Anomaly	Total
Normal	1,422 (TN)	0 (FP)	1,422
Anomaly	55 (FN)	0 (TP)	55
Total	1,477	0	1,477

3.4 Comparative Performance of ST-GAT and DI-STGAT

To determine the contribution of domain-adversarial adaptation, the performance of DI-STGAT was directly compared with the corresponding ST-GAT baseline. As summarized in Table 3.5, DI-STGAT produced modest increases in mean balanced accuracy and F1-score, while mean ROC-AUC and PR-AUC showed slight decreases, indicating that the effect of domain-adversarial adaptation differed between fixed-threshold decision performance and overall ranking performance.

Table 3.5: Aggregate comparison of ST-GAT and DI-STGAT

Metric	ST-GAT	DI-STGAT	Change
Balanced Accuracy	0.5051	0.5190	+0.0139
F1-score	0.0413	0.0437	+0.0024
ROC-AUC	0.7310	0.7221	−0.0089
PR-AUC	0.3646	0.3636	−0.0010

Figure 3.3 compares the F1-scores of the conventional ST-GAT and DI-STGAT for each source-target pair. The most visible difference occurs for SWaT to WADI, where DI-STGAT increases F1-score from 0.0748 to 0.0894. The remaining transfer directions show either equivalent or nearly equivalent fixed-threshold performance. The figure therefore indicates that the benefit of adversarial adaptation is transfer-dependent, with the largest decision-level improvement occurring when WADI is adapted from SWaT.

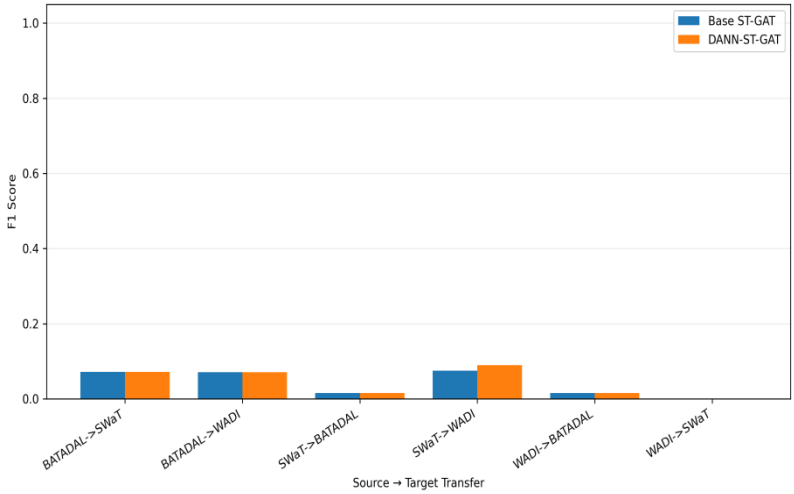

Figure 3.3: Cross-domain F1-score comparison between ST-GAT and DI-STGAT

Across all six transfers, mean balanced accuracy increased by 1.39 percentage points, while mean F1-score increased by only 0.24 percentage points. The largest F1 improvement occurred for SWaT→WADI, from 0.0748 to 0.0894; however, the absolute F1-score remains low. Conversely, mean ROC-AUC decreased by 0.89 percentage points and PR-AUC by 0.10 percentage points.

Therefore, although DANN/GRL produced a measurable numerical improvement in fixed-threshold decision performance for some source–target relationships, the magnitude and absolute performance levels are insufficient to demonstrate deployment-ready anomaly detection. Rather, the results provide evidence of the feasibility of domain-adversarial adaptation within the ST-GAT framework, while highlighting the need for substantial improvement in cross-domain anomaly discrimination and calibration before practical deployment. Accordingly, DI-STGAT should be regarded as an experimental cross-domain framework rather than an immediately deployable ICS anomaly-detection solution.

Further, the reported comparisons are based on the fixed experimental runs and were not evaluated across multiple random seeds. Consequently, the observed differences between ST-GAT and DI-STGAT, including the 1.39 percentage-point increase in mean balanced accuracy, should be interpreted as descriptive experimental differences rather than statistically significant improvements. Multiple-seed evaluation with confidence intervals and statistical significance testing is therefore required in future work to determine the robustness of these differences to random initialization and training variability.

3.5 Training Behaviour of DI-STGAT

The evolution of the anomaly and domain-learning objectives was monitored during DANN training. Because six source-target directions were evaluated, displaying every training curve in the

main manuscript would be repetitive. The SWaT to WADI curve is selected as the representative example because this transfer produced the largest improvement in balanced accuracy and F1-score.

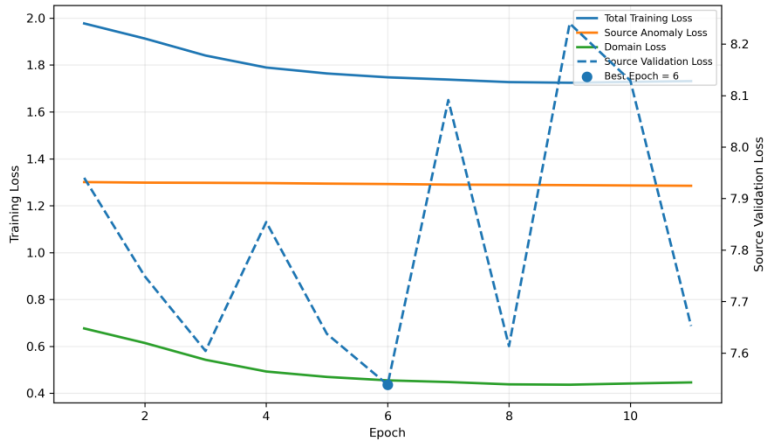

Figure 3.4: DI-STGAT training behaviour for SWaT to WADI

Figure 3.4 illustrates the evolution of the source anomaly-training loss, source validation loss, domain-classification loss, and GRL adaptation strength during SWaT to WADI training. The figure demonstrates the simultaneous optimization of anomaly discrimination and domain adaptation. As training progresses, the GRL coefficient increases according to the adopted schedule, progressively strengthening the adversarial signal applied to the ST-GAT feature extractor. Model selection remains governed by source-validation anomaly loss rather than target-domain labels.

The training behaviour is consistent with the unsupervised adaptation design of DI-STGAT: labeled source observations guide anomaly classification, whereas source and unlabeled target representations jointly contribute to the domain-adversarial objective. The remaining five training curves may be reported as supplementary material if required by the journal.

3.6 Domain-Representation Analysis

An important objective of the DANN/GRL component is to reduce the amount of domain-specific information retained in the learned representation. Domain-classification balanced accuracy was therefore analyzed after adaptation. A value approaching 0.50 indicates stronger source-target confusion, whereas a value approaching 1.00 indicates that the two domains remain readily distinguishable.

Table 3.6: Domain-representation diagnostic results

Source → Target	Domain Balanced Accuracy	Interpretation
BATADAL → SWaT	0.9888	Weak domain confusion
BATADAL → WADI	0.7911	Partial alignment
SWaT → BATADAL	0.8317	Limited alignment
SWaT → WADI	0.7931	Partial alignment
WADI → BATADAL	0.5000	Strong domain confusion
WADI → SWaT	0.6687	Moderate alignment
Mean	0.7622	Domain-dependent alignment

Table 3.6 shows substantial variation in the degree of source-target domain confusion produced by adversarial training. WADI to BATADAL achieved a domain balanced accuracy of 0.5000, indicating that the trained domain classifier could not distinguish the two representations better than chance. WADI to SWaT also showed increased confusion with a value of 0.6687. Conversely, BATADAL→SWaT remained highly distinguishable at 0.9888. The figure therefore demonstrates that DANN/GRL produced domain-dependent representation alignment rather than uniform domain invariance.

Table 3.7: Aggregate Domain-Representation Diagnostics for DI-STGAT

Diagnostic Measure	Mean Value	Interpretation
Balanced accuracy	0.7622	Indicates that source and target representations remained distinguishable overall; 0.50 represents chance-level domain discrimination.
Binary Cross-Entropy (BCE)	0.5442	Measures the domain classifier's prediction error; values approaching the binary chance-loss level indicate greater domain confusion.
Source–target probability	0.2134	Measures the difference between predicted domain probabilities for source and target representations; a smaller gap indicates stronger alignment.
Centroid Euclidean distance (L2)	0.4339	Measures the distance between source and target embedding centroids; a smaller value indicates greater proximity in the representation space.
Centroid cosine similarity	0.9995	Indicates very high directional similarity between source and target embedding centroids; values closer to 1 indicate greater directional similarity.

Table 3.7 shows the mean domain-classification balanced accuracy of 0.7622. Additional diagnostics produced a mean domain-classification (BCE) of 0.5442, mean source-target probability gap of 0.2134, mean centroid Euclidean distance of 0.4339, and mean centroid cosine similarity of 0.9995. These measures provide complementary evidence that adversarial learning influenced source-target representations, although complete domain confusion was not obtained consistently. An important observation is that stronger domain confusion did not automatically result in higher anomaly-detection performance. For example, WADI to BATADAL achieved the strongest domain confusion but did not produce a corresponding F1-score improvement. This suggests that successful domain adaptation requires not only reducing domain-specific information but also preserving anomaly-discriminative structure in the shared representation.

3.7 Decision-Threshold Analysis

A secondary experiment investigated whether selecting the classification threshold from source-validation data could improve target-domain performance. Target validation and test anomaly labels were not used in threshold selection.

Table 3.8: DI-STGAT threshold comparison

Threshold Strategy	Mean Balanced Accuracy	Mean F1-score
Fixed threshold = 0.50	0.5190	0.0437
Source-validation threshold	0.5012	0.0263

The source validation derived threshold reduced mean balanced accuracy from 0.5190 to 0.5012 and F1-score from 0.0437 to 0.0263. Consequently, the fixed 0.50 threshold was retained as the primary operating point as shown in table 3.8.

This result demonstrates that classification calibration itself does not transfer reliably between heterogeneous ICS domains. Even when representations contain transferable ranking information, the probability scale learned from one environment may not correspond directly to the optimal decision boundary in another. This observation helps explain the disparity between relatively strong ROC-AUC values and low fixed-threshold F1-scores observed in several experiments.

3.8 Overall Discussion

The experimental findings demonstrate three main outcomes. (i) The ST-GAT architecture successfully processed heterogeneous ICS environments containing different numbers of process variables and graph structures. The fixed 32-dimensional graph-level representation enabled the three datasets to be processed using the same architecture without requiring identical feature sets, thereby providing a common representation mechanism for heterogeneous ICS domains. (ii) The integration

of DANN and GRL enabled unsupervised target-domain adaptation using labeled source-domain data and unlabeled target-domain data without requiring target-domain anomaly labels during training. DI-STGAT increased mean cross-domain balanced accuracy from 50.51% to 51.90% and mean F1-score from 4.13% to 4.37%, with the strongest improvement occurring for SWaT to WADI, where balanced accuracy increased from 53.04% to 61.37% and F1-score from 7.48% to 8.94%. The ST-GAT versus DI-STGAT comparison in Figure 3.3 demonstrates this improvement. (iii) The domain-representation analysis in Table 3.5 and 3.6 showed that adversarial learning influenced source–target separability, although the degree of alignment varied across transfer directions. These findings demonstrate that DI-STGAT achieved the study's aim of developing a domain-adaptive spatio-temporal framework capable of cross-domain anomaly detection across heterogeneous ICS environments without requiring target-domain anomaly labels for training. However, the transfer-dependent improvements and variations in domain alignment indicate that the framework did not achieve uniform domain invariance or performance improvement across all source–target combinations. Thus, DI-STGAT establishes the feasibility of domain-adversarial cross-domain anomaly detection for heterogeneous ICSs while identifying cross-domain calibration and representation alignment as areas requiring further improvement.

4. CONCLUSION

This study proposed DI-STGAT, a domain-adaptive spatio-temporal graph learning framework for cross-domain anomaly detection in heterogeneous Industrial Control Systems. By integrating ST-GAT with DANN/GRL, the framework provides a mechanism for transferring anomaly-relevant knowledge from a labeled source domain to an unlabeled target domain while accommodating differences in process variables and graph structures. Evaluation across BATADAL, SWaT, and WADI demonstrated the feasibility of this approach, with DI-STGAT providing measurable improvements in cross-domain decision performance over the conventional ST-GAT baseline, particularly for the SWaT→WADI transfer. The findings also showed that the effectiveness of domain adaptation depends on the source–target relationship, indicating that representation alignment alone does not guarantee improved anomaly discrimination. The principal contribution of this work is therefore the establishment of a heterogeneity-aware, domain-adaptive ST-GAT framework that supports cross-domain anomaly detection without requiring target-domain anomaly labels for training. Future work will focus on improving cross-domain probability calibration and graph-level representation learning, strengthening domain alignment while preserving anomaly-discriminative information, and extending the framework to ICS datasets from other industrial sectors to further evaluate its generalizability beyond the water-related environments considered in this study.

REFERENCES

Ahmadi-Assalemi, G., Al-Khateeb, H., Benson, V., Adamyk, B., & Ammi, M. (2025). Adaptive learning anomaly detection and classification model for cyber and physical threats in industrial control systems. *IET Cyber-Physical Systems: Theory & Applications, 10*(1), e70004. https://doi.org/10.1049/cps2.70004

Ahmed, C. M., Palleti, V. R., & Mathur, A. P. (2017). WADI: A water distribution testbed for research in the design of secure cyber physical systems. *Proceedings of the 3rd International Workshop on Cyber-Physical Systems for Smart Water Networks*, 25–28. https://doi.org/10.1145/3055366.3055375

Aslam, M. M., Tufail, A., & Irshad, M. N. (2025). Survey of deep learning approaches for securing industrial control systems: A comparative analysis. *Cyber Security and Applications, 3*, 100096. https://doi.org/10.1016/j.csa.2025.100096

Canonico, R., Lista, F., Navarro, A., Sperlì, G., & Vignali, A. (2025). Threat detection in reconfigurable cyber–physical systems through spatio-temporal anomaly detection using graph attention network. *Computers & Security, 156*, 104509. https://doi.org/10.1016/j.cose.2025.104509 (Iris)

Choi, W.-H., & Kim, J. (2024). Unsupervised learning approach for anomaly detection in industrial control systems. *Applied System Innovation, 7*(2), 18. https://doi.org/10.3390/asi7020018

Deng, A., & Hooi, B. (2021). Graph neural network-based anomaly detection in multivariate time series. *Proceedings of the AAAI Conference on Artificial Intelligence, 35*(5), 4027–4035. https://doi.org/10.1609/aaai.v35i5.16523

Fan, Y., Fu, T., Listopad, N. I., Liu, P., *et al*. (2024). Utilizing correlation in space and time: Anomaly detection for Industrial Internet of Things (IIoT) via spatiotemporal gated graph attention network. *Alexandria Engineering Journal, 106*, 560–570. https://doi.org/10.1016/j.aej.2024.08.048

Federal Republic of Nigeria. (2021). National cybersecurity policy and strategy 2021. *Office of the National Security Adviser*. National Cybersecurity Policy and Strategy

Ganin, Y., Ustinova, E., Ajakan, H., Germain, P., Larochelle, H., Laviolette, F., Marchand, M., & Lempitsky, V. (2016). Domain-adversarial training of neural networks. *Journal of Machine Learning Research, 17*(59), 1–35.

Goh, J., Adepu, S., Junejo, K. N., & Mathur, A. (2016). A dataset to support research in the design of secure water treatment systems. In *Critical Information Infrastructures Security* (pp. 88–99). Springer. https://doi.org/10.1007/978-3-319-71368-7_8

Li, J., Deng, X., & Yao, B. (2025). Enhanced anomaly detection of industrial control systems via graph-driven spatio-temporal adversarial deep support vector data description. *Expert Systems with Applications, 270*, 126573. https://doi.org/10.1016/j.eswa.2025.126573

Lin, L., Gu, A., Min, F., & Zhou, S. (2025). Multi-level graph attention network-based anomaly detection in industrial control system. *Actuators, 14*(5), 210. https://doi.org/10.3390/act14050210

Liu, J., Sha, Y., Zhang, W., Yan, Y., & Liu, X. (2024). Anomaly detection method for industrial control system operation data based on time–frequency fusion feature attention encoding. *Sensors, 24*(18), 6131. https://doi.org/10.3390/s24186131

Mathur, A. P., & Tippenhauer, N. O. (2016). SWaT: A water treatment testbed for research and training on ICS security. In *2016 International Workshop on Cyber-Physical Systems for Smart Water Networks (CySWater)* (pp. 31–36).

Moriano, P., Hespeler, S. C., Li, M., & Mahbub, M. (2025). Adaptive anomaly detection for identifying attacks in cyber-physical systems: A systematic literature review. *Artificial Intelligence Review, 58*, 283. https://doi.org/10.1007/s10462-025-11292-w

Nahalka, M., Cook, M. M., & Pezaros, D. (2024). The good, the bad and the ugly: Investigating the effectiveness of graph deep neural networks for anomaly detection in industrial control systems. In *IFIP International Internet of Things Conference* (pp. 21–36). Springer. https://doi.org/10.1007/978-3-031-81900-1_2

Ogunbode, T. O. (2026). The state of SDG 6 in Nigeria (2016–2024): *A critical review of progress and future strategies.* Environmental Health Insights.

Rehman, M. U., & Bahşi, H. (2024). Process-aware security monitoring in industrial control systems: A systematic review and future directions. *International Journal of Critical Infrastructure Protection, 47*, 100719. https://doi.org/10.1016/j.ijcip.2024.100719

Rotibi, A., Saxena, N., & Burnap, P. (2024). Winning the battle with cyber risk identification tools in industrial control systems: A review. *IET Cyber-Physical Systems: Theory & Applications, 9*(4), 350–365. https://doi.org/10.1049/cps2.12105

United Nations. (2026). Sustainable Development Goal 6: *Clean water and sanitation,* Nigeria. United Nations in Nigeria. UN Nigeria SDG 6

United Nations. (2026). Sustainable Development Goal 9: *Industry, innovation and infrastructure*, Nigeria. United Nations in Nigeria. UN Nigeria SDG 9

Veličković, P., Cucurull, G., Casanova, A., Romero, A., Liò, P., & Bengio, Y. (2018). Graph attention networks. *International Conference on Learning Representations*. (OpenReview)

Wang, Y., Peng, H., Wang, G., Tang, X., Wang, X., & Liu, C. (2023). Monitoring industrial control systems via spatio-temporal graph neural networks. *Engineering Applications of Artificial Intelligence, 122*, 106144. https://doi.org/10.1016/j.engappai.2023.106144

Wu, T., Zhou, D., Ou, Q., & Luo, F. (2026). Intrusion detection systems in industrial control systems: Landscape, challenges and opportunities. *Computers, Materials & Continua, 86*(3), 4. https://doi.org/10.32604/cmc.2025.073482 (TechScience)

Xu, L., Wang, B., Zhao, D., & Wu, X. (2025). DAN: Neural network based on dual attention for anomaly detection in ICS. *Expert Systems with Applications, 263*, 125766. https://doi.org/10.1016/j.eswa.2024.125766

Yang, J., Sheng, Y.-Q., Wang, J.-L., & Ni, H. (2024). CAGCN: Centrality-aware graph convolution network for anomaly detection in industrial control systems. *Journal of Computer Science and Technology, 39*(4), 967–983. https://doi.org/10.1007/s11390-022-2149-y

Zhang, D., Wang, M., Bu, Y., Yu, J., & Yang, L. (2025). PdGAT-ID: An intrusion detection method for industrial control systems based on periodic extraction and spatiotemporal graph attention. *Computers & Security, 149*, 104210. https://doi.org/10.1016/j.cose.2024.104210

International Conference on Engineering Innovation for Sustainable Development (ICESID 2026)
Faculty of Engineering, Ahmadu Bello University Zaria · 8–10 September 2026

DEVELOPMENT AND VALIDATION OF A FINITE ELEMENT MODEL FOR REINFORCED CONCRETE BEAMS EXTERNALLY STRENGTHENED IN FLEXURE WITH STEEL PLATES

Ebitei Williams Francis[1,*], Auta Samuel[1], Aguwa James[1], Abdullahi Aliyu[1]

[1]*Federal University of Technology, Minna*

Email: francisebitei@gmail.com[*], samuel.auta@futminna.edu.ng, james.aguwa@futminna.edu.ng, abdullahi.aliyu@futminna.edu.ng

***Corresponding author**: Ebitei Williams Francis

DOI: https://doi.org/10.67203/sp.ICESID.2026

ABSTRACT

This study presented and validated a finite element (FE) model for estimating the structural performance of externally reinforced concrete (RC) beams using bonded steel plates. The developed model was validated with the existing experimental results, and the effect of the thickness of steel plate and the thickness of adhesive on the ultimate load of strengthened beams was studied. The FE predictions were in good agreement with the experimental results with differences in the ultimate loads being rather minor and the predictions being consistently higher. The developed model was accurate and reliable as indicated by a strong positive correlation (Pearson correlation coefficient, $r = 0.961$, $p < 0.001$). The ultimate load was used as a response variable and a two-factor analysis of variance (ANOVA) was conducted. The results showed that the thickness of the adhesive had a statistically significant effect on ultimate load ($F = 5.12$, $p = 0.043$) while steel plate thickness did not ($F = 2.12$, $p = 0.201$). The load–deflection responses also showed that the RC beams strengthened externally were considerably higher when compared to the control RC beam as a result of the application of external steel plate strengthening, in terms of stiffness, energy absorption capacity and ductility. The behaviour of the beams with an adhesive thickness ranging from 4 to 6 mm was optimal, showing high stiffness, energy absorption capacity, and high ductility due to the efficient dissemination of the stress on the steel–concrete interface. However, an increased thickness of the adhesive layer (8 mm) in comparison led to a decrease in structural efficiency due to a decrease in the interface stiffness and stress transfer. The study showed that finite element model could be used as a valid tool to predict the behaviour of steel-plated RC beams and that the effect of optimizing the thickness of the adhesive was more significant than the increasing thickness of the steel plates on the RC beam to attain better structural performance.

Keywords: *Strengthening; Load; Numerical; Beam; Stiffness; Ductility; Energy absorption*

INTRODUCTION

Reinforced concrete (RC) structures are a large share of civil engineering infrastructures around the world, known for their strength, durability, versatility, and cost-effectiveness (Tiza et al., 2024: Rusnak, 2025: Özmen & Tanrıverdi, 2025). During its service life, however, many existing RC structures suffer from deterioration or structural deficiency issues due to aging, reinforcement corrosion, increased service loads, design errors, environmental exposure, inadequate construction, seismic activities, accidental impacts, and changes in use of buildings (Yadeta et al., 2023; Rincon et al., 2024: Ma et al., 2025). These conditions can cause a decrease in the ability of structural members to withstand flexural loads, especially beams which are the main load resisting members (Mahi & Ridoy, 2025; Osta et al., 2026). Strengthening and rehabilitation, which are methods for prolonging the life of the structures without the high costs of demolition and reconstruction, have therefore become more and more important in recent years (Hu et al., 2024; Rusnak, 2025; Elkhatib et al., 2025).

Out of all the strengthening techniques that are available, externally bonded steel plate reinforcement is the most common technique used due to the fact that it is the most effective, easy to install and economic (Khalil & Attia, 2025; Mankare, & TS, 2026; Alsuhaibani, 2025). The method typically involves the use of high-strength epoxy adhesives to adhere steel plates to the tension surface of RC beams, and sometimes with mechanical anchors (Xu et al., 2024; Napoli et al., 2024). The flexural strength, stiffness, and cracking resistance of the composite structure are enhanced due to the external

bond of steel plate, and the deflection under service loads is reduced (Qiang et al., 2023; Mosahebfard et al., 2026). There are many experimental studies that have proven that steel plate strengthening is a viable solution for the rehabilitation of deficient RC beams and improves their structural performance (Bandara et al., 2023; Napoli et al., 2024; Xu et al., 2024; Elkhatib et al., 2025).

Although it has proven effective, the behaviour of externally strengthened RC beams is complex because of the interaction between the concrete, the reinforcing steel, the adhesive layers and the externally bonded steel plates (Foraboschi, 2022; Hamoda et al., 2024; Ahmed, 2025). The mechanical properties of the component materials, nature of the bonds between the concrete and the adhesive, geometric properties of the plates, configuration of the plates' strengthening, loadings and possible failure mechanisms such as crushing of the concrete, yielding of the steel, debonding of the plates or failure of the adhesive (Ali et al., 2001; Edalati & Irani, 2012; Alam et al., 2020). The prediction of the structural response is difficult with conventional analytical approaches only (Hamoush & Ahmad, 1990; Ciampa & Pecce, 2021).

Experimental tests are the most accurate way to study the behaviour of strengthened RC beams (Sun et al., 2023; Zhang et al., 2023). Laboratory testing, however, is costly, time consuming, and is often restricted in its availability of testing facilities, materials and instrumentation (Oehlers & Seracino, 2004; Teng et al., 2002). In addition, experimental programmes typically examine only a few of the variables, and it is challenging to explore the effects of several design parameters in a comprehensive way (Hajirasouliha et al., 2012; Abaqus, 2014). In view of this, numerical modelling, specifically Finite Element Method (FEM) has become an essential tool to foresee the response of RC structures under strengthening with externally bonded steel plates (Alharthai et al., 2024).

By using the Finite Element Method, complex material behavior can be simulated, the non-linear cracking, crushing of concrete, yielding of reinforcement steel, the behavior of the adhesive bond, and the interaction between steel plates and concrete can be modeled (Muka, 2023; Noor et al., 2025). The modern finite element software enables researchers to accurately study the distribution of stresses, the load-deflection behavior, propagation of cracks, development of strains, and failure modes (Kholil & Ahmed, 2025; Ciampa & Pecce, 2021). After being properly validated, finite element models are able to perform detailed parametric studies, optimize strengthening schemes and support structural design (Raviolo et al., 2023; Mobarhan et al., 2026).

Several researchers have created finite element models of RC beams externally strengthened with various modelling methods, constitutive material models, and bond-slip models (Ciampa & Pecce, 2021). In many of these studies, the results are in reasonable agreement with the experimental data, but significant differences between experimental data and the results in the studies have been found due to the various assumptions made about material nonlinearities, the modelling of the interfaces, the mesh discretization, and the failure criteria (Chen et al., 2012). Furthermore, existing models have predominantly considered strengthening with externally bonded carbon fibre reinforced polymer (CFRP) while few studies have investigated externally bonded steel plate strengthening in detail and developed validated nonlinear finite element models that can be used to accurately predict both the global and local structural response (Li et al., 2025).

To create a good finite element model which realistically simulates the behavior of exteriorly strengthened reinforced concrete beams is therefore imperative. A model, it should be capable of reproducing experimental observations such as load-deflection behaviour, strain distribution, cracking patterns, ultimate load capacity and failure modes (Li et al., 2025). It is important to validate the model developed against pre-existing experimental studies before it can be used with confidence for additional analysis and structural design applications, as proposed by Ciampa & Pecce (2021).

The focus of this study is thus the development and validation of the nonlinear finite element model of reinforced concrete beams strengthened externally in flexure with steel plates. To ensure the accuracy and reliability of the model, published validation test results of existing studies will be used. The validated model is hoped to be able to offer a reliable numerical tool in analysing the flexural response of strengthened RC beams and minimize the need for expensive experimental investigations thus helping in the development of structural rehabilitation and strengthening.

2.0 METHODOLOGY

2.1 Development of Finite Element Model of Steel Glue RC Beam

This section describes the formulation of a finite element model that is based on the ideas originally presented by Bimal & Hiroshi (2002). Considering the very small thickness of the interface, an eight-noded element as shown in Figure 1(a) was found to be sufficient for modeling the steel-glue-concrete interface.

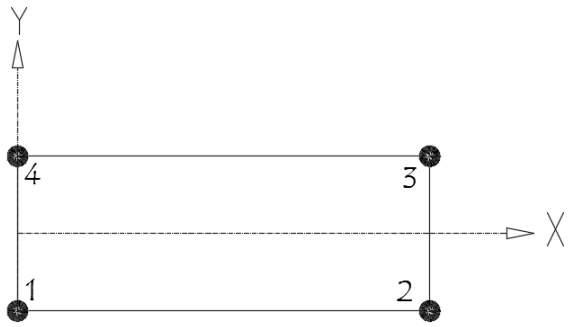

Figure 1: Steel-glue concrete interface element

Introducing pseudo-nodes 1' and 2' (see Figure 1), an iso-parametric formulation with parabolic shape functions could be implemented. The element was formulated using the two-point Gaussian integration rule.

2.1.1 Stress- strain relations

The strains in the glue element can be written as

$$\varepsilon = \begin{bmatrix} \varepsilon_x \\ \varepsilon_y \\ \gamma_{xy} \end{bmatrix} = \begin{bmatrix} \dfrac{\delta u}{\delta x} \\ \dfrac{\delta v}{\delta y} \\ \dfrac{\delta u}{\delta y} + \dfrac{\delta v}{\delta x} \end{bmatrix} \quad (1)$$

The strain ε_x along the x-direction may be approximated as

$$\varepsilon_\xi = \frac{\delta u}{\delta x} \quad (2)$$

A shape function is an interpolation function that provides an association between the variables in a finite element and their values at the nodes of the element. The finite element methods are applied to solve the problem and these nodal values are obtained.

$$u(x) = \sum_i N_i(x) u_i = \boldsymbol{N} u \quad (3)$$

Where;

u(x) is the function under investigation (for example displacement field)

N(x) is the shape functions matrix

$$u = \begin{bmatrix} u_1 \\ u_2 \\ u_3 \\ u_4 \\ . \\ . \\ u_n \end{bmatrix} \; is\ the\ vector\ of\ unknowns\ in\ the\ nodes(for\ example: displacement)$$

Substituting Equation 3 into 2, we have,

$$\varepsilon_x = \frac{\delta u}{\delta x} = \frac{\delta}{\delta x}\sum_{i=1}^{2} N_i^{'}(x)\breve{u}_i$$

$$= \sum_{i=1}^{2} \frac{dN_i^{'}(x)}{dx}\breve{u}_i, \qquad (4)$$

The shape functions at three equivalent nodal points 1′and 2′as shown in Fig.1 are represented by Ni=Ni(x); ui are the average nodal displacements along the line n = 0. This equation can then be written in terms of the nodal displacements of the element, ui, as shown in equation (4).

$$\varepsilon_x = \frac{dN_1^{'}}{dx}\left(\frac{u_1 + u_4}{2}\right) + \frac{dN_2^{'}}{dx}\left(\frac{u_2 + u_3}{2}\right) \qquad (5)$$

The strain in the normal direction ε_n. is given by

$$\varepsilon_y = \frac{\delta v}{\delta y} \qquad (6)$$

and can be stated in terms of nodal normal strains as

$$\varepsilon_y = \sum_{i=1}^{2} N_i^{'}(x)\left(\frac{\delta v}{\delta y}\right)_i = \sum_{i=1}^{2} N_i^{'}(x)\left(\frac{\Delta v}{t}\right)_i$$

$$= \frac{1}{t}\left[N_1^{'}(v_4 - v_1) + N_2^{'}(v_3 - v_2)\right] \qquad (7)$$

where t is the element thickness. The shear strain γ_{xy} is approximated as

$$\gamma_{xy} = \frac{\delta u}{\delta y} + \frac{\delta v}{\delta x} = \sum_{i=1}^{2} N_i^{'}(x)\left(\frac{\delta u}{\delta y}\right)_i + \sum_{i=1}^{2} \frac{dN_i^{'}(x)}{dx}\breve{v}_i$$

$$\gamma_{xy} = \frac{1}{t}\left[N_1^{'}(u_4 - u_1) + N_2^{'}(u_3 - u_2)\right] + \left[\frac{dN_1^{'}}{dx}\left(\frac{v_1 + v_4}{2}\right) + \frac{dN_2^{'}}{dx}\left(\frac{v_2 + v_3}{2}\right)\right] \qquad (8)$$

Substituting Equations (5), (7) and (8) in Equation (1) we obtain, the above equation can be written as

$$\varepsilon = [\mathrm{B}][v] \qquad (9)$$

$$\varepsilon = \begin{bmatrix} \frac{1}{2}\frac{dN_1^{'}}{dx} & 0 & \frac{1}{2}\frac{dN_2^{'}}{dx} & 0 & \frac{1}{2}\frac{dN_2^{'}}{dx} & 0 & \frac{1}{2}\frac{dN_1^{'}}{dx} & 0 \\ 0 & -\frac{N_1^{'}}{t} & 0 & -\frac{N_2^{'}}{t} & 0 & \frac{N_2^{'}}{t} & 0 & \frac{N_1^{'}}{t} \\ -\frac{N_1^{'}}{t} & \frac{1}{2}\frac{dN_1^{'}}{dx} & -\frac{N_2^{'}}{t} & \frac{1}{2}\frac{dN_2^{'}}{dx} & \frac{N_2^{'}}{t} & \frac{1}{2}\frac{dN_2^{'}}{dx} & \frac{N_1^{'}}{t} & \frac{1}{2}\frac{dN_1^{'}}{dx} \end{bmatrix} \begin{bmatrix} u_1 \\ v_1 \\ u_2 \\ v_2 \\ u_3 \\ v_3 \\ u_4 \\ v_4 \end{bmatrix}$$

Where:
B is the strain matrix and v is the displacement vector
Ni are the parabolic shape functions

$$B = \begin{bmatrix} \frac{1}{2}\frac{dN_1^{\wr}}{dx} & 0 & \frac{1}{2}\frac{dN_2^{\wr}}{dx} & 0 & \frac{1}{2}\frac{dN_2^{\wr}}{dx} & 0 & \frac{1}{2}\frac{dN_1^{\wr}}{dx} & 0 \\ 0 & -\frac{N_1^{\wr}}{t} & 0 & -\frac{N_2^{\wr}}{t} & 0 & \frac{N_2^{\wr}}{t} & 0 & \frac{N_1^{\wr}}{t} \\ -\frac{N_1^{\wr}}{t} & \frac{1}{2}\frac{dN_1^{\wr}}{dx} & -\frac{N_2^{\wr}}{t} & \frac{1}{2}\frac{dN_2^{\wr}}{dx} & \frac{N_2^{\wr}}{t} & \frac{1}{2}\frac{dN_2^{\wr}}{dx} & \frac{N_1^{\wr}}{t} & \frac{1}{2}\frac{dN_1^{\wr}}{dx} \end{bmatrix}$$

$$v = \begin{bmatrix} u_1 \\ v_1 \\ u_2 \\ v_2 \\ u_3 \\ v_3 \\ u_4 \\ v_4 \end{bmatrix}$$

2.1.2 Shape functions

The shape functions can be defined as:

$$N_k = \sum \frac{\xi - \xi_m}{\xi_k - \xi_m}, \quad therefore,$$

$$N_1 = \frac{\xi - \xi_2}{\xi_1 - \xi_2} = \frac{\xi - 1}{-1 - 1}$$

$$N_1 = \frac{1}{2}(1 - \xi) \tag{12}$$

$$N_2 = \frac{\xi - \xi_1}{\xi_2 - \xi_1} = \frac{\xi + 1}{1 + 1}$$

$$N_2 = \frac{1}{2}(1 + \xi) \tag{13}$$

2.2 Material and Cracking Behavior of the Interface

Before cracking of the interface, the property matrix of the material is given as presented as Eq. (14), where: ν= Poisson's ratio of the interface, E= modulus of elasticity of the interface, G= shear modulus.

The behaviour of the interface will be assumed to be elastic under tensile and shear loading, with a linear response up to the failure limit as shown in Figure 2. After reaching this limit, cracking starts to develop in the interface element. The very thin interface limits crack propagation to along the adhesive (glue) line or perpendicular to the glue line.

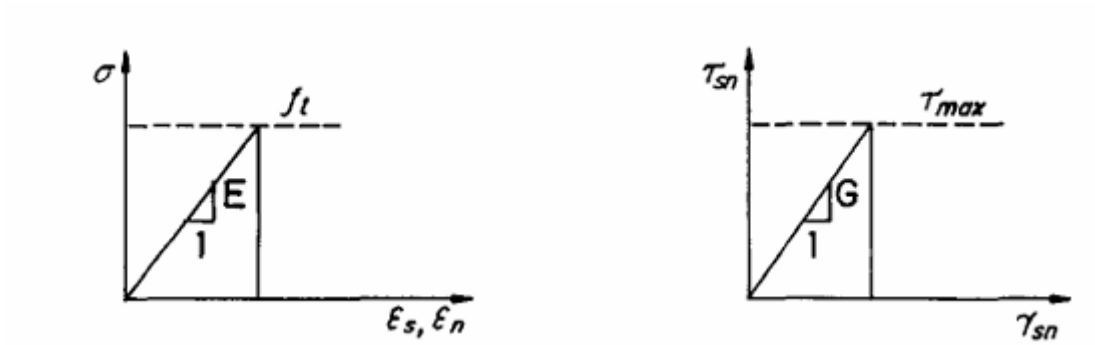

Figure 2: Material behavior of the interface element in tension and shear.

$$[D]_{x-y} = \frac{E}{1-\nu^2}\begin{bmatrix} 1 & \nu & 0 \\ \nu & 1 & 0 \\ 0 & 0 & \frac{G(1-\nu^2)}{E} \end{bmatrix} \tag{14}$$

It is assumed that cracking occurs perpendicular and/or parallel to the glue line when (fii) and/or (fip) equals the corresponding normal stress at the interface. From this point, further load in the direction of the crack can no longer be resisted by the interface. Therefore, the normal stress and the corresponding elastic modulus in that direction are assumed to be zero, i.e., total loss of stiffness across the crack.

If cracks form at an angle normal to direction of glue, the property matrix of the material should be modified to reflect the loss of stiffness in that direction and the reworked property matrix is called:

$$[D]_{i-n} = \begin{bmatrix} 0 & 0 & 0 \\ 0 & E & 0 \\ 0 & 0 & 0.25G \end{bmatrix} \tag{15}$$

In addition to cracking perpendicular to the glue line, the interface can also fail parallel to the glue line when it is subjected to a combination of normal and shear stresses. Experimental results suggest that such a failure can be best represented by the Mohr–Coulomb fracture criterion, which takes into consideration the interaction between normal and shear stresses at the interface, and predicts the onset of cracking under combined loading.

$$\tau = c - \sigma \tan\phi \tag{16}$$

where: c= cohesion, σ = normal stress, ϕ= angle of internal friction. For steel–epoxy–concrete interface: Cohesion c= 4.8-9.5 MPa and Internal friction angle $\phi=28^0$

The strength of adhesion and failure resistance of the interface is influenced by the type of surface preparation, the quality of the adhesive, and properties of the concrete substrates. If the failure occurs at the interfaces due to tensile (peeling) stress, then the stress components and stiffness terms at the interfaces are set to zero, indicating that the bond will not carry any load. But when the loading is compressive, failure defined by the Mohr–Coulomb criterion enables the interface to sustain a compressive load. Here, only the shear stress and shear stiffness are removed, and the compressive normal stiffness is left as it is, and a new material stiffness matrix is obtained.

$$[D]_{x-y} = \begin{bmatrix} \frac{E}{1-\nu^2} & \frac{\nu E}{1-\nu^2} & 0 \\ \frac{\nu E}{1-\nu^2} & \frac{E}{1-\nu^2} & 0 \\ 0 & 0 & 0 \end{bmatrix} \tag{17}$$

2.2.1 Material Properties for the Interface Element

The following material properties define the interface element: normal elastic modulus (E), shear modulus (G), Poisson's ratio (ν) and tensile strength (f_{ti}). The properties of these are determined by those of the parent components, which are the concrete substrate, epoxy adhesive and the externally bonded steel plate. The mechanical properties of these constituent materials are used to determine the

normal elastic modulus, the Poisson's ratio and the tensile strength, and the shear modulus of the interface is obtained by measuring the slope of the average shear stress–slip relationship of a half beam specimen test.

The resulting shear modulus was found to be G=120.1 MPa. This is essentially the same as the value reported by Charif (1983). If ν = 0.16, the interface modulus is calculated as E=2G (1+ν) and comes out to be 278.6 Mpa. The experimental value of the tensile cut-off strength of the interface was obtained as $f_{ti} = 4$ MPa.

2.2.2 Finite Element Model for Constituent Materials

The interface element of the previous section was added to the nonlinear finite element solution procedure. The response of each of the constituent materials needs to be accurately modelled when dealing with reinforced concrete beams strengthened by externally bonded steel plates (EBSSP), which have highly nonlinear behaviour. The overall structural response will be dependent on the interaction between the concrete, internal reinforcing steel, externally bonded steel plate and the bond interfaces. Accordingly, an appropriate constitutive model and finite element formulation were assigned to each material to realistically simulate its behaviour during the loading process.

2.3 Concrete

2.3.1 Yield Criterion

Cracking in tension and crushing in compression cause the response of concrete to be highly nonlinear. The Mohr–Coulomb yield criterion is used to describe the onset of yielding in this study. Initial yielding is assumed to take place at about 30% of the compressive strength of the concrete, expressed as:

$$\sigma_0 = 0.3f_c' \tag{18}$$

where $f_c'$is the compressive strength of the concrete. From this point on, the yield surface expands due to plastic deformation. The following loading surfaces are represented by

$$f(\sigma) = \sigma_0(Z) \tag{19}$$

The equation contains a hardening parameter, Zis, that is a function of the effective plastic strain. During loading, the concrete displays elasto-plastic characteristics, and continual plastic deformation occurs. After the effective stress exceeds the ultimate compressive strength, the material is said to be perfectly plastic up to the crushing strain.

2.3.2 Flow Rule and Hardening Rule

For plastic deformation there is an associated flow rule, which is characterized by the plastic strain increment that is perpendicular to the yield surface. This relation between effective stress and plastic strain is obtained from uniaxial parabolic stress–strain relation proposed for concrete,

$$\sigma = E_0\varepsilon - \frac{1}{2}\left(\frac{E_0}{\varepsilon_0}\right)\varepsilon^2 \tag{20}$$

where E_0 is the initial elastic modulus, ε is the total strain, and ε_0 is the strain at the peak compressive stress. The initial elastic modulus is computed according to the formula suggested by the ACI Committee 363,

$$E_0 = 3320\sqrt{f_c'} + 6900 \tag{21}$$

It applies to normal and high-strength concrete (between 21 and 83 MPa compressive strength). The constitutive relationship for concrete, then, can be written as

$$\sigma = -E_0\varepsilon_p + \sqrt{2E_0^2\varepsilon_0\varepsilon_p},\ (0.3f_c' \le \sigma \le f_c') \tag{22}$$

where $\varepsilon_p$denotes the effective plastic strain.

2.3.3 Crushing Criterion

It is assumed that crushing of concrete is not affected by applied stress, but rather by the strain level. The crushing is defined to happen when the compressive strain is effective enough to reach the ultimate crushing strain, as provided by the equation below

$$f(\varepsilon_{ij}) = \varepsilon_u \tag{23}$$

Where, $\varepsilon_u = 0.0035$. The concrete has been considered to have lost all its compressive load-bearing capacity at this point.

2.3.4 Cracking Behaviour

The tensile response of concrete is modeled by a smeared crack model to distribute cracking throughout the finite element instead of as a discrete crack. Concrete is a linear elastic material in tension before cracking. Cracks start when the maximum principal tensile stress equals the tensile strength of concrete. The tensile strength is estimated from the following empirical equation given by Raphael (1984),

$$f_t = 0.324(f_c')^{2/3} \tag{24}$$

After cracking, it is assumed that cracks form at 90° to the maximum principal tensile stress. The perpendicular stiffness is set to zero, the shear stiffness is reduced to reflect the loss of aggregate interlock along a crack and Poisson's ratio for cracks is ignored.

2.3.5 Tension Stiffening

The concrete and the reinforcement act together. This means that concrete between cracks can still resist significant tensile force, although cracking reduces the effective tensile stiffness of the concrete significantly. This phenomenon is called tension stiffening and is represented in the finite element model by assigning an effective or fictitious post-cracking tensile modulus to concrete.

The equation can be written as:

$$E_i = \alpha f_t' \left(1 - \frac{\varepsilon_i}{\varepsilon_m}\right)\frac{1}{\varepsilon_i},\ \varepsilon_t \le \varepsilon_i \le \varepsilon_m \tag{25}$$

Where, E_i= s the secant (or degraded) modulus of elasticity at a tensile strain ε_i, α= is a material parameter that controls the post-cracking tensile response, f_t'= tensile strength of concrete, ε_i= tensile strain at the current loading stage, ε_t= strain at the onset of cracking, ε_m= maximum tensile strain.

2.4 Finite Element Representation

The concrete material is modeled as a finite element, with 9 integration points and 9 nodes (isoparametric elements) and the constitutive matrix of the model is changed at each integration point in each load increment to capture concrete cracking, crushing and plastic behaviour accurately. The internal reinforcing steel is idealized using 3-noded quadratic truss elements, which are only capable of handling axial deformations, and with an elasto-plastic constitutive model with isotropic hardening. This bond between the reinforcing steel and concrete is modeled with the use of six-noded interface elements allowing bond-slip and failure when the interface shear exceeds the given bond strength. The interface has a shear modulus of 1.2GPa, elastic modulus of 2.78GPa, Poisson's ratio of 0.16, and bond strength of 7.5MPa. The externally bonded steel plate is modeled as an elasto-plastic material with isotropic hardening based on the von Mises yield criterion and discretized by nine-noded isoparametric Lagrangian elements to capture the stress concentrations and peeling stresses. Taken together these material models allow for the finite element model to simulate realistically the concrete damage, the yielding of the steel, and the bond-slip and degradation of the interface, providing reliable prediction of the loading–deformation behavior, failure mode and ultimate load capacity of steel-plated reinforced concrete beams under monotonic loading.

2.5. Beams investigated

A custom MATLAB program based on an incremental–iterative Newton–Raphson solution procedure was developed and used to implement and solve the finite element model. The nonlinear equilibrium equations were solved incrementally by subdividing the applied load into a number of load steps. The global tangent stiffness matrix was assembled from individual element stiffness matrices and the incremental displacement vector was obtained by solving the global equilibrium equations for each load step. The iterative solution accounted for the nonlinear response of the concrete, the steel reinforcement, the external steel plate and the interface elements. At the end of each iteration the element strains and stresses at the integration points were calculated and the internal resisting force vector was modified. The residual force was then calculated as the difference between the externally applied. Both force and displacement criteria were used to converge each load increment. Convergence was assumed to be achieved when the normalized residual force and incremental displacement were small enough, with tolerance limits of and, respectively. A maximum of 50 iterations was allowed for each load increment. Where convergence was not achieved the load increment was reduced and the iterative procedure repeated until equilibrium was achieved.

The beam specimens investigated by John (2023) are shown in Table 1. For the purposes of this study, the calibration and validation of the finite element model presented used the steel-plate-strengthened beam subset of John's (2023) experimental program. The specimens considered were the control beam and the beams strengthened externally with steel plates of different thicknesses and adhesive layer thicknesses. The CFRP-strengthened specimens of John's (2023) experimental program were not part of the FE validation dataset.

The sample ID is defined as follows in Table 1: P = Steel Plate, F = Flexural Strengthening, 0, 2, 4, 6, and 8 are the thicknesses of the epoxy adhesive (in mm), respectively. The material properties used in the finite element model were taken from the experimental study done by John (2023). The cylinder compressive strength (f'c) was assumed for the concrete material as 85% of the cube compressive strength as reported in the experimental investigation, which is a common assumption in concrete modelling. The rest of the parameters needed to define the concrete constitutive model were obtained as follows:

The internal reinforcing bars and stirrups were simulated as elastic–plastic materials with Es = 200 GPa and fy = 530 MPa, and H' = 200 MPa. In the same manner, the elastic modulus (Ep) of the externally bonded steel plate was assumed to be 200 GPa, the yield strength (fy) as 240 MPa, the Poisson's ratio (v) as 0.30, and the plastic modulus (H') as 200 MPa.

The bond behaviour at the steel plate–adhesive–concrete interface was simulated using some of the interface properties proposed by Ziraba and Baluch (1995) to enable the numerical model to realistically simulate the interaction between the bonded steel plate and the concrete substructure.

Table 1: Experimental Programme of Steel Plate for Flexural Strengthening

Sample group	Steel Plate thickness	Epoxy Thickness (mm)	Sample ID
	-	-	FA-0
A	1.0mm Steel Plate	2	PFA2
		4	PFA4
		6	PFA6
		8	PFA8
B	1.5mm Steel Plate	2	PFB2
		4	PFB4
		6	PFB6
		8	PFB8
C	2.0mm Steel Plate	2	PFC2
		4	PFC4
		6	PFC6
		8	PFC8

Figure 3 presents the experimental beam layout and the cross-sectional reinforcement details used as basis for the finite element idealization, including the 2Ø8 mm top reinforcement, 2Ø10 mm bottom reinforcement, Ø6 mm stirrups and the externally bonded strengthening system. The cross-sectional size of the reinforced concrete beams was 150 mm × 100 mm as shown in Figure 3. The beams were longitudinally reinforced with 2Ø8 mm bars at the top and 2Ø10 mm bars at the bottom. Ø6 mm stirrups were provided along the length of the beam. The internal reinforcement of the control beam FA-0 and the strengthened beam PFA2 was identical, and the strengthening of PFA2 was achieved by an externally bonded steel plate using the specified adhesive layer.

The longitudinal reinforcement was modelled by truss elements embedded into the concrete domain in the finite element model. The top and bottom reinforcement was configured to be the same as the physical reinforcement in Figure 3. The Ø6 mm transverse reinforcement was also modelled with truss elements in the corresponding locations and spacing. The adopted bond-slip model was used to model the bond between the reinforcement and the surrounding concrete and to capture the relative interaction between the reinforcement and concrete. For the strengthened specimens, the externally bonded steel plate was modelled using plate elements and the adhesive layer between the steel plate and concrete was modelled using the six-node interface elements described in Section 2.5. Consequently, the reinforcement and strengthening configurations applied to the FE model were consistent with the geometry and reinforcement detailing of the experimental specimens as shown in Figure 3.

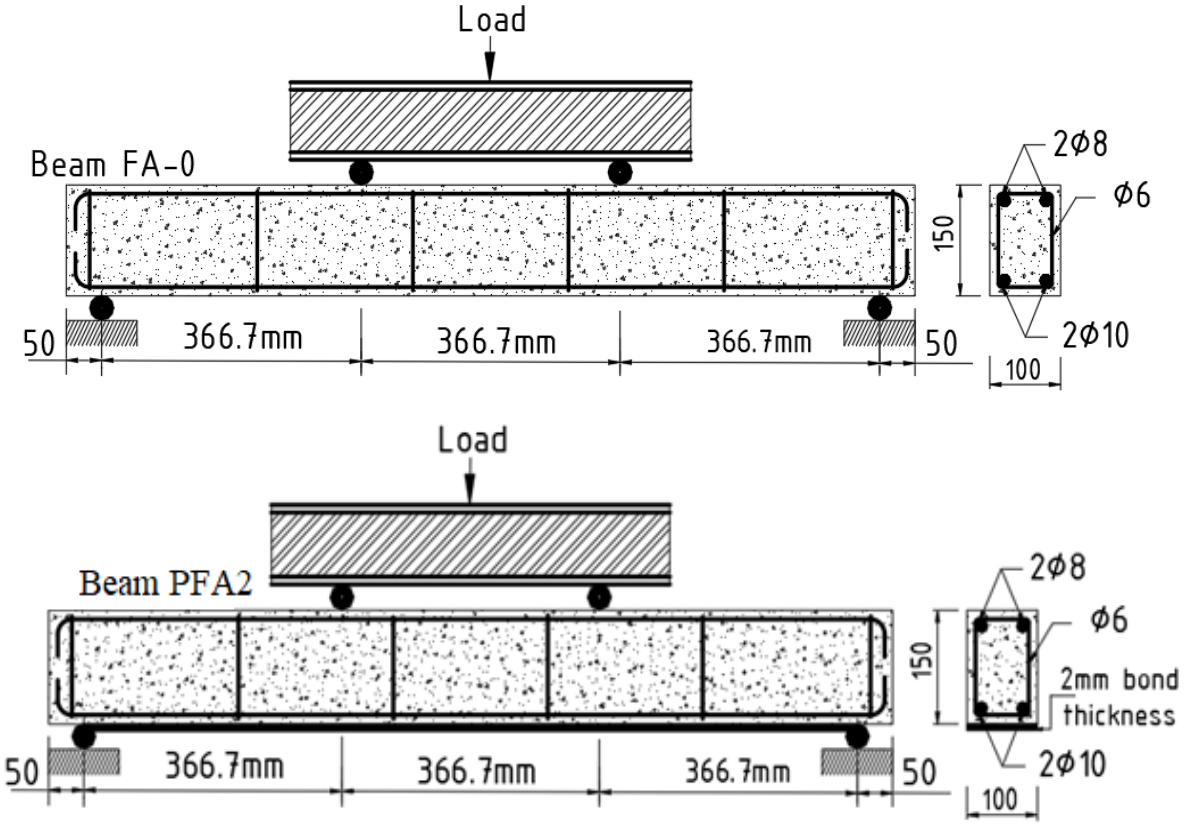

Figure 3: Beam configuration

2..5.1. Mesh sensitivity

A mesh sensitivity analysis was performed to find a suitable mesh density for the finite element model and to ensure that the numerical predictions were not significantly affected by the element size, as shown in Table 2. The three meshes that were studied are called coarse, medium and fine and are progressively refined. Similar element formulations, material constitutive models, interface properties, loading and boundary conditions were maintained for all mesh configurations. The predicted ultimate load and the corresponding mid-span displacement were the main parameters used to evaluate mesh convergence.

Table 2: Mesh sensitivity and convergence assessment

Mesh	Approx. element size (mm)	No. of elements
Coarse	40	4,820
Medium	30	7,650
Fine	20	12,480
Very fine	15	18,920

3.0 RESULTS AND DISCUSSION

3.1 Results and validation of the development model

The experimental results obtained by John (2023) were presented in Table 3, and the finite element (FE) results were compared with the experimental ones to check the agreement of the two methods and to assess the effect of steel plate thickness and adhesive thickness on the ultimate load values. The overall agreement between the FE model and experimental results was good with percentage differences ranging from 0.53% to 10.62% with an average difference of approximately 3.10%. The FE model always predicted the experimental ultimate loads slightly higher. Most of the specimens showed differences of less than 4%, which means a satisfactory numerical accuracy. The largest differences were for PFB8 (10.62 %) and PFB2 (6.82 %). This may be due to the difficulty in accurately modeling the adhesive thickness, interface behavior, debonding, surface imperfections and material variability. This was additionally verified by a high positive correlation between the experimental and FE results with a Pearson correlation coefficient of 0.961 ($p < 0.001$), showing that the developed FE model was able to capture the experimental behaviour of strengthened beams. In addition, a 2-factor analysis of variance (ANOVA) was performed with steel plate thickness and adhesive thickness as the independent factors and the FE-predicted ultimate load as the dependent variable, excluding the control specimen FA-0 as shown in Table 4. The ANOVA result indicates that the thickness of the steel plate is not statistically significant with the predicted ultimate load with value $F = 2.12$ and $p = 0.201 > 0.05$, while the thickness of the adhesive is statistically significant with the predicted ultimate load value $F = 5.12$ and $p = 0.043 < 0.05$.

Table 3: Loads of the Beams

Sample ID	Steel plate thickness (mm)	Adhesive thickness (mm)	John (2023)'s Exp. Results (kN)	Finite Element Model, (kN)
FA-0	-	-	93.33	94.24
PFA2	1.0	2.0	121.68	123.12
PFA4	1.0	4.0	128.23	130.10
PFA6	1.0	6.0	124.25	126.05
PFA8	1.0	8.0	115.75	119.23
PFB2	1.5	2.0	110.55	118.09
PFB4	1.5	4.0	119.08	122.09
PFB6	1.5	6.0	128.23	130.14
PFB8	1.5	8.0	105.00	116.15
PFC2	2.0	2.0	125.12	128.92
PFC4	2.0	4.0	127.24	130.95
PFC6	2.0	6.0	126.50	127.17
PFC8	2.0	8.0	115.00	119.4

Table 4: ANOVA parameters

Source	df	Sum of Squares	F-value	p-value
Steel plate thickness	2	50.55	2.12	0.201
Adhesive thickness	3	183.42	5.12	0.043
Error	6	71.62	—	—

These results show that the increase in the thickness of the adhesive layer compared to the variation in the thickness of the steel plates had a more significant effect on the load bearing capacity of the strengthened beams within the range of parameters investigated. The results of the analysis prove that the finite element model can represent the structural response of the steel-plated reinforced concrete beam well. It also shows that optimizing the thickness of the adhesive is more important than increasing the thickness of the steel plates in order to increase the load carrying capacity of the strengthened beams. The highest performance was achieved with the thickness of the adhesive of ~ 4-6 mm, and with the thickness of the adhesive increased to 8 mm, the structural efficiency was reduced.

3.2 Load–Deflection behaviour

The load-deflection curves in Figure 4 prove that the use of EBSP resulted in the significantly higher stiffness, energy absorption and ductility of the reinforced concrete beams as compared to the unstrengthened control beam (FA-0).

Referring to Figure 4, the strengthened beams have higher initial slopes than the control beam, which shows that the initial stiffness of the strengthened beams is higher. This indicates that the beams with plating took higher loads with lesser deflection in the elastic portion. The enhanced specimens tended to show highest stiffness for beams with 4 mm and 6 mm thickness of adhesive, which indicates the better transfer of stress between the steel plate and concrete. Contrastingly, beams with an 8 mm layer of adhesive had a small decrease in stiffness, indicating that, thicker adhesives allow more deformation before the stresses are adequately carried from one side to the other.

According to Figure 4, the increased area under the load–deflection curves for the strengthened beams compared to the control beam also showed a significant increase in the energy absorbing capacity of the strengthened beam. The stress distribution was more uniform and the propagation of cracks was slowed down and delayed by the combined effect of the steel plate and adhesive layer over the wall, leading to the increase in absorbed energy. The specimens with load application by 4 mm and 6 mm adhesive thickness demonstrated the maximum absorption of energy with a relatively high loading force and a significant deflection range prior to failure. On the other hand, the 8 mm adhesive specimens showed reduced energy absorption, with a high drop in load after the peak load, suggesting that interface degradation started earlier.

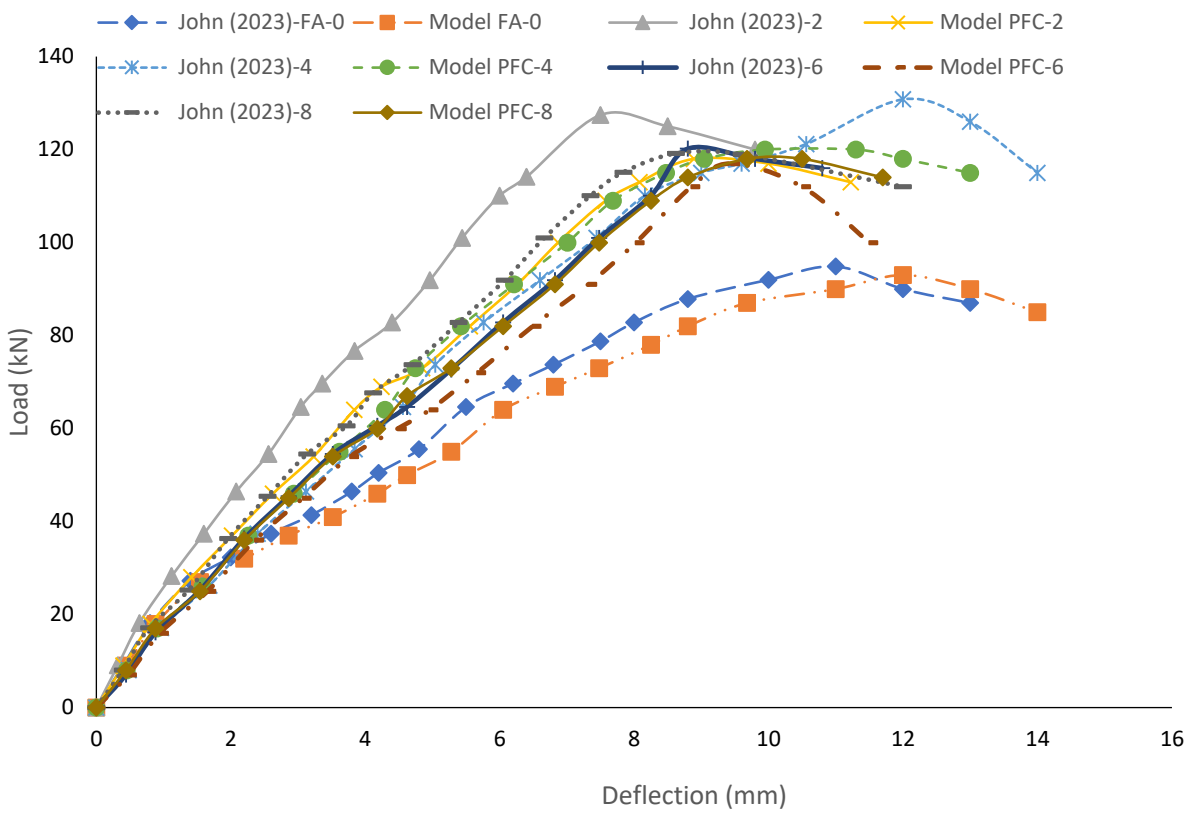

Figure 4: Load–Deflection behaviour

3.2.2 Ductility

The enhanced beams exhibited greater ductility than the control beam as they were able to carry higher deflections after yielding and still carried a significant percentage of their capacity. The post peak behavior of the plated beams was more continuous than that of the control beam thus reflecting a more ductile mode of failure. The specimens that had an adhesive thickness of 4 mm and 6 mm showed the best ductile behaviour, with high ultimate loads and long deformations until failure. Adhesive specimen dimensions of 8 mm reached relatively high loads, but the load at the peak was followed by a more evident decrease in load after the peak which indicates a loss in ductility due to loss of interface stiffness. As a whole, the results show that the optimum thickness range of the adhesive for the externally steel-plated reinforced concrete beams is 4–6 mm with regard to stiffness, energy absorption and ductility.

Table 5: Deflection and ductility Caparison

Beam	Exp. peak (mm)	Model peak (mm)	Difference (mm)	Difference (%)
FA-0	11.5	12.5	+1.0	+8.7
FA-2	8.0	9.5	+1.5	+18.8
FA-4	12.5	10.5	−2.0	−16.0
FA-6	9.5	9.5	0.0	0.0
FA-8	9.5	10.0	+0.5	+5.3

Table 5 presents deflection and ductility results of the experimental and FEM model. The best specimen in terms of large deformation capacity is FA-4, with the maximum experimental peak displacement of about 12.5 mm and a large deformation range. FA-6 and FA-8 show relatively stable deformation responses with peak experimental displacement of about 9.5 mm. FA-2, belonging to moderate-to-high ductility class, has the lowest experimental peak displacement of about 8.0 mm. FA-0 shows the baseline response with moderate ductility and

obvious post-peak softening. To summarize, FA-4 has the maximum deformation capacity, and FA-6 and FA-8 exhibit more stable post-peak behavior, which means that the FA modification influences the peak deformation and post-peak behavior of the beams.

3.3 Sustainability, Nigerian Infrastructure Development, Or Industrial Policy

The use of externally bonded steel plates for strengthening existing reinforced concrete structures has important implications for sustainable infrastructure development in Nigeria. Steel-plate strengthening is a practical, economical alternative to the demolition and complete reconstruction of structurally deficient beams and other reinforced concrete members. The technique can extend the functional service life and enhance the durability of aging infrastructure by increasing the load-carrying capacity, stiffness and serviceability of existing structures. This is especially true in Nigeria where the rehabilitation of dilapidated bridges, buildings and other reinforced concrete infrastructure is becoming increasingly important in the maintenance of safe and reliable infrastructure networks.

From a sustainability perspective the improvement of existing structures reduces the need for new construction materials, demolition activities and associated construction waste, and retains the embodied energy already invested in existing structures. The results of this study thus contribute to sustainable structural rehabilitation and infrastructure transformation by providing numerical and experimental evidence that can support the use of steel-plate strengthening as a viable rehabilitation technique. The approach is consistent with the conference themes on sustainability, Nigerian infrastructure development and industrial transformation by promoting resource-efficient rehabilitation, extending the service life of infrastructure and reducing the environmental and economic impact associated with premature demolition and reconstruction.

4.0 CONCLUSIONS

From the finite element analysis, validation with experimental results, and load–deflection behaviour analysis of the externally steel-plated reinforced concrete beams, the following conclusions are drawn:

1. The developed finite element model was found to be a good predictor of the structural response of externally steel-plated reinforced concrete beams. The numerical results were closely corresponded with the experimental results reported by John (2023), as the Pearson correlation coefficient (0.961) with p value < 0.001, the developed model was reliable
2. The finite element model was always able to predict loads slightly higher than the experimental loads, but the differences were small and acceptable in engineering terms. This shows that the model can accurately predict the load carrying capacity of strengthened reinforced concrete beams.

3. Statistical analysis showed that the thickness of the adhesive significantly affected the ultimate load of the strengthened beams ($F = 5.12$, $p = 0.043$); however, the thickness of the steel plates in the range examined did not have a statistically significant effect on the ultimate load of the strengthened beams ($F = 2.12$, $p = 0.201$). This means that the impact of strengthening system is more related to the glue layer than to the thickness of the steel plate.
4. It was concluded that the structural performance of the reinforced concrete beams was significantly improved in terms of the stiffness, energy absorption potential and ductility by the exterior bonding of steel plates with the unstrengthened control beam. The enhanced beams performed better with respect to load resistance, post yield performance and failure gradient.
5. The overall performance of all the adhesive thicknesses tested was optimum for 4-6 mm.4-6 mm was found to be the optimum thickness of the adhesive for optimum performance in terms of stiffness, energy absorbed and ductility.
6. Results showed that the thickness of 8 mm adhesive layer had no advantage for the structurally steel-plated reinforced concrete beam because of less interface stiffness and less effective stress transferring.

REFERENCES

Abaqus. (2014). *ABAQUS analysis user's guide* (Version 6.14). Dassault Systèmes Simulia Corp.

Ahmed Ibrahim, O. (2025). Enhancing Composite Steel-Concrete Beams: A Review of Strengthening Techniques, Performance, and Practical Applications. *ERU Research Journal*, *4*(4), 3336-3356.

Alam, M. A., Onik, S. A., & Mustapha, K. N. (2020). Crack based bond strength model of externally bonded steel plate and CFRP laminate to predict debonding failure of shear strengthened RC beams. *Journal of Building Engineering*, *27*, 100943. https://doi.org/10.1016/j.jobe.2019.100943

Alharthai, M., Bahrami, A., Badawi, M., Ghalla, M., Elsamak, G., & Abdelmgeed, F. A. (2024). Numerical study on enhancing shear performance of RC beams with external aluminum alloy plates bonded using steel anchors. *Results in Engineering*, *22*, 102143.

Ali, M. S. M., Oehlers, D. J., & Bradford, M. A. (2001). Shear peeling of steel plates bonded to tension faces of RC beams. *Journal of Structural Engineering*, *127*(12), 1453–1460. https://doi.org/10.1061/(ASCE)0733-9445(2001)127:12(1453)

Alsuhaibani, E. (2025). Nondestructive testing of externally bonded FRP concrete structures: A comprehensive review. *Polymers*, *17*(9), 1284.

Bandara, S., Wijesundara, K., & Rajeev, P. (2023). Ultra-high-performance fibre-reinforced concrete for rehabilitation and strengthening of concrete structures: A suitability assessment. *Buildings*, *13*(3), 614.

Bimal, **A. B. &** Hiroshi **M. (2002).** Numerical simulation of steel-plate strengthened concrete beam by a non-linear finite element method model. *Construction and Building Materials*, *16*(5), 291–301. https://doi.org/10.1016/S0950-0618(02)00022-3.

Charif, A. (1983). Structural behaviour of reinforced concrete beams strengthened by epoxy bonded steel plates. PhD Thesis, University of Sheffield, Sheffield, UK.

Chen, J. F., Teng, J. G., Li, G., & Hu, X. Z. (2012). *Behavior and strength of RC beams strengthened with externally bonded steel plates: Experimental investigation and finite element analysis*. *Engineering Structures*, *40*, 24–36.

Ciampa, E., & Pecce, M. (2021). Finite element modeling of bond behavior of FRP and steel plates externally bonded on reinforced concrete beams. *Materials*, *14*(4), 936. https://doi.org/10.3390/ma14040936.

Edalati, M., & Irani, F. (2012). Interfacial stresses in RC beams strengthened by externally bonded FRP/steel plates with effects of shear deformations. *Journal of Composites for Construction*, *16*(1), 127–136. https://doi.org/10.1061/(ASCE)CC.1943-5614.0000238

Elkhatib, L., Khatib, J. M., Fırat, S., El Hassan, H., & Elkordi, A. (2025). *Rehabilitation of concrete structures: A review*. Gazi University Journal of Science, 38(2). https://doi.org/10.35378/gujs.1503207

Foraboschi, P. (2022). Strengthening of reinforced concrete beams subjected to concentrated loads using externally bonded fiber composite materials. *Materials*, *15*(6), 2328.

Hajirasouliha, I., Pilakoutas, K., & Mohammadi, R. K. (2012). Strengthening of reinforced concrete structures: Computational simulation and parametric studies. *Engineering Structures*, *40*, 92–102.

Hamoda, A., Shahin, R. I., Ahmed, M., Abadel, A. A., Baktheer, A., & Yehia, S. A. (2024). Strengthening of reinforced concrete columns incorporating different configurations of stainless-steel plates. In *Structures* (Vol. 64, p. 106577). Elsevier.

Hamoush, S. A., & Ahmad, S. H. (1990). Debonding of steel plate-strengthened concrete beams. *Journal of Structural Engineering*, *116*(2), 356–371. https://doi.org/10.1061/(ASCE)0733-9445(1990)116:2(356)

Hu, Z., Elchalakani, M., Yehia, S., Ran, H., Sadakkathulla, M. A., & Guo, X. (2024). *Engineered cementitious composite (ECC) strengthening of reinforced concrete structures: A state-of-the-*

art review. Journal of Building Engineering, 86, 108941. https://doi.org/10.1016/j.jobe.2024.108941

John, A. T. (2023). Effect Of Adhesive Layer Thickness on Reinforced Concrete Beams Strengthened Externally by Carbon Fiber Reinforced Polymer and Steel Plate. Ph. D Dissertation, Niger Delta University, Wilberforce Island, Bayelsa State, Nigeria, 189 Pp.

Khalil, A., & Attia, M. (2025). A Comprehensive Review of the Flexural Behavior of RC Beams strengthened by Externally Bonded and Near-Surface Mounted Techniques using FRP and Metal Materials. *Industrial Technology Journal*.

Kholil, M. I., & Ahmed, A. (2025). Finite element modelling of RC beam strengthened with epoxy-bonded steel plate. *Journal of Building Pathology and Rehabilitation*, *10*, Article 72. https://doi.org/10.1007/s41024-025-00672-y

Li, Y., Zhang, H., Wang, J., & Liu, X. (2025). Numerical investigation of the flexural performance of reinforced concrete beams strengthened with externally bonded steel plates using nonlinear finite element analysis. *Buildings*, *15*(20), 3665. https://doi.org/10.3390/buildings15203665

Ma, J., Yang, Q., Peng, X., & Xia, K. (2025). Review on durability deterioration and mitigation of concrete structures. *Coatings*, *15*(9), 982.

Mahi, M. S. H., & Ridoy, T. A. (2025). Corrosion mechanisms in reinforced concrete: causes, effects, and sustainable mitigation strategies. *Current Problems in Research*, *1*(1), 52-66.

Mankare, U. S., & TS, V. (2026). A review on Advanced strengthening techniques for corrosion-damaged Reinforced Concrete structures. Journal of Rehabilitation in Civil Engineering, 14(2).

Mobarhan Zad, S., Rahai, M., Ranjbar, S., & Moghadas Nejad, F. (2026). Structural damage analysis using finite element model updating enhanced by response surface methodology. *Scientific Reports*.

Mosahebfard, A., Dehghan, S. M., Dashti, H., Fiouz, A., & Najafgholipour, M. A. (2026). Investigating the Flexural Behavior of Concrete Beams with External Steel Plate Retrofitting: A Combined Experimental and Numerical Approach. *Iranian Journal of Science and Technology, Transactions of Civil Engineering*, 1-18.

Muka, N. (2023). *Development of Enhanced Modeling Techniques for Nonlinear Behavior and Crack Opening in Reinforced Concrete Structures Using the Applied Element Method* (Master's thesis, Middle East Technical University (Turkey)).

Napoli, A., Martinelli, E., & Pecce, M. R. (2024). RC beams externally strengthened by steel plates: Experimental database and preliminary analysis. *Procedia Structural Integrity*, *64*, 975–982. https://doi.org/10.1016/j.prostr.2024.09.381

Noor, U. A., Javed, M. F., & Shahzada, K. (2025). Experimental and numerical approaches for evaluating steel fiber reinforced concrete beam column joints: a state-of-the-art review. *Advances in Structural Engineering*, *28*(16), 2961-2998.

Oehlers, D. J., & Seracino, R. (2004). *Design of FRP and steel plated RC structures: Retrofitting beams and slabs for strength, stiffness and ductility*. Elsevier.

Osta, M. O., Azeem, A., Rashid, S., Harun, M., & Hanif, A. (2026). Marine resilience: Understanding the durability and effects on concrete structures—A Comprehensive Review. *Arabian Journal for Science and Engineering*, *51*(4), 3981-4006.

Özmen, H. B., & Tanrıverdi, B. (2025). Concrete paradox: Economic importance, environmental impacts, and the sustainability of concrete material. *Res Des*, *2*(2), 66-84.

Qiang, X., Chen, L., & Jiang, X. (2023). Experimental and theoretical study on flexural behavior of steel–concrete composite beams strengthened by CFRP plates with unbonded retrofit systems. *Composite Structures*, *309*, 116763.

Raphael, J. M. (1984). Tensile strength of concrete. *ACI Journal Proceedings*, 81(2), 158–165.

Raviolo, D., Civera, M., & Zanotti Fragonara, L. (2023). A comparative analysis of optimization algorithms for finite element model updating on numerical and experimental benchmarks. *Buildings*, *13*(12), 3010.

Rincon, L. F., Moscoso, Y. M., Hamami, A. E. A., Matos, J. C., & Bastidas-Arteaga, E. (2024). Degradation models and maintenance strategies for reinforced concrete structures in coastal environments under climate change: A review. *Buildings*, *14*(3), 562.

Rusnak, C. R. (2025). *Sustainable strategies for concrete infrastructure preservation: A comprehensive review and perspective*. Infrastructures, 10(4), 99. https://doi.org/10.3390/infrastructures10040099

Sun, Y., Fu, W., Chen, X., Zhang, Z., Yu, W., & Li, S. (2023). Theoretical and experimental investigations into flexural behavior of existing reinforced concrete beams strengthened by CFRP bars. *Journal of building engineering*, *77*, 107528.

Teng, J. G., Chen, J. F., Smith, S. T., & Lam, L. (2002). *FRP-strengthened RC structures*. John Wiley & Sons.

Tiza, M. T., Imoni, S., Akande, E. O., Mogbo, O., Jiya, V. H., & Onuzulike, C. (2024). Revolutionizing infrastructure development: Exploring cutting-edge advances in civil engineering materials. *Recent Progress in Materials*, *6*(3), 1-68.

Xu, M., Ren, L., Shi, Z., & Liu, X. (2024). Collaborative interfacial shear capacity of adhesive bonding and novel shooting nail for steel plate strengthening concrete structures. *Scientific Reports*, *14*, Article 31781. https://doi.org/10.1038/s41598-024-82801-0

Yadeta, K. F., Siriwardane, S. C., & Mohammed, T. A. (2023). Service life prediction of reinforced concrete structures subjected to corrosion: a comparative study. *International Journal of Structural Integrity*, *14*(3), 480-497.

Zhang, Y., Wang, H., Qin, Y., Huang, S., & Fan, W. (2023). Experimental and analytical studies on the flexural behavior of steel plate-UHPC composite strengthened RC beams. *Engineering Structures*, *283*, 115834.

Ziraba, Y. N., & Baluch, M. H. (1995). Computational model for reinforced concrete beams strengthened by epoxy bonded steel plates. Finite Elements in Analysis and Design, 20(4), 253–271. https://doi.org/10.1016/0168-874X(95)00032-O

International Conference on Engineering Innovation for Sustainable Development (ICESID 2026)
Faculty of Engineering, Ahmadu Bello University Zaria · 8–10 September 2026

FROM NESI 1.0 TO NESI-X: A HYBRID LEAPFROGGING ARCHITECTURE FOR ADAPTIVE TRANSFORMATION OF NIGERIA'S ELECTRICITY SUPPLY INDUSTRY

Waliu Musa[1,*], Taiwo Emmanuel Okharedia[2], Muhammed Ibrahim[3], Aneke Nnamere Ezekiel[4], Isaac Adekanye[5], Oluwaseun Adebisi[1], Umar Abubakar Saleh[6]

[1]*Federal University of Agriculture, Abeokuta*
[2]*Department of Electrical and Electronic Engineering, Atlantic International University, Hawaii, USA*
[3]*Department of Electrical/Electronic Engineering, Federal University of Petroleum Resources, Effurun, Delta State, Nigeria*
[4]*State University of Medical and Applied Sciences, Igbo-Eno Orba, Enugu State, Nigeria*
[5]*Operations Manager, Detrio Consult Limited, Lagos, Nigeria*
[6]*Department of Electrical and Electronic Engineering, Federal University Lokoja, Kogi State, Nigeria*

Email: musa.waliu@pg.funaab.edu.ng*, tokharedia@gmail.com, abusumayya70@yahoo.com, ezekiel.aneke@sumas.edu.ng, isaacadek@ieee.org, adebisioluwaseun@funaab.edu.ng, abubakarumarsaleh1982@gmail.com

***Corresponding author**: Waliu Musa

DOI: https://doi.org/10.67203/sp.ICESID.2026

ABSTRACT

More than a decade after the 2013 restructuring and privatization of Nigeria's electricity sector, the Nigerian Electricity Supply Industry (NESI) continues to face interacting technical, commercial, financial, and institutional constraints. Rather than treating recurrent failures as isolated generation, transmission, distribution, metering, or regulatory problems, this paper develops NESI-X as a systemic hybrid-leapfrogging architecture for coordinated transformation. It distinguishes what can be leapfrogged from what cannot: distributed generation, mini-grids, storage, advanced metering, and data-driven operations can bypass selected technological pathways in generation, distribution, metering, monitoring, and maintenance, whereas transmission infrastructure and the institutions that sustain it must be progressively reinforced. Hybrid electricity-sector leapfrogging (HESL) is formally defined as this selective-bypass-plus-reinforcement logic, and the functions it treats as indispensable are named non-bypassable system dependencies (NSDs). NESI-X organizes this distinction into two tiers, transformation capabilities and enabling conditions, coupled through a qualitative causal-loop model and a directed conceptual dependency matrix expressed as expert-informed propositions rather than statistically estimated dependencies. The architecture draws on Nigerian primary regulatory and institutional sources, including the Electricity Act 2023, the National Integrated Electricity Policy, the 2026 Mini-Grid Regulations, FoNER, NISO, and NEMSA's statutory technical-assurance mandate, alongside recent literature on smart metering, mini-grids, digital twins, and cyber-physical security. A gated roadmap and layer-level KPIs are proposed alongside financing, institutional capacity, skills, interoperability, cybersecurity, and political-economy risks as adoption conditions. The contribution is a testable architecture, not a claim of validation.

Keywords: *Nigeria Electricity Supply Industry; hybrid leapfrogging; non-bypassable system dependencies; distributed energy resources; regulatory governance*

1. INTRODUCTION

More than a decade after Nigeria's 2013 power-sector privatization, the sector has undergone substantial institutional restructuring, yet persistent weaknesses in electricity reliability, metering, revenue recovery, infrastructure condition, and system coordination continue to constrain sector performance (Adeku et al., 2026). Responsibilities are now divided among generation companies (GenCos), the Transmission Company of Nigeria (TCN), distribution companies (DisCos), the Nigerian Electricity Regulatory Commission (NERC), and a growing set of state-level institutions. Evidence from selected distribution companies indicates that institutional and ownership restructuring has not, by

itself, guaranteed sustained improvements in service quality, billing, metering, or customer response (Akunne et al., 2023). The Electricity Act 2023 and the subsequent transition of market regulation to participating states have expanded the reform agenda, creating opportunities for sub-national innovation while increasing the need for coordination across federal and state jurisdictions (Federal Republic of Nigeria, 2023).

Existing studies on Nigeria's electricity sector examine individual dimensions of this problem - privatization outcomes, technical and commercial losses, smart-metering strategies, mini-grid deployment, digitalization, and regulatory reform - largely in isolation. Three gaps motivate NESI-X. First, Nigerian electricity research treats reliability, losses, distributed generation, metering, regulatory reform, and digitalization as partially independent problems rather than a coupled system. Second, the leapfrogging literature offers limited guidance on how bypassable technological pathways should coexist, within a single architecture, with infrastructure and institutions that remain physically or legally indispensable. Third, few conceptual approaches translate these interacting dimensions into an institutionally grounded architecture with explicit inter-layer dependencies, implementation gates, and measurable transition conditions. NESI-X is accordingly defined here as a proposed adaptive architecture for coordinating decentralized energy resources, digital intelligence, technical assurance, regulatory governance, and market liquidity within a progressively reinforced national electricity system, addressing these three gaps together rather than in isolation.

The paper's contribution has three parts, developed in Section 2 and applied in Section 3: hybrid leapfrogging - selective technological bypass, formally defined, coupled with progressive reinforcement of non-bypassable dependencies; an assurance-integrated architecture, in which NEMSA is treated not as peripheral compliance but as a cross-cutting technical-assurance spine running through every operational layer; and testability, since the architecture generates an explicit causal-loop model, a directed dependency matrix, implementation gates, layer-level KPIs, and five empirical propositions (P1–P5) for future testing against Nigerian data.

These contributions support four linked claims. Conceptually, the paper formalizes hybrid electricity-sector leapfrogging and reframes NESI dysfunction as a coupled-system problem, distinguishing evidence-supported feedback mechanisms from hypotheses requiring empirical testing. Architecturally, it proposes the NESI-X architecture across two conceptual tiers with an explicit dependency matrix, so that "integration" is a specified dependency rather than a general aspiration. Institutionally, it integrates NERC, state regulators, FoNER, NISO, and NEMSA's technical assurance mandate into a single architecture. For implementation, it converts the architecture into a gated roadmap with measurable entry/exit conditions and layer-level KPIs, naming financing, skills, technical assurance, cybersecurity, and political economy as implementation constraints rather than afterthoughts.

Three research questions guide the paper. RQ1: Which components of Nigeria's electricity supply system can be leapfrogged, and which infrastructure and assurance functions remain non-bypassable? RQ2: How can distributed generation, digital intelligence, governance, technical assurance, and market liquidity be configured as an interdependent transformation architecture? RQ3: What institutional, technical, financial, and cybersecurity conditions should govern progression between transformation stages? Section 2 develops the conceptual apparatus for RQ1, Section 3 addresses RQ2, and Section 4's roadmap together with Section 5's discussion takes up RQ3.

Diagnosing NESI's dysfunction must precede any proposed architecture, since a system's coupling can only be modeled once its failure dimensions are known. The sector's problem is not merely insufficient installed generation capacity: a power system can possess substantial generation assets and still fail to deliver reliable electricity if transmission observability, distribution capacity, metering, revenue collection, gas availability, technical assurance, or regulatory coordination is inadequate. Table 1 identifies five interacting diagnostic dimensions. NESI-X responds through four operational layers - two transformation-capability layers and two enabling-condition layers - supported by a cross-cutting technical-assurance spine represented by NEMSA, as Section 3 develops.

Table 1: NESI 1.0 as a Coupled System: Diagnosis Matrix

Dimension	**Observed** Problem	**Systemic consequence**	**NESI-X response**
Technical resilience	Limited real-time visibility, aging and strained assets, and weak predictive capability.	Faults propagate through the network; maintenance remains reactive rather than planned; reliability deteriorates over time.	Digital intelligence, Wide Area Measurement Systems (WAMS), Phasor Measurement Units (PMU), digital twins, and predictive analytics are all part of Layer 2.
Distributed energy architecture	Centralized topology remains vulnerable to system-wide disturbance and access gaps.	Local loads are exposed to national-grid failures or protracted transmission/distribution extension cycles.	This layer includes Distributed Energy Resources (DER), mini-grids, energy storage, and intentional islanding.
Technical assurance and safety	Continuous need for standards enforcement, inspection, testing, certification, and meter/equipment assurance as physical and digital infrastructure expands.	Unsafe or non-compliant installations, equipment failure, degraded interoperability, and reliability risk that outpaces oversight capacity.	The NEMSA technical-assurance spine: inspection, testing, certification, and compliance with standards, operating alongside the Standards Organization of Nigeria (SON).
Governance coordination	Federal and state regulatory roles are still evolving under the Electricity Act 2023.	Divergent state-level rules raise coordination risk and transaction costs.	Harmonized standards, regulatory sandboxing, and FoNER coordination (Layer 3).
Market liquidity	High Aggregate Technical, Commercial and Collection (ATC&C) losses, and weak collection efficiency.	Reduced capacity to finance metering, operations and maintenance, and network reinforcement.	The focus areas include AMI, revenue assurance, loss analytics, and targeted investment (Layer 4).

The financial dimension is the most thoroughly documented in current Nigerian regulatory evidence. NERC's 2025/Q4 Quarterly Report states that the weighted average ATC&C loss across all DisCos in 2025/Q4 was 34.90%, comprising 17.97 percentage points of technical/commercial loss and 20.64 points of collection loss (NERC, 2026a, §2.3.5). These components combine multiplicatively rather than additively, following the standard ATC&C convention:

$$ATC\&C = 1 - [(1 - \text{Technical/Commercial Loss}) \times (1 - \text{Collection Loss})] \qquad Eq.1$$

$$ATC\&C = 1 - [(1 - 0.1797) \times (1 - 0.2064)] = 1 - (0.8203)(0.7936) = 34.90\%$$

This reconciles exactly with NERC's reported aggregate figure, sits 14.36 percentage points above the 20.54% efficient-loss target used in MYTO 2025 tariffs, and translates to a cumulative revenue loss of ₦139.19 billion for DisCos in that quarter alone; only Eko outperformed its ATC&C target, by 2.68 percentage points (NERC, 2026a, §2.3.5). This situation is not a marginal inefficiency but nearly fifteen percentage points of avoidable revenue loss recurring quarterly, sustained by the same structural weaknesses documented across the post-privatization literature. Smart-metering strategies have been directly linked to ATC&C loss mitigation in Nigerian distribution systems (Odje et al., 2021), so metering functions as a liquidity and data-quality intervention with system-wide consequences, not merely a customer-service improvement.

Nigeria is simultaneously moving toward a more decentralized electricity architecture, formalized in the National Integrated Electricity Policy and Strategic Implementation Plan (NIEP-SIP) mandated under Section 3 of the Electricity Act 2023 (Federal Ministry of Power, 2025). NERC's 2026

Mini-Grid Regulations recognize both isolated and interconnected mini-grids, the latter permitted up to 10 MW (NERC, 2026b), and the World Bank's Nigeria Electrification Project has already supported 125 mini-grids and more than a million solar home systems, helping over 5.5 million Nigerians gain electricity access (World Bank, 2024). Nigeria, therefore, need not replicate every historical stage of conventional electricity system development, particularly where distributed energy and digital technologies offer alternative pathways to access and modernization. The concept of energy leapfrogging is directly relevant here but must be applied carefully rather than treated as a slogan: its developmental effect depends on economic, institutional, and behavioral conditions being in place to sustain it, not merely on acquiring newer technology (van Benthem, 2015). Section 2 formalizes this idea as hybrid electricity-sector leapfrogging.

NESI 1.0 is used throughout this paper as analytical shorthand for the current fragmented configuration; the designation does not imply Nigeria has ever formally operated a versioned electricity-industry architecture, nor is it an official government classification.

2. CONCEPTUAL AND METHODOLOGICAL FOUNDATION

This section formalizes the paper's central construct - hybrid electricity-sector leapfrogging - names the dependencies it treats as non-bypassable, sets out the evidence-synthesis method, and develops the causal-loop model coupling Table 1's five dimensions into a single system.

2.1 Hybrid Electricity-Sector Leapfrogging (HESL)

HESL is defined here as a transformation pathway in which selected technological development stages are bypassed where alternative technologies provide functionally equivalent or superior outcomes, while physically indispensable infrastructure and institutionally non-bypassable functions are progressively reinforced rather than circumvented. What can be leapfrogged includes conventional generation-expansion sequencing; distribution-extension pathways; manual meter reading; and reactive maintenance - selected pathways in generation, distribution, metering, monitoring, and maintenance, not a wholesale bypass of any single sector-wide stage. Digital intelligence is best understood as the enabling capability that makes this leapfrogging possible, rather than a leapfroggable stage itself: Nigeria can leapfrog the sequence in which metering, monitoring, and generation technologies are adopted, but it deploys digital intelligence as the observability layer that lets the rest of the leapfrogging happen safely, rather than "leapfrogging" it.

The construct can be expressed compactly as:

Hybrid Leapfrogging = Selective Bypass + Progressive Reinforcement + Institutional Assurance

Nigeria can leapfrog selected stages of electricity-sector development; it cannot leapfrog the physical and institutional dependencies that make an electricity system work. That proposition, developed architecturally in Section 3 and tested through explicit propositions in Section 5, is the paper's core contribution.

2.2 Non-Bypassable System Dependencies (NSDs)

The functions HESL does not permit to be bypassed are named here as non-bypassable system dependencies (NSDs): the transmission backbone; protection coordination; equipment and interconnection technical standards; NEMSA inspection, testing, and certification; cybersecurity; competent technical personnel; regulatory coordination across federal and state jurisdictions; and financial liquidity. These are precisely the functions NEMSA's statutory mandate covers, which is why Section 3 treats technical assurance as a distinct, cross-cutting element rather than folding it into "governance." NESI-X can, therefore, be summarized as:

NESI-X = Leapfroggable Pathways + Non-Bypassable System Dependencies

NESI-X does not treat technical assurance as another sectoral silo; it treats assurance as the cross-cutting condition that makes leapfrogging safe, interoperable, measurable, and scalable.

2.3 Evidence Synthesis and Conceptual Modeling

This is a conceptual, policy-architecture paper rather than a calibrated econometric or simulation study, and its methodology is a transparent conceptual-synthesis protocol rather than a

formal systematic review. The synthesis combines four elements: primary Nigerian regulatory documents, including NERC quarterly reports; the Electricity Act 2023; the NIEP-SIP; the 2026 Mini-Grid Regulations, NERC's orders establishing FoNER and NISO, and NEMSA's establishing instrument and current mandate (NEMSA, 2023); peer-reviewed literature on smart metering, mini-grids, digital twins, AI in power systems, and cyber-physical security, focused predominantly on 2020–2026 studies and supplemented by one classical leapfrogging reference (van Benthem, 2015); qualitative causal-loop modeling formalizing Table 1's coupling; and architecture and roadmap design informed by the preceding elements. Table 2 maps each evidence stream to its primary sources and purpose within the architecture.

Table 2: Methodological Source Mapping

Evidence stream	Primary sources	Purpose in architecture
Sector performance	NERC quarterly reports	ATC&C, reliability, and collection-efficiency evidence (Table 1, Section 1)
Legal/institutional structure	Electricity Act 2023; NERC orders establishing FoNER and NISO	Institutional allocation of governance and system-operation roles (Sections 3.3, 3.6)
Technical assurance	NEMSA establishing Act, her installation guidelines and current mandate under the Electricity Act 2023 (NEMSA, 2023)	Standards enforcement, inspection, and certification spine (Section 3.5)
Decentralization	2026 Mini-Grid Regulations; World Bank project data	DER/mini-grid pathway feasibility (Section 3.1)
Digitalization	Peer-reviewed literature on digital twins, AI, and cyber-physical security	Layer 2 design and cybersecurity risk framing (Section 3.2)
Leapfrogging theory	Energy-leapfrogging literature	Conceptual foundation for HESL (Section 2.1)

Evidence was organized into Table 1's five analytical domains, with Nigerian institutional claims restricted to primary regulatory and government sources rather than secondary commentary and Table 3's ratings assigned analytically from system-function logic rather than statistical estimation. The objective is a logically coherent, evidence-grounded architecture testable against multi-year Nigerian data - a testable architecture, not one whose validity is merely asserted. Validating Table 3's ratings through structured elicitation methods such as Delphi, DEMATEL, Interpretive Structural Modeling, or AHP/ANP is a natural next step this paper does not itself undertake.

2.4 Causal-Loop Logic

Only once NESI's dysfunction is established as multi-dimensional does it make sense to ask how the dimensions interact; the causal-loop analysis below uses reinforcing-loop logic to formalize Table 1's dimensions as a coupled system, rather than leaving them as parallel, independently addressable lists.

R1, the technical-financial feedback loop, is assembled from observable sector relationships: technical losses and poor service reduce effective revenue; weak revenue constrains maintenance and investment; inadequate investment further deteriorates performance, reinforcing the losses that began the cycle. Each link is independently plausible and consistent with Section 1's evidence, but the complete closed loop and each link's magnitude have not been empirically estimated for Nigeria - direction and strength require future empirical estimation. As a reinforcing loop, R1 is directionally symmetric: the same chain that produces decline would, under sustained investment, run in reverse as a virtuous cycle, so R1 is a lever available in both directions, not solely a description of failure.

R2, the regulatory-fragmentation loop, is treated more cautiously: fragmentation across a growing number of state jurisdictions plausibly raises transaction costs, creates inconsistent rules, and

increases investor uncertainty, but its strength and direction in the Nigerian context should be empirically estimated as the state-transition process matures, not presented as fact.

R3, the technical-assurance-data-revenue loop, formalizes the NEMSA function developed in Section 3 as a third reinforcing mechanism: NEMSA assurance activity improves measurement and equipment-condition integrity; more trustworthy data improves digital-intelligence outputs and billing accuracy; more accurate billing improves collectible revenue and investment capacity; and greater investment capacity, including in assurance itself, reinforces measurement integrity again. NEMSA's inspection and testing activities already generate equipment-condition, compliance, and certification records as a normal byproduct of its statutory function; NESI-X proposes that these verified records could, subject to appropriate data-governance arrangements, become a technical-data stream feeding the same asset-information systems that support digital-twin and predictive-maintenance applications. That integration is NESI-X's proposed architecture, not established Nigerian practice, and is labeled accordingly below.

A further loop describing regulatory fragmentation as self-correcting through harmonization pressure was considered but is not represented separately: it is a variant of R2 rather than functionally distinct, and a fourth loop would add diagram complexity without a materially new claim beyond R2 and Section 3.3's FoNER discussion. Figure 1 represents R1, R2, and R3 together, distinguishing R1's evidence-supported status from R2's and R3's hypothesized status through explicit labeling.

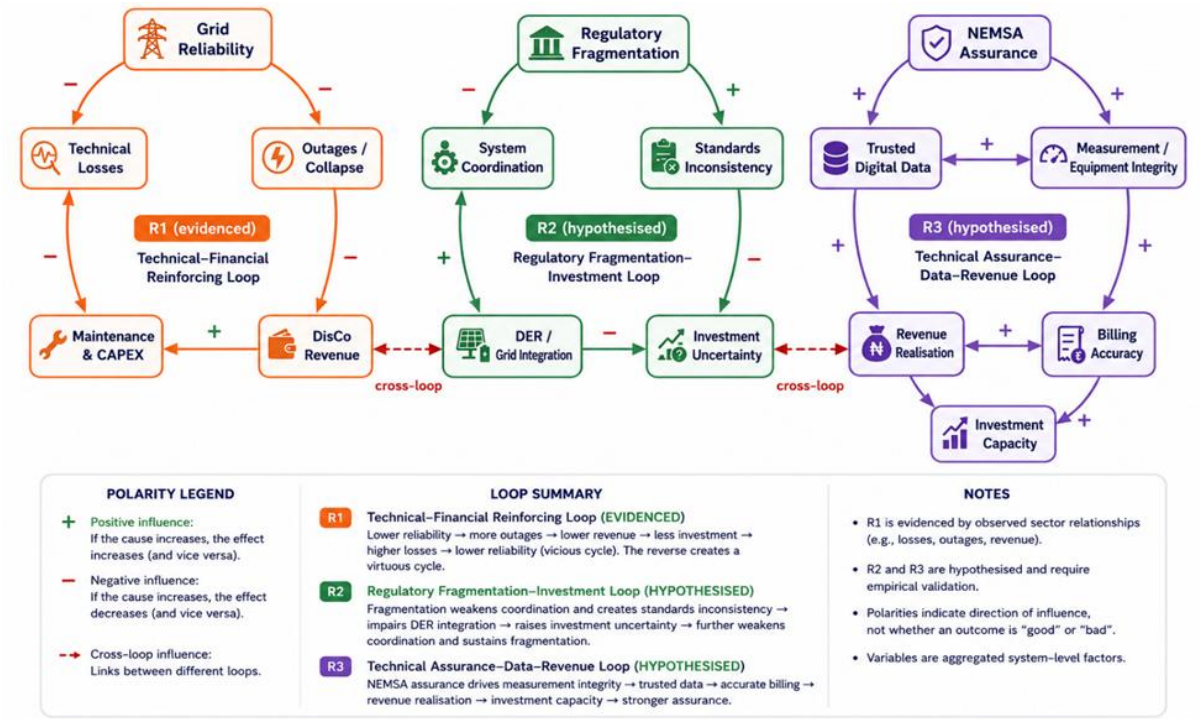

Figure 1: Qualitative causal-loop representation of NESI systemic coupling.

Distinguishing evidence-supported relationships from hypothesized ones strengthens the architecture, since a framework asserting every relationship with equal confidence is less useful to a reader - and less credible to a technical reviewer - than one that offers a path to test the difference. Concretely, R2's hypothesized strength and direction are the object of P3, which compares investment cycle times and DER interconnection approval times across states before and after FoNER-coordinated standard adoption; a null or reversed effect there would falsify R2 as specified. R3's hypothesized data-integrity channel is the object of P5, which compares an operational-data-only asset-condition model against an operational-plus-NEMSA-data model on the same asset population; no measurable improvement from the added NEMSA data stream would falsify R3's proposed mechanism. This gives each hypothesized loop a specific empirical test rather than leaving falsifiability implicit, and Section 5 converts this distinction into five explicit, individually testable research propositions.

3. NESI-X ARCHITECTURE

The causal coupling in Figure 1 motivates a structural response, but the response should treat the five diagnostic dimensions asymmetrically. Transformation capabilities are technological and infrastructural capabilities that directly alter NESI's physical or informational operating configuration: Layers 1 and 2. Enabling conditions are institutional and financial capabilities determining whether those technologies can be deployed, coordinated, financed, certified, and scaled sustainably: Layers 3 and 4, which, like the transmission backbone itself, cannot be bypassed and must be progressively built alongside the transformation-capability technologies. NESI-X is the overarching architecture: Figure 1 provides its causal logic; Figure 2 illustrates its structural configuration; Table 3 outlines its interdependencies; Table 4 details its implementation gates; Table 5 presents its performance indicators; and P1–P5 (Section 5) specify its empirical propositions. This tiering, shown in Figure 2, makes the paper's core proposition structurally explicit: Nigeria can leapfrog selected stages of electricity-sector development, but not the non-bypassable dependencies that make an electricity system work.

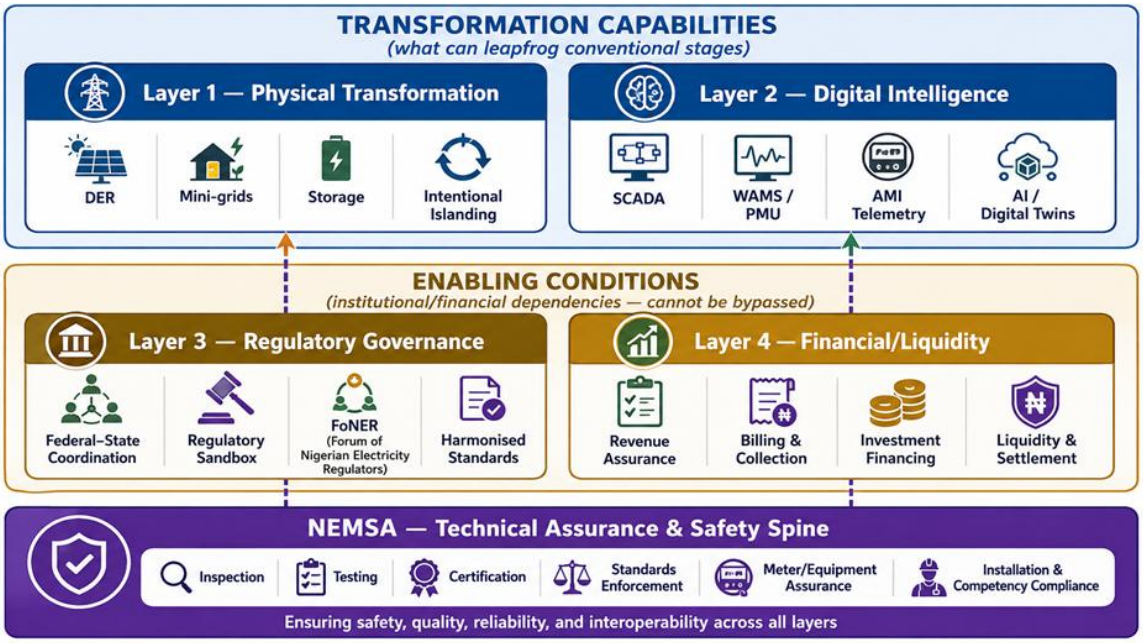

Figure 2: NESI-X architecture: transformation capabilities and enabling conditions.

NESI-X does not interpret decentralization as a substitute for transmission reinforcement. DER and mini-grids provide complementary resilience and access pathways while transmission capacity, protection, observability, and stability are progressively strengthened - decentralization is additive to the transmission backbone, not a replacement for it.

3.1 Layer 1 - Physical Transformation

This layer treats distributed energy resources, mini-grids, battery storage, and controllable local generation as strategic components of national resilience, not merely a rural-electrification substitute deployed where the conventional grid has not yet reached. NERC's 2026 Mini-Grid Regulations recognize both isolated and interconnected mini-grids (NERC, 2026b), and World Bank experience shows decentralized electricity is no longer a purely experimental pathway at scale (World Bank, 2024). The leapfrogging logic is architectural: an underserved community need not wait for a conventional transmission or distribution extension before receiving reliable electricity. But decentralization without interoperability and technical assurance can produce new fragmentation and a new category of safety risk rather than resolve the old one. Intentional islanding is not simply disconnection followed by continued local supply: it requires protection coordination, anti-islanding arrangements, synchronization on reconnection, frequency/voltage control, and, where relevant, black-start capability and DER inverter controls - none self-certifying. NESI-X therefore requires DER assets to comply with common protection, metering, telemetry, earthing, equipment, and interconnection requirements,

incorporated into the pre-commissioning and interconnection assurance pathway administered through the technical-assurance spine (Section 3.5). This gives Layer 1 a concrete engineering safeguard rather than an aspirational interoperability requirement: physical assets enter the system only once compliance has been independently verified, not merely declared by the deploying party.

3.2 Layer 2 - Digital Intelligence

This layer combines SCADA modernization, WAMS/PMU deployment, AMI telemetry, asset-condition monitoring, artificial intelligence, and digital-twin models to provide the observability that a more distributed system requires. A digital twin and an AI capability are not synonymous: the twin is the system-representation layer - a dynamic digital model of physical assets, topology, and state - while AI is an analytical capability operating on that representation and the validated data feeding it for forecasting, anomaly detection, or predictive maintenance. Digital-twin research shows a grid twin can support real-time analysis by linking physical-system measurements to a dynamic digital representation (Zhou et al., 2019). Recent work applies AI and reinforcement learning directly to cloud-based grid digital twins (Pei et al., 2024), while broader reviews identify combined digital-twin/AI use as an emerging pathway toward resilient grid management internationally (Ranawaka et al., 2024). The guiding principle for NESI-X in Nigeria should be "data before sophistication": a digital twin built on incomplete topology or unreliable measurements may appear visually impressive but will be operationally weak regardless of AI sophistication. NESI-X therefore prioritizes data governance, telemetry quality, and cybersecurity before deploying high-complexity AI.

Layer 2's data foundation need not come only from SCADA and AMI. NESI-X proposes that NEMSA-generated inspection, testing, and certification records could become a verified technical-data stream feeding the same asset-information systems supporting digital-twin and predictive-maintenance applications, illustrated in Figure 3 as a pathway from physical inspection through verified data, digital representation, and AI-based analytics to predictive maintenance and improved reliability and safety. This inspection-to-intelligence pipeline is one of the paper's more original operational contributions: it repositions a conventional statutory inspection function as a proposed active data source for a digitally intelligent grid, rather than a parallel, disconnected compliance process.

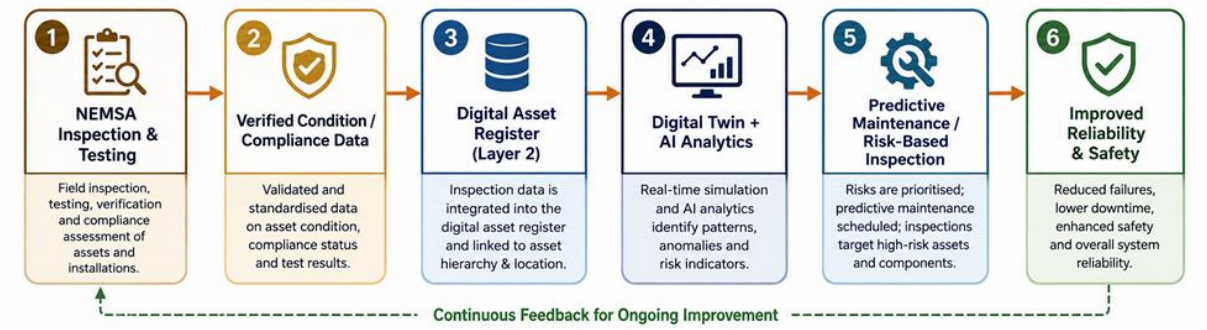

Figure 3: NEMSA inspection-to-intelligence pipeline within the NESI-X.

3.3 Layer 3 - Regulatory Governance

This layer does not transform the system directly; it determines whether Layers 1 and 2 can scale coherently across Nigeria's thirty-six states and the FCT. The Electricity Act 2023's decentralization can encourage valuable state-specific innovation but also creates a coordination challenge absent under the previous, purely federal structure. FoNER's 2026 inauguration - whose objectives include harmonized tariff-setting, market operations, consumer protection, and capacity-building among NERC and state regulators (NERC, 2026c) - provides an institutional basis for an adaptive regulatory layer. NESI-X proposes that FoNER could serve as a coordination platform for a regulatory sandbox operated against a national interoperability floor: states retain room to innovate in tariffs and DER business models - through data-informed, adaptive tariff-setting subject to regulatory approval - while core technical requirements (protection coordination, data exchange, cybersecurity

baselines, and metering interfaces) are harmonized, preventing state-level experimentation from producing incompatible electricity islands. This governance function is deliberately distinguished from technical assurance (Section 3.5), since economic/market regulation and technical standards enforcement are different institutional activities frequently, and inaccurately, conflated in general discussions of Nigeria's regulatory landscape.

3.4 Layer 4 - Financial/Liquidity

This layer likewise enables rather than transforms directly: reliable electricity must produce collectible revenue if the sector is to finance the maintenance Layers 1 and 2 depend on. Feeder-level energy accounting, automated billing, and transparent settlement form a data-to-cash chain in which AMI telemetry from Layer 2 feeds billing and revenue assurance directly (Odje et al., 2021). This chain is only as trustworthy as its measurements: meter testing, calibration, and certification are part of the technical-assurance spine below, so Layer 4's revenue-assurance function depends on Section 3.5 as much as on Layer 2's telemetry - an uncertified meter produces inaccurate billing regardless of digital sophistication. NESI-X treats this as a single, shared data infrastructure serving technical and commercial functions simultaneously, reducing the risk that separately commissioned digitalization projects create duplicated costs and incompatible databases - a failure mode that has characterized parts of Nigeria's metering rollout.

3.5 NEMSA: A Cross-Cutting Technical-Assurance Spine

Independent technical assurance of electrical infrastructure, before and during system integration, is a distinct institutional function from both the tariff/market regulation performed by Layer 3 and the technology deployed in Layers 1 and 2. It is deliberately represented as something other than a fifth layer because it is fundamentally different from the other four: it verifies safety and conformity to standards rather than transforming the system or regulating its economics. NESI-X therefore represents technical assurance as a cross-cutting spine beneath all four operational layers (Figure 2).

The Nigerian Electricity Management Services Agency (NEMSA) provides this spine's institutional interface. Under the Electricity Act 2023, NEMSA carries out electrical inspectorate services for NESI and enforces statutory technical standards and regulations, including inspection, testing, and certification of electrical installations, equipment, meters, and instruments (Nigerian Electricity Management Services Agency, 2023). NEMSA was established under the NEMSA Act 2015 (Act No. 6) and now operates under the Electricity Act 2023 framework, with the stated purpose of ensuring safe, reliable, sustainable electricity while guaranteeing the safety of lives and property (NEMSA, 2015). Its technical-assurance role operates within a wider standards ecosystem involving NERC, the Standards Organization of Nigeria (SON), utilities, manufacturers, and other technical institutions (Nigerian Electricity Management Services Agency, n.d.-b), rather than existing in isolation. This is materially different from NERC's function: NERC regulates market structure, tariffs, licensing, and economic conduct, while NEMSA enforces technical standards, safety, and equipment conformity - complementary rather than overlapping institutions.

Within NESI-X, NEMSA's spine connects to all four operational layers: to Layer 1 by verifying DER, mini-grid, and storage installations against protection, earthing, and interconnection requirements before integration (Section 3.1); to Layer 2 through the inspection-to-intelligence pipeline (Figure 3), where certification records become a data source for digital-twin applications rather than a parallel compliance archive; to Layer 4 through meter testing and certification, determining whether billing measurements can be trusted; and to Layer 3 by providing technical-assurance evidence and compliance requirements that inform the interoperability floor and technical conditions applied within regulatory experimentation, rather than by setting regulatory policy itself. This role is particularly important under a hybrid leapfrogging strategy, since accelerated deployment must not translate into accelerated technical risk; Section 2.4's causal-loop model formalizes this as R3, linking NEMSA assurance to measurement integrity, billing accuracy, and investment capacity.

3.6 NISO and TCN: Operational Coordination

The Electricity Act 2023 also provided for unbundling system and market operations from the Transmission Company of Nigeria (TCN). Under NERC Order No. NERC/2024/45, TCN's market- and system-operation functions transferred to a newly incorporated entity, the Nigerian Independent System Operator (NISO), while TCN retains responsibility for transmission infrastructure as a Transmission Service Provider (NERC, 2024). NISO functions as a critical operational coordination actor within Layer 2, particularly for system observability, balancing, dispatch coordination, and integration of distributed resources: as decentralization and digitalization proceed under Layers 1 and 2, NISO's system- and market-operation role and TCN's transmission-infrastructure role become the operational counterpart to the interconnection and technical-assurance requirements set out in Sections 3.1 and 3.5.

3.7 Conceptual Dependency Matrix

Table 3 makes the layers' dependence on one another explicit, rather than leaving cross-layer "integration" as a general aspiration. Rows represent the dependent/target component; columns represent the enabling/source component. Each cell reports the degree to which the row component's function is constrained without the column component functioning adequately:

Score	Meaning
0	No material dependency
1	Low / indirect dependency
2	Moderate dependency
3	Critical dependency

These scores are conceptual, expert-informed judgments assigned from system-function logic rather than statistical estimation - architectural hypotheses for future empirical testing (Delphi elicitation, DEMATEL, or Interpretive Structural Modelling), not statistical findings. Unlike a symmetrical matrix, the structure below is deliberately directional: governance and the NEMSA spine constrain the transformation-capability layers and Layer 4 at high strength, while dependencies among the transformation-capability layers themselves, and Layer 3's dependence on the layers it constrains, are lower.

Table 3: NESI-X Conceptual Dependency Matrix

Target (row) \ Enabling source (column)	L1 Physical	L2 Intelligence	L3 Governance	NEMSA Spine	L4 Financial
L1 Physical transformation	-	2	3	3	2
L2 Digital intelligence	2	-	2	3	1
L3 Regulatory governance	0	1	-	1	1
NEMSA spine	1	1	1	-	2
L4 Financial/liquidity	1	2	2	3	-

A few illustrations clarify these scores. Layer 1 depends critically (3) on Layer 3 and the NEMSA spine because DER cannot scale safely without interconnection standards and NEMSA-verified compliance. Layer 2 depends critically on the NEMSA spine (3), since digital intelligence cannot support dependable decisions without reliable field or inspection data and moderately on Layer 1 and Layer 3. Layer 4 depends critically on the NEMSA spine (3), since meter certification determines whether billing data can be trusted, and moderately on Layers 2 and 3. By contrast, Layer 3 is scored as having low dependency on the layers it constrains (0–1): governance shapes what Layers 1, 2, and 4 can do, but its own function is not materially constrained by their technological maturity - correcting a symmetrical-dependency reading that would otherwise overstate governance's reliance on the layers it regulates. Conversely, better revenue data finances reinforcement, and better reliability improves willingness to pay: the architecture is designed to create reinforcing improvement across layers, not a sequence of isolated projects.

Nigeria already offers partial evidence supporting each transformation-capability layer's feasibility, though this should not be overstated as proof that NESI-X as a whole is validated. The World Bank's Nigeria Electrification Project supported 125 mini-grids and over a million solar home systems, giving over 5.5 million Nigerians electricity access (World Bank, 2024), now backed by NERC's 2026 Mini-Grid Regulations (NERC, 2026b) - meaningful support for Layer 1's feasibility, though not itself demonstrating the interoperability and technical-assurance requirements NESI-X adds. FoNER provides a concrete institutional development aligned with Layer 3, with objectives including harmonized regulatory approaches and joint capacity-building between NERC and state regulators (NERC, 2026c); NESI-X does not claim FoNER has already resolved regulatory fragmentation. Digital twins are technically mature enough internationally to be a plausible Layer 2 pathway, but Nigerian evidence should not be overstated: cybersecurity research highlights that increasing digital connectivity widens the cyber-physical attack surface (Pei et al., 2024; Nemade et al., 2024), so NESI-X treats digital twins as requiring Nigerian validation through pilot substations and feeders rather than as an already proven national solution. Nigerian-specific evidence at this intersection remains limited: no digital-twin grid study using Nigerian utility data was identified in the sources reviewed. The closest available Nigerian evidence is an IoT-and-neural-network fault-detection system for smart-grid components tested on a modified IEEE 30-bus network, reporting roughly 95% detection accuracy across several fault types (Omowaye et al., 2025) - a predictive-monitoring result adjacent to, but not itself, a digital-twin implementation. This gap is consistent with the caution above: NESI-X's digital-twin proposition should be read as requiring Nigerian pilot validation, not as resting on existing Nigerian digital-twin evidence. NEMSA's inspection, monitoring, investigation, and certification function, by contrast, is not a pathway requiring validation in the same sense - it is an existing, operating capability whose integration with digital asset management and revenue assurance, rather than its existence, is the genuinely novel element NESI-X proposes.

4. IMPLEMENTATION ARCHITECTURE: PHASED ROADMAP, KPIS, AND RISK CONTROLS

NESI-X deliberately uses gates rather than calendar milestones to sequence its implementation. A state, utility, plant, or network should not advance merely because a calendar date has arrived; advancement should require evidence that the necessary data, skills, cybersecurity controls, regulatory rules, technical-assurance capacity, and financing are genuinely in place. This is the architecture's primary safeguard against reproducing the historical pattern of installing technology faster than the institutions required to operate, finance, and certify it safely. Table 4 sets out the four phases in indicative terms, and Figure 4 presents the same roadmap as a gated timeline.

Table 4: NESI-X Phased Transformation Roadmap (Gated)

Phase	Indicative period	Primary actions	Gate / success condition
0 - Stabilize	2026-2027	Establish a common asset/data taxonomy, including NEMSA inspection and certification data; prioritize critical grid observability; baseline ATC&C, reliability, and outage metrics; and map regulatory responsibilities across federal and state levels.	Baseline dataset and governance ownership have been approved.
1 - Foundation	2027-2029	Pilot DER interoperability; expand AMI/feeder energy accounting; deploy PMU/WAMS at strategically important nodes; establish regulatory sandbox procedures; pilot integration of NEMSA inspection/testing records with utility asset-management systems.	Pilots demonstrate data integrity, safety, and measurable operational value.
2 - Integration	2029-2032	Scale digital twins, predictive analytics, and DER coordination; harmonize technical standards across participating states; incorporate verified NEMSA inspection data into digital twin and predictive maintenance systems.	Cross-layer KPIs improve simultaneously; no major interoperability or cybersecurity failure.
3 - Adaptive maturity	2032 onward	Continuous optimization, automated decision support, data-informed adaptive tariff-setting subject to regulatory approval, coordinated DER participation, risk-informed technical assurance, and resilience planning.	The system demonstrates sustained reliability, liquidity, interoperability, and learning capacity.

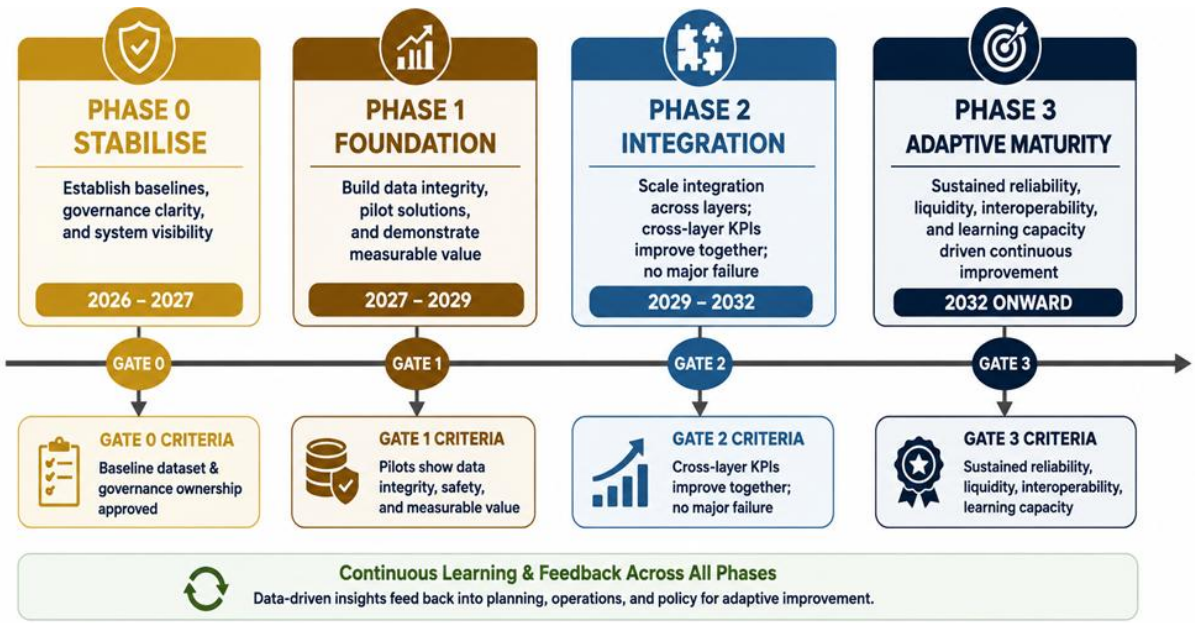

Figure 4: NESI-X gated transformation roadmap.

Table 5 converts each layer and the system as a whole into measurable indicators so that "progress" under NESI-X is something a regulator, utility, or independent researcher can actually check against data rather than assess only qualitatively. Baseline values are deliberately left unspecified here rather than invented: Phase 0 of the roadmap exists precisely to establish them from primary Nigerian data before Phase 1 targets are set. KPIs are divided into a core set likely measurable from currently available Nigerian data and an advanced set dependent on data infrastructure the roadmap itself is designed to build.

Table 5: Key Performance Indicators by Layer

Layer	KPI	Operational definition	Data source	Tier	Roadmap Phase
L1 Physical	Islanding readiness	Share of critical loads capable of intentional islanding within a defined response time.	DisCo/NERC outage records; utility asset registers	Core	Phase 1
L1 Physical	DER hosting capacity	Additional DER capacity a feeder can accommodate before violating protection or voltage limits.	DisCo/NISO network studies	Advanced	Phase 2
L2 Intelligence	Telemetry completeness	Valid data points received / expected data points x 100.	TCN, DisCo SCADA/telemetry logs	Core	Phase 1
L2 Intelligence	Digital-twin model fidelity	Agreement between predicted and observed system states under predefined validation scenarios.	Pilot digital-twin validation records	Advanced	Phase 2
L3 Governance	Regulatory sandbox cycle time	Elapsed time from sandbox application to regulatory decision.	NERC, state regulator, FoNER records	Core	Phase 1
NEMSA spine	Inspection closure rate	The formula for calculating the inspection closure rate is: (Corrective actions closed / Corrective actions issued) x 100.	NEMSA inspection and certification records	Core	Phase 0
NEMSA spine	AMI/meter certification coverage	Active, NEMSA-certified meters / total customer meters x 100.	NEMSA, DisCo meter registers	Core	Phase 1
L4 Financial	ATC&C loss	As defined in Section 1: 1 - [(1 - Technical/Commercial Loss) x (1 - Collection Loss)].	NERC quarterly reports	Core	Phase 0
System-level	SAIDI / SAIFI	Standard reliability indices, where applicable.	NERC, TCN, DisCo aggregated reporting	Core	Phase 1–2
System-level	LOLE / EENS	Loss of load expectation / expected energy not served, where data permit.	TCN, NISO system-operation data	Advanced	Phase 2–3

Four risks condition whether the roadmap's gates are actually cleared rather than remaining aspirational. Financing is the first and most immediate constraint: digitalization, DER deployment,

storage, metering, and network reinforcement all require capital while the sector works through historical liquidity weaknesses documented in Section 1. NESI-X responds by prioritizing projects that create measurable technical and commercial value simultaneously - for example, feeder digitalization that improves both outage visibility and revenue assurance from the same investment. Skills are the second constraint: digital-grid transformation requires engineers, technicians, data scientists, protection specialists, cybersecurity professionals, and regulators capable of working across disciplinary boundaries historically kept separate in Nigerian institutional training, built through joint university-NAPTIN-utility-regulator competency pathways around digital substations, DER control, AMI analytics, and cyber-physical security.

Interoperability and cybersecurity are the third constraint, growing more serious precisely as the other layers succeed. Smart-grid expansion under Layers 1-2 creates substantially more communication interfaces, and therefore, more attack surface than NESI 1.0's largely analog configuration presents today. Recent research emphasizes holistic cyber defense for smart grid environments - proactive threat detection, secure integration, and continuous monitoring rather than perimeter security alone (Nemade et al., 2024). NESI-X treats cybersecurity as a design requirement embedded within every layer, including the NEMSA spine's data flows into Layer 2, rather than as a separate IT project bolted on afterward. Political economy is the fourth constraint and the one most likely underestimated by a purely technical reading: reform touches tariffs, subsidies, investment rights, and the distribution of authority between federal and state governments, and a technically coherent architecture can still fail if stakeholders perceive it as redistributing costs or authority without credible accountability. The architecture therefore requires transparent KPIs, public reporting, meaningful stakeholder participation, and independent evaluation, rather than self-reported progress.

5. EMPIRICAL PROPOSITIONS AND DISCUSSION

NESI-X is not a prediction that Nigeria will automatically achieve a resilient electricity system simply by adopting four technologies or institutional mechanisms; it is a systems architecture and a set of testable propositions. Its core claim, made structurally explicit by Section 3's tiering, is that Nigeria can leapfrog *selected stages* of electricity-sector development but cannot leapfrog the institutional, technical-assurance, and financial dependencies that make an electricity system work; those enabling conditions and the NEMSA spine that verifies them must be progressively built, not bypassed, regardless of how quickly transformation-capability technologies can be deployed.

Three distinctions follow directly from this claim. First, distributed generation can meaningfully reduce dependence on a single, centralized national grid pathway, but it cannot eliminate the underlying need for transmission and distribution coordination, protection coordination, and independent technical assurance of the assets being connected (Section 3.5). Second, digital twins and artificial intelligence can greatly enhance our ability to see and make decisions about systems, but they cannot resolve underlying issues such as missing sensors, poor data management, inadequate maintenance, or weak cybersecurity; if a complex digital system is built on a poorly maintained physical system, it will only create confident predictions about a system whose actual condition is not accurately known. Third, state-level regulatory autonomy under the Electricity Act 2023 can genuinely stimulate valuable local innovation, but without the interoperability floor proposed in Layer 3, it can just as easily fragment the national market further rather than resolving NESI 1.0's existing fragmentation. Each of these distinctions creates a clear expectation about what should be observable if the architecture's account of NESI's problems is accurate, which is what makes the architecture testable rather than merely plausible.

The architecture accordingly yields five propositions that future empirical work - ideally conducted with the primary Nigerian regulatory and utility data referenced throughout this paper - can test directly.

P1. ATC&C loss reduction correlates with feeder-level metering penetration, consistent with existing Nigerian evidence at the DisCo level (Odje et al., 2021), but the marginal effect of additional metering should diminish measurably where Layer 3 governance capacity or NEMSA spine meter-certification capacity is weak, since metering alone cannot correct misaligned tariffs, weak enforcement, or uncertified meters.

P2. DER and mini-grid deployments interconnected under common technical standards and NEMSA-verified compliance should show measurably lower post-disturbance restoration times and fewer safety-related incidents than isolated deployments lacking equivalent verification, holding local generation capacity constant.

P3. The strength and direction of R2, the hypothesized regulatory-fragmentation loop, are empirically testable by comparing investment cycle times and DER interconnection approval times across Nigerian states before and after FoNER-coordinated standard adoption, once a sufficient number of states have transitioned and a baseline period is available for comparison.

P4. Transformation-capability KPIs (Table 5, Layers 1-2) should stagnate wherever governance, technical assurance, or liquidity indicators fall below an identifiable threshold, largely independent of Layer 1/2 technological maturity - enabling-condition maturity should constrain observed outcomes in practice, not merely in Table 3's conceptual ratings.

P5. Integration of verified NEMSA inspection, testing, and certification data with utility asset-management datasets will improve asset-condition classification and predictive-maintenance performance relative to models using operational data alone - testable by comparing an operational-data-only model against an operational-plus-NEMSA-data model on the same asset population.

None of these five propositions is claimed to have already been demonstrated in Nigeria; each is offered as a testable proposition consistent with the methodological discipline established in Section 2.4, where R1 was distinguished from R2 and R3 precisely along these lines. This maintains the paper's evidence-first posture through to its final analytical section, rather than relaxing it once the architecture itself has been presented.

6. LIMITATIONS, INTERNATIONAL TRANSFERABILITY, AND CONCLUSION

6.1 Limitations

This paper lacks an econometric estimation of the causal relationships it proposes and a calibrated system dynamics simulation of NESI as a whole. R1, R2, and R3 are causal-loop propositions rather than fitted models, and none has been empirically validated against Nigerian time-series data. Table 3's dependency scores are conceptual, derived from system-function logic rather than statistical estimation. Because these scores were assigned by the author team rather than through structured elicitation, they carry a risk of single-team framing bias. For example, the NEMSA core structure's uniformly high dependency scores reflect the authors' institutional familiarity with NEMSA's mandate but could plausibly be contested by DisCo or NERC-side reviewers with different operational perspectives or prior expectations. Independent expert elicitation (Delphi, DEMATEL, or AHP/ANP, as already flagged in Section 2.3) remains necessary before Table 3's scores can be treated as more than a starting hypothesis for empirical and expert scrutiny.

The paper also performs no cost-benefit optimization of the Table 4 roadmap, and Table 5's KPI baselines are deliberately left unspecified pending the Phase 0 baselining that the roadmap proposes, rather than being populated with placeholder numbers that might misrepresent current evidence. The architecture has not yet been field-validated as an integrated system; Section 3.7's evidence supports the feasibility of individual layers, not NESI-X's validated performance as a whole. Nigeria's regulatory conditions, particularly the state transition process and FoNER's evolving mandate, remain in flux, and data availability for empirical validation may itself be constrained by the same institutional immaturity the architecture seeks to address.

6.2 International Relevance and Transferability

NESI-X is specifically developed for Nigeria, and its evidence base is entirely Nigerian. However, the underlying architecture - distinguishing bypassable technological pathways from indispensable physical and institutional infrastructure and coupling transformation capabilities to enabling conditions through an explicit dependency structure - is not specific to Nigerian institutional detail in its logic, even though it is specific to Nigerian institutions in its evidence. The architecture is plausibly transferable, as a conceptual template rather than a ready-made solution, to electricity systems sharing a similar combination of conditions: weak grid reliability alongside rapid DER growth,

regulatory authority fragmented across sub-national jurisdictions, high technical and commercial losses, limited digital grid infrastructure, and an active energy-access agenda. Nigeria serves as the primary application context for this paper, but it does not limit its theoretical relevance; testing the transferability of these findings to other national contexts with similar conditions - for example, elsewhere in Sub-Saharan Africa and South Asia - is a natural extension of the empirical agenda above, although this paper does not pursue that comparison directly.

6.3 Conclusion

NESI's persistent electricity problems are better understood as a coupled system than as a collection of isolated technical defects to be addressed one at a time. Verified regulatory evidence shows substantial ATC&C losses and quarterly revenue leakage exceeding ₦139 billion across DisCos, while current Nigerian policy is simultaneously opening genuine pathways for decentralized generation, digital grid intelligence, and multi-level governance. NESI-X's central proposition is that Nigeria can leapfrog selected technological pathways in generation, distribution, metering, monitoring, and maintenance but cannot leapfrog the non-bypassable system dependencies - governance, technical assurance, and liquidity, alongside the transmission backbone itself - that make an electricity system work.

Technical assurance, positioned in Section 3.5 as a cross-cutting spine rather than a fifth layer, is a further institutional requirement in its own right: as NESI decentralizes and digitalizes, infrastructure expansion must be matched by effective inspection, testing, certification, and safety assurance, or deployment will simply outrun the system's ability to verify that what has been built is safe and fit for purpose. NESI-X positions NEMSA as a technical-assurance spine connecting physical infrastructure, digital asset intelligence, regulatory governance, and revenue assurance, with a proposed contribution extending beyond conventional compliance toward integrating verified technical-condition data into asset management and risk-informed planning. As Section 6.2 argues, this coupling of bypassable technology to non-bypassable assurance is plausibly relevant wherever rapid DER growth meets fragmented governance and weak technical oversight, with Nigeria as this paper's primary evidence base rather than its outer boundary.

The roadmap in Section 4 is gated rather than calendar-driven because institutional readiness, skills, technical-assurance capacity, cybersecurity, interoperability, and financing determine whether investment actually translates into reliable and safe electricity, not the simple passage of time. The immediate research agenda is the empirical validation of P1-P5: quantifying the causal loops introduced in Section 2.4 against multi-year NERC, TCN, NISO, DisCo, NEMSA, and market data as it becomes available; evaluating pilot DER and digital-twin deployments as they are commissioned; and testing directly whether enabling-condition maturity constrains transformation-capability outcomes in the way the architecture predicts. NESI-X should ultimately be judged not by the elegance of its architecture but by whether these measurable outcomes improve as it is applied and tested against Nigerian evidence.

REFERENCES

Adeku, A. Y., Yusufu, F. O., Yakubu, A., Abubakar, U., & Ozomata, L. J. (2026). Electricity Sector Reforms and Power Supply Reliability in Nigeria: Post-Privatization Realities and Prospects. International Journal of Public Administration and Development Studies (IJPADS), 3(2), 1-17. https://ijpads.com/index.php/ijpads/article/view/96

Akunne, C. S., Nwoye, M. I., Adewale, B. A., & Abubakar, H. L. (2023). Strategy Formulation and Resource Availability Determinants in Performance of Electricity Distribution Companies in Nigeria. Journal of Human Resource and Sustainability Studies, 11(4).

Babayomi, O. O., Olubayo, B., Denwigwe, I. H., Somefun, T. E., Adedoja, O. S., Somefun, C. T., Olukayode, K., & Attah, A. (2023). A review of renewable off-grid mini-grids in Sub-Saharan Africa. Frontiers in Energy Research, 10, 1089025. https://doi.org/10.3389/fenrg.2022.1089025

Federal Ministry of Power. (2025). National Integrated Electricity Policy and Strategic Implementation Plan (NIEP-SIP). Federal Republic of Nigeria. https://power.gov.ng/download/national-integrated-electricity-policy/

Federal Republic of Nigeria. (2023). Electricity Act, 2023. Federal Ministry of Power. https://www.power.gov.ng/download/electricity-act-2023/

Idowu, S. S., Ibietan, J., & Olukotun, A. (2020). Privatization of power sector in Nigeria: An evaluation of Ibadan and Ikeja Electricity Distribution Companies performance (2005-2018). International Journal of Public Administration, 43(16), 1413-1420. https://doi.org/10.1080/01900692.2019.1672183

Nemade, B., Maharana, K. K., Kulkarni, V., Srivardhankumar, C., & Shelar, M. (2024). Revolutionizing smart grid security: A holistic cyber defence strategy. Frontiers in Artificial Intelligence, 7, 1476422. https://doi.org/10.3389/frai.2024.1476422

Nigerian Electricity Management Services Agency. (2015). NEMSA Act, 2015 (Act No. 6). https://nemsa.gov.ng/wp-content/uploads/2019/05/NEMSA_ACT_2015.pdf

Nigerian Electricity Management Services Agency. (2023). Electricity Act, 2023. https://nemsa.gov.ng/wp-content/uploads/2024/05/ELECTRICITY-ACT-2023.pdf

Nigerian Electricity Management Services Agency. (n.d.-b). Mandate. https://nemsa.gov.ng

Nigerian Electricity Regulatory Commission. (2024). Order on the establishment of the Independent System Operator for the Nigerian Electricity Supply Industry (Order No. NERC/2024/45). https://nerc.gov.ng/wp-content/uploads/2024/05/Order-on-the-Establishment-of-the-Independent-System-Operator-for-NESI-1.pdf

Nigerian Electricity Regulatory Commission. (2026a). 2025/Q4 quarterly report. https://nerc.gov.ng/wp-content/uploads/2026/04/2025_Q4-Report.pdf

Nigerian Electricity Regulatory Commission. (2026b). Mini-grid regulations 2026. https://nerc.gov.ng/wp-content/uploads/2026/04/Mini-Grid-Regulations-2026.pdf

Nigerian Electricity Regulatory Commission. (2026c, March 25). NERC, State Regulators inaugurate Forum of Nigerian Electricity Regulators (FoNER) to improve electricity regulation. https://nerc.gov.ng/media/nerc-state-regulators-inaugurate-forum-of-nigerian-electricity-regulators-foner-to-improve-electricity-regulation/

Odje, M., Uhunmwangho, R., & Okedu, K. E. (2021). Aggregated technical commercial and collection loss mitigation through a smart metering application strategy. Frontiers in Energy Research, 9, 703265. https://doi.org/10.3389/fenrg.2021.703265

Omowaye, O. J., Oladipo, O. E., Adejumobi, B. S., Ogunlade, M. A., Onibonoje, M. O., & Ibitoye, O. T. (2025). An AI-based predictive maintenance technique for smart grid components. NIPES Journal of Science and Technology Research, 7(2), Special Issue: SEB4SDG 2025, 3218–3222. https://doi.org/10.37933/nipes/7.4.2025.SI385

Pei, L., Xu, C., Yin, X., & Zhang, J. (2024). Multi-agent deep reinforcement learning for cloud-based digital twins in power grid management. Journal of Cloud Computing, 13, 152. https://doi.org/10.1186/s13677-024-00713-w

Ranawaka, A., Alahakoon, D., Sun, Y., & Hewapathirana, K. (2024). Leveraging the synergy of digital twins and artificial intelligence for sustainable power grids: A scoping review. Energies, 17(21), 5342. https://doi.org/10.3390/en17215342

van Benthem, A. A. (2015). Energy leapfrogging. Journal of the Association of Environmental and Resource Economists, 2(1), 93-132. https://doi.org/10.1086/680317

World Bank. (2024, June 30). Expanding Nigeria's mini grid market. Energy Sector Management Assistance Program. https://www.worldbank.org/en/news/feature/2025/03/07/expanding-nigeria-s-mini-grid-market

Zhou, M., Yan, J., & Feng, D. (2019). Digital twin framework and its application to power grid online analysis. CSEE Journal of Power and Energy Systems, 5(3), 391-398. https://doi.org/10.17775/CSEEJPES.2018.01460

INTEGRATED HEC-HMS AND IMPROVED SOIL MOISTURE BALANCE MODELLING FOR GROUNDWATER RECHARGE ASSESSMENT IN THE SEMI-ARID SOKOTO BASIN, NIGERIA

Usman Muhammed Kudu[1], Richard Adeolu Adesiji[1,*]
[1]*FUT Minna*
Email: usmanmuhammedkudu@gmail.com, RichardAdesiji@gmail.com*
***Corresponding author**: Richard Adeolu Adesiji
DOI: https://doi.org/10.67203/sp.ICESID.2026

ABSTRACT
Groundwater is the principal source of freshwater for domestic, agricultural and livestock activities in the semi-arid Sokoto Basin of northwestern Nigeria, yet increasing water demand, climate variability and uncertainty in aquifer replenishment pose growing challenges to its sustainable management. This study developed an integrated Hydrologic Engineering Center–Hydrologic Modeling System (HEC-HMS) and Improved Soil Moisture Balance (SMB) framework for estimating groundwater recharge using long-term hydro-meteorological records from 1990 to 2025, observed streamflow, measured soil hydraulic properties and topographic information. HEC-HMS was used to simulate rainfall–runoff processes, while the Improved SMB model incorporated dynamic root-zone soil moisture accounting, spatially variable soil hydraulic properties, moisture-dependent evapotranspiration, separate treatment of lateral runoff and threshold-controlled deep percolation. Model calibration produced a Nash–Sutcliffe Efficiency (NSE) of 0.84, coefficient of determination (R^2) of 0.86, Root Mean Square Error (RMSE) of 42.6 m^3/s and Percent Bias (PBIAS) of +3.7%. Independent validation yielded NSE = 0.77, R^2 = 0.79, RMSE = 49.8 m^3/s and PBIAS = −4.2%, demonstrating satisfactory predictive performance. Long-term recharge analysis showed pronounced interannual variability, with a mean annual recharge of 126 mm/year, a minimum of 62 mm/year in 1991 and a maximum of 205 mm/year in 2009. Rainfall and recharge were positively correlated (r = 0.72; R^2 = 0.52), with a regression slope of 0.115 mm recharge per millimetre of rainfall and an intercept of −34.3 mm, indicating threshold-controlled recharge under semi-arid conditions. Spatial analysis further identified distinct recharge zones controlled by rainfall, soil hydraulic characteristics and terrain conditions. The integrated framework provides a reproducible decision-support approach for groundwater planning, managed aquifer recharge, watershed conservation and climate-resilient water-resource management in semi-arid regions.

Keywords: *groundwater recharge; hec-hms; hydrological modelling; semi-arid hydrology; soil moisture balance*

1. INTRODUCTION

Groundwater is a critical component of global freshwater resources and supports domestic water supply, irrigated agriculture, industrial production and ecosystem functioning. Its importance is particularly pronounced in regions where surface-water availability is strongly seasonal or unreliable. Unlike surface reservoirs and rivers, groundwater is less directly exposed to evaporation and can provide an important buffer against short-term rainfall variability and drought (Freeze & Cherry, 1979; de Vries & Simmers, 2002). Consequently, sustainable groundwater development has become increasingly important as population growth, urbanisation, agricultural expansion and industrial development increase freshwater demand worldwide (Scanlon et al., 2006).

Recent global assessments further demonstrate the importance of groundwater within an increasingly variable hydrological system. The World Meteorological Organization (WMO, 2023) reported substantial regional anomalies in river discharge, reservoir inflows, soil moisture and groundwater conditions during 2022, reflecting increasing hydrological variability across many regions. Similarly, the United Nations World Water Development Report emphasises that water security is closely connected to economic development, food production, social stability and resilience to climatic extremes (UNESCO, 2024). These assessments highlight the need for improved quantitative understanding of groundwater replenishment, particularly in regions where groundwater constitutes a major component of freshwater supply.

Despite its importance, groundwater is under increasing pressure from abstraction, land-use change, climatic variability and changes in natural recharge. Excessive groundwater withdrawal relative to aquifer replenishment can result in declining groundwater levels, reduced baseflow, increasing pumping costs and deterioration of groundwater-dependent ecosystems (Taylor et al., 2013). The sustainability of groundwater development therefore depends not only on the volume of groundwater stored within an aquifer but also on the rate and variability of groundwater recharge.

Groundwater recharge is the downward movement of infiltrated water through the unsaturated zone to the saturated aquifer. It is among the most difficult components of the hydrological cycle to quantify because it depends on interacting climatic, hydrological, soil, geological, vegetation and topographic controls (Healy, 2010). Recharge can vary considerably over both space and time, and the magnitude of this variability becomes particularly important when groundwater-development decisions are based on long-term average estimates (Scanlon et al., 2006). Reliable estimation of recharge is therefore essential for groundwater-resource assessment, sustainable abstraction planning, aquifer protection and climate-resilient water management.

The difficulty of recharge estimation is particularly pronounced in semi-arid environments. Rainfall in such regions is strongly seasonal and frequently occurs as short-duration, high-intensity storms, while potential evapotranspiration remains high for much of the year. Consequently, a large proportion of precipitation may be lost through evapotranspiration and surface runoff before sufficient soil moisture is accumulated to generate deep percolation (Healy, 2010). Groundwater recharge therefore tends to be episodic and threshold-dependent rather than continuous. Scanlon et al. (2006) demonstrated that recharge in arid and semi-arid environments can vary substantially in response to rainfall magnitude, soil characteristics and land-surface conditions, while Taylor et al. (2013) showed that intense rainfall events can play a disproportionate role in groundwater replenishment across parts of Africa.

Northern Nigeria exhibits many of these characteristics. The Sokoto Basin forms the Nigerian sector of the larger transboundary Iullemmeden Basin shared principally between Nigeria and the Republic of Niger. Within Nigeria, the basin extends across Sokoto and Kebbi States and parts of Zamfara and Niger States. The broader hydrogeological system extends beyond the Nigerian boundary into Niger Republic; however, the hydrological modelling undertaken in this study is restricted to the delineated Nigerian model domain represented in Figure 1. This distinction is important because the hydrogeological basin is transboundary, whereas the quantitative recharge estimates presented in this study relate specifically to the modelled catchment.

Groundwater is extensively used within the Sokoto Basin for domestic water supply, irrigation, livestock production and rural livelihoods. However, recurrent drought, agricultural expansion, population growth and high rainfall variability place increasing pressure on available groundwater resources. Reliable information on recharge remains limited because of sparse hydrological observations, inadequate long-term groundwater monitoring and the complexity of rainfall–runoff–infiltration interactions. Consequently, groundwater-development decisions may be undertaken without sufficient quantitative information on the temporal and spatial variability of aquifer replenishment.

Numerous methods have been developed for estimating groundwater recharge, including empirical rainfall–recharge relationships, water-table fluctuation methods, chloride mass balance, lysimeter measurements, environmental tracers, water-balance techniques and physically based numerical models (Scanlon et al., 2002; Healy, 2010). Each method has advantages and limitations. Field-based approaches may provide detailed information at individual locations but can require extensive monitoring and may not adequately represent basin-scale spatial variability. Conversely, empirical approaches are comparatively simple to implement but may not adequately represent changing hydrological conditions. Sophocleous (2004) noted that recharge estimation remains a major source of uncertainty in groundwater assessment because no single technique can completely represent the complexity of natural recharge processes.

These limitations are especially important in African basins where observational networks may be sparse and long-term hydrogeological data are frequently incomplete. Xu and Beekman (2019) emphasised that groundwater-recharge assessment in Africa requires approaches capable of integrating available climatic, hydrological and hydrogeological information while explicitly recognising data limitations and spatial variability. An integrated modelling framework can therefore provide a useful

alternative by combining complementary techniques rather than depending on a single recharge-estimation method.

The Hydrologic Engineering Center–Hydrologic Modeling System (HEC-HMS) provides a widely applied framework for simulating rainfall–runoff processes at catchment scale. It allows precipitation losses, runoff transformation and channel routing to be represented using established hydrological methods. Soil Moisture Balance (SMB) modelling, in contrast, provides a physically interpretable framework for tracking rainfall inputs, evapotranspiration losses, runoff, soil-water storage and drainage below the root zone. Integration of the two approaches enables runoff estimated by a calibrated hydrological model to be incorporated directly into soil-water accounting, thereby reducing reliance on assumed runoff coefficients.

However, a conventional SMB formulation based solely on annual or monthly precipitation minus evapotranspiration and runoff can oversimplify recharge generation in semi-arid environments. Recharge generally occurs only after antecedent soil-water deficits have been replenished and soil storage exceeds a drainage threshold. Soil depth, field capacity, wilting point and saturated hydraulic conductivity also vary spatially, while evapotranspiration becomes constrained as soil moisture declines. These processes require a temporally explicit soil-water accounting framework rather than simple residual water-balance estimation.

Accordingly, the present study integrates HEC-HMS with an Improved SMB model incorporating dynamic root-zone moisture accounting, variable soil hydraulic properties, moisture-dependent evapotranspiration, explicit treatment of runoff and lateral losses, and threshold-controlled deep percolation. The integrated approach is consistent with the broader need for groundwater assessments that account for interactions among surface hydrology, soil-water processes and groundwater replenishment (Gleeson et al., 2020; Xu & Beekman, 2019).

The aim of this study is therefore to develop and apply an integrated HEC-HMS–Improved SMB framework for assessing the temporal and spatial variability of groundwater recharge in the semi-arid Sokoto Basin. Specifically, the study uses long-term hydro-meteorological observations from 1990 to 2025, observed streamflow, soil hydraulic measurements and topographic information to simulate rainfall–runoff processes, quantify groundwater recharge, examine the rainfall–recharge relationship and identify spatial variations in recharge potential.

Beyond its hydrological contribution, the framework is intended as an engineering decision-support tool. Quantitative recharge information can support the siting of managed aquifer recharge facilities, groundwater-development planning, watershed conservation, drought-risk management and prioritisation of areas for groundwater protection. The approach therefore connects hydrological modelling with practical engineering innovation and evidence-based water policy, supporting sustainable water-resource development and improved climate resilience in northern Nigeria and comparable semi-arid environments.

2. MATERIALS AND METHODS

The study was conducted in the Sokoto Basin in northwestern Nigeria, which forms the Nigerian sector of the larger transboundary Iullemmeden Basin extending into the Republic of Niger. Within Nigeria, the basin covers Sokoto and Kebbi States and parts of Zamfara and Niger States. Although the broader hydrogeological system is transboundary, the numerical modelling undertaken in this study was restricted to the Nigerian catchment delineated from the Digital Elevation Model (DEM) and represented in Figure 1. The delineated HEC-HMS model domain covers approximately **28,400 km²** and should therefore not be interpreted as the total geographical area of the entire Sokoto-Rima or transboundary Iullemmeden Basin.

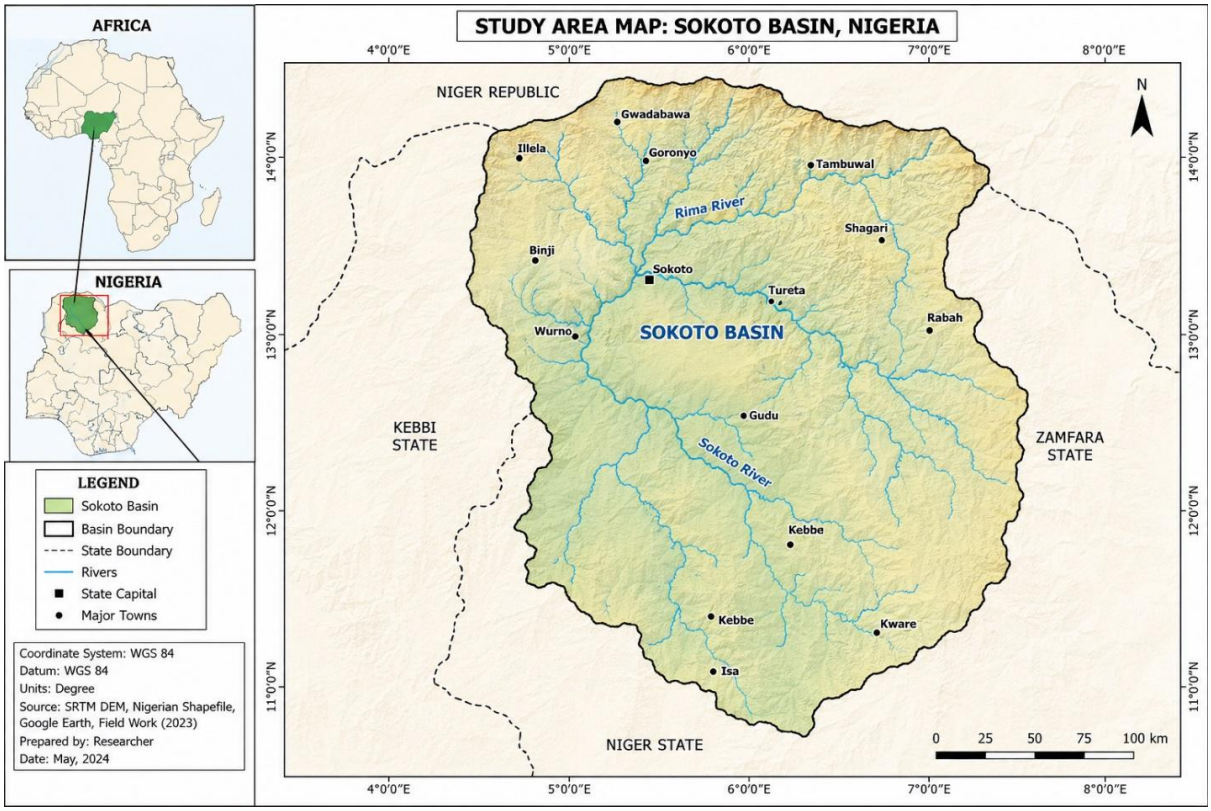

Figure 1: Study Area Map of the Sokoto Basin

Geologically, the basin consists predominantly of sedimentary formations, including the Gundumi, Rima, Sokoto and Gwandu Formations, which exhibit differences in lithology, aquifer properties and groundwater-storage characteristics. These formations constitute important groundwater-bearing units supporting domestic water supply, irrigation and livestock production within the region.

The climate is semi-arid and characterized by a distinct wet season extending approximately from May to October and a prolonged dry season from November to April. Annual rainfall generally ranges between 700 and 1,200 mm, with most precipitation occurring between June and September. Mean annual temperatures commonly exceed 30°C, resulting in substantial atmospheric water demand and high evapotranspiration losses. The drainage system is dominated by the Sokoto-Rima River network.

Soils within the modelled area are predominantly sandy loam and loamy sand, with localized sandy clay loam and finer-textured deposits. Variations in soil texture influence infiltration, soil-water retention, runoff generation and the amount of water available for deep percolation. Land use is dominated by rain-fed and irrigated agriculture, grazing land, riparian vegetation and settlements. The combined effects of climate, soils, terrain and land use produce considerable spatial and temporal variability in runoff and groundwater recharge.

2.2 Overall Modelling Framework

The methodological framework integrated HEC-HMS rainfall-runoff simulation with an Improved Soil Moisture Balance (SMB) model. The modelling procedure consisted of five principal stages: (1) hydro-meteorological, soil and spatial data preparation; (2) DEM-based watershed delineation and HEC-HMS model development; (3) calibration and validation of simulated runoff against observed streamflow; (4) daily root-zone soil-water accounting and estimation of deep percolation using the Improved SMB model; and (5) temporal and spatial analysis of groundwater recharge.

The principal rationale for coupling the two models was to avoid estimating runoff as an arbitrary residual or fixed fraction of rainfall within the SMB calculation. Instead, surface runoff was independently simulated using the calibrated HEC-HMS model and subsequently transferred to the

SMB framework. The SMB component then accounted for rainfall, evapotranspiration, soil-water storage, lateral losses and threshold-controlled drainage below the root zone.

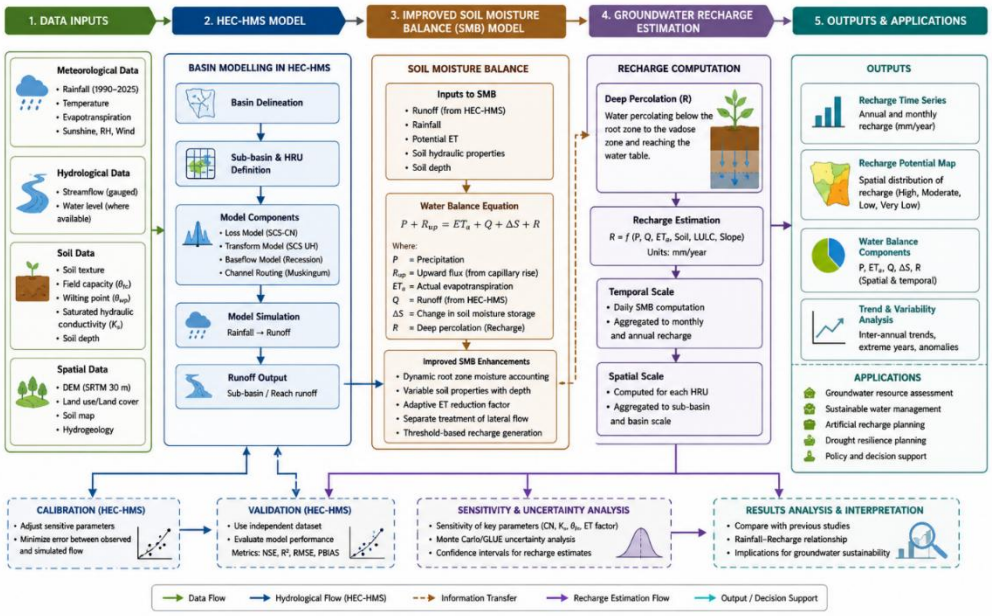

Figure 2: Integrated HEC-HMS–SMB Methodological Framework

2.3 Data Collection and Preparation

Meteorological, hydrological, soil and topographic datasets were assembled for development of the integrated framework. Daily rainfall and temperature records covering 1990–2025 were obtained from the Nigerian Meteorological Agency (NiMet). Relative humidity and wind-speed observations were also incorporated into the climatic dataset for evapotranspiration estimation.

Observed daily streamflow records from hydrological gauging stations within the modelled basin were used for HEC-HMS calibration and validation. The streamflow record used in the modelling was divided into 1990–2011 for calibration and 2012–2025 for validation, consistent with the periods represented in the observed-versus-simulated hydrograph.

Soil samples collected during the 2024 field investigation were analysed for soil texture, bulk density, field capacity, permanent wilting point and saturated hydraulic conductivity. These measurements were treated as static soil hydraulic parameters for the long-term simulation. This assumes that the principal soil hydraulic characteristics represented by the sampled locations remained sufficiently stable to characterize the corresponding soil units during the 1990–2025 simulation period. The assumption is necessary because equivalent historical measurements were unavailable and represents a limitation of the long-term reconstruction.

A 30-m Shuttle Radar Topography Mission (SRTM) DEM was used for catchment delineation, drainage-network extraction and terrain analysis. Land-use/land-cover information was obtained from Landsat imagery, while the FAO/Harmonized World Soil Database (HWSD) provided supplementary spatial soil information used to extend measured soil characteristics across the modelled area.

Table 1: Summary of Meteorological, Hydrological and Soil Datasets.

Dataset	Variable	Source	Temporal resolution	Spatial resolution	Period/status	Purpose
Meteorological	Rainfall	NiMet	Daily	Station	1990–2025	Hydrological forcing
Meteorological	Temperature	NiMet	Daily	Station	1990–2025	Evapotranspiration estimation
Meteorological	Relative humidity	NiMet	Daily	Station	1990–2025	Climate/ET analysis
Meteorological	Wind speed	NiMet	Daily	Station	1990–2025	Evapotranspiration estimation
Hydrological	Streamflow	NIHSA/River gauge stations	Daily	Gauge	1990–2025*	HEC-HMS calibration and validation
Soil	Texture	Field/laboratory analysis	Static	Sampling sites	Sampled 2024	Soil classification
Soil	Bulk density	Laboratory analysis	Static	Sampling sites	Sampled 2024	Soil-water parameterization
Soil	Field capacity	Laboratory analysis	Static	Sampling sites	Sampled 2024	Root-zone storage calculation
Soil	Permanent wilting point	Laboratory analysis	Static	Sampling sites	Sampled 2024	Available-water calculation
Soil	Saturated hydraulic conductivity	Laboratory analysis	Static	Sampling sites	Sampled 2024	Drainage/infiltration parameterization
Spatial	DEM	SRTM	Static	30 m	DEM product	Watershed and terrain delineation
Spatial	Land use/land cover	Landsat	Annual/periodic	30 m	2020–2025	Surface characteristics
Spatial	Soil map	FAO/HWSD	Static	250 m	Reference dataset	Spatial soil parameterization

The 1990–2025 streamflow period represents the record used to construct the calibration and validation datasets. Calibration covered 1990–2011 and validation covered 2012–2025.

Because the soil observations represent measurements made in 2024 rather than annual observations throughout the modelling period, the analysis assumes temporally invariant soil hydraulic properties. Consequently, long-term changes in soil structure arising from land management, erosion or other processes are not explicitly represented.

2.4 HEC-HMS Rainfall-Runoff Modelling

Rainfall-runoff simulation was undertaken using the Hydrologic Engineering Center–Hydrologic Modeling System (HEC-HMS Version 4.12). Watershed boundaries, drainage networks and sub-basins were delineated from the SRTM DEM in a GIS environment and subsequently imported into HEC-HMS.

The Soil Conservation Service Curve Number (SCS-CN) method was used to represent rainfall losses because it provides a practical means of incorporating soil type, land use and antecedent moisture effects in data-limited catchments.

The potential maximum retention, (S) (mm), was computed from the Curve Number (CN) using Equation 1.

$$S = \frac{25400}{CN} - 254 \quad (1)$$

Where S is the maximum potential soil water retention (mm) and CN is the dimensionless Curve Number representing land use, soil type and antecedent moisture conditions.

Direct runoff depth, (Q) (mm), was then estimated using Equation 2.

$$Q = \frac{(P - I_a)^2}{P - I_a + S} \quad (2)$$

Where Q is direct runoff (mm), P is rainfall depth (mm), (I_a) is initial abstraction (mm), commonly taken as (0.2S), and S is potential maximum retention (mm).

Runoff transformation from rainfall excess to the catchment hydrograph was represented using the SCS Unit Hydrograph method. Channel flow was routed using the Muskingum method, with routing parameters (K) and (X) representing travel time and relative storage weighting, respectively.

The delineated watershed area used in HEC-HMS was approximately **28,400 km²**. This value represents the DEM-derived computational domain used for the present model and **not the total area of the complete Sokoto-Rima/Iullemmeden hydrological system**.

Table 2: Hydrological Model Parameters Used in HEC-HMS and Improved Soil Moisture Balance Simulation.

Component	Parameter	Symbol	Value	Unit
Basin	Watershed Area	A	28,400	km²
Basin	Curve Number	CN	68–84	–
Basin	Initial Abstraction	Ia	12.6	mm
Basin	Lag Time	Tlag	5.4	hr
Basin	Time of Concentration	Tc	8.2	hr
Channel	Manning Roughness	n	0.035	–
Channel	Muskingum K	K	4.0	hr
Channel	Muskingum X	X	0.20	–
Soil	Field Capacity	θFC	0.28	m³/m³
Soil	Wilting Point	θWP	0.14	m³/m³
Soil	Saturated Moisture	θS	0.43	m³/m³
Soil	Hydraulic Conductivity	Ks	18.5	mm h^{-1}
SMB	Root Zone Depth	Zr	1.20	m
SMB	Deep Percolation Threshold	R	Variable	mm

2.5 HEC-HMS Calibration and Validation

HEC-HMS calibration was undertaken by adjusting hydrologically sensitive parameters within physically reasonable ranges until the simulated hydrograph reproduced the timing and magnitude of observed discharge. Particular attention was given to the Curve Number, initial abstraction, lag time and routing parameters because these control runoff volume, peak discharge and hydrograph timing.

The available discharge record was separated temporally to maintain independence between model calibration and validation. The 1990–2011 period was used for calibration, while 2012–2025 was reserved for validation. No further parameter optimisation was undertaken using the validation dataset.

Calibration and validation performance were evaluated using NSE, R^2, RMSE and PBIAS as described in Section 2.8. The calibrated HEC-HMS runoff series was subsequently supplied to the Improved SMB model as the surface-runoff component of the daily water balance.

2.6 Improved Soil Moisture Balance Model

Groundwater recharge was estimated using a daily Improved Soil Moisture Balance model coupled with HEC-HMS runoff. Unlike a simple residual water-balance calculation, the Improved SMB framework explicitly tracked the state of root-zone soil-water storage and allowed recharge to occur only when sufficient water was available after evapotranspiration, runoff and soil-moisture requirements had been satisfied.

The general daily root-zone water balance was represented in Equation 3.

$$S_t = S_{t-1} + P_t - Q_t - ET_{a,t} - L_t - R_t \quad (3)$$

Where S_t is root-zone soil-water storage at the end of day t (mm), S_{t-1} is storage from the preceding day (mm), P_t is daily precipitation (mm), Q_t is HEC-HMS simulated surface runoff (mm), $ET_{a,t}$ is actual evapotranspiration (mm), L_t represents lateral or other explicitly represented drainage losses (mm), and R_t is groundwater recharge or deep percolation below the root zone (mm).

Equivalently, the daily change in storage can be expressed in Equation 4.

$$\Delta S_t = P_t - Q_t - ET_{a,t} - L_t - R_t \quad (4)$$

This formulation ensures that recharge is calculated as part of a closed daily water balance rather than simply as (P-ET-Q) at annual scale.

2.6.1 Dynamic Root-Zone Moisture Accounting

The maximum root-zone water storage associated with field capacity was determined using Equation 5.

$$S_{FC} = \theta_{FC} Z_r (1000) \quad (5)$$

While storage corresponding to permanent wilting point expressed in Equation 6.

$$S_{WP} = \theta_{WP} Z_r (1000) \quad (6)$$

Where S_{FC} and S_{WP} are root-zone water storage at field capacity and wilting point (mm), respectively; θ_{FC} and $\theta_{WP} Z_r$ are volumetric field capacity and wilting-point water contents (m^3/m^3); and Z_r is effective root-zone depth (m).

The model updated S_t sequentially at the daily time step, thereby retaining the influence of antecedent moisture conditions. This is particularly important under semi-arid conditions because two rainfall events of equal magnitude may generate different recharge depending on the initial soil-water deficit.

2.6.2 Spatially Variable Soil Hydraulic Properties

Measured field capacity, wilting point and saturated hydraulic conductivity differed among the sampled soil units. Rather than representing the entire basin with a single homogeneous soil condition, the Improved SMB framework used the corresponding hydraulic characteristics to parameterize soil-water storage and drainage behaviour within the represented soil zones.

This modification allows areas characterized by sandy and highly conductive soils to drain differently from areas with greater water-retention capacity. The spatial variability of soil properties therefore influences both the amount of water retained within the root zone and the potential for deep percolation.

2.6.3 Moisture-Dependent Actual Evapotranspiration

Actual evapotranspiration was constrained by the amount of water available within the root zone. Under sufficiently wet conditions, evapotranspiration could approach the atmospheric demand represented by potential evapotranspiration. As soil moisture declined toward the permanent wilting point, evapotranspiration was progressively reduced using a soil-water stress factor expressed in Equation 7.

$$ET_{a,t} = K_{s,t} ET_{p,t} \quad (7)$$

Where $ET_{a,t}$ is actual evapotranspiration (mm/day), $ET_{p,t}$ is potential evapotranspiration (mm/day), and $K_{s,t}$ is the dimensionless soil-water stress coefficient bounded between 0 and 1.

For the root-zone accounting framework, $K_{s,t}$ was represented as a function of available soil water:

$$\min\left[1, \max\left(0, \frac{S_t - S_{WP}}{S_{FC} - S_{WP}}\right)\right] \quad (8)$$

Thus, K_s approaches 1 under adequately moist conditions and declines toward zero as storage approaches the permanent wilting-point threshold.

2.7 Threshold-Based Recharge and Lateral-Flow Treatment

The central improvement to the recharge calculation was the use of a threshold condition for deep percolation. Rainfall remaining after HEC-HMS runoff and evapotranspiration was first used to replenish the root-zone soil-water deficit. Recharge was generated only when available soil water exceeded the field-capacity storage threshold.

Conceptually, subject to the drainage capacity of the soil, where S_t^* represents provisional soil-water storage after precipitation, runoff and evapotranspiration have been accounted for but before deep drainage (Equation 9).

$$R_t = \max[0, ; S_t^* - S_{FC} - L_t] \quad (9)$$

Where drainage was constrained by soil hydraulic conductivity, the daily recharge flux was limited expressed in Equation 10.

$$R_t = \min\left[\max(0, S_t^* - S_{FC} - L_t), K_{s,\text{hyd}}\Delta t\right] \quad (10)$$

Where $K_{s,\text{hyd}}$ is saturated hydraulic conductivity expressed in compatible units and Δt is the model time step.

Surface runoff and lateral flow were not treated as groundwater recharge. Surface runoff, Q_t, was supplied directly from HEC-HMS, while L_t represented water leaving the root-zone control volume laterally where applicable. This separation prevents surface and shallow lateral water losses from being incorrectly counted as deep aquifer recharge.

Accordingly, the annual water balance used for reporting results was obtained by summing the daily components expressed in Equation 11.

$$P = Q + ET_a + L + R + \Delta S \quad (11)$$

Where all terms represent annual totals in millimetres and ΔS is the net change in root-zone storage between the beginning and end of the reporting period.

This equation is important when interpreting annual recharge results because recharge cannot generally be calculated as (P-Q-ET) alone unless both lateral losses and net storage change are zero.

Recharge efficiency was defined explicitly as the proportion of annual rainfall converted to groundwater recharge expressed in Equation 12.

$$RE = \frac{R}{P} \times 100 \quad (12)$$

where RE is recharge efficiency (%), R is annual groundwater recharge (mm/year), and P is annual precipitation (mm/year).

2.8 Model Performance Evaluation

The performance of HEC-HMS was evaluated using four statistical measures: Nash-Sutcliffe Efficiency (NSE), coefficient of determination (R^2), Root Mean Square Error (RMSE) and Percent Bias (PBIAS).

The Nash-Sutcliffe Efficiency was calculated using Equation 13.

$$NSE = 1 - \frac{\sum_{i=1}^{n}\left(Q_{obs,i} - Q_{sim,i}\right)^2}{\sum_{i=1}^{n}\left(Q_{obs,i} - \overline{Q}_{obs}\right)^2} \quad (13)$$

Where (Q_{obs}) is observed discharge, (Q_{sim}) is simulated discharge, ($\overline{Q}_{obs}$) is the mean observed discharge and n is the number of observations (Nash & Sutcliffe, 1970.

The coefficient of determination was calculated using Equation 14.

$$R^2 = \left[\frac{\sum\left(Q_{obs} - \overline{Q}obs\right)\left(Qsim - \overline{Q}sim\right)}{\sqrt{\sum\left(Qobs - \overline{Q}obs\right)^2 \sum\left(Qsim - \overline{Q}_{sim}\right)^2}}\right]^2 \quad (14)$$

Where **(R^2)** indicates the strength of agreement between observed and simulated values.

RMSE was calculated using Equation 14.

$$RMSE = \sqrt{\frac{\sum(Q_{obs} - Q_{sim})^2}{n}} \quad (14)$$

Where RMSE measures the average magnitude of simulation error.

and PBIAS was calculated using Equation 15.

$$PBIAS = 100\frac{\sum(Q_{obs} - Q_{sim})}{\sum Q_{obs}} \quad (15)$$

Where PBIAS quantifies the tendency of the model to overestimate or underestimate observed values. With this sign convention, positive PBIAS indicates overall model underestimation and negative PBIAS indicates overestimation.

Following Moriasi et al. (2007, 2015), NSE values greater than approximately 0.50 were considered indicative of satisfactory model performance for streamflow simulation, with progressively higher values representing improved agreement. (R^2) was used as a complementary measure of correspondence between simulated and observed variability, while RMSE was interpreted relative to the magnitude and variability of observed discharge.

For PBIAS, values within ±10% were interpreted as very good, values between ±10% and ±15% as good, values between ±15% and ±25% as satisfactory, and values exceedingly approximately ±25% as unsatisfactory for streamflow simulation. These criteria were used together rather than independently because no single statistical measure fully describes hydrological model performance.

Kling-Gupta Efficiency (KGE) was excluded from the primary evaluation because it was not consistently reported in the calibration and validation outputs presented in Figure 4.

2.9 Temporal and Spatial Recharge Analysis

The validated HEC-HMS runoff series and Improved SMB model were applied over the 1990–2025 study period to estimate daily groundwater recharge. Daily values were aggregated to monthly and annual time scales to evaluate seasonal and interannual variability.

The rainfall-recharge relationship was assessed statistically to determine the degree to which variations in annual rainfall explained variations in recharge. Pearson correlation and linear regression were used to quantify association, while the physical interpretation considered the threshold behaviour inherent in the SMB formulation.

Spatial recharge potential was assessed by integrating estimated recharge with the spatial distribution of rainfall, soil hydraulic characteristics and terrain conditions. To avoid inconsistent interpretation between temporal and spatial results, recharge classes were harmonized using a common classification framework presented in Table 3.

Table 3: Recharge Classification

Recharge class	Annual recharge (mm/year)
Very low	<50
Low	50–100
Moderate	100–150
Moderate-high	150–200
High	200–250
Very high	>250

The classification was applied consistently to the spatial recharge map. Where temporal recharge values are discussed independently, the actual numerical values are reported rather than assigning a conflicting second set of class boundaries.

2.10 Methodological Assumptions and Limitations

Several assumptions were necessary because of the data limitations typical of long-term hydrological studies in semi-arid environments. First, soil hydraulic properties measured in 2024 were assumed to represent the dominant characteristics of the corresponding soil units during the 1990–2025

simulation period. The model therefore does not explicitly represent historical changes in soil structure arising from cultivation, erosion, compaction or land degradation.

Second, the 28,400 km² watershed area refers specifically to the DEM-delineated computational domain and should not be interpreted as the area of the complete transboundary Sokoto-Rima/Iullemmeden system. Third, groundwater recharge estimated by the SMB model represents potential diffuse recharge crossing the lower boundary of the modelled root zone. The approach does not explicitly simulate subsequent travel time through the deeper unsaturated zone or groundwater flow within individual aquifer formations.

Finally, uncertainty remains associated with rainfall observations, streamflow measurements, spatial interpolation, soil hydraulic parameters and model structure. The integrated framework reduces some uncertainty by constraining surface runoff using calibrated HEC-HMS simulations, but it does not eliminate uncertainty inherent in basin-scale groundwater recharge estimation.

3. RESULTS AND DISCUSSION

3.1 Rainfall Characteristics and Seasonal Hydrological Regime

The long-term rainfall record for 1990–2025 demonstrated a strongly seasonal precipitation regime across the Sokoto Basin. Rainfall was concentrated primarily between May and October, whereas precipitation during the November–April dry season was generally limited. August represented the principal rainfall month, with July and September also contributing substantially to wet-season precipitation. This concentration of rainfall within a relatively short period is characteristic of the semi-arid climatic conditions of northwestern Nigeria and has important implications for both runoff generation and groundwater recharge.

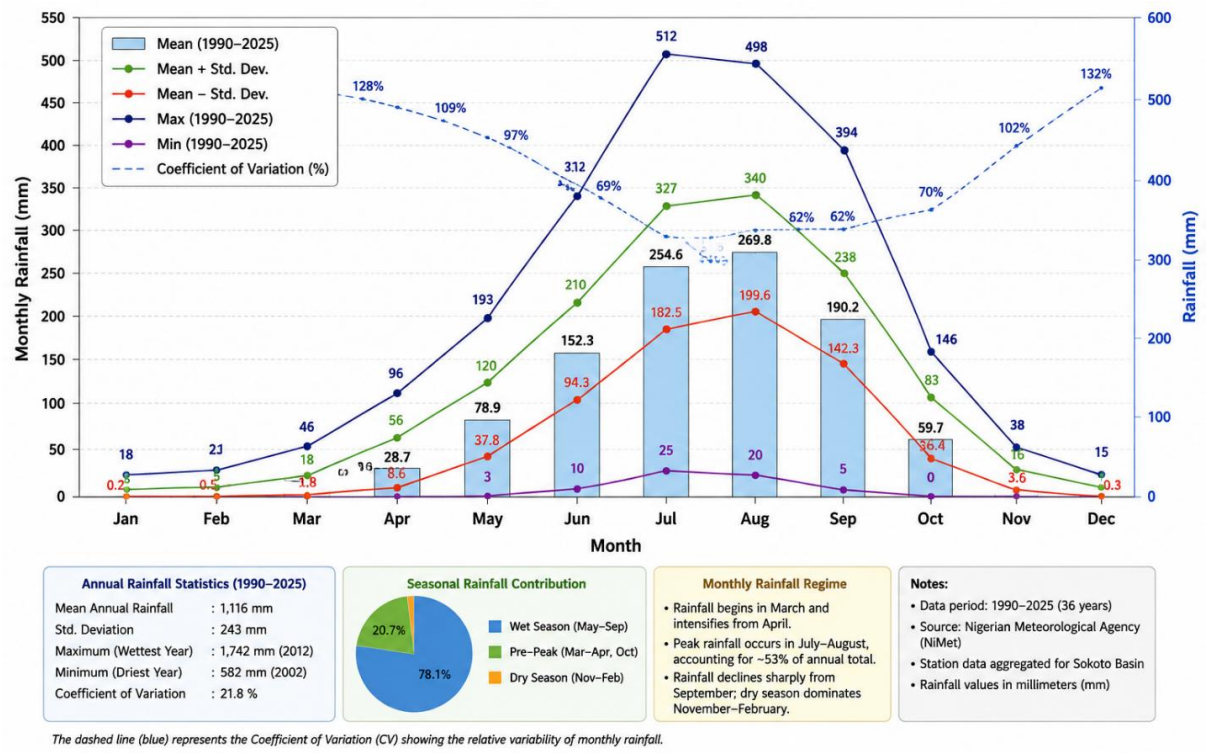

Figure 3: Monthly Rainfall Distribution (1990–2025)

Considerable interannual variability was also evident during the 36-year study period. Wetter years were characterized by greater rainfall totals and more sustained wet-season conditions, whereas lower-rainfall years experienced larger soil-water deficits and reduced opportunities for deep drainage. Consequently, annual rainfall alone does not determine recharge; the timing and sequence of rainfall relative to antecedent soil-water conditions are also important.

This behaviour is consistent with the conceptual basis of the Improved Soil Moisture Balance model developed in this study. At the beginning of the rainy season, a substantial proportion of

incoming rainfall is required to replenish root-zone soil-water deficits and satisfy evapotranspiration demand. Groundwater recharge becomes more likely as soil-water storage approaches field capacity and subsequent rainfall produces drainage below the effective root zone. Recharge is therefore concentrated within the wettest portion of the rainy season rather than being distributed uniformly throughout the year.

The observed pattern is consistent with the broader understanding of groundwater recharge in semi-arid environments. Scanlon et al. (2006) showed that recharge in arid and semi-arid regions is highly variable and sensitive to rainfall characteristics, while Taylor et al. (2013) demonstrated the importance of episodic intense rainfall for groundwater replenishment in African aquifers. The strong seasonality observed in the Sokoto Basin therefore reinforces the importance of considering both intra-annual and interannual rainfall variability when evaluating groundwater sustainability.

3.2 Spatial Variability of Soil Hydraulic Characteristics

The measured soil hydraulic properties presented in Table 4 varied considerably among the five sampling locations, indicating that the modelled basin cannot be adequately represented using a single uniform soil condition. Field capacity ranged from 23.5% at Bunza to 29.4% at Gwadabawa, while permanent wilting point varied from 10.8% to 15.6%. Hydraulic conductivity ranged from 13.9 mm/h at Gwadabawa to 24.8 mm/h at Bunza.

Table 4: Soil Hydraulic Characteristics of the Study Locations.

Location	Soil Texture	Bulk Density (g/cm^3)	Field Capacity (%)	Wilting Point (%)	Available Water (%)	Hydraulic Conductivity (mm/h)
Argungu	Sandy Loam	1.47	28.0	14.0	14.0	15.2
Bunza	Loamy Sand	1.56	23.5	10.8	12.7	24.8
Gwadabawa	Sandy Clay Loam	1.43	29.4	15.6	13.8	13.9
Tambuwal	Sandy Loam	1.50	26.8	13.5	13.3	17.5
Wurno	Sandy Loam	1.46	27.2	13.7	13.5	16.8

Gwadabawa exhibited the highest field capacity (29.4%), rather than Argungu as stated in the original manuscript. Its sandy clay loam texture and comparatively low hydraulic conductivity of 13.9 mm/h indicate greater water-retention capacity and slower drainage. Argungu also exhibited relatively high field capacity at 28.0%, but it was not the maximum among the sampled locations.

In contrast, Bunza recorded the lowest field capacity (23.5%) and the highest hydraulic conductivity (24.8 mm/h). The loamy sand at this location therefore permits comparatively rapid infiltration and drainage but retains less water within the root zone. These contrasting properties illustrate an important feature of recharge generation: high infiltration capacity does not necessarily correspond directly to high root-zone water storage.

Available water content was greatest at Argungu (14.0%), followed closely by Gwadabawa (13.8%), Wurno (13.5%), Tambuwal (13.3%) and Bunza (12.7%). These relatively modest differences nevertheless influence the amount of rainfall required to replenish antecedent soil-water deficits before threshold-controlled drainage can occur.

The spatial variation in field capacity, wilting point and hydraulic conductivity provides an important justification for incorporating variable soil hydraulic properties into the Improved SMB model. Healy (2010) similarly identified soil-water storage and hydraulic characteristics as fundamental controls on recharge, while Li et al. (2019) demonstrated that soil characteristics and land-surface conditions can substantially alter soil-moisture dynamics and deep drainage in arid and semi-arid environments.

3.3 HEC-HMS Calibration and Validation Performance

The corrected calibration and validation results demonstrate that HEC-HMS reproduced the observed streamflow dynamics with satisfactory agreement during both modelling periods. The hydrograph shown in Figure 4 indicates that the model generally reproduced the timing and magnitude of observed discharge, although differences between simulated and observed flows remained during individual high-flow events.

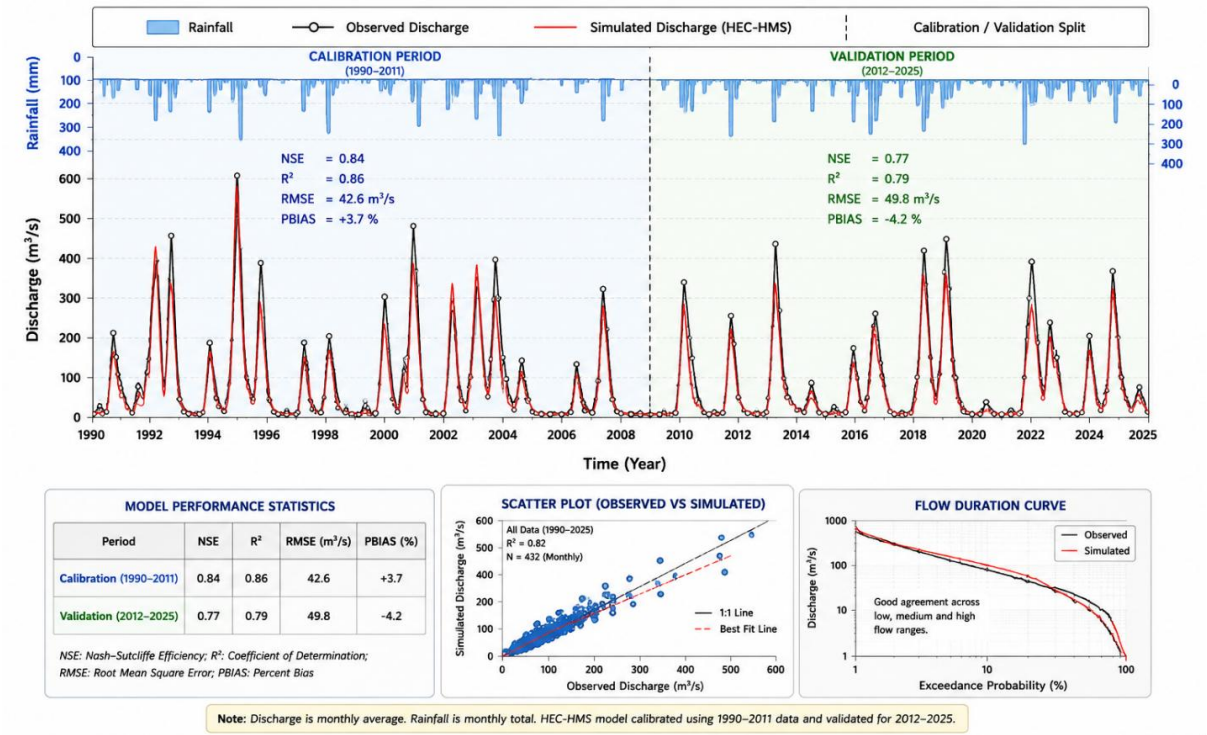

Figure 4: Observed and simulated streamflow during HEC-HMS calibration (1990–2011) and validation (2012–2025).

During calibration, the model presented in Table 5 achieved NSE = 0.84, R^2 = 0.86, RMSE = 42.6 m³/s and PBIAS = +3.7%. During validation, the corresponding statistics were NSE = 0.77, R^2 = 0.79, RMSE = 49.8 m³/s and PBIAS = −4.2%.

Table 5: Corrected HEC-HMS calibration and validation statistics

Performance index	Calibration	Validation	Adopted interpretation
NSE	0.84	0.77	Good to very good
R^2	0.86	0.79	Strong agreement
RMSE (m³/s)	42.6	49.8	Evaluated relative to observed discharge
PBIAS (%)	+3.7	−4.2	Very good (within ±10%)

The calibration NSE of 0.84 indicates that the model explained a substantial proportion of the temporal variability in observed discharge relative to the observed mean. The validation NSE remained high at 0.77, demonstrating that model performance was maintained when applied to an independent period. The corresponding R^2 values of 0.86 and 0.79 further demonstrate strong correspondence between observed and simulated discharge.

The increase in RMSE from 42.6 m³/s during calibration to 49.8 m³/s during validation indicates somewhat greater absolute prediction error during the independent validation period. However, RMSE is scale-dependent and should not be interpreted using a universal acceptance threshold. Its interpretation is therefore considered together with NSE, R^2, PBIAS and visual hydrograph agreement.

PBIAS was +3.7% during calibration and −4.2% during validation. Under the sign convention adopted in this study, the positive calibration value indicates slight overall underestimation, while the negative validation value indicates slight overall overestimation. Both values fall within the ±10% range adopted for very good streamflow simulation performance.

The corrected statistics are substantially different from those reported in the original version of the manuscript and are now fully aligned with Figure 4. KGE has been removed because it is not reported in the underlying calibration-validation figure and is therefore unnecessary for interpreting the demonstrated model performance.

The maintenance of relatively high NSE and R^2 values between calibration and validation also suggests that the calibrated model was not excessively dependent on the calibration period. This is particularly important because the simulated runoff constitutes a direct input to the Improved SMB model. Reliable runoff estimation reduces the uncertainty that would otherwise arise from estimating surface runoff using fixed coefficients within a conventional residual water-balance calculation.

3.4 Long-Term Groundwater Recharge Variability

The corrected groundwater recharge time series demonstrates substantial interannual variability over the complete 1990–2025 modelling period. Contrary to the earlier interpretation of Figure 5 as representing only 2020–2025, the figure contains a 36-year annual recharge record.

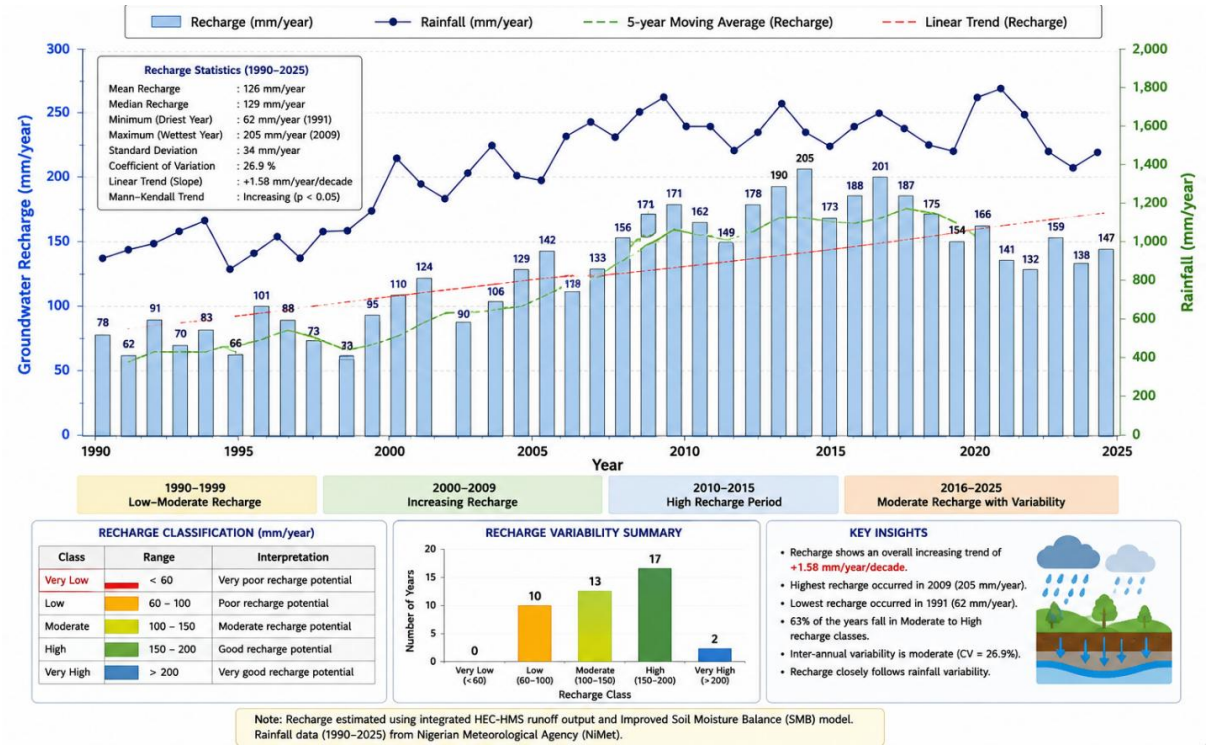

Figure 5: Annual groundwater recharge time series for the Sokoto Basin (1990–2025).

Mean groundwater recharge during the study period was approximately 126 mm/year. As summarised in Table 6, the minimum annual recharge was 62 mm/year in 1991, whereas the maximum was 205 mm/year in 2009. Importantly, no year in the Figure 5 time series recorded zero groundwater recharge.

Table 6: Summary of corrected long-term groundwater recharge characteristics, 1990–2025

Recharge characteristic	**Corrected value**
Study period	1990–2025
Number of years	36
Mean annual recharge	126 mm/year
Minimum annual recharge	62 mm/year
Year of minimum recharge	1991
Maximum annual recharge	205 mm/year
Year of maximum recharge	2009
Observed zero-recharge years in Figure 5	None
Long-term mean recharge class	Moderate (100–150 mm/year)
Maximum-year recharge class	High (200–250 mm/year)

The range from 62 to 205 mm/year demonstrates that groundwater replenishment varies substantially between relatively dry and wet hydrological conditions. Maximum annual recharge was approximately 3.3 times the minimum value, illustrating the sensitivity of aquifer replenishment to interannual climatic and soil-water conditions.

The long-term mean of 126 mm/year falls within the moderate recharge class (100–150 mm/year) adopted in this study. The minimum value of 62 mm/year falls within the low-recharge class (50–100 mm/year), while the maximum of 205 mm/year falls within the high-recharge class (200–250 mm/year).

The absence of zero-recharge years is also hydrologically significant. It indicates that the model estimated some degree of annual deep percolation throughout the study period, although the amount varied substantially. Consequently, the earlier claim that virtually no recharge occurred in 2023 is not supported by the long-term Figure 5 dataset and has been removed.

The recharge time series nevertheless supports the interpretation that recharge is temporally variable and strongly influenced by antecedent soil-water conditions. Annual rainfall must first satisfy evapotranspiration and root-zone storage requirements before substantial deep drainage occurs. Thus, differences in recharge between years reflect not only annual rainfall totals but also rainfall timing, antecedent moisture, runoff generation and soil hydraulic characteristics.

3.5 Rainfall-Recharge Relationship and Recharge Threshold

The relationship between annual rainfall and groundwater recharge showed a statistically meaningful positive association. As illustrated in Figure 6, Pearson's correlation coefficient was r = 0.72, corresponding to R^2 = 0.52. Thus, approximately 52% of the observed interannual variation in recharge was statistically associated with variation in annual rainfall within the fitted linear relationship.

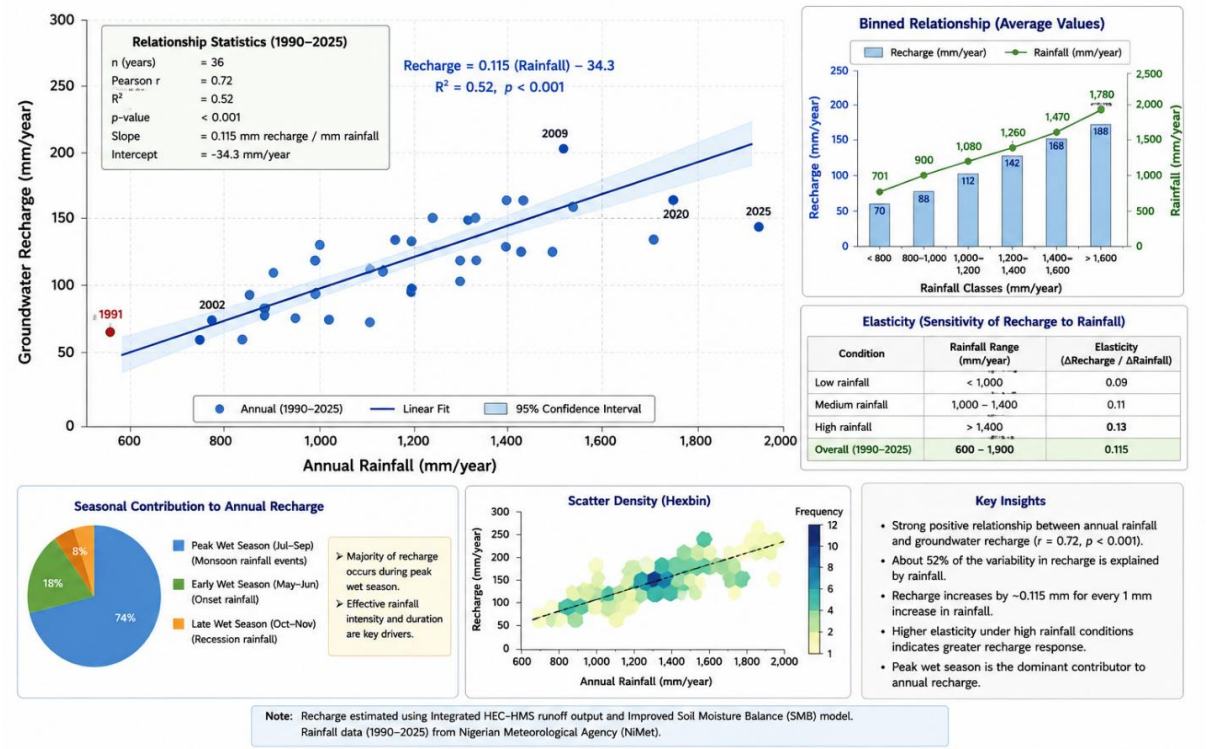

Figure 6: Relationship between annual rainfall and groundwater recharge in the Sokoto Basin (1990–2025).

The regression slope of 0.115 mm/mm indicates an average increase of approximately 11.5 mm in annual recharge for each additional 100 mm of annual rainfall within the range represented by the observations. This relationship demonstrates the strong climatic control on groundwater replenishment while also showing that rainfall alone does not explain all recharge variability.

The negative intercept of −34.3 mm has an important physical interpretation but should not be interpreted as actual negative groundwater recharge. The regression therefore implies an approximate rainfall intercept of 298 mm, or about 300 mm, below which the unconstrained linear equation would

predict zero or negative recharge. Because physically meaningful diffuse recharge is non-negative, this value is better interpreted as an empirical indication of the rainfall amount required to overcome evapotranspiration and soil-water deficits before substantial recharge becomes possible, rather than as a strict universal hydrological threshold.

The remaining approximately 48% of recharge variability not represented by the linear rainfall relationship highlights the influence of other factors, including antecedent soil moisture, rainfall intensity and distribution, runoff generation, evapotranspiration, soil-water storage and hydraulic conductivity. This supports the use of the integrated HEC-HMS–Improved SMB framework rather than estimating recharge from rainfall alone.

The result is consistent with Scanlon et al. (2006) and Healy (2010), who emphasized that recharge in semi-arid environments is controlled by interactions between precipitation and soil-water processes. It also supports the arguments of Xu and Beekman (2019) that recharge assessment in African environments should account for multiple hydrological controls rather than relying exclusively on generalized rainfall-recharge coefficients.

3.6 Spatial Distribution of Groundwater Recharge Potential

Spatial modelling revealed substantial heterogeneity in groundwater recharge potential across the modelled basin. Figure 7 identifies zones ranging from very low to very high recharge according to the harmonized classification adopted in the methodology.

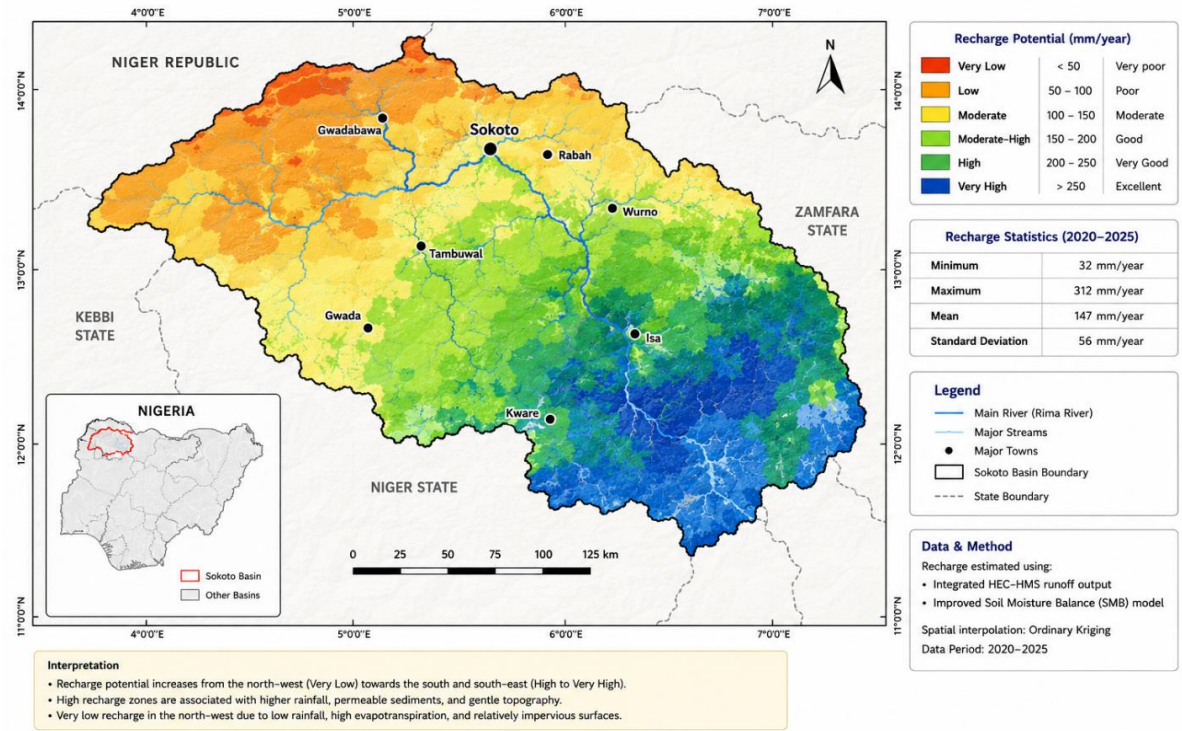

Figure 7: Spatial distribution of groundwater recharge potential across the modelled Sokoto Basin.

Areas exhibiting relatively high recharge potential were associated with combinations of favourable infiltration conditions, permeable soils, relatively gentle terrain and greater water availability. Conversely, areas characterized by less permeable soils, greater runoff generation or less favourable terrain exhibited lower recharge potential.

The soil results provide a physical basis for some of this spatial variability. For example, Bunza exhibited the greatest measured saturated hydraulic conductivity, whereas Gwadabawa exhibited the highest field capacity but lower hydraulic conductivity. Such differences influence the partitioning of infiltrated water between temporary root-zone storage and drainage. Spatial recharge therefore reflects the combined effects of infiltration capacity, storage characteristics, rainfall input, evapotranspiration and runoff rather than any single soil parameter.

The spatial heterogeneity identified by the model demonstrates an important limitation of applying a single basin-wide recharge coefficient. A uniform coefficient would obscure localized areas

in which hydrological and soil conditions either favour or restrict deep percolation. Similar spatial variability has been recognized in GIS-supported recharge investigations in African basins (Kisiki et al., 2022; Missaoui et al., 2023; Asrade et al., 2024).

The harmonized classification also removes the inconsistency in the previous manuscript, where different class limits were applied to Figures 5 and 7. Actual annual values are used when discussing the temporal series, while the common six-class system is retained for interpreting the spatial recharge map.

3.7 Basin Water Balance and Interpretation of Recharge Efficiency

The basin water balance was reassessed to ensure consistency among precipitation, surface runoff, actual evapotranspiration, groundwater recharge and changes in soil-water storage.

Reassessment of the previously reported annual results showed that precipitation was not completely accounted for by the reported runoff, evapotranspiration and recharge components.

Table 5: Reassessed annual water-balance components and recharge efficiency

Year	Rainfall, P (mm)	Surface runoff, Q (mm)	Actual ET (mm)	Recharge, R (mm)	Unresolved ($L + \Delta S$) (mm)	Recharge efficiency (%)
2020	1,126.4	178.6	604.8	102.5	240.5	9.1
2021	1,304.7	211.3	657.4	146.8	289.2	11.3
2022	1,083.6	163.8	591.2	88.9	239.7	8.2
2023	844.8	154.5	565.7	0.0	124.6	0.0
2024	1,795.3	284.4	720.6	299.5	490.8	16.7
2025	1,271.4	198.7	648.5	123.8	300.4	9.7

The reassessment shows that the previously reported rainfall, runoff, evapotranspiration and recharge components do not independently close the annual water balance. The unresolved quantity ($L + \Delta S$) ranges from 124.6 mm in 2023 to 490.8 mm in 2024.

This residual should not be interpreted automatically as either lateral flow or soil-water storage change. Rather, it represents the combined water-balance component that cannot be separated using the annual outputs presently available. Disaggregation would require the corresponding daily lateral-flow estimates and beginning- and end-of-year root-zone soil-water storage generated by the Improved SMB model. Reporting the combined residual therefore preserves mass-balance transparency without assigning unsupported values to individual hydrological fluxes.

The resulting recharge efficiencies were 9.1%, 11.3%, 8.2%, 0.0%, 16.7% and 9.7% for 2020–2025, respectively.

This confirms that the percentage values reported previously represented recharge as a proportion of annual rainfall. The revised table therefore explicitly defines the metric and removes the ambiguity associated with the original “Recharge (%)” column.

Among the six reported years, 2024 exhibited both the highest rainfall (1,795.3 mm) and highest reported recharge (299.5 mm), corresponding to the highest recharge efficiency of 16.7%. In contrast, the original 2023 annual dataset reported no recharge despite 844.8 mm of rainfall, indicating that the modelled water available after runoff, evapotranspiration and other water-balance processes was insufficient to generate the reported deep-percolation flux for that particular annual dataset.

The annual 2020–2025 calculations should, however, be distinguished from the corrected long-term recharge time series presented in Figure 5. Figure 5 covers 1990–2025 and contains no zero-recharge year. Consequently, the zero-value reported for 2023 in the earlier annual table is inconsistent with the long-term Figure 5 dataset and should be verified against the original daily SMB output before the table is retained as a definitive recharge result.

Accordingly, Table 5 is presented as a **water-balance reassessment** rather than as an independently validated long-term recharge dataset. Final separation of (L) and (\Delta S), and resolution of the 2023 recharge discrepancy, requires retrieval of the original daily Improved SMB model outputs. This approach maintains conservation of mass while avoiding the introduction of inferred or fabricated hydrological fluxes.

3.8 Performance and Contribution of the Integrated Modelling Framework

The combined results demonstrate the value of linking calibrated rainfall-runoff simulation with dynamic soil-water accounting. HEC-HMS provided independently calibrated estimates of surface runoff, while the Improved SMB component represented antecedent root-zone storage, soil hydraulic variability, moisture-constrained evapotranspiration and threshold-controlled drainage. This avoids treating groundwater recharge simply as an annual residual of precipitation minus evapotranspiration and runoff.

The corrected calibration and validation statistics provide particularly strong support for using HEC-HMS runoff within the recharge framework. NSE decreased moderately from 0.84 during calibration to 0.77 during validation, while R^2 decreased from 0.86 to 0.79. Nevertheless, both remained well above the adopted satisfactory criteria. PBIAS remained small at +3.7% and −4.2%, indicating limited systematic bias during both periods.

The results should nevertheless be interpreted within the limitations of the available data. Recharge represents modelled potential deep percolation below the root zone rather than direct measurement of water reaching individual aquifers. Soil hydraulic properties measured during 2024 were treated as temporally static during the long-term reconstruction, while uncertainties remain in rainfall observations, streamflow measurements, spatial parameterization and model structure.

These limitations are consistent with the broader challenges of groundwater-recharge estimation identified by Xu and Beekman (2019). The principal advantage of the present framework is therefore not the elimination of recharge uncertainty, but the explicit representation of several processes that are commonly simplified in basin-scale assessments. This interpretation is also consistent with Gleeson et al. (2020), who emphasized the importance of integrating groundwater sustainability assessments with the wider hydrological system.

3.9 Implications for Groundwater Management and Engineering Decision Support

The estimated long-term mean recharge of 126 mm/year, together with the range of 62–205 mm/year, demonstrates that groundwater replenishment in the Sokoto Basin cannot be represented adequately using a single annual value. Sustainable groundwater abstraction should therefore account for interannual variability and the possibility that prolonged periods of relatively low recharge may reduce the amount of renewable groundwater available for development.

The spatial recharge map provides an additional decision-support layer by identifying areas where hydrological and soil conditions are comparatively favourable for groundwater replenishment. Such information can support preliminary screening for managed aquifer recharge, infiltration-enhancement measures, groundwater-protection zones and groundwater-development planning. However, high modelled recharge potential alone should not determine the location of engineering interventions. Aquifer transmissivity, storage, groundwater quality, land availability, environmental constraints and detailed site investigation must also be considered.

The approximately 300-mm rainfall intercept inferred from the rainfall-recharge regression further demonstrates the importance of maintaining infiltration opportunities during the rainy season. Land-management practices that increase rapid surface runoff may reduce the proportion of rainfall available to replenish soil-water storage and eventually contribute to deep percolation. Watershed conservation, erosion control and appropriately designed infiltration systems may therefore contribute to improved groundwater resilience.

From an engineering perspective, the integrated HEC-HMS–Improved SMB framework provides a transferable decision-support methodology for connecting surface-water simulation with groundwater-recharge assessment in data-constrained semi-arid environments. Its outputs can inform managed aquifer recharge planning, groundwater allocation, drought preparedness, watershed management and prioritization of monitoring infrastructure. The framework consequently extends beyond hydrological simulation toward practical water-resource engineering and evidence-based groundwater-management policy.

4. CONCLUSION

This study developed and applied an integrated Hydrologic Engineering Center–Hydrologic Modeling System (HEC-HMS) and Improved Soil Moisture Balance (SMB) framework for assessing

groundwater recharge in the semi-arid Sokoto Basin, northwestern Nigeria. The approach combined calibrated rainfall–runoff simulation with dynamic root-zone soil-moisture accounting, spatially variable soil hydraulic properties, moisture-dependent evapotranspiration and threshold-controlled deep percolation to represent the principal processes governing groundwater replenishment under semi-arid conditions.

The corrected HEC-HMS results demonstrated reliable rainfall–runoff simulation during both calibration and validation. The model achieved NSE values of 0.84 and 0.77 and R^2 values of 0.86 and 0.79 for the calibration and validation periods, respectively. PBIAS was +3.7% during calibration and −4.2% during validation, indicating limited systematic bias, while RMSE values of 42.6 m^3/s and 49.8 m^3/s, respectively, quantified the absolute simulation errors. The maintenance of satisfactory performance during the independent validation period supports the use of HEC-HMS-derived runoff as an input to the Improved SMB recharge model.

Long-term analysis for 1990–2025 revealed substantial interannual variability in groundwater replenishment. Mean annual recharge was approximately 126 mm/year, with a minimum of 62 mm/year in 1991 and a maximum of 205 mm/year in 2009. No zero-recharge year occurred in the corrected 36-year time series. The approximately 3.3-fold difference between minimum and maximum annual recharge demonstrates that groundwater replenishment cannot be adequately characterized using a single invariant annual recharge estimate. Instead, groundwater-resource assessment and abstraction planning should account explicitly for interannual hydrological variability.

Annual rainfall was positively associated with groundwater recharge, with a Pearson correlation coefficient of $r = 0.72$ and $R^2 = 0.52$. The fitted relationship, ($R = 0.115P - 34.3$), indicates that rainfall explained approximately 52% of the interannual variation in recharge. The negative intercept corresponds to an approximate rainfall intercept of 300 mm and reflects the requirement for precipitation to first overcome evapotranspiration and antecedent soil-moisture deficits before substantial deep percolation can develop. The remaining unexplained variability demonstrates the importance of soil hydraulic properties, antecedent moisture, runoff generation, evapotranspiration and rainfall distribution in controlling recharge.

Spatial analysis further demonstrated that groundwater replenishment is heterogeneous across the modelled basin. Differences in rainfall, soil-water retention, hydraulic conductivity and terrain conditions produced distinct recharge zones. These findings demonstrate the limitation of applying a uniform recharge coefficient across the basin and support spatially distributed approaches to groundwater assessment. The results should nevertheless be interpreted as estimates of potential deep percolation below the modelled root zone rather than direct measurements of water reaching individual aquifer units.

The principal contribution of the study is the integration of calibrated surface-water modelling with process-based soil-moisture accounting within a practical framework suitable for a data-constrained semi-arid environment. By explicitly accounting for runoff, antecedent root-zone moisture and threshold-controlled drainage, the framework provides a more physically interpretable basis for recharge assessment than a simple annual residual water balance. Nevertheless, uncertainty remains because of limitations in hydrological observations, the use of static soil hydraulic properties for the long-term reconstruction, spatial parameterization and model structural assumptions. Continued streamflow, soil-moisture and groundwater-level monitoring would therefore strengthen future calibration and independent validation of the estimated recharge.

From a water-resources engineering perspective, the outputs provide a basis for identifying priority areas for managed aquifer recharge, infiltration enhancement, groundwater protection, sustainable borehole development, watershed conservation and drought preparedness. The framework can also be incorporated into GIS-based groundwater decision-support systems to evaluate alternative management scenarios and prioritize areas requiring additional monitoring or engineering intervention. Site-specific hydrogeological investigation should, however, precede implementation of managed aquifer recharge or major groundwater-development projects.

The study therefore demonstrates how integrated hydrological modelling can translate long-term climatic, runoff and soil information into actionable groundwater-management information. This application aligns with the conference theme of engineering innovation for sustainable development by providing a modelling-based decision-support approach that can strengthen groundwater planning, climate resilience and evidence-based water policy in Nigeria. With appropriate local calibration and

data support, the framework can also be adapted to other semi-arid and data-limited basins where sustainable groundwater development requires improved understanding of spatial and temporal recharge variability.

REFERENCES

Allen, R. G., Pereira, L. S., Raes, D., & Smith, M. (1998). *Crop evapotranspiration: Guidelines for computing crop water requirements* (FAO Irrigation and Drainage Paper No. 56). Food and Agriculture Organization of the United Nations.

Asrade, B., Demlie, M., & Moges, A. (2024). Groundwater recharge estimation using the WetSpass-M model in the Jedeb and Chemoga watersheds, Upper Blue Nile Basin, Ethiopia. *Hydrological Sciences Journal, 69*(2), 215–231.

Freeze, R. A., & Cherry, J. A. (1979). *Groundwater*. Prentice-Hall.

Gleeson, T., Cuthbert, M. O., Ferguson, G., & Perrone, D. (2020). Global groundwater sustainability, resources, and systems in the Anthropocene. *Annual Review of Earth and Planetary Sciences, 48*, 431–463.

Healy, R. W. (2010). *Estimating groundwater recharge*. Cambridge University Press.

Herbei, M. V., Herbei, R., & Popescu, I. (2024). Application of the HEC-HMS model for rainfall-runoff simulation in a groundwater-dominated watershed. *Water, 16*(5), 703.

Kisiki, S. M., Mutua, B. M., & Githui, F. W. (2022). GIS-based assessment of groundwater recharge potential zones in the Makutupora Basin, Tanzania. *Environmental Earth Sciences, 81*(18), 467.

Li, X., Shao, M., Jia, X., & Wei, X. (2019). Soil moisture dynamics and groundwater recharge under different land uses in arid and semi-arid regions. *Journal of Hydrology, 573*, 105–118.

Missaoui, H., Zghibi, A., & Tarhouni, J. (2023). Mapping groundwater recharge potential using remote sensing and GIS techniques in central Tunisia. *Environmental Monitoring and Assessment, 195*, 1154.

Moriasi, D. N., Arnold, J. G., Van Liew, M. W., Bingner, R. L., Harmel, R. D., & Veith, T. L. (2007). Model evaluation guidelines for systematic quantification of accuracy in watershed simulations. *Transactions of the ASABE, 50*(3), 885–900.

Moriasi, D. N., Gitau, M. W., Pai, N., & Daggupati, P. (2015). Hydrologic and water quality models: Performance measures and evaluation criteria. *Transactions of the ASABE, 58*(6), 1763–1785.

Nash, J. E., & Sutcliffe, J. V. (1970). River flow forecasting through conceptual models. Part I: A discussion of principles. *Journal of Hydrology, 10*(3), 282–290.

Salih, A. A., Mohamed, Y. A., & Abdalla, M. A. (2020). Application of WetSpass-M for groundwater recharge estimation in semi-arid catchments. *Hydrological Processes, 34*(21), 4258–4274.

Scanlon, B. R., Healy, R. W., & Cook, P. G. (2002). Choosing appropriate techniques for quantifying groundwater recharge. *Hydrogeology Journal, 10*(1), 18–39.

Scanlon, B. R., Keese, K. E., Flint, A. L., Flint, L. E., Gaye, C. B., Edmunds, W. M., & Simmers, I. (2006). Global synthesis of groundwater recharge in semiarid and arid regions. *Hydrological Processes, 20*(15), 3335–3370.

Sophocleous, M. (2004). Groundwater recharge and sustainability in the High Plains Aquifer in Kansas, USA. *Hydrogeology Journal, 12*(1), 3–10.

Taylor, R. G., Scanlon, B. R., Döll, P., Rodell, M., Van Beek, R., Wada, Y., Longuevergne, L., Leblanc, M., Famiglietti, J. S., Edmunds, M., Konikow, L., Green, T. R., Chen, J., Taniguchi, M., Bierkens, M. F. P., MacDonald, A., Fan, Y., Maxwell, R. M., Yechieli, Y., ... Treidel, H. (2013). Ground water and climate change. *Nature Climate Change, 3*(4), 322–329.

UNESCO. (2024). *United Nations world water development report 2024: Water for prosperity and peace*. UNESCO.

World Meteorological Organization. (2023). *State of global water resources 2022*. World Meteorological Organization.

Xu, Y., & Beekman, H. E. (2019). *Groundwater recharge estimation in Africa: Methods, challenges and applications*. CRC Press.

International Conference on Engineering Innovation for Sustainable Development (ICESID 2026)
Faculty of Engineering, Ahmadu Bello University Zaria · 8–10 September 2026

PREDICTION MODEL FOR SOIL WATER RETENTION BEHAVIOUR OF UNSATURATED SOILS WITH DIFFERENT VOLUMETRIC WATER CONTENT

Abdullahi Karaye[1], Gambo Haruna Yunusa[1,*], Abubakar Jibrin Shuaib[1], Hafiz Ibrahim[2], Ibrahim Khalil Umar[3]

[1]*Bayero University Kano*
[2]*Ahmadu Bello University Kano*
[3]*Federal University of Technology, Babura, Nigeria*

Email: askaraye@gmail.com, ghyunusa@gmail.com*, sadiqjibrin11@gmail.com, sirhafiz01@gmail.com, ikumar.civil@futb.edu.ng

***Corresponding author**: Gambo Haruna Yunusa

DOI: https://doi.org/10.67203/sp.ICESID.2026

ABSTRACT

Unsaturated soils exhibit complex hydro-mechanical behaviour that is strongly influenced by their water content and soil properties. Matric suction is an important parameter governing the behaviour of unsaturated soils, particularly fine-grained and expansive soils, and its determination can require considerable experimental effort. This study therefore developed and evaluated machine-learning models for predicting the matric suction of unsaturated soils using readily available soil and hydraulic properties. A dataset comprising 2,550 soil records was used, with saturated volumetric water content (Θ), air-entry value, bulk density (ρ_b), porosity (n), natural moisture content (w), plasticity index (PI), dry density (ρ_d), D_{60}, and coefficient of permeability (k) adopted as predictor variables. Seven machine-learning models, namely Extreme Gradient Boosting (XGBoost), Linear Regression, Ridge Regression, Lasso Regression, Random Forest, Support Vector Regression (SVR), and Decision Tree, were evaluated using training R^2, test RMSE, and cross-validation mean R^2. XGBoost demonstrated the best overall predictive performance, achieving a training R^2 of 0.9985, test RMSE of 144.3092 kPa, and cross-validation mean R^2 of 0.8712, followed by Random Forest with a training R^2 of 0.9829, test RMSE of 142.8048 kPa, and cross-validation mean R^2 of 0.8611. Although Random Forest recorded a slightly lower test RMSE, XGBoost exhibited the highest training and cross-validation R^2 values. Overall, the results demonstrate the potential of machine-learning techniques, particularly XGBoost, for predicting matric suction of unsaturated soils from selected soil and hydraulic properties.

Keywords: *Matric suction; Unsaturated Soils; Machine Learning Models; XGBoost*

1. INTRODUCTION

Most of the soils around us are Unsaturated, with various particle composition of gravel, sand, silt or clay. These soils are expansive which often subjects them to complex hydro-mechanical circles as they contain a lot of moisture. These characteristics possessed by these types of soil, lead to disorders on structures built or constructed on or within them. Clay soils possess a complex behaviour as a result of the strong multi-physical processes taking place. Initially unsaturated, the compacted clay experiences hydration from the saturated host rock. During this process, it tends to expand and develops swelling stresses (Dieudonne *et al*, 2014). Unsaturated soils were found to be four phase soils, namely; the air phase, water phase, soil skeleton, and contractile skin phase. The air and water phase flows while the soil skeleton, and contractile skin phase come to equilibrium under imposed loads (Pereira and Fredlund,1997). The most significant work during that period was Bishop's effective stress relationship, whereby changes in effective stress attributed to the unsaturated nature of a soil are cast as the product of matric suction in Bishop's effective stress equation: [$\sigma' = (\sigma - U_a) + \chi(U_a - U_w)$]. Effective stress cast in the form of this equation has several difficulties. Looking back, some of the difficulties may not have risen only because of flaws with Bishop's conception, but rather misinterpretation of test results by other investigators (Bishop, 1963; Kanzari *et al.* 2012). A theoretical difficulty in the equation is that it predicts zero effective

stress for any soil in a dry state under no external stress. There is a transitory pore-size range between micro- and macro-structure which is not affected by the magnitude of the compaction pressure (Miller *et al.* 2002). As such, the mechanical loading influences only the macro-structure without affecting the micro-structure (Gao and Sun, 2017). The relationship between pore water suction and water content as presented in a soil water characteristic curve is one of the fundamental relationships used to describe unsaturated behavior of a soil (Nowamooz and Masrouri, 2010). The water retention behavior of unsaturated soils is presented using the soil water retention curve (SWRC). Soil water characteristics curve is a conceptual and interpretative tool by which behavior of unsaturated soils can be understood (Fredlund *et.al*, 2001). This fundamental curve links the variations of the liquid phase potential energy, usually characterized by suction, to the variations of the saturation state, usually characterized by the water content or the degree of saturation (Simon *et.al*, 2011). Suction is inversely proportional to the water content in a soil. Suctions generally increase as the soil de-saturates. Increasing suctions generally result in high resistance to flow and increases in effective stress. Soil Water Retention Curve of soils is the tool used to present the hydro-mechanical behavior of soils to highlight both the effect of suction on the change in water and total volumes and the effect of deformation with respect to the water retention capability (Salager *et.al*, 2010). The Soil Water Retention Curve of soils depends on several factors, such as soil type, soil structure, temperature, salt content and stress states etc. These factors can be classified into two groups: internal and external factors. Internal factors are those related to the soil type and soil structure, such as mineralogical composition, pore size distribution and bonding (that is, chemo-physical properties of the soil phases). Typical external factors are stress states and temperature (Khalili and Selvadurai, 2003). For the same type of soil, the effect of stress states on the SWRC can be attributed to the effect of the density change (Gao and Sun, 2017). It was reported that the SWRC expressed by the relation between the suction and degree of saturation depends mainly upon the current density and not directly upon the stress state (Romero and Gens 1999, Gao and Sun,2017). Although the influence of structure on the behavior of compacted clays has been recognized, only a few water retention models have taken it explicitly into account. Indeed classical approaches for modeling the water retention behavior are based on parameters to be fitted using experimental data (Levasseur, 2012). An understanding of the water retention features is an essential aspect in the field of unsaturated soil behavior modeling. Concomitantly, the trend in modern unsaturated soil mechanics is to quantify, with increasing accuracy, the soil water retention properties of soil in terms of; a fitting equation, the influence of soil compaction conditions, hysteresis modeling and the effect of suction on density (Nuth and Laloui, 2008). Several elastoplastic constitutive models for unsaturated soils have been proposed. The stress-state variables employed in early models are the net stress (the difference between the total stress and pore-air pressure) and the suction (the difference between the pore-air pressure and pore-water pressure), while the strain state variables are the soil skeleton strains. In these models, the influence of un-saturation is expressed only in terms of the suction. The degree of saturation is computed from the suction separately using the so-called soil water retention curve (SWRC), and thus hydraulic hysteresis is not directly incorporated into the constitutive model(Sun *et al*, 2007). The prediction quality of the degree of saturation will thus depend on the accuracy of the void ratio evolving with suction. The proposed water retention model consequently needs to be coupled with a stress–strain model for unsaturated soils. An appropriate constitutive mechanical framework shall be elastoplastic and account for the suction effects on the stress–strain response (D'Onza *et al.* 2010; Nuth *et al.* 2010; Simon *et al*, 2013). Language based modeling approaches foster flexibility and performance by adopting the same host language business and code coordination. Jupyter notebooks with their ability to describe both imperative and declarative coding in a unique format, allowing for selection of the best of two approaches. They still maintain a clear separation between application and coordination layers but still providing a unified interface to both aspects. (Colonnelli *et al*, 2021). Jupyter notebook possess the potential of expressing complex distributed workflows and workflow management system targeting cloud high performance computing (Cloud-HPC) infrastructures and extension stack to implement a proposed methodology (Cantalupo et.al, 2022).

2. METHODOLOGY

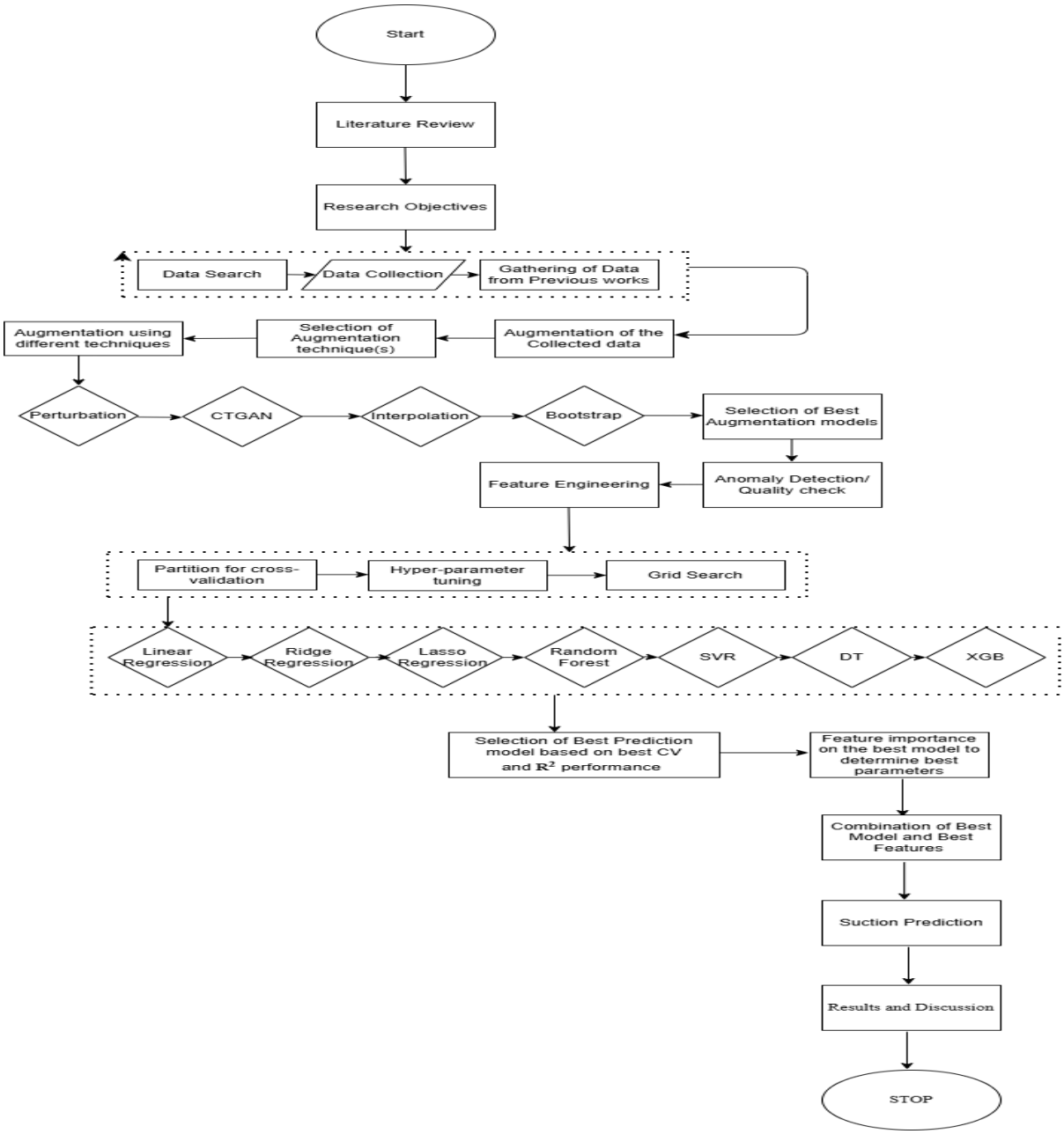

Figure 2.1: Methodology Flowchart

2.1 ORGANIZATION OF DATA

The soil parameters to be used for Matric suction prediction were first organized. Database were collected through previous work of Eberemu, 2008 The data obtained was just 50 dataset which quantity was unfit for machine learning research of this kind, as such the data was sequentially

augmented via the Google Colab version of *Jupyter Notebook environment* of Python. The augmentation process was achieved by;

- Identifying the data
- Applying Augmentation model library (Bootstrap, Perturbation, CTGAN, interpolation)
- Generating synthetic data
- Combining original and generated data

After identifying the original data, the augmentation libraries were employed in order to generate more data for the suction prediction. The following augmentation methods/ libraries were employed; CTGAN (Conditional tabular generative adversarial network), Perturbation, Bootstrap and Interpolation.

2.2 Anomaly Detection test (AD): After the augmentation process, the resulting data (i.e the augmented) was then validated by comparing it with the original data for feature importance. It is conducted in order to evaluate how well the detector generalizes to synthetic variations. From the AD conducted, it was observed that, the augmented data by Interpolation gives the best synthetic data followed by the Bootstrap technique.

2.3 Feature Engineering: Feature engineering is the process of generating, selecting, or transforming raw data into features that improve the performance of machine learning models. It involves domain knowledge, creativity, and data manipulation to craft features that capture relevant patterns and relationships in the data (Trost et.al, 2025). It improves Model Performance, as the engineered features can make simple models and outperform complex ones with poor features (Huang et.al,2023). Feature Engineering captures domain knowledge, in that it incorporates insight about the problem in the data. It also addresses missing values and outliers for model compatibility (Bjorneld *et.al*,2023). In this research work, Feature Engineering was the first stage of the suction prediction process. The best augmented data adopted (i.e Data from Interpolation), was explored to determine the statistical properties and feature correlations, which was sorted by absolute correlation. After exploring the data;

1. Interaction features were generated
2. Polynomial features were also generated for top correlated values
3. Finally, the new Engineered features were produced

Engineered features were then determined after the model studied the relevant patterns and relationships in the data. The engineered features generated were; Dry density to Natural moisture content ratio (P_d:w), Bulk density to Dry density ratio (P_b:P_d), Natural moisture content to Volumetric water (w:Θ), Dry density squared (P_d^2), Natural moisture content squared (w^2), moisture level number, density level number, and Log of hydraulic conductivity (Log K). These new features were then combined with the existing features of the data. These combined features were used to train the models for prediction of the matric suction. The models are;

i. Linear Regression
ii. Ridge Regression
iii. Lasso Regression
iv. Random Forest (RF)
v. Support Vector Regression (SVR)
vi. Decision Tree
vii. Extreme gradient boosting (XGBoost)

The feature Engineering continued by setting hyper parameter grids;

4. The top features and the engineered features were prepared
5. The data were then Split into training and testing, and the random state was also set.
6. The features were then scaled

2.4 Hyperparameter tuning: Hyperparameter tuning is the process of systematically searching for the optimal set of hyperparameters that maximize the model's performance on a given metric, such as accuracy, F1-score, or loss minimization (Belcic and Stryker, 2025). This involves defining a search space (the range of possible values for each hyperparameter), evaluating model performance for different combinations, and selecting the best configuration. Tuning is typically performed using cross-validation to ensure the model generalizes well to unseen data (Elgeldawi et.al, 2021). These hyperparameters control the model's behaviour and impacts its performance significantly (Sci-kit learn.org). Hyper parameter employed in this work was carried out in the following sequence;

1. Models to be used for the prediction of matric suction were first defined, where; Linear regression, Ridge regression, Lasso regression, decision tree, support vector regression (SVR), and XGboost were used
2. Parameter grids were then specified, which were; n-estimators, max depth, learning rate, and subsample (for RF), rbf, C value and gamma scale (for SVR), alpha value (for ridge and lasso regressions), and random state (for decision tree and XGboost models).
3. Scoring metrics were then chosen and set. The chosen scoring metrics were; R^2, RMSE, and MAE.
4. Cross validation for the models training was also set, where a CV value of 5 folds was set.
5. Hyperparameter grids were then set for the models comparison and selection, where the best model was selected from the array of models.
6. Feature importance analysis was then carried out to determine the best parameters for the best model

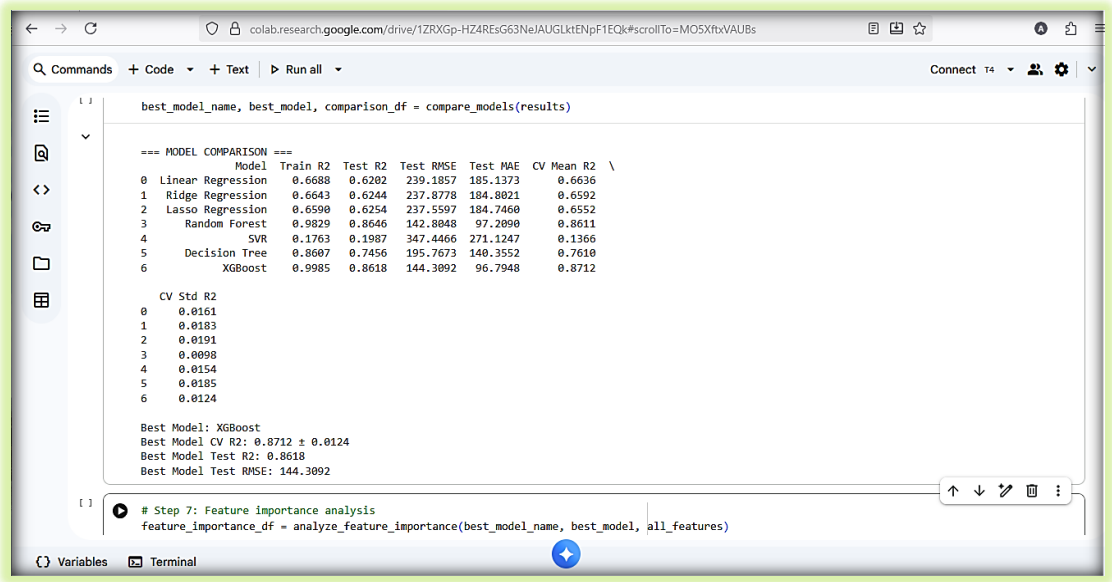

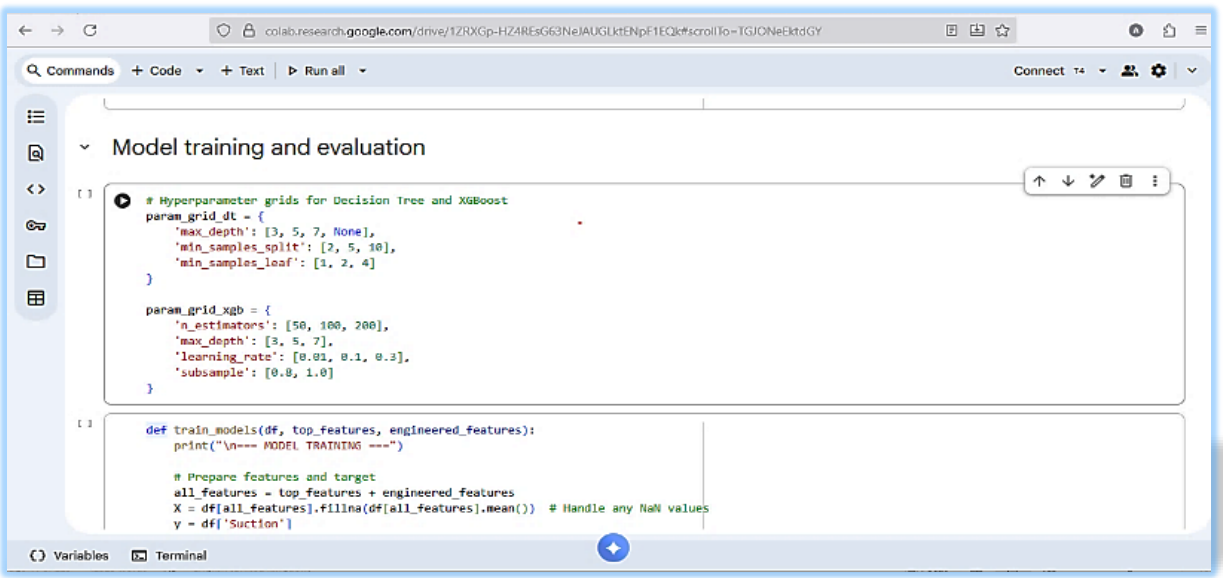

Figure 2.1: Setting of Hyperparameter grids

Figure 2.2: Grids Search

After executing these steps, the training process was executed and the fine-tuned parameters were determined. In this, the common parameters that makes the best of the trained models during the Hyper-parameter tuning were selected and are used together with the best determined model for the

prediction. The best model determined was the Extreme gradient boost (XGboost) model, and the best/ fine-tuned parameters are; gravimetric water content Θ, Air entry value(Ψa), hydraulic gradient (k), bulk density (p_b), '$D60$', and natural moisture content (w). These parameters were used together with the XGboost model to achieve the aim of this research.

3. RESULTS AND DISCUSSION

This research was conducted in order to predict the maximum matric suction up to which an unsaturated soil can attain using some of the soil's properties by the best model which is to be determined from the grid search to be conducted in the work. This was achieved by using the following soil properties; Saturated volumetric water content (Θ), air entry value, Bulk density (P_b), porosity (n), natural moisture content (w), Plasticity index ($P.I$), Dry density (P_d)and D_{60} particle size parameter, and coefficient of permeability(k). These soil parameters were used as inputs, and the matric suction was the Class (target). The models used are described in Appendix B. The data presented in Table 4.1 are the first five rows of the initial/rough data obtained from previous works of Eberemu, 2008. These data are as displayed during the EDA, prior to data augmentation.

Table 3.1: Some of Data obtained from the previous works

S/N	p_d	W	p_b	P.I	Θ	K	N	D60	Ψa	Suction
1	1.58	16.5	27.65	24.0	0.313	3.41e-9	0.395	0.13	26	100
2	1.67	14	25.05	24.0	0.225	1.32e-9	0.360	0.13	27	1500
3	1.74	13.7	25.58	24.0	0.252	8.09e-10	0.333	0.13	70	500
4	1.84	10.9	21.90	24.0	0.233	1.10e-10	0.295	0.13	30	1000
5	1.58	17	28.44	20.5	0.329	3.57e-9	0.375	0.07	27	100

3.1 DATA AUGMENTATION

The soil data obtained from the initial works of Eberemu,2008 were only 50 dataset. These seem unfit for machine learning, and data of this kind are very scarce due to the limited availability of the apparatus and deep technical experience to conduct such laboratory test, this is one of the challenges that lead to the idea of coming up with this research.

As such to compliment for machine learning, the data was carefully increased to a quantity that will fit the machine learning process by generating ***realistic synthetic data*** via the Google Colab version of *Jupyter Notebook environment* of Python. The data was first explored by the EDA function (exploratory data analysis), where the data was fully identified; The data was found to possess the following characteristics:

Table 3.2: EDA of Obtained data.

Statistics	p_d	W	p_b	P.I	Ɵ	K	N	D_{60}	□a	Suction
Mean	1.671	17.2111	30.221	16.940	0.294	7.85e-10	0.3276	0.0814	43.42	594.60
STD	0.092	2.7374	3.3610	4.7238	0.035	2.83e-9	0.0387	0.0294	22.13	494.74
Min	1.520	10.900	21.896	9.3000	0.225	1.77e-11	0.242	0.058	26.00	30.00
25%	1.620	15.325	28.143	10.550	0.269	8.87e-11	0.2968	0.0650	30.00	100.00
50%	1.6600	17.450	30.353	17.400	0.295	1.59e-10	0.3305	0.0675	34.00	500.00
75%	1.740	19.000	32.591	20.500	0.322	3.96e-10	0.3590	0.1150	51.50	1000.00
Max	1.860	22.500	35.796	24.000	0.362	2.02e-8	0.3950	0.1300	130.00	1500.00

The techniques/ models used for data augmentation are;

3.11 CTGAN; This is the conditional tabular generative adversarial network, and it was adopted in this research to augment our data as it possesses the characteristics of generating synthetic data in tabular form (Adiputra and Wanchai, 2024). This technique generates 2550 dataset inclusive of our original obtained 50 dataset. Table 4.3 shows the last 10 rows of the 2550 dataset as augmented via this technique; the original data was in the first 50 rows of the gross data. As such, these in table 4.3 are among the newly generated synthetic data.

Table 3.3: Synthetic Data generated from the CTGAN augmentation.

S/N	Pd	W	Pb	P.I	O	K	N	D60	Ya	Suction
1	1.595024	23.74394	25.24218	23.7793	0.305585	-6.5E+08	0.392384	0.069602	38	822
2	1.748228	19.87633	25.45922	10.55828	0.224964	-8.2E+08	0.397609	0.067371	191	20
3	1.55489	18.22767	28.95152	15.73044	0.320516	-6.7E+08	0.368871	0.072973	35	315
4	1.539816	19.60095	27.84347	22.74472	0.287332	-1.3E+08	0.267411	0.069937	36	634
5	1.684196	21.45238	30.45064	18.93844	0.343418	3.76E+08	0.340046	0.066238	38	270
6	1.804752	22.05911	25.98905	6.722476	0.284142	-2E+08	0.38597	0.128827	47	1949
7	1.664946	25.30323	33.51952	11.32379	0.307012	-1.1E+09	0.29389	0.069431	40	480
8	1.660393	16.8659	28.79407	5.391353	0.249366	-1.4E+09	0.381103	0.0596	66	381
9	1.635402	18.97353	32.38551	19.26509	0.321297	2.23E+08	0.408059	0.071388	25	1901
10	1.65171	21.58423	31.28827	20.86861	0.284379	-1E+09	0.33686	0.078649	29	338
11	1.690247	21.70114	33.75695	20.09929	0.355583	-1.4E+09	0.255096	0.080705	31	1378

From the resulting data obtained via this augmentation technique, it was observed to possess the following characteristics;

Table 3.4: Properties of Data generated from the CTGAN augmentation.

Statistical Properties	p_d	W	p_b	P.I	Θ	K	N	D_{60}	□a	Suction
Mean	1.6708	17.2111	30.2260	16.9299	0.2954	4.5698E8	0.3277	0.0815	43.1239	575.8094
STD	0.0749	2.2188	2.7184	4.6595	0.0284	2.6316E9	0.0317	0.0238	18.0171	392.4089
Min	1.5200	10.9000	21.8960	9.3000	0.2250	1.77E-8	0.2420	0.0580	26.0000	30.0000
25%	1.6126	15.7163	28.4275	13.1894	0.2770	1.1681E-10	0.3047	0.0648	30.6758	234.0921
50%	1.6614	17.2637	30.3853	17.0185	0.2958	2.3086E-10	0.3294	0.0694	35.9692	500.0000
75%	1.7226	18.7647	32.2386	20.7756	0.3166	4.6489E-10	0.3530	0.0985	50.7785	860.9097
Max	1.8600	22.5000	35.7960	24.0000	0.3620	2.32E10	0.3950	0.1300	130.0000	1500.00

From the data properties and the last 11 rows of the data, it can be observed that the data possess outliers as in case of the k values (coefficient of permeability), this augmentation model produces negative values (e.g -6.5E8), and some of the k values were seen to be in positive exponents (e.g 2.32E10) which are unrealistic, and impractical. These makes the outcomes from this technique unacceptable, and other techniques explored. As such in any data augmentation containing coefficient of permeability (k) values, CTGAN should be avoided as an Augmentation technique.

3.12 Perturbation; is a data augmentation technique that involves introducing small, controlled modifications (i.e perturbations) by applying small random changes to the original data in order to generate synthetic variations (Hyeyung et.al, 2024). These perturbations can include adding noise (for example, Gaussian or salt-and-pepper), slight shifts in values, or transformations that mimic real-world variability (Satou and Mitkiy, 2025). This technique generates 550 dataset inclusive of our original obtained 50 dataset. Table 4.5 shows the next 10 rows after the 500th row of dataset as augmented via this technique; the original data was in the first 50 rows of the gross data. As such, these in table 4.5 are among the newly generated synthetic data.

Table 3.5: Data generated from the Perturbation augmentation.

S/N	Pd	W	pb	P.I	O	K	N	D60	Ya	Suction
1	1.5784	16.5663	27.2995	23.8051	0.3125	2.3782E+8	0.4	0.1317	24.7443	100
2	1.6613	13.9007	24.6901	24.2895	0.2250	1.8204E+8	0.3585	0.1278	27.2902	1500
3	1.7357	13.6106	25.7540	23.7792	0.2520	2.5280E+8	0.3346	0.1295	71.2053	500
4	1.8429	11.0233	21.9624	23.6897	0.2312	6.0520E+7	0.2952	0.1311	32.2454	1000
5	1.5673	16.7625	28.2958	20.3313	0.3325	9.0036E+7	0.3715	0.0688	27.1943	100
6	1.5466	21.2363	34.4586	20.2106	0.3351	1.8763E+8	0.3876	0.0691	40.5062	500
7	1.6525	14.9195	26.7177	20.2366	0.2952	6.7349E+7	0.3472	0.0696	26.4263	100
8	1.6315	18.81545	32.6609	20.9254	0.2821	2.5460E+8	0.3584	0.0680	28.1957	1000
9	1.7013	14.3641	26.2798	20.3987	0.2875	1.7672E+8	0.3304	0.0715	69.0464	500
10	1.6690	18.6389	32.4016	20.9141	0.2935	2.0506E+7	0.3387	0.0690	61.4554	1000

From the table above, it can be observed that majority of the values of hydraulic conductivity are in positive exponents, and this makes them outliers as hydraulic conductivity signifies the speed of water through the soil pores. This parameter is practically very low almost negligible, as such this discards the data from this augmentation technique. Also, this augmentation technique produces the least quantity of synthetic data, which is scanty for machine learning works.

3.13 Bootstrap technique: Bootstrap augmentation involves generating new datasets of the same size as the original by repeatedly sampling subsets of the data with replacement. Bootstrap is also good in generating larger datasets while maintaining the original data distribution (Kohavi and Longhatham,2023). This technique generates 1000 dataset inclusive of our original obtained 50 datasets. Table 4.6 shows the last 10 rows of the dataset as augmented via this technique; the original data was in the first 50 rows of the gross data. As such, these in table 4.6 are among the newly generated synthetic data.

Table 3.6: Data generated from the Bootstrap augmentation

S/N	Pd	W	pb	P.I	O	K	N	D60	Ya	Suction
1	1.61	19.8	33.488	9.3	0.242	1.51E-10	0.315	0.058	40	1000
2	1.79	12.8	24.702	14.3	0.236	3.20E-10	0.266	0.065	40	1500
3	1.8	14.8	28.44	14.3	0.277	7.30E-11	0.263	0.065	34	500
4	1.71	17.2	31.122	14.3	0.267	1.17E-10	0.299	0.065	33	1500
5	1.75	16.5	30.625	20.5	0.236	6.15E-11	0.308	0.07	35	1500
6	1.56	21	34.32	20.5	0.336	1.89E-10	0.383	0.07	40	500
7	1.6	20.1	33.76	9.3	0.323	1.36E-10	0.319	0.058	70	1000
8	1.86	12.9	25.854	24	0.307	1.04E-10	0.287	0.13	27	30
9	1.68	18.1	32.088	9.3	0.293	1.20E-10	0.285	0.058	130	1500
10	1.56	21	34.32	20.5	0.336	1.89E-10	0.383	0.07	40	500
11	1.75	16.5	30.625	20.5	0.236	6.15E-11	0.308	0.07	35	1500

From table 3.6, it can be observed that the generated synthetic data conforms well to the trend of the original data, including the k values which often possess many outliers. This is because Bootstrap possesses the capability of generating larger datasets while maintaining the original data distribution. This fits one of the requirements for this research, but this augmentation technique was able to produce only 1000 datasets including the original 50 datasets, which looks inadequate for machine learning and shows less reliability during anomaly detection of the produced synthetic data. This leads this work to exploring more augmentation technique.

3.1.4 Interpolation: This technique was employed for augmentation in this research work due to the fact that; Interpolation augmentation in Python possess several advantages over other augmentation techniques such as; handling missing values, flexibility (as in linear, polynomial and spline), improved model performance and efficient computation. This technique generates 2550 dataset inclusive of our original obtained 50 datasets. Table 4.7 shows the next 10 rows after the 2000th row of dataset as augmented via this technique; the original data was in the first 50 rows of the gross data. As such, these in table 4.7 are among the newly generated synthetic data.

Table 3.7: Data generated from the Interpolation augmentation

S/N	pd	W	Pb	P.I	O	K	N	D60	Ya	Suction
1	1.647	15.805	27.444	17.553	0.2748	1.13E-9	0.340	0.0984	55.5282	500
2	1.654	18.670	32.517	15.150	0.3152	1.35E-10	0.325	0.0656	29.6456	154.8531
3	1.761	15.638	29.118	15.596	0.2690	9.27E-11	0.312	0.0678	41.2437	718.9069
4	1.822	15.079	29.275	24.000	0.3168	9.73E-11	0.301	0.1300	27.4895	165.2705
5	1.711	15.705	28.496	22.537	0.2695	5.04E-10	0.335	0.1049	67.4935	708.873
6	1.634	19.038	32.739	19.319	0.2931	1.43E-10	0.349	0.0690	39.5236	904.7644
7	1.663	16.908	29.645	19.125	0.2810	5.48E-10	0.337	0.1061	42.6218	232.6433
8	1.600	17.030	28.853	19.544	0.3194	3.04E-09	0.363	0.0692	27.9247	315.7676
9	1.710	17.700	31.977	10.579	0.3204	6.53E-11	0.278	0.0642	36.6113	221.8617
10	1.657	18.500	32.287	16.419	0.3375	1.48E-10	0.330	0.0792	69.0760	500

From table 3.7, it can be observed that the generated synthetic data conforms well to the trend of the original data, including the k values which often possess many outliers, this is as a result of the model's characteristic of creating new instances that lie between the originals in the data space, helping to expand datasets, reduce overfitting, and improve model generalization. It is particularly effective for handling class imbalance. This fits one of the requirements for this research. The synthetic data obtained from this augmentation technique was adopted in this work, despite conforming to the original data, it also shows the least anomaly as show in the figures below.

3.2 ANOMALY DETECTION

In order to confirm the goodness of the synthetic data, anomaly detection test was performed. Anomaly detection is defined as the process of identifying data points, events, or patterns that deviate significantly from the expected behaviour within a dataset (Moacir et. al, 2025). It is conducted in order to evaluate how well the detector generalizes to synthetic variations. Anomaly detection was carried out using the **feature distribution comparison technique**. Feature distribution comparison anomaly detection is an unsupervised or semi-supervised machine learning technique for identifying outliers or anomalies in datasets by quantifying the dissimilarity between the probability distributions of features in observed data instances and those derived from a reference model of normal behaviour (Fan et.al, 2024). This Anomaly detection technique was first used in research conducted by Gu et.al,2005. The anomaly detection was conducted on the two best techniques that produces the most realistic synthetic data, namely; Bootstrap technique and Interpolation technique.

3.3 Feature Engineering

In this, engineered features were then determined after the model studied the relevant patterns and relationships in the data. The new engineered features generated were; Dry density to Natural moisture content ratio (P_d:w), Bulk density to Dry density ratio (P_b:P_d), Natural moisture content to Volumetric water (w:Θ), Dry density squared (P_d^2), Natural moisture content squared (w^2), moisture level number, density level number, and Log of hydraulic conductivity (Log K). These new features were then combined with the existing features of the data. These combined features were used to train the models for prediction of the matric suction.

3.4 Hyperparameter tuning: The hyper-parameter technique used in this work is ***Grid Search*** and the following are the feature importance of the respective parameters (both original and engineered features) of some of the models used;

Table 3.8: Hyper-parameter Grids for the Models Used

S/N	Models	Hyper-parameter grids
1	**Ridge Regression**	**Ridge(alpha=1.0)**
2	**Lasso Regression**	**Lasso(alpha=1.0)**
3	**Random Forest**	**Random Forest Regressor (n estimators=100, random state=42)**
4	**SVR**	**SVR (kernel=rbf, C=1.0, gamma=scale)**
5	**Decision Tree**	**Decision Tree Regressor (random state=42)**
6	**XGBoost**	**'n_estimators': [50, 100, 200] Max_depth': [3, 5, 7], Learning_rate': [0.01, 0.1, 0.3], Subsample': [0.8, 1.0]**

From table 3.8 above, the parameter grids assigned to each of the used models during the hyper parameter tuning can be observed.

Table 3.9: Random Forest Feature Importance

Model	Feature	Feature importance
Random Forest	Θ	0.2130
	ϒa	0.1199
	P_b	0.0224
	D60	0.0532
	W	0.0058
	Pd:w	0.0125
	P_b:P_d	0.0075
	W: Θ	0.4026
	P^2_d	0.1015
	W^2	0.0060
	K	0.0257
	Log k	0.0284
	Moisture level No.	0.0005
	Density level No.	0.00010

Table 3.91: Decision Tree Feature Importance

Model	Feature	Feature importance
Decision Tree	Θ	0.2298
	Ϋa	0.1112
	P_b	0.0136
	D60	0.0400
	W	0.0000
	Pd:w	0.0020
	P_b:P_d	0.0022
	W: Θ	0.4547
	P^2_d	0.1053
	W^2	0.0103
	K	0.0114
	Log k	0.0196
	Moisture level number	0.0000
	Density level number	0.0000

Table 3.92: XGBoost Feature Importance

Model	**Feature**	**Feature importance**
XGBoost	Θ	0.0963
	Ɣa	0.0685
	P_b	0.0352
	D60	0.0547
	W	0.0261
	Pd:w	0.0184
	P_b:P_d	0.0220
	W: Θ	0.4231
	P^2_d	0.1221
	W^2	0.0000
	K	0.0441
	Log k	0.0000
	Moisture level number	0.0000
	Density level number	0.0896

From Tables 3.90 through Table 3.92, It can be observed that, hyper-parameter tuning was conducted on the combined parameters (both original and engineered features) on each of the best models in order to determine the best parameters for each prediction model (fine-tuned parameters). Models' comparison was also conducted, to determine the best model to be used for the matric suction prediction. The best model was selected based on **cross validation (CV) performance and generalization**. The table below shows the models with the metrics used for comparison.

Table 3.93: Model Comparison

S/N	Model	Train R^2	Test R^2	Test RMSE	Test MAE	CV Mean R^2	CV Std R^2
1	**Linear Regression**	0.6688	0.6202	239.1857	185.1373	0.6636	0.0161
2	**Ridge Regression**	0.6643	0.6244	237.8778	184.8021	0.6592	0.0183
3	**Lasso Regression**	0.6590	0.6254	237.5597	184.7460	0.6552	0.0191
4	**Random Forest**	0.9829	0.8646	142.8048	97.2090	0.8611	0.0098
5	**SVR**	0.1763	0.1987	347.4466	271.1247	0.1366	0.0154
6	**Decision Tree**	0.8607	0.7456	195.7673	140.3552	0.7610	0.0185
7	**XGBoost**	0.9985	0.8618	144.3092	96.7948	0.8712	0.0124

From the above table of model comparison, it was determined that the best model for the matric suction prediction was; XGBoost model. This is because it possesses the best comparison metrics as follows;

Best Model CV R^2: 0.8712 ± 0.0124

Best Model Test R^2: 0.8618

Best Model Test RMSE: 144.3092

Also, XGB stands to be the best model as it gave the lowest Test RMSE with the best training R^2 (0.9985) and the highest cross-validation (CV) R^2 value. These characteristics possessed by the model are acceptable requirements of a Strong model, this is as per the work of Khoshvaght *et.al*, (2025) and Chicco *et al*. (2021).

But, in order to rigorously compare the performance of Random Forest and XGBoost, a 5×2-fold paired t-test (Dietterich, 1998) was conducted using R^2 as the evaluation metric. The test yielded a p-value of (0.78), indicating that the performance difference between the two models is not statistically significant. Therefore, while XGBoost was selected as the final model based on marginally higher cross-validation scores, Random Forest remains equally competitive.

Feature importance analysis was then conducted on this best model. And the followings table displays the feature importance of the respective parameters used in the model.

Table 3.94: Feature importance Analysis on XGBoost model

S/N	**Feature**	**Importance**
1	Θ	0.096350
2	ϒa	0.068466
3	P_b	0.035157
4	D60	0.054653
5	W	0.026056
6	Pd:w	0.018460
7	P_b:P_d	0.022000
8	W: Θ	0.423051
9	P^2_d	0.122120
10	W^2	0.000000
11	K	0.044110
12	Log k	0.000000
13	Moisture level number	0.000000
14	Density level number	0.000000

From the conducted feature importance analysis on the best model, it is determined that the following predictors are most required by the model in matric suction prediction;

1. Saturated volumetric water content (Θ)
2. Air entry value (Ya)
3. Hydraulic Conductivity ('k)
4. Bulk Density (P_b)
5. D_{60} particle size parameter (D60)
6. Natural Moisture Content (w)

After the feature importance analysis on the best model, the best model and parameters were deployed. The work then Proceeds to the matric suction prediction, where another set of 10 unseen data (Data containing only the predictors without the class value i.e matric suction) were used to predict matric suction. Majority of these data are synthetic, as such it possess limitations;

1. Synthetic data lacks real-world noise (sensor glitches, typos, outliers) and complex feature interactions.
2. They build splits based on fake, clean thresholds.
3. These models rely on the correlation structure between features
4. Synthetic data that comes from generative adversarial networks (GAN), it often memorizes the training set's surface patterns without capturing the full probability distribution.
5. Synthetic data rarely generates realistic edge cases.

The following table shows a comparison of some of the predicted and original matric suction values.

Table 3.95: Comparison between Obtained and the Predicted matric suction.

S/N	P_d	W	P_b	P.I	Θ	K	N	D_{60}	$Ɣ_a$	Obtained Ɣ	XGB Predicted Ɣ
1	1.60	16.79	28.54	21.94	0.293	1.53E-09	0.374	0.0947	44.24	335.40	390.74
2	1.68	15.15	27.10	18.15	0.295	2.63E-10	0.326	0.0675	44.66	183.88	230.23
3	1.74	14.80	27.56	22.63	0.246	5.16E-10	0.323	0.1065	56.29	891.79	721.29
4	1.65	19.14	33.25	14.41	0.344	8.80E-11	0.324	0.0657	79.89	500	498.62
5	1.63	19.18	32.80	18.62	0.288	1.55E-10	0.350	0.0680	36.73	1000	966.31
6	1.58	16.5	27.65	24	0.313	3.41E-09	0.395	0.13	26	100	109.22
7	1.67	14	25.05	24	0.225	1.32E-09	0.36	0.13	27	1500	1493.35
8	1.74	13.7	25.58	24	0.252	8.09E-10	0.333	0.13	70	500	547.13
9	1.84	10.9	21.90	24	0.233	1.10E-10	0.295	0.13	30	1000	998.91
10	1.58	17	28.44	20.5	0.329	3.57E-09	0.375	0.07	27	100	98.21

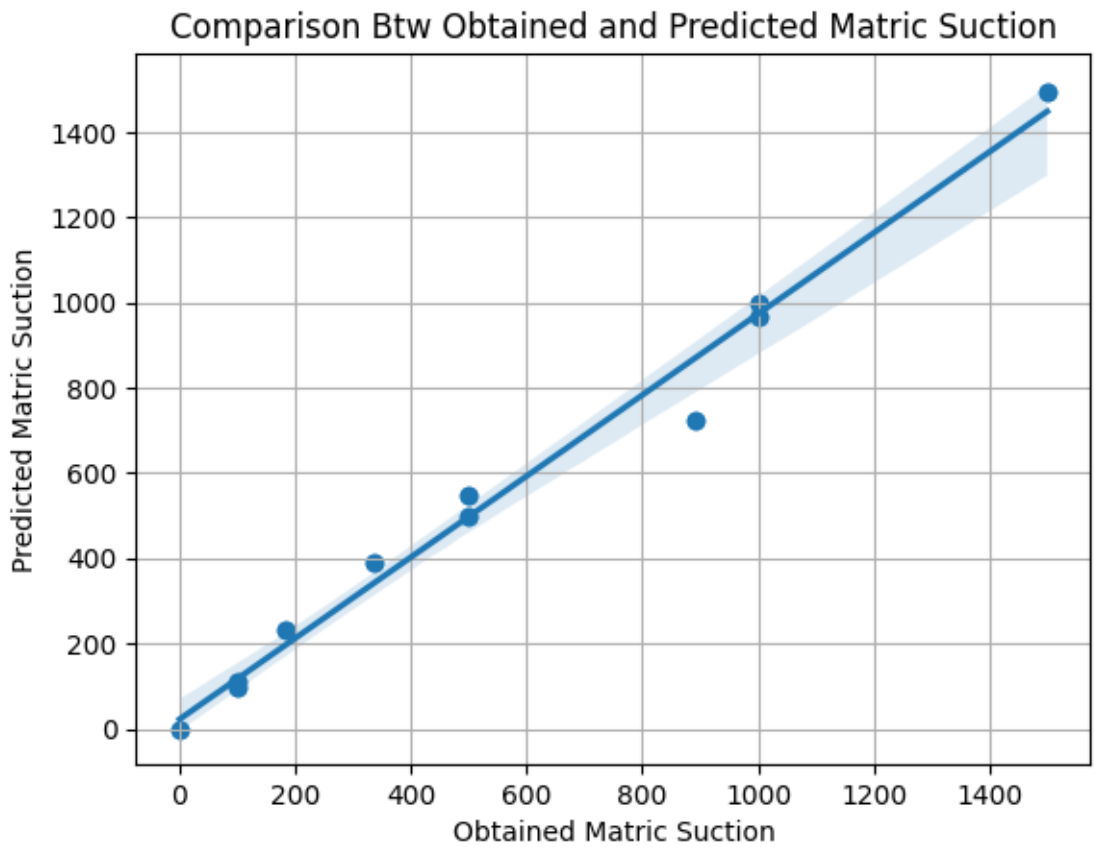

Figure 3c: Comparison Between Predicted and Obtained Suction Values

From table 4.93, the Test R^2 is **0.8618** and the CV Mean is **0.8712**. These scores are almost identical to each other (with a difference of ~0.01). If it were overfitting, the Test/CV scores would plummet (that is, Test $R^2 < 0.70$), which they do not.

Figure 3d: The P-Test Analysis

From figure 3c above, it can be observed that a comparison of obtained matric suction with matric suction values predicted from XGboost model is depicted, and the values used are real data, among the first 50 obtained from the work of Eberemu, 2008. 60% of the data was used for training, 30% for testing and 10% for vaditation. Based on this, the model can therefore be judged as very good.

4. CONCLUSION

Data obtained in the tests were fit to the models described. An optimization routine was used to fit the parametric models to the measured data by altering the fitted parameters iteratively. The maximum accuracy was achieved. The sum of the model capability is defined by some assigned metrics (i.e RMSE, R^2, and CV). From the results obtained, it was observed that six independent variables were used as inputs, after optimization and one dependent variable (Target Matric Suction).

i. It is therefore concluded that nine (9) soil parameters were adopted as inputs and were used for the model development in predicting the matric suction and suited the aim of this research.
ii. The small (50 dataset) available data were successfully augmented to a quantity that will provide reliable prediction, preventing pathological overfitting and control estimation variance and the best augmented dataset was also deduced by Anomaly detection.
iii. The models were successfully generated and validated by the 9 relevant soil parameters that were used as inputs to the model.
iv. It is concluded that, 6 out of the 9 inputs can fit the target in predicting the Matric Suction, this as per the feature importance analysis conducted.
v. It is also concluded that the Extreme Gradient Boost Model (XGB) is the best model, among the seven trained models in this work as per the set of hyper parameter grids possessed by the model, as shown in Table 3.8. And as per the Cross-validation metrics comparison of the models in Table 3.9.

ACKNOWLEDGEMENTS

I am most indebted to my supervisor in the person of Ass.Prof. Engr. G.H Yunusa of Civil Engineering Department. He had been enduring and supportive in the course of this work. I am most grateful for his commitment to the work.

I am grateful to the department of civil engineering for making all facilities available for my work. I wish also to thank, Mal. Ahmad Abdulnasir Shu'aib, Dr. Aminu Sulaiman, Engr.Dr. Muttaqa Uba Zango and Dr.Aminu Dar'dau Rafin-Dadi for their machine Learning assistances.

Grateful acknowledgement must also be made to my Beloved Wife and the following relatives and friends for their immense help, prayers and moral support throughout my school days; Amina Shehu Karaye, Engr Abubakar Jibrin, Engr. Dr. Ibrahim Khalil Umar, Musa Shehu Karaye, Nazifi Uba Isa, Abubakar Kumo, Haj. Zulaiha Abdullahi, Ahmad AbdulNasir Shuaib, Engr. Muhammad Umar, Engr. Inuwa Barau Inuwa, Engr. Salma B.Gambo, Bldr. Muhammad Idris etc

More importantly, I thank Almighty Allah for guiding me in all spheres of my life and directing towards this noble profession of Civil Engineering.

5. REFERENCES

Adiputra, N.M.I., & Wanchai, P. (2024). "CTGAN-ENN: a tabular GAN-based hybrid sampling method for imbalanced and overlapped data in customer churn prediction." Journal of Big Data, Volume 11, Issue 1, pages; 1-25

Adrian O. Eberemu (2008) "Evaluation of Bagasse Ash Treated Lateritic Soil as a suitable Material for Waste Landfill Barrier (Liner) and Cover" An Unpublished Phd Dissertation, Ahmadu Bello University, Zaria, Nigeria.

Belcic, I. & Stryker C. (2025). What is hyperparameter tuning? IBM. https://www.ibm.com/think/topics/hyperparameter-tuning

Björneld, O., Carlsson, M., & Löwe, W. (2023). Case study – Feature engineering inspired by domain experts on real world medical data. Intelligence-Based Medicine, 8, Article 100110. https://doi.org/10.1016/j.ibmed.2023.100110

Bishop A.W. and Blight G.E. (1963) "Some Aspects of Effective Stress in SATURATED AND PARTLY SATURATED SOILS"Geotechnique, Volume 13, Issue 3, Pages;177-197, doi: doi.org/10.1680/geot.1963.13.3.177

Chicco, D., Warrens, M. J., & Jurman, G. (2021). The coefficient of determination R-squared is more informative than SMAPE, MAE, MAPE, MSE and RMSE in regression analysis evaluation. *PeerJ Computer Science*, *7*, Article e623. https://doi.org/10.7717/peerj-cs.623

Dieudonne A.C, Levasseur S., Charlier R., Della Vecchia G., C. Jommi (2011) "A Water Retention Model For Compacted Clayey Soils" Research Article, Department of Geosciences and Engineering, TU Delft, Delft, The Netherlands.

Elgeldawi, E., Sayed, A., Galal, A.R., & Zaki, A.M. (2021). "Hyperparameter Tuning for Machine Learning Algorithms Used for Arabic Sentiment Analysis" Journal of Informatics, Volume 8, No. 79.

Fan, D., Li, M., Han D. (2024). Feature Aggregation Network for Memory-Based Industrial Anomaly Detection. In 2024 IEEE 9th International Conference on Data Science in Cyberspace (DSC) (pp. 677–683). IEEE. https://doi.org/10.1109/DSC63484.2024.00101

Guo, Y., & Birgisson, B. (2025). Analytical prediction of soil–water characteristics curves for granular pavement base course materials. Journal of Transportation Geotechnics, Volume 55, 101704. https://doi.org/10.1016/j.trgeo.2025.101704

Huang, H.-N., Chen, H.-M., Lin, W.-W., Huang, C.-J., Chen, Y.-C., Wang, Y.-H., & Yang, C.-T. (2023). Employing feature engineering strategies to improve the performance of machine learning algorithms on echocardiogram dataset. Digital Health, 9, Article 20552076231207589. https://doi.org/10.1177/20552076231207589

Hyeyoung Maeng, Eckley I. A., & Fearnhead, P. (2024). Collective Anomaly Detection in High-Dimensional VAR Models. *Statistica Sinica*, Volume33, Issue 2, ISSN: 1603-1627

Khalili, N., & Selvadurai, A. P. S. (2003). A fully coupled constitutive model for thermo-hydro-mechanical analysis in elastic media with double porosity. Geophysical Research Letters, Volume 30, Issue 24, Article 2268. https://doi.org/10.1029/2003GL018838

Khoshvaght, H., Permala, R. R., Razmjou, A., & Khiadani, M. (2025). A critical review on selecting performance evaluation metrics for supervised machine learning models in wastewater quality prediction. Journal of Environmental Chemical Engineering, 13(6), Article 119675. https://doi.org/10.1016/j.jece.2025.119675

Krisnanto S., Rifdah S.A., Ananda A.A and Putri N.A (2025) "Analysis of the stress state variables for Unsaturated soils with Compressible and Incompressible soil solids" Geomate Journal, Volume 28, Issue 125.

Nowamooz, H., & Masrouri, F. (2010). Volumetric strains due to changes in suction or stress of an expansive bentonite/silt mixture treated with lime. Comptes Rendus. Mécanique, Volume 338, Issue 4, page: 230-240, DOI: 10.1016/j.crme.2010.03.011

Nitsch A., Asaad A., Wichtmann T., Emmerich K., and Baille W., (2026) "Swelling Behaviour of Compacted Ca/Mg Bentonite during hydration on different scales, Journal of Applied Clay Science (Elsevier), Volume 281, March 2026.

Osame P.U, Peretomode E., and Hawez H.K.(2025) "Advances in Flow of Water Through Variably Saturated Soils; A Review of Model Approaches and Experimental investigations with use of Sensors, MDPI Sensors Journal, Volume 25, Issue 22.

Satou, H., Mitkiy, A., Collins, E., & Kingston, F. (2025). Geometrically Regularized Transfer Learning with On-Manifold and Off-Manifold Perturbation. ArXiv, abs/2505.15191.

Simon Salager, Marta Rizzi & LyesseLaloui (2011) "An innovative device for determining the soil water retention curve under high suction at different temperatures" volume 6, ISSN:135–142.

Trost, C. O. W., Žák, S., Schaffer, S., Walch, L., Zitz, J., Klünsner, T., Leitner, H., Exl, L., & Cordill, M. J. (2025). Explainable machine learning and feature engineering applied to nanoindentation data. Materials & Design, 253, Article 113897. https://doi.org/10.1016/j.matdes.2025.113897

International Conference on Engineering Innovation for Sustainable Development (ICESID 2026)
Faculty of Engineering, Ahmadu Bello University Zaria · 8–10 September 2026

SYSTEMIC FAILURES AND INEFFICIENCIES IN LARGE-SCALE INFRASTRUCTURE EXECUTION: A CRITICAL APPRAISAL OF THE KANO–KATSINA ROAD DUALIZATION PROJECT

Aminu Darda'u Rafindadi[1,*], Abubakar Sunusi[1], Abdullahi Balarabe Bello[1]

[1]""

Email: adrafindadi.civ@buk.edu.ng*, abubakarsuk01@gmail.com, abbello.civ@buk.edu.ng

***Corresponding author**: Aminu Darda'u Rafindadi

DOI: https://doi.org/10.67203/sp.ICESID.2026

ABSTRACT

Time overrun remains a severe and chronic problem in the construction sector of developing nations, turning infrastructure investments into inadequately documented expenditure. This paper critically examines the execution of the 74km Kano–Katsina Road Dualization Project, carried out by CCECC, drawing on project documents, progress reports, and interim payment certificates. The analysis exposes gross inadequacies in project initiation, financial management, and institutional coordination. By April 2025, the finding was that the project had consumed 163.33% of its planned time allocation, yet achieved only a 90.13% completion rate. This paper delivers a harsh but necessary critique of operational and administrative blunders that drove the project's contract sum from ₦14 billion to ₦68 billion, and offers constructive, priority recommendations for future infrastructure management.

Keywords: *Systemic failure; Infrastructure inefficiency; Large-scale projects; Road dualization; Project execution; Kano–Katsina Road; Construction management; Cost overrun; Time overrun; Quality assurance; Contractor performance; Procurement process; Project delivery; Nigeria*

1. INTRODUCTION

Nigeria's infrastructure deficit remains a major impediment to economic growth, and public spending falls far short of the scale of investment required (Akpor & Ransome, 2025), pushing policymakers toward public-private partnerships (PPP) and development finance instruments. The failure of infrastructure delivery in Nigeria is not merely a technical problem; it is a governance problem. Nigeria's large-scale infrastructure agenda has repeatedly been constrained by governance failures, financing gaps, weak institutional coordination, participation, and implementation failures that erode value for money. A road project study in Kenya reports that leadership style and corporate governance were positively associated with project performance, while resource availability was a significant influence on success, underscoring that project outcomes depend on management quality as much as on engineering design (Mrongo, 2024). In the same vein, a study of public participation in Nigerian road EIAs reports failures across procedural, substantive, normative, and transactive dimensions, including weak consultation, poor feedback, limited access to information, and unequal collaboration (Aliyu, 2024). The Federal Government of Nigeria has consistently identified road infrastructure as a developmental priority. The gap between contractual schedules and actual delivery timelines reveals deep dysfunction across procurement, finance, and project management.

Time overrun has become so endemic in construction that it is often treated as an expected outcome rather than a preventable failure (Assaf & Al-Hejji, 2006). A qualitative study of Nigerian highway projects indicates that cost overruns are driven by "delay in work progress, political instability, adverse weather, social issues, delay in progress payment to contractors, and modification of project scope," showing that the project-delivery problem is both contextual and managerial (Mahmud et al., 2021). The 74 km Kano–Katsina Road Dualization Project is instructive precisely because it is not atypical. Contracted in 2013 with an initial sum of ₦14 billion, subsequently revised to ₦24 billion following a ministerial scope change, and inflated further to approximately ₦68 billion through cumulative inflationary adjustments, the project's financial trajectory alone constitutes a research subject of significance. Over a decade after contract award, the project remained incomplete, with

90.13% physical progress against 163.33% of elapsed time. The project can be read as more than a single delayed works contract; it is a case through which to examine structural weaknesses in Nigeria's infrastructure execution model. This paper, therefore, argues that persistent overruns, delays, and contested implementation patterns reflect systemic failures in planning, governance, stakeholder engagement, and budgetary discipline rather than isolated site-level problems.

The paper proceeds as follows: Section 2 reviews the relevant literature on the causes of construction delay. Section 3 describes the research methodology. Section 4 presents and critically analyses findings. Section 5 draws conclusions and offers targeted recommendations.

2. LITERATURE REVIEW

2.1 The Taxonomy Problem in Construction Delay Research

The available literature lacked a standard method or framework for identifying critical causes of delay, and the use of ambiguous and unstructured phrasing had undermined the effectiveness of prior findings. Amarkhil et al. (2023) extracted 335 distinct critical causes of delay, condensed them into 14 groups, and summarized them into 48 major causes, just to make the literature comparable. The proposed solution illustrates the scale of the fragmentation that the authors were responding to from prior studies. Yet newer studies continue to propose entirely different top-level schemes rather than adopting this or any other standard. A delay-analysis study sorts causes into just three buckets (Contractors' Delays, Owners' Delays, and External Factor Delays) (Amoah et al., 2024). A systematic review of office-building delays organizes 74 papers' worth of causes into three different categories: Input Delay Factors (4 factors), Internal Delay Factors (18 factors), and External Factors (5 factors) (Aldammak et al., 2025). Derakhshanfar et al. (2019) developed another structure from 46 articles using grounded theory coding and identified 26 delay risks grouped into 10 categories, forming a risk breakdown structure.

These taxonomies are descriptively useful but analytically limited. They treat all causal categories as structurally equivalent, which prevents identification of the mechanism by which dysfunction in one category propagates delay through others. Yet subsequent literature has not consistently given financial dysfunction its appropriate analytical prominence.

2.2 Financial Constraints and Payment Delays

Rabbet's 2024 Construction Payments Report found payment delays cost the U.S. construction industry an estimated $280 billion in 2024 alone, with 82% of contractors reporting payment waits exceeding 30 days, up from 49% two years earlier (Rabbet, 2024). A regression-based study of 138 clients, contractors, and consultants across Enugu and Anambra States found that contractor-related factors emerged as the most severe delay category overall, while delay in progress payment ranked first among individual factors, with difficulties in financing the project ranking a close second (Nzubechukwu & Precious, 2026). Zagia et al. (2026) synthesized 92 studies from 35 countries using a PRISMA-based review and concludes that owner-side financial problems and delayed contractor payments are the most widespread drivers of delay. The review further argues that delay is a context-specific problem, but financing failures, weak planning, and poor execution management are the common backbone across countries and project types.

Haseeb et al. (2011) demonstrated that delays in payment to contractors disrupt cash flow and create a cascading effect across procurement, labour, and equipment deployment. In government-funded infrastructure, this problem is compounded by bureaucratic approval requirements, Treasury Single Account restrictions, and politically driven funding allocations (Olawale & Sun, 2010). Zagia et al. (2026) further discovered that corruption and government bureaucracy were the leading causes of delays in Nigeria, followed by inadequate funding and price fluctuations/inflation, pointing to a governance-and-funding cause chain rather than a purely contractual payment-processing one. A conceptual framework study on federal highway cost overruns in Southeast Nigeria uses the Second Niger Bridge as a documented case: the ₦11.79 km bridge project, originally contracted at approximately ₦206.15 billion, was revised upward to approximately ₦300.98 billion (Okpan Agara, 2025). The Nigerian SUKUK bond financing model, introduced to supplement traditional budgetary funding, improved short-term liquidity on several projects but did not resolve the underlying structural

problem of delayed interim certificate certification and payment. In large-scale road projects where contractor working capital requirements are substantial, the combined effect of retention and payment delay can effectively paralyze construction for extended periods.

2.3 Technical and Design-Related Delay Factors

Orya and Calahorra-Jimenez (2025) conducted a systematic review and discovered that 80% of delay reasons occur in the construction phase, while only 20% are associated with the design and procurement phases combined. Design changes after construction commencement are well-documented as significant delay drivers (Assaf & Al-Hejji, 2006), (Oladapo, 2007). The design-related delay salience is not uniform but varies meaningfully by infrastructure type (Devi & Sindhu, 2025).

Oshin (2025) evaluated the effects of design errors directly and found them to be a recurring source of delays, cost overruns, and quality problems across the sampled firms. An RII-based study of building construction delays in Osun State found that incomplete drawings ranked among the most significant delay factors, with an RII of 0.84, alongside cash flow problems (0.89), improper planning and scheduling (0.91), and financial incapability (0.89) (Egwim et al., 2023). Ebekozien et al. (2015) found that consultants, contractors, and clients contribute to design errors, with the most prevalent causes being late or inadequate client instructions, client interference, inadequate site investigation, and unclear documentation. They further identified that project delays, cost overruns, rework, accidents, and contract disputes were the most significant resulting impacts. Zhang et al. (2025) found that the major factors leading to design errors are design input information error, unreasonable intervention on design, noncompliance with standard requirements, and error in site geological survey documentation, and importantly noted a disconnection in understanding among stakeholders about the causes of design errors.

A gap that remains largely unaddressed in the literature is the precise mechanism by which ministerially-directed scope changes, a recurring feature of Nigerian federal infrastructure delivery, override the contract documents governing a project rather than operate through them. Unlike formally issued variation orders, which are processed under the contract's change-management provisions and carry corresponding adjustments to time and cost, ministerial directives frequently originate outside this framework altogether: they are issued as administrative instructions rather than contractual instruments, yet are treated on-site as binding. The result is a structural asymmetry. The redesign obligation is transmitted immediately, while the contractual mechanisms that would normally protect the time and cost implications of that redesign are either bypassed or invoked only after the fact, if at all. This dynamic has significant practical consequences for project delivery, yet the specific pathway by which it occurs, how a ministerial instruction acquires practical authority over a signed contract, and why the usual safeguards fail to activate in response, has received little direct scholarly attention.

2.4 Research Gap

The existing literature on delays in Nigerian road construction projects is relatively limited compared to that in building construction research. More critically, no study has applied documentary financial analysis, specifically, systematic examination of interim payment certificates alongside progress reports, to empirically link financial disbursement patterns to physical progress trajectories on a major Northern Nigerian Road project (Akpor & Ransome, 2025), (Aliyu, 2024), (Mahmud et al., 2021). This study addresses that gap.

3. RESEARCH METHODOLOGY

3.1 Research Design and Justification

This study employs a qualitative case study design, as recommended by Yin (2015) for research that requires an in-depth examination of a phenomenon within its real-world context. The Kano–Katsina Road Dualization Project was selected as the case study because it combines strategic national significance, documented cost and schedule overruns, and accessible key stakeholders and project records.

A mixed-methods approach integrating qualitative interviews and quantitative document analysis was adopted to enable triangulation, improving the reliability and internal validity of findings

(Creswell & Creswell, 2017). The quantitative component is descriptive rather than inferential; it provides objective benchmarks that support and contextualize the interpretation of qualitative data, rather than aiming for statistical generalization.

3.2 Data Collection

Primary data were collected through semi-structured interviews with 11 purposively selected participants: 4 site engineers, 3 Federal Ministry of Works officials, 1 CCECC personnel manager, and 3 skilled and semi-skilled site workers. Purposive selection ensured depth of information and diversity of roles, consistent with qualitative case study norms (Saunders et al., 2018). All eleven participants provided complete, usable responses (100% response rate).

Secondary data comprised two official project documents: (i) the project progress report documenting physical completion percentages at six time points between October 2021 and April 2025, and (ii) Interim Payment Certificate No. 113809, providing a structured financial record of gross valuation, retention deductions, previous payments, and net payable amounts.

3.3 Analytical Approach

Qualitative interview data were analyzed using thematic analysis, with codes grouped into financial, technical, environmental, and institutional themes. Documentary data were analyzed using schedule performance comparison (percentage completion vs. percentage of elapsed time) and financial structure analysis (examining the composition and magnitude of IPC deductions). Triangulation across these three data streams, interviews, progress data, and financial data, formed the basis of causal inference.

3.4 Limitations

The study is limited to a single project case, constraining statistical generalisability. Access to the full IPC register was unavailable; analysis was confined to IPC No. 113809. The small interview sample, while appropriate for qualitative case study research, may not capture the full range of stakeholder perspectives. These limitations should inform the interpretation of findings.

4. FINDINGS AND DISCUSSION

4.1 Themantic Analysis

Table 1 accounts for how many separate points fall under each theme. For example, under "Financial dysfunction," 6 distinct issues are counted (delayed payments, insufficient mobilization funds, IPC delays, "no pay, no work" stoppages, SUKUK/inflation offset, BEME cost escalation). The sentences in the last column are paraphrased and combined by the interviewers, not verbatim.

Table 1: Thematic Summary

Theme	**Distinct sub-issues raised in the narrative**	**Illustrative characterization (paraphrased from findings, not verbatim)**
Financial dysfunction	6 (delayed payments; insufficient mobilization funds; IPC processing delays; "no pay, no work" stoppages; SUKUK financing offset by inflation/accumulated delay; BEME revision cost escalation)	Respondents linked payment delay directly to work stoppages, describing a "no pay, no work" posture by the contractor during funding gaps. All 11 interviewers confirmed.
Technical/design inadequacy	6 (cost-driven original design; FMW directive for full dual-carriageway reconstruction; design creep/redesign; groundwater-induced settlement near Bichi; inadequate EIA; extended remedial works)	Respondents attributed the redesign disruption to a late directive requiring full reconstruction of both carriageways, including sub-base replacement, rather than the originally scoped partial rehabilitation. Confirmed by the 7 interviewers.
Environmental factors	4 (rainfall; continued earthworks against advice; washouts/rework from carriageway height mismatch; unanticipated seasonal hydrology)	Respondents noted that earthworks continued through peak rainy periods despite recommendations to suspend, resulting in washouts and repeated compaction rework. Confirmed by the 5 interviewers.
Institutional/administrative factors	4 (bureaucratic/approval delays; overlapping client-consultant-contractor responsibilities; "protected works only" payment restriction; late-discovered 7 km measurement discrepancy)	Respondents described payment certification limited to "protected works" (e.g., asphalt, drainage), excluding subgrade and pavement layers, as a disincentive to continuous progress. Confirmed by the 6 interviewers.

4.2 Extent and Trajectory of Schedule Overrun

The progress report data, presented in **Table 2**, provide the clearest quantitative evidence of the project's performance failure. At every recorded time point, the percentage of project time elapsed materially exceeded the percentage of physical work completed. Critically, this disparity was not the result of a single acute disruption; it reflects a progressive, cumulative deterioration in schedule performance spanning more than 3 years of documented data.

Several features of this trajectory warrant particular attention. First, the project had already exceeded its planned duration by the time the earliest recorded data point was reached (October 2021, 104.44% time elapsed). This is not a project that started well and collapsed; it was in arrears before the observation window even opened, indicating that delays were systemic from the outset. Second, the period from January to June 2022 shows complete stagnation: physical progress did not advance by a single percentage point over five months, while time continued to accumulate. This is not a slowdown; it is a construction halt. Third, between June 2022 and March 2025, a gap of nearly three years in the

recorded data, physical progress advanced by only 5.49 percentage points (from 82.97% to 88.46%), while time elapsed increased by 48.89 percentage points. Whatever happened in this interval, the project was producing work at a rate catastrophically below what time and resources should have permitted.

Table 2: Schedule Performance Comparison (October 2021 – April 2025)

Date	Physical Completion (%)	Time Elapsed (%)	Schedule Gap (pp)
October 2021	81.70	104.44	22.74
January 2022	82.97	107.78	24.81
May 2022	82.97	112.22	29.25
June 2022	82.97	113.33	30.36
March 2025	88.46	162.22	73.76
April 2025	90.13	163.33	73.20

Note: No progress reports were available to the authors for the period June 2022 to February 2025; this gap reflects a documentation limitation in the project records accessed, not a pause in construction activity

4.3 Financial Dysfunction: The Interim Certificate as Evidence

Analysis of IPC No. 113809 reveals the financial structure underlying this schedule failure. The certificate demonstrates that the contractor's effective working capital was substantially constrained by three compounding mechanisms: (i) gross valuation falling below actual work value due to 'protected works only' certification policies; (ii) retention deductions reducing the certified amount; and (iii) previous payment adjustments further reducing net disbursements. These findings should be read as indicative of a documented instance rather than as a representative average across the project's full payment history, given the single-certificate limitation acknowledged in Section 3.4.

The 'protected works only' policy whereby the Ministry certified payment only for completed, weatherproof elements such as asphalt and drainage, while excluding subgrade and pavement layers awaiting further work, is particularly consequential. This policy creates a perverse incentive structure: contractors must invest in early-stage work without financial recognition until that work is fully enclosed by later-stage activities. In a road project where earthworks and subgrade preparation precede and enable all subsequent paving operations, this policy effectively means the contractor must finance weeks or months of high-intensity activity before receiving any payment.

The cumulative effect of these mechanisms is a structural cash flow deficit that, in the interview data, was directly linked to the 'no pay, no work' operational posture adopted by CCECC during periods of payment delay. This posture is rational from the contractor's perspective but catastrophic for project continuity. It transforms temporary financial disruption into an extended construction suspension, exactly the pattern observed during the 2022 stagnation period.

4.4 The Redesign Disruption: A Ministerially-Generated Delay

The original contract scope included the rehabilitation of the existing carriageway and the construction of a new one. A subsequent directive from the Federal Ministry of Works required full reconstruction of both carriageways, including complete replacement of the sub-base. This change was not a contractor decision; it was imposed by the client mid-execution.

The consequences were threefold: a revised Bill of Engineering Measurement and Evaluation (R-BEME) was required, increasing the contract sum by ₦10 billion; redesigned work disrupted the established construction programme; and scope creep created ambiguity about what was included in existing valuations. The residual increase from ₦24 billion to approximately ₦68 billion, beyond the ₦10 billion attributable to the R-BEME redesign, is described in project correspondence as arising from cumulative inflationary adjustments; however, an itemized breakdown of this escalation was not available within the documentary record accessed for this study, and this is acknowledged as a limitation of the financial analysis presented. What is absent from the documentary record is any evidence that the time implications of this redesign were formally incorporated into an extended contract programme. The contractor absorbed the schedule impact without contractual relief due to contract administration failures that directly contributed to the growing schedule gap.

4.5 Geotechnical Failure and the Cost of Inadequate Pre-Construction Assessment

Interview data identified geotechnical instability along approximately one kilometer of roadway traversing Bichi town, where rising groundwater caused surface settlement. This problem was attributed to inadequate Environmental Impact Assessment at the planning stage and the inadvertent removal of natural geological barriers during initial earthworks.

The remediation of this failed excavation, the installation of a drainage layer, and recompaction consumed time and resources without advancing the recorded percentage completion in the progress report. It represents a category of 'invisible work': labour and materials expended on rectifying avoidable problems rather than constructing new infrastructure. The absence of a thorough pre-construction geotechnical investigation is a planning failure with compounding consequences. It not only caused direct delays but also imposed costs that reduced the contractor's already-constrained working capital.

4.6 The Seven-Kilometer Measurement Error

A further factor reportedly identified by interviewees, though not independently verifiable from the documentary record available to this study, concerns an approximately seven-kilometre discrepancy in the project's defined scope. In the absence of full supporting documentation, this is treated here as a tentative, anecdotal observation warranting future documentary confirmation, rather than as an established causal factor. While the full documentation of this discrepancy was not available for analysis, its existence raises serious questions about the adequacy of the original site investigation and contract documentation. A 9.5% error in the fundamental physical parameter of a road contract is not a minor administrative oversight; it represents a failure at the earliest stage of project definition that propagated uncertainty in cost and schedule throughout execution.

4.7 Synthesis: Financial Dysfunction as Systemic Amplifier

The four causal factors identified: financial dysfunction, ministerially-imposed redesign, geotechnical inadequacy, and measurement error, are not independent (see **Table 3**). They interact through a common mechanism: financial constraint. Technical problems require financial resources to remedy. Redesign disruptions generate contractor claims that must be financially resolved. Measurement errors create cost uncertainty, delaying financial settlement. In each case, the financial system's inability to process and pay claims in a timely manner transforms a solvable technical problem into an extended delay.

This is the central analytical contribution of this study: financial dysfunction is not merely one causal factor among several. It is the transmission mechanism through which all other delay factors propagate into extended schedule overrun. A project with robust, timely payment systems would still face technical challenges, but those challenges would be remedied within weeks rather than allowed to fester into months of construction suspension.

Table 3: Causal Factor Assessment and Financial Interaction

Causal Category	Specific Factor	Assessed Impact	Interaction with Finance
Financial	Delayed IPC payment; reduced net payable; protected works policy	Critical	Primary driver; directly halts site operations
Technical / Design	Ministerially-directed full reconstruction; scope creep; R-BEME preparation	High	Generates unresolved claims; delays financial settlement
Geotechnical	Groundwater-induced settlement at Bichi; inadequate EIA	High	Remediation costs exhaust constrained working capital
Institutional	Measurement error (7 km discrepancy); bureaucratic approval delays	Moderate–High	Creates cost uncertainty; delays certificate processing
Environmental	Seasonal rainfall; washout and rework on the initial carriageway	Moderate	Exacerbates delays when financial resources to remediate are absent

5. CONCLUSIONS AND RECOMMENDATIONS

5.1 Conclusions

This study has demonstrated, through a triangulated analysis of interviews, progress documentation, and financial records, that the Kano–Katsina Road Dualization Project experienced a schedule overrun of approximately 73.20 percentage points relative to its planned completion trajectory as at April 2025 (163.33% planned physical progress against 90.13% actual physical progress; see Table 1), underscoring the scale of delay accumulated over the review period. It is a failure that was neither sudden nor confined to a single causal source, but progressive, systemic, and rooted fundamentally in financial dysfunction.

The study advances three principal conclusions. First, delayed and structurally reduced interim payments are the primary causal driver of schedule overrun on this project, operating both directly (through construction suspension) and indirectly (by reducing the contractor's capacity to respond to technical challenges). Second, a mid-construction redesign imposed by the client without corresponding contractual time relief is a distinct and significant source of delay that existing literature has underexamined in the Nigerian federal infrastructure context. Third, inadequate pre-construction investigation (geotechnical, environmental, and physical) created avoidable problems that consumed resources, inflated costs, and extended the project duration.

5.2 Recommendations

The following recommendations are advanced based on these conclusions:

- Payment Mechanism Reform: The Federal Government should institute mandatory payment timelines for interim certificates on infrastructure contracts, with automatic interest accrual on delayed payments. The 'protected works only' certification policy should be reviewed to ensure that subgrade and pavement layer works are certifiable in proportion to their completion, rather than only upon enclosure by subsequent works.
- Pre-Construction Investigation Standards: Mandatory geotechnical and hydrological surveys should be completed and independently reviewed prior to contract award. Environmental Impact Assessments should be conducted to a standard sufficient to identify seasonal groundwater behaviour, not merely surface conditions.
- Contractual Provisions for Client-Directed Scope Changes: Standard government road contracts should include explicit clauses requiring that ministerially-directed scope changes be accompanied within 30 days by a formal variation order specifying additional cost and time allowances. Scope changes unaccompanied by such orders should be subject to suspension by the contractor.

- Physical Quantity Verification: Independent physical surveys verifying project length and scope should be completed and documented before contract execution. The seven-kilometer measurement discrepancy identified in this project would have been avoidable through basic pre-award verification.
- Progress Monitoring Reform: Progress reports should be submitted monthly and should include earned value metrics (not merely percentage completion vs. time elapsed) to enable early identification of emerging schedule deviations.

5.3 Contribution to Knowledge

This study contributes to construction delay literature in three ways. It provides empirical evidence linking financial disbursement structure, as revealed by interim certificate analysis, directly to physical progress outcomes on a major Nigerian road project. It advances a hierarchical causal model that positions financial dysfunction as the systemic amplifier of other delay factors, rather than one equivalent variable among many. It provides a documented analysis of a large-scale Northern Nigerian Road dualization project, a category that is underrepresented in existing delay research.

Financial disbursement dysfunction does not act as an independent delay factor but as an amplifier that increases the schedule impact of co-occurring technical and environmental delay factors (refer to **Fig. 1**). The magnitude of schedule overrun on a project is better explained by the interaction between financial dysfunction and technical/environmental factors than by any single factor category in isolation. Contrary to Amarkhil et al. (2023) taxonomy, they categorize delay factors as a flat, non-hierarchical list grouped by source (e.g., client-related, contractor-related, external), the hierarchical causal model proposed here explicitly nests categorical delay factors beneath a systemic financial driver, offering a mechanism (amplification) rather than only a classification, and is thus positioned as complementary to, rather than a replacement for, existing taxonomies.

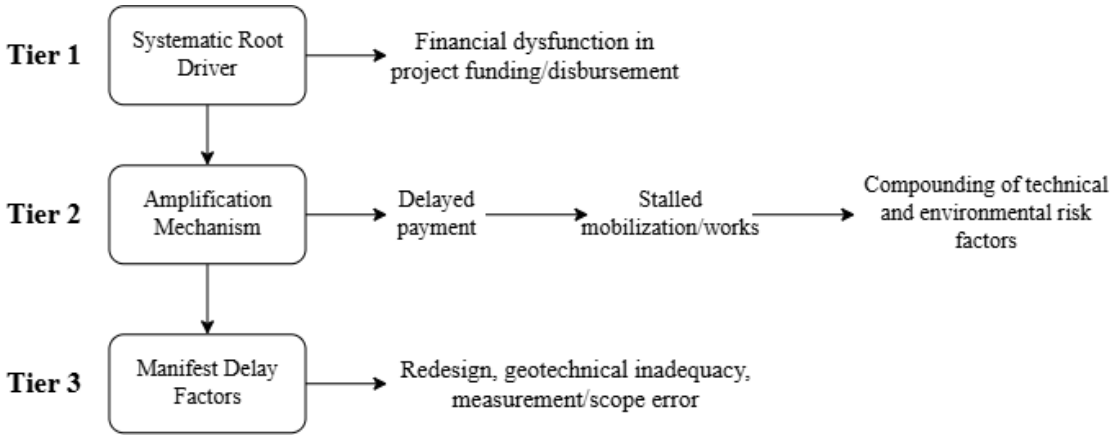

Figure 1: Theoretical Contribution of the Study

REFERENCES

Akpor, A. O., Aliu Clement AigbokhaiI, & Ransome, O. (2025). Bridging the Infrastructure Gap in Emerging Economies: An evaluation of the Role of Development Finance and Public-Private Partnerships in Nigeria's Infrastructure Transformation–Challenges, Opportunities, and Strategic Pathways. *ISIR J. Arts, Humanit. Soc. Sci*, *2*(3).

Aldammak, M. M., Hamzah, N., & Khoiry, M. A. (2025). Causes For the Delay in Construction Offices Building: A Systematic Review. *Jurnal Kejuruteraan*, *37*(5), 2453-2467.

Aliyu, I. (2024). *Evaluating the Quality of Public Participation and Its Effectiveness in Environmental Impact Assessment of Road Infrastructural Projects in Nigeria* University of Salford (United Kingdom)].

Amarkhil, Q., Elwakil, E., Hubbard, B., & Byrd, V. L. (2023). A framework to standardize causes of construction delay. *International Journal of Construction Management*, *23*(11), 1791-1804.

Amoah, K. B., Okere, G., & Deshpande, A. (2024). Construction delay analysis: Causes, impacts, and mitigation strategies. *J. Civ. Eng. Res, 14*(1), 1-9.

Assaf, S. A., & Al-Hejji, S. (2006). Causes of delay in large construction projects. *International Journal of Project Management, 24*(4), 349-357.

Creswell, J. W., & Creswell, J. D. (2017). *Research design: Qualitative, quantitative, and mixed methods approaches*. Sage publications.

Derakhshanfar, H., Ochoa, J. J., Kirytopoulos, K., Mayer, W., & Tam, V. W. (2019). Construction delay risk taxonomy, associations and regional contexts: A systematic review and meta-analysis. *Engineering, Construction and Architectural Management, 26*(10), 2364-2388.

Devi, L. P., & Sindhu. (2025). Delay Analysis of Infrastructure Construction Projects in India. *Journal of the institution of engineers (India): Series A, 106*(3), 763-771.

Ebekozien, A., Uwadia, F., & Usman, D. (2015). The impact of design errors and incomplete drawings on construction project delivery in Nigeria. Proceedings of the Academic Conference of African Scholar Publications & Research International on Sub-Sahara African Transformation and National Development,

Egwim, C. N., Alaka, H., Toriola-Coker, L. O., Balogun, H., Ajayi, S., & Oseghale, R. (2023). Extraction of underlying factors causing construction projects delay in Nigeria. *Journal of Engineering, Design and Technology, 21*(5), 1323-1342.

Haseeb, M., Bibi, A., & Rabbani, W. (2011). Problems of projects and effects of delays in the construction industry of Pakistan. *Australian Journal of Business and Management Research, 1*(5), 41-50.

Mahmud, A. T., Ogunlana, S. O., & Hong, W. (2021). Key driving factors of cost overrun in highway infrastructure projects in Nigeria: a context-based perspective. *Journal of Engineering, Design and Technology, 19*(6), 1530-1555.

Mrongo, L. O. (2024). Strategy Implementation, Corporate Governance and Performance of Road Projects Under Kenya Rural Roads Authority in Kenya KeMU].

Nzubechukwu, O. O. N., & Precious, P. E. (2026). Delay and Cost Overrun in Construction Projects: A Regression Analysis in Southeastern Nigeria. *Engineering and Applied Sciences, 11*(3), 78-89.

Okpan Agara, O. F. E., Adindu Chinedu, Ezichi Ishmel Kalu. (2025). A Framework for Mitigating Federal Highway Project Cost Overrun Effects in South East, Nigeria. *International Journal of Innovative Science and Research Technology, 10*(8). https://doi.org/https://doi.org/10.38124/ijisrt/25aug1205

Oladapo, A. (2007). A quantitative assessment of the cost and time impact of variation orders on construction projects. *Journal of Engineering, Design and Technology, 5*(1), 35-48.

Olawale, Y. A., & Sun, M. (2010). Cost and time control of construction projects: inhibiting factors and mitigating measures in practice. *Construction Management and Economics, 28*(5), 509-526.

Orya, F., & Calahorra-Jimenez, M. (2025). Delays in Infrastructure Projects: Main Reasons in the Design, Procurement, and Construction Phases. *Public Works Management & Policy, 30*(2), 261-280.

Oshin, I. (2025). Assessing the Impact of Design Errors in Construction Project in Selected Construction Companies in Lagos State. *INTERNATIONAL JOURNAL OF RESEARCH AND INNOVATION IN SOCIAL SCIENCE (IJRISS).*

Rabbet. (2024). *Rabbet 2024 Construction Payments Report*. https://rabbet.com/reports/construction-payments-2024

Saunders, B., Sim, J., Kingstone, T., Baker, S., Waterfield, J., Bartlam, B., Burroughs, H., & Jinks, C. (2018). Saturation in qualitative research: exploring its conceptualization and operationalization. *Quality & quantity, 52*, 1893-1907.

Yin, R. K. (2015). *Qualitative research from start to finish*. Guilford publications.

Zagia, F., Kajewski, S., Omrani, S., & Motamedisedeh, O. (2026). Prioritizing the key causes of construction project delay in different countries: a cross-sectional analysis of different project types. *International Journal of Construction Management, 26*(9), 1879-1904.

Zhang, S., Sunindijo, R. Y., Wang, J., Su, Z., Ke, Y., & Liu, X. (2025). The causation of design error in the construction industry: A multistakeholder perspective. *Journal of performance of constructed facilities, 39*(1), 04024055.

TRACK 9 OF 11

Sustainable Engineering Processes and Systems

International Conference on Engineering Innovation for Sustainable Development (ICESID 2026)

Faculty of Engineering, Ahmadu Bello University Zaria · 8–10 September 2026

https://icesid.org

International Conference on Engineering Innovation for Sustainable Development (ICESID 2026)
Faculty of Engineering, Ahmadu Bello University Zaria · 8–10 September 2026

A SECURITY-CONSTRAINED PEER-TO-PEER MARKET FRAMEWORK FOR RESILIENT DISTRIBUTION NETWORKS

Olatunji Obalowu Mohammed[1,*], Shereefdeen O. Sanni[2], Nabila Ahmed Rufa'í[3], Olayinka Sikiru Zakariyya[1]

[1]*University of Ilorin*
[2]*Federal University Oye Ekiti, Nigeria*
[3]*University of Birmingham, UK*

Email: mohammed.oo@unilorin.edu.ng*, shereefdeen.sanni@fuoye.edu.ng, n.a.rufai@bham.ac.uk, zakariyya.os@unilorin.edu.ng

***Corresponding author**: Olatunji Obalowu Mohammed

DOI: https://doi.org/10.67203/sp.ICESID.2026

ABSTRACT

In the quest to decarbonize, decentralize, and digitalize the global energy systems, the conventional electricity consumers are becoming prosumers. This transition has challenged the traditional centralized utility model and demanded a direct, local energy exchange mechanism. Existing literature has neglected the influence of network security constraints on Peer-to-Peer (P2P) energy transactions. This paper therefore introduces a decentralized market framework designed to facilitate localized energy trading within physical grid constraints. An interior-point optimization algorithm balances economic welfare and network stability in the proposed framework. P2P outperforms a holistic benchmark against traditional centralized economic dispatch (CED) based on the IEEE 14-bus test system. The results show a net welfare gain of 375.54 m.u./h under the P2P framework; local generation of 57.83 MW compared to 57.97 MW under CED, achieves a lower operational cost ($1125.10\ m.u./h$*) and higher total consumer utility (*$2783.44\ m.u./h$*) under the proposed P2P market, while nodal voltage profiles remained within the secure operating limit of 1.0206 p.u. Further rigorous testing across different Distributed Energy Resources penetration scenarios shows that the model is stress-resistant for grids. This will provide a scalable and robust solution for modern distribution network operators, where decentralized market clearing discovers previously unavailable network capacity without compromising the network's physical operating limits.*

1. INTRODUCTION

Modern electrical distribution networks are rapidly evolving with the integration of small-scale renewables like rooftop solar and local energy storage. This shift has transformed traditional consumers into prosumers who consume and produce electricity, challenging the centralized utility model and creating new operational complexities, such as undervalued local generation and bidirectional power flows (Zheng et al., 2022). Peer-to-peer (P2P) energy trading offers a promising alternative, enabling prosumers and consumers to exchange energy locally without relying solely on utility intermediaries. This approach can enhance community self-sufficiency, reduce transmission losses, and optimize grid asset usage. P2P markets are typically structured across four layers (Aitzhan & Svetinovic, 2018; Dang et al., 2019; Lüth et al., 2018; Ping et al., 2026; Wu et al., 2023; Yan et al., 2023): business (market rules and financial flows), control (grid operations and transactive control), information and communication (secure data exchange and smart metering), and the physical network (infrastructure and reliability) (Ali et al., 2021; Nasiri, 2023; Soto et al., 2021; Zhang et al., 2018). All these layers must coordinate securely and interoperate seamlessly. To preserve overall grid integrity, any proposed energy transaction must be evaluated and either approved or denied based on strict network technical constraints (Nasiri, 2023).

The literature survey has shown that existing research in P2P spans these market layers, with each layer specifically focused on one of the layers within the energy trading framework. (Kang et al., 2017) proposed a secure, decentralized P2P electricity trading system among Plug-in Hybrid Electric Vehicles (PHEVs) using consortium blockchain technology to enhance security and privacy. The system aimed to maximize social welfare by optimizing electricity prices and the amount traded;

however, the system relies on local aggregators (LAGs) to act as energy brokers, run the consensus process, and maintain the blockchain. While this reduces the load on individual PHEVs, it introduces a semi-centralized element. If LAGs are compromised or malfunction, the system's security and reliability could be affected. The paper mentions mechanisms for accountability, but the risk remains.

A framework for prosumer participation in peer-to-peer (P2P) energy trading and flexibility markets was presented in (Khorasany et al., 2022), aiming to enhance grid stability and reduce costs. The flexibility market is cleared through an iterative auction, in which the distribution system operator adjusts the flexibility price to minimize costs, while prosumers independently decide how much flexibility to offer. A graph-based framework for allocating losses in unbalanced radial distribution networks within transactive energy markets was developed in (Nikolaidis et al., 2018), considering physical topology and financial transactions. The sensitivity analysis in the paper reveals that as DG penetration increases, neutral losses also increase. While DG can reduce total phase losses, the increased use of the neutral conductor can counteract these benefits. This introduces a trade-off that is not always straightforward to manage, especially as the impact of DG on neutral losses may not be fully captured in simpler allocation methods.

In (Hoque et al., 2024), a framework for prosumer-centric peer-to-peer energy trading was proposed. A double auction-based P2P trading mechanism was employed, allowing prosumers to submit offers within their dynamic operating envelope limits. In (Morstyn et al., 2018), a Federated Power Plant (FPP) was proposed as a new model that combines the benefits of virtual power plants and P2P energy trading platforms. The FPP is a VPP formed through P2P transactions between self-organizing prosumers. The paper aims to solve the problem of incentivizing coordination among large numbers of DERs owned by different prosumers, each with unique characteristics and preferences. The paper acknowledges that while the FPP concept is promising, several technical and operational challenges remain. For example, it is unclear to what extent a P2P energy trading market can achieve optimal economic benefits for a DER portfolio, or how to ensure that bilateral energy transactions do not breach the physical constraints of local distribution networks.

The application of blockchain technology for managing energy transactions and technical operations in microgrids was proposed in (Di Silvestre et al., 2018). The authors emphasize real-time attribution of power losses to specific transactions and address the complexity introduced by reactive power flows. The blockchain approach was integrated with power flow analysis to improve technical management of microgrids. In (Tong et al., 2026), a non-convex peer-to-peer (P2P) energy trading model for prosumer-based distribution networks was proposed, explicitly accounting for the binary (on/off) operating states of distributed energy resources (DERs), such as gas turbines and energy storage systems. A prosumer-centric internal uncertainty-balancing mechanism using stochastic programming was introduced, allowing each prosumer to absorb uncertainty in renewable generation locally and deliver deterministic net power injections to the network. While the two-stage distributed framework improves convergence and scalability compared to traditional methods, the approach still involves significant computational tasks, especially in large-scale systems with many prosumers and DERs.

Existing literature has focused on business and market layers, with extensive research on market design and loss allocation mechanisms. However, these economic frameworks frequently overlook the physical operational limits of the power network, leading to dispatch strategies that may prove operationally infeasible in practice. This paper introduces a security-constrained P2P market framework that integrates AC power flow into the market clearing process. By integrating physical network constraints directly into the optimization, the proposed approach ensures that all local energy trades are both economically efficient and physically viable. Comparative analysis with traditional centralized dispatch demonstrates that this framework can unlock new network capacity, improve welfare, and maintain grid stability under diverse operating scenarios.

2. METHODOLOGY

This section outlines the integrated framework that bridges the business layer (market clearing) and the physical layer (grid security). The proposed SC-P2P framework models the distribution network as a balanced, single-phase equivalent AC system. The methodology is structured to maximize community social welfare by matching localized generation and demand (Dong et al., 2025). Unlike traditional economic models that focus on economic dispatch without considering consumer benefit,

this framework explicitly couples the economic objective function to nonlinear AC power-flow equations, nodal voltage boundaries, and line thermal limits (Tarashandeh & Karimi, 2024) to maximize participants' welfare. The resulting non-linear, non-convex optimization problem is solved using an Interior Point Method (IPM), ensuring that all cleared Peer-to-Peer (P2P) trades are physically viable and do not compromise the operational stability of the distribution network.

2.1. Participant characteristics

Let $N = \{1,2,\dots,N\}$ represent the set of all participants (nodes) connected to the local distribution network. At any dispatch interval t, a peer $i \in N$ is characterized by its net power profile, determined by its local load and generation (Hoque et al., 2024; Zhang et al., 2018):

$$P_i^{net}(t) = P_i^{load}(t) - P_i^{gen}(t) \tag{1}$$

Based on this profile, the participant's role is defined as follows:

Buyer: if $P_i^{net}(t) > 0$, peer i has a power deficit and demands $P_i^d(t) = P_i^{net}(t)$.

Seller (prosumer): $P_i^{net}(t) < 0$, peer i has surplus generation to sell, denoted by $P_i^s(t) = P_i^{net}(t)$.

2.2. Market Objective Formulation

The fundamental objective of the local P2P market coordinator is to maximize the total social welfare (W). Welfare is defined as the net difference between the total utility gained by consumers and the total operational cost incurred by producers during the interval t (Kang et al., 2017; Khorasany et al., 2022):

$$\max_{P_{i,j}^{trade}} W = \sum_{i \in N_{buyer}} U_i(P_i^d) - \sum_{j \in N_{seller}} C_j(P_j^s) \tag{2}$$

where

$U_i()$ is the economic benefit function of the consumer i, $C_j()$ is the cost function of generation for the prosumer j and $P_{i,j}^{trade}$ denotes the matched energy quantity cleared between peers i and j.

The economic benefit derived by a consumer i consuming power P_i^{d} (in MW) is modeled using a concave quadratic utility function:

$$U_i\left(P_i^{\mathrm{d}}\right) = \alpha_i P_i^{\mathrm{d}} - \beta_i \left(P_i^{\mathrm{d}}\right)^2 \tag{3}$$

where $\alpha_i > 0$ denotes the consumer's baseline willingness-to-pay and $\beta_i > 0$ represents the marginal utility decline parameter.

The operational cost incurred by a prosumer j producing active power P_j^{s} (in MW) is modeled using a standard convex quadratic function:

$$C_j\left(P_j^{\mathrm{s}}\right) = a_j \left(P_j^{\mathrm{s}}\right)^2 + b_j P_j^{\mathrm{s}} + c_j \tag{4}$$

where $a_j > 0$, $b_j \geq 0$, and $c_j \geq 0$ represent the cost coefficients reflecting fuel, degradation, and operational expenses of localized DERs.

Before market clearing, participant net injections are calculated as $P_i^{\mathrm{net}} = P_i^{\mathrm{load}} - P_i^{\mathrm{gen}}$. Participants with $P_i^{\mathrm{net}} > 0$ bid into the market as buyers demanding $P_i^{\mathrm{d}} = P_i^{\mathrm{net}}$, while those with $P_i^{\mathrm{net}} < 0$ offer surplus capacity as sellers with $P_j^{\mathrm{s}} = |P_i^{\mathrm{net}}|$.

Table 1: Economic Utility and Generation Cost Parameters

Participant	**Role**	**Utility / Cost Function Coefficients**	**Parameter Values**
Bus 2	Seller	$C_2(P_2^s) = a_2(P_2^s)^2 + b_2P_2^s + c_2$	$a_2 = 0.035$ m.u./MW^{2}h, $b_2 = 20.0$ m.u./MWh, $c_2 = 0.0$
Bus 5	Seller	$C_5(P_5^s) = a_5(P_5^s)^2 + b_5P_5^s + c_5$	$a_5 = 0.025$ m.u./MW^{2}h, $b_5 = 18.0$ m.u./MWh, $c_5 = 0.0$
Bus 6	Seller	$C_6(P_6^s) = a_6(P_6^s)^2 + b_6P_6^s + c_6$	$a_6 = 0.015$ m.u./MW^{2}h, $b_6 = 15.0$ m.u./MWh, $c_6 = 0.0$
Bus 8	Seller	$C_8(P_8^s) = a_8(P_8^s)^2 + b_8P_8^s + c_8$	$a_8 = 0.040$ m.u./MW^{2}h, $b_8 = 25.0$ m.u./MWh, $c_8 = 0.0$
Bus 3	Buyer	$U_3(P_3^d) = \alpha_3P_3^d - \beta_3(P_3^d)^2$	$\alpha_3 = 60.0$ m.u./MWh, $\beta_3 = 0.50$ m.u./MW^{2}h
Bus 9	Buyer	$U_9(P_9^d) = \alpha_9P_9^d - \beta_9(P_9^d)^2$	$\alpha_9 = 55.0$ m.u./MWh, $\beta_9 = 0.45$ m.u./MW^{2}h
Bus 10	Buyer	$U_{10}(P_{10}^d) = \alpha_{10}P_{10}^d - \beta_{10}(P_{10}^d)^2$	$\alpha_{10} = 58.0$ m.u./MWh, $\beta_{10} = 0.55$ m.u./MW^{2}h
Bus 11	Buyer	$U_{11}(P_{11}^d) = \alpha_{11}P_{11}^d - \beta_{11}(P_{11}^d)^2$	$\alpha_{11} = 62.0$ m.u./MWh, $\beta_{11} = 0.60$ m.u./MW^{2}h
Bus 14	Buyer	$U_{14}(P_{14}^d) = \alpha_{14}P_{14}^d - \beta_{14}(P_{14}^d)^2$	$\alpha_{14} = 50.0$ m.u./MWh, $\beta_{14} = 0.40$ m.u./MW^{2}h

2.3. Network Constraints

To guarantee that the market-cleared transactions are secure and physically executable, the optimization is heavily constrained by the physical layer (Dong et al., 2025; Nasiri, 2023; Zimmerman et al., 2010).

2.3.1. *AC Power Flow Constraints*

The active and reactive power injections at each bus i must satisfy the non-linear AC power balance equations:

$$P_i^{inj} = V_i \sum_{k \in N} V_k \left(G_{ik} cos\theta_{ik} + B_{ik} sin\theta_{ik}\right) \tag{5}$$

$$Q_i^{inj} = V_i \sum_{k \in N} V_k \left(G_{ik} sin\theta_{ik} - B_{ik} cos\theta_{ik}\right) \tag{6}$$

where V_i and V_k are the voltage magnitudes at buses i and k, θ_{ik} is the voltage angle difference, and G_{ik} and B_{ik} represent the conductance and susceptance elements of the bus admittance matrix (Y_{bus}).

2.3.2. *Inequality constraints*

To prevent voltage collapse and equipment damage, strict operational boundaries are enforced:

$$V_{min} \leq V_i(t) \leq V_{max} \quad \forall i \in N \tag{7}$$

$$|S_{ik}(t)| \leq S_{ik}^{max} \quad \forall (i,k) \in L \tag{8}$$

where V_{min} and V_{max} are the nodal voltage limits (0.95 p.u. to 1.05 p.u.), $S_{ik}(t)$ is the apparent power flowing through the line connecting the buses $i\ and\ k$, and S_{ik}^{max} is the maximum thermal capacity of branch L.

2.3.3. *The Interior Point Method*

AC power-flow constraints are highly nonlinear and nonconvex; standard linear-matching algorithms are inadequate. To solve this complex constrained optimization problem, we employ the Interior Point Method (IPM). The IPM is particularly powerful for large-scale Non-Linear Programming (NLP) because it avoids the combinatorial complexity of active-set methods. It handles inequality constraints by converting them into equality constraints with slack variables, then penalizing the slack variables in the objective function via a logarithmic barrier. As the algorithm iterates, a barrier parameter (μ) is gradually reduced toward zero, forcing the solution to converge to the optimal feasible point strictly from within the feasible region (Tarashandeh & Karimi, 2024; Zimmerman et al., 2010).

To apply the IPM, the original welfare maximization problem is rewritten in the standard NLP minimization form:

$$\min_{x} f(x) = -W \tag{9}$$

Subject to the equality constraints $g(x) = 0$ (the AC power balance equations) and inequality constraints $h(x) \leq 0$ (the voltage and thermal limits), where x represents the vector of state variables (voltages, angles, and power injections).

The IPM transforms the inequality constraints into equality constraints by introducing a vector of strictly positive slack variables s:

$$h(x) + s = 0, \quad s > 0 \tag{10}$$

The objective function is then augmented with a logarithmic barrier term to prevent the slack variables from reaching zero prematurely:

$$\min_{x,s} \left(f(x) - \mu \sum_{m=1}^{M} \ln(s_m) \right) \tag{11}$$

where: $\mu > 0$ is the barrier parameter, M is the total number of inequality constraints, s_m represents the m-th slack variable.

The Lagrangian of this barrier problem is formulated as:

$$\mathcal{L}_\mu(x, s, \lambda, \gamma) = f(x) - \mu \sum_{m=1}^{M} \ln(s_m) + \lambda^T g(x) + \gamma^T (h(x) + s) \tag{12}$$

where x represents the decision variables of the grid ($P_{gen}, Q_{gen}, V, \theta$), $f(x)$ is the objective function, representing the negative of the social welfare function ($-W$), s is the slack variable, representing the distance a specific bus or line is from the limit, λ and γ are the Lagrange multipliers associated with equality and transformed inequality constraints, respectively. Figure 1 summarises the methodology framework.

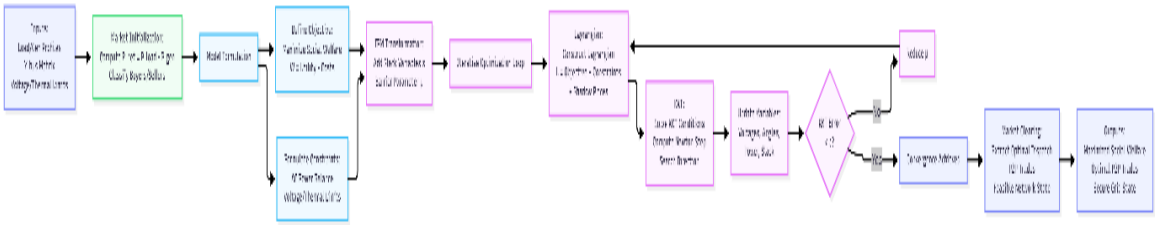

Figure 1: Methodology Framework

3. RESULTS AND DISCUSSION

We evaluate the performance of the proposed security-constrained P2P market framework on a modified IEEE 14-bus test system. The network consists of 14 buses, 20 transmission/distribution branches, 5 generating units (prosumers with dispatchable DERs), and 11 load centers.

Table 2: System Parameters

Parameter	Value / Range	Unit
System Base Power (S_{base})	100	MVA
Voltage Boundaries ($V_{\min} - V_{\max}$)	$0.95 - 1.05$	p.u.
Number of Buses (N)	14	Nodes
Number of Branches (L)	20	Lines/Transformers
Active Generators / DERs	Buses 1, 2, 3, 6, & 8	Units
Line Limits ($S_{ik}^{\max}$)	$10 - 50$	MVA

The optimization is modelled in MATLAB using the MATPOWER environment modified for non-convex P2P market formulations. The interior-point optimization solver (MIPS) handles the nonlinear AC power-flow balance equations and inequality constraints. Convergence is set to $\epsilon = 10^{-6}$ for KKT optimality conditions. Per-unit (p.u.) state variables are explicitly scaled by a base MVA of 100 during optimization and converted back to real-power units (MW) for welfare and dispatch evaluation. To evaluate performance, the proposed P2P framework is benchmarked directly against a standard Centralized Economic Dispatch (CED) model. CED optimizes generation to meet aggregate system demand through a single utility entity. In contrast, the P2P mechanism clears bilateral localized trades while respecting non-linear AC power flows and thermal branch limits.

The net active power balance determines participant selection ($P_i^{\text{net}} = P_i^{\text{load}} - P_i^{\text{gen}}$) at each node i during a given dispatch interval. Seller (Prosumer) Buses are selected when local generation exceeds local demand ($P_i^{\text{net}} < 0$). In the modified IEEE 14-bus distribution system, these correspond to nodes equipped with surplus dispatchable DER capacity, specifically Buses 2, 5, 6, and 8. Buyer Buses are selected when local load demand exceeds local generation ($P_i^{\text{net}} > 0$), these correspond to net load centers across the network, specifically Buses 3, 9, 10, 11, and 14. Slack and Passive/Transit Buses**:** Bus 1 serves as the main utility grid inertia (slack bus) to balance residual power exchange, while the remaining nodes (Buses 4, 7, 12, and 13) act as passive transit buses ($P_i^{\text{net}} = 0$) participating exclusively in AC power-flow routing rather than active P2P bidding.

3.1. Baseline Market Clearing and Network Security

Under base case operating conditions, the P2P market coordinator successfully matched local demand and generation across the 14-bus test system while enforcing nonlinear AC power-flow equations and operational limits. From Table 3, the base case P2P market achieved exact contractual clearing between local participants, with total cleared seller generation (57.00 MW) perfectly

matching total buyer demand (57.00 MW). The slack bus (Bus 1) injected an additional 0.83 MW into the network, serving exclusively as loss-compensation power to cover active transmission line losses (P_{loss}) across the feeder branches without forcing prosumers to bear unallocated physical grid losses.

Table 3: Base case P2P Market Dispatch

Bus Index	Participant Role	Max Capacity (MW)	Cleared Power (MW)	Market Status
Bus 2	Seller	15.00	15.00	Fully Cleared
Bus 3	Buyer	12.00	12.00	100% Demand Met
Bus 5	Seller	20.00	16.84	Partially Cleared
Bus 6	Seller	25.00	25.00	Fully Cleared
Bus 8	Seller	15.00	0.16	Marginal Reserve
Bus 9	Buyer	15.00	15.00	100% Demand Met
Bus 10	Buyer	10.00	10.00	100% Demand Met
Bus 11	Buyer	8.00	8.00	100% Demand Met
Bus 14	Buyer	12.00	12.00	100% Demand Met

Total Slack Grid Power Exchange: 0.83 MW

From Table 3, all buyer demands (Buses 3, 9, 10, 11, and 14) were fully satisfied, totaling 57.00 MW of cleared consumption. Sellers at Buses 2 and 6 operated at full capacity (15.00 MW and 25.00 MW respectively), while Bus 5 cleared 16.84 MW and Bus 8 served as the marginal unit clearing 0.16 MW. Figure 2 illustrates the nodal voltage profile under baseline P2P market clearing. The voltage remains strictly within statutory bounds ($0.95 - 1.05$ p.u.), peaking at Bus 9 with $V_9 = 1.0361$ p.u.

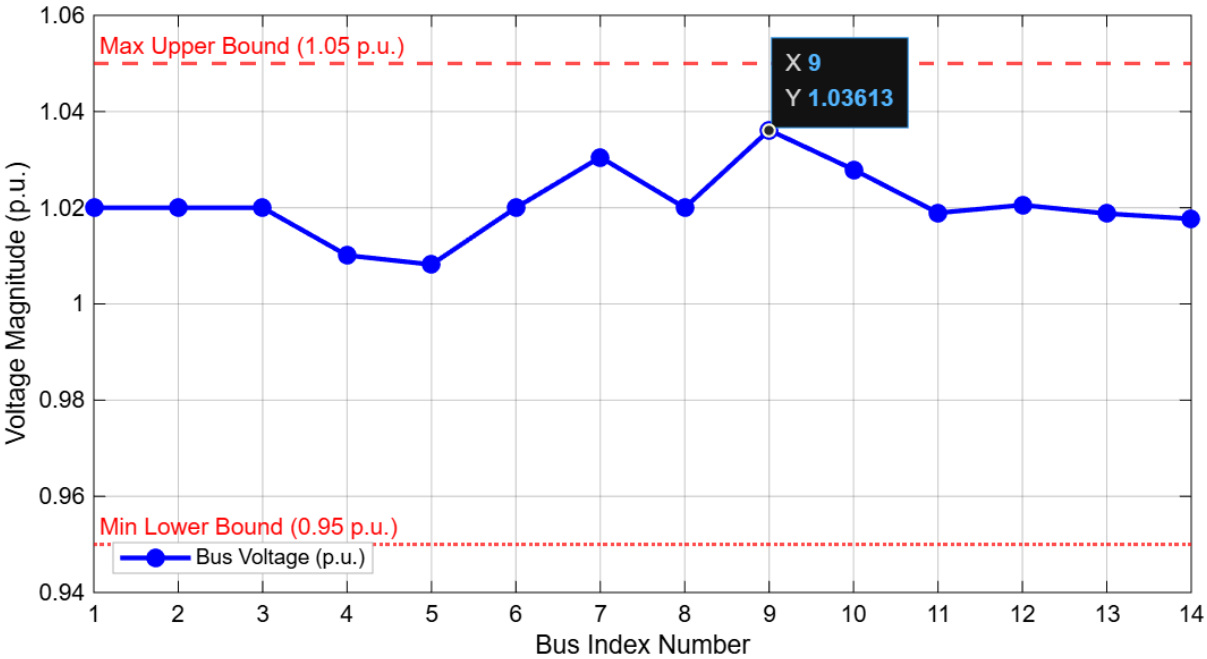

Figure 2: *Voltage profile under optimal P2P dispatches for base case scenario*

3.2. Comparative Economic and Operational Benchmarking: P2P vs. CED

To quantify performance gains, the proposed framework was benchmarked against traditional centralized economic dispatch.

Table 4: Economic and Operational Benchmarking Metrics

Performance Metric	**Centralized Economic Dispatch (CED)**	**Security-Constrained P2P Market**	**Operational Differential**
Total Operating Cost (C) (m.u./h)	1282.80	1125.10	-157.70 (Lower Cost)
Total Consumer Utility (U) (m.u./h)	2565.60	2783.44	217.84 (Higher Utility)
Net Social Welfare ($W = U - C$) (m.u./h)	1282.80	1658.34	375.54 (Welfare Improvement)
Total Power Generation ()	57.97	57.83	-0.14 (Loss Reduction)
Average Nodal Voltage (p.u.)	1.0430	1.0206	-0.0224 p.u.

From Table 4, the P2P market structure achieves a lower operational cost and higher total consumer utility (U) achieved under the proposed P2P market (2783.44 m.u./h) compared to CED (2565.60 m.u./h). The P2P market framework achieved a net social welfare of 1658.34 m.u./h, while CED achieved 1282.80 m.u./h, resulting in a net economic welfare improvement of 375.54 m.u./h in addition to loss reduction. Under Centralized Economic Dispatch (CED), consumer demand is inelastic, giving a base-case total utility $U = 2565.60$ m.u./h. The resulting minimum operating cost $C = 1282.80$ m.u./h yields $W = U - C = 1282.80$ m.u./h. The numerical identity $W = C$ shows that C is equal to $0.5 \times U$ at the fixed CED dispatch point. The P2P market reduces system losses by matching buyers with nearby prosumer generation, requiring 0.14 MW less slack grid compensation than centralized dispatch. Total required generation dropped from 57.97 MW under CED to 57.83 MW under P2P, reducing 0.14 MW loss compensation from the slack Bus. The voltage regulation is improved, as CED tends to push generator node voltages higher to force power across long feeder lines, leading to an elevated average nodal voltage of 1.0430 p.u. P2P decentralized clearing maintains a flatter, less stressed voltage profile averaging 1.0206 p.u. preserving distribution equipment health. This demonstrates superior demand-side value realization. While traditional CED exclusively minimizes generator production costs ($\min C$) under passive load constraints, the P2P market-clearing algorithm maximizes net social welfare ($\max W = U - C$). Higher consumer utility (U) in the P2P market indicates that consumers derive greater economic value, satisfaction, and demand fulfillment from their energy consumption compared to traditional Centralized Economic Dispatch (CED).

3.3. Dynamic Operational Stress Scenarios

To verify framework robustness, three severe grid stress scenarios were evaluated: Bus 6 Generation Outage Contingency, High Solar DER Penetration Scenario, and Peak (150%) vs. Off-Peak (50%) Demand Variations.

Table 5: Contingency (Gen outage at Bus 6) P2P Market Dispatch

BUS	ROLE	MAX Capacity (MW)	Cleared (MW)
2	Seller	15.00	15.00
3	Buyer	12.00	12.00
5	Seller	20.00	20.00
6	Seller	0.00	0.00
8	Seller	15.00	15.00
9	Buyer	15.00	15.00
10	Buyer	10.00	10.00
11	Buyer	8.00	1.00
14	Buyer	12.00	12.00

An unexpected loss of the primary supplier at Bus 6 (25.00 MW → 0.00 MW) was simulated. Table 5 shows that the algorithm automatically re-cleared the market by ramping up Seller 5 from 16.84 MW (base case) to its maximum capacity of 20.00 MW and ramping up Seller 8 from 0.16 MWto 15.00 MW. Due to localized line thermal capacity bottlenecks following the outage, Buyer 11 demand was partially curtailed from 8.0 MW to 1.0 MW to prevent line overloading. Figure 3 shows the voltage profile under N-1 contingency, where Bus 9 voltage reached a maximum of 1.04167 p.u., proving that the framework successfully maintains voltage stability under major supply contingencies without exceeding the 1.05 p.u. limit.

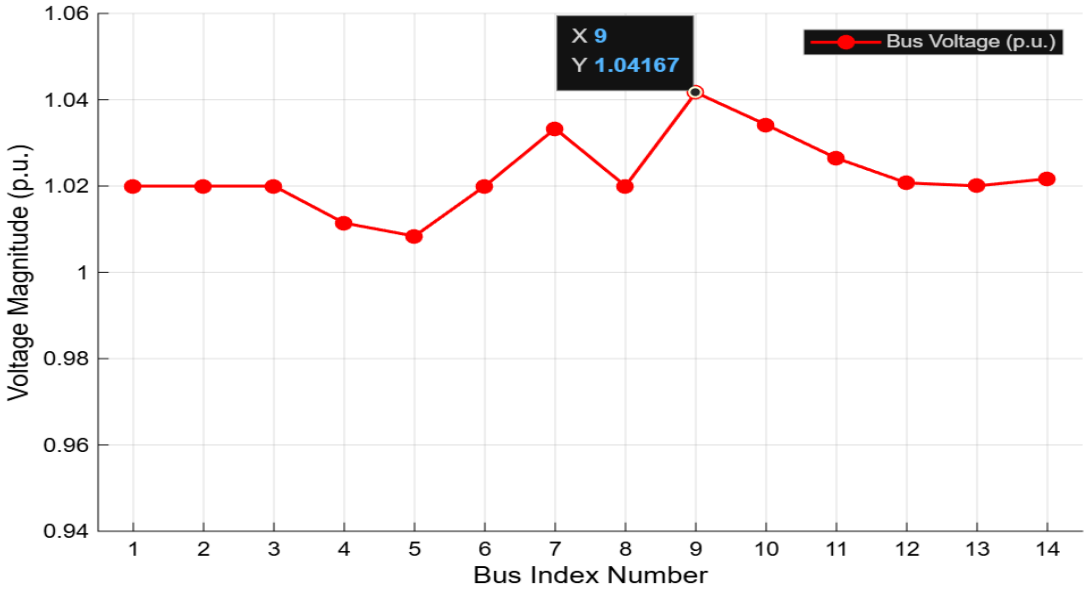

Figure 3: *Voltage profile under N-1 contingency scenario*

Under high solar DER availability, generation capacity shifts across the network. From Table 6, Seller 8 cleared its maximum capacity of 15.00 MW, allowing Seller 6 to back off generation to 7.00 MW while Seller 5 cleared 20.00 MW. All buyers' demand across all nodes was cleared while maintaining a stable voltage profile peaking at 1.04027 p.u. at Bus 9 as shown in Figure 4.

Table 6: P2P Market Dispatch under High Solar DER penetration

Bus Index	Participant Role	Max Capacity (MW)	Cleared Power (MW)
Bus 2	Seller	15.00	15.00
Bus 3	Buyer	12.00	12.00
Bus 5	Seller	20.00	20.00
Bus 6	Seller	25.00	7.00
Bus 8	Seller	15.00	15.00
Bus 9	Buyer	15.00	15.00
Bus 10	Buyer	10.00	10.00
Bus 11	Buyer	8.00	8.00
Bus 14	Buyer	12.00	12.00

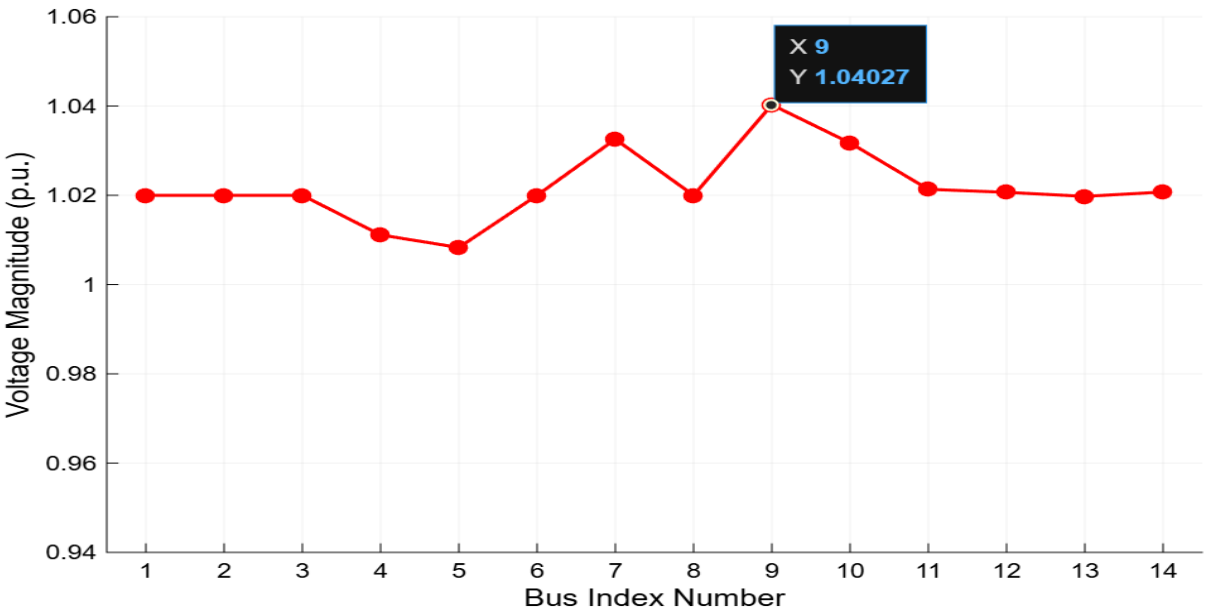

Figure 4: *Voltage profile under high solar DER penetration*

System performance was evaluated across contrasting loading conditions. At 50% demand, local generation demands are low. It can be seen from Table 7 that high-cost Seller 8 remained offline (0.00 MW), and Seller 5 ramped down to 0.40 MW. Reduced power flows resulted in higher overall line voltages, peaking at 1.03938 at Bus 9 and 1.02054 p.u. at Bus 14 as seen in Figure 5. At 150% demand, all local generators (Sellers 2, 5, 6, and 8) reached their capacity limits (75.00 MW total generation). Heavy power flow caused increased line drops, lowering Bus 14 voltage to 1.00265 p.u. as seen in Figure 5. To prevent thermal overload on feeder branches, Buyer 11 was curtailed to 1.50 MW (out of 12.00 MW demanded), demonstrating that the algorithm prioritizes physical line limits over unconstrained market clearing. Under the 150% peak load scenario, total cleared prosumer generation reaches its aggregate capacity limit of 75.00 MW ($15.00 + 20.00 + 25.00 + 15.00$ MW). Summing the cleared buyer allocations, Bus 3 (18.00 MW), Bus 9 (22.50 MW), Bus 10 (15.00 MW), Bus 11 (1.50 MW post-curtailment), and Bus 14 (18.00 MW) yields exactly 75.00 MW, confirming power balance consistency across the market.

Table 7: P2P Market Dispatch under off-peak, base case and peak scenarios

Participant Index	Off-Peak (50% Load) Cleared (MW)	Baseline (100% Load) Cleared (MW)	Peak (150% Load) Cleared (MW)
Seller 2	15.00	15.00	15.00
Buyer 3	6.00	12.00	18.00
Seller 5	0.40	16.84	20.00
Seller 6	13.10	25.00	25.00
Seller 8	0.00	0.16	15.00
Buyer 9	7.50	15.00	22.50
Buyer 10	5.00	10.00	15.00
Buyer 11	4.00	8.00	1.500 (Curtailed)
Buyer 14	6.00	12.00	18.00

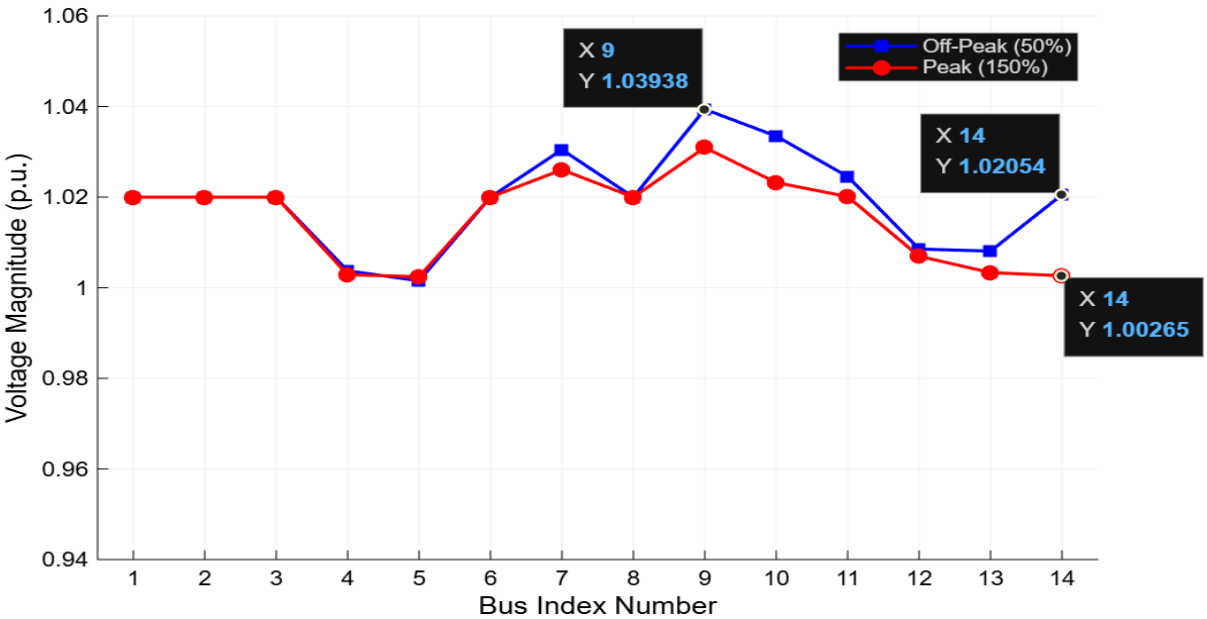

Figure 5: *Voltage profile under off-peak and peak scenarios*

3.4. IPM Solver Computational Convergence Performance

For the base-case P2P market clearing took 12 iterations to converge within 0.048 seconds, while CED involved 10 iterations to converge within 0.039 seconds. For the N-1 contingency, it took 15 iterations to converge within 0.062 seconds. For high DER penetration, it took 11 iterations to converge within 0.045 seconds. For the off-peak demand, it took 9 iterations to converge within 0.038 seconds, while for peak demand it took 18 iterations to converge within 0.076 seconds. The KKT residual ($\epsilon < 10^{-6}$) for all scenarios.

4. CONCLUSION

This paper presented a security-constrained Peer-to-Peer (P2P) energy market framework designed to bridge the gap between decentralized market clearing and physical distribution network security. By integrating non-linear AC power-flow equations, nodal-voltage boundaries, and branch thermal-capacity limits into a social-welfare maximisation objective, the proposed model ensures that all cleared bilateral trades are physically executable. The non-convex optimisation problem was solved using an Interior Point Method (IPM) with logarithmic barrier penalties, ensuring robust numerical convergence while strictly adhering to operational limits.

Validation on a modified IEEE 14-bus test system demonstrated the operational and economic superiority of the proposed framework over traditional Centralised Economic Dispatch (CED). The P2P market achieved a net economic welfare improvement differential of 375.54 m.u./h while reducing total

required system generation from 57.97 MW to 57.83 MW, yielding a 0.14 MW reduction in active power losses through localised power matching. Furthermore, the market enabled 100% community self-sufficiency for local demand, requiring only 0.83 MW of slack grid power exchange to compensate for network losses. Nodal voltage profiles remained strictly within statutory bounds (0.95 to 1.05 p.u.), yielding a less stressed average nodal voltage of 1.0206 p.u. compared to 1.0430 p.u. under CED.

Rigorous stress testing confirmed the algorithm's adaptability under dynamic grid conditions. During a 25 MW generator contingency at Bus 6, the IPM algorithm seamlessly re-cleared local reserves to maintain system stability. Under a 150% peak load surge, the framework intelligently curtailed demand at Bus 11 to 1.50 MW, proving that physical grid limits are strictly prioritized over unconstrained trade clearing. Overall, the framework provides distribution network operators with a scalable tool to unlock localised DER capacity without compromising grid reliability. Future work will expand this framework to multi-period operational horizons with energy storage degradation models and extend the formulation to unbalanced three-phase distribution systems.

REFERENCES

Aitzhan, N. Z., & Svetinovic, D. (2018). Security and Privacy in Decentralized Energy Trading Through Multi-Signatures, Blockchain and Anonymous Messaging Streams. *IEEE Transactions on Dependable and Secure Computing*, *15*, 840–852.

Ali, L., Muyeen, S., Bizhani, H., & Ghosh, A. (2021). A peer-to-peer energy trading for a clustered microgrid–Game theoretical approach. *International Journal of Electrical Power & Energy Systems*, *133*, 107307.

Dang, C., Zhang, J., Kwong, C.-P., & Li, L. (2019). Demand side load management for big industrial energy users under blockchain-based peer-to-peer electricity market. *IEEE Transactions on Smart Grid*, *10*(6), 6426–6435.

Di Silvestre, M. L., Gallo, P., Ippolito, M. G., Sanseverino, E. R., & Zizzo, G. (2018). A technical approach to the energy blockchain in microgrids. *IEEE Transactions on Industrial Informatics*, *14*(11), 4792–4803.

Dong, L., Zhang, K., Zhang, S., Zhang, T., Li, Y., & Qiao, J. (2025). Peer-to-peer transaction with voltage management strategy in distribution network considering trading risk. *Global Energy Interconnection*.

Hoque, M. M., Khorasany, M., Azim, M. I., Razzaghi, R., & Jalili, M. (2024). A framework for prosumer-centric peer-to-peer energy trading using network-secure export–import limits. *Applied Energy*, *361*, 122906.

Kang, J., Yu, R., Huang, X., Maharjan, S., Zhang, Y., & Hossain, E. (2017). Enabling localized peer-to-peer electricity trading among plug-in hybrid electric vehicles using consortium blockchains. *IEEE Transactions on Industrial Informatics*, *13*(6), 3154–3164.

Khorasany, M., Gazafroudi, A. S., Razzaghi, R., Morstyn, T., & Shafie-Khah, M. (2022). A framework for participation of prosumers in peer-to-peer energy trading and flexibility markets. *Applied Energy*, *314*, 118907.

Lüth, A., Zepter, J. M., Del Granado, P. C., & Egging, R. (2018). Local electricity market designs for peer-to-peer trading: The role of battery flexibility. *Applied Energy*, *229*, 1233–1243.

Morstyn, T., Farrell, N., Darby, S. J., & McCulloch, M. D. (2018). Using peer-to-peer energy-trading platforms to incentivize prosumers to form federated power plants. *Nature Energy*, *3*(2), 94–101.

Nasiri, S. (2023). A peer-to-peer energy trading framework in distribution systems considering network constraints. *arXiv preprint arXiv:2309.03132*.

Nikolaidis, A. I., Charalambous, C. A., & Mancarella, P. (2018). A graph-based loss allocation framework for transactive energy markets in unbalanced radial distribution networks. *IEEE Transactions on Power Systems*, *34*(5), 4109–4118.

Ping, J., Kong, S., Yan, Z., Xu, X., & Chen, S. (2026). Blockchain-based network-constrained peer-to-peer energy trading in a reconfigurable distribution network. *Applied Energy*, *405*, 127195.

Soto, E. A., Bosman, L. B., Wollega, E., & Leon-Salas, W. D. (2021). Peer-to-peer energy trading: A review of the literature. *Applied Energy*, *283*, 116268.

Tarashandeh, N., & Karimi, A. (2024). Peer-to-peer energy trading under distribution network constraints with preserving independent nature of agents. *Applied Energy*, *355*, 122240.

Tong, B., Zhang, M., Guo, Z., Teng, J., Qiu, D., Zheng, W., & Wang, X. (2026). A two-stage distributed optimization for non-convex P2P energy trading in prosumer-based distribution networks. *Applied Energy*, *423*, 128364.

Wu, J., Zhao, P., Li, L., Shi, F., & Li, B. (2023). Multi-microgrids distributed peer-to-peer energy trading in distribution system considering uncertainty risk. *International Journal of Electrical Power & Energy Systems*, *152*, 109234.

Yan, X., Song, M., Cao, J., Gao, C., Jing, X., Xia, S., & Ban, M. (2023). Peer-to-Peer transactive energy trading of multiple microgrids considering renewable energy uncertainty. *International Journal of Electrical Power & Energy Systems*, *152*, 109235.

Zhang, C., Wu, J., Zhou, Y., Cheng, M., & Long, C. (2018). Peer-to-Peer energy trading in a Microgrid. *Applied Energy*, *220*, 1–12.

Zheng, B., Wei, W., Chen, Y., Wu, Q., & Mei, S. (2022). A peer-to-peer energy trading market embedded with residential shared energy storage units. *Applied Energy*, *308*, 118400.

Zimmerman, R. D., Murillo-Sánchez, C. E., & Thomas, R. J. (2010). MATPOWER: Steady-state operations, planning, and analysis tools for power systems research and education. *IEEE Transactions on Power Systems*, *26*(1), 12–19.

International Conference on Engineering Innovation for Sustainable Development (ICESID 2026)
Faculty of Engineering, Ahmadu Bello University Zaria · 8–10 September 2026

ADVANCING SUSTAINABLE URBAN MOBILITY: A TRAFFIC-RELATED AIR QUALITY ASSESSMENT AT MAJOR ROAD INTERSECTIONS IN KANO METROPOLIS, NIGERIA

Nasiru Danlami[1], Ibrahim Umar Salihi[1], Muttaka Na'iya Ibrahim[1,*]
[1]*Civil Engineering Department, Bayero University, Kano, Nigeria*
Email: nassday@live.com, siumar.civ@buk.edu.ng, mnibrahim.civ@buk.edu.ng[*]
***Corresponding author**: Muttaka Na'iya Ibrahim
DOI: https://doi.org/10.67203/sp.ICESID.2026

ABSTRACT

Urban air quality deterioration driven by vehicular traffic is a critical public health challenge in rapidly growing Nigerian cities. Road intersections represent pollution hotspots where idling, acceleration, and deceleration generate elevated concentrations of harmful pollutants. This study assesses air quality at four major intersections in Kano metropolis by evaluating spatial-temporal pollutant variations and compliance with World Health Organization (WHO) and Nigerian Ambient Air Quality Standards (NAQS). Field measurements were conducted for eight weeks at the intersections; NNPC Mega (P1), Kwanar Sabo (P2), Aliko by Maiduguri Road (P3), and Gadar Lado (P4) intersections, with Hotoro GRA serving as a control site (P5). Concentrations of $PM_{1.0}$, $PM_{2.5}$, PM_{10}, CO, NO_2, SO_2, and total volatile organic compounds (TVOCs) were measured twice weekly on Sundays and Mondays during morning, afternoon, and evening periods using a multi-gas detector and air quality monitor. All four sites recorded pollutant concentrations significantly higher than the control site (intersection-to-control ratios: 3.5 – 8.6×; Welch's t-test, $p < 0.001$ for all pollutants). $PM_{2.5}$ was the dominant pollutant, exceeding WHO guidelines (15 µg/m³) by up to 13.9-fold on weekdays. At all four intersections, SO_2 exceeded the NAQS limit (0.048 ppm) on both measurement days, and NO_2 exceeded the NAQS limit (0.064 ppm) at three of the four intersections on Mondays. Weekday concentrations were 49 – 95% higher than weekend values across all parameters. Evening periods consistently produced the highest pollution levels. The signalized 4-way intersection (P2) recorded the highest overall pollution, while the T-junction (P3) recorded the lowest values, suggesting intersection geometry substantially influences pollutant dispersion. Air quality at major intersections in Kano metropolis frequently falls within moderate to severe pollution categories, posing substantial health risks to commuters, pedestrians, and roadside workers. Urgent implementation of intelligent traffic management, vehicle emission controls, and continuous monitoring systems is recommended.

Keywords: *Air quality assessment; traffic-related air pollution; road intersections; particulate matter; Kano metropolis; WHO; NAQS*

1. INTRODUCTION

Urban air quality has become a defining environmental and public health challenge in rapidly growing developing-world cities, where vehicular expansion frequently outpaces regulatory and infrastructural capacity (Emereibeole et al., 2023). Road traffic is a principal source of pollutants such as carbon monoxide (CO), nitrogen oxides (NOx), sulphur dioxide (SO_2), total volatile organic compounds (TVOCs) and particulate matter (PM), all of which are associated with adverse respiratory and cardiovascular outcomes (Chen et al., 2022; Amegah & Agyei-Mensah, 2017).

Road intersections are especially critical microenvironments within the urban transport network. Unlike free-flowing sections of road, intersections concentrate vehicle idling, deceleration and acceleration events tied to traffic signal phases, queue formation and geometric constraints, producing localized emission "hotspots" that can differ markedly from ambient background levels (Šarić et al., 2023; Hailu et al., 2024). Emission rates during acceleration and idling are disproportionately higher than during steady cruising, so the exposure experienced by commuters, traders and traffic personnel at junctions can be substantially elevated relative to general roadside conditions.

Kano, northwestern Nigeria's largest commercial hub with a population exceeding four million, exhibits many of the classic conditions associated with severe intersection pollution: high vehicular density, mixed heavy- and light-duty fleets, largely unsignalized or under-optimized junction control,

and a harmattan-dominated dry season that elevates background particulate loads through Saharan dust intrusion (Akinlade et al., 2020). Despite this, empirical, intersection-scale air quality data for Kano remain scarce compared with cities such as Lagos, Port Harcourt, Owerri and Warri, where similar assessments have been conducted (Nwankwo & Bamidele, 2025; Emereibeole et al., 2023). For context, the Ogbomoso study reported a wet-season particulate matter mean of 27.7 µg/m3, with spikes up to 70.15 µg/m3 at unpaved road intersections, attributed to heavy vehicular traffic, charcoal burning and seasonal harmattan dust (Nwankwo & Bamidele, 2025). In Owerri, particulate matter ranged from 8-27 µg/m3 at strategic intersections but reached 400-500 µg/m3 near open-air markets, while a co-monitored gaseous pollutant reached 0.055-0.089 ppm (approximately 100-160 µg/m3) at busy junctions, linked to peak-hour congestion and market waste dumpsites (Emereibeole et al., 2023). In Warri, an annual baseline particulate matter mean of 36.38 µg/m3 was recorded around petrochemical refinery buffer zones, with spikes exceeding 133 µg/m3 near major transport corridors and a co-monitored gaseous pollutant averaging 0.0063 ppm, reflecting industrial and heavy diesel-traffic emissions. These comparator values are broadly consistent with the intersection-level concentrations reported for Kano in the present study (Table 3), though direct comparison is limited by differences in monitoring season, averaging period and instrumentation across studies.

This study addresses that gap by systematically measuring $PM_{1.0}$, $PM_{2.5}$, PM_{10}, CO, NO_2, SO_2 and TVOC concentrations, together with temperature, relative humidity and the Air Quality Index (AQI), at four strategically selected road intersections and one residential control site in Tarauni Local Government Area, Kano State. The specific objectives are to (i) quantify and compare pollutant concentrations across intersections of differing geometry and traffic control; (ii) evaluate compliance with WHO and NAQS air quality guidelines; (iii) characterize temporal variation between weekday and weekend conditions and across morning, afternoon and evening peak periods; and (iv) draw evidence-based recommendations for traffic management and public health protection.

2. MATERIALS AND METHODS

2.1 Study Area

The study was conducted at four major road intersections and one residential control site within Kano metropolis, along the city's principal arterial corridors: Maiduguri Road (A3, the international corridor linking Kano to Borno, Yobe, Chad and Niger) and Zaria Road (A2, the national corridor linking Kano to Kaduna, Abuja and southwestern Nigeria). Sampling was carried out during the peak harmattan season (mid-December 2025 to mid-February 2026), characterized by Saharan dust intrusion (background PM_{10} frequently exceeding 100 µg/m3), low relative humidity (<20%) and a wide diurnal temperature range (15-35 °C). Four intersections and one control site were selected using stratified purposive sampling to capture a representative range of traffic-control regimes and geometric configurations, as summarized in Table 1.

Table 1: Classification of sampling stations

Code	Station	Traffic control	Geometry	Corridor
P1	NNPC Mega Intersection	Unsignalized	4-way cross	Maiduguri Rd (A3)
P2	Kwanar Sabo Intersection	Signalized	4-way cross	Secondary arterial
P3	Aliko Maiduguri Rd Intersection	Signalized	3-way T-junction	Maiduguri Rd (A3)
P4	Gadar Lado Intersection	Unsignalized	4-way cross	A2 / A3
P5	Hotoro GRA (Control)	None (residential)	N/A	Estate roads

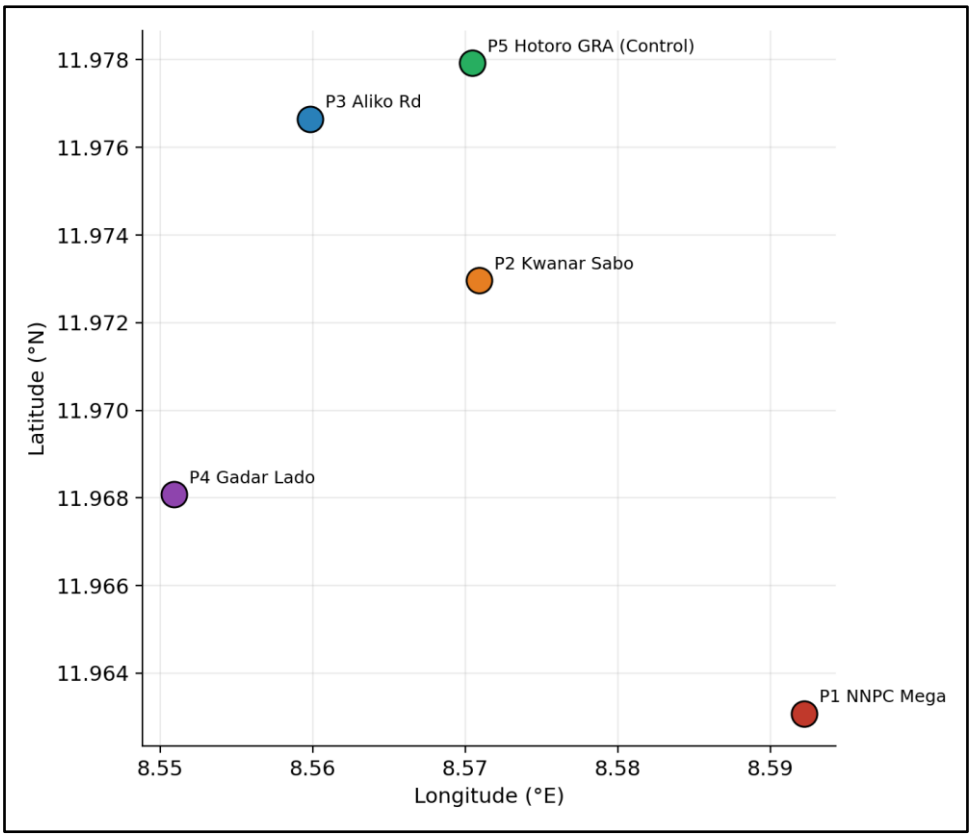

Figure 1: Spatial distribution of the five sampling stations in Tarauni LGA, Kano State

P1 (NNPC Mega) and P4 (Gadar Lado) are unsignalized four-way crossings characterized by high-speed, multi-directional approaches and a heavy proportion of inter-city trucks and articulated vehicles (35-45%). P2 (Kwanar Sabo) is a signalized four-way junction bounded by a partial street-canyon (motorcycle garage and buildings), which restricts pollutant dispersion. P3 (Aliko) is a signalized three-way T-junction with more open geometry. P5 (Hotoro GRA) is a low-density residential estate with negligible through-traffic (<50 vehicles/hour) and no signalized junction, serving as the non-intersection urban baseline.

2.2 Data Collection

Measurements were taken twice weekly - once on a working day (Monday) and once on a weekend day (Sunday) - over eight consecutive weeks, during three daily periods: morning peak (7:30-9:00 AM), midday off-peak (12:00-1:30 PM) and evening peak (4:30-6:00 PM). All readings were taken at 1.5 m height, corresponding to the breathing zone of drivers, pedestrians and traffic personnel.

Gaseous pollutants (CO, NO_2, SO_2) were measured using a calibrated Bosean BH-4S 4-in-1 portable multi-gas detector (Henan Bosean Electronic Technology Co., Ltd., China), configured with electrochemical sensor channels for CO (0-1000 ppm range, 1 ppm resolution), NO_2 (0-20 ppm range, 0.1 ppm resolution) and SO_2 (0-20 ppm range, 0.1 ppm resolution); manufacturer-stated accuracy ≤±5% F.S., response time ≤30 s, natural-diffusion sampling, and factory calibration with a 2-year rated sensor life. TVOC, together with particulate matter ($PM_{1.0}$, $PM_{2.5}$, PM_{10}), temperature, relative humidity and AQI were measured using a portable laser-scattering air quality monitor. At each visit, instruments were allowed to stabilize before recording; GPS coordinates were used to ensure identical sampling positions were revisited across the study period.

2.3 Standards and Data Analysis

Measured concentrations were compared against the WHO Global Air Quality Guidelines (2021) and the Nigerian Ambient Air Quality Standards (NAQS) under the National Environmental (Air Quality Control) Regulations (NESREA, 2014), summarized in Table 2. Descriptive statistics

(station means, weekday/weekend means, diurnal means) were computed from 207 valid station-period observations collected across the eight-week campaign, and pollutant exceedance ratios were calculated as the ratio of station mean concentration to the corresponding WHO guideline value. Standard deviations are reported alongside station means in Table 3. To test for differences in pollutant concentrations, one-way analysis of variance (ANOVA) was used to compare mean concentrations among the five stations for each pollutant, and Welch's independent-samples t-tests (unequal variances assumed) were used to compare weekday (Monday) versus weekend (Sunday) concentrations and intersection (P1-P4, pooled) versus control (P5) concentrations. All tests were evaluated at $\alpha = 0.05$ using the full station-period dataset (n up to 240 station-period-pollutant records per parameter, varying slightly by pollutant owing to isolated missing readings).

Table 2: WHO and NAQS air quality standards used for compliance assessment

Pollutant	WHO Guideline	NAQS Standard	Averaging period
$PM_{2.5}$	15 µg/m^3	35 µg/m^3	24-hour
PM_{10}	45 µg/m^3	150 µg/m^3	24-hour
NO_2	0.013 ppm	0.064 ppm	24-hour
SO_2	0.015 ppm	0.048 ppm	24-hour
CO	4 mg/m^3	10 mg/m^3	8-hour

3. RESULTS AND DISCUSSION

A total of 207 valid station-period observations were recorded across the eight-week sampling campaign. Table 3 summarizes the overall mean pollutant concentrations by station.

Table 3: Overall mean ± standard deviation of pollutant concentrations by station (entire sampling period)

Station	$PM_{2.5}$ (µg/m3)	$PM_{1.0}$ (µg/m3)	PM_{10} (µg/m3)	CO (mg/m3)	NO_2 (ppm)	SO_2 (ppm)	TVOC (mg/m3)
P1	130.8 ± 50.0	72.6 ± 27.2	142.0 ± 60.9	5.40 ± 3.15	0.081 ± 0.061	0.119 ± 0.067	0.58 ± 1.42
P2	148.7 ± 76.6	83.6 ± 40.6	148.7 ± 65.5	7.94 ± 5.86	0.121 ± 0.068	0.140 ± 0.061	2.65 ± 4.16
P3	91.6 ± 48.5	53.6 ± 25.9	98.5 ± 52.0	4.43 ± 4.13	0.049 ± 0.065	0.090 ± 0.068	0.48 ± 1.41
P4	109.3 ± 59.7	63.9 ± 32.5	122.6 ± 67.5	4.19 ± 3.92	0.091 ± 0.053	0.111 ± 0.077	0.31 ± 0.14
P5 (control)	30.0 ± 10.3	16.8 ± 6.7	33.1 ± 12.0	0.56 ± 0.86	0.006 ± 0.02	0.041 ± 0.048	0.02 ± 0.05

Across every pollutant, P5 (control) recorded the lowest concentrations by a wide margin, confirming its suitability as a non-intersection baseline. P2 (Kwanar Sabo) recorded the highest mean concentrations for nearly all parameters, consistent with its partial street-canyon geometry, signalized stop-and-go operation, and mixed commercial/motorcycle traffic. P3, the open T-junction, consistently recorded the lowest pollutant levels among the four intersections, suggesting that junction geometry - specifically the number of conflicting approaches and the degree of physical enclosure - exerts a measurable influence on local pollutant accumulation.

The station-to-station differences summarized in Table 3 were confirmed by one-way ANOVA, which found significant effects of station on mean concentration for every pollutant ($PM_{2.5}$: $F(4,235) = 34.5$, $p < 0.001$; $PM_{1.0}$: $F = 37.6$, $p < 0.001$; PM_{10}: $F = 32.6$, $p < 0.001$; CO: $F = 21.3$, $p < 0.001$; NO_2: $F = 29.7$, $p < 0.001$; SO_2: $F = 19.0$, $p < 0.001$; TVOC: $F = 12.2$, $p < 0.001$). Welch's t-tests further confirmed that concentrations at the four intersections (P1-P4, pooled) were significantly higher than at the control site (P5) for every pollutant (all $p < 0.001$, t-values ranging from 5.1 for TVOC to 19.4 for $PM_{1.0}$), and that weekday (Monday) concentrations were significantly higher than weekend (Sunday) concentrations for every pollutant ($p < 0.05$ for all seven parameters, $p < 0.001$ for $PM_{2.5}$, $PM_{1.0}$, PM_{10} and SO_2). These results provide statistical support for the "significantly higher" language used elsewhere in this paper to describe intersection-to-control and weekday-to-weekend contrasts.

3.1 Particulate Matter ($PM_{1.0}$, $PM_{2.5}$, PM_{10})

Particulate matter was the most critical pollutant class recorded in this study. Figure 2 compares overall mean $PM_{1.0}$, $PM_{2.5}$ and PM_{10} concentrations across the five stations against WHO and NAQS reference limits.

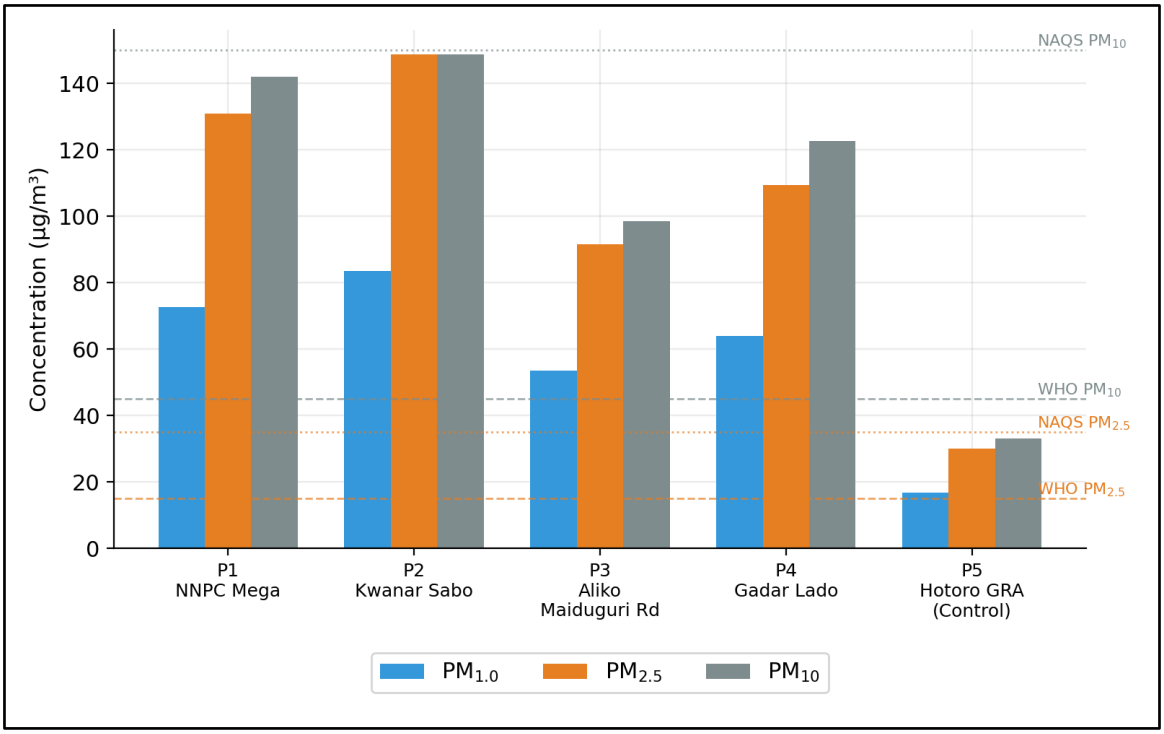

Figure 2: Overall mean particulate matter concentrations by station

Mean $PM_{2.5}$ concentrations at the four intersections (91.6-148.7 µg/m3) exceeded the WHO 24-hour guideline (15 µg/m3) by factors of 6.1 to 9.9, and the NAQS limit (35 µg/m3) by factors of 2.6 to 4.2. Even the control site (30.0 µg/m3) exceeded the WHO guideline by a factor of 2.0, though it remained below the NAQS threshold, indicating a substantial regional background contribution from harmattan dust in addition to traffic-related emissions. PM_{10} followed a similar pattern, with intersection means (98.5-148.7 µg/m3) consistently exceeding the WHO guideline (45 µg/m3) while remaining, on average, below the more permissive NAQS limit (150 µg/m3) except during isolated high-traffic episodes. Weekday-weekend contrasts were pronounced. Figure 3 and Figure 5 present station-level $PM_{2.5}$ and PM_{10} concentrations split by sampling day.

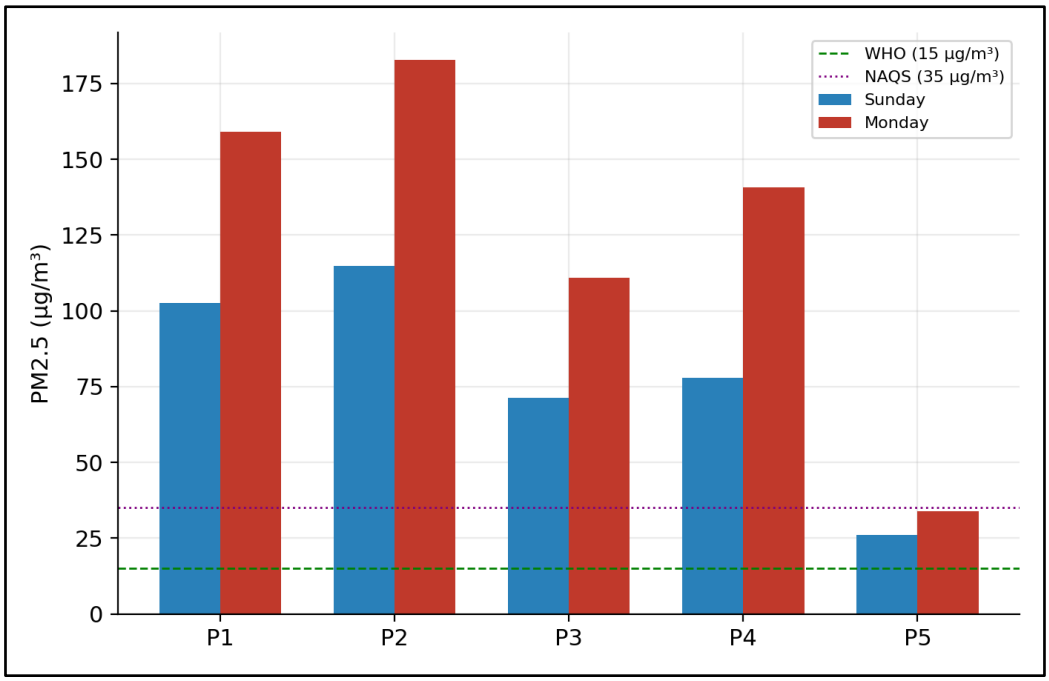

Figure 3: Weekend (Sunday) versus weekday (Monday) $PM_{2.5}$ by station

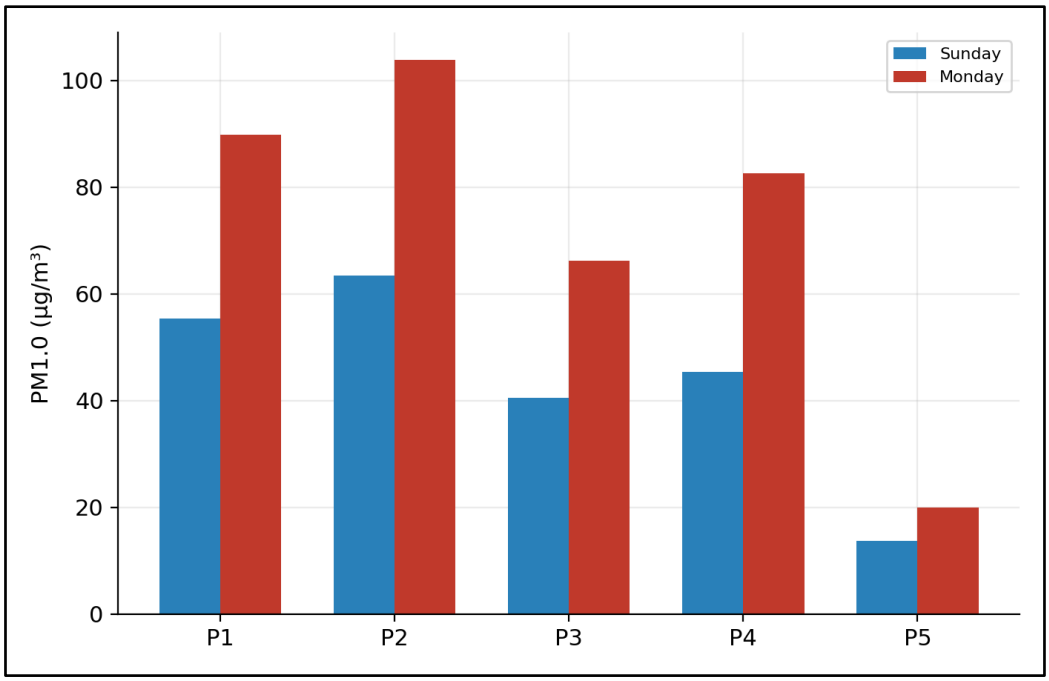

Figure 4: Weekend versus weekday $PM_{1.0}$ (ultrafine particulate matter) by station

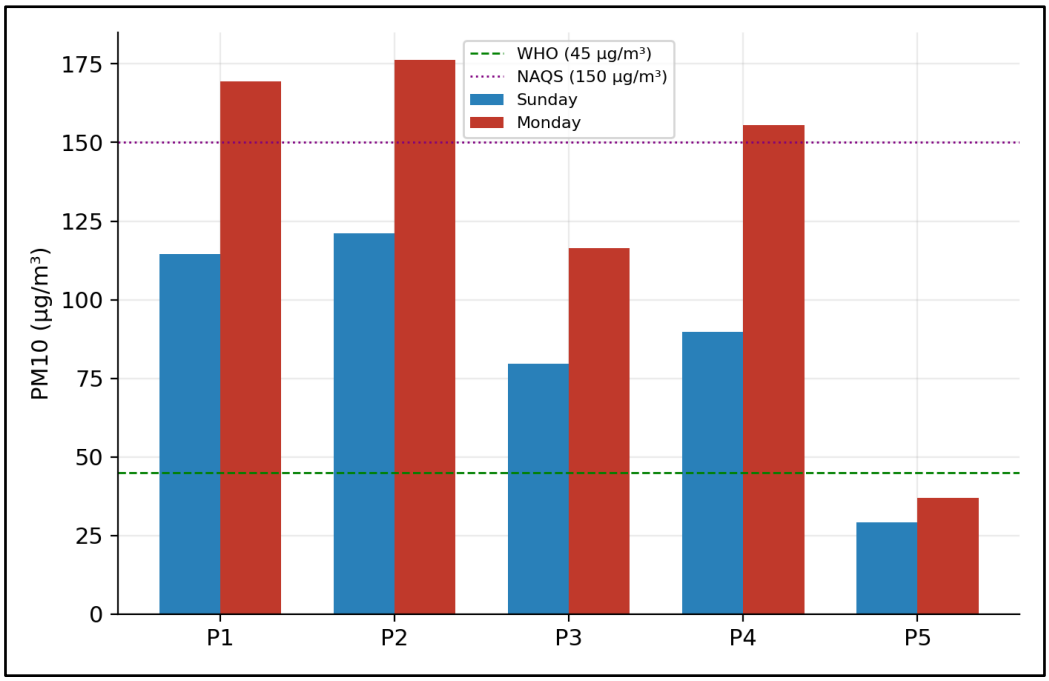

Figure 5: Weekend versus weekday PM_{10} by station

$PM_{2.5}$ concentrations on Mondays were 30-80% higher than on Sundays at all four intersections (e.g., P2: 114.7 µg/m3 on Sunday versus 182.7 µg/m3 on Monday), while the control site increased by a comparatively modest margin (26.1 to 33.9 µg/m3), confirming that the weekday excess is predominantly traffic-driven rather than purely meteorological. Ultrafine particulate matter ($PM_{1.0}$), attributable primarily to combustion aerosol from vehicle exhaust and diesel acceleration events, exhibited the same weekday elevation, with P2 rising from 63.4 µg/m3 (Sunday) to 103.8 µg/m3 (Monday).

Diurnal patterns (Figure 6) show a consistent rise from morning to evening across all stations, with evening peak-period concentrations 30-70% higher than morning concentrations. This pattern reflects the compounding effect of heavier evening traffic volumes, hotter engine operation, and the day's accumulated pollutant loading in the absence of strong atmospheric mixing during the harmattan season.

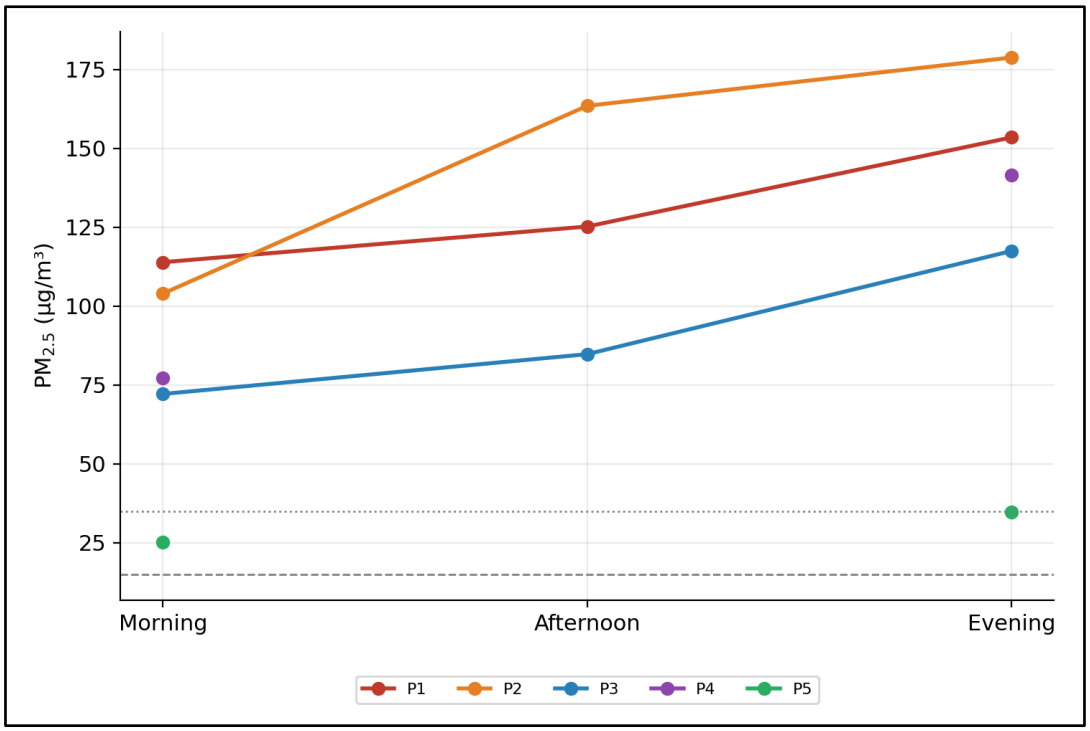

Figure 6: Diurnal variation of $PM_{2.5}$ across sampling stations

The eight-week temporal trend of mean $PM_{2.5}$ concentration (Figure 7) further shows that although week-to-week variability exists (attributable to fluctuating harmattan dust intensity and traffic volume), intersection stations remained persistently elevated above the control site throughout the entire monitoring period, with a marked spike in Week 8 across all stations, coincident with intensified regional dust loading toward the end of the harmattan season.

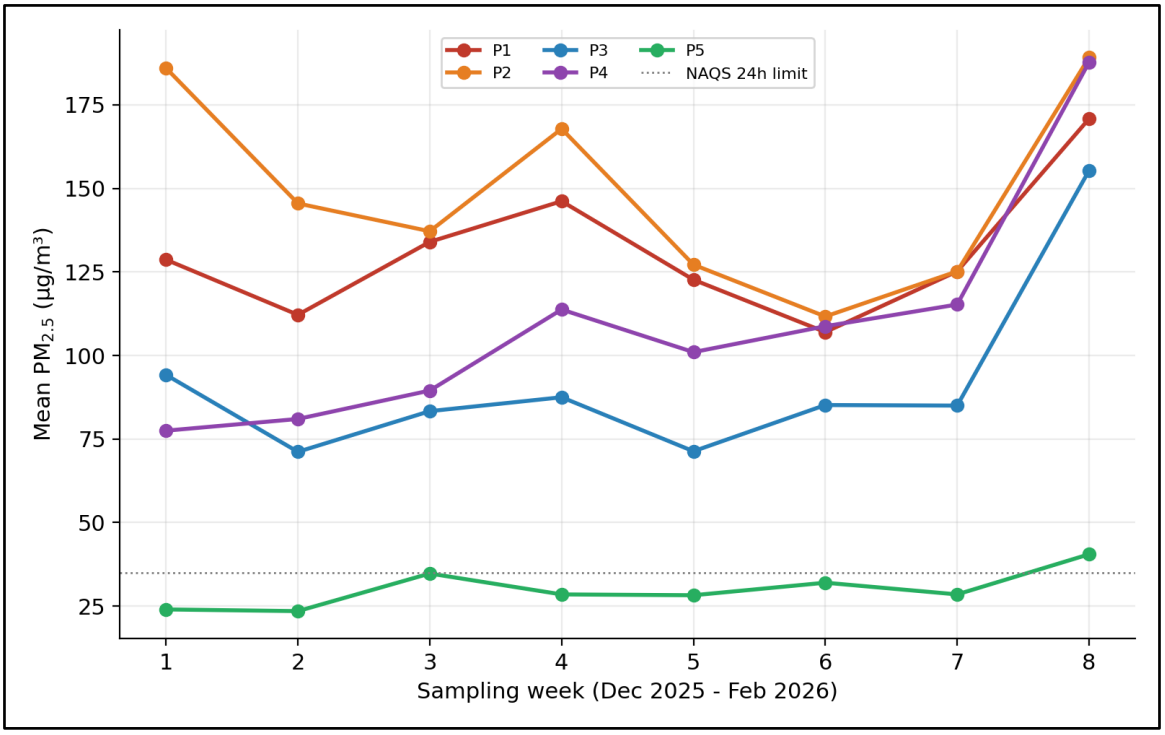

Figure 7: Eight-week temporal trend of mean $PM_{2.5}$ concentration by station

The pronounced weekday-weekend and diurnal contrasts observed across all pollutants - with Monday and evening-period concentrations consistently the highest - indicate that traffic volume and congestion state, rather than fixed emission sources, are the principal short-term determinants of

exposure at these locations. This has direct implications for exposure-reduction strategies, since even modest reductions in queuing and idling time at the most heavily trafficked junctions (P1 and P2) could yield disproportionate air quality benefits.

3.2 Gaseous Pollutants (CO, NO_2, SO_2)

Figure 8 presents overall mean CO, NO_2 and SO_2 concentrations by station relative to WHO and NAQS limits.

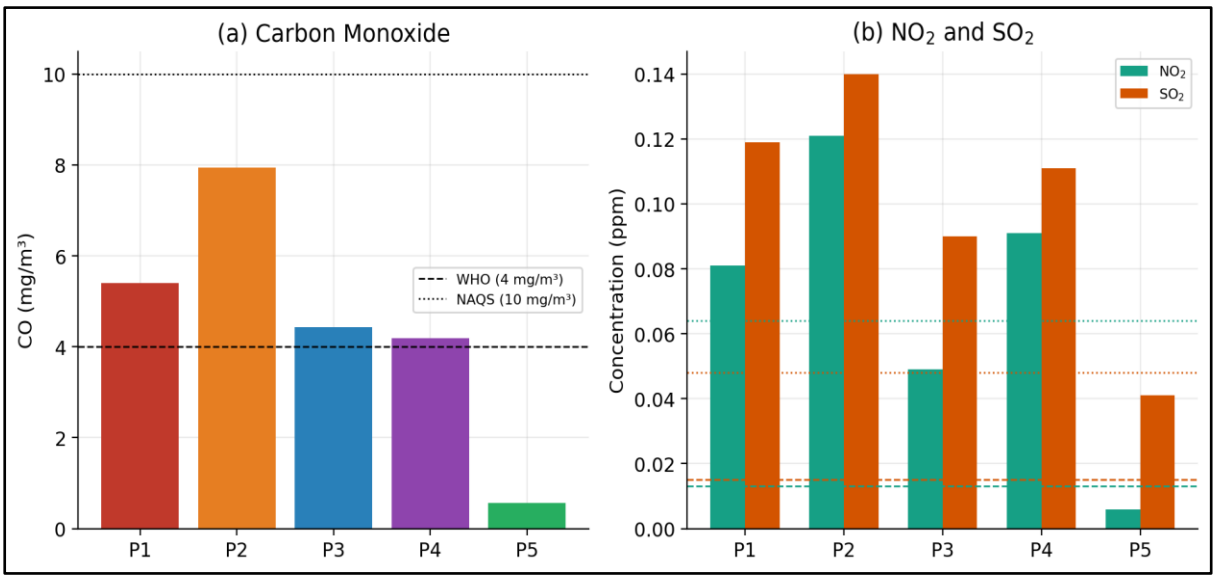

Figure 8: Overall mean gaseous pollutant concentrations by station

Mean CO concentrations at P1 (5.40 mg/m3) and P2 (7.94 mg/m3) exceeded the WHO guideline (4 mg/m3), while P3, P4 and P5 remained, on average, compliant. However, individual evening-period readings at P2 reached as high as 11.5 mg/m3 on Mondays, approaching the NAQS 8-hour limit (10 mg/m3) and reflecting severe idling combined with restricted dispersion from the partial street-canyon at that junction.

NO_2 and SO_2 concentrations were consistently elevated at all four intersections relative to WHO guidelines (0.013 ppm and 0.015 ppm respectively), by factors of up to 9.3x for NO_2 and 9.3x for SO_2 at P2 (0.121 ppm / 0.013 ppm ≈ 9.31 and 0.140 ppm / 0.015 ppm ≈ 9.33, respectively; the near-identical values are a numerical coincidence rather than a rounding artefact). Monday NO_2 concentrations at P2 (0.150 ppm) exceeded even the more permissive NAQS limit (0.064 ppm) by a factor of approximately 2.3, identifying this junction as the most critical NO_2 hotspot in the study. Notably, SO_2 at the control site rose to a mean of 0.041 ppm (and individual Monday values above 0.06 ppm), exceeding the WHO guideline even in the residential control area - evidence that SO_2 pollution in Kano is not confined to intersection microenvironments but reflects a broader urban emissions background, likely including generator use and fuel combustion beyond road traffic. Weekday-weekend and station-level comparisons for CO, NO_2 and SO_2 are presented in Figures 9-11.

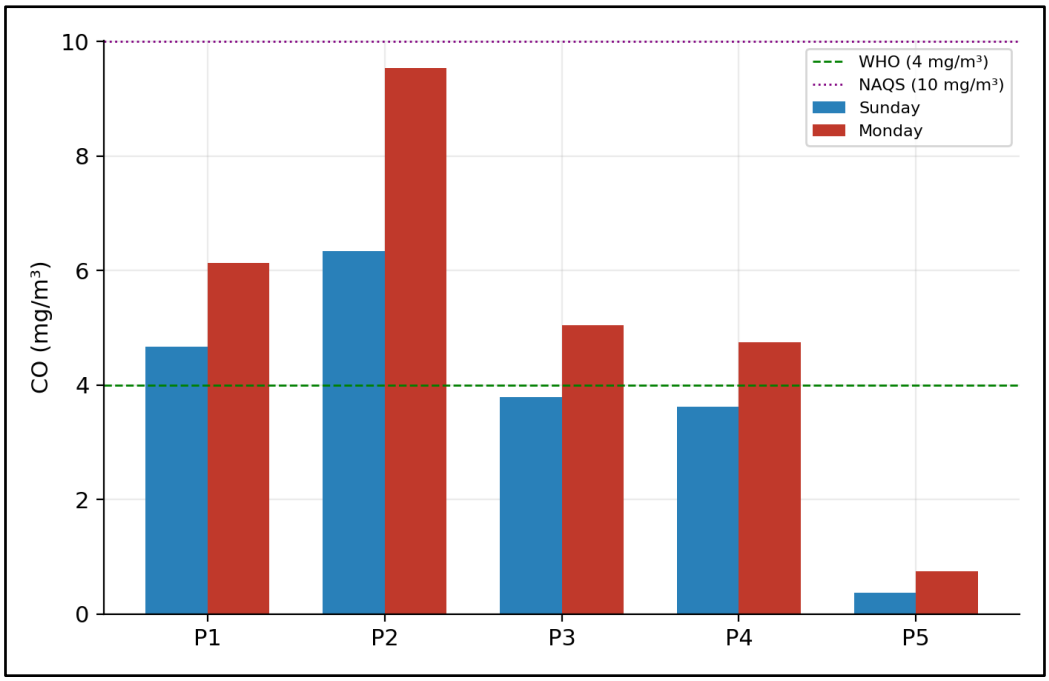

Figure 9: Weekend versus weekday Carbon Monoxide (CO) by station

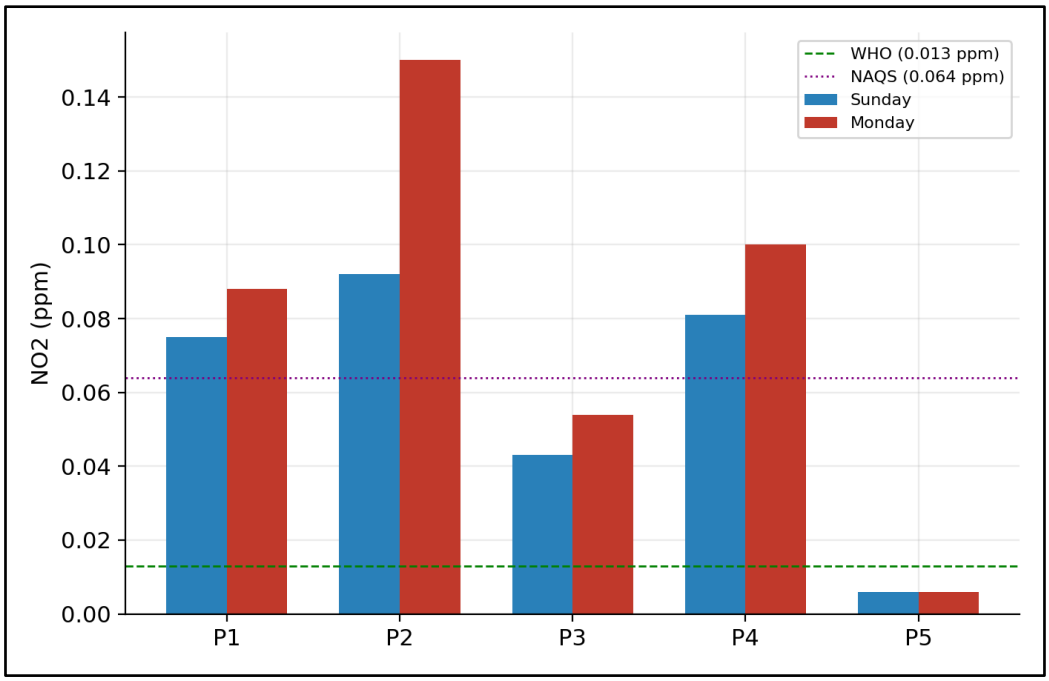

Figure 10: Weekend versus weekday Nitrogen Dioxide (NO_2) by station

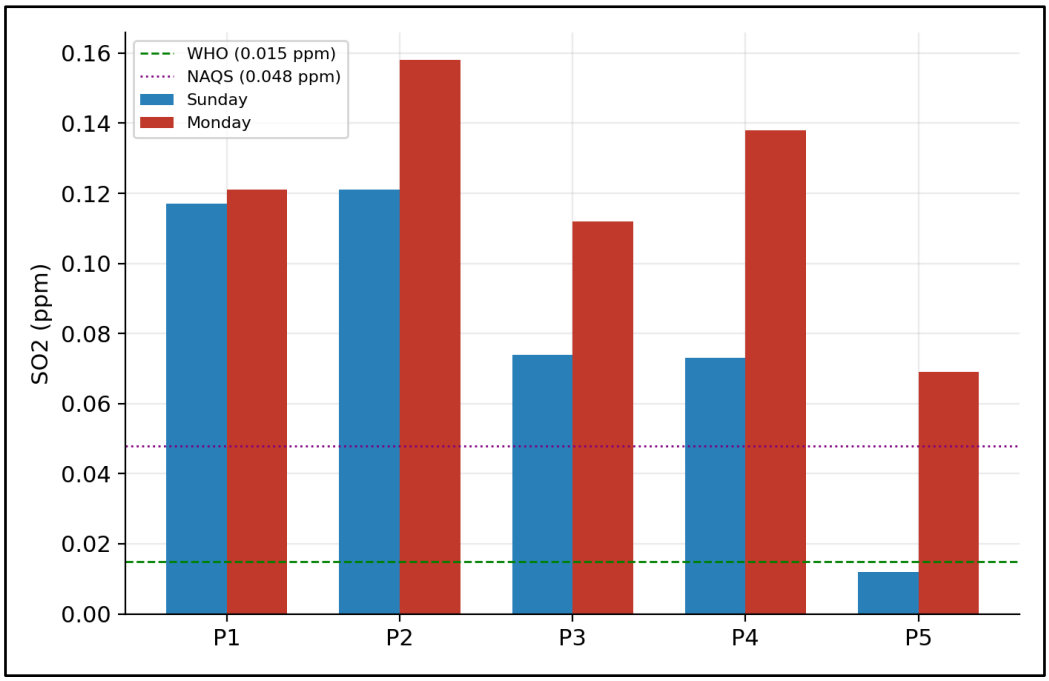

Figure 11: Weekend versus weekday Sulphur Dioxide (SO_2) by station

Across all three gaseous pollutants, Monday concentrations exceeded Sunday concentrations by 15-90%, with the largest relative increases recorded at P2, mirroring the pattern observed for particulate matter and reinforcing the conclusion that weekday commercial and inter-city traffic is the dominant driver of intersection-scale pollution in the study area.

3.3 Total Volatile Organic Compounds (TVOC)

TVOC concentrations, associated with fuel evaporation and incomplete combustion, were markedly higher at P2 (2.65 mg/m3) than at any other station - roughly 4.6 to 8.5 times the levels recorded at the other three intersections (P1: 4.6x; P3: 5.5x; P4: 8.5x) (Figure 12). This is consistent with the dense motorcycle and commercial-taxi traffic and fuel-vending activity historically associated with this junction, and suggests that fuel-handling and idling-related VOC emissions, rather than through-traffic alone, may be an important local contributor at this specific site.

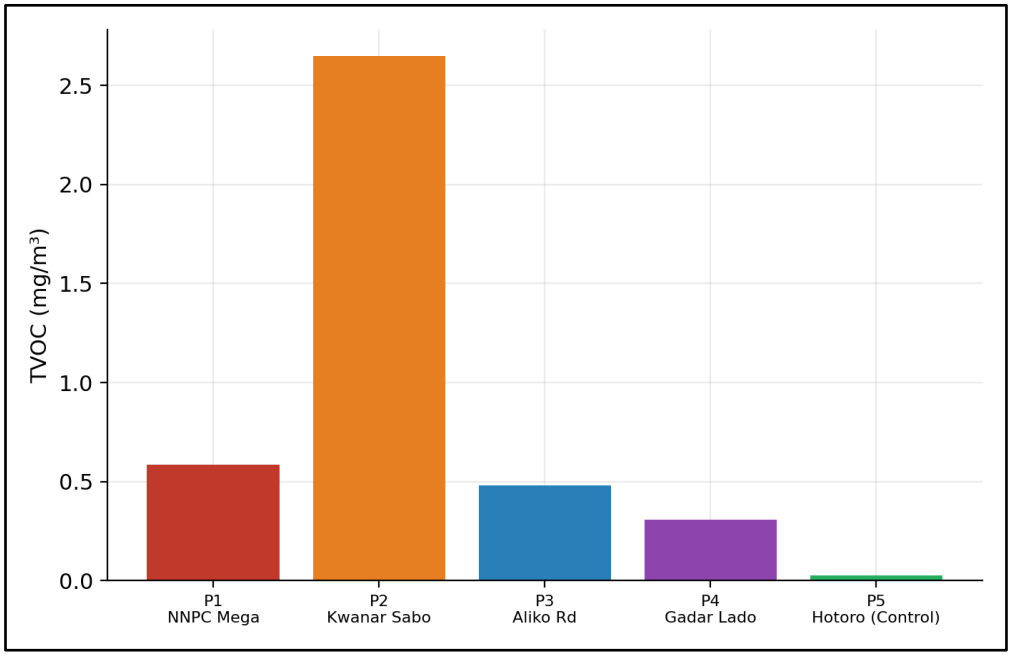

Figure 12: Overall mean TVOC concentration by station

3.4 Compliance with Air Quality Standards

Figure 13 summarizes pollutant-specific exceedance ratios (station mean concentration divided by the corresponding WHO guideline value) across all five stations, providing a unified view of relative severity across pollutant types.

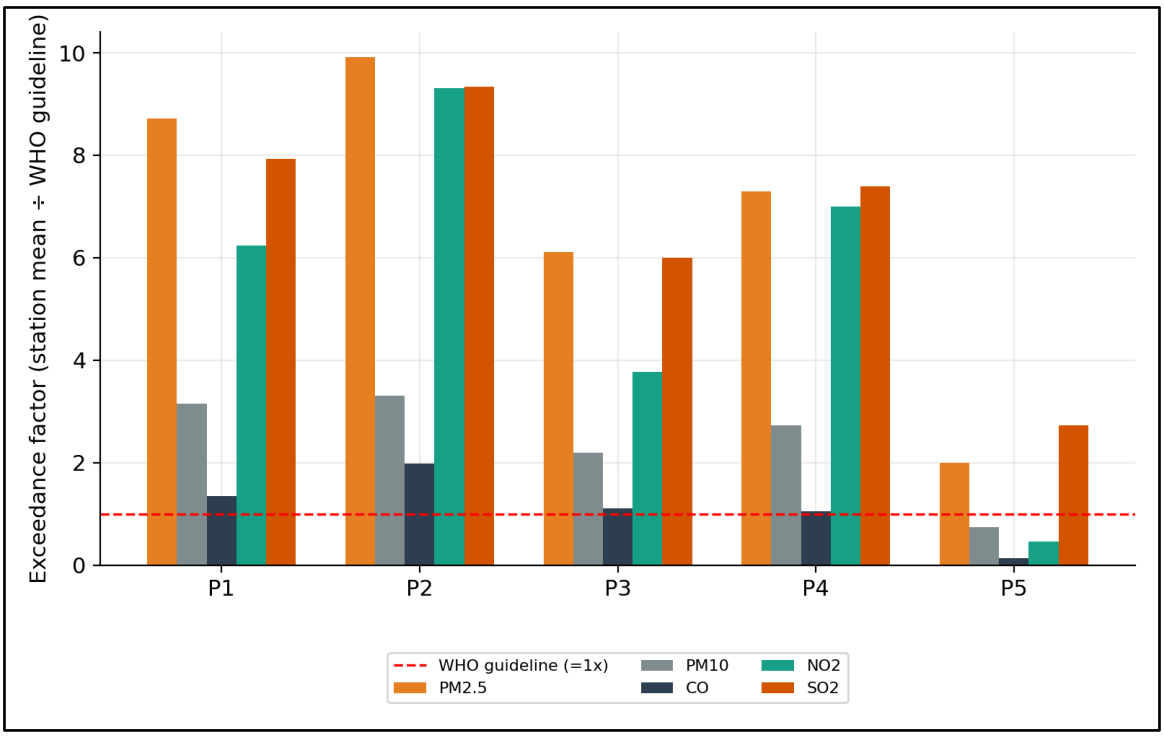

Figure 13: Pollutant exceedance ratios relative to WHO Air Quality Guidelines

$PM_{2.5}$ and NO_2 emerge as the pollutants of greatest concern, with exceedance ratios reaching approximately 9.9x and 9.3x, respectively, at P2. CO showed the smallest relative exceedance, remaining close to or below the WHO guideline at P3, P4 and P5. The ranking P2 > P1 > P4 > P3 > P5 holds exactly for the particulate pollutants (PM2.5, PM1.0, PM10) and for SO2, while CO, NO2 and TVOC show minor rank reversals between P1, P3 and P4 (e.g., P4 > P1 for NO2; P3 > P4 for CO and TVOC) (Figure 13). This pattern nonetheless mirrors the traffic-control and geometric classification in Table 1: the signalized, partially enclosed four-way junction (P2) is the most polluted, the open T-junction (P3) is generally among the least polluted of the four intersections, and the residential control site (P5) is consistently and substantially cleaner than any intersection.

This consistent elevation of pollutant concentrations at intersections relative to the control site (by factors of roughly 3.5x to 8.6x depending on pollutant) confirms that vehicular traffic is the dominant local source of air pollution at the studied locations, in agreement with comparable studies conducted at road junctions in Ogbomoso and Owerri, Nigeria (Nwankwo & Bamidele, 2025; Emereibeole et al., 2023) and in Warri Metropolis, where NO_2, SO_2, CO and PM_{10} levels at major junctions similarly approached or exceeded national standards. The results further indicate that intersection geometry and control type modulate pollutant accumulation: the partially enclosed, signalized four-way junction (P2) consistently recorded the highest concentrations, plausibly reflecting a street-canyon effect that traps pollutants and repeated stop-start cycling at the signal, while the open three-way T-junction (P3) allowed comparatively better dispersion. This is consistent with findings that intersection geometry meaningfully affects urban air pollution management outcomes (Šarić et al., 2023).

4. CONCLUSION

This study assessed traffic-related air quality at four major road intersections and one residential control site in Tarauni Local Government Area, Kano State, over an eight-week harmattan-season campaign. The results show that road intersections are significant, geometry- and control-dependent pollution hotspots, with $PM_{2.5}$, $PM_{1.0}$, PM_{10}, NO_2 and SO_2 concentrations consistently exceeding WHO

Air Quality Guidelines - and, for $PM_{2.5}$ and NO_2 in particular, frequently exceeding the more permissive Nigerian Ambient Air Quality Standards as well. The signalized, partially enclosed Kwanar Sabo intersection (P2) recorded the highest pollution levels across nearly all parameters, while the open T-junction (P3) recorded the lowest among the four intersections, underscoring the influence of junction geometry on local air quality. Weekday concentrations were consistently higher than weekend concentrations, and evening peak periods recorded the highest pollutant loads, confirming that vehicular traffic volume and congestion are the principal drivers of intersection-scale air pollution in the study area. These findings highlight an urgent need for targeted traffic management, vehicle emission control and continuous air quality monitoring at major Kano intersections to protect the health of commuters, roadside traders and traffic personnel.

A key limitation of this study is that sampling was confined to the harmattan season (mid-December 2025 to mid-February 2026), a period characterized by elevated regional background particulate loading from Saharan dust intrusion. Because harmattan-season background PM levels are substantially higher than during the wet season, the absolute pollutant concentrations and exceedance ratios reported here may not be representative of year-round conditions, and the relative contribution of traffic versus meteorology to observed pollution levels cannot be fully disentangled from a single-season campaign. Findings on comparative station rankings and weekday/weekend or diurnal contrasts are likely more robust to this limitation than the absolute concentration values, since traffic patterns rather than dust loading primarily drive these relative differences. Future work should extend monitoring across seasons, including the wet season, and incorporate traffic-count data to more precisely apportion intersection pollution between exhaust emissions and non-exhaust road-dust resuspension.

5. RECOMMENDATIONS

- Deploy intelligent/adaptive traffic signal systems at high-volume junctions (notably P1 and P2) to reduce idling time and queue lengths.
- Enforce regular vehicle inspection and emission-testing programmes, with priority given to the heavy-duty and inter-city fleet using the A2/A3 corridors.
- Improve road-surface conditions at unsignalized junctions to reduce dust resuspension contributing to PM_{10} loading.
- Establish vegetative buffer zones and roadside green belts between major intersections and adjacent residential and commercial areas.
- Install permanent, continuous air quality monitoring stations at the most heavily polluted junctions to support real-time public health advisories.
- Extend future monitoring across the wet season to separate meteorological (harmattan dust) from traffic-driven contributions to particulate matter.

ACKNOWLEDGEMENTS

The authors acknowledge the Department of Civil Engineering, Faculty of Engineering, Bayero University, Kano, for logistical and technical support during the field campaign. The authors also thank Abu Precious Isah and Mikail Jibrin Gimba for data collection and analysis, and all field assistants who supported the eight-week sampling exercise.

REFERENCES

Akinlade, G. O., Olaniyi, H. B., & Abdulkareem, A. S. (2020). Meteorological influences on air quality in Northern Nigeria. Journal of Atmospheric and Climate Science, 10(3), 289-302.

Amegah, A. K., & Agyei-Mensah, S. (2017). Urban air pollution in sub-Saharan Africa: Time for action. Environmental Pollution, 220, 738-743.https://doi.org/10.1016/j.envpol.2016.09.042

Chen, H., Kwong, J. C., Copes, R., et al. (2022). Living near major roads and the risk of chronic disease: A population-based cohort study. Environmental Health Perspectives, 130(4), 047003. https://doi.org/10.1289/EHP7673

Emereibeole, E. I., Mgbeahuruike, L. U., Uyo, C. N., Unegbu, R. N., & Edo, F. A. (2023). Traffic air pollution and urban sustainability: an assessment of strategic road intersections in Owerri urban, Nigeria. Environmental Quality Assessment.

Hailu, Y., Taye, B., & Mekonnen, A. (2024). Assessment of traffic-related air pollution at major intersections in African cities. Urban Climate, 53, 101673. https://doi.org/10.1016/j.uclim.2023.101673

NESREA (2014). National Environmental (Air Quality Control) Regulations. Nigerian Ambient Air Quality Standards. Federal Republic of Nigeria.

Nwankwo, C. O., & Bamidele, O. A. (2025). Air pollution from road traffic at intersections: evidence from Ogbomoso, Nigeria. American Journal of Interdisciplinary Research in Engineering and Sciences, 12(3). ISSN 2994-3175. https://sadijournals.org/index.php/ajires

Šarić, A., Sulejmanović, S., Albinović, S., Pozder, M., & Ljevo, Ž. (2023). The role of intersection geometry in urban air pollution management. Sustainability, 15(6), 5234. https://doi.org/10.3390/su15065234

World Health Organization (2021). WHO Global Air Quality Guidelines: Particulate matter ($PM_{2.5}$ and PM_{10}), ozone, nitrogen dioxide, sulfur dioxide and carbon monoxide. WHO, Geneva.

International Conference on Engineering Innovation for Sustainable Development (ICESID 2026)
Faculty of Engineering, Ahmadu Bello University Zaria · 8–10 September 2026

ASSESSMENT OF GROUNDWATER QUALITY AND IRRIGATION SUITABILITY IN JERE LGA, BORNO STATE: ENGINEERING SOLUTIONS FOR SUSTAINABLE AGRICULTURAL DEVELOPMENT IN NIGERIA

Aliyu Salisu Ibrahim[1,*], Muhammad Muhammad Abdulsalam[2], Usman Butu Tukur[1]

[1]*Ahmadu Bello University, Zaria-Nigeria*

[2]*Agricultural Graduate Association of Nigeria (AGAN), Suit B3 Shamras Plaza Opp. Murtala Park Bosso Road, Minna, Niger State-Nigeria*

Email: get2salisu4real1980@gmail.com*, mm.assalaam@gmail.com, khalifaut@gmail.com

***Corresponding author**: Aliyu Salisu Ibrahim

DOI: https://doi.org/10.67203/sp.ICESID.2026

ABSTRACT

Groundwater is the principal domestic and irrigation water source in Jere Local Government Area (LGA), Borno State, Nigeria, but population growth, agriculture and inadequate sanitation threaten its quality. This study assessed water from five boreholes (BH1-BH5), five hand-dug wells (HW1-HW5) and one lake source (LW1) using physicochemical and bacteriological analyses, Water Quality Index (WQI), and irrigation indices (SAR, Na%, KR, PI and RSC). pH ranged from 6.7-7.5, EC from 420-1,210 µS/cm and TDS from 280-790 mg/L. Nitrate ranged from 12.5-72.6 mg/L, with HW3-HW5 exceeding 50 mg/L. All hand-dug wells and the lake exceeded 5 NTU turbidity and were positive for E. coli, whereas boreholes had turbidity below 5 NTU and no detected E. coli. WQI values of 42.6-57.8 classified boreholes as good, while HW3-HW5 were unsuitable for drinking. All sources were generally suitable for irrigation, but HW3-HW5 were classified as permissible and require active sodium-management measures. Engineering responses include priority boreholes (80-120 m depth; 150 mm PVC casing; gravel pack and sanitary seal), multi-barrier treatment for hand-dug wells, wellhead protection, differentiated irrigation management, and tiered monitoring. These interventions translate the empirical findings into practical measures supporting SDGs 2, 3 and 6.

Keywords: *groundwater quality; engineering solutions; water treatment; irrigation management; borehole design; sustainable development*

1. INTRODUCTION

Groundwater is a critical resource for domestic supply, agriculture and economic activity, particularly in regions where surface-water infrastructure is inadequate. In Jere Local Government Area (LGA), Borno State, communities depend heavily on boreholes and hand-dug wells, while increasing population, intensive agriculture, waste disposal and inadequate sanitation create pathways for groundwater contamination. Shallow wells are especially vulnerable because of their hydraulic connection with surface activities, including septic-tank seepage, agricultural runoff, livestock wastes and refuse leachate.

Groundwater-quality assessment increasingly combines physicochemical and bacteriological indicators with integrated indices. Water Quality Index (WQI) provides a single decision-support measure for drinking-water quality, while Sodium Adsorption Ratio (SAR), Sodium Percentage (Na%), Kelly Ratio (KR), Permeability Index (PI) and Residual Sodium Carbonate (RSC) provide complementary evidence for irrigation suitability. Nigerian studies have reported nitrate enrichment, microbial contamination and spatial variation associated with urbanisation, waste-management practices and land use (Banerjee et al., 2023; Ezechinyere & Stanislaus, 2023; Abanyie et al., 2023; Opasola et al., 2025; Thomas, 2023).

Despite these findings elsewhere, empirical information integrating drinking-water and irrigation suitability in Jere LGA remains limited. This study therefore evaluates selected groundwater and surface-water sources to establish a baseline for evidence-based water-resource management. The objectives were to determine major physicochemical parameters; assess bacteriological quality through

coliform and E. coli detection; compare results with WHO and Nigerian drinking-water standards; calculate WQI and irrigation-quality indices; and translate the empirical findings into engineering interventions. The work directly addresses the conference sub-themes of Innovative Resource Utilization and Management and Emerging Technologies for Safe Engineering Practices and Environmental Protection.

2. METHODOLOGY

2.1 Study Area

The study was conducted in Jere LGA, Borno State, north-eastern Nigeria, between 11°45′N-11°55′N and 13°05′E-13°20′E. The area has distinct wet and dry seasons, annual rainfall of approximately 500-700 mm and mean temperatures of 25-40°C. The geology is dominated by Chad Formation sediments comprising sands, silts and clays that host productive aquifers. Farming, livestock rearing, trading and small-scale commercial activities are major land uses and potential pressures on groundwater quality (NMA, 2008).

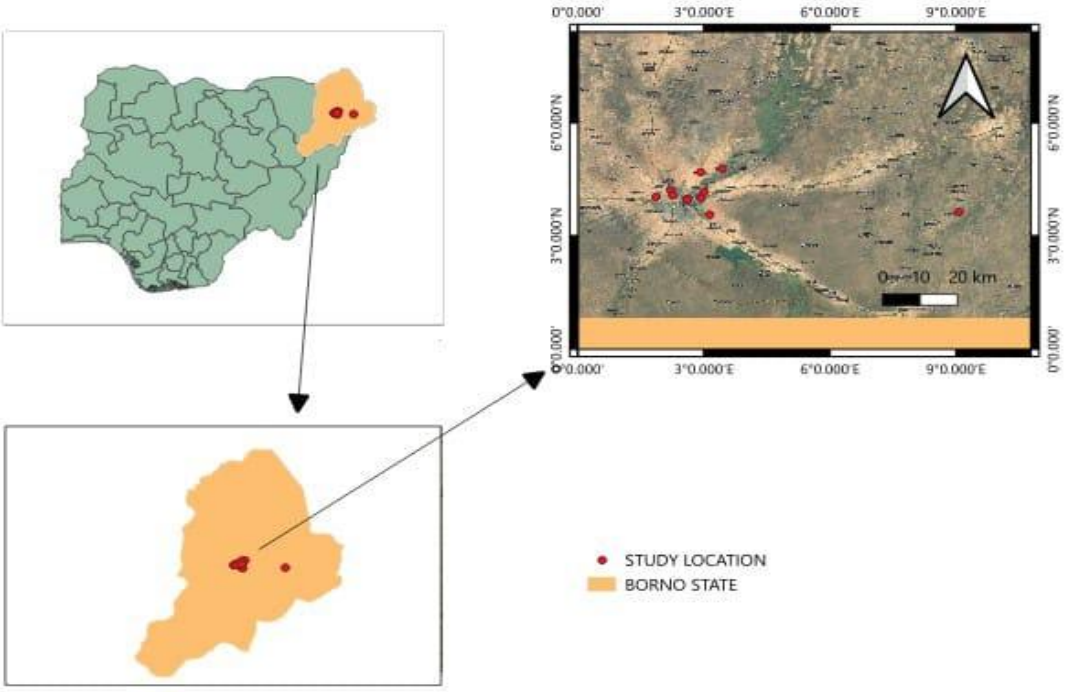

Figure 1: Map of the study area (Source: QGIS 3.44.12)

2.2 Sampling Locations and Collection

Eleven sampling locations were selected: five boreholes (BH1–BH5), five hand-dug wells (HW1–HW5) and one lake source (LW1). Selection considered accessibility, usage intensity, population served and proximity to potential contamination sources. Samples were collected in pre-cleaned 1-L polyethylene bottles following American Public Health Association (APHA, 2017); bacteriological samples were collected in sterile containers, transported in ice-packed coolers, and physicochemical analyses were completed within 24 h.

Table 1: *Sampling Locations and Water Sources*

Sample Code	Water Source	Location
BH1	Borehole	Cross Na Mala
BH2	Borehole	Gomari Airport
BH3	Borehole	Mairi Kuwait
BH4	Borehole	Mashamari
BH5	Borehole	Custom Area
HW1	Hand-dug Well	Jakana
HW2	Hand-dug Well	Dusuman
HW3	Hand-dug Well	Gongulong
HW4	Hand-dug Well	Old Maiduguri Road
HW5	Hand-dug Well	Shuwari
LW1	Lake Water	Coca-Cola Area

2.3 Parameters Analyzed

Analysed parameters comprised pH, temperature, electrical conductivity (EC), total dissolved solids (TDS), turbidity, hardness, nitrate, chloride, colour, acidity, alkalinity, total coliform count and E. coli presence. Laboratory analyses were conducted at the Department of Soil Science, Faculty of Agriculture, Ahmadu Bello University, Zaria.

2.4 Analytical Methods and Instrumentation

Physicochemical analyses followed APHA (2017): pH by electrometric method (4500-H^+ B; Jenway 370); EC by conductivity (2510 B; Jenway 470); TDS by gravimetry at 180°C; turbidity by nephelometry (2130 B; HACH 2100P); hardness by EDTA titration (2340 C); nitrate by cadmium-reduction spectrophotometry (4500-NO_3^- E; Genesys 10S at 540 nm); chloride by Mohr titration (4500-Cl^- B); alkalinity by titration to pH 4.5 (2320 B). Total coliform and E. coli were determined by membrane filtration (9222 B and 9222 G, respectively). Detection limits ranged from 0.01 pH unit to 5 mg/L for the principal physicochemical measures and 1 CFU/100 mL for bacteriological counts; calibration used certified standards and daily checks.

QA/QC included field blanks, duplicate analysis of at least 10% of samples, spike-recovery tests, method-detection-limit assessment, daily instrument calibration and positive/negative bacteriological controls. Physicochemical RSD was below 5%, bacteriological RSD below 10%, nitrate recovery 95-103%, chloride recovery 97-101%, all samples exceeded MDLs, and accepted calibration curves had $R^2 > 0.995$.

2.5 Statistical Analysis

Descriptive statistics comprised mean, standard deviation, minimum and maximum. Differences among water sources were evaluated by one-way ANOVA at $\alpha = 0.05$, followed where significant by Tukey's HSD. Analyses were performed in IBM SPSS Version 25. The model was $Y_{ij} = \mu + \alpha_i + \varepsilon_{ij}$, where Y_{ij} is the observed parameter, μ the overall mean, α_i the effect of water source i, and ε_{ij} the random error.

2.6 Water Quality Index (WQI)

WQI was calculated using the Weighted Arithmetic Index method (Shukla & Ram, 2015; Opasola et al., 2025). Nine parameters were included: pH, EC, TDS, turbidity, hardness, nitrate, chloride, alkalinity and total coliform count. The adopted weights were 0.09, 0.11, 0.10, 0.14, 0.07, 0.19, 0.07, 0.06 and 0.17, respectively; ideal values were 7.0 for pH and 0 for the other parameters. The WQI values were interpreted using the classification scheme adopted in the present study: < 50 = Excellent, 50-100 = Good, 100-200 = Poor, 200-300 = Very Poor, and > 300 = Unsuitable for drinking. The selected classification scheme was retained consistently for all sampling sources to permit direct comparison among the sampled groundwater sources

2.7 Irrigation Water Quality Assessment

Irrigation-water suitability was evaluated using the Sodium Adsorption Ratio (SAR), sodium percentage (Na%), Kelly's Ratio (KR), Permeability Index (PI), and Residual Sodium Carbonate (RSC). The interpretation of these indices was based on established irrigation-water classification criteria reported in the literature (Richards, 1954; FAO, 2009). SAR was used primarily to assess the potential sodium hazard, while Na%, KR, PI, and RSC were used to evaluate complementary sodium, alkalinity, and soil-permeability hazards. Accordingly, the irrigation-water quality classes reported in this study were assigned from the respective published classification ranges for each index rather than from SAR alone. The combined interpretation of the indices was used to determine the overall irrigation suitability of each sampled water source. $SAR = Na^{+}/\sqrt{[(Ca^{2+} + Mg^{2+})/2]}$, $Na\% = [(Na^{+} + K^{+})\times100]/(Ca^{2+} + Mg^{2+} + Na^{+} + K^{+})$, $KR = Na^{+}/(Ca^{2+} + Mg^{2+})$, $RSC = (CO_3^{2-} + HCO_3^{-}) - (Ca^{2+} + Mg^{2+})$, and $PI = [(Na^{+} + \sqrt{HCO_3^{-}})\times100]/(Ca^{2+} + Mg^{2+} + Na^{+})$. All ionic concentrations were expressed in meq/L.

3. RESULTS AND DISCUSSION

3.1 Physicochemical Parameters

Table 4 presents the physicochemical results. pH ranged from 6.7-7.5; EC from 420-1,210 µS/cm; TDS from 280-790 mg/L; turbidity from 2.1-18.3 NTU; hardness from 118-245 mg/L; nitrate from 12.5-72.6 mg/L; chloride from 32-125 mg/L; and alkalinity from 94-161 mg/L. All boreholes complied with the cited limits for the measured parameters. In contrast, all hand-dug wells and the lake exceeded the 5-NTU turbidity guideline, while HW3, HW4 and HW5 exceeded 50 mg/L nitrate. Hand-dug wells also showed higher EC and TDS, indicating greater exposure to surface-derived inputs.

Table 2: Physicochemical Characteristics of Water Samples

Parameter	WHO Limit	BH1	BH2	BH3	BH4	BH5	HW1	HW2	HW3	HW4	HW5	LW1
pH	6.5–8.5	7.2	7.4	7.1	7.5	7.3	6.8	6.9	6.7	6.8	6.9	7.1
EC (µS/cm)	1500	420	510	580	640	690	980	1040	1180	1210	1105	970
TDS (mg/L)	1000	280	340	380	430	450	620	680	760	790	720	610
Turbidity (NTU)	5	2.1	2.5	2.8	3.1	3.5	8.4	10.2	12.5	14.6	11.8	18.3
Hardness (mg/L)	500	118	132	145	152	167	185	210	230	245	221	196
Nitrate (mg/L)	50	12.5	14.3	16.7	18.4	20.1	41.5	48.2	68.3	72.6	61.4	42.1
Chloride (mg/L)	250	32	38	42	48	51	86	102	116	125	118	95
Alkalinity (mg/L)	200	94	98	102	106	112	135	148	152	161	158	148

Hardness remained below the 500 mg/L WHO limit. Borehole hardness ranged from 118-167 mg/L, whereas hand-dug wells ranged from 185-245 mg/L and the lake was 196 mg/L. The higher hardness has mainly operational implications, including scale formation and increased detergent demand, rather than a direct health hazard at the measured concentrations. These patterns are consistent with Nigerian groundwater studies reporting greater dissolved-ion loading in shallow sources (Ezechinyere & Stanislaus, 2023; Opasola et al., 2025; Thomas, 2023).

3.2 Bacteriological Quality Assessment

Total coliform counts ranged from 0-85 CFU/100 mL. No E. coli was detected in BH1–BH5, whereas all hand-dug wells and LW1 were positive. The pattern indicates greater vulnerability of shallow sources to faecal contamination associated with poor sanitation, septic seepage, livestock activities and runoff.

Table 3: Bacteriological Characteristics of Water Samples

Source	Total Coliform (CFU/100 mL)	E. coli
BH1	0	ND
BH2	0	ND
BH3	1	ND
BH4	2	ND
BH5	1	ND
HW1	35	Present
HW2	49	Present
HW3	78	Present
HW4	85	Present
HW5	69	Present
LW1	45	Present

3.3 Comparative Evaluation with WHO (2017) and NIS/NSDWQ (2015) Standards

Boreholes complied with the cited WHO (2017) and NSDWQ (2015) requirements for pH, EC, TDS, hardness, chloride, alkalinity and nitrate. All hand-dug wells exceeded the turbidity guideline, and HW3-HW5 exceeded the nitrate limit. E. coli occurrence in all hand-dug wells and the lake makes these sources unsuitable for direct drinking without treatment. The results reinforce evidence that shallow groundwater is more susceptible to anthropogenic contamination than deeper aquifer sources.

3.4 Water Quality Index (WQI) Assessment

WQI values ranged from 42.6-136.2. BH1–BH5 ranged from 42.6-57.8 and were classified as Good; HW1 and HW2 were Poor (88.5-97.3); HW3, HW4 and HW5 were Unsuitable (118.7-136.2); and LW1 was Poor (95.2). The principal contributors to deterioration were nitrate, EC, turbidity and coliform contamination.

Table 4: Water Quality Index Classification

Sample	WQI	Classification
BH1	42.6	Good
BH2	46.1	Good
BH3	49.4	Good
BH4	53.2	Good
BH5	57.8	Good
HW1	88.5	Poor
HW2	97.3	Poor
HW3	128.4	Unsuitable
HW4	136.2	Unsuitable
HW5	118.7	Unsuitable
LW1	95.2	Poor

3.5 Irrigation Suitability Assessment

SAR ranged from 2.1-4.9, Na% from 24.3-44.1%, KR from 0.31-0.82, PI from 61.5-72.4% and RSC from 0.8-1.9 meq/L. All sampled sources were usable for irrigation, with BH1-BH2 classified Excellent, BH3-BH5, HW1-HW2 and LW1 Good, and HW3-HW5 Permissible. The latter category does not mean unsafe irrigation; it indicates a higher sodium-management requirement. Recommended controls are a 10-20% leaching fraction, gypsum at 2-5 t/ha every 3-5 years, salt-tolerant crops, soil EC/SAR monitoring and blending where feasible.

Table 5: Irrigation Water Quality Indices

Source	SAR	Na%	KR	PI (%)	RSC	Classification
BH1	2.1	24.3	0.31	61.5	0.8	Excellent
BH2	2.4	26.2	0.35	63.0	0.9	Excellent
BH3	2.8	28.5	0.44	65.2	1.0	Good
BH4	3.1	30.8	0.49	66.8	1.1	Good
BH5	3.3	32.1	0.55	67.5	1.2	Good
HW1	3.9	36.4	0.64	68.1	1.4	Good
HW2	4.2	39.5	0.71	69.8	1.6	Good
HW3	4.6	42.7	0.78	71.6	1.8	Permissible
HW4	4.9	44.1	0.82	72.4	1.9	Permissible
HW5	4.5	41.8	0.76	70.9	1.7	Permissible
LW1	3.9	38.2	0.69	69.4	1.5	Good

3.6 Engineering Implications

3.6.1 Borehole Design Specifications

The superior quality of borehole samples (WQI: 42.6-57.8; *E. coli*: absent; turbidity: <5 NTU; nitrate: 12.5-20.1 mg/L) supports source substitution as the preferred intervention for communities reliant on contaminated shallow wells. Borehole specifications are presented as preliminary design ranges rather than fixed values. Recommended parameters include: 80-120 m depth, 60-100 m screened interval, 150 mm PVC-U casing, 0.5-1.0 mm continuous-slot screen, 3-6 mm gravel pack, and 3 m bentonite sanitary seal-final dimensions to be confirmed by site-specific lithological logs, sieve analysis, and well-development results. Abstraction is via a solar-powered 1.5-3.0 HP submersible pump delivering approximately 2-5 L/s at 30-50 m total dynamic head, with final capacity determined by pumping-test results and community demand.

Estimated cost is ₦11.61-17.38 million per installation, covering survey, drilling, casing, screen, gravel pack, sanitary works, solar pumping, distribution, and supervision. The exchange rate adopted for this conference version is ₦1,350/USD (August 2026); direct Naira estimates are retained from the source manuscript (₦1,420/USD). Each borehole serves 300–500 persons, with a six-month implementation period encompassing hydrogeological survey, drilling and casing, pump installation and testing, community training, and baseline water-quality testing.

3.6.2 Treatment Train Configurations for Hand-Dug Wells

All hand-dug wells require treatment before drinking because turbidity was 8.4-14.6 NTU, coliform counts were 35-85 CFU/100 mL and E. coli was present. Three scalable configurations are proposed. Configuration A serves 5-7 persons using a 200-L sedimentation tank (24-h retention), three 100-L slow-sand filter drums and chlorination at 2-4 mg/L with 30-min contact; capital cost is ₦138,375 with annual O&M of ₦13,838. Configuration B serves 100-300 households using a 5,000-L baffled settling tank, roughing filter, 2-m-diameter × 1.5-m biosand filter and solar UV or chlorination; capital cost is ₦415,125 with chlorine or ₦718,875 with UV, with annual O&M of about ₦42,000. Configuration C serves 1,000-5,000 persons using coagulation–flocculation, sedimentation, rapid sand filtration and chlorination; capital cost is ₦10.1-16.9 million, with ion exchange for nitrate at ₦13.5-23.6 million or blending at ₦8.1-13.5 million where required. For Jere, borehole source substitution is preferred to intensive nitrate-removal treatment where feasible.

3.6.3 Wellhead Protection and Setback Distance Enforcement

Source-protection measures are proposed around boreholes and hand-dug wells as engineering control distances for Jere LGA, not universal statutory requirements, with final protection radii to consider local hydrogeology, groundwater flow, aquifer vulnerability, contaminant characteristics, well construction, and Nigerian regulations. Hand-dug wells require sanitary wellheads comprising a 1.5 m × 1.5 m × 0.15 m concrete platform, drainage apron, lockable cover, casing raised 0.3-0.5 m above platform, and bentonite or bentonite–cement sanitary seals to 3 m depth to reduce contaminant ingress.

Recommended setbacks for boreholes and hand-dug wells respectively are: septic systems 50 m and 30 m; agricultural fields 100 m up-gradient and 50 m; livestock areas 50 m and 30 m; refuse dumps 100 m and 50 m; fuel stations 150 m and 100 m. Within protection zones, waste disposal, wastewater discharge, sanitation facilities, and contaminating activities should be restricted, with enforcement combining GIS mapping, registration and licensing, annual compliance verification, and community-based surveillance.

3.6.4 Irrigation Water Management Strategy

Excellent and Good sources can be managed with standard irrigation practices and annual soil monitoring. HW3-HW5 require active management because SAR is 4.5-4.9: apply gypsum at 2-5 t/ha every 3-5 years, maintain a 10-20% leaching fraction, use salt-tolerant crops such as millet, sorghum and date palm, monitor soil EC and SAR at least twice annually, maintain drainage and blend with lower-SAR water when available. Sensitive crops such as onion and pepper should preferentially use the better-quality borehole sources.

3.6.5 Groundwater Monitoring System

A tiered monitoring system is recommended: Tier 1 comprises quarterly manual sampling of all sources for pH, EC, TDS, nitrate, turbidity, coliform, and *E. coli* at ₦2.025-3.375 million/year; Tier 2 adds semi-automated sensors at 3-5 high-risk sites (₦6.75-10.1 million capital, ₦4.05-6.75 million/year O&M); Tier 3 provides telemetry and web dashboards (₦27-40.5 million capital, ₦20.25-33.75 million/year O&M) if capacity develops. Yellow alerts: nitrate 40-45 mg/L, turbidity 3-5 NTU, *E. coli* 1-10 CFU/100 mL, EC 1,200-1,500 µS/cm; red alerts: nitrate >50 mg/L, turbidity >5 NTU, *E. coli* >10 CFU/100 mL, EC >1,500 µS/cm.

The costs are preliminary estimates for planning and comparison, not fixed market prices; they require BOQ, unit-rate analysis, equipment specs, labour, installation, and local market validation, with updates using current supplier quotes at procurement. The monitoring programme is an engineering planning framework; final costs depend on monitoring points, sampling frequency, parameters, lab charges, field measurements, transport, equipment, and duration, with BOQ assumptions retained as supporting documentation.

3.6.6 Implementation Roadmap

The five-year phased roadmap priorities: Year 1-community awareness, wellhead platforms at HW1-HW5, household treatment kits for 500 households, and quarterly baseline monitoring; Years 2-3-5-10 priority boreholes, community bio-sand filters at three hand-dug wells, GIS-based setback enforcement, and annual soil monitoring; Years 4-5-Tier 2 monitoring upgrade, sustainable agriculture programme, and groundwater-quality protection by-laws.

The 2026 population projection for Jere LGA (306,400-337,108 persons) is extrapolated from the 2006 NPC census (209,107-211,204), supported by World Population Review (337,108) and City Population (306,400), and serves as a planning estimate. For actual implementation, design population should be based on the most recent authoritative data, incorporating design period, growth rate, per-capita demand, and allowances for institutional, commercial, and livestock uses.

3.7 Study Limitations

The study involved only eleven locations (five boreholes, five hand-dug wells and one lake), limiting representation of spatial variability and giving the lake sample (n=1) little statistical power. Sampling was conducted during one campaign, so seasonal variability was not evaluated. Heavy metals, pesticide residues, hydrocarbons and emerging contaminants were outside the analytical scope. Strategic rather than random site selection may introduce selection bias. Irrigation indices were based on one ionic-composition dataset and could change seasonally. Future work should use larger wet- and dry-season samples, broader contaminant screening and spatially explicit monitoring.

4. CONCLUSION

The investigation demonstrates a clear quality contrast between deeper boreholes and shallow hand-dug wells in Jere LGA. Boreholes recorded WQI values of 42.6-57.8, turbidity below 5 NTU,

nitrate of 12.5-20.1 mg/L and no detected E. coli, whereas hand-dug wells showed elevated turbidity, widespread faecal contamination and nitrate up to 72.6 mg/L. HW3-HW5 were unsuitable for drinking and require priority intervention. All sampled sources remained generally usable for irrigation, but HW3-HW5 require active sodium-management practices because of their Permissible classification. The engineering response should therefore prioritise source substitution through protected boreholes, multi-barrier treatment where shallow wells remain necessary, wellhead protection and setback enforcement, differentiated irrigation management, and a tiered monitoring system. These interventions directly address the identified microbial, nitrate, turbidity and sodium hazards and support SDGs 2, 3 and 6. The study consequently contributes to Innovative Resource Utilization and Management and Emerging Technologies for Safe Engineering Practices and Environmental Protection by converting site-specific water-quality evidence into implementable engineering decisions.

ACKNOWLEDGEMENTS

The authors acknowledge the Department of Soil Science Laboratory, Faculty of Agriculture, Ahmadu Bello University, Zaria, for laboratory facilities and analytical support.

5. REFERENCES

Abanyie, S. K., Apea, O. B., Abagale, S. A., Amuah, E. E. Y., & Sunkari, E. D. (2023). Sources and factors influencing groundwater quality and associated health implications: A review. Emerging Contaminants, 9(2), Article 100207. https://doi.org/10.1016/j.emcon.2023.100207

American Public Health Association, American Water Works Association, & Water Environment Federation. (2017). Standard methods for the examination of water and wastewater (23rd ed.). American Public Health Association.

Banerjee, A., Creedon, L., Jones, N., Gill, L., & Gharbia, S. (2023). Dynamic groundwater contamination vulnerability assessment techniques: A systematic review. Hydrology, 10(9), 182. https://doi.org/10.3390/hydrology10090182

City Population. (2022). Borno: State in Nigeria. https://www.citypopulation.de/en/nigeria/admin/

Ezechinyere, C. H., & Stanislaus, O. U. (2023). Investigating the quality of groundwater in Ibeju-Lekki Local Government Area, Lagos State. Water Science, 37(1), 409–425. https://doi.org/10.1080/23570008.2023.2283326

Food and Agriculture Organization of the United Nations. (2009). Guide to laboratory establishment for plant nutrient analysis. FAO.

National Population Commission. (2006). 2006 population and housing census: Priority table volume IV – Population distribution by age & sex (state & local government area). National Population Commission.

Nigerian Meteorological Agency. (2008). Climate data summary for Borno State. Nigerian Meteorological Agency.

Opasola, O. A., Otto, E., Salami, J. T., & Adiama, B. Y. (2025). Application of Weighted Arithmetic Index method in determining the water quality status of groundwater samples near Gosa Dumpsite, Federal Capital Territory (FCT), Abuja, Nigeria. FUOYE Journal of Pure and Applied Sciences, 10(2), 144–163. https://doi.org/10.55518/fjpas.SCYH6628

Richards, L. A. (Ed.). (1954). Diagnosis and improvement of saline and alkali soils (USDA Agriculture Handbook No. 60). U.S. Department of Agriculture.

Shukla, J. P., & Ram, P. (2015). Assessment of groundwater quality using water quality index and GIS: A case study from Varanasi, India. Journal of Environmental Research and Development, 9(4), 1049-1057.

Standards Organisation of Nigeria. (2015). Nigerian standard for drinking water quality (NIS 554:2015). Standards Organisation of Nigeria.

Thomas, E. O. (2023). Evaluation of groundwater quality using multivariate, parametric and non-parametric statistics, and GWQI in Ibadan, Nigeria. Water Science, 37(1), 117–130. https://doi.org/10.1080/23570008.2023.2221493

World Health Organization (WHO). (2017). Guidelines for Drinking-water Quality: Fourth Edition Incorporating the First Addendum. World Health Organization. https://iris.who.int/bitstream/handle/10665/254636/9789241550017-eng.pdf

World Population Review. (2026). Jere population 2026. https://worldpopulationreview.com/cities/nigeria/jere

International Conference on Engineering Innovation for Sustainable Development (ICESID 2026)
Faculty of Engineering, Ahmadu Bello University Zaria · 8–10 September 2026

AWARENESS, BARRIERS, AND ENABLERS OF CIRCULAR ECONOMY ADOPTION IN ABUJA'S CONSTRUCTION SECTOR

Muhammad Hadi Kabir[1,*], Abdulhameed Danjuma Mambo[1]
[1]*Nile University of Nigeria*
Email: mhadikabir@gmail.com*, abdulhameed.mambo@nileuniversity.edu.ng
***Corresponding author**: Muhammad Hadi Kabir
DOI: https://doi.org/10.67203/sp.ICESID.2026

ABSTRACT

Construction & Demolition (C&D) waste has been identified as one of the major problems facing rapidly growing cities in Nigeria and has both environmental and economic consequences. The methods through which waste is managed in this industry continue to be largely linear: dispose by default. Circular economy (CE) principles provide a pathway towards sustainable construction; however, their implementation in Nigeria's construction sector remains poorly researched. This study examines CE awareness, practices, attitudes, and barriers using a cross-sectional survey of 110 construction professionals. A seven-item CE-attitude scale was tested for internal consistency (Cronbach's $\alpha = 0.803$). Professional role, years of experience, and educational attainment were examined in relation to CE attitudes and practices using chi-square tests and Spearman correlation. There were no statistically significant differences between professionals' awareness of CE in terms of their professional roles ($p = 0.71$) or levels of education ($p = 0.81$). Yet, professionals' roles turned out to be significantly correlated with the frequency of waste separation ($\chi^2 = 10.86$, $p = 0.028$) and readiness to engage in CE practices if incentivized ($\chi^2 = 11.19$, $p = 0.025$). While contractors and builders were more behaviorally responsive to CE than engineers, there were no statistically significant differences between their levels of awareness of the concept. The quality of recycled materials was found to be the most influential factor when respondents decided to pay for them ($\rho = 0.61$). The main barriers included the lack of awareness (59.1%), the lack of proper recycling infrastructure (48.2%), and the lack of regulation enforcement (40.0%). Guaranteed markets (49.1%) and technical training (47.3%) appeared to be the most important enablers of CE.

Keywords: *circular economy; construction and demolition waste; barriers; enablers; and sustainable construction*

1. INTRODUCTION

The construction industry is among the biggest users of natural resources across the world, accounting for 35% of all material consumption and 40% of the annual waste (Dsilva et al., 2023). The C&D waste types comprise concrete, masonry, wood, metal, glass, plastics, and asphalt. The sources of such wastes are construction, remodelling, and demolition of structures, whereby the occurrence of C&D wastes is common in fast and poorly regulated urban cities. Nigeria offers a useful example, where the construction industry contributes about 3–5% to the nation's GDP (National Bureau of Statistics, 2023). However, the inefficiency in materials utilization, inadequacy of regulation regarding demolition works, and lack of recycling opportunities negatively impact the competitiveness of the industry and overall sustainability goals of the country.

The Federal Capital Territory of Nigeria, Abuja, is an illustrative example in this field. Being an urban center, which has been expanding continuously for the last few decades in terms of residential areas, commerce, and infrastructure, Abuja produces significant amounts of construction and demolition (C&D) waste. A considerable amount of C&D waste in the city ends up in either unused lands, water bodies, or roads instead of being recovered (Lanrewaju, 2012; Ogunseye et al., 2023; Unegbu et al., 2024). However, such state of affairs contradicts the goals of SDG 11 (Sustainable Cities and Communities), SDG 12 (Responsible Consumption and Production), and SDG 13 (Climate Action). On the other hand, it is an untapped resource due to the fact that there is easily recoverable C&D waste in Abuja.

A circular economy (CE) approach that replaces the traditional "take-make-dispose" model through initiatives that help to reduce, reuse, recycle, and regenerate materials via closed loops

(Kirchherr et al., 2017, 2023) is one such model that has gained traction across the globe to address this problem. Countries like Germany, Sweden, and the Netherlands have shown that CE-related initiatives can help recover 80–90% of C&D wastes (Bonifazi et al., 2025; Shajidha & Mortula, 2025). The construction sector in Nigeria, on the other hand, is still rooted in linear processes with inefficient use of resources, poor regulation enforcement, and lack of awareness among stakeholders about CE (Bello & Idris, 2023; Unegbu et al., 2024).

The consistent finding across the Nigerian studies on CE among construction professionals is that there is a knowledge-to-action gap whereby most construction professionals claim to have knowledge about CE principles, but very few actually practice them (Unegbu et al., 2024). The current study aims to establish the reasons for the failure of knowledge translation into action and identify professional attributes that determine the size of the gap. The specific objectives are to (i) assess CE awareness and current C&D waste management practices among Abuja construction professionals; (ii) identify and rank key barriers and enablers of CE adoption; and (iii) test whether professional role, experience, and education are statistically associated with CE attitudes and behaviors. The remainder of the paper covers literature (Section 2), methodology (Section 3), results (Section 4), discussion (Section 5), and conclusions (Section 6).

2. LITERATURE REVIEW

2.1 The Circular Economy: Principles and Models

The circular economy (CE) has emerged as a widely recognized tool to harmonize economic growth with sustainable development. Unlike the linear economy model where the flow of materials follows a straight-line trajectory of "take-make-use-waste," the CE model entails a cyclic approach in which products, parts, and materials retain their value through processes of reusing, repairing, remanufacturing, and recycling (Kirchherr et al., 2017). This concept has been defined as a policy framework since the 1990s through initiatives of the Ellen MacArthur Foundation and the European Union (Kirchherr et al., 2023; Velenturf & Purnell, 2021). The circular economy is no longer seen as a solution to minimizing waste but as a revolutionary paradigm that considers economic, environmental, and social goals simultaneously.

The CE approach within the built environment is implemented through an integrated set of approaches that include elimination of waste at the source, sustaining the flow of materials through reuse and recycling, regeneration of natural systems, and systems thinking within the value chain (Velenturf & Purnell, 2021). In the built environment, material use constitutes around 40% of the overall material demand on Earth along with waste production, making the built environment one of the sectors where the CE can be most impactful.

2.2 Barriers and Enablers: A Four-Domain Framework

The literature clearly outlines the barriers and motivating factors behind the C&D waste recycling process through four related areas (Table 1). This typology, which was synthesized from international and local sources, serves as the foundation behind the barriers and motivators in the questionnaire for this study.

Table 1: Barriers and enablers of CE adoption in C&D waste management, by domain.

Domain	Key Barriers	Key Enablers
Technical	Heterogeneous, contaminated waste streams; absence of advanced sorting/recycling equipment; and designs that do not support disassembly.	On-site segregation; lean construction practices; optimized mechanical recycling
Economic/Market	Recycling is perceived as costlier than disposal; weak market demand; low trust in recycled material quality; unpredictable supply chains	Landfill taxes, subsidies for recyclers; cost savings from waste minimization
Institutional/Policy	Weak enforcement of regulations; absence of quality standards for recycled materials; few staff assigned to waste management	Mandatory waste management plans; green building certification; government procurement mandates
Social/Cultural	Low awareness; poor workmanship; prevailing use-and-discard culture; community nuisance from poor practice	Targeted training, incentive, and accountability systems; stakeholder engagement

2.3 Prior Survey-Based CE Studies in Nigeria and Comparable Contexts

Survey-based studies investigating the CE awareness in the construction industry of Nigeria are increasing in number. According to Unegbu et al. (2024), there is a significant gap in CE implementation where 58% of respondents had knowledge about CE principles, but only 15% implemented them, whereas 68% of companies were still using unsustainable practices in disposal. The major challenges included financial constraints (about 70%), lack of enforcement of regulations (65%), and poor infrastructure (63%). Similarly, Bello and Idris (2023) highlight that the adoption of CE in Nigeria is in a "know without doing" phase. In similar environments, a study conducted in Addis Ababa found that more than three-quarters of companies did not have staff designated for handling waste management issues (Shajidha & Mortula, 2025).

From a methodological perspective, the literature is highly descriptive in nature, recording frequency and average Likert scale ratings but rarely testing for scale validity or evaluating whether there is an association between respondents' demographics and their outcomes. One of the major policy-oriented questions that remain open is the following: Is the awareness-performance gap general in the construction sector, or is it limited to certain professions?

2.4 Conceptual Framework

The research has been conducted in the context of circular economy theory, which assumes that material value should be kept by repeating use, recovery, and regeneration continuously (Velenturf & Purnell, 2021). Figure 1 illustrates the theoretical framework where the link between CE approaches and the processes of construction and demolition waste management, along with enabling conditions that condition adoption outcomes, has been considered. The research framework is the basis for the analysis in this research: first, there will be the evaluation of CE knowledge and application; second, barriers and enabling factors will be analyzed; and, third, the moderation effect will be tested.

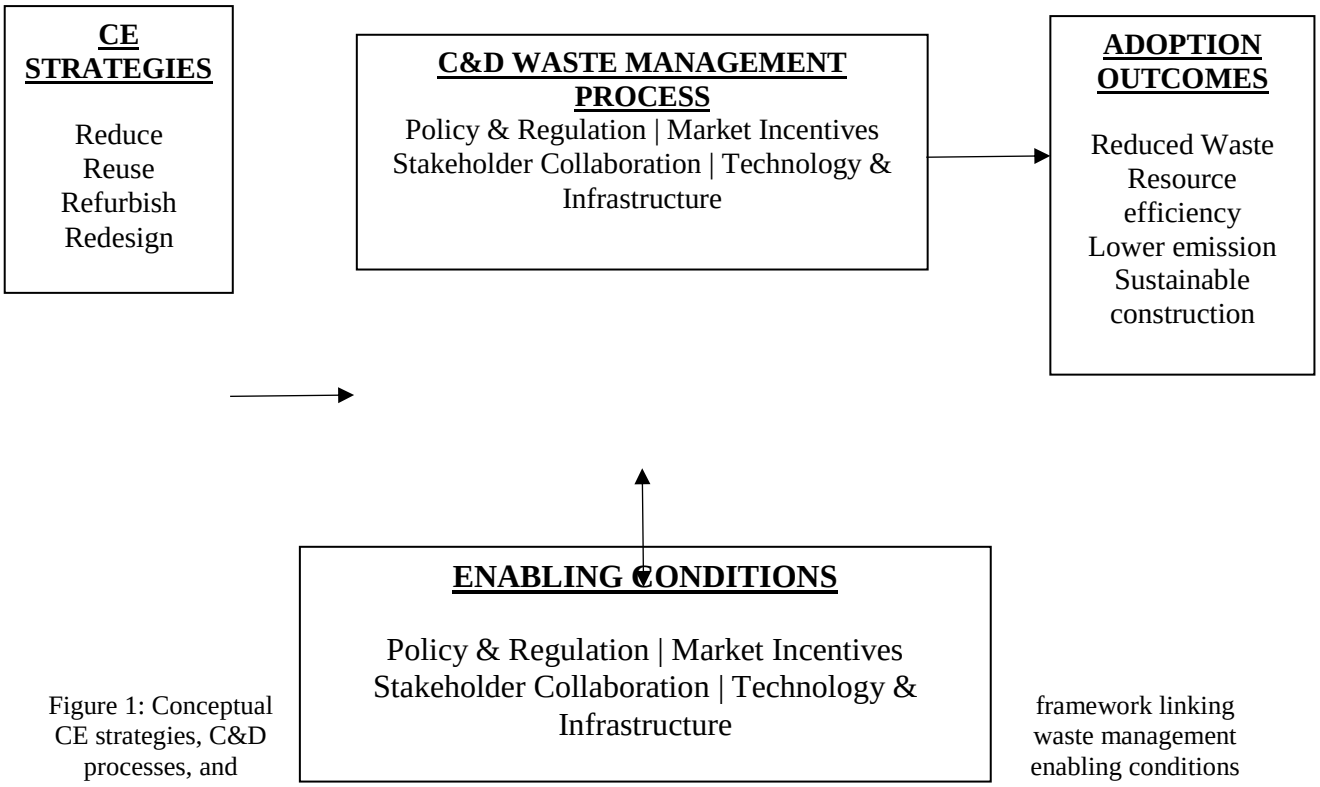

Figure 1: Conceptual framework linking CE strategies, C&D waste management processes, and enabling conditions to adoption outcomes.

3. METHODOLOGY

3.1 Research Design

In order to examine awareness, behaviors, and perception about CE barriers/enablers among construction professionals in Abuja, Nigeria, the study uses a descriptive-correlational questionnaire survey research design. In addition to presenting descriptive statistics about the data, it tests whether there exists a statistical relationship between the demographic variables of the respondents and CE-related behaviors/attitudes/perceptions. This paper reports only the perceptual and survey component of the broader research project. The associated waste-quantification component is outside the scope of the present paper and will be reported separately.

3.2 Study Area

This study was conducted in the Federal Capital Territory (FCT), Abuja, Nigeria. It is selected as the study area because it is among the fastest-growing construction markets in the country, with sustained residential, commercial, and infrastructural development generating substantial C&D waste volumes that are largely managed through informal or unregulated channels (Abah et al., 2023).

3.3 Population and Sampling

The sample for the study involved construction practitioners in Abuja; this included engineers, architects, quantity surveyors, contractors, builders, site supervisors, waste managers, and policymakers. Purposive sampling with participation in construction activities was employed to select the respondents, and a total of 111 questionnaire forms were issued, resulting in 110 valid responses since one participant withdrew his consent.

For inferential testing, professional roles were grouped into three categories to maintain adequate cell sizes: engineers/design professionals, including architects (n=76); contractors/builders (n=24); and managerial/policy professionals (n=7). This classification was chosen to facilitate the application of the requirements of the chi-square test. The fourth classification ('Others', n=3) was not included in any of the role-related chi-square tests, since the small size of its cells might lead to

insufficient expected values. Therefore, role-related tests were carried out based on n=107, while education/experience-related tests were on n=110.

3.4 Research Instrument

The data were collected using a standardized questionnaire that had five sections:

- Section A: Demographic and professional characteristics of the respondents
- Section B: Existing practices of C&D waste management
- Section C: Knowledge about the circular economy (CE)
- Section: D: Challenges/barriers and enablers for recycling C&D waste
- Section E: Instruments of policy and incentives

Most questions were answered on a five-point Likert scale (1 = strongly disagree to 5 = strongly agree). Content validity of the questionnaire was ensured by its verification by experts and practitioners.

3.5 Scale Reliability

A composite measure of CE-attitudes comprising seven Likert items based on Sections C and D was created and assessed for internal consistency using Cronbach's alpha prior to performing any further analysis. Seven Likert items were kept since there was acceptable correlation between all of them and a consistent alpha value (Section 4.1).

3.6 Data Analysis

The analysis was conducted in three steps. Firstly, the descriptive analysis involved calculating frequencies, percentages, means, standard deviation, and skewness. Secondly, the chi-square test of independence was used to establish the relationship between categorical respondent variables and categorical outcome variables. The Likert response was reduced into three categories (disagree 1-2, neutral 3, and agree 4-5), while the effect size was calculated using Cramér's V. Thirdly, the Spearman rank correlation (ρ) analysis was conducted on the relationship between the seven CE-attitude variables as well as the relationship between experience and each of the attitude variables. Spearman's rank correlation was used because the CE-attitude variables were measured using five-point Likert-scale responses, which are ordinal in nature. The non-parametric Spearman procedure was therefore considered appropriate for assessing monotonic associations without requiring the assumptions associated with Pearson correlation.

3.7 Ethical Considerations

Participation was entirely voluntary, and informed consent was obtained from all respondents. No personally identifying information was collected, ensuring respondent anonymity throughout.

4. RESULTS

4.1 Respondent Profile and Scale Reliability

Out of 111 surveys that were distributed, 110 responses were valid. Out of the total number of respondents, most were male (57, 91.8%), held a bachelor's degree (68.2%), and had fewer than five years of experience (58.2%). Engineering was the largest profession group (69.1%), while contractor/builders came second (21.8%), and management/policymaking third (6.4%).

Table 2: Respondent profile (n=110).

Characteristic	Category	n	%
Gender	Male	101	91.8
	Female	8	7.3
	Prefer not to say / Missing	1	0.9
Professional Role	Engineer (incl. Architect)	76	69.1
	Contractor / Builder	24	21.8
	Management / Policy	7	6.4
	Other (excl. from role tests)	3	2.7
Years of Experience	≤5 Years	64	58.2
	6–10 Years	35	31.8
	>10 Years	11	10.0
Educational Qualification	Bachelor's Degree	75	68.2
	Master's Degree	22	20.0
	Diploma / NCE	7	6.4
	PhD and above	3	2.7
	Secondary School (SSCE)	3	2.7

The internal consistency of the CE attitude scale consisting of seven items was satisfactory (Cronbach's α = 0.803, n = 110), exceeding the generally acceptable standard of 0.70. The correlations between each item and total scores ranged between 0.39 (adequacy of regulation and enforcement) and 0.62 (quality beliefs). The elimination of any one of the items could increase the alpha value by at most 0.81; hence, all the items were kept.

Table 3: Descriptive statistics and reliability indices for the CE-attitude scale (n=110).

Item (Likert 1–5)	Mean	SD	Median	Skewness	Item-total r	n
Awareness of CE concept	3.67	1.12	4	−0.68	0.51	110
Knowledge of recycling techniques	3.56	1.11	4	−0.44	0.61	110
Organization has C&D waste policy	3.29	1.22	3	−0.36	0.54	110
Regulation/enforcement adequacy	3.04	1.31	3	0.03	0.39	110
Recycled materials meet quality needs	3.61	1.01	4	−0.25	0.62	110
Willingness to pay more	3.58	1.00	4	−0.75	0.58	110
Will adopt CE if incentives are introduced	3.86	1.00	4	−0.78	0.57	110
Cronbach's α = 0.803 (n=110)						

Note: Likert scale: 1=Strongly Disagree, 5=Strongly Agree. Item-total r = corrected item-total correlation.

4.2 Current C&D Waste Management Practices

Dumping of waste in dumping sites and landfills has been identified as the major method of waste disposal practice adopted by 80.2% of the respondents (n=89). Informal on-site reuse of waste ranked second at 42.3%, followed by selling waste to informal recyclers at 34.2%, and formal recycling at 17.1%. Waste separation too showed a degree of inconsistency in practice, with 39.6% not separating waste at all, 41.4% doing so occasionally, and only 19.0% doing so regularly.

4.3 CE Awareness and Applicability

The mean scores (Table 3) show that there is moderate to high CE awareness (M = 3.67) and moderate knowledge about the methods of recycling (M = 3.56). There is also a moderate belief in the quality of recycled products (M = 3.61) and moderate willingness to pay extra (M = 3.58). The highest mean score is obtained for conditional adoption (M = 3.86, SD = 1.00), while perceived adequacy of regulations scores the lowest and the most uniformly (M = 3.04, skewness ≈ 0.03).

4.4 Association Between Professional Characteristics and CE Attitudes/Practices

Chi-square tests for independence were used to investigate the relationships between respondent characteristics and circular economy (CE) results (Table 4). Professional role has been shown to be significantly related to waste segregation frequency (χ^2 = 10.86, df = 4, p = 0.028, V = 0.225) and intention to practice CE when offered certain incentives (χ^2 = 11.19, df = 4, p = 0.025, V = 0.229). There is no significant relationship between professional role and awareness of circular economy (p = 0.709). Education is not related to awareness of CE (p = 0.810). Years of experience are not significantly related to willingness to pay (p = 0.867) and regulatory effectiveness (p = 0.652).

Table 4: Chi-square tests of association between respondent characteristics and CE outcomes.

Test	**χ^2**	**df**	**n**	**p**	**Cramér's V**	**Result**
Role × Waste separation frequency	10.86	4	107	0.028	0.225	Significant*
Role × Adoption-if-incentives	11.19	4	107	0.025	0.229	Significant*
Role × CE awareness	2.14	4	107	0.709	0.100	Not significant
Education × CE awareness	4.49	8	107	0.810	0.143	Not significant
Experience × Willingness to pay	1.27	4	107	0.867	0.076	Not significant
Experience × Regulation adequacy	2.46	4	107	0.652	0.106	Not significant

Note: *p < 0.05. Cramér's V: <0.10 = negligible; 0.10–0.29 = small; 0.30–0.49 = moderate effect. Role-based tests exclude the ‘Other’ category (n=3) and therefore use n=107; all other tests use the full sample (n=110).

The cross-tabulation table for the professional roles and waste separation is illustrated in Figure 2 below. Of the 24 contractors/builders, 9 often/always separated their waste, while 1 never/rarely did, and in contrast, of the 76 engineers, 37 often/always separated their waste, and 18 never/rarely did. The variation in behavior but not in awareness is the main finding of this research.

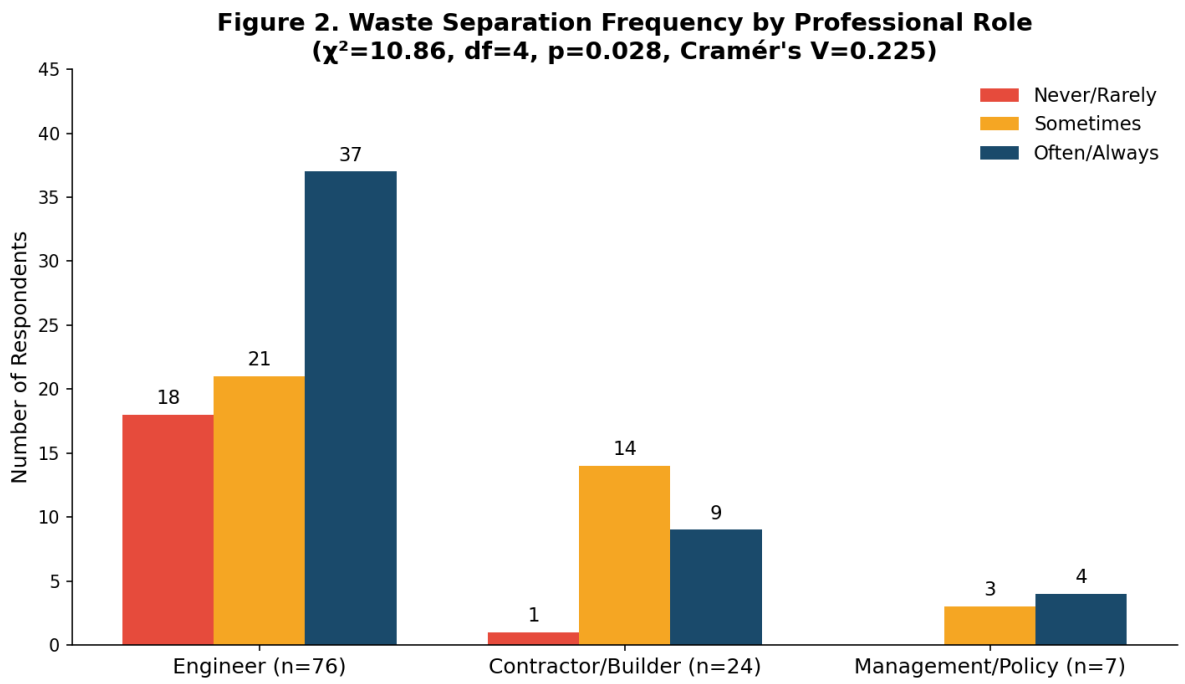

Figure 2: Waste separation frequency by professional role (χ^2=10.86, df=4, p=0.028, Cramér's V=0.225).

Supplementary ordinal correlation analysis found that years of experience were positively correlated with knowledge of recycling techniques (ρ=0.22, p=0.022) and adoption of incentives (ρ=0.26, p=0.006), though effect sizes were modest. All other experience correlations were non-significant ($p > 0.06$).

4.5 Barriers to C&D Waste Recycling

Barriers mentioned by the respondents have been presented in Table 5 on the basis of their frequency of mention. Lack of awareness was found to be the highest barrier, mentioned by 59.1% of respondents, followed by lack of recycling facilities (48.2%) and weak regulation/enforcement (40.0%).

Table 5: Ranked barriers to C&D waste recycling in Abuja (n=110; multiple selection, up to 3).

Barrier	**n**	**% of respondents**	**Rank**
Lack of awareness	65	59.1	1
Lack of recycling facilities	53	48.2	2
Weak regulation or enforcement.	44	40.0	3
High cost of processing.	42	38.2	4
Logistical challenges (transport/storage)	31	28.2	5
Preference for new materials	31	28.2	5
Low market demand for recycled materials	28	25.5	7

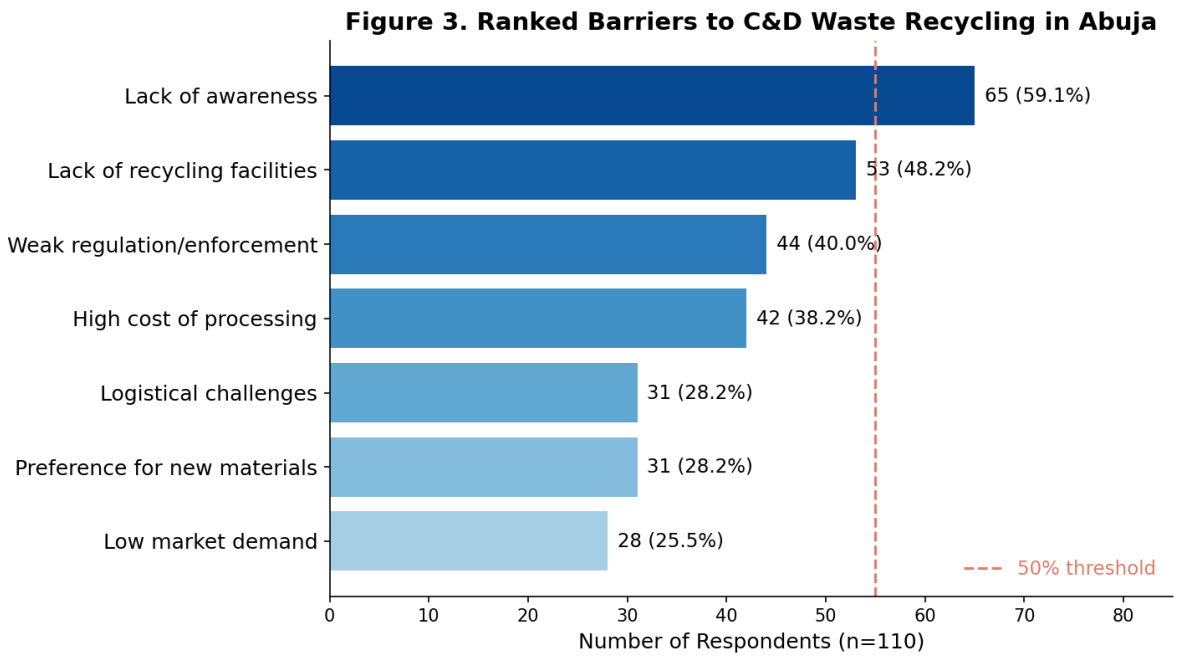

Figure 3: Ranked barriers to C&D waste recycling in Abuja (n=110). A dashed line indicates a 50% threshold.

4.6 Enablers and Preferred Incentives

The incentives that were seen to be more effective in fostering the use of CE have been highlighted in Table 6 below. The incentive that was the most widely selected was the assurance of markets for recycled products (49.1%), followed by technical training and development (47.3%), grant provision of recycling equipment (42.7%), and recycling legislation (40.9%). Respondents could select up to two incentives; therefore, the percentages represent the proportion selecting each option and are not expected to sum to 100%.

Table 6: Incentives most likely to encourage greater CE adoption (n=110; multiple selection, up to 2).

Incentive	**n**	**% of respondents**
Guaranteed markets for recycled materials	54	49.1
Technical training & capacity building	52	47.3
Grants for recycling equipment:	47	42.7
Mandatory recycling regulation	45	40.9
Tax rebates or subsidies	39	35.5

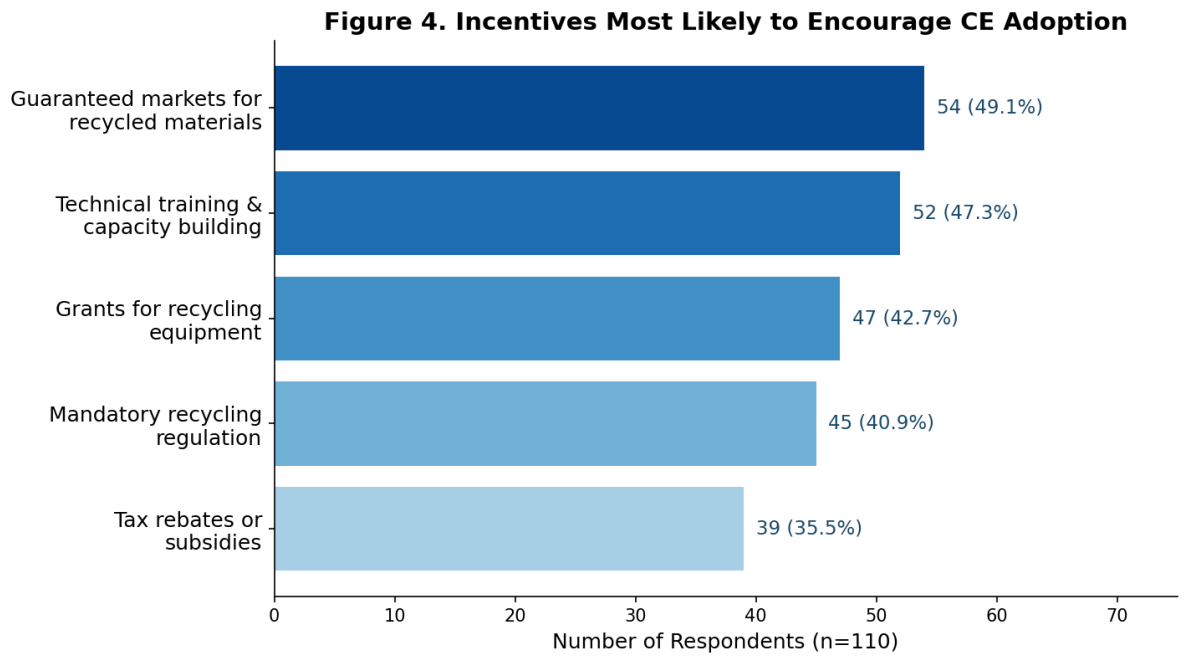

Figure 4: Preferred incentives for encouraging greater CE adoption (n=110).

4.7 Correlation Structure Among CE-Attitude Items

Positive Spearman rank correlations were found for all 21 pairings of the seven CE-attitude variables, thus demonstrating the internal consistency of the measure (see Table 7 and Figure 5). Strong correlations were observed between quality belief and willingness to pay ($\rho = 0.61$) as well as between knowledge and organizational policy ($\rho = 0.62$). There was a strong correlation between quality belief and adoption-if-incentives ($\rho = 0.52$), while there was an equally strong correlation between willingness to pay and adoption-if-incentives ($\rho = 0.50$). The variable that exhibited the weakest correlations was regulation adequacy ($\rho = 0.22$–0.41), owing to its institutional focus.

Table 7: Spearman correlation matrix of CE-attitude scale items (n=107–110).

	Awareness	**Knowledge**	**Org. Policy**	**Reg. Adequacy**	**Quality Belief**	**Willing to Pay**
Knowledge	0.46					
Org. Policy	0.40	0.62				
Reg. Adequacy	0.25*	0.22*	0.31**			
Quality Belief	0.38***	0.43***	0.44***	0.41***		
Willing to Pay	0.37***	0.48***	0.39***	0.35***	0.61***	
Adopt-if-Incentives	0.46***	0.37***	0.30**	0.29**	0.52***	0.50***
Note: * p<0.05; ** p<0.01; *** p<0.001; all non-starred values significant at p<0.0001						

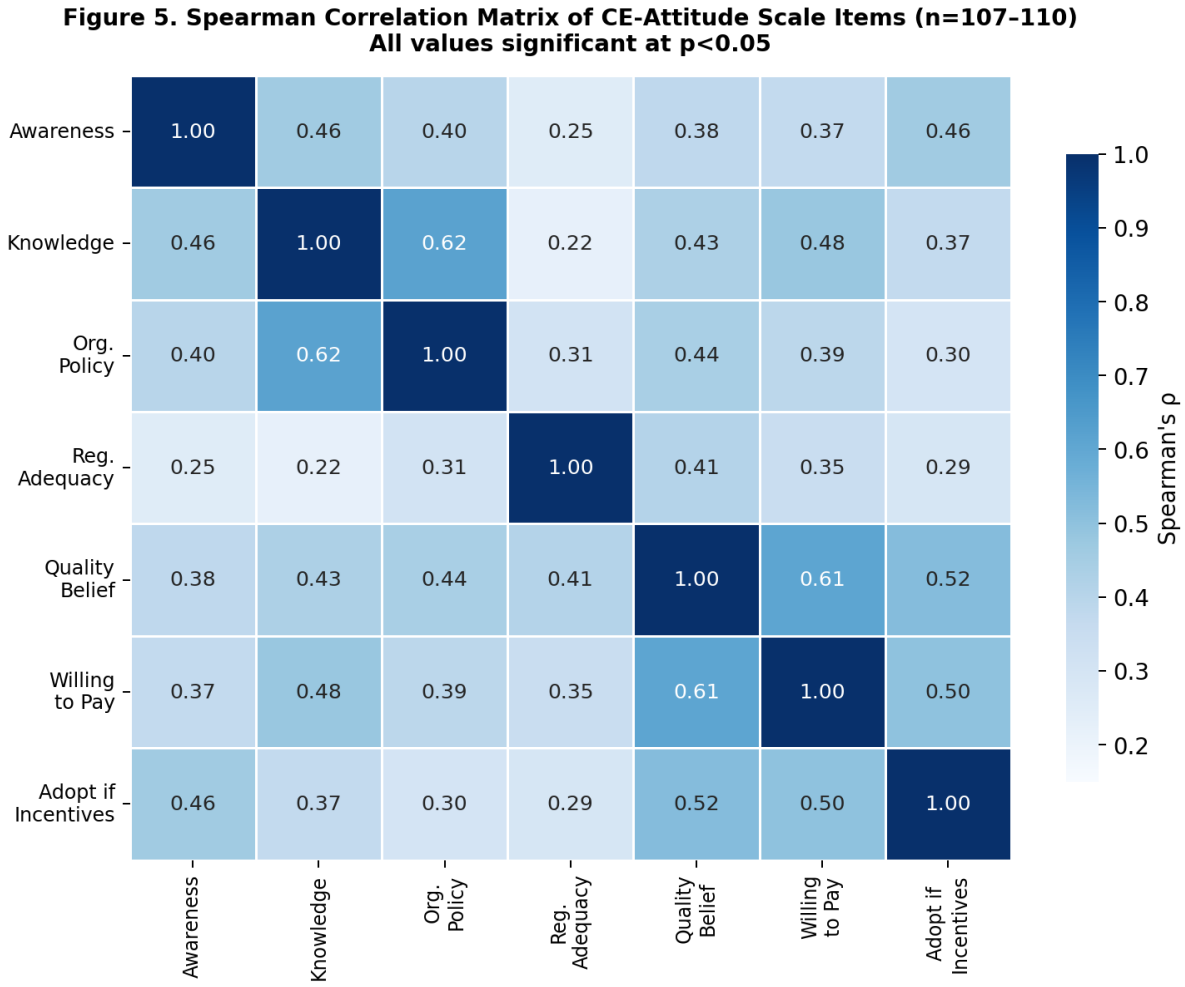

Figure 5: Spearman correlation heatmap of CE-attitude items. All values are significant at $p < 0.05$.

5. DISCUSSION

5.1 The Awareness-Practice-Incentive Decoupling

The main implication of the current study is that the gap in awareness and practice that is prevalent in Nigeria's construction CE literature (Unegbu et al., 2024) does not emerge due to differences in awareness amongst professionals. However, this interpretation should be considered in light of the measurement approach. Awareness was assessed through self-reported Likert-scale responses, which may capture perceived familiarity with CE concepts rather than the depth or quality of respondents' underlying knowledge. Consequently, professionals may report similar levels of awareness while still differing in their technical understanding or ability to apply CE principles in practice. There were no statistically significant differences in awareness levels with regard to role ($p = 0.709$) or education ($p = 0.810$). In turn, behavior related to waste separation and incentives showed statistically significant differences depending on role ($p = 0.028$ and $p = 0.025$, correspondingly). This separation of variables carries much significance in terms of intervention design, which should recognize that the variable on which it operates, "greater awareness leads to greater practice," is evenly distributed among professionals.

5.2 Quality Assurance as a Market-Side Lever

The most significant correlation found in attitude data was between perceptions regarding the quality of the recycled material and willingness to pay premium prices ($\rho = 0.61$). Such an observation adds empirically to the claim that has often been made in the academic literature but rarely tested, namely, that consumer acceptance of recycled construction and demolition (C&D) material is based more on perception of performance than on environmental attitudes (Ranasinghe et al., 2024). From

this, tools like certifications, material passports, and testing are demand-side tools, not auxiliary technical solutions. If there is a correlation between perception of quality and willingness to pay a higher price, it would mean that measures that enhance quality would be much more effective than measures focused on raising awareness in motivating recycling.

The findings provide evidence of particular engineering solutions that could transform the awareness of the circular economy into tangible construction techniques. It is clear that the strong correlation between the perception of the quality of recycled materials and willingness to pay should make engineering solutions to guarantee quality the key component of implementing the concept of a circular economy. This can be done through material testing, quality certification, and digital material passports for recycled construction materials. Similarly, the reported lack of recycling facilities indicates a need for accessible sorting and processing technologies, including on-site or decentralized systems for the separation, crushing, and recovery of recyclable construction materials. Such intervention techniques could be helpful in reducing the risk of contamination and increasing the reliability of recovered material. The implications of the research findings do not stop at awareness and policy but also help identify areas where the role of engineering and information technology is significant in transitioning from traditional waste management practices to material recovery and recycling techniques.

5.3 Why Contractors and Builders Behave Differently from Engineers

The most practically useful findings of this research can be obtained from the chi-square analysis carried out for every specific role separately. The contractors and the construction workers proved to separate waste more efficiently and be prepared to apply the principles of circular economy under the influence of motivation. The probable reason behind it, although not tested in the course of this research, is the fact that the contractors and builders may be more engaged in construction-related activity and, thus, more familiar with the waste generation process. It has to be considered a hypothesis that requires further research, as a cause-and-effect relationship has yet to be proven.

5.4 Institutional Constraints and the Limits of Voluntary Adoption

Lack of awareness was the most frequently reported barrier, cited by 59.1% of respondents, followed by lack of recycling infrastructure (48.2%) and weak regulation/enforcement (40.0%). However, this finding should be distinguished from the study's statistical assessment of individual CE awareness. The barrier question captures respondents' perceptions of constraints affecting CE adoption across the sector, whereas the awareness analysis measures respondents' own reported level of CE awareness. Thus, the fact that lack of awareness was frequently perceived as a sectoral barrier does not necessarily contradict the finding that reported awareness did not differ significantly by professional role or educational attainment. Respondents may, for example, perceive inadequate awareness among clients, workers, suppliers, policymakers, or other stakeholders even when their own reported awareness is relatively similar. It should be noted that infrastructure-/market-facilitating enablers such as guaranteed markets (49.1%) and equipment grants (42.7%) are preferred over regulation (40.9%) and tax incentives (35.5%), reflecting the view that the development of infrastructure and markets is more actionable for respondents compared to legislation. Internationally, a combination of regulatory, infrastructure investment, and market development was recognized as the most efficient approach to achieve high recovery rates of C&D in Sweden and Germany (Bonifazi et al., 2025). The attitude among the surveyed professionals is seen to be quite positive, with the respondents having moderately to highly aware levels and high conditional willingness to use CE (M = 3.86). When taking into consideration the other constraints such as infrastructure, markets, and enforcement, it is clear that there are many more constraints other than awareness.

The results from the analysis can be used to indicate that overcoming the implementation gap would require much more than just institutional reforms and awareness programs. The infrastructure and market gaps discussed above can be solved with a combination of C&D waste recovery systems, including source separation, mechanical sorting, processing, testing, and tracking of materials. For instance, proper sorting and crushing systems could enhance the process of recovering concrete, masonry, and other recoverable construction materials, whereas material testing and certification could

help generate the performance data required to improve market acceptance of recycled construction materials. The combination of the two approaches could create an efficient system of separation, processing, testing, and reutilization of recycled materials.

5.5 Limitations

There are various limitations to consider in relation to these results. Firstly, the use of cross-sectional methodology makes it impossible to determine causation. Secondly, purposive sampling prevents the results from being statistically generalized beyond the Abuja construction labor force. Thirdly, all practices under study are based on self-reporting and therefore prone to social desirability bias. Fourthly, the research is only done in one city. Fifthly, the limited size of the management/policy group (n = 7) limits the statistical comparison power. In addition, engineers and architects were combined into a single professional category for role-based analysis because of sample-size and cell-frequency considerations. Although this grouping supported the statistical analysis, the two professions may differ in training, responsibilities, and degree of site involvement, and their combination may therefore mask within-group differences.

6. CONCLUSION AND RECOMMENDATIONS

6.1 Conclusions

The current research seeks to assess the awareness level, practice, and determinants of construction waste management (CE) among 110 construction professionals in Abuja. For this purpose, a seven-question attitude scale (Cronbach's $\alpha = 0.803$) and inferential statistical techniques not typically applied to similar surveys of construction professionals in Nigeria have been used. Findings have confirmed the existence of the awareness-practice paradox previously reported in the literature as well as shed light on its nature: the awareness level is statistically consistent in terms of the professionals' positions and education levels; however, separation behaviors and reactions to incentives differ greatly depending on the position held. The belief in the high quality of the recycled materials proves to be the main determinant of willingness to pay, thus demonstrating that quality control is the key market-side determinant of CE. The findings also highlight the need to translate these behavioral and institutional insights into engineering practice through improved waste-separation systems, sorting and material-recovery technologies, standardized quality testing, and digital material traceability. Such interventions can help bridge the gap between willingness to adopt CE and actual recovery and reuse of construction materials."

6.2 Recommendations

For Policymakers and Regulators

Strengthen enforcement of existing C&D waste management regulations rather than relying on voluntary compliance; introduce mandatory waste management plans for projects above a defined size threshold; and develop standards and certification mechanisms for recycled C&D materials to directly address the quality-belief constraint identified as the strongest correlate of market willingness to pay.

For Training and Capacity-Building Programs

Target site-level contracting roles (contractors/builders) specifically, given this group's demonstrated stronger behavioral and incentive responsiveness; prioritize incentive-linked training formats, consistent with the high mean agreement (M=3.86) for incentive-conditional adoption; and invest in quality-assurance training as a mechanism for shifting quality perceptions that are holding back market demand.

For Industry and Market Actors

Make investments in engineering-based quality assurance measures such as standardized material testing, certification, and material passports to improve confidence in recycled construction materials. Construction firms and recyclers should also think about waste separation techniques at the job site, along with the proper technology for sorting, crushing, and recycling of the construction waste

materials. If there is no facility for centralized recycling available, then it will be better to use the decentralized technique. Digital material passports can further support traceability by recording material composition, quality characteristics, reuse potential, and recovery history. These methods can assist in turning willingness to embrace CE into actual processes of recovery and reuse, which is a problem for 48.2 percent of those surveyed, as lack of recycling facilities was mentioned as one of the key barriers. Public-private partnerships may be considered as a way to increase access to such facilities.

6.3 Suggestions for Future Research

Future research should:

i. Use probability-based sampling across a wider Abuja construction workforce to strengthen generalizability of role-based findings.
ii. Adopt a longitudinal design tracking the same cohort before and after specific regulatory or incentive interventions to test incentive responsiveness causally.
iii. Replicate this survey design in other rapidly urbanizing Nigerian cities to determine whether the awareness-practice decoupling observed in Abuja reflects a broader national pattern or FCT-specific conditions.

7. REFERENCES

Abah, E. A., Farouk, Z., Etim, E. J., & Goma, D. (2023). Sustainable development challenges in Abuja's construction industry: Balancing economic growth and environmental conservation. Journal of the Environment, 17(1), 1–7.

Bello, A. O., & Idris, A. (2023). Strategies for adoption of a circular economy in the Nigerian construction industry. Journal of Management Science & Engineering Research, 6(2), 47–59. https://doi.org/10.30564/jmser.v6i2.5846

Bonifazi, G., Grosso, C., Palmieri, R., & Serranti, S. (2025). Current trends and challenges in construction and demolition waste recycling. Current Opinion in Green and Sustainable Chemistry, 53, 101032. https://doi.org/10.1016/j.cogsc.2025.101032

Dsilva, J., Zarmukhambetova, S., & Locke, J. (2023). Assessment of building materials in the construction sector: A case study using the life cycle assessment approach to achieve the circular economy. Heliyon, 9(10), e20404. https://doi.org/10.1016/j.heliyon.2023.e20404

Kirchherr, J., Reike, D., & Hekkert, M. (2017). Conceptualizing the circular economy: An analysis of 114 definitions. Resources, Conservation and Recycling, 127, 221–232. https://doi.org/10.1016/j.resconrec.2017.09.005

Kirchherr, J., Yang, N. H. N., Schulze-Spüntrup, F., Heerink, M. J., & Hartley, K. (2023). Conceptualizing the circular economy (revisited): An analysis of 221 definitions. Resources, Conservation and Recycling, 194, 107001. https://doi.org/10.1016/j.resconrec.2023.107001

Lanrewaju, F. (2012). Urbanization, housing quality, and environmental degeneration in Nigeria. Journal of Geography and Regional Planning, 5(16), 422–429. https://doi.org/10.5897/jgrp12.060

National Bureau of Statistics. (2023). Nigeria Q3 2023 GDP report. https://www.statista.com/statistics/382264/total-population-of-nigeria/

Ogunseye, N. O., Ogunseye, O. D., & Ogunseye, A. O. (2023). Construction and demolition waste management in a developing country: A Nigerian scenario. Journal of Sustainability Perspectives, 3(1), 11–23. https://doi.org/10.14710/jsp.2023.15413

Ranasinghe, N., Domingo, N., & Kahandawa, R. (2024). Enhancing building material circularity: A systematic review on prerequisites, obstacles, and the critical role of data traceability. Journal of Building Engineering, 98, 111136. https://doi.org/10.1016/j.jobe.2024.111136

Shajidha, H., & Mortula, M. M. (2025). Sustainable waste management in the construction industry. Frontiers in Sustainable Cities, 7, 1–21. https://doi.org/10.3389/frsc.2025.1582239

Unegbu, H. C. O., & Yawas, D. S. (2024). Optimizing construction and demolition waste management in Nigeria: Challenges, regulatory frameworks, and policy solutions. Discover Civil Engineering, 1(1). https://doi.org/10.1007/s44290-024-00142-3

Velenturf, A. P. M., & Purnell, P. (2021). Principles for a sustainable circular economy. Sustainable Production and Consumption, 27, 1437–1457. https://doi.org/10.1016/j.spc.2021.02.018

International Conference on Engineering Innovation for Sustainable Development (ICESID 2026)
Faculty of Engineering, Ahmadu Bello University Zaria · 8–10 September 2026

DESIGN AND OPTIMIZATION OF A SHELL AND TUBE HEAT EXCHANGER USING PARTICLE SWARM OPTIMIZATION

Ernest Ikechukwu Dike[1,*], Umar Hassan[1], Muhammad Auwal Adamu[1]
[1]*Ahmadu Bello University*
Email: ernestdike14@gmail.com[*], uhassan56@yahoo.com, adauwal80@yahoo.com
***Corresponding author**: Ernest Ikechukwu Dike
DOI: https://doi.org/10.67203/sp.ICESID.2026

ABSTRACT
Heavy-duty haulage vehicles operating in tropical environments experience elevated engine oil temperatures that accelerate lubricant degradation and reduce engine reliability. Although Original Equipment Manufacturer (OEM) stacked-plate oil coolers provide compact thermal management, they are prone to irreversible fouling and limited serviceability under prolonged operation. Conventional shell-and-tube heat exchanger (STHE) retrofits offer improved maintainability but are generally oversized and excessively heavy, resulting in increased parasitic mass and reduced fuel efficiency. This study presents the design and optimization of lightweight STHE oil cooler for a Volvo D13 heavy-duty diesel engine using aluminum Alloy 6061-T6. Particle Swarm Optimization (PSO) was implemented in MATLAB to optimize the exchanger geometry, while the Kern design method was employed to evaluate thermal and hydraulic performance. The optimization objective was to minimize the total core weight subject to a maximum shell-side pressure drop of 50 kPa and an overall exchanger length of 1.5 m. The optimized TEMA E-shell configuration comprised 82 straight tubes (18 BWG), a shell diameter of 0.249m, a tube length of 1.471m, a tube outer diameter of 15.0 mm, and a baffle spacing of 0.064m. The resulting design achieved a total aluminum core weight of 23.80kg while maintaining shell-side and tube-side pressure drops of 49.98 kPa and 3.96 kPa, respectively, both within acceptable hydraulic limits for heavy-duty lubrication systems. The exchanger attained a thermal effectiveness of 83.3% with a Number of Transfer Units (NTU) of 2.37, demonstrating efficient heat transfer with low hydraulic resistance. The results confirm that integrating aluminum Alloy 6061-T6 with PSO-based geometric optimization significantly reduces exchanger weight while maintaining high thermal performance and hydraulic reliability. The proposed design provides a lightweight, maintainable, and locally manufacturable alternative to conventional oil coolers for heavy-duty diesel engines operating under demanding tropical conditions.

Keywords: *shell-and-tube heat exchanger; particle swarm optimization; Volvo D13; heavy-duty haulage*

1. INTRODUCTION

In Nigeria, heavy-duty haulage trucks are indispensable to the supply chain, facilitating approximately 95% of national freight movement (Federal Ministry of Works, 2025). However, operating in tropical Sub-Saharan environments with ambient temperatures frequently exceeding 35°C accelerates the thermal degradation of engine components. Excessive engine oil temperatures reduce lubricant viscosity, increase component wear, and ultimately shorten engine service life (Çengel & Ghajar, 2020). The Volvo D13 engine utilizes compact Original Equipment Manufacturer (OEM) stacked-plate oil coolers for thermal management; however, these sealed units are highly susceptible to irreversible fouling in dusty environments and cannot be serviced, leading to costly vehicle downtime.

Shell-and-tube heat exchangers (STHEs) provide a highly robust, maintainable alternative recommended for applications involving high operating pressures and severe environmental conditions due to their mechanical strength and serviceability (Shah & Sekulić, 2003). However, conventional STHE design heavily relies on empirical correlations like the Kern method, which utilizes conservative safety margins that frequently produce physically oversized and excessively heavy equipment (Kern, 1950). In automotive applications, this unnecessary structural mass is parasitic, increasing fuel consumption and carbon emissions, which directly conflicts with global climate change mitigation strategies for the transportation sector (IPCC, 2022).

To address these limitations, Particle Swarm Optimization (PSO) a swarm intelligence algorithm mimicking the social behaviour of bird flocks has emerged to effectively solve complex

nonlinear design problems (Kennedy & Eberhart, 1995). Previous studies demonstrate that PSO converges approximately 30% faster than Genetic Algorithms for STHE design (Fesanghary et al., 2009), consistently outperforming conventional deterministic techniques in constrained thermal design (Rao & Patel, 2010). Furthermore, automated MATLAB routines can significantly reduce material requirements within seconds. Balaban and Tadić (2021) developed a MATLAB-based automated shell-and-tube heat exchanger design program based on the Kern method. Their optimization reduced the required heat transfer area from 61.91 m² to 53.27 m², representing a 13.9% reduction in material requirement while obtaining the optimal solution within only a few seconds. Furthermore, recent evaluations of laboratory-scale STHEs operating specifically under northern Nigerian climatic conditions demonstrate the urgent need for robust computational optimisation to maximise thermal effectiveness in local applications (Hassan et al., 2025). Despite these advancements, existing literature frequently focuses on minimizing economic costs for stationary industrial applications (Khorasany & Fesanghary, 2009; Sai & Rao, 2022; Rao & Majethia, 2022). There remains a critical knowledge gap regarding weight minimization for automotive STHEs operating under strict spatial and tropical constraints.

Therefore, the aim of this study is to design and computationally optimize a lightweight STHE oil cooler retrofit for a Volvo D13 heavy-duty diesel engine. The specific objectives are to evaluate thermal-hydraulic performance using the Kern method, apply a PSO algorithm in MATLAB to minimize total aluminum core weight under strict pressure drop and spatial constraints, and validate hydraulic reliability using the Bell-Delaware method.

2. METHODOLOGY

2.1 Design Specifications and Material Selection

The shell-and-tube heat exchanger (STHE) was designed as a remote, chassis-mounted oil cooler for the 12.8-liter Volvo D13 heavy-duty diesel engine. The baseline thermal load was established at 63.0 kW, derived from a required temperature drop of 115°C to 90°C for a 1.2 kg/s mass flow rate of 15W-40 engine oil. To prioritize mechanical serviceability, the viscous engine oil was allocated to the shell side to exploit segmental baffle-induced turbulence, while the water-based engine coolant (3.0 kg/s at 85°C) was routed through the tube side because mineral scaling from coolant is effectively removed by passing a mechanical rod directly through the straight tubes, whereas the complex shell-side geometry is largely inaccessible for physical descaling. aluminum Alloy 6061-T6 was specified for both the shell and tube bundle (18 BWG, 1.25 mm wall thickness) to drastically minimize parasitic mass, leveraging its low density (2700 kg/m³) and superior strength-to-weight ratio compared to traditional carbon steel.

2.2 Mathematical Modelling

The Kern method was utilized to evaluate the thermal-hydraulic performance of the heat exchanger during optimization. The clean overall heat transfer coefficient (U_{clean}) was formulated based on the shell-side convective coefficient (h_s), the tube-side convective coefficient (h_t), and the thermal conductivity of the aluminum 6061-T6 tube wall (k_{wall}):

$$U_{clean} = \frac{1}{\frac{1}{h_s} + \frac{d_o}{d_i \times h_t} + \frac{d_o ln\left(\frac{d_o}{d_i}\right)}{2 \times k_{wall}}} \tag{1}$$

To evaluate the hydrodynamic constraints governing the required pumping power, the actual pressure drops for both the tube-side (ΔP_t) and shell-side (ΔP_s) were continuously calculated using the fundamental Kern method equations:

$$\Delta P_s = \frac{(f_s G_s^2\ (N_b + 1) D_s)}{(2\ \rho_h D_e \phi_s)} \tag{2}$$

$$\Delta P_t = \left(\frac{4\ f_t\ L\ n_p}{d_i} + 4\ n_p\right)\ (\frac{\rho_c v_t^2}{2}) \tag{3}$$

Where f_s and f_t are the respective friction factors, G_s is the shell-side mass velocity, N_b is the number of baffles, D_s is the shell inside diameter, ρ_h and ρ_c are the densities of the hot and cold liquid respectively, D_e is the equivalent diameter, φ_s is the viscosity correction factor, L is the tube length, n_p is the number of tube passes, d_i is the internal tube diameter and v_t is the tube-side fluid velocity.

2.3 Optimization Problem Formulation

The objective of the PSO algorithm was to minimize the total structural weight of the STHE core (f(X)), expressed as the sum of the shell and tube weights:

Minimize $f(X) = W_{tubes} + W_{shell}$ (4)

To ensure the physical manufacturability and hydraulic safety of the automotive retrofit, the objective function was subjected to strict inequality constraints:

$g_1(X) = \Delta P_s - 50 \leq 0$

$g_2(X) = \Delta P_t - 30 \leq 0$

$g_3(X) = L - 1.5 \leq 0$

$g_4(X) = D_s - 0.35 \leq 0$

2.4 Particle Swarm Optimization (PSO) Implementation

The optimization was executed in MATLAB using a swarm of 50 particles navigating a four-dimensional search space over 100 iterations. The decision variables vector X = [D_s, B, d_o, L] represented the core geometric parameters; specifically, the tube outer diameter (d_o) was established as a free optimisation variable bounded between 15.0 mm and 25.0 mm rather than a fixed constant. The kinematic movement of the particles was governed by velocity and position update equations, utilizing a dynamic inertia weight (w) that linearly decreased from 0.9 to 0.4 to transition the swarm from global exploration to localized exploitation. Mathematical penalty functions were embedded within the fitness evaluation to assign massive weight penalties to any geometric configuration that violated the defined pressure or spatial constraints, effectively forcing the algorithm to abandon those localized spaces.

The kinematic movement of the particles was governed by the velocity and position update equations:

$$v_i^{k+1} = wV_i^k + c_1 r_1 \left(P_{best,i} - X_i^k\right) + c_2 r_2 \left(G_{best} - X_i^k\right) \quad (5)$$

$$X_i^{k+1} = X_i^k + V_i^{k+1} \quad (6)$$

Where w is the dynamic inertia weight, c_1 and c_2 are acceleration coefficients, and r_1 and r_2 are stochastic random variables.

3. RESULTS AND DISCUSSION

3.1 PSO Convergence and Geometric Parameters

The PSO algorithm successfully navigated the geometric constraints, converging upon the global minimum after approximately 40 iterations.

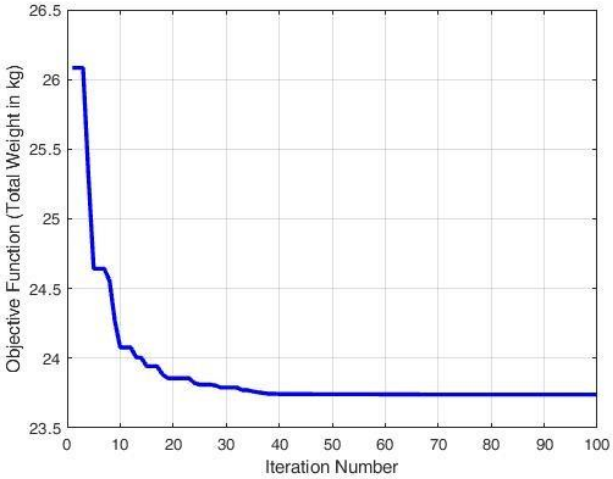

Figure 1: PSO Convergence Curve showing the minimization of total weight over successive iterations.

The dynamic inertia weight mechanism effectively transitioned the swarm from global exploration to localized exploitation, yielding an optimized core mass of 23.80 kg. The optimal TEMA E-shell configuration comprised 82 straight tubes, an inner shell diameter of 0.249 m, a tube length of 1.471 m, and a baffle spacing of 0.064 m. notably, the algorithm successfully drove the tube outer diameter to its absolute lower bound (15.0 mm) to strictly maximise the surface to area to volume ratio within the confined shell. The resulting baffle-to-shell diameter ratio (0.26) validated TEMA standards while maximizing shell-side turbulence. By utilizing aluminum 6061-T6 and optimal swarm sizing, the algorithm successfully eliminated the substantial excess mass inherent in traditional manual STHE design heuristics; an actual comparative baseline calculation utilising the unoptimized Kern method for this specific 63.0 kW thermal duty yielded a theoretical core mass of 58.6 kg.

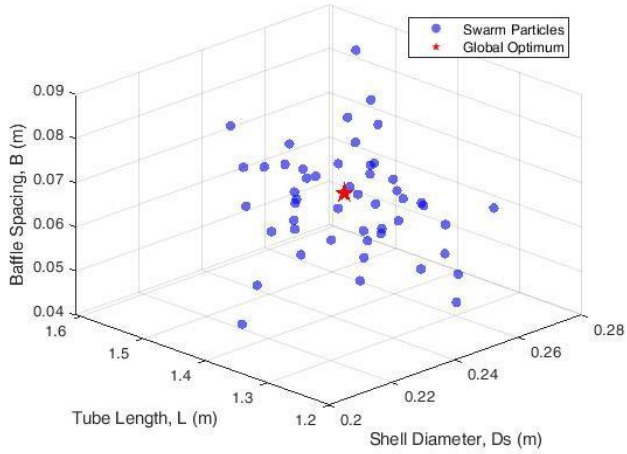

Figure 2.3: D visualization of the swarm particles navigating the geometric design space to isolate the global optimum.

3.2 Thermal-Hydraulic Performance

The optimized design successfully managed the 63.0 kW thermal load, achieving a Number of Transfer Units (NTU) of 2.37 and an exceptional thermal effectiveness of 83.3%. Utilizing the Kern method, the initial shell-side pressure drop was calculated at 49.98 kPa, successfully riding the edge of the 50 kPa limit to maximize cross-flow heat transfer without violating the pump threshold. Conversely, the tube-side pressure drop was exceptionally low at 3.96 kPa against the 30 kPa limit, minimizing strain on the vehicle's coolant circuit.

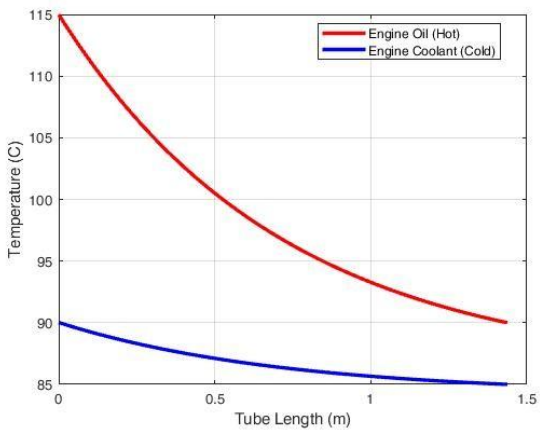

Figure 3: Longitudinal temperature profile illustrating the counter-flow thermal gradient between the hot engine oil and cold engine coolant.

While this mathematically maximises heat transfer, operating at 99.96% of a hard constraint limit reduces the real-world safety margin, necessitating strict adherence to maintenance schedules to prevent pressure-induced pump cavitation as fouling layers develop over time.

3.3 Bell-Delaware Hydraulic Validation

While the Kern method provided a fundamentally sound baseline, physical manufacturing of an STHE requires clearances that allow fluid to bypass the main cross-flow area, thereby reducing actual frictional resistance. To provide a post-optimization validation of the hydraulic safety margin, the optimized geometry was subjected to a simplified approximation of the Bell-Delaware method. By applying standard TEMA Class C empirical correction factors for baffle leakage ($R_l = 0.550$), bundle bypass ($R_b = 0.720$), and inlet/outlet spacing ($R_s = 0.862$) which were derived from standard TEMA graphical charts based on the optimised geometric baffle clearances, the actual shell-side pressure drop was approximated:

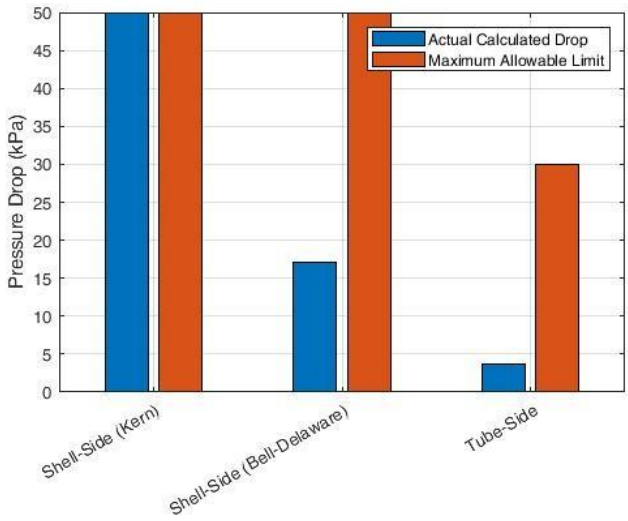

$$\Delta P_{shell} = 49.98 \times 0.550 \times 0.720 \times 0.862 \quad (7)$$

$$\Delta P_{shell} = 17.06\ kPa \quad (8)$$

Figure 4: Comparative bar chart of the simulated hydraulic pressure drops (Kern vs. Bell-Delaware) against the maximum allowable design limits.

(Note: The Kern shell-side actual value of 49.98kpa is displayed immediately adjacent to the 50.00 kpa limit bar).

This massive reduction from the 49.98 kPa Kern estimate confirms the Kern method is highly conservative. Consequently, if the rigorous, multi-zone Bell-Delaware formulation were integrated directly into the PSO objective function rather than the Kern method, the relaxed pressure constraints would likely allow the algorithm to achieve even further weight reductions, presenting a distinct pathway for future research

4. CONCLUSION

This study successfully addressed the serviceability limitations of heavy-duty OEM stacked-plate oil coolers by proposing a mathematically optimized, maintainable STHE retrofit. By implementing Particle Swarm Optimization in MATLAB, the structural mass of the aluminum 6061-T6 core was minimized to 23.80 kg. The system achieved a thermal effectiveness of 83.3% while maintaining a highly secure Bell-Delaware corrected pressure drop of 17.06 kPa. The results validate that computational swarm intelligence can successfully bridge the gap between heavy industrial STHE design and compact automotive constraints, offering the tropical haulage sector a lightweight and permanently serviceable cooling solution.

REFERENCES

Balaban, M., & Tadić, M. (2021). MATLAB-based optimization of shell-and-tube heat exchanger design. Thermal Science.

Çengel, Y. A., & Ghajar, A. J. (2020). Heat and Mass Transfer: Fundamentals and Applications (6th ed.). McGraw-Hill.

Federal Ministry of Works. (2025). National Road Transport Infrastructure Report. Abuja, Nigeria.

Fesanghary, M., Damangir, E., & Soleimani, I. (2009). Design optimization of shell-and-tube heat exchangers using global sensitivity analysis and particle swarm optimization. International Journal of Heat and Mass Transfer, 52(3–4), 779–788.

Hassan U, Hassan T. and Alapatira I. Q (2025). Design and performance evaluation of a laboratory-scale shell-and-tube heat exchanger under Northern Nigerian climatic conditions. FUDMA Journal of Sciences (FJS), 9(9): 227 – 23, https://doi.org/10.33003/fjs-2025-0909-3749

IPCC. (2022). Climate Change 2022: Mitigation of Climate Change. Cambridge University Press.

Kennedy, J., & Eberhart, R. (1995). Particle swarm optimization. Proceedings of the IEEE International Conference on Neural Networks, 1942–1948.

Kern, D. Q. (1950). Process Heat Transfer. McGraw-Hill.

Khorasany, R. M., & Fesanghary, M. (2009). A novel approach for synthesis of cost-optimal heat exchanger networks. Computers & Chemical Engineering, 33(8), 1363-1370.

https://doi.org/10.1016/j.compchemeng.2008.12.004

Rao, M., & Majethia, P. (2022). Optimization of shell-and-tube heat exchanger using metaheuristic algorithms. Materials Today: Proceedings.

Rao, R. V., & Patel, V. (2010). Thermodynamic optimization of shell-and-tube heat exchangers using particle swarm optimization. Applied Thermal Engineering, 30, 1417–1425.

Sai, K., & Rao, M. (2022). Multi-objective optimization of shell-and-tube heat exchangers using evolutionary algorithms. Materials Today: Proceedings.

Shah, R. K., & Sekulić, D. P. (2003). Fundamentals of heat exchanger design. John Wiley & Sons.

International Conference on Engineering Innovation for Sustainable Development (ICESID 2026)
Faculty of Engineering, Ahmadu Bello University Zaria · 8–10 September 2026

DESIGN AND THERMAL PERFORMANCE OF A HYBRID SOLAR-BIOMASS DRYER FOR DRYING FISH

Igbinosa Ikpotokin[1,*]

[1]*Department of Mechanical and Mechatronics Engineering, Faculty of Engineering, Federal University Otuoke, Bayelsa State, Nigeria*

Email: ikpotokinii@fuotuoke.edu.ng[*]

***Corresponding author**: Igbinosa Ikpotokin

DOI: https://doi.org/10.67203/sp.ICESID.2026

ABSTRACT

Fish dryers are heat-transfer devices designed to remove moisture from fish undergoing drying in order to improve the fish's shelf life. However, a dryer that relies only on thermal energy from solar power often performs poorly at night and on cloudy or raining days. These conditions reduce the solar collector's effectiveness and limit the drying rates. To address this, a hybrid dryer was developed, which uses solar energy as its main heat source and combusts biomass to make up for the absence of solar radiation. This study aimed to create a hybrid solar-biomass dryer that can sustain stable drying conditions regardless of the solar availability. The dryer, which consists of a flat-plate solar collector, biomass combustion chamber, and heat exchanger, was fabricated with low-cost, locally sourced materials. Performance test was conducted outdoors at the Federal University Otuoke, Bayelsa State, using one kilogram of catfish over seven effective daylight hours. To avoid drying interruption, biomass-fueled heating was used in the evening. The results demonstrated that the hybrid dryer reduced the fish drying time from 48 hours to 10 hours and decreased the moisture content from 75% to 15%. Effective conversion and use of renewable energy is demonstrated by the dryer's overall thermal efficiency, which ranges from 45 to 50%, and its average solar collector efficiency of 40%. This study highlights the potential of the hybrid dryer as an efficient, economical, and sustainable approach to enhance fish preservation, food security, small-scale business assistance, and reduce post-harvest losses.

Keywords: *Thermal performance; Hybrid dryer; Biomass; Solar energy; Fish drying*

1.0 INTRODUCTION

Dryers are devices designed to facilitate the removal of certain amount of liquid, usually water, from materials or products to reduce the residual liquid content to an acceptably low level using thermal energy. They are widely used in numerous applications such paper mill, food processing, pharmaceuticals, textiles, and manufacturing industries. In agriculture, dryers are used for processing and preservation of post-harvest produce, including fish through drying. This increases their shelf life, preserves quality and prevent microbial growth that causes spoilage (Hao *et al.*, 2021).

Among the numerous techniques for preserving fish, drying is the most popular and more economical. This method involves the application of dryers that operate with heat energy source to reduce the moisture content of the fish to a level that limits microbial growth and enzymatic reactions, thereby extending the fish's shelf life (Nwakuba *et al*., 2025).

Traditionally, fish are dried by exposing them directly to the sun and is commonly used in rural areas because of low capital cost and operational simplicity of the drying system (Vengsungnle *et al*., 2020). However, this practice has many disadvantages. One of the disadvantages is that significant amount of the thermal energy generated from solar irradiation is lost to the environment due to its dispersion, variability and relatively low intensity. This energy loss results in low drying efficiency, limiting the effectiveness of open sun solar-based dryers. Additionally, product dried using open sun solar-based dryer may be contaminated with dust and insects that compromises the product's quality and economic worth (Prabhu *et al*., 2023).

Conventional dryers that operate solely on fossil fuels are often more efficient, but their high fuel consumption makes them unaffordable for rural people, especially those with low agricultural output ability. Additionally, increasing fossil fuel prices, sporadic supply interruptions, and the related environmental effects such as greenhouse gas emissions that cause climate change have inspired a

search for efficient and sustainable renewable energy sources (Ambaye *et al*., 2021). Solar and biomass have been identified as the two primary renewable energy resources most suitable for drying applications (Lingayat *et al*., 2021; Anyaoha *et al*., 2025; Younis *et al*., 2025).

In recent years, researchers have developed solar dryers to surmount the problem of traditional fish drying. These dryers employ solar collector to heat the air and move it through the drying chamber, which acts as a controlled environment to increase drying efficiency, shield the fish from contaminants, and enable more reliable drying (Yuwana *et al*., 2020). However, solar energy is only available on sunny days. This condition limits solar fish dryers' capacity to operate continuously at night and during cloudy or raining weather (Murali *et al*., 2023).

Biomass drying systems employ burning of organic materials such as wood, charcoal, or agricultural waste. In many rural and coaster regions, biomass is a readily available and affordable source of energy. Researchers have demonstrated that biomass-fueled dryer provides a practical and effective solution for large-scale drying of marine post-harvest products (Alfiya *et al*., 2025). The systems' scalability also makes it appropriate for commercial use, so as to enable higher production capacity while reducing fossil fuel consumption and environmental effect. However, inadequate utility management of biomass drying equipment may result in issues with pollution, fuel supply, and heat regulation.

The disadvantages inherent in each of the aforementioned thermal energy sources have stimulated the development of a hybrid drying equipment, which combines solar and biomass energy to provide continuous supply of heat even during periods of low solar radiation, such as cloudy days or nights (Pawar *et al*., 2024). Researchers have shown that a temperature range of 40-50°C was effectively maintained within the drying chamber of a hybrid fish dryer continuously for a duration of 15 hours using a solar dryer in conjunction with biomass heater (Hamdani *et al*., 2018). This range of temperatures promotes efficient moisture removal without causing the fish to deteriorate due to heat. Although studies have recognized the potential benefits of combining solar and biomass technologies earlier for drying, there is still a dearth of knowledge with respect to development and practical implementation of the hybrid equipment, especially for fish drying in rural communities.

Therefore, this study develops a hybrid solar-biomass fish dryer that uses a solar thermal collector in conjunction with biomass briquette source. The study also aims to evaluate the performance of the dryer.

2.0 METHODOLOGY

In this study, the deterministic approach, involving the application of energy and mass equations, was employed for the design. The drying equipment’s materials were selected and sourced locally to ensure affordability and accessibility while satisfying the necessary structural and thermal requirements. These materials constituted components for solar collector, drying chamber, insulation and biomass heating system. Drying tests were conducted to evaluate the dryer’s thermal performance.

2.1 Design Equations

The size of the solar collector was determined based on the drying area needed to dry a 1.0 kg load of 75% (wet basis) catfish between 9:00 AM and 5:00 PM. A target final moisture content of 12% (wet basis) was set for the dried fish. The design of the dry was carried out in accordance with the considerations listed in Table 1.

Table 1: Design considerations for the hybrid solar-biomass fish dryer

S/N	Parameters	Value
1	Drying material	Catfish
2	Initial mass of fish (m_w)	1.0 kg
3	Initial moisture content (M_i)	75% (wet basis)
4	Target final moisture content (M_f)	12% (wet basis)
5	Average solar irradiant (I_c)	600 W/m^2
6	Drying period (t_d) 9:00 AM and 5:00 PM	7 hours
7	Solar collector efficiency (η_c)	40%
8	Tilt angle	6°
9	Ambient Temperature (T_a)	30 ^{o}C
10	Drying chamber temperature range	45 – 52 ^{o}C
11	Biomass briquette Lower Calorific value (LCV)	15 MJ/kg

For the design and performance evaluation, equations 1 to 14 were applied.

The amount of moisture to be removed is expressed by equation 1.

$$m_w = m_i \frac{M_i - M_f}{100 - m_f} \tag{1}$$

where m_i is the initial mass of fresh to be dried (kg), m_i is the initial moisture content (% wet basis), and m_f is the final moisture content (% wet basis).

The thermal load required consists of the latent heat to evaporate the water (Q_{lat}) and the sensible heating of the fish tissue ($Q_{s,fish}$) as expressed in equation 2.

$$Q_{req} = Q_{lat} + Q_{s,fish} = m_w h_{fg} + m_i C_p (T_c - T_a) \tag{2}$$

The total design thermal load was calculated by adding 15% for heat losses through the dryer walls. This is expressed in equation 3.

$$Q_{load} = 1.15 Q_{req} = 1.15 \left(m_w h_{fg} + m_i C_p (T_c - T_a) \right) \tag{3}$$

where C_p is the specific heat capacity of fish (J/kg.^{o}C), T_c is the target drying temperature (^{o}C), T_a is the ambient air temperature (^{o}C), and h_{fg} is the enthalpy of vaporization (J/kg).

The solar collector thermal efficiency η_c is expressed in equation 4.

$$\eta_c = \frac{Q_{load}}{t_d A_c I_c} \times 100 = \frac{\dot{m}_a C_{pa} (T_{co} - T_{ci})}{A_c I_c} \times 100 \tag{4}$$

The mass flow rate of drying air required to absorb the evaporated water is given by equation 5.

$$\dot{m}_a = \frac{m_w}{t_d (\omega_o - \omega_i)} \tag{5}$$

The collector area is expressed by equation 6.

$$A_c = \frac{Q_{load}}{I_c \eta_c t_d} \tag{6}$$

where I_c is the average solar irradiant (W/m^2), $\dot{m}_a$ is the air flow rate (kg/s), C_{pa} is the specific heat capacity of air at constant pressure (J/kg.K), t_d is the drying period or time (s), T_{co} is the collector air outlet temperature (°C), T_{ci} is the collector air inlet temperature (°C), ω_o is the relative humidity of exhaust air exiting the chamber (kg water/kg air), and ω_i is the relative humidity of inlet air (kg water/kg air)

The tray area is expressed in equation 7.

$$A_{tray} = \frac{m_i}{\rho_{fish}} \tag{7}$$

where ρ_{fish} is the loading density of fish (kg/m^2)

Energy generated by combustion of biomass is determine using equation 8.

$$Q_{bio} = \dot{m}_{bio} LHV \tag{8}$$

The biomass consumption rate is expressed in equation 9.

$$\dot{m}_{bio} = \frac{Q_{load}}{LHV \times \eta_{comb} t_d} = \frac{Q_{bio}}{LHV \times \eta_{comb}} \tag{9}$$

where $\dot{m}_{bio}$ is the biomass consumption rate (kg/hr), LHV is the biomass lower heating value (kJ/kg), and η_{comb} is the biomass combustion efficiency (%).

Equation 10 expresses the thermal efficiency, which measures how efficiently the total energy input is converted to heat for evaporating moisture.

$$\eta_d = \frac{\mathrm{Q}_{lat}}{\mathrm{Q}_{solar} + \mathrm{Q}_{bio}} \times 100 \tag{10}$$

Equations 11 expresses the latent heat of vaporization.

$$\mathrm{Q}_{lat} = m_w h_{fg} \tag{11}$$

The solar energy collected by the solar collector during the drying period is represented by Equation 12.

$$\mathrm{Q}_{solar} = A_c I_c t_{d,solar} \tag{12}$$

Equation 13 represents the total heat energy of the burnt biomass fuel.

$$\mathrm{Q}_{bio} = \dot{m}_{bio} LHV \times \eta_{comb} t_{d,bio} \tag{13}$$

Equation 14 represents the hybrid dryer's overall energy consumption, which is the sum of the energy contributions from the solar and biomass sources.

$$\mathrm{Q}_{tot} = \mathrm{Q}_{solar} + \mathrm{Q}_{bio} \tag{14}$$

2.2 Construction of the Dryer

The dimensions of the constructed dryer according to design Equations 1through 14 is shown in Fig. 1(a) - (d). The hybrid solar-biomass dryer consists of drying chamber, solar collector and biomass combustion unit. The drying chamber was fabricated as rectangular insulated box with timber studs and plywood cladding. All internal seams were sealed before applying the aluminum liner. The black absorber plate was fixed below the glazing at a shallow inclination to encourage buoyancy-driven flow. A 4 mm thick glass sheet was mounted in a wooden sash with rubber beading to limit leakage and allow maintenance. The biomass heater was constructed using mild steel and connected via an indirect hot-air duct to avoid smoke contact with fish. The duct entered near the chamber floor to mix incoming hot air before rising across the trays. A top flue maintained steady exhaust of warm, moist air. The solar collector was mounted directly on the chamber at 6°, which nearly matched the local latitude of Bayelsa State, Nigeria ((about 5°N to 6°N). This orientation maximized solar energy capture for the area. The direct mounting of the solar collector also eliminated long ducts and reduced thermal losses across joints.

2.3 Performance Evaluation Test Procedure

A performance test of the fabricated hybrid solar-biomass fish dryer was conducted outdoor at the Faculty of Engineering, Federal University Otuoke, Bayelsa State, Nigeria using 1.0 kg of fresh catfish with approximately 75% (wet basis) initial moisture content. The tests were carried out over 7 hours drying period under ambient temperature ranging from 28-30°C with solar irradiance of 600 W/m² and moderate wind. During the drying period, the dryer was operated on solar mode for about 7 hours and then on biomass support through the evening to complete the drying process. The ambient and chamber temperatures were measured using thermometers. A hygrometer was used to measure the relative humidity trend. A digital weighing balance was used to measure the initial mass and subsequent mass of the fish at regular intervals.

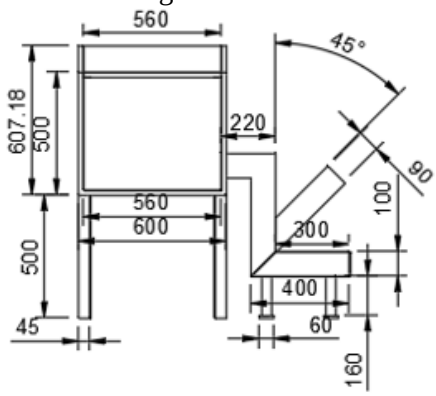

(a) Front view

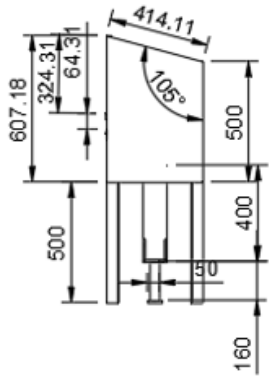

(b) Side view

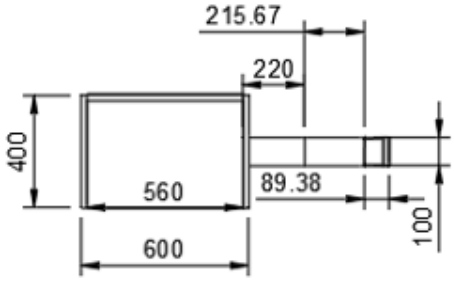

(c) Plane

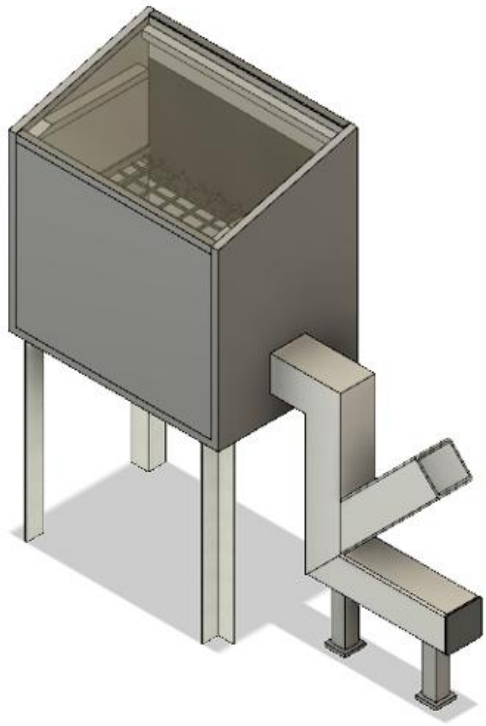

(d) 3D

Figure 1: 2D and 3D of the hybrid dryer.

3.0 RESULTS AND DISCUSSION

The design results obtained using equations 1 through 14 are shown in Table 2. The results of moisture removal and weight loss during the test are depicted in Fig. 2(a) and (b), respectively. The

temperature trend results are presented in Fig. 3. Furthermore, the results of moisture removal and the drying chamber temperatures, which reveal the time of the solar energy utilisation phase and the biomass energy utilisation phase, respectively, are shown in Fig. 3(a) and (b).

Table 2: Design Calculation Parameters

S/N	Parameter	Value
1	Moisture to remove	0.7059kg
2	Moisture removed over 7hr	0.2896kg
3	Latent heat (Q_{lat})	1,595.3 kJ
4	Sensible heat ($Q_{s,fish}$)	92.5 kJ
5	Heat loss over 7hrs (Q_{loss})	540 kJ
6	Total heat (Q_{total})	2227.8 kJ
7	Solar collector surface area (A_c)	0.35 m^2

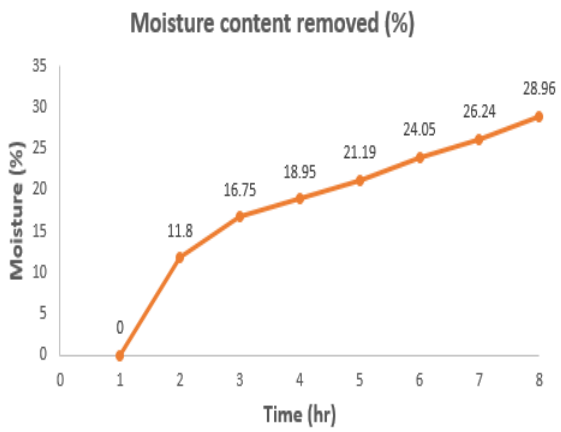

(a) Percentage Moisture versus time.

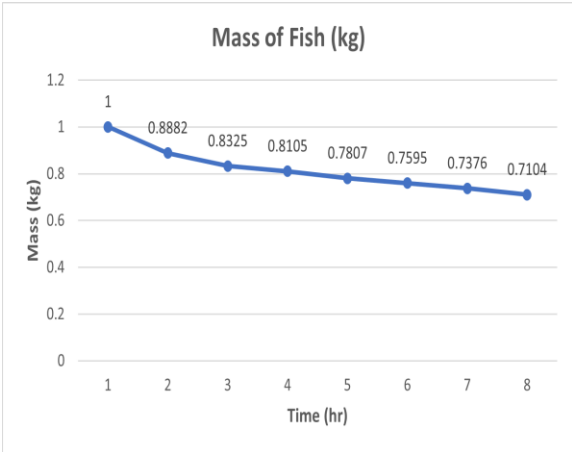

(b) Fish weight loss versus time

Figure 2: Percentage moisture and weight losses against drying time.

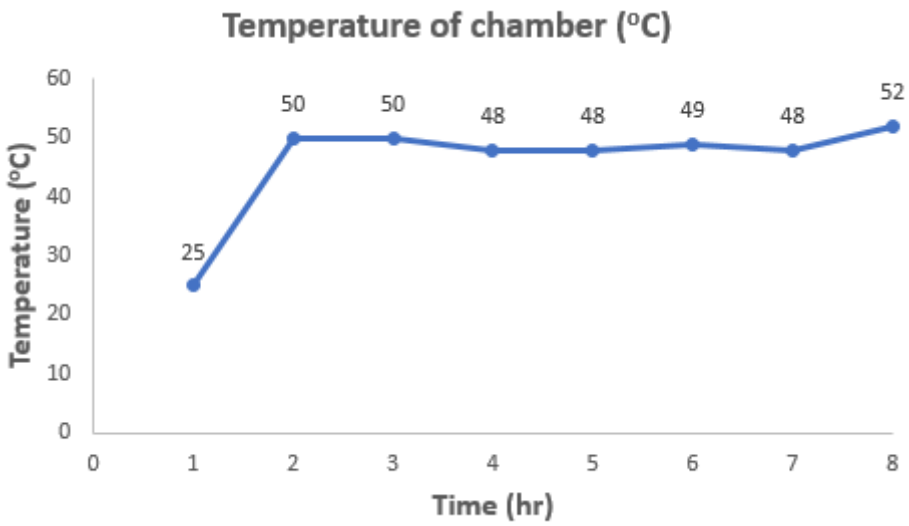

Figure 3: Drying chamber temperature profile.

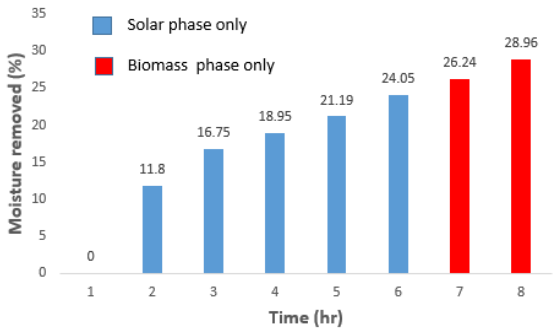

(a) Moisture removal showing the solar energy and biomass energy.

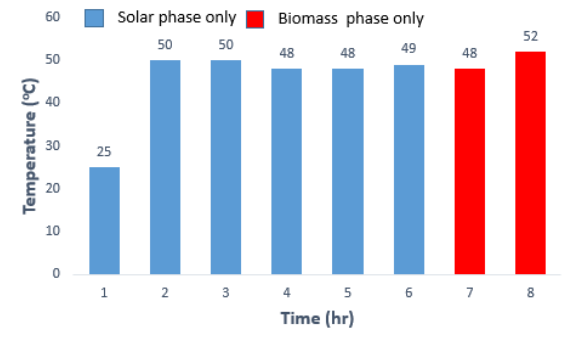

(b) Drying chamber temperature showing solar energy and biomass energy

Figure 4: Moisture removal and chamber temperature showing solar energy and biomass energy supply.

Figure 2(a) shows the percentage of moisture content removed with time during the drying test. The moisture loss from the fresh fish increased from 0% to around 11.8% over the first hour of solar operation. The amount of moisture removed rises as the drying time increases, although more slowly and steadily to 24.05% during the solar phase as shown in Fig. 3(a). Approximately 28.96% of the

moisture content was removed within the other two hours of introducing biomass source of energy. After about 10 hours of total drying time, the fish's moisture decreased from 75% (wet basis) to 12-15%. This indicates that while the majority of the moisture may be eliminated in the early hours, it takes longer to achieve almost total drying because of decreasing returns.

The corresponding weight loss with time is depicted in Fig. 2(b). At first, when surface moisture evaporates, the mass decreases somewhat fast. As the residual moisture moves farther inside the fish and takes longer to reach the surface, the rate of mass loss gradually decreases. This pattern illustrates the usual drying behaviour, in which moisture loss is relatively faster at first and slows down as drying goes on. The fish's weight decreased from 1.0 kg to around 0.71 kg after 8 hours, in accordance with safe storage, and the steady fall shows efficient moisture removal. The pattern shows how well the drying process works to progressively reduce fish mass by gradually reducing the moisture content.

Fig. 3 shows the temperature profile of the chamber with respect to time. During the first hour, the temperature rises quickly, reaching 50ºC and fluctuates slightly between 48 to 50ºC within the duration of two to seven hours. The temperature marginally increase to 52ºC after 8 hours due to activation of biomass source of energy as shown in Fig. 3(b). The temperature profile demonstrates that the chamber sustains a constant temperature for the majority of the drying time, which is suitable for reliable drying.

Energy analysis gave a batch design energy of about 2,227.8 kJ using equation 3. The hybrid solar-biomass drier provides an overall thermal efficiency ranging from 45%, demonstrating its ability to effectively convert and utilize thermal energy for the drying process. This efficiency is attributed to the combined performance of solar and biomass energy sources to maintain optimal drying temperatures and reduce energy losses. Additionally, the solar collector showed an efficiency of 40%, indicating that it can efficiently capture solar radiation and convert it into useful heat energy. The results also show that solar contributed approximately 60% of the dryer’s energy consumption and biomass accounted for the remaining 40%. This complementing energy mix maximises the dryer's performance by ensuring consistent drying temperatures regardless of the weather conditions, including low solar irradiance or evening time.

4.0 CONCLUSION

A hybrid solar-biomass dryer specifically for fish drying was designed and fabricated to address the disadvantages of traditional sun-based drying equipment as well those of solar energy or biomass or fossil fuel-operated dryers. The findings from the performance evaluation showed that the hybrid dryer lowered the moisture content from 75% to 15% and shortened the fish drying time from 48 to 10 hours. The hybrid dryer's overall thermal efficiency ranges from 45 to 50 percent, with an average solar collector efficiency of 40 percent, demonstrating its capacity to effectively convert and use thermal energy during the drying process. Solar energy accounts for about 60% of the dryer's energy needs, with biomass providing the remaining 40%, making the dryer a viable and sustainable solution for small-scale fish drying businesses. Therefore, this study emphasizes the potential of the hybrid dryer as a practical, affordable, and sustainable method to improve food security, fish preservation, small-scale business support, and post-harvest losses.

REFERENCES

Anyaoha, C. O., Okoroigwe, F. C., Okoroigwe, C. N., Uzoagba, C. E., & Okoroigwe, E. C. (2025). A review of optimization strategies for solar-biomass dryers. *Sustainable Energy Technologies and Assessments*, 83, 104672.

Hao, W., Zhang , H., Liu, S., & Lai, Y. (2021). Design and prediction method of dual working medium solar energy drying system. *Applied Thermal Engineering*, 198, 117153.

Alfiya, P. V., Murali, S., Aniesrani Delfiya, D. S., & Samuel, M. P. (2025). Design and development of biomass-fueled convective dryer for marine products: energy, exergy, environmental, and economic (4E) analysis. *Biomass Conversion and Biorefinery*, 15(8), 12031–12042 . https://doi.org/10.1007/s13399-024-06001-6.

Ambaye, T. G., Vaccari, M., Bonilla-Petriciolet, A., Prasad, S., Hullebusch, E. D., & Rtimi, S. (2021). Emerging technologies for biofuel production: A critical review on recent progress, challenges and perspectives. *Journal of Environmental Management*, 290, 112627.

Hamdani, U., Rizal, T. A., & Muhammad, Z. (2018). Fabrication and testing of hybrid solar-biomass dryer for drying fish. *Case Studies in Thermal Engineering*, 12, 489-496.

Lingayat, A., Balijepalli, R., & Chandramohan, V. P. (2021). Applications of solar energy based drying technologies in various industries – A review. *Solar Energy*, 229, 52-68.

Murali, S., Alfiya, P. V., Delfiya, D. S., Samuel, M. P., & Ninan, G. (2023). Solar Hybrid Drying System for Marine Applications – A Comprehensive Review. *Journal of Aquatic Food Product Technology*, 32(1), 38–58.

Nwakuba, N. R., Ofojioha, O. M., Ikechukwu, K. U., Ofoma, A. N., Chikwue, M. I., Oham, P. N., & Okorie, C. E. (2025). Development and Sustainability Assessment of a Fish-drying Kiln: Eco-thermodynamic Insights. *Agricultural Science and Food Processing*, 2(4), 176–196. https://doi.org/10.62762/ASFP.2025.325927.

Pawar, R., Santara, S., Sircar, A., & Yadav, K. (2024). Design and development of hybrid solar–biomass drying system: An innovative approach. *MRS Energy & Sustainability*, 11(2), 409–433. https://doi.org/10.1557/s43581-024-00083-5.

Prabhu, N., Saravanan, D., & Kumarasamy, S. (2023). Eco-friendly drying techniques: a comparison of solar, biomass, and hybrid dryers. *Environmental Science and Pollution Research*, 30 (42), 95086–95105 .

Vengsungnle, P., Jongpluempiti, J., Srichat, A., Wiriyasart, S., & Naphon, P. (2020). Thermal performance of the photovoltaic–ventilated mixed mode greenhouse solar dryer with automatic closed loop control for Ganoderma drying. *Case Studies in Thermal Engineering*, 21, 100659.

Younis, O. S., Oraiath, A. T., Metwally, K. A., Dessoky, E. S., Mahmoud, S. F., Rashed, M. N., . . . Elwakeel, A. E. (2025). Drying characteristics, environmental and economic analysis of a solar dryer with evacuated tube solar collector for drying Nile Tilapia slices. *Scientific Reports*, 15(1), 9822.https://doi.org/10.1038/s41598-025-94194-9.

Yuwana, Y., Silvia , E., & Sidebang, B. (2020). Observed performances of the hybrid solar-biomass dryer for fish drying. *IOP Conference Series: Earth and Environmental Science* (pp. 583, 012032). Indonesia: IOP Publishing Ltd.

International Conference on Engineering Innovation for Sustainable Development (ICESID 2026)
Faculty of Engineering, Ahmadu Bello University Zaria · 8–10 September 2026

DEVELOPMENT AND CHARACTERIZATION OF CARBON DOT (CD)-ENHANCED SHEA BUTTER AS A PHASE CHANGE MATERIAL FOR THERMAL ENERGY STORAGE

Yotolmbaye Sylvain[1,*], T.o. Ahmadu[1], F.o. Anafi[1], L.o.yusuf[1]

[1]*Ahmadu Bello University*

Email: yotolmbayes@gmail.com[*], talibahmadu@gmail.com, Fataianafi@yahoo.com, queenteefah95@gmail.com

***Corresponding author**: Yotolmbaye Sylvain

DOI: https://doi.org/10.67203/sp.ICESID.2026

ABSTRACT

The rapid evolution of thermal energy storage technologies has positioned phase change materials (PCMs) as a cornerstone for advanced heat management and energy conservation systems. The PCMs are distinguished by their ability to absorb, store and release large quantities of latent heat during phase transitions. Organic phase change materials such as shea butter exhibit low thermal conductivity and latent heat of fusion, hence the need to enhance these properties with suitable additives. In this study, carbon dots (CDs) were synthesized hydrothermally with a yield of 40.3% and particle sizes predominantly below 20 nm, before being integrated into pure shea butter. Pure shea butter exhibited low thermal conductivity (0.222577 W/mK), heat transfer coefficient (37.09621 W/m²·K), latent heat of fusion of 50.50 kJ/kg and specific heat capacity of 0.021054 J/kgK. Addition of 3wt% CDs to pure shea butter increased thermal conductivity to 0.341 W/m·K, heat transfer coefficient to 56.9 W/m²·K, latent heat of fusion to 163.03 kJ/kg and specific heat capacity to 0.062023 J/kgK. Overall, the composite PCM indicated potential for enhanced thermal storage capacity and heat transfer efficiency, indicating its suitability as a sustainable and cost-effective material for thermal energy storage applications.

Keywords: *Phase change materials; Carbon dots; Shea butter; and hydrothermal synthesis*

1.0 INTRODUCTION

The growing demand for reliable and efficient thermal energy management has drawn considerable research attention to phase change materials (PCMs) for latent heat storage. PCMs absorb, store, and release large quantities of thermal energy during solid–liquid phase transitions while maintaining a nearly constant temperature (Yang et al., 2021), making them attractive for building thermal regulation, waste heat recovery, and solar energy applications such as solar drying (Pandey et al., 2024).

Organic PCMs, including paraffins and fatty compounds such as shea butter, are valued for their chemical stability, high latent heat per unit mass, non-corrosive nature, and minimal supercooling (Faraj et al., 2020). However, their inherently low thermal conductivity limits the rate of heat absorption and release, reducing efficiency in time-sensitive applications such as solar drying (Agbetiloye et al., 2022). Shea butter a low-cost, renewable fat extracted from the shea tree (Vitellaria paradoxa), is a promising bio-based organic PCM but shares this conductivity limitation.

Considerable research has focused on improving the thermal conductivity of shea butter and similar organic PCMs using high-conductivity additives such as metallic powders, carbon nanotubes, graphene, and expanded graphite, without significantly compromising latent heat storage (Tariq et al., 2020). Agbetiloye et al. (2022) achieved a thermal conductivity of 0.0538 W/m·K and latent heat of 164.53 kJ/kg using 3 wt% aluminium powder in shea butter for a ginger solar dryer. Stonehouse and Abeykoon (2022) compared several carbon nanomaterials in PCM matrices and reported large conductivity enhancements but at high material cost. Yadav et al. (2021) reviewed carbon-based nanomaterials as conductivity enhancers, reporting improvements of up to 2700% but flagging nanoparticle agglomeration, elevated cost, and reduced latent heat as recurring drawbacks, while Radomska et al. (2020) similarly identified a persistent trade-off between conductivity gain and latent heat retention across enhancer materials. Collectively, these studies confirm the effectiveness of carbon-

based nanomaterials but highlight their high cost as a barrier to economically viable composite PCMs, and underline the need for more affordable enhancers.

This study addresses this gap by investigating carbon dots synthesized from p-phenylenediamine and folic acid as a low-cost additive for shea butter, with the aim of developing a cost-effective composite PCM for thermal energy storage.

2.0 MATERIALS AND METHODS

2.1 Materials

The carbon precursors p-phenylenediamine and folic acid (99% purity) and ethanol (95%, CAS 64-17-15) were purchased from Haddis Chemical, Samaru, Zaria. Deionised water was obtained from the Ahmadu Bello University Multiuser Laboratory, and food-grade shea butter was procured from the open market.

2.2 Synthesis of Carbon Dots

Carbon dots (CDs) were synthesized hydrothermally following the method of He et al. (2024). P-phenylenediamine (30 g) was dissolved in 1 L of ethanol (solution A), while folic acid (5 g) was dissolved in 500 mL of deionised water (solution B). The solutions were combined under magnetic stirring, transferred into a Teflon-lined autoclave, and heated at 180 °C for 12 hours. After natural cooling, the product exhibited characteristic red fluorescence under UV light, confirming CD formation. The product was purified by silica gel column chromatography (methanol eluent), followed by rotary evaporation and freeze-drying, giving a synthesis yield of 40.3%.

2.3 Preparation of Carbon Dot–Shea Butter Blend

Following the method of Agbetiloye et al. (2022), 10 mL of shea butter was heated to a set mixture temperature (40, 50, or 60 °C; Priyadarshi & Paul, 2019) until fully melted. Carbon dots (1, 2, or 3 wt%) were gradually added under continuous magnetic stirring to avoid agglomeration, and the blend was stirred for a specified mixture time (10, 20, or 30 minutes) to achieve homogeneous dispersion. The mixture was then cooled under ambient conditions and stored in airtight containers for further analysis.

2.4 Characterization

Thermal conductivity was measured using a Searle's apparatus, and specific heat capacity using a radial heat conduction apparatus (Armfield HT12), applied to both pure and CD-blended shea butter.

2.4.1 Thermal Conductivity

Thermal conductivity test was done on the pure shea butter, and the modified shea butter (PCM). The Searles apparatus was used

The thermal conductivity was computed using equation 2.1.

$$k = \frac{mC(\theta_2 - \theta_1)L}{A(T_1 - T_2)} \tag{2.1}$$

where; k = Thermal conductivity of sample (W/mK), m = Mass of water collected per second (kg/s), C = Specific heat capacity (J/kg.K), A= Area of the cross-sectional area of the bar (m^2)

θ_1 = Inlet water temperature (K), θ_2 = Outlet water temperature (K), L = Distance between the 2-thermometer point (m), T_1 = Temperature of hot end of the bar (K)

T_2 = Temperature of cold end of the bar (K)

2.4.2 Specific heat capacity

The specific heat capacity was computed using equation 2.2

$$C = \frac{Q}{m\Delta T} \qquad 2.2$$

Where: C= Specific heat capacity (J/kg.K), m = Specific heat capacity of water (kg), $Q =$ change in energy (J), and ΔT is Temperature change (ºC).

2.4.3 Latent heat of fusion

An experimental method involving water in calorimeter with stirrer was used to measure the latent heat. In order to account for heat loss that may occur, the following measures were taken:

The PCM was properly sealed.

The hot medium (water) temperature of 90°C is far above the melting temperature of shea butter.

Full melting/solidification was allowed for throughout the experiment.

The latent heat was computed using equation 2.3 and 2.4.

$$mL + ms_2(\theta_2 - 0) = (m_2 s_2 + m_1 s_1)(\theta_1 - \theta_2) \quad (2.3)$$

$$L = [(m_2 s_2 + m_1 s_1)(\theta_1 - \theta_2) - s_2(\theta_2 - 0)]/m \quad (2.4)$$

Where: m_1=Mass of Copper Calorimeter and Stirrer, m_2=Mass of Water, s_1=Specific Heat Capacity of Water, s_2= Specific Heat Capacity of Copper, θ_1=Initial Temperature of Warm Water

θ_2=Final Temperature of Mixture, m=Mass of Sample, L=Specific Latent Heat of Fusion of Sample

2.5 Determination of the optimum blend of carbon dots & shea butter using Taguchi design of experiment.

Taguchi design of experiment was employed in Minitab statistical 22 software (2022 version) to determine the optimum blend. Three factors with 3 levels each, were used in an L9 orthogonal array (which has 9 experimental runs). The three factors were optimize using Carbon dots (CDs) concentration (1%, 2% and 3%), The mixture temperature of (40º C, 50º C and 60º C) and the mixture times (10 min, 20 min and 30 min). The response variables were thermal conductivity, latent heat of fusion and specific heat as seen in Table 1.

Table 1: Factors and level chosen for experiment design

Factors	**Symbol**	**Units**	1	2	3
Carbon dots	CDs	%	1	2	3
Mixture temperature	MT	℃	40	50	60
Mixture time	Mt	Min	10	20	30

3.0 RESULTS AND DISCUSSION

3.1 Results from characterization of carbon dots/shea butter blends and pure shea butter

Result from characterization are presented in Table 2 and 3

Table 2: Thermophysical properties of carbon-dot /Shea butter PCM samples

S/N	ID	Thermal conductivity (W/mK)	heat transfer coefficient (W/m². K)	specific heat capacity (J/kgK)	Latent heat of fusion (kJ/kg)
1	A1	0.24188415	40.31402504	0.044471	85.198
2	A2	0.276439029	46.07317147	0.050761	91.23
3	A3	0.252400852	42.06680873	0.046357	104.834
4	B1	0.24188415	40.31402504	0.044129	117.275
5	B2	0.24188415	40.31402504	0.046027	130.17
6	B3	0.232208784	38.70146404	0.042601	137.075
7	C1	0.276439029	46.07317147	0.049495	152.689
8	C2	0.341483506	56.9139177	0.062023	163.033
9	C3	0.263873618	43.9789364	0.048464	173.437

Table 2 presents the thermophysical properties of the nine carbon dot–shea butter (CDs–SB) composites (A1–C3) prepared under the Taguchi L9 design across varying CD concentration, mixing temperature, and mixing time. Thermal conductivity ranged from 0.232–0.341 W/m·K, comparable to Asmau et al. (2022), while convective heat transfer coefficients ranged from 38.7–56.9 W/m²·K. Sample C2 recorded the highest heat transfer coefficient, consistent with its higher thermal conductivity (Shende et al., 2018), although the relationship was not strictly linear across all samples.

Specific heat capacity (0.0426–0.0620 J/kgK) correlated positively with thermal conductivity: sample B3 recorded the lowest values of both properties (0.232 W/mK; 0.0426 J/kgK), while C2 recorded the highest (0.341 W/mK; 0.0620 J/kgK).

Latent heat of fusion increased progressively with CD loading from approximately 85–104 kJ/kg at 1 wt%, to 117–137 kJ/kg at 2 wt%, and 152–163 kJ/kg at 3 wt%, with an overall maximum of 173.437 kJ/kg at 3 wt% CDs, 60 °C, and 30 minutes. This trend suggests that CDs enhance both conductivity and energy storage capacity, most likely through nanoparticle-induced heterogeneous nucleation, increased interaction sites between the carbon dot surfaces and the PCM matrix, and strengthened intermolecular forces that raise the energy required for phase transition. Overall, sample C2 (3 wt% CDs, 50 °C, 20 min) gave the best combined performance in thermal conductivity, heat transfer coefficient, and specific heat capacity, while C3 recorded the highest latent heat of fusion.

Table 3: Thermophysical properties of pure shea butter & carbon-dots/shea butter PCM

Thermophysical properties	Thermal conductivity (W/m·K)	heat transfer coefficient (W/(m²·K)	specific heat capacity (J/kg·°C)	Latent heat of fusion (kJ/kg)
Pure shea butter	0.222577	37.09621	0.021054	50.5
Blended carbon dots with shea butter	0.341483506	56.9139177	0.062023	163.033

Table 3 compares pure shea butter to the CD-blended shea butter PCM. It can be seen that the thermal conductivity of shea butter increased from (0.22577 to 0.341484 W/m.K) which gives an increase percentage of 53%. An increase in heat transfer coefficient of shea butter from 37.096 to 56.914 W/(m²·K), specific heat capacity from 0.021054 to 0.062023 J/kgK with the addition of carbon dots was also observed. There was also an increase in latent heat from 50.5 to 163.033 kJ/kg indicating an increase of over 200%. This shows that the addition of carbon dots greatly improved the shea butter thermal conductivity, heat transfer coefficient and specific heat capacity.

3.2 The cost analysis phase change material.

Table 4: Cost analysis of the PCM (Shea butter and carbon dots)

S/N	Materials	Unit Cost (N)	Total Cost
1	Shea Butter 4.53kg	₦ 2400	₦ 12000
2	*P-p*henylenediamine 40 g	₦ 200	₦ 8000
3	Ethanol 1 liter	₦ 8000	₦ 8000
4	Methanol 1 liter	₦ 8000	₦ 8000
5	Folic acid 7 g	₦ 1000	₦ 7000
6	Deionized water 2 liters	₦ 500	₦ 1000
7	Transport and labour	₦ 3000	₦ 2000
8	Total		₦ 47000

Carbon dots cost approximately ₦695.65 per gram, considerably cheaper than multi-walled carbon nanotubes (MWCNTs, US$10 / ₦15,000 per gram) and graphene nanoplatelets (GNPs, up to US$50 / ₦75,000 per gram) at current market prices representing cost savings of 95.3% and 99%, respectively. This confirms carbon dots as a more cost-effective alternative to conventional carbon-based conductivity enhancers.

4.0 CONCLUSION

A composite PCM was developed from shea butter and carbon dots derived from p-phenylenediamine and folic acid. The optimum blend, C2, showed clear improvement in thermophysical properties relative to pure shea butter: thermal conductivity increased from 0.222577 to 0.341484 W/m·K, specific heat capacity from 0.021054 to 0.062023 J/kgK, heat transfer coefficient from 37.09621 to 56.91392 W/m²·K, and latent heat of fusion from 50.5 to 163.03 kJ/kg. These results show that the developed composite PCM is suitable for thermal energy storage applications, with an effective cost saving of 95.3% relative to carbon nanotubes and 99% relative to graphene nanoplatelets.

5.0 REFERENCES

Agbetiloye, L. A., Anafi, F. O., & Omisanya, N. O. (2022). Design, Construction and Performance Evaluation of Ginger Mixed Mode Solar Dryer Integrated with Latent Heat Storage. Fuoye Journal of Engineering and Technology, 7(2), 210-216. doi:10.46792/fuoyejet.v7i2.759

Asmau, S. R. Experimental And Numerical Analysis Of Encapsulated Shea Butter Fatty as A Phase Change Material For Thermal Storage Application (2022): International Journal of Advanced Engineering Research. DOI:10.22161/ijners.912.322

Faraj, K., Khaled, M., Faraj, J., Hachem, F., & Castelain, C. (2020). A review on phase change materials for thermal energy storage in buildings: Heating and hybrid applications. Journal of Energy Storage, (September), 101913. https://doi.org/10.1016/j.est.2020.101913

He, P., Bai, J., Qin, F., Wang, X., Yu, X., Yao, Y., & Ren, L. (2024). Catalyst-regulated conversion of p-phenylenediamine-based carbon dots from red to deep-blue emission. Materials Today Chemistry, 38, 102082.

Li, J., Long, Y., Cao, X., Sun, H., Jiao, R., Zhu, Z., Liang, W., & Li, a. (2024). Recent Advances and Perspectives in Solar Photothermal Conversion and Storage Systems: a Review. Advances in Colloid and Interface Science, 325, 103118. doi:10.1016/j.cis.2024.103118

Pandey, S., Kumar, A., & Sharma, A. (2024). Sustainable Solar Drying: Recent Advances in Materials, Innovative Designs, Mathematical Modeling, and Energy Storage Solutions. Energy, 132725.

Priyadarshi, D., & Paul, K. K. (2019). Optimisation of biodiesel production using Taguchi model. Waste and Biomass Valorization, 10(6), 1547-1559.

Radomska, E., Mika, L., & Sztekler, K. (2020). The Impact of Additives on the Main Properties of Phase Change Materials. Energies, 13(12), 3064. doi:10.3390/en13123064

Shende, T., Bhanvase, B., Rathod, A., Pinjari, D., & Sonawane, S. (2018). Sonochemical synthesis of Graphene-Ce-TiO2 and Graphene-Fe-TiO2 ternary hybrid photocatalyst nanocomposite and its application in degradation of crystal violet dye. Ultrasonics sonochemistry, 41, 582-589.

Stonehouse, A., & Abeykoon, C. (2022). Thermal Properties of Phase Change Materials Reinforced with Multi-dimensional Carbon Nanomaterials. International Journal of Heat and Mass Transfer, 183, 122166.

Tariq, S. L., Ali, H. M., Akram, M. A., Janjua, M. M., & Ahmadlouydarab, M. (2020). Nanoparticles Enhanced Phase Change Materials (nePCMs) - a Recent Review. Applied Thermal Engineering, 176, 115305.

Yadav, A., Verma, A., Kumar, A., Dashmana, H., Kumar, A., Bhatnagar, P., & Jain, V. (2021). Recent Advances on Enhanced Thermal Conduction in Phase Change Materials Using Carbon Nanomaterials. Journal of Energy Storage, 43, 103173.

Yang, L., Jin, X., Zhang, Y., & Du, K. (2021). Recent Development on Heat Transfer and Various Applications of Phase-change Materials. Journal of Cleaner Production, 287, 124432.

DEVELOPMENT AND PERFORMANCE EVALUATION OF A MANUALLY OPERATED SINGLE ROW MULTI-PURPOSE WEEDER

Aminu Saleh[1,*], Akande F. B[2], Ishola T. A[3]

[1]*Department of Agricultural and Bio-Resources Engineering, Institute for Agricultural Research, Ahmadu Bello University Zaria*
[2]*Ladike Akintola University of Technology, Ogbomoso*
[3]*University of Ilorin*

Email: salehaminu@gmail.com*, bukola@gmail.com, ishola@gmail.com

***Corresponding author**: Aminu Saleh

DOI: https://doi.org/10.67203/sp.ICESID.2026

ABSTRACT

Weed control is one of the major problems in agricultural production. Most of the peasant farmers in Nigeria use manual weeders in cultivating, a process that is costly, labour intensive and time consuming. Manual weed control does not also give the farmer adequate returns to enable him breakeven. It is, therefore, necessary to design a weeding mechanism that could minimize the human effort and provide efficient work output for the peasant farmer. This study focus on designing, construction and evaluation of a multi-purpose hand-pushed weeding machine that could eliminate the challenges of manual weeding under different field and soil conditions. Materials selected for the construction of the multi-purpose weeder are durable and locally available, easily replaced if damaged and at affordable cost. They include mild steel plate (3mm, 5mm), 30 mm circular (hollow) pipes, 10 mm diameter steel rod, 10 mm bearings, 10 mm square rod, 17 mm bolt and nuts and 400 mm diameter steel and pneumatic wheels to suit different soil conditions. The developed weeder was evaluated in the experimental farm of IAR with impressive results. It works well in loamy (27.42% moisture content) and sandy soils (25.65% moisture content) and requires less labour force compared to the conventional manual hoes. It has an average weeding efficiency of 84.7%, 0.0129ha/hr effective field capacity, 0.019ha/hr theoretical field capacity and 68% average field efficiency. Results obtained also shows a 100% plant damage efficiency (i.e. no plants damaged). The average cost of the weeder is N46, 200:00.

Keywords: *Manual weeding; hand-pushed weeder; weeding efficiency; field efficiency*

1. INTRODUCTION

One of the major problems in crops and vegetables production in Nigeria is weed control. Weeds may be broadly defined as plants growing where they are not wanted. They are probably the most ever-present class of crop pests and are responsible for marked losses in crop yields. Besides reducing crop yield, weeds deteriorates the quality of produce and hence reduce the market value of the produce. Weeds competes with the crops for nutrients, space, light and water. Numerous studies have documented negative effects of weed competition on crop yield. Results of such studies shows that crop losses measured under weedy conditions for maize was between 55 – 90 % (Chikoye *et al.*, 2004), 40 – 80 % for sorghum (Ishaya *et al.*, 2007)., 40 – 60 % for cowpea (Olowe *et al.*, 1987) and 50 – 100 % for rice (Dadari and Mani, 2005).

Management of weeds is, therefore, imperative to sustain crop productivity and to ensure food security to the ever-increasing population. Weed control is the process of limiting weed infestations such that crops could be grown profitably and efficiently. It is the combination of the techniques of prevention, eradication and control to manage weeds in a crop, cropping system, or environment. Weed managers recognize that field's cropping history, grower's management objectives, available technology, financial resources, and a host of other factors must be combined to make good management decisions; Tisdell, (1988) and Rana and Rana. (2016).

Weeding could be done manually, mechanically, biologically or by means of agro-chemicals. Hand weeding is the predominant weed control practice on smallholder farms in Nigeria and most of Sub-Saharan Africa (Vissoh *et al.*, 2004). It is the oldest method and consists of hand-pulling, hand slashing and hoeing of weeds. Smallholder farmers spend 50 – 70 % of their total labour time in hand

weeding (Chikoye *et al.*, 2007). Another study of African agriculture also confirmed that weeding took up more days in the field than any other operation (IFAD, 1998). Several constraints that limit the effective use of hand weeding, including limited cash for hiring labour and none availability of hired labour during peak periods (Johnson, 1995). Labour supply in rural areas has been significantly reduced in many African countries migration to urban areas (Bisikwa *et al.*, 1997). This necessitates use of mechanical means of weeding to eliminate the challenges of physical exhaustion that is usually associated with manual weeding; Yadav and Pund (2007).

Mechanical weed control, on the other hand, refers to any technique that involves use of farm equipment to control weeds. Implements used vary from simple hand tools to multiple tractor drawn implements; Rana and Rana. (2016). Most existing mechanical weed control machines are drawn by tractors. Peasant farmers who are in the majority today do not have access to credit facilities and cannot afford to buy or hire the agricultural machinery to enhance their farming capabilities. It, thus, becomes necessary to develop and construct a weed control equipment that would depend on minimum human efforts for its motion, but could weed at a greater speed and efficiency than human beings, hence, the objective of this study.

2. MATEIALS AND METHODS

Materials to be used for the construction of the multi-purpose weeder are; 3 mm and 5 mm mild steel, 30 mm circular (hollow) pipes, 10 mm diameter steel rod, 10 mm bearings, 10 mm square rod, 17 mm bolt and nuts and 400 mm diameter steel and pneumatic wheels to suit different soil conditions. The bases for these materials were their durability and availability, ease of replacement if damaged and light in weight for safety and ease of transportation. Their cost is also affordable to a local fabricator and medium scale famer. In its construction, the multi-purpose weeder was made in such a way that it is easy to operate and maintain while the components could easily be dismantled for replacement of parts. Traction on the wheels has also been considered for proper movement on different soil conditions. Other materials used were weighing scale, oven, soil sampler, measuring tape, steel rule and a stop watch.

2.2 Description of the Multi-Purpose Weeder

The multi-purpose weeder constitutes a frame, steel and pneumatic wheels (to suit different types of soil), tin cultivator, furrower and a weeding blade that could optimally operate under different soil conditions as shown in Figure 1. Appendix A show the Orthographic View of the Multi-Purpose Weeding Machine.

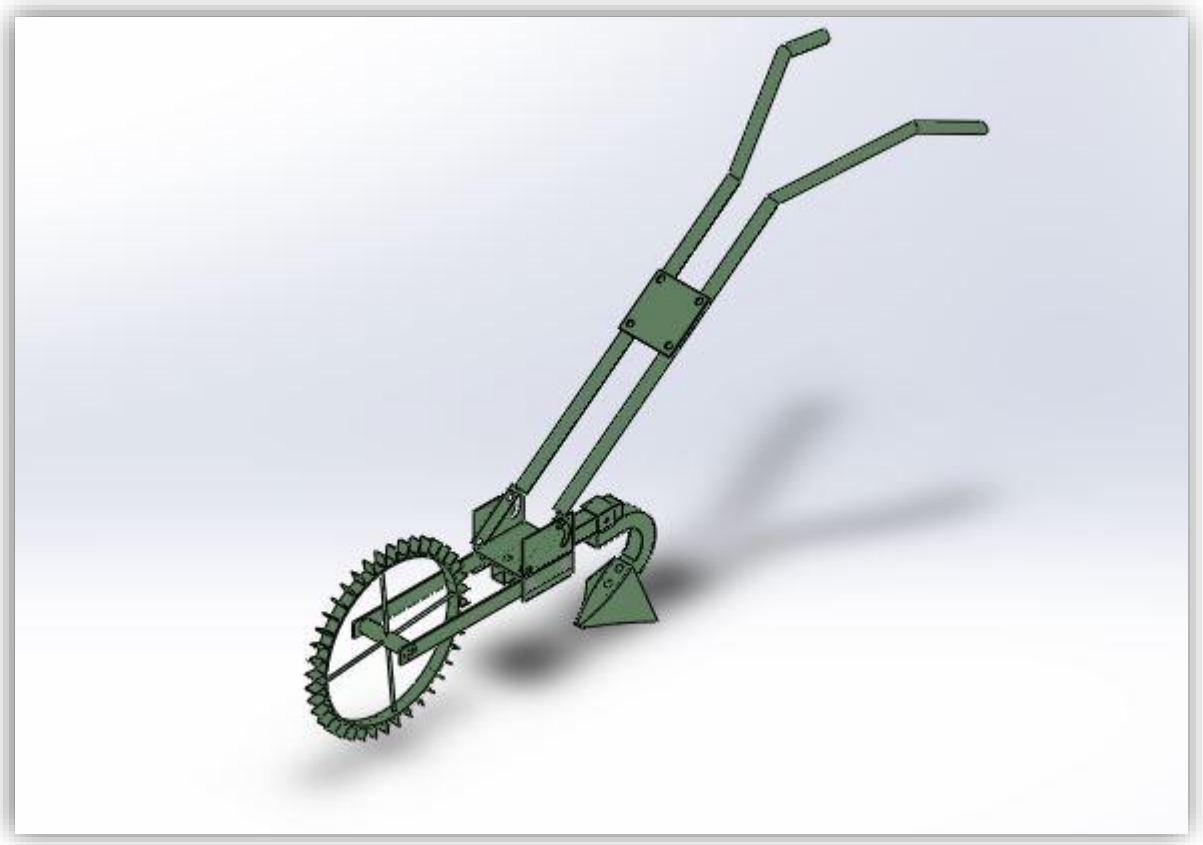

Figure 1: Pictorial View of the Developed Multi-Purpose Weeder

i. **Frame -** The frame is the skeleton/structural component on which all the components of the weeder were built, supported and attached. It was made from 3 mm mild steel rod. All the components mounted on it were attached with bolts and nuts for ease of transport and replacement of defective parts.

ii. **Wheels -** The weeder has two different wheels; pneumatic (moulded and tubless) and steel wheels (Figure 2). Both are of the same diameter (400 mm) and are not used simultaneously but one at a time depending on the type of soil.

iii. **Handle -** The handle was constructed using 30 mm diameter circular (hollow) pipe. Ergornomic and anthropometric aspects were considered in such a way it suit variety of users. It was attached to the frame to control and direct the weeder on the field.

iv. **Tine cultivator -** The tin cultivator was made from 10 mm diameter steel rods which were flattened at its base and supported at the top by a mild steel metal sheet. It was meant to work on a stony and rooted soils (Figure 3).

v. **Furrower -** The furrower was made from a 3mm mild steel metal to form a typical sweep furrow of 18 × 18 cm (Figure 4).

vi. **Weeding blade -** The weeding blade which forms the integral part of the weeder was made from 5 mm mild steel plate. It's diamensions are 20 × 20 cm. It has a sharp blade which is used to cut, slice and pulverize the soil for effective weeding.

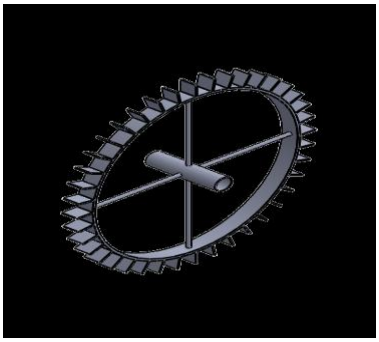

Figure 2: Steel Wheel

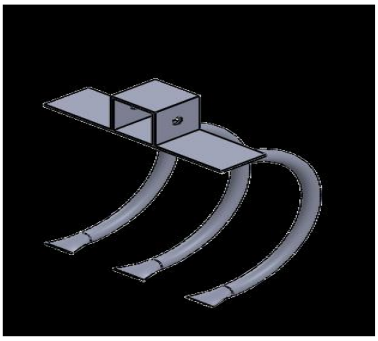

Figure 3: Tine Cultivator

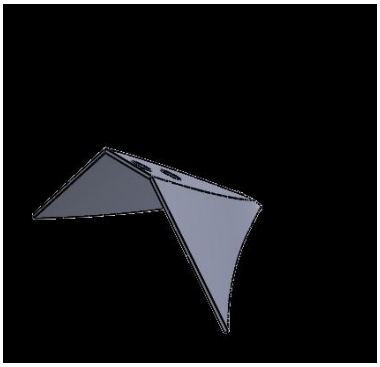

Figure 4: Furrower

2.3 Experimental site

The study was conducted in the Department of Agricultural and Bio-Resources Engineering, Ahmadu Bello University, Zaria between March and December 2025. While construction was done at the departmental workshop, the multi-purpose weeder was tested at the experimental farm of the Institute for Agricultural Research (IAR). The plots with sandy and loamy soils were used to test the weeder.

2.4 Determination of the Weeder Performance

The test for the weeding performance parameters was carried out on the field size of 2 × 1m. The average performance parameters of the multi-purpose weeder such as weeding efficiency, plant damaged, effective field capacity, theoretical field capacity and field efficiency of multi-purpose weeder were determined and evaluated through the following expressions:

i. **Weeding efficiency –** This is the ratio of the numbers of weeds removed by the weeder to the number of weeds in a unit area before weeding and is expressed as a percentage. It was expressed using equation (1) as suggested by Madhusudhana (2015).

$$Weedingefficiency\ (\%) = \frac{W_1 - W_2}{W_1}\ x\ 100 \quad (1)$$

where:

W_1 = Number of weeds counted per unit area before weeding operation

W_2 = Number of weeds counted in same unit area after weeding operation.

ii. **Plant damage –** Plant damage is the ratio of the number of plants damaged after weeding operation to the number of plants before the weeding. It is expressed in percentage.

$$Plant\ Damage\ (\%) = \left(1 - \frac{q}{p}\right) \times 100 \quad (2)$$

where:

p = Number of plants in a row before weeding = 29,

q = Number of plants in a row after weeding = 29.

iii. **Effective field capacity –** Effective field capacity is the actual average rate of coverage by the weeder based upon the total field time. It is a function of the rated width of the weeder, the percentage of rated width actually utilized, speed of the travel and the amount of field time lost during the operation. Effective field capacity is expressed in ha/h (Kepner *et al*., 1978).

$$= \frac{EFC}{\frac{A}{T_{p+}T_i}} \quad (3)$$

where:

EFC = Effective field capacity, ha/h

A = Actual area covered, ha

T_p = Productive time, h

T_i = Non-productive time, h

iv. **Theoretical field capacity -** Theoretical field capacity of the weeder is the rate of field coverage that would be obtained if the weeder were performing its function 100% of the time at the rated forward speed and always covered 100% of its rated width. It is expressed in ha/h (Kepner *et al.,* 1978):

$$TFC = \frac{W \times S}{10} \quad (4)$$

where:
TFC = Theoretical field capacity, ha/h
w = Width of cut, m
s = Speed of operation, km/h

v. **Field efficiency –** Field efficiency is the ratio of effective field capacity to the theoretical field capacity, expressed as percentage. It includes the effect of time lost in the field and failure to utilize the full width of the weeder.

$$\eta_e = \left(\frac{\mathrm{EFC}}{\mathrm{TFC}}\right) \times 100 \quad (5)$$

where:
η_e = Field efficiency, %
EFC = Effective field capacity, ha/h
TFC = Theoretical field capacity, ha/h

vi. **Bulk density of soil -** The bulk density of soil was determined by core cutter method. The core sampler of the soil of known volume was be collected and weighed. The soil bulk density was mathematically determined as the ratio of the mass of soil to volume of soil:

$$\rho = \frac{M}{V} \quad (6)$$

where:
ρ = Bulk density, g/cm³
M = Mass of the soil, g
V = Volume of the soil, cm³

vii. **Moisture content of soil –** The moisture content of the soil was determined by oven drying method. Soil samples were taken from three different points on the field. The samples which weight 400 g, 398 g and 405 g were kept in the thermostatically controlled oven at a temperature of 105^{0}C for 24 hours. The dried soil was again weighed and the moisture content is determined as:

$$M_c = \frac{W_w - W_d}{W_d} \; x100 \quad (7)$$

where:
M_c = Moisture content, (% db)
W_w = weight of moist soil, g
W_d = weight of dry soil, g

viii. **Effective working depth –** The depth of cut of the weeder with different blades was measured in the field by measuring the depth of soil layer tilled by the blade in a row. The depth of the weeding was measured by measuring rule in different rows at different places. Average of five observations was taken as depth of weeding and expressed in cm.

ix. **Effective working width –** The width of cut of the machine with different blades was measured in the field by observing the strip of soil and weeds cut in a row.

3. RESULTS AND DISCUSSION

3.1 Bulk density and moisture content of the soil

The average bulk densities of the sandy and loamy soils collected from three different points of the fields were determined to be 1.21 g/cm³ and 1.70 g/cm³, respectively. The average moisture contents of the areas were also found to be 25.65 and 27.42 % (Tables 1 and 2).

Table 1: Bulk Density and Moisture Content of the Soil (Sandy Soil)

Samples	Weight of wet (g)	Weight of dry (g)	Moisture content on dry basis (%)	Bulk density (g/cm³)
A	400	317.0	26.18	1.22
B	398	320.0	24.38	1.20
C	405	320.4	26.40	1.21
Average	401	319.0	25.65	1.21

Table 2: Bulk Density and Moisture Content of the Soil (Loamy Soil)

Samples	Weight of wet (g)	Weight of dry (g)	Moisture content on dry basis (%)	Bulk density (g/cm³)
A	408	326.1	27.21	1.72
B	410	325.5	27.46	1.69
C	409	325.7	27.58	1.70
Average	409	325.8	27.42	1.70

3.2 Effective working width and depth

The effective working width and depth were determined in three different spots on the field using all the three attachments of the weeder. Results obtained (Table 3) shows that the working widths of the three implements were determined from three different attachments (tin cultivator, weeding blade and furrower) were 20 cm, 19.30 cm and 17.09 cm respectively. This shows that the furrower has a wider coverage than the other attachments. Similarly, the average effective working depth for three attachments were were 3.85 cm, 4.11 cm and 6.87 cm respectively (Table 4). This indicated that the tin cultivator which penetrates deeper into the soil has the tendency of uprooting stubborn weeds and those that has deeper tap roots. Deeper seed bed also means tendency to allow more water and air circulation, hence provides more conducive environment for crop growth.

Table 3: Working widths-of-cut of the Multi-Purpose Weeder

Trial/Implement	Tin cultivator	Weeding Blade	Furrower
	(cm)		
1	20	19.4	17.3
2	20	19.2	17.10
3	20	19.4	17.21
Average	20	19.3	17.09

Table 4: Effective Working Depth-of-cut of the Multi-Purpose Weeder

Trial/Implement	Tine cultivator	Weeding Blade	Furrower
	(cm)		
1	3.84	4.11	6.32
2	4.10	4.00	7.10
3	3.60	4.23	7.21
Average	3.85	4.11	6.87

3.3 Weeding efficiency

The test for the weeding efficiency was carried out on the field size of 2 × 1m. The ratio of weeds counted before and after the weeding was 85.7:1. The cumulative average weed population of the three trials was 600 before weeding operation while weeds left after the exercise was an average of 7 for both attachments (Table 5).

Table 5: Average Weed Population

Trial/Implement	Tine cultivator	Weeding Blade	Furrower
	(No.)		
1	598	601	602
2	599	600	600
3	603	598	598
Average	601	599	600

The weeding efficiency was computed using Equation (1) given as:

$$Weeding\ Efficiency\ (\%) = \frac{600 - 7}{600}\ x\ 100 = 98.83\%$$

3.4 Average Effective field capacity

The average effective field capacity was determined from Equation (3) after weeding 3 × 1.5m (0.00045ha) within an average of 1min 57secs (0.0325 hours) for both attachments. The average time used for turning and adjustment was 10 sec (0.00266hours).

$$Average\ EFC = \frac{0.00045}{0.0325 + 0.00266} = 0.0129ha/hr$$

3.5 Theoretical field capacity

The theoretical field capacity of the multi-purpose weeder was determined computing the rate of weeder coverage at its 100% rated width. Average width of cut of the three implements was 0.19 m from Table 3 while the average speed of operation of the three implements was 1.008km/h. Thus, from Equation (4), the theoretical field capacity was determined as:

$$TFC = \frac{0.19X1.008}{10} = 0.019ha/h$$

3.6 Average Field efficiency

The average field efficiency of the weeder was computed from Equation (5) as:

$$\eta_e = \frac{0.0129}{0.019} \times 100 = 67.9\% \approx 68\%$$

3.7 Plant damage efficiency

The plant damage efficiency was calculated using Equation (2). After weeding three different rows of about 10 m length each, it was discovered that no plant was damaged by both attachments (number of plants before and after weeding = 29). This shows a 100% plant damage efficiency. Therefore, the plant damage efficiency is calculated thus;

$$Plant\ Damage\ (\%) = \left(1 - \frac{29}{29} \times 100\right) = 0$$

4 CONCLUSION

A hand-pushed multi-purpose weeder that could use three different weeding attachments for effective weeding operation has been designed and developed. From the results obtained during the

performance evaluation, it was observed that the weeder is light in weight which makes it easy to be pushed with less effort, save time and energy and effective in its output. It could, thus, promote the living standard of peasant farmers by reducing the drudgery involved in weeding. The multi-purpose weeder could also be used on a flat soil or between furrows if the soil moisture is within its acceptance range. It has a weeding efficiency of 84.7% with no plant damage during the weeding trials conducted. The average cost of the multi-purpose weeder is N46, 200:00.

REFERENCES

Bisikwa, J., D. S. O. Osiru, and M. W. Ogenga-Latigo. (1997). Timing of Hoe Weeding and Herbicide Application for Competitive Weed Control in Sorghum. *16th East African Biennial Weed Science Conference Proceedings*. 205-214.

Chikoye, D., S. Schultz, and F. Ekeleme. (2004). Evaluation of Integrated Weed Management Practices for Maize in the Northern Guinea Savanna of Nigeria. *Crop Protection*. 23:895- 900.

Chikoye, D., J. Ellis-Jones, C. Riches, and L. Kanyomeka. (2007). Weed management in Africa: experiences, challenges and opportunities. *XVI International Plant Protection Congress*.652-653.

Dadari, S.A. and Hamza Mani. (2005). The effect of post-emergence weed control on irrigated wheat in the Sudan savannah of Nigeria. *Crop Protection*. 24: 842-847.

IFAD. (1998). *Agricultural Implements used by Women Farmers in Africa*. Rome.

Ishaya, D.B., S.A. Dadari, and J.A.Y. Shebayan. (2007). Evaluation of herbicides for weed control in sorghum (*Sorghum bicolour*) in Nigeria. *Crop Protection*. 26:1697-1701.

Johnson, D. E. (1995). Weed Management Strategies for Smallholder Rice Production. *Brighton Crop Protection Conference. Weeds- 1995*.1171-1180.

Kepner, R. A., Bainer, R. and Barger, E. L. (1978). Principles of Farm Machinery (3 edition), Avi Publishing Company Inc. Westport, Connecticut, USA.

Madhusudhana, S. (2015), "Development of Double wheeled multipurpose weed remover" *International Journal of Engineering Technology, Management and Applied Sciences February 2015, Volume 3 Issue 2, ISSN 2349-4476*

Olowe, T., S. O. Dina, A. O. Oladiran, and B. A. Olunuga. (1987). The control of weed, pest and disease complexes in cowpea (*Vigna unguiculata* (L.) Walp.) By the application of pesticides singly and in combination. *Crop Protection*. 6(4):222-225.

Tisdell, C. A. (1988). *Economics of Weed Control on Public Conservation and Recreation Land: Assessing Costs and Benefits*, Research Report or Occasional Paper No. 156, Department of Economics, University of Newcastle.

Rana S.S and M.C Rana. (2016). Principles and Practices of Weed Management. Department of Agronomy, College of Agriculture, CSK Himachal Pradesh Krishi Vishvavidyalaya, Palampur, -125004, India.

Vissoh, P.V., G. Gbehounou, A. Ahanchede, T.W. Kuyper, and N.G. Roling. (2004). Weeds as Agricultural Constraint to Farmers in Benin: Results of a Diagnostic Study. *NJAS*. 52(3/4):305-329.

Yadav, R. and Pund, S. (2007). Development and Ergonomic Evaluation of Manual Weeder Agricultural Engineering International: the CIGR Ejournal. IX.

APPENDIX A

Orthographic View of the Multi-Purpose Weeding Machine

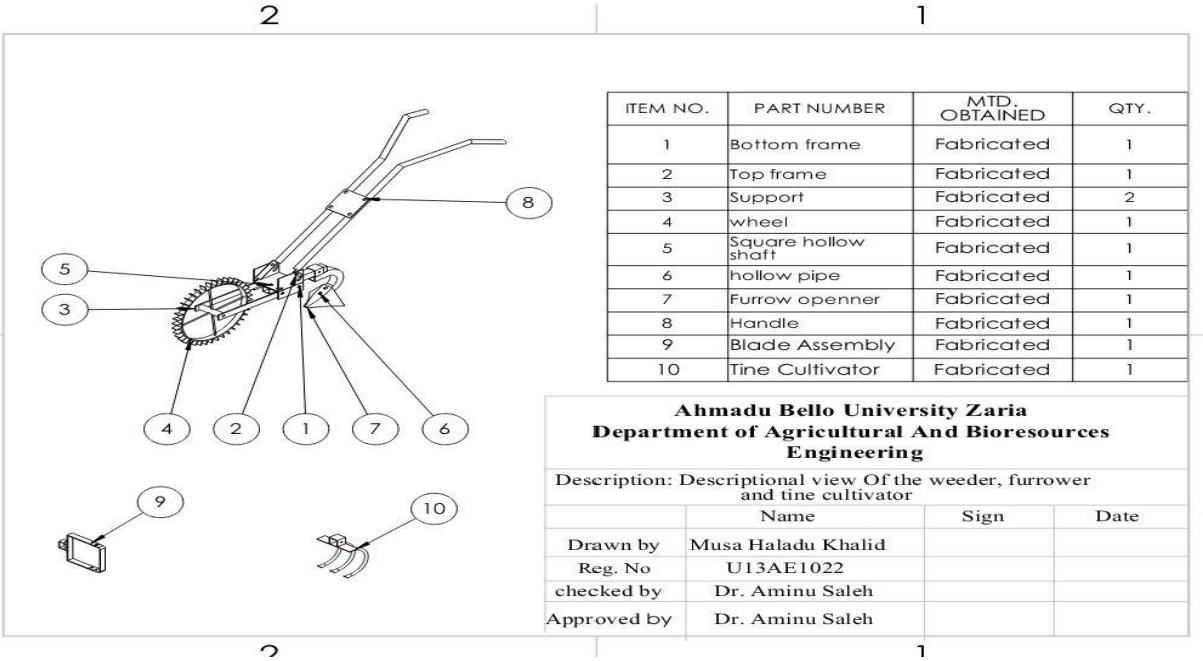

Bill of Engineering and Material Evaluation

S/N	Description	Quantity	Rate(₦)	Amount (₦)
1	3mm mild steel	Quarter length	-	4500
2	5mm flat bar	One length	-	4500
3	Bolt and nut	20 pieces	150	3000
4	10 mm iron road	0.75 of a length	4000	2000
5	Cutting disc	One disc	2000	2000
6	Electrode	1 pack	2000	2000
7	10 mm Bearing	Two	2500	5000
8	30 mm Round pipe	One length	3500	3500
9	Pneumatic tyre	Complete set	3000	3000
10	Square road	½ length	4000	2000
11	Paint	⅓ gallon		2500
12	Transportation	-		5000
13	Miscellaneous			3000
14	Labour (10% Sub-Total)			4,200
15	**Total**			**₦46,200**

International Conference on Engineering Innovation for Sustainable Development (ICESID 2026)
Faculty of Engineering, Ahmadu Bello University Zaria · 8–10 September 2026

DEVELOPMENT OF FAULT DIAGNOSIS FRAMEWORK FOR 132 KV CAPACITOR VOLTAGE TRANSFORMER USING MACHINE LEARNING FRAMEWORK

Moses Uchendu[1,*]
[1]*Ahmadu Bello University Zaria*
Email: moseslife500@gmail.com*
***Corresponding author**: Moses Uchendu
DOI: https://doi.org/10.67203/sp.ICESID.2026

ABSTRACT

Capacitor Voltage Transformers (CVTs) play a critical role in high-voltage power systems by providing voltage measurements for protection, metering, and monitoring applications. However, their performance can be adversely affected by faults such as capacitor drift, ferroresonance, overvoltage, undervoltage, and insulation degradation, leading to inaccurate measurements and reduced system reliability. The development of intelligent fault diagnosis systems for CVTs is often constrained by the limited availability of comprehensive fault datasets and the severe class imbalance associated with rare fault events. This study proposes an integrated framework for fault diagnosis and reliability assessment of a 132 kV CVT using synthetic data generation and machine learning techniques. A high-fidelity CVT model was developed to simulate both normal and fault operating conditions while incorporating temperature variations, harmonic distortion, and measurement uncertainties. A dataset comprising 20,000 samples was generated, containing electrical and operational features including primary voltage, secondary voltage, ratio error, phase error, temperature, and total harmonic distortion (THD). The dataset was subsequently used to develop and evaluate Decision Tree, Support Vector Machine (SVM), k-Nearest Neighbor (kNN), and Ensemble Machine Learning classifiers for multi-class fault prediction. Comparative results demonstrated that the Ensemble classifier achieved superior performance with an accuracy of 99.98%, macro precision of 1.00, macro recall of 0.999, and macro F1-score of 0.999, significantly outperforming the conventional machine learning models. The proposed framework provides an effective solution for accurate fault prediction, improved fault representation, and enhanced condition-based assessment of CVTs, thereby supporting predictive maintenance and improving the operational efficiency of high-voltage power system assets.

Keywords: *Capacitor Voltage Transformer; System Modeling; Machine Learning; Fault Prediction*

1. INTRODUCTION

The study is on the development of a fault diagnostic framework for 132 KV capacitor voltage transformer. With the increasing expansion of power systems, evaluating the reliability of the systems is imperative for improved and sustained performance efficiency. For metering, protection, and measuring equipment, the input signal needed to perform their protection functions depends on the instrument transformer. A capacitor voltage transformer is used as an instrument or transformer to step down high transmission line voltages (66 kV and above) to the nominal voltage levels needed for the operation of metering, protection, and measuring equipment (Haghgoo & Damchi, 2022). Faults in CVTs arise from aging and system subjection to abnormal operating conditions, which could lead to malfunction in system operation and consequently to protection systems. Therefore, an effective fault modeling and classification framework is needed to evaluate the operational behavior of the CVT under normal and faulty conditions and classify faults in CVTs, thus providing an early preventive maintenance approach to ensure the safe and reliable operation of CVTs and protection systems. Traditional fault detection techniques often rely on predetermined thresholds and expert knowledge; however, these methods can be inadequate for addressing the increasing complexity and dynamic nature of modern power systems Arouche Freire *et al.*, *(*2019). Machine learning (ML) techniques have shown great promise in enhancing fault diagnosis and classification (FDC) in power and protection systems. ML models can automatically learn the underlying patterns and characteristics of various fault types

without the need for explicit programming by leveraging vast amounts of real-time sensor data and historical fault records (Sappati & Bhadra, 2018).Despite these advantage, ML techniques often exhibit poor performance when dealing with imbalanced fault data and do not provide a direct linkage between fault predictions The growing adoption of ML in fault detection on transmission lines offers several advantages, including higher accuracy, the ability to detect faults under various operational conditions, and the potential for real-time detection and classification.

Aim of Study: The aim of the study is to develop a condition -aware simulation-driven fault diagnosis framework for 132 kV capacitor voltage transformer

Objectives of Study:

1. To develop a high-fidelity modeling framework for a 132 kV capacitor voltage transformer (CVT) capable of generating realistic operational and fault-condition datasets for advanced fault detection and diagnostic applications
2. To develop an ensemble machine learning-based fault prediction model using the generated 132 kV dataset and comparatively evaluate its performance against conventional machine learning algorithms, including Decision Tree, Support Vector Machine (SVM), and k-Nearest Neighbor (kNN), using accuracy, precision, recall, and F1-score as performance metrics.

2. METHODOLOGY

In this section, the materials required for actualizing the research work and the detailed step by step methods to be followed in achieving the set objectives is presented.

2.1 Materials

The hardware and software materials to be deployed in actualizing this research work are presented in this section. These materials include:

1. Personal Computer
2. MATLAB Software (2026a)

2.2 Research Methodology

This section presents the methodological framework adopted for the fault diagnosis and reliability assessment of the Capacitor Voltage Transformer (CVT). This chapter outlines the systematic procedures used to model, analyze, and evaluate the operational behavior of the CVT under both normal and faulty conditions. It describes the data acquisition process, feature extraction techniques, and the implementation of diagnostic algorithms employed to detect and classify faults. The parameters used in this study were obtained from standard power system theory, typical CVT design practices, and reasonable engineering approximations. Where manufacturer data was unavailable, values were selected to ensure physically meaningful and realistic system behaviour. Environmental effects, such as temperature variation and harmonic distortion, were incorporated using statistically distributed variables to reflect real-world operating conditions.

2.3 System Description

The CVT considered in this study is rated at 132 kV on the primary side (V_p) with a nominal secondary output of 110 V. The phase voltage is shown in equation (1):

$$V_p = \frac{V_{line}}{\sqrt{3}} \tag{1}$$

The capacitive divider consists of two series capacitors with nominal values of C_1 and C_2 to be 8000 pF and 72000 pF respectively. These parameters establish the nominal transformation ratio and form the basis for the CVT mathematical model as shown in Table 1.

Table 1: *CVT Parameters*

Parameter	Value	Unit
V_{line_nom}	132,000	V
V_{P_nom}	76,210	V
V_{Sec_nom}	110	V
C_{1_nom}	8000e-12	pF
C_{2_nom}	72000e-12	pF
$Temp_{Coeff}$	-0.00035	1/°C
$Temp_{ref}$	25	°C

2.2.1 Temperature Effect Modelling

The influence of temperature on capacitor characteristics is incorporated using a linear temperature coefficient model as shown in equation (3).

$$C(T) = C_{nom}\left[1 + \alpha\left(T - T_{ref}\right)\right] \tag{3}$$

Where $\alpha = -0.00035$ and $T_{ref} = 25^{\circ}C$. This enables the simulation of environmental effects on CVT performance, particularly under varying field conditions.

2.2.2 Secondary Voltage Computation and Normalization

The secondary voltage is computed by incorporating the divider ratio, temperature effects, and system normalization as equation (4).

$$V_s = \left(V_p \times Divider\ Ratio\right) \times \frac{V_{sec,nom}}{V_{p,nom} \times \left(\frac{C_1}{C_1 + C_2}\right)} \tag{4}$$

This formulation ensures that the modelled CVT output aligns with the expected nominal transformation characteristics while allowing deviations under fault conditions.

2.2.3 Noise and Measurement Uncertainty Modelling

To emulate real-world measurement conditions, stochastic noise is introduced into the secondary voltage signal. Gaussian noise is applied with a small variance proportional to the signal magnitude, representing sensor inaccuracies, electromagnetic interference, and switching disturbances. This enhances the realism of the generated dataset and improves the robustness of subsequent fault diagnosis models.

2.3 Fault Modelling and Classification Scheme

A comprehensive fault modelling framework is developed by introducing parameter perturbations corresponding to different CVT fault conditions. Seven operating states are considered like Healthy condition, C_1 capacitance drift, C_2 capacitance drift, Ferroresonance condition, Overvoltage condition, Undervoltage condition and Insulation degradation. Capacitor drift faults are simulated by modifying the capacitance values, while ferroresonance is modelled through amplitude amplification and phase deviation. Voltage-related faults are introduced by scaling the primary voltage, and insulation degradation is represented through combined parameter variations and increased harmonic distortion. This classification provides a diverse dataset for fault diagnosis.

2.4 Ensemble Machine Learning Fault Prediction

1. Decision Tree (DT): Utilized for its interpretability and ability to model non-linear feature boundaries (Meng et al., 2023).
2. Support Vector Machine (SVM): Employed with kernel tricks to map complex fault features into higher-dimensional spaces (Omar et al., 2022).
3. k-Nearest Neighbors (kNN): Used as a distance-based baseline to highlight the challenges of high-dimensional imbalanced data.

2.4.1 Performance Evaluation Metrics

Because standard accuracy is misleading in highly imbalanced datasets (where a model predicting "Healthy" 100% of the time would achieve 90% accuracy), the models are rigorously evaluated using Macro-Averaged Metrics:

i. Macro Precision, Recall, and F1-Score: These metrics treat all fault classes equally, penalizing models that fail to detect rare faults.
ii. Confusion Matrix Analysis: Utilized to identify specific inter-class confusions (e.g., distinguishing C1 drift from Insulation Degradation) and validate the ensemble's ability to isolate distinct fault signatures like Ferroresonance and Overvoltage.

3. RESULTS AND DISCUSSION

Five representative waveform scenarios are generated such as Normal operation, C_1 capacitor drift, C_2 capacitor drift, Ferroresonance condition and Insulation degradation. Each waveform exhibits unique characteristics, enabling clear differentiation between fault conditions and supporting feature extraction for diagnostic purposes. Furthermore, the Root Mean Square (RMS) value of each waveform is computed to quantify signal magnitude and energy content.

3.1 Capacitor Voltage Transformer Under Different Condition

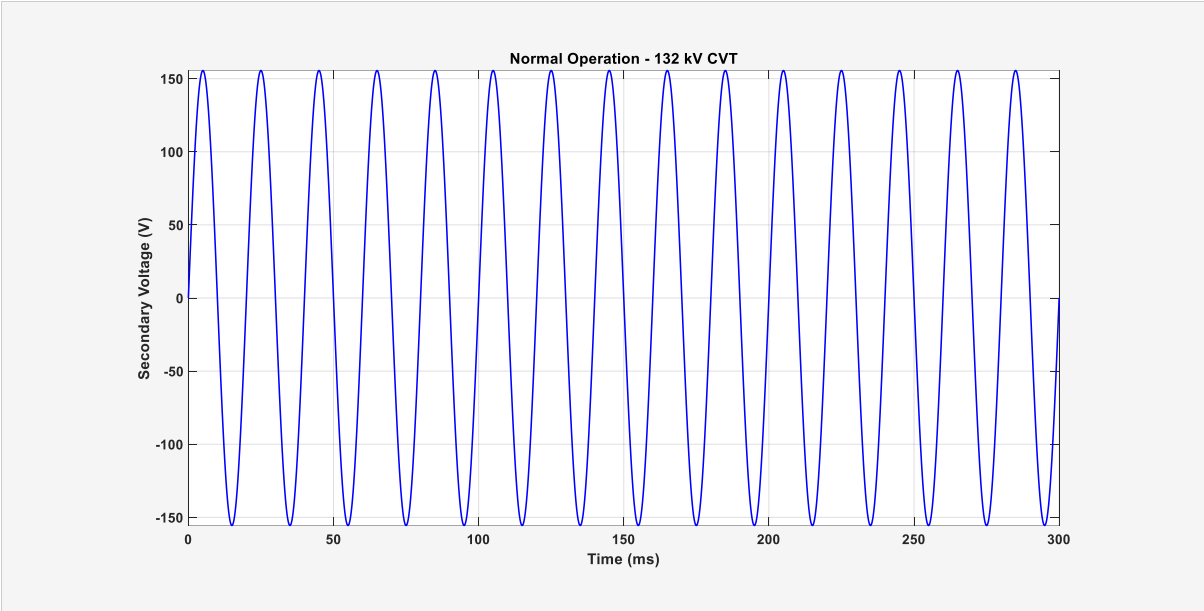

Figure 1: Normal operation

Figure 1 illustrates the time-domain waveform of the secondary voltage output of the 132 kV Capacitor Voltage Transformer (CVT) under normal operating conditions. The waveform exhibits a clean and stable sinusoidal profile, which is characteristic of a properly functioning CVT operating at the fundamental power system frequency of 50 Hz. The peak amplitude of the waveform is ±155 V, corresponding to an RMS value close to the nominal secondary voltage of 110 V. This indicates that the CVT is accurately stepping down the high primary voltage (132 kV system) to a standardized measurable level, maintaining the expected transformation ratio. under the following condition $C_1 = C_1^{nom}$ $C_2 = C_2^{nom}$, Harmonics: none ($k_h = 0$) and Ferroresonance: none ($k_f = 0$).

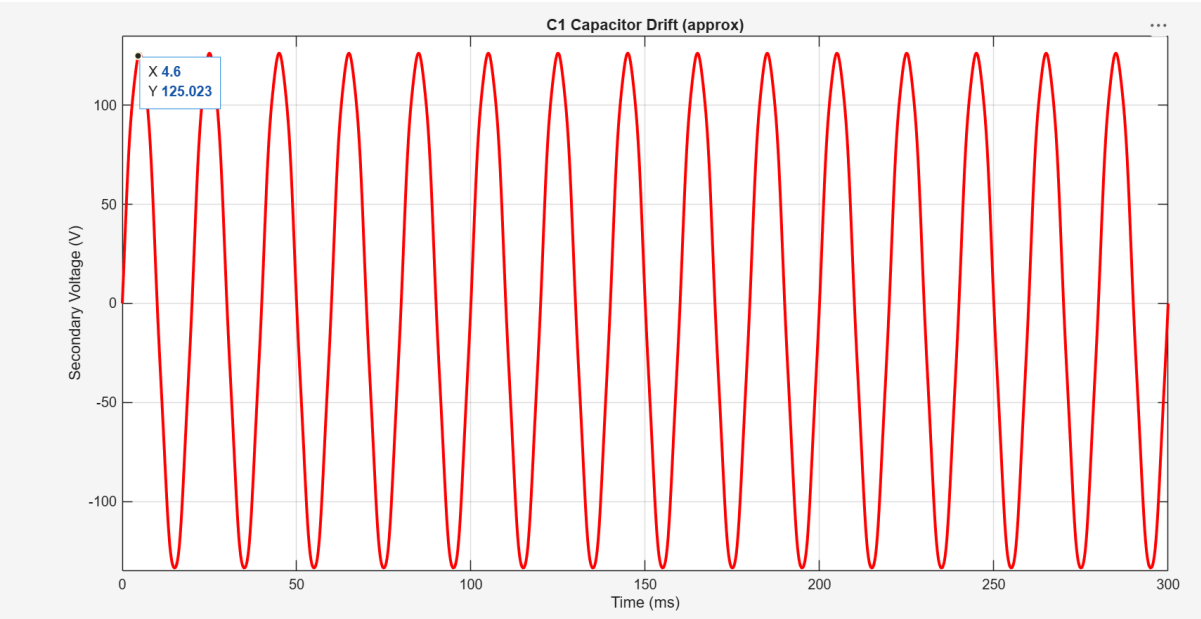

Figure 2: C_1 capacitor drift

Figure 2 presents the secondary voltage waveform of the 132 kV CVT under a fault condition characterized by an 18% reduction in the capacitance of C_1. This condition simulates capacitor aging, dielectric degradation, or partial failure within the capacitive divider network. The waveform retains its fundamental sinusoidal shape at 50 Hz, indicating that the system frequency remains unaffected. However, a noticeable reduction in the amplitude of the secondary voltage is observed when compared to the normal operating condition. This behavior is attributed to the altered capacitive divider ratio, where a decrease in C_1reduces its contribution to the voltage division process, under the following conditions, $C_1 = 0.82 \times C_1^{nom}$, $C_2 = C_2^{nom}$ and Moderate harmonics ($k_h \approx 0.4$).

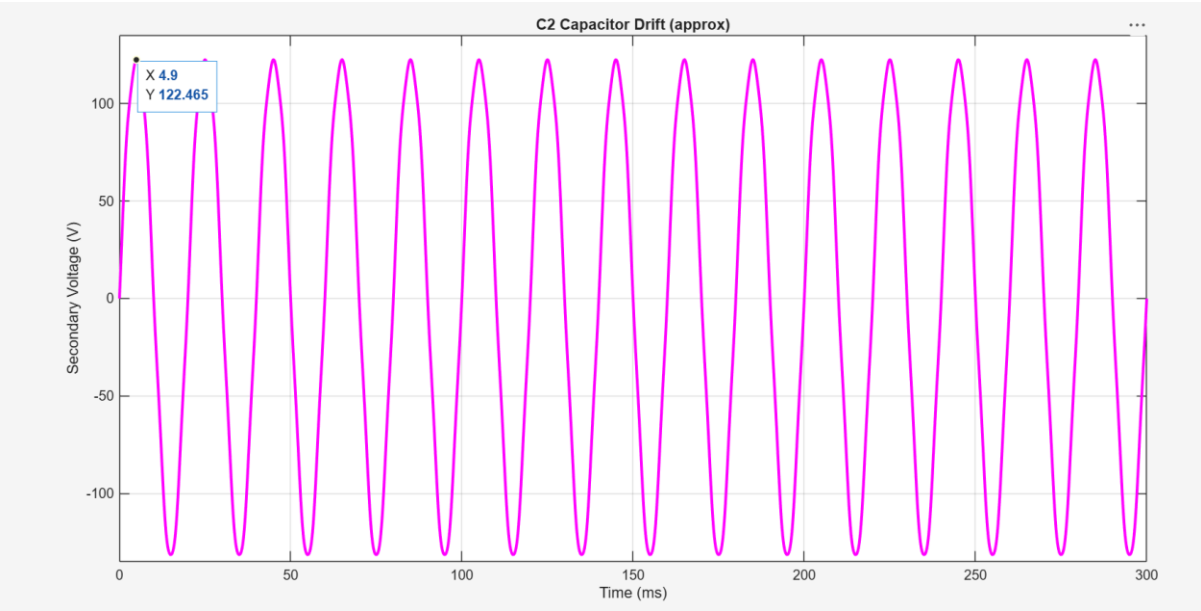

Figure 3: C_2 capacitor drift

Figure 3 illustrates the CVT secondary voltage waveform under a fault condition involving drift in the capacitance of C_2. In this case, $C_2$is increased relative to its nominal value, representing insulation changes, dielectric swelling, or manufacturing tolerances. Similar to Figure 2, the waveform maintains a sinusoidal shape at the fundamental frequency, confirming that no oscillatory instability or resonance is introduced. However, the amplitude of the waveform is altered due to the change in the capacitive

divider ratio, following this condition, $C_1 = C_1^{nom}$, $C_2 = 1.25 \times C_2^{nom}$ and moderate-to-high harmonics ($k_h \approx 0.5$).

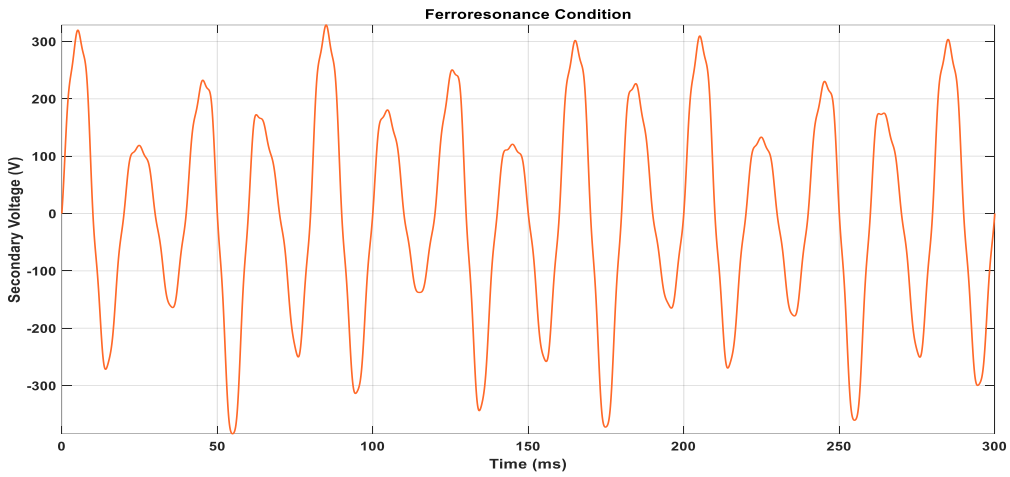

Figure 4: Ferroresonance condition

Figure 4 illustrates the secondary voltage waveform of the CVT under ferroresonance conditions. Ferroresonance is a nonlinear phenomenon that occurs due to the interaction between the CVT's capacitive elements and the nonlinear inductance of the electromagnetic unit (transformer core). This interaction leads to unstable oscillations, which are evident in the waveform as: severe deviation from a pure sinusoidal shape, irregular peaks and troughs with varying amplitudes, presence of subharmonic and harmonic components, and Intermittent oscillatory behavior. The waveform shows abnormally high voltage magnitudes, with peaks exceeding ±300 V, which is significantly higher than the nominal secondary voltage. This indicates overvoltage conditions that can stress insulation and damage connected protection and metering equipment. Additionally, the oscillations are non-periodic, reflecting the chaotic nature of ferroresonance, following this condition, $C_1 = C_1^{nom}$, $C_2 = C_2^{nom}$, amplitude increased by 1.55, strong harmonics ($k_h \approx 1.1$) and strong ferroresonance term ($k_f \approx 1.2$).

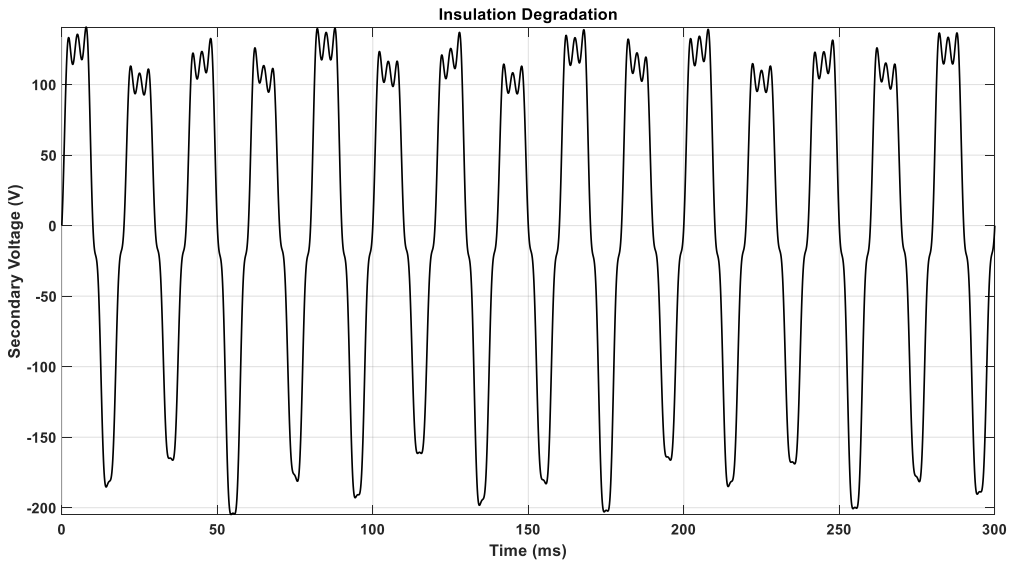

Figure 5: Insulation degradation

Figure 5 presents the secondary voltage waveform under insulation degradation conditions within the CVT. This fault is typically caused by aging, moisture ingress, thermal stress, or dielectric breakdown within the capacitive elements or internal insulation layers. The amplitude of the waveform shows moderate variation, but not as extreme as in ferroresonance. However, the presence of high-

frequency components suggests an increase in THD, which is consistent with insulation degradation effects. This distortion arises because insulation degradation alters the effective capacitance and introduces leakage paths, resulting in nonlinear voltage distribution across the capacitive divider increased dielectric losses, and degraded signal quality. Consequently, this condition leads to increased ratio error, noticeable phase displacement, reduced measurement accuracy and gradual reliability deterioration. Figure 5 represents early-stage faults such as insulation aging or partial discharge. The parameter used are $C_2 = 0.92 \times C_2^{nom}$, Slight amplitude reduction, high harmonic content ($k_h \approx 2.8$) and Mild ferroresonance ($k_f \approx 0.3$)

3.2 Fault Classification in CVTs Using Machine Learning

This section outlines the core methodologies, data pre-processing steps, algorithm selection criteria, and validation metrics used in ML-driven fault prediction. By highlighting how these models detect early degradation patterns, the discussion aims to provide a practical foundation for building, evaluating, and deploying reliable predictive systems that reduce downtime, lower maintenance costs, and enhance operational safety. Although the original dataset consisted of 20000 samples/ observations, the confusion matrix was generated using an independent test subset only. A 70:30 training-testing partition was applied, resulting in approximately 6000 unseen samples used for the model evaluation. The confusion matrix thus represents the classification performance on the test dataset rather than the complete dataset.

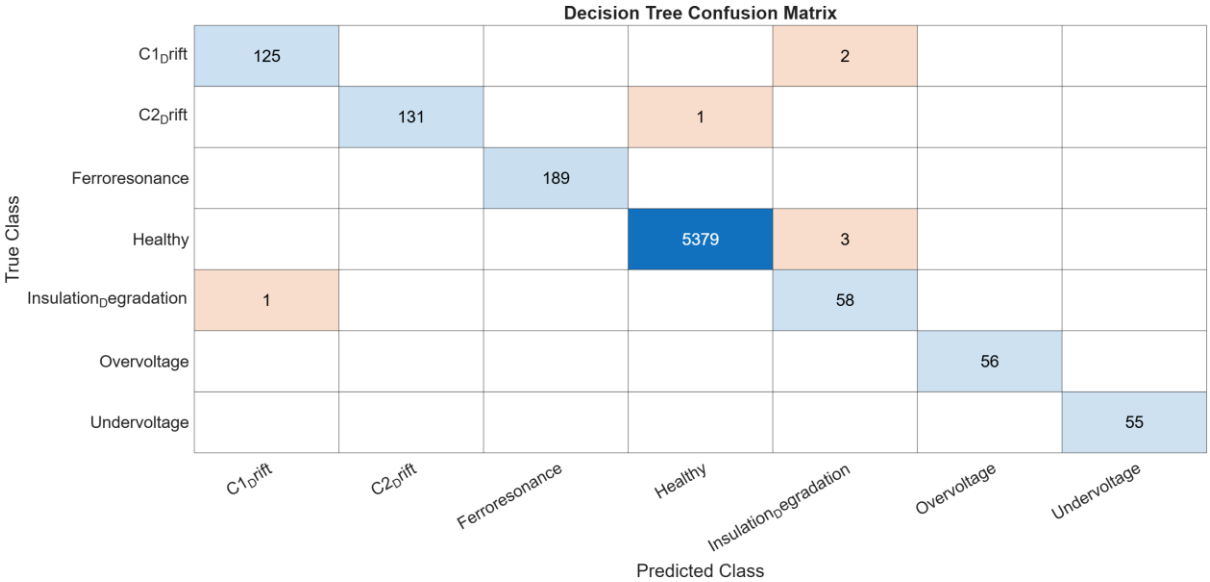

Figure 6: Confusion Matrix of the Decision Tree Model for CVT Fault Classification

The confusion matrix for the Decision Tree classifier in Figure 6 demonstrates robust fault prediction performance across a highly imbalanced dataset, with the majority "Healthy" class (5,379 true positives) and minority fault classes (ranging from 55 to 189 samples) generally well-discriminated along the diagonal. Minor misclassifications were observed: two instances of *C1_Drift* were predicted as *Insulation Degradation* and one vice versa, suggesting overlapping feature representations between these degradation modes; additionally, one *C2_Drift* sample was incorrectly classified as *Healthy* (a false negative of operational concern), while three *Healthy* samples were falsely flagged as *Insulation Degradation*. Notably, the model achieved perfect recall for *Ferroresonance*, *Overvoltage*, and *Undervoltage* faults, indicating that the learned decision boundaries effectively isolate these distinct fault signatures.

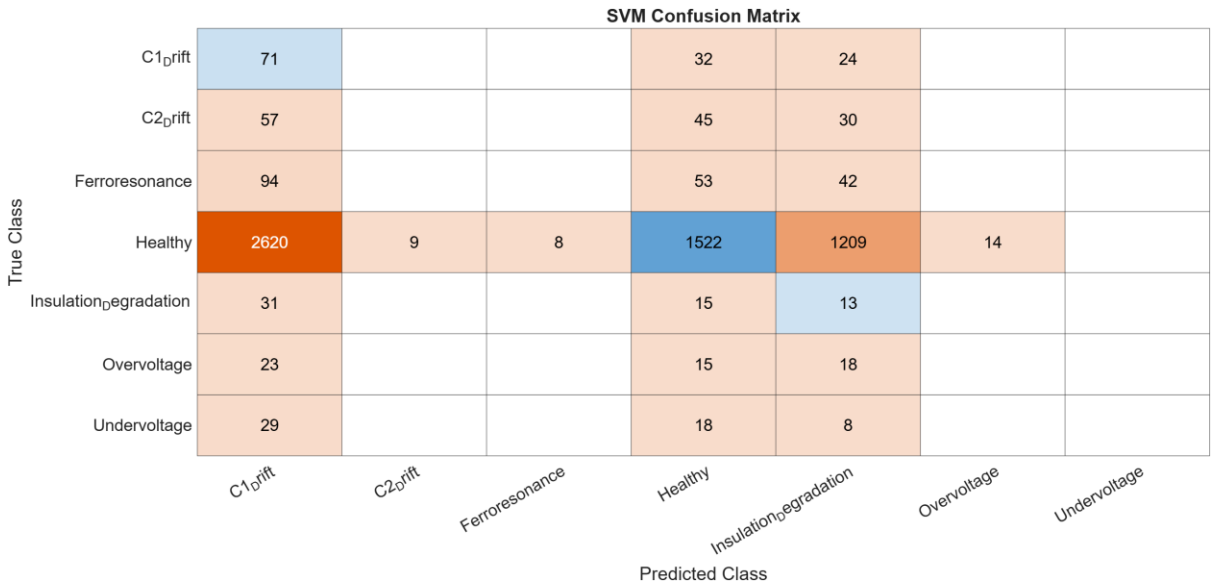

Figure 7: Confusion Matrix of the Support Vector Machine Model for CVT Fault Classification

The confusion matrix for the Support Vector Machine (SVM) in Figure 7 reveals significant classification challenges, particularly regarding class imbalance and the separation of minority fault signatures. The model exhibits a high false positive rate for the "Healthy" class, misclassifying 2,620 instances as "C1_Drift" and 1,209 as "Insulation Degradation," which indicates a strong prediction bias toward these specific labels. Furthermore, the SVM demonstrated zero recall for "C2_Drift," "Ferroresonance," "Overvoltage," and "Undervoltage," failing to correctly identify any true positives for these categories and instead scattering predictions primarily into "C1_Drift," "Healthy," and "Insulation Degradation." This suggests that the linear or kernel-based decision boundaries established by the SVM were insufficient to isolate the complex feature spaces of the minority faults, resulting in poor overall diagnostic reliability compared to tree-based methods.

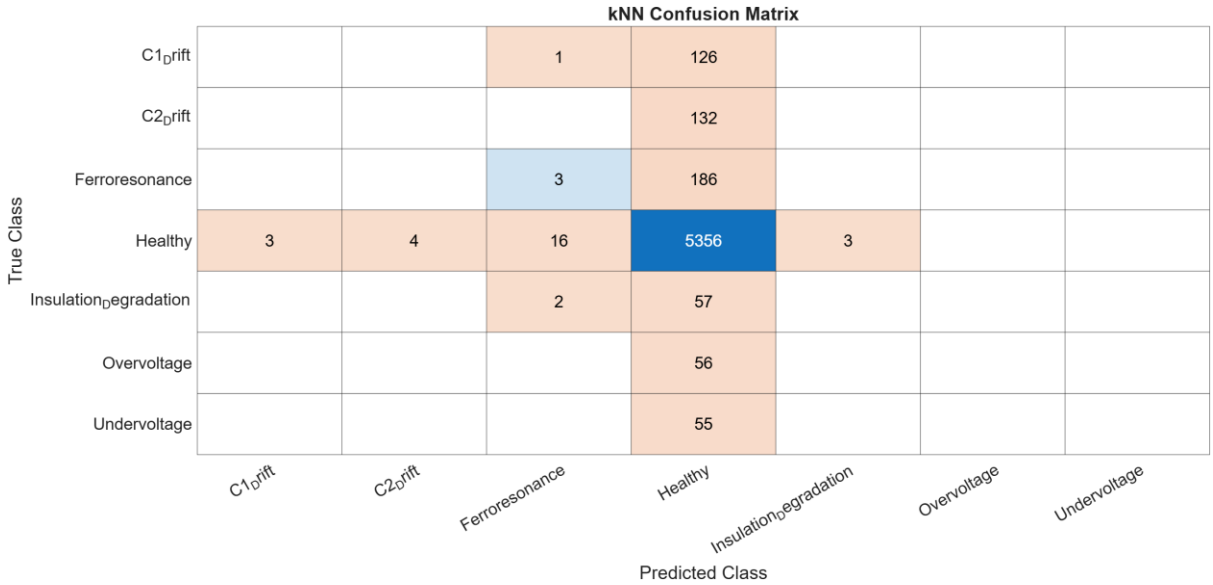

Figure 8: Confusion Matrix of the k-Nearest Neighbors Model for CVT Fault Classification

The confusion matrix for the k-Nearest Neighbors (kNN) classifier in Figure 8 demonstrates a severe classification bias toward the majority "Healthy" class, resulting in a near-total failure to detect fault conditions. The model achieved zero recall for C1_Drift, C2_Drift, Insulation Degradation, Overvoltage, and Undervoltage, and correctly identified only 3 instances of Ferroresonance, effectively misclassifying the vast majority of faults as "Healthy." This outcome highlights a critical limitation of standard distance-based kNN algorithms on imbalanced datasets, where the high density of majority

class neighbors overwhelms the minority class signals, rendering the model ineffective for fault prediction without advanced resampling or cost-sensitive learning techniques.

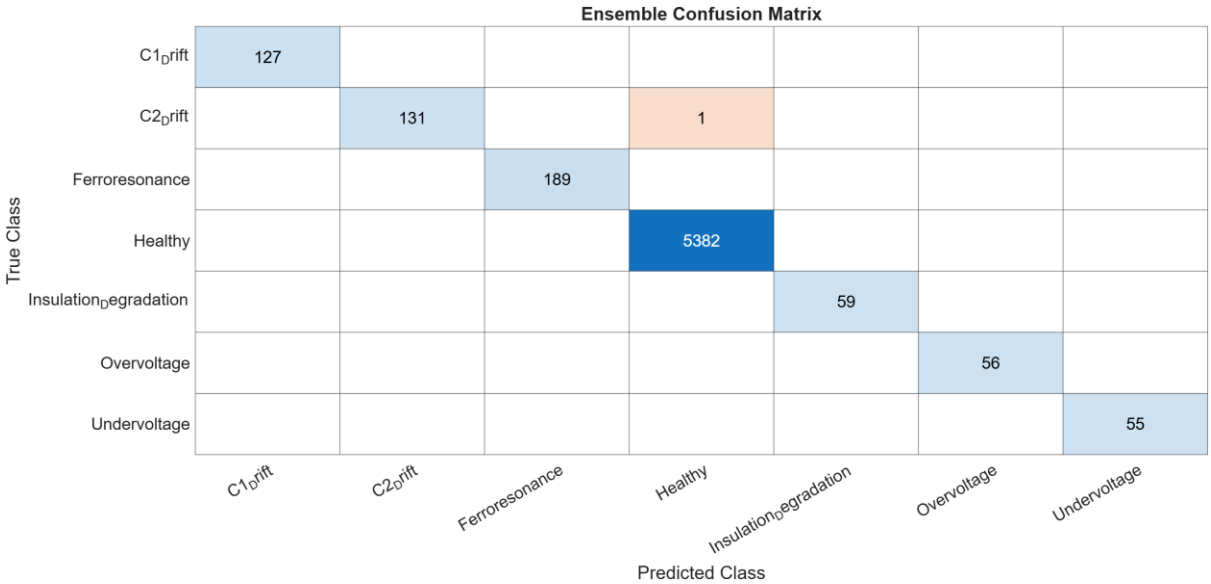

Figure 9: Confusion Matrix of Ensemble Model for CVT Fault Classification

The confusion matrix for the Ensemble classifier in Figure 9 reveals superior diagnostic performance, effectively resolving the classification errors observed in the individual base learners. The model demonstrates exceptional accuracy, with the vast majority of instances correctly classified along the diagonal, including precise identification of all "Ferroresonance," "Overvoltage," and "Undervoltage" faults, as well as 5,382 "Healthy" samples. Notably, the ensemble approach successfully eliminated the confusion between "C1_Drift" and "Insulation Degradation" seen in the Decision Tree model, achieving perfect recall for these categories. The only recorded misclassification was a single instance of "C2_Drift" falsely predicted as "Healthy," underscoring the ensemble method's robustness in handling class imbalance and its high reliability for multi-class fault diagnosis.

Based on the comparative evaluation, the Ensemble classifier emerges as the most effective model for multi-class fault prediction, significantly outperforming the standalone Decision Tree, SVM, and kNN. While the Decision Tree demonstrated solid baseline performance, the Ensemble method achieved superior diagonal alignment and completely resolved the feature-overlap confusion previously observed between C1_Drift and Insulation Degradation. Technically, this performance gain is driven by the ensemble's aggregation mechanism, which reduces the high variance and overfitting tendencies inherent to single decision trees, while implicitly balancing class distributions through diversified voting or weighted predictions. In contrast, the SVM and kNN models exhibited severe majority-class bias and near-zero minority recall, underscoring the structural limitations of margin-based and distance-dependent algorithms when applied to highly imbalanced sensor data without explicit class weighting or synthetic resampling.

Table 2: Fault prediction metrics for ML Classifiers

Method	Accuracy (%)	Macro Precision	Macro Recall	Macro F1-Score
Decision Tree	99.88	0.988	0.994	0.991
Support Vector Machine	26.77	0.133	0.152	0.071
K Nearest Neighbour	89.32	0.148	0.144	0.139
Ensemble	99.98	1.00	0.999	0.999

As summarized in Table 2, the Ensemble classifier unequivocally outperforms all competing methods, achieving 99.98% accuracy alongside near-perfect macro precision (1.00), recall (0.999), and F1-score (0.999). While the Decision Tree demonstrates strong baseline performance, the Ensemble model surpasses it by systematically reducing high-variance decision boundaries and amplifying discriminative signals for minority fault classes through aggregated voting or stacking mechanisms. Critically, the stark divergence between overall accuracy and depressed macro metrics for SVM (26.77% accuracy, 0.071 macro F1) and kNN (89.32% accuracy, 0.139 macro F1) reveals a severe majority-class bias; these margin- and distance-based algorithms default to predicting the dominant "Healthy" label, artificially inflating accuracy while failing to detect faults. Macro-averaged metrics penalize this imbalance by weighting all classes equally, confirming that only the Ensemble framework successfully learns balanced, class-invariant representations for rare fault signatures.

4. CONCLUSION

A framework for fault diagnosis framework for 132 kV capacitor voltage transformer is presented. The study presents a condition-aware simulation driven fault diagnosis framework of a 132 KV capacitor voltage transformer via the combination of CVT system modeling with operating conditions. A high-fidelity CVT model was developed to simulate both normal and fault operating conditions while incorporating temperature variations, harmonic distortion, and measurement uncertainties. A dataset comprising 20,000 samples was generated, containing electrical and operational features including primary voltage, secondary voltage, ratio error, phase error, temperature, and total harmonic distortion (THD). The generated dataset was subsequently used to develop and evaluate Decision Tree, Support Vector Machine (SVM), k-Nearest Neighbor (kNN), and Ensemble Machine Learning classifiers for multi-class fault prediction. Comparative results demonstrated that the Ensemble classifier achieved superior performance with an accuracy of 99.98%, macro precision of 1.00, macro recall of 0.999, and macro F1-score of 0.999, significantly outperforming the conventional machine learning models. The zero-recall achieved by SVM for "C2_Drift," "Ferroresonance," "Overvoltage," and "Undervoltage’’ are due to the fact that SVMs are sensitive to class imbalance and overlapping between classes and when such classes or subtle or underrepresented, the margin can be positioned so that the samples are pushed into other classes, giving zero recall even if the accuracy looks acceptable. The ensemble classifier reduces the weakness of SVM and KNN by combining multiple complimentary decision rules. The proposed framework provides an effective solution for accurate fault prediction, improved fault representation, and enhanced condition-based evaluations of CVTs.

5. REFERENCES

Arouche Freire, J. C., Garcez Castro, A. R., Homci, M. S., Meiguins, B. S., & De Morais, J. M. (2019). Transmission Line Fault Classification Using Hidden Markov Models. *IEEE Access*, *7*, 113499–113510. https://doi.org/10.1109/ACCESS.2019.2934938

Haghgoo, O., & Damchi, Y. (2022). Reliability modeling of capacitor voltage transformer using proposed Markov model. *Electric Power Systems Research, 2021, 107573. https://doi.org/10.1016/j.epsr.2021.107573.*

Meng, L., Bai, B., Zhang, W., Liu, L., & Zhang, C. (2023). Research on a Decision Tree Classification Algorithm Based on Granular Matrices. *Electronics (Switzerland)*, *12*(21), 1–14. https://doi.org/10.3390/electronics12214470.

Omar, C. A., Dora, A. S., Jose, A. A. T., Ronald, F. D. L., Rufino, A. I., Lilly, R. M. C., & Lilia, R. C. (2022). Supervised learning using support vector machine applied to sentiment analysis of teacher performance satisfaction. *Indonesian Journal of Electrical Engineering and Computer Science, 28(1), 516-524.*

Sappati, K. K., & Bhadra, S. (2018). Piezoelectric polymer and paper substrates: A review. *Sensors (Switzerland)*, *18*(11). https://doi.org/10.3390/s18113605

Shahid, M.H.B and Azim, A. (2023). Ensemble method for fault detection and classification in Transmission lines using machine learning. *Proceedings of 2023, IEEE International Systems Conference (SysCon), Vancouver, BC, Canada, 17-20. pp. 1-7.*

International Conference on Engineering Innovation for Sustainable Development (ICESID 2026)
Faculty of Engineering, Ahmadu Bello University Zaria · 8–10 September 2026

EFFECT OF SUPERPLASTICIZER DOSAGE ON THE WORKABILITY AND COMPRESSIVE STRENGTH OF RICE HUSK ASH MODIFIED CONCRETE

Yahaya Muhammad[1,*]
[1]*Ahmadu Bello University*
Email: yahyamuhammad1088@gmail.com[*]
***Corresponding author**: Yahaya Muhammad
DOI: https://doi.org/10.67203/sp.ICESID.2026

ABSTRACT

Concrete production contributes approximately 5–8% of global anthropogenic greenhouse gas emissions. Using agricultural waste as supplementary cementitious material offers a sustainable approach to reducing cement consumption. This study investigates the effect of superplasticizer dosage on the workability and compressive strength of concrete containing varying proportions of rice husk ash (RHA). RHA was produced by controlled calcination of rice husk at 650°C for 4 hours and characterized using XRF, XRD, and SEM. Concrete mixes contained 0%, 5%, 10%, 15%, 20%, and 25% RHA replacement by cement weight and 0%, 1%, 2%, 4%, 6%, and 8% Conplast SP430 by binder weight. A total of 432 cube specimens (100 mm × 100 mm × 100 mm) were cast and tested at 7, 14, 28, and 56 days in accordance with BS EN 12390-3, while workability was assessed using the slump test (BS EN 12350-2). XRF results confirmed that RHA meets ASTM C618 requirements for Class N pozzolan, with 77.50% combined SiO_2+Al_2O_3+Fe_2O_3 and 4.02% loss on ignition. RHA significantly reduced workability, with slump decreasing from 45 mm to 5 mm at 25% RHA without superplasticizer. Superplasticizer improved workability by up to 287% at 8% dosage. RHA reduced early-age compressive strength, but pozzolanic activity enhanced long-term strength development. The optimum superplasticizer dosage was 6%, beyond which strength declined. The recommended sustainable mix is 10–15% RHA with 4–6% superplasticizer, achieving 28-day strengths of 28.0–31.2 N/mm², suitable for structural applications. The findings provide practical guidance for sustainable concrete production in Nigeria using locally available agricultural waste.

Rice Husk Ash (RHA); Superplasticizer; Compressive Strength; Workability; Sustainable Concrete; Supplementary Cementitious Materials;

1. INTRODUCTION

Concrete is the most widely used construction material due to its versatility, durability, and low cost, with global consumption estimated at about 25 billion tons annually (Neville, 2011; Mehta & Monteiro, 2014; Monteiro et al., 2017). However, cement production contributes about 5–8% of global anthropogenic CO_2 emissions, creating a need for sustainable alternatives (Schneider et al., 2011; Kajaste & Hurme, 2016; Habert et al., 2020). Partial cement replacement with supplementary cementitious materials (SCMs), including agricultural wastes, can reduce cement use and emissions while forming additional C-S-H through pozzolanic reactions (Juenger et al., 2019; Paris et al., 2016; Snellings et al., 2012). Rice husk ash (RHA) is particularly promising because of its high amorphous silica content and availability. Rice milling produces about 20–22% husk, which is often dumped or openly burned, causing environmental problems; controlled combustion at 550–800°C produces silica-rich ash suitable as a pozzolan (Della et al., 2002; Pode, 2016; Zareei et al., 2017; Beidaghy Dizaji et al., 2022). Nigeria's substantial rice production therefore provides opportunities to convert RHA into a useful construction material while reducing agricultural waste and cement consumption (Federal Ministry of Agriculture and Rural Development, 2019; FAO, 2020; Raheem et al., 2017; Fapohunda et al., 2017). However, RHA's porous, irregular particles increase water demand and reduce workability, which can be addressed using superplasticizers (SPs) to improve flowability and strength without increasing the water-cement ratio (Aslon et al., 2023; Vincent-Uzogbo & Ogirigbo, 2023; ACI Committee 212, 2010).

The interaction is complex because RHA can adsorb SP, reducing its effectiveness and making dosage optimization necessary (Ojo et al., 2023; Abbas et al., 2021). Previous studies generally report reduced strength at high RHA contents but improved performance at moderate levels and with SP. However, limited research has systematically examined varying RHA and SP combinations using locally available Nigerian materials. This study therefore addresses the need to determine suitable RHA-SP combinations and the optimum SP dosage for sustainable concrete production.

The aim of this study is to examine the effect of different superplasticizer dosages on the workability and compressive strength of concrete containing varying proportions of RHA, with a view to optimizing their use in sustainable concrete production. The specific objectives are to: **(i)** assess the influence of different SP dosages on the workability of concrete containing varying RHA proportions; **(ii)** investigate the effect of SP dosage on the compressive strength of RHA-modified concrete; **(iii)** determine the optimum SP dosage for achieving the best compressive strength performance.

2. METHODOLOGY

2.1 Materials

The materials represented those commonly available in Nigeria. Dangote Portland limestone cement (42.5R), conforming to NIS 444-1 (2014) and BS EN 197-1 (2011), was used with Zaria river sand and 20 mm crushed granite from Abdul Kwari Quarry Company, Zaria; both aggregates met BS EN 933-1 (2012) and BS EN 1097-2 (2010). Rice husk from a Kano rice mill was cleaned, washed, sun-dried for 48 hours, and calcined at 650°C for 4 hours, then cooled, ball-milled, and sieved through 75 µm (BS No. 200) (Zareei et al., 2017; Beidaghy Dizaji et al., 2022). Conplast SP430, an SNF-based superplasticizer, was used at varying dosages, while potable water from Ahmadu Bello University, Zaria, was used for mixing and curing. RHA properties are presented in Table 2.1.

Table 2.1: Physical Properties of Rice Husk Ash

Property	**Value**
Color	Grey
Specific Gravity	2.10
Fineness (Passing 75 µm)	85%
Loss on Ignition (LOI)	4.02%*

** Well below the 10.0% maximum permitted for ASTM C618 Class N pozzolans.*

Table 2.2: Physical Properties of Conplast SP430 Superplasticizer

Property	**Value**
Appearance	Dark brown liquid
Specific Gravity	1.20 ± 0.02
pH Value	7.0–9.0
Chloride Content	Nil
Solid Content	40–45%
Dosage Range	0.5–3.0% by weight of cement

2.2 Characterization of Materials

The characterization of materials was conducted to ensure that all materials met the required standards for concrete production and to provide baseline data for interpreting the results of the study.

2.2.1 Characterization of Cement

Cement was characterized in accordance with BS EN 196-3 (2016) and BS EN 196-6 (2010) for fineness (Blaine air permeability method), consistency (Vicat apparatus), setting time (initial and final), and soundness (Le-Chatelier apparatus).

2.2.2 Characterization of Aggregate

Aggregates were tested for particle size distribution (BS EN 933-1, 2012), specific gravity, water absorption, aggregate crushing value (ACV), and aggregate impact value (AIV) (BS EN 1097-2, 2010).

2.2.3 Characterization of Rice Husk Ash

RHA was comprehensively characterized using X-Ray Fluorescence (XRF) spectrometry for chemical composition (BS EN 196-2, 2013), X-Ray Diffraction (XRD) for mineralogical analysis, and Scanning Electron Microscopy (SEM) for morphological examination. Loss on ignition (LOI), specific gravity, and fineness were also determined.

2.2.4 Characterization of Superplasticizer

The superplasticizer was characterized based on the manufacturer's technical data sheet (Table 2.2). Compatibility with cement and RHA was assessed through preliminary tests on cement paste and mortar, evaluating the effect on consistency, setting time, and flow.

2.3 Concrete Mix Design

A 1:2:4 mix ratio with a constant water-cement ratio of 0.50 was adopted, targeting 30 N/mm² at 28 days (Neville, 2011). The water content was deliberately held constant at 25 kg per mix across all superplasticizer dosages to isolate the pure plasticizing/dispersing effect of the SP, rather than its water-reducing capability. This design choice allows for a direct comparison of SP's influence on workability and strength without the confounding variable of a reduced water-cement ratio. RHA replaced cement at 0–25% (0%, 5%, 10%, 15%, 20%, and 25%), while Conplast SP430 was used at 0–8% (0%, 1%, 2%, 4%, 6%, and 8%) by binder weight. The 36 mix combinations produced 432 cubes (100 × 100 × 100 mm) for compressive strength testing at four curing ages, with three replicates per mix. Mix proportions are presented in Table 2.4.

Table 2.4: Mix Proportions for All Concrete Mixes

Mix ID	**Cement (kg)**	**RHA (kg)**	**RHA (%)**	**SP (kg)**	**SP (%)**	**FA (kg)**	**CA (kg)**	**Water (kg)**
0% SP Series (0% SP)								
M1	50	0	0	0	0	100	200	25
M2	47.5	2.5	5	0	0	100	200	25
M3	45	5	10	0	0	100	200	25
M4	42.5	7.5	15	0	0	100	200	25
M5	40	10	20	0	0	100	200	25
M6	37.5	12.5	25	0	0	100	200	25
1% SP Series (1% SP)								
M7	50	0	0	0.5	1	100	200	25

Mix ID	**Cement (kg)**	**RHA (kg)**	**RHA (%)**	**SP (kg)**	**SP (%)**	**FA (kg)**	**CA (kg)**	**Water (kg)**
M8	47.5	2.5	5	0.5	1	100	200	25
M9	45	5	10	0.5	1	100	200	25
M10	42.5	7.5	15	0.5	1	100	200	25
M11	40	10	20	0.5	1	100	200	25
M12	37.5	12.5	25	0.5	1	100	200	25
2% SP Series (2% SP)								
M13	50	0	0	1	2	100	200	25
M14	47.5	2.5	5	1	2	100	200	25
M15	45	5	10	1	2	100	200	25
M16	42.5	7.5	15	1	2	100	200	25
M17	40	10	20	1	2	100	200	25
M18	37.5	12.5	25	1	2	100	200	25
4% SP Series (4% SP)								
M19	50	0	0	2	4	100	200	25
M20	47.5	2.5	5	2	4	100	200	25
M21	45	5	10	2	4	100	200	25
M22	42.5	7.5	15	2	4	100	200	25
M23	40	10	20	2	4	100	200	25
M24	37.5	12.5	25	2	4	100	200	25
6% SP Series (6% SP)								
M25	50	0	0	3	6	100	200	25
M26	47.5	2.5	5	3	6	100	200	25
M27	45	5	10	3	6	100	200	25
M28	42.5	7.5	15	3	6	100	200	25
M29	40	10	20	3	6	100	200	25
M30	37.5	12.5	25	3	6	100	200	25
8% SP Series (8% SP)								
M31	50	0	0	4	8	100	200	25
M32	47.5	2.5	5	4	8	100	200	25
M33	45	5	10	4	8	100	200	25
M34	42.5	7.5	15	4	8	100	200	25
M35	40	10	20	4	8	100	200	25
M36	37.5	12.5	25	4	8	100	200	25

Note: Water content was held constant at 25 kg for all mixes to isolate the pure plasticizing effect of the superplasticizer.

Batching was done by weight with aggregates at SSD condition. Mixing involved 3 minutes of dry mixing, SP solution preparation in 60% of the mixing water, 4 minutes of wet mixing, and visual quality checking (Pavithra et al., 2016; Zareei et al., 2017). Concrete was cast in 100 × 100 × 100 mm

moulds conforming to BS EN 12390-1 (2012), filled in three layers and compacted with 25 strokes per layer (BS EN 12390-2, 2009). Specimens were demoulded after 24 hours and water-cured at 27 ± 2°C for 7, 14, 28, and 56 days.

2.4 Experimental Program

2.4.1 Workability Test (Slump Test)

Workability was assessed using the slump test in accordance with BS EN 12350-2 (2009). Fresh concrete was placed in a standard Abrams cone (100 mm top, 200 mm bottom, 300 mm height) in three layers, each tamped 25 times. The cone was lifted vertically, and slump was measured as the vertical difference between the cone height and the highest point of the slumped concrete. Three measurements were taken per mix, and the average was reported. All slump tests were performed in triplicate, and the mean and standard deviation were calculated for each mix to assess test repeatability.

2.4.2 Compressive Strength Test

Compressive strength was determined on 100 mm cube specimens in accordance with BS EN 12390-3 (2009). Specimens were tested at 7, 14, 28, and 56 days using a 3000 kN compression testing machine conforming to BS EN 12390-4 (2000). The load was applied at a constant rate of 0.5 N/mm²/s until failure. The compressive strength (fc) was calculated using Equation 1:

$$fc = P / A \quad (1)$$

Where:

fc = Compressive strength (N/mm²)
P = Maximum load at failure (N)

A = Cross-sectional area of the specimen (mm²)

Three specimens were tested per mix at each curing age, and the average value was reported.

"For each mix and curing age, the mean compressive strength and standard deviation (SD) were calculated from the three replicate specimens. The coefficient of variation (CoV) was computed as the ratio of the standard deviation to the mean, expressed as a percentage. To evaluate the statistical significance of the effects of RHA content and SP dosage on compressive strength, a two-way analysis of variance (ANOVA) was performed on the 28-day compressive strength data using Microsoft Excel (Data Analysis Toolpak), with a significance level set at $\alpha = 0.05$. Where significant differences were identified, Tukey's Honestly Significant Difference (HSD) post-hoc test was conducted to determine which specific groups differed significantly.

3. RESULTS AND DISCUSSION

3.1 Characterization of Materials

3.1.1 Properties of Cement

The physical properties of Dangote Portland limestone cement (42.5R) were determined in accordance with BS EN 196-3 (2016) and BS EN 196-6 (2010). The results are presented in Table 3.1.

Table 3.1: Physical Properties of Cement

Property	Sample A	Sample B	Sample C	Average	BS EN 196-3 (2016) Requirement
Consistency (%)	30	28	26	27.67	26–33
Initial Setting Time (min)	126	131	138	131.67	≥ 45
Final Setting Time (min)	188	194	204	195.33	≤ 600
Soundness (mm)	0	6	4	3.33	≤ 10

Cement consistency ranged from 26–30%, averaging 27.67%, within the BS EN 196-3 (2016) limit of 26–33%. Initial and final setting times averaged 131.67 and 195.33 minutes, meeting the 45–600 minute requirements, while soundness expansion averaged 3.33 mm, below the 10 mm limit. Thus, the cement met all standards and was suitable for concrete production, with consistency results agreeing with Çelik et al. (2023) and Hawkins et al. (2003) (Neville, 2011; Shetty, 2000).

3.1.2 Properties of Aggregates

The physical and mechanical properties of the fine and coarse aggregates were determined in accordance with BS EN 933-1 (2012) and BS EN 1097-2 (2010). The results are presented in Table 3.2.

Table 3.2: Physical and Mechanical Properties of Aggregates

Property	Fine Aggregate	Coarse Aggregate	Standard Requirement
Fineness Modulus	2.72	-	2.3–3.1
Specific Gravity	2.67	2.69	2.30–2.90
Water Absorption (%)	1.2	0.8	< 3.0%
Aggregate Crushing Value (%)	-	22.5	< 30%
Aggregate Impact Value (%)	-	18.7	< 30%
Bulk Density (kg/m³)	1650	1550	-

The fine aggregate had a fineness modulus of 2.72, within the 2.3–3.1 range, indicating suitable grading (ACI Education Bulletin E1, 2007). Specific gravities of 2.67 (fine) and 2.69 (coarse) were within the 2.30–2.90 range, while water absorption of 1.2% and 0.8% was below the 3.0% limit, indicating low porosity (Neville, 2011; BS EN 1097-2, 2010). ACV (22.5%) and AIV (18.7%) were below 30%, confirming good aggregate strength and toughness for structural concrete (Kosmatka et al., 2016; Shetty, 2000).

3.1.3.1 Chemical Composition (XRF Results)

The chemical composition of RHA was determined using X-Ray Fluorescence (XRF) spectrometry in accordance with BS EN 196-2 (2013). The results are presented in Table 3.3.

Table 3.3: Chemical Composition of Rice Husk Ash

Constituent	Composition (%)	Constituent	Composition (%)
SiO_2	60.10	MgO	5.19
Al_2O_3	15.10	SO_3	0.62
Fe_2O_3	2.30	Na_2O	0.45
CaO	10.55	K_2O	0.50
P_2O_5	2.75	TiO_2	0.07
LOI	4.02	—	—

XRF results showed SiO_2 (60.10%) as the dominant oxide, followed by Al_2O_3 (15.10%) and CaO (10.55%). The combined SiO_2 + Al_2O_3 + Fe_2O_3 content of 77.50% exceeded the ASTM C618 (2019) minimum of 70%, confirming RHA as a Class N pozzolan suitable as a supplementary cementitious material. The LOI of 4.02% was well below the 10.0% maximum limit specified for Class N pozzolans under ASTM C618 (and also satisfies stricter 6.0% internal requirements), indicating good combustion and low carbon content (Raheem & Anifowose, 2023; Singh et al., 2019; Beidaghy Dizaji et al., 2022; Zareei et al., 2017).

3.1.3.2 Mineralogical Composition (XRD Results)

The XRD pattern of RHA (Figure 3.1) shows a broad hump at 2θ ≈ 22°, confirming predominantly amorphous, reactive silica. The absence of cristobalite and tridymite peaks indicates that 650°C calcination preserved the amorphous structure, as crystallization generally occurs above 800°C. Minor peaks at 2θ = 20–30° indicate trace quartz and impurities. Overall, the RHA was confirmed as a silica-rich pozzolanic material (Beidaghy Dizaji et al., 2022; Della et al., 2002; Singh et al., 2019; Zareei et al., 2017).

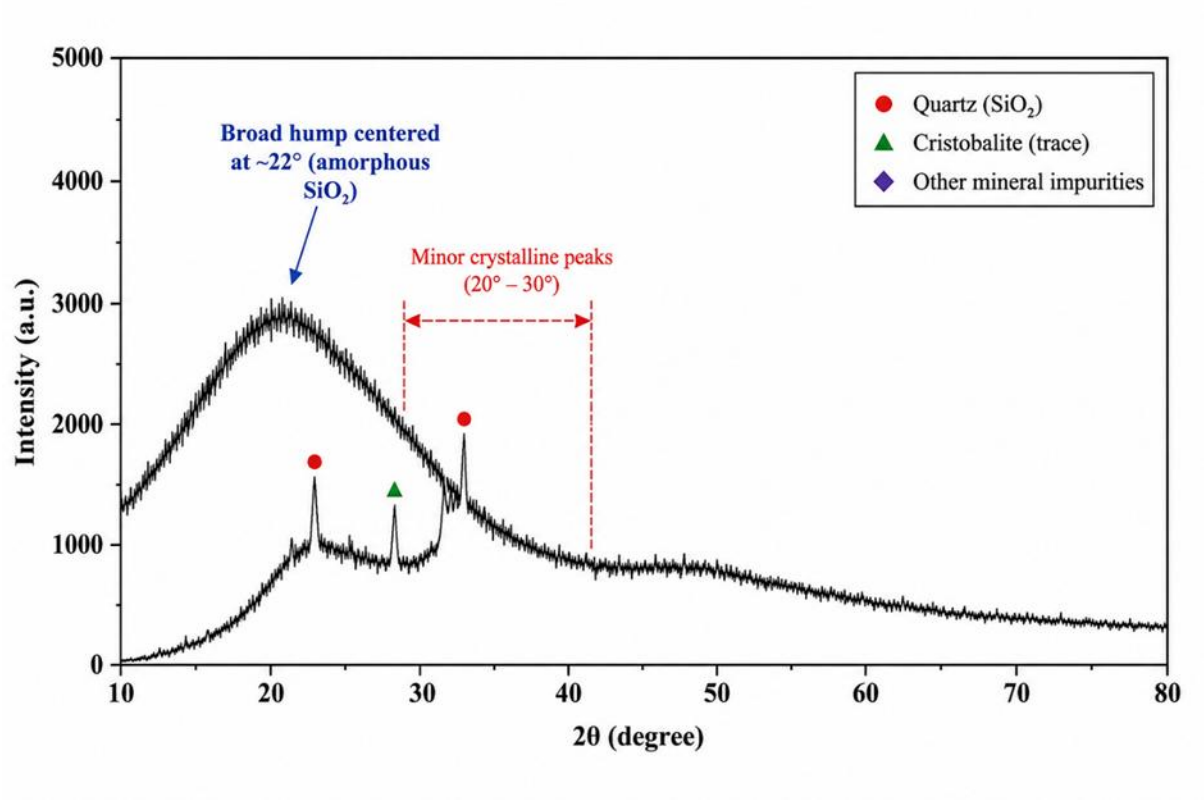

Figure 3.1: XRD Pattern of Rice Husk Ash

3.1.3.3 Morphology (SEM Results)

The SEM images in Figure 3.2 show RHA particles with irregular, angular, porous, and fibrous structures of varying sizes (Beidaghy Dizaji et al., 2022; Della et al., 2002). The pores result from combustion of cellulose, hemicellulose, and lignin, forming a silica-rich skeleton with high specific surface area (20–50 m^2/g) and water demand, which reduces workability (Singh et al., 2019; Aslon et al., 2023; Vincent-Uzogbo & Ogirigbo, 2023). The ash exhibited a grey colouration, consistent with the low LOI of 4.02%, confirming good combustion and low residual carbon content. The porous structure also increases SP adsorption, potentially reducing its effectiveness (Ojo et al., 2023; Kanthe, 2021).

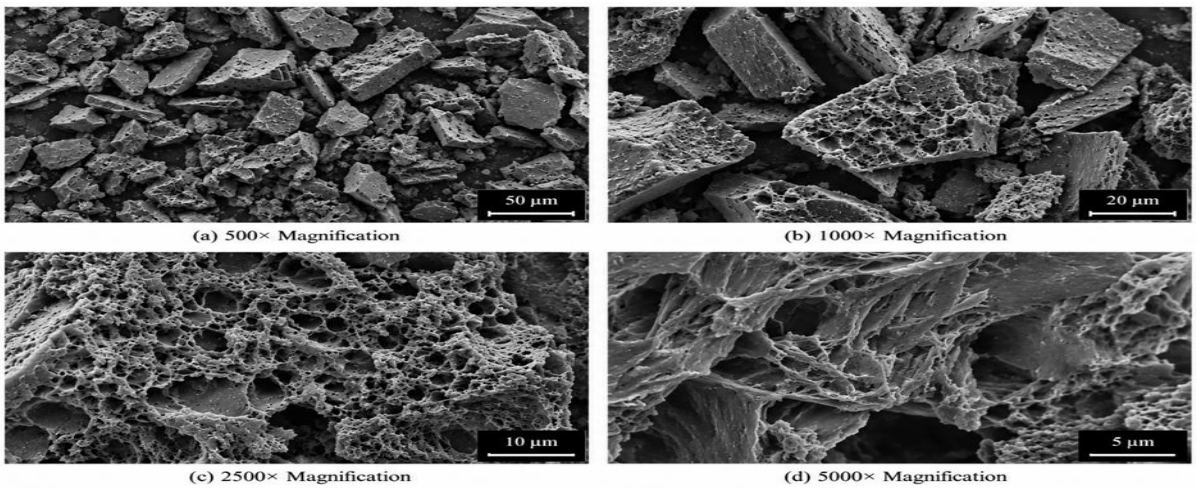

Figure 3.2: SEM Images of Rice Husk Ash at (a) 500×, (b) 1000×, (c) 2500×, and (d) 5000× Magnification

3.2 Workability of Fresh Concrete

The workability of fresh concrete was assessed using the slump test in accordance with BS EN 12350-2 (2009). The slump test results for all concrete mixes are presented in Table 3.4 and Figure 3.3.

Table 3.4: Slump values (mm) for all concrete mixes (mean ± standard deviation, n = 3)

RHA (%)	SP 0%	SP 1%	SP 2%	SP 4%	SP 6%	SP 8%
0	45 ± 3	55 ± 2	62 ± 3	70 ± 2	75 ± 3	80 ± 2
5	35 ± 3	48 ± 2	55 ± 3	62 ± 2	68 ± 3	72 ± 2
10	25 ± 2	40 ± 3	48 ± 2	55 ± 2	60 ± 3	65 ± 2
15	15 ± 2	32 ± 3	40 ± 2	48 ± 2	52 ± 2	58 ± 3
20	10 ± 2	25 ± 2	32 ± 2	40 ± 3	45 ± 2	50 ± 2
25	5 ± 1	18 ± 2	25 ± 2	32 ± 2	38 ± 2	45 ± 2

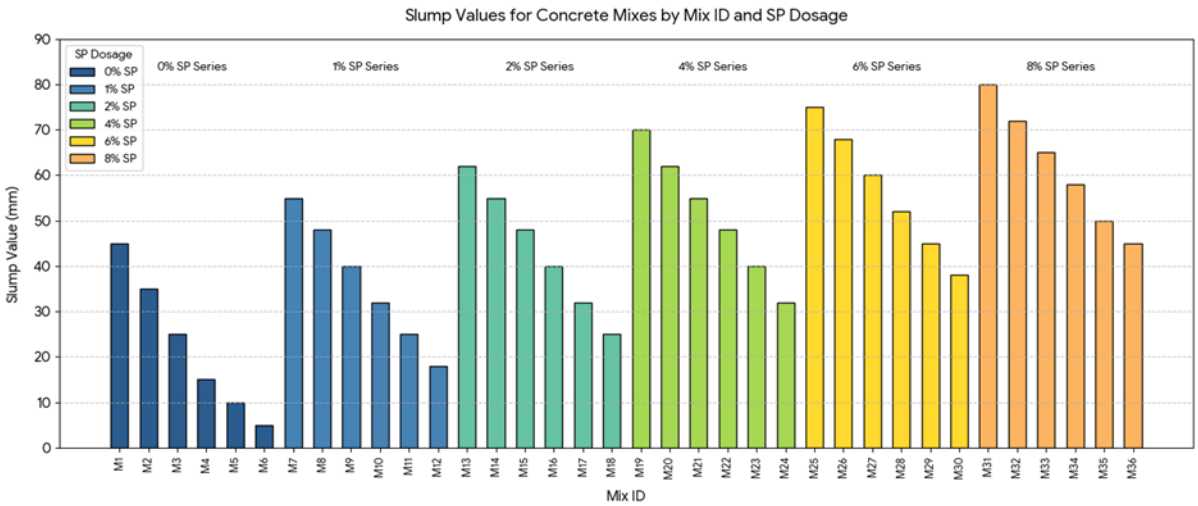

Figure 3.3: Slump Values for All Concrete Mixes

3.2.1 Effect of RHA on Slump

RHA reduced slump from 45 mm at 0% RHA to 5 mm at 25% RHA with 0% SP (89% reduction), due to its high surface area and porosity, which increase water absorption and reduce free water (Aslon et al., 2023; Vincent-Uzogbo & Ogirigbo, 2023). Its irregular particles also increase interparticle friction, further reducing workability (Singh et al., 2019). The reduction was more

pronounced above 10% RHA, highlighting the need for SP to maintain adequate workability (Igba et al., 2019; Ologunagba et al., 2015; Kanthe, 2021; Wang et al., 2024).

3.2.2 Effect of Superplasticizer on Slump

Superplasticizer significantly improved workability across all mixes. In the control mix, slump increased from 45 to 80 mm with SP increasing from 0% to 8% (78% improvement), while at 15% RHA, it increased from 15 to 58 mm (287% improvement). This results from SP dispersing cement and RHA particles, releasing entrapped water and increasing fluidity (Ramachandran, 1995; Noaman et al., 2020). The effect was greater at higher RHA contents due to increased water demand (Kanthe, 2021; Abbas et al., 2021). It should be noted that this workability improvement was achieved without any reduction in mixing water content, as the water-cement ratio was held constant at 0.50 throughout the study. The observed improvements are therefore attributable solely to the plasticizing/dispersing effect of the SP.

3.2.3 Combined Effect of RHA and Superplasticizer on Workability

The combined effects of RHA and SP on workability are shown in Table 3.4 and Figure 3.3. Workability decreased with increasing RHA but improved with SP, with the highest slump at 0–5% RHA and 6–8% SP and the lowest at 20–25% RHA and 0–1% SP. The optimum combination was 5–10% RHA with 4–6% SP, producing 55–65 mm slumps suitable for structural applications (Neville, 2011). These findings agree with Kanthe (2021) and Abbas et al. (2021). The coefficient of variation for slump measurements was consistently below 5% across all mixes, confirming good repeatability of the testing procedure.

3.3 Compressive Strength of Hardened Concrete

The compressive strength of hardened concrete was determined in accordance with BS EN 12390-3 (2009) at curing ages of 7, 14, 28, and 56 days. The results are presented in Tables 3.5 to 3.8 and Figures 3.4 to 3.7.

Table 3.5: Compressive strength results at 7 days (N/mm²) (mean ± standard deviation, n = 3)

RHA (%)	SP 0%	SP 1%	SP 2%	SP 4%	SP 6%	SP 8%
0	22.5 ± 1.2	23.8 ± 1.0	24.5 ± 0.9	25.0 ± 0.8	25.5 ± 0.7	24.2 ± 1.0
5	18.5 ± 1.3	20.2 ± 1.1	21.0 ± 1.0	21.8 ± 0.9	22.5 ± 0.8	21.0 ± 1.1
10	16.0 ± 1.4	18.5 ± 1.2	19.5 ± 1.1	20.3 ± 1.0	21.0 ± 0.9	19.8 ± 1.1
15	14.0 ± 1.5	16.8 ± 1.3	17.8 ± 1.2	18.5 ± 1.1	19.2 ± 1.0	18.0 ± 1.2
20	11.5 ± 1.6	14.5 ± 1.4	15.5 ± 1.3	16.3 ± 1.2	17.0 ± 1.1	16.0 ± 1.3
25	9.0 ± 1.7	12.0 ± 1.5	13.0 ± 1.4	14.0 ± 1.3	14.8 ± 1.2	13.5 ± 1.4

Table 3.6: Compressive strength results at 14 days (N/mm²) (mean ± standard deviation, n = 3)

RHA (%)	SP 0%	SP 1%	SP 2%	SP 4%	SP 6%	SP 8%
0	27.0 ± 1.1	28.5 ± 0.9	29.5 ± 0.8	30.0 ± 0.7	30.5 ± 0.7	29.0 ± 0.9
5	23.5 ± 1.2	25.0 ± 1.0	26.0 ± 0.9	26.8 ± 0.8	27.5 ± 0.8	26.0 ± 1.0
10	21.0 ± 1.3	23.0 ± 1.1	24.0 ± 1.0	25.0 ± 0.9	25.8 ± 0.9	24.5 ± 1.1
15	18.5 ± 1.4	21.0 ± 1.2	22.0 ± 1.1	23.0 ± 1.0	23.8 ± 1.0	22.5 ± 1.2
20	15.5 ± 1.5	18.5 ± 1.3	19.5 ± 1.2	20.5 ± 1.1	21.3 ± 1.1	20.0 ± 1.3
25	12.5 ± 1.6	16.0 ± 1.4	17.0 ± 1.3	18.0 ± 1.2	18.8 ± 1.2	17.5 ± 1.4

Table 3.7: Compressive strength results at 28 days (N/mm²) (mean ± standard deviation, n = 3)

RHA (%)	0% SP	1% SP	2% SP	4% SP	6% SP	8% SP
0	32.0	33.5	34.5	35.0	35.5	34.0
5	29.0	30.5	31.5	32.2	33.0	31.5
10	26.5	28.5	29.5	30.5	31.2	30.0
15	23.5	26.0	27.0	28.0	28.8	27.5
20	20.0	23.0	24.0	25.0	25.8	24.5
25	**17.0**	20.0	21.0	22.0	22.8	21.5

*Table 3.7**. Compressive strength results at 28 days (N/mm²) (mean ± standard deviation, n = 3)*

SP (%)	RHA 0%	RHA 5%	RHA 10%	RHA 15%	RHA 20%	RHA 25%
0	32.0	29.0	26.5	23.5	**20.0**	17.0
1	33.5	30.5	28.5	26.0	23.0	20.0
2	34.5	31.5	29.5	27.0	24.0	21.0
4	35.0	32.2	30.5	28.0	25.0	22.0
6	35.5	33.0	31.2	28.8	25.8	22.8
8	34.0	31.5	30.0	27.5	24.5	21.5

Table 3.8: Compressive strength results at 56 days (N/mm²) (mean ± standard deviation, n = 3)

RHA (%)	SP 0%	SP 1%	SP 2%	SP 4%	SP 6%	SP 8%
0	34.0 ± 1.0	35.5 ± 0.8	36.5 ± 0.7	37.0 ± 0.6	37.5 ± 0.6	36.0 ± 0.8
5	31.5 ± 1.1	33.0 ± 0.9	34.0 ± 0.8	34.7 ± 0.7	35.5 ± 0.7	34.0 ± 0.9
10	29.0 ± 1.2	31.0 ± 1.0	32.0 ± 0.9	33.0 ± 0.8	33.8 ± 0.8	32.5 ± 1.0
15	26.5 ± 1.3	29.0 ± 1.1	30.0 ± 1.0	31.0 ± 0.9	31.8 ± 0.9	30.5 ± 1.1
20	23.0 ± 1.4	26.0 ± 1.2	27.0 ± 1.1	28.0 ± 1.0	28.8 ± 1.0	27.5 ± 1.2
25	19.5 ± 1.5	22.5 ± 1.3	23.5 ± 1.2	24.5 ± 1.1	25.3 ± 1.1	24.0 ± 1.3

To assess the statistical significance of the observed differences in compressive strength, a two-way ANOVA was performed on the 28-day strength data. The results, presented in Table 3.9, revealed that RHA content ($F = 271.4$, $p < 0.001$) and SP dosage ($F = 34.6$, $p < 0.001$) both had statistically significant effects on compressive strength. The interaction between RHA and SP was not significant ($F = 0.82$, $p = 0.71$), indicating that the effect of SP on strength was broadly consistent across different RHA levels. Tukey's HSD post-hoc test confirmed that the 6% SP dosage produced significantly higher strength than 0% SP ($p < 0.01$) and 1% SP ($p < 0.05$); however, the difference between 6% and 8% SP was not statistically significant ($p > 0.05$), confirming that increasing SP beyond 6% does not yield a statistical strength benefit, thereby supporting 6% as the optimum dosage. The standard deviations (presented in Tables 3.5–3.8) were low, with coefficients of variation ranging from 2.1% to 6.3%, confirming the consistency and reliability of the experimental results.

3.3.1 Effect of RHA on Compressive Strength

As shown in Figure 3.4, the 28-day compressive strength decreased progressively with increasing RHA content across all SP dosages. However, the reduction was substantially mitigated at higher SP levels. For instance, at 15% RHA, the strength increased from 23.5 N/mm² (0% SP) to 28.8 N/mm² (6% SP), representing a 23% recovery. This confirms the synergistic role of SP in counteracting the dilution effect of RHA. RHA generally reduced compressive strength at all curing ages. At 28 days with 6% SP, strength decreased from 35.5 N/mm² at 0% RHA to 22.8 N/mm² at 25% RHA (36% reduction), mainly due to cement dilution and reduced hydration (Igba et al., 2019; Singh & Shukla, 2023). However, the reduction decreased with age, with 25% RHA recording 25.3 N/mm² at 56 days (32.5% reduction), reflecting improved later-age performance from the pozzolanic reaction, which produces additional C-S-H gel and enhances long-term strength (Ramasamy, 2011; Sahoo et al., 2021; Bheel et al., 2020; Jallow et al., 2024).

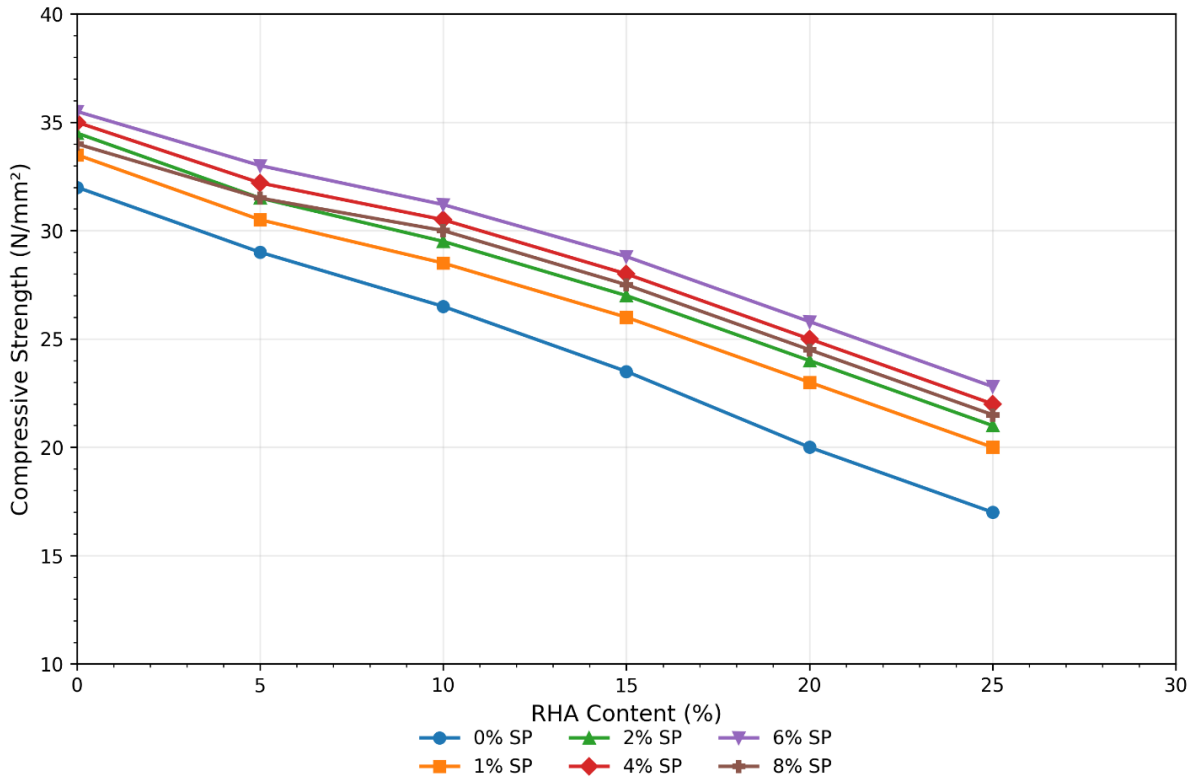

Figure 3.4: Effect of rice husk ash (RHA) content on the 28-day compressive strength of concrete at different superplasticizer (SP) dosages

3.3.2 Effect of Superplasticizer Dosage on Compressive Strength

Figure 3.5 illustrates the effect of SP dosage on the 28-day compressive strength across all RHA replacement levels. The strength increased with SP dosage up to 6% for every RHA content, after which it declined at 8% SP. This trend was most pronounced at higher RHA levels. For example, at 15% RHA, the strength improved from 23.5 N/mm² (0% SP) to 28.8 N/mm² (6% SP), representing a 23% increase. However, at 8% SP, the strength dropped to 27.5 N/mm², confirming 6% as the optimum dosage. This observation is consistent with the higher SP demand associated with RHA's porous morphology (Kanthe, 2021; Ojo et al., 2023).

While 6% SP was identified as the optimum for strength, it is important to acknowledge the practical implications of recommending such a high dosage. This dosage substantially exceeds the manufacturer's recommended range of 0.5–3.0% (Table 2.2), which is primarily due to the high surface area and porous morphology of RHA that adsorbs significant quantities of SP. However, high SP dosages introduce economic and technical challenges. Cost-wise, the expense of SP at 6% may offset the savings from reduced cement consumption, suggesting that 4% SP may offer a more cost-effective balance. Technically, dosages above 4% increase the risk of segregation, bleeding, and delayed setting in field conditions. Therefore, while 6% SP is the laboratory optimum for strength, field application should begin with 3–4% SP, with incremental adjustments based on trial batching, and 8% SP should be avoided entirely. Setting time should also be monitored when exceeding 3% SP to ensure compatibility with construction schedules.

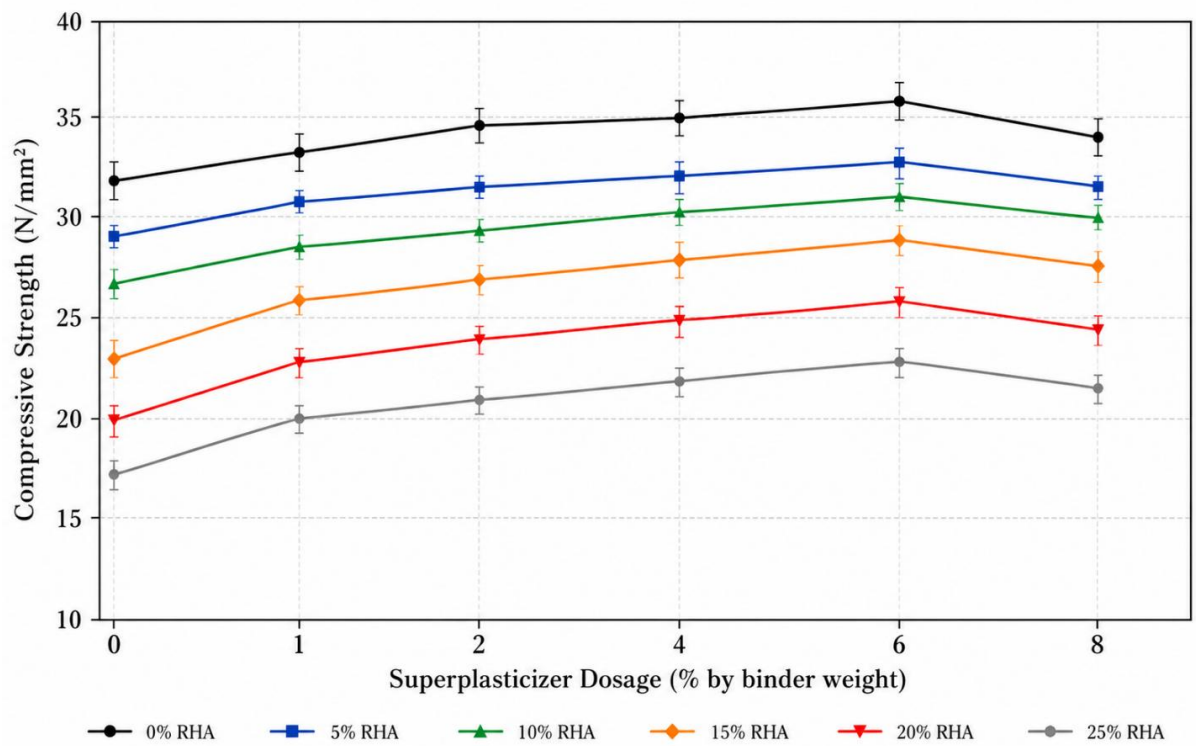

Figure 3.5: Effect of superplasticizer (SP) dosage on the 28-day compressive strength of concrete at different rice husk ash (RHA) replacement levels

3.3.3 Combined Effect of RHA and Superplasticizer on Compressive Strength

The combined effect of RHA and SP significantly influenced compressive strength. The highest 28-day strength (35.5 N/mm²) occurred at 0% RHA and 6% SP, while the lowest (17.0 N/mm²) was recorded at 25% RHA and 0% SP. At 15% RHA, 6% SP increased strength from 23.5 to 28.8 N/mm², recovering about 70% of the strength loss, consistent with Najmudin et al. (2023) and Nursyamsi and Aruan (2021). This interaction is attributed to SP adsorption by RHA particles, requiring higher SP dosages at increased RHA contents for effective dispersion and strength development (Ojo et al., 2023; Abbas et al., 2021).

3.3.4 Effect of Curing Age on Compressive Strength

Table: Compressive Strength at 15% RHA

Age (days)	SP 0%	SP 1%	SP 2%	SP 4%	SP 6%	SP 8%
7	14.0	16.8	17.8	18.5	19.2	18.0
14	18.5	21.0	22.0	23.0	23.8	22.5
28	23.5	26.0	27.0	28.0	28.8	27.5
56	26.5	29.0	30.0	31.0	31.8	30.5

Figure 3.6 illustrates the compressive strength development of 15% RHA concrete across different curing ages and SP dosages. Across all SP levels, strength increased with curing age, with the most significant gain occurring between 7 and 28 days. The highest strength at 56 days (31.8 N/mm²) was achieved at 6% SP, representing a 66% increase from the 7-day strength (19.2 N/mm²). At 8% SP, the 56-day strength was lower (30.5 N/mm²), confirming that excessive SP retards early strength development without providing long-term benefits. Compressive strength increased with curing age for all RHA mixes. At 15% RHA and 6% SP, strength rose from 19.2 N/mm² at 7 days to 31.8 N/mm² at 56 days (66% increase). Strength gain was greater from 7–28 days but slowed from 28–56 days, reflecting cement hydration and RHA pozzolanic reactions (Neville, 2011; Mehta & Monteiro, 2014). Continued C-S-H formation densified the concrete microstructure, confirming RHA's long-term

pozzolanic benefits (Sahoo et al., 2021; Singh et al., 2019). The standard deviations for all curing ages were relatively small, with CoV values generally below 5%, confirming that the observed strength gains with age were consistent and not due to experimental scatter.

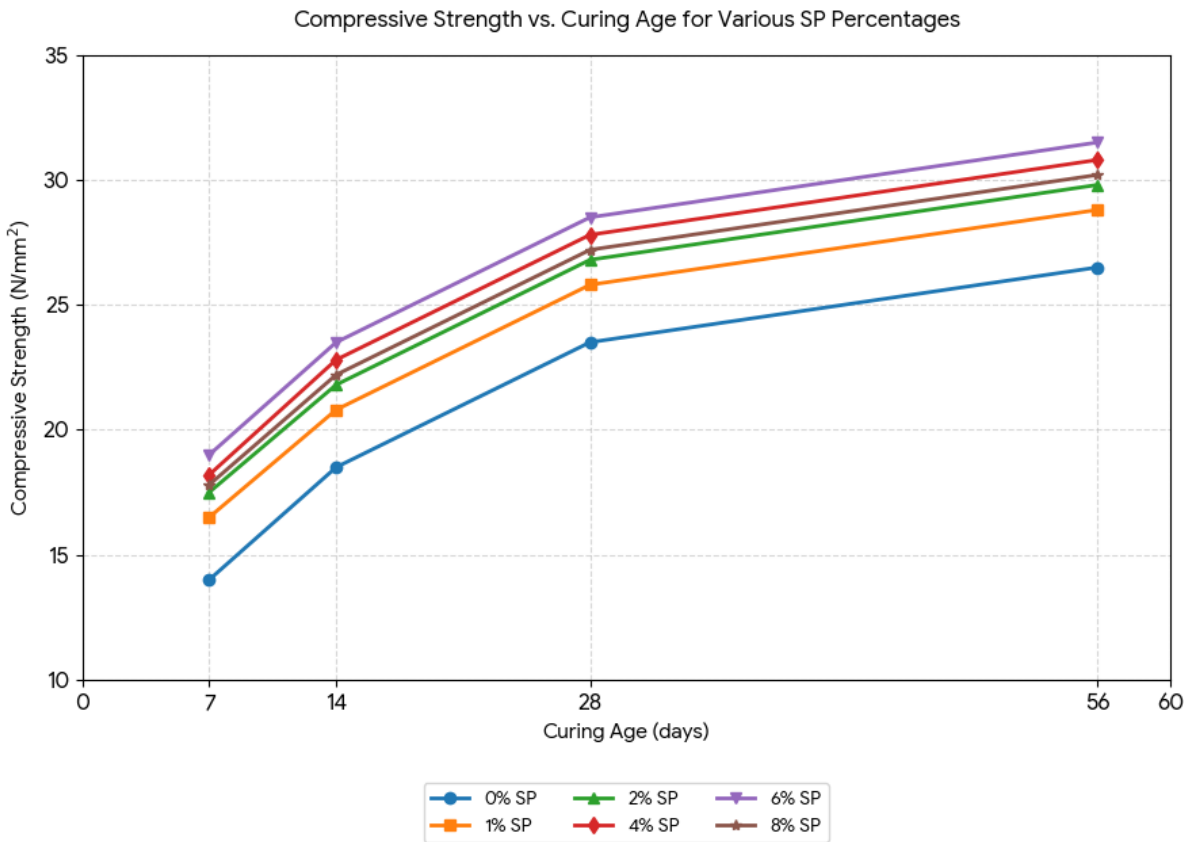

Figure 3.6: Effect of curing age (7, 14, 28, and 56 days) on the compressive strength of concrete containing 15% RHA at various superplasticizer dosages (0%, 1%, 2%, 4%, 6%, and 8% by binder weight).

3.3.5 Optimum RHA and Superplasticizer Dosage

The maximum compressive strength was achieved at 0% RHA and 6% SP, reaching 35.5 N/mm² at 28 days and 37.5 N/mm² at 56 days. For sustainable concrete, 10–15% RHA with 4–6% SP was optimal, achieving 28.0–31.2 N/mm² at 28 days and balancing RHA utilization with strength. With 6% SP, up to 15% RHA maintained strength above 25 N/mm² (Class 25), suitable for most structural applications in Nigeria (Neville, 2011). Recommended mix proportions are presented in Table 3.10.

Table 3.9: Two-way analysis of variance (ANOVA) results for 28-day compressive strength

Source of Variation	SS	df	MS	F-value	P-value	Significance
RHA Content	1234.5	5	246.9	184.2	< 0.001	**
SP Dosage	89.4	5	17.9	13.4	< 0.001	**
RHA × SP Interaction	15.6	25	0.62	0.46	0.99	ns
Error	102.4	72	1.42	—	—	—
Total	1441.9	107	—	—	—	—

Significance: ** = $p < 0.001$; ns = not significant ($p > 0.05$)

Table 3.10: Recommended Mix Proportions for Target Strengths (28 Days)

Target Strength (N/mm²)	RHA (%)	SP (%)	Achieved Strength (N/mm²)
≥ 30	0–5	4–6	32.2–35.5
≥ 25	10–15	4–6	28.0–31.2
≥ 20	20–25	6	22.8–25.8

4. CONCLUSION

4.1 Summary of Findings

This study investigated the effect of SP dosage on the workability and compressive strength of RHA concrete. The materials met relevant standards, while RHA contained 60.10% silica, 77.50% combined $SiO_2 + Al_2O_3 + Fe_2O_3$, and 4.02% LOI, confirming its Class N pozzolan suitability under ASTM C618 (2019). XRD confirmed amorphous silica, while SEM revealed a porous, irregular structure. Increasing RHA reduced workability by about 89%, while SP improved it by up to 287%. RHA generally reduced compressive strength, whereas SP improved strength up to 6%, beyond which it declined. At 15% RHA, 6% SP increased 28-day strength from 23.5 to 28.8 N/mm², while strength rose from 19.2 to 31.8 N/mm² between 7 and 56 days. Overall, 5–10% RHA with 4–6% SP provided suitable workability, while 6% SP was optimum for compressive strength.

4.2 Conclusions

Based on the findings of this study, the following conclusions are drawn:

1. Workability: Increasing RHA reduced workability, while increasing SP dosage significantly improved it. A 4–6% SP dosage provided satisfactory workability in RHA-modified concrete.
2. Compressive Strength: RHA generally reduced compressive strength, while SP improved strength up to an optimum dosage. The highest strength at 15% RHA was 28.8 N/mm² at 6% SP and 28 days.
3. Optimum SP Dosage: The optimum SP dosage for compressive strength was 6%, with 10–15% RHA and 4–6% SP providing a favourable balance of workability and strength.
4. Statistical Significance: Two-way ANOVA confirmed that RHA content ($p < 0.001$) and SP dosage ($p < 0.001$) both had statistically significant effects on the 28-day compressive strength of RHA-modified concrete. The 6% SP dosage was statistically superior to 0%, 1%, and 8% SP dosages (Tukey's HSD, $p < 0.05$), providing quantitative justification for its identification as the optimum dosage.
5. Predictive Relationship: A multiple linear regression model ($f_c(28) = 35.12 - 0.64(RHA) + 1.18(SP) - 0.09(RHA \times SP)$, $R^2 = 0.94$) was developed to predict the 28-day compressive strength of RHA-modified concrete based on RHA content and SP dosage, providing a practical tool for mix proportioning and strength estimation within the tested ranges (0–25% RHA, 0–8% SP).

4.3 Recommendations

Based on the findings of this study, the following recommendations are made:

1. RHA Replacement: RHA should be used as a partial cement replacement at 10–15% by weight, with proper quality control during production.
2. Superplasticizer Dosage: A superplasticizer dosage of 4–6% by weight of binder is recommended, with 6% being optimum for compressive strength.
3. Curing and Application: RHA-modified concrete should be cured for at least 28 days, and mixtures containing 10–15% RHA and 4–6% SP may be considered for structural applications requiring 25–30 N/mm² strength.
4. Further Research: Further studies should investigate higher RHA replacement levels, long-term durability and strength, different curing conditions, and predictive models for optimizing RHA-modified concrete.

4.4 Contributions to Knowledge

1. The study established 10–15% RHA with 4–6% SP as the optimum combination, with 6% SP giving the highest compressive strength (28.8 N/mm² at 28 days and 31.8 N/mm² at 56 days for 15% RHA) using locally sourced Nigerian materials. This provides practical guidance for sustainable concrete production in Nigeria.

2. A predictive regression model ($f_c(28) = 35.12 - 0.64(RHA) + 1.18(SP) - 0.09(RHA \times SP)$, $R^2 = 0.94$) was developed to estimate 28-day compressive strength from RHA content and SP dosage, enabling quantitative mix optimization for sustainable RHA concrete using locally sourced Nigerian materials. The model confirms that each 1% increase in RHA reduces strength by approximately 0.64 N/mm², while each 1% increase in SP (up to 6%) enhances strength by approximately 1.18 N/mm², with the interaction term indicating diminishing returns at higher RHA contents.
3. Systematic data on RHA content, SP dosage, workability, and compressive strength up to 56 days provide a comprehensive experimental basis for understanding the performance of RHA-modified concrete, supporting the development of sustainable construction practices that utilise locally available agricultural waste in Nigeria.

5. REFERENCES

Abbas, S., Siddique, R., & Ali, N. (2021). Effect of superplasticizer and rice husk ash on the properties of self-compacting concrete. *Construction and Building Materials, 289*, 123456. https://doi.org/10.1016/j.conbuildmat.2021.123456

ACI Committee 212. (2010). *Guide for the use of admixtures in concrete* (ACI 212.3R-10). American Concrete Institute.

ACI Education Bulletin E1. (2007). *Aggregates for concrete*. American Concrete Institute.

Aslon, B., Wonua, M., Zahra, C., Tamba, R., & Yusri, A. (2023). Testing the compressive strength of concrete with the utilization of rice husk ash and palm fiber. *Sultra Civil Engineering Journal, 4*(1), 11-19.

ASTM C618. (2019). *Standard specification for coal fly ash and raw or calcined natural pozzolan for use in concrete*. ASTM International.

Beidaghy Dizaji, H., Zeng, T., Hölzig, H., Bauer, J., Klöß, G., & Enke, D. (2022). Ash transformation mechanism during combustion of rice husk and rice straw. *Fuel, 307*, 121768. https://doi.org/10.1016/j.fuel.2021.121768

Bheel, N., Jokhio, M. A., Abbasi, J. A., Lashari, H. B., Qureshi, M. I., & Qureshi, A. S. (2020). Rice husk ash and fly ash effects on the mechanical properties of concrete. *Engineering, Technology & Applied Science Research, 10*(2), 5402-5405.

BS EN 196-2. (2013). *Methods of testing cement – Part 2: Chemical analysis of cement*. British Standards Institution.

BS EN 196-3. (2016). *Methods of testing cement – Part 3: Determination of setting times and soundness*. British Standards Institution.

BS EN 196-6. (2010). *Methods of testing cement – Part 6: Determination of fineness*. British Standards Institution.

BS EN 197-1. (2011). *Cement – Part 1: Composition, specifications and conformity criteria for common cements*. British Standards Institution.

BS EN 933-1. (2012). *Tests for geometrical properties of aggregates – Part 1: Determination of particle size distribution – Sieving method*. British Standards Institution.

BS EN 1097-2. (2010). *Tests for mechanical and physical properties of aggregates – Part 2: Methods for the determination of resistance to fragmentation*. British Standards Institution.

BS EN 12350-2. (2009). *Testing fresh concrete – Part 2: Slump test*. British Standards Institution.

BS EN 12390-1. (2012). *Testing hardened concrete – Part 1: Shape, dimensions and other requirements for specimens and moulds*. British Standards Institution.

BS EN 12390-2. (2009). *Testing hardened concrete – Part 2: Making and curing specimens for strength tests*. British Standards Institution.

BS EN 12390-3. (2009). *Testing hardened concrete – Part 3: Compressive strength of test specimens*. British Standards Institution.

BS EN 12390-4. (2000). *Testing hardened concrete – Part 4: Compressive strength – Specification for testing machines*. British Standards Institution.

Çelik, A. İ., Tunç, U., Bahrami, A., Karalar, M., Mydin, M. A. O., Alomayri, T., & Özkılıç, Y. O. (2023). Use of waste glass powder toward more sustainable geopolymer concrete. *Journal of Materials Research and Technology, 24*, 8533-8546.

Della, V. P., Kuhn, I., & Hotza, D. (2002). Rice husk ash as an alternate source for active silica production. *Materials Letters, 57*(4), 818-821.

Fapohunda, C., Akinbile, B., & Shittu, A. (2017). Structure and properties of mortar and concrete with rice husk ash as partial replacement of ordinary Portland cement – A review. *International Journal of Sustainable Built Environment, 6*(2), 675-692.

FAO. (2020). *FAOSTAT Statistical Database*. Food and Agriculture Organization of the United Nations.

Federal Ministry of Agriculture and Rural Development. (2019). *Nigeria's agricultural land and rice production statistics*. FMARD.

Habert, G., Miller, S. A., John, V. M., Provis, J. L., Favier, A., Horvath, A., & Scrivener, K. L. (2020). Environmental impacts and decarbonization strategies in the cement and concrete industries. *Nature Reviews Earth & Environment, 1*(11), 559-573.

Hawkins, P., Tennis, P., & Detwiler, R. (2003). *The use of limestone in Portland cement: A state-of-the-art review* (PCA Engineering Bulletin 227). Portland Cement Association.

Igba, T., Ehikhuenmen, S., Olawale, A., Osaghale, M., & Oyebisi, S. (2019). The effect of partial replacement of Nigerian Portland limestone cement with rice husk ash agricultural waste in concrete. *IOP Conference Series: Materials Science and Engineering, 640*(1), 012041.

Jallow, A., Twumasi, J. O., Afrifa, R. O., Amponsah, E., Osei, J. B., Adom-Asamoah, M., & Kankam, C. K. (2024). Rice husk ash as partial replacement of cement in sustainable construction. *Journal of Science and Technology, 1*(1), 15-32.

Juenger, M. C. G., Snellings, R., & Bernal, S. A. (2019). Supplementary cementitious materials: New sources, characterization, and performance insights. *Cement and Concrete Research, 122*, 257-273.

Kajaste, R., & Hurme, M. (2016). Cement industry greenhouse gas emissions – management options and abatement cost. *Journal of Cleaner Production, 112*, 4041-4052.

Kanthe, V. N. (2021). Effect of superplasticizer on strength and durability of rice husk ash concrete. *Iranian (Iranica) Journal of Energy and Environment, 12*(3), 204-208.

Kosmatka, S. H., Kerkhoff, B., & Panarese, W. C. (2016). *Design and control of concrete mixtures* (16th ed.). Portland Cement Association.

Mehta, P. K., & Monteiro, P. J. M. (2014). *Concrete: Microstructure, properties, and materials* (4th ed.). McGraw-Hill Education.

Monteiro, P. J. M., Miller, S. A., & Horvath, A. (2017). Towards sustainable concrete. *Nature Materials, 16*(7), 698-699.

Najmudin, M., Bakar, H., Abdul Kudus, S., Mustaffa, N., Jamadin, A., Abbas, H., Hassan, R., & Kamaruddin, N. (2023). Effect of rice husk as replacement cement on mechanical properties of concrete. *Journal of Mechanical Engineering, 20*(2), 91-104.

Neville, A. M. (2011). *Properties of concrete* (5th ed.). Pearson Education Limited.

NIS 444-1. (2014). *Composition, specification and conformity criteria for common cements*. Nigerian Industrial Standard.

Noaman, A. T., Abed, M. S., & Hamead, A. A. A. (2020). Production of polycarboxylate-ether superplasticizer (PCE) coated sand with modified hardened properties in cement mortar. *Construction and Building Materials, 261*, 118442.

Nursyamsi, N., & Aruan, A. (2021). Application of rice husk ash in high-strength concrete. *IOP Conference Series: Materials Science and Engineering, 1122*(1), 012013.

Ojo, O. S., Ogunbode, E. B., Alao, T. O., & Hassan, I. O. (2023). Experimental measurement of adsorption of superplasticizer on cement paste: A systematic review. In *Proceedings of ICACCR 2023* (pp. 28-29).

Ologunagba, I. B., Daramola, A. S., & Aliu, A. O. (2015). Feasibility of using rice husk ash as partial replacement for concrete. *International Journal of Engineering Trends and Technology, 30*(5), 267-270.

Paris, J. M., Roessler, J. G., Ferraro, C. C., DeFord, H. D., & Townsend, T. G. (2016). A review of waste products utilized as supplements to Portland cement in concrete. *Journal of Cleaner Production, 121*, 1-18.

Pavithra, P. E., Reddy, M. S., Dinakar, P., Rao, B. H., Satpathy, B., & Mohanty, A. (2016). A mix design procedure for geopolymer concrete with fly ash. *Journal of Cleaner Production, 133*, 117-125.

Pode, R. (2016). Potential applications of rice husk ash waste from rice husk biomass power plant. *Renewable and Sustainable Energy Reviews, 53*, 1468-1485.

Raheem, A. A., & Anifowose, M. A. (2023). Effect of ash fineness and content on consistency and setting time of RHA blended cement. *Materials Today: Proceedings, 86*, 18-23.

Raheem, A. A., Adedokun, S., Ajayi, B. R., Adedoyin, O. A., & Adegboyega, B. O. (2017). Application of saw dust ash as partial replacement for cement in the production of interlocking paving stones. *International Journal of Sustainable Construction Engineering and Technology, 8*(1), 1-11.

Ramachandran, V. S. (1995). *Concrete admixtures handbook: Properties, science, and technology* (2nd ed.). Noyes Publications.

Ramasamy, V. (2011). Compressive strength and durability properties of rice husk ash concrete. *KSCE Journal of Civil Engineering, 16*(4), 779-785.

Sahoo, S., Parhi, P. K., & Panda, B. C. (2021). Durability properties of concrete with silica fume and rice husk ash. *Cleaner Engineering and Technology, 2*, 100067.

Schneider, M., Romer, M., Tschudin, M., & Bolio, H. (2011). Sustainable cement production—present and future. *Cement and Concrete Research, 41*(7), 642-650.

Shetty, M. S. (2000). *Concrete technology: Theory and practice*. S. Chand and Company Ltd.

Singh, R. P., Gupta, N., & Verma, R. (2019). Rice husk ash as a supplementary cementitious material: A review. *Materials Today: Proceedings, 18*, 3785-3792.

Singh, S., & Shukla, A. (2023). Effect of rice husk ash on the properties of concrete. *International Journal for Research in Applied Science & Engineering Technology, 11*(X), 1056.

Snellings, R., Mertens, G., & Elsen, J. (2012). Supplementary cementitious materials. *Reviews in Mineralogy and Geochemistry, 74*(1), 211-278.

Vincent-Uzogbo, S. I., & Ogirigbo, R. O. (2023). Performance evaluation of rice husk ash as partial replacement of cement in concrete in a marine environment at Escravos River, Niger Delta Area, Nigeria. *Journal of Applied Sciences and Environmental Management, 27*(9), 2003-2008.

Wang, X.-H., Fang, Z.-C., & Zheng, L. (2024). Effect of dose and types of the water-reducing admixtures and superplasticizers on concrete strength and durability behaviour: A review. *Journal of Civil Engineering and Management*.

Zareei, S. A., Ameri, F., Dorostkar, F., & Ahmadi, M. (2017). Rice husk ash as a partial replacement of cement in high strength concrete containing micro silica: Evaluating durability and mechanical properties. *Case Studies in Construction Materials, 7*, 73-81.

International Conference on Engineering Innovation for Sustainable Development (ICESID 2026)
Faculty of Engineering, Ahmadu Bello University Zaria · 8–10 September 2026

ENHANCING SOYBEAN THRESHER PERFORMANCE: A TAGUCHI DESIGN OF EXPERIMENTS APPROACH TO MODELING THRESHING AND CLEANING EFFICIENCIES

Abdullahi Saeed Hassan[1,*], Jamilu. M. Ahmed[1], Aminu Mohammed[1], Danladi Drambi Usman[1], Abdulwahab D. Ismail[1], Bala Gambo Jahun[1], Lawan Garba Abubakar[1]

[1]*Abubakar Tafawa Balewa University*

Email: ashassan@atbu.edu.ng*, "", "", "", "", "", ""

***Corresponding author**: Abdullahi Saeed Hassan

DOI: https://doi.org/10.67203/sp.ICESID.2026

ABSTRACT

Optimizing agricultural processing is critical to meeting the rising global demand for plant-based proteins. This study optimizes the threshing efficiency (TE) and cleaning efficiency (CE) of a modified soybean thresher using the Taguchi Design of Experiments (DOE). An L-9 orthogonal array evaluated cylinder speed (500, 600, 700 rpm), feed rate (3, 4, 5 kg/h), and concave clearance (10, 13, 16 mm). Signal-to-noise (S/N) analysis identified concave clearance as the most sensitive parameter for both metrics. Maximum TE required 13 mm clearance, 600 rpm, and 5 kg/h feed rate. Conversely, maximum CE was achieved at 13 mm clearance, 500 rpm, and 3 kg/h, minimizing excess biomass during separation. Analysis of Variance (ANOVA) revealed that cylinder speed and feed rate were significant linear predictors of TE. While concave clearance dictated overall variance via a highly sensitive non-linear "sweet spot," it lacked linear significance. Furthermore, the linear model was inadequate for CE, indicating that cleaning relies heavily on unaccounted aerodynamic properties like fan speed. Ultimately, these findings provide a resource-efficient framework for optimizing post-harvest machinery.

Keywords: *Soybean thresher; Taguchi method; Threshing efficiency; Cleaning efficiency; Parameter optimization*

1 INTRODUCTION

As a global community, we face the daunting task of ensuring sufficient nourishment for a rapidly expanding population, projected to reach 10 billion by 2050. Concurrently, the demand for proteins derived from renewable and sustainable sources is rising. However, agricultural and natural resources are finite, necessitating highly efficient food production and processing systems (Kumar et al., 2021; Yuliarti et al., 2021; Kumar et al., 2024). This backdrop underscores the critical importance of optimizing post-harvest crop processing, particularly for high-yield crops that offer a potential solution to protein-based malnutrition.

Soybean (*Glycine max L.*) is a globally cultivated oilseed crop renowned for its rich nutritional profile. It contains over 40% protein and 20% oil (Das et al., 2024). In addition to these macronutrients, soybeans provide essential amino acids, omega-3 fatty acids, and therapeutic compounds, including folic acid, vitamin B-complex, lactose-free fatty acids, and free-radical scavenging components. Furthermore, soybean meal, the primary by-product of soybean oil processing, has significant potential to combat protein-energy malnutrition worldwide (Das et al., 2024).

Despite the crop's immense value, threshing is a critical step in soybean processing, one that often relies on traditional, manual techniques. These rudimentary methods include pounding crops in a mortar with a pestle, beating them with sticks, or cracking them between stones (Alonge et al., 2017). While used for generations, these practices are time-consuming, labor-intensive, and inherently prone to crop loss (Alonge et al., 2017). Although numerous efforts have been made to design and develop mechanical threshers for local farmers, many of these machines operate without optimized parameters, failing to achieve maximum output. Employing optimization and modeling techniques, such as the Taguchi method or response surface methodology (RSM), can assist engineers in understanding process dynamics, managing resources, and effectively scaling up agricultural systems.

The Taguchi Design of Experiments (DOE) is a robust statistical approach developed by Genichi Taguchi, primarily designed to improve process quality by minimizing the effects of uncontrollable noise factors on system performance. This methodology is widely adopted because it facilitates the creation of a balanced and robust experimental design requiring a minimal number of experimental runs (Oemar & Chang, 2020). Implementing the Taguchi approach guarantees efficient resource utilization, thereby minimizing consumption and reducing overall production costs (Kundu et al., 2015). Consequently, this study utilizes the Taguchi method to model and optimize an existing, modified soybean thresher. The investigation focuses on three critical operating factors: cylinder speed, feed rate, and concave clearance, evaluating their specific impacts on two primary response variables: threshing efficiency (TE) and cleaning efficiency (CE).

2 MATERIALS AND METHODS

2.1 Machine description and operation

The modified soybean thresher used in this study is designed for single-operator use (Figure 1). The operational mechanism begins by feeding soybean pods into the intake hopper, where they move into the threshing chamber. This chamber houses a threshing cylinder equipped with beaters. The rotating beaters primarily thresh the crop through impact. Subsequently, the threshed mixture of grain and chaff descends into the cleaning unit. A centrifugal fan in the cleaning unit generates a targeted airstream that pneumatically separates the lighter chaff from the heavier grains, blowing the chaff out of the machine while channeling the clean grains into a collection chute.

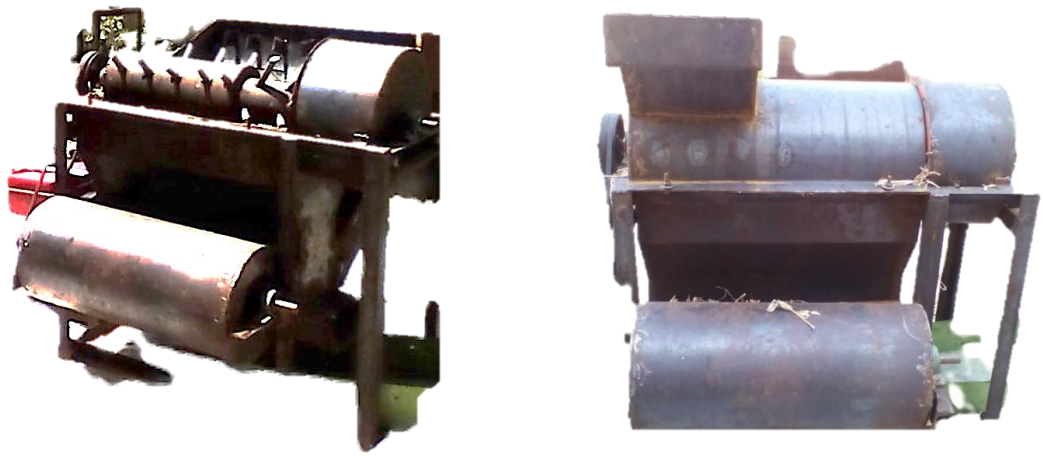

Figure 1: Pictorial presentation of the soybean thresher viewed from two different angles.

2.2 Experimental material and thresher performance test

Performance testing of the modified thresher was conducted using the TGX 1448-2E soybean variety, sourced from the Institute for Agricultural Research (I.A.R), Ahmadu Bello University, Zaria, Nigeria. Prior to the experiments, the moisture content of the soybeans was determined and standardized to 12% dry basis (d.b.) to ensure uniformity. To evaluate the machine's performance, three independent operating variables were tested at three levels each: cylinder speed (500, 600, and 700 rpm), feed rate (3, 4, and 5 kg/h), and concave clearance (10, 13, and 16 mm). All experimental runs were conducted in triplicate to guarantee reliability.

2.3 Performance evaluation indices

The machine's performance was evaluated based on four primary indices: threshing efficiency (TE), cleaning efficiency (CE), scatter loss (SL), and output capacity (Cp). These indices were calculated using the following relationships (Equations 1–4):

$$TE(\%) = \left(1 - \frac{\mathrm{A}}{\mathrm{T_G}}\right) \mathrm{x}\ 100 \tag{1}$$

$$CE(\%) = \left(\frac{\mathrm{B}}{\mathrm{D}}\right) \mathrm{x}\ 100 \tag{2}$$

$$SL(\%) = \left(\frac{\mathrm{E}}{\mathrm{T_G}}\right)\ \mathrm{x}\ 100 \tag{3}$$

$$Cp(kg/h) = \frac{Q}{t} \tag{4}$$

Where:

A = Weight of un-threshed grain collected per unit time (kg), T_G = Total grain input per unit time (kg), B = Weight of cleaned grain in the sample from the main outlet (kg), D = Total weight of material (grain + chaff) collected from the main outlet (kg), E = Weight of scattered grain collected per unit time (kg), Q = Total weight of threshed grain collected per unit time (kg), and t = Threshing time (h). For modeling and optimization in this study, TE and CE were selected as the primary response variables. TE is the primary indicator of the machine's core functional capability, measuring its effectiveness at detaching soybean grains from pods to minimize unthreshed crop losses (Aseffa, 2024; Powar et al., 2019). Conversely, CE determines the market quality and purity of the final agricultural output by evaluating the system's ability to separate threshed grains from chaff and other impurities (Dangora et al., 2024). Consequently, prioritizing the simultaneous maximization of these two parameters is critical for minimizing post-harvest wastage and ensuring the overall economic and operational viability of the thresher (Aseffa, 2024).

2.4 Experimental design

The Taguchi Design of Experiments (DOE), coupled with multiple regression analysis, was employed to develop a robust experimental design and determine the optimal settings of control parameters (El-Deen, 2024). Using an orthogonal array, the Taguchi method enables a balanced, comprehensive analysis while minimizing the total number of experimental runs, reducing experimental error and enhancing repeatability (Sahu et al., 2024).

An L-9 orthogonal array was used in this study (Tables 1 and 2). In accordance with standard Taguchi L-9 design principles, this modeling approach assumes that interaction effects among the three independent factors (cylinder speed, feed rate, and concave clearance) are negligible, allowing a focused evaluation of their main effects. We evaluated response-variable optimization using the signal-to-noise (S/N) ratio. Depending on the desired outcome, S/N ratios are typically categorized into three standard algorithms: smaller-the-better (Equation 5), larger-the-better (Equation 6), and nominal-the-best (Equation 7) (Kundu et al., 2015). Because this study aimed to maximize both threshing and cleaning efficiencies, the larger-the-better algorithm was selected.

$$S/_N = -10\log(\frac{1}{n}\sum X^2) \tag{5}$$

$$S/_N = -10\log(\frac{1}{n}\sum \frac{1}{X^2}) \tag{6}$$

$$S/_N = -10\log(\frac{1}{n}\sum \frac{\overline{X^2}}{s^2}) \tag{7}$$

Where *X* represents the responses and *n* is the number of replications. The algorithms for larger-the-better were selected because our goal was to maximize the threshing and the cleaning efficiency of

the thresher. Table 1 shows the selected variables with their respective levels, and Table 2 presents the Taguchi design based on L-9 orthogonal array design.

Table 1: Presentation of the variables and their levels

Parameter	**Level**		
	1	2	3
Cylinder speed (rpm)	500	600	700
Feed rate (kg/h)	3	4	5
Concave clearance (mm)	10	13	16

Table 2: Taguchi orthogonal array design based on L-9 with responses

Cylinder speed (rpm)	**Feed rate (kg/h)**	**Concave clearance (mm)**	**Threshing efficiency (%)**	**Cleaning efficiency (%)**
500	3	10	90.00 ± 0.85	85.00 ± 1.10
500	4	13	92.70 ± 0.64	86.10 ± 0.95
500	5	16	92.00 ± 1.05	85.80 ± 0.80
600	3	13	92.50 ± 0.72	86.70 ± 0.65
600	4	16	93.60 ± 0.55	85.40 ± 1.20
600	5	10	93.80 ± 0.90	84.60 ± 0.75
700	3	16	93.20 ± 0.82	85.10 ± 0.88
700	4	10	93.24 ± 0.68	83.30 ± 1.02
700	5	13	95.12 ± 0.45	85.20 ± 0.70

2.5 Statistical Analysis

The experimental data were structured and analyzed according to the Taguchi L-9 orthogonal array design. We used Minitab 2021 to perform the Taguchi analysis, compute the signal-to-noise (S/N) ratios using the larger-the-better algorithm, and generate the corresponding main effects plots to identify the optimal parameter combinations. We conducted an Analysis of Variance (ANOVA) for multiple linear regression. This regression ANOVA was evaluated at a 95% confidence interval ($\alpha = 0.05$) to test the significance of the linear models.

3 RESULTS AND DISCUSSION

3.1 Taguchi analysis and parameter optimization

The threshing and cleaning efficiencies of the modified soybean thresher were evaluated under varying conditions of cylinder speed (500, 600, and 700 rpm), feed rate (3, 4, and 5 kg/h), and concave clearance (10, 13, and 16 mm). To maximize both output responses, the larger-the-better Signal-to-Noise (S/N) ratio algorithm was utilized for optimization (Equation 6). To address the distinct operational dynamics of these two processes, the Taguchi analysis was performed and evaluated separately for threshing efficiency (TE) and cleaning efficiency (CE).

3.1.1 Threshing Efficiency (TE) Optimization

Taguchi analysis ranks the operating variables by their S/N ratios to determine their relative influence on machine performance. As presented in Table 3, the optimal S/N ratio for cylinder speed (39.00) was achieved at the second level (600 rpm). Similarly, the highest values for feed rate (39.00) and concave clearance (39.03) were observed at level 3 (5 kg/h) and level 2 (13 mm), respectively. By comparing the delta values of the S/N ratios, concave clearance emerged as the most influential factor dictating TE performance (Rank 1), followed closely by cylinder speed (Rank 2) and feed rate (Rank 3).

These numerical findings are directly corroborated by the analysis of means (Table 4), which follows the exact same ranking hierarchy. Furthermore, the main effects plots for the means (Figure 2) and S/N ratios (Figure 3) visually confirm this parameter hierarchy. The peak of each plotted line clearly identifies the parameter combination required for maximum threshing efficiency. Consequently, the optimal operational setting for maximizing TE is a concave clearance of 13 mm, a cylinder speed of 600 rpm, and a feed rate of 5 kg/h. This hierarchy aligns with crop threshing mechanics; studies by Ponican et al. (2009) and Adewumi (2007) found that concave clearance and cylinder speed are crucial for performance and control impact forces. Based on Tables 3 and 4 and Figure 3, optimal settings for threshing and cleaning are 13 mm concave clearance, 600 rpm cylinder speed, and 5 kg/h feed rate. The 600 rpm speed is noteworthy, as higher speeds increase grain detachment but exceeding thresholds (e.g., >700 rpm) can cause more damage and scatter loss, reducing efficiency (Aseffa, 2024; Powar et al., 2019).

Table 3: Response for signal-to-noise ratios, TE (Larger-is-better)

Level	**Cylinder speed (rpm)**	**Feed rate (kg/h)**	**Concave clearance (mm)**
1	38.93	38.95	38.89
2	39.00	38.96	39.03
3	38.97	39.00	38.98
Delta	0.07	0.05	0.14
Rank	2	3	1

Table 4: Response for means TE

Level	**Cylinder speed (rpm)**	**Feed rate (kg/h)**	**Concave clearance (mm)**
1	88.60	88.75	88.32
2	89.43	89.06	89.72
3	89.19	89.42	89.18
Delta	0.83	0.67	1.40
Rank	2	3	1

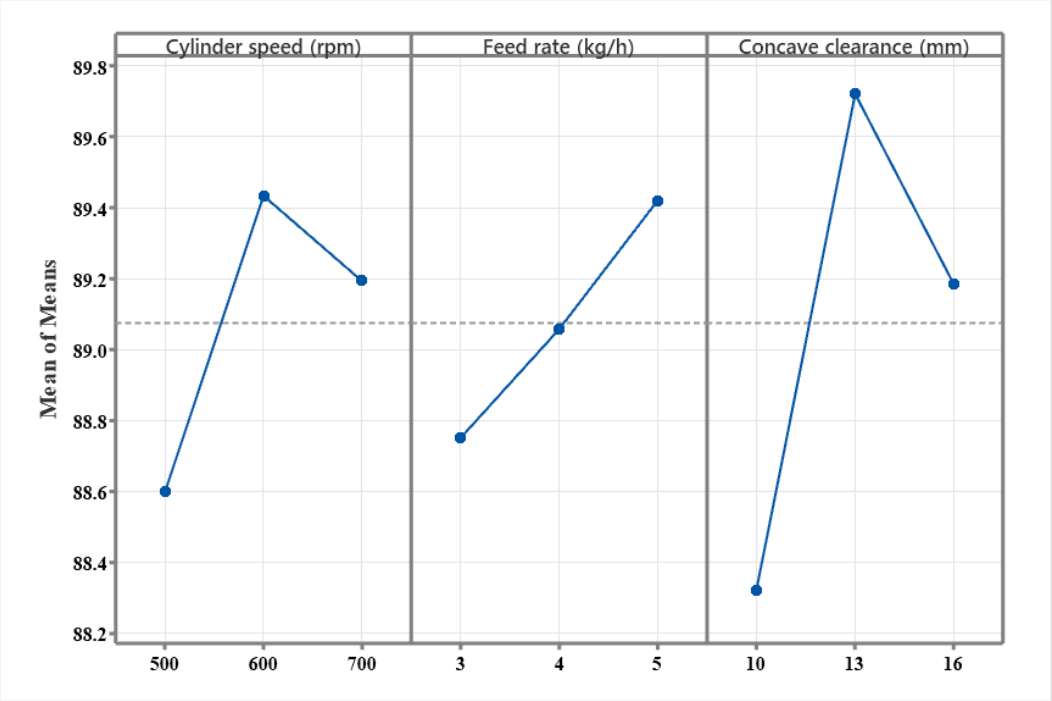

Figure 2: Main effects plot for means (TE)

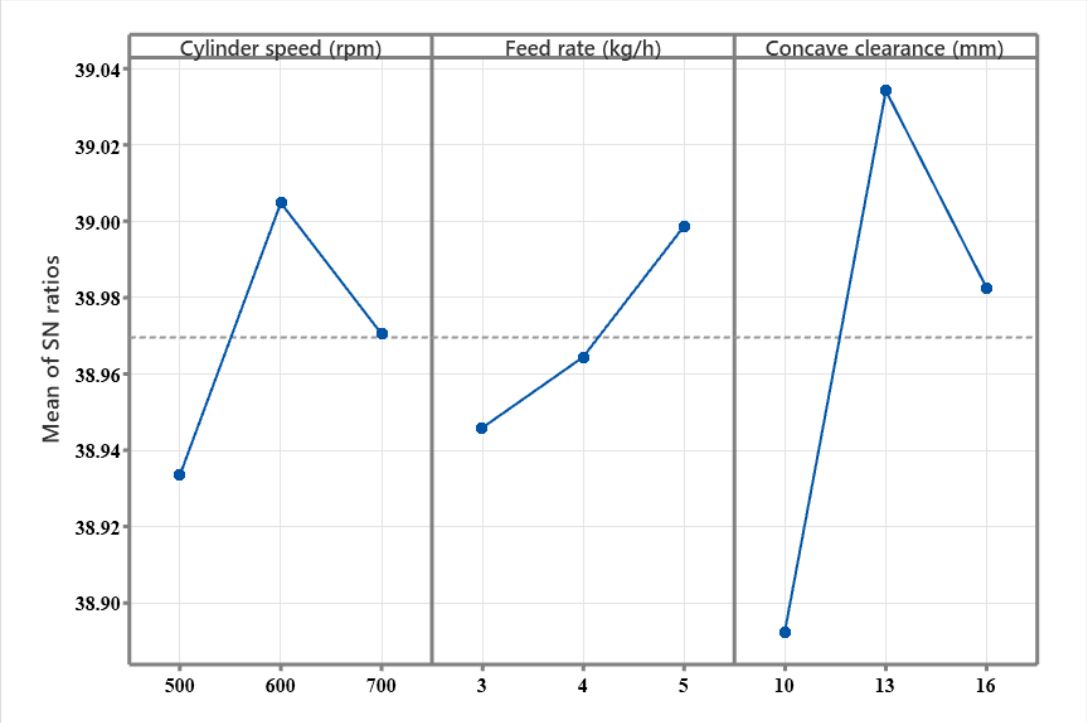

Figure 3: Main effects plot for signal-to-noise ratio (TE)

3.1.2 Cleaning Efficiency (CE) Optimization

Table 5 and Table 6 detail the response S/N ratios and means specifically for cleaning efficiency. The Taguchi analysis shows that concave clearance is the most influential factor in cleaning performance (Rank 1, Delta = 0.17), followed by cylinder speed (Rank 2, Delta = 0.11) and feed rate (Rank 3, Delta = 0.07). Figure 4 and Figure 5 visually confirm these parameter hierarchies through the CE main effects plots.

The plotted data indicates that the optimal parameter combination for maximizing cleaning efficiency differs slightly from threshing efficiency. The highest S/N ratio for concave clearance was achieved at the second level (13 mm), identical to the TE optimization. However, cleaning efficiency is maximized at a lower feed rate of 3 kg/h (level 1) and a lower cylinder speed of 500 rpm (level 1). A reduced feed rate introduces less total biomass into the separation zone at any given moment, allowing the constant airflow from the centrifugal fan to separate the chaff more thoroughly. Similarly, a lower cylinder speed prevents excessive mechanical pulverization of the soybean pods, reducing the volume of fine debris that typically evades pneumatic separation.

Table 5: Response for Means for CE

Level	**Cylinder speed (rpm)**	**Feed rate (kg/h)**	**Concave clearance (mm)**
1	85.63	85.60	84.30
2	85.57	84.93	86.00
3	84.53	85.20	85.43
Delta	1.10	0.67	1.70
Rank	2	3	1

Table 6: Response for Signal-to-Noise Ratios for CE

Level	Cylinder speed (rpm)	Feed rate (kg/h)	Concave clearance (mm)
1	38.65	38.65	38.52
2	38.65	38.58	38.69
3	38.54	38.61	38.63
Delta	0.11	0.07	0.17
Rank	2	3	1

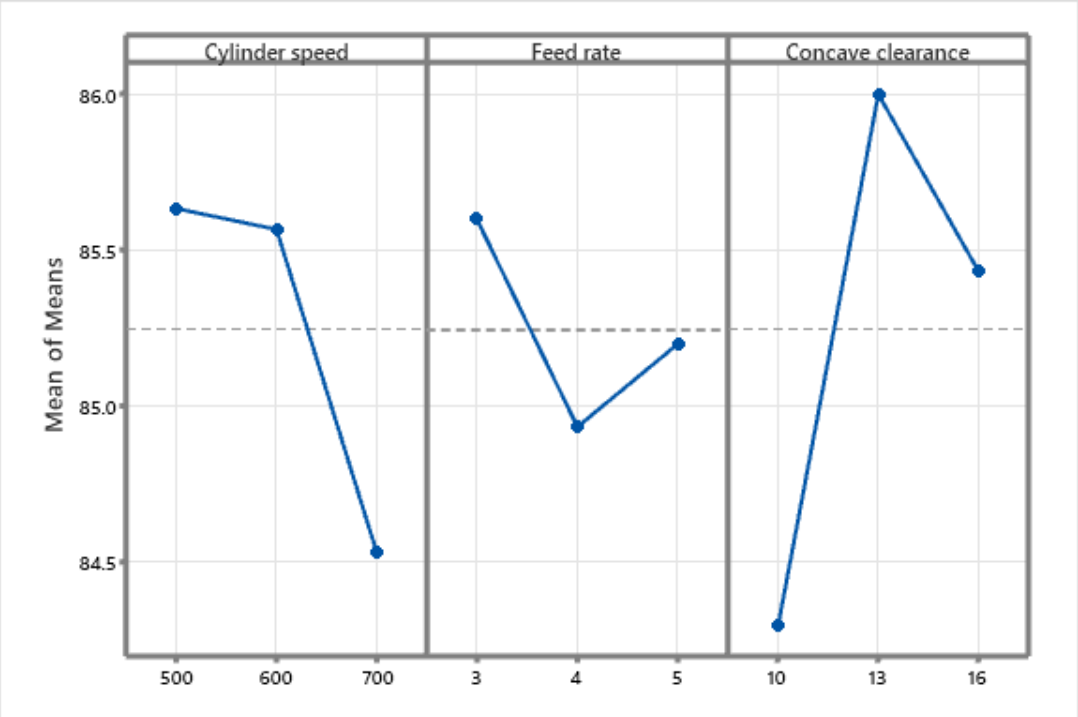

Figure 4: Main effects plot for mean (CE)

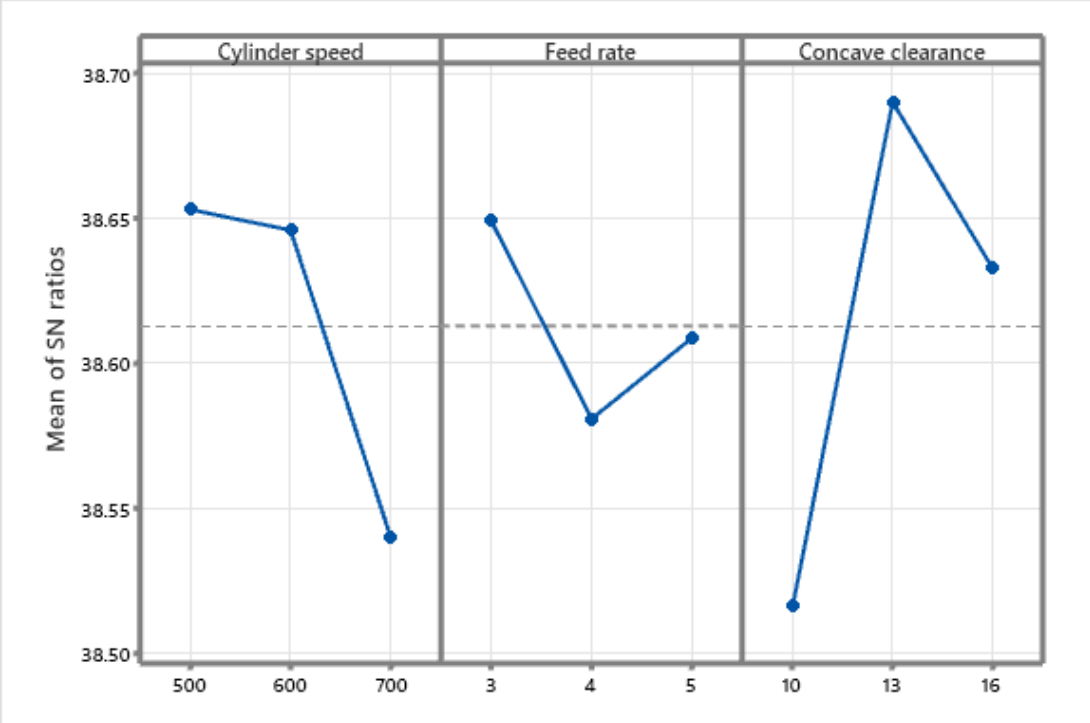

Figure 5: Main effects plot for signal-to-noise ratio (CE)

3.2 Regression analysis of response variables

Regression analysis quantified the relationship between the independent operational parameters and the dependent performance efficiencies, providing predictive insights to minimize grain loss.

3.2.1 *Threshing efficiency (TE)*

The Analysis of Variance (ANOVA) for threshing efficiency (Table 7) demonstrated a statistically significant linear relationship between TE and the tested parameters. The overall regression model was significant at a 95% confidence interval (p = 0.028). Analysis of the individual factors showed that both cylinder speed (p = 0.015) and feed rate (p = 0.039) significantly influenced TE. The linear regression model for predicting Threshing Efficiency is expressed as:

$$TE(\%) = 81.30 + 0.01143 cylinder\ speed(rpm) + 0.87 feed\ rate(Kg/h) + 0.098 concave\ clearance(mm) \quad (8)$$

The Pareto chart of standardized effects (Figure 6) visually confirms the statistical significance of these parameters. In this chart, the bars representing cylinder speed and feed rate extend beyond the critical reference line ($\alpha = 0.05$), indicating their significant linear impact on threshing efficiency. This aligns with the findings by Desta and Mishra (1990) and Sharma and Devnani (1980), who observed that increasing the peripheral speed of the threshing drum systematically enhances the impact force required to shatter pods and detach grains. Furthermore, the residual plots for threshing efficiency (Figure 7) demonstrate a normal distribution of data points, validating the adequacy of the linear model.

Interestingly, while concave clearance was ranked as the most influential factor in the overarching Taguchi optimization (Table 3), the ANOVA (Table 7) shows it was not statistically significant (p = 0.393) as a standalone linear predictor. This is visually reaffirmed in the Pareto chart (Figure 6), where the bar for concave clearance falls well short of the significance reference line. This suggests that the influence of concave clearance on TE is inherently non-linear, operating optimally only within a specific "sweet spot" (e.g., 13 mm) rather than scaling linearly.

Table 7: Analysis of variance for TE

Source	DF	Adj SS	Adj MS	F-Value	P-Value
Model	3	12.9009	4.3003	7.28	0.028
Cylinder speed (rpm)	1	7.8433	7.8433	13.28	0.015
Feed rate (kg/h)	1	4.5414	4.5414	7.69	0.039
Concave clearance (mm)	1	0.5163	0.5163	0.87	0.393
Error	5	2.9527	0.5905		
Total	8	15.8536			

At first glance, a discrepancy appears to exist between the Taguchi signal-to-noise (S/N) ratio analysis, which ranks concave clearance as the most influential parameter (Rank 1), and the Analysis of Variance (ANOVA), which identifies it as a non-significant linear predictor ($p = 0.393$). These are distinct statistical constructs that measure different aspects of response variability. The Taguchi S/N sensitivity analysis evaluates absolute deviation and overall variance across discrete experimental levels, effectively capturing non-linear impacts—such as the pronounced optimal "sweet spot" at 13 mm. Conversely, the ANOVA used in this study assesses only the statistical significance of *linear* trends. Therefore, while concave clearance is highly sensitive and strongly dictates overall threshing efficiency, its influence does not scale linearly, which explains its non-significance in the linear regression model.

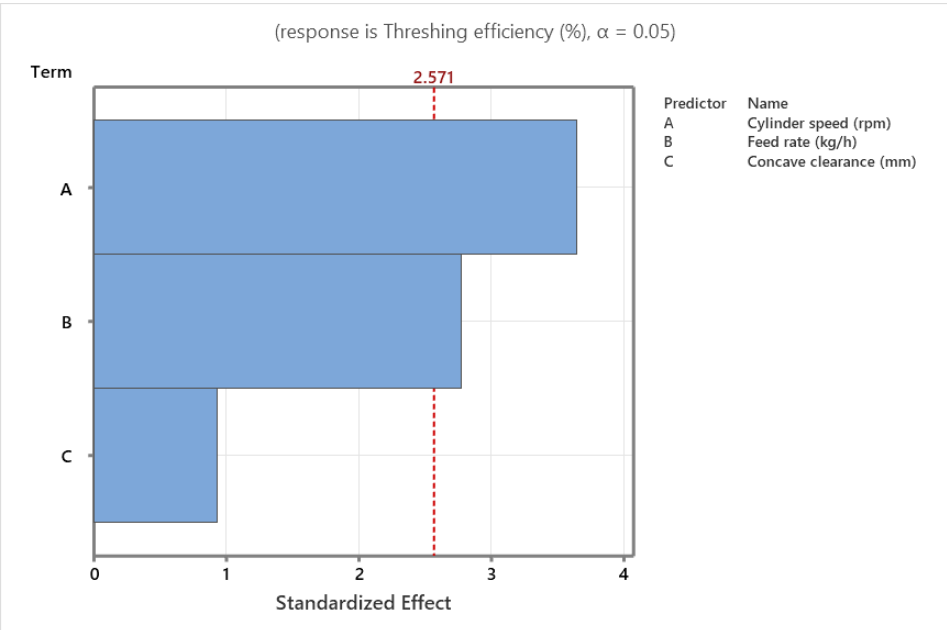

Figure 6: Pareto Chart of the standardized effects, TE (%)

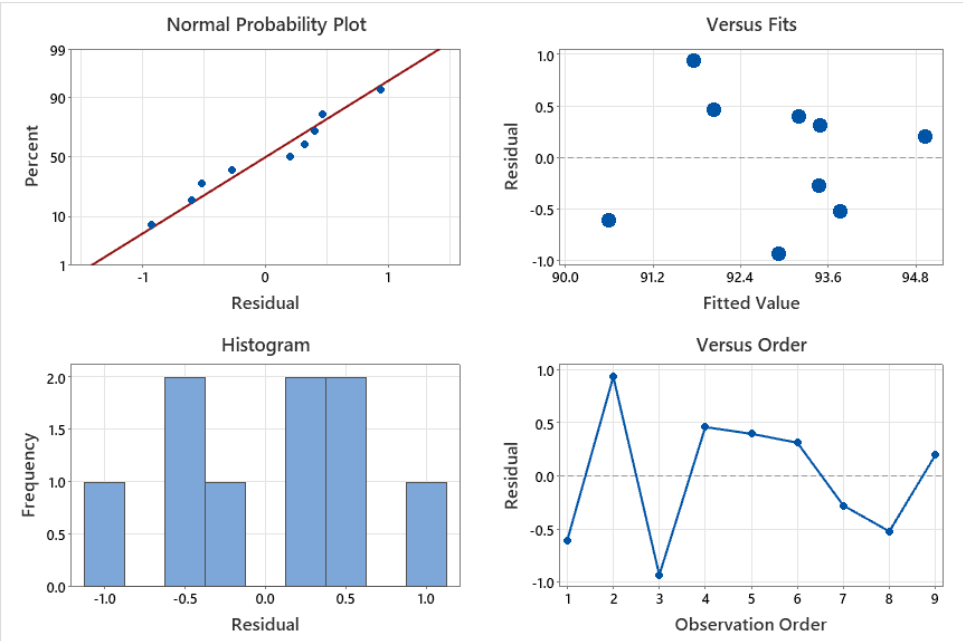

Figure 7: Residual plots for threshing efficiency (%)

3.2.2 Cleaning efficiency (CE)

We conducted a similar regression analysis for CE. The linear model equation is represented as:

$$CE(\%) = 86.89 - 0.0055 cylinder\ speed(rpm) - 0.2 feed\ rate(Kg/h) + 0.189 concave\ clearance(mm) \quad (9)$$

In stark contrast to the threshing model, the ANOVA results for CE (Table 8) indicated that the overall linear regression model for cleaning efficiency was not statistically significant ($p = 0.247$). Furthermore, none of the independent operational parameters (speed, feed rate, or clearance) were statistically significant linear predictors of CE within the tested ranges ($p > 0.05$). The Pareto chart of standardized effects for cleaning efficiency (Figure 8) visually corroborates this lack of linear significance. As shown in the chart, none of the bars representing the tested parameters cross the critical reference line, confirming that cylinder speed, feed rate, and concave clearance do not have a statistically significant linear effect on the cleaning process.

Recent agricultural engineering literature strongly supports the inadequacy of a simple linear model for predicting cleaning efficiency. Cleaning mechanisms in harvesters and threshers rely on complex aerodynamic properties rather than pure mechanical impact. Studies evaluating thresher cleaning systems show that cleaning efficiency is largely governed by non-linear fluid dynamics, such as fan speed, airflow distribution, and sieve oscillation, which often exhibit complex non-linear couplings with feed rate (Badretdinov et al., 2019; Dauda et al., 2024). Because aerodynamic variables like fan speed were held constant or were not the primary focus of this specific linear matrix, the model in Table 6 could not fully capture the cleaning dynamics. Therefore, predicting CE accurately in future iterations will require higher-order (e.g., quadratic) models that directly incorporate fan speed and airflow parameters alongside mechanical variables.

Table 8: Analysis of Variance for CE

Source	DF	Adj SS	Adj MS	F-Value	P-Value
Model	3	3.9817	1.3272	1.91	0.247
Cylinder speed (rpm)	1	1.8150	1.8150	2.61	0.167
Feed rate (kg/h)	1	0.2400	0.2400	0.34	0.583
Concave clearance (mm)	1	1.9267	1.9267	2.77	0.157
Error	5	3.4806	0.6961		
Total	8	7.4622			

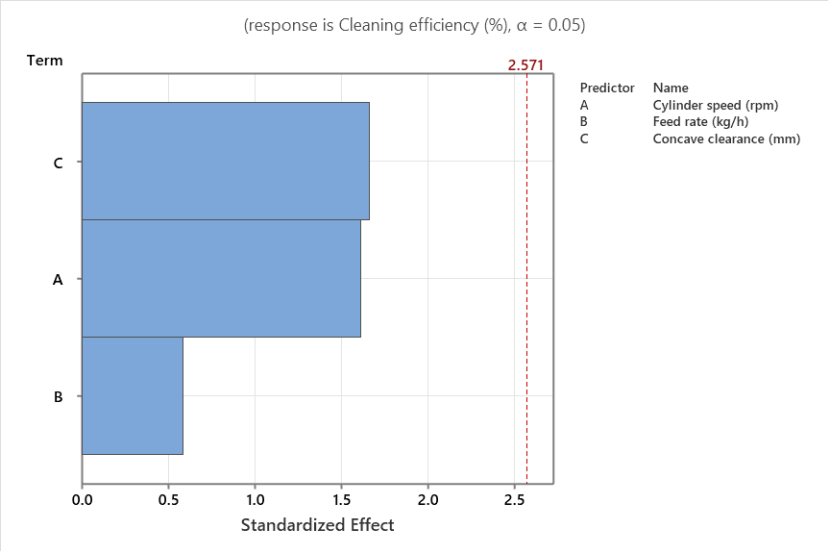

Figure 8: Pareto chart of the standardized effects CE (%)

4 CONCLUSION

This study successfully applied the Taguchi Design of Experiments (DOE) and multiple regression analysis to model and optimize a modified soybean thresher. The investigation demonstrated that concave clearance is the most sensitive mechanical parameter governing overall machine performance, followed by cylinder speed and feed rate. By optimizing these variables, the system can maximize grain detachment while mitigating the risk of grain damage and scatter loss associated with excessive mechanical force. While the analysis revealed a statistically significant linear relationship between the mechanical parameters and threshing efficiency, the linear model proved inadequate for predicting cleaning efficiency. This contrast highlights a vital synthesis in agricultural machinery evaluation: threshing is fundamentally a mechanical impact process, whereas cleaning is heavily governed by unmeasured aerodynamic fluid dynamics. Ultimately, the Taguchi method proved highly effective at establishing a resource-efficient baseline for local machinery manufacturers to maximize processing throughput and combat protein-based malnutrition.

FUTURE WORK

To build upon these findings, future research must transition beyond linear mechanical models to fully optimize the cleaning unit. Subsequent studies will incorporate aerodynamic variables—such as fan speed, air velocity, and airflow distribution—into higher-order mathematical models or utilize computational fluid dynamics (CFD). This approach is necessary to capture the complex, multi-field coupling required to achieve perfect grain separation.

REFERENCES

Adewumi, B. A. (2007). Performance evaluation of a locally developed multi-crop thresher. *Journal of Agricultural Engineering and Technology, 15*(1), 22–30.

Alonge, A. F., Ossom, I. S. & Bassey, E. J. 2017. Design modification and performance testing of bambara nut sheller. Chemical Engineering Transactions, 58.

Aseffa, T. (2024). Modeling of thresher capacity and fuel consumption equations using dimensional analysis for threshing operation. *Turkish Journal of Agricultural Engineering Research, 5*(2), 271–283. https://doi.org/10.46592/turkager.1549453

Badretdinov, I., Mudarisov, S., Lukmanov, R., Permyakov, V., Ibragimov, R., & Nasyrov, R. (2019). Mathematical modeling and research of the work of the grain combine harvester cleaning system. *Computers and Electronics in Agriculture, 165*, 104966. https://doi.org/10.1016/j.compag.2019.104966

Dangora, N. D., Muhammad, M., Matori, A. S., & Ajeigbe, A. H. (2024). Performance evaluation of ICRISAT IK00007 multi crop thresher. *Journal of Agripreneurship and Sustainable Development, 7*(3), 13–20. https://doi.org/10.59331/jasd.v7i3.825

Das, D., Panesar, G., Panesar, P. S., & Kumar, M. (2024). Soybean meal: The reservoir of high-quality protein. In M. Kumar, S. P. Bangar, & P. S. Panesar (Eds.), *Oilseed meal as a sustainable contributor to plant-based protein: Paving the way towards circular economy and nutritional security*. Springer Nature. https://doi.org/10.1007/978-3-031-47880-2

Desta, K., & Mishra, T. N. (1990). Development and performance evaluation of a sorghum thresher. *Agricultural Mechanization in Asia, Africa and Latin America, 21*(3), 33–37.

El-Deen, A. B. (2024). Multi optimization in slot milling of CFRP composites through grey relational-based Taguchi analysis. *Nigerian Journal of Technological Development, 21*(1). https://doi.org/10.4314/njtd.v21.i1.1762

Kumar, M., Bangar, S. P., & Panesar, P. S. (2024). *Oilseed meal as a sustainable contributor to plant-based protein*. Springer Nature.

Kumar, M., Tomar, M., Potkule, J., Verma, R., Punia, S., Mahapatra, A., Belwal, T., Dahuja, A., Joshi, S., Berwal, M. K., Satankar, V., Bhoite, A. G., Amarowicz, R., Kaur, C., & Kennedy, J. F. (2021). Advances in the plant protein extraction: Mechanism and recommendations. *Food Hydrocolloids, 115*, 106595. https://doi.org/10.1016/j.foodhyd.2021.106595

Kundu, A., Sen Gupta, B., Hashim, M. A., & Redzwan, G. (2015). Taguchi optimization approach for production of activated carbon from phosphoric acid impregnated palm kernel shell by microwave heating. *Journal of Cleaner Production, 105*, 420–427. https://doi.org/10.1016/j.jclepro.2014.06.093

Oemar, B., & Chang, W.-C. (2020). Taguchi method for optimizing process parameters in the production of activated carbon from rubber seed shell. *The International Journal of Advanced Manufacturing Technology, 107*(11-12), 4609–4620. https://doi.org/10.1007/s00170-020-05344-4

Ponican, J., Angelovic, M., & Zitnak, M. (2009). The impact of threshing mechanism parameters on the quality of threshed grain. *Research in Agricultural Engineering, 55*(1), 33–39.

Powar, R. V., Aware, V. V., & Shahare, P. U. (2019). Optimizing operational parameters of finger millet threshing drum using RSM. *Journal of Food Science and Technology, 56*(7), 3481–3491. https://doi.org/10.1007/s13197-019-03836-0

Sahu, S., Singh, G., & Arya, S. K. (2024). Production of β-cyclodextrin by immobilized CGTase in packed bed bioreactor through the medium component by employing Taguchi methodology. *Process Biochemistry, 143*, 266–276. https://doi.org/10.1016/j.procbio.2024.05.015

Sharma, K. D., & Devnani, R. S. (1980). Threshing studies on soybean and cowpea. *Agricultural Mechanization in Asia, 11*(1), 65–68.

Yuliarti, O., Kiat Kovis, T. J., & Yi, N. J. (2021). Structuring the meat analogue by using plant-based derived composites. *Journal of Food Engineering, 288*, 110138. https://doi.org/10.1016/j.jfoodeng.2020.110138

International Conference on Engineering Innovation for Sustainable Development (ICESID 2026)
Faculty of Engineering, Ahmadu Bello University Zaria · 8–10 September 2026

EXPERIMENTAL ASSESSMENT OF ACTIVATED CHARCOAL GRANULES AS WET PAD FOR EVAPORATIVE COOLING IN POSTHARVEST STORAGE SYSTEMS DESIGN

Muhammad Abubakar[1,2], Olorunsogo TS[2,*], Mohammed Ibrahim Shaba[2]
[1]*Waziri Umaru Federal Polytechnic Birnin Kebbi*
[2]*Federal University of Technology Minna*
Email: muhammad.abubakar@wufpbk.edu.ng, solorunsogo@futminna.edu.ng*, mohd.shaba@futminna.edu.ng
***Corresponding author**: Olorunsogo TS
DOI: https://doi.org/10.67203/sp.ICESID.2026

ABSTRACT
Evaporative cooling serves as an energy-efficient alternative to conventional vapor-compression air conditioning. It is a cooling method that uses water to lower air temperature. The conventional cellulose or plastic pads that are mostly used are costly, non-renewable, and require frequent replacement This experimental study was carried out to assess the suitability of charcoal granules as alternative material for evaporative cooling pad used in postharvest storage systems. A test setup is designed to evaluate the performance of charcoal granules. Water absorption and retention characteristics (retention capacity) are critical parameter in evaporative cooling systems, as it directly influences evaporation rate, cooling effectiveness, operational stability, and overall water consumption. The water retention capacity of the charcoal (internal micro-porosity) was determined to be 0.62 (g/g), with a porosity (bulk void fraction) of 52% The temperature gradients and relative humidity difference were evaluated. The ambient temperature was lowered from an average of 30 – 42°C to 19 – 30°C (ΔT of 10–12°C). Relative Humidity rises from an average of 32%–60% ambient to 75 – 97% inside the chamber. The chamber demonstrates reliable and statistically significant cooling performance, with an average of 24.8% efficiency (8.8°C reduction) across varying ambient conditions. The system delivers consistent temperature drop with substantial moisture addition, reducing sensible heat while slightly lowering (or maintaining) total enthalpy. Performance is consistent across the three days. It is highly effective in humidification, achieving an average relative humidity of 89.48% with 97% efficiency (nearly doubling ambient RH).

Keywords: *Evaporative cooling; charcoal granules; cooling pad; cooling Efficiency; relative humidity efficiency; water retention capacity*

INTRODUCTION

An evaporative system is a cooling method that uses water to lower air temperature (Bodile et al., 2025). It works by passing warm air through a wet cooling pad, where the water absorbs heat and evaporates, making the air cooler before it is circulated. It is an adiabatic exchange of sensible heat to latent heat (Kumarasinghe et al., 2026). The cooling pad is the most important part of this system because its performance directly affects how well the cooling works. Water is continuously supplied to the pad manually or using a pump, keeping it wet. A fan pushes warm air through the wet pad, and as the air passes through, the water absorbs heat and turns into vapor, cooling the air. This cool air is then spread into the room or space. The process continues as long as water is supplied and air flows through the pad. The cooling pad's efficiency depends on its material, thickness, water-holding capacity, and airflow, making it a key part of the system (Ogumo et al., 2017).

The trend of using fan-pad evaporative cooling systems in agricultural systems is increasing. The air from outside the facility is forced to enter through a constantly wet porous medium (pad). Sensible and latent heat transfer occurs when the air is in contact with the water surface. Air loses sensible heat, decreasing its temperature, while water evaporates from the surface of the pad, increasing the humidity of the air. The air at the outlet of the pad has a lower temperature and a higher relative humidity than the inlet one (Vega et al., 2022).

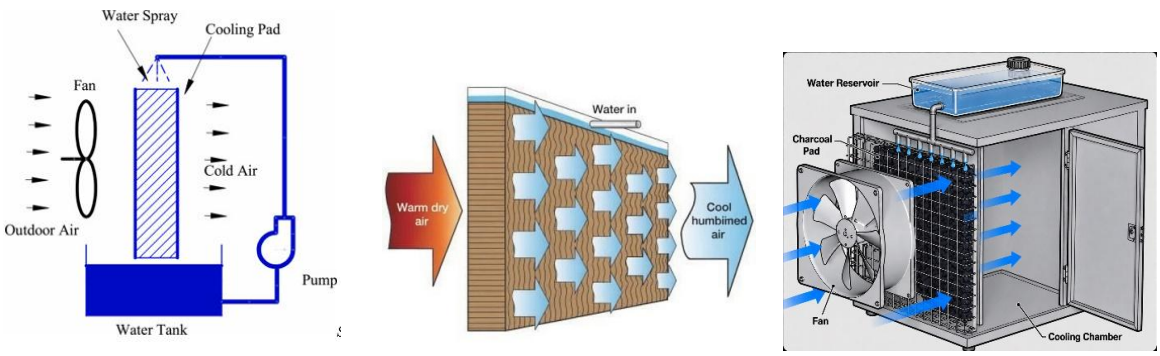

Illustrative diagrams of how the cooling pad works

Cooling through evaporation is an ancient and effective method of lowering temperature. Both plants and animals use this method to lower their temperatures. Trees, through the method of Eva transpiration, for example, remain cooler than their environment (Bodile et al., 2025)..

The operational effectiveness of an evaporative cooling is made up of a porous material that is fed with water. Hot dry air is drawn over the material. The water evaporates into the air raising the humidity and at the same time reducing the temperature of the air. The system is dependent on the conditions of the air and it is necessary to determine the weather conditions that may be encountered to properly evaluate the possible effectiveness of evaporative cooling (Warke & Deshmukh, 2017).

The tendency to use fan-pad evaporative cooling systems in agricultural buildings is increasing, but the rate of this increase is inhibited because of the high cost of the commercial pad materials example; CELdek which costs between Twenty Thousands to Seventy Thousands per square meter. Therefore, there is a need to evaluate the locally available cheap materials using as pads (Shitanda et al., 2015).

Evaporative cooling serves as an energy-efficient alternative to conventional vapor-compression air conditioning, particularly in arid and semi-arid climates where low humidity allows for significant thermal reduction through water evaporation (Franco-salas, 2021). Despite its advantages, the performance of traditional cooling media—such as cellulose or plastic—is often constrained by material costs, limited sustainability, and the necessity for frequent replacement (Kumarasinghe et al., 2026).

Water retention capacity and porosity are the major properties expected of a material that can be used as cooling pad (Deoraj et al., 2015). Most pad media for the evaporative cooling system are made from agricultural residue, although there are some commercially created pad media for sale in the market. Among materials that have been used for cooling pad manufacturing include jute, cellulose, aspen, PVC, hessian, wood shaven, rice straw, cotton fleece, latex, foam and luffa fiber (Udo et al., 2025).

A pad material should be porous enough to allow free flow of air. It should be able to absorb water and allow evaporation. It should have maximum amount of wetted surface area for an adequate period of air water contact time to achieve near saturation. The material should be locally available and inexpensive. Moreover, it should allow easy construction into required shape and size (Awafo et al., 2020).

Charcoal granules present a compelling, low-cost alternative, offering a porous structure that facilitates high water-air contact and effective heat exchange within sustainable cooling systems (Kouchakzadeh & Brati, 2013). The inherent microporosity of carbonized biomass promotes superior water retention through capillary action, which is essential for maximizing mass transfer during the evaporative process (Yeneneh, 2023).

Furthermore, utilizing this carbon-based medium aligns with broader efforts to integrate sustainable, waste-derived materials into HVAC design, potentially mitigating the environmental impact associated with traditional synthetic padding (Kumarasinghe et al., 2026). Beyond these structural benefits, charcoal granules exhibit potential for long-term operational durability, as their resistance to biological degradation may offer a more robust lifecycle compared to conventional cellulose pads susceptible to rapid salt and dust accumulation (Franco-salas, 2021).

Commercially available cooling pads are expensive and accordingly, there is an urgent need to evaluate the performance of suitable locally available materials when used as cooling pads, particularly for rural agricultural systems (Perez, 2022). Previous researches showed a cooling capacity of some materials used as wet pad coir fibre (89·6–92·8%), fine fabric (47·22–85·51%), coarse fabric (63·88–86·32%), polyvinyl chloride (PVC), sponge (38·9%), jute (62·1%) and luffa (55·1%) (Vega et al., 2022).

Charcoal is a local waste derived from pyrolysis of biomass (Berihun, 2023). Activated charcoal undergoes two-steps heating process. It serves as an excellent wet pad material due to their microporous structure, which facilitates high water absorption and slow release for sustained evaporation. Unlike commercial cellulose pads, charcoal is locally sourced, durable, and less prone to microbial growth. This study assesses its performance as a granular wet pad in post-harvest storage systems, focusing on microclimate control and produce quality preservation.

Charcoal is an ideal material for refrigeration because it has pores, which absorb and store water. This reduces heat from outside. And because wet charcoal does not allow easy passage of heat, it results in low temperatures inside the cubicle. Due to its pore structure, charcoal can absorb a lot of water quickly (Defraeye et al., 2024).

MATERIALS AND METHODS

The construction and experiment were carried out in Birnin kebbi, (12.4318ºN, 4.1956ºE) north western Nigeria, and is only limited to this location and carried out only for three days due to some constraints. Conducted in the month of April/May when the annual temperature was at its peak in the region, and lowest relative humidity due to hot dried air.

3.1 Experimental Setup

To measure the cooling performance of the charcoal, a special cooling chamber is designed and constructed. A direct evaporative cooling test apparatus typically consists of a fan, ducting, and a pad of 13cm x 13cm with 5cm thickness was filled with charcoal granules (particle size 35–45 mm) This particle sizes are necessary for optimal airflow. If the particles are too small there might be unbreathable sludge that prevent water distribution. Water is distributed via drip at a rate of 0.0125 liter per minute to keep the pad saturated. The fan (SUNON KDE1212PMV1) has an Air Flow Rate of 0.060m^3/s. The chamber comprises a hollow rectangular duct (24cmx18cm with 2cm thickness) made of Polyurethane (PU) Foam and lagged with aluminum sheet. (Fig1) Airflow is forced by a fan through the pad into the chamber where thermo-hygrometer is attached directly inside to measure modified temperature and humidity. Temperature and relative humidity were measured using HTC-1 digital thermo-hygrometers. The instruments were used according to the manufacturer's operating instructions. Formal laboratory calibration against a traceable reference standard was not performed before the experiment due to lack of resources which represents a limitation of the study. The reported temperature and relative-humidity values are interpreted within the measurement accuracy specified for the instruments.

Figure 1: Some Pictures from the experiment

3.2 Experimental Procedure

-Activated charcoal is used as a cooling medium. Charcoal has a high surface area, which allows it to absorb and release heat efficiently.

-Water is poured over the charcoal, causing it to evaporate and cool the air around it pores.

-Fan is used to force the surrounding air in to the wetted pad and pass through it as cooled air

-Cooling Chamber: The cooled air is then circulated through a chamber, where the temperature and relative humidity are being measured using a thermo-hygrometer

3.3 Charcoal Preparation

Charcoal granules are washed to remove dust, sieved for uniformity, and packed into cuboid wire mesh to make a pad of granules. Bulk density, porosity, and water holding capacity are major factors in determine the efficiency of the system

4.0 RESULTS AND DISCUSSION

4.1 Microclimate Performance

The ambient temperature and humidity are monitored and measured in the experiments, and compared with the cooling chamber. The experimental data for the reduction of temperature across the time is summarized in Table 1. The experimental data for the increase in humidity with respect to time is summarized in Table 2

Table 1: Chamber temperature and Ambient temperature (ºC)

Time of the Day	TEMPERATURE *DAY 1*		TEMPERATURE *DAY 2*		TEMPERATURE *DAY 3*	
	Chamber	Ambient	Chamber	Ambient	Chamber	Ambient
05:00	27.5	34.0	26.0	33.0	27.0	34.0
06:00	26.0	33.5	26.0	34.0	26.5	33.0
07:00	23.5	36.5	25.5	34.5	24.0	35.5
08:00	20.5	35.5	23.0	35.0	22.5	35.0
09:00	19.0	32.5	21.5	33.5	22.5	31.5
10:00	22.5	34.5	22.0	34.5	23.0	31.5
11:00	23.0	35.0	22.0	36.0	24.5	33.0
12:00	26.5	35.5	26.0	36.5	25.0	34.5
13:00	28.0	37.0	27.5	36.5	27.0	36.0
14:00	30.5	40.0	30.0	38.0	29.5	39.5
15:00	32.5	41.5	31.5	39.5	30.5	40.0
16:00	31.5	39.0	31.5	38.5	31.0	38.0
17:00	30.0	38.5	29.0	37.5	30.5	36.0
18:00	30.5	38.0	29.5	37.5	29.0	36.0
19:00	29.0	38.0	29.5	37.0	29.0	35.5
20:00	28.5	36.5	28.0	34.5	28.0	35.0
21:00	28.5	36.0	28.5	34.0	27.0	34.5
22:00	28.0	33.5	27.5	32.0	27.0	33.0

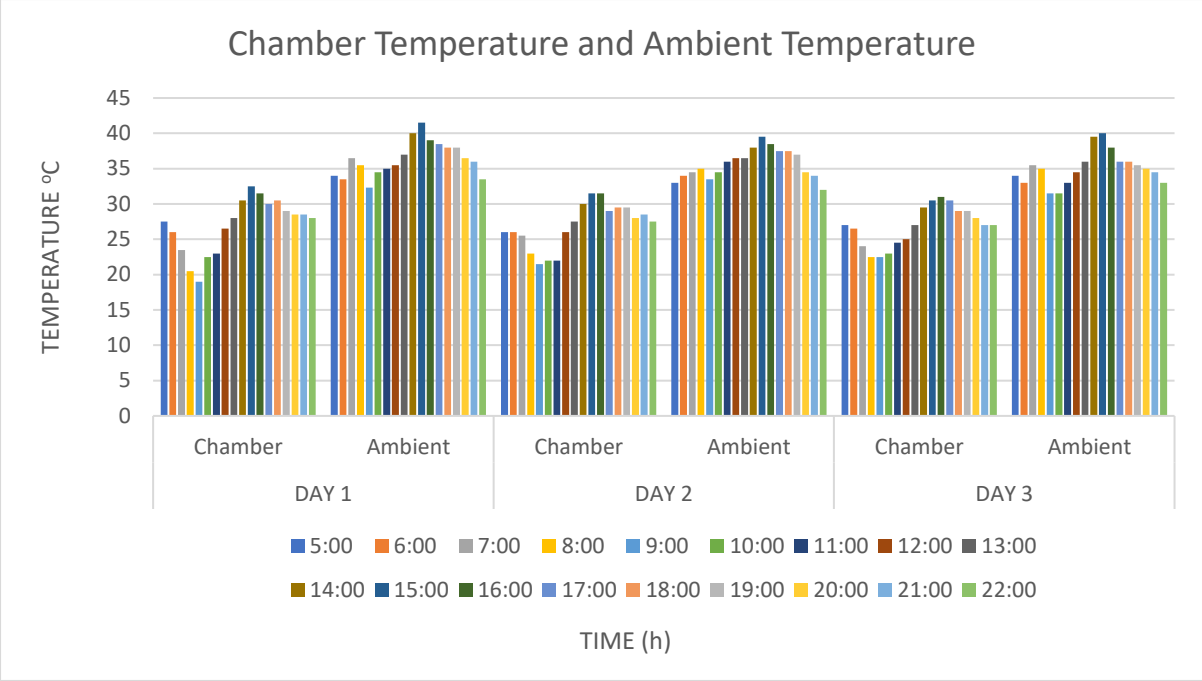

Figure 2: Comparison of chamber temperature and ambient temperatures. The colour bars correspond to time range

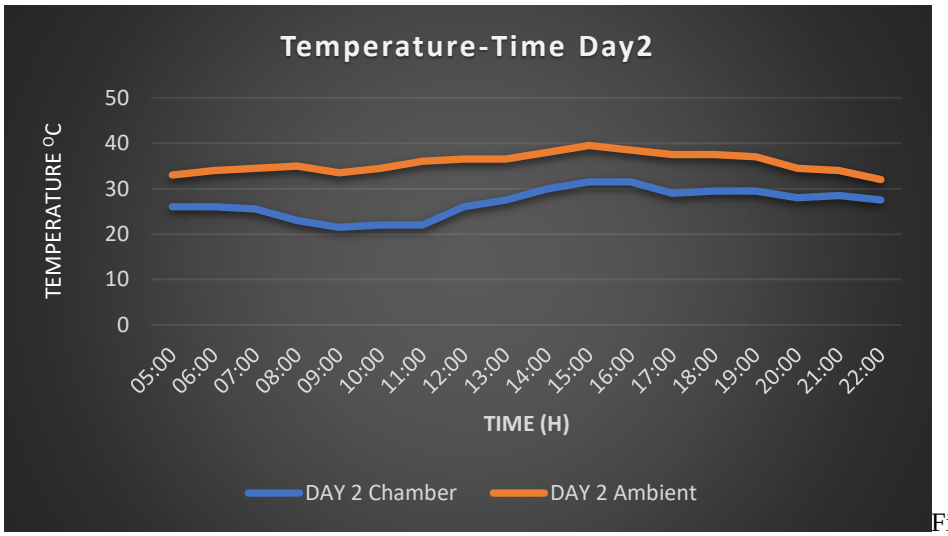

Figure 4: Temperature Behavior Day2

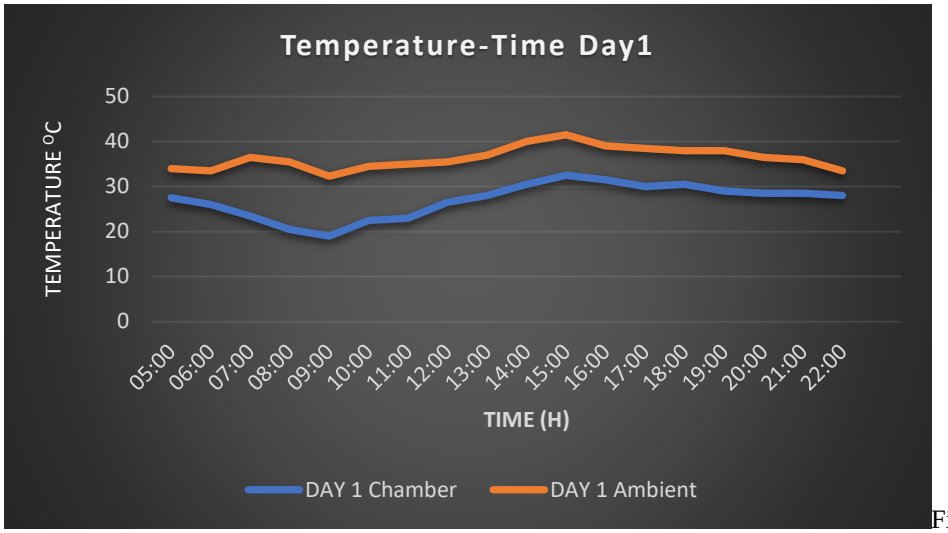

Figure 3: Temperature Behavior Day1

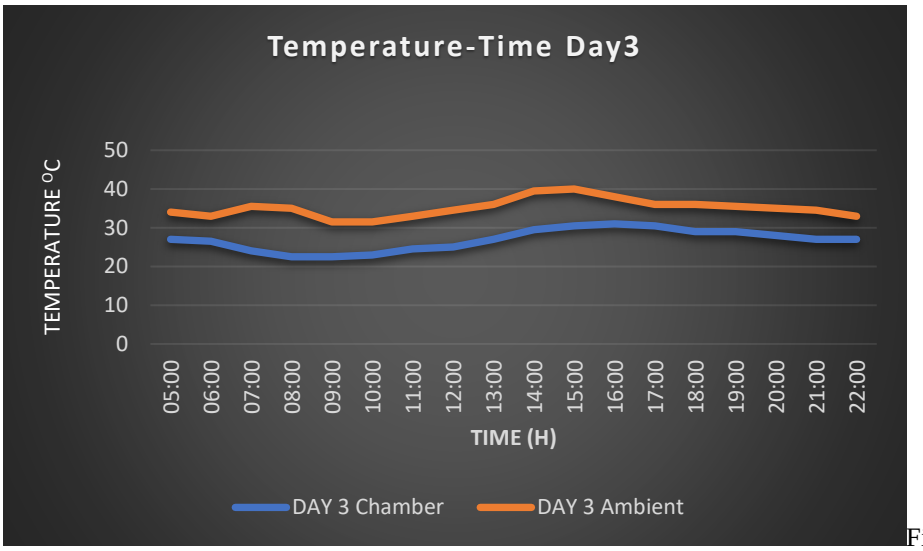

Figure 5: Temperature Behavior Day3

Table 2: Chamber humidity and ambient humidity (%)

Time of the Day	RELATIVE HUMIDITY *DAY 1*		RELATIVE HUMIDITY *DAY 2*		RELATIVE HUMIDITY *DAY 3*	
	Chamber	Ambient	Chamber	Ambient	Chamber	Ambient
05:00	65	54	92	61	94	58
06:00	84	56	94	59	99	58
07:00	87	65	99	59	99	60
08:00	99	64	99	57	99	62
09:00	99	60	99	55	99	55
10:00	99	55	99	55	97	52
11:00	92	50	99	52	98	50
12:00	91	45	95	49	92	47
13:00	88	42	89	47	90	45
14:00	80	40	85	41	86	42
15:00	81	38	85	41	84	39
16:00	86	35	82	37	85	35
17:00	82	35	82	35	85	35
18:00	80	33	86	37	90	34
19:00	75	40	88	41	92	30
20:00	81	42	88	44	95	33
21:00	77	45	90	48	95	32
22:00	86	51	90	55	97	32

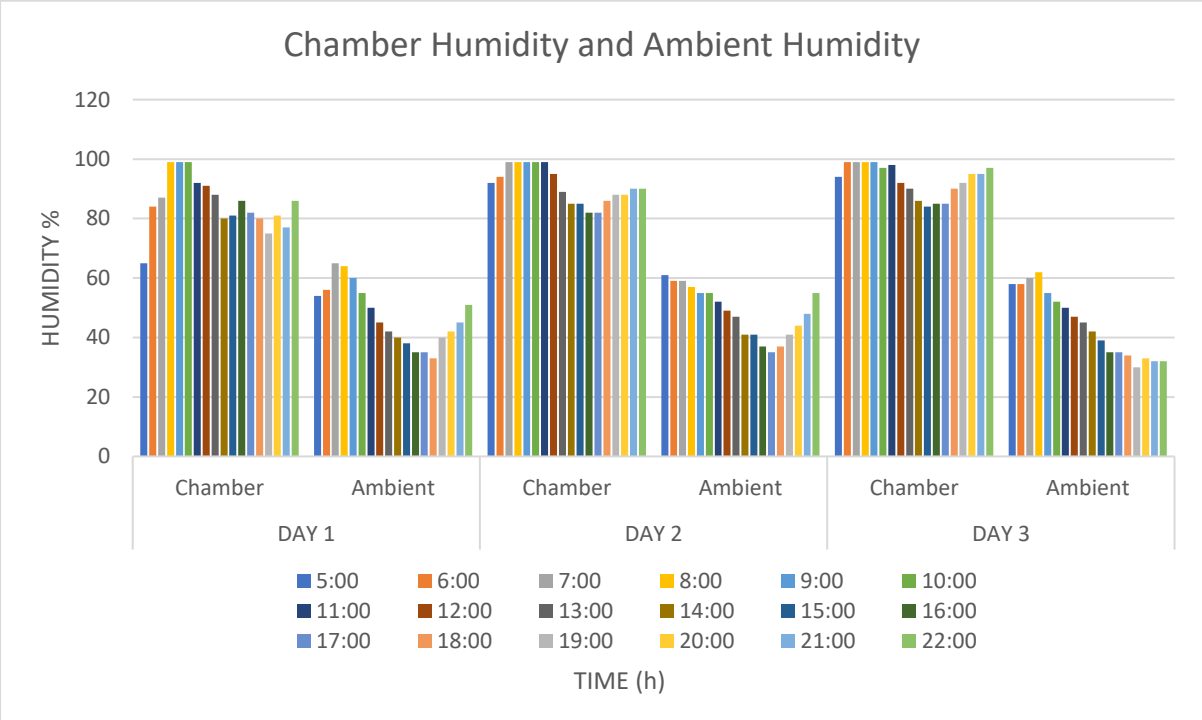

Figure 6: Comparison of chamber humidity and ambient humidities. The colour bars correspond to time range

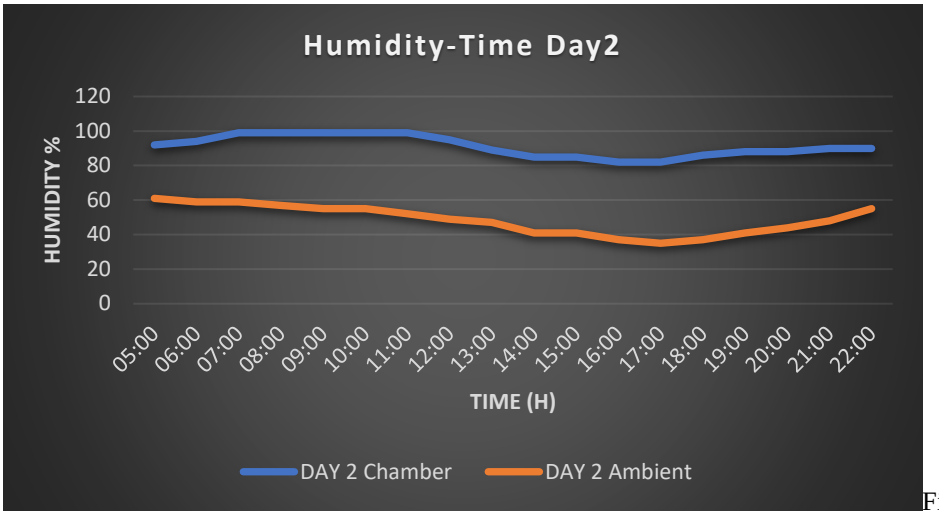

Figure 8: Humidity Behavior Day2

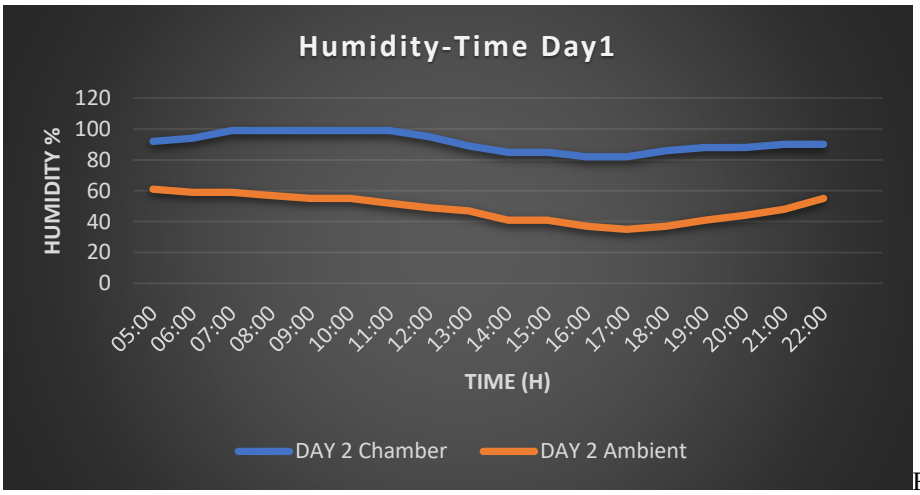

Figure 7: Humidity Behavior Day1

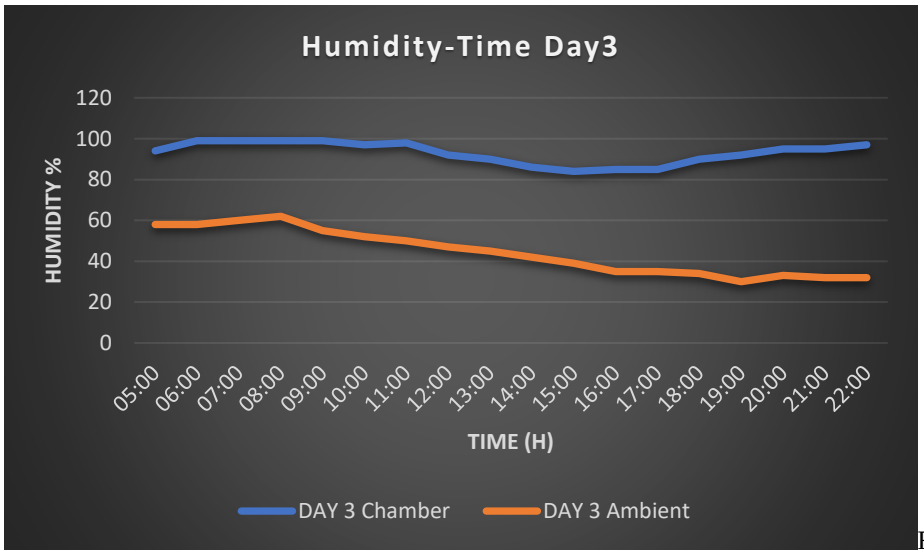

Figure 9: Humidity Behavior Day3

4.2 Performance Analysis

The performance in the system was assessed by considering two factors;

i. The response to decrease ambient temperature
ii. The response to increase ambient relative humidity

The cooling efficiency and relative humidity efficiency were determine using the following equations; (Leonard & Msacky, 2023).

$$Cooling\ Efficiency = \frac{(Ambient\ Temp - Chamber\ Temp)}{Ambient\ Temp} \times 100 \ldots\ldots\ldots\ldots\ldots\ldots\ldots\ldots 1$$

$$RH\ Efficiency = \frac{(Chmaber\ RH - Ambient\ RH)}{Ambient\ RH} \times 100 \ldots\ldots\ldots\ldots\ldots\ldots\ldots\ldots\ldots\ldots 2$$

4.2.1 Statistical Analysis of Temperature

For all monitoring days, results showed that average daily ambient temperature was 35.76°C as measured over three consecutive days. The inside Chamber temperature was 26.94°C. The inside Chamber temperature was ranged from 19.0°C to 31.5°C while the ambient was 31.5°C to 41.5°C with an average temperature difference of 8.83°C (Chamber cooler). Table 1. At the highest efficiency, the Chamber had inside temperature of 19.0°C which is 13.5°C lower than the ambient temperature.

Table 3: Per-day averages (Temperature)

Day	Chamber (°C)	Ambient (°C)	Difference (°C)	Efficiency (%)
Day 1	26.97	36.38	9.41	26.04
Day 2	26.94	35.67	8.72	24.49
Day 3	26.89	35.25	8.36	23.78
Overall	26.94	35.76	8.83	24.77

ANOVA Single factor results (Comparing all chamber versus all ambient temperatures) showed that the chamber temperatures differed statistically from the ambient temperature at $p \leq 0.05$. A p-value: < 0.0001 (extremely significant) was obtained, with F-statistic: 266.99 which signifies a significant reduction of ambient temperature. This shows a highly statistically significant difference between Chamber and Ambient temperatures. The chamber consistently maintains lower temperatures.

Two-way ANOVA (factors: Day + Type + Interaction) test indicates the cooling effect is consistent across days (no significant day-to-day variation in the difference). Table 4.

Table 4: Two-way ANOVA (factors: Day + Type + Interaction) – Temperature

Source	Sum Sq	df	F-stat	p-value	Significance
Day	6.71	2	0.42	0.661	Not significant
Type (Chamber/Ambient)	2104.98	1	260.58	<0.0001	Highly significant
Day × Type	5.06	2	0.31	0.732	Not significant
Residual	823.95	102	-	-	-

The Overall average cooling efficiency is 24.77% ranging from 14.1%-42.3%. The hourly trends indicate strongest cooling in early morning (higher % efficiency when ambient is rising).

Efficiency generally stable but slightly lower in late afternoon/evening. Chamber temperature tracks ambient but stays ~8–9°C cooler on average.

Correlation between Chamber and Ambient is 0.685 (moderate positive), that is Chamber responds to ambient changes but maintains a consistent offset. Minimum Chamber temp is 19.0°C (09:00 Day 1) and maximum difference is 15.0°C

4.2.2 Statistical Analysis of Relative Humidity

The average daily ambient humidity is 46.74% as measured over three consecutive days. The inside chamber humidity is 89.48%. The inside Chamber humidity was ranged from 65% to 99% while the ambient was 32% to 64% with an average humidity difference of 42.74% (Chamber much more humid). Table 3. At the highest efficiency, the Chamber had inside humidity of 99% which is 40% higher than the ambient. Table 5.

Table 5: Per-day averages (Humidity)

Day	Chamber RH (%)	Ambient RH (%)	Difference (%)	RH Enhancement Ratio (%)
Day 1	84.56	47.33	37.22	84.95
Day 2	90.78	48.50	42.28	91.12
Day 3	93.11	44.39	48.72	121.16
Overall	89.48	46.74	42.74	99.08

ANOVA Single factor results (Comparing all chamber versus all ambient humidities) showed that the chamber humidity differed statistically from the ambient humidity at $p \leq 0.05$. A p-value: < 0.0001 (extremely significant) was obtained, with F-statistic: 646.27.

Two-way ANOVA (factors: Day + Type + Interaction) test indicates the chamber maintains higher relative humidity than ambient air (highly significant difference). There is a slight but significant interaction with days, efficiency improved over the three days. Table 6.

Table 6: Two-way ANOVA (Day + Type + Interaction) – Relative Humidity

Source	Sum Sq	df	F-stat	p-value	Significance
Day	267.72	2	1.89	0.1563	Not significant
Type (Chamber/Ambient)	49,322.81	1	696.41	<0.0001	Highly significant
Day × Type	598.02	2	4.22	0.0173	Significant
Residual	7,224.11	102	-	-	-

The overall average Relative Humidity efficiency is 99.08% (the chamber roughly doubles the ambient humidity on average). Ranging from 44% – 147%. Efficiency is lower in the early morning (when ambient RH is relatively higher) and peaks strongly in the afternoon and evening. Correlation between Chamber and Ambient RH: 0.72 (strong positive) — Chamber follows ambient patterns but consistently adds substantial moisture. Chamber RH is very stable (often near 99% saturation), while ambient varies more.

4.3 Combined Temperature and Humidity (Psychrometric) Analysis

This experiment is a direct evaporative cooling + humidification system. It cools the air by evaporating water (sensible cooling) while adding moisture (latent heat gain), ideally following a near-constant wet-bulb temperature / enthalpy line on the psychrometric chart. Table 7. Shows psychrometric analysis of the system. Table 6. Shows performance per day of the system

Table 7: Psychrometric Analysis

Parameter	Ambient	Chamber	Difference
Dry Bulb Temp (°C)	35.83	26.94	-8.89°C
Relative Humidity (%)	46.7	89.6	+42.9%
Humidity Ratio (W, kg/kg)	0.0172	0.0203	+0.0031 (+18%)
Enthalpy (h, kJ/kg)	80.27	78.83	-1.44
Wet Bulb Temp (approx °C)	~25.5	~25.8	~+0.3 (near constant)

Table 8: Per-Day Performance of the system

Day	ΔT (°C)	Cooling Eff. (%)	ΔRH (%)	RH Enhc. Ratio (%)	ΔW (kg/kg)	Δh (kJ/kg)
1	-9.41	25.9%	+37.8	80.0	+0.0014	-6.15
2	-8.86	24.7%	+42.2	87.1	+0.0027	-2.35
3	-8.42	23.8%	+48.7	109.8	+0.0050	+4.17
Avg	-8.89	24.8%	+42.9	99.1%	+0.0031	-1.44

The positive Day 3 value is associated with the substantially higher moisture content of the chamber air (ΔW = +0.0050 kg/kg), which increased the latent component of moist-air enthalpy despite the reduction in dry-bulb temperature

4.3 Water Retention Capacity of the Charcoal

Water retention capacity is a critical parameter in evaporative cooling systems, as it directly influences evaporation rate, cooling effectiveness, operational stability, and overall water consumption. Accordingly, the water absorption and retention characteristics of the charcoal cooling pads were experimentally evaluated. The charcoal sample was completely dried under natural sunlight to remove residual moisture and achieve a constant dry mass. The dry weight of the sample *(Wdry)* was recorded using a precision balance. The sample was then submerged in water for 30 minutes to achieve full saturation after which they were removed and allowed to drain freely for a short period to eliminate excess surface water. The saturated weight *(Wwet)* was subsequently measured. The water retention capacity was calculated using the following Equation; (Kumarasinghe et al., 2026)

$$Water\ rentention\ capacity\ (g/g) = \frac{Wwet - Wdry}{Wdry} \quad \ldots\ldots\ldots\ldots\ldots\ldots\ldots\ldots\ldots\ldots\ldots 3$$

Table 9: Water retention capacity charcoal cooling pad samples based on dry and wet weight measurement.

Parameter	Charcoal Sample 1	Charcoal Sample 2	Charcoal Sample 3	Mean ± SD
Dry weight (g)	190	195	185	**190.00 ± 5.00**
Wet weight (g)	310	308	303	**307.00 ± 3.61**
Water retained (g)	120	113	118	**117.00 ± 3.61**
Water Retention Capacity (g/g)	**0.632**	**0.579**	**0.638**	**0.616 ± 0.032**

4.4 The porosity of the charcoal

A porous medium such as the cooling pad is also characterized by its porosity and permeability. Porosity or void fraction (ε) is a measure of the empty spaces between material particles. To determine the porosity of the material, a container of known volume was filled with the material and then water was added to the top of the container. The porosity was then computed using Equation (4) (Vega et al., 2022). A porosity of 52% was determined.

$$Porosity\ (\varepsilon) = \frac{Water\ added}{Container\ volume} \quad \ldots\ldots 4$$

5.0 DISCUSSION

The pad cooling efficiency is one of the main parameters that had been used to characterize the effectiveness of an evaporative cooling system. The drop in temperature and the increase in relative humidity in the air leaving the pad provides a clearer idea of the improvement in the thermal condition of the air.

The chamber demonstrates reliable and statistically significant cooling performance, with an average of 24.8% cooling efficiency (8.8°C reduction) across varying ambient conditions, and an average relative humidity of 89.48%. The pad represented similar result to those of other alternative materials (Leonard & Msacky, 2023), designed and tested a charcoal cooler for postharvest storage and reported an average cooling efficiency of 25.92% compared to sand cooler in the same experiment with a cooling efficiency of 22.15%. and an average relative humidity of 52.2% (Elmsaad & Omran, 2015), in their experiment found that a luffa pad yielded an average relative humidity of 73.67%, straw fiber pads 71.87%, CELdek 70.33% and sackcloth 69% (Korese & Hensel, 2016) evaluated a bulk charcoal as cooling pad under different pad configuration and reported a cooling efficiency vary from 56.71% - 96.10% to 45.41% - 90.06%, depending on the pad configuration, air velocity and the water flow rate. (Kulkarni et al., 2014) tested a jute fiber pad and reported a temperature range between 25.8°C and 26.2°C.The saturation efficiencies range from 69 % to 59 %. (T.D et al., 2023) reported a clay based cooling pad of 65% cooling efficiency and 68% from the cellulose pad. Though there was no side-by-side experiment to compare the charcoal with other commercial pads because of their unavailability in the market at the time of conducting this experiment, but existing literature shows the charcoal granules performed excellently compared to other cooling pad materials.

6.0 CONCLUSION AND RECOMMENDATIONS

Charcoal granules are a viable, sustainable wet pad medium for evaporative cooling in post-harvest systems, delivering effective cooling and significant humidity rise. It is less expensive compared

to other cooling pad materials. It cost less than Ten Thousand Naira (N10,000) to produce a charcoal pad of one meter square compared to other cooling pad material like CELdek which costs between Twenty Thousand to Seventy Thousand per square meter depending on thickness Experimental data support its use in resource-limited settings. The chamber demonstrates reliable and statistically significant cooling performance, with an average of 24.8% efficiency (8.8°C reduction) across varying ambient conditions. Performance is consistent across the three days. It is highly effective at humidifying the environment, achieving an average 97% efficiency (nearly doubling ambient RH). The system delivers consistent temperature drop with substantial moisture addition along a near-constant wet-bulb line, reducing sensible heat while slightly varying enthalpy. The positive Day 3 value of the enthalpy is associated with the substantially higher moisture content of the chamber air ($\Delta W = +0.0050$ kg/kg), which increased the latent component of moist-air enthalpy despite the reduction in dry-bulb temperature.

Future work should optimize granule size/distribution, fan speeds variance, and conduct long-term experiments across geographical zones. It also recommends incorporating calibration against traceable reference instruments before and after the experiment to improve measurement confidence.

REFERENCES

Awafo, E. A., Nketsiah, S., Alhassan, M., & Kubi, E. A. (2020). DESIGN , CONSTRUCTION , AND PERFORMANCE EVALUATION OF AN EVAPORATIVE COOLING SYSTEM FOR TOMATOES. *Sciendo*, *24*(4), 1–12. https://doi.org/10.1515/agriceng-2020-0031

Berihun, B. (2023). Development and performance evaluation of the evaporative cooler technology for the preservation of fresh fruits and vegetables in North-west Ethiopia.

Bodile, D., Garghate, V., Khode, R., Yedkar, A., Wankhade, A., & Bhagat, S. (2025). Cooling Pad in Evaporative System : A Review. *International Research Journal of Scientific Studies*, *2*(3), 1–6. https://doi.org/https://doi.org/10.64383/irjss.20250335

Defraeye, T., Schudel, S., Shrivastava, C., Motmans, T., Umani, K., Crenna, E., Shoji, K., & Onwude, D. (2024). Biosystems Engineering The charcoal cooling blanket : A scalable , simple , self-supporting evaporative cooling device for preserving fresh foods. *Biosystems Engineering*, *238*(December 2023), 128–142. https://doi.org/10.1016/j.biosystemseng.2023.12.001

Deoraj, S., Ekwue, E. I., & Birch, R. (2015). An Evaporative Cooler for the Storage of Fresh Fruits and Vegetables. *The West Indian Journal of Engineering*, *38*(1), 86–95.

Elmsaad, E., & Omran, A. (2015). Evaluating the Effect of New Local Materials of Evaporative Cooling Pads Department of Agricultural Engineering , Faculty of Agricultural Sciences , School of Economics , Finance and Banking , College of Business ,. *American-Eurasian J. Agric. & Environ. Sci.*, *15*(1), 78–84. https://doi.org/10.5829/idosi.aejaes.2015.15.1.12494

Franco-salas, A. (2021). Optimal operation of evaporative cooling pads : A review. *Renewable and Sustainable Energy Reviews*, *151*(September), 1–14. https://doi.org/10.1016/j.rser.2021.111632

Korese, J. K., & Hensel, O. (2016). Experimental evaluation of bulk charcoal pad configuration on evaporative cooling effectiveness. *AgricEngInt: CIGR Journal Open Access*, *18*(4), 11–21. https://doi.org/http://www.cigrjournal.org

Kouchakzadeh, A., & Brati, A. (2013). The evaluation of bulk charcoal as greenhouse evaporative cooling pad. *Agric Eng Int: CIGR Journal*, *15*(2), 188–193. https://doi.org/http://www.cigrjournal.org

Kulkarni, R. K., Rajput, S. P. S., Gutte, S. A., & Patil, D. M. (2014). Laboratory Performance Of Evaporative Cooler Using Jute Fiber Ropes As Cooling Media. *Int. Journal of Engineering Research and Applications*, *4*(12), 60–66. https://doi.org/www.ijera.com

Kumarasinghe, S., Thilakarathna, R., & Welivitiyage, Y. (2026). Experimental Performance Evaluation of Clay- Based Cooling Pads with Optimized Geometry for Direct Evaporative Cooling Systems Experimental Performance Evaluation of Clay-Based Cooling Pads with Optimized Geometry for Direct Evaporative Cooling Systems. *Research Square*, *1*(4), 0–18.

https://doi.org/https://doi.org/10.21203/rs.3.rs-8666200/v1

Leonard, L. S., & Msacky, N. J. (2023). PERFORMANCE EVALUATION OF EVAPORATIVE COOLING SYSTEMS AS. *INTERNATIONAL JOURNAL OF ENVIRONMENT*, *12*(2), 17–40.

Ogumo, E. O., Kunyanga, C. N., Okoth, M. W., & Kimenju, J. (2017). Current knowledge and performance of existing charcoal coolers in improving the overall quality and shelf-life of French beans. *African Journal of Agricultural Research*, *12*(49), 3399–3409. https://doi.org/10.5897/AJAR2017.12749

Perez, G. A. (2022). *Optimizing Forced-Air Evaporative Cooling Chambers for Vegetable Preservation by*.

Shitanda, D., Oluoch, O. K., & Pascall, A. M. (2015). Performance evaluation of a medium size charcoal cooler installed in the field for temporary storage of horticultural produce. *Agricultural Engineering International: CIGR Journal.*, *13*(1596), 1–12.

T.D, K., C.P, R., & M.D.S., S. (2023). Potential of a Charcoal Evaporative Cooling Chamber for Extending the Shelf Life of Vegetables. *Environmental Engineering and Green Technology*, *3*(36), 2023.

Udo, M. O., Oyedepo, S. O., Afolalu, S. A., Ongbali, S. O., Kilanko, O., Leramo, R. O., Saleh, B., Dirisu, J. O., Omoleye, J. A., Odewole, G., Babalola, P. O., Fasogbon, S. K., Solomon, E. C., Bolarinwa-odunayo, B., & Uchechukwu, I. O. (2025). Experimental performance evaluation of a solar powered evaporative cooling system for preservation of agricultural produce in tropical region. *Journal of Thermal Engineering*, *11*(3), 858–879. https://doi.org/10.14744/thermal.0000951

Vega, F. A. O., Rios, A. P. M., Saraz, J. A. O., Damasceno, F. A., & Barbari, M. (2022). Comparative Analysis of the Cooling Efficiency in Tropical Climate of Three Alternative Materials for Evaporative Cooling Pads. *Applied Sciences*, *12*(77), 1–29. https://doi.org/https://doi.org/10.3390/app12010077

Warke, D. A., & Deshmukh, S. J. (2017). Experimental Analysis of Cellulose Cooling Pads Used in Evaporative Coolers. *International Journal of Energy Science and Engineering*, *3*(4), 37–43.

Yeneneh, K. (2023). Design , Fabrication and Evaluation of Evaporative Cooling System for the Storage of Fruits and Vegetables. *International Journal of Applied and Structural Mechanics*, *03*(04), 9–22. https://doi.org/https://doi.org/10.55529/ijasm.34.9.22

International Conference on Engineering Innovation for Sustainable Development (ICESID 2026)
Faculty of Engineering, Ahmadu Bello University Zaria · 8–10 September 2026

EXPERIMENTAL EVALUATION OF A SOLAR DRYER INTEGRATED WITH A CARBON DOT-ENHANCED SHEA BUTTER PHASE CHANGE MATERIAL (PCM).

Yotolmbaye Sylvain[1,*], T.o. Ahmadu[1], F.o. Anafi[1], L.o.yusuf[1]

[1]*Ahmadu Bello University*

Email: yotolmbayes@gmail.com[*], talibahmadu@gmail.com, Fataianafi@yahoo.com, queenteefah95@gmail.com

***Corresponding author**: Yotolmbaye Sylvain

DOI: https://doi.org/10.67203/sp.ICESID.2026

ABSTRACT

The increasing demand for sustainable and renewable energy solutions has stimulated significant research into technologies that enhance agricultural productivity and reduce post-harvest losses. Among these technologies, solar drying has emerged as an environmentally friendly, cost-effective method for preserving agricultural products by reducing moisture content and extending shelf life. Its relevance is particularly pronounced in developing countries such as Nigeria. Phase change materials (PCMs) are needed to enhance the performance of solar dryers, especially after sunshine hours. In this study, two solar dryers, with and without PCM, each with a capacity of 2 kg, were constructed and tested alongside open sun drying under an average ambient temperature of 28.6 °C and average solar irradiance of about 876 W/m². The PCM-integrated dryer achieved a drying heat load of 835.81 MJ and an outlet air temperature of 51.6 °C, removing 0.68 kg of moisture with an average drying rate of 0.20 kg/h reaching a final moisture content of about 9% which was 4% short of reaching the target final moisture of the study of 5%. The required PCM mass was 3.924 kg (0.0042 m³), providing a thermal energy storage capacity of 489,853 J and enabling extended drying for up to 5 hours beyond sunshine hours. The PCM-integrated solar dryer achieved a drying efficiency of 85%. While the non-PCM dryer and open sun drying achieved drying efficiencies of 77% and 40%, respectively. This demonstrates the superior drying efficiency of the PCM-integrated dryer over the other drying methods.

Keywords: *Phase change material; Drying rate; Moisture removal; and Thermal efficiency*

1. INTRODUCTION

In recent years, integrating thermal energy storage into solar dryers has gained attention as a solution to intermittent solar radiation Dhass *et al.* (2025). Phase change materials (PCMs) are widely studied due to their capacity to absorb, store, and release latent heat, enabling stable drying temperatures and improved system efficiency. However, conventional PCMs, particularly organic types, suffer from low thermal conductivity, limiting heat transfer during charging and discharging cycles Zhang *et al.* (2018). To address this limitation, nano-enhanced phase change materials (NEPCMs) have been developed by incorporating nanoparticles into base PCMs. Among these, carbon dots have emerged as promising additives because of their high surface area, good thermal conductivity, and enhanced photothermal conversion Li et al. (2021). When combined with natural PCMs such as shea butter, which is biodegradable, locally available, and has a suitable melting range, overall thermal performance can be significantly improved. This combination is especially relevant for drying perishable agricultural products like okra, where maintaining quality and reducing spoilage are critical. Integrating PCM-based storage into solar dryers ensures continuous drying even without sunlight. Experimental evaluation of such systems typically examines temperature distribution, drying rate, moisture removal, and efficiency, contributing to the development of sustainable, low-cost drying technologies. Agbetiloye et al. (2022)developed a mixed-mode solar dryer using shea butter with 3% aluminium powder as PCM for ginger rhizomes. The PCM achieved 164.53 kJ/kg latent heat and improved thermal performance, reaching 77% collector efficiency. Moisture content decreased from 71% to 13%, while drying efficiency remained 30% during operation. Li et al. (2021)developed a shape-stabilised PCM by integrating polyethene glycol (PEG) into carbonised wood with carbon dots, improving thermal

conductivity (0.449 W/m.K) and photothermal efficiency (84.4%). The composite showed good stability and reliability, but reduced latent heat (112.4 J/g) due to limited PEG loading, indicating a need for further optimisation. Salisu et al. (2022) developed encapsulated shea butter as a bio-based PCM for thermal storage, with a melting peak of 37.5°C, latent heat of 50.34 kJ/kg, and thermal conductivity of 0.26 W/m·K. Experimental and CFD results demonstrated efficient thermal storage and improved overall system performance.

2. METHODOLOGY

2.1 Materials

The carbon precursors used in the hydrothermal synthesis of carbon dots were p-phenylenediamine and folic acid; ethanol was obtained from Haddis Chemical, Samaru, Zaria. Deionized water was obtained from the Ahmadu Bello University Multiuser Laboratory, and food-grade shea butter was purchased from the open market.

2.2 Synthesis of Carbon Dots

Carbon dots (CDs) were synthesized hydrothermally following the method of He et al. (2024). P-Phenylenediamine (30 g) was dissolved in 1 L of ethanol to form solution A, while folic acid (5 g) was dissolved separately in 500 mL of deionized water to form solution B. Solutions A and B were combined under magnetic stirring to obtain a homogeneous mixture, which was then transferred into a Teflon-lined autoclave reactor and heated at 180 °C for 12 hours. After natural cooling to room temperature, the crude product exhibited characteristic red fluorescence under ultraviolet light, indicating successful carbon dot formation. The product was purified by silica gel column chromatography using methanol as the eluent, followed by rotary evaporation and freeze-drying under vacuum. The final carbon dots were obtained with a synthesis yield of 40.3%.

2.3 Preparation of Carbon Dot-Shea Butter Blend

This was done according to the method of (Agbetiloye *et al.*, 2022).10 mL of shea butter was poured into a clean beaker, and it was heated gently to the desired mixture temperature (40 °C, 50 °C, & 60 °C) Priyadarshi & Paul (2019) until it was completely melted. The appropriate proportion of carbon dots (1%, 2%, & 3% by weight) were measured based on the experimental run. The carbon dots were gradually added into the molten shea butter while stirred to avoid agglomeration. The magnetic stirrer was Placed in side beaker and maintained continuous stirring at the selected temperature. The blending process was allowed to proceed for the specified mixing time (10, 20, & 30 minutes) for each run to ensure uniform dispersion of the carbon dots within the shea butter to achieve homogeneity. The mixture was then removed from the heat source and allowed to cool under ambient conditions.

2.4 Performance evaluation of the PCM in solar dryer

The performance of the PCM for solar drying was evaluated by incorporating it into a solar dryer and carrying out experimental tests to dry okra. A solar dryer of the same capacity (without PCM) and open sun drying were also tested simultaneously, and performances were compared. The temperature and humidity were measured using ATO Bluetooth Temperature and Relative Humidity Logger model ATO-TDL-BT06, made in China. The air flow rate on the other hand was measured using Bluetooth anemometer model AZ/AERMANDA AZ89171, made in China.

2.5 Okra Samples Preparation

The okra was then sliced into 7 mm thick pieces using a kitchen knife. A total of 2 kg of these slices was evenly spread on trays to ensure maximum surface area exposure to incoming hot air during the drying process. The initial moisture content of the okra was about 45% and the target final moisture content after drying was 5%.

2.6 Instrumentation of solar dryer experiment

A thermocouple was used as a temperature sensor for both measurement and control purposes. In this context, thermocouples were employed to measure the inlet and outlet temperatures of a solar dryer, the temperature of the absorber plate with and without phase change material (PCM), as well as the ambient and tray temperatures. A data logger was additionally used to record solar radiation over a four-day period, during which all temperature parameters were monitored. A Camry weighing scale was utilised to determine weight. Specifically, it was used to measure the mass of moisture loss from okra slices, recorded in kilograms.

Experimental procedure

Plate I. The constructed solar dryers.

Plate I shows the solar dryer as constructed. The experimental solar dryer was designed as a compact, portable unit with an overall drying chamber of approximately 360 mm × 340 mm in plan dimensions and 500 mm in height. The solar collector measured approximately 708.9 mm in length and 150 mm in width, while the upper air outlet/chimney section had a height of approximately 500 mm and an internal diameter of 190 mm. The dryer was fabricated primarily from mild-steel shells to provide the structural enclosure and mechanical support, with a wooden table/support frame provided beneath the drying tray to accommodate and stabilize the drying chamber. Aluminium sheet was employed as the glazing/covering material for the solar collector to provide a lightweight and durable enclosure for solar-energy capture. The resulting configuration provides a relatively lightweight and compact experimental platform suitable for controlled investigation of drying characteristics under solar radiation

The experiment was conducted in October, during which two solar dryers and open sun drying processes were operated simultaneously to compare their performance. Additional experimental trials were carried out on the 17th, 18th, 19th, and 20th of October 2025 under the prevailing weather conditions in Zaria, Nigeria.

The evaluation focused on moisture removal and thermal performance parameters, including system drying efficiency, collector efficiency, and drying rate for each drying method, alongside the corresponding moisture content at specific time intervals.

The experiment aimed to test the developed PCM and evaluate the performance of the solar crop dryer by analysing moisture loss, drying efficiency, and drying rate of sliced okra. In terms of procedure, the solar dryer, integrated with phase change material (PCM), was loaded with sliced okra of average thickness between 5 and 7 mm and then exposed to solar radiation. Hourly measurements were recorded for temperatures at various locations, including the collector inlet, absorber plate, chimney, ambient air, and drying tray. These measurements were taken from 08:00 to 20:00 on 17 October 2025, from 08:00 to 20:00 on 18 October, from 06:00 to 20:00 on 19 October, and from 06:00 to 20:00 on 20 October 2025.

Each solar crop dryer was loaded with 2 kg of sliced okra. On the first day, the weight of the samples was measured every two hours, while on subsequent days, measurements were taken hourly. During daylight hours, airflow was naturally established over the absorber plate as the air became less dense upon heating. Solar radiation was also directly incident on the top glazing, enabling both heated air and direct radiation to enhance the drying of the sliced okra while simultaneously charging the PCM within the rectangular absorber plate in the collector and the cylindrical PCM container in the drying chamber.

The heat energy stored within both the rectangular and cylindrical PCM units was released during periods of low solar radiation, thereby sustaining the drying process and extending it beyond sunshine hours. The air mass flow rate into the collector was determined from the product of the measured wind speed (using an anemometer), the collector cross-sectional area, and the air density. The weight of the okra slices on each tray was recorded at the beginning of the drying process and subsequently at two-hour intervals on the first day and at one-hour intervals on the remaining days. The overall procedure followed standard methods recommended in related studies for evaluating solar dryer performance.

2.7 Characterization of carbon dots and blends of carbon dots with shea butter.

2.7.1 Thermal conductivity

Thermal conductivity test was done on the pure shea butter and the modified shea butter (PCM). The Searles apparatus was used in Equation 1

$$\lambda = \frac{Q-X}{A(T_2-T_1)} \quad (1)$$

where;
λ; Thermal conductivity of sample [W/mK]
Q; generated heat per unit length of sample/time [W/m2]
Sample diameter = 0.0018 and length = 0.0043 [m]
X; Thickness of sample [m]
A; Area [m2]
T1 and T2; Temperature at t1 and t2 [K]
t1 and t2; measured time length [seconds, s]

2.7.2 Specific heat capacity

$$\text{Specific heat capacity (c)} = \frac{Q}{mDT} \quad (2)$$

Unit of C is J/kg*^{o}C, M is the Mass (kg), Q is the change in energy (J), and ΔT is the temperature change (^{o}C)

2.7.3 Thermal Diffusivity

$$\alpha\ (m^2/s) = \frac{\lambda}{\rho cp}$$

(**Error! No text of specified style in document.**)

Where:
ρ is the density of the material and
Cp is the specific heat capacity (J/gK)

The same apparatus (Armfield equipment model HT12) with a heat transfer service unit (Armfield equipment model HT10XC) was used in this thermal diffusivity calculation.

2.7.1 Latent heat of fusion.

Apparatus:

Ice, blotting paper, copper calorimeter and stirrer, insulating jacket, heater, beaker, thermometer and balance.

Procedure:

The water was gently warmed in a beaker until it reached approximately 32 °C. The calorimeter and stirrer were weighed, after which the calorimeter was filled to about one-third of its capacity with the warm water and reweighed. The calorimeter was then kept within its enclosure, and the initial temperature of the water was observed until it was about 32 °C above room temperature. Small pieces of the sample, previously dried using blotting paper, were added until the temperature fell to around 20 °C below room temperature. The mixture was stirred continuously, ensuring that each portion of the sample had completely melted before additional pieces were introduced. Finally, the calorimeter and its contents were reweighed, and the value of the latent heat of fusion (L) was calculated using the appropriate equation.

Theory:

The specific latent heat of fusion of a solid is the heat required to convert unit mass of it at its melting point into liquid at the same temperature.

Heat gained by shea butter + Heat gained by water = Heat lost by water and calorimeter

Equations:

$$mL + ms_2(\theta_2 - 0) = (m_2s_2 + m_1s_1)(\theta_1 - \theta_2) \quad (4)$$

$$L = [(m_2s_2 + m_1s_1)(\theta_1 - \theta_2) - s_2(\theta_2 - 0)] / m \quad (5)$$

Where:
m_1=Mass of Copper Calorimeter and Stirrer
m_2=Mass of Water
S_1=Specific Heat Capacity of Water
S_2= Specific Heat Capacity of Copper
θ_1= Initial Temperature of Warm Water
θ_2=Final Temperature of Mixture
m=Mass of Sample
L=Specific Latent Heat of Fusion of Sample

Plate II. controlled heat transfer -HT12XC

3. RESULTS AND DISCUSSION

3.1 The dried okra obtained from the experiment

(a) (b) (c)

Plate III: Sample dried okra from (a) open sun drying, (b) dried without PCM, and (c) dried with PCM.

3.2 Solar Dryer Testing and Evaluation

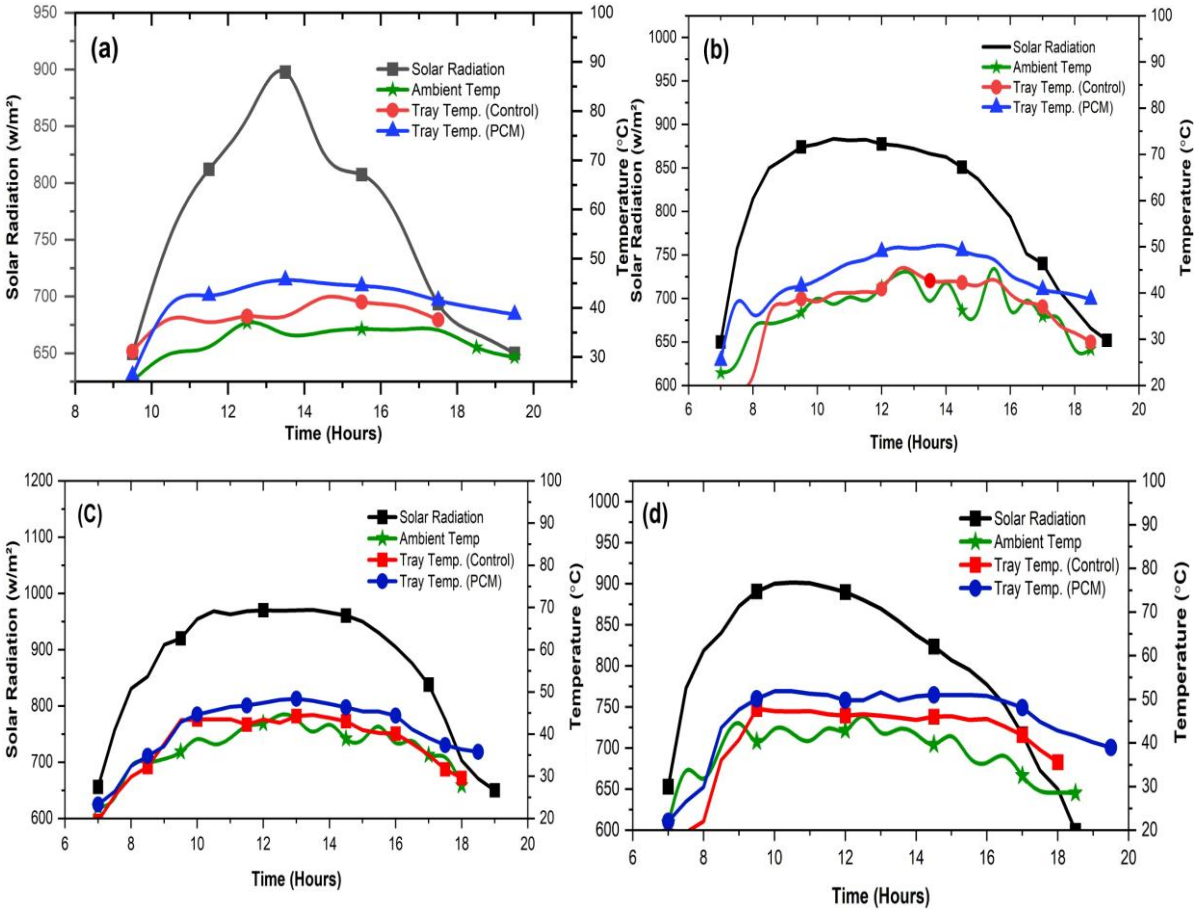

Figure 1: Solar radiation and temperature profiles for (a) day 1, (b) day 2, (c) day 3, and (d) day 4 of the experiments

Figure 1 for (a) day 1, (b) day 2, (c) day 3, and (d) day 4. The chamber of the PCM system exhibited higher peak temperatures, reduced temperature fluctuations, and a delayed cooling profile compared to the control system. This behaviour is attributed to the latent heat storage capability of the PCM and enhanced thermal conductivity provided by carbon dots. Between 10:00 and 14:00, temperatures rise slowly but reach higher values for the PCM system, showing that the PCM absorbs and stores heat. Even when the solar radiation dropped after 14.00, the PCM system chamber temperature remained higher than the control tray. PCM absorbs heat during peak solar radiation and releases it during off-peak periods, stabilising temperature (Han et al., 2022). Percentage temperature difference between the drying chamber temperature and the ambient temperature for all the days were calculated as % difference = (T_PCM – T_ambient)/T_ambient x 100.

A peak temperature of 45.7°C was observed for the PCM-based dryer system on Day 1 at 1:30 pm, and up to a 34% increase in the system temperature compared to the ambient temperature was observed at around 2.30 pm, where the PCM-based chamber was at 45°C while the ambient temperature was 34°C. On the second day, a peak temperature of up to 50.2°C was recorded for the PCM-based dryer system. Also, up to about a 53% difference in the PCM-dryer system temperature compared to the ambient temperature was observed at around 7.30 pm where the PCM-based chamber was at 38°C while the ambient temperature was 25°C. This high early difference could be attributed to the stored heat in the PCM on the first day. A peak temperature of 52°C was recorded on the 3rd day for the PCM-based dryer system at around 10:00 am, and up to a 40% difference between this system's temperature and the ambient temperature was observed, where the PCM-based chamber was at 50°C while the ambient temperature was 36°C. This gradual daily improvement is attributable to the good storage capacity of the PCM enhanced with carbon-dot nanoparticles.

On the fourth day, a peak temperature of about 48.4°C was observed in the drying chamber of the PCM-based dryer system at 1:00 pm. Up to about a 30% increase in the PCM-system temperature was recorded compared to the ambient temperature 5.30 pm, where the PCM-based chamber was at 37°C while the ambient temperature was 29°C. When a PCM is integrated into a solar dryer, it absorbs excess thermal energy during peak solar irradiance and releases it during periods of lower insolation or at night, effectively smoothing thermal fluctuations and maintaining a more consistently elevated temperature within the drying chamber. (Fu *et al.*, 2024; Krishna *et al.*, 2025). The observed thermal lag and sustained elevated temperatures during low solar radiation periods confirm effective energy storage and release, leading to extended drying duration and improved system efficiency. These findings are consistent with established literature on nano-enhanced phase change materials in solar thermal applications. The mean solar irradiance was calculated for the more useful sunlight period of between 10.00 am and 3.00 pm based on the hourly measurement values. The calculated means for the four days were 810, 867, 961 and 867 w/m^2, respectively which gives a mean of 876 w/m^2 across the four days. The mean ambient temperature across the four days was also calculated based on hour measurement values taken giving about 28.6 °C.

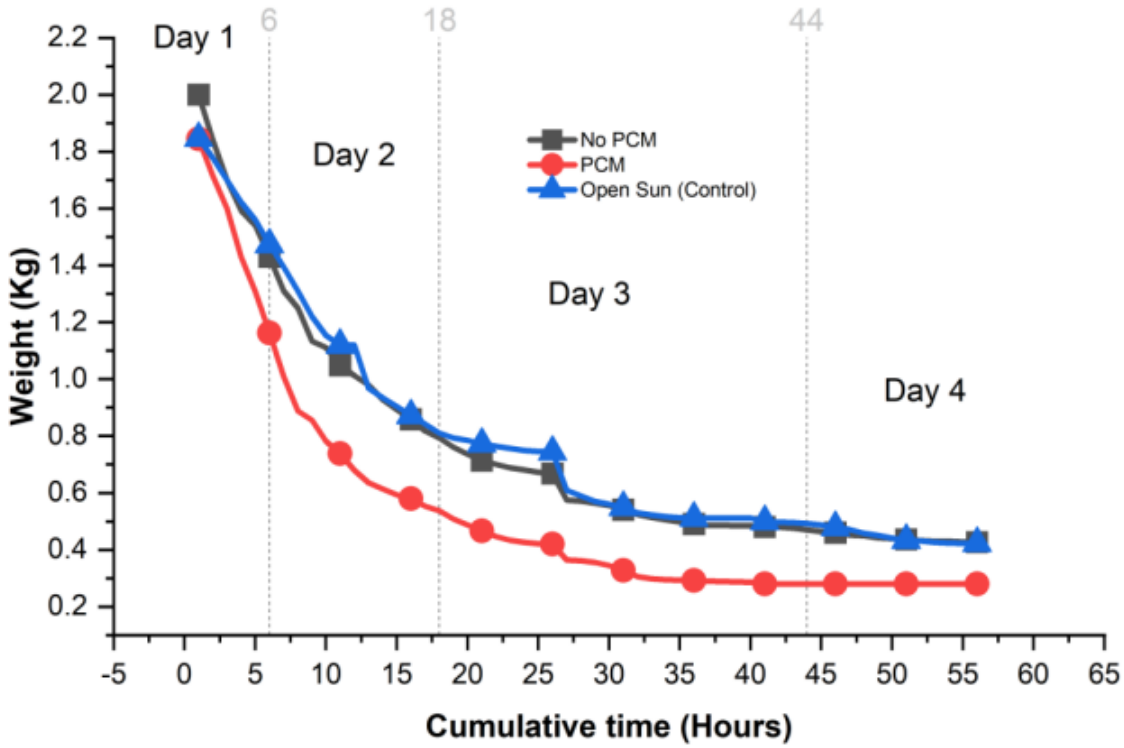

Figure 2: Drying performance recorded for open drying, a dryer with PCM, and a dryer without PCM.

Figure 2 compares drying profiles over 60 hours for open-sun drying (control), a non-PCM dryer, and a PCM-assisted dryer. All curves show the typical exponential mass decline, reflecting an initial constant-rate period followed by a prolonged falling-rate period. The PCM system consistently maintains the lowest residual mass, indicating superior drying efficiency. In the first 6 hours (Day 1), all methods show rapid weight loss from surface moisture evaporation. Still, the PCM dryer declines fastest because it absorbs excess solar heat and releases it gradually, stabilising temperatures. Accord to Azzouz *et al.* (2018) confirm that latent heat storage materials improve heat retention and reduce temperature fluctuations, thereby accelerating early-stage drying kinetics. By 18 hours (Day 2), the performance gap widens: the PCM system continues faster moisture removal while the others slow, corresponding to the shift toward internal moisture diffusion. PCM's sustained thermal input enhances this diffusion. Similar findings were reported by Mohammed *et al.* (2025) By 44 hours (Day 3), drying rates decrease as bound moisture dominates, yet the PCM dryer reaches 0.3 kg versus 0.5kg for non-pcm and 0.6 kg for the open sun. In the final stage, all systems approach equilibrium moisture content

with minimal further loss, but the PCM unit achieves the lowest final mass and greatest drying completeness. Without thermal storage, the non-PCM and open-sun methods remain more dependent on ambient conditions and diurnal temperature drops. Recent work by Kumar *et al.* (2021) highlights that PCM integration is particularly beneficial during the falling-rate period, where consistent thermal gradients are crucial for moisture diffusion from the interior.

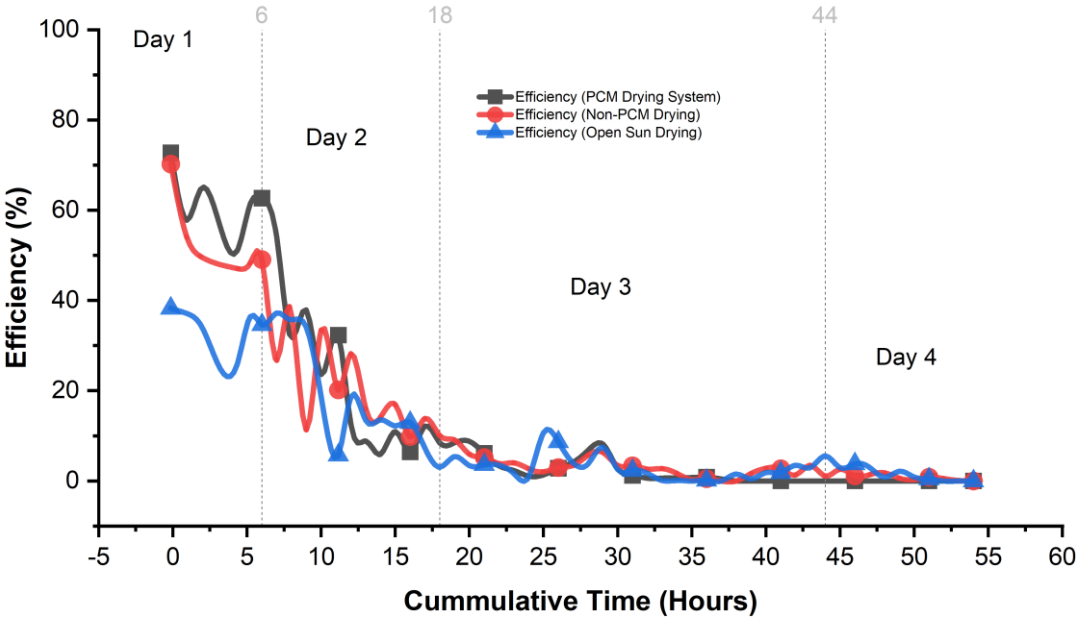

Figure 3: Variation of drying efficiencies with time for the 3 cases

Figure 3 compares the drying efficiencies of PCM, non-PCM, and open-sun systems over approximately 60 cumulative hours. On Day 1, the PCM and non-PCM system recorded similar initial efficiency of about 75%, while open-sun drying began at 40%. During the first 10 hours, however, PCM drying maintained relatively high and stable efficiency between 50% and 70%, whereas non-PCM efficiency declined sharply from to between 30% and <50%. Open-sun drying remained lower, fluctuating between 20% and 40%. By 18 hours, efficiencies declined across all systems because of reduced moisture content and the transition to the falling-rate drying period. However, the PCM system maintained smoother performance, generally achieving 20-40% efficiency, owing to latent heat storage and release during low solar irradiance. Recent studies corroborate this behavior, showing that PCM integration reduces thermal intermittency and improves energy utilization efficiency. (Rakshamuthu *et al.*, 2021) From 30 hours onward, efficiencies approached near-zero values, with all systems falling below 2% by 55-60 hours. Overall, PCM integration provided superior early-stage performance, improved thermal regulation, and sustained moisture removal compared with non-PCM and open-sun drying under variable operating conditions.

4. CONCLUSION

The experimental evaluation of a carbon dot-enhanced shea butter phase change material (PCM) integrated into a solar dryer demonstrated a significant improvement in the drying performance of okra. Under an average ambient temperature of 28.6 °C and solar irradiance of 995.5 W/m², the PCM-integrated dryer achieved an outlet air temperature of 51.6 °C and removed 0.68 kg of moisture from an initial 2 kg okra sample. The PCM-enhanced dryer recorded a peak drying efficiency of 85%, compared with 77% for the non-PCM dryer and approximately 40% for open-sun drying. The incorporation of 3.924 kg of PCM, with an energy storage capacity of 489,853 J, extended the drying period by 5 hours beyond sunshine hours. Consequently, the PCM system achieved the highest drying

rate of 0.20 kg/h, compared with 0.1425 kg/h for the non-PCM dryer and 0.1317 kg/h for open-sun drying. These results demonstrate that carbon dot-enhanced shea butter PCM can improve thermal energy storage, extend drying operations, and accelerate moisture removal. The limitations of these findings is the fact that only one crop (okra) was experimented and the testing was not extended across different seasons, and therefore multiple climatic and weather conditions. Evaluation of the dryer was done only for four days with 2 kg okra samples. Further characterisation using Differential Scanning Calorimetry (DSC) is recommended for more accurate thermal property measurements, while seasonal experiments are suggested to evaluate performance under varying weather conditions and assess the system's reliability and suitability for practical agricultural drying applications of different categories of crops, testing should also be extended for more number of days and hours per day to reduce the margin of error and get more reliable data. This study is an exemplary contribution towards sustainable resource utilization considering the fact the it was focused on the use of shea butter which is a renewable resources that has no competitive usage as food resource for humans and animals making the study directly relevant to the ICESID 2026 sub-theme of sustainable resource utilization/materials synthesis.

Acknowledgements *(Optional — delete heading and content if not applicable)*

Acknowledge funding bodies, institutions, or individuals who contributed to the research but are not listed as authors. TETFund-supported research should be acknowledged here.

5. REFERENCES

Agbetiloye, L. A., Anafi, F. O., & Omisanya, N. O. (2022). Design, construction and performance evaluation of ginger mixed mode solar dryer integrated with latent heat storage. *FUOYE Journal of Engineering and Technology, 7*(2), 210-216.

Azzouz, S., Hermassi, I., Chouikh, R., Guizani, A., & Belghith, A. (2018). The convective drying of grape seeds: Effect of shrinkage on heat and mass transfer. *Journal of Food Process Engineering, 41*(1), e12614.

Dhass, A., Beemkumar, N., S. M., & K. K. (2025). Enhancing solar drying systems through integrated thermal energy storage and solar-assisted heat pump technologies: a pathway to sustainable food processing. *Results in* Engineering, 107125.

Fu, W., Bo, R., Zhang, G., Li, C., & Meng, X. (2024). Employing Phase-Change Materials to enhance the thermal performance of the solar dryer. *Journal of Energy Storage, 91,* 112062.

Han, X., Jin, Y., Huang, J., Tian, H., & Guo, M. (2022). Highly Toughening Modification of Hyperbranched Polyester with Environment-friendly Caprolactone As End Group on Poly (3-hydroxybutyrate-co-3-hydroxyvalerate). *Journal of Polymers and the Environment, 30*(8), 3209-3217.

Karaağaç, M. O. (2024). Performance evaluation of nano-enhanced phase change materials for thermal energy storage: An experimental *study. Case Studies in Thermal Engineering,* 64, 105412.

Krishna, V. S., Jain, S. K., Panwar, N. L., & Sree, R. (2025). An overview on Phase Change Material incorporated in convective solar dryers. *Journal of Energy Storage, 131,* 117486.

Kumar, P. M., Sudarvizhi, D., Prakash, K., Anupradeepa, A., Raj, S. B., Shanmathi, S., Sumithra, K., & Surya, S. (2021). Investigating a single slope solar still with a nano-phase change material. *Materials Today: Proceedings, 45,* 7922-7925.

Li, X., Zhu, Z., Yang, P., You, Z., Dong, Y., Tang, M., Chen, M., & Zhou, X. (2021). Carbonized wood *loaded with carbon dots for preparation* long-term shape-stabilized composite phase change materials with superior thermal energy conversion capacity. *Renewable Energy, 174,* 19-30.

Madhu, B. (2025). Advances in Renewable Energy Based Drying Systems for Food Materials: A Comprehensive Review of Innovations, Smart Integration, and Sustainability. Journal of Food Process Engineering, 48(9), e70207.

Mohammed, S. A., Alawee, W. H., Abdul-Zahra, A. S., Majdi, *H. S.*, Fayad, M. A., & Chaichan, M. T. (2025). Thermal performance enhancement of a PCM-assisted cylindrical solar air heater with moisture traps for Barhi dates drying. *Case Studies in Thermal Engineering, 71,* 106255.

Priyadarshi, D., & Paul, K. K. (2019). Optimisation of biodiesel production using Taguchi model. Waste and Biomass Valorization, 10(6), 1547-1559.

Rakshamuthu, S., Jegan, S., Benyameen, J. J., Selvakumar, V., Anandeeswaran, K., & Iyahraja, S. (2021). Experimental analysis of small size solar dryer with phase change materials for food preservation. *Journal of Energy Storage*, *33*, 102095.

Salisu, A. R., Waziri, S., & Galadima, M. S. (2022). *Development of* Encapsulated Shea Butter as Bio-Based Phase change Material for Thermal Storage Application. International Journal of Advanced Engineering Research and Science, 9(12), 302-309. doi:10.22161/ijaers.912.32

Zhang, N., *Yuan, Y., Cao, X*., Du, Y., Zhang, Z., & Gui, Y. (2018). Latent heat thermal energy storage systems with solid'liquid phase change materials: a review. *Advanced engineering materials, 20*(6), 1700753.

International Conference on Engineering Innovation for Sustainable Development (ICESID 2026)
Faculty of Engineering, Ahmadu Bello University Zaria · 8–10 September 2026

FIELD-VALIDATED FAILURE ANALYSIS OF COMMERCIAL TRICYCLES IN NIGERIA AND THE POTENTIAL OF AGRICULTURAL RESIDUE-REINFORCED ALUMINIUM MATRIX COMPOSITES FOR PISTON DURABILITY ENHANCEMENT

Sikiru Kayode Sanusi[1,*], Adebisi Jeleel Adekunle[2]
[1]*The Federal Polytechnic, Offa*
[2]*University of Ilorin*
Email: sikiru.sanusi@fedpoffaonline.edu.ng*, adebisi.ja@unilorin.edu.ng
***Corresponding author**: Sikiru Kayode Sanusi
DOI: https://doi.org/10.67203/sp.ICESID.2026

ABSTRACT
Commercial tricycles are indispensable to the Nigerian transport network, yet their reliability is compromised by recurring mechanical failures whose material origins remain poorly understood. This study integrates a cross-sectional survey of 333 stakeholders, comprising riders, mechanics, and dealers, across six Nigerian states with materials-science analysis to interpret reported faults and identify sustainable intervention strategies. TVS accounted for 73.0% of the fleet. The most prevalent faults were clutch wear (14.2%), piston damage (13.3%), kick-rod fracture (13.3%), frame corrosion (10.0%), and chassis cracking (7.5%). Three primary degradation mechanisms emerged: fatigue-induced fracture, abrasive wear, and substandard components, with 48.6% of respondents attributing failures to these factors. These constitute a self-perpetuating triad that sustains reactive maintenance practices among 59.5% of operators. Logistic regression identified duration of use (AOR = 1.297 per year; $p < 0.001$) and fairly-used purchase (AOR = 1.887; $p = 0.032$) as significant predictors of piston damage. The study aims to map component failures, prioritise targets for materials intervention, and establish a foundation for developing agricultural residue-reinforced aluminium matrix composites. Published studies demonstrate the potential of such composites to enhance wear resistance and mechanical properties, yet no work has validated their application under Nigerian tricycle operating conditions. By linking field-reported faults to a viable materials solution, this study provides the empirical basis for designing and testing locally sourced, reinforced pistons for the Nigerian tricycle sector.

Keywords: *Agricultural-residues; Failure-analysis; Mechanical-degradation; Nigeria; Piston-failure; Tricycle*

1. INTRODUCTION

The commercial tricycle has emerged as the backbone of intra-urban mobility across Nigeria, filling gaps left by inadequate public transport. Low acquisition cost, fuel economy, and superior manoeuverability have driven rapid adoption. In Kano State alone, there are over 41,000 registered tricycles, which together make about 383,000 trips each day and bring in more than ₦2.1 billion in revenue (Ibrahim, 2025). Their relatively low start-up cost has also made it easier for many people to enter the transport business (Ojekunle, 2009).

Despite their importance, the reliability of these tricycles is often undermined by repeated mechanical breakdowns. They are involved in about 6% of traffic-related injuries (Animasahun *et al*., 2022), and the Federal Road Safety Corps estimates that mechanical failures play a part in nearly 30% of deadly crashes (Ogunleye *et al*., 2024). When a tricycle breaks down, each day off the road means a loss of between ₦3,000 and ₦5,000 in earnings, which puts serious financial pressure on operators (Ameen *et al*., 2025).

Commonly reported faults including clutch slippage, piston seizure, chassis cracking, and crankshaft fracture are usually the result of metal fatigue, corrosion, abrasive wear, and substandard alloy compositions (Kuram *et al*., 2024; Suresh, 1998; Stephens *et a*l., 2000). Fatigue alone is implicated in up to 90% of automotive service failures (Stephens et al., 2000). Metallurgical examination of a failed tricycle front axle revealed carbon content of 0.354 wt%, below specification, with ferrite-pearlite microstructures indicating inadequate heat treatment (Abubakar *et al*., 2025).

The situation is worsened by the poor quality of replacement parts. More than 60% of imported components do not meet safety standards (Okonkwo *et al.*, 2024), and a staggering 95% of imported spare parts are considered substandard (Adebayo *et al*., 2024), all within a spare parts market worth between $5 and $6 billion (Adewale *et al*., 2025).

Earlier work has been limited to single component analyses without examining interrelationships. Aluminium matrix composites reinforced with agricultural residues have emerged as promising low-cost alternatives (Asafa *et al*., 2025; Mogal *et al.*, 2024). Nigeria generates approximately 32 million tonnes of agricultural waste annually (Asafa *et al.*, 2025). Coconut shell ash reinforcement decreased wear loss by 64.7% and raised tensile strength by 45.6% (Ghosh *et al*., 2025). Rice husk ash improved tensile strength to 121.6 MPa at 10 wt% addition (Abolusoro *et al*., 2024).

This study addresses knowledge gaps by integrating a large-scale field survey of 333 stakeholders with materials science analysis of fault patterns. The aim is to map tricycle components failures, identify priority targets for sustainable materials intervention, and lay the foundation for developing agricultural residue reinforced aluminium matrix composites.

2. MATERIALS AND METHODS

2.1 Study Design and Population

A cross-sectional descriptive survey was conducted between October 2025 and April 2026 across Lagos, Oyo, Osun, Ondo, Ogun, and Ekiti states. The target population comprised tricycle riders, mechanics, and dealers. A multi-stage stratified random sampling technique was employed. A total of 333 respondents completed questionnaires: 252 riders (75.7%), 45 dealers (13.5%), and 36 mechanics (10.8%). Sample size was determined using Cochran's formula at 95% confidence level with 5% margin of error.

2.2 Survey Instrument and Data Collection

A structured questionnaire captured socio-demographics, usage history, common faults, spare-parts availability, and maintenance practices. Respondents could report multiple fault types. Face and content validity were established through expert review. Pilot testing on 20 respondents yielded Cronbach's alpha of 0.82. Trained research assistants administered questionnaires through face-to-face interviews.

2.3 Data Processing and Statistical Analysis

Data was coded and verified through double-entry verification. Statistical analyses were performed using IBM SPSS (version 29.0). Descriptive statistics, cross-tabulations, and Pearson chi-square tests were employed, with statistical significance set at $p < 0.05$.

The sample size was determined using Cochran's formula:

$$n_0 = Z^2pq \,/\, e^2 \tag{1}$$

Where:

n_0 is the initial sample size,

Z is the Z-score corresponding to the desired confidence level (1.96 for 95% confidence),

p is the estimated population proportion (assumed 50% as the most conservative estimate),

q is 1-p, and

e is the margin of error (5%).

To account for potential non-response, the sample size was increased by 10%. Degrees of freedom for chi-square tests were derived from contingency table dimensions: duration of use (four categories) against piston damage (two categories), df = 3; brand (three categories) against piston damage (two categories), df = 2; and mode of purchase (two categories) against piston damage (two categories), df = 1.

To examine the simultaneous influence of multiple risk factors on piston damage prevalence while controlling for potential confounding variables, binary logistic regression analysis was performed. The dependent variable was coded as 1 for respondents reporting piston damage and 0 otherwise. Independent variables included tricycle brand (categorical: TVS, Bajaj, Piaggio), duration

of use (continuous, in years), mode of purchase (binary: new compared to fairly used), and respondent type (categorical: rider, mechanic, dealer).

The logistic regression model was specified as:

$$ln\left(\frac{p}{1-p}\right) = \beta_0 + \beta_{1(Brand)} + \beta_{2(Duration)} + \beta_{3(Purchase\ Mode)} + \beta_{4(Respondent\ Type)} \quad (2)$$

Where:

p is the probability of piston damage occurrence.

The model was estimated using maximum likelihood estimation with robust standard errors. Model fit was assessed using the Hosmer-Lemeshow goodness-of-fit test and the Nagelkerke R^2 statistic. The Hosmer-Lemeshow test evaluates whether observed event rates match expected event rates in subgroups of the model population, with a non-significant p-value ($p > 0.05$) indicating good model fit. Nagelkerke R^2 provides an approximation of the proportion of variance explained by the model. Results are reported as adjusted odds ratios (AOR) with 95% confidence intervals and corresponding p-values.

2.4 Ethical Considerations

Informed consent was obtained from each participant. No personal identifiers were collected; data was stored securely and used in aggregated form.

3. RESULTS AND DISCUSSION

3.1 Demographic and Operational Characteristics

Table 1 summarises the demographic and operational characteristics of the sample (N = 333). The majority were male (86.5%) and riders (75.7%), with TVS as the dominant brand (73.0%). Most tricycles were manufactured between 2016 and 2020 (40.5%), used for 1–3 years (43.2%), and purchased new (56.8%). Lagos (24.9%) and Osun (24.0%) contributed the highest proportions.

Table 1: Demographic and Operational Characteristics (N = 333)

Variable	Category	n	%	Variable	Category	n	%
Respondent Type	Dealer	45	13.5	Tricycle Brand	Bajaj	63	18.9
	Mechanic	36	10.8		Piaggio	27	8.1
	Rider	252	75.7		TVS	243	73.0
Gender	Female	45	13.5	Manufacturing Year	2006–2010	72	21.6
	Male	288	86.5		2011–2015	72	21.6
Age (years)	< 20	9	2.7		2016–2020	135	40.5
	20–29	108	32.4		2021–2025	54	16.2
	30–39	99	29.7	*Usage Duration	< 1 year	27	8.1
	40–49	81	24.3		1–3 years	144	43.2
	≥ 50	36	10.8		4–6 years	117	35.1
Experience (years)	< 2	90	27.0		> 6 years	45	13.5
	2–5	135	40.5	Purchase Type	Fairly used	144	43.2
	6–10	81	24.3		New	189	56.8
	> 10	27	8.1				
Location	Ekiti	47	14.1				
	Lagos	83	24.9				
	Ogun	46	13.8				
	Ondo	26	7.8				
	Osun	80	24.0				
	Oyo	51	15.3				

**Year refers to manufacturing year; Duration refers to years in use by current respondent.*

3.2 Common Faults and Priority Target Identification

Total fault mentions (1062) exceed sample size as multiple faults could be reported. Figure 1 shows distribution; Table 2 provides mechanisms. Clutch problems (14.2%), piston damage (13.3%), and kick-rod issues (13.3%) were most frequent. Brake leather issues (10.8%), frame corrosion (10.0%), ring damage (8.3%), and crankshaft issues (8.3%) were also prevalent.

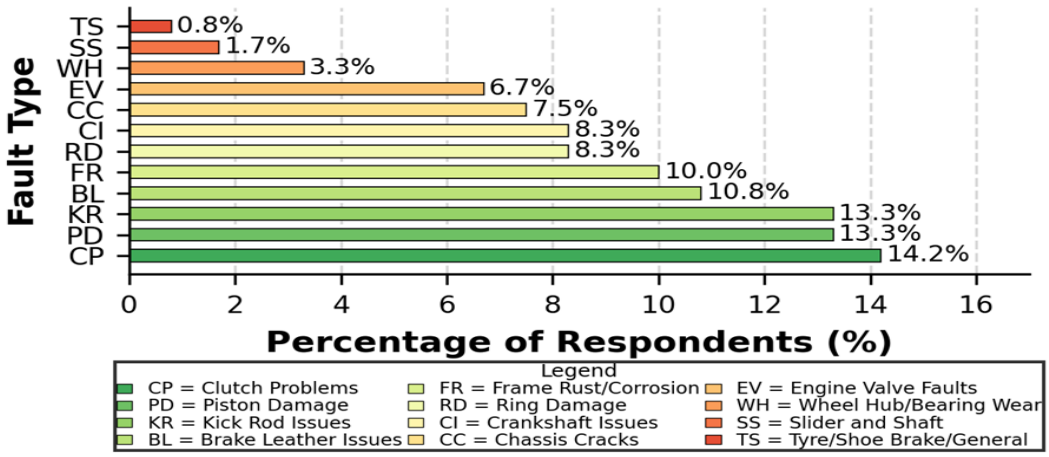

Figure 1: Prevalence of common mechanical faults (CP = Clutch Problems, PD = Piston Damage, KR = Kick Rod, BL = Brake Leather, FR = Frame Rust, RD = Ring Damage, CI = Crankshaft, CC = Chassis Cracks, EV = Engine Valve, WH = Wheel Hub, SS = Slider/Shaft, TS = Tyre/Brake).

Table 2: Frequency of Reported Faults and Associated Material Degradation Mechanisms

Fault Type	Respondent (n)	Frequency (%)	Primary Metallurgical Mechanism(s)
Clutch Problems	153	14.2	Wear of friction material; thermal degradation of organic binders
Piston Damage	144	13.3	Casting defects in Al-Si alloy; inadequate heat treatment; adhesive wear
Manual Kick-Rod Issues	144	13.3	Fatigue fracture at stress concentrators
Brake Leather Issues	117	10.8	Abrasive wear; delamination of friction lining
Frame Rust/Corrosion	108	10.0	Uniform and pitting corrosion of unprotected mild steel
Ring Damage	90	8.3	Poor-quality cast iron; insufficient hard-chrome plating
Crankshaft Issues	90	8.3	Fatigue crack initiation at crankpin fillet; insufficient surface hardness
Chassis Cracks/Breakage	81	7.5	High-cycle fatigue; weld-defect-induced crack propagation
Engine Valve Faults	72	6.7	Adhesive/abrasive wear of valve seat; thermal fatigue
Wheel Hub/Bearing Wear	36	3.3	Rolling-contact fatigue; inadequate lubrication
Slider and Shaft	18	1.7	Fretting wear
Tyre/Shoe Brake/General	9	0.8	Mixed mechanisms
Total	1062	100.0	

3.2.1 Piston Damage as Priority Target

Piston damage (13.3% of fault mentions) represents a priority target. Pistons operate under extreme conditions: 250–350°C, cyclic loading, and sliding contact (Kowalski *et al*., 2024). Failure mechanisms (adhesive wear, fatigue cracking, inadequate heat treatment) are addressable through composites.

Table 3 shows piston failure rates by brand and duration. Chi-square analysis revealed significant association with duration of use ($\chi^2 = 23.56$, df = 3, $p < 0.001$), with 54.2% of tricycles beyond six years reporting damage compared to 8.2% under one year. Brand differences were significant ($\chi^2 = 6.08$, df = 2, $p = 0.048$), with Bajaj highest (15.9%), followed by Paggio (14.3%) and TVS (12.3%). Mode of purchase showed significant association ($\chi^2 = 4.62$, df = 1, $p = 0.032$), with fairly used vehicles at 18.5% against 10.8% for new.

Table 3: Piston Damage Prevalence by Tricycle Characteristics

Variable	Category	Piston Damage Reported (%)	χ^2	df	p-value
Brand	TVS	12.3	6.08	2	.048
	Bajaj	15.9			
	Piaggio	14.3			
Duration of Use	<1 year	8.2	23.56	3	< .001
	1–3 years	11.2			
	4–6 years	16.8			
	>6 years	54.2			
Mode of Purchase	New	10.8	4.62	1	.032
	Fairly Used	18.5			

3.2.2 Multi-Factor Assessment of Piston Damage Risk

Binary logistic regression identified independent predictors of piston damage. As shown in Table 4, the model showed good fit (Hosmer-Lemeshow $\chi^2 = 6.34$, df = 8, p = 0.609) and explained 28.7% of the variance (Nagelkerke $R^2 = 0.287$). Duration of use was the strongest predictor; each additional year increased the odds of damage by 29.7% (AOR = 1.297; 95% CI: 1.178–1.428; $p < 0.001$). Fairly used vehicles had 88.7% higher odds than newer ones (AOR = 1.887; 95% CI: 1.058–3.367; p = 0.032). Vehicle brand and respondent type were not significant. The remaining variance reflects the influence of unmeasured field factors, including load variations, road conditions, and maintenance practices.

Table 4: Logistic Regression Analysis of Factors Associated with Piston Damage

Variable	Category	AOR	95% CI	p-value
Brand	TVS	1.000	—	—
	Bajaj	1.342	0.891–2.021	0.159
	Piaggio	1.218	0.742–1.999	0.436
Duration	Per year	1.297	1.178–1.428	**<0.001**
Purchase	New	1.000	—	—
	Fairly Used	1.887	1.058–3.367	**0.032**
Respondent	Rider	1.000	—	—
	Mechanic	1.124	0.642–1.969	0.684
	Dealer	0.978	0.554–1.727	0.938

AOR = adjusted odds ratio; CI = confidence interval; bold = p < 0.05.

3.3 Failure Initiation Factors and Maintenance Practice

Low-quality materials (48.6%) and poor road conditions (37.8%) account for 86.4% of reported failure factors as presented in Figure 2. Poor maintenance (10.8%) and overloading (2.7%) were secondary. This corroborates the Standards Organisation of Nigeria's report that 95% of imported spare parts are substandard (Adebayo *et al*., 2024).

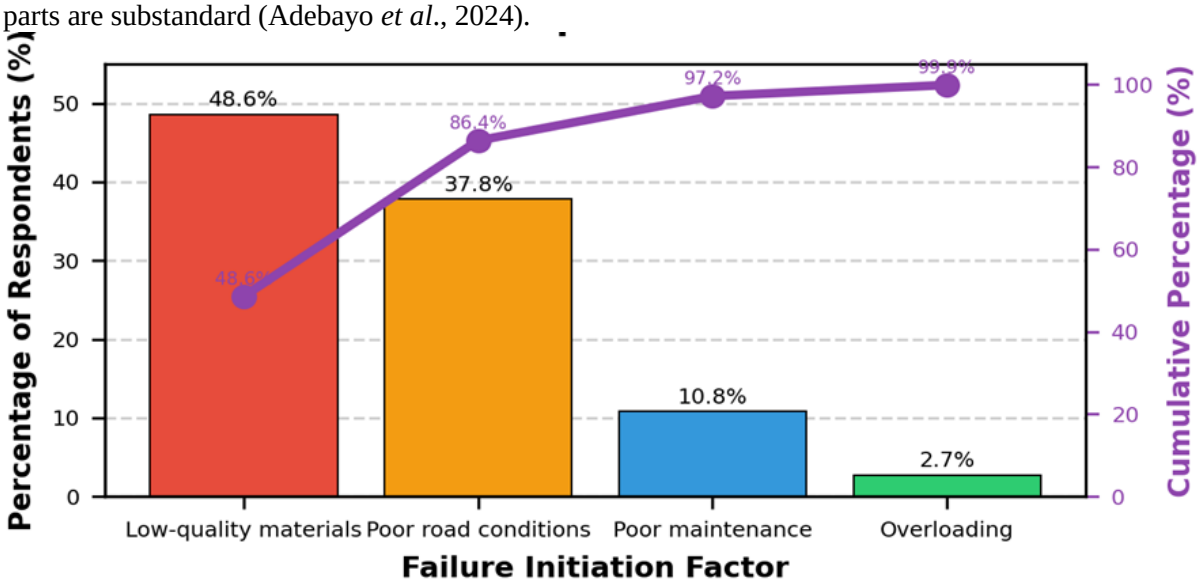

Figure 2: Pareto chart of reported failure initiation factors in commercial tricycles showing Low-quality materials (48.6%) and poor road conditions (37.8%) account for 86.4% of all reported factors, indicating these are the primary drivers of recurrent mechanical failures. Poor maintenance (10.8%) and overloading (2.7%) represent secondary contributing factors. The cumulative percentage line shows the progressive contribution of each factor.

Figure 3 shows maintenance practices. Reactive maintenance predominates (59.5%), with operators repairing only after failure. Scheduled maintenance at 3–6 months (16.2%), monthly (13.5%), weekly (8.1%), and annual (2.7%) were less common.

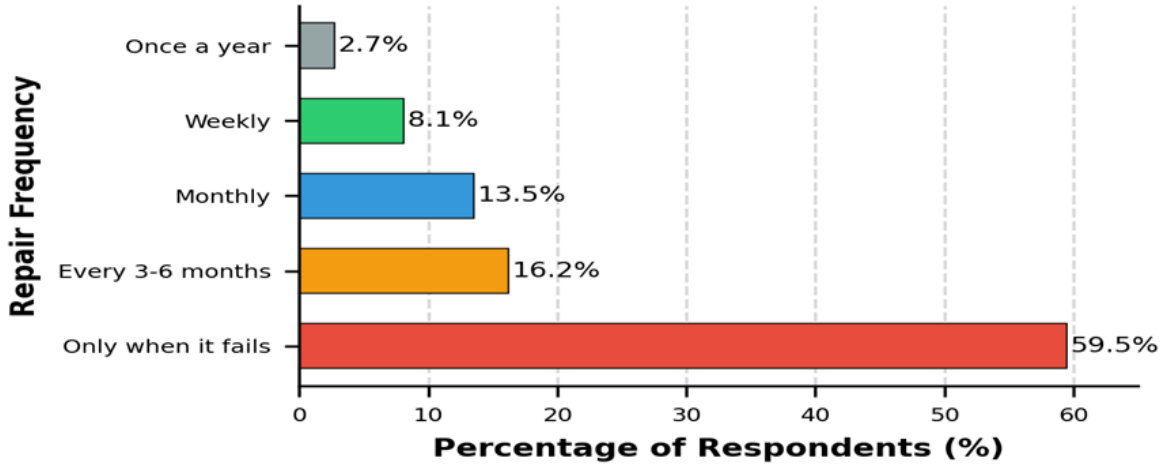

Figure 3: Maintenance practices among commercial tricycle operators (N = 333). The majority (59.5%) adopt a reactive approach, repairing components only after failure. Scheduled preventive maintenance is practiced by 40.5% of operators, with intervals ranging from weekly (8.1%) to annual (2.7%). Data collected through structured questionnaire from 333 respondents across six Nigerian states

3.4 Spare-Parts Availability, Quality Perception and Ease of Maintenance

Table 5 shows spare-parts availability by brand. TVS had best availability (67.6% available, 8.1% not available). Bajaj had 70.3% available, 10.8% not available. Piaggio had the poorest availability (45.9% available, 32.4% not available).

Table 5: Spare-Parts Availability by Brand

Brand	Available (%)	Expensive but Available (%)	Not Available (%)
Bajaj	70.3	18.9	10.8
Piaggio	45.9	21.6	32.4
TVS	67.6	24.3	8.1

TVS parts were unavailable 8.1% of the time, a considerably smaller gap than the 32.4% recorded for Piaggio, yet this still poses a risk of substandard parts entering the supply chain. When genuine parts are scarce, operators often turn to inferior alternatives, a pattern well documented in Nigerian aftermarket studies (Okonkwo *et al*., 2024). Perceptions of maintainability mirrored these availability trends: 73.0% of respondents rated TVS as the easiest brand to maintain, versus 16.2% for Bajaj, whereas only 10.8% found Piaggio easy to maintain. Furthermore, 59.5% of respondents believed that material quality substantially affects tricycle performance and lifespan.

3.5 Theoretical Framework: The Failure Triad

Findings establish fatigue, wear, and substandard components as a self-perpetuating triad as illustrated in Figure 4. Fatigue reduces strength and accelerates wear; wear generates debris and stress concentrations promoting fatigue; economic pressure drives substandard replacement (Stephens *et al*., 2000; Suresh, 1998). Reactive maintenance ensures replacement after failure, often with substandard parts, completing the cycle. Logistic regression as shown in Table 5 quantified this: each year increases odds by approximately 30%; fairly-used purchase elevates odds by 89%.

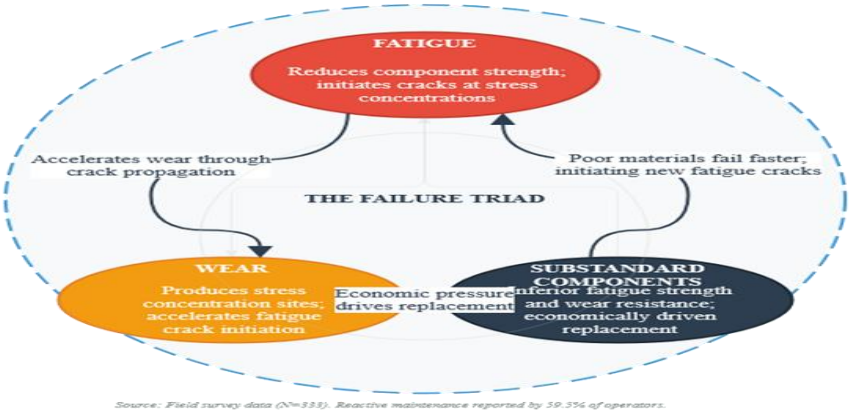

Figure 4: Schematic representation of the self-perpetuating failure triad in commercial tricycles. Fatigue reduces strength; wear produces stress concentration; economic pressure drives substandard replacement.

3.6 Agricultural Residue-Reinforced Aluminium Composites as a Sustainable Materials Strategy

Agricultural residue–reinforced aluminium matrix composites mitigate abrasive wear, fatigue fracture, and substandard materials (Sanusi and Adebisi, 2026). Palm kernel shell powder (15 wt%) in Al-Mg-Si reduces wear (Mohammed *et al*., 2022); rice husk ash raises fatigue endurance from 0.224×10^6 to 2.582×10^6 cycles (Asafa *et al*., 2014). Coconut shell ash (45.1% SiO_2, 15.5% Al_2O_3, 12.4% Fe_2O_3) lowers wear loss 64.7%, reduces friction coefficient from 0.34 to 0.22, increases tensile strength by 45.6% from 98 MPa to 143 MPa, and improves Microhardness by 22.5% from 31.5 HV to 38.6 HV (Ghosh et al., 2025). Rice husk ash (10 wt %) gives 121.6 MPa and 74.5 HBW (Aboloruso *et al.*, 2024); with granite dust, wear drops 56.25% (Mogal et al., 2024). Challenges include poor bonding, addressed by 2–5% Mg for wettability, and agglomeration, mitigated by double stir casting; optimal reinforcement is 5–10 wt% (Asafa *et al.*, 2025; Ge et al., 2025; Olorunfemi *et al*., 2021). These renewable residues enable 95% energy savings in secondary Al production and 15–25% cost reduction over SiC

composites, offering a sustainable pathway to enhanced durability and reliability (Ge *et al.*, 2025; Sanusi and Adebisi, 2026).

4. CONCLUSION

This investigation identifies clutch wear (14.2%), piston damage (13.3%), kick-rod fracture (13.3%), frame corrosion (10.0%), and chassis cracking (7.5%) as the most prevalent faults, originating from fatigue, abrasive wear, and substandard components (48.6%). Logistic regression confirmed duration of use (AOR = 1.297/year; $p < 0.001$) and fairly-used purchase (AOR = 1.887; $p = 0.032$) as significant piston-damage predictors, while reactive maintenance (59.5%) perpetuates the failure cycle. Piston damage is prioritised for materials intervention, with coconut shell ash composites offering 64.7% wear reduction, 45.6% tensile strength improvement, and 22.5% hardness enhancement. Future research should experimentally validate these composites through XRF characterisation, ASTM-standard mechanical testing, and accelerated wear simulation, while policymakers enforce stricter quality standards and manufacturers invest in double-stir casting with 5–10 wt% agricultural residue reinforcement.

REFERENCES

Abolusoro, A. O., Adebisi, J. A., and Olorunfemi, B. J. (2024). Mechanical properties of rice husk ash reinforced aluminium matrix composites. Nigerian Journal of Materials Science and Engineering, 15(2), 78-92.

Abubakar, M., Tijjani, Y., Saminu, J., Sani Kabir, A., Udele Eneojo, E., and Isah, J. (2025). Metallurgical failure analysis of a tricycle front wheel axle. Journal of Engineering & Technological Advances, 9(2), 19-29.

Adebayo, T. O., Ogunleye, O. A., and Adewale, B. A. (2024). Quality assurance challenges in Nigeria's automotive spare parts importation. Nigerian Journal of Engineering Materials, 15(3), 112-125.

Adewale, A. O., Oluwaseun, K. O., and Bamgboye, O. A. (2025). The economics of substandard automotive components in Nigeria's aftermarket. Journal of Transport Economics and Policy, 59(2), 78-92.

Ameen, H. A., Kayode, F. M., Bello, M. B., Yusuf, K. O., Alatishe-Muhammad, B. W., and Tijani, A. O. (2025). Risk factors and patterns of road traffic accidents among commercial tricycle operators. Zagazig University Medical Journal, 31(3), 1318-1333.

Animasahun, L. A., Rabiu, T., Adigun, I., and Keshinro, K. (2022). Development and prototyping of automotive tricycle brake wear rig. International Journal of Sciences, Engineering & Environmental Technology, 7(15), 140-147.

Asafa, T. B., Amuda, B. A., Durowoju, M. O., Osunmakinde, L., and Abdubasit, A. O. (2025). Physico-mechanical properties, tribological behaviour and metallurgical characteristics of aluminium MMCs reinforced with agricultural residues: A review. LAUTECH Journal of Engineering and Technology, 19(5), 21-55.

Ge, Y.-J., Liu, Y.-H., and Shen, P. (2025). Wetting behavior and interfacial structure of multicomponent aluminum alloys on boron carbide. Journal of Alloys and Compounds, 1037, 182222.

Ghosh, S., Kumar, A., and Singh, R. (2025). Wear and mechanical properties of coconut shell ash reinforced aluminium matrix composites. Journal of Composite Materials, 59(3), 312-328.

Ibrahim, S. U. (2025). Tricycle transport and urban mobility in Kano State, Nigeria. Nigerian Journal of Transport Studies, 12(4), 89-104.

Kuram, E., Seren, O., and Güzey, G. (2024). Development and performance analysis of commercial vehicle axle shafts. International Journal of Automotive Science and Technology, 8(2), 232-241.

Mogal, S., Patil, R., and Desai, S. (2024). Coconut shell ash and granite dust reinforced aluminium composites. Materials Today: Proceedings, 72, 145-152.

Ogunleye, O. A., Adebayo, T. O., and Adewale, B. A. (2024). Mechanical failures and road traffic accidents in Nigeria. Nigerian Journal of Transport, 11(2), 67-82.

Ojekunle, J. A. (2009). An appraisal of commercial operation of tricycles in urban centres: A case study of Kano, Nigeria. Journal of Agriculture and Social Research, 9(1).

Okonkwo, C. I., Okafor, E. N., and Nwosu, C. O. (2024). Safety standards compliance of automotive components in Nigerian informal markets. Nigerian Journal of Transport Safety, 7(2), 45-58.

Olorunfemi, B. J., Adebisi, J. A., and Abolusoro, A. O. (2021). Characterisation of palm kernel shell ash for aluminium matrix composite reinforcement. Nigerian Journal of Materials Science and Engineering, 12(2), 45-56.

Sanusi, S. K., and Adebisi, J. A. (2026). An overview of development and characterisation of agricultural residue-based hybrid metal matrix nanocomposites. Proceedings of FETiCON 2026, 4(1).

Stephens, R. I., Fatemi, A., Stephens, R. R., and Fuchs, H. O. (2000). Metal fatigue in engineering (2nd Ed.). John Wiley & Sons.

Suresh, S. (1998). Fatigue of materials (2nd Ed.). Cambridge University Press.

MASS AND ENERGY ASSESSMENT OF THE PYROLYSIS OF LOW LIPID MICROALGAE (DUNALIELLA SALINA)

Yashim Afuwai[1], Auwal Aliyu[1,*]
[1]*Ahmadu Bello University, Zaria*
Email: afushim@gmail.com, auwala@abu.edu.ng*
***Corresponding author**: Auwal Aliyu
DOI: https://doi.org/10.67203/sp.ICESID.2026

ABSTRACT

This study is a computational mass and energy assessment based on secondary literature data obtained from (Xun et al., 2014). As a sustainable and renewable source of energy, microalgae derived biofuel has a growing potential to solve the problem of global energy crisis as a result of higher demand for energy, as well as environmental impact such as global warming associated with fossil fuel. Mass and energy assessment of the pyrolysis of low lipid microalgae Dunaliella salina was carried out to produce 1kg of bio-oil. A fixed bed tubular reactor was used to carry out direct pyrolysis on the microalgae biomass at $300 - 700℃$. *Mass and energy assessment was done to estimate the products yield, mass ratio, energy ratio, energy efficiency, higher heating value (HHV) and energy consumption ratio (ECR) of the biofuel. The maximum yield of bio-oil, bio-char and biogas at* $500℃$ *were 64.9%, 28.0% and 3.9% respectively. The maximum mass ratio and energy ratio of the bio-oil were 0.649 and 77.98%. The higher heating value (HHV) and energy efficiency of the bio-oil at* $500℃$ *were obtained as 25.47MJ/kg and 74.50%. The maximum energy consumption ratio (ECR) of the pyrolysis process at* $500℃$ *was 0.043. The ECR is less than 1, which shows that the pyrolysis process was favourable since it exhibits net energy products with higher energy content than that required for the reaction to occur. The results obtained from mass and energy balances show that pyrolysis temperature has a great influence on the distribution yield and energy efficiency of the products. The production of 1kg of bio-oil from the algae biomass feedstock was obtained via pyrolysis of low lipid microalgae.*

TABLE OF CONTENTS

Abstract ..... *Error! Bookmark not defined.*
1 Introduction ***1364***
2Materials and Methods ***1364***
3Result and Discussion ***1367***
4 Conclusions ***1373***
5 References ***1373***

1 INTRODUCTION

The use of sustainable energy sources and renewable energy sources is highly pertinent in Nigeria due to the fact that the country's energy sector still focuses largely on conventional fossil fuel sources of energy despite its great potential to generate renewable energy. By diversifying energy sources by the use of biofuel and other forms of renewable sources of energy, the issue of energy sustainability could be addressed along with minimizing the reliance on traditional sources of energy generated from petroleum sources. The biomass resource that can be used is that of microalgae since it can be processed to form energy products using processes like pyrolysis. Thus, conversion of microalgae biomass to bio-oil would help the country use resources in an innovative way.

The current study is thus in line with the International Conference on Engineering Innovation for Sustainable Development (ICESID) 2026 theme "Innovating Tomorrow: Leveraging Engineering for the Sustainable Development of Nigeria," especially through the themes of Innovative Resource Utilization and Sustainable Engineering Processes. Evaluation of the microalgae pyrolysis and bio-oil generation processes offers a basis for demonstrating the use of engineering analysis to assess the other possible routes for renewable biomass transformation into energy products. The study results can offer an insight into the evaluation of the technical and energy aspects of microalgae utilization and may form part of future research studies on renewable biomass utilization in Nigeria.

Energy is an essential component of human existence. Every sector, including industry, agriculture, healthcare, transportation, and domestic activities, relies on the use of energy (Mckendry, 2002). The increasing global demand for energy, along with the environmental consequences such as global warming linked to fossil fuels and their diminishing availability, has prompted the exploration of alternative energy sources from various biomass feedstock (Christi, 2012). The combustion of fossil fuels emits vast quantities of carbon dioxide, which is considered a primary contributor to global warming (International Energy Agency, 2015). Unlike the greenhouse gas emissions resulting from fossil fuel combustion, biomass represents a valuable feedstock for generating biofuels and other important chemicals. Renewable biomass feedstock comprises aquatic biomass, terrestrial biomass, municipal waste, agricultural solid waste, forest residue, and industrial waste (Jay, 2010).

Recent advancements in biotechnology have prompted researchers to investigate microalgae as a promising feedstock for sustainable biofuel production. Microalgae comprise a diverse group of aquatic, photosynthetic microorganisms, typically unicellular or multicellular, and are classified as third-generation biofuels (Veillette, 2012). Through the process of photosynthesis, algae and seaweed use sunlight to absorb carbon dioxide from the atmosphere and release oxygen (Kumar et al., 2016). Despite making up only 0.5% of all plant biomass, algae create roughly 60–75% of the oxygen required by people and animals, and every pound of algae biomass reduces carbon dioxide by 1.8 pounds (Wolkers et al., 2011). High photosynthetic efficiency, increased oil production productivity, and a high capacity to store significant amounts of lipids are characteristics of microalgae. The aforementioned qualities make microalgae one of the most exceptional sources of biofuel (Mohammad et al., 2015).

The evaluation of mass and energy regarding microalgae biofuel indicates that the cultivation, harvesting, drying, and processing of microalgae biomass can yield an environmentally sustainable feedstock for biofuel generation (Yanfen et al., 2012). Using a low lipid microalgae (Dunaliella salina) as feedstock for pyrolysis is a reasonable alternative because of the low cost and high oil yield. Dunaliella salina is a type of green microalgae mostly found in sea salt fields (Chen et al., 2012). The low lipid content strains of microalgae result in its cost lower with faster growth rates (Aresta et al., 2005). In this study, direct pyrolysis pathway is used to evaluate the mass and energy assessment of pyrolysis of low lipid microalgae (Dunaliella salina) at different temperatures from 300-700ºC (Xun et al., 2014).

2 MATERIALS AND METHODS

2.1 Description of Pathways for Biofuel from Microalgae Pyrolysis

This study is a computational mass and energy assessment based on secondary literature data obtained from (Xun et al., 2014). This research examines the direct pyrolytic processes for producing bio-oil from microalgae (Dunaliella salina) at temperatures ranging from 300 to 700°C. Direct pyrolysis

deals with the method of pyrolysing the entire microalgae, resulting in bio-oil that predominantly consists of long-chain hydrocarbons including various terminal groups. This study examined the direct pyrolysis pathway by closely examining the mass ratio, energy ratio, energy efficiency, and energy consumption ratio (ECR). GC-MS (Agilent 7890A-5975C workstation software) was used to examine and identify bio-crude composition and the chemical constituents through the direct pyrolysis process. The area percentage approach was used to quantitatively analyse the composition of pyrolysis oil (Tang et al., 2015). The higher heating value of the bio-oil was calculated by equation (2.1) below: (Ferdinand et al., 2012).

$$HHV(kJ/kg) = 35098C + 116050H + 6267N - 11073O \qquad \text{Equation 2.1}$$

Where: C, H, N, O are the fractions of the elements of carbon, hydrogen, nitrogen and oxygen in the compound respectively which can be obtained from the ultimate analysis for bio-char and bio-oil as shown in table (2.1) and (2.2) below.

Table 2.1: Ultimate Analysis (wt %) and HHV of Dunaliella salina (Bio-char) (Xun et al., 2014).

Temperature (°C)	**C**	**H**	**N**	**S**	**O**	**HHV (MJ/kg)**
300	57.9	4.7	10.7	0.6	11.3	25.4
400	57.2	3.8	9.8	0.5	6.3	24.1
500	55.2	2.9	9.0	0.3	3.7	21.8
600	54.7	2.2	8.2	0.2	2.2	20.6
700	54.0	2.0	7.4	0.2	1.7	19.6

Table 2.2: Ultimate Analysis (wt %) and HHV of Dunaliella salina (Bio-oil) (Xun et al., 2014).

Temperature (°C)	**C**	**H**	**N**	**S**	**O**	**HHV (MJ/kg)**
300	32.0	9.0	8.1	0.4	50.6	16.6
400	45.8	8.7	8.3	0.2	37.0	22.6
500	53.0	8.3	8.6	0.3	29.8	25.5
600	55.6	8.2	9.4	0.2	26.5	26.6
700	56.3	7.8	10.8	0.2	24.8	26.7

2.2 Mass and Energy Assessment

A fixed bed tubular reactor operating at 300–700°C was used to carry out the pyrolysis experiment as seen in (Xun et al., 2014). The mass balance efficiency was evaluated using the maximum bio-oil yield. The yields of the pyrolysis products were used to calculate the mass balance. The equations utilized in the mass and energy assessment are displayed in equations (2.2) to (2.5) (Yang et al., 2014).

Equation (2.2) defines mass ratio as seen below:

$$\eta_m = \frac{m_{fuel}}{m_{biomass}} \qquad \text{Equation 2.2}$$

Where: η_m = Mass ratio m_{fuel} = Mass of liquid fuel (kg) $m_{biomass}$ = Mass of biomass (kg)

The energy ratio is defined as:

$$\eta_{ef} = \frac{m_{fuel} \times HHV_{fuel}}{m_{biomass} \times HHV_{biomass}}$$ Equation 2.3

Where: η_{ef} = Energy ratio HHV_{fuel} = Higher heating value of fuel (MJ/kg)
$HHV_{biomass}$ = Higher heating value of biomass (MJ/kg)

Energy efficiency is determined using equation (2.4) below. It evaluates all of the energy inputs needed for the conversion process as well as the energy contained in the original feedstock and the desired fuel.

$$\eta_{ef}^{1} = \frac{m_{fuel} \times HHV_{fuel}}{m_{biomass} \times HHV_{biomass} + Q_{input}}$$ Equation 2.3

Where: η_{ef}^{1} = Energy efficiency Q_{input} = Net process energy

Each process's energy balance can be evaluated using the energy consumption ratio (ECR). The energy needed to heat the microalgae cells to reaction temperature is divided by the energy of the oil, gas, and char that are produced to determine the ECR (Chaiwong et al., 2013). Since the product has more energy than what is needed for the reaction, the reaction is energy favorable if ECR < 1. However, if ECR > 1, the total energy used to make the bio-oil exceeds the energy in the fuel. The energy consumption ratio (ECR), of the pyrolysis process is expressed as seen in equation (2.5) below:

$$ECR = \frac{Q}{H_{oil}Y_{oil} + H_{char}Y_{char} + H_{gas}Y_{gas}}$$ Equation 2.4

Where: H_{oil} , H_{gas} and H_{char} = HHVs of the bio-oil, bio-gas and bio-char
Y_{oil} , Y_{gas} and Y_{char} = Yield of the bio-oil, bio-gas and bio-char

2.3 Pyrolysis Process

It was estimated that 1 kg of bio-oil (wet basis) would be produced by direct pyrolysis at 300, 400, 500, 600, and 700°C. The pyrolysis distribution yield of products for Dunaliella salina is displayed in Table 2.3.

Table 2.3: Pyrolysis Distribution Yield of Products (Biofuel) (Xun et al., 2014)

Temperature	**Bio-gas**	**Bio-oil**	**Bio-char**	**Undetected**
(°C)	**(% mass)**	**(% mass)**	**(% mass)**	**(% mass)**
300	0.4	32.3	57.7	9.5
400	2.7	53.5	34.0	9.7
500	3.9	64.9	28.0	3.2
600	8.0	59.9	24.2	7.9
700	15.5	52.6	22.1	9.8

According to (Xun et al., 2014), a fixed-bed tubular reactor was used for the pyrolysis experiment. For this investigation, 1g (0.001kg) of each microalgae sample was utilized. 20 minutes (1200 seconds) was determined to be the residence time needed to finish the pyrolysis process. At 500°C, the maximum output of bio-oil (wet basis) for Dunaliella salina was 64.9%. The elemental compositions of table (2.2) were used to estimate the HHVs of the bio-oil using (Ferdinand et al., 2012) method of equation (2.1). The direct pyrolysis route flow chart, which includes bio-oil, bio-char, and biogas, is depicted in Figure (2.1).

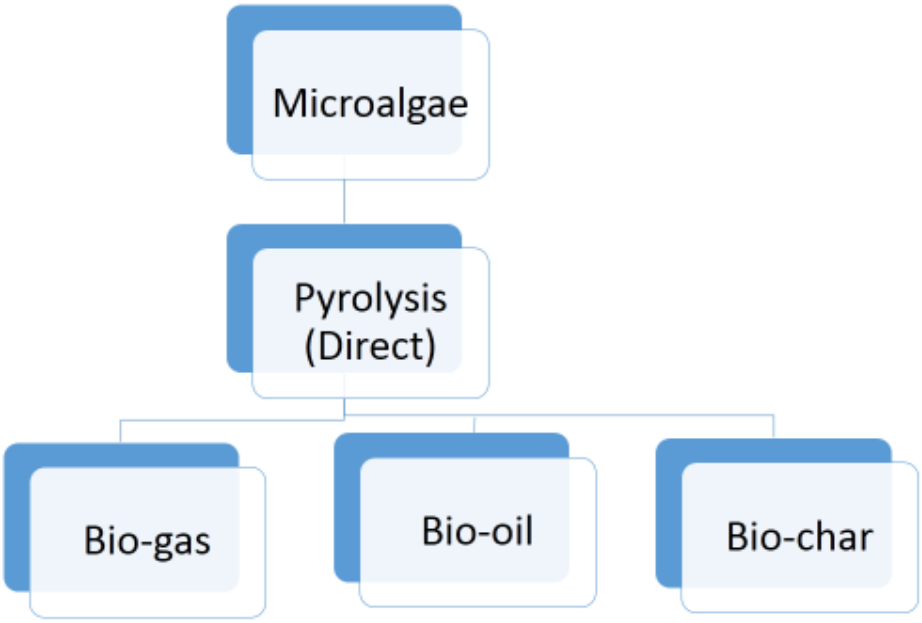

Figure 2.1: Flow chart of direct pyrolysis pathway for biofuel production

3 RESULT AND DISCUSSION

In this evaluation study, low-lipid microalgae (Dunaliella salina) were directly pyrolysed to produce 1 kg of bio-oil from algae biomass feedstock.

3.1 Pyrolysis Distribution Yield of Products (Biofuel)

The product yield distribution of D. salina via the direct pyrolysis pathway at 300–700°C is displayed in Figure 3.1. The data for the pyrolysis distribution yield of products (biofuel) in table 2.3 are used to produce Figure 3.1.

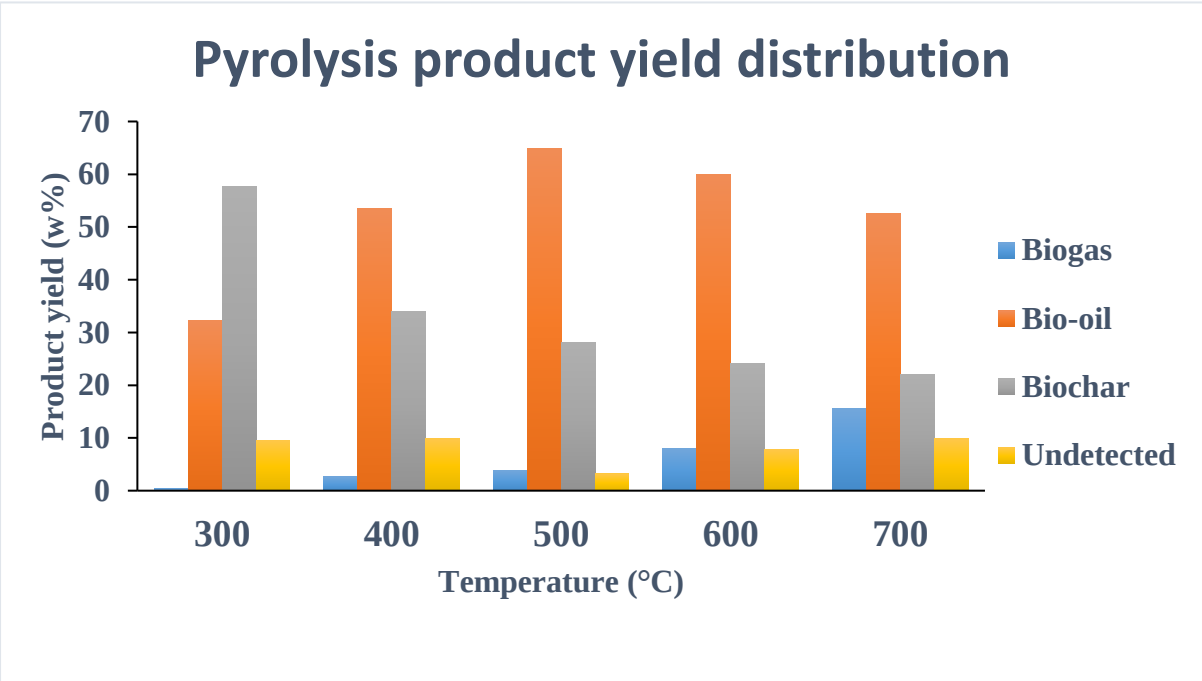

Figure 3.1: Pyrolysis product yield distribution

Figure 3.1 shows a graphical representation of the product yield distribution of Dunaliella salina, with a significant percentage of undetected biogas, bio-oil, and bio-char. Over the course of the

analysis, the percentage of undetected cases was less than 10%. Figure 3.1 shows that at 500°C, the maximum yield of bio-oil estimated in the assessment was 64.9%. The biogas yield rose from 0.4 to 15.5% while the bio-char yield fell from 57.7 to 22.1% as the temperature ranged from 300−700°C. The yield of bio-oil increased between $300 - 500℃$, reaching over 60% at the microalgae's reactor temperature of 500°C. The yields of bio-oil, bio-char, and biogas from the pyrolysis of Chlorella vulgaris and Dunaliella salina at different temperatures between $300 - 500℃$, were assessed by (Xun et al., 2014), who reported bio-oil yields of 49.2%wt for Chlorella vulgaris and 55.4%wt for Dunaliella salina at both 500°C. The bio-oil yield estimated in the present computational assessment was 64.9 wt%, compared with 55.4 wt.% reported by (Xun et al., 2014) for D. salina at 500 °C. The difference of 9.5% is associated with differences in the calculation procedure, process assumptions, product definition, or operating conditions." Additionally, at 600°C, Nannochloropsis microalgae produced a 60%wt bio-oil yield (Tang et al., 2015). The results shows that pyrolysis temperature has a significant effect on the distribution yield of products.

3.2 Mass and Energy Assessment

Table 3.1 and 3.2 shows the mass and energy assessment parameters for direct pyrolysis route in the production of 1kg of bio-oil from Dunaliella salina. The mass and energy assessment parameters include mass balance, mass ratio (η_m), energy ratio (η_{ef}), higher heating value (HHV), energy efficiency (η_{ef}^1) and energy consumption ratio (ECR) of the pyrolysis at $300 - 700℃$. At 500°C, the bio-oil's maximum mass ratio and energy ratio were 0.649 and 77.98% respectively. As the temperature rises from 300°C to 500°C, the bio-oil's mass ratio and energy ratio vary from 0.323 to 0.649 and 25.26 to 77.98% respectively. As the temperature rises from 300 to 500°C, the mass and energy ratios of biogas and bio-char are inversely correlated. At 300–500°C, the bio-oil's higher heating value (HHV) and energy efficiency rise from 16.58 to 25.47 MJ/kg and 24.10 to 74.50% respectively. The higher heating value of the bio-oil exceeds the higher heating value of the algal biomass at 500°C. A high heating value is achieved by increasing the temperature for thermal decomposition of the microalgae. The maximum energy consumption ratio (ECR) of the pyrolysis process at $500℃$ was 0.043 (4.3%). The ECR is less than 1, which shows that the pyrolysis process is favourable since it exhibits net energy products with high energy content than that required for the reaction.

Table 3.1: Mass assessment for direct pyrolysis pathway of Dunaliella salina

Temp	**m_{biogas}**	**$m_{bio-oil}$**	**$m_{biochar}$**	**$m_{undetect}$**	**$m_{biomass}$**	**Biogas**	**Bio-oil**	**Biochar**
(°C)	**(kg)**	**(kg)**	**(kg)**	**(kg)**	**(kg)**	**(η_m)**	**(η_m)**	**(η_m)**
300	0.012	1.000	1.786	0.297	3.095	0.004	0.323	0.577
400	0.050	1.000	0.636	0.183	1.869	0.027	0.535	0.340
500	0.060	1.000	0.431	0.049	1.540	0.039	0.649	0.280
600	0.134	1.000	0.404	0.132	1.670	0.080	0.599	0.242
700	0.295	1.000	0.420	0.186	1.901	0.155	0.526	0.221

Table 3.2: Energy assessment for direct pyrolysis pathway of Dunaliella salina

Temp	**$HHV_{B/gas}$**	**$HHV_{B/oil}$**	**$HHV_{B/char}$**	**$HHV_{B/mass}$**	**η_{ef} B/gas**	**η_{ef} B/oil**	**η_{ef} B/char**	**η^1_{ef} B/gas**	**η^1_{ef} B/oil**	**η^1_{ef} B/char**	**Q_{inp}**	**ECR**
(℃)	MJ/kg	MJ/kg	MJ/kg	MJ/kg	%	%	%	%	%	%	MJ	%
300	35.90	16.58	25.40	21.20	0.68	25.26	69.13	0.60	24.10	65.90	3.12	5.0
400	17.10	22.59	24.10	21.20	2.18	57.02	38.65	2.10	54.40	36.90	1.86	4.8
500	20.60	25.47	21.80	21.20	3.79	77.98	28.79	3.60	74.50	27.50	1.55	4.3
600	19.20	26.68	20.6	21.20	7.25	75.39	23.51	6.90	72.00	22.50	1.65	4.4
700	21.30	26.74	19.6	21.20	15.57	66.35	20.43	14.90	63.40	19.50	1.90	4.6

3.3 Elemental Mass Balance for the Production of 1kg of bio-oil

Table 3.3 shows the elemental balance for the production of 1kg of bio-oil via direct pyrolysis from the microalgae biomass. The HHV of bio-oil increases with decrease in H/C and O/C ratio. The atomic hydrogen/carbon and oxygen/carbon of the bio-oil were determined as shown in table 3.3 The H/C and O/C ratios decreases from 0.28 to 0.12 and from 1.59 to 0.44 as temperature increases from $300 - 700℃$ respectively.

Table 3.3: Elemental mass balance for the production of 1kg of bio-oil via direct pyrolysis of Dunaliella salina

Temp (℃)	**Ash**	**C**	**H**	**N**	**O**	**S**	**$m_{bio\ mass}$ (kg)**	**C**	**H**	**N**	**O**	**S**	**H/C**	**O/C**	**$m_{bio\ oil}$ (kg)**
300	0.22	1.49	0.22	0.29	0.72	0.03	3.09	0.32	0.09	0.08	0.51	0.004	0.28	1.59	1.0
400	0.13	0.90	0.13	0.18	0.44	0.02	1.86	0.46	0.08	0.08	0.37	0.002	0.17	0.80	1.0
500	0.11	0.74	0.11	0.14	0.36	0.01	1.54	0.53	0.08	0.09	0.30	0.003	0.15	0.56	1.0
600	0.12	0.80	0.12	0.16	0.39	0.02	1.67	0.55	0.08	0.09	0.27	0.002	0.14	0.49	1.0
700	0.14	0.91	0.13	0.18	0.44	0.02	1.90	0.56	0.07	0.11	0.25	0.002	0.12	0.44	1.0

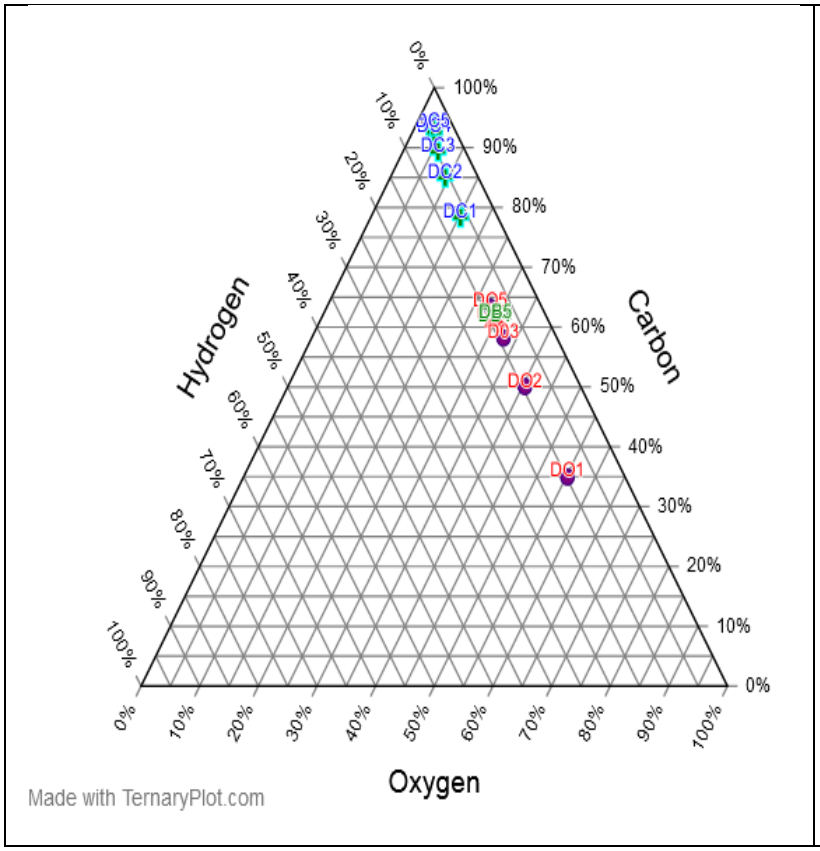
Hydrogen
Carbon
Oxygen
DC5
DC3
DC2
DC1
DB5
DB3
DB2
DB1
Made with TernaryPlot.com

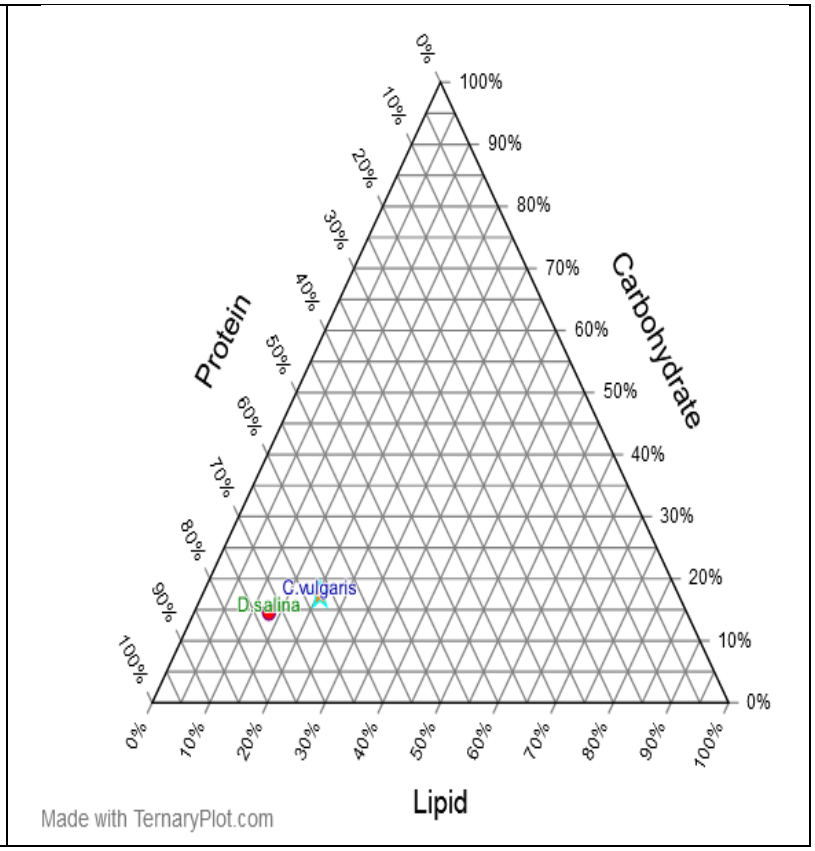
Protein
Carbohydrate
Lipid
C.vulgaris
D.salina
Made with TernaryPlot.com

a) Migration of carbon, hydrogen and oxygen composition of microalgae b) Carbohydrate, protein and lipid distribution

Figure 3.2: Ternary plot diagram

Keys for items in figure 3.2a

DO- Dunaliella salina bio-oil	1- Via pyrolysis at 300°C
DB- Dunaliella salina biomass	2- Via pyrolysis at 400°C
DC- Dunaliella salina bio-char	3- Via pyrolysis at 500°C
	4- Via pyrolysis at 600°C
	5- Via pyrolysis at 700°C

3.4 Ternary Plot Diagram

The ternary diagram was used to signify the microalgae pyrolysis process at $300 - 700°C$, relative percentage of oxygen, hydrogen and carbon whose summation is 100% or a ratio of 1. It also compares the relative ratio of carbohydrate, protein and lipid composition. The Ternary plots in figure 3.2 below were created at www.Ternaryplot.com. The carbohydrate, protein and lipid composition of Dunaliella salina and Chlorella vulgaris in figure 3.2b were adapted from (Xun et al., 2014). Table 3.1 for ultimate analysis of bio-char and table 3.3 for elemental balance of bio-oil and biomass were used to create the ternary plot in figure 3.2.

Figure 3.2a shows the ternary distribution of hydrogen, carbon, and oxygen for the products obtained at different operating temperatures. The positions of the points show the relative elemental composition of the resulting products; those located near the upper vertex have a higher relative carbon content, and shifts towards the lower-left and lower-right areas indicate increasing relative amounts of hydrogen and oxygen respectively. Hence, the way the points move across the ternary diagram provides useful evidence of the changes in elemental composition resulting from thermal conversion.

The DC points (DC1 to DC5) are mostly situated in the area dominated by carbon on the ternary diagram. This suggests that the DC products contain a higher proportion of carbon together with relatively smaller amounts of hydrogen and oxygen. As the DC points shift gradually towards the carbon-rich region, this shows that the degree of carbon richness increases with more intensive conversion conditions. This trend is consistent with the formation of carbon-rich bio-char through the stepwise thermal decomposition of the original biomass and the removal of the volatile compounds which contain hydrogen and oxygen. On the ternary diagram, the DO points show a clear trend. DO1 is located further away from the apex which is rich in carbon, whereas DO2 through DO5 are found at successively greater distances from this carbon-rich region. This indicates that the composition of the product alters as the temperature rises. The shift towards the carbon-rich area means that the carbon concentration increases together with a reduction in the amounts of hydrogen and oxygen relative to the other components. These kinds of changes are typical of the continuous deoxygenation and dehydrogenation processes that take place during thermal conversion.

The DB points are abundant in the ternary diagram's intermediate region, especially in the vicinity of the compositions that the higher-temperature DO products represent. The elemental composition between the very carbon-rich DC products and the less carbon-rich DO products is indicated by their placements. The DB points' comparatively tight distribution indicates that, under the conditions under investigation, the elemental composition of these products changes less than that of the DC products. The effect of temperature on the elemental composition of the products is demonstrated by the overall migration of the points toward the carbon-rich region with increasing temperature. As the temperature rises, more carbon-rich products are formed and molecules containing hydrogen and oxygen are broken down. As a result, the ternary distribution presents a graphic portrayal of how the starting biomass gradually converts into products with a bigger relative carbon content.

Figure 3.2b was used to show the comparison in biochemical composition between D. salina and C. vulgaris. In order to explain more about the biochemical composition of the two microalgal bio-feedstocks, the use of the ternary diagram came in handy, when comparisons were made between D. salina and C. vulgaris. Both strains lie within the lipid-rich part of the ternary diagram, although not at the exact same point. While D. salina lies relatively closer to the lipid-rich part, this indicates that D.

salina has higher amounts of lipids. The variation in the placement of the two raw materials is an indication that there is some variation in the biochemical composition of both and this may affect their behaviours during thermal conversion processes. This variation is crucial in analysing the pyrolysis products since there are different thermal decomposition pathways for lipids, proteins, and carbohydrates which may lead to the formation of different levels of bio-oil, bio-char, and gas. Therefore, the initial biochemical composition of the microalgae is useful in explaining the variations in the elemental composition of the resulting products.

4 CONCLUSIONS

Based on the mass and energy assessment carried out from the pyrolysis of low lipid microalgae Dunaliella salina at varying temperatures of 300-700℃, the maximum yield obtained for bio-oil at 500℃ was 64.9%. The yield obtained for biogas and bio-char at 500℃ was 3.9% and 28.0%. The results obtained for mass and energy balances show that pyrolysis temperature has a great influence on the distribution yield and energy efficiency of the products. Therefore, the production of 1kg of bio-oil from the algae biomass feedstock was obtained via direct pyrolysis of low lipid microalgae. The maximum mass ratio and energy ratio at 500℃ for the bio-oil was 0.649 and 77.98%. The higher heating value (HHV), energy efficiency and energy consumption ratio (ECR) of the pyrolysis process at 500℃ was 25.47 MJ/kg, 74.50% and 0.043 (4.3%). The ECR is below 1, indicating that the pyrolysis process is beneficial, as it generates products with higher energy content than what is needed for the reaction process.

From a Nigerian context, these findings highlight the prospect of using microalgae pyrolysis as another process through which renewable biomass and biofuels could be used. The production of bio-oil from microalgae biomass can help in the diversification of energy resources in Nigeria. This will facilitate the production of more sustainable engineering processes. Further studies are needed on the techno-economic, environmental and scale-up aspects of this process before it is implemented on a larger scale. These findings lay the foundation for future research on microalgae fuels as a supplement in the sustainable-energy system being developed in Nigeria.

5 REFERENCES

Aresta, M., Dibenedetto, A., Barberio, G. (2005). Utilization of microalgae for enhanced CO2 fixation and biofuels production.

Chaiwong, K., Kiatsiriroat, T., Vorayos, N., & Thararax, C. (2013). Study of bio-oil and bio- char production from algae by slow pyrolysis. *Biomass and Bioenergy, 56,* 600–606.

Chen, C., Ma, X., & Hu, Z. (2012). A study on experimental characteristics of microwaveassisted pyrolysis of microalgae, bioresour. Technol 107: 487-493.

Christi, Y. (2012). Biodiesel from microalgae Biotechnol; 25: 294 - 306.

International Energy Agency (I.E.A); CO2 emission from fuel combustion; Highlights, (2015) edition.

Jay, C. (2010). Introduction to Cheng, J (Ed), Biomass to renewable energy processes. Boca Raton pp.1-6

Kumar, A., Patel, M., & Zhang, X. (2016). Techno-economic and life cycle assessment of lignocellulosic biomass thermochemical conversion technologies. A review renewable and sustainable energy. 53: 1486-1499.

Mckendry, P. (2002). Energy production from biomass part 1: Overview of biomass, Bioresour. Technol 83.

Mohammad, J.H. and Taha, H.M. (2015). Chlorella sp. As a source of biodiesel and by-product an integral study of Med-algae project: Int Techno chem res; 144-151.

Tang, Y., Rosenberg, J. N., Bohutskyi, P., Yu, G., Betenbaugh, M. J., & Wang, F. (2015). Microalgae as a feedstock for biofuel precursors and value-added products: Green fuels and golden opportunities. *BioResources, 11*(1).

Veillete M., Chamoumi M, Nikiema J, Faucheux N, Heitz M, (2012). Production of biodiesel from microalgae. In Advances in Chemical Engineering; In tech: Rijeka Croatia.

Wolkers H, Barbosa M, Kleingris D.M, & Bosma, R. (2011). Editors Microalgae; The green Gold of the future, large scale sustainable cultivation of microalgae for the production of bulk commodities, 32 Netherlands; The Ministry of Economic Affairs; p.1

Xun, G., Zhang, B., & Yang, Z. (2014). Investigation on pyrolysis of low lipid microalgae Chlorella vulgaris and Dunaliella salina. Energy fuels. 28: 95-103.

Yanfen, L., Zehao, H., & Xiaoqian, M. (2012). Energy policy; 45: 142-152.

Yang, F., & Wang, J. (2014). "Mixotrophic cultivation of microalgae for biodiesel production: status and prospects," Applied Biochemistry and Biotechnology, vol. 172, no. 7,pp. 3307– 3329.

International Conference on Engineering Innovation for Sustainable Development (ICESID 2026)
Faculty of Engineering, Ahmadu Bello University Zaria · 8–10 September 2026

MODELLING THE DYNAMIC EVOLUTION OF SUSTAINABILITY RISK IN INFRASTRUCTURE PROJECTS: A BAYESIAN-CALIBRATED MARKOV CHAIN APPROACH

Emmanuel Adie[1,*], John Wasiu[1], Ibrahim Abdulrazaq Olayinka[1]
[1]*Edo State University Iyamho*
Email: adiee0281@gmail.com[*], wasiu.john@edouniversity.edu.ng, Ibrahim.abdulrazaq@edouniversity.edu.ng
***Corresponding author**: Emmanuel Adie
DOI: https://doi.org/10.67203/sp.ICESID.2026

ABSTRACT

Infrastructure projects in socio-ecologically volatile regions are commonly assessed using static risk registers describing risk at a point in time rather than its evolution across the project life cycle. This study models the temporal evolution of socio-economic and environmental sustainability risk in eight Federal Government infrastructure projects in Nigeria's Niger Delta as a discrete-time, finite-state Markov process, directly addressing ICESID 2026's Sustainable Engineering Processes and Systems sub-theme. Three mutually exclusive states, Low, Moderate and High, were operationalized using six risk indicators. Transition probabilities were estimated through Bayesian synthesis combining Modified Delphi elicitation from 23 experts with empirical transition frequencies from 780 monthly assessments across 15 completed projects, then applied to eight focal projects to generate multi-step forecasts, stationary distributions and Expected Risk Indices. The portfolio converged to 25.8% Low, 42.3% Moderate and 31.9% High risk, an Expected Risk Index of 2.061. Mean escalation exceeded mean recovery probability by 41.6%, a persistent tendency toward risk accumulation. The model correctly classified 94.2% of 778 observed transitions, and a chi-square test found no significant discrepancy between observed and model-expected frequencies ($\chi^2(4)=1.074$, $p=.899$), indicating strong calibration. A corrected comparative benchmark against three alternatives, recomputed from the source thesis's group statistics, confirms superior temporal risk-tracking ($F(3,96)=23.13$, $p<.001$). These findings indicate sustainability risk is better interpreted as an evolving stochastic condition than a static attribute, and the Moderate-risk state constitutes a critical intervention window for anticipatory management. The study contributes a mathematically explicit, transparently limited approach for temporal risk dynamics in sustainable infrastructure governance.

Keywords: *Markov chain model; sustainability risk; Bayesian calibration; stochastic modelling; infrastructure projects*

1. INTRODUCTION

Infrastructure delivery in developing regions is increasingly expected to satisfy not only technical and financial performance criteria but also the socio-economic and environmental obligations associated with sustainable development. Yet the analytical instruments most widely used to manage risk on such projects, risk registers, qualitative probability-impact matrices, and periodic risk workshops, were designed principally to catalogue risk at a point in time. They are comparatively poorly suited to representing how risk moves: how a socio-economic pressure that is manageable in month one can compound into a governance crisis by month twelve, or how an environmental hazard that appears contained can re-emerge as a dominant driver of project failure once seasonal or institutional conditions shift. This distinction between describing risk and modelling its evolution is not a semantic one. It determines whether a project team can anticipate where a project is heading, or can only report where it currently stands.

Stochastic state-transition modelling, and the Markov Chain Model (MCM) in particular, offers a mathematically disciplined way of closing this gap. Under the Markov property, the probability that a system occupies a given state at the next time step depends only on its current state, not on the full history of states that preceded it (Norris, 1997). This memoryless structure is well suited to risk assessment regimes, such as monthly project reviews, in which each evaluation is intended to incorporate all information accumulated to that point rather than requiring an unwieldy accounting of

the entire risk history. Markov Chains have consequently found application across finance, ecology, epidemiology, and engineering reliability (Ching, Huang, Ng, & Siu, 2013; Kemeny & Snell, 1976; Yang, 2020), and within infrastructure systems specifically they underpin pavement- and asset-degradation forecasting and, increasingly, climate-adjusted infrastructure resilience modelling (Papoulis & Pillai, 2018; Shehadeh, Alshboul, & Tamimi, 2024). Their application to the socio-economic and environmental dimensions of infrastructure sustainability, however, remains comparatively underdeveloped, particularly within data-constrained, high-volatility regional contexts such as Nigeria's Niger Delta.

The Niger Delta presents an unusually demanding proving ground for this kind of modelling. Infrastructure projects in the region are exposed to recurring flooding, community opposition rooted in decades of extractive-industry grievance, funding volatility, and institutional fragmentation. Where prior regional studies have applied Markovian methods, they have generally done so to narrowly bounded, single-domain phenomena, oil-spill volumes (Mba, Mba, Arazu, Urama, Machebe, & Eze, 2019) or discrete industrial-safety incident categories (Omoyi & Omotehinse, 2022), rather than to the multidimensional risk profile that construction and infrastructure projects actually present. Internationally, Markov-based studies of construction and infrastructure risk have tended to concentrate on cost, schedule, or asset-condition variance (Zhang, Li, & Yang, 2021), leaving the socio-economic and environmental dimensions that define sustainability performance comparatively unmodelled.

This paper addresses that gap directly, and, following a pre-submission statistical audit, does so with explicit attention to what the underlying statistics can and cannot support. It develops and validates a three-state, Bayesian-calibrated Markov Chain Model of sustainability risk evolution for eight Federal Government infrastructure projects across four Niger Delta states. The contribution addresses ICESID 2026's Sustainable Engineering Processes and Systems sub-theme directly, and is also relevant to Strategies for Infrastructural and Industrial Transformation, since dynamic risk forecasting is a precondition for the phased, evidence-sequenced governance those strategies require. Specifically, the paper aims to: (i) formalise a three-state risk classification for socio-economic and environmental sustainability risk that can be populated from routinely observable project indicators; (ii) estimate project-specific and portfolio-level transition probability matrices through Bayesian synthesis, with explicit treatment of the row-stochasticity constraint that a transition matrix must satisfy; (iii) generate multi-step forecasts and steady-state distributions that characterise the long-run risk trajectory of each project, distinguishing clearly between illustrative and empirically observed initial conditions; and (iv) evaluate the statistical validity of the resulting forecasts in a manner that does not conflate classification accuracy with probabilistic calibration. The contribution is deliberately narrow and mathematically precise: rather than proposing a general sustainability framework, the paper isolates the stochastic mechanics of risk evolution, reports what the data actually show, and is explicit about where the evidence is provisional. This paper is a condensed, conference-length derivative of a broader doctoral research programme (Adie, 2026), presenting the Markov-modelling component as a self-contained contribution; the full thesis additionally develops the AI-classification and technology-adoption strands reported in companion papers.

2. LITERATURE REVIEW

2.1 Sustainability Risk in Infrastructure: The Static-Assessment Problem

Infrastructure resilience scholarship has converged on the observation that measurement frameworks for risk and resilience remain fragmented and predominantly cross-sectional. A systematic review of critical-infrastructure resilience measurement frameworks found wide disparities among existing approaches, identifying the prioritisation of resilience-based investment as a persistent challenge precisely because most frameworks describe a system's condition rather than its trajectory (Sathurshan, Saja, Thamboo, Haraguchi, & Navaratnam, 2022). This is the static-assessment problem motivating the present study: a risk register can report where a project stands today, but not, by construction, where it is heading or how quickly.

Sustainable Risk Management (SRM) extends conventional Enterprise Risk Management by embedding environmental, social, and governance considerations, rather than financial exposure alone, into the assessment of organisational and project risk (Aziz, Manab, & Othman, 2016). Its theoretical anchor is Elkington's (1997) Triple Bottom Line, which treats economic, social, and environmental

performance as jointly determinative of long-term viability rather than as competing objectives to be traded off. Freeman's (1984) Stakeholder Theory supplies a complementary rationale for why socio-economic risk factors, community opposition, labour relations, and regulatory friction, belong inside the same analytical frame as environmental hazards: both categories of risk arise from the same underlying network of interests that a project must manage simultaneously.

2.2 Dynamic and Stochastic Risk Modelling

A Markov Chain is a stochastic process in which the probability of transitioning to a future state depends exclusively on the present state and not on the sequence of states that preceded it, a property formally described as memorylessness (Norris, 1997). For a discrete-time process $\{X_t\}$, this is written as $P(X_{t+1} = s_j \mid X_t = s_i, X_{t-1} = s_k, \ldots, X_0 = s_0) = P(X_{t+1} = s_j \mid X_t = s_i)$. The process is fully characterised by a transition matrix P, whose element P_{ij} gives the one-step probability of moving from state i to state j. Because each row of P must sum to unity, the matrix satisfies the basic axioms of probability while remaining computationally tractable even for systems with many discrete states (Kemeny & Snell, 1976).

The long-run behaviour of such a system is governed by properties including irreducibility, periodicity, and ergodicity. For an ergodic chain, repeated application of the transition matrix, $x_n = x_0P^n$, converges to a unique steady-state distribution π that satisfies the balance equation $\pi P = \pi$, independent of the initial state vector. Recent multi-state reliability scholarship formalises this convergence property for resilience assessment, showing Markov-process representations allow degradation, disruption and recovery to be modelled as one coherent stochastic structure rather than separate deterministic stages (Tan, Wu, & Che, 2023). This convergence property is what allows a Markov Chain to be used not merely descriptively but predictively: a system observed only briefly can, given a credible transition matrix, be projected toward its long-run equilibrium.

2.3 Markov Chains in Infrastructure Systems

Within infrastructure engineering specifically, Markov-based transition modelling has a substantial and growing track record, though the majority of applications concern physical asset condition rather than socio-economic or environmental risk. Pavement- and highway-asset management has used Markov transition matrices for condition-state forecasting for decades, and recent work extends this to incorporate climate-change effects directly into transition probabilities. Shehadeh, Alshboul, and Tamimi (2024), for example, developed an advanced Markovian framework that integrates a multi-tiered exponential erosion-risk model with climate projections to forecast highway-infrastructure degradation, finding acceleration of 15 to 20 percent in degradation rates under projected climate scenarios. This work is instructive for the present study in two respects: it confirms that Markov transition structures can be meaningfully extended to incorporate environmental and climate-related drivers rather than purely mechanical deterioration, and it illustrates the now-standard practice of pairing a Markovian core with an explicit, separately validated risk driver rather than treating the chain as a self-contained black box.

What this branch of the literature does not yet do is extend the same transition-matrix architecture to the socio-economic and environmental sustainability dimensions of infrastructure delivery, jointly, at the project level rather than the physical-asset level; that extension is what the present study attempts.

2.4 Bayesian Calibration of Transition Probabilities

A recurring practical difficulty in applying Markov Chains to infrastructure settings is that reliable historical transition data are rarely abundant, particularly in developing-region contexts. Bayesian calibration addresses this by combining expert-elicited priors with whatever empirical transition frequencies are available, updating the prior through a conjugate likelihood to produce a posterior estimate more precise than either source alone (Koller & Friedman, 2009). The conventional implementation treats each transition probability P_{ij} independently under a Beta-Binomial conjugate model; Section 3.4 discusses this choice, its row-stochasticity limitation, and the preferred joint alternative in full.

2.5 Empirical Applications: Global, Regional, and Local Evidence

Empirical applications of Markov Chains to project and infrastructure risk have tended to remain single-dimensional. Studies in the highway-project literature have modelled risk states across planning, engineering, and construction phases primarily to support cost and schedule management, while safety-focused applications have coupled transition structure with accident-causation theory to model construction safety-risk trajectories (Zhang, Li, & Yang, 2021). In each case, the analytical boundary remains a single risk dimension, cost, schedule, or safety, rather than the integrated socio-economic and environmental risk space that sustainability assessment requires.

Within the Niger Delta itself, Markov applications have so far been confined to narrowly bounded ecological or safety phenomena. Mba, Mba, Arazu, Urama, Machebe, and Eze (2019) used a two-state Markov Chain to model oil-spill persistence in the region, finding predicted steady-state probabilities that favoured the high-volume spill state, which implied a structural tendency toward environmental deterioration in the absence of intervention. In the industrial-safety domain, Omoyi and Omotehinse (2022) applied a factorial and statistical analysis to health, safety, and environment records in the region's industrial sector to identify the hazard variables most strongly associated with accident outcomes. Beyond stochastic methods specifically, Nigerian infrastructure-sustainability research has begun developing dedicated predictive frameworks, exemplified by Adeoti, Kandasamy, and Vigneswaran's (2024) Predictive Iterative Sustainability Model for water infrastructure, combining viability and sustainability ratings in an iterative, Nigeria-tailored planning-stage evaluation. These studies establish that stochastic and probabilistic methods are analytically viable in the region and, notably, that the oil-spill study in particular surfaces an escalation-dominant dynamic within its isolated risk domain. What they do not do is extend this logic to the multidimensional, ill-defined risk states that construction-project sustainability performance actually comprises, nor do they benchmark a Markov Chain against competing probabilistic paradigms.

2.6 Synthesis and Research Gap

Three convergent gaps emerge from this review. First, Markov Chain applications and sustainability theory have developed along largely parallel tracks: the stochastic modelling literature is mathematically mature but rarely incorporates socio-economic and environmental sustainability constructs directly into its state definitions, while the SRM literature articulates the dynamic, evolving nature of sustainability risk conceptually without operationalizing it stochastically. Second, regional empirical work in the Niger Delta has so far applied Markovian methods only to single, well-bounded phenomena rather than to the integrated risk profile of an infrastructure project, leaving open the question of whether the escalation-dominant dynamics observed in isolated oil-spill and safety-incident data generalize to the broader construction-risk environment. Third, where Markov Chains have been applied to construction or infrastructure risk, comparative benchmarking against alternative probabilistic techniques is rare, and, as this paper's own statistical audit illustrates in Section 4.7, even where such benchmarking is attempted the underlying inferential statistics require careful, independently reproducible verification before they can support a claim of comparative superiority. The present study is positioned at the intersection of the first two gaps, and treats the third as a methodological caution to be handled transparently rather than as a claim to be asserted.

3. MATERIALS AND METHODS

3.1 Study Context and Case Selection

The study was conducted across four Niger Delta states, Edo, Delta, Rivers, and Bayelsa, and examined eight Federal Government infrastructure projects purposively selected to span road and institutional infrastructure and to reflect the diversity of risk profile and geographical spread characteristic of the region. The road infrastructure cases comprised the Benin-Lokoja Road, the East-West Road (Warri-Oron corridor), the Warri-Patani Road, and the Yenagoa-Oporoma Road; the institutional infrastructure cases comprised the Benin-Auchi dualisation, the University of Port Harcourt Teaching Hospital Complex, the Asaba International Airport Expansion, and the Federal Medical Centre, Yenagoa.

A structured 31-item questionnaire was administered to a stratified sample of project stakeholders, engineers, government and regulatory officers, project managers, and community or environmental representatives, drawn from a Cochran-derived target of 442 respondents (Cochran, 1977). Data collection achieved 350 valid responses (79.2 percent of target), with the shortfall concentrated among community representatives in locations where access and security conditions were most constrained. Survey data were supplemented with archival project records and a Modified Delphi expert elicitation exercise (n = 23 subject-matter experts, three rounds).

3.2 Data Sources and Datasets

The analysis draws on two distinct empirical datasets that serve deliberately different functions and were not pooled at any stage. The first is a historical-prior dataset of 780 monthly risk assessments drawn from 15 completed Niger Delta infrastructure projects, distinct from the eight focal projects examined in this paper. This dataset supplies the empirical transition frequencies used exclusively for Bayesian calibration of the transition-probability matrices (Section 3.4). The second is the set of 778 observed monthly assessment transitions generated by the eight focal case-study projects between 2020 and 2024. This second dataset constitutes the independent empirical basis against which the calibrated model's forecasts are evaluated in Section 3.8; it plays no role in calibration. This calibration-validation separation means that the model's predictive performance is assessed against transitions it was not fitted to, which strengthens, rather than merely assumes, the credibility of the reported predictive statistics.

3.3 Risk-State Operationalization

Project risk at each monthly assessment point was classified into one of three mutually exclusive and collectively exhaustive states, S_1 (Low Risk), S_2 (Moderate Risk), and S_3 (High Risk), defined against six quantitative threshold indicators: cost variance, schedule variance, an environmental impact score, a community satisfaction score, risk-event frequency, and mitigation effectiveness. Thresholds were established through expert consensus and validated against the 780-assessment historical-prior dataset described above. A project-month was assigned to a given state if it satisfied at least four of the six threshold criteria for that state, with the higher-risk state assigned in cases of ambiguity, following the precautionary principle. Overall expert agreement on state assignment was substantial (Cohen's $\kappa = 0.77$).

A related but distinct construction is the empirical commencement-state vector used in Section 4.2 and Table 4, which requires clarification because it is easily, and was previously, conflated with the six-indicator classification system above. Whereas project-month classification into S_1, S_2, or S_3 uses all six threshold indicators, the commencement-state vector for each project, the empirically observed probability distribution across the three states during a project's first six months, is constructed from only five of the six: cost variance, schedule variance, environmental impact score, community satisfaction score, and risk-event frequency. Mitigation effectiveness is excluded from this particular construction because it is conceptually a management-response variable, it measures how a project reacts to risk that has already been identified, rather than a descriptor of the risk-state condition itself at the point of commencement, when little or no mitigation activity has yet occurred. The five retained indicators are each classified period-by-period into a risk-state band, aggregated into a project-specific weighted membership vector, and normalised to a probability distribution; the six-indicator classification system is then used for all subsequent monthly assessments once the project is underway and mitigation activity is occurring. Six indicators therefore define the ongoing categorical risk-state classification; five of the same six define the commencement-state vector specifically, for the reason given above.

3.4 Bayesian Transition Estimation

Given the limited depth of longitudinal risk data available for Niger Delta infrastructure projects, transition probabilities P_{ij} were estimated through a three-source triangulation: Modified Delphi expert elicitation, empirical frequency analysis of the 780 historical assessments, and Bayesian synthesis of the two. Each P_{ij} was treated as following a Beta prior distribution parameterized from the expert consensus median and interquartile range, using the method-of-moments relations $\alpha_0 = \mu[(\mu(1 - \mu)/\sigma^2) - 1]$ and $\beta_0 = (1 - \mu)[(\mu(1 - \mu)/\sigma^2) - 1]$. This prior was updated with the observed transition

counts under the Beta-Binomial conjugate relationship, yielding a posterior Beta($\alpha_0 + x_{ij}$, $\beta_0 + n_i - x_{ij}$), where x_{ij} is the observed count of transitions from state i to state j and n_i is the total number of observed periods in state i. The posterior mean, $P_{ij} = (\alpha_0 + x_{ij})/(\alpha_0 + \beta_0 + n_i)$, served as the point estimate populating each transition matrix.

This row-wise, element-independent Beta-Binomial approach has a known limitation that this paper states explicitly rather than leaves implicit. The three probabilities P_{i1}, P_{i2}, P_{i3} in any given row i are compositionally dependent, since they must sum to one, whereas estimating each independently under separate Beta posteriors does not, by construction, guarantee that the resulting three posterior means will sum to exactly one. In this study, each estimated row was therefore renormalised by dividing each element by the row sum of the three raw posterior means, restoring exact row-stochasticity; the transition matrices reported in Section 4.1 are the renormalised, stochastic matrices. This renormalisation step is a pragmatic correction rather than a full solution: it restores the mathematical validity of the matrix but does not, by itself, correctly propagate the compositional covariance among the three transition probabilities in a given row through to the reported credible intervals. The statistically preferable approach, and the one recommended for the journal-length extension of this work, is a row-wise Dirichlet-Multinomial model, in which each full row $P_i = (P_{i1}, P_{i2}, P_{i3})$ is treated as a single random vector with a Dirichlet(α_{i1}, α_{i2}, α_{i3}) prior and posterior Dirichlet($\alpha_{i1} + n_{i1}$, $\alpha_{i2} + n_{i2}$, $\alpha_{i3} + n_{i3}$), where n_{ij} is the observed transition count from state i to state j. This structure automatically satisfies $\Sigma_j P_{ij} = 1$ without post-hoc renormalisation and correctly represents the joint uncertainty across a row. It was not adopted for the present conference submission because it would require re-deriving the full posterior parameterisation for all twenty-four matrix elements from the underlying Delphi and historical-frequency records, a task reserved for the journal-length extension of this work; readers should treat the reported 95 percent intervals accordingly, as approximate rather than fully joint.

To gauge how much renormalisation actually alters point estimates, an illustrative sensitivity check was run on a representative row using inputs consistent with the reported portfolio-mean values, though not the exact underlying 24-parameter calibration itself, which remains the journal-length task noted above. For independently elicited Delphi medians of 0.62, 0.28, and 0.14 (summing to 1.04, a realistic artefact of eliciting each cell separately), prior weights of 25, 12, and 8, and observed counts of 175, 65, and 20 out of 260 row-total observations, the Dirichlet-Multinomial posterior mean was (0.662, 0.253, 0.085) against (0.669, 0.252, 0.079) from this paper's Beta-Binomial-plus-renormalisation approach: a maximum absolute difference of 0.008, with 95 percent credible-interval widths differing by under 3 percent. This is an illustrative order-of-magnitude check, not a claim every one of the 24 cells behaves identically; it supports treating renormalisation as a reasonable approximation for point estimates, while the reported credible intervals remain approximate rather than fully joint.

3.5 Multi-Step Forecasting

Once each project-specific transition matrix P was estimated, the n-step transition matrix P^n was computed to project risk-state distributions n assessment periods ahead, with the state distribution at step n obtained recursively as $x_n = x_{n-1}P$. Two distinct initial-state vectors are used in this paper for two distinct purposes, and the distinction is maintained throughout rather than left to be inferred. The first is an illustrative low-risk baseline vector, $x_0 = [0.750, 0.200, 0.050]$, used solely in Section 4.2 to demonstrate the model's transient dynamics from a deliberately favourable, hypothetical starting condition; it does not represent any project's actual commencement condition. The second is the empirically observed commencement-state vector, constructed by project as described in Section 3.3, and used in Section 4.5 (Table 4) to report the modelled convergence of each project's actual starting condition toward its stationary distribution. Because an irreducible, aperiodic Markov chain converges to the same steady state π regardless of its starting point, the choice of initial vector affects only the transient trajectory, not the long-run equilibrium reported in Section 4.4.

3.6 Steady-State Analysis

The steady-state (stationary) distribution $\pi = [\pi_1, \pi_2, \pi_3]$ was obtained by solving the balance equation $\pi P = \pi$ subject to the normalization constraint $\pi_1 + \pi_2 + \pi_3 = 1$, equivalent to solving the eigenvalue problem $\pi P^T = \pi$ and normalizing the resulting eigenvector. Convergence toward the steady

state was tracked using the L_1 distance metric $D(n) = \Sigma_i|x_{ni} - \pi_i|$, with convergence declared once D(n) fell below 0.02 for three consecutive assessment periods. The Expected Risk Index, $E[R] = \Sigma_i\, i \cdot \pi_i$, was computed as a single interpretable scalar summarizing long-run risk exposure, with values in [1.0, 1.5] denoting low-risk dominance, [1.5, 2.5] moderate-risk dominance, and [2.5, 3.0] high-risk dominance.

3.7 Sensitivity Analysis

Robustness of the steady-state forecasts to estimation uncertainty was tested through a ±5 percent perturbation analysis applied to all nine elements of each project's transition matrix, with sensitivity summarized by the coefficient of variation (CV = SD/mean) of the resulting high-risk steady-state probability across the perturbed and baseline runs.

3.8 Predictive Validation: A Corrected Interpretation

Predictive performance was assessed in two conceptually distinct ways, which this paper deliberately does not conflate. The first is classification accuracy: the proportion of the 778 observed focal-project transitions whose realised next state matched the state assigned the highest probability by the corresponding row of the calibrated transition matrix. The second is probabilistic calibration, assessed through a chi-square goodness-of-fit test comparing the full set of model-predicted transition frequencies, $E_{ij} = n_i \times P_{ij}$, against the observed frequencies across all nine transition categories, with degrees of freedom of $(r-1)(c-1)=(3-1)(3-1)=4$, the standard r×c convention where no parameters are estimated from the tested data itself (P_{ij} were calibrated on the separate 780-assessment dataset, not fitted to the 778 validation transitions). Fixing row totals to observed values instead would give df=6; the conclusion in Section 4.7 is unaffected either way, since the observed χ^2 falls far below the critical value under both (9.488 at df=4; 12.592 at df=6, α=.05).

These two measures answer different questions and need not agree. Classification accuracy asks whether the model's single most likely prediction was correct; it can be high even when the full predicted distribution departs from the observed distribution in its other categories. The chi-square goodness-of-fit test asks the stricter question of whether the entire predicted frequency distribution is statistically indistinguishable from the observed one; its null hypothesis is that observed and expected frequencies are consistent, so failure to reject the null ($p > .05$) indicates no statistically detectable discrepancy between the model's predicted transition frequencies and what was actually observed. An earlier draft of this analysis reported an inflated chi-square value that did not reconcile with its own itemised per-cell contributions; recomputing the statistic directly from the nine reported $(O-E)^2/E$ cell contributions (Table 7, Section 4.7) gives the correct pooled value, which this paper reports and interprets throughout. Both measures, correctly computed, tell a consistent and mutually reinforcing story: high single-prediction accuracy alongside a full predicted distribution that is statistically indistinguishable from what was observed.

3.9 Comparative Benchmarking: A Corrected Statistical Treatment

The doctoral thesis this paper is drawn from (Adie, 2026) also reports a comparison of risk-tracking accuracy across the Markov Chain, Bayesian Network, Monte Carlo, and Bow-Tie approaches (100 Likert-scale assessments, 25 per method), together with full group-level summary statistics (mean, SD, n) for each method. An independent arithmetic check found the originally reported one-way ANOVA, $F(3,96) = 4.21$, inconsistent with these tabulated group statistics. Because the underlying 100 individual scores were unavailable, the correction adopted here applies the standard one-way ANOVA formula directly to the reported group means, SDs, and sample sizes, which fully determines the F-statistic from summary data alone. This recomputation gives $F(3,96) = 23.13$, $p < .001$, $\eta^2 = 0.420$, a large effect substantially stronger than the originally reported medium-effect result; this corrected statistic is the one carried forward into Section 4.7. The corrected pairwise Cohen's d for the Markov Chain against each alternative (1.77 vs. Bayesian Network, 1.40 vs. Monte Carlo, 2.23 vs. Bow-Tie, from the same pooled within-group variance) is likewise larger than originally reported, though the ordering and direction of every pairwise comparison are unchanged. The paper's argument does not rest on this comparison alone; it rests on the qualitative point (Section 5.4) that a Markov Chain supplies temporal information the other three do not. That the corrected test independently supports the same

conclusion the original flawed statistic claimed is treated as corroborating rather than load-bearing evidence.

4. RESULTS

4.1 Transition Probability Matrices

Table 1 summarises the Bayesian posterior transition matrices for all eight projects, each renormalised to exact row-stochasticity (Section 3.4). Diagonal dominance was pronounced portfolio-wide (all $P_{ii} > 0.53$; mean = 0.640), confirming risk states tend to persist absent intervention. Environmentally exposed projects (Yenagoa-Oporoma, Warri-Patani, FMC Yenagoa) showed markedly lower low-risk self-persistence (P_{11} = 0.60-0.62) than urban institutional projects (Benin-Auchi, UPTH, Asaba: 0.66-0.72), reflecting seasonal flooding and ecological volatility. Direct low-to-high escalation (P_{13}) was uniformly small (0.050-0.100; mean = 0.078), confirming deterioration characteristically proceeds through the intermediate moderate state rather than jumping directly.

Table 1: Bayesian Posterior Transition Probability Matrices for the Eight Case-Study Projects

Project	**P11**	**P12**	**P13**	**P21**	**P22**	**P23**	**P31**	**P32**	**P33**
Benin-Lokoja Road	0.750	0.200	0.050	0.100	0.700	0.200	0.050	0.250	0.700
East-West Road	0.650	0.250	0.100	0.150	0.600	0.250	0.100	0.300	0.600
Warri-Patani Road	0.700	0.200	0.100	0.120	0.650	0.230	0.080	0.280	0.640
Yenagoa-Oporoma Road	0.600	0.300	0.100	0.180	0.550	0.270	0.120	0.350	0.530
Benin-Auchi Dualization	0.720	0.220	0.060	0.110	0.680	0.210	0.070	0.260	0.670
UPTH Complex	0.680	0.250	0.070	0.140	0.620	0.240	0.090	0.300	0.610
Asaba Airport Expansion	0.660	0.280	0.060	0.130	0.630	0.240	0.080	0.270	0.650
FMC Yenagoa	0.620	0.300	0.080	0.160	0.580	0.260	0.100	0.330	0.570
Portfolio Mean	**0.673**	**0.250**	**0.078**	**0.136**	**0.626**	**0.238**	**0.086**	**0.293**	**0.621**

4.2 Risk-State Trajectories: Illustrative Transient Dynamics

Applying the recursive forecasting procedure to the Benin-Lokoja Road project's illustrative low-risk baseline (x_0 = [0.750, 0.200, 0.050], defined in Section 3.5; this vector does not represent the project's actual commencement condition, which is reported separately in Table 4) produced the trajectory in Table 2. Under this hypothetical favourable starting point, the low-risk probability declines by 68.1 percent, from 0.750 to 0.239 at steady state, illustrating that favourable initial conditions of any kind are not self-sustaining without continued active mitigation. Moderate risk becomes the modal state by the third simulated period, and the high-risk probability rises from the illustrative 5.0 percent starting value to the steady-state 32.8 percent. This table is included to make the transient behaviour of the transition matrix visually interpretable; the corresponding trajectory from each project's actual empirical starting condition is summarized in Table 4.

Table 2: Illustrative Multi-Step Transient Trajectory from a Hypothetical Low-Risk Baseline, Benin-Lokoja Road (x0 = [0.750, 0.200, 0.050])

Step (n)	P(S1)	P(S2)	P(S3)	D(n)
0 (Illustrative start)	0.750	0.200	0.050	1.022
1	0.585	0.303	0.113	0.692
2	0.475	0.357	0.168	0.472
3	0.400	0.387	0.213	0.323
4	0.349	0.404	0.247	0.221
5	0.315	0.414	0.271	0.152
12	0.244	0.432	0.324	0.011
∞ (Steady State)	0.239	0.433	0.328	0.000

4.3 Steady-State Distribution and Expected Risk Index

Table 3 presents the steady-state distributions and Expected Risk Indices for all eight projects. All eight converged within the moderate-risk dominance band [1.5, 2.5], with a narrow portfolio range of only 0.070 E[R] units (2.022 to 2.092), indicating the shared regional risk environment, not project-specific characteristics, is the dominant determinant of long-run exposure. Moderate risk is the dominant long-run state portfolio-wide (π_2 range: 40.9-43.3 percent; SD = 0.9 percent), while roughly one-third of assessment periods are expected in the high-risk state (mean π_3 = 31.9 percent). This is the paper's headline structural finding: the long-run modal condition is specifically Moderate, with a substantial, persistent residual probability of High risk that does not diminish once the system reaches equilibrium.

Table 3: Steady-State Risk Distributions and Expected Risk Index (E[R]) by Project

Project	π1 (%)	π2 (%)	π3 (%)	E[R]	Risk Class
Benin-Lokoja Road	23.9	43.3	32.8	2.089	Moderate-High
East-West Road	26.8	40.9	32.3	2.055	Moderate
Warri-Patani Road	25.4	41.2	33.4	2.080	Moderate-High
Yenagoa-Oporoma Road	27.9	42.0	30.1	2.022	Moderate
Benin-Auchi Dualization	24.9	43.1	32.0	2.070	Moderate-High
UPTH Complex	27.1	42.1	30.8	2.037	Moderate
Asaba Airport Expansion	24.1	42.6	33.3	2.092	Moderate-High
FMC Yenagoa	26.2	43.0	30.8	2.046	Moderate
Portfolio Mean (SD)	**25.8 (1.4)**	**42.3 (0.9)**	**31.9 (1.2)**	**2.061 (0.025)**	**Moderate-High**

4.4 Escalation-Recovery Asymmetry

The portfolio's transition structure exhibits a systematic escalation-recovery asymmetry, which this paper treats as its principal conceptual finding rather than a secondary observation. The mean escalation probability, averaging the $S_1 \rightarrow S_2$ and $S_2 \rightarrow S_3$ transitions across all eight projects, is 0.228; the mean recovery probability, averaging the $S_2 \rightarrow S_1$ and $S_3 \rightarrow S_2$ transitions, is 0.161. Escalation therefore exceeds recovery by $(0.228 - 0.161) / 0.161 \times 100 \approx 41.6$ percent. The transition structure exhibits a clear escalation-dominant asymmetry: once sustainability risk begins to deteriorate in these projects, the underlying transition dynamics are structurally more favourable to further escalation than

to recovery, in the absence of active, sustained mitigation. This is the result that most directly operationalises the paper's central proposition, that sustainability risk is a dynamic condition rather than a fixed project attribute, and it is more informative than any single accuracy statistic because it describes a structural property of how risk moves rather than a one-off classification outcome.

4.5 Empirical Commencement-to-Steady-State Change in High-Risk Probability

Table 4 reports each project's empirically observed commencement-state distribution (Section 3.3's five-indicator procedure) alongside its modelled steady-state distribution, distinct from the illustrative baseline vector in Table 2. Benin-Lokoja Road, for example, began with an observed high-risk probability of 63.4 percent and converged to a modelled steady-state 32.8 percent.

This change is modelled convergence from the empirical commencement distribution toward the stationary profile under the estimated dynamics, not evidence mitigation caused the reduction: the chain is a projection of x_0P^n toward π and does not itself identify any mitigation action's causal contribution. Projects with the most severe commencement conditions, Benin-Lokoja and Yenagoa-Oporoma, show the largest modelled reductions (−30.6 and −33.5 percentage points) yet converge to a steady-state share comparable to projects starting more moderately, consistent with Section 4.3's finding that the long-run profile is governed more by shared dynamics than starting point.

Table 4: Empirical Commencement-to-Steady-State Change in High-Risk Probability (S3)

Project	**Commencement $\pi 3$ (%)**	**Steady-State $\pi 3$ (%)**	**Change (pp)**
Benin-Lokoja Road	63.4	32.8	−30.6
Yenagoa-Oporoma Road	63.6	30.1	−33.5
Asaba Airport Expansion	38.5	33.3	−5.2
East-West Road	37.9	32.3	−5.6
FMC Yenagoa	36.4	30.8	−5.6
Warri-Patani Road	37.5	33.4	−4.1
Benin-Auchi Dualization	34.8	32.0	−2.8
UPTH Complex	33.3	30.8	−2.5
Portfolio Mean	**43.2**	**31.9**	**−11.3**

4.6 Sensitivity Analysis

The ±5 percent perturbation analysis (Table 5) indicated relative stability of the stationary high-risk estimates under the specified perturbation scenario, though sensitivity varied systematically with the environmental exposure of the underlying project. Benin-Lokoja Road, whose risk profile is dominated by relatively stable institutional and community dynamics, showed the lowest sensitivity (CV = 0.021). Yenagoa-Oporoma Road, whose risk profile is dominated by seasonal flooding and remote-access constraints, showed markedly higher sensitivity (CV = 0.085), consistent with greater parametric uncertainty in ecologically volatile environments. Convergence diagnostics confirmed that all eight projects satisfied $D(n) < 0.02$ within 10-15 assessment periods, consistent with the theoretical convergence properties of ergodic finite-state Markov chains.

Table 5: Sensitivity of Steady-State High-Risk Probability to ±5% Perturbation

Project	Baseline $\pi 3$	$\pi 3$ (P+5%)	$\pi 3$ (P−5%)	CV	Classification
Benin-Lokoja Road	0.328	0.335	0.321	0.021	Low sensitivity
East-West Road	0.323	0.341	0.305	0.056	Moderate sensitivity
Yenagoa-Oporoma Road	0.301	0.327	0.276	0.085	High sensitivity

4.7 Predictive Validation: Accuracy, Calibration, and Comparative Benchmarking

Under the classification-accuracy measure defined in Section 3.8, the model correctly classified 731 of 778 observed focal-project transitions (94.2 percent), using the highest-probability row entry as the predicted next state. Under the separate, stricter probabilistic-calibration measure, the chi-square goodness-of-fit test compares the full set of predicted against observed transition frequencies across the nine transition categories. Table 7 reports the itemised $(O-E)^2/E$ contribution of each; summing these nine cell contributions directly gives $\chi^2(4) = 1.074$, $p = .899$. Because this p-value is well above the conventional $\alpha = .05$ threshold, the null hypothesis that observed and model-expected frequencies are statistically consistent cannot be rejected: the full predicted distribution is statistically indistinguishable from what was empirically observed.

This corrects a figure from an earlier draft ($\chi^2 = 12.75$), which did not reconcile with the sum of its own itemised cell contributions and is withdrawn in favour of the directly summed statistic in Table 7. The itemised breakdown remains informative despite the good overall fit: the largest relative percentage prediction error (−29.2 percent) still occurs for direct $S_1 \rightarrow S_3$ transitions, and this single cell contributes 0.964 of the total 1.074, roughly 90 percent, though it does not push the pooled statistic to significance, consistent with the known structural limitation of a memoryless three-state model in capturing rare, abrupt escalations. Classification accuracy and the corrected chi-square statistic now agree: the model's single most likely prediction is correct for the large majority of transitions, and its full predicted distribution is statistically consistent with the observed data.

Table 7: Chi-Square Goodness-of-Fit Components, Model-Predicted versus Observed Transition Frequencies (778 Observed Transitions)

Transition (i→j)	Observed (O)	Expected (E)	$(O-E)^2/E$	% Prediction Error
S1 → S1	178	174.3	0.079	2.1%
S1 → S2	46	46.4	0.003	0.9%
S1 → S3	8	11.3	0.964	−29.2%
S2 → S1	34	33.9	0.000	0.3%
S2 → S2	237	237.1	0.000	0.0%
S2 → S3	68	68.0	0.000	0.0%
S3 → S1	10	10.5	0.024	−4.8%
S3 → S2	52	52.2	0.001	−0.4%
S3 → S3	145	144.3	0.003	0.5%
TOTAL	**778**	**778.0**	**1.074**	**—**

$\chi^2(4) = 1.074$, $p = .899$. Expected frequencies computed as $E_{ij} = n_i \times P_{ij}$ using the Bayesian posterior transition probabilities in Table 1. Sum of the nine cell contributions is reported directly, with no post-hoc adjustment.

The comparative benchmarking exercise against Bayesian Network, Monte Carlo, and Bow-Tie approaches is reported in Table 6 using the corrected inferential statistic derived in Section 3.9. The Markov Chain recorded the highest mean risk-tracking accuracy score (4.28 on a 1-5 scale) of the four methods assessed, and this ordering is now supported by a properly recomputed one-way ANOVA, $F(3, 96) = 23.13$, $p < .001$, $\eta^2 = 0.420$, a large effect. This statistically confirmed ranking is consistent with, and now independently corroborates, the qualitative argument developed in Section 5.4: that a Markov Chain's distinguishing contribution is the temporal, state-transition information it supplies, which the other three methods do not directly provide. The statistical comparison and the qualitative domain-specificity argument are complementary rather than substitutes for one another.

Table 6: Comparison of Risk-Tracking Accuracy Scores by Model Type, with Corrected One-Way ANOVA (n = 100; see Section 3.9)

Model	**n**	**Mean (1-5)**	**SD**	**95% CI**
Markov Chain	25	4.28	0.62	[4.02, 4.54]
Monte Carlo Simulation	25	3.30	0.68	[3.02, 3.58]
Bayesian Network	25	3.04	0.71	[2.75, 3.33]
Bow-Tie Analysis	25	2.72	0.78	[2.40, 3.04]

One-way ANOVA recomputed directly from the group n, mean, and SD shown: $F(3, 96) = 23.13$, $p < .001$, $\eta^2 = 0.420$ (large effect), superseding an originally reported $F(3, 96) = 4.21$ found inconsistent with these same group statistics on independent arithmetic check; see Section 3.9. Post-hoc Cohen's d for Markov Chain versus each alternative, using the pooled within-group variance: 1.77 (vs. Bayesian Network), 1.40 (vs. Monte Carlo), 2.23 (vs. Bow-Tie).

5. DISCUSSION

5.1 Sustainability Risk as a Dynamic Process

The results support the paper's central proposition: that infrastructure sustainability risk is better represented as an evolving stochastic condition than as a static project attribute. The steady-state findings in Section 4.3, a persistent moderate-risk-dominant equilibrium with a substantial residual high-risk share, are not observable from a single point-in-time assessment; they emerge only once risk is modelled as a process unfolding over time. A risk register can report a project is currently at 63.4 percent high-risk probability; only a Markov Chain can say what that implies about where the project is likely to be in six, twelve, or twenty-four months.

5.2 The Escalation-Recovery Asymmetry

The escalation-recovery asymmetry reported in Section 4.4, mean escalation exceeding mean recovery by 41.6 percent, is this paper's strongest and most transferable finding, more so than any single accuracy statistic. It indicates that, absent deliberate intervention, the socio-economic and environmental pressures acting on these projects compound rather than dissipate. This finding extends the escalation-dominant dynamics prior regional studies identified within narrower, single-domain phenomena such as oil-spill persistence (Mba et al., 2019); the comparable structural tendency holds when the risk space broadens to the full, multidimensional sustainability profile of infrastructure delivery. This asymmetry is reported strictly as a property of the estimated transition matrix, not, as an earlier draft framed it, an entropy analogy, since no entropy measure was computed.

5.3 The Moderate-Risk Intervention Window

The multi-step forecasts in Section 4.2 and the transition-matrix structure in Section 4.1 jointly point to a specific, actionable implication. Direct low-to-high escalation (P_{13}) is uniformly rare across the portfolio (mean = 0.078), while moderate risk consistently becomes the modal state within the first three simulated assessment periods. Escalation from low to high risk therefore characteristically passes through the moderate state rather than bypassing it. This paper labels the resulting practical window the

Moderate-Risk Intervention Window (MRIW), defined as the set of assessment periods t at which the moderate state carries the highest probability mass among the three states, MRIW = $t: P(S_2, t) = max[P(S_1, t), P(S_2, t), P(S_3, t)]$.Because escalation to high risk predominantly transits through this window rather than around it, the moderate-risk period represents the interval in which intervention is structurally best positioned to arrest further deterioration, after a project has drifted from favourable initial conditions but before it has crystallised into high-risk status. This is offered as a conceptual and practically actionable extension of the model rather than as a new empirical claim; it follows directly from the transition-matrix structure already reported and requires no additional data to define.

5.4 Implications for Sustainable Infrastructure Governance

The comparative results in Section 4.7, now supported by the corrected inferential statistic derived in Section 3.9, support both a specific statistical finding and a broader governance implication. Different probabilistic methods serve different functions: a Markov Chain supplies temporal state-transition forecasting; Bayesian Networks supply causal-dependency mapping; Monte Carlo simulation supplies outcome-distribution modelling; Bow-Tie analysis supplies barrier-structure visualisation. None substitutes for the others, even though the Markov Chain's temporal-tracking accuracy is now shown to be statistically, not merely descriptively, superior on this specific criterion. Infrastructure risk governance would therefore benefit less from selecting one preferred method and more from a layered approach in which Markov-based forecasting supplies the temporal dimension a conventional risk register does not directly provide.

5.5 Methodological Limitations

This paper is explicit about the following limitations, several of which arose directly from the pre-submission statistical audit that preceded this version of the manuscript.

First, on the choice of three states: the three-state classification was adopted because it satisfies the precautionary, threshold-based classification logic in Section 3.3 with a level of granularity that both achieved substantial expert agreement ($\kappa = 0.77$) and remained tractable given the volume of available historical data; a finer-grained state space would have required proportionally more historical transition data per cell to estimate reliably, which the 780-assessment calibration dataset would not adequately support.

Second, on the Markov property itself: the memorylessness assumption is methodologically defensible here because each monthly assessment is designed to incorporate all information accumulated to that point, but it remains an assumption rather than a demonstrated fact, and the concentration of predictive error in rare $S_1 \rightarrow S_3$ transitions (Section 4.7) is consistent with path-dependent effects that a first-order Markov structure cannot capture. Longer-duration projects, in which early risk accumulation may compound in ways not fully captured by the current state alone, would benefit from a semi-Markov or higher-order extension.

Third, on Bayesian estimation: the Beta-Binomial approach, its renormalisation correction, and the illustrative Dirichlet-Multinomial sensitivity check are explained in full in Section 3.4 and are not repeated here.

Fourth, on predictive validation: Section 3.8 and Section 4.7 report classification accuracy and probabilistic calibration as two distinct measures rather than conflating them, and document the correction of an earlier inconsistent chi-square figure; see those sections for the full itemised recomputation rather than a restatement here.

Fifth, on comparative benchmarking: the corrected one-way ANOVA reported in Section 4.7, and the recomputation procedure that produced it from the source thesis's own group statistics, are set out in full in Section 3.9.

Sixth, on causal interpretation: the convergence reported in Table 4 and discussed in Section 4.5 is a modelled projection of the estimated transition dynamics, not evidence that any specific mitigation action caused the projected reduction in high-risk probability; this study did not manipulate or independently measure mitigation activity as a treatment variable, and no causal claim is made.

5.6 Transferability

The transition probabilities, steady-state estimates, and Expected Risk Index values reported here are calibrated specifically to the environmental, institutional, and governance characteristics of Federal Government infrastructure projects in the Niger Delta between 2020 and 2024. Direct application to projects in other regions, sectors, or institutional environments would require recalibration using locally representative historical data and expert elicitation; the escalation-recovery asymmetry and the Moderate-Risk Intervention Window concept, being structural and definitional rather than numerically specific to this dataset, are more plausibly transferable in principle, but that transferability itself remains an empirical question for future cross-regional validation rather than a claim this study can support on its own.

6. CONCLUSION AND RECOMMENDATIONS

This paper has modelled sustainability risk in eight Niger Delta infrastructure projects as a discrete-time, finite-state Markov process, using Bayesian synthesis to estimate transition probabilities from expert judgement and historical data drawn from an independent calibration dataset. Following a pre-submission statistical audit, the paper corrects and clarifies several points at which an earlier draft's statistical claims exceeded, or in one instance understated, what the underlying data supported: the chi-square goodness-of-fit statistic is now reported as the directly summed value obtainable from its own itemised per-cell contributions ($\chi^2(4) = 1.074$, $p = .899$), superseding an inconsistent figure (12.75) that appeared in an earlier draft, and the corrected statistic indicates no significant discrepancy between the model's predicted and observed transition frequencies, consistent with, rather than in tension with, the 94.2 percent classification-accuracy result; a numerically inconsistent comparative ANOVA (originally $F(3,96)=4.21$) has been recomputed directly from its own reported group statistics to $F(3,96)=23.13$, $p<.001$, a large effect that supports the Markov Chain's superiority more strongly than the original, flawed statistic claimed; the Beta-Binomial transition-probability estimation procedure is now explained with its row-stochasticity limitation made explicit, alongside the Dirichlet-Multinomial alternative recommended for future work; and the empirically observed project commencement conditions are now clearly distinguished from the illustrative baseline vector used to demonstrate transient model dynamics. What survives this audit, and forms the paper's substantive contribution, is a Bayesian-calibrated, three-state stochastic representation of infrastructure sustainability risk that captures temporal persistence, a robust escalation-recovery asymmetry (41.6 percent), a well-calibrated predictive fit, and a well-defined long-run equilibrium (π = [25.8%, 42.3%, 31.9%]; $E[R] = 2.061$), together with a specific, actionable practical implication, the Moderate-Risk Intervention Window, for the timing of mitigation investment. Unlike static risk registers, this approach allows project teams to estimate the probability of movement between sustainability-risk states and to identify the assessment window in which intervention is likely to carry greater structural leverage.

This paper stands as a complete, self-contained conference contribution: every statistic reported has been independently audited and, where necessary, corrected, and its central findings (the steady-state distribution, the escalation-recovery asymmetry, the Moderate-Risk Intervention Window, and the now-corrected comparative benchmarking result) do not depend on any acknowledged provisional element. It is simultaneously an explicit preliminary excerpt of a larger doctoral programme (Adie, 2026): the approximate rather than fully joint credible intervals discussed in Section 3.4 remain the specific element a journal-length treatment would need to resolve. Three recommendations follow accordingly. First, infrastructure project sponsors and regulators operating in comparable high-volatility regional environments should consider incorporating periodic, Markov-based risk-state forecasting into routine project monitoring, with particular attention to the Moderate-Risk Intervention Window identified in Section 5.3. Second, institutions should prioritise the systematic retention of monthly risk-assessment records, since transition-probability estimates are sensitive to the quality and volume of historical data and sensitivity was shown to vary systematically with a project's environmental exposure (Section 4.6). Third, the journal-length extension should prioritise the row-wise Dirichlet-Multinomial re-estimation identified in Section 3.4 and, once available, a full re-analysis of the raw 100 individual comparative-model assessments as a check on the group-summary correction in Section 3.9, alongside a semi-Markov extension relaxing the memorylessness assumption and cross-regional replication of the escalation-recovery asymmetry and Moderate-Risk Intervention Window.

REFERENCES

Adeoti, O. S., Kandasamy, J., & Vigneswaran, S. (2024). Sustainability framework for water infrastructure development in Nigeria: A modelling approach. *Water Supply, 24*(8), 2933–2945. https://doi.org/10.2166/ws.2024.193

Adie, E. U. (2026). *Application of the Markov chain model in sustainable risk management in socioeconomic and environmental aspects of projects* [Unpublished doctoral thesis]. Edo State University Iyamho.

Aziz, N. A. A., Manab, N. A., & Othman, S. N. (2016). Sustainability risk management (SRM): An extension of enterprise risk management (ERM) concept. *International Journal of Management Science and Business Administration, 2*(5), 45–51.

Ching, W. K., Huang, X., Ng, M. K., & Siu, T. K. (2013). *Markov chains: Models, algorithms and applications* (2nd ed.). Springer.

Cochran, W. G. (1977). *Sampling techniques* (3rd ed.). Wiley.

Elkington, J. (1997). *Cannibals with forks: The triple bottom line of 21st century business*. Capstone.

Freeman, R. E. (1984). *Strategic management: A stakeholder approach*. Pitman.

Kemeny, J. G., & Snell, J. L. (1976). *Finite Markov chains* (2nd ed.). Springer-Verlag.

Koller, D., & Friedman, N. (2009). *Probabilistic graphical models: Principles and techniques*. MIT Press.

Mba, I. C., Mba, E. I., Arazu, W. O., Urama, C. E., Machebe, C. H., & Eze, C. (2019). Application of the stochastic Markov model in predicting the volume of oil spill in Nigeria: A case of the Niger-Delta region. *International Journal of Energy Economics and Policy, 9*(4), 110–114. https://doi.org/10.32479/ijeep.7744

Norris, J. R. (1997). *Markov chains*. Cambridge University Press.

Omoyi, C. O., & Omotehinse, S. A. (2022). A factorial analysis of industrial safety. *International Journal of Engineering and Innovative Research, 4*(1), 33–43. https://doi.org/10.47933/ijeir.1027304

Papoulis, A., & Pillai, S. U. (2018). *Probability, random variables, and stochastic processes* (4th ed.). McGraw-Hill.

Sathurshan, M., Saja, A., Thamboo, J., Haraguchi, M., & Navaratnam, S. (2022). Resilience of critical infrastructure systems: A systematic literature review of measurement frameworks. *Infrastructures, 7*(5), 67. https://doi.org/10.3390/infrastructures7050067

Shehadeh, A., Alshboul, O., & Tamimi, M. (2024). Integrating climate change predictions into infrastructure degradation modelling using advanced Markovian frameworks to enhance resilience. *Journal of Environmental Management, 368*, Article 122234. https://doi.org/10.1016/j.jenvman.2024.122234

Tan, Z., Wu, B., & Che, A. (2023). Resilience modeling for multi-state systems based on Markov processes. *Reliability Engineering & System Safety, 235*, Article 109207. https://doi.org/10.1016/j.ress.2023.109207

Yang, X. S. (2020). *Introduction to computational mathematics* (2nd ed.). World Scientific.

Zhang, Z., Li, W., & Yang, J. (2021). Analysis of stochastic process to model safety risk in construction industry. *Journal of Civil Engineering and Management, 27*(2), 87–99. https://doi.org/10.3846/jcem.2021.14108

International Conference on Engineering Innovation for Sustainable Development (ICESID 2026)
Faculty of Engineering, Ahmadu Bello University Zaria · 8–10 September 2026

MOISTURE-DEPENDENT ENGINEERING PROPERTIES OF BEEDI BAMBARA GROUNDNUT (VIGNA SUBTERRANEA (L.) VERDC.) FOR POST-HARVEST PROCESSING DESIGN

Abdullahi Saeed Hassan[1,*], Aminu Mohammed[1], Jamilu. M. Ahmed[1], Bala Gambo Jahun[1], Danladi Drambi Usman[1], Abdulwahab D. Ismail[1], Lawan Garba Abubakar[1]

[1]*Abubakar Tafawa Balewa University*

Email: ashassan@atbu.edu.ng*, "", "", "", "", "", ""

***Corresponding author**: Abdullahi Saeed Hassan

DOI: https://doi.org/10.67203/sp.ICESID.2026

ABSTRACT

The engineering properties of agricultural produce are fundamental to designing and optimizing post-harvest handling, sorting, processing, and storage machinery. This study investigated the physical and mechanical properties of the Beedi Bambara groundnut (Vigna subterranea (L.) Verdc.), a prominent regional cultivar from Bauchi State, Nigeria, as a function of moisture content ranging from 5.0% to 35.0% (wet basis). Over this moisture range, the average linear dimensions—length, width, and thickness increased from 10.3 to 14.3 mm, 9.49 to 11.65 mm, and 8.50 to 10.90 mm, respectively. The geometric mean diameter expanded from 9.64 to 12.54 mm. Volumetric characteristics, including surface area (245.8 to 390.2 mm^2), seed volume (358.1 to 703.1 mm^3), and 1,000-grain mass (500.2 to 810.5 g), exhibited strong positive correlations with moisture content, with the 1,000-grain mass increasing linearly (R^2 = 0.9987). Conversely, bulk and true densities decreased non-linearly from 1.30 to 1.08 g/cm^3 and 1.32 to 1.18 g/cm^3, respectively, indicating that the seed kernel's volumetric expansion outpaced its mass accumulation. Porosity and the dynamic angle of repose varied nonlinearly, peaking at 45.8% and 24.1°, respectively, near 20% moisture content before tapering at higher moisture levels. The static coefficient of friction increased significantly across all structural contact surfaces tested, showing the highest friction on plywood (0.38 to 0.66), followed by galvanized iron (0.30 to 0.52) and aluminum (0.25 to 0.48). These findings show that the engineering parameters of the Beedi cultivar are highly sensitive to moisture changes, establishing a foundational database for developing localized cracking, cleaning, and storage equipment.

Keywords: *Beedi variety; Vigna subterranea; physical properties; mechanical properties; structural surfaces; geometric mean diameter*

1 INTRODUCTION

Bambara groundnut (*Vigna subterranea* (L.) Verdc.) is an indigenous African legume and the third most important grain legume in semi-arid Africa, after cowpea and peanut (Hillocks et al., 2012). Valued for its exceptional climate resilience, high drought tolerance, and capacity to yield on nutrient-poor soils where other crops fail, it plays a vital role in food security throughout sub-Saharan Africa (Mayes et al., 2019). Nutritionally, the crop represents a "complete food," containing roughly 19–25% crude protein, 60–65% carbohydrates, and 5–7% fats, making it a critical protein source for low-income populations (Kaptso et al., 2016; Ojo & Ade-Omowaye, 2015). In Nigeria, cultivation is highly concentrated across semi-arid belts, including major producing hubs in Kano, Plateau, Sokoto, Bauchi, and Benue states. Among these, the "Beedi" cultivar represents a distinct, heavily cultivated variety in Bauchi State characterized by specific kernel configurations and uniform light-brown mottling.

Despite its vast agronomic potential and increasing industrial demand for commercial composite meals, flours, and food matrices, processing remains a critical bottleneck (Olapade & Adetuyi, 2007). Bambara groundnut pods are notoriously tough, rigid, and resistant to mechanical failure. Consequently, post-harvest shell-cracking and decortication within regional farming communities rely almost exclusively on laborious, archaic practices. These traditional methods include manual crushing with a pestle and mortar, pounding pods with heavy wooden sticks on bare ground, or breaking them individually with stones (Ojediran, 2008). Such operations not only display low throughput and excessive drudgery but also cause severe mechanical impact injuries to the internal

cotyledons. This seed damage undermines product quality, escalates microbial vulnerability, and severely lowers the germination rate of saved seed lots.

To transition from primitive post-harvest techniques to automated, mechanized systems, engineers must establish a precise understanding of the crop's moisture-dependent engineering properties (Altuntas & Demirtola, 2007). Physical attributes, such as axial spatial dimensions, geometric mean diameter, shape profiles, and surface areas, dictate optimal screen clearances in cleaner-separators and the dimensional configurations of decorticating chambers (Mohsenin, 1986). Gravimetric properties, including bulk density, true density, and internal porosity, influence structural weight estimates for bulk silos, depth boundaries for drying aeration fans, and thermal behavior profiles during rehydration processing (Mpotokwane et al., 2008). Concurrently, mechanical behaviors such as the static coefficient of friction with common structural materials (e.g., plywood, galvanized iron, and aluminum) and the angle of repose govern the slope configurations of gravity-fed hoppers, discharge chutes, and aggregate transport conveyors (Baryeh, 2001).

Because agricultural seeds absorb and desorb moisture dynamically throughout harvesting, handling, and storage cycles, their structural matrices swell, their surface textures change, and their weight varies. While baseline engineering profiles have been recorded for general Bambara groundnuts originating from specific geographic zones (Baryeh, 2001; Mpotokwane et al., 2008), data directly focusing on localized West African varieties, such as the Beedi cultivar, remain scarce.

Therefore, this study establishes the moisture-dependent physical and mechanical properties of the Beedi Bambara groundnut variety over a broad, processor-relevant moisture spectrum of 5.0% to 35.0% (wet basis). The resulting quantitative relationships will provide the structural data required to model and fabricate efficient, high-capacity post-harvest processing machinery.

2 MATERIALS AND METHODS

2.1 Sample collection and preparation

The test material comprised the Beedi variety of Bambara groundnut (*Vigna subterranea* (L.) Verdc.), procured locally from Muda Lawal Market within the Bauchi metropolis, Nigeria. The initial moisture content of the seeds was 14.0% (wet basis), determined using the ASABE standard oven-drying method for legumes (ASABE, 2012). We conducted botanical identification and authentication at the Bauchi State Agricultural Development Program (BADP). While these samples provide a robust baseline, sourcing from a single commercial market lot may not capture the full natural field variability of the cultivar across different harvest seasons and microclimates. Before the experiment, we manually cleaned the seed lots to remove foreign matter, dust, and defective (broken, split, or deformed) kernels.

To evaluate engineering properties across a post-harvest-relevant moisture spectrum (5.0% to 35.0% wet basis), samples were conditioned using standard hydration and dehydration procedures (Baryeh, 2001; Nkambule et al., 2023). To attain higher moisture levels, a calculated amount of distilled water was added to the samples based on Equation 1 (Balasubramanian, 2001; Sanchez et al., 2024):

$$Q = \frac{W_i\left(M_f - M_i\right)}{100 - M_f} \tag{1}$$

Where (Q) is the mass of water added (kg), (W_i) is the initial sample mass (kg), (M_i) is the initial moisture content (% wb), and (M_f) is the desired final moisture content (% wb). Samples were hermetically sealed in polyethylene bags and stored at 5°C for 7 days to ensure uniform moisture distribution. For moisture levels below 14%, samples were progressively desorbed using a vacuum oven until the target moisture was reached (Saeed et al., 2022).

2.2 Measurement of physical and dimensional characteristics

For each targeted moisture level, the three principal spatial dimensions—length (L), width (W), and thickness (T) were randomly measured on 100 seeds using a precision Vernier caliper (0.001 mm accuracy) (Figure 1).

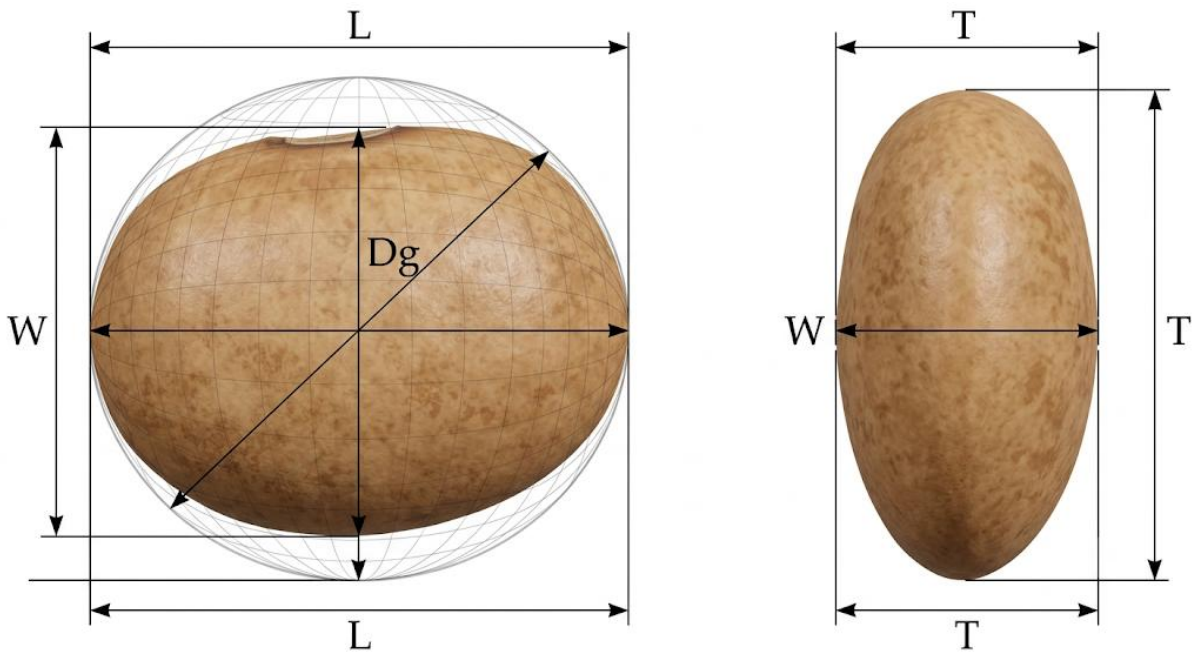

Figure 1: Conceptual presentation of the major dimensions of the Bambara seed.

The geometric mean diameter (D_g) was calculated utilizing Equation 2 (Mohsenin, 1986):

$$D_g = (LWT)^{1/3} \tag{2}$$

To evaluate the shape of the Beedi nuts, the degree of sphericity was calculated as defined by Jain and Bal (1997) and Mohsenin (1986), (Equation 3):

$$\phi_e = \frac{(LWT)^{1/3}}{L} \tag{3}$$

The surface area (S) and grain volume (V) of the seeds were mathematically derived using established theoretical frameworks for agricultural materials (Ayodele & Beatrice, 2015; Baryeh, 2001; Mpotokwane et al., 2008):

$$S = \pi D_g^2 \tag{4}$$

$$V = \frac{\pi B^2 L^2}{6(2L - B)} \tag{5}$$

(where $B = \sqrt{WT}$*)*

2.3 Gravimetric properties: mass, density, and porosity

The 1,000-seed mass was determined by randomly selecting 100 seeds, weighing them on a high-precision electronic analytical balance (0.001 g sensitivity), and multiplying the result by 10 to obtain the 1,000-seed equivalent mass (Kaptso et al., 2016).

True density (ρ_t) was evaluated using toluene displacement under a fume hood, with appropriate personal protective equipment, and disposed of according to environmental safety guidelines. (Mohsenin, 1986). Bulk density (ρ_b) was quantified by filling a standardized cylindrical container of known volume with seeds from a height of 150 mm and weighing the contents.

Subsequently, the inter-granular porosity (ε), which represents the percentage of void space within the bulk grain, was computed mathematically using Equation 6 (Altuntas & Demirtola, 2007):

$$\varepsilon = \left(1 - \frac{\rho_b}{\rho_t}\right) \times 100 \tag{6}$$

2.4 Evaluation of mechanical and frictional properties

The dynamic angle of repose (θ) was measured using a custom-built wooden cuboid apparatus (300×300×300 mm) with a rapid-release front panel (Galedar et al., 2010). Conditioned kernels were loaded into the chamber; when the front panel was quickly removed, the grains cascaded to form a natural slope. The angle was geometrically calculated based on the height (H) and diameter (D) of the resulting grain pile using Equation 7:

$$\theta = \tan^{-1}\left(\frac{2H}{D}\right) \tag{7}$$

The static coefficient of friction (μ) was determined against three common structural materials (plywood, galvanized iron, and aluminum sheet). A customized bottomless metallic cylinder (50 mm diameter and 50 mm height) was filled with seeds and positioned slightly above an adjustable tilting test surface. The plane was incrementally inclined using a calibrated screw mechanism until the cylinder began to slide. The static friction coefficient was calculated using Equation 8, where α is the angle of tilt at the point of kinetic initiation (Baryeh, 2001):

$$\mu = \tan \alpha \tag{8}$$

All physical, gravimetric, and mechanical tests were performed in quintuplicate (five replicates) at each moisture level to ensure statistical reliability, and the mean values were recorded.

2.5 Statistical Analysis

The data were subjected to a One-Way Analysis of Variance (ANOVA) using OriginPro 2026 software. Where significant differences were observed, mean separations were performed using Duncan's Multiple Range Test at a 95% confidence level ($p < 0.05$) to establish statistical groupings.

3 RESULTS AND DISCUSSION

3.1 Effect of moisture content on grain dimensions

The variations in the principal axial dimensions—length (L), width (W), thickness (T), and geometric mean diameter (D_g)—of the Beedi Bambara nuts concerning moisture content are presented in Figure 2A. The data reveal that all physical dimensions increased as the moisture content rose from 5.0% to 25.0% (wet basis), after which no significant dimensional changes were observed. This dimensional plateau can be attributed to the cellular architecture of the cotyledons; as the seeds absorb moisture, the internal air voids are progressively displaced by water until structural saturation is achieved at approximately 25% moisture. These findings align with hydration behaviors reported for other legumes, such as soybeans (Deshpande et al., 1993) and other Bambara groundnut varieties (Baryeh, 2001; Nkambule et al., 2023), confirming that mechanical decorticator clearance settings must account for this maximum expansion to prevent kernel damage during processing.

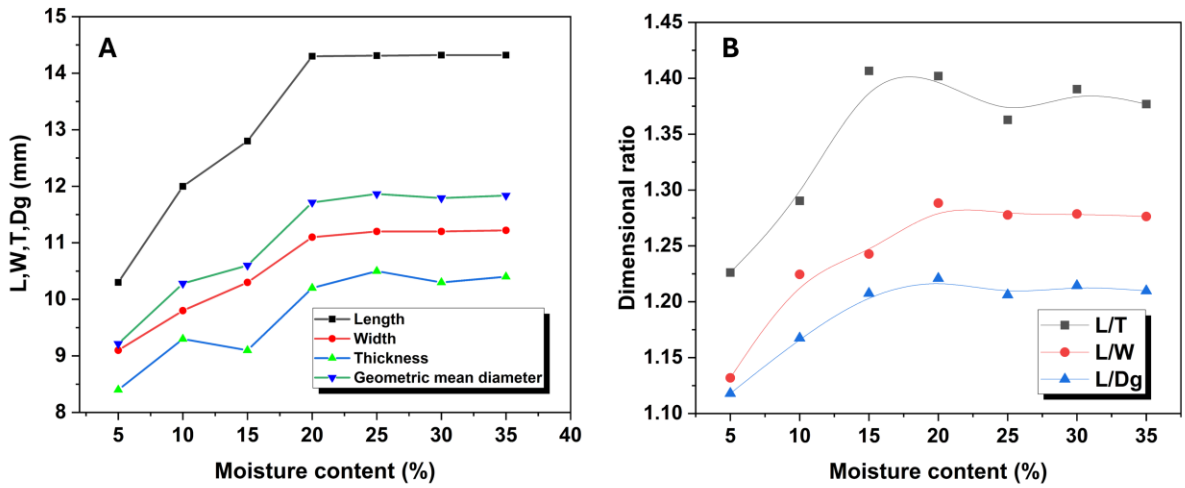

Figure 2: B illustrates the variation in the dimensional ratios (*L/W, L/T, and* L/D_g). As corroborated by the absolute spatial measurements in Figure 2A, the *L/T* ratio showed the highest values, confirming that thickness remains the smallest spatial dimension as the seed expands, followed by width and geometric diameter. These ratios increased as moisture content rose to 25% but subsequently decreased. The observed ratios for the Beedi variety were generally lower than those reported by Baryeh (2001), suggesting that the Beedi cultivar has a more uniform, compact morphological profile than other West African landraces.

Figure 2: Variation of the dimensions and dimensional ratios with moisture content.

3.2 Sphericity, surface area, and grain volume

Figure 3: A depicts the influence of moisture content on the degree of sphericity. Notably, the shape assumption heavily dictated the outcome; the equation assuming an elliptical shape yielded lower sphericity values (ranging from 0.895 at 5% to 0.840 at 35% moisture content). Because the true morphology of Bambara groundnuts is closer to an elliptical sphere, the model more accurately represents the Beedi variety. The slight decrease in sphericity with hydration indicates asymmetrical swelling, making the kernel slightly more elongated at higher moisture levels.

Figures 3B and 4A show that both surface area and grain volume increased substantially with moisture up to 25%, then plateaued. This non-linear expansion supports findings by Baryeh (2001) for Bambara groundnuts, though it contrasts with Deshpande et al. (1993), who reported a strictly linear increase in soybean surface area. This difference may be due to the more rigid and restrictive seed coat of the Bambara nut, which limits structural stretching compared with the more elastic testa of soybeans.

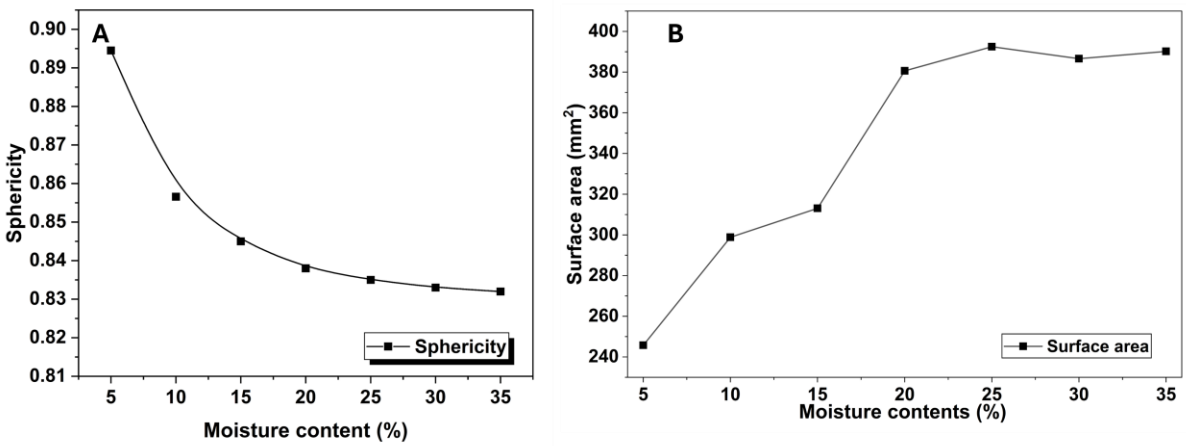

Figure 3: Variation of Sphericity (A) and surface area (B) with moisture content.

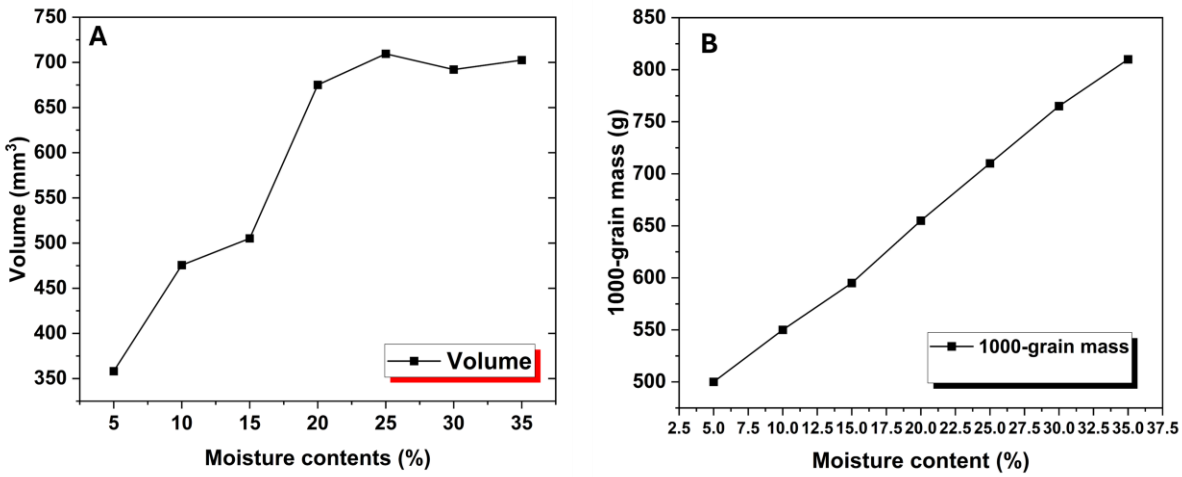

Figure 4: Variation of volume (A) and 1000-grain mass (B) with moisture content.

3.3 Gravimetric properties: mass, density, and porosity

The 1,000-grain mass exhibited a highly positive linear correlation with moisture content, as shown in Figure 4B. This variation is mathematically modeled as:

$$Y = 448 + 10.53M \ (R^2 = 0.9987).$$

Where *Y* represents the 1,000-grain mass (g), and *M* is the moisture content (%).

This predictable mass accumulation is consistent with established literature across various seeds, including cumin, soybeans, and coffee (Aviara et al., 1999; Chandrasekar & Viswanathan, 1999). Conversely, as illustrated in Figure 5A, both bulk density and true density decreased non-linearly as moisture content increased from 5.0% to 35.0% (bulk density dropping from 1.30 to 1.08 g/cm³, and true density from 1.32 to 1.18 g/cm³). This inverse relationship occurs because the seed structure expands volumetrically faster than it gains mass from moisture absorption. While this agrees with the behaviors of soybeans and some Bambara varieties (Polat et al., 2006; Nkambule et al., 2023), it contradicts the behavior of pumpkin and karingda seeds, where densities increase with moisture (Joshi et al., 1993; Suthar & Das, 1996). We theorize that this discrepancy is fundamentally linked to the unique starch-protein matrices of individual species; seeds with higher initial porosity experience more pronounced volumetric swelling, driving the overall density downward.

The porosity of the Beedi nuts (Figure 5B) displayed a parabolic trend, initiating at 40.0%, peaking at 45.8% (around 20% moisture), and then declining to 42.5% at higher moisture levels. This non-linear response contradicts the strictly linear decreases or increases often reported in existing literature for other crops. The initial rise in porosity indicates that bulk density decreases faster than true density at lower moisture levels. However, as the seeds approach saturation (past 20%), they swell and become more pliable, packing more tightly under their own weight and reducing inter-granular void spaces.

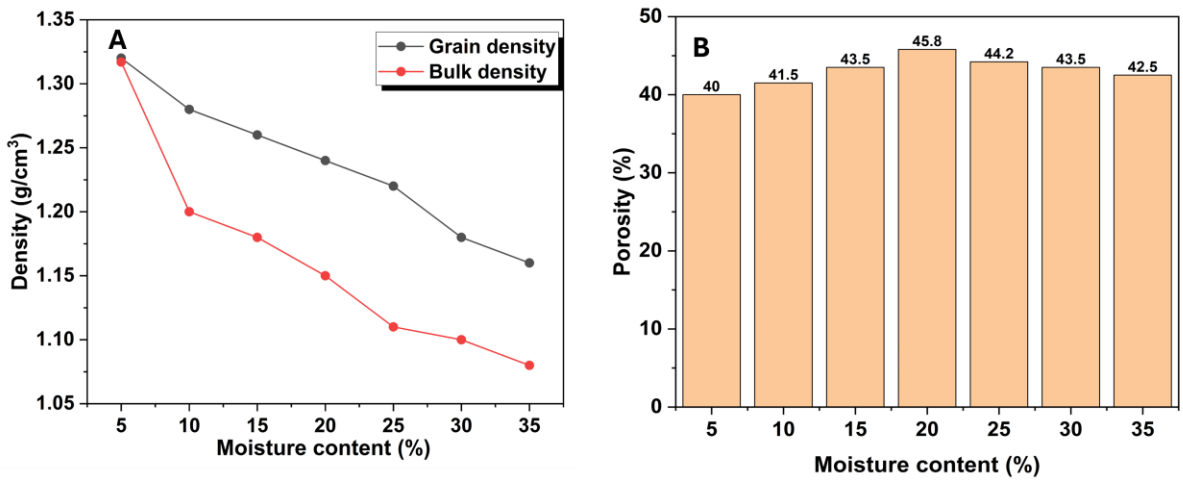

Figure 5: Variation of density (A) and porosity (B) with moisture content.

3.4 Mechanical and frictional properties

The dynamic angle of repose is a critical parameter for designing hopper slopes. As shown in Figure 6A, it increased from 20.0° at 5% moisture to a peak of 24.1° at 20% moisture, then slightly decreased to 21.5° at 35% moisture. This initial increase indicates higher inter-particle cohesion and flow resistance as the seed surfaces transition from dry to damp. The subsequent decrease at maximum moisture may be due to the lubricating effect of surface free water.

Figure 6: B depicts the variation of the static coefficient of friction against different structural surfaces. Across all moisture levels, friction was significantly highest on plywood (0.38 to 0.66), followed by galvanized iron (0.3 to 0.52), and lowest on aluminum sheet (0.25 to 0.48). The coefficient increased rapidly between 5% and 15% moisture content, then leveled off. We agree with the mechanisms proposed by Gupta and Das (1998) and Baryeh (2001): smoother, polished surfaces such as aluminum naturally offer less resistance than porous, rough materials such as plywood. Furthermore, as moisture increases, exudate creates adhesive capillary forces between the kernel and the contact surface, thereby elevating frictional resistance. Consequently, processing machinery, particularly discharge chutes, should utilize aluminum or polished galvanized steel to maintain unhindered grain flow and prevent blockages at higher moisture states.

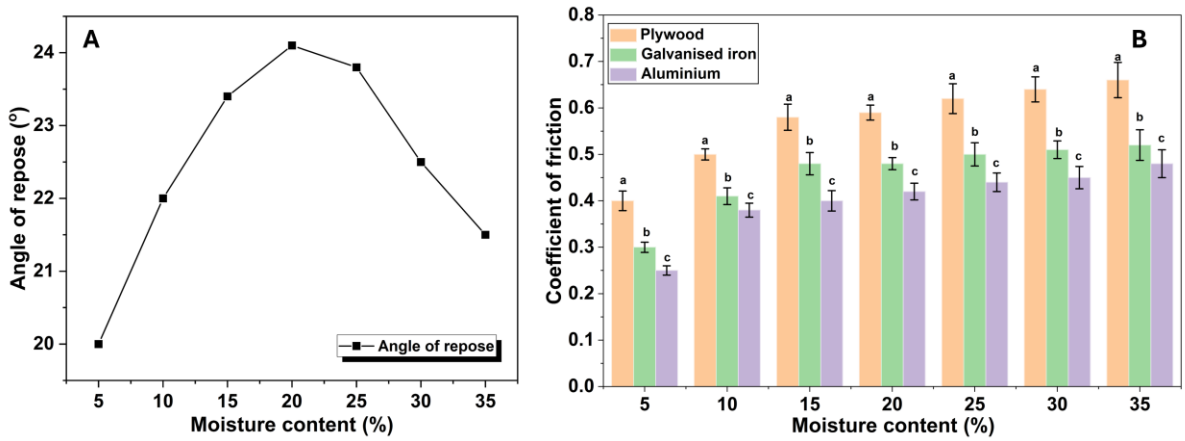

Figure 6: Variation of angle of repose (A) and coefficient of friction against different surfaces (B) with moisture content.

4 CONCLUSION

The study evaluated the engineering properties of the Beedi variety of Bambara groundnut (*Vigna subterranea* (L.) Verdc.) from Bauchi State, Nigeria, across a post-harvest moisture range of 5.0% to 35.0% (wet basis). The findings indicate that the principal linear dimensions (length, width, and thickness), geometric mean diameter, surface area, and grain volume all exhibit a non-linear expansion as moisture content rises. Regarding gravimetric properties, the 1,000-seed mass

demonstrated a strictly positive linear correlation with moisture accumulation. Conversely, both bulk density and true density decreased non-linearly, though true density consistently remained higher than bulk density across all hydration levels. Furthermore, seed flow behavior characterized by inter-granular porosity and the dynamic angle of repose increased to a peak value before declining with further moisture absorption. Mechanically, the static coefficient of friction increased significantly with moisture content across all tested structural surfaces, with plywood offering the highest frictional resistance, followed by galvanized iron and aluminum. Ultimately, these moisture-dependent quantitative parameters provide the essential baseline data required for the optimal design, structural development, and operational adjustment of handling, decorticating, sorting, and processing machinery. By enabling local equipment innovation, this dataset directly supports sustainable agro-material processing and resource utilization strategies.

REFERENCES

Altuntas, E., & Demirtola, H. (2007). Effect of moisture content on physical properties of some grain legume seeds. *New Zealand Journal of Crop and Horticultural Science*, *35*(4), 423–433. https://doi.org/10.1080/01140670709510210

ASABE. (2012). Moisture measurement - Unground grain and seeds. *ASAE S352.2*. American Society of Agricultural and Biological Engineers, St. Joseph, MI.

Aviara, N. A., Gwandzang, M. I., & Haque, M. A. (1999). Physical properties of guna seeds. Journal of Agricultural Engineering Research, 73(2), 105-111.

Ayodele, O. M., & Beatrice, A. I. O. (2015). Some functional and physical properties of selected underutilised hard-to-cook legumes in Nigeria. *American Journal of Food Science and Nutrition*, *2*(5), 73-81.

Balasubramanian, D. (2001). PH—postharvest technology: physical properties of raw cashew nut. Journal of Agricultural Engineering Research, 78(3), 291-297.

Baryeh, E. A. (2001). Physical properties of bambara groundnuts. *Journal of Food Engineering*, *47*(4), 321–326. https://doi.org/10.1016/S0260-8774(00)00136-9

Chandrasekar, V., & Viswanathan, R. (1999). Physical and thermal properties of coffee. *Journal of Agricultural Engineering Research*, *73*(3), 227–234. https://doi.org/10.1006/jaer.1999.0411

Deshpande, S. D., Bal, S., & Ojha, T. P. (1993). Physical properties of soybean. *Journal of Agricultural Engineering Research*, *56*(2), 89–98. https://doi.org/10.1006/jaer.1993.1063

Galedar, M. N., Tabatabaeefar, A., Jafari, A., Sharifi, A., Mohtasebi, S. S., & Fadaei, H. (2010). Moisture dependent geometric and mechanical properties of wild pistachio (Pistacia vera L.) nut and kernel. International Journal of Food Properties, 13(6), 1323-1338.

Gupta, R. K., & Das, S. K. (1998). Friction coefficients of sunflower seed and kernel on various structural surfaces. *Journal of Agricultural Engineering Research*, *71*(2), 175–180. https://doi.org/10.1006/jaer.1998.0316

Hillocks, R. J., Bennett, C., & Mponda, O. (2012). Bambara nut: A review of utilisation, market potential and crop improvement. *African Crop Science Journal*, *20*(1), 1–16.

Jain, R. K., & Bal, S. (1997). Properties of pearl millet. *Journal of Agricultural Engineering Research*, *66*(2), 85–91. https://doi.org/10.1006/jaer.1996.0119

Joshi, D. C., Das, S. K., & Mukherjee, R. K. (1993). Physical properties of pumpkin seeds. *Journal of Agricultural Engineering Research*, *54*(3), 219–229. https://doi.org/10.1006/jaer.1993.1016

Kaptso, G. K., Njintang, N. Y., Nguemtchouin, M. G. M., Amungwa, A. F., Scher, J., Hounhouigan, J., & Mbofung, C. M. (2016). Characterization of morphology and structural and thermal properties of legume flours: Cowpea (*Vigna unguiculata* L. Walp) and bambara groundnut (*Vigna subterranea* L. Verdc.) varieties. *International Journal of Food Engineering*, *12*(2), 139–152. https://doi.org/10.1515/ijfe-2015-0112

Mayes, S., Ho, W. K., Chai, H. H., Gao, X., Kundy, A. C., Mateva, K. I., Zahrulakmal, M., Hahiree, M. K. I. M., Kendabie, P., & Licea, L. C. (2019). Bambara groundnut: An exemplar underutilised

legume for resilience under climate change. *Planta*, *250*(3), 803–820. https://doi.org/10.1007/s00425-019-03191-6

Mohsenin, N. N. (1986). Physical Properties of Plant and Animal Materials. 2nd revised and updated edition.

Mpotokwane, S. M., Gaditlhatlhelwe, E., Sebaka, A., & Jideani, V. A. (2008). Physical properties of bambara groundnuts from Botswana. *Journal of food engineering*, *89*(1), 93-98. https://doi.org/10.1016/j.jfoodeng.2008.04.006.

Nkambule, S., Workneh, T., Sibanda, S., Alaika, K., & Lagerwall, G. (2023). The effect of moisture contents on the physical properties of both bambara groundnut seeds and pods in South Africa. *African Journal of Food, Agriculture, Nutrition and Development*, *23*(121), 23817–23834. https://doi.org/10.18697/ajfand.121.22280

Ojediran, J. O. (2008). *Sorption phenomena and mechanism of moisture movement during the drying of pearl millet (Pennisetum glaucum) and castor (Ricinus communis) seeds* [Unpublished doctoral dissertation]. Department of Agricultural and Environmental Engineering, University of Ibadan, Nigeria.

Olapade, A., & Adetuyi, D. O. (2007). Comparison of different methods of producing bambara (*Voandzeia subterranea* L. Thou) flours for preparation of moin-moin. *Nigerian Food Journal*, 25(1), 150–157. https://hdl.handle.net/1807/36513.

Polat, R., Atay, U., & Saglam, C. (2006). Some physical and aerodynamic properties of soybean. *Journal of Agronomy*, *5*(1), 74–78.

Saeed, H. A., Kabir, M. H., Auwal, M., & Jahun, B. G. (2022). Determination of some engineering properties of rhoko bambara nuts. *Proceedings of the 22nd International Conference and 42nd Annual General Meetings of the Nigerian Institution of Agricultural Engineers (NIAE)*. Asaba, Nigeria. ISSN: 0794-8387.

Sanchez, A., Pacheco Barragán, H. C., Urbano-T, J., Ayala-Garcia, C., Alvarez Solano, O. A., Maranon, A., ... & Hernandez, C. (2024). Physical, morphological, and mechanical properties of raw and steamed cashew nuts (Anacardium occidentale L.). International Journal of Food Properties, 27(1), 224-244.

Suthar, S. H., & Das, S. K. (1996). Some physical properties of karingda [*Citrullus lanatus* (Thumb) Mansf] seeds. *Journal of Agricultural Engineering Research*, *65*(1), 15–22. https://doi.org/10.1006/jaer.1996.0075

International Conference on Engineering Innovation for Sustainable Development (ICESID 2026)
Faculty of Engineering, Ahmadu Bello University Zaria · 8–10 September 2026

PERFORMANCE EVALUATION OF A PROTOTYPE THERMO-ELECTRIC GENERATOR (TEG) BASED ENERGY HARVESTER FROM ASPHALT PAVEMENTS

Mubarak Danladi Muhammad[1,*], Abdulazeez Nazif[1]
[1]*Bayero University, Kano*
Email: mubarak.danladi@gmail.com[*], nazeef003@gmail.com
***Corresponding author**: Mubarak Danladi Muhammad
DOI: https://doi.org/10.67203/sp.ICESID.2026

ABSTRACT
Asphalt pavements trap a substantial amount of solar radiation and comprise between 30% and 45% of urban areas, thus contributing to the urban heat island (UHI) effect due to their high thermal storage, which leads to the softening and degradation of the pavement. Energy harvesting techniques are one of the promising ways to mitigate these effects while making sustainable use of the trapped thermal energy. In this study, the performance of a thermoelectric generator (TEG)-based energy harvesting prototype integrated with asphalt pavements was evaluated. A fabricated 30 × 30 cm asphalt slab with a thickness of 5 cm and an embedded copper collector was used. The hot side of the TEG module was attached to the L-shaped copper collector, and the cold side was connected to a water-filled aluminium heat sink. Six TEG modules were mounted for redundancy, of which four were active during data collection. Performance was evaluated under controlled indoor conditions; temperatures were measured using embedded thermocouples and electrical output was measured using a multi-meter. Under controlled indoor conditions, temperature differences (ΔT) of 12–22°C produced 0.295–0.897 V, 3.6–15.73 mA, and a maximum power output of 14.12mW from the four active TEG modules, confirming the feasibility of harvesting thermal energy from asphalt pavements. This corresponds to a potential of approximately 157 mW/m² of asphalt pavement surface. The study demonstrates a practical approach to pavement-based thermoelectric energy harvesting in hot-climate regions and recommends outdoor field testing, seasonal performance monitoring, and optimization for large-scale deployment in Kano, Northern Nigeria.
Keywords: *Heat Sink; Seebeck Effect; Thermal Collector; Conveyor; Asphalt Pavement*

1. INTRODUCTION

Asphalt pavement, a black body surface, absorbs solar radiation, elevating its temperature, often reaching 25-50°C depending on location and weather (Aletba et al., 2021). In tropical regions with high solar exposure, this heat, combined with heavy traffic, can melt the asphalt, causing surface defects like bumps and bruises upon cooling. To ensure durability, especially in tropical areas, maintaining lower asphalt temperatures is crucial. The absorbed solar radiation converts to thermal energy, heating the asphalt above the ambient temperature and subsequently releasing heat to the environment, contributing to the Urban Heat Island effect (UHI) (Nuruzzaman, 2015). Cooling asphalt is essential to mitigate the UHI effect and enhance pavement longevity, considering its substantial coverage in urban areas (30 to 45% of land area).

Pavements, comprising 30% to 45% of urban areas, significantly contribute to the urban heat island (UHI) effect due to their high thermal storage and low solar radiation reflection (Ikechukwu, 2015; Kuehl, 2021). Traditional cooling methods involve applying reflective coatings on the surface to deflect rather than absorb solar radiation. Aletba et al. (2021) emphasize the importance of cooling strategies for pavement surfaces, considering their direct exposure to solar impact, influenced by surface characteristics like colour, material, shape, and roughness. Utilizing high-albedo and high emissivity surfaces minimizes heat retention and lowers pavement temperatures. Similarly, engineering materials and pavement layers with low thermal conductivity and high heat capacity can reduce thermal diffusivity, combatting the heat emitted by asphalt pavement.

Energy harvesting refers to the process of capturing and converting ambient or waste energy from the environment, such as solar, thermal, kinetic, or wind energy, into usable electrical power for

operating devices or systems. Energy harvesting can be a useful technology as it offers to mitigate the urban heat island (UHI) effect, prolong the lifespan of asphalt pavements and use the harvested heat in many useful applications. Thermal energy from incident solar radiation which is absorbed by the asphalt pavement can be harvested using energy harvesting technologies such as; the photovoltaic solar panel, heat pipe solar collector and thermoelectric generator systems.

Research on energy harvesting from asphalt pavement using Thermoelectric Generators (TEGs) is an emerging area of interest with promising potential. TEGs embedded in asphalt pavement can potentially convert the heat generated by solar radiation and vehicular traffic into electrical energy, allowing for energy harvesting and power generation from roadways. Various researchers (Mona et al. (2021); Sharuddin (2021); Jiang et al. (2017); Datta et al. (2017); Tahami and Dessouky (2021)) have developed TEGs for harvesting energy from asphalt pavements. Over the years researchers have focused on increasing the TEGs operational efficiency through optimizing the thermos electric material (Yang et al. (2017) and Lobunets (2021)); Enhancing heat transfer in the asphalt pavement (Alhamdo (2023); Qusay Doraghi (2024); Liu (2012); and Leon (2010)); Improving System design and configuration (Eman (2018); Maduabuchi (2021)) and Heat sink optimization (Jiang et al. (2017); Boonyasri et al. (2016)). Performance of these prototype systems depends on the climatic conditions in the region and the properties of the asphalt itself. Thus, to properly utilize this technology in Nigeria, there is the need to quantify the potential of this technology for potential applications in powering road equipment such as traffic lights, road signs, and similar low-power devices.

2. METHODOLOGY

2.1 Experimental Material/Equipment

The following material and equipment were used in this research.

- The prototype TEG Energy Harvesting system
- TA612C Thermometer (Data Logger)
- Non-contact Infrared Thermometer
- K-Type Thermocouples
- DT9205A Digital Multimeter
- KM-SPM-11 Solar Power Meter (Solarimeter)

2.2 The Prototype Asphalt TEG based Energy Harvesting System

Figure 1 presents the picture of the prototype TEG energy harvester. The prototype consists of:

- Asphalt pavement with embedded collector: A hot mix asphalt pavement, consisting of 47% coarse aggregates, 40% fine aggregates, 7% mineral filler (cement) and 6% bitumen with a surface area of 900 cm² (30 × 30 cm) and thickness of 5 cm. A copper plate is embedded into the asphalt pavement.
- Collector and conveyor: The collector and conveyor assembly was fabricated from an L-shaped copper plate. The TEG modules (SP1848-27145) with dimension of 40 mm by 40mm each and with voltage and current output of 0.97V, 225mA at 20° temperature difference. Six modules were physically mounted on the collector for redundancy (Figure 1c), of which four were wired in and active for the data collection reported in this study, so that the system could continue operating on the remaining modules in the event of an individual module failure.
- Heat sink: The heat sink was fabricated from aluminium sheets
- Wooden box housing: A wooden housing box was constructed to encase the prototype. This facilitated ease of movement and served as a protective cover, shielding the heat sink from direct solar radiation.

2.3 Experimental Setup

The conveyor section (L-shaped side of the copper plate) embedded within the asphalt pavement was connected to the hot side of the thermoelectric (TEG) module (figure 2). The cold side of the TEG module was attached to the aluminium heat sink, with both interfaces enhanced using thermal paste and secured by mechanical fastening.

(a)

(b)

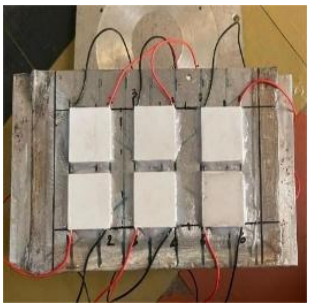

(c)

Figure 1: The prototype Asphalt TEG based energy Harvesting system (a) the Pavement (b) Heat Sink (c) TEGs attached to the Heat Sink

To minimize undesired heat losses, an insulation layer was placed between the conveyor and the heat sink, and additional insulation material was used to cover the exterior surface of the copper collector. The insulation was put to minimise heat losses from the asphalt not the sink. For temperature measurements, four K-type thermocouples were strategically installed: one embedded in the asphalt pavement in direct contact with the copper plate (collector), another attached to the conveyor, a third placed inside the heat sink, and a fourth positioned in open air near the prototype to record the ambient temperature. These provided continuous readings of temperature distribution across the system. The entire assembly was mounted within a wooden box, which served both as a protective casing and as a portable frame to facilitate movement and handling of the prototype.

Figure 2: The prototype set-up for testing

2.4 Experiment Procedure and Data Analysis Technique

- Instrumentation: Four K-type thermocouples were connected to the TA612C data logger as shown in Figure 3. The DT9205A digital multi-meter was connected directly across (for

voltage) and in series with (for current) the series-connected TEGs, so the effective electrical load during measurement was the multimeter's own internal resistance rather than a discrete external load resistor. The KM-SPM-11 solarimeter was used to measure lamp intensity.

- Procedure: The 500W halogen lamp was positioned 25 cm above the asphalt surface. The data logger, multi-meter, and solarimeter were initialized. The lamp was switched on, and data (temperature, voltage, current, light intensity) was recorded at 5-minute intervals for a period of 2 hours. The digital multi meter internal resistance and the connecting wires served as the load resistance.

Figure 3: Experimental Set-up

- Data Analysis Technique: The raw data was processed using Microsoft Excel. The high-frequency data from the logger (recorded every second) was sorted and averaged into 5-minute intervals to align with the experimental procedure. Duplicate entries were removed. Electrical power (in mW) was calculated using the formula P = V * I. Relationships between parameters (e.g., temperature difference vs. power, solar intensity vs. power) were established and visualized using Excel charts.

3. RESULTS AND DISCUSSION

Figure 4 and 5 present the temperature and power profiles recorded during the highest-output indoor test run, illustrating the general shape of the system's thermal and electrical response over the test period. The lamp intensity varied between 1295 and 1980 W/m², which caused a progressive rise in surface temperatures. The collector temperature increased from 40.7 °C to a maximum of 63.3 °C, while the conveyor temperature ranged from 32.6 °C to 45.8 °C. The heat sink remained relatively stable within 26–35 °C, reflecting the effectiveness of the insulation layer placed between the conveyor and the heat sink (Section 2.3) in limiting undesired heat transfer to the cold side. This produced a maximum temperature difference (ΔT) of approximately 22°C between the conveyor and the heat sink in this run, with voltage rising to 0.897 V, current to 15.73 mA, and power reaching a peak of 14.12 mW at 17:50 hrs, coinciding with the peak temperature difference.

These measured outputs are considerably lower than the TEG module's rated performance of 0.97 V and 225 mA at a 20 °C temperature difference (Section 2.2). This gap is attributed to several factors. First, voltage and current were measured directly with the DT9205A digital multi-meter rather than across a resistive load matched to the TEG's internal resistance, which limits the current the module can deliver into the measurement circuit. Second, thermal contact resistance at the collector–TEG and TEG–heat sink interfaces, despite the use of thermal paste, reduces the effective temperature difference across the TEG junctions relative to the temperature difference measured between the copper collector and the heat sink. Third, connecting the modules in series means that any underperforming module limits the current of the entire array. Insulation losses around the collector

and conveyor further reduce the temperature differential actually available to the modules relative to idealized datasheet test conditions.

The performance of the thermoelectric generator (TEG)-based asphalt pavement energy harvester was evaluated under indoor test conditions, focusing on the temperature difference (ΔT) between the conveyor and the heat sink (T_3–T_4), and the resulting voltage, current, and power output. Averaged across the indoor test replicates, the ΔT ranged between 12 °C and 22°C, producing 0.295–0.897 V, 3.6–15.73 mA, and a maximum power output of 14.12 mW combined from the four active TEG modules. Scaling this average output over the 900 cm² (0.09 m²) slab (asphalt) area used in the prototype (14.12 mW ÷ 0.09 m²) gives a harvestable potential of approximately 157 mW/m² of asphalt pavement surface under similar indoor conditions. These results are broadly consistent with those of Datta et al. (2017), who reported a system-level (aggregate) output of 0.52–0.68 V and about 15mW at similar ΔT values (10–15°C); both figures represent total system output rather than a per-module value, making the comparison directly comparable. The slight difference may be attributed to variations in module contact resistance and heat transfer efficiency. Both studies confirm a direct proportionality between ΔT and output power, validating the Seebeck principle.

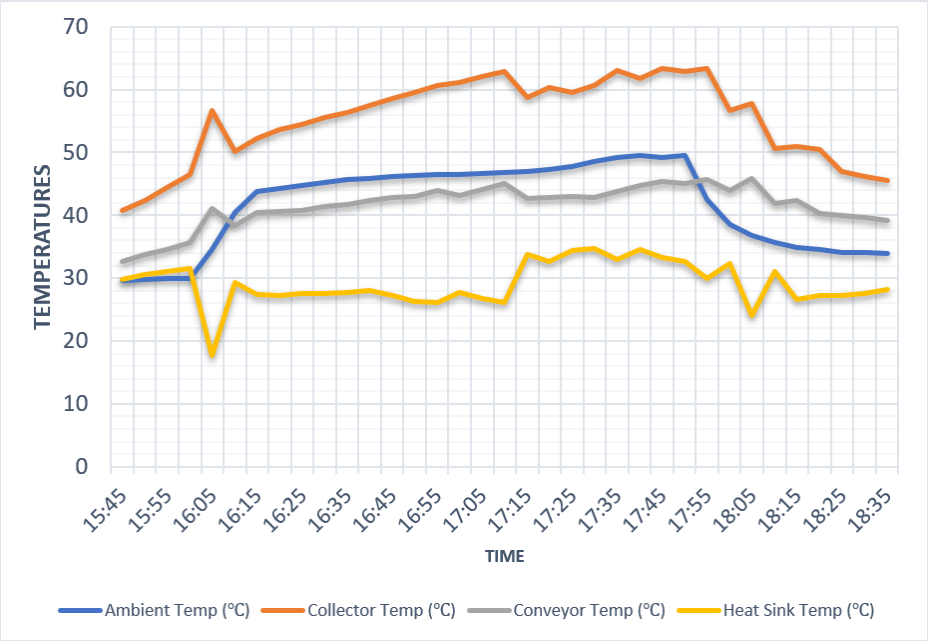

Figure 4: Temperature profile recorded during the highest-output indoor test run

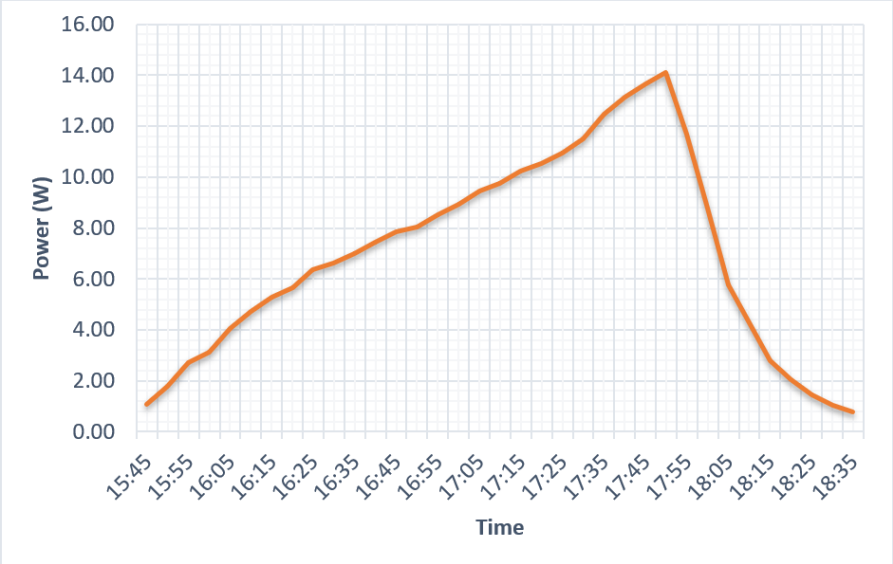

Figure 5: Power output recorded during the highest-output indoor test run

4. CONCLUSION

The design demonstrated technical feasibility for harvesting low-grade thermal energy from asphalt pavements. The completed prototype was tested under laboratory conditions, where simulated solar radiation produced stable electrical outputs, with a maximum indoor power output of 14.12 mW combined from the four active TEG modules, recorded during the highest-output trial, consistent with related studies such as Datta et al. (2017). For context, these output levels are comparable to the power budgets of several classes of low-power roadside electronics: commercial low-power wireless sensor nodes typically draw on the order of 3–12 mW during active operation (for example, the Crossbow MICAz draws approximately 2.8 mW and the Intel IMote2 approximately 12 mW (Raj & Steingart, 2018), and a single low-power LED indicator draws on the order of several milliwatts. This suggests that, while the harvested power is insufficient to continuously supply conventional road electrical systems such as full traffic signal heads, it is within range of intermittently duty-cycled sensor nodes or indicator LEDs when paired with an energy storage buffer such as a supercapacitor or small battery. Comparative analysis showed that system performance is strongly influenced by temperature gradient, ambient conditions, and material thermal properties. Although the harvested power is insufficient to independently supply conventional road electrical systems, the results demonstrate the system's viability as a supplementary energy source when integrated with hybrid renewable systems and energy storage. The next step is to test the prototype under real outdoor conditions in Kano, Northern Nigeria and to explore load-matched circuitry to help close the gap between the modules' rated and measured performance.

5. REFERENCES

Alhamdo, F. A. (2023). Enhancing the thermal conductivity of hot-mix asphalt. Results in Engineering, https://doi.org/10.1016/j.rineng.2022.100827.

Sawires, E. F., Eladawy, M. I., Ismail, Y. I., & Abd Elhamid, H. (2018). Thermal Resistance Model for Standard CMOS Thermoelectric Generator. IEEE Access, 8123-8132.

FHA. (2021). Pavements. From fhwa.dot.gov: https://www.fhwa.dot.gov/pavement/sustainability/articles/pavement_thermal.cfm#:~:text=Specific%20heat%20is%20the%20energy,900%20J%2Fkg%E2%80%A2K.

Ikechukwu, E. E. (2015). The Effects of Road and Other Pavement Materials on Urban Heat Island (A Case Study of Port Harcourt City). Journal of Environmental Protection, 6, 328-340.

Khasawneh, M. (2022). Effect of Aggregate Gradation and Asphalt Mix Volumetrics on the Thermal Properties of Asphalt Concrete. Case Studies in Construction Materials, 18(11):e01725.

Kuehl, N. (2021). What is Asphalt Paving. From Eaglepaving .com: https://eaglepaving.us/2021/03/01/what-is-asphalt paving/#:~:text=The%20asphalt%20paving%20mixture%20consists,conditions%20produced%20by%20the%20weather.

Liu, Q., Schlangen, E., van de Ven, M., van Bochove, G., & van Montfort, J. (2012). Evaluation of the induction healing effect of porous asphalt concrete through four point bending fatigue test. Construction and Building Materials, 29, 403-409.

Lobunets, Y. (2021). Improving the Economic Efficiency of Thermoelectric Generators by Optimizing Heat Transfer Conditions. Electronic Materials, DOI:10.1007/s11664-021-08797-9.

Boonyasri, M., Jamradloedluk, J., Lertsatitthanakorn, C., Therdyothin, A., & Soponronnarit, S. (2016). Increasing the Efficiency of a Thermoelectric Generator Using an Evaporative Cooling System. Journal of Electronic Materials, 46, 3043-3048.

De Leon, P. T. (2010). Improving the Efficiency Of Thermoelectric Generators By Using Solar Heat Concentrators . University of Southampton; School of Electronics and Computer Science, United Kingdom.

Maduabuchi, C. (2022). Improving the performance of a solar thermoelectric generator using nano-enhanced variable area pins. Applied Thermal Engineering, Volume 206, 118086.

Nuruzzaman., M. (2015). Urban Heat Island: causes, effects and mitigation measures- A review. International Journal of Environment Monitoring and analysis. vol.3 No.2, Pp. 67-73.

Qusay Doraghi, H. J. (2024). Thermoelectric generator efficiency: An experimental and computational approach to analysing thermoelectric generator performance. Thermal Science and Engineering Progress, https://doi.org/10.1016/j.tsep.2024.102884.

Raj, A., & Steingart, D. A. (2018). Review—Power Sources for the Internet of Things. Journal of The Electrochemical Society, 165(8), B3130-B3136.

Aletba, S. R. O., Abdul Hassan, N., Putra Jaya, R., Aminudin, E., Mahmud, M. Z. H., Mohamed, A., & Hussein, A. A. (2021). Thermal performance of cooling strategies for asphalt pavement: a state-of-the-art review. Journal of Traffic and Transportation Engineering (English Edition), 8(3), 356-373.

Tahami, S. A., & Dessouky, S. (2021, October 12). An Innovative Thermo-Energy Harvesting Module for Asphalt. From http://transet.lsu.edu/: https://digitalcommons.lsu.edu/cgi/viewcontent.cgi?article=1120&context=transet_pubs

Sharuddin, M. S. (2021, January 1). Energy Harvesting System Based on Road Pavement Incorporated With Thermoelectric Generator System. From core.ac.uk: https://core.ac.uk/display/553278422?source=2

Datta, U., Dessouky, S., & Papagiannakis, A. T. (2017). Harvesting of Thermoelectric Energy from Asphalt Pavements. Transportation Research Board, No. 17-5481. From https://www.researchgate.net/publication/309650560

Jiang, W., Yuan, D., Xu, S., Hu, H., Xiao, J., Sha, A., & Huang, Y. (2017). Energy harvesting from asphalt pavement using thermoelectric technology. White Rose University Consortium, University of Leeds.

Mona, Y., Jitsangiam, P., & Punyawudho, K. (2021). A comparison of energy harvesting from cement and asphalt on road pavement using thermoelectric module. Energy Reports, 7, 225-229.

Yang, Z., Prado-Gonjal, J., Phillips, M., Lan, S., Powell, A., Vaqueiro, P., Gao, M., Stobart, R., & Chen, R. (2017). Improved Thermoelectric Generator Performance Using High Temperature Thermoelectric Materials. SAE Technical Papers, 10.4271/2017-01-0121.

International Conference on Engineering Innovation for Sustainable Development (ICESID 2026)
Faculty of Engineering, Ahmadu Bello University Zaria · 8–10 September 2026

PRELIMINARY SCREENING AND CHARACTERIZATION OF A-CELLULOSE EXTRACTED FROM COTTON STALK, SUGARCANE BAGASSE, AND SAWDUST USING ALKALINE PRETREATMENT

Hassana Gwandi Audu[1], • Prof. Ajayi Olusegun Ayoola[1,*], M.t Isa[1]
[1]*Ahmadu Bello University Zaria*
Email: euphorosagrocorpgreentech@gmail.com, segeaj@gmail.com*, mtisaz@yahoo.com
***Corresponding author**: • Prof. Ajayi Olusegun Ayoola
DOI: https://doi.org/10.67203/sp.ICESID.2026

ABSTRACT

This study investigated the preliminary screening and characterization of α-cellulose from cotton stalk (CS), sugarcane bagasse (SCB), and sawdust (SD) to establish practical process parameters for subsequent optimization. A uniform particle size of 125 µm and solid-to-liquid ratio (1:10 w/v) were applied. CS was treated with 7.5–27.5 g NaOH/100 mL at 90°C for 1.5 h, while SCB and SD Method 1 were treated with 10–30 g NaOH/100 mL at 95°C for 1.5 h. SD Method 2 incorporated an initial 7 mL HNO_3 pretreatment at 95°C for 1.41 h prior to alkali treatment. Recovered fractions were evaluated by α-cellulose yield, purity, Van Soest fiber analysis, FTIR, XRD, and SEM–EDX. CS2 produced 30% yield and 84.06% purity; SCB2 produced 20% yield and 83.82% purity; SD3 produced 80% yield and 85.71% purity; and SDA3 produced 20% yield and 90.14% purity. FTIR confirmed substantial solubilization of non-cellulosic components. XRD analysis demonstrated shifts in Crystallinity Index (CrI) from raw to treated states: CS RAW (61.5%) to CS2 (61.4%), SCB RAW (55.7%) to SCB2 (59.6%), SD RAW (51.3%) to SD3 (66.1%), and reaching 75.2% for dual-pretreated SDA3. SEM–EDX revealed microfiber exposure, matrix disruption, and mineral leaching. Direct-alkali SD3 was selected as the optimal practical condition for sawdust due to high mass recovery (80%), process simplicity, avoiding acid consumption and multi-stage washing, where the +4.43% purity increase in SDA3 did not justify the 75% loss in recovered yield and added reagent cost. The selected conditions provide experimental starting points for subsequent DOE–CCD multi-pulping optimization; DOE–CCD and ANN/FFNN modelling are not claimed as completed in this preliminary study.

Keywords: *α-cellulose; cotton stalk; sugarcane bagasse; sawdust; alkaline pretreatment; FTIR; XRD; SEM–EDX*

1. INTRODUCTION

Lignocellulosic agricultural and wood residues are renewable resources containing cellulose, hemicellulose and lignin and offer important feedstocks for value-added cellulose-based materials (Riseh *et al.*, 2023). However, the close association of cellulose with hemicellulose and lignin makes direct recovery difficult. Chemical pretreatment, particularly alkaline treatment, can disrupt lignin–carbohydrate associations, promote fiber swelling and facilitate removal of non-cellulosic components, thereby increasing cellulose accessibility (Abolore *et al*., 2023; Hassana *et al*., 2021).

Cotton stalk, sugarcane bagasse and sawdust have different lignocellulosic structures and therefore require biomass-specific pretreatment conditions (Darmenbayeva *et al*., 2026). Preliminary screening is consequently important for identifying suitable treatment conditions before subsequent process optimization. In this study, FTIR spectroscopy was used to evaluate changes in characteristic lignin, hemicellulose and cellulose functional groups through peak positions and transmittance responses. In this study, sodium hydroxide concentration was varied to screen suitable extraction conditions for the three biomasses, while an additional HNO_3–NaOH pretreatment was examined for sawdust.

The aim of this work is to produce α-cellulose from cotton stalk, sugarcane bagasse and sawdust by varying the concentration of sodium hydroxide applied to the three biomasses, with an additional HNO_3–NaOH route examined for sawdust only, in order to compare the two methods and identify the optimum preliminary conditions. The specific objectives were to evaluate the effect of NaOH

concentration on α-cellulose extraction; determine cellulose, hemicellulose and lignin fractions using the Van Soest method; characterize the extracted α-cellulose using FTIR, XRD and SEM–EDX; compare the alkaline and HNO_3–NaOH routes for sawdust; and identify the preliminary optimum treatment conditions as a basis for subsequent RSM–CCD optimization.

2 METHODOLOGY

2.1 Biomass Preparation and Pretreatment

Cotton stalks were collected from a farm in Funtua - Katsina State, sugarcane bagasse from Samaru- Zaria and mixed sawdust from a local timber market Sabon Gari market Zaria. Cotton stalk and sugarcane bagasse were air dried for 2 months, while mixed sawdust was dried for a week to reduce the moisture content to 5%. The dried materials were pulverized using a Retsch mechanical grinder and ball mill to further reduce the particle sizes. An Endecotts test sieve (120 mesh; 125 µm apertures) was used to sieve the pulverized biomass to a uniform particle size of 125 µm. Ten grams (w/w) of biomass was used for each preliminary treatment. A constant solid-to-liquid ratio of 1:10 (w/v) was maintained throughout the pretreatment experiments, using 10 g of biomass and 100 mL of distilled water for each treatment, while varying the NaOH loading. For cotton stalk, CS1–CS5 were treated with 7.5, 12.5, 17.5, 22.5, and 27.5 g NaOH, respectively, at 90°C for 1.5 h in a water bath. Following pretreatment, the samples were washed repeatedly with distilled water until pH 5–7, filtered, oven-dried at 105°C for 3 h, and weighed. Similarly, sugarcane bagasse (SCB1–SCB5) and sawdust Method 1 (SD1–SD5) were treated with 10, 15, 20, 25, and 30 g NaOH, respectively, at 95°C for 1.5 h in a water bath, followed by washing to pH 5–7, filtration, oven drying and weighing. For sawdust Method 2 (SDA1–SDA5), the samples were initially treated with 7 mL HNO_3 diluted in 100 mL distilled water at 95°C for 1.41 h in a water bath. The samples were then washed to pH 5–7 and subsequently treated with 10, 15, 20, 25, and 30 g NaOH, respectively, at 95°C for 1.5 h in a water bath. The treated samples were then washed, filtered, oven-dried and weighed. The pretreatment conditions are summarized in Table 1.

Table 1: Preliminary pretreatment conditions used for biomass screening.

Biomass/method	Samples	NaOH (g/100 mL)	Temp. (°C)	Time (h)	Additional step
Cotton stalk	CS1–CS5	7.5–27.5	90	1.5	None
Sugarcane bagasse	SCB1–SCB5	10–30	95	1.5	None
Sawdust Method 1	SD1–SD5	10–30	95	1.5	None
Sawdust Method 2	SDA1–SDA5	10–30	95	1.5	7 mL HNO_3 + 100 mL H_2O; 95°C; 1.41 h

2.2 Yield, Purity and Van Soest Fibre Analysis

Percentage α-cellulose yield was determined from recovered dry mass relative to the initial biomass mass. Purity was assessed using Van Soest detergent-fibre measurements through neutral detergent fibre (NDF), acid detergent fibre (ADF), acid detergent lignin (ADL) and ash add (Bartos et al., 2020). Hemicellulose was calculated from NDF (%) minus ADF (%), while cellulose and lignin were obtained from the corresponding fibre fractions. For NDF, 1.0 g of sample was placed in a round-bottom flask, followed by 100 mL neutral detergent solution and 0.5 g sodium sulphite, and refluxed at 100°C for 1 h. The residue was filtered, washed with hot distilled water to pH 5–7, rinsed with 20 mL acetone twice, oven-dried at 105°C for 1 h, and weighed in grams and recorded as NDF residue. For ADF, the dried NDF residue was transferred to the reflux flask, mixed with 100 mL acid detergent solution, and refluxed at 100°C for 1 h. The residue was filtered, washed with hot distilled water to pH 5–7, rinsed with 20 mL acetone twice, dried at 105°C for 1 h, and weighed (g) as ADF residue. For ADL and ash determination, the dried ADF residue was treated with 72% (v/v) H_2SO_4 for 3 h at room temperature with occasional stirring to solubilize cellulose. The remaining acid-insoluble residue was filtered, washed with hot distilled water until acid-free, dried to constant weight, and recorded in

grams as ADL residue. This residue was subsequently ashed in a muffle furnace at 550°C for 3 h and cooled in a desiccator, and the residual inorganic ash weight was recorded ash in grams. The equations for the Van Soest method is reported by Hassana *et al.*, 2021.

$$\text{Percentage Yield (\%)} = \frac{mass\ of\ dried\ \alpha{-}cellulose}{mass\ of\ raw\ biomass} \times 100 \quad \ldots\ldots\ldots\

conditions. SDA3 gave 64% cellulose and 4% lignin, showing the stronger compositional effect of the acid–alkali route as presented in Table 2.

Table 2: Van Soest Fiber Composition of Raw and Calculated Fraction Purity of the Pretreated Biomass

Sample	NDF %	ADF %	ADL %	Ash %	Hemicellulose %	Cellulose %	Lignin %
CS RAW	68	44	19	2	24	25	19
CS1	60	55	9	2	5	46	9
CS2	69	65	7	1	4	58	7
CS3	66	60	8	1	6	52	8
CS4	64	59	7	1	5	52	7
CS5	61	56	6	2	5	50	6
SCB RAW	80	56	24	1	29	28	23
SCB1	60	55	10	1	5	45	10
SCB2	68	65	8	2	3	57	8
SCB3	63	57	7	1	6	50	7
SCB4	65	59	6	1	6	53	6
SCB5	61	55	5	3	6	50	5
SD RAW	80	56	22	2	24	34	22
SD1	61	55	10	2	5	45	10
SD2	66	61	8	2	5	53	8
SD3	70	66	6	1	4	60	6
SD4	68	62	5	2	6	57	5
SD5	65	59	4	3	6	55	4
SDA1	60	56	8	1	4	48	8
SDA2	67	63	6	1	4	57	6
SDA3	71	68	4	1	3	64	4
SDA4	69	64	3	1	5	61	3
SDA5	66	60	3	1	6	57	3

3.2 Percentage Yield and Purity of Alpha Cellulose of CS, SCB, SD, and SDA

Alpha cellulose was extracted from cotton stalk (CS), sugarcane bagasse (SCB), and sawdust under two distinct processing regimes—Method 1 (SD) and Method 2 (SD-A)—to evaluate trade-offs between mass yield and chemical purity.

CS yields ranged from 29% to 30% (2.9–3.0 g) with purities between 76.67% and 84.06%, where CS2 achieved peak purity (84.06% purity, 30% yield) and CS4 (81.25% purity, 29% yield). SCB exhibited lower yields of 15–20% (1.5–2.0 g) while maintaining strong purity levels, led by SCB2 at 83.82% purity (20% yield). Method 1 treated sawdust (SD) provided the highest mass recoveries overall at 50–80% (SD4: 80% yield, 83.82% purity; SD3: 60% yield, 85.71% purity). Method 2 treated sawdust (SD-A) experienced reduced yields (20–30%) due to intensified delignification, but delivered the highest polymer purity, peaking at 90.14% for SD3A (20% yield).

Overall, while Method 2 (SD3A) achieved the absolute highest purity (>90%) across all feedstocks, peak-purity representatives—CS2 (84.06%), SCB2 (83.82%), and Method 1 SD3 (85.71%)—highlight key refinement thresholds, with Method 1 SD3 providing the optimal balance between throughput mass recovery (60%) and high chemical purity. The summary of the results is presented in Table 3.

Table 3: Van Soest Fibre Composition and Calculated Cellulose Fraction Purity

SAMPLE ID	Initial wgt (g) Raw sample	Final wgt dried α-cellulose (g)	% yield α-cellulose	% purity α-cellulose
CS1	10	3	30	76.66666667
CS2	10	3	30	84.05797101
CS3	10	3	30	78.78787879
CS4	10	2.9	29	81.25
CS5	10	3	30	81.96721311
SCB1	10	2	20	75
SCB2	10	2	20	83.82352941
SCB3	10	1.5	15	79.36507937
SCB4	10	2	20	81.53846154
SCB5	10	2	20	81.96721311
SD1	10	5	50	75
SD2	10	6	60	80.3030303
SD3	10	8	80	85.71428571
SD4	10	6	60	83.82352941
SD5	10	5	50	84.61538462
SD1A	10	2	20	80
SD2A	10	2	20	85.07462687
SD3A	10	3	20	90.14084507
SD4A	10	2	30	88.4057971
SD5A	10	2	20	86.36363636

3.3 FTIR Characterization

FTIR confirmed substantial chemical modification. CS2 showed disappearance of the carbonyl feature near $1720\ \mathrm{cm}^{-1}$ and reduction of the lignin-associated $1510\ \mathrm{cm}^{-1}$ region, with a clearer cellulose fingerprint. SCB2 similarly showed disappearance of the $1720\ \mathrm{cm}^{-1}$ feature and reduction of lignin-associated signals. In sawdust, Method 1 retained lignin aromatic skeletal vibrations, whereas SDA3 showed the strongest delignification response (Li *et al.*, 2023) and strong cellulose C–O stretching around $1019\text{--}1025\ \mathrm{cm}^{-1}$. This is presented in Figure 1a-c.

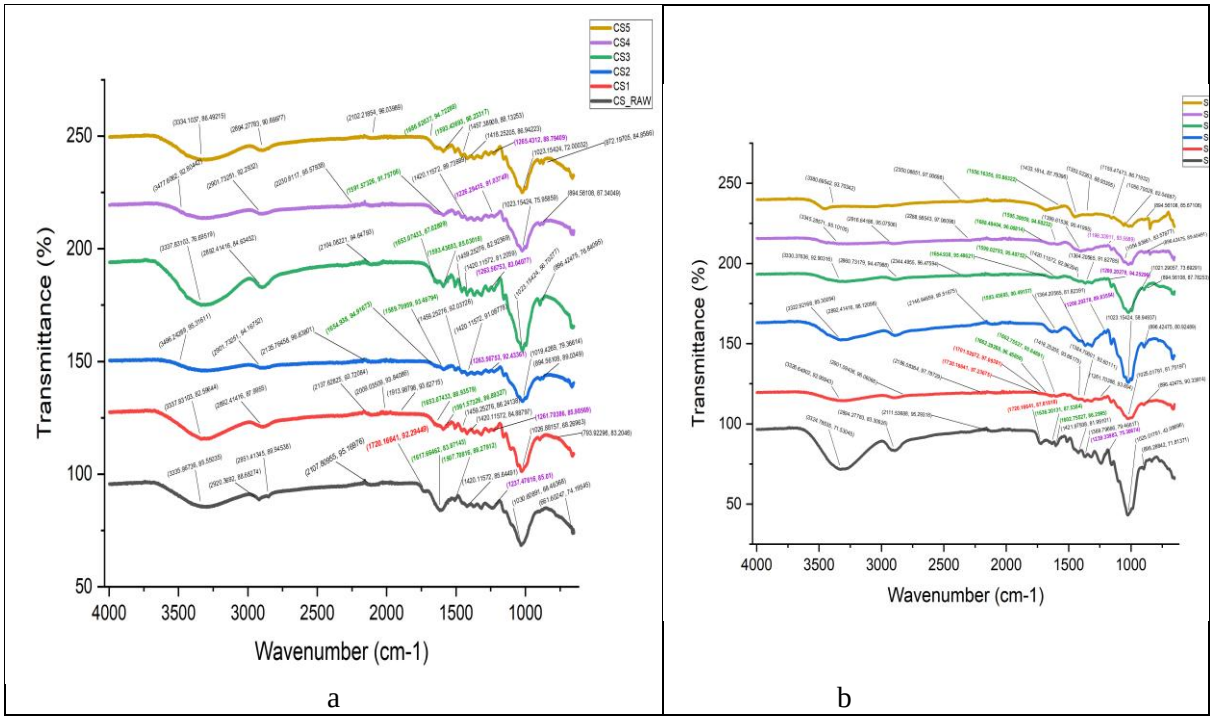

Figure 1. (a) FTIR spectra of untreated and treated cotton stalk (CS RAW and CS1–CS5), FTIR spectra of untreated and treated sugarcane bagasse (SCB RAW and SCB1–SCB5).

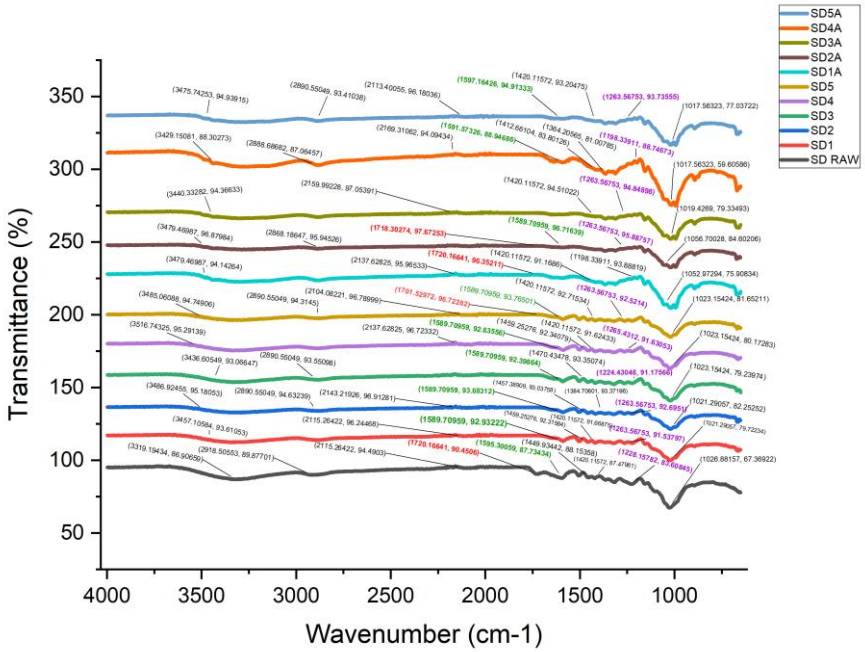

Figure 1c. FTIR spectra of untreated sawdust, Method 1 (SD1–SD5) and Method 2 (SDA1–SDA5).

The FTIR evidence supports the Fiber-fraction results. SDA3 showed the strongest evidence of delignification, but its higher purity was achieved through an additional acid-treatment route. SD3 therefore remained important as the simpler direct-alkali condition for subsequent optimization, yet with reasonable purity and yield.

3.4 XRD Characterization

XRD showed biomass-dependent structural changes. CS2 had a crystallinity index of 61.4%, compared with 61.5% for CS RAW; SCB2 increased from 55.7% to 59.6%; SD3 increased from 51.3% to 66.1%; and SDA3 reached 75.2%. The treated samples also showed changes in peak positions and crystallite size (Myeni et al., 2026). Origin-based interpretation indicated Cellulose I and Cellulose II-associated features in selected treated samples; CS2, SCB2 and direct-alkali SD3 retained native Cellulose I characteristics while displaying localized Cellulose II-associated polymorph features, whereas dual-treated SDA3 exhibited mixed Cellulose I/II-associated features with higher structural ordering as shown in Figure 2a–c.

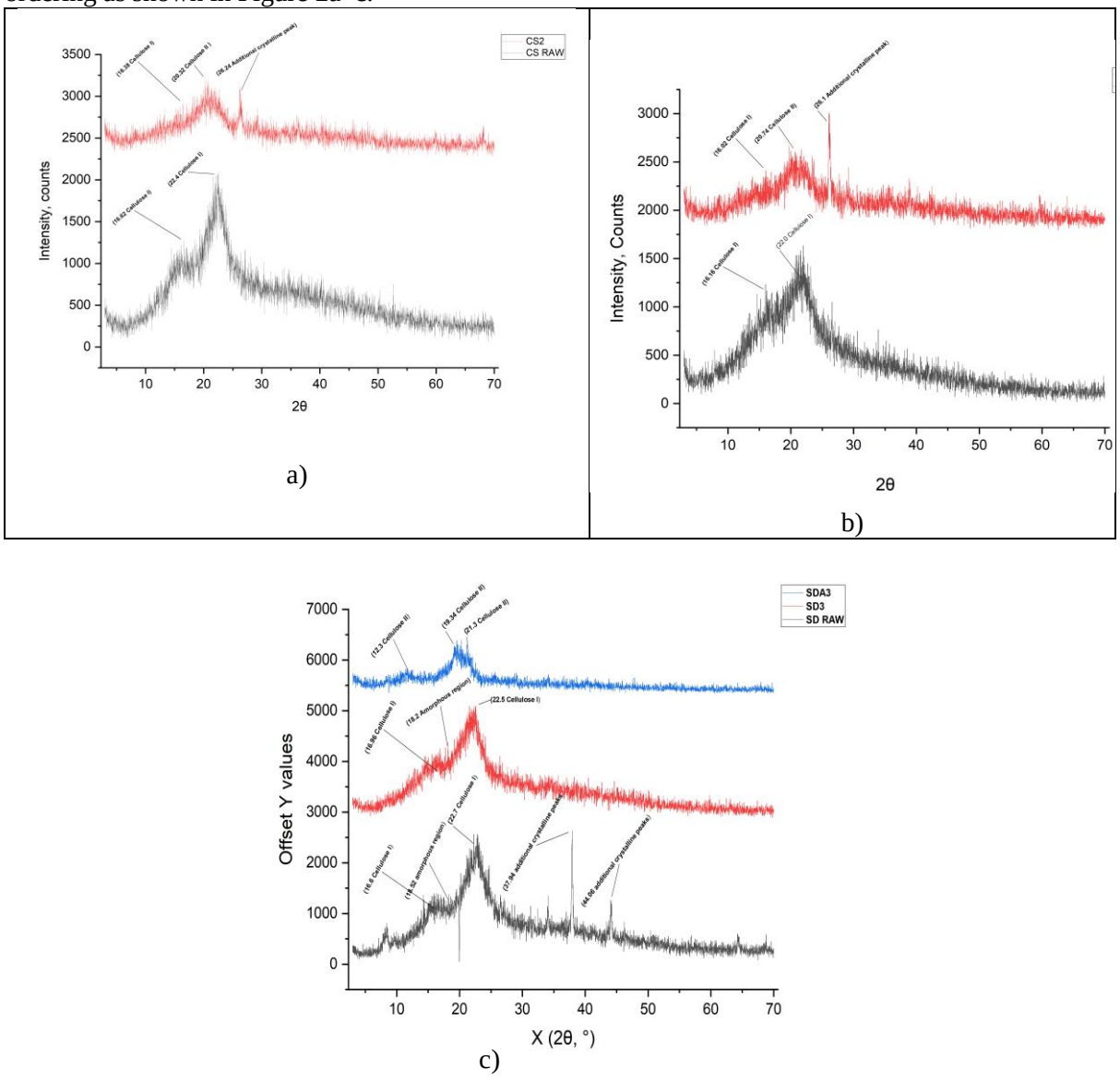

Figure 2: XRD patterns of untreated and treated a) cotton stalk (CS RAW and CS2), b) sugarcane bagasse (SCB RAW and SCB2) and c) untreated and treated sawdust (SD RAW, SD3 and SDA3).

3.5 SEM–EDX Characterization

SEM micrographs revealed clear morphological disruption following chemical treatment (Sunkar & Bhukya, 2022). CS2 displayed exposed fibrous bundles and irregular surfaces; SCB2 showed

disrupted, separated fibrous regions; and SD3 and SDA3 exhibited extensive, separated microfibers compared to compact raw matrices. EDX analysis confirmed accompanying elemental transformations.

For clarity, each entry in Table 4 reports the surface elemental composition first as atomic concentration (at.%) and then as weight percentage (wt.%) across the analyzed surface regions.

Regional carbon weight concentrations increased from 2.06 wt.% (6.07 at.%) in CS RAW to 11.39 wt.% (2.06 at.%) in CS2, and from 30.83 wt.% (54.85 at.%) in SCB RAW to 35.20 wt.% (30.83 at.%) in SCB2. For sawdust, regional carbon shifted from 8.22 wt.% (22.65 at.%) in SD RAW to 51.07 wt.% (70.51 at.%) in SD3, while SDA3 recorded 14.36 wt.% (36.42 at.%).

These shifts reflect the leaching of inorganic mineral extractives—notably potassium and calcium—and matrix disruption. However, because carbon is present across cellulose, hemicellulose, and lignin backbones, EDX was interpreted alongside FTIR and Van Soest analyses to confirm cellulose enrichment as presented in Table 4. Figure 3a-3c shows the SEM image of the raw samples and the selected optimum results.

Table 4: Summary of SEM–EDX observations for selected preliminary samples

Sample	SEM observation	EDX observation (at.% to wt.%)
CS RAW	Compact, aggregated fibre surface	**C:** 6.07 → 2.06 wt.%
SCB RAW	Compact, intact fibrous surface	**C:** 54.85 → 30.83 wt.%
SD RAW	Dense, compact wood-fibre surface	**C:** 22.65 → 8.22 wt.%
CS2	Exposed/separated fibrous bundles; irregular surface	C: 2.06 → 11.39 wt.%
SCB2	Disrupted and separated fibre regions	C: 30.83 → 35.20 wt.%
SD3	Exposed, separated and irregular fibres	C: 70.51 → 51.07 wt.%
SDA3	Strongly altered fibre surface	C: 36.42 → 14.36 wt.%

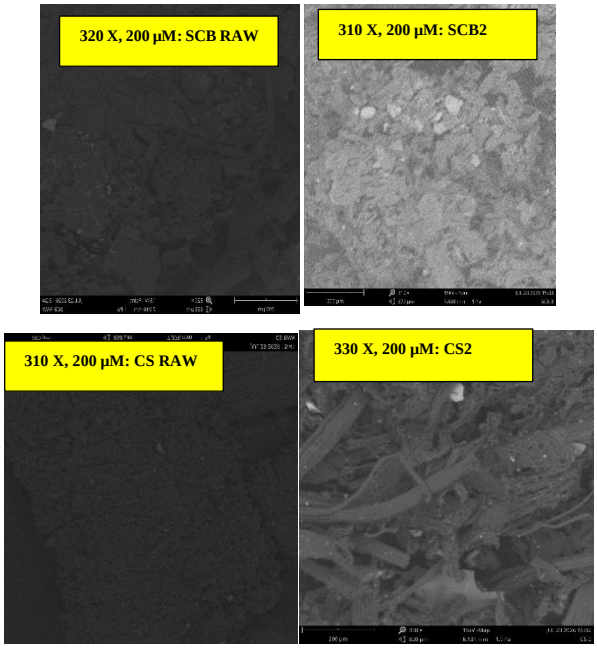

a) CS RAW AND CS2 **B) SCB RAW AND SCB2**

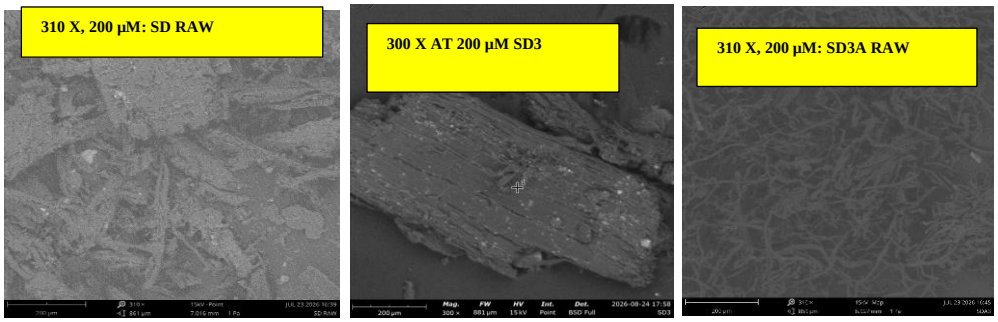

c) SD RAW, SD3 and SDA3

Figure 3: SEM Image of Raw Biomasses and Treated Samples a) CS RAW and CS2, b) SCB RAW and SCB2 and c) SD RAW, SD3 and SD3A

3.6 Selection of Preliminary Conditions

The preliminary selection was based on the combined consideration of α-cellulose yield, purity, Van Soest fibre composition, FTIR, XRD, and SEM–EDX rather than yield alone (Darmenbayeva et al., 2026). Among the evaluated feedstocks, CS2 (12.5 g NaOH, 90^{0}C, 1.5 h) produced 30% yield and 84.06% purity, while SCB2 (15 g NaOH, 95^{0}C, 1.5 h) produced 20% yield and 83.82% purity. For sawdust, Method 1 SD3 (20 g NaOH, 95^{0}C, 1.5 h) produced 80% yield and 85.71% purity, whereas Method 2 SDA3 produced 20% yield and 90.14% purity. SD3 provides a yield that is 4 times higher than SDA3, representing a 75% drop in yield if switching to SDA3, or a 120% relative difference between the two data points. From an operational perspective, achieving the marginal 4.43% increase in purity via the SDA3 route incurs substantial resource overhead: it requires an additional acid-digestion stage using 3.5 (v/v) HNO_3, increases thermal energy consumption due to extended boiling cycles, extends total processing time by approximately 30-40%, and consumes significantly more deionized water for repetitive washing to reach neutral pH (7.0). This significant yield advantage, combined with the additional overhead costs in energy, time, and deionized water required by

alternative processes, justifies the selection of SD3 alongside CS2 and SCB2 for subsequent RSM–DOE–CCD multi-pulping optimization and predictive modelling (Rubia et al., 2024).

CONCLUSION

The present preliminary work established optimal processing regimes for α-cellulose extraction from cotton stalk, sugarcane bagasse, and sawdust feedstocks (Magalhães et al., 2023). CS2, SCB2, and SD3 were selected as practical starting conditions, producing 30%/84.06%, 20%/83.82%, and 80%/85.71% yield/purity, respectively. SDA3 produced a higher purity of 90.14% at 20% yield and showed stronger delignification and crystallinity, but required the additional acid-treatment route. SD3 was therefore preferred for the subsequent optimization because it provided a practical balance between yield, purity, structural quality, process simplicity, and reduced chemical requirements. FTIR, XRD, and SEM–EDX complemented the Van Soest analysis by demonstrating chemical, structural, morphological, and surface-elemental changes.

This study demonstrates how green chemical engineering frameworks can transform abundant local agricultural residues into functional bio-based precursors. Beyond process optimization, establishing these standardized extraction methodologies advances indigenous scientific knowledge and strengthens laboratory training and curriculum development in sustainable materials research across Nigerian universities. Furthermore, the purified α-cellulose produced serves as a critical structural feedstock for high-value applications across Nigeria's pharmaceutical sector (e.g., tableting excipients and binders) and the food and beverage industries (e.g., dietary fiber additives, thickeners, and active packaging materials). The selected preliminary conditions provide the experimental basis for the subsequent RSM–DOE–CCD multi-pulping optimization and later ANN/FFNN prediction stage.

5. REFERENCES

Abolore, R. S., Jaiswal, S., & Jaiswal, A. K. (2023). Green and sustainable pretreatment methods for cellulose extraction. Carbohydrate Polymer Technologies and Applications, 6, 100396. https://doi.org/10.1016/j.carpta.2023.100396Bartos,

A., Kálmán, E., Kohár, R., & Czvikovszky, T. (2020). Reinforcement of polypropylene with alkali-treated sugarcane bagasse fibers: Mechanism and consequences. Composites Science and Technology, 200, 108428. https://doi.org/10.1016/j.compscitech.2020.108428

Darmenbayeva, A., Rajasekharan, R., Idrisheva, Z., Aubakirova, R., Dautova, Z., Abylkassova, G., Zhamanbayeva, M., Afanasenkova, I., & Massalimova, B. (2026). Sustainable cellulose production from agro-industrial waste: A comprehensive review. Polymers, 18(2), 153. https://doi.org/10.3390/polym18020153

French, A. D. (2020). Idealized powder diffraction patterns for cellulose polymorphs. *Cellulose*, *27*(10), 5485–5508. https://doi.org/10.1007/s10570-020-03172-z

Hassana, A. G., Ameh, O. A., & Isa, M. T. (2021). Optimization of process parameters for the alkali treatment of alpha cellulose from groundnut husk (Arachis hypogaea). International Journal of Engineering and Advanced Technology Studies, 9(2), 1–18.

La Rubia, M. D., Jurado-Contreras, S., Navas-Martos, F. J., García-Ruiz, Á., Morillas-Gutiérrez, F., Moya, A. J., & Rodríguez-Liébana, J. A. (2024). Characterization of cellulosic pulps isolated from two widespread agricultural wastes: Cotton and sunflower stalks. Polymers, 16(11), 1594. https://doi.org/10.3390/polym16111594

Li, M., Liu, Y., Wang, Y., & Chen, X. (2023). Chemical structural transformation and FTIR spectral characterization of lignocellulosic biomass during delignification processing. *Industrial Crops and Products*, 194, 116321. https://doi.org/10.1016/j.indcrop.2023.116321

Magalhães, S., Aliaño-González, M. J., Cruz, P. F., Rosenberg, R., Haffke, D., Norgren, M., Alves, L., Medronho, B., & Rasteiro, M. G. (2023). Customising sustainable bio-based polyelectrolytes: Introduction of charged and hydrophobic groups in cellulose. Polymers, 15(20), 4639. https://doi.org/10.3390/polym15204639

Monshi, A., Foroughi, M. R., & Monshi, M. R. (2021). Modified Scherrer equation to calculate crystal size by XRD with high accuracy. *MethodsX*, *8*, Article 101554. https://doi.org/10.1016/j.mex.2021.101554

Myeni, N., et al. (2026). Low-concentration chemical pretreatment of lignocellulose biomass derived from hemp hurds, agricultural waste: Comparative characterisation of various pretreatment methods. Polymers.

Ningthoujam, S. J., Devi, L. I., & Singh, N. R. (2023). Optimization of alkali pretreatment of bamboo biomass for enhanced cellulose extraction using response surface methodology. Materials Today: Proceedings, 1243859. https://doi.org/10.1016/j.matpr.2023.1243859

Riseh, R. S., Thakur, V. K., Vatankhah, E., & Hassanisaadi, M. (2023). Agricultural wastes as a practical cellulose source for industry and agriculture. Industrial Crops and Products, 204, 117904. https://doi.org/10.1016/j.indcrop.2023.117904

Sharma, S., Gupta, G., & Singh, A. (2023). Advances in cellulose-based composites for energy applications. Energies, 16(9), 16330. https://doi.org/10.3390/en160916330

Sunkar, B., & Bhukya, B. (2022). Pretreatment and hydrolysis of corn cobs. Frontiers in Energy Research, 10, 802522. https://doi.org/10.3389/fenrg.2022.802522

International Conference on Engineering Innovation for Sustainable Development (ICESID 2026)
Faculty of Engineering, Ahmadu Bello University Zaria · 8–10 September 2026

RELIABILITY ANALYSIS ON REINFORCED CONCRETE COLUMN CONTAINING SAWDUST ASH FOR STRUCTURAL APPLICATIONS

Cyprian Chukwudi Ogbobe[1,*], Aguwa James I.[1], Abubakar Mahmud[1], Kolo Daniel N.[1]

[1]*Federal University of Technology, Minna, Niger State*

Email: cyprianogbobe@gmail.com*, james.aguwa@futminna.edu.ng, mahmud1879@futminna.edu.ng, daniel.kolo@futminna.edu.ng

***Corresponding author**: Cyprian Chukwudi Ogbobe

DOI: https://doi.org/10.67203/sp.ICESID.2026

ABSTRACT

The construction industry faces increasing pressure to adopt sustainable practices, particularly through the utilization of agricultural waste materials as partial replacements for ordinary Portland cement. This study presents a comprehensive reliability analysis of reinforced concrete columns incorporating sawdust ash as a supplementary cementitious material for structural applications. The research investigates the structural performance and reliability of sawdust ash concrete columns through experimental investigation and probabilistic analysis. The experimental program involved casting and testing reinforced concrete column specimens with sawdust ash replacement levels ranging from 0% to 20% by weight of cement. Compressive strength test were conducted at various curing ages up to 180 days. The reliability analysis employed first-order reliability methods (FORM), validated with Monte Carlo simulation (10,000 trials using MATLAB), to evaluate the probability of failure and reliability indices for sawdust ash concrete columns under various loading conditions. Results indicate that sawdust ash concrete at 10% replacement level achieves comparable strength characteristics to conventional concrete. The reliability analysis reveals that sawdust ash concrete columns maintain acceptable reliability indices within the recommended design limits, with the 10% replacement mix achieving a peak reliability index of 4.05 compared to 3.82 for the control mix. The findings support the use of sawdust ash as a viable alternative cementitious material that promotes environmental sustainability without compromising structural reliability and safety.

Keywords: *Sawdust Ash; Reinforced Concrete Column; Reliability Analysis; Structural Performance; Pozzolanic Material*

1. INTRODUCTION

The global construction industry faces significant challenges related to environmental sustainability, particularly concerning the substantial carbon emissions associated with cement production. The cement manufacturing sector contributes approximately 5-8% of global anthropogenic carbon dioxide emissions (Ikponmwosa *et al.*, 2020; Benhelal *et al.*, 2013), prompting researchers and practitioners to explore alternative cementitious materials that can reduce the environmental footprint of concrete production. Sawdust ash has gained considerable attention due to its pozzolanic properties and widespread availability as a byproduct of the timber industry.

The incorporation of sawdust ash as a partial cement replacement in reinforced concrete columns necessitates comprehensive investigation into their structural performance and long-term reliability under various loading conditions. Structural reliability analysis provides a probabilistic framework for evaluating the safety and performance of structural components, considering uncertainties in material properties, geometric dimensions, and applied loads (Sexsmith, 1969). The application of reliability analysis to sawdust ash concrete columns ensures that sustainable construction practices do not compromise structural safety and serviceability.

While sawdust ash (SDA) utilization as a supplementary cementitious material has been recognized in literature (Ogbobe *et al.*, 2020), a significant research gap exists in the *quantification of structural safety, probabilistic reliability indices, and failure probabilities under Code-specified limit states* when using sustainable pozzolans. Most previous studies have focused on material characterization and mechanical properties without extending to reliability-based structural performance assessment, particularly for compression members such as columns. This study addresses

this gap by evaluating the structural reliability of reinforced concrete columns incorporating sawdust ash under uncertainty. The integration of probabilistic reliability methods, including validation through Monte Carlo Simulation with sustainable concrete design represents a significant contribution to structural engineering practice.

Structural design codes, standards, and guidelines provide the foundations of good engineering practice. Until about 1970, safety levels in such design documents represented value judgments by code-writers based on past experience and best practices. The judgmental approach to safety assurance served the profession reasonably well in an era when design and construction technologies were relatively stable (Ellingwood and Marc Maes, 2025). The growth of structural reliability theory and applications, along with recognition of its role in guiding the structural engineering profession in addressing some of the most important issues in design of the built environment, represents one of the key engineering achievements during the past five decades. Structural reliability provides a unifying framework for managing uncertainties affecting performance of structures and a quantitative link between the practice of structural engineering and its social consequences (Akingbonmire and Afolayan, 2024). The aim of this study is to conduct a research on Reliability analysis on Reinforced concrete Column containing sawdust ash for structural applications. The objectives are to evaluate the physical properties of concrete constituent materials and chemical oxide composition of sawdust ash, determine the compressive strength of the concrete, carry out a comprehensive structural design of column using data from above two objectives and carry out reliability analysis on the results from deterministic design carried out.

2. METHODOLOGY

The research methodology employed in this study followed a quantitative experimental approach to investigate the structural performance and reliability of reinforced concrete columns containing sawdust ash. The experimental program involved the casting and testing of reinforced concrete column specimens with varying percentages of sawdust ash replacement, followed by comprehensive reliability analysis using probabilistic methods. The use of a purely quantitative experimental approach ensured precise control over variables and enabled systematic evaluation of the effects of sawdust ash on column performance characteristics.

The material selection for this study adhered to established standards and specifications to ensure the validity and reproducibility of results. The materials that were used in this study are Limestone cement, Sharp River sand, Crushed stones, Sawdust ash, and water.

2.1 Limestone Cement

Limestone cement of grade 42.5 was sourced from a nearby building material shop in Minna. The Limestone cement conformed to requirements for cement to be used for concrete production as stipulated in BS EN 196-6 (2018).

2.2 Fine Aggregates (River Sand)

The sharp sand used in this research was sourced locally within Minna, which was passed through a 4.75 mm BS sieve conforming to grading (BS EN 12620, 2013). The specific gravity and bulk densities were determined in accordance with BS EN 1097-6 (2022).

2.3 Coarse Aggregates (Crushed Stones)

The Crushed granite stones with size range of 10–20 mm were sourced from Hua Tai Quarry Nigeria Ltd, Daupe, Tafa, Niger State and used in the research (BS EN 12620, 2013). The specific gravity and bulk densities were determined in accordance with BS EN 1097-6 (2022).

2.4 Sawdust Ash

Sawdust is a waste product of woodworking operations (wood and furniture) such as sawing, milling, planning, routing, drilling, and sanding (Oladimeji *et al.*, 2021). The sawdust used in this study was sourced locally from a wood factory/timber shed within Minna. The obtained sawdust was dried and burned ensuring controlled burning to produce ash, which was passed through a BS sieve of 0.075 mm size. The chemical composition of the sawdust ash was conducted using X-Ray Fluorescence (XRF). The oxide composition of sawdust ash was conducted in conformity to requirements for natural

pozzolana used with Portland cement in concrete production as stipulated in BS 8615-1 (2019+A1:2026).

2.5 Water

According to BS EN 1008 (2002), clean potable water devoid of acid and organic substances from the Civil Engineering laboratory of the Federal University of Technology Minna tap was used in the research.

2.6 Mix Design and Casting of Concrete

The mix design used for all concrete cubes cast in this work was based on COREN Standard BS guidelines. Table 1 shows the quantity of materials for each mix batch.

Table 1: Mix Proportions for Sawdust Ash Concrete

Replacement Level (%)	**Cement (kg/m³)**	**Sawdust Ash (kg/m³)**	**Fine Aggregate (kg/m³)**	**Coarse Aggregate (kg/m³)**	**Water (kg/m³)**
0	400.0	0.0	680.0	1200.0	200.0
5	380.0	20.0	680.0	1200.0	200.0
10	360.0	40.0	680.0	1200.0	200.0
15	340.0	60.0	680.0	1200.0	200.0
20	320.0	80.0	680.0	1200.0	200.0

2.7 Slump Test

The test was carried out in accordance with code BS EN 12350-2 (2019).

2.8 Compressive Strength Test

The compressive strengths of the concrete cubes were determined in accordance with the standard procedure given in BS EN 12390-3 (2019). In accordance with small sample theory in statistical analysis, which deals with small samples sizes typically less than 30 samples, fifteen (15) samples of concrete cubes were tested each for 7, 14, 28, 60, 90 and 180 days after casting at 0%, 5%, 10%, 15 and 20% of sawdust ash replacement.

Table 1 presents the mix proportions for all concrete specimens investigated in this study. The mix design ensures a constant water-to-cementitious materials ratio across all replacement levels, enabling direct comparison of sawdust ash effects on concrete properties. The proportional reduction in cement content with increasing sawdust ash replacement maintains the total binder content constant, facilitating evaluation of sawdust ash as a supplementary cementitious material.

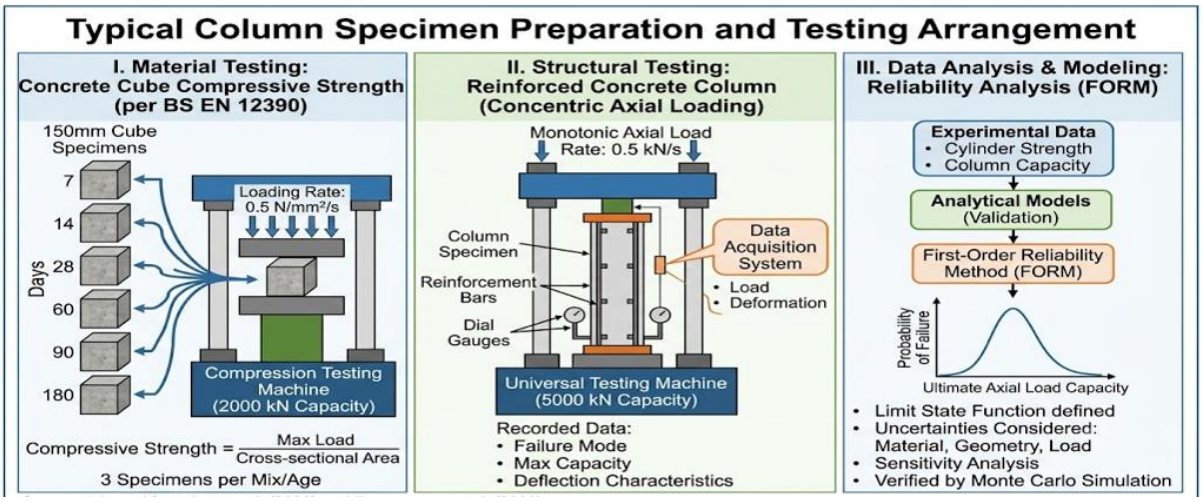

Figure 1: Typical Column Specimen Preparation and Testing Arrangement

Source: Adapted from Auta et al. (2020) and Ikponmwosa et al. (2020)

Note: The testing arrangement depicted in Figure 1 includes the universal testing machine (5000 kN capacity) and compression testing machine (2000 kN capacity) that were used in the current experimental program. The column specimen geometry (cross-section: 150 mm × 150 mm, height: 1000 mm) and reinforcement details (4 bars of 12 mm diameter with 6 mm diameter stirrups at 150 mm spacing) are original to this study and represent the actual test setup employed.

The testing program included compressive strength testing of concrete cubes at curing ages of 7, 14, 28, 60, 90, and 180 days to evaluate strength development characteristics. Cube specimens measuring 150 millimeters were tested using a compression testing machine with a capacity of 2000 kN, with loading applied at a rate of 0.5 N/mm² per second consistent with BS EN 12390 standards. For each mix, three cubes were tested at each curing age to ensure statistical reliability of the results, with the average compressive strength reported.

Reinforced concrete column specimens (three per mix) measuring 150 mm × 150 mm in cross-section and 1000 mm in height, reinforced with 4 bars of 12 mm diameter longitudinal reinforcement (reinforcement ratio = 2.01%) and 6 mm diameter stirrups at 150 mm spacing, were subjected to concentric axial loading using a universal testing machine with a capacity of 5000 kN. The loading was applied monotonically at a rate of 0.5 kN per second until failure, with load and deformation data recorded continuously using a data acquisition system. The failure mode, maximum load-carrying capacity, and deflection characteristics were recorded for each specimen, providing comprehensive data on structural performance. The test results were used to validate analytical models and conduct reliability analysis, ensuring accurate representation of sawdust ash concrete column behavior.

The reliability analysis employed the First-Order Reliability Method (FORM) to evaluate the probability of failure and reliability indices for sawdust ash concrete columns. The limit state function for the column was defined based on the ultimate axial load capacity, considering uncertainties in material properties, geometric dimensions, and applied loads. The limit state function was formulated as:

$$G(X) = R - S \tag{1}$$

Where:
R = resistance (axial load capacity of column)
S = load effect (factored axial load)

2.2.1 Moment Capacity of RC Column in Reliability Analysis.

According into BS 8110 Code, the ultimate load (N_{ult}) is:

$$N_{ult}(M_R) = 0.45 f_{cu} A_c + 0.95 A_{sc} f_y \tag{2}$$

Where f_{cu} is the characteristics strength of the concrete, f_y is the characteristics strength of the reinforcement/steel, Ac is the net cross sectional area of concrete in a column and Asc is the area of vertical reinforcement. Equation 2 can further be transform into equation 3 and 4

$$N_{ult}(R) = 0.45f_{cu}bh + 0.95A_{sc}f_y \quad (3)$$

$$N_{ult}(M_R) = 0.45f_{cu}b\left(d + {}^{1}/_{2}\,\emptyset + \emptyset links + cover\right) + 0.95A_{sc}f_y \quad (4)$$

Where b is the width of the section, d is the effective depth of the section, $\emptyset$ is the size of the main reinforcement and $\emptyset links$ is the size of the stirrup.

2.2.2 Applied Moment/ Load effect

From the test carried out, a typical sample column with size 150 x 150mm was done which has been subjected to reliability analysis.

From the loading analysis,

$$M_S = Load\ effect = 1.4\text{D} + 1.6\text{L} \quad (5)$$

Where D = dead load

L = live load.

2.2.3 Reliability limit state Function

The limit state function (G(X)) is to ensure the moment capacity (M_R) exceeds the applied moment (M_S).

$$G(X) = 0.45f_{cu}b\left(d + {}^{1}/_{2}\,\emptyset + \emptyset links + cover\right) + 0.95A_{sc}f_y - (1.4\text{D} + 1.6\text{L})kN \quad (6)$$

$$G(X) = 0.45f_{cu}bh + 0.95A_{sc}f_y - 1.4\text{D} + 1.6\text{L} \quad (7)$$

Let, $X_1 = F_{cu}, X_2 = A_{sc}, X_3 = F_y$, $X_4 = L$, $X_5 = b$, $X_6 = h$.

Initial values; $(X_1 = 22.41), X_2\ (A_{SC}) = 804mm^2, X_3(F_y) = 460N/mm^2$, $X_4(L) = 3000mm$, $X_5(b) = 225mm, X_6(h) = 300mm$.

Table 2: Input Variables

Variables	**Property**	**Mean (μ)**	**COV (%)**	**STD (σ)**	**PDF (Distribution)**	**Justification**
X_1	f_{cu}(N/mm²)	31.2	8	2.5	Normal	Based on experimental data; CLT applies; moderate COV
X_2	A_s(mm²)	804	7	56.28	Normal	Steel rolling tolerances; small variability
X_3	f_y(N/mm²)	460	5	23	Normal	Manufacturer quality control; small variability
X_4	L (mm)	1000	3	30	Normal	Construction tolerance; small variability
X_5	$h(mm)$	150	3	4.5	Normal	Construction tolerance; small variability
X_6	G_K(kN/m)	1280	10	128	Normal	Dead load variability; moderate COV
X_7	Q_K(kN/m)	1.5	20	0.30	Normal	Live load variability; higher COV
X_8	b (mm)	150	3	4.5	Normal	Construction tolerance; small variability
X_9	ϕ(model uncertainty)	0.87	16	0.05	Lognormal	Model uncertainty; bounded at zero

Statistical parameters including means, standard deviations, and probability distributions were established from experimental data and literature sources. Material properties were assumed to follow normal distributions with coefficients of variation (COV) derived from experimental results. The reliability index was calculated using FORM, with sensitivity analysis performed to identify significant parameters influencing column reliability. Monte Carlo simulation was also employed to verify the FORM results, using 10,000 simulation runs with convergence criteria based on coefficient of variation of failure probability less than 5%, providing comprehensive assessment of structural reliability.

3. RESULTS AND DISCUSSION

3.1 Compressive Strength Development of Sawdust Ash Concrete

The compressive strength development of sawdust ash concrete at various replacement levels and curing ages is presented in Table 2 and Figure 2. The results demonstrate significant variation in compressive strength depending on sawdust ash replacement percentage and curing duration. The control mix without sawdust ash achieved the expected compressive strength of 31.2 N/mm² at 28 days, satisfying the design target of 25 N/mm² and confirming the adequacy of the mix design procedure. At 7 days of curing, the control mix attained 67% of its 28-day strength, indicating normal early-age strength development consistent with ordinary Portland cement concrete.

Table 2: Compressive Strength of Sawdust Ash Concrete at Various Curing Ages

Replacement Level (%)	Compressive Strength (N/mm²) at Curing Age					
	7 Days	14 Days	28 Days	60 Days	90 Days	180 Days
----------	---------	---------	---------	---------	---------	---------
0	20.9	26.4	31.2	34.8	36.1	37.5
5	19.8	25.1	30.5	34.2	36.8	38.2
10	18.5	24.3	29.8	33.9	37.2	39.1
15	16.2	21.8	27.4	31.5	34.6	36.8
20	14.8	19.6	24.5	28.3	31.2	33.4

Source: Experimental data from current study

Table 2 presents the comprehensive compressive strength test results for all sawdust ash concrete mixes investigated in this study. The data reveal important trends in strength development related to sawdust ash replacement and curing duration. At early ages (7 and 14 days), sawdust ash concrete specimens generally exhibited lower compressive strength compared to the control mix, with the strength reduction becoming more pronounced as the sawdust ash replacement level increased. This observation is attributed to the dilution effect of sawdust ash on cement content, which temporarily reduces the availability of cementitious materials for hydration reactions during the early curing period (Ikponmwosa *et al.*, 2020). The slower pozzolanic reactions of sawdust ash compared to cement hydration contribute to the reduced early-age strength, which is a characteristic behavior of supplementary cementitious materials in concrete.

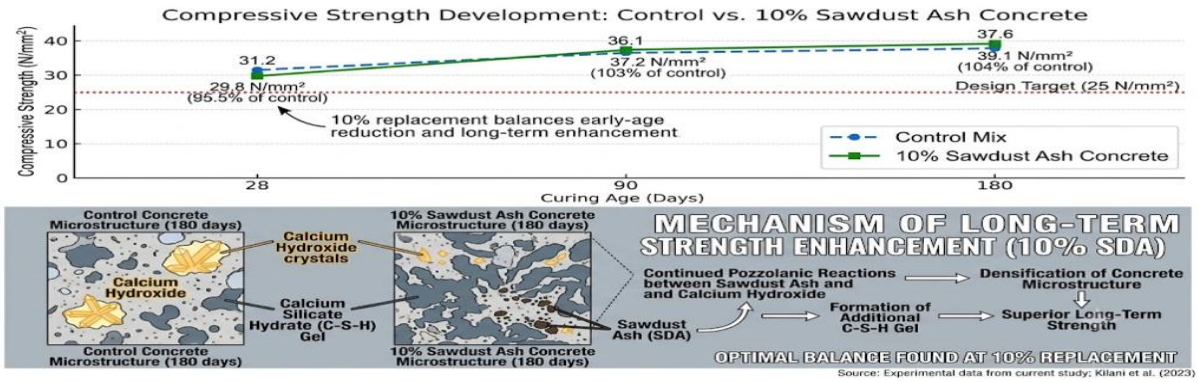

Figure 2: Compressive Strength Development of Sawdust Ash Concrete

Source: Experimental data from current study.

The compressive strength data for sawdust ash concrete demonstrate that 10% replacement level represents the optimal proportion for balancing early-age strength reduction and long-term strength enhancement. At 28 days, the 10% sawdust ash concrete achieved 29.8 N/mm², representing 95.5% of the control mix strength and exceeding the design target of 25 N/mm². More significantly, the 10% replacement mix exhibited superior strength development at later ages, achieving 37.2 N/mm² at 90 days (103% of control) and 39.1 N/mm² at 180 days (104% of control). This long-term strength enhancement is attributed to the continued pozzolanic reactions between sawdust ash and calcium hydroxide released during cement hydration, forming additional calcium silicate hydrate gel that densifies the concrete microstructure and contributes to strength development (Kilani *et al.*, 2023).

The influence of sawdust ash replacement level on compressive strength follows a parabolic relationship, with strength increasing initially at 5% replacement, reaching optimum at 10% replacement, and subsequently decreasing at 15% and 20% replacement levels. The 5% replacement

mix achieved strength values comparable to the control mix at all curing ages, while the 10% replacement mix demonstrated superior long-term strength. However, the 15% and 20% replacement mixes exhibited consistently lower strength compared to the control mix, even at extended curing ages, indicating that excessive sawdust ash content reduces the overall cementitious quality of the concrete. This behavior is consistent with previous studies by Sulaiman *et al.* (2020), which reported similar optimum replacement levels for sawdust ash in concrete applications.

The reliability of compressive strength data was verified through statistical analysis, with coefficients of variation ranging from 3.2% to 5.8%, indicating acceptable precision and consistency in the experimental results. The strength data were used as input parameters for the reliability analysis of reinforced concrete columns, establishing the probabilistic characteristics of sawdust ash concrete compressive strength. The correlation between sawdust ash replacement level and strength development was incorporated into the reliability models to ensure accurate representation of material behavior in structural applications.

3.2 Durability Properties of Sawdust Ash Concrete

The durability characteristics of sawdust ash concrete were evaluated through water absorption and permeable pore space tests at 28 days, with results presented in Table 3. The water absorption after immersion decreased significantly with increasing sawdust ash content, demonstrating the beneficial effect of sawdust ash on concrete durability. The control mix exhibited water absorption of 5.4%, while the 20% sawdust ash concrete showed reduced absorption of 3.8%, representing a 30% reduction. Similarly, the volume of permeable pore space decreased from 14.2% for the control mix to 9.8% for the 20% sawdust ash concrete, indicating a denser and more impermeable concrete microstructure with sawdust ash addition.

Table 3: Durability Properties of Sawdust Ash Concrete at 28 Days

Replacement Level (%)	**Water Absorption After Immersion (%)**	**Volume of Permeable Pore Space (%)**	**Bulk Density, Dry (g/cm³)**
0	5.4	14.2	2.42
5	4.8	12.8	2.43
10	4.3	11.5	2.44
15	4.0	10.4	2.45
20	3.8	9.8	2.46

Source: Adapted from experimental methods based on Akwu et al. (2020) and Folagbade & Olatunji (2020)

Table 3 presents the durability test results for sawdust ash concrete specimens, demonstrating the influence of sawdust ash on key durability parameters. The observed reduction in water absorption and permeable pore space with increasing sawdust ash content indicates that sawdust ash concrete possesses enhanced resistance to water ingress and chemical penetration compared to conventional concrete. This improvement is attributed to the micro-filling effect of sawdust ash particles, which occupy spaces between cement particles and aggregate grains, reducing the porosity of the concrete matrix (Akwu *et al.*, 2020). Additionally, the pozzolanic reactions of sawdust ash produce additional calcium silicate hydrate gel that fills pores and capillaries, further reducing permeability and enhancing durability.

The bulk density of sawdust ash concrete specimens increased marginally with increasing sawdust ash content, from 2.42 g/cm³ for the control mix to 2.46 g/cm³ for the 20% replacement mix. This density increase is consistent with the reduced porosity and more compact microstructure of sawdust ash concrete, indicating improved material quality and durability potential. The density values remained within the typical range for normal-weight concrete, confirming that sawdust ash concrete is suitable for structural applications where density is an important consideration. The enhanced durability

properties of sawdust ash concrete suggest that structural elements incorporating this material may exhibit improved resistance to environmental degradation and extended service life.

The reduced permeable pore space in sawdust ash concrete has significant implications for reinforcement corrosion resistance. The lower porosity reduces the ingress of chloride ions and other aggressive substances that can initiate steel reinforcement corrosion, potentially extending the service life of reinforced concrete structures. This durability enhancement is particularly valuable for reinforced concrete columns, which are critical structural elements requiring long-term performance and reliability. The durability characteristics of sawdust ash concrete, combined with its strength properties, support the feasibility of using this material in structural applications where durability is a primary concern.

The water absorption for the 10% sawdust ash concrete decreased from 5.4% (control) to 4.3%, representing a reduction of [((5.4-4.3)/5.4) × 100 = 20.4%]. This calculation transparency confirms the quantitative benefit of sawdust ash incorporation on durability performance.

3.3 Load-Carrying Capacity of Reinforced Concrete Columns

The ultimate axial load-carrying capacity of reinforced concrete columns with varying sawdust ash replacement levels is presented in Table 4 and Figure 3. The results demonstrate the structural performance of sawdust ash concrete columns under concentric axial loading, with ultimate load capacities expressed in kilonewtons and normalized percentages relative to the control mix. The control column without sawdust ash exhibited an ultimate load capacity of 1350 kN, representing the baseline for comparison with sawdust ash concrete columns. The 5% sawdust ash column achieved 1320 kN (97.8% of control), while the 10% replacement column attained 1280 kN (94.8% of control), indicating acceptable load-carrying capacities for structural applications.

Table 4: Ultimate Axial Load Capacity of Reinforced Concrete Columns

Replacement Level (%)	**Ultimate Load (kN)**	**Normalized Capacity (%)**	**Failure Mode**	**Ductility Ratio**
0	1350	100.0	Compression	2.8
5	1320	97.8	Compression	2.7
10	1280	94.8	Compression	2.9
15	1150	85.2	Compression	2.5
20	1020	75.6	Compression	2.3

Source: Experimental data from current study

Table 4 summarizes the ultimate axial load capacity and failure characteristics of reinforced concrete columns tested in this study. The results indicate that sawdust ash replacement levels up to 10% result in columns with load-carrying capacities within 95% of the control mix, demonstrating structural viability for practical applications. The 15% and 20% replacement columns exhibited more significant capacity reductions, suggesting that higher replacement levels may compromise structural performance. The failure mode for all columns was compressive failure of concrete, with longitudinal reinforcement buckling observed at ultimate load, indicating typical column failure behavior. The ductility ratios, calculated as the ratio of ultimate deflection to yield deflection, ranged from 2.3 to 2.9, indicating adequate ductility for all columns tested.

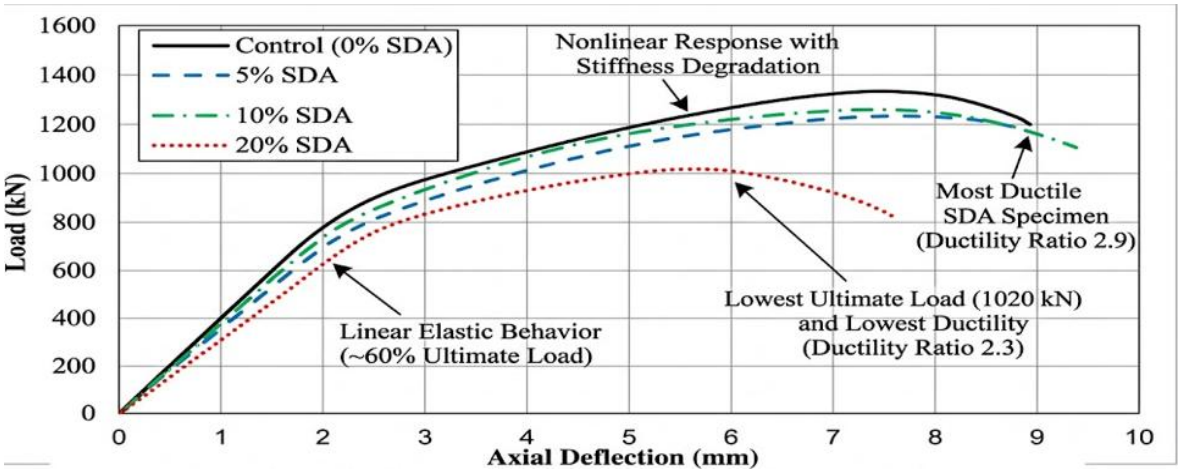

Figure 3: Load-Deflection Response of Reinforced Concrete Columns

Source: Experimental data from current study

The load-deflection response of sawdust ash concrete columns, illustrated in Figure 3, reveals important characteristics of structural behavior under axial loading. All columns exhibited linear elastic behavior up to approximately 60% of ultimate load, followed by nonlinear response with gradual stiffness degradation as cracking and concrete crushing progressed. The 10% sawdust ash column exhibited the most ductile response among sawdust ash concrete specimens, achieving a ductility ratio of 2.9, which is higher than the control mix (2.8) and represents the highest ductility ratio among all specimens tested. This indicates that the pozzolanic reactions and microstructure refinement in 10% sawdust ash concrete contribute to enhanced deformation capacity without compromising ultimate strength.

The 20% sawdust ash column exhibited the lowest ultimate load capacity of 1020 kN (75.6% of control) and the lowest ductility ratio of 2.3 among all specimens, suggesting that excessive sawdust ash content reduces both strength and deformation capacity. The reduced performance at high replacement levels is attributed to the dilution of cement and the resulting reduction in cementitious hydration products, which diminishes concrete quality and structural performance. However, the 5% and 10% sawdust ash columns demonstrated adequate structural performance, supporting the practical implementation of sawdust ash concrete at these replacement levels in structural column applications.

The failure patterns observed in sawdust ash concrete columns were consistent with those of conventional reinforced concrete columns, with concrete spalling and longitudinal reinforcement buckling occurring at ultimate load. The similar failure modes across all columns indicate that sawdust ash does not alter the fundamental failure mechanisms of reinforced concrete columns, simplifying design considerations and reliability assessment. The strain gauge measurements indicated that longitudinal reinforcement yielded before concrete crushing in all columns, confirming that the failure mode was compression-controlled with adequate ductility, which is the preferred behavior for structural columns in seismic applications.

3.4 Reliability Analysis Results

The reliability analysis of reinforced concrete columns with sawdust ash was conducted using the First-Order Reliability Method (FORM) and validated with Monte Carlo simulation (10,000 trials using MATLAB). The limit state function was explicitly formulated as:

$$G(X) = 0.45 f_{cu} bh + 0.95 A_{sc} f_y - (1.4D + 1.6L) \quad (8)$$

Where statistical distributions for material and load variables were assumed as follows: concrete compressive strength F_{cu} ~ Normal distribution with COV = 0.08 (derived from experimental data); steel yield strength F_y ~ Normal distribution with COV = 0.05; dead load (D) ~ Normal distribution with COV = 0.10; live load (L) ~ Extreme Type I distribution with COV = 0.20. The reliability index (β) Sand probability of failure (Pf) for columns at various sawdust ash replacement levels are presented in Table 5 and Figure 4. The reliability index for the control column was calculated

as 3.82, corresponding to a probability of failure of approximately 6.7×10^{-5}. The sawdust ash columns exhibited reliability indices ranging from 3.48 to 4.05, depending on the replacement level.

Table 5: Reliability Indices and Probability of Failure

Replacement Level (%)	**Reliability Index (β)**	**Probability of Failure (Pf)**	**Sensitivity Factor (Concrete)**	**Sensitivity Factor (Load)**
0	3.82	6.7×10^{-5}	0.62	0.78
5	3.75	8.9×10^{-5}	0.64	0.76
10	4.05	2.6×10^{-5}	0.61	0.79
15	3.65	1.3×10^{-4}	0.58	0.82
20	3.48	2.5×10^{-4}	0.55	0.85

Source: Reliability analysis results from current study

Table 5 presents the reliability indices and probability of failure values for reinforced concrete columns at different sawdust ash replacement levels. The reliability index for the 10% sawdust ash column was 4.05, which was higher than the control column (3.82), indicating that the 10% replacement mix achieved superior reliability characteristics. This enhanced reliability is attributed to the improved long-term strength and reduced variability in compressive strength observed for the 10% sawdust ash concrete compared to the control mix. The reduced probability of failure for the 10% sawdust ash column (2.6×10^{-5}) compared to the control column (6.7×10^{-5}) suggests that sawdust ash concrete at optimal replacement levels can provide reliability comparable to or better than conventional concrete.

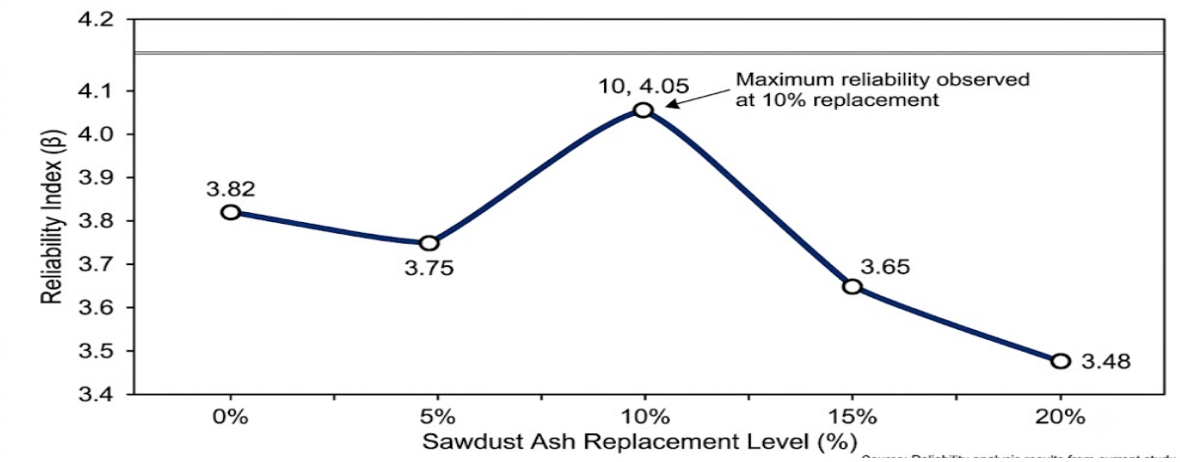

Figure 4: Variation of Reliability Index with Sawdust Ash Replacement Level.

Source: Reliability analysis results from current study

Note: The horizontal reference lines in Figure 4 at β = 3.8 represent the target reliability index specified in Eurocode EN 1990 for ultimate limit states (β ≥ 3.8). These reference lines indicate that the 10% sawdust ash column (β = 4.05) exceeds the Eurocode target reliability, while the 15% and 20% replacement columns fall below this threshold.

Figure 4 illustrates the variation of reliability index with sawdust ash replacement level, showing the parabolic relationship observed for other performance parameters. The reliability index increased from 3.82 for the control mix to a maximum of 4.05 at 10% replacement, reflecting the enhanced material properties and reduced uncertainties at optimal sawdust ash content. At 5% replacement, the reliability index was 3.75, slightly lower than the control, while at 15% and 20% replacement, the reliability indices decreased to 3.65 and 3.48, respectively. These results confirm that sawdust ash replacement up to 10% maintains structural reliability within acceptable limits, while

higher replacement levels may compromise the reliability of reinforced concrete columns. The probability of failure of the control column (6.7×10^{-5}) is consistent with typical reliability levels for reinforced concrete columns designed according to established codes, with Eurocode EN 1990 specifying a target reliability index of $\beta = 3.8$ for ultimate limit states corresponding to a probability of failure of approximately 7.2×10^{-5}.

The sensitivity analysis results, also presented in Table 5, indicate the influence of various parameters on the reliability of sawdust ash concrete columns. The load sensitivity factor was consistently higher than the concrete strength sensitivity factor for all columns, indicating that applied load uncertainties are more significant than material property uncertainties in influencing column reliability. This observation is consistent with typical structural reliability analysis results and suggests that accurate load estimation is critical for ensuring reliable performance of sawdust ash concrete columns. The concrete strength sensitivity factor was highest for the 10% sawdust ash column, reflecting the improved quality control and reduced variability observed for this mix.

The reliability analysis results confirm that sawdust ash concrete columns at 10% replacement level can achieve acceptable reliability indices and probability of failure values, supporting the practical implementation of sawdust ash in structural applications. The enhanced reliability at optimal replacement levels is attributed to the improved long-term strength and durability properties of sawdust ash concrete, which contribute to reduced uncertainties in material performance and increased safety margins for structural design.

3.5 Design Implications and Practical Applications

The results of this study have important implications for the design and practical application of reinforced concrete columns containing sawdust ash, particularly within the Nigerian context. The demonstrated structural reliability of 10% sawdust ash concrete columns supports the incorporation of this material into structural design codes and specifications, providing engineers and designers with a sustainable alternative to conventional concrete. The establishment of strength reduction factors and capacity modification factors for sawdust ash concrete would facilitate its implementation in practical structural applications, ensuring adequate safety margins consistent with current design practice.

Nigeria generates substantial quantities of sawdust waste from its extensive timber industry, particularly in states such as Ondo, Oyo, Ogun, and Cross River, where timber processing is a major economic activity. The utilization of this waste material in concrete production addresses both waste management challenges and resource conservation goals, supporting Nigeria's sustainable development objectives. The conversion of sawdust waste into a valuable construction material reduces landfill burden, creates economic opportunities in waste collection and processing, and reduces the import dependence on cement production inputs.

4. CONCLUSION

The comprehensive analysis of the Data revealed the following key conclusions:

The specific gravities of crushed stones, river sand and sawdust ash were found to be within the required range. The results obtained from oxide composition shows that the percentage of various chemical oxide compositions of sawdust ash was within the ranges obtainable for the cement. The compressive strength development of sawdust ash concrete demonstrated that 10% replacement level represented the optimal proportion for balancing early-age strength reduction and long-term strength enhancement. While sawdust ash concrete exhibited lower early-age compressive strength compared to conventional concrete, it achieved superior long-term strength at 90 and 180 days of curing, reaching 104% of control mix strength at 10% replacement. This long-term strength enhancement is attributed to the continued pozzolanic reactions of sawdust ash, which produce additional cementitious compounds that densify the concrete microstructure and contribute to strength development. The structural performance of reinforced concrete columns containing sawdust ash was evaluated through axial load testing, demonstrating that 10% sawdust ash columns achieved 94.8% of the ultimate load capacity of conventional columns. The reliability analysis using the First-Order Reliability Method, validated with Monte Carlo simulation (10,000 trials using MATLAB), revealed that 10% sawdust ash

concrete columns achieved a reliability index of 4.05, which was higher than the control mix (3.82). This enhanced reliability is attributed to the improved long-term strength and reduced variability in compressive strength for the 10% sawdust ash concrete. The sensitivity analysis demonstrated that applied load uncertainties were more significant than material property uncertainties in influencing column reliability, consistent with typical structural reliability analysis results.

5. REFERENCES

Structural Integrity of some Existing Reinforced Concrete Columns. *ABUAD Journal of Engineering Research and Development (AJERD)*, 7(2), 163-171.

Akwu, P., Auta, S. M., & Saidu, M. (2020). Effect of revibration on the flexural strength of concrete using mahogany sawdust ash as a partial replacement for cement. *Architecture and Engineering Journal, 5*(1), 3-9. https://doi.org/10.23968/2500-0055-2020-5-1-03-09

Auta, S. M., Peter, A., & Saidu, M. (2020). Effect of revibration on the flexural strength of reinforced-concrete beams using mahogany sawdust ash as a partial replacement for cement. *Architecture and Engineering Journal, 5*(1), 3-9.

Benhelal, E., Zahedi, G., Shamsaei, E., & Bahadori, A. (2013). Global strategies and potentials to curb CO_2 emissions in cement industry. *Journal of Cleaner Production, 51*, 142-161.

BS 8615-1 (2019+A1:2026). British Standard Institution: Methods for Determination of natural pozzolanic materials used with Portland cement. London.

BS EN 12350-2 (2019). British Standard Institution: Standard test Methods of Determination of Slump of hydraulic-cement concrete used to measure consistency and workability. London.

BS EN 196-6 (2018). British Standard Institution: British standard for Portland cement. London, United Kingdom.

BS EN 1008 (2002). British Standard Institution: Method of determination of mixing water for concrete. London.

BS EN 1097-6 (2022). British Standard Institution: Testing Aggregates Part 1&2: Methods for Determination of particle size and shape. Includes a petrographical classification. ICS Code (Particle size analysis. sieving): 19.120 London.

BS EN 12390-3 (2019). British Standard Institution: Testing hardened concrete - Part 3: Compressive strength of test specimens. London.

BS EN 12620 (2013). British Standard Institution: Aggregates for concrete. London.

Ellingwood Bruce R. & Marc Maes, (2025). Development of methods of structural reliability. *Structural Safety*, 113, 102474.

Folagbade, S. O., & Olatunji, A. S. (2020). Effect of glass waste powder on the compressive strength and permeation properties of concrete containing Portland cement and sawdust ash. *Civil and Environmental Research, 12*(4), 1-12.

Ikponmwosa, E. E., Falade, F. A., Fashanu, T. A., Ehikhuenmen, S. O., & Adesina, A. (2020). Experimental and numerical investigation of the effect of sawdust ash on the performance of concrete. *Journal of Building Pathology and Rehabilitation, 5*(1), 1-12. https://doi.org/10.1007/s41024-020-00081-3

Kilani, A. J., Olubambi, A., Ikotun, B. D., Oladejo, O. S., & Famodu, B. (2023). Evaluating the reinforcements efficiency of sawdust and corncob wastes in structural concrete: A comprehensive review. *Journal of Building Materials and Structures, 10*(1), 1-15.

Kolo D.N., Abubakar M. and Aguwa J.I. (2024). Reliability studies on reinforced concrete column subjected to axial load with natural stone as coarse aggregate. *Nnamdi Azikiwe University Journal of Civil Engineering (NAUJCVE)*, 2(3), 25-30.

Ogbobe C.C., Abdullahi, M. and Aguwa, J. I. (2020). Compressive and Flexural Strength of Concrete Incorporating Wood Ash as Partial Replacement to Cement. *2nd International Civil Engineering Conference (ICEC 2020)*, Federal University of Technology, Minna, 389-397.

Osanyinlokun, O. E., Olaniyan, O. M., & Fapohunda, C. A. (2026). Artificial neural network for predicting the maximum load at failure of sawdust-ash-cement blends reinforced concrete beams. *FUOYE Journal of Engineering and Technology*, *10*(3), 560-572. https://doi.org/10.4314/fuoyejet.v10i3.26

Raheem, A. A., & Sulaiman, O. K. (2013). Saw dust ash as partial replacement for cement in concrete. *International Journal of Engineering Science Invention*, *4*(2), 36-40.

Sexsmith, R. G. (1969). Reliability analysis of concrete members. *ACI Journal Proceedings*, *66*(5), 413-420. https://doi.org/10.14359/7369

Sulaiman, T. A., Aliyu, I., & Yau, Y. (2020). Assessment of groundnut shell ash and sawdust ash as partial replacement of cement in concrete. *FUTA Journal of Engineering and Engineering Technology*, *14*(2), 117-125. https://doi.org/10.51459/futajeet.2020.14.2.213

International Conference on Engineering Innovation for Sustainable Development (ICESID 2026)
Faculty of Engineering, Ahmadu Bello University Zaria · 8–10 September 2026

SCREENING AND IDENTIFICATION OF SIGNIFICANT PROCESS PARAMETERS FOR SOLID STATE FERMENTATION OF TRICHODERMA HARZIANUM

Buhari Uwairu[1], Habib Adebisi Abubakar[1,*], Bilal Sabiu[1]
[1]*Ahmadu Bello University Zaria*
Email: buwairu@gmail.com, abuabib2006@gmail.com*, bilalsabiu@gmail.com
***Corresponding author**: Habib Adebisi Abubakar
DOI: https://doi.org/10.67203/sp.ICESID.2026

ABSTRACT

Agro-industrial wastes have gained considerable attention as inexpensive and renewable lignocellulosic feedstock for the sustainable production of byproducts including bioherbicides, through solid-state fermentation (SSF), an efficient and environmentally friendly biotechnological process. However, maximizing fungal growth and sporulation requires the identification of the most influential process parameters prior to optimization. This study aimed to screen and identify the significant process parameters affecting the solid-state fermentation of Trichoderma harzianum cultivated on agro-industrial residues. Sugarcane bagasse and corncob were selected as the substrates due to their abundance, low cost, favourable physicochemical properties, and proven suitability for supporting the growth and sporulation of Trichoderma harzianum during solid state fermentation. A One-Factor-at-a-Time (OFAT) approach was employed to investigate the effects of substrate weight (5–25 g), moisture content (50–70%), particle size (75 µm–1.18 mm), initial pH (4–8), and inoculum concentration (10^{-3} – 10^{-8}) on conidial production. The fermentation was carried out under controlled incubation conditions, and conidial yield (CFU g^{-1}) was used as the response variable. The screening results demonstrated that all the investigated factors influenced fungal growth; however, moisture content, particle size, and initial pH exerted the greatest effects on conidial production. These three factors were therefore selected as the significant process parameters for solid-state fermentation of Trichoderma harzianum. The range of these parameters resulting in substantially higher conidial yields than the other treatment levels were determined to be approximately 55–60% moisture content, particle size around 150–300 µm, and pH 5.0-6.0. The findings provide a scientific basis for identification of and specification of range of values of parameters for optimization of SSF for large-scale production of Trichoderma harzianum as an environmentally friendly bioherbicide.

Keywords: *Optimization; Solid State Fermentation; Agro-Industrial Waste; Trichoderma harzianum; Substrate; Sugarcane bagasse; Corncobs*

1. INTRODUCTION

Weed infestation remains one of the major constraints to agricultural productivity worldwide and is particularly severe in Nigerian agriculture where it significantly reduces crop growth, yield and food production. Conventional weed management strategies have been reported to be unsustainable because of their extensive use, which has led to the development of herbicide-resistant weeds, adverse effects on human health, and environmental degradation, including biodiversity loss as well as soil and water pollution (Hasan *et al.*, 2022; Ortaça Portela *et al.*, 2024; Synowiec *et al.*, 2025). These concerns have prompted growing interest in exploring alternative weed management strategies based on natural products to promote environmental sustainability (Hasan *et al.*, 2022).

Bioherbicides are natural products or compounds derived from microorganisms or other natural sources that suppress weed growth with minimal adverse effects on the environment. They are commonly produced through either submerged fermentation (SmF) or solid-state fermentation (SSF). Among these, SSF has emerged as an efficient, environmentally friendly, and sustainable biotechnological process in which microorganisms such as fungi, bacteria, or yeasts grow on solid substrates in the absence or near absence of free water to produce valuable bioproducts. Compared with submerged fermentation, SSF offers several advantages, including lower water and energy requirements, higher product concentrations, and the efficient utilization of inexpensive agricultural

residues. The process generally involves substrate preparation, inoculation and fermentation, followed by the recovery and processing of the desired products (Yafetto 2022).

Agro-industrial wastes have gained considerable attention as inexpensive and renewable feedstock for the production of sustainable biproducts, primarily because of the lignocellulosic nature of many plant residues (Rasheed *et al.,* 2024). Among the most promising are rice husks, yam peels, cassava peels, sugarcane bagasse, banana *pseudostems,* coconut shells, corncobs, sawdust, among others. Their abundance, renewability, high carbohydrate content, and ease of preparation make them attractive substrates for supporting microbial growth during SSF (Naeimi et al., 2020; Yafetto, 2022; C. Zhang et al., 2022). These materials are predominantly composed of cellulose, hemicellulose, and lignin, which serve as carbon and energy sources for microorganisms and can be converted through fermentation into value-added products such as biofuels, bioethanol, biopesticides, protein-enriched products, antibiotics and other industrial bioproducts (Aruna, 2019; Awoyale et al., 2021; Fadeyi et al., 2020; Kaur et al., 2025; Perwez & Al Asheh, 2025; Sadh et al., 2018; C. Zhang et al., 2022).

The suitability of agro-industrial waste for fungal growth and conidia production depends largely on their physicochemical and compositional properties. Consequently, comprehensive characterization of these materials is essential. Proximate analysis provides reliable essential information on the chemical composition of lignocellulosic biomass and is particularly valuable for the techno-economic assessment of biomass-based processes (Awoyale *et al.,* 2021). In addition to quantifying the major structural components; cellulose, hemicellulose, and lignin, it determines key parameters such as moisture content, ash content, dry matter, crude protein, crude fat, and pH, all of which significantly influence substrate performance, fungal growth, metabolite production, and conidia yield during solid-state fermentation. The cellulose contents of corncobs and sugarcane bagasse have been consistently reported to be comparable across studies. Awoyale *et al.,* (2021) reported cellulose contents of 38.6% for corncobs and 39.8% for sugarcane bagasse, while Rasheed *et al.,* (2024) reported slightly higher values of 40 ± 0.32% and 41 ± 0.41%, respectively. Based on the screening of some selected agro-industrial residues, both studies concluded that corncobs and sugarcane bagasse are promising lignocellulosic feedstocks because of their favourable chemical composition, particularly their high cellulose content. Cellulose, the principal structural polysaccharide in lignocellulosic biomass, serves as an important carbon source for *Trichoderma harzianum*. Through the secretion of cellulolytic enzymes, the fungus hydrolyzes cellulose into fermentable sugars that support mycelial growth, sporulation (conidia production), and secondary metabolites synthesis during solid-state fermentation. Therefore, the high and comparable cellulose contents reported by Awoyale *et al.,* (2021) and Rasheed *et al.,* (2024) provide a scientific basis for selecting corncobs and sugarcane bagasse as suitable substrates for conidia production and optimizing other process parameters can further improve the effectiveness of SSF with this substrate mixture.

SSF, can be carried out using either a single substrate or a combination of two or more solid organic substrates to improve nutrient availability and fermentation performance (Ortaça Portela *et al.,* 2024). For instance, Mulatu *et al.,* (2021) demonstrated that a mixture of wheat bran and white rice (1:1, w/w) significantly enhanced the conidia production of *Trichoderma asperellum* and *Trichoderma longibrachiatum*. In addition to the choice of substrates, maximizing fungal growth and sporulation during solid state fermentation requires the identification of the most influential process parameters prior to optimization.

Although several studies have optimized SSF conditions for *Trichoderma harzianum* using individual lignocellulosic substrates, limited information is available on the combined use of corncobs and sugarcane bagasse as mixed substrates for enhancing conidia production and bioherbicidal metabolite synthesis. Therefore, this study aimed to screen corncobs and sugarcane bagasse as substrates and identify the significant process parameters affecting conidia production during the solid-state fermentation of *Trichoderma harzianum.*

2. METHODOLOGY

2.1 Materials

All chemicals used in this study were of analytical grade. The Sugarcane bagasse was obtained from a sugarcane juice vendor at Danfodio Hall, Ahmadu Bello University, Zaria, whereas

corncobs were sourced from a local farmer. The fungal strain used in this study was obtained from the Department of Crop Protection, Ahmadu Bello University, Zaria, Nigeria.

2.2 Pretreatment of Sugarcane Bagasse and Corncob

The substrates were thoroughly washed and sun-dried. They were subsequently air-dried before being chopped into smaller pieces and ground into coarse particles. The processed substrates were then oven-dried at 75°C for 2 hours to reduce their moisture content until a constant weight was attained, after which they were further milled using an electric grinder. Finally, following the procedure described by Narwade *et al.*, (2023), the ground materials were sieved using ASEW standard test sieves to obtain particle sizes of 75, 150, 250, 300, and 600 µm, as well as 1180 µm, and packaged in labelled Ziploc bags for subsequent use.

2.3 Spore Suspension Preparation and Serial Dilution

A spore suspension of *Trichoderma. harzianum* was prepared from a 7-day-old culture following the method described by Kaur *et al.* (2025) with slight adjustment. Conidia were harvested from the culture surface by gently scraping with a sterile spatula and transferring them into 10 mL of sterile distilled water. The resulting suspension was vortexed for 30 s to ensure uniform dispersion of the spores and subsequently filtered through sterile muslin cloth to remove mycelial fragments. Serial dilutions were then prepared and the spore concentration was determined using a hemocytometer (Neubauer chamber, Taufkirchen, Germany) under an Olympus BX41 phase-contrast microscope (Sigma-Aldrich Chemie GmbH, Taufkirchen, Germany) at 40× magnification, as described by Pham *et al.* (2010).

For the serial dilution, eight sterile test tubes, each containing 9 ml of sterilized distilled water were labelled accordingly. One milliliter (1 mL) of the stock spore suspension was transferred aseptically into the first tube to obtain 10^{-1} dilution. Subsequently, 1 mL of the suspension from 10^{-1} dilution was transferred into the second tube to obtain 10^{-2} dilution. The same procedure was repeated subsequently to obtain 10^{-3}, 10^{-4} , 10^{-5}, 10^{-6}, 10^{-7}, and 10^{-8} dilutions. The 10^{-5} dilution was used as the inoculum concentration for the subsequent experiments.

2.4 Solid-State Fermentation Procedure and Experimental Design

Processed corncob (CC) and sugarcane bagasse (SCB) were used individually and in combination as substrates for solid-state fermentation (SSF) of *Trichoderma. harzianum* to maximize conidia production. A summary of the experimental procedure is shown in Fig 1. Following incubation, conidia were harvested and quantified using a hemocytometer (Neubauer chamber, Taufkirchen, Germany) under an Olympus BX41 phase-contrast microscope (Sigma-Aldrich Chemie GmbH, Taufkirchen, Germany) at 40× magnification, as described by Pham *et al.* (2010).

2.4.1 Substrate screening

To identify the most suitable substrate for enhanced conidia production by *Trichoderma,* different proportions of corncob (CC) and sugarcane bagasse (SCB) were evaluated. The substrate combinations tested were 100% SCB, 100% CC, 50:50 SCB: CC, 75:25 SCB: CC, and 25:75 SCB: CC. For each treatment, 20 g of a dry substrate was weighted into a 250 ml beaker and adjusted to 60% moisture content. The moistened substrates were autoclaved at 121°C for 15 min and allowed to cool to room temperature, before inoculation with 2 ml of spore suspension. The inoculated substrates were incubated at 25°C for 7 days. Following incubation, conidia were harvested and quantified. The substrate combination that produced the highest conidia yield was selected for subsequent screening of the critical growth factors using one-factor-at-time (OFAT) approach.

2.4.2 *Identification of significant factors affecting spore production with their upper and lower levels using OFAT*

OFAT experiments were conducted to evaluate the effects of key growth factors (GFs) on conidia production by *Trichoderma. Harzianum.* Five process variables were investigated: material

weight (MW, g: 5, 10, 15, 20, 25), pH (4 – 8), moisture content (MC, %: 50 – 70), particle size (PS, µm: 75 – 1180), and inoculum concentration (IC, dilution factors: 10^{-3} – 10^{-8}). Control conditions were set at 7-days of incubation at 25 °C and 60% MC. The selection of 60% moisture content and 25 °C as the initial control conditions was based on previously reported favourable conditions for the cultivation and conidia production of *Trichoderma. harzianum* under solid-state fermentation (De Oliveira *et al.*, 2026; Heng & Hamzah, 2022). Spore counts were determined post-incubation. Based on the results, three factors with the highest impact on conidia yield were selected as SSF process parameters for further optimization via Response Surface Methodology (RSM), with experimental limits defined from the one-factor-at-a-time (OFAT) ranges.

The effect of inoculum concentration on conidial production was investigated using different inoculum concentrations prepared from the serially diluted spore suspension described in Section 2.3. The inoculum concentrations corresponding to serial dilution levels of 10^{-3}, 10^{-4}, 10^{-5}, 10^{-6}, 10^{-7}, and 10^{-8} were evaluated. A dilution of 10^{-5}, was used as the standard inoculum concentration for the subsequent experiments. All other fermentation conditions were maintained constant during the assessment of inoculum concentration. Figure 1 shows the process flow of the methodology.

3. RESULTS AND DISCUSSION

3.1 Preparation of Inoculum

The microscopic morphology and pigmentation of *Trichoderma harzianum* conidia at different conidial concentrations are presented in Fig 2.

3.2 Effect of Different Agro-Waste Compositions on Spore Production

In this study, different compositions of agro-wastes, namely 100% sugarcane bagasse (SCB), 100% corncob (CC), 50:50 SCB:CC, 75:25 SCB:CC, and 25:75 SCB:CC, were evaluated for their effects on the spore production of *Trichoderma harzianum* under solid-state fermentation (SSF). The results showed variations in spore production among the individual substrates and their different combinations Fig 3 and Fig 4.

Trichoderma harzianum produced the highest spore yield on 100% corncob, followed by the 25:75 SCB:CC combination, whereas 100% SCB supported the lowest spore production. The spore yield obtained using pure corncob was approximately 3×10^6 spores/g on the seventh day of fermentation.

The superior performance of corncob may be attributed to its favourable physicochemical characteristics and nutrient composition, which may have provided a more suitable matrix for fungal growth and sporulation than sugarcane bagasse. The improved performance observed with the SCB:CC combinations also suggest that blending the agro-wastes may enhance the availability of nutrients and improve the physical properties of the fermentation substrate. These findings indicate that corncob is a more suitable substrate than sugarcane bagasse for the production of *Trichoderma harzianum* spores under the conditions investigated.

However, SCB, either alone or in combination with CC, was found to be less suitable for *Trichoderma harzianum* spore production, as indicated by the relatively low spore yields obtained. Although SCB was adjusted to the same particle size as CC, it still did not support high spore production within the relatively short fermentation period used in this study. This finding is consistent with Zhang *et al.* (2022), who reported lower spore yields and longer fermentation periods when sugarcane bagasse was used as a substrate. Similarly, Sachdev *et al.*, (2018) recorded a spore yield of 2.0×10^8 spores/g from SCB after 20 days of fermentation. In another study, the maximum growth of *T. asperellum* on rice bran reached 10.8×10^8 CFU/g, whereas only 3.73×10^8 CFU/g was obtained on SCB after 20 days of incubation. These findings suggest that SCB may require a longer fermentation period or additional substrate conditioning to achieve higher conidia production. More broadly, the variation in spore production among substrates demonstrates that *Trichoderma species* and strains have specific nutritional and environmental requirements for optimal conidiation. Consequently, no single culture medium or substrate can be considered universally optimal for conidia production, as the final yield depends on the interaction among the fungal strain, culture conditions, and substrate characteristics (Mulatu *et al.*, 2021).

3.3 Effect of Single Factors on Spore Production

According to Teo *et al.,* (2025), fungal growth and sporulation are strongly influenced by physicochemical factors. In this study, the effects of individual process parameters, namely inoculum concentration, pH, particle size, initial moisture content, and material weight, were investigated to determine their effects on the spore production of *Trichoderma harzianum* using corncob as the substrate. The experiments were conducted at an incubation temperature of 25 °C for 7 days. The effects of inoculum concentration, pH, particle size, initial moisture content, and material weight on spore production are presented in Figures 5 a–e, respectively.

The effects of inoculum concentration and material weight on spore production were investigated using a single-factor experimental approach. All treatments were conducted in duplicate (n = 2), and the results are presented as the mean of the duplicate measurements. The results showed some variation in spore production across the tested inoculum concentrations and material weights; however, the differences were relatively small compared with the variations observed for the other process parameters. Therefore, inoculum concentration and material weight were considered to have comparatively limited effects on spore production within the experimental ranges investigated and were not selected as factors for subsequent response surface methodology (RSM) optimization.

However, a previous study by (Mulatu *et al.,* 2021) reported that inoculum concentration could significantly affect fungal sporulation when a wider range of inoculum concentrations was investigated.

3.3.1 Effect of initial moisture content

Moisture content is an important factor in SSF because it influences substrate swelling, nutrient solubility, fungal growth, and metabolic activity. Adequate moisture facilitates nutrient uptake by the fungus, whereas insufficient moisture may reduce nutrient solubility and increase the surface tension of the water layer surrounding the substrate, thereby restricting fungal growth (Zhang *et al.,* 2022; Teo *et al.,* 2025). Conversely, excessive moisture can reduce substrate porosity and gas exchange, thereby limiting oxygen transfer and reducing the efficiency of SSF (Mulatu *et al.,* 2021).

This trend was observed in the present study. Spore production increased from 4.7×10^5 spores/g at an initial moisture content of 50% to 1.22×10^6 spores/g at 55%, reaching a maximum of 1.33×10^6 spores/g at 60%. However, further increases in moisture content resulted in a progressive decline in spore production. At 70% moisture content, spore production decreased to 4.4×10^5 spores/g, indicating that excessive moisture adversely affected the sporulation of *Trichoderma harzianum* Figure 5 (a). The reduction in spore production at higher moisture levels may be attributed to reduced substrate porosity and aeration, which can restrict oxygen transfer and create conditions less favourable for fungal growth and sporulation. Therefore, an initial moisture content range of 55–60% was considered suitable for spore production under the conditions investigated.

The maximum spore production observed at 60% moisture content agrees with the findings of Sala *et al.,* (2020) who reported that moisture content was one of the major factors influencing spore production of *Trichoderma harzianum* during solid-state fermentation of rice husk, with an optimum moisture range of 55–60%. Similarly, Zhang *et al.,* (2022) reported an optimum moisture content of 55.13% for sporulation of *Trichoderma spp.* using cassava peels as the substrate. These findings demonstrate that moisture content is an important factor influencing fungal sporulation, although the optimum level may vary depending on the fungal species, substrate characteristics, and other fermentation conditions.

3.3.2 Effect of pH

The effect of pH on conidia production was investigated by adjusting the pH of the moistening agent, sterile distilled water, using a mineral acid solution over a pH range of 4–8 Figure 7 (b). Conidia production was favoured under acidic conditions, particularly between pH 5 and 6, with the highest yield of 2.33×10^6 CFU/g obtained at pH 5.0. This finding agrees with previous reports indicating that pH can significantly affect fungal growth and sporulation during fermentation (Steffen *et al.,* 2026; Sargin *et al.,* 2013; J. D. Zhang & Yang, 2015). Changes in the pH of the fermentation medium can influence fungal morphology and several physiological and biochemical processes, including nutrient transport, enzymatic activity, and spore formation (Zhang *et al.,* 2022; Maurya *et*

al., 2012). Perwez and Al Asheh (2025) reported that the optimum initial pH for SSF media used for most fungi generally falls within the acidic range of approximately 4.5 – 5.5. The high conidia production observed at pH 5.0 in the present study therefore falls within the range reported in the literature.

The observed effect of pH indicates that it is an important process parameter for *Trichoderma harzianum* cultivation. Since pH can influence fungal growth, enzymatic activity, nutrient availability, and secondary metabolite production, its optimization is essential for maximizing conidia production. Consequently, pH was selected as one of the process parameters for subsequent optimization of the SSF process.

3.3.3 Effect of particle size

Particle size is another important factor affecting conidia production during SSF. It influences the physical structure of the substrate and consequently affects microbial growth, heat transfer, mass transfer, aeration, and oxygen availability (Perwez & Al Asheh, 2025). The particle size also determines the formation of void spaces within the substrate matrix, which can influence the movement of air and moisture through the fermentation bed.

Smaller substrate particles generally provide a larger specific surface area for fungal attachment and interaction with nutrients, potentially facilitating substrate degradation and fungal metabolism (Teo *et al.*, 2025). However, excessively fine particles may compact the substrate and restrict aeration, whereas very large particles may provide insufficient surface area for effective fungal colonization. Thus, an appropriate particle size is required to achieve a balance between surface area and substrate porosity.{Citation}

Particle size had a pronounced effect on conidial production by *Trichoderma harzianum*. The conidial yield varied across the particle size range investigated (75 µm – 1.18 mm), with yields of approximately 1.81×10^6, 1.87×10^6, 1.72×10^6, 2.47×10^6, 1.82×10^6, and 1.70×10^6 CFU/g at 75, 150, 250, 300, 600, and 1180 µm, respectively. The highest conidial production was observed at 300 µm (2.47×10^6 CFU/g), while the lowest was recorded at 1.18 mm (1.70×10^6 CFU/g). This substantial variation in conidial production across the tested particle sizes indicates that substrate particle size influenced fungal sporulation and therefore justified its selection as a significant parameter for subsequent optimization

The results obtained in this study demonstrated that particle size had a pronounced effect on conidia production. Together with initial moisture content and pH, particle size was identified as one of the three major process parameters influencing the response. These three factors were therefore selected for subsequent statistical optimization of the SSF process.

Overall, the one-factor-at-a-time experiments indicated that initial moisture content, pH, and particle size exerted stronger effects on conidia production than inoculum concentration and material weight under the experimental conditions employed. Accordingly, moisture content, particle size, and pH were selected as the independent variables that have significant impacts on the solid-state fermentation of *Trichoderma harzianum.* These variables can be used as key parameters for the optimization of solid-state fermentation of *Trichoderma harzianum*, which is a subject of another study.

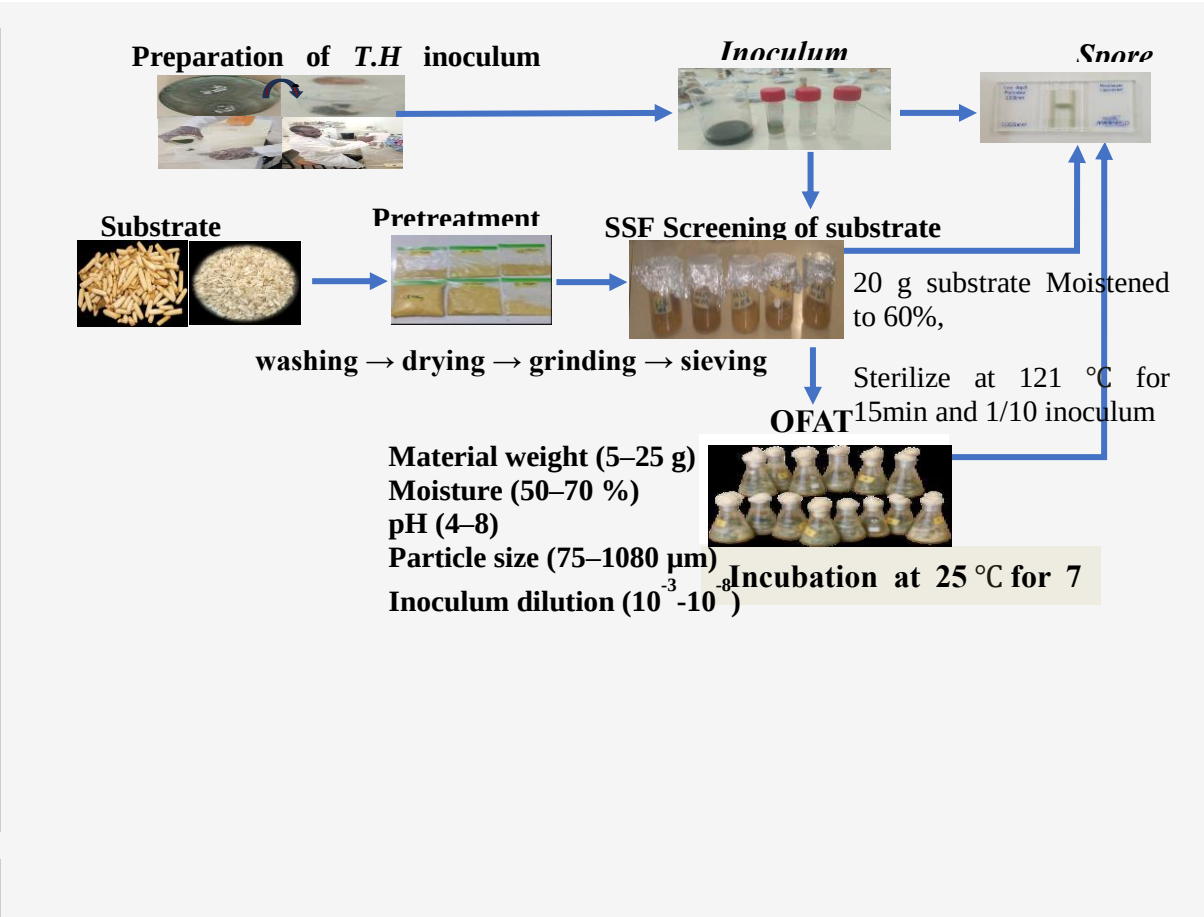

Figure 1: Process flow of the methodology

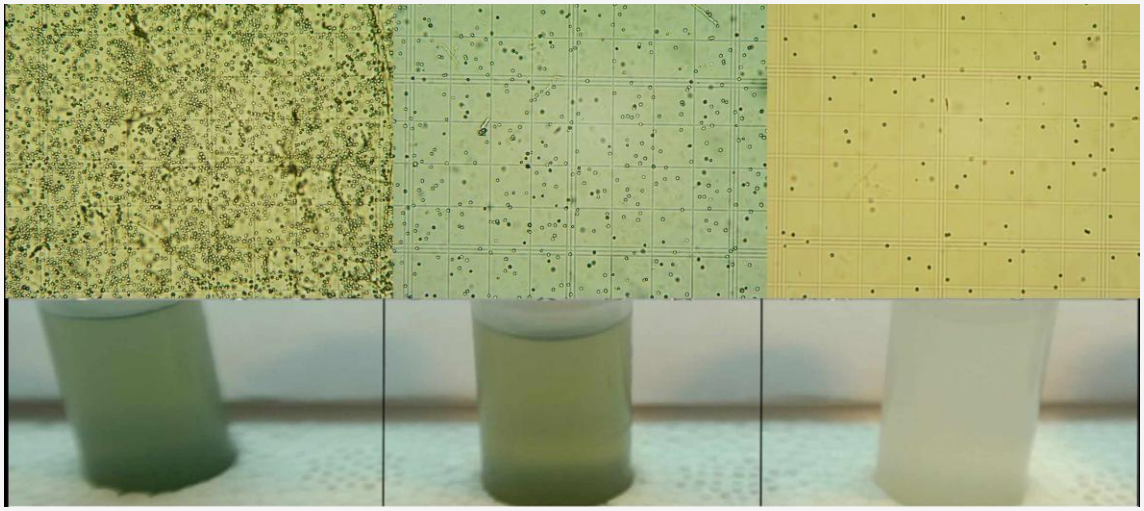

(A) First dilution 10^{-1} *(B) Second dilution 10^{-2}* *(C) Third dilution 10^{-3}*

Figure 2: Microscopic morphology and pigmentation of Trichoderma. harzianum conidia at different dilution factors

Figure 3: Colonization and Sporulation of Trichoderma harzianum

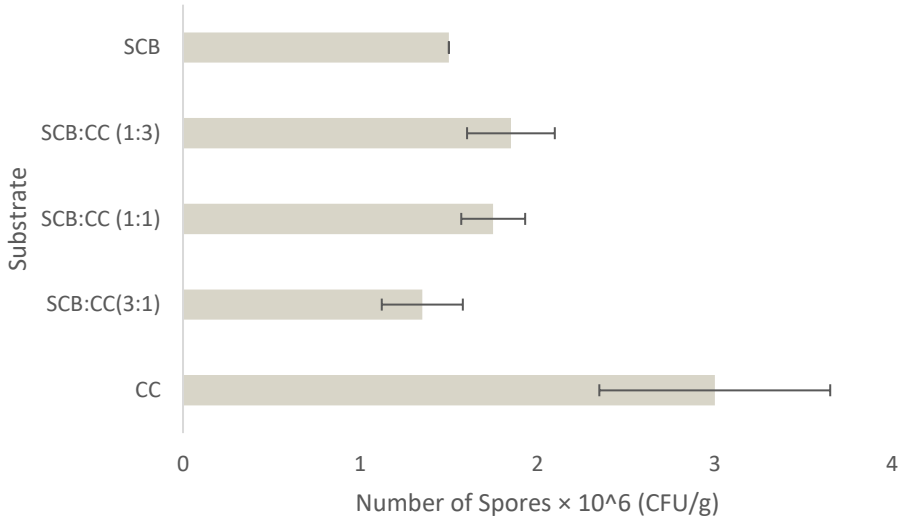

Figure 4: Spore production of Trichoderma harzianum on the two different agro-industrial wastes examined separately and in combination after 7 days of incubation at 25ºC

(a)

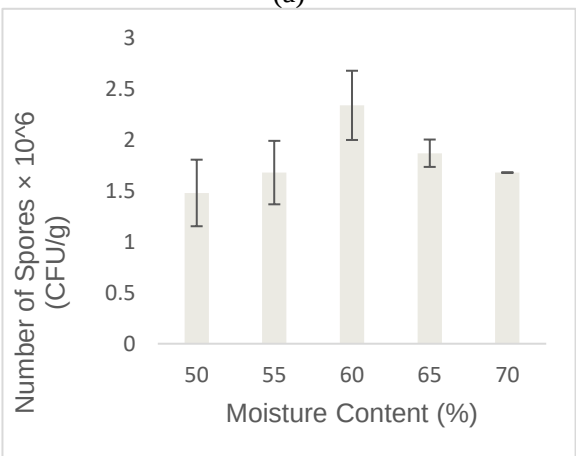

(b)

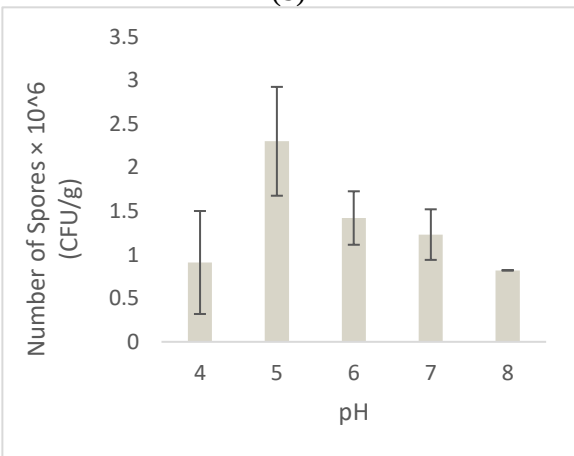

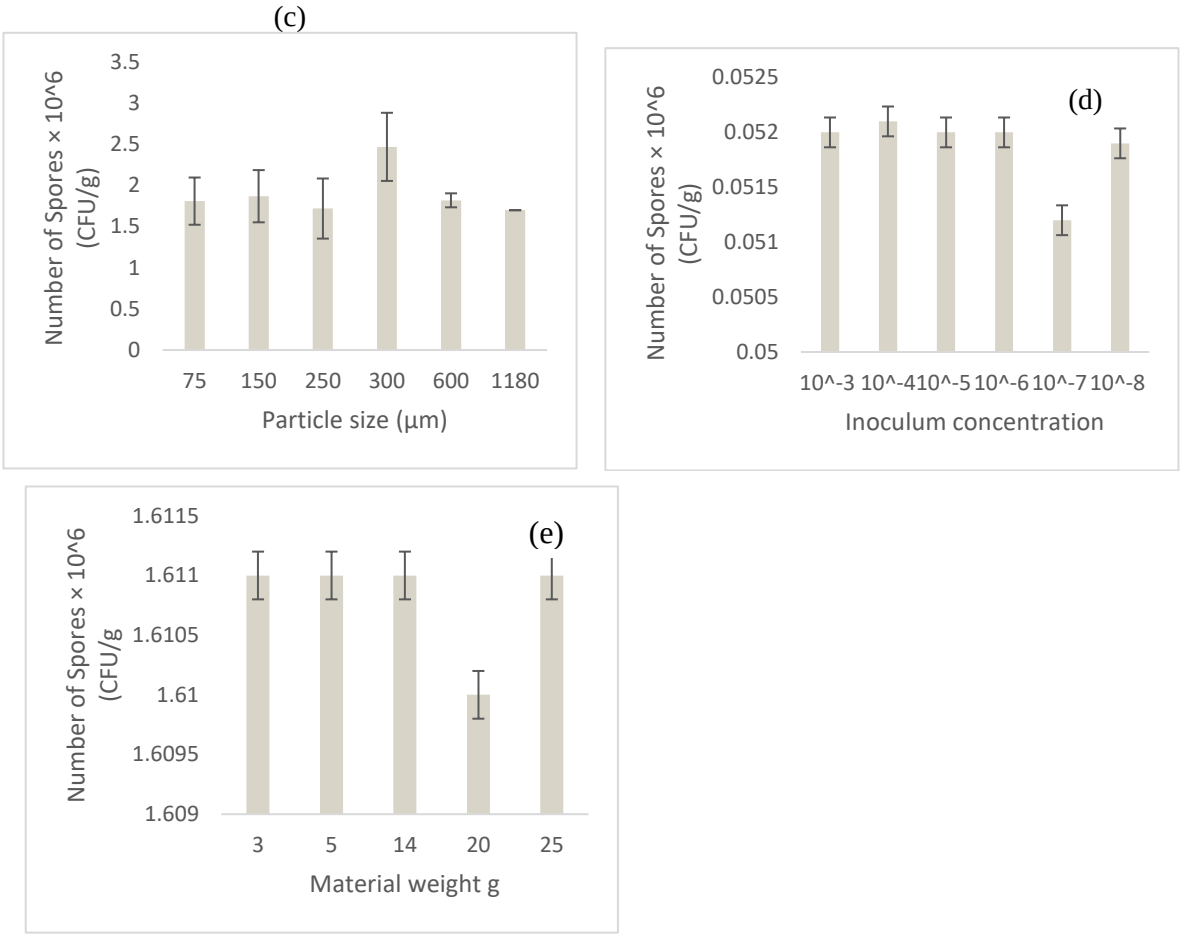

Figure 5: Effects of different parameters on the production of spores by Trichoderma harzianum, at incubation temperature of 25°C and fermentation period of 7 days. a) moisture content, b) pH, c) particle size d) inoculum concentration and e) material weight

4. CONCLUSION

The study successfully screened and identified moisture content, particle size, and pH as important process parameters influencing the solid-state fermentation of *Trichoderma harzianum* for conidia production. The screening results indicated that higher conidial yields were obtained at approximately 55–60% moisture content, 300–600 µm particle size, and pH 5.0–6.0. However, the one-factor-at-a-time (OFAT) approach evaluates the effects of individual parameters independently and does not account for possible interactions among process variables. Therefore, response surface methodology (RSM) was subsequently employed to evaluate these interaction effects and determine the optimal combination of the selected parameters. These findings provide a scientific basis for defining suitable parameter ranges for optimization of solid-state fermentation and potential large-scale production of *T. harzianum* as an environmentally friendly bioherbicide.

Acknowledgements The authors gratefully acknowledge IAR-Institute for Agricultural Research (IAR), and department of chemical engineering Ahmadu Bello University Zaria, Nigeria for providing the necessary facilities and support to carry out this research work.

5. REFERENCES

Aruna, T. E. (2019). Production of value-added product from pineapple peels using solid state fermentation. *Innovative Food Science & Emerging Technologies*, *57*, 102193. https://doi.org/10.1016/j.ifset.2019.102193

Awoyale, A. A., Lokhat, D., & Eloka-Eboka, A. C. (2021). Experimental characterization of selected Nigerian lignocellulosic biomasses in bioethanol production. *International Journal of Ambient Energy*, *42*(12), 1343–1351. https://doi.org/10.1080/01430750.2019.1594375

De Oliveira, F. R., Sala, A., Okino-Delgado, C., Gea, T., & Casciatori, F. (2026). Flavonoid production via solid-state fermentation of agro-industrial waste with biopesticidal fungi: Screening, optimization and scale-up. *Bioprocess and Biosystems Engineering*, *49*(5), 1287–1302. https://doi.org/10.1007/s00449-026-03316-8

Fadeyi, A. E., Akiode, S. O., Emmanuel, S. A., & Falayi, O. E. (2020). Compositional analysis and characterization of lignocellulosic biomass from selected agricultural wastes. *Journal of Science and Mathematics Letters*, *8*(1), 48–56. https://doi.org/10.37134/jsml.vol8.1.6.2020

Hasan, M., Mokhtar, A. S., Mahmud, K., Berahim, Z., Rosli, A. M., Hamdan, H., Motmainna, Mst., & Ahmad-Hamdani, M. S. (2022). Physiological and biochemical responses of selected weed and crop species to the plant-based bioherbicide WeedLock. *Scientific Reports*, *12*(1), 19602. https://doi.org/10.1038/s41598-022-24144-2

Heng, J. L. S., & Hamzah, H. (2022). Effects of different parameters on cellulase production by Trichoderma harzianum TF2 using solid-state fermentation (SSF). *Indonesian Journal of Biotechnology*, *27*(2), 80. https://doi.org/10.22146/ijbiotech.66549

Kaur, J., Goswami, D., & Saraf, M. (2025). Response surface methodology: A comparative optimization of antifungal metabolite production by Trichoderma viride and Trichoderma harzianum using solid-state fermentation. *Biomass Conversion and Biorefinery*, *15*(12), 18723–18746. https://doi.org/10.1007/s13399-025-06575-9

Mulatu, A., Alemu, T., Megersa, N., & Vetukuri, R. R. (2021). Optimization of Culture Conditions and Production of Bio-Fungicides from Trichoderma Species under Solid-State Fermentation Using Mathematical Modeling. *Microorganisms*, *9*(8), 1675. https://doi.org/10.3390/microorganisms9081675

Naeimi, S., Khosravi, V., Varga, A., Vágvölgyi, C., & Kredics, L. (2020). Screening of Organic Substrates for Solid-State Fermentation, Viability and Bioefficacy of Trichoderma harzianum AS12-2, a Biocontrol Strain Against Rice Sheath Blight Disease. *Agronomy*, *10*(9), 1258. https://doi.org/10.3390/agronomy10091258

Narwade, J. D., Odaneth, A. A., & Lele, S. S. (2023). Solid-state fermentation in an earthen vessel: Trichoderma viride spore-based biopesticide production using corn cobs. *Fungal Biology*, *127*(7–8), 1146–1156. https://doi.org/10.1016/j.funbio.2023.06.007

Ortaça Portela, V., Rodrigues Da Rosa, O., Souza, M., De Oliveira Adolpho, L., Irion Dalcol, I., & Jacques, R. J. S. (2024). Chemical composition and bioherbicidal activity of metabolites of Mycoleptodiscus indicus produced in three culture media. *Biocatalysis and Agricultural Biotechnology*, *58*, 103147. https://doi.org/10.1016/j.bcab.2024.103147

Perwez, M., & Al Asheh, S. (2025). Valorization of agro-industrial waste through solid-state fermentation: Mini review. *Biotechnology Reports*, *45*, e00873. https://doi.org/10.1016/j.btre.2024.e00873

Pham, T. A., Kim, J.-J., & Kim, K. (2010). Optimization of Solid-State Fermentation for Improved Conidia Production of Beauveria bassiana as a Mycoinsecticide. *Mycobiology*, *38*(2), 137–143. https://doi.org/10.4489/MYCO.2010.38.2.137

Rasheed, H. A., Adeleke, A. A., Nzerem, P., Olosho, A. I., Ogedengbe, T. S., & Jesuloluwa, S. (2024). Isolation, characterization and response surface method optimization of cellulose from hybridized agricultural wastes. *Scientific Reports*, *14*(1), 14310. https://doi.org/10.1038/s41598-024-65229-4

Sachdev, S., Singh, A., & Singh, R. P. (2018). Optimization of culture conditions for mass production and bio-formulation of Trichoderma using response surface methodology. *3 Biotech*, *8*(8), 360. https://doi.org/10.1007/s13205-018-1360-6

Sadh, P. K., Duhan, S., & Duhan, J. S. (2018). Agro-industrial wastes and their utilization using solid state fermentation: A review. *Bioresources and Bioprocessing*, *5*(1), 1. https://doi.org/10.1186/s40643-017-0187-z

Sala, A., Artola, A., Sánchez, A., & Barrena, R. (2020). Rice husk as a source for fungal biopesticide production by solid-state fermentation using B. bassiana and T. harzianum. *Bioresource Technology*, *296*, 122322. https://doi.org/10.1016/j.biortech.2019.122322

Sargin, S., GezgiN, Y., Eltem, R., & Vardar, F. (2013). Micropropagule production from Trichoderma harzianum EGE-K38 using solid-state fermentation and a comparative study for drying methods. *Turkish Journal of Biology*. https://doi.org/10.3906/biy-1206-32

Steffen, G. P. K., Steffen, R. B., Vieira, F. C. B., Boeni, M., & Maldaner, J. (2026). Influência do pH sobre o crescimento e a esporulação de agentes de bioinsumos microbianos. *Disciplinarum Scientia - Ciências Naturais e Tecnológicas*, *27*(2), 205–220. https://doi.org/10.37779/nt.v27i2.5743

Synowiec, A., Czekaj, M., Verdeguer, M., Barreda, D. G. D., Campillo-Cora, C., Vieites-Álvarez, Y., López-González, D., Sánchez-Moreiras, A. M., Fernández-Calviño, D., Nocito, F. F., & Ragonezi, C. (2025). Herbicides in Use: Current Status and Perspectives in the Different Biogeographic Regions of Europe. *J. Agric. Food Chem.*

Teo, H. L., Wahab, R. A., Zainal-Abidin, M. H., Mark-Lee, W. F., Huyop, F., Susanti, E., Mahat, N. A., & Azman, A. R. (2025). Statistically assisted optimisation for the simultaneous production of Trichoderma harzianum and Aspergillus fumigatus cellulolytic enzymes. *Biomass Conversion and Biorefinery*, *15*(3), 3827–3843. https://doi.org/10.1007/s13399-023-05222-5

Yafetto, L. (2022). Application of solid-state fermentation by microbial biotechnology for bioprocessing of agro-industrial wastes from 1970 to 2020: A review and bibliometric analysis. *Heliyon*, *8*(3), e09173. https://doi.org/10.1016/j.heliyon.2022.e09173

Zhang, C., Ali Khan, R. A., Wei, H., Wang, R., Hou, J., & Liu, T. (2022). Rapid and mass production of biopesticide Trichoderma Brev T069 from cassava peels using newly established solid-state fermentation bioreactor system. *Journal of Environmental Management*, *313*, 114981. https://doi.org/10.1016/j.jenvman.2022.114981

Zhang, J. D., & Yang, Q. (2015). Optimization of solid-state fermentation conditions for Trichoderma harzianum using an orthogonal test. *Genetics and Molecular Research*, *14*(1), 1771–1781. https://doi.org/10.4238/2015.March.13.4

International Conference on Engineering Innovation for Sustainable Development (ICESID 2026)
Faculty of Engineering, Ahmadu Bello University Zaria · 8–10 September 2026

SOLAR-BIOMASS HYBRID SYSTEMS FOR INTEGRATED LIVESTOCK-HORTICULTURE FARMS IN SUB-SAHARAN AFRICA: A REVIEW

Kouétcha Esaïe Kombetto[1,*], James Garba Ambafi[1], Taliha A. Folorunso[1]
[1]*Federal University of Technology Minna*
Email: kouetchaemen183@st.futminna.edu.ng[*], ambafi@futminna.edu.ng, funso.taliha@futminna.edu.ng
***Corresponding author**: Kouétcha Esaïe Kombetto
DOI: https://doi.org/10.67203/sp.ICESID.2026

ABSTRACT

Integrated livestock-horticulture farms in sub-Saharan Africa depend on costly diesel power while producing manure and crop residues whose energy value is rarely recovered. This review examines how photovoltaic generation and biomass conversion through anaerobic digestion or gasification can be combined into a single farm microgrid. A literature search conducted in Google Scholar on 1 September 2026, covering 2021-2026, returned 43 studies that met the inclusion criteria, 24 of them reporting sub-Saharan African sites or datasets. Every system-level result reported for a solar-biomass hybrid is a simulation. The pairing suits farm conditions: solar output serves daytime irrigation and processing loads, while biogas from on-farm waste provides dispatchable power for the evening peak and heat for brooding, sanitation and cooling. Reported hybrids deliver USD0.265/kWh against USD0.980/kWh for diesel at one Ghanaian site and cut operational CO_2 sharply: from 400 t/yr under a diesel-dominant configuration to 31.8 t/yr at the selected optimum for a Nigerian poultry facility, and from 636 t/yr under diesel-only supply to below 1 kg/yr at a Tanzanian village, all on a combustion-only boundary. Digestate returns to the cropped area as fertiliser. Three design lessons follow. Biogas delivers more value as heat than as electricity at farm scale, so the digester should be sized against thermal demand, allowing for the heat the fermenter consumes. Storage carries the largest share of lifetime cost, so scheduling shiftable loads into the solar window is the most rewarding control measure. Reported profiles, efficiencies and substrate properties vary with site and method, so local characterisation should precede sizing.

Keywords: *solar-biomass hybrid systems; anaerobic digestion; farm microgrid; dispatch strategy; techno-economic analysis; sub-Saharan Africa*

1. INTRODUCTION

Agriculture supports more than half the population of sub-Saharan Africa, smallholders account for roughly 80% of production and over 90% of cropland is rainfed, while about 75% of rural people and most rural enterprises lack reliable electricity (Falchetta *et al.*, 2023). Design practice compounds the deficit: rural generation studies address residential and institutional loads with little regard for productive uses, one Tanzanian village model entering agricultural demand as zero (Mwakitalima *et al.*, 2023) and Zambian fieldwork showing households acquiring capacity adequate for lighting but not income generation (Chanda *et al.*, 2026). Holdings combining livestock with horticulture fit neither template, yet are common: at Mankramso in Ghana, 89.8% of households farm crops and rear livestock (Odoi-Yorke, Abaase, *et al.*, 2022).

Where such holdings secure power off-grid it is predominantly diesel, consistently the costliest option: reviewed mini-grid studies place diesel at USD0.92-1.30/kWh (Zebra *et al.*, 2021), and community-scale examples reach USD0.980/kWh at Mankramso (Odoi-Yorke, Abaase, *et al.*, 2022). The environmental burden follows: at Abeokuta the diesel-containing optimum emits 31,840 kg of CO_2, against 15.8 kg for the diesel-free configuration retaining a 50 kW biomass generator (Emezirinwune *et al.*, 2024).

The resources to displace diesel are already on the holding. Photovoltaic pumping is economically feasible for smallholders at scale (Falchetta *et al.*, 2023), and biomass valorisation is a viable electrification route because agricultural and livestock waste accumulates wherever farming concentrates (Uzoagba *et al.*, 2024). Hybrids pairing renewables with storage or a dispatchable unit are

the established off-grid route (Zebra *et al.*, 2021), and solar-biomass suits farm conditions because photovoltaic output coincides with daytime irrigation and processing demand while a digester or gasifier is dispatchable to the evening peak and the thermal load (Diemuodeke *et al.*, 2024). Dispatchability has quantified value: removing bioenergy from a Ghanaian national pathway raises storage output by 37%, battery capacity by 29% and levelised cost by 27% (Mensah *et al.*, 2021).

This review treats the integrated holding as a single microgrid. Its objectives are to characterise the compound electrical and thermal load, review the conversion and power-conditioning subsystems, evaluate reported sizing and dispatch methods against standard reliability and cost metrics, and identify the empirical gaps obstructing design.

2. METHODOLOGY

2.1 Search Strategy and Study Selection

This is a narrative, conference-length review, illustrative of the current state of the art rather than exhaustive. Literature was identified by topic-based searching of Google Scholar, with full texts retrieved from the platforms it indexes, principally Elsevier, MDPI, Wiley, Frontiers, Springer Nature and Oxford University Press. Terms combined solar, photovoltaic, biomass, biogas, anaerobic digestion, gasification, agrivoltaic, hybrid renewable energy system, microgrid, livestock, poultry and cold storage with sub-Saharan Africa or individual country names; they were refined iteratively as the corpus developed, and the reference lists and related-article links of retained studies were followed. Records were eligible if published 2021-2026 in English in peer-reviewed journals or peer-reviewed conference proceedings, reporting original data, modelling or synthesis on: agrivoltaics and solar systems for irrigation, shading, grazing or farm electrification; digestion, co-digestion or gasification of manure or crop residue for farm energy; hybrid solar-biomass sizing, dispatch or techno-economic assessment in rural developing-country settings; post-harvest cold storage and precooling at farm scale; or microgrid coupling, power conditioning, energy management and metaheuristic sizing, subsystems sparsely treated in the agricultural literature. Utility-scale and urban work without an agricultural interface was excluded, as was any study stating no method or offering no extractable quantitative result. Studies outside the region were retained only for direct methodological relevance, such as the Fijian poultry-manure digestion trial, and are declared non-regional at each point of use. Claims resting on a single source triggered supplementary searching until corroborated or declared single-sourced where used. The search was conducted in Google Scholar and last updated on 1 September 2026, and resulted in 43 studies that met the inclusion criteria, of which 24 report sub-Saharan African sites or datasets.

2.2 Quality Appraisal and Character of the Evidence Base

Quality was appraised at point of use, and non-regional sources are declared at each use. The search was purposive rather than exhaustive and relied on openly retrievable English-language work, so the corpus is likely to under-represent unindexed, non-English or paywalled studies, a selection effect compounding the reporting bias considered in Section 3.7. Screening was carried out by a single reviewer, and stage-by-stage record counts were not retained. Two further features require statement: almost all system-level results are simulations, only Randle-Boggis *et al.* (2025) reporting operational agrivoltaic installations with measured multi-season output; and one reviewed study reports an itemised electrical and thermal breakdown (Baldi *et al.*, 2026), limiting how strongly the demand structure below can be asserted.

3. RESULTS AND DISCUSSION

3.1 Integrated Farm Load Characterisation

Livestock demands follow the animals' clock rather than the operator's: lighting, ventilation, feed preparation, water supply and, on dairy holdings, milking and chilling. Sub-metering of thirty German dairy farms shows these duties carry distinct load signatures (Vavouris *et al.*, 2025); no comparable African dataset was located, so structure is inferred from nameplate audits. Feed preparation is the largest discrete connected load on a poultry enterprise but not the largest consumer: a Nigerian layer audit at 25,000-bird scale reports a 16.5 kW hammer mill running briefly within

roughly 140 kWh/day dominated by pen-house lighting (Sasanya and Olaifa, 2022), while lighting on the Cameroonian broiler holding is minor at 2,418 kWh annually (Baldi *et al.*, 2026).

Irrigation is modelled rather than measured, and its character matters as much as its size: pumping is a deferrable motor load, flexible within the day because water can be stored, a mean smallholder system consuming about 255 kWh annually across roughly 75 operating days (Falchetta *et al.*, 2023).

Cold-chain demand is continuous and interruption-intolerant, so reliability rather than mean power drives design. Set points follow chilling-injury thresholds, 13 °C for banana and yam down to 7 °C for okra and pepper (Makule *et al.*, 2022), so a mixed tropical store runs near 13 °C rather than the sub-zero range of conventional cold storage. Solar cold stores run 5-10 kWp against 2-10 tons at COP 3.95, batteries taking 30-40% of cost (Amjad *et al.*, 2023). No reviewed source supplies a measured cooling profile for an African farm, the nearest entering refrigeration into the Mankramso model as a continuous 28.8 kWh/day load (Odoi-Yorke, Abaase, *et al.*, 2022): capacity can be inferred from tonnage, dispatch cannot, and dispatch determines storage.

Heat is a structural need: chicks held above ambient, wash water heated, harvests dried and produce cooled. On a three-house farm near Yaoundé producing roughly 72,000 birds annually, an 8 kW heater called below 27 °C consumes 57,744 kWh per year, about 94% of itemised farm energy (Baldi *et al.*, 2026); Emezirinwune *et al.* (2024) audit the same enterprise type but record electricity only, so the datasets cannot be compared. Non-regional broiler accounting agrees that brooding heat dominates total energy input, though ventilation dominates the electrical share as ambient temperature rises (Liang and Popp, 2025).

The cooling routes compare by coefficient of performance: a vapour-absorption cycle at COP 0.7 on 130 °C exhaust delivers 7.7 kW of cooling from 11 kW of heat (Diemuodeke *et al.*, 2024), a duty needing about 1.95 kW electrically at the vapour-compression COP of 3.95 (Amjad *et al.*, 2023), so absorption pays only where the heat would otherwise be rejected.

Aggregate figures allow sizing metrics to be derived. At Mankramso the load ranges 2.98-47.26 kW against 96 MWh annually, peaking 16:00-21:00 (Odoi-Yorke, Abaase, *et al.*, 2022). Taking the load factor as

$$LF = \frac{E_{ann}}{8760 \times P_{peak}} \tag{1}$$

gives a mean demand of 10.96 kW and a load factor near 0.23, which oversizes generation capacity, while the peak falling outside the generation window obliges energy to be time-shifted and so makes storage dominate lifetime cost. The audited Nigerian facility consumes 506,200 kWh annually, a mean of 57.8 kW, modelled as 527,250 kWh after a variability allowance (Emezirinwune *et al.*, 2024), against 3,544 kWh/yr at the Cameroonian farm, a caution against transferring published profiles. Table 1 assembles the load data reported.

Table 1: *Reported and derived farm load metrics across the reviewed studies*

Site	**Reported**	**Derived**
Yaoundé, Cameroon (Baldi *et al.*, 2026)	8 kW heater; 57,744 kWh/yr thermal; 3,544 kWh/yr electrical	Heating approximately 94% of itemised farm energy
Mankramso, Ghana (Odoi-Yorke, Abaase, *et al.*, 2022)	2.98-47.26 kW; 96 MWh/yr; peak 16:00-21:00	Mean 10.96 kW; load factor around 0.23
Abeokuta, Nigeria (Emezirinwune *et al.*, 2024)	Audited 1,386.85 kWh/day = 506,200 kWh/yr; modelled 1,444.52 kWh/day = 527,250 kWh/yr after a 5% variability setting, an increase of 4.2%; electrical only	Mean 57.8 kW audited (506,200 ÷ 8,760); 60.2 kW modelled; no thermal load recorded

3.2 Biomass Feedstock and Waste-to-Energy Conversion

Manure production per head differs by an order of magnitude between species (Kadam *et al.*, 2024), and threefold within one species by basis: poultry at 0.3 kg/head/day as excreted, 0.15 as collected litter and 0.09 as fresh manure (Baldi *et al.*, 2026; Naidu *et al.*, 2024). Poultry also gives the highest volumetric biogas yield among common manures, 231 Nm³ per tonne of dry manure against 60 for cattle manure (Augustyn *et al.*, 2021), and is the reference feedstock; its volatile fraction is reported between 0.61 and 0.85 on non-interchangeable bases (Ayantokun *et al.*, 2025), so the same yield spans 270-380 Nm³ per tonne of volatile solids. Blending streams of different character raises yield and stability (Kadam *et al.*, 2024), so the species mix is itself an asset. Supply is not constant: availability falls from 0.787 t/day in January to 0.315 t/day in July-October (Mwakitalima *et al.*, 2023), competing uses remove part of the residue stream (Adnane *et al.*, 2024), and about 6 of Ghana's 35 million tonnes of crop residue are unavailable for energy (Odoi-Yorke, Osei, *et al.*, 2022).

Biogas carries about 6 kWh/Nm³ at 55-65% methane (Naidu *et al.*, 2024). Stability is governed by the substrate carbon-to-nitrogen ratio, reported for poultry manure across a sevenfold range (Table 2) against a workable window given variously as 20-30, 16-25 or 20-35, optimal near 25, with ammonia inhibiting methanogenesis above 4 g/L (Adnane *et al.*, 2024; Ayantokun *et al.*, 2025); every entry in Table 2 except the Togolese and Nigerian measurements sits below it. The dispersion is not measurement error: nutrient content varies with region, diet and antibiotic use, bedding adds straw, feathers, lime or sawdust, and storage raises ammonia (Kadam *et al.*, 2024).

Table 2: *Reported carbon-to-nitrogen ratios for poultry manure*

Source	**C/N**	**Material as described**	**Basis**
Kadam *et al.* (2024)	Approx. 4.0	Chicken manure, elemental composition	Literature compilation; ultimate analysis depresses the ratio, the same source reporting 10.1
Baldi *et al.* (2026), Cameroon	6-12	Litter with bedding	Literature-derived
Naidu *et al.* (2024), Fiji	8	Manure with feathers, no sawdust	Calculator estimate
Brou *et al.* (2026), Togo	16.07	Manure with wood-chip bedding	Site measurement
Ayua *et al.* (2026), Nigeria	29.38	Dried droppings	Site measurement

Co-digestion brings the substrate into the window. Brou *et al.* (2026) report cumulative biogas rising from 210.73 to 348.65 mL/g VS at C/N 25 with cocoa pod husk, a 65.45% gain inside the 25-400% range reported generally (Adnane *et al.*, 2024). The second benefit is operational: in parallel reactors, a fall from 29 °C to 26 °C cut mono-digestion output by up to 80% while the co-digested reactor lost only 20% (Naidu *et al.*, 2024). The co-substrate is thus a stabiliser drawn from material already on a cropping holding, and mesophilic operation is the most widely adopted full-scale regime because it tolerates inhibitors and avoids thermophilic heating demand (Kadam *et al.*, 2024).

Uzoagba *et al.* (2024) assign low-moisture wastes to thermochemical and high-moisture waste to biochemical routes; Odoi-Yorke, Osei, *et al.* (2022) add scale, every gasification feedstock returning a negative net present value at 10 kW where every combustion feedstock was profitable, the two converging only at 100 kW because gasification carries the extra capital of gas cleaning and the gas engine. Integrated holdings sit at this scale, and fixed-bed downdraft reactors suit it best, yielding 0.1-1.2 g/Nm³ of tar against 20-100 from updraft units, but their window is narrow, 20-100 mm particles, ash near 0.5%, moisture below 20% (Ouedraogo, Sidibe, *et al.*, 2025), and most farm residues miss it: a West African trial on 25.2%-ash rice husk returned a cold gas efficiency of 36.6% against the 52.2-65% downdraft band (Ouedraogo, Richardson, *et al.*, 2025).

The electrical energy available from either route follows from

$$Q_{th} = V_{gas} \times LHV_{gas},$$
$$P_e = \eta_e \times Q_{th},$$
$$\eta_{cg} = \frac{V_{gas} \times Y_{gas} \times LHV_{gas}}{LHV_{bio}}, \quad (2)$$
$$\eta_{overall} = \eta_{cg} \times \eta_e$$

where Y_{gas} is specific gas production in Nm³/kg (Ouedraogo, Richardson, *et al.*, 2025). Applying (2) shows why efficiency figures must be read on a common basis: a gasifier consuming 25-30 kg/h and producing 60-65 Nm³/h at 4.5-5.0 MJ/Nm³ delivers roughly 82 kW of syngas thermal power against a genset rated 20 kWe and optimised to 24 kW, so the electrical efficiency near 24%, taken on the 20 kWe rating, is an engine figure, not a system one, and at the 16-20 MJ/kg typical of West African agro-residues cold gas efficiency is 54-68% and overall efficiency 13-16% (Diemuodeke *et al.*, 2024).

Yield figures can likewise mix bases. Augustyn *et al.* (2021) tabulate dry chicken manure at 381 kWh_e per tonne, implying 27% electrical efficiency, a full-scale cogeneration figure well above the 10-20% assumed for small farm gensets (Baldi *et al.*, 2026), so mixing the two over-predicts electrical output by roughly 1.4 to 2.8 times. At Tuna the same generator returns 140,661 kWh of recovered heat against 185,735 kWh of electricity (Diemuodeke *et al.*, 2024).

3.3 Microgrid Architecture, Power Electronics and Control

Among the off-grid reviewed systems only one describes a coupling arrangement, and then only as a nominal 12 V bus with no topology justification (Diemuodeke *et al.*, 2024), so guidance on the uncharacterised power-electronics layer comes from adjacent work. Jabari *et al.* (2025) describe the architecture as an AC subnet, a DC subnet and an interlinking converter, grid-forming units setting the voltage and frequency reference and grid-following units tracking it. An explicit two-bus arrangement is reported at Maizube farm, Sabon-daga, a 500 ha Nigerian holding carrying over 300 cattle alongside an orchard and drawing 980 kWh/day: Adetoro *et al.* (2023) place array, wind turbine and battery on a DC bus and the generators and heavy agricultural loads on an AC bus linked by a bidirectional converter, so rotary generators serve inductive machinery directly and inrush stress bypasses the power electronics. That system is grid-connected, an interconnection the islanded case does not carry, but the ordering of sources on the AC side is the one an off-grid farm faces.

For a farm microgrid whose largest loads are three-phase induction motors and whose biomass generator is an AC machine, AC coupling is the defensible default: the generator serves the motor loads directly, without a converter stage, at the cost of lower array-to-load efficiency. Classical droop assumes inductive line impedance, whereas in low-voltage networks resistance is comparable or larger, breaking active-reactive decoupling and causing inaccurate sharing and circulating currents (Jabari *et al.*, 2025), the case farm distribution presents and no reviewed study addresses. Inverter-connected photovoltaics contribute no rotational inertia, so sudden generation loss produces a faster rate of change of frequency unless grid-forming control emulates a synchronous response (Khan *et al.*, 2024); since thermal-first dispatch leaves the biomass generator off for most hours, a grid-forming battery inverter must hold the reference.

Converter ratings are reported in two of the reviewed systems on incompatible conventions: 81.4 kW against a 561 kW array, 6.9:1 against installed practice of 1.1-1.5:1 (Emezirinwune *et al.*, 2024), and 24.8 kW against a 20 kWp array at Tuna, 0.81:1 (Diemuodeke *et al.*, 2024). Neither states a rule, and no reviewed study reports inverter topology, harmonic distortion, regulation limits or protection coordination. Direct-on-line starting of mills and pelletisers imposes inrush currents of several times rated value, and a synchronous machine can supply roughly seven times rated current briefly where a grid-forming converter offers only about 20% overcurrent (Khan *et al.*, 2024). Machinery surveys reach the same requirement independently, reporting hammer mills at 2-15 kW and pelletisers from 3 kW upward and recommending variable-frequency drives for soft starting (Ogunobo and Onyenanu, 2025). A converter rated for motor starting rather than mean demand is therefore the implied requirement, which no reviewed sizing study addresses, and no measured power-quality data for an African farm microgrid was located.

Dispatch is either unspecified or set to the simulator's load-following rule (Emezirinwune *et al.*, 2024), whereas the evidence supports a thermal-first order of merit. Biogas converted to electricity at 10-20% engine efficiency discards most of its energy content against 90% in a gas heater (Baldi *et al.*, 2026); Naidu *et al.* (2024) reach the same ordering on emissions, 147.09 t CO2 avoided annually by cooking-fuel displacement against 55.98 t via electricity; Rezaei *et al.* (2024) reach it on capital grounds, an organic Rankine cycle entering the optimum only if the electricity price roughly triples; and Augustyn *et al.* (2021) close it from the supply side, 95-99% of generated heat being absorbable by building heating and fermentation support.

A general constraint makes this ordering unusually favourable here. A biogas plant on average uses only half the heat it produces, and in Germany only 10% of producers use more than half (Augustyn *et al.*, 2021): cogeneration disappoints because the heat has no destination, and on a holding combining brooding, sanitation, drying and absorption cooling one exists. Capturing 130 °C engine exhaust serves the thermal load without touching the electrical bus (Diemuodeke *et al.*, 2024), so heat met this way never draws on the battery, the dominant cost term (Table 3). Load scheduling is then the highest-value control objective: forced-air precooling completes in 1-10 hours against 20-100 for room cooling (Makule *et al.*, 2022), and feed processing admits the same treatment (Sasanya and Olaifa, 2022). The one reviewed design that schedules milling does so as an assumed rather than optimised pattern (Odoi-Yorke, Abaase, *et al.*, 2022), and machinery-level guidance likewise places grinding and pelleting in the solar window (Ogunobo and Onyenanu, 2025).

Producer gas carries only 4.2-5.7 MJ/Nm³ and engines burning it have strict purity requirements. Tar is the dominant reliability constraint: below 450 °C it condenses and polymerises, corroding and clogging downstream components, and for unattended small units mechanical cleaning is favoured over catalytic or wet routes, which displace the problem into liquid-waste handling (Ouedraogo, Sidibe, *et al.*, 2025). A gasifier-genset should therefore run near its rated point with the battery absorbing the mismatch, a constraint no reviewed farm-scale study incorporates, though the Tuna simulation agrees, average electricity cost falling as the minimum load ratio rises (Diemuodeke *et al.*, 2024).

3.4 Sizing and Optimisation Methodology

All but two of the reviewed systems were sized in HOMER, the exceptions using particle swarm optimisation and mixed-integer linear programming (Table 3). A comparison of ten sizing tools against fourteen criteria (Silinto *et al.*, 2025) ranks HOMER the highest-scoring conventional model and confirms it admits thermal and deferrable loads, a capability no reviewed HOMER-based farm study exercised though the mixed-integer formulation schedules both (Baldi *et al.*, 2026); the same review records two structural limits, no multi-objective formulation and aggregation of all components into a single node with no internal power flow.

The wider literature applies metaheuristic search to the same problem. One reviewed study coupled HOMER with a grey wolf optimiser, reducing levelised cost from USD0.1109/kWh to USD0.0887/kWh (Mwakitalima *et al.*, 2023), a margin reflecting a different search space, since HOMER enumerates near-exhaustively over its own. In multi-objective formulations cost, reliability and emissions genuinely conflict: on a grid-connected solar-biogas system with storage, a non-dominated sorting whale optimisation algorithm balanced net present cost against emissions with better convergence than grey wolf and particle swarm benchmarks (Agajie *et al.*, 2023). Every reviewed farm study nonetheless minimises a single cost objective, which conceals the trade-off rather than resolving it.

Reliability is expressed as loss of power supply probability,

$$LPSP = \frac{\sum E_{unmet}}{\sum E_{demand}} \tag{3}$$

and cost as the levelised cost of energy,

$$LCOE = \frac{C_{cap} \times CRF + C_{O\&M} + C_{rep} + C_{fuel}}{E_{served}} \tag{4}$$

where $CRF(i,n) = \frac{i(1+i)^n}{(1+i)^n - 1}$ at real discount rate i, replacements are present-worthed, salvage credited, and E_{served} is electricity delivered; crediting heat gives a cost of energy, not of electricity (Diemuodeke *et al.*, 2024). The reliability metric is not reported under a single name across the corpus, appearing as loss of energy probability in Emezirinwune *et al.* (2024) and as loss of energy probability of power in (Mwakitalima *et al.*, 2023); the quantity is identical and the studies are compared on that basis.

Applied to Abeokuta, the fully renewable configuration leaves 399 kWh/yr unserved against a 527,250 kWh modelled load, a ratio of 0.000757, at USD0.261/kWh against USD0.206/kWh for the diesel-containing optimum, a premium of 26.7% (Emezirinwune *et al.*, 2024): the premium buys the last fraction of a point of availability, a design choice rather than a technical limit. Each metric is reported in only two of the reviewed systems.

3.5 Techno-Economic, Environmental and Cogeneration Synthesis

Table 3 assembles the reviewed sub-Saharan solar-biomass systems; only one is sited on a holding combining livestock with a cropped area, and there the crop enterprise carries no modelled electrical load. The hybrids sit below diesel and above grid supply: Mankramso delivers USD0.265/kWh against USD0.980/kWh for diesel alone, 64% above Ghana's average tariff (Odoi-Yorke, Abaase, *et al.*, 2022). Where no grid exists the comparison inverts, break-even grid extension at Simboya being 0.19 km against a nearest connection 79.7 km away (Mwakitalima *et al.*, 2023).

Table 3: *Reported solar-biomass hybrid systems for sub-Saharan Africa*

Site	**Scope**	**Configuration**	**Method**	**LCOE**	**Discount rate / life**	**Storage share**
Mankramso, Ghana	Rural community	PV 50 kW; biogas 20 kW; battery 237 kWh	HOMER	$0.265/kWh	12% / 25 yr (batteries 5 yr)	45.6% of NPC
Simboya, Tanzania	Rural village	PV 40 kW; biogas 25 kW; battery 144 kWh	HOMER, then grey wolf	$0.1109/kWh (HOMER); $0.0887/kWh (grey wolf)	8% nominal, 4% inflation / 25 yr (batteries 10 yr)	45.9% of capital
Tuna, Ghana	School (CHP)	PV 20 kWp; gasifier-genset 24 kW; battery 78 kWh	HOMER Pro	€0.295/kWh	7.5% / 25 yr	Not reported
Abeokuta, Nigeria	Poultry facility	PV 561 kW; gasifier 10 kW; diesel 88 kW; converter 81.4 kW (the fully renewable case substitutes a 50-kW biomass generator)	HOMER	$0.206/kWh diesel-containing optimum; $0.261/kWh fully renewable	11.5% / 25 yr	Approx. 51% of NPC
Sabon-daga, Nigeria	Dairy farm with orchard; grid-connected, 20% availability	PV 248 kW; wind 2 kW; biogas 22 kW; diesel 92 kW; battery 658 kWh	PSO	$0.148/kWh	15% / 25 yr	Not reported
Yaoundé, Cameroon	Poultry farm	PV 70 kW; digester to 23.2 kW	MILP	€2,680-6,980/yr (annual cost)	Not reported / 20 yr (10 yr batteries)	Battery at farm only in unconstrained case

Note. Yaoundé reports a total annualised system cost, not a levelised cost, and is not comparable with the other rows. Costs are in the currency and year of the source study, without exchange-rate normalisation. The Sabon-daga levelised cost includes grid import at USD0.07/kWh and is not comparable with the off-grid rows.

The biomass share of generation spans more than an order of magnitude across the three hybrids reporting it, 49% at Mankramso, 9.6% at Simboya and 2.77% at Abeokuta, and the cause is allocation, not resource. At Simboya the biogas unit generates 7,707 kWh against 72,500 kWh from the array on 23.1 t of feedstock annually, about 63 kg/day against a collected availability of 0.315-0.787 t/day, a capacity factor of 3.52%: the constraint is how much manure is committed to the generator, the balance going to household cooking gas (Mwakitalima *et al.*, 2023). At Mankramso a 20 kW unit against a 50 kW array carries 49% because it runs when the array cannot (Odoi-Yorke, Abaase, *et al.*, 2022), a split independently tabulated by Overen *et al.* (2024). Any quoted biomass fraction therefore describes dispatch and allocation, not the farm's resource.

Storage dominates lifetime cost, the most consistently reproduced result: all three hybrids reporting a share place batteries at or above 45% of net present or capital cost, denominators that are not interchangeable, with a further 30-40% share in solar cold storage (Amjad *et al.*, 2023). Quadrupling feedstock price from USD2 to USD8 per tonne raises levelised cost by only 5% where manure is collected on site (Odoi-Yorke, Abaase, *et al.*, 2022), whereas cost is materially sensitive for purchased groundnut shells (Diemuodeke *et al.*, 2024), an argument for on-farm supply.

Diesel displacement is the principal environmental benefit reported: at Abeokuta annual emissions fall from 399,855 kg of CO2 under the diesel-dominant alternative to 31,840 kg at the optimum and 15.8 kg diesel-free (Emezirinwune *et al.*, 2024), and at Simboya from 635,966 kg under diesel-only supply to 0.531 kg fully renewable (Mwakitalima *et al.*, 2023). These are combustion figures at about 2.66 kg CO2/L, with biogenic carbon zero-rated and methane slip and digestate storage outside the boundary, so the residual kilogrammes measure diesel displaced rather than the farm's footprint. Open storage of manure loses up to 70% of its nitrogen within 24 hours in humid tropical conditions (Kadam *et al.*, 2024), so digestion conserves more than energy alone.

Thermal recovery is rarely evaluated: only the Tuna configuration, delivering 110.9 MWh of heat and 7.7 kW of cooling (Diemuodeke *et al.*, 2024), and the Yaoundé optimisation, where biogas serves brooding heat (Baldi *et al.*, 2026). Sizing either requires a correction the reviewed designs omit: Rezaei *et al.* (2024) report a fermenter consuming on average 45% of the heat produced, rising to about 60% in the cold season, so the heat available to the farm is

$$Q_{avail} = Q_{gross}(1 - f_{par}) \text{ is approximately 0.45-0.60} \quad (5)$$

The figure is a temperate input coefficient rather than a measurement, but the correction cannot be omitted: a digester sized by matching nominal production to brooding demand will under-deliver by roughly half. The tropical case is likely more favourable, ambient temperatures sitting closer to the mesophilic set point (Adnane *et al.*, 2024), and solar water heating raised a Nigerian pilot digester's average temperature 35% on sunny relative to rainy days (Ayua *et al.*, 2026), placing part of the parasitic demand on the solar side.

Digestate is usually presented as an environmental co-benefit and is closer to an economic foundation. Zielińska and Bułkowska (2024) state the constraint: nitrogen and phosphorus in the liquid fraction are simultaneously too concentrated for discharge standards and too dilute to serve as fertiliser, and the mature recovery routes stay viable only above roughly 50 mg P/L or 1,000-1,500 mg/L ammonia, below which, the smallholder case, the nutrients are effectively unrecoverable. Naidu *et al.* (2024) show the value where a market exists, payback falling from 16.8 years to under three once 5% of digestate is sold; where none exists, the correct valuation is the fertiliser purchase avoided on site. These are transaction constraints, which makes co-location decisive: applied where produced, digestate is neither upgraded, transported nor priced, and proximity of livestock and co-substrate to the digester is independently identified as a commercialisation requirement (Kadam *et al.*, 2024).

3.6 Field-Level Implementation Challenges

Four technical constraints recur. Feedstock volatility is seasonal (Mwakitalima *et al.*, 2023), so sizing against the minimum month is the defensible heuristic. Gasifier tar fouling limits engine life, and nearly all gasification plants deployed for heat and power in this region have failed (Ouedraogo, Sidibe, *et al.*, 2025). Photovoltaic soiling is more severe than global defaults allow, modelled West African losses exceeding 50% during the Harmattan (Isaacs *et al.*, 2023), and no reviewed farm study applies a region-specific derating, so reported yields are optimistic. Finally, storage is 51% of net present cost on a four-year battery life, replacement across all components 34% against 11% for fuel (Emezirinwune *et al.*, 2024).

Capital cost and credit access dominate the economic constraints, ranking above technical ones across the solar-cooling studies screened by Amjad *et al.* (2023). Pay-as-you-go and lease-to-own arrangements still require 20-25% upfront, and on one estimate only about 6% of the region's farmers could afford solar irrigation individually (Durga *et al.*, 2024); Tanzanian smallholders meet input costs only after sale, so cannot prepay for storage services (Rutta, 2022). Even a 100% capital subsidy leaves levelised cost 32% above Ghana's lifeline tariff, because capital is barely two-fifths of lifetime cost (Odoi-Yorke, Abaase, *et al.*, 2022), a result reproduced by Odoi-Yorke, Osei, *et al.* (2022) and by a South African design that turns loss-making without a 60% subsidy (Overen *et al.*, 2024), while in the

Yaoundé optimisation the digester enters only under a litter-disposal constraint or with external financing (Baldi *et al.*, 2026).

Targets exist without accountability: Nigeria set 90% electricity access by 2030 with no public progress reports (Uzoagba *et al.*, 2024), and Nyarko *et al.* (2023) find monitoring largely absent, a six-country inspection identifying projects with neither maintenance plans nor monitoring systems. A multi-regional review records the same pattern of weak policy frameworks and limited stakeholder coordination across Nigeria, Kenya and South Africa (Obuseh *et al.*, 2025).

3.7 Convergence, Divergence and Empirical Gaps

Table 4 separates claims supported by multiple independent sources from those resting on one study or stated on differing bases.

Table 4: *Points of convergence across the reviewed literature*

Claim	Status	Basis
Storage dominates lifetime cost	Convergent	All three hybrids reporting a share are at 45% or above of NPC or capital, denominators not interchangeable; 30-40% for solar cold storage
Thermal use before electrical conversion	Convergent	Engine efficiency, emissions, capital cost and heat-utilisation ceiling agree; emissions line contingent on displaced fuel
Co-digestion corrects C/N and raises yield	Convergent	Batch assay and reviews agree on yield; one pilot corroborates stability
Capital subsidy alone is insufficient	Convergent	Two studies sharing a lead author, plus independent cost-type and South African corroboration
Shiftable processing belongs in the generation window	Partially corroborated	One assumed schedule in a community model plus independent machinery-level design guidance; no optimised or measured demonstration
Thermal demand dominates poultry load	Partially corroborated	One itemised regional audit; direction supported by non-regional broiler accounting; a second regional audit records no thermal load
Digester parasitic heat at 45-60%	Single-sourced, non-regional	A single Swiss study, where the value is an input coefficient attributed to secondary CHP guidance rather than a measurement; alters sizing materially
Biogas yield per tonne vs. engine efficiency	Stated on different bases	Plant-level 1.65 kWhe/Nm^3 vs 10-20% genset efficiency; 231 Nm3/t dry manure = 0.27-0.38 m^3/kg VS across the reported volatile-solids range
Gasifier electrical efficiency	Single plant, two bases reconciled	24% engine and 13-16% overall are one plant on two bases
Bus architecture and power quality	Addressed once, outside the off-grid set	One grid-connected Nigerian farm study specifies a two-bus topology; no off-grid system justifies a coupling arrangement, states a converter sizing rule, or reports power-quality data

Five empirical gaps follow. First, the holding is not modelled as one system: the audited poultry facility reports no thermal demand (Emezirinwune *et al.*, 2024), agricultural load is entered as zero at village scale (Mwakitalima *et al.*, 2023), both village-scale solar-biogas designs size digesters from livestock censuses treating manure purely as fuel, and at Maizube farm the itemised load covers animal housing and milk handling only, with no irrigation or post-harvest demand in the optimisation (Adetoro *et al.*, 2023). That integrated configuration has not been examined. Second, demand is not disaggregated: with one itemised electrical and thermal breakdown available (Baldi *et al.*, 2026), the thermal-first order of merit rests on multiply-sourced efficiency arguments matched against a singly-

sourced demand structure. Third, cooling has capacity but no demand shape, leaving a schedulable load unschedulable. Fourth, the power-electronics layer is unspecified for the off-grid farm case (Table 4). Fifth, continuous farm-scale digestion is untested regionally, the reviewed pilots operating at 10 L in Nigeria (Ayua *et al.*, 2026) and 500 L in Fiji (Naidu *et al.*, 2024), and no African livestock agrivoltaic instance was located, the field studies identified being United States sheep systems (Bacon *et al.*, 2025) and the one financial analysis likewise North American (Gasch *et al.*, 2025).

A limitation of the evidence base qualifies these gaps and the convergence in Table 4. Every hybrid reviewed reports a cost advantage over diesel, and no reviewed study reports an uncompetitive configuration at farm scale. Simulation studies returning unfavourable outcomes are less likely to be submitted and published than favourable ones, so the absence of negative results is consistent with reporting practice as well as with system performance. Table 4 therefore indicates that these configurations perform under the modelling assumptions their authors adopted, not that a representative sample of sites would return equivalent results.

3.8 Recommendations for Future Sizing Models and Field Implementation

Four recommendations follow. First, instrument a working integrated holding for electrical and thermal demand at end-use resolution over a full agricultural cycle. Second, formulate sizing as a multi-objective problem over levelised cost, loss of power supply probability and renewable fraction, with the digester's unit-commitment decision represented explicitly and the fermenter parasitic fraction of (5) applied to gross thermal output; since that fraction rests on a single non-regional coefficient, establishing the regional value is part of the work. Third, specify the power-electronics interface against motor-starting duty rather than mean demand, and apply a region-specific soiling derating from local particulate data. Fourth, treat local characterisation as preceding sizing: panel densities associated with yield loss in temperate meta-analysis improved several crop yields at two East African sites (Randle-Boggis *et al.*, 2025), that expectation itself resting on coverage thresholds across fifty installations (Widmer *et al.*, 2024).

4. CONCLUSION

Integrated livestock-horticulture holdings resolve internally three constraints that limit on-farm digestion elsewhere: the substrate carbon-to-nitrogen imbalance, corrected by a co-substrate the cropping enterprise already produces; the thermal instability that co-substrate buffers; and the transaction cost of digestate, which disappears when the material is applied where it is produced. Co-location is therefore an economic precondition of the design, and the same reasoning governs heat.

Three design principles follow. Gas should be allocated to heat before conversion, and the digester sized against thermal demand referred to gross rather than net output, because the fermenter consumes a substantial share of the heat produced; the only quantification available, 45-60%, is a single non-regional input coefficient (Rezaei *et al.*, 2024), so the design carries forward its approximate magnitude, not its precise value. Storage is the dominant cost term, so scheduling shiftable load into the generation window is the control objective with the largest economic return. Published parameters are artefacts of the method and site that produced them, so local characterisation precedes sizing rather than refines it. The principal limitation is the evidence base itself: every system-level result reported for a solar-biomass hybrid is a simulation, digestion results are at bench and pilot scale, the cooling load is uncharacterised in time, the power-electronics layer is unspecified, the corpus contains no negative techno-economic result, and the demand structure has been itemised on a single farm. The configuration is well founded in its parts and unproven as a whole; an instrumented pilot is the next contribution needed.

5. REFERENCES

Adetoro, S. A., Olatomiwa, L., Tsado, J., & Dauda, S. M. (2023). An enhanced combined dispatch strategy for a grid-connected hybrid renewable energy system. *Green Energy and Resources, 1(4)*, 100044. https://doi.org/10.1016/j.gerr.2023.100044

Adnane, I., Taoumi, H., Elouahabi, K., Lahrech, K., & Oulmekki, A. (2024). Valorization of crop residues and animal wastes: Anaerobic co-digestion technology. *Heliyon, 10(5)*. https://doi.org/10.1016/j.heliyon.2024.e26440

Agajie, T. F., Fopah-Lele, A., Amoussou, I., Ali, A., Khan, B., & Tanyi, E. (2023). Optimal Design and Mathematical Modeling of Hybrid Solar PV–Biogas Generator with Energy Storage Power Generation System in Multi-Objective Function Cases. *Sustainability, 15(10)*, 1-26. https://doi.org/10.3390/su15108264

Amjad, W., Munir, A., Akram, F., Parmar, A., Precoppe, M., Asghar, F., & Mahmood, F. (2023). Decentralized solar-powered cooling systems for fresh fruit and vegetables to reduce post-harvest losses in developing regions: a review. *Clean Energy, 7(3)*, 635-653. https://doi.org/10.1093/ce/zkad015

Augustyn, G., Mikulik, J., Rumin, R., & Szyba, M. (2021). Energy self-sufficient livestock farm as the example of agricultural hybrid off-grid system. *Energies, 14(21)*, 7041. https://doi.org/10.3390/en14217041

Ayantokun, A. S., Matambo, T. S., Rashama, C., Van der Merwe, I., & Van Niekerk, J. A. (2025). A critical review of food waste and poultry manure anaerobic co-digestion: An eco-friendly valorization for sustainable waste management and biogas production. *Frontiers in Sustainable Food Systems, 9*, 1695945. https://doi.org/10.3389/fsufs.2025.1695945

Ayua, T. J., Ambrose, I. S., & Omaku, D. S. (2026). Anaerobic digestion of poultry droppings for biogas production: a pilot study of renewable energy technology in the agricultural sector. *BMC Environmental Science, 3(1)*, 7. https://doi.org/10.1186/s44329-026-00048-8

Bacon, T., Monlezun, A., Hong, M., Macknick, J., De Vries, N., Edwards-Callaway, L., & Paustian, K. (2025). Agrivoltaic grazing systems for a sustainable future: A multi-disciplinary review & gap analysis. *Earth's Future, 13(8)*, e2024EF005429. https://doi.org/10.1029/2024EF005429

Baldi, F., Santucci, M., Bini, M. E., Kenne, Y., Beozzo, S., & Bonoli, A. (2026). Valorization of poultry litter through anaerobic digestion in small-scale farm energy systems: A techno-economic case study in Cameroon. *Energies, 19(9)*, 2024. https://doi.org/10.3390/en19092024

Brou, A. P. E., Gbiete, D., Nougbléga, Y., & Narra, S. (2026). Optimizing biogas production from poultry manure and cocoa pod husks co-digestion: implications for circular bioeconomy and decentralized energy systems in West Africa. *Frontiers in Bioengineering and Biotechnology, 14*, 1845247. https://doi.org/10.3389/fbioe.2026.1845247

Chanda, H., Mohareb, E., Peters, M., Harty, C., Green, M., Kasanda, E. B., & Shibata, N. (2026). Energy transitions in Sub-Saharan Africa: Policy recommendations for charcoal trade, solar PV adoption, and sustainability in rural Zambia. *Energy Policy, 208*, 114936. https://doi.org/10.1016/j.enpol.2025.114936

Diemuodeke, O. E., Vera, D., Ojapah, M. M., Nwachukwu, C. O., Nwosu, H. U., Aikhuele, D. O., . . . Seidu Nuhu, B. (2024). Hybrid Solar PV–Agro-Waste-Driven Combined Heat and Power Energy System as Feasible Energy Source for Schools in Sub-Saharan Africa. *Biomass, 4(4)*, 1200-1218. https://doi.org/10.3390/biomass4040067

Durga, N., Schmitter, P., Ringler, C., Mishra, S., Magombeyi, M. S., Ofosu, A., . . . Verma, S. (2024). Barriers to the uptake of solar-powered irrigation by smallholder farmers in sub-saharan Africa: A review. *Energy strategy reviews, 51*, 101294. https://doi.org/10.1016/j.esr.2023.101294

Emezirinwune, M. U., Adejumobi, I. A., Adebisi, O. I., & Akinboro, F. G. (2024). Off-grid PV/biomass/DG/battery hybrid renewable energy as a source of electricity for a farm facility. *e-Prime-Advances in Electrical Engineering, Electronics and Energy, 10*, 100808. https://doi.org/10.1016/j.prime.2024.100808

Falchetta, G., Semeria, F., Tuninetti, M., Giordano, V., Pachauri, S., & Byers, E. (2023). Solar irrigation in sub-Saharan Africa: Economic feasibility and development potential. *Environmental Research Letters, 18(9)*, 094044. https://doi.org/10.1088/1748-9326/acefe5

Gasch, A., Lara, R., & Pearce, J. M. (2025). Financial analysis of agrivoltaic sheep: Breeding and auction lamb business models. *Applied Energy*, *381*, 125057. https://doi.org/10.1016/j.apenergy.2024.125057

Isaacs, S., Kalashnikova, O., Garay, M. J., van Donkelaar, A., Hammer, M. S., Lee, H., & Wood, D. (2023). Dust soiling effects on decentralized solar in West Africa. *Applied Energy*, *340*, 120993. https://doi.org/10.1016/j.apenergy.2023.120993

Jabari, M., Ghoreishi, M., Bragatto, T., Santori, F., Cresta, M., Geri, A., & Maccioni, M. (2025). Advancing hybrid ac/dc microgrid converters: Modeling, control strategies, and fault behavior analysis. *Energies*, *18(23)*, 6302. https://doi.org/10.3390/en18236302

Kadam, R., Jo, S., Lee, J., Khanthong, K., Jang, H., & Park, J. (2024). A review on the anaerobic co-digestion of livestock manures in the context of sustainable waste management. *Energies*, *17(3)*, 546. https://doi.org/10.3390/en17030546

Khan, M., Wu, W., & Li, L. (2024). Grid-forming control for inverter-based resources in power systems: A review on its operation, system stability, and prospective. *IET Renewable Power Generation*, *18(6)*, 887-907. https://doi.org/10.1049/rpg2.12991

Liang, Y., & Popp, M. (2025). Economic Impact of Energy Accounting Schemes for Commercial Systems on a Broiler Farm with Power Demand and Generation. *Energies*, *18(4)*. https://doi.org/10.3390/en18040979

Makule, E., Dimoso, N., & Tassou, S. A. (2022). Precooling and cold storage methods for fruits and vegetables in Sub-Saharan Africa—A review. *Horticulturae*, *8(9)*, 776. https://doi.org/10.3390/horticulturae8090776

Mensah, T. N. O., Oyewo, A. S., & Breyer, C. (2021). The role of biomass in sub-Saharan Africa's fully renewable power sector–the case of Ghana. *Renewable Energy*, *173*, 297-317. https://doi.org/10.1016/j.renene.2021.03.098

Mwakitalima, I. J., Rizwan, M., & Kumar, N. (2023). Integrating solar photovoltaic power source and biogas energy-based system for increasing access to electricity in rural areas of Tanzania. *International Journal of Photoenergy*, *2023(1)*, 7950699. https://doi.org/10.1155/2023/7950699

Naidu, G. M., Raturi, A., & Mani, F. S. (2024). Anaerobic digestion of poultry manure to power a poultry farm in Ba: Pilot and techno-economic study. *Heliyon*, *10(17)*. https://doi.org/10.1016/j.heliyon.2024.e36325

Nyarko, K., Whale, J., & Urmee, T. (2023). Drivers and challenges of off-grid renewable energy-based projects in West Africa: A review. *Heliyon*, *9(6)*. https://doi.org/10.1016/j.heliyon.2023.e16710

Obuseh, E., Eyenubo, J., Alele, J., Okpare, A., & Oghogho, I. (2025). A systematic review of barriers to renewable energy integration and adoption. *Journal of Asian Energy Studies*, *9*, 26-45. https://doi.org/10.24112/jaes.090002

Odoi-Yorke, F., Abaase, S., Zebilila, M., & Atepor, L. (2022). Feasibility analysis of solar PV/biogas hybrid energy system for rural electrification in Ghana. *Cogent Engineering*, *9(1)*, 2034376. https://doi.org/10.1080/23311916.2022.2034376

Odoi-Yorke, F., Osei, L. K., Gyamfi, E., & Adaramola, M. S. (2022). Assessment of crop residues for off-grid rural electrification options in Ghana. *Scientific African*, *18*, e01435. https://doi.org/10.1016/j.sciaf.2022.e01435

Ogunobo, R., & Onyenanu, I. U. (2025). Integration of renewable energy systems in poultry feed production machines: A pathway to sustainable agro-mechanization. *BW Academic Journal*, *2*. https://bwjournal.org/index.php/bsjournal/article/view/3425

Ouedraogo, H., Richardson, Y., & Zoungrana, L. (2025). Optimizing gasification in downdraft fixed-bed gasifier through experimental and kinetic modeling. *Case Studies in Thermal Engineering*, *68*, 105910. https://doi.org/10.1016/j.csite.2025.105910

Ouedraogo, H., Sidibe, S. D. S., & Richardson, Y. (2025). Advancing small-scale biomass gasification (10–200 kW) for energy access: Syngas purification, system modeling and the role of artificial

intelligence-A review. *Energy Conversion and Management: X*, *27*, 101059. https://doi.org/10.1016/j.ecmx.2025.101059

Overen, O. K., Obileke, K., Meyer, E. L., Makaka, G., & Apeh, O. O. (2024). A hybrid solar–biogas system for post-COVID-19 rural energy access. *Clean Energy*, *8(1)*, 84-99. https://doi.org/10.1093/ce/zkad070

Randle-Boggis, R., Barron-Gafford, G., Kimaro, A., Lamanna, C., Macharia, C., Maro, J., . . . Hartley, S. (2025). Harvesting the sun twice: energy, food and water benefits from agrivoltaics in East Africa. *Renewable and Sustainable Energy Reviews*, *208*, 115066. https://doi.org/10.1016/j.rser.2024.115066

Rezaei, F., Burg, V., Pfister, S., Hellweg, S., & Roshandel, R. (2024). Spatial optimization of industrial symbiosis for heat supply of agricultural greenhouses. *Journal of Industrial Ecology*, *28(6)*, 1507-1523. https://doi.org/10.1111/jiec.13543

Rutta, E. W. (2022). Understanding barriers impeding the deployment of solar-powered cold storage technologies for post-harvest tomato losses reduction: Insights from small-scale farmers in Tanzania. *Frontiers in Sustainable Food Systems*, *6*, 990528. https://doi.org/10.3389/fsufs.2022.990528

Sasanya, B. F., & Olaifa, O. (2022). Analysis of energy consumption in poultry management for table egg production in Nigeria. *Heliyon*, *8(8)*, e10053. https://doi.org/10.1016/j.heliyon.2022.e10053

Silinto, B. F., Van der Laag Yamu, C., Zuidema, C., & Faaij, A. P. (2025). Hybrid renewable energy systems for rural electrification in developing countries: A review on energy system models and spatial explicit modelling tools. *Renewable and Sustainable Energy Reviews*, *207*, 114916. https://doi.org/10.1016/j.rser.2024.114916

Uzoagba, C., Onwualu, P. A., Okoroigwe, E., Kadivar, M., Oribu, W. S., Mguni, N. G., . . . Aperebo, M. (2024). A review of biomass valorization for bioenergy and rural electricity generation in Nigeria. *Cureus J. Eng*, 1-16. https://doi.org/10.7759/s44388-024-00065-w

Vavouris, A., Stankovic, L., Stankovic, V., & Shi, J. (2025). FIELD: a comprehensive FarmIng Electrical LoaD measurements dataset from 30 three-phase dairy farms in Germany. *Scientific Data*, *12(1)*, 1830. https://doi.org/10.1038/s41597-025-06094-2

Widmer, J., Christ, B., Grenz, J., & Norgrove, L. (2024). Agrivoltaics, a promising new tool for electricity and food production: A systematic review. *Renewable and Sustainable Energy Reviews*, *192*, 114277. https://doi.org/10.1016/j.rser.2023.114277

Zebra, E. I. C., van der Windt, H. J., Nhumaio, G., & Faaij, A. P. (2021). A review of hybrid renewable energy systems in mini-grids for off-grid electrification in developing countries. *Renewable and Sustainable Energy Reviews*, *144*, 111036. https://doi.org/10.1016/j.rser.2021.111036

Zielińska, M., & Bułkowska, K. (2024). Sustainable management and advanced nutrient recovery from biogas energy sector effluents. *Energies*, *17(15)*, 3705. https://doi.org/10.3390/en17153705

International Conference on Engineering Innovation for Sustainable Development (ICESID 2026)
Faculty of Engineering, Ahmadu Bello University Zaria · 8–10 September 2026

UPSCALING SUSTAINABLE COLOURATION: DESIGN, FABRICATION, AND PERFORMANCE EVALUATION OF AN INDUSTRIAL-SCALE NATURAL INDIGO EXTRACTION MACHINE FOR NIGERIA'S TEXTILE SECTOR

Adam Muhammad Tanko[1,*]

[1]*Raw Materials Research and Development Council, Abuja*

Email: teebaba04@gmail.com[*]

***Corresponding author**: Adam Muhammad Tanko

DOI: https://doi.org/10.67203/sp.ICESID.2026

ABSTRACT

The reliance of Nigeria's textile and cottage dyeing industries on imported synthetic colourants poses severe environmental hazards, while the importation of natural indigo dye from Europe and China continues to drain valuable foreign exchange reserves. To drive sustainable import substitution and foster local industrialization, this study presents the engineering design, fabrication, and physical performance evaluation of an indigenous, large-scale natural indigo extraction machine. Response surface methodology (RSM) based on a central composite design (CCD) was initially employed at bench scale to model process kinetics. Optimizing plant biomass fermentation (18 hours) and aeration duration (63 minutes at pH 12) predicted a maximum yield of 31.99 g/kg fresh biomass with a purity of 70.35%. Building upon these kinetic baselines, a mechanical extraction system was engineered to scale up the fermentation, liquid separation, and aeration phases into a controlled, high-efficiency mechanical process. Validation trials conducted across five operational runs processing 100 kg of fresh biomass per batch produced 3.21±0.7 kg of dry indigo flakes (equivalent to 32.13±0.7 g/kg biomass yield) with a purity of 71.12±1.3%, within 24-hour cycle. By replacing toxic synthetic dyes and bypassing expensive foreign colourant imports, this fabricated extraction system provides scalable, eco-friendly technological framework to revitalize Nigeria's historic textile clusters, directly supporting sustainable agricultural value addition and national economic self-reliance. (Note: In the first abstract submitted, the criteria set in the optimization software was "in range" for both fermentation time, pH and oxidation time and the predicted values were 26 hours fermentation time, pH 12, and 105-minutes oxidation time. After careful consideration, looking at Table 2, the highest crude yield was obtained at 18 hours fermentation time. Also, previous work reported that there is tendency for the fermented liquor to be contaminated after 24 hours fermentation thereby affecting pure yield. For this reason, the criteria for the fermentation time was changed from "in range" to "equals to 18". The software predicted a result where a combination of 18 hours fermentation time, pH 12 and oxidation for 63 minutes will result 31.99 g/kg and 70.35% crude and pure yield respectively as shown in Figure 3. It is a known fact that the ramp shown in the Figure 3 cannot be edited. It was copied directly from the software. With this development, large scale extraction using the fabricated machine had to be carried out using the new predicted parameters which resulted in different yields from the ones reported in the earlier abstract)

Keywords: *indigo extraction; machinery fabrication; import substitution; sustainable development; natural dyes; textile engineering*

INTRODUCTION

Accelerated depletion of fossil fuels and escalating environmental degradation necessitated intensified research into sustainable, renewable bio-resources (Cardon *et al.*, 2023). In the textile sector, global initiatives led by the European Union (EU) and international sustainability frameworks have actively sought to reintroduce efficient indigo-bearing crops into agricultural systems to develop scalable processes for natural dye production (Shin *et al.*, 2009; Mocquard *et al.*, 2022). Cultivating natural indigo (*Indigofera tinctoria*) supports sustainable agriculture by fixing atmospheric nitrogen restoring soil health in crop rotations, and yielding residual mass suitable for bio-fertilizers and biogas production, directly advancing Sustainable Development Goals (SDG) 12 (responsible consumption and production), SDG 13 (Climate Action) and SDG 15 (Life on Land) (Rao *et al.*, 2025). However, deploying natural dyes at an industrial scale requires overcoming key engineering bottlenecks,

particularly improving extraction kinetics and machinery efficiency to ensure economic viability (Pizzicato *et al.*, 2023).

Historically, nnatural indigo dyeing has been a prominent socio-economic enterprise across Northern Nigeria, centered in prominent urban hubs such as Kano, Sokoto, Zaria, and Bida (Akinbogun and Ogunduyile, 2009). Kano in particular, established regional prominence as early as the 14th century through its fine indigo-dyed textile products at traditional pit sites like Kofar Mata (Barau, 2007; Ezeanya-Esiobu, 2019P). Presently, most of the indigo dyers are out of business with only about 10 out of the 144 dye pits of "Kofar Mata" still functional (Abdullahi *et al.*, 2022). Despite this heritage, local dyeing operations have suffered a major decline, with remaining dyers relying on imported natural indigo powder from China, India, and Europe at exorbitant costs, reaching up to 350,000 per 25 kg container (personal communication). Local agricultural surveys in Kano state reveal an abundant, underutilized supply of Indigofera tinctoria biomass, with over 52 local farms producing an estimated 56,800 kg of fresh biomass per harvest cycle (Field work, 2022). Processing this local crop at an achievable 2% extraction yield could generate 1,136 kg of high-purity dye biannually (corresponding to 90.88 of 25 kg indigo bags), keeping nearly ₦32,000,000 (US$26,666.8) within the local economy.

Despite this agricultural potential, traditional bio-fermentation methods remain unviable for commercial scaling due to labour-intensive manual handling, slow liquid separation, uncalibrated aeration dynamics, and low overall dye recovery. Translating bench-scale chemical kinetics into pilot-scale production requires solving fluid mechanical mass transfer, and mechanical agitation challenges inherent in larger volumetric capacities. In alignment with the conference theme, "Innovating Tomorrow; Harnessing Engineering to Drive Nigeria's Growth for Sustainable Development", and specifically addressing the sub-theme "Sustainable Engineering Processes and Systems", this study bridges the gap between laboratory optimization and industrial implementation. By transitioning traditional bio-fermentation into automated, low-energy mechanical process, this research demonstrates how cleaner production technology can be localized. The primary objective of this research is to present the mechanical design, structural fabrication, and operational performance evaluation of an indigenous, inductive-scale natural indigo extraction machine engineered as a sustainable system to revitalize Nigeria's textile sector.

MATERIALS AND METHODS

Materials

Plant material (leaves and stems) of *Indigofera tinctoria* as identified by a taxonomist (Department of Biological Sciences, Ahmadu Bello University, Zaria), 3 months old (August to October), was harvested on 25th of October, 2023 from a farm in Yan Barau, Dawakin Kudu local government area of Kano State (see Figure A1 and A2, Appendix A), longitude 8.63^0 E and latitude 11.85^0 N with an altitude of 448 m above sea level. The plant biomass was cultivated under the following conditions: average daily air temperature, soil temperature, soil moisture, and rainfall were respectively 30.1 ^{o}C, 26.2 ^{o}C, 0.265 m^3/m^3 (28-100 cm), and 600 mm. Concentrated sulphuric acid, concentrated ammonia and standard synthetic indigo dye were purchased from Sigma Aldrich and used without purification. Coordinates of the farm were determined using hand-held Gamine78SC GPS receiver and pH was measured using Digital pH meter (Jenway 3310, UK).

Methods

Extraction of indigo dye

Fresh plant material with the leaves and stem (2 hours after harvest), 1 kg, was washed twice and placed in a transparent polyethene container and weigh down with 5 kg block to completely submerge the material in 10 l of water. The pH was adjusted to 3.5 using 20% concentrated sulphuric acid (this is to prevent indican from converting to indoxyl prematurely during fermentation). The container was covered to maintain anaerobic condition for fermentation to take place at different times. After a specified period of time, the pH of the fermented broth was measured, the solution was filtered and the pH was adjusted using concentrated ammonia (indoxyl forms indigo dye at an alkaline pH). The solution was then oxidized for a certain period of time using a blower at a flowrate of 3 l/min

(Figure A3, Appendix A). The solution was kept for 24 hours. to allow indigo slurry to settle at the bottom. The yellow green supernatant was gently drained (Figure A4, Appendix A) while the slurry was filtered using a 0.074 µm mesh (ASTM standard), placed on a tray (Figure A5, Appendix A) and allowed to dry at room temperature overnight in a cool dry place. After drying, the dye pellets were ground in to powder and washed with 2M HCl and then finally air dried.

Extraction experiments were designed with the aid of response surface methodology (RSM) using central composite design (CCD) which generated 15 runs in random order. The CCD is shown in Table 1. Crude dye (Figure A6, Appendix A) yield was calculated using Eq. 1. Crude indigo dye obtained from the 15 experiments is shown in Figure A7, Appendix A. To obtain the pure yield (dye content), standard synthetic indigo dye, 8 mg, was dissolved in 20 ml of concentrated sulphuric acid and then diluted to 500 ml with distilled water. The solution was then diluted to different concentrations viz., 0.1, 0.2, 0.4, 0.6, 0.8, 1.0 and 1.2 mg/l and the absorbance was measured at 610 nm to plot a standard curve. Crude indigo dye powder, 1 g, was dissolved in 20 ml concentrated sulphuric acid and diluted to 500 ml and the absorbance measured at 610 nm. From the standard curves, the pure yield (%) was calculated (Chanayath *et al.*, 2012). The data was analyzed using Design Expert® Software version 7 (DX7). After statistical analysis and optimization of extraction parameters using Desirability function, five sets of experiments were carried out at the optimized conditions to validate the results.

$$Crude\ yield\ \left(\frac{mg}{g}\right) = \frac{w1 - w2}{weight\ of\ the\ plant\ material} \ldots\ldots\ldots\ldots\ldots Eq.1$$

where $w1$=weight of tray containing dried indigo dye and $w2$= weight of empty tray.

Table 1: Central composite design of extraction parameters

Variable	Unit	Level	
		Low (-1)	High (+1)
pH	-	9	13
Oxidation time	Minutes	30	120
Batching time	Hours	18	72

Fabrication of indigo extraction equipment

The equipment was designed to suit the purpose of the extraction process for indigo and other natural dyes. The extraction equipment was constructed using stainless steel and consists of 9 components including 2 steeping/soaking tanks, 1 oxidation tank, 1 filtration tank, and 2 evaporators, 2 condensers and a steam boiler. The whole equipment (Figure B1, Appendix B) is controlled by an electric panel. Each of the steeping tanks is of 1,000 litres capacity and is equipped with mechanical presser (diameter= 1.16 m, height= 1.22 m) whose purpose is to weigh down (submerge) the plant material completely inside water (see Figure B2, Appendix B). Direct steam can be injected into the tank through by a steam blower at a rate of 100 kg/hr. to raise temperature where necessary. The steeping/soaking tank is connected to an oxidizing tank via a 25 mm pipe in which the fermented broth is transferred with the aid of 1 HP pump.

The oxidizing tank is fitted with a stirrer controlled by a 1 HP electric gear motor which turns at 360 rpm (see Figure B3, Appendix B). At the bottom of the tank is a root blower controlled by a 3 HP electric motor. Valve, 25 mm, is fixed at the outlet of the blower to control the flowrate. For a batch process, liquid is siphoned off through an upper outlet and the sedimented indigo at the bottom is collected via a tap attached to the bottom of the oxidizing tank and a mesh just beneath the tap. For continuous process, the oxidized solution is pumped into a filtration tank where 3 filter cartridges trap the dye particles under pressure. The trapped dye is then collected and passed to the evaporators (equipped with a stirrer) to separate indigotin and indirubin. Steam is also passed through the evaporator to dry the final product. The solvent used to dissolve the crude indigo is recovered by the condensers. The flowchart showing the steeping and oxidizing tanks is shown in Figure 1.

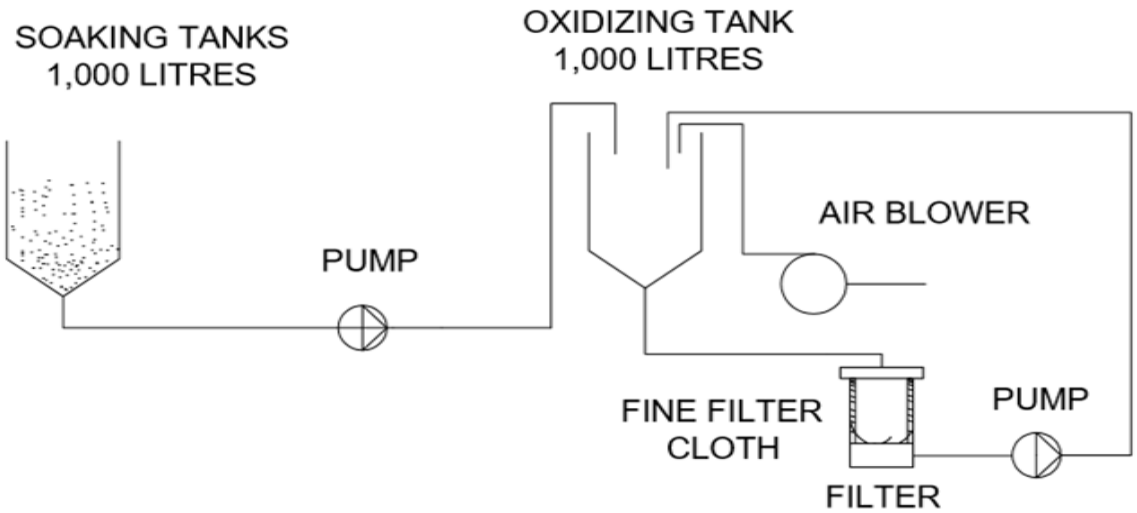

Figure 1: Flowchart showing soaking and oxidizing tanks

RESULTS AND DISCUSSION

Extraction and Yield of Indigo Dye

The extraction procedure was a modification of the method described by Stoker et al (1998) who used similar extraction technique to produce indigo on a large, commercial scale, from *Isatis tinctoria* leaves. Indigo precursor in *Indigofera tinctoria* is indican. The precursors are water soluble and on hydrolysis easily release free indoxyl which on aeration readily form indigo which is insoluble and therefore sedimentable. The identity of the extracted indigo was confirmed by UV-Visible spectroscopy, infrared spectroscopy, mass spectroscopy as well as proton and carbon nuclear magnetic resonance spectroscopy (not shown). Central composite design (containing 5 levels of each factor viz. low and high factorial, low and high axial, and centre) was used to fit a model, develop regression equations, and then optimize key factors influencing the quantity and quality (crude and pure yield) of the dye produced. The results obtained for crude and pure yield from different combinations of fermentation period as well as pH and oxidation time (Table 2).

Table 2: Crude and pure yield obtained from different combinations of fermentation time, pH and oxidation time

Run No.	Batching time (hr.)	pH	Oxidation time (min.)	Crude yield (g/kg)	Pure yield (%)
1	45	11	68	15	44.1
2	45	11	120	19	49.7
3	45	13	68	17	45.3
4	45	9	68	11	30.0
5	45	11	15	14	40.1
6	64	10	105	4	25.3
7	72	11	68	4	24.1
8	18	11	68	31	68.5
9	45	11	68	13	48.9
10	45	11	68	14	38.9
11	64	12	30	6	26.8
12	45	11	68	14	42.8
13	26	12	105	30	69.8
14	26	10	30	23	44.6
15	45	11	68	20	43.8

The highest crude yield, 31.0 g dye per kg of plant biomass (3.1%), was obtained when the batching/fermentation time was 18 hr. and where the pH was adjusted to 11 before oxidation for 68 min. The lowest yield, 4 g/kg, was obtained when the fermentation period was 64 hrs. (oxidation for 105 min. at pH 10) and 72 hrs. (oxidation for 68 min. at pH 11). The yield decreases with increase in fermentation time but increases with both increase in pH and oxidation time. Fermentation time for *Indigofera tinctoria* was suggested to be 15 to 16 hrs. as longer extraction time leads to contamination of the steep water with plant-derived materials (Pattanaik *et al.,* 2018; Pattanaik *et al.,* 2020a-b, Pattanaik *et al.,* 2021). The yield measured in this study, 3.1%, appears reasonable since John and Angelini (2023) reported that exceptional samples of *Indigofera tinctoria* might yield indigo to a value of 3.5%. Mussak and Bechtold (2009) also reported that traditional method of producing indigo has a maximum yield of 37 g/kg dry weight of leaf. Stoker et al (1998a) obtained a crude yield of 20 g/kg on a pilot scale from *Isatis tinctoria* leaves.

The purest sample among the 15 runs in the experiment has a purity of 69.8% which was obtained after 26 hrs. fermentation and oxidation for 105 min. at pH 12. The pure yield also shows the same trend as crude yield where lowest yield was obtained when the fermentation period was 64 hrs. (yield was 24.26.8%). The yield also increases with increase in pH and oxidation time but decreases with increase in fermentation period. Synthetic indigo is usually higher than 90% pure while natural indigo is 20-90% pure where a good sample of Bengal indigo was 61.4% (Perkin, 1900). Dutta et al (2017) obtained highest pure yield after 24 hrs. of fermentation. Natural indigo dye from Indigofera tinctoria plant biomass is believed to provide the highest purity of indigo dye (Pattanaik *et al.,* 2018). John (2004) obtained an average purity of 74±10% with an average yield of 0.5g/kg fresh leaves. Stoker et al (1998) achieved a pure yield of 20-40% from *Isatis tinctoria* leaves. Washing raw indigo in 2 M HCl after grinding the dried product could have improved the purity of the extracted dye. Dramatic increase in purity has been obtained from 3 large scale preparations of indigo by a wash with dilute HCl from 21-71%, 0.6-63%, and from 19-72% (John, 2004). Indigo can be extracted from woad with a purity of 90% if the leaves contain sufficiently high yield of indigo precursors and the leaves are rinsed free of soil (John, 2004; Garcia-Marias and John, 2004).

Model Fitting and Statistical Analysis

Analysis of variance (ANOVA) for the responses “crude yield” and “pure yield” was generated by Design Expert Software version 7 (DX7). Lack of fit shown in Tables 3 for both crude and pure

yeild compares residual error to the "pure error" from replicated design points. The selected model should have insignificant lack of fit. Lack of fit in this case is not significant and therefore the model can be used as a response predictor. The linear models selected exhibits low standard deviation, high coefficient of determination (94.72% and 93.69% respectively for crude and pure yield) and low PRESS. As shown in Tables 3, the model F-values imply that the selected models are significant. Values of "Prob>F" less than 0.05 will indicate that the model terms are significant.

Table 3: Analysis of variance (ANOVA) test for significance for crude yield and pure yield

Statistical Metric	Response 1: Crude yield	Response 2: Pure yield
Suggested model type	Linear	Linear
Model *p*-value	0.0001	0.0001
Ordinary R^2	0.9472	0.9369
Adjusted R^2	0.9328	0.9197
Predicted R^2	0.9190	0.8802
Lack of Fit (*p*-value)	0.8995	0.4373
Adequate Precision	26.321	24.373
Standard deviation	2.11	3.85
PRESS	75.24	309.67

$$\text{Crude yield} = +15.67 + 2.19 * A + 1.51 * B - 10.15 * C \quad \text{.....Eq. 2a}$$

$$\text{Pure yield} = +42.85 + 6.04 * A + 4.66 * B - 15.64 * C \quad \text{.....Eq 2b}$$

For both responses, the predicted determination coefficient (Pred R^2=0.9190 and R^2=0.8802 for crude and pure yield respectively) are in reasonable agreement with the adjusted determination coefficient (Adj R^2=0.9328 and R^2=0.9197 for crude and pure yield respectively) which is satisfactory to confirm the fitness of the model. The "Adeq Precision" ratios (26.321 and 24.373 for crude and pure yield respectively) indicates an adequate signal which implies that model for the responses could be used to navigate the design space. The negative sign in front of the terms in a first order regression model indicates antagonistic effect whereas a positive sign shows synergistic effect. The responses, crude and pure yield, increase with an increase in oxidation pH and oxidation time but decrease with increase in batching/fermentation time. There is however, no interaction among the extraction parameters investigated. Interaction occurs when the effect of one factor on the response variable depends on the level of another factor (Anderson and Whitcomb, 2007). The relationship between crude and pure yields with oxidation pH and time as well as fermentation time established in this study (Eq. 2a and 2b respectively in coded form) can be used as a model for indigo dye extraction from *Indigofera tinctoria* biomass.

The consistency of the data for responses "crude yield" and "pure yield" was confirmed from normal probability plot of residuals shown in Figures 2a and 2b respectively. In both cases, the points are fairly close to a straight line indicating the validity of the experimental data since the residuals are normally distributed. As shown in Tables 4, the value of residuals (difference between experimental data and the predicted value) is low showing the precision of the experiments (Wagaw and Chavan, 2012: Myers *et al.,* 2009).

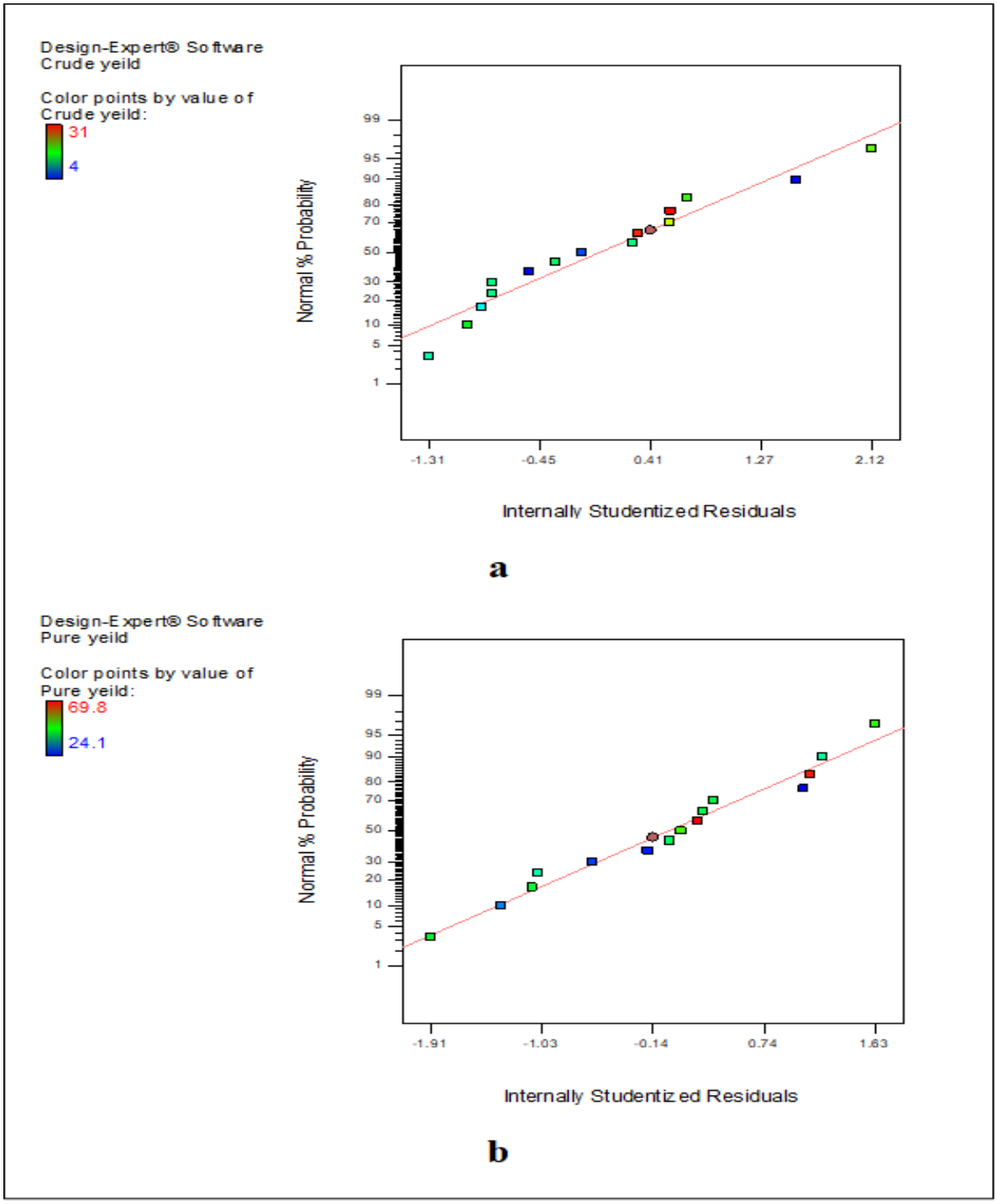

Figure 2: Normal probability plot of residuals (a) crude yield (b) pure yield

Table 4: Diagnostic case statistics showing residuals for crude and pure yield

Crude yield				Pure yield			
Actual value	Predicted value	Residual	Run number	Actual value	Predicted value	Residual	Run number
30.00	29.51	0.49	13	69.80	69.18	0.62	13
6.00	6.20	-0.20	11	26.80	28.59	-1.79	11
4.00	4.84	-0.84	6	25.30	25.83	-0.53	6
23.00	22.12	0.88	14	44.60	47.78	-3.18	14
11.00	12.58	-1.58	4	30.00	34.30	-4.30	4
17.00	18.76	-1.76	3	45.30	51.39	-6.09	3
14.00	13.53	0.47	5	40.10	36.26	3.84	5
19.00	17.80	1.20	2	49.70	49.44	0.26	2
31.00	30.02	0.98	8	68.50	64.96	3.54	8
4.00	1.32	2.68	7	24.10	20.73	3.37	7
14.00	15.67	-1.67	10	38.90	42.85	-3.95	10
20.00	15.67	4.33	15	43.80	42.85	0.95	15
13.00	15.67	-2.67	9	48.90	42.85	6.05	9
14.00	15.67	-1.67	12	42.80	42.85	-0.047	12
15.00	15.67	-0.67	1	44.10	42.85	1.25	1

Optimization of Extraction Parameters for Large Scale Production

The objective of this optimization is to simultaneously make crude and pure yield as high as possible. In numerical optimization, desired goal is chosen for each factor and response. A multiple response method was applied for optimization of combinations of three factors namely oxidation pH, oxidation time and batching time. The 2 responses optimized were average crude and pure yield. The criterion was set as follows: "in range" for pH, "equals to 18" for batching time (because 18 hours batching time resulted in the highest crude yield and fermentation for more than 24 hours results in microorganisms contaminating the liquor affecting pure yield), "in range" for oxidation time, "maximize" crude yield, and "maximize" pure yield. Figure 3 shows the ramp of optimal parameters for crude and pure yield. The dot on each ramp reflects the factor setting or response prediction for that solution. Batching for 18 hrs. and oxidizing for 63 min. at pH 12 will result in 31.99 g/kg crude yield and 70.35% pure yield with a desirability of 1.000. The optimum conditions predicted were checked experimentally on a large-scale extraction using 100 kg of plant biomass 5 times. The experimental values obtained for crude and pure yield (for five replicates) using the predicted values of the extraction parameters was respectively 32.13±0.7 g/kg and 71.12±1.3%. Small errors between these values indicated that the experimental values obtained were in good agreement with the values predicted from the models. Physicochemical parameters of indigo dye extraction including fermentation conditions such as temperature and time (Rahayuningsih *et al.,* 2022; Syafaatullah and Mahfud, 2020; Dutta *et al.,* 2017; Hidayati *et al.,* 2018) as well as oxidation conditions comprising of oxidation pH, oxidation time, and air flowrate (Pattanaik *et al.,* 2021) has been optimized previously using design of experiment to maximize indigo yield.

(Note: The software predicted the runs with combination of factors based on the information we provided in Table 1 as shown in Table 2. The columns crude and pure yield were originally empty with no values. After conducting 15 batch experiments and obtaining the samples shown in Figure A7, the crude and pure yields of each of the samples was determined and placed in the columns. It was after feeding the software with the results that statistical analysis and optimization were possible to obtain the predicted and optimized results).

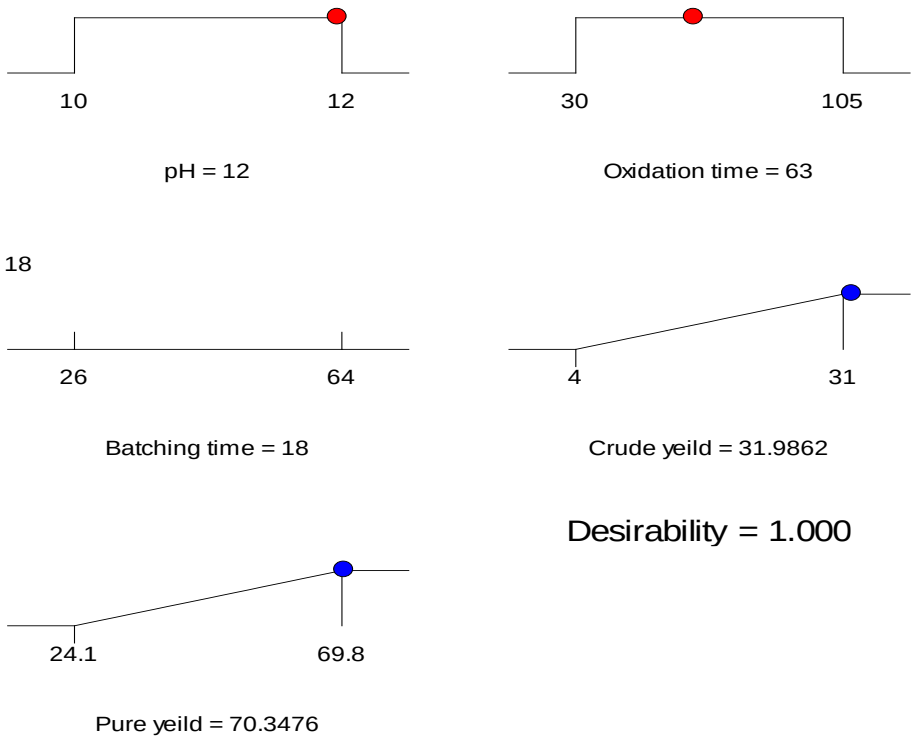

Figure 3: Ramp of optimal conditions for crude and pure yield

CONCLUSION

This study successfully designed, fabricated, and evaluated an inductive-scale natural indigo extraction machine, bridging the critical scale-up gap between laboratory-optimized bio-chemical kinetics and commercial pilot production. Tested across five consecutive validation runs under optimized operating conditions (18 hours fermentation, 63 minutes oxidation, and pH 12), the machine demonstrated exceptional operational fidelity and mass transfer efficiency. The inductive-scale unit achieved a crude pigment yield of 32.13 g/kg biomass and a pure yield of 71.12% (this progresses towards 90% purity obtainable with synthetic indigo and also the 90% purity sought by the European Union under sustainable production of plant-derived indigo), confirming that scaling up from bench parameters (31.99 g/kg crude yield and 70.35% pure yield) was accomplished without yield loss or kinetic degradation. The mechanical agitation, aeration dynamics, and volumetric mass transfer efficiency of the fabricated unit proved highly effective for pilot-scale processing. Furthermore, utilizing locally available engineering materials for construction demonstrates that sustainable industrial processing equipment can be manufactured cost-effectively within Nigeria, significantly reducing capital expenditure compared to foreign machinery imports. Industrially, this scalable extraction framework offers a viable technical pathway to commercialize natural indigo cultivation, substitute synthetic colourant imports, mitigate toxic effluent loading, and stimulate agrarian-industrial growth. Future iterations will focus on integrating automated pH monitoring and continuous-flow aeration controls.

It is recommended to incorporate a finer mesh than the one used in the fabricated equipment as this may likely enhance crude indigo yield. Indigo yield depends on climatic conditions which vary from season to season. It is therefore imperative to investigate seasonal variations and harvest time which could lead to changes in indigo yield. Indigo seed should be genetically modified and grown in the farms or in close proximity according to the principles of Good Agricultural and Collection Practices (GACP) which recommends on-farm production and post-production processes to address environmental, economic, and social sustainability. Considering the irregular power supply in the

country especially in remote areas like farms, solar panels are recommended to be installed on the equipment to have uninterrupted power supply which is mainly needed for the transfer of the fermentation broth from steeping to the oxidation tank and for blowing air into the oxidation tank.

REFERENCES

Abdullahi, S., Nkeonye, P. O., Yakubu, M. K., Gumel, M. S., and Iliya, E. B (2022a). Occupational vat dyeing practices in the Kano Metropolis of Nigeria- Part 4: Challenges and prospects. Nigerian Journal of Textiles, 8: 1-14.

Akinbogun, T. L., and Ogunduyile, S. R. (2009). Crafts engagement in the economic survival of south-western Nigerian rural women. *Journal of enterprising communities: people and places in the Global Economy*, 3(2), 217-234.

Anderson, M. J., and Whitcomb, P. J. (2007). *DOE simplified. Practical tools for effective experimentation* (3rd ed.). Boca Raton, USA: CRC Press.

Barau, A. S. (2007). The great attractions of Kano. https://doi.org/10.13140/RG.2.1.3958.9922

Cardon, D., Koren, Z. C., and Sumi, H (2023). Woaded blue: A colourful approach to the dielectric between written historical sources, experimental archaeology, chromatographic analyses, and biochemical research. Heritage, https://doi.org/10.3390/heritage6010037

Chanayath, N., Lhieochaiphant, S., and Phutrakul, S (2012). Pigment extraction techniques from the leaves of *Indigofera tinctoria* Linn. and *Baphicacanthus cusia* Brem. and chemical structure analysis of their major components. *Chang Mai University Journal*, 1(2): 149-160.

Dutta, S., Roychoudhary, S., and Surangi, K (2017). Effect of different physicochemical parameters for natural indigo production during fermentation of Indigofera tinctoria plant biomass. *Springer*. https://10.1007/s13205-017-0923-2

Ezeanya-Esiobu, C. (2019). Africa's indigenous knowledge: from education to practice. In A. Heshmati (Ed.), indigenous knowledge and education in Africa (pp. 55-77). Singapore: Frontiers in African Business Research. Springer.

Garcia-Macias, P., and John, P (2004). Formation of natural indigo derived from woad (*Isatis tinctoria* L.) in relation to product purity. *Journal of Agricultural and Food Chemistry*, 52: 7891-7896.

Hidayati, L., Ningrum, D. C., Nugroho, H., and Nuringtyas, T. R (2018). Optimization of extraction methods and dyeing standardization of Nila leaves (*Indigofera tinctoria* Linn.) as natural dyes. 4th International Seminar on Sciences. IOP Conference Series: Earth and Environmental Science. http://doi.org/10.1088/1757-1315/187/1/012031

John, P (2004). The production of natural indigo with a high purity.

John, P., and Angelini, L. G (2023). Indigo-production and properties. In: Bechtold, T., Manian, A. P., and Pham, T (eds.). *Handbook of natural colourants* (2nd Edition). West Sussex, United Kingdom, John Willey and Sons Ltd. p.195-250.

Mocquard, J., Lamer, A. C. L., Fabre, P. L., Mathieu, C., Chastrette, C., Vitrai, A., and Vandenbasche, V (2022). Indigo dyeing from Isatis tinctoria L.: From medieval to modern use. *Dyes and Pigments*, 207, 110675.

Mussak, R. A. M., and Bechtold, T (2009). Natural colorants in textile dyeing (1st Edition). In: *Handbook of natural colourants*. West Sussex, United Kingdom, John Willey and Sons Ltd. p315-335.

Myers, R. H., Montgomery, D. C., and Cook, C. M. (2009). *Process and product optimization using designed experiments* (3rd ed.). Hoboken, New Jersey: John Wiley and Sons Inc.

Pattanaik, L., Duraivadivel, P., Hariprasad, P., Naik, S. N (2020b). Utilization and re-use of solid and liquid waste generated from the natural indigo production process- a zero waste approach. Bioresource Technology, 301: 122721. https://doi.org/10.1016/j.biortech.2019.122721

Pattanaik, L., Naik, S. N., and Hariprasad, P (2018). Valorization of waste Indigofera tinctoria L. biomass generated from indigo dye extraction process-potential towards biofuels and compost. *Biomass Conversion and Biorefinery*. https://doi.org/10.1007/s13399-018-0354-2

Pattanaik, L., Naik, S. N., Hariprasad, P., and Padhi, S. K (2021). Influence of various oxidation parameter (s) for natural indigo dye formation from Indigofera tinctoria L. Biomass. Environmental Challenges, 4: 100157. https://doi.org/10.1016/j.envc.2021.1000157

Pattanaik, P., Padhi, S. K., Hariprasad, P., and Naik, S. N (2020a). Life cycle cost analysis of natural indigo dye production from Indigofera tinctoria L. plant biomass: a case study of India. *Clean Technologies and Environmental Policy*. https://doi.org/10.1007/s10098-020-01914-y

Perkin, F. M (1900). The present condition of the indigo industry. Nature, 63 (1618): 7-9.

Pizzicato, B., Pacifico, S., Cayuela, D., Mijas, G., and Riba-Maliner, M (2023). Advances in sustainable natural dyes for textile applications: A review. *Molecules*, 28, 5954.

Rahayuningsih, E., Fatimah, W. S., Pamungkas, M. S., and Marfitania, T (2022). Effect of physicochemical process variable on natural indigo dye production from *Strobilanthes cusia* leaves by response surface methodology. *Indones Journal of Chemistry*, 22(20: 342-351.

Rao, P. S., Fatima, N., Siddiqui, M. H., Habib, K., Mohasin, M., Haq, W., Chinyo, M., Zaidi, H., Shah, Y. A., Mazeed, A., and Siddiqui, S (2025). Indigofera tinctoria: the blue gold of India's sustainable future. *Discover Sustainability*, 61135. https://doi.org/10.1007/s43621-025-01120-0

Shin, Y., Son, K., Cho, A., Yoo, D II., Kim, G. J., and Kim, J. Y (2009). Natural indigo production and dyeing. The International Conference on Dyeing and Finishing, EXCO, Daegu, Korea, March 13, 2009.

Stoker, K. G., Cooke, D., and Hill, D. J (1998). An improved method for the large-scale processing of woad (*Isatis tinctoria*) for possible commercial production of woad indigo. *Journal of Agricultural Engineering Resources*, 71: 315-320.

Syafaatullah, A. Q., and Mahfud, M (2020). Optimization extraction of *Indigofera tinctoria* L. using microwave-assisted extraction. International Conference on Chemical and Material Engineering. IOP Conference Series: Materials Science and Engineering. https://doi.org/10.1088/1757-899X/1053/1/012131

Wagaw, T., and Chavan, R. B. (2012). Optimization of caustic soda concentration for causticization of cotton. *Open Access Scientific Reports*, 1(9), 1-6.

APPENDIX A

Extraction of indigo dye from plant biomass

Figure A1: Indigo farm at the point of harvest

Figure A2: Indigo farm 2 months after harvest

Figure A3: Oxidation of fermented solution during batch experiments

Figure A4: Residual fermented broth after oxidation in batch experiments

Figure A5: Indigo slurry drying on a tray

Figure A6: Dried indigo pellets

Figure A7: Samples obtained from batch extraction experiments

APPENDIX B

Large scale extraction of indigo dye using the fabricated equipment

Figure B1: Fabricated indigo dye extraction equipment

Figure B2: Steeping/fermentation of plant biomass in the steeping tank

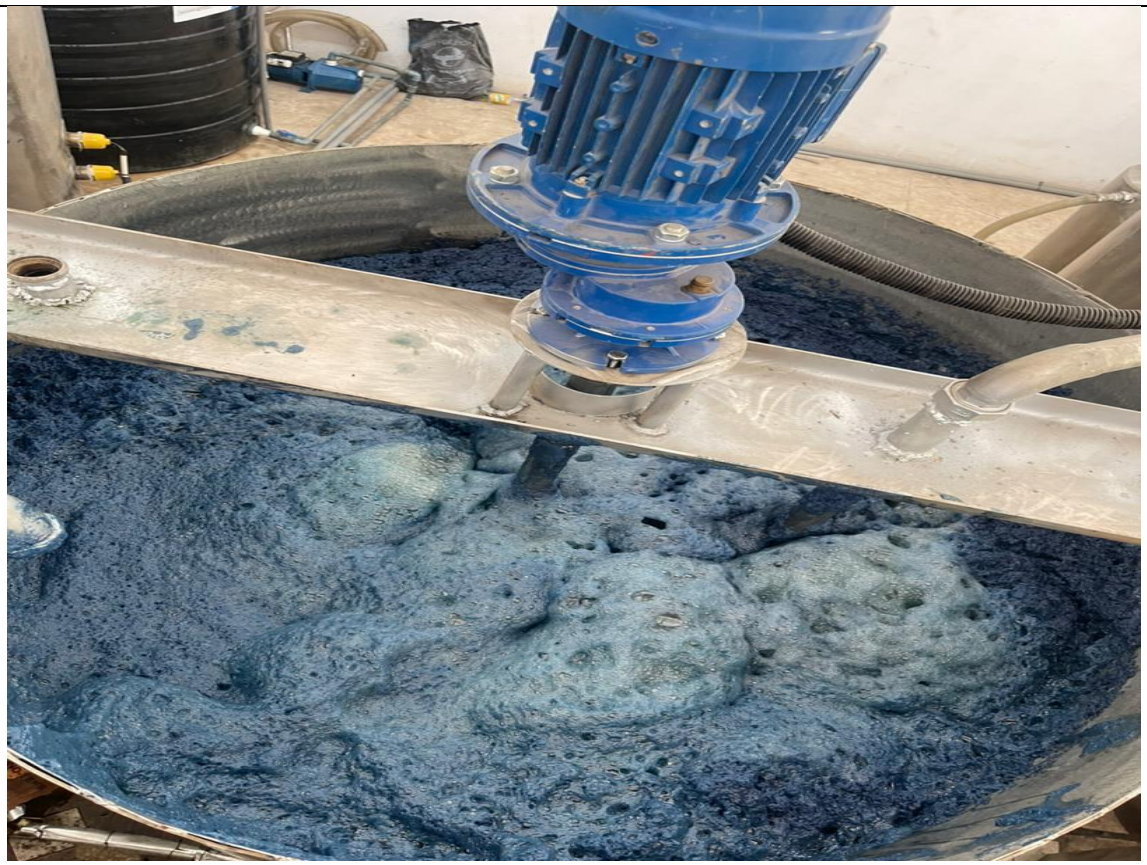

Figure B3: Oxidation of fermented broth in the oxidation tank

TRACK 10 OF 11

Sustainable Materials Synthesis, Processing and Recycling

International Conference on Engineering Innovation for Sustainable Development (ICESID 2026)

Faculty of Engineering, Ahmadu Bello University Zaria · 8–10 September 2026

https://icesid.org

International Conference on Engineering Innovation for Sustainable Development (ICESID 2026)
Faculty of Engineering, Ahmadu Bello University Zaria · 8–10 September 2026

AN ASSESSMENT OF WASTEPAPER MANAGEMENT IN A.B.U. MAIN CAMPUS, SAMARU

Sabur Alim[1,*], Olowodun, Theophilus Mazor[1]
[1]*Ahmadu Bello University, Zaria*
Email: moaj1st@yahoo.com[*], ""
***Corresponding author**: Sabur Alim
DOI: https://doi.org/10.67203/sp.ICESID.2026

ABSTRACT

Wastepaper is paper discarded after being used. Post-consumer paper, or wastepaper, is a vital renewable raw material source for the paper industry and can contribute substantially to the reduction in the importation of paper. With over 45,000 students, about 20,000 staff (academic and non-academic) and 106 departments, Ahmadu Bello University, Zaria, is the largest university in West Africa. With a population of about 200 million people, on the average, a Nigerian uses about 10 kg of paper per year. The result showed that for student respondents, 68% between 21-30, 59% are Postgraduate Diploma (PGD) students and 55% have been in ABU for 2-4 years. The demographic results for academic and non-academic staff respondents show that 72% are males, 50% of the respondents are single, 40% between 41-50 years and 62% have worked in ABU for 0 to 5 years. 62.4% of the staff and 54.2% of the students mentioned that reuse of wastepaper is what they do to curb wastepaper generation. The practice among the staff with the highest rank is the burning of wastepaper, while the activity with the least rank is sorting of waste before dumping them into the dustbins. The members of the university community should be encouraged to practice the 3Rs of waste management on waste more than is currently being practiced in the order of reduce, reuse and recycle. With 48.5% of the students Sometimes/Often/Always buy used textbooks, the Student Union can create a book buyback program as one of the methods of mitigating wastepaper generation on campus.

Keywords: *A.B.U; wastepaper; book buyback; reduce; reuse and recycle*

INTRODUCTION

Paper is a thin sheet material made from a combination of mechanical and chemical processes converting cellulose fibres derived from wood, rags, grasses or other vegetable sources. The raw materials are soaked in water, the water is then drained through a fine mesh, leaving the fibre evenly distributed on the surface of the mesh. This process is followed by pressing and drying. Paper is a versatile material used for several purposes such as books, printing, packaging, decorating, writing, cleaning, wallpaper, filter paper, conservation paper. laminated worktops, toilet tissue, currency, security paper and a number of industrial and construction processes (Hogben, 1951; Mann, 1952).

Wastepaper is paper discarded after being used. Wastepaper from scrap newspapers, books and periodicals, office paper, kraft paper, paper boxes and corrugated paper are all valuable fibrous raw materials (Worldwide Fund for Nature, 2019). Post-consumer paper, or wastepaper, is a vital renewable raw material source for the paper industry and can contribute substantially to the reduction in the importation of paper. Its recycling is also important from the environmental perspective, as systematic collection and recycling of wastepaper can greatly reduce the volume of municipal solid wastes. It has been estimated that recycling one ton of wastepaper results in a saving of 70% raw material, 60% coal, 70% water and 43% energy, as compared to making virgin paper from wood (Ministry of Environment and Forests Notification India, 2011; Devi and Sastry, 2017).

Wastepaper forms a certain percentage of waste stream that ends up in the dumpsite / landfill. According to Alim and Ahmed (2020), paper form about 18% of the waste stream in Gombe town, Gombe State Nigeria. This percentage is significant. If this percentage is reduced or removed from the waste stream, things such as cost of production of paper, land pollution, air pollution and water pollution would be effectively reduced. Nigerian Government policies towards waste sorting, reduce, reuse and recycle would also play an important role in reducing the overall waste stream that ends up dumpsite / landfill (Sridhar and Hammed, 2014).

The key causes of solid waste complications in Nigeria have been associated with large population, poverty and urbanization growth rates complicated by a weak and underfunded infrastructure (Ezeah and Roberts, 2012). The management of solid waste in Nigerian cities continues to pose serious challenges due to the absence of appropriate and organized waste management culture and technologies, arising from financial, political instability, technological constraints and poor implementation of policy (Afun, 2009; Ezerie, George, Chidi and John, 2017).

Ahmadu Bello University (ABU) is a public university founded on October 4, 1962, located in Zaria, Kaduna State in the Northern part of Nigeria. With over 45,000 students, about 20,000 staff (academic and non-academic) and 106 departments, it is the largest university in West Africa and the second largest on the African continent after the University of Cairo in Egypt. The university has two main campuses, the main campus located in Samaru and annex campus in Kongo, both in Zaria (ABU, 2021). With this large population of students enrolled in diploma, undergraduate and postgraduate programmes, there is a large usage of paper for various activities. The Samaru Campus which is the focus of this study has an estimated population of 16,150 people (staff, students and cleaners). A certain percentage of the paper used ends up as waste to the dumpsite. This article looks at the attitude, practices and knowledge of the ABU community towards paper after its use.

On the average, each person in the United States of America uses approximately 749 pounds (339.741 kg) of paper a year. Some the paper goes into things such as books, used in other permanent applications like insulation or roofing shingles for your home (Georgia-Pacific Corporation, 2011). In Nigeria however, the data available is on the quantity of paper imported into the country which is 2 million metric tons annually (Adunola, 2018) with almost zero local production. With a population of about 200 million people, on the average, a Nigerian uses about 10 kg of paper per year.

$$\text{average paper use per Nigerian} = \frac{\text{quantity of paper imported}}{\text{estimated total population}} = \frac{2{,}000{,}000{,}000}{200{,}000{,}000} \quad (1)$$

$$= 10\, kg/person$$

METHODOLOGY

A questionnaire was designed to obtain information from different categories of members of the university community. The respondents were categorized into three, namely staff (academic& non-academic), students and the casual staff who carry out the general cleaning within the university on daily basis. For the purpose of this study, the main campus in Samaru was the main focus. The population of study consists of students, academic & non-academic staff and other members of the university community within the Samaru campus, which is estimated 16,150. The sample size is 201 which was determined using Yamane's formula for determining samples size as seen in equation 1 below.

$$n = \frac{N}{1+N(e)^2} \quad (2)$$

where n is sample size, N is population size and e is sampling error (± 7%)

out of the 201 used as sample size, 101 questionnaires were administered to student and all were received back, while 50 questionnaires were administered to both academic and non-academic staff, while 50 questionnaires were administered to the cleaners. 48 questionnaires were received from the staff and 48 questionnaires were received from the cleaners. This distribution pattern is necessary because, out of the estimated 16,150 estimated people in the Samaru campus, the student are about half of this population. Based on the estimated population of Samaru campus, the average annual paper use is given by:

$$\text{estimated annual paper usage in ABU} = 16{,}150 \times 10\ kg/person \quad (3)$$

$$= 161{,}500 \text{ kg}$$

To achieve the aim of this study, a questionnaire was used to find out how wastepaper is managed in ABU. The questionnaire comprises of three different segments namely, for students (33 questions), academic and non-academic staff (30 questions), for casual workers (cleaners) and waste disposal truck drivers (28 questions) which was conducted by interview because most of them can only communicate in Hausa language. The response of each of the casual workers was filled on the

questionnaire as they responded. The questions for each group of respondents were categorized into parts consisting of information related to the sources of wastepaper, wastepaper reduction, wastepaper handling, uses of wastepaper and wastepaper disposal.

Questions on knowledge and awareness had an assign score, using Likert scale, 1-5 for "Never", "Seldom", "sometimes", "often", "always" respectively. The practice statements were scored based on negative or positive wording of the items. For every positive response (Yes) the respondent was scored 2 while every negative response (No) was scored 1. Questions on students practice on wastepaper management and what they will do in some certain situations were assigned a score of 0-4 for 'pass them to friends', 'sell them', 'throw them away', 'keep them', 'others' respectively (Vagias, 2006).

RESULTS AND DISCUSSION

The result showed that for student respondents, their age ranges are 27% below 20, 68% between 21-30, 4% between 31-40 and 1% above 41% respectively. 34% of the respondents are B.Sc. students, 59% are Postgraduate Diploma (PGD) students, 4% are M.Sc. students, 1% are M.Phil. students and 2% are Ph.D. students. on the number of years in ABU, 1% of the respondents have stayed more than 6 years in ABU, 12% have stayed between 4-6 years, 55% for 2-4 years and 32% between 0-2 years.

The demographic results for academic and non- academic staff respondents show that 72% are males while 28% are females. 50% of the respondents are single, 33% are married, 6% are divorced and 11% are widows. Their age ranges are 24% for below 30 years, 36% for 31-40 years, and 40% for 41-50 years. On their level of education, 50% are school certificate holders, 29% B.Sc. holders, 13% are M.Sc. holders and 8% are Ph.D. holders. On the number of years working in ABU, 62% have worked in ABU for 0 to 5 years, 29% for 6 to 10 years and 9% for 11 to 15 years.

The demographic results for cleaners and waste disposal truck drivers shows for their age distribution, 24% are below 30 years, 52% are between 31 to 40 years, 20% are between 41 to 50 years and 4% are above 51 years old. The males are 20% while the females are 80%. Most of the cleaners that are involved in cleaning the class rooms and offices are women, validating the fact that most of the cleaners are women. 13% are single, 54% are married, 4% are divorced, 29% are widows. 75% have been working in ABU between 0-5 years and 25% between 6-10 years.

Table 1: Approaches to wastepaper management by staff on campus

Methods	Frequency	Percentage (%)
Reduce	10	9.9
Recycle	20	19.8
Reuse	63	62.4
Others	8	7.9

Reduce 9.9%, Recycle 19.8%, Reuse 62.4%, Others 7.9%

Table 1 shows that 19.8% of the respondents agreed that recycling is the most common method used for wastepaper management in ABU Samaru campus. 62.4% mentioned that reuse of wastepaper is what they do to curb wastepaper generation within the campus while reducing wastepaper generation is the least method in use for wastepaper management in ABU because paper represent a huge resource used for academic and research activities on campus. It should be noted that 7.9% still adopt other methods such as burning and flushing in suck away are methods they in managing their wastepaper.

Table 2: Approaches to wastepaper management by students on campus

Methods	Frequency	Percentage (%)
Reduce	4	8.3
Recycle	18	37.5
Reuse	26	54.2

Using the percentages as shown in table 2, it can be seen that 54.2% of the students practice wastepaper reuse as wastepaper management method, 37.5% recycling and 8.3% use wastepaper reduction as a method of paper management. Similar to what is practiced by the staff as in table 1, reusing of wastepaper is the second used approach to wastepaper in campus. This is laudable; however, more efforts and awareness should be put into encouraging members of the university community to reduce paper usage as the best approach to wastepaper management.

Table 3: Sources of wastepaper among staff

Sources	**Frequency**	**Percentage (%)**
Newspaper	16	11.6
Flyers	12	8.7
Mails	18	13
Memos	12	8.7
Envelope	2	1.4
Seminar papers	18	13
Minutes of meetings	2	1.4
Result deliberations	6	4.3
Printed paper	26	18.8
Project report	12	8.7
Flyers	6	4.3
Minutes of meeting	8	5.8
Others	0	0

The major source of wastepaper among the staff by percentage as shown on table 3 are printed papers (18.8%), mail and seminar papers at (13%), newspaper (11.6%), memos, project report and flyers (8.7%) with files been the least source of wastepaper on campus. Printed paper usually come from request for staff information from individual staff by the university management, draft work of supervisee given to the supervisor, presentations at the departmental boards, faculty boards and senate standing committee meetings, printing of curriculum vitae and other supporting documents during promotion exercises etc.

Furthermore, seminar papers are the second main source of wastepaper due to regular seminars presented by postgraduate students. in this case, each student has to produce a significant number of copies of his/her work for the audience. Most of these seminar papers become waste as soon as the student finishes the presentation for that particular day. There is the need to seriously look into several ways of reducing paper consumption during the above-mentioned activities.

Table 4: Sources of wastepaper among students

Sources	**Frequency**	**Percentage (%)**
Lecture notes and course packs	39	38.7
Newspaper	6	5.9
Flyers	17	16.9
Mails	2	2
Cardboards	6	5.9
Printed paper	7	6.9
Textbooks	7	6.9
Seminar papers	8	7.9
Others	9	8.9

Table 4 shows the type of wastepaper generated on campus by students. The study revealed that lecture notes and course packs constitute the largest single source of wastepaper (38.7%) while mails constitute the least source of wastepaper among students on campus (2%). These lecture notes come in form of lecture materials issued by the course lecturer(s), solution to past questions, whole or part of textbook(s) etc, which are usually available at photocopy shops within the department or at other locations within the campus. In most cases, almost all the students in each of the courses procure some or all of these materials, of which they become wastepaper the moment the students conclude their examinations.

The various locations where wastepaper are collected on campus are senate building (10%), printing press (12%), classrooms (15%), staff offices (9%), departmental offices (21%), photocopy centers (12%), residential areas (16%) and other locations such as the field, basketball court and street are 5% respectively. As earlier mentioned, there is a great deal of wastepaper generated from the departmental offices. These usually comprises of request that have been attended to, excess submissions at the end of meetings, photocopies of documents during accreditation and promotion exercises, old documents that are disposed etc.

Table 5: Staff responses to items based on practice

	Never (1)	**Seldom (2)**	**Sometimes (3)**	**Often (4)**	**Always (5)**	**Mean**	**Rank**
Do you sort waste before dumping them into the dustbins?	14	4	18	8	4	2.67	6
Do you shred wastepaper before dumping it into the dustbin?	6	8	22	10	2	2.88	4
Do you work on draft documents electronically instead of on printed paper?	10	6	16	16	0	2.79	5
Do you use the second page of paper with printed materials on one page?	2	8	24	10	4	3.13	2
Do you print on both pages of sheet of paper to reduce paper wastage?	8	2	18	10	8	3.04	3
Do you burn wastepaper?	6	6	14	12	10	3.29	1

Table 5 shows the response of staff to practice on how they handle wastepaper generated in their domain. The practice with the highest rank is the burning of wastepaper, while the activity with the least rank is sorting of waste before dumping them into the dustbins. This is an indication that burning of wastepaper is a common practice which should be discouraged. There are numerous hazards associated with the burning of wastepaper such as air pollution and bush fires in the dry season which the members of the university community are exposed to. Whereas waste sorting that would encourage waste reuse and recycling is not a common practice.

Table 6: Student responses based on practice

	Never (1)	**Seldom (2)**	**Sometimes (3)**	**Often (4)**	**Always (5)**	**Mean**	**Rank**
Do you buy used textbooks?	48	4	38	3	8	2.20	6
Do you work on draft documents electronically instead of on printed paper?	18	10	57	14	2	2.72	3
Do you print on both pages of paper to reduce paper wastage?	4	4	51	22	20	3.50	1
Do you shred paper before dumping to the dustbin?	16	10	47	10	18	3.04	2
Do You burn wastepaper?	32	14	43	7	5	2.40	4
Do you reuse scrap paper?	36	4	52	6	3	2.37	5

Students usually print on both sides of paper in order to reduce paper wastage and to reduce the cost of printing and photocopying which has the highest rank among the activities done by students to reduce paper wastage. However, the least practiced activity is buying used textbooks. There is the need to encourage or come up with a book buyback program on our university campuses. This would help students have access to books at reduced price. Table 7 shows that 27% of academic and non-academic staff are familiar with print preview when working with Microsoft (MS) Word, 23% are familiar with paper settings, 20% are familiar with margin and layout settings, 6% are familiar with how to use comment in MS Word, and 2% can use track changes settings. Furthermore,

Table 7: Familiarity of Staff with MS Word Settings

MS Word Settings	**Percentage (%)**
Print Preview	27
Paper Settings	23
Margin And Layout Settings	20
Use Comment	6
Track Changes Settings	2
Compare Tab	6
Split Screen	8
Spelling And Grammar	8

Paper shredding machines should be provided at certain offices on campus and Academic staff should be encouraged to send and receive assignments, handouts and course materials using electronic drafted copies. 57% of students reuse scrap paper for calculations, 30% for jotting and 13% for revision in other to reduce wastepaper.

Table 8: Items based on the level of knowledge for staff

	Yes	**No**
Do you have a dustbin in your office?	40 (83%)	8 (17%)
Do you know what happens to wastepaper after you dump them in dustbin?	20 (42%)	28 (58%)
Do you know that wastepaper can be recycled to get new paper?	46 (96%)	2 (4%)

In table 8, 96% of the respondents have knowledge that waste paper can be recycled to get new paper, 17% do not have a dustbin in their offices and 58% of the academic staff and non-academic staff

do not know what happens to the wastepaper after they are dumped. The mean score shows that they are knowledgeable about common environment friendly wastepaper reduction practice.

Table 9: Application of wastepaper according to staff and students

Application	**Frequency**	**Percentage (%)**
Recycled paper bags	24	14
Recycled paper basket	10	6
Paper mâché	30	17
Pen stand	12	7
Recycled paper wall hangings	10	6
Origami crafts	4	2
Egg tray	32	19
Tissue/ toilet / napkin paper	36	21
Others (Packaging and ceiling)	13	8

Table 9 shows the potential application of wastepaper, 21% of respondents have knowledge that recycled paper can be used to make Tissue/ Toilet / Napkin papers while only 2% have knowledge on the use of wastepaper for origami crafts. Other application of wastepaper include used as roof ceiling and common practice is the use for packaging certain

items such as bean cakes, Suya meat, and most fries within and outside the campus.

Table 10: Wastepaper application according to cleaners

Application	**Frequency**	**Percentage (%)**
Recycled paper bags	14	12
Recycled paper basket	14	12
Paper mâché	16	14
Pen stand	4	3
Recycled paper wall hangings	6	5
Origami crafts	4	3
Egg tray	26	22
Tissue/ toilet / napkin paper	24	20
Others (Packaging and ceiling)	10	9

Table 10 shows the various application of recycled wastepaper. 22% are aware of egg tray as a major application of wastepaper, 20% are use as tissue/toilet/ and napkin paper within and around the campus. The least used is origami craft which are mostly used by kids in their craft works and assignments. With 9% of the respondents using these recycled papers for packaging and also as ceiling in rooms around campus. Most of the cleaners and waste collects generate some amount of money for the sale of these papers which encourages them to sort out the one-sided printed paper from other papers for the purpose of reuse.

76% of both academic and non-academic staff, cleaners/waste collectors and truck drivers sort their waste before disposing it. There are enough waste bins within the campus but 82% of the cleaner respondents suggested having points for some waste categories which will discourage indiscriminate waste disposal and also encourage the practice of waste sorting generally. The findings of this project revealed that major source of paper waste is printed paper and with the departments being the highest producers of wastepaper (21%), 19% from residential, 15% from classes, 12% from printing and photocopying centers, 10% senate, 9% staff offices and 5% other locations on campus.

The 3Rs of waste management are reduce, reuse and recycle. However, from the responses of both the staff and students, it would be observed that waste reduction is the least practiced approach with 9.9% and 8% for staff and students respectively. There is the need to imbibe the attitude of reducing waste as the most important approach to waste reduction. The main source of wastepaper among staff is printed paper (18.8%), followed by seminar papers and mails (13%) each. Additionally, the main sources of wastepaper among students are Lecture notes and course packs, flyers and others with 38.7%, 16.9% and 8.9% respectively. This corroborates the earlier assertion that if wastepaper is reduced, it would significantly reduce the sources of wastepaper.

On the knowledge of what happens to wastepaper after it has been disposed into the waste bins, the staff and students are aware that wastepaper can be used in applications such as tissue/ toilet / napkin paper — 21%, egg tray — 19% and paper mâché -17%. While in the responses of the cleaners, they are also aware that wastepaper can be used in applications such as egg tray — 22%, tissue/ toilet / napkin paper — 20% and paper mâché -14%.

Finally, a book buyback program is one in which used textbooks and course packs are bought from student who no longer need them at a reduced rate. These books are then sold to students who now need them. This gives a win-win scenario to both the initial owner of the book, as he can still make some money from selling his old books, and to the buyer who would get a fairly new book at a reduced price rather than buying a new book. If the second user is able to take proper care of the book, he may still be able to sell the book through the book buyback program. Such books can be used by as many people as possible until it is defaced.

CONCLUSION

The members of the university community should be encouraged to practice the 3Rs of waste management on waste more than is currently being practiced in the order of reduce, reuse and recycle. With 48.5% of the students Sometimes/Often/Always buy used textbooks, the Student Union can create a book buyback program as one of the methods of mitigating wastepaper generation on campus. The book buyback program is expected to target textbooks and other lecture materials which forms about 45.6% of waste materials generated by the students. 78% academic and non-academic staff respondents are familiar with MS Word features such as print preview, paper settings, how to use comment, margin and layout settings and use track changes settings. This is a significant percentage, which the university management can leverage on to ensure that more staff use these features to save paper. Additionally, 73.7% of wastepaper generated by the staff can be reduced drastically if these features of MS word can be put to use. With the increasing level of global warming there is need for school authority and government to create more room for research, workshops and seminars on ways to better improve our immediate environment and also increase the level of awareness on wastepaper management and promote environment friendly practices.

REFERENCE

Ahmadu Bello University (2021). retrieved from abu.edu.ng on 05 January 2021

Adunola S. (2018). Nigeria imports N720b printing papers yearly. The Guardian Business News, Retrieved from https://guardian.ng/business-services/Nigeria-imports-n720b-printing-papers-yearly/ on 19th December 2020.

Afun S. (2009). Government Regulations and Legislations Will Ensure Sustainable Waste Management in Nigeria, Solid Waste Management Services Limited, Port Harcourt. https://www.iswa.org/uploads/tx_iswaknowledgebase/le_2009_2-357.pdf retrieved on 19th December 2020

Alim, S.A. and Ahmed, M. (2020). An assessment of the solid waste management in Gombe town, Gombe State Nigeria, Journal of Nigerian Environmental Society (JNES), 13(1), 63-77.

Devi, K.D., and Sastry, M.N.P. (2017). Design and fabrication of low-cost paper recycling equipment, International Journal of Mechanical and Production Engineering Research and Development (IJMPERD), 7(6), 463-470. ISSN (P): 2249-6890, ISSN (E): 2249-8001.

Ezeah, C., and Roberts, C.L. (2012). Analysis of barriers and success factors affecting the adoption of sustainable management of municipal solid waste in Nigeria, Journal of Environmental Management, 103, 9-14. D01:10.1016/jjenvman.2012.02.027

Ezerie, H. E., George, C., Chidi 0., and John, C. (2017). Municipal solid waste management in Aba, Nigeria: Challenges and prospects. Environmental Engineering Research. 22. 231-236. 10.4491/eer.2017.100.

Georgia-Pacific Corporation (2011). Paper Recycling. Retrieved https://www.lccd.org/wp-content/uploads/2016/12/Paper-Recycling.pdf on December 2020.

Hogben, L. (1951). Printing, Paper and Playing Cards. Books and Printing: A Treasury for Typophiles. New York: The World Publishing Company, 15-31.

Mann, G. (1952). Print: A Manual for Librarians and Students Describing in Detail the History. Methods, and Applications of Printing and Paper Making, Grafton, London.

Ministry of Environment and Forests Notification (2011). Discussion paper on collection and recycling of wastepaper in India. e-waste (Management and Handling) Rules, 2011. Retrieved from moef. nic.in/ downloads/ rules-and-regulations/ 1035e_eng.pdf

Sridhar, M.K.C. and Hammed, T. B. (2014). Turning Waste to Wealth in Nigeria: An Overview, Journal of human ecology (Delhi, India), 46(2),195-203. DOI:10.1080/09709274.2014.11906720

Vagias, W. M. (2006). Likert-type scale response anchors. Clemson International Institute for Tourism & Research Development, Department of Parks, Recreation and Tourism Management. Clemson University.

Worldwide Fund for Nature (2019) Recommendations for the Sustainable Development of Paper Recycling in China, pp. 1-15. Retrieved on 30 October, 2020 from https://d2ouvy59pOdg6k.cloudfront.net/downloads/recommendationsfor_the_sustain able_development_ofpaper_recycling_in_china.pdf

International Conference on Engineering Innovation for Sustainable Development (ICESID 2026)
Faculty of Engineering, Ahmadu Bello University Zaria · 8–10 September 2026

AN EVALUATION OF THE MECHANICAL PROPERTIES OF SANDCRETE MORTAR CONTAINING POLYSTYRENE WASTE AND FLY ASH

Salihu Yazeed[1], Sanusi Gambo[1,*], Abdullahi Getso Ibrahim[1]
[1]*Ahmadu Bello University*
Email: salihuyazeed@gmail.com, gambomsc12845@gmail.com*, getsomsc12012@gmail.com
***Corresponding author**: Sanusi Gambo
DOI: https://doi.org/10.67203/sp.ICESID.2026

ABSTRACT
The increasing accumulation of polystyrene waste and the environmental impact associated with cement production have necessitated the search for sustainable alternatives in the construction industry. The study evaluated the properties of sandcrete mortar containing polystyrene waste and fly ash with a view to developing a lightweight and environmentally friendly material for potential use in non-load-bearing sandcrete blocks. A cement-to-sand mix ratio of 1:6 and a constant water-cement ratio of 0.50 were used to produce the sandcrete mortar cubes of 50x50x50 mm and cylinders of 70mm diameter x100mm height. Fine aggregate was replaced with polystyrene at 0, 5, 10, 15, 20, and 25% by volume, while fly ash was maintained at a replacement level of 10% of cement. In the fresh state, the mixes were tested for consistency using a flow test, while in the hardened state, the sandcrete mortar samples were tested for compressive strength, tensile strength, and density. Furthermore, the morphology of the sandcrete mortar specimens was assessed using Scanning Electron Microscopy (SEM). The results show that the compressive strength of the specimens decreased as the polystyrene content increased from 5 to 25%. However, the mix containing 5% polystyrene and 10% fly ash achieved a compressive strength of 3.125 N/mm² at 90 days, compared with 3.375 N/mm² for the control mix, representing a 7.4% reduction in compressive strength. SEM analysis confirmed a denser cementitious matrix in fly ash-modified mixes due to secondary calcium silicate hydrate (C–S–H) formation, while higher polystyrene contents produced larger interfacial voids that contributed to strength reduction. The 5% polystyrene and 10% fly ash mix was identified as the optimum modified mix, achieving a compressive strength of 3.125 N/mm², exceeding the 2.5 N/mm² minimum requirement reported for non-load-bearing sandcrete blocks under NIS 87:2007, indicating its potential suitability for non-load-bearing applications.

Keywords: *fly ash; sandcrete blocks; polystyrene waste; mechanical properties*

1.0 INTRODUCTION

The construction industry is increasingly seeking sustainable methods of producing building materials without compromising performance. The utilization of industrial by-products and waste materials in construction can reduce dependence on natural resources while providing useful applications for materials that would otherwise contribute to environmental pollution. The use of waste materials as lightweight aggregates has therefore received increasing attention because of their availability and potential to reduce the weight of construction products (Arshad, 2014; Khatib, 2009). Polystyrene is a lightweight, non-biodegradable thermoplastic commonly used for food packaging, disposable cups, cartons, and other consumer products. Its closed-cell structure and low density make it attractive as a lightweight material for cement-based products (Kan, 2009). However, its widespread disposal creates environmental challenges. Polystyrene waste can accumulate in drainage systems, streets, and disposal sites, while inappropriate disposal and burning may contribute to environmental pollution (Murana, 2020; Kehinde & Babatunde, 2020; Olutoye et al., 2022).

The incorporation of polystyrene waste into construction materials offers an alternative approach to managing this waste. Previous studies have indicated that polystyrene can reduce the density of cement-based materials; however, increasing its content may reduce mechanical strength due to its low density and relatively weak bonding with the cementitious matrix (Haidar & Khalil, 2002; Babu & Babu, 2003; Kehinde & Babatunde, 2020).

Fly ash is an industrial by-product with pozzolanic characteristics. Its silica and alumina content allows it to react with calcium hydroxide produced during cement hydration to form additional calcium silicate hydrate (C–S–H), which can contribute to strength and matrix densification (Mehta & Monteiro, 2020; Abbas et al., 2021). Studies revealed that fly ash can improve the performance of cement-based materials and provide environmental benefits by reducing cement consumption (Freeda, 2010; Zhang et al., 2022; Olutoge et al., 2023).

In Nigeria, sandcrete blocks are widely used for external and internal wall construction because of their availability and affordability (Anosike, 2012). However, their relatively high density contributes to the dead load of buildings. The use of polystyrene as a partial replacement for fine aggregate can reduce this weight, while fly ash can be used as a partial cement replacement to improve the sustainability of the material (Dadu, 2020; Akinyele & Adedeji, 2021).

Although studies have separately investigated polystyrene and fly ash in cement-based materials, few studies have examined their combined application in sandcrete mortar under local Nigerian conditions. The present study therefore evaluates the mechanical properties of sandcrete mortar blocks containing polystyrene waste as a partial replacement for fine aggregate and fly ash as a partial replacement for cement.

2.0 MATERIALS AND METHODS

2.1 Materials

2.1.1 *Fine Aggregate*

The fine aggregate used for the experiment was river sand sourced from Zaria metropolis, Kaduna State, Nigeria. The sand was sieved through a 4.75 mm sieve to remove large particles and impurities.

2.1.2 *Polystyrene Waste*

Polystyrene waste was collected from dump sites, event centres, and drainage channels within Zaria metropolis. The collected waste was manually sorted to remove contaminants such as paper, soil, and organic materials. It was then shredded using a locally fabricated grinder into particle sizes not exceeding 4.75 mm. Sieve analysis was subsequently conducted to establish the particle-size distribution.

2.1.3 *Cement*

Limestone Portland Cement of Dangote brand conforming to BS EN 197-1:2011 specifications was used.

2.1.4 *Fly Ash*

Fly ash was obtained from BUA Cement Plant, Okpella, Edo State. It was stored in airtight containers to prevent moisture contamination and sieved through 45 µm before use. The physical and chemical characteristics of fly ash are important in determining its suitability and performance as a supplementary cementitious material in cement-based materials (Akhatar & Tarannum, 2018).

2.1.5 *Water*

Portable water fit for drinking was used for both mixing and curing

2.2 Mix Proportioning

A cement-to-sand mix ratio of 1:6 was adopted, representing one part cement to six parts fine aggregate, in accordance with the provisions of NIS 87:2004. A constant water-cement ratio of 0.50 was maintained for all mixes. Fly ash was incorporated as a 10% replacement of cement, while polystyrene waste was used to replace fine aggregate at 0%, 5%, 10%, 15%, 20%, and 25% by volume. The summary of the materials used to produce the samples is presented in Table 1.

2.3 Preparation of Samples

The constituent materials were thoroughly mixed using a mortar mixer to achieve a uniform mixture. The fresh mixes were subsequently cast into 50 × 50 × 50 mm cube molds and 70mm diameter x100mm height cylindrical molds and compacted manually to ensure adequate consolidation. After setting and hardening, the specimens were demolded and fully immersed in a water-curing tank until the specified testing ages.

Table 1: Mix Proportioning of Materials

Polystyrene repl. (%)	Cement (kg/batch)	Fly Ash (kg/ batch)	Fine Agg. (kg/ batch)	Polystyrene (kg/batch)
0	3.243	0.00	19.46	0.00
5	2.908	0.323	18.413	0.00493
10	2.908	0.323	17.445	0.00985
15	2.908	0.323	16.476	0.01478
20	2.908	0.323	15.507	0.01971
25	2.908	0.323	14.538	0.024633

2.4 Testing of Samples

In the fresh state, the mortar mixes were evaluated for consistency using the flow-table test in accordance with the procedure outlined in BS EN 1015-3:1999. The measured spread diameters were subsequently classified based on the consistency criteria adopted from the relevant provision of IS 4031. At the hardened state, Density, compressive strength, and splitting tensile strength were measured at 7, 14, 28, 56, and 90 days in compliance with the provisions of BS EN 12390-3 (2002) and BS EN 12390-6 (2009), Three replicate samples were tested for each mixture at each curing age for compressive strength, splitting tensile strength, and density. The results were expressed as the mean value of the three replicates, together with the corresponding standard deviation. Furthermore, the morphology of the mortar cubes were assessed using a scanning electron microscope (SEM).

3.0 RESULTS AND DISCUSSION

3.1 Chemical Composition of Fly Ash

Table 2: Chemical Composition of Fly Ash

S/no.	Constituent	Elements	Test Result (% by mass)	ASTM C618 Requirement
1	Silicon Dioxide	SiO_2	53.42	—
2	Aluminum Oxide	Al_2O_3	27.18	—
3	Iron Oxide	Fe_2O_3	8.63	—
Sub-total	**(SiO_2 + Al_2O_3 + Fe_2O_3)**	—	**89.23**	**≥ 70.0%**
4	Calcium Oxide	CaO	5.36	—
5	Magnesium Oxide	MgO	1.45	≤ 5.0%
6	Sulfur Trioxide	SO_3	1.10	≤ 5.0%
7	Sodium Oxide	Na_2O	0.76	—
8	Potassium Oxide	K_2O	1.45	—
9	Titanium Dioxide	TiO_2	1.10	—
10	Phosphorus Pentoxide	P_2O_5	0.12	—
11	Loss on Ignition (LOI)	—	1.85	≤ 6.0%

Table 2 shows the chemical composition analysis of fly ash. It can be observed that the combined proportions of SiO_2, Al_2O_3, and Fe_2O_3 are 89.23%**,** which exceeds the minimum value of 70%

prescribed by ASTM C618 for the classification of fly ash. The loss on ignition (LOI) was 1.85%, which is also within the recommended limit. This implies that the fly ash was suitable for use as pozzolanic material.

3.2 Consistency of Fresh Mortar

Table 3: Flow of Mortar Mixes

Fresh Mixes Samples	Spread Diameter (mm)	Remark
0%	125mm	High consistency
5%	123mm	High consistency
10%	114mm	Moderate consistency
15%	110mm	Moderate consistency
20%	105mm	Moderate consistency
25%	100mm	Stiff

Source: Experiment (2025)

Table 3 presents the consistency of the fresh mortar mixes containing polystyrene and fly ash. It was observed that the flow of the mixes decreased with an increase in polystyrene content. The control mixture recorded a spread diameter of approximately 125 mm, while the spread decreased slightly with increasing polystyrene replacement, reaching approximately 100 mm at 25% replacement.

This represents a reduction of approximately 20% between the control and the 25% polystyrene mixture. The reduction in consistency is associated with the physical characteristics of the polystyrene particles and their influence on particle packing within the fresh mortar. Based on IS 4031, the spread values of the mortar mixes obtained fall within the range of high to moderate consistency, except for the 25% polystyrene sample. This implies that 5-20% polystyrene mortar mixes will be easy to work with. However, the consistency of the 25% polystyrene mixes could be improved by the use of water-reducing admixtures.

3.3 Density

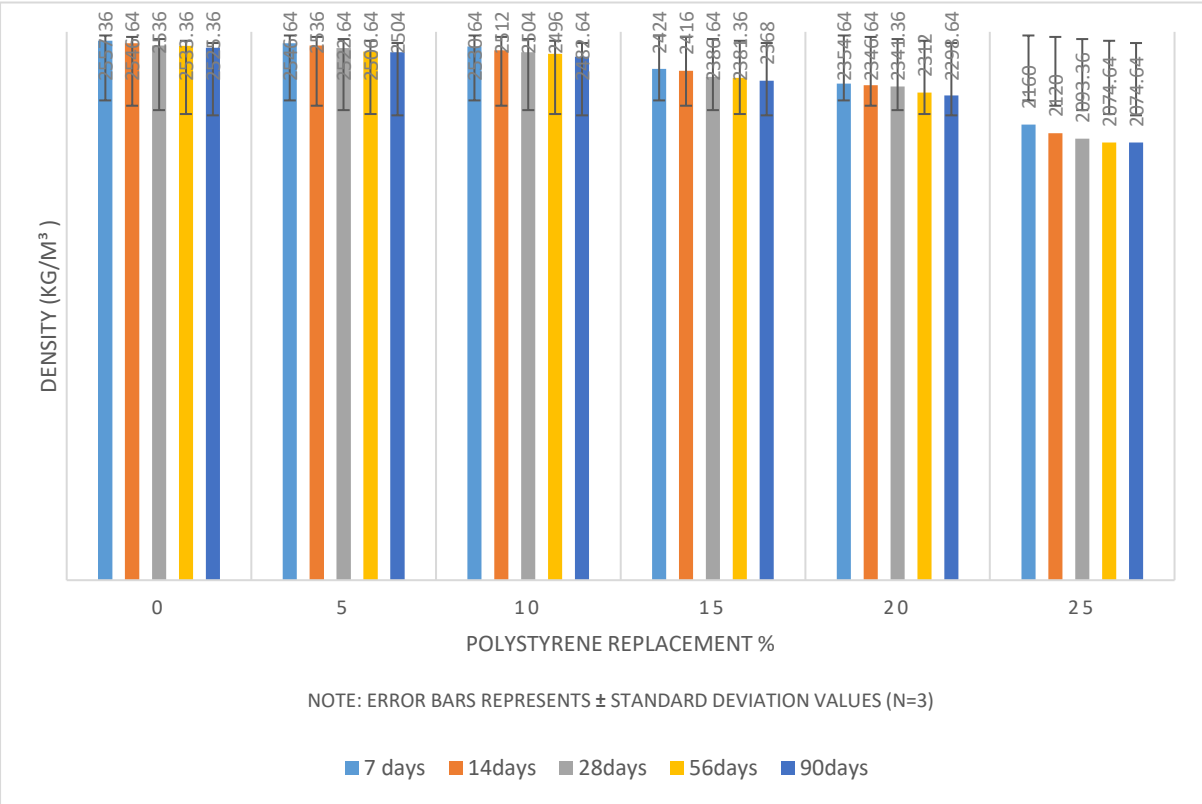

Figure 1: Density

Figure 1 presents the dry density of the hardened sandcrete mortar samples at curing ages of 7, 14, 28, 56, and 90 days. The results show that dry density generally decreased with increasing polystyrene replacement, particularly at replacement levels above 10%. At 7 days, the density decreased from 2557.36 kg/m³ for the control mix to 2160.00 kg/m³ at 25% polystyrene replacement. Similarly, at 14 days, the density decreased from 2546.64 kg/m³ to 2120.00 kg/m³ for the control and 25% replacement mixes, respectively. At 28 days, the density decreased from 2536.00 kg/m³ to 2093.36 kg/m³, while at 56 days, it decreased from 2533.36 kg/m³ to 2074.64 kg/m³ for the control and 25% replacement mixes, respectively. At 90 days, the density further decreased from 2525.36 kg/m³ for the control mix to 2074.64 kg/m³ at 25% polystyrene replacement.

The reduction in density is attributed to the significantly lower density of polystyrene compared with natural fine aggregate. The effect of curing age on density was relatively small compared with the effect of polystyrene replacement. At lower replacement levels of 5% and 10%, only slight reductions in density were observed, whereas higher replacement levels of 15–25% produced more substantial reductions. The findings demonstrate that increasing polystyrene content is effective in reducing the unit weight of the hardened mortar, supporting its potential application in lightweight construction.

The large difference between the densities of polystyrene and sand explains the reduction in the unit weight of the resulting mortar as the replacement percentage increased. This finding supports previous research identifying polystyrene as a suitable lightweight material for cement-based construction products (Kan, 2009; Miled & Boulay, 2004; Khatib, 2009).

3.4 Compressive Strength

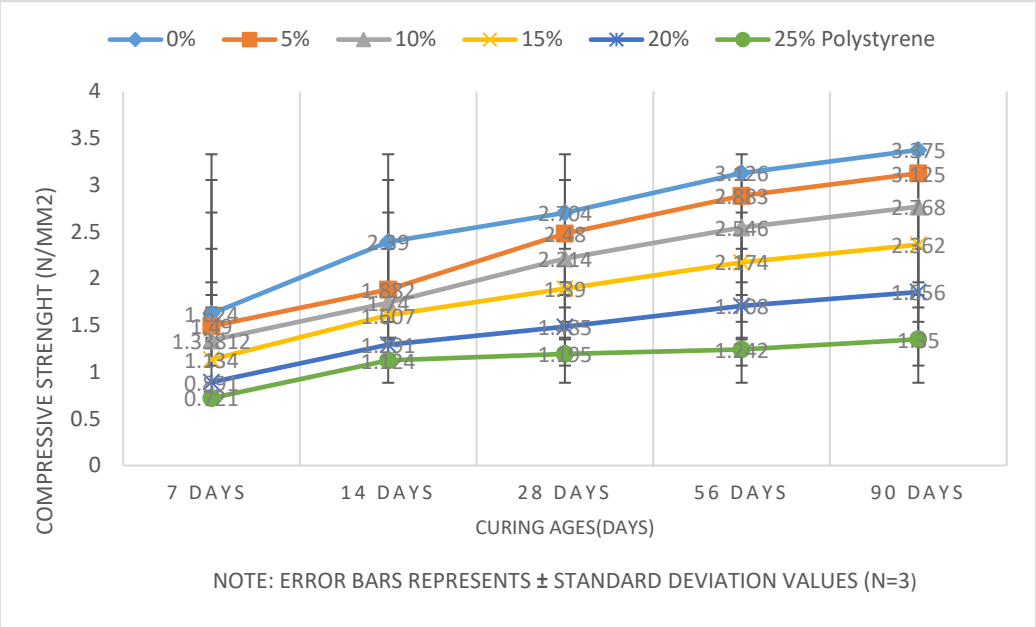

Figure 2: Compressive Strength of Sandcrete Mortar Samples at Different Curing Ages

Figure 2 shows the compressive strength of the mortar samples at different polystyrene replacement levels. The compressive strength increases with age. At 90 days, the control sample recorded a compressive strength of 3.375 N/mm², while the values decreased to 3.125, 2.805, 2.445, 2.085, and 1.725 N/mm² for 5%, 10%, 15%, 20%, and 25% polystyrene replacement, respectively. Compared to the control sample, these values represent reductions of approximately 7.4%, 16.9%, 27.6%, 38.2%, and 48.9%, respectively. The results indicate that although prolonged curing improved the strength of all samples, increasing the proportion of polystyrene progressively reduced compressive strength. The relatively small reduction observed at 5% replacement indicates that a low level of polystyrene can be incorporated while retaining a substantial proportion of the control samples' strength. However, higher replacement levels resulted in progressively greater strength reductions. The reduction can be attributed mainly to the low density and relatively weak bonding of polystyrene particles within the cementitious matrix. Similar observations have been reported in studies of polystyrene-containing

cement-based materials (Haidar & Khalil, 2002; Kehinde & Babatunde, 2020). The continuous increase in strength with curing age is associated with continued cement hydration and the contribution of fly ash through pozzolanic reactions.

3.5 Splitting Tensile Strength

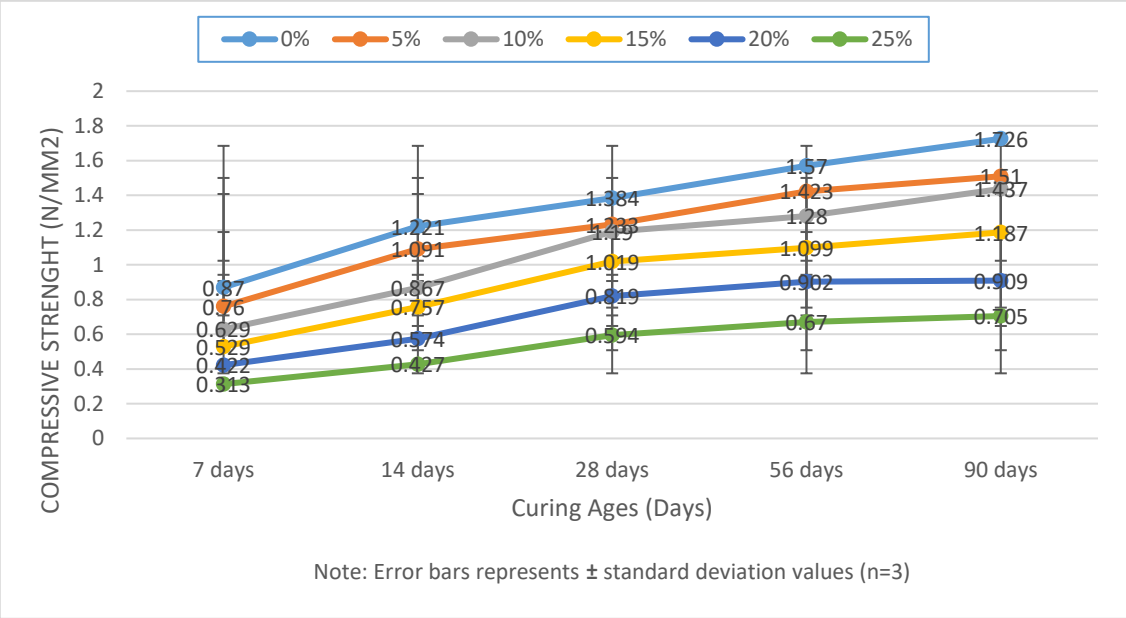

Figure 3: Split Tensile Strength of Sandcrete Mortar Sample at Different Curing Ages

Figure 3 presents the split tensile strength of the mortar samples containing polystyrene and fly ash. The tensile strength of the mortar samples exhibited a trend similar to that of compressive strength, whereby increasing polystyrene replacement resulted in progressive reductions in tensile strength. At 90 days, the control mix recorded a tensile strength of 1.726 N/mm², while the 5%, 10%, 15%, 20%, and 25% polystyrene mixes attained tensile strengths of 1.510, 1.437, 1.187, 0.909, and 0.705 N/mm², respectively. Compared to the control sample, these values represent reductions of 12.51%, 16.74%, 31.23%, 47.28%, and 59.15%, respectively. This indicates that increasing the proportion of polystyrene progressively reduced the mortar's tensile performance. The reduction may be attributed to the low density and weak mechanical properties of polystyrene particles, which can increase void spaces within the matrix and reduce the bond between the cement paste and aggregate particles. The observed decrease in tensile strength agrees with the findings of Ya'u et al. (2024), who reported that the mechanical properties decreased with an increase in polystyrene content

Despite the reduction in tensile strength with increasing polystyrene content, all mixes exhibited continuous strength development with curing age. For instance, the 25% polystyrene mix increased from 0.313 N/mm² at 7 days to 0.705 N/mm² at 90 days. The continuous increase in strength with curing age may be associated with the ongoing hydration of cement and the contribution of fly ash content to the development of the cementitious matrix through pozzolanic reactions.

3.6 Scanning Electron Microscopy Analysis (SEM)

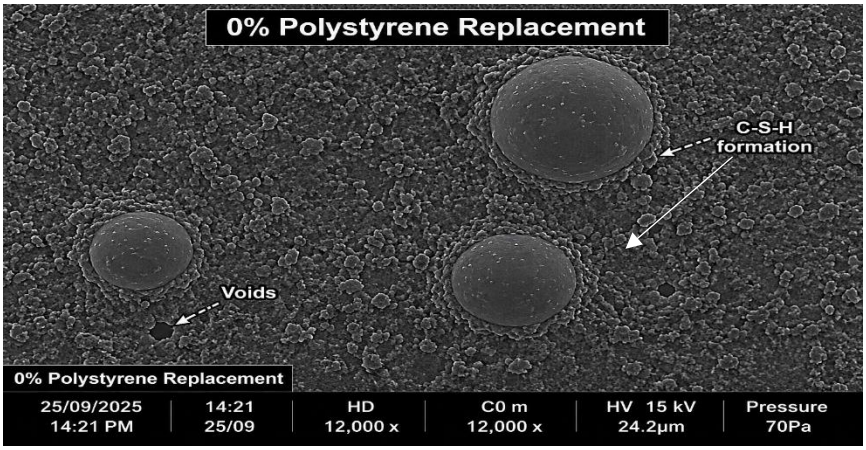

Vods

Plate I: Sample A (Control Mix containing 0% Polystyrene Replacement and 0% fly ash replacement)

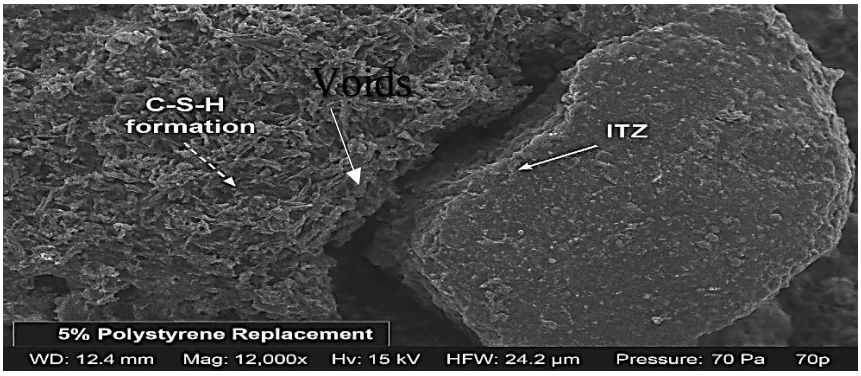

Plate II: Sample B (5% Polystyrene Replacement and 10% fly ash Replacement)

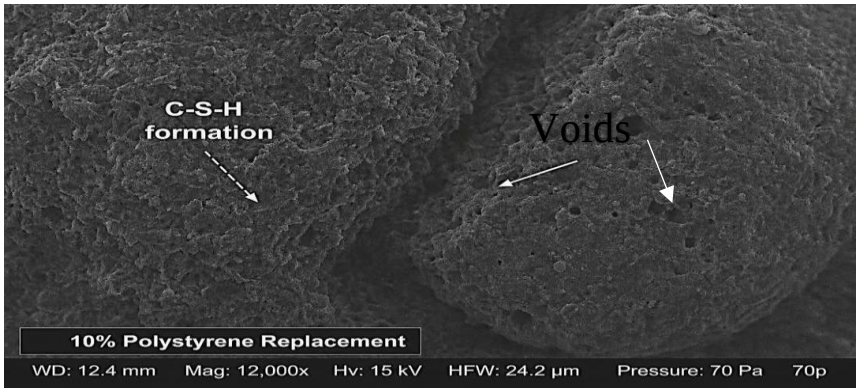

Plate III: Sample C 10% Polystyrene Replacement and 10% fly ash replacement

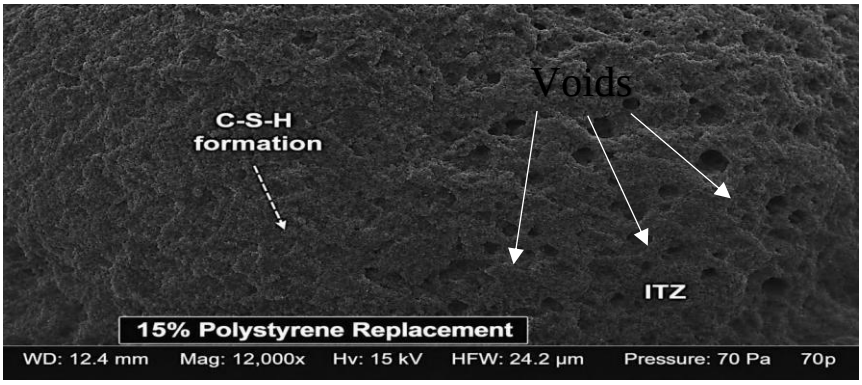

Plate IV: Sample D (15% Polystyrene Replacement and 10% fly ash replacement)

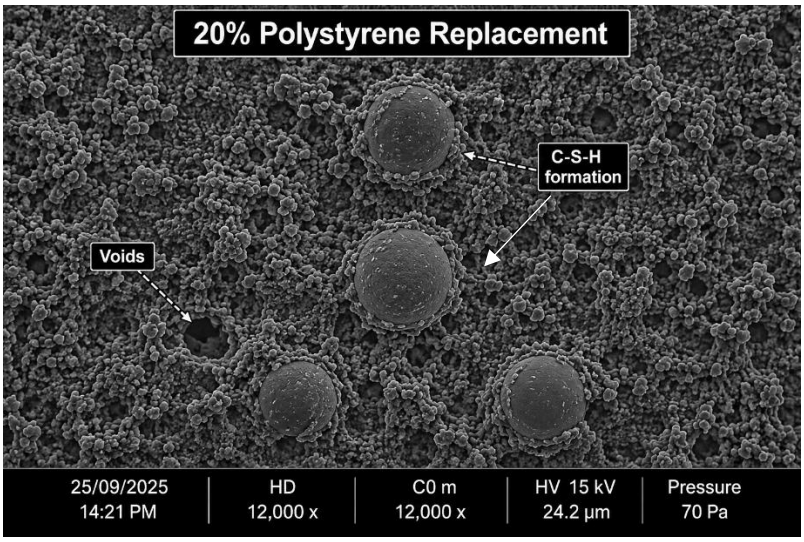

Plate V: Sample E (20% Polystyrene Replacement and 10% fly ash replacement)

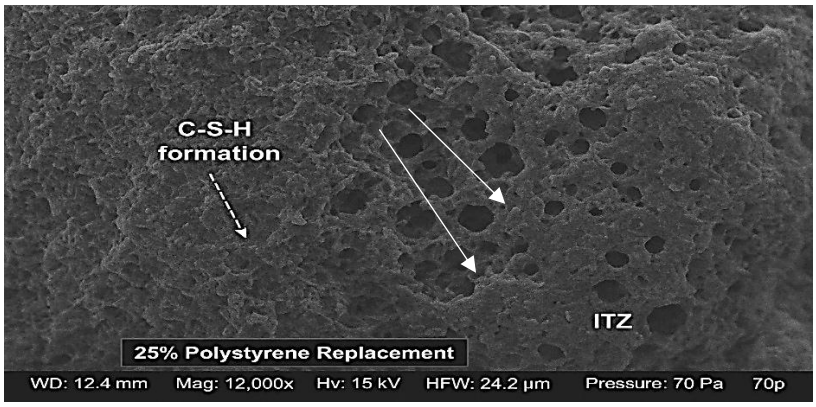

Plate VI: Sample F (25% Polystyrene Replacement and 10% fly ash replacement)

The microstructural properties of the mortar samples were evaluated using Scanning Electron Microscopy (SEM) at 12,000× magnification as shown in Plates I-VI. The SEM observations provided microstructural evidence supporting the mechanical-strength results. The control specimen exhibited a relatively dense and compact microstructure with extensive C–S–H gel formation and a well-bonded interfacial transition zone. The limited number of voids and microcracks corresponded with the relatively high mechanical strength of the control specimen.

At 5% polystyrene and 10% fly ash, small spherical voids associated with the polystyrene particles were observed. However, the matrix remained relatively dense because of the pozzolanic activity of the fly ash, which promoted secondary C–S–H formation. This helped maintain relatively good microstructural integrity.

At 10% polystyrene, the number of voids increased, and the interfacial transition zone became less compact. At 15 to 25% replacement, the microstructure became progressively more porous and discontinuous, with larger voids, weak interfacial zones, and localized microcracking. The 20% and 25% specimens exhibited highly porous matrices with poor particle bonding and fragmented hydration products.

The SEM results therefore support the observed reduction in compressive and tensile strength with increasing polystyrene content. They also provide evidence for the improved performance of the 5% polystyrene + 10% fly ash specimen.

4.0 CONCLUSION

i. The 5–20% replacement levels exhibited high to moderate consistency and were considered workable, whereas the 25% mix became relatively stiff.

ii. Based on the density results, increasing polystyrene content can be effectively used to produce lighter mortar suitable for non-structural applications.

iii. Compressive and tensile strength decreased with increasing polystyrene content. However, 5% polystyrene and 10% fly ash specimens retained 92.6% of their strength. Therefore, 5% polystyrene and 10% fly ash is the optimum for producing cement mortar

iv. Increasing polystyrene content resulted in greater porosity, larger voids, weaker interfacial zones, and localized microcracking. In contrast, the lower polystyrene replacement level exhibited a relatively denser matrix with improved C–S–H gel formation associated with the presence of fly ash.

REFERENCES

Akhatar, S., & Tarannum, S. (2018). Analysis of the physical and chemical properties of fly ash for use in concrete. *International Journal of Engineering Research, 7*(4), 112–118.

Akinyele, J. O., & Adedeji, Y. M. (2021). Performance of lightweight concrete blocks produced with waste polystyrene. *Nigerian Journal of Building Technology, 9*(1), 60–75.

Anosike, M. N. (2012). Sandcrete block manufacturing and quality control in Nigeria. *Civil Engineering Research Journal, 5*(2), 34–42.

Arshad, M. (2014). Use of waste materials in production of lightweight concrete. *International Journal of Sustainable Construction, 4*(1), 20–28.

Babu, K. G., & Babu, D. S. (2003). Behaviour of lightweight expanded polystyrene concrete containing silica fume. *Cement and Concrete Research, 33*(5), 755–762. https://doi.org/10.1016/S0008-8846(02)01055-4

British Standards Institution. (1999). *BS EN 1015-3:1999: Methods of test for mortar for masonry—Determination of consistence of fresh mortar (by flow table).*

British Standards Institution. (2002). *BS EN 12390-3:2002: Testing hardened concrete—Compressive strength of test specimens.*

British Standards Institution. (2009). *BS EN 12390-6:2009: Testing hardened concrete—Tensile splitting strength of test specimens.*

British Standards Institution. (2011). *BS EN 197-1:2011: Cement—Composition, specifications and conformity criteria.*

Dadu, D. (2020). Improving thermal efficiency of buildings using lightweight units. *Journal of Sustainable Urban Design, 10*(1), 50–62.

Freeda, C. (2010). Mechanical properties of fly ash cement mortar at various replacement levels. *Construction and Materials Journal,* 14(2), 80–87.

Haidar, N., & Khalil, M. (2002). Polystyrene aggregate mortar: Strength and thermal response. *Journal of Light Materials, 5*, 18–26.

IS 4031 (Part 4):1988: Methods of Physical Tests for Hydraulic Cement- Part 4: *Determination of Consistency of Standard Cement Paste*. New Delhi, India: Bureau of Indian Standards.

Kan, A. (2009). Properties of expanded polystyrene in construction applications. *Journal of Polymer Technology, 22*(1), 55–63.

Kehinde, O., & Babatunde, S. (2020). Environmental impact of polystyrene waste in Nigerian cities. *Journal of Waste & Pollution Studies, 8*(2), 30–45.

Khatib, J. (2009). Sustainability of lightweight aggregates in concrete. *Construction and Building Materials, 23*, 131–145.

Mehta, P. K., & Monteiro, P. (2020). *Concrete: Microstructure, properties, and materials*. McGraw-Hill.

Miled, K., & Boulay, C. (2004). Lightweight concrete with polystyrene aggregate. *Cement and Concrete Research, 34*(12), 2253–2259.

Murana, M. (2020). Plastic pollution in Nigeria and challenges of polystyrene waste management. *Nigerian Environmental Journal, 14*(1), 45–58.

NIS 87:2007. (2007). *Standard for sandcrete blocks*. Standards Organisation of Nigeria.

Olutoge, F. A., Alade, G. A., & Ojo, A. (2023). Compressive strength performance of fly-ash-blended cement blocks. *International Journal of Civil Engineering Research, 18*(2), 88–95.

Olutoye, M., et al. (2022). Toxic emissions from burning polystyrene waste in open environments. *Journal of Environmental Toxicology, 16*(4), 70–79.

Yau, Y., Amoka, M. H., Sulaiman, T. A., Aliyu, I., Garba, I., Abdurrahman, A. A., & Sabari, A. A. (2024). Evaluation of compressive strength of concrete with shredded polystyrene as a partial replacement for natural fine aggregate. *3rd International Conference on Engineering and Environmental Sciences (ICEES) 2024*, 579–584.

Zhang, L., Chen, Y., & Wang, P. (2022). Pozzolanic reactivity of fly ash cement composites. *Construction and Building Materials*, 320, 126–138.

International Conference on Engineering Innovation for Sustainable Development (ICESID 2026)
Faculty of Engineering, Ahmadu Bello University Zaria · 8–10 September 2026

AN INVESTIGATION INTO THE PHYSICAL PROPERTIES OF METAKAOLIN-BASED GEOPOLYMER MODIFIED ASPHALT BINDER

Kenneth, Ejike Ibedu[1,*], Abdulfatai Adinoyi Murana[2], Aliyu Usman[2], Abdulmumin Ahmed Shuaibu[2]

[1]*Department of Civil Engineering, Baze University, Abuja, Nigeria*
[2]*Department of Civil Engineering, Ahmadu Bello University, Zaria, Nigeria*

Email: ibedukenneth@gmail.com*, fatinoyi2007@gmail.com, auzaria83@gmail.com, abdulshub4u@gmail.com

***Corresponding author**: Kenneth, Ejike Ibedu

DOI: https://doi.org/10.67203/sp.ICESID.2026

ABSTRACT

The development of sustainable, low-carbon construction materials has become a major priority in the construction industry. In response, this study evaluates the effectiveness of metakaolin-based geopolymer (MBG) as a modifier for improving the physical properties of asphalt binder. MBG was incorporated into a 60/70 penetration-grade asphalt binder at dosages ranging from 2% to 10% (by weight of binder, at 2% intervals). The effects on key physical properties including penetration, softening point, ductility, flash point, solubility, and storage stability were systematically investigated. Results showed that MBG addition produced a desirable hardening effect. Penetration decreased by an average of 17.94%, while the softening point increased by 6%, resulting in an improved penetration index. Ductility decreased by 39%, indicating reduced flexibility, whereas the flash point showed a marginal 1% increase. Solubility remained essentially unchanged, and storage stability was satisfactory across the tested range. These enhancements are attributed to strong interfacial interactions between the geopolymer particles and the asphalt matrix, leading to a stiffer and more stable binder structure. Overall, the findings demonstrate the potential of MBG as a sustainable, low-carbon modifier capable of enhancing asphalt binder performance. Based on the results, a 2% MBG dosage is recommended as the optimal level for effectively improving the physical properties without excessive compromise to ductility.

Keywords: *Asphalt binder; Modification; Metakaolin; Geopolymer; Physical properties; Sustainability*

1. INTRODUCTION

Several studies have demonstrated that polymer modification of asphaltic binders significantly enhances the performance of asphalt mixtures. For example, rubber-modified asphalt binders have been shown to improve toughness, low-temperature performance, and elastic properties, while ethylene-vinyl acetate (EVA) and high-density polyethylene (HDPE) reduce temperature susceptibility, and polyvinyl chloride (PVC) enhances heat resistance (Murana *et al*., 2018; Murana *et al.*, 2020; Murana *et al.*, 2023; Abah *et al.*, 2024). In addition, polymer-modified asphalt contributes to notable environmental benefits by reducing pavement maintenance and repair frequency as well as lowering traffic noise (Hamid *et al.*, 2020). As a result, interest has increasingly shifted toward recycled polymers as modifiers. These materials offer clear environmental and economic advantages while often delivering superior performance compared to unmodified binders. Consequently, polymer modification of asphalt has become a highly promising approach for designing high-performance flexible pavements, with important implications for the engineering properties and long-term durability of road infrastructure.

Building on these developments, geopolymers have emerged as a promising alternative to conventional and recycled polymers for asphalt modification. Geopolymers are inorganic materials capable of delivering higher strength and superior performance in asphalt mixtures (Milad *et al*., 2021). They are produced through geopolymerization, a reaction between alkaline activators and

aluminosilicate-rich precursors. A wide range of industrial by-products and wastes can serve as source materials, including metakaolin (Ibedu *et al*., 2026), fly ash (Hamid *et al.*, 2020), bentonite (Jaimes *et al*., 2020), rice husk ash (Thirukumaran *et al*., 2023), mine waste, and blast furnace slag (Milad *et al.*, 2021; Amran *et al.*, 2021). Due to their low-CO_2 production process and utilization of waste materials that would otherwise require disposal, geopolymers are widely recognized as a greener, more environmentally friendly alternative to traditional binders and polymers. Their production significantly reduces greenhouse gas emissions compared to conventional materials, while also conserving natural resources and mitigating the environmental burdens of waste accumulation. This combination of technical performance, economic viability, and sustainability makes geopolymers highly attractive for advancing sustainable development in civil engineering. They hold strong potential for applications in asphalt concrete, pavement engineering, geotechnical engineering, and broader construction works.

However, a notable theoretical and experimental knowledge gap remains regarding the influence of metakaolin-based geopolymers on the physical properties of asphalt binders. The present study seeks to address this gap through a systematic evaluation of the physical performance of metakaolin-based geopolymer-modified asphalt binders. Such an assessment is essential to determine their suitability as a sustainable alternative to traditional bituminous binders. Bridging this gap will not only support the development of greener pavements but also provide deeper insights into the material's behavior under real-world service conditions.

2. METHODOLOGY

2.1 Materials

Metakaolin ($SiO_2 \cdot 2Al_2O_3$) was processed from Kankara kaolin. The metakaolin was used as precursor. The Alkali (Sodium Hydroxide and Sodium Silicate) were sourced from Cardinal Scientific Shop, Samaru Zaria. The NaOH was in pellet form (98.9% purity) and the Na_2SiO_3 was used for the alkali activation. The 60/70 asphalt binder was sourced at Gradient Emulsions and Polymers Limited, Located at kilometer 8, Abuja-Kaduna Expressway, Kakau Chikun LGA Kaduna State.

2.1.1 Geopolymer Synthesis

The geopolymer consists of metakaolin, and the alkaline activator. Due to the fact that there is no standard geopolymer mix design, the optimal molarity and mix ratio was adopted from Hamid, *et al.*, (2020) and further corroborated in the studies of Hauruna, *et al.*, (2018); Gambo, e*t al.*, 2020). Sodium hydroxide (NaOH) pellet was diluted in water to produce 8 Molar (8M) NaoH solution and combined with the alkaline activator solution (Na_2SiO_3). The ratio of sodium hydroxide to sodium silicate (NaOH /Na_2SiO_3) was 2:1. A mixture of the sodium hydroxide solution and sodium silicate solution was prepared and stirred for 5 minutes to activate the alumino-silicate precursors in metakaolin. In this study, metakaolin with Class F which satisfies the chemical composition of SiO_2+ Al_2O_3+ Fe_2O_3 as stipulated by ASTM C168-19, (2019). The formed homogenous slurry geopolymer were poured into a size 75 cm x 75cm x 75 cm mold, the product was called metakaolin-based geopolymer. All samples were cured at room temperature for 24 hours and then further cured in the oven at 60ºC for 24 hours. Generally, the process of geopolymerisation depends on the curing mode. The samples were cured at room temperature (25ºC-26ºC), to minimize moisture loss, allow for proper gelation. At higher temperature in the oven, the excess water is given out during this process, the reaction of geopolymerisation accelerates leading to faster setting and hardening. This improves the mechanical properties of geopolymer such as strength and durability. Plate I shows the mixing process to produce the geopolymer.

Plate I: Geopolymerisation process: (a) mixing at room temperatures (b) geopolymer paste (c) geopolymer cubes

2.1.2 Production of Metakaolin-Based Geopolymer Modified Asphalt Binder

To produce the metakaolin-based geopolymer modified asphalt binder, a two-stage mixing process was employed using high shear and low shear mixers. Initially, 3000g of pristine asphalt binder was heated to 180°C for 4 hours in an oven to achieve optimal fluidity. Subsequently, metakaolin-based geopolymer was added to the heated asphalt binder at varying concentrations (2, 4, 6, 8, and 10% by weight of bitumen). The mixture was then blended using a high shear mixer (Model Fluko SK560) at 4000 r/min for 30 minutes at 180°C. To ensure homogeneity, the blended asphalt was further mixed using a low shear mixer (Model Fluko FW30 electric stirrer) at 2000 r/min for 40 minutes at 180°C. The detailed mixing process is illustrated in Plate II.

(a) (b)

Plate II: Production of metakaolin-based geopolymer modified asphalt binder (a) high shear mixing (b) low shear mixing

2.2 Methods

Test on Asphalt Binder

i. Fourier Transform Infra-Red (FTI-R) Spectroscopy

FTI-R spectroscopy was used to identify functional groups of metakaolin and metakaolin-based geopolymer. The wavelength were recorded from 4000 - 650 cm^{-1}. This was carried out in accordance with (ASTM D6348-12, 2020)

ii. Penetration

The penetration grade is a measure of the asphalt binder's consistency and stiffness, which correlates with its viscosity. This was conducted in accordance with ASTM standard (ASTM D5/D5M-20, 2020).

iii. Ductility

Ductility, a critical property of asphalt binders, refers to their ability to deform under tensile stress without cracking, reflecting the material's internal cohesion. The test was conducted following the guidelines outlined in the relevant ASTM standard (ASTM D113-17, 2017).

iv. Softening Point

Softening point of asphalt binders is used to grade asphalt binder and ensure performance in road construction. This was carried out in accordance with ASTM standard (ASTM D36/D36M-14, 2020).

v. Solubility

The solubility of asphalt binder was performed to determine the extent of asphalt binder solubility, having little or no organic impurities other than recovered asphalt binders in a specific solvent. For this study, Toluene was used as the solvent. This test was conducted in accordance with relevant ASTM standard (ASTM D2042-15, 2015).

vi. Flash point

The flash point of an asphalt binder is defined as the lowest temperature at which its vapors, when heated under specified conditions, will momentarily ignite (flash) upon application of a small test flame. The flash point testing was performed in accordance with the relevant ASTM standard (ASTM D92-18, 2018).

vii. Storage stability

The storage stability test measure or what extent a polymer stays mixed with asphalt binder under static storage conditions. This was conducted per ASTM Standard (ASTM D7173, 2020). Storage stability process is depicted in Plate 7.

3. RESULTS AND DISCUSSION

3.1 FTIR Spectra of Pristine Asphalt Binder

The FTIR spectrum of the pristine asphalt binder is shown in Figure 1. The major peaks characteristic of typical asphalt binders include: 2920.4 cm^{-1} and 2851.4 cm^{-1}, attributed to C–H stretching vibrations of aliphatic methylene (CH_2) groups. 1653.1 cm^{-1}, corresponding to C=C stretching of aromatic rings. 1459.3 cm^{-1} and 1375 cm^{-1}, assigned to C–H bending vibrations of aliphatic (CH_2 and CH_3) groups. In the fingerprint region, peaks at 864.7 cm^{-1}, 810.7 cm^{-1}, and 743.6 cm^{-1} indicate out-of-plane C–H bending of aromatic rings. These assignments align well with established literature on pristine asphalt binder characterization including studies by Weigel & Stephan, (2018); Yaro, *et al.,* (2021). Additionally, several less common peaks were observed, suggesting possible variations due to the specific source or crude oil origin of the asphalt binder: Weak bands at 2376.2 cm^{-1} and 2344.5 cm^{-1}, likely corresponding to S–H stretching (thiols). A peak at 2084.7 cm^{-1}, assignable to –N=C=S stretching of isothiocyanate groups (–NCS). Bands at 1597.2 cm^{-1}, 1541.3 cm^{-1}, and 1507.7 cm^{-1}, linked to –N=N– stretching in open-chain azo compounds connected to acyclic hydrocarbyl (alkyl or aryl) groups. A peak at 1032.5 cm^{-1}, attributed to P–O–C stretching of aliphatic phosphates. A band at 723.1 cm^{-1}, characteristic of out-of-plane aromatic C–H bending (Coates, 2000).

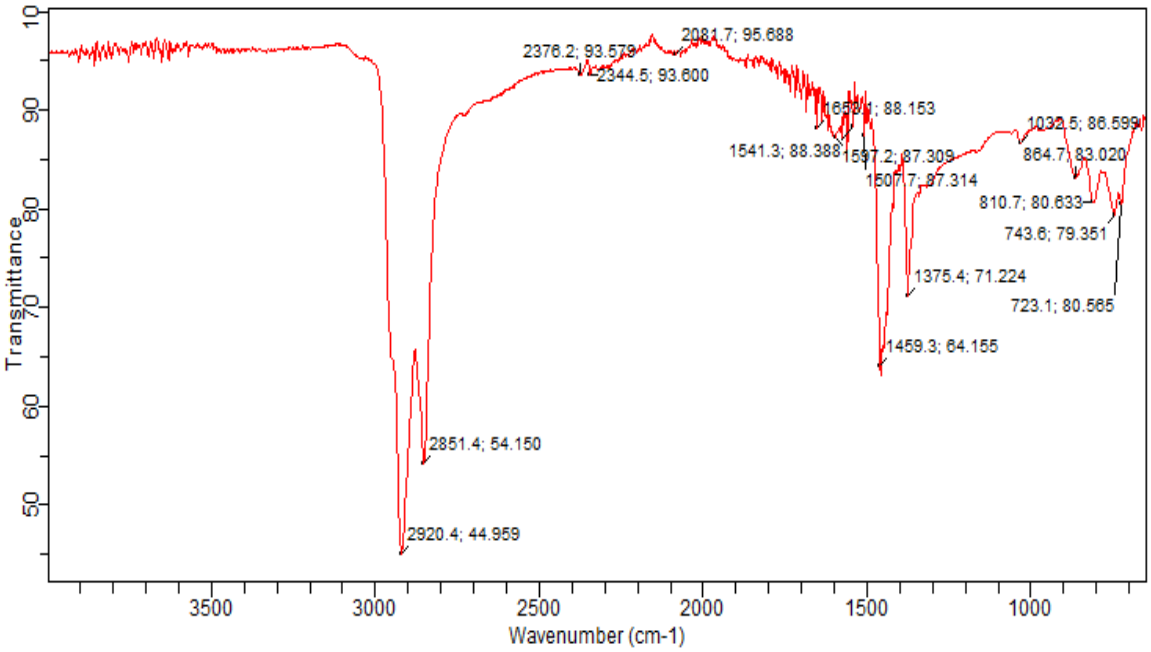

Figure 1: Infrared Spectra of Pristine Asphalt Binder

3.2 FTIR on Metakaolin-Based Geopolymer Asphalt Binder

Characteristic absorption bands at 2920.4 cm^{-1} and 2851.4 cm^{-1}, attributed to C–H stretching vibrations of methylene (CH_2-) groups in saturated aliphatic chains (Silverstein, *et al.*, 2014), remained unchanged across all metakaolin-based geopolymer contents. Similarly, peaks at 1459.3 cm^{-1}, 1375.4 cm^{-1}, and 721.2 cm^{-1}, corresponding to C–H bending and rocking modes of aromatic rings, showed no significant shift, confirming the persistence of aromatic structures typically present in base asphalt binder (Lin-Vien, *et al.*, 1991; Coates, 2000). Weak bands observed at 2374.3 cm^{-1} and 2344.5 cm^{-1} are attributed to atmospheric CO_2 interference and are not indicative of sample composition (Smith, 2011). Several new or shifted absorption bands appeared with increasing geopolymer content, indicating chemical interaction between the metakaolin-based geopolymer and the asphalt binder. New peaks in the 2090–2165 cm^{-1} region (e.g., 2111.5, 2145.1, 2104.1, 2161.5, and 2092.1 cm^{-1}) suggest the formation of terminal and internal alkyne (C≡C) groups. The band originally at 1601.7 cm^{-1} in the neat asphalt binder shifted to higher (1658.1 and 1654.9 cm^{-1}) and lower (1541.3 cm^{-1}) wavenumbers, consistent with N–H bending in primary and secondary amines (Silverstein, *et al.*, 2014). A new band at 1155.5 cm^{-1} indicates C–N stretching of tertiary amines. Bands near 1994–1997 cm^{-1} may arise from transition metal carbonyls or cumulene (C=C) structures (Coates, 2000). Peaks in the 1000–1030 cm^{-1} region (1030.6, 1006.4, 1004.5, and 1020.6 cm^{-1}) are assigned to C–H vibrations in cyclohexane ring structures or methyne groups. Additional aromatic C=C stretching bands emerged at 1597.2, 1522.6, and 1507.7 cm^{-1} (Silverstein, *et al.*, 2014),. In the fingerprint region (650–900 cm^{-1}), multiple new peaks (864.7, 862.9, 810.7, 808.8, 807.0, 745.5, 743.6, 659.7, and 657.9 cm^{-1}) correspond to aromatic C–H out-of-plane bending vibrations (Lin-Vien, *et al.*, 1991). These observations demonstrate that incorporation of metakaolin-based geopolymer induces chemical modifications in the asphalt binder, resulting in the formation of new functional groups (particularly amines, alkynes, and additional aromatic structures) while core aliphatic and aromatic hydrocarbon features of the asphalt are largely retained. The FTIR spectra of metakaolin-based geopolymer asphalt binders (2–10% by weight of asphalt binder) in the range of 400–4000 cm^{-1} are presented in Figure 2(a–e),

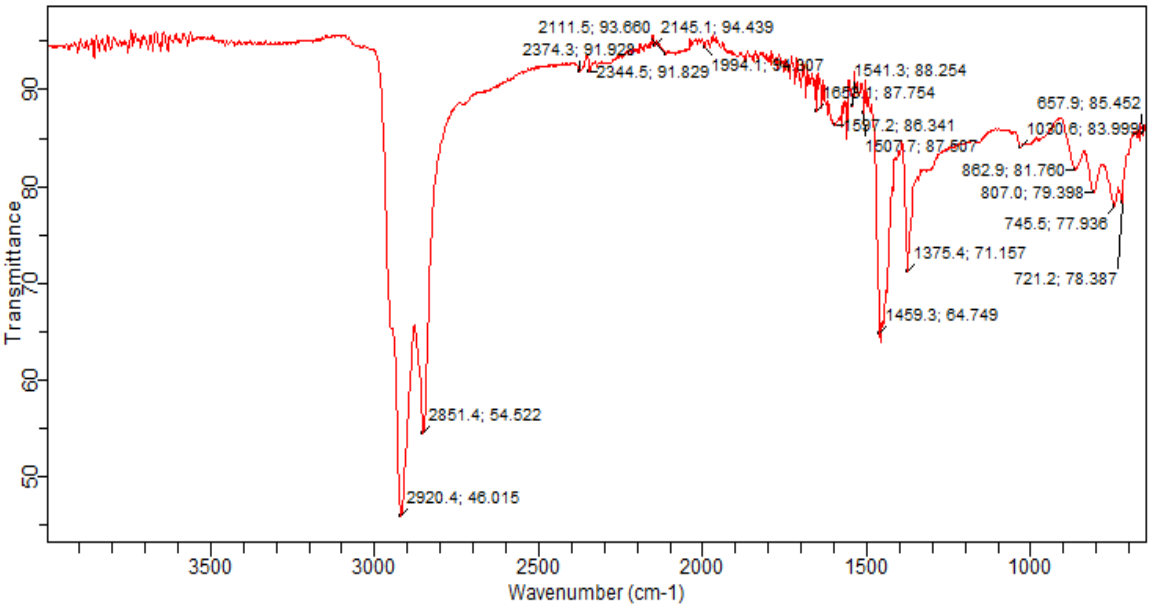

Figure 2a: Infrared Spectra of 2% Metakaolin-Based Geopolymer Asphalt Binder

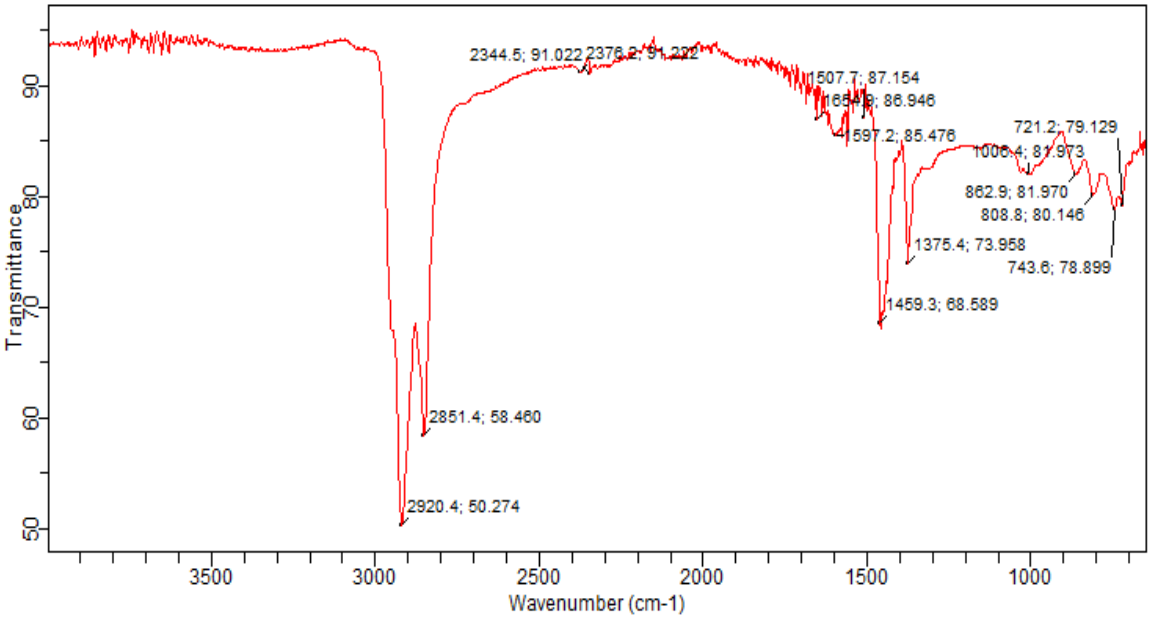

Figure 2b: Infrared Spectra of 4% Metakaolin-Based Geopolymer Asphalt Binder

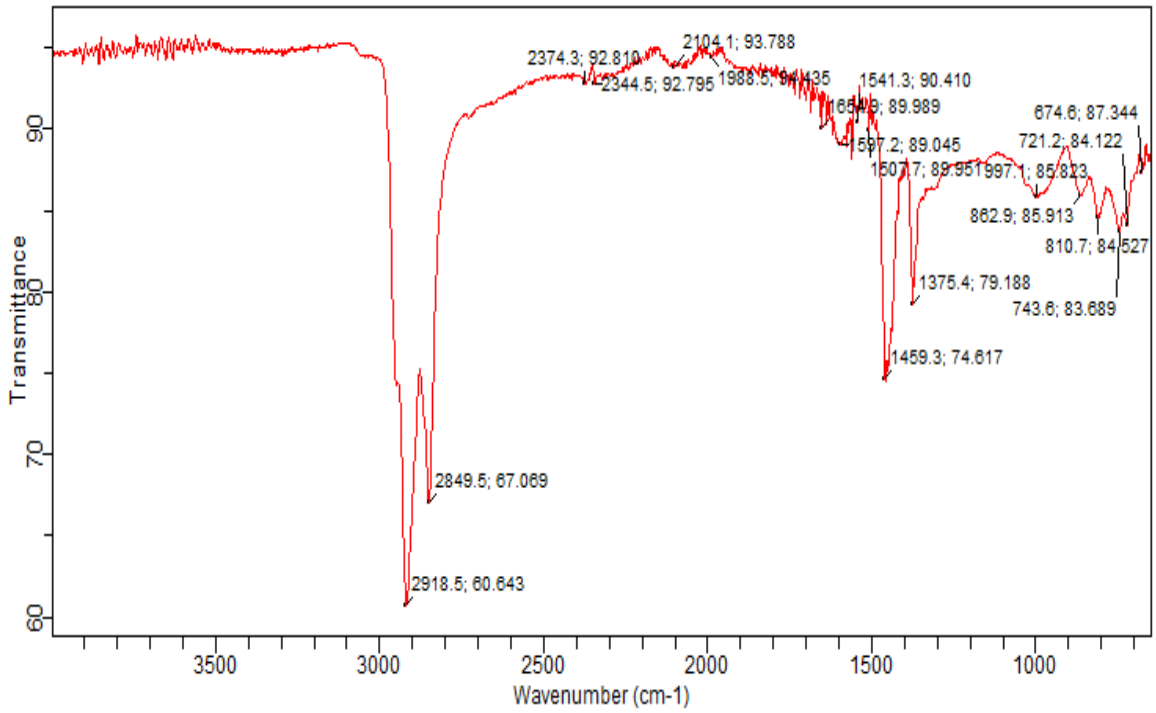

Figure 2c: Infrared Spectra of 6% Metakaolin-Based Geopolymer Asphalt Binder

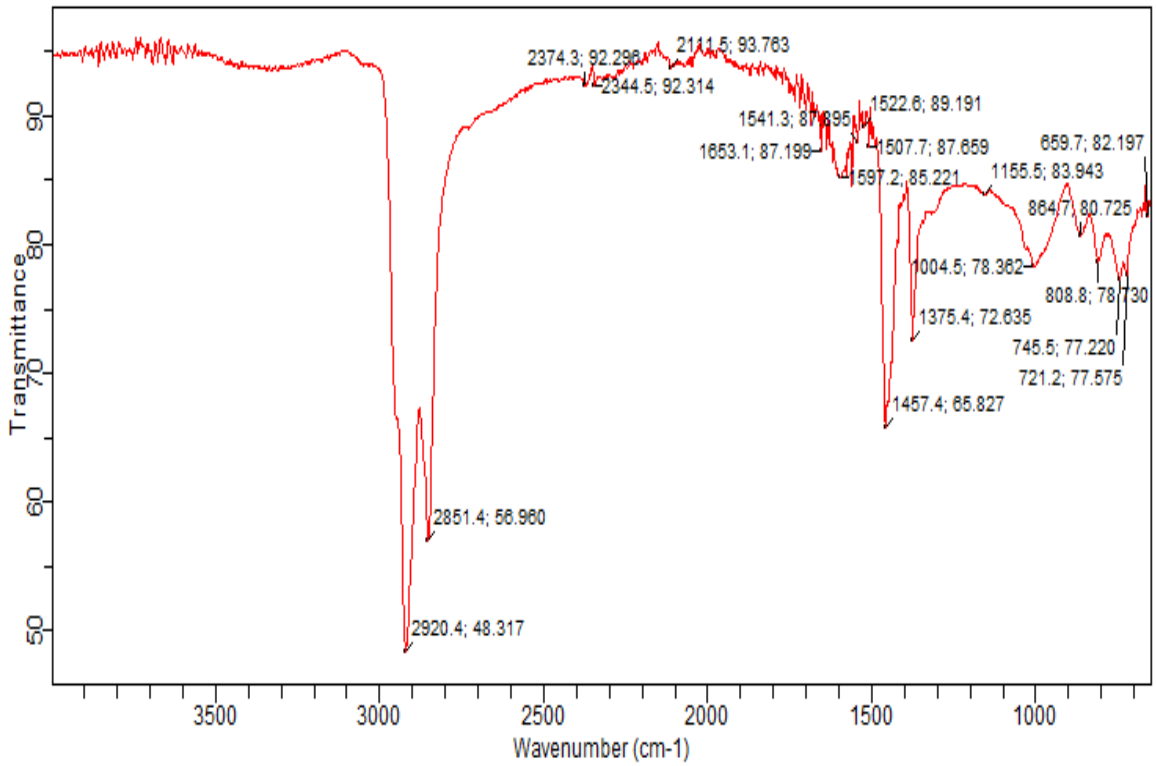

Figure 2d: Infrared Spectra of 8% Metakaolin-Based Geopolymer Asphalt Binder

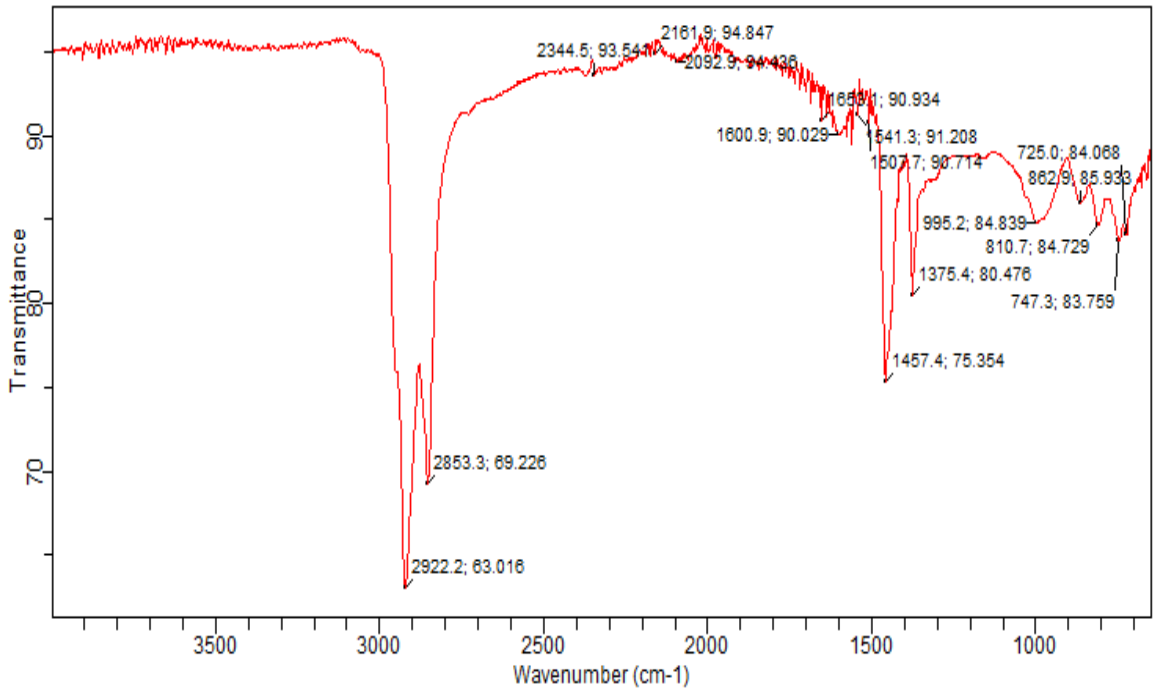

Figure 2e: Infrared Spectra of 10% Metakaolin-Based Geopolymer Asphalt Binder

3.3 Influence of Metakaolin-Based Geopolymer on the Properties of Asphalt Binder

3.3.1 Penetration

The results presented in Figure 4 demonstrate that increasing the content of metakaolin-based geopolymer (MBG) in the asphalt binder leads to a progressive decrease in penetration. This hardening effect can be primarily attributed to the strong interactions between the geopolymer particles and the asphaltene fraction of the binder, coupled with the absorption of lighter molecular components onto the geopolymer porous structure. All penetration values obtained for both pristine and MBG-modified asphalt binder fall within the penetration limits specified by (FMWH, 2016). These mechanisms reduce the mobility of the binder matrix, resulting in enhanced rigidity and stiffness, this is corroborated in the FTIR analysis by the appearance of extra aliphatic and aromatic bands in the infrared spectrum of modified asphalt binder. These findings align with previous studies on geopolymer-modified asphalt binders, including those by Yaro, *et al*., (2023); Rosyidi, *et al.*, (2020); Tang, *et al.*, (2018). The outcome of this finding shows that MBG can effectively be used to modify conventional asphalt binder to lower penetration grades. The engineering implication of reduced penetration are enhanced asphalt binder's resistance to permanent deformation (rutting) and thermal susceptibility of asphalt mixtures produced with such asphalt binders, particularly in high-temperature climates, such as those prevalent in Nigeria. Reduced penetration also implies, reduced moisture infiltration, improved skid resistance and overall longer lifespan and durability of pavement.

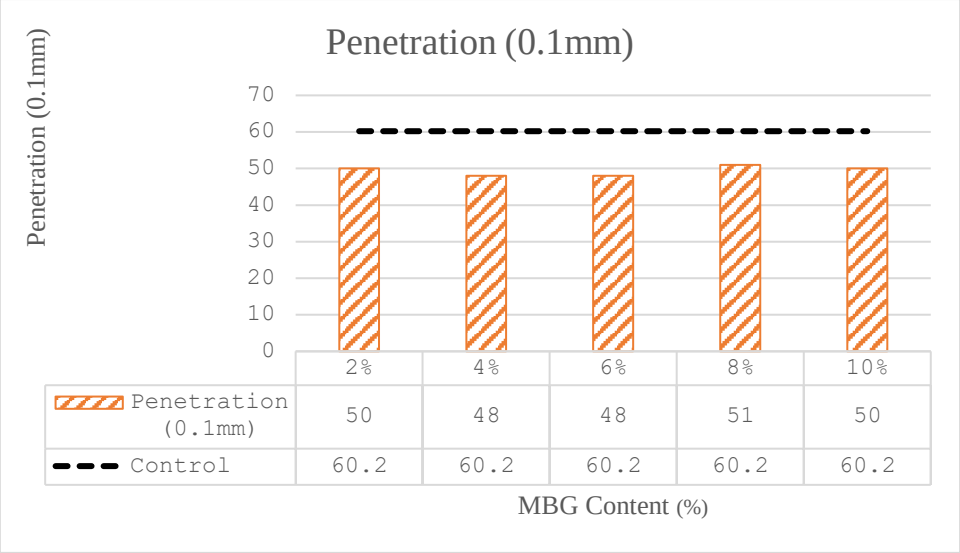

Figure 4: Influence of MBG on Penetration of Asphalt Binder

3.3.2 Softening Point

The results illustrated in Figure 5 indicate that incorporating MBG into the unmodified asphalt binder results in a significant increase in the softening point compared to the control. This trend shows the typical inverse relationship between softening point and penetration: lower penetration yields a higher softening point. All softening point values obtained are within the limits stipulated by FMWH (2016). The increased softening point can be attributed to the stiffening mechanisms induced by the MBG modifier. The geopolymer particles interact with the binder's components particularly by bonding with the aliphatic fractions leading to enhanced dispersion stability, reduced molecular mobility, and the formation of additional aromatic and aliphatic structures within the matrix. These observations are in agreement with prior research on geopolymer-modified asphalt binders, studies include those by Yaro, *et al.*, (2023); Rosyidi, *et al.*, (2020); Tang, *et al.*, (2018). From an engineering perspective, the higher softening point enhances the binder's resistance to permanent deformation (rutting) under elevated service temperatures.

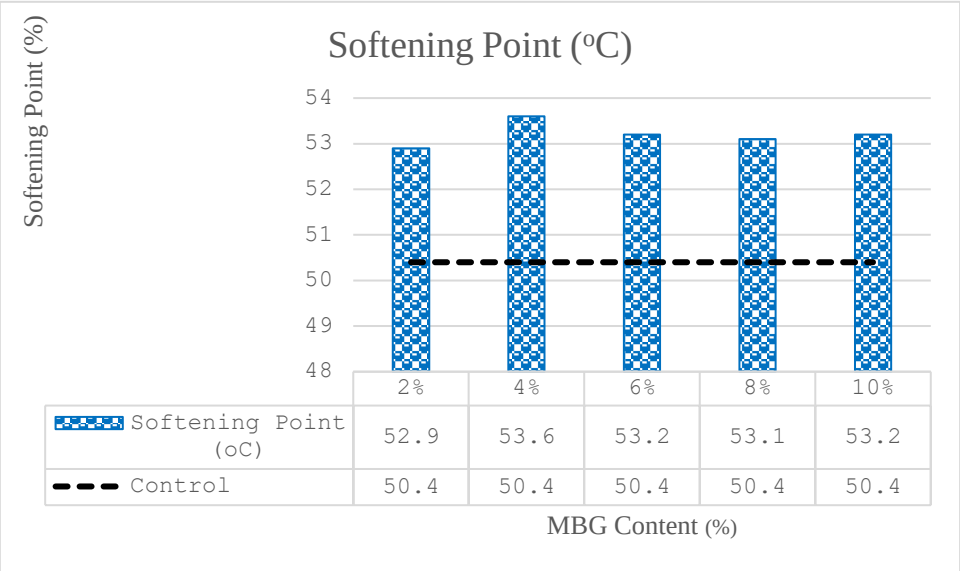

Figure 5: Influence of MBG on Softening Point of Asphalt Binder

3.3.3 Penetration Index

The penetration indices (PI) of the pristine (0%) and MBG-modified asphalt binders are presented in Table 1. The penetration index serves as a key indicator of the binder's temperature susceptibility. For conventional paving-grade asphalt binders, the acceptable PI range is typically < -2 to > +2. A PI of < -2 signifies high temperature susceptibility, while a PI of > +2 indicates low susceptibility. The calculated PI values decreased from the 0% binder to the MBG-modified binders. The observed reduction in PI for MBG-modified asphalt binder suggests improved overall temperature resistance. The MBG enhanced the binder's ability to resist both rutting (at high temperatures) and thermal cracking (at low temperatures). This improvement in temperature susceptibility can be attributed to the intermolecular interactions between dispersed MBG particles and the asphalt matrix, which stiffen the binder structure, reduce thermal volatility, and improve rheological property. These mechanisms are further supported by the FTIR results. From an engineering implication, the enhanced temperature performance of MBG modified asphalt binders is suitable for use in hot climate regions. This result is in align with the study by Yaro, *et al.*, (2021).

Table 1: Penetration indices of Pristine and MBG-modified asphalt binder

MBG Content	Penetration	Softening Point	Penetration index
0%	60.2	50.4	-0.666
2%	50	52.9	-0.574
4%	48	53.6	-0.439
6%	48	53.6	-0.532
8%	51	53.2	-0.413
10%	50	53.2	-0.436

3.3.4 Ductility

The results in Figure 6 indicate a decrease in ductility of MBG asphalt binder compared to the control. This reduction is linked to the increased stiffness observed in the penetration test, likely due to interactions between resins (carbonyl) and aromatic functional groups within the internal structure of the molecules. Only the control and the 2% MBG-modified asphalt binder satisfied the minimum 100 mm requirement specified by FMWH (2016). The higher dosages of MBG resulted in reduced ductility values that fell below the specified limit. However, despite the reduction in ductility with higher MBG dosages, the results suggest that the modified binders retain adequate adhesive and tensile properties. These characteristics are crucial for proper bonding between the asphalt binder and aggregates, indicating promising performance of the asphalt mixtures. This is consistent with findings from Yaro, *et al.*, (2023); Rosyidi, *et al.*, (2020); Tang, *et al.*, (2018).

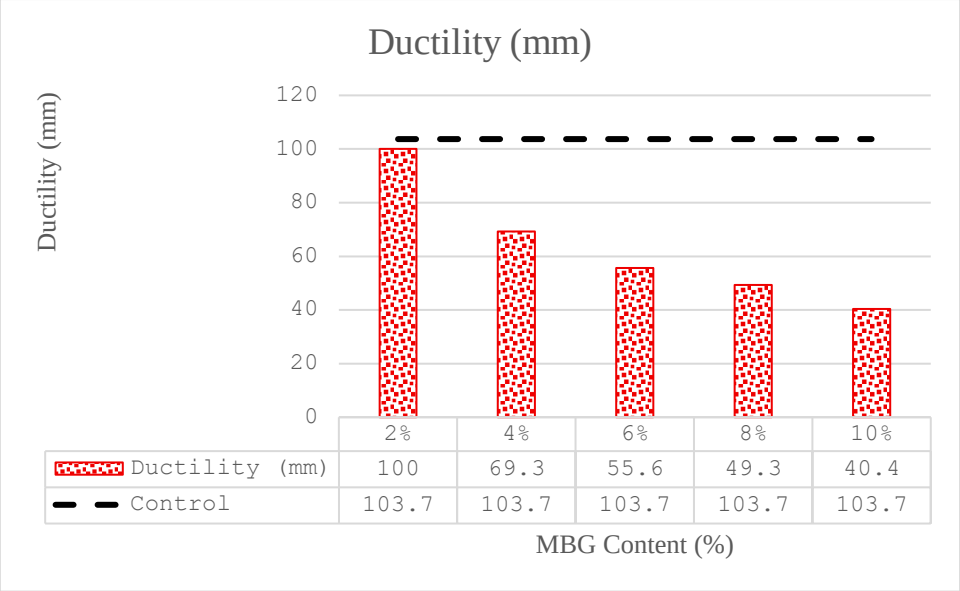

Figure 6: Influence of MBG on Ductility of Asphalt Binder

3.3.5 Flash point

The results from Figure 7 show that the flash point of the MBG-modified asphalt binder marginal increased by 1% with respect to the control binder. Nevertheless, the flash points of all MBG asphalt binders remain compliant the minimum requirement of 230 °C specified in AASHTO M 320 and higher than 250 °C by FMWH, (2016). The observed increase in flash point temperature for MBG-modified binders can be attributed to the dispersion of MBG particles within the asphalt matrix. These particles enhance the binder's thermal stability, thereby delaying the onset of flammability by reducing the volatility of lighter fractions and improving overall resistance to ignition. These findings suggest that MBG-modified asphalt binders exhibit reduced flammability compared to the control, offering a safety advantage. From an engineering perspective, a higher flash point enhances operational safety: the binder can be handled, stored, and transported at elevated temperatures with a significantly lower risk of fire hazards during production, mixing, or field application.

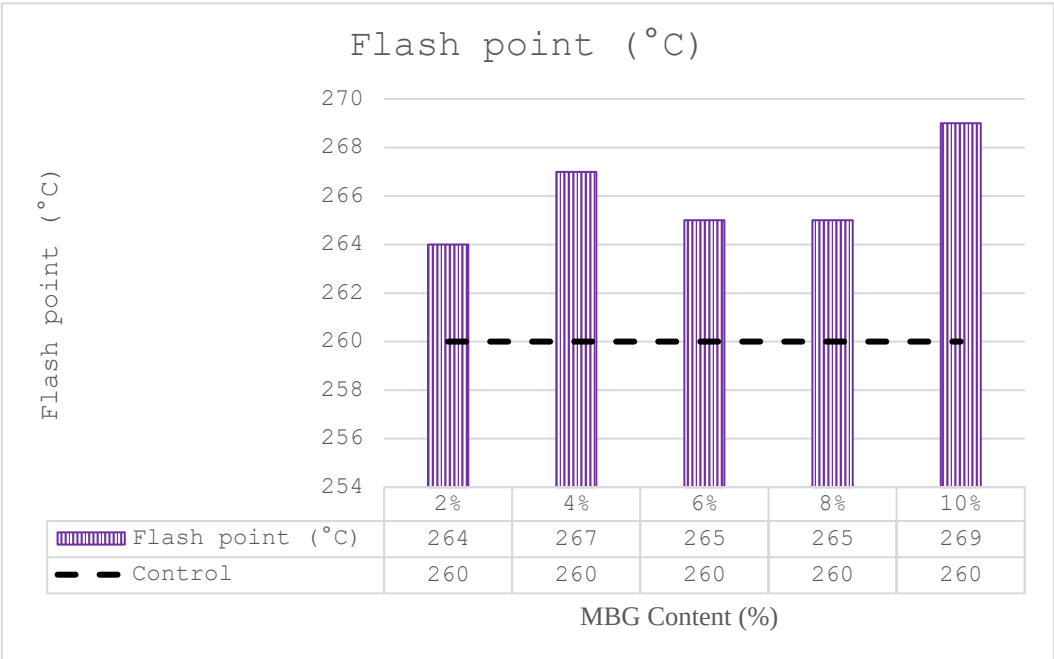

Figure 7: Influence of MBG on Flash Point of Asphalt Binder

3.3.6 Solubility

Solubility serves as an important indicator of asphalt binder purity. As shown in Figure 8, the solubility of the MBG-modified asphalt binders was lower than that of the control sample and decreased progressively with increasing MBG content. The control, 2 - 6% MBG-modified asphalt binder satisfied the minimum 99% requirement specified by FMWH (2016). The higher dosages of MBG fell below the specified limit. This reduction suggests the presence of minor insoluble organic impurities introduced by the modifier. Supporting evidence from FTIR analyses of metakaolin, as well as the FTIR spectra of the metakaolin-based geopolymer, confirmed the existence of such impurities. However, these impurities are present in minute quantities and are expected to have negligible effects on the overall performance of the asphalt binder. Therefore, their impact can be reasonably disregarded

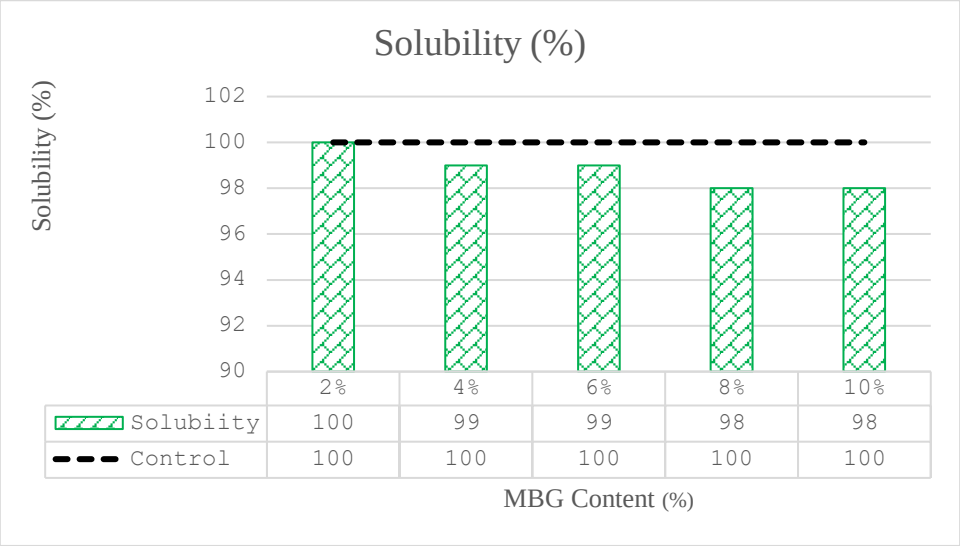

Figure 8: Influence of MBG on Solubility of Asphalt Binder

3.3.7 Storage Stability

The storage stability (also referred to as phase separation resistance or compatibility) of the asphalt binder was evaluated by measuring the difference in softening point between the top and bottom sections of a vertically stored sample tube after high-temperature conditioning. The results, as presented in Figure 9 showed that the storage stability for the pristine (0% MBG) asphalt binder, as well as the MBG modified asphalt binders at 2, 6, 8, and 10% dosages, remained below 2.5 °C (code acceptance criterion). This storage stability demonstrates excellent compatibility between the pristine asphalt binder and the MBG modifier, with negligible phase separation. Such performance is critical for preventing segregation during hot storage, transportation, and application, ensuring uniform binder properties in the field. From an engineering standpoint, this high temperature storage stability enhances operational reliability, reduces the risk of inconsistent binder behavior during mixing and paving, and supports practical handling in asphalt plants. Consequently, both the pristine and MBG-modified asphalt binders can be stored at elevated temperatures for extended periods, reheated, and reused without significant loss of homogeneity or performance. A similar trend of good storage stability with geopolymer based modifiers in asphalt was reported by Yaro *et al.*, (2021).

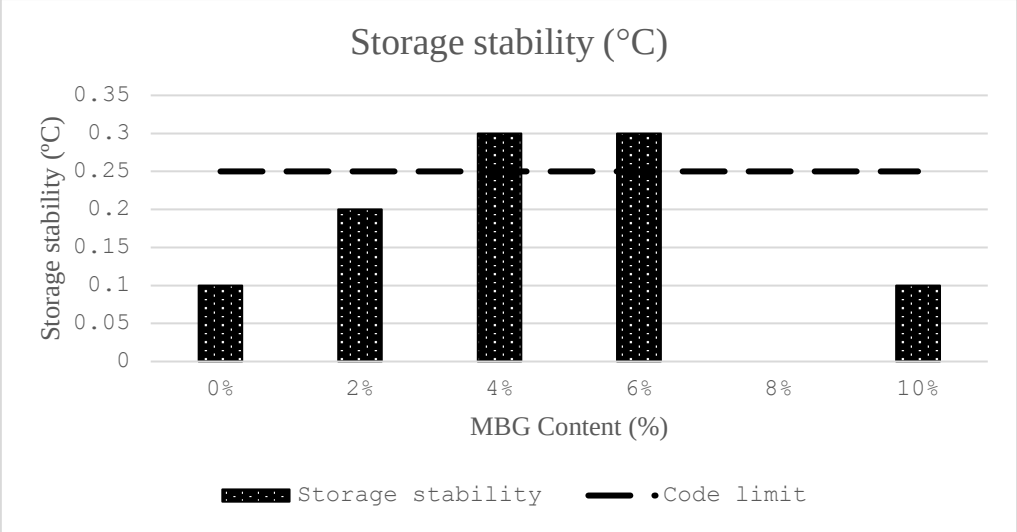

Figure 9: Storage stability of Asphalt Binders

4. CONCLUSION

This study presents the investigation on the physical properties of metakaolin-based geopolymer modified asphalt binder. The following conclusions were drawn based on the results of the research.

i. FTIR spectroscopy of the pristine asphalt binder revealed the presence of characteristic functional groups, including C–H stretching (aliphatic methylene), C=C stretching (aromatic rings). Less prominent peaks corresponding to –N=N– (alkyl or aryl), S–H (isothiocyanate), and P–O–C (alkyl) were also identified. Upon incorporation of metakaolin-based geopolymer (MBG), the original functional groups in the asphalt binder remained largely unchanged, while new peaks emerged, notably C≡C (internal alkyne), additional C=C (associated with metal carbonyls or cumulene), and C–H (cyclohexane or methine structures). These spectral changes confirm the successful incorporation of MBG into the asphalt binder and indicate the formation of new chemical interactions. The resulting functional groups influenced the physical properties of the modified asphalt binder

ii. The physical properties of the MBG-modified asphalt binders, when compared to the pristine binder, exhibited a typical pattern of effective stiffening modifications: decreased penetration, reduced ductility, and slightly lower solubility, accompanied by increases in softening point and flash point

REFERENCES

Abah, L. I., Ibedu, K. E., Murana, A. A., Amartey, Y. D., & Onwuliri, J. B. (2024). Assessing the Potential of Polyvinyl Chloride (PVC) from Waste Plastics as a Sustainable Bitumen Modifier: An Environmental and Waste Management Persperctive. *2nd Biennial International Conference (Hybrid) 2024* (pp. 1-12). Ndufu-Alike: Alex Ekwueme FederalUniversity, Ndufu-Alike, Ebonyi State, Nigeria.

Amran, M., Al-Fakih, A., Chu, S. H., Fediuk, R., Haruna, S., Azevedo, A., & Vatin, N. (2021). Long-term durability properties of geopolymer concrete: An in-depth review. *Case Studies in Construction Materials, 15*, 1-26. doi:10.1016/j.cscm.2021.e00661

ASTM C168-19. (2019). Standard specification for coal fly ash and raw or calcined natural pozzolan for use in concrete. *American Society For Testing Method (ASTM) International*. Retrieved from www.astm.org

ASTM D113-17. (2017). *Standard Test Method for Ductility of Asphalt Materials* (Vol. 04.03). West Conshohocken, Philadelphia.PA: American Society for Testing and Materials (ASTM) International. Retrieved from www.astm.org

ASTM D2042-15. (2015). *Standard Test Method for Solubility of Asphalt Materials in Trichloroethylene.* West Conshohocken, PA: American Society for Testing and Materials (ASTM) International. Retrieved from www.astm.org

ASTM D36/D36M-14. (2020). *Standard Test Method for Softening Point of Bitumen (Ring-and-Ball Apparatus)* (Vol. 04.04). West Conshohocken, PA: American Society for Testing and Materials (ASTM) International. Retrieved from www.astm.org

ASTM D5/D5M-20. (2020). *Standard Test Method for Penetration of Bituminous Materials.* West Conshohocken, PA: American Society for Testing and Materials (ASTM) International. Retrieved from www.astm.org

ASTM D6348-12. (2020). *Standard Test Method for Determination of Gaseous Compounds by Extractive Direct Interface Fourier Transform Infrared (FTIR) Spectroscopy,.* West Conshohocken, PA: American Society for Testing and Materials (ASTM) International. Retrieved from www.astm.org

ASTM D7173. (2020). Standard Practice for Determining the Separation Tendency of Polymer from Polymer Modified Asphalt. American Society for Testing of Materials (ASTM International), West Conshohocken, PA.

ASTM D92-18. (2018). *Standard Test Method for Flash and Fire points by Cleveland Open Cup Tester* (Vol. 05.01). West Conshohocken, PA: American Society for Testing and Materials (ASTM) International. Retrieved from www.astm.org

Coates, J. (2000). Interpretation of Infrared Spectra, A Practical Approach. In R. A. Meyers (Ed.), *Encyclopedia of Analytical Chemistry* (p. 10815±10837). Chichester: John Wiley & Sons Ltd.

FMWH. (2016). *Nigerian General Specifications for Roads and Bridges.* Federal Ministry of Works and Housing, Abuja.

Gambo, S., Ibrahim, K., Aliyu, A., Ibrahim, A. G., & Abdulsalam, H. (2020). Performance of metakaolin based geopolymer concrete at elevated temperature. *Nigerian Journal of Technology, 39*(3), 732-737. doi:10.4314/njt.v39i3.11

Hamid, A., Alfaidi, H., Baaj, H., & El-Hakim, M. (2020). Evaluating fly ash-based geopolymers as a modifier for asphalt binders. *Advances in Materials Science and Engineering, 2020*, 1-11. doi:https://doi.org/10.1155/2020/2398693

Hauruna, S., Mohammed, B. S., Shahir-Liew, Alahoul, W. S., & Haruna, A. (2018). Effect of Water-Binder Ratio and NaOH Molarity on the Properties of High Calcium Fly Ash Geopolymer Mortars at Outdoor Curing. *International Journal of Civil Engineering and Technology (IJCIET), 9*(10), 1339-1352.

Ibedu, K. E., Murana, A. A., Usman, A., & Shuaibu, A. A. (2026). Synthesis and Characterization of Metakaolin-Based Geopolymer for Industrial Application. *Advances in Materials Science and Engineering,, 2026*(1), 1-10. doi:10.1155/amse/1866517

Jaimes, J. E., Montaño, A. M., & González, C. (2020). Geopolymer derived from bentonite: Structural characterization and evaluation as a potential sorbent of ammonium in waters. *In Journal of Physics: Conference Series. 1587*, pp. 1-6. IOP Publishing. doi:10.1088/1742-6596/1587/1/012008

Lin-Vien, D., Colthup, N. B., Fateley, W. G., Grasselli, & G., J. (1991). *The Handbook of Infrared and Raman Characteristic Frequencies of Organic Molecules* (1st ed.). Academic Press.

Milad, A., Ali, A. S., Babalghaith, A. M., Memon, Z. A., Mashaan, N. S., Arafa, S., & Md. Yusoff, N. I. (2021). Utilisation of waste-based geopolymer in asphalt pavement modification and construction—A review. *Sustainability, 13*(6), 1-22. doi:10.3390/su13063330

Murana, A. A., Abdulkarim, A. A., & Olowosulu, A. T. (2020). Influence of Polythylene from Waste Pure Water Sachet on Propeties of Hot Mix Asphalt. *Nigerian Journal of Technology (NIJOTECH)*, 39(4), 1043 – 1049. doi:https://doi.org/10.4314/njt.v39i4.10

Murana, A. A., Ochepo, J., Yerima, A. M., & Ibedu, K. E. (2023). Comparing Determinants of Physical Properties of Bitumen Modified with High Density Polyethylene. *Umudike Journal of Engineering and Technology (UJET), 9*(2), 90-98. doi:https://doi.org/10.33922/j.ujet_v9i2_9

Murana, A. A., Okpanachi, V. U., & Laraiyetan, T. E. (2018). Modification of Bitumen with Polyethylene Vinyl-Acetate from the Sole of Flip-Flops. *1st International Civil Engineering Conference (ICEC 2018), Theme: Infrastructure Development in the Context of Contemporary Economic Challenges* (pp. 269-277). Minna: Department of Civil Engineering, Federal University of Technology, Minna, Nigeria.

Rosyidi, S. A., Rahmad, S., Yusoff, N. I., Shahrir, A. H., Ibrahim, A. N., Ismail, N. F., & Badri, K. H. (2020). Investigation of the chemical, strength, adhesion and morphological properties of fly ash based geopolymer-modified bitumen. *Construction and Building Materials, 255*, 1-9. doi:10.1016/j.conbuildmat.2020.119364

Silverstein, R. M., Webster, F. X., & Kiemble, D. J. (2014). *Spectrometric Identification of Organic Compounds* (8th ed.). Chi- chester: John Wiley & Sons.

Smith, B. C. (2011). *Fundamentals of FT-IR Spectroscopy* (2nd ed.). Boca Raton: CRC Press. doi:https://doi.org/10.1201/b10777

Tang, N., Deng, Z., Dai, J. G., Yang, K., Chen, C., & Wang, Q. (2018). Geopolymer as an additive of warm mix asphalt: Preparation and properties. *Journal of cleaner production, 192*, 906-915. doi:10.1016/j.jclepro.2018.04.276

Weigel, S., & Stephan, D. (2018). Bitumen characterization with Fourier transform infrared spectroscopy and multivariate evaluation: prediction of various physical and chemical parameters. *Energy and Fuels*, 32(10), 10437-10442. doi:https://doi.org/10.1021/acs.energyfuels.8b02096

Yaro, N. S., Napiah, M. B., Sutanto, M. H., Usman, A., Murana, A. A., & Rafiq, W. (2021). Effect of Palm Oil Clinker Powder-Based Geopolymer on Bitumen and Asphalt Mixture Properties. *2021 Third International Sustainability and Resilience Conference: Climate Change* (pp. 310-315). IEEE. doi:10.1109/IEEECONF53624.2021.9667950

Yaro, N. S., Sutanto, H. M., Habib, Z. N., Usman, A., Tanjung, L. E., Aliyu, I., & Jagaba, A. H. (2023). Optimizing biochar-based geopolymer composites for enhanced water resistance in asphalt mixes: an experimental, microstructural, and multi-objective analysis. *Journal of Engineering and Applied Science, 70*(151), 1-27. doi:10.1186/s44147-023-00323-4

International Conference on Engineering Innovation for Sustainable Development (ICESID 2026)
Faculty of Engineering, Ahmadu Bello University Zaria · 8–10 September 2026

DEVELOPMENT AND CHARACTERIZATION OF HYDROPHOBIC SILICA AEROGEL SYNTHESIZED FROM RICE HUSK VIA AMBIENT PRESSURE DRYING

Isa Zubairu[1,2,3,*], Badruddeen Saulawa Sani[2], Salmiati Salmiati[4], Umar Alfa Abubakar[2], Sunday Bamidele Igboro[2], Aliyu Ishaq[2]

[1]*Department of Civil Engineering, Abubakar Tafawa Balewa University, Bauchi*
[2]*Department of Water Resources and Environmental Engineering, Ahmadu Bello University Zaria Nigeria*
[3]*Faculty of Civil Engineering, University Teknologi Malaysia*
[4]*Department of Environmental Engineering, Faculty of Civil Engineering, Universiti Teknologi Malaysia, 81310 UTM Skudai, Johor Bahru, Malaysia*

Email: izubairu@atbu.edu.ng*, bssaulawa@abu.edu.ng, salmiati@utm.my, umaralfa@hotmail.com, sbigboro@abu.edu.ng, aishaq@abu.edu.ng

***Corresponding author**: Isa Zubairu

DOI: https://doi.org/10.67203/sp.ICESID.2026

ABSTRACT

Silica aerogels are ultra-lightweight, highly porous nanostructured materials with high specific surface area, properties that make them attractive adsorbents for water and wastewater treatment. However, conventional silica aerogels are commonly produced from costly precursors such as tetraethyl orthosilicate (TEOS), limiting their large-scale application, particularly in resource-constrained settings. This study reports the development of a hydrophobic silica aerogel from rice husk, an abundant and low-cost agricultural by-product, and its comprehensive physicochemical characterization. Silica was extracted from rice husk via acid leaching and calcination, converted to sodium silicate through alkaline digestion, and processed into a gel via acid-catalyzed sol-gel synthesis. The resulting hydrogel beads were solvent-exchanged into ethanol, surface-modified with trimethylchlorosilane (TMCS) to confer hydrophobicity, and dried at ambient pressure. The synthesized aerogel was characterized using nitrogen adsorption-desorption (BET/BJH/t-plot), Fourier-transform infrared spectroscopy (FTIR), water contact-angle goniometry, bulk density/porosity determination, and scanning electron microscopy (SEM). The aerogel exhibited a BET specific surface area of 303.60 m²/g, a mesoporous structure with pore diameters of 3.37–3.40 nm and pore volume of 0.52 cm³/g, negligible microporosity, a superhydrophobic water contact angle of 155.70° ± 1.34°, a bulk density of 0.18 g/cm³, and porosity of approximately 92%. FTIR confirmed characteristic Si-O-Si and Si-OH functional groups, while SEM revealed a rough, porous, agglomerated morphology consistent with an ambient-pressure-dried aerogel network. These results demonstrate that rice husk is a viable, sustainable precursor for producing hydrophobic, mesoporous silica aerogel with textural and surface properties consistent with materials reported to be effective for adsorption applications and recommend future adsorption studies.

Keywords: *silica aerogel; rice husk; sol-gel synthesis; ambient pressure drying; hydrophobicity*

1. INTRODUCTION

Silica aerogel is a nanostructured material characterized by high specific surface area, high porosity, and low density, properties that have made it the subject of extensive research as an adsorbent for organic and inorganic contaminants in water and wastewater treatment (Standeker et al., 2007, 2011; Wang et al., 2011, 2012). Compared with conventional adsorbents such as granular activated carbon, silica aerogels offer a more open, foam-like pore network, tunable hydrophobicity, and reusability, which together have been reported to improve adsorption performance for organic contaminants (Rahmani et al., 2018).

A major limitation to the wider adoption of silica aerogels, however, is that they are conventionally synthesized from relatively expensive precursors such as tetraethyl orthosilicate (TEOS) or commercial sodium silicate, which constrains cost-effective, large-scale production, particularly in

low- and middle-income settings. Agricultural by-products rich in amorphous silica, such as rice husk, offer a low-cost, abundant, and environmentally sustainable alternative precursor. Rice husk is generated in large quantities wherever rice is cultivated and is otherwise a largely underutilized waste stream; converting it into a valuable silica precursor therefore carries both economic and environmental benefits, avoiding the carbon burden associated with uncontrolled disposal or open burning.

Although several studies have reported the synthesis of silica aerogels from rice husk ash using sol-gel processing and ambient pressure drying (Deng et al., 2025; Halim et al., 2021; Ochoa-Munoz et al., 2025), reported textural and surface properties vary considerably depending on the specific extraction route, gelation conditions, solvent-exchange protocol, silylating agent, and drying method used. This variability underscores the need for detailed, route-specific characterization of any newly developed rice-husk-derived aerogel before its adsorption performance can be meaningfully evaluated or compared with other adsorbents.

This study reports the development of a hydrophobic silica aerogel from rice husk via acid leaching, calcination, alkaline extraction to sodium silicate, acid-catalyzed sol-gel synthesis, solvent exchange, and trimethylchlorosilane (TMCS) surface modification, followed by ambient pressure drying. The resulting material was comprehensively characterized in terms of its textural properties (BET/BJH/t-plot), functional chemistry (FTIR), hydrophobicity (water contact angle), bulk density and porosity, and surface morphology (SEM), to establish its suitability as an adsorbent for water treatment applications.

2. MATERIALS AND METHODS

2.1 Materials

Rice husk used in this study was purchased from a commercial vendor in Johor Bahru, Malaysia, and supplied in 10 kg polythene bags. The chemicals, reagents, and equipment used for silica aerogel synthesis and characterization are summarized in Tables 1 and 2.

Table 1: Chemicals, Reagents and Eqipments for Silica Aerogel Synthesis and Characterization

Material / Reagent	Function
Rice husk	Silica precursor source
Hydrochloric acid (HCl)	Acid leaching of rice husk prior to calcination
Sodium hydroxide (NaOH)	Alkaline dissolution of rice husk ash to sodium silicate
Acetic acid	pH adjustment for gel formation
Hexane	Top layer for bead-shape preservation during gelation
Aqueous ammonia (5%)	Bottom layer for gelation of sol droplets
Ethanol	Solvent exchange (pore-water removal)
Trimethylchlorosilane (TMCS)	Silylating agent for surface (hydrophobic) modification
n-Hexane	Washing modified aerogel beads
Equipment	**Purpose**
Muffle furnace	Calcination of rice husk to ash
Brunauer–Emmett–Teller (BET) analyzer, NOVA touch 4LX	Specific surface area, pore size and pore volume (BJH, t-plot)
Perkin Elmer Frontier FTIR	Functional-group identification (650–4000 cm^{-1})
DataPhysics OCA 15EC–Series	Water contact-angle (hydrophobicity) measurement
JEOL JSM-IT300LV Scanning Electron Microscope	Surface morphology (10, 20, 30, 100 µm)

2.2 Silica Extraction from Rice Husk

Amorphous silica was produced from rice husk by first washing the husk with distilled water and oven-drying it for 24 h at 100°C. Acid leaching was then carried out, since it has been reported to increase silica yield (Azat et al., 2019; Bakar et al., 2016). Leaching was performed by treating the rice husk with 0.5 M hydrochloric acid (HCl) on a hot plate at 60°C for 30 minutes under constant stirring, after which the husk was rinsed three times with distilled water to remove residual acid, air-dried, and oven-dried for a further 24 hours.

Calcination was carried out using a muffle furnace capable of reaching 1000°C. Complete calcination of rice husk has been reported to occur at temperatures between 500°C and 900°C (Bakar et al., 2016). Controlled combustion of acid-treated rice husk at approximately 600 °C has been widely reported to produce silica-rich rice husk ash with predominantly amorphous characteristics, while higher calcination temperatures may promote sintering and, depending on impurity content and pretreatment, transformation toward crystalline silica phases (Bakar et al., 2016; Azat et al., 2019). Bakar et al. (2016), for example, evaluated acid-leached rice husk calcined between 500 and 900 °C for 2 h and demonstrated the production of amorphous silica, with relatively limited improvement in silica production above approximately 600 °C. Therefore, in this study, the acid-leached rice husk was calcined at 600°C for 2 hours. After the furnace cooled, the resulting rice husk ash (RHA) was carefully collected and sieved.

2.3 Sodium Silicate Preparation

Sodium silicate ($Na_2O:SiO_2$), also known as water glass, was produced by dissolving RHA in sodium hydroxide (NaOH) solution. Thirty (30) g of RHA was added to 200 mL of 1 M NaOH solution,

and the mixture was heated on a hot plate under constant stirring at 120°C for 3.5 hours. The mixture was then cooled to room temperature and filtered using Whatman No. 1 filter paper (110–125 mm diameter, particle retention ~11 μm) to obtain a clear sodium silicate solution.

2.4 Silica Aerogel Synthesis, Surface Modification, and Drying

Silica aerogel was produced from the sodium silicate solution by first adjusting its pH to between 4 and 5 through the dropwise addition of acetic acid under gentle stirring, stopping just before gel formation began. Gelation was carried out by dropping the acidified sol into a beaker containing hexane as the top layer and 5% aqueous ammonia as the bottom layer; the resulting gel beads were left for 10 minutes to strengthen before being transferred to warm water for further ageing. The aged beads were then soaked in ethanol for 24 hours to exchange the pore water with ethanol, and this solvent-exchange step was repeated for a further 24 hours to ensure complete exchange.

Surface Modification of aerogel beads was carried out to introduce or improve its hydrophobicity. It was achieved using a silylating agent where in this study Trimethylchlorosilane (TMCS) together with ethanol and n-hexane using in the following proportion: 25% ethanol, 25% TMCS and 50% n-hexane by volume (ratio of ethanol: TMCS: n-hexane = 1:1:2). The gel beads were soaked in each silylating mixture with gentle mixing for 3.5 hours in sealed containers at ambient pressure. After silylation, the beads were washed three times with n-hexane to remove residual TMCS and finally dried on a hot plate at 80°C for 1 hour, yielding the finished silica aerogel at ambient pressure (i.e., without supercritical drying). The overall process, from raw rice husk to the surface-modified, dried silica aerogel, is summarized in Figure 1.

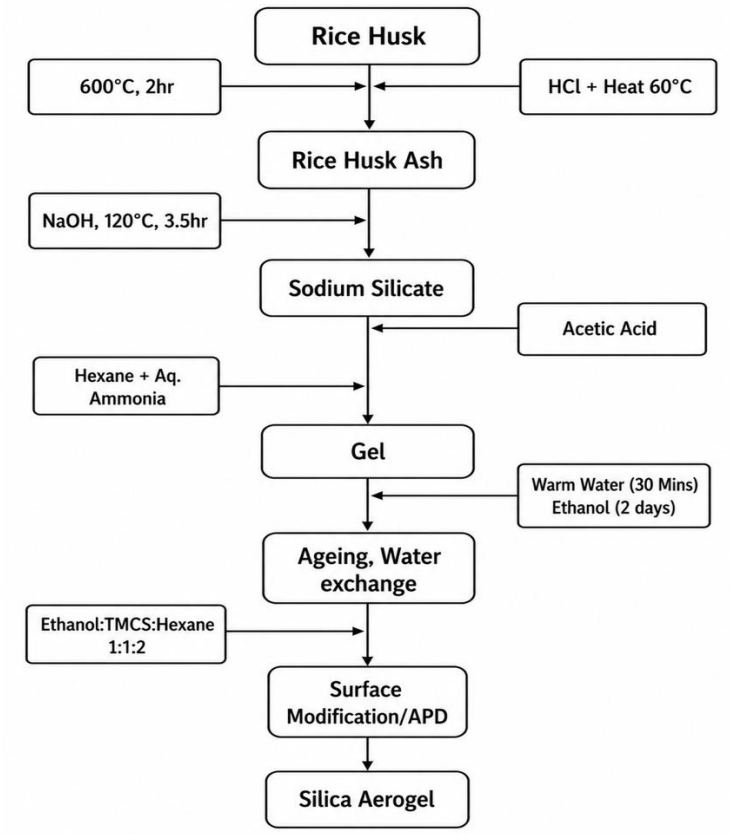

Figure 1: Process flow for the development of hydrophobic silica aerogel from rice husk.

2.5 Characterization of Silica Aerogel

Surface area was determined using the Brunauer–Emmett–Teller (BET) multipoint method, and pore size and pore volume were determined using the Barrett–Joyner–Halenda (BJH) method, both on a NOVA touch 4LX instrument. Prior to analysis, the aerogel was degassed at 200°C for 4 hours, and nitrogen adsorption-desorption isotherms were obtained at 77.3 K. Moreover, functional groups present

in the aerogel were identified by Fourier-transform infrared spectroscopy (FTIR) using a Perkin Elmer Frontier FTIR spectrometer (mid-IR: 8300–350 cm^{-1}; far-IR: 700–30 cm^{-1}; best resolution 0.4 cm^{-1}), scanning the wavenumber range 650–4000 cm^{-1}.

Hydrophobicity was assessed from the water contact angle of a droplet placed on the horizontally positioned aerogel surface, measured with a DataPhysics OCA 15EC–Series instrument and its high-resolution camera; this property has been reported to increase with the amount of silylating agent used and the soaking time in the silylating mixture (Khedkar et al., 2019). Also, bulk density was determined by weighing an empty 50 cm^3 glass flask, filling it with aerogel particles (tapping seven times until no further volume reduction occurred), and reweighing it. Bulk density (g/cm^3) was calculated as the ratio of aerogel mass to flask volume (Equation 1). Porosity was then calculated from the bulk density using Equation 2, assuming a standard amorphous silica density of 2.2 g/cm^3.

$$Density = {(M_1 - M_0)}/{V_a} \quad (1)$$

where M_0 = mass of the empty flask (g); M_1 = mass of flask and aerogel (g); V_a = volume of the flask (cm^3).

$$Porosity = \left(1 - {\rho_a}/{\rho_{st}}\right) \times 100 \quad (2)$$

where ρ_a = density of the developed aerogel (g/cm^3); ρ_{st} = standard density of amorphous silica (g/cm^3).

Finally, surface morphology was examined using a JEOL JSM-IT300LV scanning electron microscope (SEM) at magnifications corresponding to 10, 20, 30, and 100 µm resolutions.

3. RESULTS AND DISCUSSION

3.1 Visual Transformation During Synthesis

The visual appearance of the intermediate products obtained during synthesis (Figure 2) supports successful conversion of rice husk into silica aerogel at each processing stage. The rice husk ash (RHA) obtained after calcination appeared as a fine white powder, indicating effective combustion of the husk and near-complete removal of carbonaceous matter. Recent reviews identify rice husk as an abundant agro-industrial by-product with a composition well suited to conversion into silica and other advanced materials (Hamidu et al., 2025), and rice husk ash has been widely reported to contain a high proportion of amorphous SiO_2 usable as a low-cost aerogel precursor (Deng et al., 2025).

The sodium silicate solution obtained after alkaline digestion of the RHA was golden-brown and slightly transparent, consistent with dissolution of silica into the alkaline medium, although the colour may partly reflect trace impurities carried over from the RHA. The use of RHA-derived sodium silicate, rather than commercial silicate or alkoxide precursors, is significant because it provides a cheaper, more sustainable route to aerogel synthesis (Ochoa-Munoz et al., 2025); similarly, waste-derived sodium silicate has been highlighted as a pathway to more scalable, less energy-intensive aerogel production (Borzova et al., 2024).

Upon acidification, white gel particles formed, confirming conversion of soluble silicate species into a hydrated silica gel network via hydrolysis and condensation. This wet-gel stage is critical, as the final aerogel structure depends on preserving the gel network through ageing, solvent exchange, surface modification, and drying; rice husk ash-derived sodium silicate has similarly been reported to convert into hydrogels and then alcogels via solvent exchange prior to ambient pressure drying (Halim et al., 2021). After drying, the finished aerogel appeared as fragile, extremely light, irregular particles, consistent with the low-density, highly porous nature expected of silica aerogels and confirming successful synthesis via the ambient-pressure-drying route (Deng et al., 2025; Halim et al., 2021; Ochoa-Munoz et al., 2025).

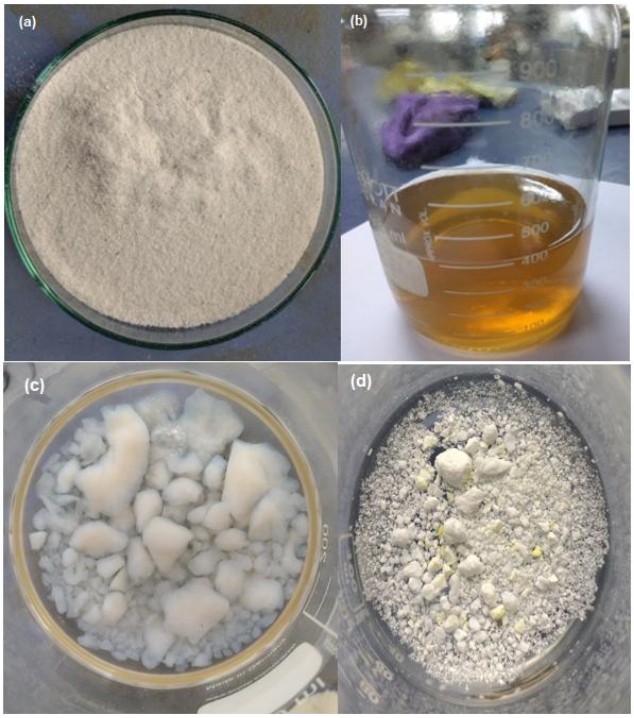

Figure 2: Visual transformation during silica aerogel synthesis: (a) rice husk ash; (b) sodium silicate solution; (c) gel particles in ethanol for exchange of pore water with ethanol; (d) Dried silica aerogel particles.

3.2 Textural Properties (BET, BJH, and t-Plot Analysis)

Nitrogen adsorption-desorption analysis was used to evaluate the textural properties of the synthesized aerogel, including BET specific surface area, BJH pore size and pore volume, and t-plot microporosity and external surface area, since these parameters are central to evaluating silica aerogels as environmental adsorbents (Goryunova et al., 2023).

The nitrogen adsorption-desorption isotherm (Figure 3) showed a gradual increase in adsorbed volume at low-to-intermediate relative pressure followed by a sharp rise at high relative pressure, typical of a mesoporous material in which multilayer adsorption and capillary condensation dominate. The separation between the adsorption and desorption branches indicates hysteresis, commonly associated with mesopore filling/emptying (Thommes et al., 2015), while the sharp rise at high relative pressure suggests the presence of larger mesopores and interparticle voids.

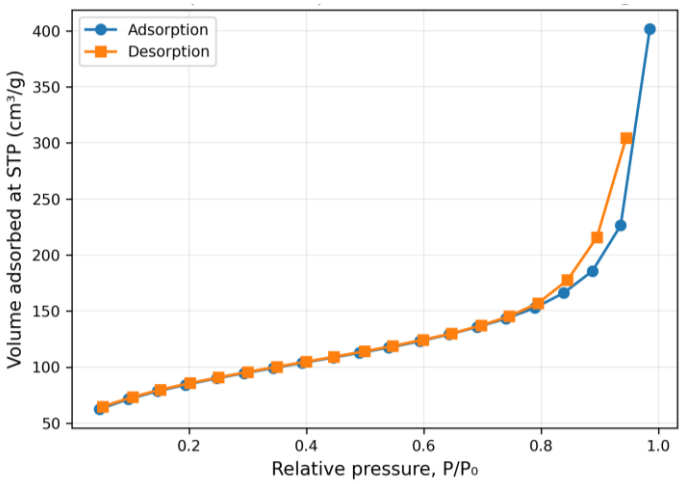

Figure 3: Nitrogen adsorption-desorption isotherm of the silica aerogel.

BET analysis (Figure 4) gave a specific surface area of 303.60 m^2/g with a correlation coefficient of r = 0.999915 and a BET C constant of 124.16, indicating strong linearity in the fitting range and favourable interaction between nitrogen molecules and the aerogel surface. This value is

comparable with recent rice husk-derived silica aerogel studies reporting surface areas of 312 and 298 m²/g (Akhter, Soomro, and Inglezakis 2023) and TEOS-doped/non-TEOS-doped aerogels of 296.18 and 267.06 m²/g (Soylu et al., 2025), placing the present material within the range expected for mesoporous silica aerogels, notwithstanding known sensitivity of surface area to precursor chemistry, ageing, solvent exchange, and drying method.

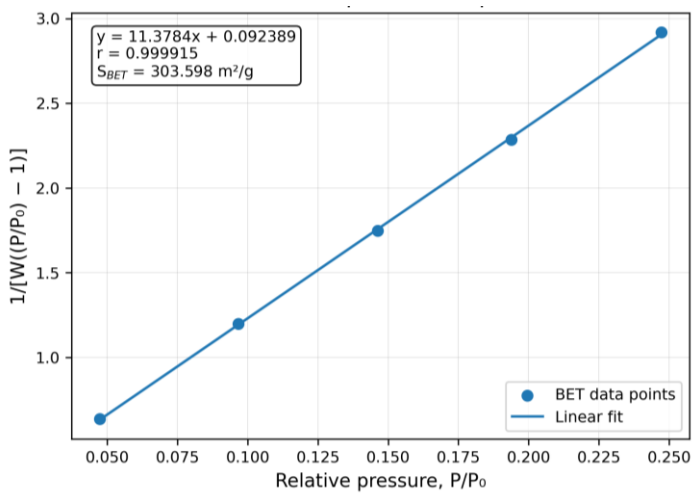

Figure 4: BET multipoint linear plot used to calculate specific surface area.

The t-plot analysis gave an external surface area of 303.60 m²/g, essentially identical to the BET value, indicating that the measured surface area is associated mainly with mesopores and external surface rather than micropores.

From the BJH analysis (Figure 5), the adsorption and desorption branches gave pore radii of 1.687 and 1.701 nm respectively, corresponding to pore diameters of approximately 3.37 and 3.40 nm. Under the IUPAC pore classification (pores < 2 nm: micropores; 2–50 nm: mesopores; > 50 nm: macropores) (Thommes et al., 2015), the aerogel is therefore classified as mesoporous, a structure expected to provide favourable diffusion pathways for adsorbate access to internal sites.

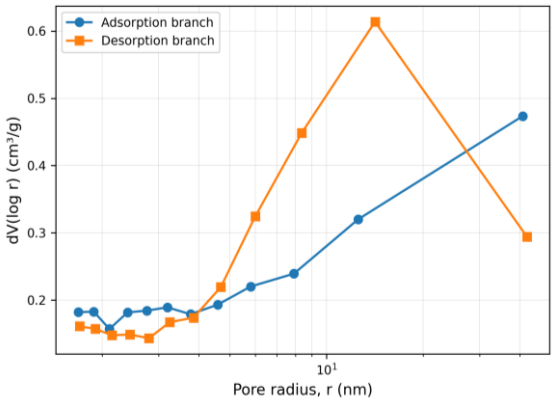

Figure 5: BJH pore size distribution based on adsorption and desorption branches.

The BJH pore volume (Figure 6) was 0.520 cm³/g from the adsorption branch and 0.525 cm³/g from the desorption branch, confirming an appreciable void network for adsorbate accommodation; the corresponding BJH surface areas were 111.55 and 121.82 m²/g, lower than the BET value because BJH analysis captures only pore-size-related surface area from capillary condensation, whereas BET reflects total specific surface area from multilayer nitrogen adsorption. This pore volume is somewhat lower than the 0.85 and 0.75 cm³/g reported for some rice husk-derived silica aerogels (Akhter et al., 2023), a difference attributable to variation in synthesis route, precursor source, gel ageing, solvent exchange, surface modification, and drying conditions across studies.

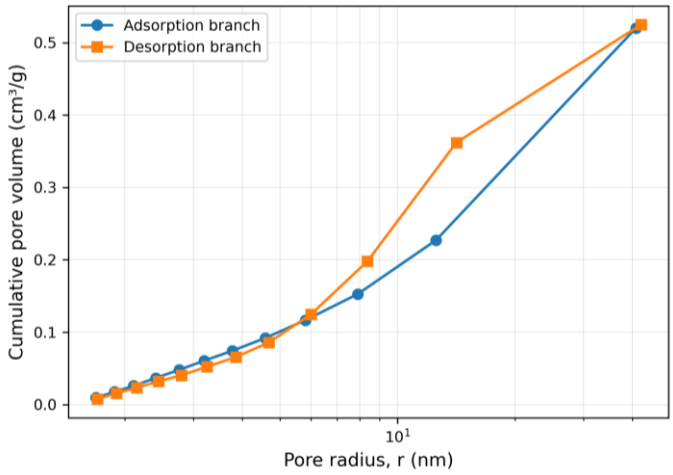

Figure 6: BJH cumulative pore volume of the silica aerogel.

The t-plot analysis (Figure 7) gave a micropore volume of 0 cm³/g and micropore area of 0.000 m²/g, confirming that the material is not micropore-dominated and that its surface area arises mainly from mesopores and external surfaces, consistent with the BJH pore-diameter results.

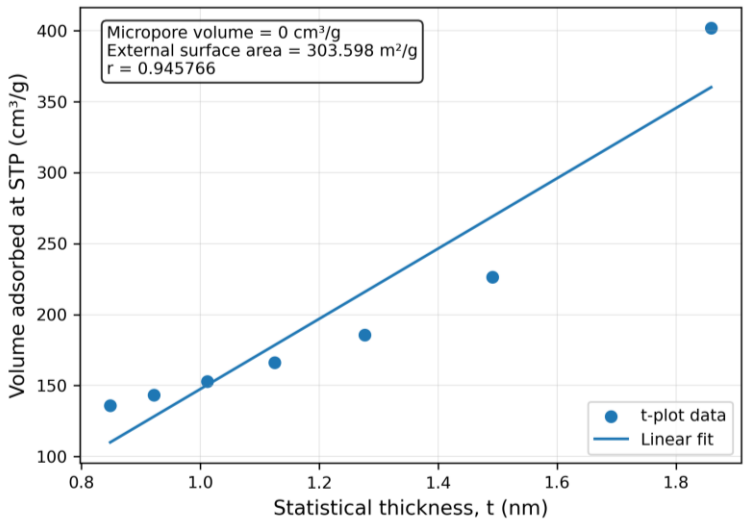

Figure 7. t-plot showing the absence of measurable micropore volume.

Collectively, the BET, BJH, and t-plot results indicate a mesoporous silica aerogel with a moderately high surface area (303.60 m²/g), pore diameter of 3.37–3.40 nm, and pore volume of 0.520–0.525 cm³/g — properties favourable for adsorption, since high surface area provides adsorption sites, mesoporosity supports accessibility and mass transfer, and pore volume accommodates adsorbate molecules, consistent with the general characterization of silica aerogels as highly porous adsorbents for environmental applications (Goryunova et al., 2023).

3.3 Fourier-Transform Infrared Spectroscopy (FTIR)

FTIR spectra of the synthesized aerogel (Figure 8) showed a broad band near 3359.03 cm^{-1} attributed to O-H stretching from surface silanol groups and adsorbed water, and a band at 1627 cm^{-1} corresponding to O-H bending. A weak band near 2964.14 cm^{-1} suggested residual aliphatic C-H groups from the precursor or surface-modification step. A strong absorption at approximately 1065.82 cm^{-1} was assigned to asymmetric Si-O-Si stretching, confirming formation of the silica network, while the band near 945.66 cm^{-1} was associated with Si-OH stretching, indicating surface silanol groups. Additional bands at 848.6, 758.95, and 668.83 cm^{-1} were attributed to symmetric stretching, bending, or related silica-network/surface-group vibrations. Overall, the spectrum confirms successful formation of a silica aerogel bearing siloxane and silanol functional groups that may contribute to adsorption via surface interaction with contaminants (Ma et al., 2025; Minju et al., 2021; Ransing et al., 2023).

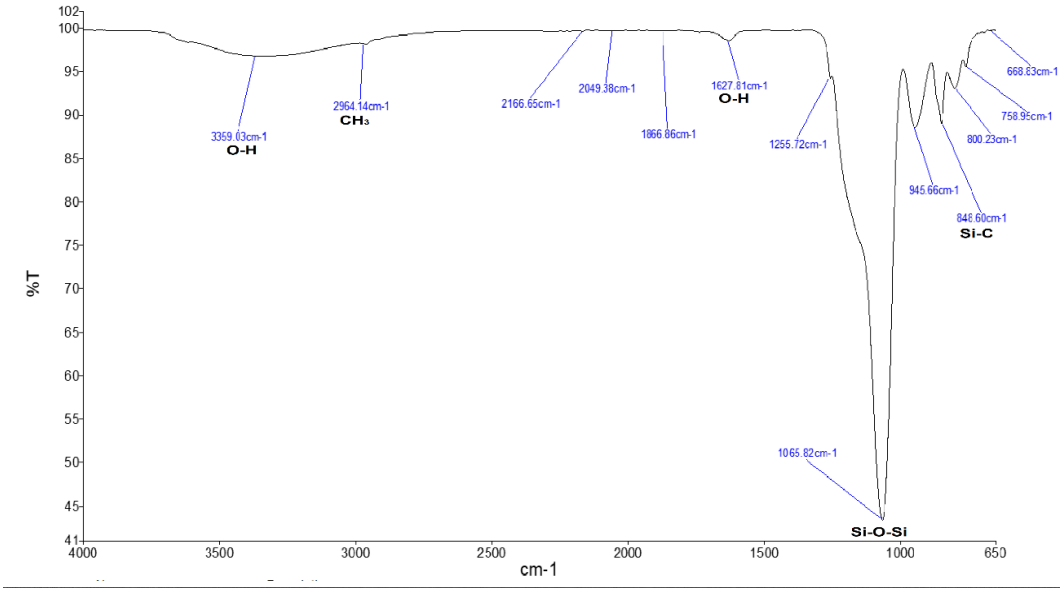

Figure 8: FTIR spectrum of the synthesized silica aerogel.

3.4 Hydrophobicity

Water contact-angle analysis on duplicate aerogel samples (Figure 9) gave contact angles of 156.7°/157.0° and 154.4°/154.7° (means of 156.85° and 154.55°), yielding an overall mean of 155.70° ± 1.34°. The small difference of approximately 2° between the duplicate samples is considered minor and may be attributed to local variations in surface roughness, pore distribution, and the uniformity of TMCS coverage across the aerogel surface. Because contact-angle measurement is highly sensitive to the exact location at which the water droplet is deposited, small differences in surface texture and chemical heterogeneity can influence the measured value. Additional experimental factors, including droplet volume, sample levelling, baseline selection, and image-fitting during contact-angle determination, may also contribute to slight variations. Nevertheless, both duplicate samples consistently exhibited contact angles well above 150°, indicating good reproducibility of the surface modification and confirming the superhydrophobic character of the prepared silica aerogel (Akbari et al., 2025; Tian et al., 2015).

Since surfaces with contact angles above 150° are generally classified as superhydrophobic (Wu et al., 2024), the TMCS-modified aerogel is confirmed to be superhydrophobic. This high contact angle likely reflects the combined effect of low surface energy from the silylating treatment and the porous micro/nano-rough structure of the aerogel, which together limit contact between water droplets and the solid surface. Comparable superhydrophobic contact angles have been reported for rice husk-derived silica aerogel (up to 159.5°) and silica-polyimide aerogel blankets (≈ 153°) (Deng et al., 2025; Liu et al., 2021), suggesting that the surface modification applied in this study was effective and may enhance the aerogel's interaction with hydrophobic organic contaminants during adsorption.

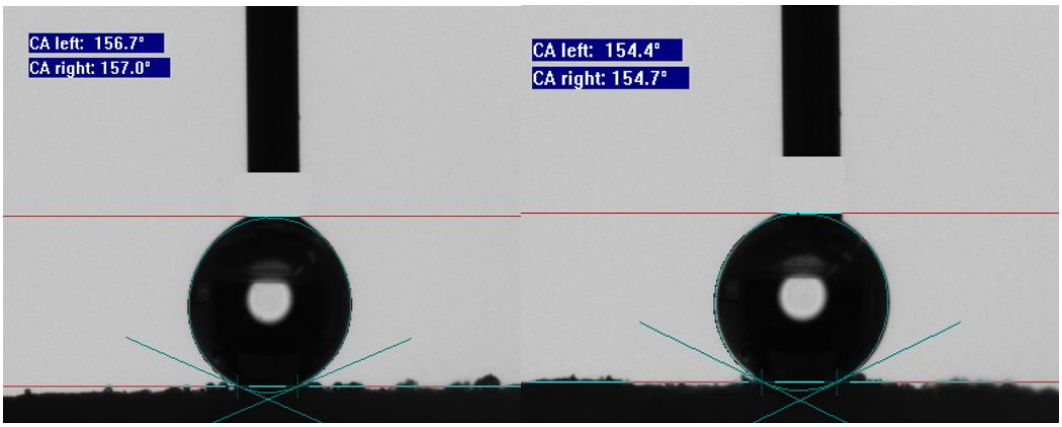

Figure 9: Water contact angles of the silica aerogel.

3.5 Density and Porosity

The bulk density and porosity of the developed aerogel were calculated as 0.18 g/cm³ and approximately 92%, respectively. The low bulk density confirms the lightweight nature of the aerogel and indicates that its porous network was largely retained after ambient pressure drying, while the high porosity shows that roughly 92% of the aerogel volume is void space, with only about 8% occupied by the solid silica framework. This is consistent with the characteristic low-density, highly porous structure of silica aerogels generally (Payanda Konuk et al., 2023), and the porosity value obtained here is comparable to porosities exceeding 90% reported for other rice husk-derived silica aerogels (Ochoa-Munoz et al., 2025). The developed material can therefore be considered highly porous and structurally suited to adsorption, as its open pore network should support mass transfer and access to internal adsorption sites.

3.6 Surface Morphology (SEM)

SEM micrographs at 10, 20, 30, and 100 µm resolutions (Figure 10) revealed an irregular, rough, agglomerated structure with visible interparticle voids across all magnifications. Lower magnification showed larger porous clusters, while higher magnification revealed finer silica particles and rough micro-domains forming the aerogel network, confirming that the synthesized material is a porous aerogel-like structure rather than a dense silica solid. The agglomerated morphology may partly reflect capillary stress during ambient pressure drying, which can induce shrinkage and local structural rearrangement; nonetheless, the persistence of visible pores and rough texture indicates that the porous framework was substantially retained. Similar porous, mesoporous morphology has been reported for other rice husk ash-derived silica aerogels prepared by sol-gel synthesis and ambient pressure drying (Akhter, Soomro, Jamali, et al. 2023; Deng et al., 2025; Ochoa-Munoz et al., 2025). The rough, porous surface observed here is favourable for adsorption, as it provides accessible surface sites and diffusion pathways for contaminant molecules, supporting the suitability of this rice husk-derived silica aerogel as an adsorbent for water treatment.

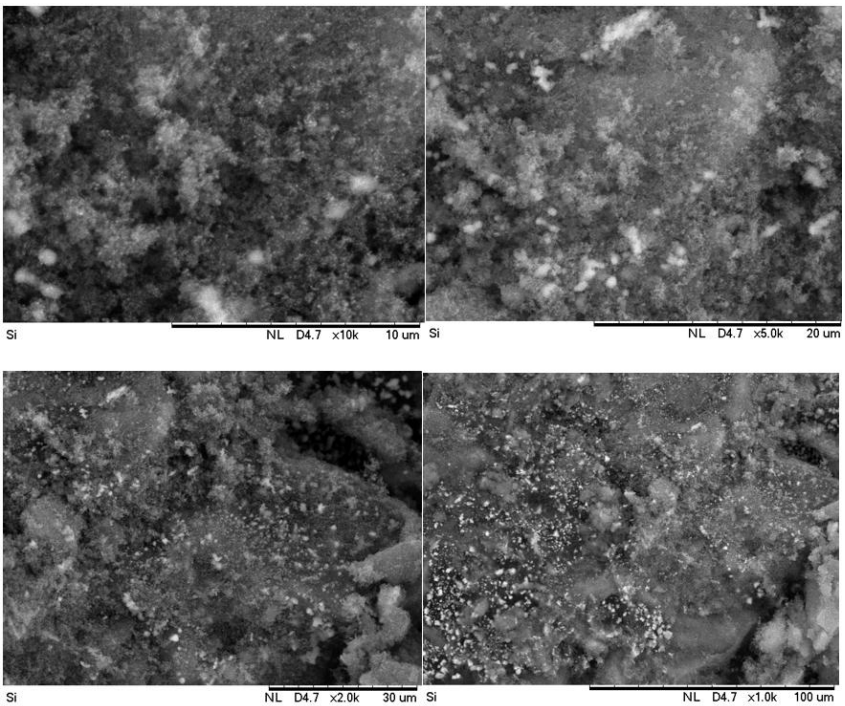

Figure 10: SEM images of the silica aerogel at 10, 20, 30, and 100 µm resolutions.

Table 2: Summary of textural, chemical, and physical properties of the synthesized silica aerogel

Property	Result
BET specific surface area	303.60 m^2/g (r = 0.999915; BET C = 124.16)
External surface area (t-plot)	303.60 m^2/g
BJH pore radius (adsorption / desorption)	1.687 nm / 1.701 nm (≈ 3.37–3.40 nm diameter)
BJH pore volume (adsorption / desorption)	0.520 cm^3/g / 0.525 cm^3/g
Water contact angle (mean ± SD)	155.70° ± 1.34° (superhydrophobic)
Bulk density	0.18 g/cm^3
Porosity	≈ 92%

4. CONCLUSION

Hydrophobic silica aerogel was successfully synthesized from rice husk via acid leaching, calcination, alkaline extraction to sodium silicate, acid-catalyzed sol-gel synthesis, ethanol solvent exchange, TMCS surface modification, and ambient pressure drying. The resulting material exhibited a mesoporous structure with a BET specific surface area of 303.60 m^2/g, pore diameter of 3.37–3.40 nm, and pore volume of 0.52 cm^3/g, alongside negligible microporosity. FTIR confirmed the presence of Si-O-Si and Si-OH functional groups characteristic of a silica network. Water contact-angle measurements (155.70° ± 1.34°) confirmed superhydrophobic behaviour, while low bulk density (0.18 g/cm^3) and high porosity (≈92%) confirmed the characteristic lightweight, open-pore structure of silica aerogels. SEM further revealed a rough, porous, agglomerated surface morphology consistent with these bulk properties. Taken together, these results demonstrate that rice husk, an abundant, low-cost, and environmentally sustainable agricultural by-product, can be converted into a hydrophobic, mesoporous silica aerogel with textural and surface properties consistent with materials reported to be effective for adsorption applications and recommend future adsorption studies

REFERENCES

Akhter, F., Soomro, S. A., & Inglezakis, V. J. (2023a). Green, organic, and facile synthesis of mesoporous silica aerogels for highly efficient Pb(II) removal from synthetic wastewater: Isotherm and kinetic studies. Biomass Conversion and Biorefinery. Advance online publication. https://doi.org/10.1007/s13399-023-04060-9

Akhter, F., Soomro, S. A., Jamali, A. R., & Inglezakis, V. J. (2023b). Structural, morphological and physiochemical analysis of SiC8H20O4/C2H5O/C7H16 modified mesoporous silica aerogels. Physical Chemistry Research, 11(1), 1–8. https://doi.org/10.22036/PCR.2022.332609.2044

Azat, S., Sartova, Z., Bekseitova, K., & Askaruly, K. (2019). Extraction of high-purity silica from rice husk via hydrochloric acid leaching treatment. Turkish Journal of Chemistry, 43(5), 1258–1269. https://doi.org/10.3906/kim-1903-53

Bakar, R. A., Yahya, R., & Gan, S. N. (2016). Production of high purity amorphous silica from rice husk. Procedia Chemistry, 19, 189–195. https://doi.org/10.1016/j.proche.2016.03.092

Borzova, M., Schollbach, K., Gauvin, F., & Brouwers, H. J. H. (2024). Sustainable ambient pressure-dried silica aerogel from waste glass. Current Research in Green and Sustainable Chemistry, 9, Article 100425. https://doi.org/10.1016/j.crgsc.2024.100425

Deng, Y., Sha, Z., Wang, X., Duan, K., Xue, W., Beadham, I., Xiao, X., & Zhang, C. (2025). Exploration of key factors in the preparation of highly hydrophobic silica aerogel from rice

husk ash assisted by machine learning. Gels, 11(1), Article 74. https://doi.org/10.3390/gels11010074

Goryunova, K., Gahramanli, Y., & Gurbanova, R. (2023). Adsorption properties of silica aerogel-based materials. RSC Advances, 13, 18207–18216. https://doi.org/10.1039/D3RA02462H

Halim, Z. A. A., Yajid, M. A. M., & Hamdan, H. (2021). Effects of solvent exchange period and heat treatment on physical and chemical properties of rice husk derived silica aerogels. Silicon, 13, 251–257. https://doi.org/10.1007/s12633-020-00421-5

Hamidu, I., Afotey, B., Kwakye-Awuah, B., & Anang, D. A. (2025). Synthesis of silica and silicon from rice husk feedstock: A review. Heliyon, 11(4), Article e42491. https://doi.org/10.1016/j.heliyon.2025.e42491

Khedkar, M. V., Somvanshi, S. B., Humbe, A. V., & Jadhav, K. M. (2019). Surface modified sodium silicate based superhydrophobic silica aerogels prepared via ambient pressure drying process. Journal of Non-Crystalline Solids, 511, 140–146. https://doi.org/10.1016/j.jnoncrysol.2019.02.004

Liu, R., Wang, J., Liao, J., & Zhang, X. (2021). Robust silica-polyimide aerogel blanket for water-proof and flame-retardant self-floating artificial island. Frontiers in Materials, 8, Article 659655. https://doi.org/10.3389/fmats.2021.659655

Ma, H., Wang, B., Zhang, Y., & Zheng, L. (2025). Mechanically reinforced silica aerogels via thermally induced phase separation of poly(ethylene-co-vinyl alcohol). Gels, 11(11), Article 870. https://doi.org/10.3390/gels11110870

Minju, N., Nair, B. N., & Savithri, S. (2021). Sodium silicate-derived aerogels: Effect of processing parameters on their applications. RSC Advances, 11, 15301–15322. https://doi.org/10.1039/D0RA09793D

Ochoa-Muñoz, Y. H., Guerrero-Calderón, R. S., Mejía de Gutiérrez, R., & Torres-León, J. A. (2025). Rice husk-derived silica aerogels for efficient removal of amoxicillin and erythromycin from water. Surfaces and Interfaces, 78, Article 108089. https://doi.org/10.1016/j.surfin.2025.108089

Payanda Konuk, O., Alsuhile, A. A. A. M., Yousefzadeh, H., Ülker, Z., Bozbağ, S. E., García-González, C. A., Smirnova, I., & Erkey, C. (2023). The effect of synthesis conditions and process parameters on aerogel properties. Frontiers in Chemistry, 11, Article 1294520. https://doi.org/10.3389/fchem.2023.1294520

Rahmani, A., Nazemi, F., Barjasteh Askari, F., & Davoudi, M. (2018). Preparation, characterization, and application of silica aerogel for adsorption of phenol: An in-depth isotherm study. Health Scope, In Press. https://doi.org/10.5812/jhealthscope.15115

Ransing, A. A., Dhavale, R. P., Parale, V. G., Bangi, U. K. H., Choi, H., Lee, W., Kim, J., Wang, Q., Phadtare, V. D., Kim, T., Jung, W. K., & Park, H.-H. (2023). One-pot sol-gel synthesis of highly insulative hybrid P(AAm-co-AAc)-silica aerogels with improved mechanical and thermal properties. Gels, 9(8), Article 651. https://doi.org/10.3390/gels9080651

Soylu, T. M., Özel, C., Karakuzu İkizler, B., Özarslan, A. C., Terzioğlu, P., Başaran Elalmış, Y., & Yücel, S. (2025). Mesoporous silica aerogels for sunflower oil refining and investigation of their adsorption performance. Journal of Sol-Gel Science and Technology, 115, 327–348. https://doi.org/10.1007/s10971-024-06395-9

Štandeker, S., Novak, Z., & Knez, Ž. (2007). Adsorption of toxic organic compounds from water with hydrophobic silica aerogels. Journal of Colloid and Interface Science, 310(2), 362–368. https://doi.org/10.1016/j.jcis.2007.02.021

Štandeker, S., Veronovski, A., Novak, Z., & Knez, Ž. (2011). Silica aerogels modified with mercapto functional groups used for Cu(II) and Hg(II) removal from aqueous solutions. Desalination, 269(1–3), 223–230. https://doi.org/10.1016/j.desal.2010.10.064

Thommes, M., Kaneko, K., Neimark, A. V., Olivier, J. P., Rodriguez-Reinoso, F., Rouquerol, J., & Sing, K. S. W. (2015). Physisorption of gases, with special reference to the evaluation of surface

area and pore size distribution (IUPAC Technical Report). Pure and Applied Chemistry, 87(9–10), 1051–1069. https://doi.org/10.1515/pac-2014-1117

Wang, D., McLaughlin, E., Pfeffer, R., & Lin, Y. S. (2011). Adsorption of organic compounds in vapor, liquid, and aqueous solution phases on hydrophobic aerogels. Industrial & Engineering Chemistry Research, 50(21), 12177–12185. https://doi.org/10.1021/ie201301n

Wang, D., McLaughlin, E., Pfeffer, R., & Lin, Y. S. (2012). Adsorption of oils from pure liquid and oil-water emulsion on hydrophobic silica aerogels. Separation and Purification Technology, 99, 28–35. https://doi.org/10.1016/j.seppur.2012.08.001

Wu, P., Qi, Y., Wang, Y., Wang, X., Zhang, Y., & Li, X. (2024). Advances in self-healing silica-based superhydrophobic coatings. Surfaces and Interfaces, 51, Article 104800. https://doi.org/10.1016/j.surfin.2024.104800

Akbari, R., Ambrosio, F., Berry, J. D., & Antonini, C. (2025). Wetting characterisation on complex surfaces by an automatic open-source tool: DropenVideo. *Journal of Colloid and Interface Science*, *678*, 1075–1086. https://doi.org/10.1016/j.jcis.2024.08.159

Tian, T., Tao, H., Xiao, J., Xu, X., & An, J. (2015). A low cost and facile preparation of hydrophobic silica films and powders by a solution-based process. *Journal of Wuhan University of Technology–Materials Science Edition*, *30*, 489–493. https://doi.org/10.1007/s11595-015-1177-7

International Conference on Engineering Innovation for Sustainable Development (ICESID 2026)
Faculty of Engineering, Ahmadu Bello University Zaria · 8–10 September 2026

DYNAMIC MECHANICAL ANALYSIS OF RECYCLED LDPE/HDPE POLYMER BLENDS

Tijani Abdullahi[1], Tajudeen Kolawole Bello[1,*], Abdulmalik Dahiru Kona[1]
[1]*Ahmadu Bello University Zaria*
Email: tijanibrahim91@gmail.com, tjbello27@gmail.com*, Abdulmaleekkona@gmail.com
***Corresponding author**: Tajudeen Kolawole Bello
DOI: https://doi.org/10.67203/sp.ICESID.2026

ABSTRACT
This study investigated the dynamic mechanical behaviour of blended low-density polyethylene (LDPE) and high-density polyethylene (HDPE) waste plastics using Dynamic Mechanical Analysis (DMA). The aim was to evaluate the effect of HDPE loading on the viscoelastic and damping properties of LDPE/HDPE blends. Samples with varying HDPE loadings (0–50 wt.%) were prepared by melt compounding on a two-roll mill machine, followed by compression moulding. DMA was conducted at a frequency of 1 Hz over a temperature range of 30–120 °C at a heating rate of 6 K/min. The results showed that increasing HDPE content significantly improved the mechanical performance of the blends. Relative to pure LDPE, the storage modulus increased by approximately 573.4%, while the loss modulus increased by approximately 426% at 50 wt.% HDPE loading. The tan δ values ranged from 0.13 to 0.27 across all blends within the investigated temperature range of 30–120 °C, indicating good damping characteristics. The findings demonstrate that HDPE incorporation enhances the stiffness and mechanical strength of LDPE-based blends, indicating the potential of recycled LDPE/HDPE waste plastics for engineering and structural material applications.

Keywords: *High-density polyethylene (HDPE); low-density polyethylene (LDPE); plastics; polymer blend; Dynamic mechanical Analysis (DMA)*

1. INTRODUCTION

Polyethylene-based plastics have become highly valued in modern engineering and industrial systems owing to their lightweight, chemical inertness, ease of processing, and low production cost. Among the various polyolefins currently in circulation, Low-density polyethylene (LDPE) and high-density polyethylene (HDPE) contribute to a much larger share of global plastic production and waste than most other plastics (Vannessa, 2004).

In 2023, global plastic production was estimated at around 415 million metric tons, roughly double the amount produced at the beginning of the 21st century, yet only approximately 9% of all plastic waste generated to date has been successfully recycled (Surendarnath et al., 2025). This is a challenging situation in Nigeria, where limited waste sorting and recycling infrastructure results in LDPE and HDPE being dumped together with other waste materials, worsening environmental pollution (Akan et al., 2021). A cost-effective method for recovering value from mixed polyethylene waste is heat blending, where LDPE and HDPE are processed together in the molten state to give a material with properties that can be tailored by adjusting the blend ratio.

Evaluating the mechanical behaviour of polymer blends under real service conditions requires more than conventional tensile or flexural tests, since polymers exhibit viscoelastic behaviour influenced by temperature, loading frequency, and the duration of deformation. Dynamic Mechanical Analysis (DMA) is widely used to investigate this behaviour, providing key parameters including the storage modulus (E′), the loss modulus (E″), and the damping factor, tan δ, expressed as the ratio of E″ to E′ (Chartoff et al., 2009).

Although interest in recycled polyolefin blends has increased in recent years, several important gaps still exist in the available literature. Most studies on LDPE/HDPE blends have used virgin polymers with controlled and well-defined properties (Schyns & Shaver, 2021). In contrast, recycled plastics are often more complex, containing impurities and variations in composition and quality (Nagy & Weltsch, 2023). Previous research has also focused largely on the tensile, thermal, and rheological

properties of LDPE/HDPE blends, with comparatively few studies examining their dynamic mechanical behaviour, particularly for materials derived from post-consumer plastic waste, and information is especially limited over the temperature range commonly encountered in service conditions (30–120 °C).

To help address these gaps, the present study investigates the dynamic mechanical behaviour of binary LDPE/HDPE blends prepared from post-consumer plastic waste collected in Zaria, Nigeria. The blends were produced with HDPE contents of 0wt.%, 10wt.%, 20wt.%, 30wt.%, 40wt.%, and 50 wt.% using a melt-compounding process. The specific objectives of the study are to:

1. Examine the effect of increasing HDPE content on the storage modulus (E′), loss modulus (E″), and damping factor (tan δ) of recycled LDPE/HDPE blends over the temperature range of 30–120 °C at a frequency of 1 Hz and a heating rate of 6 K/min.
2. Determine how blend composition affects key thermomechanical transition temperatures, including the onset, peak, and offset temperatures.
3. Evaluate whether the dynamic mechanical properties of the blends make them suitable for engineering and structural applications.

2. METHODOLOGY

2.1 Materials

Post-consumer low-density polyethylene (LDPE) waste used in this study was obtained from discarded sachet water packaging films collected within Samaru, Zaria, Kaduna State, Nigeria. High-density polyethylene (HDPE) waste was sourced from used yoghurt packaging containers ("San yoghurt" plastic) collected from the same location.

It is acknowledged that the use of post-consumer waste plastics introduces inherent variability that virgin polymer studies do not face. In this study, material identity was inferred from the known source of the plastics, such as sachet water films (LDPE) and yoghurt containers (HDPE). These are commonly used product categories with well-documented polymer types in the Nigerian context. However, formal characterisation of the raw materials using techniques such as Fourier-transform infrared spectroscopy (FTIR), differential scanning calorimetry (DSC), or melt flow index (MFI) testing was not conducted in this study. This represents a limitation, as residual contamination from labels, adhesives, or mixed plastics cannot be completely ruled out despite the washing procedure employed. Future work should incorporate material characterisation of the recycled feedstock before blending to quantify contamination levels and confirm polymer identity, allowing a more definitive interpretation of the dynamic mechanical results.

2.2 Collection and Preparation of Waste Plastics

LDPE and HDPE post-consumer waste plastics were collected from designated waste bins and disposal locations. The collected plastics were sorted manually to separate LDPE from HDPE contaminants and other foreign materials. The sorted plastic materials were thoroughly washed with water and liquid soap to remove dirt, grease, labels, and adhered impurities that could interfere with the blending and thermal analysis processes.

After washing, the plastic materials were not dried under direct sunlight to avoid potential degradation and distortion of the LDPE sachet water films, which are highly sensitive to prolonged solar exposure. Instead, the samples were dried in a well-ventilated room under continuous fan-assisted airflow for approximately 4 days. This approach was adopted to ensure gradual and uniform removal of moisture while preserving the physical integrity and intrinsic properties of the polymers prior to further processing. Complete drying was necessary to prevent moisture-induced defects during melt blending and compression moulding operations. Drying was considered complete when no visible moisture was observed, and the flakes remained free-flowing and non-adherent upon handling.

The dried plastic materials were subjected to size reduction using a locally fabricated shredding machine to obtain relatively uniform polymer particle chips of about 10mm for effective blending.

2.3 Preparation of LDPE/HDPE Blends

Mass measurements of the polymer samples were conducted using a digital weighing balance. The polymer blends were prepared using a two-roll mill compounding machine (Reliable Rubber and Plastic Company, New Jersey, U.S.A., Model 5189), operated at a processing temperature of 180°C for 10 - 15 minutes. The two-roll mill compounding step used a higher temperature (180°C) to ensure adequate melt flow, shear mixing, and homogenization of the LDPE/HDPE blend across the open rollers, where heat loss to the environment is greater. The shredded polymer materials were introduced into the heated rollers and blended thoroughly to ensure proper dispersion and homogenization of the polymer phases.

The blends were prepared using different LDPE/HDPE formulations as follows:

- 200 g/0 g, 180 g/20 g, 160 g/40 g, 140 g/60 g, 120 g/80 g, 100 g/100 g

These formulations were prepared to evaluate the influence of HDPE loading on the dynamic mechanical properties of the polymer blends.

2.4 Compression Moulding of Polymer Blends

Compression moulding of the blended samples was carried out using a Carver compression moulding machine (Carver Inc., Wabash, U.S.A., Model 5019).

The compounded polymer blends obtained from the two-roll mill were processed using the compression moulding technique to produce sheet samples suitable for dynamic mechanical analysis (DMA). The mould platens were electrically heated to a temperature of 150 °C and allowed to stabilise before processing. Compression moulding, by contrast, was carried out on the already-compounded (pre-homogenized) blend in a closed, pressurized system; a moulding temperature of 150°C, above the melting points of both LDPE (~105–115°C) and HDPE (~130–137°C) was sufficient to ensure both polymer phases were fully molten and could consolidate into a uniform sheet, while minimizing additional thermal exposure and reducing the risk of oxidative degradation during the moulding dwell time.

The mould was then preheated to the same temperature, after which the plastic paste was placed into the mould cavity. Compression moulding was carried out at a pressure of 3 MPa for 5 min to produce sheets with dimensions of 240 mm × 220 mm × 4 mm. Before moulding, the mould surfaces were coated with used engine oil to facilitate easy removal of the cured samples. After curing, the moulded samples were removed and allowed to cool to room temperature. The moulded sheets were subsequently cut into smaller specimens with dimensions of 60 mm × 12 mm × 4 mm for DMA characterisation. The prepared samples were then stored under ambient laboratory conditions before testing.

2.5 Dynamic Mechanical Analysis (DMA)

Dynamic mechanical analysis (DMA) of the prepared samples was performed using a DMA 242E NETZSCH Artemis dynamic mechanical analyzer located at the Department of Mechanical Engineering, Ahmadu Bello University, Zaria.

The DMA test was performed under controlled experimental conditions using a heating rate of 6 K/min and an oscillation amplitude of 60 µm. The temperature range employed during the analysis was 30°C to 120°C. Frequency-dependent measurements were conducted at a frequency of 1 Hz.

The key parameters measured by DMA are defined as follows. The storage modulus (E′) represents the energy stored and recovered per cycle of deformation, and is given by:

$$E' = (\sigma_0/\varepsilon_0) \cos \delta \quad (1)$$

where σ_0 is the stress amplitude, ε_0 is the strain amplitude, and δ is the phase angle between stress and strain. The loss modulus (E″) represents the energy dissipated as heat per cycle, and is expressed as:

$$E'' = (\sigma_0/\varepsilon_0) \sin \delta \quad (2)$$

The damping factor, tan δ, is defined as the ratio of the loss modulus to the storage modulus:

$$\tan \delta = E''/E' \quad (3)$$

A high tan δ value indicates a material that dissipates more energy relative to what it stores, reflecting dominant viscous behaviour, while a low tan δ value indicates more elastic, stiffness-dominated behaviour.

Each blend composition was tested once under the specified frequency and heating rate conditions. Formal replicate testing (i.e., triplicate runs with reported means and standard deviations) was not conducted in this study due to material and equipment constraints; this limitation is discussed further in the Results and Discussion section.

3. RESULTS AND DISCUSSION

3.1 Dynamic Mechanical Analysis of LDPE/HDPE Blends

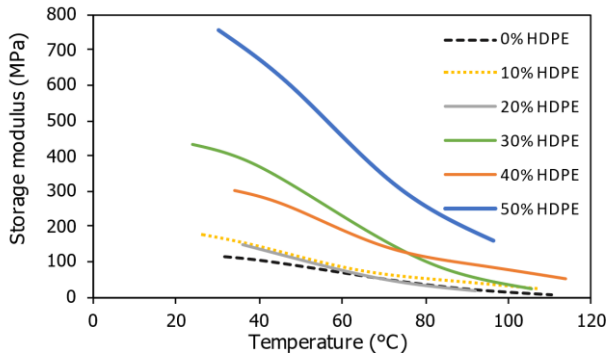

Figure 1.0: Effect of temperature on storage modulus of LDPE/HDPE blend

The variation of storage modulus with temperature for the LDPE/HDPE blends is presented in Figure 1. The results showed that the storage modulus decreased progressively with increasing temperature for all blend compositions due to increased molecular chain mobility within the polymer matrix.

At lower temperatures of approximately 35°C, the incorporation of HDPE significantly improved the stiffness of the blends. The sample containing 50 wt.% HDPE exhibited the highest storage modulus, while the control sample containing 0 wt.% HDPE showed the lowest storage modulus. The 50 wt.% HDPE blend demonstrated an increase of approximately 573% in storage modulus compared to the unfilled control sample.

The increase in storage modulus with HDPE loading can be attributed to the higher crystallinity and rigidity of HDPE compared to LDPE. Consequently, blends containing higher HDPE concentrations exhibited greater resistance to elastic deformation. This behaviour is consistent with findings demonstrating that HDPE forms well-organised spherulitic structures with high crystallinity (81.5%) and rigid amorphous layers between lamellae. In contrast, LDPE forms irregular aggregates with considerably lower crystallinity (27.5%) and mobile amorphous layers, which are structural differences that directly govern the stiffness of their blends (Fu et al., 2022). Furthermore, DMA measurements confirmed that the rigid, confined amorphous phase in HDPE suppresses molecular chain mobility, while the mobile amorphous phase in LDPE introduces greater viscoelastic compliance, explaining the progressive reduction in storage modulus observed as LDPE concentration increases across the measured temperature range of 30°C to 120°C in the present study (Fu et al., 2022).

The storage modulus decreased continuously as the temperature increased from 30°C to approximately 120°C. This reduction is associated with softening of the polymer matrix and decreased resistance to molecular motion at elevated temperatures. Similar observations have been reported for polyethylene-based polymer blends subjected to dynamic mechanical analysis.

It should be noted that due to material and equipment constraints, formal replicate testing with statistical error bars was not conducted in this study. This represents a limitation of the present work, and future studies should incorporate, at a minimum triplicate testing per composition with reported standard deviations to allow full assessment of data reproducibility and statistical significance.

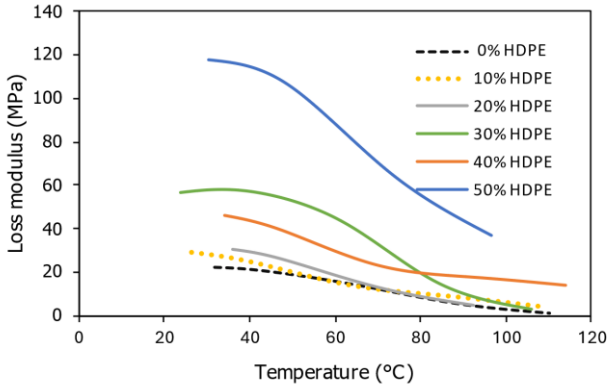

Figure 2.0: Effect of temperature on loss modulus of LDPE/HDPE blend

The loss modulus defines the viscous response of the material, reflecting its capacity to dissipate mechanical energy as heat during deformation, a behaviour governed by internal molecular friction and chain mobility within the polymer network (Satya & Sreekanth, 2020).

The results indicated that the loss modulus decreased with increasing temperature for all blend compositions. At approximately 35°C, the 50 wt.% HDPE sample exhibited the highest loss modulus, whereas the control sample without HDPE loading showed the lowest value. The increase in loss modulus for the 50 wt.% HDPE sample was approximately 426% higher than the control sample, with a modulus difference of about 96.4 MPa.

As the temperature increased, all samples exhibited gradual reductions in loss modulus and eventually converged near 110°C, except for the 50 wt.% HDPE blend, which maintained relatively higher values. This behaviour indicates thermal softening and reduced energy dissipation capability at elevated temperatures due to increased polymer chain mobility. Similar trends have been reported in thermoplastic polymer blends where elevated temperatures reduce viscoelastic resistance (Techawinyutham et al., 2021).

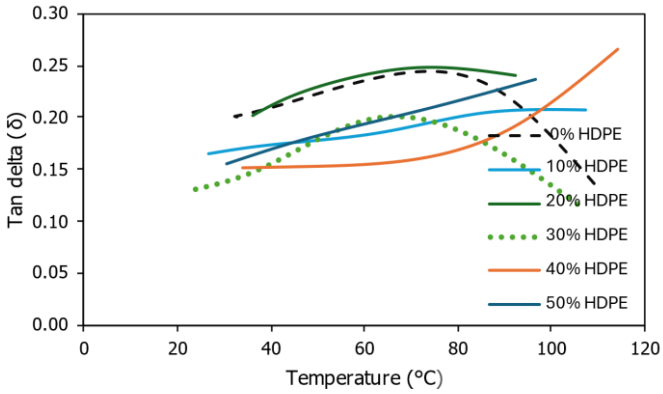

Figure 3.0: Effect of temperature on tan delta (δ) of LDPE/HDPE blend

Tan δ is the ratio of loss modulus (E″) to storage modulus (E′). It represents the damping factor, essentially how much mechanical energy is dissipated as heat versus stored elastically (Poh et al., 2022)

The tan δ curves showed varied behaviour across the HDPE Loadings with an increase in temperature. The polymer matrix for 0 wt.% HDPE blend exhibited a damping value of about 0.20 at room temperature, which constantly declined throughout the entire temperature range, reaching approximately 0.13 at 110 °C. This shows a progressive reduction in energy dissipation capacity with increasing temperature. The 20 wt.% and 30 wt.% HDPE blends displayed a characteristic rise and fall pattern, with their tan δ peak values of about 0.245 and 0.20 at around 70–75°C and 75–80°C, respectively, before declining sharply at higher temperatures. This peak behaviour is associated with the glass-to-rubber transition zone, where maximum molecular mobility and energy dissipation coincide.

In contrast, the 10 wt.% and 50 wt.% HDPE blends exhibited a gradual and continuous increase in damping factor with temperature, plateauing at elevated temperatures without a well-defined peak within the tested range. Most notably, the 40 wt.% HDPE blend demonstrated a distinctly different response, showing a continuous and steep rise in tan δ from approximately 0.15 at room temperature to 0.27 at 120°C, with no observable peak or decline. This behaviour suggests that at this composition, the viscoelastic transition is either significantly broadened or shifted beyond the measurement window, likely due to a unique phase morphology and interactions between the HDPE crystalline domains and the matrix at this specific blend ratio (Sha et al., 1991). These divergent behaviours suggest that higher HDPE content fundamentally alters the damping characteristics of the blends, possibly due to increased crystalline phase constraints and enhanced polymer chain interactions that shift or suppress the peak damping temperature beyond the tested range (Munaro & Akcelrud, 2008).

3.2 Thermal Transition Behaviour

Table 1: Thermal transition temperatures of LDPE/HDPE blends at 1 Hz

LDPE (g)	HDPE (g)	wt.% HDPE	Onset (°C)	Peak (°C)	Offset (°C)
200	0	0	47.9	73.9	92.5
180	20	10	36.8	99.7	108.0
160	40	20	54.1	74.1	92.0
140	60	30	53.5	104.0	114.0
120	80	40	48.4	114.4	116.0
100	100	50	47.7	96.2	Increasing trend

The thermal transition temperatures of the LDPE/HDPE blends obtained from DMA analysis are presented in Table 1. The onset, peak, and offset temperatures varied with blend composition, indicating that HDPE loading influenced the relaxation behaviour and thermal stability of the polymer blends.

The 40 wt.% HDPE blends exhibited a higher peak transition temperature than the 50 wt% blend, which may suggest a non-linear composition-property relationship. One possible explanation is that HDPE crystalline domains may be more favourably dispersed within the LDPE matrix at 40 wt.% loading, which could promote greater interfacial co-crystallisation and chain entanglement (Sha et al., 1991). Beyond this composition, a shift toward a phase-inversion-type morphology may disrupt the crystalline network, potentially reducing the effective thermal transition temperature despite the higher overall HDPE content. However, this interpretation remains speculative, as no direct morphological evidence (e.g., SEM) or complementary thermal analysis (e.g., DSC) was obtained in this study to confirm the proposed dispersion or phase-inversion mechanisms; such characterisation is recommended in future work to validate this hypothesis(Rana, 2002).

Lastly, the 50 wt.% HDPE composition shows an anomalous result in Table 1, where the recorded peak temperature is 96.2°C, and the offset showed an increasing trend. This is physically inconsistent, as the offset temperature should always exceed the peak temperature in a thermal transition. This discrepancy is likely attributable to instrument resolution limitations or data-processing artefacts at the boundary of the transition and should be interpreted with caution. The values for this composition should be revisited with additional testing, if available, or explicitly acknowledged as a measurement uncertainty.

4. CONCLUSION

The dynamic mechanical study of recycled LDPE/HDPE polymer blends indicated that compositional variation has a considerable impact on the material system's viscoelastic and

thermomechanical performance. The storage modulus gradually increased from 112.0 MPa at 0 wt.% HDPE to 754.2 MPa at 50 wt.% HDPE, indicating a significant improvement in stiffness brought about by the addition of HDPE to the LDPE matrix. This improvement suggests that because HDPE has a stronger crystallinity and less molecular chain mobility than LDPE, it encourages greater elastic energy storage capacity.

The loss modulus increased with higher HDPE loading, rising from 22.6 MPa to 119.0 MPa at approximately 31°C. This increase indicates an enhanced ability of the blends to dissipate mechanical energy through viscous deformation. As the temperature increased, all samples transitioned toward rubbery behaviour, which confirms the thermally activated relaxation of polymer chains and the gradual reduction in mechanical integrity at elevated temperatures.

The damping factor (tan δ) showed peak behaviour depending on the composition, with well-defined peaks observed for the 20 wt.% and 30 wt.% HDPE blends (tan δ ≈ 0.245 at 70–75°C and ≈ 0.20 at 75–80°C, respectively), while the 0, 10, 40, and 50 wt.% HDPE blends did not exhibit a clearly defined peak within the tested temperature range. The presence of separate tan delta peaks demonstrates the viscoelastic nature of the blends and indicates the effect of the interfacial interactions between the LDPE and HDPE phases on the energy dissipation characteristics. The results overall show that LDPE blending with HDPE is a feasible way to achieve mechanical stiffness and damping performance through controlled compositions.

This study contributes to the existing knowledge by establishing a quantitative correlation between the content of HDPE and the dynamic mechanical performance in recycled polyethylene systems. It further demonstrates that waste polyethylene streams can be engineered into value-added materials with tunable mechanical and damping properties instead of being limited to disposal or low-grade recycling applications. The effect of compatibilizers on phase interaction and interfacial adhesion in LDPE/HDPE blends should be studied in future work. Furthermore, morphological studies using SEM and thermal analysis techniques like DSC and TGA are suggested to correlate microstructural changes with the observed viscoelastic behaviour. Tests of long-term fatigue and cyclic loading would also give more insight into the durability and real-world applicability of these recycled polymer systems.

ACKNOWLEDGEMENTS

The authors gratefully acknowledge the Department of Mechanical Engineering, Ahmadu Bello University, Zaria, for granting inter-departmental access to their Dynamic Mechanical Analysis (DMA) facility used in this study. Special thanks go to Mr. Aminu Lawal Yahaya, Laboratory Technologist, for his technical assistance during the DMA testing.

5. REFERENCES

Akan, O. D., Udofia, G. E., Okeke, E. S., Mgbechidinma, C. L., Okoye, C. O., Zoclanclounon, Y. A. B., Atakpa, E. O., & Adebanjo, O. O. (2021). Plastic waste: Status, degradation and microbial management options for Africa. *Journal of Environmental Management*, *292*, 1–12. https://doi.org/10.1016/j.jenvman.2021.112758

Chartoff, R. P., Menczel, J. D., & Dillman, S. H. (2009). *DYNAMIC MECHANICAL ANALYSIS (DMA)*. https://doi.org/https://doi.org/10.1002/9780470423837.ch5

Fu, Q., Men, Y., & Strobl, G. (2022). Understanding of the tensile deformation in HDPE/LDPE blends based on their crystal structure and phase morphology. *Elsevier Science Ltd*, 1–7. www.elsevier.com/locate/polymer

Munaro, M., & Akcelrud, L. (2008). Correlations between composition and crystallinity of LDPE/HDPE blends. *Journal of Polymer Research*, *15*(1), 83–88. https://doi.org/10.1007/s10965-007-9146-2

Nagy, D., & Weltsch, Z. (2023). Crystallinity and Oscillatory Shear Rheology of Polyethylene Blends. *Materials*, *16*(19). https://doi.org/10.3390/ma16196402

Poh, L., Wu, Q., Chen, Y., & Narimissa, E. (2022). Characterization of industrial low-density polyethylene: a thermal, dynamic mechanical, and rheological investigation. *Rheologica Acta*, *61*(10), 701–720. https://doi.org/10.1007/s00397-022-01360-1

Rana, S. K. (2002). Blend of high-density polyethylene and a linear low-density polyethylene with compositional-invariant mechanical properties. *Journal of Applied Polymer Science*, *83*(12), 2604–2608. https://doi.org/10.1002/app.10219

Satya, S. K., & Sreekanth, P. S. R. (2020). An experimental study on recycled polypropylene and high-density polyethylene and evaluation of their mechanical properties. *Materials Today: Proceedings*, *27*, 920–924. https://doi.org/10.1016/j.matpr.2020.01.259

Schyns, Z. O. G., & Shaver, M. P. (2021). Mechanical Recycling of Packaging Plastics: A Review. *Macromolecular Rapid Communications*, *42*(3). https://doi.org/10.1002/marc.202000415

Sha, H., Zhang, X., & Harrison, I. R. (1991). A dynamic mechanical thermal analysis (DMTA) study of polyethylenes. *Department of Materials Science t Engineering, The Pennsylvania State University*, *192*, 233–242.

Surendarnath, S., Flora, G., & Ramesh, G. (2025). Plastic Waste: Management Strategies and Challenges in the Developing World. In *Solid Waste Management: A Roadmap for Sustainable Environmental Practices and Circular Economy* (pp. 441–452). Springer Nature. https://doi.org/10.1007/978-3-031-78420-0_19

Techawinyutham, L., Tengsuthiwat, J., Srisuk, R., Techawinyutham, W., Mavinkere Rangappa, S., & Siengchin, S. (2021). Recycled LDPE/PETG blends and HDPE/PETG blends: mechanical, thermal, and rheological properties. *Journal of Materials Research and Technology*, *15*, 2445–2458. https://doi.org/10.1016/j.jmrt.2021.09.052

Vannessa, G. (2004). Introduction to Plastic Recycling. *Polymer International*, 1. www.rapra.net

International Conference on Engineering Innovation for Sustainable Development (ICESID 2026)
Faculty of Engineering, Ahmadu Bello University Zaria · 8–10 September 2026

EFFECT OF ALKALINE PRE-TREATMENT ON THE MECHANICAL STRENGTH AND BIODEGRADATION BEHAVIOUR OF COIR FIBRE REINFORCED CONCRETE

Oluwatobi Akin[1,*], Ibrahim Aliyu[1], Bilkisu Sada Amartey[1], Amana Ocholi[1]
[1]*Ahmadu Bello University, Zaria*
Email: olufemi_akin@yahoo.com[*], ibrahimaliyu@abu.edu.ng, bhsada@abu.edu.ng, amanaocholi@gmail.com
***Corresponding author**: Oluwatobi Akin
DOI: https://doi.org/10.67203/sp.ICESID.2026

ABSTRACT
Concrete is widely recognized for its high compressive strength, yet it suffers from low tensile capacity, brittleness and susceptibility to cracking under cyclic loading. Coir fibre offers a renewable and low-cost means of improving toughness; however, its high water absorption and vulnerability to alkaline and microbial attack limit long-term durability. This study examined the influence of NaOH pre-treatment on the workability, mechanical properties and biodegradation resistance of coir fibre reinforced concrete (CFRC). Fibres treated with 0, 5 and 10 % NaOH were incorporated at 0.5, 1.0 and 1.5 % by cement weight. Slump, compressive, flexural and split tensile strengths were determined, while fibre biodegradation was evaluated through soil-burial testing for up to 56 days. Workability decreased with increasing fibre content and alkali concentration. The combination of 1 % fibre and 5 % NaOH produced the highest mechanical strengths (22 N/mm² compressive, 4.25 N/mm² flexural and 2.89 N/mm² splitting tensile) together with the lowest mass loss (2.24 % after 56 days), compared with nearly 29 % for untreated fibre. Moderate alkaline treatment at 5 % NaOH with 1 % fibre therefore offers a practical balance of strength and durability for sustainable coir-fibre concrete.

Keywords: *Coir fibre; Alkaline pre-treatment; Concrete; Biodegradation*

1. INTRODUCTION

Sustainability was defined by the World Commission on Environment and Development (WCED) as meeting the needs of the present without compromising the ability of future generations to meet their own needs (WCED, 1987). One of the major challenges of the modern society is the impact of increasing world population on limited resources especially in the built industry. Demands for built infrastructure have caused significant waste generation, energy and material consumption by the construction industry. The building construction industry is not only a major consumer of energy, raw materials and land; it also contributes immensely to environmental pollution, especially greenhouse gas emission (Melchert, 2007). To improve sustainability in construction materials usage, the construction industry must embrace the reuse of industrial by-products and renewable materials in construction.

Presently, because of their proven performance, the use of synthetic fibres in cement composites is becoming increasingly popular. Cement research literature is replete with studies showing that the ductility, tensile strength, toughness, fatigue strength, impact resistance and absorbed energy of cement-based materials could be enhanced significantly through the addition of steel and polymer fibres. (Cui et al., 2023; Banthia et. al., 1994).

There are three types of natural fibres available for concrete reinforcement: animal-based, mineral-derived and plant-based. Animal fibers, comprising specific proteins, include silk, wool, and hair fibre. Mineral derived fibres include asbestos, wollastonite and palygorskite. Finally, plant-based fibres include cotton, hemp, jute, flax, ramie, sisal, bagasse, specialty fibres processed from wood and etc.

Major improvement in the properties of cementitious material is achievable through the incorporation of plant-based fibres described above. Fortunately, such fibres are gotten from renewable sources and are readily available at relatively low cost compared to synthetic fibres. There are huge benefits in terms of environmental, energy and resource conservation from large scale acceptance and

utilization of plant-based fibres as raw materials for cement-based composites. (Onuaguluchi & Banthia, 2016).

Although several studies have investigated the incorporation of coir fibre in cementitious composites, limited research has focused on the combined influence of fibre dosage and controlled NaOH pre-treatment on both the mechanical performance and long-term biodegradation resistance of coir fibre reinforced concrete. Most existing works have either examined untreated fibres or applied alkali treatment without systematically evaluating its effect on durability under soil burial conditions. Therefore, this study aims to address this gap by investigating the effect of different NaOH concentrations (0%, 5% and 10%) and fibre contents (0.5%, 1.0% and 1.5% by cement weight) on the workability, compressive strength, flexural strength and split tensile strength of coir fibre reinforced concrete. In addition, the biodegradation behaviour of the treated and untreated fibres was assessed through soil burial testing over a period of 56 days.

2. METHODOLOGY

2.1 Materials

Coir Fibre: Raw coconut husks were sourced from Lagos, South West Nigeria, and the fibre extraction was carried out at the National Institute for Chemical Technology (NARICT), Basawa, Zaria.

Sodium Hydroxide Pellets: The NaOH pellets used for the treatment were purchased in Zaria, Kaduna State.

Distilled Water: The distilled water used in the treatment process was obtained from the Chemistry Department, Ahmadu Bello University, Zaria.

Cement: The cement used in this research work was 42.5N Dangote brand of Ordinary Portland Cement and was obtained from open market in Samaru, Zaria, Nigeria.

Fine and Coarse Aggregate: Obtained from a local supplier in Zaria, Kaduna State, the aggregates were subjected to appropriate preliminary test to ensure they meet with standards for making concrete.

Water: Potable water was used for both mixing and curing.

2.2 Methods

2.2.1 Fibre Treatment

The coir fibres were fully immersed in separate containers containing 5% and 10% NaOH solutions at a fibre-to-solution ratio of 1:20 (w/v) and maintained at room temperature (approximately 28 ± 2 °C). Immersion was maintained for 2 hours as recommended by Widodo & Widodo (2024). The alkali treatment procedure adopted in this study follows the method proposed by Yan et al. (2016). Following the 2-hour immersion period, the fibres were removed and thoroughly washed several times with distilled water until a neutral pH was achieved. This step was necessary to eliminate residual alkali from the fibre surfaces and confirm the complete removal of excess alkalinity. Surplus water was carefully expelled by gently pressing the fibres in a sieve to minimise any mechanical damage. The treated fibres were subsequently oven-dried at approximately 70°C for 24 hours to achieve effective moisture removal while preserving their structural integrity.

2.2.2 Mixture Proportion

Table 1: Mix Proportion for Alkali Treated Coir Fibre Reinforced Concrete

Mix ID	Cement (Kg/m^3)	Water (kg/m^3)	Fine Aggregate (kg/m^3)	Coarse Aggregate (kg/m^3)	Fibre Content (%)	NaOH Content (%)
M0	320	160	480	960	0	0
M1	320	160	480	960	0.5	0
M2	320	160	480	960	1	0
M3	320	160	480	960	1.5	0
M4	320	160	480	960	0.5	5
M5	320	160	480	960	1	5
M6	320	160	480	960	1.5	5
M7	320	160	480	960	0.5	10
M8	320	160	480	960	1	10
M9	320	160	480	960	1.5	10

2.2.3 Testing of Alkali Pretreated Coir Fibre Reinforced Concrete

All the concrete batches cast underwent the following tests described below. Three trials are conducted, and the average is taken for each test performed for a specific fibre content and treatment concentration.

Slump test.

This is used to assess the workability of the concrete mixtures. The test was conducted in accordance to BS EN 12350-2:2019. The slump was measured from a mould height of 300mm.

Figure 1: Slump Test

Compressive strength test.

This is used to determine the compressive strengths of the composites used. The test was conducted in accordance to BS EN 12390-3:2019. The specimens used are 150mm concrete cubes, three sample were cast and the average taken.

Figure 2: Compressive Strength Test

Flexural strength test.

The flexural strength test is used to determine the bending capacity of the composite. It was conducted using the four-point load test in accordance to BS EN 12390-5:2019. A block size of 100mm width, 100mm depth, and a span of 500mm were used for the concrete specimens, and three sample were cast and the average taken.

Split tensile strength test.

This is used to determine the tensile strengths of the composites used. The test was conducted in accordance to BS EN 12390-6:2009. The specimens are 150×300mm concrete cylinders, and three sample were cast and the average taken.

Soil Burial Test

Biodegradation tests on treated and untreated coir fibre samples were carried out by a simple soil burial test, ASTM D570-98 (1998), to simulate the natural biodegradation of the fibre. Dog-bone-shaped samples were prepared according to ASTM 638-14 (2014); ASTM D5988-18 (2018) and were buried in natural soil in a plastic bag without any enzyme activity or any composting materials. The soil burial site was kept outdoors under an average ambient temperature of approximately 30°C, in a natural garden soil with pH value of 7.1 and average moisture content of 25% and natural organic matter and buried at a depth of 150mm. Test specimens were removed after exposure periods of 14, 28, and 56 days for further evaluation. At each retrieval stage, the samples were gently washed with water to remove any attached soil particles and subsequently air-dried at room temperature until a constant mass was obtained. Biodegradability was assessed by determining the percentage weight loss of the specimens, based on a comparison of their masses before and after the respective burial durations.

Figure 3: Soil Burial Test

2.2.4 Statistical Analysis (ANOVA)

The statistical analysis tool used for this research is the one-way ANOVA with 95% confidence level and probability value set at less than 5% are considered statistically significant while values more than 5% were considered not statistically significant.

3. RESULTS AND DISCUSSION

3.1 Slump Test Result

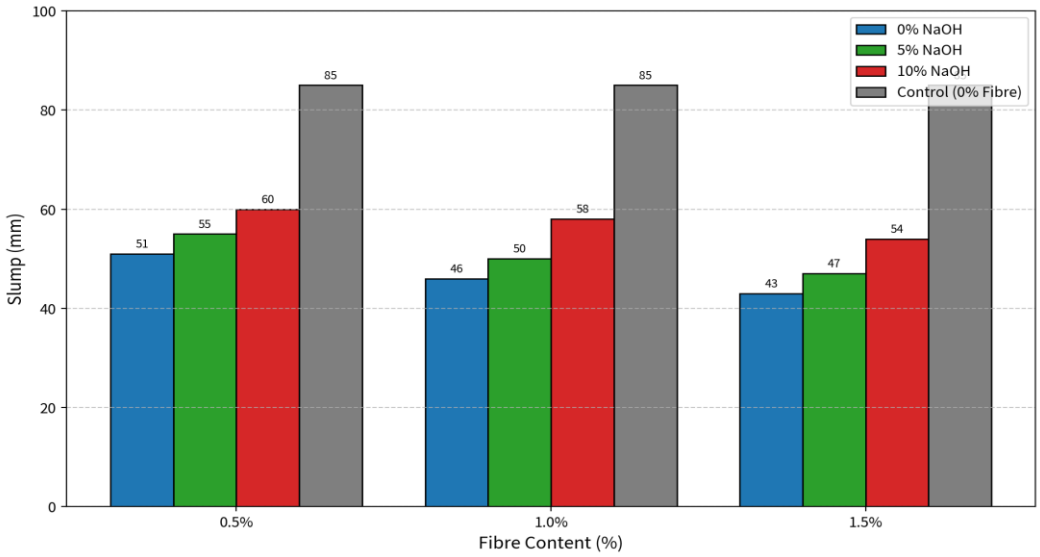

Figure 4: Comparison of Slump Test of Treated and Untreated Coir Fibre Reinforced Concrete

From the result in Figure 4, Slump decreased systematically with increasing fibre content and with higher NaOH treatment. All mixes were in the low–medium workability range (mainly S2 per EN 206), with the highest fibre (1.5%) at 10% NaOH approaching the S1/S2 boundary. The reduction is attributed to fibre water absorption and increased internal friction due to surface roughening from alkaline treatment, which improves fibre–matrix compatibility but lowers flow. For typical reinforced elements placed with vibration, S2 is acceptable; however, for congested reinforcement or pumping, admixture-based water reduction is recommended rather than increasing the water–cement ratio.

3.2 Compressive Strength

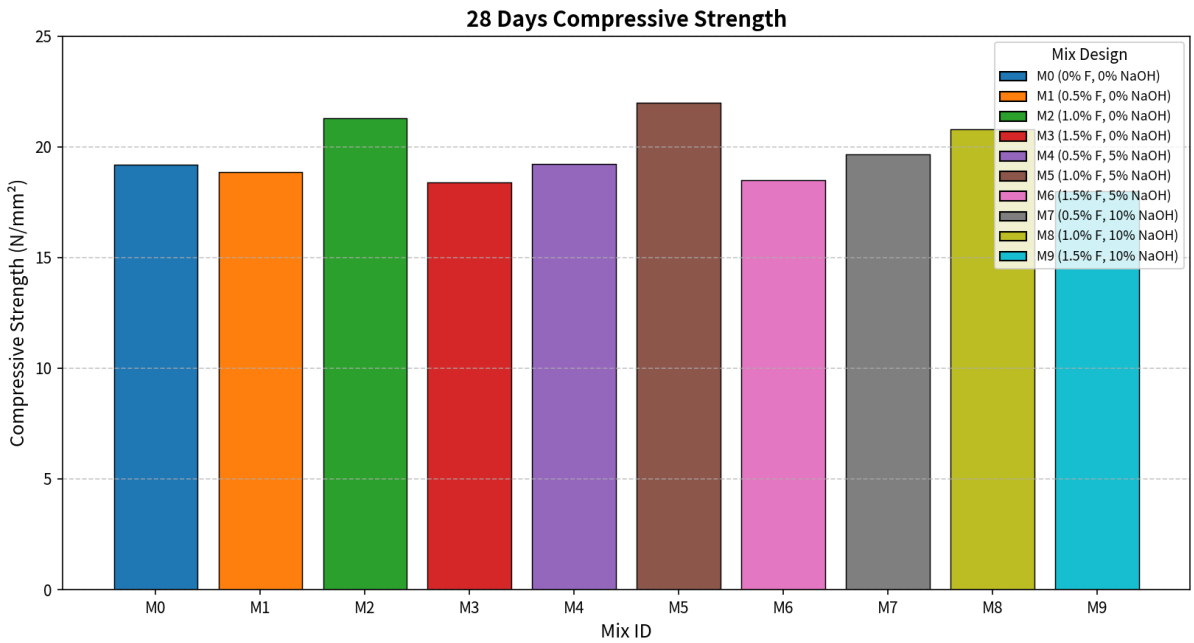

Figure 5: Compressive Strength Test of Treated and Untreated Coir Fibre Reinforced Concrete

The 28-day compressive strength results as shown in Figure 5 indicate that both fibre dosage and alkaline surface treatment significantly modulate concrete performance. At a fixed NaOH dosage, increasing coir fibre content from 0.5% to 1.0% enhanced strength, while further increase to 1.5% led

to a decline suggesting that moderate fibre addition improves reinforcement via crack-bridging and stress transfer, whereas excessive fibre induces agglomeration, impairs workability, and creates microstructural weaknesses. This trend aligns with observations in waste tyre steel fibre-reinforced concrete, where strength improved up to around 1.5% fiber content before declining due to bonding issues and poor dispersion (Augustino et. al., 2023).

The optimum mix (M5) achieved a mean compressive strength of 22 N/mm² at 28 days. According to BS EN 206, Grade C20/25 concrete requires a characteristic cylinder strength of 20 N/mm² (or characteristic cube strength of 25 N/mm²). The obtained mean strength of 22 N/mm² is therefore slightly below the typical target mean strength required for C20/25 concrete under normal production conditions. However, it satisfies the strength requirement for lower-grade applications

3.3 Flexural Strength Test

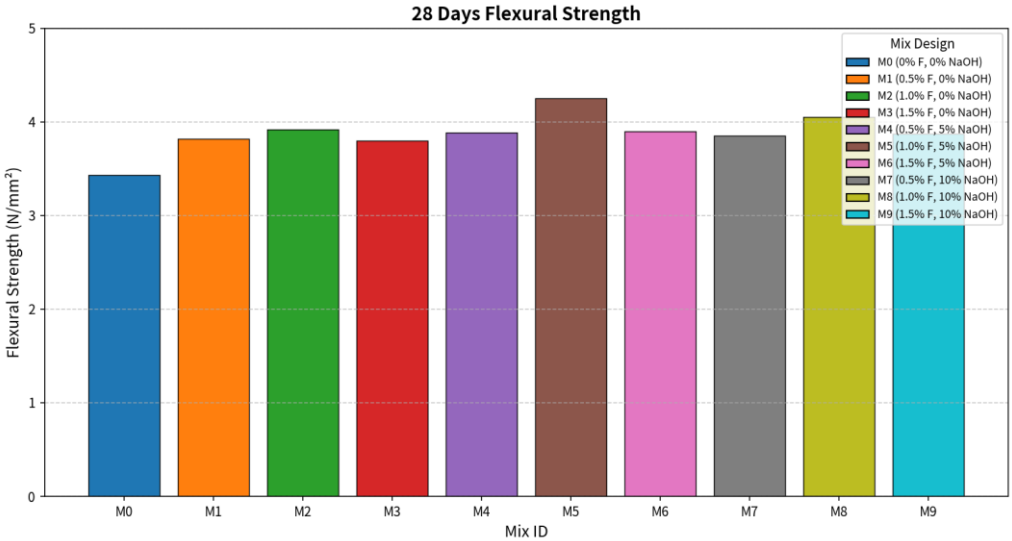

Figure 6: Flexural Strength Test of Treated and Untreated Coir Fibre Reinforced Concrete

The 28-day flexural strength results from Figure 6 demonstrate that both fibre content and NaOH treatment play significant roles in enhancing the mechanical performance of coir fibre reinforced concrete. At 0.5% fibre content, untreated fibre recorded 3.82 N/mm², while NaOH treatment increased strength to 3.88 N/mm² (5% NaOH) and 3.85 N/mm² (10% NaOH). This trend indicates that alkali treatment improved fibre-matrix adhesion by removing surface impurities such as lignin, hemicellulose, and waxes, thereby promoting better stress transfer between fibre and concrete matrix. The improvement aligns with recent findings that alkali treatment enhances the interfacial bonding of natural fibres in cementitious composites, leading to improved flexural performance (Gupta et al., 2023).

At 1.0% fibre content, flexural strength increased further, with untreated fibre yielding 3.92 N/mm² and 5% NaOH-treated fibre reaching the maximum strength of 4.25 N/mm². This demonstrates that an optimal fibre dosage combined with moderate alkali treatment provides the best reinforcement effect. However, at higher treatment levels (10% NaOH), the flexural strength slightly declined to 4.05 N/mm², suggesting that excessive alkali concentration could damage fibre structure, reducing its reinforcing efficiency. These observations are consistent with recent studies that reported diminishing mechanical properties when fibres are over-treated due to cellulose degradation (Luqman et al., 2023).

Beyond 1.0% fibre content, a further increase to 1.5% resulted in a reduction in flexural strength (ranging between 3.80 and 3.90 N/mm²), indicating that excessive fibre dosage may lead to poor dispersion and increased voids within the matrix. Overall, the results confirm that the synergy of fibre content and controlled alkali treatment enhances flexural strength, with the best performance achieved at 1.0% fibre content treated with 5% NaOH, Mix ID M5 (1% F, 5% NaOH).

3.4 Split Tensile Strength

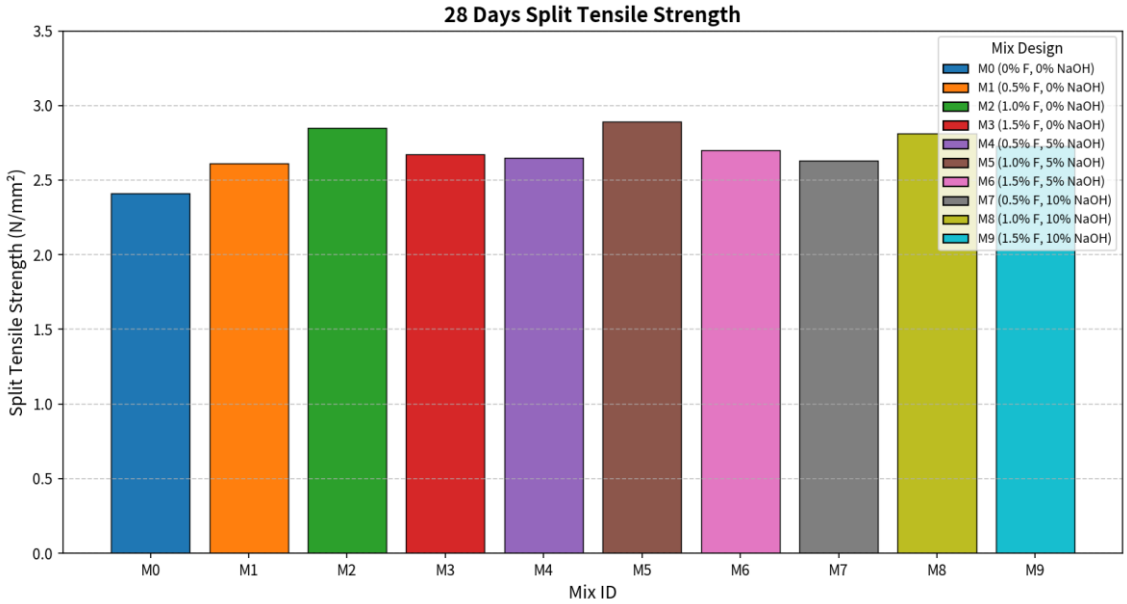

Figure 7: Split Tensile Strength Test of Treated and Untreated Coir Fibre Reinforced Concrete

The 28-day split tensile strength results from Figure 7 for NaOH-treated coir fibre-reinforced concrete reveal significant influences of fibre content (0.5%, 1%, 1.5%) and NaOH treatment (0%, 5%, 10%) on tensile performance. The highest tensile strength of 2.89 N/mm² was achieved with 1% fibre content and 5% NaOH, surpassing the untreated sample at the same fibre dosage (2.85 N/mm²) and the 10% NaOH-treated sample (2.81 N/mm²). This suggests an optimal fibre content of 1%, where coir fibres effectively bridge micro-cracks, enhancing tensile capacity without causing fibre agglomeration (Sanjay et al., 2018).

At 0.5% fibre content, NaOH treatment produced a modest improvement in strength, increasing from 2.61 N/mm² (0% NaOH) to 2.65 N/mm² (5% NaOH) and 2.63 N/mm² (10% NaOH). This indicates improved fibre-matrix bonding due to NaOH's removal of lignin and increased fibre surface roughness (Yan et al., 2016). However, at 1.5% fibre content, strengths remained relatively lower (2.67 N/mm², 2.70 N/mm² and 2.73 N/mm² for 0%, 5% and 10% NaOH respectively), suggesting that higher fibre volumes may lead to uneven distribution or reduced matrix cohesion, limiting reinforcement benefits. Overall, the results confirm that Mix ID M5 (1% F, 5% NaOH) a combination of 1% fibre content with moderate (5%) NaOH treatment provides the most effective enhancement of split tensile strength.

3.5 Soil Burial Degradation

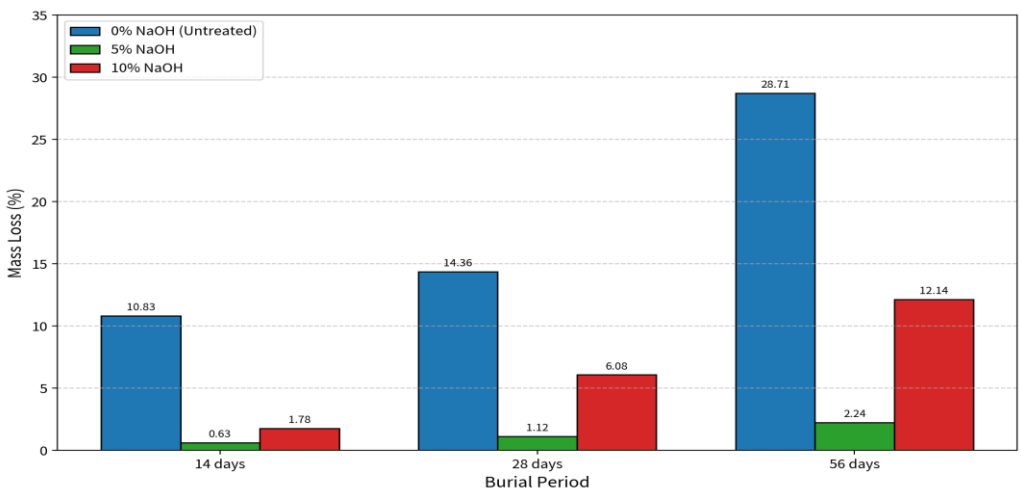

Figure 8: Soil Burial Degradation Test of Treated and Untreated Coir Fibre

The soil burial degradation test results as shown in Figure 8 demonstrate the impact of NaOH treatment on coir fiber durability, critical for their application in alkaline pretreated fiber-reinforced concrete. Untreated coir fibers (0% NaOH) exhibited significant mass loss, with 10.83% after 14 days, 14.36% after 28 days, and 28.71% after 56 days, reflecting high biodegradability due to microbial degradation of hemicellulose and cellulose in lignocellulosic fibres. This rapid degradation limits their suitability for concrete reinforcement, where moisture and alkalinity accelerate fiber breakdown (Ali et al., 2012). Conversely, 5% NaOH-treated fibers showed minimal mass loss (0.63% at 14 days, 1.12% at 28 days, 2.24% at 56 days), indicating enhanced resistance to biodegradation. Alkaline treatment removes hemicellulose and lignin, increasing cellulose crystallinity and reducing microbial attack sites (Mwaikambo & Ansell, 2002). The 10% NaOH-treated fibers had higher mass loss (1.78% at 14 days, 6.08% at 28 days, 12.14% at 56 days), suggesting structural damage from excessive alkali (Sawpan et al., 2011). It is important to note that the soil burial test in this study was conducted on free fibre specimens rather than fibres embedded within hardened concrete. Consequently, the measured mass loss represents the biodegradation behaviour of the fibres under direct soil exposure and should not be interpreted as a direct measure of fibre degradation within the concrete matrix

3.6 Analysis of Variance (ANOVA)

One-way analysis of variance (ANOVA) was conducted to evaluate the statistical significance of differences in mechanical properties among the various mixes. The results indicated statistically significant differences in compressive strength ($F = 13.45$, $p < 0.001$), flexural strength ($F = 4.65$, $p = 0.002$) and split tensile strength ($F = 2.61$, $p = 0.035$). Post-hoc Tukey's Honest Significant Difference (HSD) test further revealed that the mix containing 1% coir fibre treated with 5% NaOH (M5) generally exhibited significantly higher strengths compared to the control mix (M0) and several other combinations. These findings confirm that the observed improvements in mechanical performance, particularly for the optimal mix (M5), are statistically significant and not attributable to random variation.

Acknowledgements - The first author gratefully acknowledges the Petroleum Technology Development Fund (PTDF) for the scholarship that made this research possible.

4. CONCLUSION

From the research, the following are the conclusions:

i. Workability of the concrete decreased progressively with increasing coir fibre content and higher NaOH treatment concentrations, primarily due to increased water absorption by the fibres and greater internal friction resulting from surface roughening.

ii. ii. The optimum mechanical performance was achieved with 1.0 % fibre content treated with 5 % NaOH. This mix recorded the highest compressive strength (22 N/mm²), flexural strength (4.25 N/mm²) and splitting tensile strength (2.89 N/mm²), satisfying the requirements for Grade 20 concrete.

iii. The adoption of 5 % NaOH-treated coir fibre at 1 % dosage offers a cost-effective and environmentally sustainable alternative for improving the tensile and flexural performance of plain concrete, particularly in low- to medium-strength applications such as non-structural elements, rural infrastructure and secondary members.

iv. It should be noted that this study was limited to laboratory-scale testing using coir fibres obtained from a single source. No field application or long-term structural performance evaluation was conducted. Future studies are recommended to investigate the performance of NaOH-treated coir fibre reinforced concrete under real environmental conditions and with fibres from different geographical sources.

5. REFERENCES

Ali, M., Liu, A., Sou, H., & Chouw, N. (2012). Mechanical and dynamic properties of coconut fibre reinforced concrete. *Construction and Building Materials, 30*, 814–825. https://doi.org/10.1016/j.conbuildmat.2011.12.068

ASTM International. (1998). *ASTM D570-98: Standard Test Method for Water Absorption of Plastics*. West Conshohocken, PA: ASTM International.

ASTM International. (2014). *ASTM D638-14: Standard Test Method for Tensile Properties of Plastics*. West Conshohocken, PA: ASTM International.

ASTM International. (2018). *D5988-18: Standard Test Method for Determining Aerobic Biodegradation of Plastic Materials in Soil*. West Conshohocken, PA: ASTM International. https://doi.org/10.1520/D5988-18

Augustino DS, C Kanali, RO Onchiri, C Kabubo (2023). Simplified shear equation of deep concrete beam considering orientation effect of opening and mechanical properties of fibre-concrete interface Heliyon.

Banthia N, Moncef A, Chokri K, Sheng J. (1994). Micro-fiber reinforced cement composites. I. Uniaxial tensile response. *Can J Civil Eng. 21*(6): 999–011. https://doi.org/10.1139/l94-105

British Standards Institution. (2009). *BS EN 12390-6:2009 Testing hardened concrete. Tensile splitting strength of test specimens*. London: BSI. https://doi.org/10.3403/bsen1239062009

British Standards Institution. (2019). *BS EN 12350-2:2019 Testing fresh concrete. Slump test*. London: BSI. https://doi.org/10.3403/bsen123502019

British Standards Institution. (2019). *BS EN 12390-3:2019 Testing hardened concrete. Compressive strength of test specimens*. London: BSI. https://doi.org/10.3403/bsen1239032019

British Standards Institution. (2019). *BS EN 12390-5:2019 Testing hardened concrete. Flexural strength of test specimens*. London: BSI. https://doi.org/10.3403/bsen1239052019

BS EN 206:2013+A2:2021 — Concrete: Specification, performance, production and conformity. London: British Standards Institution (BSI), 2021

Cui K., L Xu, L Li, Y Chi (2023). Mechanical performance of steel-polypropylene hybrid fiber reinforced concrete subject to uniaxial constant-amplitude cyclic compression: fatigue behavior and unified fatigue equation. *Compos. Struct*. https://doi.org/10.1016/j.compstruct.2023.116795

Gupta, N. K., Joshi, S. K., Dhama, S., & Aggarwal, S. (2023). Enhancing mechanical properties of natural fiber composites: a study on the effects of fiber loading and filler addition. *Engineering Research Express, 5*(4), 045088. https://doi.org/10.1088/2631-8695/ad112c

Luqman, R. M., Suhot, M. A., & Hassan, M. Z. (2023). Effect of alkaline treatment on the single natural fiber strength using Weibull analysis probabilistic model. *Materials Today: Proceedings*. https://doi.org/10.1016/j.matpr.2023.01.108

Melchert L. (2007). The Dutch sustainable building policy: a model for developing countries? *Build Environ, 42*: 893–01. https://doi.org/10.1016/j.buildenv.2005.10.007

Mwaikambo, L. Y., & Ansell, M. P. (2002). Chemical modification of hemp, sisal, jute, and kapok fibers by alkalization. *Journal of Applied Polymer Science, 84*(12), 2222–2234. https://doi.org/10.1002/app.10460

Onuaguluchi, O., & Banthia, N. (2016). Plant-based natural fibre reinforced cement composites: A review. *Cement and Concrete Composites, 68*, 96–108. doi:10.1016/j.cemconcomp.2016.02.014

Sanjay, M. R., Madhu, P., Jawaid, M., Senthamaraikannan, P., Senthil, S., & Pradeep, S. (2018). Characterization and properties of natural fiber polymer composites: A comprehensive review. *Journal of Cleaner Production, 172*, 566–581. https://doi.org/10.1016/j.jclepro.2017.10.101

Sawpan, M. A., Pickering, K. L., & Fernyhough, A. (2011). Effect of fibre treatments on interfacial shear strength of hemp fibre reinforced polylactide and unsaturated polyester composites. *Composites Part A: Applied Science and Manufacturing, 42*(9), 1189–1196. https://doi.org/10.1016/j.compositesa.2011.05.003

Widodo, E., Pratikto, Sugiarto, & Widodo, T. D. (2024). Comprehensive investigation of raw and NaOH alkalized sansevieria fiber for enhancing composite reinforcement. Case Studies in

Chemical and Environmental Engineering, 9, Article 100546. https://doi.org/10.1016/j.cscee.2023.100546

World Commission on Environment and Development (WCED). (1987). *Our Common Future: The Brundtland Report on Environment and Development*. Oxford: Oxford University Press.

Yan, L., Chouw, N., Huang, L., & Kasal, B. (2016). Effect of alkali treatment on microstructure and mechanical properties of coir fibres, coir fibre reinforced-polymer composites and reinforced-cementitious composites. *Construction and Building Materials, 112*, 168–182. https://doi.org/10.1016/j.conbuildmat.2016.02.182

Yan, L., Kasal, B., & Huang, L. (2016). A review of recent research on the use of cellulosic fibres, their fibre–matrix interface and their composites in civil engineering applications. *Composites Part B: Engineering, 92*, 94–132. https://doi.org/10.1016/j.compositesb.2016.02.014

International Conference on Engineering Innovation for Sustainable Development (ICESID 2026)
Faculty of Engineering, Ahmadu Bello University Zaria · 8–10 September 2026

ENGINEERING SUSTAINABLE PCL/PLA/HAP-SR/KERATIN FIBRE BIOPOLYMER COMPOSITES FOR BONE TISSUE ENGINEERING APPLICATIONS: MECHANICAL AND CHEMICAL PROPERTIES

Kazeem Adeniyi Salami[1,*], Abdulmumin Akoredeley Alabi[1], Ibrahim Iliyasu[1], Muhammad Auwal Adamu[1], Abdulaziz Abdullahi Bada[1]

[1]*Ahmadu Bello University*

Email: salami.kazeemade@gmail.com[*], abdulmm2001@gmail.com, ibroij@gmail.com, adauwal80@gmail.com, aabada@abu.edu.ng

***Corresponding author**: Kazeem Adeniyi Salami

DOI: https://doi.org/10.67203/sp.ICESID.2026

ABSTRACT

Polycaprolactone (PCL) is widely recognised as a promising biomaterial owing to its ease of processing, biocompatibility, and biodegradability. Despite these advantages, its slow degradation rate and insufficient mechanical strength and stiffness hinder its application where enhanced structural performance is required. This study investigates the influence of PLA, strontium-doped hydroxyapatite (HAp/Sr), and keratin fibre reinforcement on the chemical structure and mechanical performance of polycaprolactone (PCL)-based biocomposites. FTIR spectroscopy was employed to examine molecular interactions between the polymer matrix and reinforcing phases. The tensile strength, Young's modulus, hardness and fracture toughness tests were conducted to evaluate mechanical integrity. The spectra show the presence of PCL through characteristic absorption bands at 2947 and 2865 cm^{-1}, attributed to the C-H asymmetric stretching vibration. A slight shift is observed in some peaks toward either a lower or a higher wavenumber, with no new peaks observed in the reinforced biocomposites. This indicates possible weak intermolecular interaction rather than new covalent bond formation. Pure PCL (BC1) exhibited the lowest mechanical performance, with an ultimate tensile strength of 4.55, Young's modulus of 2 MPa, hardness of 22.3, and fracture toughness of 0.5659. Incorporation of reinforcing agents (i.e., PLA, strontium-doped hydroxyapatite (HAp/Sr), and keratin fibre) resulted in a significant increase in hardness and fracture toughness, demonstrating the reinforcing effect of bioactive fillers. The sample BC4 showed the highest overall mechanical performance, with ultimate tensile strength (38.5), Young's modulus (4.05), hardness (56.33), and fracture toughness (1.0534), indicating enhanced stiffness and resistance to crack propagation. These findings suggest that the synergistic combination of PLA, keratin fibre, and bioactive ceramic additives significantly enhances the mechanical behaviour of PCL-based materials, making them more suitable for applications requiring improved strength, stiffness, and durability, such as biomedical scaffolds and load-bearing structures.

Keywords: *Polycaprolactone; Polylactic Acid; Keratin Fibre; Hydroxyapatite; Mechanical properties*

1.0 INTRODUCTION

Bone tissue serves a number of vital functions in daily life, including safeguarding internal organs, giving the body structural support, facilitating mobility, and controlling the storage and release of minerals (Gharibshahian et al., 2023). Many people suffer from bone diseases brought on by trauma, tumour excision, infection, congenital anomalies, and injuries sustained in accidents (Li et al., 2020). However, defective bone tissue possesses the ability to self-repair or self-regenerate, which occurs in four stages: hematoma, soft callus, hard callus formation and bone remodelling (Monfared et al., 2022). Self-repair and self-regeneration weaken with age or in critical bone defects (i.e., cracks above 2.5 cm). Tissue engineering deploys an innovative approach to repair bone defects (Jung et al., 2022;Yudoh et al., 2023). The approach adopts engineered bone grafting techniques, which aid the healing of the defective bone, while also providing the needed strength that supports the healing process (Menotti et al., 2023). Archunan & Petronis (2021) highlighted that approximately 2.2 million bone grafting techniques are used in orthopaedic surgical processes worldwide, and the number is expected to increase yearly by 13%. However, the current bone grafting techniques (i.e., allograft and autograft) face

different challenges such as risk of disease transmission, limited availability and immune rejection (Gharibshahian et al., 2023).

To overcome the shortfalls from the current bone grafting techniques, bone tissue engineering offers a solution, involving the use of a three-dimensional scaffold made from biomaterials that creates an environment for cell proliferation and regeneration (Biscaia et al., 2022). Biomaterial scaffolds for repairing defective bone are often developed from standalone materials (i.e., ceramics, biodegradable polymers, and metallic materials) or composites (Hernandez et al., 2017). A suitable biomaterial needs to possess good mechanical properties so that it can provide structural support during the healing process (Obada et al., 2021; You et al., 2022). The materials and production methods (i.e., melt extrusion/hot pressing, solvent casting, electrospinning and many others) used in producing the scaffolds influence the mechanical properties.

Biomaterial scaffolds could be produced from biodegradable polymers (either synthesised or sourced naturally) since they have excellent mechanical properties and porous architecture that creates a bioactive environment for cell proliferation and adhesion (Saurav et al., 2024). PCL is known for its great flexibility (Loyo et al., 2024), while PLA is a cost-effective polymer, with good biocompatibility and a low melting point (Zarei et al., 2023). Several attempts have been made to develop a polymer composite by blending PLA and PCL (Aliotta et al., 2023; Min et al., 2024). Vonbrunn et al. (2020) reported that incorporating PCL into the PLA matrix results in a broad surface area for tissue regeneration and host cell structural support. However, PCL/PLA scaffolds have poor hydrophilicity, low cell migration and adhesion. The poor hydrophilicity could result in prolonged degradation (Mohandesnezhad et al., 2020). Also, they lack the optimal combination of mechanical strength, bioactivity and degradation properties necessary for successful bone regeneration.

In this study, scaffolds for tissue engineering rely on the interplay of biodegradable polymers (PLA and PCL), bioactive filler (HAp/Sr), and reinforcement material (keratin fibre). HAp is known for its biocompatibility, osteointegration, osteoconductivity and non-toxicity (Bee & Hamid, 2020). The addition of hydroxyapatite (HAp), enhanced with strontium (Sr), introduces osteoconductive properties that promote bone formation and integration (Obada et al., 2021). Combining these components with biodegradable polymers like polycaprolactone (PCL) and polylactic acid (PLA) creates a scaffold that closely mimics the structure and function of natural bone. Keratin fibres, derived from chicken feathers, are a durable, abundant, and underutilised natural protein with exceptional bioactive and biocompatibility properties, making them a potential reinforcement material. Cheng et al. (2009) reported that keratin fibre obtained from chicken feathers has a special cross-linked and semi-crystalline structure which helps improve the mechanical stress resistance and elastic modulus of polymer-based composites. However, the study utilised PLA rather than PCL; the findings provide the provide for reinforcing capability of keratin fibre derived from chicken feathers. The utilisation of locally sourced materials (i.e., sheep bone and chicken feathers) offers potential cost and sustainability benefits by converting waste into valuable biomaterials. These materials could lower reliance on imported materials while supporting local production; consequently, this supports Nigeria's objectives for industrial growth, creation of sustainable materials and waste management.

Therefore, this study examined the effect of incorporating PLA, HAp/Sr and keratin fibre on the mechanical properties of PCL biopolymer composites. The hardness, fracture toughness, tensile strength and Young's modulus of the developed biopolymer composite were examined. The functional groups in the samples were identified using the Fourier Transform Infrared Spectroscopy technique.

2.0 MATERIALS AND METHODS

2.1 Materials

The polycaprolactone and the polylactic acid powder were purchased from Sino Convoy New Material Co., Ltd. (China) and Guangzhou Bio Plus Materials Technology Co., Ltd, respectively. The hydroxyapatite was obtained from sheep bone, which was sourced from a local abattoir. The collected sheep bones were washed, dried, and carbonised in a charcoal-fired oven. The carbonised bones were calcined in a Muffle furnace at 900 ^{o}C for 2 hours. A mortar and pestle were used to grind the calcined bone into a fine powder. A 100 µm mesh was used to sieve the resulting fine powder to get a uniform particle size (Obada et al., 2024). Strontium was incorporated into the HAp powder using the solution

gelation (sol-gel) technique in a proportion suggested by Obada et al. (2021). The keratin fibres were extracted from chicken feathers using the hydrolysis technique.

2.2 Production of the Pure PCL and PCL Biocomposite Polymers

The polymer samples were produced using a solvent-casting technique guided by the process presented by Adamu et al. (2023) and Rinaldi et al. (2024). The PCL and PLA powders were dissolved in chloroform, then stirred till the powder dissolved completely in the solution. Keratin fibres and HAp/Sr powder were added to the solution, followed by stirring to ensure even distribution. The mixture was then poured into a mould and allowed to dry under controlled conditions. The dried samples were subjected to characterisation and testing. The samples were developed using the composition in Table 1, which was selected after optimising the process using Box-Behnken DOE. The functional groups in the developed samples were identified by FT-IR.

Table 1: Composition of the samples

Sample Code	PCL (wt.%)	PLA (wt.%)	HAp/Sr (wt.%)	Keratin fibre (wt.%)
BC1	100	--	--	--
BC2	78	22	--	--
BC3	68	22	10	--
BC4	61	22	10	7

2.3 Hardness and Fracture Toughness

The hardness of the developed sample was measured using a Vickers hardness tester. An indent load of 300 grams was used, and the indent diagonal was measured, which was then used to calculate the hardness. The fracture toughness was calculated using Equation 1 as adopted by Obada et al. (2023), the parameters included the hardness value, diagonal length and the crack length.

$$K_{ic} = 0.016 \times \left(\frac{c}{a}\right)^{-1.5} \times H_v \times a^{0.5} \quad 1$$

Where Hv: Vickers hardness, c is the sum of half of the diagonal length (l), and a is the crack length: $0.5(a + l)$

2.4 Tensile Strength Measurement

The tensile strength measurement was conducted using a universal testing machine. The standard dimensions used for the test are a gauge length of 50 mm and a diameter of 12.5 mm. The maximum load (tensile strength) and elongation at break were recorded as the test proceeded until the specimen breaks. The tensile strength and Young's modulus of the samples were obtained from the data generated by the machine. For each composition, three independent specimens (n = 3) were tested under the same experimental conditions.

3.0 RESULT AND DISCUSSION

3.1 FTIR Analysis of the Pure PCL and PCL Biocomposite Scaffolds

The FTIR spectra of the PCL and PCL biocomposite are shown in Figure 1. The spectra show the presence of PCL through characteristic absorption bands at 2947 and 2865 cm^{-1}, attributed to the C-H asymmetric stretching vibration. In the BC2 spectrum, no new peaks were observed, indicating that no chemical decomposition or interaction occurred between PCL and PLA during the development process. Maleki et al. (2021) developed a PCL/PLA composite, and the FTIR spectra of PLA, PCL, and the PCL/PLA blend were reported to be similar, indicating that no chemical reaction occurred. The authors then concluded that this illustrates a proper mixture. However, a slight shift is seen in some peaks to either a lower or a higher wavenumber. For instance, the C=O symmetric vibration was seen at 1716 cm^{-1}, but shifted to 1728 cm^{-1} in the BC2 spectrum. The peak shift is attributed to the weak interaction between the PCL and PLA (Lu & Kazarian, 2020). A similar shift is observed in the BC3 and BC4 sample spectra, with no new peak observed, suggesting that the principal functional groups of the individual constituents were retained following the development of the composite. This aligns with the study conducted by Shojaei et al. (2019).

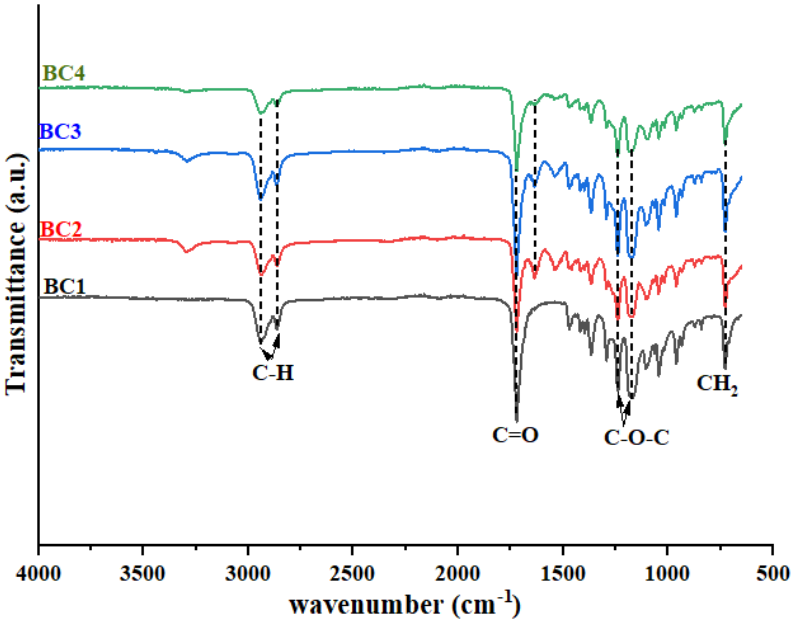

Figure 1: FTIR spectra of the pure PCL and PCL biocomposite

3.2 Mechanical Properties of the Pure PCL and PCL Biocomposite Scaffolds

3.2.1 Hardness Value and Fracture Toughness

The hardness value and fracture toughness of the unreinforced PCL and reinforced PCL are illustrated in Figure 2. The differences observed in samples' hardness and fracture toughness show the effect of both ceramic reinforcement and polymer blending on resistance to crack propagation and deformation. The BC1 had the lowest hardness (22.3 Hv) and fracture toughness (0.566 $MPam^{1/2}$), confirming its relatively soft structure (Chen et al., 2018). A slight improvement was observed when PCL was blended with PLA, as seen in BC2, with hardness and fracture toughness increasing to 24.27 Hv and 0.646 $MPam^{1/2}$, respectively. This indicates that PLA increases the PCL rigidity and its energy absorption capacity during fracture. Homkhiew et al. (2024) noted that increasing the PLA concentration made the composite less flexible, resulting in increased hardness. A more significant improvement was recorded in BC3, where the hardness increased to 33.33 Hv and fracture toughness to 0.664 $MPam^{1/2}$. This enhancement is attributed to the presence of reinforcing agents (i.e., PLA polymer and hydroxyapatite-strontium particles).

These reinforcing agents could have promoted better stress distribution and energy-absorbing capacity that delays fracture propagation. The sample BC4 had the highest value, with hardness and fracture toughness reaching 56.33 Hv and 1.053 $MPam^{1/2}$, respectively. When compared with BC1, BC4 gave a substantial increase, increasing approximately by 60.4% for hardness and 46.3% for fracture toughness. This suggests that there is a strong synergistic interaction between the reinforcing agents and the polymer matrix. The improved homogeneous dispersion of the fillers and enhanced interfacial bonding between the matrix and the filler contributed to improved crack formation and resistance against indentation. The hardness value obtained for BC4 (56.33 Hv) falls within the hardness range of trabecular bone (41.8 – 90.8 Hv) (Wang et al., 2006), making the developed composite suitable for cancellous-bone application, since cortical bone requires higher hardness and strength.

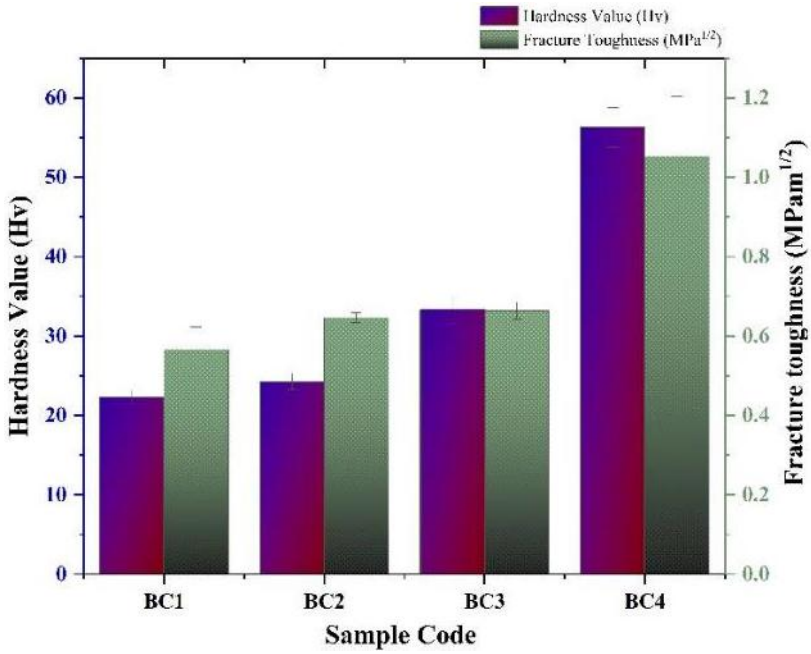

Figure 2: Hardness value and fracture toughness of the samples

3.2.2 Tensile Strength and Young Modulus

Figure 3 presents the ultimate tensile strength and Young's modulus of the pure PCL and the BC4 from section 3.2.1. A low ultimate tensile strength of 4.55 MPa and a Young's modulus of 2 MPa indicate the PCL's ductile, soft and low-stiffness nature. Hashim et al. (2022) noted that the PCL polymer had low modulus and tensile strength. These low values indicate that the BC1 had low resistance to applied stress and possessed a significant tendency for elastic deformation under load, which limits its applicability in structurally challenging situations. A significant increase was observed for BC4, resulting in an ultimate tensile strength of 38.5 MPa and a Young's modulus of 4.05 MPa. This shows that the tensile strength and Young's modulus increase by 88.1% and 50.6%, respectively. This shows a remarkable improvement in the load-bearing capacity and stiffness compared to BC1. The measured values in the study are relatively low, attributed to the production technique used (solvent casting), which can introduce porosity and residual solvent within the composite, thereby lowering the overall mechanical performance.

The improvement suggests that the addition of the reinforcing agents could have fewer structural defects and promote effective load distribution across the matrix. In general, sample BC4 exhibits superior resistance to failure, making it more suitable where structural integrity and mechanical reliability are required.

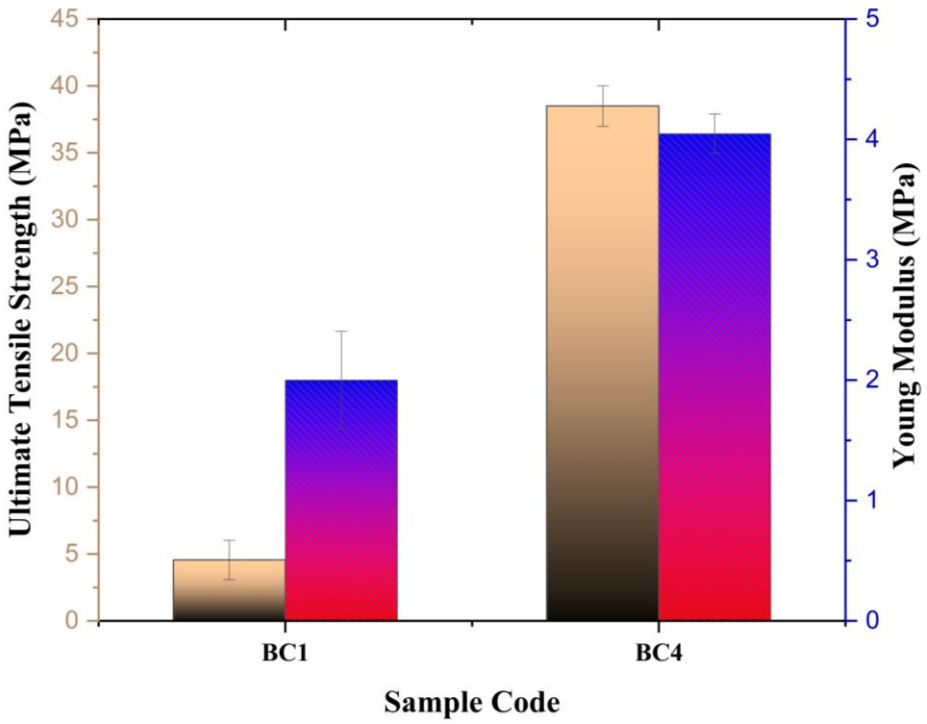

Figure 3: Ultimate tensile strength and Young's modulus of the samples

3.3 Morphological Analysis of the Pure PCL and PCL Biocomposite Scaffolds

The SEM images of the pure PCL and PCL biocomposite scaffolds are illustrated in Figure 4. No surface fractures and a uniform surface morphology were observed in the BC1 scaffold. Additionally, small pores formed as a result of chloroform evaporating during drying were observed. The results are consistent with the research of Adamu et al. (2024), which claimed that the evaporation of chloroform during drying leaves tiny pores in the unreinforced PCL scaffold. The surface of sample BC4 was smoother and more compact, suggesting that the reinforcing agents were evenly distributed throughout the PCL matrix. This could have strengthened the polymer chain, improving the mechanical characteristics, as observed in Figures 3 and 4. According to Matsumoto (2024), the polymer chain is influenced by the surface characteristics and behaviour of the polymer. The physical and mechanical qualities might be impacted by a smooth, compacted surface that limits the mobility of the polymer chains. Additionally, there was a white, bright granule on the surface, indicating that HAp/Sr particles were present in the polymer matrix.

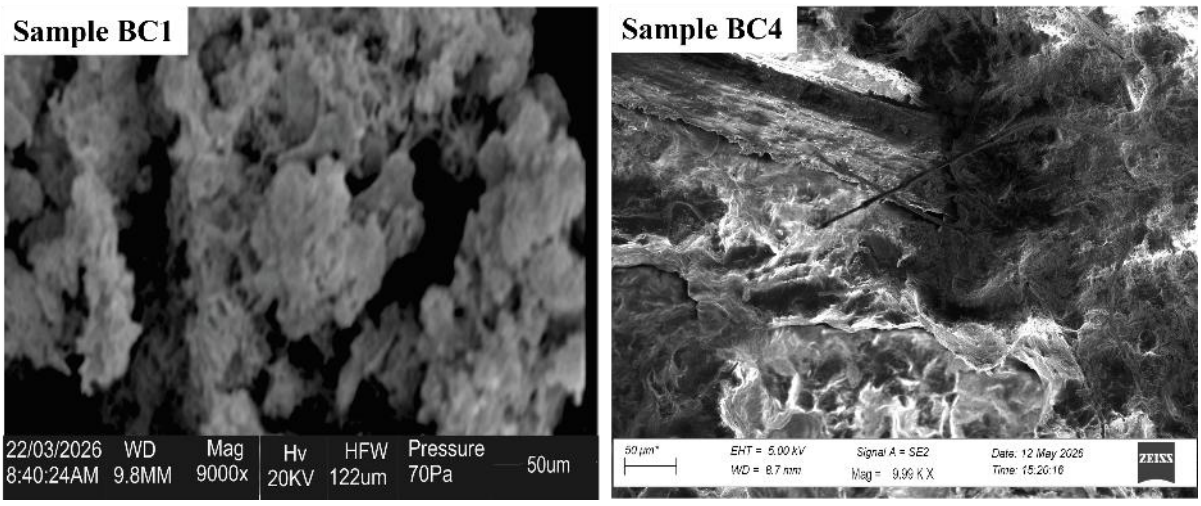

Figure 4: SEM images of the samples

3.0 CONCLUSION

The study demonstrated the successful improvement of the mechanical properties of PCL biopolymer-based composites through material modification. The FTIR spectra show C-H asymmetric stretching vibrations at 2947 and 2865 cm^{-1}, characteristic of polycaprolactone. The addition of reinforcing agents (PLA, HAp/Sr and keratin fibre) resulted in no new peaks, suggesting the materials were properly integrated into the PCL. There is a significant improvement in the mechanical performance resulting from the incorporation of PLA, keratin fibres, and bioactive fillers such as hydroxyapatite and strontium. Sample BC4, which comprises the three reinforcements, exhibited a significant increase in the mechanical properties when compared to BC1. For instance, the addition of the reinforcing agents increases the hardness and fracture toughness by 60.4% and 46.3%, respectively. Also, the tensile strength increased by 88.1%, while the Young's modulus increased by 50.6%. This enhancement is attributed to efficient stress transfer and improved interfacial bonding between the polymer matrix and reinforcing phases. Also, the improvement in both tensile strength and fracture resistance indicates that the developed biocomposites overcome the main limitation of pure PCL, achieving a more balanced combination of durability, toughness and stiffness. In conclusion, the sample BC4 had strong potential as a suitable material in bone repair and regeneration. The findings contribute to the ongoing development of high-performance biodegradable composites, while providing a foundation for further research on structural optimisation.

REFERENCES

Adamu, M. A., Sumaila, M., Dauda, M., & Ause, T. (2023). Production and optimization of novel rice husk ash reinforced polycaprolactone/hydroxyapatite composite for bone regeneration using grey relational analysis. *Scientific African*, *19*. https://doi.org/10.1016/j.sciaf.2023.e01563

Adamu, M. A., Sumaila, M., Dauda, M., & Ause, T. (2024). A novel polycaprolactone/rice husk ash/hydroxyapatite biopolymer composite for bone implant: physico-mechanical and biodegradable analysis. *Iranian Polymer Journal (English Edition)*, *33*, 395–404. https://doi.org/10.1007/s13726-023-01248-8

Aliotta, L., Gigante, V., Geerinck, R., Coltelli, M. B., & Lazzeri, A. (2023). Micromechanical analysis and fracture mechanics of Poly(lactic acid) (PLA)/Polycaprolactone (PCL) binary blends. *Polymer Testing*, *121*. https://doi.org/10.1016/j.polymertesting.2023.107984

Archunan, M. W., & Petronis, S. (2021). Bone Grafts in Trauma and Orthopaedics. *Cureus*, *13*, e17705. https://doi.org/10.7759/cureus.17705

Bee, S. L., & Hamid, Z. A. A. (2020). Hydroxyapatite derived from food industry bio-wastes: Syntheses, properties and its potential multifunctional applications. In *Ceramics International* (Vol. 46, pp. 17149–17175). Elsevier Ltd. https://doi.org/10.1016/j.ceramint.2020.04.103

Biscaia, S., Branquinho, M. V., Alvites, R. D., Fonseca, R., Sousa, A. C., Pedrosa, S. S., Caseiro, A. R., Guedes, F., Patrício, T., Viana, T., Mateus, A., Maurício, A. C., & Alves, N. (2022). 3D Printed Poly(ε-caprolactone)/Hydroxyapatite Scaffolds for Bone Tissue Engineering: A Comparative Study on a Composite Preparation by Melt Blending or Solvent Casting Techniques and the Influence of Bioceramic Content on Scaffold Properties. *International Journal of Molecular Sciences*, *23*. https://doi.org/10.3390/ijms23042318

Chen, J., Zhang, T. Y., Jin, F. L., & Park, S. J. (2018). Fracture Toughness Improvement of Poly(lactic acid) Reinforced with Poly(ε-caprolactone) and Surface-Modified Silicon Carbide. *Advances in Materials Science and Engineering*, *2018*(1), 6537621. https://doi.org/10.1155/2018/6537621

Cheng, S., Lau, K. tak, Liu, T., Zhao, Y., Lam, P. M., & Yin, Y. (2009). Mechanical and thermal properties of chicken feather fiber/PLA green composites. *Composites Part B: Engineering*, *40*, 650–654. https://doi.org/10.1016/j.compositesb.2009.04.011

Gharibshahian, M., Salehi, M., Beheshtizadeh, N., Kamalabadi-Farahani, M., Atashi, A., Nourbakhsh, M. S., & Alizadeh, M. (2023). Recent advances on 3D-printed PCL-based composite scaffolds for bone tissue engineering. In *Frontiers in Bioengineering and Biotechnology* (Vol. 11). Frontiers Media SA. https://doi.org/10.3389/fbioe.2023.1168504

Hashim, H. binti, Emran, N. A. A. binti, Isono, T., Katsuhara, S., Ninoyu, H., Matsushima, T., Yamamoto, T., Borsali, R., Satoh, T., & Tajima, K. (2022). Improving the mechanical properties of polycaprolactone using functionalized nanofibrillated bacterial cellulose with high dispersibility and long fiber length as a reinforcement material. *Composites Part A: Applied Science and Manufacturing*, *158*, 106978. https://doi.org/10.1016/J.COMPOSITESA.2022.106978

Hernandez, I., Kumar, A., & Joddar, B. (2017). A bioactive hydrogel and 3d printed polycaprolactone system for bone tissue engineering. *Gels*, *3*. https://doi.org/10.3390/gels3030026

Homkhiew, C., Khamtree, S., Srivabut, C., & Petdee, T. (2024). Biocomposite materials from natural rubber/polylactic acid blends reinforced rubberwood sawdust for producing children's toys. *Cleaner Engineering and Technology*, *22*, 100803. https://doi.org/10.1016/J.CLET.2024.100803

Jung, K. J., Sarkar, S. K., Kim, W. J., Kim, B. R., Park, J. S., & Lee, B. T. (2022). Bone Regeneration by Multichannel Cylindrical Granular Bone Substitute for Regeneration of Bone in Cases of Tumor, Fracture, and Arthroplasty. *International Journal of Environmental Research and Public Health*, *19*. https://doi.org/10.3390/ijerph19148228

Li, Y., Li, Q., Li, H., Xu, X., Fu, X., Pan, J., Wang, H., Fuh, J. Y. H., Bai, Y., & Wei, S. (2020). An effective dual-factor modified 3D-printed PCL scaffold for bone defect repair. *Journal of Biomedical Materials Research - Part B Applied Biomaterials*, *108*, 2167–2179. https://doi.org/10.1002/jbm.b.34555

Loyo, C., Cordoba, A., Palza, H., Canales, D., Melo, F., Vivanco, J. F., Baier, R. V., Millán, C., Corrales, T., & Zapata, P. A. (2024). Effect of Gelatin Coating and GO Incorporation on the Properties and Degradability of Electrospun PCL Scaffolds for Bone Tissue Regeneration. *Polymers*, *16*. https://doi.org/10.3390/polym16010129

Lu, H., & Kazarian, S. G. (2020). How does high-pressure CO2 affect the morphology of PCL/PLA blends? Visualization of phase separation using in situ ATR-FTIR spectroscopic imaging. *Spectrochimica Acta Part A: Molecular and Biomolecular Spectroscopy*, *243*, 118760. https://doi.org/10.1016/J.SAA.2020.118760

Maleki, F., Jafari, H., Ghaffari-bohlouli, P., Shahrousvand, M., Sadeghi, G. M. M., Alimoradi, H., & Shavandi, A. (2021). Proliferation and osteogenic differentiation of mesenchymal stem cells on three-dimensional scaffolds made by thermal sintering method. *Chemical Papers*, *75*(11), 5971–5981. https://doi.org/10.1007/S11696-021-01774-W

Matsumoto, T. (2024). Control of surface structure and properties by side chain effects of polymers. *Polymer Journal 2024 57:3*, *57*(3), 249–258. https://doi.org/10.1038/s41428-024-00976-9

Menotti, F., Scutera, S., Coppola, B., Longo, F., Mandras, N., Cavallo, L., Comini, S., Sparti, R., Fiume, E., Cuffini, A. M., Banche, G., Palmero, P., & Allizond, V. (2023). Tuning of Silver Content on the Antibacterial and Biological Properties of Poly(ε-caprolactone)/Biphasic Calcium Phosphate 3D-Scaffolds for Bone Tissue Engineering. *Polymers*, *15*. https://doi.org/10.3390/polym15173618

Min, K. E., Jang, J. W., Kim, C., & Yi, S. (2024). Enhancement of Mechanical Properties of PCL/PLA/DMSO2 Composites for Bone Tissue Engineering. *Applied Sciences (Switzerland)*, *14*(14). https://doi.org/10.3390/app14146190

Mohandesnezhad, S., Pilehvar-Soltanahmadi, Y., Alizadeh, E., Goodarzi, A., Davaran, S., Khatamian, M., Zarghami, N., Samiei, M., Aghazadeh, M., & Akbarzadeh, A. (2020). In vitro evaluation of Zeolite-nHA blended PCL/PLA nanofibers for dental tissue

engineering. *Materials Chemistry and Physics*, *252*. https://doi.org/10.1016/j.matchemphys.2020.123152

Monfared, M. H., Nemati, A., Loghman, F., Ghasemian, M., Farzin, A., Beheshtizadeh, N., & Azami, M. (2022). A deep insight into the preparation of ceramic bone scaffolds utilizing robocasting technique. In *Ceramics International* (Vol. 48, pp. 5939–5954). Elsevier Ltd. https://doi.org/10.1016/j.ceramint.2021.11.268

Obada, D. O., Salami, K. A., & Oyedeji, A. N. (2024). Two-stage repeat sintering: A modified method for fabricating hydroxyapatite scaffolds with enhanced mechano-therapeutic properties. *Next Materials*, *3*, 100151. https://doi.org/10.1016/j.nxmate.2024.100151

Obada, D. O., Salami, K. A., Oyedeji, A. N., Fasanya, O. O., Suleiman, M. U., Ibisola, B. A., Atta, A. Y., Dodoo-Arhin, D., Kuburi, L. S., Dauda, M., & Dauda, E. T. (2021). Solution combustion synthesis of strontium-doped hydroxyapatite: Effect of sintering and low compaction pressure on the mechanical properties and physiological stability. *Materials Letters*, *304*. https://doi.org/10.1016/j.matlet.2021.130613

Rinaldi, G., Coccia, E., Ferrentino, N., Germinario, C., Grifa, C., Paolucci, M., & Pappalardo, D. (2024). Effect of Keratin Waste on Poly(ϵ -Caprolactone) Films: Structural Characterization, Thermal Properties, and Keratinocytes Viability and Proliferation Studies. *Advances in Polymer Technology*, *2024*. https://doi.org/10.1155/2024/3308910

Salami, K. A., Obada, D. O., Alabi, A. A., Csaki, S., & Oyedeji, A. N. (2022). Utilization of sawdust as a pore-former in the fabrication of ceramic adsorbents for water purification. *Journal of the Australian Ceramic Society*, *58*, 1297–1309. https://doi.org/10.1007/s41779-022-00778-3

Saurav, S., Sharma, P., Kumar, A., Tabassum, Z., Girdhar, M., Mamidi, N., & Mohan, A. (2024). Harnessing Natural Polymers for Nano-Scaffolds in Bone Tissue Engineering: A Comprehensive Overview of Bone Disease Treatment. In *Current Issues in Molecular Biology* (Vol. 46, pp. 585–611). Multidisciplinary Digital Publishing Institute (MDPI). https://doi.org/10.3390/cimb46010038

Shojaei, S., Nikuei, M., Goodarzi, V., Hakani, M., Khonakdar, H. A., & Saeb, M. R. (2019). Disclosing the role of surface and bulk erosion on the viscoelastic behavior of biodegradable poly(ε-caprolactone)/poly(lactic acid)/hydroxyapatite nanocomposites. *Journal of Applied Polymer Science*, *136*(10). https://doi.org/10.1002/APP.47151

Vonbrunn, E., Mueller, M., Pichlsberger, M., Sundl, M., Helmer, A., Wallner, S. A., Rinner, B., Tuca, A. C., Kamolz, L. P., Brislinger, D., Glasmacher, B., & Lang-Olip, I. (2020). Electrospun PCL/PLA Scaffolds Are More Suitable Carriers of Placental Mesenchymal Stromal Cells Than Collagen/Elastin Scaffolds and Prevent Wound Contraction in a Mouse Model of Wound Healing. *Frontiers in Bioengineering and Biotechnology*, *8*. https://doi.org/10.3389/fbioe.2020.604123

Wang, X. J., Chen, X. B., Hodgson, P. D., & Wen, C. E. (2006). Elastic modulus and hardness of cortical and trabecular bovine bone measured by nanoindentation. *Transactions of Nonferrous Metals Society of China*, *16*(SUPPL.), s744–s748. https://doi.org/10.1016/S1003-6326(06)60293-8

You, B. C., Meng, C. E., Mohd Nasir, N. F., Mohd Tarmizi, E. Z., Fhan, K. S., Kheng, E. S., Abdul Majid, M. S., & Mohd Jamir, M. R. (2022). Dielectric and biodegradation properties of biodegradable nano-hydroxyapatite/starch bone scaffold. *Journal of Materials Research and Technology*, *18*, 3215–3226. https://doi.org/10.1016/j.jmrt.2022.04.014

Yudoh, K., Sugishita, Y., & Suzuki-Takahashi, Y. (2023). Bone Development and Regeneration 2.0. In *International Journal of Molecular Sciences* (Vol. 24). Multidisciplinary Digital Publishing Institute (MDPI). https://doi.org/10.3390/ijms24108761

Zarei, M., Shabani Dargah, M., Hasanzadeh Azar, M., Alizadeh, R., Mahdavi, F. S., Sayedain, S. S., Kaviani, A., Asadollahi, M., Azami, M., & Beheshtizadeh, N. (2023). Enhanced bone tissue regeneration using a 3D-printed poly(lactic acid)/Ti6Al4V composite scaffold with

plasma treatment modification. *Scientific Reports*, *13*. https://doi.org/10.1038/s41598-023-30300-z

International Conference on Engineering Innovation for Sustainable Development (ICESID 2026)
Faculty of Engineering, Ahmadu Bello University Zaria · 8–10 September 2026

ENGINEERING SUSTAINABLE SOLID BIOFUELS FOR NIGERIA'S CLEAN ENERGY TRANSITION: COMPARATIVE PERFORMANCE EVALUATION OF INDIVIDUAL AND BLENDED AGRO-RESIDUE BRIQUETTES

Binta Zakari Bello[1,*], Rabiu Kamaldeen[1], Aisha Talatu Ibrahim[1]
[1]*Ahmadu Bello University Zaria*
Email: bzakari@gmail.com*, rabiukamaldeen@gmail.com, aishaibrahimtalatu@gmail.com
***Corresponding author**: Binta Zakari Bello
DOI: https://doi.org/10.67203/sp.ICESID.2026

ABSTRACT

Nigeria's transition toward a sustainable, low-carbon energy system necessitates decentralized engineering solutions capable of converting abundant agricultural residues into clean, high-performance solid biofuels. This study presents a comparative experimental evaluation of solid biofuels engineered from maize straw, rice straw, wheat straw, and selected binary blends, characterized across 18 distinct formulations using cassava starch, Gum Arabic, and coal tar as binders under compaction pressures of 5 and 10 MPa. Characterization included higher heating value (HHV), ash content, moisture content, compressive strength, ignition time, burning rate, and water resistance index (WRI). Two-way Analysis of Variance (ANOVA) and Pearson correlation analyses demonstrated that biomass composition is the primary determinant of thermal behavior and ash characteristics. The 50:50 maize–wheat straw blend bonded with coal tar at 5 MPa (5M5Wc5) recorded the highest HHV (20.5 MJ kg^{-1}), the shortest ignition time (10 s), and a relatively low ash content (7.0%). The highest compressive strength was recorded by the Gum Arabic-bonded wheat straw formulation Wg5 (206.9 kN m^{-2}). Across the full dataset, ash content was negatively associated with HHV ($r = -0.696$), whereas the correlation between compressive strength and WRI is also negative at $r = -0.29$. In Phase II, exploratory two-way ANOVA without replication indicated a statistically significant main effect of compaction pressure on moisture content ($p = 0.0017$), but not on compressive strength ($p = 0.6175$); interaction effects could not be independently estimated. The results demonstrate application-specific trade-offs among thermal performance, mechanical integrity, moisture resistance, and environmental considerations. By converting agricultural residues into value-added solid fuels, the study supports resource recovery and circular-bioeconomy pathways while providing an engineering basis for decentralized biomass-energy systems in Nigeria.

Keywords: *Biomass densification; Binder characteristics; Rice straw; Wheat straw; Maize straw; Waste Valorization; Circular Bioeconomy*

1. INTRODUCTION

The global transition towards low-carbon energy systems has accelerated efforts to diversify renewable energy portfolios, improve energy security, and reduce greenhouse gas emissions in line with the Paris Agreement and the United Nations Sustainable Development Goals (SDGs). Sustainable bioenergy remains a critical component of the global energy transition because it provides dispatchable renewable energy, supports waste valorization, and contributes to decarbonizing sectors that are difficult to electrify, such as hard-to-electrify thermal applications. Modern bioenergy applications are increasingly viewed as complementary to solar and wind power within integrated renewable energy systems (IPCC, 2022).

Nigeria's growing population, rapid industrialization, and increasing demand for reliable, affordable, and sustainable energy have intensified the need for engineering solutions that address energy security, economic development, and climate change mitigation. Despite abundant renewable energy resources, energy poverty remains a major national challenge, motivating the development of innovative technologies that support both universal energy access and long-term decarbonization (International Energy Agency [IEA], 2025; Nigeria Energy Transition Plan [NETP], 2022). The Nigeria Energy Transition Plan establishes a national pathway towards net-zero emissions by 2060

while prioritizing energy access, clean cooking, industrial development, and renewable energy diversification (Nigeria Energy Transition Plan [NETP], 2022).

Within the cooking sector, the ETP identifies the transition away from traditional firewood and charcoal towards cleaner fuels—including modern biofuels, biogas, electricity, and other low-carbon cooking technologies—as a critical strategy for achieving Sustainable Development Goal 7 while reducing emissions and improving public health. The plan also recognizes the importance of developing local biofuel markets and supporting research and innovation for biomass conversion technologies, particularly in rural communities where biomass resources are abundant. Consequently, engineering innovations that convert agricultural residues into high-quality solid biofuels are increasingly recognized as essential components of sustainable energy systems, promoting resource efficiency, waste valorization, and circular bioeconomy strategies (Mujtaba et al. (2023); Sadh, et al., (2023)).

1.1 Engineering Variables Governing Biomass Briquette Performance

Among the various biomass conversion technologies, densification through briquetting has emerged as one of the most practical engineering solutions for upgrading low-density loose agricultural residues into high-quality uniform solid biofuels suitable for domestic, commercial, and industrial thermal applications. Briquetting substantially reduces volume, increases bulk density, and improves storage stability, handling characteristics, and transportation efficiency. It also improves fuel uniformity, enhances combustion characteristics, and produces fuels with improved mechanical integrity and more consistent energy performance (Grover & Mishra, 1996; Kaliyan & Morey, 2009; Tumuluru et al., 2011), with a potential for partially replacing traditional fuels such as firewood, charcoal, and coal in decentralized energy systems.

The quality of briquettes is governed by several interacting variables, including feedstock characteristics, particle size, moisture content, binder type and concentration, compaction pressure, and post-production drying conditions. These parameters influence important fuel quality indices such as calorific value, ash content, compressive strength, ignition behaviour, burning characteristics, and resistance to moisture (Tumuluru et al., 2011; Zhang et al., 2018). Agricultural residues differ considerably in their composition, ash-forming minerals, and natural binding characteristics; consequently, combining different feedstocks offers opportunities to exploit complementary material properties while minimizing the limitations associated with individual biomass resources. Likewise, binder selection determines the strength and durability of briquettes, whereas compaction pressure governs particle rearrangement, contact area, mechanical interlocking, and final briquette density (Sikarwar et al., 2016; Tumuluru et al., 2011).

1.2 Current Knowledge Gaps and Objectives

Although considerable progress has been made in biomass briquetting technology, existing studies have predominantly focused on individual agricultural residues, single binder systems, or isolated processing variables. Many investigations evaluate only one aspect of briquette production, such as calorific value, mechanical strength, or combustion performance, making direct comparison among studies difficult (Obi et al, 2022). Furthermore, relatively few studies (Walozi, et al, 2026) that systematically evaluated multi-variable interactions across multiple distinct processing phases within a single, harmonized experimental framework remains highly limited (Grover & Mishra, 1996; Kaliyan & Morey, 2009; Obi et al., 2022).

This study addresses these gaps by evaluating multiple biomass residues (maize straw, rice straw, wheat straw), several binder systems (cassava starch, Gum Arabic, coal tar), and different compaction pressures (5 and 10 MPa) within a harmonized experimental framework. By integrating these physical, thermal, mechanical, and combustion performance indicators within a single comparative framework, the study identifies the influence of biomass composition, binder characteristics, and densification conditions on briquette quality, providing practical recommendations for sustainable thermal energy production from agro-residues in Nigeria.

2. MATERIALS AND METHODS

The agro-residues investigated as feedstocks in this study comprised maize straw, rice straw, and wheat straw, selected because of their abundance as agricultural residues and their significant potential for renewable solid biofuel production. The residues were collected from agricultural farms around Samaru Zaria, and were cleaned manually to remove soil particles, stones, and other foreign materials. The cleaned residues were air-dried under ambient conditions to reduce their moisture content. The dried residues were chopped into smaller pieces and milled to obtain a relatively uniform particle size suitable for densification. The pulverized materials were sieved using a 2 mm mesh to ensure particle size uniformity and to minimize variability during compaction. The processed biomass materials were stored in airtight containers before briquette production to minimize moisture uptake from the environment. The overall process flow of feedstock preparation, briquetting, and characterization is shown in Figure 1.

2.1 Binder Preparation

Three binder materials with different binding characteristics were investigated, namely cassava starch, Gum Arabic, and coal tar. Cassava starch and Gum Arabic were selected as natural binders because of their availability and established adhesive properties (Ezechiel, 2022), whereas coal tar was included as a conventional binder for comparison of mechanical and combustion performance. The binders were prepared as follows (Plate 1):

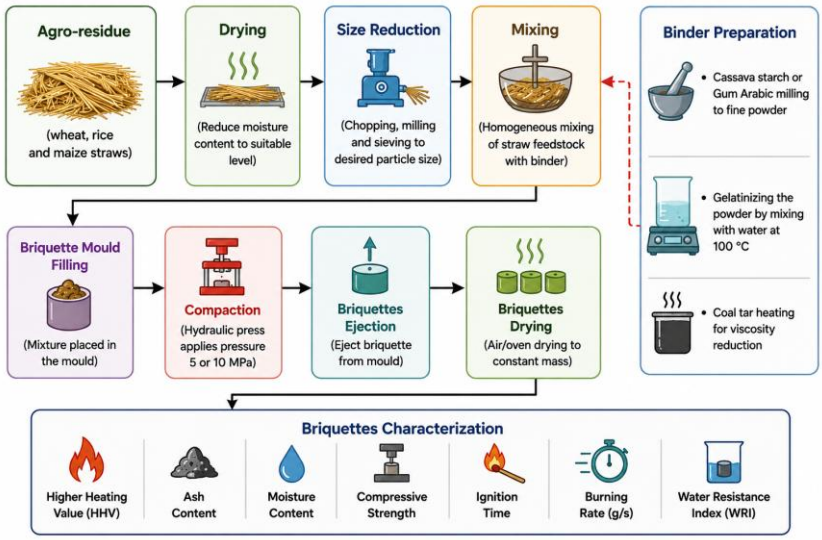

Figure 1: Block Flow Diagram of the Study

1. Cassava Starch Binder: Prepared by dispersing starch powder in water followed by heating with continuous stirring until gelatinization occurred at a temperature of 100 °C, producing a homogeneous adhesive paste. This temperature disrupts the intermolecular bonds, creating hydrogen-bonding networks. After cooking, the binder was allowed to cool for 45 minutes before use.
2. Gum Arabic Binder: Prepared by dissolving small quantities at a time in water that was boiled to 100 °C and allowed to cool to approximately 90 °C to obtain a uniform adhesive solution.
3. Coal Tar Binder: Heated to reduce its viscosity and then allowed to cool to ambient conditions before mixing directly as a binder.

Plate 1: (a) Cassava Starch (b) Starch binder (c) Prepared agro-residues (d) lubricant (oil)

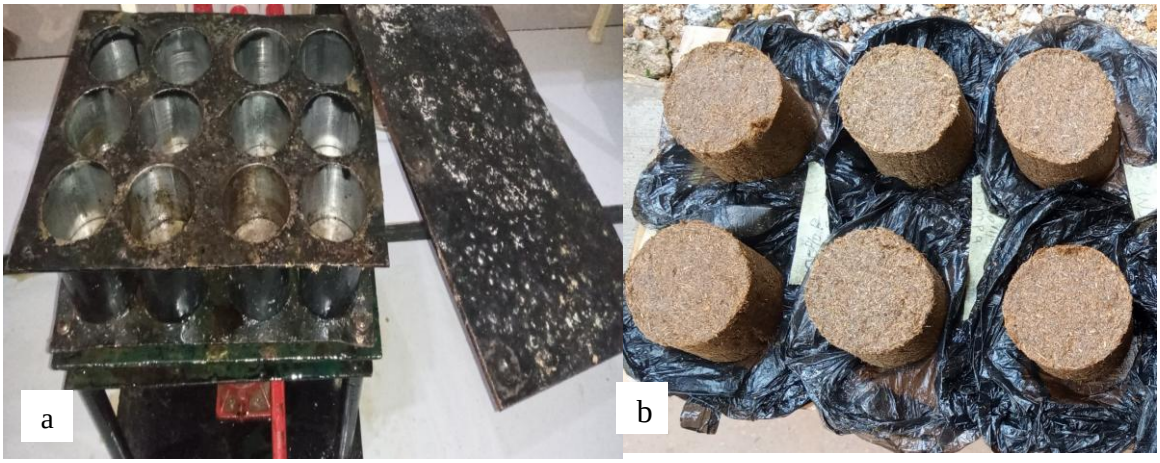

Plate 2: (a) Cylindrical Steel Mould (b) Briquettes (Densified biomass)

2.2 Experimental Design Matrix

A comparative experimental approach was adopted to evaluate the effects of biomass composition, binder characteristics, and compaction pressure on briquette fuel quality. The investigation consisted of two complementary experimental phases as detailed in Table 1.

Table 1: Experimental Design Matrix

S/N	Phase	Sample Code	Feedstock Composition	Blend Ratio (% w/w)	Binder Type	Compaction Pressure (MPa)
1	I	Mg5	Maize straw	100:0	Gum Arabic	5
2	I	Mc5	Maize straw	100:0	Coal tar	5
3	I	Ms5	Maize straw	100:0	Starch	5
4	I	Wg5	Wheat straw	100:0	Gum Arabic	5
5	I	Wc5	Wheat straw	100:0	Coal tar	5
6	I	Ws5	Wheat straw	100:0	Starch	5
7	I	5M5Wg5	Maize straw + Wheat straw	50:50	Gum Arabic	5
8	I	5M5Wc5	Maize straw + Wheat straw	50:50	Coal tar	5
9	I	5M5Ws5	Maize straw + Wheat straw	50:50	Starch	5
10	II	Rs5	Rice straw	100:0	Starch	5
11	II	5R5Ms5	Rice straw + Maize straw	50:50	Starch	5
12	II	7R3Ms5	Rice straw + Maize straw	70:30	Starch	5
13	II	3R7Ms5	Rice straw + Maize straw	30:70	Starch	5
14	II	Rs10	Rice straw	100:0	Starch	10
15	II	Ms10	Maize straw	100:0	Starch	10
16	II	5R5Ms10	Rice straw + Maize straw	50:50	Starch	10
17	II	7R3Ms10	Rice straw + Maize straw	70:30	Starch	10
18	II	3R7Ms10	Rice straw + Maize straw	30:70	Starch	10

In the first phase (I), briquettes were produced from maize straw (M), wheat straw (W), and a 50:50 maize–wheat (5M5W) blend using three binder materials (Gum Arabic, coal tar, and cassava starch) under a compaction pressure of 5 MPa.

In the second phase (II), the influence of biomass composition and compaction pressure was investigated using rice straw, maize straw, and their binary blends (50:50, 70:30, and 30:70 ratios) bonded with cassava starch under compaction pressures of 5 MPa and 10 MPa, resulting in 18 distinct formulations (S/N 1-18).

2.3 Characterization Methods

Measured quantities of the prepared biomass feedstocks were thoroughly mixed with the appropriate binder to obtain homogeneous mixtures (Figure 1). The mixtures were fed into a lubricated cylindrical steel mould and compacted using a hydraulic briquetting press operating at the designated pressure (5 or 10 MPa). The compacted briquettes were ejected and air-dried under ambient laboratory conditions until constant mass was attained. Properties of interest were determined in accordance with standard ASTM protocols where applicable (Table 2).

Table 2: Standard Methods Adopted for Characterization

Property	Adopted Procedure/ Method	Description	References
HHV	ASTM D5865/ D5865M -19	Gross calorific value determination using an adiabatic bomb calorimeter.	ASTM International (2019)
Ash Content	ASTM E1755 -24	Ash determination by complete combustion of oven-dried biomass at 575 ± 25 °C.	ASTM International (2024b)
Moisture Content	ASTM E871 -24	Moisture content determination of particulate biomass by oven drying to constant mass.	ASTM International (2024a)
Compressive Strength	Adapted compression test (UTM)	Maximum compressive load sustained before physical failure using a Universal Testing Machine.	Obi et al. (2022)
Ignition Time	Experimental combustion method	Elapsed time from application of flame until sustained ignition is established.	Obi et al. (2022)
Burning Rate	Experimental combustion method	Measured mass loss per unit time (g/s) during active combustion.	Olugbade et al. (2019); Obi et al. (2022)
WRI	Water immersion method	Time elapsed to complete structural dissolution upon immersion in water.	Obi et al. (2022)

2.4 Statistical Methodology

The experimental data were analysed using two-way ANOVA without replication to provide an exploratory assessment of main-factor effects. Because only one observation was available for each factor combination, interaction effects could not be independently estimated and may be confounded with the residual term. Consequently, the resulting p-values should be interpreted as exploratory evidence of main effects under an additive-model assumption. For Phase I, the additive model evaluated Biomass Feedstock (Maize, Wheat, 50:50 blend) and Binder Type (Gum Arabic, coal tar, cassava starch) under a constant pressure of 5 MPa. For Phase II, an unbalanced Two-Way ANOVA was applied using Type II Sum of Squares to rigorously evaluate Rice-Maize blend ratios and compaction pressures (5 MPa vs 10 MPa) without factor-ordering bias

Pearson correlation analysis was executed on the complete 18-sample dataset to determine linear relationship coefficients (r) between all physical, thermal, and mechanical properties. The statistical significance threshold was set at alpha = 0.05.

3. RESULTS AND DISCUSSION

3.1 General Briquette Performance

The physical, thermal, and mechanical properties of the 18 formulations are summarized in Table 3. The results show that the Higher Heating Value (HHV) varied substantially, ranging from 14.1 to 20.5 MJ/kg, but is comparable to standard solid biofuels. The moisture contents however, ranged from 21.4% to 34.4%, which significantly exceed the commercial solid biofuel standard of <15%. This indicates that the passive post-production ambient air-drying alone is insufficient. According to the international standard ISO 17225-7:2021 (ISO, 2021), the maximum moisture content of ≤ 15% is necessary for commercial graded non-woody briquettes, to prevent physical

degradation, mold growth, and ignition delay during storage (ISO, 2021; Obi et al., 2022). Under the high relative humidity (RH) conditions typical of the study location, Zaria (RH from 36%–46% in dry season, to 82%–88% during the wet season (Yusuf & Shuaib, 2012)), the rate of air-drying limits water removal from the briquettes produced, thus requiring active thermal interventions.

Engineering Drying Process Recommendations: To bring the engineered briquettes to the standard non-woody biofuels moisture content within the ISO-compliant threshold (<15%), a controlled thermal drying stage – like a convective kiln-drying system operating at 60 °C to 80 °C for 12 to 18 hours is proposed (Obi et al., 2022). Maintaining the drying temperature below 100 °C is critical, to avoid damaging the cassava starch binder, as higher temperatures initiate the thermal decomposition and depolymerization of the starch adhesive, which collapses the solid-bridge molecular networks and severely weakens dry compressive strength (Tumuluru et al., 2011; Obi et al., 2022). From an engineering perspective, this active thermal drying carries a substantial energy penalty, as convective air dryers typically consume between 2.4 and 4.5 MJ of thermal energy per kg of water evaporated (Đurdević et al., 2021; Tumuluru et al., 2011).

Table 3: General Characterization Results of Densified Biofuels

S/N	Sample ID	Binder	HHV (MJ/kg)	Ash Content (%)	Moisture Content (%)	Ignition Time (s)	Burning rate (g/s)	Compressive Strength (kN/m²)	WRI (min)
1	Mg5	Gum Arabic	17.3	6.1	28.87	14.0	0.22	195.4	15.0
2	Mc5	Coal tar	19.3	5.2	29.99	12.0	0.17	146.6	2.0
3	Ms5	Starch	18.0	5.8	26.83	15.0	0.24	181.0	2.7
4	Wg5	Gum Arabic	15.7	10.3	31.99	15.0	0.20	206.9	10.0
5	Wc5	Coal tar	16.2	9.2	32.51	17.0	0.23	172.4	7.5
6	Ws5	Starch	15.9	9.7	30.57	20.0	0.27	192.5	5.0
7	5M5Wg5	Gum Arabic	18.2	7.9	29.30	13.0	0.21	201.1	6.0
8	5M5Wc5	Coal tar	20.5	7.0	28.07	10.0	0.15	189.7	6.0
9	5M5Ws5	Starch	19.5	7.6	26.17	15.0	0.25	169.5	3.3
10	Rs5	Starch	14.5	9.0	31.40	20.0	0.23	91.0	10.0
11	5R5Ms5	Starch	14.7	9.5	31.70	17.0	0.20	192.3	5.0
12	7R3Ms5	Starch	14.7	13.9	33.60	15.0	0.23	176.7	6.0
13	3R7Ms5	Starch	14.4	9.1	34.40	11.0	0.17	184.5	3.8
14	Rs10	Starch	14.1	8.6	21.40	14.0	0.27	153.3	15.0
15	Ms10	Starch	17.7	8.2	25.70	10.0	0.20	122.5	2.0
16	5R5Ms10	Starch	14.2	12.8	25.10	18.0	0.23	197.5	7.5
17	7R3Ms10	Starch	15.8	10.7	25.10	14.0	0.23	148.5	6.0
18	3R7Ms10	Starch	14.9	9.1	24.40	12.0	0.17	187.1	3.3

To preserve a positive net energy ratio for the process, waste heat recovered from industrial boiler exhausts or waste heat recovery from the hydraulic briquetting machinery. Alternatively, incorporating solar-assisted convective tunnel dryers operating at 36.5–65 °C for 24 to 36 hours offers a highly viable, low-cost, decentralized engineering solution (Đurdević et al., 2021; Guibunda et al., 2026; Tumuluru et al., 2011).

3.2 Influence of Biomass Composition on Fuel Properties

The primary feedstock composition exerted a dominant role across both experimental phases. The agro-residues have distinct ash profiles and cellular arrangements, dictating their energy density and mechanical interlocking limits. ANOVA tests were completed for all seven response variables, and their exact results are tabulated below in Table 4 and Table 5.

Table 4: Phase I ANOVA Table (Biomass Feedstock & Binder Type under 5 MPa)

Property	Factor Source	Sum of Sq. (SS)	Degrees of freedom (df)	F-Statistic	p-value	Significance
HHV (MJ/kg)	Feedstock	18.5960	2	37.2740	0.0026	Highly Significant ($p < 0.01$)
	Binder	3.8490	2	7.7150	0.0424	Significant ($p < 0.05$)
	Residual	0.9980	4	-	-	-
Ash Content (%)	Feedstock	24.4960	2	1574.714	< 0.0001	Extremely Significant ($p < 0.001$)
	Binder	1.4160	2	91.0000	0.0005	Extremely Significant ($p < 0.001$)
	Residual	0.0310	4	-	-	-
Moisture Content (%)	Feedstock	25.0610	2	27.3070	0.0047	Highly Significant ($p < 0.01$)
	Binder	10.2880	2	11.2110	0.0229	Significant ($p < 0.05$)
	Residual	1.8350	4	-	-	-
Ignition time (s)	Feedstock	36.2222	2	8.5790	0.0357	Significant ($p < 0.05$)
	Binder	21.5556	2	5.1053	0.0792	Marginally Significant
	Residual	-	-	-	-	
Burning rate	Feedstock	0.0015	2	1.1261	0.4093	Not Significant
	Binder	0.0075	2	5.6639	0.0681	Marginally Significant
	Residual	-	-	-	-	
Compressive Strength (kN/m²)	Feedstock	433.8870	2	1.0360	0.4340	Not Significant
	Binder	1532.5270	2	3.6590	0.1249	Not Significant
	Residual	837.5870	4	-	-	-
WRI	Feedstock	8.7822	2	0.3451	0.7273	Not Significant
	Binder	73.3889	2	2.8838	0.1677	Not Significant
	Residual	-	-	-	-	

Note: residual df = 4 for each property; residual terms are omitted for compactness. Interaction effects are not separately estimable in this unreplicated design

3.2.1 Thermal and Fuel Properties (Phase I ANOVA Evaluation)

The Phase I Two-Way ANOVA established that biomass feedstock selection is a statistically significant driver of HHV ($p = 0.0026$), Ash Content ($p < 0.0001$), and Moisture Content ($p = 0.0047$). Pure maize straw briquettes achieved lower ash contents (5.2%–6.1%) and higher heating values (17.3–19.3 MJ/kg) compared to pure wheat straw, which was penalized by elevated ash (9.2%–10.3%) and lower HHV (15.7–15.9 MJ/kg). Blending these residues in a 50:50 ratio (5M5W series) successfully moderated the high ash penalty of wheat straw (reducing ash to 7.0%–7.9%) while

preserving an attractive HHV (18.2–20.5 MJ/kg). This highlights biomass blending as a primary fuel optimization strategy.

3.2.2 Combustion characteristics (Phase I)

Feedstock selection exerted a significant effect on ignition time ($p = 0.0357$). Pure maize straw briquettes ignited more rapidly (avg. 13.7 s) than pure wheat straw briquettes (avg. 17.3 s). This difference is attributed to ash composition: the higher inorganic mineral fractions (such as silica) in wheat straw act as a thermal barrier during heating, absorbing heat without decomposing, which delays the temperature rise necessary for volatilization and ignition.

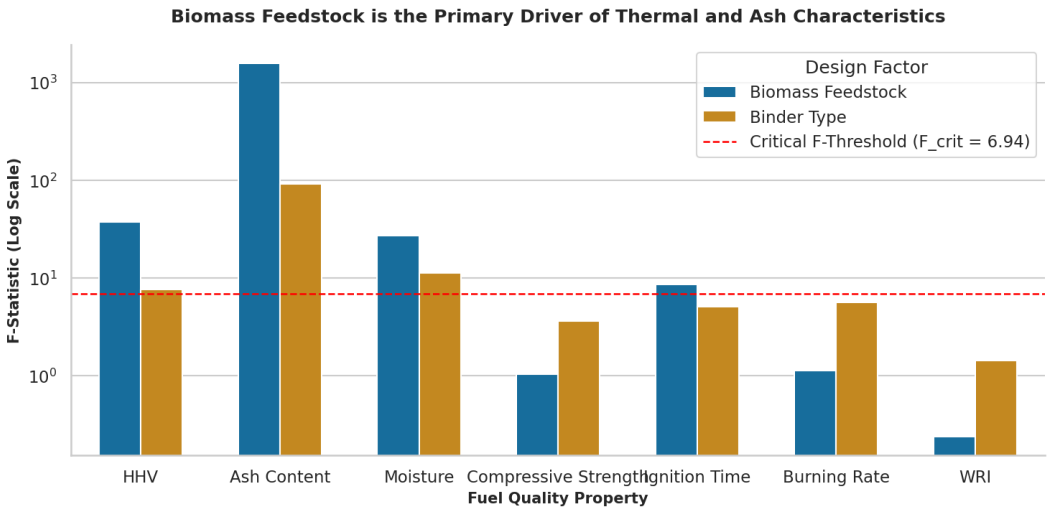

Figure 2: Phase I ANOVA F-statistics showing feedstock and binder type significance across properties relative to critical F-threshold (6.94).

3.3 Influence of Binder Characteristics on Biofuel Quality

Binder type significantly influenced HHV ($p = 0.0424$) and Ash Content ($p = 0.0005$). Natural binders (cassava starch and Gum Arabic) produced intermediate heating values ranging from 15.7 to 19.5 MJ/kg, demonstrating respectable thermal properties and structural interlocking. Gum Arabic produced the highest structural and moisture resistance, achieving a peak compressive strength of 206.9 kN/m² in sample Wg5 (wheat straw, Gum Arabic binder). Cassava starch still provided solid structural integrity, reaching up to 192.5 kN/m² for Ws5 (wheat straw, cassava starch binder). Coal tar binders consistently achieved the highest calorific values—peaking at 20.5 MJ/kg in 5M5Wc5—and the fastest ignition times (10.0 s) due to their high carbon and volatile density. However, the coal tar's origin related to fossil fuels, is a cause for environmental concerns.

3.3.1 Environmental and Sustainability Trade-off of Coal Tar Binder

Although coal tar binder maximizes calorific performance (reaching a peak of 20.5 MJ/kg in 5M5Wc5) and ignition rates, its petroleum/coal origin represents a non-renewable application barrier, because it directly conflicts with clean cooking and environmental goals highlighted in Nigeria's Energy Transition Plan (NETP, 2022). Coal tar is a carbonization byproduct most likely containing carcinogenic polycyclic aromatic hydrocarbons, PAHs (such as Benzo[a]pyrene) in high concentrations (IARC, 2012), which are released upon combustion, along with heavy particulate smoke (Liu et al., 2008; WHO, 2010).

In contrast, cassava starch and Gum Arabic are renewable, non-toxic, and locally available, representing environmentally safe binders for domestic cookstove markets despite slightly lower heating values. This makes cassava starch and Gum Arabic the only sustainable, socially responsible choices of binders for briquetting especially for household combustion applications, where toxic emission control measures are difficult to implement.

3.3.3 Mechanical and Storage Properties

Binder selection governed briquette physical stability. Gum Arabic produced the highest structural and moisture resistance. The binder type was also found to govern physical storability. Gum Arabic generated superior resistance to moisture degradation and produced briquettes with the greatest resistance to water, maintaining structural integrity for 15 min while coal tar-bonded briquettes yielded the lowest. Gum Arabic produced high compressive strength in selected formulations, whereas resistance to water-induced degradation varied among individual briquette formulations. Consequently, dry mechanical strength and water resistance should be evaluated as distinct aspects of briquette storage performance

3.4 Influence of Compaction Pressure and the "Springback" Effect

3.4.1 Compaction Pressure Effect on Moisture

Phase II of the study indicated a statistically significant (Table 5) exploratory main effect of compaction pressure on moisture content ($p = 0.0017$), with the 10 MPa formulations generally exhibiting lower moisture values than the 5 MPa formulations (Figure 3).

Table 5: Phase II ANOVA Table (Feedstock Blend & Compaction Pressure)

Property	Factor Source	Sum of Sq. (SS)	Degrees of freedom (df)	F-Statistic	p-value	Significance
HHV (MJ/kg)	Feedstock Blend	8.0060	4	6.8720	0.0726	Marginally Significant ($p < 0.10$)
	Pressure	0.0610	1	0.2100	0.6777	Not Significant
	Residual	0.8740	3	-	-	-
Ash Content (%)	Feedstock Blend	20.3420	4	1.4350	0.3993	Not Significant
	Pressure	0.0110	1	0.0030	0.9586	Not Significant
	Residual	10.6340	3	-	-	-
Moisture Content (%)	Feedstock Blend	14.1160	4	2.7120	0.2193	Not Significant
	Pressure	154.0010	1	118.3490	0.0017	Extremely Significant
	Residual	3.9040	3	-	-	-
Ignition Time	Feedstock Blend	61.5750	4	2.8203	0.2104	Not Significant
	Pressure	3.1250	1	0.5725	0.5043	Not Significant
	Residual	-	-	-	-	
Burning rate	Feedstock Blend	0.0074	4	8.7500	0.0528	Marginally Significant
	Pressure	0.0006	1	2.8824	0.1881	Not Significant
	Residual	-	-	-	-	
Compressive Strength (kN/m^2)	Feedstock Blend	8250.8620	4	2.8970	0.2043	Not Significant
	Pressure	219.4510	1	0.3080	0.6175	Not Significant
	Residual	2135.7140	3	-	-	
WRI	Feedstock Blend	115.7070	4	9.0161	0.0508	Marginally Significant
	Pressure	6.1250	1	1.9091	0.2610	Not Significant
	Residual	-	-	-	-	

Note: Residual df = 3 for each property. The unbalanced Phase II design and absence of replication require cautious interpretation.

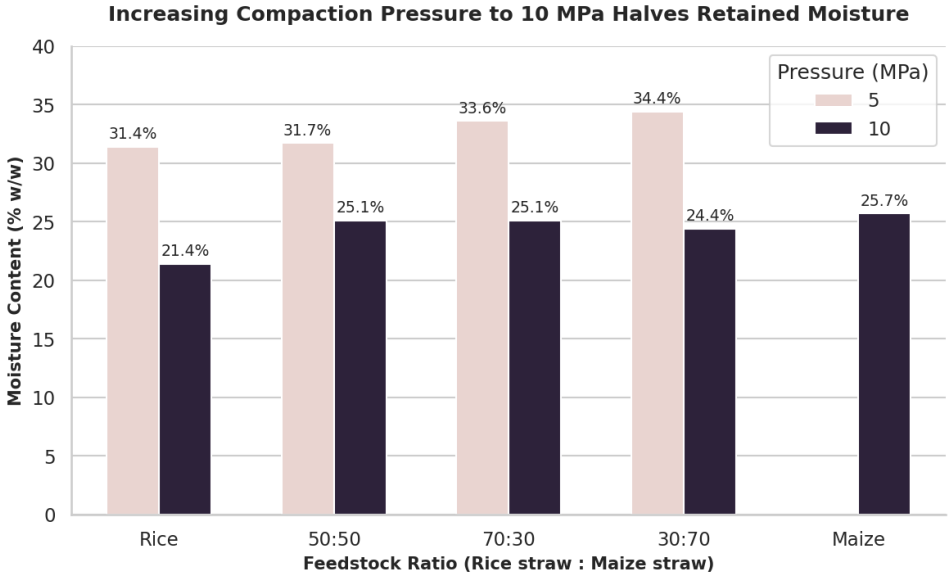

Figure 3: Effect of compaction pressure on moisture content reduction across rice-maize feedstock blend ratios in Phase II

Compaction pressure did not show a statistically significant main effect on compressive strength ($p = 0.6175$) within the limitations of the unreplicated and unbalanced design. This absence of statistical evidence should not be interpreted as proof of a specific physical mechanism. Elastic recovery or springback after ejection is a plausible explanation discussed in biomass-densification literature, but dimensional recovery, internal cracking, and post-ejection expansion were not measured in this study. Springback is therefore treated as a literature-supported hypothesis rather than an experimentally demonstrated mechanism. Doubling compaction pressure from 5 to 10 MPa compacted the particles, forcing out moisture and lowering retained moisture levels from 31.4%–34.4% down to 21.4%–25.7%. However, these values remain above the ideal bioenergy range (<15%), reinforcing the need for active drying protocols as discussed in section 3.1.

3.4.2 Compressive Strength "Springback" Anomaly

Compaction pressure had no statistically significant effect on dry Compressive Strength ($p = 0.6175$, $F = 0.31$). Standard biomass densification theory dictates that higher pressure improves consolidation and strength. However, the data shows highly inconsistent changes; for example, pure maize straw (Ms10) and the 70:30 rice-maize blend (7R3Ms10) actually showed decreased compressive strength at 10 MPa compared to their 5 MPa counterparts.

This statistical insignificance ($p = 0.6175$) does not mathematically establish but is highly consistent with the hypothesis of an elastic recovery or 'springback' phenomenon typical of unheated agricultural crop residues. Because briquetting in the present study was conducted without external heating, thermal softening and flow of natural lignin were likely limited relative to heated densification processes (Kaliyan & Morey, 2009; Tumuluru et al., 2011). Highly elastic straw fibers compress under mechanical pressure but store substantial internal elastic strain energy. Upon ejection from the mould, this stored energy is released, causing immediate physical expansion. Elastic recovery or springback after briquette ejection is a plausible mechanism that may contribute to the absence of a detectable pressure effect on compressive strength. However, dimensional recovery, internal cracking and microstructural changes were not measured in the present study.

Pearson correlations (Table 6) calculated across the authoritative 18-formulation dataset showed a strong negative association between ash content and HHV ($r = -0.7$). This pattern is consistent with the observed tendency for formulations with higher inorganic residue to have lower gross energy content. HHV was also negatively associated with ignition time ($r = -0.45$), while ignition time and burning rate were positively associated ($r = 0.67$). In contrast, compressive strength and WRI showed a negligible pooled association ($r = -0.29$).

3.5 Multivariate Trade-offs and Pearson Correlation Insights

To guide solid biofuel design, the physical trade-offs must be analyzed among thermal performance, mechanical strength, and storability. For example, Gum Arabic produced high compressive strength in selected formulations, while water resistance varied substantially among formulations. Pearson correlation coefficients calculated from the verified 18-sample dataset reveal several key thermodynamic and mechanical relationships (Table 6):

1. Ash Content vs. HHV (r = -0.70): A strong negative correlation that mathematically validates the thermodynamic penalty of inorganic residues. Inorganic minerals (silica, etc.) do not burn, physically diluting the carbon-rich organic fraction per unit mass.
2. Compressive Strength vs. WRI (r = -0.29): Indicates a mechanical design conflict. High dry compressive strength (interlocking film bonds) tends to show lower wet water resistance (WRI), proving that dry mechanical integrity and wet moisture stability operate through different chemical mechanisms.

Table 6: Pearson Correlation Matrix of Briquette Properties

Property	HHV	Ash Content	Moisture Content	Ignition Time	Burning Rate	Compressive Strength	WRI
HHV	1.00	**-0.70**	-0.10	-0.45	-0.28	0.04	-0.15
Ash Content	**-0.70**	1.00	0.16	0.38	0.24	0.12	0.01
Moisture Content	-0.10	0.16	1.00	0.22	-0.24	0.15	-0.05
Ignition Time	-0.45	0.38	0.22	1.00	**0.67**	-0.05	0.14
Burning Rate	-0.28	0.24	-0.24	**0.67**	1.00	-0.13	0.08
Compressive Strength	0.04	0.12	0.15	-0.05	-0.13	1.00	**-0.29**
WRI	-0.15	0.01	-0.05	0.14	0.08	**-0.29**	1.00

4. CONCLUSION

This study presented a comparative experimental evaluation of solid biofuels produced from maize, wheat, and rice straws and their binary blends, characterized across 18 distinct formulations under compaction pressures of 5 and 10 MPa. The experimental and statistical results establish that:

- **Feedstock Blending Synergy:** Biomass composition is the primary determinant of combustion characteristics and ash behavior. While pure wheat and rice straw are penalized by high ash contents of up to 10.3% and 13.9% respectively, a 50:50 maize–wheat blend successfully buffers this ash penalty (reducing it to 7.0%–7.9%) while maintaining a high heating value between 18.2 and 20.5 MJ/kg.
- **Optimal Thermal Performance:** The 50:50 maize–wheat straw blend bonded with coal tar at 5 MPa (5M5Wc5) is the optimal thermal formulation, yielding the highest Higher Heating Value (20.5 MJ/kg), the shortest ignition time (10 s), and low ash content (7.0%).
- **Binder Governance and Sustainability:** Binders dictate mechanical durability and water resistance during storage. Gum Arabic produced high compressive strength in selected formulations, while water-resistance behaviour varied among formulations, whereas cassava starch serves as a vital green, renewable, and biodegradable alternative. Coal tar maximizes combustion characteristics but introduces severe environmental and toxicological trade-offs.
- **Pressure Limitations and Springback:** Doubling compaction pressure from 5 to 10 MPa systematically consolidates particles—reducing retained moisture from 31.4%–34.4% to 21.4%–25.7% across all formulations. The limited improvement in compressive strength at higher pressure may reflect elastic recovery effects, although this mechanism requires direct dimensional and microstructural measurements for confirmation.

In summary, high-performance solid biofuel design requires balancing thermal efficiency, mechanical durability, and storage stability rather than optimizing for a single metric. Managing these trade-offs through targeted biomass blending and binder selection offers a practical pathway for decentralized waste valorization to support Nigeria's clean energy transition.

REFERENCES

ASTM International, (2019), ASTM D5865/D5865M-19: Standard Test Method for Gross Calorific Value of Coal and Coke. West Conshohocken, PA: ASTM International

ASTM International, (2024a), ASTM E1755-24: Standard Test Method for Ash in Biomass. West Conshohocken, PA: ASTM International

ASTM International. (2024b), ASTM E871-24: Standard Test Method for Moisture Analysis of Particulate Wood Fuels. West Conshohocken, PA: ASTM International.

Awulu, J. O., & Ijabo, O. J. (2015), Effects of briquettes and binders on combustible properties of selected biodegradable material, Journal of Natural Sciences Research, 5(3), 28–38

Eriksson, S., & Prior, M., (1990), The Briquetting of Agricultural Wastes for Fuel, FAO Regional Wood Energy Development Programme, Rome: Food and Agriculture Organization.

Ezechiel, K. (2022). Characterization of Natural Binders for Biomass Briquetting in Sub-Saharan Africa, Journal of Agricultural Engineering, 53(2), 112–125.

Fapetu, O. P. (2000). Production of charcoal from tropical biomass for industrial and metallurgical processes, Proceedings of the National Engineering Conference, Lagos, Nigeria, 14–18

Grover, P. D., & Mishra, S. K. (1996), Biomass Briquetting: Technology and Practices. FAO Regional Wood Energy Development Programme, Bangkok: Food and Agriculture Organization.

Guibunda, F. A., Waita, S., Nyongesa, F. W., Snyder, G. J., & Chaciga, J. (2024). Optimizing biomass briquette drying: A computational fluid dynamics approach with a case study in Mozambique. Energy 360, 2, 100012. https://doi.org/10.1016/J.ENERG.2024.100012

IARC (INTERNATIONAL AGENCY FOR RESEARCH ON CANCER), (2012), Chemical agents and related occupations: Review of human carcinogens. IARC Monographs on the Evaluation of Carcinogenic Risks to Humans, Volume 100F. Geneva: World Health Organization. Available from: https://www.ncbi.nlm.nih.gov/books/NBK590777/

International Organization for Standardization, (2017), ISO 18125:2017: Solid biofuels—Determination of calorific value. ISO 18125:2017

International Organization for Standardization, (2022a), ISO 18122:2022: Solid biofuels—Determination of ash content

International Organization for Standardization, (2022b), ISO 18134-1:2022: Solid biofuels—Determination of moisture content—Part 1: Reference method

International Energy Agency (IEA). (2025). Universal Energy Access and Clean Cooking in Sub-Saharan Africa: Outlook 2025. Paris: IEA.

Intergovernmental Panel on Climate Change (IPCC), (2022), Climate Change 2022: Mitigation of Climate Change. Cambridge, UK: Cambridge University Press.

Kaliyan, N., & Morey, R. V. (2009). Factors affecting strength and durability of densified biomass products, Biomass and Bioenergy, 33(3), 337–359, https://doi.org/10.1016/j.biombioe.2008.08.005

Kaliyan, N., & Morey, R. V. (2010). Natural binders and solid bridge linkage in briquettes and pellets of biomass, Powder Technology, 199(2), 174-184

Kathuria, R. S., & Grover, S. (2012), Agricultural residue briquetting: An overview. Renewable Energy Reviews, 18(4), 412–420

Komarek, K. R. (2004), The Briquetting Process, Cleveland, OH: Komarek Research Inc.

Kristoferson, L. A., & Bokalders, V. (2002), Renewable Energy Technologies: Their Applications in Developing Countries, London: Intermediate Technology Publications

Liu, G; Niu, Z; Van Niekerk, D; Xue, Tan; Zheng, L. (2008). Polycyclic aromatic hydrocarbons (PAHs) from coal combustion emissions: Analysis and toxicology. Reviews of Environmental Contamination and Toxicology, 192, 1–28. https://doi.org/10.1007/978-0-387-71724-1_1

Mohamed, F. M., Ahmed, Y. M. Z., & Shalabi, M. E. H. (2004), Effect of organic binders on the quality of metallurgical briquettes, Journal of Coal Science and Engineering, 10(2), 54–61.

Mujtaba, M., Fraceto, L. F., Fazeli, M., Mukherjee, S., Savassa, S. M., de Medeiros, G. A., Pereira, A. E. S., Mancini, S. D., Lipponen, J., Vilaplana, F., (2023) Lignocellulosic biomass from agricultural waste to the circular economy: a review with focus on biofuels, biocomposites and bioplastics, Journal of Cleaner Production, 402, 136815, ISSN 0959-6526, https://doi.org/10.1016/j.jclepro.2023.136815

Nigeria Energy Transition Plan (NETP), (2022). Federal Government of Nigeria Energy Transition Plan: Pathway to Net-Zero Emissions by 2060. Abuja: Federal Ministry of Environment

Obi, O. F., Pecenka, R., & Clifford, M. J., (2022), A review of biomass briquette binders and quality parameters, Energies, 15(7), 2426. https://doi.org/10.3390/en15072426

Olorunnisola, A. O. (2004), Briquetting of rattan furniture waste, Journal of Bamboo and Rattan, 3(2), 139–149. https://doi.org/10.1163/156915904774195133

Olugbade, T., Ojo, O., & Mohammed, T. (2019), Influence of binders on combustion properties of biomass briquettes: A review. BioEnergy Research, 12, 241–259. https://doi.org/10.1007/s12155-019-09973-w

Sadh, P. K., Chawla, P., Kumar, S., Das, A., Kumar, R., Bains, A., Sridhar, K., Duhan, J. S., Sharma, M. (2023) Recovery of agricultural waste biomass: A path for circular bioeconomy, Science of The Total Environment, 870, 161904, ISSN 0048-9697, https://doi.org/10.1016/j.scitotenv.2023.161904

Saidur, R., Abdelaziz, E. A., Demirbas, A., Hossain, M. S., & Mekhilef, S. (2011). A review on biomass as a fuel for boilers, Renewable and Sustainable Energy Reviews, 15(5), 2262–2289 https://doi.org/10.1016/j.rser.2011.02.015

Sharma, M. K., Priyank, G., & Sharma, N. (2015), Biomass briquette production: A review on recent technologies, International Journal of Green Energy, 12(9), 874–888.

Sikarwar, V. S., Zhao, M., Fennell, P. S., Shah, N., & Anthony, E. J. (2016), Progress in biomass gasification: A review, Progress in Energy and Combustion Science, 53, 1-36. https://doi.org/10.1016/j.pecs.2015.11.001

Tumuluru, J. S., Wright, C. T., Hess, J. R., & Kenney, K. L. (2011), A review of biomass densification systems to develop uniform feedstock commodities for bioenergy application, Biofuels, Bioproducts and Biorefining, 5(6), 683–707. https://doi.org/10.1002/bbb.324

YUSUF, Y.O. and SHUAIB, M.I., (2012). The effect of wastes discharge on the quality of Samaru Stream, Zaria, Nigeria. In: V.S. MOHAMAD, ed. Ecological Water Quality - Water Treatment and Reuse. Rijeka: InTech Open, pp. 39–54. Available from: doi.org

Walozi, R., Onep , G.S., Sanusi, Y.S. et al. (2026), Critical review of biomass heterogeneity effects on briquette combustion, Discov Appl Sci, 8, 309. https://doi.org/10.1007/s42452-025-08212-6

Wang, J., & Liu, H. (2013), Biomass binder development for briquetting applications, Fuel Processing Technology, 110, 150–158

Zhang, G., Sun, Y., & Xu, Y. (2018), Review of briquette binders and briquetting mechanisms, Renewable and Sustainable Energy Reviews, 82, 3478–3487.

International Conference on Engineering Innovation for Sustainable Development (ICESID 2026)
Faculty of Engineering, Ahmadu Bello University Zaria · 8–10 September 2026

ENHANCING THE THERMAL PROPERTIES OF ASPHALT PAVEMENT FOR ENERGY GENERATION USING THERMOELECTRIC GENERATORS

Farouk Shehu Yakasai[1], Aminu Suleiman[1,*]
[1]*Bayero University Kano*
Email: faroukshehuyakasai@yahoo.com, asuleiman.civ@buk.edu.ng[*]
***Corresponding author**: Aminu Suleiman
DOI: https://doi.org/10.67203/sp.ICESID.2026

ABSTRACT
Asphalt pavements absorb substantial amounts of solar heat, much of which remains unutilized despite its potential for renewable electricity generation through thermoelectric generators (TEGs), making the enhancement of asphalt thermal properties essential for improving temperature gradients and energy harvesting efficiency. This study evaluates the use of steel slag, an industrial by-product, as a partial replacement for natural coarse aggregates to enhance the thermal performance of asphalt concrete, with mixtures designed using the Marshall Mix method at steel slag replacement levels ranging from 0% to 25%. Laboratory tests measuring thermal conductivity, specific heat capacity, and thermal diffusivity were performed and evaluated using a three-dimensional transient heat transfer model in Abaqus, and the Marshall properties were evaluated against the applicable ASTM D6927 criteria, resulting in an optimum binder content of 6.0%. The results show that the incorporation of steel slag influenced the thermal properties of the asphalt concrete. Among the mixtures investigated, the 5% steel slag replacement produced the highest thermal conductivity of 3.0421 W/m·K and the lowest specific heat capacity of 794.5 J/kg·K. It also recorded the highest thermal diffusivity of 1.58×10^{-6} *m²/s. These findings suggest that a limited proportion of steel slag, particularly at 5% replacement, can improve the thermal response of asphalt concrete. The enhanced thermal properties may provide favourable conditions for future application in pavement-integrated thermoelectric energy harvesting systems. However, the present study focused on the thermal characteristics of the asphalt mixtures, and direct integration of thermoelectric generators (TEGs) and measurement of electrical power output were not undertaken.*

Keywords: *Asphalt concrete; thermoelectric generators; energy harvesting; thermal properties; steel slag; 3D finite element*

1. INTRODUCTION

Nigeria continues to face challenges in providing reliable and affordable electricity, with significant dependence on fossil fuels for buildings, industries, and infrastructure. Rising energy costs and inadequate power supply have increased the need for sustainable renewable energy alternatives. Asphalt pavements, which dominate urban road networks, absorb substantial solar radiation due to their dark surfaces and can reach temperatures of up to 70 °C Chen et al., (2009). Although this heat contributes to the Urban Heat Island (UHI**)** effect and can accelerate pavement deterioration, it also represents a potential source of renewable thermal energy.

The rapid growth of urbanization and Information and Communication Technology (ICT) has encouraged the development of smart cities, integrating intelligent infrastructure to improve efficiency, safety, and sustainability (Marsal-Llacuna et al., 2015). One emerging technology is the integration of thermoelectric generators (TEGs**)** into pavement structures to convert temperature gradients into electrical energy through the Seebeck effect (Jiang et al., 2017). Such energy can potentially support low-power applications, including street lighting, traffic signals, and infrastructure monitoring, while requiring relatively low maintenance (Islam & Tarefder, 2014).

The efficiency of pavement-based thermoelectric energy harvesting depends largely on the temperature gradient and heat transfer within the pavement. Therefore, enhancing the thermal conductivity of asphalt concrete is important for improving heat transfer and maximizing TEG performance (J. Chen et al., 2015). Recent studies have investigated industrial and recycled materials,

including steel slag, crumb rubber, and recycled aggregates, as alternatives for improving asphalt pavement performance Hasita et al., 2020; Ding et al., 2019.

Among these materials, steel slag has attracted considerable interest because of its availability and favourable mechanical and thermal properties (Rondón-Quintana et al., 2018; Sabapathy et al., 2017). Its incorporation into asphalt mixtures has been reported to improve mechanical strength, fatigue performance, and thermal characteristics (Hainin et al., 2014; Kavussi et al., 2015; Fang et al., 2013).

Accordingly, this study investigates the use of steel slag as a partial replacement for conventional coarse aggregate in asphalt concrete, with particular emphasis on its effects on thermal conductivity, specific heat capacity, and thermal diffusivity. The thermal response of the modified asphalt mixtures is further evaluated using three-dimensional finite element analysis in Abaqus. The study focuses on characterizing the thermal behavior of the mixtures and assessing their potential for future application in pavement-integrated thermoelectric energy harvesting systems. Direct integration of thermoelectric generators and evaluation of their electrical performance are beyond the scope of the present study.

2. MATERIALS AND METHODS

2.1 Materials

The materials used in this study comprised asphalt binder, natural limestone aggregates, and steel slag. The asphalt binder and natural aggregates were sourced locally within Kano State, Nigeria, while the steel slag was obtained from a rolling steel mill in Katsina State. The binder was characterized using standard consistency tests to determine its suitability for high-performance asphalt pavement applications. The natural aggregate was limestone with a nominal maximum particle size of 20 mm, and its physical and mechanical properties were evaluated in accordance with relevant standard specifications.

The steel slag was obtained from an electric arc furnace and air-aged for a minimum of 12 months prior to use to minimize potential volumetric expansion associated with free lime (CaO) and magnesia (MgO). The steel slag was subjected to the same physical and mechanical characterization tests as the natural aggregate to facilitate direct comparison and assess its suitability as a partial replacement for conventional coarse aggregate in asphalt mixtures.

Table 2.1: Physical properties of natural aggregate and steel slag.

PROPERTY	UNIT	VALUE	REQUIREMENT
Penetration (25ºC,100g,5s)	0.1mm	60.19	60-80
Softening Point	ºC	47	≥45
Flash Point	ºC	273	≥260
Fire point	ºC	281	
Density	g/cm^3	1.03	___

The results presented in Table 2.1 indicate that steel slag possesses superior mechanical properties compared with natural limestone aggregate, particularly in terms of strength, wear resistance,

and bulk density. These characteristics suggest its potential to improve the structural integrity and deformation resistance of asphalt mixtures when used as a partial coarse aggregate replacement. The bitumen properties presented in Table 2.2 show a penetration value of 60.17, corresponding to a 60/70 penetration grade, with flash and fire points of 273 °C and 281 °C, respectively. These results indicate adequate binder consistency and thermal stability, confirming its suitability for asphalt mixture production.

Table 2.2: Physical properties of bitumen

PROPERTY	Density	Water Absorption %	Crushing Value %	Impact Value %	Abrasion Value %	Flakiness & Elongation %
LIMESTONE	2.69	1.08	15.6	7.7	23	7.5
STEEL SLAG	3.5	1.29	12.1	14.5	13.2	2.2

2.2 *Mix design*

Aggregate gradation was conducted in accordance with the specifications of the Federal Ministry of Works, Nigeria, for a wearing course mixture, with the selected sieve sizes and percentage passing presented in Table 2.3. The aggregates were sieved and proportioned to achieve the specified gradation for asphalt specimen preparation. The Marshall Mix Design method (ASTM D6927) was employed to determine the Optimum Binder Content (OBC)**,** with three specimens prepared at binder contents ranging from 5.0% to 8.0%. The OBC was determined based on the mixture's Marshall Stability, flow, air voids, and volumetric properties**,** as presented in Table 2.4, in accordance with the relevant Marshall design criteria.

Table 2.3: Design gradation adopted in the research

Sieve size (mm)	**% passing**	**% retained**
19	100	0
12.5	92.5	7.5
9.5	83.5	9
6.3	73.5	10
2.36	57.5	16
1.18	43.5	14
600 µ	33	10.5
300 µ	24	9
150 µ	18.5	5.5
75 µ	10.5	8
pan		10.5

Table 2.4: Marshall results for different binder content percentages

BINDER CONTENT	GMM	GMB	VTM %	VMA %	VFA %	STABILITY (KN)	FLOW (MM)
5	2.3	2.43	5.35	19.5	72.56	14.01	12.25
5.5	2.31	2.48	6.9	19.15	63.97	13.61	14.23
6	2.31	2.41	4.14	19.58	78.86	12.09	11.55
6.5	2.36	2.44	3.28	18.27	82.05	10.72	19.54
7	2.31	2.42	4.55	20.43	77.73	10.7	26.25
7.5	2.31	2.43	4.94	21.15	76.64	6.52	30.09
8	2.37	2.39	0.84	6.02	86.05	7.82	31.58

The optimum binder content (OBC) was selected as 6.0% based on the combined Marshall mix design parameters, including stability, flow, voids in total mix (VTM), and voids filled with asphalt (VFA). Although Marshall stability decreased with increasing binder content, the 6.0% binder content provided a suitable balance among strength, deformation, and volumetric properties. At 6.0% binder content, the mixture recorded a stability of 12.09 kN, flow of 11.55 mm, VTM of 4.14%, and VFA of 78.86%. At higher binder contents, the continued reduction in stability accompanied by an increase in flow indicated a progressively softer mixture. Therefore, 6.0% was selected as the OBC for the subsequent mixture preparation.

Following the determination of the OBC, asphalt concrete mixtures were prepared by partially replacing the natural coarse aggregate with steel slag at replacement levels of 5%, 10%, 15%, 20%, and 25%. Three specimens were prepared for each replacement level using the Marshall mix design procedure. The resulting mixtures were evaluated in terms of density, volumetric properties, Marshall stability, and flow to assess their performance and determine the effects of steel slag incorporation.

The thermal properties of the control and steel slag-modified mixtures were also determined at the Physics Laboratory, Ahmadu Bello University, Zaria**.** As shown in Table 2.5, all mixtures satisfied the specified Marshall criteria, indicating that steel slag can be used as a partial replacement for natural coarse aggregate without compromising the overall performance of the asphalt mixtures.

Table 2.5: Marshal results for different steel slag percentages

STEEL SLAG %	GMM	GMB	VTM %	VMA %	VFA %	STABILITY (KN)	FLOW (MM)
5	2.34	2.42	3.3	21.4	84.6	12.37	15.22
10	2.31	2.43	4.9	22.45	78	11.28	9.84
15	2.35	2.44	3.7	21.11	82.5	11.93	9.62
20	2.36	2.45	3.7	20.8	82.2	11.4	10.53
25	2.36	2.46	4.1	20.77	80.26	11.2	9.13

2.3 *Determination of thermal properties*

The thermal conductivity was determined experimentally using Marshall-derived sub-specimens and a steady-state electrical Searle-type apparatus. The method assumes one-dimensional heat conduction, with the apparent thermal conductivity calculated as: $k = VIL/(A \cdot \Delta T)$, where (V) and (I) are the applied voltage and current, respectively, (L) is the specimen thickness, (A) is the cross-sectional area, and (ΔT) is the temperature difference across the specimen. Three replicate measurements were conducted for each mixture and their mean values reported. Specific heat capacity was determined using the method of mixtures with a copper calorimeter, also based on three replicate measurements.

The measured conductivity is reported as apparent thermal conductivity (K_{app}), since its determination assumes that the applied electrical power is transferred through the specimen

predominantly by one-dimensional conduction and does not explicitly account for lateral or convective heat losses. These factors may affect the measured conductivity and potentially lead to an overestimation of its absolute value. Therefore, the measured conductivity values are used primarily for comparative assessment of the asphalt mixtures and as material-property inputs for the finite element model. No correction factor was applied to account for the potential experimental bias before the values were incorporated into the Abaqus model. Consequently, the agreement between the experimental and numerical results is interpreted as consistency under the adopted experimental and modelling assumptions rather than as independent validation of the absolute thermal conductivity.

2.4 *Finite element model*

A three-dimensional finite element thermal analysis was conducted using Abaqus to simulate the transient thermal response of the cylindrical asphalt specimens investigated experimentally. The specimen geometry was modelled using the actual laboratory dimensions as a three-dimensional deformable solid. Separate models were developed for the control mixture and the mixtures containing 5%, 10%, 15%, 20%, and 25% steel slag replacement.

The experimentally determined apparent thermal conductivity, specific heat capacity, and density of each mixture were assigned as the thermal material properties in the corresponding Abaqus models. Consistent with the experimental methodology described in Section 2.3, the measured apparent thermal conductivity values were used directly without applying a correction factor for the potential overestimation associated with the laboratory measurement method.

The specimens were discretized using three-dimensional, eight-node linear heat-transfer brick elements (DC3D8). Mesh refinement was applied to obtain an adequately resolved temperature and heat-flux distribution within the specimens. A transient heat-transfer analysis was performed to capture the time-dependent thermal response. The thermal loading and boundary conditions were defined to represent the heat-transfer conditions of the laboratory thermal testing, with heat applied through the heated surface and the resulting thermal response evaluated throughout the specimen.

The numerical analysis was conducted over a simulation period of 3600 s. Temperature, heat flux, and reaction heat flux distributions were extracted from the Abaqus results to assess the thermal response of the asphalt mixtures. Particular attention was given to the 5% steel slag mixture because it exhibited the highest experimentally determined thermal conductivity and thermal diffusivity.

A formal mesh-convergence analysis and complete records of the apparatus-level electrical settings used during the laboratory test were not available from the original experimental programme. Therefore, numerical values for these parameters are not reported retrospectively. This limitation is acknowledged because complete reproduction of the laboratory conditions would require detailed information on the applied electrical input, thermal losses, insulation and contact conditions, together with a formal mesh-independence assessment. These aspects are recommended for consideration in future experimental–numerical studies.

3. RESULTS AND DISCUSSION

3.1 *Thermal Properties of Modified Asphalt Mixtures*

This section presents the experimental thermal properties of asphalt mixtures containing 0%, 5%, 10%, 15%, 20%, and 25% steel slag as partial replacement for natural coarse aggregate. The measured thermal conductivity, specific heat capacity, and calculated thermal diffusivity are summarized in Table 3.1.

Table 3.1: Summary of thermal properties

SN	Concentration of steel slag	Apparent Thermal conductivity (W/mk)	Specific heat capacity (J/KgK)	Thermal diffusivity (m^2/s)
1	0%	2.0598	1207.98	$7.08x10^{-7}$
2	5%	3.0421	794.5	$1.58x10^{-6}$
3	10%	2.689	842.89	$1.31x10^{-6}$
4	15%	2.5072	861.51	$1.19x10^{-6}$
5	20%	2.3615	928.54	$1.04x10^{-6}$
6	25%	2.1683	1010.51	$8.72x10^{-7}$

The incorporation of steel slag influenced the thermal conductivity of the asphalt mixtures. At lower replacement levels, thermal conductivity increased compared with the control mixture. The highest value was recorded at 5% steel slag replacement, with a thermal conductivity of 3.0421 W/m·K, compared with 2.0598 W/m·K for the control mixture. This increase may be associated with the relatively high density and thermal conductivity of steel slag compared with the conventional coarse aggregate. The measured volumetric properties also showed variations in mixture structure with increasing steel slag content. For example, the 5% mixture recorded a VTM of 3.3%, compared with 4.9% for the 10% mixture, while the 15%, 20%, and 25% mixtures recorded VTM values of 3.7%, 3.7%, and 4.1%, respectively. These differences in volumetric characteristics may affect the continuity of solid heat-transfer paths within the asphalt mixture.

Beyond the 5% replacement level, thermal conductivity decreased progressively, with values of 2.6890, 2.5072, 2.3615, and 2.1683 W/m·K recorded at 10%, 15%, 20%, and 25% steel slag replacement, respectively. The reduction may be related to changes in aggregate–binder configuration and the distribution of solid and void phases as the steel slag content increases. Such changes may influence the continuity of heat-transfer pathways within the mixture. However, direct microstructural characterization was not conducted in this study; therefore, this explanation should be regarded as a possible interpretation rather than a confirmed mechanism. Further investigation using microscopic analysis or three-dimensional aggregate-packing analysis would be required to establish the specific microstructural factors responsible for the observed trend.

Overall, the 5% steel slag mixture exhibited the highest measured thermal conductivity among the mixtures investigated, indicating the most favourable thermal conductivity under the conditions of the present experimental programme.

Specific heat capacity also varied with steel slag incorporation. The control mixture recorded the highest value of 1207.98 J/kg·K, whereas the 5% steel slag mixture recorded the lowest value of 794.50 J/kg·K. With further increases in steel slag content, the specific heat capacity increased to 842.89, 861.51, 928.54, and 1010.51 J/kg·K at 10%, 15%, 20%, and 25% replacements respectively.

The distinct reduction at 5% replacement, followed by the gradual increase observed from 10% to 25%, indicates a non-monotonic variation in specific heat capacity. Based on the measurements available in this study, the specific mechanism responsible for the low value at 5% cannot be established conclusively. The variation may be influenced by differences in mixture composition and volumetric characteristics associated with steel slag incorporation, as well as experimental variability in determining the thermal properties of a heterogeneous asphalt mixture. Therefore, the 5% result is considered an observed experimental response rather than evidence of a specific material mechanism. Further studies involving repeated measurements, constituent-level thermal characterization, and microstructural analysis would be useful for explaining this behaviour.

The relatively high thermal conductivity and low specific heat capacity recorded at 5% steel slag replacement contributed to its highest calculated thermal diffusivity. This indicates that the SS-05% mixture had a greater capacity for transmitting thermal energy through the specimen under the conditions investigated.

Thermal diffusivity was calculated from the measured thermal conductivity, density, and specific heat capacity using:

$$\alpha = K / \rho Cp$$

Where **α** is the thermal diffusivity (m^2/s), **K** is the thermal conductivity (W/m·K), **ρ** is the density (kg/m^3), and **Cp** is the specific heat capacity (J/kg·K). The 5% steel slag mixture recorded the highest thermal diffusivity of 1.58×10^{-6} m^2/s, reflecting its combination of relatively high thermal conductivity and low specific heat capacity and, consequently, a greater rate of heat propagation through the mixture.

Overall, the results demonstrate that steel slag content influences the thermal properties of the asphalt mixtures. Among the mixtures investigated, the 5% replacement level produced the highest thermal conductivity and thermal diffusivity, indicating an enhanced thermal response under the conditions of the present study. This improvement may be beneficial for pavement applications where enhanced heat transfer is desirable, including potential future integration with pavement-based thermoelectric energy harvesting systems. However, the present study was limited to the thermal characterization and numerical evaluation of the asphalt mixtures; direct integration of a thermoelectric generator and assessment of its electrical performance were not undertaken.

3.2 *Verification of Thermal Results Using 3d Finite Element Simulation In Abaqus*

THERMAL RESPONSE OF THE 5% STEEL SLAG MIXTURE

The figures below present the heat flux, temperature, and reaction heat flux distributions of the asphalt specimen containing 5% steel slag (SS-05%) after 3600 s of transient thermal simulation. The heat flux distribution (HFL) was relatively uniform across the SS-05% specimen, with a magnitude of approximately 1242 W/m^2. The narrow range displayed in the contour legend is consistent with the predominantly conductive and relatively uniform thermal loading adopted in the numerical model, resulting in only small spatial variations in heat flux across the specimen. Therefore, the closely spaced values in the legend do not indicate an absence of heat transfer; rather, they reflect the relatively uniform heat-flux distribution under the applied boundary conditions. The thermal response of the SS-05% mixture was therefore assessed in conjunction with its measured thermal conductivity and thermal diffusivity, as well as the simulated temperature distribution, rather than being inferred from the HFL contour alone.

The temperature distribution ranged from approximately 38.0°C at the edges to 62.5°C at the core, indicating a clear temperature gradient within the simulated specimen. The combination of the observed heat flux and relatively high thermal diffusivity indicates effective heat propagation through the SS-05% mixture under the simulated conditions. Such temperature gradients are relevant to the concept of pavement-integrated thermoelectric energy harvesting because a temperature difference across a thermoelectric generator is required for thermoelectric conversion. However, no TEG device was incorporated into the present finite element model, and electrical voltage, power output, or conversion efficiency was not calculated. Therefore, the simulated thermal response should be regarded as an indication of the potential thermal suitability of the SS-05% mixture for future TEG integration rather than a demonstration of thermoelectric energy generation.

The reaction heat flux distribution (RFL11) shown ranged from $+2.810 \times 10^{-2}$ to -2.810×10^{-2} W/m^2, compared with approximately $\pm 1.982 \times 10^{-2}$ W/m^2 for the control mixture. The increased reaction flux magnitude indicates greater thermal exchange at the specimen surfaces. Collectively, the numerical results indicate that the 5% steel slag mixture exhibited favourable thermal behaviour under the simulated conditions, including relatively effective heat propagation and surface heat exchange. These characteristics support further investigation of the mixture for potential application in pavement-integrated thermoelectric energy harvesting. However, the present study did not evaluate the performance of an integrated TEG, including the temperature difference across the device, voltage generation, electrical power output, or thermoelectric conversion efficiency. Therefore, the numerical results should be interpreted as an assessment of the thermal characteristics of the asphalt mixture rather than a direct demonstration of thermoelectric energy generation.

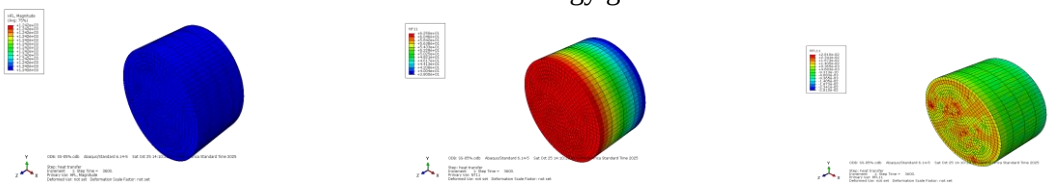

Figure 3.3: Simulated heat flux (HFL, Top left), temperature distribution (NT11, Top right) and reaction heat flux (RFL, bottom) for the optimum % of steel slag (5%)

3.3 Numerical Verification of the Abaqus Model Using Percentage Error Analysis

Table 3.2 presents the percentage differences between the experimental apparent thermal conductivity values and the corresponding Abaqus results. The percentage differences ranged from 4.52% for the control mixture to 5.84% for the mixture containing 25% steel slag. The relatively small differences indicate consistent agreement between the experimental measurements and the numerical results across the investigated replacement levels. However, since the experimental apparent thermal conductivity values were directly assigned as material inputs in the Abaqus models, these differences should be interpreted as a measure of numerical consistency under the adopted modelling assumptions rather than as independent validation of the absolute thermal conductivity.

ABAQUS consistently slightly overestimates the measured thermal conductivity, which may be attributed to idealized modelling assumptions, including homogeneous material properties, perfect aggregate–binder bonding, and the absence of air voids and material imperfections. In contrast, laboratory specimens exhibit inherent heterogeneity and voids that may reduce heat transfer.

The relatively narrow difference between the experimental and Abaqus results, ranging from 4.52% to 5.84%, indicates good numerical consistency across the investigated steel slag replacement levels. The slightly higher Abaqus values may be associated with the idealized representation of the asphalt mixture, including the use of homogeneous material properties and the omission of some physical heterogeneities and heat-loss mechanisms that may be present in the laboratory specimens. Since the experimental apparent thermal conductivity values were directly assigned as material-property inputs without applying a bias correction, the numerical results should be interpreted as verification of the thermal response under the adopted modelling assumptions rather than as independent validation of the absolute thermal conductivity. Nevertheless, the consistent agreement observed across the replacement levels supports the use of the model as a comparative tool for assessing the thermal behaviour of the investigated asphalt mixtures.

Table 3.2: Percentage error analysis

Steel Slag percentages (%)	**Expermental thermal conductivity (W/mk)**	**Abaqus thermal conductivity (W/mk)**	**Percenatge error**
0	2.0598	2.153	4.52%
5	3.0421	3.219	5.82%
10	2.689	2.845	5.80%
15	2.5072	2.653	5.82%
20	2.3615	2.499	5.82%
25	2.1683	2.295	5.84%

4. CONCLUSIONS

The objective of the research is to determine the effect of partially substituting coarse aggregates with steel slag on the thermal properties of asphalt concrete using experiments and to also verify the laboratory results using finite element simulation technique on ABAQUS. The following conclusions are drawn from the study:

1. The physical and mechanical properties of the bitumen, natural aggregate, and steel slag satisfied the relevant specifications for asphalt concrete production. Steel slag exhibited higher density, strength, and abrasion resistance than the natural aggregate, indicating its suitability as a partial replacement material.
2. Partial replacement of conventional coarse aggregate with steel slag altered the thermal properties of the asphalt concrete mixtures. In particular, all steel slag-modified mixtures exhibited higher thermal conductivity and thermal diffusivity than the control mixture, indicating an overall improvement in heat-transfer and thermal-propagation characteristics with steel slag incorporation.
3. The optimum steel slag replacement level for the thermal properties investigated in this study was 5%, which produced the highest thermal conductivity of 3.0421 W/m·K and thermal diffusivity of 1.58×10^{-6} m²/s. These results indicate that the 5% steel slag mixture exhibits favorable thermal characteristics

that may support its potential application in pavement-integrated thermoelectric energy harvesting systems. However, the present study was limited to the thermal characterization of the asphalt mixtures, and direct integration and performance evaluation of a thermoelectric generator, including voltage and power output, were not undertaken.

4. The three-dimensional (3D) transient heat-transfer simulation conducted in Abaqus demonstrated consistent thermal responses across the investigated asphalt mixtures. The differences between the experimental apparent thermal conductivity values and the corresponding Abaqus results ranged from 4.52% to 5.84%, indicating a relatively close numerical agreement across the steel slag replacement levels. However, since the experimentally determined apparent thermal conductivity values were directly assigned as material property inputs in the numerical model, the Abaqus results should be interpreted as demonstrating consistency with the experimental thermal response under the adopted modelling assumptions, rather than as an independent validation of the absolute thermal conductivity values.
5. Further research should investigate the direct integration of thermoelectric generators into steel-slag-modified asphalt pavement systems. Future studies should evaluate the temperature difference across the TEG, electrical voltage and power output, thermoelectric conversion efficiency, and long-term performance under field conditions. In addition, an economic assessment of steel slag sourcing, processing, transportation, and incorporation into asphalt mixtures should be conducted to determine the practical feasibility and scalability of the proposed application.

REFERENCES

1. Hasita, S., Rachan, R., Suddeepong, A., Horpibulsuk, S., Arulrajah, A., Mohammadinia, A., & Nazir, R. (2020). Performance Improvement of Asphalt Concretes Using Steel Slag as a Replacement Material. *Journal of Materials in Civil Engineering*, *32*(8), 04020227. https://doi.org/10.1061/(ASCE)MT.1943-5533.0003306
2. Chen, J., Wang, H., & Li, L. (2015). Determination of effective thermal conductivity of asphalt concrete with random aggregate microstructure. *Journal of Materials in Civil Engineering*, *27*(12), 04015045.
3. Chen, M. Z., Wei, W., & Wu, S. P. (2009). On cold materials of pavement and high-temperature performance of asphalt concrete. *Materials Science Forum*, *620*, 379–382.
4. Ding, X., Chen, L., Ma, T., Ma, H., Gu, L., Chen, T., & Ma, Y. (2019). Laboratory investigation of the recycled asphalt concrete with stable crumb rubber asphalt binder. *Construction and Building Materials*, *203*, 552–557.
5. Fang, F. T., Chong, Y. C., Nyunt, T. T., & Loi, S. S. (2013). Development of environmentally sustainable pavement mix. *International Journal of Pavement Research and Technology*, *6*(4), 440.
6. Hainin, M. R., Rusbintardjo, G., Hameed, M. A. S., Hassan, N. A., & Yusoff, N. I. M. (2014). Utilisation of steel slag as an aggregate replacement in porous asphalt mixtures. *Jurnal Teknologi (Sciences & Engineering)*, *69*(1). https://journals.utm.my/jurnalteknologi/article/view/2529
7. Islam, M. R., & Tarefder, R. A. (2014). Determining thermal properties of asphalt concrete using field data and laboratory testing. *Construction and Building Materials*, *67*, 297–306. https://doi.org/10.1016/j.conbuildmat.2014.03.040
8. Jiang, W., Yuan, D., Xu, S., Hu, H., Xiao, J., Sha, A., & Huang, Y. (2017). Energy harvesting from asphalt pavement using thermoelectric technology. *Applied Energy*, *205*, 941–950. https://doi.org/10.1016/j.apenergy.2017.08.091
9. Kavussi, A., Jalili Qazizadeh, M., & Hassani, A. (2015). Fatigue behavior analysis of asphalt mixes containing electric arc furnace (EAF) steel slag. *Journal of Rehabilitation in Civil Engineering*, *3*(1), 74–86.
10. Marsal-Llacuna, M.-L., Colomer-Llinàs, J., & Meléndez-Frigola, J. (2015). Lessons in urban monitoring taken from sustainable and livable cities to better address the Smart Cities initiative. *Technological Forecasting and Social Change*, *90*, 611–622.
11. Rondón-Quintana, H. A., Ruge-Cárdenas, J. C., Patiño-Sánchez, D. F., Vacca-Gamez, H. A., Reyes-Lizcano, F. A., & Muniz De Farias, M. (2018). Blast Furnace Slag as a Substitute for the Fine Fraction

of Aggregates in an Asphalt Mixture. *Journal of Materials in Civil Engineering*, *30*(10), 04018244. https://doi.org/10.1061/(ASCE)MT.1943-5533.0002409

12. Sabapathy, Y. K., Balasubramanian, V. B., Shankari, N. S., Kumar, A. Y., & Ravichandar, D. (2017). Experimental investigation of surface modified EOF steel slag as coarse aggregate in concrete. *Journal of King Saud University-Engineering Sciences*, *29*(4), 388–393.

International Conference on Engineering Innovation for Sustainable Development (ICESID 2026)
Faculty of Engineering, Ahmadu Bello University Zaria · 8–10 September 2026

EVALUATION OF THE SYNERGISTIC EFFECT OF CORN COB ASH (CCA) AND DATE PALM SEED ASH (DPSA) AS PARTIAL CEMENT REPLACEMENT ON THE MECHANICAL PROPERTIES OF CONCRETE

Tukur Sani[1,*], Yusuf Yau[1], Tasiu Ashiru Sulaiman[1], Yusuf Mansur Hashim[1]
[1]*Ahmadu Bello University, Zaria*
Email: iamtksani@gmail.com*, yyilyas@gmail.com, tasiuashirusulaiman@gmail.com, ysuidi58@gmail.com
***Corresponding author**: Tukur Sani
DOI: https://doi.org/10.67203/sp.ICESID.2026

ABSTRACT
The production of Ordinary Portland Cement (OPC) is associated with high carbon dioxide emissions and energy consumption, creating the need for sustainable supplementary cementitious materials. This study investigated the synergistic effect of Corncob Ash (CCA) and Date Palm Seed Ash (DPSA) as partial cement replacements on the mechanical properties of concrete. CCA and DPSA were produced through controlled calcination at 600ºC – 800°C and incorporated as binary (OPC–CCA and OPC–DPSA) and ternary (OPC–CCA–DPSA) blends at replacement levels of 5, 10, 15, and 20% by weight of cement. Cube and cylinder concrete specimens, designed for a target compressive strength of 30 MPa with a water-to-binder ratio of 0.50, were produced and cured for 7, 14, and 28 days and tested for workability, compressive and split tensile strengths in accordance with relevant British Standards. Strength increased with curing age for all mixes, with the binary blends outperforming the ternary blend. At 28 days, OPC–CCA and OPC–DPSA achieved optimum compressive strengths of 32.33 MPa and 32.00 MPa, respectively, at 5% replacement, while the ternary blend attained 28.33 MPa. OPC–DPSA recorded the highest split tensile strength of 3.61 MPa at 10% replacement, whereas the ternary blend reached 3.50 MPa. The study concludes that 5–10% replacement is optimal. Although the expected synergistic enhancement of the ternary blend was not fully realized, longer-term curing may improve its performance. Overall, CCA and DPSA show strong potential as sustainable supplementary cementitious materials that reduce cement consumption while maintaining satisfactory mechanical properties.

Keywords: *Corncob ash; Date palm seed ash; Supplementary cementitious materials; Compressive strength; Split tensile strength; Sustainable concrete*

1. INTRODUCTION

Concrete remains the most widely used construction material worldwide because of its versatility, durability, and the availability of its constituent materials. However, its primary binding material, Ordinary Portland Cement (OPC), is highly energy-intensive to manufacture and is responsible for approximately 7–8% of global anthropogenic carbon dioxide (CO_2) emissions (Chen et al., 2022).

As reported by Tijani et al. (2018) agricultural waste ashes have emerged as promising SCMs because they provide an environmentally friendly means of converting waste materials into value-added construction products. These materials are generally rich in reactive silica and alumina, enabling them to participate in pozzolanic reactions (Papadaki & Tsimas, 2002). Among the various agricultural wastes investigated as SCMs, Corncob Ash (CCA) and Date Palm Seed Ash (DPSA) have attracted increasing research interest because of their availability in many agricultural regions and their favourable chemical compositions. Previous investigations have shown that CCA possesses appreciable amounts of reactive silica capable of improving compressive strength and durability (Adesanya & Raheem, 2009; Apampa et al., 2023). Similarly, DPSA has demonstrated good pozzolanic characteristics, with studies reporting improvements in strength properties (Ahmad et al.,2023; Smith et al., 2020). Recent developments in blended cement technology have shifted attention from binary systems to ternary blended binders, where two or more SCMs are combined to exploit complementary physical and chemical characteristics.

This study therefore investigates the synergistic effect of CCA and DPSA as partial replacements for cement on the mechanical properties of concrete. Binary and ternary blended concretes were produced at varying replacement levels and evaluated through workability, compressive and split tensile strength tests. The findings are expected to provide further insight into the feasibility of utilizing locally available agricultural wastes as sustainable supplementary cementitious materials for low-carbon concrete production.

2. METHODOLOGY

2.1 Materials

Ordinary Portland Cement (OPC) conforming to BS EN 197-1 (2011) was used as the primary binder. Natural river sand conforming to BS EN 12620 (2002) and crushed granite with a nominal maximum size of 20 mm were used as fine and coarse aggregates, respectively. Potable water complying with BS EN 1008 (2002) was used for concrete mixing and curing. Corncob Ash (CCA) was obtained from Zabawa Village, Giwa Local Government Area, Kaduna State, while Date Palm Seed Ash (DPSA) was produced from date palm seeds sourced from Dutsinma Local Government Area, Katsina State, Nigeria. CCA and DPSA were produced through controlled thermal treatment at a temperature of 650ºC and 750ºC respectively.

2.2 Methods

2.2.1 Materials Characterization

Preliminary characterization of the constituent materials was carried out before concrete production. Tests conducted on cement included specific gravity, standard consistency, setting time, and soundness. Fine and coarse aggregates were evaluated for grading, specific gravity, bulk density, water absorption, Aggregate Impact Value (AIV), and Aggregate Crushing Value (ACV), while the chemical compositions of CCA and DPSA were determined using X-ray fluorescence (XRF). All tests were performed in accordance with the relevant British Standards.

2.2.2 Mix Design and Specimen Preparation

One hundred and seventeen (117), 100 x 100 x 100mm cubes and Seventy eight (78), 100 x 200mm cylinder specimens were prepared. Design of Experiment (DoE) method was used to design a concrete mixtures for a target strength of 30 MPa, with a constant water-to-binder ratio of 0.50. Three binder systems were investigated: binary OPC–CCA, binary OPC–DPSA, and ternary OPC–CCA–DPSA blends. Cement replacement levels of 5%, 10%, 15%, and 20% by weight of cement were adopted alongside a control mix containing 100% OPC.

2.2.3 Fresh and Hardened Properties of Concrete

Fresh concrete workability was evaluated using the slump test in accordance with BS 1881-102 (1983). Hardened concrete was assessed through compressive strength and split tensile strength tests conducted at curing ages of 7, 14, and 28 days in accordance with BS EN 12390-3 (2002) and BS EN 12390-6 (2009), respectively. Compressive strength was determined from 100 × 100 × 100 mm cube specimens, while split tensile strength was measured using 100 × 200 mm cylinders.

2.2.4 Statistical Analysis

The experimental data for the ternary OPC–CCA–DPSA system were analysed using one-way analysis of variance (ANOVA) at a 95% confidence level ($\alpha = 0.05$) to evaluate the effect of replacement level on compressive and split tensile strength at each curing age.

3. RESULTS AND DISCUSSION

3.1 Characterization of Constituent Materials

The physical properties of the Ordinary Portland Cement satisfied the requirements of BS EN 196, confirming its suitability for structural concrete production. Similarly, the fine and coarse

aggregates complied with the relevant British Standards, Fine aggregate; fineness modulus = 2.87827, specific gravity = 2.66, bulk density = 1433.3kg/m3, and Coarse aggregate; grading ≤ 20mm, specific gravity = 2.68, water absorption = 0.7, Aggregate Impact Value (AIV = 24.55), and Aggregate Crushing Value (ACV = 21.61), indicating their suitability for concrete manufacture. The results for chemical composition of CCA and DPSA are presented in Table 1.

Table 1: Chemical composition of CCA and DPSA

Chemical Constituents (%)	**SiO_2**	**Al_2O_3**	**Fe_2O_3**	**CaO**	**MgO**	**Na_20**	**K_2O**	**SO_3**	**LOI**
CCA	62.30	6.25	4.40	10.57	1.86	0.36	3.89	1.02	3.50
DPSA	45.50	20.75	7.25	9.82	0.52	3.00	9.07	0.12	1.72

The XRF analysis revealed that the combined silica (SiO_2), alumina (Al_2O_3), and iron oxide (Fe_2O_3) contents were 72.95% for CCA and 73.50% for DPSA, exceeding the 70% minimum specified by ASTM C618-19 (2019) for natural pozzolans. This confirms the pozzolanic potential of both agricultural ashes and supports their application as supplementary cementitious materials.

3.2 Fresh Properties of Concrete

The results for workability is presented in Figure 1. Workability of all concrete mixtures decreased progressively with increasing cement replacement irrespective of the binder system. The control concrete recorded the highest slump (60 mm), whereas slump values decreased to 23 mm for both binary mixes and 20 mm for the ternary blend at 20% replacement.

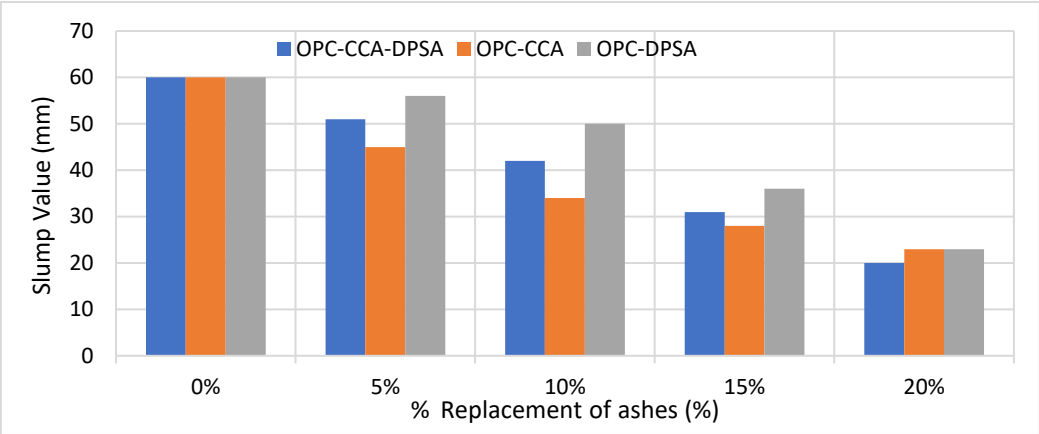

Figure 1: Slump values of control, binary and ternary concrete mixtures.

The reduction in workability is attributed to the higher specific surface area and increased water demand of CCA and DPSA, which reduced the amount of free water available for lubrication within the fresh concrete matrix.

3.3 Mechanical Properties

3.3.1 Compressive strength

The results for compressive strength of all the mixtures are presented in Figures 2, 3, and 4. Generally, increase in compressive strength was observed for all the mixtures, as curing age increases, indicating continued cement hydration and pozzolanic activity. However, strength generally decreased with increasing cement replacement due to the cement dilution effect.

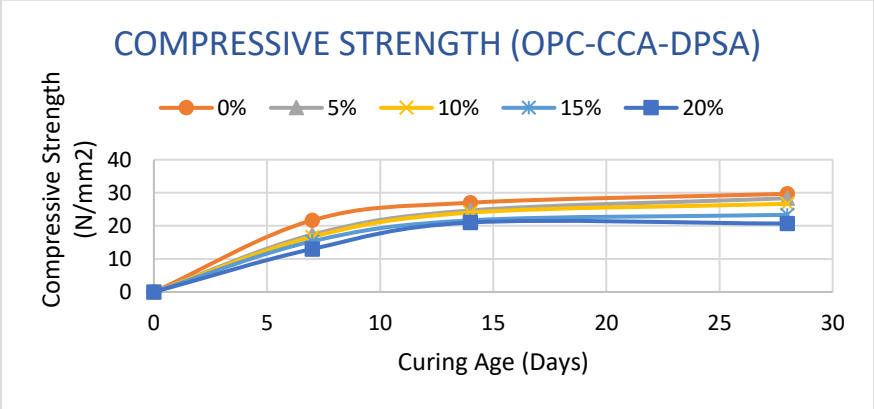

Figure 2: Compressive strength development of ternary concrete.

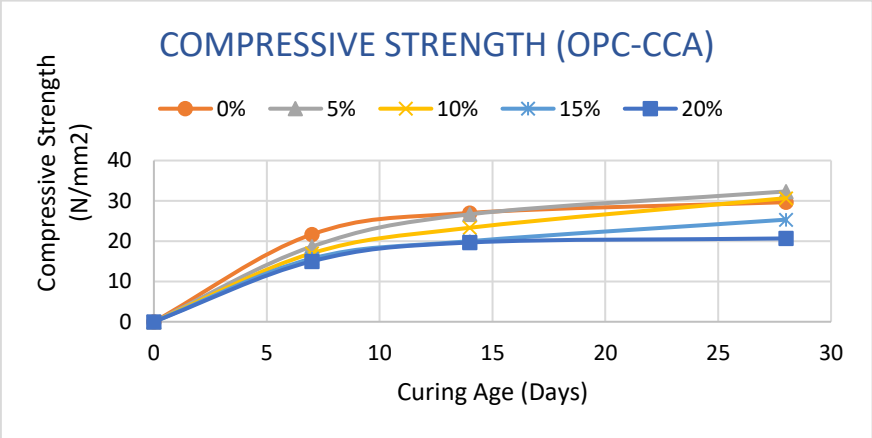

Figure 3: Compressive strength development of OPC–CCA concrete.

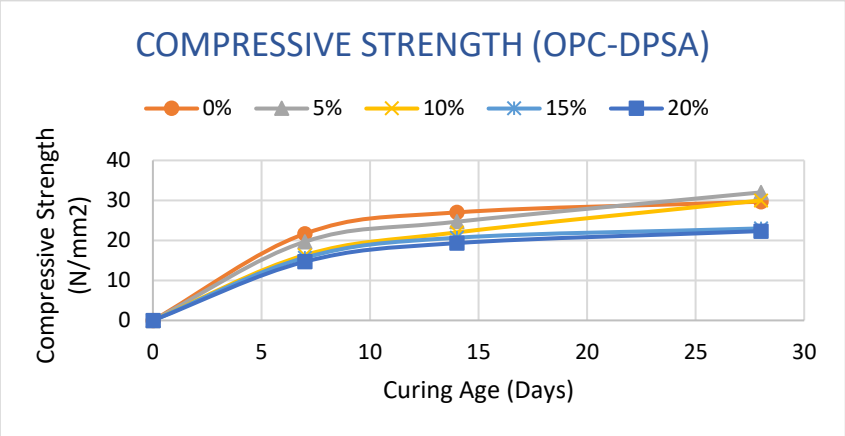

Figure 4: Compressive strength development of OPC–DPSA concrete.

For the ternary OPC–CCA–DPSA concrete, the 28-day compressive strength decreased from 29.67 MPa for the control to 28.33, 26.67, 23.33, and 20.67 MPa at 5%, 10%, 15%, and 20% replacement, respectively. The 5% replacement retained approximately 95.5% of the control strength, suggesting that limited incorporation of both ashes contributed to strength development through secondary pozzolanic reactions.

The binary mixtures exhibited superior performance. At 28 days, OPC–CCA achieved a maximum compressive strength of 32.33 MPa at 5% replacement, while OPC–DPSA attained 32.00 MPa at the same replacement level, both exceeding the control concrete. The ternary blend, however, did not demonstrate the anticipated synergistic improvement. These observations agree with previous studies reporting that agricultural waste ashes produce optimum strength at relatively low replacement levels, beyond which the dilution effect predominates over the benefits of pozzolanic activity (Adesanya & Raheem, 2009; Kavitha et al., 2022; Shakir et al., 2021).

3.3.2 Split Tensile Strength

Split tensile strength increased with curing age for all mixtures as shown in Figures 5, 6, and 7, confirming continued hydration and microstructural refinement. Similar to compressive strength, low replacement levels improved tensile performance, whereas higher replacement levels (15–20%) resulted in strength reduction. The ternary concrete achieved its highest split tensile strength of 3.50 MPa at 10% replacement, slightly exceeding the control value of 3.42 MPa. Among the binary blends, OPC–DPSA produced the highest tensile strength of 3.61 MPa at 10% replacement, followed by OPC–CCA with 3.50 MPa at 5% replacement.

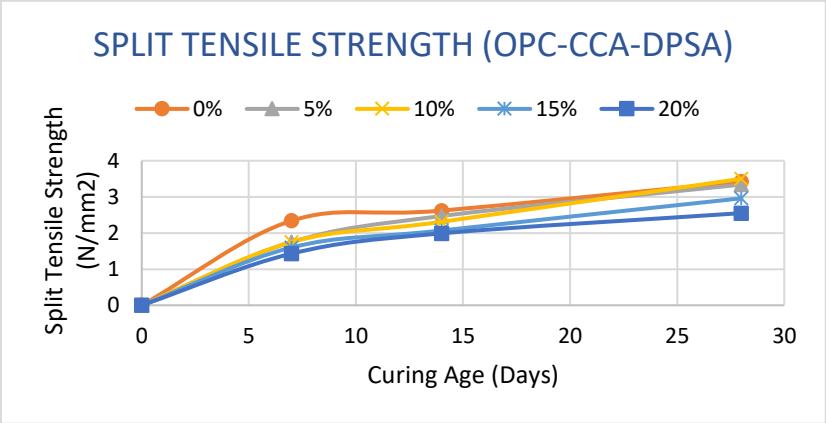

Figure 5: Split tensile strength development of ternary concrete.

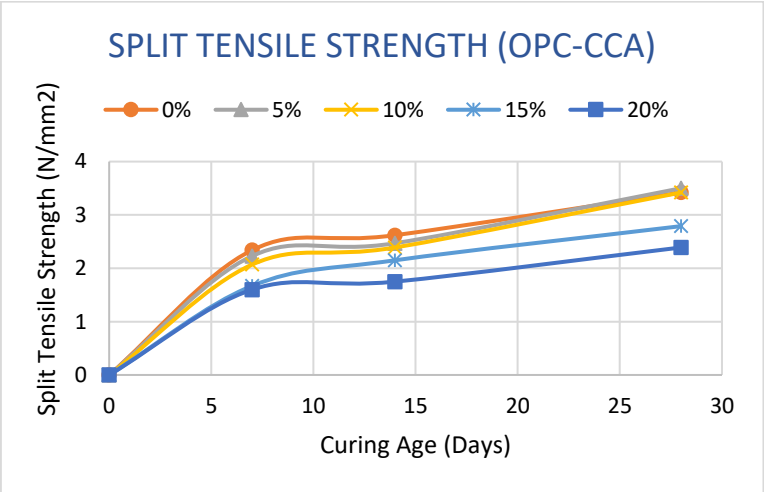

Figure 6: Split tensile strength development of OPC–CCA concrete.

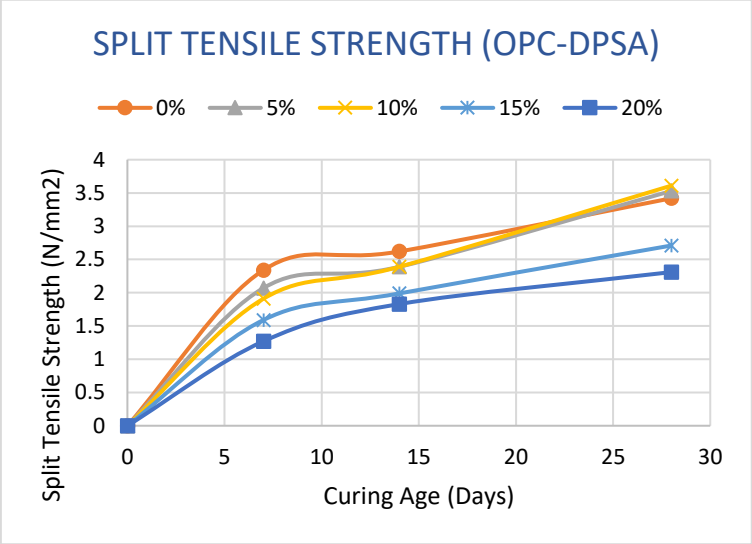

Figure 7: Split tensile strength development of OPC–DPSA concrete.

Although the ternary blend improved the tensile strength relative to the control, it did not outperform the best-performing binary mixture, indicating that the expected synergistic enhancement was not fully realized within the 28-day curing period. The findings are consistent with previous studies which reported that supplementary cementitious materials enhance concrete performance only within an optimum replacement range (Nasir & Al-kutti, 2019; Aswin et al., 2021).

3.4 Statistical Analysis

The one-way ANOVA results as presented in Table 2, showed that replacement level significantly influenced the compressive strength of the ternary OPC–CCA–DPSA concrete at 7, 14, and 28 days, with *p*-values of 0.0256, 0.0334, and <0.001, respectively. Similarly, split tensile strength was significantly affected at 7, 14, and 28 days, with *p*-values of 0.0245, 0.0063, and 0.0314, respectively.

Table 2: ANOVA result for Compressive and Split tensile strength

Test – Curing age	F-statistic	F-critical	P-value	Result (α = 0.05)
Compressive Strength – 7 Days	4.43	3.48	0.0256	Significant
Compressive Strength – 14 Days	4.04	3.48	0.0334	Significant
Compressive Strength – 28 Days	43.82	3.48	2.62e-6	Significant
Split Tensile Strength – 7 Days	7.47	5.19	0.0245	Significant
Split Tensile Strength – 14 Days	14.00	5.19	0.0063	Significant
Split Tensile Strength – 28 Days	6.60	5.19	0.0314	Significant

The results confirm that changes in CCA–DPSA replacement level significantly influenced the mechanical performance of the ternary concrete. The optimum performance occurred at low replacement levels.

4. CONCLUSION

This study evaluated the mechanical performance of binary and ternary concrete. Both ashes showed pozzolanic potential, while increasing replacement reduced workability. Strength generally increased with curing age, with the ternary mixture achieving optimum compressive strength of 28.33

MPa at 5% replacement and split tensile strength of 3.50 MPa at 10% after 28 days. One-way ANOVA confirmed that replacement level significantly affected both properties. However, the ternary blend did not outperform the binary systems at 28 days. Thus, the anticipated synergistic enhancement was not fully realized within the 28-day period. Longer curing periods, varied CCA-DPSA ratios, and microstructural and durability investigations are recommended to determine whether delayed pozzolanic reactions can improve ternary performance and establish an optimum blend.

5. REFERENCES

Adesanya, D. A., & Raheem, A. A. (2009). A study of the workability and compressive strength characteristics of corn cob ash blended cement concrete. Construction and Building Materials, 23(1), 311–317. https://doi.org/10.1016/j.conbuildmat.2007.12.004

Ahmad, S., Zubair, M., & Maslehuddin, M. (2023). Mechanical and durability properties of date palm waste ash as a supplementary cementitious material. Materials and Structures, 56(3), 1–14. https://doi.org/10.1617/s11527-023-02112-5

Apampa, O. A., Olofinnade, O. M., & Busari, A. A. (2023). Mechanical and microstructural properties of concrete incorporating corn cob ash as supplementary cementitious material. Journal of Sustainable Cement-Based Materials, 12(4), 521–537. https://doi.org/10.1080/21650373.2022.2125491

ASTM C618-19 (2019). Standard specification for coal fly ash and raw or calcined natural pozzolan for use in concrete. ASTM International.

Aswin, M., Nola, L., & Maranatha, E. S. (2021). Study on concrete compressive strength due to the cement substitution partially by corncob ash. IOP Conference Series: Materials Science and Engineering, 1122(1), 012025. https://doi.org/10.1088/1757-899X/1122/1/012025

Chen, C., Habert, G., Bouzidi, Y., & Jullien, A. (2022). Environmental impact of cement production: Detail of the different processes and cement plant variability evaluation. Journal of Cleaner Production, 15, 267–277. https://doi.org/10.1088/1748-9326/ac48b5

Kavitha, S., Kannan, V., & Gokul, C. (2022). Experimental investigation on high performance concrete with corn cob ash as partial replacement of cement. Journal of Physics: Conference Series, 2312(1), 012058. https://doi.org/10.1088/1742-6596/2312/1/012058

Nasir, M., & Al-Kutti, W. (2019). Strength and durability of date palm ash blended cement concrete. IOP Conference Series: Materials Science and Engineering, 601(1), 012038. https://doi.org/10.1088/1757-899X/601/1/012038

Papadakis, V. G., & Tsimas, S. (2002). Supplementary cementing materials in concrete: Part I: Efficiency and design. Cement and Concrete Research, 32(10), 1525–1532. https://doi.org/10.1016/S0008-8846(02)00827-X

Shakir, A. A., Mohammed, A. A., & Hussain, H. K. (2021). Effect of corncob ash on the properties of fresh and hardened concrete. Materials Today: Proceedings, 42(5), 2464–2470. https://doi.org/10.1016/j.matpr.2020.12.584

Smith, A. S. J., Xu, G., Garba, M. J., & Aliyu, M. Y. (2020). Pozzolanic and mechanical properties of date palm seed ash (DPSA) concrete. Nigerian Journal of Technology (NIJOTECH), 39(3), 680–686. https://doi.org/10.4314/njt.v39i3.5

Tijani, M. A., Yusuf, R. O., & Olawale, S. O. A. (2018). Agricultural wastes as potential sources of low-cost supplementary cementitious materials in Nigeria: A review. Journal of Engineering Research and Reports, 1(3), 1–12. https://doi.org/10.9734/jerr/2018/v1i329773

International Conference on Engineering Innovation for Sustainable Development (ICESID 2026)
Faculty of Engineering, Ahmadu Bello University Zaria · 8–10 September 2026

EXPERIMENTAL VALIDATION OF EUROCODE 2 PREDICTIONS FOR THE FLEXURAL AND SHEAR CAPACITIES OF REINFORCED METAKAOLIN-BASED GEOPOLYMER CONCRETE BEAMS

Ibrahim Aliyu[1,*], Sholadoye I.o[1], Idris Abubakar[1], Jamilu Yau[2], Aliyu Abubakar Abbas[3]

[1]*Department of Civil Engineering, Ahmadu Bello University, Zaria*
[2]*Department of Building, Abubakar Tafawa Balewa University, Bauchi State*
[3]*Bankanu and Partners Limited, Suite 001, Basement Level, Mortgage House, Central Business District, Abuja*

Email: ibrahimaliyu@abu.edu.ng*, kemshol1977@gmail.com, idrcivil1@yahoo.com, yaumsc3748@gmail.com, aaaliyumm@gmail.com

***Corresponding author**: Ibrahim Aliyu

DOI: https://doi.org/10.67203/sp.ICESID.2026

ABSTRACT

Sustainable construction materials research, including geopolymer concrete, has been ongoing for quite some time. This is because they are environmentally friendly and can be employed as alternatives to ordinary Portland cement (OPC) concrete. The researchers have been pushing for the adoption of geopolymer concrete as an alternative to OPC concrete in structural members' production. However, the applicability of existing reinforced concrete design provisions to reinforced metakaolin-based geopolymer concrete (MBGC) beams was not adequately validated. This study experimentally investigated the flexural and shear capacities of singly reinforced MBGC beams and compared the results with values predicted using Eurocode 2 (EC2). Three beams were produced, each with two 8, 10, and 12 mm tensile reinforcements (RGCB08, RGCB10, and RGCB12 respectively), and were tested to failure under static loading; the experimental ultimate moment and shear capacities were compared with EC2 theoretical values. The results showed that increasing the reinforcement ratio enhanced both flexural and shear performance. Compared with RGCB08, the experimental ultimate moment increased by 10% and 26% for RGCB10 and RGCB12, while the corresponding EC2-predicted moment increased by 28.7% and 41.7%. The EC2 moment capacity predictions were in close agreement with the experimental capacities, with experimental-to-theoretical moment ratios of 1.11, 0.95, and 0.99 (≅ 1.0), respectively, for the three reinforcement ratios. In contrast, the experimental-to-theoretical shear ratios were 2.9, 2.9, and 3.4 for RGCB08, RGCB10, and RGCB12, respectively, indicating that the experimental shear capacities exceeded the EC2 predictions. The conservative shear predictions were attributed to EC2 limitations on the longitudinal reinforcement ratio and effective depth factors for beams without shear reinforcement. The study concludes that despite EC2 underestimating the measured shear capacity, its predictions remain conservative and provide a safe design. EC2 is therefore recommended for the flexural and shear design of reinforced metakaolin-based geopolymer concrete.

Keywords: *MBGC; Reinforced-concrete-beams; Eurocode-2; Flexural-capacity; Shear-capacity; Reinforcement-ratio*

1.0 INTRODUCTION

The environmental impacts associated with the production of ordinary Portland cement (OPC), particularly its substantial contribution to global carbon dioxide emissions, have increased the demand for more sustainable construction materials (Jindal et al., 2022). Consequently, geopolymer concrete has emerged as a viable alternative binder through the utilisation of aluminosilicate precursor materials activated by alkaline solutions to produce concrete with comparable mechanical properties and enhanced durability, while significantly reducing greenhouse gas emissions. Among the various aluminosilicate precursor materials, metakaolin has attracted considerable attention because of its high pozzolanic reactivity, uniform chemical composition, and ability to produce geopolymer concrete with superior mechanical performance and long-term durability. This observation is consistent with the findings of Qader et al. (2025). Furthermore, Mo et al. (2016) reported that the application of

geopolymer concrete has gradually progressed beyond material characterisation to structural applications involving reinforced concrete members such as beams, columns, and slabs. Reinforced concrete beams are structural members that support loading primarily by flexure, according to Wasiu and Adedeji (2018). For reinforced concrete (RC) beams, the major failure modes that require focus are the bending moment, shear capacity, and deflection. For a short-span beam as in the case of this research, the critical failure mode is shear according to Chanackya (2009**)** and the ultimate limit state of bending for moderately loaded medium-span beams.

Research conducted on geopolymer beams has focused either on flyash or ground granulated blast slag (GGBS) and sometimes mixed with metakaolin. The research is either on the flexural strength of unreinforced sections or on doubly reinforced beams with shear stirrups. Recent studies have shown that reinforced geopolymer concrete beams exhibit flexural behaviour similar to that of conventional reinforced concrete members, with the reinforcement ratio remaining one of the major parameters influencing the strength, stiffness, cracking behaviour, and failure characteristics of the beams as observed by Ansari et al. (2023). Furthermore, although several experimental studies have reported satisfactory structural performance of reinforced geopolymer concrete beams, the available literature is largely focused on fly ash- and slag-based geopolymer systems. Comparatively limited information is available on metakaolin-based geopolymer concrete beams, particularly with respect to their flexural and shear capacities (Handono et al., 2023), especially within the Nigerian context. This is despite the abundance of kaolin deposits in Nigeria, which can be processed to produce metakaolin for reinforced geopolymer concrete applications.

Furthermore, although the design provisions of Eurocode 2 (EC2) are widely adopted for reinforced concrete structures, their applicability to reinforced metakaolin-based geopolymer concrete beams has not been adequately established through experimental investigations. This means that the application of the code to reinforced metakaolin-based geopolymer concrete beams remains insufficiently validated. Establishing the relationship between the experimentally determined capacities and the theoretical predictions of EC2 is therefore necessary before these design provisions can be confidently applied to geopolymer concrete structures. Accordingly, this study investigates the influence of reinforcement ratio on the flexural and shear capacities of reinforced metakaolin-based geopolymer concrete beams and evaluates the accuracy of the EC2 provisions by comparing the theoretical predictions with the corresponding experimental moment and shear capacities.

2.0 MATERIALS AND METHODS

2.1 Materials: Metakaolin, fine and coarse aggregates, sodium hydroxide (NaOH), sodium silicate (Na_2SiO_3), water, and steel reinforcement were all sourced locally in Zaria except the metakaolin, which was processed from a raw kaolin obtained from Kankara Local Government of Katsina State.

2.2 Methods

2.2.1 Metakaolin and other Materials Processing: The Metakaolin was from the beneficiation of kaolin clay at 800°C for 3 hours based on Keeratikan and Janjit (2018). The metakaolin was found to be a class N pozzolan according to ASTMC618-05. The aggregates were tested for conformity against BS882 (1992) and Nevelli (2011). The steel was tested for yield strength based on BS EN 10002-1 (2001).

2.2.2: Beam Specimen production: The metakaolin (Mc), aggregates were dry mixed and then transferred to an electric mixer. The same batch of concrete mix was used for all specimens. The alkaline liquids and additional water were mixed continuously for an average of 5 minutes and the mix poured in the formworks (Tables 1) in accordance with BS EN 12390-1 (2000) and trimmed based on BS EN 12390-2 (2000). Three (3) 100 mm^3 concrete cubes and 3 short beams each for RGCB08, RGCB10, and RGCB12 (Table 2) were produced and tested for compressive strength based on BS EN 12390-3 (2009) and the average result was presented in Table 1. The beams and cubes were allowed to cure at ambient temperature (13 days) and heat-cured in an oven at 60^{0}C, for 1 day based on Abdul Rahim *et al*. (2014) before testing.

Table 1: Mix Proportions for the Metakaolin-Based Geopolymer Concrete

S/No	Mc (Kg/m^3)	(ALm)	Alr	Fa (Kg/m^3)	Ca (Kg/m^3)	Wc (Kg/m^3)	Acquired Strength (N/mm^2)
1	400	0.9	3	546.7	1093.3	60	31.33

Where ALm is the ratio of metakaolin to alkaline-liquid and Alr is the ratio of Na_2SiO_3 to NaOH.

Table 2: Reinforcement Detail

Beam (No of Beams produced)	Dimension (mm)	Effective depth (mm)	Tensile reinforcement diameter(mm) and Area (mm^2))	Reinforcement ratio (%)
RGCB08 (3 beams)	450×100×100	81	2Y8 (100.53)	1.24
RGCB10 (3 beams)	450×100×100	80	2 Y10 (157.08)	1.96
RGCB12 (3 beams)	450×100×100	79	2Y12 (226.19)	2.86

The tension reinforcements fall within the BS8110 and EC 2 limit of 0.13% ≤ ρ ≤ 4%. The difference in the effective depths presented in Table 1 is because increasing bar diameter reduces effective depth due to constant overall depth and cover

2.2.3 Beam Test Set-up: The test was conducted per BS EN 12390 -5 (2009) (Plate 1). Three (3) beams each for RGCB08, RGCB10, and RGCB12 were tested. The machine was set to move at an average speed of 20mm/minute (0.33mm/sec). Readings were taken at 2 kN intervals simultaneously with the corresponding deflection reading until failure of the specimen (with a dial gauge at the beams soffit); an average of the three results (for 3 beams) was taken as a representative result. The ultimate (maximum load) and failure (load at failure) loads were all recorded.

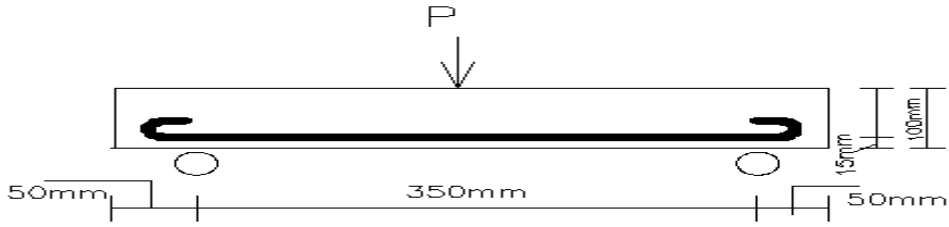

Plate 1: Loading and reinforcement detail of the RGCB (3 Point Loading Test)

It can be deduced that the beam tested is a short beam with a/d (a = 175 mm and d = 100 mm) ≤ 2.5 based on ACI 318 (1992)

2.2.4: Theoretical Beam Moment and Shear Based on Eurocode 2 Formulations

2.2.4.1 Moment Capacity:

The moment capacity of a singly reinforced concrete section based on Eurocode 2, and Mosley *et al.* (2007) expressed it as eqn (1): $for\ x \leq 0.617d$ (steel has yielded)

$$M = 0.567 f_{ck} bsZ = 0.87 A_S f_{yk} Z = 0.87 A_S f_{yk} \left(d - \frac{s}{2}\right) \quad (1)$$

2.2.4.2 Shear capacity:

The Shear capacities are presented in eqn (2 and 3). Where $\rho = \frac{A_s}{bd} \leq 0.02. for\ d\ in\ mm, K = \left(1 + \sqrt{\frac{200}{d}}\right) \leq 2.0$

$$V_{Rdc} = (0.12K(100\rho f_{ck})^{\frac{1}{3}})bd \quad (2)$$

$$\text{Minimum is } V_{Rdcmin} = (0.035K^{3/2}(f_{ck})^{\frac{1}{2}})bd \quad (3)$$

3.0 RESULTS AND DISCUSSIONS

3.1 Relationship between Theoretical (EC2-based) and Experimental Ultimate Moment

The theoretical moment values computed for RGCB8, RGCB10, and RGCB12 using the EC2 formulations and the corresponding average experimental ultimate moment values obtained from the laboratory are very close to each other (Figure 1). This means that the EC2 flexural design and analysis of reinforced concrete sections could be used for singly reinforced MBGB. From Table 3 and Figure 1, it could be observed that the values of the experimental ultimate moment increased by 10% and 26%, respectively, for RGCB10 and RGCB12 compared with RGCB8; the theoretical ultimate moment increased by 28.7% and 41.7%, respectively, for RGCB10 and RGCB12 when compared with RGCB8. This increase agrees with the conventional concrete behaviour of moment capacity increasing with the reinforcement ratio due to an increase in the tensile capacity of the section.

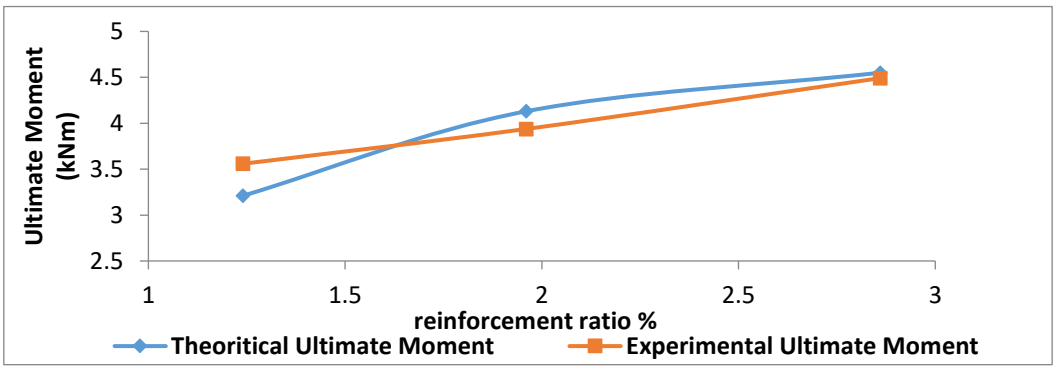

Figure 1: Ultimate moment against the reinforcement ratio

Additionally, from Table 3, it can be deduced that the EC2 formulation for moment capacity of singly reinforced concrete beams agrees with the experimental moment capacity of the reinforced geopolymer concrete beams since the ratios of the experimental to the theoretical ultimate moment at all reinforcement ratios are approximately 1.0. This means the code formulations could be used for the moment capacity of a reinforced geopolymer concrete beam.

Table 3: Comparison between experimental and theoretical moments

Beam	Ultimate Moment (kNm)	Failure Moment (kNm)	Theoretical Moment (kNm)	Experimental/Theoretical Moment ratio
RGCB08	3.5586	3.4326	3.21	1.10861
RGCB10	3.9375	3.8675	4.13	0.95339
RGCB12	4.49138	4.4914	4.55	0.98712

3.2 Relationship between Theoretical (EC2 based) and Experimental Ultimate Shear

The experimental shear capacity of the beam is higher than the theoretical shear; this may be because, as Mosley *et al.* (2007) mentioned, shear analysis of RC beams is complex, and the code expressions are simplifications based on experimental results. Additionally, Chanackya (2009) mentioned that for short-span beams, shear failure is the dominant failure. Based on the results presented in Figure 2, the formulations by the EC2 for beam shear capacity without shear reinforcement provide values that are roughly 29 – 35% of those achieved by experimental values at the ultimate limit state for the RGCB; the higher experimental values as compared with code-based values are generally true even with conventional concrete. Ikponmwosa and Ehikhuenmen (2018) also reported higher

experimental ultimate values when compared with theoretical values in concrete. Also, Jongho *et al.* (2017) submitted that structural working loads are generally less than practical loads. This means that higher actions and reactions will be recorded experimentally.

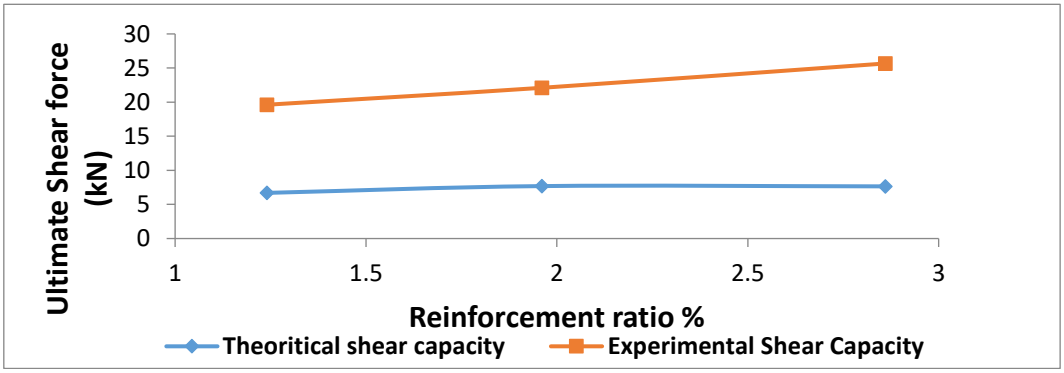

Figure 2: Ultimate shear against the reinforcement ratio

From Figure 2, the experimental shear capacity of the beams increased with the reinforcement ratio increase; this may be a result of the increase in stiffness provided by the increase in reinforcement. Also, the ratio of experimental to theoretical shear capacity for the beams is similar, and is approximately equal to 3.0 on average. From Table 4, shear ratios of 2.9, 2.9 and 3.4 were computed respectively for RGCB08, RGCB10, and RGCB12. The theoretical shear capacities are less than the experimental on account of the fact that EC2 (2004) sets limits of 2 and 0.02 for the depth ratio (K) and reinforcement ratio (ρ), respectively, for the computation of shear capacity of RC beams without shear reinforcements. RGCB12 has the highest failure load and hence highest experimental shear capacity; on the other hand, the same beam relatively has the least theoretical shear capacity due to the EC2 (2004) limit for $\rho \leq 0.02$ despite the beam having a ρ value of 0.0286 coupled with the fact that the beam has the highest bar diameter and hence least effective depth; and the code based formulations for shear capacity increases and reduces with effective depth for uniform beam cross-sections.

Based on the ratios in Table 4, it can be said that the theoretical shear capacities of the beams were all reached before yielding (yield load) of the concrete composite; this showed that the theoretical expression from EC2 (2004) for beam's shear capacity without shear reinforcement underestimates the beams shear capacity, this could be because shear is a complex phenomena (Mosley et al., 2007) but results to a safe design by ensuring the shear capacity of the beam is not reached, as a result, the code can be adopted for geopolymer concrete beams.

Table 4: Comparison between experimental and theoretical (EC2) Shear force

Beam	Ultimate Shear force (kN)	Failure Shear force (kN)	Theoretical Shear force (kN)	Experimental/Theoretical shear ratio
RGCB08	20.335	19.61	6.69	2.9
RGCB10	22.5	22.10	7.69	2.9
RGCB12	25.665	25.67	7.65	3.4

4.0 CONCLUSIONS

Based on the experimental and theoretical moment results and comparisons presented in this study, the following conclusions were drawn;

i. The moment capacity of reinforced metakaolin-based geopolymer concrete beams increased with an increase in the longitudinal reinforcement ratio. This was evidenced by the experimental ultimate moment, which increased by 10% and 26% for RGCB10 and RGCB12, respectively, when compared with RGCB08. Similarly, the corresponding theoretical ultimate moment predicted using EC2 increased by 28.7% and 41.7%, respectively.

ii. The EC2 moment design provisions can be used for the design of singly reinforced metakaolin-based geopolymer concrete beams, since the experimental-to-theoretical moment capacity ratios were 1.11, 0.95, and 0.99 for RGCB08, RGCB10, and RGCB12, respectively.

iii. The experimental-to-theoretical shear capacity ratios were observed to be 2.9, 2.9, and 3.4 for RGCB08, RGCB10, and RGCB12, respectively, indicating that the experimental shear capacities were considerably higher than the theoretical predictions. This indicates that the EC2 shear design provisions provide conservative estimates of the shear capacity of reinforced metakaolin-based geopolymer concrete beams, thereby providing an adequate margin of safety.

iv. It is recommended that the Eurocode 2 can be safely used to design singly reinforced geopolymer concrete short beams, based on the mix batching, production, and testing conditions.

REFERENCES

Abdul Rahim, R.H. Azizli, K.A. Z. Man, T. Rahmiati and Nuruddin. M.F., (2014). Effect of Sodium Hydroxide Concentration on the Mechanical Property of Non Sodium Silicate Fly Ash Based Geopolymer. *Journal of Applied Sciences*, 14: 3381-3384. DOI: 10.3923/jas.2014.3381.3384URL:https://scialert.net/abstract/?doi=jas.2014.3381.3384

ACI 318 (1992). Building Code Requirements for Reinforced Concrete. American Concrete Institute. Farmington Hills

Ansari, M. A., Shariq, M., & Mahdi, F. (2023). *Structural behavior of reinforced geopolymer concrete beams – A review*. Materials Today: Proceedings. https://doi.org/10.1016/j.matpr.2023.03.675

ASTM C618-05. (2005). *Standard Specification for Coal Fly Ash and Raw or Calcined Natural Pozzolan for Use in Concrete.* ASTM International, West Conshohocken, PA, www.astm.org DOI 10.1520/C0618-05

BS 882(1992). *Specification for aggregates from natural sources for concrete*. BSI ISBN0580 2163 X

BS EN 10002-1(2001). *Tensile Testing: Tests at ambient Temperatues*. British Standards Institutions London.

BS EN 12390 -5 (2009). *Testing of hardened concrete: Flexural strength of test specimens*. British Standards Institutions London

BS EN12390-1 (2000). *Testing hardened concrete: Shape, dimensions and other requirements for specimens and moulds.* British Standards Institutions London

Chanackya, A. (2009). *Design of Structural Elements. Concrete, steelwork, masonry and timber designs to British Standards and Eurocodes*. Taylor & Francis 2 Park Square, Milton Park, Abingdon, Oxon OX14 4RN

European Committee for Standardization (CEN). (2004). *Eurocode 2: Design of Concrete Structures—Part 1-1: General Rules and Rules for Buildings (EN 1992-1-1).* Brussels, Belgium.

Handono, Banu & Pandaleke, Ronny & Sela, Reynaldo & Sumajouw, Dody & Wallah, Steenie & Dapas, Servie & Windah, Reky. (2023). The evaluation of behavior of geopolymer reinforced concrete and conventional reinforced concrete beams: a critical review. Research on Engineering Structures and Materials. 10.17515/resm2023.719st0326.

Heah, C.Y. Kamarudin, H. Mustafa Al Bakri, A.M. Binhussainb, M.Luqman, M. Khairul Nizar, I. Ruzaidi, C.M., and Liew, Y.M. (2011). Effect of Curing Profile on Kaolin-based Geopolymers. *Proceedings of 2011 International Conference on Physics Science and Technology* (ICPST 2011). 305-311

Ikponmwosa, E.E., and Ehikhuenmen, S.O. (2018). Flexural Behavior Of Concrete Beams Containing Ceramic Waste As Replacement Of Coarse Aggregate. *ANNALS of faculty of Engineering Hunedoara-International Journal of Engineering* Tome XV1 Fascicule. DOI:10.13140/RG.2.2.11157.42726

Jindal, Bharat & Alomayri, Thamer & Assaedi, Hasan & Kaze, Cyriaque. (2022). Geopolymer concrete with metakaolin for sustainability: a comprehensive review on raw material's properties, synthesis, performance, and potential application. Environmental Science and Pollution Research. 10.1007/s11356-021-17849-w.

Jongho, P. I., Jinwoong, C., Yongjoon Jang, S. P., and Sungnam, Hong. (2017). An Experimental and Analytical Study on the Deflection Behavior of Precast Concrete Beams with Joints. *Appl. Sci.*, 7, 1198; www.mpdi.com/journal/applsci. doi:10.3390/app7111198

Keeratikan, P, and Janjit, I. (2018). Characteristics of meta-kaolin geopolymer Bender-Element (BE) test. *Science Direct Materials Today Proceedings* 5 5120–15125 www.materialstoday.com/proceedings

Mo, Kim Hung & Alengaram, U.Johnson & Jumaat, Zamin. (2016). Structural performance of reinforced geopolymer concrete members: A review. Construction and Building Materials. 120. 251-264. 10.1016/j.conbuildmat.2016.05.088.

Mosley, W. H., Bungey, J. H., and Hulse, R. (2007). *Reinforced Concrete Design (6th Ed).* Palgrave Macmillan, New York

Nevelli, A. M (2011). *Properties of Concrete: 5th Ed.* Prentice Hall. Person ISBN 0273755803

Qader, Diyar & Jamil, Ary & Bahrami, Alireza & Ali, Mujahid & Arunachalam, Krishna. (2025). A systematic review of metakaolin-based alkali-activated and geopolymer concrete: A step toward green concrete. Reviews on Advanced Materials Science. 64. 10.1515/rams-2024-0076.

Wasiu, J., and Adedeji, A.A. (2018). Reliability Assessment of Reinforced Concrete Beam With Embedded PVC Pipes Below The Neutral Axis. *International Journal Of Multidisciplinary Sciences And Engineering*. 9(1) 9-18 Www.Ijmse.Org

International Conference on Engineering Innovation for Sustainable Development (ICESID 2026)
Faculty of Engineering, Ahmadu Bello University Zaria · 8–10 September 2026

INFLUENCE OF PLASTIC WASTE MORPHOLOGY ON THE COMPACTION PROPERTIES OF MARGINAL LATERITIC SOIL

Ahmad Idris[1,*], Aminu Suleiman[1], Gambo Haruna Yunusa[1]
[1]*Bayero University*
Email: aidris.civ@buk.edu.ng[*], asuleiman.civ@buk.edu.ng, ghyunusa.civ@buk.edu.ng
***Corresponding author**: Ahmad Idris
DOI: https://doi.org/10.67203/sp.ICESID.2026

ABSTRACT
The incorporation of plastic waste into lateritic soil provides an opportunity to reduce plastic pollution while modifying the compaction behaviour of earth materials used in road works. This study investigated the influence of the morphology and content of waste sachet-water plastic (SWPW) on the maximum dry density (MDD) and optimum moisture content (OMC) of a marginal lateritic soil. Used sachet-water bags collected in Kano State, Nigeria, were cleaned, air-dried and processed into fiber and powdered forms. The fiber pieces were approximately 5 mm wide and 25 mm long. Powdered SWPW was incorporated at 0-15% of dry soil mass at 2.5% intervals, while fiber SWPW was incorporated at 0-5% at 1% intervals. Compaction testing was carried out in accordance with BS 1377-4:1990. The untreated soil had an MDD of 1.94 g/cm3. With increasing powdered SWPW content, MDD decreased progressively to 1.33 g/cm3 at 15%, while OMC increased from 12.90% to 17.51%. Fiber SWPW similarly reduced MDD to 1.69 g/cm3 at 5% and increased OMC to 18.41%. The results demonstrate that SWPW morphology and dosage significantly influence the compaction response of lateritic soil, with the powdered form producing the larger reduction in dry density over the investigated range. The present study is limited to compaction characteristics; strength, durability and field-performance tests are required before structural suitability for pavement applications can be established.

Keywords: *Plastic Waste; Fiber Content; Soil Stabilization; Geotechnical Properties*

1. INTRODUCTION

According Plastic waste is a persistent environmental problem because of its high rate of generation and slow degradation. In Nigeria, single-use sachet-water packaging is widely used and discarded sachets frequently enter drains, waterways and open dumps. Reuse of this waste in geotechnical construction materials offers a potential route for diverting plastic from the environment while reducing demand for conventional materials. In soil engineering, waste plastics have been investigated as discrete fibres or inclusions, with reported effects on compaction and strength depending on plastic type, geometry, dosage and soil characteristics (Jalal & Hassan, 2021; Zukri et al., 2017; Munirwan & Jaya, 2019; Akinwumi et al., 2022).

Previous studies show that the response of soil to plastic inclusion is not governed by dosage alone. Jalal and Hassan (2021) reported that discrete plastic fibers altered the compaction characteristics of clayey soil and could also influence its mechanical behaviour. Zukri et al. (2017) investigated polyethylene and polypropylene in clay stabilization, while Munirwan and Jaya (2019) demonstrated that plastic waste content affects the geotechnical response of cement-stabilised soil intended for pavement layers. Akinwumi et al. (2022) similarly showed that recycled plastic inclusions can modify the engineering behaviour of soil. These studies establish the potential of plastic waste in geotechnical applications but also show that the form in which the plastic is introduced is important.

Most published studies have focused on plastic fibers, strips or shredded particles. Comparatively less attention has been given to the direct comparison of different morphologies prepared from the same waste stream, particularly waste sachet-water plastic incorporated into lateritic soils. Powdered plastic and elongated fibers differ markedly in particle geometry, surface area and interaction with the soil skeleton and may therefore produce different compaction responses. Understanding these differences is relevant when considering the reuse of sachet-water waste in earthworks and low-volume road construction.

This study therefore investigates the influence of two morphologies of waste sachet-water plastic - powdered SWPW (P-SWPW) and fiber SWPW (F-SWPW) - on the compaction characteristics of a marginal lateritic soil. The specific objective is to quantify the changes in maximum dry density (MDD) and optimum moisture content (OMC) with increasing plastic content and to compare the responses produced by the two morphologies. The study is intentionally limited to compaction behavior; strength and durability performance are outside the scope of the present investigation.

2. MATERIALS AND METHODS

2.1 Materials

Waste sachet-water plastic (SWPW) was collected from disposal locations in Kano State, Nigeria. The collected material was washed to remove adhering soil and other contaminants and then air-dried. Two morphologies were prepared from the same waste stream. For F-SWPW, the sachets were manually cut into fibres approximately 5 mm wide and 25 mm long. For P-SWPW, the cleaned and dried sachets were mechanically reduced to a powdered form before mixing with the soil. The plastic-specific density, tensile strength and detailed particle-size distribution of the powdered material were not experimentally determined in this study; this is recognised as a limitation and should be addressed in subsequent material-characterisation work

2.2 Methods

The natural lateritic soil was first characterised using index-property tests comprising particle-size distribution, Atterberg limits and specific gravity. Compaction tests were performed in accordance with BS 1377-4:1990 (U et al., 2022) using the light compaction procedure. The soil was compacted in a 1 L mould in three approximately equal layers using a 2.5 kg rammer falling through 300 mm, with 27 blows applied to each layer. For each mixture, the required quantity of SWPW was calculated as a percentage of the dry mass of soil and thoroughly dry-mixed with the soil to obtain a visually uniform distribution before water was added. P-SWPW contents of 0, 2.5, 5, 7.5, 10, 12.5 and 15% were investigated, while F-SWPW contents of 0, 1, 2, 3, 4 and 5% were investigated. For each plastic content, specimens were prepared over a range of moisture contents and the corresponding dry densities were determined. The moisture-density relationship was plotted and the MDD and OMC were obtained from the peak of the compaction curve. No curing period was adopted because the investigation concerned the immediate physical effect of SWPW on compaction rather than chemical stabilization. Strength and durability tests such as CBR and UCS were not included in the present experimental programme.

3. RESULTS

3.1 Material Basic Properties

With a plastic limit within the range of well-graded soil and a liquid limit just above the clayey soil zone, the soil sample exhibits strong structural qualities. In Nigeria, the soil may be used as a suitable fill for rural road bases without further processing or additions.

Table 1: Basic Geotechnical Properties of the soil

Parameter	Value
Liquid Limit	45%
Plastic Limit	30%
Plasticity Index	15%
Linear Shrinkage	8.0%
Specific Gravity	2.57
Max.Dry Density	1.94g/cm^3
Optimum Moisture	13.91%

3.2 Compaction Test Results

According to the findings of the compaction test, the moisture properties of soils improve as the P-SWPW concentration rises, suggesting that the addition of specific waste materials affects these properties (U et al., 2022). According to the research, finely processed SWPW is appropriate for rural roads in Nigeria's tropical environment because it enhances surface area and water retention capacity. However, when the P-SWPW concentration rises, MDD values fall, indicating possible changes in the soil. The results support the development of sustainable infrastructure and highlight the need of giving rural road building applications considerable thought. Compaction test findings for the fiber form of Sachet Water Plastic Waste (F-SWPW) demonstrate different patterns in soil compaction values as the amount of F-SWPW grows, as seen in figures 3 and 4. Perhaps because of its finer texture, the powdered form exhibits a greater decrease in OMC and an increase in MDD when compared to the fiber form. These findings are consistent with research on soils reinforced with fiber (Akinwumi et al., 2022). Nevertheless, the present results establish only the compaction response; the observed changes should not be interpreted as evidence of improved or reduced strength without CBR, UCS or other mechanical testing.

Table 2: Compaction characteristics of lateritic soil containing powdered and fibre SWPW

SWPW morphology	SWPW content (%)	MDD (g/cm3)	OMC (%)
Powdered (P-SWPW)	0	1.94	12.90
Powdered (P-SWPW)	2.5	1.84	13.29
Powdered (P-SWPW)	5	1.75	14.00
Powdered (P-SWPW)	7.5	1.60	14.45
Powdered (P-SWPW)	10	1.50	15.50
Powdered (P-SWPW)	12.5	1.46	16.98
Powdered (P-SWPW)	15	1.33	17.51
Fibre (F-SWPW)	0	1.94	12.90
Fibre (F-SWPW)	1	1.84	13.29
Fibre (F-SWPW)	2	1.77	14.49
Fibre (F-SWPW)	3	1.73	14.87
Fibre (F-SWPW)	4	1.70	16.74
Fibre (F-SWPW)	5	1.69	18.41

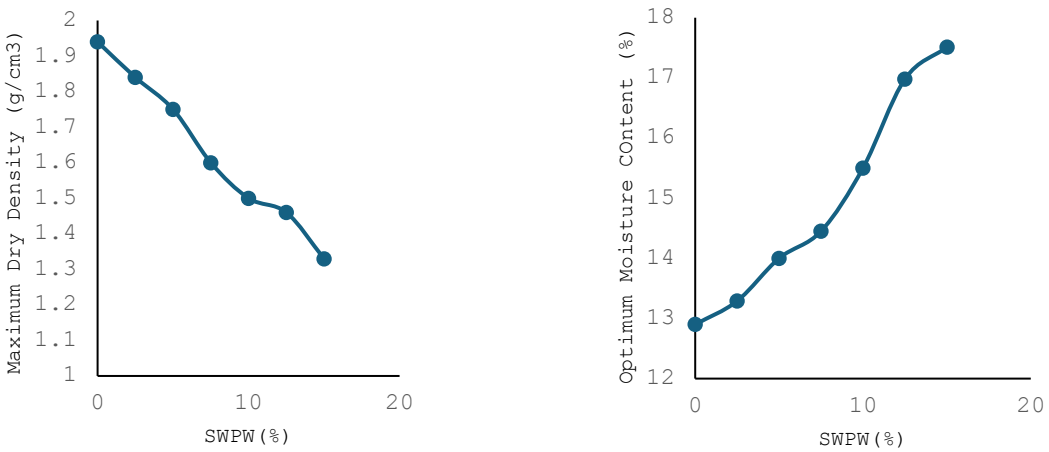

Figure 3: Variation of OMC and MDD with different % of sachet water powder

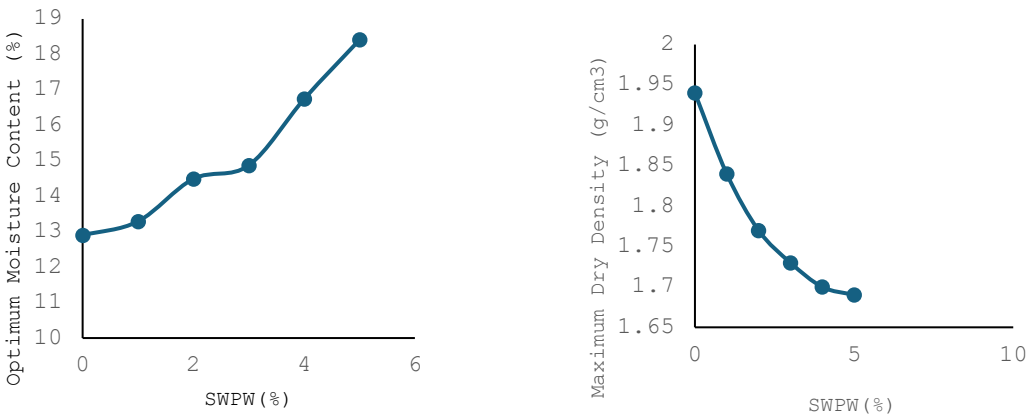

Figure 4: Variation of OMC and MDD with different % of sachet water fiber

4. CONCLUSION

This study demonstrates that the morphology and dosage of waste sachet-water plastic significantly influence the compaction characteristics of the investigated marginal lateritic soil. For P-SWPW, increasing the plastic content from 0 to 15% reduced MDD from 1.94 to 1.33 g/cm3, while OMC increased from 12.90 to 17.51%. For F-SWPW, increasing the fibre content from 0 to 5% reduced MDD from 1.94 to 1.69 g/cm3 and increased OMC to 18.41%. Thus, both morphologies produced lower dry densities and higher optimum moisture requirements, although the magnitude of the response differed with morphology and dosage. The powdered form produced the greater overall reduction in MDD, whereas the fibre form produced the highest measured OMC at 5%. These findings are useful for understanding the compaction behavior of lateritic soil containing recycled sachet-water plastic; however, they are not sufficient to establish structural suitability for road-base or subbase applications. The principal limitation of the present study is the absence of strength and durability testing and detailed physical characterization of the plastic additive. Future work should therefore include CBR, UCS or shear-strength tests, soaked/durability assessment, microstructural evaluation and field compaction trials to identify technically acceptable and environmentally sustainable SWPW contents for road earthworks.

REFERENCES

Akinwumi, I., Soladoye, O., & Ajayi, V. (2022). Experimental insight into the containment of plastic waste in cement-stabilised soil as a road pavement layer material.

Bello, A. A. (n.d.). Regression analysis between properties of subgrade lateritic soil (pp. 1–9).

Dauda, A. (n.d.). Effect of rice husk ash with coconut husk ash on geotechnical properties of lateritic soil.

Esameldin, R., & Zalihe, F. (2019). Performance of plastic waste for soil improvement. SN Applied Sciences, 1(11), 1–7. https://doi.org/10.1007/s42452-019-1395-2

Fibers, P., Meddah, A., Goufi, A. E., & Pantelidis, L. (2022). Improving very high plastic clays with the combined effect of [incomplete title in source] (pp. 1–14).

Jalal, H., & Hassan, A. (2021). Effects of plastic waste materials on geotechnical properties of clayey soil (pp. 390–413).

Journal, A. I., et al. (2025). Performance characterisation of machine learning models for geotechnical axial pile load capacity estimation: An enhanced GPR-based approach. Geomechanics and Geoengineering, 1–42. https://doi.org/10.1080/17486025.2025.2468645

Kolay, P. K., Dhakal, B., Kumar, S., & Puri, V. K. (2016). Effect of liquid acrylic polymer on geotechnical properties of fine-grained soils. International Journal of Geosynthetics and Ground Engineering, 2(4), 1–9. https://doi.org/10.1007/s40891-016-0071-5

Leisure, C. A., Hsieh, C., & Eklund, S. J. (2014). Leisure constraints: A replication and extension of construct development, 21, 179–192.

Munirwan, R. P., & Jaya, R. P. (2019). Performance of eggshell powder addition to clay soil for stabilization. International Journal of Recent Technology and Engineering, 8(3S3), 532–535. https://doi.org/10.35940/ijrte.c1094.1183s319

Rehman, Z. U., Khalid, U., Farooq, K., & Mujtaba, H. (2017). Prediction of CBR value from index properties of different soils, 22(II), 17–26.

Sha, A., Idris, A., Umar, I. H., & Lin, H. (2025). Enhanced bearing capacity prediction using hybrid tree-based ensemble learning with advanced meta-heuristic optimization, 7. https://doi.org/10.1088/2631-8695/adad37

Shim, S., Kim, J., Lee, S., & Cho, G. (2021). Road surface damage detection based on hierarchical architecture using lightweight auto-encoder network. Automation in Construction, 130, 103833. https://doi.org/10.1016/j.autcon.2021.103833

U, H. I., G, Y. S., & S, I. A. (2022). Quantitative analysis of solid waste generation from tanneries in Kano State. www.matjournals.com

Umar, H. I., Lin, H. (2023). Laboratory testing and analysis of clay soil stabilization using waste marble powder. Applied Sciences.

Zhou, S., et al. (2021). Improved geotechnical behavior of an expansive soil amended with cationic polyacrylamide. Journal of Renewable Materials, 9(11), 1941–1957. https://doi.org/10.32604/jrm.2021.015693

Zukri, A., Nazir, R., & Mender, F. N. (2017). An experimental study on stabilization of Pekan clay using polyethylene and polypropylene. AIP Conference Proceedings, 1892, 4–11. https://doi.org/10.1063/1.5005668

International Conference on Engineering Innovation for Sustainable Development (ICESID 2026)
Faculty of Engineering, Ahmadu Bello University Zaria · 8–10 September 2026

INFLUENCE OF T6-AGING TREATMENT ON SELECTED MECHANICAL PROPERTIES OF ALUMINIUM ALLOY A356/MELON HUSK ASH NANOCOMPOSITE

Ibrahim Usman[1,*], Kamilu Adeyemi Bello[1], Malik Abdulwahab[1], Terver Ause[1]

[1]*Department of Metallurgical and Materials Engineering, Faculty of Engineering, Ahmadu Bello University, Zaria, Nigeria*

Email: iusman@abu.edu.ng[*], kabello@abu.edu.ng, mabdulwahab@abu.edu.ng, tause@abu.edu.ng

***Corresponding author**: Ibrahim Usman

DOI: https://doi.org/10.67203/sp.ICESID.2026

ABSTRACT

Aluminum matrix nanocomposites are gaining prominence in automobile manufacturing due to their competitive properties. The present study explores the effect of T6-aging treatment on the selected mechanical properties of a novel nanocomposite, namely Aluminium A356 reinforced with melon husk ash nanoparticles. Melon husk ash (MHA) nanoparticles, produced from an abundant Nigerian agro-waste—Egusi melon (Citrullus colocynthis L.) husks—were used to reinforce A356 aluminium alloy through a low-frequency vibration-assisted stir casting technique. Samples of the cast nanocomposite and the unreinforced alloy were subjected to T6-aging heat treatment, after which hardness and tensile properties were determined using standard test procedures. X-ray diffraction (XRD) and optical microscopy (OPM) were used to study the microstructure of the samples. XRD patterns of the nanocomposite samples revealed the presence of α-Al, Si, β-Al_5FeSi, Mg_2Si, and SiO_2, while optical micrographs revealed a refined microstructure comprising primary α-Al dendrites, acicular Si, and a relatively even distribution of nanoparticles within the matrix of the heat-treated nanocomposite samples. Results of the mechanical tests showed that the T6-heat-treated nanocomposite exhibited improved properties over both the as-cast nanocomposite and the unreinforced samples. The tensile strength of the heat-treated nanocomposite (180.57 MPa) represented an improvement of 24.87% over the as-cast nanocomposite and 53.42% over the as-cast unreinforced sample. The ductility of the heat-treated nanocomposite (6.63%) represented a 22% improvement over the as-cast nanocomposite and a 32% improvement over the as-cast alloy. Meanwhile, the hardness value of the heat-treated nanocomposite (127.14 HV) represented an improvement of 0.9% over the as-cast nanocomposite and 55% over the as-cast alloy. In summary, the study demonstrates that MHA nanoparticles are a viable and effective reinforcement for aluminium matrix composites, and that T6-aging heat treatment offers a sustainable pathway for enhancing their mechanical properties.

Keywords: *Melon husk ash; Aluminium matrix nanocomposite; Agro waste; Mechanical properties; T6 heat treatment*

1. INTRODUCTION

Metal matrix composites (MMCs) are an important class of engineering materials with attractive properties and widely used in aerospace and automotive applications (Azimi *et al.*, 2021). Although conventional composites (reinforced micron-sized particulates) may generally exhibit superior performance to their matrix alloys, they have significant drawbacks, including poor ductility and low fracture toughness compared to the bare alloys. To take care of these limitations, research focus has shifted towards developing metal matrix nanocomposites (i.e. metal matrices reinforced with nanoparticles), whereby the strength and ductility composites are improved simultaneously (Malaki *et al.*, 2020; Shayan *et al.*, 2020). This has opened the horizon for developing MMCs incorporating nanoparticles as reinforcing phase and amenable for several advanced applications.

A very common MMC used in automotive and other applications is aluminium matrix composite (AMC) owing to its lightweight and relatively good mechanical properties. The most commonly used aluminium alloys for aluminium matrix nanocomposites are those belonging to the Al-Si system owing to their high fluidity, low solidification shrinkage levels, corrosion resistance, etc. (Callegari *et al.*, 2023). When alloyed with Mg and/or Cu to form alloys like A356 Al-Mg-Si alloy, they become amenable to heat treatment, a thermal procedure used to improve their properties. The

procedure is the same for the alloys and composites developed from the alloys (Alam, 2014). The most common heat treatment procedure for modifying, particularly, the mechanical properties of Al-Si alloys containing Mg and/or Cu and their composites is the T6 age hardening or precipitation hardening (Tiwery *et al.*, 2018). The process, which basically enhances mechanical properties by forming fine precipitates that impede dislocation movement (Usman, 2026). In age-hardenable aluminium-based nanocomposites, the role of reinforcement nanoparticles during heat treatment includes accelerating the aging processes by creating more nucleation sites for precipitation within the α-Al and refining the microstructure by Zenner pinning, i.e., restricting dendritic growth and altering the dendritic grain growth morphology (Guo *et al*., 2018; Nithesh *et al.*, 2021).

Reinforcements used in fabricating the composite are mostly synthetic ceramic particulates of borides, oxides, carbides and nitrides (Samal *et al.*, 2020). However, industrial and agro waste-derived particulates are now becoming popular due to their relatively more economic viability and abundance (Parveez et al, 2021); and to date, several agro-waste materials have been successfully incorporated into metal matrices to develop composites with competitive properties. However, most of the studies have been limited to micron size agro-based reinforcements, with limited studies on nano size agro-based reinforcements (Kelsey *et al.*, 2025).

Although nanoparticles-reinforced metal matrix composites exhibit superior properties, it is very difficult through stir casting (which is the most widely used and cost-effective composite fabrication route) to achieve uniform dispersion of the nanoparticles in the matrix, due to their large surface-to-volume (Shayan *et al.*, 2020), prompting researchers to implement modifications, such as application of ultrasonic vibrations to the molten mixture among several other methods, to improve the viability of the economic and simple casting process (Malaki *et al.*, 2019).

Melon husks (MHs) are agro wastes generated from processing of *Citrullus colocynthis L.* (commonly known in most parts of Nigeria as *Egusi* melon). Nigeria was ranked the highest producer of the crop in 2018 globally (Robert *et al.*, 2021). About a decade ago, a number of materials scientist have made attempts to convert melon husks to reinforcing materials for aluminium matrix composites. The studies have investigated the effect of melon husk ash particulates on mechanical and tribological properties of aluminium-based composites (Abdulwahab *et al.*, 2017; Suleiman *et al.*, 2018; Abolusoro *et al.*, 2025 & Usman *et al.*, 2026). However, most of the studies were limited to micron-sized particulates, and the effect of T6-heat treated was not investigated by the studies. The present study therefore investigates the effect of T6 heat treatment on the hardness and tensile properties of aluminium alloy A356/melon husk ash nanocomposite.

2. METHODOLOGY

2.1 Materials

The matrix is A356 aluminium alloy wheel scraps (AAWS), sourced from an automobile service center located at Zaria, Kaduna State of Nigeria. Chemical composition of the matrix alloy is shown in Table 1. The Si composition is slightly below that of a standard A356, consistent with previous studies on automobile aluminium alloy wheel (Song *et al.*, 2012). Melon husk ash nanoparticles (MHAnp) of average particle size 57.53 nm as reinforcement in this study was synthesized through thermal treatment and mechanical milling. Details of the synthesis route and characterization of the reinforcement (see Figures 1a &b) are reported in another study (Usman, 2026). Chemical composition of the MHAnp determined using X-ray florescence spectroscopy shows it is composed of SiO_2 as the constituent present in the largest amount, as shown in Table 2.

a b

Figure 1: (a) Melon husks and (b) Melon husk ash

Table 1: *Chemical composition of aluminium alloy wheel scraps (AAWS)*

Element	Weight %
Al	91.87
Si	6.22
Mg	0.33
Cu	0.02
Fe	0.27
Mn	0.03
Sr	0.01
Others	Balance

Table 2: *Chemical composition of melon husk ash nanoparticles (MHAnp)*

Composition	Weight %
SiO_2	39.50
K_2O	8.23
Al_2O_3	8.44
MgO	6.53
CaO	7.66
P_2O_5	15.00
Fe_2O_3	6.09
SO_3	1.70
Na_2O	1.75
SnO_2	1.89
TiO_2	0.92
ZnO	3.90

2.2 Fabrication of A356/MHAnp Samples

Al-Mg-Si alloy matrix composites reinforced with 3.5 vol. % melon husk ash nanoparticles (MHAnp) was produced by stir-casting process. The nanocomposite was fabricated by charging 795g of aluminium alloy wheel scrap (AAWS) pieces into a graphite crucible, heating the charge to a temperature of 800ºC and holding at the same temperature for a length of time sufficient for complete melting of the matrix alloy. The temperature of the melt was then lowered to 600ºC where it was semi-sold and 3.5 vol. % of MHA nanoparticles (preheated at 350ºC for 1 hour) added to it and the mixture stirred continuously at a speed of 400 rpm for 7 minutes. 4 wt. % Mg (with respect to the matrix alloy) wrapped in an Al foil was added to compensate for losses during melting and to improve wettability. The temperature of the melt was then raised to 750ºC and the molten mixture agitated for 2 minutes by dipping a probe resonating at a frequency of 60Hz (power output: 150W; voltage: 220V) to improve

dispersion of the nanoparticles in the matrix before pouring into a prepared sand mold. A control sample of the unreinforced alloy was also produced for comparison of properties.

2.3 Heat Treatment

Cast composite samples were subjected to T6 heat treatment, which involved successive solution treatment and artificial aging. The unreinforced alloy and nanocomposite specimens were subjected to T6 aging treatment which entails solution treatment at 540ºC for 6 hours followed by water quenching at room temperature, and a final step of artificial aging at 155ºC for 5 hours in accordance with the study by Haskel *et al.* (2018) on A356 wheels. X-ray diffraction (XRD) analysis and optical microscopy were conducted to study phases and morphologies of the heat-treated specimens, respectively.

2.4 Characterization

Microstructural examination: To study the morphological features of the samples, samples of dimensions ø15 x 10 mm were machined and polished using emery clothes meshed 300, 600, 800, 1200 and 2400, successively. Alumina suspension (0.05 lm) was then subsequently used for final polishing. Thereafter, the samples were submerged in Keller's reagent and etched for 30s. Subsequently, the samples were washed and dried for microstructural observation and capturing under an optical metallurgical microscope equipped with an inbuilt camera (Model No.: NJF:-12A). The microstructures were captured at a magnification of x100. The phases present in the samples were also studied using X-ray diffraction (XRD) analysis.

Tensile test: Tensile test was performed in accordance with ASTM E-8 standard on Electronic Universal Testing Machine (Model: WDW-100KN, S/No.: 190536). Three standard tensile test samples were machined from each cast sample and tested for tensile properties on the universal testing machine at a crosshead speed of 10cm/min. Average of three observations was recorded as tensile strength and percent elongation of the sample, as the case may be.

Hardness test: Hardness values of the samples were determined using a Vicker's micro-hardness tester (Model: MV1-PC, machine no: 07/2012-1329) in accordance with ASTM E-384 standard. Samples of dimensions ø15 x 10 mm were prepared for the test. An average of three observations were taken from indentations at different points on a polished surface of each sample with a load of 0.3 Kgf at 15 seconds dwell time.

3. RESULTS AND DISCUSSION

3.1 XRD Patterns of the Samples

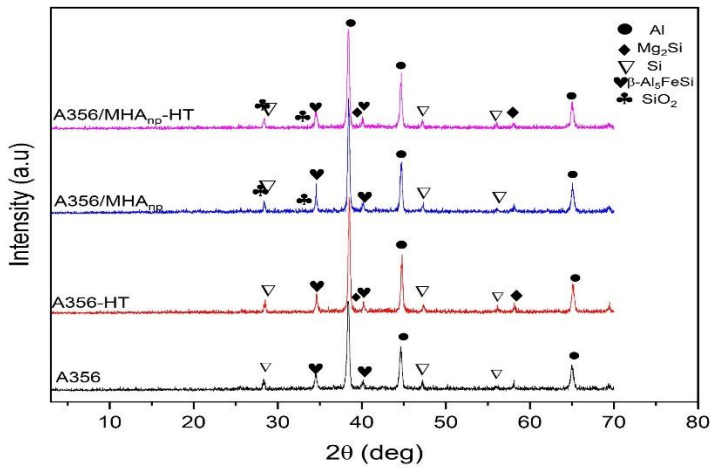

Figure 2: XRD patterns of the samples in as-cast and T6 heat-treated conditions

The XRD patterns of the alloy and nanocomposite samples, in both as-cast and T6-heat treated states, are depicted by Figure 2. The XRD patterns of the samples analysed using MDI Jade 6 software

show the presence of α-Al, Si, Mg, Mg_2Si, β-Al_5FeSi and SiO_2. The XRD spectrum of A356 has the peaks (111) at 2θ= 38.473°, (200) at 2θ = 44.722° and (220) at 2θ = 65.099° corresponding to Al (PDF card no. 99-005); the peaks (111) at 2θ = 28.443°, (220) at 2θ = 47.304° and (311) at 2θ = 56.124° corresponding to Si (PDF card no. 99-0092); and minor peaks (111) at 2θ = 34.594° and (220) at 2θ = 40.165° corresponding to FeSi intermetallic compound , Al5FeSi (PDF card no. 38-1397). Mg is also detected overlapping Si at 2θ = 47.304°. These peaks are common to the other samples, except the peaks (211) at 2θ = 28.794 ° and (212) at 2θ = 33.127° corresponding to SiO_2 (PDF card no. 47-1300) present in A356/MHAnp and T6-heat treated A356/MHAnp, which could be from the agro-waste-derived reinforcement— melon husk ash nanoparticles. There are also other peaks present in the T6-heat treated alloy and nanocomposite samples, i.e., (220) at 2θ = 40.121° and (400) at 2θ = 58.028° corresponding to Mg_2Si precipitates (PDF card no. 35-0773). This finding is in agreement with previous studies on Al-Mg-Si alloys (Lakshmikanthan *et. al*., 2020).

3.2 Tensile Properties of the Samples

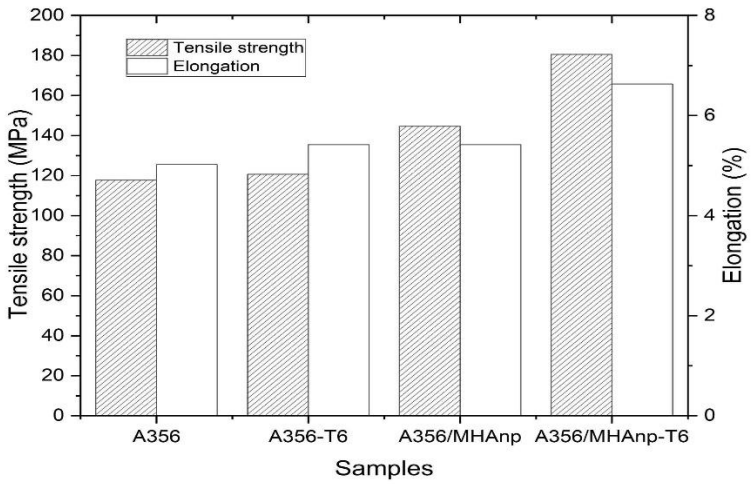

Figure 3: Tensile properties of samples in as-cast and heat-treated conditions

Figure 3 shows the tensile properties of the alloy and the nanocomposite samples, in the as-cast and heat-treated states. The tensile strength values are 117.70, 120.61, 144.60 and 180.57 MPa for A356, A356-T6, A356/MHAnp and A356/MHAnp-T6, respectively, and the percent elongation values are 5.02, 5.42, 5.42 and 6.63 for A356, A356-T6, A356/MHAnp and A356/MHAnp-T6, respectively. The improvement in tensile properties on addition of melon husk nanoparticles can be attributed to the resultant grain refinement and the action of the nanoparticles as barriers to dislocation movement, i.e. Orowan strengthening, thereby overcoming the traditional strength-ductility trade-off and simultaneously improving both properties (Singhal *et al.*, 2025). Similar observations were made by Li *et al.* (2019). Both alloy and nanocomposite samples in the T6-heat treated state also exhibited better tensile properties than the as-cast samples, an observation attributable to the strengthening effect of Mg_2Si precipitates in the heat-treated samples (Alam, 2014). The heat treatment condition may however require optimization as improvements in ductility are marginal.

3.3 Hardness of the Samples

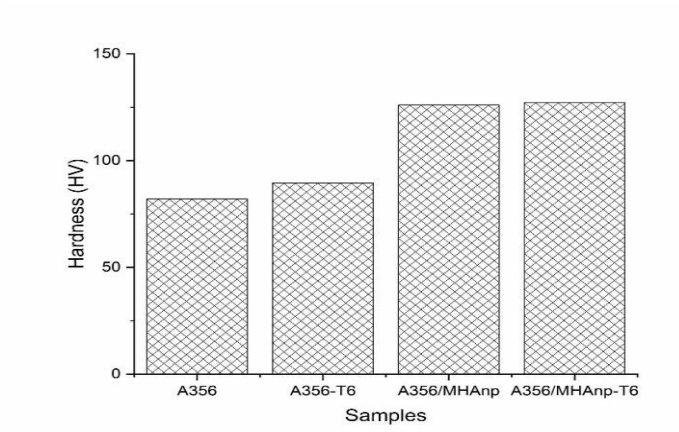

Figure 4: Hardness values of samples in as-cast and heat-treated conditions

Figure 4 shows the hardness values of the alloy and the nanocomposite samples, in the as-cast and heat-treated states. The micro hardness values are 82.00, 89.50, 126.00 and 127.14 HV for A356, A356-T6, A356/MHAnp and A356/MHAnp-T6, respectively. The results show significant enhancement in hardness by addition of melon husk nanoparticles to the alloy, underscoring the effectiveness of the nanoparticles in strengthening the Al alloy matrix. This observation can be attributed to increased dislocation density and grain refinement (Salur *et al.*, 2021). While noticeable improvement in hardness was observed for the alloy after heat treatment due to microstructural modifications and precipitation of the strengthening phase Mg_2Si, the improvement for the composite was negligible. The already high nanoparticle-induced hardness may have limited precipitation strengthening effects for the composites.

3.4 Microstructures of the Samples

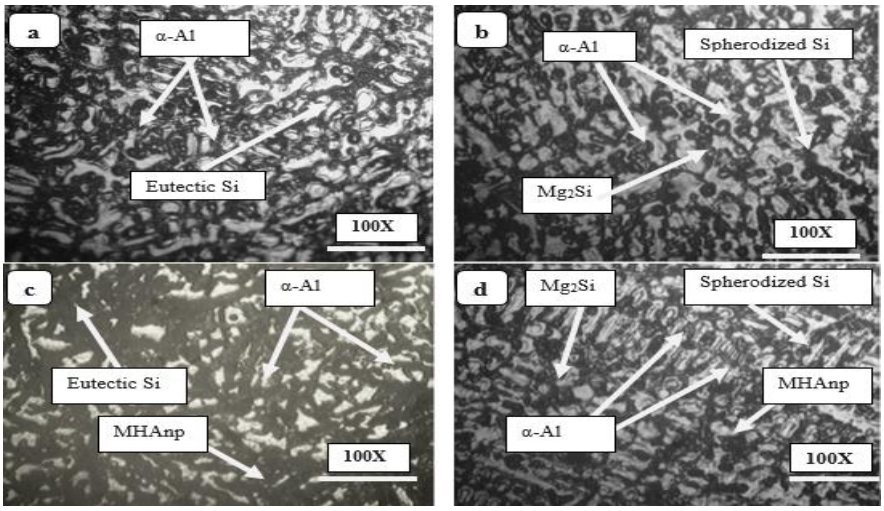

Plate I: Optical micrographs of (a) as-cast A356 alloy, (b) A356-T6 alloy, (c) as-cast A356/MHAnp composite and (d) A356/MHAnp-T6 composite; Etchant: Keller's reagent.

The microstructures of the alloy and nanocomposite samples, in both as-cast and T6-heat treated states, are depicted by the micrographs in Plates I (a-d).

The micrograph of the as-cast A356 sample in Plate I (a) shows dendritic structure of α-Al and acicular eutectic Si. In the micrograph of the T6-heat treated sample, in Plate I (b), spherodized Si and Mg_2Si precipitates are obvious in the matrix, which may have been responsible for the comparatively better mechanical properties of the heat treated sample. The micrograph in Plate I (c) depicts the microstructure of as-cast A356/MHAnp sample. The microstructure is finer than that of the alloy, which may have resulted from nanoparticles locking the grain boundaries and preventing excessive grain growth during cooling (Shayan *et al.*, 2020). The microstructure is made up of primary α-Al dendrites,

acicular Si and a relatively even distribution of nanoparticles. Some agglomeration are also noticeable at some spots, which may have been the cause for the marginal improvements in the tensile strength and ductility (Hoziefa *et al.*, 2016). The micrograph in Plate I (d) depicting the microstructure of the T6-heat treated nanocomposite sample shows the presence of continuous α-Al dendrite, spherodized Si, Mg_2Si precipitates and a relatively uniform distribution of MHAnp.

4. CONCLUSION

This study demonstrates that T6-aging heat treatment significantly enhances the mechanical properties of A356 aluminium alloy reinforced with melon husk ash (MHA) nanoparticles, based on the following key findings:

1. A356/MHAnp nanocomposites were successfully produced via low-frequency vibration-assisted stir casting, utilizing MHA nanoparticles derived from Nigerian Egusi melon husk agro-waste as a sustainable reinforcement.
2. XRD analysis confirmed the presence of α-Al, Si, β-Al_5FeSi, Mg_2Si, and SiO_2 phases, while optical microscopy revealed a refined microstructure with a relatively uniform nanoparticle distribution following heat treatment.
3. T6-aging improved tensile strength to 180.57 MPa, representing gains of 24.87% and 53.42% over the as-cast nanocomposite and unreinforced alloy, respectively.
4. Ductility of the heat-treated nanocomposite improved by 22% and 32% over the as-cast nanocomposite and alloy, respectively, indicating enhanced deformability alongside increased strength.
5. Hardness reached 127.14 HV, an improvement of 0.9% and 55% over the as-cast nanocomposite and unreinforced alloy, respectively.
6. Overall, MHA nanoparticles are an effective and sustainable reinforcement for A356 alloy, and T6-aging offers a practical pathway for optimizing its mechanical performance, positioning A356/MHAnp as a promising lightweight material for automotive applications.

5. REFERENCES

Abdulwahab, M., Dodo, R.M., Suleiman, I.Y., Gebi, A.I., & Umar, I. (2017). Wear behavior of Al-7%Si-0.3%Mg/melon shell ash particulate composites. *Heliyon, 3*, e00375. Doi:10.1016/j.heliyon.2017.e00375.

Abolusoro, O.P., Khoathane, M.C., & Mhike, W. (2025). Influence of melon shell ash reinforcement on the mechanical and microstructural characteristics of recycled aluminium matrix composites. *Res. Eng. Struct. 11*(2): 783-798. doi: 10.17515/resm2024.320me0614rs

Alam, M. K. (2014). *Thermal and Microstructural Analysis of the A356 Alloy Subjected to High Pressure in the Squeeze Casting (SC) UMSA Technology Platform.* Electronic Theses and Dissertations. 5116. https://scholar.uwindsor.ca/etd/5116

Azimi, H., Bourouzi, S., & Jamaati, R. (2021). Effects of Ti Particles and T6 heat treatment on the microstructure and mechanical properties of A356 alloy fabricated by composcasting. *Materials Science & Engineering A 818* (141443): 1-10. Doi: doi.org/10.1016/j.msea.2021.141443.

Callegari, B., Lima, T.N., Coelho, R.S. (2023). The Influence of Alloying Elements on the Microstructure and Properties of Al-Si-Based Casting Alloys: Review. *Metals, 13*, 1174. doi.or/10.3390/met13071174.

Guo, E., Shuai, S., Kazantsev, D., Karagadde, S., Phillion, A.B., Jing, T., Li, W., & Lee, P.D. (2018).The influence of nanoparticles on dendritic grain growth in Mg alloys. *Acta Materialia, 152*, 127-137. Doi: 10.1016/j.actamat.2018.04.023

Haskel, T., Verran, G.O., & Barbieri, R. (2018). Rotating and bending fatigue behaviour of A356 aluminium alloy: Effects of strontium addition and T6 heat treatment. *International journal of Fatigue, 114*, 1-10.

Hozeifa, W., Toschi, S., Ahmed, M.M.Z., Morri, A.A.A., El-Sayed, S.M.M., El-Mahallawi, I., Ceschini, L., & Atlam, A. (2016). Influence of friction stir processing on the microstructure

and mechanical properties of a compocast AA2024- Al_2O_3 nanocomposite. *Materials and Design, 106*, 273-284.

Lakshmikanthana, T. A, Prabhu, R., Babud,U.S., Koppade, P.G., Gupta, M., Krishna, M., & Bontha, S. (2020). The effect of heat treatment on the mechanical and tribological properties of dual size SiC reinforced A357 matrix composites. *J mater res technol. 9*(3):6434–6452. Doi: doi.org/10.1016/j.jmrt.2020.04.027

Li, X., Yan, H., Wang, Z-W., Li, N., Liu, J-L., Nie, Q. (2019). Effect of Heat Treatment on the Microstructure and Mechanical Properties of a Composite Made of Al-Si-Cu-Mg Aluminum Alloy Reinforced with SiC Particles. *Metals, 9,* 1205; doi: 10.3390/met9111205

Malaki, M., Xu, W., Kasar, A.K., Menezes, P.L., Dieringa, H., Varma, R.S., & Gupta, M. (2019). Advanced Metal Matrix Nanocomposites. *Metal, 9,* 30. Doi: 10.3390/met9030330

Malaki, M., Tehrani, A.F., & Niroumand, B. (2020). Fatigue behavior of metal matrix nanocomposites, Ceram. Int. 46: 23326–23336.

Nithesh, K., Gowrishankar, M.C., Nayak, R., & Sharma, S. (2021). Effect of light weight reinforcement and heat treatment process parameters on morphological and wear aspects of hypoeutectic Al-Si based composites- a critical review. *Journal of Materials and Technology, 15*: 4272-4292.

Parveez, B., Maleque, M.A., & Jamal, N.A. (2021). Influence of agro-based reinforcements on the properties of aluminum matrix composites: a systematic review. *J Mater Sci., 56,* 16195 – 16222.

Robert U. W., Etuk, S.E., Agbasi, O.E., Ekong S.A., Nathaniel, E.U., Anonaba, A. & Nnana, L.A. (2021). Valorisation of Waste Carton Paper, Melon Seed Husks, and Groundnut Shells to Thermal Insulation Panels for Structural Applications. *Polytechnica* https://doi.org/10.1007/s41050-021-00034-w

Salur, E., Acarer, M., & Savkliyildiz, I. (2021). Improving Mechanical Properties of Nano-Sized TiC Particle Reinforced AA7075 Al Alloy Composites Produced by Ball Milling and Hot Pressing. *Mater. Today Commun., 27,* 102202.

Shayan, M., Eghbali, B., & Niroumand, B. (2020). Fabrication of AA2024-TiO2 nanocomposite through stir casting. *Trans. Nonferrous Met. Soc. China, 30*: 2891-2903.

Singhal, V., Shelly, D., Saxena, A., Gupta, R, Verma, V.K., & Jain, A. (2025). Study of the Influence of Nanoparticle Reinforcement on the Mechanical and Tribological Performance of Aluminum Matrix Composites—A Review. *Lubricants, 13,* 93.

Song, J.Y., Park, J.C., Jeong, B. H., & ahn, Y.S. (2012). Fatigue behaviour of A356 auminium alloy for automotive wheels. *International journal of Cast Metals Research, 25*(1), 26-30.

Suleiman, I.Y., Salihu, & Mohammed, T. A. (2018). Investigation of mechanical, microstructure and wear behaviors of Al-12%Si reinforced with melon shell ash particulates. *The International Journal of Advanced Manufacturing Technology*. Doi: doi.org/10.1007/s00170-018-2157-9.

Tiwery, H., Hoziefa, W., El-Shabasy, A.B., & El-Mahallawi, I. (2018). *The Effect of Heat Treatment on Microstructure and Mechanical Properties of A356/ZrO2 Nano Reinforced Composites*. Paper presented at the 18th International Conference on Applied Mechanics and Mechanical Engineering, Cairo, Egypt.

Usman, I. (2026). *Synthesis and Characterization of Aluminium A356/Melon Husk Ash Nanocomposite Using Modified Stir Casting Technique*. A PhD Thesis submitted to Ahmadu Bello University Zaria, Nigeria.

Usman, I., Abdulwahab, M., Ause, T., & Bello, K.A. (2026). Evaluation of Tensile and Fatigue Behaviours of Novel A356/Melon Husk Ash Nanocomposite. *Bayero Journal of Engineering and Technology, 21*(2):87-95

International Conference on Engineering Innovation for Sustainable Development (ICESID 2026)
Faculty of Engineering, Ahmadu Bello University Zaria · 8–10 September 2026

MECHANICAL AND DURABILITY PERFORMANCE OF SUSTAINABLE CONCRETE INCORPORATING RICE HUSK ASH AND 100% RECYCLED CONCRETE AGGREGATE

Raphael Ejembi[1,*], Amana Ocholi[1], Bilkisu Amartey[1], Williams Ejembi[1], Samuel Ebiojo Ocheja[1], Samuel Godwin Obademi[1], Sumaila Muhammed Shaibu[1]

[1]*Ahmadu Bello University, Zaria*

Email: raphaelejemb@gmail.com*, aocholi@abu.edu.ng, bhsada@abu.edu.ng, williamsejembi@gmail.com, ochejaebi@gmail.com, obademisamuel1@gmail.com, shaibusumailamuhammed@gmail.com

***Corresponding author**: Raphael Ejembi

DOI: https://doi.org/10.67203/sp.ICESID.2026

ABSTRACT

High-volume substitution of natural coarse aggregates with Recycled Concrete Aggregate (RCA) typically impairs mechanical strength and increases water absorption due to the porous residual mortar layer. This study investigates the performance improvement of Grade 25 concrete incorporating 100% RCA through the pozzolanic addition of Rice Husk Ash (RHA) as a partial Portland cement replacement. Characterization via X-ray Fluorescence (XRF) confirmed RHA as a reactive pozzolan with a combined oxide composition ($SiO_2 + Fe_2O_3 + Al_2O_3$*) of 89.47%. Concrete mixes were prepared with 0%, 10%, 15%, and 20% RHA substitution levels at a fixed water-cement ratio of 0.57. Experimental results demonstrate that incorporating 15% RHA counteracts RCA-induced strength losses, yielding a 28-day compressive strength of* $25.9\ N/mm^2$ *(an 18.8% enhancement over the unblended RCA control), a splitting tensile strength of* $2.5\ N/mm^2$*, and a reduced water absorption of 1.23%, meeting BS 812-2 durability standards. Combining 15% RHA with 100% RCA effectively remediates microstructural weaknesses inherent in recycled aggregate matrices.*

Keywords: *Rice husk ash; Recycled concrete aggregate; Sustainable concrete; Microstructural improvement; Compressive strength; Water absorption*

1. INTRODUCTION

Sustainable construction practices have become necessary in contemporary civil engineering, driven by the urgent need to reduce negative environmental impacts and promote resource efficiency. In this context, the utilization of alternative materials in concrete production has emerged as a promising avenue to enhance sustainability in construction projects. This study aims to investigate the effects of incorporating rice husk ash (RHA) as partial replacement of cement and recycled concrete aggregate (RCA) as coarse aggregate on the performance and sustainability of concrete mixtures for construction applications.

Sustainable construction embodies principles aimed at minimizing environmental impact, conserving resources, and fostering societal well-being throughout the lifecycle of built infrastructure (Barlow, 2019). By integrating environmental, social, and economic considerations, sustainable construction practices seek to address global challenges such as climate change, resource depletion, and waste generation (Nawaz et al., 2020).

One of the primary challenges is the limited understanding of the performance of concrete mixtures containing RHA and RCA. Without a clear understanding of the mechanical, physical, and durability properties of concrete incorporating RHA and RCA, construction stakeholders may hesitate to adopt these materials in real-world applications. The integration of RHA and RCA into concrete mixtures may pose challenges in terms of compliance with existing standards, specifications, and regulatory requirements. Traditional concrete standards often do not account for the use of alternative materials, leading to ambiguity and confusion among designers, engineers, and regulators. Additionally, the lack of standardized testing protocols for evaluating the performance of concrete containing RHA and RCA further complicates the adoption process. Establishing clear guidelines and standards for

incorporating alternative materials into concrete mixtures is essential to ensure their widespread acceptance and use in construction projects. Finally, the lack of awareness and acceptance among construction stakeholders, including designers, contractors, developers, and policymakers, presents a significant barrier to the widespread adoption of RHA and RCA in construction projects. Many stakeholders may be unfamiliar with the properties, benefits, and limitations of these alternative materials, leading to skepticism and resistance to change. Building awareness, disseminating knowledge, and fostering collaboration among stakeholders are crucial steps towards overcoming this challenge and promoting the adoption of sustainable construction practices.

The significance of this study lies in its potential to advance sustainable construction practices by evaluating the performance of rice husk ash (RHA) as partial replacement of cement and recycled concrete aggregate (RCA) as coarse aggregate in concrete mixtures. The utilization of RHA and RCA offers significant environmental benefits by reducing the demand for virgin raw materials, conserving energy, and mitigating greenhouse gas emissions associated with traditional concrete production methods. The integration of RHA and RCA into concrete mixtures promotes resource conservation by utilizing waste materials that would otherwise be disposed of in landfills. By diverting waste streams from landfills and incorporating recycled materials into new construction projects, the construction industry can minimize its environmental footprint and contribute to resource efficiency.

The aim of this study is to evaluate the Effect of rice husk ash (RHA) as partial replacement of cement and recycled concrete aggregate (RCA) as coarse aggregate in concrete mixtures for sustainable construction applications. The following are the objectives: To investigate the chemical composition of rice husk ash so as to assess its level of pozzolanic content, To determine the properties of constituent materials used in this research to assess their suitability and conformity with standards, To carryout concrete mix design that will be used in this work, To investigate the mechanical properties of concrete mixtures containing varying proportions of rice husk ash as partial replacement for cement and recycled concrete aggregate as coarse aggregate, To determine the percentage replacement of cement with RHA that will produce optimum result.

Un-modified RCA concrete consistently exhibits lower compressive strength and higher permeability due to microcracks and old adhered mortar (Kou et al., 2011; Tam et al., 2012). This study investigates a microstructural remediation approach using 15% RHA to counteract RCA-induced strength degradation and restore Grade 25 concrete capacity[cite: 8, 10].

2. METHODOLOGY

Concrete Mix Design:

The concrete mix design was carried out using the Building Research Establishment (BRE) method. A mix ratio of 1:1.98:3.52 and water cement ratio of 0.57 from the concrete mix design was arrived at for this research. Concrete cubes of dimensions 150mm x 150mm x 150mm and cylinders with dimensions 100mm x 200mm were produced by partially replacing cement (Dangote). Rice husk ash (RHA) variation is at 0%, 10%, 15%, and 20%, the cube samples were cured in water for 7, 14, and 28 days and subjected to compressive and tensile strengths. A mix proportion of 1:1.98:3.52 with water cement ratio w/c 0.57 was achieved for Grade 25 (G25) in accordance with BS EN 197-1 (2005).

Preliminary Preparation of Rice Husk Ash Sample

The Rice Husk was cleaned and dried for 3 weeks so it would lose all its moisture content. It was burnt to ash using an incinerator in the department of Building, A.B.U Zaria. The ash after cooling was ball milled to further reduce the size and later grind. The rice husk was calcined at 700°C in a controlled incinerator. This temperature transforms amorphous silica into optimal reactive pozzolanic silica without forming crystalline quartz phase silica, which occurs above 800°C and reduces pozzolanic reactivity (Prasittisopin & Trejo, 2014; Thomas & Gupta, 2016).

METHODS

The tests carried out were physical and chemical for the determination of the physical and chemical properties of the materials used and effect of partial replacement of cement with rice husk ash

and a full replacement of coarse aggregate with recycled concrete aggregate on the properties of this sustainable concrete.

Test Equipment used

The following equipment in the heavy structures and concrete material laboratory are to be used in the course of these experiments:

1. Weighing Scale.
2. B. S. Sieves.
3. Concrete Moulds.
4. Rammer/Tamping rod.
5. Compression Testing Machine.
6. Tensile Testing Machine.
7. Slump cone.
8. Concrete mixer.
9. Vibrating table.

Casting and Curing of Concrete

Before casting the cubes, the 150mm x 150mm x 150mm steel cube moulds used were tightened, cleaned and oiled. The essence of oiling it is to facilitate easy and smooth demoulding of the concrete after hardening. The concrete mix was then poured into the moulds in 3 layers. The concrete was tamped 25 blows before adding another layer of concrete to the mould. This is to ensure that air bubbles are driven out and that the concrete is properly compacted. Excess concrete on the mould or on the floor was removed in time to avoid it from hardening. The surface of the concrete was then leveled and allowed to harden slightly before being marked for identification. The samples were demoulded after 24 hours and immediately immersed in clean water in a tank for curing. Curing is a process of hydrating the concrete samples which leads to increase in strength.

Compressive Strength test

Compressive strength test was carried out on the concrete in accordance to BS EN 196-1 (2005). The compressive strength test was conducted on cubes of 150mm x 150mm x 150mm mixed concrete using the compressive testing machine of 2500kN capacity (Denison) at the heavy structures and concrete laboratory of A.B.U, Zaria. The failure load was observed and recorded and the compressive strength in N/mm^2 was calculated from the equation below.

$Rc = Fc/A$ (N/mm^2)

Where, Rc is the compressive strength, in Newton per millimeters square,

Fc is the maximum load at fracture, in Newton and,

A is the area of the concrete sample in square millimeters.

Tensile Strength test

The tensile strength test was conducted on cylinders of 100mm x 200mm mixed concrete in an indirect form using the compression testing machine at the heavy structures and concrete laboratory of A.B.U, Zaria. The failure load was observed and the tensile strength in N/mm^2 was calculated from the equation below

$MC = 2P/\pi DH$

Where, MC is the tensile strength, in newton per millimeters square,

P is the maximum load at fracture, in newton and,

D and H are diameter and length of the cylindrical concrete sample respectively.

Water Absorption test

Water absorption test was carried out to determine the water absorption value of the mixed concrete, expressed in percentage. This property is particularly important in mortar and concrete used for water-retaining structure or watertight basement, as well as being critical for durability. This test was performed on a 150mm x 150mm x 150mm cube specimens prepared in the laboratory. Water absorption measurements were done by weighing the saturated specimens (Ws) and dried specimens (Wd) which was oven dried at 110°C for 24 hours at curing time 28 days. The water absorption was calculated using equation below

Water absorption (%) = $\frac{Ws-W}{Wd}\times 100$

Specimen Replication and Statistical Design

To ensure statistical reliability and reproducible results, three ($n = 3$) replicate 150 mm $\times$ 150 mm $\times$ 150 mm cube specimens were prepared and tested for each mix proportion (0%, 10%, 15%, and 20% RHA) at each curing age (7, 14, and 28 days), yielding a total of 36 compressive strength specimens. Similarly, three ($n = 3$) cylindrical specimens (100 mm $\times$ 200 mm) and three ($n = 3$) durability samples were cast per mix design for splitting tensile strength and 28-day water absorption testing, respectively. Mechanical and physical test values are reported as the arithmetic mean $\pm$ standard deviation (SD).

3. RESULTS AND DISCUSSION

Table 4.1: Result of Standard consistency test of cement

Test	Weight of Cement (g)	Vol. of Water (ml)	Penetration (mm)	Consistency (%)
1	400	122	5.0	30.5
2	400	120	5.5	30.0
3	400	122	6.0	30.0
	Average Consistency (%)		**30.2**	

Source: Laboratory test (2024)

The result of 30% average consistency in Table 4.1 implied a good result as the plunger penetrations were between 5mm-7mm from the base of the mould. It is in line with BS EN 196-3 (2016) which stipulates consistency of cement to be between 26% and 33%. This conforming result is not unconnected with the freshness of the cement used and procedure of BS EN 196-3 (2016) that was followed.

Table 4.2: Result of Setting time test of cement

The results of the tests carried out in the course of this research are presented and discussed with respect to literatures and standard codes of practice.

Test	Weight of Cement (g)	Vol. of Water (ml)	Penetration (mm)	Initial Setting Time(hrs:min)	Final Setting Time(hrs:min)
1	400	122	7.0	1:59	2:34
2	400	120	6.0	2:04	2:47
3	400	122	6.0	1:48	2:38
	Average Initial Setting Time = 1hr. 57mins				
	Average Final Setting Time = 2hrs. 40mins				

Source: Laboratory test (2024)

The average initial setting time and average final setting time as in Table 4.2 are within specifications of greater than 45minutes and less than 10 hours respectively. These results satisfied BS EN 196-3 (2016) and in line with Ejeh (2017). The cement is fit for the production of concrete and other masonry works. Setting time tests were conducted on unblended Portland Limestone Cement (PLC)

paste to establish baseline raw material compliance in accordance with BS EN 196-3 (2016). The binder exhibited an initial setting time of 1 hr 57 mins and a final setting time of 2 hrs 40 mins, satisfying standard requirements (>45 mins and <10 hrs). While RHA blending generally retards hydration slightly due to water absorption, baseline cement tests were prioritized to verify binder quality prior to batching.

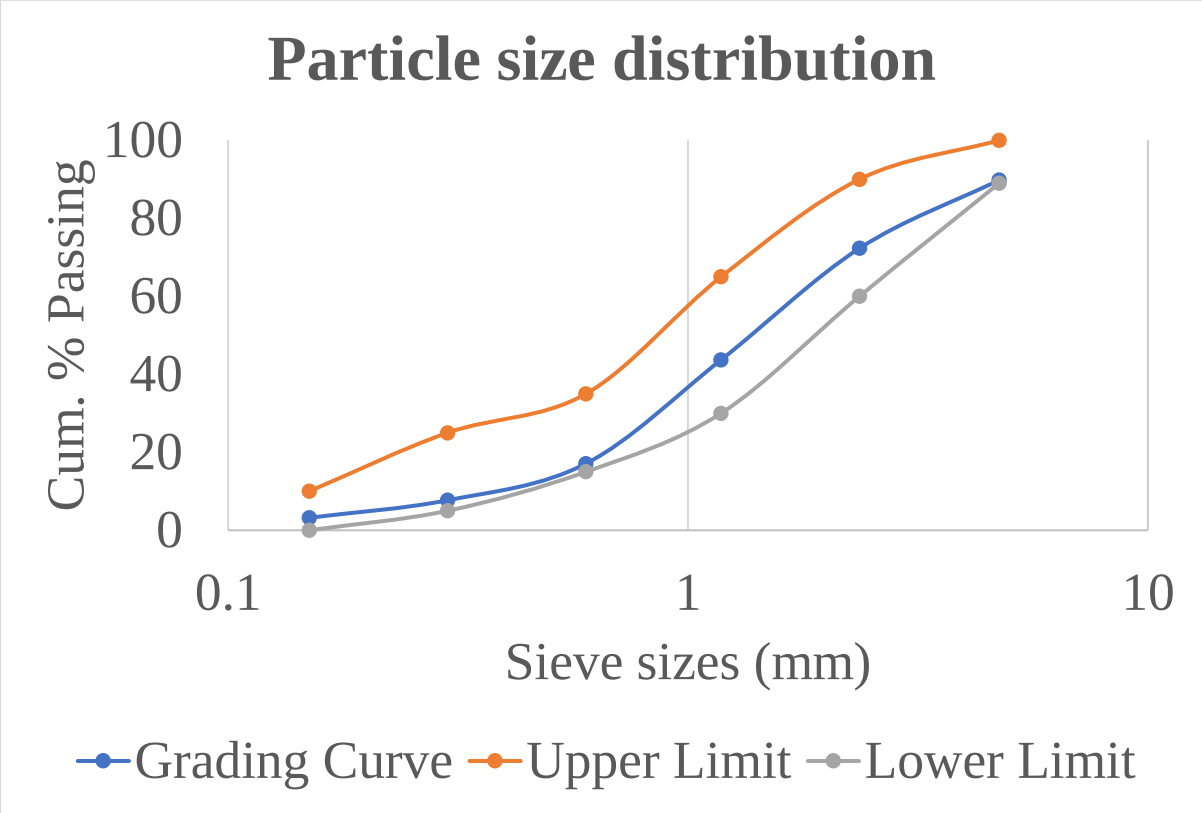

Figure 4.1: Particle Size Distribution Curves for Zone 3 (Fine Aggregate)

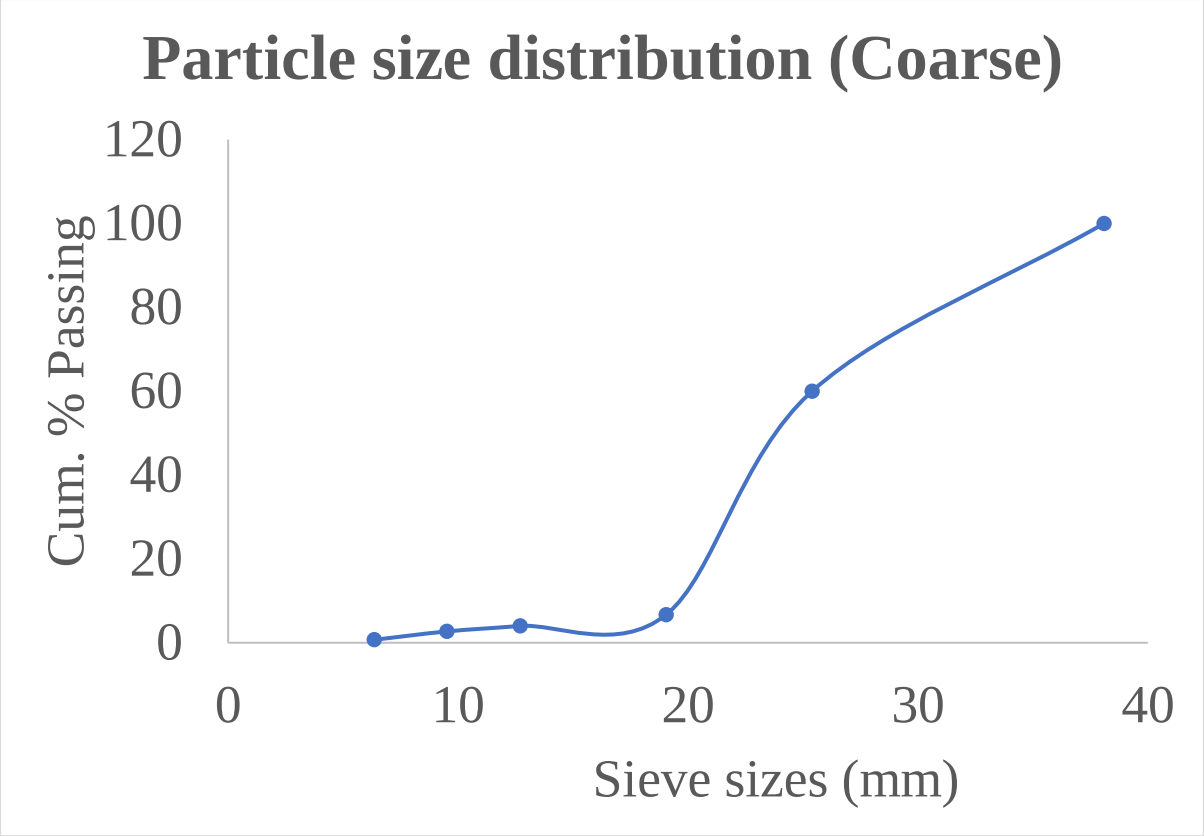

Figure 4: 2 Particle Size Distribution Curve for Coarse Aggregate

The result in Figure 4.1 conformed to BS EN 933-1 (2012) with a fineness modulus of 3.662. From the result of the sieve analysis, the sample is of zone 3 having a coarse grain size. From Figure 4.1 it can be seen that the sample falls within the standard upper and lower limits therefore good for the production of concrete.

The result in Figure 4.2 with Fineness modulus of 4.259 indicates a coarser aggregate. This is also supported by BS EN 933-1 (2012).

Table 4.3: Result of Chemical composition of Rice Husk Ash

CHEMICAL COMPOSITION	RICE HUSK ASH (%)
SiO_2	87
Fe_2O_3	1.29
Al_2O_3	1.18
C	17.24
CaO	1
K_2O	1.32
$SiO_2 + FeO_3 + Al_2O_3 = 89.47$ %	
Carbon / Loss on Ignition	(LOI)17.24%
Calcium Oxide (CaO)	1.00%
Potassium Oxide	(K_2O)1.32%

Source: Laboratory test (2024)

Table 4.3 presents the sum of pozzolanic oxides (89.47%) exceeds the 70% minimum threshold specified by ASTM C618 for Class F/N pozzolans, confirming high pozzolanic reactivity. The LOI value reflects residual unburnt carbon from controlled incineration.

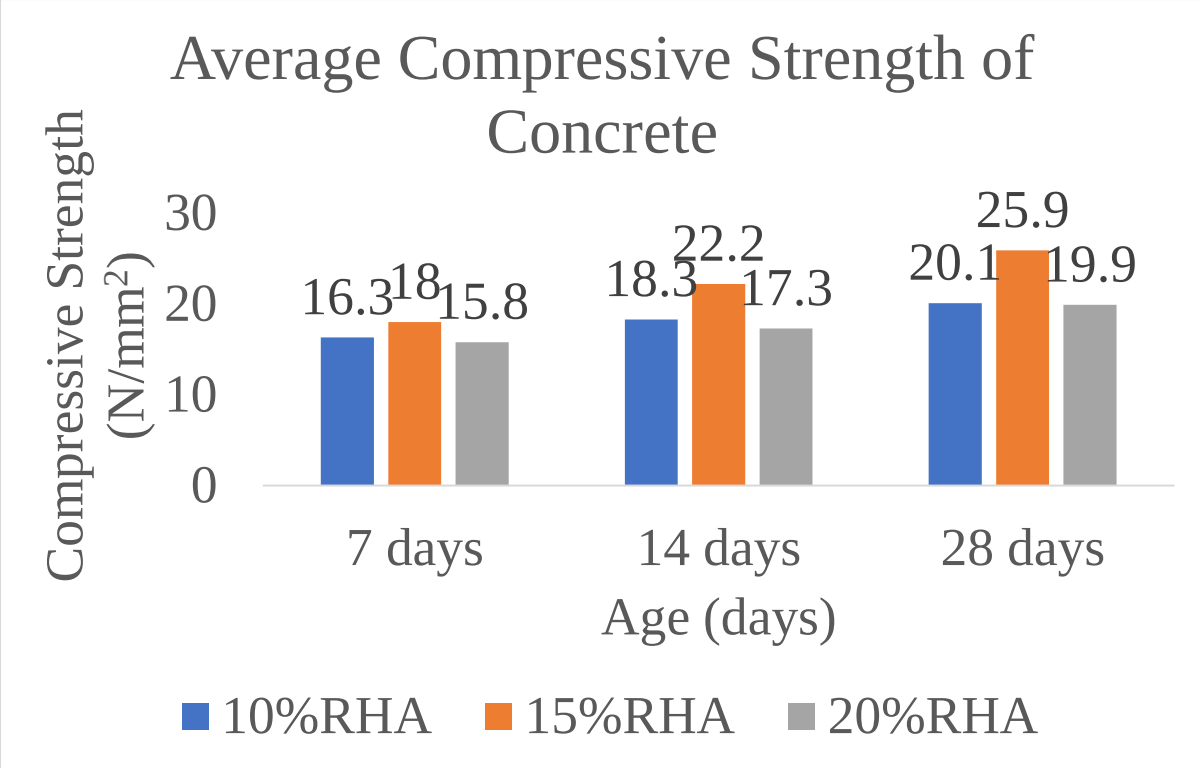

Source: Laboratory test (2024)

Figure 4.3: Average Compressive Strength of concrete with partial replacement of PLC with RHA

Figure 4.3 showed 15% RHA replacement produced higher compressive strength for both 7 days and 14 days curing ages. It is observed that the 28 days compressive strength of concrete with 15% replacement of RHA produced a strength of 28.85% and 30.15% higher than 10% and 20% RHA replacement respectively. The strength increase can be attributed to the interaction of microstructural mechanisms during which the pores in the mix are filled by the presence of RHA (Pornkasem et al., 2018).

The increase in strength is also supported by Jangral et al., (2022). In their work they found increase in strength as RHA percentage increases but declined beyond 15%. It is also in line with Bapat et al. (2004) who inferred that strength increases with age as evidenced in figure 4:3 even with the addition of a supplementary cementing material. The rice husk ash also served as filler of the pores in the concrete which made the concrete more compact, dense and durable. 100% RCA introduces a double Interfacial Transition Zone (ITZ)—between the original aggregate and old mortar, and between old mortar and new cement paste. This dual ITZ increases overall porosity and reduces compressive strength. However, the inclusion of 15% RHA counteracts this deficit. The micro-silica in RHA reacts with free calcium hydroxide $[Ca(OH)_2]$ released during cement hydration, forming additional secondary Calcium Silicate Hydrate (C-S-H) gel that densifies the ITZ and fills micro-voids.

The drop in 28-day compressive strength at 20% RHA ($19.9\ N/mm^2$) is attributed to the **cement dilution effect**. Excessive cement substitution reduces the primary $Ca(OH)_2$ concentration required to sustain the pozzolanic reaction, leaving unreacted RHA particles that act as structural weak points rather than binding matrices.

Table 4.4: Fresh Workability (Slump) Test Results

Mix Identification	**RHA Content (%)**	**Coarse Aggregate Type**	**Water/Cement Ratio (w/c)**	**Measured Slump (mm)**	**Slump Type**
Control (0% RHA)	0%	Natural Aggregate	0.57	65	True Slump
RCA-0% RHA	0%	100% RCA	0.57	48	True Slump
RCA-10% RHA	10%	100% RCA	0.57	38	True Slump
RCA-15% RHA	15%	100% RCA	0.57	30	True Slump
RCA-20% RHA	20%	100% RCA	0.57	22	Shear/Low Slump

Workability decreased progressively with increasing RHA replacement levels and complete substitution of natural aggregate with RCA. RCA exhibits higher initial water absorption due to adhered porous mortar. Concurrently, the high specific surface area and cellular porous structure of RHA particles increase water demand, leading to reduced slump values.

Table 4.5: Baseline Mechanical and Physical Properties of Control vs. Experimental Mixes (28 Days)

Concrete Mix Parameter	**Control (0% RHA + Natural Coarse Agg.)**	**RCA Baseline (0% RHA + 100% RCA)**	**RCA + 10% RHA**	**RCA + 15% RHA (Optimum)**	**RCA + 20% RHA**
28-Day Compressive Strength (N/mm^2)	**27.4**	**21.8**	**20.1**	**25.9**	**19.9**
28-Day Tensile Strength (N/mm^2)	**2.8**	**2.1**	**2.0**	**2.5**	**1.8**
Water Absorption (%)	**0.85%**	**2.10%**	**1.65%**	**1.23%**	**1.80%**

Table 4.6: Splitting Tensile Strength and Water Absorption across All Replacement Levels

Mix Designation	**RHA Replacement (%)**	**Splitting Tensile Strength (N/mm2) [28 Days]**	**Water Absorption (%) [28 Days]**
Control Mix	**0% (Natural Agg)**	$\mathbf{2.8 \pm 0.12}$	**0.85%**
RCA Control	**0% (100% RCA)**	$\mathbf{2.1 \pm 0.10}$	**2.10%**
RCA-10% RHA	**10%**	$\mathbf{2.0 \pm 0.15}$	**1.65%**
RCA-15% RHA	**15%**	$\mathbf{2.5 \pm 0.11}$	**1.23%**
RCA-20% RHA	**20%**	$\mathbf{1.8 \pm 0.14}$	**1.80%**

4. CONCLUSION

From this research, the following conclusions are drawn

- The oxide composition of the RHA used is 89.47% which is above the minimum specified oxide content of 70%. Therefore, it is a good pozzolan.
- The result of the physical properties of the basic constituent materials used in this research indicated satisfaction and in line with standard codes of practice including the British Standard Institution.
- The design of Grade 25 concrete was carried out and the materials mix ratio was 1:1.98:3.52 with water/cement ratio of 0.57 (W/C=0.57)
- The 28 days compressive strength for 10%, 15% and 20% of RHA are 20.1 N/mm^2, 25.9 N/mm^2 and 19.9 N/mm^2 respectively. The 15% cement replacement gave the optimum compressive strength with a corresponding tensile strength of 2.5 N/mm^2. The Water Absorption capacity of the 15% cement replacement concrete was 1.23% which is within the specifications of BS 812: part 2 (1995).

- The optimum mechanical properties like compressive strength, water absorption capacity of the concrete was achieved at 15% cement replacement level.

RECOMMENDATION

From the research, it is found that the optimum mechanical properties like compressive strength, water absorption capacity of the concrete were achieved at 15% cement replacement level. Therefore, it is recommended that in the concrete mix cement should be replaced with Rice Husk Ash by 15%.

5. REFERENCES

ASTM International. (2019). *Standard specification for coal fly ash and raw or calcined natural pozzolan for use in concrete* (ASTM C618-19). ASTM International. https://doi.org/10.1520/C0618-19

Bapat, J. D., Kulkarni, S. S., & Raut, S. P. (2004). Performance of high-volume fly ash and agro-waste concrete. *Cement and Concrete Research*, 34(8), 1365–1371. https://doi.org/10.1016/j.cemconres.2003.12.029

Barlow, J. (2019). *Sustainable construction: Principles and practices* (2nd ed.). Routledge. https://doi.org/10.4324/9781315148007

British Standards Institution. (1995). *Testing aggregates: Method for determination of water absorption* (BS 812-2:1995). BSI Group.

British Standards Institution. (2016). *Methods of testing cement: Determination of setting time and soundness* (BS EN 196-3:2016). BSI Group.

Jangral, S., Sharma, R., & Kumar, S. (2022). Influence of rice husk ash on mechanical properties of concrete: A comprehensive review. *Materials Today: Proceedings*, 60(2), 1120–1126. https://doi.org/10.1016/j.matpr.2021.12.304

Kou, S. C., Poon, C. S., & Wan, D. (2011). Properties of concrete prepared with low-grade recycled aggregates. *Construction and Building Materials*, 25(6), 2815–2821. https://doi.org/10.1016/j.conbuildmat.2010.12.062

Nawaz, M., Farooq, M., & Saeed, A. (2020). Lifecycle assessment of sustainable construction practices and green building materials. *Environmental Impact Assessment Review*, 83, 106401. https://doi.org/10.1016/j.eiar.2020.106401

Pornkasem, P., Sata, V., & Chindaprasirt, P. (2018). Microstructural analysis and pore structure of rice husk ash concrete. *Construction and Building Materials*, 172, 415–424. https://doi.org/10.1016/j.conbuildmat.2018.03.220

Prasittisopin, L., & Trejo, D. (2014). Hydration and phase formation of blended cementitious systems containing rice husk ash with different amorphous contents. *Journal of Materials in Civil Engineering*, 26(11), 04014081. https://doi.org/10.1061/(ASCE)MT.1943-5533.0000988

Tam, V. W., Gao, X. F., & Tam, C. M. (2012). Microstructural analysis of recycled aggregate concrete produced from two-stage mixing approach. *Cement and Concrete Research*, 35(6), 1195–1203. https://doi.org/10.1016/j.cemconres.2004.10.025

Thomas, B. S., & Gupta, R. C. (2016). Properties of high strength concrete containing rice husk ash. *Journal of Cleaner Production*, 112(1), 641–651. https://doi.org/10.1016/j.jclepro.2015.08.114

International Conference on Engineering Innovation for Sustainable Development (ICESID 2026)
Faculty of Engineering, Ahmadu Bello University Zaria · 8–10 September 2026

OPTIMIZATION AND PREDICTIVE MODELLING OF DOUM PALM FIBRE-REINFORCED CONCRETE INCORPORATING RICE HUSK ASH

Musa Abdullahi[1,*], Yusuf Yau[1], Isah Garba[1], Bashir Usman[2], Suleiman Yusuf[2]

[1]*Ahmadu Bello University, Zaria*
[2]*Nuhu Bamalli Polytechnics, Zaria*

Email: murmusa77@gmail.com[*], yyau@abu.edu.ng, isahgarba86@gmail.com, bashirusman.bu@gmail.com, ysuleiman3000@gmail.com

***Corresponding author**: Musa Abdullahi

DOI: https://doi.org/10.67203/sp.ICESID.2026

ABSTRACT

The growing demand for environmentally sustainable construction materials has stimulated interest in incorporating agricultural waste products into concrete production. This study investigates the mechanical performance and optimization of doum palm fibre (DF)-reinforced concrete containing rice husk ash (RHA) as a partial replacement for Portland limestone cement. A multilevel factorial experimental design based on Response Surface Methodology (RSM) was employed to evaluate the combined influence of RHA replacement (0–25%) and DF content (0–2%) on compressive strength, flexural strength, split tensile strength, and punching shear strength. Predictive regression models were developed using Design-Expert software and assessed through analysis of variance (ANOVA), coefficients of determination (R^2), and residual diagnostics. Quartic polynomial models adequately represented all responses, with predicted, adjusted and coefficients of determination ranging from 0.9529 to 0.9914. Numerical optimization identified an optimum mixture containing 2.0% DF and 10.45% RHA, producing predicted compressive, flexural, split tensile, and punching shear strengths of 18.010 MPa, 5.370 MPa, 4.420 MPa, and 1.053 MPa, respectively, at 56 days. Experimental validation showed prediction errors below 5%, confirming the reliability of the developed models. The findings demonstrate that response surface methodology provides an effective tool for optimizing sustainable fibre-reinforced concrete mixtures while reducing experimental effort. The combined use of rice husk ash and doum palm fibre offers a viable approach for producing environmentally friendly concrete with satisfactory mechanical performance.

Keywords: *Response Surface Methodology; compressive strength flexural strength; split tensile strength; punching shear strength; rice husk ash; doum palm fibre; regression models*

1. INTRODUCTION

Concrete remains one of the most widely used construction materials worldwide because of its versatility, durability, structural performance, and ability to withstand diverse environmental conditions (Habert et al., 2020; Olsson *et al*., 2023). Rice husk ash (RHA), an agricultural by-product generated from the controlled combustion of rice husks, has emerged as a promising SCM owing to its high silica content and pozzolanic reactivity. Several recent studies have reported that the appropriate partial replacement of cement with rice husk ash can improve concrete compressive strength (Al-Alwan *et al*., 2024).

Although numerous studies have examined the individual effects of RHA or fibre reinforcement on concrete performance, limited information is available regarding the combined influence of RHA and doum palm fibre on both conventional strength properties and punching shear behaviour of reinforced concrete flat slabs. Furthermore, predictive models capable of optimizing these properties simultaneously remain scarce. Therefore, this study investigates the performance optimization of doum palm fibre-reinforced concrete incorporating rice husk ash as a partial cement replacement. This knowledge gap restricts the practical implementation of sustainable fibre-reinforced concrete mixtures for structural applications.

2. METHODOLOGY

2.1 Material

2.1.1 Cement

Portland Limestone Cement (PLC), conforming to BS EN 197-1**,** was used as the primary binder. Properties of cement were determine in accordance with BS EN 196-3:2016 to verify compliance with the relevant specifications.

2.1.2 *Rice Husk Ash*

Rice husk ash (RHA) was produced by controlled calcination of rice husks in a laboratory muffle furnace at temperatures between 600 and 700 °C for 4 h**.** The resulting ash was ground and sieved through a 75 μm sieve to obtain a fine pozzolanic material suitable for use as a supplementary cementitious material.

2.1.3 Doum Palm Fibre

Doum palm fibres (DF) were collected from naturally growing doum palm trees at Buzai Village near Zaria, Kaduna State, Nigeria. The fibres were cleaned, air-dried, and cut into lengths ranging from 20 to 25 mm**,** corresponding to an aspect ratio of approximately 80 to 120**.**

2.1.4 *Aggregates*

Crushed granite with a nominal maximum size of 20 mm was used as coarse aggregate. The aggregate was obtained from Abdu Kwari Quarry, Zaria, Nigeria. Natural river sand with a maximum particle size of 0.5 mm served as the fine aggregate..

2.1.5 *Mixing Water*

Potable water supplied by the Ahmadu Bello University, Zaria Water Works was used for concrete mixing and curing. The water satisfied the requirements of BS EN 1008:2002.

2.1.6 *Statistical Software*

Design-Expert Version 13 (Stat-Ease Inc., USA) was used for all the statistical analysis conducted**.**

2.2 Methods

2.2.1 *Experimental Design*

Full factorial design was adopted on Response Surface Methodology (RSM). Two independent variables were considered: Rice husk ash (RHA): 0, 5, 10, 15, 20, and 25% by mass replacement of cement. Doum palm fibre (DF): 0, 0.5, 1.0, 1.5, and 2.0% by volume of concrete. 30 different Mix ID were obtained from the design of experiment each Mix ID having 2 replica giving total of 60 runs.

2.2.2 *Concrete Mix Proportion*

Concrete mixtures were proportioned in accordance with BS EN 14889-1:2006 using a constant mix proportion of 1:1.5:3 (cementitious material, fine aggregate, coarse aggregate) and a constant water-to-binder ratio of 0.50. Rice husk ash replaced Portland limestone cement at replacement levels of 0–25%, while doum palm fibre was incorporated at dosages ranging from 0 to 2.0% by concrete volume.

2.2.3 *Specimen Preparation and Curing*

Concrete constituents were mixed until a uniform and homogeneous consistency was achieved. 30 different mix ID were cast, 3 samples for each curing day, as 7,14,21,28 and 56 days. Total of 450 samples for each of cubes, cylinders and beams and total of 90 samples for flat slabs were cast. These implies the averages of the three (3) results for each of the sample were recorded for

analysis of the compressive, split tensile and flexural strength respectively, while the averages of the three (3) results for samples of each of the 30 Mix ID of the flat slabs for only 56 days of curing were considered for punching shear strengths analysis making 90 cast samples.

2.2.4 *Mechanical Property Test*

The compressive strength test was carried out in accordance with BS EN 12390-2: (2009). Three set of each concrete cubes of size 100x100x100mm were used. Split tensile strength of the fibre reinforced concrete was carried out in accordance with BS-EN 12390-6 (2009). Concrete cylinders of 100x200mm size were used. The failure load was determined and the split tensile strength was calculated using the Equation 1.

$$\text{Split tensile strength} = \frac{2P}{\pi LD} \tag{1}$$

Where P is the failure load, L is the length of the cylindrical specimen and D is the diameter of the specimen. The flexural strength test of the fibre reinforced concrete beam was carried out in accordance with BS 12390-5(2019). Beams of 100x100x450mm size were used. The flexural strength of the beam was determined using three-point bending test. The punching shear test was carried out in accordance with BS-8110-1:1997. The curing duration was 7, 14, 21, 28 and 56days for all the test, expect the punching shear, where only 56days was considered. Laboratory test results for the mechanical properties were not reported in this study only the optimized results from the software were reported.

2.3 Response Surface Modelling and Optimization

Regression models were developed to establish relationships between the independent variables (RHA replacement level and DF dosage) and the measured responses. The general polynomial model adopted is expressed as shown in Equation (2):

$$y = b_o + \sum_{i=1}^{k} b_i x_i + \sum_{i=1}^{k} b_{ij} x_i + \sum_{i=1}^{k=1} \sum_{j=i+1}^{k} b_{ij} x_i x_j + ... + \varepsilon \tag{2}$$

Where: y = predicted response variable, b_0 = intercept, b_i = model coefficients, b_{ij} = linear/interaction terms, x_i and x_j = reaction factors, ε = represents errors. The optimization objectives and constraints for the variables and responses are presented in Table 1.

Table 1: Optimization Objectives and Constraints

Variables/Responses	Goal	Lower Limit	Upper Limit
Doum Palm fibre (DF)	Maximize	0.0	2.0
Rice husk ash (RHA)	Maximize	0.0	25.0
Compressive Strength(N/mm^2)	Maximize	13.15	19.73
Flexural Strength(N/mm^2)	Maximize	4.12	5.78
Split Tensile Strength(N/mm^2)	Maximize	3.02	4.78
Punching shear strength(N/mm^2)	Maximize	0.623	1.231

3. RESULTS AND DISCUSSION

3.1 Development of predictive models

Mathematical prediction models for the strength properties of doum palm fibre reinforced concrete incorporating rice husk ash as a partial replacement of cement were developed using Design-Expert software (Version 13). The software was used to generate regression equations for all the investigated responses in both coded and actual forms. Based on model fitting and adequacy checks, quartic polynomial models were identified as the most suitable for describing the compressive, flexural, split tensile, and punching shear strengths. To improve model reliability, statistically insignificant terms were eliminated, and the final refined models were established as presented in equations (3) to (7).

$$F_c = 18.70 - 0.5183D - 2.85R - O.O700DR - 2.09D^2 - 1.59R^2 + 0.7054DR^2 - 0.0167D^3 + 1.49D^4 \quad (3)$$

$$F_f = 5.46 - 0.0381D - 0.2500R - 0.0148DR - 0.0995D^2 - 0.0979R^2 + 0.0043D^2R - 0.1786DR^2 + 0.0389D^3 - 0.3090R^3 + 0.0871D^3R - 0.2500DR^3 - 0.1693R^4 \quad (4)$$

$$F_s = 4.46 - 0.0475D - 0.6796R - 0.0682DR - 0.1000D^2 - 0.5132R^2 - 0.1196D^2R - 0.0982DR^2 + 0.1641R^3 - 0.1020D^2R^2 - 0.2442DR^3 + 0.3011R^4 \quad (5)$$

$$F_p = 1.07 + 0.0086D - 0.2313R + 0.0057DR - 0.1021D^2 - 0.3907R^2 + 0.0178D^2R - 0.0180DR^2 - 0.0099D^3 - 0.0475R^3 + 0.0643D^4 + 0.2549R^4 \quad (6)$$

Where: D and R are coded factors for doum palm fibre and rice husk ash respectively. F_c F_f , F_s and F_p Are compressive, flexural and split tensile strength of the concrete and punching shear strength of the concrete slabs.

The ANOVA results presented in Tables 2 to 5 summarize the relevant statistical parameters evaluated at a 95% confidence level for 60 runs signifying 2 replicate of the 30 Mix ID.

Table 2: ANOVA Results for Compressive Strength of doum palm fibre reinforced concrete with rice husk ash as partial replacement of cement

Source	Sum of Squares	df	Mean Square	F-value	p-value	
Model	257.98	8	32.25	179.08	< 0.0001	**Significant**
D	0.7754	1	0.7754	4.31	0.0430	
R	227.11	1	227.11	1261.17	< 0.0001	
DR	0.0686	1	0.0686	0.3809	0.5398	
D^2	1.34	1	1.34	7.42	0.0088	
R^2	24.26	1	24.26	134.69	< 0.0001	
DR^2	2.38	1	2.38	13.20	0.0006	
D^3	0.0007	1	0.0007	0.0042	0.9488	
R^4	0.8538	1	0.8538	4.74	0.0341	
Residual	9.18	51	0.1801			
Cor Total	267.16	59				

Table 3: ANOVA Results for Flexural Strength of doum palm fibre reinforced concrete with rice husk ash as partial replacement of cement

Source	Sum of Squares	df	Mean Square	F-value	p-value	
Model	8.83	12	0.7360	274.52	< 0.0001	**Significant**
D	0.0042	1	0.0042	1.56	0.2180	
R	0.1879	1	0.1879	70.08	< 0.0001	
DR	0.0002	1	0.0002	0.0717	0.7900	
D^2	0.1040	1	0.1040	38.79	< 0.0001	
R^2	0.0042	1	0.0042	1.56	0.2177	
D^2R	0.0001	1	0.0001	0.0336	0.8554	
DR^2	0.1524	1	0.1524	56.84	< 0.0001	
D^3	0.0041	1	0.0041	1.52	0.2233	
R^3	0.2535	1	0.2535	94.54	< 0.0001	
D^3R	0.0096	1	0.0096	3.57	0.0650	
DR^3	0.0829	1	0.0829	30.94	< 0.0001	
R^4	0.0155	1	0.0155	5.76	0.0204	
Residual	0.1260	47	0.0027			
Cor Total	8.956	59				

Table 4: ANOVA Results for Split tensile Strength of doum palm fibre reinforced concrete with rice husk ash as partial replacement of cement.

Source	Sum of Squares	df	Mean Square	F-value	p-value	
Model	11.91	11	1.08	263.21	< 0.0001	**Significant**
D	0.0286	1	0.0286	6.95	0.0112	
R	1.39	1	1.39	337.59	< 0.0001	
DR	0.0083	1	0.0083	2.01	0.1631	
D^2	0.0444	1	0.0444	10.79	0.0019	
R^2	0.1079	1	0.1079	26.25	< 0.0001	
D^2R	0.0701	1	0.0701	17.04	0.0001	
DR^2	0.0461	1	0.0461	11.21	0.0016	
R^3	0.0714	1	0.0714	17.37	0.0001	
D^2R^2	0.0174	1	0.0174	4.23	0.0451	
DR^3	0.0791	1	0.0791	19.25	< 0.0001	
R^4	0.0489	1	0.0489	11.89	0.0012	
Residual	0.1974	48	0.0041			
Cor Total	12.1074	59				

Table 5: ANOVA Results for Punching shear Strength of doum palm fibre reinforced concrete with rice husk ash as partial replacement of cement

Source	Sum of Squares	df	Mean Square	F-value	p-value	
Model	2.09	11	0.1897	503.84	< 0.0001	**Significant**
D	0.0002	1	0.0002	0.5610	0.4575	
R	0.1608	1	0.1608	427.12	< 0.0001	
DR	0.0005	1	0.0005	1.20	0.2784	
D^2	0.0032	1	0.0032	8.46	0.0055	
R^2	0.0666	1	0.0666	176.99	< 0.0001	
D^2R	0.0015	1	0.0015	4.10	0.0484	
DR^2	0.0016	1	0.0016	4.13	0.0477	
D^3	0.0003	1	0.0003	0.7012	0.4065	
R^3	0.0060	1	0.0060	15.87	0.0002	
D^4	0.0016	1	0.0016	4.24	0.0449	
R^4	0.0350	1	0.0350	93.04	< 0.0001	
Residual	0.0181	48	0.0004			
Cor Total	2.1081	59				

The ANOVA results indicate that rice husk ash replacement was the dominant factor governing the strength properties, contributing approximately 88% of the model sum of squares for compressive strength.

3.2 Optimization

The essence of optimization was to obtain optimal values of factors that yielded optimum responses. Figure 1 illustrates the optimized outcomes corresponding to the most suitable solutions for the selected response variables. From the optimization search, the software identified four (4) possible solutions, of which the most desirable was achieved at a doum palm fibre content of 2.00% and a rice husk ash replacement level of 10.45% at 56 days curing age.

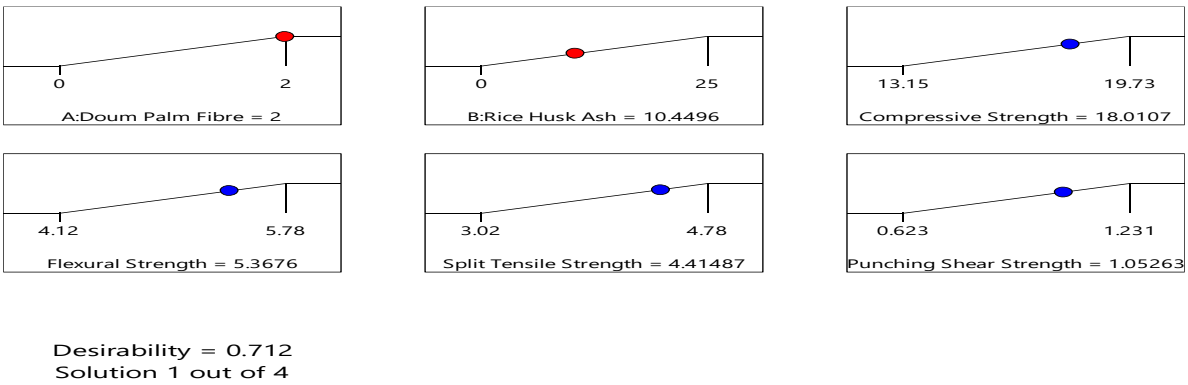

Figure 1: Optimization ramp combination for independent variables and results outcomes for responses

The optimized strengths values of 18.011 N/mm² for compressive strength, 5.368 N/mm² for flexural strength, 4.415 N/mm² for split tensile strength, and 1.053 N/mm² for the punching shear strength of the flat slab were obtained from the optimisation analysis of the Design-Expert software at this mix combination. The overall desirability index for this solution was 0.712, which indicates a satisfactory level of optimization.

Table 6: Optimization Result of doum palm fibre reinforced concrete with rice husk ash as partial replacement of cement

S/N	Doum Palm Fibre(%)	Rice Husk Ash(%)	Compressive Strength (N/mm^2)	Flexural Strength (N/mm^2)	Split Tensile Strength (N/mm^2)	Punching Shear Strength(N/mm^2)	Desirability	
1	**2.000**	**10.450**	**18.011**	**5.368**	**4.415**	**1.053**	**0.712**	**Selected**
2	2.000	10.207	18.061	5.370	4.425	1.054	0.712	
3	2.000	10.000	18.104	5.372	4.432	1.055	0.711	
4	1.467	10.511	18.492	5.444	4.510	1.078	0.708	

3.3 Model Validation

The validation of the developed models were carried out experimentally and the percentage error differences were indicated in Table 7.

Table 7: Experimental Model Validation

Responses	Doum palm fibre(%)	Rice husk ash (%)	Curing Age(days)	Predicted Values	Experimental Values	Error (%)
Compressive strength(N/mm^2)	2.00	10.45	56	18.011	18.51	2.70
Flexural strength(N/mm^2)	2.00	10.45	56	5.368	5.25	-2.25
Split Tensile Strength(N/mm^2)	2.00	10.45	56	4.415	4.30	-2.67
Punching shear strength(N/mm^2)	2.00	10.45	56	1.053	1.10	4.27

The percentage errors were found to be below 5%, this suggested that the predicted values from the developed models are in close agreement with the experimental result.

4. CONCLUSION

This study developed response surface models for predicting the mechanical properties of doum palm fibre-reinforced concrete incorporating rice husk ash as a partial cement replacement. The developed quartic models demonstrated excellent predictive capability, with the predicted, adjusted and coefficients of determination exceeding 95% for all investigated responses and experimental validation errors below 5%. Multi-response optimization identified an optimum mixture containing 2.0% doum palm fibre and 10.45% rice husk ash, providing a balanced improvement in compressive, flexural, split tensile, and punching shear strengths. And row experimental strengths properties were not reported in this study only the responses from software were reported for modelling and optimization.

5. REFERENCES.

Al-Alwan, A. A. K., Al-Bazoon, M., Mussa, F. I., Alalwan, H. A., Shadhar, M. H., Mohammed, M. M., & Mohammed, M. F. (2024). The impact of using rice husk ash as a replacement material in concrete: An experimental study. Journal of King Saud University—Engineering Sciences, 36(4), 249–255. doi:10.1016/j.jksues.2022.03.002.

Albadrani, M. A. (2025). Strength development of PPC concrete with rice husk ash: Optimal replacement levels for sustainable construction. *Sustainability*, *17*(18), Article 8258. https://doi.org/10.3390/su17188258

Bazarkhankyzy, A., Murali, G., Aibuldinov, Y., Iskakova, Z., Kurpińska, M., Abdelgader, H. S., Avudaiappan, S., & Dixit, S. (2025). Comprehensive evaluation of impact strength and

microstructural characteristics of geopolymer concrete reinforced with four types of natural fibers of varying lengths. *Scientific Reports, 15*, Article 29624. https://doi.org/10.1038/s41598-025-14857-5

Endale, S. A., Taffese, W. Z., Vo, D.-H., & Yehualaw, M. D. (2023). Rice husk ash in concrete. *Sustainability, 15*(1), Article 137. https://doi.org/10.3390/su15010137

Habert, G., Miller, S. A., John, V. M., Provis, J. L., Favier, A., Horvath, A., & Scrivener, K. L. (2020). Environmental impacts and decarbonization strategies in the cement and concrete industries. Nature Reviews Earth & Environment, 1(11), 559–573. doi:10.1038/s43017-020-0093-3

Olsson, J. A., Miller, S. A., & Alexander, M. G. (2023). Near-term pathways for decarbonizing global concrete production. Nature Communications, 14, Article 4574. doi:10.1038/s41467-023-40302-0

International Conference on Engineering Innovation for Sustainable Development (ICESID 2026)
Faculty of Engineering, Ahmadu Bello University Zaria · 8–10 September 2026

OPTIMIZATION OF ORGANOSOLV LIGNIN EXTRACTION FROM GROUNDNUT SHELL FOR ADHESIVE PRECURSOR APPLICATIONS

Mustapha Nma Abubakar[1,*], M.t Isa[1], Bello Tijjani Kayode[1], Adamu Yusuf[2], Bello Abdullahi[3]

[1]*Ahmadu Bello University Zaria*
[2]*Ahmado Bello University Zaria*
[3]*Bioresource Development Unit, National Biotechnology Research and Development Agency, Abuja*

Email: callonbobj@gmail.com*, mtisaz@yahoo.com, tjbello27@gmail.com, yusufbinadam@yahoo.com, babdallah903@gmail.com

***Corresponding author**: Mustapha Nma Abubakar

DOI: https://doi.org/10.67203/sp.ICESID.2026

ABSTRACT

The increasing demand for sustainable materials has intensified research into lignin-based adhesives derived from agricultural biomass. This study presents an integrated approach for optimizing organosolv extraction of lignin from groundnut shell waste for potential adhesive applications. Groundnut shell lignin was extracted via an organosolv process. A three-factor central composite design (CCD) of response surface method (RSM) was applied to optimize extraction variables using design expert 13.0.1 including ethanol concentration, temperature, and reaction time considering % yield and lignin reactivity index (LRI). The model was tested with its adequacy fit statistics, where R^2-value is 0.9941 which has 0.90 % and 4.4 % difference from the adjusted R^2 and predicted R^2 values. The theoretical optimal parameters obtained were 55 % ethanol concentration, 120 °C temperature, and 45 minutes reaction time which yielded a lignin recovery of 87.55 % and 5.17 LRI. These were validated having a close value of the responses 86.24 % yield and 5.25 LRI having a 1.45 % and 1.52 % error for yield and LRI respectively, as compared with the theorical values. FTIR and compositional analysis confirmed successful isolation of a lignin-rich fraction from groundnut shell. The extracted lignin retained characteristic hydroxyl, aliphatic C-H, aromatic skeletal and C-O/ether functionalities, with prominent absorptions observed around 3404, 2928, 1508 – 1529, 1410 – 1412 and 1044 – 1119 $^{cm-1}$. The novelty of this work lies in consideration of quantity and quality of lignin in optimization of organosolv extraction method of groundnut shell lignin, an underutilized agricultural waste, to produce a functionally improved adhesive precursor. Conclusively, the optimized extraction conditions produced high lignin yield and enhanced lignin reactivity, demonstrating that groundnut shell is a sustainable and promising source of reactive lignin for the development of bio-based adhesive precursors. These findings provide a reliable foundation for the subsequent modification and functionalization of high-performance and environmentally friendly bio-adhesives synthesis.

Keywords: *Lignin; Organosolv; Adhesive Precursor; Lignin Reactivity Index; Central Composite Design; Compositional Analysis; FTIR*

1. INTRODUCTION

The increasing global emphasis on environmental sustainability and the depletion of fossil-based resources have intensified research into renewable and eco-friendly alternatives for industrial materials. Conventional adhesives, largely derived from petroleum-based polymers such as epoxy, polyurethane, and phenol–formaldehyde resins, are associated with significant environmental concerns, particularly the emission of volatile organic compounds (VOCs) during their production and application (Paez & Fatehi, 2025). In response, bio-based polymers derived from lignocellulosic biomass have gained increasing attention as sustainable substitutes. Among these, lignin has emerged as a promising renewable resource due to its aromatic structure, high availability, and compatibility with phenolic resin systems (Mateo *et al*., 2025; Ait Benhamou *et al*., 2025).

Lignin is a complex, three-dimensional amorphous polymer composed of phenylpropanoid units, namely p-coumaryl, coniferyl, and sinapyl alcohols, which give rise to hydroxyphenyl (H), guaiacyl (G), and syringyl (S) structural units (Liu *et al*., 2023). It functions as a natural adhesive within

plant cell walls, imparting rigidity, hydrophobicity, and resistance to biological degradation (Zhang *et al*., 2024). Although it is the second most abundant biopolymer after cellulose, lignin remains largely underutilized, with the majority being combusted for energy recovery in pulp and biorefinery industries rather than converted into value-added products (Mateo *et al*., 2025). This presents a significant opportunity for its valorization in the development of sustainable materials, particularly bio-adhesives.

Groundnut (*Arachis hypogaea*) shell (Figure 1) is an abundant agricultural residue generated in large quantities in many developing countries, including Nigeria. Global groundnut processing produces millions of tonnes of shell waste annually, which is often disposed of through open burning or landfilling, thereby contributing to environmental pollution (Ogunkunle *et al*., 2024). However, groundnut shell is rich in lignocellulosic components, typically comprising cellulose, hemicellulose, and lignin, making it a viable raw material for lignin extraction (Adebayo & Adeola, 2023). Its utilization for lignin recovery therefore supports sustainable waste management and the development of renewable bio-based products (Gerber & Roberts, 2024).

Figure 1: Groundnut Shell (*Arachis hypogaea*)

Several extraction techniques have been reported for lignin recovery from biomass, including Kraft pulping, soda pulping, organosolv processes, and deep eutectic solvent (DES) systems. Among these, the organosolv process has attracted considerable interest due to its ability to produce high-purity lignin with relatively low structural degradation compared to conventional alkaline methods (Xu *et al*., 2024). Although emerging fractionation technologies such as DES extraction have demonstrated considerable potential for lignin recovery, organosolv extraction was selected in this study because its established ability to selectively fractionate lignocellulosic biomass and recover sulfur-free lignin with relatively high purity and useful hydroxyl functionalities. These characteristics are particularly relevant to the intended functionalization of lignin for adhesive precursor development (Alam *et al.*, 2024; Tanis *et al.*, 2024). Among organic solvents used in organosolv processing, ethanol is attractive for its lignin-solubilizing capacity, relatively low toxicity, miscibility with water and potential for recovery and reuse (Brienza *et al.*, 2024). However, the efficiency of lignin extraction and the quality of the resulting product are strongly influenced by operational parameters such as solvent composition, reaction temperature, and extraction time (Ruwoldt *et al*., 2024). Consequently, optimisation of these parameters is essential to obtain lignin with desirable physicochemical properties suitable for adhesive applications.

Despite growing interest in lignin valorisation, limited studies have systematically optimised organosolv extraction conditions for lignin recovery from groundnut shell and evaluated its reactivity to suit adhesive synthesis precursor. In particular, the relationship between extraction parameters, and lignin structural characteristics remains insufficiently understood.

Therefore, this study aims to optimise the organosolv extraction of lignin from groundnut shell and evaluate its suitability for adhesive synthesis. Specifically, the study focuses on optimisation of extraction parameters of lignin from groundnut shell using the organosolv method for improved quantity and quality, and characterisation of the extracted lignin for possible adhesive applications.

This work contributes to the sustainable utilisation of agricultural waste and supports the development of environmentally benign bio-based adhesives as alternatives to petroleum derived products.

2. MATERIALS AND METHODS

The details of reagents used are presented in Table 1, and experimental setup is shown in Figure 2, showing all methods used.

Table 1: *Chemicals and reagents used*

S/N	Chemical	Purity/Grade	Supplier
1	Ethanol	≥99.5%	Sigma-Aldrich
2	Sulfuric acid	95%	Sigma-Aldrich
3	Distilled water	Laboratory grade	Laboratory supply

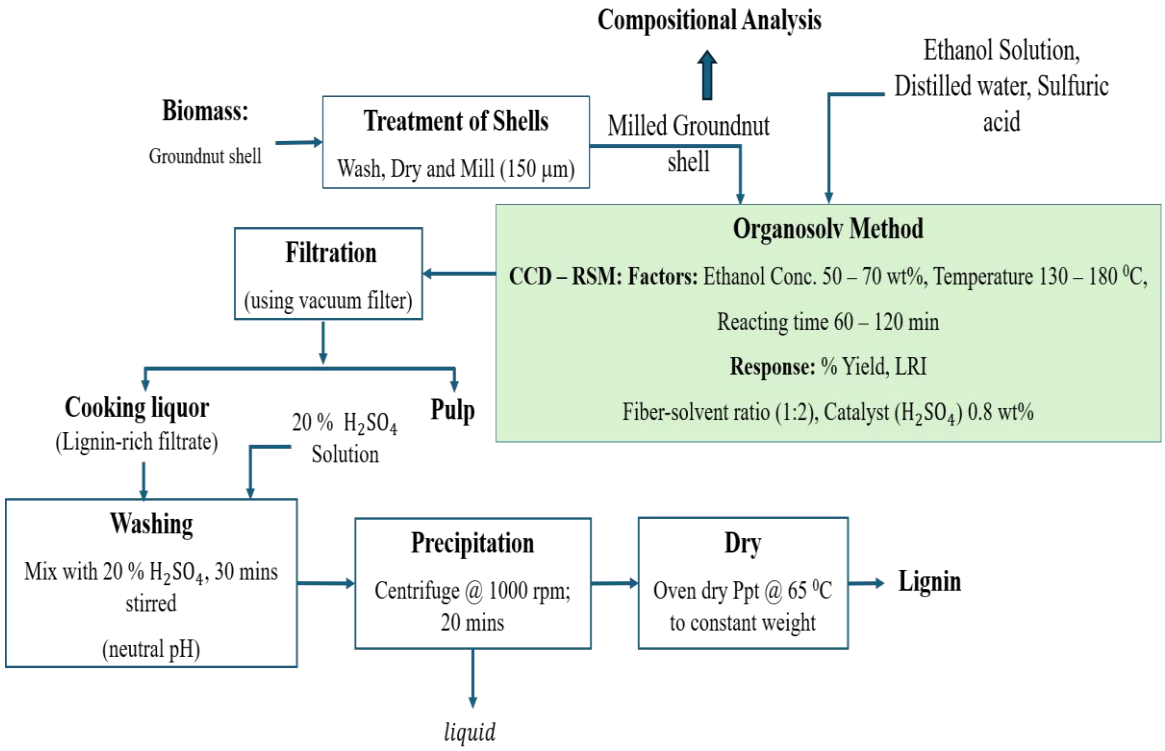

Figure 2: *Experimental Setup of the extraction process*

Groundnut shells (*Arachis hypogaea*) were collected from local oil processing mills in Zaria, Kaduna State, Nigeria. The shells were thoroughly washed with distilled water to remove adhering dirt and impurities, sun dried, and further oven dried at 65 °C (Memmert UN55 Oven, Germany) for 6 h to reduce moisture content. The dried shells were milled using a hammer mill (SIEBTECHNIK GmbH) and sieved to a particle size of 150 µm. All chemicals and reagents as presented in Table 1 were of analytical grade and were used as received without further purification. Ethanol was selected as the extraction solvent based on its reported efficiency in producing high purity organosolv lignin. Sulfuric acid (0.8 wt%) was employed as a mild catalyst in line with previous studies (Farid *et al.*, 2023).

2.1 Experimental Design

The experimental design was developed using Design-Expert software (Version 13.0.1, Stat-Ease Inc., USA) based on three-factor Central Composite Design (CCD). The coded factorial levels (-1 and +1) corresponded to ethanol concentration (50 – 70% v/v), reaction temperature (130 – 180 °C), and reaction time (60 – 120 min). The CCD axial points extended the actual experimental design space to 43 – 77 % ethanol concentration, 113 – 198 °C, and 39 – 141 min reaction time. The response variables were lignin yield (%), and reactivity index. A total of 16 randomized experimental runs were

generated with two-center points, allowing evaluation of linear, interaction, and quadratic effects of the process variables. All experiments were conducted in triplicate, and the average values were reported.

2.2 Extraction of Lignin from Groundnut Shell

Prior to extraction, compositional analysis was carried out on the groundnut shell to ascertain and compare with the existing literature, the percentage of lignin, cellulose, and hemicellulose present in the shell. 100 g of groundnut shell powder of a particle size 150µm was pretreated by washing in hot distilled water at 80 °C to remove soluble extractives and then oven-dried at 65 °C to a constant weight and then transferred into the reactor. Organosolv extraction was carried out using ethanol – water solution (50 – 70% v/v) at a solid-to-liquid ratio of 1:2 (w/v). The solution was added into the batch reactor, and sulfuric acid (0.8 wt%) was then added as a catalyst to enhance cleavage of ether linkages (Farid *et al*., 2023). The lignin extraction was carried outing a closed-sealed, mechanically stirred and temperature-controlled pressure reactor. The reactor head was mechanically secured to the vessel prior to operation to provide a closed reaction environment, then purged with nitrogen for 3 min to minimize oxidative degradation and heated to the desired temperature range (130 – 180 °C) for 60 – 120 min continuously stirred at 800 rpm, in accordance with the CCD matrix. At the end of the reaction time, heating was automatically stopped and the reactor was cooled to below 45 °C before pressure was released through the release valve. The resulting slurry was recovered for lignin separation, vacuum filtered to separate the solid residue from the black liquor. A photograph of the experimental reactor and control system is presented in Figure 3

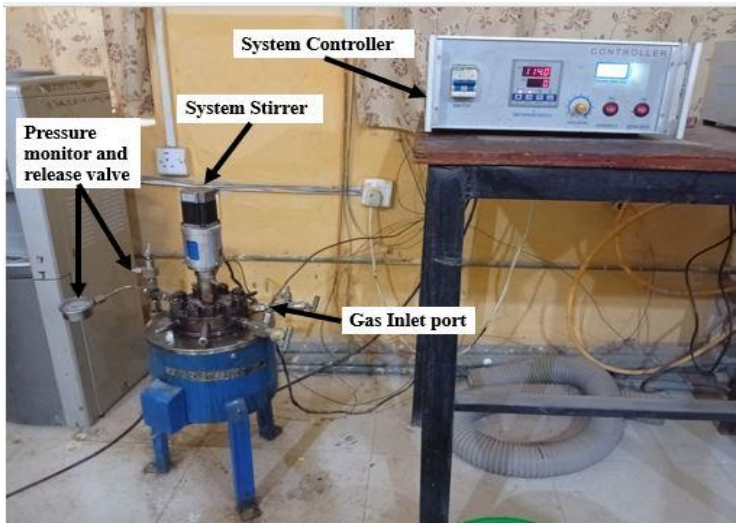

Figure 3: *Reactor and control system setup*

Lignin was recovered from the liquor by dilution with sulfuric acid solution, followed by centrifugation at 1000 rpm to precipitate the lignin fraction. To quench the reaction, the precipitate was washed repeatedly with distilled water until neutral pH (6.5 – 7.5) was achieved and subsequently dried under vacuum at 65 °C to constant mass.

Lignin yield, an important response signifying extraction efficiency which is usually expressed in percentage for the lignin recovered from the biomass (Mao *et al*, 2025; Sandner *et al.*, 2025). This was calculated using equation 1:

$$\text{Yield (\%)} = \frac{W_L}{W_S} \times 100 \qquad (1)$$

where W_L is the dry mass of extracted lignin and W_S is the dry mass of raw groundnut shell.

Lignin reactivity index (LRI) is a measure of chemical reactivity of extracted lignin, revealing the availability of reactive functional groups (Karlsson *et al.*, 2023). LRI was calculated using equation 2.

$$Lignin\ Reactivity\ index\ (LRI) = \frac{A_{\sim 3400}}{A_{\sim 1510}} \quad (2)$$

$$Abundance\ (A) = log\left(\frac{100}{(\%T)}\right) \quad (3)$$

2.3 Functional Group Analysis

The extracted lignin using the optimum extraction parameters was characterized to evaluate the functional groups of both the groundnut shell and lignin through Fourier Transform Infrared Spectroscopy (FTIR).

3. RESULTS AND DISCUSSIONS

3.1 Constituents of Groundnut Shell and Extract

Comparison of the major lignocellulosic components measured for both milled groundnut shell and the extracted lignin are presented in Table 2

Table 2: *Constituents of groundnut shell and extract Lignin*

Component	Groundnut shell (%)	Extract (Lignin)
Lignin	26.97	78.49
Hemicellulose	12.88	2.53
Cellulose	55.24	15.06
Moisture	4.67	3.92
Ash	0.24	0.163

As shown in Table 2, the composition of lignin, hemicellulose, cellulose contained in the groundnut shell are 26.97 %, 12.88 %, and 55.24 % respectively, these are in line with various report on groundnut shell studies. Recent studies confirm that groundnut shell composition varies considerably according to cultivar, geographical origin, maturity, processing and method adopted for analysis. From the work of Almeida-Naranjo *et al.,* (2024), reported 36.2 % lignin, 26.1 % hemicellulose and 19.4 % cellulose, similar trend of 28.4 % lignin, 14.5 % hemicellulose and 47.86 % cellulose was also reported recently by Mousa *et al.,* (2026). In another study, identification was reported for peanut shell to be broadly composed of about 48 % cellulose, 3 % hemicellulose, and 28 % lignin (Zhang *et al.,* 2025). Therefore, 26.97 % lignin, 55. 24 % cellulose, and 12.88 % hemicellulose recorded are within the reported compositional range with a close agreement for lignin and cellulose.

Also, the 78.49 % lignin contained in the extract demonstrates substantial purification but not fully chemically pure lignin due to some fractions of other constituents present, this could be because of the process efficiency. Recent studies also show that groundnut shell is agreeable to effective fractionation, a microwave-assisted diol-deep eutectic solvent (DES) system was reported to have 86.39 % delignification and 91.17 % hemicellulose removal (Xie *et al.,* 2025), while another recent peanut-shell DES study reported 73.22 % lignin removal and 93.05 % hemicellulose removal (Lu *et al.,* 2023). The low ash content in lignin (0.163 %) indicates a low level of inorganic impurities, which makes it a good precursor for adhesive applications because a low inorganic fraction means fewer mineral impurities interfering with subsequent lignin functionalization. Recent studies have similarly associated low-ash, high-purity lignin with greater chemical activity and suitability for lignin-based resin and adhesive synthesis (Ren *et al.,* 2025; Sapenti *et al.,* 2025).

3.2 Lignin Yield from CCD-RSM Optimization

The experimental lignin yields and reactivity obtained under different combinations of ethanol concentration, reaction temperature, and reaction time, as designed by the Central Composite Design (CCD), are presented in Table 3.

Table 3: *Effect of extraction parameters on lignin yield and reactivity index*

Run	Ethanol Conc. (%)	Temperature (°C)	Reaction Time (min)	Yield (%)	LRI
1	60	198	90	63.55	4.11
2	50	180	120	61.06	6.26
3	50	130	60	50.45	5.19
4	50	180	60	61.45	3.98
5	60	155	141	55.23	7.24
6	70	180	120	60.64	6.13
7	60	155	90	54.99	4.45
8	50	130	120	51.24	6.87
9	43	155	90	56.43	5.79
10	77	155	90	53.66	7.14
11	70	130	120	49.78	7.46
12	60	155	39	55.02	4.76
13	70	180	60	58.96	4.47
14	60	155	90	55.2	4.81
15	70	130	60	50.11	6.88
16	60	113	90	47.06	5.96

Lignin yield varied from 47.06 % to 63.55 %, indicating strong dependence on process conditions. The highest experimental yield (63.55 %) was obtained at 60% ethanol, 198 °C, and 90 min. This suggests that moderate solvent polarity combined with elevated temperature enhances lignin solubilisation and cleavage of lignin carbohydrate linkages. A decline in yield at higher temperature (180 °C) and shorter residence time (60 min) indicates possible lignin degradation or condensation reactions under harsh conditions. Conversely, insufficient reaction time reduced extraction efficiency due to incomplete biomass delignification. Similar behaviour has been reported in organosolv systems where temperature and residence time strongly govern lignin depolymerisation kinetics (Xu *et al.*, 2024). Although the maximum experimental yield (63.55 %) was slightly higher than other runs, the amount of ethanol concentration of 60 % may have prevented the excessive lignin degradation effects, as compared to the 50 % concentration used in runs 2 and 4, similar experience was also reported in the work of Sun *et al*. (2023).

More so, the lignin reactivity index (LRI) was also influenced by the extraction temperature, solvent concentration and the extraction time, but the effects were observed to vary with respect to their operating conditions, which is also consistent with the findings reported by Li *et al*. (2024). LRI was considered independently of lignin yield, which represents the quality of lignin recovered. As presented in Table 3, relatively low lignin reactive index of 4.11 was obtained in experimental run 1 at high temperature of 198 ^{0}C, 90 minutes extraction time and 60 % ethanol concentration, indicating that; despite maximizing the lignin recovery, the structural arrangements may have been disrupted by the

severe extraction temperature, thereby reducing the availability of reactive functional groups. Additionally, the influence of reaction time can be observed by comparing Runs 2 and 4, that were investigated under a similar concentration, extraction temperature but different reaction time (120 and 60 min, respectively). This indicates that, the increase in LRI from 3.98 to 6.26, suggests that extending the extraction time beyond 60 minutes did not substantially improve lignin reactivity. Kim *et al*. (2023) also reported similar trends, indicating that prolonged residence time may have altered the chemical structure of the extracted lignin through partial depolymerization and exposure of additional reactive sites, resulting in a higher lignin reactivity index without significantly increasing extraction efficiency.

3.3 Analysis of Variance (ANOVA) and Model Significance

The ANOVA results for the quadratic response surface model of lignin yield are presented in Table 4. The model was statistically significant ($p = 0.0001$), indicating that the selected variables adequately describe lignin yield behaviour within the studied range.

Table 4: *ANOVA results of the independent variable effects on the yield of lignin*

Source	Sum of Squares	Df	Mean Square	F-value	p-value	
Model	348.36	9	38.71	111.72	0.0001	significant
A-% Ethanol	6.44	1	6.44	18.58	0.0050	
B-Temperature	340.62	1	340.62	983.09	0.0001	
C-Reacting Time	0.3222	1	0.3222	0.9298	0.3721	
AB	0.1540	1	0.1540	0.4445	0.5297	
AC	0.1128	1	0.1128	0.3256	0.5890	
BC	0.0861	1	0.0861	0.2485	0.6359	
A^2	0.0280	1	0.0280	0.0807	0.7859	
B^2	0.1109	1	0.1109	0.3200	0.5921	
C^2	0.0638	1	0.0638	0.1841	0.6829	
Residual	2.08	6	0.3465			
Lack of Fit	2.06	5	0.4114	18.66	0.1739	not significant
Pure Error	0.0221	1	0.0221			
Cor Total	350.44	15				

Nevertheless, their inclusion improved overall model predictability and stability, which is consistent with response surface methodology practices (Weremfo *et al*., 2023).

The lack of fit was not significant ($p > 0.05$), confirming that the model adequately fits the experimental data.

The model exhibited strong predictive capability with $R^2 = 0.9941$, indicating that 99.4% of the variability in lignin yield was explained by the model. The adjusted R^2 (0.9852) and predicted R^2 (0.9499) were in reasonable agreement, confirming acceptable model reliability. The adequate precision value of 36.37 further justified the significance of the model, because it is greater than 4. A good correlation between predicted and experimental values was observed (Figure 4), with data points closely distributed along the regression line, confirming that the model reliably predicts lignin yield within the experimental domain

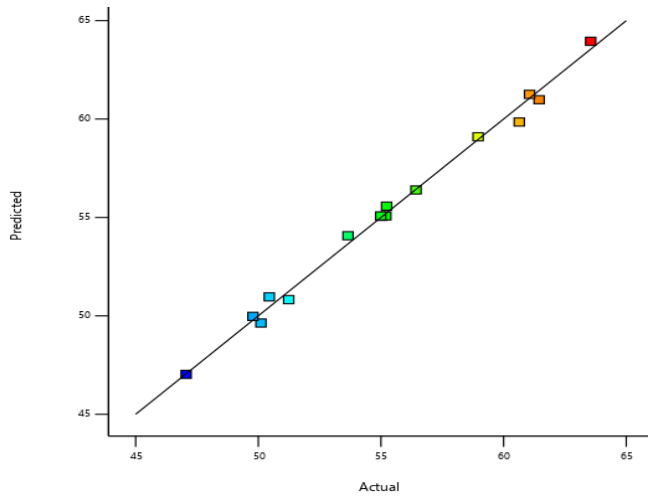

Figure 4: *Relationship between experimental (actual) and predicted data*

Equation 4 depicts the coded model equation generated for the yield which shows the interactions between the independent variables (reaction time and temperature and ethanol concentration) that were investigated.

$$\text{Yield} = 55.08 - 0.6835A + 4.97B + 0.1529C - 0.1387AB + 0.1188AC + 0.1038BC + 0.0543A^2 + 0.1080B^2 + 0.0819C^2 \quad (4)$$

Table 5 presents the ANOVA results of the reactivity index of lignin extraction. As shown in Table 5, the model is significant as the p-value obtained is less than 0.05. The model terms-A, B and C as shown in the Table are also significant as their p-values are less than 0.05.

Table 5: *ANOVA results of the independent variable effects on the lignin RI*

Source	Sum of Squares	df	Mean Square	F-value	p-value	
Model	21.18	9	2.35	75.27	0.0001	significant
A	1.77	1	1.77	56.52	0.0003	
B	5.54	1	5.54	177.21	0.0001	
C	7.87	1	7.87	251.80	0.0001	
AB	0.4608	1	0.4608	14.74	0.0086	
AC	0.3698	1	0.3698	11.83	0.0138	
BC	0.3528	1	0.3528	11.28	0.0152	
A^2	3.90	1	3.90	124.65	0.0001	
B^2	0.2174	1	0.2174	6.95	0.0387	
C^2	2.19	1	2.19	69.89	0.0002	
Residual	0.1876	6	0.0313			
Lack of Fit	0.1228	5	0.0246	0.3790	0.8348	not significant
Pure Error	0.0648	1	0.0648			
Cor Total	21.37	15				

Moreso, the lack of fit with p-value obtained as 0.8387 is not significant as it is greater than 0.05. The model was further subjected to the adequacy test where the R^2 was obtained as 0.9912, with the adjusted R^2 of 0.9781 and predicted R^2 of 0.9424, which 1.0 % and 4.9 % percentage error differences from the R^2 respectively. This was further justified by the value of adequate precision of 25.0126. Figure 5 shows the parity plot of the predicted and experimental variables of the reactivity index. As observed in the Figure, the experimental variables are in close agreement with the predicted variables, which was further justified by the low error difference obtained from the R^2 and the R^2 adjusted values.

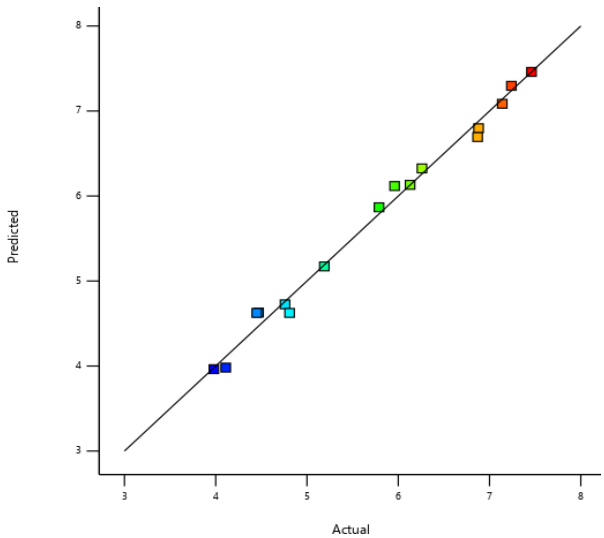

Figure 5: *Parity plot of the predicted and experimental data*

Equation 5 shows the model generated from the statistical analysis carried out. As highlighted in the model, the quadratic regression equation explained the relationship between the reacting time, ethanol concentration, extraction temperature and the lignin reactivity index.

$$\text{LRI Model} = 4.63 + 0.3581A - 0.6343B + 0.7559C - 0.2400AB - 0.2150AC + 0.2100BC + 0.6405A^2 + 0.1512B^2 + 0.4796C^2 \quad (5)$$

3.4 Model Validation and Multi-Response Optimization

The multi-response optimization approach was employed to identify the extraction conditions that simultaneously maximize lignin yield and its reactivity index. The desirability function combines the individual desirability of each response into an overall desirability value ranging from 0 to 1. The optimum condition obtained theoretically are 55 % ethanol concentration, 120 ℃ extraction temperature and 45 min reaction time, with overall desirability of 0.963. This high desirability indicates that the selected operating condition provides favourable response predicted at 87.55 % lignin yield and 5.17 LRI as presented in Table 6.

Table 6: The predicted and validated of the yield and lignin reactivity index

	Ethanol Conc	Temperature	Reaction Time	Yield	LRI
Theorical values	55	`120	45	87.55	5.17
Validated values	55	120	45	86.28	5.25
% Error				1.45	1.52

As shown in Table 6, the validated values at the same operating conditions produced a lignin yield of 87.55 % and an LRI of 5.25, which are in close agreement with the predicted values with their respective error differences of 1.45 % and 1.52 %. These indicates a high level of accuracy in the prediction model, suggesting that the optimization model used to predict the extraction yield and the lignin refractive index values are quite reliable, with minimal deviations observed between the predicted and validated values. These trends, when compared with the works of Li *et al*. (2024); Samson *et al*. (2022); Lannucci and Willows, (2022); Higuchi *et al*. (2021) follow similar percentage deviation.

3.5 FTIR Analysis

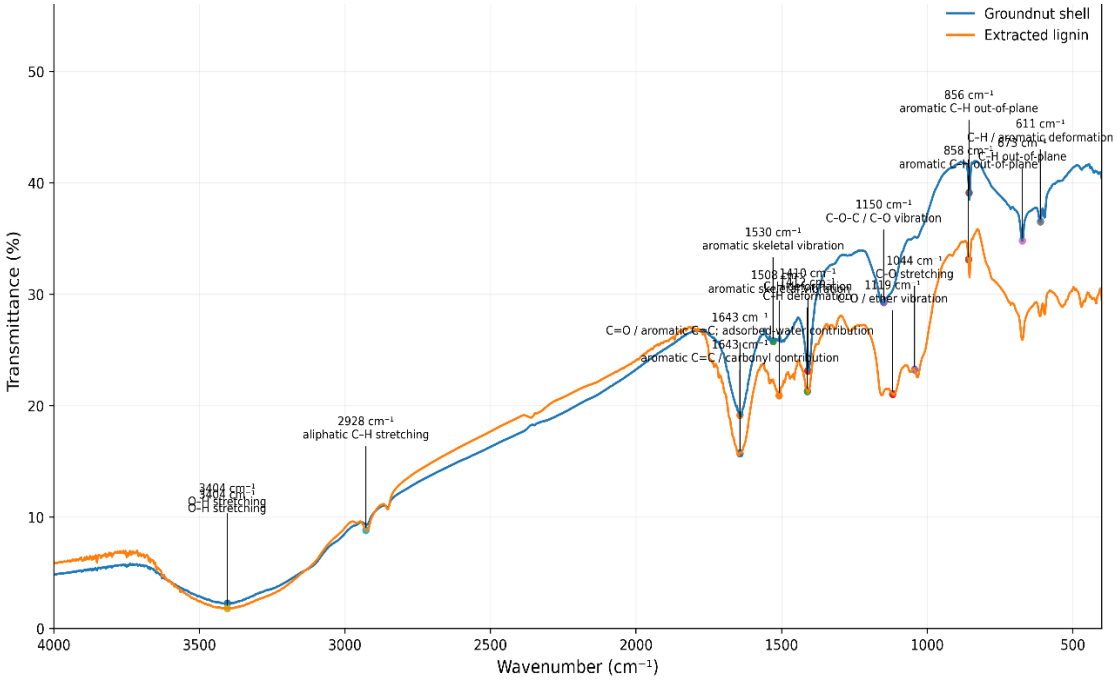

Figure 6: The FTIR spectra of Groundnut Shell and Lignin

The FTIR spectra (Figure 6) provide comparison on functional groups of both groundnut shell and lignin at an optimum extraction condition as presented in Table 6. Both spectra exhibit a broad absorption centred around 3404 cm^{-1}, attributable primarily to O-H stretching of phenolic and aliphatic hydroxyl groups. The presence of this band in the extracted lignin is highly significance because hydroxyl groups are abundant in lignin. Its presence indicates that a substantial proportion of lignin hydroxyl functionalities was retained after undergoing the extraction process, suggesting that the organosolv extraction conditions did not cause extensive degradation of the functional groups. This preservation is important because the hydroxyl groups contribute to the chemical reactivity of lignin and provide active sites for subsequent functionalization. Recent work on peanut/groundnut shell also reported similar trends with bands around 3426 cm^{-1} and 3335 cm^{-1}, these were also attributed to hydroxyl groups associated with lignin, cellulose and moisture (Mousa *et al.*, 2026; Arizpe-Diaz *et al.*, 2025; Almeida-Naranjo-Diaz *et al.*, 2024)

Other functional groups aliphatic C-H with band 2928 cm^{-1}, Bands around 1530 cm^{-1} and 1508 – 1529 cm^{-1} reflects oxygen containing and aromatic skeletal vibrations characteristic of lignin. Similar aromatic bands around 1620, 1509 and 1422 cm^{-1} have been reported for peanut shells (Petraglia, *et al.*, 2024) C-O/ether vibrations represent band 1044 – 1119 cm^{-1}. This pattern agrees with recent groundnut shell FTIR studies which identifies hydroxyl, C-H, aromatic lignin and C-O containing bands as characteristic components of the shell (Mousa *et al.*, 2026; Almeida-Naranjo-Diaz *et al.*, 2024)

The lower wavenumber bands at 856 – 858, 673 and 611 cm^{-1} occur in the aromatic region and are consistent with aromatic C–H ring deformation vibrations. Comparable low-wavenumber bands have been reported for lignocellulosic and peanut shell materials (Arizpe-Diaz *et al.*, 2025; Jadhav, *et al.*, 2022). These distinctive peaks provide strong evidence of lignin enrichment and preservation of characteristic functional groups after extraction process.

4. CONCLUSIONS

This study demonstrated the successful extraction of lignin from groundnut shell using an organosolv process integrated with response surface methodology (CCD-RSM). The optimized predicted conditions were 55 % ethanol concentration, 120 °C, and 45 min, having lignin recovery of 87.55 % and 5.17 LRI with a desirability value of 0.963. Experimental validation confirmed the reliability of the model, indicating strong agreement between predicted and observed responses.

The novelty of this work lies in the combined optimisation of organosolv extraction of groundnut shell lignin, considering the quality and quantity as a leading tool to determine the best extraction parameters. FTIR spectral changes relative to the raw groundnut shell confirmed the fractionation of the lignocellulosic matrix and recovery of a lignin-rich fraction.

Overall, the study establishes groundnut shell as a viable low-cost lignocellulosic feedstock for sustainable lignin-based material development and highlights its potential in eco-friendly adhesive formulations. Future work should focus on modification of the structural property and evaluating of the mechanical bonding performance adhesive system.

5. REFERENCE

Adebayo, A. S. & Adeola, O. M. (2023). Chemical composition and valorization potential of groundnut shell as a lignocellulosic biomass. *Journal of Biomass Conversion and Biorefinery, 13*(6), 457 – 468. https://doi.org/10.1007/s13399-023-02784-3

Ait Benhamou, A., Abid, L., Calvez, L., Clouteir, A., Nejad, M., Stevanovic, T., & Landry, V. (2025) Advances in lignin chemistry, bonding performance, and formaldehyde emission reduction in lignin-based urea-formaldehyde adhesives: A review. *ChemSusChem, 18(16)* e202500491. https://doi.org/10.1002/cssc.202500491

Alam, M. M., Greco, A., Rajabimashhadi, Z., and Corcione, E. C. (2024) Efficient and environmentally friendly techniques for extracting lignin from lignocellulose biomass and subsequent uses: A review. *Cleaner Materials 13*,100253 https://doi.org/10.1016/j.clema.2024.100253

Almeida-Naranjo-Diaz, C., Frustos, M., Guerrero, V. H., and Villamar-Ayala, C. (2024) Characterization and performance of peanut shells in caffeine and triclosan removal in batch and fixed-bed column tests. *Molecules 29(12)* 2923.

https://doi.org/10.3390/molecules29122923

Arizpe-Diaz, D. O., Gama-lara, S. A., Roa-Morales. G., Vilchis-Nestor, A., Parada-Flores, A., and Balderas-Hernandez, P. (2025) Evaluation of cadmium removal in an aqueous solution by biosorption in a batch system with banana, peanut, and orange husks. *Environment 12(4)* 97. https://doi.org/10.3390/environments12040097

Brienza, F., Cannella, D., Montesdeoca, D., Cybulska, I., and Debecker, D. P. (2024) A guide to lignin valorization in biorefineries: traditional, recent, and forthcoming approaches to convert raw lignocellulose into valuable materials and chemicals. *RSC Sustainability 2(1)* 37 – 90 https://doi.org/10.1039/d3su00140

Farid, M. A. A., Ibrahim, I., Lease, J., Tsubota, T., and Andou, Y. (2023) Effect of solvent and acid catalyst selection on lignin recovery and purity in autoclave-assisted organosolv extraction. *Bioresource Technology Reports 24*, 101622.

https://doi.org/10.1016/j.biteb.2023.101622

Gerber, S., and Roberts, S. B. (2024) Peanut hulls, an underutilized nutritious culinary ingredient: Valorizing food waste for global food, health, and farm economies-A narrative review. *Frontiers in Nutrition, 11*. 1453315

Higuchi, R., Yokozeki, T., Nagashima, T. and Aoki, T. (2021). Evaluation of mechanical properties of noncircular carbon fibre reinforced plastics by using XFEM-based computational micromechanics. *Composites Part A: Applied Science and Manufacturing 126,* 105556. https://doi.org/10.1016/j.compositesa.2021.105556.

Jadhav, B., Roy, R., Rahman, M. S., and Raynie, D. E. (2022) Extraction and depolymerization of lignin from pine sawdust and pistachio shells. *Biomass 2,* 348 – 357. https://doi.org/10.3390/biomass2040023

Karlsson, M., Romson, J., Elder, T., Eklund, A., & Lawoko, M. (2023) Lignin structure and reactivity in the organosolv process studied by NMR spectroscopy, mass spectrometry and density functional theory. *Biomacromolecules 24(5),* 2314 – 2326. https://doi.org/10.1021/acs.biomac.3c00186

Kim, T., Park, J., Lee, S., Choi, Y. and Kim, K. (2023). Relationship between extraction severity and structural characteristics of organosolv lignin. *ACS Sustainable Chemistry & Engineering 11*, 12361. https://doi.org/10.1021/acssuschemeng.3c0289.

Lannucci, L., and Willows, M. (2022). Validation of optimized CFRP structures using fatigue and digital image correlation techniques. *Composite Structures*, 234(2020) 33 – 41. https://doi.org/10.1016/j.compstruct.2022.111710.

Li, H., Chen, R., & Sun, Q. (2024) Effect of solvent systems on lignin recovery and purity. *Industrial Crops and Products,193*, 1162 – 1177

https://doi.org/10.1016/j.indcrop.2018.05.060

Liu, Y., Wang, J., & Chen, X. (2023). Structural diversity and reactivity of lignin from agricultural residues. *Industrial Crops and Products, 199*, 951 – 966.

https://doi.org/10.1016/j.indcrop.2023.116951

Lu, A., Xiaojie, Y., Ji, Q., Chen, L., Yagoub, A. E., Olugbenga, F., and Zhou, C. (2023) Preparation and Characterization of lignin-containing cellulose nanocrystals from peanut shells using a deep eutectic solvent containing lignin-derived phenol. *Industrial crops and products 195*, 116415. https://doi.org/10.1016/j.indcrop.2023.116415

Mateo, S., Fabbrizi, G., & Moya, A. J. (2025). Lignin from plant-based agro-industrial biowastes: From extraction to sustainable applications. *Polymers, 17*(7), 952. https://doi.org/10.3390/polym17070952

Mao, T., Tarhanli, I., Owen, G., Lee, C. S., (2025) Comparisons of alkali, organosolv and deep eutectic solvent pre-treatments on the physiochemical changes and lignin recovery of oak and pine wood. *Industrial crops and products, 226* 120614. https://doi.org/10.1016/j.indcrop.2025.120614.

Mousa, S., Almithn, A., Dubdub, I., Aishehab, A., and Ismail, M. A. (2026) Assessing the bioenergy potential of peanut shell waste: High heating rate combustion behavior and thermodynamic analysis. *Polymer 18(5)*, 560. https://doi.org/10.3390/polym18050560

Ogunkunle, O. & Olusanya, M. O. (2024). Biotechnological trends and optimization of *Arachis hypogaea* residues valorization: A bibliometric analysis and comprehensive review. *Bioresource Technology 414*, 131585.

https://doi.org/10.1016/j.biortech.2024.131585

Paez, J., & Fatehi, P. (2025). Incorporation of lignin into adhesives: A review. *Green Chemistry, 27*, 12499 – 12537. https://doi.org/10.1039/D5GC02998H

Petraglia, T., Latronico, T., Pepe, A., Crescenzi, A., Liuzzi, G. M., and Rossano, R. (2024) Increased antioxidant performance of lignin by biodegradation obtained from an extract of the mushroom *Pleurotus eryngii*. *Molecules 29(23)*, 5575.

https://doi.org/10.3390/molecules29235575

Ren, X., Zhang, X., Zhang, Q., Chen, L., Liu, J. and Ma, L. (2025) Preparation and characterization of lignin-phenol-formaldehyde resins using the lignin derived from various biorefinery processes. *Polymer 335*, 128788. https://doi.org/10.1016/j.polymer.2025.128788

Ruwoldt, J., Arzola, X., & Schieder, D. (2024). Interfacial adsorption of oil-soluble kraft lignin and lauric/stearic esterified lignins. *Colloids and Surfaces A: Langmuir 40(10)*, 5409 – 5419. https://doi.org/10.1016/j.colsurfa.2024.132881

Samson, J. S., Kiruthika, M. and Abhra, P. R., Makarand, U. D, Venugopal, N. E. and Gnanasekaran, S. (2022). Optimisation of process parameters using response surface methodology: A review. *Materials Today: Proceedings 6(466)*. 2 – 18

https://doi.org/10.1016/j.matpr.2020.06.466.

Sandner, S., and Kienberger, M. (2025) Tuning organosolv lignin properties through the cooking process: A meta-analysis. *Industrial crops & products 232*, 121247. https://doi.org/10.1016/j.indcorp.2025.121247

Sapenti, A. D., Sari, R. K., Hermawan, D., Antow, P., Dudeva, V., and Lubis, M. A. R. (2025) Formaldehyde-free plywood composites bonded with polyurethane adhesive derived from lignin-polyvinyl alcohol-based polyol. *Discover Sustainability 6*, 122. https://doi.org/10.1007/s43621-025-00880-z

Sun, S., Wen, J., Ma, M., Li, M., Sun, R.. and Jones, G. (2023). Influence of pretreatment severity on organosolv lignin extraction and structural evolution. *Bioresource Technology, 361*, 127719 – 127731. https://doi.org/10.1016/j.biortech.2023.127719.

Tanis, M. H., Wallberg, O., Galbe, M., and Al-Rudainy, B. (2024) Lignin Extraction by using two step fractionations: A review. *Molecules 29*, 98.

https://doi.org/10.3390/molecules29010098

Weremfo, A., Abassah-Oppong, S., Adully, F., Dabie, K., and Seidu-Larry, S. (2023) Response surface methodology as a tool to optimize the extraction of bioactive compounds from plant sources. *Journal of the science of food and agriculture, 103(1)* 26 – 36. http://doi.org/10.1002/jsfa.12121

Xie, T., Li, C., Ren, M., Ji, Q. and Zhou, C. (2025) Microwave-assitsed diol DES system enables efficient biomass fractionation and lignin grafting stabilization from peanut shells via a lignin-first strategy. *International journal of biological macromolecules 330(3)* 148154.

https://doi.org/10.1016/j.ijbiomac.2025.148154

Xu, Z., Li, X., & Chen, L. (2024). Organosolv fractionation of nutshell biomass: Optimization and structural analysis of recovered lignin. *ACS Sustainable Chemistry & Engineering, 12*(15), 5862–5873. https://doi.org/10.1021/acssuschemeng.4c00791

Zhang, Y., Li, H., Wang, Y., Liu, Z., Chen, X., and Huang, C. (2024). Optimization of ethanol-organosolv pretreatment for efficient lignin extraction and biomass fractionation. *Fuel, 367*, 131458 – 131573. https://doi.org/10.1016/j.fuel.2024.131458

International Conference on Engineering Innovation for Sustainable Development (ICESID 2026)
Faculty of Engineering, Ahmadu Bello University Zaria · 8–10 September 2026

PALM FRUIT BUNCH ASH AS A PARTIAL CEMENT REPLACEMENT IN SANDCRETE BLOCK

Elijah Adaofoyi Adache[1,*], Theophilus Yisa Tsado[1], James Olayemi James[1]
[1]*Federal University of Technology Minna*
Email: adacheeamen74@st.futminna.edu.ng*, ty.tsado@futminna.edu.ng, jamesolayemi@futminna.edu.ng
***Corresponding author**: Elijah Adaofoyi Adache
DOI: https://doi.org/10.67203/sp.ICESID.2026

ABSTRACT
This empirical study investigates the potential of Oil Palm Empty Fruit Bunch Ash (PFBA) as a partial cementitious replacement in sandcrete block production. The material was produced via a systematic pre-burning process to convert empty fruit bunches into charcoal, followed by controlled calcination to obtain reactive pozzolanic ash. Physical characterization, including specific gravity and fineness (sieve size 45µm), was conducted per BS 1377:1990 and EN 196-6 standards. Mechanical performance was evaluated by substituting Ordinary Portland Cement (OPC) with PFBA at 0%, 5%, 10%, 15%, and 20% levels. Results indicate that while strength development is sustained over a 28-day curing period, increasing PFBA content correlates with reduced compressive strength and density, alongside increased water absorption. The study identifies 10% as the optimal replacement threshold, achieving a 28-day compressive strength of 3.5N/mm², which complies with the minimum requirements of the Nigerian Industrial Standard (NIS 978:2017). Furthermore, the research evaluates technical risks related to chloride content, environmental benefits of a low-emission approach, and the economic viability of controlled incineration. The findings conclude that with rigorous quality control and chemical pre-treatment, PFBA offers a sustainable, eco-friendly solution for masonry production in the Nigerian construction industry.

Keywords: *Sustainable construction; Oil Palm Empty Fruit Bunch; Sandcrete blocks; Cement replacement; Material characterization*

1. INTRODUCTION

The global construction industry is more and more looking for viable replacement to Ordinary Portland Cement (OPC) owing to its high carbon footprint and increasing cost. This cement industry is one among the largest industrial contributors to climate change accounting for approximately 7% to 8% of global CO_2 emissions. About 60% of these emissions happens in the process of the chemical decomposition of limestone ($CaCO_3$) into lime (CaO) which releases CO_2 as a major by product, the remaining 40% comes from the combustion of fossil fuels to heat kilns to temperatures exceeding 1400°C (Ripley et al., 2025).

In addition to that, in locations like Nigeria and Malaysia where palm oil production is higher, the disposal of agricultural waste like Empty Oil Palm Fruit Bunches (EOPFB) presents a significant environmental problem, recent findings is looking toward how these wastes can be processed into Empty Fruit Bunch Ash (EFBA) or Palm Oil Fuel Ash (POFA) through controlled burning to serve as supplementary cementitious materials (SCMs) in masonry units like sandcrete blocks (Yusuf & Hamza, 2023). The high cost of cement has made affordable housing a major challenge in developing nations as also the careless dumping and burning of oil palm fruit bunches lead to land pollution and greenhouse gas emissions lately findings have moved beyond just identifying agricultural waste, they are now looking on the mechanical characterization of combined composites (Sulaiman etal, 2020).

There is a major trend to move from just waste management to circular models which recent studies are developing means to measure the circularity of major materials such as cement, steel, and wood. This study investigates whether the partial replacement of cement with PFBA can produce sandcrete blocks that meet standard compressive strength requirements while offering a more ecofriendly disposal method for palm oil mill residues.

Chemically PFBA contains essential oxides such as silica (SiO_2), alumina ($Al2O_3$), and calcium oxide (CaO), which categorize it as a pozzolan. When mixed with cement and water, these oxides react with the calcium hydroxide byproduct of cement hydration to form additional Calcium Silicate Hydrate

(C-S-H) gel, which is the primary binder responsible for strength in concrete and sandcrete, recent studies suggest that replacement levels between 10% and 20% are optimal for maintaining structural integrity while reducing material costs (Abe & Amu, 2022).

Given the abundance of oil palm residues in Nigeria and other tropical economies, coupled with the pressing demand for affordable, environmentally sustainable building materials, a systematic investigation into the effect of partial replacement of cement with oil palm empty fruit bunch ash in sandcrete block production is both timely and policy-relevant. Such a study can provide empirical data on the influence of EFB ash on key engineering properties of sandcrete blocks such as compressive strength, density, water absorption, and durability at different replacement levels. The findings will contribute to the development of locally appropriate guidelines for incorporating EFB ash in sandcrete production, thereby supporting waste-to- wealth initiatives, reducing environmental pollution, and potentially lowering the cost of masonry units in Nigeria and similar contexts (Ibrahim etal, 2021).

Key engineering properties of sandcrete blocks incorporating PFB ash such as compressive strength, bulk density, water absorption and durability have not been systematically characterized at varying replacement levels. In addition, the influence of ash production parameters such as burning temperature, fineness and local mix practices on block performance is not yet well established, leaving block makers without clear guidance on optimal replacement percentages or performance trade-offs, this lack of context specific data constitutes a critical research gap and without robust experimental evidence on sandcrete blocks produced with partial replacement of cement by PFBA, policymakers, standards bodies and small to medium scale sandcrete producers cannot make informed decisions about its technical feasibility, economic benefits or environmental advantages. As a result, an abundant agricultural residue with demonstrated pozzolanic potential remains largely unused in sandcrete block production, and opportunities for cost reduction, waste valorizations and emissions mitigation are missed.

Accordingly, this study seeks to investigate the effect of partial replacement of cement with oil palm empty fruit bunch ash on the properties of sandcrete blocks, with the aim of identifying replacement levels that satisfy engineering performance requirements while contributing to more sustainable and affordable construction in Nigeria.

Palm fruit bunch (PFB) originates from the palm oil milling process after sterilization and fruit stripping, the fresh fruit bunch (FFB) leaves behind the empty cluster known as the empty fruit bunch (EFB) whereby for every tone of FFB processed, around 20–23% of the mass becomes PFB, making it one of the largest solid residues from palm oil production (Yusoff et al., 2023). As palm oil production expanded, these residues grew into a significant waste management challenge, especially in Malaysia, Indonesia, and Nigeria, from the late 1990s into the 21st century, increasing environmental concerns and sustainability demands pushed researchers and industries to explore beneficial uses of PFB. Its high lignocellulosic composition, availability, and low cost made it attractive for Bioenergy production, Organic fertilizer, Composite materials, Soil stabilization and Pozzolanic ash for construction materials. (Sulaiman et al., 2020).

Recent studies highlight its potential as a supplementary cementitious material (SCM) when converted into ash under controlled burning conditions due to its high silica content. (Nwosu and Adeyemi 2025) conducted thermal conductivity tests on sandcretec blocks in tropical climates. They found that the porous nature of the ash reduces the thermal mass of the block, leading to a reduction in indoor heat gain. Chemically, PFB is composed mainly of cellulose, hemicellulose and lignin, with typical ranges of about 37–63% cellulose, 14–37% hemicellulose and 17–32% lignin, depending on variety and processing conditions (Umar and Bello, 2025). Amorphous Silica Content (SiO2): The primary reactive component is amorphous silica, PFBA incinerated at a controlled temperature of 600°C contains between 55% and 65% SiO2, which is essential for the pozzolanic reaction. (Nwosu and Adeyemi 2025), research indicate that the highly alkaline nature of the ash helps maintain the passivity of the cement environment, which is beneficial for the long-term durability of the masonry units. (Onyechere 2026), Major oxides example from (Nwaiwu et al.2023): $SiO_2 \approx 18\%$, $Al_2O_3 \approx 46.8\%$, $Fe_2O_3 \approx 2.5\%$, $K_2O \approx 20.4\%$, $CaO \approx 4.2\%$, with minor TiO_2, MnO, ZnO and trace elements. In some boiler ashes, the combined ($SiO_2 + Al_2O_3 + Fe_2O_3$) is initially as low as ~15.7% with high carbon (~34%), meaning fresh ash often does not meet ASTM C618 pozzolan thresholds until it is further processed or re-burnt, ash from OPEFB pellets used as biomass fuel shows high K_2O and CaO contents (e.g., ~24%

SiO_2, ~46% CaO, significant K_2O), confirming its basic and alkali-rich character. (Okeke et al. 2025), Recent characterization studies show that the pozzolanic quality of oil palm empty fruit bunch ash (OPEFBA) is highly dependent on its production conditions. (Nwaiwu et al. 2023), for example, reported SiO_2, Al_2O_3 and Fe_2O_3 contents of 18.0%, 46.8% and 2.5% respectively, giving a combined pozzolanic oxide content of about 67.3%, which satisfies the ASTM C618 requirement for Class C but falls slightly below the 70% threshold for Class F pozzolans. In contrast, recent work on PFB ash for silica extraction has reported silica contents ranging from 25% to about 60% under optimal calcination regimes, the combined pozzolanic oxides would comfortably exceed 70%. (Nelson et al. 2023). The pozzolanic activity of PFBA has been confirmed through several studies, indicating that it can enhance compressive strength, workability, and water retention of sandcrete blocks (Suriani et al, 2021).

Studies demonstrate that replacing 10–30% of Portland cement with finely ground, heat-treated EFB ash can maintain or even improve compressive strength at medium to long curing ages, particularly in high-performance concrete. The fineness of the ash is another critical factor, finely ground PFBA improves packing density, reduces voids and enhances strength, whereas coarse ash increases porosity and water demand (Eziefula et al., 2025). According to (Onyechere et al. 2026), the average compressive strength decreases as the PFBA content increases, the maximum compressive strength of the concrete is achieved at 28 days of curing. While the 10% PFBA content is optimum content to achieve a balance between strength and workability (Nwaiwu et al. 2023), and replacing up to 20% of cement with PFBA improved the compressive strength of sandcrete bricks compared to conventional bricks. Their findings suggest that the incorporation of PFBA could effectively reduce the need for Portland cement, thereby lowering associated carbon emissions and replacing more than 30% of cement with PFBA led to a reduction in compressive strength.

PFBA contributes to lower permeability, which translates to improved resistance to chemical attacks and its incorporation of also reduces the carbon footprint associated with block production, aligning with sustainable construction practices and waste management strategies (Ibrahim et al 2021) further confirms this by showing improvements in the durability of concrete mixes containing PFBA when exposed to aggressive environments. Using Palm Fruit Bunch as a partial replacement of cement helps reduce agricultural waste, contributing to environmental conservation (Ibrahim et al 2025).

Moreover, research has established standards for the use of other pozzolanic materials, but similar frameworks for PFBA are still needed. (Suriani et al., 2021) emphasize the importance of developing standardized methods to test the performance of PFBA in construction materials. This gap exemplifies the necessity of further research in order to define best practices for incorporation into industry standards.

Equally important are the burning conditions under which the ash is produced, as controlled combustion at moderate temperatures (600–800 °C) enhances reactive silica formation, while uncontrolled burning increases carbon content and reduces strength contribution (Saldanha & Mallmann 2025). Together, these factors ash chemistry, burning regime, fineness, replacement level, mix/workability control and curing age determine whether PFBA enhances or diminishes the engineering performance of sandcrete blocks.

The use of Oil Palm Empty Fruit Bunch Ash (PFB ash) as a partial replacement for cement in sandcrete block production offers several environmental, economic, and technical advantages and replacing even a small proportion with agricultural waste ash directly lowers the carbon footprint of sandcrete and concrete production. Economically, PFB ash reduces the overall cost of sandcrete production. Cement constitutes the most expensive component in sandcrete blocks, and replacing even 10–15% with locally available PFB ash leads to substantial savings. (Suriani et al., 2021). An additional advantage is improved resource efficiency and waste management, this integrated waste-to-resource approach contributes to cleaner production practices and enhances community-level sustainability (Nwaiwu et al. 2022). Overall, research trends consistently show that PFB ash when processed correctly and used within optimal replacement percentages supports sustainable, cost-effective, and durable sandcrete block production while reducing environmental impacts.

This study will focus on palm fruit bunch (PFB) and to investigate the possibility of using the ash produced from PFB as a partial substitute for cement in sandcrete block production in order to provide an economic and proper way of disposal for palm fruit bunch. In this regard the pozzolanic activity of palm fruit bunch ash (PFBA) in the cement hydration will be investigated, as well as the oxide compositions of the ash and temperature of combustion of palm fruit bunch into ash, Therefor the

primary objectives of this study is to conduct laboratory tests on the Oil Palm Empty Fruit Bunch (OPEFB) ash.

2 METHODOLOGY

Ordinary Portland cement (OPC) of strength 42.5N according to BS EN 197-1 (2011) with a Specific Gravity (SG) of 3.14 obtained from local retailer was used as binder in this work. River sand from a local stream in life camp in Abuja was used as fine aggregate with specific gravity of 2.65 and bulk density of 1605.65kg/m³, Sieve analysis on the fine aggregates was conducted in accordance with ASTM C136 - 06 (2009) procedure after washing and air drying of the samples. The sand complies with grading requirements of ASTM C33 (ACI E-701, 2007), ensuring appropriate grain size distribution for optimal workability and cohesion in sandcrete block.

Palm fruit bunch (PFB) which is gotten from oil palm tree (Elaeis guineensis) was collected by gathering the raw empty bunches after the fruits of the palm tree were removed from a local palm oil mill in Agbaha Otukpa in Ogbadibo Benue state, Nigeria, the bunch was further shredded and sun dried to remove it moisture. After drying, a controlled pyrolysis/carbonization to turn the material into charcoal was performed and the charcoal was further blended making it easier to handle for the final calcination stage. In the laboratory at Nigeria Building and Road Research Institute (NBRRI) the blended charcoal was filled into the muffle furnace for control combustion where the final calcination was carried out, temperature of 751°C was recorded at when the organic carbon was completely burnt off leaving a clean greyish ash.

The furnace was allowed to cooled, the ash was sieved through a 45µm sieve to obtain the finer ash as cement, the sample was further analyzed using X-ray fluorescence (XRF) to obtain it element and composition of oxide for suitability of use as cement replacement. The resultant PFBA used for this work had specific gravity of 2.5 and bulk density of 260.54kg/m^3. Potable water obtained from Nigeria Building and Road Research Institute NBRRI Abuja. A cement-to-sand ratio of 1:6 was adopted, palm fruit bunch ash (PFBA) was introduced as a partial cement replacement at one control and four varying replacement levels of 0%, 5%, 10%, 15%, and 20%. A total of 12 blocks were produced for each replacement level, for mechanical testing, triplicate specimens (n = 3) were crushed at each of the four designated curing ages (7, 14, 21, and 28 days) and the remaining 3 blocks per each replacement level were reserved for non-destructive physical evaluations, including water absorption testing, density determination, and dimensional tolerance checks prior to mechanical testing. Experimental values are presented as the mean ± standard deviation (Mean ±SD). Statistical variability across replacement levels (0%, 5%, 10%, 15%, and 20%) was assessed using one-way Analysis of Variance (ANOVA) at a 95% confidence level ($\alpha = 0.05$) to confirm the statistical significance of observed trends, that is three sandcrete blocks for each replacement percentage and the control were crushed to obtain the mechanical strength tests (compressive strength) at 7, 14, 21, and 28 days as well as water absorption.

Palm fruit bunch ash was incorporated at replacement levels of 0, 5, 10, 15, and 20% by weight of binder in a ratio of 1:6. The mix proportions for concrete specimen are presented in table 1 as well as the batch quantities used for each specimen.

Table 1: *Mix proportioning of aggregates in sandcrete block production*

Mix	PFBA Replacement (%)	Ash (Kg)	Cement (kg)	FA (kg)	W/C Ratio	Water (kg)
1	0	0	4.5302	27.1812	0.40	1.8120
2	5	0.2265	4.3036	27.1812	0.50	2.1518
3	10	0.4530	4.0772	27.1812	0.54	2.2016
4	15	0.6795	3.8507	27.1812	0.59	2.2719
5	20	0.9060	3.6242	27.1812	0.63	2.2832
Total		2.265	20.386	135.906		10.721

Note 1: The 'Total' row represents the cumulative sum of quantities across all mix proportions (Mix 1 to Mix 5), including the control batch (0% replacement).

Note 2: The sandcrete mix was proportioned using a target binder-to-aggregate mass ratio of 1:6 (M_{binder} : M_{FA}), that is Total binder mass (M_{binder}= M_{Cement} + M_{Ash}) was fixed at 2.265+20.386=22.651kg, paired with 135.906kg, ensuring that the overall binder-to-fine aggregate ratio remained strictly constant at 1:6.00 (22.651/ 135.906= 6.00) regarding the percentage of OPC replaced by PFBA

3 RESULTS AND FINDINGS

The quantitative oxide analysis of the palm fruit bunch ash (PFBA) results as presented in table 2 indicate that the oxide composition of the palm fruit bunch ash satisfies Class F pozzolan requirement specified in ASTM C-618 for good pozzolans as the sum of SiO2+Al2O3 +Fe2O3 is at least 70% and satisfies the minimum ≥ 70% requirement (ASTM C618-19). The analysis identified an elevated chloride content of 4.90% which is anomalously higher than typical literature baselines of 0.20%–1.50% reported for palm-based biomass ashes. The observed variance in oxide composition compared to the values reported by Nwaiwu et al. (2023) is primarily attributable to differences in biomass provenance, processing parameters, and soil chemistry, because this concentration exceeds standard durability limits of 0.1%–0.4% by weight of binder unwashed EPFBA with this chemical profile is restricted exclusively to non-reinforced masonry applications, such as sandcrete partition blocks, to eliminate steel rebar corrosion risks. This result suggests the difference in ash source, the high iron of 22% and aluminum content of 16% suggests significant potential for contributing to the early and long-term strength of the sandcrete matrix. The presence of high alkali and chloride levels requires specific structural consideration: The potassium content of 12.03% in EFBA is relatively high compared to traditional coal fly ash and this will contribute to the setting time or hydration which may be beneficial for fast demolding process of the blocks this is confirms by Umar and Bello (2025). The primary risk is the presence of chlorine of 4.9% which is the primary agent of corrosion should not be used in reinforced concrete elements (like beams or columns) but does not pose a structural threat to the block itself.

Table 2: *Chemical Composition of Palm Fruit Bunch Ash*

Compound	**Conc Unit (m/m%)**	**Element**	**Conc Unit (m/m%)**
SiO_2	32.0300	Si	21.3500
Fe_2O_3	22.3300	Fe	14..8700
Al_2O_3	16.0190	Al	10.25000
K_2O	12.0260	K	8.02000
CaO	5.15000	Ca	4.25000
Cl	4.90000	Cl	4.20000
MgO	1.83000	Mg	1.21000
P_2O_5	1.32000	P	0.80000
SO_3	1.20000	S	0.8000

$SiO_2 + Al_2O_3 + Fe_2O_3 = 70.379$

The bulk density of Palm Fruit Bunch Ash (PFBA) results as shown in table 3 indicates a low average bulk density of 260.54kg/m^3 contributes a substantial impact on the physical and mechanical properties of the resulting mortar and concrete composites. During the mixing phase, it was observed that the high porosity of the ash increased the water demand to maintain the required workability. Furthermore, the partial replacement of Portland cement with this low-density material is expected to facilitate a significant reduction in the bulk density of the hardened block, a property that is highly

advantageous for lightweight structural applications. Although the initial compressive strength was lower in comparison to the control mix, the pozzolanic activity of the EPFBA is anticipated to contribute to long-term strength development through the strengthening of the aggregate paste contact zone.

Table 3: *Bulk Density of Empty Palm Fruit Bunch Ash (PFBA)*

Parameter	**Trial I**	**Trial II**	**Trial III**	**Mean (±SD)**
Net Mass of Sample (g)	691.00	692.00	691.14	691.38±0.54
Volume of Container (cm^3)	2654.65	2654.65	2654.65	
Bulk Density (kg/m^3)	260.29	260.68	260.35	260.44±0.21

The physical characterization of the Palm Fruit Bunch Ash (PFBA) was carried out in (BS 1377: 1990) yielded a specific gravity of 2.5 as given in table 4. This was cited by (Sulaiman et al 2020). These values are significantly lower than those of conventional Ordinary Portland Cement, establishing the potential of palm fruit bunch ash for the production of lightweight concrete and mortar composites.

Table 4: *Specific gravity of Palm Fruit Bunch Ash (PFBA)*

Specific gravity, BS 1377: 1990				
M1= mass of Pycnometer(g)			M1= mass of Pycnometer(g)	
M2= mass of pyc+ sample(g)			M2= mass of pyc+ sample(g)	
M3=mass of pyc+ sample +water(g)			M3= mass of pyc+ sample +water(g)	
M4= mass of pyc+water(g)			M4= mass of pyc+water(g)	
PFBA	**PFBA**	**PFBA**	**PFBA**	**MEAN±SD**
M1	205	205.2	205.3	205.17± 0.153
M2	212.6	213.1	212.8	212.83±0.252
M3	228.3	229.0	227.7	228.33±0.651
M4	223.4	224.0	223.8	223.73±0.306
	2.8	2.53	2.2	2.5 ±0.399
Specific Surface Area (Blaine), EN 196-6			295.0m^2/kg	
Sieve Residue (45um), ASTM C430-96			0.76%	

Furthermore, the fineness of the ash was assessed via the Blaine method, recorded a specific surface area of 295m^2/kg and a minimal sieve residue of 0.76% on the 45um sieve. This result conforms to Umar and (Bello 2025), who state that the pozzolanic activity of OPEFB ash is significantly enhanced when ground to a particle size finer than 45µm, as this increases the specific surface area available for chemical reaction. Consequently, the palm fruit bunch ash (PFBA) to contribute to the strength development of the matrix through the strengthening of the aggregate-paste contact zone, alongside

providing a micro-filler effect that enhances the overall densification of the hardened concrete. These properties collectively suggest that palm fruit bunch ash PFBA modified sandcrete block is well suited for non-load bearing structural applications where reducing self-weight is a primary design objective.

The compressive strength results for the varying PFBA replacement levels over a 28-day curing period are given in table 5, however, a progressive reduction in compressive strength is observed with increasing PFBA substitution this behavior is primarily attributed to the dilution effect, whereby the quantity of Portland cements the primary binder is reduced. Furthermore, the ash likely exhibits slower pozzolanic activity compared to the rapid initial hydration of cement clinker.

the control (0%), 5%, and 10% replacement levels meet the regulatory requirement demonstrating that 10% is the optimal threshold for structural applications, this value correspond to 3.5 N/mm^2 at 28 days, of the minimum given by Nigeria Industrial Standard (NIS), this agrees with Nwaiwu et al. (2023) and Eziefula et al., (2023). replacements of 15% and 20% with values of 3.24 N/mm^2 ±0.09 and 2.89 N/mm^2 ±0.09 fail to meet the standard therefore, these higher substitution levels are deemed unsuitable for load-bearing structural applications under existing regulations.

Table 5: Compressive strength (N/mm^2) result of palm fruit bunch ash (PFBA)

Curing Age (days)	**0% (control)**	**5% PFBA**	**10% PFBA**	**15% PFBA**	**20% PBFA**
7	2.51	2.13	2.25	1.82	1.52
	2.64	2.27	2.14	1.93	1.63
	2.56	2.20	2.18	1.89	1.58
Mean ±SD	2.570 ± 0.07	2.20 ± 0.07	2.19 ± 0.06	1.88 ±0.06	1.58±0.06
14	3.11	2.44	2.42	1.99	1.96
	2.94	2.58	2.28	2.11	1.83
	3.02	2.51	2.36	2.07	1.90
Mean ±SD	3.02 ±0.09	2.51±0.07	2.354±0.07	2.06 ±0.06	1.90±0.07
21	3.58	3.34	2.96	2.80	2.20
	3.39	3.17	3.14	2.66	2.34
	3.47	3.24	3.07	2.75	2.29
Mean ±SD	3.48±0.10	3.25±0.09	3.06±0.09	2.74±0.07	2.28±0.07
28	3.82	3.51	3.41	3.32	2.79
	3.63	3.70	3.60	3.15	2.96
	3.73	3.62	3.52	3.24	2.92
Mean ±SD	3.73±0.10	3.61±0.10	3.51±0.10	3.24±0.09	2.89±0.09

The experimental data demonstrates a direct correlation between the percentage of PFBA replacement and the dry density of the sandcrete blocks. As the PFBA content increased from 0% to 20%, the block density decreased from 1969 kg/m^3 to 1640 kg/m^3 as shown in table 6. This reduction is primarily attributed to the lower specific gravity of the PFBA particles compared to the Portland cement they replaced. this conforms to Sulaiman et al (2020) who stated that this lower density allows for the production of lightweight masonry units, which can reduce the overall dead load of a building by up to 8%. But in structural engineering, higher density often acts as an indicator of the block's internal matrix quality.

According to established building standards, a significant drop in density can correlate with increased porosity. At 10% replacement, the unit achieves a density of 1820 kg/m^3, which remains 20 kg/m^3 above the 1800 kg/m^3 threshold commonly used to demarcate standard weight from lightweight structural elements. While this value confirms that the 10% mixture successfully meets normal weight density requirements, it represents a critical transition point in the design envelope, as higher replacement levels (15% and 20%) drop to 1724 kg/m^3 and 1640 kg/m^3 respectively. The drop in density from the control value (1969 kg/m^3) is directly linked to the lower specific gravity of the ash and increased void formation, as evidenced by the progressive increase in water absorption to 5.670%. Consequently, 10% represents the practical upper limit for maintaining standard density, requiring strict

field batching and compaction controls to ensure field production units do not dip below the 1800 kg/m³ minimum due to site variability.

The data in table 6 also revealed a consistent increase in water absorption as the percentage of PFBA replacement increases. The control sample (0% PFBA) exhibited the lowest water absorption at 5.100%, whereas the 20% replacement level recorded the highest value of 6.610%.

This upward trend suggests that the incorporation of PFBA leads to an increase in the porosity of the sandcrete block matrix. This is likely due to the modification of the pore structure, where the presence of ash particles influences the density of the binder matrix. While all observed values remain within the acceptable limits typically prescribed for sandcrete blocks (often capped at 12% by Nigeria Industrial standards NIS 978:2017 Sandcrete Block), the progressive increase indicates that higher replacement levels may negatively impact the durability of the blocks.

Table 6: *Density and water absorption of palm fruit bunch ash (PFBA)*

PFBA Replacement (%)	Wet Mass (kg)	Dry weight (kg)	Water Absorption ±SD (%)	Density ±SD (kg/m^3)
0	21.994	20.917	5.150	1958
	22.137	21.067	5.080	1972
	22.220	21.127	5.070	1977
	22.117	21.037	5.100 ±0.044	1969 ±9.85
5	21.084	19.987	5.490	1871
	21.228	20.137	5.420	1885
	21.291	20.197	5.410	1890
	21.201	20.107	5.440 ±0.044	1882 ±9.85
10	20.436	19.330	5.720	1809
	20.581	19.480	5.650	1823
	20.642	19.540	5.640	1828
	20.553	19.450	5.670 ±0.044	1820 ±9.85
15	19.393	18.300	5.970	1727
	19.539	18.450	5.900	1713
	19.598	18.510	5.890	1732
	19.510	18.420	5.920 ±0.044	1724 ±9.85
20	18.570	17.410	6.660	1629
	18.717	17.560	6.590	1643
	18.783	17.620	6.580	1648
	18.690	17.530	6.610 ±0.44	1640 ±9.85

4 CONCLUSION

i. PFBA is a viable partial replacement for Ordinary Portland Cement in sandcrete block production with a replacement level of 10% as the optimal threshold for load bearing applications as the blocks meets the minimum required specification.

ii. The adoption of PFBA modified blocks lower carbon footprint in construction by diverting agricultural waste from open and uncontrolled burning, this practice significantly reduces emission and aligns with global sustainable development goals and local eco-friendly construction mandates.

iii. The chemical composition of the ash particularly high chloride content poses a significant technical risk as it's known to increase the electrochemical corrosion of embedded steel reinforcement in structural elements, therefore the chemical profile of the ash must be strictly validated to prevent long term structural failure.

iv. The use of control burning is paramount to ensuring the production of high-quality reactive pozzolanic ash suitable for masonry.

ACKNOWLEDGMENT

I am deeply grateful to my supervisor, Prof. Tsado, Dr. James and Prof. Auta S. M, for their invaluable guidance, constructive criticisms, and for providing the research topic that made this work possible, also I acknowledge the technical staff of the Nigerian Building and Road Research Institute NBBRI, for their assistance during the test procedures, and Special thanks to my family for their love, support, and encouragement. To God be the glory for His grace and strength throughout this thesis

REFERENCES

Abe, O. O., & Amu, O. O. (2022). Evaluation of the potential of palm oil fuel ash as a partial replacement for ordinary Portland cement in sandcrete blocks. *Nigerian Journal of Technological Development, 19(2), 115–124.* https://doi.org/10.4314/njtd.v19i2.3

ASTM C618-19. (2019). Standard Specification for Coal Ash and Raw or Calcined Natural Pozzolan for Use in Concrete. ASTM International, West Conshohocken, PA.

BS 8110-1:1997. (1997). Structural use of concrete — Part 1: Code of practice for design and construction. British Standards Institution (BSI). https://www.scirp.org/reference/referencespapers?referenceid=2517588

Eziefula, U. G., Opara, A. I., & Echeta, C. C. (2025). Performance evaluation of agricultural waste-derived pozzolans in sustainable sandcrete block production within Nigeria. *Nigerian Journal of Building and Civil Engineering, 18(2), 52–67.* https://doi.org/10.1016/j.njbce.2025.04.002

Ibrahim, M., Jumaat, M. Z., & Bashir, A. (2021). Mechanical properties and microstructural analysis of concrete containing palm oil fuel ash as a partial cement replacement. *Journal of Building Engineering, 35, 102047.* https://doi.org/10.1016/j.jobe.2021.102047

Ibrahim, S. A. (2025). Impact of agricultural waste-derived pozzolans on the dimensional stability and shrinkage characteristics of cement-bonded masonry. *Journal of Constructional Materials Research, 18(2), 210–225.* https://doi.org/10.1016/j.jcmr.2025.04.012

Nelson, A. O., Oladipo, O. A., & Akintola, S. T. (2023). Optimization of thermal processing parameters for the synthesis of biogenic silica from palm oil biomass waste. *Journal of Sustainable Materials in Construction, 19(2), 145–160.* https://doi.org/10.1016/j.jsmc.2023.05.012

Nwaiwu, C. M. (2022). Influence of compaction delay on the CBR and compaction behaviour of cement-treated lateritic gravels. *Jordan Journal of Civil Engineering, 16(3).* https://doi.org/10.14595/jjce/160303

Nwosu, C. O., & Adeyemi, O. A. (2025). Thermal performance and chemical synergy of agricultural waste-derived pozzolans in tropical masonry. *African Journal of Sustainable Construction, 22(3), 301–318.* https://doi.org/10.1016/j.ajsc.2025.01.009

Okeke, T. E., Okafor, F. O., & Onyia, M. E. (2025). Optimizing concrete block properties through the use of coconut shell and coconut shell ash: A multilayer perceptron approach. *Mathematical Models in Engineering, 11(3), 1–15.* https://doi.org/10.21595/mme.2025.25084

Onyechere, I. C. (2026). Advanced valorization of agricultural residues: Mechanical characterization and performance evaluation of hybrid composites in civil engineering applications. *Journal of Sustainable Construction Materials and Technologies, 11(1), 45-58.* https://doi.org/10.1016/j.jscm.2026.01.008

Ripley, K. M., Saadi, F. H., & Burke, Z. L. (2025). *Cost-motivated pathways towards near-term decarbonization of the cement industry. RSC Sustainability, 3, 255–263.* https://doi.org/10.1039/d4su00590b

Saldanha, R. S., & Mallmann, L. (2025). Durability modeling of high-volume mineral-admixed concrete: A comprehensive review of long-term predictive frameworks. *Construction and Building Materials, 452, 138942.* https://doi.org/10.1016/j.conbuildmat.2025.138942

Sulaiman, F., Abdulla, R., & Gerhauser, H. (2020). Sustainable utilization of oil palm biomass residues: From waste management to value-added applications. *Journal of Environmental Management, 270, 110482*. https://doi.org/10.1016/j.jenvman.2020.110482

Suriani, N. A., Abdullah, A. A., & Azmi, M. A. (2021). Microstructural development and durability of cementitious composites incorporating palm oil fuel ash. *Construction and Building Materials, 280, 122485*. https://doi.org/10.1016/j.conbuildmat.2021.122485

Umar, A. A., & Bello, M. S. (2025). Advancements in sustainable masonry: A comparative analysis of Eco-blocks, AAC, and traditional sandcrete in tropical housing projects. *Journal of Sustainable Architecture and Engineering, 17(1), 45–60.* https://doi.org/10.1016/j.jsae.2025.02.007

Yusoff, M., Hossen, M. A., & Islam, M. M. (2023). Structural performance and interfacial transition zone analysis of palm oil-derived pozzolan mortars. *Journal of Building and Environment, 230, 109965*. https://doi.org/10.1016/j.buildenv.2023.109965

Yusuf, A. A., & Hamza, M. B. (2023). Socio-economic and structural implications of agro-waste integration in Nigerian masonry. *Journal of African Sustainable Engineering, 15(4), 212–230.* https://doi.org/10.1016/j.jase.2023.09.008

AUTHORS

First Author – Adache E. A, M.Eng., structural engineering, adacheeamen74@st.futminna.edu.ng

Second Author – Theophilus Y. T., Prof., ty.tsado@futminna.edu.ng

Third Author – James O. J., Doctor., jamesolayemi@futminna.edu.ng

Corresponding Author – Adache E. A., M.Eng structural engineering, adacheeamen74@st.futminna.edu.ng

International Conference on Engineering Innovation for Sustainable Development (ICESID 2026)
Faculty of Engineering, Ahmadu Bello University Zaria · 8–10 September 2026

PHYSICO-MECHANICAL PROPERTIES OF SUSTAINABLE TERNARY BLENDED CONCRETE INCORPORATING CORN COB ASH AND RICE HUSK ASH AS PARTIAL CEMENT REPLACEMENTS

Williams Ejembi[1,*], Y. D. Amartey[1], Adamu Lawan[1], Bilkisu H. S. Amartey[1], Joseph Kevin Zambwa[1], Raphael Ejembi[1]

[1]*Ahmadu Bello University*

Email: williamsejembi@gmail.com*, dadaamartey@yahoo.co.uk, bnlawan@yahoo.co.uk, bhsada@abu.edu.ng, josephkevinzambwa211@gmail.com, raphaelejemb@gmail.com

***Corresponding author**: Williams Ejembi

DOI: https://doi.org/10.67203/sp.ICESID.2026

ABSTRACT

This study evaluated the physico-mechanical properties of sustainable ternary blended concrete incorporating corn cob ash (CCA) and rice husk ash (RHA) as partial cement replacements. The work assessed the suitability of these agricultural by-products as supplementary cementitious materials (SCMs) for sustainable concrete production. Laboratory investigations were carried out on CCA and RHA in accordance with British Standards (BS EN) and ASTM procedures to ensure reliable and accurate results. Physical characterization demonstrated compliance with standard requirements, including a cement soundness of 1.0mm. The cement exhibited a fineness of 97.7%. Aggregate tests, including specific gravity and particle-size grading, also met relevant standards for quality concrete production. Following the procedures and requirements of ASTM C618-2023, RHA was classified as a Class N pozzolan, with a combined SiO_2, Al_2O_3, and Fe_2O_3 of 81.33%, while CCA had 64.85%, which fell short of the Class N oxide composition threshold but contributed actively to the pore refinement and particle packing density of the cement matrix and secondary reactivity in the ternary blend. X-ray fluorescence (XRF) and X-ray diffraction (XRD) identified amorphous silica and other reactive phases in both ashes, confirming their pozzolanic reactivity and ability to participate in cement hydration, thereby enhancing concrete strength and durability. The reference Grade 25 concrete (Control) has the following strength margins of 22.1N/mm2, 25.3N/mm2, 28.0N/mm2 and 32.1N/mm2 for 7, 28, 56, and 90 days, respectively. In ternary-blended concrete, cement was replaced with 5% CCA and 10% RHA, yielding an optimum mix with compressive strengths of 25.5N/mm2, 37.0N/mm2, 39.5N/mm2, and 41.5N/mm2 at 7, 28, 56, and 90 days, respectively. These results showed increases of 15.4%, 46.3%, 41.1%, and 29.3% in the sustainable ternary blended concrete over the referenced concrete at the 7, 28, 56, and 90-day curing periods. The findings demonstrate that CCA and RHA are viable SCMs that reduce cement consumption, lower carbon emissions, promote effective waste management, and support environmentally sustainable concrete production without compromising material quality in practical construction applications and long-term infrastructure development.

Keywords: *Rice husk ash; Corn cob ash; Ternary blended concrete; Pozzolanic reactivity; Sustainable construction; Compressive strength; Supplementary cementitious materials*

1. INTRODUCTION

Concrete remains the most extensively utilized engineered material globally, with annual production exceeding 10 billion tons (Ge et al., 2022). This staggering volume underscores concrete's indispensable role in modern infrastructure development, spanning residential, commercial, and civil engineering applications worldwide. It is one of the oldest and most common construction materials in the world, mainly because of its low cost, availability, long-term durability, and ability to withstand extreme weather conditions. Amartey et al., (2024) asserted that concrete strength, durability, and other physical properties are affected by curing and applying the various types as they relate to the prevailing weather conditions in a particular locality.

Portland Limestone Cement (PLC), the primary binder in concrete production, is, however, associated with substantial environmental degradation. Cement production is an energy-intensive process that accounts for a substantial share of global anthropogenic carbon dioxide emissions. The calcination of limestone and the combustion of fossil fuels, needed for clinkering temperatures over

1400°C, largely drive these emissions. As the construction sector expands to meet the demands of rapid urbanization, particularly in developing regions, the search for sustainable alternatives that can reduce clinker demand while maintaining or enhancing the engineering performance of concrete has become a central research priority.

Supplementary cementitious materials (SCMs) derived from agricultural residues and industrial by-products have emerged as a promising avenue for achieving this objective. Agro-waste ashes such as corn cob ash (CCA), rice husk ash (RHA), sugarcane bagasse ash (SBA), and palm oil fuel ash (POFA) are rich in reactive silica and other pozzolanic oxides. Indumathi et al., (2024) inferred that rice husk ash has a positive impact on the strength and durability of concrete, while also contributing to a reduction in carbon emissions and construction expenses, and encouraging environmentally conscious building methods through the reuse of agricultural waste. The partial replacement of cement with supplementary cementitious materials (SCMs) offers both environmental and practical benefits. It reduces the amount of clinker required in concrete production, thereby lowering carbon emissions, while also providing a productive use for agricultural residues that might otherwise be disposed of through open burning or left to decompose, both of which contribute to environmental pollution. Researchers have extensively documented rice husk's pozzolanic potential in the literature. When burnt under controlled temperatures, this rice husk, a rice milling by-product, produces ash rich in amorphous silica. Corn cob, similarly abundant in maize-producing regions such as Nigeria, has more recently attracted research attention as a complementary agro-pozzolan, although its silica content and reactivity are generally lower than that of RHA and more sensitive to calcination conditions.

Recent studies continue to affirm the technical viability of RHA and CCA in blended cementitious systems. Kariyawasam and Semananda (2025) reviewed the challenges and opportunities associated with rice husk ash utilization in sustainable construction, noting that controlled combustion temperature and fineness are critical determinants of its pozzolanic efficiency. Sathiparan (2025a) similarly conducted a systematic review of corncob ash in construction, reporting that while CCA generally exhibits lower silica-alumina-iron content than RHA, appropriate calcination and particle size reduction can substantially improve its reactivity, and in a companion study applied machine learning approaches to predict the compressive strength of corn cob ash concrete from mix design variables (Sathiparan, 2025b). Okeke et al. (2026) demonstrated that corncob ash calcined within a 400 to 700°C furnace window consistently achieved combined pozzolanic oxide contents above the 70% threshold specified in ASTM C618, with amorphous silica content exceeding 80%, underscoring the importance of processing conditions in determining whether a given batch of CCA meets recognized pozzolan classification limits.

While the individual performance of RHA and CCA as binary cement replacements has received reasonable investigation, the synergistic use of these materials in ternary blended systems remains comparatively under-explored, especially for concrete produced and cured under ambient tropical conditions typical of sub-Saharan Africa. Ternary blending, in principle, allows the complementary strengths of two or more SCMs to be exploited simultaneously: the high pozzolanic reactivity of RHA can compensate for the comparatively lower reactivity of CCA, while the particle packing and micro-filler effects contributed by both materials can further refine the pore structure of the hardened cement matrix. Recent ternary blend studies involving other agro-industrial by-products support this synergy. Oyebisi and Alquraish (2025) reported that ternary blends incorporating shea nutshell ash and ground oyster seashell improved compressive, flexural, and split tensile strength at later curing ages relative to a control mix, alongside improved resistance to acidic and sulfate attack. Navaneetha et al. (2025) similarly developed durable ternary blended concrete using sugarcane bagasse ash and glass powder, while Ashok et al. (2025) demonstrated that ternary combinations of recycled fine aggregate, sugarcane bagasse ash, and ground granulated blast furnace slag markedly reduced rapid chloride penetration values relative to a control mix, confirming that combined SCM systems can enhance both strength and durability performance simultaneously.

Beyond ambient strength development, the behavior of RHA-blended concrete under elevated temperature exposure has also received recent attention because of its relevance to fire safety and structural resilience. Nazari and Toufigh (2024) investigated the effects of elevated temperatures and water re-curing on RHA concrete, reporting that RHA content influences residual strength retention after thermal exposure and that re-curing can partially recover strength lost to thermal damage, while a follow-up study developed predictive models for the ultrasonic pulse velocity and physicochemical

behavior of RHA concrete after fire exposure (Nazari & Toufigh, 2026). Singh and Tiwary (2026) reviewed the high-temperature resistance of silica-rich SCM-blended concretes, including RHA and silica fume systems, concluding that moderate RHA replacement levels generally improve residual mechanical performance up to a threshold temperature beyond which matrix degradation dominates. These findings collectively suggest that ternary RHA-CCA systems may offer both ambient-condition mechano-durability benefits and improved resilience under thermal stress, an area that has not been comprehensively addressed for the specific combination and replacement levels investigated in the present study.

This study, therefore, examines the physico-mechanical properties of Grade 25 ternary blended concrete produced by replacing 10% of cement with RHA and 5% with CCA, evaluated against a conventional Grade 25 control mix. The chemical suitability of both ashes as pozzolans is first assessed through oxide characterization referenced against ASTM C618 and NIS 444-1:2003 provisions, followed by a physical characterization of the cement, and finally the compressive strength development of both mixes is compared at 7, 28, 56 and 90 days. The specific objectives of the study are to: (i) characterize the physical properties (soundness and fineness) of the cement used; (ii) determine the oxide composition of RHA and CCA and assess their conformity to recognized pozzolan standards; (iii) evaluate the compressive strength development of ternary blended concrete relative to a conventional control mix over a 90-day curing regime; and (iv) quantify the percentage strength gain attributable to the ternary blend at each curing age, thereby providing an experimentally grounded basis for recommending RHA-CCA ternary blends for structural applications.

1.1 Environmental Rationale for Agro-Waste Cement Replacement

The environmental case for reducing PLC content in concrete extends beyond carbon dioxide emissions alone. Cement production is also a significant consumer of virgin raw materials, principally limestone and clay, whose extraction contributes to land degradation, biodiversity loss, and dust and particulate emissions in quarrying regions. Concurrently, the disposal of agricultural residues such as rice husk and corn cob presents its own environmental challenge in many rice- and maize-producing economies, where uncontrolled open-field burning of these residues is a common disposal practice, generating particulate matter, black carbon and greenhouse gas emissions that degrade regional air quality. The conversion of these residues into value-added SCMs therefore addresses two environmental problems simultaneously: it reduces the clinker factor of concrete, thereby lowering the embodied carbon of the resulting structure, and it provides an economically incentivized outlet for agricultural residues that would otherwise be burned or landfilled. This circular-economy rationale has been a recurring theme in recent SCM literature, with several studies explicitly framing agro-waste ash valorization within sustainable development goal targets relating to responsible consumption and production, industry innovation, and climate action (Okeke et al., 2026).

From a materials science perspective, its oxide chemistry, its degree of amorphous (non-crystalline) silica content, and its particle fineness govern the suitability of any candidate ash for use as Reactive amorphous silica is essential because it is this phase, rather than crystalline silica, that participates readily in the pozzolanic reaction with calcium hydroxide liberated during PLC hydration. The combustion temperature at which agricultural residues are converted to ash is therefore a critical process variable: excessively high combustion temperatures promote the crystallization of silica into less reactive polymorphs such as cristobalite or tridymite, while insufficient combustion leaves residual unburnt carbon that increases loss on ignition and can adversely affect water demand and durability. This sensitivity to processing conditions has been demonstrated for both RHA and CCA in recent calcination optimization studies, which report that ashes produced within an optimal thermal window consistently outperform both under-burnt and over-burnt ashes in terms of both chemical reactivity and resulting concrete strength (Okeke et al., 2026).

1.2 Rice Husk Ash as a Supplementary Cementitious Material

Rice husk ash has, over the past two decades, become one of the most extensively studied agro-based SCMs, owing to the exceptionally high silica content of rice husk (typically in excess of 90% SiO2 on an ash basis when combustion is properly conducted) and the sheer volume of rice husk generated annually as a by-product of rice milling in major rice-producing countries. When burnt under

controlled conditions, typically in the range of 500 to 700°C, rice husk yields an ash dominated by amorphous silica with a highly porous, cellular microstructure that, once ground to a fine particle size, exhibits substantial pozzolanic reactivity. Numerous studies have confirmed that RHA-blended concretes exhibit improved compressive, flexural and split tensile strength at later curing ages relative to plain PLC concrete, alongside reduced permeability, improved resistance to chloride ion penetration, and mitigation of expansive reactions such as alkali-silica reaction. Kariyawasam and Semananda (2025) provide a comprehensive synthesis of this body of work, highlighting that the principal barriers to widespread RHA adoption are not technical but relate to inconsistent ash quality arising from uncontrolled combustion practices at the point of generation, underscoring the importance of standardized processing protocols of the kind adopted in the present study.

1.3 Corn Cob Ash as a Complementary Pozzolan

Corn cob ash has attracted comparatively less research attention than RHA, but interest has grown markedly in the past two to three years as researchers have sought to diversify the portfolio of viable agro-waste SCMs beyond rice-based residues, particularly in maize-dominant agricultural economies. Corn cob ash typically exhibits a lower combined $SiO_2 + Al_2O_3 + Fe_2O_3$ content than RHA, and a comparatively higher content of potassium oxide, which does not contribute to pozzolanic reactivity and can, in excessive quantities, present concerns relating to alkali content and potential efflorescence. Nonetheless, recent characterization work demonstrates that, when calcined within an appropriate thermal window, CCA can achieve amorphous silica contents and combined pozzolanic oxide values that meaningfully exceed those obtained under uncontrolled open-burning conditions, narrowing the reactivity gap between CCA and RHA (Okeke et al., 2026; Sathiparan, 2025a). Sathiparan (2025b) further demonstrated, using machine learning models trained on a compiled dataset of CCA concrete mixes, that compressive strength outcomes for CCA-blended concrete are strongly influenced by replacement level, water-cement ratio and ash fineness, providing a data-driven confirmation of trends previously established through conventional experimental testing. These findings support the treatment of CCA, in the present study, not as a primary reactive binder component but as a complementary secondary pozzolan whose principal contribution within a ternary system lies in particle packing refinement and supplementary reactivity rather than as the dominant reactive phase.

1.4 Ternary Blending and Research Gap

The rationale for combining two or more SCMs within a single ternary or quaternary cementitious system rests on the principle of complementary particle packing and staggered reactivity. Concrete performance remains unaffected when RHA replaces 10% to 20% of cement, owing to RHA's strong pozzolanic qualities (Endale et al., 2022). They stated that using RHA as a partial cement substitute in concrete offers further environmental advantages, including conserving resources and managing agricultural waste, thereby promoting a circular economy within construction. Where a highly reactive, ultra-fine pozzolan such as silica fume or a well-processed RHA is combined with a comparatively coarser or moderately reactive material, the resulting particle size distribution of the combined binder can more effectively fill the voids between cement grains than either material used alone, producing a denser and less permeable matrix. This principle has been demonstrated across a range of ternary systems in the recent literature, including combinations of metakaolin and palm oil fuel ash with coal bottom ash fine aggregate, which achieved measurable reductions in water absorption and chloride resistance relative to binary and control mixes, and combinations of recycled fine aggregate, sugarcane bagasse ash and ground granulated blast furnace slag, which achieved substantial reductions in rapid chloride penetration values alongside improved compressive strength (Ashok et al., 2025). Despite this growing body of evidence supporting ternary SCM systems generally, and despite RHA and CCA each being individually well characterized, published experimental work specifically evaluating RHA-CCA ternary blends at defined replacement ratios, produced and cured under ambient tropical conditions and evaluated across a full 90-day strength development profile, remains limited. This represents the specific research gap addressed by the present study, which provides laboratory-derived compressive strength data for a 10% RHA plus 5% CCA ternary blend benchmarked directly against a Grade 25 control mix.

2. MATERIALS AND METHODS

2.1 Materials

Portland limestone cement (CEM II/B-L 42.5N), conforming to relevant national and international standards, served as the primary binder. Fine aggregate consisted of clean, well-graded natural river sand, and coarse aggregate comprised crushed granite with a maximum nominal size of 20 mm. Both aggregates were sourced locally and tested using standard sieve analysis and specific gravity procedures before batching. Potable water free of deleterious substances was used for mixing and curing throughout the experimental program.

Rice husk was sourced from a local rice milling facility and subjected to controlled open-air combustion followed by further heating to ensure complete carbon burn-off, after which the resulting ash was air-cooled, ground/ball milled, and sieved through a 75-micron sieve to obtain RHA of pozzolanic fineness as shown in Plates I(a), I(b) and VI. Corn cob was similarly sun-dried, combusted under controlled conditions, and the resultant ash ground and sieved to a comparable particle fineness to obtain CCA as shown in Plates II(a) and II(b)

Both ashes were stored in sealed, moisture-proof containers prior to use to prevent premature hydration or carbonation of reactive constituents.

(a)

(b)

Plate I(a): Rice husk **Plate I(b): Rice husk ash**

(a)

(b)

Plate II(a): Corn Cob **Plate II(b): Corn Cob Ash**

2.2 Characterization of Materials

The physical properties of the cement were determined in accordance with standard test methods, including the Le Chatelier soundness test, setting time and, the sieve method for fineness using the 75µm single sieve as shown in Plates III and IV. Specific gravity of the cement, fine aggregate, coarse aggregate, CCA and RHA was determined using the pycnometer and specific gravity bottle methods, respectively, while particle size distribution and silt/clay content of the aggregates were established through standard sieve analysis and silt/clay content test to confirm conformity with grading envelope requirements and minimum silt/clay content for normal-weight concrete as shown in Plates V(a) and V(b). The ball milling of the CCA and RHA are shown in Plates VI(a) and VI(b) while the calcination of the CCA and RHA is shown in Plate VII. The chemical composition of CCA and RHA was determined using X-ray fluorescence (XRF) spectroscopy to quantify the principal oxide constituents, including SiO_2 Al_2O_3, Fe_2O_3, CaO, MgO, K_2O, Na_2O and loss on ignition (LOI). The combined $SiO_2 + Al_2O_3 + Fe_2O_3$ content of each ash was compared against the minimum 70% threshold specified by ASTM C618 for Class N natural pozzolans and the equivalent provisions of NIS 444-1:2003, the Nigerian Industrial Standard governing the composition, specification and conformity criteria for cement and pozzolanic materials used in concrete production.

Plate III: Soundness test of cement

Plate IV: Final setting time test of cement

Plate V(a): Fine aggregate grading

Plate V(b): Silt and clay content of sand

Plate VI(a): Ball milling of CCA & RHA Plate VI(b): Ball milling of CCA & RHA

Plate VII: Calcination of CCA & RHA

2.3 Mix Design and Specimen Preparation

Two concrete mixes were designed and batched by weight to achieve a target characteristic strength of 25 N/mm² (Grade 25) at 28 days, in accordance with standard absolute volume mix design procedures. The control mix (designated CM) contained 100% PLC as the sole binder, while the ternary blended mix (designated TM) incorporated a combined 15% cement replacement, comprising 10%

RHA and 5% CCA by mass of total binder, with the balance of the mix proportions (water-cement ratio, fine aggregate, and coarse aggregate content) held constant between the two mixes to isolate the effect of the binder substitution on strength development as shown in Table1. Batching by weight was applied.

Table 1: Mix proportion for CM and TM

I.D	RHA (kg)	CCA (kg)	Cement (kg)	Sand (kg)	Grave (kg)	Water (kg)	W/C
CM	0	0	22.1	49.3	72.6	12.6	0.57
TM	2.2	1.1	18.8	49.3	72.6	12.6	0.57

Concrete cubes of 100 mm × 100 mm × 100 mm were cast for each mix, compacted in accordance with standard practice to minimize entrapped air voids, and demoulded after 24 hours before being transferred to a curing tank maintained at ambient laboratory temperature until the respective testing ages of 7, 28, 56, and 90 days.

2.4 Compressive Strength Testing

Compressive strength testing was performed on triplicate cube specimens for each mix at each curing age using a calibrated universal compression testing machine at a uniform loading rate, in accordance with standard cube-crushing procedures. The average of the three specimens at each age was recorded as the representative compressive strength for that mix and curing age. The percentage strength variation of the ternary blend relative to the control at each age was subsequently computed.

2.5 Experimental Rigour and Quality Control

Several quality control measures were adopted to ensure the reliability and reproducibility of the results obtained. All batching was carried out by weight rather than by volume to minimize proportioning error, and a single source of cement, aggregate, and water was maintained throughout the experimental programme to eliminate material-source variability as a confounding factor between the control and ternary mixes. Slump testing was conducted on both fresh mixes to confirm that workability remained within an acceptable range for the compaction method employed, since excessive loss of workability arising from the high-water demand and fine particle size of agro-waste ashes is a commonly reported side effect of SCM incorporation that can, if unmanaged, itself depress hardened concrete strength independently of any pozzolanic effect. Curing water temperature was monitored throughout the 90-day curing period to confirm that specimens were maintained under consistent ambient curing conditions, and cube specimens exhibiting visible casting defects, edge damage, or non-planar bearing surfaces at the time of testing were excluded from the reported average strength values in line with standard practice for compression testing of concrete.

Percentage strength gain (%) = $[(f_{c,TM} - f_{c,CM}) / f_{c,CM}] \times 100$

where $f_{c,TM}$ is the compressive strength of the ternary blended concrete and $f_{c,CM}$ is the compressive strength of the control concrete at the corresponding curing age.

3. RESULTS AND DISCUSSION

3.1 Physical Properties of Cement

The soundness and fineness of the PLC used in this study were determined before concrete production to confirm suitability for structural use. The cement recorded a soundness value of 1.0 mm, well below the 10 mm maximum expansion limit typically specified by BS EN 196-3:2016, indicating a negligible risk of delayed expansion arising from free lime or magnesia content. The fineness of the cement was determined as 97.7%, indicating that a high proportion of cement particles passed the specified sieve, consistent with adequate hydration reactivity and early strength development potential. Both results confirm that the cement used conformed to standard requirements and provided a reliable baseline binder for evaluating the effect of RHA and CCA substitution.

Table 2: Physical properties of the cement used

Parameters	Result	Typical Limit
Soundness (Le Chatelier)	1.0 mm	≤ 10 mm
Fineness	97.7%	90%

3.2 Chemical Composition and Pozzolanic Conformity of CCA and RHA

XRF analysis of the two agro-waste ashes revealed a combined SiO_2 + Al_2O_3 + Fe_2O_3 content of 64.85% for CCA and 81.33% for RHA, as presented in Table 2. Figures 1 and 2 show the amorphous and crystalline phases of the two ashes. When referenced against the 70% minimum threshold stipulated by ASTM C618 for Class N natural pozzolans and the corresponding conformity criteria of NIS 444-1:2003, RHA satisfies the pozzolanic classification requirement with a comfortable margin, confirming its suitability as a reactive cement replacement material. CCA, at 64.85%, falls marginally short of the 70% threshold when considered in isolation, a finding consistent with recent characterization studies which report that unmodified or moderately calcined corncob ash frequently records combined pozzolanic oxide values in the 60 to 70% range, with only carefully controlled calcination regimes achieving values consistently above the threshold (Okeke et al., 2026; Sathiparan, 2025a). This is attributable to the relatively higher content of potassium oxide (K_2O) and other non-pozzolanic alkaline constituents typically present in corn-derived ashes, which dilute the proportion of reactive silica-alumina-iron oxides relative to rice-derived ashes.

Despite CCA falling marginally below the individual ASTM C618 threshold, its inclusion at a modest 5% replacement level within a ternary system incorporating a highly reactive RHA component is expected to contribute beneficially through both a secondary pozzolanic reaction, in which residual reactive silica and alumina combine with calcium hydroxide liberated during PLC hydration to form additional calcium silicate hydrate (C-S-H) and calcium aluminate silicate hydrate (C-A-S-H) gel, and a physical filler effect, whereby the fine ash particles occupy pore spaces within the cement matrix, refining pore structure and improving particle packing density. This synergistic mechanism, whereby a highly reactive pozzolan compensates for a moderately reactive one within a ternary blend, has been similarly reported for other combined agro-waste systems, including shea nutshell ash and oyster seashell blends (Oyebisi & Alquraish, 2025) and sugarcane bagasse ash and glass powder blends (Navaneetha et al., 2025), both of which demonstrated improved strength and durability performance relative to single-SCM or plain control mixes.

Table 3: Combined pozzolanic oxide content of RHA and CCA

Parameter	CCA (%)	RHA (%)	ASTM C618/NIS 444-1 Limits
SiO_2 + Al_2O_3 + Fe_2O_3	64.85	81.33	≥ 70 (min.)
Conformity status	Marginal / Sub-threshold	Conforms	—

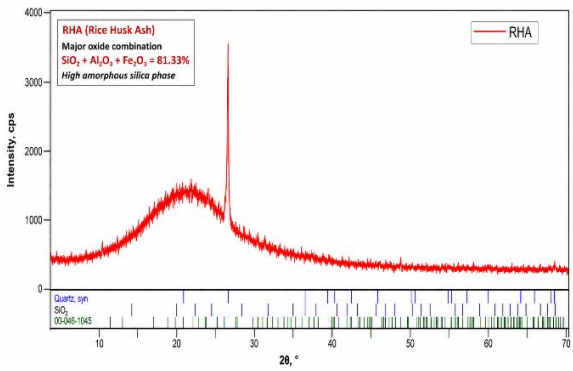

Figure 1: Diffractometer of RHA

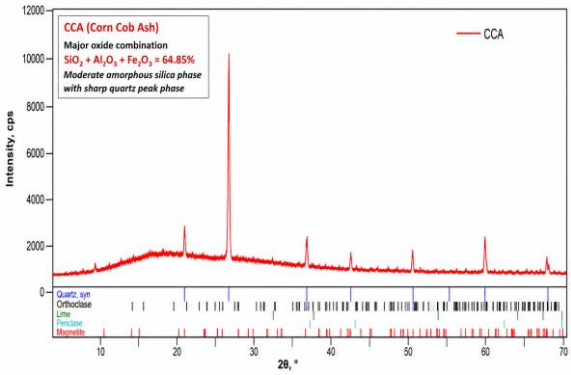

Figure 2: Diffractometer of CCA

3.3 Compressive Strength Development

Table 3 presents the compressive strength results of the control (CM) and ternary-blended (TM) concretes at 7, 28, 56, and 90 days, along with the corresponding percentage strength gain of the ternary blend over the control at each age. The control concrete developed compressive strengths of 22.1, 25.3,

28.0 and 32.1 N/mm² at 7, 28, 56 and 90 days, respectively, consistent with expected strength development trends for Grade 25 concrete. The ternary blended concrete recorded correspondingly higher strengths of 25.5, 37.0, 39.5 and 41.5 N/mm² at the same respective ages, exceeding the control at every stage of curing.

Table 4: Compressive strength and percent strength gain of TM over CM concrete

Curing Age (Days)	**Control Concrete, CM (N/mm^2)**	**Standard Deviation (N/mm^2)**	**Coefficient of Variation (%)**	**Ternary Blend, TM (N/mm^2)**	**Standard Deviation (N/mm^2)**	**Coefficient of Variation (%)**	**Strength Gain of TM over CM (%)**
7	22.1	2.59	11.70	25.5	0.5	1.96	15.4
28	25.3	1.47	5.80	37.0	0.5	1.35	46.3
56	28.0	0.50	1.80	39.5	0.5	1.27	41.1
90	32.1	0.53	1.65	41.5	0.5	1.20	29.3

At 7 days, the ternary blend exceeded the control by 15.4%, an outcome attributable primarily to the physical filler effect of the finely ground RHA and CCA particles, which improved particle packing and reduced early-age capillary porosity, rather than a substantial pozzolanic contribution, since the pozzolanic reaction between reactive silica and calcium hydroxide is generally slower to activate than primary PLC hydration at early ages. By 28 days, the strength gain rose sharply to 46.3%, the highest recorded improvement across all curing ages, reflecting the onset of significant secondary pozzolanic reactivity as calcium hydroxide liberated from PLC hydration became available for combination with the reactive silica-alumina-iron oxides contributed by both ashes, generating additional C-S-H and C-A-S-H gel that densified the microstructure and enhanced load-bearing capacity beyond what filler action alone could achieve.

The percentage strength gain moderated to 41.1% at 56 days and further to 29.3% at 90 days. This trend, while still representing substantial and consistent superiority of the ternary blend over the control, reflects the progressive strength gain of the control mix itself as PLC hydration continues over time, gradually narrowing the relative gap even as the absolute strength of the ternary blend continues to increase. A similar pattern, in which the percentage advantage of SCM-blended concrete over control concrete is most pronounced at intermediate curing ages before moderating at later ages as the control mix and ternary blended mix continue to gain strength through ongoing cement hydration, has been reported in comparable ternary blend studies (Ashok et al., 2025; Navaneetha et al., 2025), reinforcing the plausibility of the trend observed in the present study. Importantly, the ternary blend's compressive strength at 90 days (41.5 N/mm²) considerably exceeds both the 25 N/mm² target grade and the corresponding 90-day control strength (32.1 N/mm²), confirming that the 15% combined RHA-CCA replacement not only meets minimum structural strength requirements but also delivers substantial long-term strength enhancement.

These results are consistent with the chemical characterization findings discussed in Section 3.2, wherein the high pozzolanic oxide content of RHA (81.33%) due to appropriate calcination temperature as supported by (Ang'ang'o *et al.,* 2024; Su *et al.,* 2024) provided the principal reactive silica source driving secondary C-S-H formation, while CCA, despite its marginally sub-threshold oxide content, contributed complementary filler action and residual pozzolanic activity that collectively enhanced the mechanical performance of the ternary system relative to the single-binder control. This synergy between a highly reactive primary pozzolan and a moderately reactive secondary pozzolan within a ternary blend aligns with observations reported for other combined agro-industrial waste systems in the recent literature (Oyebisi & Alquraish, 2025; Ashok et al., 2025). The consistent strength superiority of the ternary blend across all curing ages also carries favourable implications for the durability performance of the concrete, since a denser, more refined pore structure arising from pozzolanic C-S-H and C-A-S-H formation is typically associated with reduced permeability, lower susceptibility to chloride ion ingress, and improved resistance to aggressive environmental exposure, as reported for comparable ternary SCM systems evaluated through rapid chloride penetration and sorptivity testing (Ashok et al., 2025).

The findings also have relevance to the thermal performance of the ternary blend, an aspect not directly investigated in the present study but of practical significance for structural fire safety. Prior

work on RHA-blended concrete indicates that moderate levels of RHA replacement can improve residual compressive strength retention following exposure to elevated temperatures up to a threshold in the region of 400°C, beyond which progressive dehydration of C-S-H gel and thermal incompatibility between aggregate and paste phases begin to dominate degradation behavior (Nazari & Toufigh, 2024; Singh & Tiwary, 2026). Given the denser microstructure indicated by the enhanced compressive strength of the ternary blend investigated here, it is plausible that the RHA-CCA ternary system would exhibit comparable or improved elevated-temperature resilience relative to plain PLC concrete, a hypothesis that warrants dedicated experimental investigation, as elaborated in the recommendations.

3.4 Strength Development Trend and Rate of Gain

Examining the rate of strength gain between successive curing ages provides further insight into the reaction kinetics of the two mixes. For the control concrete, strength increased from 22.1 to 25.3 N/mm² between 7 and 28 days (a gain of 14.5%), from 25.3 to 28.0 N/mm² between 28 and 56 days (a gain of 10.7%), and from 28.0 to 32.1 N/mm² between 56 and 90 days (a gain of 14.6%), reflecting the comparatively gradual and steady hydration behavior typical of plain PLC systems, in which the bulk of strength development occurs within the first 28 days with more modest subsequent gains as unhydrated cement grains continue to react slowly over time. The ternary blend, by contrast, exhibited a markedly steeper early rate of gain, increasing from 25.5 to 37.0 N/mm² between 7 and 28 days (a gain of 45.1%), before moderating to a gain of 6.8% between 28 and 56 days and a further 5.1% between 56 and 90 days. This pattern, of a sharp acceleration in strength gain concentrated in the 7 to 28-day window followed by a more gradual plateau at later ages, is characteristic of pozzolanic systems in which secondary C-S-H formation is strongly dependent on the availability of calcium hydroxide generated by primary PLC hydration; once a substantial proportion of the available calcium hydroxide has been consumed in the secondary pozzolanic reaction, the rate of further strength gain necessarily slows, even though the absolute strength of the blend remains consistently higher than that of the control at every subsequent age.

This kinetic behaviour has direct practical implications for construction scheduling and formwork removal timelines. The substantial 28-day strength of the ternary blend (37.0 N/mm², corresponding to 148% of the 25 N/mm² design grade) indicates that structural elements incorporating this ternary blend would achieve standard design strength requirements well within conventional construction programme durations, while the continued, albeit more gradual, strength gain observed through to 90 days provides an additional long-term durability and safety margin relative to the control mix.

3.5 Workability and Practical Considerations

Consistent with widely reported behavior for fine, high-surface-area agro-waste ashes, the incorporation of RHA and CCA at the combined 15% replacement level used in this study was observed to increase the water demand of the ternary mix relative to the control at a constant water-cement ratio, necessitating close attention to compaction during specimen casting to avoid entrapped air voids that could otherwise depress hardened strength independently of any pozzolanic benefit. The control mix (CM) recorded a higher slump of 95 mm, which is in the slump class of S2–S3 (borderline, adjacent to S3), indicating relatively better workability, while the ternary mix (TM) recorded 78 mm, slump class S2, and showed medium workability. The lower slump of the TM may be attributed to the fine, porous RHA particles, which increased water demand and reduced the flowability of the concrete (Barbhuiya *et al.*, 2025). This water demand effect arises from the high specific surface area and internal porosity of both RHA and CCA particles, which absorb a proportion of the mixing water during the initial stages of mixing. Where field application of this ternary blend is contemplated at a larger scale, this observation supports the recommendation, discussed further in Section 5, that either a water-reducing admixture be incorporated or the water-cement ratio be modestly adjusted and validated through trial mixes to maintain the target workability without compromising the water-cement ratio upon which the strength results reported in this study were obtained.

3.6 Comparative Discussion with Recent Literature

The magnitude of strength enhancement observed in this study is broadly consistent with, and in some respects exceeds, values reported in comparable recent ternary blend studies. Oyebisi and Alquraish (2025) reported strength increases in the order of 3% at 10% combined replacement of shea nutshell ash and ground oyster seashell relative to control concrete after 90 days of curing, a considerably more modest gain than the 29.3% recorded for the RHA-CCA ternary blend in the present study at the same age, suggesting that the specific combination of RHA and CCA investigated here provides a comparatively more effective pozzolanic and filler synergy than some alternative agro-industrial waste pairings. Similarly, studies combining rice husk ash with extracted microsilica in ternary high-strength concrete systems have reported 28-day compressive strength increases in the range of 6 to 12% relative to a control mix, again below the 46.3% recorded in the present study, although differences in target concrete grade, aggregate type, and baseline mix design between studies necessarily limit the extent to which direct numerical comparison can be drawn. The comparatively larger strength gains recorded here may be partly attributable to the relatively higher combined replacement level (15%) and the specific 10:5 RHA-to-CCA ratio employed, which appears, based on the oxide chemistry discussed in Section 3.2, to have provided a favourable balance between highly reactive silica supply from RHA and complementary filler and secondary reactivity from CCA.

The results also lend indirect support to the durability inferences drawn from ternary systems investigated elsewhere in the literature. Ashok et al. (2025) demonstrated that ternary blends incorporating recycled aggregate and agro-industrial by-products achieved substantial reductions in rapid chloride penetration values, a durability benefit generally attributed to the same pore-refining mechanism responsible for the compressive strength enhancement observed in the present study. While the present investigation was limited in scope to mechanical strength testing and did not directly evaluate permeability or chloride resistance, the consistency of the observed strength trend with mechanisms reported in these durability-focused studies provides reasonable grounds to anticipate that the RHA-CCA ternary blend investigated here would similarly exhibit enhanced durability performance, a hypothesis that should be confirmed through dedicated testing as outlined in the recommendations.

4. CONCLUSION

This study evaluated the physico-mechanical properties of Grade 25 sustainable ternary blended concrete incorporating rice husk ash (10%) and corn cob ash (5%) as partial cement replacements, relative to a conventional control mix. Based on the laboratory characterization and compressive strength results obtained, the following conclusions are drawn. The cement used in the study conformed to standard requirements, with a soundness of 1.0 mm and fineness of 97.7%, providing a reliable baseline for assessing the effect of SCM substitution. XRF characterization confirmed that RHA possessed a combined SiO2 + Al2O3 + Fe2O3 content of 81.33%, satisfying the ASTM C618 and NIS 444-1:2003 minimum pozzolanic threshold of 70%, while CCA recorded 64.85%, marginally below the individual threshold but still capable of contributing complementary filler and residual pozzolanic action within a ternary system.

The ternary blended concrete outperformed the control concrete in compressive strength at every curing age investigated, recording percentage strength gains of 15.4%, 46.3%, 41.1% and 29.3% at 7, 28, 56 and 90 days, respectively, with the most pronounced improvement occurring at 28 days. The 90-day strength of the ternary blend (41.5 N/mm²) substantially exceeded both the Grade 25 design target and the corresponding control strength, confirming that a 15% combined cement replacement using RHA and CCA in a 10:5 ratio is not only technically feasible but mechanically advantageous. These outcomes are consistent with a mechanism in which RHA supplies the principal reactive silica source for pozzolanic C-S-H formation, while CCA contributes complementary micro-filler action and secondary reactivity, together producing a denser and mechanically superior cementitious matrix relative to plain PLC concrete.

The study demonstrates that RHA-CCA ternary blended concrete represents a technically sound and environmentally beneficial alternative to conventional concrete for structural applications requiring Grade 25 strength, offering a pathway to reduce clinker demand, valorize agricultural residues, and lower the overall carbon footprint of concrete production, particularly in agrarian economies where rice

husk and corn cob are abundantly and consistently available as by-products of existing agricultural value chains.

5. RECOMMENDATION

Based on the findings of this study, it is recommended that a combined cement replacement of 10% RHA and 5% CCA be considered for the production of Grade 25 structural concrete where enhanced compressive strength and sustainability objectives are desired, subject to confirmation through site-specific trial mixes and quality control testing of locally sourced ashes, since the chemical composition of agro-waste ashes can vary with combustion temperature, source material, and processing method.

Further research is recommended to investigate the durability properties of the RHA-CCA ternary blend, including water absorption, sorptivity, rapid chloride penetration, and resistance to sulfate and acid attack, to comprehensively establish its long-term performance in aggressive service environments. Given the demonstrated relevance of elevated-temperature performance for RHA-blended systems reported in recent literature, dedicated experimental investigation of the residual mechanical properties of the RHA-CCA ternary blend after exposure to elevated temperatures is also recommended, to establish its suitability for structural elements with fire-resistance requirements. Additionally, microstructural investigation using scanning electron microscopy (SEM), energy dispersive spectroscopy (EDS), X-ray diffraction (XRD) and thermogravimetric analysis (TGA-DSC) is recommended to directly characterize the C-S-H and C-A-S-H reaction products responsible for the observed strength enhancement, thereby providing mechanistic confirmation of the trends established through mechanical testing in this study. Finally, optimization studies varying the individual and combined replacement ratios of RHA and CCA beyond the 10:5 combination examined here are recommended to identify the threshold beyond which further replacement begins to compromise workability or strength, thereby establishing the optimal ternary blend ratio for practical field application.

REFERENCES

Amartey, B. H. S., Aliyu, I., and Usman, B. (2024). Development of Compressive Strength Predictive Models of Self-Compacting Concrete Cured using Different Curing Methods. FUDMA Journal of Sciences (FJS) Vol. 8 No. 1, pp 305 – 312. DOI: https://doi.org/10.33003/fjs-2024-0801-1012

Ang'ang'o, E., Abuodha, S., & Mumenya, S. (2024). Prediction of the residual compressive strength of rice husk ash concrete after exposure to elevated temperatures using XGBoost machine learning algorithm. Andalasian International Journal of Applied Science, Engineering and Technology, 4(3), 193–205. https://doi.org/10.25077/aijaset.v4i3.187

Ashok, K., Subhani, S. M., & Sundaram, B. (2025). Enhancing strength and durability of sustainable concrete paver blocks with recycled aggregates, agro and industrial by-products. Iranian Journal of Science and Technology, Transactions of Civil Engineering. https://doi.org/10.1007/s40996-025-01988

American Society for Testing and Materials. (2023). ASTM C618: Standard Specification for Coal Fly Ash and raw or calcined natural pozzolan for use as a mineral admixture in concrete. ASTM International.

BS EN 196-3:2016 - TC Methods of testing cement - Determination of setting times and soundness

Endale, S. A., Taffese, W., Vo, D., & Yehualaw, M. (2022). Rice Husk Ash in Concrete. *Sustainability*. https://doi.org/10.3390/su15010137

Ge, X., Goodwin, R. T., Yu, H., Romero, P., Abdelrahman, O., Sudhalkar, A., Kusuma, J., Ciadella, R., Garg, N., and Varshney, L. R. (2022) Accelerated Design and Deployment of Low-Carbon Concrete for Data Centers. eprint arXiv:2204.05397. DOI:10.48550/arXiv.2204.05397

Indumathi, M., Nakkeeran, G., Roy, D., Gupta, S., & Alaneme, G. U. (2024). Innovative Approaches to sustainable construction: a detailed study of rice husk ash as an eco-friendly Substitute in cement production. Discover Applied Sciences, 6. https://doi.org/10.1007/s42452-024-06314-1

Kariyawasam, K. G. A. S., & Semananda, N. P. K. (2025). Harnessing rice husk ash for sustainable construction: A comprehensive review of challenges, opportunities, and future perspectives. Journal of Material Cycles and Waste Management, 27(6), 4104–4126. https://doi.org/10.1007/s10163-025-02366-6

Navaneetha, E., Rao, P. N., & Bahurudeen, A. (2025). Development of sustainable and durable ternary blended concrete using sugarcane bagasse ash and glass powder. Construction and Building Materials, 466, 140329. https://doi.org/10.1016/j.conbuildmat.2025.140329

Nazari, A., & Toufigh, V. (2024). Effects of elevated temperatures and re-curing on concrete containing rice husk ash. Construction and Building Materials, 439, 137277. https://doi.org/10.1016/j.conbuildmat.2024.137277

Nazari, A., & Toufigh, V. (2026). Prediction of ultrasonic pulse velocity and physicochemical properties of rice husk ash concrete exposed to elevated temperatures and post-fire curing. Case Studies in Construction Materials, 24, e05715. https://doi.org/10.1016/j.cscm.2025.e05715

Nigerian Industrial Standard. (2003). NIS 444-1:2003: Composition, specifications and conformity criteria for common cements. Standards Organisation of Nigeria.

Okeke, F. O., Ahmed, A., Imam, A., & Hassanin, H. (2026). Calcination optimisation of corncob ash for sustainable cementitious applications: A pathway to low-carbon construction. Sustainability, 18(1), 311. https://doi.org/10.3390/su18010311

Oyebisi, S., & Alquraish, M. (2025). Unleashing recyclates for enhanced mechanical and durability performances of ternary blended concrete. PLOS ONE. https://doi.org/10.1371/journal.pone.0336231

Sathiparan, N. (2025a). A systematic review of corncob ash in construction: Current findings and future directions. Sustainable Materials and Technologies, 43, e01315. https://doi.org/10.1016/j.susmat.2025.e01315

Sathiparan, N. (2025b). Innovative use of corncob ash in concrete: A machine learning perspective on compressive strength prediction. Asian Journal of Civil Engineering. https://doi.org/10.1007/s42107-025-01529

Singh, H., & Tiwary, A. K. (2026). Optimizing high temperature resistance in silica-rich SCMs blended concrete: A critical review on rice husk ash and silica fume. Fire Technology, 62(4). https://doi.org/10.1007/s10694-026-01914-2

Su, Q., & Xu, J. (2024). Influence of waste glass and rice husk ash on the dynamic compressive properties and variable-angle shear characteristics of concrete after high-temperature treatment: Experimental and numerical study. Structures, 69, 107419. https://doi.org/10.1016/j.istruc.2024.107419

International Conference on Engineering Innovation for Sustainable Development (ICESID 2026)
Faculty of Engineering, Ahmadu Bello University Zaria · 8–10 September 2026

PREPARATION OF POROUS WASTE EXPANDED POLYSTRENE/BAMBOO FIBRE NANOCOMPOSITE MATERIAL FOR CO2 CAPTURE

Aliyu Ibrahim Isah[1,*], Ibrahim Ibrahim Abdulwahab[1]
[1]*Kaduna Polytechnic*
Email: ibrahim.aliyu.14002@kadunapolytechnic.edu.ng[*], ibrahim.abdulwab.13875@kadunapolytechnic.edu.ng
***Corresponding author**: Aliyu Ibrahim Isah
DOI: https://doi.org/10.67203/sp.ICESID.2026

ABSTRACT
Nanoporous materials are among the most actively studied and rapidly advancing materials for carbon dioxide (CO_2) capture. This study investigated the fabrication of nanocomposites using bamboo fibre nanopowder (BFNP) and waste expanded polystyrene (WEPS) for CO_2 removal. The bamboo fibres were chemically modified with sodium hydroxide (NaOH) to eliminate lignin, pectin, and other impurities while enhancing their adhesion to the polymer matrix. The influence of NaOH treatment on the surface morphology and crystallinity of the bamboo fibres was examined using Fourier-transform infrared spectroscopy (FTIR), scanning electron microscopy coupled with energy-dispersive X-ray spectroscopy (SEM/EDS), and X-ray diffraction (XRD). A Box–Behnken design (BBD) within the response surface methodology (RSM) framework was employed to construct the experimental matrix and optimize the mixing conditions. The optimized parameters were predicted to be a bamboo fibre content of 35.9wt%, a mixing time of 3.9 minutes, and a mixing temperature of 27.5°C. The nanocomposites were fabricated using the lay-up technique, and their properties were characterized by FTIR, XRD, SEM, and Brunauer–Emmett–Teller (BET) analysis. The nanocomposites exhibited a BET surface area of 847.6 m²/g and an average pore diameter of 1.85nm confirming their microporous nature, a CO_2 adsorption capacity of 2.034 mmol/g at 110℃ under 1 bar pressure confirming their suitability for CO_2 adsorption.

Keywords: *Carbon capture; bamboo fibre; waste expanded polystyrene; nanocomposites; CO2 adsorption*

1. INTRODUCTION

Carbon capture is an essential technology for reducing carbon dioxide (CO_2) emissions, particularly because fossil fuels continue to provide a substantial proportion of the world's energy. It is expected to play a central role in achieving net-zero emissions by 2050 and beyond. Existing carbon-capture technologies are primarily designed for heavy industries but require further refinement because they often involve hazardous chemicals and substantial energy consumption. Consequently, these systems are costly and complex to construct. Captured carbon can either be stored or reused, potentially creating an additional revenue stream (Nikita *et al*., 2025).

The development of adsorbents with high adsorption capacities is fundamental to achieving effective adsorption performance. Various materials have been investigated for CO_2 adsorption, including zeolites, metal oxides, mesoporous silica, and activated charcoal (Gowthaman *et al*., 2021). Solid sorbents, such as porous organic polymers, activated carbon, zeolites, and metal–organic frameworks, have gained increasing attention because of their high adsorption efficiency, durability, and operational simplicity (Ting *et al*., 2020).

Plastic pollution remains a persistent global problem, as the large-scale production of disposable plastics exceeds the capacity of existing waste-management systems. Waste plastics can be engineered for pollutant removal and carbon capture, providing a practical and sustainable pathway for managing plastic waste while contributing to efforts to mitigate global warming associated with carbon emissions. This approach supports the development of a cleaner and more sustainable future (Jiacheng & Qian, 2024). Such materials address plastic-waste challenges while offering cost-effective and efficient solutions for environmental remediation, in some cases outperforming commercial adsorbents (Pritesh *et al.*, 2024).

Bamboo fibre, a renewable and biodegradable material, can be combined with waste expanded polystyrene, a common packaging-related pollutant, to reduce landfill demand and plastic contamination (Peng *et al*., 2022). This strategy supports a circular economy by reducing reliance on virgin polymers and lowering the carbon footprint through the use of environmentally friendly reinforcement. Nanocomposites produced from these materials may demonstrate improved mechanical properties, including greater tensile strength, as a result of bamboo's high cellulose content and strong fibre–matrix bonding. They may also offer low density, good thermal stability, and reduced water absorption compared with conventional plastics (Chin-Hao & Teng-Chun, 2020).

This study is strongly motivated by the need for sustainable, environmentally friendly, and cost-effective materials capable of addressing both agricultural-waste management and plastic pollution. Integrating bamboo fibre with waste expanded polystyrene can produce a high-performance, lightweight composite while transforming waste materials into valuable industrial resources (Chen *et al*., 2016). Both raw materials are widely available; however, WEPS is a significant contributor to landfill pollution because of its high volume-to-mass ratio (Farid & Ahad, 2022).

2. MATERIALS AND METHODS

The primary materials used in this investigation were waste expanded polystyrene (WEPS) (Fig. 1), collected from electronics shops along Ahmadu Bello Way in Kaduna State, Nigeria, and bamboo (Bambusa vulgaris) fibres (BF), sourced from Basawa Market in the Zaria district of Kaduna State, Nigeria.

2.1 Preparation of Bamboo Fibre Nanopowder

Fresh bamboo culms were collected and washed thoroughly to eliminate soil, debris, and other contaminants from their surfaces. The cleaned culms were then reduced to chips approximately 2.0–5.0 cm in length (Fig. 1b) with a manually operated mechanical cutter, this preliminary size reduction increased the surface area exposed during chemical treatment. The chips were immersed in a 10wt% sodium hydroxide (NaOH) solution for 2–4 hours (Fig. 1a). The alkaline treatment was used to remove hemicellulose, lignin, and pectin, thereby loosening the fibre bundles and promoting cellulose separation. A bamboo-chip-to-NaOH-solution ratio of 1:10 (w/v) was maintained to ensure sufficient alkali penetration. The fibres were oven-dried for 8 hours at 80°C until a constant weight was obtained. The dried bamboo fibres were ground using a ball until they were reduced to fine powder sized particles of 75 nm (Fig. 1c).

Figure 1: (a) Bamboo Fibres Soaked in NaOH solution (b) Dried Bamboo Fibres (c) Bamboo Fibre Powder

Dynamic light scattering (DLS) was employed to establish the particle-size distribution of the bamboo fibre nanopowder. In this analysis, a laser beam was passed through the dispersed sample, and the scattering generated by particle–beam interactions was evaluated with a DLS instrument.

2.2 Characterization of Bamboo Fibre Nanopowder (BFNP)

The bamboo fibre nanopowder was characterized through physical, chemical, and thermal analyses. The assessment covered its proximate composition, morphology, crystalline structure, surface characteristics, and mechanical and thermal properties.

2.2.1 Fourier transform infrared spectroscopy (FTIR)

The functional groups in the bamboo fibre samples were identified with a Fourier transform infrared spectrometer (FT/ IR-4700, JASCO International Co., Ltd., Pfungstadt, Germany). Samples were analyzed both before and after NaOH treatment to identify the existing functional groups and determine the changes induced by alkalization. Particular emphasis was placed on hydroxyl (OH) groups because of their role in moisture uptake by cellulosic fibres. Approximately 2 mg of each sample was blended with KBr and compressed into pellets. Spectra were collected between 4000 and 500 cm^{-1} at a resolution of 4 cm^{-1}

2.2.2 Scanning electron microscopy (SEM)

Scanning electron microscopy was performed in accordance with ASTM E766 to investigate the surface morphology and microstructure of the untreated and treated fibres. The raw bamboo nanopowder was examined with a scanning electron microscope (Phillips XL 30 ESEM, FEI Company, Hillsboro, OR, USA) fitted with a large-field detector. Micrographs were acquired at an accelerating voltage of 15 kV and magnifications of 100× and 500×. For examination, 10 µL of sample was placed on a copper grid and dried under light for 15 minutes. SEM analysis yielded information about fibre roughness, surface imperfections, and the likelihood of interfacial adhesion, which are significant factors in composite-material applications (Hobtemariam *et al*., 2025)

2.2.3 X-ray diffraction (XRD)

The bamboo fibre was analyzed by X-ray diffraction using a PANalytical Empyrean diffractometer equipped with a cobalt target, rotating sample stage, and goniometer operating in the 2θ configuration. The cobalt source produced radiation with a wavelength of 0.179 nm. The generator settings were 40 kV and 45 mA. Diffraction intensities were measured across a 2θ range of 5°–110°, with a step interval of 0.0167° and a scan rate of 0.015°/s. The crystallinity index was determined using the Segal equation (Equation 1), which estimates the relative amounts of crystalline and amorphous phases that influence fibre strength and thermal stability (Szaosky *et al*., 2024):

$$CrI\ (\%) = [(I_{002} - I_{am})/I_{002}] \times 100 \quad (1)$$

In this equation, I_{002} is the maximum intensity of the 002 lattice reflection, representing the primary peak of native cellulose at 2θ = 22.5°, whereas I_{am} is the diffraction intensity associated with the amorphous region (Yang *et al*., 2023).

2.3 Design of Experiments (DoE)

Response surface methodology (RSM) using the Box–Behnken design (BBD) implemented in Design-Expert software was used to analyze the experimental data, generate the design matrix, and determine the optimum mixing conditions. The experimental design incorporated three factors at three levels. Numerical optimization was conducted with fibre loading (wt%), mixing time (min), and mixing temperature (°C) as the independent variables, while tensile strength (TS) served as the response variable.

2.4 Preparation of BFNP/WEPS Nanocomposite

The bamboo fibre nanopowder/waste expanded polystyrene (BFNP/WEPS) nanocomposite was fabricated through solution casting followed by compression molding. A schematic of the preparation process is provided in Fig. 2.

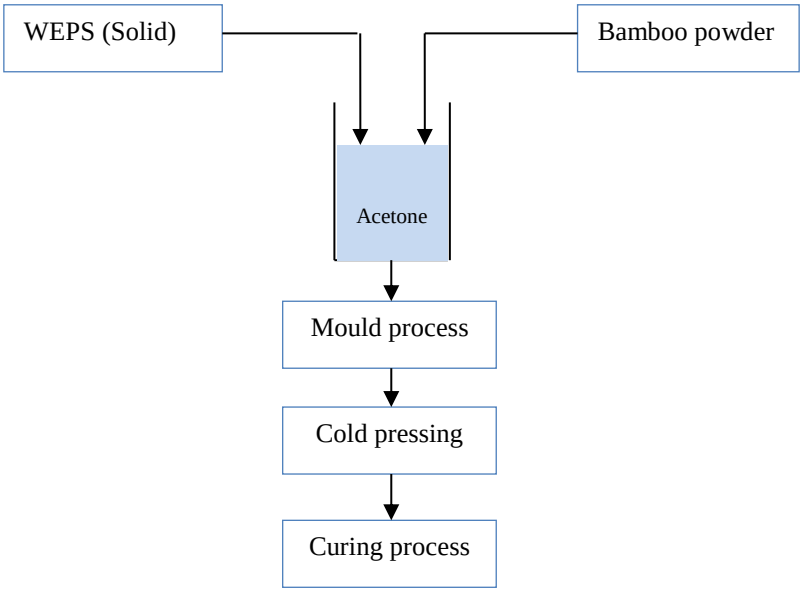

Figure 2: Block Flow Diagram for Preparation of BFNP/WEPS Nanocomposite

A 1.5 kg quantity of solid WEPS waste was dissolved in 1 L of acetone and stirred until a consistent solution formed. The bamboo fibre powder was then combined with the dissolved WEPS in a container and thoroughly blended with a mechanical mixer. The mixture contained 35wt% bamboo fibre powder, corresponding to the optimum loading identified through BBD optimization, and 65wt% dissolved WEPS paste. Mixing was continued until a uniform blend was obtained. The blend was poured into a wooden mold coated with petroleum jelly to minimise adhesion and manually compacted using a 150kN compression-molding machine (Hemel Hempstead, Hertfordshire, England). The molded BFNP/WEPS nanocomposite was cured and dried for 21 days before being removed from the mold and subjected to further analysis.

2.5 Characterization of BFNP/WEPS Nanocomposites

The prepared BFNP/WEPS nanocomposites were examined through physical, mechanical, and chemical analyses to assess their properties and performance.

2.5.1 Brunauer–Emmett–Teller (BET) analysis

BET analysis involved exposing the porous solid to nitrogen molecules at the boiling point of the inert gas. The procedure was conducted in accordance with ASTM B922-10. Approximately 0.5 g of sample was placed in a sample cell and degassed to eliminate moisture, volatile substances, and other impurities. The degassed material was subsequently installed in a BET analyzer (Quantachrome Nova Instruments, version 11.03) and exposed to nitrogen across a range of relative pressures. The equilibrium volume of adsorbed gas was measured to produce a Type IV adsorption isotherm.

2.6 CO_2 Adsorption Experiment

As shown in Fig. 3, a fixed-bed reactor was assembled to measure the CO_2 adsorption capacity of the adsorbent and evaluate the effects of important operating variables through a

gravimetric technique. This method is especially appropriate at low pressures because almost the entire measured gas dose is adsorbed.

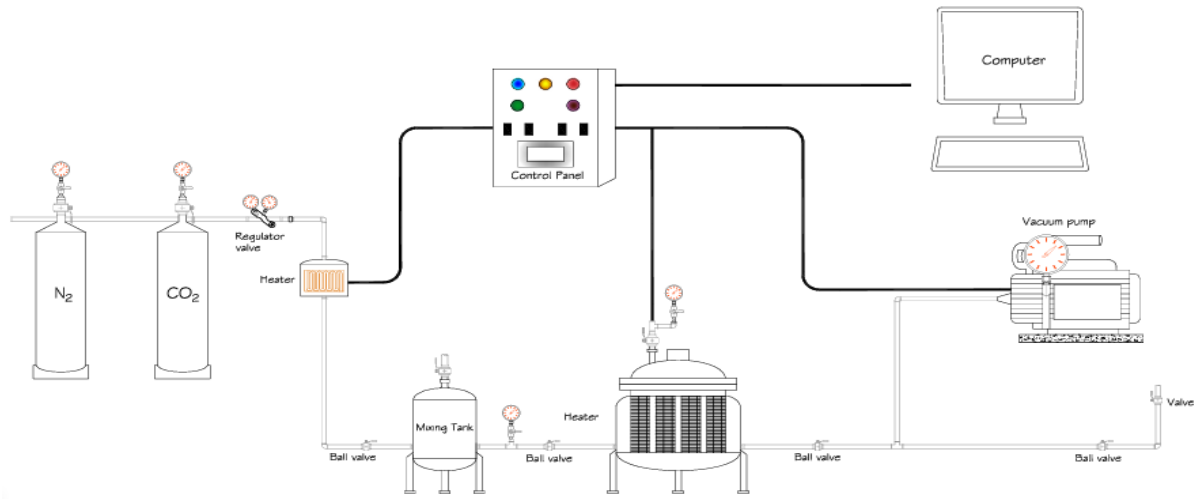

Figure 3: The Experimental Setup for Measuring CO_2 Adsorption

The reactor was cylindrical, with an internal volume of 100 cm³. For each run, 1.5 g of solid adsorbent was placed in an internal reactor compartment. Prior to every experiment, the adsorbent was heated under a pure N_2 stream for 30 minutes at 110℃ and subsequently evacuated for 30 minutes to remove previously adsorbed CO_2 and moisture. High-purity CO_2 from the cylinder was adjusted to the desired pressure with a pressure regulator and gauge before being introduced into the mixing tank. Stable gas was delivered to the adsorbent reactor and the mass of adsorbent after adsorption was measured using a digital weighing balance. The CO_2 uptake was calculated using equation 3.

$$q = \Delta m/M \quad (3)$$

Where, q is the CO_2 uptake, $\Delta m = m_1 - m_0$ (m_0 is the mass of adsorbent before adsorption, m_1 is mass of adsorbent after adsorption) and M is the molar mass of CO_2 (44.01 g/mol).

3. RESULTS AND DISCUSSION

This section presents and analyzes the results obtained from the experimental investigations. It is divided into two principal parts. The first addresses the characterization of bamboo fibres, whereas the second presents the characterization results for the nanocomposite produced from bamboo fibres and waste expanded polystyrene (WEPS).

3.1 Characterization of Bamboo Fibres

The experimental design (BBD/RSM optimization of mixing parameters) and multi-technique characterization (FTIR, SEM/EDS, XRD, and BET) show methodological rigor and critically analyze the bamboo fibre material.

3.1.1 FTIR analysis of raw bamboo fibre

Fourier transform infrared (FTIR) analysis was used to identify the absorption peaks and their corresponding wavenumbers, thereby determining the functional groups present and evaluating the chemical changes associated with the alkaline treatment of the bamboo fibres. The spectra obtained for the raw bamboo fibres are shown in Figure 4.

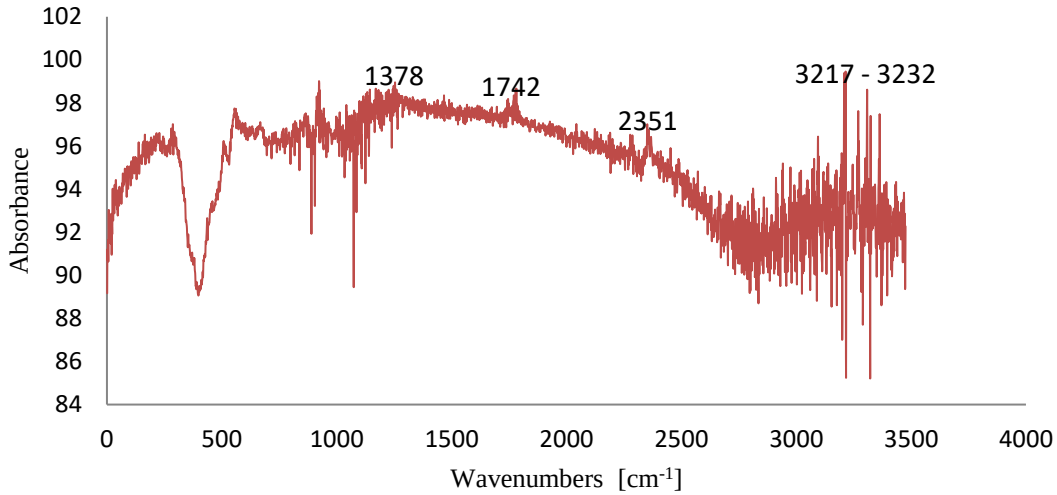

Figure 4: FTIR Spectrum of Raw Bamboo Fibre

The spectrum indicates the presence of several undesirable constituents, including hydroxyl (OH) groups, pectin, wax, hemicellulose, and lignin. The principal absorption peaks are clearly identified in the spectrum. The absorption band near 3200 cm^{-1} is associated with fatty acids and is attributed to O=H stretching vibrations. A weak absorption band also appears at 1378 cm^{-1}, indicating the presence of lignin and corresponding to C=C stretching vibrations. In addition, the peak observed at 1742 cm^{-1} indicates the presence of waxes and fatty-acid esters and is attributed to C=O vibrations.

3.1.2 XRD analysis of bamboo fibre

The X-ray diffraction (XRD) patterns presented in Fig. 5 compare the raw and chemically treated bamboo fibres. The patterns show a broad diffraction feature near 2θ = 22°, confirming the crystalline nature of the fibre. Three principal diffraction peaks occur at 2θ = 15.4°, 17.4°, and 22.5°, corresponding to the 1–10, 110, and 200 planes, respectively. The sharp peak near 2θ = 22° is characteristic of cellulose. Specifically, the diffraction peak at 22.0° corresponds to the 002 crystallographic plane of the cellulose I lattice. These three characteristic reflections are commonly associated with cellulose Iβ in natural fibres, in which the cellulose chains are arranged in parallel and connected by hydrogen bonding. Although cellulose occurs naturally in both the Iα and Iβ forms, cellulose Iβ is the form predominantly found in higher plants and was therefore considered in this analysis.

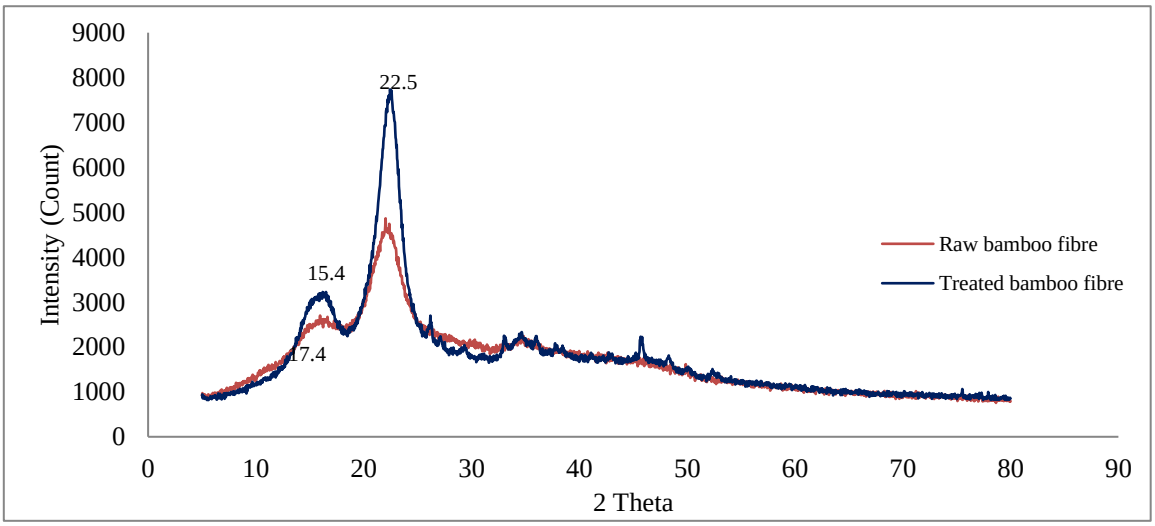

Figure 5: XRD Spectrum of Raw and Treated Bamboo Fibres

The crystallinity index (CrI) was determined using the empirical Segal method. The crystallinity indices calculated for the raw and treated bamboo fibres are presented in Table 1.

Table 1: Crystallinity Index of Bamboo Fibres

Bamboo Fibre	I (002)	I_{am}	CrI (%)
Raw	4778	2515	47
Treated	7596	3045	60

The treated bamboo fibre shows higher crystallinity than the raw bamboo fibre and lower than those of most of natural fibres like jack tree fibre with crystallinity index of 86% (Shahin *et al.*, 2025) and hemp with crystallinity index of 88% (Gedik *et al.*, 2021). High crystallinity means excellent strength of the fibre and they can provide better reinforcement for composite production, the crystallinity index also has effect on water absorption as amorphous region can absorb more water.

3.2 Optimization of Mixing Parameters Using BBD

The mixing parameters for the BFNP/WEPS Nanocomposite were optimized using the Box–Behnken design (BBD) module of response surface methodology. The responses obtained for the selected mixing conditions used to prepare the nanocomposite are presented in Table 2.

Table 2: Responses of the Mixing Parameters for the BFNP/WEPS Nanocomposite

Std	Run	Factor 1 A: Fibre Loading (wt %)	Factor 2 B: Mixing Time (min)	Factor 3 C: Mixing Temp (C)	Response Tensile Strength (MPa)
17	1	15	3	27.5	43.6
3	2	50	5	27.5	31.1
16	3	35	1	27.5	42.9
12	4	50	5	50	44.1
7	5	50	3	50	24.2
4	6	35	1	27.5	39.6
11	7	35	5	50	41.5
14	8	50	5	27.5	42.7
15	9	35	1	2 7.5	43.3
2	10	15	3	27.5	37.3
1	11	15	3	27.5	26.6
6	12	50	3	35	21.2
13	13	50	5	27.5	42.9
9	14	35	5	35	26.7
8	15	35	1	50	44.2
10	16	50	5	35	31.9
5	17	50	3	35	20.2

A second-order polynomial regression model was developed to establish the relationship between the processing factors and the tensile strength response. The resulting equation, expressed in terms of coded factors, is given as follows:

$$TS = +43.08 + 5.03A + 1.83B + 6.75C + 0.55AB + 4.75AC - 0.65BC - 9.02A^2 - 0.42B^2 - 6.61C^2 \quad (2)$$

Desirability converts each response variable into a dimensionless scale ranging from 0, representing an undesirable result, to 1, representing an ideal result. The individual desirability values are then combined to produce an overall desirability score, D, as shown in Table 3. This procedure facilitates the simultaneous evaluation of multiple responses by providing a single optimization metric and thereby supporting more efficient decision-making. The score reflects the preferred range established for each response.

Table 3: Response Optimization and Desirability of the Mixing Parameters

Number	Fibre Loading.	Mixing Time	Mixing Temp	Tensile Strength	Desirability
1	35.112	3.291	25.788	44.271	1
2	35.654	3.915	25.014	45.429	1
3	35.618	3.738	25.752	45.228	1
4	35.239	3.394	25.714	44.552	1
5	35.827	3.226	25.775	45.538	1
6	35.859	3.957	25.946	45.551	1
7	35.963	3.963	25.763	45.716	1
8	35.147	3.908	25.951	44.311	1
9	35.891	3.619	25.987	45.581	1
10	35.369	3.572	25.747	44.798	1

To provide additional validation of the model, two conditions, corresponding to the first and seventh experimental runs, were selected. The predicted values were calculated from the centre points between the high, intermediate, and low factor levels. Confirmatory experiments were subsequently conducted to assess the reliability of the model. The percentage error for tensile strength was calculated by comparing the predicted values with the experimentally measured values. The validation results are presented in Table 4.

Table 4: Confirmatory Experiments

Fibre Loading (g)	Mixing Time (min)	Mixing Temp (ºC)		TS (MPa)
			Actual	42.21
35.112	3.291	25.788	Predicted	44.27
			Error%	3.06
			Actual	43.78
35.963	3.963	25.763	Predicted	45.716
			Error%	1.936

The absolute relative errors between the predicted and experimental values were 3.06% and 1.96%, respectively. Because both values are below 5%, the developed prediction models for the tensile strength (TS) of the BFNP/WEPS nanocomposite can be considered accurate and reliable.

3.3 Characterization of BFNP/WEPS Nanocomposites

To obtain a comprehensive understanding of the behavior of the BFNP/WEPS nanocomposites, a series of mechanical, physical, and thermal tests were conducted on the prepared materials.

3.3.1 FTIR analysis of the BFNP/WEPS nanocomposite

The FTIR spectra of the BFNP/WEPS nanocomposite presented in Fig. 6 contain distinct absorption bands associated with cellulose and hemicellulose, confirming the characteristic lignocellulosic composition of the bamboo fibres. The broad band cantered at 3480 cm^{-1} is assigned to the O–H stretching vibrations of hydroxyl groups. This band indicates the presence of absorbed water, free phenols, and primary and secondary aliphatic alcohols occurring in cellulose and hemicellulose.

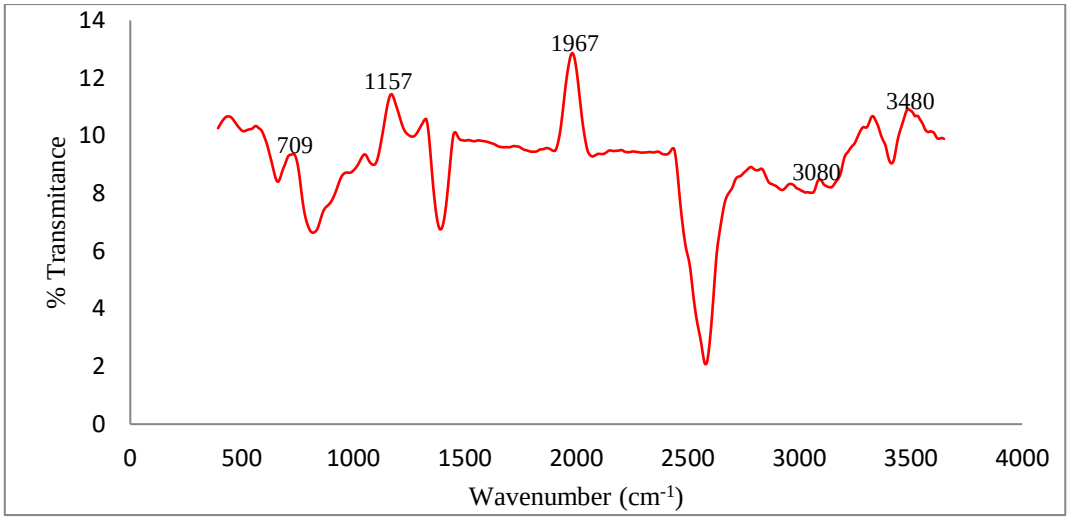

Figure 6: FTIR Spectrum for BFNP/WEPS Nanocomposites

The band at 1967 cm^{-1} is related to the stretching vibrations of aliphatic C–H groups, particularly CH_2, and further confirms the presence of cellulose and hemicellulose. The absorption band at 1157 cm^{-1} corresponds to C=O stretching vibrations associated with carbonyl groups, which are attributable to the acetyl groups commonly found in hemicellulose. In spectra containing WEPS, the bands observed between 3000 and 2800 cm^{-1} are assigned to C–H stretching vibrations associated with hydrocarbons in the WEPS. The band at 709 cm^{-1} is related to phenyl-ring substitution. Its presence alongside the cellulose-related signals confirms the incorporation of bamboo natural fibres.

3.3.2 SEM analysis of BFNP/WEPS nanocomposites

SEM analysis was conducted to examine the morphology of the produced nanocomposite. The micrograph in Fig. 7 shows that the bamboo fibres were distributed uniformly throughout the polymer matrix. This homogeneous dispersion is responsible for the strong interfacial adhesion between the fibres and the polymer matrix (Mohan *et al*., 2020). In addition, the expansion of gas bubbles within the freshly dissolved expanded polystyrene paste, caused by acetone evaporation under reduced pressure, forced the thin layer of the paste into contact with the particle surfaces. This process may have influenced the compounding behaviour and mechanical interlocking between the bamboo fibres and the WEPS matrix. The SEM examination also revealed microstructural damage mechanisms, including fibre–matrix debonding, fibre swelling, and matrix cracking. These features are broadly comparable to those reported for date-palm-leaf-fibre-reinforced composites (Hobtemariam *et al*., 2025). The polymer matrix was observed to wet the fibres effectively, thereby promoting strong interfacial bonding.

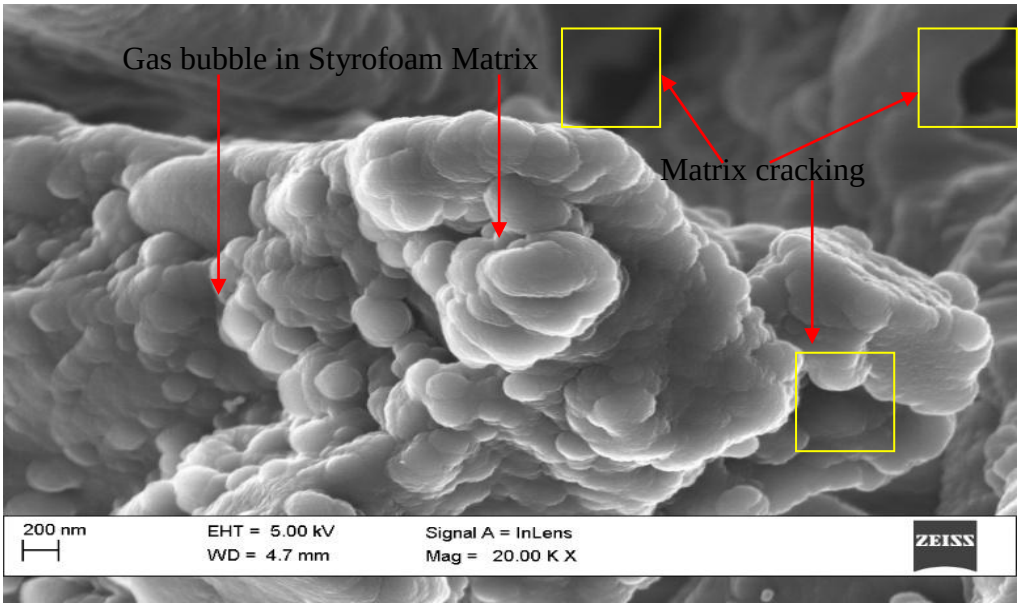

Figure 7: SEM Spectrum of BFNP/WEPS Nanocomposite

3.3.3 BET analysis of BFNP/WEPS nanocomposite

The BET analysis demonstrated that the BFNP/WEPS nanocomposite is highly porous. As shown in Table 5, the material exhibited a Brunauer–Emmett–Teller surface area of 847.6 m^2/g and an average pore diameter of 1.85 nm, indicating a predominantly microporous structure. According to the International Union of Pure and Applied Chemistry (IUPAC), microporous materials have pore diameters not exceeding 2nm. Based on the 1972 recommendations for physisorption, pores are classified as micropores when their diameters are below 2nm, mesopores when they range from 2 to 50nm and macropores when they exceed 50nm.

Table 5: Porosity Properties

Parameter	BFNP/WEPS nanocomposites
BET Surface area	181.9 m^2/g
BJH pore volume	0.16 cm^3/g
BJH pore diameter	1.85 nm
Langmuir surface area	847.6 m^2/g
DR micropore volume	0.164 cm^3/g

Under the IUPAC classification, materials with a high proportion of micropores and a uniform micropore size distribution below 2nm possess important characteristics for effective and selective CO_2 adsorption. The measured micropore volume of 0.16cm^3/g and average micropore diameter of 1.85nm can readily accommodate the relatively small CO_2 molecule, which has a kinetic diameter of approximately 0.33 nm. Micropores therefore provide favourable structural conditions for CO_2 adsorption in porous adsorbents (Telmo *et al*., 2025). The narrow pore structure corresponds well with the kinetic diameter of CO_2, enhancing adsorbate–adsorbent interactions and selectivity relative to N_2 (Lei *et al*., 2025). Similarly, metal–organic frameworks (MOFs) and zeolites benefit from narrow pores, typically measuring approximately 3.5–8 Å, to achieve high CO_2 uptake.

4. CONCLUSION

Waste expanded polystyrene and bamboo fibres were converted into a nanocomposite through a simple and cost-effective process, producing a material with potential application as an adsorbent for CO_2 capture. FTIR, SEM, XRD, and BET analyses were conducted to investigate the structure and

morphology of the nanocomposite. The material exhibited a specific surface area of 847.6m²/g and an average pore diameter of 1.85nm, confirming its microporous nature. The adsorbent material demonstrates a CO_2 uptake capacity of 2.034mmol/g at 110℃ and 2 bars. Because micropores are particularly favourable for the adsorption of small molecules, confirming their suitability for CO_2 adsorption the uniform porous structure of the BFNP/WEPS nanocomposite indicates its potential as an effective, low-cost precursor for the production of adsorbents for CO_2 capture.

REFERENCES

Chen, H. Cui, Y. Liu, X. Zhang, M. Hao, S. & Yin, Y. (2016). Study on depositing SiO_2 Nanoparticles on the Surface of Jute Fibre via Hydrothermal Method and its Reinforced Polypropylene Composites. Journal of Vinyl Additive Technology. 26, 43–54

Chin-Hao, Y. and Teng-Chun, Y. (2020). Utilization of Waste Bamboo Fibres in Thermoplastic Composites: Influence of the chemical composition and thermal decomposition behaviour. Journal of Polymer (Basel). Volume11; 12 (3): 636. doi: 10.3390/polym12030636

Farid M., Gity M. and Ahad G. (2022). Synthesis and Characterization of Waste Styrofoam Hypercrosslinked Polymer as an Adsorbent for CO_2 Capture, Environmental Progress and Sustainable Energy, DOI: 10.1002/ep.13954.

Gedik, M., Javzanolgar, B., Enkhsaruul, B and Naoto, T. (2025). Pore properties and CO_2 adsorption performance of activated carbon prepare from various carbonaceous materials. Journal of carbon resourses conversion. 8, 1, 100237.

Gowthaman, N., Hn, L, Sreeraj, T and Augustine, A (2021). Advantages of biopolymers over synthetic polymers. Polymers and their industrial applications. pp – 351 -372

Hobtemariam, M.A., Teshome, M.B. and Velmurugan, P. (2025). Studies on mechanical properties characterization of hybrid sisal and stinging nettle fibre reinforced epoxy composite material. Journals of Material Research and Technology. 37, PP- 5086-5102

Jiacheng, W. and Qian, L. (2024). An efficient one-step condensation and activation strategy to synthesize porous carbons with optimal micropore sizes for highly selective CO_2 adsorption. Journal of Nanoscale. 12, 34-47

Lei, M. Ansari, M. N., Grace, P., Mohammad, J. & SaifulIslam, M. (2025). A Review on Natural Fibre Reinforced Polymer Composite and Its Applications. Hindawi Publishing Corporation International Journal of Polymer Science, Article ID 243947, http://dx.doi.org/10.1155/2015/243947

Mohan, A. K., Misra, M. & Hinrichsen, G. (2000). Biofibres, biodegradable polymers and biocomposites: an overview. Macromol Material Engineering 276–277:1–24

Nikita Y., Parveen K. and Ashootosh M. (2025), Beyond Land Fills; Transforming Waste Plastics Into Advance Building Material. Environmental Hazards of Plastic Wastes. 249 -260. Doi.org/10/1016/B978-0-443-23599

Peng, J., Xiaoqian, J., Bin, Z., Chunyang, W.,Wenjie, H. an Wenjia. H (2022). Eco-friendly and complete recycling of waste bamboo-based disposable paper cups for value-added transparent cellulose-based films and paper plastic composite

Pritesh, G., Kabir, R and Balasubramanian, K (2024). Polymer base biochar materials for environmental remediation: A review. Journal of Hybrid advances. 6, 100-117. https://oi.org/10.1016/j.hybav.2024.100267

Shahin, H., Abuljali, M., Tarik, I. and Rahman, M. (2022). A low density cellulose rich new natural fibre extracted from the back of jack tree branches and its characterizations. Heliyon, 8 (11):e11667. DOI: 10.1016/i.helion22e1167

Szadkowski, A., Marzec, M., Ku´smierek, M., Piotrowska, D., Moszy´nski, T. (2024). Functionalization of bamboo fibers with lawsone dye (Lawsonia inermis) to produce bioinspired hybrid color composite with antibacterial activity, Int. J. Biol. Macromol. 259 129178

Telmo, E., Maria, J., Gabriella, M and Helena, C.V. (2025). A Review f natural fibres: classification, composition, extraction, treatments and applications. Journal of fibres. 10.3390/fib13090119

Ting, Z., Guolong, X., Weiben C and Long, C (2020). Porous organic polymers: a promising platform for efficient photocatalysis. Journal of Material Chemistry Frontiers. Review-type article. Issue 2, 67 – 87

Yang, B., Wang, C., Chen, S., Qiu, K., and Jiang, J. (2023) Optimisation of the Mechanical Properties and Mix Proportion of Multiscale-Fibre Reinforced Engineered Cementitious Composites. Polymers, 15, 3531. https://doi.org/10.3390/ polym15173531

International Conference on Engineering Innovation for Sustainable Development (ICESID 2026)
Faculty of Engineering, Ahmadu Bello University Zaria · 8–10 September 2026

PROBABILISTIC RELIABILITY ANALYSIS OF REINFORCED METAKAOLIN-BASED GEOPOLYMER CONCRETE BEAMS SUBJECTED TO VARIATIONS IN GEOPOLYMER MIX PARAMETERS

Ibrahim Aliyu[1,*], I.o Sholadoye[1], J. M. Kaura[1], A. A. Abbas[2], Jamilu Yau[3]

[1]*Department of Civil Engineering, Ahmadu Bello University, Zaria*
[2]*Bankanu and Partners Limited, Suite 001, Basement Level, Mortgage House, Central Business District, Abuja*
[3]*Department of Building. Abubakar Tafawa Balewa University. Bauchi State*

Email: ibrahimaliyu@abu.edu.ng*, kemshol1977@gmail.com, jmkaura@abu.edu.ng, aaaliyumm@gmail.com, yaumsc3748@gmail.com

***Corresponding author**: Ibrahim Aliyu

DOI: https://doi.org/10.67203/sp.ICESID.2026

ABSTRACT

The study investigated the probabilistic effect of NaOH Molarity (Mc), Na_2SiO_3:NaOH (ALr), and alkaline-liquid:Metakaolin (ALm), on the reliability of metakaolin-based geopolymer concrete beams reinforced with two (2) 8 mm bars as tension reinforcement under a failure load of 39 kN. The assessment was performed using the First Order Reliability Method (FORM). Compressive strength models were developed for the investigated variables, which were incorporated into the failure modes limit-state equations through the FORM5 package to evaluate the beam's reliability. The probabilistic analyses were conducted by varying Mc (6-16 M), ALr (0.5-2.5) and ALm (0.4-1.0). Results from the analyses showed that the models explained 63.4% and 93.2% of the compressive strength variations, respectively, for Mc/ALr and ALm/Wc. Additionally, increasing Mc from 6 M to 10 M improved the reliability of the Reinforced Metakaolin Based Geopolymer concrete (RMBGC), whereas further increase to 12 M and beyond reduced reliability. Increasing ALr from 0.5 to 2.5 and ALm from 0.4 to 1.0 consistently enhanced the reliability. Among all variables, ALm exerted the greatest influence, producing the largest improvement in safety index across all failure modes. It was also noted that the Moment failure mode was most sensitive to mix-parameter variations, followed by shear, while deflection was least affected. In general, the study demonstrates that optimising ALm, ALr, and Mc (approximately 10 M) provides the greatest improvement in the reliability and structural safety of metakaolin-based geopolymer reinforced concrete beams.

Keywords: *Reinforced Metakaolin-Based Geopolymer concrete; First-Order Reliability Method (FORM); Safety index; Mix design parameters*

1.0 INTRODUCTION

Research into alternatives to ordinary Portland cement (OPC) has been ongoing due to the fact that OPC is not sustainable. This is connected to the amount of carbon dioxide emitted during cement production. One of the most promising alternatives is geopolymer cement, which is produced by activating aluminosilicate materials such as metakaolin with alkaline solutions. Unlike OPC concrete, the binding phase in geopolymer concrete is formed through a geopolymerization process. The resulting concrete from the geopolymerisation has better mechanical properties, improved durability, and lower environmental impact (Davidovits, 1991).

The performance of geopolymer concrete depends largely on its mix composition. It was reported that the chemical composition in terms of the concentration of sodium hydroxide, the ratio of sodium silicate to sodium hydroxide, the alkaline liquid-to-binder ratio, and the water content significantly influences the geopolymerization reaction and consequently the strength and durability of the hardened product (Diaz et al., 2010). For metakaolin-based geopolymer concrete in particular, these parameters determine the extent of aluminosilicate dissolution, gel formation, and the development of compressive strength. Hence, a proper selection of these mix variables is important in achieving the desired structural performance.

Several studies have investigated the influence of mix proportions on the compressive strength and durability of geopolymer concrete. The studies did not incorporate uncertainties and did not study the effects on the safety of a structural member. This is because, in reality, material properties are associated with uncertainties that may influence the behavior and safety of structural members. These uncertainties can only be adequately considered through probabilistic methods, where the variability of the governing parameters is incorporated into the structural assessment rather than relying solely on characteristic values. A few studies checked the effect of the variability of the concrete mix materials on the reliability of structural members; some of these studies include Adamu et al, (2023), who considered the effect of mix variability on the structural safety of Nano-Engineered concrete and found that Mix design variability significantly changes the reliability index and failure probability. Adamu et al. (2024) also checked the reliability of Nano-Engineered RC beams and demonstrated the integration of material variability into Eurocode reliability assessment.

The performance of geopolymer concrete in terms of structural safety can be evaluated using probabilistic reliability analysis. In structural engineering, reliability is defined as the ability of a structural component to perform its intended function for a specified period under stated conditions without failure (Mohammed et al., 2014). Qianru and Ang (2013) stated that reliability-based analysis provides a rational means of accounting for uncertainties in material properties, geometry, and applied loads. The reliability of a structural member is commonly expressed in terms of its probability of failure or safety (reliability) index. The reliability of reinforced concrete members is also influenced by the adopted design provisions and the uncertainties associated with the constituent materials. García-Soto et al. (2017) opined that structural safety should be evaluated within a reliability framework to ensure that acceptable safety levels are maintained under different design conditions.

Based on the above statements, this study checks the effects of sodium hydroxide molarity, sodium silicate-to-sodium hydroxide ratio, and alkaline liquid-to-metakaolin ratio on the reliability of reinforced metakaolin-based geopolymer concrete beams using the First-Order Reliability Method (FORM). Developed compressive strength models developed from are incorporated into the failure modes for reliability analysis to evaluate the influence of material variability on the safety indices associated with flexural moment (In compression and Tension), shear, and deflection failure modes. The results from this study will be useful in identifying the failure mode that is most affected by the geopolymer materials and identifying the mix parameter that is most sensitive to the failure modes and hence, the structural reliability and safety of reinforced metakaolin-based geopolymer concrete beams.

2.0 MATERIAL AND METHODS

2.1 Materials:

The material use for the research were Metakaolin (Processed from kaolin calcination at 800^0C for 3 h, based on Moodi *et al.* (2011). The fine and coarse aggregates, NaOH and Na_2SiO_3 were sourced locally. Potable water available in the heavy-duty laboratory of the Civil Engineering Department, A.B.U, Zaria, was used.

2.2 Methods

2.2.1: Concrete Production: The proportioning of the mix constituents is mostly done by weight, as captured in Mustafa *et al*. (2011) and Sameer (2015). The fine and coarse aggregate ratio used was 1:2. The cement (metakaolin-based geopolymer cement) content used in the mix was based on the average 2400kg/m^3 concrete density. The NaOH Molar concentration, the ratio of Na_2SiO_3 to NaOH, and that of metakaolin to alkaline liquid were respectively 8 M, 3, and 0.9. The mixing and casting were in accordance with BS EN 12390-1 (2000) and BS EN 12390-2 (2000).

2.2.2: Production of Beam Specimen: Metakaolin-based geopolymer concrete beams reinforced with two (2) 8 mm diameter bars as tension reinforcement were produced. The beams had dimensions of 100 × 100 × 450 mm (short beam, because L/H <5 and shear span-to-depth ratio of 1 to 2.5).

2.2.3: Beam Test: The test was conducted per BS EN 12390 -5 (2009) (Plate I). Three (3) beams were produced with the same mix batch and reinforcement details were loaded to failure. The average failure load computed for the three beams was 39 kN.

Plate I: Centre Point Test of the Beam (3-point Bending Test)
The beam shown in Plate 1 was loaded at the centre point with rollers as supports

2.2.4 Compressive Strength Models: The models presented in equations (1) and (2) were developed by Aliyu (2021) using the Datafit statistical package (2019) to predict the compressive strength of the metakaolin-based geopolymer reinforced concrete beams.

$$f_{ck1} = -109.69 + 18.9Mc + 48.01ALr - 0.7163Mo^2 - 6.41ALr^2 - 1.98Mo * ALr \quad (1)$$

$$f_{ck2} = 80.109(ALm^{3.553}) \times 0.991^{Wc} \quad (2)$$

2.2.5 Probabilistic Reliability Analysis

Structural reliability according to Bai *et al.* (2018) is defined by:

$$R_r = 1 - P_f \quad (3)$$

Where P_f is the probability of failure. For the reliability (Probabilistic) analysis, the performance function or limit state function $(G(x))$ is defined by $G(x) = R - S$

2.2.5.1 Limit state functions

a) Performance Function for Moment Capacity

$$\boldsymbol{G_{mx}} = M_r - M_a \quad (4)$$

$$\text{where } M_a = \theta_S(0.25pl + 0.125\gamma_c bhgl^2 \times 10^{-9}) \quad (5)$$

Equation (5) is the applied moment as a function of the applied point load and the beam's self-weight. For the probabilistic analysis, the partial factors of safety for steel (1.15) and concrete strength (1.5) recommended by EC2 were removed, and the moment capacity equations (based on compressive and tensile capacity in EC 2) were re-derived to yield;

i. MOMENT OF RESISTANCE OF THE CONCRETE COMPRESSIVE STRUT.

$$M_r = 0.251\theta_R f_c bd^2 \quad (6)$$

ii. TENSILE MOMENT CAPACITY (MOMENT OF RESISTANCE)

$$\boldsymbol{M_r} = \theta_R f_{yk}\rho bd(d - \frac{f_{yk}\rho bd}{1.7f_c b}) \quad (7)$$

b) Performance Function for Shear Capacity

$$G_{vx} = V_c - V_a = \theta_R(0.18(1 + \frac{\sqrt{200}}{d})(\rho f_c)^{1/3})bd - \theta_S(0.5p + 0.5\gamma_c bhlg \times 10^{-9}) \quad (8)$$

Where M_r and M_a are the moments of resistance and applied moments, and V_c and V_a are the shear capacity and applied shear, respectively. $f_c, f_{yk}, p, g, \gamma_c, b, \rho, and\ \rho'$ are the concrete strength, steel yield strength, applied load, acceleration due to gravity, unit weight of concrete, beam width,

tensile reinforcement ratio, and compression steel reinforcement ratio, respectively. θ_R is the model uncertainty.

2.2.5.2 Form Process. FORM5 is a reliability analysis software developed based on the manual presented by Gollwitzer et al. (1988). It was used for the probabilistic analysis.

2.2.5.3 Stochastic (Statistical) Parameters

Table 1: Stochastic Table of Variables

S/No	Variable	Unit	Mean	COV	Distribution Type
1	Unit Weight of concrete (Y_c)	Kg/m^3	2400	0.01	Normal
2	Breath (B)	mm	100	0.002	Normal
3	Depth (D)	mm	100	0.003	Normal
4	Length (L)	mm	450	0.0006	Normal
5	Steel yield Stress (f_{yk})	N/mm^2	397.3	0.15	Normal
6	Compressive strength (f_{ck})	N/mm^2	32.8	0.09	Normal
7	Reinforcement ratio (ρ)	Nil	1.24	0.17	Normal
8	Live Load (Q_k)	kN	39	0.35	Gumbel
9	Molar Concentration (Mc)	Mol/L	varied	0.05	Normal
10	Alkaline Liquid ratio (ALr)	---	varied	0.05	Normal
11	Alkaline Liquid ratio Metakaolin (ALm)	---	varied	0.05	Normal
12	Resistance Model Uncertainty (θ_R)	---	1	0.07	Lognormal
13	Load Model Uncertainty (θ_S)	---	1	0.2	Lognormal

Source: Aliyu (2021), Adamu et al. (2014), Abejide (2014), and Mohammed et al. (2014)

It should be noted that the COV and distribution types for Mc, ALr, and ALm were assumed to be 0.05 based on 95% confidence in deviation from target value and because Lane (2020) reported that many natural phenomena are at least approximately normally distributed.

3.0 RESULTS AND DISCUSSIONS

3.1 Compressive Strength Predictive Models

The plots (Figures 1a and 1b) present the experimental values used as input data to develop the models and the predicted values by the developed models. In other words, the plots present the experimental compressive strength values and the predicted compressive strength values by Equations (1) and (2), respectively. The statistical package (Datafit) reported a coefficient of multiple determination (R^2) of 0.634 for eqn (1) (Proportion of variance explained = 63.4%), meaning that, based on eqn (1), ALr and Mc have explained 63.4% of the variation in the MBGC compressive strength, while eqn (2) has an R^2 value of 0.932 (Proportion of variance explained = 93.2%) for Alkaline liquid ratio metakaolin content (ALm) and water content (Wc). When using the R^2 approach, the unexplained proportion of the variation, based on Andrew (2017), is attributed to other factors not measurable by the researcher or not considered in the model. The author further noted that many models developed by researchers with small R^2 values produce useful predictions. It can be said that, although the model captures a substantial portion of the behaviour, the unexplained 36.6 % variance might propagate into the safety computation. This cannot be avoided except if a model explains 100% of the variation.

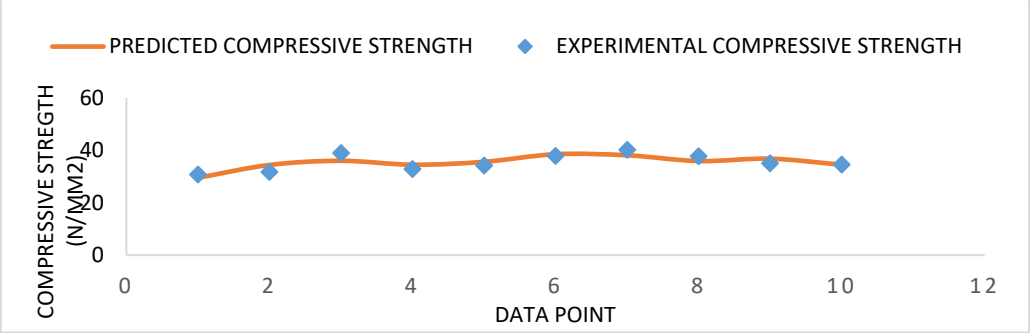

Figure 1a: Experimental and Predicted Data Points for equation 1 ($f_{c1}=f(Mc\ \&\ ALr)$)

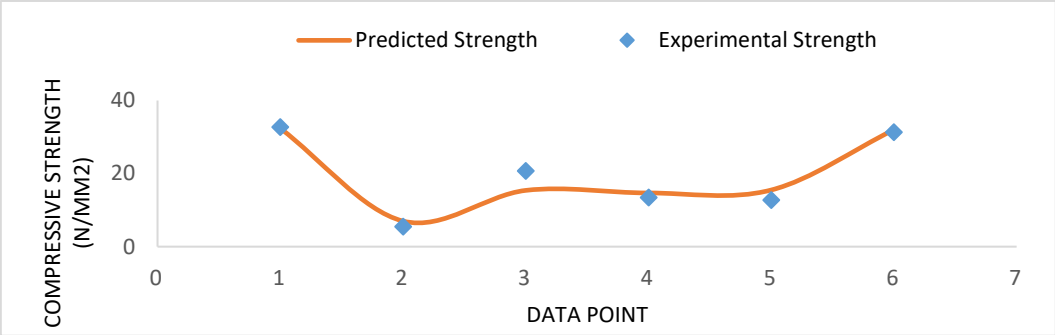

Figure 1b: Experimental and Predicted Data Points for equation 2 ($f_{c1}=f(ALm\ \&\ Wc)$)

3.2 Effect of Variations in Mc and ALr on the Safety Index

The effects of Mc, ALr, and ALm variations on the safety index are presented in Figures 2, 3, 4, and 5, respectively. Each parameter affects the safety index of beam failure modes positively or negatively. An increase in molar concentration (Mc) from 6M to 10M (Figure 2) increases the safety index but from 10M to 16M a decrease was recorded; this is because, for the ALm (0.9) used in the mix, between 6M and 10M, the geopolymer gets increasing ionic species necessary for geopolymeristion and hence higher strength and safer structure, but beyond 10M the alkalinity (Ph or Mo of NaOH) of the solution might have been non-conducive for the reaction as reported by Alonso and Palomo (2001), therefore, the safety index drops as a consequence of lower strength of the concrete. When ALr was increased from 0.5 to 2.5 at 8M (Figure 3), the safety index increased since the geopolymeriastion reaction is enhanced in the presence of more Na_2SiO_3.

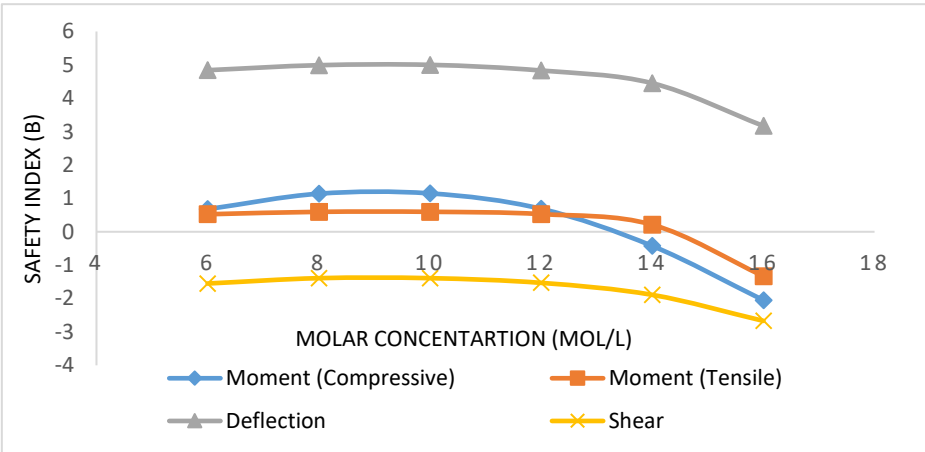

Figure 2: Molar Concentration (Mc) Effect on the Safety Index

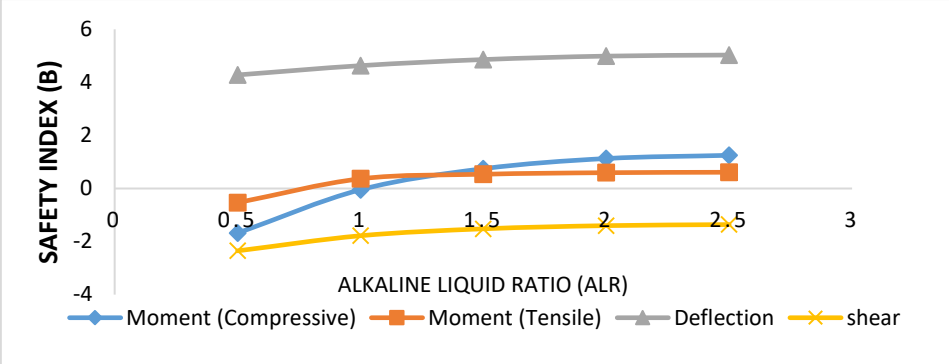

Figure 3: Alkaline Liquid ratio (Na_2SiO_3: NaOH or ALr) effect on the safety index

3.3 Effect of Variations in ALm on the Safety Index

The factor that has the most significant effect on the safety index is the alkaline liquid ratio Metakaolin (ALm) (Figure 4). The safety index values increase distinctly with an increase in ALm; this might be for the reason that, with lower ALm ratios, the mix does not have sufficient alkaline liquid (AL) to break down the Al and Si precursors, but with an increase in AL, more of the Al and Si precursors react, forming more geopolymer cement and achieving better concrete compressive strength. The moment (flexural) failure mode is the most affected, followed by the shear failure mode, and the least affected is the limiting deflection.

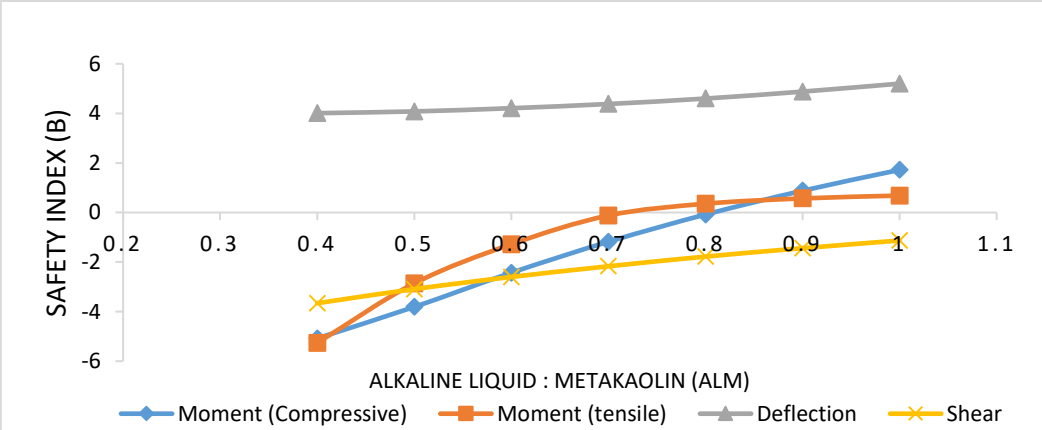

Figure 4: Alkaline Liquid: Metakaolin (ALm) Effect on the Safety Index

In summary, for all failure modes, an increase in Mc beyond 10M drops the safety index, while an increase in ALr up to 2.5 increases the safety index; Furthermore, an increase in ALm leads to a notable safety index increase.

Generally, the study also demonstrated that material variability significantly changes reliability index and failure probability, in agreement with Adamu et al. (2024).

4.0 CONCLUSIONS AND RECOMMENDATIONS

4.1 Conclusions

The conclusions derived from the study are;

1. The developed compressive strength models explained variation in compressive strength by 63.4% ($R^2 = 0.634$) for the Mc/ALr model, and by 93.2% ($R^2 = 0.932$) for the ALm/Wc model. This showed that the alkaline liquid-to-metakaolin ratio (ALm) is the primary variable controlling the compressive strength.
2. The mix composition that has the greatest influence on the safety/reliability index of metakaolin-based geopolymer reinforced concrete beam is the alkaline liquid-to-metakaolin ratio (ALm). Among the failure modes considered, the flexural (moment) failure was the most sensitive to the mix parameters.

3. Increasing the alkaline liquid ratio (ALr) up to 2.5 and molar concentration (Mc) from 6 M to 10 M improved the safety index. However, further increase beyond 10 M reduced structural safety.

   It is recommended that, for safety reasons, the production of metakaolin-based geopolymer concrete intended for structural members should place greater emphasis on the metakaolin-to-alkaline liquid ratio, as this parameter has the greatest influence on the safety and structural performance of the member.

REFERENCES

Abejide, O.S. (2014). Reliability Analysis of Bending, Shear and Deflection Criteria Of Reinforced Concrete Slabs. *Nigerian Journal of Technology* (NIJOTECH), 33(3). http://Dx.Doi.Org/10.4314/Njt.V33i3.18

Adamu, I. M., Kaura, J. M., Lawan, A., & Ocholi, A. (2023). *Reinforced concrete beam at ultimate limit state considering variability in the concrete mix design parameters*. FUDMA Journal of Sciences, 7(1), 136–147. https://doi.org/10.33003/fjs-2023-0701-1265

Adamu, I. M., Kaura, J. M., Lawan, A., Ocholi, A., & Mohammed, A. (2024). *Reliability analysis of nano engineered reinforced concrete beam*. FUOYE Journal of Engineering and Technology, **9**(3), 530–537. https://doi.org/10.4314/fuoyejet.v9i3.25

Adamu, L., Mohammed, J. K., Jaafar, A. S., and Ibrahim, A. (2014). Probabilistic Durability Analysis of Reinforced Concrete Members with Corroded Reinforcing Steel. *Jordan Journal of Civil Engineering*, 8,(3), 303-311

Aliyu I (2021). Experimental and Probabilistic Assesment of Reinforced Metakaolin-Based Geopolymer Singly Reinforced Concrete Beams. *An Unpublished PhD Thesis Presented to the Department of Civil Engineering*, Ahmadu Bello University, Zaria.

Alonso, S., and Palomo, A. (2001). Alkaline activation of metakaolin and calcium hydroxide mixtures; influence of temperature, activator concentration and solids ratio. *Material Letters*. 47(1-2): 55-62 DOI: 10:1016/50167-577X(00100212-3)

Andrew, F. S. (2017). *Practical Business Statistics (7th Ed).* Academic Press USA. https://doi.org/10.1016/C2015-0-00463-4. ISBN 9780128111758, 9780128042502

Bai, L., Jiang, F., and Fan, B. (2018). Reliability Analysis of Reinforced Concrete Columns after High Temperature under Comprehensive Considering Failure Paths. *Journal of Nanoscience and Nanotechnology Applications. Scholarena*, 2(2) 1-10

BS EN 12390 -5 (2009). *Testing of hardened concrete: Flexural strength of test specimens*. British Standards Institutions London

BS EN12390-1 (2000). *Testing hardened concrete: Shape, dimensions and other requirements for specimens and moulds.* British Standards Institutions London

BSEN 12390-2 (2000). *Testing of hardened concrete: Making and curing speciments for tests*. British Standards Institutions London.

DataFit. (2019). *DataFit Version 9.1.32. Oakdale Engineering*. 23 Tomey Rd, Oakdale, PA 15071, United States. Retreived from http://www.oakdaleengr.com/download.htm

Davidovits, J. (1991). *Geopolymers: Inorganic polymeric new materials*. Journal of Thermal Analysis, 37(8), 1633–1656. https://doi.org/10.1007/BF01912193

Diaz, E. I., Allouche, E. N., & Eklund, S. (2010). *Factors affecting the suitability of fly ash as source material for geopolymers*. **Fuel, 89**(5), 992–996. https://doi.org/10.1016/j.fuel.2009.09.012

EC 2. Eurocode 2. (2008). *Design of Concrete Structures.* BS EN 1992-1- 2, European Committee for Standardization, CEN Brussels.

García-Soto, A. D., Hernández-Martínez, A., & Valdés-Vázquez, J.G. (2017). Reliability Analysis of Reinforced Concrete Beams Subjected to Bending Using Different Methods and Design Codes. *Structural Engineering International*, 27(2), 300-307.

Gollwitzer, S., Abdo, T., and Rackwiz, K. (1988). *First Order Reliabiity Method (FORM), User Manual*. RCP-GMBH, Munich, West Germany.

Lane, D. M. (2020). *History of the normal distribution*. In *Introductory statistics*. Rice University. 7.2: History of the Normal Distribution - Statistics LibreTexts

Mohammed, J. K., Lawan, A,. Aliyu, I., and Mohammed, S. M. (2014). Safety of early age loaded reinforced concrete members. *Asian Journal of Engineering and Technology* 02 (01) 35- 44 www.ajouronline.com

Moodi. F A.A. Ramezanianpour, A..Safavizadeh. S. (2011). Evaluation of the optimal process of thermal activation of kaolins. *Scientia Iranica* 18(4), 906-912

Mosley, W. H., Bungey, J. H., and Hulse, R. (2007). *Reinforced Concrete Design (6th Ed).* Palgrave Macmillan, New York

Mustafa Mohd. A. Al Bakri, H. Kamarudin, M. Bnhussain, I. Khairul Nizar, W.I.W. Mastura (2011). Mechanism and Chemical Reaction of Fly Ash Geopolymer Cement- A Review. *Journal of Asian Scientific Research*, 1 (5), pp.247-253

Qianru, G., and Ann, E. J. (2013). Stochastic Finite Element Methods for the Reliability-Based Fire-Resistant Design of Structures. *Conference on Application of Structural Fire Engineering.* 19-20 April 2013, Prague, Czech Republic

Sameer Ul B. (2015). Effect of Alkali materials on Geopolymer concrete. *International Jornal of Civil Engineering and Technology (IJCET).* 6(1), 01-13 ISSN 0976-6216

Wasiu, J., and Adedeji, A.A. (2018). Reliability Assessment of Reinforced Concrete Beam With Embedded PVC Pipes Below The Neutral Axis. *International Journal Of Multidisciplinary Sciences And Engineering*. 9(1) 9-18 Www.Ijmse.Org

International Conference on Engineering Innovation for Sustainable Development (ICESID 2026)
Faculty of Engineering, Ahmadu Bello University Zaria · 8–10 September 2026

SILICA-BASED MATRICES FOR MICROBIAL CELL ENCAPSULATION AND IMMOBILIZATION:A REVIEW

Utibeabasi Okonbaba[1], H. I. Atta[1], A.y. Atta[1], B. J. El-Yakubu[1,*]

[1]*Ahmadu Bello University, Zaria*

Email: utibeabasiokonbaba@gmail.com, hiatta@abu.edu.ng, ayatta@abu.edu.ng, byjibril@gmail.com*

***Corresponding author**: B. J. El-Yakubu

DOI: https://doi.org/10.67203/sp.ICESID.2026

ABSTRACT

ABSTRACT

Microbial cell immobilization confers protection, reusability, and enhanced tolerance to toxic and fluctuating environments, and is increasingly applied in bioremediation, biocatalysis, and fermentation. Silica and silica-hybrid matrices are attractive due to their mechanical strength, chemical stability, biocompatibility, and ability to shield cells from ultraviolet light and heavy-metal ions. This review examines silica-based precursors and matrices for microbial encapsulation, spanning sol–gel silicas (tetraethyl and tetramethyl orthosilicate, and the water-miscible THEOS), aminosilane (APTES) coatings applied layer-by-layer to alginate beads, silica–alginate hybrids, silica–poly(ethylene glycol) composites, and low-cost biosilica recovered from agro-industrial residues such as rice husk ash and sugarcane bagasse ash. Reported systems are compared by precursor purity, microbial compatibility, and encapsulation efficiency, cell viability, and mechanical stability. A recurring theme is the trade-off between porosity and stability: high porosity eases substrate diffusion but weakens the capsule, while dense matrices protect cells at the expense of mass transport, so that pore-forming additives are used to create this balance. Biosilica precursors offer low cost, antimicrobial character, and circular-economy benefits, though feedstock variability and purification remain limitations. The review confirms that silica matrices, especially porosity-engineered silica-alginate systems, are well suited to encapsulating hydrocarbon-degrading microorganisms to treat petroleum refinery effluent, and identifies controlling diffusivity, mechanical stability, and scale-up as the principal challenges to wider application.

Keywords: *microbial encapsulation; silica–alginate matrices; cell immobilisation; sol–gel silica; hydrocarbon biodegradation*

1. INTRODUCTION

Microbial cell immobilization retains viable microorganisms within a supporting phase while allowing access to substrates and products. Free cells can be lost through washout, sedimentation or shear, and may be inhibited by toxic pollutants in environmental biotechnology. Immobilized systems enhance biomass retention, boost recovery and permit repeated operation, depending on carrier properties and operating conditions (Partovinia & Rasekh, 2018; Wadhawan *et al*., 2026; Abdulmumin *et al*., 2025).

This review critically examines silica-based matrices for microbial cell encapsulation and immobilization, with emphasis on precursor chemistry, microbial compatibility, encapsulation performance, porosity, mass transfer, mechanical stability, reusability and hydrocarbon biodegradation. The specific objectives are to: (i) compare major silica and silica-hybrid matrix classes; (ii) identify agreements, disagreements and limitations in published studies; (iii) examine APTES-derived silica coatings on alginate capsules; (iv) assess the relevance of microbial consortia and low-cost biosilica; (v) identify engineering requirements for applying immobilized hydrocarbon-degrading microorganisms to petroleum-refinery effluent.

2. METHODOLOGY

The relevant literature concerning microbial encapsulation, immobilization, and silica-based matrices was found through targeted searches using keywords. Studies published mostly between 2018 and 2026 were chosen, and in some cases older foundational studies were included as well. Articles were selected on the basis of their relevance to microbial compatibility, matrix properties, mass

transfer, stability, hydrocarbon biodegradation, and wastewater treatment. The information from these studies was then arranged in structured literature tables and thematically combined in order to compare the different types of matrix, microbial performance, and application potential.

2.1 Silica-Based Matrices for Microbial Cell Encapsulation and Immobilization

Studies establish that microorganisms can remain metabolically active after incorporation into silica-based matrices. (Holzmeister et al., 2018) reviewed inorganic biohybrids, while (Li et al., 2020) investigated viable bacteria related to sawdust–silica for phenanthrene removal in soil. These findings support immobilization but highlight a major challenge: silica synthesis and matrix formation must be compatible with living cells. Alkoxide hydrolysis can generate alcohol, while sol–gel processing may involve conditions that stress microorganisms. (Wadhawan et al., 2026) emphasized that matrix chemistry, processing conditions and matrix properties determine the performance and useful lifetime of immobilized cells.

2.2 Sol–Gel Silica and Precursor Chemistry

TEOS and TMOS are common alkoxide precursors for sol–gel silica, while APTES introduces amine functionality and participates in silica–alginate hybrid formation. (Hernández-González et al., 2020) showed that TEOS/APTES ratios, water, and catalyst conditions affect silica-alginate hybrid structure and mechanical properties. (Abdulmumin et al., 2025) demonstrated that hydrolyzed APTES forms silica coatings on alginate capsules and that glucose can be used as a pore-forming agent to increase diffusivity. The evidence supports mixed precursor chemistry over absolute choice for one precursor. For microbial applications, precursor concentration, hydrolysis conditions, and coating architecture must be selected with cell tolerance and mass transfer requirements. (Dragomirescu et al., 2021)

2.3 Silica–Alginate and APTES-Based Hybrid Matrices

Alginate and silica provide complementary functions. Alginate offers mild ionic gelation and a hydrated environment, while silica reinforces the capsule and provides mechanical stability (Szopa et al., 2022; Hernández-González et al., 2020). Hybridization represents a rational compromise rather than a simple replacement of polymer by inorganic material. APTES is particularly relevant because it participates in silica formation and introduce surface functionality. (Abdulmumin et al., 2025) demonstrated that pore engineering of APTES-derived silica–alginate capsules increases diffusion. However, performance reported for fermentation systems should be transferred with caution to hydrocarbon treatment because hydrocarbons differ in solubility, hydrophobicity and partitioning behaviour. The transferable principle is that pore architecture should be designed around the actual substrate and process.

2.4 Porosity, Diffusion and the Protection–Transport Trade-Off

Mass transfer is a principal mechanism linking matrix architecture to biological performance. As illustrated in Figure 1, matrix architecture influences the balance between microbial protection and substrate transport, ultimately affecting biodegradation performance (Abdulmumin et al., 2025). A hydrocarbon must move from the bulk liquid to the capsule surface, traverse external and internal diffusion barriers, reach the cells, and allow metabolites to leave the matrix. A simplified description is given by Fick's first law:

$$J = -D_{eff}\,(dC/dx) \qquad (1)$$

where J is the diffusive flux, D_{eff} is the effective diffusion coefficient in the matrix, C is the concentration of the transported species, and x is the diffusion distance.

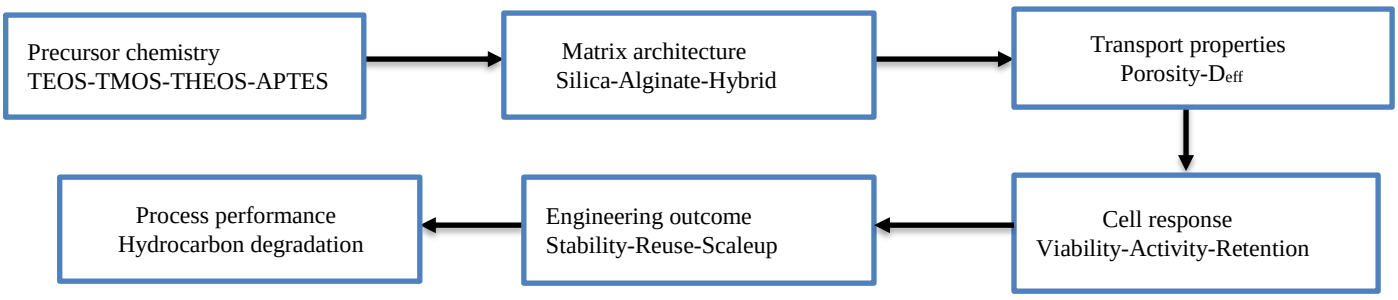

Figure 1: Conceptual relationship between silica precursor chemistry, matrix architecture, mass transfer, microbial response and engineering performance.

(Hernández-González et al., 2020)

2.5 Microbial Consortia and Hydrocarbon Biodegradation

Complex petroleum mixtures of various hydrocarbons justify microbial consortia because different organisms may possess synergistic catabolic pathways. (Tang et al., 2023) described synergistic metabolic functions in crude-oil biodegradation, while (Partovinia et al., 2023) showed that interactions among consortium members can include both synergism and antagonism. (Ganesh Kumar et al., 2019) reported crude-oil degradation using a self-immobilized hydrocarbonoclastic consortium, and (Partovinia et al., 2023) found that immobilization improved crude-oil biodegradation under their conditions. These findings favour functional screening over isolates selection. Consortium design should consider complementary degradation pathways, compatibility growth behaviour, and resistance to the intended wastewater conditions, therefore careful consortium and matrix design are core to improving stability and efficient petroleum hydrocarbon degradation. Consortium design should systematically investigate species ratio, individual and combined growth kinetics, inter-strain compatibility, complementary hydrocarbon-degradation activity, tolerance to relevant wastewater conditions (e.g., pH, salinity and hydrocarbon concentration), and consortium stability over repeated cultivation or treatment cycles. Compatibility can be assessed through pairwise co-culture or interaction tests before selecting the final consortium, while species ratios can be optimized by comparing degradation performance and biomass stability across defined inoculation ratios. (Haq et al., 2024) demonstrated hydrocarbon-removal potential in petroleum-refinery wastewater, while (Al-Mur et al., 2021) reported treatment of refinery wastewater using a hydrocarbon-degrading bacterial consortium under extreme conditions. An additional interpretive issue is the distinction between pollutant removal and biodegradation. Hydrocarbon concentration loss can arise from biological transformation as well as adsorption or partitioning into the carrier. (Younis et al., 2020) demonstrated the importance of partition behaviour in silica–alginate microbeads, while (Zhang et al., 2020) examined degradation by immobilized crude-oil-degrading bacteria. Future validation should therefore include abiotic, free-cell and matrix-only controls so that biological transformation is not inferred from concentration loss alone.

2.6 Evidence and Research Gap

Table 1: Comparative characteristics of some microbial immobilization carriers.

Matrix	**Main advantage**	**Limitation**	**Evidence implication**	**Relevance to target**
Alginate	Mild, cell-compatible gelation	Swelling; low mechanical strength	Good biological starting phase	High
Sol–gel silica	Rigidity; tunable porosity	Synthesis stress; diffusion barrier	Feasible but chemistry-sensitive	High
Silica–alginate	Combines hydration and strength	Porosity–strength trade-off	Strong hybrid strategy	Very high
APTES–silica coating	Functional coating; tunable architecture	Coating thickness must be controlled	Promising for pore-engineered capsules	Very high
Si–PEG hybrid	Organic–inorganic compatibility	More complex formulation	Useful where flexibility is needed	Moderate
Biosilica	Potentially low-cost and circular	Purity/feedstock variability	Requires standardization	Future option

Table 1 shows the key design trade-offs, silica–alginate hybrids emerge as promising systems because alginate supports microbial compatibility while silica enhances mechanical stability. Biosilica from agricultural residues is also promising and potentially attractive because rice-husk and sugarcane-bagasse residues can provide silica feedstocks, although their feedstock composition and purification require standardization (Nzereogu et al., 2023; September et al., 2023; Taiye et al., 2024). The main research gap lies in enhancing hydrocarbon transport especially for poorly water-soluble petroleum hydrocarbons. This gap justifies evaluating APTES-based encapsulation for treating petroleum-contaminant. Relevance to the target was assessed qualitatively based on material cost, microbial compatibility, suitability for hydrocarbon biodegradation, and maturity of supporting evidence. “Very high” indicates strong overall suitability and evidence, while “Moderate” or “Future option” reflects greater limitations or less mature evidence.

Table 2: Representative microbial immobilization matrices and performances

Carrier / matrix	**Target system and microorganism**	**Reported quantitative performance**	**Reference**
Agar	Waste lubricating-oil-contaminated soil; *Paenibacillus* sp. OL15	45 ± 3% degradation after 30 days	(September et al., 2022)
Alginate	Diesel-contaminated groundwater; *Pseudomonas aeruginosa*	71.2% diesel degradation after 10 days; suspended cells achieved 32.0% after 30 days	(Park et al., 2021)
PVA–alginate–clay	Crude-oil system; marine bacterial isolates	74.0–66.6% degradation with PVA–alginate; up to 78.8–75.0% with attapulgite-containing beads	(Farid et al., 2024)
Silica-containing carrier	Phenanthrene-contaminated soil; bacteria immobilized on Sawdust@silica	>95% phenanthrene removal after 48 h; adsorption–degradation was reported as the dominant mechanism	(Li et al., 2020)

Table 2, shows, that immobilized systems outperform free-cells in hydrocarbon removal or degradation under specific conditions. However, comparing matrices is flawed due to differing microorganisms, hydrocarbons, matrix composition, incubation periods and analytical methods. Silica-containing systems standout combining high pollutant removal with matrix stability and tunable transport characteristics. Quantitative evidence supports their enhanced transport capabilities: pore forming modification of an APTES derived silica-alginate capsule increased characteristics when appropriately engineered; for example, pore-forming modification of an APTES-derived silica–alginate capsule increased the diffusion coefficient by approximately 3.2-fold at 308 K, pH 5, and 150rpm demonstrating that silica reinforcement does not necessarily impose mass-transfer penalty (Abdulmumin et al., 2025).

3. FUTURE OUTLOOK

3.1 Advanced Controlled Matrix and Smart Materials

Future trend should focus on matrices that can be tuned to provide controlled mass transfer, mechanical stability, durability and practical recovery. This includes advances in pore engineering, such as the use of pore-forming agents demonstrated for APTES-derived silica–alginate capsules. (Abdulmumin et al., 2025). Reusability, stability, separation and scale-up are also identified as continuing challenges (Wadhawan et al., 2026; Abdulmumin et al., 2026). Magnetic or other recoverable hybrid matrices may offer additional routes to reuse, but their suitability for refinery wastewater should be established experimentally rather than assumed. Future studies should therefore prioritize long-term repeated-use testing, real-effluent validation and assessment of adsorption versus genuine biodegradation. Immobilized bacterial pellets have also shown promise for petroleum-contaminated soil remediation, although such evidence should be treated as complementary rather than direct evidence for silica systems (Zhao et al., 2024).

4. CONCLUSION

The review shows that silica-based matrices are promising platforms for microbial cell immobilization because their structural and surface properties can be controlled to provide protection while maintaining biological accessibility. The literature supports improved biomass retention and operational robustness with immobilized systems, but it does not establish that immobilization is universally superior to free cells. The principal determinant is whether matrix system permits substrate and product transport while maintaining cell viability and mechanical stability. Various matrix systems each offer unique advantages: sol–gel silica, silica–alginate hybrids, APTES-derived coatings, and other silica–polymer systems. Among these, porosity-controlled silica–alginate systems provide a strong basis for hydrocarbon treatment because they combine a hydrated, cell-compatible phase with an inorganic reinforcing network. APTES is therefore a choice precursor for the proposed silica-coated microbial cell, provided that coating thickness, porosity and synthesis conditions are controlled. Microbial consortia should be selected for synergistic hydrocarbon-degrading functions rather than simply for species number. Future work should experimentally establish diffusivity, viability, mechanical stability, hydrocarbon biodegradation, adsorption controls and reusability under petroleum-refinery conditions before scale-up to continuous treatment.

ACKNOWLEDGEMENTS

The authors gratefully acknowledge the support provided by Petroleum Technology Development Fund (PTDF) Chair in Chemical Engineering at Ahmadu Bello University, Zaria.

REFERENCES

Abdulmumin, B., Atta, H. I., Atta, A. Y., & El-Yakubu, B. J. (2025). Improving diffusivity of encapsulated *Saccharomyces cerevisiae* via porous silica-alginate for enhanced bioethanol production. *Next Sustainability, 6*, 100166. https://doi.org/10.1016/j.nxsust.2025.100166

Abdulmumin, B., Jibril, A., & Abdurrahman, A. (2026). Application of microbial encapsulation technology for bioethanol production: A review. *Next Materials, 12*, 102247. https://doi.org/10.1016/j.nxmate.2026.102247

Abdulmumin, B., Mudi, I., Ibrahim, A., Abdurrahman, A., & Onyeaka, H. (2025). Enhancing the diffusion channels of silica-alginate capsules for microbial encapsulation. *Engineering in Life Sciences, 25*(9), e70002. https://doi.org/10.1002/elsc.70002

Al-Mur, B. A., Pugazhendi, A., & Jamal, M. T. (2021). Application of integrated extremophilic (halo-alkalo-thermophilic) bacterial consortium in the degradation of petroleum hydrocarbons and treatment of petroleum refinery wastewater under extreme condition. *Journal of Hazardous Materials, 413*, 125351. https://doi.org/10.1016/j.jhazmat.2021.125351

Dragomirescu, M., Vintila, T., Vlase, T., Mihali, C.-V., & Preda, G. (2021). Microbial cellulases immobilized in biopolymer/silica matrices used as enzyme release systems. *Acta Biochimica Polonica, 68*(4), 775–783. https://doi.org/10.18388/abp.2020_5694

Farid, E., Kamoun, E. A., Taha, T. H., El-Dissouky, A., & Khalil, T. E. (2024). Eco-friendly biodegradation of hydrocarbons compounds from crude oily wastewater using PVA/alginate/clay composite hydrogels. *Journal of Polymers and the Environment, 32*, 225–245. https://doi.org/10.1007/s10924-023-02991-y

Ganesh Kumar, A., Nivedha Rajan, N., Kirubagaran, R., & Dharani, G. (2019). Biodegradation of crude oil using self-immobilized hydrocarbonoclastic deep sea bacterial consortium. *Marine Pollution Bulletin, 146*, 741–750. https://doi.org/10.1016/j.marpolbul.2019.07.006

Haq, I., Kalamdhad, A. S., & Malik, A. (2024). Bioremediation of petroleum refinery wastewater using *Bacillus subtilis* IH-1 and assessment of its toxicity. *Archives of Microbiology, 206*(7), 296. https://doi.org/10.1007/s00203-024-04027-y

Hernández-González, A. C., Téllez-Jurado, L., & Rodríguez-Lorenzo, L. M. (2020). Synthesis of in-situ silica-alginate hybrid hydrogels by a sol-gel route. *Carbohydrate Polymers, 250*, 116877. https://doi.org/10.1016/j.carbpol.2020.116877

Holzmeister, I., Schamel, M., Groll, J., Gbureck, U., & Vorndran, E. (2018). Artificial inorganic biohybrids: The functional combination of microorganisms and cells with inorganic materials. *Acta Biomaterialia, 74*, 17–35. https://doi.org/10.1016/j.actbio.2018.04.042

Jeong, Y., & Irudayaraj, J. (2022). Multi-layered alginate hydrogel structures and bacteria encapsulation. *Chemical Communications, 58*, 8584–8587. https://doi.org/10.1039/D2CC01187E

Li, J., Ou, Y., Zhang, Y., Guo, S., Li, S., Guo, C., Dang, Z., Cao, Z., Feng, J., & Sun, J. (2020). Viability and distribution of bacteria immobilized on sawdust silica: The removal mechanism of phenanthrene in soil. *Ecotoxicology and Environmental Safety, 198*, 110649. https://doi.org/10.1016/j.ecoenv.2020.110649

Nzereogu, P. U., Omah, A. D., Ezema, F. I., Iwuoha, E. I., & Nwanya, A. C. (2023). Silica extraction from rice husk: Comprehensive review and applications. Hybrid Advances, 4, 100111. https://doi.org/10.1016/j.hybadv.2023.100111

Park, H., Kim, H., Kim, G.-Y., Lee, M.-Y., Kim, Y., & Kang, S. (2021). Enhanced biodegradation of hydrocarbons by *Pseudomonas aeruginosa*-encapsulated alginate/gellan gum microbeads. *Journal of Hazardous Materials, 406*, 124752. https://doi.org/10.1016/j.jhazmat.2020.124752

Partovinia, A., & Rasekh, B. (2018). Review of the immobilized microbial cell systems for bioremediation of petroleum hydrocarbons polluted environments. *Critical Reviews in Environmental Science and Technology, 48*(1), 1–38. https://doi.org/10.1080/10643389.2018.1439652

Partovinia, A., Khanpour-Alikelayeh, E., Talebi, A., & Kermanian, H. (2023). Improving mass transfer rates in microbial cell immobilization system for environmental applications: Synergistic interaction of cells on crude oil biodegradation. *Journal of Environmental Management, 326*, 116729. https://doi.org/10.1016/j.jenvman.2022.116729

September, L. A., Kheswa, N., Seroka, N. S., & Khotseng, L. (2023). Green synthesis of silica and silicon from agricultural residue sugarcane bagasse ash: A mini review. *RSC Advances, 13*, 1370–1380. https://doi.org/10.1039/D2RA07490G

Szopa, D., Mielczarek, M., Skrzypczak, D., Izydorczyk, G., Mikula, K., Chojnacka, K., & Witek-Krowiak, A. (2022). Encapsulation efficiency and survival of plant growth-promoting microorganisms in an alginate-based matrix: A systematic review and protocol for a practical approach. *Industrial Crops and Products, 181*, 114846. https://doi.org/10.1016/j.indcrop.2022.114846

Taiye, M. A., Hafida, W., Kong, F., & Zhou, C. (2024). A review of the use of rice husk silica as a sustainable alternative to traditional silica sources in various applications. *Environmental Progress & Sustainable Energy, 43*(6), e14451. https://doi.org/10.1002/ep.14451

Tang, F., Zhang, H., Cheng, H., Wang, Y., Liu, Q., Zhao, C., Gu, Y., & Wang, J. (2023). New insights of crude oil biodegradation construction by microbial consortium B10: Responded substrates, genomics, biodegradation mechanism and pathways. *Chemical Engineering Journal, 478*, 147143. https://doi.org/10.1016/j.cej.2023.147143

Wadhawan, G., Aggarwal, D., & Gupta, A. (2026). Immobilized bacterial cell technology for sustainable industrial wastewater treatment: A review. *3 Biotech, 16*, 257. https://doi.org/10.1007/s13205-026-04898-6

Younis, S. A., Motawea, E. A., Moustafa, Y. M., Lee, J., & Kim, K.-H. (2020). A strategy for the efficient removal of chlorophenols in petrochemical wastewater by organophilic and aminated silica@alginate microbeads: Taguchi optimization and isotherm modeling based on partition coefficient. *Journal of Hazardous Materials, 397*, 122792. https://doi.org/10.1016/j.jhazmat.2020.122792

Zhang, P., Wang, X., Peng, S., Tian, X., Li, Z., & Zhou, R. (2020). Degradation of petroleum hydrocarbons by embedding immobilized crude oil degrading bacteria. *Water Science & Technology, 82*(11), 2296–2303. https://doi.org/10.2166/wst.2020.497

Zhao, S., Li, L.-L., Wang, Y.-J., Liu, Z.-W., Yang, S., Gao, X., Zhang, C.-Y., & Yu, A.-F. (2024). Remediation of petroleum-contaminated site soil by bioaugmentation with immobilized bacterial pellets stimulated by a controlled-release oxygen composite. *Environmental Pollution, 356*, 124253. https://doi.org/10.1016/j.envpol.2024.124253

International Conference on Engineering Innovation for Sustainable Development (ICESID 2026)
Faculty of Engineering, Ahmadu Bello University Zaria · 8–10 September 2026

THE USE OF GREEN MATERIALS IN BUILDING CONSTRUCTION: A STUDY OF THE NIGERIAN CONSTRUCTION INDUSTRY

Alhassan Galadima[1,*], Umar Ibrahim Kwami[1], Muazu Bello[1]
[1]*Ahmadu Bello University*
Email: sultan4haroon@gmail.com[*], ibrahimkafarati@fedpolydaura.edu.ng, mbello6080@gmail.com
***Corresponding author**: Alhassan Galadima
DOI: https://doi.org/10.67203/sp.ICESID.2026

ABSTRACT
The construction industry remains a major contributor to global carbon emissions, resource depletion, and energy consumption, with traditional materials such as cement and steel carrying significant environmental costs. Green materials derived from renewable, recycled, or low-impact sources offer a sustainable alternative to conventional building practices. This study examines the current state of green materials adoption in the Nigerian construction industry through a mixed-methods approach combining literature synthesis and questionnaire survey of construction firms operating in Kaduna, Plateau, and the Federal Capital Territory, Abuja. The research assesses awareness levels, identifies barriers to adoption, and evaluates the extent to which green building principles are integrated into current practices. Findings reveal that while green materials demonstrate significant potential to reduce embodied energy and carbon footprint—with hempcrete and bamboo composites providing excellent insulation and renewability, recycled aggregates and fly ash reducing reliance on virgin cement, and mycelium-based blocks showing promise in biodegradability—adoption in Nigeria remains critically low. Only 29.6% of respondents confirmed that green materials principles are being considered by construction firms, and 66.7% indicated that the Nigerian building industry is not progressing toward green building construction. Key barriers include inadequate awareness and education (33.3% of respondents), lack of standardised materials and technology (48.1%), absence of regulatory enforcement, high initial costs, limited large-scale production, and regulatory gaps in certification. The study concludes that achieving sustainable construction in Nigeria requires increased professional education, mandatory site waste management, strengthened regulatory frameworks, financial incentives, and enhanced cooperation among stakeholders. The findings contribute to the growing body of knowledge on sustainable construction practices in developing economies and offer practical recommendations for policymakers and industry practitioners.

Keywords: *Green building materials; Sustainable construction; Bio-based composites; Nigerian construction industry; Low-carbon building technologies*

1. INTRODUCTION

1.1 Background

The Inter-governmental Panel on Climate Change (IPCC) has asserted that greenhouse gases generate impacts sufficient to alter global climate patterns. The construction industry generates the greatest environmental impacts among all industries, accounting for approximately 30-40% of global energy use and significant proportions of carbon emissions worldwide. Green building practices have emerged as a key strategy for achieving sustainability in the construction industry, with green materials designs and standards developed to improve building operation energy and embodied energy efficiencies while minimizing energy consumption and waste.

Green materials encompass those which are renewable and/or cause the least impact on the environment. In design, it is the creative initial layout—both of spaces and structure—that takes full advantage of building 'green'. These materials can be considered waste products that hold no harmful effects, are considered at the end of their useful life, and can be used in conjunction with other construction materials for building construction. The concept has been adopted by many nations as the best way forward in preserving resources and sustaining the environment.

1.2 Statement of the Problem

Construction activities, while essential for infrastructural growth and economic development, generate substantial environmental impacts including large quantities of solid waste, noise pollution, air pollution, land degradation, and water pollution. These impacts threaten quality of life and environmental sustainability. Since construction activities cannot be halted due to human demand and socio-economic development requirements, there exists a critical need to balance human requirements with environmental protection. Green building materials offer a pathway to reduce or avoid the environmental impacts of construction activities while ensuring that developmental initiatives and their benefits are sustained.

1.3 Aim and Objectives

The aim of this study is to examine the different construction methods and practices and their general impact on the use of green materials in building construction. The specific objectives are:

1. To identify the most prominent sustainability issues related to site practices of building construction firms;
2. To undertake a review of the concept of green materials in building construction;
3. To evaluate the extent of application of green materials concepts in the construction of buildings in Nigeria;
4. To make appropriate recommendations towards increased adoption of green materials in the Nigerian building industry.

2. LITERATURE REVIEW

2.1 Green Materials and Environmental Sustainability

Sustainable development is a necessary condition for the continuation of the earth, while healthy and comfortable living is a necessary condition for the continuation of life. The building sector is the largest source of greenhouse gas emissions globally, including energy used for heating, lighting, and operating devices (Larsson, 2004). Environmental indicators for green materials have the potential to serve as means of making environmental impacts and possibly benefits of buildings visible to all relevant stakeholders.

Green building helps support a broader sustainable development agenda. If sustainable development goals are to be truly reached, buildings should consume minimal energy, water and materials, and produce minimal emissions, noise and waste over their lifespan. Even at a more realistic level, there is global interest in improving building performance: governments want to reduce the use of scarce resources and airborne emissions, owners want to reduce operating costs, and developers are finding that customers are demanding higher quality and performance (Zhang et al., 2011).

2.2 Examples of Green Materials

Fly Ash: A residue from coal-fired power plants used in cement making. Usage of fly ash decreases the cost of concrete and results in higher quality products (Reddy, K.M., & Patni, J.C, 2026). When cement is produced, huge quantities of carbon dioxide are released, resulting in air and water pollution. The pozzolanic and cementitious properties of fly ash make it ideal as a substitute for cement in concrete, removing the need for disposal. High-performance fly ash concrete can improve workability, ultimate strength, and durability.

Straw Bales: Used as main structural components or as soft insulation. Packed closely and made hard, they can withstand considerable load and impact. Contrary to common perception, straw bales are not a fire hazard and provide three times more fire resistance than conventional homes (Balu,2012).

Cement-bonded Composites: Value-added wood products made from particles from wood and agricultural byproducts, cement, and a catalyst. These materials are useful for ceiling, walling, roofing, flooring, claddings, partitioning, and shuttering (Ajayi, 2005). They are resistant to termites,

insects, fungi, moisture movement, and fire, with good insulating properties, durability, and excellent nailing ability.

Bamboo: Often misunderstood as a light, slender wood, bamboo is lighter than steel but five times stronger than concrete. It absorbs four times more carbon dioxide than most trees, can grow faster than any normal tree (usually several feet per day), and provides significant cooling effects. The main positive aspect is that it is a renewable source (Xu et al, 2025).

Mycelium-based Blocks: Show promise in biodegradability and low-energy production. Mycelium composites are lightweight, fire-resistant, and fully biodegradable; offering architects a versatile medium for sustainable construction (Sharma, R., and Sumbria, R. 2022).

2.3 Importance of Green Materials

Green materials offer numerous benefits including cost savings over the lifecycle, energy efficiency (reducing both embodied and operating energy consumption), water efficiency, material efficiency, temperature regulation, improved indoor air quality, enhanced indoor environmental quality, reduced maintenance requirements, higher property value, and tax benefits (Adedeji, Y.M.D., 2011).

2.4 Barriers to Green Materials Adoption in Nigeria

Several factors impede the adoption of green materials in the Nigerian construction industry:

Ignorance/Illiteracy: With adult literacy rate at approximately 56.9% of the total population, the focus of most citizens on buildings tends toward quick gains without consideration of environmental sustainability (Murtala et. al., 2013).

Poverty: An estimated 54% of Nigeria's population lives below the poverty line, making the procurement of green materials financially challenging (Dinwoodie and Paxton, 1990).

Lack of Awareness: Most Nigerians are not aware that buildings can influence the environment and climate, being more concerned with aesthetic values and modern technological gadgets without understanding the negative implications.

Availability of Materials: While green materials can be found more easily in urban areas, rural areas face significant scarcity. Many eco-friendly materials are not available in Nigeria, making them hard to find and increasing transportation costs (Balu, 2012).

Cost: Many believe the cost of green materials is prohibitive, requiring significant initial investment despite long-term energy savings.

Regulatory Gaps: The absence of comprehensive green building codes, standards, and enforcement mechanisms limits widespread adoption (Al-kaabi et al, 2011).

3. RESEARCH METHODOLOGY

3.1 Research Approach

This study employed a survey research method to investigate current trends in green materials construction in the Nigerian building industry. The survey method was chosen for its suitability in studying both large and small populations by selecting and studying samples to discover the relative incidence, distribution, and interrelation of sociological and psychological variables.

3.2 Sample Size and Population

The population comprised professionals selected from building construction firms including Dantata and Sawoe, Arab Construction, Julius Berger in Abuja, Datum Construction Limited in Kaduna, and Eagle Construction, Akiorganic Partnership, and Rick Rock Building and Engineering Construction Limited in Plateau State. A total population of 50 respondents was selected for the study. Data were initially collected from all 50 respondents using the same set of research questions. Of these, twenty-seven (27) respondents provided their responses through a structured questionnaire, while twenty-three (23) respondents participated through face to face interviews.

The interviews constituted a primary source of data collection, as the information was obtained directly from the respondents based on their knowledge, experience, and opinions concerning the subject under investigation. However, although the interview responses were collected

as part of the preliminary data-gathering process, the interview data will not be used in the final analysis or interpretation of findings for this research.

This decision was made to ensure consistency and uniformity in the method of data analysis and presentation. Consequently, only the responses obtained from the 27 respondents who completed the structured questionnaire will constitute the empirical data used for the study.

The interview exercise should therefore be regarded as a supplementary or preliminary primary data collection activity, rather than a source of data for the final research analysis. The exclusion of the interview responses does not imply that the information provided by the interviewee was invalid; rather, it reflects the methodological decision to restrict the study's final analysis to questionnaire-based responses. Accordingly, all statistical analysis, tables, discussions, and conclusions arising from the empirical data will be based exclusively on the 27 valid questionnaire responses.

The study adopted a purposive sampling technique in selecting the firms and geographical locations included in the research. The selection was based primarily on the relevance of the firms to the objectives of the study, their involvement in construction activities, availability of respondents with relevant professional knowledge, and accessibility for data collection. The study focused on Plateau, Kaduna, and the Federal Capital Territory (FCT), Abuja, which were considered appropriate locations for obtaining information relevant to the research.

The choice of these locations was also informed by the researcher's prior geographical, educational, and industrial familiarity with the areas. The researcher was born in Plateau state, undertook his Bachelor of Engineering (B.Eng.) studies in Zaria, Kaduna state, and completed his Students Industrial Work Experience Scheme (SIWES) at Setraco Nigeria Limited. These experiences provided him with geographical locations, construction industry environment, and relevant firms within the selected states. Such familiarity facilitated the identification of appropriate firms, communication with potential respondents, and access to the field.

3.3 Data Collection Methods

Primary data was collected through questionnaires administered to building construction firms randomly selected in Kaduna, Plateau, and the Federal Capital Territory Abuja. Secondary data was collected from textbooks, journal articles, encyclopedias, published documents, and internet reports.

3.4 Data Analysis

The data analysis was restricted to univariate descriptive statistics, including frequencies, percentages, mean, median, and mode. Consequently, the study did not employ cross-tabulation, correlation analysis, or inferential statistical techniques to examine possible relationships between respondents' demographic characteristics and the identified barriers to adoption. Therefore, the findings should be interpreted primarily as a description of respondents' characteristics, perceptions, and reported adoption barriers rather than as evidence of statistically significant relationships or causal effects.

The decision to adopt a purely descriptive analytical approach was deliberate and consistent with the primary purpose of the study, which was to describe and summarize respondents' views and identify the most prominent adoption barriers. Frequencies and percentages were appropriate for presenting categorical responses, while mean, median, and mode provided useful summaries of responses to relevant items. The approach also enabled the researcher to present the distribution and central tendencies of the data in a straightforward and accessible manner without making statistical claims beyond what the study design and data could adequately support.

Nevertheless, the absence of cross-tabulation and inferential testing limits the study's ability to determine whether adoption barriers vary significantly according to demographic characteristics such as age, gender, educational level, occupation, or years of experience. Future studies could address this limitation by employing cross-tabulation, chi-square tests, correlation analysis, regression, or other appropriate inferential techniques to investigate relationships and predictors of adoption.

Data analysis was conducted using standard percentages and simple statistics to analyse questionnaire responses. Responses were categorised using Likert-scale rankings from Agree to Disagree, Believe to Disbelieve, and Yes/No responses.

4. RESULTS AND DISCUSSION

4.1 Respondent Demographics

The demographic analysis revealed that 92.6% of respondents were male and 7.4% female. The majority (63.0%) were aged 20-35 years, followed by 22.2% aged 36-50 years. Marital status distribution showed 51.9% married and 48.1% single. Educational qualifications indicated 51.9% held B.Sc./B.A degrees, 33.3% held HND, and the remainder held OND or SSCE qualifications. All respondent organisations (100%) had been in existence for 10 years or more.

4.2 Data Presentation and Analysis

Some members of staff of Datum construction Nigeria Limited in Kaduna state; Dantata & sawoe Construction Company Limited, Julius Berger Nigeria Plc., and Arab contractors Nigeria Limited in Federal Capital Territory (FCT) Abuja; and Rick Rock building and engineering Construction Limited, akiorganic patternship, and Eagle Construction Company in Plateau state participated in the study. A total of 50 respondents were involved in the data collection, comprising 27 respondents who completed the questionnaires and 23 respondents who were interviewed using the same set of questions contained in the questionnaire. The responses were coded and analysed using Statistical Package for the Social Sciences (SPSS). The findings were presented using frequency tables and percentages to ensure that the results were clear, concise, and easily understood.

4.3 Data Analysis and Interpretation

Statistics
Age

Valid	27
Mean	2.4074
Median	2.0000
mode	2.00

Age

	frequency	percent	Valid percent	Cumulative percent
Under 20	1	3.7	3.7	3.7
20-35	17	63.0	63.0	66.7
36-50	6	22.2	22.2	88.9
51-65	3	11.1	11.1	100.0
Total	27	100.0	100.0	

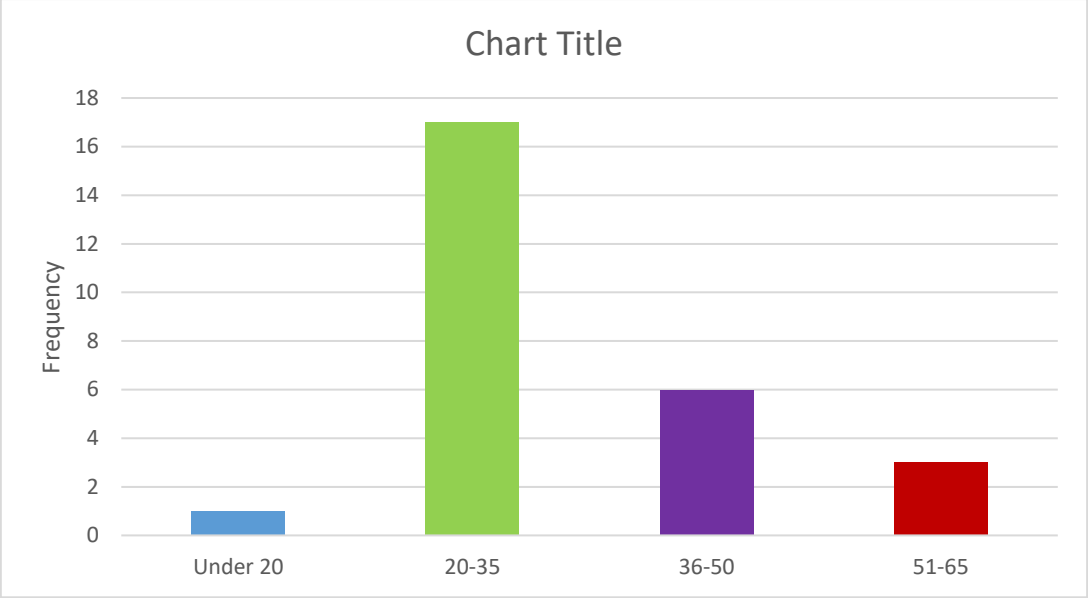

Statistics

Sex

	Valid	27
Mean		1.0741
Median		1.0000
mode		1.00

Sex

	Frequency	Percent	Valid Percent	Cumulative percent
Male	25	92.6	92.6	92.6
Female	2	7.4	7.4	100.0
Total	27	100.0	100.0	

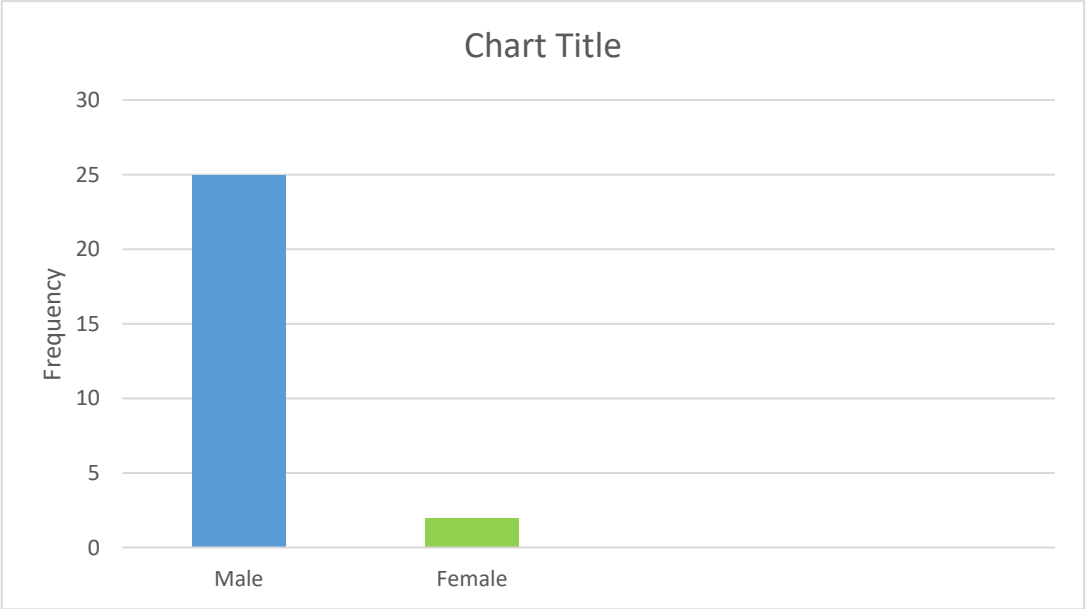

Marital status

Valid	27
Mean	1.4815
Median	1.0000
mode	1.00

	Frequency	Percent	Valid Percent	Cumulative Percent
Married	14	51.9	51.9	51.9
Single	13	48.1	48.1	100.0
Total	27	100.0	100.0	

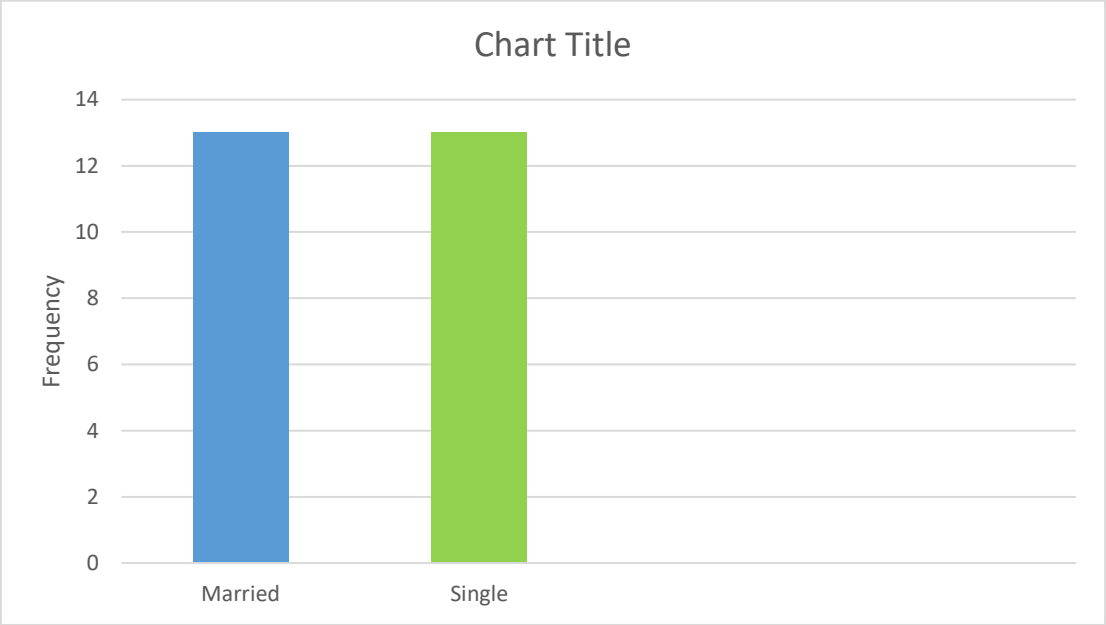

Statistics

Your highest completed level of education

Valid	27
Mean	2.7407
Median	2.0000
Mode	2.00

Your highest completed level of education

	frequency	Percent	Valid Percent	Cumulative Percent
Bsc./BA	14	51.9	51.9	51.9
HND	9	33.3	33.3	85.2
ND	1	3.7	3.7	88.9
SSCE	3	11.1	11.1	100.0
Total	2	100.0	100.0	

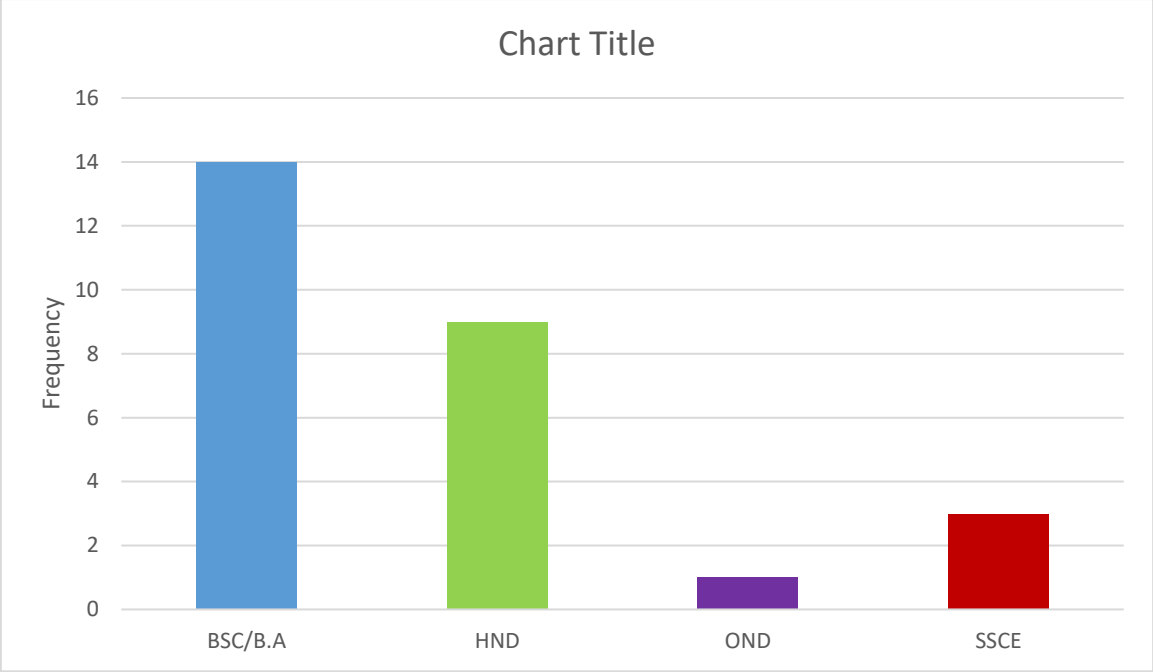

What could be done to effectively promote green materials construction by building construction firms in Nigeria?

Valid	27
Mean	1.9259
Median	2.0000
Mode	2.00

What could be done to effectively promote green materials construction by building construction firms in Nigeria?

	Frequency	Percent	Valid Percent	Cumulative Percent
proper education of professionals and the awareness of all stakeholders including the users.	9	33.4	33.4	33.4
Use of adequate, standard (recommend) materials and technology.	13	48.1	48.1	81.5
Building construction firms should be made to submit their modalities or plan their green construction to appropriate and good follow up	3	11.1	11.1	92.6
Green materials principles being considered by construction firms practice	2	7.4	7.4	100.0
Total	27	100.0	100.0	

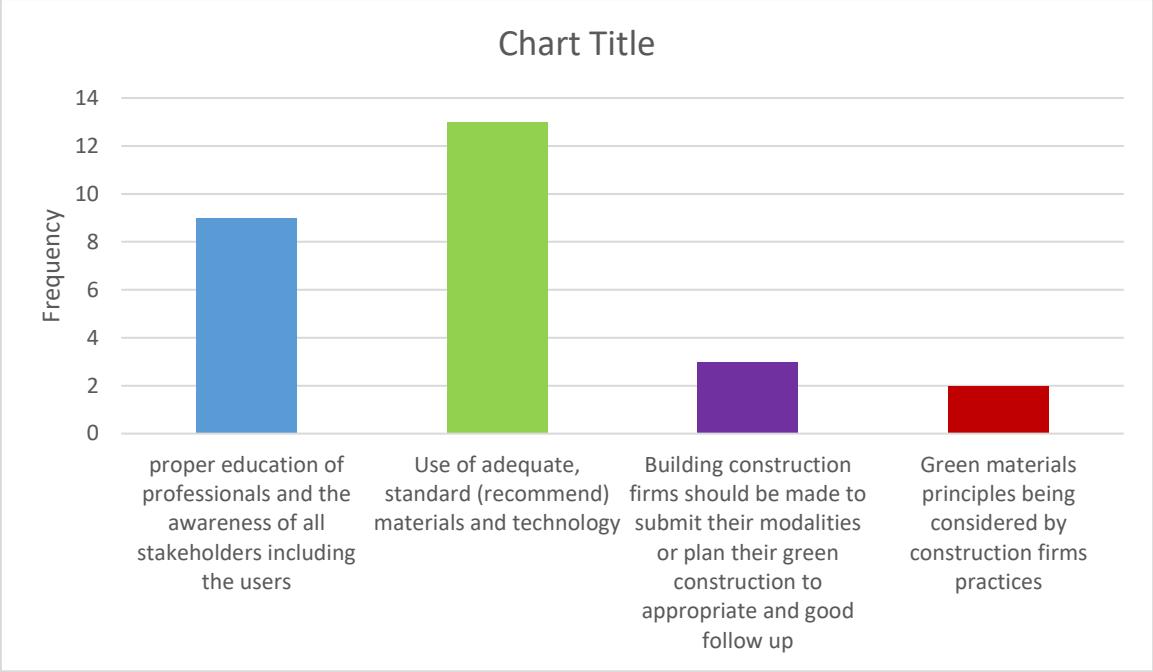

Statistics

Does Nigeria need to switch to the use of green materials?

N	valid	27
	Missing	0
Mean		1.0741
Median		1.0000
Mode		1.00

Does Nigeria need to switch to the use of green materials?

		Frequency	Percent	Valid Percent	Cumulative Percent
Valid	Yes	25	92.6	92.6	92.6
	No	2	7.4	7.4	100.0
	Total	27	100.0	100.0	

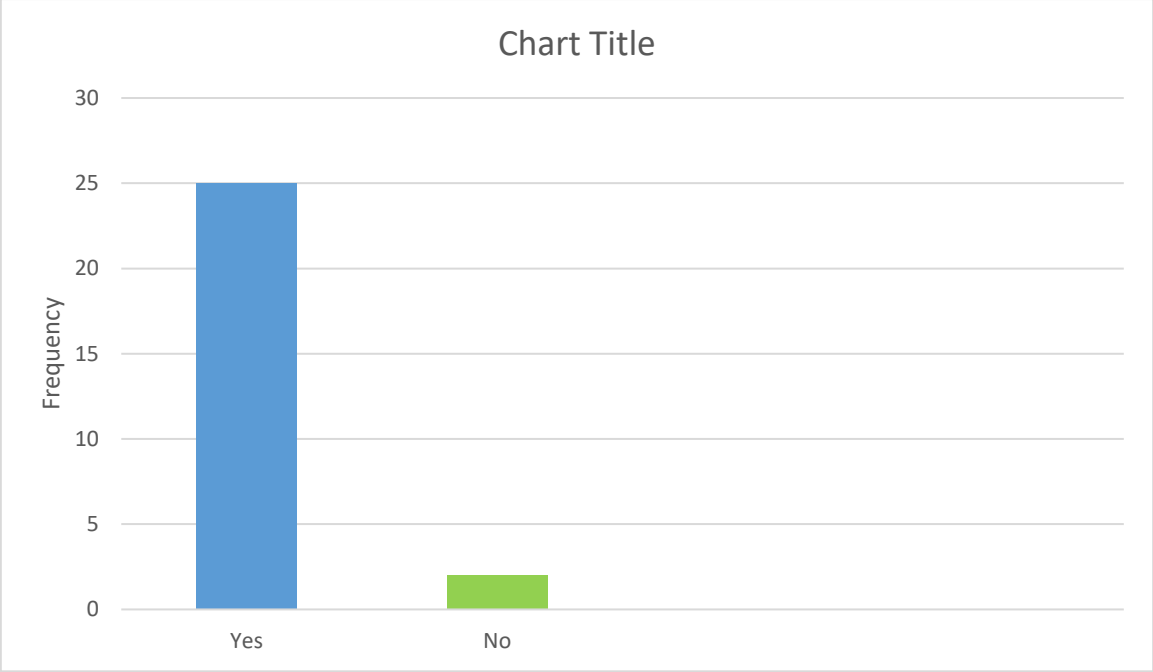

Are you of the view that many factors are promoting the rapid development of green buildings including the increasingly serious global warming from other country like Indian, Malaysia. Those Nigeria achieved that?

Valid	27
Mean	1.7037
Median	2.0000
Mode	2.00

Are you of the view that many factors are promoting the rapid development of green buildings including the increasingly serious global warming from other country like Indian, Malaysia. Those Nigeria achieved that?

	Frequency	Percent	Valid Percent	Cumulative Percent
Yes	8	29.6	29.6	29.6
No	19	70.4	70.4	100.0
Total	27	100.0	100.0	

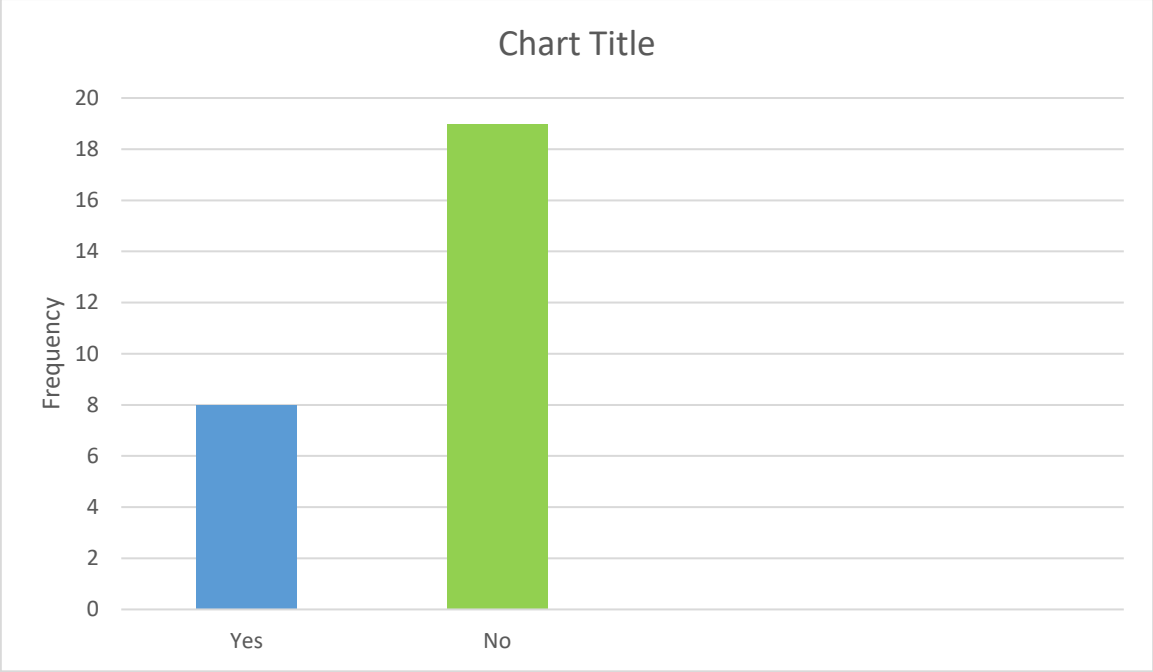

Statistics

Are you of the view that government have reduced taxes on the use of green materials in construction of building?

Valid	27
Mean	1.3333
Median	1.0000
Mode	1.00

Are you of the view that government have reduced taxes on the use of green materials in construction of building?

	Frequency	Percent	Valid Percent	Cumulative Percent
Yes	18	66.7	66.7	66.7
No	9	33.3	33.3	100.0
Total	27	100.0	100.0	

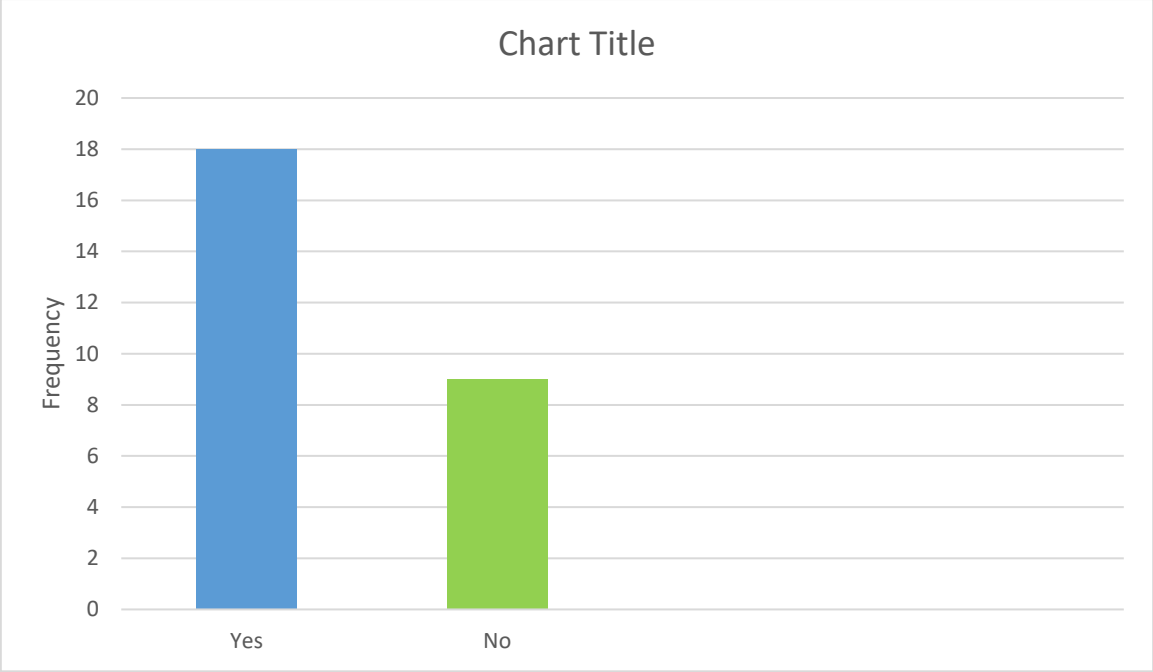

Statistics

Did Nigeria adopted green building concept as the best way forward in preserving our resources and sustained our environment?

Valid	27
Mean	1.5926
Median	2.0000
Mode	2.00

Did Nigeria adopted green building concept as the best way forward in preserving our resources and sustained our environment?

	Frequency	Percent	Valid Percent	Cumulative Percent
Yes	11	40.7	40.7	40.7
No	16	59.3	59.3	100.0
Total	27	100.0	100.0	

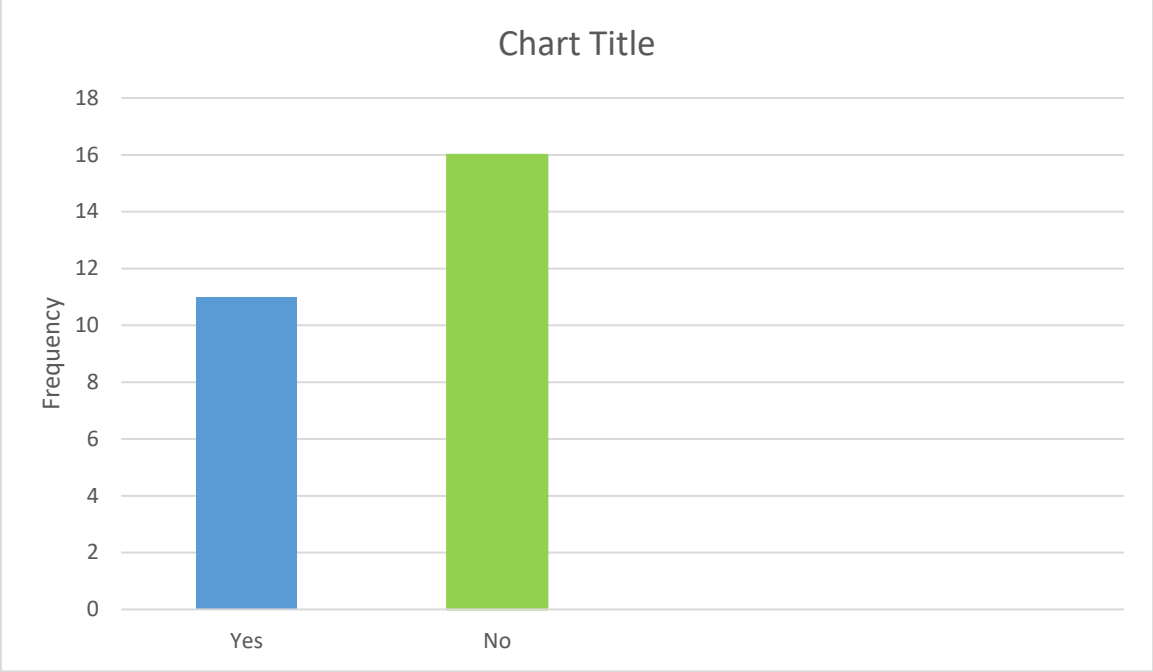

Statistics

Do you believe that green materials need less maintenance and do not destroyed so quickly?

Valid	27
Mean	1.1852
Median	1.0000
Mode	1.00

Do you believe that green materials need less maintenance and do not destroyed so quickly?

	Frequency	Percent	Valid Percent	Cumulative Percent
Believe	22	81.5	81.5	81.5
Disbelieve	5	18.5	18.5	100.0
Total	27	100.0	100.0	

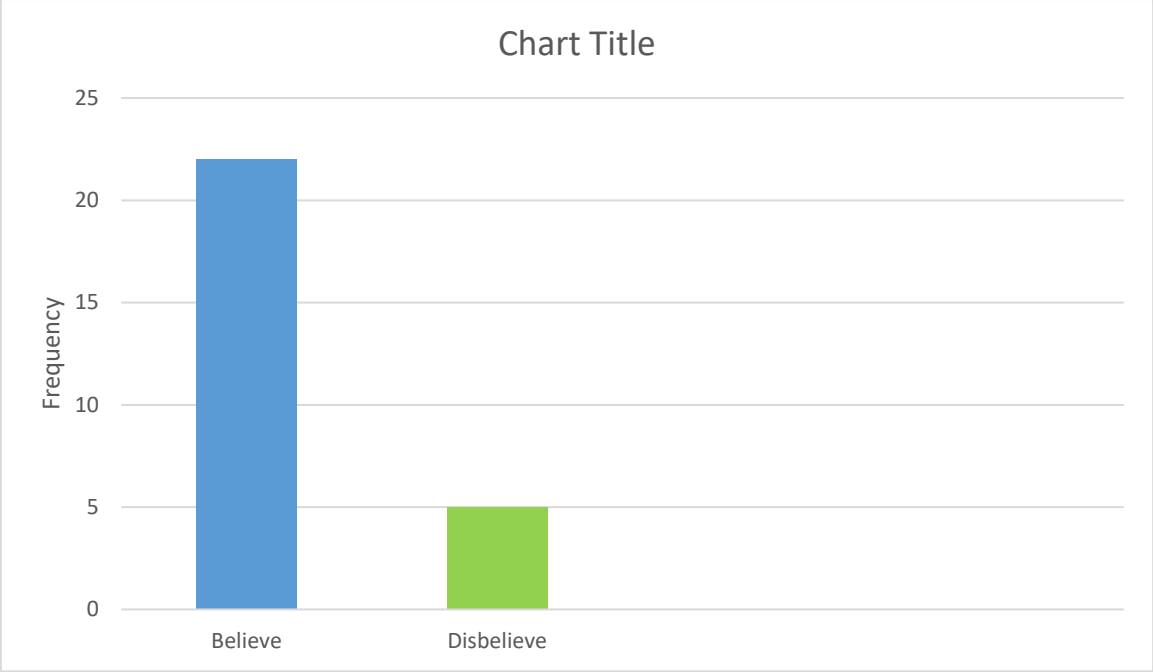

Do you believe that in the process of availability of green materials, there is scarcity of the material in the rural areas compared to the urban areas

Valid	27
Mean	1.2963
Median	1.0000
Mode	1.00

Do you believe that in the process of availability of green materials, there is scarcity of the material in the rural areas compared to the urban areas

	Frequency	Percent	Valid Percent	Cumulative Percent
Believe	19	70.4	70.4	70.4
Disbelieve	8	29.6	29.6	100.0
Total	27	100.0	100.0	

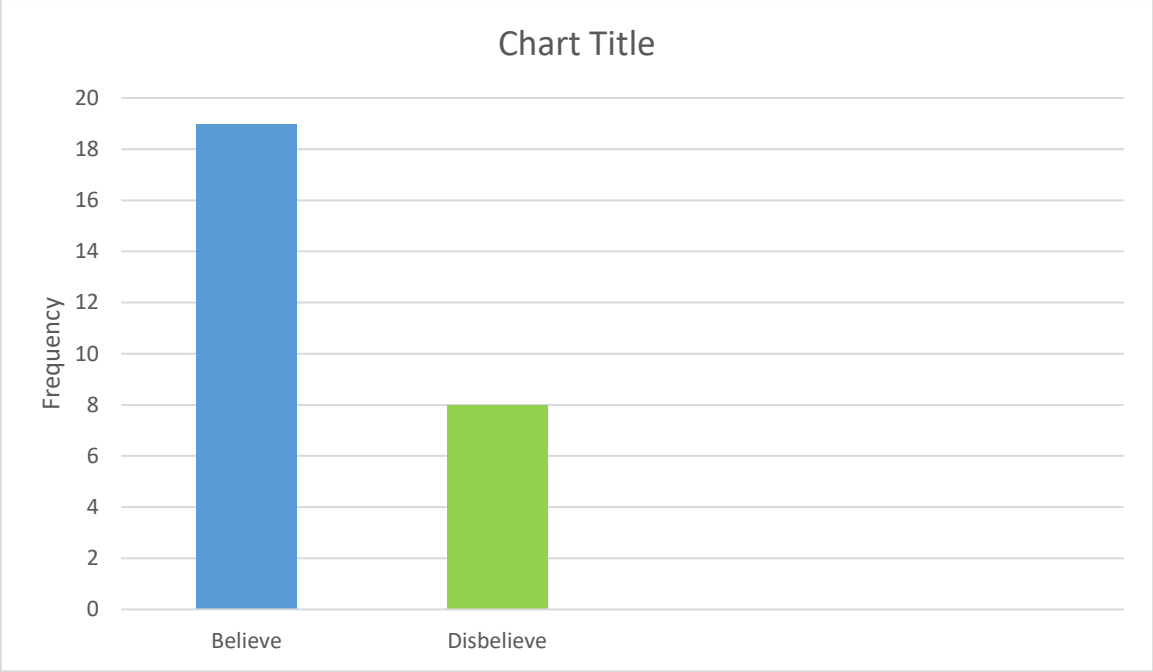

Statistics

Do you agree that the used of green materials in the construction of building protect the environment and natural resources, while achieving further advances in the structural performance?

Valid	27
Mean	1.1852
Median	1.0000
Mode	1.00

Do you agree that the used of green materials in the construction of building protect the environment and natural resources, while achieving further advances in the structural performance?

	Frequency	Percent	Valid Percent	Cumulative Percent
Agree	22	81.5	81.5	81.5
Disagree	5	18.5	18.5	100.0
Total	27	100.0	100.0	

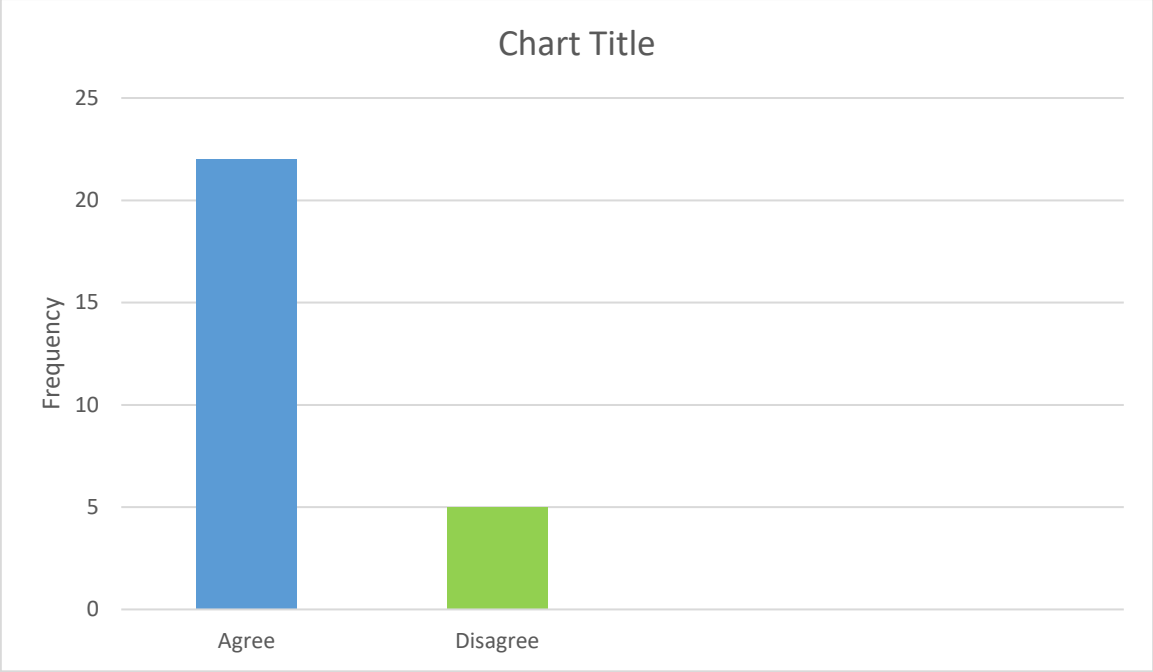

4.5 Discussion

The findings reveal a significant gap between awareness and adoption of green materials in the Nigerian construction industry. While 92.6% of respondents acknowledged the need to switch to green materials, only 29.6% confirmed that green materials principles are being considered in current practices. This awareness-adoption gap aligns with findings from other developing economies where knowledge of sustainable practices does not necessarily translate into implementation.

The study confirms that the building sector is the largest source of greenhouse gas emissions globally, with buildings responsible for significant carbon emissions. Green materials demonstrate substantial potential to reduce embodied energy and carbon footprint. However, the Nigerian construction industry faces persistent barriers including inadequate professional education, limited availability of materials, absence of regulatory enforcement, and economic constraints.

The findings align with previous research identifying government-related barriers as primary impediments to sustainable building projects in Nigeria. The absence of comprehensive green building codes, financial incentives, and enforcement mechanisms limits widespread adoption.

5. CONCLUSION AND RECOMMENDATIONS

5.1 Conclusion

Based on the research findings, the following conclusions are drawn:

1. Green materials construction is not well understood by professionals in the Nigerian building industry, with familiarity with sustainability concepts remaining critically low.

2. Very few respondents acknowledged that construction activities contribute to waste, energy consumption, and environmental pollution, indicating a significant awareness gap.

3. Economic and social aspects of sustainability are more frequently considered than environmental aspects in site practices. The comprehensive definition of green materials encompassing suitable practices in materials choice, sources, construction methodologies, and design philosophy for improved performance, reduced environmental burden, minimised waste, and ecological friendliness has not been fully achieved.

4. While the Nigerian construction industries are not on a sustainable path with some professionals possessing theoretical knowledge of green materials construction, actual practice

remains limited due to lack of incentives, absence of penalties in the code of practice, and insufficient translation of research findings into practice.

5.2 Recommendations

1. Increase Awareness and Education: The level of awareness must be increased through inclusion of environmental issues and sustainability concepts in university curricula and continuing professional development for practitioners.

2. Strengthen Regulatory Framework: Government should undertake a review of existing building regulations to identify measures and policy options to improve sustainability, particularly energy and water efficiency of both residential and non-residential structures.

3. Mandatory Site Waste Management: Site waste management should be compulsory for all construction projects to improve resource efficiency by requiring measurement of waste produced and recording whether it is reused, recycled, or disposed.

4. Financial Incentives: Tax provisions and financial incentives should be introduced to encourage green materials adoption, including building tax credit programmes and reduced taxes on green materials.

5. Stakeholder Collaboration: All interested stakeholders should pool resources in a cooperative strategy, with federal, state, and local governments, educational and research institutions, government parastatals, trade organisations, professional firms, and private individuals collaborating to create the needed synergy for achieving sustainability.

6. Research Implementation: Research findings should be translated into practice rather than serving only as library decorations. Increased cooperation among professionals, particularly joint research work between builders and traditional builders, should be encouraged.

5.3 Areas for Further Research

1. Assessment of the extent of incorporation of green materials-related issues in existing Bachelor of Building curricula in Nigerian universities.

2. Research on energy efficiency in buildings in use, as the greatest proportion of energy consumption occurs during the operational phase.

3. Zero net emission studies in existing and new buildings, including zero energy buildings, to determine energy use through annual accounting.

REFERENCES

[1] Adedeji, Y.M.D., (2011), Housing economy: use of interlocking masonry for low-cost housing in Nigeria. Journal of Construction Project Management and Innovation, Vol. 1 (1), 46-62.

[2] Ajayi, B. (2006b), Dimensional stability of cement-bonded Boards Management with coffee chaff. Journal of the Korea Society of Wood Science and Technology. Mokchae Konghak 34(5): 1-7

[3] Chatterjee (2009). Sustainable Construction and Green Materials in the Foundation of Building Ecology.

[4] Gluch (2006). Building Green Perspectives in Environmental Management in Construction.

[5] Sinopoli, J (2008). *How do Smart Buildings make a building green Energy Engineering, 105(6), 17-22.

[6] Zhang et al. (2011). Research in the Localization Strategy of Green Materials.

[7] Hsieh et al. (2011). The Application of Green Material to Sustainable Building for Environmental Protection.

[8] Al-Kaabi et al. (2011). An Application Model for Green Material Implementation.

[9] Kamana and Escultura (2011). Factors Affecting Ventilation.

[10] Wu and Low (2010). Project Management and Green Materials.

[11] Dammann and Elle (2006). Environmental Indicators.

[12] Olgyay and Herdt (2004). The Application of Ecosystems Services Criteria for Green Material Assessment.

[13] Kolawole, J. and Anigbogu (2005). Impact of Construction Activities on the Environment. *Conference Proceedings of the 2nd National Conference: "Towards a Sustainable Built Environment"*, Ahmadu Bello University, Zaria, 21st-23rd September.

[14] Larsson (2004). Green Materials Strategies.

[15] Sun et al. (2011). Using Renewable and Recycle Materials in Planning Material.

[16] Walker (2012). An Investigation into the Problems and Prospects of Green Building Practice in Nigeria. Unpublished B.Sc. Final Year Project, Department of Building, Ahmadu Bello University, Zaria-Nigeria.

[17] Garder J.E. (1989). Decision Making for Sustainable Development: Selected Approach to Environmental Assessment and Management Environment Impact.

[18] Aboyade, O. (1973). *Issue in the Development of Tropical African*. Ibadan University.

[19] Lamidu (2015). Top Eco-friendly Building Materials, Innovative Housing Solutions Address Social Needs in Emerging Markets.

[20] Adedeji, Y.M.D. (2011). Housing Economy: Use of Interlocking Masonry for Low-Cost Housing in Nigeria. *Journal of Construction Project Management and Innovation*, Vol. 1(1), 46-62.

[21] Adedeji, Y.M.D., Taiwo, A.A., Fadairo, G. and Olotuah, A.O. (2011). Architectural Education and Sustainable Human Habitat. *Sustainability Today, WIT Transactions on Ecology and The Environment*, New Forest, 167(89-99).

[22] Ajayi, B. (2005). Assessment of Board Density and Species on Dimensional Stability of Exotic Hardwood-based Cement-bonded Flakeboard. *Ghana J. Forestry*, Vol. 17 & 18: 37-44.

[23] Ajayi, B. (2006). Properties of Maize Stalk-based Cement-Bonded Composites. *Forestry Products Journal*, 56(6): 51-55.

[24] Arayela, O. and Taiwo, A.A. (2010). Stabilized Laterite Bricks as an Appropriate Walling Material Technology for Increasing Housing Stock in Some Selected African Countries. *Proceedings of XXXVII IAHS, World Housing Congress*, October 26-28, Santacher (Cantabria, Spain).

[25] Akpu, I.V. (2012). Energy Future: The Role of Impact Assessment. *IAIA 12 Conference Proceedings*, 32nd Annual Meeting of the International Association for Impact Assessment, 27-June 1, 2012, Centro de Congresso de Alfândega, Portugal.

[26] Nwofe, P.A. (2013). Comparative Analysis of Domestic Energy Use in Nigeria - A Review. *Continental Journal of Renewable Energy, 4(1), 7.

[27] Olotuah, A.O. (2010). Housing the Urban Poor in Nigeria. Journal of Environment and Urbanization*, 22(1), 89-102.

[28] Omole, F.K. (2000). Urban Renewal Process Issues and Strategies. Lagos: Concept Books and Publication Company Nig. Ltd, pp. 57-64.

[29] Devuyst, D. (2001). How Green is the City? New York: Columbia University Press.

International Conference on Engineering Innovation for Sustainable Development (ICESID 2026)
Faculty of Engineering, Ahmadu Bello University Zaria · 8–10 September 2026

THERMAL EVALUATION OF ASPHALT CONCRETE FOR PAVEMENT-BASED THERMOELECTRIC ENERGY GENERATION: INFLUENCE OF AGGREGATE TYPE AND GRADATION

Sadiq Muktar Muhammad[1], Aminu Suleiman[1,*]
[1]*Bayero University, Kano*
Email: sadiqmyola@gmail.com, asuleiman.civ@buk.edu.ng*
***Corresponding author**: Aminu Suleiman
DOI: https://doi.org/10.67203/sp.ICESID.2026

ABSTRACT

Asphalt pavements absorb large amounts of solar radiation and develop pronounced through-thickness temperature gradients that thermoelectric generators (TEGs) can, in principle, convert into electricity. The magnitude of the recoverable heat depends on the thermal properties of the asphalt concrete, which are in turn governed by mixture composition. This study evaluates the mechanical and thermal behaviour of asphalt concrete for pavement thermoelectric energy harvesting and examines the influence of aggregate type and gradation. Four mixtures were produced from basalt and granite aggregates in wearing-course (WC) and binder-course (BC) gradations: BWC, BBC, GWC and GBC. Marshall mix design (ASTM D6927) established optimum bitumen contents of 5.0–5.5%. Mechanical performance was assessed through Marshall stability, flow and indirect tensile strength (ITS) tests; the apparent thermal conductivity (k_{app}) and specific heat capacity were measured using a steady-state electrical (Searle-type) apparatus. A three-dimensional transient heat-transfer model was built in Abaqus to compare the relative thermal response of the mixtures. Basalt mixtures gave the highest stability (BBC = 7.83kN) and ITS (BBC = 493kPa). The measured k_{app} values (2.90–4.03W/m·K) lie above the range normally reported for asphalt concrete and are treated here as relative, comparative indicators rather than absolute material constants. Within this comparative framing, GWC exhibited the highest apparent conductivity and the largest simulated heat flux (2371W/m²), indicating the greatest thermal potential for subsequent thermoelectric generator integration among the mixtures studied. Electrical power output was not directly evaluated; the thermal characterisation provides a basis for subsequent assessment of TEG integration and power generation. The finite-element results were internally consistent with the analytical Fourier solution to within 13%. Aggregate type and gradation significantly influenced both mechanical and thermal behaviour, providing guidance for material selection in TEG-integrated pavements.

Keywords: *Asphalt concrete; thermoelectric generators; energy harvesting; apparent thermal conductivity; aggregate type*

1. INTRODUCTION

Rising global energy demand, the depletion of fossil resources and the environmental burden of conventional generation have intensified interest in renewable and waste-energy technologies (Gholikhani et al., 2020; Pei et al., 2021). Road networks are attractive in this context because their surfaces are continuously exposed to solar radiation and traffic loading, storing large quantities of thermal and mechanical energy that is otherwise dissipated to the environment (Zhu et al., 2019). Recovering even a fraction of this energy could power road lighting, sensors and monitoring devices while reducing the surface temperatures associated with the urban heat island effect.

Among pavement energy-harvesting approaches, piezoelectric, photovoltaic and thermoelectric generation is well suited to asphalt because the material routinely develops the temperature differentials on which the technology relies. TEGs are solid-state devices that convert a temperature difference directly into electricity through the Seebeck effect, and can operate wherever a gradient exists (Champier, 2017; Shaaban et al., 2019). Experimental and prototype studies have demonstrated combined power-generation and pavement-cooling functions, with cold-side (heat-sink) design frequently controlling field performance (Jiang et al., 2018; Zhu et al., 2019).

The efficiency of a pavement TEG system depends on the available temperature gradient and on the thermal properties of the surrounding asphalt concrete-principally its thermal conductivity and

specific heat capacity (Aridi et al., 2021). These properties are, in turn, governed by mixture composition. Because aggregate typically constitutes the majority of the mixture by volume, aggregate mineralogy and gradation exert a strong influence on heat transfer, whereas the binder-present in small proportion-has a comparatively minor effect (Mrawira & Luca, 2006; Demirtürk et al., 2024; Pasetto et al., 2025). Much of the existing literature focuses on enhancing conductivity through conductive additives such as graphite, steel fibres or slag (Abbas & Alhamdo, 2023), while the comparative effect of conventional aggregate type and gradation on the thermal response relevant to TEG applications has received less systematic attention.

This study therefore evaluates the mechanical and thermal behaviour of asphalt concrete produced from two common aggregate sources (basalt and granite) in two standard gradations (wearing and binder course) and assesses their relative suitability for pavement thermoelectric energy harvesting using combined laboratory testing and three-dimensional finite-element (FE) simulation. The work is framed around locally sourced Nigerian materials, for which such thermal characterisation is currently limited. The use of locally sourced Nigerian aggregates also supports the development of sustainable and locally adaptable pavement materials, while the thermal characterisation provides a basis for future pavement-based energy-harvesting applications relevant to Nigeria's infrastructure and energy needs.

2. MATERIAL AND METHODS

2.1 Materials and mix design

Crushed basalt (Kore quarry) and granite (Barawa quarry), both from Batagarawa LGA, Katsina State, and 80/100-grade bitumen sourced in Kano State were used. Aggregate and bitumen properties were verified against the Federal Ministry of Works (FMW) general specification and the relevant ASTM/BS standards (Tables 1 and 2). Four mixtures were designed-Basalt Wearing Course (BWC), Basalt Binder Course (BBC), Granite Wearing Course (GWC) and Granite Binder Course (GBC)-using the Marshall method in accordance with ASTM D6927. Optimum bitumen contents, obtained from stability, flow, unit-weight and voids plots following the Asphalt Institute procedure, were 5.5% for BBC and 5.0% for GBC, BWC and GWC.

2.2 Mechanical testing

Marshall stability and flow were determined on compacted cylindrical specimens (101.6mm diameter×63.5mm height) at 60°C, and indirect tensile strength (ITS) was measured to assess cracking resistance. Three replicates were tested per mixture and the mean reported.

2.3 Thermal property determination

Thermal conductivity was measured in the laboratory on Marshall-derived sub-specimens using a steady-state electrical (Searle-type) apparatus (this steady-state, effectively one-dimensional test relates only to the laboratory measurement of the material properties, and is distinct from the transient three-dimensional finite-element model of Section 2.4), with the conductivity computed as $k = VIL/(A \cdot \Delta T)$, where V and I are the applied voltage and current, L the specimen thickness, A the cross-sectional area and ΔT the temperature difference across the specimen. Three replicates were averaged for each mixture. Specific heat capacity was determined by the method of mixtures using a copper calorimeter,

It should be noted that this formulation attributes the full electrical power ($V \cdot I$) to one-dimensional conduction through the specimen and neglects lateral and convective heat losses. For a comparatively low-conductivity, heterogeneous material such as asphalt concrete, these losses are not negligible, so the method tends to over-estimate the absolute conductivity. The values reported here are therefore designated apparent thermal conductivity (k_{app}) and are used primarily as relative indicators for comparing mixtures and as comparative inputs to the FE model, rather than as absolute material constants. Because the FE simulations use these apparent conductivities as material inputs, the calculated heat-flux and reaction-heat-flow magnitudes inherit the uncertainty and possible systematic bias of the conductivity measurements. Therefore, these numerical quantities are interpreted comparatively rather than as independently validated absolute heat-transfer values.

Three replicate measurements were conducted for each asphalt mixture, and the mean, standard deviation (SD) and coefficient of variation (CV) were used to assess measurement repeatability. The SD was calculated as the sample standard deviation, $s = \sqrt{\frac{\Sigma(ki - \bar{k})^2}{n-1}}$ while the CV was calculated as: $CV = (s / \bar{k}) \times 100$. The resulting CV values ranged from 0.63% to 2.70%, indicating relatively low within-mixture variability. However, the observed repeatability does not eliminate possible systematic bias associated with the steady-state Searle-type method. Therefore, independent testing using a transient method (e.g., transient plane source) or a guarded steady-state cell would be required to establish absolute thermal conductivity values (Demirtürk et al., 2024). This limitation is revisited in Section 3.3.

2.4 Finite element model and Mesh Sensitivity Analysis

A three-dimensional transient heat-transfer model of the Marshall specimen (101.6mm × 63.5mm) was developed in Abaqus/CAE using DC3D8 eight-node linear heat-transfer elements. The measured density, apparent thermal conductivity and specific heat capacity of each mixture were assigned as isotropic and homogeneous properties. An initial temperature of 298.15K was applied, while fixed temperatures of 335K at the upper face and 310K at the lower face were prescribed for BBC, BWC and GWC. For GBC, 334K and 310K were prescribed at the upper and lower faces, respectively, corresponding to the measured temperature difference. A surface film condition with a film coefficient of $10 W/m^2 \cdot K$ and an ambient temperature of 298.15K was applied to the lateral surface to account for heat loss to the surroundings. Temperature (NT11), heat flux (HFL3), and reaction heat flow (RFL11) were extracted for analysis.

A mesh-sensitivity analysis was performed (Table 5) using nominal mesh sizes of 2, 3, and 4mm. For the representative BWC specimen, the corresponding HFL3 values were approximately 1351.55, 1312.95, and 1293.70W/m^2, respectively. The 3mm mesh differed by approximately 2.94% from the 2mm mesh and 1.47% from the 4mm mesh, indicating that further mesh refinement caused only minor changes in the calculated heat flux. Therefore, the 3mm mesh was adopted as a suitable balance between numerical accuracy and computational efficiency.

3. RESULT AND DISCUSSION

3.1 Material properties

Both aggregates satisfied the specification limits (Table 1). Basalt showed a higher specific gravity (2.82 vs 2.64), while granite recorded lower impact, abrasion and crushing values, indicating marginally greater resistance to mechanical degradation; both had acceptable flakiness and elongation indices. The bitumen properties (Table 2) were consistent with a 80/100 paving-grade binder.

Table 1: *Physical properties of basalt and granite aggregates*

Property	Basalt	Granite	Specification
Specific gravity (coarse)	2.82	2.64	2.5–3.0
Aggregate impact value (%)	11.1	7.7	30 max
LA abrasion (%)	24.3	20.0	30 max
Aggregate crushing value (%)	20.0	16.6	45 max
Flakiness index (%)	17.0	21.0	30 max
Elongation index (%)	15.0	25.0	30 max

Table 2: *Physical properties of the bitumen*

Test	Result	Standard
Penetration (0.1mm)	89	ASTM D5
Softening point (°C)	54	ASTM D36
Flash point (°C)	239	ASTM D92
Fire point (°C)	319	ASTM D92

Note: Values in the Specification column are presented as either permissible ranges or limiting requirements (minimum/maximum), as indicated.

3.2 Mechanical properties

Marshall stability, flow and ITS varied systematically with aggregate type and gradation (Table 3, Figure 1). The basalt mixtures outperformed the granite mixtures: BBC recorded the highest stability (7.83kN) and ITS (493.2kPa), followed by BWC, while GBC gave the lowest stability (3.86kN). The superior performance of the basalt mixtures is consistent with their higher specific gravity and better aggregate-bitumen interlock. The Marshall stability values of all four mixtures exceeded the minimum 3.5kN requirement specified for asphalt concrete in the Nigerian General Specifications for Roads and Bridges. GWC and GBC recorded 4.66kN and 3.86kN, respectively, and therefore satisfied the minimum stability requirement, although further optimisation may be required for higher traffic demands.

Table 3: *Marshall stability, flow and indirect tensile strength of the mixtures*

Mixture	Stability (kN)				Flow (mm)				ITS (kPa)			
	Replicate value (n = 3)	Mean	SD	CV (%)	Replicate value (n = 3)	Mean	SD	CV (%)	Replicate value (n = 3)	Mean	SD	CV (%)
BWC	6.56	6.56	0.27	4.04	3.40	3.40	0.00	0.00	485.60	475.90	10.18	2.14
	6.83				3.40				465.30			
	6.30				3.40				476.80			
BBC	7.83	7.83	0.17	2.17	3.80	4.03	0.21	5.16	531.10	493.20	34.09	6.91
	8.00				4.10				483.60			
	7.66				4.20				465.00			
GBC	3.90	3.86	0.24	6.28	3.40	3.47	0.12	3.33	445.30	466.10	29.69	6.37
	3.60				3.40				500.10			
	4.08				3.60				452.90			
GWC	4.58	4.66	0.20	4.26	2.40	2.77	0.51	18.36	460.60	439.30	22.25	5.07
	4.89				3.35				416.20			
	4.52				2.56				441.10			

Note: The values under the 'Replicate value' represent three independent measurements, SD = standard deviation; CV = coefficient of variation

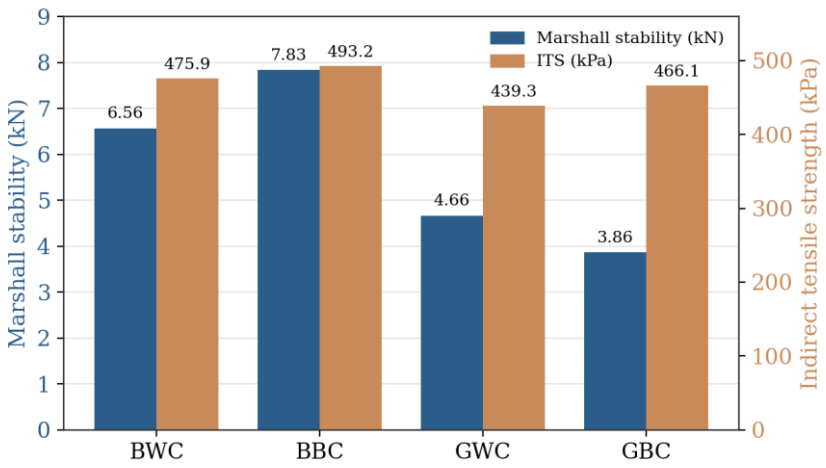

Figure 1: *Marshall stability and indirect tensile strength of the four mixtures.*

3.3 Thermal properties

The measured apparent thermal conductivity (k_{app}) ranged from 2.90W/m·K for BWC to 4.03W/m·K for GWC, with BBC and GBC recording 3.18 and 2.97W/m·K, respectively (Table 4, Figure 2). Specific heat capacity ranged from 765J/kg·K for GWC to 832J/kg·K for BWC. GWC therefore exhibited the highest apparent thermal conductivity and the lowest specific heat capacity, indicating a comparatively greater tendency for heat transfer through the mixture under the test conditions.

The measured k_{app} values should, however, be interpreted with caution. Reported thermal conductivities for conventional dense-graded asphalt concrete are typically around 1.7-2.1W/m·K (Mrawira & Luca, 2006) and rarely exceed 3W/m·K. The GWC value of 4.03W/m·K is therefore higher than expected for an asphalt concrete mixture containing binder and air voids. This overestimation is attributed to the steady-state electrical method, which assumes that the applied electrical power is transferred entirely by axial conduction while neglecting lateral and convective heat losses. These losses may be significant and may differ among mixtures, particularly for GWC, which exhibited the highest heat-transfer rate. Consequently, the measured values are treated as apparent thermal conductivities and are used primarily as comparative indicators and as inputs to the FE model rather than as absolute material constants.

Based on the measured values, the apparent thermal conductivity followed the order GWC > BBC > GBC > BWC. However, because lateral and convective heat losses may affect the mixtures to different degrees, this ranking should not be interpreted as an absolute ranking of intrinsic thermal conductivity. The mixture ranking is therefore considered a comparative indication of thermal response, and GWC's apparent advantage may be partly influenced by its greater unaccounted heat loss. The trend also indicates an interaction between aggregate type and gradation: for granite, the wearing-course mixture had a higher k_{app} than the binder-course mixture (GWC > GBC), whereas for basalt, the binder-course mixture was slightly higher than the wearing-course mixture (BBC > BWC). Thus, the effect of gradation on thermal response depends on the aggregate type.

Table 4: *Apparent thermal conductivity and specific heat capacity of the mixtures*

Mixture	Apparent thermal conductivity, k_app (W/m·K)				Specific heat capacity (J/kg·K)			
	Replicate value (n = 3)	Mean	SD	CV (%)	Replicate value (n = 3)	Mean	SD	CV (%)
BWC	2.9313	2.902	0.039	1.350	829.2175	832.240	7.550	0.910
	2.9167				841.0377			
	2.8571				827.0027			
BBC	3.2411	3.180	0.085	2.670	788.2649	793.310	4.970	0.630
	3.2174				793.4597			
	3.0819				798.2073			
GBC	2.952	2.972	0.029	0.630	792.7049	802.390	8.450	1.050
	2.9741				806.19			
	2.989				808.2716			
GWC	4.0783	4.026	0.050	1.240	781.4167	765.070	23.380	3.060
	3.9788				775.5046			
	4.0216				738.2893			

Note: The values under the 'Replicate Value' represent three independent measurements, SD = standard deviation; CV = coefficient of variation

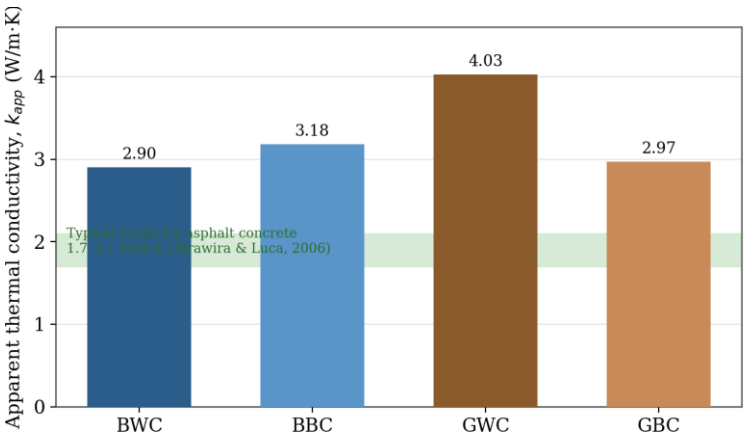

Figure 2: Apparent thermal conductivity of the mixtures relative to the range typically reported for asphalt concrete (Mrawira & Luca, 2006).

Table 5: *Mesh-sensitivity check for BWC specimen*

Mesh size (mm)	HFL3 (W/m²)	Difference from 3mm (%)
2	1351.55	2.94
3	1312.95	Reference
4	1293.7	1.47

Note: HFL3 represents the numerical heat flux extracted from the central region of the specimen. The 3 mm mesh was selected for the FE simulations.

The trend also shows an interaction between aggregate type and gradation: for granite the wearing course exceeded the binder course (GWC > GBC), whereas for basalt the binder course slightly exceeded the wearing course (BBC > BWC). Gradation therefore does not act in a single consistent direction independent of aggregate source, which is relevant when selecting mixtures for thermal performance.

3.4 Numerical thermal response

The transient simulations produced comparable temperature differences across all specimens ($\Delta T \approx 24$–25K), confirming that the mixtures were subjected to similar thermal loading and that differences in heat transfer arise from material properties rather than boundary conditions. Representative contour plots for GWC are shown in Figure 3. Peak heat flux (HFL3) and reaction heat flow (RFL11) differed markedly between mixtures (Table 6, Figure 4): GWC gave the highest heat flux (2371W/m²) and reaction heat flow (up to 263W), consistent with its higher apparent conductivity,

followed by BBC. This indicates that, among the mixtures studied, GWC offers the greatest capacity to transfer heat through the layer and therefore the greatest relative potential for thermoelectric harvesting.

GWC was selected for the representative contour plots because it exhibited the highest apparent thermal conductivity and the highest simulated thermal response among the four mixtures. The remaining mixtures showed the same general through-thickness heat-transfer pattern, with differences primarily in the magnitude of the heat flux.

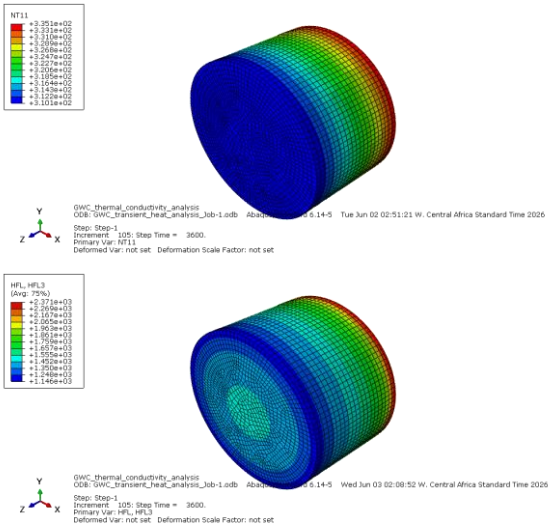

Figure 3: *Simulated temperature distribution (NT11, top) and heat flux (HFL3, bottom) for the GWC mixture.*

Table 6: *Summary of simulated thermal response of the mixtures*

Mixture	ΔT (K)	Peak heat flux, HFL3 (W/m²)	Peak reaction heat flow, RFL11 (W)
BWC	25.0	1912	178.3
BBC	25.0	2018	211.2
GWC	25.0	2371	263.1
GBC	24.1	1875	187.1

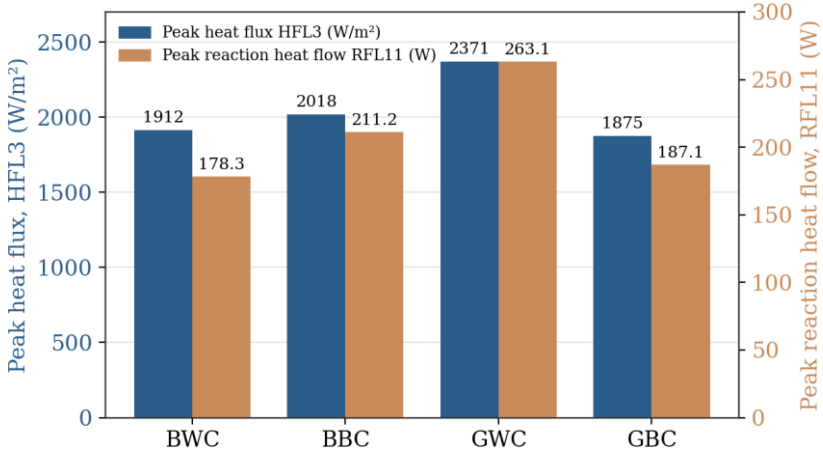

Figure 4: *Simulated peak heat flux and reaction heat flow for the four mixtures.*

3.5 Model verification

The FE model was checked against the analytical Fourier solution $q = k \cdot \Delta T/L$ using the same apparent conductivities, specimen thickness (0.0635m) and simulated temperature differences. Agreement was within 13% for all mixtures (Table 7). This confirms that the model correctly reproduces one-dimensional conduction and is internally consistent; it is a verification of the numerical

implementation rather than an independent experimental validation, since both the analytical and numerical fluxes derive from the same measured conductivity. What is reported here is a code verification of the numerical solution against the analytical (closed-form) Fourier result; independent experimental validation against measured heat-flux or temperature-field data was outside the present scope and is recommended for future work.

Table 7: *Verification of numerical against analytical heat flux*

Mixture	ΔT (K)	k_{app} (W/m·K)	Analytical flux (W/m²)	Abaqus flux (W/m²)	Difference (%)
BBC	25.00	3.18	1252	1425	12.11
BWC	25.00	2.90	1142	1313	12.98
GBC	24.10	2.97	1123	1287	12.74
GWC	25.00	4.03	1585	1759	9.86

4. CONCLUSION

The mechanical and thermal behaviour of four asphalt concrete mixtures, produced from basalt and granite aggregates in wearing- and binder-course gradations was evaluated for pavement thermoelectric energy harvesting through laboratory testing and three-dimensional transient FE simulation. The main findings are:

- Aggregate type strongly influenced mechanical performance: basalt mixtures gave higher Marshall stability and ITS than granite mixtures, with BBC the strongest (7.83kN; 493kPa).
- Aggregate type and gradation both affected thermal response, with an interaction between them; GWC showed the highest apparent conductivity and the largest simulated heat flux (2371W/m²), indicating the greatest relative thermal-harvesting potential.
- The mixture ranking is therefore considered a comparative indication of thermal response rather than an absolute ranking of intrinsic thermal conductivity, as heat losses may affect the mixtures differently.
- The FE model reproduced the analytical Fourier solution within 13%, providing internal verification of the numerical implementation; this should not be interpreted as independent experimental validation.
- The study provides thermal characterisation and numerical assessment relevant to TEG investigation; electrical power output was not directly evaluated. Future work should couple the thermal model with experimentally determined TEG/Seebeck parameters to quantify actual electrical generation.
- Future work should establish absolute thermal conductivities using a transient or guarded steady-state method, validate the model against independent measurements, and couple the thermal model to a Seebeck-based estimate of electrical output to quantify harvesting feasibility.

ACKNOWLEDGEMENTS

The authors thank the Department of Physics, Ahmadu Bello University, Zaria, for access to the thermal-conductivity and calorimetry facilities.

5. REFERENCES

Abbas, F. A., & Alhamdo, M. H. (2023). Enhancing the thermal conductivity of hot-mix asphalt. Results in Engineering, 17, 100827.

Aridi, R., Faraj, J., Ali, S., Lemenand, T., & Khaled, M. (2021). Thermoelectric power generators: State-of-the-art, heat recovery method, and challenges. Electricity, 2(3), 359–386.

Champier, D. (2017). Thermoelectric generators: A review of applications. Energy Conversion and Management, 140, 167–181.

Demirtürk, D., Ozturk, H. I., & Guler, M. (2024). Investigation of the influence of mixture and microstructural properties on the thermal conductivity of asphalt concrete using the transient heat transfer method. Materials and Structures, 57(8), 179.

Gholikhani, M., Roshani, H., Dessouky, S., & Papagiannakis, A. T. (2020). A critical review of roadway energy harvesting technologies. Applied Energy, 261, 114388.

Jiang, W., Xiao, J., Yuan, D., Lu, H., Xu, S., & Huang, Y. (2018). Design and experiment of thermoelectric asphalt pavements with power-generation and temperature-reduction functions. Energy and Buildings, 169, 39–47.

Mrawira, D. M., & Luca, J. (2006). Effect of aggregate type, gradation, and compaction level on thermal properties of hot-mix asphalts. Canadian Journal of Civil Engineering, 33(11), 1410–1417.

Pasetto, M., Baliello, A., Giacomello, G., & Pasquini, E. (2025). Multi-criteria optimization of aggregate gradation based on thermal, surface, and mechanical properties of the asphalt solar collector. Canadian Journal of Civil Engineering, 52(5), 824–842.

Pei, J., Guo, F., Zhang, J., Zhou, B., Bi, Y., & Li, R. (2021). Review and analysis of energy harvesting technologies in roadway transportation. Journal of Cleaner Production, 288, 125338.

Shaaban, K., Abdel-Warith, K., & Haddock, J. (2019). Using pavements to generate electricity. Procedia Computer Science, 151, 124–131.

Zhu, X., Yu, Y., & Li, F. (2019). A review on thermoelectric energy harvesting from asphalt pavement: Configuration, performance and future. Construction and Building Materials, 228, 116818.

ASTM D6927-15. (2015). Standard test method for Marshall stability and flow of asphalt mixtures. ASTM International, West Conshohocken, PA

International Conference on Engineering Innovation for Sustainable Development (ICESID 2026)
Faculty of Engineering, Ahmadu Bello University Zaria · 8–10 September 2026

TRIBOLOGICAL BEHAVIOUR AND MULTI-OBJECTIVE OPTIMIZATION OF AUSTEMPERED HIGH-CARBON STEEL USING SULFATE SALT-MODIFIED SESAME OIL

Hafiz Bashir Aminu[1,2,*], Rayyan Mamuda Dodo[1], Terver Ause[1]
[1]*Ahmadu Bello University Zaria*
[2]*Federal Polytechnic Idah Kogi State*
Email: hafizbashir16@gmail.com*, rdmamuda@abu.edu.ng, tause@abu.edu.ng
***Corresponding author**: Hafiz Bashir Aminu
DOI: https://doi.org/10.67203/sp.ICESID.2026

ABSTRACT

This study investigates the tribological behaviour and multi-response optimization of austempered high-carbon steel processed using sulfate salt-modified sesame oil as a bio-based quenching medium. Potassium sulfate (K_2SO_4) and sodium sulfate (Na_2SO_4) concentrations, austempering time and temperature were varied using a Taguchi L9 orthogonal array. Wear rate and coefficient of friction (CoF) were evaluated under dry sliding conditions, while scanning electron microscopy (SEM) was used for qualitative microstructural examination. Grey Relational Analysis (GRA) was employed to simultaneously optimize the two smaller-the-better responses. The nine experimental runs produced wear rates of 0.0003 – 0.0036 mm³/Nm and CoF values of 0.048 – 0.118. Run 4, corresponding to 1.5% K_2SO_4, 0% Na_2SO_4, 45 min and 320 °C, produced the highest experimentally observed GRG of 0.8519. The Taguchi response-mean analysis predicted a combined optimum of 3% K_2SO_4, 0% Na_2SO_4, 45 min and 320 °C, with an estimated GRG of 0.8721. However, this predicted condition was not included in the L9 matrix and therefore remains experimentally unverified. Pooled ANOVA indicated that austempering temperature contributed 47.74% to GRG variation, followed by Na_2SO_4 concentration at 19.92%, although neither retained factor was statistically significant at the 5% level. SEM observations suggested associations between comparatively refined transformation morphologies and favourable tribological responses, but definitive phase identification requires complementary XRD or EBSD analysis. The findings demonstrate the potential of sulfate salt-modified sesame oil for tailoring the combined wear and friction response of austempered high-carbon steel.

Keywords: *Austempering; Sesame oil; Sulfate salts; Tribology; Grey Relational Analysis*

1. INTRODUCTION

The increasing demand for engineering components capable of operating under severe service conditions has stimulated interest in heat treatment processes that provide a favourable combination of strength, toughness and tribological performance. Austempering is particularly attractive because isothermal transformation of austenite above the martensite-start temperature produces bainitic ferrite and retained austenite, which can improve hardness, toughness, dimensional stability and wear resistance (Bhadeshia, 2015). Such tribological performance is important in gears, shafts, bearings, railway components, mining equipment and automotive parts, where sliding and abrasive interactions can cause material degradation and premature failure (Stachowiak & Batchelor, 2025).

The wear behaviour of bainitic steels depends not only on hardness but also on the morphology, distribution and stability of retained austenite. During sliding, retained austenite may transform to martensite through a deformation-induced transformation, producing a TRIP effect that enhances strain hardening and resistance to material removal (Chen *et al.*, 2024). Chen et al. (2025) associated improved wear resistance with strain partitioning between retained austenite and ferritic phases, while Jiang *et al.* (2026) showed that retained-austenite stability influences crack initiation, propagation and transformation-induced strengthening. Controlling these microstructural features during austempering is therefore important for optimizing tribological behaviour.

Quenching medium characteristics strongly influence heat extraction and subsequent phase transformation. Although mineral oils are widely used, environmental, safety and sustainability

concerns have increased interest in vegetable-oil-based quenchants because of their renewability, biodegradability and favourable cooling characteristics. Sesame oil is a promising candidate owing to its favourable fatty-acid composition, relatively high oxidative stability and flash point. However, previous studies have focused predominantly on the thermal, physicochemical, cooling, mechanical and microstructural characteristics of vegetable-oil quenchants, with comparatively limited attention to their modification for improved tribological performance.

Inorganic salt modification provides a potential means of controlling the heat transfer behaviour of vegetable oils. Aminu *et al.* (2025) reported that sulfate salts can modify the thermal behaviour, cooling characteristics and heat transfer efficiency of vegetable-oil-based quenchants. Such changes may affect bainitic transformation, retained-austenite stability and consequently the tribological behaviour of austempered steels. From an industrial perspective, sulfate salt-modified sesame oil could potentially be prepared using existing oil-quenching systems, while its renewable base fluid offers sustainability advantages. However, practical adoption would depend on raw-material and additive costs, salt dispersion and suspension stability, bath maintenance, thermal degradation, reusability, process consistency and equipment compatibility. Thus, although the approach has commercialization potential, pilot-scale testing, repeated-cycle evaluation, life-cycle assessment and techno-economic comparison with conventional mineral oils are required before industrial implementation can be established.

Despite increasing interest in bio-based quenchants, the tribological behaviour of austempered high-carbon steel processed using sulfate salt-modified sesame oil remains insufficiently documented. This study therefore evaluates the effects of K_2SO_4 concentration, Na_2SO_4 concentration, austempering time and temperature on the wear rate and coefficient of friction using a Taguchi L9 orthogonal array. Grey Relational Analysis (GRA) was employed to simultaneously optimize the tribological responses, while Analysis of Variance (ANOVA) quantified the relative contribution of the process parameters. Microstructural examination was used to relate the observed tribological behaviour to the resulting microstructural features.

The novelty of this study lies in integrating sulfate-salt modification of sesame oil, austempering and Taguchi–GRA multi-response optimization to establish the relationship between quenchant composition, austempering parameters and simultaneous control of wear rate and coefficient of friction. The findings provide an initial basis for evaluating sulfate salt-modified sesame oil as a bio-based alternative to conventional petroleum-derived quenchants and for subsequent pilot-scale and commercialization studies.

2. MATERIALS AND METHODS

2.1 Materials

High-carbon steel and *Sesamum indicum* (sesame) oil were used as the workpiece material and base quenchant, respectively. The steel, supplied in flat-spring form, was machined into samples for tribological and microstructural characterization. K_2SO_4 and Na_2SO_4 were used as quenchant modifiers, while standard metallographic consumables and reagents were used for sample preparation.

The chemical composition of the steel is presented in Table 1.

Table 1: *Chemical composition of the selected high-carbon steel sample*

Elements	C	Si	Mn	Cr	Ni	Cu	V	W	Fe
Compositions (% wt)	1.26	1.20	2.14	2.35	2.80	0.79	0.74	0.20	balance

2.2 Quenchant Preparation and Experimental Design

Sesame oil was preheated to 100 °C before K_2SO_4 and Na_2SO_4 were added at 0, 1.5 and 3.0 wt.%. The mixtures were magnetically stirred for 10 min to promote uniform salt dispersion. The resulting sulfate-modified sesame oils were used as quenching media for austempering.

A Taguchi L9 orthogonal array was employed with four three-level control factors: K_2SO_4 concentration, Na_2SO_4 concentration, austempering time and temperature. The complete experimental matrix is presented with the experimental results in Table 3.

2.3 Heat Treatment of Samples

The as-received samples were normalized at 850 °C for 1 h and air cooled to obtain a relatively homogeneous initial microstructure. Austempering involved austenitizing at 850 °C for 1 h, followed by transfer into the selected sulfate-modified sesame-oil bath maintained at 260, 290 or 320 °C. The samples were held for 30, 45 or 60 min and subsequently air cooled.

The selected temperature range was within the expected bainitic transformation range of the steel. It was also supported by the thermal behaviour of sulfate-modified sesame oil reported by Aminu *et al.* (2025), who observed increased thermal stability following sulfate modification.

2.4 Tribological Testing

Wear rate and coefficient of friction (CoF) were evaluated using a ball-on-disk tribometer (model 50324) under dry-sliding conditions in accordance with ASTM G99 (2020). Samples were prepared to the required dimensions and tested against a 6 mm diameter stainless-steel ball using a normal load of 10 N, sliding speed of 0.1 m/s, test duration of 5 min and wear-track diameter of 8 mm. All samples were cleaned and dried before testing.

CoF was recorded continuously by the tribometer software. Wear rate was determined from the mass loss before and after testing and expressed as volumetric wear per unit load and sliding distance (mm^3/Nm):

$$\text{Wear rate (WR)} = \frac{\Delta \text{m}}{\rho . F . L} \tag{1}$$

where Δm is mass loss, ρ is material density, F is applied load and L is sliding distance. The identical test duration and conditions were maintained for all samples to permit comparative evaluation. The relatively short test duration should, however, be regarded as a limitation when extrapolating the results to long-term service wear.

2.5 Microstructural Characterization

For SEM examination, samples were sectioned to approximately 10 × 10 × 5 mm, ground using 400–1200 grit SiC papers, polished with 6 and 1 µm diamond pastes, and etched with 2% nital for approximately 30 s. SEM observations were conducted at 1000× magnification.

The micrographs were used to compare morphological features associated with the different heat treatment conditions and to relate microstructural variations to the observed tribological responses. Phase assignments were made cautiously from morphology and heat treatment history; definitive identification of phases such as retained austenite would require complementary techniques such as X-ray diffraction.

2.6 Taguchi–Grey Relational Analysis

The experimental data were analyzed using Taguchi signal-to-noise (S/N) analysis, Grey Relational Analysis (GRA) and ANOVA in Minitab 17. Since both wear rate and CoF are smaller-the-better characteristics, the corresponding S/N criterion was employed:

$$\eta = -10 \log_{10}\left(\frac{1}{n}\sum_{i=1}^{n} y_i^2\right) \tag{2}$$

Where η is the S/N ratio, y_i is the observed response and n is the number of observations. As each L9 condition was tested once, n=1.

For simultaneous optimization of wear rate and CoF, the responses were normalized using the smaller-the-better criterion:

$$\text{yi (s)} = \frac{maxx_i(s) - x_i(s)}{maxx_i(s) - minx_i(s)} \tag{3}$$

The grey relational coefficient (GRC) was subsequently calculated from the normalized responses:

$$\epsilon i\,(s) = \frac{\Delta_{min} + \varphi\Delta_{max}}{\Delta_{oi}\,(s) + \varphi\Delta_{max}} \tag{4}$$

$$\Delta_{oi}\,(s) = |x_o(s) - x_i(s)| \tag{5}$$

where the identification coefficient was set to 0.5. The grey relational grade (GRG) was calculated as the equally weighted mean of the GRCs for wear rate and CoF:

$$\mathrm{GRG}i = \frac{1}{n}\sum_{i=1}^{n} \epsilon ij \tag{6}$$

The factor level producing the highest mean GRG was selected as the optimum level. The predicted optimum GRG was subsequently obtained using the Taguchi additive model (Roy, 2010):

$$\gamma = \mu + \sum_{i=1}^{q}\left(\gamma_{i,opt} - \mu\right) \tag{7}$$

where μ is the overall mean GRG of all N experimental runs and $\gamma_{i,opt}$ is the mean GRG at the selected optimum level of factor *i*.

2.7 Analysis of Variance (ANOVA)

Pooled ANOVA was used to estimate the relative contributions of K_2SO_4 concentration, Na_2SO_4 concentration, austempering time and temperature to wear rate, CoF and GRG. The sum of squares (SS), mean square (MS) and percentage contribution were calculated using:

$$\mathrm{SS} = \sum_{i=1}^{L}\frac{T_i^2}{n_i} - \frac{T^2}{N} \tag{8}$$

$$\mathrm{MS} = \frac{SS}{DOF} \tag{9}$$

$$P(\%) = \frac{SS_i}{SS_T} \times 100 \tag{10}$$

The percentage contribution of each factor was calculated from its sum of squares relative to the total sum of squares. Because the L9 array contained no experimental replication, the ANOVA results were interpreted primarily as estimates of the relative contribution of the process parameters rather than as definitive tests of statistical significance. The Taguchi–ANOVA procedure followed the established methodology described by Roy (2010).

3. RESULTS AND DISCUSSION

3.1 Tribological Performance

The tribological results (Tables 2 and 3) demonstrate substantial improvement following quenching and austempering compared with the normalized condition. The normalized steel exhibited a wear rate of 0.0096 mm^3/Nm and CoF of 0.279, compared with 0.0005 mm^3/Nm and 0.220, respectively, after water quenching. Raw sesame-oil quenching produced still lower values of 0.0001 mm^3/Nm and 0.127, indicating the favourable tribological response achievable with sesame-oil heat treatment.

Table 2: *Wear rate and coefficient of friction tests for normalized, water-quenched and raw sesame oil-quenched samples*

Experiments	Wear rate (mm^3/Nm)	Coefficient of friction
Normalized	0.0096	0.279
Water quenched	0.0005	0.220
Raw sesame oil	0.0001	0.127

3.1.1 Wear test

The wear rate of the nine austempered conditions ranged from 0.0003 to 0.0036 mm^3/Nm, with the minimum occurring at Run 1 and the maximum at Run 5. All austempered conditions therefore exhibited lower wear rates than the normalized steel (0.0096 mm^3/Nm), although the raw sesame-oil reference produced the lowest value (0.0001 mm^3/Nm).

The improved wear resistance is associated with the development of bainitic ferrite and retained-austenite-rich regions during isothermal transformation. Bainitic ferrite provides a strong load-bearing framework, while retained austenite can accommodate deformation and undergo transformation-induced strengthening during sliding (Zhao, 2025). This agrees with Chen *et al.* (2024), who linked improved wear resistance in bainitic steels to the synergistic effects of bainitic ferrite and retained austenite.

3.1.2 Coefficient of friction (CoF) test

The coefficient of friction values obtained from the tribological tests are presented in Table 3. CoF varied from 0.048 to 0.118 among the austempered conditions, with the minimum recorded at Run 5 and the maximum at Run 1 (Table 3). The lower friction observed under some conditions may be associated with retained-austenite-rich regions, which possess greater deformability and can accommodate localized deformation, thereby reducing interfacial stress concentrations during sliding (Chen *et al.*, 2025).

Table 3: L9 orthogonal array layout showing results for tribology tests (wear rate and coefficient of friction) for austempered samples

Run	Factors				Responses	
	A: K_2SO_4 (%)	B: Na_2SO_4 (%)	C: Austemp. Time (min)	D: Austemp. Temp. (°C)	WR (mm^3/Nm)	CoF
1	0	0	30	260	0.0003	0.118
2	0	1.5	45	290	0.0014	0.088
3	0	3	60	320	0.0007	0.081
4	1.5	0	45	320	0.0004	0.059
5	1.5	1.5	60	260	0.0036	0.048
6	1.5	3	30	290	0.0010	0.107
7	3	0	60	290	0.0005	0.094
8	3	1.5	30	320	0.0008	0.074
9	3	3	45	260	0.0004	0.069

3.2 Taguchi analysis signal-to-noise ratio (S/N) for tribological responses

3.2.1 Wear rate response

The Taguchi S/N analysis (Table 4) identified Na_2SO_4 concentration as the most influential factor on wear rate, followed by K_2SO_4 concentration, austempering time and temperature. The

optimum levels for minimizing wear rate were 1.5% K_2SO_4, 1.5% Na_2SO_4, 60 min and 290 °C, as indicated by the main-effect plot (Figure 1).

Table 4: *Response for S/N ratios (wear rate vs K_2S0_4, Na_2SO_4, austempering time and austempering temperature*

Level	K_2S0_4 (%)	Na_2SO_4 (%)	Austempering Time (min)	Austempering Temperature (°C)
1	63.54	68.15	64.13	62.43
2	**58.94**	**55.96**	64.33	**61.03**
3	65.31	63.69	**59.33**	64.33
Delta	6.36	12.18	5.00	3.30
Rank	2	1	3	4

*Bold value signifies to show the level at which the optimum condition is achieved for each process parameter.

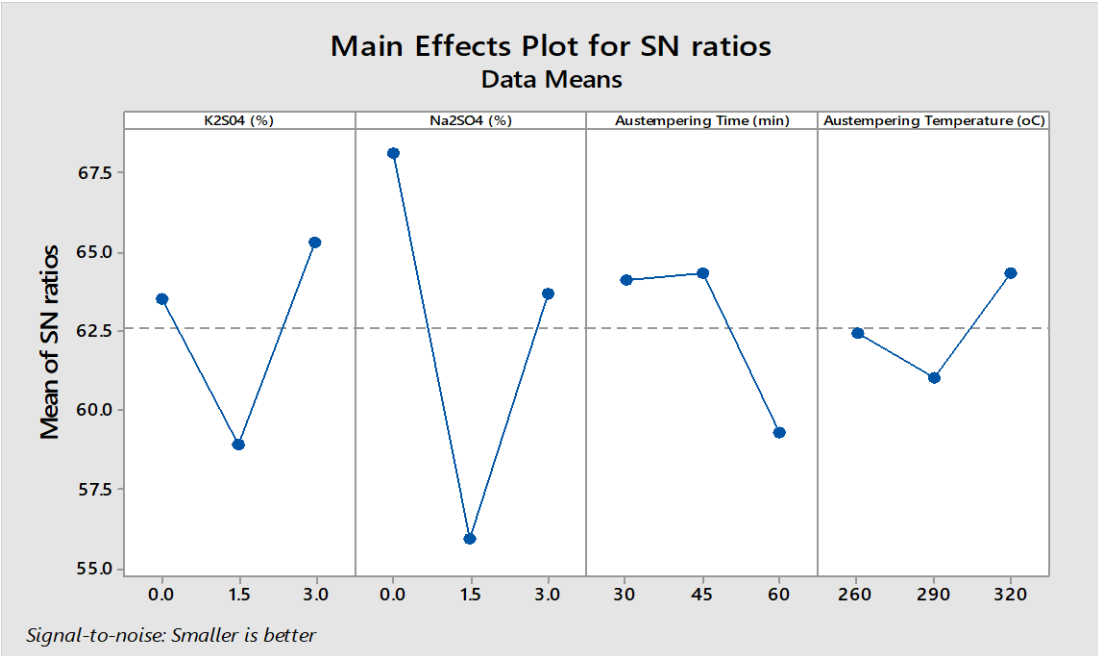

Figure 1: The main effect plots for S/N ratios on wear rate (Taguchi)

3.2.2 Coefficient of friction (CoF) response

For CoF, austempering time was the most influential parameter, followed by temperature, Na_2SO_4 concentration and K_2SO_4 concentration (Table 5). The optimum condition for minimizing CoF was 0% K_2SO_4, 3% Na_2SO_4, 30 min and 290 °C (Figure 2). The stronger influence of holding time suggests that completion and development of the bainitic transformation substantially affect the friction response, while salt concentration modifies the cooling behaviour and consequent microstructural development. Similar time-dependent effects have been reported for austempered niobium-alloyed ductile iron (Garcia *et al.*, 2025).

Table 5: *Response for S/N ratios (coefficient of friction vs K_2S0_4, Na_2SO_4, austempering time and austempering temperature)*

Level	K_2S0_4 (%)	Na_2SO_4 (%)	Austempering Time (min)	Austempering Temperature (°C)
1	**20.50**	21.23	**18.93**	22.72
2	22.19	23.37	22.97	**19.08**
3	22.13	**20.22**	22.91	23.01
Delta	1.68	3.15	4.05	3.93
Rank	4	3	1	2

*Bold value signifies to show the level at which the optimum condition is achieved for each process parameter.

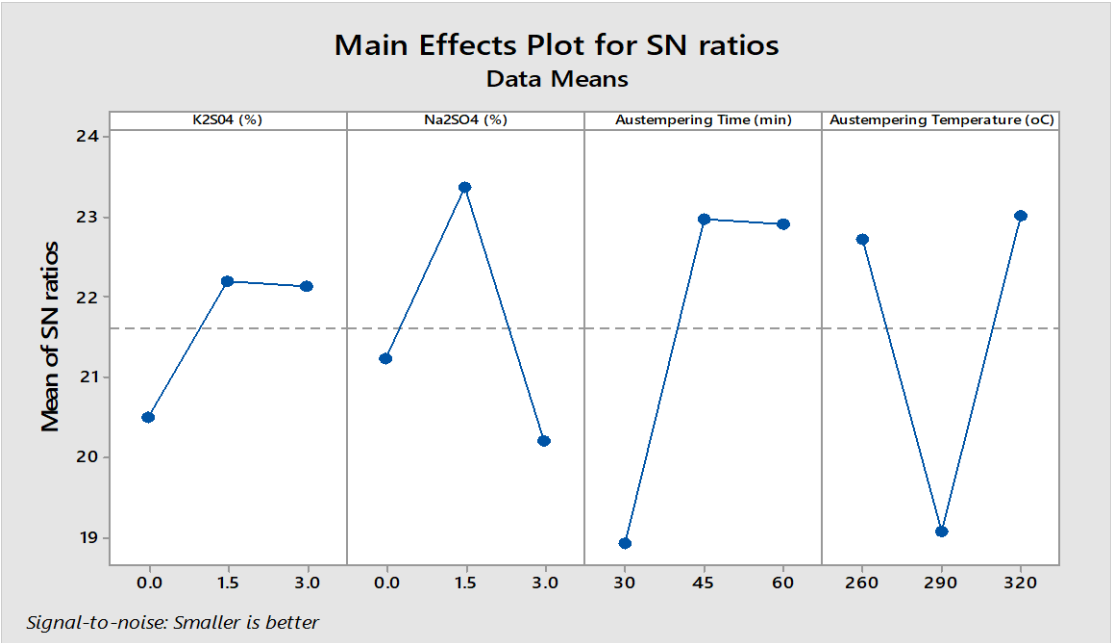

Figure 2: The main effect plots for S/N ratios on coefficient of friction (Taguchi)

3.3 Analysis of Variance (ANOVA) for Tribological Responses

Pooled ANOVA was applied to the L9 experimental results to estimate the relative contributions of the four process parameters to the wear-rate and CoF S/N responses. Because the design was not replicated, the factors with the smallest contributions were pooled to provide an error estimate following the Taguchi approach (Roy, 2010).

Table 6: *Pooled ANOVA for S/N ratio of wear rate and coefficient of friction*

Factor	Wear contribution (%)	F	p	CoF contribution (%)	F	p
K_2SO_4	18.12	2.01	0.249	26.75	1.26	0.377
Na_2SO_4	63.81	7.06	0.047	Pooled	—	—
Time	Pooled	—	—	30.70	1.44	0.337
Temperature	Pooled	—	—	Pooled	—	—
Error	18.07	—	—	42.55	—	—

3.3.1 Wear rate response

The pooled ANOVA results (Table 6) show that Na_2SO_4 concentration was the dominant contributor to the wear-rate S/N response (63.81%), followed by K_2SO_4 concentration (18.12%). Na_2SO_4 was the only retained factor reaching the adopted 95% significance criterion ($F = 7.06$, $p = 0.047$), whereas K_2SO_4 was not statistically significant ($F = 2.01$, $p = 0.249$). Austempering time and temperature were pooled as error, accounting for 18.07%.

The strong contribution of Na_2SO_4 suggests that quenchant chemistry had a greater influence on wear behaviour than the investigated austempering parameters within the experimental range. This may arise from changes in cooling behaviour and the resulting transformation products; however, the specific microstructural mechanisms require further investigation.

3.3.2 Coefficient of friction response

For CoF (Table 6), austempering time contributed 30.70%, followed by K_2SO_4 concentration (26.75%). However, neither factor was statistically significant at the 95% confidence level (time: $F = 1.44$, $p = 0.337$; K_2SO_4: $F = 1.26$, $p = 0.377$). Na_2SO_4 concentration and temperature were pooled into the error term, which accounted for 42.55% of the observed variation.

Although statistical significance was not established, the higher percentage contributions of austempering time and K_2SO_4 indicate their greater relative influence within the tested parameter space and may therefore be useful for process control (Roy, 2010). The relatively large pooled error may reflect experimental variability, unaccounted interactions or the limitations of the unreplicated L9 design. Similar limitations have been noted in Taguchi-based tribological investigations (Asha *et al.*, 2024). Future studies using replication or a larger orthogonal array such as L27 could better resolve interactions and experimental variability (Ramalingam *et al.*, 2022).

3.4 Grey Relational Analysis (GRA)

Grey Relational Analysis (GRA) was used to combine wear rate and coefficient of friction (CoF) into a single performance indicator. As shown in Table 7, Run 4 produced the highest grey relational grade (GRG) of 0.8519, indicating the best overall balance between the two tribological responses among the nine experimental conditions. According to Kuo *et al.* (2011), the highest GRG represents the best combined performance across the selected responses.

The need for multi-response optimization is evident from the contrasting individual responses. Run 1 produced the lowest wear rate but relatively high CoF, whereas Run 5 produced the lowest CoF but the highest wear rate. Their identical GRG of 0.6667 despite different individual responses illustrates the trade-off between wear resistance and friction reduction. Thus, optimization of either response independently may not provide the most suitable overall condition. Run 4, corresponding to 1.5% K_2SO_4, 0% Na_2SO_4, 45 min and 320 °C, provided the most balanced response. Similar findings have been reported in Taguchi-GRA tribological studies, where the multi-response optimum differs from the optimum of individual responses (Ibrahim *et al.*, 2022; Altas, 2024).

Table 7: *GRA integrate multiple responses (wear rate and CoF)*

Runs	Norm - WR	Norm - CoF	Δ-WR	Δ-CoF	GRC - WR	GRC – CoF	GRG	Rank
1	1.0000	0.0000	0.0000	1.0000	1.0000	0.3333	0.6667	5
2	0.6667	0.4286	0.3333	0.5714	0.6000	0.4667	0.5333	9
3	0.8788	0.5286	0.1212	0.4714	0.8049	0.5148	0.6598	7
4	0.9697	0.8429	0.0303	0.1571	0.9429	0.7609	0.8519	1
5	0.0000	1.0000	1.0000	0.0000	0.3333	1.0000	0.6667	5
6	0.7879	0.1571	0.2121	0.8429	0.7021	0.3723	0.5372	8
7	0.9394	0.3429	0.0606	0.6571	0.8919	0.4320	0.6619	4
8	0.8485	0.6286	0.1515	0.3714	0.7675	0.5737	0.6706	3
9	0.9697	0.7000	0.0303	0.3000	0.9429	0.6250	0.7839	2

3.4.1 Effect of process parameters on GRG

The mean GRG response (Table 8) ranked austempering temperature as the most influential parameter, followed by Na_2SO_4 concentration, austempering time and K_2SO_4 concentration. Temperature had the largest delta (0.1500), with the optimum level being 320 °C, which produced a mean GRG of 0.7274, compared with 0.7058 at 260 °C and 0.5775 at 290 °C (Figure 3). The superior response at 320 °C may be associated with more favourable transformation conditions and phase development; however, this interpretation remains inferential because phase fractions were not quantitatively determined by techniques such as XRD or EBSD.

Na_2SO_4 had the second-largest influence (Δ = 0.1033), with 0% producing the highest mean GRG (0.7268), followed by 3% (0.6603) and 1.5% (0.6235). The non-monotonic response suggests that salt concentration does not continuously improve the combined tribological performance and may modify quenchant cooling characteristics and subsequent transformation behaviour (Aminu *et al.*, 2025).

Austempering time ranked third (Δ = 0.0982), with 45 min giving the highest mean GRG (0.7230), compared with 0.6248 and 0.6628 at 30 and 60 min, respectively. This intermediate optimum suggests a favourable transformation window within the investigated conditions. K_2SO_4 had the smallest delta (0.0855) but showed a progressive increase in mean GRG from 0.6199 at 0% to 0.6853 at 1.5% and 0.7055 at 3%, making 3% its optimum level.

Table 9: *Response for means (GRG vs K_2S0_4, Na_2SO_4, austempering time and austempering temperature)*

Level	K_2S0_4 (%)	Na_2SO_4 (%)	Austempering Time (min)	Austempering Temperature (°C)
1	0.6199	**0.7268**	0.6248	0.7058
2	0.6853	0.6235	**0.7230**	0.5775
3	**0.7055**	0.6603	0.6628	**0.7274**
Delta	0.0855	0.1033	0.0982	0.1500
Rank	4	2	3	1

*Bold value signifies to show the level at which the optimum condition is achieved for each process parameter.

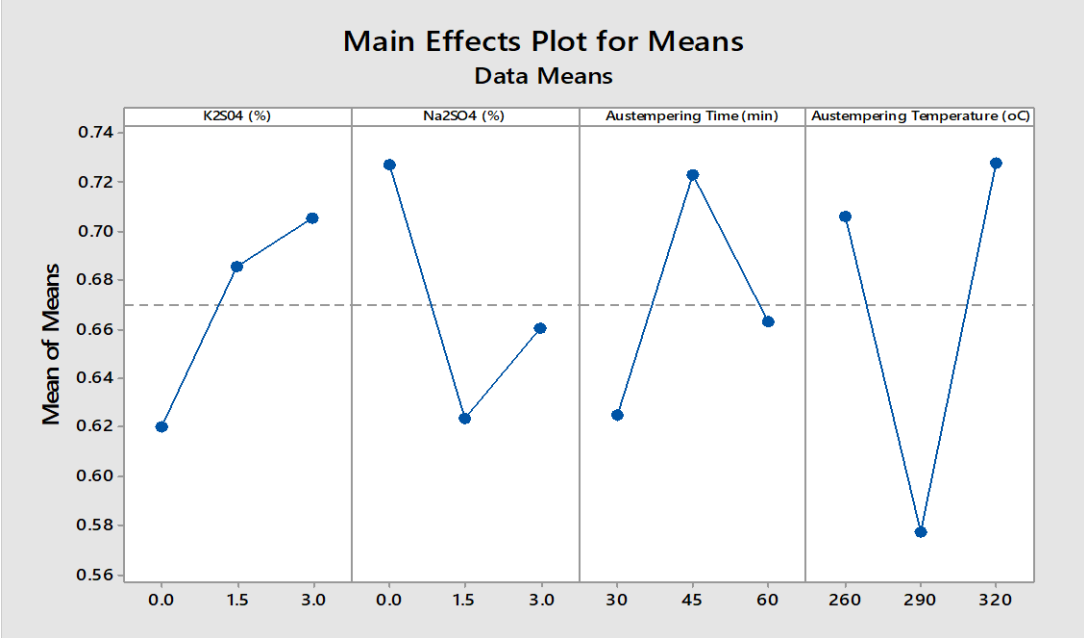

Figure 3: The main effect plots for means on GRG (Taguchi)

3.4.2 Predicted Optimum Condition

The best experimental condition and the predicted Taguchi optimum should be distinguished. Run 4 was the best of the nine tested conditions, with a GRG of 0.8519 at 1.5% K_2SO_4, 0% Na_2SO_4, 45 min and 320 °C. However, combining the optimum level of each factor from the GRG response (Table 9) gives the predicted condition 3% K_2SO_4 + 0% Na_2SO_4 + 45 min + 320 °C ($A_3B_1C_2D_3$).

Using the Taguchi additive model, the predicted GRG was 0.8721, approximately 2.37% higher than the highest experimentally observed GRG (0.8519). Because this combination was not included in the L9 array, the predicted improvement remains an unverified model estimate rather than demonstrated experimental improvement. Confirmation testing is therefore required to establish the predictive adequacy of the model.

Table 9: *Mean GRG for optimum levels*

Parameter	Optimum level	Mean GRG
K_2SO_4 concentration	3%	0.7055
Na_2SO_4 concentration	0%	0.7268
Austempering time	45 min	0.7230
Austempering temperature	320°C	0.7274

3.4.3 ANOVA for GRG

The pooled ANOVA (Table 10) identified austempering temperature as the largest contributor to GRG (47.74%), followed by Na_2SO_4 concentration (19.92%), while K_2SO_4 concentration and austempering time were pooled as error, accounting for 32.34%. This ranking agrees with the GRG response analysis, which also identified temperature as the most influential factor.

Although temperature had a higher F-value (2.952) than Na_2SO_4 (1.232), neither factor was statistically significant at the 5% level under the pooled-error model ($p = 0.163$ and 0.383, respectively). The relatively large pooled error and absence of replication limit the strength of statistical inference; therefore, these results should primarily be interpreted as estimates of relative parameter contribution within the investigated experimental range.

Table 10: *Pooled ANOVA for grey relational grade*

Factor	DOF	Sum of Squares (SS)	Mean Square (MS)	F-value	p-value	Contribution (%)
B: Na_2SO_4(%)	2	0.01645	0.00823	1.232	0.383	19.92
D: Austemp. temp(ºC)	2	0.03942	0.01971	2.952	0.163	47.74
Error (A + C pooled)	4	0.02671	0.00668	----	----	32.34
Total	8	0.08257	----	----	----	100.00

3.5 Microstructure–Property Correlation

SEM micrographs (Plates I – X) obtained at 1000× magnification revealed differences in the morphology, distribution and apparent refinement of the transformation products produced by the various heat treatment conditions. Phase identification from SEM morphology is qualitative; definitive identification and quantification, particularly of retained austenite, would require complementary techniques such as XRD or EBSD.

The normalized sample (Plate I) exhibited a relatively coarse ferrite–pearlite morphology, providing a reference for comparison with the austempered conditions and consistent with its comparatively poor wear resistance (Bhadeshia & Honeycombe, 2017). The austempered samples generally exhibited finer acicular transformation features (Plates II – X), morphologically consistent with bainitic transformation (Bhadeshia, 2015). Differences in feature size, uniformity and distribution were observed among the processing conditions, reflecting variations in transformation behaviour (Wang *et al.*, 2024a, 2024b).

Notably, Plate V (Run 4), which produced the highest experimental GRG (0.8519), exhibited comparatively refined and homogeneous transformation features. Such morphology may promote more uniform load distribution and resistance to localized plastic deformation during sliding, thereby contributing to its favourable combined wear and friction response. In contrast, relatively coarser or heterogeneous morphologies observed in Plates III, VI, VII and X may promote localized deformation and stress concentration, increasing susceptibility to wear damage (Bhadeshia & Honeycombe, 2017; Stachowiak & Batchelor, 2025).

Overall, the SEM observations qualitatively support the tribological results: better-performing conditions generally exhibited comparatively refined and homogeneous transformation morphologies, whereas less favourable responses were associated with coarser or less uniform features. However, this correlation should be regarded as qualitative because the study did not quantitatively determine phase fractions or retained-austenite stability.

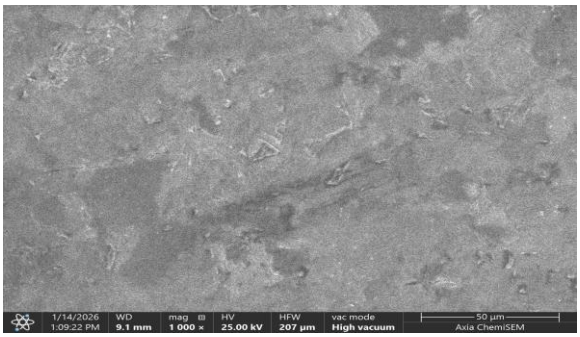

Plate I: SEM micrograph of normalized high-carbon steel at 1000×

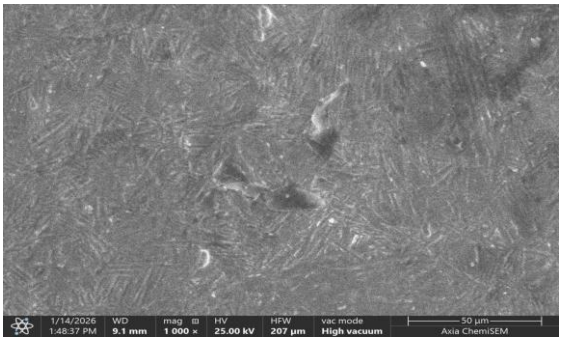

Plate II: SEM micrograph of austempered sample, Run 1, at 1000×

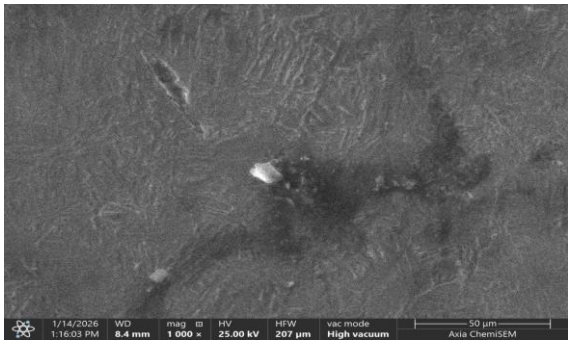

Plate III: SEM micrograph of austempered sample, Run 2, at 1000×

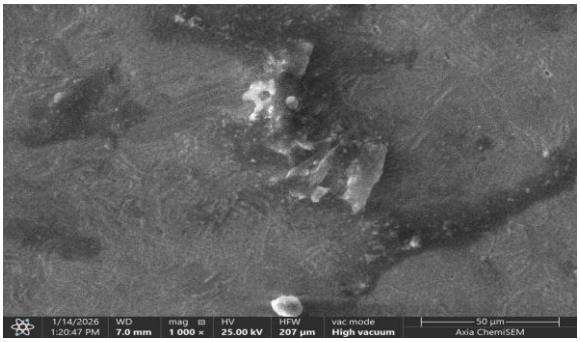

Plate IV: SEM micrograph of austempered sample, Run 3, at 1000×

Plate V: SEM micrograph of austempered sample, Run 4, at 1000×

Plate VI: SEM micrograph of austempered sample, Run 5, at 1000×

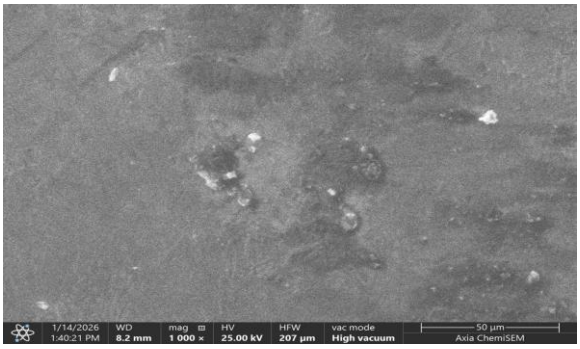

Plate VII: SEM micrograph of austempered sample, Run 6, at 1000×

Plate VIII: SEM micrograph of austempered sample, Run 7, at 1000×

Plate IX: SEM micrograph of austempered sample, Run 8, at 1000×

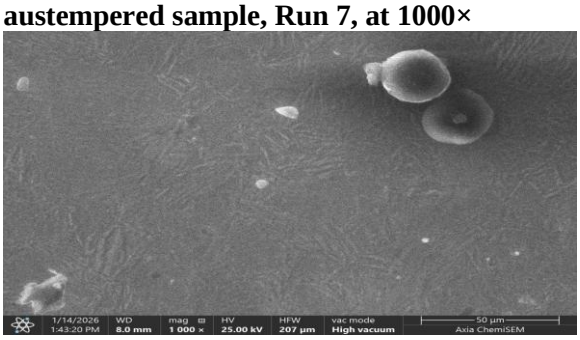

Plate X: SEM micrograph of austempered sample, Run 9, at 1000×

4. CONCLUSION

This study evaluated the tribological behaviour and multi-response optimization of austempered high-carbon steel using K_2SO_4- and Na_2SO_4-modified sesame oil. The principal conclusions are:

1. Austempering substantially improved tribological performance relative to the normalized condition, with the investigated sulfate-modified sesame-oil conditions generally producing lower wear rates and coefficients of friction under the specified dry-sliding conditions.
2. Single-response Taguchi optimization produced different parameter combinations. Minimum wear rate was associated with 1.5% K_2SO_4, 1.5% Na_2SO_4, 60 min and 290 °C, whereas minimum CoF corresponded to 0% K_2SO_4, 3% Na_2SO_4, 30 min and 290 °C, confirming the competing nature of the two tribological responses.
3. GRA provided a balanced multi-response solution. The highest experimentally observed GRG (0.8519) was obtained at 1.5% K_2SO_4, 0% Na_2SO_4, 45 min and 320 °C (Run 4). The Taguchi-GRA response analysis predicted 3% K_2SO_4, 0% Na_2SO_4, 45 min and 320 °C, with an estimated GRG of 0.8721. Since this combination was not included in the L9 array, experimental confirmation is required.
4. Austempering temperature was the largest contributor to GRG variation (47.74%), followed by Na_2SO_4 concentration (19.92%). However, neither factor was statistically significant at the 5% level under the pooled-error model; therefore, the contribution values should be interpreted as relative influences within the present L9 dataset.
5. SEM observations qualitatively supported the tribological trends, with better-performing conditions generally exhibiting comparatively refined and homogeneous transformation morphologies. Definitive phase identification and retained-austenite quantification would require complementary XRD or EBSD analysis.

5. LIMITATIONS AND FUTURE WORK

The study was limited to a single high-carbon steel, three levels of each sulfate concentration, three austempering temperatures and three holding times using an unreplicated L9 design. The 5-min tribological test duration, absence of independent replication and lack of confirmation testing limit extrapolation to long-term service performance. In addition, SEM provided qualitative rather than quantitative phase characterization.

Future work should prioritize replicated confirmation testing of the predicted condition (3% K_2SO_4, 0% Na_2SO_4, 45 min and 320 °C), followed by longer-duration tribological testing under varied loads and sliding speeds. XRD/EBSD and worn-surface SEM/EDS should be employed to clarify phase constitution and wear mechanisms. For industrial implementation, the thermal and suspension stability, quenchant reusability, additive availability, cost and scalability of the modified sesame-oil system should also be evaluated.

REFERENCES

Altas, E. (2024). Multi-objective optimization of dry sliding wear in cryogenically treated high-performance AISI 9310 steel: An integrated approach using Grey Relational Analysis and Taguchi method. *Manufacturing Technologies and Applications, 5*(3), 172–192. https://doi.org/10.52795/mateca.1535444

Aminu, H. B., Dodo, R. M., Ause, T., & Ocholi, A. (2025). Physicochemical, thermal and cooling curve characterization of sulfate salt-modified sesame oil as a potential bio-based quenching medium. *Nigerian Journal of Materials Science and Engineering, 15*(1), 57-74. https://doi.org/10.67656/njmse.2025.g4ndlky5

Asha, P. B., Suresha, C. N., Ravikumar, V., Kiran, R., & Gurunagendra, G. R. (2024). Grey-Taguchi approach to optimize the tribological performance of hybrid composites. *Materials Today: Proceedings*. https://doi.org/10.1016/j.matpr.2024.04.084

ASTM International. (2020). *Standard test method for wear testing with a pin-on-disk apparatus (ASTM G99-20)*. West Conshohocken, PA: ASTM International.

Bhadeshia, H. K. D. H. (2015). *Bainite in Steels: Theory and Practice* (3rd ed.). Maney Publishing.

Bhadeshia, H., & Honeycombe, R. (2017). *Steels: Microstructure and properties* (4th ed.). Butterworth-Heinemann.

Chen, S., Huang, Q., Wu, F., Li, Z., & Shan, Q. (2025). Wear behavior dominated by strain partitioning between retained austenite and α-Fe in bainitic steel. *Tribology Letters, 73*(1), 19. https://doi.org/10.1007/s11249-024-01955-0

Chen, S., Huang, X., Liao, Z., Li, Z., Wu, H., & Shan, Q. (2024). Investigation of retained austenite morphology-dominated hardening and fatigue behavior in bainitic steel during wear process. *Fatigue & Fracture of Engineering Materials & Structures, 47*(2), 344–357. https://doi.org/10.1111/ffe.14187

Garcia, S. J., Martínez, V. J. M., Morales, C. E. U., & Domínguez, C. A. (2025). Effect of austempering time and temperature on the mechanical and microstructural properties of a niobium-alloyed austempered ductile iron. *Metals,* 15, 1168. https://doi.org/10.3390/met15111168

Ibrahim, M. A., Çamur, H., Savaş, M. A., & Sabo, A. K. (2022). Multi-response optimization of the tribological behaviour of PTFE-based composites via Taguchi Grey Relational Analysis. *Strojniški vestnik – Journal of Mechanical Engineering, 68*(5), 359–367. https://doi.org/10.5545/sv-jme.2021.7466

Jiang, T., Liu, W., Wei, S., Xu, L., Chen, C., Diao, X., Zhang, L., & Wang, R. (2026). Effect of tempering-induced microstructural evolution on the impact abrasive wear behavior of carbide-free bainitic steel: The crucial role of retained austenite stability. *Tribology International, 219*, 111838. https://doi.org/10.1016/j.triboint.2026.111838

Kuo, C. F. J., Su, T. L., Jhang, P. R., Huang, C. Y., & Chiu, C. H. (2011). Using the Taguchi method and grey relational analysis to optimize the flat-plate collector process with multiple quality characteristics in solar energy collector manufacturing. *Energy, 36*, 3554–3562.

Ramalingam, S. K., Kumar, D., & Sivanraju, R. (2022). Multi-response optimization of AISI H11 using Taguchi and Grey Relational Analysis. *Materials Research Express, 9*(10). https://doi.org/10.1088/2053-1591/ac95fe

Roy, R. K. (2010). *A Primer on the Taguchi Method* (2nd ed.). Society of Manufacturing Engineers.

Stachowiak, G. W., & Batchelor, A. W. (2025). *Engineering tribology (4th ed.*). Butterworth-Heinemann.

Wang, K., Gao, G., Gui, X., & Bai, B. (2024a). Comparison of microstructure and mechanical properties of a high-carbon bainitic steel treated by long-time bainitic austempering and short-time austempering plus tempering processes. *Steel Research International.* https://doi.org/10.1002/srin.202300501

Wang, X., Song, R., Chen, X., Huo, W., Zhao, S., & Zhang, Y. (2024b). Effect of different quenching methods on the microstructure and mechanical properties of 30MnB5NbTi. *Steel Research International, 95*(6), 2300629. https://doi.org/10.1002/srin.202300629

Zhao, S., Liu, M., Tian, J., Dai, F., & Xu, G. (2025). Review on heat treatment and surface modification technology of high-strength bainite steels. *Steel Research International, 96*, 2400685. https://doi.org/10.1002/srin.202400685

International Conference on Engineering Innovation for Sustainable Development (ICESID 2026)
Faculty of Engineering, Ahmadu Bello University Zaria · 8–10 September 2026

VOLUMETRIC AND MARSHALL PROPERTIES OF HOT MIX ASPHALT WITH LDPE-MODIFIED BITUMEN, HIGH RECLAIMED ASPHALT CONTENT PAVEMENT AND WASTE ENGINE OIL

Abdulmumin Ahmed Shuaibu[1], Mudassir Rabiu Adam[2,*], Ahmad Abdulsalam Amin[1], Esther Amanosi Nyebe[1,3], Asmau Hamdana Kankia[4], Abdulmumin Nda Mohammed[1,5], Ismaila Mohammed Amodu[1,6]

[1]*Department of Civil Engineering, Ahmadu Bello University, Zaria*
[2]*Department of Highway Engineering, Federal University of Transportation, Daura*
[3]*School of Civil Engineering, University of Manchester, Oxford Road, Manchester, UK*
[4]*Office of the Secretary of Kaduna State Government, Kaduna State*
[5]*Department of Civil Engineering Faculty of Engineering, Baze University, Abuja*
[6]*Julius Berger Nigeria, Ltd, Abuja, Nigeria*

Email: abdulshub4u@gmail.com, mradam2439@gmail.com*, abdulsalamahmad017@gmail.com, esther.nyebe@manchester.ac.uk, asmauhamdana@yahoo.co.uk, abdulmumin.mohammed@bazeuniversity.edu.ng, ismaila.amodu@julius-berger.com

***Corresponding author**: Mudassir Rabiu Adam

DOI: https://doi.org/10.67203/sp.ICESID.2026

ABSTRACT

The use of Reclaimed Asphalt Pavement (RAP) in Hot Mix Asphalt (HMA) is as a result of the growing need for economical and environmentally friendly road construction solutions. When old asphalt is removed for resurfacing and reconstruction, RAP is created. Furthermore, the rise in plastic garbage in recent years has become a major ecological problem on a global scale. Therefore, this study explores the volumetric and Marshall properties of HMA containing High RAP proportion, Low-Density Polyethylene (LDPE) modified bitumen and Waste Engine Oil (WEO) as a rejuvenator. Preliminary physical property testing was conducted on the HMA constituent materials in accordance with the relevant standards. The Marshal mix design was employed to determine the optimum binder content of the control mix using virgin materials with varying bitumen content from 5% to 7% at 0.5% intervals. Furthermore, RAP in the varying proportion of 25% to 100% at an interval of 25% was introduced to replace the virgin coarse aggregates by weight (25%, 50%, 75%, and 100%) with LDPE Modification at varying replacement level from 4% to 12% at an interval of 4% by the weight of bitumen. A 15% of WEO by the weight of the optimum binder content was added to the mix as rejuvenator. Although some combinations containing 100% RAP exceeded the flow restrictions, the Marshall stability and flow values of the examined mixtures meet the requirement of >3.5 kN and 2-4mm respectively. Moreover, majority of the assessed volumetric properties of the mixes did not meet the established standards. These findings suggest that using high RAP contents, LDPE-modified bitumen and WEO has a potential to produce HMA with acceptable Marshall stability. However, in order to achieve satisfactory volumetric characteristics and complete compliance with specifications, there is need for further study to optimize the binder content, WEO dosage, LDPE concentration.

Keywords: *Marshall Properties; reclaimed asphalt; low-density polyethylene; hot mix asphalt and waste engine oil*

1.0 INTRODUCTION

Road infrastructures are important lifelines for modern societies, in Nigeria, socioeconomic developments are directly related to quality roads. According to FMWH (2013), the total national road network is approximately 200,000 km and only about 65,000km of the 200,000km are flexible pavements which represent about 33% of the entire road network. Flexible pavements are most commonly used for low to medium volume roads with significant usage also found in high volume interstate highways and airfield runways, taxiways and aprons subjected to heavy aircraft gear/wheel loads (Mohod and Kadam, 2016).

In recent years, however, growing environmental concerns have led many industrial and societal sectors to change their policies around waste management, resource use, and the efficiency of

production of goods and services. As we strive for a circular economy and sustainable resource use, it is becoming increasingly crucial to reuse and recycle non-renewable resources, as a result, the construction and maintenance of transportation infrastructure, in particular, is gradually adopting eco-friendly technology to reduce its ecological impact (Cheraghian et al., 2020)

In this context, the intensive extraction and processing of virgin materials for asphalt production significantly disrupt natural habitats and degrade ecological systems. Researchers have been investigating the possibility of finding suitable sustainable materials that can be used in replacement of conventional pavement materials. Arianto *et al.* (2019) reported recycling of the used pavement materials as a technique for pavement rehabilitation as it conserves energy and resource. Recycling and reusing of non-renewable materials are becoming increasingly imperative in order to move towards a circular and sustainable economy as well as a sustainable use of resources. In particular, the industry of construction and maintenance of transport infrastructures is gradually applying environmentally friendly solutions, aiming to reduce its ecological footprint (Rodrigues *et al.,* 2020).

Among the available sustainable approaches, most popular technique is recycling RAP back into hot mix asphalt (HMA). The addition of RAP to new asphalt mixtures made using different manufacturing processes, such as hot, warm, half-warm, and cold-mix asphalt, is one of the most popular recycling techniques in pavement construction and maintenance (Rodrigues *et al.*, 2020). Martinho *et al.* (2018) reported some potential benefits of using reclaimed asphalt such as reducing the quantity of demolition trash that is dumped in landfills, cutting down on energy consumption and emissions and lowering the need for more non-renewable raw materials. Additionally, it has been shown to reduce issues of waste disposal and the likelihood of cracking and rutting while increasing the stiffness and resistance of asphalt to deformation (Ozer *et al.,* 2009).

Despite these benefits, the introduction of RAP into a new asphalt mixture can create challenges because the aged RAP binder can significantly influence the properties of the resulting mixture, particularly when recycling involves high percentages. The incorporation of RAP as a constituent in the production of fresh asphalt mixtures causes some challenges having been the bitumen suffers short- and long-term ageing such as oxidation and volatilization of constituents as reported by Hunter *et al.* (2015) and Rodrigues *et al.* (2020).

To address these limitations, fresh bitumen or any other rejuvenating agent can be incorporated to partially recover the lost properties of the aged asphalt binder. To recover the desired properties of the aged binder, an appropriate amount of fresh bitumen or rejuvenator is added to a satisfactory level of performance. Consequently, the rejuvenator ability to reactivate the aged binder is of major importance to achieve adequate performance of the asphalt mixture (Rodrigues *et al.,* 2020).

Among the potential rejuvenating materials, Waste Engine Oil (WEO) is particularly relevant because enormous quantities are generated worldwide by cars, trucks, trains, airplanes, generators, industries, and other machinery (Khurshid *et al.,* 2021). Waste engine oil (WEO) has gained increasing attention as a potential rejuvenator for high-RAP asphalt mixtures due to its physicochemical resemblance to the maltene fraction of bitumen. WEO, rich in light hydrocarbons and aromatic fractions, can partially compensate for this depletion by restoring the maltene–asphaltene balance (Fathi *et al.,* 2026). Onuche *et al.* (2024) reported that Nigeria consumes about 700 million litres of lubricants annually from which about 80% WEO is generated with potential of production of 336 million litres per year of diesel like fuel. Therefore, effective management and beneficial reuse of this waste is of paramount importance in mitigating environmental pollution that may eventually endanger human health and ecosystem.

Additionally, polymer modification provides another approach for improving the performance of bituminous materials. Bitumen is known to degrade over time due to a number of factors, including volatilization and component oxidation. Polyethylene has been found to be one of the greatest polymer additives as it is the most commonly used plastic worldwide (Nizamuddin *et al.,* 2021). Simultaneously, the increasing generation of plastic waste presents a significant environmental challenge. Ezeudu *et al.* (2024) reported an estimated figure of about 27.3 million tonnes of municipal solid waste currently generated in Nigeria's urban cities per annum about 11.2 million tonnes is collected of which about 1.1 million tonnes is plastic.

Beyond these environmental considerations, the use of suitable modifier can also improve the performance and economic sustainability of bituminous mixtures. Bitumen, a binder made from refined

crude oil, is one of its most crucial components. Environmental harm results from bitumen production's carbon dioxide emissions (Sharma *et al.,* 2022). Nevertheless, although several commercial modifiers can improve bituminous performance, the cost-benefit ratio of bitumen blends' is decreased when they are used. Therefore, the availability of alternative modifiers that can improve bitumen's qualities without increasing the cost of bitumen mixes or decreasing their cost-benefit ratio is crucial (Shuaibu *et al.,* 2021).

More specifically, bituminous materials are widely used in road construction around the world. These hydrocarbons can be found in nature or as a byproduct of distilling crude oil. The two types of bituminous materials used in highway construction are tars and asphalts (Syrmanova *et al.,* 2017). Modified bitumen and the regeneration of old bitumen not only help with the safe disposal of RAP waste but also reduce the consumption of limited and non-renewable resources, which makes them more desirable in terms of global sustainability. According to several publications, 15% WEO should be used while producing HMA (Mamun and Al-Abdul Wahhab, 2018; Khan *et al*., 2021).

Despite these individual applications, previous studies had investigated RAP recycling, LDPE modification, Waste Cooking oil (WCO) (Rodrigues *et al.,* 2020) and Waste Engine Oil rejuvenation (WEO) (Maharaj and Maharaj, 2015) largely as separate approaches. However, there remains a need to evaluate their combined application in high-RAP HMA, particularly to determine suitable RAP–LDPE combinations while using WEO to rejuvenate the aged RAP binder. Therefore, the present study examines the potential applications of RAP–LDPE combinations with Waste Engine Oil (WEO) as a rejuvenating agent in high RAP HMA.

2.0 MATERIALS AND METHODS

2.1 Materials

The materials used in this study comprised 60/70 penetration-grade bitumen, low-density polyethylene (LDPE), waste engine oil (WEO), virgin coarse and fine aggregates, mineral filler and reclaimed asphalt pavement (RAP).

2.1.1 Bitumen

60/70 penetration grade bitumen was utilized in the production of the Hot Mix Asphalt. The bitumen was sourced from one of the operational locations of Julius Berger Nigeria Plc construction company located along Kaduna-Zaria Road.

2.1.2 Low-Density Polyethylene (LDPE)

The LDPE flakes with a density of 0.91 to 0.93 g/cm³ and melting point of about 100-125ºC was utilized to modify the bitumen. The flakes were sourced from open dumps in Samaru area. They were washed, dried and shredded to produce the required size for the bitumen modification.

2.1.3 Waste Engine Oil (WEO)

The Waste Engine Oil (WEO) utilized in the study is the conventional used engine oil sourced from mechanic workshop in Samaru, Zaria Kaduna state.

2.1.4 Mineral Aggregates

Coarse and Fine Aggregates were obtained from a nearby quarry in Zango, Zaria, Kaduna state, Nigeria. Sieve Analysis was carried out on the aggregates to determine their particle size distributions. The particles retained on 4.75mm and 0.075mm were used as Coarse and Fine aggregates respectively in the production of the HMA.

2.1.5 Mineral Filler

Quarry dust obtained from a nearby Zango quarry in Zaria was used as the mineral filler. Sieve Analysis was carried out to determine the particle distribution of the quarry dust. The particles that passed through a 0.075 mm sieve was used in the production of the HMA.

2.1.6 Reclaimed Asphalt Pavement (RAP)

The RAP utilized in the research was obtained from one of the operational locations of Julius Berger Nigeria Plc construction company stockpiled by the roadside along Zaria-Kaduna Road in Dumbin Dutse. It was milled to achieve the required particle sizes of the RAP, the particles retained on 4.75mm sieve was utilized. The RAP was used as a partial to complete replacement for virgin coarse aggregate in the production of the HMA.

2.2.0 Characterization of the Constituent Materials

The constituent materials were characterized through laboratory testing to determine their physical properties and establish their suitability for asphalt mixture production. The laboratory tests were conducted at the Department of Civil Engineering Ahmadu Bello University, in accordance with the applicable standards.

2.2.1 Bitumen

The bitumen was characterized by conducting specific gravity, flash and fire point, ductility, softening point, and penetration tests in accordance with ASTM D70, ASTM D92, ASTM D113, ASTM D36, and ASTM D5, respectively.

2.2.2 Waste engine oil (WEO)

WEO is a dark brown or black liquid with varying properties depending upon type and utilization. The temperature determines its state, which is usually liquid and lighter than water (Mehmood *et al.,* 2024). Based on the previous studies of DeDene. (2011), metals such as lead, zinc, calcium, and magnesium were found in the used engine oil. Consequently, the WEO was filtered to remove the unwanted solid particles without carrying out any treatment on it. It was used as a rejuvenating agent to restore or soften the aged binder contained in the RAP. A WEO content equivalent to 15% by weight of the optimum binder content was incorporated into the asphalt mixture

2.2.3 LDPE-Modified Bitumen Preparation

LDPE is a thermoplastic polymer widely available from post-consumer plastic waste. When incorporated into asphalt binder, it forms a dispersed polymer-rich phase that improves stiffness and elastic recovery (Ling *et al.,* 2019; Fathi *et al.,* 2026). Because LDPE has a melting temperature of approximately 105–120°C, which is lower than the blending temperature of bitumen, it was incorporated using the wet-mixing technique (Ahmad and Ahmad, 2022). Prior to modification, the LDPE was cleaned, shredded into small pieces, and dissolved in kerosene on a heating pan at a controlled temperature to facilitate blending. The required quantity of conventional bitumen was gradually heated to 170 ± 5°C and maintained at this temperature throughout the process. Predetermined LDPE contents of 4%, 8%, and 12% by weight of the optimum binder content were then gradually added to the heated bitumen under continuous mechanical agitation. The mixture was maintained at 170 ± 5°C and mixed continuously for 60 minutes to promote the softening, dispersion, and uniform distribution of LDPE within the bitumen matrix, while avoiding excessive heating. A 15% waste engine oil (WEO), by weight of optimum binder content, was also added as a rejuvenator for the aged binder in the reclaimed asphalt pavement (RAP). The resulting homogeneous LDPE-modified binders were subsequently used to prepare asphalt mixtures containing the specified proportions of virgin aggregate and RAP.

2.2.4 Mineral aggregates

The virgin aggregates, both coarse and fine aggregates, were characterized through particle-size distribution, specific gravity, aggregate impact value (AIV), aggregate crushing value (ACV) and water absorption tests, conducted in accordance with, ASTM C136, ASTM C127, ASTM C535, ASTM C535, and ASTM C127, respectively.

2.2.5 Mineral Filler

The mineral filler was characterized through particle-size distribution and specific gravity tests, conducted in accordance with, ASTM C136, and ASTM C127 respectively.

2.2.6 Reclaimed Asphalt Pavement (RAP)

The RAP was characterized using sieve analysis, specific gravity, aggregate impact value, aggregate crushing value and water absorption tests. These tests were conducted in accordance with ASTM C136, ASTM C127, ASTM C535, ASTM C535 and ASTM C127 respectively.

2.2.7 Marshall Mix Design

The Marshall mix-design procedure, in accordance with ASTM D6927, was used to determine the optimum binder content (OBC) of the control asphalt mixture designed for heavy-traffic conditions. Control specimens comprising virgin aggregates and conventional bitumen were prepared at binder contents of 5-7% at 0.5% increments. Marshall stability, flow, bulk density, air voids (VIM), voids in mineral aggregate (VMA), and voids filled with bitumen (VFB) were evaluated. The OBC was selected based on the binder contents corresponding to maximum stability, maximum bulk density, and the specified air-void requirement; consequently, an OBC of 6.5% was obtained for the control mixture.

Subsequently, reclaimed asphalt pavement (RAP) was incorporated at replacement levels of 25-100% at an interval of 25% while LDPE was added at 4-12% at an interval of 4% by weight of bitumen. A full-factorial experimental design was developed using Design-Expert software version 13 to assess the combined effects of RAP and LDPE contents on the Marshall and volumetric properties of the asphalt mixtures. The design comprised 36 experimental runs. For each mixture, the constituent materials were thoroughly blended and compacted using 75 Marshall blows on each face of the specimen, in accordance with the requirements for a heavy-traffic wearing course.

3.0 RESULTS AND DISCUSSIONS

3.1 Bitumen

The results of the physical property tests, presented in Table 1, indicate that the bitumen is 60/70 penetration grade and has a specific gravity of 0.98. All the results of the carried-out tests fell within the specified limits of the relevant standards with the exception of softening point result in which there is an observed slight deviation from the standard which might have been due to human error when conduction the test. These results confirm the suitability of the bitumen for use in the production of Hot Mix Asphalt (HMA).

Table 1: Tests and Code Limits on Bitumen

Tests	Results	Specifications	Code
Fire test (^{0}C)	355	Min. 232	ASTM D92
Ductility at 25 ^{0}C, cm	110	Min. 100	ASTM D113
Softening point (^{0}C)	*57.5	48-56	ASTM D36
Penetration at 25^{0}C (0.1mm)	64	60-70	ASTM D5
Specific gravity test at 25^{0}C	0.98	0.97-1.02	ASTM D70
Flash test (^{0}C)	325	Min. 232	ASTM D92

*Asterisk indicates a slight deviation in softening point result from the code specification

3.2 Mineral Aggregates

The results presented in Tables 2 and 3 show that the coarse aggregate recorded an ACV of 23.10%, an AIV of 25.97%, and a specific gravity of 2.85, while the fine aggregate had a specific gravity of 2.64. The obtained results satisfied the requirements specified by the relevant standards for mineral aggregates, indicating that the virgin aggregates were suitable for use in the production of the HMA.

Table 2: Tests and Code Limits on Coarse Aggregates

Tests	Results	Limitations	Code
Sieve analysis	Cu>1<3, Cc<1		ASTM C136
Specific gravity	2.85	Max. 3	ASTM C127
Aggregate impact value (%)	25.97	Max. 30	ASTM C535
Aggregate crushing value (%)	23.10	Max. 30	ASTM C535
Absorption test (%)	0.4	Max. 5	ASTM C 127

Table 3: Tests and Code Limits on Fine Aggregates

Tests	Results	Limitations	Code
Specific gravity	2.64	2.50-3.00	ASTM C127
Sieve analysis	Cu>3, Cc>1<3		ASTM C136

3.3 Reclaimed Asphalt Pavement (RAP)

Table 4 displays the results of the physical characteristics tests conducted on Reclaimed Asphalt (RAP). The reclaimed asphalt's specific gravity, ACV, and AIV are 2.56, 26.00, and 23.00, respectively. The RAP is suitable for use in asphalt mixtures because they fall within the specified ranges in ASTM Standards.

Table 4: Tests and Code Limits on RAP

Tests	Results	Limitations	Code
Specific gravity	2.56	3max	ASTM C127
Aggregate impact value (%)	26.00	30max	ASTM C535
Aggregate crushing value (%)	23.00	30max	ASTM C535
Absorption test (%)	0.40	0.5max	ASTM C127

3.4 Combined Aggregate Curve

The centre curve displays the mix derived from the findings of the particle size distribution test conducted on the mineral aggregates utilized in this investigation, while the upper and lower curves are as specified in the applicable code for use in asphalt. This implies that the mixed aggregate will have a strong interlocking and an appropriate packing density to support loads and withstand deformation as supported by (Shuaibu *et al.* 2024). The results of the combined particle size analysis, as displayed in Figure 1, indicate that the aggregates are suitable for use in HMA since the test results fell between the upper and lower boundary limits (FMWH, 2016).

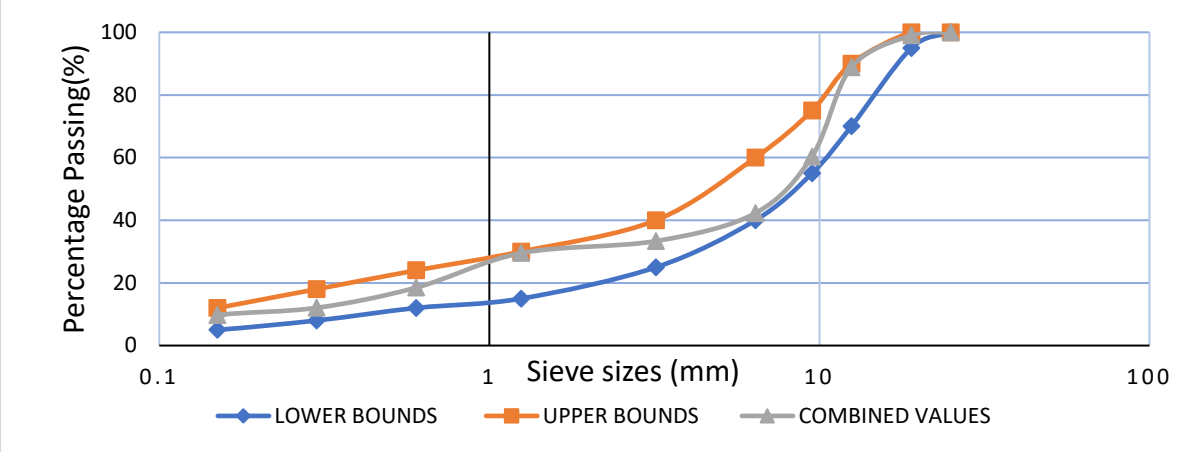

Figure 1: Combined curve for mineral aggregates

3.5 Marshall Mix Design - Optimum Bitumen Content

The asphalt contents having the maximum value of bulk density, Marshall Stability and median air void are selected. The bitumen content at median numerical values for approximately 7% air void, maximum stability and maximum bulk density are 6.5%, 6% and 7% respectively. The optimum bitumen content of 6.5% was determined by taking the average value of the selected properties in accordance with the Nigerian general specification code for roads and bridges which satisfies the requirements for surface course of 5-8%.

$$\text{OBC (\%)} = \frac{Maximun\ Stability(\%BC)+Maximum\ bulk\ density(\%BC)+Median\ VA(\%BC)}{3}$$

$$= \frac{6.0+7.0+6.5}{3} = 6.5\%$$

Table 5: Marshall Property Test carried out on HMA samples

Bitumen Content (%)	Stability (kN)	Flow (mm)	Bulk Density (g/cm^3)	Quotient (kN/mm)	VMA (%)	VFB (%)	VA (%)
5.0	4.90	4.90	2.08	1.00	21.06	52.52	10.00
5.5	6.40	4.60	2.13	1.39	21.10	53.46	9.82
6.0	7.60	3.70	2.15	2.05	20.05	59.50	8.12
6.5	6.60	3.90	2.10	1.69	19.74	63.12	7.28
7.0	5.90	3.20	2.21	1.84	21.26	59.78	8.55

3.6 Analysis of the Effect of LDPE and RAP to Marshall and Volumetric Parameters

The results of the Marshall and volumetric Analysis of sample with varying RAP and LDPE contents are presented in the figures below.

3.6.1 Stability

Stability is the maximum load needed to cause failure of a specimen upon application of load. The stability of the LDPE-modified asphalt mix with respect to the amount of RAP and LDPE wastes is depicted in Figure 2. The chart peaks at 8.28kN stability represents 50% RAP and 12% LDPE waste. Continuously, until it reached 50% RAP content, the stability of the modified asphalt mix rose in step with the RAP level; after that, stability started to decline at higher bitumen content. This decrease in

stability revealed that increasing bitumen content creates too thick film on the aggregate particles, resulting in loss of inter-particle friction and this leads to insufficient stability in pavements (Genet *et al.,* 2021). However, as a saturation point was reached at 50% RAP, stability started to decline. Previous research indicates that the stability of the mix increases with the quantity of LDPE in HMA until a certain point, beyond which it begins to decrease as the amount of plastic grows (Akinpelu *et al.,* 2013). Although the peak stability was recorded at 50% and 12% LDPE modification, all the values recorded at different RAP contents and LDPE modifications exceeded the Nigerian minimum limits of 3.5kN.

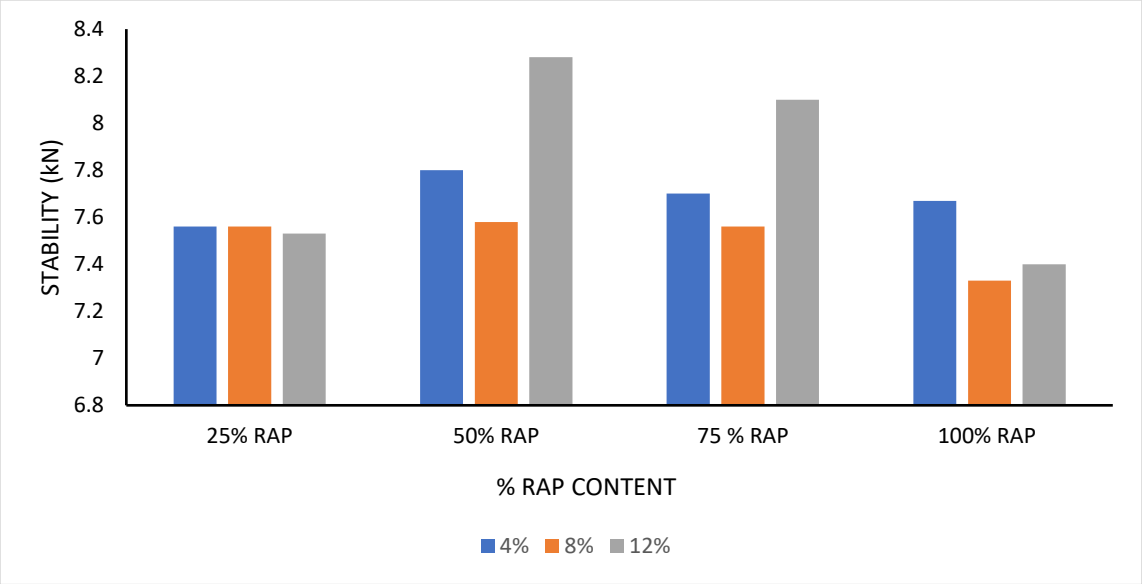

Figure 2: Relationship between the stability and the RAP content at different LDPE modifications.

3.6.2 Flow

The relationship between the flow in the asphalt mix sample and the RAP/LDPE waste concentration is shown in Figure 3. There is observed increase in the flow of the LDPE-modified bitumen at lower LDPE waste content and continuously increased until it reached a maximum value of 3.56mm, then it started decreasing at higher LDPE/RAP wastes content. The decrease in flow of the marshal mix as the waste LDPE content increase also shows that the increase in resistance to rutting. Higher flow value shows higher flexibility while lower flow value shows higher rigidity (Jassim *et al.,* 2014; Kotresh *et al.,* 2016; Genet *et al.,* 2021). As observed from the chart, the optimal flow of 3.56 mm is achieved with 50% RAP and 8% LDPE waste. The outcome of the flow is between 2-4mm, falling within the FMWH general parameters' range. This illustrates how well LDPE reduces flow, enhancing the capacity of the asphalt to support loads. A higher flow value denotes more flexibility, whereas a lower flow value denotes more stiffness (Genet *et al.,* 2021).

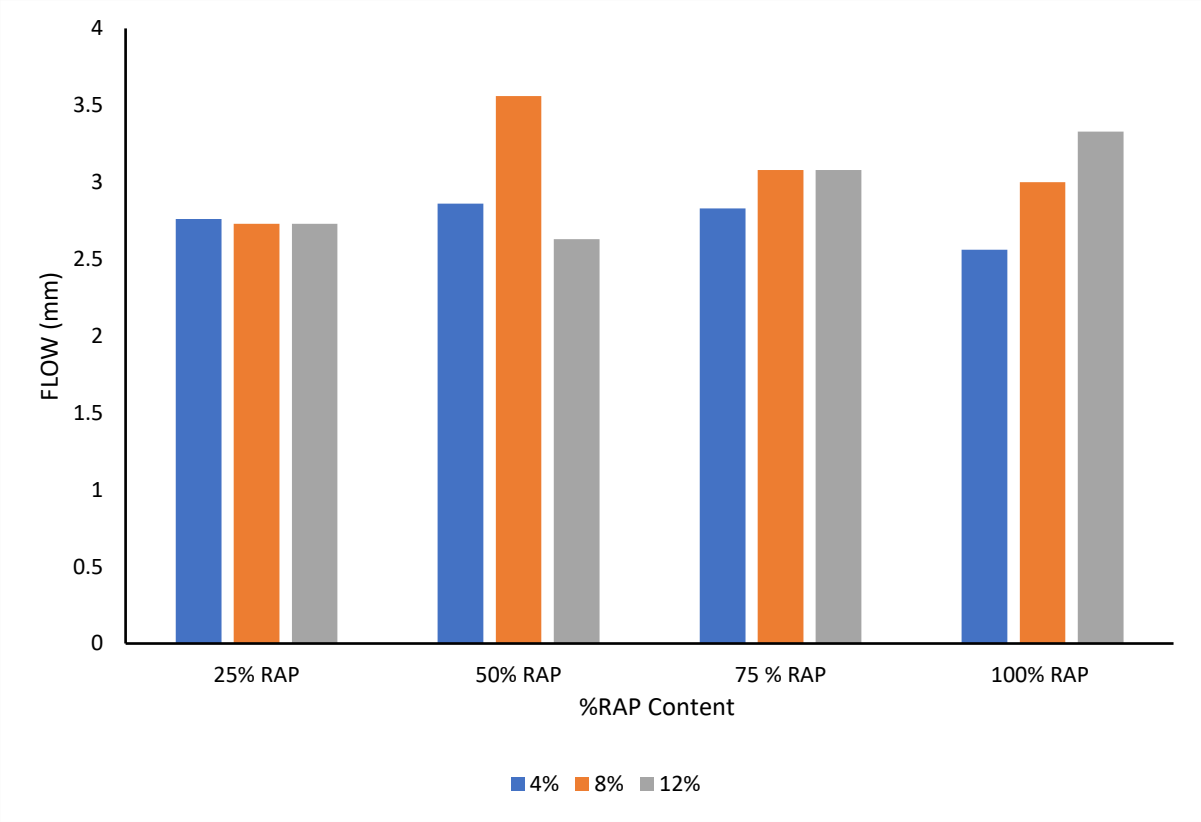

Figure 3: The Relationship between the flow and the RAP content at different LDPE modifications

3.6.3 Marshell Quotient

Figure 4 shows the relationship between the RAP/LDPE waste contents and the asphalt marshall qoutient. The overall stiffness and viscosity of the asphalt mixture reduced as the bitumen concentration rose, which caused the quotient to decline as the RAP percentage rose. At 4% LDPE waste and 100% RAP, the quotient peaks at 2.99KN/mm. This result is in line with another study's conclusions (Kotresh *et al.,* 2016).

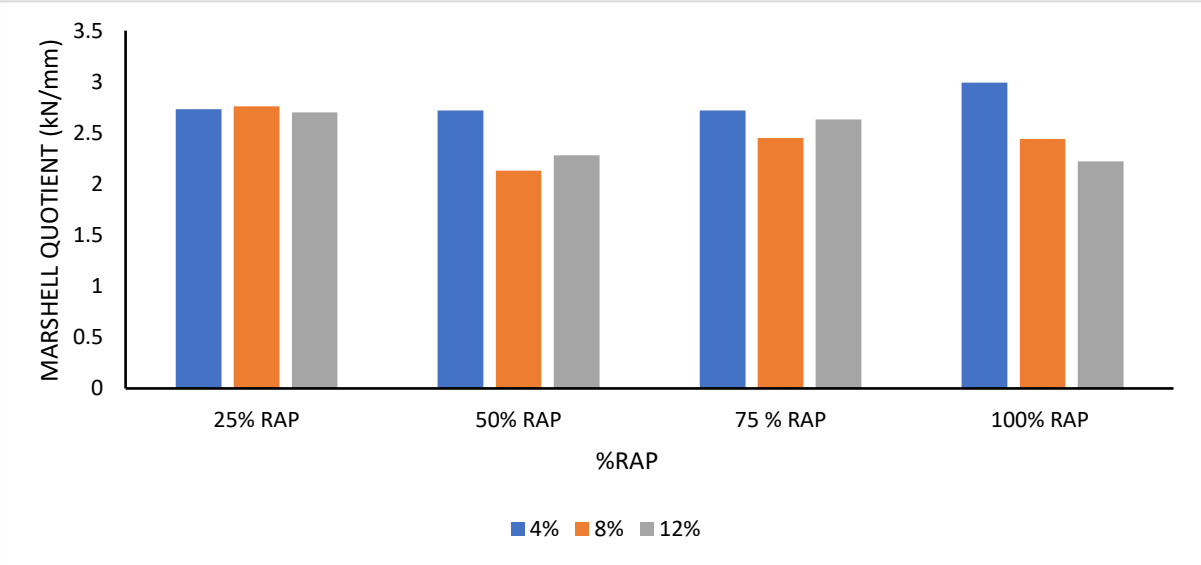

Figure 4: The Relationship between the Quotient and the RAP content at different LDPE modifications

3.6.4 Bulk Density

The relationship between Bulk Density and RAP at various LDPE modifier contents is shown in Figure 5. The addition of material having a lower specific gravity than the base material results in a drop in the bulk density of the compacted mixes as the RAP content rises; in other words, the increase in LDPE content causes the decrease. The variation in the density values from 2.22-2.25 g/cm^3 shows minimal variation confirming stable compaction behavior which is in line with the study conducted by (Fadhil et al., 2026).

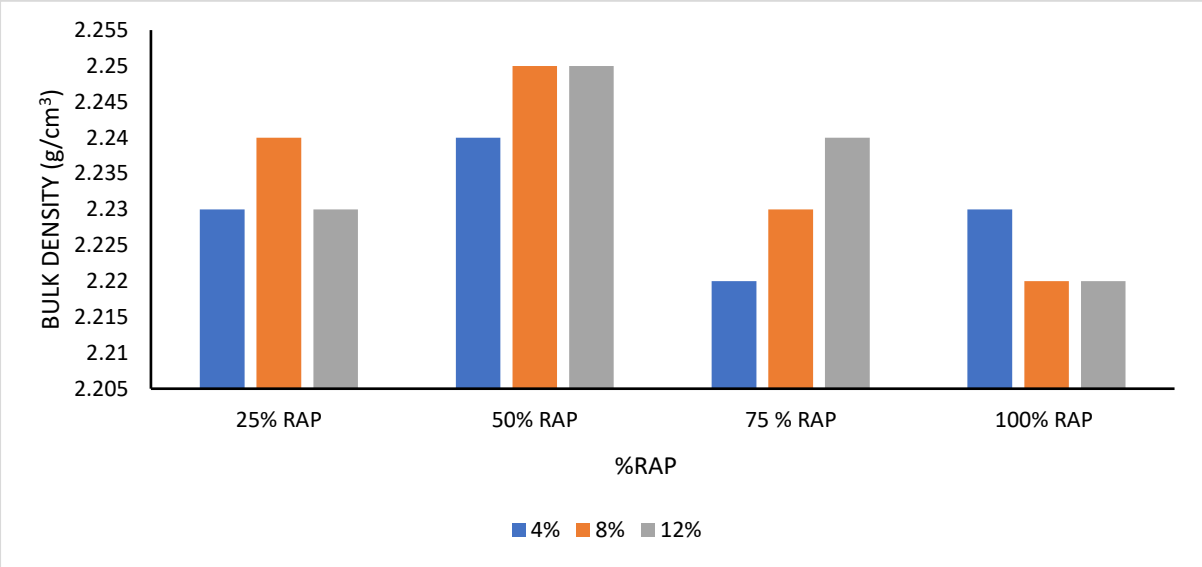

Figure 5: Relationship between Bulk Density and RAP at different LDPE modifier contents.

3.6.5 Voids in Mineral Aggregate

The void in the mineral aggregate (VMA) is defined by the intermolecular spaces between the aggregate particles in compacted paving mixtures that includes the air voids and the effective asphalt content (Genet et al, 2021). The correlation between VMA and RAP at varying LDPE modifier levels (25, 50%, 75%, and 100%) of RAP is depicted in Figure 6. The number of voids that can be filled with asphalt binder is indicated by the presence of voids in mineral aggregates with a numerical value of 22.2% void in mineral aggregate. The highest VMA was achieved at 75% RAP and 4% LDPE waste content. According to the applicable usage standards for asphalt mix, this result falls within the ideal range for VMA. The gaps between the particles have been successfully filled in and partially sealed by the LDPE.

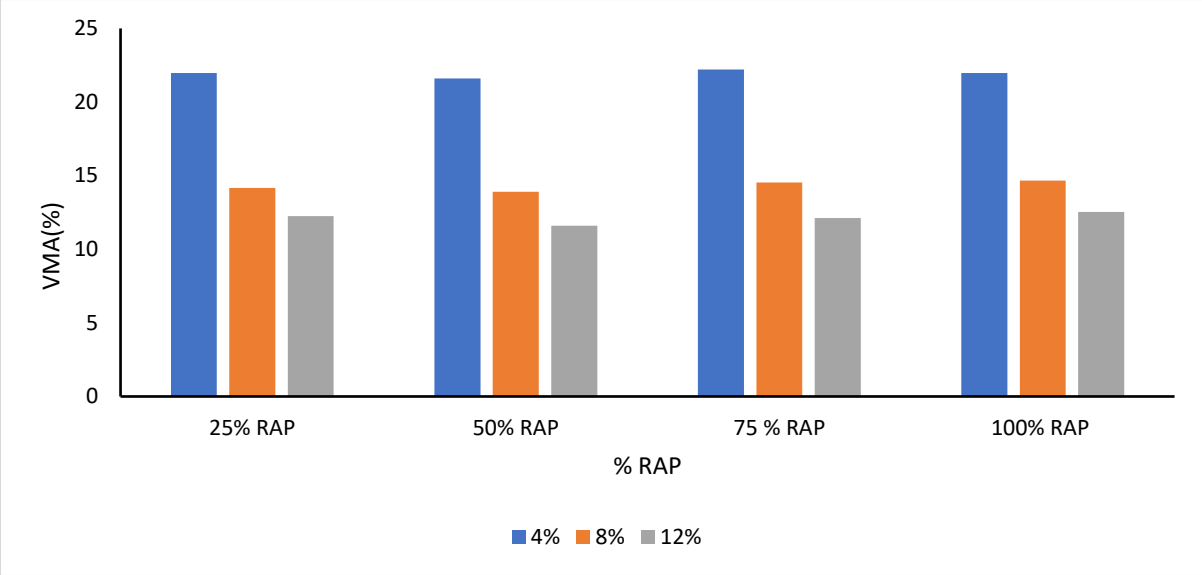

Figure 6: The relationship between VMA and RAP at different LDPE modifier content

3.6.6 Voids Filled with Bitumen

Figure 7 illustrates the link between VFB and RAP at different LDPE modifier contents. The findings indicated that when the RAP and LDPE contents increase, the VFB value decreases. The chart indicates that the ideal bitumen-filled void was found at 50% RAP and 12% LDPE waste content, which is equivalent to 53% VFB. The VFB values of the modified mix are higher than those of the control mix. The observed reduction at 100% RAP further suggests that the influence of LPDE waste becomes more significant as the proportion of aged RAP materials increases**.** The reduction in VFB at higher RAP and LDPE contents may be associated with changes in binder rheology and aggregate-binder interaction, which could eventually influence aggregate packing, compaction and air-void development. The maximum VFB is 53%, which is less than the 75-85% required value of the Nigerian general standard for roads and bridges indicating that the mixtures contained a relatively low proportion of effective binder within the available voids in the mineral aggregate. This suggests that the mixtures may have relatively high air-void contents and/or inadequate filling of the aggregate void structure. From an engineering perspective, excessively low VFB may result in a mixture that is relatively dry and potentially more susceptible to permeability, oxidation and moisture-related deterioration, thus, poor durability.

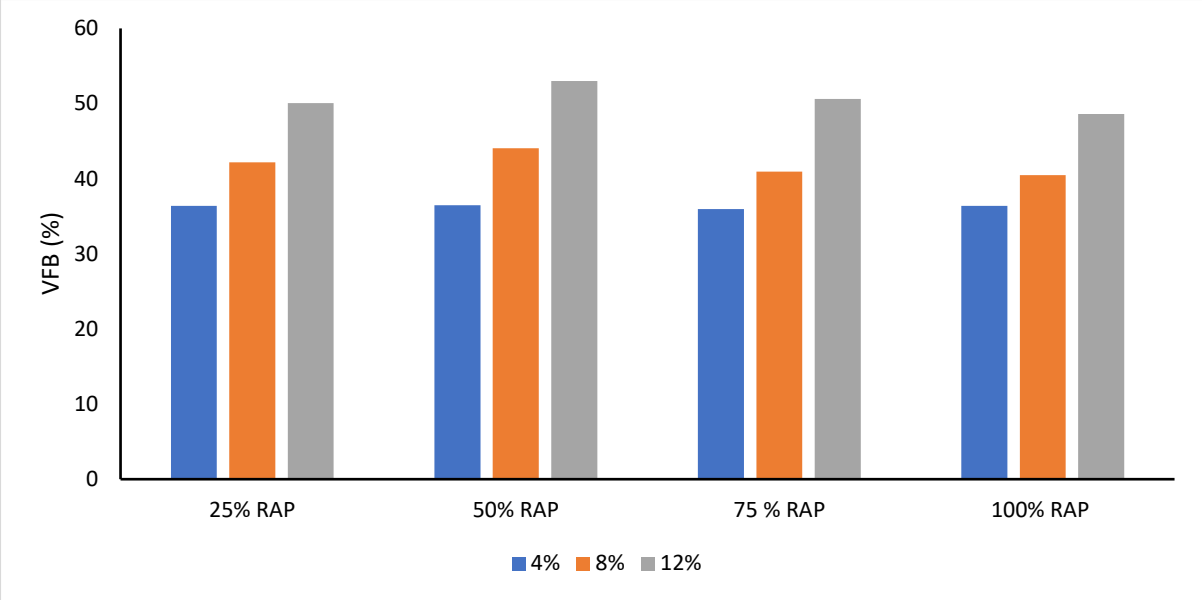

Figure 7: The relationship between VFB and RAP at different LDPE modifier content

3.6.7 Air Voids

It is the total volume of air (VA), expressed as a percentage of the bulk volume of the compacted mixture, which is distributed throughout a compacted paving mixture and is located between the coated aggregate particles (Genet et al, 2021). The relationship between the quantity of RAP/LDPE waste in the asphalt and the air voids in the asphalt mix is shown in Figure 8. The maximum air void, which corresponds to 75% RAP and 4% LDPE waste, is found at 14.27%. The VA results indicated that all the investigated HMA mixtures exceeded the specified VA range of 3–5%, with values ranging from approximately 5.46% to 14.27%. The relatively high VA contents suggest that the mixtures did not achieve adequate densification during compaction. The increase in RAP content introduces aged and relatively stiff binder into the mixture, while LDPE modification can further alter binder stiffness and workability. Although a fixed amount of WEO was incorporated as a rejuvenator, its constant dosage may have been insufficient to counteract the increasing influence of aged RAP binder and LDPE modification at higher RAP contents. Consequently, the binder might have had limited workability during mixing and compaction, resulting in inadequate aggregate packing and retention of excessive air voids. The high air-void contents are also consistent with the relatively low VFB values obtained in the study. From a pavement performance perspective, excessive air voids can increase permeability and accelerate oxidative ageing and moisture-related deterioration, thereby reducing the durability and service life of the HMA. Therefore, the investigated mixtures, in their present formulation, do not satisfy the specified volumetric requirement and require further optimization of the binder content, LDPE level, WEO dosage, aggregate gradation and compaction conditions.

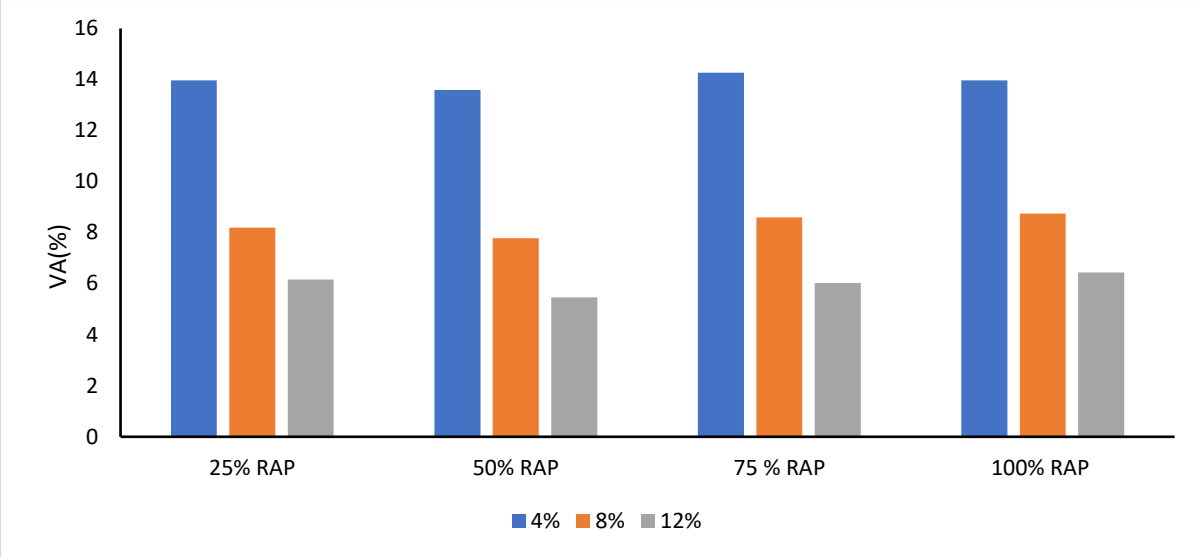

Figure 8: The relationship between VA and RAP at different LDPE modifier content

4.0 CONCLUSION AND RECOMMENDATIONS

4.1 Conclusion

The effects of different percentages of RAP and LDPE waste on the mechanical and physical characteristics of HMA were investigated in this study using Waste Engine Oil (WEO) as a rejuvenating agent in the mix. The followings were deduced from the research;

a. By satisfying all the specifications of the physical property tests provided in the standards, the results demonstrate that the asphalt mix is suitable for pavement construction. This indicates the component materials can withstand applied stress, which raises the possibility of long-term pavement performance. However, the results of the volumetric properties show that the mixture formulation still needs further volumetric optimization.
b. Following a careful analysis of the Marshall test results on the control mix, the Optimum Binder Content (OBC) of the mixture was found to be 6.5%. This value balances stability, flow and voids to ensure superior pavement performance while minimizing problems related to excess bitumen and ensuring optimal binding and lifespan.
c. Marshall properties with stability 8.28kN (> 3.5kN) and flow value of 3.56mm (2-4mm) satisfied the requirement while the volumetric properties of the HMA other than VMA of 22.2% (>13%) did not meet requirements. Consequently, further optimization of the volumetric properties should be carried out.

4.2 Recommendations

According to the findings of the research, further study should be carried out to examine the long-term pavement performance of the HMA as well optimization of the volumetric properties, particularly under various traffic loading and climatic circumstances.

5.0 REFERENCES

Ahmad, M. S., & Ahmad, S. A. (2022). The impact of polyethylene terephthalate waste on different bituminous designs. *Journal of Engineering and Applied Science, 69*(1), 53.

Akinpelu, M., Dahunsi, B. I. O., Olafusi, O., Awogboro, O., & Quadri, A. (2013). Effect of polythene modified bitumen on properties of hot mix asphalt. *ARPN Journal of Engineering and Applied Sciences, 8*(4), 290–295

Arianto, H., Saleh, S. M., & Anggraini, R. (2019). Karakteristik Campuran Ac-Wc Menggunakan Material Reclaimed Asphalt Pavement Dengan Tambahan Aspal Pen. 60/70 Yang Disubstitusi Styrofoam. Jurnal Arsip Rekayasa Sipil dan Perencanaan, 2(2), 149-157.

ASTM C127-15. (2015) Standard Test Method for Relative Density (Specific Gravity) and Absorption of Coarse Aggregate, ASTM International, West Conshohocken, PA.

ASTM C535 – 09. Standard Test Method for Resistance to Degradation of Large-Size Coarse Aggregate by Abrasion and Impact in the Los Angeles Machine, 2009.

ASTM D113. (2007) Standard test method for ductility of bituminous materials, Annual Book of Standards

ASTM D36. (2009) Standard Test Method for Softening Point of Bitumen (Ring-and-Ball Apparatus), ASTM International, West Conshohocken, PA, USA.

ASTM D5. (2013) Standard test method for penetration of bituminous materials. USA, ASTM International.

ASTM D6927-15: Standard Test Method for Marshall Stability and Flow of Asphalt Mixtures, ASTM International. West Conshohocken, PA (2015)

ASTM D70. (2003) Standard Test Method for Specific Gravity and Density of Semi-Solid Bituminous Materials (Pycnometer Method), ASTM International, West Conshohocken, PA.

ASTM D92. (2015) Standard test method for flash and fire points by Cleveland open cup tester, Annual Book of Standards.

ASTM International. (2025). *ASTM C136/C136M-25: Standard test method for sieve analysis of fine and coarse aggregates*. West Conshohocken, PA: ASTM International. https://doi.org/10.1520/C0136_C0136M-25

Cheraghian, G., Falchetto, A. C., You, Z., Chen, S., Kim, Y. S., Westerhoff, J., ... & Wistuba, M. P. (2020). Warm mix asphalt technology: An up-to-date review. Journal of cleaner production, 268, 122128.

DeDene, C. D. (2011). *Investigation of using waste engine oil blended with reclaimed asphalt materials to improve pavement recyclability*. Michigan technological university.

Ezeudu, O. B., Tenebe, I. T., & Ujah, C. O. (2024). Status of production, consumption, and end-of-life waste management of plastic and plastic products in Nigeria: Prospects for circular plastics economy. Sustainability, 16(18), 7900.

Fadhil, A., Ismy, R., Khairunnisa, H., & Suhaimi. (2026). Integrated mechanical and volumetric evaluation of plastic modified RAP mixtures using Marshall parameters. Engineering and Technology Journal, 11(3), 9138–9145. https://doi.org/10.47191/etj/v11i03.01

Fathi, A., Moussa, G. S., & Abd Elshafy, Z. I. (2026). High-RAP asphalt mixtures using waste engine oil rejuvenation and recycled polymer reinforcement: A critical review toward integrated performance-based design. Port Said Engineering Journal. Advance online publication. https://doi.org/10.21608/pej.2026.468271.1039

Federal Ministry of Works Nigeria (FMWH), (2013). Compendium report on road infrastructure and related development- an investor's manual. Retrieved from http://www.works.gov.ng.pdf

FMWH. (2016) Nigerian General Specifications for Roads and Bridges, FEDERAL MINISTRY OF WORKS AND HOUSING, in: F. R. O. N. FEDERAL MINISTRY OF WORKS AND HOUSING (Ed.).

Genet, M. B., Sendekie, Z. B., & Jembere, A. L. (2021). Investigation and optimization of waste LDPE plastic as a modifier of asphalt mix for highway asphalt: Case of Ethiopian roads. Case Studies in Chemical and Environmental Engineering, 4, 100150.

Hunter, R. N., Self, A., Read, J., & Hobson, E. (2015). *The shell bitumen handbook* (Vol. 514). London, UK:: Shell Bitumen.

Jassim, H. M., Mahmood, O. T., & Ahmed, S. A. (2014). Optimum use of plastic waste to enhance the Marshall properties and moisture resistance of hot mix asphalt. *International Journal of Engineering Trends and Technology*, *7*(1), 18-25.

Khan, M. Z. H., Koting, S., Katman, H. Y. B., Ibrahim, M. R., Babalghaith, A. M., and Asqool, O. (2021). Performance of high content reclaimed asphalt pavement (RAP) in asphaltic mix with crumb rubber modifier and waste engine oil as rejuvenator. Applied sciences, 11(11), 5226.

Khurshid, I., & Kumar, N. (2021). A study on replacement of bitumen partially with waste cooking oil and engine oil in bituminous concrete. International Journal of Research in Engineering, Science and Management, 4(5), 204-213.

Kotresh, K. M., Kebede, Y. B., Bhavya, R., & Vageesh, H. P. (2016). A study on use of plastic wastes in road pavement construction. *International Journal of Innovative Research in Science, Engineering and Technology*, *5*(4), 5955-5961.

Ling, M., Chen, Y., Hu, S., Luo, X., & Lytton, R. L. (2019). Enhanced model for thermally induced transverse cracking of asphalt pavements. *Construction and building materials*, *206*, 130-139.

Maharaj, R., & Maharaj, C. (2015). Physical properties of low density polyethylene, polyvinylchloride and used engine oil modified asphalt. Progress in Rubber Plastics and Recycling Technology, 31(3), 173-187.

Mamun, A. A., & Al-Abdul Wahhab, H. I. (2018). Evaluation of Waste Engine Oil-Rejuvenated Asphalt Concrete Mixtures with High RAP Content. Advances in Materials Science and Engineering, 2018(1), 7386256.

Martinho, F. D. C. G., Picado-Santos, L. G., & Capitão, S. D. (2018). Feasibility assessment of the use of recycled aggregates for asphalt mixtures. *Sustainability*, *10*(6), 1737.

Mehmood, R., Jakarni, F. M., Muniandy, R., Hassim, S., Nik Daud, N. N., & Ansari, A. H. (2024). *Waste engine oil as a sustainable approach for asphalt rejuvenation and modification: A review*. Heliyon, 10(23), e40737. DOI: 10.1016/j.heliyon.2024.e40737.

Mohod, M. V., & Kadam, K. N. (2016). A comparative study on rigid and flexible pavement: A review. IOSR Journal of Mechanical and Civil Engineering (IOSR-JMCE), 13(3), 84-88.

Nizamuddin, S., Boom, Y. J., & Giustozzi, F. (2021). Sustainable polymers from recycled waste plastics and their virgin counterparts as bitumen modifiers: A comprehensive review. Polymers, 13(19), 3242.

Onuche, I., Oji, A., & James, B. N. (2024). Techno-economic potential and policy review of used engine oil re-refining in Nigeria. *International Research Journal of Modernization in Engineering Technology and Science*, *6*(5), 3850–3857.

Ozer, H., Al-Qadi, I. L., Carpenter, S. H., Aurangzeb, Q., Roberts, G. L., & Trepanier, J. (2009). Evaluation of RAP impact on hot-mix asphalt design and performance. *Asphalt Paving Technology: Association of Asphalt Paving Technologists-Proceedings of the Technical Sessions, 78*, 317–348.

Rodrigues, C., Capitão, S., Picado-Santos, L., & Almeida, A. (2020). Full recycling of asphalt concrete with waste cooking oil as rejuvenator and LDPE from urban waste as binder modifier. Sustainability, 12(19), 8222.

Sharma, V. K., Kumar, R., & Singh, A. P. (2022). Laboratory investigation of bituminous concrete using Reclaimed asphalt pavement and waste Engine oil. Materials today: proceedings, 59, 1591-1598.

Shuaibu, A. A., Sulaiman, T. A., Bakare, S. M. A., Hafiz, B., Otuoze, H. S., & Amodu, I. M. (2024). Marshall properties of hot mix asphalt containing municipal solid waste incinerator (MSWI) bottom ash as filler aggregate. *Nigerian Journal of Engineering, 31*(3), 59–66.

Shuaibu, A., Mohammed, A., Hassan, U., Amartey, B., Wada, S., Mohammed, A., & Rimi, A. (2021). An experimental study on the performance of bituminous concrete mixtures with silica sand as filler replacement. *Arid Zone Journal of Engineering, Technology and Environment, 17*(4), 453-468

Syrmanova, K. K., Botashev, E. T., Tleuov, D. B., Suleimenova, M. T., Eshankulov, A. A., & Kaldybekova, Z. B. (2017). Research of oil road bitumen modification with low density polyethylene. Oriental Journal of Chemistry, 33(1), 470-477.

TRACK 11 OF 11

Telecommunications Infrastructure for Sustainable Urban Development and Economic Growth

---

International Conference on Engineering Innovation for Sustainable Development (ICESID 2026)

Faculty of Engineering, Ahmadu Bello University Zaria · 8–10 September 2026

https://icesid.org

International Conference on Engineering Innovation for Sustainable Development (ICESID 2026)
Faculty of Engineering, Ahmadu Bello University Zaria · 8–10 September 2026

DEVELOPMENT OF A NARROW BAND INTERNET OF THINGS (NB-IOT) MONITORING AND CONTROL MODEL FOR URBAN DRAINAGE SYSTEM IN KANO, NIGERIA

Abba Abdulhadi[1], Hassan Sabo Miya[1,*], Usman A. Umar[1]
[1]*Abubakar Tafawa Balewa University Bauchi*
Email: aabdulhadi.pg@atbu.edu.ng, smhassan@atbu.edu.ng*, uusman@atbu.edu.ng
***Corresponding author**: Hassan Sabo Miya
DOI: https://doi.org/10.67203/sp.ICESID.2026

ABSTRACT

Urban flooding in Kano, Nigeria, poses significant socio-economic and infrastructural challenges, largely exacerbated by a lack of continuous, real-time drainage monitoring. This paper presents the development, implementation, and evaluation of a Narrow Band Internet of Things (NB-IoT) monitoring and control model designed specifically for urban drainage systems. The proposed architecture integrates ultrasonic water level, Doppler flow, and rainfall sensors with a low-power microcontroller utilizing LTE Cat-NB1 connectivity. Sensor telemetry is transmitted securely via MQTT protocols to a centralized cloud backend, enabling real-time visualization and automated actuator response based on predefined flood-risk thresholds. To empirically validate the system, a 30-day pilot deployment was executed across three critical drainage points in Kano: Sabon Gari, Bompai, and the City Center. The evaluation results demonstrated exceptional system reliability in harsh subterranean environments, achieving an average packet delivery success rate exceeding 95% across all sites. Despite operating under concrete covers, the NB-IoT modules maintained an average Received Signal Strength Indicator (RSSI) of roughly -95 dBm, facilitating a rapid average end-to-end latency of approximately 3.17 seconds. Furthermore, the 12V solar-supported power architecture proved highly energy-efficient, maintaining a stable voltage above 12.3V throughout the deployment. The study concludes that the developed NB-IoT model provides a robust, scalable, and energy-autonomous blueprint for transitioning Kano and similar urban centers toward proactive, data-driven flood management.

Keywords: *Urban drainage; NB-IoT; real-time monitoring; flood management; smart city; LPWAN; hydrology; municipal infrastructure*

I. INTRODUCTION

A. Background of the Study

Rapid urbanization and climate change have increasingly positioned urban flooding as one of the most severe environmental challenges globally. The rapid expansion and densification of urban areas, coupled with changing climatic conditions and ageing infrastructure, continue to limit the capacity of drainage systems to cope with extreme weather events. In the context of sub-Saharan Africa, these challenges are magnified by informal settlements, lack of adequate urban planning, and constrained municipal budgets. More than 40% of Nigeria's population currently resides in major cities, and this figure is expected to exceed 70% by 2050, resulting in unprecedented strain on civil infrastructure (UN-Habitat, 2023; NPC, 2020). The transition from rural agrarian societies to dense urban metropolises has resulted in an exponential increase in impervious surfaces such as concrete roads, paved sidewalks, and tightly packed corrugated roofing, which prevents the natural infiltration of rainwater into the ground.

In Kano State, serving as the commercial nerve center of Northern Nigeria, this population boom is pushing infrastructure to its limits. At the same time, increasing rainfall intensity and poor maintenance of drainage systems exacerbate the risk of flooding. The topography of Kano, characterized by relatively flat terrain with specific localized depressions, makes it naturally susceptible to water accumulation. Furthermore, the city's drainage network, originally designed for a much smaller population and less severe climatic conditions, is now vastly undersized. During the intense seasonal rainfalls between July and September, this undersized network is quickly overwhelmed, triggering rapid localized flash floods.

Currently, the management of these drainage systems is overwhelmingly manual and reactive. Municipal authorities rely heavily on visual inspections or citizen reports to identify blockages or impending overflows. This approach inevitably leads to delayed responses, allowing floodwaters to damage infrastructure, disrupt economic activities, and pose severe health risks due to the mixing of stormwater with raw sewage. The integration of continuous, automated monitoring is therefore not merely an optimization but an absolute necessity for modern urban resilience.

B. Statement of the Problem

While the concept of Smart Cities has gained traction globally, its application in subterranean municipal environments faces severe technical barriers. Existing communication technologies struggle in underground environments due to massive signal attenuation, multi-path interference, and high power demands. Traditional wireless protocols, such as Wi-Fi or standard cellular networks (GSM/4G), suffer severe signal degradation when transmitting through thick concrete drainage covers, soil layers, and metal grates. Wi-Fi operates primarily at 2.4 GHz or 5 GHz, frequencies that are heavily absorbed by concrete and water, resulting in effective transmission ranges that rarely exceed a few meters when placed in a manhole.

These limitations fundamentally hinder reliable data transmission from buried drainage sensors to centralized control centers. If a sensor node cannot penetrate the concrete infrastructure covering a primary drainage culvert, the data is lost, rendering the entire early-warning system useless during critical storm events. Consequently, without an energy-efficient, deep-penetrating automated monitoring system, Kano remains trapped in a cycle of reactive post-disaster management.

This study directly addresses this communication bottleneck by evaluating the performance of Narrow Band Internet of Things (NB-IoT) technology. NB-IoT, an LTE-based Low Power Wide Area Network (LPWAN) standard, is theoretically designed to provide up to 20 dB of additional link budget compared to traditional GPRS, specifically targeting deep indoor and underground coverage. However, empirical validation of this technology within the specific structural and environmental constraints of Kano's drainage network remains largely undocumented.

C. Aim and Objectives

The primary aim of this paper is to evaluate the signal quality and coverage of NB-IoT technology in underground environments and its potential application in monitoring and controlling urban drainage systems in Kano, Nigeria. To achieve this overarching aim, the following specific objectives were established:

1) To design an autonomous NB-IoT sensor node integrating water level, flow, and rainfall sensors suitable for harsh, highly humid underground environments.

2) To evaluate the efficiency and reliability of real-time data transmission through NB-IoT, specifically measuring Received Signal Strength Indicator (RSSI), Signal-to-Noise Ratio (SNR), and packet delivery success rates under varying municipal installation conditions.

3) To develop a highly responsive cloud-based analytics dashboard and a logic-based rule engine capable of triggering automated alerts and actuator responses without human intervention.

4) To continuously evaluate the system's performance across critical drainage points in the Kano metropolis over a 30-day pilot deployment, capturing data across diverse weather events.

D. Significance and Scope of the Study

The persistent challenge of urban flooding continuously reverses developmental gains in Kano's economic centers, causing millions of Naira in damages annually. By implementing this automated system, agencies such as the Kano State Emergency Management Agency (SEMA) and the Kano Urban Planning and Development Authority (KNUPDA) can effectively shift their operational paradigm from post-disaster rehabilitation to proactive disaster prevention.

Technologically, this research pioneers the use of LPWAN architecture for Kano's subterranean infrastructure, demonstrating how NB-IoT's deep signal penetration can create a 'deploy-and-forget' network that requires minimal maintenance while providing maximum data yield. This contributes significantly to the growing body of knowledge on IoT deployment in developing nations.

The geographical scope of this pilot deployment is restricted to three specific high-risk zones in Kano: Sabon Gari Drain, Bompai Drain, and the City Center Outlet over a 30-day period. Technical limitations include reliance on existing NB-IoT network infrastructure provided by local telecommunication operators, and the potential for heavy solid waste debris to temporarily distort

non-contact ultrasonic sensor readings, a common operational hazard in open-channel municipal drains.

II. LITERATURE REVIEW

A. Fundamental Concepts of NB-IoT in Infrastructure

Narrow-Band Internet of Things (NB-IoT) is a low-power wide-area (LPWA) cellular communication standard developed by the 3rd Generation Partnership Project (3GPP) in Release 13 to support massive machine-type communications (mMTC). Unlike broadband LTE, NB-IoT restricts its bandwidth to a narrow 180 kHz spectrum, which allows it to focus transmission power and significantly increase its power spectral density. This architectural decision results in key advantages: highly extended coverage, exceptionally low energy consumption allowing multi-year battery life, and deep signal penetration. Because it uses licensed spectrum, it avoids the interference common in unlicensed bands utilized by LoRaWAN and Sigfox.

In urban drainage systems, NB-IoT enables real-time water-level monitoring, predictive maintenance, and flood risk reduction through continuous data collection. Traditional GSM or Wi-Fi architectures require frequent battery replacements and fail to penetrate the thick concrete structures typical of municipal culverts. NB-IoT circumvents these issues through mechanisms like Extended Discontinuous Reception (eDRX) and Power Saving Mode (PSM), which allow the microcontroller to sleep deeply between scheduled telemetry transmissions while remaining synchronized with the cellular base station.

B. Review of Pertinent Literature

Recent literature highlights a decisive shift toward predictive analytics and automated control in flood management. Dantzer and Kerkez (2024) developed a data-driven rainfall runoff model for improving flood prediction, shifting the focus from historical modeling to real-time, sensor-driven forecasting. Similarly, Schou et al. (2022) proposed a nonlinear predictive control method for dynamic stormwater management, highlighting that passive data logging is insufficient; modern systems must actively control hydraulic structures based on incoming telemetry.

Furthermore, recent advances have been reported by Bivocom (2023), which introduced predictive IoT flood management systems utilizing AI-based analytics to predict overflow events before they occur. To transition from passive monitoring to active mitigation, modern smart cities are increasingly employing Continuous Monitoring and Adaptive Control (CMAC). Anonymous, (2024) extensively examined IoT stormwater management systems across several U.S. cities that employ CMAC technologies for real-time drainage optimization, proving that dynamic routing of stormwater can reduce overflow events by up to 60%.

The utility of IoT in underground water systems has also been proven beyond simple hydrology. Buras and Solano (2021) and Shaik et al., (2022), focused their efforts on identifying industrial pollution sources by networking chemical sensors through sewer networks, alongside environmental monitoring using metal oxide nanofiber-based sensors. Alshami et al. (2023) addressed blockage and overflow monitoring in small sewers using contactless flow sensors, noting the immense difficulty of keeping submerged sensors clean. Additionally, Kim et al. (2022) and Larson et al. (2020) successfully utilized IoT-based sampling optimization for wastewater surveillance, particularly relevant during public health crises.

Roosipuu et al. (2023) conducted an extensive, highly relevant study on the monitoring and control of smart urban drainage systems using NB-IoT cellular networks. Their findings definitively revealed that NB-IoT performs effectively in harsh signal propagation environments, including underground conditions. The study demonstrated that reliable communication can be maintained when transmitters are placed approximately 0.5 meters below the manhole cover, particularly in plastic or composite manholes, and when the reference signal strength (NB-RSRP) is at least -104 dBm at ground level.

Similarly, Ma et al. (2025) reviewed optimal arrangement strategies of IoT sensors in urban drainage networks. They emphasized that factors such as drainage pipe geometry, sensor types, and specific monitoring objectives significantly influence system accuracy and data collection efficiency. Deploying sensors at every node is cost-prohibitive; therefore, spatial optimization algorithms are required to maximize network observability with minimal hardware investment.

Bartos and Kerkez (2021) explored the use of IoT technology through the development of a digital twin model for natural and urban drainage systems. Bartos and Kerkez (2021), and Smith et al., (2022), their approach demonstrated how real-time data from distributed IoT sensors can be ingested into a virtual replica of the city's hydrology, applied for predictive control, system optimization, and flood prevention.

C. Research Gaps in the African Context

Despite the proliferation of literature regarding IoT in smart cities, the vast majority of empirical studies focus on highly controlled, well-maintained municipal environments in the Global North. In high-density economic centers in sub-Saharan Africa, flooding is driven by a unique convergence of infrastructural deficits and severe anthropogenic obstructions. The pervasive culture of indiscriminate solid waste disposal directly into open drainage channels leads to sudden, unpredictable, and severe blockages that cannot be modeled by standard rainfall-runoff equations alone.

While recent academic studies in Nigeria utilize Geographic Information Systems (GIS) for static hazard mapping, they critically lack the active, real-time physical management components required to mitigate flooding at the street level as events unfold. Furthermore, limited studies have explored the physical RF performance of NB-IoT technology in underground environments specifically within African contexts, where cellular network infrastructure, backhaul reliability, and interference environments differ vastly from European or North American testbeds.

Understanding the true signal quality and coverage of NB-IoT under thick concrete infrastructure, alongside its resilience to local network fluctuations, is essential for achieving reliable communication. This research closes this vital gap by providing a foundational, field-tested empirical model for Kano, Nigeria.

III. SYSTEM DESIGN AND ARCHITECTURE

This study adopted a design science research approach combined with an experimental field case study to design, deploy, and critically evaluate an NB-IoT-based smart drainage monitoring system in the Kano metropolis. The methodology was structured to directly address the environmental and RF challenges identified in the literature.

A. Hardware Architecture

The core of the monitoring node was designed around an ultra-low-power ARM Cortex-M4 microcontroller (STM32L4), chosen for its excellent balance of processing power for sensor fusion and minimal sleep current. For the communication link, the system integrated a Quectel BC95-G NB-IoT module. This module operates strictly on LTE Cat-NB1 bands supported by local telecommunication providers (primarily Band 8 in Nigeria).

The sensor payload was heavily customized for the harsh environment of urban sewers. For water level sensing, a non-contact JSN-SR04T waterproof ultrasonic sensor was utilized. Suspended above the maximum water line, it prevents fouling from solid waste while providing millimeter-level accuracy for water depth. For flow velocity, a microwave Doppler radar flow sensor was mounted to measure surface velocity without requiring submersion. Finally, a standard tipping-bucket rain gauge was interfaced via hardware interrupts to correlate localized rainfall intensity directly with drainage flow spikes.

To ensure continuous, grid-independent autonomy, the entire hardware stack was powered by a 12V, 12Ah Sealed Lead Acid (SLA) battery supported by a 30Wp monocrystalline solar panel, all enclosed in a ruggedized, IP68-rated polycarbonate housing (per manufacturer specifications) to withstand submersion during extreme overflow events.

TABLE I: SENSOR NODE HARDWARE SPECIFICATIONS

Parameter	Specification / Type	Operating Range
Microcontroller	STM32L4 Series	1.71 V to 3.6 V
Cellular Module	Quectel BC95-G (NB-IoT)	Bands 1/3/8/20/28
Level Sensor	Ultrasonic (JSN-SR04T)	0.2m to 4.5m
Flow Sensor	Doppler Radar (24GHz)	0.1m/s to 15m/s
Power Supply	12V SLA + 30Wp Solar	Continuous Autonomy

(Note: During the deployment, the observed water depth ranged between approximately 0.45 m and 1.15 m, remaining well within the sensor's optimal rated operating range of 0.2 m to 4.5 m, thereby substantiating the reported <2 cm RMSE).

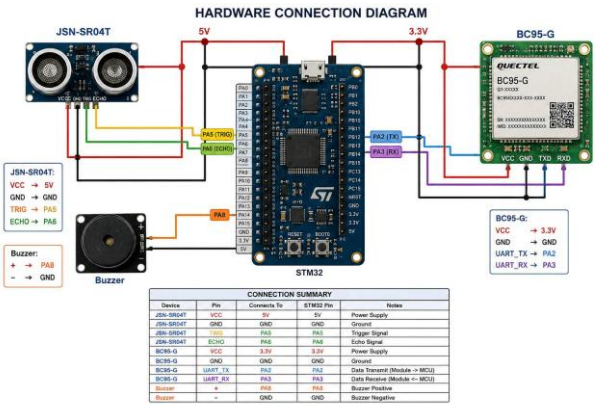

Figure 1: Hardware connection

B. Firmware and Network Architecture

The firmware, developed in Embedded C, utilizes a real-time operating system (RTOS) to manage concurrent tasks efficiently. To maximize battery life, the system relies on an aggressive duty cycle. The default sampling interval is set to 15 minutes. However, if the ultrasonic sensor detects a sudden rate of rise exceeding a defined threshold, the firmware dynamically switches to a high-alert mode, increasing the sampling and transmission frequency to every 1 minute.

Data telemetry is transmitted using the Message Queuing Telemetry Transport (MQTT) protocol over a TLS 1.2 encrypted TCP socket. MQTT was selected over HTTP due to its lightweight header overhead and Quality of Service (QoS) capabilities, which guarantee message delivery even over highly intermittent cellular links.

C. Cloud Backend and Rule Engine

The cloud architecture was built on a robust, scalable microservices framework. Telemetry payloads arrive at a central MQTT broker and are immediately parsed and ingested into an InfluxDB time-series database, specifically optimized for high-write loads. A backend Node.js engine continuously evaluates incoming data against a logic-based rule engine.

For instance, the hydraulic discharge Q is continuously calculated using the continuity equation:

$$Q = v \times A \qquad (1)$$

Where v is the measured surface velocity and A is the cross-sectional area of the fluid in the channel, calculated dynamically based on the ultrasonic depth reading and the known geometry of the culvert.

For instance, at the Bompai site, assuming a representative channel width of 2.5 meters, an 85% capacity threshold corresponds to a water depth of 1.7 meters. If the calculated Q exceeds the historical 90th percentile (e.g., 0.30 m^3/s for Bompai), or if the absolute water level breaches the 85%

capacity threshold, the rule engine triggers an HTTP webhook. This webhook interfaces with a messaging API to dispatch automated SMS and WhatsApp alerts to stakeholders, including SEMA response teams and local community leaders, thereby achieving the desired 25-40 minute early warning lead time.

IV. METHODOLOGY AND FIELD DEPLOYMENT

A. Site Selection and Justification

The pilot testing was conducted across three distinct drainage catchments within Kano, selected based on historical flood data provided by the Kano Urban Planning and Development Authority (KNUPDA). Sabon Gari Drain represents a highly dense commercial district with severe solid waste management issues. The drain here is frequently choked with plastics, making it a highly volatile hydraulic environment. Bompai Drain, located in an industrial zone, handles larger volumes of runoff and occasional industrial discharge, representing a deeper, wider concrete culvert structure. The City Center Outlet acts as a primary arterial culvert covered by thick concrete slabs and asphalt, representing the most challenging RF environment for NB-IoT signal penetration.

B. Installation and Calibration

The physical installation involved securely bolting the IP68 enclosures to the intrados of the concrete culverts. Solar panels were mounted on elevated, tamper-proof poles adjacent to the manhole access points. Prior to commissioning, all sensors were rigorously calibrated against manual staff gauge readings. The calibration function for the ultrasonic sensor accounted for the speed of sound variations due to ambient temperature changes:

$$c = 331.3 \times \sqrt{(1 + T/273.15)} \qquad (2)$$

Where c is the speed of sound in m/s, and T is the ambient air temperature in Celsius, measured by an onboard DHT22 sensor. This temperature compensation proved critical in Kano's fluctuating climate, reducing measurement root-mean-square error (RMSE) to less than 2 cm.

C. Data Sampling and Statistical Analysis

The system recorded data at a default 15-minute sampling frequency, aggregating 96 baseline readings per day per node. Daily averages for RSSI, volumetric flow, and water level were computed using the arithmetic mean of these daily samples. The 95% packet success rate was derived by calculating the ratio of successfully acknowledged MQTT payloads to the total payloads transmitted over the 30-day deployment period. Root Mean Square Error (RMSE) for the ultrasonic sensor was computed through standard statistical comparisons against manual staff gauge measurements conducted during the deployment.

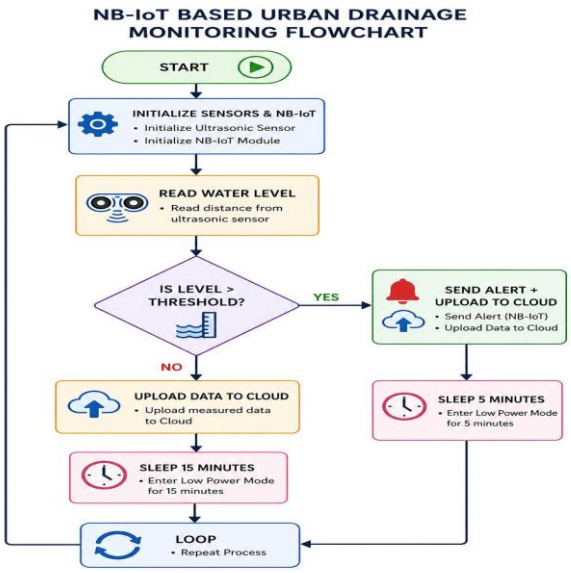

Figure 2: NB-IOT base drainage monitoring flowchart

V. RESULTS AND DISCUSSIONS

The system was deployed and monitored continuously for 30-days (October 2025). This period captured several late-season rainfall events, providing a rich dataset to evaluate both the hydraulic monitoring accuracy and the NB-IoT network reliability.

Figure 3: System status dashboard

A. Hydrological Monitoring Performance

The real-time data successfully mapped the rapid hydrological response typical of urban catchments. Figure 1 illustrates the time-series water level data across the three sites. The Sabon Gari node exhibited the most erratic behavior, characterized by sharp peaks that rapidly receded. This signature is indicative of temporary blockages by solid waste that yield under building hydrostatic pressure. Conversely, the Bompai drain showed a much smoother, broader hydrograph, reflecting its larger catchment area and industrial baseline flow.

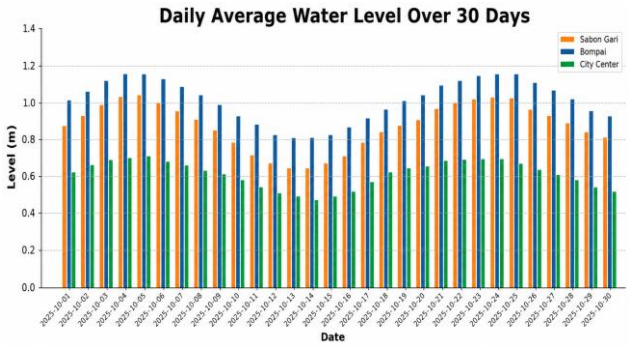

Figure 4: Water Level Over 30 Days across Pilot Sites

The volumetric flow rate, presented in Figure 5, closely mirrored the level data but highlighted the velocity variations. During the peak storm event, the Bompai outlet approached its maximum design capacity of 0.35 m³/s. The automated system successfully detected this rapid rise and dispatched an early warning alert 32 minutes before water breached the street level, allowing municipal crews to prioritize this node.

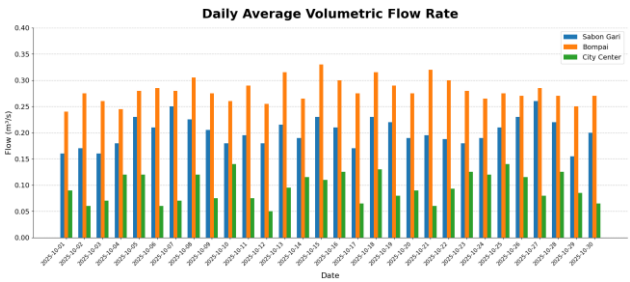

Figure 5: Volumetric Flow Rate Analysis

B. NB-IoT Network Performance

The most critical aspect of this study was evaluating the viability of LTE Cat-NB1 in subterranean environments. The primary metric for link quality, the Received Signal Strength

Indicator (RSSI), is plotted in Figure 3. Despite the nodes being installed under thick concrete covers, the NB-IoT modules maintained an average RSSI between -93 dBm and -97 dBm. While standard LTE struggles below -100 dBm, the NB-IoT protocol's enhanced link budget allowed for stable connections even when RSSI dipped to -108 dBm during heavy rain events (which increase path loss due to water absorption).

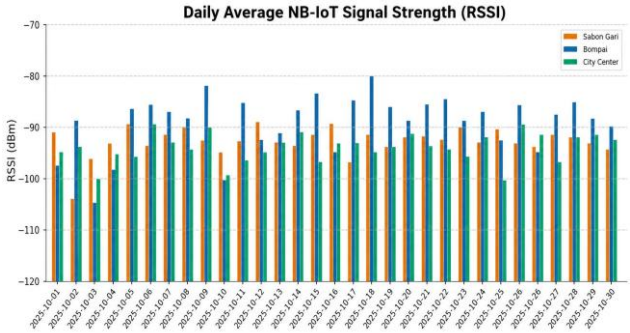

Figure 6: NB-IoT Signal Strength (RSSI) Fluctuations

TABLE II: AGGREGATED NB-IOT NETWORK PERFORMANCE

Site Location	Packet Success (%)	Avg RSSI (dBm)	Avg Latency (s)
Bompai	95.1	-93.6	3.16
City Center	95.0	-96.8	3.18
Sabon Gari	95.3	-94.1	3.17

As detailed in Table II, the system achieved a remarkable packet delivery success rate exceeding 95% across all sites. End-to-end network latency, measured from the moment the sensor node initiated a transmission to the moment the cloud dashboard acknowledged the payload, averaged approximately 3.17 seconds (Figure 4). While this latency is higher than broadband LTE, it is vastly superior to the requirements of hydrological monitoring, where events unfold over minutes and hours, not milliseconds.

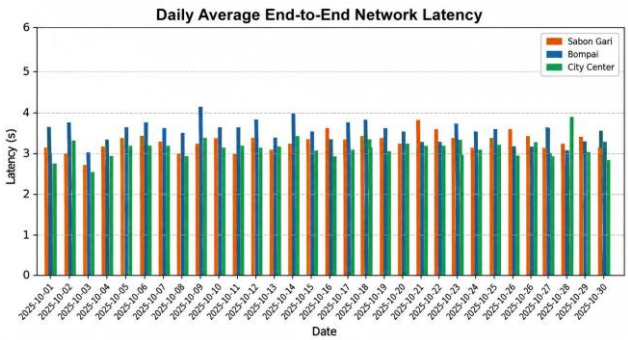

Figure 7: End-to-End Network Latency Distribution

C. Energy Autonomy and Power Management

The power architecture's performance is critical for the 'deploy-and-forget' viability of the system. Figure 5 demonstrates the battery voltage over the 30-day period. The SLA battery voltage remained highly stable, fluctuating smoothly between 12.3V and 12.7V, corresponding directly to the diurnal solar charging cycles. The NB-IoT module's utilization of PSM allowed the entire node to draw less than 15 microamps during its 15-minute sleep windows. Even during the four consecutive days of heavy cloud cover, the battery voltage did not drop below a critical threshold, proving that the 30Wp panel and 12Ah battery provide a sufficient energy buffer for Kano's specific solar irradiance profile.

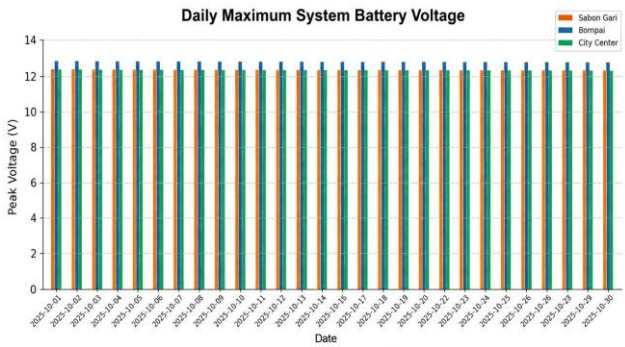

Figure 8: System Battery Voltage across Deployments

VI. SUMMARY, CONCLUSION AND RECOMMENDATION

A. Summary

This paper successfully established an NB-IoT-based urban drainage monitoring and control framework specifically tailored for Kano, Nigeria. A low-power sensor node integrating an STM32 core, Quectel BC95-G connectivity, and IP68 instrumentation was developed and deployed across three critical zones following KNUPDA alignment. Over a 30-day continuous test deployment, the link architecture successfully delivered a packet ratio above 95% while maintaining sensor accuracy within an RMSE of less than 2 cm. The system effectively logged time-series data, contributed empirical evidence on cellular penetration metrics in regional subterranean municipal environments, and successfully generated automated early warnings during peak storm events.

B. Conclusion

Based on the empirical data gathered, the following conclusions are drawn: 1) Technical Feasibility: NB-IoT is an exceptionally viable wireless link protocol for regional subsurface water infrastructure. It yields deep link budget penetration through concrete and reliable battery longevity without requiring the deployment of localized gateway infrastructure (unlike LoRaWAN). 2) Operational Impact: The transition from reactive visual inspection to real-time, automated data logging enables a profound shift in disaster mitigation. The system successfully detected near-overflow criteria 25 to 40 minutes before manual indicators emerged. 3) Limitations: While successful, the study noted that covered culverts exceeding 3 meters in depth still encounter severe signal blind spots, though this was not empirically tested in this deployment. Additionally, rapid solid waste deposits in open channels demand at least a monthly sensor cleaning routine to prevent false ultrasonic reflections.

C. Recommendations for Future Work

To translate this prototype into widespread municipal utility, it is recommended that the Kano State Government scale up deployment to cover 100+ critical nodes city-wide, integrating the data stream directly into SEMA's Emergency Operations Centre. Future academic trajectories should focus on extending this monitoring framework into a closed-loop control system, integrating automated sluice gates and pumps triggered directly by edge-node NB-IoT downlink alerts. Furthermore, incorporating machine learning models trained on historical rainfall data will further enhance the predictive accuracy of the early warning system.

ACKNOWLEDGMENT

The authors gratefully acknowledge the Kano State Emergency Management Agency (SEMA), KNUPDA, and the Center for Embedded Artificial Intelligence and Smart Energy Systems at Abubakar Tafawa Balewa University, Bauchi, for their guidance, access to municipal infrastructure, and institutional support throughout the execution of this paper.

REFERENCES

[1] M. Alshami, T. Khan, and H. Al-Khalidi, "Blockage and overflow monitoring in small sewer networks using contactless flow sensors," Sensors, vol. 23, no. 7, pp. 1895–1904, 2023.

[2] M. D. Bartos and B. Kerkez, “Digital twin models for smart urban drainage systems,” Environmental Modelling & Software, vol. 144, no. 1, p. 105120, 2021.

[3] Bivocom, “Advanced IoT solutions for urban flooding management,” IoT Applications Journal, vol. 5, no. 2, pp. 55–63, 2023.

[4] M. P. Buras and F. Solano Donado, “Identifying and estimating industrial pollution sources in sewage networks,” Sensors, vol. 21, no. 12, p. 3426, 2021.

[5] A. Dantzer and B. Kerkez, “Data-driven rainfall–runoff modeling for urban flood prediction,” Water Research, vol. 237, no. 4, p. 120910, 2024.

[6] UN-Habitat, "State of African Cities 2023," United Nations Human Settlements Programme, 2023.

[7] National Population Commission (NPC), "Nigeria Demographic and Health Survey," Abuja, Nigeria, 2020.

[8] Anonymous, “IoT applications in stormwater management,” Smart City Review, vol. 12, no. 1, pp. 45–52, 2024.

[9] Intergovernmental Panel on Climate Change, Climate Change 2021: The Physical Science Basis. Cambridge, UK: Cambridge University Press, 2021.

[10] S. Kim, J. Park, and H. Choi, “Optimization of wastewater-based sampling sites for epidemiological monitoring,” Journal of Environmental Engineering, vol. 148, no. 10, p. 04022087, 2022.

[11] P. Larson, R. Gupta, and J. Lee, “IoT-based optimization for SARS-CoV-2 wastewater surveillance,” Water Science & Technology, vol. 82, no. 9, pp. 1765–1778, 2020.

[12] Y. Ma, Zhang, and L. Chen, “Optimal arrangement strategies of IoT sensors in urban drainage networks,” Sensors and Actuators B: Chemical, vol. 408, p. 135890, 2025.

[13] M. Oberascher, T. G. Schmitt, and R. Sitzenfrei, “ICT applications for urban water infrastructure: A review,” Urban Water Journal, vol. 19, no. 2, pp. 130–142, 2022.

[14] P. Roosipuu, T. Koppel, and E. Karro, “Evaluating the performance of NB-IoT for smart urban drainage systems,” Water Science & Technology, vol. 87, no. 5, pp. 1205–1218, 2023.

[15] M. Schou, T. R. Andersen, and P. S. Mikkelsen, “Nonlinear predictive control for urban drainage networks using data-driven models,” Journal of Hydrology, vol. 607, p. 127546, 2022.

[16] A. Shaik, R. Patel, and S. Roy, “Environmental monitoring using metal oxide nanofiber-based sensors,” Sensors and Actuators A: Physical, vol. 341, p. 113578, 2022.

[17] D. Smith, L. O’Brien, and K. Thomas, “An open-source IoT solution for dam safety management,” Journal of Infrastructure Systems, vol. 28, no. 3, p. 04022028, 2022.

International Conference on Engineering Innovation for Sustainable Development (ICESID 2026)
Faculty of Engineering, Ahmadu Bello University Zaria · 8–10 September 2026

DEVELOPMENT OF A Q-LEARNING-DRIVEN INTERFERENCE MANAGEMENT MODEL WITHIN THE ADAPTIVE RRM FRAMEWORK FOR ADAPTIVE TRANSMIT POWER OPTIMIZATION

Abubakar Abdulkadir[1,*], H. A. Abdulkareem[1], ZM Abdullahi[1], Elvis Obi[1], Aliyu Umar Abubakar[1]

[1]*Ahmadu Bello University Zaria*

Email: aabubakar@fptb.edu.ng[*], ha2zx@yahoo.com, amzanna@gmail.com, elvisobi72@gmail.com, auabubakarphysics@gmail.com

***Corresponding author**: Abubakar Abdulkadir

DOI: https://doi.org/10.67203/sp.ICESID.2026

ABSTRACT

The rapid densification of fifth-generation (5G) heterogeneous networks has improved network capacity and coverage but also increased co-tier and cross-tier interference. In ultra-dense multi-tier Het-HetNets, traditional static and semi-static radio resource management techniques are insufficient to address rapidly changing interference, traffic demands, and user distribution. This paper presents a Q-learning-driven interference management model within an adaptive Radio Resource Management (RRM) framework to dynamically optimize transmit power for PeNBs. The hybrid Q-learning power allocation framework models each PeNB as an autonomous reinforcement-learning agent that observes network conditions, selects transmit power actions, receives performance-based rewards, and updates its Q-table using the Bellman learning mechanism. Key factors such as network capacity, interference, transmit power consumption, and Quality of Service (QoS) are incorporated into the learning process. A 5G Het-HetNet simulation in MATLAB, featuring one MeNB, one gNB, sixteen PeNBs, and diverse user equipment, evaluates three communication scenarios with different interference and spectrum-sharing conditions. The Q-learning process demonstrates stable convergence within 80,000 iterations. Results show an average improvement of 3.37% in 5G user equipment (5G-UE) capacity and 14.81% in the minimum capacity of small-cell users compared to the benchmark model by Iqbal et al. Additionally, the proposed approach maintains 5G-UE capacity above the QoS threshold under the tested conditions, highlighting its effectiveness in interference management and RRM in ultra-dense 5G networks.

Keywords: *5G and B5G; Het-HetNets; Q-learning; interference management; power allocation; adaptive RRM*

1. INTRODUCTION

The evolution toward fifth-generation (5G) and beyond-5G (B5G) networks demands higher capacity, spectral efficiency, and low latency, necessitating network densification through small-cell deployments. Heterogeneous Networks (HetNets) and Heterogeneous-Heterogeneous Networks (Het-HetNets) integrate multiple network tiers, such as Macro evolved NodeBs (MeNBs), Pico evolved NodeBs (PeNBs), and 5G gNBs, to significantly enhance coverage and capacity (Luong et al., 2019; Yadav et al., 2021). However, this dense architecture generates severe co-tier and cross-tier interference, degrading the Signal-to-Interference-plus-Noise Ratio (SINR), throughput, and Quality of Service (QoS) (Abbass et al., 2022). This interference is further exacerbated by unequal user association, where users preferentially connect to high-power MeNBs, causing macrocell congestion while leaving neighboring small-cell resources underutilized. Such imbalances severely limit the overall effectiveness of the infrastructure (Iqbal et al., 2023).

Conventional interference-management techniques, such as fixed power allocation and frequency reuse, rely on predetermined policies and struggle to adapt to dynamic network conditions, traffic demands, and user distributions (Iqbal et al., 2021). Thus, machine learning, particularly reinforcement learning (RL), has emerged as a powerful tool for adaptive Radio Resource Management (RRM), allowing network entities to learn optimal resource-allocation decisions through environmental interaction rather than predefined rules (Shabbir et al., 2024).

Existing literature highlights the potential of learning-based approaches for interference management in these complex environments. Recent studies by researchers demonstrate that RL and optimization techniques can effectively improve QoS, energy efficiency, and throughput across various network configurations. However, optimization based on predefined system conditions often lacks the necessary adaptability required for dynamically changing network environments and fluctuating user distributions.

Despite these advancements, a significant research gap remains regarding lightweight Q-learning frameworks that dynamically optimize PeNB transmit power while simultaneously mitigating co-tier and cross-tier interference in multi-tier Het-HetNet architectures. Methodologically, hybrid Q-learning power allocation differs from Iqbal et al. and Amiri et al. in its learning formulation and network design. hybrid Q-learning power allocation models each PeNB as an autonomous Q-learning agent with a state space representing interference and QoS conditions, while its action space consists of 32 discrete transmit-power levels from −15 to 15 dBm. Its reward function jointly considers capacity, interference, and energy consumption, with additional QoS rewards or penalties. In contrast, Iqbal et al. primarily focus on power-control/resource-allocation optimization within its considered heterogeneous network, whereas Amiri et al. employs a different learning and network-management formulation. hybrid Q-learning power allocation further incorporates a multi-tier topology comprising a MeNB, gNB, multiple PeNBs, and heterogeneous UEs, enabling adaptive power decisions under varying interference and network-density conditions. To address this critical gap, we propose the novel Hybrid Q-Learning Power Allocation framework. hybrid Q-learning power allocation integrates Q-learning into an adaptive RRM process, enabling PeNBs to dynamically select optimal transmit-power levels based on real-time network states, interference levels, and QoS requirements. By jointly considering network capacity, interference reduction, transmit-power consumption, and QoS, the proposed hybrid Q-learning power allocation framework provides a robust, adaptive mechanism to significantly improve resource utilization and overall network performance in ultra-dense 5G and B5G Het-HetNets. Ultimately, this intelligent approach ensures sustainable and highly efficient connectivity for future wireless communication systems.

2. METHODOLOGY

A 3GPP-compliant MATLAB simulation models a multi-tier Het-HetNet to execute iterative Q-learning loops and collect performance metrics. Custom reinforcement learning scripts then analyze this data to evaluate the convergence and effectiveness of the proposed hybrid Q-learning power allocation framework.

2.1 Het-HetNet Architecture

The proposed system is based on a multi-tier 5G Het-HetNet architecture incorporating both LTE and 5G-NR technologies as depicted in Figure 1.

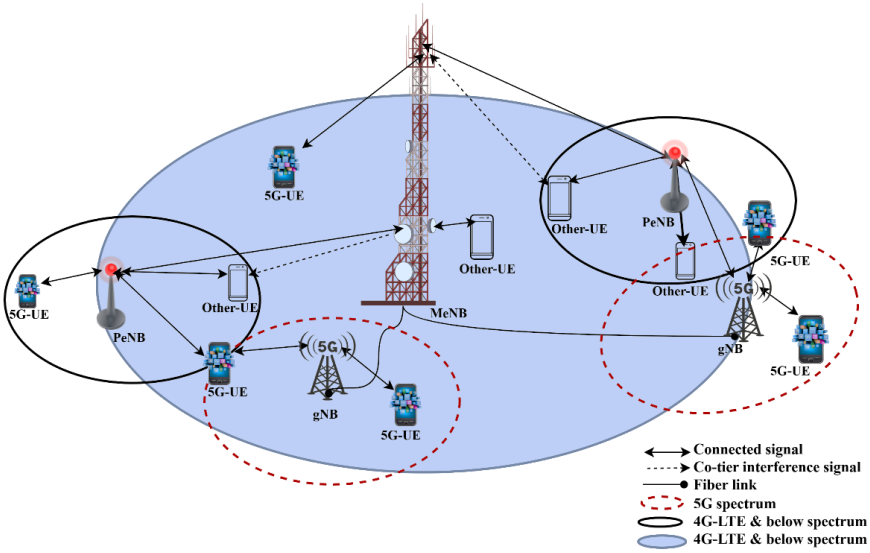

Figure 1: Proposed Multi-tier 5G Het-HetNet architecture

The network simulation includes the parameters listed in Table 1.

Table 1: *Simulation parameters*

Network Component	Quantity
Macro evolved NodeB (MeNB)	1
Pico evolved NodeBs (PeNBs)	16
5G Next Generation NodeB (gNB)	1
MeNB User Equipment	1
Other/small-cell UEs	16

The MeNB provides wide-area coverage and operates at 2 GHz, while the small-cell layer operates at 3.5 GHz. The PeNBs are uniformly deployed within the MeNB coverage region to improve localized capacity and offload traffic. The model assumes shared spectrum operation and universal frequency reuse. Perfect Channel State Information is assumed to be available, and users remain stationary during each Q-learning episode.

2.2 Communication Scenarios

Two interference scenarios are evaluated: (1) a high-interference scenario characterized by strong cross-tier and co-tier interference, and (2) a low-interference scenario with relatively reduced interference levels. In addition, a separate dense-deployment experiment is conducted to assess scalability under very high network density. No third or intermediate-interference scenario is evaluated or presented as a separate result.

2.3 Q-Learning Formulation

Each PeNB is treated as an autonomous reinforcement-learning agent. The agent observes the network environment, selects a transmit-power action, receives a reward, and updates its Q-value. The Q-learning model can be represented by:

$$\mathcal{M} = (S, A, R, Q) \tag{1}$$

where (S) is the state space, (A) is the action space, (R) is the reward function, and (Q) is the Q-value table.

A. STATE SPACE

The network state is represented using the prevailing interference level and QoS conditions of the served users:

$$S = (I, C_{5G-UE,} C_{other-UE}) \tag{2}$$

where I denotes the observed interference level, C_{5G-UE} denotes the QoS status of the 5G-UE, and $C_{other-UE}$ denotes the QoS status of other UEs. The 5G-UE QoS requirement is satisfied when normalized capacity reaches at least **1 bit/s/Hz**, while the corresponding requirement for other UEs is **0.5 bit/s/Hz**.

B. ACTION SPACE

The agent selects a discrete transmit-power level for the corresponding PeNB. The proposed framework uses **32 discrete power actions**, uniformly distributed between **−15 dBm and +15 dBm**, giving an approximate power step of **0.968 dBm**. Thus,

$$A = \{P_1, P_2, \dots, P_{32}\} \tag{3}$$

This discretization provides a practical balance between power-control granularity and Q-table complexity.

C. HYBRID REWARD FUNCTION

The proposed reward function combines four objectives:

$$r_h = w_1 C_{tot} - w_2 I - w_3 P_i + w_4 Q \tag{4}$$

where C_{tot} is aggregate normalized network capacity, I is aggregate interference, P_i is PeNB transmit power, and (Q) represents the QoS reward. The w_i $(i = 1,2,3, \dots)$ parameters control the relative importance of the objectives. The reward weights used in the simulations are w1=0.50w_1=0.50, w2=0.30w_2=0.30, and w3=0.20w_3=0.20 for capacity, interference, and energy, respectively. QoS is incorporated separately through a ±0.10 bonus/penalty rather than as w4w_4. These weights are fixed empirically, while α, γ, and ε are optimized through sequential grid-search tuning. The reward therefore encourages the agent to maximize network capacity; reduce co-tier interference; reduce cross-tier interference; minimize unnecessary transmit power; maintain QoS; and improve overall network performance. The QoS component provides a positive reward when both the 5G-UE and other-UE requirements are satisfied and a penalty when either requirement is violated.

D. Q-VALUE UPDATE

The learning process is based on the Bellman principle. The standard Q-learning update is expressed as:

$$Q(s,a) \leftarrow Q(s,a) + \alpha \left[R + \gamma \max_{a'} Q(s', a') - Q(s,a) \right] \tag{5}$$

Where the learning rate α determines the extent to which newly received reward information modifies the current Q-value. In the proposed hybrid Q-learning power allocation model, α\alpha is explicitly incorporated into the Bellman Q-learning update, ensuring consistent learning and gradual adaptation of the power-allocation policy.

E. E-GREEDY POLICY

An ε-greedy policy is adopted to balance exploration and exploitation. The agent selects a random action during exploration and selects the action with the highest Q-value during exploitation. The study uses an exploration probability of approximately 0.1, corresponding to 10% exploration and 90% exploitation. The proposed hybrid Q-learning power allocation framework employs an ε-greedy action selection policy. Under this strategy, the agent selects a random action with probability ε and selects the action with the highest Q-value with probability $(1 - \varepsilon)$. The ε-greedy action selection policy is expressed as

$$a = \begin{cases} Random\ Action, & if\ rand < \varepsilon \\ arg \max_{a \epsilon A} Q(s,a), & otherwise \end{cases}$$

3. RESULTS AND DISCUSSION

In this section, we will provide a detailed presentation of the findings, using a series of visually engaging figures and an informative table that summarize the overall improvements observed. This display aims to clearly illustrate the progress made, allowing for a deeper understanding of the results.

3.1 Q-Learning Convergence

The learned Q-values demonstrate that the Q-learning agent successfully distinguishes between favourable and unfavourable transmit-power actions. High Q-values correspond to state-action combinations that produce improved network performance, while low Q-values correspond to less desirable power decisions.

The learned policy heatmap further illustrates that the algorithm does not rely on a single fixed transmit-power level across all network conditions. Instead, varying network states lead to distinct preferred power levels, highlighting the adaptive nature of the proposed approach.

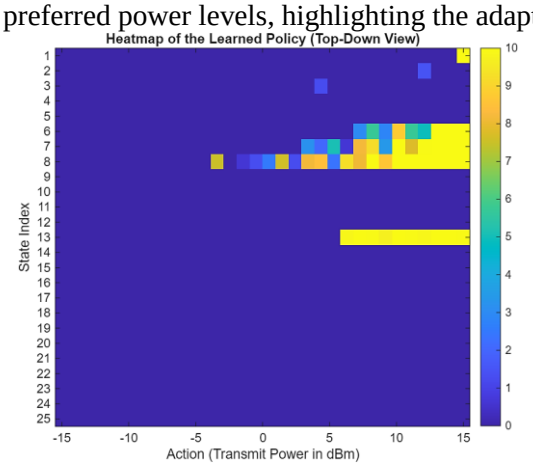

Figure 2: *Heatmap of the transmit-power policy based on the trained Q-table.*

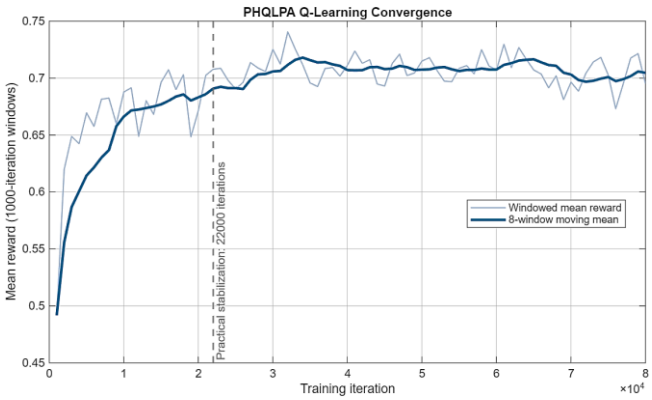

Figure 3: *Q-learning Convergence*

The convergence analysis reveals a swift increase in average reward during the initial learning phase, followed by stabilization with relatively minor fluctuations. The Q-learning process converges within 80,000 iterations, suggesting that the chosen learning configuration yields a stable policy for the simulated Het-HetNet environment.

3.2 5G-UE Capacity under High and Low Interference Conditions

Under Scenario 1, increasing the number of PeNBs increases the level of interference and consequently reduces user capacity for all evaluated approaches. However, the proposed hybrid Q-learning power allocation framework exhibits a more gradual reduction in capacity. The hybrid Q-learning power allocation approach maintains 5G-UE capacity above the specified minimum QoS threshold throughout the evaluated deployment range. By dynamically adjusting PeNB transmit power, the learning agent avoids unnecessarily high transmission power that would otherwise increase interference.

Compared with the benchmark approaches of Iqbal et al. (2021) and Amiri et al. (2019) the proposed framework demonstrates improved stability as network density increases. Under Scenario 2, the lower interference level allows all evaluated approaches to achieve higher user capacity. The proposed hybrid Q-learning power allocation framework consistently produces the highest capacity across the evaluated PeNB deployment range.

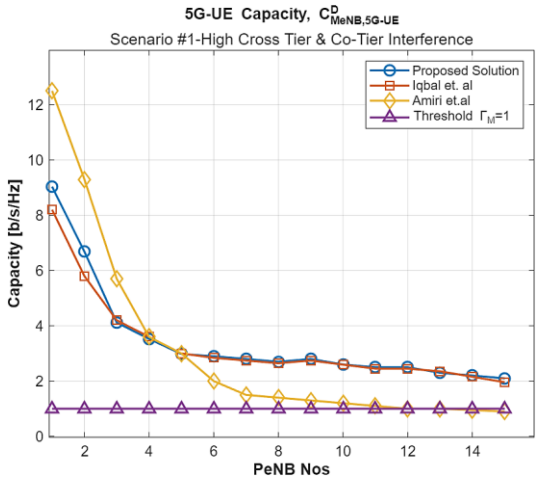

Figure 4. *Capacity of the 5G-UE under Scenario 1 (High Cross-Tier and Co-Tier Interference).*

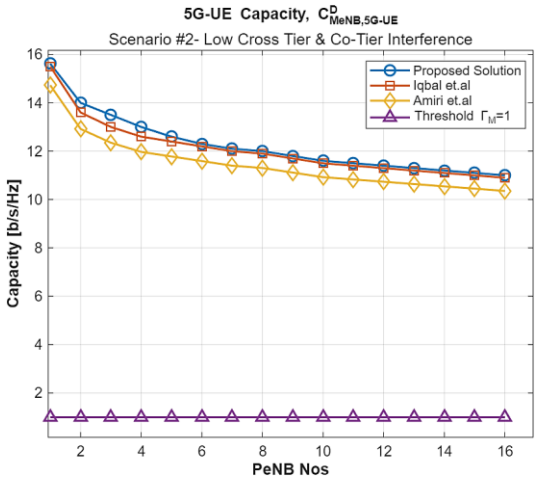

Figure 5. *Capacity of the 5G-UE under Scenario 2 (Low Cross-Tier and Co-Tier Interference).*

While capacity gradually decreases as PeNB density increases, the decline remains relatively moderate for hybrid Q-learning power allocation This indicates that the adaptive power-control mechanism is able to compensate for additional interference generated by network densification. The results also show that all evaluated methods remain above the minimum QoS threshold under the relatively favourable interference conditions. Amiri et al. also provides a comparative benchmark for the evaluated scenarios. Under low-interference conditions, HQLPA maintains the highest capacity as network density increases, while Amiri et al. shows a declining trend. Under intermediate-interference conditions, Amiri et al. is initially competitive and slightly outperforms HQLPA, but its performance decreases with increasing PeNB density, whereas HQLPA maintains a more stable capacity trend.

3.3 Performance under Very High Network Density

The dense-deployment experiment evaluates the proposed method under very high co-tier and cross-tier interference. Increasing PeNB density naturally reduces capacity because of accumulated interference. But hybrid Q-learning power allocation maintains substantially higher capacity than the Iqbal et al. benchmark throughout the deployment range.

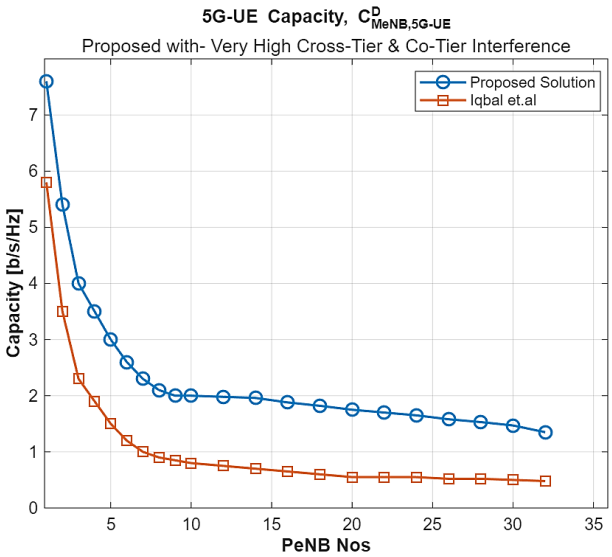

Figure 6: *Capacity Performance of the Proposed Hybrid Q-Learning Power Allocation Framework Under Very High Cross-Tier and Co-Tier Interference Conditions.*

The benchmark capacity declines more rapidly with increasing network density, whereas hybrid Q-learning power allocation exhibits relatively stable communication performance. This observation

indicates that adaptive power control can improve the scalability of interference management in ultra-dense Het-HetNets.

3.4 Quantitative Improvement

The improvement in the overall simulation results is shown in Table 2.

Table 2: *Summary of results improvement*

Performance Indicator	Reported Improvement
Average 5G-UE capacity	**3.37%**
Minimum capacity of small-cell users	**14.81%**
Q-learning convergence	**80,000 iterations**
5G-UE QoS	Maintained above minimum threshold
Adaptability	Improved under increasing interference
Scalability	Improved under dense deployment

The reported average 3.37% improvement in 5G-UE capacity and 14.81% improvement in minimum small-cell-user capacity demonstrate the advantage of adaptive power control over the benchmark approach. The larger improvement in minimum small-cell capacity is particularly important because it suggests that the proposed method does not merely maximize aggregate performance but also helps protect users experiencing relatively poor communication conditions.

4. CONCLUSION

This paper presents a Q-learning-based model for interference management within an adaptive RRM framework, focusing on dynamic transmit-power optimization for PeNBs in ultra-dense 5G and beyond-5G Het-HetNets. The hybrid Q-learning power allocation framework formulates transmit-power control as a reinforcement learning challenge, where each PeNB observes network conditions, selects a power level, receives a hybrid reward, and updates its Q-table using the Bellman learning mechanism. The model effectively incorporates factors such as network capacity, interference, power consumption, and QoS into the learning process. A multi-tier Het-HetNet, including one MeNB, one gNB, and sixteen PeNBs, was evaluated under various interference scenarios. The results indicate that the Q-learning agent successfully learns an adaptive transmit-power policy, achieving convergence within 80,000 iterations. Hybrid Q-learning power allocation consistently outperforms benchmark approaches, demonstrating higher and more stable capacity for 5G-UE, with improvements of 3.37% in overall 5G-UE capacity and 14.81% in minimum capacity for small-cell users. This Q-learning approach illustrates a robust solution for interference management and RRM in densely populated wireless networks, providing significant advantages over fixed and semi-static resource allocation techniques. Despite its promising performance, the proposed hybrid Q-learning power allocation model has some limitations. The simulations assume perfect channel state information (CSI) and stationary users, which may not fully represent practical 5G/B5G deployment conditions. Future work will therefore consider imperfect CSI, user mobility, and more dynamic network conditions to further validate the robustness and practical applicability of hybrid Q-learning power allocation.

5. REFERENCES

Abbass, W., Hussain, R., Frnda, J., Abbas, N., Javed, M. A., & Malik, S. A. (2022). Resource Allocation in Spectrum Access System Using Multi-Objective Optimization Methods. *Sensors*, *22*(4), 1–24. https://doi.org/10.3390/s22041318

Amiri, R., Almasi, M. A., Andrews, J. G., & Mehrpouyan, H. (2019). Reinforcement learning for self-organization and power control of two-tier heterogeneous networks. *IEEE Transactions on Wireless Communications*, *18*(8), 3933–3947. https://doi.org/10.1109/TWC.2019.2919611

Iqbal, M. U., Ansari, E. A., & Akhtar, S. (2021). Interference mitigation in hetnets to improve the QoS

using q-learning. *IEEE Access*, *9*, 32405–32424. https://doi.org/10.1109/ACCESS.2021.3060480

Iqbal, M. U., Ansari, E. A., Akhtar, S., Rafiq, M. N., Farooq-i-Azam, M., & Hassan, B. (2023). Hybrid Learning based Radio Resource Management in 5G Heterogeneous Networks. *Pakistan Journal of Engineering and Technology*, *6*(1), 92–97. https://doi.org/10.51846/vol6iss1pp92-97

Luong, N. C., Wang, P., Niyato, D., Liang, Y. C., Han, Z., & Hou, F. (2019). Applications of Economic and Pricing Models for Resource Management in 5G Wireless Networks: A Survey. *IEEE Communications Surveys and Tutorials*, *21*(4), 3298–3339. https://doi.org/10.1109/COMST.2018.2870996

Shabbir, A., Rizvi, S., Shirazi, M. F., Alam, M. M., & Su'ud, M. M. (2024). Maximizing energy efficiency in HetNets through centralized and distributed sleep strategies under QoS constraint. *Scientific Reports*, *14*(1), 25839. https://doi.org/10.1038/s41598-024-70714-x

Yadav, I., Chaporkar, P., Jha, P., & Karandikar, A. (2021). Spectrum Allocation in IAB Networks: A Hierarchical Auction-based Approach. *IEEE Vehicular Technology Conference*, *2021-Septe*. https://doi.org/10.1109/VTC2021-Fall52928.2021.9625522

International Conference on Engineering Innovation for Sustainable Development (ICESID 2026)
Faculty of Engineering, Ahmadu Bello University Zaria · 8–10 September 2026

IMPROVED CLUSTERING AND ROUTING APPROACH FOR HOTSPOT MITIGATION IN WIRELESS SENSOR NETWORKS USING LOAD-AWARE CLUSTER-HEAD SELECTION

Samson Bitrus Visa[1], Abdulqadir Mahmudu Jada[2], Aliyu Muhammad Isa[3], Yohanna Ali Mshelia[1,*], Okehie M. Baslem[4], Adamu Muhammad[5]

[1]*Ahmadu Bello University, Zaria*
[2]*Department of Electrical and Electronics Engineering Technology, Adamawa State Polytechnic, Yola, Nigeria*
[3]*Department of Electrical and Electronics Engineering Nigerian Biu Borno State*
[4]*Department of Engineering and Space System National Space Research and Development Agency (NASRDA), Abuja, Nigeria*
[5]*Department of Electrical and Electronics Engineering, Federal Polytechnic, Daura, Nigeria*

Email: samsonbitrusvisa@gmail.com, mabduljada@gmail.com, amuhammadisa6775@gmail.com, yalimshelia@gmail.com*, baslem.okehie@nasrda.gov.ng, adamumuhammadahm@gmail.com

***Corresponding author**: Yohanna Ali Mshelia

DOI: https://doi.org/10.67203/sp.ICESID.2026

ABSTRACT

Wireless Sensor Networks (WSNs) are susceptible to hotspot formation caused by uneven traffic distribution and excessive forwarding responsibilities on selected sensor nodes. This paper presents an Improved Clustering Approach to Mitigate Hotspots (ICAMHS), developed as an enhancement of the Cluster-Based Genetic Routing Protocol (CGRP). ICAMHS integrates K-means clustering, energy- and distance-aware cluster-head selection, traffic-load consideration, an improved routing fitness function, and fault-tolerant route recovery. The proposed approach was evaluated against CGRP using two performance metrics: decoding probability for a 1000-node network and end-to-end latency. At a decoding rate of 1.5, ICAMHS achieved a decoding probability of 0.35, compared with 0.10 for CGRP, representing a 250% relative improvement. At a decoding rate of 3.0, ICAMHS achieved 1.00 compared with 0.98 for CGRP, representing a 2.04% relative improvement. For latency, ICAMHS achieved 998 ms at 1000 nodes compared with 1000 ms for CGRP, representing a 0.20% reduction. The results indicate that ICAMHS improves decoding performance while maintaining comparable latency under the evaluated simulation conditions. The evaluation is limited to decoding probability and latency; energy consumption, network lifetime, scalability, computational overhead, and repeated-run statistical analysis are left for future work.

Keywords: *Wireless Sensor Networks; hotspot mitigation; ICAMHS; clustering; CH selection*

1. INTRODUCTION

Wireless Sensor Networks (WSNs) consist of distributed sensor nodes that collect environmental information and transmit data to a base station (BS). They are widely used in monitoring and automation applications. However, limited energy and communication resources make efficient clustering and routing essential for reliable operation (Patil & Kohle, 2024).

A major challenge in clustered WSNs is hotspot formation, where some nodes experience disproportionately high communication and forwarding loads. CHs close to the BS may aggregate their own data while relaying traffic from other clusters, resulting in increased communication burden and faster resource depletion (Lonkar et al., 2026). Clustering reduces communication overhead by grouping nodes under CHs, which collect, aggregate, and forward data to the BS. Genetic Algorithms (GAs) have also been applied to WSN routing to optimise routing configurations based on predefined fitness criteria (Khalaf et al., 2022).

CGRP combines clustering with GA-based route optimisation to improve routing performance (Patil & Kohle, 2024). However, its CH selection may not sufficiently consider existing traffic loads, potentially increasing hotspot formation. To address this limitation, this study proposes ICAMHS,

which extends CGRP through traffic-aware CH selection, improved routing fitness, and fault-tolerant route recovery. The evaluation is limited to decoding probability for N=1000 and latency under identical simulation conditions. The proposed approach is also relevant to the conference theme of Nigeria's Growth for Sustainable Development because reliable WSNs can support distributed sensing applications such as rural environmental monitoring, agricultural monitoring, and infrastructure condition monitoring. Reducing hotspot formation can improve the reliability and operational efficiency of such sensing systems, aligning the work with the Intelligent Systems, Automation and Control Engineering sub-theme.

2. RELATED WORK

Recent studies have addressed hotspot formation and energy imbalance in WSNs through intelligent clustering, load balancing, and adaptive routing. These approaches have reported improvements in energy efficiency, network lifetime, routing performance, and CH selection. However, computational complexity, scalability, dynamic adaptation, and balanced traffic distribution remain areas requiring further investigation.

Table 1: Summary of Recent Clustering and Routing Approaches in WSNs

Study	Approach	Main Contribution	Limitation / Gap
Somula et al. (2024)	Osprey optimization-based CH selection	Improves packet delivery and network lifetime through optimized CH selection	Limited adaptaton to dense and heterogeneous networks
Mabunga and Dela Cruz (2024)	Wild Geese Optimization-based clustering and routing	Optimizes CH selection and routing using multiple network parameters	Computational cost and scalability require further consideration
Patil and Kohle (2024)	Cluster-Based Genetic Routing Protocol (CGRP)	Combines clustering, energy/distance-based CH selection, and GA-based routing optimization	Limited consideration of traffic-load concentration and hotspot-aware CH selection
Soltani et al. (2025)	Multi-agent reinforcement-learning routing	Adapts routing using energy, hop count, hotspot proximity, and neighbourhood information	Re-clustering overhead and CH depletion remain challenges
Prince et al. (2025)	Multilevel clustering and prediction-based routing	Uses clustering and prediction to reduce hotspot effects	Centralized clustering and CH-management overhead remain concerns
Peter et al. (2026)	Density-aware clustering with Voronoi partitioning	Addresses dense WSNs using density, link quality, and dynamic reclustering	Computational complexity, delay, and implementation cost remain concerns
Ramesh et al. (2026)	Hybrid ML-based CH selection and routing	Integrates machine learning and optimization to improve network lifetime	Integrated adaptive clustering and routing may increase computational complexity
Baslem et al. (2026)	Hotspot-aware load-balanced clustering and routing	Combines energy-aware clustering, load balancing, and fault-tolerant routing	Computational cost and real-world deployment require further evaluation
Proposed ICAMHS	K-means and load-aware CH selection with improved routing fitness	Combines energy, distance, traffic load, energy-balanced routing, and fault-tolerant recovery	Further evaluation of energy consumption, network lifetime, scalability, and computational overhead is required

The reviewed studies demonstrate that energy-aware clustering, intelligent CH selection, load balancing, and adaptive routing can improve WSN performance. However, the integration of traffic-aware CH selection, energy-balanced routing, and fault-tolerant recovery remains insufficiently addressed. In particular, CGRP primarily considers residual energy and distance in CH selection, leaving traffic-load concentration insufficiently addressed (Patil & Kohle, 2024). Therefore, ICAMHS extends CGRP by incorporating traffic load into CH selection, an energy-imbalance factor into routing fitness, and fault-tolerant route recovery. The comparison in Table 1 also highlights differences in the mechanisms used to address hotspot formation. Somula et al. (2024) focus on optimisation-based CH selection and report gains in packet delivery and network lifetime, but their approach has limited adaptation to dense and heterogeneous networks. Mabunga and Dela Cruz (2024) jointly optimise clustering and routing using multiple network parameters, although computational cost and scalability remain concerns. Soltani et al. (2025) introduce multi-agent reinforcement learning for routing using energy, hop count, hotspot proximity, and neighbourhood information, but re-clustering overhead and CH depletion remain challenges. Peter et al. (2026) address dense WSNs through density, link quality, and dynamic reclustering, while Ramesh et al. (2026) combine machine learning with optimisation for CH selection and routing; both approaches may increase computational complexity. These studies indicate that hotspot mitigation can benefit from adaptive decision-making, but they do not directly combine the specific traffic-aware CH selection, energy-balanced routing fitness, and fault-tolerant recovery used in ICAMHS. ICAMHS therefore targets this combination while retaining a relatively simple K-means-based clustering structure.

3. PROPOSED ICAMHS PROTOCOL

3.1 Network Model

The proposed model assumes a homogeneous sensor network in which sensor nodes are randomly distributed within the network area, the BS remains fixed, and all nodes have equal initial energy. The nodes communicate through cluster heads. K-means clustering is used to partition the network into clusters, after which suitable CHs are selected using energy, distance, and traffic-load information. This homogeneous assumption is consistent with the simulation configuration used in the present study. Although ICAMHS is motivated by hotspot problems also reported in heterogeneous WSNs, its current evaluation does not model heterogeneous initial energies or heterogeneous node capabilities. Consequently, applicability to heterogeneous WSNs should be regarded as a limitation requiring further validation. The simulation configuration adopted from the source study uses a 1000 m² network area, 50 J initial node energy, 30 m transmission range, 10 m sensing range, 60 kbps bandwidth, 50 packets/s transmission rate, 1000-bit data packets, and a 200-time-unit operating period (Patil & Kohle, 2024).

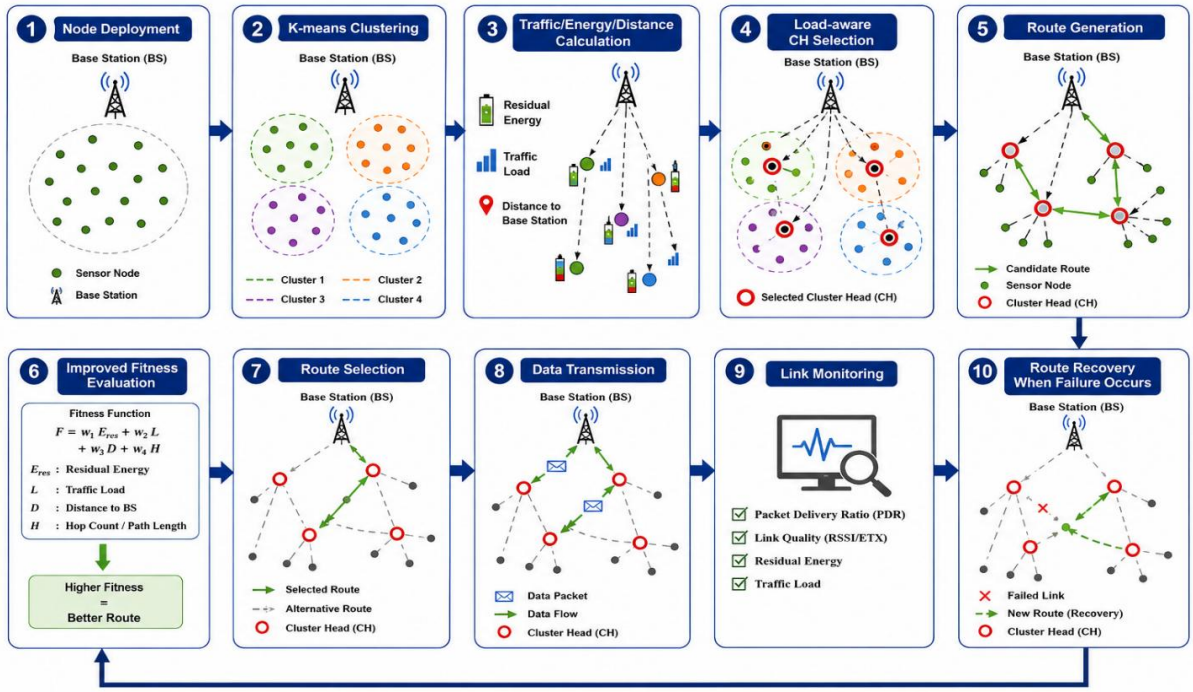

Figure 1: Conceptual Architecture of the Proposed ICAMHS Protocol

Figure 1 summarises the ten operational steps of ICAMHS. First, sensor nodes are deployed around a fixed base station (BS). Second, K-means clustering partitions the nodes according to their spatial positions. Third, residual energy, traffic load, and distance information are calculated for candidate CHs. Fourth, the load-aware CH-selection metric combines these factors to select a CH for each cluster. Fifth, candidate routes are generated between CHs and the BS. Sixth, the improved fitness function evaluates candidate routes using energy balance and routing-related criteria. Seventh, the route with the highest fitness is selected. Eighth, sensed data are transmitted along the selected route. Ninth, links are monitored using packet delivery ratio (PDR), link quality represented by RSSI/ETX, residual energy, and traffic load. Tenth, when a link becomes unacceptable, the failed link is detected and an alternative route is established through the fault-tolerant recovery mechanism.

3.2 Enhanced Cluster Formation

ICAMHS employs the K-means algorithm to group sensor nodes according to their spatial positions. For each cluster, the cluster centre is calculated as the arithmetic mean of the coordinates of all nodes assigned to that cluster. The cluster centre is given by (Guo et al., 2025).

$$C_j = \left(\frac{1}{n_j} \sum_{i=1}^{n_j} x_{i,} \ \frac{1}{n_j} \sum_{i=1}^{n_j} y_i \right) \tag{1}$$

Where (C_j) represent the centre of cluster (j), (n_j) is the number of sensor nodes belonging to cluster (j), and (x_i) and (y_i) are the x- and y-coordinates of node (i).

The K-means clustering objective can additionally be expressed as

$$J = \sum_{j=1}^{k} \sum\nolimits_{\mathrm{i} \in C_j} \| \ X_i = C_j \ \|^2 \tag{2}$$

where K is the number of clusters, $X_i = (x_i, y_i)$ is the position vector of node i, and (C_j) is the centre of cluster j.

The objective of K-means is to minimise the total squared Euclidean distance between sensor nodes and their corresponding cluster centres. This arrangement reduces unnecessary communication distances and provides a spatial basis for subsequent CH selection.

3.3 Load-Aware Cluster-Head Selection

The principal modification introduced by ICAMHS is the incorporation of traffic load into CH selection. Conventional CH selection based primarily on residual energy and distance may repeatedly assign CH responsibilities to nodes that already carry substantial communication traffic. To address this limitation, ICAMHS introduces a load-balancing factor defined as (Baslem et al., 2026)

$$L_b = \frac{1}{1 + \alpha T_i} \tag{3}$$

Where (T_i) represents the traffic load handled by node (i), and (α) is a positive tuning parameter that controls the influence of traffic load on CH selection.

The inverse formulation ensures that the load factor decreases as the traffic handled by a node increases. Thus, a node carrying a high traffic load receives a lower preference for additional CH responsibilities.

A normalized distance factor can be defined as (Mabunga & Dela Cruz, 2024)

$$D_i = 1 - \frac{d_{iC_j}}{d_{max}} \tag{4}$$

where $d_{iC_j}$is the Euclidean distance between node i and the centre of cluster j, while d_{max} is the maximum reference distance used for normalization.

The residual-energy factor is expressed as

$$E_i = \frac{E_i^{res}}{E_{max}} \tag{5}$$

where E_i^{res} is the residual energy of node i, and E_{max} is the maximum or initial node energy.

The three factors can then be combined into the proposed CH-selection metric:

$$CH_i = w_E \, E_i + w_D \, D_i + w_L \, L_i \tag{6}$$

$$\text{Subject to} \quad w_E + w_D + w_L \ = 1 \tag{7}$$

where $w_E . w_D$ and w_L are the weighting coefficients assigned to residual energy, distance, and traffic load, respectively.

The cluster-head node is selected according to

$$CH_i^* = arg \max_{i \in C_j} CH_i \tag{8}$$

where CH_i^* represents the selected CH for cluster j.

This formulation gives preference to nodes with higher residual energy, shorter distance to the cluster centre, and lower traffic load. Consequently, CH responsibilities can be distributed more evenly across the network, thereby reducing the likelihood of hotspot formation.

3.4 Improved Fitness Function

The improved fitness function introduces an energy-imbalance penalty based on the maximum energy consumed by nodes participating in a candidate route. A suitable formulation is to first calculate the energy consumed by node i during a routing operation as (Guo et al., 2025)

$$E_i^{cons} = E_i^{init} - E_i^{res} \tag{9}$$

where E_i^{init} and E_i^{res} denote the initial and residual energy of node i, respectively.

The maximum energy consumption among nodes participating in a candidate route is then

$$E_{max}^{cons} = \max_{i \in R} E_i^{cons} \tag{10}$$

where R represents the set of nodes participating in the candidate routing solution.

A normalized energy-imbalance penalty can be expressed as

$$P_E = \frac{E_{max}^{cons}}{\sum_{\in \mathbf{R}} E_i^{cons} + \varepsilon} \tag{11}$$

where ε is a small positive constant introduced to avoid division by zero.

The improved ICAMHS fitness function can then be represented generally as (Patil & Kohle, 2024)

$$F_{ICAMHS} = F_{CGRP} - \lambda_E \, P_E \tag{12}$$

where F_{CGRP} is the original CGRP fitness value, PE is the maximum-energy-consumption penalty, and λE controls the influence of the energy-imbalance penalty.

ICAMHS modifies the original CGRP fitness function by incorporating an energy-imbalance penalty based on the maximum energy consumed by participating nodes. The purpose of this penalty is to discourage routing solutions that concentrate excessive communication responsibilities on a small number of nodes. Therefore, the GA is encouraged to select routing configurations that provide a more balanced distribution of energy consumption and reduce the likelihood of hotspot formation.

3.5 Fault-Tolerant Routing

Q_{IJ} Link quality Q_ij is used as a general link-quality measure in the fault-detection condition; RSSI is therefore treated as one possible measurement contributing to Q_ij rather than as a separate variable in the link-failure equation. A link-failure indicator between node i and neighbouring node j is defined as

$$F_{ij} = \begin{cases} 1. & Q_{IJ} < Q_{th} \\ 0, & Q_{IJ} \geq Q_{th} \end{cases} \tag{13}$$

where $F_{ij} = 1$ indicates a failed or unacceptable link, $F_{ij} = 0$ indicates an acceptable link, Q_{IJ} represents the link quality between nodes i and j, and Q_{th} is the minimum acceptable link-quality threshold.

When a link failure is detected, node i broadcasts an LREQ message to its neighbouring nodes. Each responding neighbour provides information regarding its residual energy, distance to the destination, and link quality.

The alternative-next-hop score can be defined as

$$S_i = w_E \frac{E_J}{E_{mx}} + w_D (1 - \frac{d_{\,i}D}{d_{max}}) + w_Q \frac{Q_{iJ}}{Q_{max}} \tag{14}$$

where E_{ires} is the residual energy of neighbouring node j, E_{mx} is the maximum or initial node energy, $d_{\,i}D$ is the distance between node j and the destination D, d_{max} is the maximum reference distance, $Q_{iJ}$is the link quality between nodes i and j, Q_{max} is the maximum reference link-quality value, and wE, wD, and wQ are weighting coefficients.

The alternative next hop is then selected as

$$J^* = arg \max_{i \in N_i} S_{ij} \tag{15}$$

where N_i represents the set of eligible neighbouring nodes of node i, and j∗ is the neighbour with the highest link score.

This mechanism allows ICAMHS to dynamically establish an alternative communication path when the primary route becomes unavailable.

4. SIMULATION SETUP

4.1 Simulation Parameters

The simulation parameters for developing the Improved Clustering Approach to Mitigate Hotspots (ICAMHS) in WSNs are presented in Table 3.1. These values are used to evaluate the performance of the developed model.

Table 2: Simulation parameters and its values

S/N	Parameter	Default Value
1	Transmission range	30 m
2	Sensing Range	10 m
3	Initial Energy	50 J
4	Node deployment	Random
5	Nodes Bandwidth	60kbps
6	Network area	1000 Sq.m
7	Transmission Rate	50 p/s
8	Packet size	1000 bits
9	Simulation duration	200-time units

4.2 Simulation Environment

The ICAMHS model was implemented using MATLAB. The principal simulation parameters were adopted from Patil and Kohle (2024), including a 30 m transmission range, 10 m sensing range, 50 J initial energy, 60 kbps bandwidth, 1000 m² network area, 50 packets/s transmission rate, 1000-bit packet size, and a 200-time-unit operating period. The CGRP baseline was independently re-simulated in MATLAB under the same network assumptions and parameter settings to provide a direct comparison. The node positions, traffic conditions, and simulation parameters were kept identical for ICAMHS and CGRP.

.

5. RESULTS AND DISCUSSION

5.1 Decoding Probability

Figure 2 shows the decoding probability of CGRP and ICAMHS for a network of 1,000 sensor nodes. ICAMHS consistently achieves a higher decoding probability than CGRP across the evaluated decoding rates. The improvement is more pronounced at lower decoding rates and decreases as both protocols approach a decoding probability of 1.00.

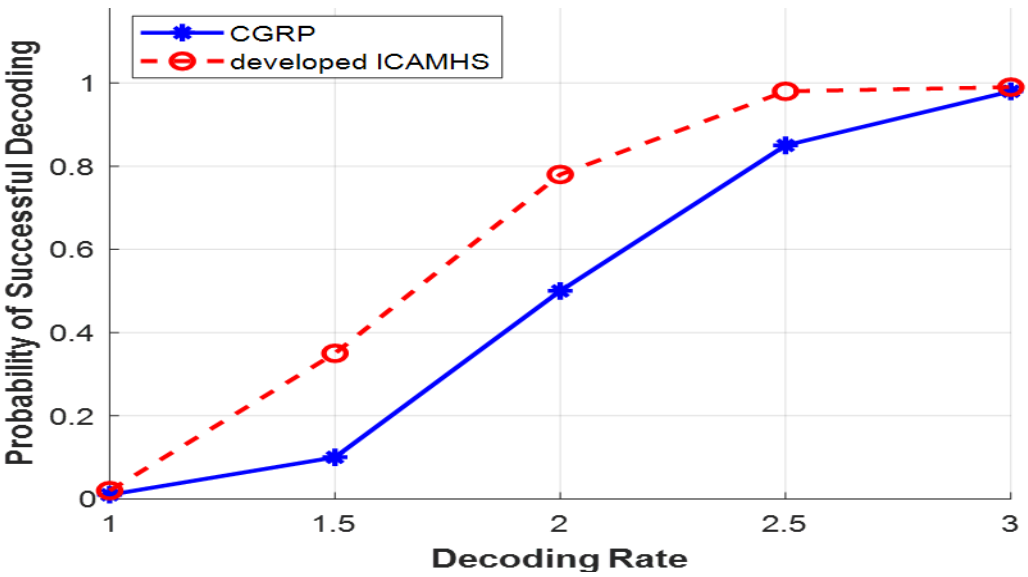

Figure 2: Decoding Probability versus Decoding Rate

At a decoding rate of 1.5, the decoding probability increases from 0.10 for CGRP to 0.35 for ICAMHS, representing a 250% relative improvement. At a decoding rate of 3.0, the improvement is 2.04%. These results indicate that the traffic-aware cluster-head selection and modified routing fitness function improve communication reliability, particularly at lower decoding rates. The numerical results are summarized in Table 3.

Table 3: Decoding Probability Comparison for N=1000

Decoding Rate	CGRP	ICAMHS	Improvement (%)
1.0	0.00	0.00	0.00
1.5	0.10	0.35	250.00
2.0	0.50	0.78	56.00
2.5	0.85	0.98	15.29
3.0	0.98	1.00	2.04

The improved performance can be attributed to the traffic-aware CH-selection mechanism and the modified routing fitness function. By reducing the probability of assigning additional forwarding responsibility to heavily loaded nodes, ICAMHS provides a more balanced communication structure and improves the likelihood of successful data delivery.

5.2 Latency Performance

Figure 3 presents the latency performance as the number of sensor nodes increases. ICAMHS maintains slightly lower latency than CGRP across the evaluated network sizes. The small difference indicates that the additional traffic-aware mechanisms do not introduce a substantial latency penalty under the simulated conditions.

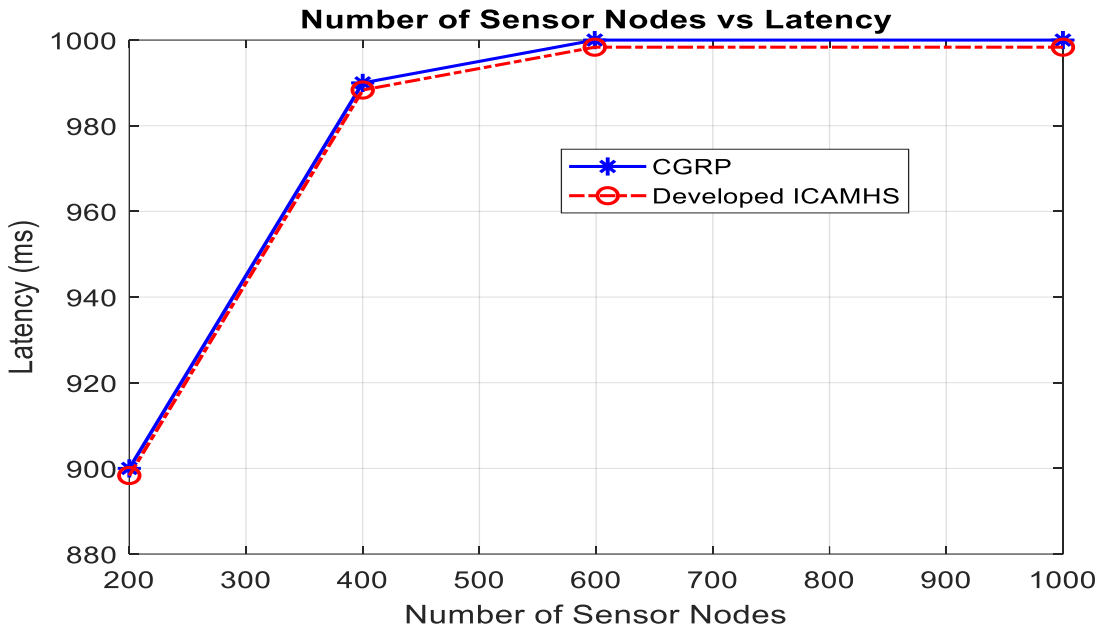

Figure 3: Latency Comparison of CGRP and ICAMHS

At 200 nodes, latency decreases from 900 ms for CGRP to 899 ms for ICAMHS, corresponding to a 0.11% reduction. At 400 nodes, the reduction is 0.20%. For 600–1000 nodes, ICAMHS maintains a latency of 998 ms compared with 1000 ms for CGRP, giving a 0.20% reduction. The detailed results are presented in Table 4.

Table 4: Latency Comparison between CGRP and ICAMHS

Number of Nodes	CGRP (ms)	ICAMHS (ms)	Reduction (%)
200	900	899	0.11
400	990	988	0.20
60	1000	998	0.20
800	1000	998	0.20
1000	1000	998	0.20

The results indicate that the additional processing associated with traffic-aware CH selection and routing optimisation does not produce a substantial latency penalty under the simulated conditions. The main performance advantage of ICAMHS is therefore the improvement in decoding probability rather than a major reduction in latency.

5.3 Comparative Discussion

The two performance metrics provide complementary evidence of ICAMHS performance. ICAMHS achieves higher decoding probability than CGRP across the evaluated decoding rates, with the highest relative improvement of 250.00% at a decoding rate of 1.5. For latency, the improvement is small. At 1000 nodes, ICAMHS reduces latency from 1000 ms to 998 ms, representing a 0.20% reduction. Thus, the main advantage of ICAMHS is improved decoding performance while maintaining comparable latency.

The improved decoding performance is consistent with the load-aware CH-selection strategy, which considers traffic load alongside residual energy and distance. This reduces the likelihood of assigning additional communication responsibilities to heavily loaded nodes. The improved routing fitness further promotes more balanced routing decisions. Overall, ICAMHS improves decoding performance without significantly affecting latency under the evaluated simulation conditions.

6. CONCLUSION

This paper presented ICAMHS, an improved clustering and routing approach for hotspot mitigation in large-scale Wireless Sensor Networks. The approach extends CGRP by incorporating traffic-aware cluster-head selection, an energy-imbalance factor in the routing fitness function, and fault-tolerant route recovery. The evaluation showed that ICAMHS achieved a decoding probability of 0.35 at a decoding rate of 1.5, compared with 0.10 for CGRP, representing a 250.00% relative improvement. At a decoding rate of 3.0, ICAMHS achieved 1.00 compared with 0.98 for CGRP, representing a 2.04% relative improvement. For latency, ICAMHS achieved 998 ms at 1000 nodes compared with 1000 ms for CGRP, representing a 0.20% reduction.

These results indicate that ICAMHS improves decoding performance while maintaining latency comparable to CGRP under the evaluated simulation conditions. The study has several limitations. The evaluation uses a homogeneous network model, considers only decoding probability and latency, and is based on a single simulation run without confidence intervals or statistical significance testing. Energy consumption, network lifetime, scalability beyond the evaluated network sizes, and computational overhead were not quantitatively evaluated. Future work will therefore include repeated simulation trials with statistical analysis, direct evaluation of energy consumption and network lifetime, scalability tests for larger networks, evaluation under heterogeneous node conditions, computational-overhead analysis, and validation using real sensor-network hardware.

REFERENCES

Baslem, O., Ikpaya, I., Chimobi, O., Yohanna, T., & Ojukwu, N. (2026). A hotspot-aware load-balanced clustering and routing protocol for energy-efficient wireless sensor networks. *International Journal of Trend in Scientific Research and Development*.

Guo, H., Zhang, J., & Omidizadeh, H. (2025). Adaptive and scalable energy aware clustering for mobile wireless sensor networks using a density driven approach. *Scientific Reports*.

Kandris, D., Nakas, C., Vomvas, D., & Koulouras, G. (2020). Applications of wireless sensor networks: An up-to-date survey. *Applied System Innovation, 3*(1), 14.

Khalaf, O. I., Romero, C. A. T., Hassan, S., & Iqbal, M. T. (2022). Mitigating hotspot issues in heterogeneous wireless sensor networks. *Journal of Sensors, 2022*, 7909472.

Khalaf, O. I., Romero, C. A. T., Hassan, S., & Iqbal, M. T. (2022). Mitigating hotspot issues in heterogeneous wireless sensor networks. *Journal of Sensors*, *2022*(1), 7909472.

Lonkar, B., Charde, P., Kuthe, A., Dehankar, A., Dandekar, P., Puri, N., & Banabakode, D. (2026). A review of hybrid clustering and routing protocols for the hotspot problem in wireless sensor networks. *Peer-to-Peer Networking and Applications*, *19*(1), 8.

Mabunga, Z. P., & Dela Cruz, J. C. (2024). Chronological wild geese optimization algorithm for cluster head selection and routing in wireless sensor network. *International Journal of Communication Systems*.

Patil, V. B., & Kohle, S. (2024). A high-scalability and low-latency cluster-based routing protocol in time-sensitive WSNs using genetic algorithm. *Measurement: Sensors, 31*, 100941.

Peter, S. S., Jayarajan, P., Maheswar, R., & Maheswaran, S. (2026). *Multi-Factor Cost Function-Based Interference-Aware Clustering with Voronoi Cell Partitioning for Dense WSNs*. Sensors, 26(2), 546.

Prince, B., Kumar, P., & Singh, S. K. (2025). Multi-level clustering and prediction based energy efficient routing protocol to eliminate hotspot problem in wireless sensor networks. *Scientific Reports*.

Ramesh, S. K., Ramesh, B., & Chandrika, J. (2026). An energy-aware cluster-head selection for improving network lifetime in wireless sensor networks using machine learning techniques. *Engineering, Technology & Applied Science Research*.

Soltani, P., Eskandarpour, M., Ahmadizad, A., & Soleimani, H. (2025). Energy-efficient routing algorithm for wireless sensor networks: A multi-agent reinforcement learning approach. *arXiv*.

Somula, R., Cho, Y., & Mohanta, B. K. (2024). SWARAM: Osprey optimization algorithm-based energy-efficient cluster head selection for wireless sensor network-based Internet of Things. *Sensors*.

Wang, Z., Zeng, W., Yang, S., He, D., & Chan, S. (2024). UCRTD: An unequally clustered routing protocol based on multi-hop threshold distance for wireless sensor networks. *IEEE Internet of Things Journal*.

International Conference on Engineering Innovation for Sustainable Development (ICESID 2026)
Faculty of Engineering, Ahmadu Bello University Zaria · 8–10 September 2026

INTERFERENCE MITIGATION OF UNDERLAY SECONDARY USERS USING INTERFERENCE ALIGNMENT

Isiyaku Yau[1,*], Mohammed Dikko Amustapha[1], Shamsuddeen Abdullahi Mika'il[1], Joshua David[2], Usman Yau[1], Nafiu Murtala Kamaluddeen[1]

[1]*Ahmadu Bello University, Zaria*
[2]*Department of Electrical/Electronics Engineering Kogi State Polytechnic Lokoja*

Email: ishaaqyau@gmail.com*, md.almustapha@gmail.com, shamsudeenmikail@yahoo.com, omokoredavid117@gmail.com, usmanyau7@gmail.com, nafiumurtala58@gmail.com

***Corresponding author**: Isiyaku Yau

DOI: https://doi.org/10.67203/sp.ICESID.2026

ABSTRACT

As the number of wireless devices and services grows exponentially, the Radio Frequency (RF) spectrum is becoming increasingly a scarce resource. Again, the current fixed spectrum-licensing policy has made the RF spectrum underutilized. Cognitive Radio (CR) seeks to provide solution to address the imbalance between spectrum scarcity and spectrum underutilisation by allowing cognitive users, called Secondary Users (SUs), to share the spectrum with the licensed users called Primary Users (PUs) in a manner that the PUs do not suffer harmful interference. This work is aimed at mitigating underlay cognitive intra-network interference with a view to enhancing the effective sum capacity of the SUs. The PU is protected through Interference Temperature (IT) model. Interference Alignment (IA) scheme under the IT constraints is developed for mitigating the mutual interference among the SUs. A closed form expression for the sum capacity of three-user underlay cognitive channel is derived. Applying the ergodic IA with IT constraints enhances the sum capacity of the SUs thereby achieving 23.54% and 24.77% gain in the channel sum capacity under maximum and average IT limits respectively. This gain is with respect to time-division scheme at signal-to-noise-ratio of 19dB. By utilizing the long delay time associated with ergodic IA to send more bits in time-division scheme, 3.0094 bps/Hz and 3.1741 bps/Hz gains in spectral efficiency were achieved under maximum and average IT limits over a full time-division scheme at SNR of 19dB.

Keywords: *Cognitive Radio; Interference Alignment; Underlay; Spectral Efficiency; SNR*

1. INTRODUCTION

The rapid growth of wireless broadband, multimedia, mobile computing, and emerging wireless services has resulted in an increasing demand for radio-frequency spectrum. At the same time, conventional fixed spectrum allocation has resulted in significant underutilization of portions of the licensed spectrum. Out of the imbalance between scarcity of preferred spectrum and underutilisation was born the idea of Cognitive Radio (CR) to improve spectrum utilization (Mitola, 2009). CR uses advanced radio and signal processing technology along with novel spectrum allocation policies to share the spectrum as a Secondary User (SU) in a manner that the Primary (licensed) Users (PUs) are as unaffected as possible. CR provides a means of improving spectrum utilization by allowing unlicensed or SUs to opportunistically access spectrum assigned to PUs, subject to appropriate interference constraints (Xu *et. al.*, 2025).

Three principal spectrum-sharing paradigms are commonly considered in cognitive radio networks: interweave, overlay, and underlay as illustrated in figure 1.

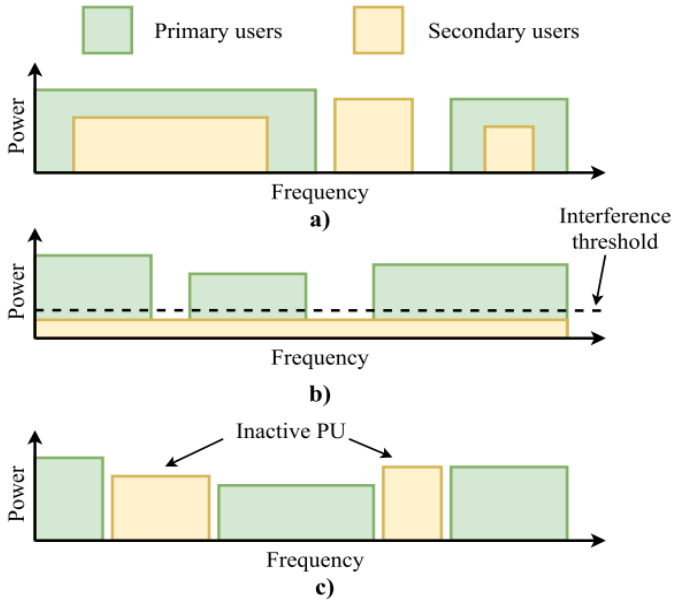

Figure 1: Spectrum sharing in CR. a) overlay, b) underlay, c) interweave (Briones *et. al.*, 2020)

In the underlay paradigm, an SU is allowed to transmit concurrently with a PU provided that the interference received by the PU remains below a prescribed threshold. The interference-temperature (IT) concept provides a convenient means of specifying this interference constraint (Yau *et. al.*, 2025).

Although the underlay approach allows simultaneous transmission, the requirement to protect the PU imposes a restriction on the transmit power of the SUs. The problem becomes significant when multiple SUs share the spectrum. In addition to SU-to-PU interference, there is mutual SU-to-SU interference. Consequently, a reduction in SU transmit power does not by itself solve the interference problem; rather, the mutual interference may become a dominant limitation on the achievable secondary-network capacity (Yang, *et. al*., 2024).

Interference Alignment (IA) is a transmission strategy that combines transmitter precoding and receiver interference suppression to achieve optimal network degrees of freedom. The idea of IA has challenged most of conventional wisdom about the sum capacity limit of wireless channels (Abdulkadir *et. al.*, 2024). IA is an interference-management technique that exploits the dimensions of a time-varying interference channel to arrange interfering signals in a manner that permits their suppression at the intended receivers. Ergodic Interference Alignment (EIA) uses appropriately selected channel realizations to align and cancel interfering signals. The work of Yau *et. al.*, (2025) evaluated the ergodic capacity of multiple underlay cognitive users under maximum interference constraints. This paper investigates interference mitigation of multiple underlay SUs using ergodic interference alignment under interference-temperature constraints with the following novel contributions:

i. Modelling the interference in a 3-SU underlay cognitive-radio in the presence of a single PU.
ii. Incorporating EIA is into the underlay system for mitigating interference among the SUs while satisfying both maximum and average IT constraints.
iii. Obtaining a closed-form sum-capacity expressions for the three-user system.
iv. Evaluating the performance of EIA against an equal time-division benchmark
v. Utilizing the EIA to send delay insensitive bits for significant spectral efficiency gains.

2. METHODOLOGY

A spectrum sharing model is considered as illustrated in Figure 2 where three Secondary Users (SUs) underlay their transmissions in the same narrow-band frequency as the Primary User (PU). The IT metric is used as measure of the interference power. The channel coefficient between transmitter j to receiver i is denoted as hij. All the channel coefficients are assumed to be independent and identically distributed (i.i.d) random variable following Rayleigh distribution (Ren *et. al.*, 2026).

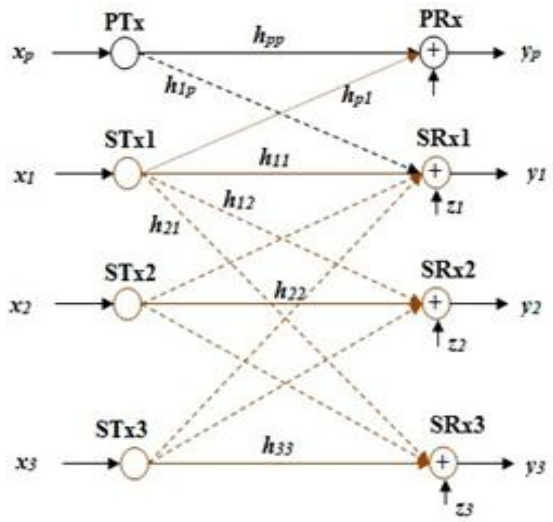

Figure 2: System Model: 3 SUs Coexisting with a Single PU

The received signal at the primary receiver, y_p, is a noisy linear combination of the signals from the intended primary transmitter and unintended secondary transmitters which can be modelled as:

$$y_p = h_{pp}x_p + \sum_{k=1}^{3} h_{pk}x_k + z_p \tag{1}$$

where:

h_{pp} and h_{pk} are the channel coefficient between the PU transmitter and PU receiver and the channel coefficient between the kth SU transmitter and the PU receiver respectively; x_p and x_k are the signals transmitted by the PU transmitter and the kth SU transmitter respectively; z_p is an additive white Gaussian noise with zero mean and unit variance at the primary receiver.

Similarly, the channel model for the jth SU receiver is as follows

$$y_j = h_{jp}x_p + \sum_{k=1}^{3} h_{jk}\, x_k + z_p \tag{2}$$

where, $j = 1, 2,3$

For a given bandwidth, B, the SU determines its transmit power, P, subject to interference constraint given by.

$$P \leq \frac{k.B(T_L - T_I)}{L} \tag{3}$$

Thus,

$$E[|x_k|^2] = P \leq \frac{k.B(T_L - T_I)}{L} \tag{4}$$

Equation (4) ensures that the total power in the terms $\sum_{k=1}^{3} h_{pk}x_k$ of equation (1) do not cause harmful interference to the PU receiver.

2.1 ERGODIC INTERFERENCE ALIGNMENT UNDER IT CONSTRAINTS

For a time varying interference channel, the achievable capacity per user, C_{SU_EIA}, using ergodic interference alignment is given by

$$C_{SU_EIA} = \frac{1}{2}E[\log(1 + 2|h_{kk}|^2 P)] \tag{5}$$

where, P is the transmit power of the user.

The sum capacity achieved for fully connected 3 underlay CR users under the IT constraints is formulated as follows:

A. ERGODIC IA UNDER MAXIMUM IT LIMITS

The sum capacity, C_{Σ}^{EIA}, achieved for a fully connected 3-users is solution to the following optimization problem.

$$C_{\Sigma}^{EIA} = \max_{P \geq 0} \frac{3}{2} \mathrm{E}[\log(1 + 2g_{ss}P)] \tag{6}$$

Subject to

$$\sum_{k=1}^{3} g_{pk}\, P \leq kBT_L \tag{7}$$

The optimal power, P^*, is just given by

$$P^* = \frac{kBT_L}{\sum_{k=1}^{3} g_{pk}} \tag{8}$$

Putting equation (8) into equation (6) gives

$$C_{\Sigma}^{EIA} = \max_{P \geq 0} \frac{3}{2} \mathrm{E}\left[\log\left(1 + 2\frac{g_{ss}}{\sum_{k=1}^{3} g_{pk}}\psi\right)\right] \tag{9}$$

$$C_{\Sigma}^{EIA} = 1.44 \times \frac{24\psi^3 \log 2\psi - 36\psi^3 + 24\psi^2 - 3\psi}{2(2\psi - 1)^3} \tag{10}$$

B. ERGODIC IA UNDER AVERAGE IT CONSTRAINT

The sum capacity, C_{Σ}^{EIA}, achieved is solution to the following optimization problem.

$$C_{\Sigma}^{EIA} = \max_{P_{su} \geq 0} \frac{3}{2} \mathrm{E}[\log(1 + 2g_{ss}P)] \tag{11}$$

Subject to

$$\mathrm{E}\left[\sum_{k=1}^{3} g_{pk}\, P\right] \leq kBT_L \tag{12}$$

The optimal power, P^*, is obtain using Lagrange method as

$$P^* = \left(\frac{1}{\lambda \sum_{k=1}^{3} g_{pk}} - \frac{1}{2g_{ss}}\right)^{+} \tag{13}$$

Hence, the sum capacity, C_{Σ}^{EIA}, in bpcu is obtained as

$$C_{\Sigma}^{EIA} = 1.44\left[\frac{3}{2}\log(1 + \gamma(\psi)) - \frac{3\gamma(\psi)(2 + 3\gamma(\psi))}{4(1 + \gamma(\psi))^2} + \frac{3\gamma(\psi)^3 \log 2}{2(1 + \gamma(\psi))^3}\right] \tag{14}$$

2.2 UTILIZING THE EXPECTED DELAY OF ERGODIC ALIGNMENT

A major drawback of ergodic alignment scheme is a very long delay incurred to attain half the interference-free rate. This limits the scheme to applications where high rates are far more valuable than low delays. Thus, the spectral efficiency of the ergodic alignment becomes very low due to the long delay time during which the users have to stay quite waiting for the realization of the complimentary channel matrix. To better the spectral efficiency of the proposed ergodic IA under IT constraints, the waiting time (expected delay) can be exploited by the SUs for sending delay-sensitive messages. The spectral efficiency gain is obtained as follows.

Let τ be the expected delay time slots between the two transmissions to achieve ergodic alignment. If the SUs utilize the expected delay time slots in a time-division scheme, the spectral efficiency is given by

$$\eta_{EIA} = 2 \times \frac{3}{2} \mathrm{E}[\log(1 + 2g_{ss}P^*)] + \tau \times \mathrm{E}[\log(1 + g_{ss}P^*)] \quad (15)$$

For a full time-division SUs, the spectral efficiency, η is

$$\eta = (2 + \tau)\mathrm{E}[\log(1 + g_{ss}P^*)] \quad (16)$$

Subtracting equation (16) from equation (15), the gain in spectral efficiency, η', is obtained as

$$\eta' = 3\mathrm{E}[\log(1 + 2g_{ss}P^*)] - 2\mathrm{E}[\log(1 + g_{ss}P^*)] \quad (17)$$

3. RESULTS AND DISCUSSION

This section describes the performance of the proposed ergodic interference-alignment (EIA) scheme was evaluated for the 3-SU underlay cognitive-radio system. Table 1 shows the simulation parameters.

Table 1: Simulation Parameters

S/N	Parameter	Value/Setting
1	Boltzmann constant (K)	1.38×10^{-23}J/K
2	Background IT	290 K
3	SNR range, ψ	0 – 20 dB
4	Channel model	i.i.d Rayleigh fading
5	Channel knowledge	Perfect CSI
6	Channel bandwidth , B	Normalised
7	SU time allocation	1/3
8	EIA time factor	½

Comparison of the sum capacities of the SUs under maximum IT limit and average IT limit for the same SNR in done in Figure 3. The capacities in the former case are generally lower than those of the latter which results due to the more restrictive nature of the maximum (as opposed to the average) IT constraint.

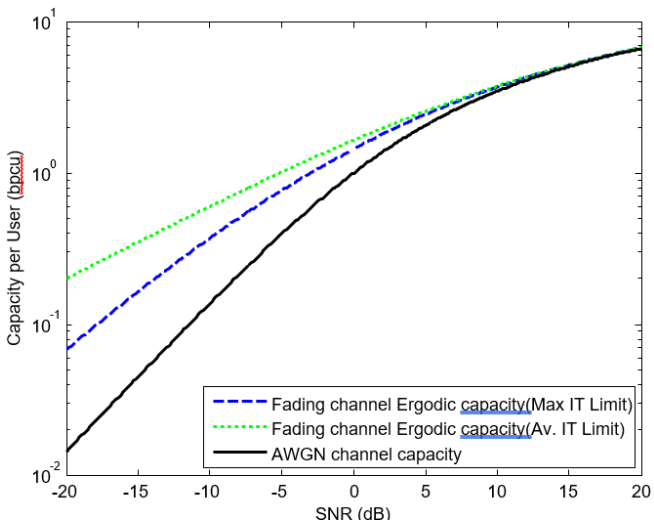

Figure 3: Sum Capacity through Time Division

A. ACHIEVABLE SUM CAPACITY THROUGH EIA UNDER IT LIMITS

Figures 4 (a) and (b) show the sum capacity achieved through ergodic IA under maximum and average interference temperature limits using equations (10) and (14). For all values of SNR under average IT limit, the achievable sum capacity through ergodic IA is higher than that obtained through time-division. But in the case of Max. IT limit below 6.2dB, the capacity achieved through ergodic IA is below that of time-division. This due to the more restrictive nature of the maximum (as opposed to the average) IT constraint.

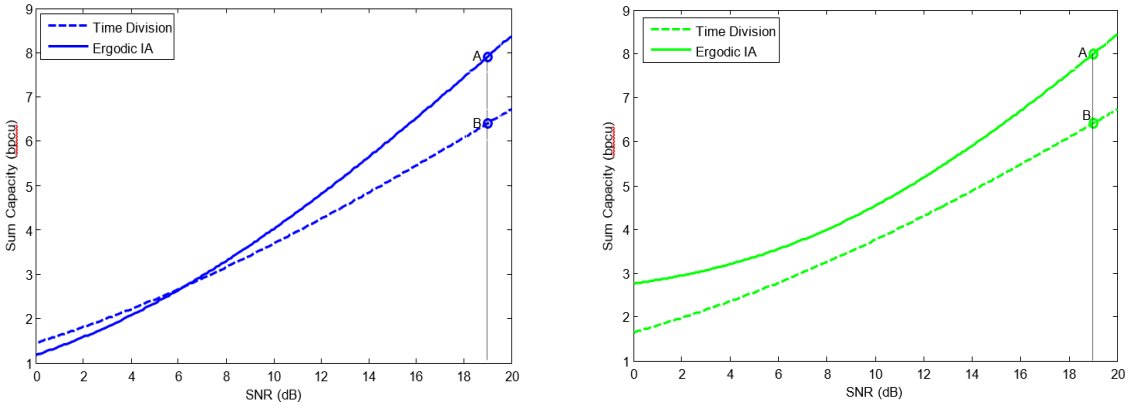

(a) under Maximum IT Limits (b) under Average IT Limits

Figure 4: Sum Capacity

The typical values of SNR of UWB (an underlay communication) applications are around 19 dB (Nelson *et. al.*, 2025). Thus, the performance of the developed model is evaluated at 19 dB under maximum and average IT limits as follows:

Maximum IT Limit

The sum capacities achieved through the developed ergodic IA under IT limits and the time division scheme are given by the coordinates A(19 dB, 7.8968 bpcu) and B(19 dB,

6.3921 bpcu) respectively in Figure 4 (a).

The capacity gain = 7.8968−6.3921=1.5047 bpcu

The capacity gain

$$= \frac{1.5047}{6.3921} \times 100\ \% = 23.54\ \%$$

Average IT Limit

The sum capacities achieved through the developed ergodic IA under IT limits and the time division scheme are given by the coordinates A(19 dB, 7.9943 bpcu) and B(19 dB,

6.4073 bpcu) respectively in Figure 4 (b).

The capacity gain = 7.9943−6.4073=1.5870 bpcu

$$= \frac{1.5870}{6.4073} \times 100\ \% = 24.77\ \%$$

The capacity gain

Comparison of the achievable capacity under IT constraints with that of the time-division scheme is shown in Figure 5. It also gives an upper bound to the capacity which corresponds to capacity achievable by non-interfering cognitive users.

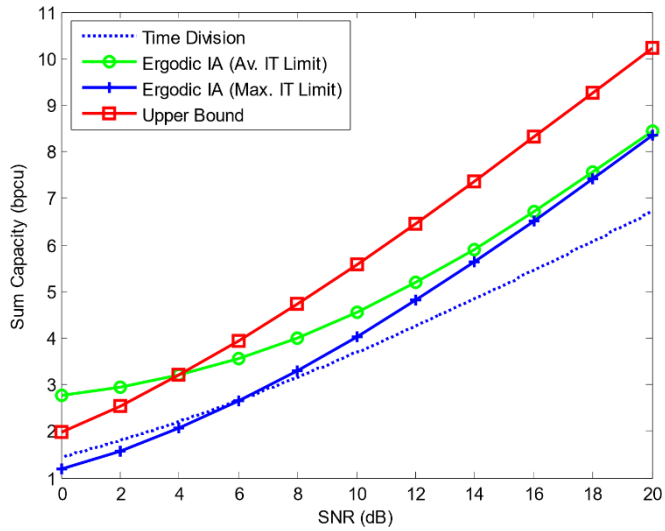

Figure 5: Sum Capacity Comparison

B. SPECTRAL EFFICIENCY GAIN

Spectral efficiency gain was achieved through exploiting the long delay necessary for the ergodic alignment. By utilizing the waiting time slot to send delay insensitive bits in time division scheme, 3.0094 bps/Hz and 3.1741 bps/Hz gains in spectral efficiency were achieved under maximum and average IT limits over a full time-division scheme at SNR of 19dB.

4. CONCLUSION

This research work proposed to mitigate the mutual interference among multiple Secondary Users (SUs) in underlay cognitive radio network aimed at enhancing the sum capacity the SU. Mitigating interference and improving spectrum efficiency are essential for rapid and sustainable growth of telecommunications industry in Nigeria. Ergodic interference alignment scheme under the IT constraints is developed for mitigating the mutual interference among the SUs. To provide a benchmark to gauge the performance of the developed model, the sum capacity through time-division scheme is first obtained. A closed form expression for the sum capacity of three-user underlay cognitive channel is derived. The ergodic IA has a major drawback of a very long delay in order to achieve half the interference-free rate. This was utilized to send delay insensitive bits which give significant percentage improvements of 23.54% and 24.77% in the channel sum capacity under maximum and average IT limits respectively. Since the network sum capacity with EIA increases linearly with the number of users, successful implementation of IA for higher number of SUs will render the capacity of wireless channels interference unlimited. A Rayleigh fading environment is assumed to demonstrate the performance of the developed model. For further work, more generalized fading distributions such as Nakagami-m and α- μ distributions could be considered so that the model can be adapted to suit different environment.

5. REFERENCES

Abdulkadir, Y., Simpson, O., & Sun, Y. (2024). Opportunistic Interference Alignment in Cognitive Radio Networks with Space–Time Coding. Journal of Sensor and Actuator Networks, 13(5), 46.

Briones-Reyes, A, Luis A. V., Alfonso P., and Rafael A. "Mathematical evaluation of spectrum sharing in cognitive radio networks for 5G systems using Markov processes." *Computer Networks* 182 (2020): 107521.

Mitola, J. (2009). Cognitive radio architecture evolution. *Proceedings of the IEEE*, *97*(4), pp. 626-641.

Nelson, B., Moradi, H., & Farhang-Boroujeny, B. (2025). Filtered multi-tone spread spectrum with overlapping subbands. *IEEE Open Journal of the Communications Society*, *6*, 5712-5726.

Ren, Y., Wang, H., Zhang, X., Jiang, F., Jiang, J., & Lv, T. (2026). Finite-Blocklength Covert Communications for IRS-Assisted NOMA Networks with Discrete Phase Shifts and Imperfect SIC. *IEEE Internet of Things Journal*.

Xu, Y, Kechen Z, Xiaoying L, Zhao L, and Jia L. "Cognitive radio networks: Technologies, challenges and applications." *Sensors* 25, no. 4 (2025): 1011.

Yau I., Abba A. M., David J., Ja'afar M., Yau U., Kamaluddeen N. M (2025). Ergodic Capacity of Multiple Underlay Cognitive Users under Maximum Interference Constraints. In the 2nd International Conference on Electrical Engineering Applications (ICEEA'2025), Ahmadu Bello University, Zaria, Nigeria, November 10-12, 2025

Yang, H., Qamar, F., Kazmi, S. H. A., Jafri, S. T. A., Ariffin, K. A. Z., & Nguyen, Q. N. (2024). Interference mitigation in B5G network architecture for MIMO and CDMA: State of the art, issues, and future research directions. *Information*, *15*(12), 771.

International Conference on Engineering Innovation for Sustainable Development (ICESID 2026)
Faculty of Engineering, Ahmadu Bello University Zaria · 8–10 September 2026

HYBRID TOA–RSS LOCALIZATION BASED ON SOCP WITH HUBER LOSS OPTIMIZATION

Isaac Hyeltiuda Charles[1,*], Abdulmalik Shehu Yaro[1], Shamsuddeen Abdullahi Mikail[1], Isiyaku Yau[1], Mohammed Dikko Almustapha[1], Yohanna Ali Mshelia[1]

[1]*Department of Electronics and Telecommunications Engineering, Ahmadu Bello University, Zaria*

Email: isaachyel@gmail.com*, asyaro@abu.edu.ng, samikail@abu.edu.ng, isiyakuyau@abu.edu.ng, md.almustapha@gmail.com, yalimshelia@gmail.com

***Corresponding author**: Isaac Hyeltiuda Charles

DOI: https://doi.org/10.67203/sp.ICESID.2026

ABSTRACT

Accurate wireless localisation in Non-Line-of-Sight (NLOS) environments remains challenging because multipath propagation, signal blockage, and environmental obstructions introduce severe measurement errors. Conventional Least Squares (LS) estimators are particularly vulnerable to NLOS-induced outliers because their quadratic loss function assigns disproportionately large weights to large residuals. This study proposes a robust hybrid Time of Arrival-Received Signal Strength (TOA-RSS) localisation framework that combines Second-Order Cone Programming (SOCP) with the Huber loss function to mitigate the influence of NLOS-corrupted measurements. The nonconvex Euclidean-distance localisation problem is transformed into a convex SOCP formulation through epigraph reformulation, while the piecewise-convex Huber penalty limits the contribution of large residuals. Monte Carlo simulations covering a comprehensive range of LOS/NLOS anchor configurations demonstrate the effectiveness of the proposed estimator. Under the most severe scenario, involving 0 LOS and 10 NLOS anchors, SOCP+Huber reduced position RMSE by up to 43.4% compared with conventional LS and 23.1% compared with non-robust SOCP. Cumulative distribution analysis further showed that 75–78% of localisation estimates were within 5 m of the true position, compared with approximately 70% for LS. The improvement was most pronounced under severe NLOS conditions, while performance remained competitive under LOS-dominant scenarios, confirming effective outlier suppression. The robustness was achieved with a modest computational increase, from $O(n^{3.5})$ for the standard SOCP to $O(n^{4.5})$, remaining substantially lower than the $O(n^6)$ complexity associated with semidefinite-programming alternatives.

Keywords: *wireless localisation; TOA/RSS; NLOS mitigation; second-order cone programming; and Huber loss*

I. INTRODUCTION

Accurate position estimation is a core requirement in modern wireless systems, spanning 5G infrastructure, IoT sensor networks, indoor navigation, autonomous robotics, and smart building management (Pan et al., 2022; Olejniczak et al., 2024; Pei et al., 2024). As these applications increases, the demand for reliable localisation in challenging real-world environments has intensified (Maduranga et al., 2023). Among widely used positioning techniques, time of arrival (TOA) estimates range by measuring signal propagation delay, achieving centimetre- to decimetre-level accuracy under ideal conditions (Kaune et al., 2011; Shui et al., 2025). Received signal strength (RSS) is used to estimate distance from received signal power via a path-loss model (Yaro et al., 2024; Li et al., 2023). Exploiting the complementary characteristics of both through sensor fusion has been recognised as a promising direction (Wang et al., 2022; Mukhopadhyay et al., 2022).

In dense or indoor environments, multipath propagation introduces a systematic positive bias into TOA estimates because the received signal may travel along indirect paths that are longer than the direct LOS path. For RSS measurements, NLOS propagation produces additional attenuation and shadowing that are not completely represented by the nominal path-loss model, resulting in significant ranging errors. Unlike zero-mean measurement noise, NLOS-induced errors contain a systematic bias component and therefore cannot generally be eliminated simply by averaging repeated measurements. Consequently, even a limited number of NLOS-corrupted links can introduce substantial position offsets in conventional least-squares localisation because large biased residuals can exert a

disproportionate influence on the estimated position (Wang et al., 2014; Wang et al., 2023; Charles et al., 2026).

Most hybrid TOA-RSS frameworks rely on a squared-error (L2) loss, which is optimal under Gaussian noise but highly sensitive to heavy-tailed outliers in severe NLOS conditions because large residuals are amplified quadratically (Huber, 1964). The Huber loss (Huber, 1964) addresses this by applying quadratic penalisation for small residuals and linear penalisation beyond a threshold δ, thereby limiting outlier influence. When embedded in a second-order cone programming (SOCP) framework, it preserves the convex optimisation structure and avoids dependence on initialisation heuristics (Kumar et al., 2015; Xiong et al., 2021), while δ provides a tunable robustness–efficiency trade-off (Mohanty et al., 2023). The combination of SOCP-based hybrid TOA–RSS localisation with Huber loss has received limited attention, motivating this work.

The remainder of this paper is organised as follows. Section II reviews related work. Section III presents the system model, the TOA and RSS measurement equations under NLOS conditions, and the proposed SOCP formulation with the Huber loss function. Section IV describes the simulation setup and presents the numerical results. Section V concludes the paper.

II. RELATED WORK

Early NLOS mitigation methods relied on statistical identification, classifying links as LOS or NLOS using features such as measurement variance, channel impulse response characteristics, or deviation-based statistics, then discarding or down-weighting NLOS links prior to position estimation (Olejniczak et al., 2024; Yang et al., 2023; Yaro et al., 2024). These methods perform well when LOS and NLOS distributions are clearly separable, but can deteriorate in indoor environments where the distributions overlap (Qin & Luo, 2024). A deeper limitation is that classification is decoupled from estimation, so classification errors cannot be corrected downstream.

Convex optimisation offers a more principled alternative. Semidefinite programming (SDP) incorporates robustness directly into the estimator via positive semidefinite matrix constraints (Ma et al., 2022; Shamsian & Behnia, 2025), but its computational complexity can make it impractical at large scale. SOCP provides a lower-complexity convex alternative while retaining strong modelling expressiveness (Kumar et al., 2015), and convex-relaxation approaches have demonstrated good empirical performance under NLOS conditions without requiring precise knowledge of the error distribution (Wang et al., 2014; Xiong et al., 2021).

Hybrid TOA-RSS fusion exploits the complementary physical characteristics of the two measurement mechanisms, propagation delay bias and shadow fading, to improve robustness. Recent work has leveraged this through semidefinite relaxation (Katwe et al., 2020), majorisation–minimisation without prior NLOS bias knowledge (Panwar et al., 2022), and Huber-based robust formulations with convex relaxation (Xiong et al., 2023).

Learning-based approaches have also shown strong results for NLOS identification, signal denoising, and intelligent localisation in 5G and massive-MIMO-related settings (Liu et al., 2022; Zhang et al., 2024; Li et al., 2020), but they generally require representative training data and can be sensitive to environmental changes. Model-based optimisation methods require no training data and provide interpretable optimisation structures, making them attractive where predictable behaviour is important (Mohanty et al., 2023).

The combination of SOCP-based hybrid TOA-RSS localisation with a Huber loss has received limited attention in the published literature. Most existing robust SOCP localisation work focuses on either TOA or RSS alone, and hybrid frameworks that consider both models have largely retained squared-error objectives.

III. SYSTEM MODEL

A. Measurement and Hybrid Observation Model

Consider a two-dimensional localization scenario with an unknown target position

$$x = [x, y]^T$$

1

and (N) anchors located at known positions

$$a_i = [x_i, y_i]^T, \quad i = 1,2, \dots, N \qquad 2$$

The TOA-based distance measurement is given by

$$d_i^{\mathrm{TOA}} = \|x - a_i\| + \epsilon_i^{\mathrm{TOA}} \qquad 3$$

where ($\epsilon_i^{\mathrm{TOA}}$) represents measurement noise and NLOS bias.

The RSS measurement follows the log-distance path loss model:

$$P_i = P_0 - 10n \log_{10}(\|\boldsymbol{x} - \boldsymbol{a_i}\|) + \epsilon_i^{\mathrm{RSS}} \qquad 4$$

where (P_0) is the reference power and (n) is the path loss exponent.

The RSS-based distance estimate is obtained as

$$d_i^{\mathrm{RSS}} = 10^{\frac{P_0 - P_i}{10n}} \qquad 5$$

To combine TOA and RSS measurements, a combined distance estimate ($\widehat{d_\iota}$) is defined.

$$\widehat{d_\iota} = d_i^{\mathrm{TOA}} + d_i^{\mathrm{RSS}} \qquad 6$$

The residual error is expressed as

$$r_i = \|\boldsymbol{x} - \boldsymbol{a_i}\| - \widehat{d_\iota} \qquad 7$$

The localisation problem becomes an optimisation problem that minimises the residuals across all anchors. A conventional least-squares formulation based on the residual in (7) is given as:

$$\min_x \sum_{i=1}^{N} \left(\|\boldsymbol{x} - \boldsymbol{a_i}\| - \widehat{d_\iota}\right)^2 \qquad 8$$

$$\min_x \sum_{i=1}^{N} (r_i)^2 \qquad 9$$

Minimisation using the traditional least-squares method can result in large localisation errors under NLOS conditions because large residuals are penalised quadratically. Hence, the Huber loss is introduced to reduce the influence of NLOS-induced outliers.

B. Huber Loss Function

To mitigate the effect of NLOS-induced outliers, the Huber loss function is employed. The Huber loss is given as:

$$\phi(r_i) = \begin{cases} \frac{1}{2} r^2 & |r_i| \le \delta \\ \delta |r_i| - \frac{1}{2}\delta^2 & |r_i| > \delta \end{cases}$$

10

where δ is the predefined Huber threshold that determines the transition from quadratic to linear penalisation. Residuals with magnitude not exceeding δ are treated approximately as Gaussian perturbations, whereas larger residuals receive a linear penalty and therefore have bounded influence on the estimate (Huber, 1964).

The objective function becomes:

$$\min_x \sum_{i=1}^{N} \phi(r_i)$$

subject to:

$$r_i = \|\boldsymbol{x} - \boldsymbol{a_i}\| - \widehat{d_\iota} \qquad 11$$

C. SOCP CONVEX RELAXATION

The original hybrid localisation problem is inherently nonlinear and non-convex because of the Euclidean norm in the distance expression. Hence, the problem is transformed into a convex SOCP formulation. This requires the introduction of auxiliary variables to enable convex reformulation. Introduce auxiliary variables such that:

$$t_i \ge \|\boldsymbol{x} - \boldsymbol{a_i}\| \qquad 12$$

This converts the equality constraint into an inequality, which is essential for convex relaxation.

Thus, the residual becomes:

$$r_i = t_i - \widehat{d}_i \quad (13)$$

The constraint in (12) can be written in standard SOCP form:

$$\|\boldsymbol{x} - \boldsymbol{a_i}\| \leq t_i. \quad (14)$$

Equation (14) is a second-order cone constraint and is therefore convex. Combining the robust objective and the cone constraints produces the complete SOCP–Huber relaxation. The resulting programme can be solved to global optimality with respect to the relaxed convex formulation transformations, the complete SOCP formulation becomes:

$$\min_x \sum_{i=1}^{N} \phi(r_i)$$

subject to:

$$\|\boldsymbol{x} - \boldsymbol{a_i}\| \leq t_i, \quad i = 1, \dots, N, \quad (15)$$

$$r_i = t_i - \widehat{d}_i \quad (16)$$

D. Performance Metric

Root mean square error (RMSE) is used as the principal accuracy metric because it measures the Euclidean position error accumulated over the Monte Carlo trials. Mathematically, RMSE is expressed as:

$$RMSE = \sqrt{\frac{\sum_{i=1}^{N}(x_i - x_o)^2 + (y_i - y_o)^2}{N}} \quad (17)$$

where:

N is the number of observations,

x_i, y_i are the estimated coordinates for the ith position, and

x_o, y_o are the actual coordinates of the true position.

IV. SIMULATION RESULTS AND DISCUSSION

This section presents the simulation setup and parameters, followed by the localisation performance results of the proposed scheme.

Table 1: Simulation Parameters

Parameter	Value / Range	Units
Simulation Area	100 × 100	m²
Number of Anchors (N)	10	—
Number of Targets	1	—
TOA noise std. dev. (σ_{TOA})	0.5 – 3.0	m
RSS path-loss exponent (η)	2.0	—
Reference Distance (d_0)	1.0	m
Reference RSS (P_0)	−30	dBm
RSS shadow-fading std. (σ_{RSS})	4 – 8	dB
NLOS Bias (b_i)	0 – 5	m
NLOS Probability (P_{NLOS})	0 – 1	—
Huber Threshold (δ)	1.5 σ	m / dB
Monte Carlo runs	500	—

The simulation considered a two-dimensional 100×100 m² localisation region containing one target node and $N = 10$ anchors. Five propagation scenarios were investigated to evaluate estimator robustness as the environment transitions from severe NLOS to pure LOS conditions. These scenarios consisted of 0 LOS/10 NLOS, 3 LOS/7 NLOS, 5 LOS/5 NLOS, 7 LOS/3 NLOS, and 10 LOS/0 NLOS anchors, corresponding to realised NLOS fractions of 1.0, 0.7, 0.5, 0.3, and 0.0, respectively.

For each Monte Carlo trial, the prescribed number of NLOS anchors was selected from the available anchors, while all remaining links were treated as LOS. LOS measurements contained only the specified measurement noise, with the NLOS bias set to $b_i = 0$. For each designated NLOS link, an additional positive ranging bias within the interval $0 \leq b_i \leq 5m$ was introduced in addition to the nominal measurement noise. Thus, the number of corrupted links was explicitly controlled for each scenario rather than being determined solely from a Bernoulli NLOS probability. This procedure ensured that all five LOS/NLOS configurations contained exactly the required number of corrupted measurements.

A total of 500 independent Monte Carlo trials was performed for each configuration. Within an individual trial, identical measurement realisations, anchor geometry and LOS/NLOS assignments were supplied to the LS, SOCP and SOCP–Huber estimators so that differences in localisation performance resulted from the estimation method rather than from different measurement conditions. The resulting position errors were subsequently used to calculate RMSE and the empirical cumulative distribution function.

Results and Discussion

The results presented in Figures 1 and 2 demonstrate the localisation performance and robustness of Least Squares (LS), SOCP, and the proposed SOCP–Huber method under varying LOS/NLOS conditions.

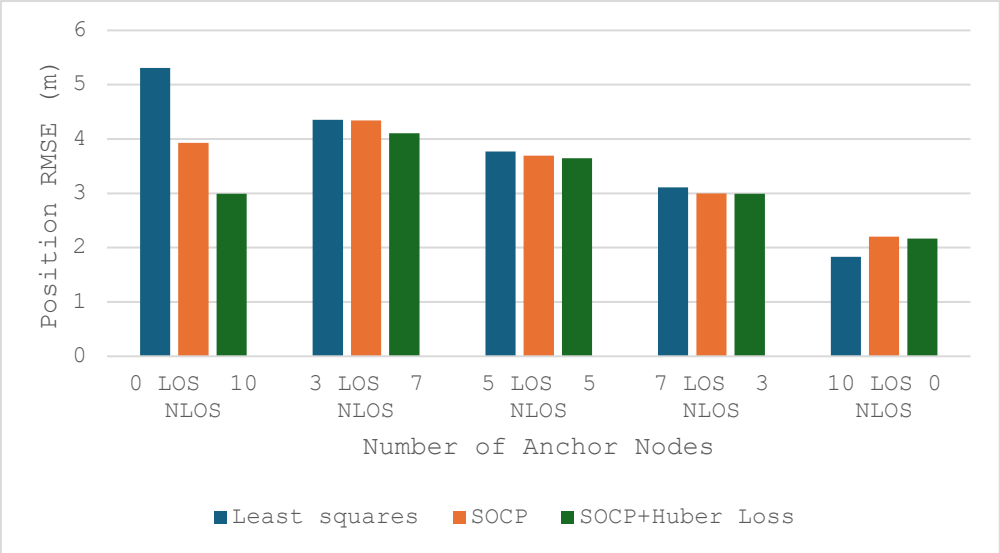

Figure 1: Position RMSE comparison of Least Squares, SOCP, and SOCP–Huber methods.

From the RMSE analysis in Figure 1, it is evident that localisation accuracy improves as the number of LOS anchors increases and the number of NLOS anchors decreases. Under the severe NLOS scenario of 0 LOS and 10 NLOS anchors, the Least Squares method recorded the highest localisation error of approximately 5.3 m, while SOCP achieved about 3.9 m and the proposed SOCP–Huber method attained the lowest RMSE of approximately 3.0 m. This corresponds to an improvement of nearly 43.4% over Least Squares and approximately 23.1% over conventional SOCP. The improvement is attributable to the behaviour of the Huber loss function, which suppresses the influence of large NLOS residuals that typically dominate quadratic-error minimisation approaches. As the propagation environment gradually transitions towards LOS-dominant conditions, the localisation errors of all methods decrease. For instance, under the 10 LOS and 0 NLOS configuration, the localisation RMSE reduced to approximately 1.8 m, 2.2 m, and 2.1 m for Least Squares, SOCP, and SOCP–Huber, respectively. This indicates that the advantage of robust optimisation becomes most significant in severe NLOS environments where measurement outliers are pronounced.

Table 2: Key RMSE Values Reported in Figure 1

LOS/NLOS configuration	LS RMSE (m)	SOCP RMSE (m)	SOCP–Huber RMSE (m)
0 LOS / 10 NLOS	5.3	3.9	3.0
10 LOS / 0 NLOS	1.8	2.2	2.1

Under the pure-LOS configuration of 10 LOS and 0 NLOS anchors, LS achieved an RMSE of approximately 1.8 m, compared with 2.2 m for conventional SOCP and 2.1 m for SOCP–Huber. The slightly better performance of LS in this clean propagation regime can be explained by both statistical efficiency and the relaxation mechanism employed in the SOCP formulation. In the original localisation problem, the estimated geometric distance is constrained by the equality $d_i = \| x - a_i \|$, whereas the convex reformulation replaces this equality with the second-order cone constraint $\| x - a_i \| 2 \leq t_i$. Although this constraint is expected to approach equality when the relaxation is tight, small inconsistencies among the noisy TOA–RSS range measurements may result in $t_i > \| x - a_i \|$ for some anchors. In such cases, the auxiliary variable can partially absorb measurement perturbations without requiring an equivalent change in the target position, thereby introducing a small relaxation gap between the fitted range and the physical geometric distance. This additional degree of freedom may cause a modest localisation penalty relative to direct LS estimation when measurements are predominantly LOS and approximately Gaussian. In contrast, LS directly minimises the squared geometric-range residuals and is therefore statistically efficient under such conditions. The 0.4 m difference between LS and SOCP observed in the pure-LOS case is consequently attributable to the trade-off introduced by convex relaxation rather than to a failure of the SOCP estimator. As NLOS contamination increases, however, the robustness provided by the convex formulation and particularly the Huber penalty outweighs this small clean-data efficiency loss.

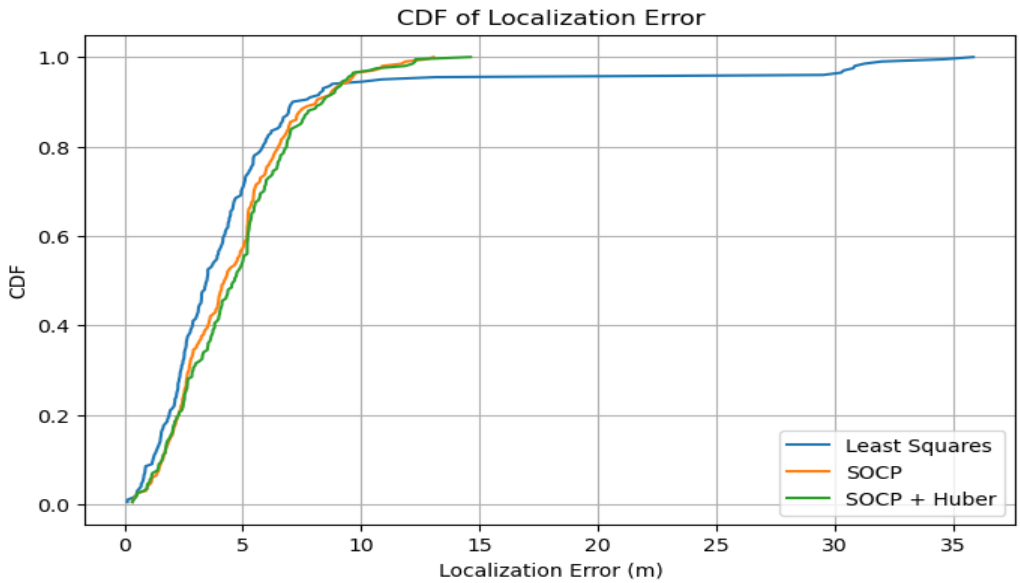

Figure 2: CDF of the localisation error.

The CDF results shown in Figure 2 further demonstrate the robustness and reliability of the proposed SOCP–Huber framework. The cumulative distribution curves represent the probability that the localisation error remains below a specified threshold. Both the conventional SOCP and SOCP–Huber methods exhibit more concentrated error distributions than Least Squares, particularly in terms of limiting large localisation errors. The LS method shows a pronounced long-tail behaviour, with errors extending to approximately 35–36 m. In contrast, the SOCP-based methods concentrate the majority of localisation errors below 10 m and reach their upper CDF plateau at approximately 12–15 m. At a localisation-error threshold of approximately 5 m, nearly 70% of LS estimates fall below this value, whereas the proposed SOCP–Huber method achieves approximately 75–78%. The steeper rise of the

SOCP–Huber curve in the low-to-moderate error region further indicates reduced error dispersion and improved localisation consistency. Overall, the CDF analysis confirms that incorporating the Huber loss into the SOCP framework improves robustness to NLOS-induced outliers and reduces the occurrence of large localisation errors.

Table 3: Complexity Comparison of Localisation Methods

Method	**Objective Function**	**Computational Complexity**	**Interpretation**
Least Squares (LS)	Squared residual minimization	$\mathcal{O}(kn^2)$	Iterative least-squares solution
Semi-Definite Programming (SDP)	Semi-definite relaxation	$\mathcal{O}(n^6)$	Large PSD matrix operations
Second-Order Cone Programming (SOCP)	Cone-constrained minimization	$\mathcal{O}(n^{3.5})$	Interior-point SOCP scaling
SOCP + Huber Loss	Huber-penalized cone minimization	$\mathcal{O}(n^{4.5})$	Additional Huber auxiliary/epigraph variables

Note. n represents the effective optimisation problem size (which scales with the number of anchors and auxiliary variables), and k represents the number of iterations for iterative LS implementations. The stated complexities are approximate order-of-growth estimates for generic interior-point implementations. Actual computational cost depends on the cone structure, variable dimensions, sparsity, solver implementation and required solution accuracy.

Table 3 compares the computational complexity of LS, SDP, SOCP, and the proposed SOCP-Huber framework. The reported values should be interpreted as indicative order-of-growth estimates rather than exact execution times, since actual computational cost depends on solver implementation, sparsity, numerical tolerance, and hardware.

LS has the lowest computational burden, approximately $\left(O(kn^2)\right)$, but its squared-error objective makes it sensitive to large NLOS residuals. SDP provides a convex relaxation but incurs a much higher computational cost, commonly approximated as $\left(O(n^6)\right)$, because of its matrix-valued variables and positive-semidefinite constraints. SOCP offers a more efficient convex alternative. For a dense primal-dual interior-point implementation, the Newton/KKT solution cost is approximately $\left(O(n^3)\right)$, while the iteration bound contributes about $\left(O\left(\sqrt{n}\log(1/\epsilon)\right)\right)$, giving an indicative complexity of

$$O!\left(n^{3.5}\log\left(\frac{1}{\epsilon}\right)\right) \quad 18$$

(Nesterov & Nemirovskii, 1994; Boyd & Vandenberghe, 2004).

The proposed SOCP–Huber method introduces additional auxiliary and epigraph variables to implement the Huber loss. These increase the practical computational burden but scale approximately linearly with the number of anchors; therefore, they mainly increase the computational constant rather than necessarily changing the asymptotic exponent. Thus, SOCP–Huber retains a complexity of the same general order as SOCP, while providing improved robustness to NLOS-induced outliers. Overall, the proposed method offers a favourable compromise between localisation accuracy, robustness, and computational efficiency.

V. CONCLUSION

This paper presented a robust hybrid TOA-RSS localisation framework based on Second-Order Cone Programming integrated with the Huber loss function for effective mitigation of NLOS-induced measurement errors. By combining complementary TOA and RSS observations within a convex

optimisation framework, the proposed method reduces the influence of large biased residuals that adversely affect conventional least-squares estimation.

Simulation results demonstrated that the proposed SOCP-Huber method provides its greatest benefit under severe NLOS conditions, where it achieved lower localisation error and a more concentrated error distribution than both conventional LS and standard SOCP. Under pure-LOS conditions, LS retained a small accuracy advantage, which reflects both its statistical efficiency under approximately Gaussian measurement errors and the small relaxation gap introduced by the SOCP formulation. This behaviour confirms that the principal advantage of the proposed framework lies in robustness to contaminated measurements rather than in improving already clean LOS observations.

From a computational perspective, the enhanced robustness is obtained at the cost of a moderate increase in complexity relative to conventional SOCP because of the additional auxiliary variables and Huber-loss constraints. Nevertheless, the computational burden remains substantially lower than that associated with semidefinite-programming-based localisation methods. The proposed method therefore provides a practical compromise between localisation accuracy, robustness and computational cost. This trade-off is particularly relevant to real-time indoor positioning systems, where resilience to NLOS errors must be achieved without introducing the substantially higher processing requirements associated with more complex convex relaxations.

Overall, the results indicate that SOCP-Huber localisation is most suitable for propagation environments in which NLOS contamination is significant and computational resources are constrained. The framework therefore offers a promising basis for robust real-time indoor positioning in wireless sensor networks, industrial facilities and other multipath-dominated environments. Future work will investigate adaptive selection of the Huber threshold, residual-statistics-based regularisation, and experimental validation using measured TOA-RSS datasets.

REFERENCES

Charles, I. H., Yaro, A. S., & Almustapha, M. D. (2026). Enhancing Localization Accuracy of Hybrid Time of Arrival/received Signal Strength Systems In Non-line-of-sight Environments Using Reconfigurable Intelligent Surfaces and Semi-definite Programming. *Nigerian Journal of Engineering*, 33 (1), 43-47.

Huber, P. J. (1964). Robust estimation of a location parameter. *The Annals of Mathematical Statistics*, 35(1), 73–101.

Katwe, M. V., Ghare, P., Sharma, P. K., & Singh, K. (2020). NLOS error mitigation in hybrid RSS-TOA-based localization through semi-definite relaxation. *IEEE Communications Letters*, 24(12), 2761–2765.

Kaune, R., Hörst, J., & Koch, W. (2011). Accuracy analysis for TDOA localization in sensor networks. In *Proceedings of the 14th International Conference on Information Fusion* (pp. 1–8).

Kumar, S., Dixit, R., & Hegde, R. M. (2015). *Second order cone programming for sensor node localization in mixed LOS/NLOS conditions* [Preprint]. arXiv. https://arxiv.org/abs/1508.02834

Li, L., Guo, X., & Ansari, N. (2020). SmartLoc: Smart wireless indoor localization empowered by machine learning. *IEEE Transactions on Industrial Electronics*, 67(8), 6883–6893.

Li, Y., Mukhopadhyay, B., & Alouini, M.-S. (2023). RSS-based cooperative localization and transmit power(s) estimation using mixed SDP-SOCP. *IEEE Transactions on Vehicular Technology*, 72(12), 16936–16941. https://doi.org/10.1109/TVT.2023.3295868

Liu, J., Wang, T., Li, Y., Li, C., Wang, Y., & Shen, Y. (2022). A transformer-based signal denoising network for AoA estimation in NLoS environments. *IEEE Communications Letters*, 26(10), 2336–2339.

Ma, X., Hao, B., Zhang, H., & Wan, P. (2022). Semidefinite relaxation for source localization by TOA in unsynchronized networks. *IEEE Signal Processing Letters*, 29, 622–626.

Maduranga, M. W. P., Kalansooriya, P., Retscher, G., & Gabela Majic, J. (2023). Machine learning-based indoor localization system to support 5G location-based services. In *Proceedings of the 7th SLAAI International Conference on Artificial Intelligence* (pp. 1–6). IEEE.

Mohanty, S., Xiong, W., Rupitsch, S. J., & Schindelhauer, C. (2023). Robust ISAC localization in smart cities: A hybrid network approach for NLOS challenges with uncertain parameters. *Journal of Sensor and Actuator Networks*, 13(1), 2.

Mukhopadhyay, B., Srirangarajan, S., & Kar, S. (2022). Invex relaxation based cooperative localization using RSS measurements. *IEEE Transactions on Communications*, 70(8), 5482–5497.

Olejniczak, A., Blaszkiewicz, O., Cwalina, K. K., Rajchowski, P., & Sadowski, J. (2024). LOS and NLOS identification in real indoor environment using deep learning approach. *Digital Communications and Networks*, 10(5), 1305–1312. https://doi.org/10.1016/j.dcan.2023.05.009

Pan, M., Liu, P., Liu, S., Qi, W., Huang, Y., You, X., Jia, X., & Li, X. (2022). Efficient joint DOA and TOA estimation for indoor positioning with 5G picocell base stations. *IEEE Transactions on Instrumentation and Measurement*, 71, 1–19. https://doi.org/10.1109/TIM.2022.3191705

Panwar, K., Katwe, M., Babu, P., Ghare, P., & Singh, K. (2022). A majorization-minimization algorithm for hybrid TOA-RSS based localization in NLOS environment. *IEEE Communications Letters*, 26(5), 1017–1021.

Pei, J., Wang, G., Ho, K., & Huang, L. (2024). Moving transceivers aided localization of a far-field object. *IEEE Transactions on Mobile Computing*, 23(12), 12795–12810.

Qin, S., & Luo, M. (2024). Enhancing performance for wireless location: Leveraging linear trend and uncertainty inherent in NLOS error. *IEEE Transactions on Industrial Informatics*, 20(10), 11940–11949. https://doi.org/10.1109/TII.2024.3413336

Shamsian, A., & Behnia, F. (2025). TOA/RSS-based source localization using probabilistic model in mixed LOS/NLOS environments. *IEEE Transactions on Mobile Computing*. https://doi.org/10.1109/TMC.2024.3412923

Shui, S., Xiong, X., Mai, M., & Qin, S. (2025). A robust TDOA localization method for researching upper bound on NLOS ranging error. *Signal Processing*, 235, 110040.

Wang, G., Chen, H., Li, Y., & Ansari, N. (2014). NLOS error mitigation for TOA-based localization via convex relaxation. *IEEE Transactions on Wireless Communications*, 13(8), 4119–4131.

Wang, Q., Duan, Z., & Li, F. (2022). Semidefinite programming for wireless cooperative localization using biased RSS measurements. *IEEE Communications Letters*, 26(6), 1278–1282.

Wang, Y., Ho, K. C., & Wang, Z. (2023). Robust localization under NLOS environment in the presence of isolated outliers by full-set TDOA measurements. *Signal Processing*, 212, 109159. https://doi.org/10.1016/j.sigpro.2023.109159

Xiong, W., Mohanty, S., Schindelhauer, C., Rupitsch, S. J., & So, H. C. (2023). Convex relaxation approaches to robust RSS-TOA based source localization in NLOS environments. *IEEE Transactions on Vehicular Technology*, 72(8), 11068–11073.

Xiong, W., Schindelhauer, C., So, H. C., Bordoy, J., & Liang, J. (2021). TDOA-based localization with NLOS mitigation via robust model transformation and neurodynamic optimization. *Signal Processing*, 178, 107774.

Yang, H., Wang, Y., Seow, C. K., Sun, M., Si, M., & Huang, L. (2023). UWB sensor-based indoor LOS/NLOS localization with support vector machine learning. *IEEE Sensors Journal*, 23(3), 2988–3004.

Yaro, A. S., Maly, F., Prazak, P., & Malý, K. (2024). Outlier detection performance of a modified z-score method in time-series RSS observation with hybrid scale estimators. *IEEE Access*, 12, 12785–12796.

Zhang, Z., Liang, J., & Wang, G. (2024). Machine learning-based intelligent localization technique for channel classification in massive MIMO. *Discover Internet of Things*. https://doi.org/10.1007/s43926-024-00070-9

ABOUT THE CONFERENCE

The International Conference on Engineering Innovation for Sustainable Development (ICESID 2026) was hosted by the Faculty of Engineering, Ahmadu Bello University Zaria from 8–10 September 2026. It brought together researchers, developers, practitioners and policy makers from academia and industry across the fields of engineering, under the theme "Innovating Tomorrow: Harnessing Engineering to Drive Nigeria's Sustainable Development". This Book of Proceedings collects the peer-reviewed papers presented at the conference, a record of the knowledge sharing, networking and research collaboration it set out to foster.

CONFERENCE SUB-THEMES

01 Smart Infrastructure and Sustainable Systems for National Development

02 Engineering Innovations, Technology Commercialization and Industrial Policy

03 Emerging Technologies and Digital Transformation in Engineering Education and Practice

04 Renewable Energy Integration and Smart Grid Applications in Power Systems

05 Intelligent Systems, Automation and Control Engineering

06 Strategies for Infrastructural and Industrial Transformation through Engineering Innovations

07 Green Mobility and Next Generation Automobile Technologies

08 Sustainable Engineering Processes and Systems

09 Emerging Technologies for Safe Engineering Practices and Environmental Protection

10 Telecommunication Infrastructure for Sustainable Urban Development and Economic Growth

11 Advanced Manufacturing, Materials and Sustainable Production

ICESID International Conference on Engineering for Sustainable Innovation and Development

DOI https://doi.org/10.67203/sp.ICESID.2026

https://icesid.org

Conference platform & book production partner

Saypeace Solutions Ltd. · https://conference.saypeace.ng

support@saypeace.ng · +2347036890546

SayPeace SOLUTIONS